

Publications Jorgen D'Hondt



First measurement of the cross section for top quark pair production with additional charm jets using dileptonic final states in pp collisions at $\sqrt{s} = 13$ TeV

The CMS Collaboration ^{*}

CERN, Geneva, Switzerland



ARTICLE INFO

Article history:

Received 17 December 2020

Received in revised form 11 June 2021

Accepted 30 July 2021

Available online 4 August 2021

Editor: M. Doser

Keywords:

CMS

Top quark

Dilepton

Charm quark

Charm-tagging

Heavy-flavour

ABSTRACT

The first measurement of the inclusive cross section for top quark pairs ($t\bar{t}$) produced in association with two additional charm jets is presented. The analysis uses the dileptonic final states of $t\bar{t}$ events produced in proton-proton collisions at a centre-of-mass energy of 13 TeV. The data correspond to an integrated luminosity of 41.5 fb^{-1} , recorded by the CMS experiment at the LHC. A new charm jet identification algorithm provides input to a neural network that is trained to distinguish among $t\bar{t}$ events with two additional charm ($t\bar{t}c\bar{c}$), bottom ($t\bar{t}b\bar{b}$), and light-flavour or gluon ($t\bar{t}LL$) jets. By means of a template fitting procedure, the inclusive $t\bar{t}c\bar{c}$, $t\bar{t}b\bar{b}$, and $t\bar{t}LL$ cross sections are simultaneously measured, together with their ratios to the inclusive $t\bar{t}$ + two jets cross section. This provides measurements of the $t\bar{t}c\bar{c}$ and $t\bar{t}b\bar{b}$ cross sections of 10.1 ± 1.2 (stat) ± 1.4 (syst) pb and 4.54 ± 0.35 (stat) ± 0.56 (syst) pb, respectively, in the full phase space. The results are compared and found to be consistent with predictions from two different matrix element generators with next-to-leading order accuracy in quantum chromodynamics, interfaced with a parton shower simulation.

© 2021 The Author(s). Published by Elsevier B.V. This is an open access article under the CC BY license (<http://creativecommons.org/licenses/by/4.0/>). Funded by SCOAP³.

1. Introduction

The modelling of top quark pair ($t\bar{t}$) production in association with jets from the hadronization of bottom (b) or charm (c) quarks, referred to as b jets and c jets, respectively, in proton-proton (pp) collisions at the CERN LHC is challenging. Calculations of the production cross section for top quark pairs with additional pairs of b jets ($t\bar{t}b\bar{b}$) are available at next-to-leading order (NLO) in quantum chromodynamics (QCD) [1–5], but suffer from large uncertainties due to the choice of factorization (μ_F) and renormalization (μ_R) scales. The uncertainties arise from the different energy (or mass) scales in $t\bar{t}b\bar{b}$ production, which range from the large scales associated with the top quark mass (m_t), to the relatively small scales associated with additional jets resulting mostly from gluon splitting into $b\bar{b}$ pairs. To better understand the $t\bar{t}b\bar{b}$ process, the ATLAS and CMS experiments have conducted several measurements in pp collisions at centre-of-mass energies of 7, 8, and 13 TeV [6–13].

The production of a $t\bar{t}$ pair with an additional pair of c jets ($t\bar{t}c\bar{c}$) has received far less attention, both theoretically and experimentally. Whereas the experimental signature of a b jet looks quite different from that of a light-flavour (LF) or gluon jet, the

differences are much less pronounced for c jets. This explains the challenge of simultaneously separating $t\bar{t}c\bar{c}$ and $t\bar{t}b\bar{b}$ events from a large background of $t\bar{t}$ events with additional LF or gluon jets ($t\bar{t}LL$). With the development of a charm jet identification algorithm (“c tagger”) [14], these signatures can now be more efficiently disentangled. We present the first measurement of the inclusive $t\bar{t}c\bar{c}$ cross section and its ratio to the inclusive $t\bar{t}$ + two jets ($t\bar{t}jj$) cross section. A fully consistent treatment of the different additional jet flavours is ensured using a technique that simultaneously extracts the $t\bar{t}c\bar{c}$, $t\bar{t}b\bar{b}$, and $t\bar{t}LL$ cross sections. The measurement is performed in the dileptonic decay channel of the $t\bar{t}$ events using a data sample of pp collisions at a centre-of-mass energy of 13 TeV, collected with the CMS detector in 2017, corresponding to an integrated luminosity of 41.5 fb^{-1} [15]. This data set benefits from the upgrade of the pixel tracking detector [16], which was installed in winter 2016–2017 and which has been shown to significantly improve the performance of heavy-flavour (HF) jet identification [17].

Although the additional b jets in $t\bar{t}b\bar{b}$ events are predominantly produced via gluon splitting into $b\bar{b}$ pairs, they can also originate from the decay of a Higgs boson (H). Previous measurements of Higgs boson production in association with a top quark pair, where the Higgs boson decays into a pair of b quarks ($t\bar{t}H$, $H \rightarrow b\bar{b}$) [18–21], suffer from a nonresonant background of gluon-

^{*} E-mail address: cms-publication-committee-chair@cern.ch.

induced $t\bar{t}b\bar{b}$ events, and to a lesser extent also from $t\bar{t}c\bar{c}$ events due to the misidentification of c jets as b jets. The techniques described here provide a basis for a simultaneous measurement of the $t\bar{t}b\bar{b}$ and $t\bar{t}c\bar{c}$ processes from data that can be adopted in future $t\bar{t}H$ analyses to significantly reduce the uncertainties related to these backgrounds.

2. The CMS detector

The central feature of the CMS apparatus is a superconducting solenoid of 6 m internal diameter, providing a magnetic field of 3.8 T. Within the solenoid volume are a silicon pixel and strip tracker, a lead tungstate crystal electromagnetic calorimeter (ECAL), and a brass and scintillator hadron calorimeter (HCAL), each composed of a barrel and two endcap sections. The silicon tracker measures charged particles within the pseudorapidity range $|\eta| < 2.5$. During the LHC running period when the data used for this analysis were recorded, the silicon tracker consisted of 1856 silicon pixel and 15 148 silicon strip detector modules. For nonisolated particles of $1 < p_T < 10$ GeV and $|\eta| < 2.5$, the track resolutions are typically 1.5% in p_T and 20–75 μm in the transverse impact parameter [22]. Forward calorimeters extend the η coverage provided by the barrel and endcap detectors. Muons are detected in gas-ionization chambers embedded in the steel flux-return yoke outside the solenoid. A more detailed description of the CMS detector, together with a definition of the coordinate system used and the relevant kinematic variables, can be found in Ref. [23].

Events of interest are selected using a two-tiered trigger system [24]. The first level, composed of custom hardware processors, uses information from the calorimeters and muon detectors to select events at a rate of around 100 kHz within a fixed time interval of about 4 μs . The second level, known as the high-level trigger, consists of a farm of processors running a version of the full event reconstruction software optimized for fast processing, and reduces the event rate to around 1 kHz before data storage.

3. Event simulation

Samples of signal and background events are simulated using Monte Carlo (MC) event generators based on a fixed-order perturbative QCD calculation with up to four noncollinear high- p_T partons, supplemented with parton showering (PS) and multiparton interactions. The matrix element (ME) generation of $t\bar{t}$ events is performed with POWHEG (v2) [25–29] at NLO in QCD using the five-flavour scheme, followed by a simulation of the PS using PYTHIA8.230 [30] (referred to as PYTHIA8 in the following), using the CP5 underlying event tune [31] and the NNPDF3.1 [32] parton distribution functions (PDFs). The first additional hard radiation from the $t\bar{t}$ system is included in the NLO ME calculation, whereas higher additional jet multiplicities result from radiation simulated in the PS. A value of $m_t = 172.5$ GeV is used in the event generation and the values of μ_R and μ_F are set to a dynamic scale given by $\sqrt{m_t^2 + p_{T,t}^2}$, where $p_{T,t}$ denotes the transverse momentum of the top quark in the $t\bar{t}$ rest frame. The $t\bar{t}$ cross section is scaled to a theoretical prediction at next-to-next-to-leading order in QCD including resummation of next-to-next-to-leading logarithmic soft-gluon terms, which yields $\sigma_{t\bar{t}} = 832^{+39.9}_{-45.8}$ pb [33]. The results are also compared to those from $t\bar{t}$ production simulated with the MADGRAPH5_AMC@NLO (v2.4.2) [34] ME generator at NLO accuracy using the five-flavour scheme, with FxFx jet matching [35] and including up to two jets in addition to the $t\bar{t}$ system in the NLO ME calculation. No dedicated simulations have been used to model separately $t\bar{t}c\bar{c}$ or $t\bar{t}b\bar{b}$ events, ensuring a consistent treatment between $t\bar{t}c\bar{c}$, $t\bar{t}b\bar{b}$, and $t\bar{t}LL$ events in the inclusive $t\bar{t}$ samples mentioned above.

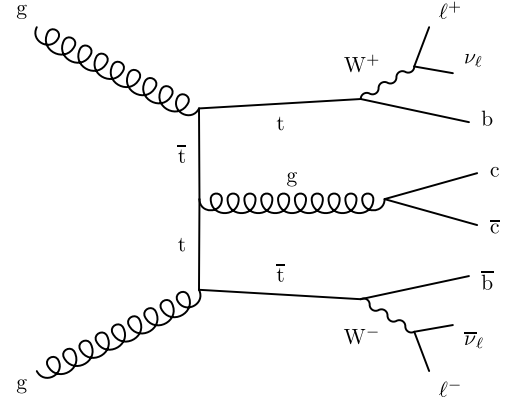


Fig. 1. Example of a Feynman diagram at the lowest order in QCD, describing the dileptonic decay channel of a top quark pair with an additional $c\bar{c}$ pair produced via gluon splitting.

The background processes for this analysis consist mainly of Drell–Yan (DY) and single top quark events, with additional minor contributions from $W + \text{jets}$, diboson, triboson, $t\bar{t}Z$, $t\bar{t}W$, and $t\bar{t}H$ events (collectively referred to as rare backgrounds). For all these samples, the PS is simulated using PYTHIA8. The ME generation of the DY, $W + \text{jets}$, triboson, $t\bar{t}Z$, and $t\bar{t}W$ events is handled using MADGRAPH5_AMC@NLO at leading order in QCD, with MLM jet matching [36]. The $t\bar{t}H$ events are generated at NLO using POWHEG. Single top quark production in the t and s channels are simulated at NLO in the four-flavour scheme using POWHEG and MADGRAPH5_AMC@NLO, respectively, while the tW channel is simulated at NLO with POWHEG in the five-flavour scheme. The diboson samples are simulated at leading order in QCD using PYTHIA8 for both the ME calculations and PS description.

The interactions between particles and the material in the CMS detector are simulated using GEANT4 (v10.02) [37]. The effect of additional pp interactions in the same or nearby beam crossings as the hard-scattering process (pileup) is modelled by adding simulated minimum bias collisions generated in PYTHIA8.

4. Signal definition

A typical Feynman diagram describing the dileptonic $t\bar{t}c\bar{c}$ process is shown in Fig. 1. To provide an unambiguous interpretation of the results, a generator-level definition of the event categories is needed, based on the flavours of the additional jets. The HF jets are identified at the generator level using the procedure of ghost matching [38], where in addition to the reconstructed final-state particles, the generated b and c hadrons are clustered into the jets. However, the modulus of the hadron four-momentum is set to a small number to prevent these generated hadrons from affecting the reconstructed jet momentum and to ensure that only their directional information is retained. Jets that contain both b and c hadrons are labelled as b jets, since the c hadrons most likely originate from a decay of a b hadron. The results of this measurement are reported in terms of the fiducial and full phase spaces.

Fiducial phase space: In the definition of the fiducial phase space, all of the final-state particles (except for the neutrinos) resulting from the decay chain: $pp \rightarrow t\bar{t}jj \rightarrow \ell^+ \nu_\ell b \ell^- \bar{\nu}_\ell \bar{b} j j$ are required to be within the region of the detector in which these objects can be properly reconstructed. The fiducial phase space is therefore defined by the presence of two oppositely charged electrons, muons, or τ leptons (ℓ) at the generator level with $p_T > 25$ GeV and $|\eta| < 2.4$. Each lepton is required to originate from a decay of a W boson, which in turn results from a top quark decay. Particle-level jets are defined by clustering generated final-state particles with a mean lifetime greater than 30 ps, excluding neutrinos, us-

ing the anti- k_T algorithm [39,40] with a distance parameter of 0.4. We demand two particle-level b jets from the top quark decays with $p_T > 20$ GeV and $|\eta| < 2.4$. Besides these two b jets, at least two additional particle-level jets must be present, with the same kinematic requirements imposed. Jets that lie within $\Delta R = \sqrt{(\Delta\eta)^2 + (\Delta\phi)^2} < 0.4$ of either one of the leptons from the W boson decays, where ϕ denotes the azimuthal angle, are excluded. The above requirements define the inclusive $t\bar{t}jj$ signal, which is then subdivided based on the flavour content of the additional particle-level jets (not from the top quark decays) into the following categories:

- $t\bar{t}b\bar{b}$: At least two additional b jets are present, each containing at least one b hadron.
- $t\bar{t}bL$: Only one additional b jet is present, containing at least one b hadron. In addition, at least one additional LF or c jet is present. This category results from $t\bar{t}b\bar{b}$ events in which one of the two additional b jets is outside the acceptance, or two b jets are merged into one.
- $t\bar{t}c\bar{c}$: No additional b jets are present, but at least two additional c jets are found, each containing at least one c hadron.
- $t\bar{t}cL$: No additional b jets are present, and only one additional c jet is found, containing at least one c hadron. In addition, at least one additional LF jet is present. This category results from $t\bar{t}c\bar{c}$ events in which one of the two additional c jets is outside the acceptance, or two c jets are merged into one.
- $t\bar{t}LL$: No additional b or c jets are present, but at least two additional LF jets are within the acceptance.

All other $t\bar{t}$ events that do not fit in any of the above categories, because they do not fulfill the acceptance requirements described in the definition of the fiducial phase space, are labelled as “ $t\bar{t}$ +other”. These could for example be events with semileptonic or fully hadronic $t\bar{t}$ decays that pass the event selection criteria outlined in Section 6, or dileptonic $t\bar{t}$ events for which the leptons or the particle-level jets as described above are not within the fiducial detector volume. These contributions are estimated from the same simulations as those used for the signal events.

Full phase space: The definition of the full phase space comprises dileptonic, semileptonic, and fully hadronic $t\bar{t}$ decays that contain in addition at least two particle-level jets with $p_T > 20$ GeV and $|\eta| < 2.4$. These jets must not originate from the decays of the top quarks or W bosons. There are no requirements imposed on the generator-level leptons or on the particle-level jets that result from the top quark and W boson decays. The measurement in the fiducial phase space is extrapolated to the full phase space by applying an acceptance factor, estimated from simulations, to each signal category based on the additional jet flavours.

The definition of the fiducial phase space is much closer to the reconstructed phase space in which the measurement is performed, and therefore expected to suffers less from theoretical uncertainties that affect the extrapolation from the fiducial to the full phase space. However, the full phase space definition is better suited for comparison with theoretical calculations.

5. Object reconstruction

The global event reconstruction is based on the particle-flow algorithm [41], which aims to reconstruct and identify each individual particle in an event by combining information from the various elements of the CMS detector. The energy of photons is obtained from the ECAL measurement. The energy of electrons is determined from a combination of the electron momentum at the primary interaction vertex as determined by the tracker, the energy of the corresponding ECAL cluster, and the energy sum of all bremsstrahlung photons spatially compatible with originating from

the electron track. The energy of muons is obtained from the curvature of the corresponding track. The energy of charged hadrons is determined from a combination of their momentum measured in the tracker and the matching ECAL and HCAL energy deposits, corrected for zero-suppression effects and for the response function of the calorimeters to hadronic showers. Finally, the energy of neutral hadrons is obtained from the corresponding corrected ECAL and HCAL energies.

For each event, hadronic jets are clustered from these reconstructed particles using the infrared and collinear safe anti- k_T algorithm with a distance parameter of 0.4. Jet momentum is determined as the vectorial sum of all particle momenta in the jet, and is found from simulations to be, on average, within 5 to 10% of the true momentum over the whole p_T spectrum and detector acceptance. Pileup interactions can contribute additional tracks and calorimetric energy depositions, increasing the apparent jet momentum. To mitigate this effect, tracks identified as originating from pileup vertices are discarded and an offset correction is applied to correct for remaining contributions. Jet energy corrections are derived from simulation studies so that the average measured response of jets becomes identical to that of particle-level jets. In situ measurements of the momentum balance in dijet, photon+jets, Z + jets, and multijet events are used to determine any residual differences between the jet energy scale in data and simulations [42], and appropriate corrections are made. Additional selection criteria are applied to each jet to remove jets potentially dominated by instrumental effects or reconstruction failures.

The missing transverse momentum vector \vec{p}_T^{miss} is computed as the negative of the vector sum of the \vec{p}_T of all the particle-flow candidates in an event, and its magnitude is denoted as p_T^{miss} [43]. The \vec{p}_T^{miss} is modified to account for corrections to the energy scale of the reconstructed jets in the event.

The candidate vertex with the largest value of summed physics-object p_T^2 is taken to be the primary pp interaction vertex. The physics objects are the jets and the associated p_T^{miss} .

Jets originating from the hadronization of b and c quarks are identified using the deep combined secondary vertex (DeepCSV) algorithm [14], which uses information on the decay vertices of long-lived mesons and the impact parameters of the charged particle tracks as input to a deep neural network (NN) classifier. For the identification of b jets, a medium working point is chosen, corresponding to a $\approx 70\%$ efficiency for correctly selecting b jets and a misidentification probability for LF (c) jets of $\approx 1(12)\%$, derived from simulated $t\bar{t}$ events. The same algorithm also provides discriminators to distinguish c jets from LF and b jets, which are collectively referred to as c tagging discriminators. The information from the distributions of these observables plays a key role in this analysis, and the calibration of the c tagger is further discussed in Section 8.

6. Event selection

An event selection has been employed to select a subset of events that consists almost exclusively (more than 95% as evaluated from simulations) of dileptonic $t\bar{t}$ events with at least two additional jets. Exactly two reconstructed, oppositely charged leptons (either electrons or muons) are required to be present. This procedure also selects τ leptons that decay into an electron or a muon. The electrons and muons are required to have $p_T > 25$ GeV and $|\eta| < 2.4$, and should be isolated from other objects in the event. At least four jets are required in the event, all of which must be spatially separated from the isolated leptons by imposing $\Delta R(\ell, \text{jet}) > 0.5$. Only jets with $p_T > 30$ GeV and $|\eta| < 2.4$ are considered. An assignment of the jets to the expected partons is made to identify the b jets from top quark decays and jets originating from additional radiation (described in detail in Section 7). The

two jets assigned to the b quarks from the top quark decays are required to be b tagged. Neutrinos from leptonically decaying W bosons are not detected, but instead contribute to the p_T^{miss} , which is required to exceed 30 GeV in events with two electrons (ee) or two muons ($\mu\mu$), in order to reduce contributions from DY events. In events with one electron and one muon ($e\mu$), no requirement is imposed on p_T^{miss} . In order to further reduce the contribution from DY production in ee and $\mu\mu$ events, the invariant mass of the two leptons ($m_{\ell\ell}$) is required to be outside of the Z boson mass window, $m_{\ell\ell} \notin [m_Z - 15, m_Z + 15]$ GeV, with $m_Z = 91.2$ GeV [44]. For all events, it is required that $m_{\ell\ell} > 12$ GeV in order to minimize contributions from low-mass resonances.

7. Matching jets to partons

The distinction among the $t\bar{t}c\bar{c}$, $t\bar{t}b\bar{b}$, and $t\bar{t}L\bar{L}$ categories relies on the correct identification of the additional jets not coming from the decay of the top quarks. Assuming a 100% branching fraction for the decay $t \rightarrow bW$, and focusing on the dileptonic decay channel, two b jets are expected from the top quark decays and at least two additional jets are required through the other event selection criteria. In practice, not all b jets from top quark decays will be reconstructed within the acceptance of the detector and additional jets will also not necessarily pass the reconstruction and selection criteria. In this section, a matching procedure is described to achieve the most accurate correspondence between the final-state jets and the expected partons. This is done by considering all possible permutations of four jets in the collection of jets passing the selection criteria described in Section 6 and training a NN to identify the correct jet-parton assignment.

Whether a given permutation corresponds to a correct jet-parton assignment can be inferred from different quantities, such as the jet kinematic variables, b and c tagging discriminators, and angular separations and invariant masses between pairs of jets (and between jets and leptons). The NN processes, for each event, all possible jet-parton assignments and is trained on the aforementioned observables to give the highest possible score to the correct permutation. For the $t\bar{t}L\bar{L}$, $t\bar{t}c\bar{c}$, and $t\bar{t}cL$ categories, the b and c tagging discriminators dominate the decision made by the NN. For the $t\bar{t}b\bar{b}$ category all four partons have the same flavour, so the correct assignment of the four b jets relies mainly on the angular separations and invariant masses between jets or leptons. The best assignment for the $t\bar{t}bL$ category benefits from a combination of all these observables.

The main objective is to identify additional HF jets in the event. In the assignment of b jets from the $t\bar{t}$ decays, it does not matter which b jet is matched to the decay of the top quark or anti-quark. Any permutation for which these b jets are reversed can still be considered appropriate for this measurement. If at least one additional b or c jet is present, a correct permutation has to identify these as the first or second additional jets. The NN is also trained to choose a permutation in which the first additional jet has a larger b tagging discriminator value than the second additional jet. With these considerations in mind, three output classes are defined. One of the NN outputs denotes the probability for a given permutation to correspond to the correct jet-parton assignment (P^+). Another output class refers to those permutations for which the additional jets are correctly matched, but the b jets from the $t\bar{t}$ decays are reversed as explained above (P^\times). The third output represents all permutations for which the matching is wrong (P^-), meaning that either at least one of the b jets from the $t\bar{t}$ decays is not correctly matched, or an additional HF jet is found but is not identified as either the first or the second additional jet. The best jet-parton assignment is then identified by selecting the permutation with the highest value of:

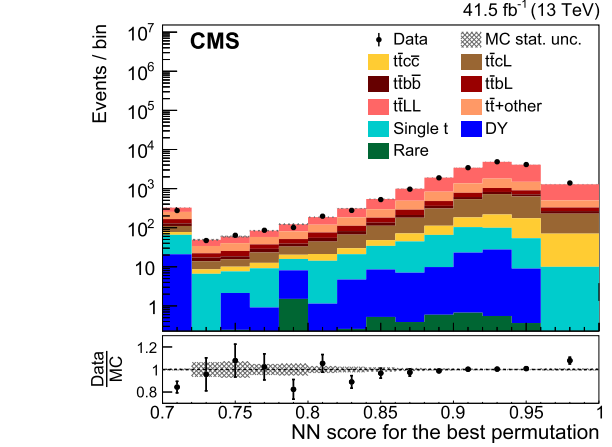


Fig. 2. Comparison between data (points) and simulated predictions (histograms) for the distribution of the NN score for the best permutations of jet-parton assignments found in each event. Underflow is included in the first bin. The distributions are found after the event selections outlined in Section 6, but before fitting the predicted signal yields to the data. The lower panel shows the ratio of the yields in data to those predicted in simulations. The vertical bars represent the statistical uncertainties in data, while the hatched bands show the statistical uncertainty in the simulated predictions.

$$\max\left(\frac{P^+}{P^+ + P^-}, \frac{P^\times}{P^\times + P^-}\right). \quad (1)$$

The NN is trained using the KERAS deep learning library [45], interfaced to TENSORFLOW [46] as a back end. Its architecture is composed of two fully connected hidden layers with 50 neurons each, and with a rectified linear unit activation function. The training is performed using an independent data set of simulated $t\bar{t}$ events that pass all the event selections outlined in Section 6, except for the b tagging requirement. Only events for which the two generator-level b quarks from top quark decays lie within $\Delta R < 0.3$ of a reconstructed b jet are used for the training. These constitute $\approx 76\%$ of the simulated $t\bar{t}$ events with at least two additional jets. Of those, the NN correctly identifies the two additional c (b) jets in 50 (30)% of the cases for $t\bar{t}c\bar{c}$ ($t\bar{t}b\bar{b}$) events. For $t\bar{t}b\bar{b}$ events, the matching is more challenging because the HF tagging information cannot help in separating additional b jets from those originating from top quark decays. A comparison between data and simulations of the NN score for the best permutation in each event is shown in Fig. 2, indicating good agreement between the two.

8. Charm jet identification and calibration

The DeepCSV HF tagging algorithm has a multiclass output structure that predicts the probabilities for each jet to contain a single b hadron ($P(b)$), two b hadrons ($P(bb)$), one or more c hadrons ($P(c)$), or no b or c hadrons ($P(\text{udsg})$). The b tagger used throughout this analysis is constructed from the sum $P(b) + P(bb)$. However, different combinations of output values provide different types of discrimination. Since the displacements of tracks and secondary vertices for c jets are on average smaller than those for b jets and larger than those for LF jets, a charm jet identification algorithm uses a combination of two discriminators. The first is used to distinguish c jets from LF jets (CvsL) and the second separates c jets from b jets (CvsB). The CvsL and CvsB discriminators are defined from the multiclass output structure of the DeepCSV algorithm as:

$$\begin{aligned} \text{CvsL} &= \frac{P(c)}{P(c) + P(\text{udsg})}, \\ \text{CvsB} &= \frac{P(c)}{P(c) + P(b) + P(\text{bb})}. \end{aligned} \quad (2)$$

The c tagging discriminators require calibration with the data, given that these algorithms are trained on simulated events and are therefore prone to mismodelling effects in the input variables. The observed initial discrepancies between the data and the simulated predictions can be as large as 50%, as can be seen from the distributions before calibration in Appendix A. In order to use these c tagger discriminators for the fit of the template distributions (as discussed in Section 9), the shape of the two-dimensional (CvsL, CvsB) distribution is corrected to reproduce the distribution observed in data. To this end, a novel calibration technique is employed that uses three control regions selecting for semileptonic $t\bar{t}$, $W + c$, and $DY + \text{jets}$ events, which are enriched in b , c , and LF jets, respectively [47]. By means of an iterative fit in these three control regions, a set of scale factors for each jet flavour is derived, as a function of both the CvsL and CvsB discriminator values of a given jet. The effectiveness of this calibration for different jet flavours has been validated in the three corresponding control regions outlined above, showing that the calibrated distributions in simulations indeed match those in data within the associated uncertainties. Additionally, the method shows no bias when applied to pseudo-data constructed from simulated events that have artificial scale factors applied to them.

After applying this calibration to the simulated events, the distributions of the CvsL and CvsB discriminators provide a good description of the data, as shown in Fig. 3 for the first (upper row) and second (lower row) additional jet. The uncertainties related to this calibration are further discussed in Section 10.

9. Fit to an event-based neural network discriminator

The extraction of the $t\bar{t}c\bar{c}$, $t\bar{t}b\bar{b}$, and $t\bar{t}LL$ cross sections proceeds by means of a template fit to an observable that can distinguish among the different flavour categories. Since the differentiation relies mainly on the additional-jet flavour, the c tagging discriminators of the first and second additional jets provide a natural choice for separating the different signals. The CvsL discriminator distinguishes the $t\bar{t}c\bar{c}$ and $t\bar{t}b\bar{b}$ from the $t\bar{t}LL$ events, whereas the CvsB discriminator provides additional information that can be used to distinguish between the $t\bar{t}c\bar{c}$ and $t\bar{t}b\bar{b}$ events. The flavour tagging information for the second additional jet allows the $t\bar{t}cL$ and $t\bar{t}bL$ processes to be identified. Additional information is extracted from two kinematic variables. The first is the angular separation ΔR between the two additional jets. In the $t\bar{t}c\bar{c}$ and $t\bar{t}b\bar{b}$ processes, the additional jets arise predominantly from gluon splitting into $c\bar{c}$ and $b\bar{b}$ pairs, respectively, and are therefore expected to be more collimated. The second is the NN score for the best permutation (shown in Fig. 2), which is expected to be larger on average for $t\bar{t}LL$ events because the additional jets are well distinguished from the b jets from top quark decays. This observable indirectly incorporates information on the event kinematic features through its input variables.

Using the six aforementioned observables, a NN is trained. Given the relatively small number of inputs, an architecture for the NN is chosen with one hidden layer that comprises 30 neurons with a rectified linear unit activation function. This NN predicts output probabilities for five output classes: $P(t\bar{t}c\bar{c})$, $P(t\bar{t}cL)$, $P(t\bar{t}b\bar{b})$, $P(t\bar{t}bL)$, and $P(t\bar{t}LL)$. To obtain the distributions that are used in the fit, these probabilities are projected onto a two-dimensional phase space spanned by two derived discriminators:

Table 1

Selection efficiencies and acceptance factors for events in different signal categories. The values are obtained from simulated $t\bar{t}$ events.

Event category	$t\bar{t}b\bar{b}$	$t\bar{t}bL$	$t\bar{t}c\bar{c}$	$t\bar{t}cL$	$t\bar{t}LL$
Efficiency ϵ (%)	12.0	8.5	6.8	5.6	4.5
Acceptance \mathcal{A} (%)	2.9	2.5	2.0	2.0	2.3

$$\begin{aligned} \Delta_b^c &= \frac{P(t\bar{t}c\bar{c})}{P(t\bar{t}c\bar{c}) + P(t\bar{t}b\bar{b})}, \\ \Delta_L^c &= \frac{P(t\bar{t}c\bar{c})}{P(t\bar{t}c\bar{c}) + P(t\bar{t}LL)}. \end{aligned} \quad (3)$$

These discriminators can be interpreted as topology-specific c tagger discriminators that augment the information on the jet flavour of the two additional jets with additional event kinematic features to optimally distinguish different signal categories. The two-dimensional distributions of these discriminators, normalized to unit area, are shown in Fig. 4 for simulated dileptonic $t\bar{t}$ events. The different signal categories occupy different parts of this phase space, demonstrating that a fit of templates derived from these distributions to the data can be used to extract the $t\bar{t}c\bar{c}$, $t\bar{t}b\bar{b}$, and $t\bar{t}LL$ cross sections. It can be seen that the lower right corner of this phase space is almost exclusively populated with $t\bar{t}b\bar{b}$ events, whereas the upper right corner is dominated by $t\bar{t}c\bar{c}$ events.

Templates are constructed separately for each dilepton channel (ee , $\mu\mu$, and $e\mu$) and are fitted simultaneously to data by means of a binned maximum likelihood fit assuming Poisson statistics. The negative logarithm of the likelihood is minimized using the ‘‘Combine’’ framework developed for the combined Higgs boson measurements performed by ATLAS and CMS [48,49]. Uncertainties are included as nuisance parameters in the definition of the likelihood.

A first fit is performed to extract the absolute cross section (σ) of the $t\bar{t}c\bar{c}$, $t\bar{t}b\bar{b}$, and $t\bar{t}LL$ events in the fiducial phase space, where the expected yield in each bin is parametrized using the function:

$$\begin{aligned} F_i(\sigma_{t\bar{t}c\bar{c}}, \sigma_{t\bar{t}b\bar{b}}, \sigma_{t\bar{t}LL}) = \\ \mathcal{L}^{\text{int}} \left\{ \sigma_{t\bar{t}c\bar{c}} \epsilon_{t\bar{t}c\bar{c}} \left(f_{t\bar{t}c\bar{c},i}^{\text{norm}} + \frac{N_{t\bar{t}c\bar{c}}^{\text{MC}}}{N_{t\bar{t}c\bar{c}}^{\text{MC}}} f_{t\bar{t}cL,i}^{\text{norm}} \right) \right. \\ + \sigma_{t\bar{t}b\bar{b}} \epsilon_{t\bar{t}b\bar{b}} \left(f_{t\bar{t}b\bar{b},i}^{\text{norm}} + \frac{N_{t\bar{t}bL}^{\text{MC}}}{N_{t\bar{t}b\bar{b}}^{\text{MC}}} f_{t\bar{t}bL,i}^{\text{norm}} \right) \\ \left. + \sigma_{t\bar{t}LL} \epsilon_{t\bar{t}LL} \left(f_{t\bar{t}LL,i}^{\text{norm}} + \frac{N_{t\bar{t}+other}^{\text{MC}}}{N_{t\bar{t}LL}^{\text{MC}}} f_{t\bar{t}+other,i}^{\text{norm}} \right) \right\} \\ + \mathcal{L}^{\text{int}} \sigma_{\text{bkg}} f_{\text{bkg},i}^{\text{norm}}. \end{aligned} \quad (4)$$

Here, \mathcal{L}^{int} denotes the total integrated luminosity and f_i^{norm} represents a given bin (with index i) of the simulated two-dimensional template, normalized to unit area. The measurements in the reconstructed phase space are corrected to the fiducial phase space through an efficiency (ϵ). To extract the result in the full phase space, an additional acceptance factor, \mathcal{A} , is applied to the extracted fiducial cross section to account for the difference in acceptance between the fiducial and full phase spaces. The efficiency and acceptance factors are summarized in Table 1, and are calculated from simulations. The largest contribution to the acceptance can be attributed to the extrapolation from the dileptonic to the fully inclusive decays of the $t\bar{t}$ pairs. The remaining contributions are due to changes in kinematic requirements on the generator-level objects. As discussed in Section 4, the $t\bar{t}cL$ and $t\bar{t}bL$ categories result from $t\bar{t}c\bar{c}$ and $t\bar{t}b\bar{b}$ events, respectively, where one of the additional HF jets is outside the acceptance or both are merged

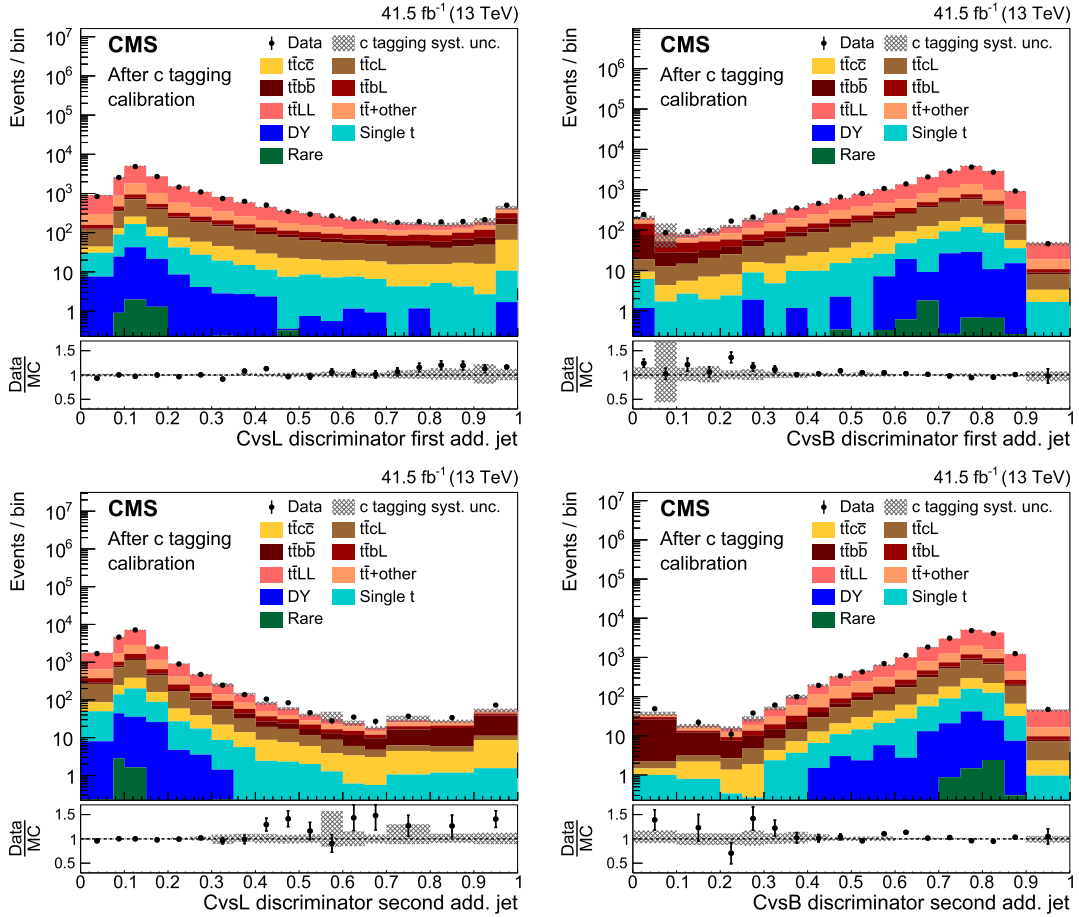


Fig. 3. Comparison between data (points) and simulated predictions (histograms) for the CvsL (left column) and CvsB (right column) c tagging discriminator distributions of the first (upper row) and second (lower row) additional jet after applying the c tagging calibration. The distributions are found after the event selections outlined in Section 6, but before fitting the predicted signal yields to the data. The lower panels show the ratio of the yields in data to those predicted in simulations. The vertical bars represent the statistical uncertainties in data, while the hatched bands show the systematic uncertainty from the c tagging calibration only.

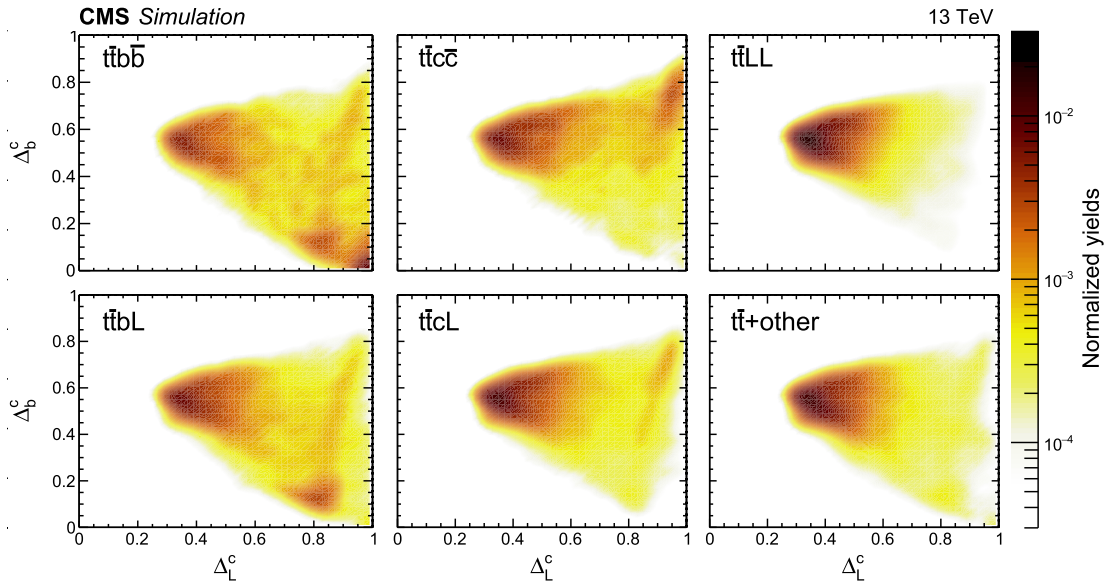


Fig. 4. Normalized two-dimensional distributions of Δ_b^c vs. Δ_L^c in simulated dileptonic $t\bar{t}$ events, for each of the event categories outlined in Section 4. The colour scale on the right shows the normalized event yields.

into one jet. Therefore, these components are scaled with the same factors as the $t\bar{t}c\bar{c}$ and $t\bar{t}b\bar{b}$ templates, respectively, such that the relative yield of $t\bar{t}cL$ ($t\bar{t}bL$) with respect to $t\bar{t}c\bar{c}$ ($t\bar{t}b\bar{b}$) events is fixed to that predicted in the simulations. The predicted yields from the simulations are denoted by N_k^{MC} , where k denotes the signal process. The $t\bar{t}$ +other component is scaled with the same factor as the $t\bar{t}LL$ component, motivated by their similar LF content. Uncertainties in the ratios of simulated yields are taken into account in the fit. The background processes are summed together into one template and their yield is fixed to the predictions from simulations, with uncertainties taken into account as discussed in Section 10. The sum of the cross sections for the background processes (obtained from simulations) is denoted as σ_{bkg} .

A second binned maximum likelihood fit is performed assuming Poisson statistics to extract the ratios of the $t\bar{t}c\bar{c}$ and $t\bar{t}b\bar{b}$ cross sections to the overall inclusive $t\bar{t}jj$ cross section (denoted R_c and R_b , respectively) in the fiducial phase space, with the expected yield in bin i calculated using the function:

$$F_i(\sigma_{t\bar{t}jj}, R_c, R_b) = \mathcal{L}^{\text{int}} \sigma_{t\bar{t}jj} \left\{ R_c \epsilon_{t\bar{t}c\bar{c}} \left(f_{t\bar{t}c\bar{c},i}^{\text{norm}} + \frac{N_{t\bar{t}cL}^{MC}}{N_{t\bar{t}c\bar{c}}^{MC}} f_{t\bar{t}cL,i}^{\text{norm}} \right) + R_b \epsilon_{t\bar{t}b\bar{b}} \left(f_{t\bar{t}b\bar{b},i}^{\text{norm}} + \frac{N_{t\bar{t}bL}^{MC}}{N_{t\bar{t}b\bar{b}}^{MC}} f_{t\bar{t}bL,i}^{\text{norm}} \right) + (1 - R_c - R_{cL} - R_b - R_{bL}) \epsilon_{t\bar{t}LL} \left(f_{t\bar{t}LL,i}^{\text{norm}} + \frac{N_{t\bar{t}+other}^{MC}}{N_{t\bar{t}LL}^{MC}} f_{t\bar{t}+other,i}^{\text{norm}} \right) \right\} + \mathcal{L}^{\text{int}} \sigma_{bkg} f_{bkg,i}^{\text{norm}},$$

with

$$\begin{cases} R_{cL} = R_c \left(\frac{N_{t\bar{t}cL}^{MC} \epsilon_{t\bar{t}c\bar{c}}}{N_{t\bar{t}c\bar{c}}^{MC} \epsilon_{t\bar{t}cL}} \right), \\ R_{bL} = R_b \left(\frac{N_{t\bar{t}bL}^{MC} \epsilon_{t\bar{t}b\bar{b}}}{N_{t\bar{t}b\bar{b}}^{MC} \epsilon_{t\bar{t}bL}} \right). \end{cases} \quad (6)$$

The parameters R_{cL} and R_{bL} are used to denote, respectively, the ratios of the $t\bar{t}cL$ and $t\bar{t}bL$ cross sections to the inclusive $t\bar{t}jj$ cross section, and are defined as a function of R_c and R_b in Eq. (6).

10. Systematic uncertainties

This section summarizes the systematic uncertainties related to the extraction of the $t\bar{t}c\bar{c}$, $t\bar{t}b\bar{b}$, and $t\bar{t}LL$ cross sections (and the ratios R_c and R_b), as well as corrections applied to the simulated events to account for differences with respect to data. Systematic uncertainties are treated as nuisance parameters in the template fit to data that can affect both the shapes of the templates and the yields of the signal and background processes. A smoothing procedure [50] is applied to the templates that describe the uncertainty variations affecting the template shape. The sources of systematic uncertainties are subdivided into experimental and theoretical components and are discussed below.

Experimental uncertainties: These uncertainties affect both the shape and normalization of the templates. The jet energy resolution is known to be worse in data than in simulations, and a corresponding additional smearing is applied to the simulated jet energies [42]. Systematic uncertainties are estimated by varying the smearing of the jet energy within its uncertainties in the calculation of the cross sections. Similarly, we take into account corrections and uncertainties from observed differences in the jet

energy scale. These corrections are evaluated and applied in different regions of jet p_T and $|\eta|$. Observed differences in electron and muon identification, isolation, reconstruction, and trigger efficiencies between data and simulations are taken into account through p_T - and η -dependent scale factors, with the corresponding uncertainties accounted for. The distribution of the number of pileup collisions in simulated events is reweighted to match the distribution observed in data, using an inelastic pp cross section of 69.2 mb [51]. An uncertainty related to this correction is applied by varying this inelastic cross section by $\pm 4.6\%$. An uncertainty of 2.3% [15] in the total integrated luminosity is also taken into account. The scale factors extracted from the c tagging calibration are applied to the simulated events, and corresponding uncertainties are considered. Uncertainties related to this calibration are found to be dominated by the choice of μ_R and μ_F in the $W + c$ and $DY + jets$ control regions, affecting scale factors for c and LF jets, respectively, and by PS uncertainties in semileptonic $t\bar{t}$ events that affect scale factors for b jets, together with a significant contribution from statistical uncertainties for all jet flavours. Most of the theoretical and experimental sources of uncertainty are in common between the control regions in which the c tagging calibration is derived and the $t\bar{t}$ dileptonic signal region considered in this analysis. In such cases, the common uncertainties are considered fully correlated and evaluated simultaneously.

Theoretical uncertainties: In the ME calculation, the choice of μ_R and μ_F can have an impact on the kinematic distributions of the final-state objects. Uncertainties in these scales are taken into account by rescaling μ_F and μ_R up or down by a factor of two at the ME level [52,53]. The choice was made not to include the difference between PYTHIA and alternative PS simulations as a systematic uncertainty in this analysis. Instead a variety of parameters in PYTHIA, sensitive to the PS and hadronization, are consistently varied to assess the uncertainty in an unambiguous way. In the PS, the uncertainty in the value of the strong coupling constant (α_S) evaluated at m_Z is taken into account by varying the renormalization scale of QCD emissions in the initial- and final-state radiation up and down by a factor of two. Similarly, uncertainties in the momentum transfer from b quarks to b hadrons (b fragmentation) in the PS have been included. The b fragmentation in PYTHIA is parametrized using a Bowler–Lund model [54–56], with uncertainties calculated by tuning the internal parameters of this model to measurements from the ALEPH [57], DELPHI [58], OPAL [59] and SLD [60] experiments. In practice, it was found that this parametrization can be varied within its uncertainties by a reweighting at the generator level of the so-called “transfer function”, $x_b = p_T(b \text{ hadron})/p_T(b \text{ jet})$. No such detailed assessment of the c fragmentation uncertainties has yet been performed, but a similar level of variation is observed when comparing the available experimental measurements [61] with the default PYTHIA tune used in this analysis [62]. We verified that variations of the c jet transfer function ($x_c = p_T(c \text{ hadron})/p_T(c \text{ jet})$) induce similar variations of the c jet p_T and c tagging discriminator distributions as the analogous variations in b fragmentation for b jets, and found that these effects are comfortably covered by an uncertainty a factor of two larger than that for b fragmentation. This uncertainty is modelled as an uncertainty in the $t\bar{t}c\bar{c}$ and $t\bar{t}cL$ yields in the fit in the fiducial phase space, and an additional uncertainty in the acceptance correction from the full to the fiducial phase space. Uncertainties associated with the PDF, as well as with the value of α_S in the PDF of the proton are considered, following the PDF4LHC prescription [63]. For all of the aforementioned theoretical sources of uncertainty (except for the c fragmentation uncertainty), the effects of these variations on the shape of the fitted templates are taken into account in the fit, whereas their impact on the signal yields is considered as an uncertainty in the theoretical prediction to which the measurement is compared in Section 11. The resid-

Table 2

Sources of theoretical uncertainties in the acceptance, used to extrapolate the results from the fiducial to the full phase space, for different signal categories, together with their individual impact in percent. The last row of the table quotes the total relative uncertainty in the acceptance, calculated by adding in quadrature the effects from individual sources. A dash indicates that the uncertainty is not applicable for that signal category.

Sources	Uncertainty in the acceptance (%)				
	$t\bar{t}c\bar{c}$	$t\bar{t}cL$	$t\bar{t}b\bar{b}$	$t\bar{t}bL$	$t\bar{t}LL$
μ_R and μ_F	1.0	0.8	0.4	0.6	0.5
PS scale	1.6	1.6	1.2	1.4	1.5
PDF	0.6	0.8	1.2	1.2	0.9
Underlying event	1.0	1.2	1.8	1.1	0.3
ME-PS matching	2.1	2.3	1.0	2.5	1.7
b fragmentation	2.2	2.0	4.2	2.6	2.3
c fragmentation	4.5	2.0	–	–	–
Total	5.9	4.3	5.0	4.2	3.4

ual theoretical uncertainty that enters the measured cross sections through the ϵ_i terms in Eqs. (4) and (5) is accounted for by a separate theoretical uncertainty in the efficiency. The experimental uncertainties in the efficiency are already taken into account through the uncertainties in the normalization of the templates. The matching between the ME and PS is governed by a parameter called h_{damp} . The value of this parameter is varied according to $h_{\text{damp}} = \left(1.379^{+0.926}_{-0.505}\right) m_t$ [31] in a separate simulation. Since the size of this simulated data set is insufficient to reliably estimate the effect on the shapes of the templates, this uncertainty is conservatively estimated through its effect on the overall yield. The remnants of the pp collisions that do not take part in the hard scattering are referred to as the underlying event. Their kinematic distributions are tuned in the generators to match those observed in the data [31]. The resulting parametrization of the CP5 tune, used in this analysis, is varied within its uncertainties in separate simulations. Here too the effect of the uncertainty in the overall yield, rather than in the template shapes, is propagated to the measured cross sections. The effects of the theoretical uncertainties listed above on the fixed ratios of $t\bar{t}bL$ to $t\bar{t}b\bar{b}$, $t\bar{t}cL$ to $t\bar{t}c\bar{c}$, and $t\bar{t}$ -other to $t\bar{t}LL$ yields, taken from simulations in Eqs. (4) and (5), are also included in the fit. An uncertainty of 25% is assigned to the total cross section of all background processes, based on the precision of recent measurements of the dominant background processes [64,65]. The statistical uncertainty due to the finite size of the simulated samples is taken into account in the fit. In extrapolating the results from the fiducial to the full phase space, some of these theoretical uncertainties also affect the acceptance for the different signal categories. The individual and combined impacts of different sources of uncertainty in the acceptance are summarized in Table 2.

The individual impacts from each source of uncertainty in the cross sections (and ratios) for the fiducial phase space after the fit are summarized in Table 3. The fitted nuisance parameters do not deviate significantly from their initial values and are not significantly constrained. No strong correlations between any of the nuisance parameters and the fitted cross sections or ratios are observed. The dominant systematic uncertainties are related to the c tagging calibration, followed by jet energy scale and fragmentation uncertainties, as well as uncertainties related to the matching between ME and PS, and the choice of μ_R and μ_F scales in the ME calculation.

11. Results

The binning of the two-dimensional Δ_L^c vs. Δ_b^c distribution is chosen to be:

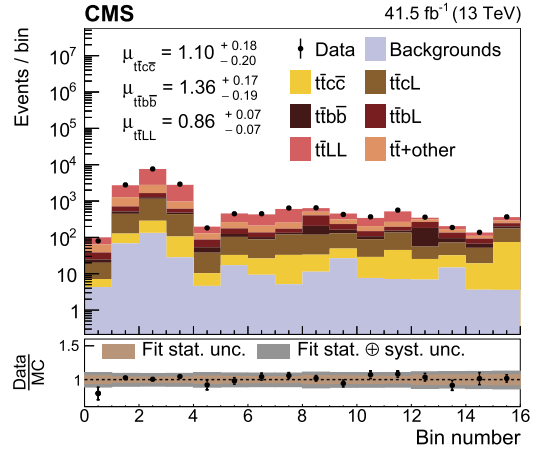


Fig. 5. A one-dimensional representation of the two-dimensional Δ_L^c vs. Δ_b^c distributions, in the simulations (histograms) and in data (points), after normalizing the simulated templates according to the fitted cross sections. The lower panel shows the ratio of the yields in data to those predicted in the simulations. The brown and grey uncertainty bands denote, respectively, the statistical and total uncertainties from the fit. The factors (μ) by which the templates of the different processes (using the POWHEG ME generator) are scaled, are also displayed, together with their combined statistical and systematic uncertainties.

$$\Delta_L^c \otimes \Delta_b^c : \quad (7)$$

$$[0, 0.55, 0.65, 0.85, 1.0] \otimes [0, 0.35, 0.5, 0.6, 1.0].$$

This gives a total of 16 bins with varying compositions of signal categories. From these 16 bins, a one-dimensional histogram is created in which the first four bins correspond to the first bin in Δ_b^c , with increasing values of Δ_L^c , and then analogously for the remainder of the bins. This histogram is shown in Fig. 5 after normalizing the simulated templates according to the fitted cross sections. The factors by which the templates of the $t\bar{t}c\bar{c}$, $t\bar{t}b\bar{b}$, and $t\bar{t}LL$ processes (using the POWHEG ME generator) are scaled to match the data are denoted $\mu_{t\bar{t}c\bar{c}}$, $\mu_{t\bar{t}b\bar{b}}$, and $\mu_{t\bar{t}LL}$, respectively. Their measured values from the fit are displayed in the top panel of Fig. 5, together with their combined statistical and systematic uncertainties. An improved agreement between data and simulated predictions is also observed for the c tagging discriminators of the first and second additional jets after normalizing the simulated templates according to the fitted cross sections. This is demonstrated in Appendix B and can be directly compared to the agreement before the fit in Fig. 3.

The measured cross sections in the fiducial and full phase spaces, together with their statistical and systematic uncertainties, are summarized in Table 4 and compared to predictions using the POWHEG and MADGRAPH5_AMC@NLO ME generators. Uncertainties in the measured values of the cross sections and ratios are determined from the points where the decrease in the logarithm of the profiled likelihood from the best-fit value intersects with 0.5. The inclusive $t\bar{t}c\bar{c}$ cross section and the ratio R_c are measured here for the first time. They are in agreement with the predictions from both ME generators, within the uncertainties.

In addition, two-dimensional likelihood scans are performed over different combinations of cross sections or ratios. These are shown in Fig. 6 for the measurements in the fiducial phase space. The 68 and 95% confidence level contours are shown, along with the predictions from the POWHEG and MADGRAPH5_AMC@NLO ME generators. Agreement is observed at the level of one to two standard deviations between the measured values and simulated predictions for the $t\bar{t}c\bar{c}$, $t\bar{t}b\bar{b}$, and $t\bar{t}LL$ processes. The most significant tension is observed in the ratio R_b , at the level of 2.5 standard deviations. Results for $\sigma_{t\bar{t}b\bar{b}}$ and R_b are consistent with previous measurements targeting specifically this signature [6–13] and show the

same tendency to be slightly above the predictions from simulations.

12. Summary

The production of a top quark pair ($t\bar{t}$) in association with additional bottom or charm jets at the LHC provides challenges both in the theoretical modelling and experimental measurement of this process. Whereas $t\bar{t}$ production with two additional bottom jets ($t\bar{t}b\bar{b}$) has been measured by the ATLAS and CMS Collaborations at different centre-of-mass energies [6–13], this analysis presents the first measurement of the cross section for $t\bar{t}$ production with two additional charm jets ($t\bar{t}c\bar{c}$). The analysis is conducted using data from proton-proton collisions recorded by the CMS experiment at a centre-of-mass energy of 13 TeV, corresponding to an integrated luminosity of 41.5 fb^{-1} . The measurement is performed in the dileptonic channel of the $t\bar{t}$ decays and relies on the use of recently developed charm jet identification algorithms (c tagging). A template fitting method is used, based on the outputs of

a neural network classifier trained to identify the signal categories defined by the flavour of the additional jets. This allows the simultaneous extraction of the cross section for the $t\bar{t}c\bar{c}$, $t\bar{t}b\bar{b}$, and $t\bar{t}$ with two additional light-flavour or gluon jets ($t\bar{t}LL$) processes. A novel multidimensional calibration of the shape of the c tagging discriminator distributions is employed, such that this information can be reliably used in the neural network classifier.

The $t\bar{t}c\bar{c}$ cross section is measured for the first time to be $0.207 \pm 0.025 \text{ (stat)} \pm 0.027 \text{ (syst)} \text{ pb}$ in the fiducial phase space (matching closely the sensitive region of the detector) and $10.1 \pm 1.2 \text{ (stat)} \pm 1.4 \text{ (syst)} \text{ pb}$ in the full phase space. The ratio of the $t\bar{t}c\bar{c}$ to the inclusive $t\bar{t}$ + two jets cross sections is found to be $(3.01 \pm 0.34 \text{ (stat)} \pm 0.31 \text{ (syst)})\%$ in the fiducial phase space and $(3.36 \pm 0.38 \text{ (stat)} \pm 0.34 \text{ (syst)})\%$ in the full phase space. These results are compared with predictions from two different matrix element generators with next-to-leading order accuracy in quantum chromodynamics, in which an inclusive description of the $t\bar{t}$ process, with up to two additional radiated hard gluons at the

Table 3

Classes of systematic uncertainties in the measured parameters and their individual impact in percent after the fit for the fiducial phase space. The upper (lower) rows of the table list uncertainties related to the experimental conditions (theoretical modelling). For classes describing contributions from multiple nuisance parameters, the quoted numbers are obtained by adding the impacts from individual sources within that class in quadrature. The last row gives the overall systematic uncertainty in each quantity, which results from the nuisance parameter variations in the fit and is not the quadrature sum of the individual components.

Sources	Systematic uncertainty (%)				
	$\Delta\sigma_{t\bar{t}c\bar{c}}$	$\Delta\sigma_{t\bar{t}b\bar{b}}$	$\Delta\sigma_{t\bar{t}LL}$	ΔR_c	ΔR_b
Jet energy scale	4.0	3.2	4.7	2.8	2.1
Jet energy resolution	2.3	1.0	0.9	2.5	1.3
c tagging calibration	7.0	3.2	2.5	7.3	3.5
Lepton identification and isolation	0.8	1.0	1.3	0.6	0.3
Trigger	2.0	2.0	2.0	< 0.1	< 0.1
Pileup	0.3	0.2	0.3	0.5	< 0.1
Total integrated luminosity	2.3	2.4	2.3	< 0.1	< 0.1
μ_R and μ_F scales in ME	3.3	6.2	2.1	3.8	6.8
PS scale	0.4	1.6	0.3	0.5	1.6
PDF	0.3	0.1	0.1	0.2	0.1
ME-PS matching	7.1	5.7	3.5	2.6	1.5
Underlying event	1.9	2.3	1.1	0.5	0.9
b fragmentation	0.4	1.9	0.8	0.3	2.4
c fragmentation	4.6	< 0.1	< 0.1	3.9	0.7
$t\bar{t}b\text{(cL)}/t\bar{t}b\bar{b}\text{(c}\bar{c}\text{)} \text{ and } t\bar{t}\text{+other}/t\bar{t}LL$	2.4	1.8	1.1	1.8	1.5
Efficiency (theoretical)	2.4	2.1	2.0	< 0.1	< 0.1
Simulated sample size	3.2	2.6	1.1	3.1	2.5
Background normalization	0.5	0.7	0.6	0.1	0.1
Total	13.7	11.4	8.2	10.9	9.2

Table 4

Measured parameter values in the fiducial (upper rows) and full (lower rows) phase spaces with their statistical and systematic uncertainties listed in that order. The last two columns display the expectations from the simulated $t\bar{t}$ samples using the POWHEG or MADGRAPH5_AMC@NLO ME generators. The uncertainties quoted for these predictions include the contributions from the theoretical uncertainties listed in the lower rows of Table 3, as well as the uncertainty in the $t\bar{t}$ cross section.

	Result	POWHEG	MADGRAPH5_AMC@NLO
Fiducial phase space			
$\sigma_{t\bar{t}c\bar{c}}$ [pb]	$0.207 \pm 0.025 \pm 0.027$	0.187 ± 0.038	0.189 ± 0.032
$\sigma_{t\bar{t}b\bar{b}}$ [pb]	$0.132 \pm 0.010 \pm 0.015$	0.097 ± 0.021	0.101 ± 0.023
$\sigma_{t\bar{t}LL}$ [pb]	$5.15 \pm 0.12 \pm 0.41$	5.95 ± 1.02	6.32 ± 0.94
R_c [%]	$3.01 \pm 0.34 \pm 0.31$	2.53 ± 0.18	2.43 ± 0.17
R_b [%]	$1.93 \pm 0.15 \pm 0.18$	1.31 ± 0.12	1.30 ± 0.16
Full phase space			
$\sigma_{t\bar{t}c\bar{c}}$ [pb]	$10.1 \pm 1.2 \pm 1.4$	9.1 ± 1.8	8.9 ± 1.5
$\sigma_{t\bar{t}b\bar{b}}$ [pb]	$4.54 \pm 0.35 \pm 0.56$	3.34 ± 0.72	3.39 ± 0.66
$\sigma_{t\bar{t}LL}$ [pb]	$220 \pm 5 \pm 19$	255 ± 43	261 ± 37
R_c [%]	$3.36 \pm 0.38 \pm 0.34$	2.81 ± 0.20	2.72 ± 0.19
R_b [%]	$1.51 \pm 0.11 \pm 0.16$	1.03 ± 0.08	1.03 ± 0.09

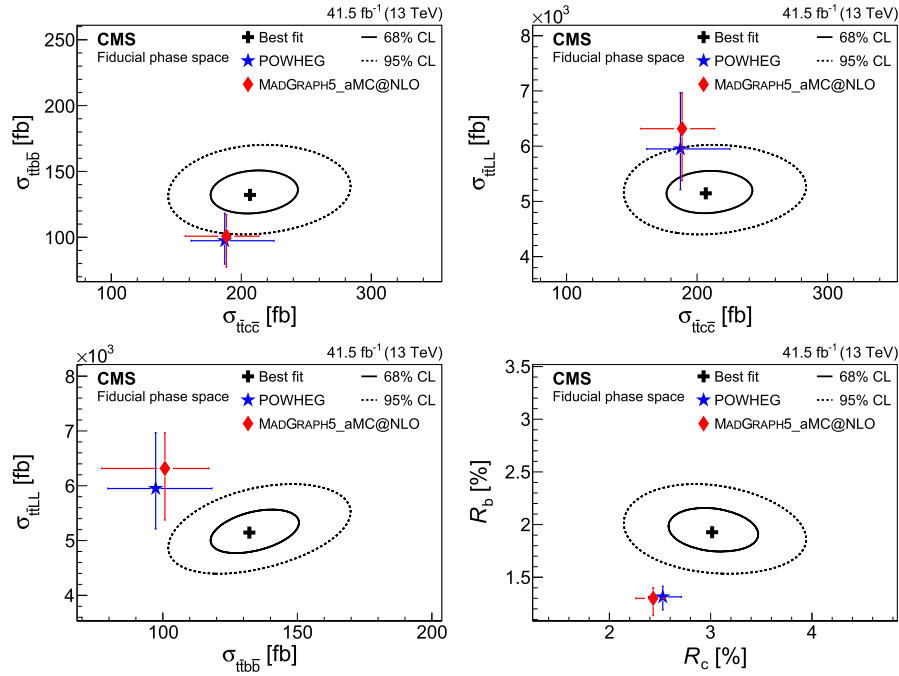


Fig. 6. Results of the two-dimensional likelihood scans for several combinations of the parameters of interest in the fiducial phase space. The best-fit value (black cross) with the corresponding 68% (full) and 95% (dashed) confidence level (CL) contours are shown, compared to the theoretical predictions using either the POWHEG (blue star) or MADGRAPH5_aMC@NLO (red diamond) ME generators. Uncertainties in the theoretical predictions are displayed by the horizontal and vertical bars on the markers.

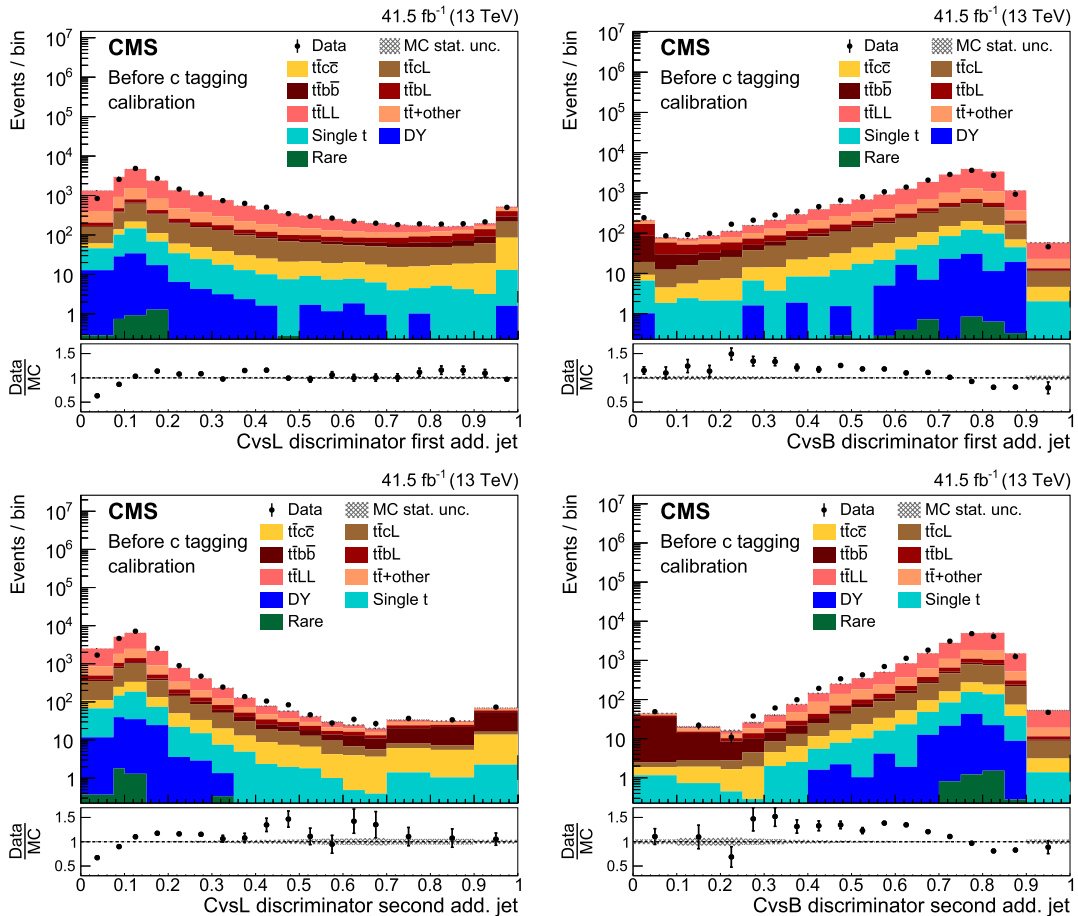


Fig. 7. Comparison between data (points) and simulated predictions (histograms) for the CvsL (left column) and CvsB (right column) c tagging discriminator distributions of the first (upper row) and second (lower row) additional jet before applying the c tagging calibration. The lower panels show the ratio of the yields in data to those predicted in simulations. The vertical bars represent the statistical uncertainties in data, while the hatched bands show the statistical uncertainty in the simulated predictions.

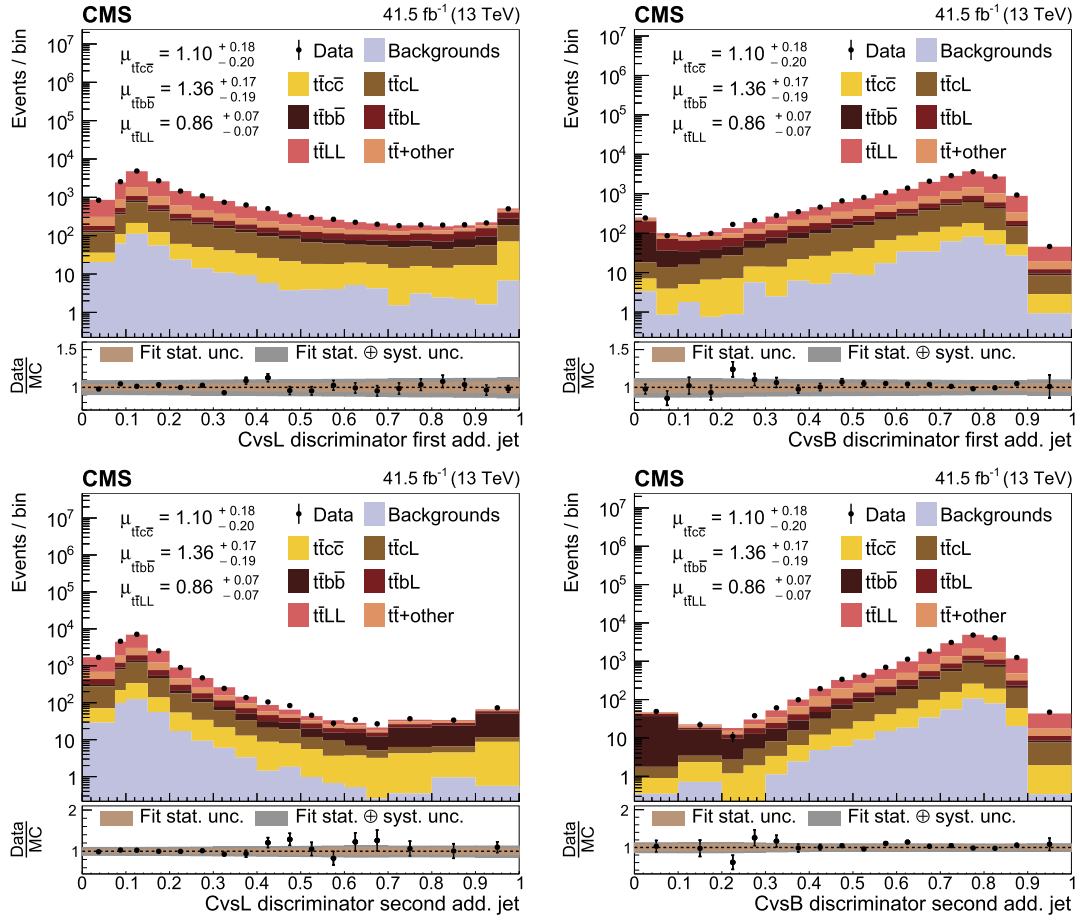


Fig. 8. Comparison between data (points) and simulated predictions (histograms) for the CvsL (left column) and CvsB (right column) c tagging discriminator distributions of the first (upper row) and second (lower row) additional jet, after normalizing the simulated templates according to the fitted cross sections. The lower panels show the ratio of the yields in data to those predicted in the simulations. The brown and grey uncertainty bands denote, respectively, the statistical and total uncertainties from the fit. The factors (μ) by which the templates of the different processes (using the POWHEG ME generator) are scaled, are also displayed, together with their combined statistical and systematic uncertainties.

ME level, is interfaced with a parton shower simulation to generate the additional radiation. Agreement is observed at the level of one to two standard deviations between the measured values and simulated predictions for the $t\bar{t}c\bar{c}$, $t\bar{t}b\bar{b}$, and $t\bar{t}LL$ processes. The observed ratio of the $t\bar{t}b\bar{b}$ to the inclusive $t\bar{t}$ + two jets cross sections exceeds the predictions by about 2.5 standard deviations, consistent with the tendency seen in previous measurements.

Declaration of competing interest

The authors declare that they have no known competing financial interests or personal relationships that could have appeared to influence the work reported in this paper.

Acknowledgements

We congratulate our colleagues in the CERN accelerator departments for the excellent performance of the LHC and thank the technical and administrative staffs at CERN and at other CMS institutes for their contributions to the success of the CMS effort. In addition, we gratefully acknowledge the computing centres and personnel of the Worldwide LHC Computing Grid for delivering so effectively the computing infrastructure essential to our analyses. Finally, we acknowledge the enduring support for the construction and operation of the LHC and the CMS detector provided by the following funding agencies: BMBWF and FWF (Austria); FNRS and FWO (Belgium); CNPq, CAPES, FAPERJ, FAPERGS, and FAPESP

(Brazil); MES (Bulgaria); CERN; CAS, MOST, and NSFC (China); COLCIENCIAS (Colombia); MSES and CSF (Croatia); RIF (Cyprus); SENESCYT (Ecuador); MoER, ERC PUT and ERDF (Estonia); Academy of Finland, MEC, and HIP (Finland); CEA and CNRS/IN2P3 (France); BMBF, DFG, and HGF (Germany); GSRT (Greece); NKfIA (Hungary); DAE and DST (India); IPM (Iran); SFI (Ireland); INFN (Italy); MSIP and NRF (Republic of Korea); MES (Latvia); LAS (Lithuania); MOE and UM (Malaysia); BUAP, CINVESTAV, CONACYT, LNS, SEP, and UASLP-FAI (Mexico); MOS (Montenegro); MBIE (New Zealand); PAEC (Pakistan); MSHE and NSC (Poland); FCT (Portugal); JINR (Dubna); MON, ROSATOM, RAS, RFBR, and NRC KI (Russia); MESTD (Serbia); SEIDI, CPAN, PCTI, and FEDER (Spain); MoSTR (Sri Lanka); Swiss Funding Agencies (Switzerland); MST (Taipei); ThEPCenter, IPST, STAR, and NSTDA (Thailand); TUBITAK and TAEK (Turkey); NASU (Ukraine); STFC (United Kingdom); DOE and NSF (USA).

Individuals have received support from the Marie-Curie programme and the European Research Council and Horizon 2020 Grant, contract Nos. 675440, 724704, 752730, and 765710 (European Union); the Leventis Foundation; the A.P. Sloan Foundation; the Alexander von Humboldt Foundation; the Belgian Federal Science Policy Office; the Fonds pour la Formation à la Recherche dans l'Industrie et dans l'Agriculture (FRIA-Belgium); the Agentschap voor Innovatie door Wetenschap en Technologie (IWT-Belgium); the F.R.S.-FNRS and FWO (Belgium) under the "Excellence of Science – EOS" – be.h project n. 30820817; the Beijing Municipal Science & Technology Commission, No. Z191100007219010; the Ministry of Education, Youth and Sports

(MEYS) of the Czech Republic; the Deutsche Forschungsgemeinschaft (DFG) under Germany's Excellence Strategy – EXC 2121 “Quantum Universe” – 390833306; the Lendület (“Momentum”) Programme and the János Bolyai Research Scholarship of the Hungarian Academy of Sciences, the New National Excellence Program ÚNKP, the NKFI research grants 123842, 123959, 124845, 124850, 125105, 128713, 128786, and 129058 (Hungary); the Council of Science and Industrial Research, India; the HOMING PLUS programme of the Foundation for Polish Science, cofinanced from European Union, Regional Development Fund, the Mobility Plus programme of the Ministry of Science and Higher Education, the National Science Center (Poland), contracts Harmonia 2014/14/M/ST2/00428, Opus 2014/13/B/ST2/02543, 2014/15/B/ST2/03998, and 2015/19/B/ST2/02861, Sonata-bis 2012/07/E/ST2/01406; the National Priorities Research Program by Qatar National Research Fund; the Ministry of Science and Higher Education, project no. 0723-2020-0041 (Russia); the Tomsk Polytechnic University Competitiveness Enhancement Program; the Programa Estatal de Fomento de la Investigación Científica y Técnica de Excelencia María de Maeztu, grant MDM-2015-0509 and the Programa Severo Ochoa del Principado de Asturias; the Thalís and Aristeia programmes cofinanced by EU-ESF and the Greek NSRF; the Rachadapisek Sompot Fund for Postdoctoral Fellowship, Chulalongkorn University and the Chulalongkorn Academic into Its 2nd Century Project Advancement Project (Thailand); the Kavli Foundation; the Nvidia Corporation; the SuperMicro Corporation; the Welch Foundation, contract C-1845; and the Weston Havens Foundation (USA).

Appendix A. Charm tagging discriminators before calibration

The c tagging algorithms are trained on simulated events and are therefore prone to mismodelling effects in the input variables. The initial C_{vsL} and C_{vsB} c tagging discriminator distributions of the first and second additional jet are shown in Fig. 7. Discrepancies between the data and the simulated predictions of up to 50% are observed, demonstrating the need for the c tagging calibration described in Section 8.

Appendix B. Charm tagging discriminators after scaling to the fitted cross sections

After scaling the simulated templates of the c tagging discriminators to their fitted yields, the agreement between data and simulations is shown in Fig. 8. This can be compared to the agreement before the fit was performed in Fig. 3, and indeed shows an improved agreement especially in those bins which have a relatively large contribution from $t\bar{t}b\bar{b}$ and $t\bar{t}c\bar{c}$ events.

References

- [1] A. Bredenstein, A. Denner, S. Dittmaier, S. Pozzorini, NLO QCD corrections to $t\bar{t}b\bar{b}$ production at the LHC: 1. Quark-antiquark annihilation, *J. High Energy Phys.* 08 (2008) 108, <https://doi.org/10.1088/1126-6708/2008/08/108>, arXiv:0807.1248.
- [2] A. Bredenstein, A. Denner, S. Dittmaier, S. Pozzorini, NLO QCD corrections to $pp \rightarrow t\bar{t}b\bar{b} + X$ at the LHC, *Phys. Rev. Lett.* 103 (2009) 012002, <https://doi.org/10.1103/PhysRevLett.103.012002>, arXiv:0905.0110.
- [3] F. Cascioli, P. Maierhöfer, N. Moretti, S. Pozzorini, F. Siegert, NLO matching for $t\bar{t}b\bar{b}$ production with massive b quarks, *Phys. Lett. B* 734 (2014) 210, <https://doi.org/10.1016/j.physletb.2014.05.040>, arXiv:1309.5912.
- [4] T. Ježo, J.M. Lindert, N. Moretti, S. Pozzorini, New NLOPS predictions for $t\bar{t} + b$ jet production at the LHC, *Eur. Phys. J. C* 78 (2018) 502, <https://doi.org/10.1140/epjc/s10052-018-5956-0>, arXiv:1802.00426.
- [5] F. Buccioni, S. Kallweit, S. Pozzorini, M.F. Zoller, NLO QCD predictions for $t\bar{t}b\bar{b}$ production in association with a light jet at the LHC, *J. High Energy Phys.* 12 (2019) 015, [https://doi.org/10.1007/JHEP12\(2019\)015](https://doi.org/10.1007/JHEP12(2019)015), arXiv:1907.13624.
- [6] ATLAS Collaboration, Study of heavy-flavour quarks produced in association with top quark pairs at $\sqrt{s} = 7$ TeV using the ATLAS detector, *Phys. Rev. D* 89 (2014) 072012, <https://doi.org/10.1103/PhysRevD.89.072012>, arXiv:1304.6386.
- [7] CMS Collaboration, Measurement of the cross section ratio $\sigma_{t\bar{t}b\bar{b}}/\sigma_{t\bar{t}ij}$ in pp collisions at $\sqrt{s} = 8$ TeV, *Phys. Lett. B* 746 (2015) 132, <https://doi.org/10.1016/j.physletb.2015.04.060>, arXiv:1411.5621.
- [8] ATLAS Collaboration, Measurements of fiducial cross sections for $t\bar{t}$ production with one or two additional b jets in pp collisions at $\sqrt{s} = 8$ TeV using the ATLAS detector, *Eur. Phys. J. C* 76 (2016) 11, <https://doi.org/10.1140/epjc/s10052-015-3852-4>, arXiv:1508.06868.
- [9] CMS Collaboration, Measurement of $t\bar{t}$ production with additional jet activity, including b quark jets, in the dilepton decay channel using pp collisions at $\sqrt{s} = 8$ TeV, *Eur. Phys. J. C* 76 (2016) 379, <https://doi.org/10.1140/epjc/s10052-016-4105-x>, arXiv:1510.03072.
- [10] CMS Collaboration, Measurements of $t\bar{t}$ cross sections in association with b jets and inclusive jets and their ratio using dilepton final states in pp collisions at $\sqrt{s} = 13$ TeV, *Phys. Lett. B* 776 (2018) 355, <https://doi.org/10.1016/j.physletb.2017.11.043>, arXiv:1705.10141.
- [11] ATLAS Collaboration, Measurements of inclusive and differential fiducial cross sections of $t\bar{t}$ production with additional heavy-flavour jets in proton-proton collisions at $\sqrt{s} = 13$ TeV with the ATLAS detector, *J. High Energy Phys.* 04 (2019) 046, [https://doi.org/10.1007/JHEP04\(2019\)046](https://doi.org/10.1007/JHEP04(2019)046), arXiv:1811.12113.
- [12] CMS Collaboration, Measurement of the $t\bar{t}b\bar{b}$ production cross section in the all-jet final state in pp collisions at $\sqrt{s} = 13$ TeV, *Phys. Lett. B* 803 (2020) 135285, <https://doi.org/10.1016/j.physletb.2020.135285>, arXiv:1909.05306.
- [13] CMS Collaboration, Measurement of the cross section for $t\bar{t}$ production with additional jets and b jets in pp collisions at $\sqrt{s} = 13$ TeV, *J. High Energy Phys.* 07 (2020) 125, [https://doi.org/10.1007/JHEP07\(2020\)125](https://doi.org/10.1007/JHEP07(2020)125), arXiv:2003.06467.
- [14] CMS Collaboration, Identification of heavy-flavour jets with the CMS detector in pp collisions at 13 TeV, *J. Instrum.* 13 (2018) P05011, <https://doi.org/10.1088/1748-0221/13/05/P05011>, arXiv:1712.07158.
- [15] CMS Collaboration, CMS luminosity measurement for the 2017 data-taking period at $\sqrt{s} = 13$ TeV, CMS Physics Analysis Summary CMS-PAS-LUM-17-004, CERN, <https://cds.cern.ch/record/2621960>, 2018.
- [16] CMS Collaboration, CMS technical design report for the pixel detector upgrade, CMS Technical Design Report CERN-LHCC-2012-016, CMS-TDR-011, CERN, 2012, <https://cds.cern.ch/record/1481838>.
- [17] CMS Collaboration, Performance of b tagging algorithms in proton-proton collisions at 13 TeV with Phase 1 CMS detector, CMS Detector Performance Note CMS-DP-2018-033, CERN, <https://cds.cern.ch/record/2627468>, 2018.
- [18] CMS Collaboration, Observation of $t\bar{t}H$ production, *Phys. Rev. Lett.* 120 (2018) 231801, <https://doi.org/10.1103/PhysRevLett.120.231801>, arXiv:1804.02610.
- [19] CMS Collaboration, Search for $t\bar{t}H$ production in the $H \rightarrow b\bar{b}$ decay channel with leptonic $t\bar{t}$ decays in proton-proton collisions at $\sqrt{s} = 13$ TeV, *J. High Energy Phys.* 03 (2019) 026, [https://doi.org/10.1007/JHEP03\(2019\)026](https://doi.org/10.1007/JHEP03(2019)026), arXiv:1804.03682.
- [20] ATLAS Collaboration, Observation of Higgs boson production in association with a top quark pair at the LHC with the ATLAS detector, *Phys. Lett. B* 784 (2018) 173, <https://doi.org/10.1016/j.physletb.2018.07.035>, arXiv:1806.00425.
- [21] ATLAS Collaboration, Search for the standard model Higgs boson produced in association with top quarks and decaying into a $b\bar{b}$ pair in pp collisions at $\sqrt{s} = 13$ TeV with the ATLAS detector, *Phys. Rev. D* 97 (2018) 072016, <https://doi.org/10.1103/PhysRevD.97.072016>, arXiv:1712.08895.
- [22] CMS Collaboration, Track impact parameter resolution in the 2017 dataset with the CMS phase-1 pixel detector, CMS Detector Performance Note CMS-DP-2020-032, CERN, <https://cds.cern.ch/record/2723305>, 2020.
- [23] CMS Collaboration, The CMS experiment at the CERN LHC, *J. Instrum.* 3 (2008) S08004, <https://doi.org/10.1088/1748-0221/3/08/S08004>.
- [24] CMS Collaboration, The CMS trigger system, *J. Instrum.* 12 (2017) P01020, <https://doi.org/10.1088/1748-0221/12/01/P01020>, arXiv:1609.02366.
- [25] P. Nason, A new method for combining NLO QCD with shower Monte Carlo algorithms, *J. High Energy Phys.* 11 (2004) 040, <https://doi.org/10.1088/1126-6708/2004/11/040>, arXiv:hep-ph/0409146.
- [26] S. Frixione, P. Nason, C. Oleari, Matching NLO QCD computations with parton shower simulations: the powheg method, *J. High Energy Phys.* 11 (2007) 070, <https://doi.org/10.1088/1126-6708/2007/11/070>, arXiv:0709.2092.
- [27] S. Alioli, P. Nason, C. Oleari, E. Re, A general framework for implementing NLO calculations in shower Monte Carlo programs: the powheg BOX, *J. High Energy Phys.* 06 (2010) 043, [https://doi.org/10.1007/JHEP06\(2010\)043](https://doi.org/10.1007/JHEP06(2010)043), arXiv:1002.2581.
- [28] J.M. Campbell, R.K. Ellis, P. Nason, E. Re, Top-pair production and decay at NLO matched with parton showers, *J. High Energy Phys.* 04 (2015) 114, [https://doi.org/10.1007/JHEP04\(2015\)114](https://doi.org/10.1007/JHEP04(2015)114), arXiv:1412.1828.
- [29] S. Frixione, P. Nason, G. Ridolfi, A positive-weight next-to-leading-order Monte Carlo for heavy-flavour hadroproduction, *J. High Energy Phys.* 09 (2007) 126, <https://doi.org/10.1088/1126-6708/2007/09/126>, arXiv:0707.3088.
- [30] T. Sjöstrand, S. Ask, J.R. Christiansen, R. Corke, N. Desai, P. Ilten, S. Mrenna, S. Prestel, C.O. Rasmussen, P.Z. Skands, An introduction to PYTHIA8.2, *Comput. Phys. Commun.* 191 (2015) 159, <https://doi.org/10.1016/j.cpc.2015.01.024>, arXiv:1410.3012.
- [31] CMS Collaboration, Extraction and validation of a new set of CMS PYTHIA8 tunes from underlying-event measurements, *Eur. Phys. J. C* 80 (2020) 4, <https://doi.org/10.1140/epjc/s10052-019-7499-4>, arXiv:1903.12179.

- [32] R.D. Ball, et al., NNPDF, Parton distributions from high-precision collider data, *Eur. Phys. J. C* 77 (2017) 663, <https://doi.org/10.1140/epjc/s10052-017-5199-5>, arXiv:1706.00428.
- [33] M. Cacciari, M. Czakon, M. Mangano, A. Mitov, P. Nason, Top-pair production at hadron colliders with next-to-next-to-leading logarithmic soft-gluon resummation, *Phys. Lett. B* 710 (2012) 612, <https://doi.org/10.1016/j.physletb.2012.03.013>, arXiv:1111.5869.
- [34] J. Alwall, R. Frederix, S. Frixione, V. Hirschi, F. Maltoni, O. Mattelaer, H.S. Shao, T. Stelzer, P. Torrielli, M. Zaro, The automated computation of tree-level and next-to-leading order differential cross sections, and their matching to parton shower simulations, *J. High Energy Phys.* 07 (2014) 079, [https://doi.org/10.1007/JHEP07\(2014\)079](https://doi.org/10.1007/JHEP07(2014)079), arXiv:1405.0301.
- [35] R. Frederix, S. Frixione, Merging meets matching in MC@NLO, *J. High Energy Phys.* 12 (2012) 061, [https://doi.org/10.1007/JHEP12\(2012\)061](https://doi.org/10.1007/JHEP12(2012)061), arXiv:1209.6215.
- [36] J. Alwall, S. Höche, F. Krauss, N. Lavesson, L. Lonnblad, F. Maltoni, M.L. Mangano, M. Moretti, C.G. Papadopoulos, F. Piccinini, S. Schumann, M. Treccani, J. Winter, M. Worek, Comparative study of various algorithms for the merging of parton showers and matrix elements in hadronic collisions, *Eur. Phys. J. C* 53 (2008) 473, <https://doi.org/10.1140/epjc/s10052-007-0490-5>, arXiv:0706.2569.
- [37] S. Agostinelli, et al., GEANT4, Geant4 – a simulation toolkit, *Nucl. Instrum. Methods A* 506 (2003) 250, [https://doi.org/10.1016/S0168-9002\(03\)01368-8](https://doi.org/10.1016/S0168-9002(03)01368-8).
- [38] M. Cacciari, G.P. Salam, Pileup subtraction using jet areas, *Phys. Lett. B* 659 (2008) 119, <https://doi.org/10.1016/j.physletb.2007.09.077>, arXiv:0707.1378.
- [39] M. Cacciari, G.P. Salam, G. Soyez, The anti- k_T jet clustering algorithm, *J. High Energy Phys.* 04 (2008) 063, <https://doi.org/10.1088/1126-6708/2008/04/063>, arXiv:0802.1189.
- [40] M. Cacciari, G.P. Salam, G. Soyez, FastJet user manual, *Eur. Phys. J. C* 72 (2012) 1896, <https://doi.org/10.1140/epjc/s10052-012-1896-2>, arXiv:1111.6097.
- [41] CMS Collaboration, Particle-flow reconstruction and global event description with the CMS detector, *J. Instrum.* 12 (2017) P10003, <https://doi.org/10.1088/1748-0221/12/10/P10003>, arXiv:1706.04965.
- [42] CMS Collaboration, Jet energy scale and resolution in the CMS experiment in pp collisions at 8 TeV, *J. Instrum.* 12 (2017) P02014, <https://doi.org/10.1088/1748-0221/12/02/P02014>, arXiv:1607.03663.
- [43] CMS Collaboration, Performance of missing transverse momentum reconstruction in proton-proton collisions at $\sqrt{s} = 13$ TeV using the CMS detector, *J. Instrum.* 14 (2019) P07004, <https://doi.org/10.1088/1748-0221/14/07/P07004>, arXiv:1903.06078.
- [44] Particle Data Group, P.A. Zyla, et al., Review of particle physics, *Prog. Theor. Exp. Phys.* 2020 (2020) 083C01, <https://doi.org/10.1093/ptep/ptaa104>.
- [45] F. Chollet, et al., <https://github.com/keras-team/keras>, 2015, software available from GitHub.
- [46] A. Martín, et al., TensorFlow: large-scale machine learning on heterogeneous systems, software available from <https://www.tensorflow.org/>, 2015.
- [47] CMS Collaboration, Calibration of charm jet identification algorithms using proton-proton collision events at $\sqrt{s} = 13$ TeV, CMS Physics Analysis Summary CMS-PAS-BTV-20-001, CERN, <https://cds.cern.ch/record/2758866>, 2021.
- [48] G. Aad, et al., ATLAS, CMS, Measurements of the Higgs boson production and decay rates and constraints on its couplings from a combined ATLAS and CMS analysis of the LHC pp collision data at $\sqrt{s} = 7$ and 8 TeV, *J. High Energy Phys.* 08 (2016) 045, [https://doi.org/10.1007/JHEP08\(2016\)045](https://doi.org/10.1007/JHEP08(2016)045), arXiv:1606.02266.
- [49] CMS Collaboration, Precise determination of the mass of the Higgs boson and tests of compatibility of its couplings with the standard model predictions using proton collisions at 7 and 8 TeV, *Eur. Phys. J. C* 75 (2015) 212, <https://doi.org/10.1140/epjc/s10052-015-3351-7>, arXiv:1412.8662.
- [50] A. Savitzky, M. Golay, Smoothing and differentiation of data by simplified least squares procedures, *Anal. Chem.* 36 (1964) 1627, <https://doi.org/10.1021/ac60214a047>.
- [51] CMS Collaboration, Measurement of the inelastic proton-proton cross section at $\sqrt{s} = 13$ TeV, *J. High Energy Phys.* 07 (2018) 161, [https://doi.org/10.1007/JHEP07\(2018\)161](https://doi.org/10.1007/JHEP07(2018)161), arXiv:1802.02613.
- [52] M. Cacciari, S. Frixione, M.L. Mangano, P. Nason, G. Ridolfi, The $t\bar{t}$ cross section at 1.8 and 1.96 TeV: a study of the systematics due to parton densities and scale dependence, *J. High Energy Phys.* 04 (2004) 068, <https://doi.org/10.1088/1126-6708/2004/04/068>, arXiv:hep-ph/0303085.
- [53] S. Catani, D. de Florian, M. Grazzini, P. Nason, Soft gluon resummation for Higgs boson production at hadron colliders, *J. High Energy Phys.* 07 (2003) 028, <https://doi.org/10.1088/1126-6708/2003/07/028>, arXiv:hep-ph/0306211.
- [54] M.G. Bowler, e^+e^- production of heavy quarks in the string model, *Z. Phys. C* 11 (1981) 169, <https://doi.org/10.1007/BF01574001>.
- [55] B. Andersson, G. Gustafson, G. Ingelman, T. Sjöstrand, Parton fragmentation and string dynamics, *Phys. Rep.* 97 (1983) 31, [https://doi.org/10.1016/0370-1573\(83\)90080-7](https://doi.org/10.1016/0370-1573(83)90080-7).
- [56] T. Sjöstrand, Jet fragmentation of nearby partons, *Nucl. Phys. B* 248 (1984) 469, [https://doi.org/10.1016/0550-3213\(84\)90607-2](https://doi.org/10.1016/0550-3213(84)90607-2).
- [57] A. Heister, et al., ALEPH, Study of the fragmentation of b quarks into B mesons at the Z peak, *Phys. Lett. B* 512 (2001) 30, [https://doi.org/10.1016/S0370-2693\(01\)00690-6](https://doi.org/10.1016/S0370-2693(01)00690-6), arXiv:hep-ex/0106051.
- [58] J. Abdallah, et al., DELPHI, A study of the b quark fragmentation function with the DELPHI detector at LEP I and an averaged distribution obtained at the Z pole, *Eur. Phys. J. C* 71 (2011) 1557, <https://doi.org/10.1140/epjc/s10052-011-1557-x>, arXiv:1102.4748.
- [59] G. Abbiendi, et al., OPAL, Inclusive analysis of the b quark fragmentation function in Z decays at LEP, *Eur. Phys. J. C* 29 (2003) 463, <https://doi.org/10.1140/epjc/s2003-01229-x>, arXiv:hep-ex/0210031.
- [60] K. Abe, et al., SLD, Measurement of the b quark fragmentation function in Z^0 decays, *Phys. Rev. D* 65 (2002) 092006, <https://doi.org/10.1103/PhysRevD.66.079905>, arXiv:hep-ex/0202031.
- [61] R. Barate, et al., ALEPH, Study of charm production in Z decays, *Eur. Phys. J. C* 16 (2000) 597, <https://doi.org/10.1007/s100520000421>, arXiv:hep-ex/9909032.
- [62] P. Skands, S. Carrazza, J. Rojo, Tuning pythia 8.1: the Monash 2013 tune, *Eur. Phys. J. C* 74 (2014) 3024, <https://doi.org/10.1140/epjc/s10052-014-3024-y>, arXiv:1404.5630.
- [63] J. Butterworth, et al., PDF4LHC recommendations for LHC run II, *J. Phys. G* 43 (2016) 023001, <https://doi.org/10.1088/0954-3889/43/2/023001>, arXiv:1510.03865.
- [64] CMS Collaboration, Electroweak production of two jets in association with a Z boson in proton-proton collisions at $\sqrt{s} = 13$ TeV, *Eur. Phys. J. C* 78 (2018) 589, <https://doi.org/10.1140/epjc/s10052-018-6049-9>, arXiv:1712.09814.
- [65] CMS Collaboration, Measurement of the single top quark and antiquark production cross sections in the t channel and their ratio in proton-proton collisions at $\sqrt{s} = 13$ TeV, *Phys. Lett. B* 800 (2020) 135042, <https://doi.org/10.1016/j.physletb.2019.135042>, arXiv:1812.10514.

The CMS Collaboration

A.M. Sirunyan[†], A. Tumasyan

Yerevan Physics Institute, Yerevan, Armenia

W. Adam, T. Bergauer, M. Dragicevic, A. Escalante Del Valle, R. Frühwirth¹, M. Jeitler¹, N. Krammer, L. Lechner, D. Liko, I. Mikulec, F.M. Pitters, J. Schieck¹, R. Schöfbeck, M. Spanring, S. Templ, W. Waltenberger, C.-E. Wulz¹, M. Zarucki

Institut für Hochenergiephysik, Wien, Austria

V. Chekhovsky, A. Litomin, V. Makarenko

Institute for Nuclear Problems, Minsk, Belarus

M.R. Darwish², E.A. De Wolf, X. Janssen, T. Kello³, A. Lelek, M. Pieters, H. Rejeb Sfar, P. Van Mechelen, S. Van Putte, N. Van Remortel

Universiteit Antwerpen, Antwerpen, Belgium

F. Blekman, E.S. Bols, J. D'Hondt, J. De Clercq, D. Lontkovskyi, S. Lowette, I. Marchesini, S. Moortgat, A. Morton, D. Müller, A.R. Sahasransu, S. Tavernier, W. Van Doninck, P. Van Mulders

Vrije Universiteit Brussel, Brussel, Belgium

D. Beghin, B. Bilin, B. Clerbaux, G. De Lentdecker, B. Dorney, L. Favart, A. Grebenyuk, A.K. Kalsi, K. Lee, I. Makarenko, L. Moureaux, L. Pêtré, A. Popov, N. Postiau, E. Starling, L. Thomas, C. Vander Velde, P. Vanlaer, D. Vannerom, L. Wezenbeek

Université Libre de Bruxelles, Bruxelles, Belgium

T. Cornelis, D. Dobur, M. Gruchala, I. Khvastunov⁴, G. Mestdach, M. Niedziela, C. Roskas, K. Skovpen, M. Tytgat, W. Verbeke, B. Vermassen, M. Vit

Ghent University, Ghent, Belgium

A. Bethani, G. Bruno, F. Bury, C. Caputo, P. David, C. Delaere, M. Delcourt, I.S. Donertas, A. Giammanco, V. Lemaître, K. Mondal, J. Prisciandaro, A. Taliercio, M. Teklishyn, P. Vischia, S. Wertz, S. Wuyckens

Université Catholique de Louvain, Louvain-la-Neuve, Belgium

G.A. Alves, C. Hensel, A. Moraes

Centro Brasileiro de Pesquisas Físicas, Rio de Janeiro, Brazil

W.L. Aldá Júnior, E. Belchior Batista Das Chagas, H. Brandao Malbouisson, W. Carvalho, J. Chinellato⁵, E. Coelho, E.M. Da Costa, G.G. Da Silveira⁶, D. De Jesus Damiao, S. Fonseca De Souza, J. Martins⁷, D. Matos Figueiredo, C. Mora Herrera, L. Mundim, H. Nogima, P. Rebello Teles, L.J. Sanchez Rosas, A. Santoro, S.M. Silva Do Amaral, A. Sznajder, M. Thiel, F. Torres Da Silva De Araujo, A. Vilela Pereira

Universidade do Estado do Rio de Janeiro, Rio de Janeiro, Brazil

C.A. Bernardes^a, L. Calligaris^a, T.R. Fernandez Perez Tomei^a, E.M. Gregores^{a,b}, D.S. Lemos^a, P.G. Mercadante^{a,b}, S.F. Novaes^a, Sandra S. Padula^a

^a *Universidade Estadual Paulista, São Paulo, Brazil*

^b *Universidade Federal do ABC, São Paulo, Brazil*

A. Aleksandrov, G. Antchev, I. Atanasov, R. Hadjiiska, P. Iaydjiev, M. Misheva, M. Rodozov, M. Shopova, G. Sultanov

Institute for Nuclear Research and Nuclear Energy, Bulgarian Academy of Sciences, Sofia, Bulgaria

A. Dimitrov, T. Ivanov, L. Litov, B. Pavlov, P. Petkov, A. Petrov

University of Sofia, Sofia, Bulgaria

T. Cheng, W. Fang³, Q. Guo, M. Mittal, H. Wang, L. Yuan

Beihang University, Beijing, China

M. Ahmad, G. Bauer, Z. Hu, Y. Wang, K. Yi^{8,9}

Department of Physics, Tsinghua University, Beijing, China

E. Chapon, G.M. Chen¹⁰, H.S. Chen¹⁰, M. Chen, T. Javaid¹⁰, A. Kapoor, D. Leggat, H. Liao, Z.-A. Liu¹⁰, R. Sharma, A. Spiezia, J. Tao, J. Thomas-Wilsker, J. Wang, H. Zhang, S. Zhang¹⁰, J. Zhao

Institute of High Energy Physics, Beijing, China

A. Agapitos, Y. Ban, C. Chen, Q. Huang, A. Levin, Q. Li, M. Lu, X. Lyu, Y. Mao, S.J. Qian, D. Wang, Q. Wang, J. Xiao

State Key Laboratory of Nuclear Physics and Technology, Peking University, Beijing, China

Z. You

Sun Yat-Sen University, Guangzhou, China

X. Gao³, H. Okawa

Institute of Modern Physics and Key Laboratory of Nuclear Physics and Ion-beam Application (MOE) – Fudan University, Shanghai, China

M. Xiao

Zhejiang University, Hangzhou, China

C. Avila, A. Cabrera, C. Florez, J. Fraga, A. Sarkar, M.A. Segura Delgado

Universidad de Los Andes, Bogota, Colombia

J. Jaramillo, J. Mejia Guisao, F. Ramirez, J.D. Ruiz Alvarez, C.A. Salazar González, N. Vanegas Arbelaez

Universidad de Antioquia, Medellin, Colombia

D. Giljanovic, N. Godinovic, D. Lelas, I. Puljak

University of Split, Faculty of Electrical Engineering, Mechanical Engineering and Naval Architecture, Split, Croatia

Z. Antunovic, M. Kovac, T. Sculac

University of Split, Faculty of Science, Split, Croatia

V. Brigljevic, D. Ferencek, D. Majumder, M. Roguljic, A. Starodumov¹¹, T. Susa

Institute Rudjer Boskovic, Zagreb, Croatia

M.W. Ather, A. Attikis, E. Erodotou, A. Ioannou, G. Kole, M. Kolosova, S. Konstantinou, J. Mousa, C. Nicolaou, F. Ptochos, P.A. Razis, H. Rykaczewski, H. Saka, D. Tsiakkouri

University of Cyprus, Nicosia, Cyprus

M. Finger¹², M. Finger Jr.¹², A. Kveton, J. Tomsa

Charles University, Prague, Czech Republic

E. Ayala

Escuela Politecnica Nacional, Quito, Ecuador

E. Carrera Jarrin

Universidad San Francisco de Quito, Quito, Ecuador

A.A. Abdelalim^{13,14}, S. Abu Zeid¹⁵, S. Elgammal¹⁶

Academy of Scientific Research and Technology of the Arab Republic of Egypt, Egyptian Network of High Energy Physics, Cairo, Egypt

M.A. Mahmoud, Y. Mohammed

Center for High Energy Physics (CHEP-FU), Fayoum University, El-Fayoum, Egypt

S. Bhowmik, A. Carvalho Antunes De Oliveira, R.K. Dewanjee, K. Ehataht, M. Kadastik, J. Pata, M. Raidal, C. Veelken

National Institute of Chemical Physics and Biophysics, Tallinn, Estonia

P. Eerola, L. Forthomme, H. Kirschenmann, K. Osterberg, M. Voutilainen

Department of Physics, University of Helsinki, Helsinki, Finland

E. Brücken, F. Garcia, J. Havukainen, V. Karimäki, M.S. Kim, R. Kinnunen, T. Lampén, K. Lassila-Perini, S. Lehti, T. Lindén, H. Siikonen, E. Tuominen, J. Tuominiemi

Helsinki Institute of Physics, Helsinki, Finland

P. Luukka, T. Tuuva

Lappeenranta University of Technology, Lappeenranta, Finland

C. Amendola, M. Besancon, F. Couderc, M. Dejardin, D. Denegri, J.L. Faure, F. Ferri, S. Ganjour, A. Givernaud, P. Gras, G. Hamel de Monchenault, P. Jarry, B. Lenzi, E. Locci, J. Malcles, J. Rander, A. Rosowsky, M.Ö. Sahin, A. Savoy-Navarro¹⁷, M. Titov, G.B. Yu

IRFU, CEA, Université Paris-Saclay, Gif-sur-Yvette, France

S. Ahuja, F. Beaudette, M. Bonanomi, A. Buchot Perraguin, P. Busson, C. Charlot, O. Davignon, B. Diab, G. Falmagne, R. Granier de Cassagnac, A. Hakimi, I. Kucher, A. Lobanov, C. Martin Perez, M. Nguyen, C. Ochando, P. Paganini, J. Rembser, R. Salerno, J.B. Sauvan, Y. Sirois, A. Zabi, A. Zghiche

Laboratoire Leprince-Ringuet, CNRS/IN2P3, Ecole Polytechnique, Institut Polytechnique de Paris, Palaiseau, France

J.-L. Agram¹⁸, J. Andrea, D. Bloch, G. Bourgatte, J.-M. Brom, E.C. Chabert, C. Collard, J.-C. Fontaine¹⁸, U. Goerlach, C. Grimault, A.-C. Le Bihan, P. Van Hove

Université de Strasbourg, CNRS, IPHC UMR 7178, Strasbourg, France

E. Asilar, S. Beauceron, C. Bernet, G. Boudoul, C. Camen, A. Carle, N. Chanon, D. Contardo, P. Depasse, H. El Mamouni, J. Fay, S. Gascon, M. Gouzevitch, B. Ille, Sa. Jain, I.B. Laktineh, H. Lattaud, A. Lesauvage, M. Lethuillier, L. Mirabito, K. Shchablo, L. Torterotot, G. Touquet, M. Vander Donckt, S. Viret

Université de Lyon, Université Claude Bernard Lyon 1, CNRS-IN2P3, Institut de Physique Nucléaire de Lyon, Villeurbanne, France

A. Khvedelidze¹², Z. Tsamalaidze¹²

Georgian Technical University, Tbilisi, Georgia

L. Feld, K. Klein, M. Lipinski, D. Meuser, A. Pauls, M.P. Rauch, J. Schulz, M. Teroerde

RWTH Aachen University, I. Physikalisches Institut, Aachen, Germany

D. Eliseev, M. Erdmann, P. Fackeldey, B. Fischer, S. Ghosh, T. Hebbeker, K. Hoepfner, H. Keller, L. Mastrolorenzo, M. Merschmeyer, A. Meyer, G. Mocellin, S. Mondal, S. Mukherjee, D. Noll, A. Novak, T. Pook, A. Pozdnyakov, Y. Rath, H. Reithler, J. Roemer, A. Schmidt, S.C. Schuler, A. Sharma, S. Wiedenbeck, S. Zaleski

RWTH Aachen University, III. Physikalisches Institut A, Aachen, Germany

C. Dziwok, G. Flügge, W. Haj Ahmad¹⁹, O. Hlushchenko, T. Kress, A. Nowack, C. Pistone, O. Pooth, D. Roy, H. Sert, A. Stahl²⁰, T. Ziemons

RWTH Aachen University, III. Physikalisches Institut B, Aachen, Germany

H. Aarup Petersen, M. Aldaya Martin, P. Asmuss, I. Babounikau, S. Baxter, O. Behnke, A. Bermúdez Martínez, A.A. Bin Anuar, K. Borras²¹, V. Botta, D. Brunner, A. Campbell, A. Cardini, P. Connor, S. Consuegra Rodríguez, V. Danilov, A. De Wit, M.M. Defranchis, L. Didukh, D. Domínguez Damiani, G. Eckerlin, D. Eckstein, L.I. Estevez Banos, E. Gallo²², A. Geiser, A. Giraldi, A. Grohsjean, M. Guthoff, A. Harb, A. Jafari²³, N.Z. Jomhari, H. Jung, A. Kasem²¹, M. Kasemann, H. Kaveh, C. Kleinwort, J. Knolle, D. Krücker, W. Lange, T. Lenz, J. Lidrych, K. Lipka, W. Lohmann²⁴, T. Madlener, R. Mankel, I.-A. Melzer-Pellmann, J. Metwally, A.B. Meyer, M. Meyer, J. Mnich, A. Mussgiller, V. Myronenko, Y. Otariid, D. Pérez Adán, S.K. Pflitsch, D. Pitzl, A. Raspereza, A. Saggio, A. Saibel, M. Savitskyi, V. Scheurer, C. Schwanenberger, A. Singh, R.E. Sosa Ricardo, N. Tonon, O. Turkot, A. Vagnerini, M. Van De Klundert, R. Walsh, D. Walter, Y. Wen, K. Wichmann, C. Wissing, S. Wuchterl, O. Zenaiev, R. Zlebcik

Deutsches Elektronen-Synchrotron, Hamburg, Germany

R. Aggleton, S. Bein, L. Benato, A. Benecke, K. De Leo, T. Dreyer, M. Eich, F. Feindt, A. Fröhlich, C. Garbers, E. Garutti, P. Gunnellini, J. Haller, A. Hinzmann, A. Karavdina, G. Kasieczka, R. Klanner, R. Kogler, V. Kutzner, J. Lange, T. Lange, A. Malara, C.E.N. Niemeyer, A. Nigamova, K.J. Pena Rodriguez, O. Rieger, P. Schleper, M. Schröder, S. Schumann, J. Schwandt, D. Schwarz, J. Sonneveld, H. Stadie, G. Steinbrück, A. Tews, B. Vormwald, I. Zoi

University of Hamburg, Hamburg, Germany

J. Bechtel, T. Berger, E. Butz, R. Caspart, T. Chwalek, W. De Boer, A. Dierlamm, A. Droll, K. El Morabit, N. Faltermann, K. Flöh, M. Giffels, J.o. Gosewisch, A. Gottmann, F. Hartmann²⁰, C. Heidecker, U. Husemann, I. Katkov²⁵, P. Keicher, R. Koppenhöfer, S. Maier, M. Metzler, S. Mitra, Th. Müller, M. Musich, M. Neukum, G. Quast, K. Rabbertz, J. Rauser, D. Savoie, D. Schäfer, M. Schnepf, D. Seith, I. Shvetsov, H.J. Simonis, R. Ulrich, J. Van Der Linden, R.F. Von Cube, M. Wassmer, M. Weber, S. Wieland, R. Wolf, S. Wozniewski, S. Wunsch

Karlsruher Institut fuer Technologie, Karlsruhe, Germany

G. Anagnostou, P. Asenov, G. Daskalakis, T. Geralis, A. Kyriakis, D. Loukas, G. Paspalaki, A. Stakia

Institute of Nuclear and Particle Physics (INPP), NCSR Demokritos, Aghia Paraskevi, Greece

M. Diamantopoulou, D. Karasavvas, G. Karathanasis, P. Kontaxakis, C.K. Koraka, A. Manousakis-Katsikakis, A. Panagiotou, I. Papavergou, N. Saoulidou, K. Theofilatos, E. Tziaferi, K. Vellidis, E. Vourliotis

National and Kapodistrian University of Athens, Athens, Greece

G. Bakas, K. Kousouris, I. Papakrivopoulos, G. Tsipolitis, A. Zacharopoulou

National Technical University of Athens, Athens, Greece

I. Evangelou, C. Foudas, P. Gianneios, P. Katsoulis, P. Kokkas, K. Manitaras, N. Manthos, I. Papadopoulos, J. Strologas

University of Ioánnina, Ioánnina, Greece

M. Csanad, M.M.A. Gadallah²⁶, S. Lökös²⁷, P. Major, K. Mandal, A. Mehta, G. Pasztor, O. Surányi, G.I. Veres

MTA-ELTE Lendület CMS Particle and Nuclear Physics Group, Eötvös Loránd University, Budapest, Hungary

M. Bartók²⁸, G. Bencze, C. Hajdu, D. Horvath²⁹, F. Sikler, V. Veszpremi, G. Vesztergombi[†]

Wigner Research Centre for Physics, Budapest, Hungary

S. Czellar, J. Karancsi²⁸, J. Molnar, Z. Szillasi, D. Teyssier

Institute of Nuclear Research ATOMKI, Debrecen, Hungary

P. Raics, Z.L. Trocsanyi³⁰, B. Ujvari

Institute of Physics, University of Debrecen, Debrecen, Hungary

T. Csorgo³¹, F. Nemes³¹, T. Novak

Eszterhazy Karoly University, Karoly Robert Campus, Gyongyos, Hungary

S. Choudhury, J.R. Komaragiri, D. Kumar, L. Panwar, P.C. Tiwari

Indian Institute of Science (IISc), Bangalore, India

S. Bahinipati³², D. Dash, C. Kar, P. Mal, T. Mishra, V.K. Muraleedharan Nair Bindhu³³, A. Nayak³³, N. Sur, S.K. Swain

National Institute of Science Education and Research, HBNI, Bhubaneswar, India

S. Bansal, S.B. Beri, V. Bhatnagar, G. Chaudhary, S. Chauhan, N. Dhingra³⁴, R. Gupta, A. Kaur, S. Kaur, P. Kumari, M. Meena, K. Sandeep, J.B. Singh, A.K. Viridi

Panjab University, Chandigarh, India

A. Ahmed, A. Bhardwaj, B.C. Choudhary, R.B. Garg, M. Gola, S. Keshri, A. Kumar, M. Naimuddin, P. Priyanka, K. Ranjan, A. Shah

University of Delhi, Delhi, India

M. Bharti³⁵, R. Bhattacharya, S. Bhattacharya, D. Bhowmik, S. Dutta, S. Ghosh, B. Gomber³⁶, M. Maity³⁷, S. Nandan, P. Palit, P.K. Rout, G. Saha, B. Sahu, S. Sarkar, M. Sharan, B. Singh³⁵, S. Thakur³⁵

Saha Institute of Nuclear Physics, HBNI, Kolkata, India

P.K. Behera, S.C. Behera, P. Kalbhor, A. Muhammad, R. Pradhan, P.R. Pujahari, A. Sharma, A.K. Sikdar

Indian Institute of Technology Madras, Madras, India

D. Dutta, V. Jha, V. Kumar, D.K. Mishra, K. Naskar³⁸, P.K. Netrakanti, L.M. Pant, P. Shukla

Bhabha Atomic Research Centre, Mumbai, India

T. Aziz, S. Dugad, G.B. Mohanty, U. Sarkar

Tata Institute of Fundamental Research-A, Mumbai, India

S. Banerjee, S. Bhattacharya, S. Chatterjee, R. Chudasama, M. Guchait, S. Karmakar, S. Kumar, G. Majumder, K. Mazumdar, S. Mukherjee, D. Roy

Tata Institute of Fundamental Research-B, Mumbai, India

S. Dube, B. Kansal, S. Pandey, A. Rane, A. Rastogi, S. Sharma

Indian Institute of Science Education and Research (IISER), Pune, India

H. Bakhshiansohi³⁹, M. Zeinali⁴⁰

Department of Physics, Isfahan University of Technology, Isfahan, Iran

S. Chenarani⁴¹, S.M. Etesami, M. Khakzad, M. Mohammadi Najafabadi

Institute for Research in Fundamental Sciences (IPM), Tehran, Iran

M. Felcini, M. Grunewald

University College Dublin, Dublin, Ireland

M. Abbrescia^{a,b}, R. Aly^{a,b,42}, C. Aruta^{a,b}, A. Colaleo^a, D. Creanza^{a,c}, N. De Filippis^{a,c}, M. De Palma^{a,b}, A. Di Florio^{a,b}, A. Di Pilato^{a,b}, W. Elmetenawee^{a,b}, L. Fiore^a, A. Gelmi^{a,b}, M. Gul^a, G. Iaselli^{a,c}, M. Ince^{a,b}, S. Lezki^{a,b}, G. Maggi^{a,c}, M. Maggi^a, I. Margjeka^{a,b}, V. Mastrapasqua^{a,b}, J.A. Merlin^a, S. My^{a,b}, S. Nuzzo^{a,b}, A. Pompili^{a,b}, G. Pugliese^{a,c}, A. Ranieri^a, G. Selvaggi^{a,b}, L. Silvestris^a, F.M. Simone^{a,b}, R. Venditti^a, P. Verwilligen^a

^a INFN Sezione di Bari, Bari, Italy

^b Università di Bari, Bari, Italy

^c Politecnico di Bari, Bari, Italy

G. Abbiendi^a, C. Battilana^{a,b}, D. Bonacorsi^{a,b}, L. Borghonovi^a, S. Braibant-Giacomelli^{a,b}, R. Campanini^{a,b}, P. Capiluppi^{a,b}, A. Castro^{a,b}, F.R. Cavallo^a, C. Ciocca^a, M. Cuffiani^{a,b}, G.M. Dallavalle^a, T. Diotallevi^{a,b}, F. Fabbri^a, A. Fanfani^{a,b}, E. Fontanesi^{a,b}, P. Giacomelli^a, L. Giommi^{a,b}, C. Grandi^a, L. Guiducci^{a,b}, F. Iemmi^{a,b}, S. Lo Meo^{a,43}, S. Marcellini^a, G. Masetti^a, F.L. Navarria^{a,b}, A. Perrotta^a, F. Primavera^{a,b}, A.M. Rossi^{a,b}, T. Rovelli^{a,b}, G.P. Siroli^{a,b}, N. Tosi^a

^a INFN Sezione di Bologna, Bologna, Italy

^b Università di Bologna, Bologna, Italy

S. Albergo ^{a,b,44}, S. Costa ^{a,b}, A. Di Mattia ^a, R. Potenza ^{a,b}, A. Tricomi ^{a,b,44}, C. Tuve ^{a,b}

^a INFN Sezione di Catania, Catania, Italy

^b Università di Catania, Catania, Italy

G. Barbagli ^a, A. Cassese ^a, R. Ceccarelli ^{a,b}, V. Ciulli ^{a,b}, C. Civinini ^a, R. D'Alessandro ^{a,b}, F. Fiori ^a,
E. Focardi ^{a,b}, G. Latino ^{a,b}, P. Lenzi ^{a,b}, M. Lizzo ^{a,b}, M. Meschini ^a, S. Paoletti ^a, R. Seidita ^{a,b},
G. Sguazzoni ^a, L. Viliani ^a

^a INFN Sezione di Firenze, Firenze, Italy

^b Università di Firenze, Firenze, Italy

L. Benussi, S. Bianco, D. Piccolo

INFN Laboratori Nazionali di Frascati, Frascati, Italy

M. Bozzo ^{a,b}, F. Ferro ^a, R. Mulargia ^{a,b}, E. Robutti ^a, S. Tosi ^{a,b}

^a INFN Sezione di Genova, Genova, Italy

^b Università di Genova, Genova, Italy

A. Benaglia ^a, A. Beschi ^{a,b}, F. Brivio ^{a,b}, F. Cetorelli ^{a,b}, V. Ciriolo ^{a,b,20}, F. De Guio ^{a,b}, M.E. Dinardo ^{a,b},
P. Dini ^a, S. Gennai ^a, A. Ghezzi ^{a,b}, P. Govoni ^{a,b}, L. Guzzi ^{a,b}, M. Malberti ^a, S. Malvezzi ^a, A. Massironi ^a,
D. Menasce ^a, F. Monti ^{a,b}, L. Moroni ^a, M. Paganoni ^{a,b}, D. Pedrini ^a, S. Ragazzi ^{a,b}, T. Tabarelli de Fatis ^{a,b},
D. Valsecchi ^{a,b,20}, D. Zuolo ^{a,b}

^a INFN Sezione di Milano-Bicocca, Milano, Italy

^b Università di Milano-Bicocca, Milano, Italy

S. Buontempo ^a, N. Cavallo ^{a,c}, A. De Iorio ^{a,b}, F. Fabozzi ^{a,c}, F. Fienga ^a, A.O.M. Iorio ^{a,b}, L. Lista ^{a,b},
S. Meola ^{a,d,20}, P. Paolucci ^{a,20}, B. Rossi ^a, C. Sciacca ^{a,b}

^a INFN Sezione di Napoli, Napoli, Italy

^b Università di Napoli "Federico II", Napoli, Italy

^c Università della Basilicata, Potenza, Italy

^d Università G. Marconi, Roma, Italy

P. Azzi ^a, N. Bacchetta ^a, D. Bisello ^{a,b}, P. Bortignon ^a, A. Bragagnolo ^{a,b}, R. Carlin ^{a,b}, P. Checchia ^a,
P. De Castro Manzano ^a, T. Dorigo ^a, F. Gasparini ^{a,b}, U. Gasparini ^{a,b}, S.Y. Hoh ^{a,b}, L. Layer ^{a,45},
M. Margoni ^{a,b}, A.T. Meneguzzo ^{a,b}, M. Presilla ^{a,b}, P. Ronchese ^{a,b}, R. Rossin ^{a,b}, F. Simonetto ^{a,b},
G. Strong ^a, M. Tosi ^{a,b}, H. Yarar ^{a,b}, M. Zanetti ^{a,b}, P. Zotto ^{a,b}, A. Zucchetta ^{a,b}, G. Zumerle ^{a,b}

^a INFN Sezione di Padova, Padova, Italy

^b Università di Padova, Padova, Italy

^c Università di Trento, Trento, Italy

C. Aime ^{a,b}, A. Braghieri ^a, S. Calzaferri ^{a,b}, D. Fiorina ^{a,b}, P. Montagna ^{a,b}, S.P. Ratti ^{a,b}, V. Re ^a,
M. Ressegotti ^{a,b}, C. Riccardi ^{a,b}, P. Salvini ^a, I. Vai ^a, P. Vitulo ^{a,b}

^a INFN Sezione di Pavia, Pavia, Italy

^b Università di Pavia, Pavia, Italy

G.M. Bilei ^a, D. Ciangottini ^{a,b}, L. Fanò ^{a,b}, P. Lariccia ^{a,b}, G. Mantovani ^{a,b}, V. Mariani ^{a,b}, M. Menichelli ^a,
F. Moscatelli ^a, A. Piccinelli ^{a,b}, A. Rossi ^{a,b}, A. Santocchia ^{a,b}, D. Spiga ^a, T. Tedeschi ^{a,b}

^a INFN Sezione di Perugia, Perugia, Italy

^b Università di Perugia, Perugia, Italy

K. Androsov ^a, P. Azzurri ^a, G. Bagliesi ^a, V. Bertacchi ^{a,c}, L. Bianchini ^a, T. Boccali ^a, E. Bossini, R. Castaldi ^a,
M.A. Ciocci ^{a,b}, R. Dell'Orso ^a, M.R. Di Domenico ^{a,d}, S. Donato ^a, A. Giassi ^a, M.T. Grippo ^a, F. Ligabue ^{a,c},
E. Manca ^{a,c}, G. Mandorli ^{a,c}, A. Messineo ^{a,b}, F. Palla ^a, G. Ramirez-Sanchez ^{a,c}, A. Rizzi ^{a,b}, G. Rolandi ^{a,c},
S. Roy Chowdhury ^{a,c}, A. Scribano ^a, N. Shafiei ^{a,b}, P. Spagnolo ^a, R. Tenchini ^a, G. Tonelli ^{a,b}, N. Turini ^{a,d},
A. Venturi ^a, P.G. Verdini ^a

^a INFN Sezione di Pisa, Pisa Italy

^b Università di Pisa, Pisa Italy

^c Scuola Normale Superiore di Pisa, Pisa Italy^d Università di Siena, Siena, Italy

F. Cavallari ^a, M. Cipriani ^{a,b}, D. Del Re ^{a,b}, E. Di Marco ^a, M. Diemoz ^a, E. Longo ^{a,b}, P. Meridiani ^a,
 G. Organtini ^{a,b}, F. Pandolfi ^a, R. Paramatti ^{a,b}, C. Quaranta ^{a,b}, S. Rahatlou ^{a,b}, C. Rovelli ^a,
 F. Santanastasio ^{a,b}, L. Soffi ^{a,b}, R. Tramontano ^{a,b}

^a INFN Sezione di Roma, Rome, Italy^b Sapienza Università di Roma, Rome, Italy

N. Amapane ^{a,b}, R. Arcidiacono ^{a,c}, S. Argiro ^{a,b}, M. Arneodo ^{a,c}, N. Bartosik ^a, R. Bellan ^{a,b}, A. Bellora ^{a,b},
 J. Berenguer Antequera ^{a,b}, C. Biino ^a, A. Cappati ^{a,b}, N. Cartiglia ^a, S. Cometti ^a, M. Costa ^{a,b},
 R. Covarelli ^{a,b}, N. Demaria ^a, B. Kiani ^{a,b}, F. Legger ^a, C. Mariotti ^a, S. Maselli ^a, E. Migliore ^{a,b},
 V. Monaco ^{a,b}, E. Monteil ^{a,b}, M. Monteno ^a, M.M. Obertino ^{a,b}, G. Ortona ^a, L. Pacher ^{a,b}, N. Pastrone ^a,
 M. Pelliccioni ^a, G.L. Pinna Angioni ^{a,b}, M. Ruspa ^{a,c}, R. Salvatico ^{a,b}, F. Siviero ^{a,b}, V. Sola ^a, A. Solano ^{a,b},
 D. Soldi ^{a,b}, A. Staiano ^a, M. Tornago ^{a,b}, D. Trocino ^{a,b}

^a INFN Sezione di Torino, Torino, Italy^b Università di Torino, Torino, Italy^c Università del Piemonte Orientale, Novara, Italy

S. Belforte ^a, V. Candelise ^{a,b}, M. Casarsa ^a, F. Cossutti ^a, A. Da Rold ^{a,b}, G. Della Ricca ^{a,b}, F. Vazzoler ^{a,b}

^a INFN Sezione di Trieste, Trieste, Italy^b Università di Trieste, Trieste, Italy

S. Dogra, C. Huh, B. Kim, D.H. Kim, G.N. Kim, J. Lee, S.W. Lee, C.S. Moon, Y.D. Oh, S.I. Pak,
 B.C. Radburn-Smith, S. Sekmen, Y.C. Yang

Kyungpook National University, Daegu, Republic of Korea

H. Kim, D.H. Moon

Chonnam National University, Institute for Universe and Elementary Particles, Kwangju, Republic of Korea

B. Francois, T.J. Kim, J. Park

Hanyang University, Seoul, Republic of Korea

S. Cho, S. Choi, Y. Go, B. Hong, K. Lee, K.S. Lee, J. Lim, J. Park, S.K. Park, J. Yoo

Korea University, Seoul, Republic of Korea

J. Goh, A. Gurtu

Kyung Hee University, Department of Physics, Seoul, Republic of Korea

H.S. Kim, Y. Kim

Sejong University, Seoul, Republic of Korea

J. Almond, J.H. Bhyun, J. Choi, S. Jeon, J. Kim, J.S. Kim, S. Ko, H. Kwon, H. Lee, S. Lee, K. Nam, B.H. Oh,
 M. Oh, S.B. Oh, H. Seo, U.K. Yang, I. Yoon

Seoul National University, Seoul, Republic of Korea

D. Jeon, J.H. Kim, B. Ko, J.S.H. Lee, I.C. Park, Y. Roh, D. Song, I.J. Watson

University of Seoul, Seoul, Republic of Korea

S. Ha, H.D. Yoo

Yonsei University, Department of Physics, Seoul, Republic of Korea

Y. Choi, C. Hwang, Y. Jeong, H. Lee, Y. Lee, I. Yu

Sungkyunkwan University, Suwon, Republic of Korea

Y. Maghrbi

College of Engineering and Technology, American University of the Middle East (AUM), Dasman, Kuwait

V. Veckalns⁴⁶

Riga Technical University, Riga, Latvia

M. Ambrozas, A. Juodagalvis, A. Rinkevicius, G. Tamulaitis, A. Vaitkevicius

Vilnius University, Vilnius, Lithuania

W.A.T. Wan Abdullah, M.N. Yusli, Z. Zolkapli

National Centre for Particle Physics, Universiti Malaya, Kuala Lumpur, Malaysia

J.F. Benitez, A. Castaneda Hernandez, J.A. Murillo Quijada, L. Valencia Palomo

Universidad de Sonora (UNISON), Hermosillo, Mexico

G. Ayala, H. Castilla-Valdez, E. De La Cruz-Burelo, I. Heredia-De La Cruz⁴⁷, R. Lopez-Fernandez, C.A. Mondragon Herrera, D.A. Perez Navarro, A. Sanchez-Hernandez

Centro de Investigacion y de Estudios Avanzados del IPN, Mexico City, Mexico

S. Carrillo Moreno, C. Oropeza Barrera, M. Ramirez-Garcia, F. Vazquez Valencia

Universidad Iberoamericana, Mexico City, Mexico

I. Pedraza, H.A. Salazar Ibarguen, C. Uribe Estrada

Benemerita Universidad Autonoma de Puebla, Puebla, Mexico

J. Mijuskovic⁴, N. Raicevic

University of Montenegro, Podgorica, Montenegro

D. Krofcheck

University of Auckland, Auckland, New Zealand

S. Bheesette, P.H. Butler

University of Canterbury, Christchurch, New Zealand

A. Ahmad, M.I. Asghar, A. Awais, M.I.M. Awan, H.R. Hoorani, W.A. Khan, M.A. Shah, M. Shoib, M. Waqas

National Centre for Physics, Quaid-I-Azam University, Islamabad, Pakistan

V. Avati, L. Grzanka, M. Malawski

AGH University of Science and Technology Faculty of Computer Science, Electronics and Telecommunications, Krakow, Poland

H. Bialkowska, M. Bluj, B. Boimska, T. Frueboes, M. Górski, M. Kazana, M. Szleper, P. Traczyk, P. Zalewski

National Centre for Nuclear Research, Swierk, Poland

K. Bunkowski, K. Doroba, A. Kalinowski, M. Konecki, J. Krolikowski, M. Walczak

Institute of Experimental Physics, Faculty of Physics, University of Warsaw, Warsaw, Poland

M. Araujo, P. Bargassa, D. Bastos, A. Boletti, P. Faccioli, M. Gallinaro, J. Hollar, N. Leonardo, T. Niknejad, J. Seixas, K. Shchelina, O. Toldaiev, J. Varela

Laboratório de Instrumentação e Física Experimental de Partículas, Lisboa, Portugal

S. Afanasiev, D. Budkouski, P. Bunin, M. Gavrilenko, I. Golutvin, I. Gorbunov, A. Kamenev, V. Karjavine, A. Lanev, A. Malakhov, V. Matveev^{48,49}, V. Palichik, V. Perelygin, M. Savina, D. Seitova, V. Shalaev, S. Shmatov, S. Shulha, V. Smirnov, O. Teryaev, N. Voytishin, A. Zarubin, I. Zhizhin

Joint Institute for Nuclear Research, Dubna, Russia

G. Gavrillov, V. Golovtsov, Y. Ivanov, V. Kim⁵⁰, E. Kuznetsova⁵¹, V. Murzin, V. Oreshkin, I. Smirnov, D. Sosnov, V. Sulimov, L. Uvarov, S. Volkov, A. Vorobyev

Petersburg Nuclear Physics Institute, Gatchina (St. Petersburg), Russia

Yu. Andreev, A. Dermenev, S. Gninenko, N. Golubev, A. Karneyeu, M. Kirsanov, N. Krasnikov, A. Pashenkov, G. Pivovarov, D. Tlisov[†], A. Toropin

Institute for Nuclear Research, Moscow, Russia

V. Epshteyn, V. Gavrillov, N. Lychkovskaya, A. Nikitenko⁵², V. Popov, G. Safronov, A. Spiridonov, A. Steppenov, M. Toms, E. Vlasov, A. Zhokin

Institute for Theoretical and Experimental Physics named by A.I. Alikhanov of NRC 'Kurchatov Institute', Moscow, Russia

T. Aushev

Moscow Institute of Physics and Technology, Moscow, Russia

R. Chistov⁵³, M. Danilov⁵⁴, A. Oskin, P. Parygin, S. Polikarpov⁵³

National Research Nuclear University 'Moscow Engineering Physics Institute' (MEPhI), Moscow, Russia

V. Andreev, M. Azarkin, I. Dremin, M. Kirakosyan, A. Terkulov

P.N. Lebedev Physical Institute, Moscow, Russia

A. Belyaev, E. Boos, V. Bunichev, M. Dubinin⁵⁵, L. Dudko, A. Gribushin, V. Klyukhin, N. Korneeva, I. Lokhtin, S. Obraztsov, M. Perfilov, V. Savrin, P. Volkov

Skobeltsyn Institute of Nuclear Physics, Lomonosov Moscow State University, Moscow, Russia

V. Blinov⁵⁶, T. Dimova⁵⁶, L. Kardapoltsev⁵⁶, I. Ovtin⁵⁶, Y. Skovpen⁵⁶

Novosibirsk State University (NSU), Novosibirsk, Russia

I. Azhgirey, I. Bayshev, V. Kachanov, A. Kalinin, D. Konstantinov, V. Petrov, R. Ryutin, A. Sobol, S. Troshin, N. Tyurin, A. Uzunian, A. Volkov

Institute for High Energy Physics of National Research Centre 'Kurchatov Institute', Protvino, Russia

A. Babaev, A. Iuzhakov, V. Okhotnikov, L. Sukhikh

National Research Tomsk Polytechnic University, Tomsk, Russia

V. Borchsh, V. Ivanchenko, E. Tcherniaev

Tomsk State University, Tomsk, Russia

P. Adzic⁵⁷, M. Dordevic, P. Milenovic, J. Milosevic

University of Belgrade: Faculty of Physics and VINCA Institute of Nuclear Sciences, Belgrade, Serbia

M. Aguilar-Benitez, J. Alcaraz Maestre, A. Álvarez Fernández, I. Bachiller, M. Barrio Luna, Cristina F. Bedoya, C.A. Carrillo Montoya, M. Cepeda, M. Cerrada, N. Colino, B. De La Cruz, A. Delgado Peris, J.P. Fernández Ramos, J. Flix, M.C. Fouz, O. Gonzalez Lopez, S. Goy Lopez, J.M. Hernandez, M.I. Josa, J. León Holgado, D. Moran, Á. Navarro Tobar, A. Pérez-Calero Yzquierdo, J. Puerta Pelayo, I. Redondo, L. Romero, S. Sánchez Navas, M.S. Soares, L. Urda Gómez, C. Willmott

Centro de Investigaciones Energéticas Medioambientales y Tecnológicas (CIEMAT), Madrid, Spain

C. Albajar, J.F. de Trocóniz, R. Reyes-Almanza

Universidad Autónoma de Madrid, Madrid, Spain

B. Alvarez Gonzalez, J. Cuevas, C. Erice, J. Fernandez Menendez, S. Folgueras, I. Gonzalez Caballero, E. Palencia Cortezon, C. Ramón Álvarez, J. Ripoll Sau, V. Rodríguez Bouza, S. Sanchez Cruz, A. Trapote

Universidad de Oviedo, Instituto Universitario de Ciencias y Tecnologías Espaciales de Asturias (ICTEA), Oviedo, Spain

J.A. Brochero Cifuentes, I.J. Cabrillo, A. Calderon, B. Chazin Quero, J. Duarte Campderros, M. Fernandez, C. Fernandez Madrazo, P.J. Fernández Manteca, A. García Alonso, G. Gomez, C. Martinez Rivero, P. Martinez Ruiz del Arbol, F. Matorras, J. Piedra Gomez, C. Prieels, F. Ricci-Tam, T. Rodrigo, A. Ruiz-Jimeno, L. Scodellaro, N. Trevisani, I. Vila, J.M. Vizan Garcia

Instituto de Física de Cantabria (IFCA), CSIC-Universidad de Cantabria, Santander, Spain

M.K. Jayananda, B. Kailasapathy⁵⁸, D.U.J. Sonnadara, D.D.C. Wickramaratna

University of Colombo, Colombo, Sri Lanka

W.G.D. Dharmaratna, K. Liyanage, N. Perera, N. Wickramage

University of Ruhuna, Department of Physics, Matara, Sri Lanka

T.K. Aarrestad, D. Abbaneo, E. Auffray, G. Auzinger, J. Baechler, P. Baillon, A.H. Ball, D. Barney, J. Bendavid, N. Beni, M. Bianco, A. Bocci, E. Brondolin, T. Camporesi, M. Capeans Garrido, G. Cerminara, S.S. Chhibra, L. Cristella, D. d'Enterria, A. Dabrowski, N. Daci, A. David, A. De Roeck, M. Deile, R. Di Maria, M. Dobson, M. Dünser, N. Dupont, A. Elliott-Peisert, N. Emriskova, F. Fallavollita⁵⁹, D. Fasanella, S. Fiorendi, A. Florent, G. Franzoni, J. Fulcher, W. Funk, S. Giani, D. Gigi, K. Gill, F. Glege, L. Gouskos, M. Guilbaud, M. Haranko, J. Hegeman, Y. Iiyama, V. Innocente, T. James, P. Janot, J. Kaspar, J. Kieseler, M. Komm, N. Kratochwil, C. Lange, S. Laurila, P. Lecoq, K. Long, C. Lourenço, L. Malgeri, S. Mallios, M. Mannelli, F. Meijers, S. Mersi, E. Meschi, F. Moortgat, M. Mulders, S. Orfanelli, L. Orsini, F. Pantaleo²⁰, L. Pape, E. Perez, M. Peruzzi, A. Petrilli, G. Petrucciani, A. Pfeiffer, M. Pierini, T. Quast, D. Rabady, A. Racz, M. Rieger, M. Rovere, H. Sakulin, J. Salfeld-Nebgen, S. Scarfi, C. Schäfer, C. Schwick, M. Selvaggi, A. Sharma, P. Silva, W. Snoeys, P. Sphicas⁶⁰, S. Summers, V.R. Tavolaro, D. Treille, A. Tsiros, G.P. Van Onsem, M. Verzetti, K.A. Wozniak, W.D. Zeuner

CERN, European Organization for Nuclear Research, Geneva, Switzerland

L. Caminada⁶¹, A. Ebrahimi, W. Erdmann, R. Horisberger, Q. Ingram, H.C. Kaestli, D. Kotlinski, U. Langenegger, M. Missiroli, T. Rohe

Paul Scherrer Institut, Villigen, Switzerland

M. Backhaus, P. Berger, A. Calandri, N. Chernyavskaya, A. De Cosa, G. Dissertori, M. Dittmar, M. Donegà, C. Dorfer, T. Gadek, T.A. Gómez Espinosa, C. Grab, D. Hits, W. Lustermann, A.-M. Lyon, R.A. Manzoni, M.T. Meinhard, F. Micheli, F. Nessi-Tedaldi, J. Niedziela, F. Pauss, V. Perovic, G. Perrin, S. Pigazzini, M.G. Ratti, M. Reichmann, C. Reissel, T. Reitenspiess, B. Ristic, D. Ruini, D.A. Sanz Becerra, M. Schönenberger, V. Stampf, J. Steggemann⁶², R. Wallny, D.H. Zhu

ETH Zurich – Institute for Particle Physics and Astrophysics (IPA), Zurich, Switzerland

C. Amsler⁶³, C. Botta, D. Brzhechko, M.F. Canelli, R. Del Burgo, J.K. Heikkilä, M. Huwiler, A. Jofrehei, B. Kilminster, S. Leontsinis, A. Macchiolo, P. Meiring, V.M. Mikuni, U. Molinatti, I. Neutelings, G. Rauco, A. Reimers, P. Robmann, K. Schweiger, Y. Takahashi

Universität Zürich, Zurich, Switzerland

C. Adloff⁶⁴, C.M. Kuo, W. Lin, A. Roy, T. Sarkar³⁷, S.S. Yu

National Central University, Chung-Li, Taiwan

L. Ceard, P. Chang, Y. Chao, K.F. Chen, P.H. Chen, W.-S. Hou, Y.y. Li, R.-S. Lu, E. Paganis, A. Psallidas, A. Steen, E. Yazgan

National Taiwan University (NTU), Taipei, Taiwan

B. Asavapibhop, C. Asawatangtrakuldee, N. Srimanobhas

Chulalongkorn University, Faculty of Science, Department of Physics, Bangkok, Thailand

F. Boran, S. Damarseckin⁶⁵, Z.S. Demiroglu, F. Dolek, C. Dozen⁶⁶, I. Dumanoglu⁶⁷, E. Eskut, G. Gokbulut, Y. Guler, E. Gurpinar Guler⁶⁸, I. Hos⁶⁹, C. Isik, E.E. Kangal⁷⁰, O. Kara, A. Kayis Topaksu, U. Kiminsu, G. Onengut, K. Ozdemir⁷¹, A. Polatoz, A.E. Simsek, B. Tali⁷², U.G. Tok, S. Turkcapar, I.S. Zorbakir, C. Zorbilmez

Çukurova University, Physics Department, Science and Art Faculty, Adana, Turkey

B. Isildak⁷³, G. Karapinar⁷⁴, K. Ocalan⁷⁵, M. Yalvac⁷⁶

Middle East Technical University, Physics Department, Ankara, Turkey

B. Akgun, I.O. Atakisi, E. Gülmez, M. Kaya⁷⁷, O. Kaya⁷⁸, Ö. Özçelik, S. Tekten⁷⁹, E.A. Yetkin⁸⁰

Bogazici University, Istanbul, Turkey

A. Cakir, K. Cankocak⁶⁷, Y. Komurcu, S. Sen⁸¹

Istanbul Technical University, Istanbul, Turkey

F. Aydogmus Sen, S. Cerci⁷², B. Kaynak, S. Ozkorucuklu, D. Sunar Cerci⁷²

Istanbul University, Istanbul, Turkey

B. Grynyov

Institute for Scintillation Materials of National Academy of Science of Ukraine, Kharkov, Ukraine

L. Levchuk

National Scientific Center, Kharkov Institute of Physics and Technology, Kharkov, Ukraine

E. Bhal, S. Bologna, J.J. Brooke, A. Bundock, E. Clement, D. Cussans, H. Flacher, J. Goldstein, G.P. Heath, H.F. Heath, L. Kreczko, B. Krikler, S. Paramesvaran, T. Sakuma, S. Seif El Nasr-Storey, V.J. Smith, N. Stylianou⁸², J. Taylor, A. Titterton

University of Bristol, Bristol, United Kingdom

K.W. Bell, A. Belyaev⁸³, C. Brew, R.M. Brown, D.J.A. Cockerill, K.V. Ellis, K. Harder, S. Harper, J. Linacre, K. Manolopoulos, D.M. Newbold, E. Olaiya, D. Petyt, T. Reis, T. Schuh, C.H. Shepherd-Themistocleous, A. Thea, I.R. Tomalin, T. Williams

Rutherford Appleton Laboratory, Didcot, United Kingdom

R. Bainbridge, P. Bloch, S. Bonomally, J. Borg, S. Breeze, O. Buchmuller, V. Cepaitis, G.S. Chahal⁸⁴, D. Colling, P. Dauncey, G. Davies, M. Della Negra, G. Fedi, G. Hall, G. Iles, J. Langford, L. Lyons, A.-M. Magnan, S. Malik, A. Martelli, V. Milosevic, J. Nash⁸⁵, V. Palladino, M. Pesaresi, D.M. Raymond, A. Richards, A. Rose, E. Scott, C. Seez, A. Shtipliyski, A. Tapper, K. Uchida, T. Virdee²⁰, N. Wardle, S.N. Webb, D. Winterbottom, A.G. Zecchinelli

Imperial College, London, United Kingdom

J.E. Cole, A. Khan, P. Kyberd, C.K. Mackay, I.D. Reid, L. Teodorescu, S. Zahid

Brunel University, Uxbridge, United Kingdom

S. Abdullin, A. Brinkerhoff, K. Call, B. Caraway, J. Dittmann, K. Hatakeyama, A.R. Kanuganti, C. Madrid, B. McMaster, N. Pastika, S. Sawant, C. Smith, C. Sutantawibul, J. Wilson

Baylor University, Waco, USA

R. Bartek, A. Dominguez, R. Uniyal, A.M. Vargas Hernandez

Catholic University of America, Washington, DC, USA

A. Buccilli, O. Charaf, S.I. Cooper, D. Di Croce, S.V. Gleyzer, C. Henderson, C.U. Perez, P. Rumerio, C. West

The University of Alabama, Tuscaloosa, USA

A. Akpinar, A. Albert, D. Arcaro, C. Cosby, Z. Demiragli, D. Gastler, J. Rohlf, K. Salyer, D. Sperka, D. Spitzbart, I. Suarez, S. Yuan, D. Zou

Boston University, Boston, USA

G. Benelli, B. Burkle, X. Coubez²¹, D. Cutts, Y.t. Duh, M. Hadley, U. Heintz, J.M. Hogan⁸⁶, K.H.M. Kwok, E. Laird, G. Landsberg, K.T. Lau, J. Lee, J. Luo, M. Narain, S. Sagir⁸⁷, E. Usai, W.Y. Wong, X. Yan, D. Yu, W. Zhang

Brown University, Providence, USA

R. Band, C. Brainerd, R. Breedon, M. Calderon De La Barca Sanchez, M. Chertok, J. Conway, R. Conway, P.T. Cox, R. Erbacher, C. Flores, F. Jensen, O. Kukral, R. Lander, M. Mulhearn, D. Pellett, M. Shi, D. Taylor, M. Tripathi, Y. Yao, F. Zhang

University of California, Davis, Davis, USA

M. Bachtis, R. Cousins, A. Dasgupta, A. Datta, D. Hamilton, J. Hauser, M. Ignatenko, M.A. Iqbal, T. Lam, N. Mccoll, W.A. Nash, S. Regnard, D. Saltzberg, C. Schnaible, B. Stone, V. Valuev

University of California, Los Angeles, USA

K. Burt, Y. Chen, R. Clare, J.W. Gary, G. Hanson, G. Karapostoli, O.R. Long, N. Manganeli, M. Olmedo Negrete, W. Si, S. Wimpenny, Y. Zhang

University of California, Riverside, Riverside, USA

J.G. Branson, P. Chang, S. Cittolin, S. Cooperstein, N. Deelen, J. Duarte, R. Gerosa, L. Giannini, D. Gilbert, V. Krutelyov, J. Letts, M. Masciovecchio, S. May, S. Padhi, M. Pieri, V. Sharma, M. Tadel, A. Vartak, F. Würthwein, A. Yagil

University of California, San Diego, La Jolla, USA

N. Amin, C. Campagnari, M. Citron, A. Dorsett, V. Dutta, J. Incandela, M. Kilpatrick, B. Marsh, H. Mei, A. Ovcharova, H. Qu, M. Quinnan, J. Richman, U. Sarica, D. Stuart, S. Wang

University of California, Santa Barbara – Department of Physics, Santa Barbara, USA

A. Bornheim, O. Cerri, I. Dutta, J.M. Lawhorn, N. Lu, J. Mao, H.B. Newman, J. Ngadiuba, T.Q. Nguyen, M. Spiropulu, J.R. Vlimant, C. Wang, S. Xie, Z. Zhang, R.Y. Zhu

California Institute of Technology, Pasadena, USA

J. Alison, M.B. Andrews, T. Ferguson, T. Mudholkar, M. Paulini, I. Vorobiev

Carnegie Mellon University, Pittsburgh, USA

J.P. Cumalat, W.T. Ford, E. MacDonald, R. Patel, A. Perloff, K. Stenson, K.A. Ulmer, S.R. Wagner

University of Colorado Boulder, Boulder, USA

J. Alexander, Y. Cheng, J. Chu, D.J. Cranshaw, K. Mcdermott, J. Monroy, J.R. Patterson, D. Quach, A. Ryd, W. Sun, S.M. Tan, Z. Tao, J. Thom, P. Wittich, M. Zientek

Cornell University, Ithaca, USA

M. Albrow, M. Alyari, G. Apollinari, A. Apresyan, A. Apyan, S. Banerjee, L.A.T. Bauerdick, A. Beretvas, D. Berry, J. Berryhill, P.C. Bhat, K. Burkett, J.N. Butler, A. Canepa, G.B. Cerati, H.W.K. Cheung, F. Chlebana, M. Cremonesi, K.F. Di Petrillo, V.D. Elvira, J. Freeman, Z. Gecse, L. Gray, D. Green, S. Grünendahl, O. Gutsche, R.M. Harris, R. Heller, T.C. Herwig, J. Hirschauer, B. Jayatilaka, S. Jindariani, M. Johnson, U. Joshi, P. Klabbers, T. Klijsma, B. Klima, M.J. Kortelainen, S. Lammel, D. Lincoln, R. Lipton, T. Liu, J. Lykken, K. Maeshima, D. Mason, P. McBride, P. Merkel, S. Mrenna, S. Nahn, V. O'Dell, V. Papadimitriou, K. Pedro, C. Pena⁵⁵, O. Prokofyev, F. Ravera, A. Reinsvold Hall, L. Ristori, B. Schneider, E. Sexton-Kennedy, N. Smith, A. Soha, L. Spiegel, S. Stoynev, J. Strait, L. Taylor, S. Tkaczyk, N.V. Tran, L. Uplegger, E.W. Vaandering, H.A. Weber

Fermi National Accelerator Laboratory, Batavia, USA

D. Acosta, P. Avery, D. Bourilkov, L. Cadamuro, V. Cherepanov, F. Errico, R.D. Field, D. Guerrero, B.M. Joshi, M. Kim, J. Konigsberg, A. Korytov, K.H. Lo, K. Matchev, N. Menendez, G. Mitselmakher, D. Rosenzweig, K. Shi, J. Sturdy, J. Wang, X. Zuo

University of Florida, Gainesville, USA

T. Adams, A. Askew, D. Diaz, R. Habibullah, S. Hagopian, V. Hagopian, K.F. Johnson, R. Khurana, T. Kolberg, G. Martinez, H. Prosper, C. Schiber, R. Yohay, J. Zhang

Florida State University, Tallahassee, USA

M.M. Baarmand, S. Butalla, T. Elkafrawy¹⁵, M. Hohmann, R. Kumar Verma, D. Noonan, M. Rahmani, M. Saunders, F. Yumiceva

Florida Institute of Technology, Melbourne, USA

M.R. Adams, L. Apanasevich, H. Becerril Gonzalez, R. Cavanaugh, X. Chen, S. Dittmer, O. Evdokimov, C.E. Gerber, D.A. Hangal, D.J. Hofman, C. Mills, G. Oh, T. Roy, M.B. Tonjes, N. Varelas, J. Viinikainen, X. Wang, Z. Wu, Z. Ye

University of Illinois at Chicago (UIC), Chicago, USA

M. Alhusseini, K. Dilsiz⁸⁸, S. Durgut, R.P. Gandrajula, M. Haytmyradov, V. Khristenko, O.K. Köseyan, J.-P. Merlo, A. Mestvirishvili⁸⁹, A. Moeller, J. Nachtman, H. Ogul⁹⁰, Y. Onel, F. Ozok⁹¹, A. Penzo, C. Snyder, E. Tiras⁹², J. Wetzel

The University of Iowa, Iowa City, USA

O. Amram, B. Blumenfeld, L. Corcodilos, M. Eminizer, A.V. Gritsan, S. Kyriacou, P. Maksimovic, C. Mantilla, J. Roskes, M. Swartz, T.Á. Vámi

Johns Hopkins University, Baltimore, USA

C. Baldenegro Barrera, P. Baringer, A. Bean, A. Bylinkin, T. Isidori, S. Khalil, J. King, G. Krintiras, A. Kropivnitskaya, C. Lindsey, N. Minafra, M. Murray, C. Rogan, C. Royon, S. Sanders, E. Schmitz, J.D. Tapia Takaki, Q. Wang, J. Williams, G. Wilson

The University of Kansas, Lawrence, USA

S. Duric, A. Ivanov, K. Kaadze, D. Kim, Y. Maravin, T. Mitchell, A. Modak

Kansas State University, Manhattan, USA

F. Rebassoo, D. Wright

Lawrence Livermore National Laboratory, Livermore, USA

E. Adams, A. Baden, O. Baron, A. Belloni, S.C. Eno, Y. Feng, N.J. Hadley, S. Jabeen, R.G. Kellogg, T. Koeth, A.C. Mignerey, S. Nabili, M. Seidel, A. Skuja, S.C. Tonwar, L. Wang, K. Wong

University of Maryland, College Park, USA

D. Abercrombie, R. Bi, S. Brandt, W. Busza, I.A. Cali, Y. Chen, M. D'Alfonso, G. Gomez Ceballos, M. Goncharov, P. Harris, M. Hu, M. Klute, D. Kovalskyi, J. Krupa, Y.-J. Lee, P.D. Luckey, B. Maier, A.C. Marini, C. Mironov, X. Niu, C. Paus, D. Rankin, C. Roland, G. Roland, Z. Shi, G.S.F. Stephans, K. Tatar, D. Velicanu, J. Wang, T.W. Wang, Z. Wang, B. Wyslouch

Massachusetts Institute of Technology, Cambridge, USA

R.M. Chatterjee, A. Evans, P. Hansen, J. Hiltbrand, Sh. Jain, M. Krohn, Y. Kubota, Z. Lesko, J. Mans, M. Revering, R. Rusack, R. Saradhy, N. Schroeder, N. Strobbe, M.A. Wadud

University of Minnesota, Minneapolis, USA

J.G. Acosta, S. Oliveros

University of Mississippi, Oxford, USA

K. Bloom, M. Bryson, S. Chauhan, D.R. Claes, C. Fangmeier, L. Finco, F. Golf, J.R. González Fernández, C. Joo, I. Kravchenko, J.E. Siado, G.R. Snow[†], W. Tabb, F. Yan

University of Nebraska-Lincoln, Lincoln, USA

G. Agarwal, H. Bandyopadhyay, L. Hay, I. Iashvili, A. Kharchilava, C. McLean, D. Nguyen, J. Pekkanen, S. Rappoccio

State University of New York at Buffalo, Buffalo, USA

G. Alverson, E. Barberis, C. Freer, Y. Haddad, A. Hortiangtham, J. Li, G. Madigan, B. Marzocchi, D.M. Morse, V. Nguyen, T. Orimoto, A. Parker, L. Skinnari, A. Tishelman-Charny, T. Wamorkar, B. Wang, A. Wisecarver, D. Wood

Northeastern University, Boston, USA

S. Bhattacharya, J. Bueghly, Z. Chen, A. Gilbert, T. Gunter, K.A. Hahn, N. Odell, M.H. Schmitt, K. Sung, M. Velasco

Northwestern University, Evanston, USA

R. Bucci, N. Dev, R. Goldouzian, M. Hildreth, K. Hurtado Anampa, C. Jessop, K. Lannon, N. Loukas, N. Marinelli, I. Mcalister, F. Meng, K. Mohrman, Y. Musienko⁴⁸, R. Ruchti, P. Siddireddy, M. Wayne, A. Wightman, M. Wolf, L. Zygala

University of Notre Dame, Notre Dame, USA

J. Alimena, B. Bylsma, B. Cardwell, L.S. Durkin, B. Francis, C. Hill, A. Lefeld, B.L. Winer, B.R. Yates

The Ohio State University, Columbus, USA

F.M. Addesa, B. Bonham, P. Das, G. Dezoort, P. Elmer, A. Frankenthal, B. Greenberg, N. Haubrich, S. Higginbotham, A. Kalogeropoulos, G. Kopp, S. Kwan, D. Lange, M.T. Lucchini, D. Marlow, K. Mei, I. Ojalvo, J. Olsen, C. Palmer, D. Stickland, C. Tully

Princeton University, Princeton, USA

S. Malik, S. Norberg

University of Puerto Rico, Mayaguez, USA

A.S. Bakshi, V.E. Barnes, R. Chawla, S. Das, L. Gutay, M. Jones, A.W. Jung, S. Karmarkar, M. Liu, G. Negro, N. Neumeister, C.C. Peng, S. Piperov, A. Purohit, J.F. Schulte, M. Stojanovic¹⁷, J. Thieman, F. Wang, R. Xiao, W. Xie

Purdue University, West Lafayette, USA

J. Dolen, N. Parashar

Purdue University Northwest, Hammond, USA

A. Baty, S. Dildick, K.M. Ecklund, S. Freed, F.J.M. Geurts, A. Kumar, W. Li, B.P. Padley, R. Redjimi, J. Roberts[†], W. Shi, A.G. Stahl Leiton

Rice University, Houston, USA

A. Bodek, P. de Barbaro, R. Demina, J.L. Dulemba, C. Fallon, T. Ferbel, M. Galanti, A. Garcia-Bellido, O. Hindrichs, A. Khukhunaishvili, E. Ranken, R. Taus

University of Rochester, Rochester, USA

B. Chiarito, J.P. Chou, A. Gandrakota, Y. Gershtein, E. Halkiadakis, A. Hart, M. Heindl, E. Hughes, S. Kaplan, O. Karacheban²⁴, I. Laflotte, A. Lath, R. Montalvo, K. Nash, M. Osherson, S. Salur, S. Schnetzer, S. Somalwar, R. Stone, S.A. Thayil, S. Thomas, H. Wang

Rutgers, The State University of New Jersey, Piscataway, USA

H. Acharya, A.G. Delannoy, S. Spanier

University of Tennessee, Knoxville, USA

O. Bouhali⁹³, M. Dalchenko, A. Delgado, R. Eusebi, J. Gilmore, T. Huang, T. Kamon⁹⁴, H. Kim, S. Luo, S. Malhotra, R. Mueller, D. Overton, D. Rathjens, A. Safonov

Texas A&M University, College Station, USA

N. Akchurin, J. Damgov, V. Hegde, S. Kunori, K. Lamichhane, S.W. Lee, T. Mengke, S. Muthumuni, T. Peltola, S. Undleeb, I. Volobouev, Z. Wang, A. Whitbeck

Texas Tech University, Lubbock, USA

E. Appelt, S. Greene, A. Gurrola, W. Johns, C. Maguire, A. Melo, H. Ni, K. Padeken, F. Romeo, P. Sheldon, S. Tuo, J. Velkovska

Vanderbilt University, Nashville, USA

M.W. Arenton, B. Cox, G. Cummings, J. Hakala, R. Hirosky, M. Joyce, A. Ledovskoy, A. Li, C. Neu, B. Tannenwald, E. Wolfe

University of Virginia, Charlottesville, USA

P.E. Karchin, N. Poudyal, P. Thapa

Wayne State University, Detroit, USA

K. Black, T. Bose, J. Buchanan, C. Caillol, S. Dasu, I. De Bruyn, P. Everaerts, C. Galloni, H. He, M. Herndon, A. Hervé, U. Hussain, A. Lanaro, A. Loeliger, R. Loveless, J. Madhusudanan Sreekala, A. Mallampalli, A. Mohammadi, D. Pinna, A. Savin, V. Shang, V. Sharma, W.H. Smith, D. Teague, S. Trembath-Reichert, W. Vetens

University of Wisconsin – Madison, Madison, WI, USA

[†] Deceased.

¹ Also at Vienna University of Technology, Vienna, Austria.

² Also at Institute of Basic and Applied Sciences, Faculty of Engineering, Arab Academy for Science, Technology and Maritime Transport, Alexandria, Egypt, Alexandria, Egypt.

- ³ Also at Université Libre de Bruxelles, Bruxelles, Belgium.
- ⁴ Also at IRFU, CEA, Université Paris-Saclay, Gif-sur-Yvette, France.
- ⁵ Also at Universidade Estadual de Campinas, Campinas, Brazil.
- ⁶ Also at Federal University of Rio Grande do Sul, Porto Alegre, Brazil.
- ⁷ Also at UFMS, Nova Andradina, Brazil.
- ⁸ Also at Nanjing Normal University Department of Physics, Nanjing, China.
- ⁹ Now at The University of Iowa, Iowa City, USA.
- ¹⁰ Also at University of Chinese Academy of Sciences, Beijing, China.
- ¹¹ Also at Institute for Theoretical and Experimental Physics named by A.I. Alikhanov of NRC 'Kurchatov Institute', Moscow, Russia.
- ¹² Also at Joint Institute for Nuclear Research, Dubna, Russia.
- ¹³ Also at Helwan University, Cairo, Egypt.
- ¹⁴ Now at Zewail City of Science and Technology, Zewail, Egypt.
- ¹⁵ Also at Ain Shams University, Cairo, Egypt.
- ¹⁶ Now at British University in Egypt, Cairo, Egypt.
- ¹⁷ Also at Purdue University, West Lafayette, USA.
- ¹⁸ Also at Université de Haute Alsace, Mulhouse, France.
- ¹⁹ Also at Erzincan Binali Yildirim University, Erzincan, Turkey.
- ²⁰ Also at CERN, European Organization for Nuclear Research, Geneva, Switzerland.
- ²¹ Also at RWTH Aachen University, III. Physikalisches Institut A, Aachen, Germany.
- ²² Also at University of Hamburg, Hamburg, Germany.
- ²³ Also at Department of Physics, Isfahan University of Technology, Isfahan, Iran, Isfahan, Iran.
- ²⁴ Also at Brandenburg University of Technology, Cottbus, Germany.
- ²⁵ Also at Skobeltsyn Institute of Nuclear Physics, Lomonosov Moscow State University, Moscow, Russia.
- ²⁶ Also at Physics Department, Faculty of Science, Assiut University, Assiut, Egypt.
- ²⁷ Also at Eszterhazy Karoly University, Karoly Robert Campus, Gyongyos, Hungary.
- ²⁸ Also at Institute of Physics, University of Debrecen, Debrecen, Hungary, Debrecen, Hungary.
- ²⁹ Also at Institute of Nuclear Research ATOMKI, Debrecen, Hungary.
- ³⁰ Also at MTA-ELTE Lendület CMS Particle and Nuclear Physics Group, Eötvös Loránd University, Budapest, Hungary, Budapest, Hungary.
- ³¹ Also at Wigner Research Centre for Physics, Budapest, Hungary.
- ³² Also at IIT Bhubaneswar, Bhubaneswar, India, Bhubaneswar, India.
- ³³ Also at Institute of Physics, Bhubaneswar, India.
- ³⁴ Also at G.H.G. Khalsa College, Punjab, India.
- ³⁵ Also at Shoolini University, Solan, India.
- ³⁶ Also at University of Hyderabad, Hyderabad, India.
- ³⁷ Also at University of Visva-Bharati, Santiniketan, India.
- ³⁸ Also at Indian Institute of Technology (IIT), Mumbai, India.
- ³⁹ Also at Deutsches Elektronen-Synchrotron, Hamburg, Germany.
- ⁴⁰ Also at Sharif University of Technology, Tehran, Iran.
- ⁴¹ Also at Department of Physics, University of Science and Technology of Mazandaran, Behshahr, Iran.
- ⁴² Now at INFN Sezione di Bari^a, Università di Bari^b, Politecnico di Bari^c, Bari, Italy.
- ⁴³ Also at Italian National Agency for New Technologies, Energy and Sustainable Economic Development, Bologna, Italy.
- ⁴⁴ Also at Centro Siciliano di Fisica Nucleare e di Struttura Della Materia, Catania, Italy.
- ⁴⁵ Also at Università di Napoli 'Federico II', NAPOLI, Italy.
- ⁴⁶ Also at Riga Technical University, Riga, Latvia, Riga, Latvia.
- ⁴⁷ Also at Consejo Nacional de Ciencia y Tecnología, Mexico City, Mexico.
- ⁴⁸ Also at Institute for Nuclear Research, Moscow, Russia.
- ⁴⁹ Now at National Research Nuclear University 'Moscow Engineering Physics Institute' (MEPhI), Moscow, Russia.
- ⁵⁰ Also at St. Petersburg State Polytechnical University, St. Petersburg, Russia.
- ⁵¹ Also at University of Florida, Gainesville, USA.
- ⁵² Also at Imperial College, London, United Kingdom.
- ⁵³ Also at P.N. Lebedev Physical Institute, Moscow, Russia.
- ⁵⁴ Also at Moscow Institute of Physics and Technology, Moscow, Russia, Moscow, Russia.
- ⁵⁵ Also at California Institute of Technology, Pasadena, USA.
- ⁵⁶ Also at Budker Institute of Nuclear Physics, Novosibirsk, Russia.
- ⁵⁷ Also at Faculty of Physics, University of Belgrade, Belgrade, Serbia.
- ⁵⁸ Also at Trincomalee Campus, Eastern University, Sri Lanka, Nilaveli, Sri Lanka.
- ⁵⁹ Also at INFN Sezione di Pavia^a, Università di Pavia^b, Pavia, Italy, Pavia, Italy.
- ⁶⁰ Also at National and Kapodistrian University of Athens, Athens, Greece.
- ⁶¹ Also at Universität Zürich, Zurich, Switzerland.
- ⁶² Also at Ecole Polytechnique Fédérale Lausanne, Lausanne, Switzerland.
- ⁶³ Also at Stefan Meyer Institute for Subatomic Physics, Vienna, Austria, Vienna, Austria.
- ⁶⁴ Also at Laboratoire d'Annecy-le-Vieux de Physique des Particules, IN2P3-CNRS, Annecy-le-Vieux, France.
- ⁶⁵ Also at Şirnak University, Şirnak, Turkey.
- ⁶⁶ Also at Department of Physics, Tsinghua University, Beijing, China, Beijing, China.
- ⁶⁷ Also at Near East University, Research Center of Experimental Health Science, Nicosia, Turkey.
- ⁶⁸ Also at Beykent University, Istanbul, Turkey, Istanbul, Turkey.
- ⁶⁹ Also at Istanbul Aydin University, Application and Research Center for Advanced Studies (App. & Res. Cent. for Advanced Studies), Istanbul, Turkey.
- ⁷⁰ Also at Mersin University, Mersin, Turkey.
- ⁷¹ Also at Piri Reis University, Istanbul, Turkey.
- ⁷² Also at Adiyaman University, Adiyaman, Turkey.
- ⁷³ Also at Ozyegin University, Istanbul, Turkey.

- ⁷⁴ Also at Izmir Institute of Technology, Izmir, Turkey.
- ⁷⁵ Also at Necmettin Erbakan University, Konya, Turkey.
- ⁷⁶ Also at Bozok Universitetesi Rektörlüğü, Yozgat, Turkey, Yozgat, Turkey.
- ⁷⁷ Also at Marmara University, Istanbul, Turkey.
- ⁷⁸ Also at Milli Savunma University, Istanbul, Turkey.
- ⁷⁹ Also at Kafkas University, Kars, Turkey.
- ⁸⁰ Also at Istanbul Bilgi University, Istanbul, Turkey.
- ⁸¹ Also at Hacettepe University, Ankara, Turkey.
- ⁸² Also at Vrije Universiteit Brussel, Brussel, Belgium.
- ⁸³ Also at School of Physics and Astronomy, University of Southampton, Southampton, United Kingdom.
- ⁸⁴ Also at IPPP Durham University, Durham, United Kingdom.
- ⁸⁵ Also at Monash University, Faculty of Science, Clayton, Australia.
- ⁸⁶ Also at Bethel University, St. Paul, Minneapolis, USA, St. Paul, USA.
- ⁸⁷ Also at Karamanoğlu Mehmetbey University, Karaman, Turkey.
- ⁸⁸ Also at Bingol University, Bingol, Turkey.
- ⁸⁹ Also at Georgian Technical University, Tbilisi, Georgia.
- ⁹⁰ Also at Sinop University, Sinop, Turkey.
- ⁹¹ Also at Mimar Sinan University, Istanbul, Istanbul, Turkey.
- ⁹² Also at Erciyes University, KAYSERI, Turkey.
- ⁹³ Also at Texas A&M University at Qatar, Doha, Qatar.
- ⁹⁴ Also at Kyungpook National University, Daegu, Korea, Daegu, Republic of Korea.

Higgs Boson studies at future particle colliders

J. de Blas,^{a,b} M. Cepeda,^c J. D'Hondt,^d R.K. Ellis,^e C. Grojean,^{f,g} B. Heinemann,^{f,h}
 F. Maltoni,^{i,j} A. Nisati,^k E. Petit,^l R. Rattazzi^m and W. Verkerkeⁿ

^a*Dipartimento di Fisica e Astronomia Galileo Galilei, Università di Padova,
 Via Marzolo 8, I-35131 Padova, Italy*

^b*INFN — Sezione di Padova, Via Marzolo 8, I-35131 Padova, Italy*

^c*Centro de Investigaciones Energéticas, Medioambientales y Tecnológicas (CIEMAT),
 Avda. Complutense 40, 28040, Madrid, Spain*

^d*Inter-University Institute for High Energies (IIHE),
 Vrije Universiteit Brussel, Brussels, 1050, Belgium*

^e*IPPP, University of Durham, Durham DH1 3LE, U.K.*

^f*Deutsches Elektronen-Synchrotron (DESY), Hamburg, 22607, Germany*

^g*Institut für Physik, Humboldt-Universität, Berlin, 12489, Germany*

^h*Albert-Ludwigs-Universität Freiburg, Freiburg, 79104, Germany*

ⁱ*Centre for Cosmology, Particle Physics and Phenomenology, Université catholique de Louvain,
 Louvain-la-Neuve, 1348, Belgium*

^j*Dipartimento di Fisica e Astronomia, Università di Bologna and INFN — Sezione di Bologna,
 via Irnerio 46, 40126 Bologna, Italy*

^k*INFN — Sezione di Roma, P.le A. Moro 2, I-00185 Roma, Italy*

^l*Aix Marseille Univ, CNRS/IN2P3, CPPM, Marseille, France*

^m*Theoretical Particle Physics Laboratory (LPTP), EPFL, Lausanne, Switzerland*

ⁿ*Nikhef and University of Amsterdam, Science Park 105, 1098XG Amsterdam, the Netherlands*

E-mail: Jorge.DeBlasMateo@pd.infn.it, maria.cepada@cern.ch,
Jorgen.DHondt@vub.be, keith.ellis@durham.ac.uk,
christophe.grojean@desy.de, beate.heinemann@desy.de,
fabio.maltoni@uclouvain.be, nisati@cern.ch, Elisabeth.Petit@cern.ch,
riccardo.rattazzi@epfl.ch, verkerke@nikhef.nl

ABSTRACT: This document aims to provide an assessment of the potential of future colliding beam facilities to perform Higgs boson studies. The analysis builds on the submissions made by the proponents of future colliders to the European Strategy Update process, and takes as its point of departure the results expected at the completion of the HL-LHC program. This report presents quantitative results on many aspects of Higgs physics for future collider projects of sufficient maturity using uniform methodologies.

KEYWORDS: e⁺-e⁻ Experiments, Electroweak interaction, Higgs physics

ARXIV EPRINT: [1905.03764](https://arxiv.org/abs/1905.03764)

Contents

1	Introduction	1
2	Methodology	5
3	The Higgs boson couplings to fermions and vector bosons	7
3.1	The kappa framework	8
3.1.1	Choice of parametrization	8
3.1.2	Modeling of invisible and untagged Higgs decays	9
3.1.3	Fitting scenarios	9
3.2	Results from the kappa-framework studies and comparison	10
3.3	Effective field theory description of Higgs boson couplings	12
3.4	Results from the EFT framework studies	22
3.4.1	SMEFT fit results	24
3.4.2	Results for BSM-motivated effective Lagrangians	30
3.5	Impact of Standard Model theory uncertainties in Higgs calculations	35
4	The Higgs boson self-coupling	38
5	Rare Higgs boson decays	47
6	Sensitivity to Higgs CP	51
7	The Higgs boson mass and full width	54
8	Future studies of the Higgs sector, post-European Strategy	56
8.1	Higgs prospects at the muon collider	56
8.2	Higgs physics at multi-TeV electron-positron colliders	58
8.3	What and why: Higgs prospect studies beyond this report	58
9	Summary	63
A	Mandate agreed by RECFA in consultation with the PPG “Higgs physics with future colliders in parallel and beyond the HL-LHC”	64
B	Theoretical cross sections and partial width uncertainties	65
C	Inputs	67
C.1	Inputs for Higgs studies	67
C.2	Inputs for electroweak precision observables	72
D	Correlation matrices	74
E	Additional Kappa scenario fits	75

F	Additional comparisons	76
G	Electroweak precision constraints on oblique parameters	82
H	Consistency of electroweak precision data	85
I	Improvement with respect to HL-LHC	86

1 Introduction

This article presents the results of the Standard Model (SM) Higgs boson studies performed by the *Higgs@FutureColliders* group based on the input submitted to the Update of the European Strategy by the various proponents of new high-luminosity energy-frontier particle accelerator projects beyond the *High Luminosity LHC* (HL-LHC). This report fulfils part of the mandate given to this group by the restricted ECFA (REFCA) committee, see appendix A. The exploration of the Higgs boson through direct searches and precision measurements at future colliders is among the most important aspects of their scientific programmes.

The colliders considered for this document are High-Energy LHC (HE-LHC), Future Circular Colliders (FCC-ee,eh,hh) [1], the Circular Electron-Positron Collider (CEPC) [2], the International Linear Collider (ILC) [3, 4], the Compact Linear Collider (CLIC) [5], and the Large Hadron electron Collider [6] (LHeC or HE-LHeC¹). The physics results that are expected by the completion of HL-LHC are assumed to represent the scenario from where these future colliders would start. Furthermore, a muon collider is also briefly illustrated, but given the less advanced stage, it is not part of the default analyses performed. The potential of a $\gamma\gamma$ collider (based on an e^+e^- collider and laser beams) for Higgs boson physics has been studied a while ago [7, 8] and more recently again in context of plasma-wakefield driven accelerators [9]. Plasma-wakefield driven accelerators also offer promise to provide multi-TeV e^+e^- colliders (e.g. [9]) and are addressed briefly later in this report.

A table of the colliders and their parameters (type, \sqrt{s} , polarisation \mathcal{P} , integrated luminosity \mathcal{L} , the run time) is given in table 1. A graphical display of the time line and luminosity values is shown in figure 1. The parameters used are taken from the references also given in that table. For the purpose of this study, only inputs as provided by the various collaborations are used, and there is no attempt to make any judgement on the validity of the assumptions made in estimating the projected measurement uncertainties (see also mandate in appendix A). In addition to the collider runs shown in table 1, a few other scenarios are considered such as FCC-hh with $\sqrt{s} = 37.5$ TeV [10] and $\mathcal{L} = 15$ fb⁻¹, FCC-ee with 4 instead of 2 IPs (doubling the total integrated luminosity), and CLIC and ILC with a dedicated running period of 1–3 years to collect $\mathcal{L} = 100$ fb⁻¹ at $\sqrt{s} \approx M_Z$ [4, 11]. These are discussed in appendix F.

¹For HE-LHeC no analysis was performed here, but it is expected that the relative improvements w.r.t. LHeC are expected to be similar as from HL-LHC to HE-LHC.

Collider	Type	\sqrt{s}	\mathcal{P} [%] [e^-/e^+]	N(Det.)	$\mathcal{L}_{\text{inst}}$ [10^{34}] $\text{cm}^{-2}\text{s}^{-1}$	\mathcal{L} [ab^{-1}]	Time [years]	Refs.	Abbreviation
HL-LHC	pp	14 TeV	—	2	5	6.0	12	[13]	HL-LHC
HE-LHC	pp	27 TeV	—	2	16	15.0	20	[13]	HE-LHC
FCC-hh ^(*)	pp	100 TeV	—	2	30	30.0	25	[1]	FCC-hh
FCC-ee	ee	M_Z	0/0	2	100/200	150	4	[1]	FCC-ee ₂₄₀ FCC-ee ₃₆₅ (1y SD before $2m_{\text{top}}$ run)
		$2M_W$	0/0	2	25	10	1–2		
		240 GeV	0/0	2	7	5	3		
		$2m_{\text{top}}$	0/0	2	0.8/1.4	1.5	5 (+1)		
ILC	ee	250 GeV	$\pm 80/\pm 30$	1	1.35/2.7	2.0	11.5	[3, 14]	ILC ₂₅₀
		350 GeV	$\pm 80/\pm 30$	1	1.6	0.2	1		ILC ₃₅₀
		500 GeV	$\pm 80/\pm 30$	1	1.8/3.6	4.0	8.5 (+1)	(1y SD after 250 GeV run)	ILC ₅₀₀
		1000 GeV	$\pm 80/\pm 20$	1	3.6/7.2	8.0	8.5 (+1-2)	[4] (1–2y SD after 500 GeV run)	ILC ₁₀₀₀
CEPC	ee	M_Z	0/0	2	17/32	16	2	[2]	CEPC
		$2M_W$	0/0	2	10	2.6	1		
		240 GeV	0/0	2	3	5.6	7		
CLIC	ee	380 GeV	$\pm 80/0$	1	1.5	1.0	8	[15]	CLIC ₃₈₀
		1.5 TeV	$\pm 80/0$	1	3.7	2.5	7		CLIC ₁₅₀₀
		3.0 TeV	$\pm 80/0$	1	6.0	5.0	8 (+4)		CLIC ₃₀₀₀ (2y SDs between energy stages)
LHeC	ep	1.3 TeV	—	1	0.8	1.0	15	[12]	LHeC
HE-LHeC	ep	1.8 TeV	—	1	1.5	2.0	20	[1]	HE-LHeC
FCC-eh	ep	3.5 TeV	—	1	1.5	2.0	25	[1]	FCC-eh

Table 1. Summary of the future colliders considered in this report. The number of detectors given is the number of detectors running concurrently, and only counting those relevant to the entire Higgs physics programme. The instantaneous and integrated luminosities provided are those used in the individual reports, and for e^+e^- colliders the integrated luminosity corresponds to the sum of those recorded by the detectors. For HL-LHC this is also the case while for HE-LHC and FCC_{hh} it corresponds to 75% of that. The values for \sqrt{s} are approximate, e.g. when a scan is proposed as part of the programme this is included in the closest value (most relevant for the Z , W and t programme). For the polarisation, the values given correspond to the electron and positron beam, respectively. For HL-LHC, HE-LHC, FCC, CLIC and LHeC the instantaneous and integrated luminosity values are taken from ref. [12]. For these colliders the number of seconds per year is 1.2×10^7 based on CERN experience [12]. CEPC (ILC) assumes 1.3×10^7 (1.6×10^7) seconds for the annual integrated luminosity calculation. When two values for the instantaneous luminosity are given these are before and after a luminosity upgrade planned. The last column gives the abbreviation used in this report in the following sections. When the entire programme is discussed, the highest energy value label is used, e.g. ILC₁₀₀₀ or CLIC₃₀₀₀. It is always inclusive, i.e. includes the results of the lower-energy versions of that collider. Also given are the shutdowns (SDs) needed between energy stages of the machine. SDs planned during a run at a given energy are included in the respective energy line. (*) For FCC-hh a value of $\sqrt{s} = 37.5$ TeV is also considered, see appendix F. Additional scenarios where ILC/CLIC accumulate 100 fb^{-1} on the Z -pole, and where FCC-ee has 4 IPs are also discussed in appendix F.

	T_0	+5	+10	+15	+20	...	+26
ILC	0.5/ab 250 GeV		1.5/ab 250 GeV	1.0/ab 500 GeV	0.2/ab $2m_{top}$	3/ab 500 GeV	
CEPC	5.6/ab 240 GeV		16/ab M_Z	$\frac{2.6}{ab}$ $2M_W$			SppC =>
CLIC	1.0/ab 380 GeV			2.5/ab 1.5 TeV			5.0/ab => until +28 3.0 TeV
FCC	150/ab ee, M_Z	10/ab ee, $2M_W$	5/ab ee, 240 GeV		1.7/ab ee, $2m_{top}$		hh.eh =>
LHeC	0.06/ab		0.2/ab	0.72/ab			
HE-LHC	10/ab per experiment in 20y						
FCC eh/hh	20/ab per experiment in 25y						

Figure 1. Time line of various collider projects starting at time T_0 as submitted to the European Strategy Update process. Some possible extensions beyond these baseline run plans have been discussed and are presented in more detail in appendix F. For the clarification of the meaning of a year of running, see the caption of table 1. Figure 13 in appendix C shows an alternative version of this figure using the earliest possible start date (i.e. the calendar date of T_0) given by the proponents.

For the following sections the tables and plots are labelled using the acronyms given in table 1. The energy subscript indicates the highest energy stage of the given collider, and the results always assume that it is combined with results from the lower energy stages.

At the heart of the Higgs physics programme is the question of how the Higgs boson couples to Standard Model elementary particles. Within the SM itself, all these couplings are uniquely determined. But new physics beyond the SM (BSM) can modify these couplings in many different ways. The structure of these deformations is in general model-dependent. One important goal of the Higgs programme at the future colliders is to identify, or at least constrain, these deformations primarily from the measurements the Higgs production cross section, σ , times decay branching ratio, BR.² Ultimately, these studies will be used to assess the fundamental parameters of the new physics models. For the time being, in the absence of knowledge of new physics, we need to rely on a parametrisation of our ignorance in terms of continuous deformations of the Higgs boson couplings. Different assumptions allow to capture different classes of new physics dynamics. First, in the so-called κ -framework [16, 17], often used to interpret the LHC measurements, the Higgs couplings to the SM particles are assumed to keep the same helicity structures as in the SM. While it offers a convenient exploration tool that does not require other computations than the SM ones and still captures the dominant effects of well motivated new physics scenarios on a set of on-shell Higgs observables, the κ -framework suffers from some limitations that will be discussed later and it includes some biases that will prevent to put the Higgs programme in perspective with other measurements, see e.g. the discussion in

²The Higgs couplings could be constrained less directly from processes with no Higgs in the final state or without even a non-resonant Higgs. But the main focus of the study presented in this report will be on the information obtained from the measured $\sigma \times BR$. Still, note that, at lepton colliders, the ZH associated production can be measured without the decay of the Higgs.

ref. [18] and at the beginning of section 3. An alternative approach, based on *Effective Field Theory* (EFT), considers new Higgs couplings with different helicity structures, with different energy dependence or with different number of particles. They are not present in the SM but they can potentially be generated by new heavy degrees of freedom.

Furthermore, the sensitivity of the data to the Higgs self-coupling is analysed based on single-Higgs and di-Higgs production measurements by future colliders. Due to lack of access to the simulated data of the collaborations, in particular differential kinematical distributions, it is not possible in this case to perform a study for the Higgs self-coupling with similar rigour as the analysis of the single-Higgs-coupling described in the previous paragraph.

The Higgs width determination is also discussed as is the possible decay of the Higgs bosons into new particles that are either “invisible” (i.e. observed through missing energy - or missing transverse energy) or “untagged”, to which none of the Higgs analyses considered in the study are sensitive. Rare decays and CP aspects are also discussed.

All colliders have provided extensive documentation on their Higgs physics programme. However, sometimes different choices are made e.g. on which parameters to fit for and which to fix, what theoretical uncertainties to assume, which operators to consider in e.g. the EFT approach. This would lead to an unfair comparison of prospects from different future colliders, with consequent confusing scientific information. In this report, we aim to have a single clear and reasonable approach to the assumptions made when comparing the projections for the future.

In general, one should not over-interpret 20% differences between projected sensitivities for partial widths of different future projects. In many cases, these are likely not significant. For instance, CEPC and FCC-ee at $\sqrt{s} = 240$ GeV expect to acquire a very similar luminosity and should obtain very similar results if both use two optimized detectors and analyses. Differences between the projected sensitivities, when considering only results from the $\sqrt{s} = 240$ GeV run, originate likely from different choices made in the analyses at this stage or, in some cases, because an analysis has not yet been performed. For the EFT analysis the measurements at different \sqrt{s} values play an important role, and this results in significant differences as CEPC and FCC-ee have proposed different integrated luminosities at the different \sqrt{s} values and CEPC lacks a run at $\sqrt{s} = 365$ GeV. It is also useful to keep in mind that the target luminosity values have some uncertainties, and historically colliders have sometimes exceeded them (e.g. LHC by a factor of about two in instantaneous luminosity) and sometimes fallen short.

In this document only inclusive cross section times branching ratio measurements, and in some cases ratios of inclusive measurements, are used. It is well known that probing the Higgs boson at high p_T enhances the sensitivity to new physics and the analysis presented here does not capture this. As a result of this, the true power of high-energy colliders (where $\sqrt{\hat{s}} \gg m_H$) for probing Higgs physics is underestimated.

This document is organised as follows. Section 2 discusses the methodology, including the systematic uncertainties on the theoretical calculations which are common to all colliders. Section 3 presents the study made on the Higgs boson couplings to SM elementary particles. The results found in the context of the κ -framework (briefly summarised in sec-

tion 3.1) are presented in section 3.2. Likewise, the results from the EFT fits (summarised in section 3.3) are collected in section 3.4. The impact of theory uncertainties on the Higgs projections is discussed in section 3.5. Particular attention is dedicated to the Higgs self-coupling in section 4 and the Higgs boson rare decays, in section 5. The prospects for measurements of Higgs boson CP properties are given in section 6, and the prospects for precision measurements of the mass and width are summarized in section 7.

Section 8 presents future studies that would be important to deepen to get a more complete view of the Higgs physics potential at future colliders. The Muon Collider (section 8.1) and plasma-wakefield accelerators (section 8.2) are discussed first, and then phenomenological studies that relate the precision measurements to new physics models are discussed (section 8.3).

In the appendix, all theoretical and experimental input parameters related to the Higgs observables are provided, and some results that seemed too detailed for the main body, are also shown.

2 Methodology

The various colliders measure values for the cross sections times branching ratios, $\sigma \times \text{BR}$. At hadron colliders the main processes are gluon-gluon-fusion (ggF), vector boson fusion (VBF), Higgs-strahlung (VH, where $V = Z, W$) and $t\bar{t}H$ production. At lepton colliders, Higgs-strahlung (ZH) dominates at low values of \sqrt{s} , while at high \sqrt{s} values the VBF process becomes dominant. At lepton-hadron colliders, the Higgs boson is dominantly produced via WW or ZZ fusion in the t -channel.

The extraction of the couplings of the Higgs boson relies on a simultaneous fit of all the projected measurements of $\sigma \times \text{BR}$, and their comparison to the SM values. As such, it is sensitive to both the experimental uncertainties as well as theoretical uncertainties on the production cross sections and branching ratios.

At the HL-LHC, these theoretical uncertainties are taken from the S2 scenario of the HL-LHC [13], which assumes that the current uncertainties can be reduced by a factor of two by the end of the HL-LHC running in twenty years.³ For the studies at future lepton colliders we use the future projections for the theory uncertainties on the partial width values given in table 19. At the FCC-hh a 1% total uncertainty is assumed, combined for the luminosity and cross section normalisation [1]. It is expected that this 1% is dominated by the luminosity uncertainty and that theory uncertainties will be negligible in comparison, also thanks to the PDF uncertainty reduction from FCC-eh and/or LHeC. For HL-LHC and HE-LHC a luminosity uncertainty of 1% is assumed. For LHeC the theoretical uncertainties on the charged-current and neutral-current production processes are taken to be 0.5% [19]. For the decays the uncertainties as given in table 19 are used.

Some caution must be taken when studying the HE-LHC results provided here. They are derived from the same inputs as the HL-LHC ones evolved with integrated luminosity and increased cross section. This is a simplified approach, and all the HE-LHC results are

³Apart from improved theoretical calculations, part of this reduction would require a more precise knowledge of PDFs and α_S , which could be possible with an ep machine such as the LHeC.

thus approximations. As in ref. [13], we consider 2 scenarios: one where we use the same S2 assumptions as for the HL-LHC; and a second scenario, denoted S2', which assumes a further reduction in the signal theoretical systematic uncertainties by another factor of two with respect to the S2 scenario at the HL-LHC, i.e. roughly four times smaller than current studies from Run 2. It must be noted that such reduction of the uncertainty is not motivated on solid theoretical grounds and it is simply a hypothesis, based on the reasoning that the time available to make progress is significantly longer for HE-LHC than HL-LHC. When combined with the HL-LHC, the theory systematics are assumed to be fully correlated between HL-LHC and HE-LHC, using the same uncertainties, S2 or S2', for both colliders.

For the purpose of the analyses presented here, it is assumed that all observables of relevance have the SM value and there are no new physics effects present in the simulated data. If new physics effects are observed e.g. in the data from the 2nd or 3rd LHC run, either in the Higgs sector or otherwise, the analysis method and assumptions made will likely change significantly.

The combination of any future data with HL-LHC results is done assuming no correlations between the colliders, except for those between HL-LHC and HE-LHC which are treated as discussed above.

In the input HL-LHC predictions it is assumed that the intrinsic theory systematic uncertainties for the various production modes are uncorrelated. A consequence of this assumption is that, when Higgs model parameters are constructed that represent (directly or indirectly) an average over independent measurements with independent theory uncertainties that are all interpreted to measure the same physics quantity (e.g. the global signal strength μ , or the EFT parameter c_ϕ in eq. (3.19) below), such averages can have smaller (theory) uncertainties than the component measurements. This reduced average uncertainty occurs by virtue of the choices:

- to consider the input systematic uncertainties to be independent;
- to interpret different classes of measurement to measure the same physics.

The impact of the choice of correlation between theory systematic uncertainties should be carefully investigated in the future, but was not possible with the set of inputs provided for the preparation of this document. Where the effect of theory error averaging was observed to be prominent in the presented results, e.g. in section 3.4, it is mentioned.

Electroweak precision observables also contribute significantly in the EFT-based analysis. At present, LEP still provides the best constraints in many cases, and these are used here, except when new higher precision measurements are expected to be made by the given collider. For instance, for the HL-LHC and HE-LHC projections, LEP values are used for the constraints on electroweak precision observables, whilst all FCC machines use the values expected from FCC-ee.

The fits presented in this report have been produced using the fitting framework of the `HEPfit` package [20], a general tool to combine information from direct and indirect searches and test the Standard Model and its extensions [21–24]. We use the Markov-Chain

Monte-Carlo implementation provided by the Bayesian Analysis Toolkit [25], to perform a Bayesian statistical analysis of the sensitivity to deformations from the SM at the different future collider projects. The experimental projections for the different observables included in the fits are implemented in the likelihood assuming Gaussian distributions, with SM central values and standard deviations given by the corresponding projected uncertainties. Model parameters are assumed to have flat priors. Finally, theory uncertainties, when included, are introduced via nuisance parameters with Gaussian priors.

The projected uncertainties of all measurements of observables, relevant to the various analyses presented in this article, are listed in appendix C.

3 The Higgs boson couplings to fermions and vector bosons

Within the SM, all the Higgs couplings are uniquely fixed in terms of the Fermi constant and the masses of the different particles. Measuring the Higgs couplings thus requires a parametrization of the deviations from the SM induced by new physics. The κ -framework is the simplest parametrization directly related to experimental measurements of the Higgs boson production and decay modes. For this reason, it has been widely used by the community. It only compares the experimental measurements to their best SM predictions and does not require any new BSM computations *per se*. From a more theoretical perspective, its relevance arises from the fact that it actually fully captures the leading effects in single Higgs processes of well motivated scenarios. For instance, in the minimal supersymmetric standard model with R-parity, all dominant corrections to the Higgs couplings induced by the new super-partners are of order m_H^2/m_{SUSY}^2 relative to the SM predictions (m_{SUSY} is the mass of the new particles) and they appear as shifts of the Higgs couplings with the *same* SM helicity structures while new helicity structures are only generated as subleading effects further suppressed by a loop factor. In scenarios where the Higgs boson arises from a strongly-interacting sector as a composite (pseudo-Goldstone) boson, the leading deformations to the SM scale like $\xi = (g_\star^2/g_{\text{SM}}^2) m_W^2/m_\star^2$ (m_\star and g_\star are the overall mass scale of the strong sector resonances and their mutual coupling respectively) and they all preserve the helicity structure of the interactions already present in the SM. The constraints derived in the κ analysis can thus be readily exploited to derive constraints on the new physics parameters. This kappa-framework has, however, its own limitations when Higgs measurements need to be put in perspective and compared to processes with different particle multiplicities or combined with other measurements done in different sectors or at different energies. An effective field theory (EFT) approach naturally extends the kappa-framework. First, it allows to exploit polarisation- and angular-dependent observables that a κ -analysis will remain blind to. Second, an EFT analysis constitutes a useful tool to probe the Higgs boson in the extreme kinematical regions relevant for colliders operating far above the weak scale, exploring the tails of kinematical distributions, even though these observables have not been fully exploited yet in the studies presented by the different future collider collaborations. Third, the EFT offers a consistent setup where predictions can be systematically improved via the inclusion of both higher loop corrections in the SM couplings and further new physics corrections encoded in operators of even higher dimensions.

Both approaches will be studied in this document and we will report the fits to the experimental projected measurements obtained in these two frameworks. As an illustration, a concrete interpretation of the results obtained will be done in the context of composite Higgs models.

3.1 The kappa framework

3.1.1 Choice of parametrization

The kappa framework, described in detail in ref. [16, 17], facilitates the characterisation of Higgs coupling properties in terms of a series of Higgs coupling strength modifier parameters κ_i , which are defined as the ratios of the couplings of the Higgs bosons to particles i to their corresponding Standard Model values. The kappa framework assumes a single narrow resonance so that the zero-width approximation can be used to decompose the cross section as follows

$$(\sigma \cdot \text{BR})(i \rightarrow H \rightarrow f) = \frac{\sigma_i \cdot \Gamma_f}{\Gamma_H}, \quad (3.1)$$

where σ_i is the production cross section through the initial state i , Γ_f the partial decay width into the final state f and Γ_H the total width of the Higgs boson. The κ parameters are introduced by expressing each of the components of eq. (3.1) as their SM expectation multiplied by the square of a coupling strength modifier for the corresponding process at leading order:

$$(\sigma \cdot \text{BR})(i \rightarrow H \rightarrow f) = \frac{\sigma_i^{\text{SM}} \kappa_i^2 \cdot \Gamma_f^{\text{SM}} \kappa_f^2}{\Gamma_H^{\text{SM}} \kappa_H^2} \rightarrow \mu_i^f \equiv \frac{\sigma \cdot \text{BR}}{\sigma_{\text{SM}} \cdot \text{BR}_{\text{SM}}} = \frac{\kappa_i^2 \cdot \kappa_f^2}{\kappa_H^2}, \quad (3.2)$$

where μ_i^f is the rate relative to the SM expectation (as given in tables 18 and 19) and κ_H^2 is an expression that adjusts the SM Higgs width to take into account of modifications κ_i of the SM Higgs coupling strengths:

$$\kappa_H^2 \equiv \sum_j \frac{\kappa_j^2 \Gamma_j^{\text{SM}}}{\Gamma_H^{\text{SM}}}. \quad (3.3)$$

When all κ_i are set to 1, the SM is reproduced. For loop-induced processes, e.g. $H \rightarrow \gamma\gamma$, there is a choice of either resolving the coupling strength modification in its SM expectation, i.e. $\kappa_\gamma(\kappa_t, \kappa_W)$ or keeping κ_γ as an effective coupling strength parameter.

For the results presented in the document, we choose to describe loop-induced couplings with effective couplings, resulting in a total of 10 κ parameters: $\kappa_W, \kappa_Z, \kappa_c, \kappa_b, \kappa_t, \kappa_\tau, \kappa_\mu$, and the effective coupling modifiers κ_γ, κ_g and $\kappa_{Z\gamma}$. The couplings $\kappa_s, \kappa_d, \kappa_u$ and κ_e that are only weakly constrained from very rare decays are not included in the combined κ -framework fits presented in this section, their estimated limits are discussed separately in section 5. We note the parameter κ_t is only accessible above the tH threshold as the processes involving virtual top quarks are all described with effective coupling modifiers

$(\kappa_g, \kappa_{Z\gamma}, \kappa_\gamma)$, hence standalone fits to low-energy (lepton) colliders have no sensitivity to κ_t in the κ -framework fits considered here.⁴

3.1.2 Modeling of invisible and untagged Higgs decays

The κ -framework can be extended to allow for the possibility of Higgs boson decays to invisible or untagged BSM particles. The existence of such decays increases the total width Γ_H by a factor $1/(1 - BR_{\text{BSM}})$, where BR_{BSM} is the Higgs branching fraction to such BSM particles. Higgs boson decays to BSM particles can be separated in two classes: decays into invisible particles, which are experimentally directly constrained at all future colliders (e.g $ZH, H \rightarrow \text{invisible}$), and decays into all other ‘untagged’ particles.

Reflecting this distinction we introduce two branching fraction parameters BR_{inv} and BR_{unt} so that:

$$\Gamma_H = \frac{\Gamma_H^{\text{SM}} \cdot \kappa_H^2}{1 - (BR_{\text{inv}} + BR_{\text{unt}})}, \tag{3.4}$$

where κ_H^2 is defined in eq. (3.3).

For colliders that can directly measure the Higgs width, BR_{unt} can be constrained together with κ_i and BR_{inv} from a joint fit to the data. For standalone fits to colliders that cannot, such as the HL-LHC, either an indirect measurement can be included, such as from off-shell Higgs production, or additional theoretical assumptions must be introduced. A possible assumption is $|\kappa_V| \leq 1$ ($V = W, Z$), which is theoretically motivated as it holds in a wide class of BSM models albeit with some exceptions [26] (for more details see [17], section 10).

3.1.3 Fitting scenarios

To characterise the performance of future colliders in the κ -framework, we defined four benchmark scenarios, which are listed in table 2. The goal of the kappa-0 benchmark is to present the constraining power of the κ -framework under the assumption that there exist no light BSM particles to which the Higgs boson can decay. The goal of benchmarks kappa-1,2 is to expose the impact of allowing BSM Higgs decays, in combination with a measured or assumed constraint on the width of the Higgs, on the standalone κ results. Finally, the goal of the kappa-3 benchmark is to show the impact of combining the HL-LHC data with each of the future accelerators. In all scenarios with BSM branching fractions, these branching fractions are constrained to be positive definite.

Experimental uncertainties — defined as statistical uncertainties and, when provided, experimental systematic uncertainties, background theory uncertainties and signal-acceptance related theory uncertainties — are included in all scenarios. Theory uncertainties on the Higgs branching fractions predictions for all future colliders and uncertainties

⁴At high Higgs/jet p_T , $gg \rightarrow H$ becomes directly sensitive to κ_t . However, high- p_T regions are not separately considered in the κ -framework fits reported here. Furthermore, there is no sensitivity to the sign of the κ parameters as the loop-induced processes with sensitivity to the sign have all been described with effective modifiers. Single top production is sensitive to the sign but not used in the κ fits presented here (but used in the CP studies). Finally, note that, for vector-boson-fusion, the small interference effect between W- and Z boson fusion is neglected.

Scenario	BR_{inv}	BR_{unt}	include HL-LHC
kappa-0	fixed at 0	fixed at 0	no
kappa-1	measured	fixed at 0	no
kappa-2	measured	measured	no
kappa-3	measured	measured	yes

Table 2. Definition of the benchmark scenarios used to characterize future colliders in the κ -framework.

on production cross section predictions for hadron colliders, as described in section 2, are partially included; intrinsic theory uncertainties, arising from missing higher-order corrections, are *not* included in any of the benchmarks, while parametric theory uncertainties arising from the propagation of experimental errors on SM parameters *are* included in all scenarios. A detailed discussion and assessment of the impact of theory uncertainties is given in section 3.5.

3.2 Results from the kappa-framework studies and comparison

The κ -framework discussed in the previous section was validated comparing the results obtained with the scenarios described as kappa-0 and kappa-1 to the original results presented by the Collaborations to the European Strategy. In general, good agreement is found.

The results of the kappa-0 scenario described in the previous section are reported in table 3. In this scenario, no additional invisible or untagged branching ratio is allowed in the fits, and colliders are considered independently. This is the simplest scenario considered in this report, and illustrates the power of the kappa framework to constrain new physics in general, and in particular the potential to constrain new physics at the proposed new colliders discussed in this report. In general the precision is at the per cent level, In the final stage of the future colliders a precision of the order of a few per-mille would be reachable for several couplings, for instance κ_W and κ_Z . Cases in which a particular parameter has been fixed to the SM value due to lack of sensitivity are shown with a dash (-). Examples of this are κ_c , not accessible at HL-LHC and HE-LHC, and κ_t , only accessible above the ttH/tH threshold. Not all colliders reported results for all possible decay modes in the original reference documentation listed in table 1, the most evident example of this being the $Z\gamma$ channel. In this standalone collider scenario, the corresponding parameters were left to float in the fits. They are indicated with * in the tables.

This kappa-0 scenario can be expanded to account for invisible decays (kappa-1) and invisible and untagged decays (kappa-2), still considering individual colliders in a standalone way. The overall effect of this additional width is a slight worsening of the precision of the kappa parameters from the kappa-0 scenario to the kappa-1, and further on to the kappa-2. It is most noticeable for κ_W , κ_Z and κ_b . For comparison of the total impact, the kappa-2 scenario results can be found in tables 28 and 29 in appendix E.

Table 4 shows the expected precision of the κ parameters in the final benchmark scenario discussed in this paper in which 95% CL limits on BR_{unt} and BR_{inv} are set, for

kappa-0	HL-LHC	LHeC	HE-LHC		ILC			CLIC			CEPC	FCC-ee		FCC-ee/eh/hh
			S2	S2'	250	500	1000	380	15000	3000		240	365	
κ_W [%]	1.7	0.75	1.4	0.98	1.8	0.29	0.24	0.86	0.16	0.11	1.3	1.3	0.43	0.14
κ_Z [%]	1.5	1.2	1.3	0.9	0.29	0.23	0.22	0.5	0.26	0.23	0.14	0.20	0.17	0.12
κ_g [%]	2.3	3.6	1.9	1.2	2.3	0.97	0.66	2.5	1.3	0.9	1.5	1.7	1.0	0.49
κ_γ [%]	1.9	7.6	1.6	1.2	6.7	3.4	1.9	98*	5.0	2.2	3.7	4.7	3.9	0.29
$\kappa_{Z\gamma}$ [%]	10.	–	5.7	3.8	99*	86*	85*	120*	15	6.9	8.2	81*	75*	0.69
κ_c [%]	–	4.1	–	–	2.5	1.3	0.9	4.3	1.8	1.4	2.2	1.8	1.3	0.95
κ_t [%]	3.3	–	2.8	1.7	–	6.9	1.6	–	–	2.7	–	–	–	1.0
κ_b [%]	3.6	2.1	3.2	2.3	1.8	0.58	0.48	1.9	0.46	0.37	1.2	1.3	0.67	0.43
κ_μ [%]	4.6	–	2.5	1.7	15	9.4	6.2	320*	13	5.8	8.9	10	8.9	0.41
κ_τ [%]	1.9	3.3	1.5	1.1	1.9	0.70	0.57	3.0	1.3	0.88	1.3	1.4	0.73	0.44

Table 3. Expected relative precision (%) of the κ parameters in the kappa-0 scenario described in section 2 for future accelerators. Colliders are considered independently, not in combination with the HL-LHC. No BSM width is allowed in the fit: both BR_{unt} and BR_{inv} are set to 0, and therefore κ_V is not constrained. Cases in which a particular parameter has been fixed to the SM value due to lack of sensitivity are shown with a dash (–). A star (★) indicates the cases in which a parameter has been left free in the fit due to lack of input in the reference documentation. The integrated luminosity and running conditions considered for each collider in this comparison are described in table 1. FCC-ee/eh/hh corresponds to the combined performance of FCC-ee₂₄₀+FCC-ee₃₆₅, FCC-eh and FCC-hh. In the case of HE-LHC, two theoretical uncertainty scenarios (S2 and S2') [13] are given for comparison.

the three possibilities using the LHC tunnel: HL-LHC, LHeC, and HE-LHC. The results correspond to the kappa-3 scenario.

As discussed before, for these hadron colliders a constraint on $|\kappa_V| \leq 1$ is applied in this case, as no direct access to the Higgs width is possible.

Table 5 shows the corresponding kappa-3 scenario for the different lepton colliders and a final FCC-ee/eh/hh combination, all combined with the HL-LHC results. The integrated luminosity and running conditions considered for each collider in this comparison are taken for table 1. The constraints on Γ_H derived from the fit parameters using eq. (3.4) are discussed in detail in section 7. In this case when HL-LHC is combined with a lepton collider the assumption $|\kappa_V| \leq 1$ is no longer necessary, and therefore it is not used as a constrain in these kappa-3 fits. For those particular analyses not reported in the original reference documentation listed in table 1 (e.g. $\kappa_{Z\gamma}$) the HL-LHC prospects drive the combination. They are indicated with * in the tables.

We have examined the correlations of the lepton collider kappa-3 fits. In the initial stage of ILC (ILC₂₅₀), κ_W , κ_g , κ_b , κ_t and κ_τ show sizeable correlations (> 70%), with the largest corresponding to κ_b and κ_τ (93%). There is practically no correlation between κ_W and κ_Z (8%). The untagged branching fraction is not particularly correlated with the couplings, with the largest correlation corresponding to κ_Z (50%), and an anti correlation (-20%) seen for $\kappa_{Z\gamma}$ where the only information comes from the HL-LHC data. In the case of FCC-ee₃₆₅, we see a slight correlation between κ_Z and κ_W (30%), and a similar correlation

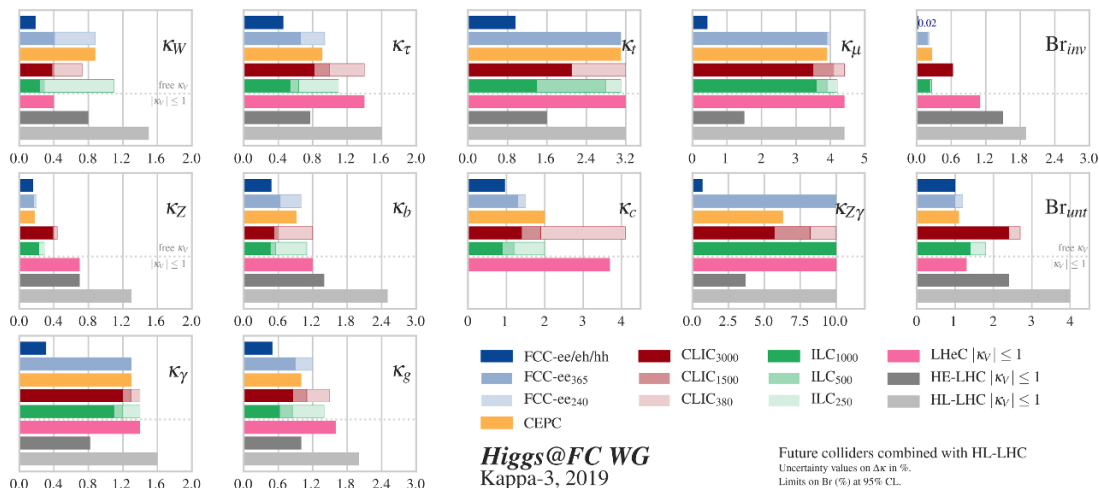


Figure 2. Expected relative precision (%) of the κ parameters in the kappa-3 scenario described in section 2. For details, see tables 4 and 5. For HE-LHC, the S2' scenario is displayed. For LHeC, HL-LHC and HE-LHC a constrained $\kappa_V \leq 1$ is applied.

between these and the untagged branching fraction (30–50%). The correlations between κ_b , κ_τ , κ_g and κ_W are mild, with the largest value corresponding once again to κ_b and κ_τ (74%). In this case there is also no strong correlation between the untagged branching fraction and the couplings, with the largest correlation corresponding to κ_Z (50%), followed by κ_b (30%). Again an anti correlation (-20%) is seen for $\kappa_{Z\gamma}$. For CLIC₃₀₀₀ the situation is markedly different, with large correlations between κ_Z and κ_W (80%), and between the untagged branching fraction and κ_Z , κ_W and κ_b (90%, 80%, 70% respectively). The correlations between κ_b , κ_Z , κ_τ , κ_g and κ_W are not negligible, with the highest corresponding to κ_b and κ_W (70%). In this case, κ_b and κ_τ are correlated to 45%. These correlations can be seen graphically in figure 14 in the appendix.

The results of the kappa-3 benchmark scenario are also presented graphically in figure 2. Note that while hadron colliders and lepton colliders are shown together, the caveat that a bound on $|\kappa_V| \leq 1$ is required for HL-LHC, HE-LHC and LHeC still applies. Parameters fixed to the Standard Model value are not displayed.

Intrinsic theoretical uncertainties for future lepton colliders are omitted in tables 3, 4 and 5. Their effect is discussed in detail in section 3.5.

3.3 Effective field theory description of Higgs boson couplings

As already discussed, the κ -framework provides a convenient first parametrization of new physics in single Higgs processes. By construction, it is perfectly suitable to spot a deviation from the SM, but it does not provide a systematic description of new physics. As such it does not permit to correlate different processes nor to describe their energy dependence, which is certainly a drawback when trying to develop a strategic perspective. When aiming at a more systematic approach one must distinguish the two cases of light and heavy new physics. In the first case, there is no simple and systematic description. One must proceed case by case, perhaps with the aid of simplified models. While we are not aware of any

kappa-3	HL-LHC	HL-LHC &		
		LHeC	HE-LHC (S2)	HE-LHC (S2')
$1 \geq \kappa_W > (68\%)$	0.985	0.996	0.988	0.992
$1 \geq \kappa_Z > (68\%)$	0.987	0.993	0.989	0.993
κ_g (%)	$\pm 2.$	± 1.6	± 1.6	$\pm 1.$
κ_γ (%)	± 1.6	± 1.4	± 1.2	± 0.82
$\kappa_{Z\gamma}$ (%)	$\pm 10.$	$\pm 10. *$	± 5.5	± 3.7
κ_c (%)	–	± 3.7	–	–
κ_t (%)	± 3.2	$\pm 3.2 *$	± 2.6	± 1.6
κ_b (%)	± 2.5	± 1.2	$\pm 2.$	± 1.4
κ_μ (%)	± 4.4	$\pm 4.4 *$	± 2.2	± 1.5
κ_τ (%)	± 1.6	± 1.4	± 1.2	± 0.77
$\text{BR}_{\text{inv}} (< \%, 95\% \text{ CL})$	1.9	1.1	1.8 *	1.5 *
$\text{BR}_{\text{unt}} (< \%, 95\% \text{ CL})$	inferred using constraint $ \kappa_V \leq 1$			
	4.	1.3	3.3	2.4

Table 4. Expected relative precision (%) of the κ parameters in the kappa-3 scenario described in section 2 for the HL-LHC, LHeC, and HE-LHC. A bound on $|\kappa_V| \leq 1$ is applied since no direct access to the Higgs width is possible, thus the uncertainty on κ_W and κ_Z is one-sided. For the remaining kappa parameters one standard deviation is provided in \pm . The corresponding 95%CL upper limit on BR_{inv} is also given. In this kappa-3 scenario BR_{unt} is a floating parameter in the fit, to propagate the effect of an assumed uncertain total width on the measurement of the other κ_i . Based on this constraint the reported values on BR_{unt} are inferred. Cases in which a particular parameter has been fixed to the SM value due to lack of sensitivity are shown with a dash (–). An asterisk (*) indicates the cases in which there is no analysis input in the reference documentation, and HL-LHC dominates the combination. In the case of κ_t sensitivity at the LHeC, note that the framework relies as input on $\mu_{t\bar{t}H}$, and does not take into consideration μ_{tH} . The integrated luminosity and running conditions considered for each collider in this comparison are described in table 1. In the case of HL-LHC and HE-LHC, both the S2 and the S2' uncertainty models [13] are given for comparison.

attempt at a general analysis, it should be noted that light degrees of freedom carrying electroweak quantum numbers seem disfavored, and that the less constrained options involve portal type interactions of the Higgs to SM singlets. Examples in the latter class can involve mixing with a new light CP-even scalar S , or the trilinear couplings to scalar (hS^2) or fermion ($h\bar{\psi}\psi$) bilinears. In these cases, besides the presence of new processes, e.g. the production of a sequential Higgs-like scalar, the effect on single Higgs production and decay are well described by the κ -framework, including the option for an invisible width into new physics states. Heavy new physics can instead be systematically described in the effective Lagrangian approach. This fact, and the richer set of consistent and motivated heavy new physics options, gives particular prominence to the effective Lagrangian approach. One can distinguish two broad classes of heavy new physics depending on the origin of the corresponding mass scale, which we henceforth indicate by Λ . In the first class, Λ is controlled by the Higgs VEV (v) and is expected to be bounded to be less than $4\pi v \sim 3 \text{ TeV}$. The

kappa-3	HL-LHC &									
	ILC ₂₅₀	ILC ₅₀₀	ILC ₁₀₀₀	CLIC ₃₈₀	CLIC ₁₅₀₀	CLIC ₃₀₀₀	CEPC	FCC-ee ₂₄₀	FCC-ee ₃₆₅	FCC-ee/eh/hh
κ_W [%]	1.0	0.29	0.24	0.73	0.40	0.38	0.88	0.88	0.41	0.19
κ_Z [%]	0.29	0.22	0.23	0.44	0.40	0.39	0.18	0.20	0.17	0.16
κ_g [%]	1.4	0.85	0.63	1.5	1.1	0.86	1.	1.2	0.9	0.5
κ_γ [%]	1.4	1.2	1.1	1.4*	1.3	1.2	1.3	1.3	1.3	0.31
$\kappa_{Z\gamma}$ [%]	10.*	10.*	10.*	10.*	8.2	5.7	6.3	10.*	10.*	0.7
κ_e [%]	2.	1.2	0.9	4.1	1.9	1.4	2.	1.5	1.3	0.96
κ_t [%]	3.1	2.8	1.4	3.2	2.1	2.1	3.1	3.1	3.1	0.96
κ_b [%]	1.1	0.56	0.47	1.2	0.61	0.53	0.92	1.	0.64	0.48
κ_μ [%]	4.2	3.9	3.6	4.4*	4.1	3.5	3.9	4.	3.9	0.43
κ_τ [%]	1.1	0.64	0.54	1.4	1.0	0.82	0.91	0.94	0.66	0.46
BR _{inv} (<%, 95% CL)	0.26	0.23	0.22	0.63	0.62	0.62	0.27	0.22	0.19	0.024
BR _{unt} (<%, 95% CL)	1.8	1.4	1.4	2.7	2.4	2.4	1.1	1.2	1.	1.

Table 5. Expected relative precision (%) of the κ parameters in the kappa-3 (combined with HL-LHC) scenario described in section 2 for future accelerators beyond the LHC era. The corresponding 95%CL upper limits on BR_{unt} and BR_{inv} and the derived constraint on the Higgs width (in %) are also given. No requirement on κ_V is applied in the combination with HL-LHC, since the lepton colliders provide the necessary access to the Higgs width. Cases in which a particular parameter has been fixed to the SM value due to lack of sensitivity are shown with a dash (-). An asterisk (*) indicates the cases in which there is no analysis input in the reference documentation, and HL-LHC dominates the combination. The integrated luminosity and running conditions considered for each collider in this comparison are described in table 1. FCC-ee/eh/hh corresponds to the combined performance of FCC-ee₂₄₀+FCC-ee₃₆₅, FCC-eh and FCC-hh.

effective Lagrangian corresponds here to the so-called Higgs-EFT, which cannot be written as a polynomial expansion in gauge invariant operators [27, 28]. In this scenario, which is in this respect analogous to Technicolor, deviations in Higgs couplings and EWPT are expected to exceed their present bounds, unless the new physics effect can be tuned to be small for each and every coupling, which makes it rather implausible. In the second class, basically including all the more plausible scenarios, Λ is not controlled by the Higgs VEV, and can virtually be arbitrarily large. In that case the effective Lagrangian corresponds to the so-called SMEFT. It is polynomial in gauge invariant operators and organised as an expansion in inverse powers of Λ :

$$\mathcal{L}_{\text{Eff}} = \mathcal{L}_{\text{SM}} + \frac{1}{\Lambda}\mathcal{L}_5 + \frac{1}{\Lambda^2}\mathcal{L}_6 + \frac{1}{\Lambda^3}\mathcal{L}_7 + \frac{1}{\Lambda^4}\mathcal{L}_8 + \dots, \quad \mathcal{L}_d = \sum_i c_i^{(d)} \mathcal{O}_i^{(d)}. \quad (3.5)$$

In the previous equation, each $\mathcal{O}_i^{(d)}$ is a local $SU(3)_c \times SU(2)_L \times U(1)_Y$ -invariant operator of canonical mass dimension d , built using only fields from the light particle spectrum. Moreover, \mathcal{L}_{SM} represents the renormalizable SM Lagrangian that nicely complies with basically all the measurements made so far in particle physics, with the exception of the tiny neutrino masses, which are however nicely described by the next term, \mathcal{L}_5 . The contribution of the higher order terms $\mathcal{L}_{d \geq 5}$ to physical amplitudes is suppressed by $(E/\Lambda)^{d-4}$, where E is the relevant energy scale of the process. The *Wilson coefficients* $c_i^{(d)}$ encode the virtual effects of the heavy new physics in low-energy observables. Their precise form in terms of masses and couplings of the new particles can be obtained via *matching* with an ultraviolet (UV) completion of the SM [29], or inferred using *power-counting* rules [30, 31].

The success of \mathcal{L}_{SM} in explaining the data indicates that either the scale of new physics Λ is large, or that the structure of the terms $\mathcal{L}_{d \geq 5}$ is particularly elaborate, or perhaps a combination of both. Moreover it is important to stress that in general we expect new physics at multiple and even widely separated scales, and that the parametrization in terms of a single scale Λ is a simplification. It is however clear that given the good but limited precision of future high energy experiments only the lowest scale is expected to matter. In particular, given the observed suppression of lepton and baryon number violation, the operators mediating such violation, which appear already in \mathcal{L}_5 and \mathcal{L}_6 , must be further suppressed if Λ is as low as to be interesting in collider physics. That suppression could be due to approximate symmetries or simply because the dynamics generating these processes is $\gg \Lambda$. The same remarks apply to flavour and CP violation.

Assuming lepton and baryon numbers are conserved independently, all relevant operators in the previous expansion are of even dimension. Therefore new physics effects start at dimension $d = 6$. In this report we work under the assumption that Λ is large enough for $d = 6$ to dominate over $d \geq 8$ (but see comment below) and restrict our studies to the effective Lagrangian truncated part $d = 6$. The resulting Lagrangian is that of the so-called dimension-6 Standard Model Effective Field Theory (SMEFT). In a bottom-up approach, one can write a complete basis for the dimension-6 SMEFT Lagrangian using a total of 59 types of operators [32], for a total of 2499 taking into account flavour indices [33]. For most of the calculations presented in this report we use the dimension-six basis first presented

in [32], the so-called *Warsaw basis*, with minor modifications.⁵ In the discussion presented in this section, however, we will use a different parameterization, which is usually deemed to be more transparent from the point of view of Higgs physics.

One must notice that in any realistic situation there will be structure in the coefficients of the 2499 operators of dimension 6. For instance, if they were a set of structureless $O(1)$ numbers, then the experimental constraints from flavour and/or CP violation on Λ would already be much stronger than from any foreseeable study of Higgs and EW processes. Moreover in realistic situations we should also expect structure in the coefficients of flavour preserving operators. In other words some coefficients may be significantly smaller than others. This remark, together with a sensitivity limited to Λ 's that are not very much above the energy of the processes, implies that it may in principle happen that operators of dimension 8 are equally or more important than the dimension 6 operators. We shall later mention a natural example of this phenomenon. In structured scenarios like the SILH [30], it is easy to address this caveat, also thanks to the fact that the operators that matter in \mathcal{L}_6 are much fewer than in the general case (even after imposing flavour violation). The message here is that the reduction to pure dimension 6, with full neglect of dimension 8, while reasonable and useful, contains nonetheless an assumption which may not be universally true for all observables even in simple motivated models.

When considering Higgs data, one can reasonably focus on a relatively small subset of the 2499 operators in \mathcal{L}_6 . In particular the vast subset of 4-fermion operators, whether flavour and CP preserving or not, can be more strongly constrained by other processes. Thus, it makes sense to neglect this whole class, with the exception of one particular four-fermion interaction that contributes to the muon decay and thus directly affects the Fermi constant, see caption in table 6. The dipole operators, instead do directly affect Higgs production, however under very general and plausible assumptions on the flavour structure of new physics, the coefficients of these operators display the same structure and the same chiral suppression of Yukawa couplings. The consequence is that, with the possible exception of processes involving the top quark, their effect in Higgs production is expected to be negligible given that the leading SM contribution (for instance in $e^+e^- \rightarrow ZH$) as well as the other new physics effects are not chirally suppressed. Furthermore, as far as Higgs decays are concerned, the dipole operators only contribute to three (or more)-body final states (for instance $H \rightarrow \bar{b}b\gamma$) and as such they are easily seen to be negligible. In what follows we shall thus neglect this whole class, and leave the consideration of their effect in top sector to future studies. Eliminating these two classes, there remain three other classes: 1) purely bosonic operators, 2) generalized Yukawas, 3) Higgs-fermion current operators. Neglecting CP violating operators in class 1, the corresponding structures are shown in table 6. Operators in class 2 and 3, per se, can still contain CP- or flavour-violating terms, on which experimental constraints are rather strong. In order to proceed we shall consider two alternative scenarios to minimize the remaining flavour and/or CP violations:

⁵By using a perturbative field redefinition we trade the operators $\mathcal{O}_{\phi WB}$ and $\mathcal{O}_{\phi D}$ in ref. [32] for the operators $iD^\mu \phi^\dagger \sigma_a D^\nu \phi W_{\mu\nu}^a$ and $iD^\mu \phi^\dagger D^\nu \phi B_{\mu\nu}$.

1. *Flavour Universality*, corresponding to

$$Y_u^{(6)} \propto Y_u, \quad Y_d^{(6)} \propto Y_d, \quad Y_e^{(6)} \propto Y_e, \quad \text{and} \quad \Delta_{ij}^{q,u,d,l,e,ud}, \Delta_{ij}^{lq}, \propto \delta_{ij}, \quad (3.6)$$

where $Y_f^{(6)}$ are the coefficients of dimension-6 operators of class 2, which control the flavour structure of the modifications to the SM Yukawa matrices Y_f . Similarly, Δ^f and Δ'^f represent the combinations of dimension-6 operators of class 3, which induce flavour-dependent modifications of the neutral and charged current couplings of the fermions to the EW vector bosons. In terms of the Wilson coefficients of the operators in table 6 one has $Y_f^{(6)} = c_{f\phi}$ ($f = u, d, e$); $\Delta^f = c_{\phi f}$ for the operators involving the right-handed fermion multiplets ($f = u, d, e, ud$); and $\Delta^f = c_{\phi f}^{(1)}$, $\Delta'^f = c_{\phi f}^{(3)}$ for the left-handed ones ($f = q, l$). The choice in (3.6) corresponds to *Minimal Flavour Violation* (MFV) [34] in the limit where terms only up to linear in the Yukawa matrices are considered. Notice that *Minimal Flavour Violation* corresponds to the assumption that the underlying dynamics respects the maximal flavour symmetry group $SU(3)^5$. A more appropriate name would then perhaps be *Maximal Flavour Conservation*.

2. *Neutral Diagonality*, corresponding to a scenario where $Y_{u,d,e}^{(6)}$ while not proportional to the corresponding Yukawa matrices are nonetheless diagonal in the same basis. That eliminates all flavour-changing couplings to the Higgs boson. Similarly the $\Delta_{ij}^{q,u,d,l,e,ud}$, Δ_{ij}^{lq} , while not universal, are such that no flavour-changing couplings to the Z-boson are generated. In fact we shall work under the specific assumption where flavour universality is respected by the first two quark families, and violated by the third quark family and by leptons. This choice, per se, does not correspond to any motivated or even plausible scenario (it is rather cumbersome to produce sizeable flavour non-universality without any flavour violation). We consider it principally to test the essential constraining power of future machines and because it is widely studied by the community. Moreover non-universality limited to the third quark family is an often recurring feature of scenarios motivated by the hierarchy problem. That is simply because the large top Yukawa makes it intricately involved in the EW symmetry breaking dynamics and calls for the existence of various top partners.

Working in the unitary gauge and performing suitable redefinition of fields and input parameters the effective Lagrangian can be conveniently expressed in the parameterization of [35, 36], the so-called *Higgs basis*. Considering only the terms that are relevant for our analysis, we can identify five classes of terms.⁶

Higgs trilinear:

$$\Delta\mathcal{L}_6^{\text{h,self}} = -\delta\lambda_3 v h^3. \quad (3.7)$$

The impact of this coupling in single Higgs processes and its extraction from Higgs pair production will be discussed in section 4.

⁶In this paper we shall refer to the doublet Higgs field as ϕ . After symmetry breaking the field for the Higgs boson will be referred to as h . The Higgs particle will be referred to as H .

	Operator	Notation	Operator	Notation	
Class 1	X^3	$\varepsilon_{abc} W_\mu^{a\nu} W_\nu^{b\rho} W_\rho^{c\mu}$	\mathcal{O}_W		
	ϕ^6	$(\phi^\dagger \phi)^3$	\mathcal{O}_ϕ		
	$\phi^4 D^2$	$(\phi^\dagger \phi) \square (\phi^\dagger \phi)$	$\mathcal{O}_{\phi \square}$	$(\phi^\dagger D_\mu \phi) ((D^\mu \phi)^\dagger \phi)$	$\mathcal{O}_{\phi D}$
	$X^2 \phi^2$	$\phi^\dagger \phi B_{\mu\nu} B^{\mu\nu}$	$\mathcal{O}_{\phi B}$	$\phi^\dagger \phi W_{\mu\nu}^a W^{a\mu\nu}$	$\mathcal{O}_{\phi W}$
$\phi^\dagger \sigma_a \phi W_{\mu\nu}^a B^{\mu\nu}$		$\mathcal{O}_{\phi WB}$	$\phi^\dagger \phi G_{\mu\nu}^A G^{A\mu\nu}$	$\mathcal{O}_{\phi G}$	
Class 2	$\psi^2 \phi^2$	$(\phi^\dagger \phi) (\bar{l}_L^i \phi e_R^j)$	$(\mathcal{O}_{e\phi})_{ij}$		
		$(\phi^\dagger \phi) (\bar{q}_L^i \phi d_R^j)$	$(\mathcal{O}_{d\phi})_{ij}$	$(\phi^\dagger \phi) (\bar{q}_L^i \tilde{\phi} u_R^j)$	$(\mathcal{O}_{u\phi})_{ij}$
Class 3	$\psi^2 \phi^2 D$	$(\phi^\dagger i \overleftrightarrow{D}_\mu \phi) (\bar{l}_L^i \gamma^\mu l_L^j)$	$(\mathcal{O}_{\phi l}^{(1)})_{ij}$	$(\phi^\dagger i \overleftrightarrow{D}_\mu^a \phi) (\bar{l}_L^i \gamma^\mu \sigma_a l_L^j)$	$(\mathcal{O}_{\phi l}^{(3)})_{ij}$
		$(\phi^\dagger i \overleftrightarrow{D}_\mu \phi) (\bar{e}_R^i \gamma^\mu e_R^j)$	$(\mathcal{O}_{\phi e})_{ij}$		
		$(\phi^\dagger i \overleftrightarrow{D}_\mu \phi) (\bar{q}_L^i \gamma^\mu q_L^j)$	$(\mathcal{O}_{\phi q}^{(1)})_{ij}$	$(\phi^\dagger i \overleftrightarrow{D}_\mu^a \phi) (\bar{q}_L^i \gamma^\mu \sigma_a q_L^j)$	$(\mathcal{O}_{\phi q}^{(3)})_{ij}$
		$(\phi^\dagger i \overleftrightarrow{D}_\mu \phi) (\bar{u}_R^i \gamma^\mu u_R^j)$	$(\mathcal{O}_{\phi u})_{ij}$	$(\phi^\dagger i \overleftrightarrow{D}_\mu \phi) (\bar{d}_R^i \gamma^\mu d_R^j)$	$(\mathcal{O}_{\phi d})_{ij}$
		$(\tilde{\phi}^\dagger i D_\mu \phi) (\bar{u}_R^i \gamma^\mu d_R^j)$	$(\mathcal{O}_{\phi ud})_{ij}$		

Table 6. Dimension six operators considered in the SMEFT analysis. The hermitian derivatives \overleftrightarrow{D} and \overleftrightarrow{D}^a are defined as: $\overleftrightarrow{D}_\mu \equiv \overrightarrow{D}_\mu - \overleftarrow{D}_\mu$ and $\overleftrightarrow{D}_\mu^a \equiv \sigma_a \overrightarrow{D}_\mu - \overleftarrow{D}_\mu \sigma_a$, while $B_{\mu\nu}$, $W_{\mu\nu}^a$ and $G_{\mu\nu}^A$ denote the SM gauge boson field-strengths. See text for details. Apart from these, the effects of the four-lepton operator $(\mathcal{O}_{ll})_{1221} = (\bar{l}_1 \gamma_\mu l_2) (\bar{l}_2 \gamma^\mu l_1)$, which modifies the prediction for the muon decay amplitude, must also be included in the fit since we use the Fermi constant as one of the SM input parameters.

Higgs couplings to vector bosons:

$$\begin{aligned}
 \Delta \mathcal{L}_6^{\text{hVV}} = & \frac{h}{v} \left[2\delta c_w m_W^2 W_\mu^+ W_\mu^- + \delta c_z m_Z^2 Z_\mu Z_\mu \right. \\
 & + c_{ww} \frac{g^2}{2} W_{\mu\nu}^+ W_{\mu\nu}^- + c_{w\square} g^2 (W_\mu^- \partial_\nu W_{\mu\nu}^+ + \text{h.c.}) \\
 & + c_{gg} \frac{g_s^2}{4} G_{\mu\nu}^a G_{\mu\nu}^a + c_{\gamma\gamma} \frac{e^2}{4} A_{\mu\nu} A_{\mu\nu} + c_{z\gamma} \frac{e\sqrt{g^2 + g'^2}}{2} Z_{\mu\nu} A_{\mu\nu} \\
 & \left. + c_{zz} \frac{g^2 + g'^2}{4} Z_{\mu\nu} Z_{\mu\nu} + c_{z\square} g^2 Z_\mu \partial_\nu Z_{\mu\nu} + c_{\gamma\square} g g' Z_\mu \partial_\nu A_{\mu\nu} \right], \quad (3.8)
 \end{aligned}$$

where only c_{gg} , δc_z , $c_{\gamma\gamma}$, $c_{z\gamma}$, c_{zz} , $c_{z\square}$ are independent parameters:

$$\begin{aligned}
 \delta c_w &= \delta c_z + 4\delta m, \\
 c_{ww} &= c_{zz} + 2 \sin^2 \theta_w c_{z\gamma} + \sin^4 \theta_w c_{\gamma\gamma}, \\
 c_{w\square} &= \frac{1}{g^2 - g'^2} [g^2 c_{z\square} + g'^2 c_{zz} - e^2 \sin^2 \theta_w c_{\gamma\gamma} - (g^2 - g'^2) \sin^2 \theta_w c_{z\gamma}], \\
 c_{\gamma\square} &= \frac{1}{g^2 - g'^2} [2g^2 c_{z\square} + (g^2 + g'^2) c_{zz} - e^2 c_{\gamma\gamma} - (g^2 - g'^2) c_{z\gamma}], \quad (3.9)
 \end{aligned}$$

where θ_w denotes the weak mixing angle while δm is an independent parameter from \mathcal{L}_6 controlling the deviation of m_W^2 with respect to its tree level SM value.

Trilinear gauge couplings:

$$\begin{aligned} \Delta\mathcal{L}^{\text{aTGC}} &= ie\delta\kappa_\gamma A^{\mu\nu}W_\mu^+W_\nu^- \\ &+ ig \cos\theta_w \left[\delta g_{1Z} (W_{\mu\nu}^+W^{-\mu} - W_{\mu\nu}^-W^{+\mu})Z^\nu + \left(\delta g_{1Z} - \frac{g'^2}{g^2}\delta\kappa_\gamma \right) Z^{\mu\nu}W_\mu^+W_\nu^- \right] \\ &+ \frac{ig\lambda_z}{m_W^2} (\sin\theta_w W_\mu^{+\nu}W_\nu^{-\rho}A_\rho^\mu + \cos\theta_w W_\mu^{+\nu}W_\nu^{-\rho}Z_\rho^\mu), \end{aligned} \quad (3.10)$$

where of the three coefficients $g_{1,z}$ and $\delta\kappa_\gamma$ depend on $c_{gg}, \delta c_z, c_{\gamma\gamma}, c_{z\gamma}, c_{zz}, c_{z\Box}$:

$$\begin{aligned} \delta g_{1,z} &= \frac{1}{2}(g^2 - g'^2) [c_{\gamma\gamma}e^2g'^2 + c_{z\gamma}(g^2 - g'^2)g'^2 - c_{zz}(g^2 + g'^2)g'^2 - c_{z\Box}(g^2 + g'^2)g^2], \\ \delta\kappa_\gamma &= -\frac{g^2}{2} \left(c_{\gamma\gamma}\frac{e^2}{g^2 + g'^2} + c_{z\gamma}\frac{g^2 - g'^2}{g^2 + g'^2} - c_{zz} \right), \end{aligned} \quad (3.11)$$

while λ_z is an independent parameter.

Yukawa couplings:

$$\Delta\mathcal{L}_6^{\text{hff}} = -\frac{h}{v} \sum_{f \in u,d,e} \hat{\delta}y_f m_f \bar{f}f + \text{h.c.}, \quad (3.12)$$

where $\hat{\delta}y_f m_f$ should be thought as 3×3 matrices in flavour space. FCNC are avoided when $\hat{\delta}y_f$ is diagonal in the same basis as m_f . Under the assumption of *Flavour Universality* ($\hat{\delta}y_f)_{ij} \equiv \delta y_f \times \delta_{ij}$, corresponding to a total of three parameters $\delta y_u, \delta y_d, \delta y_e$. The assumption of *Neutral Diagonality* corresponds instead to $(\hat{\delta}y_f)_{ij} \equiv \delta(y_f)_i \times \delta_{ij}$ (no summation) corresponding to 9 parameters $\delta_u, \delta_c, \delta_t$ for the ups and similarly for downs and charged leptons. In practice only $\delta_{t,c}, \delta_b$ and $\delta_{\tau,\mu}$ are expected to matter in plausible models and in the experimental situations presented by all future colliders. This adds two parameters with respect to *Flavour Universality*.

Vector couplings to fermions:

$$\begin{aligned} \Delta\mathcal{L}_6^{vff,hvff} &= \frac{g}{\sqrt{2}} \left(1 + 2\frac{h}{v} \right) W_\mu^+ \left(\hat{\delta}g_L^{W\ell} \bar{\nu}_L \gamma^\mu e_L + \hat{\delta}g_L^{Wq} \bar{u}_L \gamma^\mu d_L + \hat{\delta}g_R^{Wq} \bar{u}_R \gamma^\mu d_R + \text{h.c.} \right) \\ &+ \sqrt{g^2 + g'^2} \left(1 + 2\frac{h}{v} \right) Z_\mu \left[\sum_{f=u,d,e,\nu} \hat{\delta}g_L^{Zf} \bar{f}_L \gamma^\mu f_L + \sum_{f=u,d,e} \hat{\delta}g_R^{Zf} \bar{f}_R \gamma^\mu f_R \right] \end{aligned} \quad (3.13)$$

where, again, not all terms are independent:⁷

$$\hat{\delta}g_L^{W\ell} = \hat{\delta}g_L^{Z\nu} - \hat{\delta}g_L^{Ze}, \quad \hat{\delta}g_L^{Wq} = \hat{\delta}g_L^{Zu} V_{CKM} - V_{CKM} \hat{\delta}g_L^{Zd}. \quad (3.14)$$

⁷Here we choose a slightly different convention for the dependent couplings with respect to [35, 36], and we express everything in terms of the modifications of the neutral currents.

In the case of *Flavour Universality*, all the $\hat{\delta}g$ are proportional to the identity corresponding to a total of 8 parameters: $(\hat{\delta}g_L^{Zu})_{ij} \equiv \delta g_L^{Zu} \times \delta_{ij}$, etc. However the right handed charged current, associated with $\hat{\delta}g_R^{Wq}$ does not interfere with the SM amplitudes in the limit $m_q \rightarrow 0$ and can be neglected, reducing the number of parameters to 7.

In the case of *Neutral Diagonality*, the assumption $\hat{\delta}g_{ij} \propto \delta_{ij}$ is relaxed, allowing for the four coefficients associated with the third quark family $(\hat{\delta}g_L^{Zu})_{33}, (\hat{\delta}g_L^{Zd})_{33}, (\hat{\delta}g_R^{Zu})_{33}, (\hat{\delta}g_R^{Zd})_{33}$ as well as all diagonal coefficients associated with leptons to be different. This adds 10 further parameters with respect to the flavour Universal case.

In conclusion considering single Higgs and EW processes (i.e. neglecting the Higgs trilinear) in the scenarios of *Flavour Universality* and *Neutral Diagonality* we end up with respectively 18 and 30 independent parameters:⁸

$$\begin{aligned} \text{SMEFT}_{\text{FU}} \equiv & \{ \delta m, c_{gg}, \delta c_z, c_{\gamma\gamma}, c_{z\gamma}, c_{zz}, c_{z\Box}, \delta y_u, \delta y_d, \delta y_e, \lambda_z \} \\ & + \left\{ \delta g_L^{Zu}, \delta g_L^{Zd}, \delta g_L^{Z\nu}, \delta g_L^{Ze}, \delta g_R^{Zu}, \delta g_R^{Zd}, \delta g_R^{Ze} \right\}, \end{aligned} \quad (3.15)$$

$$\begin{aligned} \text{SMEFT}_{\text{ND}} \equiv & \{ \delta m, c_{gg}, \delta c_z, c_{\gamma\gamma}, c_{z\gamma}, c_{zz}, c_{z\Box}, \delta y_t, \delta y_c, \delta y_b, \delta y_\tau, \delta y_\mu, \lambda_z \} \\ & + \left\{ (\delta g_L^{Zu})_{q_i}, (\delta g_L^{Zd})_{q_i}, (\delta g_L^{Z\nu})_\ell, (\delta g_L^{Ze})_\ell, (\delta g_R^{Zu})_{q_i}, (\delta g_R^{Zd})_{q_i}, (\delta g_R^{Ze})_\ell \right\}_{\substack{q_1=q_2 \neq q_3, \\ \ell=e,\mu,\tau}}. \end{aligned} \quad (3.16)$$

While we have chosen to present the degrees of freedom used in the different fitting scenarios described above using the parameterization of the Higgs basis, one can of course do the same in any other basis. In particular, the mapping between the Higgs basis parameters in the previous Lagrangians and the Wilson coefficients in other popular dimension-6 bases in the literature can be found in section 3 and appendices A and B in [35].

The previous two scenarios will be used to study the sensitivity at future colliders to general departures from the SM in the global fit to EW precision observables (EWPO), Higgs boson rates and diboson production. We will, however, also consider another more simplified scenario, designed exclusively to study (1) the interplay between the EW and Higgs constraints, and (2) the impact of the SM theory uncertainties in Higgs boson processes. The impact of the EW precision constraints on Higgs boson measurements will be illustrated comparing the results of the fit in the SMEFT_{ND} scenario, with the analogous ones assuming the electroweak precision observables are known with infinite accuracy, both from experiment and theory. We will refer to this idealized case as a scenario with *perfect EW* constraints. In practice, this means that any new physics contributions to the EWPO are bounded to be exactly zero. This includes all possible corrections to the Vff vertices as well as any possible modification to the W mass, i.e.

$$\left\{ \delta m, (\delta g_L^{Zu})_{q_i}, (\delta g_L^{Zd})_{q_i}, (\delta g_L^{Z\nu})_\ell, (\delta g_L^{Ze})_\ell, (\delta g_R^{Zu})_{q_i}, (\delta g_R^{Zd})_{q_i}, (\delta g_R^{Ze})_\ell \right\} \equiv 0. \quad (3.17)$$

As also mentioned above, in this scenario it is also implicit that the SM theory uncertainties on EWPO are negligible, which makes it suitable to isolate the effect of the SM theory

⁸The impact at NLO of the relatively poorly constrained Higgs self-coupling on the determination of the single-Higgs couplings will be discussed in section 4.

uncertainties in Higgs processes in the fit. Imposing the previous constraints in eq. (3.16) we are thus left with a total of 12 parameters for this scenario assuming *perfect EW* constraints:

$$\text{SMEFT}_{\text{PEW}} \equiv \{ c_{gg}, \delta c_z, c_{\gamma\gamma}, c_{z\gamma}, c_{zz}, c_{z\Box}, \delta y_t, \delta y_c, \delta y_b, \delta y_\tau, \delta y_\mu, \lambda_z \}. \quad (3.18)$$

Finally, while the setup described above aims at some generality, it makes sense to add some perspective on the nature of the UV theory and to frame the EFT results in terms of particularly well-motivated scenarios. Understandably, heavy new physics is more visible in low energy observables the more strongly it is coupled. In this respect models with a Composite Higgs (CH) are the natural arena in which to perform indirect studies of new physics. The basic idea of CH models is that all the degrees of freedom of the SM apart from the Higgs are elementary. The Higgs instead arises as a bound state from a strong dynamics. In the simplest possible situation such dynamics is roughly described by two parameters, the overall mass scale and its overall coupling strength, respectively m_* and g_* . The prototypical template for such a two-parameter description is offered by large N gauge theories, which are characterized by the overall mass of their resonances (m_*) and by their mutual coupling $g_* \sim 4\pi/\sqrt{N}$. Concrete and largely calculable realizations of the scenario have been constructed in the context of warped compactifications and of their holographic interpretation, for reviews see e.g. [37, 38] (there are also attempts to build explicit composite models in 4D, see e.g. [39, 40]). Of course, as in all matters, it is easy to imagine more elaborate situations, but at the very least the minimal case can provide a first perspective on future machines. Indeed a more interesting variation concerns the top quark, which in motivated scenarios can become partially and even fully composite. Under the assumptions described in [30, 31], the low energy signatures of these kind of models can be parameterized in terms of the following effective Lagrangian:

$$\begin{aligned} \mathcal{L}_{\text{SILH}} = & \frac{c_\phi}{\Lambda^2} \frac{1}{2} \partial_\mu (\phi^\dagger \phi) \partial^\mu (\phi^\dagger \phi) + \frac{c_T}{\Lambda^2} \frac{1}{2} (\phi^\dagger \overleftrightarrow{D}_\mu \phi) (\phi^\dagger \overleftrightarrow{D}^\mu \phi) - \frac{c_6}{\Lambda^2} \lambda (\phi^\dagger \phi)^3 \\ & + \left(\frac{c_{y_f}}{\Lambda^2} y_{ij}^f \phi^\dagger \phi \bar{\psi}_{Li} \phi \psi_{Rj} + \text{h.c.} \right) \\ & + \frac{c_W}{\Lambda^2} \frac{ig}{2} \left(\phi^\dagger \overleftrightarrow{D}_\mu^a \phi \right) D_\nu W^{a\mu\nu} + \frac{c_B}{\Lambda^2} \frac{ig'}{2} \left(\phi^\dagger \overleftrightarrow{D}_\mu \phi \right) \partial_\nu B^{\mu\nu} \\ & + \frac{c_{\phi W}}{\Lambda^2} ig D_\mu \phi^\dagger \sigma_a D_\nu \phi W^{a\mu\nu} + \frac{c_{\phi B}}{\Lambda^2} ig' D_\mu \phi^\dagger \sigma_a D_\nu \phi B^{\mu\nu} \\ & + \frac{c_\gamma}{\Lambda^2} g'^2 \phi^\dagger \phi B^{\mu\nu} B_{\mu\nu} + \frac{c_g}{\Lambda^2} g_s^2 \phi^\dagger \phi G^{A\mu\nu} G_{\mu\nu}^A - \frac{c_{2W}}{\Lambda^2} \frac{g^2}{2} (D^\mu W_{\mu\nu}^a) (D_\rho W^{a\rho\nu}) \\ & - \frac{c_{2B}}{\Lambda^2} \frac{g'^2}{2} (\partial^\mu B_{\mu\nu}) (\partial_\rho B^{\rho\nu}) - \frac{c_{2G}}{\Lambda^2} \frac{g_s^2}{2} (D^\mu G_{\mu\nu}^A) (D_\rho G^{A\rho\nu}) \\ & + \frac{c_{3W}}{\Lambda^2} g^3 \varepsilon_{abc} W_\mu^a \nu W_\nu^b \rho W_\rho^c \mu + \frac{c_{3G}}{\Lambda^2} g_s^3 f_{ABC} G_\mu^A \nu G_\nu^B \rho G_\rho^C \mu, \end{aligned} \quad (3.19)$$

where the different Wilson coefficients can be written in terms of the couplings and masses of the resonances, denoted in short by $g_* \lesssim 4\pi$ and m_* , as

$$\begin{aligned} \frac{c_{\phi,6,y_f}}{\Lambda^2} & \sim \frac{g_*^2}{m_*^2} \equiv \frac{1}{f^2}, & \frac{c_T}{\Lambda^2} & \sim \frac{y_t^4}{16\pi^2 m_*^2}, \\ \frac{c_{W,B,\phi W,\phi B,\gamma,g}}{\Lambda^2} & \sim \frac{1}{m_*^2}, & \frac{c_{2W,2B,2G,3W,3G}}{\Lambda^2} & \sim \frac{1}{g_*^2} \frac{1}{m_*^2}, \end{aligned} \quad (3.20)$$

up to $O(1)$ factors. The expression for c_T has been derived under the most favorable hypothesis where the new physics preserves custodial symmetry. Note also that, for the relevant case of a pseudo-Nambu-Goldstone-boson (pNGB) Higgs, $c_{g,\gamma}$ benefit from a further suppression $\sim y_t^2/16\pi^2$. Moreover, in explicit constructions based on warped compactifications $c_{\phi W, \phi B, 3W, 3G}$ arise at “loop level” and have a further suppression $\sim g_*^2/16\pi^2$, which of course matters only when g_* is not maximally strong.

A few remarks concerning the above effective Lagrangian are in order. First, notice that the only effects enhanced by the strong coupling g_* are those on the first line and involving non linearities in the Higgs field. That is not surprising given that in CH, the Higgs itself is strongly interacting while the other SM degrees of freedom are not. In view of that, see discussion in section 8.3, in CH the measurements of Higgs couplings compete very well with much more precise measurements, like EWPT, which are not directly zooming in on the strongly coupled nature of the Higgs boson. Second, notice that in CH the whole set $\psi^2\phi^2D$ is subdominant and neglected in lowest approximation. However, the operator basis used above, which is the one naturally dictated by the structure of the model, is not precisely the one we used for our global analysis. In particular, the operators associated with $c_{2W, 2B, 2G}$ can be turned, by a field redefinition, into a particular combination of 4-fermion operators and one particular and flavour universal combination of the $\psi^2\phi^2D$. Third, the CH models, when considering $gg \rightarrow HH$ at high energy, offer a nice example of dim-8 operators potentially winning over dim-6 ones. Indeed, as mentioned above, when the Higgs is a composite pNGB, the coefficient of the dim-6 operator is further suppressed by a top loop factor $y_t^2/16\pi^2$ [41]. However that is not the case for the dim-8 operator $D_\rho\phi^\dagger D^\rho\phi G_{\mu\nu}^A G^{A\mu\nu}$ which simply comes with coefficient $\sim g_s^2/m_*^4$. One can then easily see that when the experimental accuracy in the measurement of $gg \rightarrow HH$ is worse than $O(y_t^2/16\pi^2)$, the sensitivity on m_* is dominated by the dim-8 operator.

Although the particular structure of the previous Lagrangian is not fully general, it provides a theoretically sound benchmark to interpret the results of our studies from a more BSM-oriented perspective. The contributions from the different SILH Wilson coefficients in the Lagrangian (3.19) to the parameters of the Higgs basis can be found in [35].

3.4 Results from the EFT framework studies

In the previous section we have detailed the counting of the degrees of freedom that enter in the different SMEFT fit scenarios using the so-called Higgs basis. While physical results do not depend on the choice of basis, in some cases a particular basis may be convenient for computational, presentational or interpretational purposes (note that the physical interpretation of each dimension-six operator does depend on the basis). From the point of view of the results presented in this section, however, we are mostly interested in comparing the sensitivity to deformations with respect to the SM in the Higgs couplings at the different future collider projects. To assess these deformations with respect to the SM in a basis-independent way one can *project* the results of the SMEFT fit onto a set of on-shell properties of the Higgs boson, via the following *Higgs effective couplings*:

$$g_{HX}^{\text{eff } 2} \equiv \frac{\Gamma_{H \rightarrow X}}{\Gamma_{H \rightarrow X}^{\text{SM}}}. \tag{3.21}$$

By definition, these quantities, constructed from physical observables, are basis independent. These definitions are also convenient to compare in a straightforward manner the SMEFT results with those of the κ framework for the single Higgs couplings. Such definition is, however, not phenomenologically possible for the top-Higgs coupling and the Higgs self-interaction. For the present report we will sidestep these issues by: (1) defining the effective top coupling in a similar way to all other fermions; (2) to connect and compare with all current studies of the Higgs self-interaction, we will define $g_{HHH} \equiv \lambda_3/\lambda_3^{\text{SM}}$.

Note that, at the dimension-six level and truncating the physical effects at order $1/\Lambda^2$ one can always express the previous effective couplings in terms of the dimension-six operators via a linear transformation. Provided one has a large enough set of such effective couplings, one can then map the effective coupling result into Wilson coefficients, and vice-versa (of course, the former are not a basis per se and the connection is only well-defined at a fixed order in perturbation theory and in the EFT expansion). The single Higgs couplings plus g_{HHH} are however not enough to match the number of free parameters in the SMEFT fits, even in the simplified scenario SMEFT_{PEW} in eq. (3.18). In particular, the on-shell couplings $g_{HZZ,HWW}^{\text{eff}}$ in eq. (3.21) do not capture all possible linear combinations of the different types of EFT interactions contributing to the HZZ and HWW vertices.⁹ For that reason we will also present our results by adding the predictions for the anomalous Triple Gauge Coupling (aTGC), a (pseudo)-observable obtained from the di-boson analysis. These extra parameters offer a measure of the Higgs couplings to gauge bosons with a non-SM Lorentz structure. As long as we restrict the analysis to observables around the Higgs mass scale, this approach with on-shell effective couplings and aTGC is perfectly appropriate. When high-energy observables are considered, like in section 3.4.2, it would have to be revisited. (In that section, however, we will present the results directly in terms of the Wilson coefficients, for easier interpretation in terms of BSM scenarios.) Even after adding the aTGC, in the SMEFT_{PEW} scenario where $\delta m \equiv 0$ the $g_{HZZ,HWW}^{\text{eff}}$ couplings are not independent, and therefore we will present the results reporting only the coupling to Z bosons.

In the global fit scenarios SMEFT_{FU} and SMEFT_{ND}, where we also add those combinations of operators that can contribute to EWPO, extra information needs to be added to illustrate the constraints on the different degrees of freedom included in the fit. Since δm is now a free parameter, we report separately the $g_{HZZ,HWW}^{\text{eff}}$ couplings. Following a similar approach as for the Higgs couplings, one can report the sensitivity to modifications in the effective couplings of the Z to fermions, which can be defined from the Z -pole measurements of the Z decays and asymmetries, e.g.

$$\Gamma_{Z \rightarrow e^+e^-} = \frac{\alpha M_Z}{6 \sin^2 \theta_w \cos^2 \theta_w} (|g_L^e|^2 + |g_R^e|^2), \quad A_e = \frac{|g_L^e|^2 - |g_R^e|^2}{|g_L^e|^2 + |g_R^e|^2}. \quad (3.22)$$

In what follows, we discuss the results of the SMEFT fit from the point of view of the expected sensitivity to modifications of the Higgs couplings in the scenarios SMEFT_{FU} and

⁹We note, however, that, from the point of view of the interpretation in terms of motivated scenarios like those described below eq. (3.20), the contributions to such interactions are dominated only by c_ϕ , unless $g_* \sim g$.

SMEFT_{ND}. As was done in the fits in the κ framework, we will present the results assuming that at future colliders only the SM theory uncertainties associated with the knowledge of the SM input parameters are non-negligible. (As also discussed there, for the HL-LHC and HE-LHC scenarios we always consider the uncertainties adopted by the studies in [13].) The impact of these and other SM theory uncertainties in Higgs processes will be discussed afterwards in section 3.5, using for that purpose the results in the benchmark SMEFT_{PEW}.

3.4.1 SMEFT fit results

The main results of this section are summarised in table 7, where we compare the 68% probability sensitivity to deviations in the Higgs couplings from the global SMEFT fit to Higgs, di-boson and EWPO at future colliders. We show the projections for the fits with and without flavour universality assumptions, given by the scenarios SMEFT_{FU} and SMEFT_{ND}, respectively. Note that the SMEFT_{ND} scenario not only has $g_{Htt}^{\text{eff}} \neq g_{Hcc}^{\text{eff}}$, $g_{H\tau\tau}^{\text{eff}} \neq g_{H\mu\mu}^{\text{eff}}$, but also treats in a family-dependent way the corrections to $Zf\bar{f}$ couplings, which typically leads to less stringent constraints from EWPO. The impact of the EWPO in the fit will be discussed below. The results for the more general scenario SMEFT_{ND} are also shown in figure 3 where we compare the results across colliders. In the lower panel of figure 3 we also show the relative improvement compared to the HL-LHC results. In both table and figure we illustrate the impact of the data taking at different energy stages at each collider. As in the previous sections, we distinguish between the initial energy stage when each collider can start operating as a Higgs factory, and subsequent upgrades to higher energies. In the case of FCC, we also consider the results in combination with the other collider options foreseen as part of the FCC integrated program.

Although in this section we will be mainly interested in the comparison of the sensitivities to modifications of Higgs couplings, for completeness we show in figure 4 and table 8 the results of the remaining degrees of freedom included in the SMEFT_{ND} fit, i.e. the precisions for the corresponding $Zf\bar{f}$ couplings. These are constrained mainly by the future projections for EWPO. In this regard, it must be noted that, unlike most of the Higgs results, where the uncertainties are expected to be controlled by the statistical component, the future projections for EWPO are expected to be dominated, in most cases, by systematic errors. Because of that, the results for the $Zf\bar{f}$ couplings have a significant dependence on what assumptions are made by the different collider projects in terms of these systematics. Whenever large differences between these assumptions were identified, we tried to unify them in order to provide a more coherent comparison. This is the case of the results for heavy flavour measurements of the Z properties ($A_{b,c}$ and $R_{b,c}$), where clearly different assumptions were made in terms of the expected size of future theory uncertainties associated with QCD corrections. These are expected to be collider independent (i.e. apply equally to linear or circular collider) and greatly affect the projections for the heavy flavor asymmetries A_f . Because of this, we chose 2 different scenarios for the systematics applied to these observables. We take as a base scenario one where the systematic uncertainties on the asymmetries are given by the main “collider-dependent” uncertainty quoted by each project. For linear colliders, where A_f are determined from a left-right forward backward asymmetry, this is the uncertainty on the knowledge of the

beam polarization. In absence of polarization, at circular colliders the A_f parameters are derived from an unpolarized forward-backward asymmetry, $A_{FB}^f = \frac{3}{4}A_e A_f$, and therefore are subject to the uncertainty associated to the knowledge of A_e . To illustrate the impact of the QCD uncertainties, in figure 4 we compare the result of this first scenario with a different one, obtained assuming the QCD uncertainties at future lepton colliders will be reduced by a factor of 2 compared to LEP. (The results for this latter scenario are indicated with the red marks in the figure.) In any case, the difference in the results between similar machines must therefore be interpreted with caution. For instance, the final CEPC capabilities from the point of view of the EWPO should not be significantly different than those for FCC-ee, at least regarding those measurement possible below 240 GeV.¹⁰ Finally, the scenarios considered here for linear colliders correspond to the baseline presented by the corresponding projects, which do not foresee a Z -pole run. Some results including that possibility, i.e. the Giga- Z factory, are presented in appendix F.

Focusing our attention on the results for the Higgs couplings, from the results we observe that the LHeC and HE-LHC would help in pushing the knowledge of some of the Higgs couplings close to the 2% level. This may be surprising compared to the results obtained in the κ framework (kappa-0), especially for the LHeC case, where the couplings to W and Z bosons were obtained with slightly below 1% accuracy. This deterioration in the precision of the EFT results is due to the absence of projections for improved measurements of the aTGC. This limits the constraining power on the non-SM tensor structures that are present in the EFT formalism but not in the κ framework. One must also note that the improvement at the HE-LHC S'_2 on the Higgs couplings is mostly dominated by the assumptions on the reduction of theory and systematics with respect to HL-LHC which, as explained in section 2, are reduced by fiat, rather than by a detailed workplan for the reduction of uncertainties. If such hypothesised improvement is not realised, the HE-LHC reach would be, with a few exceptions, not far from the HL-LHC one, as illustrated by the HE-LHC S_2 results in table 7. A future lepton collider could achieve below 1-percent accuracy for several of the g_{HX}^{eff} parameters.

Even at a low energy run, all future lepton colliders can bring the precision of the Higgs coupling to vector bosons to the 0.5% level or below (note also that lepton colliders are the only type of Higgs factory able to provide an absolute normalization for the Higgs couplings, via the measurement of the $e^+e^- \rightarrow ZH$ cross section using the recoil mass method). With similar luminosities collected at 240 GeV, the overall performances of CEPC and the 240 GeV run of FCC-ee are expected to be comparable.¹¹ In particular, both machines would be able to measure the effective HZZ coupling with a precision of $\sim 0.5\%$. After running at 365 GeV and completing the 14 year physics program of the FCC-ee collider¹² the precision of the HZZ coupling would be further reduced to $\sim 0.3\%$,

¹⁰The absence of a run around the $t\bar{t}$ threshold would, however, prevent measuring the top quark mass with increased precision, which is also a key observable in the EWPO analysis.

¹¹The differences between the CEPC and FCC-ee results at 240 GeV are simply due to the details of the available projections from each collider project. In particular, the better sensitivity to the $HZ\gamma$ coupling at CEPC is simply due to the absence of a projections for the $H \rightarrow Z\gamma$ channel at the FCC-ee.

¹²Note that this also includes the runs at the Z pole and WW threshold, which are crucial for the EW precision program. The total run time as Higgs factory is 8 years.

nearly a factor of 2 improvement. This of course could also be achieved at the CEPC, if a similar run at such energies were included in their physics program. For the ILC, running at 250 GeV would bring a precision of $\sim 0.4\%$ for g_{HZZ}^{eff} . This would be pushed down to 0.2% with an increase of the centre-of-mass energy to 500 GeV and after collecting 4 ab^{-1} of data, with a total combined run time of 22 years. A further ILC upgrade to energies of 1 TeV would bring an extra $\sim 30\%$ gain in precision. Finally, the determination of the different Higgs couplings to W and Z bosons obtained from the 380 GeV run of CLIC would be comparable to that of the circular colliders at 240 GeV. As in the ILC case, the CLIC data taken at high-energies would help to reach/surpass the two per-mille accuracy on the Higgs coupling to vector bosons after the 1.5 TeV/3 TeV run, concluding a 23-year program.

Turning our attention to the Higgs couplings to fermions, a similar pattern of improvements can be observed for the couplings to bottom quark and τ lepton. The top quark Yukawa is not directly accessible for lepton colliders running below the ttH threshold. Indeed, below threshold the top quark coupling can only be accessed via its contribution to the SM loop-induced processes, e.g. $H \rightarrow gg$. In the EFT framework, however, these can also receive corrections from new local operators, preventing the extraction of g_{Htt}^{eff} . In these cases, only a minor improvement can be achieved in the SMEFT_{ND} scenario,¹³ due to the more precise determinations of the other couplings involved in the extraction of g_{Htt}^{eff} from the ttH channels at the HL-LHC. The high-energy runs of the lepton machines would give access to the ttH threshold. ILC studies at 500 GeV –included in this study– project a determination of g_{Htt}^{eff} with a precision $\sim 6\text{--}7\%$. This could be significantly improved by running slightly above threshold, at 550 GeV, where due to the increased statistics it would be possible to access the same coupling at the 3% level [3]. Similar precision is projected for the CLIC run at 1500 GeV. Note that in order to take full advantage of these studies it is necessary to also have an adequate determination of the $Zt\bar{t}$ couplings. These also contribute to the ttH process and are not precisely constrained by current data. Here we use the results from [42] for ILC at 500 GeV and from [3, 43] for CLIC. In any case, these projected uncertainties for g_{Htt}^{eff} would still be similar to the one from the HL-LHC determination of the top Yukawa coupling. Only the FCC project would be able to surpass that precision on its own, after including in the picture the measurements possible at the 100 TeV pp collider. The improvement in this case comes from the measurement of the ttH/ttZ cross sections, which then also relies on a precise measurement of the $Zt\bar{t}$ coupling. For the FCC this would come from the FCC-ee run at 365 GeV [44]. It should be recalled that in all these studies of the ttH or ttZ processes, both at hadron and lepton colliders, we are making explicit use of the assumption that other interactions such as four-fermion or dipole operators can be neglected. A fully global analysis of these processes has to include those operators as well, including the corresponding constraints.

Finally, even after the full physics program of any of the future leptonic machines, there are several couplings whose precision are still above the one percent threshold, mainly those

¹³We remind that in the SMEFT_{FU} scenario, the corrections to the Yukawa interactions of the different fermion families are universal. Therefore, in that scenario, the apparent improvement on the top coupling is in most instances directly linked to the percent level precision of the measurement of the coupling to charm quarks.

associated to rare decays and that are statistically limited. Only a future lepton collider combined with a high-luminosity hadron machine like the FCC-hh would be able to bring down all the main Higgs couplings below 1%, as can be seen in the last column in table 7. In this regard, we also note the role of the FCC-eh measurements, which would help to further increase the precision in the determination of the couplings to vector bosons and b quarks, after the completion of the FCC-ee program.

A comparison between the results of the global fit with those obtained assuming perfect EW measurements –scenario SMEFT_{PEW}– illustrates the relative importance of the EWPO in the extraction of the different Higgs couplings from the global fit [45]. Figure 5 compares the two results for the future Higgs factories at lepton colliders. For what concerns the Higgs couplings, in most cases the impact is quite mild and, in the case of FCC-ee and CEPC, almost nonexistent due to the rich program for measuring the EWPO at the Z pole and above. The default analysis presented in this report includes the preliminary studies of the radiative return process $e^+e^- \rightarrow Z\gamma$ at 250 GeV (380 GeV) with polarized beams at ILC (CLIC). The results are also shown for the case when a Giga- Z run is also included, with on 100 fb^{-1} of data at $\sqrt{s} \sim m_Z$. It is seen that for ILC and CLIC₃₈₀ there is a clear degradation of the uncertainty on the g_{HVV} without the Giga- Z run, which is largely reduced by a dedicated Giga- Z run [3, 4, 11] since the uncertainties on the fermion asymmetries and partial width ratios are reduced by a factor of ~ 10 (see table 27). For these W and Z couplings, such loss of precision can also be minimized by including the information from a high-energy run, as can be seen for CLIC₃₀₀₀, where there is little impact on the precision of the same HVV effective couplings. However, for the aTGC parameters δg_{1Z} and $\delta\kappa_\gamma$, there is still a substantial degradation compared to perfect knowledge of the EWPO values. A significant improvement in the measurements of the electron EW interactions is therefore still needed, if one wants to extract the maximum precision across all the different couplings at e^+e^- colliders [45].

One must take into account that, with the set of projections available from each future collider project, the global fit results presented here are, in some cases, not entirely consistent, due to some approximations present in the projections for $e^+e^- \rightarrow W^+W^-$. Indeed, these are typically reported in terms of the precision on the aTGC but, except for the CLIC studies presented in [46], they are obtained assuming that new physics can only modify δg_{1Z} , $\delta\kappa_\gamma$ and λ_Z , but not the other couplings involved in the production or decays of the WW pairs.¹⁴ This explains the large difference for those parameters in the CLIC results between the global fit and the ones computed under the assumption of perfect EW measurements, see figure 5. The *aTGC dominance* assumption was a good approximation at LEP2, due to the comparatively more precise constraints from the Z -pole measurements at LEP/SLD, but is something to be tested at future colliders, especially for those projects where a run at the Z -pole will not happen. In those cases, the results presented here must therefore be interpreted with caution [45].

¹⁴For the ILC studies [3, 18, 47] part of this dependence is taken into account, adding those contributions from dimension-6 operator coefficients that are enhanced by a factor $s/2m_W^2$. This approximation, justified in the high-energy limit, may not be a good assumption for the ILC run at 250 GeV, but should work well for the aTGC projections at 500 GeV. (These were not available in [3] and we take them from [18].)

	Benchmark	HL-LHC	LHeC	HE-LHC		ILC			HL-LHC + CLIC			CEPC		FCC-ee		FCC-ee/eh/hh
				S_2	S'_2	250	500	1000	380	1500	3000	240	365			
$g_{HZZ}^{\text{eff}} [\%]$	SMEFT _{FU} SMEFT _{ND}	3.2 3.6	1.9 2.1	2.8 3.2	2.4 2.8	0.37 0.39	0.21 0.22	0.16 0.16	0.48 0.5	0.2 0.2	0.16 0.16	0.44 0.45	0.47 0.47	0.26 0.26	0.13 0.13	
$g_{HWW}^{\text{eff}} [\%]$	SMEFT _{FU} SMEFT _{ND}	2.9 3.2	1.6 1.8	2.5 2.8	2.1 2.4	0.38 0.41	0.22 0.22	0.17 0.17	0.49 0.5	0.19 0.19	0.15 0.15	0.42 0.43	0.45 0.46	0.27 0.27	0.13 0.13	
$g_{H\gamma\gamma}^{\text{eff}} [\%]$	SMEFT _{FU} SMEFT _{ND}	3.3 3.6	2. 2.2	2.8 3.1	2.3 2.6	1.3 1.3	1.2 1.2	1.1 1.1	1.4 1.4	1.3 1.3	1.1 1.1	1.3 1.3	1.3 1.3	1.2 1.2	0.33 0.34	
$g_{Hgg}^{\text{eff}} [\%]$	SMEFT _{FU} SMEFT _{ND}	11. 11.	10. 10.	6.1 6.3	4.2 4.5	8.8 9.6	6.8 6.8	6.6 6.7	9.6 9.7	4.6 4.6	3.6 3.7	6.2 6.3	9.9 9.8	9.3 9.3	0.66 0.7	
$g_{H\tau\tau}^{\text{eff}} [\%]$	SMEFT _{FU} SMEFT _{ND}	2.3 2.3	1.6 1.6	1.8 1.8	1.2 1.2	1.1 1.1	0.79 0.79	0.55 0.55	1.3 1.3	0.95 0.96	0.74 0.75	0.75 0.76	0.95 0.95	0.81 0.82	0.42 0.49	
$g_{Htt}^{\text{eff}} [\%]$	SMEFT _{FU} SMEFT _{ND}	3.5 3.5	2.5 3.2	2.9 2.8	1.8 1.7	1.6 3.2	1.1 2.9	0.75 1.5	2.5 3.2	1.4 2.2	1.2 2.1	1.6 3.1	1.3 3.1	1.2 3.1	0.66 1.7	
$g_{Hcc}^{\text{eff}} [\%]$	SMEFT _{FU} SMEFT _{ND}	—	4.	—	—	Same as g_{Htt}^{eff}			4.	1.8	1.4	1.8	1.4	1.2	0.95	
$g_{Hbb}^{\text{eff}} [\%]$	SMEFT _{FU} SMEFT _{ND}	4.9 5.3	1.7 1.9	4.1 4.4	3.1 3.5	0.77 0.78	0.51 0.52	0.42 0.43	0.97 0.99	0.44 0.44	0.37 0.37	0.62 0.63	0.7 0.71	0.56 0.56	0.39 0.44	
$g_{H\tau\tau}^{\text{eff}} [\%]$	SMEFT _{FU} SMEFT _{ND}	3.1 3.4	2. 2.2	2.6 2.9	2.2 2.5	0.79 0.81	0.58 0.59	0.49 0.5	1.2 1.3	0.91 0.93	0.73 0.74	0.64 0.66	0.69 0.7	0.57 0.57	0.3 0.46	
$g_{H\mu\mu}^{\text{eff}} [\%]$	SMEFT _{FU} SMEFT _{ND}	5.5	4.7	3.6	2.9	Same as $g_{H\tau\tau}^{\text{eff}}$			4.4	4.1	3.5	3.8	4.	3.8	0.42	
$\delta g_{1,Z} [\times 10^2]$	SMEFT _{FU} SMEFT _{ND}	0.63 0.66	0.48 0.52	0.45 0.49	0.39 0.45	0.068 0.091	0.043 0.047	0.04 0.044	0.044 0.045	0.013 0.013	0.011 0.011	0.087 0.087	0.085 0.085	0.036 0.037	0.017 0.018	
$\delta \kappa_\gamma [\times 10^2]$	SMEFT _{FU} SMEFT _{ND}	2.9 3.2	2.2 2.4	2.4 2.7	2.2 2.5	0.098 0.12	0.069 0.076	0.062 0.068	0.078 0.079	0.032 0.032	0.025 0.025	0.089 0.089	0.086 0.086	0.049 0.049	0.047 0.047	
$\lambda_Z [\times 10^2]$	SMEFT _{FU} SMEFT _{ND}	3.2 3.2	3. 3.	3. 3.	3. 3.	0.041 0.042	0.02 0.021	0.014 0.014	0.043 0.043	0.0053 0.0053	0.0018 0.0018	0.11 0.11	0.1 0.1	0.05 0.051	0.045 0.045	

Table 7. Sensitivity at 68% probability to deviations in the different effective Higgs couplings and aTGC from a global fit to the projections available at each future collider project. Results obtained for the Global SMEFT fit benchmarks denoted as SMEFT_{FU} and SMEFT_{ND} in the text. The numbers for all future colliders are shown *in combination* with the HL-LHC results. For ILC and CLIC results from the Z boson radiative return events are included.

	HL-LHC		LHeC		HE-LHC		ILC			CLIC			CEPC		FCC-ee		FCC
			S_2	S_2'	250	500	1000	380	1500	3000	240	365	ee/eh/hh				
$g_L^{e^+e^-}$ [%]	1.3	0.97	1.3	1.2	0.082	0.048	0.043	0.027	0.013	0.011	0.032	0.028	0.028				
$g_L^{\nu\mu}$ [%]	1.2	1.2	1.2	1.2	0.11	0.088	0.085	0.16	0.14	0.14	0.036	0.03	0.03				
$g_L^{\nu\tau}$ [%]	1.6	1.4	1.6	1.5	0.12	0.095	0.092	0.16	0.14	0.14	0.038	0.034	0.033				
g_L^e [%]	0.08	0.079	0.079	0.079	0.048	0.037	0.035	0.035	0.022	0.02	0.014	0.0095	0.0073				
g_R^e [%]	0.098	0.098	0.098	0.098	0.055	0.041	0.037	0.047	0.035	0.031	0.016	0.0097	0.0089				
g_R^{μ} [%]	0.39	0.39	0.39	0.39	0.072	0.07	0.069	0.17	0.17	0.17	0.031	0.0094	0.007				
g_R^{τ} [%]	0.61	0.6	0.6	0.6	0.09	0.087	0.087	0.24	0.24	0.24	0.047	0.0099	0.0092				
g_L^t [%]	0.2	0.2	0.2	0.2	0.076	0.073	0.073	0.17	0.17	0.17	0.016	0.0099	0.0076				
g_R^t [%]	0.29	0.29	0.29	0.29	0.094	0.091	0.091	0.24	0.24	0.24	0.018	0.01	0.0094				
$g_L^{u=c}$ [%]	0.97	0.96	0.95	0.95	0.24	0.23	0.23	0.26	0.26	0.26	0.051	0.05	0.05				
$g_R^{u=c}$ [%]	3.6	3.6	3.5	3.5	0.35	0.35	0.35	0.43	0.44	0.43	0.08	0.066	0.066				
g_L^b [%]	11.	11.	11.	11.	11.	0.84	0.78	2.4	0.65	0.52	11.	11.	1.5				
g_R^b [%]	—	—	—	—	—	2.	1.9	6.	1.6	1.7	—	—	3.5				
$g_L^{t=s}$ [%]	0.88	0.81	0.77	0.75	0.23	0.21	0.21	0.25	0.24	0.24	0.056	0.051	0.051				
$g_R^{t=s}$ [%]	27.	25.	23.	22.	4.8	3.9	3.8	5.9	5.3	5.1	1.4	1.1	1.1				
g_L^b [%]	0.35	0.35	0.35	0.35	0.071	0.068	0.067	0.13	0.13	0.13	0.017	0.011	0.011				
g_R^b [%]	11.	11.	11.	11.	0.51	0.51	0.51	3.	3.	3.	0.29	0.088	0.088				

Table 8. Sensitivity at 68% probability to deviations in the different effective EW couplings from a global fit to the projections available at each future collider project. Results obtained for the Global SMEFT fit benchmark denoted as SMEFT_{ND} in the text. The numbers for all future colliders are shown *in combination* with the HL-LHC results. The results for ILC and CLIC are shown without a dedicated Giga-Z run. Appendix F includes the results with a Giga-Z run in table 34.

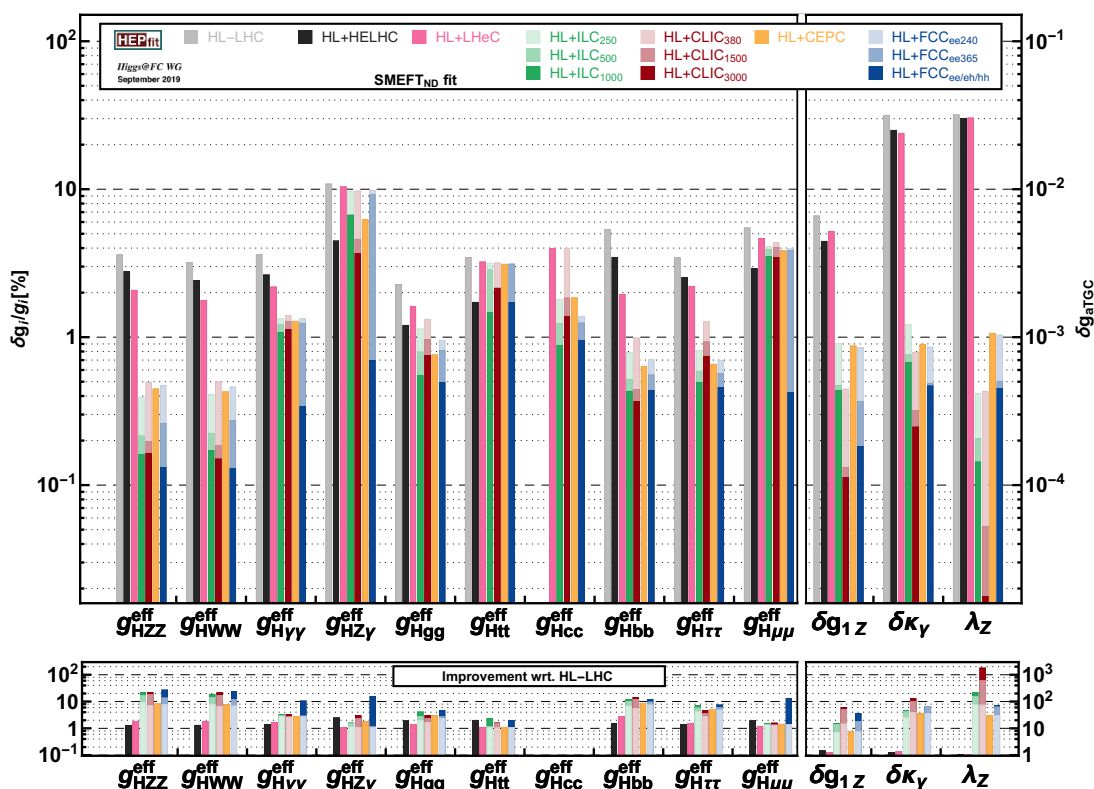


Figure 3. Sensitivity at 68% probability to deviations in the different effective Higgs couplings and aTGC from a global fit to the projections available at each future collider project. Results obtained within the SMEFT framework in the benchmark SMEFT_{ND}. The HE-LHC results correspond to the S_2^J assumptions for the theory systematic uncertainties in Higgs processes [13].

3.4.2 Results for BSM-motivated effective Lagrangians

In this subsection, we adopt a more BSM-oriented perspective and present the global fit results in a way that can be easily matched to theory-motivated scenarios, such as composite Higgs models. For that purpose, we will restrict the results to the set of dimension-6 interactions in the effective Lagrangian in eq. (3.19) and adopt the usual presentation of results in terms of the bounds on the dimension-6 operator coefficients. We will also extend the global fits presented in previous sections, adding further studies available in the literature about high-energy probes of the EFT. These are designed to benefit from the growth with energy of the contributions of certain dimension-6 operators in physical processes, leading to competitive constraints on new physics, without necessarily relying on extreme experimental precision. In this regard, we note that these studies are usually not performed in a fully global way within the EFT framework, but rather focus on the most important effects at high energies. Therefore, the results when such processes dominate in the bounds on new physics should be considered with a certain amount of caution, although they should offer a reasonable approximation under the assumptions in (3.19) and (3.20). In particular, we will add the following high-energy probes using di-boson and

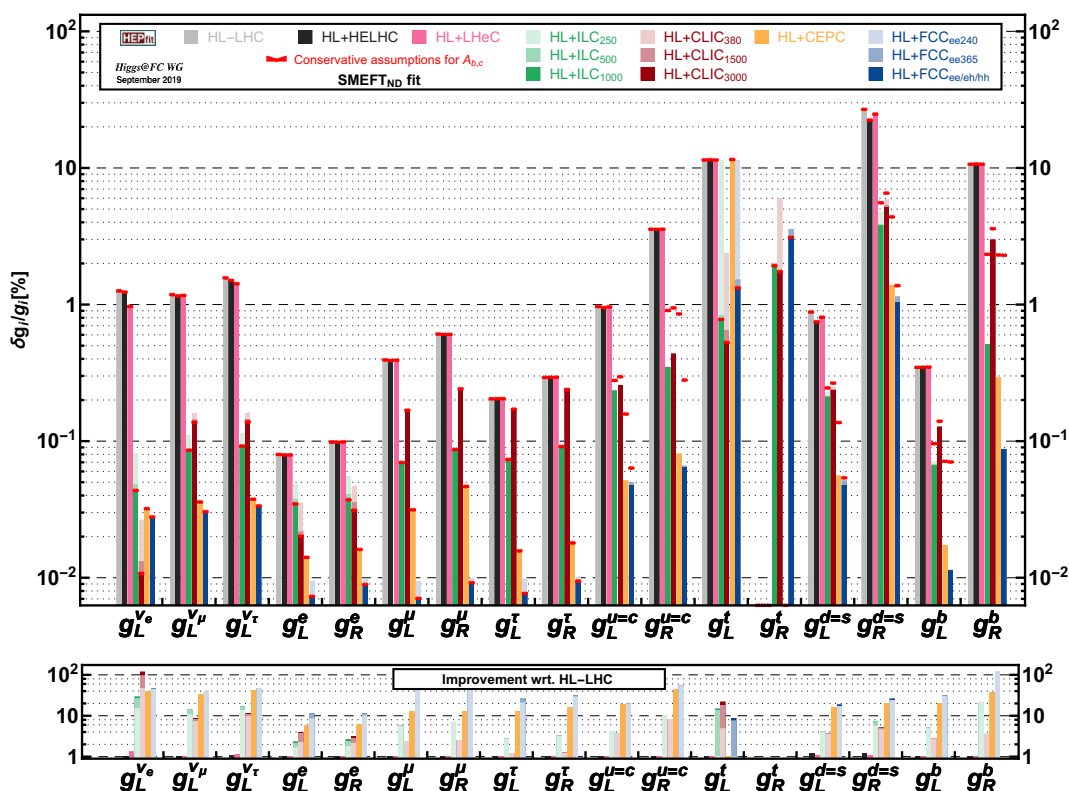


Figure 4. Sensitivity at 68% probability to deviations in the different EW couplings from a global fit to the projections available at each future collider project. Results obtained within the SMEFT framework in the benchmark SMEFT_{ND}. Note that Z-radiative return measurements at ILC and CLIC are included in the fit. Two different assumptions are considered for the systematic errors. The HE-LHC results correspond to the S'_2 assumptions for the theory systematic uncertainties in Higgs processes [13]. See text for details.

di-fermion processes:

- The constraints on the W and Y oblique parameters [48] (which can be mapped into $c_{2W;2B}$) from fermion pair production at the HL-LHC, HE-LHC [13], FCC-hh [49], ILC at 250, 500 and 1000 GeV [4] and CLIC [46].¹⁵

It must be noted that, for the HE-LHC, only the sensitivity to W and Y from $pp \rightarrow \ell^+ \ell^-$ is available in [13]. There is no sensitivity reported from charged-current process, which can constrain W independently. No studies on the reach for the W and Y parameters were available for CEPC or the FCC-ee. For this section for these two lepton colliders it has been estimated following the studies in ref. [4, 46].¹⁶

¹⁵The studies in [46] and [4] make use of significantly different assumptions for the systematic uncertainties and efficiencies for each $e^+e^- \rightarrow f\bar{f}$ channel. The apparent small difference in terms of reach at the highest energy stages for CLIC/ILC is, however, due to the high luminosity assumed at ILC, as well as the use of positron polarization, which allow to partially compensate the lower energy achievable compared to CLIC.

¹⁶We obtain alues of $\delta W_{\text{CEPC}} \sim 5.3 \times 10^{-5}$, $\delta Y_{\text{CEPC}} \sim 4.7 \times 10^{-5}$, with a correlation of -0.5 ; $\delta W_{\text{FCC-ee}(240)} \sim 5.4 \times 10^{-5}$, $\delta Y_{\text{FCC-ee}(240)} \sim 4.9 \times 10^{-5}$, with the same -0.5 correlation; and $\delta W_{\text{FCC-ee}} \sim 3.2 \times 10^{-5}$, $\delta Y_{\text{FCC-ee}} \sim 2.9 \times 10^{-5}$, with a correlation of -0.53 .

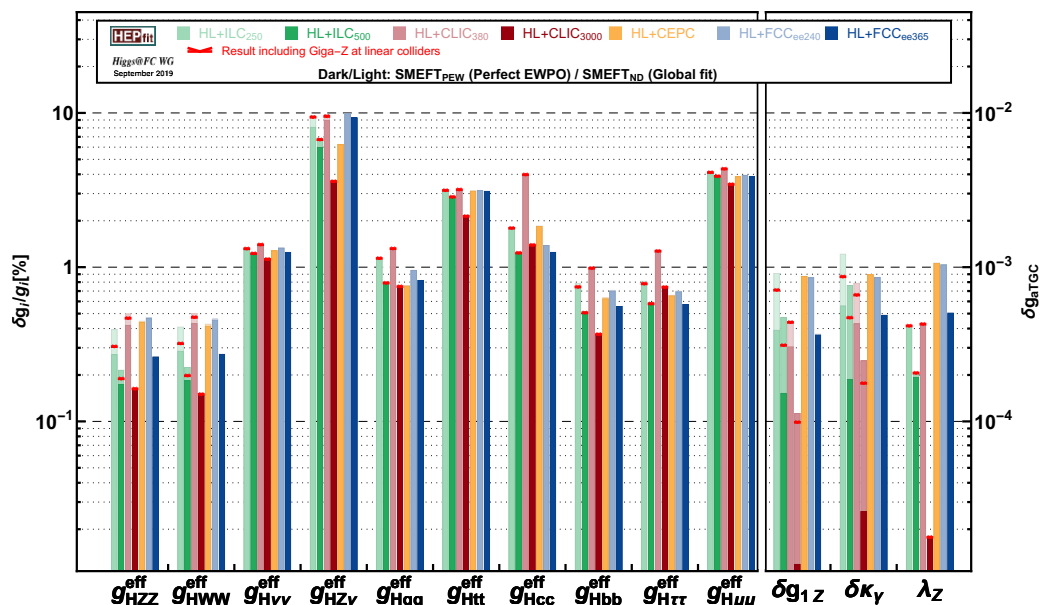


Figure 5. 68% probability reach on Higgs couplings and aTGC values for the different lepton colliders from the Global fit SMEFT_{ND}, compared with the results obtained assuming infinite precision for the EWPO (scenario SMEFT_{PEW}). The difference (partially) illustrates the impact of the EW constraints on the Higgs results. See text for discussion and caveats which apply to this study. The measurements based on Z bosons from radiative return at ILC and CLIC are included in the default fit, and the horizontal red marks indicate the coupling reach when additionally a dedicated Z -pole run is taken.

- The study in ref. [50] of the M_{ZH} distribution in $pp \rightarrow ZH, H \rightarrow b\bar{b}$ in the boosted regime for the HL-LHC [13] and FCC-hh [1]. (This was not available for the HE-LHC.) Note that both CLIC (and to a lesser extent ILC) have access to similar physics in the leptonic case, from the ZH measurements at 1.5/3 TeV (500/1000 GeV). Current ILC projections for Higgs production at 1 TeV [4] are only available for the W boson fusion channel. For the fits presented in this section, for $\sigma_{ZH} \times BR(H \rightarrow b\bar{b})$ at ILC at 1 TeV an uncertainty of 1.3% is assumed for each polarization [51].
- The p_{TV} distribution in $pp \rightarrow WZ$ from ref. [52] for the HL-LHC, HE-LHC and FCC-hh.

These are of course only a sample of the high-energy precision probes that could be tested at future colliders (and at HL-LHC) so the results presented are not an exhaustive study of the potential of the different machines in this regard (see e.g. [53, 54].)

The results of this fit are shown in figure 6 after the full run of each future collider project, and in table 9. Apart from the 68% probability bounds for each operator from the global fit, we also present the results assuming only one operator is generated by the UV dynamics. The difference between both results is indicative of the correlations between the different operators in the fit. These can, in some cases, be rather large. A full study of such correlations goes beyond the scope of this report, but it is worth mentioning that some of the largest correlations typically occur between $\mathcal{O}_\gamma, \mathcal{O}_{\phi W}, \mathcal{O}_{\phi B}, \mathcal{O}_W, \mathcal{O}_B$ where

all contribute to the Higgs interactions with neutral vector bosons. Large correlations also connect \mathcal{O}_g and \mathcal{O}_{y_u} . These are typically constrained along the $H \rightarrow gg$ direction with better precision than the one obtained for \mathcal{O}_{y_u} from the corresponding ttH process at the different colliders.

For those operators whose effects are mainly constrained by Higgs observables, e.g. \mathcal{O}_ϕ and \mathcal{O}_{y_f} , the evolution of the results in the table follows essentially the same pattern as in the discussion of the Higgs coupling results of the SMEFT fit. Likewise, similar considerations must be taken into account when comparing the results across colliders, in particular regarding the dependence of the HE-LHC results on the assumptions of the reduction of the theory/systematic uncertainties, which control most of the improvement with respect to HL-LHC. (See comment on the S2' assumptions in section 2.) Also regarding the results at high luminosity/energy upgrades of the LHC, some of the numbers in table 9, namely those involving a single operator fit to c_ϕ , may look surprising, given that the projections for most Higgs observables at such machines are expected to be dominated by the theory/systematic uncertainties. These results are marked with a \dagger in the table. For instance, the HL-LHC result corresponds to a precision in an overall Higgs coupling modification at the level of 0.8%. This is below the dominant signal theory uncertainties assumed in the HL-LHC S2 hypothesis. As explained in section 2, this is a consequence of the assumptions in the treatment of theory/systematic uncertainties in the simplified set of inputs used in this report for the HL-LHC fits. A rough estimate of the bound that would result from assuming 100% correlated signal theory uncertainties would return, for the same case, $c_\phi/\Lambda^2 \sim 0.42 \text{ TeV}^{-2}$, illustrating the impact of the choice of assumption in the treatment of these theory systematics. Given the implications of these bounds in terms of constraining BSM scenarios (as will be illustrated below, c_ϕ sets some of the most important constraints in composite Higgs models), this is an issue that should be carefully studied at hadron colliders, as it will become (even more) relevant at the end of the HL-LHC era. There is another caveat affecting the results presented in the table 9 that concerns the HE-LHC limits for c_{2B} and c_{2W} , also marked with a \dagger . In this case, the reaches for c_{2B} and c_{2W} , which can be mapped into the W and Y oblique parameters, are limited by the lack of constraints from the charged current channel at HE-LHC since no projections were provided at this time. The charged current channel is sensitive to the W parameter and, via its correlation with Y , can also affect the results for the latter in the global fit.

A meaningful interpretation of these results in terms of a broad class of composite Higgs models can be obtained under the assumptions leading to the dependence of the Wilson coefficients on new physics coupling, g_\star , and mass, m_\star , described in eq. (3.20) and below (i.e. we assume $c_{g,\gamma}$ and $c_{\phi V,3V}$ are loop suppressed in y_t and g_\star , respectively). In figure 7 we translate the results of the fit in figure 6 in terms of the 95% probability constraints in the (g_\star, m_\star) plane under such assumptions, and setting all $O(1)$ coefficients exactly to 1, i.e.

$$\begin{aligned}
 \frac{c_{\phi,6,y_f}}{\Lambda^2} &= \frac{g_\star^2}{m_\star^2}, & \frac{c_{W,B}}{\Lambda^2} &= \frac{1}{m_\star^2}, & \frac{c_{2W,2B,2G}}{\Lambda^2} &= \frac{1}{g_\star^2} \frac{1}{m_\star^2}, & \frac{c_T}{\Lambda^2} &= \frac{y_t^4}{16\pi^2} \frac{1}{m_\star^2}, \\
 \frac{c_{\phi W,\phi B}}{\Lambda^2} &= \frac{g_\star^2}{16\pi^2} \frac{1}{m_\star^2}, & \frac{c_{\gamma,g}}{\Lambda^2} &= \frac{y_t^2}{16\pi^2} \frac{1}{m_\star^2}, & \frac{c_{3W,3G}}{\Lambda^2} &= \frac{1}{16\pi^2} \frac{1}{m_\star^2}.
 \end{aligned}
 \tag{3.23}$$

[TeV ⁻²]	HL-LHC +										FCC-ee	FCC-ee/eh/hh		
	HL-LHC	LHeC	HE-LHC		ILC		CLIC		CEPC	240			365	
$\frac{c_6}{\Lambda^2}$	0.53 (0.28) [†]	0.15 (0.11)	0.43 (0.21) [†]	S_2' 0.31 (0.16) [†]	0.13 (0.061)	0.057 (0.041)	0.038 (0.033)	0.14 (0.076)	0.049 (0.04)	0.033 (0.027)	0.14 (0.038)	0.15 (0.044)	0.1 (0.038)	0.036 (0.029)
$\frac{c_7}{\Lambda^2}$	0.0056 (0.002)	0.0056 (0.002)	0.0056 (0.002)	0.0055 (0.002)	0.0018 (0.0013)	0.0016 (0.0011)	0.0016 (0.001)	0.0029 (0.001)	0.0025 (0.001)	0.0023 (0.001)	0.00097 (0.0008)	0.0007 (0.0007)	0.0004 (0.0002)	0.0003 (0.0002)
$\frac{c_{8V}}{\Lambda^2}$	0.33 (0.022)	0.28 (0.022)	0.24 (0.0098)	0.19 (0.0098)	0.06 (0.011)	0.046 (0.0073)	0.037 (0.004)	0.065 (0.011)	0.042 (0.0037)	0.035 (0.0015)	0.092 (0.0076)	0.11 (0.0051)	0.072 (0.0036)	0.032 (0.0029)
$\frac{c_9}{\Lambda^2}$	0.32 (0.028)	0.27 (0.028)	0.24 (0.028)	0.19 (0.028)	0.057 (0.011)	0.045 (0.0084)	0.037 (0.0053)	0.066 (0.013)	0.048 (0.0079)	0.041 (0.0035)	0.088 (0.0081)	0.11 (0.005)	0.069 (0.0035)	0.031 (0.0035)
$\frac{c_{9V}}{\Lambda^2}$	0.32 (0.034)	0.27 (0.033)	0.24 (0.01)	0.19 (0.01)	0.07 (0.026)	0.058 (0.012)	0.041 (0.0047)	0.078 (0.02)	0.044 (0.0039)	0.036 (0.0014)	0.086 (0.021)	0.11 (0.021)	0.08 (0.015)	0.032 (0.0043)
$\frac{c_{10}}{\Lambda^2}$	0.32 (0.18)	0.28 (0.18)	0.24 (0.099)	0.19 (0.067)	0.086 (0.048)	0.054 (0.016)	0.039 (0.0066)	0.093 (0.035)	0.05 (0.0092)	0.04 (0.0034)	0.086 (0.062)	0.11 (0.066)	0.086 (0.042)	0.031 (0.011)
$\frac{c_{11}}{\Lambda^2}$	0.0052 (0.004)	0.0049 (0.004)	0.0042 (0.0031)	0.0026 (0.0021)	0.0043 (0.0039)	0.004 (0.0038)	0.0035 (0.0033)	0.0048 (0.004)	0.0042 (0.0039)	0.0036 (0.0035)	0.004 (0.0038)	0.0041 (0.0039)	0.004 (0.0038)	0.0012 (0.0010)
$\frac{c_{12}}{\Lambda^2}$	0.0012 (0.0005)	0.0009 (0.0005)	0.001 (0.0004)	0.0006 (0.0003)	0.0006 (0.0004)	0.0005 (0.0003)	0.0003 (0.0002)	0.001 (0.0004)	0.0006 (0.0003)	0.0005 (0.0002)	0.0006 (0.0002)	0.0005 (0.0003)	0.0005 (0.0003)	0.0003 (0.0001)
$\frac{c_{13}}{\Lambda^2}$	0.25 (0.2)	0.23 (0.18)	0.18 (0.13)	0.11 (0.091)	0.14 (0.096)	0.097 (0.079)	0.079 (0.07)	0.21 (0.17)	0.15 (0.13)	0.11 (0.1)	0.1 (0.072)	0.11 (0.078)	0.094 (0.071)	0.052 (0.044)
$\frac{c_{14}}{\Lambda^2}$	0.57 (0.24)	0.42 (0.19)	0.44 (0.19)	0.26 (0.12)	0.26 (0.14)	0.19 (0.099)	0.12 (0.072)	0.42 (0.16)	0.23 (0.11)	0.19 (0.085)	0.25 (0.091)	0.2 (0.11)	0.19 (0.099)	0.11 (0.052)
$\frac{c_{15}}{\Lambda^2}$	0.46 (0.25)	0.23 (0.13)	0.37 (0.19)	0.26 (0.14)	0.13 (0.084)	0.088 (0.066)	0.071 (0.059)	0.18 (0.098)	0.077 (0.063)	0.059 (0.055)	0.091 (0.064)	0.1 (0.068)	0.092 (0.064)	0.071 (0.057)
$\frac{c_{16}}{\Lambda^2}$	0.08 (0.069)	0.08 (0.069)	0.028 [†] (0.013)	0.028 [†] (0.013)	0.025 (0.023)	0.0083 (0.0078)	0.0029 (0.0027)	0.031 (0.028)	0.0064 (0.0059)	0.0023 (0.0021)	0.042 (0.034)	0.042 (0.029)	0.028 (0.021)	0.0034 (0.0034)
$\frac{c_{17}}{\Lambda^2}$	0.008 (0.0069)	0.008 (0.0069)	0.0053 [†] (0.0024) [†]	0.0053 [†] (0.0024) [†]	0.0062 (0.0058)	0.0032 (0.003)	0.0012 (0.0011)	0.0062 (0.0058)	0.0016 (0.0014)	0.0006 (0.0005)	0.0069 (0.0062)	0.0062 (0.0057)	0.0056 (0.0049)	0.0003 (0.0003)
$\frac{c_{18}}{\Lambda^2}$	1.7 (1.6)	1.6 (1.6)	1.6 (1.6)	1.6 (1.6)	0.023 (0.022)	0.011 (0.011)	0.0076 (0.0075)	0.024 (0.024)	0.0031 (0.0031)	0.001 (0.001)	0.036 (0.02)	0.034 (0.019)	0.026 (0.015)	0.021 (0.015)
$\frac{c_{19}}{\Lambda^2}$	8.4 (7.8)	8.1 (7.7)	2.5 (2.4)	2.4 (2.3)	8.1 (4.7)	3.5 (3.1)	1.5 (1.4)	8.1 (7.7)	4.8 (4.5)	1.8 (1.7)	8. (2.8)	8. (3.2)	5.3 (3.1)	0.81 (0.79)

Table 9. 68% probability reach on the different Wilson coefficients in the Lagrangian eq. (3.19) from the global fit. In parenthesis we give the corresponding results from a fit assuming only one operator is generated by the UV physics. See text for details, in particular regarding the results marked with a †.

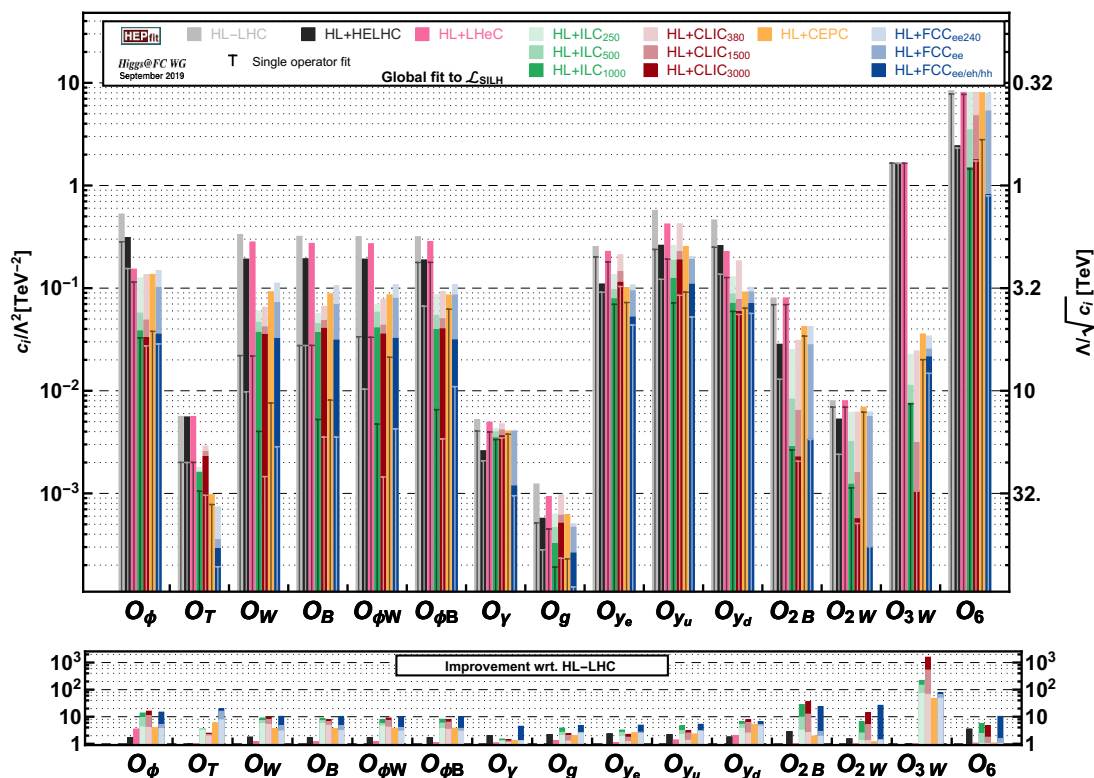


Figure 6. Global fit to the EFT operators in the Lagrangian (3.19). We show the marginalized 68% probability reach for each Wilson coefficient c_i/Λ^2 in eq. (3.19) from the global fit (solid bars). The reach of the vertical “T” lines indicate the results assuming only the corresponding operator is generated by the new physics. The HE-LHC results correspond to the S'_2 assumptions for the theory systematic uncertainties in Higgs processes [13].

We focus the comparison, again, on the full physics program at each future collider project (solid regions), but also show the region delimited by the low energy runs, or the FCC-ee for the case of the FCC project (the boundaries are indicated by the dashed lines). In the right panel of that figure we also show, for illustration purposes, the individual constraints set by several of the operators in (3.19) for the FCC fit. The modifications of the on-shell Higgs properties discussed in this report are mainly controlled, within the SILH assumptions, by the contributions to the operators \mathcal{O}_ϕ and \mathcal{O}_{y_f} , both of which set similar constraints in the global fit for this collider. These give the leading constraints in strongly coupled scenarios. Electroweak precision measurements, on the other hand, are more affected by a combination of $\mathcal{O}_{W,B}$ and set bounds independently of the new physics coupling. Finally, some of the high-energy probes included in the analysis provide the most efficient way of testing weakly coupled scenarios.

3.5 Impact of Standard Model theory uncertainties in Higgs calculations

As important as it is to have very precise experimental measurements of the different Higgs processes, it is also fundamental from the point of view of their physical interpretation to

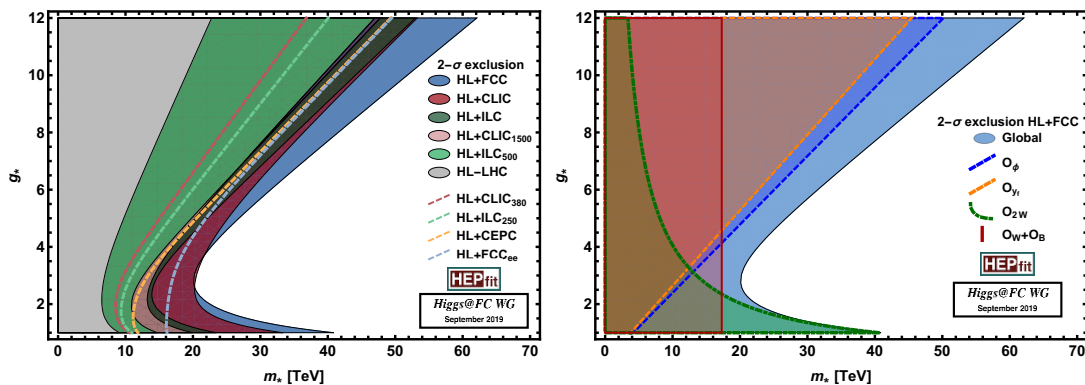


Figure 7. (Left) $2\text{-}\sigma$ exclusion regions in the (g_*, m_*) plane from the fit presented in figure 6, using the SILH power-counting described in eq. (3.20) and below (solid regions). Dashed lines indicate the regions constrained by the corresponding low-energy runs (or FCC-ee only for the case of the FCC project). (Right) The same comparing the results from the global fit with the constraints set by some of the operators individually, for the illustrative case of the HL-LHC+FCC-ee/eh/hh. In this case, the constraints from the on-shell Higgs measurements mainly affect \mathcal{O}_ϕ and \mathcal{O}_{y_f} .

have theoretical calculations for the predictions of such processes with comparable or better precision. In this sense, to quantify to what extent an experimental measurement with uncertainty δ_{exp} can be translated into a constraint on new physics,¹⁷ one needs to know the corresponding uncertainty δ_{SM} for the SM prediction. In order to extract the maximum experimental information, ideally, $\delta_{\text{SM}} \ll \delta_{\text{exp}}$. The sources of the SM uncertainty are typically separated in two types of contributions:

- *Parametric theory uncertainties* (Th_{Par}). For a given observable O , this is the error associated to the propagation of the experimental error of the SM input parameters to the SM prediction O_{SM} .
- The second source of uncertainty is due to the fact that, in practice, O_{SM} is only known to a finite order in perturbation theory. The estimate of the net size associated with the contribution to O_{SM} from missing higher-order corrections is usually referred to as *intrinsic theory uncertainty* (Th_{Intr}).

Of course, in the interpretation of any measurement in a particular extension of the SM, there are also errors associated with the missing corrections in the expansion(s) including the new physics parameters. In the particular case of the EFT framework, these would come from NLO corrections in the perturbative expansion including dimension-6 interactions or, from the point of view of the EFT expansion, from q^4/Λ^4 effects coming from either the square of the dimension-6 contributions to the amplitudes, or the SM interference with amplitudes involving dimension-8 operators or double insertions of the dimension-6 ones. Note that all these corrections affect the interpretation of a measurement in terms of pinpointing what is the source of the deformation from the SM, i.e. which particular operator and how large its coefficient can be, but not on the size of the overall deformation

¹⁷Or, equivalently, to what extent a measurement agrees with the SM.

per se. The latter is only controlled by the SM theoretical uncertainty. Because of that, and in the absence of a fully developed program including such contributions in the SMEFT framework, we restrict the discussion in this section to SM uncertainties only.

In the previous sections the results for future colliders after the HL/HE-LHC era were presented taking into account parametric uncertainties only. This was done to illustrate the final sensitivity to BSM deformations in Higgs couplings, as given directly by the experimental measurements of the different inputs (i.e. Higgs rates, diBoson measurements, EWPO or the processes used to determine the values of the SM input parameters). On the other hand, for this scenario to be meaningful, it is crucial to also study the effect in such results of the projections for the future intrinsic errors. This is needed to be able to quantify how far we will be from the assumption that such intrinsic errors become subdominant and, therefore, which aspects of theory calculations should the theory community focus on to make sure we reach the maximum experimental sensitivity at future colliders.

In this section we discuss more in detail the impact of the two types of SM theory errors described above, from the point of view of the calculations of the predictions for Higgs observables. This will be done both within the κ framework and also in the context of the EFT results. For the results from the κ -framework we will use the most general scenario considered in section 3.1, i.e. kappa-3, which allows non-SM decays. On the EFT side, we will use the scenario SMEFT_{PEW}, where the uncertainty associated with the precision of EWPO has already been “factorized”. In this scenario each fermion coupling is also treated separately, thus being sensitive to the uncertainties in the different $H \rightarrow f\bar{f}$ decay widths. Finally, we will also restrict the study in this subsection to the case of future lepton colliders only (we always consider them in combination with the HL-LHC projections). For the latter we keep the theory uncertainties as reported by the WG2 studies [13]).

In table 10 we show the results of the κ fit for the benchmark scenario kappa-3, indicating the results obtained including/excluding the different sources of SM theory uncertainties. Similarly, table 11 shows the results of the EFT fit for the benchmark scenario SMEFT_{PEW}. For the EFT results the impact of the different theory uncertainties is also illustrated in figure 8. As can be seen, if the SM errors were reduced to a level where they become sub-dominant, the experimental precision would allow to test deviations in some of the couplings at the one per-mille level, e.g. the coupling to vector bosons at CLIC in the SMEFT framework (the presence of extra decays would however reduce the precision to the 0.4% level, as shown in the kappa-3 results). The assumed precision of the SM theory calculations and inputs, however, prevents reaching this level of sensitivity. The most notable obstacle to achieve this close to per-mille level of precision are the intrinsic uncertainties for the $e^+e^- \rightarrow ZH$ and, especially, in $e^+e^- \rightarrow H\bar{\nu}\nu$, estimated to be $\sim 0.5\%$. In reaching this level of theoretical precision it was assumed that predictions at NNLO in the EW coupling for both processes will be available. This is within reach for ZH production, but it may be more challenging for $e^+e^- \rightarrow H\bar{\nu}\nu$ (and $H \rightarrow VV^* \rightarrow 4f$). However, with enough effort on the theory side [55–57], this type of uncertainties can be reduced. If the necessary resources are dedicated to develop these types of calculations, it should be possible to achieve, or even surpass, the required level of precision. This is not the case for the SM parametric errors, which depend on the experimental measurements of the corresponding input parameters.

From the results of the fits, the largest effect of this type of uncertainty on the determination of the fermion couplings affects the effective coupling of the bottom to the Higgs. The corresponding SM error in $H \rightarrow b\bar{b}$ depends on the precision of the bottom quark mass, whose projected future determination was assumed to be ~ 13 MeV. Taking into account the projected improvements from Lattice QCD calculations, this should be a conservative estimate [55]. Other parametric uncertainties, e.g. in $H \rightarrow c\bar{c}, gg$ and associated with m_c and α_S , are larger than the one for $H \rightarrow b\bar{b}$ but have a smaller effect in the results due to the also larger experimental errors expected in the corresponding channels. From the point of view of the Higgs decays into vector bosons, the predictions of $H \rightarrow ZZ^*, WW^*$ have a strong dependence on the value of the Higgs mass. It is therefore important to accompany the precise measurements of the Higgs couplings with equally precise measurements of the Higgs mass, to the level of 10 MeV. This would be possible at 240/250 GeV lepton colliders but more challenging at CLIC, where the final precision on M_H is expected at the level of 20–30 MeV (see section 7). In the kappa-framework, the fact that the dependence of the production e^+e^- Higgs cross sections on M_H is less severe helps to reduce the impact of the M_H uncertainty in the CLIC results. This is no longer the case once we move to the more general description of the SMEFT. In that case, non-SM like interactions contribute to the effective HZZ and HWW couplings, and the information on $H \rightarrow WW^*$ becomes relevant to determine g_{HZZ}^{eff} . The measurement of M_H at the HL-LHC at the 10–20 MeV level prevents this from becoming an issue at the lower energy stages at CLIC. But there is still a factor ~ 2 deterioration in the precision of the g_{HZZ}^{eff} coupling in the final CLIC results, emphasising again the necessity of a precise determination of M_H .

4 The Higgs boson self-coupling

The Higgs field is responsible for the spontaneous breaking of the electroweak symmetry, and for the generation of all the SM particle masses, because its potential features a global minimum away from the origin. Within the SM, this potential is fully characterised by two parameters, the Higgs mass m_h , and v , which can be experimentally inferred from the measurements of the Fermi constant ($v = 1/\sqrt{\sqrt{2}G_F} \approx 246$ GeV).

$$V(h) = \frac{1}{2}m_H^2 h^2 + \lambda_3 v h^3 + \frac{1}{4}\lambda_4 h^4, \quad \text{with} \quad \lambda_3^{\text{SM}} = \lambda_4^{\text{SM}} = \frac{m_H^2}{2v^2}. \quad (4.1)$$

However, the Higgs potential could show sizeable departures from the SM form, described in eq. (4.1). The understanding of EW symmetry breaking will remain hypothetical until experimental measurements reconstruct the shape of the Higgs potential. The *measurement* of the Higgs potential is therefore a high priority goal on the physics programme of all future colliders.

Unfortunately, the Higgs self-interactions, apart from the simple kinematical 2-point interaction that corresponds to the Higgs boson mass, are not physical observables. Therefore, a theoretical framework is needed to infer their values from experimental measurements. One needs a general parametrisation of the departures from the SM that allows the various Higgs couplings to vary continuously. Within this framework, one makes accurate predictions of various observables as a function of the modified Higgs couplings and

	Benchmark kappa-3	HL-LHC +								
		ILC			CLIC			CEPC	FCC-ee	
		250	500	1000	380	1500	3000		240	365
κ_W [%]	ExpStat	1.	0.28	0.24	0.73	0.4	0.38	0.87	0.87	0.4
	ExpStat + ThPar	1.	0.29	0.24	0.73	0.4	0.38	0.88	0.88	0.41
	ExpStat + ThIntr	1.	0.51	0.47	0.82	0.53	0.49	0.89	0.89	0.56
	ExpStat + Th	1.	0.51	0.47	0.81	0.53	0.63	0.89	0.89	0.56
κ_Z [%]	ExpStat	0.28	0.22	0.22	0.44	0.4	0.39	0.17	0.19	0.16
	ExpStat + ThPar	0.29	0.23	0.22	0.44	0.4	0.39	0.18	0.2	0.17
	ExpStat + ThIntr	0.32	0.27	0.26	0.46	0.42	0.41	0.23	0.24	0.22
	ExpStat + Th	0.32	0.27	0.27	0.46	0.42	1.2	0.23	0.24	0.23
κ_g [%]	ExpStat	1.3	0.83	0.58	1.5	1.1	0.83	1.	1.1	0.87
	ExpStat + ThPar	1.4	0.85	0.63	1.5	1.1	0.86	1.	1.2	0.9
	ExpStat + ThIntr	1.4	0.97	0.8	1.6	1.1	0.95	1.1	1.2	1.
	ExpStat + Th	1.4	0.99	0.82	1.6	1.1	2.1	1.1	1.2	1.
κ_γ [%]	ExpStat	1.4	1.2	1.1	1.4	1.3	1.2	1.3	1.3	1.3
	ExpStat + ThPar	1.4	1.2	1.1	1.4	1.3	1.2	1.3	1.3	1.3
	ExpStat + ThIntr	1.4	1.3	1.1	1.5	1.3	1.2	1.3	1.3	1.3
	ExpStat + Th	1.4	1.3	1.1	1.4	1.3	5.9	1.3	1.4	1.3
$\kappa_{Z\gamma}$ [%]	ExpStat	10.	10.	10.	10.	8.2	5.7	6.3	10.	10.
	ExpStat + ThPar	10.	10.	10.	10.	8.2	5.7	6.3	10.	10.
	ExpStat + ThIntr	10.	10.	10.	10.	8.2	5.7	6.3	10.	10.
	ExpStat + Th	10.	10.	10.	10.	8.2	17.	6.3	10.	10.
κ_c [%]	ExpStat	1.9	1.1	0.74	4.	1.8	1.3	1.9	1.4	1.2
	ExpStat + ThPar	2.	1.2	0.9	4.1	1.9	1.4	2.	1.5	1.3
	ExpStat + ThIntr	1.9	1.2	0.84	4.	1.8	1.4	1.9	1.5	1.2
	ExpStat + Th	2.	1.3	0.99	4.1	1.9	3.6	2.	1.5	1.3
κ_t [%]	ExpStat	3.1	2.8	1.4	3.2	2.1	2.1	3.1	3.1	3.1
	ExpStat + ThPar	3.1	2.8	1.4	3.2	2.1	2.1	3.1	3.1	3.1
	ExpStat + ThIntr	3.2	2.9	1.4	3.2	2.1	2.1	3.1	3.1	3.1
	ExpStat + Th	3.1	2.8	1.4	3.2	2.1	7.	3.1	3.1	3.1
κ_b [%]	ExpStat	1.1	0.47	0.36	1.2	0.5	0.41	0.82	0.91	0.56
	ExpStat + ThPar	1.1	0.56	0.47	1.2	0.59	0.52	0.9	0.98	0.64
	ExpStat + ThIntr	1.1	0.64	0.54	1.2	0.64	0.54	0.86	0.94	0.68
	ExpStat + Th	1.2	0.71	0.62	1.3	0.71	0.87	0.93	1.	0.76
κ_μ [%]	ExpStat	4.2	3.9	3.6	4.4	4.1	3.5	3.9	4.	3.9
	ExpStat + ThPar	4.2	3.9	3.6	4.4	4.1	3.5	3.9	4.	3.9
	ExpStat + ThIntr	4.2	3.9	3.6	4.4	4.1	3.5	3.9	4.	3.9
	ExpStat + Th	4.2	4.	3.6	4.4	4.1	4.4	3.9	4.	3.9
κ_τ [%]	ExpStat	1.1	0.64	0.53	1.4	0.99	0.81	0.91	0.94	0.65
	ExpStat + ThPar	1.1	0.64	0.54	1.4	1.	0.82	0.91	0.94	0.66
	ExpStat + ThIntr	1.1	0.74	0.64	1.4	1.	0.85	0.93	0.96	0.74
	ExpStat + Th	1.1	0.75	0.65	1.4	1.	3.3	0.94	0.96	0.75
$BR_{inv}^{95\%} <$	ExpStat	0.26	0.22	0.23	0.63	0.62	0.62	0.27	0.22	0.19
	ExpStat + ThPar	0.26	0.23	0.22	0.63	0.62	0.62	0.27	0.22	0.19
	ExpStat + ThIntr	0.26	0.23	0.23	0.63	0.62	0.62	0.27	0.22	0.19
	ExpStat + Th	0.26	0.23	0.23	0.63	0.62	0.69	0.27	0.22	0.19
$BR_{unt}^{95\%} <$	ExpStat	1.8	1.4	1.4	2.8	2.4	2.4	1.1	1.2	1.
	ExpStat + ThPar	1.8	1.4	1.4	2.7	2.4	2.4	1.1	1.2	1.
	ExpStat + ThIntr	1.8	1.4	1.4	2.8	2.4	2.4	1.1	1.2	1.
	ExpStat + Th	1.8	1.4	1.4	2.7	2.4	2.4	1.1	1.2	1.1

Table 10. Comparison of the sensitivity at 68% probability to deviations in the different Higgs couplings modifiers in the kappa-3 fit, under different assumptions for the SM theory uncertainties. We compare the results obtained neglecting both intrinsic and parametric uncertainties, including each of them separately, and adding the full SM uncertainty.

	Benchmark SMEFT _{PEW}	HL-LHC +								
		ILC			CLIC			CEPC	FCC-ee	
		250	500	1000	380	1500	3000		240	365
$g_{HZZ}^{\text{eff}}[\%]$	ExpStat	0.26	0.16	0.12	0.4	0.14	0.089	0.43	0.46	0.25
	ExpStat + Th _{Par}	0.27	0.17	0.13	0.42	0.19	0.16	0.44	0.46	0.26
	ExpStat + Th _{Intr}	0.33	0.29	0.28	0.45	0.33	0.32	0.47	0.5	0.34
	ExpStat + Th	0.34	0.3	0.29	0.47	0.36	0.34	0.48	0.5	0.35
$g_{HWW}^{\text{eff}}[\%]$	ExpStat	0.28	0.17	0.13	0.41	0.14	0.091	0.41	0.45	0.26
	ExpStat + Th _{Par}	0.29	0.18	0.14	0.43	0.18	0.15	0.41	0.45	0.27
	ExpStat + Th _{Intr}	0.37	0.32	0.31	0.48	0.36	0.34	0.47	0.5	0.37
	ExpStat + Th	0.37	0.33	0.32	0.5	0.38	0.36	0.47	0.51	0.38
$g_{H\gamma\gamma}^{\text{eff}}[\%]$	ExpStat	1.3	1.2	1.1	1.4	1.3	1.1	1.3	1.3	1.2
	ExpStat + Th _{Par}	1.3	1.2	1.1	1.4	1.3	1.1	1.3	1.3	1.3
	ExpStat + Th _{Intr}	1.4	1.3	1.1	1.5	1.4	1.2	1.4	1.4	1.3
	ExpStat + Th	1.4	1.3	1.2	1.5	1.4	1.2	1.4	1.4	1.3
$g_{HZZ\gamma}^{\text{eff}}[\%]$	ExpStat	8.1	5.9	5.4	8.9	4.3	3.5	6.2	9.9	9.3
	ExpStat + Th _{Par}	8.1	6.	5.5	9.	4.4	3.5	6.2	9.9	9.3
	ExpStat + Th _{Intr}	8.1	6.6	6.1	9.	5.3	4.2	6.2	9.9	9.6
	ExpStat + Th	8.1	6.5	6.1	9.1	5.3	4.2	6.2	9.9	9.5
$g_{Hgg}^{\text{eff}}[\%]$	ExpStat	1.1	0.78	0.54	1.3	0.95	0.74	0.75	0.94	0.81
	ExpStat + Th _{Par}	1.1	0.79	0.54	1.3	0.96	0.75	0.75	0.95	0.82
	ExpStat + Th _{Intr}	1.2	0.82	0.6	1.4	0.99	0.78	0.78	0.98	0.85
	ExpStat + Th	1.2	0.82	0.6	1.4	1.	0.79	0.78	0.98	0.85
$g_{Htt}^{\text{eff}}[\%]$	ExpStat	3.1	2.8	1.5	3.2	2.1	2.1	3.1	3.1	3.1
	ExpStat + Th _{Par}	3.2	2.8	1.5	3.2	2.1	2.1	3.1	3.1	3.1
	ExpStat + Th _{Intr}	3.1	2.8	1.5	3.2	2.1	2.1	3.1	3.1	3.1
	ExpStat + Th	3.2	2.8	1.5	3.2	2.1	2.1	3.1	3.1	3.1
$g_{Hcc}^{\text{eff}}[\%]$	ExpStat	1.7	1.1	0.72	3.9	1.8	1.3	1.8	1.3	1.1
	ExpStat + Th _{Par}	1.8	1.2	0.88	4.	1.9	1.4	1.8	1.4	1.3
	ExpStat + Th _{Intr}	1.7	1.2	0.77	4.	1.8	1.3	1.8	1.3	1.2
	ExpStat + Th	1.8	1.3	0.92	4.	1.9	1.4	1.9	1.4	1.3
$g_{Hbb}^{\text{eff}}[\%]$	ExpStat	0.66	0.4	0.29	0.92	0.3	0.17	0.52	0.61	0.46
	ExpStat + Th _{Par}	0.73	0.5	0.42	0.96	0.44	0.37	0.62	0.7	0.56
	ExpStat + Th _{Intr}	0.7	0.49	0.41	0.97	0.45	0.38	0.57	0.66	0.53
	ExpStat + Th	0.76	0.58	0.52	1.	0.56	0.5	0.67	0.74	0.62
$g_{H\tau\tau}^{\text{eff}}[\%]$	ExpStat	0.77	0.57	0.48	1.3	0.92	0.73	0.64	0.69	0.57
	ExpStat + Th _{Par}	0.77	0.57	0.48	1.3	0.93	0.74	0.65	0.69	0.57
	ExpStat + Th _{Intr}	0.79	0.61	0.53	1.3	0.95	0.77	0.67	0.72	0.61
	ExpStat + Th	0.79	0.61	0.53	1.3	0.95	0.78	0.68	0.72	0.62
$g_{H\mu\mu}^{\text{eff}}[\%]$	ExpStat	4.1	3.9	3.5	4.3	4.1	3.5	3.9	3.9	3.8
	ExpStat + Th _{Par}	4.1	3.9	3.5	4.3	4.1	3.4	3.9	3.9	3.9
	ExpStat + Th _{Intr}	4.1	3.9	3.5	4.3	4.1	3.5	3.9	3.9	3.9
	ExpStat + Th	4.1	3.9	3.5	4.3	4.1	3.5	3.9	3.9	3.9
$\delta g_{1Z}[\times 10^2]$	ExpStat	0.039	0.015	0.013	0.03	0.0034	0.0012	0.087	0.085	0.036
	ExpStat + Th _{Par}	0.039	0.015	0.013	0.03	0.0034	0.0012	0.087	0.085	0.036
	ExpStat + Th _{Intr}	0.039	0.015	0.013	0.031	0.0034	0.0012	0.087	0.086	0.037
	ExpStat + Th	0.039	0.015	0.013	0.031	0.0034	0.0012	0.088	0.086	0.037
$\delta\kappa_\gamma[\times 10^2]$	ExpStat	0.056	0.019	0.015	0.043	0.0073	0.0026	0.089	0.086	0.049
	ExpStat + Th _{Par}	0.056	0.019	0.015	0.043	0.0074	0.0026	0.089	0.086	0.049
	ExpStat + Th _{Intr}	0.056	0.02	0.016	0.044	0.0074	0.0026	0.09	0.086	0.05
	ExpStat + Th	0.056	0.02	0.016	0.044	0.0074	0.0026	0.09	0.086	0.05
$\lambda_Z[\times 10^2]$	ExpStat	0.041	0.019	0.014	0.042	0.0053	0.0018	0.11	0.1	0.05
	ExpStat + Th _{Par}	0.041	0.019	0.014	0.042	0.0053	0.0018	0.11	0.1	0.05
	ExpStat + Th _{Intr}	0.041	0.019	0.014	0.043	0.0053	0.0018	0.11	0.1	0.05
	ExpStat + Th	0.041	0.019	0.014	0.042	0.0053	0.0018	0.11	0.1	0.05

Table 11. Comparison, within the SMEFT_{PEW} fit, of the sensitivity at 68% probability to deviations in the different effective Higgs couplings and aTGC under different assumptions for the SM theory uncertainties. We compare the results obtained neglecting both intrinsic and parametric uncertainties, including each of them separately, and finally adding the full SM uncertainty.

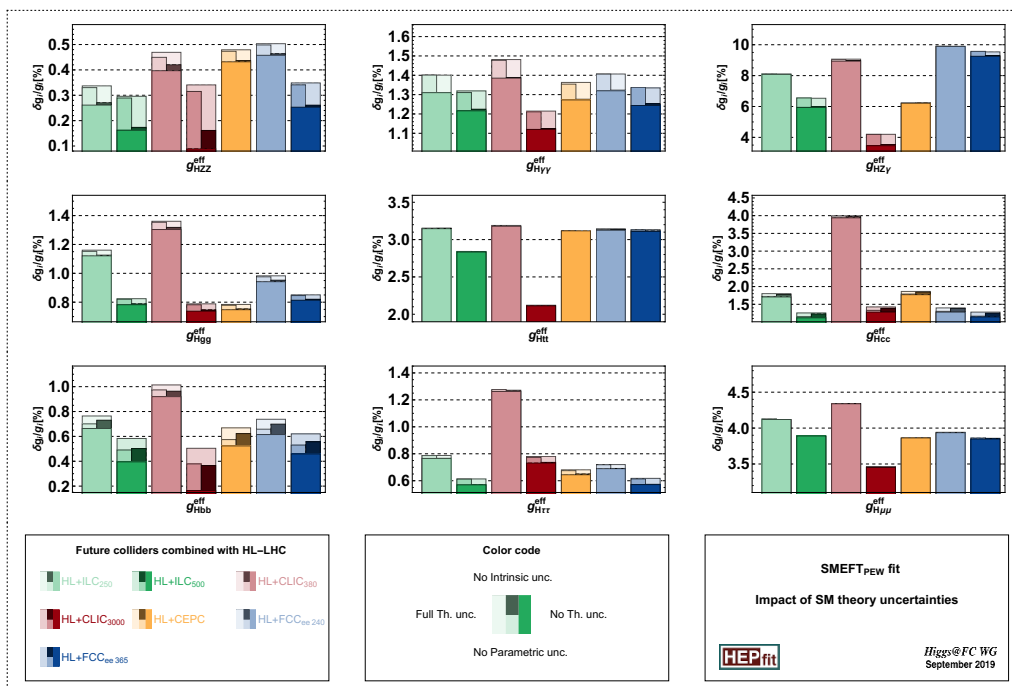


Figure 8. Impact of the different sources of SM theory uncertainties in the coupling reach at the different lepton-collider projects based on the SMEFT_{PEW} fit. Using dark to light shades we show the results without SM theory uncertainties (darkest shade), only with the intrinsic uncertainty (medium), and the full SM error (lightest shade). The solid line indicates the result with SM parametric uncertainties only. The most significant differences are found for the effective coupling to vector bosons (dominated by intrinsic uncertainties) and to bottom quarks (controlled by the parametric error associated with m_b). See table 11 and text for details.

a global fit then leads to a determination of all these couplings. Effective Field Theory offers us such a theoretically sound framework in which higher order calculations can be performed to provide solid and improvable predictions able to cope with systematic and statistic experimental uncertainties. As in section 3.3, we will focus our attention on EFT where the EW symmetry is linearly realised, i.e. under the assumption that no new heavy degree of freedom acquires its mass from the Higgs expectation value. In that case, there are only two dimension-6 operators that induce a deviation of the Higgs self-couplings

$$\mathcal{L} = \mathcal{L}^{\text{SM}} + \frac{c_\phi}{2\Lambda^2} \partial_\mu |\phi|^2 \partial^\mu |\phi|^2 - \frac{c_6 \lambda_3^{\text{SM}}}{\Lambda^2} |\phi|^6$$

$$\Rightarrow \kappa_3 \equiv \frac{\lambda_3}{\lambda_3^{\text{SM}}} = 1 + \left(c_6 - \frac{3}{2} c_\phi \right) \frac{v^2}{\Lambda^2}, \quad \kappa_4 \equiv \frac{\lambda_4}{\lambda_4^{\text{SM}}} = 1 + \left(6c_6 - \frac{25}{3} c_\phi \right) \frac{v^2}{\Lambda^2}. \quad (4.2)$$

In particular, the operator proportional to c_ϕ requires a non-linear field definition to keep the Higgs boson kinetic term canonically normalised. The modifications of the cubic and quartic self-interactions are related in this model. Independent modifications are only obtained when operators of dimension 8 are considered.

The most direct way to assess the Higgs cubic self-interaction is through the measurement of double Higgs production either at hadron colliders, where the production is

dominated by gluon fusion, $gg \rightarrow HH$, or at lepton colliders via double Higgs-strahlung, $e^+e^- \rightarrow ZHH$, particularly relevant at low energies, or via vector boson fusion (VBF), $e^+e^- \rightarrow HH\nu_e\bar{\nu}_e$, more important at centre-of-mass energies of 1 TeV and above. At leading order, double Higgs production receives a contribution proportional to the cubic coupling, for both pp and e^+e^- collisions, as shown in figure 9. Figure 10 shows the dependence of the inclusive double Higgs production cross section when the value of the Higgs cubic coupling is varied, assuming no other deviation from the SM. Gluon fusion production at a hadron collider has been computed within the SM at NNLO accuracy in the infinite top mass limit [58–61] and at NLO with the full top mass dependence [62–64], leading to a prediction whose theoretical and parametric uncertainties are of the order of a few percent.

For the LHC at 14 TeV, the cross section is predicted to be $36.69^{+2.1\%}_{-4.9\%}$ fb, about three orders of magnitude smaller than the single Higgs production, which makes the double Higgs channel a challenging process to observe. The most up-to-date analysis relies on the combination of the $b\bar{b}\gamma\gamma$ and $b\bar{b}\tau\tau$ decay channels to reach almost 5 standard deviation evidence for double Higgs production at HL-LHC (see table 55 and figure 65 of ref. [13]), which can be translated into a 68% CL bound of order 50% on the deviation of the Higgs cubic coupling relative to the SM prediction. Note that the mapping of the inclusive $gg \rightarrow HH$ cross section onto a value of the Higgs cubic self-coupling is not unique: for instance, at 14 TeV LHC, a value of the cross section equal to the SM prediction corresponds either to $\kappa_3 = 1$ or to $\kappa_3 \approx 6.2$. This ambiguity can however be resolved by analysing the shape of the invariant mass distribution of the reconstructed two Higgs boson system: the larger the value of κ_3 , the closer to threshold the m_{HH} distribution is peaked. This kinematic information is a crucial element of Boosted Decision Trees (BDT) based analysis performed at HL-LHC. However the BDT and the final selection cuts are often devised to optimise the significance of the SM cross section for double Higgs production and therefore it is not necessarily optimised for the determination of the Higgs self-coupling directly, leaving room for possible improvement towards an even higher sensitivity. At lepton colliders, double Higgs-strahlung, $e^+e^- \rightarrow ZHH$, gives stronger constraints on positive deviations ($\kappa_3 > 1$), while VBF is better in constraining negative deviations, ($\kappa_3 < 1$). While at HL-LHC, values of $\kappa_3 > 1$, as expected in models of strong first order phase transition, result in a smaller double-Higgs production cross section due to the destructive interference, at lepton colliders for the ZHH process they actually result in a larger cross section, and hence into an increased precision. For instance at ILC₅₀₀, the sensitivity around the SM value is 27% but it would reach 18% around $\kappa_3 = 1.5$.

Modified Higgs self-interactions can also affect, at higher orders, the single Higgs processes [67–69] and even the electroweak precision observables [70–72]. Since the experimental sensitivities for these observables are better than for double Higgs production, one can devise alternative ways to assess the value of the Higgs self-interactions. For a 240 GeV lepton collider, the change of the ZH production cross section at NLO induced by a deviation of the Higgs cubic coupling amounts to

$$\sigma_{ZH}^{\text{NLO}} \approx \sigma_{ZH}^{\text{NLO,SM}}(1 + 0.014 \delta\kappa_3). \tag{4.3}$$

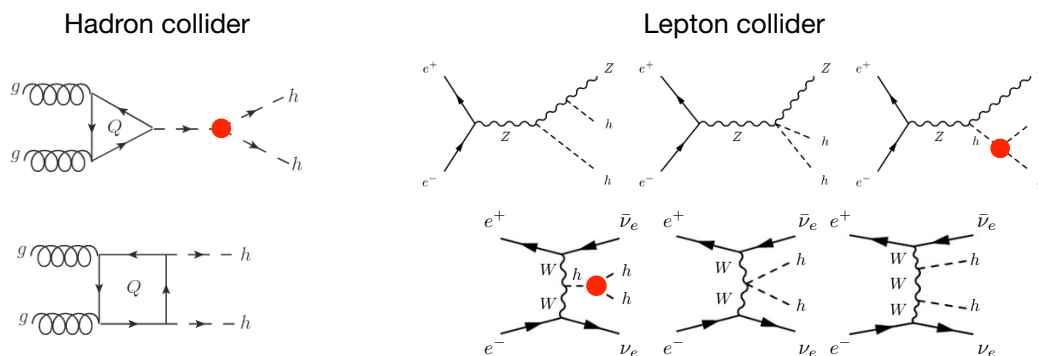


Figure 9. Representative Feynman diagrams for the leading contribution to double Higgs production at hadron (left) and lepton (right) colliders. Extracting the value of the Higgs self-coupling, in red, requires a knowledge of the other Higgs couplings that also contribute to the same process. See table 18 for the SM rates. At lepton colliders, double Higgs production can also occur via vector boson fusion with neutral currents but the rate is about ten times smaller. The contribution proportional to the cubic Higgs self-coupling involves an extra Higgs propagator that dies off at high energy. Therefore, the kinematic region close to threshold is more sensitive to the Higgs self-coupling.

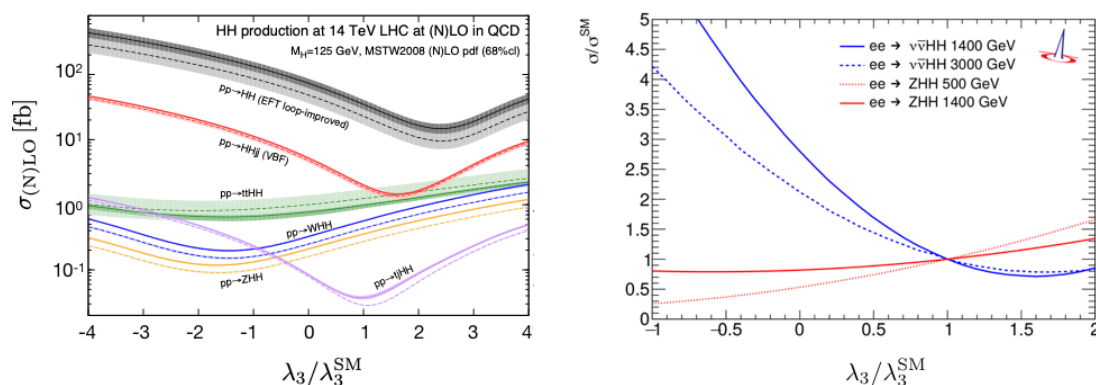


Figure 10. Double Higgs production at hadron (left) [65] and lepton (right) [66] colliders as a function of the modified Higgs cubic self-coupling. See table 18 for the SM rates. At lepton colliders, the production cross sections do depend on the polarisation but this dependence drops out in the ratios to the SM rates (beam spectrum and QED ISR effects have been included).

Thus, to be competitive with the HL-LHC constraint, the ZH cross section needs to be measured with an accuracy below 1%, but this is expected to be achieved by e^+e^- Higgs factories at 240/250 GeV. However, one needs to be able to disentangle a variation due to a modified Higgs self-interaction from variations due to another deformation of the SM. This cannot always be done relying only on inclusive measurements [73, 74] and it calls for detailed studies of kinematical distributions with an accurate estimate of the relevant uncertainties [75]. Inclusive rate measurements performed at two different energies also help lifting the degeneracy among the different Higgs coupling deviations (see for instance the κ_3 sensitivities reported in table 12 for FCC-ee₂₄₀ vs FCC-ee₃₆₅; it is the combination

of the two runs at different energies that improve the global fit, a single run at 365 GeV alone would not improve much compared to a single run at 240 GeV).

In principle, large deformations of κ_3 could also alter the fit of single Higgs processes often performed at leading order, i.e. neglecting the contribution of κ_3 at next-to-leading order. The results presented in section 3.4 were obtained along that line. It was shown in [73] that a 200% uncertainty on κ_3 could for instance increase the uncertainty in g_{Htt} or g_{Hgg}^{eff} by around 30–40%. The fact that HL-LHC from the double Higgs channel analysis will limit the deviations of κ_3 to 50% prevents such a large deterioration of the global fits to single Higgs couplings when also allowing κ_3 to float. In the effective coupling basis we are considering in this report, the effect of κ_3 would be mostly in the correlations among the single Higgs couplings. In other bases, like the Warsaw basis, there would be a deterioration up to 15-20% in the sensitivity of the operator $\mathcal{O}_{\phi\Box}$. Anyway, one should keep in mind that such a deterioration only concerns specific models where the deviations of the Higgs self-coupling is parametrically larger than the deviations of the single Higgs couplings and in generic situations, the results of section 3.4 hold.

In order to set quantitative goals in the determination of the Higgs self-interactions, it is useful to understand how large the deviations from the SM could be while remaining compatible with the existing constraints on the different single Higgs couplings. From an agnostic point of view, the Higgs cubic coupling can always be linked to the independent higher dimensional operator $|H|^6$ that does not alter any other Higgs couplings. Still, theoretical considerations set an upper bound on the deviation of the trilinear Higgs couplings. Within the plausible linear EFT assumption discussed above, perturbativity imposes a maximum deviation of the Higgs cubic self-interaction, relative to the SM value, of the order of [27, 73]

$$|\kappa_3| \lesssim \text{Min}(600 \xi, 4\pi), \tag{4.4}$$

where ξ is the typical size of the deviation of the single Higgs couplings to other SM particles [30]. However, the stability condition of the EW vacuum, i.e. the requirement that no other deeper minimum results from the inclusion of higher dimensional operators in the Higgs potential, gives the bound [27, 76]

$$|\kappa_3| \lesssim 70 \xi. \tag{4.5}$$

At HL-LHC, ξ can be determined with a precision of 1.5% at best, corresponding to a sensitivity on the Higgs self-coupling of about 100%, and thus somewhat inferior but roughly comparable to the direct sensitivity of 50% [13]. Parametric enhancements of the deviations of Higgs cubic self-coupling relative to the single Higgs couplings require a particular dynamics for the new physics. An example is encountered in Higgs portal models where the Higgs boson mixes with a SM neutral scalar field, possibly contributing to the dark matter relic abundance [41, 73]. In more traditional scenarios addressing the hierarchy problem, such as supersymmetric or composite models, the deviation of κ_3 is expected to be of the order ξ and is likely to remain below the experimental sensitivity.

The sensitivity of the various future colliders to the Higgs cubic coupling can be obtained using five different methods (1, 2(a), 2(b), 3, and 4):

1. an exclusive analysis of HH production, i.e., a fit of the double Higgs cross section considering only deformation of the Higgs cubic coupling;
2. a global analysis of HH production, i.e., a fit of the double Higgs cross section considering also all possible deformations of the single Higgs couplings that are constrained by single Higgs processes;
 - (a) the global fit does not consider the effects at higher order of the modified Higgs cubic coupling to single Higgs production and to Higgs decays;
 - (b) these higher order effects are included;
3. an exclusive analysis of single Higgs processes at higher order, i.e., considering only deformation of the Higgs cubic coupling; technically, this will be a one-dimensional EFT fit where only the linear combination of the two operators of eq. (4.2) corresponding to the κ_3 deformation is turned on;
4. a global analysis of single Higgs processes at higher order, i.e., considering also all possible deformations of the single Higgs couplings. Technically, this will be a 30-parameter EFT fit done within the scenario SMEFT_{ND} scenario of eq. (3.16). The contribution of κ_3 to EWPO at 2-loop could also be included but for the range of κ_3 values discussed here, the size of effects would be totally negligible.

Most of the studies of the Higgs self-couplings at Future Colliders were done following Method (1). In order to maximize the sensitivity to λ_3 , the analyses rely on sophisticated BDTs, and a simple recasting within an EFT framework is not an easy task. A pragmatic approach was followed along the line of what was proposed in [73]: different bins in m_{HH} are considered and the experimental uncertainty on the total rate is distributed in the different bins according to their number of expected events. This certainly ignores the bin-to-bin correlations and it does not take into account either that the background itself has a non-trivial shape as a function of m_{HH} . Nevertheless, the results obtained that way are in good agreement with those quoted by the different collaborations. This approach has the advantage that it can be easily generalised to a global EFT analysis that considers all the operators modifying also the single Higgs couplings, Methods (2). One should keep in mind that the bounds derived that way represent a crude estimate that waits for a proper experimental study.¹⁸

For most colliders, the single Higgs constraints are strong enough that they give a contribution to the double Higgs production below its experimental sensitivity. And Method (1) and Method (2) lead to rather similar bound on κ_3 . A notable exception is at FCC-hh where the 1% uncertainty on the top Yukawa coupling results in a deviation of the double Higgs production rate at a level comparable to the one induced by a shift of κ_3 by

¹⁸A detailed m_{HH} binned analysis was not available for HE-LHC, hence we could not estimate the κ_3 sensitivity along Method (2) for that collider. Similarly, for CLIC₃₀₀₀, the granularity of the available information was not sufficient to match the announced sensitivity, and therefore we did not venture into a complete study along Method (2) either. In both cases, our checks led to the conclusion that there will not be any noticeable difference between the sensitivity obtained in Methods (1) and (2).

5%. While a parametric enhancement of the deviation in κ_3 compared to the other Higgs couplings deviations could make its higher order contributions to single Higgs processes as important as the leading order ones and thus could in principle modify the global fit, in practice, the constraints set by the double Higgs production are strong enough that there is hardly any difference in the results obtained using Methods (2a) and (2b). Methods (3) and (4) are particularly relevant for low-energy colliders below the double Higgs production threshold. Above this threshold, these methods can still be relevant to complement results from the double Higgs analysis, for instance by helping to resolve the degeneracy between the SM and a second minimum of the likelihood. While this does not modify the 1σ bound on κ_3 , it can impact the bound starting at the 2σ level due to the non-Gaussian profile of the likelihood. It should be remembered that the single Higgs data used in Methods (3) and (4) have not been optimised for the extraction of the Higgs self-coupling that would benefit from further differential information. Therefore, the bounds on κ_3 should be considered as conservative and are certainly improvable.

Table 12 reports the sensitivity at the various colliders for the Higgs cubic coupling determination. For the global EFT fits, we limit ourselves to the SMEFT_{ND} scenario, see eq. (3.16), extended with eq. (3.7). For all results a simple combination with the HL-LHC results is done, i.e. by using a 50% uncertainty on κ_3 . It is seen that the results for Methods (1) and (2) are very similar, showing that the determination of κ_3 is dominated by the di-Higgs measurements when these are included. When comparing Methods (3) and (4) one observes that the exclusive results appear to be more constraining than the global results. But they overestimate the sensitivity as *a priori* it is not known which operator coefficients to fix and the same single-Higgs data should be used to constrain all operators. Method (4) is significantly more robust than Method (3). In the following we focus on Methods (1) and (4).

The results are also summarised in figure 11 for these two methods. Even though the likelihood is not a symmetric function of κ_3 , the current level of precision in this EFT analysis is not good enough to robustly assess an asymmetric error and we report only symmetrised bounds in the figure.

Based on di-Higgs measurements, with a 50% sensitivity on κ_3 , HL-LHC will exclude the absence of the Higgs self-interaction ($\kappa_3 = 0$) at 95%CL. Several of the proposed FCs (HE-LHC, LE-FCC and LHeC) will reach a sensitivity of order 20% based on di-Higgs production, thus establishing the existence of the self-interaction at 5σ . Even more remarkable, CLIC₃₀₀₀ and ILC₁₀₀₀ are expected to reach a sensitivity of order 10% and FCC_{hh} of the order of 5%, where one could start probing the size of the quantum corrections to the Higgs potential directly.

With single-Higgs production at FCC-ee and ILC₅₀₀ and ILC₁₀₀₀, in combination with di-Higgs results from HL-LHC, a sensitivity of $\sim 30\%$ can be reached. For FCC-ee with 4 interaction points (IPs) this is reduced to 24%. For the other collider options with $\sqrt{s} < 400$ GeV no improvement w.r.t. the HL-LHC result is seen.

Even though we do not report any sensitivity on κ_3 at muon-collider, we note that preliminary studies [77] indicate that a 10 TeV (resp. 30 TeV) machine could reach a 3% (resp. 1%) sensitivity.

collider	di-Higgs		single-Higgs		
	(1) excl.	(2.a) glob.	(3) excl.		(4) glob.
			with HL-LHC	w/o HL-LHC	
HL-LHC	$^{+60}_{-50}\%$ (50%)	52%	47%	–	50%
HE-LHC	10-20% (n.a.)	n.a.	40%	80%	50%
ILC ₂₅₀	–	–	29%	37%	49%
ILC ₃₅₀	–	–	28%	37%	46%
ILC ₅₀₀	27% (27%)	27%	27%	32%	38%
ILC ₁₀₀₀	10% (n.a.)	10%	25%	30%	36%
CLIC ₃₈₀	–	–	46%	120%	50%
CLIC ₁₅₀₀	36% (36%)	36%	41%	78%	49%
CLIC ₃₀₀₀	$^{+11}_{-7}\%$ (n.a.)	n.a.	35%	63%	49%
FCC-ee ₂₄₀	–	–	19%	21%	49%
FCC-ee ₃₆₅	–	–	19%	21%	33%
FCC-ee ₃₆₅ ^{4IP}	–	–	14%	14%	24%
FCC-eh	17-24% (n.a.)	n.a.	n.a.	n.a.	n.a.
FCC-ee/eh/hh	5% (5%)	6%	18%	19%	25%
LE-FCC	15% (n.a.)	n.a.	n.a.	n.a.	n.a.
CEPC	–	–	17%	18%	49%

Table 12. Sensitivity at 68% probability on the Higgs cubic self-coupling at the various future colliders. All the numbers reported correspond to a simplified combination of the considered collider with HL-LHC, which is approximated by a 50% constraint on κ_3 . The numbers in the first column (i.e. “di-H excl.” or Method (1)) correspond to the results given by the future collider collaborations and in parenthesis, we report our derived estimate obtained in the binned analysis described in the text. In the three last columns, i.e. Methods (2a), (3) and (4), we report the results computed by the Higgs@FC working group. For the leptonic colliders, the runs are considered in sequence. For the colliders with $\sqrt{s} \lesssim 400$ GeV, Methods (1) and (2.a) cannot be used, hence the dash signs in the corresponding cells. No sensitivity was computed along Method (2.a) for HE-LHC and CLIC₃₀₀₀ but our initial checks do not show any difference with the sensitivity obtained for Method (1). In the global analyses, Methods (2.a) and (4), we consider the flavour scenario of *Neutral Diagonality* (the results show little difference compared to the ones reported in the first version of this report within the *Neutral Diagonality* scenario). Due to the lack of results available for the ep cross section in SMEFT, we do not present any result for LHeC nor HE-LHeC, and only results with Method (1) for FCC-eh. For Method (3) results are shown with and without combination with HL-LHC for many of the colliders (in several cases, the fit for Method (4) does not converge for the standalone collider without HL-LHC input).

5 Rare Higgs boson decays

There are many reasons for the interest in rare Higgs boson decays. First, they provide access to Higgs couplings which are expected to be small in the SM and have not yet been directly probed. A leading example is the coupling to second and first generation fermions, whose determination would test the hypothesis that the same Higgs doublet is responsible for the mass generation of the lighter states of the SM. More specifically, the measurement of several Yukawa couplings will allow the comparison of ratios of couplings

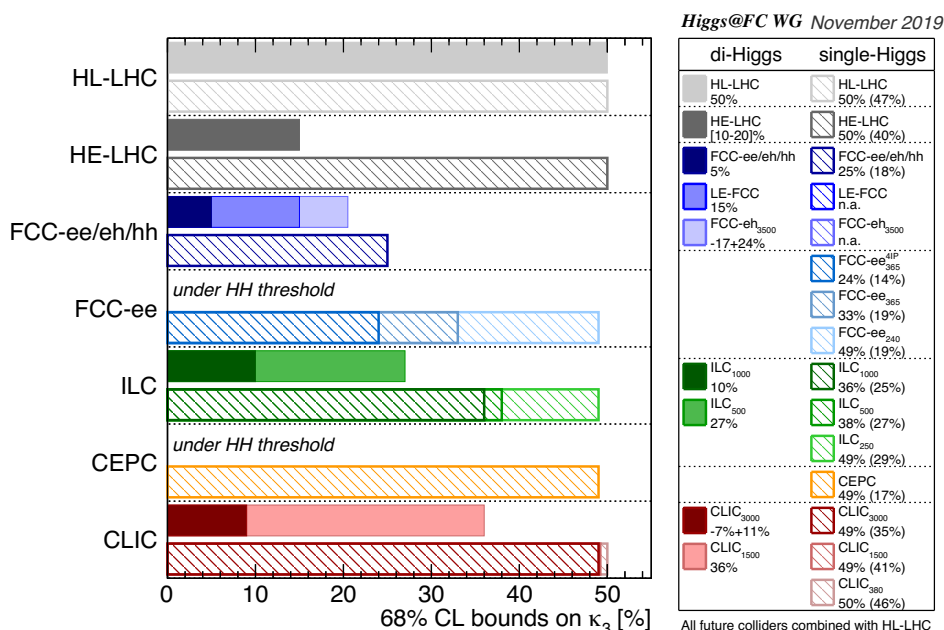


Figure 11. Sensitivity at 68% probability on the Higgs cubic self-coupling at the various FCs. All values reported correspond to a simplified combination of the considered collider with HL-LHC. Only numbers for Method (1), i.e. “di-H excl.”, corresponding to the results given by the future collider collaborations, and for Method (4), i.e. “single-H glob.” are shown (the results for Method (3) are reported in parenthesis). For Method (4) we report the results computed by the Higgs@FC working group. For the leptonic colliders, the runs are considered in sequence. For the colliders with $\sqrt{s} \lesssim 400$ GeV, Method (1) cannot be used, hence the dash signs. Due to the lack of results available for the ep cross section in SMEFT, we do not present any result for LHeC nor HE-LHeC, and only results with Method (1) for FCC-eh. When uncertainties are asymmetric (CLIC and FCC-eh) or a range is given (HE-LHC) the mid value is displayed.

with ratios of masses on the one hand, and test constants of proportionality on the other. The second motivation is that processes which are predicted to be rare in the SM, offer enhanced sensitivity to new physics residing at high scales. A leading example is the search for flavour-changing neutral interactions, which are extremely suppressed in the SM and if detected would reliably point to the existence of new physics. Third, peculiar and rare final state signatures can have a special connection with BSM scenarios. One example is H decaying to invisible particles, which is used to constrain scenarios featuring DM candidates. In the SM, the Higgs boson can decay invisibly via $H \rightarrow 4\nu$ with a branching ratio of 0.11%. Finally, Yukawa interactions with first generation fermions are the cornerstone of the low-energy constraints on CP violation of the couplings on the third generation. The typical example here are limits obtained by the EDM’s on the CP -odd interaction of the third generation fermions (section 6).

The reach of various colliders for rare decays, depends in the first place on the available statistics of the Higgs bosons being produced. The expected rates are presented in the appendix B, table 18.

	HL-LHC	HL-LHC+						
		LHeC	HE-LHC	ILC ₅₀₀	CLIC ₃₀₀₀	CEPC	FCC-ee ₂₄₀	FCC-ee/eh/hh
κ_u	560.	320.	430.	330.	430.	290.	310.	280.
κ_d	260.	150.	200.	160.	200.	140.	140.	130.
κ_s	13.	7.3	9.9	7.5	9.9	6.7	7.	6.4
κ_c	1.2		0.87			measured directly		

Table 13. Upper bounds on the κ_i for u, d, s and c (at hadron colliders) at 95% CL, obtained from the upper bounds on BR_{unt} in the kappa-3 scenario.

In the following, we restrict ourselves to a summary of the prospects to bound or determine the size of the interactions of the Higgs to the other SM particles through decays. These can occur either directly, through a process which is proportional to a tree-level coupling squared, i.e. all decays $H \rightarrow \bar{f}f$, where f is any SM fermion of the first or second generation, or indirectly, i.e. through interfering amplitudes or loops, such as $H \rightarrow \gamma\gamma$ and $H \rightarrow \gamma Z$. We will also briefly present results on very rare exclusive decays, which could provide indirect information on the light-quark Yukawa couplings. We follow the notation introduced in the κ -framework and consider the rescaling factors $\kappa_i = y_i/y_i^{\text{SM}}$ introduced previously for the couplings to quarks $\kappa_u, \kappa_d, \kappa_c, \kappa_s$ and for κ_μ , and for the loop induced processes, κ_γ and $\kappa_{Z\gamma}$. The values of $\kappa_\mu, \kappa_\gamma, \kappa_{Z\gamma}, \kappa_c$ have been obtained from the kappa-3,-4 fits presented in section 3.2 and we do not reproduce them here, while the upper bounds on $\kappa_u, \kappa_d, \kappa_s$ (κ_c for hadron colliders) are obtained from the upper limits on BR_{unt} . Constraints on flavour-changing Higgs boson interactions are not reported here.

The constraints of the couplings to first and second generation quarks are given in table 13 and displayed in figure 12, based on the results on BR_{unt} . For κ_c the hadron colliders reach values of $\mathcal{O}(1)$, and lepton colliders and LHeC are expected to improve the precision by about two orders of magnitude, to a 1-2%. For the strange quarks the constraints are about 5-10 \times the SM value while for the first generation it ranges between 100-600 \times the SM value. For the latter, future colliders could improve the limits obtained at the HL-LHC by about a factor of two. For HL-LHC, HE-LHC and LHeC, the determination of BR_{unt} relies on assuming $\kappa_V \leq 1$. For $\kappa_\gamma, \kappa_{Z\gamma}$ and κ_μ the lepton colliders do not significantly improve the precision compared to HL-LHC but the higher energy hadron colliders, HE-LHC and FCC_{hh} , achieve improvements of factor of 2-3 and 5-10, respectively, in these couplings.

For the electron Yukawa coupling, the current limit $\kappa_e < 611$ [78] is based on the direct search for $H \rightarrow e^+e^-$. A preliminary study at the FCC-ee [79] has assessed the reach of a dedicated run at $\sqrt{s} = m_H$. At this energy the cross section for $e^+e^- \rightarrow H$ is 1.64 fb, which reduces to 0.3 with an energy spread equal to the SM Higgs width. According to the study, with 2 ab⁻¹ per year achievable with an energy spread of 6 MeV, a significance of 0.4 standard deviations could be achieved, equivalent to an upper limit of 2.5 times the SM value, while the SM sensitivity would be reached in a five year run.

While the limits quoted on κ_c from hadron colliders (see table 13) have been obtained indirectly, we mention that progress in inclusive direct searches for $H \rightarrow c\bar{c}$ at the LHC

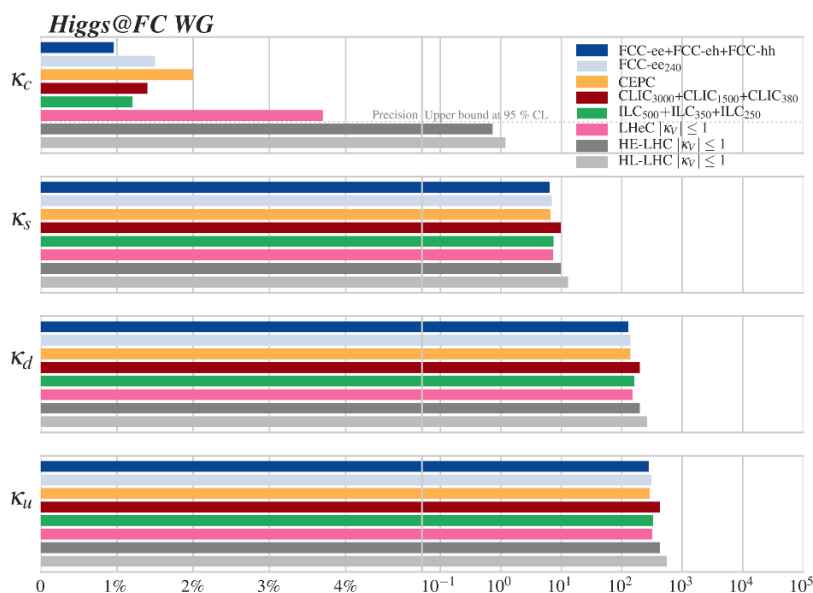


Figure 12. Summary plot illustrating the limits that can be obtained from rare Higgs decays on the couplings.

Collider	95% CL upper bound on				
	BR _{inv} [%]			BR _{unt} [%]	
	Direct	kappa-3	BR _{inv} only	kappa-3	BR _{unt} only
HL-LHC	2.6	1.9	1.9	4.0	3.6
HL-LHC + HE-LHC(S'_2)		1.5	1.5	2.4	1.9
FCC-hh	0.025	0.024	0.024	1.0	0.36
HL-LHC + LHeC	2.3	1.1	1.1	1.3	1.3
HL-LHC + CEPC	0.3	0.27	0.26	1.1	0.49
HL-LHC + FCC-ee ₂₄₀	0.3	0.22	0.22	1.2	0.62
HL-LHC + FCC-ee ₃₆₅		0.19	0.19	1.0	0.54
HL-LHC + ILC ₂₅₀	0.3	0.26	0.25	1.8	0.85
HL-LHC + ILC ₅₀₀		0.23	0.22	1.4	0.55
HL-LHC + ILC ₁₀₀₀		0.22	0.20	1.4	0.43
HL-LHC + CLIC ₃₈₀	0.69	0.63	0.56	2.7	1.0
HL-LHC + CLIC ₁₅₀₀		0.62	0.40	2.4	0.51
HL-LHC + CLIC ₃₀₀₀		0.62	0.30	2.4	0.33

Table 14. Expected upper limits on the invisible and untagged BRs of the Higgs boson. The SM decay, $H \rightarrow 4\nu$, has been subtracted as a background. Given are the values of the direct searches using missing (transverse) momentum searches, the constraint derived from the coupling fit (see table 5) in the kappa-3 scenario, and the result from a fit in the κ framework where only modifications of BR_{inv} are allowed. The last two columns show the corresponding information for untagged BR of the Higgs, BR_{unt}. For all fits the direct search for invisible decays is included.

has been reported from ATLAS together with a projection for the HL-LHC. Currently the upper bound on the charm coupling is $\kappa_c \lesssim 10$ [80]. With HL-LHC, it is expected to improve the sensitivity to values of $\kappa_c < 2.1$ (based on ref. [81]), while LHCb, with the foreseen detector improvement, could reach a sensitivity on κ_c of 2-3 [13].

Exclusive Higgs decays to a vector meson (V) and a photon, $H \rightarrow V\gamma$, $V = \rho, \omega, \phi, J/\psi, \Upsilon$ directly probe the Higgs bottom, charm strange, down and up quark Yukawas [82–84]. Within the LHC, the Higgs exclusive decays are the only direct probe of the u and d Yukawa couplings, while if s -tagging could be implemented at the LHC [84], then the strange Yukawa could be probed both inclusively and exclusively. On the experimental side, both ATLAS and CMS have reported upper bounds on $H \rightarrow J/\psi\gamma$ [85, 86], $H \rightarrow \phi\gamma$ and $h \rightarrow \rho\gamma$ [87, 88]. These processes receive contributions from two amplitudes, only one of which is proportional to the Yukawa coupling. Since the contribution proportional to the Yukawa is smaller, the largest sensitivity to the Higgs q -quark coupling is via the interference between the two diagrams. The prospects for probing light quark Yukawas within future LHC runs employing the direct probe from exclusive decays are not competitive with indirect limits that can be set from production or global fit or inclusive search for c -Yukawa [13, 81]. However, the information coming from exclusive decays will be relevant regardless of the global fit sensitivity. For example, a limit of $|y_s/y_b| \lesssim 50$ could be set HL-LHC [13] and $y_s/y_b \lesssim 25$ at FCC_{hh} [1].

The constraints on invisible and untagged BRs to new particles are reported in table 14. For the invisible decays the SM $H \rightarrow 4\nu$ process ($\text{BR}_{\text{inv}}^{\text{SM}} = \text{BR}(H \rightarrow 4\nu) = 0.11\%$) is treated as background. Shown are the estimated projections for direct searches for invisible decays using signatures of missing transverse or total energy, and the results from the kappa-3 fit presented earlier in table 5. Also shown is a kappa-fit where all SM BR values are fixed and only BR_{inv} is free in the fit. It is seen that the e^+e^- colliders generally improve the sensitivity by about a factor 10 compared to HL-LHC. FCC-hh improves it by another order of magnitude and will probe values below that of the SM. Comparing the three determinations of the BR_{inv} for the various colliders, it is seen that in most cases the difference is small, indicating that the BR_{inv} is mostly constrained by the direct search. An exception is LHeC where the kappa-fits improve the direct search result by a factor two.

Finally, comparing the bounds on the invisible and untagged BR one notices the latter are always weaker as the untagged BR is not constrained by any direct search here. For the untagged BR, the kappa-3 fit sensitivity is significantly worse than that obtained by fitting only BR_{unt} as the kappa-3 fit implicitly takes into account the experimental uncertainties on all other BR values.

6 Sensitivity to Higgs CP

Barring the strong-CP problem, in the SM the only source of CP violation stems from fermion mixing in the charged currents, while the Higgs boson is predicted to have CP-even, flavour-diagonal interactions. Detecting non-zero CP-odd components in the Higgs interactions with the SM particles, would therefore clearly point to physics beyond the Standard Model. Departures from the SM can be efficiently parametrised in terms of a

limited set of (flavour conserving) dimension-6 operators. Employing the Higgs basis, the (P-violating/C-conserving) CP-violating (CPV) HVV couplings are given by

$$\delta\mathcal{L}_{\text{CPV}}^{hVV} = \frac{h}{v} \left[\tilde{c}_{gg} \frac{g_s^2}{4} G_{\mu\nu}^a \tilde{G}_{\mu\nu}^a + \tilde{c}_{aa} \frac{e^2}{4} A_{\mu\nu} \tilde{A}_{\mu\nu} + \tilde{c}_{za} \frac{e\sqrt{g^2 + g'^2}}{2} Z_{\mu\nu} \tilde{A}_{\mu\nu} + \tilde{c}_{zz} \frac{g^2 + g'^2}{4} Z_{\mu\nu} \tilde{Z}_{\mu\nu} + \tilde{c}_{ww} \frac{g^2}{2} W_{\mu\nu}^+ \tilde{W}_{\mu\nu}^- \right], \quad (6.1)$$

where, g_s , g and g' are the $SU(3)$, $SU(2)_L$ and $U(1)_Y$ gauge coupling constants and $\tilde{V}_{\mu\nu} = \frac{1}{2}\epsilon^{\mu\nu\rho\sigma}V_{\rho\sigma}$. Out of the four electroweak parameters, only three are independent at this order in the EFT expansion. In particular,

$$\tilde{c}_{ww} = \tilde{c}_{zz} + 2\sin^2\theta_w \tilde{c}_{za} + \sin^4\theta_w \tilde{c}_{aa}. \quad (6.2)$$

The (P-violating/C-violating) CP-violating (yet flavour-diagonal) interactions of the Higgs boson with fermions can be parametrised as

$$\mathcal{L}_{\text{CPV}}^{hff} = -\bar{\kappa}_f m_f \frac{h}{v} \bar{\psi}_f (\cos\alpha + i\gamma_5 \sin\alpha) \psi_f, \quad (6.3)$$

where the angle α parametrizes the departure from the CP-even case. Another, equivalent parametrization employs $\kappa_f = \bar{\kappa}_f \cos\alpha$ and $\tilde{\kappa}_f = \bar{\kappa}_f \sin\alpha$, where $\kappa_f = 1 + \delta y_f$ in the notation used for the CP conserving cases in the κ -framework (with $\kappa > 0$). The pure scalar coupling corresponds to $\alpha = 0$ ($\tilde{\kappa}_f = 0$), a pure pseudoscalar coupling to $\alpha = 90^\circ$ ($\kappa_f = 0$), while CP violation occurs in all other intermediate cases.

Sensitivity to the CP-odd operators can arise from two distinct classes of observables. The first class includes CP-even observables, such as total cross sections or single particle inclusive distributions. In this case, CP-odd operators contribute in a way that is analogous to CP-even operators, i.e. affecting rates and shapes. The second class includes observables that are built to be directly sensitive to CP violation, i.e. they are zero (at the lowest order) if CP is conserved. Limits obtained from this second class are therefore automatically insensitive to the presence of higher-dimensional CP-conserving operators and deviations from zero would uniquely point to CP violation.

Sensitivity to the CP-odd hgg interaction comes from gluon fusion processes at the inclusive level, while direct sensitivity to CP violation can arise only starting from final states featuring at least two jets in the final state. Studies performed at the LHC exist, yet no dedicated investigation for future colliders has been documented. Sensitivity to the CP-odd hVV weak operators comes from Higgs-strahlung processes (WH and ZH), the vector boson fusion and the Higgs decay into four charged leptons ($H \rightarrow 4\ell$). Studies have been performed both at the level of rates/distributions and via CP-sensitive observables [13].

CP-violation effects in the couplings to fermions have been considered for the top quark and the tau lepton. Proposals to access information on CP violation in top quark interactions exist for both classes of observables, yet studies at future colliders have been mostly based on rates and distributions. These focus on ttH at hadron colliders and on ttH and tH final states at e^+e^- colliders and ep colliders, respectively, which are also sensitive

Name	α_τ	\tilde{c}_{zz}	Ref.
HL-LHC	8°	0.45 (0.13)	[13]
HE-LHC	—	0.18	[13]
CEPC	—	0.11	[2]
FCC-ee ₂₄₀	10°	—	[1]
ILC ₂₅₀	4°	0.014	[3]

Table 15. Upper bounds on the CP phase α of the Yukawa coupling for τ leptons and the CP-violating coefficient \tilde{c}_{zz} entering the HZZ coupling. The result in parenthesis for the HL-LHC is obtained with the same method used for the CEPC study.

to the absolute signs of CP-even and CP-odd interactions through interference effects. For example, by studying distributions in ttH , the HL-LHC will be able to exclude a CP-odd Higgs at 95%CL with about 200 fb^{-1} of integrated luminosity. CLIC 1.5 TeV foresees to measure the mixing angle for the top quark, α_t in $t\bar{t}H$ to better than 15° . At LHeC, a Higgs interacting with the top quarks with a CP-odd coupling can be excluded at 3σ with 3 ab^{-1} . At FCC_{eh} a precision of 1.9% could be achieved on α_t .

The most promising direct probe of CP violation in fermionic Higgs decays is the $\tau^+\tau^-$ decay channel, which benefits from a relatively large branching fraction (6.3%). Accessing the CP violating phase requires a measurement of the linear polarisations of both τ leptons and the azimuthal angle between them. This can be done by analysing the angular distribution of the various components of the tau decay products and by building suitable CP sensitive quantities (such as triple products of three-vectors or acoplanarities). The estimated sensitivities for the CP-violating phases, α_τ of the τ Yukawa coupling and \tilde{c}_{zz} extracted from CP-sensitive variables are collected in table 15.

Before concluding this section, we recall that CP-violating Yukawa couplings are well constrained from bounds on the electric dipole moments (EDMs) [89–94] under the assumptions of i) no cancellation with other contributions to EDMs, ii) SM values for the CP-even part of the Yukawa couplings.

CP violation in the top quark sector can be constrained by the EDM of the electron, giving $\tilde{\kappa}_t < 0.001$ once the latest limits of the ACME collaboration are considered [95]. For the bottom and charm Yukawas the strongest limits come from the neutron EDM, $\tilde{\kappa}_b < 5$ and $\tilde{\kappa}_c < 21$ when theory errors are taken into account. For the light quark CPV Yukawas, measurements of the neutron EDM give a rather weak constraint on the strange quark Yukawa of $\tilde{\kappa}_s < 7.2$, while the bound on the mercury EDM translates into strong bounds on the up and down Yukawas of $\tilde{\kappa}_u < 0.11$ and $\tilde{\kappa}_d < 0.05$ (no theory errors, 90% CL). For the τ Yukawa coupling, using the latest ACME measurement gives $\tilde{\kappa}_\tau < 0.3$, while for the electron Yukawa, provides an upper bound of $\tilde{\kappa}_e < 1.9 \times 10^{-3}$.

Assuming a SM Yukawa coupling of the Higgs to the electron, one can easily compare the indirect limits from EDMs with the prospects for direct ones. Using the relations between $(\bar{\kappa}, \alpha)$ and $(\kappa, \tilde{\kappa})$ one can convert the results for both the top quark (given above) and for the τ lepton (collected in table 15). One finds that the direct top quark limits are not competitive with the indirect ones, while those on the τ lepton are comparable with the current indirect ones.

7 The Higgs boson mass and full width

The current best measurement of the Higgs boson mass, based on the ATLAS and CMS analyses of $H \rightarrow ZZ^*$ and $H \rightarrow \gamma\gamma$ events in the LHC Run-2 data is 125.18 ± 0.16 GeV [96]. Future accelerators are expected to substantially improve the precision of this mass measurement.

The mass measurements at lepton colliders in the centre-of-mass energy range 240-350 GeV analyse the recoil mass of the Higgs boson in $e^+e^- \rightarrow ZH$ events, with $Z \rightarrow e^+e^-, \mu^+\mu^-$. Only the statistical uncertainties on the mass measurements are shown, as systematic uncertainties in this recoil mass analysis are expected to be negligible. The CLIC mass measurements at higher centre-of-mass energies analyse the $H \rightarrow b\bar{b}$ invariant mass distribution in $e^+e^- \rightarrow H(\rightarrow b\bar{b})\nu\nu$ events. The quoted mass resolutions based on m_{bb} measurements account only for statistical uncertainties, but are sensitive to b -jet energy scale uncertainties. This systematic uncertainty can be constrained with a $e^+e^- \rightarrow Z(\rightarrow b\bar{b})\nu\nu$ calibration sample which is expected to yield comparable statistics to the Higgs sample. The mass measurement at HL-LHC is based on the analysis of $H \rightarrow Z(l^+l^-)Z(l^+l^-)$ events. While the calibration of lepton momentum scales has not been studied in detail, a resolution of 10-20 MeV is projected to be plausibly in reach with the assumption that the higher statistics can help to significantly improve muon p_T systematic uncertainties.

Table 16 summarizes the expected precision of Higgs boson mass measurements of future accelerators. Also shown is the impact of the m_H uncertainty on the $H \rightarrow ZZ^*$ partial decay width. Already with HL-LHC, it will be possible to reduce this impact to the level of about 0.2%. At this value, the parametric uncertainty on Higgs partial widths, (primarily on ZZ^*, WW^*) is much smaller than the expected precision at any hadron collider. For the e^+e^- colliders the precision on the W and Z couplings is of that order, so that the m_H precision needs to be further improved to about 10 MeV to avoid any limitations on the Higgs coupling extraction precision (assuming the uncertainty due to higher order processes gets improved in the future, see table 19).

In the SM, the width of a 125 GeV H boson is predicted to be around 4 MeV, i.e. three orders of magnitude smaller than that of the weak bosons and of the top quark. It is therefore very challenging to measure it directly. All methods considered so far at colliders are in fact indirect and model dependent to various degrees. Three methods have been proposed at the LHC, and are considered for future hadron colliders.

The most direct method involves the diphoton decay mode and it is based on the measurement of the shape of the invariant mass of the diphoton close to the Higgs boson mass. This observable has a dependence on the width from signal-background interference effects. The foreseen sensitivity, however, will not allow to probe values close to the SM predictions, and can provide constraints of about $8 - 22 \times \Gamma_{\text{SM}}$ [13].

A second method extracts the width indirectly from a global fit of the Higgs boson couplings by employing specific assumptions. For example, in the κ -framework, assuming $\kappa_Z \leq 1$ and $\text{BR}_{\text{unt}} = 0$ one can determine the width from the fit.¹⁹

¹⁹In fact, the width and the branching ratio to undetected final states are not independent observables. In the analysis presented in section 3.2 we opted to fit BR_{unt} and calculate Γ_H from eq. (3.4).

Collider	Strategy	δm_H (MeV)	Ref.	$\delta(\Gamma_{ZZ^*})$ [%]
LHC Run-2	$m(ZZ), m(\gamma\gamma)$	160	[96]	1.9
HL-LHC	$m(ZZ)$	10-20	[13]	0.12-0.24
ILC ₂₅₀	ZH recoil	14	[3]	0.17
CLIC ₃₈₀	ZH recoil	78	[98]	0.94
CLIC ₁₅₀₀	$m(bb)$ in $H\nu\nu$	30 ²⁰	[98]	0.36
CLIC ₃₀₀₀	$m(bb)$ in $H\nu\nu$	23	[98]	0.28
FCC-ee	ZH recoil	11	[99]	0.13
CEPC	ZH recoil	5.9	[2]	0.07

Table 16. Overview of expected precision of Higgs boson mass measurements for future accelerators scenarios. For the lepton colliders (ILC, CLIC, CEPC) the projected uncertainties listed are statistical only. The impact of δm_H on $\delta\Gamma_{ZZ^*}$ reported in this table is calculated as $1.2\% \cdot (\delta m_H / 100 \text{ MeV})$, following ref. [97].

A third method is based on the combination of two independent measurements in gluon fusion production of a H boson with subsequent decay into a ZZ final state: $gg \rightarrow H \rightarrow ZZ^*$, where the H boson is on shell (and at least one of the final state Z off shell) and $gg \rightarrow ZZ$ with two on-shell Z bosons, where the H boson contribution is off shell [100]. The ratio of the off-shell over the on-shell rate is directly proportional to the total width [101]. Even though in generic BSM scenarios including the EFT, the interpretation of the off-shell/on-shell ratio as an extraction of the width is model dependent, this ratio can provide useful information on other key aspects of the Higgs couplings, e.g. their energy dependence [102]. It is foreseen that, with the HL-LHC and improvements in the theoretical calculations, Γ_H can be measured with a precision of up to 20% using this method [13].

At lepton colliders, the mass recoil method allows to measure the inclusive cross section of the ZH process directly, without making any assumption about the Higgs BR's. This possibility is unique to lepton colliders as it relies on the precise knowledge of the total initial energy of the event. In combination with measurements of exclusive Higgs decay cross sections, it allows to extract the total width Γ_H with a mild model dependence. The simplest way is to consider the ratio of the ZH cross section (from the recoil method) with the $H \rightarrow ZZ$ branching ratio (extracted from the $ZH, H \rightarrow ZZ^*$ rate)

$$\frac{\sigma(e^+e^- \rightarrow ZH)}{\text{BR}(H \rightarrow ZZ^*)} = \frac{\sigma(e^+e^- \rightarrow ZH)}{\Gamma(H \rightarrow ZZ^*)/\Gamma_H} \simeq \left[\frac{\sigma(e^+e^- \rightarrow ZH)}{\Gamma(H \rightarrow ZZ^*)} \right]_{\text{SM}} \times \Gamma_H, \quad (7.1)$$

where the last approximate equality assumes a cancellation of new physics effects, which holds, for instance, in the κ -framework. This method is limited by the relatively poor statistical precision of the $H \rightarrow ZZ$ BR measurement. More in general, even in scenarios where such a cancellation does not hold, e.g. in an EFT, a global fit can be performed to extract information on the width, using other decays (particularly the bb and WW decays)

²⁰In ref. [98] the values are 36 MeV (for $\sqrt{s} = 1.5 \text{ TeV}$) and 28 MeV (for $\sqrt{s} = 3 \text{ TeV}$) are based on unpolarized beams. The values quoted here are for the default scenario of 80% electron polarisation assumed throughout.

Collider	$\delta\Gamma_H$ [%] from ref.	Extraction technique for standalone result	$\delta\Gamma_H$ [%] kappa-3 fit
ILC ₂₅₀	2.3	EFT fit [3, 4]	2.2
ILC ₅₀₀	1.6	EFT fit [3, 4, 14]	1.1
ILC ₁₀₀₀	1.4	EFT fit [4]	1.0
CLIC ₃₈₀	4.7	κ -framework [98]	2.5
CLIC ₁₅₀₀	2.6	κ -framework [98]	1.7
CLIC ₃₀₀₀	2.5	κ -framework [98]	1.6
CEPC	2.8	κ -framework [103, 104]	1.7
FCC-ee ₂₄₀	2.7	κ -framework [1]	1.8
FCC-ee ₃₆₅	1.3	κ -framework [1]	1.1

Table 17. Overview of expected precision of Higgs boson width measurements for future accelerator scenarios. The result given in the second column refers to the width extraction as performed by the future lepton colliders using the stated technique, and as provided in the references given. The last column of the table lists the width extracted from the kappa-3 scenario fit. It also includes the HL-LHC measurements (but excludes the constraint $\kappa_V < 1$ that is used in HL-LHC-only fits).

and channels ($e^+e^- \rightarrow H\nu\bar{\nu}$). This method is used for CEPC. For FCC-ee and CLIC the κ -formalism is used to extract the width, similar to what is done in this report for table 5. For ILC, the width reported here was extracted using an EFT formalism that does not assume that there is only one operator that governs the interactions between the Higgs boson and the Z boson (as is done implicitly in the κ -framework). In this determination of Γ_H , angular distributions and polarisation asymmetries are used to constrain the free parameters that result from relaxing this assumption [18], in addition to the parameters used by the κ -formalism for the other lepton colliders. This fit is different from the EFT fits performed in section 3.4.

Table 17 summarizes the expected relative precision that can be reached on the Higgs width at future lepton colliders, comparing the estimates of the standalone estimates of the future lepton colliders to the results of the kappa-3 scenario fits performed in this article (with HL-LHC data included). It is seen that the result obtained in the kappa-3 fit is generally more constraining than the results quoted in the references, primarily as this result also includes the constraint from the HL-LHC data, and, in some cases, uses a different approach to modelling changes to the total width. In both cases, the best precision is obtained for the ILC₅₀₀ and FCC-ee₃₆₅ scenarios.

8 Future studies of the Higgs sector, post-European Strategy

8.1 Higgs prospects at the muon collider

Electron-positron colliders offer a well-defined value of the collision energy of the hard-scattering process and a relatively clean event, as opposed to hadron collisions where the underlying event and the high-level of event pileup challenge the reconstruction of the hard scattering event and its measurement.

The main limitation to the collision energy of circular electron-positron colliders is due to the low mass of the electrons/positrons which leads to large fraction of their energy emitted as synchrotron radiation. The solutions pursued so far to reach high lepton collision energies are based on limiting the energy loss by synchrotron radiation by reducing the curvature either by increasing the radius of the circular colliders or by employing linear colliders. However, the beam acceleration does require a number of RF cavities imposing a machine of large dimensions.

With a mass of about two hundred times that of electrons, muons do not suffer significant energy losses due to synchrotron radiation (the loss goes as the inverse of the fourth power of the mass) and therefore could be accelerated up to multi-TeV collision energies. For example, if the LHC ring were used, with the proposed HE-LHC dipoles (Nb₃Sn, 16 T), muons would collide at an energy close to $\sqrt{s} = 14$ TeV, compared to the 0.2 to 0.4 TeV of an electron-positron collider.

Alternatively, a collider with $\sqrt{s} = 125$ GeV could be a very compact (diameter ~ 60 m) Higgs factory using s -channel production of Higgs bosons [105]. However, it should be noted that the expected rate of produced Higgs bosons by s -channel is small, given the instantaneous luminosity possible at this machine [106], and the limited production cross section (taking into account both the beam energy spread and the initial state radiation effects) [107–109]. Estimates of the achievable precision on Higgs couplings for such a machine are given in [110].

Muon production, cooling, lifetime and physics background [111] pose severe challenges to the accelerator and detector technologies. Although the study of a Muon Collider (machine and physics prospects) is not as mature as those of other future proposed colliders, its physics potential certainly merits consideration.

Currently, two different configurations have been proposed for the muon collider. In the first configuration, muons are produced by the decay of hadronically produced charged pions or kaons, and cooled before they undergo the acceleration [106]. In the second configuration, muons are produced at threshold (in the centre of mass frame) by high energy positron collisions with atomic electrons [112]. The first configuration has been originally proposed for $\mu^+\mu^-$ collision at the Higgs boson pole ($\sqrt{s} \sim 125$ GeV), while the second is mainly considered for very high energy collisions, in the range of $O(10)$ TeV.

At muon collision c.m. energies $\sqrt{s} \gtrsim 10$ TeV, assuming the *point cross section* $\sigma \simeq 4\pi\alpha^2/(3s) \simeq 1 \text{ fb} \cdot (10 \text{ TeV}/\sqrt{s})^2$, the requirement of a percent statistical precision in the measurement of heavy particle pair production would imply an integrated luminosity of the order $L \sim 10 \text{ ab}^{-1} (\sqrt{s}/10 \text{ TeV})^2$. This could correspond to a 10-year physics run with an instantaneous luminosity of the order $10^{35} (\sqrt{s}/10 \text{ TeV})^2 \text{ cm}^{-2} \text{ s}^{-1}$ [113]. At such large values of \sqrt{s} , both the single-Higgs and the multi-Higgs production mechanisms are dominated by vector-boson fusion (VBF) processes, which provides very large statistical Higgs samples [77]. As an example, at $\sqrt{s} \sim 14$ TeV, with 20 ab^{-1} , one would produce about 20 million single Higgs, 90,000 Higgs pairs, and 140 triple Higgs final states, with presumably quite moderate background. Although there is currently only preliminary analysis of the Higgs production in such an environment this would be a robust basis to considerably advance on the Higgs couplings determination. The Higgs self-coupling

sector might be explored with unprecedented precision. In particular, with the above Higgs production statistics, and no unexpectedly difficult background, an accuracy of few percent for the trilinear Higgs coupling, and a few tens of percent for the quadrilinear Higgs coupling might be reached at $\sqrt{s} \sim 14$ TeV, with 20 ab^{-1} , assuming all the remaining Higgs and EW parameters at their SM value. Many other investigations of the Higgs properties might significantly benefit from such collider configuration [77, 113].

8.2 Higgs physics at multi-TeV electron-positron colliders

The length of linear accelerators proposed today, is largely determined by the electric field gradients that can be achieved with RF cavities. For the superconducting RF technology used by ILC the limit is about 35 MV/m while for the drive-beam technology, envisaged for CLIC, it is about 100 MV/m.

Much higher gradients (up to 1000 times more acceleration compared to RF) can be achieved using plasma-wakefield acceleration, where laser pulses [114–117], electron [118, 119] or proton [120] bunches (called drivers) can excite ultra-high fields in plasma devices. Thus this is a very promising technique for future high energy e^+e^- and $\gamma\gamma$ colliders.²¹ The ALEGRO Collaboration [9] has been formed with the goal of designing an Advanced Linear Collider (ALIC) based on this technology. A summary of the facilities operating today and planned for the future, as well as the R&D needed, are given in [9]. The physics opportunities of an e^+e^- collider with \sqrt{s} up to 100 TeV are also discussed there.

The minimum instantaneous luminosity that needs to be achieved for probing cross sections of new particles interacting weakly at energies in the 10 – 100 TeV is found to be $10^{36} \text{ cm}^{-2}\text{s}^{-1}$. With such a collider, an integrated luminosity of 30 ab^{-1} could be collected within a few years. With this dataset, the Higgs physics programme is similar to that of a Multi-TeV muon collider outlined above. It is also being considered to have such a collider at lower collision energies, in the range between m_Z and 3 TeV. Here, it would have the same physics programme as the other proposed colliders, assuming that comparable luminosity values can be achieved and background conditions are similar.

The proposed ALIC collider [9] would achieve $\sqrt{s} = 30$ TeV with a peak luminosity of $10^{36} \text{ cm}^{-2}\text{s}^{-1}$ in a tunnel of 9 km length. While the principle of acceleration has been proven, there are many issues that need to be resolved before a collider based on plasma-technology can be achieved, but none are considered to be show-stoppers at present. The primary focus of the R&D programme is the beam quality which is addressed at lower-energy applications (e.g. free-electron lasers, fixed target experiments) and will benefit the development of a collider based on this technology.

8.3 What and why: Higgs prospect studies beyond this report

The purpose of this subsection is to place the Higgs coupling measurements in perspective with other new physics studies performed at future colliders with the aim of providing answers to the following two questions: *What are we going to learn?*, *What can we possibly*

²¹For $\gamma\gamma$ colliders it is sufficient to accelerate two e^- beams which is technically less demanding than accelerating positrons.

discover? The unknown territory of energy and precision to be explored may have different discoveries in store, including unexpected ones. Given the scope of this document, a discussion of the various options would hardly be self-contained, and would miss, by definition, the most exciting case of unexpected discoveries. On the other hand, by focusing on some open problems in particle physics, it is possible to structure a self-contained discussion at least around the first question. The hierarchy problem (HP), dark matter (DM) and the electroweak phase transition (EW Φ T) are issues on which we shall definitely make progress. Flavour could also be added to this list, but mostly in the measure in which it is connected to the HP.

In view of its centrality, and of the controversial regard in which it is sometimes held, a succinct but modern appraisal of the HP is needed. The HP is a paradox challenging the modern effective field theory (EFT) view of particle physics. The challenge is presented by the clash between infrared (IR) Simplicity and Naturalness. IR Simplicity is an unavoidable feature of any EFT when making observations at energies much below its fundamental scale Λ_{UV} . In practice that is due to the decoupling of the infinite (complicated) set of non-renormalizable couplings in favor of the finite (simple) set of renormalizable ones. Naturalness instead arises by viewing EFT parameters as functions of more fundamental ones: in this point of view it is expected that any specific structure, like the presence of a very small parameter, should be accounted for by symmetries and selection rules rather than by accidents. Now, the structure of the SM is such that several crucial experimental facts like approximate baryon and lepton numbers, lightness of neutrinos, GIM suppression of FCNC, custodial symmetry *all* remarkably and beautifully follow from IR Simplification. That is by assuming $\Lambda_{UV} \gg m_{weak}$. However when considering the Higgs mass parameter, one famously finds that $\Lambda_{UV} \gg m_H$ is inconsistent with the predicate of Naturalness. In the SM, IR Simplicity can thus only be obtained at the price of un-Naturalness. But this is only half of the problem. The other half is that models realizing Naturalness, like supersymmetry (SUSY) or Composite Higgs (CH), invariably sacrifice Simplicity. Indeed all these natural extensions have concrete structural difficulties in reproducing the observed simplicity in flavour, CP violating and electroweak observables. In order to meet the corresponding experimental constraints, these scenarios must rely on *clever* constructions mostly associated with *ad hoc* symmetries, like flavour symmetries or custodial symmetry, which in the SM are either not needed or automatic. The paradoxical tension between Simplicity and Naturalness is what defines the hierarchy problem: no win-win scenario seems to be available.

The paradox could already be formulated before LEP, and gained in importance with more and more precise flavour and electroweak data that demands a more elaborate structure in natural models. Furthermore, the ever stronger bounds from direct searches for ‘Natural’ agents at Tevatron and LHC imply the need for some amount of un-Naturalness, or fine tuning, even in models like SUSY or CH that aimed at full Naturalness. Depending on the scenario, the finesse of the cancellation in the Higgs mass parameter needed to lift new physics out of LHC reach can be quantified to roughly range from 1/10 to 1/10³.

The test of Naturalness vs. Simplicity offers one concrete criterion to compare future machines across their reach in three different sets of measurements: direct searches, Higgs couplings, EW precision tests (EWPT).

- *Direct searches*: natural models all possess computational control over the Higgs squared mass. The result varies in a finite range, and a small or vanishing result can only be achieved by tuning different contributions against one another. Indicating by Δm_H^2 the most sizeable contribution, the tuning is simply measured by

$$\epsilon \equiv m_H^2 / \Delta m_H^2, \tag{8.1}$$

with m_H the observed Higgs mass. Because of its large Yukawa coupling, the most sizeable effects come from coloured states associated with the top, the so-called top-partners. Models can be broadly classified into three classes according to the dependence of Δm_H^2 on the top partner mass m_T :

- *Soft*: $\Delta m_H^2 \sim m_T^2$. This situation is realized in SUSY with soft terms generated at a high scale. In the absence of any tuning $m_T \sim m_H \sim 100$ GeV, within the energy range of LEP and Tevatron.
- *SuperSoft*: $\Delta m_H^2 \sim (3y_t^2)/(4\pi^2) m_T^2$. This situation is realized in SUSY with low scale mediation and in CH. Without any tuning one expects $m_T \sim m_H / \sqrt{3y_t^2/4\pi^2} \sim 450$ GeV, within the reach of the LHC.
- *HyperSoft*: $\Delta m_H^2 \sim (3\lambda_h)/(16\pi^2) m_T^2$. The mechanism of Neutral Naturalness is a prime example. The top partner mass is naturally pushed around 1.5 TeV.

A ~ 10 TeV reach on m_T like offered by FCC-hh or muon-collider (the top partners have often EW quantum numbers) will thus probe Naturalness down to $\epsilon = 10^{-4}, 10^{-3}, 10^{-2}$ in respectively Soft, SuperSoft and HyperSoft scenarios.

- *Higgs couplings*: the deviations δg_h from the SM in single and multi-Higgs couplings satisfy

$$\delta g_H / g_H^{\text{SM}} \sim c \epsilon, \tag{8.2}$$

with c a coupling-dependent coefficient, and ϵ the Higgs mass correction defined in (8.1). In basically all models, there always exists a set of couplings where $c \sim O(1)$. The only exception is strictly supersoft SUSY, where one can cleverly go down to $c \sim 0.1$. Not surprisingly full Naturalness basically mandates $O(1)$ deviations in Higgs couplings.

The best measurements that will be carried out at future machines aim at 10^{-3} precision on some of the Higgs couplings, in particular g_{HWW} and g_{HZZ} . This should be compared to the reach in ϵ in direct searches. In particular, Higgs couplings probe less than direct searches in the simplest high scale SUSY models. But one must not forget that these models admit countless variants, with additional states, in particular SM singlets, and with a spread spectra. So one cannot completely discount the relevance of Higgs couplings to probe these models. In any case, one should not underestimate the value of Higgs precision programme that can measure the Higgs couplings with a 10^{-3} precision. The equal relevance of Higgs studies and direct searches for CH models seems robust.

In view of parametric uncertainties, 10^{-3} seems like a limiting (or at least a critical) sensitivity to BSM deviations in single Higgs production near threshold. However these deviations are all associated with operators of dimension ≥ 6 , whose effects grow with energy when considering processes with a sufficient number of legs, like $gg \rightarrow HH, hV_L$ or $VV \rightarrow HH, V_L V_L$. And one must then consider the possibility of obtaining a better sensitivity by measuring such processes. For instance, FCC-hh can probe $gg \rightarrow HV_L$ and $VV \rightarrow VV$ up to $\epsilon \sim 1\%$ [79]. Lepton machines might compete better: while CLIC can reach a sensitivity to $\epsilon \sim 10^{-2}$ in $VV \rightarrow HH$ [121], still one order of magnitude poorer than single Higgs measurements, a recent analysis [77] of a muon collider shows the $\epsilon = 10^{-3}$ wall is beaten for a CM energy of 10 TeV. A μ -dream machine running at 30 TeV could go down to $\epsilon = 2 \times 10^{-4}$ [77], which competes well even with the reach on top partners (~ 14 TeV) for such a machine.

- *EWPT*: while Higgs couplings are prime sensors of Naturalness, EWPT sense the dynamics of EWSB indirectly, via loops. To make this concrete, consider the \hat{S} parameter, defined with the normalization of [48]. For all models, encompassing supersymmetry, CH or technicolor one can write a parametric formula

$$\hat{S} \sim \frac{\alpha_W}{4\pi} \frac{g_*^2 v^2}{m_*^2} N \lesssim \frac{m_W^2}{m_*^2}, \tag{8.3}$$

where m_*, g_* indicate overall mass and coupling of the new dynamics (the most obvious expectation being $m_* \sim m_T$), while N measures the number of new degrees of freedom. Theoretical considerations set the upper bound $g_* \sqrt{N} \lesssim 4\pi$, which is saturated in CH and technicolor where $\hat{S} \sim m_W^2/m_*^2$. In these models a measurement of \hat{S} translates into an indirect measurement of the scale m_* . In the case of CH, one obtains $\hat{S} \equiv 3 \times 10^{-2} \epsilon$, indicating that a sensitivity to $\hat{S} \sim \text{few} \times 10^{-5}$ corresponds to 10^{-3} sensitivity in Higgs couplings/fine tuning. Supersymmetric models are instead well below the saturation of the upper bound, as in that case the g_* is of the order of SM couplings, principally g_W and y_t , while the multiplicity N is $O(1)$ [122]. One can then very roughly write $\hat{S} \sim (\alpha_W/4\pi)(m_{weak}^2/m_*^2)$ implying $m_* \gtrsim 1$ TeV is enough to make $\hat{S} \lesssim 10^{-5}$, below the wildest dreams of an FCC-ee.

Very much like for Higgs couplings, we can consider the sensitivity to the same class of dim-6 operators contributing to \hat{S} in processes with more legs, where the growth with energy can be exploited. A crucial comparison here is that between the reach of a Z -pole machine like the FCC-ee and CLIC which can study processes such as $e^+e^- \rightarrow hZ, h\gamma, WW$ at higher energies.²² The available CLIC studies estimate its reach as $\hat{S} \simeq 0.5 \times 10^{-5}$. This should be compared to the estimated reach of 5×10^{-5} at FCC-ee. Again the systematics of the two measures would be drastically different, with CLIC dominated by statistics and with FCC-ee dominated by parametric and intrinsic systematics.

²²The latter processes are sensitive to slightly different combinations of operator coefficients than \hat{S} at low energy, but in well motivated models like CH, this difference is often subdominant, and at worse they represent equally interesting but different combinations.

The above analysis also offers the starting point for the consideration of other motivations and other viewpoints. As we mentioned at the beginning the EW phase transition and DM offer alternative motivations. We will discuss them briefly in what follows.

The interest in the order of the EW phase transition is largely related to baryogenesis. A strongly first order transition with sizeable sources of CP violation from BSM dynamics could generate the observed cosmological baryon asymmetry. The corresponding new physics would impact both future colliders and precision low energy studies. In particular a first order phase transition implies a $O(1)$ change in the Higgs potential at finite temperature, indicating the possibility for important effects also at zero temperature, the regime we can test at colliders. The connection between $T \neq 0$ and $T = 0$ is however model dependent and one can broadly distinguish two scenarios. In the absence of new symmetries $T \neq 0$ and $T = 0$ are directly connected and the Higgs trilinear is expected to be $O(1)$ off its SM prediction (see e.g. [123]). On the other hand in the presence of extra symmetries [124] there could be a further phase separation between $T \neq 0$ and $T = 0$ in which case deviations can be smaller but hardly smaller than a few % [125]. The low energy implications of EW baryogenesis concern electric dipole moments (edms) from new sources of CP violation. Here it must be noticed that the present bound $d_e < 10^{-29}$ e-cm on the electron edm is already very strongly constraining many scenarios. Moreover there are serious plans to improve the sensitivity on d_e by a few orders of magnitude in the future. A thorough analysis is not available to our knowledge, but it would be interesting in order to better appreciate the impact of such improved measurements on the space of possibilities, as that conditions the importance of Higgs trilinear studies. It should however be kept in mind that the EW Φ T could be viewed as interesting *per se*, regardless of baryogenesis, as it is an essential part of the history of our Universe. It also offers a new bridge between Higgs physics and gravitational physics: in case of a strong first order phase transition, the EW Φ T would be the source of a stochastic gravitational wave (GW) background and future GW experiments like LISA could proffer complementary probes of the Higgs potential [126].

The search for Dark Matter (DM) at future colliders is a broad field whose implications cannot be even partially described here. One crucial strength of a machine with a reach in the multi-TeV range is that it should be able to discover the minimal incarnation of DM, the one which arises from the purely radiatively split EW multiplets. Amazingly, this simple and well motivated class of models is hardly directly detectable in view of its loop suppressed spin independent cross section (see table 1 in [127]). Focussing on Higgs studies the basic question is: to what extent can an invisible Higgs width be associated with DM? The answer is given in figure 4 of ref. [128]: considering all present constraints there remains a very small region around $m_{DM} = m_H/2$, and part of this region will be explored, by direct DM detection experiments a long time before the future precision Higgs studies. The chance that DM sits in this region seems slim but a discovery in direct detection would certainly add to the Higgs programme. One should also keep in mind that the Higgs boson can decay invisibly to new particles that are not by themselves stable with the right relic abundance, but that would be part of a more complex DM sector whose abundance would not set by its interactions with the Higgs but rather by its own internal

dynamics. Twin sectors of Mirror Twin Higgs models [129] and strongly coupled dark sectors [130] are examples of this type and they offer a motivation to search for invisible decays of the Higgs.

9 Summary

The precision study of the Higgs boson will be the primary guaranteed deliverable of any future collider facility. The apparent uniqueness of the Higgs boson, as the only fundamental scalar boson thus far discovered, justifies the importance which it is accorded in planning for future facilities.

Several future colliders have been proposed in the context of the update of the European Strategy for Particle Physics. The potential of these machines for Higgs boson physics has been intensely studied by the proponents of these machines. The purpose of the Higgs@FutureCollider Working Group (Higgs@FC WG) and this report is to provide a coherent comparison of the reach of these machines in the exploration of the Higgs sector. We have assumed the baseline provided by the approved programme of the HL-LHC and quantified the additional information that would be provided by each of the future facilities.

Taking into account the inputs submitted to the strategy process and our dedicated discussions with proponents of future colliders, we provide this report on the comparisons achieved, using both the simplified kappa framework and an alternative EFT framework. The comparisons are made in reasonable frameworks developed based on current knowledge, with the prime objective to allow a clear and coherent comparison. Where relevant we note the potential caveats in the approaches taken. We have also reported on the rare decays of the Higgs boson, on measurements of its mass and width, and on the expectations for CP violation studies.

Acknowledgments

We would like to express our appreciation to the numerous colleagues who have presented and discussed material to our working group, and in addition for the valuable comments made on a draft of this report by representatives of the future collider projects.

We wish to express special thanks to J. Gu for discussions, for providing some of the inputs for the EFT studies in this report, and for his help in producing some of the results presented in section 4. We are also very grateful to J. Tian for his cross-checks of the EFT fit results and to J. Reuter for his results on the double Higgs cross-sections at lepton colliders.

We thank S. Heinemeyer and collaborators for kindly sharing an updated version of their study of the theory uncertainties in electroweak and Higgs precision observables, whose results were also include in this report. We also benefited from helpful discussions with R. Contino, G. Durieux, G.F. Giudice, M. Kumar, M. Mangano, M. McCullough, G. Panico, A. Paul, M.E. Peskin, A. Pomarol, J. Reuter, F. Riva, A. Shivaji, Y. Soreq, E. Vryonidou, A. Wulzer and X. Zhao.

The work of CG and BH was in part funded by the Deutsche Forschungsgemeinschaft under Germany’s Excellence Strategy-EXC 2121 “Quantum Universe” — 390833306. The work of JDH and FM was partly supported by F.R.S.-FNRS under the “Excellence of Science — EOS” — be.h project n. 30820817.

A Mandate agreed by RECFA in consultation with the PPG “Higgs physics with future colliders in parallel and beyond the HL-LHC”

In the context of exploring the Higgs sector, provide a coherent comparison of the reach with all future collider programmes proposed for the European Strategy update, and to project the information on a timeline.

- For the benefit of the comparison, motivate the choice for an adequate interpretation framework (e.g. EFT, κ , ...) and apply it, and map the potential prerequisites related to the validity and use of such framework(s).
- For at least the following aspects, where achievable, comparisons should be aim for:
 - Precision on couplings and self-couplings (through direct and indirect methods);
 - Sensitivities to anomalous and rare Higgs decays (SM and BSM), and precision on the total width;
 - Sensitivity to new high-scale physics through loop corrections;
 - Sensitivities to flavour violation and CP violating effects.
- In all cases the future collider information is to be combined with the expected HL-LHC reach, and the combined extended reach is to be compared with the baseline reach of the HL-LHC.
- In April 2019, provide a comprehensive and public report to inform the community.
- ECFA helps in the creation of a working group relevant for the Strategy process, especially for the Physics Preparatory Group (PPG).
- Towards the Open Symposium the working group will work together with the PPG to provide a comprehensive and public report to inform the community, i.e. this is not an ECFA report.
- The working group has a scientific nature, i.e. not a strategic nature; it uses the input submitted to the Strategy process to map the landscape of Higgs physics at future colliders.
- The convenors in the PPG who are connected to this specific topic (Beate Heinemann and Keith Ellis) and the ECFA chair will be included as *ex-officio* observers.

B Theoretical cross sections and partial width uncertainties

pp collider	Cross Section σ [pb]							
	Total	ggH	VBF	WH	ZH	$t\bar{t}H$	tH	$ggHH$
LHC (13 TeV)	56	48.6	3.77	1.36	0.88	0.510	0.074	0.031
HL-LHC	62	54.7	4.26	1.50	0.99	0.613	0.090	0.037
HE-LHC	168	147	11.8	3.40	2.47	2.86	0.418	0.140
FCC _{hh}	936	802	69	15.7	11.4	32.1	4.70	1.22

e^+e^- collider ($\mathcal{P}_{e^-}/\mathcal{P}_{e^+}$)	Cross Section σ [fb]				
	Total	VBF CC/NC	ZH	$t\bar{t}H$	ZHH (CC VBF)
CEPC	199	6.19/0.28	192.6		
FCC-ee	199	6.19/0.28	192.6		
ILC ₂₅₀ (-80/30)	313	15.4/0.70	297		
ILC ₅₀₀ (-80/30)	262	158/7.8	96	0.41	0.2
CLIC ₃₈₀ (0/0)	160	40/7.4	113	—	0.029 (0.0020)
CLIC ₁₅₀₀ (0/0)	329	290/30	7.5	1.3	0.082 (0.207)
CLIC ₃₀₀₀ (0/0)	532	480/49	2	0.48	0.037 (0.77)
CLIC ₃₈₀ (-80/0)	209	68/8.7	133	—	0.034 (0.0024)
CLIC ₁₅₀₀ (-80/0)	574	528/35	8.8	1.70	0.97 (0.37)
CLIC ₃₀₀₀ (-80/0)	921	860/57	2.4	0.61	0.043 (1.38)
CLIC ₃₈₀ (+80/0)	112	13/6.0	93	—	0.024 (0.0016)
CLIC ₁₅₀₀ (+80/0)	91	59/24	6.2	0.89	0.068 (0.045)
CLIC ₃₀₀₀ (+80/0)	138	96/40	1.7	0.34	0.30 (1.56)

e^-p collider (\mathcal{P}_{e^-})	Cross Section σ [fb]			
	Total	VBF CC/NC	tH	HH (CC VBF)
LHeC (0)	130	110/20	0.07	0.01
HE-LHeC (0)	247	206/41	0.37	0.04
FCC _{eh} (0)	674	547/127	4.2	0.26
LHeC (-80)	221	197/24	0.12	0.02
HE-LHeC (-80)	420	372/48	0.67	0.07
FCC _{eh} (-80)	1189	1040/149	7.6	0.47

Table 18. Cross sections for the main production channels expected for Higgs boson production at the different types of colliders (as defined in table 1).

Decay	Γ [keV]	current unc. $\Delta\Gamma/\Gamma$ [%]			future unc. $\Delta\Gamma/\Gamma$ [%]			
		Th_{Intr}	$\text{Th}_{\text{Par}}(m_q)$	$\text{Th}_{\text{Par}}(\alpha_s)$	Th_{Intr}	$\text{Th}_{\text{Par}}(m_q)$	$\text{Th}_{\text{Par}}(\alpha_s)$	$\text{Th}_{\text{Par}}(m_H)$
$H \rightarrow b\bar{b}$	2379	< 0.4	1.4	0.4	0.2	0.6	< 0.1	—
$H \rightarrow \tau^+ \tau^-$	256	< 0.3	—	—	< 0.1	—	—	—
$H \rightarrow c\bar{c}$	118	< 0.4	4.0	0.4	0.2	1.0	< 0.1	—
$H \rightarrow \mu^+ \mu^-$	0.89	< 0.3	—	—	< 0.1	—	—	—
$H \rightarrow W^+ W^-$	883	0.5	—	—	0.4	—	—	0.1
$H \rightarrow gg$	335	3.2	< 0.2	3.7	1.0	—	0.5	—
$H \rightarrow ZZ$	108	0.5	—	—	0.3	—	—	0.1
$H \rightarrow \gamma\gamma$	9.3	< 1.0	< 0.2	—	< 1.0	—	—	—
$H \rightarrow Z\gamma$	6.3	5.0	—	—	1.0	—	—	0.1

Table 19. Partial decay widths for the Higgs boson to specific final states and the uncertainties in their calculation [97]. The uncertainties arise either from intrinsic limitations in the theoretical calculation (Th_{Intr}) and parametric uncertainties (Th_{Par}). The parametric uncertainties are due to the finite precision on the quark masses, $\text{Th}_{\text{Par}}(m_q)$, on the strong coupling constant, $\text{Th}_{\text{Par}}(\alpha_s)$, and on the Higgs boson mass, $\text{Th}_{\text{Par}}(M_H)$. The columns labelled “partial width” and “current uncertainty” and refer to the current precision [97], while the predictions for the future are taken from ref. [131]. For the future uncertainties, the parametric uncertainties assume a precision of $\delta m_b = 13$ MeV, $\delta m_c = 7$ MeV, $\delta m_t = 50$ MeV, $\delta\alpha_s = 0.0002$ and $\delta M_H = 10$ MeV.

C Inputs

In this section we report some information relative to the inputs to the strategy process. Figure 13 shows the start date and extent of the runs of proposed future projects, using the earliest start time provided in the submitted documentation.

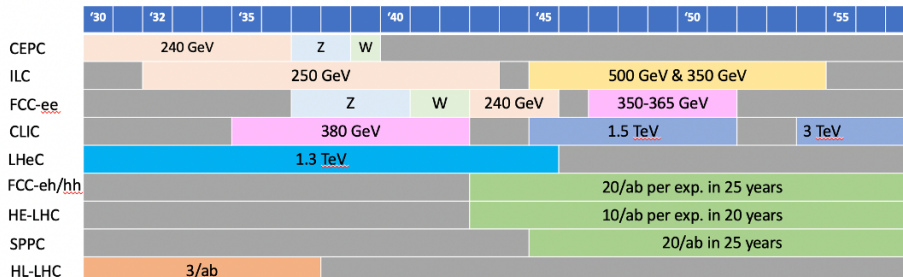


Figure 13. Sketch of timeline of various collider projects starting at the “earliest start time” stated in the respective documents. For FCC-eh/hh this figure assumes that it is not preceded by FCC-ee. If it comes after FCC-ee it would start in the early 2060s. Only scenarios as submitted to the European Strategy by Dec. 2018 are displayed. Additional scenarios considered in this report (e.g. Giga-Z at ILC/CLIC, ILC at 1 TeV, LE-FCC) are not shown.

C.1 Inputs for Higgs studies

The uncertainties on inputs for all the colliders used in our analysis are listed in tables 20–26. In all cases the relative uncertainty on the measurement is given corresponding to a Gaussian $1\text{-}\sigma$ uncertainty.

	FCC-ee ₂₄₀	FCC-ee ₃₆₅	CEPC
$\delta\sigma_{ZH}$	0.005	0.009	0.005
$\delta\mu_{ZH,bb}$	0.003	0.005	0.0031
$\delta\mu_{ZH,cc}$	0.022	0.065	0.033
$\delta\mu_{ZH,gg}$	0.019	0.035	0.013
$\delta\mu_{ZH,WW}$	0.012	0.026	0.0098
$\delta\mu_{ZH,ZZ}$	0.044	0.12	0.051
$\delta\mu_{ZH,\tau\tau}$	0.009	0.018	0.0082
$\delta\mu_{ZH,\gamma\gamma}$	0.09	0.18	0.068
$\delta\mu_{ZH,\mu\mu}$	0.19	0.40	0.17
$\delta\mu_{ZH,Z\gamma}$	—	—	0.16
$\delta\mu_{\nu\nu H,bb}$	0.031	0.009	0.030
$\delta\mu_{\nu\nu H,cc}$	—	0.10	—
$\delta\mu_{\nu\nu H,gg}$	—	0.045	—
$\delta\mu_{\nu\nu H,ZZ}$	—	0.10	—
$\delta\mu_{\nu\nu H,\tau\tau}$	—	0.08	—
$\delta\mu_{\nu\nu H,\gamma\gamma}$	—	0.22	—
BR _{inv}	<0.0015	<0.003	<0.0015

Table 20. Inputs used for CEPC and FCC-ee projections. All uncertainties are given as fractional 68% CL intervals and are taken to be symmetric. The upper limits are given at 68% CL. A dash indicates the absence of a projection for the corresponding channel.

ILC ₂₅₀		
Polarization:	$e^-: -80\% e^+: +30\%$	$e^-: +80\% e^+: -30\%$
$\delta\sigma_{ZH}/\sigma_{ZH}$	0.011	0.011
$\delta\mu_{ZH,bb}$	0.0072	0.0072
$\delta\mu_{ZH,cc}$	0.044	0.044
$\delta\mu_{ZH,gg}$	0.037	0.037
$\delta\mu_{ZH,ZZ}$	0.095	0.095
$\delta\mu_{ZH,WW}$	0.024	0.024
$\delta\mu_{ZH,\tau\tau}$	0.017	0.017
$\delta\mu_{ZH,\gamma\gamma}$	0.18	0.18
$\delta\mu_{ZH,\mu\mu}$	0.38	0.38
$\delta\mu_{\nu\nu H,bb}$	0.043	0.17
BR _{inv}	<0.0027	<0.0021

ILC ₃₅₀		
Polarization:	$e^-: -80\% e^+: +30\%$	$e^-: +80\% e^+: -30\%$
$\delta\sigma_{ZH}/\sigma_{ZH}$	0.025	0.042
$\delta\mu_{ZH,bb}$	0.021	0.036
$\delta\mu_{ZH,cc}$	0.15	0.26
$\delta\mu_{ZH,gg}$	0.11	0.20
$\delta\mu_{ZH,ZZ}$	0.34	0.59
$\delta\mu_{ZH,WW}$	0.076	0.13
$\delta\mu_{ZH,\tau\tau}$	0.054	0.094
$\delta\mu_{ZH,\gamma\gamma}$	0.53	0.92
$\delta\mu_{ZH,\mu\mu}$	1.2	2.1
$\delta\mu_{\nu\nu H,bb}$	0.025	0.18
$\delta\mu_{\nu\nu H,cc}$	0.26	1.9
$\delta\mu_{\nu\nu H,gg}$	0.10	0.75
$\delta\mu_{\nu\nu H,ZZ}$	0.27	1.9
$\delta\mu_{\nu\nu H,WW}$	0.078	0.57
$\delta\mu_{\nu\nu H,\tau\tau}$	0.22	1.6
$\delta\mu_{\nu\nu H,\gamma\gamma}$	0.61	4.2
$\delta\mu_{\nu\nu H,\mu\mu}$	2.2	16
BR _{inv}	<0.0096	<0.015

Table 21. Inputs used for ILC projections at the 250 and 350 GeV energy stages and two polarizations. All uncertainties are given as fractional 68% CL intervals and are taken to be symmetric. The upper limits are given at 68% CL.

ILC ₅₀₀		
Polarization:	$e^-: -80\% e^+: +30\%$	$e^-: +80\% e^+: -30\%$
$\delta\sigma_{ZH}/\sigma_{ZH}$	0.017	0.017
$\delta\mu_{ZH,bb}$	0.010	0.010
$\delta\mu_{ZH,cc}$	0.071	0.071
$\delta\mu_{ZH,gg}$	0.059	0.059
$\delta\mu_{ZH,ZZ}$	0.14	0.14
$\delta\mu_{ZH,WW}$	0.030	0.030
$\delta\mu_{ZH,\tau\tau}$	0.024	0.024
$\delta\mu_{ZH,\gamma\gamma}$	0.19	0.19
$\delta\mu_{ZH,\mu\mu}$	0.47	0.47
$\delta\mu_{\nu\nu H,bb}$	0.0041	0.015
$\delta\mu_{\nu\nu H,cc}$	0.035	0.14
$\delta\mu_{\nu\nu H,gg}$	0.023	0.095
$\delta\mu_{\nu\nu H,ZZ}$	0.047	0.19
$\delta\mu_{\nu\nu H,WW}$	0.014	0.055
$\delta\mu_{\nu\nu H,\tau\tau}$	0.039	0.16
$\delta\mu_{\nu\nu H,\gamma\gamma}$	0.11	0.43
$\delta\mu_{\nu\nu H,\mu\mu}$	0.4	1.7
$\delta\mu_{ttH,bb}$	0.20	0.20
BR _{inv}	<0.0069	<0.0050
Direct constraint on Higgs self-interaction		
$\delta\kappa_3$		0.27

ILC ₁₀₀₀		
Polarization:	$e^-: -80\% e^+: +20\%$	$e^-: +80\% e^+: -20\%$
$\delta\mu_{\nu\nu H,bb}$	0.0032	0.010
$\delta\mu_{\nu\nu H,cc}$	0.017	0.064
$\delta\mu_{\nu\nu H,gg}$	0.013	0.047
$\delta\mu_{\nu\nu H,ZZ}$	0.023	0.084
$\delta\mu_{\nu\nu H,WW}$	0.0091	0.033
$\delta\mu_{\nu\nu H,\tau\tau}$	0.017	0.064
$\delta\mu_{\nu\nu H,\gamma\gamma}$	0.048	0.17
$\delta\mu_{\nu\nu H,\mu\mu}$	0.17	0.64
$\delta\mu_{ttH,bb}$	0.045	0.045
Direct constraint on Higgs self-interaction		
$\delta\kappa_3$		0.10

Table 22. Inputs used for ILC projections at the 500 and 1000 GeV energy stages and two polarisations. All uncertainties are given as fractional 68% CL intervals and are taken to be symmetric. The upper limits are given at 68% CL.

CLIC ₃₈₀		
Polarization:	$e^-: -80\% e^+: 0\%$	$e^-: +80\% e^+: 0\%$
$\delta\sigma_{ZH,Z\rightarrow ll}/\sigma_{ZH,Z\rightarrow ll}$	0.036	0.041
$\delta\sigma_{ZH,Z\rightarrow qq}/\sigma_{ZH,Z\rightarrow qq}$	0.017	0.020
$\delta\mu_{ZH,bb}$	0.0081	0.0092
$\delta\mu_{ZH,cc}$	0.13	0.15
$\delta\mu_{ZH,gg}$	0.057	0.065
$\delta\mu_{ZH,WW}$	0.051	0.057
$\delta\mu_{ZH,\tau\tau}$	0.059	0.066
$\delta\mu_{\nu\nu H,bb}$	0.014	0.041
$\delta\mu_{\nu\nu H,cc}$	0.19	0.57
$\delta\mu_{\nu\nu H,gg}$	0.076	0.23
BR _{inv}	<0.0027	<0.003

CLIC ₁₅₀₀		
Polarization:	$e^-: -80\% e^+: 0\%$	$e^-: +80\% e^+: 0\%$
$\delta\mu_{ZH,bb}$	0.028	0.062
$\delta\mu_{\nu\nu H,bb}$	0.0025	0.015
$\delta\mu_{\nu\nu H,cc}$	0.039	0.24
$\delta\mu_{\nu\nu H,gg}$	0.033	0.20
$\delta\mu_{\nu\nu H,WW}$	0.0067	0.04
$\delta\mu_{\nu\nu H,ZZ}$	0.036	0.22
$\delta\mu_{\nu\nu H,\gamma\gamma}$	0.1	0.6
$\delta\mu_{\nu\nu H,Z\gamma}$	0.28	1.7
$\delta\mu_{\nu\nu H,\tau\tau}$	0.028	0.17
$\delta\mu_{\nu\nu H,\mu\mu}$	0.24	1.5
$\delta\mu_{eeH,bb}$	0.015	0.033
$\delta\mu_{ttH,bb}$	0.056	0.15

CLIC ₃₀₀₀		
Polarization:	$e^-: -80\% e^+: 0\%$	$e^-: +80\% e^+: 0\%$
$\delta\mu_{ZH,bb}$	0.045	0.10
$\delta\mu_{\nu\nu H,bb}$	0.0017	0.01
$\delta\mu_{\nu\nu H,cc}$	0.037	0.22
$\delta\mu_{\nu\nu H,gg}$	0.023	0.14
$\delta\mu_{\nu\nu H,WW}$	0.0033	0.02
$\delta\mu_{\nu\nu H,ZZ}$	0.021	0.13
$\delta\mu_{\nu\nu H,\gamma\gamma}$	0.05	0.3
$\delta\mu_{\nu\nu H,Z\gamma}$	0.16	0.95
$\delta\mu_{\nu\nu H,\tau\tau}$	0.023	0.14
$\delta\mu_{\nu\nu H,\mu\mu}$	0.13	0.8
$\delta\mu_{eeH,bb}$	0.016	0.036
Direct constraint on Higgs self-interaction		
$\delta\kappa_3$		0.11

Table 23. Inputs used for CLIC projections at the three energy stages and two polarisations. All uncertainties are given as fractional 68% CL intervals and are taken to be symmetric. The upper limits are given at 68% CL.

Observable	LHeC	FCC-eh
$\delta\mu_{WBF,bb}$	0.008	0.0025
$\delta\mu_{WBF,cc}$	0.071	0.022
$\delta\mu_{WBF,gg}$	0.058	0.018
$\delta\mu_{ZBF,bb}$	0.023	0.0065
$\delta\mu_{WBF,WW}$	0.062	0.019
$\delta\mu_{WBF,ZZ}$	0.120	0.038
$\delta\mu_{WBF,\tau\tau}$	0.052	0.016
$\delta\mu_{WBF,\gamma\gamma}$	0.15	0.046
$\delta\mu_{ZBF,cc}$	0.200	0.058
$\delta\mu_{ZBF,gg}$	0.160	0.047
$\delta\mu_{ZBF,WW}$	0.170	0.050
$\delta\mu_{ZBF,ZZ}$	0.350	0.100
$\delta\mu_{ZBF,\tau\tau}$	0.15	0.042
$\delta\mu_{ZBF,\gamma\gamma}$	0.42	0.120

Table 24. Inputs used for LHeC and FCC-eh projections. All uncertainties are given as fractional 68% CL intervals and are taken to be symmetric.

FCC-hh		FCC-hh	
$\delta\mu_{ggF,4\mu}$	0.019	(Extra inputs used in κ fits)	
$\delta\mu_{ggF,\gamma\gamma}$	0.015	$\delta(\sigma_{WH}^{H\rightarrow\gamma\gamma}/\sigma_{WZ}^{Z\rightarrow e^+e^-})$	0.014
$\delta\mu_{ggF,Z\gamma}$	0.016	$\delta(\sigma_{WH}^{H\rightarrow\tau\tau}/\sigma_{WZ}^{Z\rightarrow\tau\tau})$	0.016
$\delta\mu_{ggF,\mu\mu}$	0.012	$\delta(\sigma_{WH}^{H\rightarrow bb}/\sigma_{WZ}^{Z\rightarrow bb})$	0.011
$\delta(\text{BR}_{\mu\mu}/\text{BR}_{4\mu})$	0.013	$\delta(\sigma_{WH}^{H\rightarrow WW}/\sigma_{WH}^{H\rightarrow\gamma\gamma})$	0.015
$\delta(\text{BR}_{\gamma\gamma}/\text{BR}_{2e2\mu})$	0.008		
$\delta(\text{BR}_{\gamma\gamma}/\text{BR}_{\mu\mu})$	0.014		
$\delta(\text{BR}_{\mu\mu\gamma}/\text{BR}_{\gamma\gamma})$	0.018		
$\delta(\sigma_{ttH}^{bb}/\sigma_{ttZ}^{bb})$	0.019		
Invisible decays			
BR_{inv}	<0.00013		
Direct constraint on Higgs self-interaction			
$\delta\kappa_3$	0.05		

Table 25. (Left) Inputs used for FCC-hh. All uncertainties are given as fractional 68% CL intervals and are taken to be symmetric. (Right) Extra inputs used in the κ fit studies.

LE-FCC	
$\delta(\text{BR}_{\mu\mu}/\text{BR}_{4\mu})$	0.029
$\delta(\text{BR}_{\gamma\gamma}/\text{BR}_{2e2\mu})$	0.015
$\delta(\text{BR}_{\gamma\gamma}/\text{BR}_{\mu\mu})$	0.028
$\delta(\text{BR}_{\mu\mu\gamma}/\text{BR}_{\gamma\gamma})$	0.06
$\delta(\sigma_{ttH}^{bb}/\sigma_{ttZ}^{bb})$	0.04–0.06
Direct constraint on Higgs self-interaction	
$\delta\kappa_3$	0.15

Table 26. Inputs used for a low-energy FCC-hh running at 37.5 TeV (LE-FCC). All uncertainties are given as fractional 68% CL intervals and are taken to be symmetric.

C.2 Inputs for electroweak precision observables

The uncertainties on several electroweak precision observables related to the properties (masses and couplings) of the electroweak vector bosons are presented in table 27. We also report the expected uncertainties on the top-quark mass, which enters in the analysis as an input of the global electroweak fit.

For the extraction of m_{top} from a $t\bar{t}$ scan threshold at e^+e^- colliders the current theoretical uncertainty is ~ 40 MeV [132]. As it was done for the other intrinsic theory uncertainties, this is expected to improve in the future and is neglected in the baseline fits. We therefore use a common statistical uncertainty of ~ 20 MeV for all lepton colliders running at the $t\bar{t}$ threshold.

For the circular colliders, the asymmetries A_f and partial-width ratios R_f are not given for $\sqrt{s} \gg 90$ GeV as the statistical precision is much higher at the Z pole, and the Z -pole run is part of the default programme. For the linear colliders a Giga- Z run is not part of the running plan submitted to the EPPSU, but it is used in some of the results presented in this report to illustrate the impact of such a run in the EW and Higgs programmes. For the ILC and CLIC Giga- Z option, an integrated luminosity of 100 fb^{-1} is assumed, and polarisations as stated in table 1. Note that the asymmetry parameters A_f can be extracted in different ways depending on the access of polarization of the initial and/or final states. For instance, at linear colliders with polarized beams A_b can be directly extracted from a left-right forward-backward asymmetry. Without polarized beams, circular colliders can access that quantify via a forward-backward asymmetry $A_{FB}^b = \frac{3}{4}A_e A_b$, but it requires to know A_e . On the other hand, both circular and linear colliders could access A_e and A_τ separately, measuring the polarization of the final states in $e^+e^- \rightarrow \tau^+\tau^-$. We refer to the discussion in section 3.4.1 for the assumptions adopted in the treatment of systematic uncertainties for the heavy flavor observables included the fits.

For ILC all values are taken from ref. [4]. For CLIC all values are taken from refs. [5, 11]. For CEPC they are taken from either ref. [2] or from ref. [133]. For FCC-ee they are taken from refs. [79, 134–136].

Quantity	Current	HL-LHC	FCC-ee	CEPC	ILC		CLIC	
					Giga-Z	250 GeV	Giga-Z	380 GeV
δm_{top} [MeV]	~ 500 ^{a)}	~ 400 ^{a)}	20 ^{b)}	–	–	17 ^{b)}	–	20-22 ^{b)}
δM_Z [MeV]	2.1	–	0.1	0.5	–	–	–	–
$\delta \Gamma_Z$ [MeV]	2.3	–	0.1	0.5	1	–	1	–
$\delta \Gamma_{Z \rightarrow \text{had}}$ [MeV]	2.0	–	–	–	0.7	–	0.7	–
$\delta \sigma_{\text{had}}^0$ [pb]	37	–	4	5	–	–	–	–
δM_W [MeV]	12	7	0.7	1.0 (2-3) ^{c)}	–	2.4 ^{d)}	–	2.5
$\delta \Gamma_W$ [MeV]	42	–	1.5	3	–	–	–	–
$\delta \text{BR}_{W \rightarrow e\nu}$ [10^{-4}]	150	–	3	3	–	4.2	–	11
$\delta \text{BR}_{W \rightarrow \mu\nu}$ [10^{-4}]	140	–	3	3	–	4.1	–	11
$\delta \text{BR}_{W \rightarrow \tau\nu}$ [10^{-4}]	190	–	4	4	–	5.2	–	11
$\delta \text{BR}_{W \rightarrow \text{had}}$ [10^{-4}]	40	–	1	1	–	–	–	–
δA_e [10^{-4}]	140	–	1.1 ^{e)}	3.2 ^{e)}	5.1	10	10	42
δA_μ [10^{-4}]	1060	–	–	–	5.4	54	13	270
δA_τ [10^{-4}]	300	–	3.1 ^{e)}	5.2 ^{e)}	5.4	57	17	370
δA_b [10^{-4}]	220	–	–	–	5.1	6.4	9.9	40
δA_c [10^{-4}]	400	–	–	–	5.8	21	10	30
δA_{FB}^μ [10^{-4}]	770	–	0.54	4.6	–	–	–	–
δA_{FB}^b [10^{-4}]	160	–	30 ^{f)}	10 ^{f)}	–	–	–	–
δA_{FB}^c [10^{-4}]	500	–	80 ^{f)}	30 ^{f)}	–	–	–	–
δR_e [10^{-4}]	24	–	3	2.4	5.4	11	4.2	27
δR_μ [10^{-4}]	16	–	0.5	1	2.8	11	2.2	27
δR_τ [10^{-4}]	22	–	1	1.5	4.5	12	4.3	60
δR_b [10^{-4}]	31	–	2	2	7	11	7	18
δR_c [10^{-4}]	170	–	10	10	30	50	23	56
δR_ν [10^{-3}] ^{g)}	–	–	–	–	–	–	–	9.4
δR_{inv} [10^{-3}] ^{g)}	–	–	0.27	0.5	–	–	–	–

Table 27. Uncertainty on several observables related to the properties of the electroweak vector bosons. We also list the uncertainty on the top mass. For dimensionful quantities the absolute uncertainty is given, while relative errors are listed for dimensionless quantities. A few comments on some particular numbers are in order: a) For hadron colliders the top mass is not the pole mass. b) For the top mass all lepton colliders require a dedicated top threshold scan to achieve the uncertainty given here. (For ILC the quoted value comes from a dedicated run at 350 GeV.) c) From direct reconstruction in the ZH run 2-3 MeV can be achieved [2]. d) In a 4-year dedicated run 2 MeV can be achieved by ILC [137]. e) From τ polarization measurements. f) At circular colliders, for A_b and A_c previous measurement uncertainties were dominated by the physics modelling [138] and the systematic uncertainty arising from this was only estimated by FCC-ee [135]. When these systematics are set to zero in the measurements of A_{FB}^b and A_{FB}^c the uncertainty in A_b and A_c is controlled by the statistical errors plus the uncertainty on A_e . This is the setup used for the baseline fits. See discussion in section 3.4.1 for details. g) $R_\nu \equiv \Gamma_{Z \rightarrow \text{inv}}/\Gamma_{Z \rightarrow \text{had}}$ and $R_{\text{inv}} \equiv \Gamma_{Z \rightarrow \text{inv}}/\Gamma_{Z \rightarrow \ell\ell}$.

D Correlation matrices

The correlations of three of the lepton collider kappa-3 fits, discussed in section 3.2, are shown in figure 14.

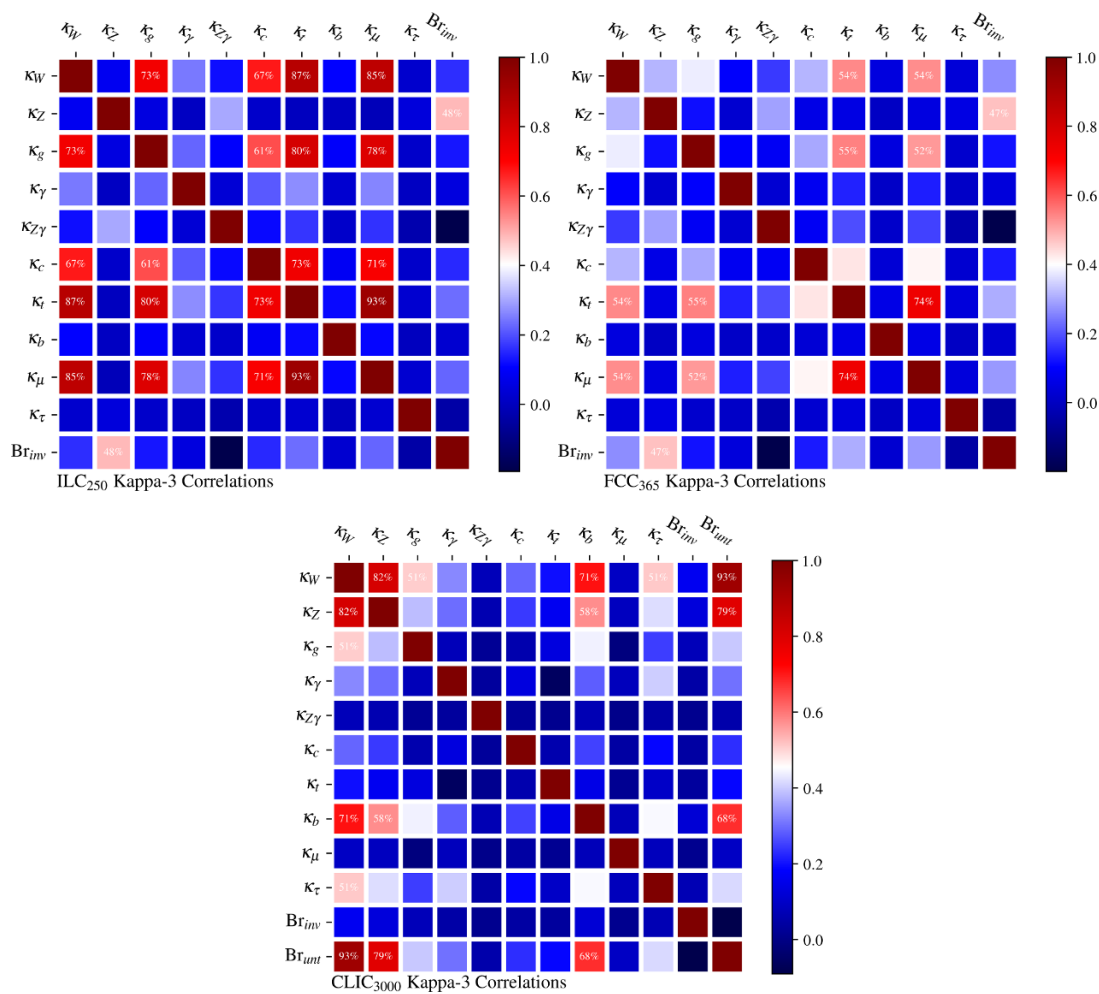


Figure 14. Correlation seen in the kappa-3 scenario fit for three future colliders as discussed in section 3.2. Top left: ILC₂₅₀. Top right: FCC₃₆₅. Bottom: CLIC₃₀₀₀.

E Additional Kappa scenario fits

This appendix contains additional kappa scenarios to complement the results shown in section 3.2. Tables 28 and 29 present the results of the different colliders in the kappa-2 scenario, in which BSM decays are allowed and future colliders are considered independently and not fitted together with the HL-LHC prospects.

kappa-2	HL-LHC	LHeC	HE-LHC (S2)	HE-LHC (S2')
$1 \geq \kappa_W > (68\%)$	0.985	0.994	0.988	0.992
$1 \geq \kappa_Z > (68\%)$	0.987	0.988	0.990	0.990
κ_g [%]	$\pm 2.$	± 3.9	± 1.6	± 1.1
κ_γ [%]	± 1.6	± 7.8	± 1.3	± 0.96
$\kappa_{Z\gamma}$ [%]	$\pm 10.$	–	± 5.6	± 3.8
κ_c [%]	–	± 4.3	–	–
κ_t [%]	± 3.2	–	± 2.6	± 1.6
κ_b [%]	± 2.5	± 2.3	± 2.0	± 1.5
κ_μ [%]	± 4.4	–	± 2.3	± 1.5
κ_τ [%]	± 1.6	± 3.6	± 1.2	± 0.85
$\text{BR}_{\text{inv}} (<\%)$	1.9	2.2	3.2★	2.4★
$\text{BR}_{\text{unt}} (<\%)$	inferred using constraint $ \kappa_V \leq 1$			
	4.	2.2	3.2	2.1

Table 28. Expected relative precision (%) of the κ parameters in the kappa-2 (standalone) scenario described in section 2 for the HL-LHC, LHeC, and HE-LHC. A bound on $|\kappa_V| \leq 1$ is applied since no direct access to the Higgs width is possible, thus the uncertainty on κ_W and κ_Z is one-sided. For the remaining kappa parameters one standard deviation is provided in \pm . The corresponding 95%CL upper limit on BR_{inv} is also given. In this scenario BR_{unt} is a floating parameter in the fit, to propagate the effect of an assumed uncertain total width on the measurement of the other κ_i . Based on this constraint the reported values on BR_{unt} are inferred. The 95% CL upper limits are given for these. Cases in which a particular parameter has been fixed to the SM value due to lack of sensitivity are shown with a dash (–). In the case of κ_t sensitivity at the LHeC, note that the framework relies as input on μ_{ttH} , and does not take into consideration μ_{tH} . A star (★) indicates the cases in which a parameter has been left free in the fit due to lack of input in the reference documentation. The integrated luminosity and running conditions considered for each collider in this comparison are described in table 1.

kappa-2	ILC	ILC	ILC	CLIC	CLIC	CLIC	CEPC	FCC-ee	FCC-ee	FCC
	250	500	1000	380	1500	3000		240	365	ee/eh/hh
κ_W [%]	1.8	0.31	0.26	0.86	0.39	0.38	1.3	1.3	0.44	0.2
κ_Z [%]	0.3	0.24	0.24	0.5	0.39	0.39	0.19	0.21	0.18	0.17
κ_g [%]	2.3	0.98	0.67	2.5	1.3	0.96	1.5	1.7	1.0	0.52
κ_γ [%]	6.8	3.5	1.9	88.*	5.	2.3	3.7	4.8	3.9	0.32
$\kappa_{Z\gamma}$ [%]	87.*	75.*	74.*	110.*	15.	7.	8.2	71.*	66.*	0.71
κ_c [%]	2.5	1.3	0.91	4.4	1.9	1.4	2.2	1.8	1.3	0.96
κ_t [%]	—	6.9	1.6	—	—	2.7	—	—	—	1.0
κ_b [%]	1.8	0.6	0.5	1.9	0.6	0.52	1.3	1.3	0.69	0.48
κ_μ [%]	15.	9.4	6.3	290.*	13.	5.9	9.	10.	8.9	0.43
κ_τ [%]	1.9	0.72	0.58	3.1	1.3	0.95	1.4	1.4	0.74	0.49
BR _{inv} (<%)	0.26	0.23	0.23	0.65	0.65	0.65	0.28	0.22	0.19	0.024
BR _{unt} (<%)	1.8	1.4	1.3	2.7	2.4	2.4	1.1	1.2	1.1	1.0

Table 29. Expected relative precision (%) of the κ parameters in the kappa-2 (standalone collider) scenario described in section 2 for future accelerators beyond the LHC era. The corresponding 95%CL upper limits on BR_{unt} and BR_{inv} and the derived constraint on the Higgs width (in %) are also given. Cases in which a particular parameter has been fixed to the SM value due to lack of sensitivity are shown with a dash (-). An asterisk (*) indicates the cases in which a parameter has been left free in the fit due to lack of input in the reference documentation. The integrated luminosity and running conditions considered for each collider in this comparison are described in table 1. FCC-ee/eh/hh corresponds to the combined performance of FCC-ee₂₄₀+FCC-ee₃₆₅, FCC-eh and FCC-hh.

F Additional comparisons

In this section additional potential scenarios for accelerators are compared. The inputs for these were mostly provided after the European Strategy meeting in Granada.

Table 30 and figure 15 show the results of the kappa-0-HL fit for various FCC scenarios. This fit is a replica of the already described kappa-0 one, which does not allow any BSM decay of the Higgs, but incorporating the HL-LHC information in a combined fit for completeness. With 4 instead of 2 IPs the uncertainties reduce by a factor of up to 1.4 due to the increased statistics. With the FCC-hh only, the uncertainties all increase by factors of 2-5. When omitting FCC-eh, the uncertainty on κ_W increases by a factor of two and that on κ_b increases by 20%, the others are mostly unaffected. When omitting FCC-ee, most uncertainties increase by about 20% and that on κ_Z increases by more than a factor of two.

Another interesting questions is what uncertainties are obtained when combining any of the lower energy stages of e^+e^- colliders with the FCC-hh. This is shown in table 31 for the kappa-0-HL fit and in table 32 for the EFT fit. The results for the various 1st-stage e^+e^- colliders are comparable within a factor of about two for the Higgs couplings in the kappa-fits. Figure 16 shows this comparison graphically. For the EFT framework, the differences are a bit larger, in particular for the aTGC values, see table 32.

kappa-0-HL	HL-LHC +						
	FCC-ee ₂₄₀	FCC-ee	FCC-ee (4 IP)	FCC-ee/hh	FCC-eh/hh	FCC-hh	FCC-ee/eh/hh
κ_W [%]	0.86	0.38	0.23	0.27	0.17	0.39	0.14
κ_Z [%]	0.15	0.14	0.094	0.13	0.27	0.63	0.12
κ_g [%]	1.1	0.88	0.59	0.55	0.56	0.74	0.46
κ_γ [%]	1.3	1.2	1.1	0.29	0.32	0.56	0.28
$\kappa_{Z\gamma}$ [%]	10.	10.	10.	0.7	0.71	0.89	0.68
κ_c [%]	1.5	1.3	0.88	1.2	1.2	–	0.94
κ_t [%]	3.1	3.1	3.1	0.95	0.95	0.99	0.95
κ_b [%]	0.94	0.59	0.44	0.5	0.52	0.99	0.41
κ_μ [%]	4.	3.9	3.3	0.41	0.45	0.68	0.41
κ_τ [%]	0.9	0.61	0.39	0.49	0.63	0.9	0.42
Γ_H [%]	1.6	0.87	0.55	0.67	0.61	1.3	0.44

Table 30. Results of kappa-0-HL fit for various scenarios of the FCC. In all cases the FCC data are combined with HL-LHC. The “4 IP” option considers 4 experiments instead of the 2 experiments considered in the CDR. For the FCC-hh scenario constraints on the b , τ and W couplings come from measurements of ratios of WH to WZ production with the H and Z decaying to b -quarks or τ leptons, see ref. [139].

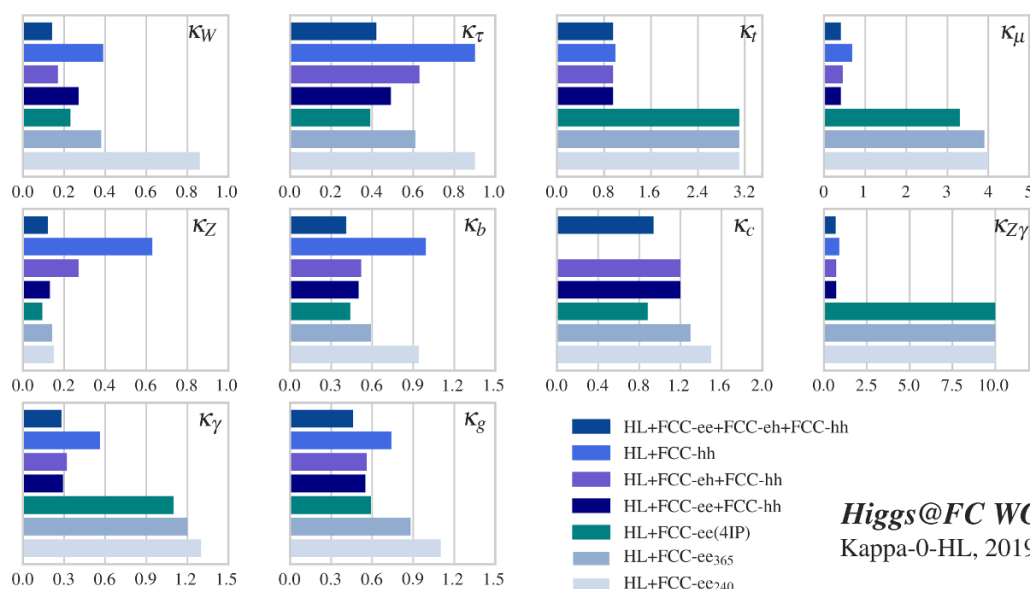


Figure 15. Comparison of the different FCC scenarios in the kappa-0-HL scenario (similar to kappa-0 in that it does not allow any BSM decay, but including HL-LHC data).

kappa-0-HL	HL-LHC + FCC-hh +			
	ILC ₂₅₀	CLIC ₃₈₀	CEPC	FCC-ee ₃₆₅
κ_W [%]	0.37	0.36	0.35	0.27
κ_Z [%]	0.19	0.26	0.12	0.13
κ_g [%]	0.65	0.69	0.55	0.55
κ_γ [%]	0.31	0.34	0.29	0.29
$\kappa_{Z\gamma}$ [%]	0.71	0.74	0.69	0.7
κ_c [%]	1.8	3.8	1.8	1.2
κ_t [%]	0.96	0.96	0.95	0.95
κ_b [%]	0.63	0.68	0.52	0.5
κ_μ [%]	0.43	0.47	0.41	0.41
κ_τ [%]	0.61	0.78	0.52	0.49
Γ_H [%]	0.90	0.98	0.74	0.67

Table 31. Results for the kappa-0-HL fit for FCC-hh combined with any of the four e^+e^- colliders proposed.

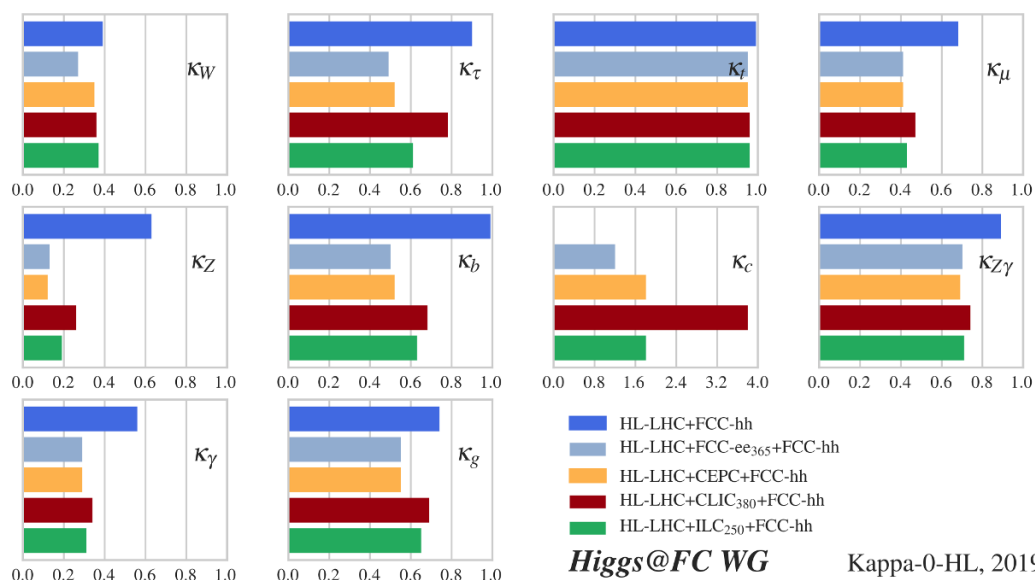


Figure 16. Combination of the different future ee colliders with FCC-hh and HL-LHC, in an extension of the kappa-0-HL scenario. Note that ILC₂₅₀ and CLIC₃₈₀ (first stages) are shown in comparison with CEPC (240) and FCC-ee₃₆₅.

The ILC and CLIC documents submitted to the European Strategy did not contain any explicit analysis related to the Z boson properties. In the meantime, it was explored what can be done either using radiative Z boson events during the standard running or by a dedicated running at $\sqrt{s} \approx M_Z$ for a period of 1-3 years, collecting 100 fb^{-1} . The results shown in the main body of this paper now include the radiative return analysis. Here, we present the additional improvement which can be made when a dedicated Z running period is considered. Table 33 shows the effective Higgs boson couplings with and without Giga- Z running for the ILC and CLIC. It is seen that for ILC₂₅₀ a Giga- Z running improves the H couplings to vector bosons by about 30%, and for other couplings the improvement

SMEFT _{ND}	HL-LHC + FCC-hh +			
	ILC ₂₅₀	CLIC ₃₈₀	CEPC	FCC-ee ₃₆₅
$g_{HZZ}^{\text{eff}}[\%]$	0.35	0.46	0.38	0.21
$g_{HWW}^{\text{eff}}[\%]$	0.36	0.46	0.36	0.21
$g_{H\gamma\gamma}^{\text{eff}}[\%]$	0.47	0.55	0.48	0.38
$g_{HZ\gamma}^{\text{eff}}[\%]$	0.78	0.83	0.76	0.72
$g_{Hgg}^{\text{eff}}[\%]$	0.73	0.88	0.54	0.56
$g_{Htt}[\%]$	3.1	2.2	3.1	1.7
$g_{Hcc}[\%]$	1.8	3.9	1.8	1.2
$g_{Hbb}[\%]$	0.75	0.95	0.58	0.51
$g_{H\tau\tau}[\%]$	0.78	1.2	0.61	0.54
$g_{H\mu\mu}[\%]$	0.54	0.61	0.53	0.46
$\delta g_{1Z}[\times 10^2]$	0.078	0.04	0.08	0.028
$\delta\kappa_\gamma[\times 10^2]$	0.12	0.079	0.089	0.048
$\lambda_Z[\times 10^2]$	0.042	0.043	0.1	0.047

Table 32. Results for the global EFT fit for FCC-hh combined with any of the four e^+e^- colliders proposed, also shown in table 31.

SMEFT _{ND}	HL-LHC +					
	ILC ₂₅₀	ILC ₂₅₀ +GigaZ	ILC ₅₀₀	ILC ₅₀₀ +GigaZ	CLIC ₃₈₀	CLIC ₃₈₀ +GigaZ
$g_{HZZ}^{\text{eff}}[\%]$	0.39	0.31	0.22	0.19	0.5	0.47
$g_{HWW}^{\text{eff}}[\%]$	0.41	0.32	0.22	0.2	0.5	0.47
$g_{H\gamma\gamma}^{\text{eff}}[\%]$	1.3	1.3	1.2	1.2	1.4	1.4
$g_{HZ\gamma}^{\text{eff}}[\%]$	9.6	9.4	6.8	6.7	9.7	9.5
$g_{Hgg}^{\text{eff}}[\%]$	1.1	1.1	0.79	0.79	1.3	1.3
$g_{Htt}[\%]$	3.2	3.1	2.9	2.8	3.2	3.2
$g_{Hcc}[\%]$	1.8	1.8	1.2	1.2	4.	4.
$g_{Hbb}[\%]$	0.78	0.74	0.52	0.51	0.99	0.98
$g_{H\tau\tau}[\%]$	0.81	0.78	0.59	0.58	1.3	1.3
$g_{H\mu\mu}[\%]$	4.1	4.1	3.9	3.9	4.4	4.3
$\delta g_{1Z}[\times 10^2]$	0.091	0.071	0.047	0.031	0.045	0.044
$\delta\kappa_\gamma[\times 10^2]$	0.12	0.087	0.076	0.047	0.079	0.066
$\lambda_Z[\times 10^2]$	0.042	0.042	0.021	0.021	0.043	0.043

Table 33. Comparison of the effective Higgs coupling sensitivities for the ILC and CLIC with and without a dedicated running at $\sqrt{s} \approx M_Z$.

is much smaller. For ILC₅₀₀ and CLIC₃₈₀ the impact of dedicated Giga-Z running is low, except for the precision on the TGC parameter $\delta\kappa_\gamma$.

Table 34 shows the impact of the Giga-Z running on the precision on the effective couplings of the Z boson to fermions. In many cases, the impact is significant, improving the precision by up to a factor of ~ 4 . Also shown are the results expected for CEPC

SMEFT _{ND}	HL-LHC +							
	ILC ₂₅₀	ILC ₂₅₀ +GigaZ	ILC ₅₀₀	ILC ₅₀₀ +GigaZ	CLIC ₃₈₀	CLIC ₃₈₀ +GigaZ	CEPC	FCC-ee
$g_L^{\nu e}$ [%]	0.082	0.058	0.048	0.032	0.027	0.024	0.032	0.028
$g_L^{\nu \mu}$ [%]	0.11	0.075	0.088	0.064	0.16	0.11	0.036	0.03
$g_L^{\nu \tau}$ [%]	0.12	0.079	0.095	0.071	0.16	0.11	0.038	0.034
g_L^e [%]	0.048	0.025	0.037	0.023	0.035	0.021	0.014	0.0073
g_R^e [%]	0.055	0.028	0.041	0.025	0.047	0.025	0.016	0.0089
g_L^μ [%]	0.072	0.023	0.07	0.022	0.17	0.022	0.031	0.007
g_R^μ [%]	0.09	0.025	0.087	0.024	0.24	0.026	0.047	0.0092
g_L^τ [%]	0.076	0.027	0.073	0.026	0.17	0.029	0.016	0.0076
g_R^τ [%]	0.094	0.031	0.091	0.03	0.24	0.034	0.018	0.0094
$g_L^{u=c}$ [%]	0.24	0.13	0.23	0.12	0.26	0.11	0.051	0.05
$g_R^{u=c}$ [%]	0.35	0.15	0.35	0.15	0.43	0.16	0.08	0.066
g_L^t [%]	11.	11.	0.84	0.84	2.4	2.3	11.	1.5
g_R^t [%]	–	–	2.	2.	6.	6.	–	3.5
$g_L^{d=s}$ [%]	0.23	0.14	0.21	0.13	0.25	0.14	0.056	0.051
$g_R^{d=s}$ [%]	4.8	3.2	3.9	2.5	5.9	3.9	1.4	1.1
g_L^b [%]	0.071	0.034	0.068	0.033	0.13	0.041	0.017	0.011
g_R^b [%]	0.51	0.31	0.51	0.32	3.	0.75	0.29	0.088

Table 34. Comparison of the effective Z -boson coupling sensitivities for the ILC and CLIC with and w/o a dedicated running at $\sqrt{s} \approx M_Z$. Also shown are the values for CEPC and FCC-ee. In all cases, the combination with HL-LHC is shown but the sensitivity is dominated by the e^+e^- collider.

SMEFT _{ND}	HL-LHC +					
	ILC ₅₀₀	ILC ₁₀₀₀	CLIC ₁₅₀₀	CLIC ₃₀₀₀	FCC-ee/hh	FCC-ee/eh/hh
g_{HZZ}^{eff} [%]	0.19	0.15	0.2	0.16	0.21	0.13
g_{HWW}^{eff} [%]	0.2	0.16	0.18	0.15	0.21	0.13
$g_{H\gamma\gamma}^{\text{eff}}$ [%]	1.2	1.1	1.3	1.1	0.38	0.34
$g_{HZ\gamma}^{\text{eff}}$ [%]	6.7	6.6	4.5	3.6	0.72	0.7
g_{Hgg}^{eff} [%]	0.79	0.55	0.97	0.75	0.56	0.49
g_{Htt} [%]	2.8	1.5	2.2	2.1	1.7	1.7
g_{Hcc} [%]	1.2	0.88	1.8	1.4	1.2	0.95
g_{Hbb} [%]	0.51	0.43	0.44	0.37	0.51	0.44
$g_{H\tau\tau}$ [%]	0.58	0.49	0.92	0.74	0.54	0.46
$g_{H\mu\mu}$ [%]	3.9	3.5	4.1	3.4	0.46	0.42
$\delta g_{1Z} [\times 10^2]$	0.031	0.03	0.012	0.0099	0.028	0.018
$\delta \kappa_\gamma [\times 10^2]$	0.047	0.044	0.022	0.018	0.048	0.047
$\lambda_Z [\times 10^2]$	0.021	0.014	0.0053	0.0018	0.047	0.045

Table 35. Effective Higgs couplings precision for the EFT fit for a selection of colliders at high energy. For the linear colliders it is assumed that 100 fb⁻¹ of dedicated running on the Z -pole, corresponding to 1-3 years of data taking, are part of the programme.

kappa-0-HL	HL-LHC+FCC-hh _{37.5} +			
	ILC ₂₅₀	CLIC ₃₈₀	CEPC	FCC-ee ₃₆₅
κ_W [%]	0.94	0.62	0.81	0.38
κ_Z [%]	0.21	0.33	0.13	0.14
κ_g [%]	1.3	1.3	0.97	0.87
κ_γ [%]	0.64	0.68	0.62	0.62
$\kappa_{Z\gamma}$ [%]	3.	3.1	2.8	3.
κ_c [%]	1.9	3.9	1.9	1.3
κ_t [%]	1.9	1.9	1.9	1.9
κ_b [%]	0.99	0.94	0.81	0.58
κ_μ [%]	1.	1.1	1.	1.
κ_τ [%]	0.96	1.2	0.83	0.6

kappa-0-HL	HL-LHC+FCC-hh+			
	ILC ₂₅₀	CLIC ₃₈₀	CEPC	FCC-ee ₃₆₅
κ_W [%]	0.37	0.36	0.35	0.27
κ_Z [%]	0.19	0.26	0.12	0.13
κ_g [%]	0.65	0.69	0.55	0.55
κ_γ [%]	0.31	0.34	0.29	0.29
$\kappa_{Z\gamma}$ [%]	0.71	0.74	0.69	0.7
κ_c [%]	1.8	3.8	1.8	1.2
κ_t [%]	0.96	0.96	0.95	0.95
κ_b [%]	0.63	0.68	0.52	0.5
κ_μ [%]	0.43	0.47	0.41	0.41
κ_τ [%]	0.61	0.78	0.52	0.49
Γ_H [%]	0.90	0.98	0.74	0.67

Table 36. Expected relative precision (%) of the κ parameters in the kappa-0-HL scenario described in section 2 for future lepton colliders combined with the HL-LHC and the FCC-hh_{37.5} (top part) and with HL-LHC and FCC-hh (bottom part). No BSM width is allowed in the fit: both BR_{unt} and BR_{inv} are set to 0.

and FCC-ee. In most cases, CEPC and FCC-ee achieve the highest precision. A notable exception is the top quark coupling which is best constrained by the ILC₅₀₀.

It is also interesting to compare the highest energy options closely. This is done in table 35. In all cases, it is assumed that the colliders also include a Giga-Z run of 1-3 years [4, 11].

After the Granada meeting, it was also studied what could be achieved with a hadron-hadron collider with $\sqrt{s} = 37.5$ TeV and $\mathcal{L} = 15 \text{ ab}^{-1}$, in conjunction with one of the e^+e^- colliders [10]. This is shown in table 36 compared to the nominal FCC-hh in combination with the various e^+e^- colliders. For most coupling parameters the sensitivity of the 37.5 TeV collider is degraded by about a factor 1.5 – 2 w.r.t. the 100 TeV collider, except for $Z\gamma$ where it is a factor of 5. For κ_Z and κ_c there is no difference as both are very much dominated by the lepton collider sensitivity.

G Electroweak precision constraints on oblique parameters

In this section we will focus on the constraints on heavy new physics that can be obtained by precise measurement of the on-shell W and Z properties. We will focus on universal effects that can be fully encapsulated in the vector boson propagators, with no direct correction to the interaction vertices with fermions. This assumption allows on the one hand to limit the analysis to a few parameters. On the other hand, it should be noted, motivated models, like the minimal composite Higgs, often satisfy this assumption to a very good approximation. When considering universal deviations from the SM one must distinguish between the number of on-shell Z and W observables and the total number of parameters, which corresponds to the total number of on- and off-shell observables.

Under the assumption of universality, the relevant on-shell observables of W and Z physics reduce to three quantities: the relative normalization of charged and neutral currents (or the Z 's axial coupling), and the two relative differences among the three possible definitions of the Weinberg angle (from $\alpha(M_Z)$, G_F , M_Z , from the Z 's vector coupling, and from M_W/M_Z). These can be nicely encapsulated in the ϵ 's of Altarelli and Barbieri [140]:

$$\begin{aligned}\epsilon_1 &= \Delta\rho, \\ \epsilon_2 &= \cos^2\theta_w\Delta\rho + \frac{\sin^2\theta_w}{\cos^2\theta_w - \sin^2\theta_w}\Delta r_W - 2s_0^2\Delta\kappa, \\ \epsilon_3 &= \cos^2\theta_w\Delta\rho + (\cos^2\theta_w - \sin^2\theta_w)\Delta\kappa.\end{aligned}\tag{G.1}$$

where we define the weak angle from $\sin^2\theta_w \cos^2\theta_w \equiv \frac{\pi\alpha(M_Z)}{\sqrt{2}G_F M_Z^2}$ and the Δr_W , $\Delta\rho$ and $\Delta\kappa$ parameters are defined from the masses and effective vector and axial couplings of the electroweak bosons:

$$\begin{aligned}\frac{M_W^2}{M_Z^2} &= \frac{1}{2}\sqrt{1 + \sqrt{1 - \frac{4\pi\alpha(M_Z)}{\sqrt{2}G_F M_Z^2}(1 - \Delta r_W)}}, \\ g_V^f &= \sqrt{1 + \Delta\rho}(T_3^f - 2Q_f(1 + \Delta\kappa)\sin^2\theta_w), \\ g_A^f &= \sqrt{1 + \Delta\rho}T_3^f.\end{aligned}\tag{G.2}$$

(T_3^f and Q_f are weak isospin and charge of the corresponding fermion.) Notice that ϵ_2 relies on the measurement of the W mass while $\epsilon_{1,3}$ do not.

The number of parameters describing universal new physics in the W, Z channel on- and off-shell is instead four.²³ They correspond to the leading effects in a derivative expansion of the vector boson self-energies, $\Pi_{VV'}(q^2)$. More precisely they correspond to the

²³For a good part of the history of EW precision tests, the community has mostly relied on a set of three quantities, S, T, U . These are however inadequate in any realistic new physics scenario: they are always either redundant or incomplete. Indeed in technicolor models, it was understood that U is negligible and the set is redundant in that case [141–144]. On the other hand S, T, U are insufficient to describe even the simplest sequential Z' models that fall into the class of universal theories. That the relevant set should be consist of 4 quantities was first realized in [145] in the context of linearly realized EW symmetry, i.e. SMEFT. The generality of this counting, and therefore its validity also in technicolor/HEFT scenarios, has been clarified in [48].

		HL-LHC	HL-LHC+					
			CLIC ₃₈₀	CLIC ₃₈₀ (+GigaZ)	ILC ₂₅₀	ILC ₂₅₀ (+GigaZ)	CEPC	FCC-ee
<i>S</i>	Full Th_{Intr} Unc.	0.053	0.032	0.013	0.015	0.012	0.01	0.0079
	No Th_{Intr} Unc.	0.053	0.032	0.011	0.012	0.009	0.0068	0.0038
	No $Th_{\text{Par+Intr}}$ Unc.	0.052	0.031	0.0091	0.011	0.0067	0.0031	0.0013
<i>T</i>	Full Th_{Intr} Unc.	0.041	0.023	0.013	0.015	0.014	0.0094	0.0058
	No Th_{Intr} Unc.	0.041	0.023	0.012	0.014	0.013	0.0072	0.0022
	No $Th_{\text{Par+Intr}}$ Unc.	0.039	0.022	0.01	0.011	0.0091	0.0041	0.0019

Table 37. Comparison of the sensitivity at 68% probability to new physics contributions to EWPO in the form of the oblique S and T parameters, under different assumptions for the SM theory uncertainties. We express the results in terms of the usually normalised parameters: $S = 4 \sin^2 \theta_w \hat{S}/\alpha$ and $T = \hat{T}/\alpha$.

leading effects in each independent channel (with the channels characterized by the relevant quantum numbers: electric charge, electroweak and custodial symmetry). Considering the vector boson self-energies, using the constraints from $U(1)_{\text{EM}}$ unbroken gauge invariance (massless photon), and subtracting the quantities that play the role of SM inputs (v, g, g'), one is left with these four leading quantities

$$\begin{aligned}
 \hat{S} &= g^2 \Pi'_{W_3 B}(0), \\
 \hat{T} &= \frac{g^2}{M_W^2} (\Pi_{W_3 W_3}(0) - \Pi_{W^+ W^-}(0)), \\
 W &= \frac{1}{2} g^2 M_W^2 \Pi''_{W_3 W_3}(0), \\
 Y &= \frac{1}{2} g'^2 M_W^2 \Pi''_{BB}(0),
 \end{aligned} \tag{G.3}$$

which can be mapped to four linear combinations of operators in the SMEFT Lagrangian. Finally, considering their effect on W, Z on-shell propagation, one finds, writing $\epsilon_i = \epsilon_{i,\text{SM}} + \delta\epsilon_i$,

$$\begin{aligned}
 \delta\epsilon_1 &= \hat{T} - W - Y \tan^2 \theta_w, \\
 \delta\epsilon_2 &= -W, \\
 \delta\epsilon_3 &= \hat{S} - W - Y.
 \end{aligned} \tag{G.4}$$

Strongly coupled models come with a parametric enhancement of \hat{S}, \hat{T} over W, Y , such that in the class of models, one can simplify further the analysis of EW data and perform a two-dimensional fit.

The results of this fit setup are presented in table 37 and figure 17, for the different future lepton-collider options, where the largest improvement in terms of measurements of the EW precision observables (EWPO) is expected. In the table and figures we also show the impact of the SM theory uncertainties in the results. The results are presented assuming the projected future improvements in SM theory calculations (*Full Th_{Intr} Unc.*), neglecting the intrinsic theory uncertainties associated to such calculations (*No Th_{Intr} Unc.*) and,

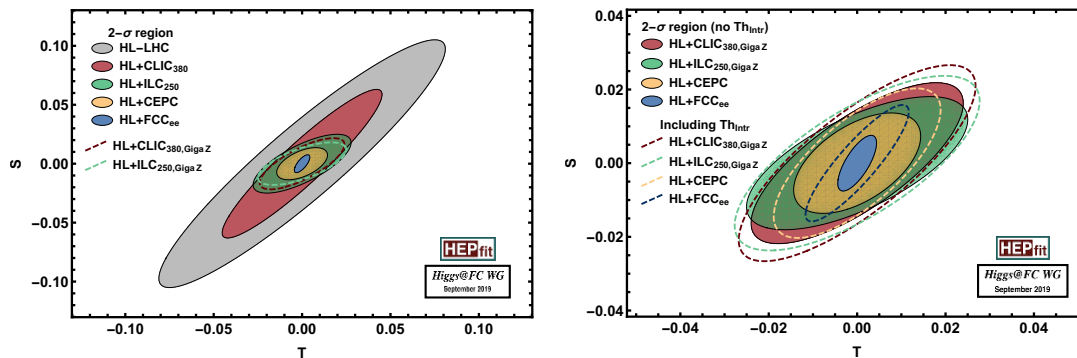


Figure 17. (Left) $2\text{-}\sigma$ regions in the $S - T$ plane at the different future colliders, combined with the HL-LHC (including also the LEP/SLD EWPO programme). We express the results in terms of the usually normalised parameters: $S = 4 \sin^2 \theta_w \hat{S}/\alpha$ and $T = \hat{T}/\alpha$. The results include the future projected parametric uncertainties in the SM predictions of the different EWPO, but not the intrinsic ones. (Right) The same illustrating the impact of neglecting such intrinsic theory errors. For each project (including the Giga-Z option for linear colliders) the solid regions show the results in the left panel, to be compared with the regions bounded by the dashed lines, which include the full projected theory uncertainty.

finally, also assuming that parametric uncertainties become subdominant (*No $Th_{\text{par+Intr}} \text{Unc.}$*). Since several of the SM EW inputs are to be measured at the future collider under consideration, the latter scenario goes beyond the physics potential of these machines. This scenario is presented only to illustrate whether the precision of the measurements of such inputs can become a limiting factor in terms of the reach of \hat{S} and \hat{T} . This seems to be the case for the circular colliders and, to a less extent, the linear collider Giga-Z options.

H Consistency of electroweak precision data

Before the discovery of a Higgs boson, the consistency of the SM has often been illustrated by comparing the direct measurement of m_W and m_{top} with the indirect constraints derived from precision measurement at the Z -pole and at low-energy experiments. Figure 18 for the future e^+e^- colliders.

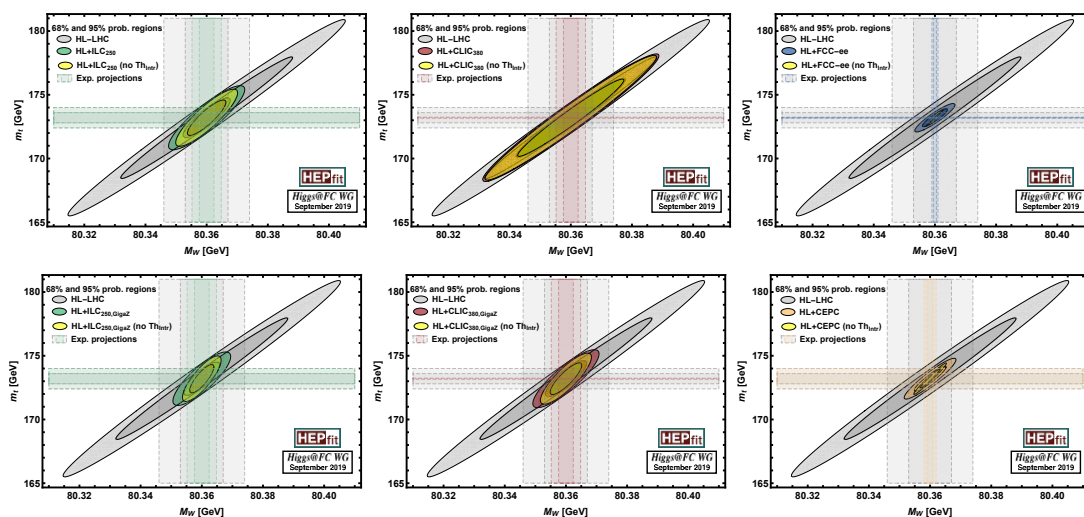


Figure 18. Constraints on m_W and m_{top} from direct measurements (horizontal and vertical lines) and indirect constraints (ellipses). In all cases the constraints from current data plus HL-LHC are compared to the ones expected for the e^+e^- collider. For ILC and CLIC the result is shown without (top row) and with a Giga-Z (bottom row) run.

I Improvement with respect to HL-LHC

Figures 19 and 20 give a graphic comparison of the improvement with respect to HL-LHC in the Kappa-3 and SMEFT-ND frameworks. This improvement is shown as the ratio of the precision at the HL-LHC over the precision at the future collider, with more darker colors corresponding to larger improvement factors. The kappa-3 result shows large improvements, up to an order of magnitude, for all future ee colliders for the measurement of the couplings to Z, W and b and the limits on the invisible branching ratio, and an ‘infinite’ improvement in the case of the coupling to charm, immeasurable at the HL-LHC. Rare, statistically dominated, couplings, as well as the coupling to the top quark are shown to be markedly improved with respect to HL-LHC only with FCC-hh. The more complete SMEFT-ND fit highlights more clearly the improvement in precision, with improvements of the order of an order of magnitude in the measurement of Z, W and b couplings for all future ee colliders. The aTGC results show an even more dramatic improvement, with factors over 100 and 1000 for the last stages of the linear colliders.

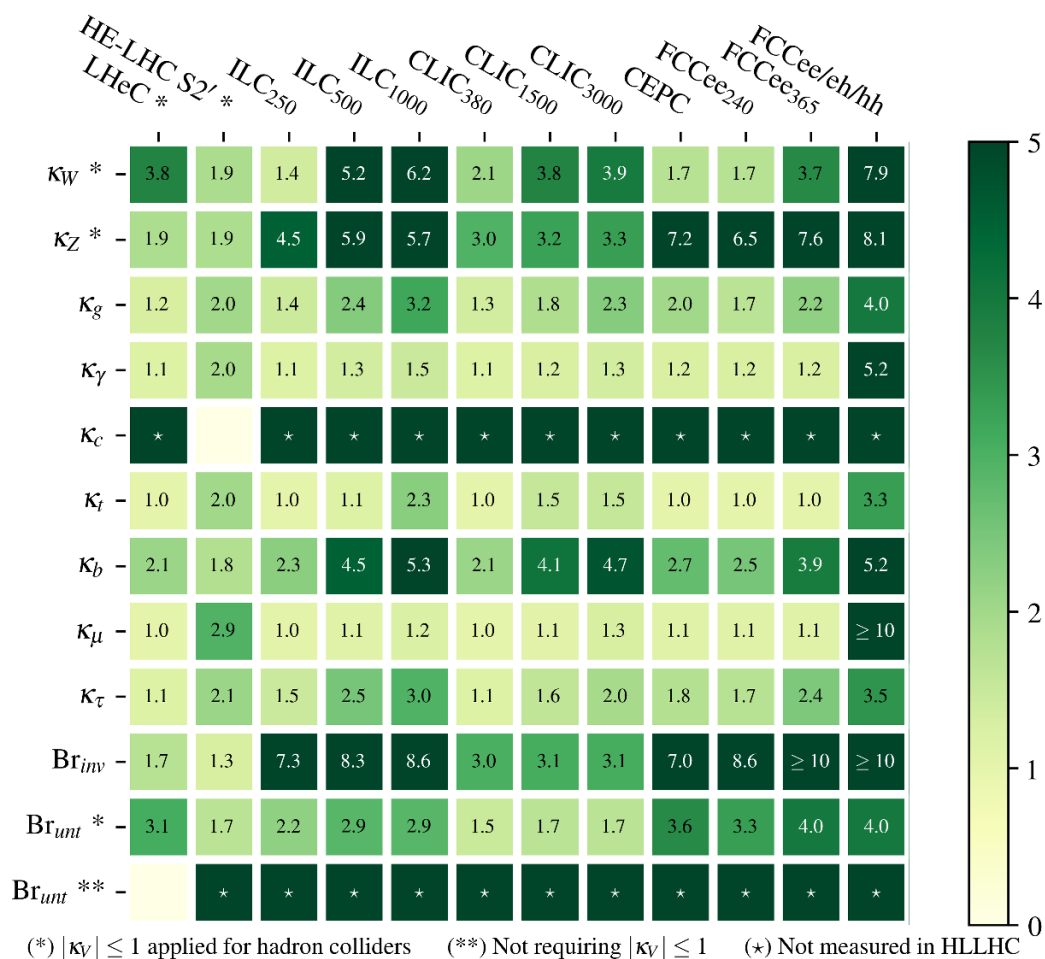


Figure 19. Graphic comparison of the improvement with respect to HL-LHC in the Kappa-3 framework.

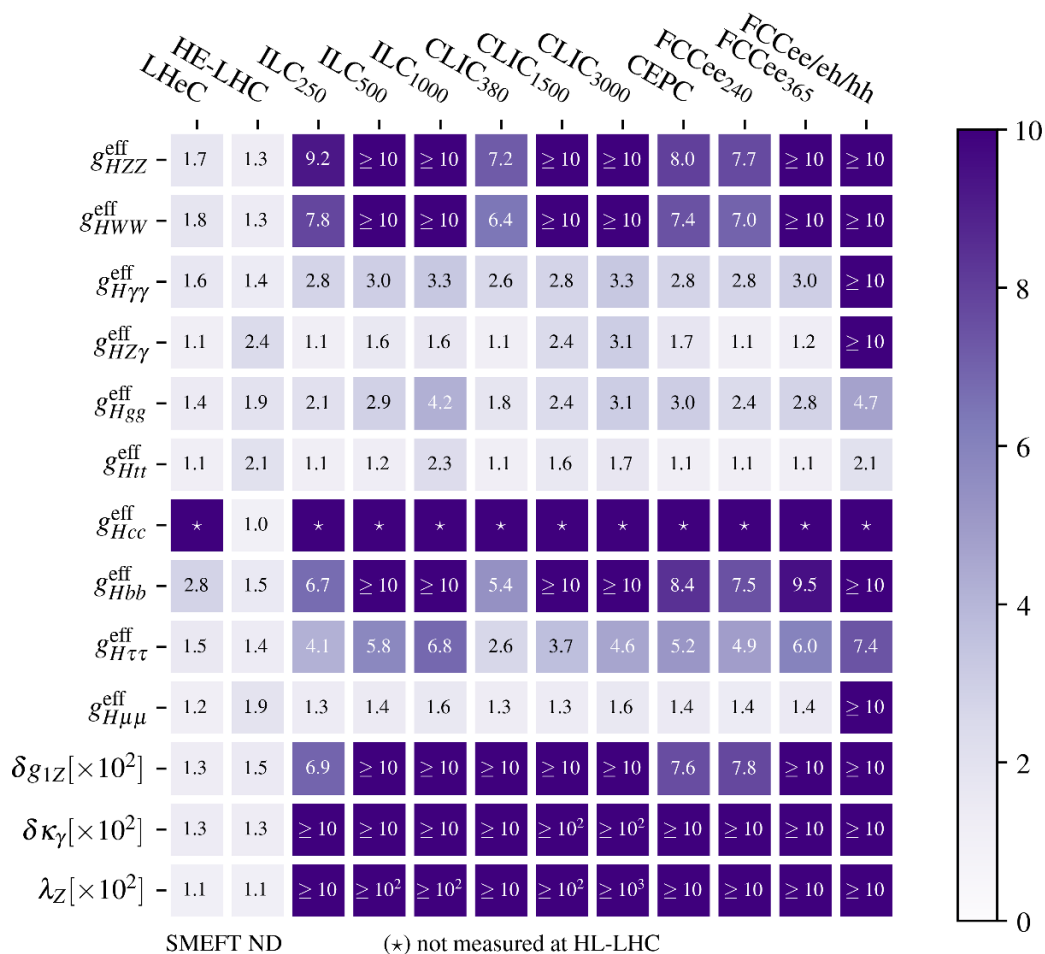


Figure 20. Graphic comparison of the improvement with respect to HL-LHC in the SMEFT-ND framework.

Open Access. This article is distributed under the terms of the Creative Commons Attribution License ([CC-BY 4.0](https://creativecommons.org/licenses/by/4.0/)), which permits any use, distribution and reproduction in any medium, provided the original author(s) and source are credited.

References

- [1] FCC collaboration, *FCC physics opportunities*, *Eur. Phys. J. C* **79** (2019) 474.
- [2] CEPC STUDY GROUP collaboration, *CEPC conceptual design report: volume 2 — Physics & detector*, [arXiv:1811.10545](https://arxiv.org/abs/1811.10545) [[INSPIRE](https://arxiv.org/abs/1811.10545)].
- [3] P. Bambade et al., *The International Linear Collider: a global project*, [arXiv:1903.01629](https://arxiv.org/abs/1903.01629) [[INSPIRE](https://arxiv.org/abs/1903.01629)].
- [4] LCC PHYSICS WORKING GROUP collaboration, *Tests of the standard model at the International Linear Collider*, [arXiv:1908.11299](https://arxiv.org/abs/1908.11299) [[INSPIRE](https://arxiv.org/abs/1908.11299)].
- [5] CLICDP, CLIC collaboration, *The Compact Linear collider (CLIC) — 2018 summary report*, *CERN Yellow Rep. Monogr.* **1802** (2018) 1 [[arXiv:1812.06018](https://arxiv.org/abs/1812.06018)] [[INSPIRE](https://arxiv.org/abs/1812.06018)].

- [6] LHEC STUDY GROUP collaboration, *A Large Hadron electron Collider at CERN: report on the physics and design concepts for machine and detector*, *J. Phys. G* **39** (2012) 075001 [[arXiv:1206.2913](#)] [[INSPIRE](#)].
- [7] D.M. Asner, J.B. Gronberg and J.F. Gunion, *Detecting and studying Higgs bosons at a photon-photon collider*, *Phys. Rev. D* **67** (2003) 035009 [[hep-ph/0110320](#)] [[INSPIRE](#)].
- [8] S.A. Bogacz et al., *SAPPHiRE: a Small Gamma-Gamma Higgs Factory*, [arXiv:1208.2827](#) [[INSPIRE](#)].
- [9] ALEGRO collaboration, *Towards an Advanced Linear International Collider*, [arXiv:1901.10370](#) [[INSPIRE](#)].
- [10] M. Mangano, *Physics potential of a low-energy FCC-hh*, [CERN-FCC-PHYS-2019-0001](#) (2019).
- [11] J.J. Blaising and P. Roloff, *Electroweak couplings of the Z boson at CLIC*, private communication.
- [12] F. Bordry et al., *Machine parameters and projected luminosity performance of proposed future colliders at CERN*, [arXiv:1810.13022](#) [[INSPIRE](#)].
- [13] M. Cepeda et al., *Report from Working Group 2, CERN Yellow Rep. Monogr.* **7** (2019) 221 [[arXiv:1902.00134](#)] [[INSPIRE](#)].
- [14] K. Fujii et al., *Physics case for the 250 GeV stage of the International Linear Collider*, [arXiv:1710.07621](#) [[INSPIRE](#)].
- [15] CLIC, CLICDP collaboration, *The Compact Linear e^+e^- Collider (CLIC): physics potential*, [arXiv:1812.07986](#) [[INSPIRE](#)].
- [16] LHC HIGGS CROSS SECTION WORKING GROUP collaboration, *LHC HXSWG interim recommendations to explore the coupling structure of a Higgs-like particle*, [arXiv:1209.0040](#) [[INSPIRE](#)].
- [17] LHC HIGGS CROSS SECTION WORKING GROUP collaboration, *Handbook of LHC Higgs cross sections: 3. Higgs properties*, [arXiv:1307.1347](#) [[INSPIRE](#)].
- [18] T. Barklow et al., *Improved formalism for precision Higgs coupling fits*, *Phys. Rev. D* **97** (2018) 053003 [[arXiv:1708.08912](#)] [[INSPIRE](#)].
- [19] M. Klein et al., *LHeC Higgs studies*, in preparation.
- [20] HEPFIT collaboration, *HEPfit: a code for the combination of indirect and direct constraints on high energy physics models*, <http://hepfit.roma1.infn.it/>.
- [21] J. de Blas et al., *Electroweak precision observables and Higgs-boson signal strengths in the Standard Model and beyond: present and future*, *JHEP* **12** (2016) 135 [[arXiv:1608.01509](#)] [[INSPIRE](#)].
- [22] J. de Blas et al., *Electroweak precision constraints at present and future colliders*, [PoS\(ICHEP 2016\)690](#) [[arXiv:1611.05354](#)] [[INSPIRE](#)].
- [23] J. de Blas et al., *The global electroweak and Higgs fits in the LHC era*, [PoS\(EPS-HEP2017\)467](#) [[arXiv:1710.05402](#)] [[INSPIRE](#)].
- [24] J. de Blas, O. Eberhardt and C. Krause, *Current and future constraints on Higgs couplings in the nonlinear effective theory*, *JHEP* **07** (2018) 048 [[arXiv:1803.00939](#)] [[INSPIRE](#)].

- [25] F. Beaujean et al., *Bayesian Analysis Toolkit: 1.0 and beyond*, *J. Phys. Conf. Ser.* **664** (2015) 072003.
- [26] A. Falkowski, S. Rychkov and A. Urbano, *What if the Higgs couplings to W and Z bosons are larger than in the Standard Model?*, *JHEP* **04** (2012) 073 [[arXiv:1202.1532](#)] [[INSPIRE](#)].
- [27] A. Falkowski and R. Rattazzi, *Which EFT*, *JHEP* **10** (2019) 255 [[arXiv:1902.05936](#)] [[INSPIRE](#)].
- [28] S. Chang and M.A. Luty, *The Higgs trilinear coupling and the scale of new physics*, [arXiv:1902.05556](#) [[INSPIRE](#)].
- [29] J. de Blas, J.C. Criado, M. Pérez-Victoria and J. Santiago, *Effective description of general extensions of the Standard Model: the complete tree-level dictionary*, *JHEP* **03** (2018) 109 [[arXiv:1711.10391](#)] [[INSPIRE](#)].
- [30] G.F. Giudice, C. Grojean, A. Pomarol and R. Rattazzi, *The strongly-interacting light Higgs*, *JHEP* **06** (2007) 045 [[hep-ph/0703164](#)] [[INSPIRE](#)].
- [31] D. Liu, A. Pomarol, R. Rattazzi and F. Riva, *Patterns of strong coupling for LHC searches*, *JHEP* **11** (2016) 141 [[arXiv:1603.03064](#)] [[INSPIRE](#)].
- [32] B. Grzadkowski, M. Iskrzynski, M. Misiak and J. Rosiek, *Dimension-six terms in the standard model lagrangian*, *JHEP* **10** (2010) 085 [[arXiv:1008.4884](#)] [[INSPIRE](#)].
- [33] R. Alonso, E.E. Jenkins, A.V. Manohar and M. Trott, *Renormalization group evolution of the standard model dimension six operators III: gauge coupling dependence and phenomenology*, *JHEP* **04** (2014) 159 [[arXiv:1312.2014](#)] [[INSPIRE](#)].
- [34] G. D'Ambrosio, G.F. Giudice, G. Isidori and A. Strumia, *Minimal flavor violation: an effective field theory approach*, *Nucl. Phys. B* **645** (2002) 155 [[hep-ph/0207036](#)] [[INSPIRE](#)].
- [35] A. Falkowski, *Higgs Basis: Proposal for an EFT basis choice for LHC HXSWG, LHCHXSWG-INT-2015-001* (2015).
- [36] A. Falkowski, *Effective field theory approach to LHC Higgs data*, *Pramana* **87** (2016) 39 [[arXiv:1505.00046](#)] [[INSPIRE](#)].
- [37] R. Contino, *The Higgs as a composite Nambu-Goldstone boson*, in the proceedings of *Physics of the large and the small (TASI 09)*, June 1–26, Boulder, Colorado, U.S.A. (2009), [arXiv:1005.4269](#) [[INSPIRE](#)].
- [38] G. Panico and A. Wulzer, *The composite Nambu-Goldstone Higgs*, *Lect. Notes Phys.* **913** (2016) 1 [[arXiv:1506.01961](#)].
- [39] G. Ferretti and D. Karateev, *Fermionic UV completions of composite Higgs models*, *JHEP* **03** (2014) 077 [[arXiv:1312.5330](#)] [[INSPIRE](#)].
- [40] G. Cacciapaglia and F. Sannino, *Fundamental composite (Goldstone) Higgs dynamics*, *JHEP* **04** (2014) 111 [[arXiv:1402.0233](#)] [[INSPIRE](#)].
- [41] A. Azatov, R. Contino, G. Panico and M. Son, *Effective field theory analysis of double Higgs boson production via gluon fusion*, *Phys. Rev. D* **92** (2015) 035001 [[arXiv:1502.00539](#)] [[INSPIRE](#)].
- [42] M.S. Amjad et al., *A precise characterisation of the top quark electro-weak vertices at the ILC*, *Eur. Phys. J. C* **75** (2015) 512 [[arXiv:1505.06020](#)] [[INSPIRE](#)].
- [43] CLICDP collaboration, *Top-quark physics at the CLIC electron-positron linear collider*, *JHEP* **11** (2019) 003 [[arXiv:1807.02441](#)] [[INSPIRE](#)].

- [44] P. Janot, *Top-quark electroweak couplings at the FCC-ee*, *JHEP* **04** (2015) 182 [[arXiv:1503.01325](#)] [[INSPIRE](#)].
- [45] J. De Blas et al., *On the future of Higgs, electroweak and diboson measurements at lepton colliders*, *JHEP* **12** (2019) 117 [[arXiv:1907.04311](#)] [[INSPIRE](#)].
- [46] J. de Blas et al., *The CLIC potential for new physics*, [arXiv:1812.02093](#) [[INSPIRE](#)].
- [47] T. Barklow et al., *Model-independent determination of the triple Higgs coupling at e^+e^- colliders*, *Phys. Rev. D* **97** (2018) 053004 [[arXiv:1708.09079](#)] [[INSPIRE](#)].
- [48] R. Barbieri, A. Pomarol, R. Rattazzi and A. Strumia, *Electroweak symmetry breaking after LEP-1 and LEP-2*, *Nucl. Phys. B* **703** (2004) 127 [[hep-ph/0405040](#)] [[INSPIRE](#)].
- [49] M. Farina et al., *Energy helps accuracy: electroweak precision tests at hadron colliders*, *Phys. Lett. B* **772** (2017) 210 [[arXiv:1609.08157](#)] [[INSPIRE](#)].
- [50] S. Banerjee, C. Englert, R.S. Gupta and M. Spannowsky, *Probing electroweak precision physics via boosted Higgs-strahlung at the LHC*, *Phys. Rev. D* **98** (2018) 095012 [[arXiv:1807.01796](#)] [[INSPIRE](#)].
- [51] K. Fujii, J. List, M. Peskin and J. Tiang, private communication.
- [52] R. Franceschini et al., *Electroweak precision tests in high-energy diboson processes*, *JHEP* **02** (2018) 111 [[arXiv:1712.01310](#)] [[INSPIRE](#)].
- [53] B. Henning, D. Lombardo, M. Riembau and F. Riva, *Measuring Higgs couplings without Higgs bosons*, *Phys. Rev. Lett.* **123** (2019) 181801 [[arXiv:1812.09299](#)] [[INSPIRE](#)].
- [54] F. Maltoni, L. Mantani and K. Mimasu, *Top-quark electroweak interactions at high energy*, *JHEP* **10** (2019) 004 [[arXiv:1904.05637](#)] [[INSPIRE](#)].
- [55] G.P. Lepage, P.B. Mackenzie and M.E. Peskin, *Expected precision of Higgs boson partial widths within the standard model*, [arXiv:1404.0319](#) [[INSPIRE](#)].
- [56] A. Blondel et al., *Theory requirements and possibilities for the FCC-ee and other future high energy and precision frontier lepton colliders*, [arXiv:1901.02648](#) [[INSPIRE](#)].
- [57] A. Blondel et al., *Standard model theory for the FCC-ee Tera-Z stage*, in the proceedings of the *Mini Workshop on Precision EW and QCD Calculations for the FCC Studies: Methods and Techniques*, January 12–13, CERN, Geneva, Switzerland (2018), [arXiv:1809.01830](#) [[INSPIRE](#)].
- [58] D. de Florian and J. Mazzitelli, *Two-loop virtual corrections to Higgs pair production*, *Phys. Lett. B* **724** (2013) 306 [[arXiv:1305.5206](#)] [[INSPIRE](#)].
- [59] D. de Florian and J. Mazzitelli, *Higgs boson pair production at next-to-next-to-leading order in QCD*, *Phys. Rev. Lett.* **111** (2013) 201801 [[arXiv:1309.6594](#)] [[INSPIRE](#)].
- [60] J. Grigo, K. Melnikov and M. Steinhauser, *Virtual corrections to Higgs boson pair production in the large top quark mass limit*, *Nucl. Phys. B* **888** (2014) 17 [[arXiv:1408.2422](#)] [[INSPIRE](#)].
- [61] D. de Florian et al., *Differential Higgs boson pair production at next-to-next-to-leading order in QCD*, *JHEP* **09** (2016) 151 [[arXiv:1606.09519](#)] [[INSPIRE](#)].
- [62] S. Borowka et al., *Higgs boson pair production in gluon fusion at next-to-leading order with full top-quark mass dependence*, *Phys. Rev. Lett.* **117** (2016) 012001 [*Erratum ibid.* **117** (2016) 079901] [[arXiv:1604.06447](#)] [[INSPIRE](#)].

- [63] S. Borowka et al., *Full top quark mass dependence in Higgs boson pair production at NLO*, *JHEP* **10** (2016) 107 [[arXiv:1608.04798](#)] [[INSPIRE](#)].
- [64] J. Baglio et al., *Gluon fusion into Higgs pairs at NLO QCD and the top mass scheme*, *Eur. Phys. J. C* **79** (2019) 459 [[arXiv:1811.05692](#)] [[INSPIRE](#)].
- [65] R. Frederix et al., *Higgs pair production at the LHC with NLO and parton-shower effects*, *Phys. Lett. B* **732** (2014) 142 [[arXiv:1401.7340](#)] [[INSPIRE](#)].
- [66] J. Reuter, WHIZARD team, private communication.
- [67] M. McCullough, *An indirect model-dependent probe of the Higgs self-coupling*, *Phys. Rev. D* **90** (2014) 015001 [Erratum *ibid.* **D 92** (2015) 039903] [[arXiv:1312.3322](#)] [[INSPIRE](#)].
- [68] G. Degrandi, P.P. Giardino, F. Maltoni and D. Pagani, *Probing the Higgs self coupling via single Higgs production at the LHC*, *JHEP* **12** (2016) 080 [[arXiv:1607.04251](#)] [[INSPIRE](#)].
- [69] W. Bizon, M. Gorbahn, U. Haisch and G. Zanderighi, *Constraints on the trilinear Higgs coupling from vector boson fusion and associated Higgs production at the LHC*, *JHEP* **07** (2017) 083 [[arXiv:1610.05771](#)] [[INSPIRE](#)].
- [70] J.J. van der Bij, *Does low-energy physics depend on the potential of a heavy Higgs particle?*, *Nucl. Phys. B* **267** (1986) 557 [[INSPIRE](#)].
- [71] G. Degrandi, M. Fedele and P.P. Giardino, *Constraints on the trilinear Higgs self coupling from precision observables*, *JHEP* **04** (2017) 155 [[arXiv:1702.01737](#)] [[INSPIRE](#)].
- [72] G.D. Kribs et al., *Electroweak oblique parameters as a probe of the trilinear Higgs boson self-interaction*, *Phys. Rev. D* **95** (2017) 093004 [[arXiv:1702.07678](#)] [[INSPIRE](#)].
- [73] S. Di Vita et al., *A global view on the Higgs self-coupling*, *JHEP* **09** (2017) 069 [[arXiv:1704.01953](#)] [[INSPIRE](#)].
- [74] S. Di Vita et al., *A global view on the Higgs self-coupling at lepton colliders*, *JHEP* **02** (2018) 178 [[arXiv:1711.03978](#)] [[INSPIRE](#)].
- [75] F. Maltoni, D. Pagani, A. Shivaji and X. Zhao, *Trilinear Higgs coupling determination via single-Higgs differential measurements at the LHC*, *Eur. Phys. J. C* **77** (2017) 887 [[arXiv:1709.08649](#)] [[INSPIRE](#)].
- [76] L. Di Luzio, R. Gröber and M. Spannowsky, *Maxi-sizing the trilinear Higgs self-coupling: how large could it be?*, *Eur. Phys. J. C* **77** (2017) 788 [[arXiv:1704.02311](#)] [[INSPIRE](#)].
- [77] *Muon Collider — Preparatory meeting*, April 10–11, CERN, Geneva, Switzerland (2019), <https://indico.cern.ch/event/801616>.
- [78] CMS collaboration, *Search for a standard model-like Higgs boson in the $\mu^+\mu^-$ and e^+e^- decay channels at the LHC*, *Phys. Lett. B* **744** (2015) 184 [[arXiv:1410.6679](#)] [[INSPIRE](#)].
- [79] FCC collaboration, *FCC-ee: the lepton collider*, *Eur. Phys. J. ST* **228** (2019) 261.
- [80] ATLAS collaboration, *Search for the decay of the Higgs boson to charm quarks with the ATLAS experiment*, *Phys. Rev. Lett.* **120** (2018) 211802 [[arXiv:1802.04329](#)] [[INSPIRE](#)].
- [81] G. Perez, Y. Soreq, E. Stamou and K. Tobioka, *Prospects for measuring the Higgs boson coupling to light quarks*, *Phys. Rev. D* **93** (2016) 013001 [[arXiv:1505.06689](#)] [[INSPIRE](#)].
- [82] G.T. Bodwin, F. Petriello, S. Stoynev and M. Velasco, *Higgs boson decays to quarkonia and the $H\bar{c}c$ coupling*, *Phys. Rev. D* **88** (2013) 053003 [[arXiv:1306.5770](#)] [[INSPIRE](#)].

- [83] G.T. Bodwin et al., *Relativistic corrections to Higgs boson decays to quarkonia*, *Phys. Rev. D* **90** (2014) 113010 [[arXiv:1407.6695](#)] [[INSPIRE](#)].
- [84] A.L. Kagan et al., *Exclusive window onto Higgs Yukawa couplings*, *Phys. Rev. Lett.* **114** (2015) 101802 [[arXiv:1406.1722](#)] [[INSPIRE](#)].
- [85] ATLAS collaboration, *Searches for exclusive Higgs and Z boson decays into $J/\psi\gamma$, $\psi(2S)\gamma$ and $\Upsilon(nS)\gamma$ at $\sqrt{s} = 13$ TeV with the ATLAS detector*, *Phys. Lett. B* **786** (2018) 134 [[arXiv:1807.00802](#)] [[INSPIRE](#)].
- [86] CMS collaboration, *Search for rare decays of Z and Higgs bosons to J/ψ and a photon in proton-proton collisions at $\sqrt{s} = 13$ TeV*, *Eur. Phys. J. C* **79** (2019) 94 [[arXiv:1810.10056](#)] [[INSPIRE](#)].
- [87] ATLAS collaboration, *Search for exclusive Higgs and Z boson decays to $\phi\gamma$ and $\rho\gamma$ with the ATLAS detector*, *JHEP* **07** (2018) 127 [[arXiv:1712.02758](#)] [[INSPIRE](#)].
- [88] CMS collaboration, *Search for a Higgs boson decaying into $\gamma^*\gamma \rightarrow \ell\ell\gamma$ with low dilepton mass in pp collisions at $\sqrt{s} = 8$ TeV*, *Phys. Lett. B* **753** (2016) 341 [[arXiv:1507.03031](#)] [[INSPIRE](#)].
- [89] J. Brod, U. Haisch and J. Zupan, *Constraints on CP-violating Higgs couplings to the third generation*, *JHEP* **11** (2013) 180 [[arXiv:1310.1385](#)] [[INSPIRE](#)].
- [90] Y.T. Chien et al., *Direct and indirect constraints on CP-violating Higgs-quark and Higgs-gluon interactions*, *JHEP* **02** (2016) 011 [[arXiv:1510.00725](#)] [[INSPIRE](#)].
- [91] W. Altmannshofer, J. Brod and M. Schmaltz, *Experimental constraints on the coupling of the Higgs boson to electrons*, *JHEP* **05** (2015) 125 [[arXiv:1503.04830](#)] [[INSPIRE](#)].
- [92] D. Egana-Ugrinovic and S. Thomas, *Higgs boson contributions to the electron electric dipole moment*, [arXiv:1810.08631](#) [[INSPIRE](#)].
- [93] J. Brod and E. Stamou, *Electric dipole moment constraints on CP-violating heavy-quark Yukawas at next-to-leading order*, [arXiv:1810.12303](#) [[INSPIRE](#)].
- [94] J. Brod and D. Skodras, *Electric dipole moment constraints on CP-violating light-quark Yukawas*, *JHEP* **01** (2019) 233 [[arXiv:1811.05480](#)] [[INSPIRE](#)].
- [95] ACME collaboration, *Improved limit on the electric dipole moment of the electron*, *Nature* **562** (2018) 355.
- [96] PARTICLE DATA GROUP collaboration, *Review of particle physics*, *Phys. Rev. D* **98** (2018) 030001.
- [97] LHC HIGGS CROSS SECTION WORKING GROUP collaboration, *Handbook of LHC Higgs cross sections: 4. Deciphering the nature of the Higgs sector*, [arXiv:1610.07922](#) [[INSPIRE](#)].
- [98] A. Robson and P. Roloff, *Updated CLIC luminosity staging baseline and Higgs coupling prospects*, [arXiv:1812.01644](#) [[INSPIRE](#)].
- [99] P. Azzi et al., *Prospective studies for LEP3 with the CMS detector*, [arXiv:1208.1662](#) [[INSPIRE](#)].
- [100] N. Kauer and G. Passarino, *Inadequacy of zero-width approximation for a light Higgs boson signal*, *JHEP* **08** (2012) 116 [[arXiv:1206.4803](#)] [[INSPIRE](#)].
- [101] F. Caola and K. Melnikov, *Constraining the Higgs boson width with ZZ production at the LHC*, *Phys. Rev. D* **88** (2013) 054024 [[arXiv:1307.4935](#)] [[INSPIRE](#)].

- [102] A. Azatov, C. Grojean, A. Paul and E. Salvioni, *Taming the off-shell Higgs boson*, *Zh. Eksp. Teor. Fiz.* **147** (2015) 410 [[arXiv:1406.6338](#)] [[INSPIRE](#)].
- [103] CEPC PHYSICS-DETECTOR STUDY GROUP collaboratio, *The CEPC input for the European strategy for particle physics — Physics and detector*, [arXiv:1901.03170](#) [[INSPIRE](#)].
- [104] F. An et al., *Precision Higgs physics at the CEPC*, *Chin. Phys. C* **43** (2019) 043002 [[arXiv:1810.09037](#)] [[INSPIRE](#)].
- [105] V.D. Barger, M. Berger, J.F. Gunion and T. Han, *Physics of Higgs factories*, *eConf C* **010630** (2001) E110 [[hep-ph/0110340](#)] [[INSPIRE](#)].
- [106] C. Rubbia, *Further searches of the Higgs scalar sector*, in *Input to the European Particle Physics Strategy Update 2018–2020*, November 1–December 19 (2018).
- [107] M. Greco, T. Han and Z. Liu, *ISR effects for resonant Higgs production at future lepton colliders*, *Phys. Lett. B* **763** (2016) 409 [[arXiv:1607.03210](#)] [[INSPIRE](#)].
- [108] T. Han and Z. Liu, *Potential precision of a direct measurement of the Higgs boson total width at a muon collider*, *Phys. Rev. D* **87** (2013) 033007 [[arXiv:1210.7803](#)] [[INSPIRE](#)].
- [109] Y. Alexahin et al., *Muon collider Higgs factory for snowmass 2013*, in the proceedings of the *2013 Community Summer Study on the Future of U.S. Particle Physics: Snowmass on the Mississippi (CSS2013)*, July 29–August 6, Minneapolis, U.S.A. (2013), [arXiv:1308.2143](#) [[INSPIRE](#)].
- [110] P. Janot, *Circular lepton colliders (FCC-ee + CEPC + Muon collider)*, <https://indico.cern.ch/event/716380/> (2018).
- [111] N. Bartosik et al., *Preliminary report on the study of beam-induced background effects at a muon collider*, [arXiv:1905.03725](#) [[INSPIRE](#)].
- [112] N. Pastrone, *Muon colliders*, in *Input to the European Particle Physics Strategy Update 2018–2020*, November 1–December 19 (2018).
- [113] J.P. Delahaye et al., *Muon colliders*, [arXiv:1901.06150](#) [[INSPIRE](#)].
- [114] S.P.D. Mangles et al., *Monoenergetic beams of relativistic electrons from intense laser-plasma interactions*, *Nature* **431** (2004) 535 [[INSPIRE](#)].
- [115] S. Lee, T.C. Katsouleas, R. Hemker and W.B. Mori, *Simulations of a meter-long plasma wake field accelerator*, *Phys. Rev. E* **61** (2000) 7014 [[INSPIRE](#)].
- [116] J. Krall and G. Joyce, *Transverse equilibrium and stability of the primary beam in the plasma wake-field accelerator*, *Phys. Plasmas* **2** (1995) 1326.
- [117] D.H. Whittum, *Transverse two stream instability of a beam with a Bennett profile*, *Phys. Plasmas* **4** (1997) 1154 [[INSPIRE](#)].
- [118] I. Blumenfeld et al., *Energy doubling of 42 GeV electrons in a metre-scale plasma wakefield accelerator*, *Nature* **445** (2007) 741 [[INSPIRE](#)].
- [119] M. Litos et al., *High-efficiency acceleration of an electron beam in a plasma wakefield accelerator*, *Nature* **515** (2014) 92.
- [120] AWAKE collaboration, *Acceleration of electrons in the plasma wakefield of a proton bunch*, *Nature* **561** (2018) 363 [[arXiv:1808.09759](#)] [[INSPIRE](#)].

- [121] R. Contino et al., *Strong Higgs Interactions at a Linear Collider*, *JHEP* **02** (2014) 006 [[arXiv:1309.7038](#)] [[INSPIRE](#)].
- [122] G. Marandella, C. Schappacher and A. Strumia, *Supersymmetry and precision data after LEP2*, *Nucl. Phys. B* **715** (2005) 173 [[hep-ph/0502095](#)] [[INSPIRE](#)].
- [123] C. Grojean, G. Servant and J.D. Wells, *First-order electroweak phase transition in the standard model with a low cutoff*, *Phys. Rev. D* **71** (2005) 036001 [[hep-ph/0407019](#)] [[INSPIRE](#)].
- [124] J.R. Espinosa, T. Konstandin and F. Riva, *Strong electroweak phase transitions in the Standard Model with a singlet*, *Nucl. Phys. B* **854** (2012) 592 [[arXiv:1107.5441](#)] [[INSPIRE](#)].
- [125] D. Curtin, P. Meade and C.-T. Yu, *Testing electroweak baryogenesis with future colliders*, *JHEP* **11** (2014) 127 [[arXiv:1409.0005](#)] [[INSPIRE](#)].
- [126] C. Grojean and G. Servant, *Gravitational waves from phase transitions at the electroweak scale and beyond*, *Phys. Rev. D* **75** (2007) 043507 [[hep-ph/0607107](#)] [[INSPIRE](#)].
- [127] M. Farina, D. Pappadopulo and A. Strumia, *A modified naturalness principle and its experimental tests*, *JHEP* **08** (2013) 022 [[arXiv:1303.7244](#)] [[INSPIRE](#)].
- [128] A. De Simone, G.F. Giudice and A. Strumia, *Benchmarks for dark matter searches at the LHC*, *JHEP* **06** (2014) 081 [[arXiv:1402.6287](#)] [[INSPIRE](#)].
- [129] Z. Chacko, D. Curtin, M. Geller and Y. Tsai, *Cosmological signatures of a mirror twin Higgs*, *JHEP* **09** (2018) 163 [[arXiv:1803.03263](#)] [[INSPIRE](#)].
- [130] R. Contino, A. Mitridate, A. Podo and M. Redi, *Gluequark dark matter*, *JHEP* **02** (2019) 187 [[arXiv:1811.06975](#)] [[INSPIRE](#)].
- [131] S. Heinemeyer et al., *Theoretical uncertainties for electroweak and Higgs-boson precision measurements at FCC-ee*, IFT-UAM/CSIC-18-021 (2019) [[TUM-HEP-1185/19](#)].
- [132] F. Simon, *Impact of theory uncertainties on the precision of the top quark mass in a threshold scan at future e^+e^- colliders*, [PoS\(ICHEP2016\)872](#) [[arXiv:1611.03399](#)] [[INSPIRE](#)].
- [133] CEPC STUDY GROUP collaboration, *CEPC electroweak precision measurements*, CEPC-PHY-EW-2019-008, private communication.
- [134] A. Abada et al., *Future circular collider*, [CERN-ACC-2018-0056](#) (2018).
- [135] N. Alipour Tehrani et al., *FCC-ee: your questions answered*, in the proceedings of the *CERN Council Open Symposium on the Update of European Strategy for Particle Physics (EPPSU)*, May 13–16, Granada, Spain (2019), [[arXiv:1906.02693](#)] [[INSPIRE](#)].
- [136] R. Tenchini, *Electroweak precision measurements at the FCC-ee*, talk given at the *Physics at the FCC: Overview of the conceptual design report*, March 4–5, CERN, Geneva, Switzerland (2019).
- [137] G.W. Wilson, *Updated study of a precision measurement of the W mass from a threshold scan using polarized e^- and e^+ at ILC*, in the proceedings of the *International Workshop on Future Linear Colliders (LCWS15)*, November 2–6, Whistler, Canada (2015), [[arXiv:1603.06016](#)] [[INSPIRE](#)].
- [138] ALEPH, DELPHI, L3, OPAL, SLD, LEP ELECTROWEAK WORKING GROUP, SLD ELECTROWEAK GROUP, SLD HEAVY FLAVOUR GROUP collaboration, *Precision electroweak measurements on the Z resonance*, *Phys. Rept.* **427** (2006) 257 [[hep-ex/0509008](#)] [[INSPIRE](#)].

- [139] M. Mangano, *Higgs physics potential of FCC-hh standalone*, [CERN-FCC-PHYS-2019-0002](#) (2019).
- [140] G. Altarelli and R. Barbieri, *Vacuum polarization effects of new physics on electroweak processes*, *Phys. Lett. B* **253** (1991) 161 [[INSPIRE](#)].
- [141] M.E. Peskin and T. Takeuchi, *A new constraint on a strongly interacting Higgs sector*, *Phys. Rev. Lett.* **65** (1990) 964 [[INSPIRE](#)].
- [142] B. Holdom and J. Terning, *Large corrections to electroweak parameters in technicolor theories*, *Phys. Lett. B* **247** (1990) 88 [[INSPIRE](#)].
- [143] M. Golden and L. Randall, *Radiative corrections to electroweak parameters in technicolor theories*, *Nucl. Phys. B* **361** (1991) 3 [[INSPIRE](#)].
- [144] M.E. Peskin and T. Takeuchi, *Estimation of oblique electroweak corrections*, *Phys. Rev. D* **46** (1992) 381 [[INSPIRE](#)].
- [145] B. Grinstein and M.B. Wise, *Operator analysis for precision electroweak physics*, *Phys. Lett. B* **265** (1991) 326 [[INSPIRE](#)].

Measurement of the top quark mass using proton-proton data at $\sqrt{s} = 7$ and 8 TeV

V. Khachatryan *et al.**

(CMS Collaboration)

(Received 14 September 2015; published 7 April 2016)

A new set of measurements of the top quark mass are presented, based on the proton-proton data recorded by the CMS experiment at the LHC at $\sqrt{s} = 8$ TeV corresponding to a luminosity of 19.7 fb^{-1} . The top quark mass is measured using the lepton + jets, all-jets and dilepton decay channels, giving values of $172.35 \pm 0.16(\text{stat}) \pm 0.48(\text{syst})$ GeV, $172.32 \pm 0.25(\text{stat}) \pm 0.59(\text{syst})$ GeV, and $172.82 \pm 0.19(\text{stat}) \pm 1.22(\text{syst})$ GeV, respectively. When combined with the published CMS results at $\sqrt{s} = 7$ TeV, they provide a top quark mass measurement of $172.44 \pm 0.13(\text{stat}) \pm 0.47(\text{syst})$ GeV. The top quark mass is also studied as a function of the event kinematical properties in the lepton + jets decay channel. No indications of a kinematic bias are observed and the collision data are consistent with a range of predictions from current theoretical models of $t\bar{t}$ production.

DOI: [10.1103/PhysRevD.93.072004](https://doi.org/10.1103/PhysRevD.93.072004)

I. INTRODUCTION

The mass of the top quark (m_t) is one of the fundamental parameters of the standard model (SM). A precise measurement of its value provides a key input to global electroweak fits and to tests of the internal consistency of the SM [1,2]. Its value leads to constraints on the stability of the electroweak vacuum [3,4] and affects models with broader cosmological implications [5,6].

The most precise measurements of m_t have been derived from combinations of the results from the CDF and D0 experiments at the Tevatron, and ATLAS and CMS at the CERN LHC. The current combination from the four experiments gives a top quark mass of 173.34 ± 0.76 GeV [7], while the latest combination from the Tevatron experiments gives a mass of 174.34 ± 0.64 GeV [8]. The Tevatron combination is currently the most precise measurement and it includes all of the current Tevatron measurements. In contrast, the current four experiment combination has not been updated since 2013 and does not include the latest Tevatron and LHC measurements, in particular the measurement from ATLAS using a combination of the lepton + jets and dilepton channels [9].

Beyond the leading order (LO) in quantum chromodynamics (QCD), the numerical value of m_t depends on the renormalization scheme [10,11]. The available Monte Carlo (MC) generators contain matrix elements at LO or next-to-leading order (NLO), while higher orders are approximated by applying parton showering. Each of the

measurements used in the combinations has been calibrated against the mass implemented in a MC program. Given the precision of the experimental results, a detailed understanding of the relationship between the measurements and the value of m_t in different theoretical schemes is needed. Current indications are that the present measurements based on the kinematic reconstruction of the top quark mass correspond approximately to the pole (“on-shell”) mass to within a precision of about 1 GeV [12].

At the LHC, top quarks are predominantly produced in quark-antiquark pairs ($t\bar{t}$) and top quark events are characterized by the decays of the daughter W bosons. This leads to experimental signatures with two jets associated with the hadronization of the bottom quarks and either a single lepton (e, μ), one undetected neutrino and two light quark jets (lepton + jets channel), or four light quark jets (all-jets channel), or two leptons ($ee, e\mu, \mu\mu$) and two undetected neutrinos (dilepton channel). While the events which contain leptonic τ decays are included in the analysis samples, they contribute very little to the mass measurements as their yields are negligible. The results presented in this paper focus on the analysis of data in these three channels recorded by the CMS experiment in the 2012 part of what is commonly referred to as Run 1 of the LHC.

The paper is organized as follows. The main features of the detector and the data are discussed in Secs. II and III. Section IV is a discussion of the analysis techniques, which lead to the measurements of Sec. V. The categorization of the systematic uncertainties is presented in Sec. VI, followed by the full results for the three decay channels in Sec. VII. Section VIII presents a study of m_t as a function of the kinematical properties of the $t\bar{t}$ system in the lepton + jets channel. This is followed in Secs. IX and X, which discuss the combination of the measurements and the final result for m_t , respectively.

*Full author list given at the end of the article.

II. THE CMS DETECTOR

The central feature of the CMS apparatus is a superconducting solenoid of 6 m internal diameter, providing a magnetic field of 3.8 T. Within the solenoid volume are a silicon pixel and strip tracker, a lead tungstate crystal electromagnetic calorimeter (ECAL), and a brass and scintillator hadron calorimeter (HCAL), each composed of a barrel and two endcap sections. The tracker has a track-finding efficiency of more than 99% for muons with transverse momentum $p_T > 1$ GeV and pseudorapidity $|\eta| < 2.5$. The ECAL is a fine-grained hermetic calorimeter with quasiprojective geometry, and is distributed in the barrel region of $|\eta| < 1.48$ and in two endcaps that extend up to $|\eta| < 3.0$. The HCAL barrel and endcaps similarly cover the region $|\eta| < 3.0$. In addition to the barrel and endcap detectors, CMS has extensive forward calorimetry. Muons are measured in gas-ionization detectors, which are embedded in the steel flux-return yoke outside of the solenoid. A more detailed description of the CMS detector, together with a definition of the coordinate system used, and the relevant kinematic variables can be found in Ref. [13].

III. DATA SETS

The measurements presented in this paper are based on the data recorded at a center-of-mass energy of 8 TeV during 2012, and correspond to an integrated luminosity of 19.7 fb^{-1} .

A. Event simulation and reconstruction

Simulated $t\bar{t}$ signal events are generated with the MADGRAPH 5.1.5.11 LO matrix element generator with up to three additional partons [14]. MADSPIN [15] is used for the decay of heavy resonances, PYTHIA 6.426 for parton showering [16] using the Z2* tune, and TAUOLA [17] for decays of τ leptons. The most recent PYTHIA Z2* tune is derived from the Z1 tune [18], which uses the CTEQ5L parton distribution function (PDF) set, whereas Z2* uses CTEQ6L [19]. A full simulation of the CMS detector based on GEANT4 [20] is used. The $t\bar{t}$ signal events are generated for seven different values of m_t ranging from 166.5 to 178.5 GeV. The W/Z + jets background events are generated with MADGRAPH 5.1.3.30. The diboson background (WW , WZ , ZZ) is simulated using PYTHIA 6.426 using the Z2* tune. The single top quark background is simulated using POWHEG 1.380 [21–25], assuming an m_t of 172.5 GeV. The $t\bar{t}$, W/Z + jets, and single top quark samples are normalized to the theoretical predictions described in Refs. [26–30]. The simulation includes the effects of additional proton-proton collisions (pileup) by overlapping minimum bias events with the same multiplicity distribution and location as in data.

Events are reconstructed using a particle-flow (PF) algorithm [31,32]. This proceeds by reconstructing and

identifying each final-state particle using an optimized combination of all of the subdetector information. Each event is required to have at least one reconstructed collision vertex. The primary vertex is chosen as the vertex with the largest value of $\sum p_T^2$ of the tracks associated with that vertex. Additional criteria are applied to each event to reject events with features consistent with detector noise and beam-gas interactions.

The energy of electrons is determined from a combination of the track momentum at the primary vertex, the corresponding ECAL energy cluster, and the sum of the reconstructed bremsstrahlung photons associated with the track [33]. The momentum of muons is obtained from the track momentum determined in a combined fit to information from the silicon trackers and the muon detectors [34]. The energy of charged hadrons is determined from a combination of the track momentum and the corresponding ECAL and HCAL energies, corrected for the suppression of small signals and calibrated for the nonlinear response of the calorimeters. Finally, the energy of the neutral hadrons is obtained from remaining calibrated HCAL and ECAL energies. As the charged leptons originating from top quark decays are typically isolated from other particles, a relative isolation variable (I_{rel}) is constructed to select lepton candidates. This is defined as the scalar sum of the p_T values of the additional particles reconstructed within an angle $\Delta R = \sqrt{(\Delta\eta)^2 + (\Delta\phi)^2}$ of the lepton direction, divided by the p_T of the lepton. Here $\Delta\eta$ and $\Delta\phi$ are the differences in the pseudorapidity and azimuthal angles between the lepton direction and other tracks and energy depositions. A muon candidate is rejected if $I_{\text{rel}} \geq 0.12$ for $\Delta R = 0.4$, and an electron candidate is rejected if $I_{\text{rel}} \geq 0.10$ for $\Delta R = 0.3$.

Jets are clustered from the reconstructed PF candidates using the anti- k_T algorithm [35] with a distance parameter of 0.5, as implemented in the FASTJET package [36]. The jet momentum is determined from the vector sum of the momenta of the particles in each jet, and is found in simulation to be within 5% to 10% of the jet momentum at hadron level for the full p_T range [37]. Corrections to the jet energy scale (JES) and the jet energy resolution (JER) are obtained from the simulation and through *in situ* measurements of the energy balance of exclusive dijet, photon + jet, and Z + jet events. Muons, electrons, and charged hadrons originating from pileup interactions are not included in the jet reconstruction. Missing transverse energy (E_T^{miss}) is defined as the magnitude of the negative vector p_T sum of all selected PF candidates in the event. Charged hadrons originating from pileup interactions are not included in the calculation of E_T^{miss} . Jets are classified as b jets through their probability of originating from the hadronization of bottom quarks, using the combined secondary vertex (CSV) b tagging algorithm, which combines information from the significance of the track impact parameters, the kinematical properties of the jets, and the

presence of tracks that form vertices within the jet. Three different minimum thresholds are used for the CSV discriminator to define the loose (CSVL), medium (CSVM), and tight (CSVT) working points. These have b tagging efficiencies of approximately 85%, 67%, and 50%, and misidentification probabilities for light-parton jets of 10%, 1%, and 0.1%, respectively [38].

B. Event selection

For the lepton + jets channel we use the data collected using a single-muon or single-electron trigger with a minimum trigger p_T threshold for an isolated muon (electron) of 24 GeV (27 GeV), corresponding to an integrated luminosity of 19.7 fb^{-1} . We then select events

that have exactly one isolated muon or electron, with $p_T > 33 \text{ GeV}$ and $|\eta| < 2.1$. In addition, at least four jets with $p_T > 30 \text{ GeV}$ and $|\eta| < 2.4$ are required. Jets originating from b quarks (denoted as b jets) are identified using the CSV algorithm at the medium working point [38]. With the requirement of exactly two b -tagged jets among the four jets with the highest p_T , 104 746 $t\bar{t}$ candidate events are selected in data. From simulation, the sample composition is expected to be 93% $t\bar{t}$, 4% single top quark, 2% W + jets, and 1% other processes. Figure 1 shows the comparison of the data and simulation for the selected events in some representative distributions. The simulation shown is not corrected for the uncertainty in the shape of the top quark p_T distribution [39], which accounts for almost all of the

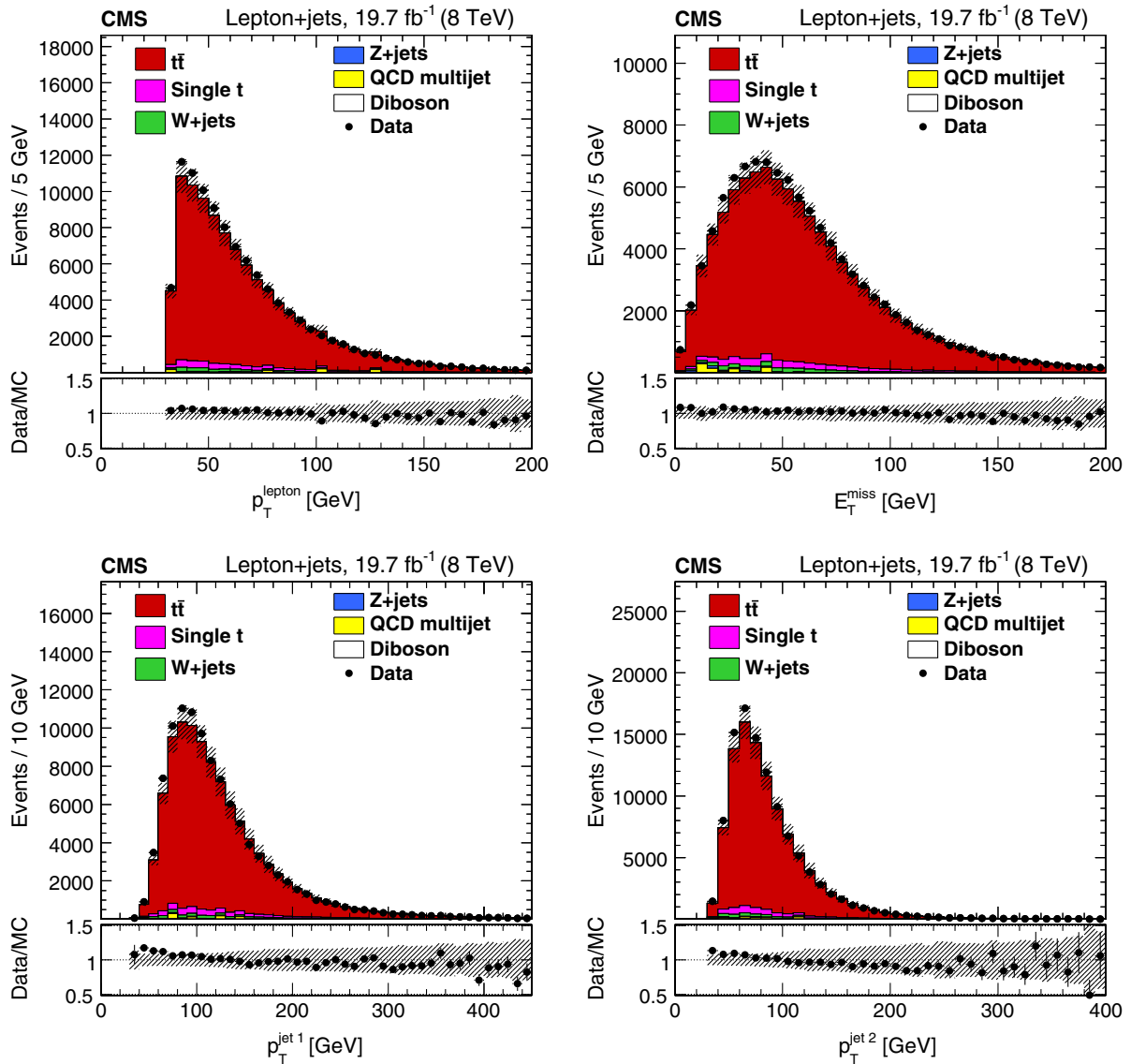


FIG. 1. Distributions for the lepton + jets channel of (upper left) lepton p_T , (upper right) missing transverse energy, (lower left) leading jet p_T , (lower right) second-leading jet p_T for data and simulation, summed over all channels and normalized by luminosity. The vertical bars show the statistical uncertainty and the hatched bands show the statistical and systematic uncertainties added in quadrature. The lower portion of each panel shows the ratio of the yields between the collision data and the simulation.

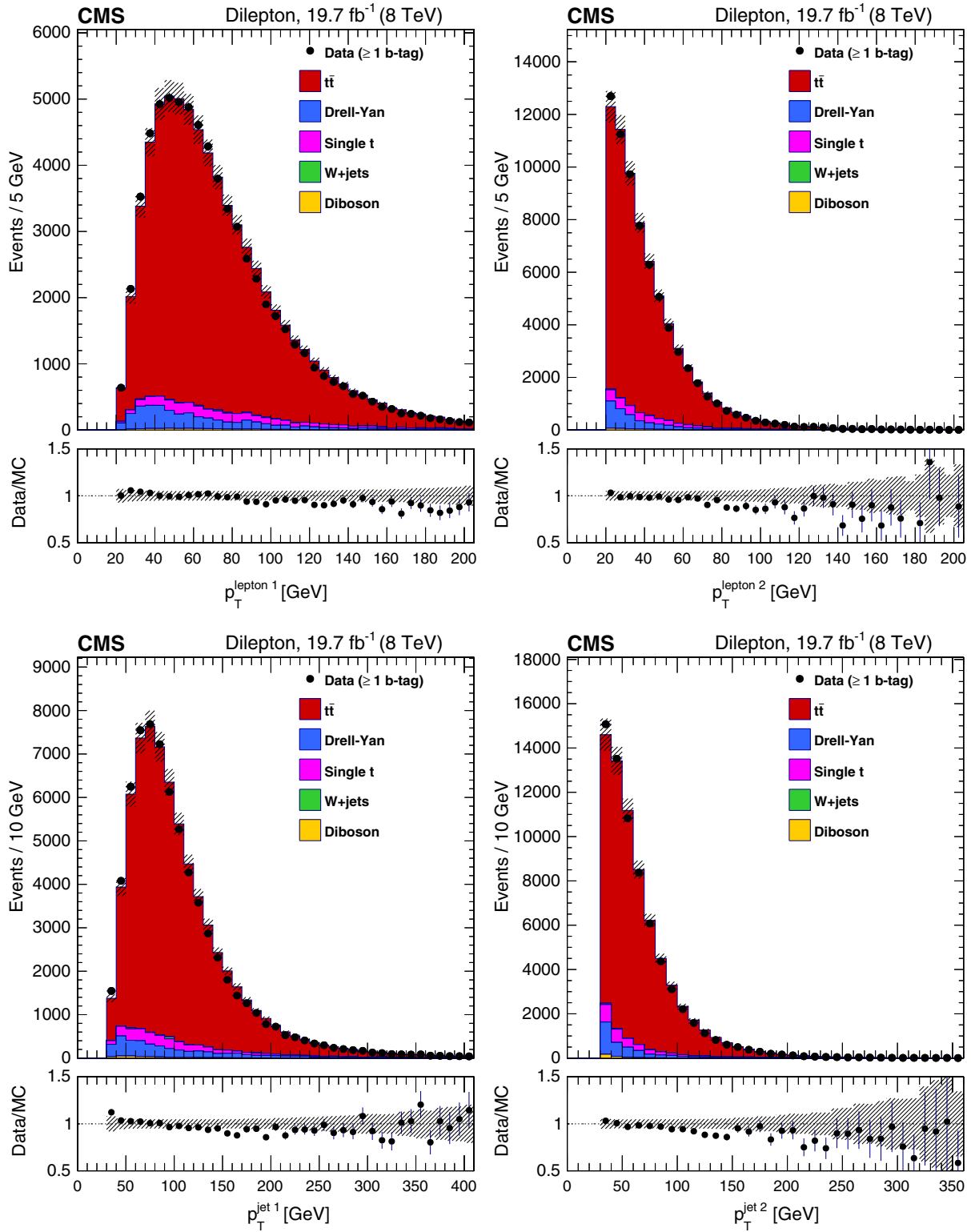


FIG. 2. Distributions for the dilepton channel: (upper left) leading lepton p_T , (upper right) second-leading lepton p_T , (lower left) leading jet p_T , (lower right) second-leading jet p_T for data and simulation, summed over all channels and normalized by luminosity. The vertical bars show the statistical uncertainty and the hatched bands show the statistical and systematic uncertainties added in quadrature. The lower portion of each panel shows the ratio of the yields between the collision data and the simulation.

slope visible in the data/MC ratio plots. However, even without making a correction, the data and simulation are consistent within the quoted uncertainties.

For the all-jets channel we use the data collected using a multijet trigger, corresponding to an integrated luminosity of 18.2 fb^{-1} . The trigger requires the presence of at least four jets, reconstructed from the energies deposited in the calorimeters, with transverse momenta $p_T > 50 \text{ GeV}$. Since fully hadronically decaying top quark pairs lead to six partons in the final state, events are required to have at least four jets with $p_T > 60 \text{ GeV}$ and a fifth and sixth jet with $p_T > 30 \text{ GeV}$. Jets originating from b quarks are identified using the CSV b algorithm at the tight working point [38]. With the requirement of exactly two b -tagged jets among the six leading ones, 356 231 candidate events are selected. From simulation, the sample is expected to be dominated by the QCD multijet background and to have a signal fraction of about 13%. The QCD multijet background cannot be reliably simulated and we determine its kinematic dependence from a control sample in the data. The background normalization is determined as a part of the fit process, which is discussed in Sec. V B.

For the dilepton channel, events are required to pass the triggers appropriate for each of the three channels. The $e\mu$ channel uses a logical OR of two triggers that require a muon of $p_T > 17$ (or 8) GeV and an isolated electron of 8 (or 17) GeV. Dimuon events must pass a trigger which requires a $p_T > 17 \text{ GeV}$ for the muon with the highest (“leading”) p_T and 8 GeV for the second-leading muon. Similarly, dielectron events must satisfy a trigger with a threshold of $p_T > 17 \text{ GeV}$ for the leading electron and 8 GeV for the second-leading electron. In this case both electrons are required to be isolated. In all three cases the amount of data corresponds to a luminosity of 19.7 fb^{-1} . We select events for analysis if they have two isolated opposite-sign leptons with $p_T > 20 \text{ GeV}$ and $|\eta| < 2.4$ (2.5) for muons (electrons). Jets originating from b quarks are identified with the CSV algorithm at the loose working point [38]. Events are retained if they have at least two b -tagged jets. Background contamination from low-mass resonances is reduced by demanding a dilepton pair invariant mass, $m_{\ell\ell}$, of at least 10 GeV. To suppress the background from Z boson decays, events with $e\bar{e}$ and $\mu\bar{\mu}$ signatures are required to have $E_T^{\text{miss}} > 40 \text{ GeV}$, and to fall outside of the dilepton invariant mass window $76 < m_{\ell\ell} < 106 \text{ GeV}$. The remaining Drell–Yan background is estimated from the data using the ratio of the event yield inside vs outside the invariant mass window [38]. After all of the requirements, we find 41 125 candidate events in data for which the sample compositions is expected to be 95% $t\bar{t}$, 3% single top quark, 2% Drell–Yan, and $< 0.3\%$ other processes. Figure 2 shows a comparison of the data and simulation for events with at least one b jet for some representative distributions. As with the lepton + jets plot (Fig. 1) the simulation is not corrected for the

discrepancy in the top quark p_T distribution, leading to the slopes visible in the data/MC plots.

IV. ANALYSIS TECHNIQUES

The measurements discussed in the following sections use analysis techniques in which either m_t alone is determined or m_t and the overall jet energy scale factor (JSF) are determined simultaneously. For the lepton + jets and the all-jets channels we use analyses based on the ideogram technique (Sec. IV A). While the ideogram technique provides the most precise measurements, it is not suitable for dilepton events where the presence of more than one neutrino introduces uncertainties in the use of the measured E_T^{miss} . Instead, for the dilepton channel, we use the analytical matrix weighting technique (AMWT) method (Sec. IV B).

A. One- and two-dimensional ideogram analyses

The ideogram method is a joint maximum likelihood fit that determines m_t and, optionally, the JSF from a sample of selected $t\bar{t}$ candidate events in the lepton + jets or all-jets channels. The observable used for measuring m_t is the mass m_t^{fit} estimated by a kinematic fit [40]. The kinematic fit constrains the candidates for the $t\bar{t}$ decay products to the hypothesis of the production of two heavy particles of equal masses, each one decaying to a W boson and a bottom quark, where the W boson invariant mass is constrained to 80.4 GeV [41]. The JSF is defined as a multiplicative factor to be applied in addition to the standard jet energy corrections (JEC) [37] to the four-momenta of the jets. The JSF is determined from the invariant masses of the jet pairs, m_W^{reco} , associated with the W bosons before the jet momenta are constrained by the kinematic fit. For the case of a simultaneous fit to both m_t and the JSF (2D approach), no prior knowledge of the JSF is assumed. If only m_t is fitted (1D approach), the jet energy scale determined from the JEC is taken as the JSF prior, fixing it to unity. A third category of fits (hybrid approach) incorporates the prior knowledge about the jet energy scale by using a Gaussian constraint, $P(\text{JSF})$, centered at 1 with a variance depending on the total JEC uncertainty. For the hybrid analysis in the lepton + jets channel, the JSF determined from the W boson decays and the jet energy scale from the JEC are given equal weight in the fit. In contrast, for the hybrid fit in the all-jets channel, the jet energy scale from the JEC contributes 80% of the information, because of the larger uncertainty on the JSF from the 2D fit.

The distributions of m_t^{fit} and m_W^{reco} are obtained from simulation for three to seven different m_t and three to five different JSF values for the $t\bar{t}$ signal, and from simulated background events (lepton + jets) or the control sample for the multijet background (all-jets). From these distributions, probability density functions are derived separately for different cases of jet-parton assignments for the signal, and

for the background contribution. The signal functions depend on m_t and JSF, and are labeled $P(m_t^{\text{fit}}|m_t, \text{JSF})$ and $P(m_W^{\text{reco}}|m_t, \text{JSF})$, respectively, for an event in the final likelihood.

The likelihood for measuring m_t and the JSF in an observed data sample can be expressed as

$$\mathcal{L}(\text{sample}|m_t, \text{JSF}) = \prod_{\text{events}} \mathcal{L}(\text{event}|m_t, \text{JSF})^{w_{\text{event}}}, \quad (1)$$

where the event weight $w_{\text{event}} = c \sum_{i=1}^n P_{\text{gof}}(i)$ is used in the lepton + jets analysis to reduce the impact of events for which the chosen permutation of the jets is incorrect. Here, c is a normalization constant and the remaining quantities are defined as in Eq. (2). For the all-jets channel, $w_{\text{event}} = 1$ is used. The event likelihoods (or *ideograms*) are given by

$$\begin{aligned} \mathcal{L}(\text{event}|m_t, \text{JSF}) &= \sum_{i=1}^n P_{\text{gof}}(i) \{f_{\text{sig}} P_{\text{sig}}(m_{t,i}^{\text{fit}}, m_{W,i}^{\text{reco}}|m_t, \text{JSF}) \\ &+ (1 - f_{\text{sig}}) P_{\text{bkg}}(m_{t,i}^{\text{fit}}, m_{W,i}^{\text{reco}})\}, \end{aligned} \quad (2)$$

where the index i runs over the n selected permutations of an event that each have a goodness-of-fit probability P_{gof} assigned from the kinematic fit. The signal fraction f_{sig} is assumed to be 1 for the lepton + jets channel and is left as a free parameter of the fit for the all-jets channel. The background term P_{bkg} is independent of both m_t and the JSF for backgrounds determined from the collision data.

As the W boson mass is fixed to 80.4 GeV in the fit, the observables m_t^{fit} and m_W^{reco} have a low correlation coefficient (less than 5%) and the probability density P can be factorized into one-dimensional expressions,

$$\begin{aligned} P(m_t^{\text{fit}}, m_W^{\text{reco}}|m_t, \text{JSF}) &= \sum_j f_j P_j(m_t^{\text{fit}}|m_t, \text{JSF}) \\ &\times P_j(m_W^{\text{reco}}|m_t, \text{JSF}), \end{aligned} \quad (3)$$

where the index j denotes the different jet-parton permutation classes defined for the measurement. Their relative fraction f_j is either determined from the simulated sample with $m_{t,\text{gen}} = 172.5$ GeV or by the fit.

The most likely m_t and JSF values are obtained by minimizing $-2 \ln \mathcal{L}(\text{sample}|m_t, \text{JSF})$ for the 2D and hybrid analyses. For the 1D analyses only m_t is determined and the JSF is set to unity during the minimization.

B. Analytical matrix weighting technique

The measurement of m_t for the dileptonic $t\bar{t}$ decays is performed using the AMWT. This is based on a matrix weighting technique used by the D0 Collaboration [42], combined with an analytical algorithm to find solutions of the kinematic equations [43]. The method allows the

determination of m_t with the assumption of JSF = 1, and in this sense, the results are comparable to the 1D fits performed in either the lepton + jets or all-jets channels (see Sec. IV A).

In dileptonic $t\bar{t}$ decays, the final state consists of two charged leptons, two neutrinos, and two b quarks, resulting in 18 unknowns: three momentum components for each of the six final state particles. Of these, we observe the momenta of the two charged leptons, the momenta of the two jets, and the momenta of all of the other charged particles and jets. If there are more than two jets in an event we have to select the jets to assign to the b quarks from the decay of the top quark pair. We preferentially assign b -tagged jets to these. Hence, after physics object reconstruction, we measure the following observables for each event:

- (i) the momenta \vec{p}_{ℓ^+} and \vec{p}_{ℓ^-} of the charged leptons from the W^+ and W^- decays,
- (ii) the momenta \vec{p}_b and $\vec{p}_{\bar{b}}$ of the b and \bar{b} quarks produced by the t and \bar{t} quark decays,
- (iii) the total transverse momentum $\vec{p}_T^{\ell\ell}$ of the $t\bar{t}$ pair.

This leaves four unknowns that must be solved analytically. Conservation of four-momentum provides the following four constraints on the kinematics, if a hypothetical value for the top-quark mass is assumed:

- (i) the masses $m_{\ell^+\nu}$ and $m_{\ell^-\bar{\nu}}$ of the lepton-neutrino pairs from the W^+ and W^- decays are constrained to be 80.4 GeV [41],
- (ii) the masses of the systems of particles from the t and \bar{t} decays must equal the hypothesized mass of the top quark.

Hence, the system of equations is appropriately constrained. However, there is not a unique solution, because the equations are nonlinear. For a given assignment of reconstructed momenta to final-state particles there can be up to four solutions for the neutrino momenta such that the event satisfies all of the constraints. There is a twofold ambiguity of assigning jet momenta to the b and \bar{b} jets, which doubles this to eight possible solutions. We follow the algorithm given in Refs. [44,45] to find these solutions. In rare cases, a latent singularity in the equations used to find these solutions can prohibit the calculation of the longitudinal momenta. In such events, a numerical method is employed to find the incalculable variables [44].

For each event, we find all solutions of neutrino momenta for hypothesized top quark masses between 100 and 600 GeV, in 1 GeV increments. In general, we expect solutions to be found for a large range of mass hypotheses. To each solution we assign a weight w given by [46]

$$\begin{aligned} w(\vec{X}|m_t) &= \left[\sum_{\text{initial partons}} F(x_1)F(x_2) \right] \\ &\times p(E_{\ell^+}|m_t)p(E_{\ell^-}|m_t), \end{aligned} \quad (4)$$

where \vec{X} represents the momentum vectors of the final state particles as obtained from the solutions of the kinematic equations. We sum the parton distribution functions $F(x)$, evaluated at $Q^2 = m_t^2$, over the possible LO initial parton states ($u\bar{u}$, $\bar{u}u$, $d\bar{d}$, $\bar{d}d$, and gg); x_1 and x_2 are the Bjorken x values for the initial-state partons which can be computed from the momenta of the final-state particles. The function $p(E|m_t)$ is the probability density of observing a charged lepton of energy E in the rest frame of a top quark of mass m_t , given by [46]

$$p(E|m_t) = \frac{4m_t E(m_t^2 - m_b^2 - 2m_t E)}{(m_t^2 - m_b^2)^2 + M_W^2(m_t^2 - m_b^2) - 2M_W^4}, \quad (5)$$

where the b quark mass, m_b , is set to 4.8 GeV, and the W boson mass, M_W , to 80.4 GeV. For each m_t hypothesis, we find an overall weight by summing the weights of all solutions found. To compensate for mismeasurements of the momenta due to finite detector resolution or the loss of correlation between the jet and quark momentum because of hard-gluon radiation, we account for the jet energy resolution during reconstruction. Every event in both the collision and simulated data is reconstructed 500 times, each time with jet momenta drawn randomly from a Gaussian distribution of widths given by the detector resolution and with means given by the measured momenta. After this randomization procedure, approximately 96% of all events in both the collision and simulated data have at least one solution, and hence a top quark mass estimator. The final weight curve of each event is given by the average of the weight distributions from each of the 500 randomizations, after excluding the cases for which there is no valid solution. This distribution serves as a measure of the relative probability that the observed event occurs for any given value of m_t .

The estimator for m_t is then the hypothesized mass with the highest average sum weight for each event, called the AMWT mass, m_t^{AMWT} .

V. MASS MEASUREMENTS

A. The lepton + jets channel

To check the compatibility of an event with the $t\bar{t}$ hypothesis and improve the resolution of the reconstructed quantities, a kinematic fit [40] is applied to the events. For each event, the inputs to the fitter are the four-momenta of the lepton and the four leading jets, the missing transverse energy, and their respective resolutions. The fit constrains these to the hypothesis of the production of two heavy particles of equal mass, each one decaying to a W boson with an invariant mass of 80.4 GeV [41] and a bottom quark. It minimizes $\chi^2 = (\mathbf{x} - \mathbf{x}^m)^T \mathbf{E}^{-1} (\mathbf{x} - \mathbf{x}^m)$ where \mathbf{x}^m is the vector of measured observables, \mathbf{x} is the vector of fitted observables, and \mathbf{E}^{-1} is the inverse error matrix which is given by the resolutions of the observables. The two b -tagged jets are candidates for the bottom quarks in the

$t\bar{t}$ hypothesis, while the two untagged jets serve as candidates for the light quarks for one of the W boson decays. This leads to two possible parton-jet assignments per event and two solutions for the z component of the neutrino momentum.

For simulated $t\bar{t}$ events, the parton-jet assignments are classified as *correct permutations*, *wrong permutations*, and *unmatched permutations*. The correct permutation class includes those events for which all of the quarks from the $t\bar{t}$ decay (after initial-state parton shower) are correctly matched to the selected jets within a distance $\Delta R < 0.3$. The wrong permutations class covers the events for which the jets from the $t\bar{t}$ decay are correctly matched to the selected jets, but where two or more of the jets are interchanged. Lastly, the unmatched permutations class includes the events for which at least one quark from the $t\bar{t}$ decay is not matched unambiguously to any of the four selected jets. To increase the fraction of correct permutations, we require $P_{\text{gof}} > 0.2$ for the kinematic fit with 2 degrees of freedom. This selects 28 295 events for the mass measurement, with an estimated composition of 96.3% $t\bar{t}$ signal and 3.7% non- $t\bar{t}$ background, which is dominated by single top quark events. In the mass extraction, the permutations are weighted by their P_{gof} values, and the effective fraction of correct permutations among the $t\bar{t}$ signal improves from 13% to 44%, while the fractions of wrong and unmatched permutations change from 16% to 21% and 71% to 35%, respectively, determined in simulation.

Figure 3 shows the distributions before and after the kinematic fit and P_{gof} selection of the reconstructed mass m_W^{reco} of the W boson decaying to a $q\bar{q}$ pair and the mass m_t^{reco} of the corresponding top quark for all possible permutations.

The ideogram method (Sec. IV A) is calibrated for each combination of the top quark mass hypothesis, m_t^{gen} and JSF values by conducting 10 000 pseudoexperiments, separately for the muon and electron channels, using simulated $t\bar{t}$ and background events. The average deviations between extracted mass and JSF and their input values are obtained as a function of m_t^{gen} and the bias is fit with a linear function for each generated JSF value. From these fits, additional small corrections for calibrating the top quark mass and the jet energy scale are derived as linear functions of both the extracted top quark mass and JSF. The corrections are approximately -0.2 GeV for m_t and -0.4% for the JSF. The statistical uncertainties of the method are also corrected by factors of approximately 1.04 that are derived from the widths of the corresponding pull distributions.

The 2D ideogram fit to the combined electron and muon channels yields

$$m_t^{2D} = 172.14 \pm 0.19(\text{stat} + \text{JSF}) \text{ GeV},$$

$$\text{JSF}^{2D} = 1.005 \pm 0.002(\text{stat}).$$

As m_t and the JSF are measured simultaneously, the statistical uncertainty in m_t combines the statistical

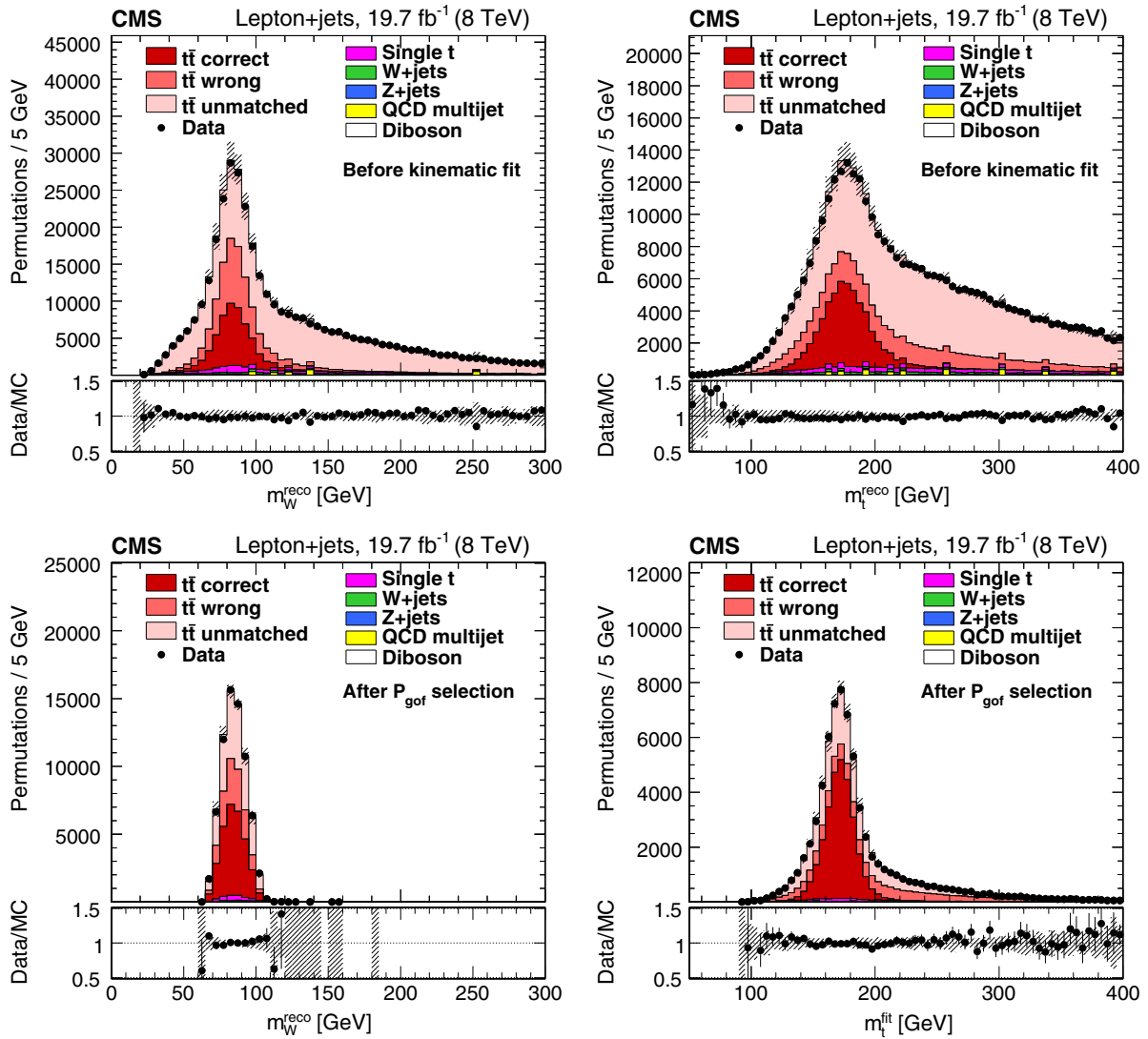


FIG. 3. Reconstructed masses of (upper left) the W bosons decaying to $q\bar{q}$ pairs and (upper right) the corresponding top quarks, prior to the kinematic fitting to the $t\bar{t}$ hypothesis. Panels (lower left) and (lower right) show, respectively, the reconstructed W boson masses and the fitted top quark masses after the goodness-of-fit selection. The total number of permutations found in simulation is normalized to be the same as the total number of permutations observed in data. The vertical bars show the statistical uncertainty and the hatched bands show the statistical and systematic uncertainties added in quadrature. The lower portion of each panel shown the ratio of the yields between the collision data and the simulation.

uncertainty arising from both components of the measurement. The uncertainty of the measurement agrees with the expected precision obtained by performing pseudoexperiments.

The results in the individual muon and electron channels are compatible within their statistical uncertainties:

$$\begin{aligned} \mu + \text{jets: } m_t^{2D} &= 172.03 \pm 0.27(\text{stat} + \text{JSF}) \text{ GeV,} \\ \text{JSF}^{2D} &= 1.007 \pm 0.003(\text{stat}), \\ e + \text{jets: } m_t^{2D} &= 172.26 \pm 0.28(\text{stat} + \text{JSF}) \text{ GeV,} \\ \text{JSF}^{2D} &= 1.003 \pm 0.003(\text{stat}). \end{aligned}$$

The 1D and hybrid analyses give results of

$$\begin{aligned} m_t^{1D} &= 172.56 \pm 0.12(\text{stat}) \text{ GeV,} \\ m_t^{\text{hyb}} &= 172.35 \pm 0.16(\text{stat} + \text{JSF}) \text{ GeV,} \\ \text{JSF}^{\text{hyb}} &= 1.002 \pm 0.001(\text{stat}), \end{aligned}$$

respectively. Both the 2D and hybrid results for the JSF (JSF^{2D} and JSF^{hyb}) are within 0.5% of one. The results for m_t and the JSF are compared in Fig. 4, which shows the two-dimensional statistical likelihoods obtained from data in the 2D and hybrid cases and m_t from the 1D analysis.

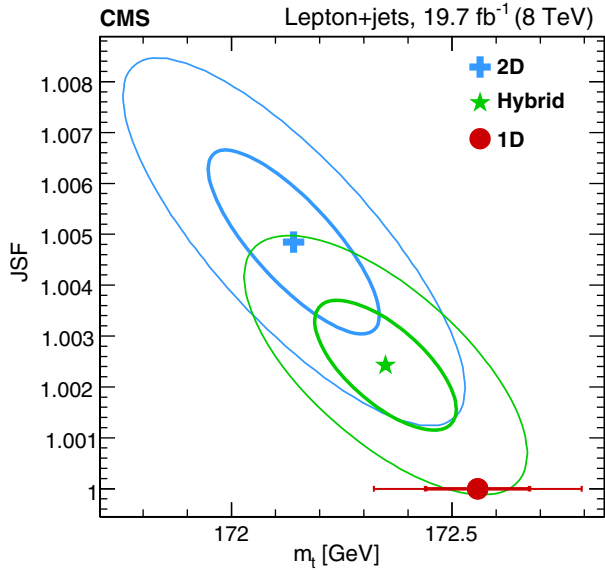


FIG. 4. The two-dimensional likelihood ($-2\Delta \log(\mathcal{L})$) for the lepton + jets channel for the 2D, hybrid, and 1D fits. The thick (thin) ellipses correspond to contours of $-2\Delta \log(\mathcal{L}) = 1(4)$ allowing the construction of the one (two) σ statistical intervals of m_t . For the 1D fit, the thick and thin lines correspond to the one and two σ statistical uncertainties, respectively.

B. The all-jets channel

As in the lepton + jets channel, a kinematic fit [47] is used to improve the resolution of the reconstructed quantities and to check the compatibility of an event with the $t\bar{t}$ hypothesis. For each event, the inputs to the fit are the four-momenta of the six leading jets. The fit constrains these to the hypothesis of the production of two heavy particles of equal masses, each one decaying to a W boson with its invariant mass constrained to 80.4 GeV [41] and a bottom quark. The two b -tagged jets are candidates for the bottom quarks in the $t\bar{t}$ hypothesis, while the four untagged jets serve as candidates for the light quarks of the W boson decays. This leads to six possible parton-jet assignments per event and the assignment that fits best to the $t\bar{t}$ hypothesis based on the χ^2 of the kinematic fit is chosen. As final selection criteria, we require $P_{\text{gof}} > 0.1$ for the kinematic fit with 3 degrees of freedom, and the two b quark jets be separated in η - ϕ space by $\Delta R_{b\bar{b}} > 2.0$. These requirements select 7049 events for the mass measurement in data and the fraction of signal events f_{sig} increases from 14% to 61% based on the simulation.

For simulated $t\bar{t}$ events, the parton-jet assignments are classified as *correct permutations* and *wrong permutations*. The correct permutation class is defined in the same way as for the lepton + jets channel (Sec. VA). The wrong permutations class consists of permutations where at least one quark from the $t\bar{t}$ decay is not unambiguously matched with a distance of $\Delta R < 0.3$ to any of the six selected jets. For correct permutations, which compose 42% of the

selected $t\bar{t}$ events, the kinematic fit improves the resolution of the fitted values of m_t from 13.8 to 7.5 GeV.

The multijet background from QCD is modeled using a control sample that is obtained from data with the same event selection but without the b tagging requirement. While this sample has a small contamination of a few percent coming from signal events, these have no influence on the results for the background model. For each event, the kinematic selection is applied to all possible assignments of the six jets to the six quarks from the $t\bar{t}$ hypothesis. The best fitting assignment is chosen and the event is used to model the background if it fulfills the P_{gof} and $\Delta R_{b\bar{b}}$ criteria. The modeled background is compared to the background predicted by an event mixing technique [48]. Both predictions are found to agree within their uncertainties that are derived from the validation of the methods on simulated multijet events.

Figure 5 compares data to the expectation from simulated $t\bar{t}$ signal and background estimate from the data for m_t^{fit} , m_W^{reco} , P_{gof} , and $\Delta R_{b\bar{b}}$.

The ideogram method is calibrated for each combination of the m_t^{en} and JSF values by conducting 10 000 pseudoexperiments. The average deviations between extracted mass and JSF and their input values are obtained as a function of m_t^{en} and the bias is fit with a linear function for each generated JSF value. From these fits, additional small corrections for calibrating the top quark mass and the jet energy scale are derived as linear functions of both the extracted top quark mass and JSF. The corrections are approximately -0.6 GeV for m_t and $+1.0\%$ for the JSF. The statistical uncertainties of the method are corrected by factors of approximately 1.005 using values derived from the widths of the corresponding pull distributions.

Applying the ideogram method on data with no prior knowledge on the JSF (2D), yields the results:

$$m_t^{2D} = 171.64 \pm 0.32(\text{stat} + \text{JSF}) \text{ GeV},$$

$$\text{JSF}^{2D} = 1.011 \pm 0.003(\text{stat}).$$

As m_t and the JSF are measured simultaneously, the statistical uncertainty in m_t combines the statistical uncertainty arising from both components of the measurement. The two additional free parameters in the fit, the signal fraction f_{sig} and the fraction of correct permutations f_{cp} , are in agreement with the expectation from simulation.

Using the JEC determined from γ/Z + jet events in combination with the JSF prior from the 2D fit yields the results in the 1D and hybrid approaches of

$$m_t^{1D} = 172.46 \pm 0.23(\text{stat}) \text{ GeV},$$

$$m_t^{\text{hyb}} = 172.32 \pm 0.25(\text{stat} + \text{JSF}) \text{ GeV},$$

$$\text{JSF}^{\text{hyb}} = 1.002 \pm 0.001(\text{stat}).$$

For the all-jets channel, the fitted results for the JSF (JSF^{2D} and JSF^{hyb}) are both within 1.1% of one. While the

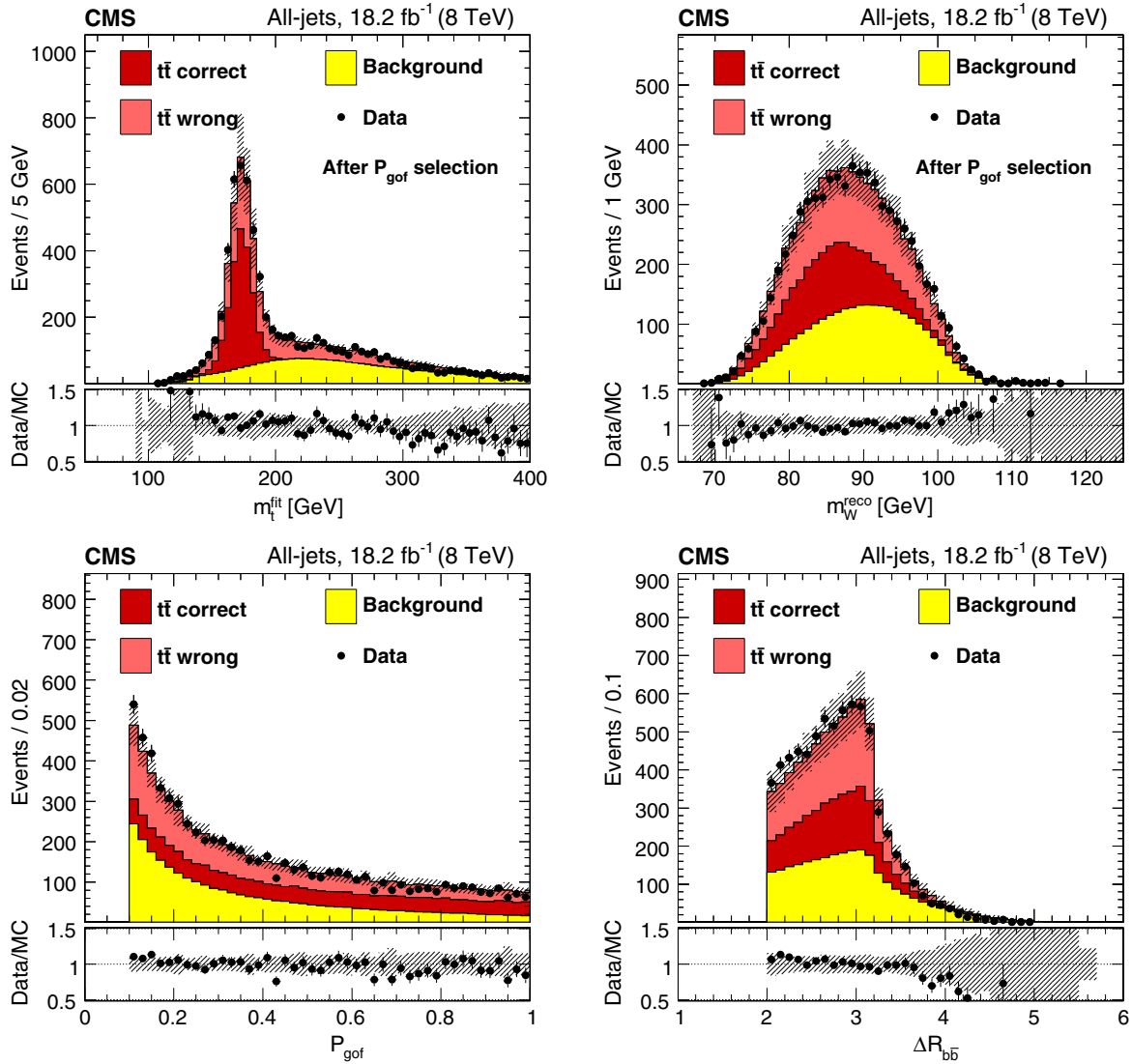


FIG. 5. Distributions of (upper left) the reconstructed top quark mass from the kinematic fit, (upper right) the average reconstructed W boson mass, (lower left) the goodness-of-fit probability, and (lower right) the separation of the two b quark jets for the all-jets channel. The simulated $t\bar{t}$ signal and the background from the control sample are normalized to data. The value of m_t used in the simulation is 172.5 GeV and the nominal jet energy scale is applied. The vertical bars show the statistical uncertainty and the hatched bands show the statistical and systematic uncertainties added in quadrature. The lower portion of each panel shows the ratio of the yields between the collision data and the simulation.

JSF results from the 2D analyses in the lepton + jets and all-jets channels differ by 0.6%, the results from the hybrid analyses agree to within 0.2%. The all-jets results for m_t and the JSF are compared in Fig. 6 which shows the two-dimensional statistical likelihoods obtained from data in the 2D and hybrid cases and m_t from the 1D analysis.

C. The dilepton channel

Figure 7 shows the distribution of m_t^{AMWT} in data compared to a simulation with $m_t = 172.5$ GeV for events containing at least one b jet. This channel is very clean with a negligible background from non- $t\bar{t}$ sources and the collision and simulated events are in good agreement.

AMWT masses are computed for all events in both the data and the simulations. The m_t^{AMWT} distributions computed for each of the seven simulated $t\bar{t}$ mass samples are added to the distributions from the background samples, and these are treated as templates in a binned likelihood fit. To minimize the effects of any bias from the poorly populated tails of the distribution, we only examine events with m_t^{AMWT} between 100 and 400 GeV. For each of the seven mass templates, a maximum likelihood fit is performed to the data distribution. A parabola is fit to the negative logarithms of the maximum likelihoods returned by the fits, and the minimum of the parabola is taken as the measured mass value.

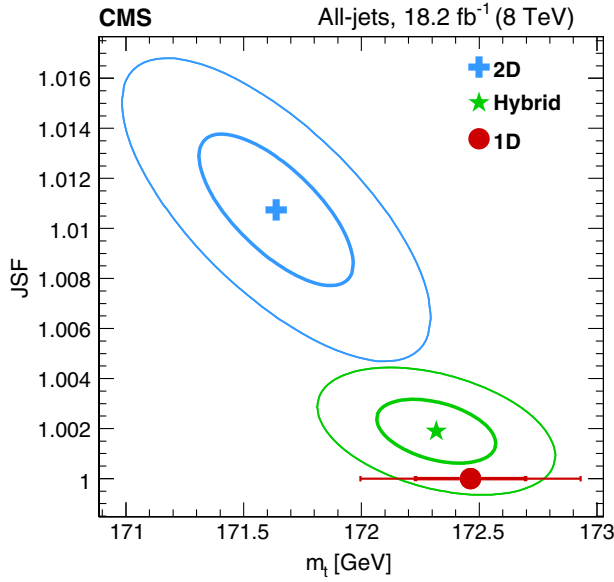


FIG. 6. The two-dimensional likelihood $[-2\Delta \log(\mathcal{L})]$ for the all-jets channel for the 2D, hybrid, and 1D fits. The thick (thin) ellipses correspond to contours of $-2\Delta \log(\mathcal{L}) = 1(4)$ allowing the construction of the one (two) σ statistical intervals of m_t . For the 1D fit, the thick and thin lines correspond to the one and two σ statistical uncertainties, respectively.

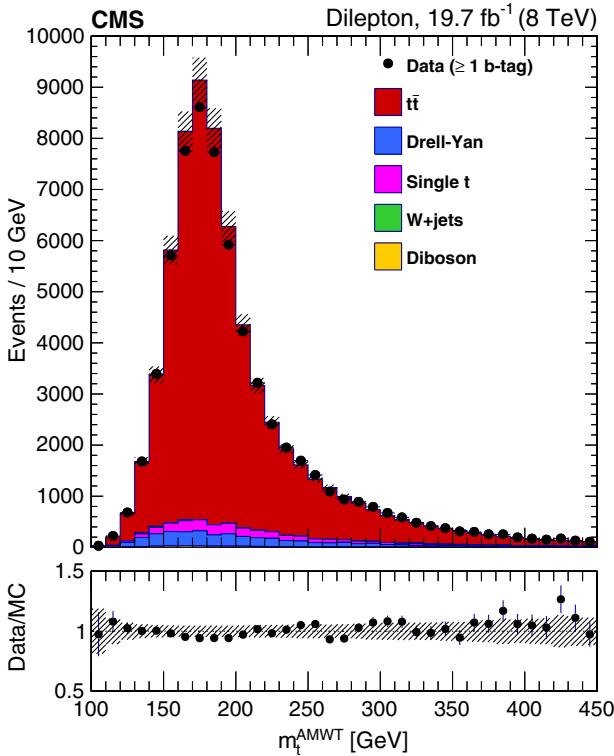


FIG. 7. Distribution of m_t^{AMWT} for the collision and simulated data with $m_t = 172.5$ GeV. The vertical bars show the statistical uncertainty and the hatched bands show the statistical and systematic uncertainties added in quadrature. The lower section of the plot shows the ratio of the yields between the collision data and the simulation.

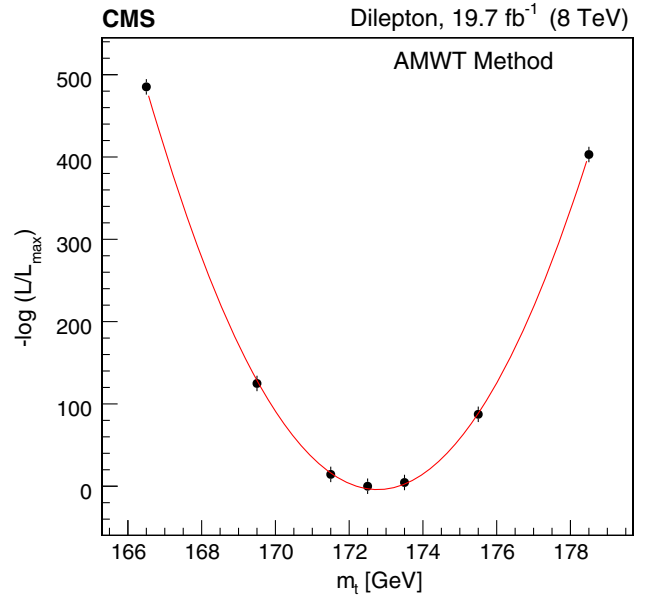


FIG. 8. Plot of the negative log likelihood for data for the dilepton analysis. The continuous line represents a parabolic fit to the points.

The fit is calibrated to correct for any biases induced by the reconstruction using pseudodata. The calibration is performed by means of a test using the simulated templates for the top quark masses between 169.5 and 175.5 GeV. We randomly draw 1000 samples of events, each selected such that the total number of events is the same as in the full data sample. For each template, the 1000 measured masses are averaged together and subtracted from the input mass to obtain a numerical value for the bias induced by the fit. The bias is then parametrized as a linear dependence on the generated value of m_t , and the resulting calibration curve is used to correct for biases in the final result.

The likelihoods obtained from a fit of each of the seven simulated templates to data, as well as a second-order polynomial fit to these values, are shown in Fig. 8. This yields an uncalibrated measured mass of $m_t = 172.77 \pm 0.19(\text{stat})$ GeV. After correcting for the fit bias, the result for the top quark mass is found to be $m_t = 172.82 \pm 0.19(\text{stat})$ GeV.

The analysis was optimized with the value of m_t blinded. The optimization of the event selection was done by minimizing the total expected (statistical + systematic) uncertainty. This resulted in the restriction of the analysis to events containing only two b jets, rather than the requirement of at least one b jet which was used initially.

VI. SYSTEMATIC UNCERTAINTIES

The systematic uncertainties affecting each of the measurements can be grouped into four distinct categories: one experimental category and three theoretical categories that describe the modeling uncertainties. The experimental

classification covers the uncertainties that arise from the precision of the calibration and resolution of the CMS detector and the effects coming from the backgrounds and pileup. The other three categories cover the modeling of the hard scattering process and the associated radiation; non-perturbative QCD effects, such as the simulation of the underlying event and color reconnection; and the modeling of the light- and b -quark hadronization. Each of these is broken down into subcategories leading to a total of 24 distinct systematic uncertainties. In each case the uncertainty is evaluated in terms of the largest shift that is observed in the value of m_t that occurs when the parameter is varied by $\pm 1\sigma$, where σ is the uncertainty assigned to that quantity. The only exception to this is if the statistical uncertainty in the observed shift is larger than the value of the calculated shift. In this case the statistical uncertainty is taken as the best estimate of the uncertainty in the parameter.

A. Experimental effects

- (i) Intercalibration jet energy correction: This is the part of the JES uncertainty originating from modeling of the radiation in the relative (p_T —and η -dependent) intercalibration procedure.
- (ii) *In situ* jet energy calibration: This is the part of the JES uncertainty coming from the uncertainties affecting the absolute JES determination using $\gamma/Z + \text{jets}$ events.
- (iii) Uncorrelated jet energy correction: This is the uncertainty source coming from the statistical uncertainty in the *in situ* jet energy calibration, the contributions stemming from the jet energy correction due to pileup effects, the uncertainties due to the variations in the calorimeter response versus time, and some detector specific effects. To give a clear indication of the contribution to the JES uncertainty coming from pileup, we have subdivided this uncertainty into nonpileup and pileup contributions.
- (iv) Lepton energy scale (LES): Analogous to the JES, the energy scale of the leptons may also induce a systematic bias. A typical variation of 0.6% is taken for electrons in the barrel region and 1.5% in the detector endcaps. For the muons, the uncertainty is negligible.
- (v) E_T^{miss} scale: Measurement of the E_T^{miss} is affected by the variation in LES and JES and by the uncertainty in scale of the unclustered energy. The unclustered energy scale is varied independently of LES and JES to obtain the E_T^{miss} uncertainty.
- (vi) Jet energy resolution: The systematic uncertainty associated with the JER in the simulation is determined by increasing or decreasing the JER by 1σ .
- (vii) b tagging: The uncertainty in the b tagging efficiency and misidentification probability of non- b jets may lead to varying background and signal

levels. This uncertainty is estimated by varying the b tagging discriminator requirements in simulations. In the lepton + jets analysis, for example, the changes in the CSVM discriminator leads to an uncertainty in the b tagging efficiency of 1.2% and the false tagging rate of 15%, both of which correspond to a 1σ variation in the value of the b tagging scale factor. The all-jets and dilepton uncertainties are computed in a similar manner for the CSVT and CSVL discriminators, respectively. Propagating the tagging efficiency uncertainty to the values of m_t leads to the systematic uncertainty.

- (viii) Trigger: This systematic uncertainty captures the uncertainties related to the modeling of the trigger efficiency, and is only significant for the all-jets measurement.
- (ix) Pileup: During the data taking period, the instantaneous luminosity increased dramatically during the year, leading to an increased number of simultaneous proton-proton interactions overlapping with the primary hard scattering (in-time pileup) and possible effects due to the detector response to previous collision events (out-of-time pileup). These effects are evaluated by using pseudoexperiments in which the average number of pileup events was varied by $\pm 5\%$.
- (x) Backgrounds: The background contamination expected from simulation is $< 5\%$ in the lepton + jets and dilepton channels. The effect of the background modeling on m_t is estimated by varying the shape and normalization for each background within their uncertainty. Uncertainties from simulated backgrounds are taken to be correlated across all the measurements. The only channel for which there is a significant non- $t\bar{t}$ background in the final fit sample is the all-jets channel. For this, the shape of the QCD multijet background is estimated from a control sample in the data. The method is validated using simulated QCD multijet events and with an alternative approach using event mixing in the data. The predicted background shapes are varied to cover the residual differences found in the validation. The uncertainties from the background estimation from control samples in the data are assumed to be uncorrelated.
- (xi) Fit calibration: For the calibration of the fits, the simulated samples are statistically limited. The uncertainty quoted is the statistical uncertainty in the residual bias in the fit calibration.

B. Theoretical and modeling uncertainties

1. Hard scattering and radiation

- (i) Parton distribution functions: PDFs are used in modeling the hard scattering in proton-proton

collisions in the simulations. The uncertainties in the PDFs and their effect on the measured value of m_t are studied by reweighting a $t\bar{t}$ sample with different PDF eigenvectors using the PDF4LHC prescription [49]. The reweighted events are used to generate pseudoexperiments and the variation in the fitted mass is quoted as the uncertainty [37].

- (ii) Renormalization and factorization scales: This uncertainty is estimated using the simultaneous

variation of the renormalization and factorization scales by factors of 2 and 0.5 in the matrix element calculation and the initial-state parton shower of the signal and the $W + \text{jets}$ background.

- (iii) ME-PS matching threshold: In the $t\bar{t}$ simulation, the matching thresholds used for interfacing the matrix elements (ME) generated with MADGRAPH to the PYTHIA parton showers (PS) are varied from the default of 40 GeV down to 30 GeV and up to 60 GeV

TABLE I. Category breakdown of the systematic uncertainties for the 2D, 1D, and hybrid measurements in the lepton + jets channel. Each term has been estimated using the procedures described in Sec. VI. The uncertainties are expressed in GeV and the signs are taken from the $+1\sigma$ shift in the value of the quantity. Thus a positive sign indicates an increase in the value of m_t or the JSF and a negative sign indicates a decrease. For uncertainties determined on independent simulated samples the statistical precision of the shift is displayed. With the exception of the flavor-dependent JEC terms (see Sec. VI), the total systematic uncertainty is obtained from the sum in quadrature of the individual systematic uncertainties.

Lepton + jets channel	m_t fit type			
	2D		1D	hybrid
	δm_t^{2D} (GeV)	δJSF	δm_t^{1D} (GeV)	δm_t^{hyb} (GeV)
Experimental uncertainties				
Method calibration	0.04	0.001	0.04	0.04
Jet energy corrections				
–JEC: intercalibration	< 0.01	< 0.001	+0.02	+0.01
–JEC: <i>in situ</i> calibration	–0.01	+0.003	+0.24	+0.12
–JEC: uncorrelated nonpileup	+0.09	–0.004	–0.26	–0.10
–JEC: uncorrelated pileup	+0.06	–0.002	–0.11	–0.04
Lepton energy scale	+0.01	< 0.001	+0.01	+0.01
E_T^{miss} scale	+0.04	< 0.001	+0.03	+0.04
Jet energy resolution	–0.11	+0.002	+0.05	–0.03
b tagging	+0.06	< 0.001	+0.04	+0.06
Pileup	–0.12	+0.002	+0.05	–0.04
Backgrounds	+0.05	< 0.001	+0.01	+0.03
Modeling of hadronization				
JEC: flavor-dependent				
–light quarks ($u d s$)	+0.11	–0.002	–0.02	+0.05
–charm	+0.03	< 0.001	–0.01	+0.01
–bottom	–0.32	< 0.001	–0.31	–0.32
–gluon	–0.22	+0.003	+0.05	–0.08
b jet modeling				
– b fragmentation	+0.06	–0.001	–0.06	< 0.01
–Semileptonic b hadron decays	–0.16	< 0.001	–0.15	–0.16
Modeling of perturbative QCD				
PDF	0.09	0.001	0.06	0.04
Ren. and fact. scales	+0.17 ± 0.08	–0.004 ± 0.001	–0.24 ± 0.06	–0.09 ± 0.07
ME-PS matching threshold	+0.11 ± 0.09	–0.002 ± 0.001	–0.07 ± 0.06	+0.03 ± 0.07
ME generator	–0.07 ± 0.11	–0.001 ± 0.001	–0.16 ± 0.07	–0.12 ± 0.08
Top quark p_T	+0.16	–0.003	–0.11	+0.02
Modeling of soft QCD				
Underlying event	+0.15 ± 0.15	–0.002 ± 0.001	+0.07 ± 0.09	+0.08 ± 0.11
Color reconnection modeling	+0.11 ± 0.13	–0.002 ± 0.001	–0.09 ± 0.08	+0.01 ± 0.09
Total systematic	0.59	0.007	0.62	0.48
Statistical	0.20	0.002	0.12	0.16
Total	0.62	0.007	0.63	0.51

and the uncertainty is taken as the maximal difference in m_t induced by this variation.

- (iv) ME generator: The sensitivity to the parton-level modeling is estimated by comparing the reference samples (MADGRAPH and PYTHIA) to samples produced using POWHEG and PYTHIA. The difference between the values of m_t obtained with the two samples is taken as the uncertainty.

- (v) Top quark p_T uncertainty: This term represents the uncertainty coming from the modeling of the top quark p_T distribution in the ME generator. The uncertainty is estimated by taking the difference in shape between the parton level p_T spectrum from the ME generator and the unfolded p_T spectrum determined from the data [39]. The uncertainty is considered fully correlated across the measurements.

TABLE II. Category breakdown of the systematic uncertainties for the 2D, 1D and hybrid measurements in the all-jets channel. Each term has been estimated using the procedures described in Sec. VI. The uncertainties are expressed in GeV and the signs are taken from the $+1\sigma$ shift in the value of the quantity. Thus a positive sign indicates an increase in the value of m_t or the JSF and a negative sign indicates a decrease. For uncertainties determined on independent simulated samples the statistical precision of the shift is displayed. With the exception of the flavor-dependent JEC terms (see Sec. VI), the total systematic uncertainty is obtained from the sum in quadrature of the individual systematic uncertainties.

All-jets channel	m_t fit type			
	2D		1D	hybrid
	δm_t^{2D} (GeV)	δJSF	δm_t^{1D} (GeV)	δm_t^{hyb} , (GeV)
Experimental uncertainties				
Method calibration	0.06	0.001	0.06	0.06
Jet energy corrections				
–JEC: intercalibration	< 0.01	< 0.001	+0.02	+0.02
–JEC: <i>in situ</i> calibration	–0.01	< 0.001	+0.23	+0.19
–JEC: uncorrelated non-pileup	+0.06	–0.001	–0.19	–0.16
–JEC: uncorrelated pileup	+0.04	< 0.001	–0.08	–0.06
Jet energy resolution	–0.10	+0.001	+0.03	+0.02
<i>b</i> tagging	+0.02	< 0.001	+0.01	+0.02
Pileup	–0.09	+0.002	+0.02	< 0.01
Backgrounds	–0.61	–0.007	–0.14	–0.20
Trigger	+0.04	< 0.001	–0.01	< 0.01
Modeling of hadronization				
JEC: flavor-dependent				
–light quarks (<i>u d s</i>)	+0.10	–0.001	–0.02	+0.00
–charm	+0.03	–0.001	–0.01	–0.01
–bottom	–0.30	+0.000	–0.29	–0.29
–gluon	–0.17	+0.002	+0.02	–0.02
<i>b</i> jet modeling				
– <i>b</i> fragmentation	+0.08	–0.001	+0.03	+0.04
–Semileptonic <i>b</i> hadron decays	–0.14	< 0.001	–0.13	–0.13
Modeling of perturbative QCD				
PDF	0.06	< 0.001	0.03	0.03
Ren. and fact. scales	$+0.29 \pm 0.16$	-0.005 ± 0.001	-0.19 ± 0.11	-0.12 ± 0.12
ME-PS matching threshold	$+0.18 \pm 0.16$	-0.002 ± 0.001	$+0.12 \pm 0.11$	$+0.13 \pm 0.12$
ME generator	-0.04 ± 0.20	-0.002 ± 0.002	-0.18 ± 0.14	-0.16 ± 0.14
Top quark p_T	+0.04	+0.001	+0.08	+0.06
Modeling of soft QCD				
Underlying event	$+0.27 \pm 0.25$	-0.002 ± 0.002	$+0.13 \pm 0.18$	$+0.14 \pm 0.18$
Color reconnection modeling	$+0.35 \pm 0.22$	-0.003 ± 0.002	$+0.14 \pm 0.16$	$+0.16 \pm 0.16$
Total systematic	0.95	0.011	0.62	0.59
Statistical	0.32	0.003	0.23	0.25
Total	1.00	0.011	0.66	0.64

2. Nonperturbative QCD

- (i) Underlying event: This represents the uncertainty in modeling the soft underlying hadronic activity in the event, which affects the simulation of both signal and background. The uncertainty is estimated by comparing PYTHIA tunes with increased and decreased underlying event activity relative to a central tune. For this we compare the results for the Perugia 2011 tune to the results obtained using the Perugia 2011 mpiHi and the Perugia 2011 Tevatron tunes [50].
- (ii) Color reconnection: The effects of possible mis-modeling of color reconnection are estimated by comparing the mass calculated using underlying event tunes with and without the inclusion of these effects. For these simulations the Perugia 2011 and Perugia 2011 no CR tunes are used [50]. The uncertainty is taken as the difference between the two computed values of m_t .

3. Hadronization

- (i) Flavor-dependent hadronization uncertainty: This is the part of the JES uncertainty that comes from differences in the energy response for different jet flavors and flavor mixtures with respect to those used in the calibration procedures. Four uncertainties are quoted that correspond to the uncertainties for light quarks (u , d , s), charm quarks, bottom quarks and gluons. These are evaluated by comparing Lund string fragmentation (PYTHIA 6 [16]) and cluster fragmentation (HERWIG++ [51]) for each category of jets. The models in PYTHIA and HERWIG allow for the differences between the jet types, and the uncertainty is determined by varying the jet energies within their respective flavor-dependent uncertainties. The full flavor-dependent uncertainty is obtained by taking a signed linear sum of these four contributions. For this we perform $\pm 1\sigma$ shifts for each of the contributions and compute the total uncertainty from the sum of the $+1\sigma$ and -1σ shifts separately. As these are symmetric, we quote the $+1\sigma$ shifts for the values of the uncertainties in Tables I–III.
- (ii) b quark fragmentation and b hadron branching fraction uncertainties: This term provides a description of the residual uncertainties not covered by the flavor-dependent hadronization term. It has two components: the uncertainty in the modeling of the b quark fragmentation function and the uncertainty from the measured b hadron semileptonic branching fractions. The b quark fragmentation function in PYTHIA is modeled using a Bowler-Lund model for the fragmentation into b hadrons. The fragmentation uncertainty is determined from the difference between a version tuned to ALEPH [52]

TABLE III. Category breakdown of the systematic uncertainties for the AMWT measurement in the dilepton channel. Each term has been estimated using the procedures described in Sec. VI. The uncertainties are expressed in GeV and the signs are taken from the $+1\sigma$ shift in the value of the quantity. Thus a positive sign indicates an increase in the value of m_t and a negative sign indicates a decrease. For uncertainties determined on independent simulated samples the statistical precision of the shift is displayed. With the exception of the flavor-dependent JEC terms (see Sec. VI), the total systematic uncertainty is obtained from the sum in quadrature of the individual systematic uncertainties.

Dilepton channel	δm_t (GeV)
Experimental uncertainties	
Method calibration	0.03
Jet energy corrections	
–JEC: intercalibration	+0.03
–JEC: <i>in situ</i> calibration	+0.24
–JEC: uncorrelated nonpileup	–0.28
–JEC: uncorrelated pileup	–0.12
Lepton energy scale	+0.12
E_T^{miss} scale	+0.06
Jet energy resolution	+0.06
b tagging	+0.04
Pileup	+0.04
Backgrounds	+0.02
Modeling of hadronization	
JEC: flavor-dependent	
–light quarks ($u d s$)	+0.02
–charm	+0.02
–bottom	–0.34
–gluon	+0.06
b jet modeling	
– b fragmentation	–0.69
–Semileptonic b hadron decays	–0.17
Modeling of perturbative QCD	
PDF	0.16
Ren. and fact. scales	–0.75 \pm 0.20
ME-PS matching threshold	–0.12 \pm 0.20
ME generator	–0.24 \pm 0.20
Top quark p_T	–0.25
Modeling of soft QCD	
Underlying event	+0.04 \pm 0.20
Color reconnection modeling	–0.11 \pm 0.20
Total systematic	1.22
Statistical	0.19
Total	1.24

and DELPHI [53] data and the PYTHIA Z2* tune. Lastly, the uncertainty from the semileptonic b hadron branching fraction is obtained by varying by -0.45% and $+0.77\%$, which is the range of the measurements from B^0/B^+ decays and their uncertainties [41].

VII. INDIVIDUAL CHANNEL RESULTS

A. The lepton + jets channel

After estimating the systematic uncertainties for the lepton + jets channel, the measurement of m_t and the JSF from the 2D analysis gives

$$m_t^{2D} = 172.14 \pm 0.19(\text{stat} + \text{JSF}) \pm 0.59(\text{syst}) \text{ GeV},$$

$$\text{JSF}^{2D} = 1.005 \pm 0.002(\text{stat}) \pm 0.007(\text{syst}).$$

The overall uncertainty in m_t is 0.62 GeV and the measured JSF is compatible with the one obtained from events with Z bosons and photons [37] within the systematic uncertainties.

The measurements from the 1D and hybrid analyses are

$$m_t^{1D} = 172.56 \pm 0.12(\text{stat}) \pm 0.62(\text{syst}) \text{ GeV},$$

$$m_t^{\text{hyb}} = 172.35 \pm 0.16(\text{stat} + \text{JSF}) \pm 0.48(\text{syst}) \text{ GeV}.$$

Thus the hybrid approach delivers the most precise measurement of the methods studied for the lepton + jets channel with a total uncertainty of 0.51 GeV.

The breakdown of the systematic uncertainties for the three fits is shown in Table I. In the lepton + jets and all-jets measurements several uncertainty sources yield opposite signs in the 1D and 2D approaches. This arises because the untagged jets used for m_W^{reco} have a softer p_T spectrum and larger gluon contamination compared to the b jets. As a consequence, the measurement of the JSF in the 2D measurement is more sensitive to low- p_T effects and radiation uncertainties than the 1D measurement where the light-jet energies are bound to fulfill the W mass constraint. The net effect, when using a flat JSF, is that the uncertainties can be overcorrected in the 2D fit and thus their signs reverse. The hybrid fit makes optimal use of the available information and leads to partial cancelation of these uncertainties, resulting in the observed improvement of the precision of the mass measurement.

B. The all-jets channel

The 2D analysis in the all-jets channel yields a measurement of

$$m_t^{2D} = 171.64 \pm 0.32(\text{stat} + \text{JSF}) \pm 0.95(\text{syst}) \text{ GeV},$$

$$\text{JSF}^{2D} = 1.011 \pm 0.003(\text{stat}) \pm 0.011(\text{syst}),$$

giving an overall uncertainty in the mass of 1.00 GeV.

The measurements from the 1D and hybrid analyses are

$$m_t^{1D} = 172.46 \pm 0.23(\text{stat}) \pm 0.62(\text{syst}) \text{ GeV},$$

$$m_t^{\text{hyb}} = 172.32 \pm 0.25(\text{stat} + \text{JSF}) \pm 0.59(\text{syst}) \text{ GeV},$$

with overall uncertainties of 0.66 and 0.64 GeV for the 1D and hybrid fits, respectively.

The breakdown of the systematic uncertainties for the three fits is shown in Table II.

C. The dilepton channel

For the dilepton channel the systematic uncertainties are defined as the difference between measurements of m_t from pseudodata events, selected at random from the MC events in the $m_t = 172.5$ GeV template. For each category of systematic uncertainty, modified templates were produced with a given systematic variable shifted, generically by $\pm 1\sigma$. The fit is repeated using the modified pseudodata and the respective mean is subtracted from the mean of the default $t\bar{t}$ MC simulation to calculate the final systematic uncertainty for each category. This yields a final mass measurement of

$$m_t = 172.82 \pm 0.19(\text{stat}) \pm 1.22(\text{syst}) \text{ GeV}.$$

The breakdown of the systematic uncertainty for the dilepton mass measurement is shown in Table III. In comparison with the lepton + jets (Table I) and the all-jets (Table II) channels, the systematic uncertainties are similar in size with the exception of the factorization and renormalization, and b fragmentation terms, both of which are significantly larger. Studies of these indicate that this is probably the result of an increased boost of the visible decay products, coupled to the weak constraint of the E_T^{miss} on the energies of the two neutrinos.

D. The 2010 and 2011 measurements

The published CMS measurements are based on $\sqrt{s} = 7$ TeV data recorded during 2010 and 2011. Although much less precise than the new measurements, they come

TABLE IV. CMS measurements of the top quark mass using the data recorded at $\sqrt{s} = 7$ TeV.

Analysis	Reference	m_t (GeV)	Statistical uncertainty (GeV)	Systematic uncertainty (GeV)
2010 dilepton (AMWT)	[54]	175.50	4.60	4.52
2011 lepton + jets (2D)	[55]	173.49	0.27	1.03
2011 all-jets (1D)	[48]	173.49	0.69	1.23
2011 dilepton (AMWT)	[43]	172.50	0.43	1.46

from independent data sets and have different sensitivities to the various systematic uncertainties. These are included in the combined mass analysis, which is discussed in Sec. IX. For completeness we summarize these measurements in Table IV below. The analysis techniques used for each of these are very similar to those used for the 2012 analyses. The dilepton results both use the AMWT method, which is described in Sec. IV B, and the lepton + jets (all-jets) result comes from the 2D (1D) ideogram technique, which is described in Sec. IV A.

VIII. MEASURED TOP QUARK MASS AS A FUNCTION OF KINEMATIC OBSERVABLES

To search for possible biases in our measurements and the potential limitations of current event generators, a series of differential measurements of m_t as a function of the kinematic properties of the $t\bar{t}$ system is performed. To maximize the accuracy of the results, the study is performed in the lepton + jets channel using the hybrid fit technique. The variables are chosen to probe potential effects from color reconnection, initial- and final-state

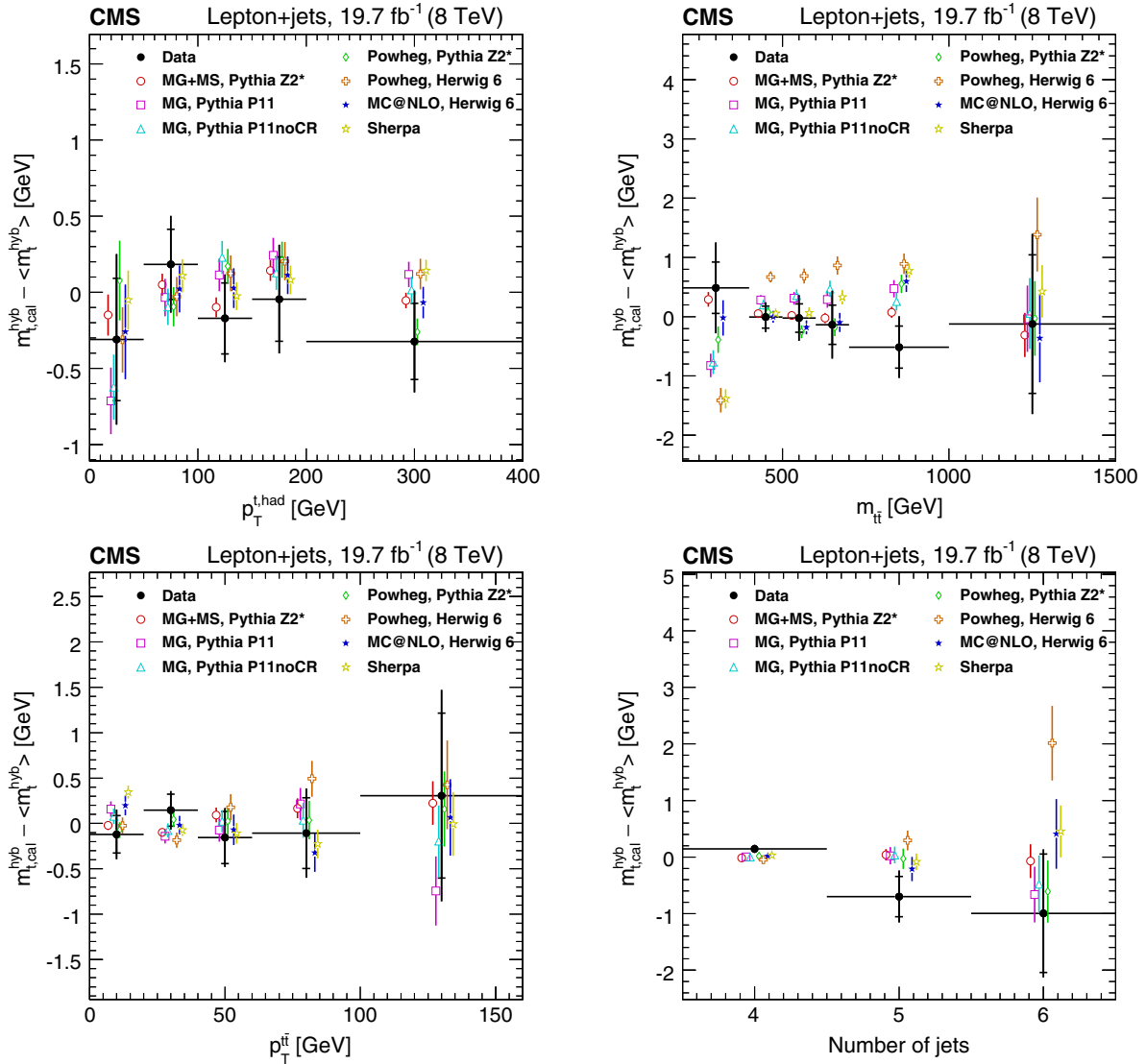


FIG. 9. Measurements of m_t as a function of the transverse momentum of the hadronically decaying top quark ($p_T^{t, \text{had}}$), the invariant mass of the $t\bar{t}$ system ($m_{t\bar{t}}$), the transverse momentum of the $t\bar{t}$ system ($p_T^{t\bar{t}}$), and the number of jets with $p_T > 30$ GeV. The filled circles represent the data, and the other symbols are for the simulations. For reasons of clarity the horizontal error bars are shown only for the data points and each of the simulations is shown as a single offset point with a vertical error bar representing its statistical uncertainty. The statistical uncertainty of the data is displayed by the inner error bars. For the outer error bars, the systematic uncertainties are added in quadrature. The open circles correspond to MADGRAPH with the PYTHIA Z2* tune, the open squares correspond to MADGRAPH with the PYTHIA Perugia 2011 tune, and the open triangles represent MADGRAPH with the PYTHIA Perugia 2011 noCR tune. The open diamonds correspond to POWHEG with the PYTHIA Z2* tune and the open crosses correspond to POWHEG with HERWIG 6. The filled stars are for MC@NLO with HERWIG 6 and the open stars are for SHERPA.

radiation, and the kinematics of the jets coming from the top quark decays.

For each measurement, the hybrid analysis method is applied to subsets of events defined according to the value of a given kinematic event observable after the kinematic fit. The contribution of the external JSF constraint is fixed to 50% to ensure consistency of all bins with the inclusive result. Constant shifts in the measured m_t values may arise due to the systematic uncertainties of the inclusive measurement or from the use of different m_t values in data and

simulations. To search for kinematics-dependent biases the value of the mean measured top quark mass is subtracted and the results are expressed in the form $m_t - \langle m_t \rangle$, where the mean comes from the inclusive measurement on the specific sample. In each case, the event sample is divided into 3 to 5 bins as a function of the value of the kinematic observable and we populate each bin using all permutations which lie within the bin boundaries. As some observables depend on the jet-quark assignment that cannot be resolved unambiguously, such as the p_T of a reconstructed top

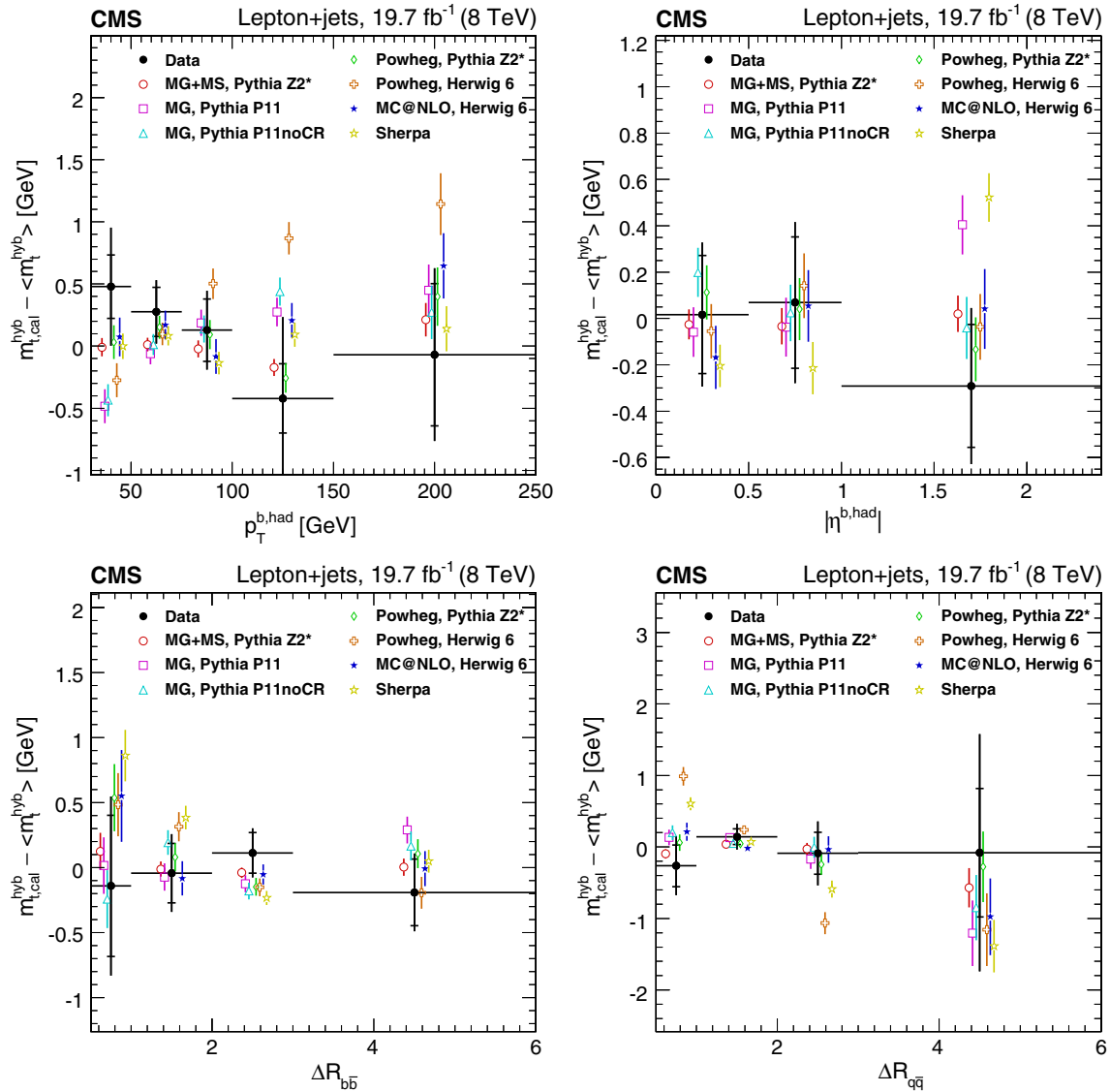


FIG. 10. Measurements of m_t as a function of the p_T of the b jet assigned to the hadronic decay branch ($p_T^{b, had}$), the pseudorapidity of the b jet assigned to the hadronic decay branch ($|\eta^{b, had}|$), the ΔR between the b jets (ΔR_{bb}), and the ΔR between the light-quark jets ($\Delta R_{q\bar{q}}$). The filled circles represent the data, and the other symbols are for the simulations. For reasons of clarity the horizontal error bars are shown only for the data points and each of the simulations is shown as a single offset point with a vertical error bar representing its statistical uncertainty. The statistical uncertainty of the data is displayed by the inner error bars. For the outer error bars, the systematic uncertainties are added in quadrature. The open circles correspond to MADGRAPH with the PYTHIA Z2* tune, the open squares to MADGRAPH with the PYTHIA Perugia 2011 tune, and the open triangles represent MADGRAPH with the PYTHIA Perugia 2011 noCR tune. The open diamonds correspond to POWHEG with the PYTHIA Z2* tune and the open crosses correspond to POWHEG with HERWIG 6. The filled stars are for MC@NLO with HERWIG 6 and the open stars are for SHERPA.

quark, a single event is allowed to contribute to multiple bins.

To aid in the interpretation of a difference between the value of $m_t - \langle m_t \rangle$ and the prediction from a simulation in the same bin, a bin-by-bin calibration of the results is performed using the MADGRAPH+PYTHIA simulation. This is performed using the same technique as for the inclusive measurement [55] except that it is performed on each bin separately. Thus, after calibration the value in each bin can be interpreted in terms of its agreement with respect to the inclusive measurement.

For eight kinematic variables the results for the calibrated mass difference, $m_t - \langle m_t \rangle$, are shown as a function of the chosen variable, and we compare the results to the predictions of seven different simulations. For each plotted point the statistical uncertainty and the dominant systematic uncertainties are combined in quadrature, where the latter include the JES (p_T -, η - and flavor-dependent), JER, pileup, b fragmentation, renormalization and factorization scales, and ME-PS matching threshold. The systematic uncertainties are assumed to be correlated among all bins, so that any constant shift is removed by subtracting $\langle m_t \rangle$. We note that this approximation may underestimate the uncertainties from the p_T/η -dependent JES.

For each plot we compare the data to simulations based on LO (MADGRAPH and SHERPA) and NLO (POWHEG and MC@NLO) matrix element calculations with both string (PYTHIA) and cluster (HERWIG) models for fragmentation. We also vary the choice of underlying event tune from Z2* to Perugia 2011 both with and without color reconnections, and the AUET2 tune. With the exception of the MC@NLO and SHERPA simulations, which are only used for this study, these are the same simulation as those discussed in Sec. III A. The simulations used for this study are

- (i) MADGRAPH with the PYTHIA Z2* tune, which is the simulation used in the mass determinations [14–16,56];
- (ii) MADGRAPH with the PYTHIA Perugia 2011 tune [14,16,50];
- (iii) MADGRAPH with the PYTHIA Perugia 2011 noCR tune [14,16,50];
- (iv) SHERPA 1.4.0 with up to 4 additional jets from the LO matrix element [57,58];
- (v) POWHEG with the PYTHIA Z2* tune [16,21–25,56];
- (vi) POWHEG with the HERWIG 6.520 AUET2 tune [21–25,59];
- (vii) MC@NLO 3.41 with the HERWIG 6.520 default tune [59–61].

The variables were chosen for their potential sensitivity to modeling the kinematics of top quark production (Fig. 9) and decay (Fig. 10). No significant deviation in the value of the measured m_t is observed, indicating that within the current precision, there is no evidence for a bias in the measurements. The agreement between the data and each of the simulations is quantified in Table V. Here we show

TABLE V. Comparison of different simulations and the data. The summed χ^2 values and number of standard deviations are computed for the 27 points entering Figs. 9 and 10 assuming two-sided Gaussian statistics.

Simulation	χ^2	Standard deviations
MG + PYTHIA 6 Z2*	17.55	0.10
MG + PYTHIA 6 P11	37.68	1.73
MG + PYTHIA 6 P11noCR	31.57	1.15
POWHEG + PYTHIA 6 Z2*	19.70	0.20
POWHEG + HERWIG 6	76.48	4.84
MC@NLO + HERWIG 6	20.47	0.24
SHERPA	46.79	2.56

the cumulative χ^2 for the 27 degrees of freedom represented by the eight distributions studied (Figs. 9 and 10) and the corresponding number of standard deviations between the data and the simulation, where we have assumed two-sided Gaussian confidence intervals for each simulation. In all cases, with the possible exception of POWHEG+HERWIG 6 simulation, the data is well described by the models.

IX. COMBINING THE MASS MEASUREMENTS

In this section, results for the combined top quark mass measurement are presented. As inputs we use the new results presented in this paper and the published CMS measurements from the 2010 [54] and 2011 [43,48,55] analyses. To combine the results, the best linear unbiased estimate method (BLUE) [62] is used. This determines a linear combination of the input measurements which takes into account statistical and systematic uncertainties by minimizing the total uncertainty of the combined result. The procedure takes account of the correlations that exist between the different uncertainty sources through the use of correlation coefficients. These are chosen to reflect the current knowledge of the uncertainties for both the correlations between measurements in a given decay channel from different years (ρ_{chan}) and between the measurements in different decay channels from the same year (ρ_{year}). The nominal values are set to either zero for uncorrelated or unity for fully correlated (see Table VI). Because the measurements from the 2012 analyses are significantly more precise, both statistically and systematically, than those from the 2010 and 2011 analyses, the use of unity coefficients for ρ_{chan} and ρ_{year} is problematic. To mitigate this, we have chosen to perform combinations in which the correlation coefficients are limited to value of less than unity. This has been done by setting the correlation coefficients for each pair of measurements in the fully correlated cases to $\rho = \sigma_i/\sigma_j$, where σ_i and σ_j are the uncorrelated components of the uncertainties in measurements i and j , respectively, and $\sigma_i < \sigma_j$. For all of the measurements, the statistical uncertainties are assumed to be uncorrelated.

TABLE VI. Nominal correlation coefficients for the systematic uncertainties, The term ρ_{chan} is the correlation factor for measurements in the same top quark decay channel, but different years and the term ρ_{year} is the correlation between measurements in different channels from the same year.

	Correlations	
	ρ_{chan}	ρ_{year}
Experimental uncertainties		
Method calibration	0	0
JEC: intercalibration	1	1
JEC: <i>in situ</i> calibration	1	1
JEC: uncorrelated nonpileup	0	1
Lepton energy scale	1	1
E_T^{miss} scale	1	1
Jet energy resolution	1	1
b tagging	1	1
Pileup	0	1
Non- $t\bar{t}$ background (data)	0	0
Non- $t\bar{t}$ background (simulation)	1	1
Trigger	0	0
Modeling of hadronization		
JEC: flavor-dependent	1	1
b jet modeling	1	1
Modeling of perturbative QCD		
PDF	1	1
Ren. and fact. scales	1	1
ME-PS matching threshold	1	1
ME generator	1	1
Top quark p_T	1	1
Modeling of soft QCD		
Underlying event	1	1
Color reconnection modeling	1	1

A. Measurement permutations

The precision of any combination of the measurements will be dominated by the set of new measurements, derived from the 2012 data. To investigate the effect of

TABLE VII. Combination results for the permutations of the 2D, 1D, and hybrid measurements. The permutation order is defined to be lepton + jets:all-jets:dilepton, thus 211 corresponds to the 2D lepton + jets:1D all-jets:AMWT dilepton combination.

Combination	m_t (GeV)	Stat + JSF uncertainty (GeV)	Syst uncertainty (GeV)
211	172.40	0.13	0.54
121	172.61	0.11	0.57
221	172.30	0.15	0.58
111	172.66	0.12	0.56
h11	172.45	0.13	0.47
hh1	172.44	0.13	0.47
2h1	172.35	0.14	0.53

the choice of fit method on the result, we perform a series of combinations in which the 2012 inputs from the lepton + jets and all-jets decay channels are varied. For simplicity of discussion, these are classified according to the type of fit used for each channel. They are labeled as follows: 2 for a 2D fit, 1 for a 1D or AMWT fit, and h for a

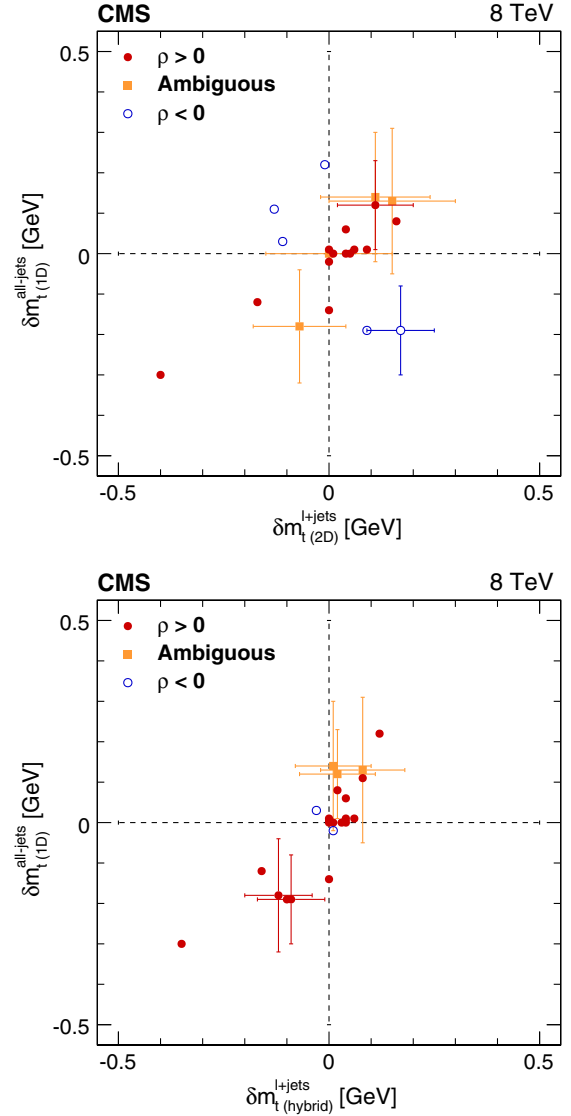


FIG. 11. Systematic uncertainty correlations for mass measurements in the lepton + jets and all-jets channels. Each point represents a single systematic uncertainty taken from Tables I and II. Top: for the 2D lepton + jets and 1D all-jets measurements; bottom: for the hybrid lepton + jets and the 1D all-jets measurements. The filled circles correspond to the systematic uncertainties which show a positive correlation between the two fit methods and the open circles to the systematic terms which show a negative correlation. The points shown as filled squares are those for which the systematic estimation is dominated by a statistical uncertainty, so no clear categorization is possible. The vertical and horizontal error bars correspond to the statistical uncertainties in the systematic uncertainties.

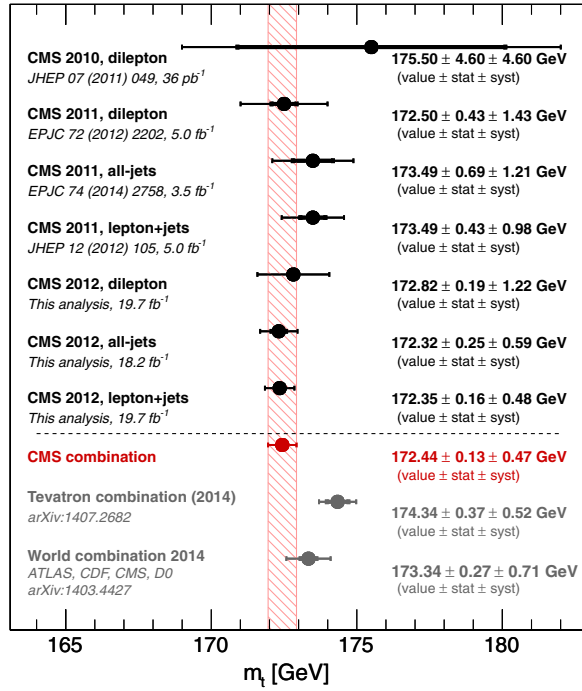


FIG. 12. Summary of the CMS m_t measurements and their combination. The thick error bars show the statistical uncertainty and the thin error bars show the total uncertainty. Also shown are the current Tevatron [8] and world average [7] combinations.

hybrid fit. Thus a lepton + jets:all-jets:dilepton fit is denoted 211 in the case of a 2D fit for the lepton + jets channel a 1D fit for the all-jets channel and the AMWT fit in the dilepton channel.

The most precise set of nonhybrid measurements corresponds to the set 211, which gives a result of

$$m_t = 172.40 \pm 0.13(\text{stat} + \text{JSF}) \\ \pm 0.54(\text{syst}) \text{ GeV (211 combination).}$$

To verify that this gives the most precise combination, combinations are performed using the other permutations of the 2012 measurements. The results, listed in Table VII,

are in good agreement with the 211 result but have less precision, as expected.

For the hybrid results, the effect of constraining the JSF factor in the mass fits can be examined. There are three significant new permutations to consider, the h11, hh1, and 2h1 combinations. The results, shown in Table VII, are in good agreement with the 211 result, with the h11 and hh1 combinations giving the most precise measurements, as expected. For these the results are

$$m_t = 172.45 \pm 0.13(\text{stat} + \text{JSF}) \\ \pm 0.47(\text{syst}) \text{ GeV (h11 combination),}$$

$$m_t = 172.44 \pm 0.13(\text{stat} + \text{JSF}) \\ \pm 0.47(\text{syst}) \text{ GeV (hh1 combination),}$$

both with an overall improvement in precision of 0.07 GeV with respect to the 211 analysis, and a total uncertainty of 0.48 GeV.

B. Anticorrelation effects

For the results presented here, the signs of most of the uncertainty contributions are well defined (i.e. for a 1σ shift in a given quantity, the statistical component of the estimated systematic uncertainty is significantly smaller than the value of the uncertainty). This allows a comparison of the signs of the systematic uncertainties for the different channels and for the different fitting techniques. An anticorrelation (i.e. opposite signs) is observed between several of the terms when comparing the results from a 2D and a 1D (or AMWT) fit. However, if the 2D fit is replaced by the corresponding hybrid result, the anticorrelations are removed. This is illustrated in Fig. 11, which shows the uncertainty correlations between the lepton + jets and all-jets channels for the 2D vs 1D and the hybrid vs 1D cases. In the 2D vs 1D plot (Fig. 11 left) we observe a significant number of anticorrelated terms (coming primarily from the JES and pileup terms), whereas in the hybrid vs 1D plot (Fig. 11 right) we see no significant anticorrelations. Given the uncertainty terms that vary between the 2D and hybrid treatments, it is believed that the observed effect arises from

TABLE VIII. Correlations between input measurements. The elements in the table are labeled according to the analysis they correspond to (rows and columns read as 2010, 2011, 2012 followed by the $t\bar{t}$ decay channel name).

		2010		2011		2012		
		dilepton	dilepton	lepton + jets	all-jets	dilepton	lepton + jets	all-jets
2010	dilepton	1.00						
	dilepton	0.15	1.00					
2011	lepton + jets	0.09	0.37	1.00				
	all-jets	0.10	0.62	0.31	1.00			
	dilepton	0.09	0.26	0.17	0.17	1.00		
2012	lepton + jets	0.05	0.21	0.30	0.26	0.26	1.00	
	all-jets	0.06	0.20	0.27	0.28	0.32	0.61	1.00

the variation in the JSF factors between the 2D, 1D, and hybrid results (Secs. VA and VB).

These effects are not considered in the standard 211 combination as the input correlation coefficients are positive for all of the correlated cases (see Table VI). To estimate the effect of including anticorrelations, the correlation coefficients are set to negative values for the cases where an anticorrelation (opposite sign) is observed and positive values where a positive (same sign) or neutral (statistically limited) correlation is observed and the 211 combination analysis is repeated. This gives a result of $172.40 \pm 0.13(\text{stat} + \text{JSF}) \pm 0.47(\text{syst})$ GeV. Thus, while the result for the mass is unchanged, the systematic uncertainty is decreased and becomes comparable to that achieved in the hybrid combinations.

X. RESULTS

Based on the expected uncertainties for each of the individual measurements (Tables I–III) and the consistency of the hybrid and 1D results for the JSF (Secs. VA, VB), the hh1 combination is chosen as the preferred result. Combining the seven input measurements (four from $\sqrt{s} = 7$ TeV and three from this analysis) gives a combined top quark mass measurement of

$$m_t = 172.44 \pm 0.13(\text{stat} + \text{JSF}) \pm 0.47(\text{syst}) \text{ GeV},$$

for which the combination χ^2 is 2.5 for 6 degrees of freedom, corresponding to a probability of 87%. This is compared to the full set of Run 1 measurements in Fig. 12 where the current world average [7] and Tevatron [8] combinations are also shown. The result is consistent with all of the published LHC measurements and is the most precise measurement to date with a precision of 0.3%.

The correlations between each of the measurements is shown in Table VIII. Figure 13 shows the combination coefficients and pulls, where the pull is defined as $(m_{\text{top}}^{\text{comb}} - m_{\text{top}}^{\text{meas}}) / \sqrt{\sigma_{\text{meas}}^2 - \sigma_{\text{comb}}^2}$ where $m_{\text{top}}^{\text{comb}}$ and $m_{\text{top}}^{\text{meas}}$ are the combined and the individual measurements of m_t , respectively, and σ_{comb} and σ_{meas} are the corresponding total uncertainties. The 2010 measurement contributes very little to the overall result. As the treatment of the systematic uncertainty for this analysis is the least sophisticated of the seven measurements, the final combination is repeated to verify that it does not influence the final result. Excluding this measurement produces negligible changes in the values of m_t or its total uncertainty, δm_t . For the combination of the remaining six measurements the χ^2 is 2.3 for 5 degrees of freedom, corresponding to a probability of 80%.

The breakdown of the systematic uncertainties for the combination is shown in Table IX. The dominant uncertainty in the measurement arises from the modeling of the hadronization, with 0.33 GeV coming from the flavor-dependent jet energy corrections and a further 0.14 GeV

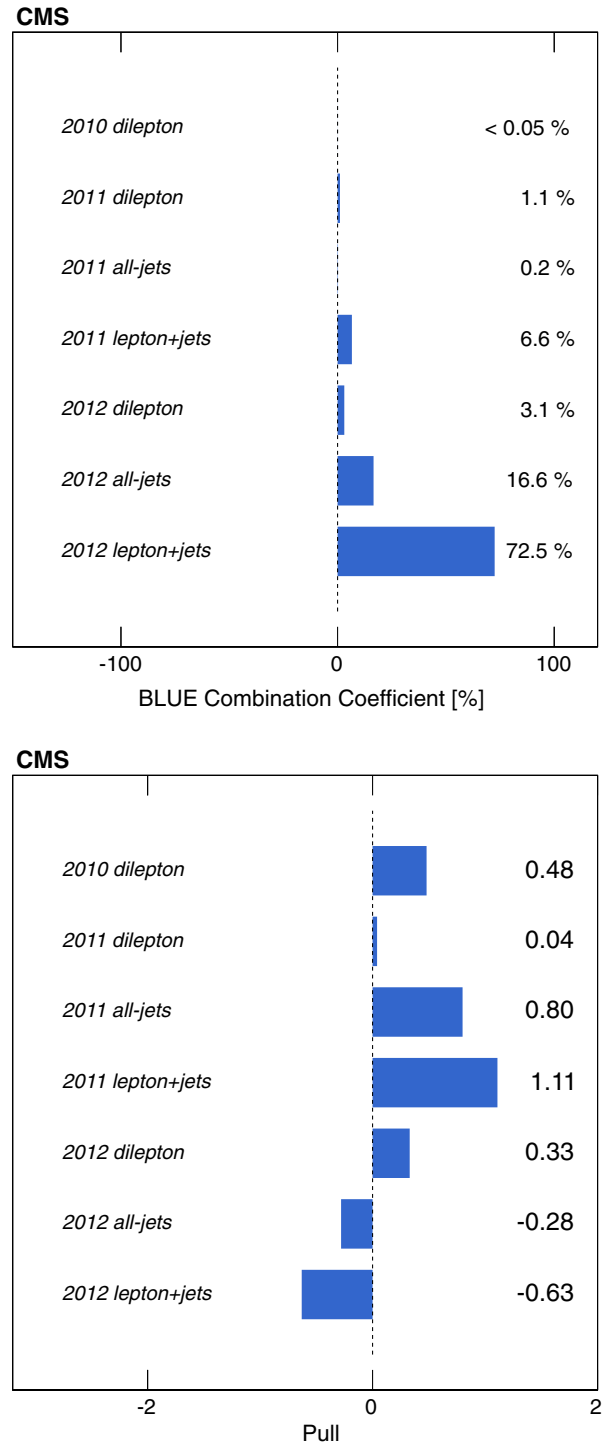


FIG. 13. Results of the BLUE combining procedure on the CMS measurements showing (left) the combination coefficients, and (right) the pulls for each contribution.

coming from the b jets. There are a further six terms with uncertainties in the range of 0.11–0.12 GeV. Of these, four are coming from theory and only two, the JEC *in situ* (0.12 GeV) and the JEC uncorrelated nonpileup (0.10 GeV) are experimental. The theoretical uncertainties

TABLE IX. Category breakdown of systematic uncertainties for the combined mass result. The uncertainties are expressed in GeV.

Combined m_t result	δm_t (GeV)
Experimental uncertainties	
Method calibration	0.03
Jet energy corrections	
–JEC: intercalibration	0.01
–JEC: <i>in situ</i> calibration	0.12
–JEC: uncorrelated nonpileup	0.10
Lepton energy scale	0.01
E_T^{miss} scale	0.03
Jet energy resolution	0.03
b tagging	0.05
Pileup	0.06
Backgrounds	0.04
Trigger	< 0.01
Modeling of hadronization	
JEC: flavor	0.33
b jet modeling	0.14
Modeling of perturbative QCD	
PDF	0.04
Ren. and fact. scales	0.10
ME-PS matching threshold	0.08
ME generator	0.11
Top quark p_T	0.02
Modeling of soft QCD	
Underlying event	0.11
Color reconnection modeling	0.10
Total systematic	0.47
Statistical	0.13
Total Uncertainty	0.48

are computed using the same models so they should be fully correlated. For the two experimental terms, the strength of the assumed correlations is varied by 50% of their nominal values to check the sensitivity to the assumed correlation strength. In both cases this produces changes of less than 0.01 GeV in m_t and δm_t . We therefore conclude that the result is quite stable against reasonable changes in the assumed correlation strength.

Although we do not believe that the use of 100% correlation strengths is appropriate to use for the correlated systematic uncertainties, for completeness we have rerun the final combination without the constraint on the correlation strengths. In this case we observe shifts of -0.28 GeV in m_t and -0.03 GeV in δm_t . For this combination, four of the seven measurements have negative combination coefficients and the central mass lies outside of the boundaries of the measurements. This corresponds to the result obtained using the standard BLUE method.

Figure 14 shows the mass values obtained from each of the three channels separately. These correspond to

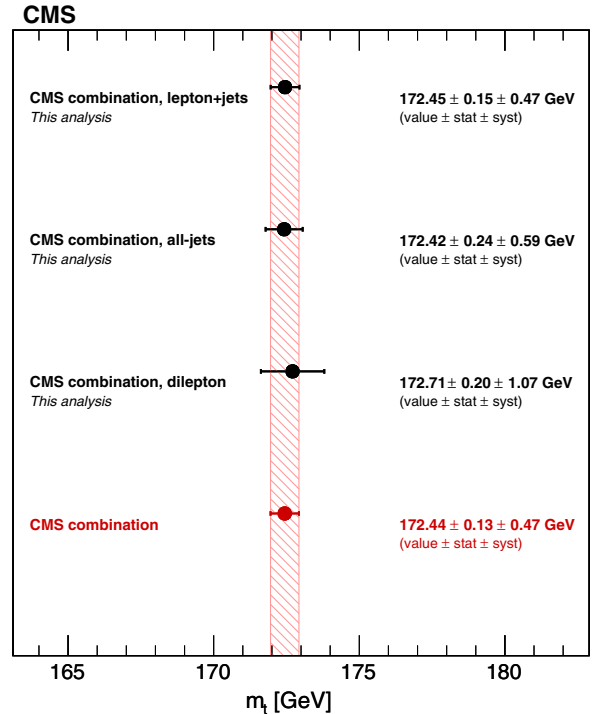


FIG. 14. The combined $\sqrt{s} = 7$ and 8 TeV measurements of m_t for each of the $t\bar{t}$ decay channels.

combinations h2 (2012, 2011) for the lepton + jets channel, h11 (2012, 2011, 2010) for the dilepton channel, and h1 (2012, 2011) for the all-jets channel, respectively. The results are all in good agreement with the combined measurement.

XI. SUMMARY

A new set of measurements of the top quark mass has been presented, based on the data recorded by the CMS experiment at the LHC at $\sqrt{s} = 8$ TeV during 2012, and corresponding to a luminosity of 19.7 fb^{-1} . The top quark mass has been measured in the lepton + jets, all-jets and dilepton decay channels, giving values of $172.35 \pm 0.16(\text{stat}) \pm 0.48(\text{syst}) \text{ GeV}$, $172.32 \pm 0.25(\text{stat}) \pm 0.59(\text{syst}) \text{ GeV}$, and $172.82 \pm 0.19(\text{stat}) \pm 1.22(\text{syst}) \text{ GeV}$, respectively. Individually, these constitute the most precise measurements in each of the decay channels studied. When combined with the published CMS results at $\sqrt{s} = 7$ TeV, a top quark mass measurement of $172.44 \pm 0.13(\text{stat}) \pm 0.47(\text{syst}) \text{ GeV}$ is obtained. This is the most precise measurement of m_t to date, with a total uncertainty of 0.48 GeV, and it supersedes all of the previous CMS measurements of the top quark mass.

The top quark mass has also been studied as a function of the event kinematical properties in the lepton + jets channel. No indications of a kinematical bias in the measurements is observed and the data are consistent with a range of predictions from current theoretical models of $t\bar{t}$ production.

ACKNOWLEDGMENTS

We congratulate our colleagues in the CERN accelerator departments for the excellent performance of the LHC and thank the technical and administrative staffs at CERN and at other CMS institutes for their contributions to the success of the CMS effort. In addition, we gratefully acknowledge the computing centers and personnel of the Worldwide LHC Computing Grid for delivering so effectively the computing infrastructure essential to our analyses. Finally, we acknowledge the enduring support for the construction and operation of the LHC and the CMS detector provided by the following funding agencies: the Austrian Federal Ministry of Science, Research and Economy and the Austrian Science Fund; the Belgian Fonds de la Recherche Scientifique, and Fonds voor Wetenschappelijk Onderzoek; the Brazilian Funding Agencies (CNPq, CAPES, FAPERJ, and FAPESP); the Bulgarian Ministry of Education and Science; CERN; the Chinese Academy of Sciences, Ministry of Science and Technology, and National Natural Science Foundation of China; the Colombian Funding Agency (COLCIENCIAS); the Croatian Ministry of Science, Education and Sport, and the Croatian Science Foundation; the Research Promotion Foundation, Cyprus; the Ministry of Education and Research, Estonian Research Council via IUT23-4 and IUT23-6 and European Regional Development Fund, Estonia; the Academy of Finland, Finnish Ministry of Education and Culture, and Helsinki Institute of Physics; the Institut National de Physique Nucléaire et de Physique des Particules/CNRS, and Commissariat à l'Énergie Atomique et aux Énergies Alternatives/CEA, France; the Bundesministerium für Bildung und Forschung, Deutsche Forschungsgemeinschaft, and Helmholtz-Gemeinschaft Deutscher Forschungszentren, Germany; the General Secretariat for Research and Technology, Greece; the National Scientific Research Foundation, and National Innovation Office, Hungary; the Department of Atomic Energy and the Department of Science and Technology, India; the Institute for Studies in Theoretical Physics and Mathematics, Iran; the Science Foundation, Ireland; the Istituto Nazionale di Fisica Nucleare, Italy; the Ministry of Science, ICT and Future Planning, and National Research Foundation (NRF), Republic of Korea; the Lithuanian Academy of Sciences; the Ministry of Education, and University of Malaya (Malaysia); the Mexican Funding Agencies (CINVESTAV, CONACYT, SEP, and UASLP-FAI); the Ministry of Business, Innovation and

Employment, New Zealand; the Pakistan Atomic Energy Commission; the Ministry of Science and Higher Education and the National Science Centre, Poland; the Fundação para a Ciência e a Tecnologia, Portugal; JINR, Dubna; the Ministry of Education and Science of the Russian Federation, the Federal Agency of Atomic Energy of the Russian Federation, Russian Academy of Sciences, and the Russian Foundation for Basic Research; the Ministry of Education, Science and Technological Development of Serbia; the Secretaría de Estado de Investigación, Desarrollo e Innovación and Programa Consolider-Ingenio 2010, Spain; the Swiss Funding Agencies (ETH Board, ETH Zurich, PSI, SNF, UniZH, Canton Zurich, and SER); the Ministry of Science and Technology, Taipei; the Thailand Center of Excellence in Physics, the Institute for the Promotion of Teaching Science and Technology of Thailand, Special Task Force for Activating Research and the National Science and Technology Development Agency of Thailand; the Scientific and Technical Research Council of Turkey, and Turkish Atomic Energy Authority; the National Academy of Sciences of Ukraine, and State Fund for Fundamental Researches, Ukraine; the Science and Technology Facilities Council, UK; the U.S. Department of Energy, and the U.S. National Science Foundation. Individuals have received support from the Marie-Curie program and the European Research Council and EPLANET (European Union); the Leventis Foundation; the A. P. Sloan Foundation; the Alexander von Humboldt Foundation; the Belgian Federal Science Policy Office; the Fonds pour la Formation à la Recherche dans l'Industrie et dans l'Agriculture (FRIA-Belgium); the Agentschap voor Innovatie door Wetenschap en Technologie (IWT-Belgium); the Ministry of Education, Youth and Sports (MEYS) of the Czech Republic; the Council of Science and Industrial Research, India; the HOMING PLUS program of the Foundation for Polish Science, cofinanced from European Union, Regional Development Fund; the OPUS program of the National Science Center (Poland); the Compagnia di San Paolo (Torino); the Consorzio per la Fisica (Trieste); MIUR project 20108T4XTM (Italy); the Thalís and Aristeia programs cofinanced by EU-ESF and the Greek NSRF; the National Priorities Research Program by Qatar National Research Fund; the Rachadapisek SomWetenschappelijk Onderzopot Fund for Postdoctoral Fellowship, Chulalongkorn University (Thailand); and the Welch Foundation, Contract No. C-1845.

[1] ALEPH, CDF, D0, DELPHI, L3, OPAL and SLD Collaborations, the LEP Electroweak Working Group, the Tevatron Electroweak Working Group and the SLD Electroweak and

Heavy Flavour Groups, Precision electroweak measurements and constraints on the standard model, [arXiv:1012.2367](https://arxiv.org/abs/1012.2367).

- [2] M. Baak, M. Goebel, J. Haller, A. Hoecker, D. Kennedy, R. Kogler, K. Mönig, M. Schott, and J. Stelzer, The electro-weak fit of the standard model after the discovery of a new boson at the LHC, *Eur. Phys. J. C* **72**, 2205 (2012), updates available from <http://gfitter.desy.de>.
- [3] G. Degrandi, S. Di Vita, J. Elias-Miró, J. R. Espinosa, G. F. Giudice, G. Isidori, and A. Strumia, Higgs mass and vacuum stability in the standard model at NNLO, *J. High Energy Phys.* **08** (2012) 1.
- [4] F. Bezrukov, M. Y. Kalmykov, B. A. Kniehl, and M. Shaposhnikov, Higgs boson mass and new physics, *J. High Energy Phys.* **10** (2012) 140.
- [5] F. Bezrukov and M. Shaposhnikov, The standard model Higgs boson as the inflaton, *Phys. Lett. B* **659**, 703 (2008).
- [6] A. De Simone, M. P. Herzberg, and F. Wilczek, Running inflation in the standard model, *Phys. Lett. B* **678**, 1 (2009).
- [7] ATLAS, CDF, CMS and D0 Collaborations, First combination of Tevatron and LHC measurements of the top quark mass, [arXiv:1403.4427](https://arxiv.org/abs/1403.4427).
- [8] The Tevatron Electroweak Working Group, Combination of the CDF and D0 results on the mass of the top quark using up to 9.7 fb^{-1} at the Tevatron, [arXiv:1407.2682](https://arxiv.org/abs/1407.2682).
- [9] ATLAS Collaboration, Measurement of the top quark mass in the $t\bar{t} \rightarrow \text{lepton} + \text{jets}$ and $t\bar{t} \rightarrow \text{dilepton}$ channels using $\sqrt{s} = 7 \text{ TeV}$ ATLAS data, *Eur. Phys. J. C* **75**, 330 (2015).
- [10] A. H. Hoang and I. W. Stewart, Top mass measurements from jets and the tevatron top quark mass, *Nucl. Phys. B, Proc. Suppl.* **185**, 220 (2008).
- [11] V. Ahrens, A. Ferroglia, M. Neubert, B. D. Pecjak, and L. L. Yang, Precision predictions for the $t\bar{t}$ production cross section at hadron colliders, *Phys. Lett. B* **703**, 135 (2011).
- [12] A. Buckley, J. Butterworth, S. Gieseke, D. Grellscheid, S. Höche, H. Hoeth, F. Krauss, L. Lönnblad, E. Nurse, P. Richardson, S. Schumann, M. H. Seymour, T. Sjöstrand, P. Skands, and B. Webber, General-purpose event generators for LHC physics, *Phys. Rep.* **504**, 145 (2011).
- [13] CMS Collaboration, The CMS experiment at the CERN LHC, *J. Instrum.* **3**, S08004 (2008).
- [14] J. Alwall, M. Herquet, F. Maltoni, O. Mattelaer, and T. Stelzer, MadGraph 5: Going beyond, *J. High Energy Phys.* **06** (2011) 128.
- [15] P. Artoisenet, R. Frederix, O. Mattelaer, and R. Rietkerk, Automatic spin-entangled decays of heavy resonances in Monte Carlo simulations, *J. High Energy Phys.* **03** (2013) 015.
- [16] T. Sjöstrand, S. Mrenna, and P. Skands, PYTHIA 6.4 physics and manual, *J. High Energy Phys.* **05** (2006) 026.
- [17] S. Jadach, Z. Was, R. Decker, and J. H. Kühn, The tau decay library TAUOLA: Version 2.4, *Comput. Phys. Commun.* **76**, 361 (1993).
- [18] R. Field, Early LHC underlying event data—Findings and surprises, [arXiv:1010.3558](https://arxiv.org/abs/1010.3558).
- [19] J. Pumplin, D. R. Stump, J. Huston, H.-L. Lai, P. Nadolsky, and W.-K. Tung, New generation of parton distributions with uncertainties from global QCD analysis, *J. High Energy Phys.* **07** (2002) 012.
- [20] S. Agostinelli *et al.* (GEANT4), GEANT4—A simulation toolkit, *Nucl. Instrum. Methods Phys. Res., Sect. A* **506**, 250 (2003).
- [21] S. Alioli, P. Nason, C. Oleari, and E. Re, NLO single-top production matched with shower in POWHEG: s - and t -channel contributions, *J. High Energy Phys.* **09** (2009) 111.
- [22] E. Re, Single-top Wt -channel production matched with parton showers using the POWHEG method, *Eur. Phys. J. C* **71**, 1547 (2011).
- [23] P. Nason, A new method for combining NLO QCD with shower Monte Carlo algorithms, *J. High Energy Phys.* **11** (2004) 040.
- [24] S. Frixione, P. Nason, and C. Oleari, Matching NLO QCD computations with parton shower simulations: The POWHEG method, *J. High Energy Phys.* **11** (2007) 070.
- [25] S. Alioli, P. Nason, C. Oleari, and E. Re, A general framework for implementing NLO calculations in shower Monte Carlo programs: The POWHEG BOX, *J. High Energy Phys.* **06** (2010) 043.
- [26] N. Kidonakis, Next-to-next-to-leading soft-gluon corrections for the top quark cross section and transverse momentum distribution, *Phys. Rev. D* **82**, 114030 (2010).
- [27] N. Kidonakis, Differential and total cross sections for top pair and single top production, [arXiv:1205.3453](https://arxiv.org/abs/1205.3453).
- [28] K. Melnikov and F. Petriello, Electroweak gauge boson production at hadron colliders through $O(\alpha_s^2)$, *Phys. Rev. D* **74**, 114017 (2006).
- [29] J. M. Campbell and R. K. Ellis, MCFM for the Tevatron and the LHC, *Nucl. Phys. B, Proc. Suppl.* **205-206**, 10 (2010).
- [30] M. Czakon, P. Fiedler, and A. Mitov, The total top quark pair production cross-section at hadron colliders through $O(\alpha_s^4)$, *Phys. Rev. Lett.* **110**, 252004 (2013).
- [31] CMS Collaboration, CMS Physics Analysis Summary Report No. CMS-PAS-PFT-09-001, 2009, <http://cdsweb.cern.ch/record/1194487>.
- [32] CMS Collaboration, CMS Physics Analysis Summary Report No. CMS-PAS-PFT-10-001, 2010, <http://cdsweb.cern.ch/record/1247373>.
- [33] CMS Collaboration, Performance of electron reconstruction and selection with the CMS detector in proton-proton collisions at $\sqrt{s} = 8 \text{ TeV}$, *J. Instrum.* **6**, P06005 (2015).
- [34] CMS Collaboration, Performance of CMS muon reconstruction in pp collision events at $\sqrt{s} = 7 \text{ TeV}$, *J. Instrum.* **7**, P10002 (2012).
- [35] M. Cacciari, G. P. Salam, and G. Soyez, The anti- k_r jet clustering algorithm, *J. High Energy Phys.* **04** (2008) 063.
- [36] M. Cacciari, G. P. Salam, and G. Soyez, FastJet user manual, *Eur. Phys. J. C* **72**, 1896 (2012).
- [37] CMS Collaboration, Determination of jet energy calibration and transverse momentum resolution in CMS, *J. Instrum.* **6**, P11002 (2011).
- [38] CMS Collaboration, CMS Physics Analysis Summary Report No. CMS-PAS-BTV-13-001, 2013, <http://cdsweb.cern.ch/record/1581306>.
- [39] CMS Collaboration, Measurement of the differential cross section for top quark pair production in pp collisions at $\sqrt{s} = 8 \text{ TeV}$, *Eur. Phys. J. C* **75**, 542 (2015).
- [40] B. Abbott *et al.* (D0 Collaboration), Direct measurement of the top quark mass at D0, *Phys. Rev. D* **58**, 052001 (1998).
- [41] K. A. Olive *et al.* (Particle Data Group), Review of particle physics, *Chin. Phys. C* **38**, 090001 (2014).

- [42] B. Abbott *et al.* (D0 Collaboration), Measurement of the Top Quark Mass Using Dilepton Events, *Phys. Rev. Lett.* **80**, 2063 (1998).
- [43] CMS Collaboration, Measurement of the top-quark mass in $t\bar{t}$ events with dilepton final states in pp collisions at $\sqrt{s} = 7$ TeV, *Eur. Phys. J. C* **72**, 2202 (2012).
- [44] L. Sonnenschein, Algebraic approach to solve $t\bar{t}$ dilepton equations, *Phys. Rev. D* **72**, 095020 (2005).
- [45] L. Sonnenschein, Analytical solution of $t\bar{t}$ dilepton equations, *Phys. Rev. D* **73**, 054015 (2006); **78**, 079902(E) (2008).
- [46] R. H. Dalitz and G. R. Goldstein, Decay and polarization properties of the top quark, *Phys. Rev. D* **45**, 1531 (1992).
- [47] J. D'Hondt, S. Lowette, O. L. Buchmüller, S. Cucciarelli, F.-P. Schilling, M. Spiropulu, S. Paktinat-Mehdiabadi, D. Benedetti, and L. Pape, CMS Note Report No. CMS-NOTE-2006-023, CERN, 2006.
- [48] CMS Collaboration, Measurement of the top-quark mass in all-jets $t\bar{t}$ events in pp collisions at $\sqrt{s} = 7$ TeV, *Eur. Phys. J. C* **74**, 2758 (2014).
- [49] M. Botje, J. Butterworth, A. Cooper-Sarkar, A. de Roeck, J. Feltesse, S. Forte, A. Glazov, J. Huston, R. McNulty, T. Sjöstrand, and R. S. Thorne, The PDF4LHC Working Group interim recommendations, [arXiv:1101.0538](https://arxiv.org/abs/1101.0538).
- [50] P. Z. Skands, Tuning Monte Carlo generators: The Perugia tunes, *Phys. Rev. D* **82**, 074018 (2010).
- [51] M. Bähr, S. Gieseke, M. A. Gigg, D. Grellscheid, K. Hamilton, O. Latunde-Dada, S. Plätzer, P. Richardson, M. H. Seymour, A. Sherstnev, and B. R. Webber, Herwig + physics and manual, *Eur. Phys. J. C* **58**, 639 (2008).
- [52] A. Heister *et al.* (ALEPH Collaboration), Study of the fragmentation of b quarks into B mesons at the Z peak, *Phys. Lett. B* **512**, 30 (2001).
- [53] J. Abdallah *et al.* (DELPHI Collaboration), A study of the b-quark fragmentation function with the DELPHI detector at LEP I and an averaged distribution obtained at the Z pole, *Eur. Phys. J. C* **71**, 1557 (2011).
- [54] CMS Collaboration, Measurement of the top-quark pair-production cross section and the top-quark mass in the dilepton channel at $\sqrt{s} = 7$ TeV, *J. High Energy Phys.* **07** (2011) 049.
- [55] CMS Collaboration, Measurement of the top-quark mass in $t\bar{t}$ events with lepton + jets final states in pp collisions at $\sqrt{s} = 7$ TeV, *J. High Energy Phys.* **12** (2012) 105.
- [56] CMS Collaboration, Measurement of the underlying event activity at the LHC with $\sqrt{s} = 7$ TeV and comparison with $\sqrt{s} = 0.9$ TeV, *J. High Energy Phys.* **09** (2011) 109.
- [57] T. Gleisberg, S. Höche, F. Krauss, M. Schönherr, S. Schumann, F. Siegert, and J. Winter, Event generation with SHERPA 1.1, *J. High Energy Phys.* **02** (2009) 007.
- [58] S. Hoeche, F. Krauss, S. Schumann, and F. Siegert, QCD matrix elements and truncated showers, *J. High Energy Phys.* **05** (2009) 053.
- [59] G. Corcella, I. G. Knowles, G. Marchesini, S. Moretti, K. Odagiri, P. Richardson, M. H. Seymour, and B. R. Webber, HERWIG 6: An event generator for hadron emission reactions with interfering gluons (including supersymmetric processes), *J. High Energy Phys.* **01** (2001) 010.
- [60] S. Frixione and B. R. Webber, Matching NLO QCD computations and parton shower simulations, *J. High Energy Phys.* **06** (2002) 029.
- [61] S. Frixione, P. Nason, and B. R. Webber, Matching NLO QCD and parton showers in heavy flavor production, *J. High Energy Phys.* **08** (2003) 007.
- [62] L. Lyons, D. Gibaut, and P. Clifford, How to combine correlated estimates of a single physical quantity, *Nucl. Instrum. Methods Phys. Res., Sect. A* **270**, 110 (1988).

V. Khachatryan,¹ A. M. Sirunyan,¹ A. Tumasyan,¹ W. Adam,² E. Asilar,² T. Bergauer,² J. Brandstetter,² E. Brondolin,² M. Dragicic,² J. Erö,² M. Flechl,² M. Friedl,² R. Frühwirth,^{2,a} V. M. Ghete,² C. Hartl,² N. Hörmann,² J. Hrubec,² M. Jeitler,^{2,a} V. Knünz,² A. König,² M. Krammer,^{2,a} I. Krätschmer,² D. Liko,² T. Matsushita,² I. Mikulec,² D. Rabady,^{2,b} B. Rahbaran,² H. Rohringer,² J. Schieck,^{2,a} R. Schöfbeck,² J. Strauss,² W. Treberer-Treberspurg,² W. Waltenberger,² C.-E. Wulz,^{2,a} V. Mossolov,³ N. Shumeiko,³ J. Suarez Gonzalez,³ S. Alderweireldt,⁴ T. Cornelis,⁴ E. A. De Wolf,⁴ X. Janssen,⁴ A. Knutsson,⁴ J. Lauwers,⁴ S. Luyckx,⁴ M. Van De Klundert,⁴ H. Van Havermaet,⁴ P. Van Mechelen,⁴ N. Van Remortel,⁴ A. Van Spilbeeck,⁴ S. Abu Zeid,⁵ F. Blekman,⁵ J. D'Hondt,⁵ N. Daci,⁵ I. De Bruyn,⁵ K. Deroover,⁵ N. Heracleous,⁵ J. Keaveney,⁵ S. Lowette,⁵ L. Moreels,⁵ A. Olbrechts,⁵ Q. Python,⁵ D. Strom,⁵ S. Tavernier,⁵ W. Van Doninck,⁵ P. Van Mulders,⁵ G. P. Van Onsem,⁵ I. Van Parijs,⁵ P. Barria,⁶ H. Brun,⁶ C. Caillol,⁶ B. Clerbaux,⁶ G. De Lentdecker,⁶ G. Fasanella,⁶ L. Favart,⁶ A. Grebenyuk,⁶ G. Karapostoli,⁶ T. Lenzi,⁶ A. Léonard,⁶ T. Maerschalk,⁶ A. Marinov,⁶ L. Perniè,⁶ A. Randle-conde,⁶ T. Reis,⁶ T. Seva,⁶ C. Vander Velde,⁶ P. Vanlaer,⁶ R. Yonamine,⁶ F. Zenoni,⁶ F. Zhang,^{6,c} K. Beernaert,⁷ L. Benucci,⁷ A. Cimmino,⁷ S. Crucy,⁷ D. Dobur,⁷ A. Fagot,⁷ G. Garcia,⁷ M. Gul,⁷ J. McCartin,⁷ A. A. Ocampo Rios,⁷ D. Poyraz,⁷ D. Ryckbosch,⁷ S. Salva,⁷ M. Sigamani,⁷ N. Strobbe,⁷ M. Tytgat,⁷ W. Van Driessche,⁷ E. Yazgan,⁷ N. Zaganidis,⁷ S. Basegmez,⁸ C. Beluffi,^{8,d} O. Bondu,⁸ S. Brochet,⁸ G. Bruno,⁸ A. Caudron,⁸ L. Ceard,⁸ G. G. Da Silveira,⁸ C. Delaere,⁸ D. Favart,⁸ L. Forthomme,⁸ A. Giammanco,^{8,e} J. Hollar,⁸ A. Jafari,⁸ P. Jez,⁸ M. Komm,⁸ V. Lemaître,⁸ A. Mertens,⁸ M. Musich,⁸ C. Nuttens,⁸ L. Perrini,⁸ A. Pin,⁸ K. Piotrkowski,⁸ A. Popov,^{8,f} L. Quertenmont,⁸ M. Selvaggi,⁸ M. Vidal Marono,⁸ N. Belyi,⁹ G. H. Hammad,⁹ W. L. Aldá Júnior,¹⁰ F. L. Alves,¹⁰ G. A. Alves,¹⁰ L. Brito,¹⁰ M. Correa Martins Junior,¹⁰ M. Hamer,¹⁰ C. Hensel,¹⁰ C. Mora Herrera,¹⁰ A. Moraes,¹⁰ M. E. Pol,¹⁰ P. Rebello Teles,¹⁰

E. Belchior Batista Das Chagas,¹¹ W. Carvalho,¹¹ J. Chinellato,^{11,g} A. Custódio,¹¹ E. M. Da Costa,¹¹ D. De Jesus Damiao,¹¹ C. De Oliveira Martins,¹¹ S. Fonseca De Souza,¹¹ L. M. Huertas Guativa,¹¹ H. Malbouisson,¹¹ D. Matos Figueiredo,¹¹ L. Mundim,¹¹ H. Nogima,¹¹ W. L. Prado Da Silva,¹¹ A. Santoro,¹¹ A. Sznajder,¹¹ E. J. Tonelli Manganote,^{11,g} A. Vilela Pereira,¹¹ S. Ahuja,^{12a} C. A. Bernardes,^{12b} A. De Souza Santos,^{12b} S. Dogra,^{12a} T. R. Fernandez Perez Tomei,^{12a} E. M. Gregores,^{12b} P. G. Mercadante,^{12b} C. S. Moon,^{12a,h} S. F. Novaes,^{12a} Sandra S. Padula,^{12a} D. Romero Abad,^{12a} J. C. Ruiz Vargas,^{12a} A. Aleksandrov,¹³ R. Hadjiiska,¹³ P. Iaydjiev,¹³ M. Rodozov,¹³ S. Stoykova,¹³ G. Sultanov,¹³ M. Vutova,¹³ A. Dimitrov,¹⁴ I. Glushkov,¹⁴ L. Litov,¹⁴ B. Pavlov,¹⁴ P. Petkov,¹⁴ M. Ahmad,¹⁵ J. G. Bian,¹⁵ G. M. Chen,¹⁵ H. S. Chen,¹⁵ M. Chen,¹⁵ T. Cheng,¹⁵ R. Du,¹⁵ C. H. Jiang,¹⁵ R. Plestina,^{15,i} F. Romeo,¹⁵ S. M. Shaheen,¹⁵ A. Spiezia,¹⁵ J. Tao,¹⁵ C. Wang,¹⁵ Z. Wang,¹⁵ H. Zhang,¹⁵ C. Asawatangtrakuldee,¹⁶ Y. Ban,¹⁶ Q. Li,¹⁶ S. Liu,¹⁶ Y. Mao,¹⁶ S. J. Qian,¹⁶ D. Wang,¹⁶ Z. Xu,¹⁶ C. Avila,¹⁷ A. Cabrera,¹⁷ L. F. Chaparro Sierra,¹⁷ C. Florez,¹⁷ J. P. Gomez,¹⁷ B. Gomez Moreno,¹⁷ J. C. Sanabria,¹⁷ N. Godinovic,¹⁸ D. Lelas,¹⁸ I. Puljak,¹⁸ P. M. Ribeiro Cipriano,¹⁸ Z. Antunovic,¹⁹ M. Kovac,¹⁹ V. Brigljevic,²⁰ K. Kadija,²⁰ J. Luetic,²⁰ S. Micanovic,²⁰ L. Sudic,²⁰ A. Attikis,²¹ G. Mavromanolakis,²¹ J. Mousa,²¹ C. Nicolaou,²¹ F. Ptochos,²¹ P. A. Razis,²¹ H. Rykaczewski,²¹ M. Bodlak,²² M. Finger,^{22,j} M. Finger Jr.,^{22,j} E. El-khateeb,^{23,k,k} T. Elkafrawy,^{23,k} A. Mohamed,^{23,l} Y. Mohammed,^{23,m} E. Salama,^{23,n,k} B. Calpas,²⁴ M. Kadastik,²⁴ M. Murumaa,²⁴ M. Raidal,²⁴ A. Tiko,²⁴ C. Veelken,²⁴ P. Eerola,²⁵ J. Pekkanen,²⁵ M. Voutilainen,²⁵ J. Härkönen,²⁶ V. Karimäki,²⁶ R. Kinnunen,²⁶ T. Lampén,²⁶ K. Lassila-Perini,²⁶ S. Lehti,²⁶ T. Lindén,²⁶ P. Luukka,²⁶ T. Mäenpää,²⁶ T. Peltola,²⁶ E. Tuominen,²⁶ J. Tuominiemi,²⁶ E. Tuovinen,²⁶ L. Wendland,²⁶ J. Talvitie,²⁷ T. Tuuva,²⁷ M. Besancon,²⁸ F. Couderc,²⁸ M. DeJardin,²⁸ D. Denegri,²⁸ B. Fabbro,²⁸ J. L. Faure,²⁸ C. Favaro,²⁸ F. Ferri,²⁸ S. Ganjour,²⁸ A. Givernaud,²⁸ P. Gras,²⁸ G. Hamel de Monchenault,²⁸ P. Jarry,²⁸ E. Locci,²⁸ M. Macheda,²⁸ J. Malcles,²⁸ J. Rander,²⁸ A. Rosowsky,²⁸ M. Titov,²⁸ A. Zghiche,²⁸ I. Antropov,²⁹ S. Baffioni,²⁹ F. Beaudette,²⁹ P. Busson,²⁹ L. Cadamuro,²⁹ E. Chapon,²⁹ C. Charlot,²⁹ T. Dahms,²⁹ O. Davignon,²⁹ N. Filipovic,²⁹ A. Florent,²⁹ R. Granier de Cassagnac,²⁹ S. Lisniak,²⁹ L. Mastrolorenzo,²⁹ P. Miné,²⁹ I. N. Naranjo,²⁹ M. Nguyen,²⁹ C. Ochando,²⁹ G. Ortona,²⁹ P. Paganini,²⁹ P. Pigard,²⁹ S. Regnard,²⁹ R. Salerno,²⁹ J. B. Sauvan,²⁹ Y. Sirois,²⁹ T. Strebler,²⁹ Y. Yilmaz,²⁹ A. Zabi,²⁹ J.-L. Agram,^{30,o} J. Andrea,³⁰ A. Aubin,³⁰ D. Bloch,³⁰ J.-M. Brom,³⁰ M. Buttignol,³⁰ E. C. Chabert,³⁰ N. Chanon,³⁰ C. Collard,³⁰ E. Conte,^{30,o} X. Coubez,³⁰ J.-C. Fontaine,^{30,o} D. Gelé,³⁰ U. Goerlach,³⁰ C. Goetzmann,³⁰ A.-C. Le Bihan,³⁰ J. A. Merlin,^{30,b} K. Skovpen,³⁰ P. Van Hove,³⁰ S. Gadrat,³¹ S. Beauceron,³² C. Bernet,³² G. Boudoul,³² E. Bouvier,³² C. A. Carrillo Montoya,³² R. Chierici,³² D. Contardo,³² B. Courbon,³² P. Depasse,³² H. El Mamouni,³² J. Fan,³² J. Fay,³² S. Gascon,³² M. Gouzevitch,³² B. Ille,³² F. Lagarde,³² I. B. Laktineh,³² M. Lethuillier,³² L. Mirabito,³² A. L. Pequegnot,³² S. Perries,³² J. D. Ruiz Alvarez,³² D. Sabes,³² L. Sgandurra,³² V. Sordini,³² M. Vander Donckt,³² P. Verdier,³² S. Viret,³² T. Toriashvili,^{33,p} Z. Tsalalaidze,^{34,j} C. Autermann,³⁵ S. Beranek,³⁵ M. Edelhoff,³⁵ L. Feld,³⁵ A. Heister,³⁵ M. K. Kiesel,³⁵ K. Klein,³⁵ M. Lipinski,³⁵ A. Ostapchuk,³⁵ M. Preuten,³⁵ F. Raupach,³⁵ S. Schael,³⁵ J. F. Schulte,³⁵ T. Verlage,³⁵ H. Weber,³⁵ B. Wittmer,³⁵ V. Zhukov,^{35,f} M. Ata,³⁶ M. Brodski,³⁶ E. Dietz-Laursonn,³⁶ D. Duchardt,³⁶ M. Endres,³⁶ M. Erdmann,³⁶ S. Erdweg,³⁶ T. Esch,³⁶ R. Fischer,³⁶ A. Güth,³⁶ T. Hebbeker,³⁶ C. Heidemann,³⁶ K. Hoepfner,³⁶ D. Klingebiel,³⁶ S. Knutzen,³⁶ P. Kreuzer,³⁶ M. Merschmeyer,³⁶ A. Meyer,³⁶ P. Millet,³⁶ M. Olschewski,³⁶ K. Padeken,³⁶ P. Papacz,³⁶ T. Pook,³⁶ M. Radziej,³⁶ H. Reithler,³⁶ M. Rieger,³⁶ F. Scheuch,³⁶ L. Sonnenschein,³⁶ D. Teyssier,³⁶ S. Thüer,³⁶ V. Cherepanov,³⁷ Y. Erdogan,³⁷ G. Flügge,³⁷ H. Geenen,³⁷ M. Geisler,³⁷ F. Hoehle,³⁷ B. Kargoll,³⁷ T. Kress,³⁷ Y. Kuessel,³⁷ A. Künsken,³⁷ J. Lingemann,^{37,b} A. Nehr Korn,³⁷ A. Nowack,³⁷ I. M. Nugent,³⁷ C. Pistone,³⁷ O. Pooth,³⁷ A. Stahl,³⁷ M. Aldaya Martin,³⁸ I. Asin,³⁸ N. Bartosik,³⁸ O. Behnke,³⁸ U. Behrens,³⁸ A. J. Bell,³⁸ K. Borras,^{38,q} A. Burgmeier,³⁸ A. Campbell,³⁸ S. Choudhury,^{38,r} F. Costanza,³⁸ C. Diez Pardos,³⁸ G. Dolinska,³⁸ S. Dooling,³⁸ T. Dorland,³⁸ G. Eckerlin,³⁸ D. Eckstein,³⁸ T. Eichhorn,³⁸ G. Flucke,³⁸ E. Gallo,^{38,s} J. Garay Garcia,³⁸ A. Geiser,³⁸ A. Gishko,³⁸ P. Gunnellini,³⁸ J. Hauk,³⁸ M. Hempel,^{38,t} H. Jung,³⁸ A. Kalogeropoulos,³⁸ O. Karacheban,^{38,t} M. Kasemann,³⁸ P. Katsas,³⁸ J. Kieseler,³⁸ C. Kleinwort,³⁸ I. Korol,³⁸ W. Lange,³⁸ J. Leonard,³⁸ K. Lipka,³⁸ A. Lobanov,³⁸ W. Lohmann,^{38,t} R. Mankel,³⁸ I. Marfin,^{38,t} I.-A. Melzer-Pellmann,³⁸ A. B. Meyer,³⁸ G. Mittag,³⁸ J. Mnich,³⁸ A. Mussgiller,³⁸ S. Naumann-Emme,³⁸ A. Nayak,³⁸ E. Ntomari,³⁸ H. Perrey,³⁸ D. Pitzl,³⁸ R. Placakyte,³⁸ A. Raspereza,³⁸ B. Roland,³⁸ M. Ö. Sahin,³⁸ P. Saxena,³⁸ T. Schoerner-Sadenius,³⁸ M. Schröder,³⁸ C. Seitz,³⁸ S. Spannagel,³⁸ K. D. Trippkewitz,³⁸ R. Walsh,³⁸ C. Wissing,³⁸ V. Blobel,³⁹ M. Centis Vignali,³⁹ A. R. Draeger,³⁹ J. Erfle,³⁹ E. Garutti,³⁹ K. Goebel,³⁹ D. Gonzalez,³⁹ M. Görner,³⁹ J. Haller,³⁹ M. Hoffmann,³⁹ R. S. Höing,³⁹ A. Junkes,³⁹ R. Klanner,³⁹ R. Kogler,³⁹ N. Kovalchuk,³⁹ T. Lapsien,³⁹ T. Lenz,³⁹ I. Marchesini,³⁹ D. Marconi,³⁹ M. Meyer,³⁹ D. Nowatschin,³⁹ J. Ott,³⁹ F. Pantaleo,^{39,b} T. Peiffer,³⁹ A. Perieanu,³⁹ N. Pietsch,³⁹ J. Poehlsen,³⁹ D. Rathjens,³⁹ C. Sander,³⁹ C. Scharf,³⁹ H. Schettler,³⁹ P. Schlexer,³⁹ E. Schlieckau,³⁹

A. Schmidt,³⁹ J. Schwandt,³⁹ V. Sola,³⁹ H. Stadie,³⁹ G. Steinbrück,³⁹ H. Tholen,³⁹ D. Troendle,³⁹ E. Usai,³⁹ L. Vanelderren,³⁹ A. Vanhoefer,³⁹ B. Vormwald,³⁹ M. Akbiyik,⁴⁰ C. Barth,⁴⁰ C. Baus,⁴⁰ J. Berger,⁴⁰ C. Böser,⁴⁰ E. Butz,⁴⁰ T. Chwalek,⁴⁰ F. Colombo,⁴⁰ W. De Boer,⁴⁰ A. Descroix,⁴⁰ A. Dierlamm,⁴⁰ S. Fink,⁴⁰ F. Frensch,⁴⁰ R. Friese,⁴⁰ M. Giffels,⁴⁰ A. Gilbert,⁴⁰ D. Haitz,⁴⁰ F. Hartmann,^{40,b} S. M. Heindl,⁴⁰ U. Husemann,⁴⁰ I. Katkov,^{40,f} A. Kornmayer,^{40,b} P. Lobelle Pardo,⁴⁰ B. Maier,⁴⁰ H. Mildner,⁴⁰ M. U. Mozer,⁴⁰ T. Müller,⁴⁰ Th. Müller,⁴⁰ M. Plagge,⁴⁰ G. Quast,⁴⁰ K. Rabbertz,⁴⁰ S. Röcker,⁴⁰ F. Roscher,⁴⁰ G. Sieber,⁴⁰ H. J. Simonis,⁴⁰ F. M. Stober,⁴⁰ R. Ulrich,⁴⁰ J. Wagner-Kuhr,⁴⁰ S. Wayand,⁴⁰ M. Weber,⁴⁰ T. Weiler,⁴⁰ C. Wöhrmann,⁴⁰ R. Wolf,⁴⁰ G. Anagnostou,⁴¹ G. Daskalakis,⁴¹ T. Geralis,⁴¹ V. A. Giakoumopoulou,⁴¹ A. Kyriakis,⁴¹ D. Loukas,⁴¹ A. Psallidas,⁴¹ I. Topsis-Giotis,⁴¹ A. Agapitos,⁴² S. Kesisisoglou,⁴² A. Panagiotou,⁴² N. Saoulidou,⁴² E. Tziaferi,⁴² I. Evangelou,⁴³ G. Flouris,⁴³ C. Foudas,⁴³ P. Kokkas,⁴³ N. Loukas,⁴³ N. Manthos,⁴³ I. Papadopoulos,⁴³ E. Paradas,⁴³ J. Strolagos,⁴³ G. Bencze,⁴⁴ C. Hajdu,⁴⁴ A. Hazi,⁴⁴ P. Hidas,⁴⁴ D. Horvath,^{44,u} F. Sikler,⁴⁴ V. Veszpremi,⁴⁴ G. Vesztergombi,^{44,v} A. J. Zsigmond,⁴⁴ N. Beni,⁴⁵ S. Czellar,⁴⁵ J. Karancsi,^{45,w} J. Molnar,⁴⁵ Z. Szillasi,⁴⁵ M. Bartók,^{46,x} A. Makovec,⁴⁶ P. Raics,⁴⁶ Z. L. Trocsanyi,⁴⁶ B. Ujvari,⁴⁶ P. Mal,⁴⁷ K. Mandal,⁴⁷ D. K. Sahoo,⁴⁷ N. Sahoo,⁴⁷ S. K. Swain,⁴⁷ S. Bansal,⁴⁸ S. B. Beri,⁴⁸ V. Bhatnagar,⁴⁸ R. Chawla,⁴⁸ R. Gupta,⁴⁸ U. Bhawandeep,⁴⁸ A. K. Kalsi,⁴⁸ A. Kaur,⁴⁸ M. Kaur,⁴⁸ R. Kumar,⁴⁸ A. Mehta,⁴⁸ M. Mittal,⁴⁸ J. B. Singh,⁴⁸ G. Walia,⁴⁸ Ashok Kumar,⁴⁹ A. Bhardwaj,⁴⁹ B. C. Choudhary,⁴⁹ R. B. Garg,⁴⁹ A. Kumar,⁴⁹ S. Malhotra,⁴⁹ M. Naimuddin,⁴⁹ N. Nishu,⁴⁹ K. Ranjan,⁴⁹ R. Sharma,⁴⁹ V. Sharma,⁴⁹ S. Bhattacharya,⁵⁰ K. Chatterjee,⁵⁰ S. Dey,⁵⁰ S. Dutta,⁵⁰ Sa. Jain,⁵⁰ N. Majumdar,⁵⁰ A. Modak,⁵⁰ K. Mondal,⁵⁰ S. Mukherjee,⁵⁰ S. Mukhopadhyay,⁵⁰ A. Roy,⁵⁰ D. Roy,⁵⁰ S. Roy Chowdhury,⁵⁰ S. Sarkar,⁵⁰ M. Sharan,⁵⁰ A. Abdulsalam,⁵¹ R. Chudasama,⁵¹ D. Dutta,⁵¹ V. Jha,⁵¹ V. Kumar,⁵¹ A. K. Mohanty,^{51,b} L. M. Pant,⁵¹ P. Shukla,⁵¹ A. Topkar,⁵¹ T. Aziz,⁵² S. Banerjee,⁵² S. Bhowmik,^{52,y} R. M. Chatterjee,⁵² R. K. Dewanjee,⁵² S. Dugad,⁵² S. Ganguly,⁵² S. Ghosh,⁵² M. Guchait,⁵² A. Gurtu,^{52,z} G. Kole,⁵² S. Kumar,⁵² B. Mahakud,⁵² M. Maity,^{52,y} G. Majumder,⁵² K. Mazumdar,⁵² S. Mitra,⁵² G. B. Mohanty,⁵² B. Parida,⁵² T. Sarkar,^{52,y} N. Sur,⁵² B. Sutar,⁵² N. Wickramage,^{52,aa} S. Chauhan,⁵³ S. Dube,⁵³ K. Kothekar,⁵³ S. Sharma,⁵³ H. Bakhshiansohi,⁵⁴ H. Behnamian,⁵⁴ S. M. Etesami,^{54,bb} A. Fahim,^{54,cc} R. Goldouzian,⁵⁴ M. Khakzad,⁵⁴ M. Mohammadi Najafabadi,⁵⁴ M. Naseri,⁵⁴ S. Paktinat Mehdiabadi,⁵⁴ F. Rezaei Hosseinabadi,⁵⁴ B. Safarzadeh,^{54,dd} M. Zeinali,⁵⁴ M. Felcini,⁵⁵ M. Grunewald,⁵⁵ M. Abbrescia,^{56a,56b} C. Calabria,^{56a,56b} C. Caputo,^{56a,56b} A. Colaleo,^{56a} D. Creanza,^{56a,56c} L. Cristella,^{56a,56b} N. De Filippis,^{56a,56c} M. De Palma,^{56a,56b} L. Fiore,^{56a} G. Iaselli,^{56a,56c} G. Maggi,^{56a,56c} M. Maggi,^{56a} G. Miniello,^{56a,56b} S. My,^{56a,56c} S. Nuzzo,^{56a,56b} A. Pompili,^{56a,56b} G. Pugliese,^{56a,56c} R. Radogna,^{56a,56b} A. Ranieri,^{56a} G. Selvaggi,^{56a,56b} L. Silvestris,^{56a,b} R. Venditti,^{56a,56b} P. Verwilligen,^{56a} G. Abbiendi,^{57a} C. Battilana,^{57a,b} A. C. Benvenuti,^{57a} D. Bonacorsi,^{57a,57b} S. Braibant-Giacomelli,^{57a,57b} L. Brigliadori,^{57a,57b} R. Campanini,^{57a,57b} P. Capiluppi,^{57a,57b} A. Castro,^{57a,57b} F. R. Cavallo,^{57a} S. S. Chhibra,^{57a,57b} G. Codispoti,^{57a,57b} M. Cuffiani,^{57a,57b} G. M. Dallavalle,^{57a} F. Fabbri,^{57a} A. Fanfani,^{57a,57b} D. Fasanella,^{57a,57b} P. Giacomelli,^{57a} C. Grandi,^{57a} L. Guiducci,^{57a,57b} S. Marcellini,^{57a} G. Masetti,^{57a} A. Montanari,^{57a} F. L. Navarria,^{57a,57b} A. Perrotta,^{57a} A. M. Rossi,^{57a,57b} T. Rovelli,^{57a,57b} G. P. Siroli,^{57a,57b} N. Tosi,^{57a,57b} R. Travaglini,^{57a,57b} G. Cappello,^{58a} M. Chiorboli,^{58a,58b} S. Costa,^{58a,58b} A. Di Mattia,^{58a} F. Giordano,^{58a,58b} R. Potenza,^{58a,58b} A. Tricomi,^{58a,58b} C. Tuve,^{58a,58b} G. Barbagli,^{59a} V. Ciulli,^{59a,59b} C. Civinini,^{59a} R. D'Alessandro,^{59a,59b} E. Focardi,^{59a,59b} S. Gonzi,^{59a,59b} V. Gori,^{59a,59b} P. Lenzi,^{59a,59b} M. Meschini,^{59a} S. Paoletti,^{59a} G. Sguazzoni,^{59a} A. Tropiano,^{59a,59b} L. Viliani,^{59a,59b,b} L. Benussi,⁶⁰ S. Bianco,⁶⁰ F. Fabbri,⁶⁰ D. Piccolo,⁶⁰ F. Primavera,⁶⁰ V. Calvelli,^{61a,61b} F. Ferro,^{61a} M. Lo Vetere,^{61a,61b} M. R. Monge,^{61a,61b} E. Robutti,^{61a} S. Tosi,^{61a,61b} L. Brianza,^{62a} M. E. Dinardo,^{62a,62b} S. Fiorendi,^{62a,62b} S. Gennai,^{62a} R. Gerosa,^{62a,62b} A. Ghezzi,^{62a,62b} P. Govoni,^{62a,62b} S. Malvezzi,^{62a} R. A. Manzoni,^{62a,62b} B. Marzocchi,^{62a,62b,b} D. Menasce,^{62a} L. Moroni,^{62a} M. Paganoni,^{62a,62b} D. Pedrini,^{62a} S. Ragazzi,^{62a,62b} N. Redaelli,^{62a} T. Tabarelli de Fatis,^{62a,62b} S. Buontempo,^{63a} N. Cavallo,^{63a,63c} S. Di Guida,^{63a,63d,b} M. Esposito,^{63a,63b} F. Fabozzi,^{63a,63c} A. O. M. Iorio,^{63a,63b} G. Lanza,^{63a} L. Lista,^{63a} S. Meola,^{63a,63d,b} M. Merola,^{63a} P. Paolucci,^{63a,b} C. Sciacca,^{63a,63b} F. Thyssen,^{63a} P. Azzi,^{64a,b} N. Bacchetta,^{64a} L. Benato,^{64a,64b} D. Bisello,^{64a,64b} A. Boletti,^{64a,64b} A. Branca,^{64a,64b} R. Carlin,^{64a,64b} P. Checchia,^{64a} M. Dall'Osso,^{64a,64b,b} T. Dorigo,^{64a} U. Dosselli,^{64a} F. Gasparini,^{64a,64b} U. Gasparini,^{64a,64b} A. Gozzelino,^{64a} M. Gulmini,^{64a,ee} K. Kanishchev,^{64a,64c} S. Lacaprara,^{64a} M. Margoni,^{64a,64b} A. T. Meneguzzo,^{64a,64b} J. Pazzini,^{64a,64b} N. Pozzobon,^{64a,64b} P. Ronchese,^{64a,64b} F. Simonetto,^{64a,64b} E. Torassa,^{64a} M. Tosi,^{64a,64b} M. Zanetti,^{64a} P. Zotto,^{64a,64b} A. Zucchetta,^{64a,64b,b} G. Zumerle,^{64a,64b} A. Braghieri,^{65a} A. Magnani,^{65a} P. Montagna,^{65a,65b} S. P. Ratti,^{65a,65b} V. Re,^{65a} C. Riccardi,^{65a,65b} P. Salvini,^{65a} I. Vai,^{65a} P. Vitulo,^{65a,65b} L. Alunni Solestizi,^{66a,66b} M. Biasini,^{66a,66b} G. M. Bilei,^{66a} D. Cianggottini,^{66a,66b,b} L. Fanò,^{66a,66b} P. Lariccia,^{66a,66b} G. Mantovani,^{66a,66b} M. Menichelli,^{66a} A. Saha,^{66a} A. Santocchia,^{66a,66b} K. Androsov,^{67a,ff} P. Azzurri,^{67a} G. Bagliesi,^{67a} J. Bernardini,^{67a} T. Boccali,^{67a} R. Castaldi,^{67a} M. A. Ciocci,^{67a,ff} R. Dell'Orso,^{67a} S. Donato,^{67a,67c,b} G. Fedi,^{67a} L. Foà,^{67a,67c†}

A. Giassi,^{67a} M. T. Grippo,^{67a,ff} F. Ligabue,^{67a,67c} T. Lomtadze,^{67a} L. Martini,^{67a,67b} A. Messineo,^{67a,67b} F. Palla,^{67a}
A. Rizzi,^{67a,67b} A. Savoy-Navarro,^{67a,gg} A. T. Serban,^{67a} P. Spagnolo,^{67a} R. Tenchini,^{67a} G. Tonelli,^{67a,67b} A. Venturi,^{67a}
P. G. Verdini,^{67a} L. Barone,^{68a,68b} F. Cavallari,^{68a} G. D'imperio,^{68a,68b,b} D. Del Re,^{68a,68b} M. Diemoz,^{68a} S. Gelli,^{68a,68b}
C. Jorda,^{68a} E. Longo,^{68a,68b} F. Margaroli,^{68a,68b} P. Meridiani,^{68a} G. Organtini,^{68a,68b} R. Paramatti,^{68a} F. Priato,^{68a,68b}
S. Rahatlou,^{68a,68b} C. Rovelli,^{68a} F. Santanastasio,^{68a,68b} P. Traczyk,^{68a,68b,b} N. Amapane,^{69a,69b} R. Arcidiacono,^{69a,69c,b}
S. Argiro,^{69a,69b} M. Arneodo,^{69a,69c} R. Bellan,^{69a,69b} C. Biino,^{69a} N. Cartiglia,^{69a} M. Costa,^{69a,69b} R. Covarelli,^{69a,69b}
A. Degano,^{69a,69b} N. Demaria,^{69a} L. Finco,^{69a,69b,b} B. Kiani,^{69a,69b} C. Mariotti,^{69a} S. Maselli,^{69a} E. Migliore,^{69a,69b}
V. Monaco,^{69a,69b} E. Monteil,^{69a,69b} M. M. Obertino,^{69a,69b} L. Pacher,^{69a,69b} N. Pastrone,^{69a} M. Pelliccioni,^{69a}
G. L. Pinna Angioni,^{69a,69b} F. Ravera,^{69a,69b} A. Romero,^{69a,69b} M. Ruspa,^{69a,69c} R. Sacchi,^{69a,69b} A. Solano,^{69a,69b}
A. Staiano,^{69a} U. Tamponi,^{69a} S. Belforte,^{70a} V. Candelise,^{70a,70b,b} M. Casarsa,^{70a} F. Cossutti,^{70a} G. Della Ricca,^{70a,70b}
B. Gobbo,^{70a} C. La Licata,^{70a,70b} M. Marone,^{70a,70b} A. Schizzi,^{70a,70b} A. Zanetti,^{70a} A. Kropivnitskaya,⁷¹ S. K. Nam,⁷¹
D. H. Kim,⁷² G. N. Kim,⁷² M. S. Kim,⁷² D. J. Kong,⁷² S. Lee,⁷² Y. D. Oh,⁷² A. Sakharov,⁷² D. C. Son,⁷²
J. A. Brochero Cifuentes,⁷³ H. Kim,⁷³ T. J. Kim,⁷³ S. Song,⁷⁴ S. Choi,⁷⁵ Y. Go,⁷⁵ D. Gyun,⁷⁵ B. Hong,⁷⁵ M. Jo,⁷⁵ H. Kim,⁷⁵
Y. Kim,⁷⁵ B. Lee,⁷⁵ K. Lee,⁷⁵ K. S. Lee,⁷⁵ S. Lee,⁷⁵ S. K. Park,⁷⁵ Y. Roh,⁷⁵ H. D. Yoo,⁷⁶ M. Choi,⁷⁷ H. Kim,⁷⁷ J. H. Kim,⁷⁷
J. S. H. Lee,⁷⁷ I. C. Park,⁷⁷ G. Ryu,⁷⁷ M. S. Ryu,⁷⁷ Y. Choi,⁷⁸ J. Goh,⁷⁸ D. Kim,⁷⁸ E. Kwon,⁷⁸ J. Lee,⁷⁸ I. Yu,⁷⁸ V. Dudenias,⁷⁹
A. Juodagalvis,⁷⁹ J. Vaitkus,⁷⁹ I. Ahmed,⁸⁰ Z. A. Ibrahim,⁸⁰ J. R. Komaragiri,⁸⁰ M. A. B. Md Ali,^{80,hh} F. Mohamad Idris,^{80,ii}
W. A. T. Wan Abdullah,⁸⁰ M. N. Yusli,⁸⁰ E. Casimiro Linares,⁸¹ H. Castilla-Valdez,⁸¹ E. De La Cruz-Burelo,⁸¹
I. Heredia-De La Cruz,^{81,jj} A. Hernandez-Almada,⁸¹ R. Lopez-Fernandez,⁸¹ A. Sanchez-Hernandez,⁸¹ S. Carrillo Moreno,⁸²
F. Vazquez Valencia,⁸² I. Pedraza,⁸³ H. A. Salazar Ibarguen,⁸³ A. Morelos Pineda,⁸⁴ D. Krofcheck,⁸⁵ P. H. Butler,⁸⁶
A. Ahmad,⁸⁷ M. Ahmad,⁸⁷ Q. Hassan,⁸⁷ H. R. Hoorani,⁸⁷ W. A. Khan,⁸⁷ T. Khurshid,⁸⁷ M. Shoaib,⁸⁷ H. Bialkowska,⁸⁸
M. Bluj,⁸⁸ B. Boimska,⁸⁸ T. Frueboes,⁸⁸ M. Górski,⁸⁸ M. Kazana,⁸⁸ K. Nawrocki,⁸⁸ K. Romanowska-Rybinska,⁸⁸
M. Szleper,⁸⁸ P. Zalewski,⁸⁸ G. Brona,⁸⁹ K. Bunkowski,⁸⁹ A. Byszuk,^{89,kk} K. Doroba,⁸⁹ A. Kalinowski,⁸⁹ M. Konecki,⁸⁹
J. Krolikowski,⁸⁹ M. Misiura,⁸⁹ M. Olszewski,⁸⁹ M. Walczak,⁸⁹ P. Bargassa,⁹⁰ C. Beirão Da Cruz E Silva,⁹⁰
A. Di Francesco,⁹⁰ P. Faccioli,⁹⁰ P. G. Ferreira Parracho,⁹⁰ M. Gallinaro,⁹⁰ N. Leonardo,⁹⁰ L. Lloret Iglesias,⁹⁰ F. Nguyen,⁹⁰
J. Rodrigues Antunes,⁹⁰ J. Seixas,⁹⁰ O. Toldaiev,⁹⁰ D. Vadrucio,⁹⁰ J. Varela,⁹⁰ P. Vischia,⁹⁰ S. Afanasiev,⁹¹ P. Bunin,⁹¹
M. Gavrilenko,⁹¹ I. Golutvin,⁹¹ I. Gorbunov,⁹¹ A. Kamenev,⁹¹ V. Karjavin,⁹¹ V. Konoplyanikov,⁹¹ A. Lanev,⁹¹
A. Malakhov,⁹¹ V. Matveev,^{91,ll,mmm} P. Moiseenz,⁹¹ V. Palichik,⁹¹ V. Perelygin,⁹¹ S. Shmatov,⁹¹ S. Shulha,⁹¹ N. Skatchkov,⁹¹
V. Smirnov,⁹¹ A. Zarubin,⁹¹ V. Golovtsov,⁹² Y. Ivanov,⁹² V. Kim,^{92,nn} E. Kuznetsova,⁹² P. Levchenko,⁹² V. Murzin,⁹²
V. Oreshkin,⁹² I. Smirnov,⁹² V. Sulimov,⁹² L. Uvarov,⁹² S. Vavilov,⁹² A. Vorobyev,⁹² Yu. Andreev,⁹³ A. Dermenev,⁹³
S. Gninenko,⁹³ N. Golubev,⁹³ A. Karneyev,⁹³ M. Kirsanov,⁹³ N. Krasnikov,⁹³ A. Pashenkov,⁹³ D. Tlisov,⁹³ A. Toropin,⁹³
V. Epshteyn,⁹⁴ V. Gavrilov,⁹⁴ N. Lychkovskaya,⁹⁴ V. Popov,⁹⁴ I. Pozdnyakov,⁹⁴ G. Safronov,⁹⁴ A. Spiridonov,⁹⁴ E. Vlasov,⁹⁴
A. Zhokin,⁹⁴ A. Bylinkin,⁹⁵ V. Andreev,⁹⁶ M. Azarkin,^{96,mmm} I. Dremin,^{96,mmm} M. Kirakosyan,⁹⁶ A. Leonidov,^{96,mmm}
G. Mesyats,⁹⁶ S. V. Rusakov,⁹⁶ A. Baskakov,⁹⁷ A. Belyaev,⁹⁷ E. Boos,⁹⁷ V. Bunichev,⁹⁷ M. Dubinin,^{97,oo} L. Dudko,⁹⁷
V. Klyukhin,⁹⁷ O. Kodolova,⁹⁷ N. Korneeva,⁹⁷ I. Lokhtin,⁹⁷ I. Myagkov,⁹⁷ S. Obraztsov,⁹⁷ M. Perfilov,⁹⁷ S. Petrushanko,⁹⁷
V. Savrin,⁹⁷ I. Azhgirey,⁹⁸ I. Bayshev,⁹⁸ S. Bitioukov,⁹⁸ V. Kachanov,⁹⁸ A. Kalinin,⁹⁸ D. Konstantinov,⁹⁸ V. Krychkin,⁹⁸
V. Petrov,⁹⁸ R. Ryutin,⁹⁸ A. Sobol,⁹⁸ L. Tourchanovitch,⁹⁸ S. Troshin,⁹⁸ N. Tyurin,⁹⁸ A. Uzunian,⁹⁸ A. Volkov,⁹⁸
P. Adzic,^{99,pp} J. Milosevic,⁹⁹ V. Rekovic,⁹⁹ J. Alcaraz Maestre,¹⁰⁰ E. Calvo,¹⁰⁰ M. Cerrada,¹⁰⁰ M. Chamizo Llatas,¹⁰⁰
N. Colino,¹⁰⁰ B. De La Cruz,¹⁰⁰ A. Delgado Peris,¹⁰⁰ D. Domínguez Vázquez,¹⁰⁰ A. Escalante Del Valle,¹⁰⁰
C. Fernandez Bedoya,¹⁰⁰ J. P. Fernández Ramos,¹⁰⁰ J. Flix,¹⁰⁰ M. C. Fouz,¹⁰⁰ P. Garcia-Abia,¹⁰⁰ O. Gonzalez Lopez,¹⁰⁰
S. Goy Lopez,¹⁰⁰ J. M. Hernandez,¹⁰⁰ M. I. Josa,¹⁰⁰ E. Navarro De Martino,¹⁰⁰ A. Pérez-Calero Yzquierdo,¹⁰⁰
J. Puerta Pelayo,¹⁰⁰ A. Quintario Olmeda,¹⁰⁰ I. Redondo,¹⁰⁰ L. Romero,¹⁰⁰ J. Santaolalla,¹⁰⁰ M. S. Soares,¹⁰⁰ C. Albajar,¹⁰¹
J. F. de Trocóniz,¹⁰¹ M. Missiroli,¹⁰¹ D. Moran,¹⁰¹ J. Cuevas,¹⁰² J. Fernandez Menendez,¹⁰² S. Folgueras,¹⁰²
I. Gonzalez Caballero,¹⁰² E. Palencia Cortezon,¹⁰² J. M. Vizán Garcia,¹⁰² I. J. Cabrillo,¹⁰³ A. Calderon,¹⁰³
J. R. Castiñeiras De Saa,¹⁰³ P. De Castro Manzano,¹⁰³ J. Duarte Campderros,¹⁰³ M. Fernandez,¹⁰³ J. Garcia-Ferrero,¹⁰³
G. Gomez,¹⁰³ A. Lopez Virto,¹⁰³ J. Marco,¹⁰³ R. Marco,¹⁰³ C. Martinez Rivero,¹⁰³ F. Matorras,¹⁰³ F. J. Munoz Sanchez,¹⁰³
J. Piedra Gomez,¹⁰³ T. Rodrigo,¹⁰³ A. Y. Rodríguez-Marrero,¹⁰³ A. Ruiz-Jimeno,¹⁰³ L. Scodellaro,¹⁰³ N. Trevisani,¹⁰³
I. Vila,¹⁰³ R. Vilar Cortabitarte,¹⁰³ D. Abbaneo,¹⁰⁴ E. Auffray,¹⁰⁴ G. Auzinger,¹⁰⁴ M. Bachtis,¹⁰⁴ P. Baillon,¹⁰⁴ A. H. Ball,¹⁰⁴
D. Barney,¹⁰⁴ A. Benaglia,¹⁰⁴ J. Bendavid,¹⁰⁴ L. Benhabib,¹⁰⁴ J. F. Benitez,¹⁰⁴ G. M. Berruti,¹⁰⁴ P. Bloch,¹⁰⁴ A. Bocci,¹⁰⁴
A. Bonato,¹⁰⁴ C. Botta,¹⁰⁴ H. Breuker,¹⁰⁴ T. Camporesi,¹⁰⁴ R. Castello,¹⁰⁴ G. Cerminara,¹⁰⁴ M. D'Alfonso,¹⁰⁴

D. d'Enterria,¹⁰⁴ A. Dabrowski,¹⁰⁴ V. Daponte,¹⁰⁴ A. David,¹⁰⁴ M. De Gruttola,¹⁰⁴ F. De Guio,¹⁰⁴ A. De Roeck,¹⁰⁴ S. De Visscher,¹⁰⁴ E. Di Marco,¹⁰⁴ M. Dobson,¹⁰⁴ M. Dordevic,¹⁰⁴ B. Dorney,¹⁰⁴ T. du Pree,¹⁰⁴ M. Dünser,¹⁰⁴ N. Dupont,¹⁰⁴ A. Elliott-Peisert,¹⁰⁴ G. Franzoni,¹⁰⁴ W. Funk,¹⁰⁴ D. Gigi,¹⁰⁴ K. Gill,¹⁰⁴ D. Giordano,¹⁰⁴ M. Girone,¹⁰⁴ F. Glege,¹⁰⁴ R. Guida,¹⁰⁴ S. Gundacker,¹⁰⁴ M. Guthoff,¹⁰⁴ J. Hammer,¹⁰⁴ P. Harris,¹⁰⁴ J. Hegeman,¹⁰⁴ V. Innocente,¹⁰⁴ P. Janot,¹⁰⁴ H. Kirschenmann,¹⁰⁴ M. J. Kortelainen,¹⁰⁴ K. Kousouris,¹⁰⁴ K. Krajczar,¹⁰⁴ P. Lecoq,¹⁰⁴ C. Lourenço,¹⁰⁴ M. T. Lucchini,¹⁰⁴ N. Magini,¹⁰⁴ L. Malgeri,¹⁰⁴ M. Mannelli,¹⁰⁴ A. Martelli,¹⁰⁴ L. Masetti,¹⁰⁴ F. Meijers,¹⁰⁴ S. Mersi,¹⁰⁴ E. Meschi,¹⁰⁴ F. Moortgat,¹⁰⁴ S. Morovic,¹⁰⁴ M. Mulders,¹⁰⁴ M. V. Nemallapudi,¹⁰⁴ H. Neugebauer,¹⁰⁴ S. Orfanelli,^{104,qq} L. Orsini,¹⁰⁴ L. Pape,¹⁰⁴ E. Perez,¹⁰⁴ M. Peruzzi,¹⁰⁴ A. Petrilli,¹⁰⁴ G. Petrucciani,¹⁰⁴ A. Pfeiffer,¹⁰⁴ D. Piparo,¹⁰⁴ A. Racz,¹⁰⁴ G. Rolandi,^{104,rr} M. Rovere,¹⁰⁴ M. Ruan,¹⁰⁴ H. Sakulin,¹⁰⁴ C. Schäfer,¹⁰⁴ C. Schwick,¹⁰⁴ M. Seidel,¹⁰⁴ A. Sharma,¹⁰⁴ P. Silva,¹⁰⁴ M. Simon,¹⁰⁴ P. Sphicas,^{104,ss} J. Steggemann,¹⁰⁴ B. Stieger,¹⁰⁴ M. Stoye,¹⁰⁴ Y. Takahashi,¹⁰⁴ D. Treille,¹⁰⁴ A. Triossi,¹⁰⁴ A. Tsirou,¹⁰⁴ G. I. Veres,^{104,v} N. Wardle,¹⁰⁴ H. K. Wöhri,¹⁰⁴ A. Zagodzinska,^{104,kk} W. D. Zeuner,¹⁰⁴ W. Bertl,¹⁰⁵ K. Deiters,¹⁰⁵ W. Erdmann,¹⁰⁵ R. Horisberger,¹⁰⁵ Q. Ingram,¹⁰⁵ H. C. Kaestli,¹⁰⁵ D. Kotlinski,¹⁰⁵ U. Langenegger,¹⁰⁵ D. Renker,¹⁰⁵ T. Rohe,¹⁰⁵ F. Bachmair,¹⁰⁶ L. Bäni,¹⁰⁶ L. Bianchini,¹⁰⁶ B. Casal,¹⁰⁶ G. Dissertori,¹⁰⁶ M. Dittmar,¹⁰⁶ M. Donegà,¹⁰⁶ P. Eller,¹⁰⁶ C. Grab,¹⁰⁶ C. Heidegger,¹⁰⁶ D. Hits,¹⁰⁶ J. Hoss,¹⁰⁶ G. Kasieczka,¹⁰⁶ W. Lustermann,¹⁰⁶ B. Mangano,¹⁰⁶ M. Marionneau,¹⁰⁶ P. Martinez Ruiz del Arbol,¹⁰⁶ M. Masciovecchio,¹⁰⁶ D. Meister,¹⁰⁶ F. Micheli,¹⁰⁶ P. Musella,¹⁰⁶ F. Nessi-Tedaldi,¹⁰⁶ F. Pandolfi,¹⁰⁶ J. Pata,¹⁰⁶ F. Pauss,¹⁰⁶ L. Perrozzi,¹⁰⁶ M. Quittnat,¹⁰⁶ M. Rossini,¹⁰⁶ A. Starodumov,^{106,tt} M. Takahashi,¹⁰⁶ V. R. Tavolaro,¹⁰⁶ K. Theofilatos,¹⁰⁶ R. Wallny,¹⁰⁶ T. K. Aarrestad,¹⁰⁷ C. Amsler,^{107,uu} L. Caminada,¹⁰⁷ M. F. Canelli,¹⁰⁷ V. Chiochia,¹⁰⁷ A. De Cosa,¹⁰⁷ C. Galloni,¹⁰⁷ A. Hinzmann,¹⁰⁷ T. Hreus,¹⁰⁷ B. Kilminster,¹⁰⁷ C. Lange,¹⁰⁷ J. Ngadiuba,¹⁰⁷ D. Pinna,¹⁰⁷ P. Robmann,¹⁰⁷ F. J. Ronga,¹⁰⁷ D. Salerno,¹⁰⁷ Y. Yang,¹⁰⁷ M. Cardaci,¹⁰⁸ K. H. Chen,¹⁰⁸ T. H. Doan,¹⁰⁸ Sh. Jain,¹⁰⁸ R. Khurana,¹⁰⁸ M. Konyushikhin,¹⁰⁸ C. M. Kuo,¹⁰⁸ W. Lin,¹⁰⁸ Y. J. Lu,¹⁰⁸ S. S. Yu,¹⁰⁸ Arun Kumar,¹⁰⁹ R. Bartek,¹⁰⁹ P. Chang,¹⁰⁹ Y. H. Chang,¹⁰⁹ Y. W. Chang,¹⁰⁹ Y. Chao,¹⁰⁹ K. F. Chen,¹⁰⁹ P. H. Chen,¹⁰⁹ C. Dietz,¹⁰⁹ F. Fiori,¹⁰⁹ U. Grundler,¹⁰⁹ W.-S. Hou,¹⁰⁹ Y. Hsiung,¹⁰⁹ Y. F. Liu,¹⁰⁹ R.-S. Lu,¹⁰⁹ M. Miñano Moya,¹⁰⁹ E. Petrakou,¹⁰⁹ J. f. Tsai,¹⁰⁹ Y. M. Tzeng,¹⁰⁹ B. Asavapibhop,¹¹⁰ K. Kovitanggoon,¹¹⁰ G. Singh,¹¹⁰ N. Srimanobhas,¹¹⁰ N. Suwonjandee,¹¹⁰ A. Adiguzel,¹¹¹ S. Cerci,^{111,vv} Z. S. Demiroglu,¹¹¹ C. Dozen,¹¹¹ I. Dumanoglu,¹¹¹ S. Girgis,¹¹¹ G. Gokbulut,¹¹¹ Y. Guler,¹¹¹ E. Gurpinar,¹¹¹ I. Hos,¹¹¹ E. E. Kangal,^{111,ww} A. Kayis Topaksu,¹¹¹ G. Onengut,^{111,xx} K. Ozdemir,^{111,yy} S. Ozturk,^{111,zz} B. Tali,^{111,vv} H. Topakli,^{111,zz} M. Vergili,¹¹¹ C. Zorbilmez,¹¹¹ I. V. Akin,¹¹² B. Bilin,¹¹² S. Bilmis,¹¹² B. Isildak,^{112,aaa} G. Karapinar,^{112,bbb} M. Yalvac,¹¹² M. Zeyrek,¹¹² E. Gülmez,¹¹³ M. Kaya,^{113,ccc} O. Kaya,^{113,ddd} E. A. Yetkin,^{113,eee} T. Yetkin,^{113,fff} A. Cakir,¹¹⁴ K. Cankocak,¹¹⁴ S. Sen,^{114,ggg} F. I. Vardarli,¹¹⁴ B. Grynyov,¹¹⁵ L. Levchuk,¹¹⁶ P. Sorokin,¹¹⁶ R. Aggleton,¹¹⁷ F. Ball,¹¹⁷ L. Beck,¹¹⁷ J. J. Brooke,¹¹⁷ E. Clement,¹¹⁷ D. Cussans,¹¹⁷ H. Flacher,¹¹⁷ J. Goldstein,¹¹⁷ M. Grimes,¹¹⁷ G. P. Heath,¹¹⁷ H. F. Heath,¹¹⁷ J. Jacob,¹¹⁷ L. Kreczko,¹¹⁷ C. Lucas,¹¹⁷ Z. Meng,¹¹⁷ D. M. Newbold,^{117,hhh} S. Paramesvaran,¹¹⁷ A. Poll,¹¹⁷ T. Sakuma,¹¹⁷ S. Seif El Nasr-storey,¹¹⁷ S. Senkin,¹¹⁷ D. Smith,¹¹⁷ V. J. Smith,¹¹⁷ K. W. Bell,¹¹⁸ A. Belyaev,^{118,iii} C. Brew,¹¹⁸ R. M. Brown,¹¹⁸ L. Calligaris,¹¹⁸ D. Cieri,¹¹⁸ D. J. A. Cockerill,¹¹⁸ J. A. Coughlan,¹¹⁸ K. Harder,¹¹⁸ S. Harper,¹¹⁸ E. Olaiya,¹¹⁸ D. Petyt,¹¹⁸ C. H. Shepherd-Themistocleous,¹¹⁸ A. Thea,¹¹⁸ I. R. Tomalin,¹¹⁸ T. Williams,¹¹⁸ W. J. Womersley,¹¹⁸ S. D. Worm,¹¹⁸ M. Baber,¹¹⁹ R. Bainbridge,¹¹⁹ O. Buchmuller,¹¹⁹ A. Bundock,¹¹⁹ D. Burton,¹¹⁹ S. Casasso,¹¹⁹ M. Citron,¹¹⁹ D. Colling,¹¹⁹ L. Corpe,¹¹⁹ N. Cripps,¹¹⁹ P. Dauncey,¹¹⁹ G. Davies,¹¹⁹ A. De Wit,¹¹⁹ M. Della Negra,¹¹⁹ P. Dunne,¹¹⁹ A. Elwood,¹¹⁹ W. Ferguson,¹¹⁹ J. Fulcher,¹¹⁹ D. Futyan,¹¹⁹ G. Hall,¹¹⁹ G. Iles,¹¹⁹ M. Kenzie,¹¹⁹ R. Lane,¹¹⁹ R. Lucas,^{119,hhh} L. Lyons,¹¹⁹ A.-M. Magnan,¹¹⁹ S. Malik,¹¹⁹ J. Nash,¹¹⁹ A. Nikitenko,^{119,ii} J. Pela,¹¹⁹ M. Pesaresi,¹¹⁹ K. Petridis,¹¹⁹ D. M. Raymond,¹¹⁹ A. Richards,¹¹⁹ A. Rose,¹¹⁹ C. Seez,¹¹⁹ A. Tapper,¹¹⁹ K. Uchida,¹¹⁹ M. Vazquez Acosta,^{119,iii} T. Virdee,¹¹⁹ S. C. Zenz,¹¹⁹ J. E. Cole,¹²⁰ P. R. Hobson,¹²⁰ A. Khan,¹²⁰ P. Kyberd,¹²⁰ D. Leggat,¹²⁰ D. Leslie,¹²⁰ I. D. Reid,¹²⁰ P. Symonds,¹²⁰ L. Teodorescu,¹²⁰ M. Turner,¹²⁰ A. Borzou,¹²¹ K. Call,¹²¹ J. Dittmann,¹²¹ K. Hatakeyama,¹²¹ H. Liu,¹²¹ N. Pastika,¹²¹ O. Charaf,¹²² S. I. Cooper,¹²² C. Henderson,¹²² P. Rumerio,¹²² D. Arcaro,¹²³ A. Avetisyan,¹²³ T. Bose,¹²³ C. Fantasia,¹²³ D. Gastler,¹²³ P. Lawson,¹²³ D. Rankin,¹²³ C. Richardson,¹²³ J. Rohlf,¹²³ J. St. John,¹²³ L. Sulak,¹²³ D. Zou,¹²³ J. Alimena,¹²⁴ E. Berry,¹²⁴ S. Bhattacharya,¹²⁴ D. Cutts,¹²⁴ N. Dhirra,¹²⁴ A. Ferapontov,¹²⁴ A. Garabedian,¹²⁴ J. Hakala,¹²⁴ U. Heintz,¹²⁴ E. Laird,¹²⁴ G. Landsberg,¹²⁴ Z. Mao,¹²⁴ R. Nally,¹²⁴ M. Narain,¹²⁴ S. Piperov,¹²⁴ S. Sagir,¹²⁴ T. Speer,¹²⁴ R. Syarif,¹²⁴ R. Breedon,¹²⁵ G. Breto,¹²⁵ M. Calderon De La Barca Sanchez,¹²⁵ S. Chauhan,¹²⁵ M. Chertok,¹²⁵ J. Conway,¹²⁵ R. Conway,¹²⁵ P. T. Cox,¹²⁵ R. Erbacher,¹²⁵ M. Gardner,¹²⁵ W. Ko,¹²⁵ R. Lander,¹²⁵ M. Mulhearn,¹²⁵ D. Pellett,¹²⁵ J. Pilot,¹²⁵ F. Ricci-Tam,¹²⁵ S. Shalhout,¹²⁵ J. Smith,¹²⁵ M. Squires,¹²⁵ D. Stolp,¹²⁵ M. Tripathi,¹²⁵ S. Wilbur,¹²⁵ R. Yohay,¹²⁵ R. Cousins,¹²⁶ P. Everaerts,¹²⁶ C. Farrell,¹²⁶ J. Hauser,¹²⁶ M. Ignatenko,¹²⁶ D. Saltzberg,¹²⁶ E. Takasugi,¹²⁶ V. Valuev,¹²⁶

M. Weber,¹²⁶ K. Burt,¹²⁷ R. Clare,¹²⁷ J. Ellison,¹²⁷ J. W. Gary,¹²⁷ G. Hanson,¹²⁷ J. Heilman,¹²⁷ M. Ivova Paneva,¹²⁷
 P. Jandir,¹²⁷ E. Kennedy,¹²⁷ F. Lacroix,¹²⁷ O. R. Long,¹²⁷ A. Luthra,¹²⁷ M. Malberti,¹²⁷ M. Olmedo Negrete,¹²⁷
 A. Shrinivas,¹²⁷ H. Wei,¹²⁷ S. Wimpenny,¹²⁷ B. R. Yates,¹²⁷ J. G. Branson,¹²⁸ G. B. Cerati,¹²⁸ S. Cittolin,¹²⁸
 R. T. D’Agnolo,¹²⁸ M. Derdzinski,¹²⁸ A. Holzner,¹²⁸ R. Kelley,¹²⁸ D. Klein,¹²⁸ J. Letts,¹²⁸ I. Macneill,¹²⁸ D. Olivito,¹²⁸
 S. Padhi,¹²⁸ M. Pieri,¹²⁸ M. Sani,¹²⁸ V. Sharma,¹²⁸ S. Simon,¹²⁸ M. Tadel,¹²⁸ A. Vartak,¹²⁸ S. Wasserbaech,^{128,kkk} C. Welke,¹²⁸
 F. Würthwein,¹²⁸ A. Yagil,¹²⁸ G. Zevi Della Porta,¹²⁸ J. Bradmiller-Feld,¹²⁹ C. Campagnari,¹²⁹ A. Dishaw,¹²⁹ V. Dutta,¹²⁹
 K. Flowers,¹²⁹ M. Franco Sevilla,¹²⁹ P. Geffert,¹²⁹ C. George,¹²⁹ F. Golf,¹²⁹ L. Gouskos,¹²⁹ J. Gran,¹²⁹ J. Incandela,¹²⁹
 N. Mccoll,¹²⁹ S. D. Mullin,¹²⁹ J. Richman,¹²⁹ D. Stuart,¹²⁹ I. Suarez,¹²⁹ C. West,¹²⁹ J. Yoo,¹²⁹ D. Anderson,¹³⁰
 A. Apresyan,¹³⁰ A. Bornheim,¹³⁰ J. Bunn,¹³⁰ Y. Chen,¹³⁰ J. Duarte,¹³⁰ A. Mott,¹³⁰ H. B. Newman,¹³⁰ C. Pena,¹³⁰
 M. Pierini,¹³⁰ M. Spiropulu,¹³⁰ J. R. Vlimant,¹³⁰ S. Xie,¹³⁰ R. Y. Zhu,¹³⁰ M. B. Andrews,¹³¹ V. Azzolini,¹³¹ A. Calamba,¹³¹
 B. Carlson,¹³¹ T. Ferguson,¹³¹ M. Paulini,¹³¹ J. Russ,¹³¹ M. Sun,¹³¹ H. Vogel,¹³¹ I. Vorobiev,¹³¹ J. P. Cumalat,¹³²
 W. T. Ford,¹³² A. Gaz,¹³² F. Jensen,¹³² A. Johnson,¹³² M. Krohn,¹³² T. Mulholland,¹³² U. Nauenberg,¹³² K. Stenson,¹³²
 S. R. Wagner,¹³² J. Alexander,¹³³ A. Chatterjee,¹³³ J. Chaves,¹³³ J. Chu,¹³³ S. Dittmer,¹³³ N. Eggert,¹³³ N. Mirman,¹³³
 G. Nicolas Kaufman,¹³³ J. R. Patterson,¹³³ A. Rinkevicius,¹³³ A. Ryd,¹³³ L. Skinnari,¹³³ L. Soffi,¹³³ W. Sun,¹³³ S. M. Tan,¹³³
 W. D. Teo,¹³³ J. Thom,¹³³ J. Thompson,¹³³ J. Tucker,¹³³ Y. Weng,¹³³ P. Wittich,¹³³ S. Abdullin,¹³⁴ M. Albrow,¹³⁴
 J. Anderson,¹³⁴ G. Apollinari,¹³⁴ S. Banerjee,¹³⁴ L. A. T. Bauerdick,¹³⁴ A. Beretvas,¹³⁴ J. Berryhill,¹³⁴ P. C. Bhat,¹³⁴
 G. Bolla,¹³⁴ K. Burkett,¹³⁴ J. N. Butler,¹³⁴ H. W. K. Cheung,¹³⁴ F. Chlebana,¹³⁴ S. Cihangir,¹³⁴ V. D. Elvira,¹³⁴ I. Fisk,¹³⁴
 J. Freeman,¹³⁴ E. Gottschalk,¹³⁴ L. Gray,¹³⁴ D. Green,¹³⁴ S. Grünendahl,¹³⁴ O. Gutsche,¹³⁴ J. Hanlon,¹³⁴ D. Hare,¹³⁴
 R. M. Harris,¹³⁴ S. Hasegawa,¹³⁴ J. Hirschauer,¹³⁴ Z. Hu,¹³⁴ B. Jayatilaka,¹³⁴ S. Jindariani,¹³⁴ M. Johnson,¹³⁴ U. Joshi,¹³⁴
 A. W. Jung,¹³⁴ B. Klima,¹³⁴ B. Kreis,¹³⁴ S. Kwan,^{134†} S. Lammel,¹³⁴ J. Linacre,¹³⁴ D. Lincoln,¹³⁴ R. Lipton,¹³⁴ T. Liu,¹³⁴
 R. Lopes De Sá,¹³⁴ J. Lykken,¹³⁴ K. Maeshima,¹³⁴ J. M. Marraffino,¹³⁴ V. I. Martinez Outschoorn,¹³⁴ S. Maruyama,¹³⁴
 D. Mason,¹³⁴ P. McBride,¹³⁴ P. Merkel,¹³⁴ K. Mishra,¹³⁴ S. Mrenna,¹³⁴ S. Nahn,¹³⁴ C. Newman-Holmes,¹³⁴ V. O’Dell,¹³⁴
 K. Pedro,¹³⁴ O. Prokofyev,¹³⁴ G. Rakness,¹³⁴ E. Sexton-Kennedy,¹³⁴ A. Soha,¹³⁴ W. J. Spalding,¹³⁴ L. Spiegel,¹³⁴
 L. Taylor,¹³⁴ S. Tkaczyk,¹³⁴ N. V. Tran,¹³⁴ L. Uplegger,¹³⁴ E. W. Vaandering,¹³⁴ C. Vernieri,¹³⁴ M. Verzocchi,¹³⁴ R. Vidal,¹³⁴
 H. A. Weber,¹³⁴ A. Whitbeck,¹³⁴ F. Yang,¹³⁴ D. Acosta,¹³⁵ P. Avery,¹³⁵ P. Bortignon,¹³⁵ D. Bourilkov,¹³⁵ A. Carnes,¹³⁵
 M. Carver,¹³⁵ D. Curry,¹³⁵ S. Das,¹³⁵ G. P. Di Giovanni,¹³⁵ R. D. Field,¹³⁵ I. K. Furic,¹³⁵ S. V. Gleyzer,¹³⁵ J. Hugon,¹³⁵
 J. Konigsberg,¹³⁵ A. Korytov,¹³⁵ J. F. Low,¹³⁵ P. Ma,¹³⁵ K. Matchev,¹³⁵ H. Mei,¹³⁵ P. Milenovic,^{135,III} G. Mitselmakher,¹³⁵
 D. Rank,¹³⁵ R. Rossin,¹³⁵ L. Shchutska,¹³⁵ M. Snowball,¹³⁵ D. Sperka,¹³⁵ N. Terentyev,¹³⁵ L. Thomas,¹³⁵ J. Wang,¹³⁵
 S. Wang,¹³⁵ J. Yelton,¹³⁵ S. Hewamanage,¹³⁶ S. Linn,¹³⁶ P. Markowitz,¹³⁶ G. Martinez,¹³⁶ J. L. Rodriguez,¹³⁶ A. Ackert,¹³⁷
 J. R. Adams,¹³⁷ T. Adams,¹³⁷ A. Askew,¹³⁷ J. Bochenek,¹³⁷ B. Diamond,¹³⁷ J. Haas,¹³⁷ S. Hagopian,¹³⁷ V. Hagopian,¹³⁷
 K. F. Johnson,¹³⁷ A. Khatiwada,¹³⁷ H. Prosper,¹³⁷ M. Weinberg,¹³⁷ M. M. Baarmand,¹³⁸ V. Bhopatkar,¹³⁸
 S. Colafranceschi,^{138,mmm} M. Hohmann,¹³⁸ H. Kalakhety,¹³⁸ D. Noonan,¹³⁸ T. Roy,¹³⁸ F. Yumiceva,¹³⁸ M. R. Adams,¹³⁹
 L. Apanasevich,¹³⁹ D. Berry,¹³⁹ R. R. Betts,¹³⁹ I. Bucinskaite,¹³⁹ R. Cavanaugh,¹³⁹ O. Evdokimov,¹³⁹ L. Gauthier,¹³⁹
 C. E. Gerber,¹³⁹ D. J. Hofman,¹³⁹ P. Kurt,¹³⁹ C. O’Brien,¹³⁹ I. D. Sandoval Gonzalez,¹³⁹ C. Silkworth,¹³⁹ P. Turner,¹³⁹
 N. Varelas,¹³⁹ Z. Wu,¹³⁹ M. Zakaria,¹³⁹ B. Bilki,^{140,nnn} W. Clarida,¹⁴⁰ K. Dilsiz,¹⁴⁰ S. Durgut,¹⁴⁰ R. P. Gandrajula,¹⁴⁰
 M. Haytmyradov,¹⁴⁰ V. Khristenko,¹⁴⁰ J.-P. Merlo,¹⁴⁰ H. Mermerkaya,^{140,ooo} A. Mestvirishvili,¹⁴⁰ A. Moeller,¹⁴⁰
 J. Nachtman,¹⁴⁰ H. Ogul,¹⁴⁰ Y. Onel,¹⁴⁰ F. Ozok,^{140,eee} A. Penzo,¹⁴⁰ C. Snyder,¹⁴⁰ E. Tiras,¹⁴⁰ J. Wetzel,¹⁴⁰ K. Yi,¹⁴⁰
 I. Anderson,¹⁴¹ B. A. Barnett,¹⁴¹ B. Blumenfeld,¹⁴¹ N. Eminizer,¹⁴¹ D. Fehling,¹⁴¹ L. Feng,¹⁴¹ A. V. Gritsan,¹⁴¹
 P. Maksimovic,¹⁴¹ C. Martin,¹⁴¹ M. Osherson,¹⁴¹ J. Roskes,¹⁴¹ A. Sady,¹⁴¹ U. Sarica,¹⁴¹ M. Swartz,¹⁴¹ M. Xiao,¹⁴¹ Y. Xin,¹⁴¹
 C. You,¹⁴¹ P. Baringer,¹⁴² A. Bean,¹⁴² G. Benelli,¹⁴² C. Bruner,¹⁴² R. P. Kenny III,¹⁴² D. Majumder,¹⁴² M. Malek,¹⁴²
 M. Murray,¹⁴² S. Sanders,¹⁴² R. Stringer,¹⁴² Q. Wang,¹⁴² A. Ivanov,¹⁴³ K. Kaadze,¹⁴³ S. Khalil,¹⁴³ M. Makouski,¹⁴³
 Y. Maravin,¹⁴³ A. Mohammadi,¹⁴³ L. K. Saini,¹⁴³ N. Skhirtladze,¹⁴³ S. Toda,¹⁴³ D. Lange,¹⁴⁴ F. Rebassoo,¹⁴⁴ D. Wright,¹⁴⁴
 C. Anelli,¹⁴⁵ A. Baden,¹⁴⁵ O. Baron,¹⁴⁵ A. Belloni,¹⁴⁵ B. Calvert,¹⁴⁵ S. C. Eno,¹⁴⁵ C. Ferraioli,¹⁴⁵ J. A. Gomez,¹⁴⁵
 N. J. Hadley,¹⁴⁵ S. Jabeen,¹⁴⁵ R. G. Kellogg,¹⁴⁵ T. Kolberg,¹⁴⁵ J. Kunkle,¹⁴⁵ Y. Lu,¹⁴⁵ A. C. Mignerey,¹⁴⁵ Y. H. Shin,¹⁴⁵
 A. Skuja,¹⁴⁵ M. B. Tonjes,¹⁴⁵ S. C. Tonwar,¹⁴⁵ A. Apyan,¹⁴⁶ R. Barbieri,¹⁴⁶ A. Baty,¹⁴⁶ K. Bierwagen,¹⁴⁶ S. Brandt,¹⁴⁶
 W. Busza,¹⁴⁶ I. A. Cali,¹⁴⁶ Z. Demiragli,¹⁴⁶ L. Di Matteo,¹⁴⁶ G. Gomez Ceballos,¹⁴⁶ M. Goncharov,¹⁴⁶ D. Gulhan,¹⁴⁶
 Y. Iiyama,¹⁴⁶ G. M. Innocenti,¹⁴⁶ M. Klute,¹⁴⁶ D. Kovalskyi,¹⁴⁶ Y. S. Lai,¹⁴⁶ Y.-J. Lee,¹⁴⁶ A. Levin,¹⁴⁶ P. D. Luckey,¹⁴⁶
 A. C. Marini,¹⁴⁶ C. Mcginn,¹⁴⁶ C. Mironov,¹⁴⁶ S. Narayanan,¹⁴⁶ X. Niu,¹⁴⁶ C. Paus,¹⁴⁶ D. Ralph,¹⁴⁶ C. Roland,¹⁴⁶
 G. Roland,¹⁴⁶ J. Salfeld-Nebgen,¹⁴⁶ G. S. F. Stephans,¹⁴⁶ K. Sumorok,¹⁴⁶ M. Varma,¹⁴⁶ D. Velicanu,¹⁴⁶ J. Veverka,¹⁴⁶

J. Wang,¹⁴⁶ T. W. Wang,¹⁴⁶ B. Wyslouch,¹⁴⁶ M. Yang,¹⁴⁶ V. Zhukova,¹⁴⁶ B. Dahmes,¹⁴⁷ A. Evans,¹⁴⁷ A. Finkel,¹⁴⁷ A. Gude,¹⁴⁷ P. Hansen,¹⁴⁷ S. Kalafut,¹⁴⁷ S. C. Kao,¹⁴⁷ K. Klapöetke,¹⁴⁷ Y. Kubota,¹⁴⁷ Z. Lesko,¹⁴⁷ J. Mans,¹⁴⁷ S. Nourbakhsh,¹⁴⁷ N. Ruckstuhl,¹⁴⁷ R. Rusack,¹⁴⁷ N. Tambe,¹⁴⁷ J. Turkewitz,¹⁴⁷ J. G. Acosta,¹⁴⁸ S. Oliveros,¹⁴⁸ E. Avdeeva,¹⁴⁹ K. Bloom,¹⁴⁹ S. Bose,¹⁴⁹ D. R. Claes,¹⁴⁹ A. Dominguez,¹⁴⁹ C. Fangmeier,¹⁴⁹ R. Gonzalez Suarez,¹⁴⁹ R. Kamalieddin,¹⁴⁹ J. Keller,¹⁴⁹ D. Knowlton,¹⁴⁹ I. Kravchenko,¹⁴⁹ F. Meier,¹⁴⁹ J. Monroy,¹⁴⁹ F. Ratnikov,¹⁴⁹ J. E. Siado,¹⁴⁹ G. R. Snow,¹⁴⁹ M. Alyari,¹⁵⁰ J. Dolen,¹⁵⁰ J. George,¹⁵⁰ A. Godshalk,¹⁵⁰ C. Harrington,¹⁵⁰ I. Iashvili,¹⁵⁰ J. Kaisen,¹⁵⁰ A. Kharchilava,¹⁵⁰ A. Kumar,¹⁵⁰ S. Rappoccio,¹⁵⁰ B. Roobahani,¹⁵⁰ G. Alverson,¹⁵¹ E. Barberis,¹⁵¹ D. Baumgartel,¹⁵¹ M. Chasco,¹⁵¹ A. Hortiangtham,¹⁵¹ A. Massironi,¹⁵¹ D. M. Morse,¹⁵¹ D. Nash,¹⁵¹ T. Orimoto,¹⁵¹ R. Teixeira De Lima,¹⁵¹ D. Trocino,¹⁵¹ R.-J. Wang,¹⁵¹ D. Wood,¹⁵¹ J. Zhang,¹⁵¹ K. A. Hahn,¹⁵² A. Kubik,¹⁵² N. Mucia,¹⁵² N. Odell,¹⁵² B. Pollack,¹⁵² A. Pozdnyakov,¹⁵² M. Schmitt,¹⁵² S. Stoynev,¹⁵² K. Sung,¹⁵² M. Trovato,¹⁵² M. Velasco,¹⁵² A. Brinkerhoff,¹⁵³ N. Dev,¹⁵³ M. Hildreth,¹⁵³ C. Jessop,¹⁵³ D. J. Karmgard,¹⁵³ N. Kellams,¹⁵³ K. Lannon,¹⁵³ S. Lynch,¹⁵³ N. Marinelli,¹⁵³ F. Meng,¹⁵³ C. Mueller,¹⁵³ Y. Musienko,^{153,II} T. Pearson,¹⁵³ M. Planer,¹⁵³ A. Reinsvold,¹⁵³ R. Ruchti,¹⁵³ G. Smith,¹⁵³ S. Taroni,¹⁵³ N. Valls,¹⁵³ M. Wayne,¹⁵³ M. Wolf,¹⁵³ A. Woodard,¹⁵³ L. Antonelli,¹⁵⁴ J. Brinson,¹⁵⁴ B. Bylsma,¹⁵⁴ L. S. Durkin,¹⁵⁴ S. Flowers,¹⁵⁴ A. Hart,¹⁵⁴ C. Hill,¹⁵⁴ R. Hughes,¹⁵⁴ W. Ji,¹⁵⁴ K. Kotov,¹⁵⁴ T. Y. Ling,¹⁵⁴ B. Liu,¹⁵⁴ W. Luo,¹⁵⁴ D. Puigh,¹⁵⁴ M. Rodenburg,¹⁵⁴ B. L. Winer,¹⁵⁴ H. W. Wulsin,¹⁵⁴ O. Driga,¹⁵⁵ P. Elmer,¹⁵⁵ J. Hardenbrook,¹⁵⁵ P. Hebda,¹⁵⁵ S. A. Koay,¹⁵⁵ P. Lujan,¹⁵⁵ D. Marlow,¹⁵⁵ T. Medvedeva,¹⁵⁵ M. Mooney,¹⁵⁵ J. Olsen,¹⁵⁵ C. Palmer,¹⁵⁵ P. Piroué,¹⁵⁵ H. Saka,¹⁵⁵ D. Stickland,¹⁵⁵ C. Tully,¹⁵⁵ A. Zuranski,¹⁵⁵ S. Malik,¹⁵⁶ V. E. Barnes,¹⁵⁷ D. Benedetti,¹⁵⁷ D. Bortoletto,¹⁵⁷ L. Gutay,¹⁵⁷ M. K. Jha,¹⁵⁷ M. Jones,¹⁵⁷ K. Jung,¹⁵⁷ D. H. Miller,¹⁵⁷ N. Neumeister,¹⁵⁷ B. C. Radburn-Smith,¹⁵⁷ X. Shi,¹⁵⁷ I. Shipsey,¹⁵⁷ D. Silvers,¹⁵⁷ J. Sun,¹⁵⁷ A. Svyatkovskiy,¹⁵⁷ F. Wang,¹⁵⁷ W. Xie,¹⁵⁷ L. Xu,¹⁵⁷ N. Parashar,¹⁵⁸ J. Stupak,¹⁵⁸ A. Adair,¹⁵⁹ B. Akgun,¹⁵⁹ Z. Chen,¹⁵⁹ K. M. Ecklund,¹⁵⁹ F. J. M. Geurts,¹⁵⁹ M. Guilbaud,¹⁵⁹ W. Li,¹⁵⁹ B. Michlin,¹⁵⁹ M. Northup,¹⁵⁹ B. P. Padley,¹⁵⁹ R. Redjimi,¹⁵⁹ J. Roberts,¹⁵⁹ J. Rorie,¹⁵⁹ Z. Tu,¹⁵⁹ J. Zabel,¹⁵⁹ B. Betchart,¹⁶⁰ A. Bodek,¹⁶⁰ P. de Barbaro,¹⁶⁰ R. Demina,¹⁶⁰ Y. Eshaq,¹⁶⁰ T. Ferbel,¹⁶⁰ M. Galanti,¹⁶⁰ A. Garcia-Bellido,¹⁶⁰ J. Han,¹⁶⁰ A. Harel,¹⁶⁰ O. Hindrichs,¹⁶⁰ A. Khukhunaishvili,¹⁶⁰ G. Petrillo,¹⁶⁰ P. Tan,¹⁶⁰ M. Verzetti,¹⁶⁰ S. Arora,¹⁶¹ A. Barker,¹⁶¹ J. P. Chou,¹⁶¹ C. Contreras-Campana,¹⁶¹ E. Contreras-Campana,¹⁶¹ D. Duggan,¹⁶¹ D. Ferencek,¹⁶¹ Y. Gershtein,¹⁶¹ R. Gray,¹⁶¹ E. Halkiadakis,¹⁶¹ D. Hidas,¹⁶¹ E. Hughes,¹⁶¹ S. Kaplan,¹⁶¹ R. Kunnawalkam Elayavalli,¹⁶¹ A. Lath,¹⁶¹ K. Nash,¹⁶¹ S. Panwalkar,¹⁶¹ M. Park,¹⁶¹ S. Salur,¹⁶¹ S. Schnetzer,¹⁶¹ D. Sheffield,¹⁶¹ S. Somalwar,¹⁶¹ R. Stone,¹⁶¹ S. Thomas,¹⁶¹ P. Thomassen,¹⁶¹ M. Walker,¹⁶¹ M. Foerster,¹⁶² G. Riley,¹⁶² K. Rose,¹⁶² S. Spanier,¹⁶² A. York,¹⁶² O. Bouhali,^{163,PPP} A. Castaneda Hernandez,^{163,PPP} M. Dalchenko,¹⁶³ M. De Mattia,¹⁶³ A. Delgado,¹⁶³ S. Dildick,¹⁶³ R. Eusebi,¹⁶³ J. Gilmore,¹⁶³ T. Kamon,^{163,qqq} V. Krutelyov,¹⁶³ R. Mueller,¹⁶³ I. Osipenkov,¹⁶³ Y. Pakhotin,¹⁶³ R. Patel,¹⁶³ A. Perloff,¹⁶³ A. Rose,¹⁶³ A. Safonov,¹⁶³ A. Tatarinov,¹⁶³ K. A. Ulmer,^{163,b} N. Akchurin,¹⁶⁴ C. Cowden,¹⁶⁴ J. Damgov,¹⁶⁴ C. Dragoiu,¹⁶⁴ P. R. Duerdo,¹⁶⁴ J. Faulkner,¹⁶⁴ S. Kunori,¹⁶⁴ K. Lamichhane,¹⁶⁴ S. W. Lee,¹⁶⁴ T. Libeiro,¹⁶⁴ S. Undleeb,¹⁶⁴ I. Volobouev,¹⁶⁴ E. Appelt,¹⁶⁵ A. G. Delannoy,¹⁶⁵ S. Greene,¹⁶⁵ A. Gurrola,¹⁶⁵ R. Janjam,¹⁶⁵ W. Johns,¹⁶⁵ C. Maguire,¹⁶⁵ Y. Mao,¹⁶⁵ A. Melo,¹⁶⁵ H. Ni,¹⁶⁵ P. Sheldon,¹⁶⁵ B. Snook,¹⁶⁵ S. Tuo,¹⁶⁵ J. Velkovska,¹⁶⁵ Q. Xu,¹⁶⁵ M. W. Arenton,¹⁶⁶ B. Cox,¹⁶⁶ B. Francis,¹⁶⁶ J. Goodell,¹⁶⁶ R. Hirosky,¹⁶⁶ A. Ledovskoy,¹⁶⁶ H. Li,¹⁶⁶ C. Lin,¹⁶⁶ C. Neu,¹⁶⁶ T. Sinthuprasith,¹⁶⁶ X. Sun,¹⁶⁶ Y. Wang,¹⁶⁶ E. Wolfe,¹⁶⁶ J. Wood,¹⁶⁶ F. Xia,¹⁶⁶ C. Clarke,¹⁶⁷ R. Harr,¹⁶⁷ P. E. Karchin,¹⁶⁷ C. Kottachchi Kankanamge Don,¹⁶⁷ P. Lamichhane,¹⁶⁷ J. Sturdy,¹⁶⁷ D. A. Belknap,¹⁶⁸ D. Carlsmith,¹⁶⁸ M. Cepeda,¹⁶⁸ S. Dasu,¹⁶⁸ L. Dodd,¹⁶⁸ S. Duric,¹⁶⁸ B. Gomer,¹⁶⁸ M. Grothe,¹⁶⁸ R. Hall-Wilton,¹⁶⁸ M. Herndon,¹⁶⁸ A. Hervé,¹⁶⁸ P. Klabbers,¹⁶⁸ A. Lanaro,¹⁶⁸ A. Levine,¹⁶⁸ K. Long,¹⁶⁸ R. Loveless,¹⁶⁸ A. Mohapatra,¹⁶⁸ I. Ojalvo,¹⁶⁸ T. Perry,¹⁶⁸ G. A. Pierro,¹⁶⁸ G. Polese,¹⁶⁸ T. Ruggles,¹⁶⁸ T. Sarangi,¹⁶⁸ A. Savin,¹⁶⁸ A. Sharma,¹⁶⁸ N. Smith,¹⁶⁸ W. H. Smith,¹⁶⁸ D. Taylor,¹⁶⁸ and N. Woods¹⁶⁸

(CMS Collaboration)

¹*Yerevan Physics Institute, Yerevan, Armenia*²*Institut für Hochenergiephysik der OeAW, Wien, Austria*³*National Centre for Particle and High Energy Physics, Minsk, Belarus*⁴*Universiteit Antwerpen, Antwerpen, Belgium*⁵*Vrije Universiteit Brussel, Brussel, Belgium*⁶*Université Libre de Bruxelles, Bruxelles, Belgium*⁷*Ghent University, Ghent, Belgium*⁸*Université Catholique de Louvain, Louvain-la-Neuve, Belgium*⁹*Université de Mons, Mons, Belgium*

- ¹⁰*Centro Brasileiro de Pesquisas Físicas, Rio de Janeiro, Brazil*
¹¹*Universidade do Estado do Rio de Janeiro, Rio de Janeiro, Brazil*
^{12a}*Universidade Estadual Paulista, São Paulo, Brazil*
^{12b}*Universidade Federal do ABC, São Paulo, Brazil*
¹³*Institute for Nuclear Research and Nuclear Energy, Sofia, Bulgaria*
¹⁴*University of Sofia, Sofia, Bulgaria*
¹⁵*Institute of High Energy Physics, Beijing, China*
¹⁶*State Key Laboratory of Nuclear Physics and Technology, Peking University, Beijing, China*
¹⁷*Universidad de Los Andes, Bogota, Colombia*
¹⁸*University of Split, Faculty of Electrical Engineering, Mechanical Engineering and Naval Architecture, Split, Croatia*
¹⁹*University of Split, Faculty of Science, Split, Croatia*
²⁰*Institute Rudjer Boskovic, Zagreb, Croatia*
²¹*University of Cyprus, Nicosia, Cyprus*
²²*Charles University, Prague, Czech Republic*
²³*Academy of Scientific Research and Technology of the Arab Republic of Egypt, Egyptian Network of High Energy Physics, Cairo, Egypt*
²⁴*National Institute of Chemical Physics and Biophysics, Tallinn, Estonia*
²⁵*Department of Physics, University of Helsinki, Helsinki, Finland*
²⁶*Helsinki Institute of Physics, Helsinki, Finland*
²⁷*Lappeenranta University of Technology, Lappeenranta, Finland*
²⁸*DSM/IRFU, CEA/Saclay, Gif-sur-Yvette, France*
²⁹*Laboratoire Leprince-Ringuet, Ecole Polytechnique, IN2P3-CNRS, Palaiseau, France*
³⁰*Institut Pluridisciplinaire Hubert Curien, Université de Strasbourg, Université de Haute Alsace Mulhouse, CNRS/IN2P3, Strasbourg, France*
³¹*Centre de Calcul de l'Institut National de Physique Nucleaire et de Physique des Particules, CNRS/IN2P3, Villeurbanne, France*
³²*Université de Lyon, Université Claude Bernard Lyon 1, CNRS-IN2P3, Institut de Physique Nucléaire de Lyon, Villeurbanne, France*
³³*Georgian Technical University, Tbilisi, Georgia*
³⁴*Tbilisi State University, Tbilisi, Georgia*
³⁵*RWTH Aachen University, I. Physikalisches Institut, Aachen, Germany*
³⁶*RWTH Aachen University, III. Physikalisches Institut A, Aachen, Germany*
³⁷*RWTH Aachen University, III. Physikalisches Institut B, Aachen, Germany*
³⁸*Deutsches Elektronen-Synchrotron, Hamburg, Germany*
³⁹*University of Hamburg, Hamburg, Germany*
⁴⁰*Institut für Experimentelle Kernphysik, Karlsruhe, Germany*
⁴¹*Institute of Nuclear and Particle Physics (INPP), NCSR Demokritos, Aghia Paraskevi, Greece*
⁴²*University of Athens, Athens, Greece*
⁴³*University of Ioánnina, Ioánnina, Greece*
⁴⁴*Wigner Research Centre for Physics, Budapest, Hungary*
⁴⁵*Institute of Nuclear Research ATOMKI, Debrecen, Hungary*
⁴⁶*University of Debrecen, Debrecen, Hungary*
⁴⁷*National Institute of Science Education and Research, Bhubaneswar, India*
⁴⁸*Panjab University, Chandigarh, India*
⁴⁹*University of Delhi, Delhi, India*
⁵⁰*Saha Institute of Nuclear Physics, Kolkata, India*
⁵¹*Bhabha Atomic Research Centre, Mumbai, India*
⁵²*Tata Institute of Fundamental Research, Mumbai, India*
⁵³*Indian Institute of Science Education and Research (IISER), Pune, India*
⁵⁴*Institute for Research in Fundamental Sciences (IPM), Tehran, Iran*
⁵⁵*University College Dublin, Dublin, Ireland*
^{56a}*INFN Sezione di Bari, Bari, Italy*
^{56b}*Università di Bari, Bari, Italy*
^{56c}*Politecnico di Bari, Bari, Italy*
^{57a}*INFN Sezione di Bologna, Bologna, Italy*
^{57b}*Università di Bologna, Bologna, Italy*
^{58a}*INFN Sezione di Catania, Catania, Italy*
^{58b}*Università di Catania, Catania, Italy*
^{58c}*CSFNSM, Catania, Italy*

- ^{59a}*INFN Sezione di Firenze, Firenze, Italy*
^{59b}*Università di Firenze, Firenze, Italy*
⁶⁰*INFN Laboratori Nazionali di Frascati, Frascati, Italy*
^{61a}*INFN Sezione di Genova, Genova, Italy*
^{61b}*Università di Genova, Genova, Italy*
^{62a}*INFN Sezione di Milano-Bicocca, Milano, Italy*
^{62b}*Università di Milano-Bicocca, Milano, Italy*
^{63a}*INFN Sezione di Napoli, Napoli, Italy*
^{63b}*Università di Napoli 'Federico II', Napoli, Italy*
^{63c}*Università della Basilicata, Potenza, Italy*
^{63d}*Università G. Marconi, Roma, Italy*
^{64a}*INFN Sezione di Padova, Padova, Italy*
^{64b}*Università di Padova, Padova, Italy*
^{64c}*Università di Trento, Trento, Italy*
^{65a}*INFN Sezione di Pavia, Pavia, Italy*
^{65b}*Università di Pavia, Pavia, Italy*
^{66a}*INFN Sezione di Perugia, Perugia, Italy*
^{66b}*Università di Perugia, Perugia, Italy*
^{67a}*INFN Sezione di Pisa, Pisa, Italy*
^{67b}*Università di Pisa, Pisa, Italy*
^{67c}*Scuola Normale Superiore di Pisa, Pisa, Italy*
^{68a}*INFN Sezione di Roma, Roma, Italy*
^{68b}*Università di Roma, Roma, Italy*
^{69a}*INFN Sezione di Torino, Torino, Italy*
^{69b}*Università di Torino, Torino, Italy*
^{69c}*Università del Piemonte Orientale, Novara, Italy*
^{70a}*INFN Sezione di Trieste, Trieste, Italy*
^{70b}*Università di Trieste, Trieste, Italy*
⁷¹*Kangwon National University, Chunchon, Korea*
⁷²*Kyungpook National University, Daegu, Korea*
⁷³*Chonbuk National University, Jeonju, Korea*
⁷⁴*Chonnam National University, Institute for Universe and Elementary Particles, Kwangju, Korea*
⁷⁵*Korea University, Seoul, Korea*
⁷⁶*Seoul National University, Seoul, Korea*
⁷⁷*University of Seoul, Seoul, Korea*
⁷⁸*Sungkyunkwan University, Suwon, Korea*
⁷⁹*Vilnius University, Vilnius, Lithuania*
⁸⁰*National Centre for Particle Physics, Universiti Malaya, Kuala Lumpur, Malaysia*
⁸¹*Centro de Investigacion y de Estudios Avanzados del IPN, Mexico City, Mexico*
⁸²*Universidad Iberoamericana, Mexico City, Mexico*
⁸³*Benemerita Universidad Autonoma de Puebla, Puebla, Mexico*
⁸⁴*Universidad Autónoma de San Luis Potosí, San Luis Potosí, Mexico*
⁸⁵*University of Auckland, Auckland, New Zealand*
⁸⁶*University of Canterbury, Christchurch, New Zealand*
⁸⁷*National Centre for Physics, Quaid-I-Azam University, Islamabad, Pakistan*
⁸⁸*National Centre for Nuclear Research, Swierk, Poland*
⁸⁹*Institute of Experimental Physics, Faculty of Physics, University of Warsaw, Warsaw, Poland*
⁹⁰*Laboratório de Instrumentação e Física Experimental de Partículas, Lisboa, Portugal*
⁹¹*Joint Institute for Nuclear Research, Dubna, Russia*
⁹²*Petersburg Nuclear Physics Institute, Gatchina (St. Petersburg), Russia*
⁹³*Institute for Nuclear Research, Moscow, Russia*
⁹⁴*Institute for Theoretical and Experimental Physics, Moscow, Russia*
⁹⁵*National Research Nuclear University 'Moscow Engineering Physics Institute' (MEPhI), Moscow, Russia*
⁹⁶*P.N. Lebedev Physical Institute, Moscow, Russia*
⁹⁷*Skobeltsyn Institute of Nuclear Physics, Lomonosov Moscow State University, Moscow, Russia*
⁹⁸*State Research Center of Russian Federation, Institute for High Energy Physics, Protvino, Russia*
⁹⁹*University of Belgrade, Faculty of Physics and Vinca Institute of Nuclear Sciences, Belgrade, Serbia*
¹⁰⁰*Centro de Investigaciones Energéticas Medioambientales y Tecnológicas (CIEMAT), Madrid, Spain*
¹⁰¹*Universidad Autónoma de Madrid, Madrid, Spain*

- ¹⁰²*Universidad de Oviedo, Oviedo, Spain*
- ¹⁰³*Instituto de Física de Cantabria (IFCA), CSIC-Universidad de Cantabria, Santander, Spain*
- ¹⁰⁴*CERN, European Organization for Nuclear Research, Geneva, Switzerland*
- ¹⁰⁵*Paul Scherrer Institut, Villigen, Switzerland*
- ¹⁰⁶*Institute for Particle Physics, ETH Zurich, Zurich, Switzerland*
- ¹⁰⁷*Universität Zürich, Zurich, Switzerland*
- ¹⁰⁸*National Central University, Chung-Li, Taiwan*
- ¹⁰⁹*National Taiwan University (NTU), Taipei, Taiwan*
- ¹¹⁰*Chulalongkorn University, Faculty of Science, Department of Physics, Bangkok, Thailand*
- ¹¹¹*Cukurova University, Adana, Turkey*
- ¹¹²*Middle East Technical University, Physics Department, Ankara, Turkey*
- ¹¹³*Bogazici University, Istanbul, Turkey*
- ¹¹⁴*Istanbul Technical University, Istanbul, Turkey*
- ¹¹⁵*Institute for Scintillation Materials of National Academy of Science of Ukraine, Kharkov, Ukraine*
- ¹¹⁶*National Scientific Center, Kharkov Institute of Physics and Technology, Kharkov, Ukraine*
- ¹¹⁷*University of Bristol, Bristol, United Kingdom*
- ¹¹⁸*Rutherford Appleton Laboratory, Didcot, United Kingdom*
- ¹¹⁹*Imperial College, London, United Kingdom*
- ¹²⁰*Brunel University, Uxbridge, United Kingdom*
- ¹²¹*Baylor University, Waco, USA*
- ¹²²*The University of Alabama, Tuscaloosa, USA*
- ¹²³*Boston University, Boston, USA*
- ¹²⁴*Brown University, Providence, USA*
- ¹²⁵*University of California, Davis, Davis, USA*
- ¹²⁶*University of California, Los Angeles, USA*
- ¹²⁷*University of California, Riverside, Riverside, USA*
- ¹²⁸*University of California, San Diego, La Jolla, USA*
- ¹²⁹*University of California, Santa Barbara, Santa Barbara, USA*
- ¹³⁰*California Institute of Technology, Pasadena, USA*
- ¹³¹*Carnegie Mellon University, Pittsburgh, USA*
- ¹³²*University of Colorado Boulder, Boulder, USA*
- ¹³³*Cornell University, Ithaca, USA*
- ¹³⁴*Fermi National Accelerator Laboratory, Batavia, USA*
- ¹³⁵*University of Florida, Gainesville, USA*
- ¹³⁶*Florida International University, Miami, USA*
- ¹³⁷*Florida State University, Tallahassee, USA*
- ¹³⁸*Florida Institute of Technology, Melbourne, USA*
- ¹³⁹*University of Illinois at Chicago (UIC), Chicago, USA*
- ¹⁴⁰*The University of Iowa, Iowa City, USA*
- ¹⁴¹*Johns Hopkins University, Baltimore, USA*
- ¹⁴²*The University of Kansas, Lawrence, USA*
- ¹⁴³*Kansas State University, Manhattan, USA*
- ¹⁴⁴*Lawrence Livermore National Laboratory, Livermore, USA*
- ¹⁴⁵*University of Maryland, College Park, USA*
- ¹⁴⁶*Massachusetts Institute of Technology, Cambridge, USA*
- ¹⁴⁷*University of Minnesota, Minneapolis, USA*
- ¹⁴⁸*University of Mississippi, Oxford, USA*
- ¹⁴⁹*University of Nebraska-Lincoln, Lincoln, USA*
- ¹⁵⁰*State University of New York at Buffalo, Buffalo, USA*
- ¹⁵¹*Northeastern University, Boston, USA*
- ¹⁵²*Northwestern University, Evanston, USA*
- ¹⁵³*University of Notre Dame, Notre Dame, USA*
- ¹⁵⁴*The Ohio State University, Columbus, USA*
- ¹⁵⁵*Princeton University, Princeton, USA*
- ¹⁵⁶*University of Puerto Rico, Mayaguez, USA*
- ¹⁵⁷*Purdue University, West Lafayette, USA*
- ¹⁵⁸*Purdue University Calumet, Hammond, USA*
- ¹⁵⁹*Rice University, Houston, USA*
- ¹⁶⁰*University of Rochester, Rochester, USA*
- ¹⁶¹*Rutgers, The State University of New Jersey, Piscataway, USA*

¹⁶²*University of Tennessee, Knoxville, USA*
¹⁶³*Texas A&M University, College Station, USA*
¹⁶⁴*Texas Tech University, Lubbock, USA*
¹⁶⁵*Vanderbilt University, Nashville, USA*
¹⁶⁶*University of Virginia, Charlottesville, USA*
¹⁶⁷*Wayne State University, Detroit, USA*
¹⁶⁸*University of Wisconsin, Madison, USA*

[†]Deceased.

^aAlso at Vienna University of Technology, Vienna, Austria.

^bAlso at CERN, European Organization for Nuclear Research, Geneva, Switzerland.

^cAlso at State Key Laboratory of Nuclear Physics and Technology, Peking University, Beijing, China.

^dAlso at Institut Pluridisciplinaire Hubert Curien, Université de Strasbourg, Université de Haute Alsace Mulhouse, CNRS/IN2P3, Strasbourg, France.

^eAlso at National Institute of Chemical Physics and Biophysics, Tallinn, Estonia.

^fAlso at Skobeltsyn Institute of Nuclear Physics, Lomonosov Moscow State University, Moscow, Russia.

^gAlso at Universidade Estadual de Campinas, Campinas, Brazil.

^hAlso at Centre National de la Recherche Scientifique (CNRS)—IN2P3, Paris, France.

ⁱAlso at Laboratoire Leprince-Ringuet, Ecole Polytechnique, IN2P3-CNRS, Palaiseau, France.

^jAlso at Joint Institute for Nuclear Research, Dubna, Russia.

^kAlso at Ain Shams University, Cairo, Egypt.

^lAlso at Zewail City of Science and Technology, Zewail, Egypt.

^mAlso at Fayoum University, El-Fayoum, Egypt.

ⁿAlso at British University in Egypt, Cairo, Egypt.

^oAlso at Université de Haute Alsace, Mulhouse, France.

^pAlso at Tbilisi State University, Tbilisi, Georgia.

^qAlso at RWTH Aachen University, III. Physikalisches Institut A, Aachen, Germany.

^rAlso at Indian Institute of Science Education and Research, Bhopal, India.

^sAlso at University of Hamburg, Hamburg, Germany.

^tAlso at Brandenburg University of Technology, Cottbus, Germany.

^uAlso at Institute of Nuclear Research ATOMKI, Debrecen, Hungary.

^vAlso at Eötvös Loránd University, Budapest, Hungary.

^wAlso at University of Debrecen, Debrecen, Hungary.

^xAlso at Wigner Research Centre for Physics, Budapest, Hungary.

^yAlso at University of Visva-Bharati, Santiniketan, India.

^zAlso at King Abdulaziz University, Jeddah, Saudi Arabia.

^{aa}Also at University of Ruhuna, Matara, Sri Lanka.

^{bb}Also at Isfahan University of Technology, Isfahan, Iran.

^{cc}Also at University of Tehran, Department of Engineering Science, Tehran, Iran.

^{dd}Also at Plasma Physics Research Center, Science and Research Branch, Islamic Azad University, Tehran, Iran.

^{ee}Also at Laboratori Nazionali di Legnaro dell'INFN, Legnaro, Italy.

^{ff}Also at Università degli Studi di Siena, Siena, Italy.

^{gg}Also at Purdue University, West Lafayette, USA.

^{hh}Also at International Islamic University of Malaysia, Kuala Lumpur, Malaysia.

ⁱⁱAlso at Malaysian Nuclear Agency, MOSTI, Kajang, Malaysia.

^{jj}Also at Consejo Nacional de Ciencia y Tecnología, Mexico city, Mexico.

^{kk}Also at Warsaw University of Technology, Institute of Electronic Systems, Warsaw, Poland.

^{ll}Also at Institute for Nuclear Research, Moscow, Russia.

^{mm}Also at National Research Nuclear University 'Moscow Engineering Physics Institute' (MEPhI), Moscow, Russia.

ⁿⁿAlso at St. Petersburg State Polytechnical University, St. Petersburg, Russia.

^{oo}Also at California Institute of Technology, Pasadena, USA.

^{pp}Also at Faculty of Physics, University of Belgrade, Belgrade, Serbia.

^{qq}Also at National Technical University of Athens, Athens, Greece.

^{rr}Also at Scuola Normale e Sezione dell'INFN, Pisa, Italy.

^{ss}Also at University of Athens, Athens, Greece.

^{tt}Also at Institute for Theoretical and Experimental Physics, Moscow, Russia.

^{uu}Also at Albert Einstein Center for Fundamental Physics, Bern, Switzerland.

^{vv}Also at Adiyaman University, Adiyaman, Turkey.

^{ww}Also at Mersin University, Mersin, Turkey.

^{xx}Also at Cag University, Mersin, Turkey.

- ^{yy} Also at Piri Reis University, Istanbul, Turkey.
- ^{zz} Also at Gaziosmanpasa University, Tokat, Turkey.
- ^{aaa} Also at Ozyegin University, Istanbul, Turkey.
- ^{bbb} Also at Izmir Institute of Technology, Izmir, Turkey.
- ^{ccc} Also at Marmara University, Istanbul, Turkey.
- ^{ddd} Also at Kafkas University, Kars, Turkey.
- ^{eee} Also at Mimar Sinan University, Istanbul, Istanbul, Turkey.
- ^{fff} Also at Yildiz Technical University, Istanbul, Turkey.
- ^{ggg} Also at Hacettepe University, Ankara, Turkey.
- ^{hhh} Also at Rutherford Appleton Laboratory, Didcot, United Kingdom.
- ⁱⁱⁱ Also at School of Physics and Astronomy, University of Southampton, Southampton, United Kingdom.
- ^{jjj} Also at Instituto de Astrofísica de Canarias, La Laguna, Spain.
- ^{kkk} Also at Utah Valley University, Orem, USA.
- ^{lll} Also at University of Belgrade, Faculty of Physics and Vinca Institute of Nuclear Sciences, Belgrade, Serbia.
- ^{mmm} Also at Facoltà Ingegneria, Università di Roma, Roma, Italy.
- ⁿⁿⁿ Also at Argonne National Laboratory, Argonne, USA.
- ^{ooo} Also at Erzincan University, Erzincan, Turkey.
- ^{ppp} Also at Texas A&M University at Qatar, Doha, Qatar.
- ^{qqq} Also at Kyungpook National University, Daegu, Korea.

Observation of $t\bar{t}H$ Production

A. M. Sirunyan *et al.**
(CMS Collaboration)

 (Received 8 April 2018; revised manuscript received 1 May 2018; published 4 June 2018)

The observation of Higgs boson production in association with a top quark-antiquark pair is reported, based on a combined analysis of proton-proton collision data at center-of-mass energies of $\sqrt{s} = 7, 8,$ and 13 TeV, corresponding to integrated luminosities of up to $5.1, 19.7,$ and 35.9 fb $^{-1}$, respectively. The data were collected with the CMS detector at the CERN LHC. The results of statistically independent searches for Higgs bosons produced in conjunction with a top quark-antiquark pair and decaying to pairs of W bosons, Z bosons, photons, τ leptons, or bottom quark jets are combined to maximize sensitivity. An excess of events is observed, with a significance of 5.2 standard deviations, over the expectation from the background-only hypothesis. The corresponding expected significance from the standard model for a Higgs boson mass of 125.09 GeV is 4.2 standard deviations. The combined best fit signal strength normalized to the standard model prediction is $1.26^{+0.31}_{-0.26}$.

DOI: [10.1103/PhysRevLett.120.231801](https://doi.org/10.1103/PhysRevLett.120.231801)

Proton-proton (pp) collisions at the CERN LHC, at the center-of-mass (c.m.) energies of $\sqrt{s} = 7, 8,$ and 13 TeV, have allowed direct measurements of the properties of the Higgs boson [1–3]. In particular, the 13 TeV data collected so far by the ATLAS [4] and CMS [5] experiments have led to improved constraints on the couplings of the Higgs boson compared to those performed at the lower energies [6], permitting more precise consistency checks with the predictions of the standard model (SM) of particle physics [7–9]. Nonetheless, not all properties of the Higgs boson have been established, in part because of insufficiently large data sets. The lack of statistical precision can be partially overcome by combining the results of searches in different decay channels of the Higgs boson and at different c.m. energies. Among the properties that are not yet well established is the tree-level coupling of Higgs bosons to top quarks.

In this Letter, we present a combination of searches for the Higgs boson (H) produced in association with a top quark-antiquark pair ($t\bar{t}$), based on data collected with the CMS detector. Results from data collected at $\sqrt{s} = 13$ TeV [10–14] are combined with analogous results from $\sqrt{s} = 7$ and 8 TeV [15]. As a result of this combination, we establish the observation of $t\bar{t}H$ production. This constitutes the first confirmation of the tree-level coupling of the Higgs boson to top quarks.

A top quark decays almost exclusively to a bottom quark and a W boson, with the W boson subsequently decaying either to a quark and an antiquark or to a charged lepton and its associated neutrino. The Higgs boson exhibits a rich spectrum of decay modes that includes the decay to a bottom quark-antiquark pair, a $\tau^+\tau^-$ lepton pair, a photon pair, and combinations of quarks and leptons from the decay of intermediate on- or off-shell W and Z bosons. Thus, $t\bar{t}H$ production gives rise to a wide variety of final-state event topologies, which we consider in our analyses and in the combination of results presented below.

In the SM, the masses of elementary fermions are accounted for by introducing a minimal set of Yukawa interactions, compatible with gauge invariance, between the Higgs and fermion fields. Following the spontaneous breaking of electroweak symmetry [16–21], charged fermions of flavor f couple to H with a strength y_f proportional to the mass m_f of those fermions, namely $y_f = m_f/v$, where $v \approx 246$ GeV is the vacuum expectation value of the Higgs field. Measurements of the Higgs boson decay rates to down-type fermions (τ leptons and bottom quarks) agree with the SM predictions within their uncertainties [22,23]. However, the top quark Yukawa coupling (y_t) cannot be similarly tested from the measurement of a decay rate since on-shell top quarks are too heavy to be produced in Higgs boson decay. Instead, constraints on y_t can be obtained through the measurement of the $pp \rightarrow t\bar{t}H$ production process. Example tree-level Feynman diagrams for this process are shown in Fig. 1. To date, $t\bar{t}H$ production has eluded definite observation, although first evidence has been recently reported by the ATLAS [24] and CMS [10] Collaborations.

The overall agreement observed between the SM predictions and data for the rate of Higgs boson production

*Full author list given at the end of the Letter.

Published by the American Physical Society under the terms of the [Creative Commons Attribution 4.0 International license](https://creativecommons.org/licenses/by/4.0/). Further distribution of this work must maintain attribution to the author(s) and the published article's title, journal citation, and DOI. Funded by SCOAP³.

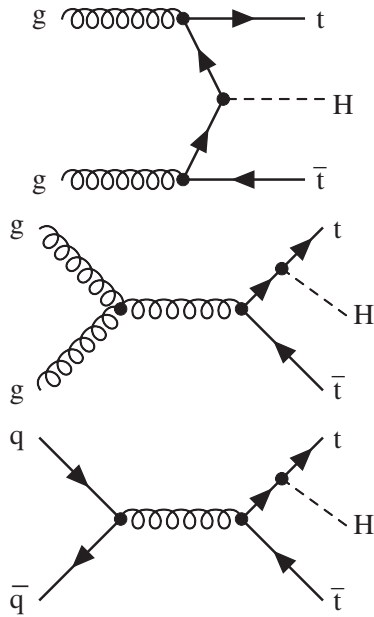


FIG. 1. Example tree-level Feynman diagrams for the $pp \rightarrow t\bar{t}H$ production process, with g a gluon, q a quark, t a top quark, and H a Higgs boson. For the present study, we consider Higgs boson decays to a pair of W bosons, Z bosons, photons, τ leptons, or bottom quark jets.

through gluon-gluon fusion and for the $H \rightarrow \gamma\gamma$ decay mode [6] suggests that the Higgs boson coupling to top quarks is SM-like, since the quantum loops in these processes include top quarks. However, non-SM particles in the loops could introduce terms that compensate for, and thus mask, other deviations from the SM. A measurement of the production rate of the tree-level $t\bar{t}H$ process can provide evidence for, or against, such new-physics contributions.

The central feature of the CMS apparatus is a superconducting solenoid of 6 m internal diameter, providing a magnetic field of 3.8 T. Within the solenoid volume are a silicon pixel and strip tracker, a lead tungstate crystal electromagnetic calorimeter, and a brass and scintillator hadron calorimeter, each composed of a barrel and two end cap sections. Forward calorimeters extend the pseudorapidity coverage provided by the barrel and end cap detectors. Muons are detected in gas-ionization chambers embedded in the steel flux-return yoke outside the solenoid. A detailed description of the CMS detector can be found in Ref. [5].

Events of interest are selected using a two-tiered trigger system [25] based on custom hardware processors and a farm of commercial processors running a version of the full reconstruction software optimized for speed. Offline, a particle-flow algorithm [26] is used to reconstruct and identify each particle in an event based on a combination of information from the various CMS subdetectors. Additional identification criteria are employed to improve

purities and define the final samples of candidate electrons, muons, hadronically decaying τ leptons (τ_h) [27,28], and photons. Jets are reconstructed from particle-flow candidates using the anti- k_T clustering algorithm [29] implemented in the FASTJET package [30]. Multivariate algorithms [31,32] are used to identify (tag) jets arising from the hadronization of bottom quarks (b jets) and discriminate against gluon and light flavor quark jets. The algorithms utilize observables related to the long lifetimes of hadrons containing b quarks and the relatively larger particle multiplicity and mass of b jets compared to light flavor quark jets. The τ_h identification is based on the reconstruction of the hadronic τ decay modes $\tau^- \rightarrow h^- \nu_\tau$, $h^- \pi^0 \nu_\tau$, $h^- \pi^0 \pi^0 \nu_\tau$, and $h^- h^+ h^- \nu_\tau$ (plus the charge conjugate reactions), where h^\pm denotes either a charged pion or kaon. More details about the reconstruction procedures are given in Refs. [10–15].

The 13 TeV data employed for the current study were collected in 2016 and correspond to an integrated luminosity of up to 35.9 fb^{-1} [33]. The 7 and 8 TeV data, collected in 2011 and 2012, correspond to integrated luminosities of up to 5.1 and 19.7 fb^{-1} [34], respectively. The 13 TeV analyses are improved relative to the 7 and 8 TeV studies in that they employ triggers with higher efficiencies, contain improvements in the reconstruction and background-rejection methods, and use more precise theory calculations to describe the signal and the background processes. For the 7, 8, and 13 TeV data, the theoretical calculations of Ref. [35] for Higgs boson production cross sections and branching fractions are used to normalize the expected signal yields.

The event samples are divided into exclusive categories depending on the multiplicity and kinematic properties of reconstructed electrons, muons, τ_h candidates, photons, jets, and tagged b jets in an event. Samples of simulated events based on Monte Carlo event generators, with simulation of the detector response based on the GEANT4 [36] suite of programs, are used to evaluate the detector acceptance and optimize the event selection for each category. In the analysis of data, the background is, in general, evaluated from data control regions. When this is not feasible, either because the background process has a very small cross section or a control region depleted of signal events cannot be identified, the background is evaluated from simulation with a systematic uncertainty assigned to account for the known model dependence. Multivariate algorithms [37–41] based on deep neural networks, boosted decision trees, and matrix element calculations are used to reduce backgrounds.

At 13 TeV, we search for $t\bar{t}H$ production in the $H \rightarrow b\bar{b}$ decay mode by selecting events with at least three tagged b jets and with zero leptons [11], one lepton [12], or an opposite-sign lepton pair [12], where “lepton” refers to an electron or muon candidate. A search for $t\bar{t}H$ production in the $H \rightarrow \gamma\gamma$ decay mode is performed in events with two

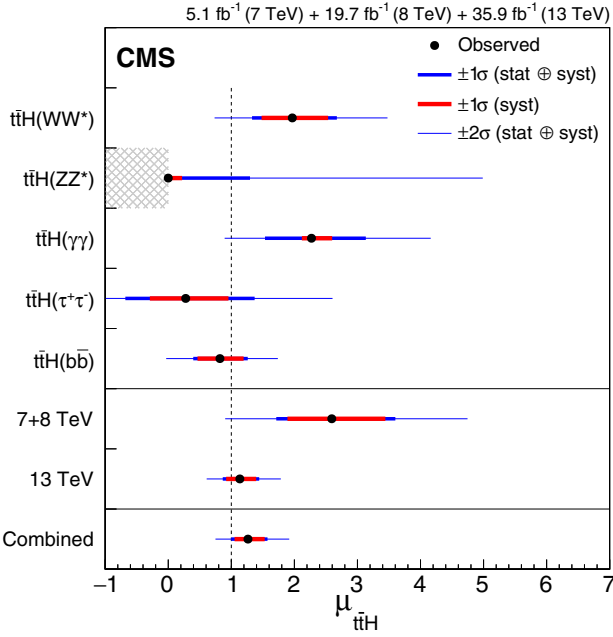


FIG. 2. Best fit value of the $t\bar{t}H$ signal strength modifier $\mu_{t\bar{t}H}$, with its 1 and 2 standard deviation confidence intervals (σ), for (upper section) the five individual decay channels considered, (middle section) the combined result for 7 + 8 TeV alone and for 13 TeV alone, and (lower section) the overall combined result. The Higgs boson mass is taken to be 125.09 GeV. For the $H \rightarrow ZZ^*$ decay mode, $\mu_{t\bar{t}H}$ is constrained to be positive to prevent the corresponding event yield from becoming negative. The SM expectation is shown as a dashed vertical line.

reconstructed photons in combination with reconstructed electrons or muons, jets, and tagged b jets [13]. The signal yield is extracted from a fit to the diphoton invariant mass spectrum. Events with combinations of jets and tagged b jets and with two same-sign leptons, three leptons, or four leptons are used to search for $t\bar{t}H$ production in the $H \rightarrow \tau^+\tau^-$, WW^* , or ZZ^* decay modes [10,14], where in this case “lepton” refers to an electron, muon, or τ_h candidate (the asterisk denotes an off-shell particle). The searches in the different decay channels are statistically independent from each other. Analogous searches have been performed with the 7 and 8 TeV data [15].

The presence of a $t\bar{t}H$ signal is assessed by performing a simultaneous fit to the data from the different decay modes and also from the different c.m. energies as described below. A detailed description of the statistical methods can be found in Ref. [42]. The test statistic q is defined as the negative of twice the logarithm of the profile likelihood ratio [42]. Systematic uncertainties are incorporated through the use of nuisance parameters treated according to the frequentist paradigm. The ratio between the normalization of the $t\bar{t}H$ production process and its SM expectation [35], defined as the signal strength modifier $\mu_{t\bar{t}H}$, is a freely floating parameter in the fit. The SM expectation is evaluated assuming the combined ATLAS

and CMS value for the mass of the Higgs boson, which is 125.09 GeV [43]. We consider the five Higgs boson decay modes with the largest expected event yields, namely, $H \rightarrow WW^*$, ZZ^* , $\gamma\gamma$, $\tau^+\tau^-$, and $b\bar{b}$. Other Higgs boson decay modes and production processes, including $pp \rightarrow tH + X$ (or $\bar{t}H + X$), with X a light flavor quark or W boson, are treated as backgrounds and normalized using the predicted SM cross sections, subject to the corresponding uncertainties.

The measured values of the five independent signal strength modifiers, corresponding to the five decay channels considered, are shown in the upper section of Fig. 2 along with their 1 and 2 standard deviation confidence intervals obtained in the asymptotic approximation [44]. Numerical values are given in Table I. The individual measurements are seen to be consistent with each other within the uncertainties.

We also perform a combined fit, using a single signal strength modifier $\mu_{t\bar{t}H}$, that simultaneously scales the $t\bar{t}H$ production cross sections of the five decay channels considered, with all Higgs boson branching fractions fixed to their SM values [35]. Besides the five decay modes

TABLE I. Best fit value, with its uncertainty, of the $t\bar{t}H$ signal strength modifier $\mu_{t\bar{t}H}$, for the five individual decay channels considered, the combined result for 7 + 8 TeV alone and for 13 TeV alone, and the overall combined result. The total uncertainties are decomposed into their statistical, experimental systematic, background theory systematic, and signal theory components. The numbers in parentheses are those expected for $\mu_{t\bar{t}H} = 1$.

Parameter	Best fit	Uncertainty			
		Statistical	Experi- mental	Background theory	Signal theory
$\mu_{t\bar{t}H}^{WW^*}$	$1.97^{+0.71}_{-0.64}$ (+0.57) (-0.54)	+0.42 -0.41 (+0.39) (-0.38)	+0.46 -0.42 (+0.36) (-0.34)	+0.21 -0.21 (+0.17) (-0.17)	+0.25 -0.12 (+0.12) (-0.03)
$\mu_{t\bar{t}H}^{ZZ^*}$	$0.00^{+1.30}_{-0.00}$ (+2.89) (-0.99)	+1.28 -0.00 (+2.82) (-0.99)	+0.20 -0.00 (+0.51) (-0.00)	+0.04 -0.00 (+0.15) (-0.00)	+0.09 -0.00 (+0.27) (-0.00)
$\mu_{t\bar{t}H}^{\gamma\gamma}$	$2.27^{+0.86}_{-0.74}$ (+0.73) (-0.64)	+0.80 -0.72 (+0.71) (-0.64)	+0.15 -0.09 (+0.09) (-0.04)	+0.02 -0.01 (+0.01) (-0.00)	+0.29 -0.13 (+0.13) (-0.05)
$\mu_{t\bar{t}H}^{\tau^+\tau^-}$	$0.28^{+1.09}_{-0.96}$ (+1.00) (-0.89)	+0.86 -0.77 (+0.83) (-0.76)	+0.64 -0.53 (+0.54) (-0.47)	+0.10 -0.09 (+0.09) (-0.08)	+0.20 -0.19 (+0.14) (-0.01)
$\mu_{t\bar{t}H}^{b\bar{b}}$	$0.82^{+0.44}_{-0.42}$ (+0.44) (-0.42)	+0.23 -0.23 (+0.23) (-0.22)	+0.24 -0.23 (+0.24) (-0.23)	+0.27 -0.27 (+0.26) (-0.27)	+0.11 -0.03 (+0.11) (-0.04)
$\mu_{t\bar{t}H}^{7+8 \text{ TeV}}$	$2.59^{+1.01}_{-0.88}$ (+0.87) (-0.79)	+0.54 -0.53 (+0.51) (-0.49)	+0.53 -0.49 (+0.48) (-0.44)	+0.55 -0.49 (+0.50) (-0.44)	+0.37 -0.13 (+0.14) (-0.02)
$\mu_{t\bar{t}H}^{13 \text{ TeV}}$	$1.14^{+0.31}_{-0.27}$ (+0.29) (-0.26)	+0.17 -0.16 (+0.16) (-0.16)	+0.17 -0.17 (+0.17) (-0.16)	+0.13 -0.12 (+0.13) (-0.12)	+0.14 -0.06 (+0.11) (-0.05)
$\mu_{t\bar{t}H}$	$1.26^{+0.31}_{-0.26}$ (+0.28) (-0.25)	+0.16 -0.16 (+0.15) (-0.15)	+0.17 -0.15 (+0.16) (-0.15)	+0.14 -0.13 (+0.13) (-0.12)	+0.15 -0.07 (+0.11) (-0.05)

considered, the signal normalizations for the Higgs boson decay modes to gluons, charm quarks, and $Z\gamma$, which are subleading and cannot be constrained with existing data, are scaled by $\mu_{\tilde{t}\tilde{t}H}$. The results combining the decay modes at 7 + 8 TeV, and separately at 13 TeV, are shown in the middle section of Fig. 2. The overall result, combining all decay modes and all c.m. energies, is shown in the lower section, with numerical values given in Table I. Table I includes a breakdown of the total uncertainties into their statistical and systematic components. The overall result is $\mu_{\tilde{t}\tilde{t}H} = 1.26^{+0.31}_{-0.26}$, which agrees with the SM expectation $\mu_{\tilde{t}\tilde{t}H} = 1$ within 1 standard deviation.

The principal sources of experimental systematic uncertainty in the overall result for $\mu_{\tilde{t}\tilde{t}H}$ stem from the uncertainty in the lepton and b jet identification efficiencies and in the τ_h and jet energy scales. The background theory systematic uncertainty is dominated by modeling uncertainties in $\tilde{t}\tilde{t}$ production in association with a W boson, a Z boson, or a pair of b or c quark jets. The dominant contribution to the signal theory systematic uncertainty arises from the finite accuracy in the SM prediction for the $\tilde{t}\tilde{t}H$ cross section because of missing higher order terms and uncertainties in the proton parton density functions [35].

To highlight the excess of data over the expectation from the background-only hypothesis, we classify each event

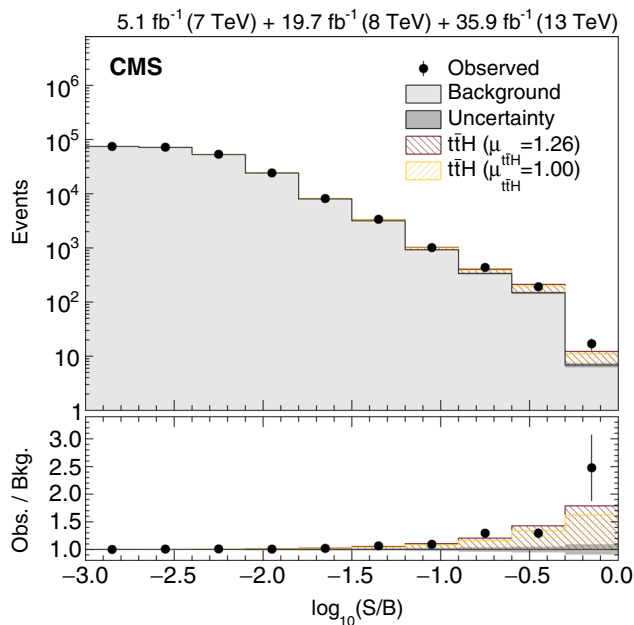


FIG. 3. Distribution of events as a function of the decimal logarithm of S/B , where S and B are the expected postfit signal (with $\mu_{\tilde{t}\tilde{t}H} = 1$) and background yields, respectively, in each bin of the distributions considered in this combination. The shaded histogram shows the expected background distribution. The two hatched histograms, each stacked on top of the background histogram, show the signal expectation for the SM ($\mu_{\tilde{t}\tilde{t}H} = 1$) and the observed ($\mu_{\tilde{t}\tilde{t}H} = 1.26$) signal strengths. The lower panel shows the ratios of the expected signal and observed results relative to the expected background.

that enters the combined fit by the ratio S/B , where S and B are the expected postfit signal (with $\mu_{\tilde{t}\tilde{t}H} = 1$) and background yields, respectively, in each bin of the distributions considered in the combination. The distribution of $\log_{10}(S/B)$ is shown in Fig. 3. The main sensitivity at high values of S/B is given by events selected in the $H \rightarrow \gamma\gamma$ analysis with a diphoton mass around 125 GeV and by events selected in the $H \rightarrow \tau^+\tau^-$, $H \rightarrow WW^*$, and $H \rightarrow b\bar{b}$ analyses with high values of the multivariate discriminating variables used for the signal extraction. A broad excess of events in the rightmost bins of this distribution is observed, consistent with the expectation for $\tilde{t}\tilde{t}H$ production with a SM-like cross section.

The value of the test statistic q as a function of $\mu_{\tilde{t}\tilde{t}H}$ is shown in Fig. 4, with $\mu_{\tilde{t}\tilde{t}H}$ based on the combination of decay modes described above for the combined fit. The results are shown for the combination of all decay modes at 7 + 8 TeV and at 13 TeV, separately, and for all decay modes at all c.m. energies. To quantify the significance of the measured $\tilde{t}\tilde{t}H$ yield, we compute the probability of the background-only hypothesis (p value) as the tail integral of the test statistic using the overall combination evaluated at $\mu_{\tilde{t}\tilde{t}H} = 0$ under the asymptotic approximation [45]. This corresponds to a significance of 5.2 standard deviations for a one-tailed Gaussian distribution. The expected significance for a SM Higgs boson with a mass of 125.09 GeV, evaluated through use of an Asimov data set [45], is 4.2 standard deviations.

In summary, we have reported the observation of $\tilde{t}\tilde{t}H$ production with a significance of 5.2 standard deviations

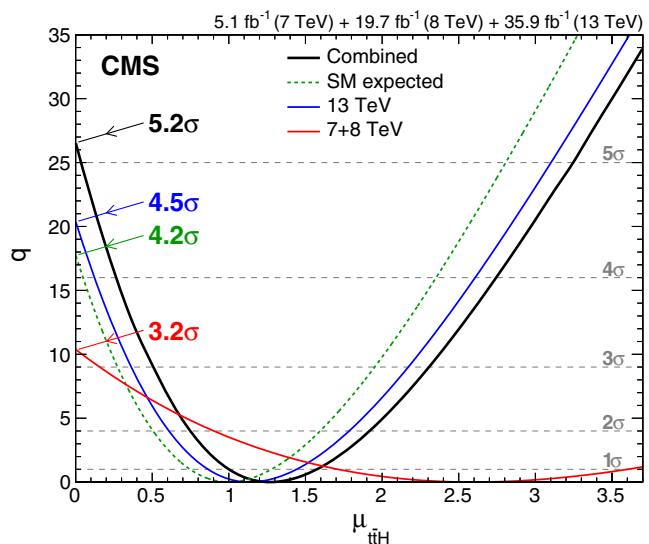


FIG. 4. Test statistic q , described in the text, as a function of $\mu_{\tilde{t}\tilde{t}H}$ for all decay modes at 7 + 8 TeV and at 13 TeV, separately, and for all decay modes at all c.m. energies. The expected SM result for the overall combination is also shown. The horizontal dashed lines indicate the p values for the background-only hypothesis obtained from the asymptotic distribution of q , expressed in units of the number of standard deviations.

above the background-only hypothesis, at a Higgs boson mass of 125.09 GeV. The measured production rate is consistent with the standard model prediction within one standard deviation. In addition to comprising the first observation of a new Higgs boson production mechanism, this measurement establishes the tree-level coupling of the Higgs boson to the top quark, and hence to an up-type quark.

We congratulate our colleagues in the CERN accelerator departments for the excellent performance of the LHC and thank the technical and administrative staffs at CERN and at other CMS institutes for their contributions to the success of the CMS effort. In addition, we gratefully acknowledge the computing centers and personnel of the Worldwide LHC Computing Grid for delivering so effectively the computing infrastructure essential to our analyses. Finally, we acknowledge the enduring support for the construction and operation of the LHC and the CMS detector provided by the following funding agencies: BMFWF and FWF (Austria); FNRS and FWO (Belgium); CNPq, CAPES, FAPERJ, and FAPESP (Brazil); MES (Bulgaria); CERN; CAS, MoST, and NSFC (China); COLCIENCIAS (Colombia); MSES and CSF (Croatia); RPF (Cyprus); SENESCYT (Ecuador); MoER, ERC IUT, and ERDF (Estonia); Academy of Finland, MEC, and HIP (Finland); CEA and CNRS/IN2P3 (France); BMBF, DFG, and HGF (Germany); GSRT (Greece); OTKA and NIH (Hungary); DAE and DST (India); IPM (Iran); SFI (Ireland); INFN (Italy); MSIP and NRF (Republic of Korea); LAS (Lithuania); MOE and UM (Malaysia); BUAP, CINVESTAV, CONACYT, LNS, SEP, and UASLP-FAI (Mexico); MBIE (New Zealand); PAEC (Pakistan); MSHE and NSC (Poland); FCT (Portugal); JINR (Dubna); MON, RosAtom, RAS, RFBR and RAEP (Russia); MESTD (Serbia); SEIDI, CPAN, PCTI and FEDER (Spain); Swiss Funding Agencies (Switzerland); MST (Taipei); ThEPCenter, IPST, STAR, and NSTDA (Thailand); TUBITAK and TAEK (Turkey); NASU and SFFR (Ukraine); STFC (United Kingdom); DOE and NSF (USA).

[1] ATLAS Collaboration, Observation of a new particle in the search for the standard model Higgs boson with the ATLAS detector at the LHC, *Phys. Lett. B* **716**, 1 (2012).
 [2] CMS Collaboration, Observation of a new boson at a mass of 125 GeV with the CMS experiment at the LHC, *Phys. Lett. B* **716**, 30 (2012).
 [3] CMS Collaboration, Observation of a new boson with mass near 125 GeV in pp collisions at $\sqrt{s} = 7$ and 8 TeV, *J. High Energy Phys.* **06** (2013) 081.
 [4] ATLAS Collaboration, The ATLAS experiment at the CERN large hadron collider, *J. Instrum.* **3**, S08003 (2008).
 [5] CMS Collaboration, The CMS experiment at the CERN LHC, *J. Instrum.* **3**, S08004 (2008).

[6] ATLAS and CMS Collaborations, Measurements of the Higgs boson production and decay rates and constraints on its couplings from a combined ATLAS and CMS analysis of the LHC pp collision data at $\sqrt{s} = 7$ and 8 TeV, *J. High Energy Phys.* **08** (2016) 045.
 [7] S. L. Glashow, Partial-symmetries of weak interactions, *Nucl. Phys.* **22**, 579 (1961).
 [8] S. Weinberg, A Model of Leptons, *Phys. Rev. Lett.* **19**, 1264 (1967).
 [9] Abdus Salam, Weak and electromagnetic interactions, in *Elementary Particle Physics: Relativistic Groups and Analyticity*, edited by N. Svartholm (Almqvist & Wiksells, Stockholm, 1968), p. 367.
 [10] CMS Collaboration, Evidence for associated production of a Higgs boson with a top quark pair in final states with electrons, muons, and hadronically decaying τ leptons at $\sqrt{s} = 13$ TeV, [arXiv:1803.05485](https://arxiv.org/abs/1803.05485) [*J. High Energy Phys.* (to be published)].
 [11] CMS Collaboration, Search for $t\bar{t}H$ in all-jet final states in proton-proton collisions at $\sqrt{s} = 13$ TeV, [arXiv:1803.06986](https://arxiv.org/abs/1803.06986) [*J. High Energy Phys.* (to be published)].
 [12] CMS Collaboration, Search for $t\bar{t}H$ production in the $H \rightarrow b\bar{b}$ decay channel with leptonic $t\bar{t}$ decays in proton-proton collisions at $\sqrt{s} = 13$ TeV, [arXiv:1804.03682](https://arxiv.org/abs/1804.03682) [*J. High Energy Phys.* (to be published)].
 [13] CMS Collaboration, Measurements of Higgs boson properties in the diphoton decay channel in proton-proton collisions at $\sqrt{s} = 13$ TeV, [arXiv:1804.02716](https://arxiv.org/abs/1804.02716) [*J. High Energy Phys.* (to be published)].
 [14] CMS Collaboration, Measurements of properties of the Higgs boson decaying into the four-lepton final state in pp collisions at $\sqrt{s} = 13$ TeV, *J. High Energy Phys.* **11** (2017) 047.
 [15] CMS Collaboration, Search for the associated production of the Higgs boson with a top-quark pair, *J. High Energy Phys.* **09** (2014) 087.
 [16] P. W. Higgs, Broken symmetries, massless particles and gauge fields, *Phys. Lett.* **12**, 132 (1964).
 [17] F. Englert and R. Brout, Broken Symmetry and the Mass of Gauge Vector Mesons, *Phys. Rev. Lett.* **13**, 321 (1964).
 [18] P. W. Higgs, Broken Symmetries and the Masses of Gauge Bosons, *Phys. Rev. Lett.* **13**, 508 (1964).
 [19] G. S. Guralnik, C. R. Hagen, and T. W. B. Kibble, Global Conservation Laws and Massless Particles, *Phys. Rev. Lett.* **13**, 585 (1964).
 [20] P. W. Higgs, Spontaneous symmetry breakdown without massless bosons, *Phys. Rev.* **145**, 1156 (1966).
 [21] T. W. B. Kibble, Symmetry breaking in non-Abelian gauge theories, *Phys. Rev.* **155**, 1554 (1967).
 [22] CMS Collaboration, Observation of the Higgs boson decay to a pair of τ leptons, *Phys. Lett. B* **779**, 283 (2018).
 [23] CMS Collaboration, Evidence for the Higgs boson decay to a bottom quark-antiquark pair, *Phys. Lett. B* **780**, 501 (2018).
 [24] ATLAS Collaboration, Evidence for the associated production of the Higgs boson and a top quark pair with the ATLAS detector, *Phys. Rev. D* **97**, 072003 (2018).
 [25] CMS Collaboration, The CMS trigger system, *J. Instrum.* **12**, P01020 (2017).

- [26] CMS Collaboration, Particle-flow reconstruction and global event description with the CMS detector, *J. Instrum.* **12**, P10003 (2017).
- [27] CMS Collaboration, Reconstruction and identification of τ lepton decays to hadrons and ν_τ at CMS, *J. Instrum.* **11**, P01019 (2016).
- [28] CMS Collaboration, Performance of Reconstruction and Identification of Tau Leptons in their Decays to Hadrons and Tau Neutrino in LHC Run-2, CMS Physics Analysis Summary CMS-PAS-TAU-16-002 CERN, 2016, <https://cds.cern.ch/record/2196972>.
- [29] M. Cacciari, G. P. Salam, and G. Soyez, The anti- k_T jet clustering algorithm, *J. High Energy Phys.* **04** (2008) 063.
- [30] M. Cacciari, G. P. Salam, and G. Soyez, FastJet user manual, *Eur. Phys. J. C* **72**, 1896 (2012).
- [31] CMS Collaboration, Identification of b-quark jets with the CMS experiment, *J. Instrum.* **8**, P04013 (2013).
- [32] CMS Collaboration, Identification of heavy-flavour jets with the CMS detector in pp collisions at 13 TeV, [arXiv:1712.07158](https://arxiv.org/abs/1712.07158) [*J. Instrum.* (to be published)].
- [33] CMS Collaboration, CMS Luminosity Measurements for the 2016 Data Taking Period, CMS Physics Analysis Summary CMS-PAS-LUM-17-001 CERN, 2017, <https://cds.cern.ch/record/2257069>.
- [34] CMS Collaboration, CMS Luminosity Based on Pixel Cluster Counting—Summer 2013 Update, CMS Physics Analysis Summary CMS-PAS-LUM-13-001 CERN, 2013, <https://cds.cern.ch/record/1598864>.
- [35] LHC Higgs Cross Section Working Group, Handbook of LHC Higgs Cross Sections: 4. Deciphering the Nature of the Higgs Sector, CYRM-2017-002 CERN, 2016.
- [36] S. Agostinelli *et al.* (GEANT4 Collaboration), GEANT4—a simulation toolkit, *Nucl. Instrum. Methods Phys. Res., Sect. A* **506**, 250 (2003).
- [37] I. Goodfellow, Y. Bengio, and A. Courville, *Deep Learning* (MIT Press, Cambridge, MA, 2016).
- [38] J. Therhaag, A. Hoecker, P. Speckmeyer, E. von Toerne, and H. Voss, TMVA—toolkit for multivariate data analysis, in *Proceedings, Int'l Conf. on Computational Methods in Science and Engineering, 2009, ICCMSE2009*, Vol. 1504 (ICCMSE, 2012), p. 1013.
- [39] V. M. Abazov *et al.* (D0 Collaboration), A precision measurement of the mass of the top quark, *Nature (London)* **429**, 638 (2004).
- [40] V. M. Abazov *et al.* (D0 Collaboration), Helicity of the W boson in lepton + jets $t\bar{t}$ events, *Phys. Lett. B* **617**, 1 (2005).
- [41] CMS Collaboration, Search for a standard model Higgs boson produced in association with a top-quark pair and decaying to bottom quarks using a matrix element method, *Eur. Phys. J. C* **75**, 251 (2015).
- [42] ATLAS Collaboration, CMS Collaboration, LHC Higgs Combination Group, Procedure for the LHC Higgs Boson Search Combination in Summer 2011, Technical Report CMS-NOTE-2011-005, ATL-PHYS-PUB-2011-11 2011, <https://cds.cern.ch/record/1379837>.
- [43] ATLAS and CMS Collaborations, Combined Measurement of the Higgs Boson Mass in pp Collisions at $\sqrt{s} = 7$ and 8 TeV with the ATLAS and CMS Experiments, *Phys. Rev. Lett.* **114**, 191803 (2015).
- [44] CMS Collaboration, Precise determination of the mass of the Higgs boson and tests of compatibility of its couplings with the standard model predictions using proton collisions at 7 and 8 TeV, *Eur. Phys. J. C* **75**, 212 (2015).
- [45] G. Cowan, K. Cranmer, E. Gross, and O. Vitells, Asymptotic formulae for likelihood-based tests of new physics, *Eur. Phys. J. C* **71**, 1554 (2011); Erratum, *Eur. Phys. J. C* **73**, 2501 (2013).

A. M. Sirunyan,¹ A. Tumasyan,¹ W. Adam,² F. Ambrogio,² E. Asilar,² T. Bergauer,² J. Brandstetter,² M. Dragicevic,² J. Erö,² A. Escalante Del Valle,² M. Flechl,² R. Frühwirth,^{2,b} V. M. Ghete,² J. Hrubec,² M. Jeitler,^{2,b} N. Krammer,² I. Krätschmer,² D. Liko,² T. Madlener,² I. Mikulec,² N. Rad,² H. Rohringer,² J. Schieck,^{2,b} R. Schöfbeck,² M. Spanring,² D. Spitzbart,² A. Taurok,² W. Waltenberger,² J. Wittmann,² C.-E. Wulz,^{2,b} M. Zarucki,² V. Chekhovsky,³ V. Mossolov,³ J. Suarez Gonzalez,³ E. A. De Wolf,⁴ D. Di Croce,⁴ X. Janssen,⁴ J. Lauwers,⁴ M. Pieters,⁴ M. Van De Klundert,⁴ H. Van Haevermaet,⁴ P. Van Mechelen,⁴ N. Van Remortel,⁴ S. Abu Zeid,⁵ F. Blekman,⁵ J. D'Hondt,⁵ I. De Bruyn,⁵ J. De Clercq,⁵ K. Deroover,⁵ G. Flouris,⁵ D. Lontkovskyi,⁵ S. Lowette,⁵ I. Marchesini,⁵ S. Moortgat,⁵ L. Moreels,⁵ Q. Python,⁵ K. Skovpen,⁵ S. Tavernier,⁵ W. Van Doninck,⁵ P. Van Mulders,⁵ I. Van Parijs,⁵ D. Beghin,⁶ B. Bilin,⁶ H. Brun,⁶ B. Clerbaux,⁶ G. De Lentdecker,⁶ H. Delannoy,⁶ B. Dorney,⁶ G. Fasanella,⁶ L. Favart,⁶ R. Goldouzian,⁶ A. Grebenyuk,⁶ A. K. Kalsi,⁶ T. Lenzi,⁶ J. Luetic,⁶ N. Postiau,⁶ E. Starling,⁶ L. Thomas,⁶ C. Vander Velde,⁶ P. Vanlaer,⁶ D. Vannerom,⁶ Q. Wang,⁶ T. Cornelis,⁷ D. Dobur,⁷ A. Fagot,⁷ M. Gul,⁷ I. Khvastunov,^{7,c} D. Poyraz,⁷ C. Roskas,⁷ D. Trocino,⁷ M. Tytgat,⁷ W. Verbeke,⁷ B. Vermassen,⁷ M. Vit,⁷ N. Zaganidis,⁷ H. Bakhshiansohi,⁸ O. Bondu,⁸ S. Brochet,⁸ G. Bruno,⁸ C. Caputo,⁸ P. David,⁸ C. Delaere,⁸ M. Delcourt,⁸ B. Francois,⁸ A. Giammanco,⁸ G. Krintiras,⁸ V. Lemaître,⁸ A. Magitteri,⁸ A. Mertens,⁸ M. Musich,⁸ K. Piotrkowski,⁸ A. Saggio,⁸ M. Vidal Marono,⁸ S. Wertz,⁸ J. Zobec,⁸ F. L. Alves,⁹ G. A. Alves,⁹ L. Brito,⁹ M. Correa Martins Junior,⁹ G. Correia Silva,⁹ C. Hensel,⁹ A. Moraes,⁹ M. E. Pol,⁹ P. Rebello Teles,⁹ E. Belchior Batista Das Chagas,¹⁰ W. Carvalho,¹⁰ J. Chinellato,^{10,d} E. Coelho,¹⁰ E. M. Da Costa,¹⁰ G. G. Da Silveira,^{10,e}

D. De Jesus Damiao,¹⁰ C. De Oliveira Martins,¹⁰ S. Fonseca De Souza,¹⁰ H. Malbouisson,¹⁰ D. Matos Figueiredo,¹⁰ M. Melo De Almeida,¹⁰ C. Mora Herrera,¹⁰ L. Mundim,¹⁰ H. Nogima,¹⁰ W. L. Prado Da Silva,¹⁰ L. J. Sanchez Rosas,¹⁰ A. Santoro,¹⁰ A. Sznajder,¹⁰ M. Thiel,¹⁰ E. J. Tonelli Manganote,^{10,d} F. Torres Da Silva De Araujo,¹⁰ A. Vilela Pereira,¹⁰ S. Ahuja,^{11a} C. A. Bernardes,^{11a} L. Calligaris,^{11a} T. R. Fernandez Perez Tomei,^{11a} E. M. Gregores,^{11b} P. G. Mercadante,^{11b} S. F. Novaes,^{11a} Sandra S. Padula,^{11a} D. Romero Abad,^{11b} A. Aleksandrov,¹² R. Hadjiiska,¹² P. Iaydjiev,¹² A. Marinov,¹² M. Misheva,¹² M. Rodozov,¹² M. Shopova,¹² G. Sultanov,¹² A. Dimitrov,¹³ L. Litov,¹³ B. Pavlov,¹³ P. Petkov,¹³ W. Fang,^{14,f} X. Gao,^{14,f} L. Yuan,¹⁴ M. Ahmad,¹⁵ J. G. Bian,¹⁵ G. M. Chen,¹⁵ H. S. Chen,¹⁵ M. Chen,¹⁵ Y. Chen,¹⁵ C. H. Jiang,¹⁵ D. Leggat,¹⁵ H. Liao,¹⁵ Z. Liu,¹⁵ F. Romeo,¹⁵ S. M. Shaheen,^{15,g} A. Spiezia,¹⁵ J. Tao,¹⁵ C. Wang,¹⁵ Z. Wang,¹⁵ E. Yazgan,¹⁵ H. Zhang,¹⁵ J. Zhao,¹⁵ Y. Ban,¹⁶ G. Chen,¹⁶ A. Levin,¹⁶ J. Li,¹⁶ L. Li,¹⁶ Q. Li,¹⁶ Y. Mao,¹⁶ S. J. Qian,¹⁶ D. Wang,¹⁶ Z. Xu,¹⁶ Y. Wang,¹⁷ C. Avila,¹⁸ A. Cabrera,¹⁸ C. A. Carrillo Montoya,¹⁸ L. F. Chaparro Sierra,¹⁸ C. Florez,¹⁸ C. F. González Hernández,¹⁸ M. A. Segura Delgado,¹⁸ B. Courbon,¹⁹ N. Godinovic,¹⁹ D. Lelas,¹⁹ I. Puljak,¹⁹ T. Sculac,¹⁹ Z. Antunovic,²⁰ M. Kovac,²⁰ V. Brigljevic,²¹ D. Ferencek,²¹ K. Kadija,²¹ B. Mesic,²¹ A. Starodumov,^{21,h} T. Susa,²¹ M. W. Ather,²² A. Attikis,²² M. Kolosova,²² G. Mavromanolakis,²² J. Mousa,²² C. Nicolaou,²² F. Ptochos,²² P. A. Razis,²² H. Rykaczewski,²² M. Finger,^{23,i} M. Finger Jr.,^{23,i} E. Ayala,²⁴ E. Carrera Jarrin,²⁵ H. Abdalla,^{26,j} A. A. Abdelalim,^{26,k,l} A. Mohamed,^{26,l} S. Bhowmik,²⁷ A. Carvalho Antunes De Oliveira,²⁷ R. K. Dewanjee,²⁷ K. Ehataht,²⁷ M. Kadastik,²⁷ M. Raidal,²⁷ C. Veelken,²⁷ P. Eerola,²⁸ H. Kirschenmann,²⁸ J. Pekkanen,²⁸ M. Voutilainen,²⁸ J. Havukainen,²⁹ J. K. Heikkilä,²⁹ T. Järvinen,²⁹ V. Karimäki,²⁹ R. Kinnunen,²⁹ T. Lampén,²⁹ K. Lassila-Perini,²⁹ S. Laurila,²⁹ S. Lehti,²⁹ T. Lindén,²⁹ P. Luukka,²⁹ T. Mäenpää,²⁹ H. Siikonen,²⁹ E. Tuominen,²⁹ J. Tuominiemi,²⁹ T. Tuuva,³⁰ M. Besancon,³¹ F. Couderc,³¹ M. Dejardin,³¹ D. Denegri,³¹ J. L. Faure,³¹ F. Ferri,³¹ S. Ganjour,³¹ A. Givernaud,³¹ P. Gras,³¹ G. Hamel de Monchenault,³¹ P. Jarry,³¹ C. Leloup,³¹ E. Locci,³¹ J. Malcles,³¹ G. Negro,³¹ J. Rander,³¹ A. Rosowsky,³¹ M. Ö. Sahin,³¹ M. Titov,³¹ A. Abdulsalam,^{32,m} C. Amendola,³² I. Antropov,³² F. Beaudette,³² P. Busson,³² C. Charlot,³² R. Granier de Cassagnac,³² I. Kucher,³² A. Lobanov,³² J. Martin Blanco,³² M. Nguyen,³² C. Ochando,³² G. Ortona,³² P. Pigard,³² R. Salerno,³² J. B. Sauvan,³² Y. Sirois,³² A. G. Stahl Leitner,³² A. Zabi,³² A. Zghiche,³² J.-L. Agram,^{33,n} J. Andrea,³³ D. Bloch,³³ J.-M. Brom,³³ E. C. Chabert,³³ V. Cherepanov,³³ C. Collard,³³ E. Conte,^{33,n} J.-C. Fontaine,^{33,n} D. Gelé,³³ U. Goerlach,³³ M. Jansová,³³ A.-C. Le Bihan,³³ N. Tonon,³³ P. Van Hove,³³ S. Gadrat,³⁴ S. Beauceron,³⁵ C. Bernet,³⁵ G. Boudoul,³⁵ N. Chanon,³⁵ R. Chierici,³⁵ D. Contardo,³⁵ P. Depasse,³⁵ H. El Mamouni,³⁵ J. Fay,³⁵ L. Finco,³⁵ S. Gascon,³⁵ M. Gouzevitch,³⁵ G. Grenier,³⁵ B. Ille,³⁵ F. Lagarde,³⁵ I. B. Laktineh,³⁵ H. Lattaud,³⁵ M. Lethuillier,³⁵ L. Mirabito,³⁵ A. L. Pequegnot,³⁵ S. Perries,³⁵ A. Popov,^{35,o} V. Sordini,³⁵ M. Vander Donckt,³⁵ S. Viret,³⁵ S. Zhang,³⁵ A. Khvedelidze,^{36,i} Z. Tsamalaidze,^{37,i} C. Autermann,³⁸ L. Feld,³⁸ M. K. Kiesel,³⁸ K. Klein,³⁸ M. Lipinski,³⁸ M. Preuten,³⁸ M. P. Rauch,³⁸ C. Schomakers,³⁸ J. Schulz,³⁸ M. Teroerde,³⁸ B. Wittmer,³⁸ V. Zhukov,^{38,o} A. Albert,³⁹ D. Duchardt,³⁹ M. Endres,³⁹ M. Erdmann,³⁹ T. Esch,³⁹ R. Fischer,³⁹ S. Ghosh,³⁹ A. Güth,³⁹ T. Hebbeker,³⁹ C. Heidemann,³⁹ K. Hoepfner,³⁹ H. Keller,³⁹ S. Knutzen,³⁹ L. Mastrolorenzo,³⁹ M. Merschmeyer,³⁹ A. Meyer,³⁹ P. Millet,³⁹ S. Mukherjee,³⁹ T. Pook,³⁹ M. Radziej,³⁹ Y. Rath,³⁹ H. Reithler,³⁹ M. Rieger,³⁹ F. Scheuch,³⁹ A. Schmidt,³⁹ D. Teyssier,³⁹ G. Flügge,⁴⁰ O. Hlushchenko,⁴⁰ T. Kress,⁴⁰ A. Künsken,⁴⁰ T. Müller,⁴⁰ A. Nehr Korn,⁴⁰ A. Nowack,⁴⁰ C. Pistone,⁴⁰ O. Pooth,⁴⁰ D. Roy,⁴⁰ H. Sert,⁴⁰ A. Stahl,^{40,p} M. Aldaya Martin,⁴¹ T. Arndt,⁴¹ C. Asawatangtrakuldee,⁴¹ I. Babounikau,⁴¹ K. Beernaert,⁴¹ O. Behnke,⁴¹ U. Behrens,⁴¹ A. Bermúdez Martínez,⁴¹ D. Bertsche,⁴¹ A. A. Bin Anuar,⁴¹ K. Borras,^{41,q} V. Botta,⁴¹ A. Campbell,⁴¹ P. Connor,⁴¹ C. Contreras-Campana,⁴¹ F. Costanza,⁴¹ V. Danilov,⁴¹ A. De Wit,⁴¹ M. M. Defranchis,⁴¹ C. Diez Pardos,⁴¹ D. Domínguez Damiani,⁴¹ G. Eckerlin,⁴¹ T. Eichhorn,⁴¹ A. Elwood,⁴¹ E. Eren,⁴¹ E. Gallo,^{41,r} A. Geiser,⁴¹ J. M. Grados Luyando,⁴¹ A. Grohsjean,⁴¹ P. Gunnellini,⁴¹ M. Guthoff,⁴¹ M. Haranko,⁴¹ A. Harb,⁴¹ J. Hauk,⁴¹ H. Jung,⁴¹ M. Kasemann,⁴¹ J. Keaveney,⁴¹ C. Kleinwort,⁴¹ J. Knolle,⁴¹ D. Krücker,⁴¹ W. Lange,⁴¹ A. Lelek,⁴¹ T. Lenz,⁴¹ K. Lipka,⁴¹ W. Lohmann,^{41,s} R. Mankel,⁴¹ I.-A. Melzer-Pellmann,⁴¹ A. B. Meyer,⁴¹ M. Meyer,⁴¹ M. Missiroli,⁴¹ G. Mittag,⁴¹ J. Mnich,⁴¹ V. Myronenko,⁴¹ S. K. Pflitsch,⁴¹ D. Pitzl,⁴¹ A. Raspereza,⁴¹ A. Saibel,⁴¹ M. Savitskyi,⁴¹ P. Saxena,⁴¹ P. Schütze,⁴¹ C. Schwanenberger,⁴¹ R. Shevchenko,⁴¹ A. Singh,⁴¹ H. Tholen,⁴¹ O. Turkot,⁴¹ A. Vagnerini,⁴¹ G. P. Van Onsem,⁴¹ R. Walsh,⁴¹ Y. Wen,⁴¹ K. Wichmann,⁴¹ C. Wissing,⁴¹ O. Zenaiev,⁴¹ R. Aggleton,⁴² S. Bein,⁴² L. Benato,⁴² A. Benecke,⁴² V. Blobel,⁴² M. Centis Vignali,⁴² T. Dreyer,⁴² E. Garutti,⁴² D. Gonzalez,⁴² J. Haller,⁴² A. Hinzmann,⁴² A. Karavdina,⁴² G. Kasieczka,⁴² R. Klanner,⁴² R. Kogler,⁴² N. Kovalchuk,⁴² S. Kurz,⁴² V. Kutzner,⁴² J. Lange,⁴² D. Marconi,⁴² J. Multhaup,⁴² M. Niedziela,⁴² D. Nowatschin,⁴² A. Perieanu,⁴² A. Reimers,⁴² O. Rieger,⁴² C. Scharf,⁴² P. Schleper,⁴² S. Schumann,⁴² J. Schwandt,⁴² J. Sonneveld,⁴² H. Stadie,⁴² G. Steinbrück,⁴² F. M. Stober,⁴² M. Stöver,⁴² D. Troendle,⁴² A. Vanhoefer,⁴² B. Vormwald,⁴² M. Akbiyik,⁴³ C. Barth,⁴³ M. Baselga,⁴³ S. Baur,⁴³ E. Butz,⁴³ R. Caspart,⁴³ T. Chwalek,⁴³ F. Colombo,⁴³

W. De Boer,⁴³ A. Dierlamm,⁴³ K. El Morabit,⁴³ N. Faltermann,⁴³ B. Freund,⁴³ M. Giffels,⁴³ M. A. Harrendorf,⁴³ F. Hartmann,^{43,p} S. M. Heindl,⁴³ U. Husemann,⁴³ F. Kassel,^{43,p} I. Katkov,^{43,o} P. Keicher,⁴³ S. Kudella,⁴³ H. Mildner,⁴³ S. Mitra,⁴³ M. U. Mozer,⁴³ Th. Müller,⁴³ M. Plagge,⁴³ G. Quast,⁴³ K. Rabbertz,⁴³ M. Schröder,⁴³ I. Shvetsov,⁴³ G. Sieber,⁴³ H. J. Simonis,⁴³ R. Ulrich,⁴³ S. Wayand,⁴³ M. Waßmer,⁴³ M. Weber,⁴³ T. Weiler,⁴³ S. Williamson,⁴³ C. Wöhrmann,⁴³ R. Wolf,⁴³ G. Anagnostou,⁴⁴ G. Daskalakis,⁴⁴ T. Gerialis,⁴⁴ A. Kyriakis,⁴⁴ D. Loukas,⁴⁴ G. Paspalaki,⁴⁴ I. Topsis-Giotis,⁴⁴ G. Karathanasis,⁴⁵ S. Kesisoglou,⁴⁵ P. Kontaxakis,⁴⁵ A. Panagiotou,⁴⁵ I. Papavergou,⁴⁵ N. Saoulidou,⁴⁵ E. Tziaferi,⁴⁵ K. Vellidis,⁴⁵ K. Kousouris,⁴⁶ I. Papakrivopoulos,⁴⁶ G. Tsiopolitis,⁴⁶ I. Evangelou,⁴⁷ C. Foudas,⁴⁷ P. Gianneios,⁴⁷ P. Katsoulis,⁴⁷ P. Kokkas,⁴⁷ S. Mallios,⁴⁷ N. Manthos,⁴⁷ I. Papadopoulos,⁴⁷ E. Paradis,⁴⁷ J. Strologas,⁴⁷ F. A. Triantis,⁴⁷ D. Tsitsonis,⁴⁷ M. Bartók,^{48,t} M. Csanad,⁴⁸ N. Filipovic,⁴⁸ P. Major,⁴⁸ M. I. Nagy,⁴⁸ G. Pasztor,⁴⁸ O. Surányi,⁴⁸ G. I. Veres,⁴⁸ G. Bencze,⁴⁹ C. Hajdu,⁴⁹ D. Horvath,^{49,u} Á. Hunyadi,⁴⁹ F. Sikler,⁴⁹ V. Veszpremi,⁴⁹ G. Vesztergombi,^{49,a} T. Á. Vámi,⁴⁹ N. Beni,⁵⁰ S. Czellar,⁵⁰ J. Karancsi,^{50,v} A. Makovec,⁵⁰ J. Molnar,⁵⁰ Z. Szillasi,⁵⁰ P. Raics,⁵¹ Z. L. Trocsanyi,⁵¹ B. Ujvari,⁵¹ S. Choudhury,⁵² J. R. Komaragiri,⁵² P. C. Tiwari,⁵² S. Bahinipati,^{53,w} C. Kar,⁵³ P. Mal,⁵³ K. Mandal,⁵³ A. Nayak,^{53,x} D. K. Sahoo,^{53,w} S. K. Swain,⁵³ S. Bansal,⁵⁴ S. B. Beri,⁵⁴ V. Bhatnagar,⁵⁴ S. Chauhan,⁵⁴ R. Chawla,⁵⁴ N. Dhingra,⁵⁴ R. Gupta,⁵⁴ A. Kaur,⁵⁴ A. Kaur,⁵⁴ M. Kaur,⁵⁴ S. Kaur,⁵⁴ R. Kumar,⁵⁴ P. Kumari,⁵⁴ M. Lohan,⁵⁴ A. Mehta,⁵⁴ K. Sandeep,⁵⁴ S. Sharma,⁵⁴ J. B. Singh,⁵⁴ G. Walia,⁵⁴ Ashok Kumar,⁵⁵ Aashaq Shah,⁵⁵ A. Bhardwaj,⁵⁵ B. C. Choudhary,⁵⁵ R. B. Garg,⁵⁵ M. Gola,⁵⁵ S. Keshri,⁵⁵ S. Malhotra,⁵⁵ M. Naimuddin,⁵⁵ P. Priyanka,⁵⁵ K. Ranjan,⁵⁵ R. Sharma,⁵⁵ R. Bhardwaj,^{56,y} M. Bharti,⁵⁶ R. Bhattacharya,⁵⁶ S. Bhattacharya,⁵⁶ U. Bhawandeep,^{56,y} D. Bhowmik,⁵⁶ S. Dey,⁵⁶ S. Dutt,^{56,y} S. Dutta,⁵⁶ S. Ghosh,⁵⁶ K. Mondal,⁵⁶ S. Nandan,⁵⁶ A. Purohit,⁵⁶ P. K. Rout,⁵⁶ A. Roy,⁵⁶ S. Roy Chowdhury,⁵⁶ G. Saha,⁵⁶ S. Sarkar,⁵⁶ M. Sharan,⁵⁶ B. Singh,⁵⁶ S. Thakur,^{56,y} P. K. Behera,⁵⁷ R. Chudasama,⁵⁸ D. Dutta,⁵⁸ V. Jha,⁵⁸ V. Kumar,⁵⁸ P. K. Netrakanti,⁵⁸ L. M. Pant,⁵⁸ P. Shukla,⁵⁸ Ravindra Kumar Verma,⁵⁹ T. Aziz,⁵⁹ M. A. Bhat,⁵⁹ S. Dugad,⁵⁹ G. B. Mohanty,⁵⁹ N. Sur,⁵⁹ B. Sutar,⁵⁹ S. Banerjee,⁶⁰ S. Bhattacharya,⁶⁰ S. Chatterjee,⁶⁰ P. Das,⁶⁰ M. Guchait,⁶⁰ Sa. Jain,⁶⁰ S. Karmakar,⁶⁰ S. Kumar,⁶⁰ M. Maity,^{60,z} G. Majumder,⁶⁰ K. Mazumdar,⁶⁰ N. Sahoo,⁶⁰ T. Sarkar,^{60,z} S. Chauhan,⁶¹ S. Dube,⁶¹ V. Hegde,⁶¹ A. Kapoor,⁶¹ K. Kotheekar,⁶¹ S. Pandey,⁶¹ A. Rane,⁶¹ S. Sharma,⁶¹ S. Chenarani,^{62,aa} E. Eskandari Tadavani,⁶² S. M. Etesami,^{62,aa} M. Khakzad,⁶² M. Mohammadi Najafabadi,⁶² M. Naseri,⁶² F. Rezaei Hosseinabadi,⁶² B. Safarzadeh,^{62,bb} M. Zeinali,⁶² M. Felcini,⁶³ M. Grunewald,⁶³ M. Abbrescia,^{64a,64b} C. Calabria,^{64a,64b} A. Colaleo,^{64a} D. Creanza,^{64a,64c} L. Cristella,^{64a,64b} N. De Filippis,^{64a,64c} M. De Palma,^{64a,64b} A. Di Florio,^{64a,64b} F. Errico,^{64a,64b} L. Fiore,^{64a} A. Gelmi,^{64a,64b} G. Iaselli,^{64a,64c} M. Ince,^{64a,64b} S. Lezki,^{64a,64b} G. Maggi,^{64a,64c} M. Maggi,^{64a} G. Miniello,^{64a,64b} S. My,^{64a,64b} S. Nuzzo,^{64a,64b} A. Pompili,^{64a,64b} G. Pugliese,^{64a,64c} R. Radogna,^{64a} A. Ranieri,^{64a} G. Selvaggi,^{64a,64b} A. Sharma,^{64a} L. Silvestris,^{64a} R. Venditti,^{64a} P. Verwilligen,^{64a} G. Zito,^{64a} G. Abbiendi,^{65a} C. Battilana,^{65a,65b} D. Bonacorsi,^{65a,65b} L. Borgonovi,^{65a,65b} S. Braibant-Giacomelli,^{65a,65b} R. Campanini,^{65a,65b} P. Capiluppi,^{65a,65b} A. Castro,^{65a,65b} F. R. Cavallo,^{65a} S. S. Chhibra,^{65a,65b} C. Ciocca,^{65a} G. Codispoti,^{65a,65b} M. Cuffiani,^{65a,65b} G. M. Dallavalle,^{65a} F. Fabbri,^{65a} A. Fanfani,^{65a,65b} P. Giacomelli,^{65a} C. Grandi,^{65a} L. Guiducci,^{65a,65b} F. Iemmi,^{65a,65b} S. Marcellini,^{65a} G. Masetti,^{65a} A. Montanari,^{65a} F. L. Navarra,^{65a,65b} A. Perrotta,^{65a} F. Primavera,^{65a,65b,p} A. M. Rossi,^{65a,65b} T. Rovelli,^{65a,65b} G. P. Siroli,^{65a,65b} N. Tosi,^{65a} S. Albergo,^{66a,66b} A. Di Mattia,^{66a} R. Potenza,^{66a,66b} A. Tricoli,^{66a,66b} C. Tuve,^{66a,66b} G. Barbagli,^{67a} K. Chatterjee,^{67a,67b} V. Ciulli,^{67a,67b} C. Civinini,^{67a} R. D'Alessandro,^{67a,67b} E. Focardi,^{67a,67b} G. Latino,^{67a} P. Lenzi,^{67a,67b} M. Meschini,^{67a} S. Paoletti,^{67a} L. Russo,^{67a,cc} G. Sguazzoni,^{67a} D. Strom,^{67a} L. Viliani,^{67a} L. Benussi,⁶⁸ S. Bianco,⁶⁸ F. Fabbri,⁶⁸ D. Piccolo,⁶⁸ F. Ferro,^{69a} F. Ravera,^{69a,69b} E. Robutti,^{69a} S. Tosi,^{69a,69b} A. Benaglia,^{70a} A. Beschi,^{70b} L. Brianza,^{70a,70b} F. Brivio,^{70a,70b} V. Ciriolo,^{70a,70b,p} S. Di Guida,^{70a,p} M. E. Dinardo,^{70a,70b} S. Fiorendi,^{70a,70b} S. Gennai,^{70a} A. Ghezzi,^{70a,70b} P. Govoni,^{70a,70b} M. Malberti,^{70a,70b} S. Malvezzi,^{70a} A. Massironi,^{70a,70b} D. Menasce,^{70a} L. Moroni,^{70a} M. Paganoni,^{70a,70b} D. Pedrini,^{70a} S. Ragazzi,^{70a,70b} T. Tabarelli de Fatis,^{70a,70b} D. Zuolo,^{70a} S. Buontempo,^{71a} N. Cavallo,^{71a,71c} A. Di Crescenzo,^{71a,71b} F. Fabozzi,^{71a,71c} F. Fienga,^{71a} G. Galati,^{71a} A. O. M. Iorio,^{71a,71b} W. A. Khan,^{71a} L. Lista,^{71a} S. Meola,^{71a,71d,p} P. Paolucci,^{71a,p} C. Sciacca,^{71a,71b} E. Voevodina,^{71a,71b} P. Azzi,^{72a} N. Bacchetta,^{72a} D. Bisello,^{72a,72b} A. Boletti,^{72a,72b} A. Bragagnolo,^{72a} R. Carlin,^{72a,72b} P. Checchia,^{72a} M. Dall'Osso,^{72a,72b} P. De Castro Manzano,^{72a} T. Dorigo,^{72a} F. Fanzago,^{72a} U. Gasparini,^{72a,72b} A. Gozzelino,^{72a} S. Y. Hoh,^{72a} S. Lacaprara,^{72a} P. Lujan,^{72a} M. Margoni,^{72a,72b} A. T. Meneguzzo,^{72a,72b} J. Pazzini,^{72a,72b} N. Pozzobon,^{72a,72b} P. Ronchese,^{72a,72b} R. Rossin,^{72a,72b} F. Simonetto,^{72a,72b} A. Tiko,^{72a} E. Torassa,^{72a} M. Zanetti,^{72a,72b} P. Zotto,^{72a,72b} G. Zumerle,^{72a,72b} A. Braghieri,^{73a} A. Magnani,^{73a} P. Montagna,^{73a,73b} S. P. Ratti,^{73a,73b} V. Re,^{73a} M. Ressegotti,^{73a,73b} C. Riccardi,^{73a,73b} P. Salvini,^{73a} I. Vai,^{73a,73b} P. Vitulo,^{73a,73b} L. Alunni Solestizi,^{74a,74b} M. Biasini,^{74a,74b} G. M. Bilei,^{74a} C. Cecchi,^{74a,74b} D. Ciangottini,^{74a,74b} L. Fanò,^{74a,74b} P. Lariccia,^{74a,74b} R. Leonardi,^{74a,74b} E. Manoni,^{74a} G. Mantovani,^{74a,74b} V. Mariani,^{74a,74b} M. Menichelli,^{74a} A. Rossi,^{74a,74b} A. Santocchia,^{74a,74b} D. Spiga,^{74a} K. Androsov,^{75a}

P. Azzurri,^{75a} G. Bagliesi,^{75a} L. Bianchini,^{75a} T. Boccali,^{75a} L. Borrello,^{75a} R. Castaldi,^{75a} M. A. Ciocci,^{75a,75b} R. Dell'Orso,^{75a}
 G. Fedi,^{75a} F. Fiori,^{75a,75c} L. Giannini,^{75a,75c} A. Giassi,^{75a} M. T. Grippo,^{75a} F. Ligabue,^{75a,75c} E. Manca,^{75a,75c}
 G. Mandorli,^{75a,75c} A. Messineo,^{75a,75b} F. Palla,^{75a} A. Rizzi,^{75a,75b} P. Spagnolo,^{75a} R. Tenchini,^{75a} G. Tonelli,^{75a,75b}
 A. Venturi,^{75a} P. G. Verdini,^{75a} L. Barone,^{76a,76b} F. Cavallari,^{76a} M. Cipriani,^{76a,76b} N. Daci,^{76a} D. Del Re,^{76a,76b}
 E. Di Marco,^{76a,76b} M. Diemoz,^{76a} S. Gelli,^{76a,76b} E. Longo,^{76a,76b} B. Marzocchi,^{76a,76b} P. Meridiani,^{76a} G. Organtini,^{76a,76b}
 F. Pandolfi,^{76a} R. Paramatti,^{76a,76b} F. Preiato,^{76a,76b} S. Rahatlou,^{76a,76b} C. Rovelli,^{76a} F. Santanastasio,^{76a,76b} N. Amapane,^{77a,77b}
 R. Arcidiacono,^{77a,77c} S. Argiro,^{77a,77b} M. Arneodo,^{77a,77c} N. Bartosik,^{77a} R. Bellan,^{77a,77b} C. Biino,^{77a} N. Cartiglia,^{77a}
 F. Cenna,^{77a,77b} S. Cometti,^{77a} M. Costa,^{77a,77b} R. Covarelli,^{77a,77b} N. Demaria,^{77a} B. Kiani,^{77a,77b} C. Mariotti,^{77a} S. Maselli,^{77a}
 E. Migliore,^{77a,77b} V. Monaco,^{77a,77b} E. Monteil,^{77a,77b} M. Monteno,^{77a} M. M. Obertino,^{77a,77b} L. Pacher,^{77a,77b} N. Pastrone,^{77a}
 M. Pelliccioni,^{77a} G. L. Pinna Angioni,^{77a,77b} A. Romero,^{77a,77b} M. Ruspa,^{77a,77c} R. Sacchi,^{77a,77b} K. Shchelina,^{77a,77b}
 V. Sola,^{77a} A. Solano,^{77a,77b} D. Soldi,^{77a} A. Staiano,^{77a} S. Belforte,^{78a} V. Candelise,^{78a,78b} M. Casarsa,^{78a} F. Cossutti,^{78a}
 G. Della Ricca,^{78a,78b} F. Vazzoler,^{78a,78b} A. Zanetti,^{78a} D. H. Kim,⁷⁹ G. N. Kim,⁷⁹ M. S. Kim,⁷⁹ J. Lee,⁷⁹ S. Lee,⁷⁹ S. W. Lee,⁷⁹
 C. S. Moon,⁷⁹ Y. D. Oh,⁷⁹ S. Sekmen,⁷⁹ D. C. Son,⁷⁹ Y. C. Yang,⁷⁹ H. Kim,⁸⁰ D. H. Moon,⁸⁰ G. Oh,⁸⁰ J. Goh,^{81,dd} T. J. Kim,⁸¹
 S. Cho,⁸² S. Choi,⁸² Y. Go,⁸² D. Gyun,⁸² S. Ha,⁸² B. Hong,⁸² Y. Jo,⁸² K. Lee,⁸² K. S. Lee,⁸² S. Lee,⁸² J. Lim,⁸² S. K. Park,⁸²
 Y. Roh,⁸² H. S. Kim,⁸³ J. Almond,⁸⁴ J. Kim,⁸⁴ J. S. Kim,⁸⁴ H. Lee,⁸⁴ K. Lee,⁸⁴ K. Nam,⁸⁴ S. B. Oh,⁸⁴ B. C. Radburn-Smith,⁸⁴
 S. h. Seo,⁸⁴ U. K. Yang,⁸⁴ H. D. Yoo,⁸⁴ G. B. Yu,⁸⁴ D. Jeon,⁸⁵ H. Kim,⁸⁵ J. H. Kim,⁸⁵ J. S. H. Lee,⁸⁵ I. C. Park,⁸⁵ Y. Choi,⁸⁶
 C. Hwang,⁸⁶ J. Lee,⁸⁶ I. Yu,⁸⁶ V. Dudenias,⁸⁷ A. Juodagalvis,⁸⁷ J. Vaitkus,⁸⁷ I. Ahmed,⁸⁸ Z. A. Ibrahim,⁸⁸
 M. A. B. Md Ali,^{88,ee} F. Mohamad Idris,^{88,ff} W. A. T. Wan Abdullah,⁸⁸ M. N. Yusli,⁸⁸ Z. Zolkapli,⁸⁸
 A. Castaneda Hernandez,⁸⁹ J. A. Murillo Quijada,⁸⁹ R. Reyes-Almanza,⁹⁰ G. Ramirez-Sanchez,⁹⁰ M. C. Duran-Osuna,⁹⁰
 H. Castilla-Valdez,⁹⁰ E. De La Cruz-Burelo,⁹⁰ I. Heredia-De La Cruz,^{90,gg} R. I. Rabadan-Trejo,⁹⁰ R. Lopez-Fernandez,⁹⁰
 J. Mejia Guisao,⁹⁰ M. Ramirez-Garcia,⁹⁰ A. Sanchez-Hernandez,⁹⁰ S. Carrillo Moreno,⁹¹ C. Oropeza Barrera,⁹¹
 F. Vazquez Valencia,⁹¹ J. Eysermans,⁹² I. Pedraza,⁹² H. A. Salazar Ibarguen,⁹² C. Uribe Estrada,⁹² A. Morelos Pineda,⁹³
 D. Krofcheck,⁹⁴ S. Bheesette,⁹⁵ P. H. Butler,⁹⁵ A. Ahmad,⁹⁶ M. Ahmad,⁹⁶ M. I. Asghar,⁹⁶ Q. Hassan,⁹⁶ H. R. Hoorani,⁹⁶
 A. Saddique,⁹⁶ M. A. Shah,⁹⁶ M. Shoaib,⁹⁶ M. Waqas,⁹⁶ H. Bialkowska,⁹⁷ M. Bluj,⁹⁷ B. Boimska,⁹⁷ T. Frueboes,⁹⁷
 M. Górski,⁹⁷ M. Kazana,⁹⁷ K. Nawrocki,⁹⁷ M. Szleper,⁹⁷ P. Traczyk,⁹⁷ P. Zalewski,⁹⁷ K. Bunkowski,⁹⁸ A. Byszuk,^{98,hh}
 K. Doroba,⁹⁸ A. Kalinowski,⁹⁸ M. Konecki,⁹⁸ J. Krolikowski,⁹⁸ M. Misiura,⁹⁸ M. Olszewski,⁹⁸ A. Pyskir,⁹⁸ M. Walczak,⁹⁸
 M. Araujo,⁹⁹ P. Bargassa,⁹⁹ C. Beirão Da Cruz E Silva,⁹⁹ A. Di Francesco,⁹⁹ P. Faccioli,⁹⁹ B. Galinhas,⁹⁹ M. Gallinaro,⁹⁹
 J. Hollar,⁹⁹ N. Leonardo,⁹⁹ M. V. Nemallapudi,⁹⁹ J. Seixas,⁹⁹ G. Strong,⁹⁹ O. Toldaiev,⁹⁹ D. Vadrucchio,⁹⁹ J. Varela,⁹⁹
 S. Afanasiev,¹⁰⁰ V. Alexakhin,¹⁰⁰ P. Bunin,¹⁰⁰ M. Gavrilenko,¹⁰⁰ A. Golunov,¹⁰⁰ I. Golutvin,¹⁰⁰ N. Gorbounov,¹⁰⁰
 V. Karjavin,¹⁰⁰ A. Lanev,¹⁰⁰ A. Malakhov,¹⁰⁰ V. Matveev,^{100,ii,jj} P. Moiseev,¹⁰⁰ V. Palichik,¹⁰⁰ V. Perelygin,¹⁰⁰ M. Savina,¹⁰⁰
 S. Shmatov,¹⁰⁰ V. Smirnov,¹⁰⁰ N. Voytishin,¹⁰⁰ A. Zarubin,¹⁰⁰ V. Golovtsov,¹⁰¹ Y. Ivanov,¹⁰¹ V. Kim,^{101,kk} E. Kuznetsova,^{101,ll}
 P. Levchenko,¹⁰¹ V. Murzin,¹⁰¹ V. Oreshkin,¹⁰¹ I. Smirnov,¹⁰¹ D. Sosnov,¹⁰¹ V. Sulimov,¹⁰¹ L. Uvarov,¹⁰¹ S. Vavilov,¹⁰¹
 A. Vorobyev,¹⁰¹ Yu. Andreev,¹⁰² A. Dermenev,¹⁰² S. Gninenko,¹⁰² N. Golubev,¹⁰² A. Karneyev,¹⁰² M. Kirsanov,¹⁰²
 N. Krasnikov,¹⁰² A. Pashenkov,¹⁰² D. Tlisov,¹⁰² A. Toropin,¹⁰² V. Epshteyn,¹⁰³ V. Gavrilov,¹⁰³ N. Lychkovskaya,¹⁰³
 V. Popov,¹⁰³ I. Pozdnyakov,¹⁰³ G. Safronov,¹⁰³ A. Spiridonov,¹⁰³ A. Stepenov,¹⁰³ V. Stolin,¹⁰³ M. Toms,¹⁰³ E. Vlasov,¹⁰³
 A. Zhokin,¹⁰³ T. Aushev,¹⁰⁴ R. Chistov,^{105,mm} M. Danilov,^{105,mm} P. Parygin,¹⁰⁵ D. Philippov,¹⁰⁵ S. Polikarpov,^{105,mm}
 E. Tarkovskii,¹⁰⁵ V. Andreev,¹⁰⁶ M. Azarkin,^{106,jj} I. Dremin,^{106,jj} M. Kirakosyan,^{106,jj} S. V. Rusakov,¹⁰⁶ A. Terkulov,¹⁰⁶
 A. Baskakov,¹⁰⁷ A. Belyaev,¹⁰⁷ E. Boos,¹⁰⁷ V. Bunichev,¹⁰⁷ M. Dubinin,^{107,nn} L. Dudko,¹⁰⁷ V. Klyukhin,¹⁰⁷ O. Kodolova,¹⁰⁷
 N. Korneeva,¹⁰⁷ I. Lokhtin,¹⁰⁷ I. Miagkov,¹⁰⁷ S. Obraztsov,¹⁰⁷ M. Perfilov,¹⁰⁷ V. Savrin,¹⁰⁷ P. Volkov,¹⁰⁷ V. Blinov,^{108,oo}
 T. Dimova,^{108,oo} L. Kardapoltsev,^{108,oo} D. Shtol,^{108,oo} Y. Skovpen,^{108,oo} I. Azhgirey,¹⁰⁹ I. Bayshev,¹⁰⁹ S. Bitioukov,¹⁰⁹
 D. Elumakhov,¹⁰⁹ A. Godizov,¹⁰⁹ V. Kachanov,¹⁰⁹ A. Kalinin,¹⁰⁹ D. Konstantinov,¹⁰⁹ P. Mandrik,¹⁰⁹ V. Petrov,¹⁰⁹
 R. Ryutin,¹⁰⁹ S. Slabospitskii,¹⁰⁹ A. Sobol,¹⁰⁹ S. Troshin,¹⁰⁹ N. Tyurin,¹⁰⁹ A. Uzunian,¹⁰⁹ A. Volkov,¹⁰⁹ A. Babaev,¹¹⁰
 S. Baidali,¹¹⁰ V. Okhotnikov,¹¹⁰ P. Adzic,^{111,pp} P. Cirkovic,¹¹¹ D. Devetak,¹¹¹ M. Dordevic,¹¹¹ J. Milosevic,¹¹¹
 J. Alcaraz Maestre,¹¹² I. Bachiller,¹¹² M. Barrio Luna,¹¹² J. A. Brochero Cifuentes,¹¹² M. Cerrada,¹¹² N. Colino,¹¹²
 B. De La Cruz,¹¹² A. Delgado Peris,¹¹² C. Fernandez Bedoya,¹¹² J. P. Fernández Ramos,¹¹² J. Flix,¹¹² M. C. Fouz,¹¹²
 O. Gonzalez Lopez,¹¹² S. Goy Lopez,¹¹² J. M. Hernandez,¹¹² M. I. Josa,¹¹² D. Moran,¹¹² A. Pérez-Calero Yzquierdo,¹¹²
 J. Puerta Pelayo,¹¹² I. Redondo,¹¹² L. Romero,¹¹² M. S. Soares,¹¹² A. Triossi,¹¹² A. Álvarez Fernández,¹¹² C. Albajar,¹¹³
 J. F. de Trocóniz,¹¹³ J. Cuevas,¹¹⁴ C. Erice,¹¹⁴ J. Fernandez Menendez,¹¹⁴ S. Folgueras,¹¹⁴ I. Gonzalez Caballero,¹¹⁴
 J. R. González Fernández,¹¹⁴ E. Palencia Cortezon,¹¹⁴ V. Rodríguez Bouza,¹¹⁴ S. Sanchez Cruz,¹¹⁴ P. Vischia,¹¹⁴

J. M. Vizan Garcia,¹¹⁴ I. J. Cabrillo,¹¹⁵ A. Calderon,¹¹⁵ B. Chazin Quero,¹¹⁵ J. Duarte Campderros,¹¹⁵ M. Fernandez,¹¹⁵ P. J. Fernández Manteca,¹¹⁵ J. Garcia-Ferrero,¹¹⁵ A. García Alonso,¹¹⁵ G. Gomez,¹¹⁵ A. Lopez Virto,¹¹⁵ J. Marco,¹¹⁵ C. Martinez Rivero,¹¹⁵ P. Martinez Ruiz del Arbol,¹¹⁵ F. Matorras,¹¹⁵ J. Piedra Gomez,¹¹⁵ C. Prieels,¹¹⁵ T. Rodrigo,¹¹⁵ A. Ruiz-Jimeno,¹¹⁵ L. Scodellaro,¹¹⁵ N. Trevisani,¹¹⁵ I. Vila,¹¹⁵ R. Vilar Cortabitarte,¹¹⁵ D. Abbaneo,¹¹⁶ B. Akgun,¹¹⁶ E. Auffray,¹¹⁶ P. Baillon,¹¹⁶ A. H. Ball,¹¹⁶ D. Barney,¹¹⁶ J. Bendavid,¹¹⁶ M. Bianco,¹¹⁶ A. Bocci,¹¹⁶ C. Botta,¹¹⁶ E. Brondolin,¹¹⁶ T. Camporesi,¹¹⁶ M. Cepeda,¹¹⁶ G. Cerminara,¹¹⁶ E. Chapon,¹¹⁶ Y. Chen,¹¹⁶ G. Cucciati,¹¹⁶ D. d'Enterria,¹¹⁶ A. Dabrowski,¹¹⁶ V. Daponte,¹¹⁶ A. David,¹¹⁶ A. De Roeck,¹¹⁶ N. Deelen,¹¹⁶ M. Dobson,¹¹⁶ M. Dünser,¹¹⁶ N. Dupont,¹¹⁶ A. Elliott-Peisert,¹¹⁶ P. Everaerts,¹¹⁶ F. Fallavollita,^{116,qq} D. Fasanella,¹¹⁶ G. Franzoni,¹¹⁶ J. Fulcher,¹¹⁶ W. Funk,¹¹⁶ D. Gigi,¹¹⁶ A. Gilbert,¹¹⁶ K. Gill,¹¹⁶ F. Glege,¹¹⁶ M. Guilbaud,¹¹⁶ D. Gulhan,¹¹⁶ J. Hegeman,¹¹⁶ V. Innocente,¹¹⁶ A. Jafari,¹¹⁶ P. Janot,¹¹⁶ O. Karacheban,^{116,s} J. Kieseler,¹¹⁶ A. Kornmayer,¹¹⁶ M. Krammer,^{116,b} C. Lange,¹¹⁶ P. Lecoq,¹¹⁶ C. Lourenço,¹¹⁶ L. Malgeri,¹¹⁶ M. Mannelli,¹¹⁶ F. Meijers,¹¹⁶ J. A. Merlin,¹¹⁶ S. Mersi,¹¹⁶ E. Meschi,¹¹⁶ P. Milenovic,^{116,rr} F. Moortgat,¹¹⁶ M. Mulders,¹¹⁶ J. Ngadiuba,¹¹⁶ S. Orfanelli,¹¹⁶ L. Orsini,¹¹⁶ F. Pantaleo,^{116,p} L. Pape,¹¹⁶ E. Perez,¹¹⁶ M. Peruzzi,¹¹⁶ A. Petrilli,¹¹⁶ G. Petrucciani,¹¹⁶ A. Pfeiffer,¹¹⁶ M. Pierini,¹¹⁶ F. M. Pitters,¹¹⁶ D. Rabady,¹¹⁶ A. Racz,¹¹⁶ T. Reis,¹¹⁶ G. Rolandi,^{116,ss} M. Rovere,¹¹⁶ H. Sakulin,¹¹⁶ C. Schäfer,¹¹⁶ C. Schwick,¹¹⁶ M. Seidel,¹¹⁶ M. Selvaggi,¹¹⁶ A. Sharma,¹¹⁶ P. Silva,¹¹⁶ P. Sphicas,^{116,t} A. Stakia,¹¹⁶ J. Steggemann,¹¹⁶ M. Tosi,¹¹⁶ D. Treille,¹¹⁶ A. Tsirova,¹¹⁶ V. Veckalns,^{116,uu} W. D. Zeuner,¹¹⁶ L. Caminada,^{117,vv} K. Deiters,¹¹⁷ W. Erdmann,¹¹⁷ R. Horisberger,¹¹⁷ Q. Ingram,¹¹⁷ H. C. Kaestli,¹¹⁷ D. Kotlinski,¹¹⁷ U. Langenegger,¹¹⁷ T. Rohe,¹¹⁷ S. A. Wiederkehr,¹¹⁷ M. Backhaus,¹¹⁸ L. Bäni,¹¹⁸ P. Berger,¹¹⁸ N. Chernyavskaya,¹¹⁸ G. Dissertori,¹¹⁸ M. Dittmar,¹¹⁸ M. Donegà,¹¹⁸ C. Dorfer,¹¹⁸ C. Grab,¹¹⁸ C. Heidegger,¹¹⁸ D. Hits,¹¹⁸ J. Hoss,¹¹⁸ T. Klijnsma,¹¹⁸ W. Lustermann,¹¹⁸ R. A. Manzoni,¹¹⁸ M. Marionneau,¹¹⁸ M. T. Meinhard,¹¹⁸ F. Micheli,¹¹⁸ P. Musella,¹¹⁸ F. Nessi-Tedaldi,¹¹⁸ J. Pata,¹¹⁸ F. Pauss,¹¹⁸ G. Perrin,¹¹⁸ L. Perrozzi,¹¹⁸ S. Pigazzini,¹¹⁸ M. Quittnat,¹¹⁸ D. Ruini,¹¹⁸ D. A. Sanz Becerra,¹¹⁸ M. Schönenberger,¹¹⁸ L. Shchutska,¹¹⁸ V. R. Tavolaro,¹¹⁸ K. Theofilatos,¹¹⁸ M. L. Vesterbacka Olsson,¹¹⁸ R. Wallny,¹¹⁸ D. H. Zhu,¹¹⁸ T. K. Aarrestad,¹¹⁹ C. Amsler,^{119,ww} D. Brzhechko,¹¹⁹ M. F. Canelli,¹¹⁹ A. De Cosa,¹¹⁹ R. Del Burgo,¹¹⁹ S. Donato,¹¹⁹ C. Galloni,¹¹⁹ T. Hreus,¹¹⁹ B. Kilminster,¹¹⁹ I. Neutelings,¹¹⁹ D. Pinna,¹¹⁹ G. Raucó,¹¹⁹ P. Robmann,¹¹⁹ D. Salerno,¹¹⁹ K. Schweiger,¹¹⁹ C. Seitz,¹¹⁹ Y. Takahashi,¹¹⁹ A. Zucchetta,¹¹⁹ Y. H. Chang,¹²⁰ K. y. Cheng,¹²⁰ T. H. Doan,¹²⁰ Sh. Jain,¹²⁰ R. Khurana,¹²⁰ C. M. Kuo,¹²⁰ W. Lin,¹²⁰ A. Pozdnyakov,¹²⁰ S. S. Yu,¹²⁰ Arun Kumar,¹²¹ P. Chang,¹²¹ Y. Chao,¹²¹ K. F. Chen,¹²¹ P. H. Chen,¹²¹ W.-S. Hou,¹²¹ Y. y. Li,¹²¹ Y. F. Liu,¹²¹ R.-S. Lu,¹²¹ E. Paganis,¹²¹ A. Psallidas,¹²¹ A. Steen,¹²¹ B. Asavapibhop,¹²² N. Srimanobhas,¹²² N. Suwonjandee,¹²² A. Bat,¹²³ F. Boran,¹²³ S. Cerci,^{123,xx} S. Damarseckin,¹²³ Z. S. Demiroglu,¹²³ F. Dolek,¹²³ C. Dozen,¹²³ I. Dumanoglu,¹²³ S. Girgis,¹²³ G. Gokbulut,¹²³ Y. Guler,¹²³ E. Gurpinar,¹²³ I. Hos,^{123,yy} C. Isik,¹²³ E. E. Kangal,^{123,zz} O. Kara,¹²³ A. Kayis Topaksu,¹²³ U. Kiminsu,¹²³ M. Oglakci,¹²³ G. Onengut,¹²³ K. Ozdemir,^{123,aaa} S. Ozturk,^{123,bbb} D. Sunar Cerci,^{123,xx} B. Tali,^{123,xx} U. G. Tok,¹²³ S. Turkcapar,¹²³ I. S. Zorbakir,¹²³ C. Zorbilmez,¹²³ B. Isildak,^{124,ccc} G. Karapinar,^{124,ddd} M. Yalvac,¹²⁴ M. Zeyrek,¹²⁴ I. O. Atakisi,¹²⁵ E. Gülmez,¹²⁵ M. Kaya,^{125,eee} O. Kaya,^{125,fff} S. Tekten,¹²⁵ E. A. Yetkin,^{125,ggg} M. N. Agaras,¹²⁶ S. Atay,¹²⁶ A. Cakir,¹²⁶ K. Cankocak,¹²⁶ Y. Komurcu,¹²⁶ S. Sen,^{126,hhh} B. Grynyov,¹²⁷ L. Levchuk,¹²⁸ F. Ball,¹²⁹ L. Beck,¹²⁹ J. J. Brooke,¹²⁹ D. Burns,¹²⁹ E. Clement,¹²⁹ D. Cussans,¹²⁹ O. Davignon,¹²⁹ H. Flacher,¹²⁹ J. Goldstein,¹²⁹ G. P. Heath,¹²⁹ H. F. Heath,¹²⁹ L. Kreczko,¹²⁹ D. M. Newbold,^{129,iii} S. Paramesvaran,¹²⁹ B. Penning,¹²⁹ T. Sakuma,¹²⁹ D. Smith,¹²⁹ V. J. Smith,¹²⁹ J. Taylor,¹²⁹ A. Titterton,¹²⁹ K. W. Bell,¹³⁰ A. Belyaev,^{130,iii} C. Brew,¹³⁰ R. M. Brown,¹³⁰ D. Cieri,¹³⁰ D. J. A. Cockerill,¹³⁰ J. A. Coughlan,¹³⁰ K. Harder,¹³⁰ S. Harper,¹³⁰ J. Linacre,¹³⁰ E. Olaiya,¹³⁰ D. Petyt,¹³⁰ C. H. Shepherd-Themistocleous,¹³⁰ A. Thea,¹³⁰ I. R. Tomalin,¹³⁰ T. Williams,¹³⁰ W. J. Womersley,¹³⁰ G. Auzinger,¹³¹ R. Bainbridge,¹³¹ P. Bloch,¹³¹ J. Borg,¹³¹ S. Breeze,¹³¹ O. Buchmuller,¹³¹ A. Bundock,¹³¹ S. Casasso,¹³¹ D. Colling,¹³¹ L. Corpe,¹³¹ P. Dauncey,¹³¹ G. Davies,¹³¹ M. Della Negra,¹³¹ R. Di Maria,¹³¹ Y. Haddad,¹³¹ G. Hall,¹³¹ G. Iles,¹³¹ T. James,¹³¹ M. Komm,¹³¹ C. Laner,¹³¹ L. Lyons,¹³¹ A.-M. Magnan,¹³¹ S. Malik,¹³¹ A. Martelli,¹³¹ J. Nash,^{131,kkk} A. Nikitenko,^{131,h} V. Palladino,¹³¹ M. Pesaresi,¹³¹ A. Richards,¹³¹ A. Rose,¹³¹ E. Scott,¹³¹ C. Seez,¹³¹ A. Shtipliyski,¹³¹ T. Strebler,¹³¹ S. Summers,¹³¹ A. Tapper,¹³¹ K. Uchida,¹³¹ T. Virdee,^{131,p} N. Wardle,¹³¹ D. Winterbottom,¹³¹ J. Wright,¹³¹ S. C. Zenz,¹³¹ J. E. Cole,¹³² P. R. Hobson,¹³² A. Khan,¹³² P. Kyberd,¹³² C. K. Mackay,¹³² A. Morton,¹³² I. D. Reid,¹³² L. Teodorescu,¹³² S. Zahid,¹³² K. Call,¹³³ J. Dittmann,¹³³ K. Hatakeyama,¹³³ H. Liu,¹³³ C. Madrid,¹³³ B. McMaster,¹³³ N. Pastika,¹³³ C. Smith,¹³³ R. Bartek,¹³⁴ A. Dominguez,¹³⁴ A. Buccilli,¹³⁵ S. I. Cooper,¹³⁵ C. Henderson,¹³⁵ P. Rumerio,¹³⁵ C. West,¹³⁵ D. Arcaro,¹³⁶ T. Bose,¹³⁶ D. Gastler,¹³⁶ D. Rankin,¹³⁶ C. Richardson,¹³⁶ J. Rohlf,¹³⁶ L. Sulak,¹³⁶ D. Zou,¹³⁶ G. Benelli,¹³⁷ X. Coubez,¹³⁷ D. Cutts,¹³⁷ M. Hadley,¹³⁷ J. Hakala,¹³⁷ U. Heintz,¹³⁷ J. M. Hogan,^{137,iii} K. H. M. Kwok,¹³⁷ E. Laird,¹³⁷ G. Landsberg,¹³⁷ J. Lee,¹³⁷ Z. Mao,¹³⁷ M. Narain,¹³⁷ S. Piperov,¹³⁷ S. Sagir,^{137,mmmm} R. Syarif,¹³⁷ E. Usai,¹³⁷

D. Yu,¹³⁷ R. Band,¹³⁸ C. Brainerd,¹³⁸ R. Breedon,¹³⁸ D. Burns,¹³⁸ M. Calderon De La Barca Sanchez,¹³⁸ M. Chertok,¹³⁸ J. Conway,¹³⁸ R. Conway,¹³⁸ P. T. Cox,¹³⁸ R. Erbacher,¹³⁸ C. Flores,¹³⁸ G. Funk,¹³⁸ W. Ko,¹³⁸ O. Kukral,¹³⁸ R. Lander,¹³⁸ M. Mulhearn,¹³⁸ D. Pellett,¹³⁸ J. Pilot,¹³⁸ S. Shalhout,¹³⁸ M. Shi,¹³⁸ D. Stolp,¹³⁸ D. Taylor,¹³⁸ K. Tos,¹³⁸ M. Tripathi,¹³⁸ Z. Wang,¹³⁸ F. Zhang,¹³⁸ M. Bachtis,¹³⁹ C. Bravo,¹³⁹ R. Cousins,¹³⁹ A. Dasgupta,¹³⁹ A. Florent,¹³⁹ J. Hauser,¹³⁹ M. Ignatenko,¹³⁹ N. Mccoll,¹³⁹ S. Regnard,¹³⁹ D. Saltzberg,¹³⁹ C. Schnaible,¹³⁹ V. Valuev,¹³⁹ E. Bouvier,¹⁴⁰ K. Burt,¹⁴⁰ R. Clare,¹⁴⁰ J. W. Gary,¹⁴⁰ S. M. A. Ghiasi Shirazi,¹⁴⁰ G. Hanson,¹⁴⁰ G. Karapostoli,¹⁴⁰ E. Kennedy,¹⁴⁰ F. Lacroix,¹⁴⁰ O. R. Long,¹⁴⁰ M. Olmedo Negrete,¹⁴⁰ M. I. Paneva,¹⁴⁰ W. Si,¹⁴⁰ L. Wang,¹⁴⁰ H. Wei,¹⁴⁰ S. Wimpenny,¹⁴⁰ B. R. Yates,¹⁴⁰ J. G. Branson,¹⁴¹ S. Cittolin,¹⁴¹ M. Derdzinski,¹⁴¹ R. Gerosa,¹⁴¹ D. Gilbert,¹⁴¹ B. Hashemi,¹⁴¹ A. Holzner,¹⁴¹ D. Klein,¹⁴¹ G. Kole,¹⁴¹ V. Krutelyov,¹⁴¹ J. Letts,¹⁴¹ M. Masciovecchio,¹⁴¹ D. Olivito,¹⁴¹ S. Padhi,¹⁴¹ M. Pieri,¹⁴¹ M. Sani,¹⁴¹ V. Sharma,¹⁴¹ S. Simon,¹⁴¹ M. Tadel,¹⁴¹ A. Vartak,¹⁴¹ S. Wasserbaech,^{141,nnn} J. Wood,¹⁴¹ F. Würthwein,¹⁴¹ A. Yagil,¹⁴¹ G. Zevi Della Porta,¹⁴¹ N. Amin,¹⁴² R. Bhandari,¹⁴² J. Bradmiller-Feld,¹⁴² C. Campagnari,¹⁴² M. Citron,¹⁴² A. Dishaw,¹⁴² V. Dutta,¹⁴² M. Franco Sevilla,¹⁴² L. Gouskos,¹⁴² R. Heller,¹⁴² J. Incandela,¹⁴² A. Ovcharova,¹⁴² H. Qu,¹⁴² J. Richman,¹⁴² D. Stuart,¹⁴² I. Suarez,¹⁴² S. Wang,¹⁴² J. Yoo,¹⁴² D. Anderson,¹⁴³ A. Bornheim,¹⁴³ J. M. Lawhorn,¹⁴³ H. B. Newman,¹⁴³ T. Q. Nguyen,¹⁴³ M. Spiropulu,¹⁴³ J. R. Vlimant,¹⁴³ R. Wilkinson,¹⁴³ S. Xie,¹⁴³ Z. Zhang,¹⁴³ R. Y. Zhu,¹⁴³ M. B. Andrews,¹⁴⁴ T. Ferguson,¹⁴⁴ T. Mudholkar,¹⁴⁴ M. Paulini,¹⁴⁴ M. Sun,¹⁴⁴ I. Vorobiev,¹⁴⁴ M. Weinberg,¹⁴⁴ J. P. Cumalat,¹⁴⁵ W. T. Ford,¹⁴⁵ F. Jensen,¹⁴⁵ A. Johnson,¹⁴⁵ M. Krohn,¹⁴⁵ S. Leontsinis,¹⁴⁵ E. MacDonald,¹⁴⁵ T. Mulholland,¹⁴⁵ K. Stenson,¹⁴⁵ K. A. Ulmer,¹⁴⁵ S. R. Wagner,¹⁴⁵ J. Alexander,¹⁴⁶ J. Chaves,¹⁴⁶ Y. Cheng,¹⁴⁶ J. Chu,¹⁴⁶ A. Datta,¹⁴⁶ K. McDermott,¹⁴⁶ N. Mirman,¹⁴⁶ J. R. Patterson,¹⁴⁶ D. Quach,¹⁴⁶ A. Rinkevicius,¹⁴⁶ A. Ryd,¹⁴⁶ L. Skinnari,¹⁴⁶ L. Soffi,¹⁴⁶ S. M. Tan,¹⁴⁶ Z. Tao,¹⁴⁶ J. Thom,¹⁴⁶ J. Tucker,¹⁴⁶ P. Wittich,¹⁴⁶ M. Zientek,¹⁴⁶ S. Abdullin,¹⁴⁷ M. Albrow,¹⁴⁷ M. Alyari,¹⁴⁷ G. Apollinari,¹⁴⁷ A. Apresyan,¹⁴⁷ A. Apyan,¹⁴⁷ S. Banerjee,¹⁴⁷ L. A. T. Bauerdick,¹⁴⁷ A. Beretvas,¹⁴⁷ J. Berryhill,¹⁴⁷ P. C. Bhat,¹⁴⁷ G. Bolla,^{147,a} K. Burkett,¹⁴⁷ J. N. Butler,¹⁴⁷ A. Canepa,¹⁴⁷ G. B. Cerati,¹⁴⁷ H. W. K. Cheung,¹⁴⁷ F. Chlebana,¹⁴⁷ M. Cremonesi,¹⁴⁷ J. Duarte,¹⁴⁷ V. D. Elvira,¹⁴⁷ J. Freeman,¹⁴⁷ Z. Gecse,¹⁴⁷ E. Gottschalk,¹⁴⁷ L. Gray,¹⁴⁷ D. Green,¹⁴⁷ S. Grünendahl,¹⁴⁷ O. Gutsche,¹⁴⁷ J. Hanlon,¹⁴⁷ R. M. Harris,¹⁴⁷ S. Hasegawa,¹⁴⁷ J. Hirschauer,¹⁴⁷ Z. Hu,¹⁴⁷ B. Jayatilaka,¹⁴⁷ S. Jindariani,¹⁴⁷ M. Johnson,¹⁴⁷ U. Joshi,¹⁴⁷ B. Klima,¹⁴⁷ M. J. Kortelainen,¹⁴⁷ B. Kreis,¹⁴⁷ S. Lammel,¹⁴⁷ D. Lincoln,¹⁴⁷ R. Lipton,¹⁴⁷ M. Liu,¹⁴⁷ T. Liu,¹⁴⁷ J. Lykken,¹⁴⁷ K. Maeshima,¹⁴⁷ J. M. Marraffino,¹⁴⁷ D. Mason,¹⁴⁷ P. McBride,¹⁴⁷ P. Merkel,¹⁴⁷ S. Mrenna,¹⁴⁷ S. Nahn,¹⁴⁷ V. O'Dell,¹⁴⁷ K. Pedro,¹⁴⁷ O. Prokofyev,¹⁴⁷ G. Rakness,¹⁴⁷ L. Ristori,¹⁴⁷ A. Savoy-Navarro,^{147,ooo} B. Schneider,¹⁴⁷ E. Sexton-Kennedy,¹⁴⁷ A. Soha,¹⁴⁷ W. J. Spalding,¹⁴⁷ L. Spiegel,¹⁴⁷ S. Stoynev,¹⁴⁷ J. Strait,¹⁴⁷ N. Strobbe,¹⁴⁷ L. Taylor,¹⁴⁷ S. Tkaczyk,¹⁴⁷ N. V. Tran,¹⁴⁷ L. Uplegger,¹⁴⁷ E. W. Vaandering,¹⁴⁷ C. Vernieri,¹⁴⁷ M. Verzocchi,¹⁴⁷ R. Vidal,¹⁴⁷ M. Wang,¹⁴⁷ H. A. Weber,¹⁴⁷ A. Whitbeck,¹⁴⁷ D. Acosta,¹⁴⁸ P. Avery,¹⁴⁸ P. Bortignon,¹⁴⁸ D. Bourilkov,¹⁴⁸ A. Brinkerhoff,¹⁴⁸ L. Cadamuro,¹⁴⁸ A. Carnes,¹⁴⁸ M. Carver,¹⁴⁸ D. Curry,¹⁴⁸ R. D. Field,¹⁴⁸ S. V. Gleyzer,¹⁴⁸ B. M. Joshi,¹⁴⁸ J. Konigsberg,¹⁴⁸ A. Korytov,¹⁴⁸ P. Ma,¹⁴⁸ K. Matchev,¹⁴⁸ H. Mei,¹⁴⁸ G. Mitselmakher,¹⁴⁸ K. Shi,¹⁴⁸ D. Sperka,¹⁴⁸ J. Wang,¹⁴⁸ S. Wang,¹⁴⁸ Y. R. Joshi,¹⁴⁹ S. Linn,¹⁴⁹ A. Ackert,¹⁵⁰ T. Adams,¹⁵⁰ A. Askew,¹⁵⁰ S. Hagopian,¹⁵⁰ V. Hagopian,¹⁵⁰ K. F. Johnson,¹⁵⁰ T. Kolberg,¹⁵⁰ G. Martinez,¹⁵⁰ T. Perry,¹⁵⁰ H. Prosper,¹⁵⁰ A. Saha,¹⁵⁰ C. Schiber,¹⁵⁰ V. Sharma,¹⁵⁰ R. Yohay,¹⁵⁰ M. M. Baarmand,¹⁵¹ V. Bhopatkar,¹⁵¹ S. Colafranceschi,¹⁵¹ M. Hohlmann,¹⁵¹ D. Noonan,¹⁵¹ M. Rahmani,¹⁵¹ T. Roy,¹⁵¹ F. Yumiceva,¹⁵¹ M. R. Adams,¹⁵² L. Apanasevich,¹⁵² D. Berry,¹⁵² R. R. Betts,¹⁵² R. Cavanaugh,¹⁵² X. Chen,¹⁵² S. Dittmer,¹⁵² O. Evdokimov,¹⁵² C. E. Gerber,¹⁵² D. A. Hangal,¹⁵² D. J. Hofman,¹⁵² K. Jung,¹⁵² J. Kamin,¹⁵² C. Mills,¹⁵² I. D. Sandoval Gonzalez,¹⁵² M. B. Tonjes,¹⁵² N. Varelas,¹⁵² H. Wang,¹⁵² X. Wang,¹⁵² Z. Wu,¹⁵² J. Zhang,¹⁵² M. Alhousseini,¹⁵³ B. Bilki,^{153,ppp} W. Clarida,¹⁵³ K. Dilsiz,^{153,qqq} S. Durgut,¹⁵³ R. P. Gandrajula,¹⁵³ M. Haytmyradov,¹⁵³ V. Khristenko,¹⁵³ J.-P. Merlo,¹⁵³ A. Mestvirishvili,¹⁵³ A. Moeller,¹⁵³ J. Nachtman,¹⁵³ H. Ogul,^{153,rrr} Y. Onel,¹⁵³ F. Ozok,^{153,sss} A. Penzo,¹⁵³ C. Snyder,¹⁵³ E. Tiras,¹⁵³ J. Wetzel,¹⁵³ B. Blumenfeld,¹⁵⁴ A. Cocoros,¹⁵⁴ N. Eminizer,¹⁵⁴ D. Fehling,¹⁵⁴ L. Feng,¹⁵⁴ A. V. Gritsan,¹⁵⁴ W. T. Hung,¹⁵⁴ P. Maksimovic,¹⁵⁴ J. Roskes,¹⁵⁴ U. Sarica,¹⁵⁴ M. Swartz,¹⁵⁴ M. Xiao,¹⁵⁴ C. You,¹⁵⁴ A. Al-bataineh,¹⁵⁵ P. Baringer,¹⁵⁵ A. Bean,¹⁵⁵ S. Boren,¹⁵⁵ J. Bowen,¹⁵⁵ A. Bylinkin,¹⁵⁵ J. Castle,¹⁵⁵ S. Khalil,¹⁵⁵ A. Kropivnitskaya,¹⁵⁵ D. Majumder,¹⁵⁵ W. Mcbrayer,¹⁵⁵ M. Murray,¹⁵⁵ C. Rogan,¹⁵⁵ S. Sanders,¹⁵⁵ E. Schmitz,¹⁵⁵ J. D. Tapia Takaki,¹⁵⁵ Q. Wang,¹⁵⁵ S. Duric,¹⁵⁶ A. Ivanov,¹⁵⁶ K. Kaadze,¹⁵⁶ D. Kim,¹⁵⁶ Y. Maravin,¹⁵⁶ D. R. Mendis,¹⁵⁶ T. Mitchell,¹⁵⁶ A. Modak,¹⁵⁶ A. Mohammadi,¹⁵⁶ L. K. Saini,¹⁵⁶ N. Skhirtladze,¹⁵⁶ F. Rebassoo,¹⁵⁷ D. Wright,¹⁵⁷ A. Baden,¹⁵⁸ O. Baron,¹⁵⁸ A. Belloni,¹⁵⁸ S. C. Eno,¹⁵⁸ Y. Feng,¹⁵⁸ C. Ferraioli,¹⁵⁸ N. J. Hadley,¹⁵⁸ S. Jabeen,¹⁵⁸ G. Y. Jeng,¹⁵⁸ R. G. Kellogg,¹⁵⁸ J. Kunkle,¹⁵⁸ A. C. Mignerey,¹⁵⁸ F. Ricci-Tam,¹⁵⁸ Y. H. Shin,¹⁵⁸ A. Skuja,¹⁵⁸ S. C. Tonwar,¹⁵⁸ K. Wong,¹⁵⁸ D. Abercrombie,¹⁵⁹ B. Allen,¹⁵⁹ V. Azzolini,¹⁵⁹ A. Baty,¹⁵⁹ G. Bauer,¹⁵⁹ R. Bi,¹⁵⁹ S. Brandt,¹⁵⁹ W. Busza,¹⁵⁹ I. A. Cali,¹⁵⁹ M. D'Alfonso,¹⁵⁹ Z. Demiragli,¹⁵⁹ G. Gomez Ceballos,¹⁵⁹ M. Goncharov,¹⁵⁹ P. Harris,¹⁵⁹ D. Hsu,¹⁵⁹ M. Hu,¹⁵⁹

Y. Iiyama,¹⁵⁹ G. M. Innocenti,¹⁵⁹ M. Klute,¹⁵⁹ D. Kovalskyi,¹⁵⁹ Y.-J. Lee,¹⁵⁹ P. D. Luckey,¹⁵⁹ B. Maier,¹⁵⁹ A. C. Marini,¹⁵⁹ C. Mcginn,¹⁵⁹ C. Mironov,¹⁵⁹ S. Narayanan,¹⁵⁹ X. Niu,¹⁵⁹ C. Paus,¹⁵⁹ C. Roland,¹⁵⁹ G. Roland,¹⁵⁹ G. S. F. Stephans,¹⁵⁹ K. Sumorok,¹⁵⁹ K. Tatar,¹⁵⁹ D. Velicanu,¹⁵⁹ J. Wang,¹⁵⁹ T. W. Wang,¹⁵⁹ B. Wyslouch,¹⁵⁹ S. Zhaozhong,¹⁵⁹ A. C. Benvenuti,¹⁶⁰ R. M. Chatterjee,¹⁶⁰ A. Evans,¹⁶⁰ P. Hansen,¹⁶⁰ S. Kalafut,¹⁶⁰ Y. Kubota,¹⁶⁰ Z. Lesko,¹⁶⁰ J. Mans,¹⁶⁰ S. Nourbakhsh,¹⁶⁰ N. Ruckstuhl,¹⁶⁰ R. Rusack,¹⁶⁰ J. Turkewitz,¹⁶⁰ M. A. Wadud,¹⁶⁰ J. G. Acosta,¹⁶¹ S. Oliveros,¹⁶¹ E. Avdeeva,¹⁶² K. Bloom,¹⁶² D. R. Claes,¹⁶² C. Fangmeier,¹⁶² F. Golf,¹⁶² R. Gonzalez Suarez,¹⁶² R. Kamalieddin,¹⁶² I. Kravchenko,¹⁶² J. Monroy,¹⁶² J. E. Siado,¹⁶² G. R. Snow,¹⁶² B. Stieger,¹⁶² A. Godshalk,¹⁶³ C. Harrington,¹⁶³ I. Iashvili,¹⁶³ A. Kharchilava,¹⁶³ C. Mclean,¹⁶³ D. Nguyen,¹⁶³ A. Parker,¹⁶³ S. Rappoccio,¹⁶³ B. Roozbahani,¹⁶³ E. Barberis,¹⁶⁴ C. Freer,¹⁶⁴ A. Hortiangtham,¹⁶⁴ D. M. Morse,¹⁶⁴ T. Orimoto,¹⁶⁴ R. Teixeira De Lima,¹⁶⁴ T. Wamorkar,¹⁶⁴ B. Wang,¹⁶⁴ A. Wisecarver,¹⁶⁴ D. Wood,¹⁶⁴ S. Bhattacharya,¹⁶⁵ O. Charaf,¹⁶⁵ K. A. Hahn,¹⁶⁵ N. Mucia,¹⁶⁵ N. Odell,¹⁶⁵ M. H. Schmitt,¹⁶⁵ K. Sung,¹⁶⁵ M. Trovato,¹⁶⁵ M. Velasco,¹⁶⁵ R. Bucci,¹⁶⁶ N. Dev,¹⁶⁶ M. Hildreth,¹⁶⁶ K. Hurtado Anampa,¹⁶⁶ C. Jessop,¹⁶⁶ D. J. Karmgard,¹⁶⁶ N. Kellams,¹⁶⁶ K. Lannon,¹⁶⁶ W. Li,¹⁶⁶ N. Loukas,¹⁶⁶ N. Marinelli,¹⁶⁶ F. Meng,¹⁶⁶ C. Mueller,¹⁶⁶ Y. Musienko,^{166,ii} M. Planer,¹⁶⁶ A. Reinsvold,¹⁶⁶ R. Ruchti,¹⁶⁶ P. Siddireddy,¹⁶⁶ G. Smith,¹⁶⁶ S. Taroni,¹⁶⁶ M. Wayne,¹⁶⁶ A. Wightman,¹⁶⁶ M. Wolf,¹⁶⁶ A. Woodard,¹⁶⁶ J. Alimena,¹⁶⁷ L. Antonelli,¹⁶⁷ B. Bylsma,¹⁶⁷ L. S. Durkin,¹⁶⁷ S. Flowers,¹⁶⁷ B. Francis,¹⁶⁷ A. Hart,¹⁶⁷ C. Hill,¹⁶⁷ W. Ji,¹⁶⁷ A. Lefeld,¹⁶⁷ T. Y. Ling,¹⁶⁷ W. Luo,¹⁶⁷ B. L. Winer,¹⁶⁷ H. W. Wulsin,¹⁶⁷ S. Cooperstein,¹⁶⁸ P. Elmer,¹⁶⁸ J. Hardenbrook,¹⁶⁸ S. Higginbotham,¹⁶⁸ A. Kalogeropoulos,¹⁶⁸ D. Lange,¹⁶⁸ M. T. Lucchini,¹⁶⁸ J. Luo,¹⁶⁸ D. Marlow,¹⁶⁸ K. Mei,¹⁶⁸ I. Ojalvo,¹⁶⁸ J. Olsen,¹⁶⁸ C. Palmer,¹⁶⁸ P. Piroué,¹⁶⁸ J. Salfeld-Nebgen,¹⁶⁸ D. Stickland,¹⁶⁸ C. Tully,¹⁶⁸ S. Malik,¹⁶⁹ S. Norberg,¹⁶⁹ A. Barker,¹⁷⁰ V. E. Barnes,¹⁷⁰ L. Gutay,¹⁷⁰ M. Jones,¹⁷⁰ A. W. Jung,¹⁷⁰ A. Khatiwada,¹⁷⁰ B. Mahakud,¹⁷⁰ D. H. Miller,¹⁷⁰ N. Neumeister,¹⁷⁰ C. C. Peng,¹⁷⁰ H. Qiu,¹⁷⁰ J. F. Schulte,¹⁷⁰ J. Sun,¹⁷⁰ F. Wang,¹⁷⁰ R. Xiao,¹⁷⁰ W. Xie,¹⁷⁰ T. Cheng,¹⁷¹ J. Dolen,¹⁷¹ N. Parashar,¹⁷¹ Z. Chen,¹⁷² K. M. Ecklund,¹⁷² S. Freed,¹⁷² F. J. M. Geurts,¹⁷² M. Kilpatrick,¹⁷² W. Li,¹⁷² B. Michlin,¹⁷² B. P. Padley,¹⁷² J. Roberts,¹⁷² J. Rorie,¹⁷² W. Shi,¹⁷² Z. Tu,¹⁷² J. Zabel,¹⁷² A. Zhang,¹⁷² A. Bodek,¹⁷³ P. de Barbaro,¹⁷³ R. Demina,¹⁷³ Y. t. Duh,¹⁷³ J. L. Dulemba,¹⁷³ C. Fallon,¹⁷³ T. Ferbel,¹⁷³ M. Galanti,¹⁷³ A. Garcia-Bellido,¹⁷³ J. Han,¹⁷³ O. Hindrichs,¹⁷³ A. Khukhunaishvili,¹⁷³ K. H. Lo,¹⁷³ P. Tan,¹⁷³ R. Taus,¹⁷³ M. Verzetti,¹⁷³ A. Agapitos,¹⁷⁴ J. P. Chou,¹⁷⁴ Y. Gershtein,¹⁷⁴ T. A. Gómez Espinosa,¹⁷⁴ E. Halkiadakis,¹⁷⁴ M. Heindl,¹⁷⁴ E. Hughes,¹⁷⁴ S. Kaplan,¹⁷⁴ R. Kunnawalkam Elayavalli,¹⁷⁴ S. Kyriacou,¹⁷⁴ A. Lath,¹⁷⁴ R. Montalvo,¹⁷⁴ K. Nash,¹⁷⁴ M. Osherson,¹⁷⁴ H. Saka,¹⁷⁴ S. Salur,¹⁷⁴ S. Schnetzer,¹⁷⁴ D. Sheffield,¹⁷⁴ S. Somalwar,¹⁷⁴ R. Stone,¹⁷⁴ S. Thomas,¹⁷⁴ P. Thomassen,¹⁷⁴ M. Walker,¹⁷⁴ A. G. Delannoy,¹⁷⁵ J. Heideman,¹⁷⁵ G. Riley,¹⁷⁵ S. Spanier,¹⁷⁵ K. Thapa,¹⁷⁵ O. Bouhali,^{176,uu} A. Celik,¹⁷⁶ M. Dalchenko,¹⁷⁶ M. De Mattia,¹⁷⁶ A. Delgado,¹⁷⁶ S. Dildick,¹⁷⁶ R. Eusebi,¹⁷⁶ J. Gilmore,¹⁷⁶ T. Huang,¹⁷⁶ T. Kamon,^{176,uuu} S. Luo,¹⁷⁶ R. Mueller,¹⁷⁶ R. Patel,¹⁷⁶ A. Perloff,¹⁷⁶ L. Perniè,¹⁷⁶ D. Rathjens,¹⁷⁶ A. Safonov,¹⁷⁶ N. Akchurin,¹⁷⁷ J. Damgov,¹⁷⁷ F. De Guio,¹⁷⁷ P. R. Duerdo,¹⁷⁷ S. Kunori,¹⁷⁷ K. Lamichhane,¹⁷⁷ S. W. Lee,¹⁷⁷ T. Mengke,¹⁷⁷ S. Muthumuni,¹⁷⁷ T. Peltola,¹⁷⁷ S. Undleeb,¹⁷⁷ I. Volobouev,¹⁷⁷ Z. Wang,¹⁷⁷ S. Greene,¹⁷⁸ A. Gurrola,¹⁷⁸ R. Janjam,¹⁷⁸ W. Johns,¹⁷⁸ C. Maguire,¹⁷⁸ A. Melo,¹⁷⁸ H. Ni,¹⁷⁸ K. Padeken,¹⁷⁸ J. D. Ruiz Alvarez,¹⁷⁸ P. Sheldon,¹⁷⁸ S. Tuo,¹⁷⁸ J. Velkovska,¹⁷⁸ M. Verweij,¹⁷⁸ Q. Xu,¹⁷⁸ M. W. Arenton,¹⁷⁹ P. Barria,¹⁷⁹ B. Cox,¹⁷⁹ R. Hirosky,¹⁷⁹ M. Joyce,¹⁷⁹ A. Ledovskoy,¹⁷⁹ H. Li,¹⁷⁹ C. Neu,¹⁷⁹ T. Sinthuprasith,¹⁷⁹ Y. Wang,¹⁷⁹ E. Wolfe,¹⁷⁹ F. Xia,¹⁷⁹ R. Harr,¹⁸⁰ P. E. Karchin,¹⁸⁰ N. Poudyal,¹⁸⁰ J. Sturdy,¹⁸⁰ P. Thapa,¹⁸⁰ S. Zaleski,¹⁸⁰ M. Brodski,¹⁸¹ J. Buchanan,¹⁸¹ C. Caillol,¹⁸¹ D. Carlsmith,¹⁸¹ S. Dasu,¹⁸¹ L. Dodd,¹⁸¹ B. Gomber,¹⁸¹ M. Grothe,¹⁸¹ M. Herndon,¹⁸¹ A. Hervé,¹⁸¹ U. Hussain,¹⁸¹ P. Klabbers,¹⁸¹ A. Lanaro,¹⁸¹ K. Long,¹⁸¹ R. Loveless,¹⁸¹ T. Ruggles,¹⁸¹ A. Savin,¹⁸¹ N. Smith,¹⁸¹ W. H. Smith,¹⁸¹ and N. Woods¹⁸¹

(CMS Collaboration)

¹Yerevan Physics Institute, Yerevan, Armenia²Institut für Hochenergiephysik, Wien, Austria³Institute for Nuclear Problems, Minsk, Belarus⁴Universiteit Antwerpen, Antwerpen, Belgium⁵Vrije Universiteit Brussel, Brussel, Belgium⁶Université Libre de Bruxelles, Bruxelles, Belgium⁷Ghent University, Ghent, Belgium⁸Université Catholique de Louvain, Louvain-la-Neuve, Belgium⁹Centro Brasileiro de Pesquisas Físicas, Rio de Janeiro, Brazil

- ¹⁰*Universidade do Estado do Rio de Janeiro, Rio de Janeiro, Brazil*
^{11a}*Universidade Estadual Paulista, São Paulo, Brazil*
^{11b}*Universidade Federal do ABC, São Paulo, Brazil*
¹²*Institute for Nuclear Research and Nuclear Energy, Bulgarian Academy of Sciences, Sofia, Bulgaria*
¹³*University of Sofia, Sofia, Bulgaria*
¹⁴*Beihang University, Beijing, China*
¹⁵*Institute of High Energy Physics, Beijing, China*
¹⁶*State Key Laboratory of Nuclear Physics and Technology, Peking University, Beijing, China*
¹⁷*Tsinghua University, Beijing, China*
¹⁸*Universidad de Los Andes, Bogota, Colombia*
¹⁹*University of Split, Faculty of Electrical Engineering, Mechanical Engineering and Naval Architecture, Split, Croatia*
²⁰*University of Split, Faculty of Science, Split, Croatia*
²¹*Institute Rudjer Boskovic, Zagreb, Croatia*
²²*University of Cyprus, Nicosia, Cyprus*
²³*Charles University, Prague, Czech Republic*
²⁴*Escuela Politecnica Nacional, Quito, Ecuador*
²⁵*Universidad San Francisco de Quito, Quito, Ecuador*
²⁶*Academy of Scientific Research and Technology of the Arab Republic of Egypt, Egyptian Network of High Energy Physics, Cairo, Egypt*
²⁷*National Institute of Chemical Physics and Biophysics, Tallinn, Estonia*
²⁸*Department of Physics, University of Helsinki, Helsinki, Finland*
²⁹*Helsinki Institute of Physics, Helsinki, Finland*
³⁰*Lappeenranta University of Technology, Lappeenranta, Finland*
³¹*IRFU, CEA, Université Paris-Saclay, Gif-sur-Yvette, France*
³²*Laboratoire Leprince-Ringuet, Ecole polytechnique, CNRS/IN2P3, Université Paris-Saclay, Palaiseau, France*
³³*Université de Strasbourg, CNRS, IPHC UMR 7178, F-67000 Strasbourg, France*
³⁴*Centre de Calcul de l'Institut National de Physique Nucleaire et de Physique des Particules, CNRS/IN2P3, Villeurbanne, France*
³⁵*Université de Lyon, Université Claude Bernard Lyon I, CNRS-IN2P3, Institut de Physique Nucléaire de Lyon, Villeurbanne, France*
³⁶*Georgian Technical University, Tbilisi, Georgia*
³⁷*Tbilisi State University, Tbilisi, Georgia*
³⁸*RWTH Aachen University, I. Physikalisches Institut, Aachen, Germany*
³⁹*RWTH Aachen University, III. Physikalisches Institut A, Aachen, Germany*
⁴⁰*RWTH Aachen University, III. Physikalisches Institut B, Aachen, Germany*
⁴¹*Deutsches Elektronen-Synchrotron, Hamburg, Germany*
⁴²*University of Hamburg, Hamburg, Germany*
⁴³*Institut für Experimentelle Teilchenphysik, Karlsruhe, Germany*
⁴⁴*Institute of Nuclear and Particle Physics (INPP), NCSR Demokritos, Aghia Paraskevi, Greece*
⁴⁵*National and Kapodistrian University of Athens, Athens, Greece*
⁴⁶*National Technical University of Athens, Athens, Greece*
⁴⁷*University of Ioánnina, Ioánnina, Greece*
⁴⁸*MTA-ELTE Lendület CMS Particle and Nuclear Physics Group, Eötvös Loránd University, Budapest, Hungary*
⁴⁹*Wigner Research Centre for Physics, Budapest, Hungary*
⁵⁰*Institute of Nuclear Research ATOMKI, Debrecen, Hungary*
⁵¹*Institute of Physics, University of Debrecen, Debrecen, Hungary*
⁵²*Indian Institute of Science (IISc), Bangalore, India*
⁵³*National Institute of Science Education and Research, Bhubaneswar, India*
⁵⁴*Panjab University, Chandigarh, India*
⁵⁵*University of Delhi, Delhi, India*
⁵⁶*Saha Institute of Nuclear Physics, HBNI, Kolkata, India*
⁵⁷*Indian Institute of Technology Madras, Madras, India*
⁵⁸*Bhabha Atomic Research Centre, Mumbai, India*
⁵⁹*Tata Institute of Fundamental Research-A, Mumbai, India*
⁶⁰*Tata Institute of Fundamental Research-B, Mumbai, India*
⁶¹*Indian Institute of Science Education and Research (IISER), Pune, India*
⁶²*Institute for Research in Fundamental Sciences (IPM), Tehran, Iran*
⁶³*University College Dublin, Dublin, Ireland*
^{64a}*INFN Sezione di Bari, Bari, Italy*
^{64b}*Università di Bari, Bari, Italy*
^{64c}*Politecnico di Bari, Bari, Italy*
^{65a}*INFN Sezione di Bologna, Bologna, Italy*

- ^{65b} *Università di Bologna, Bologna, Italy*
- ^{66a} *INFN Sezione di Catania, Catania, Italy*
- ^{66b} *Università di Catania, Catania, Italy*
- ^{67a} *INFN Sezione di Firenze, Firenze, Italy*
- ^{67b} *Università di Firenze, Firenze, Italy*
- ⁶⁸ *INFN Laboratori Nazionali di Frascati, Frascati, Italy*
- ^{69a} *INFN Sezione di Genova, Genova, Italy*
- ^{69b} *Università di Genova, Genova, Italy*
- ^{70a} *INFN Sezione di Milano-Bicocca, Milano, Italy*
- ^{70b} *Università di Milano-Bicocca, Milano, Italy*
- ^{71a} *INFN Sezione di Napoli, Napoli, Italy*
- ^{71b} *Università di Napoli 'Federico II', Napoli, Italy*
- ^{71c} *Università della Basilicata, Potenza, Italy*
- ^{71d} *Università G. Marconi, Roma, Italy*
- ^{72a} *INFN Sezione di Padova, Padova, Italy*
- ^{72b} *Università di Padova, Padova, Italy*
- ^{72c} *Università di Trento, Trento, Italy*
- ^{73a} *INFN Sezione di Pavia, Pavia, Italy*
- ^{73b} *Università di Pavia, Pavia, Italy*
- ^{74a} *INFN Sezione di Perugia, Perugia, Italy*
- ^{74b} *Università di Perugia, Perugia, Italy*
- ^{75a} *INFN Sezione di Pisa, Pisa, Italy*
- ^{75b} *Università di Pisa, Pisa, Italy*
- ^{75c} *Scuola Normale Superiore di Pisa, Pisa, Italy*
- ^{76a} *INFN Sezione di Roma, Rome, Italy*
- ^{76b} *Sapienza Università di Roma, Rome, Italy*
- ^{77a} *INFN Sezione di Torino, Torino, Italy*
- ^{77b} *Università di Torino, Torino, Italy*
- ^{77c} *Università del Piemonte Orientale, Novara, Italy*
- ^{78a} *INFN Sezione di Trieste, Trieste, Italy*
- ^{78b} *Università di Trieste, Trieste, Italy*
- ⁷⁹ *Kyungpook National University, Daegu, Korea*
- ⁸⁰ *Chonnam National University, Institute for Universe and Elementary Particles, Kwangju, Korea*
- ⁸¹ *Hanyang University, Seoul, Korea*
- ⁸² *Korea University, Seoul, Korea*
- ⁸³ *Sejong University, Seoul, Korea*
- ⁸⁴ *Seoul National University, Seoul, Korea*
- ⁸⁵ *University of Seoul, Seoul, Korea*
- ⁸⁶ *Sungkyunkwan University, Suwon, Korea*
- ⁸⁷ *Vilnius University, Vilnius, Lithuania*
- ⁸⁸ *National Centre for Particle Physics, Universiti Malaya, Kuala Lumpur, Malaysia*
- ⁸⁹ *Universidad de Sonora (UNISON), Hermosillo, Mexico*
- ⁹⁰ *Centro de Investigación y de Estudios Avanzados del IPN, Mexico City, Mexico*
- ⁹¹ *Universidad Iberoamericana, Mexico City, Mexico*
- ⁹² *Benemerita Universidad Autónoma de Puebla, Puebla, Mexico*
- ⁹³ *Universidad Autónoma de San Luis Potosí, San Luis Potosí, Mexico*
- ⁹⁴ *University of Auckland, Auckland, New Zealand*
- ⁹⁵ *University of Canterbury, Christchurch, New Zealand*
- ⁹⁶ *National Centre for Physics, Quaid-I-Azam University, Islamabad, Pakistan*
- ⁹⁷ *National Centre for Nuclear Research, Swierk, Poland*
- ⁹⁸ *Institute of Experimental Physics, Faculty of Physics, University of Warsaw, Warsaw, Poland*
- ⁹⁹ *Laboratório de Instrumentação e Física Experimental de Partículas, Lisboa, Portugal*
- ¹⁰⁰ *Joint Institute for Nuclear Research, Dubna, Russia*
- ¹⁰¹ *Petersburg Nuclear Physics Institute, Gatchina (St. Petersburg), Russia*
- ¹⁰² *Institute for Nuclear Research, Moscow, Russia*
- ¹⁰³ *Institute for Theoretical and Experimental Physics, Moscow, Russia*
- ¹⁰⁴ *Moscow Institute of Physics and Technology, Moscow, Russia*
- ¹⁰⁵ *National Research Nuclear University 'Moscow Engineering Physics Institute' (MEPhI), Moscow, Russia*
- ¹⁰⁶ *P.N. Lebedev Physical Institute, Moscow, Russia*
- ¹⁰⁷ *Skobeltsyn Institute of Nuclear Physics, Lomonosov Moscow State University, Moscow, Russia*

- ¹⁰⁸Novosibirsk State University (NSU), Novosibirsk, Russia
- ¹⁰⁹State Research Center of Russian Federation, Institute for High Energy Physics of NRC “Kurchatov Institute”, Protvino, Russia
- ¹¹⁰National Research Tomsk Polytechnic University, Tomsk, Russia
- ¹¹¹University of Belgrade, Faculty of Physics and Vinca Institute of Nuclear Sciences, Belgrade, Serbia
- ¹¹²Centro de Investigaciones Energéticas Medioambientales y Tecnológicas (CIEMAT), Madrid, Spain
- ¹¹³Universidad Autónoma de Madrid, Madrid, Spain
- ¹¹⁴Universidad de Oviedo, Oviedo, Spain
- ¹¹⁵Instituto de Física de Cantabria (IFCA), CSIC-Universidad de Cantabria, Santander, Spain
- ¹¹⁶CERN, European Organization for Nuclear Research, Geneva, Switzerland
- ¹¹⁷Paul Scherrer Institut, Villigen, Switzerland
- ¹¹⁸ETH Zurich-Institute for Particle Physics and Astrophysics (IPA), Zurich, Switzerland
- ¹¹⁹Universität Zürich, Zurich, Switzerland
- ¹²⁰National Central University, Chung-Li, Taiwan
- ¹²¹National Taiwan University (NTU), Taipei, Taiwan
- ¹²²Chulalongkorn University, Faculty of Science, Department of Physics, Bangkok, Thailand
- ¹²³Çukurova University, Physics Department, Science and Art Faculty, Adana, Turkey
- ¹²⁴Middle East Technical University, Physics Department, Ankara, Turkey
- ¹²⁵Bogazici University, Istanbul, Turkey
- ¹²⁶Istanbul Technical University, Istanbul, Turkey
- ¹²⁷Institute for Scintillation Materials of National Academy of Science of Ukraine, Kharkov, Ukraine
- ¹²⁸National Scientific Center, Kharkov Institute of Physics and Technology, Kharkov, Ukraine
- ¹²⁹University of Bristol, Bristol, United Kingdom
- ¹³⁰Rutherford Appleton Laboratory, Didcot, United Kingdom
- ¹³¹Imperial College, London, United Kingdom
- ¹³²Brunel University, Uxbridge, United Kingdom
- ¹³³Baylor University, Waco, Texas, USA
- ¹³⁴Catholic University of America, Washington DC, USA
- ¹³⁵The University of Alabama, Tuscaloosa, Alabama, USA
- ¹³⁶Boston University, Boston, Massachusetts, USA
- ¹³⁷Brown University, Providence, Rhode Island, USA
- ¹³⁸University of California, Davis, Davis, California, USA
- ¹³⁹University of California, Los Angeles, California, USA
- ¹⁴⁰University of California, Riverside, Riverside, California, USA
- ¹⁴¹University of California, San Diego, La Jolla, California, USA
- ¹⁴²University of California, Santa Barbara—Department of Physics, Santa Barbara, California, USA
- ¹⁴³California Institute of Technology, Pasadena, California, USA
- ¹⁴⁴Carnegie Mellon University, Pittsburgh, Pennsylvania, USA
- ¹⁴⁵University of Colorado Boulder, Boulder, Colorado, USA
- ¹⁴⁶Cornell University, Ithaca, New York, USA
- ¹⁴⁷Fermi National Accelerator Laboratory, Batavia, Illinois, USA
- ¹⁴⁸University of Florida, Gainesville, Florida, USA
- ¹⁴⁹Florida International University, Miami, Florida, USA
- ¹⁵⁰Florida State University, Tallahassee, Florida, USA
- ¹⁵¹Florida Institute of Technology, Melbourne, Florida, USA
- ¹⁵²University of Illinois at Chicago (UIC), Chicago, Illinois, USA
- ¹⁵³The University of Iowa, Iowa City, Iowa, USA
- ¹⁵⁴Johns Hopkins University, Baltimore, Maryland, USA
- ¹⁵⁵The University of Kansas, Lawrence, Kansas, USA
- ¹⁵⁶Kansas State University, Manhattan, Kansas, USA
- ¹⁵⁷Lawrence Livermore National Laboratory, Livermore, California, USA
- ¹⁵⁸University of Maryland, College Park, Maryland, USA
- ¹⁵⁹Massachusetts Institute of Technology, Cambridge, Massachusetts, USA
- ¹⁶⁰University of Minnesota, Minneapolis, Minnesota, USA
- ¹⁶¹University of Mississippi, Oxford, Mississippi, USA
- ¹⁶²University of Nebraska-Lincoln, Lincoln, Nebraska, USA
- ¹⁶³State University of New York at Buffalo, Buffalo, New York, USA
- ¹⁶⁴Northeastern University, Boston, Massachusetts, USA
- ¹⁶⁵Northwestern University, Evanston, Illinois, USA
- ¹⁶⁶University of Notre Dame, Notre Dame, Indiana, USA
- ¹⁶⁷The Ohio State University, Columbus, Ohio, USA

- ¹⁶⁸*Princeton University, Princeton, New Jersey, USA*
¹⁶⁹*University of Puerto Rico, Mayaguez, Puerto Rico, USA*
¹⁷⁰*Purdue University, West Lafayette, Indiana, USA*
¹⁷¹*Purdue University Northwest, Hammond, Indiana, USA*
¹⁷²*Rice University, Houston, Texas, USA*
¹⁷³*University of Rochester, Rochester, New York, USA*
¹⁷⁴*Rutgers, The State University of New Jersey, Piscataway, New Jersey, USA*
¹⁷⁵*University of Tennessee, Knoxville, Tennessee, USA*
¹⁷⁶*Texas A&M University, College Station, Texas, USA*
¹⁷⁷*Texas Tech University, Lubbock, Texas, USA*
¹⁷⁸*Vanderbilt University, Nashville, Tennessee, USA*
¹⁷⁹*University of Virginia, Charlottesville, Virginia, USA*
¹⁸⁰*Wayne State University, Detroit, Michigan, USA*
¹⁸¹*University of Wisconsin—Madison, Madison, Wisconsin, USA*

^aDeceased.

^bAlso at Vienna University of Technology, Vienna, Austria.

^cAlso at IRFU, CEA, Université Paris-Saclay, Gif-sur-Yvette, France.

^dAlso at Universidade Estadual de Campinas, Campinas, Brazil.

^eAlso at Federal University of Rio Grande do Sul, Porto Alegre, Brazil.

^fAlso at Université Libre de Bruxelles, Bruxelles, Belgium.

^gAlso at University of Chinese Academy of Sciences.

^hAlso at Institute for Theoretical and Experimental Physics, Moscow, Russia.

ⁱAlso at Joint Institute for Nuclear Research, Dubna, Russia.

^jAlso at Cairo University, Cairo, Egypt.

^kAlso at Helwan University, Cairo, Egypt.

^lAlso at Zewail City of Science and Technology, Zewail, Egypt.

^mAlso at Department of Physics, King Abdulaziz University, Jeddah, Saudi Arabia.

ⁿAlso at Université de Haute Alsace, Mulhouse, France.

^oAlso at Skobeltsyn Institute of Nuclear Physics, Lomonosov Moscow State University, Moscow, Russia.

^pAlso at CERN, European Organization for Nuclear Research, Geneva, Switzerland.

^qAlso at RWTH Aachen University, III. Physikalisches Institut A, Aachen, Germany.

^rAlso at University of Hamburg, Hamburg, Germany.

^sAlso at Brandenburg University of Technology, Cottbus, Germany.

^tAlso at MTA-ELTE Lendület CMS Particle and Nuclear Physics Group, Eötvös Loránd University, Budapest, Hungary.

^uAlso at Institute of Nuclear Research ATOMKI, Debrecen, Hungary.

^vAlso at Institute of Physics, University of Debrecen, Debrecen, Hungary.

^wAlso at IIT Bhubaneswar, Bhubaneswar, India.

^xAlso at Institute of Physics, Bhubaneswar, India.

^yAlso at Shoolini University, Solan, India.

^zAlso at University of Visva-Bharati, Santiniketan, India.

^{aa}Also at Isfahan University of Technology, Isfahan, Iran.

^{bb}Also at Plasma Physics Research Center, Science and Research Branch, Islamic Azad University, Tehran, Iran.

^{cc}Also at Università degli Studi di Siena, Siena, Italy.

^{dd}Also at Kyunghee University, Seoul, Korea.

^{ee}Also at International Islamic University of Malaysia, Kuala Lumpur, Malaysia.

^{ff}Also at Malaysian Nuclear Agency, MOSTI, Kajang, Malaysia.

^{gg}Also at Consejo Nacional de Ciencia y Tecnología, Mexico city, Mexico.

^{hh}Also at Warsaw University of Technology, Institute of Electronic Systems, Warsaw, Poland.

ⁱⁱAlso at Institute for Nuclear Research, Moscow, Russia.

^{jj}Also at National Research Nuclear University “Moscow Engineering Physics Institute” (MEPhI), Moscow, Russia.

^{kk}Also at St. Petersburg State Polytechnical University, St. Petersburg, Russia.

^{ll}Also at University of Florida, Gainesville, FL, USA.

^{mmm}Also at P.N. Lebedev Physical Institute, Moscow, Russia.

ⁿⁿAlso at California Institute of Technology, Pasadena, CA, USA.

^{oo}Also at Budker Institute of Nuclear Physics, Novosibirsk, Russia.

^{pp}Also at Faculty of Physics, University of Belgrade, Belgrade, Serbia.

^{qq}Also at INFN Sezione di Pavia, Università di Pavia, Pavia, Italy.

^{rr}Also at University of Belgrade, Faculty of Physics and Vinca Institute of Nuclear Sciences, Belgrade, Serbia.

^{ss}Also at Scuola Normale e Sezione dell’INFN, Pisa, Italy.

- ^{tt} Also at National and Kapodistrian University of Athens, Athens, Greece.
- ^{uu} Also at Riga Technical University, Riga, Latvia.
- ^{vv} Also at Universität Zürich, Zurich, Switzerland.
- ^{ww} Also at Stefan Meyer Institute for Subatomic Physics.
- ^{xx} Also at Adiyaman University, Adiyaman, Turkey.
- ^{yy} Also at Istanbul Aydin University, Istanbul, Turkey.
- ^{zz} Also at Mersin University, Mersin, Turkey.
- ^{aaa} Also at Piri Reis University, Istanbul, Turkey.
- ^{bbb} Also at Gaziosmanpasa University, Tokat, Turkey.
- ^{ccc} Also at Ozyegin University, Istanbul, Turkey.
- ^{ddd} Also at Izmir Institute of Technology, Izmir, Turkey.
- ^{eee} Also at Marmara University, Istanbul, Turkey.
- ^{fff} Also at Kafkas University, Kars, Turkey.
- ^{ggg} Also at Istanbul Bilgi University, Istanbul, Turkey.
- ^{hhh} Also at Hacettepe University, Ankara, Turkey.
- ⁱⁱⁱ Also at Rutherford Appleton Laboratory, Didcot, United Kingdom.
- ^{jjj} Also at School of Physics and Astronomy, University of Southampton, Southampton, United Kingdom.
- ^{kkk} Also at Monash University, Faculty of Science, Clayton, Australia.
- ^{lll} Also at Bethel University, Arden Hills, MN, USA.
- ^{mmm} Also at Karamanoğlu Mehmetbey University.
- ⁿⁿⁿ Also at Utah Valley University, Orem, UT, USA.
- ^{ooo} Also at Purdue University, West Lafayette, IN, USA.
- ^{ppp} Also at Beykent University, Istanbul, Turkey.
- ^{qqq} Also at Bingol University, Bingol, Turkey.
- ^{rrr} Also at Sinop University, Sinop, Turkey.
- ^{sss} Also at Mimar Sinan University, Istanbul, Istanbul, Turkey.
- ^{ttt} Also at Texas A&M University at Qatar, Doha, Qatar.
- ^{uuu} Also at Kyungpook National University, Daegu, Korea.

OPEN ACCESS

Identification of heavy-flavour jets with the CMS detector in pp collisions at 13 TeV

To cite this article: A.M. Sirunyan *et al* 2018 *JINST* **13** P05011

View the [article online](#) for updates and enhancements.

Related content

- [Identification of b-quark jets with the CMS experiment](#)
The CMS collaboration
- [Jet energy scale and resolution in the CMS experiment in pp collisions at 8 TeV](#)
V. Khachatryan, A.M. Sirunyan, A. Tumasyan *et al.*
- [Note](#)
D Benedetti, S Cucciarelli, C Hill *et al.*

Identification of heavy-flavour jets with the CMS detector in pp collisions at 13 TeV



The CMS collaboration

E-mail: cms-publication-committee-chair@cern.ch

ABSTRACT: Many measurements and searches for physics beyond the standard model at the LHC rely on the efficient identification of heavy-flavour jets, i.e. jets originating from bottom or charm quarks. In this paper, the discriminating variables and the algorithms used for heavy-flavour jet identification during the first years of operation of the CMS experiment in proton-proton collisions at a centre-of-mass energy of 13 TeV, are presented. Heavy-flavour jet identification algorithms have been improved compared to those used previously at centre-of-mass energies of 7 and 8 TeV. For jets with transverse momenta in the range expected in simulated $t\bar{t}$ events, these new developments result in an efficiency of 68% for the correct identification of a b jet for a probability of 1% of misidentifying a light-flavour jet. The improvement in relative efficiency at this misidentification probability is about 15%, compared to previous CMS algorithms. In addition, for the first time algorithms have been developed to identify jets containing two b hadrons in Lorentz-boosted event topologies, as well as to tag c jets. The large data sample recorded in 2016 at a centre-of-mass energy of 13 TeV has also allowed the development of new methods to measure the efficiency and misidentification probability of heavy-flavour jet identification algorithms. The b jet identification efficiency is measured with a precision of a few per cent at moderate jet transverse momenta (between 30 and 300 GeV) and about 5% at the highest jet transverse momenta (between 500 and 1000 GeV).

KEYWORDS: Particle identification methods; Pattern recognition, cluster finding, calibration and fitting methods; Performance of High Energy Physics Detectors

ARXIV EPRINT: [1712.07158](https://arxiv.org/abs/1712.07158)

Contents

1	Introduction	1
2	The CMS detector	2
3	Data and simulated samples	4
4	Heavy-flavour jet discriminating variables	4
4.1	Properties of heavy-flavour jets	4
4.2	Track selection and variables	6
4.3	Secondary vertex reconstruction and variables	10
4.4	Soft-lepton variables	12
5	Heavy-flavour jet identification algorithms	14
5.1	The b jet identification	14
5.1.1	Jet probability taggers	14
5.1.2	Combined secondary vertex taggers	15
5.1.3	Soft-lepton and combined taggers	22
5.1.4	Performance in simulation	23
5.2	The c jet identification	25
5.2.1	Algorithm description	25
5.2.2	Performance in simulation	29
6	Identification of b jets in boosted topologies	31
6.1	Boosted b jet identification with the CSVv2 algorithm	31
6.2	The double-b tagger	34
7	Performance of b jet identification at the trigger level	39
8	Measurement of the tagging efficiency using data	43
8.1	Comparison of data with simulation	43
8.2	The misidentification probability	47
8.3	The c jet identification efficiency	49
8.3.1	Measurement relying on W + c events	50
8.3.2	Measurement relying on the single-lepton $t\bar{t}$ events	54
8.3.3	Combination of the measured c tagging efficiencies	57
8.4	The b jet identification efficiency	58
8.4.1	Measurements relying on a muon-enriched topology	58
8.4.2	Measurements relying on the dilepton $t\bar{t}$ topology	65
8.4.3	Tag-and-probe technique using single-lepton $t\bar{t}$ events	70
8.4.4	Combination of the data-to-simulation scale factors from multijet and $t\bar{t}$ events	75

8.5	Measurement of the data-to-simulation scale factors as a function of the discriminator value	76
8.6	Comparison of the measured data-to-simulation scale factors	79
9	Measurement of the tagging efficiency for boosted topologies	82
9.1	Comparison of data with simulation	82
9.2	Efficiency for subjets	83
9.2.1	Misidentification probability	83
9.2.2	Measurement of the b tagging efficiency	84
9.3	Efficiency of the double-b tagger	86
9.3.1	Measurement of the double-b tagging efficiency	86
9.3.2	Measurement of the misidentification probability for top quarks	87
10	Summary	89
A	Parameterization of the efficiency	91
	The CMS collaboration	98

1 Introduction

The success of the physics programme of the CMS experiment at the CERN LHC requires the particles created in the LHC collisions to be reconstructed and identified as accurately as possible. With the exception of the top quark, quarks and gluons produced in pp collisions develop a parton shower and eventually hadronize giving rise to jets of collimated particles observed in the CMS detector. Heavy-flavour jet identification techniques exploit the properties of the hadrons in the jet to discriminate between jets originating from b or c quarks (heavy-flavour jets) and those originating from light-flavour quarks or gluons (light-flavour jets). The CMS Collaboration presented in ref. [1] a set of b jet identification techniques used in physics analyses performed on LHC Run 1 pp collision data, collected in 2011 and 2012 at centre-of-mass energies of 7 and 8 TeV. This paper presents a comprehensive summary of the newly developed and optimized techniques compared to our previous results. In particular, the larger recorded data set of pp collisions at a centre-of-mass energy of 13 TeV during Run 2 of the LHC in 2016, allows the study of rarer high-momentum topologies in which daughter jets from a Lorentz-boosted parent particle merge into a single jet. Examples of such topologies include the identification of boosted Higgs bosons decaying to two b quarks, and of b jets from boosted top quarks. The identification of c jets is also of significant interest, e.g. for the study of Higgs boson decays to a pair of c quarks, and for top squark searches in the c quark plus neutralino final-state topology.

The paper is organized as follows. A brief summary of particle and jet reconstruction in the CMS detector is given in section 2. Details about the simulated proton-proton collision samples and the data-taking conditions are given in section 3. The properties of heavy-flavour jets and the variables used to discriminate between these and other jets are discussed in section 4, while

the algorithms are presented in sections 5 and 6. For some physics processes, it is important to identify b jets at the trigger level. This topic is discussed in section 7. The large recorded number of proton-proton (pp) collisions permits the exploration of new methods to measure the efficiency of the heavy-flavour jet identification algorithms using data. These new methods, as well as the techniques used during the Run 1, are summarized in sections 8 and 9 for efficiency measurements in nonboosted and boosted event topologies, respectively.

2 The CMS detector

The central feature of the CMS apparatus is a superconducting solenoid of 6 m internal diameter and a magnetic field of 3.8 T. Within the solenoid volume are a silicon pixel and strip tracker, a lead tungstate crystal electromagnetic calorimeter (ECAL), and a brass and scintillator hadron calorimeter (HCAL), each composed of a barrel and two endcap sections, together providing coverage in pseudorapidity (η) up to $|\eta| = 3.0$. Forward calorimeters extend the coverage to $|\eta| = 5.2$. Muons are detected in the pseudorapidity range $|\eta| < 2.4$ using gas-ionization chambers embedded in the steel flux-return yoke outside the solenoid.

The silicon tracker measures charged particles within the range $|\eta| < 2.5$. During the first two years of Run 2 operation at a centre-of-mass energy of 13 TeV, the silicon tracker setup did not change compared to the Run 1 of the LHC. The trajectories of charged particles are reconstructed from the hits in the silicon tracking system using an iterative procedure with a Kalman filter. The tracking efficiency is typically over 98% for tracks with a transverse momentum (p_T) above 1 GeV. For nonisolated particles with $1 < p_T < 10$ GeV and $|\eta| < 1.4$, the track resolutions are typically 1.5% in p_T and 25–90 (45–150) μm in the transverse (longitudinal) impact parameter (IP) [2]. The pp interaction vertices are reconstructed by clustering tracks on the basis of their z coordinates at their points of closest approach to the centre of the beam spot using a deterministic annealing algorithm [3]. The position of each vertex is estimated with an adaptive vertex fit [4]. The resolution on the position is around 20 μm in the transverse plane and around 30 μm along the beam axis for primary vertices reconstructed using at least 50 tracks [2].

The global event reconstruction, also called particle-flow (PF) event reconstruction [5], consists of reconstructing and identifying each individual particle with an optimized combination of all subdetector information. In this process, the identification of the particle type (photon, electron, muon, charged hadron, neutral hadron) plays an important role in the determination of the particle direction and energy. Photons, e.g. coming from neutral pion decays or from electron bremsstrahlung, are identified as ECAL energy clusters not linked to the extrapolation of any charged-particle trajectory to the ECAL. Electrons, e.g. coming from photon conversions in the tracker material or from heavy-flavour hadron semileptonic decays, are identified as combinations of charged-particle tracks reconstructed in the tracker and multiple ECAL energy clusters corresponding to both the passage of the electron through the ECAL plus any associated bremsstrahlung photons. Muons, e.g. from the semileptonic decay of heavy-flavour hadrons, are identified as tracks reconstructed in the tracker combined with matching hits or tracks in the muon system, and matching energy deposits in the calorimeters. Charged hadrons are identified as charged particles not identified as electrons or muons. Finally, neutral hadrons are identified as HCAL energy clusters not matching

any charged-particle track, or as ECAL and HCAL energy excesses with respect to the expected charged-hadron energy deposit.

For each event, particles originating from the same interaction vertex are clustered into jets with the infrared and collinear safe anti- k_T algorithm [6, 7], using a distance parameter $R = 0.4$ (AK4 jets). Compared to the $R = 0.5$ jets that were used in Run 1 physics analyses, jets reconstructed with $R = 0.4$ are found to still contain most of the particles from the hadronization process, while at the same time being less sensitive to particles from additional pp interactions (known as pileup) appearing in the same or adjacent bunch crossings. For studies involving boosted topologies, jets are clustered with a larger distance parameter $R = 0.8$ (AK8 jets). The jet momentum is determined as the vectorial sum of all particle momenta in the jet. Jet energy corrections are derived from the simulation and are confirmed with in situ measurements using the energy balance in dijet, multijet, photon + jet, and leptonically decaying Z + jets events [8]. The jet energy resolution amounts typically to 15% at 10 GeV, 8% at 100 GeV, and 4% at 1 TeV [8]. For the studies presented here, jets are required to lie within the tracker acceptance ($|\eta| < 2.4$) and have $p_T > 20$ GeV. The missing transverse momentum vector is defined as the projection of the negative vector sum of the momenta of all reconstructed particles in an event on the plane perpendicular to the beams. Its magnitude is referred to as p_T^{miss} .

The reconstructed vertex with the largest value of summed physics-object p_T^2 is taken to be the primary pp interaction vertex (PV). The physics objects are the jets, clustered using the jet finding algorithm with the tracks assigned to the vertex as inputs, and the associated missing transverse momentum, taken as the negative vector sum of the p_T of those jets.

The energy of electrons is determined from a combination of the track momentum at the main interaction vertex, the corresponding ECAL cluster energies, and the energies of all bremsstrahlung photons associated with the track. The momentum resolution for electrons with $p_T \approx 45$ GeV from $Z \rightarrow ee$ decays ranges from 1.7% for nonshowering electrons, i.e. not producing additional photons and electrons, in the barrel region ($|\eta| < 1.48$), to 4.5% for showering electrons in the endcaps ($1.48 < |\eta| < 3.0$) [9]. Muons with $20 < p_T < 100$ GeV have a relative p_T resolution of 1.3–2.0% in the barrel and less than 6% in the endcaps. The p_T resolution in the barrel is better than 10% for muons with p_T up to 1 TeV [10]. The energy of charged hadrons is determined from a combination of the track momentum and the corresponding ECAL and HCAL energy deposits, corrected for zero-suppression effects and for the response function of the calorimeters to hadronic showers. Finally, the energy of neutral hadrons is obtained from the corresponding corrected ECAL and HCAL energy deposits.

Events of interest are selected using a two-tiered trigger system [11]. The level-1 trigger (L1), composed of custom hardware processors, uses information from the calorimeters and muon detectors to select events at a rate of around 100 kHz. The second level, known as the high-level trigger (HLT), consists of a farm of processors running a version of the full event reconstruction software optimized for fast processing, and reduces the event rate to less than 1 kHz before data storage.

A more detailed description of the CMS detector, together with a definition of the coordinate system used and the relevant kinematic variables, can be found in ref. [12].

3 Data and simulated samples

The results presented in this paper are based on the pp collision data set recorded at a centre-of-mass energy of 13 TeV by the CMS detector in 2016, corresponding to an integrated luminosity of 35.9 fb^{-1} . Various event generators are used to model the relevant physics processes. The interactions between particles and the material of the CMS detector are simulated using `GEANT 4` [13–15]. The data and simulated samples are used to determine the heavy-flavour jet identification efficiency in various event topologies. When measuring the heavy-flavour jet identification efficiency or when comparing the data to the simulation, the number of simulated events is large enough to neglect the statistical uncertainty in the simulation unless mentioned otherwise.

The pair production of top quarks and electroweak single top quark production is performed with the `POWHEG 2.0` generator at next-to-leading order (NLO) accuracy [16–21]. The value of the top quark mass used for the generation of the simulated samples is 172.5 GeV. The systematic uncertainty related to the value of the top quark mass m_t is evaluated by varying it by ± 1 GeV. Alternative samples are used to assess parton shower uncertainties, as well as factorization and normalization scale uncertainties at the matrix element and parton shower levels. Diboson WW, WZ, and ZZ events, referred to collectively as “VV” events, are generated at NLO accuracy with the `MADGRAPH5_AMC@NLO 2.2.2` generator [22], including `MADSPIN` [23] and the FxFx merging scheme [24] between jets from matrix element calculations and the parton shower description, or with the `POWHEG 2.0` generator [25, 26]. The Z + jets and W + jets events are generated with `MADGRAPH5_AMC@NLO 2.2.2` at leading order (LO), using the MLM matching scheme [27]. Samples of events with a Kaluza-Klein graviton [28] decaying to two Higgs bosons are also simulated with `MADGRAPH5_AMC@NLO 2.2.2` at LO for graviton masses ranging between 1 and 3.5 TeV. Background events comprised uniquely of jets produced through the strong interaction (multijet events) are generated with `PYTHIA 8.205` [29] in different \hat{p}_T bins, where \hat{p}_T is defined as the average p_T of the final-state partons. Muon-enriched multijet samples are produced by forcing the decay of charged pions and kaons into muons and by requiring a generated muon with $p_T > 5$ GeV.

`PYTHIA 8.205` is also used for the parton showering and hadronization of all the simulated samples with the CMS underlying event tunes CUETP8M1 [30] using the NNPDF 2.3 [31] parton distribution functions. In the case of top quark pair production a modification of this tune is used, CUETP8M2T4 [32] using the NNPDF 3.0 [33] parton distribution functions.

Pileup interactions are modelled by overlaying the simulated events with additional minimum bias collisions generated with `PYTHIA 8.205`. These additional simulated events are then reweighted to match the observed number of pileup interactions or the primary vertex multiplicity in data.

4 Heavy-flavour jet discriminating variables

4.1 Properties of heavy-flavour jets

Algorithms for heavy-flavour jet identification use variables connected to the properties of heavy-flavour hadrons present in jets resulting from the radiation and hadronization of b or c quarks. For instance, the lifetime of hadrons containing b quarks is of the order of 1.5 ps, while the lifetime of c hadrons is 1 ps or less. This leads to typical displacements of a few mm to one cm for b hadrons, depending on their momentum, thus giving rise to displaced tracks from which a secondary vertex

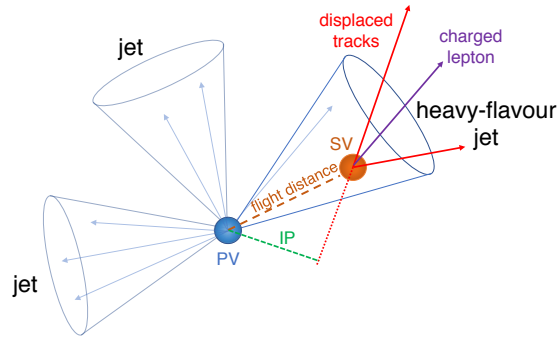


Figure 1. Illustration of a heavy-flavour jet with a secondary vertex (SV) from the decay of a b or c hadron resulting in charged-particle tracks (including possibly a soft lepton) that are displaced with respect to the primary interaction vertex (PV), and hence with a large impact parameter (IP) value.

(SV) may be reconstructed, as illustrated in figure 1. The displacement of tracks with respect to the primary vertex is characterized by their impact parameter, which is defined as the distance between the primary vertex and the tracks at their points of closest approach. The vector pointing from the primary vertex to the point of closest approach is referred to as the impact parameter vector. The impact parameter value can be defined in three spatial dimensions (3D) or in the plane transverse to the beam line (2D). The longitudinal impact parameter is defined in one dimension, along the beam line. The impact parameter is defined to be positive or negative, with a positive sign indicating that the track is produced “upstream”. This means that the angle between the impact parameter vector and the jet axis is smaller than $\pi/2$, where the jet axis is defined by the primary vertex and the direction of the jet momentum. In addition, b and c quarks have a larger mass and harder fragmentation compared to the light quarks and massless gluons. As a result, the decay products of the heavy-flavour hadron have, on average, a larger p_T relative to the jet axis than the other jet constituents. In approximately 20% (10%) of the cases, a muon or electron is present in the decay chain of a heavy b (c) hadron. Hence, apart from the properties of the reconstructed secondary vertex or displaced tracks, the presence of charged leptons is also exploited for heavy-flavour jet identification techniques and for measuring their performance in data.

In order to design and optimize heavy-flavour identification techniques, a reliable method is required for assigning a flavour to jets in simulated events. The jet flavour is determined by clustering not only the reconstructed final-state particles into jets, but also the generated b and c hadrons that do not have b and c hadrons as daughters respectively. To prevent these generated hadrons from affecting the reconstructed jet momentum, the modulus of the hadron four-momentum is set to a small number, retaining only the directional information. This procedure is known as ghost association [34]. Jets containing at least one b hadron are defined as b jets; the ones containing at least one c hadron and no b hadron are defined as c jets. The remaining jets are considered to be light-flavour (or “uds-g”) jets. Since pileup interactions are not included during the hard-scattering event generation, jets from pileup interactions (“pileup jets”) in the simulation are tentatively identified as jets without a matched generated jet. The generated jets are reconstructed with the jet clustering algorithm mentioned in section 2 applied to the generated final-state particles (excluding neutrinos). The matching between the reconstructed PF jets and the generated jets with $p_T > 8$ GeV

is performed by requiring the angular distance between them to be $\Delta R = \sqrt{(\Delta\eta)^2 + (\Delta\phi)^2} < 0.25$. Using this flavour definition, jets arising from gluon splitting to $b\bar{b}$ are considered as b jets. In sections 6, 8 and 9, these $g \rightarrow b\bar{b}$ jets are often shown as a separate category. In this case, two b hadrons without b hadron daughters should be clustered in the jet. The studies presented in sections 4 and 5 are based on simulated events. For these studies, jets are removed if they are closer than $\Delta R = 0.4$ to a generated charged lepton from a direct V boson decay. In addition, electrons or muons originating from gauge boson decays that are reconstructed as jets are removed if they carry more than 60% of the jet p_T , i.e. $p_T^\ell/p_T^{\text{jet}} < 0.6$ is required, where p_T^ℓ (p_T^{jet}) is the p_T of the lepton (jet). No additional identification or isolation requirements are applied for muons or electrons.

4.2 Track selection and variables

The properties of the tracks clustered within the jet represent the basic inputs of all heavy-flavour jet identification (tagging) algorithms. Input variables for the tagging algorithms are constructed from the tracks after applying appropriate selection criteria. In particular, to ensure a good momentum and impact parameter resolution, tracks are required to have $p_T > 1$ GeV, a χ^2 value of the trajectory fit normalized to the number of degrees of freedom below 5, and at least one hit in the pixel layers of the tracker detector. The last of these requirements is less stringent than the requirement used for b jet identification in Run 1, where at least eight hits were required in the pixel and strip tracker combined, of which at least two were pixel detector hits. The requirement on the number of hits was relaxed to cope with saturation effects that were observed at high occupancy in the readout electronics of the strip tracker during the first part of the 2016 data taking, leading to a reduced tracking and b tagging performance. The issues with the readout electronics have been fully resolved, with no side effects on the tracking performance, but the relaxed requirement on the number of hits was kept since there was no impact on the final b tagging performance. Apart from the requirements on the quality of the tracks, the presence of tracks from long-lived K_S^0 or Λ hadrons as well as from material interactions is reduced by requiring the track decay length, defined as the distance from the primary vertex to the point of closest approach between the track and the jet axis, to be less than 5 cm. The contribution from tracks originating from pileup vertices is reduced with the following set of requirements: the absolute value of the transverse (longitudinal) impact parameter of the track is required to be smaller than 0.2 (17) cm and the distance between the track and the jet axis at their point of closest approach is required to be less than 0.07 cm. Figure 2 presents typical distributions of the latter variable for jets in $t\bar{t}$ events after applying the rest of the track selection requirements, showing the origin of each track separately. The origin of a track is labelled with “ b hadron” if the track corresponds to a particle originating from a b hadron decay. A track corresponding to a particle from the decay of a c hadron that itself originates from the decay of a b hadron is also labelled as “ b hadron”. The category with the “ c hadron” label contains only tracks corresponding to a particle from the decay of a c hadron without a b hadron ancestor. The label “ uds hadron” indicates tracks corresponding to particles without heavy-flavour hadron ancestors. The label “pileup” refers to tracks from charged particles originating from a different primary vertex. A category with mismeasured tracks is defined containing tracks that are more likely to have been misreconstructed, e.g. by wrongly combining hits created by different particles. A track belongs to this category if the number of hits from the simulated charged particle closest to the track over the number of hits associated with the track, is less than 75%. This category is

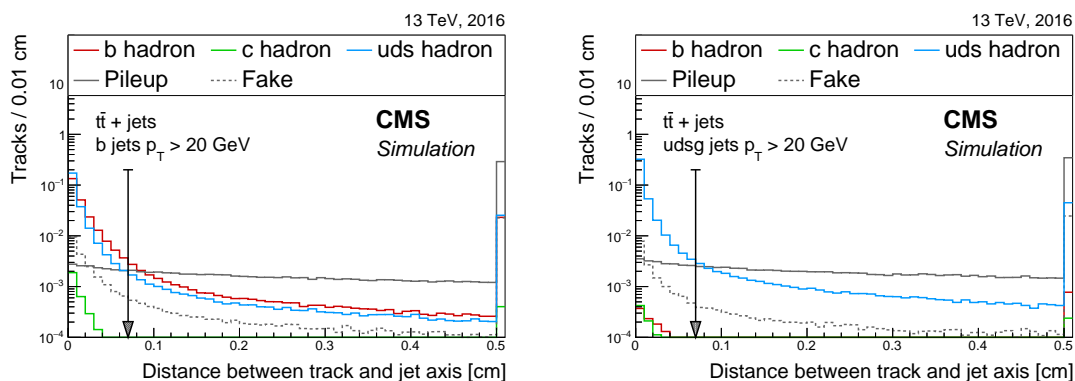


Figure 2. Distribution of the distance between a track and the jet axis at their point of closest approach for tracks associated with b (left) and light-flavour (right) jets in $t\bar{t}$ events. This distance is required to be smaller than 0.07 cm, as indicated by the arrow. The tracks are divided into categories according to their origin as defined in the text. The distributions are normalized such that their sum has unit area. The last bin includes the overflow entries.

labelled as “fake”. In figure 3, the impact of the track selection requirements on the number of tracks in a given category is shown for various jet flavours in $t\bar{t}$ events. The track selection requirements clearly enhance the fraction of tracks originating from heavy-flavour hadron decays in bottom and charm jets. The track selection requirements reduce the number of tracks in the fake and pileup categories to a few per cent for all jet flavours. Figure 4 shows the track multiplicity dependence on the jet p_T and $|\eta|$ for various jet flavours in $t\bar{t}$ events before and after applying the track selection requirements. For b jets, the average track multiplicity is higher than for light-flavour jets, before and after applying the track selection requirements, and the ratio of the average track multiplicity for b jets to other jet flavours is roughly constant. The average track multiplicity increases with increasing jet p_T for all jet flavours. Before the track selection, the average track multiplicity is almost constant with respect to the jet $|\eta|$. The small variations seen are due to the tracker geometry that has an impact on the track reconstruction efficiency. In addition, since the η of the jet is defined as the η of the jet axis, some of the charged particles in the jet are outside the tracker acceptance for high jet $|\eta|$ values, resulting in a lower track multiplicity in the highest bin. When the track selection requirements are applied, the average track multiplicity decreases with respect to the jet $|\eta|$, because of the relatively larger impact of the track selection requirements near the edge of the acceptance window for the tracker.

The aforementioned track selection requirements are always applied when reconstructing the variables used in the tagging algorithms. An exception is given by the variables relying on the inclusive vertex finding algorithm, as discussed in section 4.3. Figure 5 shows the distribution of the 3D impact parameter and its significance for the different jet flavours. The impact parameter significance is defined as the impact parameter value divided by its uncertainty, IP/σ . In addition, the lower panels in figure 5 also show the distribution of the 2D impact parameter significance for the track with the highest and second-highest 2D impact parameter significance for different jet flavours. From figure 5 it is clear that tracks in heavy-flavour jets have larger impact parameter and impact parameter significance compared to tracks in light-flavour jets. The lower left panel in

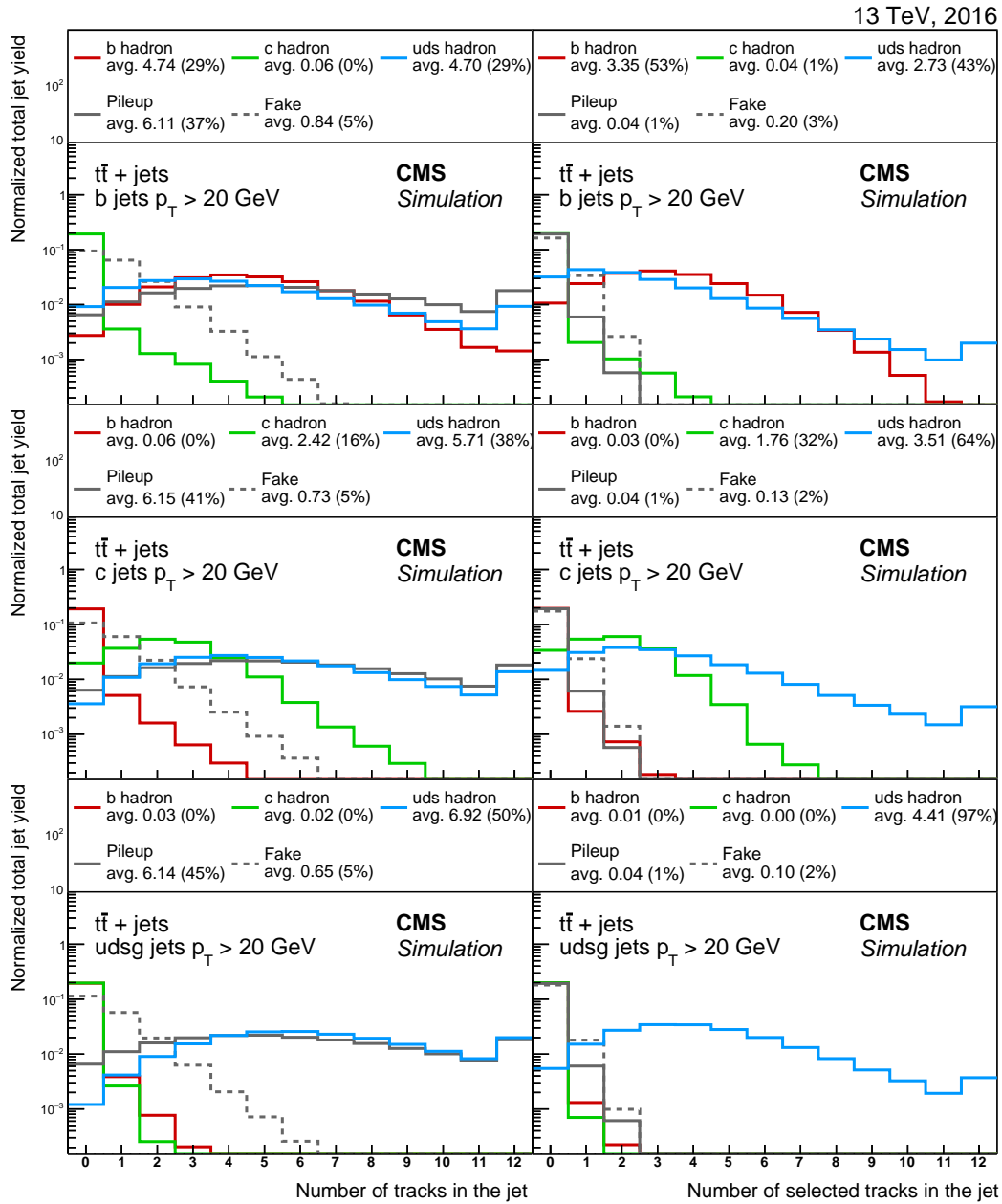


Figure 3. Fraction of tracks from different origins before (left) and after (right) applying the track selection requirements on b (upper), c (middle), and light-flavour (lower) jets in $t\bar{t}$ events. The average number of tracks of each origin is given in the legend as well as the average fraction of tracks of a certain origin with respect to the total number of tracks in the jet, indicated in per cent. The number of tracks corresponding to pileup vertices or mismeasured tracks is strongly reduced after applying the track selection requirements. The distributions are normalized such that their sum has unit area. The last bin includes the overflow entries.

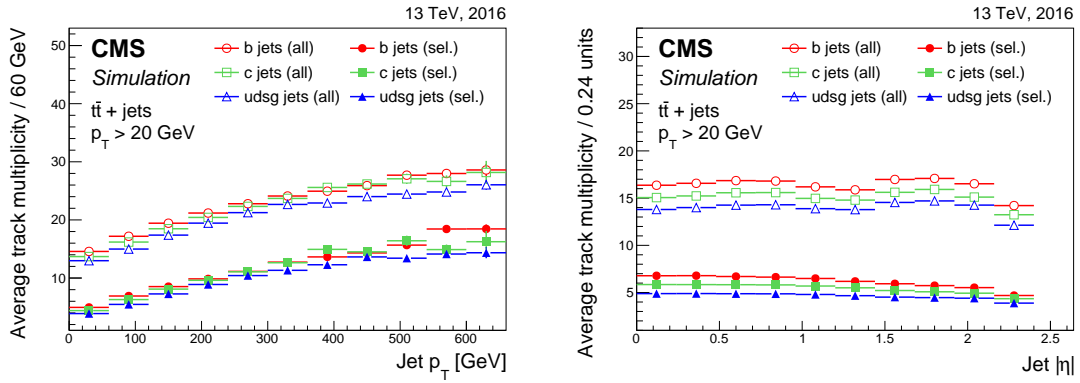


Figure 4. Average track multiplicity as a function of the jet p_T (left) and $|\eta|$ (right) for jets of different flavours in $t\bar{t}$ events before (open symbols) and after (filled symbols) applying the track selection requirements.

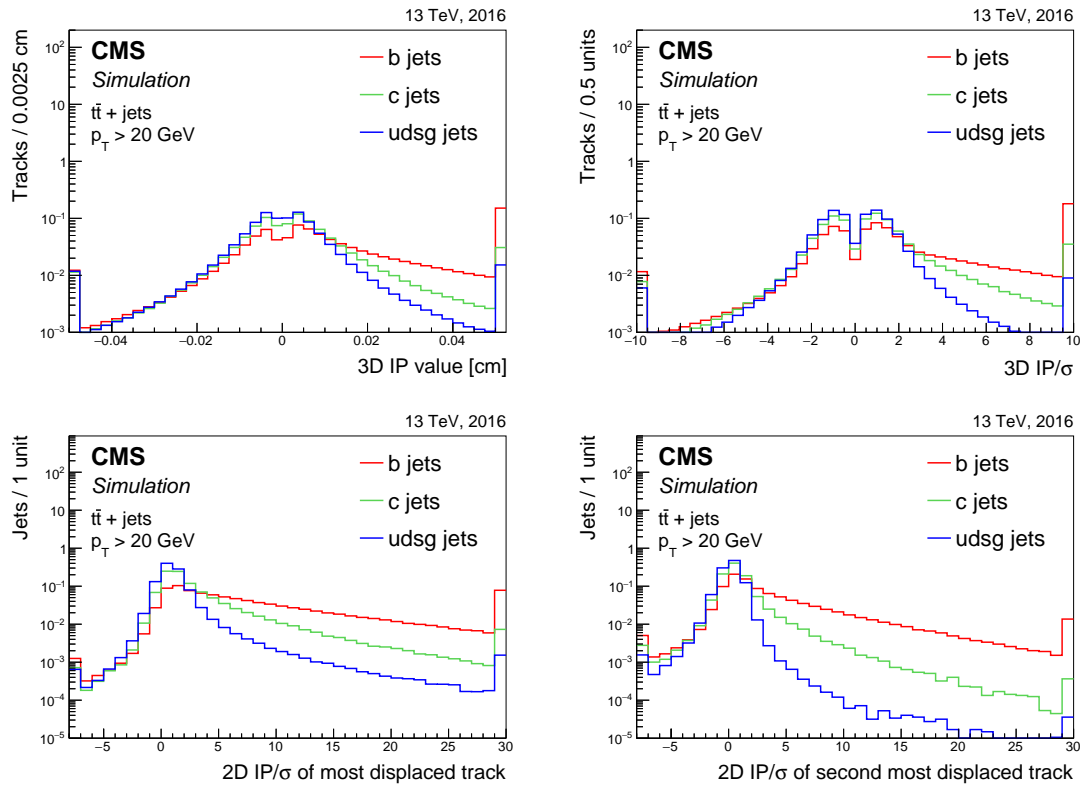


Figure 5. Distribution of the 3D impact parameter value (upper left) and significance (upper right) for tracks associated with jets of different flavours in $t\bar{t}$ events. Distribution of the 2D impact parameter significance for the track with the highest (lower left) and second-highest (lower right) 2D impact parameter significance for jets of different flavours in $t\bar{t}$ events. The distributions are normalized to unit area. The first and last bin include the underflow and overflow entries, respectively.

figure 5 shows that tracks with a large impact parameter significance are also present in light-flavour jets. These originate from the decays of relatively long-lived hadrons, for example K_S^0 or Λ , or from heavy-flavour hadrons where the tracks have been incorrectly clustered into a light-flavour jet. For the track with the second-highest impact parameter significance in light-flavour jets, the distribution is much more symmetric as expected for hadrons with a short lifetime.

4.3 Secondary vertex reconstruction and variables

If the secondary vertex from the decay of a heavy-flavour hadron is reconstructed, powerful discriminating variables can be derived from it. An example is the (corrected) secondary vertex mass, which is directly related to the mass of the heavy-flavour hadron. The corrected secondary vertex mass is defined as $\sqrt{M_{SV}^2 + p^2 \sin^2 \theta} + p \sin \theta$, where M_{SV} is the invariant mass of the tracks associated with the secondary vertex, p is the secondary vertex momentum obtained from the tracks associated with it, and θ the angle between the secondary vertex momentum and the vector pointing from the primary vertex to the secondary vertex, which is referred to as the secondary vertex flight direction. Using this definition, the secondary vertex mass is corrected for the observed difference between its flight direction and its momentum, taking into account particles that were not reconstructed or which failed to be associated with the secondary vertex. It should be noted that the energy of a track is obtained using its momentum and assuming the π^\pm mass [35]. Another example of a discriminating secondary vertex variable is its flight distance (significance), defined as the 2D or 3D distance between the primary and secondary vertex positions (divided by the uncertainty on the secondary vertex flight distance). Reconstructing the secondary vertex from the heavy-flavour hadron decay is not always possible for two main reasons: the heavy-flavour hadron decays too close to the primary vertex, or there are less than two selected tracks. The latter may be due to having less than two charged particles in the decay, less than two reconstructed tracks, or less than two tracks passing the selection requirements.

Two algorithms for reconstructing secondary vertices are used. The first one is the adaptive vertex reconstruction (AVR) algorithm [36]. This secondary vertex reconstruction algorithm was used for b jet identification by the CMS Collaboration during the LHC Run 1 [1]. The algorithm uses the tracks clustered within jets and passing the selection requirements discussed in section 4.2. In addition, the tracks are required to be within $\Delta R < 0.3$ of the jet axis and to have a track distance below 0.2 cm. The vertex pattern recognition iteratively fits all tracks with an outlier-resistant adaptive vertex fitter [4]. At each iteration, tracks close enough to the fitted vertex are removed and a new iteration is made with the remaining tracks. Given that the first iteration often finds a vertex close to the primary vertex, the first iteration is explicitly run with a constraint on the primary vertex. Vertices are rejected if it is found that they share more than 65% of their tracks with the primary vertex, or if their 2D secondary vertex flight distance is more than 2.5 cm or less than 0.01 cm. In addition, the 2D secondary vertex flight distance significance is required to be larger than 3. To reduce the impact of long-lived hadron decays and material interactions, only secondary vertices with $M_{SV} < 6.5$ GeV are considered. Pairs of tracks are rejected if they are compatible with the mass of the relatively long-lived K_S^0 hadron within 50 MeV. Additionally, the angular distance between the jet axis and the secondary vertex flight direction should satisfy $\Delta R < 0.4$. When all these requirements are fulfilled, the reconstructed AVR secondary vertex is associated with the jet.

At the start of LHC Run 2, the inclusive vertex finding (IVF) algorithm was adopted as the standard secondary vertex reconstruction algorithm used to define variables for heavy-flavour jet tagging. In contrast with AVR, which uses as input the selected tracks clustered in the reconstructed jets, IVF uses as input all reconstructed tracks in the event with $p_T > 0.8$ GeV and a longitudinal IP < 0.3 cm. The algorithm was initially developed to perform a measurement of the angular correlations between the b jets in $b\bar{b}$ pair production [37]. It is well suited for b hadron decays at small relative angle giving rise to overlapping, or completely merged, jets. The IVF procedure starts by identifying seed tracks with a 3D impact parameter value of at least $50 \mu\text{m}$ and a 2D impact parameter significance of at least 1.2. After identifying the seed tracks, the procedure includes the following steps:

- **Track clustering:** the compatibility between a seed track and any other track is evaluated using requirements on the distance at the point of closest approach of the two tracks and the angle between them. In addition, the distance between the seed track and any other track at their points of closest approach is required to be smaller than the distance between the track and the primary vertex at their points of closest approach.
- **Secondary vertex fitting and cleaning:** in order to determine the position of the secondary vertices, the sets of clustered tracks are fitted with the adaptive vertex fitter also used in the AVR algorithm. After the fit, secondary vertices with a 2D (3D) flight distance significance smaller than 2.5 (0.5) are removed. For IVF vertices used in the c tagging algorithm presented in section 5.2.1, the threshold is relaxed to 1.25 (0.25). In addition, if two secondary vertices share 70% or more of their tracks, or if the significance of the flight distance between the two secondary vertices is less than 2, one of the two secondary vertices is dropped from the collection of secondary vertices.
- **Track arbitration:** at this stage, a track could be assigned to both the primary vertex and secondary vertex. To resolve this ambiguity, a track is discarded from the secondary vertex if it is more compatible with the primary vertex. This is the case if the angular distance between the track and the secondary vertex flight direction is $\Delta R > 0.4$, and if the distance between the secondary vertex and the track is larger than the absolute impact parameter value of the track.
- **Secondary vertex refitting and cleaning:** the secondary vertex position is refitted after track arbitration and if there are still two or more tracks associated with the secondary vertex. After refitting the secondary vertex positions, a second check for duplicate vertices is performed. This time, a secondary vertex is removed from the collection of secondary vertices when it shares at least 20% of its tracks with another secondary vertex and the significance of the flight distance between the two secondary vertices is less than 10.

The selection criteria applied to the remaining IVF secondary vertices are mostly the same as in the case of the AVR vertices. However, to maximize the secondary vertex reconstruction efficiency, some requirements are relaxed. In particular, secondary vertices are rejected when they share 80% or more of their tracks, and when the 2D flight distance significance is less than 2 (1.5) for secondary vertices used in b (c) tagging algorithms. The remaining secondary vertices are then associated

with the jets by requiring the angular distance between the jet axis and the secondary vertex flight direction to satisfy $\Delta R < 0.3$.

Figure 6 shows the discriminating power between the various jet flavours for the IVF secondary vertex mass (left) and 2D flight distance significance (right). The secondary vertex mass for b jets peaks at higher values compared to that of the other jet flavours. For c jets, a peak is observed around 1.5 GeV, as expected from the lower mass of c compared to b hadrons.

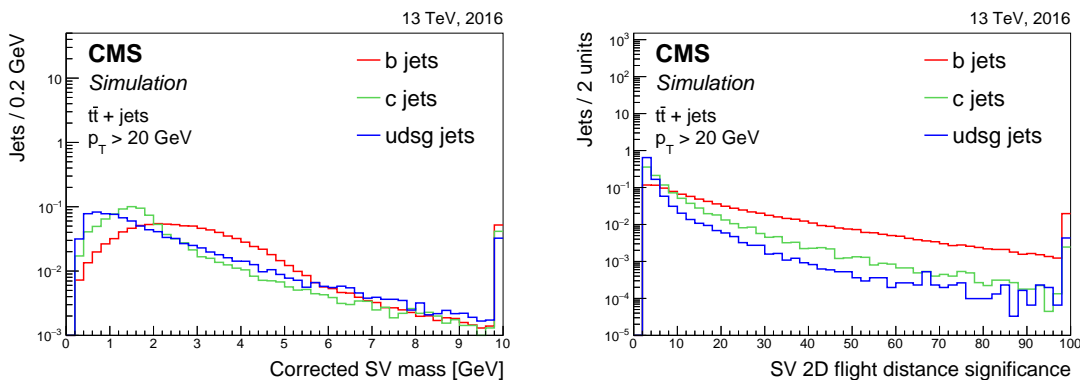


Figure 6. Distribution of the corrected secondary vertex mass (left) and of the secondary vertex 2D flight distance significance (right) for jets containing an IVF secondary vertex. The distributions are shown for jets of different flavours in $t\bar{t}$ events and are normalized to unit area. The last bin includes the overflow entries.

The secondary vertex reconstruction efficiency for jets is defined as the number of jets containing a reconstructed secondary vertex divided by the total number of jets. For jets with $p_T > 20$ GeV in $t\bar{t}$ events, the efficiency for reconstructing a secondary vertex for b (udsg) jets using the IVF algorithm is about 75% (12%), compared to 65% (4%) for reconstructing a secondary vertex with the AVR algorithm. However, the efficiency gain is largest for c jets with an IVF secondary vertex reconstruction efficiency of about 37%, compared to 23% for the efficiency of the AVR algorithm. Averaged over all jet flavours, 66% of the IVF secondary vertices in jets are also found by the AVR algorithm. The other way around, 86% of the AVR secondary vertices are also found by the IVF algorithm. Figure 7 (left) compares the number of secondary vertices in b jets for the IVF and AVR algorithms. As expected, more secondary vertices are reconstructed with the IVF algorithm because of the inclusive approach of using all tracks instead of only those associated with the jet and passing the selection requirements. The right panel in figure 7 shows the correlation between the corrected mass of the secondary vertices obtained with the two approaches. From the correlation it is clear that the same secondary vertex is found in most cases. Since the efficiency of the IVF algorithm is higher, IVF secondary vertices are used to compute the secondary vertex variables for the heavy-flavour jet identification algorithms. AVR secondary vertices are only used in one of the b jet identification algorithms discussed in section 5.

4.4 Soft-lepton variables

Although an electron or muon is present in only 20% (10%) of the b (c) jets, the properties of this low-energy nonisolated “soft lepton” (SL) permit the selection of a pure sample of heavy-flavour jets. Therefore, some of the heavy-flavour taggers use the properties of these soft leptons. Soft

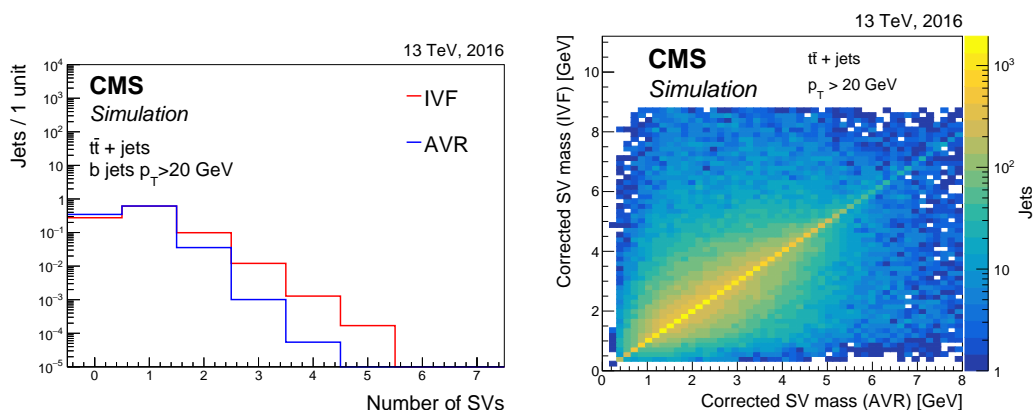


Figure 7. Distribution of the number of secondary vertices in b jets for the two vertex finding algorithms described in the text (left). The distributions are normalized to unit area. Correlation between the corrected secondary vertex mass for the vertices obtained with the two vertex finding algorithms (right). Both panels show jets in $t\bar{t}$ events.

muons are defined as particles clustered in the jet passing the loose muon identification criteria and with a p_T of at least 2 GeV [10]. Electrons are associated with a jet by requiring $\Delta R < 0.4$. Soft electrons should pass the loose electron identification criteria, have an associated track with at least three hits in the pixel layers, and be identified as not originating from a photon conversion [9].

Discriminating variables using soft lepton information are typically similar to the variables based on track information alone. As an example, figure 8 shows the distribution of the 3D impact parameter value of soft leptons associated with jets. The 3D impact parameter value of the soft

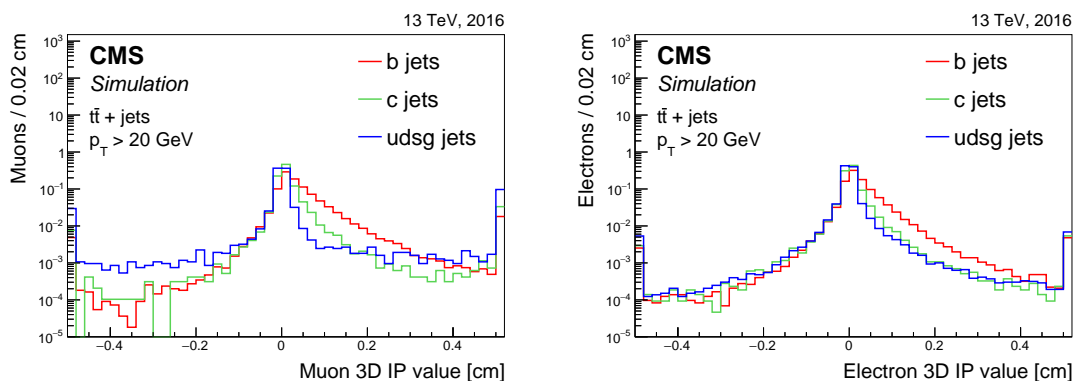


Figure 8. Distribution of the 3D impact parameter value for soft muons (left) and soft electrons (right) for jets of different flavours in $t\bar{t}$ events. The distributions are normalized to unit area. The first and last bins include the underflow and overflow entries, respectively.

lepton discriminates between the various jet flavours. For the low- p_T muons expected from the heavy-flavour hadron decays, it should be noted that the impact parameter resolution is worse than at high p_T [10], which is reflected in the relatively large spread of the impact parameter values. The soft lepton variables are used in the soft lepton algorithms discussed in section 5.1.3 and in the c tagger discussed in section 5.2.1.

5 Heavy-flavour jet identification algorithms

5.1 The b jet identification

The jet probability (JP) and combined secondary vertex (CSV) taggers used during Run 1 [1] are also used for the Run 2 analyses. Likewise, the combined multivariate analysis (cMVA) tagger, which combines the discriminator values of various taggers, was retrained. Apart from the retraining, the CSV algorithm was also optimized and the new version is referred to as CSVv2. In addition, another version of the CSV algorithm was developed that uses deep machine learning [38] (DeepCSV). These taggers are presented in more detail in the sections 5.1.1 to 5.1.3. The new developments result in a performance that is significantly better than that of the Run 1 taggers, as discussed in section 5.1.4.

5.1.1 Jet probability taggers

There are two jet probability taggers, the JP and JBP algorithms. The JP algorithm is described in ref. [1] and uses the signed impact parameter significance of the tracks associated with the jet to obtain a likelihood for the jet to originate from the primary vertex. This likelihood, or jet probability, is obtained as follows. The negative impact parameter significance of tracks from light-flavour jets reflects the resolution of the measured track impact parameter values. Hence, the distribution of the negative impact parameter significance is used as a resolution function. The probability for a track to originate from the primary vertex, P_{tr} , is obtained by integrating the resolution function $\mathcal{R}(s)$ from $-\infty$ to the negative of the absolute track impact parameter significance, $-|\text{IP}|/\sigma$:

$$P_{\text{tr}} = \int_{-\infty}^{-|\text{IP}|/\sigma} \mathcal{R}(s) ds. \quad (5.1)$$

The resolution function depends strongly on the quality of the reconstructed track, e.g. the number of hits in the pixel and strip layers of the tracker. Moreover, the probability for a given track to originate from the primary vertex will be smaller for tracks with a large number of missing hits. Therefore, different resolution functions are defined for various track quality classes. In addition, the track quality may be different in data and simulated events. To calibrate the JP algorithm, the resolution functions are determined separately for data and simulation. Using eq. (5.1), tracks corresponding to particles from the decay of a displaced particle will have a low track probability, indicating that the track is not compatible with the primary vertex. The individual track probabilities are combined to obtain a jet probability P_j as follows:

$$P_j = \Pi \sum_{\text{tr}=0}^{N-1} \frac{(-\ln \Pi)^{\text{tr}}}{\text{tr}!}, \quad (5.2)$$

where Π is the product over the track probabilities, P_{tr} , and the sum runs over the selected tracks index tr , with N the number of selected tracks associated with the jet. To avoid instabilities due to the multiplication of small track probabilities, the probability is set to 0.5% for track probabilities below 0.5%. Only tracks with a positive impact parameter and for which the angular distance between the track and the jet axis satisfies $\Delta R < 0.3$ are used. A variant of the JP algorithm also exists for which the four tracks with the highest impact parameter significance get a higher weight in the jet

probability calculation. This algorithm is referred to as jet b probability (JBP) and uses tracks with $\Delta R < 0.4$. For a light-flavour jet misidentification probability of around 10%, the JBP algorithm has a b jet identification efficiency of 80% compared to 78% for the JP algorithm. The discriminators for the jet probability algorithms were constructed to be proportional to $-\ln P_j$. Figure 9 shows the distributions of the discriminator values for the JP and JBP algorithms. The discontinuities in the discriminator distributions are due to the minimum track probability threshold of 0.5%.

The jet probability algorithms are interesting for two reasons. First, the fact that the calibration of the resolution function is performed independently for data and simulation results in a robust reference tagger. Second, these algorithms rely only on the impact parameter information of the tracks. Therefore, they are used by some methods when measuring the efficiency of other b jet identification algorithms that rely on secondary vertex or soft lepton information, as discussed in sections 8 and 9.

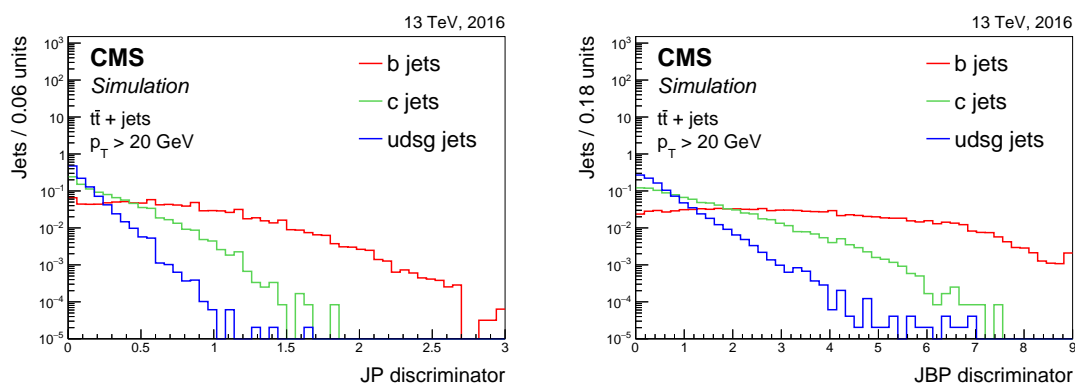


Figure 9. Distribution of the JP (left) and JBP (right) discriminator values for jets of different flavours in $t\bar{t}$ events. Jets without selected tracks are assigned a negative value. The distributions are normalized to unit area. The first and last bin include the underflow and overflow entries, respectively.

5.1.2 Combined secondary vertex taggers

The CSVv2 tagger. The CSVv2 algorithm is based on the CSV algorithm described in ref. [1] and combines the information of displaced tracks with the information on secondary vertices associated with the jet using a multivariate technique. Two variants of the CSVv2 algorithm exist according to whether IVF or AVR vertices are used. As baseline, IVF vertices are used in the CSVv2 algorithm, otherwise we refer to it as CSVv2 (AVR). At least two tracks per jet are required. When calculating the values of the track variables, the tracks are required to have an angular distance with respect to the jet axis of $\Delta R < 0.3$. Moreover, any combination of two tracks compatible with the mass of the K_S^0 meson in a window of 30 MeV is rejected. Jets that have neither a selected track nor a secondary vertex are assigned a default output discriminator value of -1 .

In a first step, the algorithm has to learn the features, e.g. input variable distributions corresponding to the various jet flavours, and combine them into a single discriminator output value. This step is the so-called “training” of the algorithm. During this step, it is important to ensure that the algorithm does not learn any unwanted behaviour, such as b jets having a higher jet p_T ,

on average, compared to other jets in a sample of $t\bar{t}$ events. To avoid discrimination between jet flavours caused by different jet p_T and η distributions, these distributions are reweighted to obtain the same spectrum for all jet flavours in the training sample. The training is performed on inclusive multijet events in three independent vertex categories:

- **RecoVertex**: The jet contains one or more secondary vertices.
- **PseudoVertex**: No secondary vertex is found in the jet but a set of at least two tracks with a 2D impact parameter significance above two and a combined invariant mass at least 50 MeV away from the K_S^0 mass are found. Since there is no real secondary vertex reconstruction, no fit is performed, resulting in a reduced number of variables.
- **NoVertex**: Containing jets not assigned to one of the previous two categories. Only the information of the selected tracks is used.

Figure 10 shows the fraction of jets of each flavour in the various vertex categories of the CSVv2 algorithm using jets in $t\bar{t}$ events with p_T above 20 GeV, where the secondary vertices in the RecoVertex category are obtained with the IVF algorithm. The following discriminating variables are combined in the algorithm.

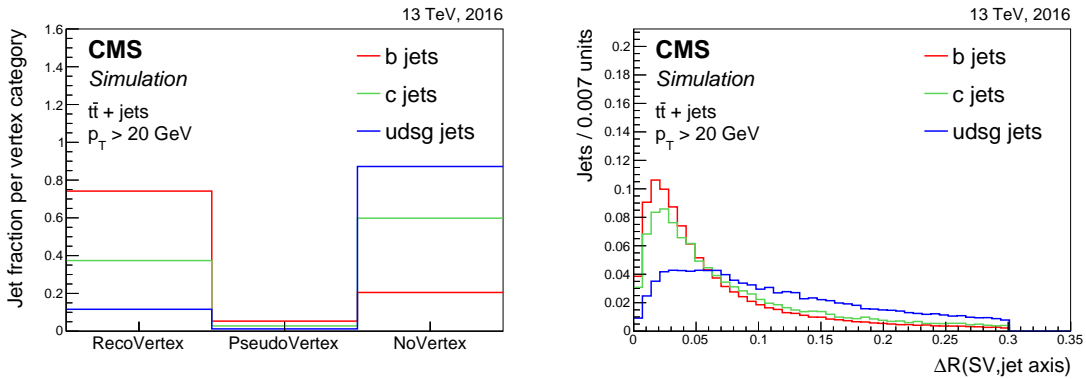


Figure 10. Vertex category for secondary vertices reconstructed with the IVF algorithm (left), and the distribution of the angular distance between the IVF secondary vertex flight direction and the jet axis (right) for jets of different flavours in $t\bar{t}$ events. The distributions are normalized to unit area.

- The “SV 2D flight distance significance”, defined as the 2D flight distance significance of the secondary vertex with the smallest uncertainty on its flight distance for jets in the RecoVertex category.
- The “number of SV”, defined as the number of secondary vertices for jets in the RecoVertex category.
- The “track η_{rel} ”, defined as the pseudorapidity of the track relative to the jet axis for the track with the highest 2D impact parameter significance for jets in the RecoVertex and PseudoVertex categories.

- The “corrected SV mass”, defined as the corrected mass of the secondary vertex with the smallest uncertainty on its flight distance for jets in the RecoVertex category or the invariant mass obtained from the total summed four-momentum vector of the selected tracks for jets in the PseudoVertex category.
- The “number of tracks from SV”, defined as the number of tracks associated with the secondary vertex for jets in the RecoVertex category or the number of selected tracks for jets in the PseudoVertex category.
- The “SV energy ratio”, defined as the energy of the secondary vertex with the smallest uncertainty on its flight distance divided by the energy of the total summed four-momentum vector of the selected tracks.
- The “ $\Delta R(\text{SV}, \text{jet})$ ”, defined as the ΔR between the flight direction of the secondary vertex with the smallest uncertainty on its flight distance and the jet axis for jets in the RecoVertex category, or the ΔR between the total summed four-momentum vector of the selected tracks for jets in the PseudoVertex category.
- The “3D IP significance of the first four tracks”, defined as the signed 3D impact parameter significances of the four tracks with the highest 2D impact parameter significance.
- The “track $p_{T,\text{rel}}$ ”, defined as the track p_T relative to the jet axis, i.e. the track momentum perpendicular to the jet axis, for the track with the highest 2D impact parameter significance.
- The “ $\Delta R(\text{track}, \text{jet})$ ”, defined as the ΔR between the track and the jet axis for the track with the highest 2D impact parameter significance.
- The “track $p_{T,\text{rel}}$ ratio”, defined as the track p_T relative to the jet axis divided by the magnitude of the track momentum vector for the track with the highest 2D impact parameter significance.
- The “track distance”, defined as the distance between the track and the jet axis at their point of closest approach for the track with the highest 2D impact parameter significance.
- The “track decay length”, defined as the distance between the primary vertex and the track at the point of closest approach between the track and the jet axis for the track with the highest 2D impact parameter significance.
- The “summed tracks E_T ratio”, defined as the transverse energy of the total summed four-momentum vector of the selected tracks divided by the transverse energy of the jet.
- The “ $\Delta R(\text{summed tracks}, \text{jet})$ ”, defined as the ΔR between the total summed four-momentum vector of the tracks and the jet axis.
- The “first track 2D IP significance above c threshold”, defined as the 2D impact parameter significance of the first track that raises the combined invariant mass of the tracks above 1.5 GeV. This track is obtained by summing the four-momenta of the tracks adding one track at the time. Every time a track is added, the total four-momentum vector is computed. The 2D impact parameter significance of the first track that is added resulting in a mass of the total

four-momentum vector above the aforementioned threshold is used as a variable. The threshold of 1.5 GeV is related to the c quark mass.

- The number of selected tracks.
- The jet p_T and η .

The discriminating variables in each vertex category are combined into a neural network, specifically a feed-forward multilayer perceptron with one hidden layer [39]. The number of nodes in the hidden layer is different for the three different vertex categories and is set to twice the number of input variables. The discriminator values of the three vertex categories are combined with a likelihood ratio taking into account the fraction of jets of each flavour expected in $t\bar{t}$ events. The fraction of jets of each flavour is obtained as a function of the jet p_T and $|\eta|$, using 19 exclusive bins in total. Two dedicated trainings are performed, one with c jets, and one with light-flavour jets as background. The final discriminator value is a linear combination of the output of these two trainings with relative weights of 1 : 3 for the output of the network trained against c and light-flavour jets, respectively. The value of these relative weights is inspired by $t\bar{t}$ events where one of the two W bosons decays into quarks and the other into leptons, and provides the best performance for a wide variety of physics topologies compared to alternative relative weights.

The main differences from the Run 1 version of the CSV algorithm are the following:

- **The secondary vertex reconstruction algorithm:** the secondary vertices are reconstructed with the IVF algorithm.
- **Input variables:** table 1 lists the variables used for the Run 1 version of the CSV algorithm and for the CSVv2 algorithm. Figure 11 shows two of the variables used for the CSVv2 algorithm and not for the CSV algorithm.
- **Multilayer perceptron:** in the previous version of the algorithm the input variables in a certain vertex category were combined with a likelihood ratio. Depending on the type of correlations present between the input variables, the likelihood ratio performs at a comparable level to the other multivariate methods. The likelihood ratio is particularly useful because of its simplicity and when a small number of variables are used. However, to increase the performance of the algorithm, more input variables were added and combined into an artificial neural network.
- **Jet p_T and η dependence:** the correlation of some of the input variables with the jet p_T and η is taken into account by including the jet kinematics as input variables, after reweighting the distributions to be the same for all jet flavours. In the past, the training was performed in bins of the jet kinematics. In the current procedure, the bins of jet kinematics are only used to combine the vertex categories after the training.

Figure 12 shows the distribution of the discriminator values for the various jet flavours for both versions of the CSVv2 algorithm.

Table 1. Input variables used for the Run 1 version of the CSV algorithm and for the CSVv2 algorithm. The symbol “x” (“—”) means that the variable is (not) used in the algorithm.

Input variable	Run 1 CSV	CSVv2
SV 2D flight distance significance	x	x
Number of SV	—	x
Track η_{rel}	x	x
Corrected SV mass	x	x
Number of tracks from SV	x	x
SV energy ratio	x	x
$\Delta R(\text{SV}, \text{jet})$	—	x
3D IP significance of the first four tracks	x	x
Track $p_{\text{T,rel}}$	—	x
$\Delta R(\text{track}, \text{jet})$	—	x
Track $p_{\text{T,rel}}$ ratio	—	x
Track distance	—	x
Track decay length	—	x
Summed tracks E_{T} ratio	—	x
$\Delta R(\text{summed tracks}, \text{jet})$	—	x
First track 2D IP significance above c threshold	—	x
Number of selected tracks	—	x
Jet p_{T}	—	x
Jet η	—	x

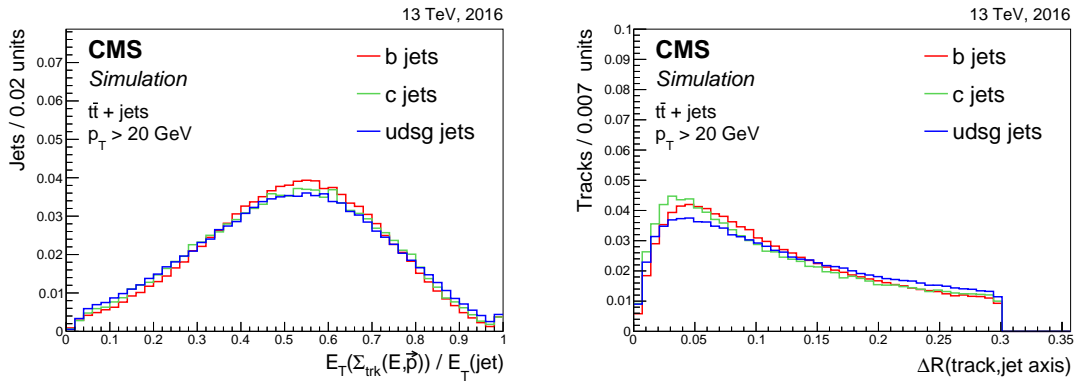


Figure 11. Distribution of the transverse energy of the total summed four-momentum vector of the selected tracks divided by the jet transverse energy (left), and angular distance between the track and the jet axis (right) for jets of different flavours in $t\bar{t}$ events. The distributions are normalized to unit area. The last bin in the left panel includes the overflow entries.

The DeepCSV tagger. The identification of jets from heavy-flavour hadrons can be improved by using the advances in the field of deep machine learning [38]. A new version of the CSVv2 tagger, “DeepCSV”, was developed using a deep neural network with more hidden layers, more nodes per

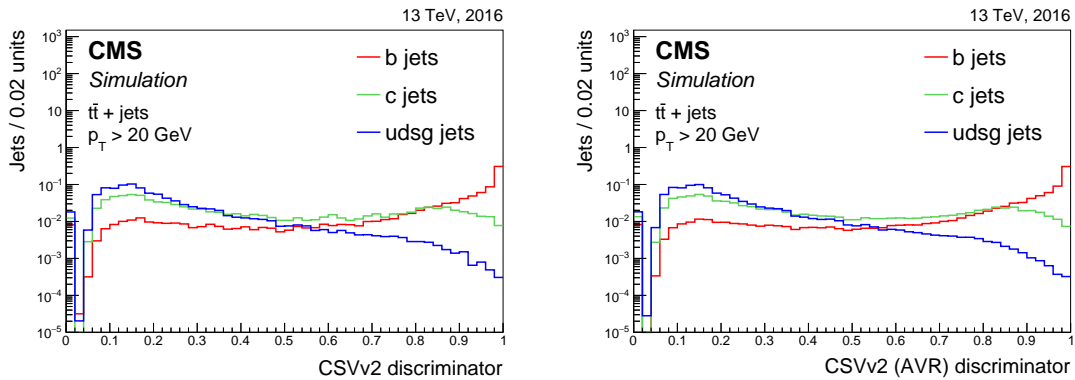


Figure 12. Distribution of the CSVv2 (left) and CSVv2(AVR) (right) discriminator values for jets of different flavours in $t\bar{t}$ events. The distributions are normalized to unit area. Jets without a selected track and secondary vertex are assigned a negative discriminator value. The first bin includes the underflow entries.

layer, and a simultaneous training in all vertex categories and for all jet flavours.

The same tracks and IVF secondary vertices are used in this approach as for the CSVv2 tagger. The same input variables are also used, with only one difference, namely that for the track-based variables up to six tracks are used in the training of the DeepCSV. Jets are randomly selected in such a way that similar jet p_T and η distributions are obtained for all jet flavours. These jet p_T and η distributions are also used as input variables in the training to take into account the correlation between the jet kinematics and the other variables. The distribution of all input variables is preprocessed to centre the mean of each distribution around zero and to obtain a root-mean-square value of unity. All of the variables are presented to the multivariate analysis (MVA) in the same way because of the preprocessing. This speeds up the training. In case a variable cannot be reconstructed, e.g. because there are less than six selected tracks (or no secondary vertex), the variable values associated with the missing track or vertex are set to zero after the preprocessing.

The training is performed using jets with p_T between 20 GeV and 1 TeV, and within the tracker acceptance. The relative ratio of the number of jets of each flavour is set to 2 : 1 : 4 for b : c : udsg jets. A mixture of $t\bar{t}$ and multijet events is used to reduce the possible dependency of the training on the heavy-flavour quark production process.

The training of the deep neural network is performed using the KERAS [40] deep learning library, interfaced with the TENSORFLOW [41] library that is used for low-level operations such as convolutions. The neural network uses four hidden layers that are fully connected, each with 100 nodes. Increasing the number of hidden layers and the number of nodes per layer had negligible effects on the performance. Each node in one of the hidden layers uses a rectified linear unit as its activation function to define the output of the node given the input values. For the nodes in the last layer, a normalized exponential function is used for the activation to be able to interpret the output value as a probability for a certain jet flavour category, $P(f)$. The output layer contains five nodes corresponding to five jet flavour categories used in the training. These categories are defined according to whether the jet contains exactly one b hadron, at least two b hadrons, exactly one c hadron and no b hadrons, at least two c hadrons and no b hadrons, or none of the aforementioned categories. Each of these categories is completely independent of the others. The reason for

defining five flavour categories in the training is to provide analyses with the possibility to identify jets containing two b or c hadrons.

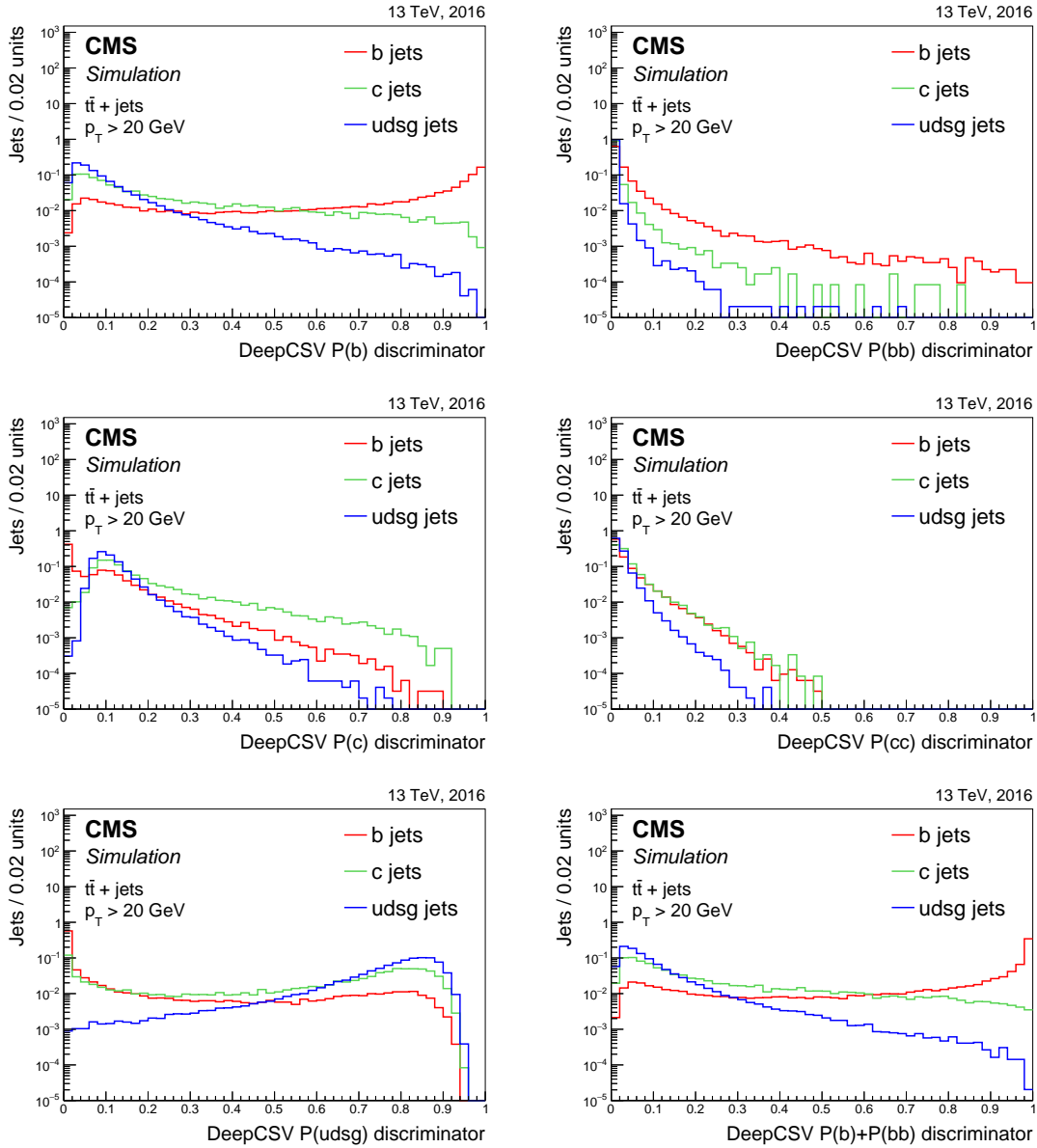


Figure 13. Distribution of the DeepCSV $P(b)$ (upper left), $P(bb)$ (upper right), $P(c)$ (middle left), $P(cc)$ (middle right), $P(udsg)$ (lower left), and $P(b) + P(bb)$ (lower right) discriminator values for jets of different flavours in $t\bar{t}$ events. Jets without a selected track and without a secondary vertex are assigned a discriminator value of 0. The distributions are normalized to unit area.

Figure 13 shows the discriminator distribution for each of the DeepCSV probabilities $P(f)$. The lower right panel in figure 13 also shows the $P(b) + P(bb)$ discriminator used to tag b jets in physics analyses. It has been checked that summing the probabilities for these two categories is equivalent to using a combined training for these categories.

5.1.3 Soft-lepton and combined taggers

Soft leptons, i.e. electrons or muons reconstructed as described in section 4.4 are sometimes present in a jet. When they are, the information related to the charged lepton is used to construct a soft-electron (SE) and soft-muon (SM) tagger. The discriminating variables that are used as input for the boosted decision tree (BDT) are the 2D and 3D impact parameter significance of the lepton, the angular distance between the jet axis and the lepton, ΔR , the ratio of the p_T of the lepton to that of the jet, and the p_T of the lepton relative to the jet axis, p_T^{rel} . In the case of the SE algorithm an MVA-based electron identification variable is also used as input. The distributions of the SE and SM discriminator values are shown in figure 14. The different range for the algorithm output values is related to different settings in the training when combining the input variables with a BDT.

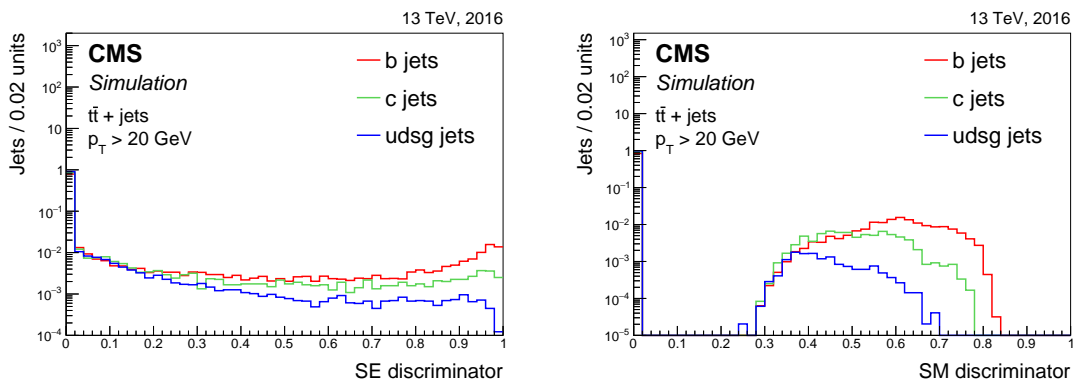


Figure 14. Distribution of the soft-electron (left) and soft-muon (right) discriminator values for jets of different flavours in $t\bar{t}$ events. Jets without a soft lepton are assigned a discriminator value of 0. The distributions are normalized to unit area.

As a soft lepton is only present in a relatively small fraction of heavy-flavour jets, the soft lepton taggers are not always able to discriminate heavy-flavour jets from other jets. Therefore they are not used standalone, but rather as input for a combined tagger. The combined tagger, cMVA_{v2}, uses six b jet identification discriminators as input variables, namely the two variants of the JP algorithm, the SE and SM algorithms, and the two variants of the CSV_{v2} algorithm. The training is performed using the open source SCIKIT-LEARN package [42] and the variables are combined using a gradient boosting classifier (GBC) as BDT. Prior to the training, the jet p_T and η distributions are reweighted to obtain a similar distribution for all jet flavours. Although the correlation between the two CSV_{v2} discriminator values is close to 100%, a small improvement is seen in the case where the vertex finding algorithms reconstruct different secondary vertices. Figure 15 shows the correlation between the input variables of the cMVA_{v2} algorithm for b jets as well as the distribution of the cMVA_{v2} discriminator values for various jet flavours obtained in a $t\bar{t}$ sample. The correlation between the input variables is similar for other jet flavours. Adding the SL taggers or one of the JP taggers as input variables for the cMVA_{v2} algorithm results in a similar large performance gain with respect to the CSV_{v2} algorithm. Adding the other JP tagger and CSV_{v2} (AVR) algorithm results only in a modest performance gain. The performance of the cMVA_{v2} tagger for discriminating b jets against other jet flavours is discussed more extensively in section 5.1.4.

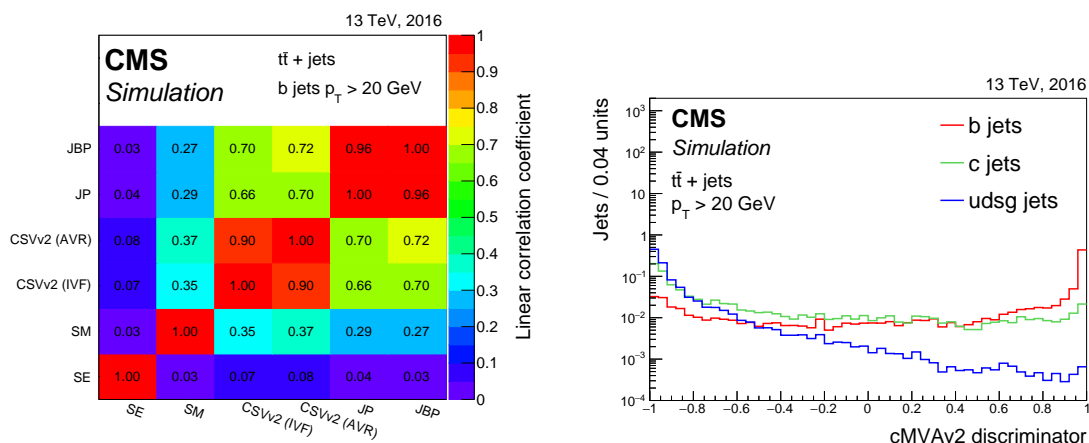


Figure 15. Correlation between the different input variables for the cMVA2 tagger for b jets in $t\bar{t}$ events (left), and distribution of the cMVA2 discriminator values (right), normalized to unit area, for jets of different flavours in $t\bar{t}$ events.

It is relevant to note that the DeepCSV discriminator output was not included as an input variable, as this algorithm was developed after the cMVA2 tagger. Further optimizations are ongoing, in particular in the context of the new pixel tracker installed in 2017 [43].

5.1.4 Performance in simulation

The tagging efficiency of the JP, CSVv2, cMVA2, and DeepCSV taggers is determined using simulated pp collision events. The efficiency (misidentification probability) to correctly (wrongly) tag a jet with flavour f is defined as the number of jets of flavour f passing the tagging requirement divided by the total number of jets of flavour f . Figure 16 shows the b jet identification efficiency versus the misidentification probability for either c or light-flavour jets in simulated $t\bar{t}$ events requiring jets with $p_T > 20$ GeV and $|\eta| < 2.4$ for various b taggers. In this figure, the tagging efficiency is integrated over the p_T and η distributions of the jets in the $t\bar{t}$ sample. The tagging efficiency is also shown for the Run 1 version of the CSV algorithm. It should be noted that the CSV algorithm was trained on simulated multijet events at centre-of-mass energy of 7 TeV using anti- k_T jets clustered with a distance parameter $R = 0.5$. Therefore, the comparison is not completely fair. The performance improvement expected from a retraining is typically of the order of 1%. The absolute improvement in the b jet identification efficiency for the CSVv2 (AVR) algorithm with respect to the CSV algorithm is of the order of 2–4% when the comparison is made at the same misidentification probability value for light-flavour jets. An additional improvement of the order of 1–2% is seen when using IVF vertices instead of AVR vertices in the CSVv2 algorithm. The cMVA2 tagger performs around 3–4% better than the CSVv2 algorithm for the same misidentification probability for light-flavour jets. The DeepCSV $P(b) + P(bb)$ tagger outperforms all the other b jet identification algorithms, when discriminating against c jets or light-flavour jets, except for b jet identification efficiencies above 70% where the cMVA2 tagger performs better when discriminating against light-flavour jets. The absolute b identification efficiency improves by about 4% with respect to the CSVv2 algorithm for a misidentification probability for light-flavour

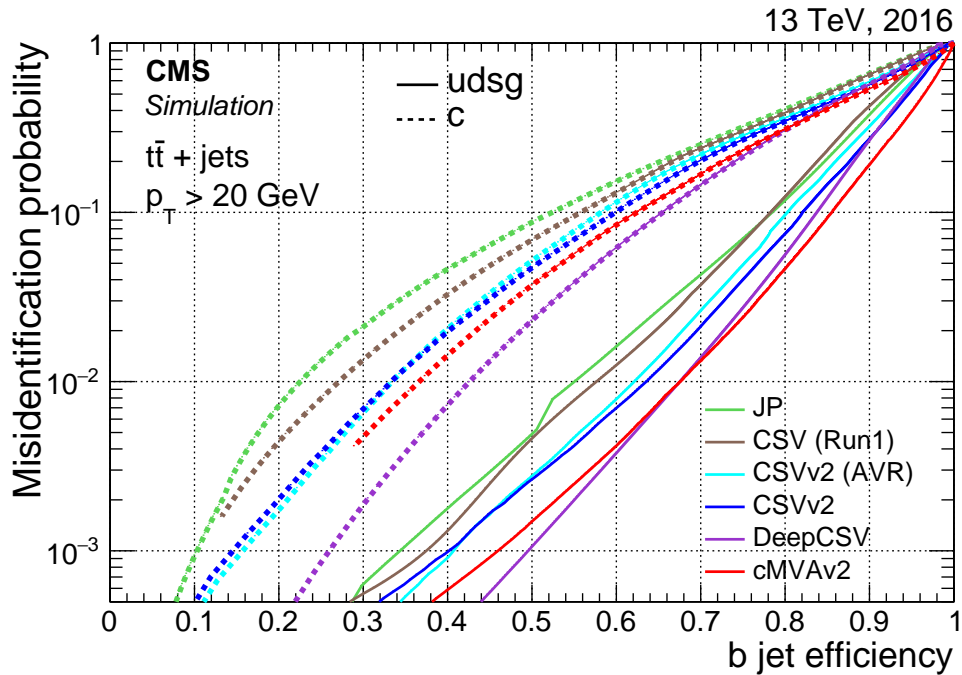


Figure 16. Misidentification probability for c and light-flavour jets versus b jet identification efficiency for various b tagging algorithms applied to jets in $t\bar{t}$ events.

jets of 1%. Three standard working points are defined for each b tagging algorithm using jets with $p_T > 30$ GeV in simulated multijet events with $80 < \hat{p}_T < 120$ GeV. The average jet p_T in this sample of events is about 75 GeV. These working points, “loose” (L), “medium” (M), and “tight” (T), correspond to thresholds on the discriminator after which the misidentification probability is around 10%, 1%, and 0.1%, respectively, for light-flavour jets. The efficiency for correctly identifying b jets in simulated $t\bar{t}$ events for each of the three working points of the various taggers is summarized in table 2.

The tagging efficiency depends on the jet p_T , η , and the number of pileup interactions in the event. This dependency is illustrated for the DeepCSV $P(b) + P(bb)$ tagger in figure 17 using jets with $p_T > 20$ GeV in $t\bar{t}$ events. A parameterization of the efficiency as a function of the jet p_T is provided in appendix A. The efficiency for correctly identifying b jets is maximal for jets with $p_T \approx 100$ GeV and decreases at low- and high- p_T values. The lower efficiency at low jet p_T is due to the larger uncertainty on the track impact parameter resolution. At high jet p_T , there are two main effects. First, the misidentification probability for light-flavour jets increases because of the larger number of tracks present in the jet, as can be seen from figure 4. Second, at higher jet transverse momenta, jets are more collimated and their charged particles are closer together, resulting in merged hits in the innermost layers of the tracking system. This effect impacts the track reconstruction efficiency and hence also the b jet identification efficiency. Due to the higher track reconstruction efficiency and the better resolution of the track parameters at small $|\eta|$ values [2], the algorithms are more efficient in identifying b jets in the barrel region of the CMS silicon tracker ($|\eta| < 1$). The efficiency for misidentifying light-flavour jets increases with an increasing number of

Table 2. Taggers, working points, and corresponding efficiency for b jets with $p_T > 20 \text{ GeV}$ in simulated $t\bar{t}$ events. The numbers in this table are for illustrative purposes since the b jet identification efficiency is integrated over the p_T and η distributions of jets.

Tagger	Working point	ε_b (%)	ε_c (%)	$\varepsilon_{\text{uds}g}$ (%)
Jet probability (JP)	JP L	78	37	9.6
	JP M	56	12	1.1
	JP T	36	3.3	0.1
Combined secondary vertex (CSVv2)	CSVv2 L	81	37	8.9
	CSVv2 M	63	12	0.9
	CSVv2 T	41	2.2	0.1
Combined MVA (cMVAv2)	cMVAv2 L	84	39	8.3
	cMVAv2 M	66	13	0.8
	cMVAv2 T	46	2.6	0.1
Deep combined secondary vertex (DeepCSV) $P(b) + P(bb)$	DeepCSV L	84	41	11
	DeepCSV M	68	12	1.1
	DeepCSV T	50	2.4	0.1

pileup interactions. This is explained as follows. First, the increasing number of pileup interactions results in a higher probability to choose the wrong primary vertex resulting in light-flavour jets that are displaced, and b jets for which the displacement is wrong. Second, the increasing number of pileup interactions results in a higher occupancy in the tracker, leading to a larger number of wrongly reconstructed tracks as well as more tracks from a different interaction vertex that are clustered in the jets associated with the primary vertex. It was checked that all taggers presented in table 2 show a similar dependence with respect to the number of pileup interactions, and jet p_T and $|\eta|$.

5.2 The c jet identification

As can be seen from figures 5, 6, and 8 in section 4, the distributions of the tagging variables for c jets lie in between the distributions for b and light-flavour jets. This is due to the lifetime of the c hadrons being shorter than that of the b hadrons. In addition, the secondary vertex multiplicity is also lower and the smaller c quark mass results in a smaller track p_T relative to the jet axis. Therefore, it is particularly challenging to efficiently identify jets originating from c quarks.

5.2.1 Algorithm description

The c jet identification algorithm uses properties related to displaced tracks, secondary vertices, and soft leptons inside the jets. The secondary vertices are obtained using the IVF algorithm with modified parameters for c jets as described in section 4.3. Based on the presence or absence of a secondary vertex associated with a jet, three secondary vertex categories are defined in the same way as for the CSVv2 algorithm. The presence or absence of a soft lepton, as discussed in the previous paragraph, leads to the definition of three soft lepton categories, independent of the secondary vertex categories:

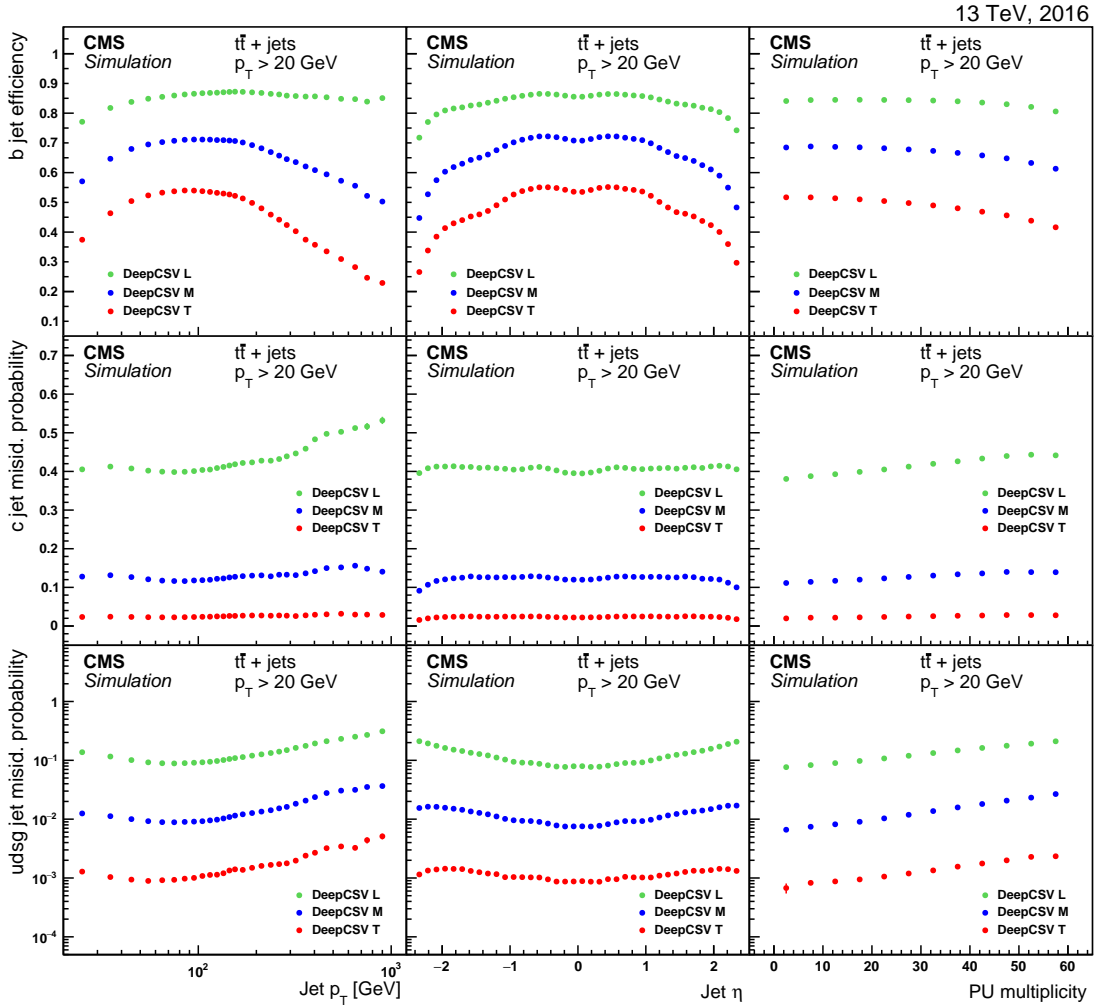


Figure 17. Efficiencies and misidentification probabilities for the DeepCSV $P(b) + P(bb)$ tagger as a function of the jet p_T (left), jet η (middle), and PU multiplicity, i.e. the number of inelastic pp collisions in the event (right), for b (upper), c (middle), and light-flavour (lower) jets in $t\bar{t}$ events. Each panel shows the efficiency for the three different working points with different colours.

- **NoSoftLepton:** including jets without soft leptons found inside the jet;
- **SoftMuon:** at least one soft muon was found inside the jet;
- **SoftElectron:** no soft muon, but at least one soft electron was found inside the jet.

With this categorization, jets containing a muon and an electron will be assigned to the SoftMuon category. Like for the b tagging algorithms, the displaced tracks are ordered by decreasing 2D impact parameter significance, and the secondary vertices are ordered by increasing uncertainty on their 3D flight distance. Some variables are only defined if a secondary vertex was reconstructed or if a soft lepton was found inside the jet. Whenever a variable is not available, a default value is assigned to it. The variables used are similar to the ones used in the CSVv2 algorithm (section 5.1.2) and in the SM or SE algorithms (section 5.1.3). For track- and lepton-based variables, up to two

tracks or leptons are used (if available), while for the secondary vertex variables only the first secondary vertex is used (if available). The list of variables used is the following:

- The vertex-lepton category.
- The 2D and 3D impact parameter significance of the first two tracks, and the 3D impact parameter significance of the first two leptons.
- The pseudorapidity of the track (lepton) relative to the jet axis for the first two tracks (leptons).
- The track (lepton) p_T relative to the jet axis, i.e. the track momentum perpendicular to the jet axis, for the first two tracks (leptons).
- The track p_T relative to the jet axis divided by the magnitude of the track momentum vector, for the first two tracks.
- The track momentum parallel to the jet direction, for the first two tracks.
- The track momentum parallel to the jet direction divided by the magnitude of the track momentum vector, for the first two tracks.
- The ΔR between the track (lepton) and the jet axis for the first two tracks (leptons).
- The distance between the track and the jet axis at their point of closest approach, for the first two tracks.
- The track decay length, i.e. the distance between the primary vertex and the track at the point of closest approach between the track and the jet axis, for the first two tracks.
- The transverse energy of the total summed four-momentum vector of the selected tracks divided by the transverse energy of the jet.
- The ΔR between the total summed four-momentum vector of the tracks and the jet axis.
- The 2D and 3D impact parameter significance of the first track that raises the combined invariant mass of the tracks above 1.5 GeV. This track is obtained by summing the four-momenta of the tracks adding one track at the time. Every time a track is added, the total four-momentum vector is computed. The 2D impact parameter significance of the first track that is added resulting in a mass of the total four-momentum vector above the aforementioned threshold is used as a variable. The threshold of 1.5 GeV is related to the c quark mass.
- The lepton p_T divided by the jet p_T , for the first two leptons.
- The lepton momentum parallel to the jet direction divided by the magnitude of the jet momentum, for the first two leptons.
- The 2D and 3D flight distance significance of the first secondary vertex.
- The secondary vertex energy ratio, defined as the energy of the secondary vertex with the smallest uncertainty on its flight distance divided by the energy of the total summed four-momentum vector of the selected tracks.

- The corrected secondary vertex mass.
- The “massVertexEnergyFraction” variable, which is defined as $X/(X + 0.04)$, where X is the corrected secondary vertex mass divided by the average b meson mass [35] multiplied by the scalar sum of the track energies (assuming the pion mass) for tracks associated with the secondary vertex divided by the scalar sum of the track energies for track associated with the jet:

$$X = \frac{m_{SV}[\text{GeV}]}{5.2794} \frac{\sum_{SV \text{ tracks}} E_i}{\sum_{jet \text{ tracks}} E_i}. \quad (5.3)$$

This variable is first defined in section 7 of ref. [44].

- The “vertexBoost” variable, defined as $Y^2/(Y^2 + 10)$, where Y is the square root of the average b meson mass [35] multiplied with the scalar sum of the track p_T for tracks associated with the vertex, divided by the product of the corrected secondary vertex mass and the square root of the jet p_T . This variable is related to the boost of the secondary vertex. This variable is first defined in section 7 of ref. [44].
- The number of tracks associated with the first secondary vertex.
- The number of secondary vertices.
- The number of tracks associated with the jet.

The training of the algorithm was performed on simulated multijet events. As in the case of the DeepCSV tagger, the variables are first preprocessed to centre their mean at zero and obtain a root-mean-square of unity. Two weights are applied for each jet in the training. To avoid introducing any unwanted dependence on the jet kinematics in the tagger, a first weight is applied to flatten the jet p_T and η distributions in the whole training sample for all jet flavours. Simultaneously, a second weight skews the relative contribution of the different secondary vertex categories in the multijet sample to fit the observed ones in the $t\bar{t}$ sample. Two trainings are performed: one for discriminating c jets from light-flavour jets (CvsL) and another one for discriminating c jets from b jets (CvsB). The training of the two discriminators was performed with the SCIKIT-LEARN package [42] using a GBC as implementation of the BDT.

The GBC settings were optimized by varying them over a wide range of values, to ensure the optimal setting was contained within the scanned range. Both the CvsL and CvsB trainings were optimized by scanning a range of the parameters and comparing the final performance curves. The best performance was achieved with the number of boosting stages set to 500, the learning rate to 0.05, the minimum number of samples required to split an internal node to 0.6% and a maximum depth of the individual regression estimators of 15 (8) for the CvsL (CvsB) training. Some of the optimized values did not change the performance visibly when being varied, but they were chosen to reduce the computation time without a loss in performance.

Figure 18 shows the output discriminator distributions for the CvsL and CvsB taggers. The discriminator distributions exhibit spikes, which originate from the default values for most input variables if a jet has no track passing the selection criteria. These spikes do not affect any

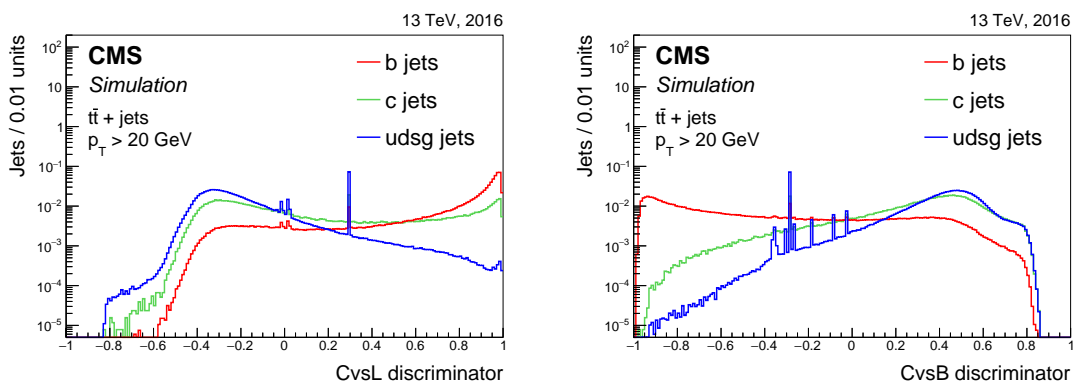


Figure 18. Distribution of the CvsL (left) and CvsB (right) discriminator values for jets of different flavours in $t\bar{t}$ events. The spikes originate from jets without a track passing the track selection criteria, as discussed in the text. The distributions are normalized to unit area.

physics analyses, as the discriminator thresholds defining the working points are not just before or after a spike.

5.2.2 Performance in simulation

The performance is evaluated using jets with $p_T > 20$ GeV and $|\eta| < 2.4$ in a sample of simulated $t\bar{t}$ events. The left panel in figure 19 shows the correlation between the CvsL and CvsB discriminators for various jet flavours. Discriminator values close to one correspond to signal-like c jets. Therefore, the c jets populate the upper right corner of this figure, whereas b jets and light-flavour jets populate the region near the bottom right and the upper left corners, respectively. In the upper left corner there is a relatively large fraction of c jets because of the similarity of c jets and light-flavour jets at CvsL discriminator values below -0.3 and CvsB discriminator values above $+0.5$, as can be seen in figure 18. In order to discriminate c jets from other jet flavours and to evaluate the performance of the c tagger, thresholds are applied on both CvsL and CvsB to select the upper right corner of this phase space. Three working points have been defined corresponding to the efficiency for correctly identifying c jets. These are indicated by the dashed lines. The loose working point has a high efficiency for c jets and rejects primarily b jets, whereas the tight working point rejects primarily light-flavour jets. Table 3 summarizes the efficiencies for the three working points.

Table 3. Efficiency for the working points of the c tagger and corresponding efficiency for the different jet flavours obtained using jets with $p_T > 20$ GeV in simulated $t\bar{t}$ events. The numbers quoted are for illustrative purposes since the efficiency is integrated over the p_T and η distributions of the jets.

Working point	ε_c (%)	ε_b (%)	ε_{udsg} (%)
c tagger L	88	36	91
c tagger M	40	17	19
c tagger T	19	20	1.2

The right panel in figure 19 shows the light-flavour and b jet misidentification probabilities for constant c tagging efficiencies. The arrows indicate the c jet identification efficiency and

misidentification probability for b and light-flavour jets corresponding to the three working points. The discontinuous transition in each of the curves for c tagging efficiencies between 0.35 and 0.7 are due to the largest spike in the CvsL distribution in the left panel in figure 18.

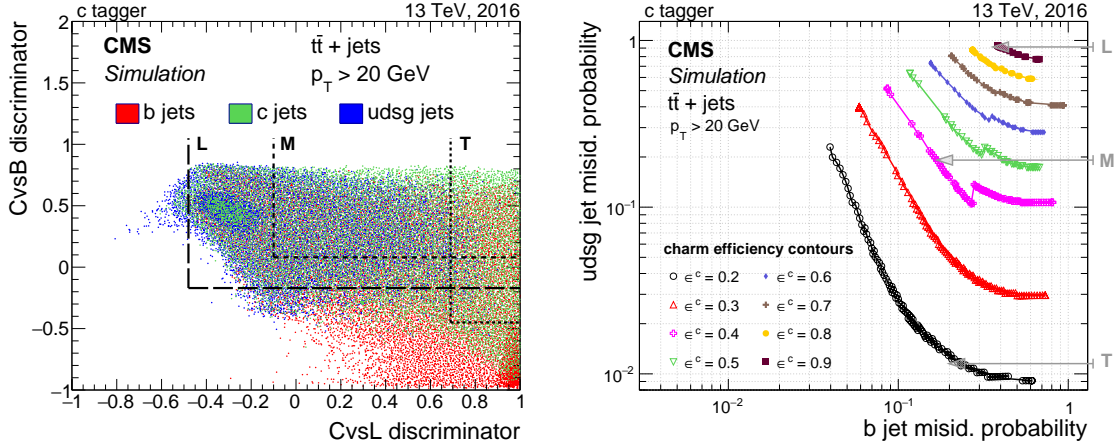


Figure 19. Correlation between CvsL and CvsB taggers for the various jet flavours (left), and misidentification probability for light-flavour jets versus misidentification probability for b jets for various constant c jet efficiencies (right) in $t\bar{t}$ events. The L, M, and T working points discussed in the text are indicated by the dashed lines (left) or arrows (right). The discontinuity in the curves corresponding to c tagging efficiencies between 0.4 and 0.7 are due to the spike in the CvsL distribution of figure 18.

In figure 20 the performance of the CvsL and CvsB taggers is compared with the cMVA_{v2} and CSV_{v2} b tagging algorithms. In the right panel of this figure, the transition in the performance of the curve for a c jet identification efficiency around 0.4 is due to the largest spike in the CvsL discriminator distribution. The performance of the CvsB tagger is similar to the performance of both b taggers, except at small b jet misidentification probabilities where the CvsB tagger is performing slightly worse than the cMVA_{v2} tagger. The CvsL tagger outperforms the cMVA_{v2} and CSV_{v2} tagger for small light-flavour jet misidentification probabilities. The DeepCSV tagger described in section 5.1.2 is outperforming the dedicated c tagger. For the discrimination between c and b jets, the DeepCSV probabilities corresponding to the five flavour categories defined in section 5.1.2, are combined in the following way:

$$\text{DeepCSV CvsB} = \frac{P(c) + P(cc)}{1 - P(\text{udsg})}, \quad (5.4)$$

where the numerator corresponds to the probability to identify c jets and the denominator to the probability to identify b or c jets. Similarly, for the discrimination between c and light-flavour jets, the discriminator is constructed:

$$\text{DeepCSV CvsL} = \frac{P(c) + P(cc)}{1 - (P(b) + P(bb))}, \quad (5.5)$$

with the numerator giving the probability to identify c jets and the denominator the probability to identify light-flavour or c jets. The comparison with the DeepCSV algorithm used for c tagging should be considered as an illustration for the performance of future c taggers since the working points are not yet defined and the efficiency in data is not yet measured.

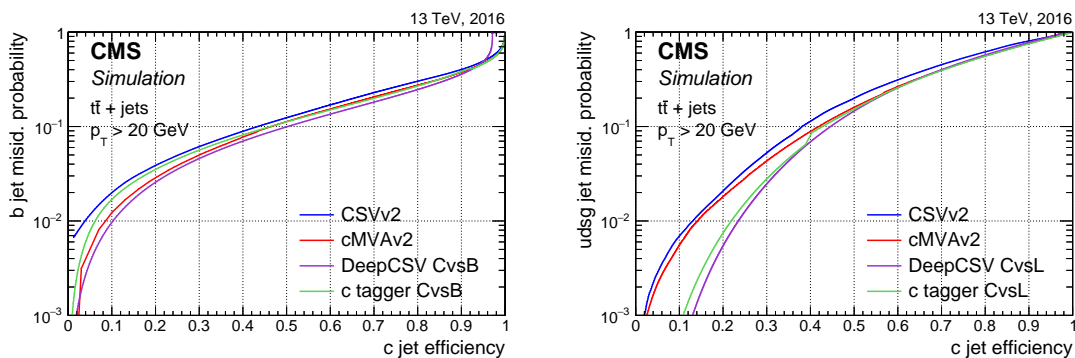


Figure 20. Misidentification probability for b jets (left) or light-flavour jets (right) versus c jet identification efficiency for various c tagging algorithms applied to jets in $t\bar{t}$ events.

6 Identification of b jets in boosted topologies

6.1 Boosted b jet identification with the CSVv2 algorithm

At the high centre-of-mass energy of the LHC, particles decaying to b quarks can be produced with a large Lorentz boost. Examples are boosted top quarks decaying to $bW \rightarrow bq\bar{q}$, or boosted Higgs or Z bosons decaying to $b\bar{b}$. As a result of the large boost of the parent particle the decay products often give rise to overlapping jets. In order to capture all the decay products, the jets are reconstructed with a distance parameter of $R = 0.8$ (AK8). Jet substructure techniques can then be applied to resolve the subjets corresponding to the decay products in the AK8 jet [45–48]. In this paper, the soft-drop algorithm [45, 46], which recursively removes soft wide-angle radiation from a jet, is used to resolve the substructure of the AK8 jets. The subjet axes are obtained by reclustering the jet constituents using the anti- k_T algorithm and undoing the last step of the clustering procedure.

When the decay of the boosted particle contains a b quark, b tagging can be applied either on the AK8 jet or on its subjets. In both cases the CSVv2 algorithm is used. In the first approach the CSVv2 algorithm is applied to the AK8 jet but using looser requirements for the track-to-jet and vertex-to-jet association criteria, consistent with the $R = 0.8$ parameter. In the second approach the CSVv2 algorithm is applied to the subjets. The two approaches are illustrated by the scheme in figure 21 (left and middle).

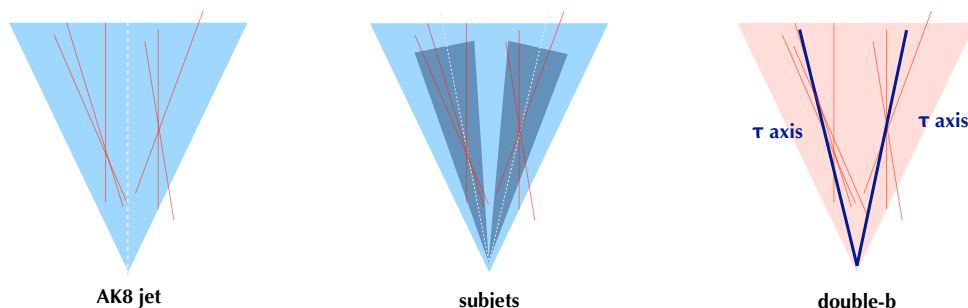


Figure 21. Schematic representation of the AK8 jet (left) and subjet (middle) b tagging approaches, and of the double-b tagger approach (right).

To illustrate the performance of b tagging in various boosted topologies, AK8 and subjet b tagging are compared in figures 22 and 23. When studying the performance of b tagging in various boosted topologies, jets originating from the decay of boosted top quarks (boosted top quark jets) are obtained from a Z' sample, where the Z' decays to $t\bar{t}$, with $t \rightarrow bW \rightarrow bq\bar{q}$. The boosted top quark jets are then defined as jets containing at least one b hadron. Jets originating from the decay of boosted Higgs bosons ($H \rightarrow b\bar{b}$ jets) are obtained from a Kaluza-Klein graviton sample, where the graviton decays to two Higgs bosons, with $H \rightarrow b\bar{b}$. The $H \rightarrow b\bar{b}$ jets are then defined as jets containing at least two b hadrons. Jets from a sample of inclusive multijet events are used to determine the misidentification probability.

To obtain a performance similar to what is expected in physics analyses, the jet mass is used to select jets consistent with the top quark or Higgs boson mass. While the jet mass for these particles arises from the kinematics of the decay products present in the jet, the single-parton jet mass arises mostly from soft-gluon radiation. This soft radiation can be removed by applying jet grooming methods [49–51], shifting the single-parton jet mass to smaller values. In this paper, jet pruning [51] is applied to the AK8 jets. The jet mass obtained from the jet four-momentum after pruning is referred to as the pruned jet mass. Jets are then selected when they have a pruned jet mass between 50 (135) and 200 GeV for b tagging boosted $H \rightarrow b\bar{b}$ (top quark) jets.

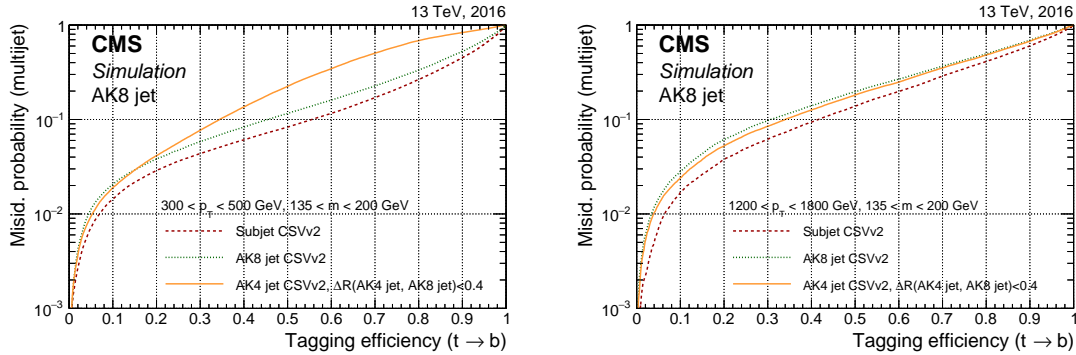


Figure 22. Misidentification probability for jets in an inclusive multijet sample versus the efficiency to correctly tag boosted top quark jets. The CSVv2 algorithm is applied to three different types of jets: AK8 jets, their subjets, and AK4 jets matched to AK8 jets. The AK8 jets are selected to have a pruned jet mass between 135 and 200 GeV, and $300 < p_T < 500$ GeV (left), or $1.2 < p_T < 1.8$ TeV (right).

Figure 22 shows the b tagging efficiency for boosted top quark jets versus the misidentification probability using jets from a background sample of multijet events. The performance of AK8 and subjet b tagging is compared. When b tagging is applied to the subjets of boosted top quark jets, at least one of the subjets is required to be tagged. In addition, the performance of b tagging applied to AK4 jets matched to AK8 jets within $\Delta R(\text{AK4}, \text{AK8}) < 0.4$ is also shown. When b tagging is applied to AK4 jets matched to the AK8 jet, at least one of the AK4 jets is required to be tagged. In figure 22 (left), for jets with $300 < p_T < 500$ GeV, the AK8 jet b tagging is more efficient than AK4 jet b tagging. In contrast, in figure 22 (right), for jets with $p_T > 1200$ GeV, AK8 and AK4 jet b tagging perform similarly. This can be understood as due to the fact that at large jet p_T most of the tracks and the secondary vertex are also present in the AK4 jet because of the larger boost.

In both cases, subjet b tagging is more efficient than AK8 jet b tagging when identifying the b jet from the boosted top quark decay.

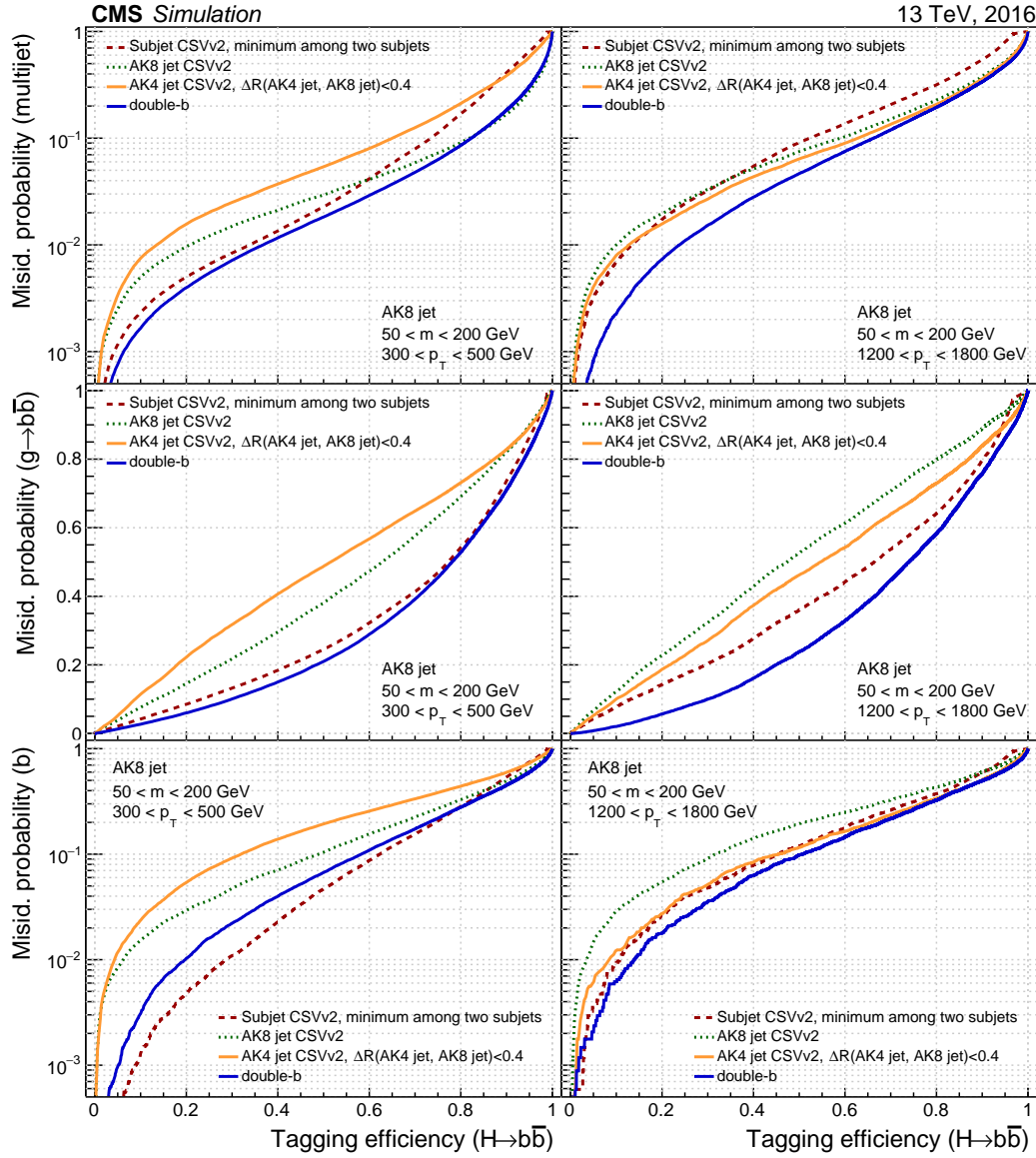


Figure 23. Misidentification probability using jets in a multijet sample (upper), for $g \rightarrow b\bar{b}$ jets (middle), and for single b jets (lower), versus the efficiency to correctly tag $H \rightarrow b\bar{b}$ jets. The CSVv2 algorithm is applied to three different types of jets: AK8 jets, their subjets, and AK4 jets matched to AK8 jets. For the subjet b tagging curves, both subjets are required to be tagged. The double-b tagger, described in section 6.2, is applied to AK8 jets. The AK8 jets are selected to have a pruned jet mass between 50 and 200 GeV, and $300 < p_T < 500$ GeV (left), or $1.2 < p_T < 1.8$ TeV (right).

Figure 23 shows the efficiency for identifying $H \rightarrow b\bar{b}$ jets versus the misidentification probability using jets from a background sample of inclusive multijet events, $g \rightarrow b\bar{b}$ jets or single b jets. When b tagging is applied to the subjets of the $H \rightarrow b\bar{b}$ jet, both subjets are required to be tagged. Similarly, both AK4 jets matched with the AK8 jet are required to be tagged.

When the misidentification probability is determined using inclusive multijet events, as illustrated in the upper panels of figure 23, AK8 jet b tagging performs well at the highest $H \rightarrow b\bar{b}$ jet tagging efficiencies, while subjet b tagging performs better at lower $H \rightarrow b\bar{b}$ jet tagging efficiencies. This can be understood as follows. Some of the input variables used in the CSVv2 tagger rely on the jet axis, as mentioned in section 5.1.2. An example is the ΔR between the secondary vertex flight direction and the jet axis. This variable is expected to have, on average, a smaller value for b jets compared to other jets, as can be seen in the right panel of figure 10. When b tagging is applied to the AK8 jet, the AK8 jet axis is used to calculate some of the variables. However, when two b hadrons are present in the jet, the ΔR between the secondary vertex flight direction and the AK8 jet axis or between the track and the AK8 jet axis may be quite large. Therefore, it is better to calculate these variables with respect to their respective subjet axes. On the other hand, at the highest $H \rightarrow b\bar{b}$ jet tagging efficiencies, subjet b tagging does not fully use variables that rely on the information of the full AK8 jet, such as the number of secondary vertices. This results in a worse performance of subjet b tagging compared to AK8 jet b tagging at the highest $H \rightarrow b\bar{b}$ jet tagging efficiencies.

The middle panels of figure 23 show the efficiency for $H \rightarrow b\bar{b}$ jets versus the misidentification probability for $g \rightarrow b\bar{b}$ in multijet events. Both for jets with $300 < p_T < 500$ GeV and $1.2 < p_T < 1.8$ TeV, subjet b tagging performs better than AK8 jet b tagging. This is understood as due to the fact that the information from both b hadrons is better used by the subjet b tagging approach.

As can be seen in the bottom panels of figure 23, also in the case where the background is composed of single b jets, subjet b tagging performs better. The lower misidentification probability at the same efficiency is explained by the fact that for the subjet b tagging, the two subjets are required to be tagged. Requiring both subjets to be tagged while there is only one b hadron present in the background jets results in a lower misidentification probability. It is worth noting that these performance curves look very similar to the performance curves obtained when b jets from boosted top quarks are considered as background instead of single b jets from multijet events.

The left panels in figure 23 demonstrate that AK8 jet b tagging is more efficient than AK4 jet b tagging using jets with $300 < p_T < 500$ GeV. The reason is that at low jet p_T not all the tracks and secondary vertex are associated with the two AK4 jets, while they are associated with the AK8 jet. In contrast, using jets with $p_T > 1200$ GeV, requiring the two AK4 jets to be tagged results in a similar performance or better than when the AK8 jet is required to be tagged. This can be explained by the fact that the high jet p_T results in tracks and secondary vertices that are more collimated and fully contained in the AK4 jets.

Figures 22 and 23 demonstrate that the performance of subjet and AK8 jet b tagging depends not only on the signal jets to be b tagged and on the background jets under consideration, but also on the jet p_T .

6.2 The double-b tagger

As mentioned in the previous section, the approaches of b tagging AK8 jets, as well as applying subjet b tagging, have limitations when identifying $H \rightarrow b\bar{b}$ jets. In this section, a novel approach is presented to discriminate $H \rightarrow b\bar{b}$ candidates from single-parton jets in multijet events. The strategy followed when developing the new “double-b” tagging algorithm is to fully use not only the presence of two b hadrons inside the AK8 jet but also the correlation between the directions of

the momenta of the two b hadrons. Although the algorithm is developed using simulated $H \rightarrow b\bar{b}$ events, any dependence of the algorithm performance on the mass or p_T of the $b\bar{b}$ pair is avoided. This strategy allows the usage of the tagger in physics analyses with a large range of jet p_T . The dependence on the jet mass is avoided as this variable is often used to define a region for the estimation of the background. In addition, this strategy also permits the use of the double-b tagger for the identification of boosted $Z \rightarrow b\bar{b}$ jets or any other boosted $b\bar{b}$ resonance where the kinematics of the decay products are similar.

A variable sensitive to the substructure is the N-subjettiness, τ_N [47], which is a jet shape variable, computed under the assumption that the jet has N subjets, and it is defined as the p_T -weighted distance between each jet constituent and its nearest subjet axis (ΔR):

$$\tau_N = \frac{1}{d_0} \sum_k p_T^k \min(\Delta R_{1,k}, \dots, \Delta R_{N,k}), \quad (6.1)$$

where k runs over all jet constituents. The normalization factor is $d_0 = \sum_k p_T^k R_0$ and R_0 is the original jet distance parameter, i.e. $R_0 = 0.8$. The τ_N variable has a small value if the jet is consistent with having N or fewer subjets. The subjet axes are used as a starting point for the τ_N minimization. After the minimization, the τ_N axes, also called τ axes, are obtained. These are then used to estimate the directions of the partons giving rise to the subjets, as schematically illustrated in figure 21 (right).

Many of the CSVv2 variables are also used in the double-b tagger algorithm. The variables rely on reconstructed tracks, secondary vertices obtained using the IVF algorithm, as well as the system of two secondary vertices. Tracks with $p_T > 1$ GeV are associated with jets in a cone of $\Delta R < 0.8$ around the jet axis. Each track is then associated with the closest τ axis, where the distance of a track to the τ axis is defined as the distance at their point of closest approach. The selection requirements applied to tracks in the CSVv2 algorithm are also applied here, using the τ axis instead of the jet axis. The reconstructed secondary vertices are associated first with jets in a cone $\Delta R < 0.7$ and then to the closest τ axis within that jet. For each τ axis, the track four-momenta of the constituent tracks from all the secondary vertices associated with a given τ axis are added to compute the secondary vertex mass and p_T for that τ axis.

Input variables are selected that discriminate between $H \rightarrow b\bar{b}$ jets and other jet flavours, and that improve the discrimination against the background from inclusive multijet production by at least 5% compared to the performance of the tagger without the variable. In addition, as mentioned earlier, variables are chosen that do not have a strong dependence on the jet p_T or jet mass. This procedure resulted in the following list of variables:

- The four tracks with the highest impact parameter significance.
- The impact parameter significance of the first two tracks ordered in decreasing impact parameter significance, for each τ axis.
- The 2D impact parameter significance, of the first two tracks (first track) that raise the total mass above 5.2 (1.5) GeV. These tracks are obtained as explained in section 5.1.2 in the context of the CSVv2 algorithm. In the case of the highest threshold, also the second track above the threshold mass is used. The thresholds of 5.2 GeV and 1.5 GeV are related to the b and c hadron masses, respectively.

- The secondary vertex energy ratio, defined as the total energy of all secondary vertices associated with a given τ axis divided by the total energy of all the tracks associated with the AK8 jet that are consistent with the primary vertex, for each of the two τ axes.
- The number of secondary vertices associated with the jet.
- The 2D secondary vertex flight distance significance, for the secondary vertex with the smallest uncertainty on the 3D flight distance, for each of the two τ axes.
- The ΔR between the secondary vertex with the smallest 3D flight distance uncertainty and its τ axis, for each of the two τ axes.
- The relative pseudorapidity, η_{rel} , of the tracks from all secondary vertices with respect to their τ axis for the three leading tracks ordered in increasing η_{rel} , for each of the two τ axes.
- The total secondary vertex mass, defined as the invariant mass of all tracks from secondary vertices associated with the same τ axis, for each of the two τ axes.
- The information related to the system of two secondary vertices, the z variable, defined as:

$$z = \Delta R(SV_0, SV_1) \frac{p_T(SV_1)}{m(SV_0, SV_1)} \quad (6.2)$$

where SV_0 and SV_1 are the secondary vertices with the smallest 3D flight distance uncertainty associated with the two τ axes, $p_T(SV_1)$ is the p_T of the secondary vertex associated with the second τ axis, and $\Delta R(SV_0, SV_1)$ is the distance between the two secondary vertices, and $m(SV_0, SV_1)$ is the invariant mass corresponding to the summed four-momenta of the two secondary vertices.

The most discriminating variables are the impact parameter significance for the most displaced tracks, the 2D impact parameter significance for the first track above the (5.2 GeV) b-hadron mass threshold, and the secondary vertex energy ratio for the secondary vertex with the smallest 3D flight distance uncertainty (SV_0).

Figure 24 shows the distributions for some of the input variables for the signal $H \rightarrow b\bar{b}$ jets and using jets from inclusive multijet production containing zero, one, or two b quarks. Distributions are shown separately for $g \rightarrow b\bar{b}$, single b quark, and light-flavour jets production. The secondary vertex multiplicity and the vertex energy ratio for SV_0 , along with the impact parameter significance of the first track raising the total invariant mass of all tracks above the b hadron mass threshold show a good separation between the $H \rightarrow b\bar{b}$ jets and the different background contributions. The z variable, eq. (6.2), shows good discrimination against $g \rightarrow b\bar{b}$ jets since it uses the different kinematic properties of the $H \rightarrow b\bar{b}$ and $g \rightarrow b\bar{b}$ decays.

Several variables related to the properties of soft leptons arising from the b hadron decay were also investigated. Despite a small gain in performance, these variables were excluded as input variables since they could introduce a bias in the efficiency measurement from data. The bias could arise when using muon information both to define input variables and to select a sample of jets containing a muon for the efficiency measurement in data, presented in section 9.

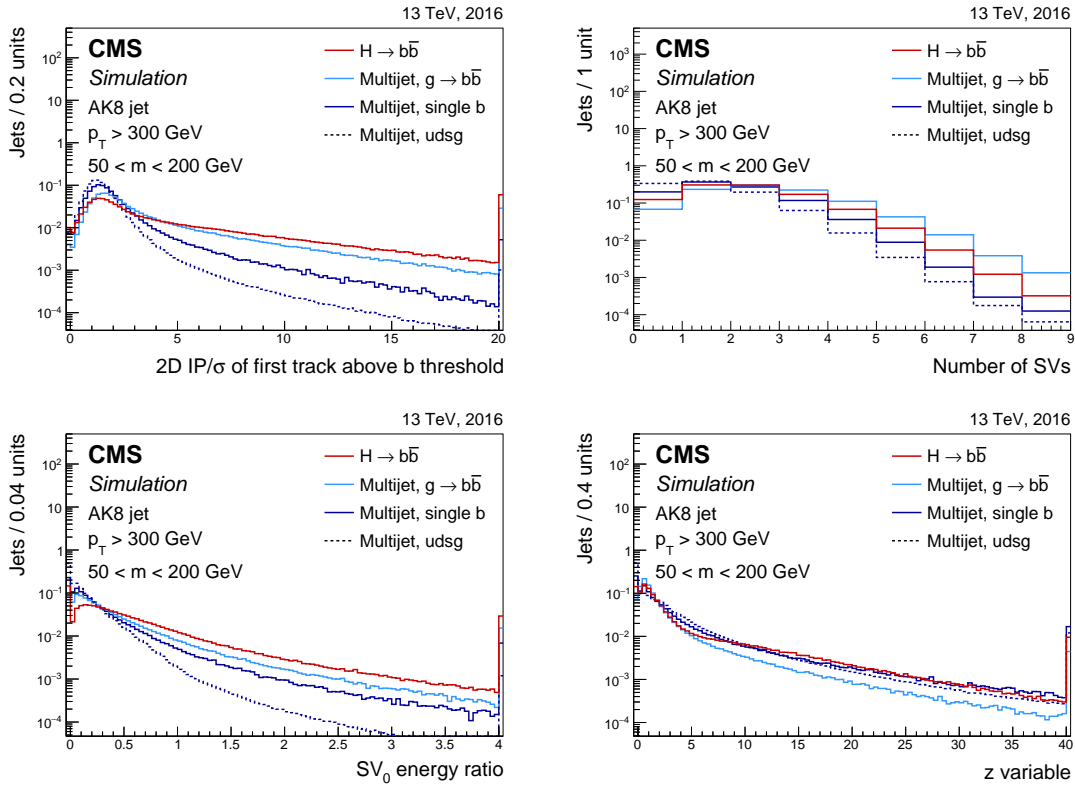


Figure 24. Distribution of 2D impact parameter significance for the most displaced track raising the mass above the b hadron mass threshold as described in the text (upper left), number of secondary vertices associated with the AK8 jet (upper right), vertex energy ratio for the secondary vertex with the smallest 3D flight distance uncertainty (lower left), and z variable described in the text (lower right). Comparison between $H \rightarrow b\bar{b}$ jets from simulated samples of a Kaluza-Klein graviton decaying to two Higgs bosons, and jets in an inclusive multijet sample containing zero, one, or two b quarks. The AK8 jets are selected with $p_T > 300$ GeV and pruned jet mass between 50 and 200 GeV. The distributions are normalized to unit area. The last bin includes the overflow entries.

The discriminating variables are combined using a BDT and the τ_{MVA} package [52]. The training is performed using $H \rightarrow b\bar{b}$ jets from simulated events with a Kaluza-Klein graviton decaying to two Higgs bosons as signal, and jets from inclusive multijet production as background. Jets are selected when they have a pruned mass between 50 and 200 GeV and p_T between 300 and 2500 GeV. The jet p_T distributions for the simulated signal and background jet samples are similar, therefore no dedicated reweighting of the samples was performed.

The distribution of the double- b discriminator values is shown in the upper panel of figure 25. Four working points are defined corresponding to about 75, 65, 45 and 25% signal efficiency for a jet p_T of about 1 TeV. The signal efficiencies and misidentification probabilities as functions of the jet p_T for these four working points are shown in the lower panels of figure 25. The decreasing signal efficiency at high jet p_T originates from the larger collimation of particles, which results in a lower track reconstruction efficiency due to close by hits. The reduced track reconstruction efficiency for high jet p_T results in a lower tagging efficiency for high jet p_T .

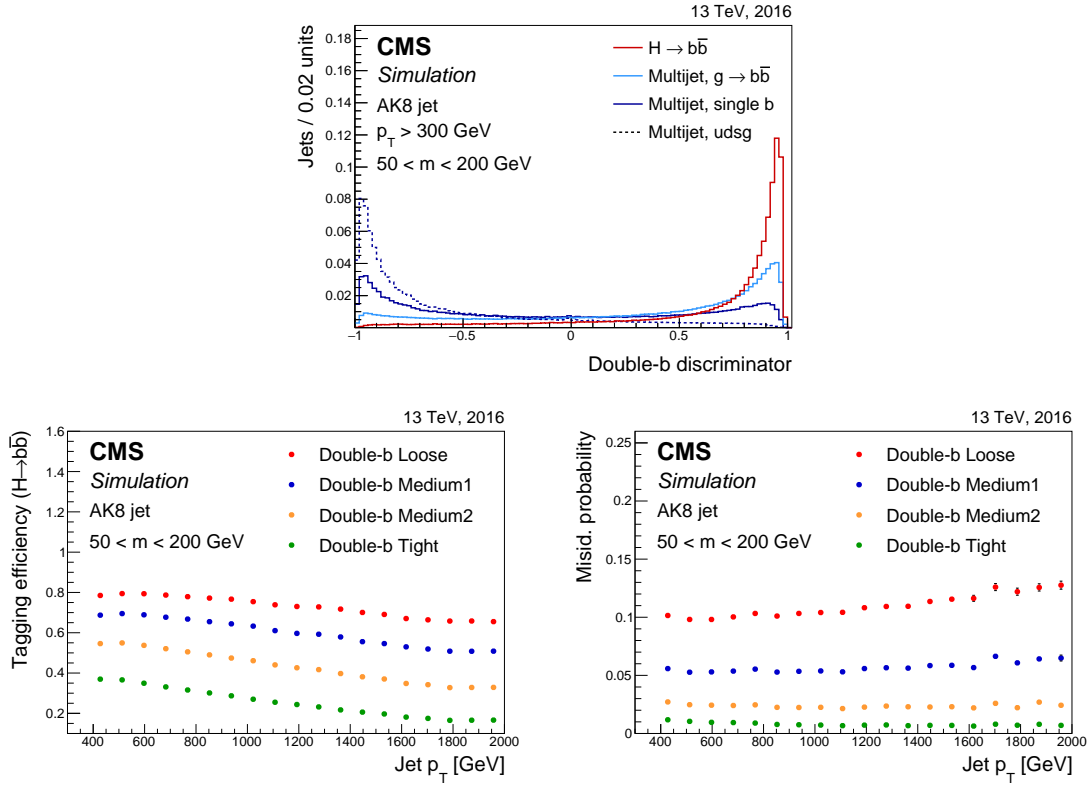


Figure 25. Distribution of the double-b tagger discriminator values normalized to unit area for $H \rightarrow b\bar{b}$ jets in simulated samples of a Kaluza-Klein graviton decaying to two Higgs bosons, and for jets in an inclusive multijet sample containing zero, one, or two b quarks (upper). Efficiency to correctly tag $H \rightarrow b\bar{b}$ jets (lower left) and misidentification probability using jets in an inclusive multijet sample (lower right) for four working points of the double-b tagger as a function of the jet p_T . The AK8 jets are selected with $p_T > 300$ GeV and pruned jet mass between 50 and 200 GeV.

The performance of the double-b tagger is compared with that of the CSVv2 tagger applied to AK8 jets or their subjets. The top and middle panels in figure 23 show the performance when the background consists of jets from inclusive multijet production or $g \rightarrow b\bar{b}$ jets. In these cases, the double-b tagger outperforms the AK8 jet and subjet b tagging approaches for all jet p_T ranges. At high jet p_T the improvement is larger compared to low jet p_T , thereby providing an important gain in the searches for heavy resonances where mostly high- p_T jets are expected. When the background is composed of single b jets, as shown in the bottom panels of figure 23, subjet b tagging outperforms the double-b tagger at low jet p_T , while the two approaches are similar at high jet p_T . The lower misidentification probability for single b jets at the same $H \rightarrow b\bar{b}$ jet tagging efficiency for subjet b tagging at low jet p_T is explained by the fact that the two subjets are very well separated at low jet p_T and the variables related to the AK8 jet used in the double-b tagger are less efficient. In contrast, at high jet p_T the subjets are much closer together, resulting in shared tracks and secondary vertices and thereby leading to a more similar performance.

Whether it is better to use subjet b tagging or the double-b tagger in a physics analysis depends strongly on the flavour composition and p_T distribution of the jets from the signal and background processes under consideration.

7 Performance of b jet identification at the trigger level

The identification of b jets at the trigger level is essential to collect events that do not pass standard lepton, jet, or missing p_T triggers, and to increase the purity of the recorded sample for analyses requiring b jets in the final state. The L1 trigger uses information from the calorimeters and muon detectors to reconstruct objects such as charged leptons and jets. Identification of b jets is not possible at that stage as it relies on the reconstructed tracks from charged particles available only at the HLT. In this section, we describe b jet identification at the HLT. A detailed description of the CMS trigger system can be found in ref. [11].

Because of latency constraints at the HLT, it is not feasible to reconstruct the tracks and primary vertex with the algorithms used for offline reconstruction. The time needed for track finding can be significantly reduced if the position of the primary vertex is known. While the position in the transverse plane is defined with a precision of $20\ \mu\text{m}$, its position along the beam line is not known [2]. However, it is possible to obtain a rough estimate of the primary vertex position along the beam line by projecting onto the z direction the position of the silicon pixel tracker hits (pixel detector hits) compatible with the jets. A pixel tracker hit in the barrel (endcap) is compatible with a jet when the difference in azimuthal angle between the hit and the jet is less than 0.21 (0.14). The region along the beam line with the highest number of projected pixel detector hits is most likely to correspond to the position of the primary vertex. This concept is illustrated in figure 26: the direction of the tracks in a jet is assumed to be approximately the same as the direction of the jet obtained using the calorimeter information.

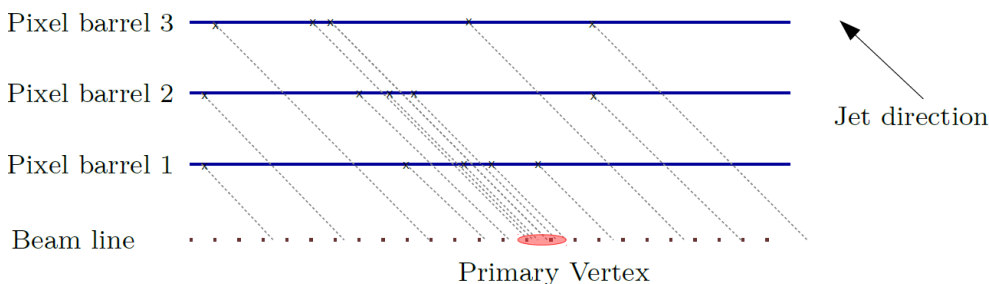


Figure 26. Scheme of the fast primary vertex finding algorithm used to determine the position of the vertex along the beam line. The pixel detector hits from the tracks in a jet are projected along the calorimeter jet direction onto the beam line.

This fast primary vertex (FPV) finding algorithm is sensitive to pixel detector hits from pileup interactions. Therefore, a number of selection requirements based on the shape of the charge deposition clusters associated with the pixel detector hits are applied to select those that most likely correspond to a particle with a large p_T . In addition, only pixel detector hits compatible with up to four leading jets with $p_T > 30\ \text{GeV}$ and $|\eta| < 2.4$ are used. Finally, each pixel detector hit is assigned a weight reflecting the probability that it corresponds to a track in one of the considered jets. The weight is obtained by using information related to the shape of the charge deposition cluster, the azimuthal angle between the jet and the cluster, and the jet p_T . Since the spread of projected hits from the primary vertex is proportional to the distance from the beam line, a larger weight is assigned to pixel detector hits closer to the beam line.

Figure 27 (left) shows that the resolution of the primary vertex along the beam line, Δz , is about 3 mm for simulated multijet events with 35 pileup interactions on average. Here, events are selected if the scalar sum of the calorimeter jet transverse momenta exceeds 250 GeV. The double-peak structure is caused by a bias in the FPV reconstruction that finds the primary vertex closer to the centre of the CMS detector than it is in reality in the simulation. This bias originates from the higher number of projected hits at the centre of the detector because of the detector geometry and pileup interactions. The efficiency of the FPV algorithm to reconstruct the primary vertex within 1.5 cm of its true position along the beam line is close to 99%.

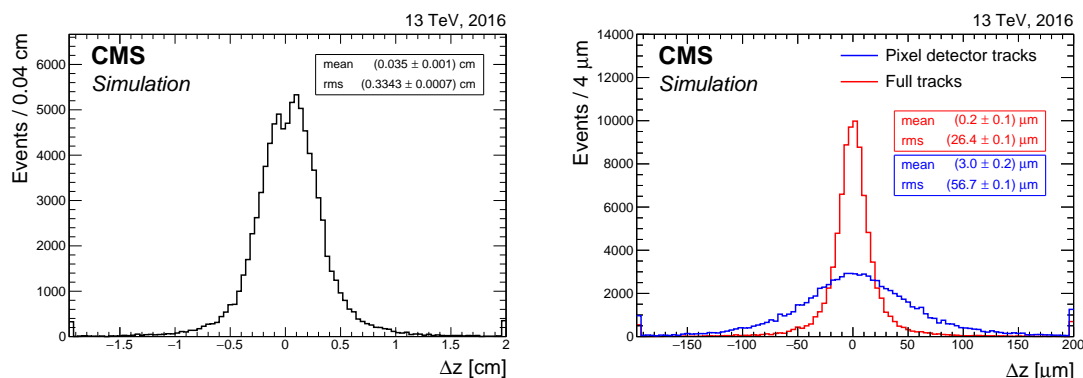


Figure 27. Distribution of residuals on the position of the primary vertex along the beam line using the fast primary vertex finding algorithm described in the text (left), and on the position of the primary vertex along the beam line after refitting with the tracks reconstructed at the HLT (right). The distributions are obtained using simulated multijet events with 35 pileup interactions on average and a flat \hat{p}_T spectrum between 15 and 3000 GeV for the leading jet. Events are selected for which the scalar sum of the p_T of the jets is above 250 GeV. The first and last bin of each histogram contain the underflow and overflow entries, respectively.

Since b tagging relies on the precise measurement of the displaced tracks with respect to the primary vertex, it is crucial to use tracks that use the information of both the pixel and the silicon strip tracker to improve the spatial and momentum resolutions. To reduce the HLT algorithm processing time, these tracks are only reconstructed when originating near the primary vertex and if they are close to the direction of the leading jets, sorted according to decreasing jet p_T . Up to eight jets with $p_T > 30$ GeV and $|\eta| < 2.4$ are considered in an event. In the first step, the trajectories of charged particles are reconstructed from the pixel detector hits. To reduce the reconstruction time, tracks are only reconstructed when they have a longitudinal (transverse) impact parameter below 15 (2) mm and are compatible with the direction of one of the jets. For simulated $t\bar{t}$ events with 35 pileup interactions on average, this approach of regional pixel tracking reduces the track reconstruction time by a factor of almost 40 with respect to pixel tracking without constraints. Using the reconstructed pixel tracks, the efficiency to find the primary vertex within 0.2 mm of its true position along the beam line is around 97.5%. To increase the efficiency even further, the variable

$$R = \frac{\sum_{j=1}^2 \sum_i p_{T}^{i,j}}{\sum_{j=1}^2 p_{T}^j} \quad (7.1)$$

is defined, where $p_{T}^{i,j}$ is the p_T of track i associated with the leading or subleading jet ($j = 1$ or 2)

and p_T^j is the p_T of jet j obtained from the calorimeter deposits. To calculate R , tracks from the two leading jets are used if they have a χ^2 of the track fit below 20, which reduces the effect of tracks reconstructed from a wrong combination of pixel hits. The impact of mismeasured tracks is reduced by setting the track p_T to 20 GeV if it is larger than this value. If the primary vertex position is not correctly reconstructed, the value of R will be small. If $R < 0.10$, the reconstruction of pixel detector tracks is run without the primary vertex position and using instead the direction of the two leading jets. The pixel detector tracks obtained in this way are then used to obtain a new position for the primary vertex, partially recovering the efficiency loss. The primary vertex position for all events is refitted using the reconstructed pixel detector tracks, resulting in a resolution that is much improved, as can be seen in figure 27 (right). Pairs of vertices that are closer than $70 \mu\text{m}$ to each other are merged into a single vertex. After the full procedure, the efficiency to find the primary vertex within 0.2 mm of its true position is larger than 98.5%, and the resolution on the position of the primary vertex along the beam line is less than $60 \mu\text{m}$, using simulated multijet events with 35 pileup interactions on average.

In the second step, the tracks are reconstructed using the information from the pixel and strip detectors. An iterative procedure is applied that is similar to the offline track reconstruction except for the number of iterations and the seeds used for track finding in each iteration. In the first iteration, the pixel tracks reconstructed as described above with $p_T > 0.9 \text{ GeV}$ are used as seeds if they have a transverse (longitudinal) impact parameter below 1 (3) mm. For the second iteration, triplets of pixel hits are used with $p_T > 0.5 \text{ GeV}$ and a transverse (longitudinal) impact parameter < 0.5 (1) mm. The last iteration uses pairs of pixel hits with $p_T > 1.2 \text{ GeV}$ and a transverse (longitudinal) impact parameter < 0.25 (0.5) mm. It is worth noting that the requirements on the impact parameter do not have a large impact on the reconstruction efficiency for displaced tracks. When refitting the primary vertex using the reconstructed tracks, the resolution on its position along the beam line further improves to less than $30 \mu\text{m}$, as shown in figure 27.

The reconstructed tracks and the refitted primary vertex are then used to reconstruct secondary vertices with the IVF vertex reconstruction algorithm. These vertices and tracks are then used as input for the CSVv2 algorithm described in section 5. No dedicated training of the CSVv2 algorithm is used at the HLT, as studies have not shown any improvement in performance. The processing time of regional tracking used for b tagging with up to eight leading jets with $p_T > 30 \text{ GeV}$ is on average 87 ms, not including the jet reconstruction time. The processing time was evaluated using data with the highest number of pileup interactions observed in 2016 (49 pileup interactions on average) and selecting events using a trigger threshold of 250 GeV on the scalar sum of the calorimeter jet transverse momenta. As a comparison, the average global processing time of the HLT farm is limited to about 200 ms per event. The b tagging algorithm was run in about 6% of the events accepted by the L1 trigger.

The performance of b tagging at the HLT is evaluated using data collected during 2016, selecting events with at least four calorimeter jets with $p_T > 45 \text{ GeV}$ and $|\eta| < 2.4$ and with the sum of the p_T of the jets at the HLT above 800 GeV. Offline CSVv2 discriminator distributions are shown in figure 28 using all jets (in red) as well as using jets with an HLT CSVv2 discriminator exceeding 0.56 (in blue). An estimate of the reduction factor for the trigger rate when requiring a single b tagged jet at HLT is determined as the number of jets passing the initial trigger, based on the sum of the p_T of the jets, divided by the number of jets passing the trigger and having an

HLT CSVv2 discriminator above 0.56. The b tagging efficiency for a threshold of 0.56 on the HLT CSVv2 discriminator is shown as a function of the offline CSVv2 discriminator value in figure 28 (right). In both panels, the structure at a discriminator value of ≈ 0.5 is caused by jets from pileup interactions. In the right panel, the discontinuity indicates that these jets do not behave exactly in the same manner at the HLT and offline, due to their different track reconstruction. The larger efficiency for CSVv2 discriminator values below 0.05 is due to jets for which the chosen primary vertex at the HLT and offline is different. In particular, the primary vertex position is wrongly reconstructed at the HLT, resulting in an apparent displaced jet with a high CSVv2 discriminator value at the HLT and a small offline CSVv2 discriminator value. The impact of this effect is relatively small since there are only a few jets with an offline CSVv2 discriminator value below 0.05, as can be seen in the left panel.

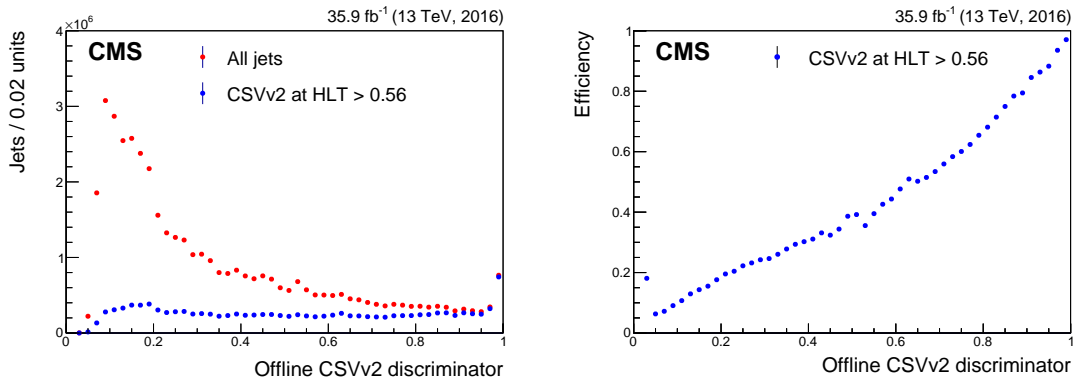


Figure 28. Offline CSVv2 discriminator distribution for all jets and for jets with a value of the CSVv2 discriminator at the HLT exceeding 0.56 (left), and b tagging efficiency at the HLT as a function of the offline CSVv2 discriminator value (right).

Figure 29 compares the HLT and offline b tagging performance using jets in simulated $t\bar{t}$ events with 35 pileup interactions on average. Events are selected if the scalar sum of the jet transverse momenta exceeds 250 GeV. Up to eight leading jets are used with $p_T > 30$ GeV and $|\eta| < 2.4$. As expected, the b tagging performance of the offline reconstruction is better than at the HLT. The maximum b jet identification efficiency at the HLT is $\approx 95\%$ because of three effects that occur more frequently at the HLT:

- The primary vertex is not reconstructed or not identified as the vertex corresponding to the jets on which the b tagging algorithm is applied.
- Since the track reconstruction efficiency at the HLT is lower, it happens more often that less than two tracks are associated with the jet, resulting in no valid discriminator value being assigned to the jet.
- There are at least two reconstructed tracks, but they do not pass the track selection requirements applied in the CSVv2 algorithm.

In the future, the b tagging performance at the HLT will be further improved by replacing the CSVv2 tagger with the DeepCSV tagger.

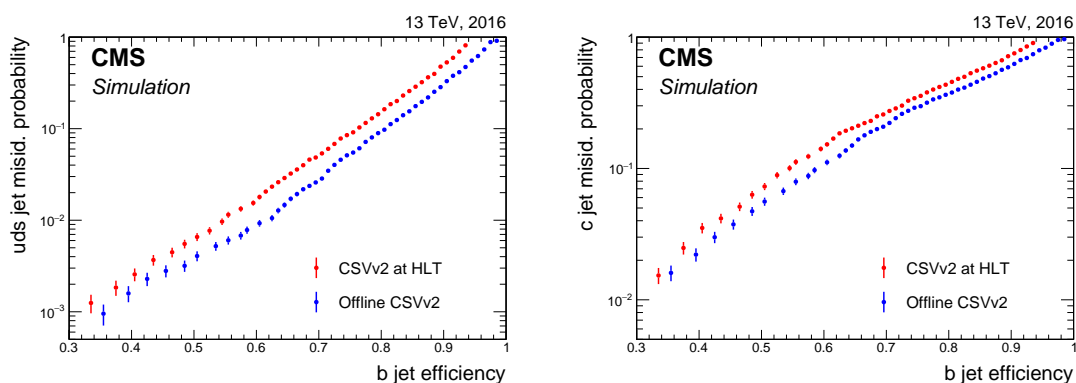


Figure 29. Comparison of the misidentification probability for light-flavour jets (left) and c jets (right) versus the b tagging efficiency at the HLT and offline for the CSVv2 algorithm applied on simulated $t\bar{t}$ events for which the scalar sum of the jet p_T for all jets in the event exceeds 250 GeV.

8 Measurement of the tagging efficiency using data

In the previous sections, the performance of the taggers was studied on simulated samples. In this section, we present the methods used to measure the efficiency of the heavy-flavour tagging algorithms applied on the data. In section 8.1, the data are compared to the simulation for a few input variables as well as for the output discriminator distributions. The measurement of the misidentification probability in the data is presented in section 8.2. The tagging efficiency for c and b jets is presented in sections 8.3 and 8.4, respectively. Section 8.5 summarizes a method to measure data-to-simulation scale factors as a function of the discriminator value for the various jet flavours. The results of the various measurements are compared and discussed in section 8.6.

8.1 Comparison of data with simulation

The data are compared to simulation in different event topologies, chosen for their different jet flavour composition, and selected according to the following criteria:

- **Inclusive multijet sample:** events are selected if they satisfy a trigger selection requiring the presence of at least one AK4 jet with $p_T > 40$ GeV. Because of the high event rates only a fraction of the events that fulfill the trigger requirement are selected (prescaled trigger). The fraction of accepted events depends on the prescale value, which varies during the data-taking period according to the instantaneous luminosity. The data are compared to simulated multijet events using jets with $50 < p_T < 250$ GeV. This topology is dominated by light-flavour jets and contains also a contribution of jets from pileup interactions.
- **Muon-enriched jet sample:** events are considered if they satisfy an online selection requiring at least two AK4 jets with $p_T > 40$ GeV of which at least one contains a muon with $p_T > 5$ GeV. Also in this case, the trigger was prescaled. The data are compared to a sample of jets with $50 < p_T < 250$ GeV and containing a muon selected from simulated muon-enriched multijet events. Because of the muon requirement this topology is dominated by jets containing heavy-flavour hadrons.

- **Dilepton $t\bar{t}$ sample:** at trigger level, events are selected by requiring the presence of at least one isolated electron and at least one isolated muon. Offline, the leading muon and electron are required to have $p_T > 25$ GeV and be isolated, as expected for leptonic W boson decays [9, 10]. Events are further considered if they contain at least two AK4 jets with $p_T > 20$ GeV. In this event sample we expect an enrichment in b jets from top quark decays. There is also a small contribution from jets from pileup interactions due to the relatively low threshold on jet p_T .
- **Single-lepton $t\bar{t}$ sample:** events are selected at trigger level by requiring the presence of at least one isolated electron or muon [9, 10]. Offline, exactly one isolated electron or muon is required, satisfying tight identification criteria. The electron (muon) is required to have a $p_T > 40$ (30) GeV and $|\eta| < 2.4$. Events are further considered if they contain at least four jets with $p_T > 25$ GeV. In this event sample a higher fraction of c jets is expected in comparison with the other samples. These c jets arise from the decay of the W boson to quarks.

The distributions of all input variables and output discriminators in the four aforementioned event topologies are monitored to assess the agreement between data and simulation. Figure 30 shows a selection of four input variables. For the secondary vertex variables that are shown the secondary vertices are reconstructed with the IVF algorithm, discussed in section 4.3. In the top left panel, the 3D impact parameter significance of the tracks is shown for jets in the dilepton $t\bar{t}$ sample. The observed discrepancy around zero is explained by the sensitivity of this variable to the tracker alignment and the uncertainty in the track parameters. The top right panel shows the corrected secondary vertex mass for the leading secondary vertex (sorted according to increasing uncertainty in the 3D flight distance), using jets in an inclusive multijet sample. The bottom left panel shows the 3D flight distance significance of the leading secondary vertex using jets in the muon-enriched jet sample. As was the case for the impact parameter significance, the disagreement between the data and the simulation is related to the sensitivity of this variable to the tracker alignment and the uncertainty in the track parameters and hence on the secondary vertex position. The bottom right panel shows the “massVertexEnergyFraction” variable, defined in section 5.2.1, using jets in the single-lepton $t\bar{t}$ sample.

While the simulation models the secondary vertex mass reasonably well, some discrepancies are observed for the impact parameter significance of the tracks and the secondary vertex flight distance. The imperfect modelling of the input variables will also have an impact on the modelling of the output discriminator distributions, which are shown in figure 31. The upper panels show the JP and cMVA_{v2} discriminators using jets in the dilepton $t\bar{t}$ sample. The discontinuities in the distribution of the JP discriminator values are due to the minimum track probability requirement of 0.5%, as explained in section 5.1.1. The middle panels show the CSV_{v2} and DeepCSV discriminators using jets in the muon-enriched sample. The lower panels show the CvsL and the CvsB discriminators, using jets in the inclusive multijet sample. The discontinuities in both distributions arise from jets for which no tracks pass the track selection criteria, as discussed in section 5.2.1. Deviations of up to 20% are observed at the highest discriminator values. These deviations may be related to the modelling of the detector in the simulation and to the accuracy of the generators in their modelling of the parton shower and hadronization. It is therefore important to measure the efficiencies directly from the data. In physics analyses, the difference between the tagging efficiency in the data and

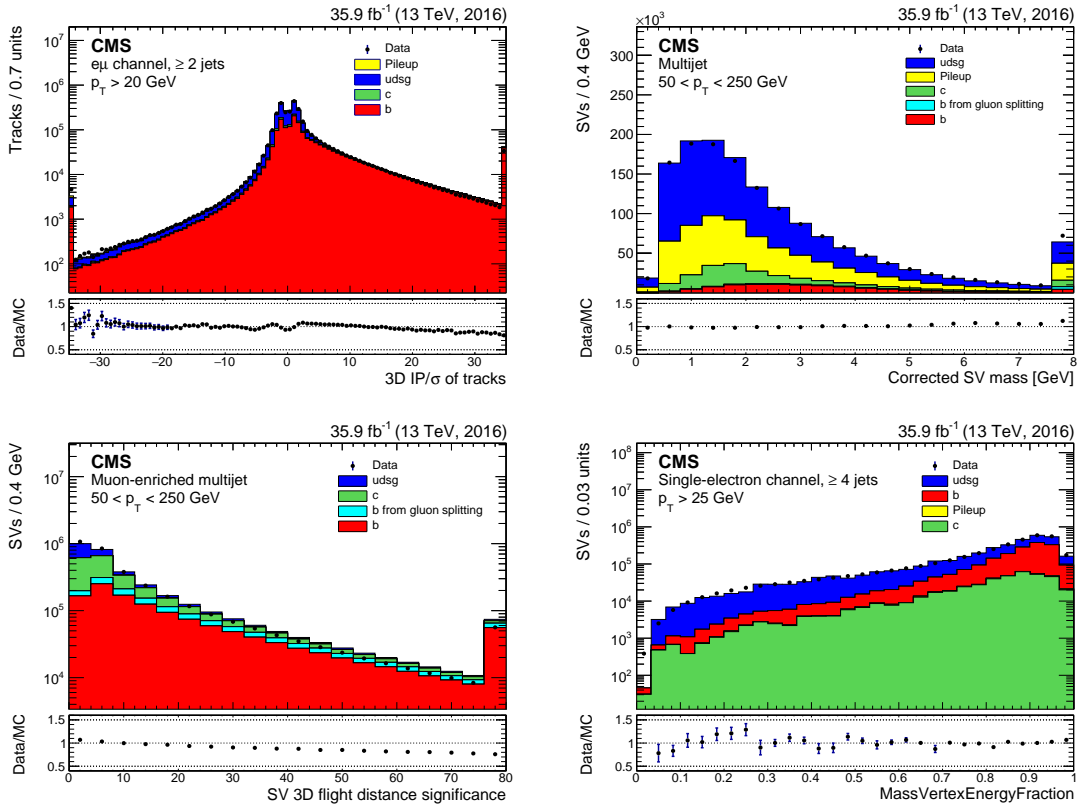


Figure 30. Examples of input variables used in heavy-flavour tagging algorithms in data compared to simulation. Impact parameter significance of the tracks in jets from the dilepton $t\bar{t}$ sample (upper left), corrected secondary vertex mass for the secondary vertex with the smallest uncertainty in the 3D flight distance for jets in an inclusive multijet sample (upper right), secondary vertex flight distance significance for jets in a muon-enriched jet sample (lower left), and distribution of the massVertexEnergyFraction variable described in the text for jets in the single-lepton $t\bar{t}$ sample (lower right). The simulated contributions of each flavour are shown with different colours. The total number of entries in the simulation is normalized to the number of observed entries in data. The first and last bin of each histogram contain the underflow and overflow entries, respectively.

simulation is then corrected for by taking into account a per jet data-to-simulation scale factor

$$SF_f = \varepsilon_f^{\text{data}}(p_T, \eta) / \varepsilon_f^{\text{MC}}(p_T, \eta), \quad (8.1)$$

where $\varepsilon_f^{\text{data}}(p_T, \eta)$ and $\varepsilon_f^{\text{MC}}(p_T, \eta)$ are the tagging efficiencies for a jet with flavour f in data and simulation, respectively. For most of the efficiency measurements, the number of jets in the data is too limited to provide a dependence on the jet $|\eta|$. For those methods, only the dependence on the jet p_T is measured. In simulation, the b/c tagging efficiency (misidentification probability) is defined as the number of b/c (light-flavour) jets that are tagged, according to the working point of a given algorithm (section 5), with respect to the total number of b/c (light-flavour) jets. Using simulated events, the number of jets with flavour f is determined by matching the jets with the generated hadrons. In data, the tagging efficiency is measured with a pure sample of jets with a

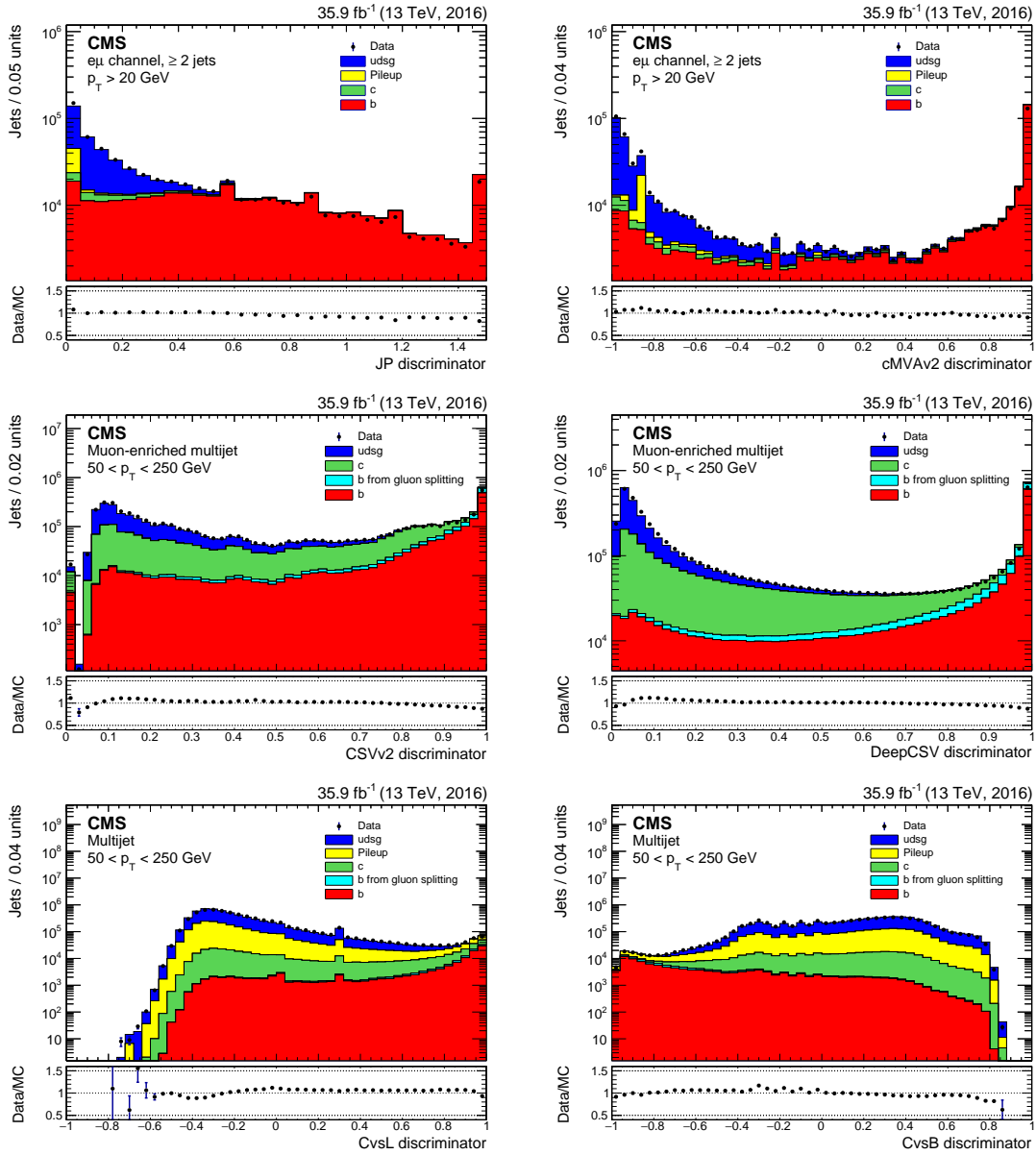


Figure 31. Examples of discriminator distributions in data compared to simulation. The JP (upper left) and cMVAv2 (upper right) discriminator values are shown for jets in the dilepton $t\bar{t}$ sample, the CSVv2 (middle left) and DeepCSV (middle right) discriminators for jets in the muon-enriched multijet sample, and the CvsL (lower left) and CvsB (lower right) discriminators for jets in the inclusive multijet sample. The simulated contributions of each jet flavour are shown with different colours. The total number of entries in the simulation is normalized to the number of observed entries in data. The first and last bin of each histogram contain the underflow and overflow entries, respectively.

certain flavour f , using selection requirements that do not bias the jets with respect to the variables used in the tagging algorithm.

8.2 The misidentification probability

The misidentification probability for light-flavour jets is measured with a sample of inclusive multijet events. The inclusive multijet data are collected using triggers requiring at least one jet above a certain p_T threshold, with $p_T > 40$ GeV being its lowest value. Because of the high trigger rates for the lowest trigger thresholds, the triggers are prescaled. The selected events are reweighted to take into account the different prescales for each trigger threshold in order to obtain the same jet p_T distribution as if unprescaled triggers were used. The simulated events are reweighted to match the distribution of the number of pileup interactions in the data.

The negative-tag method [1] is used for the measurement of the misidentification probability and the data-to-simulation scale factor, SF_1 . The method is based on the definition of positive and negative taggers, which are identical to the default algorithms, except that for each jet only tracks with either positive or negative impact parameter values and secondary vertices with either positive or negative flight distance are used. To first order, the discriminator values for negative and positive taggers are expected to be symmetric for light-flavour jets, with nonzero values of the impact parameter and flight distance arising because of resolution effects. Some asymmetries are present for light-flavour jets due to long-lived hadrons, such as K_S^0 and Λ hadrons. The positive and negative discriminator distributions are presented in figure 32 using jets with $p_T > 50$ GeV. For convenience, the discriminator values of the negative taggers are shown with a negative sign. Note that since the cMVA2 and c tagger discriminator values range between -1 and 1 , a shift was introduced such that the positive cMVA2 discriminator is defined between 0 and 2 , while the negative discriminator is shown with a negative sign and obtains values between -2 and 0 . Deviations of up to 10% are observed between the data and simulation for some discriminator values.

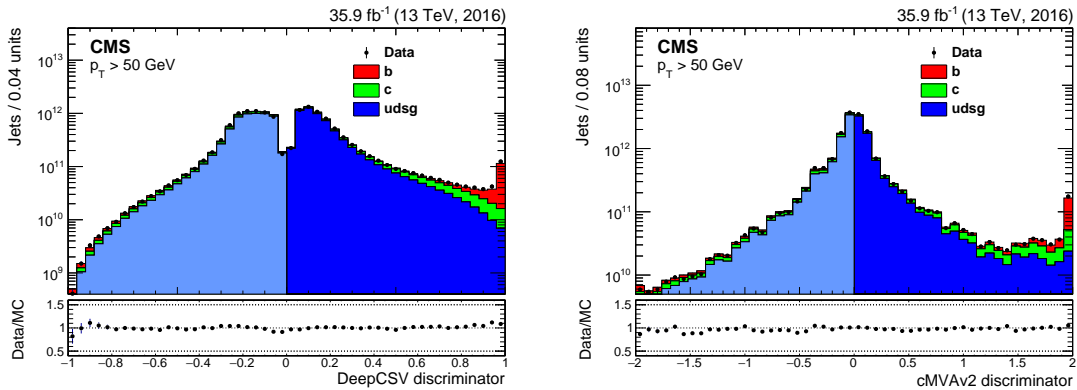


Figure 32. Distributions of the DeepCSV (left) and the cMVA2 (right) discriminators for jets in an inclusive multijet sample. For visualization purposes the discriminator output of the negative DeepCSV tagger is shown with a negative sign. For the cMVA2 tagger, the discriminator output of the positive tagger is shifted from $[-1, 1]$ to $[0, 2]$ and the discriminator values of the negative tagger are shown with a negative sign. The simulation is normalized to the number of entries in the data.

We define negative-tagged (positive-tagged) jets as the jets with a discriminator value of the negative (positive) tagger passing the working point of the tagger. The misidentification probability, ε_1 , is determined from the fraction of negative-tagged jets passing the working point, ε^- , in an

inclusive multijet sample

$$\varepsilon_1 = \varepsilon^- R_{\text{LF}} \quad (8.2)$$

where the correction factor $R_{\text{LF}} = \varepsilon_1^{\text{MC}} / \varepsilon^{-,\text{MC}}$ is the ratio of the misidentification probability of light-flavour jets to the negative tagging probability of all jets in simulation. The correction factor R_{LF} is typically between 0.3 and 1, with the exact value depending on the working point and tagger.

Systematic uncertainties in the misidentification probability are related to possible effects that may have an impact on R_{LF} . In particular, the following systematic uncertainties are evaluated:

- **Fraction of heavy-flavour jets:** if the fraction of jets from heavy-flavour quarks in the negative-tag sample increases, the value of R_{LF} decreases. The fraction of b jets has been measured by the CMS collaboration to agree with the simulation within $\pm 20\%$ [53]. To assess the effect of this systematic uncertainty, the fraction of heavy-flavour jets in the simulation is varied by $\pm 20\%$.
- **Gluon fraction:** the fraction of gluon jets affects the misidentification probability in the simulation as well as the negative tagging probability, because of the larger track multiplicity in gluon jets compared to jets originating from light-flavour quarks. In addition, the fraction of gluon jets depends on the parton density and parton showering in the simulation. The systematic effect due to the uncertainty in the fraction of gluon jets is evaluated by varying the gluon fraction by $\pm 20\%$ [54].
- **K_S^0 and Λ decays (V^0):** the observed numbers of reconstructed K_S^0 and Λ hadrons are found to be a factor of 1.30 ± 0.30 and 1.50 ± 0.50 larger than expected [55, 56], respectively. To determine the nominal value of the data-to-simulation scale factor, the amount of reconstructed K_S^0 or Λ hadrons is reweighted in the simulation to be consistent with the observed yields. To obtain the size of the systematic effect due to the reweighting, the fraction of K_S^0 and Λ hadrons is varied by the uncertainty in the measured fraction, i.e. by ± 30 and $\pm 50\%$, respectively.
- **Secondary interactions:** the rate of secondary interactions from photon conversions or nuclear interactions in the pixel tracker layers has been measured with a precision of $\pm 5\%$ [55, 56]. The number of secondary interactions is varied by this amount to obtain the systematic uncertainty in the data-to-simulation scale factor.
- **Mismeasured tracks:** according to the simulation, there are more positive- than negative-tagged jets containing a reconstructed track that cannot be associated with a genuine charged particle. This is expected because the positive-tagged light-flavour jets contain K_S^0 or Λ hadrons, resulting in more hits and hence a higher probability for a wrong combination of those hits leading to a mismeasured track. To correct for this residual effect of mismeasured tracks, a $\pm 50\%$ variation of this contribution is taken into account for the systematic uncertainty in R_{LF} .
- **Sign flip:** the number of jets with a negative tag is sensitive to the angular resolution on the jet axis and 3D impact parameter since these may affect the impact parameter sign. In particular, a difference between data and simulation in the probability of sign flips will affect the ratio of the negative tagging probability in data to that in simulation. The difference between data and

simulation on the fraction of negative-tagged jets with respect to all tagged jets is measured with a muon-enriched jet sample and used to estimate the size of this systematic effect.

- **Sampling:** the dependence of the data-to-simulation scale factor on the event topology is estimated by the trigger dependence of the scale factor. The scale factor is computed separately for each of the trigger requirements used to select the inclusive multijet sample. The maximum variation of the scale factor for these different measurements with respect to the nominal value using the unbiased jet p_T spectrum is taken as the size of the systematic effect.
- **Pileup:** the simulated events are reweighted according to the observed amount of pileup interactions in data. A 5% uncertainty in the total inelastic cross section of pp collisions [57] is propagated to the distribution of the number of pileup interactions to assess the impact of the uncertainty in the pileup reweighting.
- **Statistical uncertainty in the simulation:** the limited amount of simulated multijet events is taken into account as an additional systematic uncertainty.

Figure 33 shows an example of the measured misidentification probabilities, data-to-simulation scale factors, and relative systematic uncertainties for the medium working point of the DeepCSV and cMVA2 taggers. In the top right panel of figure 33, the “step” in the misidentification probability around 450 GeV is caused by the p_T - (and $|\eta|$ -) dependent weights for the jet flavours in the vertex categories in the training of the CSVv2 algorithm, discussed in section 5.1.2. The middle panels in figure 33 show the scale factors as a function of the jet p_T with the result of the fit superimposed. The fit functions are typically parameterized by a third degree polynomial with four free parameters. The dashed lines around the fit function represent the overall statistical and systematic uncertainty in the measurement. For jets with $p_T > 1000$ GeV the uncertainty in the scale factor is doubled. The scale factors are typically larger than one in a broad jet p_T range. The relative precision that is achieved on the scale factors for light-flavour jets when using b tagging algorithms is 5–10% for the loose working point and rises to 20–30% for the tight working point using jets with $20 < p_T < 1000$ GeV. The statistical uncertainty is typically a factor of 10 times smaller than the systematic uncertainty. For the c tagger, the relative precision varies between 3 and 7% for the loose and tight working points, respectively. The reason for the smaller uncertainty for the c tagger compared to the b taggers is the different definition of the working points. The working points for the c tagger have a much higher misidentification probability for light-flavour jets, ranging from over 90% for the loose working point to about a per cent for the tight working point, compared to 10% and 0.1%, respectively, for the b tagging algorithms (section 5). The tight working point of the c tagger corresponds to a misidentification probability that is in between the loose and medium working points of the b taggers. Taking this into account, the corresponding systematic uncertainties are of a similar size.

8.3 The c jet identification efficiency

In this section, the methods are presented to obtain a jet sample enriched in c quark content, which is subsequently employed to measure the efficiency for (mis)identifying c jets in data. The efficiency in data and simulation is then used to determine the data-to-simulation scale factor for c jets, SF_c ,

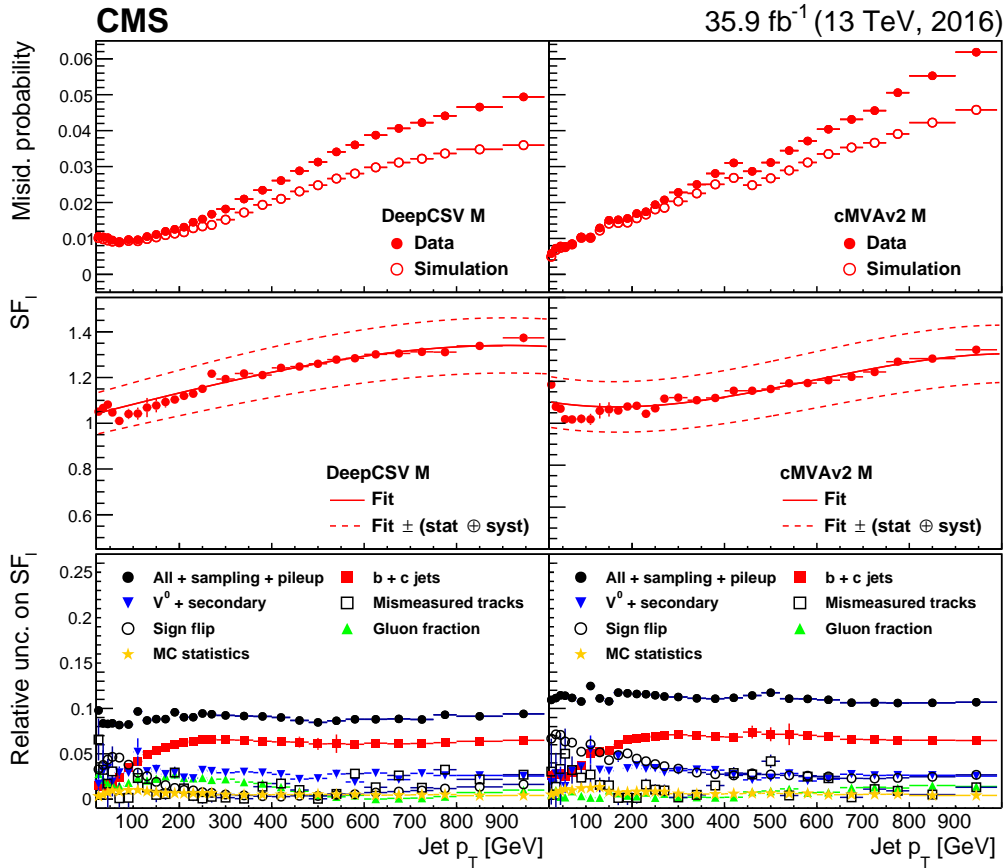


Figure 33. Misidentification probability, data-to-simulation scale factors, and relative uncertainty in the scale factors for light-flavour jets for the medium working point of the DeepCSV (left) and cMVA2 (right) algorithm. The upper panels show the misidentification probability in data and simulation as a function of the jet p_T . The middle panels show the scale factors for light-flavour jets, where the solid curve is the result of a fit to the scale factors, and the dashed lines represent the overall statistical and systematic uncertainty in the measurement. The lower panels show the relative systematic uncertainties in the scale factors for light-flavour jets. The sampling and pileup uncertainties are not shown since they are below 1%, but are included in the total systematic uncertainty covered by the black dots.

for each algorithm and working point. The first method relies on the $W + c$ topology. The second method uses c jets from the W boson decay to quarks in the single-lepton $t\bar{t}$ topology, where one of the W bosons decays into quarks and the other one into leptons.

8.3.1 Measurement relying on $W + c$ events

The efficiency to identify c jets using heavy-flavour jet identification algorithms is measured with a sample enriched in c jets obtained from events with a W boson produced in association with a c quark. At leading order, the production of a W boson in association with a c quark proceeds mainly through $s + g \rightarrow W^- + c$ and $\bar{s} + g \rightarrow W^+ + \bar{c}$ as shown in figure 34 (left and middle). A key property of this production process is that the c quark and W boson have opposite-sign (OS) electric charge. The dominant background are $W + q\bar{q}$ events, which are produced with an equal amount of OS and

same-sign (SS) events, as can be seen in figure 34 (right). After the event selection, a sample with a high purity of $W + c$ events is obtained by subtracting the SS distribution of a variable from the OS distribution for that variable. The remaining events are referred to as “OS-SS”.

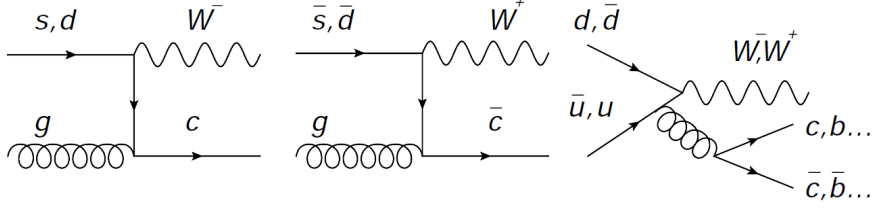


Figure 34. Leading order production of $W + c$ with opposite-sign electric charges (left and middle), and of $W + q\bar{q}$ through gluon splitting (right). In gluon splitting there is an additional c quark with the same sign as the W boson.

The $W + c$ events are selected according to the criteria of ref. [58]. Events are selected by requesting one isolated electron (muon) with a p_T^ℓ above 34 (26) GeV and satisfying medium (tight) identification criteria [9, 10]. When the event has more than one isolated electron or muon satisfying the selection criteria, the highest- p_T lepton is considered as the lepton from the W boson decay. The contribution from $Z + \text{jets}$ events is reduced by vetoing events with a same-flavour dilepton invariant mass between 70 and 110 GeV. To reduce the background from multijet events to a negligible level, the transverse mass $M_T = \sqrt{p_T^\ell p_T^{\text{miss}} [1 - \cos(\phi^\ell - \phi^{\text{miss}})]}$ is required to be larger than 55 GeV. In this expression, ϕ^ℓ and ϕ^{miss} (p_T^ℓ and p_T^{miss}) are the azimuthal angles (transverse momenta) of the isolated lepton and the \vec{p}_T^{miss} vector, respectively. At least one jet is required in the tracker acceptance, with $p_T > 25$ GeV and separated from the isolated lepton by $\Delta R > 0.5$. In addition, the leading jet should contain a nonisolated soft muon among the jet constituents with $p_T < 25$ GeV. The charge of the c quark is determined from the charge of the soft muon inside the jet. The OS (SS) events are then defined as events for which the muon in the jet has the opposite (same) charge as the isolated lepton from the W decay. After these requirements, the expected signal purity is about 60% for $W \rightarrow \mu\nu$ events and 80% for $W \rightarrow e\nu$ events. Remaining $Z + \text{jets}$ and $t\bar{t}$ events are the main sources of background for the $W \rightarrow \mu\nu$ channel, and $t\bar{t}$ events for the $W \rightarrow e\nu$ channel. As an example, the distributions of the c tagger discriminators are shown in figure 35 for the OS-SS sample, for the $W \rightarrow \mu\nu$ and $W \rightarrow e\nu$ channels combined.

The efficiency to tag a c jet using a certain working point and tagger is obtained as the fraction of tagged c jets over the total number of c jets in $W + c$ events in the OS-SS sample:

$$\varepsilon_c = \frac{N(W + c)_{\text{tagged}}^{\text{OS-SS}}}{N(W + c)^{\text{OS-SS}}}, \quad (8.3)$$

where the number of $W + c$ events in data, $N(W + c)^{\text{OS-SS}}$, is obtained as the observed number of OS-SS events times the fraction of $W + c$ events among these, derived from simulation as $f_{W+c}^{\text{MC}} = 1 - f_{\text{bkg}}^{\text{MC}}$. Analogously, $N(W + c)_{\text{tagged}}^{\text{OS-SS}}$ corresponds to the number of $W + c$ events with a tagged c jet, obtained as the observed number of OS-SS events with a tagged c jet times the fraction of expected $W + c$ events with a tagged c jet, where the fraction is obtained as $f_{W+c}^{\text{tagged,MC}} = 1 - f_{\text{bkg}}^{\text{tagged,MC}}$. The simulated c jet tagging efficiency is obtained by repeating the procedure on simulated data.

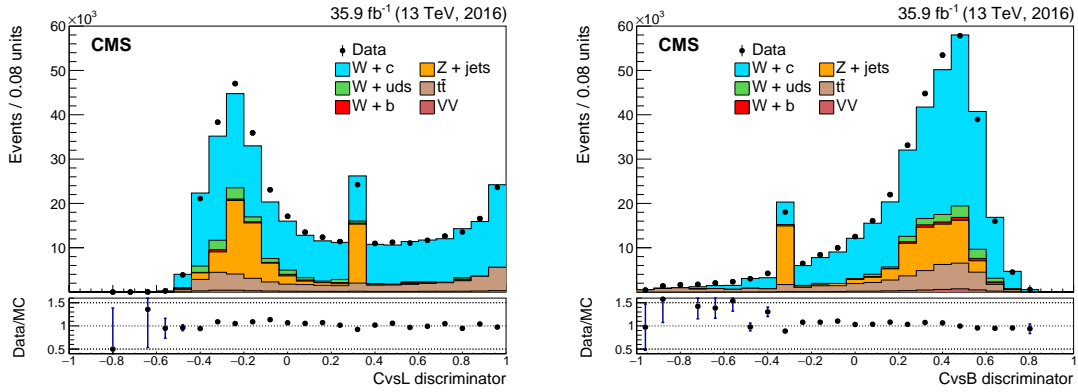


Figure 35. Distribution of the CvsL (left) and CvsB (right) discriminators in the $W \rightarrow \mu\nu$ and $W \rightarrow e\nu$ channels after the OS-SS subtraction. The spikes originate from jets without a track passing the track selection criteria, as discussed in section 5.2.1. The last bin includes the overflow entries.

Apart from the statistical uncertainty, the measurement may also be affected by several sources of systematic effects:

- **Background subtraction:** the number of $W+c$ events in data is obtained under the assumption that the fraction of (tagged) background events in data and simulation is the same. The effect of this assumption is quantified by varying $f_{\text{bkg}}^{\text{MC}}$ and $f_{\text{bkg}}^{\text{tagged,MC}}$ by 50%. The impact on the measured efficiency for tagging c jets is of the order of 2%, becoming one of the dominant uncertainties.
- **Branching fraction of $D \rightarrow \mu X$ and fragmentation of $c \rightarrow D$:** the branching fractions for $D \rightarrow \mu X$ are varied to match the latest PDG data [35]. In particular, the branching fractions are shifted by -2% for $D^+ \rightarrow \mu X$, $+13\%$ for $D^0 \rightarrow \mu X$, and $+16\%$ for $D_s \rightarrow \mu X$. In addition, also the fragmentation rate of a c quark to a D meson is varied to be consistent with the PDG data [59]. This implies the following `PYTHIA 8` variations: $+37\%$ for $c \rightarrow D^+$, -9% for $c \rightarrow D^0$, and -33% for $c \rightarrow D_s$. The difference in the measured c jet tagging efficiency after this simultaneous variation is less than 1% and is taken as a systematic uncertainty.
- **Number of tracks:** the uncertainty in the modelling of the number of selected tracks per jet in the simulation is taken into account by reweighting the distribution to match the data and remeasuring the data-to-simulation scale factor. The difference between the nominal scale factor value and the one after reweighting is less than 1%.
- **Soft-muon requirement:** requiring a muon in a jet may introduce a potential bias in the efficiency measurement when the tagger also relies on muon variables, as is the case for the c tagger and the `cMVA2` tagger. The bias may arise if the tagger response is different for jets with and without a soft lepton. The potential bias is estimated by repeating the measurement using a modified version of the tagger, which treats the muon as a track and assigns a default value to the soft-muon input variables. The difference between the values measured with the modified tagger and the default one is taken as systematic uncertainty. The effect of this variation is less than 3%. This is the dominant systematic uncertainty.

- **Jet energy scale:** since the measurements are performed in bins of jet p_T , the fraction of jets in each bin may vary depending on the jet energy corrections. The data-to-simulation scale factors are remeasured after varying the jet energies by ± 1 standard deviation of the nominal jet energy scale. The systematic effect due to this variation is less than 1%.
- **Electron and muon efficiency:** the uncertainties related to the lepton reconstruction and identification are taken into account by varying the corresponding correction factors within their uncertainty and reevaluating the efficiency for tagging c jets. The effect of this variation is smaller than 1%.
- **Pileup:** the effect of the uncertainty in the number of additional pileup interactions is evaluated as described in section 8.2, having an impact on the c tagging efficiency below 1%.
- **Factorization and renormalization scales:** in ref. [58] the normalized cross section for W+c events has been measured and the impact of the factorization and renormalization scales used at matrix element and parton shower levels was evaluated. The systematic uncertainty related to the variation of these scales was found to be well below 1% because of the cross section normalization. When measuring data-to-simulation scale factors, this systematic uncertainty also cancels in the ratio.
- **Parton distribution functions:** the NNPDF parton densities are varied within their uncertainties resulting in additional templates for the systematic uncertainty. The effect was found to be less than 1%.

The total systematic uncertainty in the data-to-simulation scale factor measurement is obtained as the quadratic sum of the individual systematic uncertainties.

The c jet tagging efficiency and the data-to-simulation scale factor SF_c are computed as a function of jet p_T and presented in figure 36 for the loose and medium working points of the c tagger. Scale factors for misidentifying c jets are also derived for the b tagging algorithms.

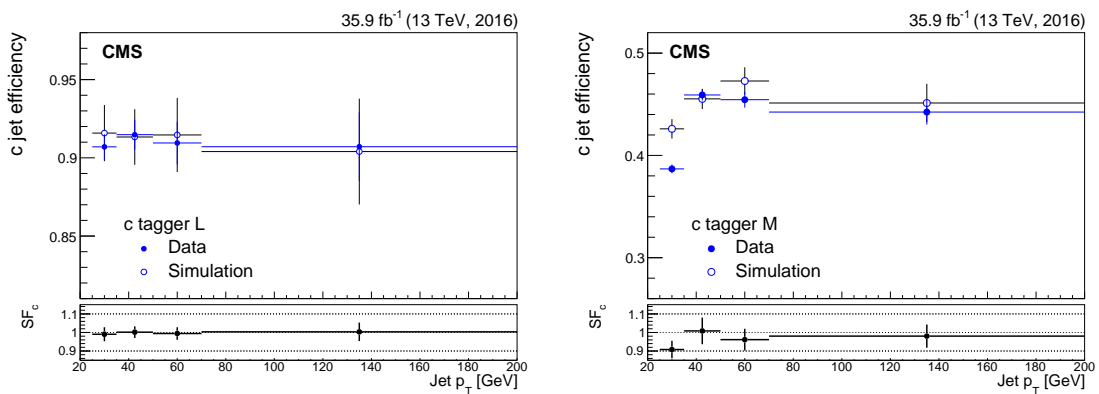


Figure 36. Efficiency for tagging c jets in data and simulation as a function of the jet p_T , and corresponding data-to-simulation scale factors (bottom panels) for the loose (left) and medium (right) working points of the c tagger.

8.3.2 Measurement relying on the single-lepton $t\bar{t}$ events

If a W boson decays hadronically, the decay contains a c quark in about 50% of the cases. Therefore, in a pure sample of single-lepton $t\bar{t}$ events, about one event out of two will contain a c jet. Because of the particular decay chain of the top quark, the energy of up-type quarks from the W boson decay is, on average, larger than for down-type quarks. This property, verified in simulated $t\bar{t}$ events, is used to obtain samples of jets enriched and depleted in c quarks. The c tagging efficiency is obtained by fitting the distribution of a variable in both of these samples simultaneously to the data, as will be explained in the following.

Events are selected by requiring exactly one isolated muon satisfying the tight identification criteria and with a p_T exceeding 30 GeV [10]. In addition, exactly four jets with $p_T > 30$ GeV are required. All objects are required to be within the tracker acceptance. The background from multijet events is reduced to a negligible level by requiring the reconstructed transverse mass formed by the muon and \vec{p}_T^{miss} , to be $M_T(\mu, p_T^{\text{miss}}) > 50$ GeV. The $t\bar{t}$ event is reconstructed by assigning the jets to the quarks from which they originate, using a mass discriminant λ_M . This mass discriminant is defined as the 2D probability for the invariant mass of a correct combination of two jets to be consistent with the W boson mass, and the invariant mass of a correct three-jet combination to be consistent with the top quark mass. The jet-quark assignment for which the negative logarithm of λ_M is minimal is chosen as the reconstructed $t\bar{t}$ topology candidate for the event. The two jets assigned to the b quarks from the top quark decay are required to be b-tagged; one jet should pass the tight working point of the CSVv2 tagger and the other one its loose working point. By requiring those jets to be b-tagged only after the jet-quark assignment is done, a bias is avoided on the c jet tagging efficiency measurement. Figure 37 shows the distribution of λ_M and of the highest (leading) and second-highest (subleading) energy for the two jets corresponding to the W decay after the full event selection. The $t\bar{t}$ simulation is divided into three different subsamples:

- **$t\bar{t}$, right W_h :** the W boson is correctly reconstructed, hence the two jets are correctly assigned to the quarks from the W boson decay.
- **$t\bar{t}$, wrong W_h :** the W boson is wrongly reconstructed, hence at least one of the two jets is not correctly assigned to the quarks from the W boson decay.
- **Other $t\bar{t}$ decay:** the generated event is not a single-lepton $t\bar{t}$ event.

The non- $t\bar{t}$ background is relatively small, with contributions from single top quark, W + jets, Z + jets, and multijet production.

From figure 37 it is clear that the λ_M distribution has discrimination power to separate jets that are correctly associated with the W boson decay and jets for which this is not the case. Therefore, this distribution is used to measure the efficiency and data-to-simulation scale factor for c jets.

Four event categories are defined according to whether or not the jets that are assigned to the W boson decay (i.e. the probe jets) pass the tagging working point for which the efficiency is to be measured:

- **Notag:** both probe jets fail the tagging requirement;
- **Leadtag:** only the most energetic probe jet passes the tagging requirement;

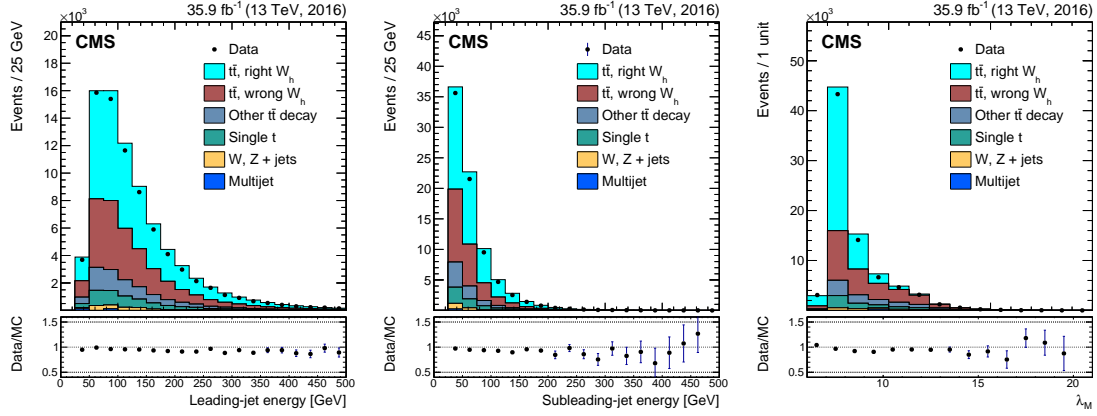


Figure 37. Distributions of the leading- (left) and subleading- (middle) jet energy as well as of the mass discriminant λ_M (right) after the full event selection, jet-quark assignment, and b tagging requirement on the two b jet candidates.

- **Subleadttag:** only the least energetic probe jet passes the tagging requirement; and
- **Ditag:** both probe jets pass the tagging requirement.

For $t\bar{t}$ events in the “right W_h ” subsample, the number of events in the various categories can be written as:

$$\begin{aligned}
 N_{\text{notag}} &= N_T((1 - \varepsilon_1^c)(1 - \varepsilon_2^{\text{LF}})f_1 + (1 - \varepsilon_1^{\text{LF}})(1 - \varepsilon_2^c)f_2 + (1 - \varepsilon_1^{\text{LF}})(1 - \varepsilon_2^{\text{LF}})(1 - f_1 - f_2)), \\
 N_{\text{leadttag}} &= N_T(\varepsilon_1^c(1 - \varepsilon_2^{\text{LF}})f_1 + \varepsilon_1^{\text{LF}}(1 - \varepsilon_2^c)f_2 + \varepsilon_1^{\text{LF}}(1 - \varepsilon_2^{\text{LF}})(1 - f_1 - f_2)), \\
 N_{\text{subtag}} &= N_T((1 - \varepsilon_1^c)\varepsilon_2^{\text{LF}}f_1 + (1 - \varepsilon_1^{\text{LF}})\varepsilon_2^c f_2 + (1 - \varepsilon_1^{\text{LF}})\varepsilon_2^{\text{LF}}(1 - f_1 - f_2)), \\
 N_{\text{ditag}} &= N_T(\varepsilon_1^c\varepsilon_2^{\text{LF}}f_1 + \varepsilon_1^{\text{LF}}\varepsilon_2^c f_2 + \varepsilon_1^{\text{LF}}\varepsilon_2^{\text{LF}}(1 - f_1 - f_2)),
 \end{aligned} \tag{8.4}$$

with N_T the total number of events, $f_{1,2}$ the fraction of leading (subscript 1) and subleading (subscript 2) c jets, and $\varepsilon_{1,2}^{c,L}$ the tagging efficiencies for leading and subleading jets for c (superscript c) and light-flavour (superscript LF) quarks. The indentation highlights the different components, namely the probability for a jet pair to be composed of (c, light), (light, c), and (light, light) jet flavours as (leading, subleading) jets from the W boson decay. The (c, c) pair is not present since it is unphysical. Instead of measuring the efficiency $\varepsilon_{1,2}^{c,\text{LF}}$, the data-to-simulation scale factor is measured. Therefore, $\varepsilon_{1,2}^{c,\text{LF}}$ is replaced with $SF_{c,l}\varepsilon_{1,2}^{c,\text{LF}}(\text{MC})$ in eq. (8.4). In the latter expression $\varepsilon_{1,2}^{c,\text{LF}}(\text{MC})$ is the efficiency obtained from simulation and SF_c (SF_l) is the scale factor for c (light-flavour) jets. To reduce the number of unknown parameters, the value for SF_l is taken to be the measured value using the negative-tag method presented in section 8.2.

A maximum likelihood fit is performed on the binned λ_M distributions using the signal and background distributions (templates) obtained from the simulated events. The measurement is performed inclusively, since the selected number of events is not sufficient for a precise measurement in bins of jet p_T . Systematic uncertainties are included in the fit as nuisance parameters that are profiled. Each nuisance parameter is floating with a Gaussian constraint around the central value with a standard deviation proportional to the systematic uncertainty. It is possible to group the systematic uncertainties in two sets based on their effect on the templates. The following systematic effects only affect the normalization of the templates:

- **Scale factor for light-flavour jets:** the data-to-simulation scale factor for the misidentification of light-flavour jets is varied within its uncertainty. This is the dominant uncertainty in the scale factor measurement for c jets.
- **Cross sections of the simulated processes:** an uncertainty of 16, 50 and 20% is assumed in the cross section of the $t\bar{t}$ [60], single top quark [61, 62], and the combined W + jets and Z + jets [63, 64] processes, respectively. The limited number of simulated W + jets and Z + jets events requires an additional uncertainty in their yield, fully uncorrelated among the event categories.
- **Integrated luminosity and pileup:** the uncertainty in the integrated luminosity measurement of 6.2% [65] and on the number of additional pileup interactions are considered as yield uncertainties. These uncertainties as well as the uncertainty in the cross sections for the simulated processes are the same for each working point probed, and are applied to the related samples in a correlated way between categories.
- **Scale factors for b tagging:** since b tagging is applied for the event selection, the uncertainty in the b tagging data-to-simulation scale factor is considered as a systematic effect. The simulation has been processed with b jet scale factors shifted by their uncertainties. In case the b-tagged jets in the event selection are actually originating from c quarks, the scale factor is varied by a conservative 50%. The size of the combined effect due to the uncertainty of correctly tagging b jets and wrongly tagging c or light-flavour jets for the event selection depends on the samples, the categories, and the working points considered. However, the effect of these uncertainties has limited impact on the final result, being fully correlated across samples and categories.

A potential source of systematic uncertainty for the normalization of the templates may arise from the uncertainty in the cross section of $t\bar{t}$ events produced in association with heavy-flavour jets, which is constrained to within 35% [66]. Such an uncertainty is covered by the systematic variation on the inclusive $t\bar{t}$ production cross section and the uncertainty in the b tagging scale factor for the event selection, which is taken to be 50% for jets arising from c quarks.

In addition to a possible impact on the normalization of the templates, the following systematic effects affect the shape of the templates:

- **Jet energy scale:** new templates are constructed by varying the jet energy scale by ± 1 standard deviation from its nominal value. The uncertainty is propagated to the fraction of c jets in leading and subleading jets.
- **Jet energy resolution:** for the nominal efficiency measurement, the jet energies in the simulation are smeared according to a Gaussian function to accommodate the slightly worse resolution in data. The uncertainty in the jet energy resolution is propagated to the data-to-simulation scale factor measurement by varying the standard deviation of the Gaussian function by its uncertainty.
- **Factorization and renormalization scales:** the factorization and renormalization scales used at matrix element and parton shower levels affect the number of additional jets from

initial-state radiation (ISR) and final-state radiation (FSR), and may impact the fraction of leading and subleading c jets. The factorization and renormalization scales used at matrix element level are varied independently and simultaneously by factors of 2 and 0.5 with respect to their default values. Also the scale for ISR (FSR) in the parton shower is varied by a factor of 2 ($\sqrt{2}$) and 0.5 ($\sqrt{0.5}$) [67]. A different way to assess the uncertainty in the modelling of ISR and FSR is to vary the “hdamp” parameter in POWHEG. This parameter is used to limit the resummation of higher-order effects using a reference energy scale. The real emissions are reweighted by a step-function $h^2/(p_T^2 + h^2)$, where h is the hdamp parameter and p_T is the transverse momentum of the top quark in the $t\bar{t}$ rest frame. The hdamp parameter is varied between $0.5m_t$ and $2m_t$ to evaluate the uncertainty related to additional jets from ISR and FSR. The variations upwards and downwards having the largest impact on the templates, are used to repeat the data-to-simulation scale factor measurements independently for ISR and FSR. The deviation from the nominal scale factor value is taken as the uncertainty. Together with the uncertainties in the jet energy scale and resolution, the effect is 1% for both the leading and subleading jets.

- **Top quark mass:** the uncertainty in the top quark mass may affect the measurement of the data-to-simulation scale factor. The size of the uncertainty is estimated using alternative simulated samples with a mass that is shifted within the uncertainty in the measured value [35].
- **Parton distribution functions:** the uncertainties in the parton densities is evaluated in the same way as in section 8.3.1 and found to be negligible.
- **Bin-by-bin statistical uncertainty:** statistical uncertainties related to the single bin population in the templates have been addressed through bin-by-bin variations, i.e. fully uncorrelated shape uncertainties in which only one bin of the template is shifted according to its uncertainty. In order to reduce the computational time required by the fit to converge, this uncertainty is only considered for template bins having an uncertainty larger than 5% of the yield observed in the same bin, thus rejecting most of the low-yield backgrounds.

Table 4 summarizes the values of the measured data-to-simulation scale factors for all tagging requirements. The uncertainty in the scale factors in the table are a combination of the statistical and systematic uncertainties obtained from the fit.

8.3.3 Combination of the measured c tagging efficiencies

In the previous sections two methods have been described to measure the c tagging efficiency. In this section, a combination of the measurements is performed. The combination is a weighted average taking into account the full covariance matrix for the uncertainties using the best linear unbiased estimator (BLUE) method [68]. This technique was also used for combining the SF_b measurements in Run 1 [1], but here it has been extended to fit all the jet p_T bins simultaneously [69], treating more correctly the bin-to-bin correlations for the systematic uncertainties. Systematic uncertainties shared by the two measurements are treated as correlated in the combination. The averaging has been done using the finer jet p_T binning of the $W + c$ topology. The relative contribution of the single-lepton $t\bar{t}$ measurement in each jet p_T bin is taken into account by assigning weights to this

Table 4. Measured data-to-simulation scale factors for c jets for various algorithms and working points in single-lepton $t\bar{t}$ events. The uncertainty in the scale factor includes both the statistical and systematic uncertainties, while the last column shows the statistical uncertainty alone.

Working point	SF_c	Statistical uncertainty
CSVv2 L	0.89 ± 0.05	± 0.02
CSVv2 M	0.87 ± 0.08	$+0.04$ -0.03
CSVv2 T	$1.15^{+0.35}_{-0.33}$	$+0.15$ -0.14
c tagger L	1.05 ± 0.03	± 0.01
c tagger M	0.93 ± 0.05	± 0.02
c tagger T	$0.88^{+0.05}_{-0.04}$	± 0.02
DeepCSV L	$0.98^{+0.05}_{-0.04}$	± 0.02
DeepCSV M	0.96 ± 0.09	± 0.04
DeepCSV T	$0.87^{+0.37}_{-0.38}$	± 0.15
cMVAv2 L	0.87 ± 0.04	± 0.02
cMVAv2 M	0.76 ± 0.09	± 0.03
cMVAv2 T	$0.86^{+0.31}_{-0.29}$	± 0.13

measurement corresponding to the fraction of jets from top quark decays expected in each of the jet p_T bins. These fractions are obtained from simulation. The result of the combination is shown in figure 38 for the loose and medium working points of the c tagger. In each panel the combined value is represented as the hatched area. The individual measurements are represented in the upper panel as markers with different colours. The inner thicker error bar represents the statistical uncertainty of the measurement. The lower panel includes a fit of the data-to-simulation scale factor dependence on the jet p_T , which is parameterized by a linear function.

For the c tagging algorithm, the relative precision on the data-to-simulation scale factors for c jets is 2% (4%) for the loose (tight) working point. For the b tagging algorithms, the relative precision is 3–5% for the loose working points, and 10–38% for the tight working points. Overall, the statistical uncertainty is 40–90% of the total uncertainty.

8.4 The b jet identification efficiency

The data-to-simulation scale factor for b jets, SF_b , is obtained using a sample of jets enriched in b quark content, e.g. by selecting multijet events with at least one jet containing a muon, or $t\bar{t}$ events that contain two b jets from the decay of the two top quarks. To enhance the purity when selecting $t\bar{t}$ events, the decay of one or both of the W bosons into leptons is required. This section describes the various SF_b measurements and their combination.

8.4.1 Measurements relying on a muon-enriched topology

Events are selected using various online criteria requiring the presence of two jets with at least one of those jets containing a muon. The different prescales of the various triggers are taken into account

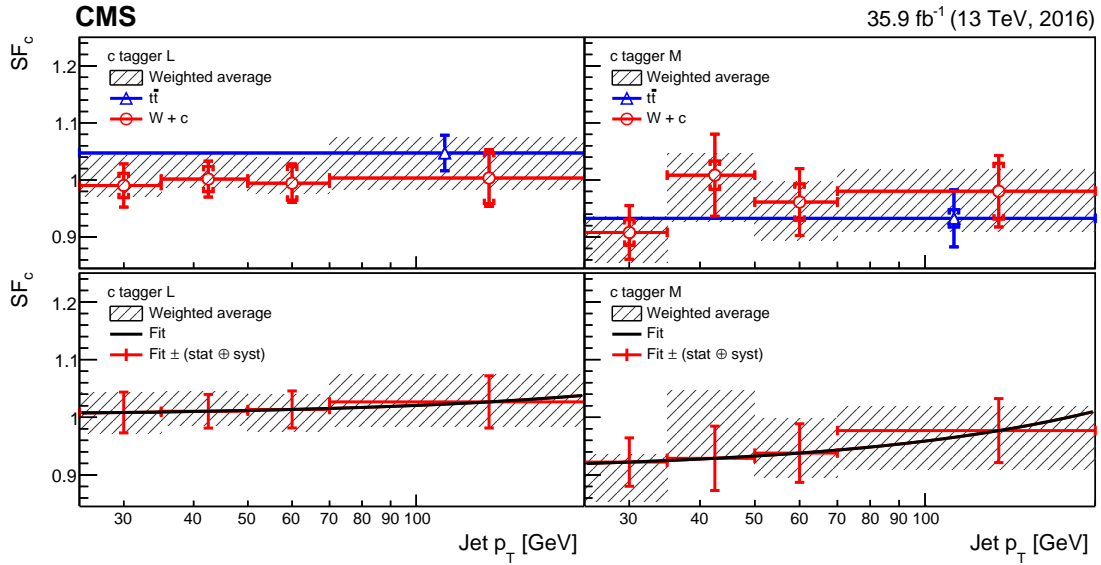


Figure 38. Data-to-simulation scale factors for c jets for the loose (left) and medium (right) working points of the c tagger. The upper panels show the scale factors for c jets as a function of the jet p_T obtained with the two methods described in the text. The inner error bars represent the statistical uncertainty and the outer error bars the combined statistical and systematic uncertainty. The combined scale factor values with their overall uncertainty are displayed as a hatched area. The lower panels show the same combined scale factor values with superimposed the result of a fit function represented by the solid curve. The combined statistical and systematic uncertainty is centred around the fit result, represented by the points with error bars. The last bin includes the overflow entries.

by reweighting the selected events according to the value of the prescale. Offline, the sample is enriched with events containing b jets by requiring that at least one jet has a muon with $p_T > 5$ GeV and with $\Delta R < 0.4$ from the jet axis, referred to as the “muon jet”. The selected simulated events are reweighted to match the pileup profile observed in the data. The muon jet sample is used for three measurements, using the PtRel, LifeTime (LT), and System-8 methods [1]. As discussed in section 8.3.1, the muon enrichment may introduce a bias for the efficiency measurement of taggers that rely on soft muon information, such as the cMVA2, CvsB, and CvsL discriminators. Therefore, the methods described in this section are only used to derive data-to-simulation scale factors for the other taggers.

PtRel method. The p_T of the muon relative to the jet axis, p_T^{rel} , is a variable that is able to discriminate between b jets and non-b jets. On average, this variable is expected to be larger for muons coming from the decay of b hadrons because of the large mass of these hadrons. Therefore, this variable can be used to measure the efficiency for tagging b jets with algorithms relying on track and secondary vertex variables. The fraction of b jets in data can be estimated by fitting the observed p_T^{rel} distribution to the sum of the templates for the different jet flavours. The p_T^{rel} templates for the different flavours are obtained from the simulated muon-enriched multijet samples. To reduce the fraction of non-b jets, the presence of a second jet is required away from the first one (“away jet”) with $\Delta R > 1.5$ and exceeding a JBP discriminator value corresponding to the medium

working point.

For light-flavour jets, a difference is observed between data and simulation in the distribution of the number of charged particles per jet. Therefore, the jets are reweighted with the ratio of the distribution of the observed number of charged particles in inclusive multijet data to that expected in simulation (without the muon enrichment). The template for b jets is corrected by applying a factor corresponding to the ratio of the p_T^{rel} distribution in data to that in simulation for b jets passing the tight JP tagging requirement. The fraction of non-b jets in the JP-tagged samples is found to be of a few per cent and is subtracted. After this correction, we apply the algorithm working point for which the efficiency is to be measured. The observed p_T^{rel} distribution is then fitted with the templates for the jet flavours to obtain the number of b jets passing (N_b^{tagged}) or failing (N_b^{vetoed}) the requirement. The b tagging efficiency in data is obtained as

$$\varepsilon_b = \frac{N_b^{\text{tagged}}}{N_b^{\text{vetoed}} + N_b^{\text{tagged}}} \quad (8.5)$$

Examples of the fitted p_T^{rel} distributions using jets passing and failing the medium working point of the CSVv2 algorithm and with $50 < p_T < 70$ GeV, are shown in figure 39.

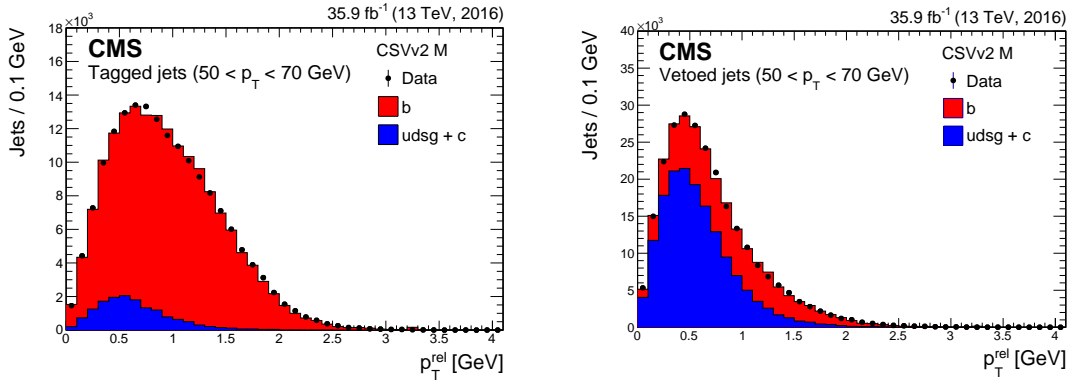


Figure 39. Fitted p_T^{rel} distribution for muon jets passing (left) and failing (right) the medium working point of the CSVv2 algorithm. The distribution is shown for jets with $50 < p_T < 70$ GeV. The simulation is normalized to the observed number of events.

LifeTime method. The muon jet sample used in the LT method is the same as for the PtRel method, except that the away jet is not required to be tagged. Also the strategy is similar to the PtRel method, but the fit is performed on the JP discriminator distribution. The track probabilities are calibrated using templates with negative impact parameter tracks in multijet events. The calibration is done separately on data and simulation to take into account a potential difference in the impact parameter resolution between both samples. The fraction of b jets is fitted including all shape systematic uncertainties via a correlation matrix. The tagging efficiency is then obtained as the ratio of the number of b jets obtained from the fit after and before applying the algorithm working point

$$\varepsilon_b = C_b \frac{N_b^{\text{tagged}}}{N_b}. \quad (8.6)$$

The factor C_b is a correction factor, which takes into account the fraction of jets for which the JP discriminant can be computed. It is defined as

$$C_b = \frac{n_{b,MC}^{\text{tag}} N_{b,MC}}{N_{b,MC}^{\text{tag}} n_{b,MC}}, \quad (8.7)$$

with $N_{b,MC}$ the number of b jets with JP information, $n_{b,MC}$ the number of all selected b jets, $N_{b,MC}^{\text{tag}}$ the number of b jets with JP information passing the algorithm working point for which the efficiency is being measured and $n_{b,MC}^{\text{tag}}$ the number of b jets passing the tagging requirement for which the data-to-simulation scale factor is being measured. The fraction of jets without a JP discriminant value is maximum at very low jet p_T (8%) and drops below 1% using jets with $p_T > 120$ GeV.

As an illustration, figure 40 shows the fitted JP distributions using jets with $200 < p_T < 300$ GeV before and after applying the medium working point of the CSVv2 algorithm.

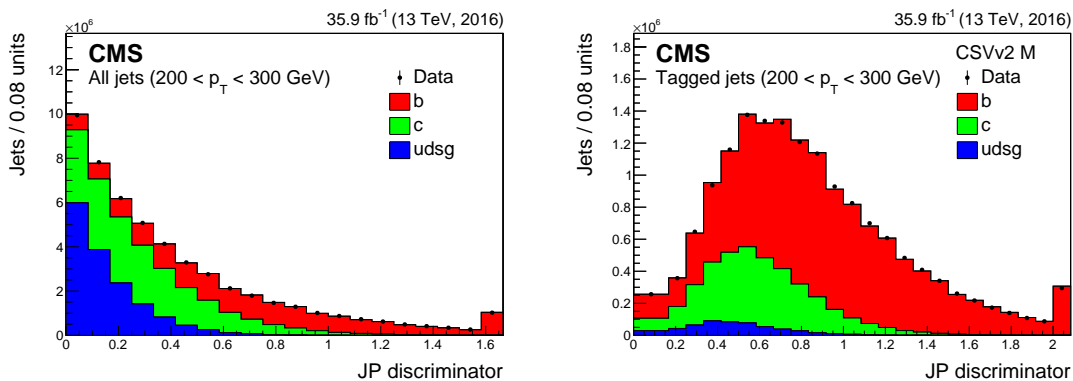


Figure 40. Fitted JP distribution for muon jets (left) and for the subsample of those jets passing the medium working point of the CSVv2 algorithm (right). The distribution is shown for jets with $200 < p_T < 300$ GeV. The simulation is normalized to the integrated luminosity for the data set. The last bin includes the overflow entries.

System-8 method. In contrast with the two methods described before, the System-8 method [70] does not rely on simulated templates of a discriminating variable. Instead, it is based on the usage of two weakly correlated b taggers and two samples containing muons within jets. The first b tagging requirement corresponds to the working point of the algorithm for which the efficiency is to be measured (tag); the second b tagging requirement is $p_T^{\text{rel}} > 0.8$ GeV. This requirement is weakly correlated with the working points for algorithms that do not rely on soft-muon information. The first sample consists of all events with a muon jet (sample n); the second sample is a subset where an away jet satisfies the medium working point of the JBP algorithm (sample p). For each combination of a sample with either zero, one of the two, or both tagging requirements applied, the observed number of jets can be written as the sum of the two (b and non-b) flavour contributions. The efficiency of the algorithm working point under study and the efficiency of the $p_T^{\text{rel}} > 0.8$ GeV requirement are assumed to be factorizable modulo a correlation factor that is determined from simulated events. In total eight equations can be written, with eight unknown parameters, namely

the b tagging efficiencies of the two requirements and the number of b and non-b jets in the two samples:

$$\begin{aligned}
n &= n_b + n_{c,\text{udsg}} \\
p &= p_b + p_{c,\text{udsg}} \\
n^{\text{tag}} &= \varepsilon_b^{\text{tag}} n_b + \varepsilon_{c,\text{udsg}}^{\text{tag}} n_{c,\text{udsg}} \\
p^{\text{tag}} &= \beta \varepsilon_b^{\text{tag}} p_b + \alpha \varepsilon_{c,\text{udsg}}^{\text{tag}} p_{c,\text{udsg}} \\
n^{p_T^{\text{rel}}} &= \varepsilon_b^{p_T^{\text{rel}}} n_b + \varepsilon_{c,\text{udsg}}^{p_T^{\text{rel}}} n_{c,\text{udsg}} \\
p^{p_T^{\text{rel}}} &= \delta \varepsilon_b^{p_T^{\text{rel}}} p_b + \gamma \varepsilon_{c,\text{udsg}}^{p_T^{\text{rel}}} p_{c,\text{udsg}} \\
n^{\text{tag}, p_T^{\text{rel}}} &= \kappa_b \varepsilon_b^{\text{tag}} \varepsilon_b^{p_T^{\text{rel}}} n_b + \kappa_{c,\text{udsg}} \varepsilon_{c,\text{udsg}}^{\text{tag}} \varepsilon_{c,\text{udsg}}^{p_T^{\text{rel}}} n_{c,\text{udsg}} \\
p^{\text{tag}, p_T^{\text{rel}}} &= \kappa_b \beta \delta \varepsilon_b^{\text{tag}} \varepsilon_b^{p_T^{\text{rel}}} p_b + \kappa_{c,\text{udsg}} \alpha \gamma \varepsilon_{c,\text{udsg}}^{\text{tag}} \varepsilon_{c,\text{udsg}}^{p_T^{\text{rel}}} p_{c,\text{udsg}}
\end{aligned} \tag{8.8}$$

where $\alpha, \beta, \gamma, \delta, \kappa_b$ and $\kappa_{c,\text{udsg}}$ are the correlation factors. This system of eight equations is solved numerically. The solution has to pass some physical constraints, e.g. the b tagging efficiency is required to be larger than the non-b tagging efficiency, and the fraction of b jets in the initial sample needs to be smaller than the fraction of non-b jets in the sample.

Systematic uncertainties. Various systematic uncertainties are taken into account that may affect the SF_b measurement. For the three measurements based on the muon-enriched jet samples, the following systematic effects are considered:

- **Gluon splitting:** a variation in the fraction of b and c jets from gluon splitting may have an important impact on the b tagging efficiency since heavy-flavour jets from gluon splitting have a higher track multiplicity. The fraction of events with b jets from gluon splitting is varied by $\pm 25\%$ [71] to estimate the potential effect. For the tight working point of the taggers, this is one of the dominating uncertainties for the System-8 method. In the case of the LT method, the fraction of events with c jets from gluon splitting is also varied by this amount. For the System-8 and PtRel methods, the fraction of c jets in the non-b template is varied when evaluating other systematic effects.
- **b quark fragmentation:** the modelling of the b quark fragmentation may affect the p_T distribution of the b jets in the sample. The size of this effect is estimated by varying the p_T of the primary b hadron in the muon jet by $\pm 5\%$, which is the observed variation between the distribution of the energy fraction of the b jet carried out by the b hadron in PYTHIA and HERWIG. This variation between PYTHIA and HERWIG is typically larger than the variation observed between PYTHIA and data.
- **Branching fraction of $D \rightarrow \mu X$ and fragmentation of $c \rightarrow D$:** these systematic effects are evaluated in the same way as described in section 8.3.1, with the exception that the PDG 2008 values [72] are used for the fragmentation rates. While the nominal values and uncertainties vary slightly in the PDG 2008 and 2016 references, they are fully consistent.
- **K_S^0 and Λ decays (V^0):** this systematic effect is evaluated in the same way as described in section 8.2.

- **Muon p_T and ΔR :** the fraction of muons that reach the muon chambers depends on the muon p_T . The threshold on the muon p_T is varied between 5 and 8 GeV to assess the size of the systematic uncertainty. In addition, the dependence of the measured data-to-simulation scale factor on the ΔR requirement is tested by tightening the requirement to $\Delta R < 0.3$. These systematic effects are among the dominant uncertainties for the System-8 method.
- **Away jet tag:** the dependence of the b tagging efficiency on the away jet tagging requirement is studied by repeating the data-to-simulation scale factor measurement after changing the tagging requirement from the medium to the loose or tight working points. The largest deviation from the scale factor value obtained using the default away-jet tagging requirement is taken as the size of the systematic effect. This systematic effect is typically the dominant uncertainty for the PtRel method, and it is one of the dominating uncertainties for the System-8 method.
- **JP correction factor C_b :** for the LT method, the fit is performed using only jets that have a JP discriminant value. The applicability of the measured data-to-simulation scale factor to all jets is ensured through the correction factor C_b . The systematic uncertainty associated with C_b is defined as $(\delta C_b)^{SF} = \pm \frac{1-C_b}{2}$. This systematic effect induces an uncertainty in the measured scale factor of a few per cent using jets in the lowest p_T bin and is negligible at high jet p_T .
- **JP calibration:** the LT method relies on the calibrated JP discriminator distribution. For the nominal data-to-simulation scale factor value, the calibration of the impact parameter resolution derived from data is applied to the data, and the calibration derived from simulated events is applied to the simulation. However, a bias could be induced in the measurement if there are significant differences between data and simulation in the distribution of track impact parameter resolutions used. Therefore, an additional uncertainty is taken into account by applying the calibration derived on simulation, also on the data. The difference in the measured scale factor is included as additional systematic uncertainty. The inverse approach was also tested, i.e. applying the JP calibration derived on data to both data and simulation. In that case, the shape changed in a similar way, yielding consistent results for the size of the systematic effect. The systematic effect due to the JP calibration is the dominating uncertainty for the LT method.
- **JP bin-to-bin correlation:** for the LT method the systematic uncertainties are taken into account via a correlation matrix. This requires an assumption on the bin-to-bin correlation factors. To assess the impact of an uncertainty in these correlation factors, the data-to-simulation scale factors were remeasured when varying the bin-to-bin factors within $\pm 25\%$. The size of the systematic effect is given by the maximal difference with the nominal SF value.
- **Muon p_T^{rel} requirement:** for the System-8 method, the default requirement of $p_T^{\text{rel}} > 0.8$ GeV on the muon is set to a value of 0.5 or 1.2 GeV. The largest deviation from the measured nominal data-to-simulation scale factor is taken as a systematic uncertainty.
- **udsg-to-c jet ratio:** in the PtRel method the c and light-flavour jets are combined in a single template. The uncertainty in the ratio of light-flavour to c jets is changed by varying it by

$\pm 30\%$ to cover the observed discrepancy in the fraction of light-flavour jets in inclusive and muon-enriched multijet events.

- **Non-b jet template correction:** for the PtRel method, the non-b jet templates are corrected to accommodate the difference in the number of selected tracks for data and simulation. The difference between the measured data-to-simulation scale factors when applying these corrections or not is considered as the size of the systematic effect.
- **b jet template correction:** similarly as in the case for the non-b jet template, also for the b jet template the difference between the nominal data-to-simulation scale factor value and that measured without template correction is taken as an additional uncertainty for the PtRel method.
- **Jet energy scale:** the impact of the uncertainty in the jet energy corrections is evaluated as described in section 8.3.1.
- **Pileup:** the effect of the uncertainty in the number of additional pileup interactions is evaluated as described in section 8.2.

For the System-8 and PtRel methods the largest deviation from the nominal data-to-simulation scale factor value is taken as the size of the systematic effects. For the LT method, the shape variations are taken into account in the template fit. Table 5 summarizes the list of systematic effects taken into account for each of the three methods to measure SF_b .

Results. The measurements of SF_b obtained on muon-enriched multijet events are combined using the BLUE method as described in section 8.3.3. The weighted average is calculated taking into account the correlations between the three methods. The combination is performed as a function of the jet p_T , ranging from 20 to 1000 GeV. Jets with a higher p_T are included in the last bin. The PtRel and LT methods provide measurements on the full jet- p_T range from 20 to 1000 GeV, while the sensitivity of the System-8 method is limited to the lower part of the spectrum, $20 < p_T < 140$ GeV.

The PtRel, System-8, and LT methods are applied on the same events. However, the requirement on the second jet is different for each method. The fraction of events with b quarks that is in common between each pair of methods is obtained from simulated events, and is used to estimate the statistical correlation in the combination of the results. Systematic uncertainties that are in common for two or three methods are treated as correlated. Some of the systematic effects that induce a large uncertainty are however related to a specific method and are treated as uncorrelated.

The data-to-simulation scale factor measurements obtained with the PtRel, System-8, and LT methods for the loose (tight) working point of the CSVv2 (DeepCSV) algorithm as a function of the jet p_T are compared in the upper panel of figure 41. For each point, the thick error bar corresponds to the statistical error and the thin one to the overall statistical and systematic uncertainty. The combined SF_b value is displayed as a hatched area in both panels with its overall uncertainty. In the lower panel the result of a fit function is superimposed. The function used in the fit is $SF_b(p_T) = \alpha \frac{1+\beta p_T}{1+\gamma p_T}$, where α , β , γ are free parameters. The combined statistical and systematic uncertainty is centred around the fit result. The measured data-to-simulation scale factors for the loose working point of the CSVv2 algorithm range from 0.96 to 1.03, and from 0.9 to 1.0 for the

Table 5. Summary of the potential sources of systematic effects taken into account for the muon-enriched SF_b measurements. The symbol “x” means that the uncertainty is considered, “—” means that it is negligible, and “n/a” that it is not applicable. The systematic effects are separated by horizontal lines according to the type of uncertainty. The first set indicates the modelling uncertainty of heavy-flavour jets in the simulation, the second set are uncertainties related to the selection requirements or to the method that is applied, and the third set covers any other type of uncertainty.

Systematic effect	PtRel	LT	System-8
Gluon splitting to $b\bar{b}$	x	x	x
b quark fragmentation	x	x	x
Branching fraction of $D \rightarrow \mu X$	n/a	x	n/a
c \rightarrow D fragmentation rate	n/a	x	n/a
K_S^0 (Λ) production fraction	n/a	x	n/a
Muon p_T and ΔR	x	—	x
Away jet tag	x	n/a	x
Fraction of jets with JP	n/a	x	n/a
JP calibration	n/a	x	n/a
JP bin-by-bin correlation	n/a	x	n/a
p_T^{rel} requirement	n/a	n/a	x
udsg-to-c jet ratio	x	n/a	n/a
Non-b template correction	x	n/a	n/a
b template correction	x	n/a	n/a
JES	x	x	x
Pileup	x	—	x

tight working point of the DeepCSV algorithm. The relative precision on the scale factors is 1–1.5% using jets with $70 < p_T < 100$ GeV and rises to 3–5% at the highest considered jet p_T .

8.4.2 Measurements relying on the dilepton $t\bar{t}$ topology

The b jet identification efficiency is also measured using dilepton $t\bar{t}$ events, where two b jets are expected from the decay of the top quark pair. Events are selected with exactly two isolated leptons (muons or electrons) fulfilling tight identification criteria [9, 10] with opposite charge and p_T above 25 GeV. Events are selected if there are at least two jets with $p_T > 30$ GeV. All aforementioned objects are required to be in the tracker acceptance.

Kinematic selection method For the kinematic selection (Kin) method, events are further selected by requiring the presence of exactly one isolated electron and one isolated muon with opposite sign and with a dilepton invariant mass $M_{\mu e} > 90$ GeV. These requirements significantly reduce the background from Z + jets events. In addition, p_T^{miss} is required to be larger than 40 GeV. While two jets are expected in dilepton $t\bar{t}$ events, it is possible that more than two jets (or the wrong two jets) are selected because of, e.g. ISR and FSR. A discriminator is constructed that is able to separate b

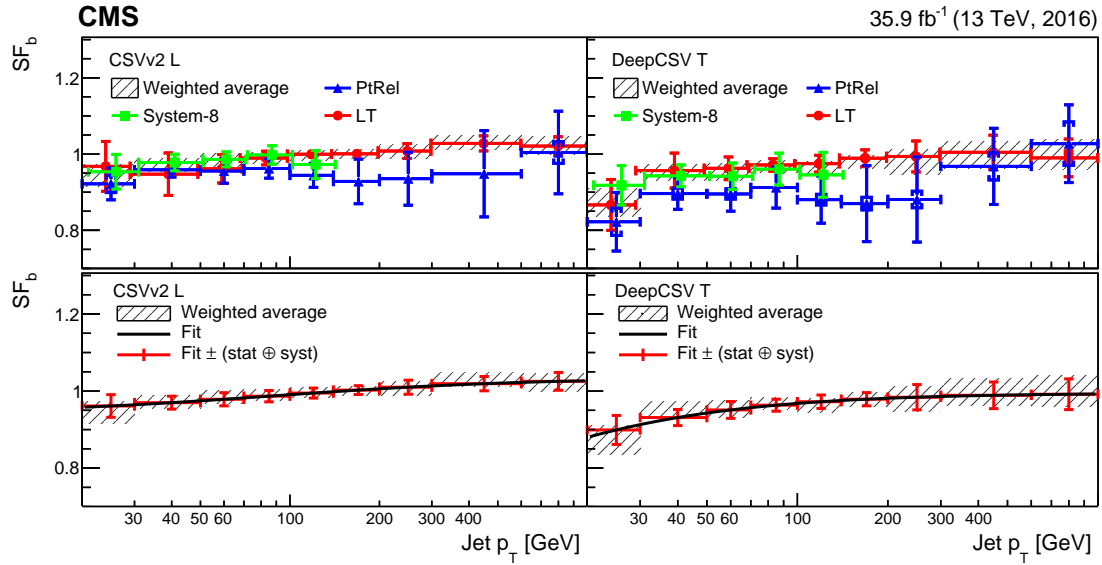


Figure 41. Data-to-simulation scale factors for b jets as a function of the jet p_T for the loose CSVv2 (left) and the tight DeepCSV (right) algorithms working points. The upper panels show the scale factors for tagging b as a function of the jet p_T measured with three methods in muon jet events. The inner error bars represent the statistical uncertainty and the outer error bars the combined statistical and systematic uncertainty. The combined scale factors with their overall uncertainty are displayed as a hatched area. The lower panels show the same combined scale factors with the result of a fit function (solid curve) superimposed. The combined scale factors with the overall uncertainty are centred around the fit result. To increase the visibility of the individual measurements, the scale factors obtained with various methods are slightly displaced with respect to the bin centre for which the measurement was performed. The last bin includes the overflow entries.

jets and non-b jets. To avoid biasing the measurement of the b jet efficiency, only variables related to the kinematics of the event are used. For each jet j in the event, the angular distance $\Delta R(\ell, j)$ is calculated between the jet and the two leptons. The following variables are calculated for each jet:

- $M(\ell, j)$: invariant mass of the (ℓ, j) pair with the smallest and the largest $\Delta R(\ell, j)$.
- $\Delta\eta(\ell, j)$ and $\Delta\phi(\ell, j)$: difference in pseudorapidity and in azimuthal angle between the lepton and jet for the (ℓ, j) pair with the smallest and the largest $\Delta R(\ell, j)$.
- $\Delta\eta(\ell\ell, \ell j)$ and $\Delta\phi(\ell\ell, \ell j)$: difference in pseudorapidity and azimuthal angle between the dilepton system and an (ℓ, j) pair for the (ℓ, j) pair with the smallest and the largest $\Delta R(\ell, j)$.
- $\Delta\eta(\ell\ell, j)$ and $\Delta\phi(\ell\ell, j)$: difference in pseudorapidity and azimuthal angle between the dilepton system and the jet.

The variables in the first two items are sensitive to (ℓ, j) pairs originating from the same top quark decay, while the variables in the two latter items use the correlation between the spin of the top quark and the top antiquark that is present in $t\bar{t}$ events [73]. The 12 variables listed above are combined with a BDT using the TMVA package [52]. Prior to the training on simulated $t\bar{t}$ events, jets in the event are classified according to their rank when ordered according to decreasing p_T . In

particular, the training is performed in three different categories for the leading, subleading, and other jets. This classification helps to better use the correlations between the variables for the signal and background, in particular for events with a high jet multiplicity. The parameters of the BDT, such as the number of trees, the depth and the shrinkage factor of the gradient learning algorithm, were roughly optimized to obtain a smooth background shape at large discriminator values without reducing the discriminating power.

A binned likelihood fit is performed on the kinematic discriminator of jets passing and failing the b tagging requirement, inclusively for all jets together. For each flavour f , the total number of jets N_f can be expressed as a function of the tagging efficiency in simulation, $\varepsilon_f^{\text{MC}}$, and the data-to-simulation scale factor SF_f :

$$\begin{cases} N_f^{\text{tagged}} = SF_f \varepsilon_f^{\text{MC}} N_f = SF_f N_f^{\text{MC, tagged}} \\ N_f^{\text{vetoed}} = (1 - SF_f \varepsilon_f^{\text{MC}}) N_f = \frac{(1 - SF_f \varepsilon_f^{\text{MC}})}{SF_f \varepsilon_f^{\text{MC}}} N_f^{\text{MC, tagged}}, \end{cases} \quad (8.9)$$

where $N_f^{\text{MC, tagged}}$ is the expected number of jets of flavour f passing the requirement determined from simulation. The templates for light-flavour and c jets are similar. The measured value of the mistag data-to-simulation scale factor, as presented in section 8.2, is used to correct for the different misidentification probability in the data and simulation. It is not necessary to use a dedicated scale factor for c jets since the fraction of c jets is expected to be less than 1% and fully covered by the systematic uncertainties. The scale factor for b jets is the only free parameter to be determined from the fit. The fit is performed simultaneously in bins of jet multiplicity, with up to four jets. For convenience, the discriminator values are transformed from $[-1, 1]$ to $[-1, 1] + 2(N_{\text{jets}} - 2)$.

Several sources of systematic uncertainties are considered:

- **Factorization and renormalization scales:** the uncertainty in the factorization and renormalization scales is evaluated in the same way as in section 8.3.2, except that the scale for FSR in the parton shower is varied by a factor of two up and down, and not by a factor of $\sqrt{2}$. In addition, both the variation of the scale in the parton shower as well as the variation of the hdamp parameter in POWHEG are taken into account to assess the impact of ISR and FSR instead of using the largest variation. Although these systematic uncertainties are correlated, they are conservatively treated as uncorrelated.
- **Cross section of background processes:** the cross section of each non- $t\bar{t}$ background process is varied by 30% to assess the systematic effect due to the uncertainty in the background contributions.
- **Top quark mass:** the uncertainty in the top quark mass is evaluated in the same way as in section 8.3.2.
- **Scale factor for non-b jets:** the data-to-simulation scale factor for light-flavour jets, SF_l , is applied to correct the expected fraction of light-flavour and c jets. To evaluate the uncertainty related to SF_l , the value is changed to $SF_l \pm 1\sigma$, where σ represents the uncertainty in SF_l . The effect of this variation on the measured value of SF_b is taken as the size of the uncertainty due to SF_l .

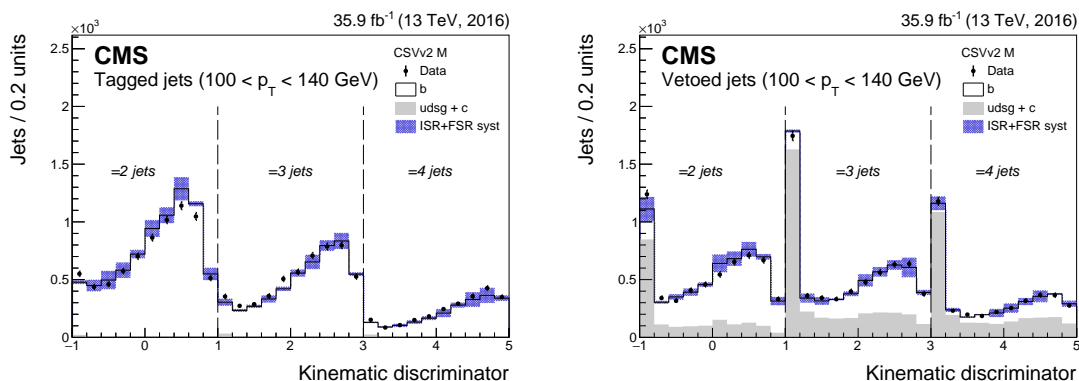


Figure 42. Fitted distribution of the kinematic discriminator for jets with $100 < p_T < 140$ GeV passing (left) and failing (right) the medium working point of the CSVv2 algorithm. The discriminator distribution is shown in bins of jet multiplicity with the discriminator output transformed from $[-1, 1]$ to $[-1, 1] + 2(N_{\text{jets}} - 2)$. The dominant systematic uncertainty due to initial- and final-state radiation is represented by the band.

- **Jet energy scale:** the uncertainty in the jet energy scale is assessed in the same way as in section 8.3.2. The variation in jet momentum is simultaneously propagated to the p_T^{miss} value for a consistent approach.
- **Jet energy resolution:** the uncertainty in the jet energy resolution is assessed in the same way as in section 8.3.2.
- **Selection efficiency:** the uncertainty in the lepton identification and isolation efficiency is propagated to the measurement by reweighting the simulation using a lepton efficiency scale factor that is shifted up or down by one standard deviation with respect to the nominal value.
- **Pileup:** the uncertainty in the pileup modelling is assessed as described in section 8.2.

The systematic effect induced by the uncertainty in the parton distribution functions is negligible.

To determine the dependence of the data-to-simulation scale factor on the jet p_T , independent fits are performed in mutually exclusive bins of jet p_T . An example of the fitted distribution in the jet p_T range between 100 and 140 GeV using jets passing and failing the medium working point of the CSVv2 algorithm is shown in left and right panels of figure 42, respectively. Discrepancies between the data and simulation are covered by the combined statistical and systematic uncertainty. The scale factor as a function of the jet p_T is shown in figure 43 for the three working points of the CSVv2 and DeepCSV algorithms.

Two-tag counting method. The two-tag counting (TagCount) method is mainly used as a cross check of the Kin method. While the Kin method is able to determine data-to-simulation scale factors at higher jet p_T , the TagCount method is a simple and robust approach to assess the size of the scale factors. The dilepton $\bar{t}t$ events are selected by requiring the dilepton invariant mass $M_{\ell\ell} > 12$ GeV. If the two leptons have the same flavour, the contribution from Z + jets events is reduced by applying a veto around the Z boson mass, $|M_{\ell\ell} - M_Z| > 10$ GeV, and requiring $p_T^{\text{miss}} > 50$ GeV. In addition, each event is required to have exactly two jets.

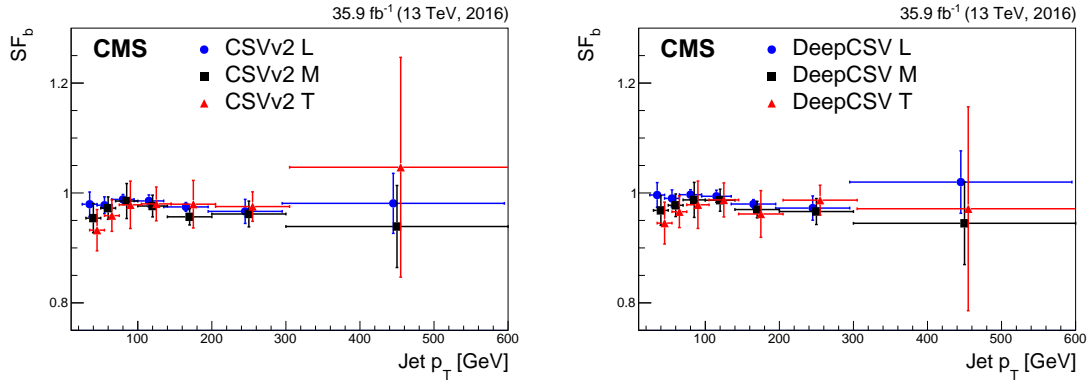


Figure 43. Data-to-simulation scale factors for b jets obtained with the Kin method as a function of the jet p_T for the three CSVv2 (left) and the three DeepCSV (right) working points. The uncertainty corresponds to the combined statistical and systematic uncertainty. For clarity, the points for the loose and tight tagging requirement are shifted by -5 and $+5$ GeV with respect to the bin centre.

The b jet identification efficiency, ε_b , can be obtained by counting the number of events with two b-tagged jets in the selected sample of events:

$$N_{2 \text{ b-tagged}} - N_{2 \text{ b-tagged}}^{\text{non-b jet}} = \varepsilon_b^2 n_{2 \text{ b jets}}, \quad (8.10)$$

where $N_{2 \text{ b-tagged}}$ is the number of events with two b-tagged jets from data, $N_{2 \text{ b-tagged}}^{\text{non-b jet}}$ is the number of events with two b-tagged jets with at least one of them being a light-flavour or c jet, and $n_{2 \text{ b jets}}$ is the number of events with two true b jets. This equation can be solved for ε_b if $N_{2 \text{ b-tagged}}^{\text{non-b jet}}$ and $n_{2 \text{ b jets}}$ are known. To reduce the dependence on the $t\bar{t}$ production cross section, the equation is divided by the number of selected events,

$$\varepsilon_b = \sqrt{\frac{F_{2 \text{ b-tagged}} - F_{2 \text{ b-tagged}}^{\text{non-b jet}}}{f_{2 \text{ b jets}}}} \quad (8.11)$$

where $F_{2 \text{ b-tagged}}$ is the fraction of events with two b-tagged jets, $F_{2 \text{ b-tagged}}^{\text{non-b jet}}$ is the fraction of events with two b-tagged jets of which at least one is a non-b jet, and $f_{2 \text{ b jets}}$ is the fraction of events with two true b jets. The two latter fractions are obtained from simulation. When the method is used to measure the efficiency as a function of the jet p_T , the two tagged jets are required to be in the same jet p_T bin.

While the method is sensitive to the uncertainties in the predicted fraction of events with non-b jets $F_{2 \text{ b-tagged}}^{\text{non-b jet}}$, using the fraction of events ensures that systematic uncertainties related to the number of $t\bar{t}$ events cancel out. The dominant uncertainties originate from the normalization of background events and the fraction of non-b jet events in the bin with two b-tagged jets. The following systematic effects were studied:

- **The fraction of non-b jets ($F_{2 \text{ b-tagged}}^{\text{non-b jet}}$):** a conservative variation of 50% is used to estimate the uncertainty in the fraction of non-b jets. This represents the leading uncertainty in the final data-to-simulation scale factor for the loose working point of the b jet identification algorithms.

- **Background yield:** the effect of the uncertainty in the background estimation for the $Z + \text{jets}$ background obtained from data is evaluated by varying its normalization by 50%. For the background yields that are estimated from the simulation, an uncertainty of 30% is assumed. This uncertainty is the subleading source of uncertainty.
- **Factorization and renormalization scales:** the uncertainty in the factorization and renormalization scales is assessed as described in section 8.3.2, except for the scale for FSR in the parton shower that is varied by a factor of two up and down, and not by factor of $\sqrt{2}$.
- **Jet energy scale:** the uncertainty in the jet energy scale is propagated to an uncertainty in the data-to-simulation scale factor as described in section 8.3.1.
- **Jet energy resolution:** the uncertainty in the jet energy resolution is addressed as described in section 8.3.2.
- **Pileup:** the systematic effect related to the uncertainty in the number of pileup interactions is evaluated as described in section 8.2.

The systematic effects related to the uncertainty in the top quark mass and the parton distribution functions are negligible compared to the impact of the uncertainty in the background yield and the number of non-b jets.

The b jet identification efficiency is determined in bins of jet p_T and the corresponding data-to-simulation scale factors are shown in figure 44. Large bin-to-bin variations are observed for low- p_T jets, in particular for the tight working points of the taggers, for which the statistical uncertainty dominates.

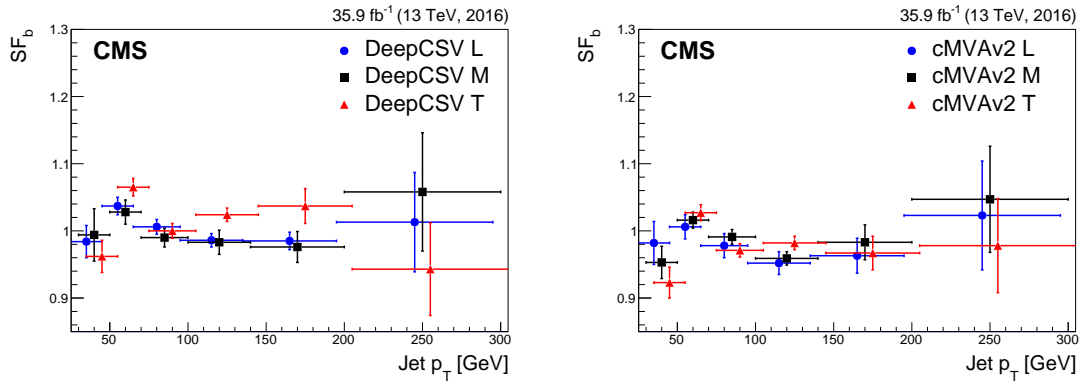


Figure 44. Data-to-simulation scale factors for b jets measured with the TagCount method as a function of the jet p_T for the three DeepCSV (left) and cMVA2 (right) working points. The uncertainty corresponds to the combined statistical and systematic uncertainty. For clarity, the points for the loose and tight tagging requirement are shifted by -5 and $+5$ GeV with respect to the bin centre.

8.4.3 Tag-and-probe technique using single-lepton $\bar{t}t$ events

In addition to dilepton $\bar{t}t$ events, one can also use the $\bar{t}t$ topology where only one of the W bosons decays to leptons. In this case, two b jets are expected from the top quark decays as well as two non-b

jets from the decay of one of the W bosons. The decay chain $t \rightarrow bW \rightarrow bq\bar{q}$ is referred to as the hadronic side, while $t \rightarrow bW \rightarrow b\ell\nu$ is the leptonic side. The event selection criteria are similar to those described in section 8.3.2, requiring exactly one isolated muon or electron with $p_T > 30$ GeV and satisfying tight identification criteria [9, 10] and exactly four jets with $p_T > 30$ GeV to reduce the possible number of jet-quark assignments.

To enhance the b quark content in the jet sample on which the b tagging efficiency will be determined, the jets need to be correctly assigned to the quarks from which they originate. To achieve this, a likelihood method is used that is described in detail in ref. [60]. The reconstruction of the $t\bar{t}$ topology is enhanced by determining first the four-momentum of the neutrino p_ν using the W boson and top quark mass constraints, $(p_\nu + p_\ell)^2 = m_W^2$ and $(p_\nu + p_\ell + p_{b,\ell})^2 = m_t^2$, with p_ℓ and $p_{b,\ell}$ being the four-momenta of the charged lepton and of the b jet candidate on the leptonic side, respectively. If both equations need to be satisfied, the possible solutions are found on an ellipsoid in the 3D momentum space of the neutrino. For each solution, the distance D_ν is computed between the ellipse projection on the transverse plane and the \vec{p}_T^{miss} vector. The solution of p_ν for which this distance is minimal, $D_{\nu,\text{min}}$, is used. More details on this procedure and its performance can be found in ref. [74]. Once the neutrino momentum is defined, the jets are assigned to the quarks by choosing the jet-quark assignment that minimizes the negative logarithm of the likelihood λ . For each permutation $-\log(\lambda)$ is obtained as:

$$-\log(\lambda) = -\log(\lambda_M) - \log(\lambda_\nu), \quad (8.12)$$

where $\lambda_M = \mathcal{P}_m(m_2, m_3)$ is the 2D probability distribution of the invariant mass of the correctly reconstructed W boson on the hadronic side (m_2) and the invariant mass of the correctly reconstructed top quark on the hadronic side (m_3), that was already introduced in section 8.3.2. Similarly, $\lambda_\nu = \mathcal{P}_\nu(D_{\nu,\text{min}})$ is the probability distribution of $D_{\nu,\text{min}}$ for the correct assignment of the b jet on the leptonic side. While λ_M is sensitive to the correct reconstruction of the top quark on the hadronic side, λ_ν is sensitive to the correct reconstruction of the top quark on the leptonic side.

Once the jets are assigned to the quarks, a tag-and-probe (TnP) technique is applied to determine the b tagging efficiency from data. As a tagging requirement, the medium working point of the CSVv2 algorithm is applied to either the b jet on the hadronic or leptonic side while the b jet from the other side is used as probe. The event is rejected if the tagging requirement is not satisfied. The probe jets are used to determine the b tagging efficiency of a given working point for each tagger under consideration. To achieve that, the distributions of $-\log(\lambda)$ and p_T^{miss} for probe jets passing and failing the tagging requirement are fitted with their expected templates to determine their number in data for the correctly-reconstructed $t\bar{t}$ events. During the fit, the normalization of the template for the non- $t\bar{t}$ background is naturally constrained by the p_T^{miss} distribution during the simultaneous fit. The b tagging efficiency in data is then obtained from the fitted fraction of probe jets passing the tagging requirement with respect to all probe jets, as in eq. (8.5). To increase the number of probe jets and to avoid a possible bias in the measurement, each b jet is used once as tag and once as probe. While the measurements are performed separately with either the b jet from the hadronic or the leptonic side as probe jet, they are afterwards combined by treating all systematic uncertainties as correlated. The measurement is performed in bins of jet p_T .

Figure 45 shows an example of the fitted $-\log(\lambda)$ and p_T^{miss} distributions for probe jets from the leptonic side, with $70 < p_T < 100$ GeV, passing and failing the medium working point of the

CSVv2 algorithm. The template distributions for correctly and wrongly reconstructed $t\bar{t}$ events are

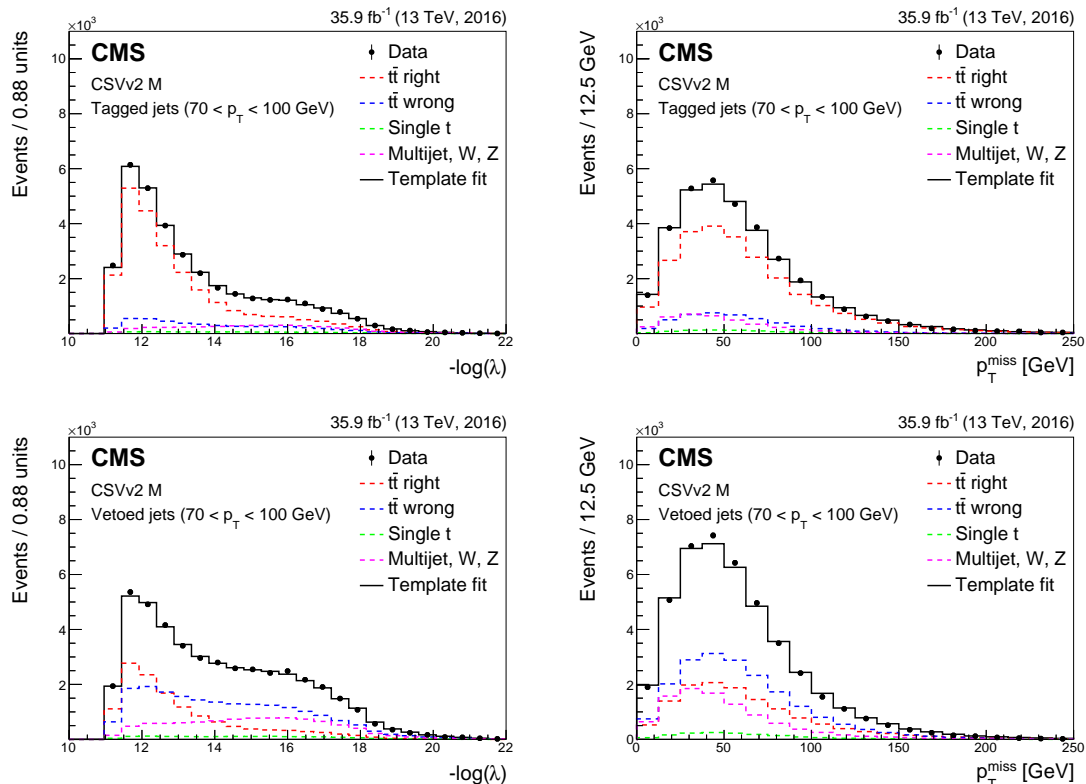


Figure 45. Distributions of fitted $-\log(\lambda)$ (left) and p_T^{miss} (right) for jets from the $t\bar{t}$ leptonic side with $70 < p_T < 100$ GeV passing (upper) and failing (lower) the medium working point of the CSVv2 algorithm.

obtained from simulation. Also the template distribution for single top quark events is taken from simulation and in addition, its normalization is constrained within 20% of the expected standard model yield. The non- $t\bar{t}$ background is composed of multijet, Z + jets, and W + jets events and the combined template for these background processes is derived from data in a control region. The control region contains the events for which the jet with the highest CSVv2 discriminator value is below 0.6.

Several sources of systematic effects may impact the measurement of the b tagging efficiency. These effects are related to the data-taking conditions or to the uncertainty in the object reconstruction, affecting the selection of events and reconstruction of the $t\bar{t}$ topology. On the other hand, systematic effects are related to the modelling of the $t\bar{t}$ production and decay. In particular the following sources of systematic effects have been taken into account:

- **Factorization and renormalization scales:** the uncertainty due to the factorization and renormalization scales is assessed as described in section 8.3.2.
- **Top quark mass:** the uncertainty in the top quark mass is propagated to the data-to-simulation scale factor measurement as described in section 8.3.2.

- **Background:** the non- $\bar{t}t$ background template is derived using events for which the jet with the highest CSVv2 discriminator value is below 0.6. The systematic effect due to this requirement is evaluated by varying its value to less than 0.3, or to values between 0.4 and 0.7. Although these alternative selections result in a different relative fraction of b and non-b jets, as well as in a different background composition, the overall template shape and the fitted value for the number of correctly reconstructed $\bar{t}t$ events is stable.
- **Gluon splitting:** the uncertainty in the gluon splitting into a heavy quark pair is estimated by reweighting events with at least one additional heavy quark that is not originating from the $\bar{t}t$ decay. Events with an additional c and b quark are reweighted by $\pm 15\%$ [75] and $\pm 25\%$ [71], respectively. As can be seen in figure 46 (right) the effect is relatively small.
- **b quark fragmentation:** the uncertainty in the b quark fragmentation function is estimated by varying the Bowler-Lund parameterization within the tune uncertainties. In particular, the parameter `StringZ:rFactB` in PYTHIA is varied by +0.184 and -0.197 to obtain alternative distributions for the ratio of the b hadron p_T to the jet p_T . The $\bar{t}t$ simulation is then reweighted using these functions and the impact on the measured data-to-simulation scale factor is taken as the size of the systematic effect.
- **Branching fraction of $B \rightarrow \ell X$:** the systematic uncertainty induced by the values of the branching fractions of the semileptonic decay of b hadrons may affect the b jet energy response. It is evaluated by reweighting the fractions to the values in ref. [35]. In particular, the branching fraction to leptons is varied by 2.7% for B^0 , by 8% B_s , by 2.5% for B^+ , and by 21% for Λ_B . As can be seen in figures 46 (right) and 47 (right), the impact of this variation, labelled “b hadron decay”, is negligible compared to the other systematic effects.
- **Jet energy scale:** the impact of the uncertainty in the jet energy scale and its propagation to p_T^{miss} is assessed as described in section 8.3.2.
- **Jet energy resolution:** the uncertainty in the jet energy resolution is propagated to the data-to-simulation scale factor measurement as described in section 8.3.2.
- p_T^{miss} : the uncertainty in the lepton, photon, and unclustered energy is estimated by changing p_T^{miss} within its uncertainty and repeating the measurement.
- **Pileup:** the uncertainty in the pileup modelling is assessed as described in section 8.2.

The TnP method is applied to derive data-to-simulation scale factors for the three working points of the CSVv2, DeepCSV, cMVA_{v2}, and c taggers. An example of the size of the systematic uncertainties as a function of the jet p_T is shown in figure 46 (right). In the same figure the scale factor SF_b as a function of the jet p_T is also shown for the medium working point of the CSVv2 algorithm. As discussed previously, SF_b is derived separately for b jets from the hadronic or leptonic side of the single-lepton $\bar{t}t$ decay. As expected, both results are consistent over the full jet p_T range. To reduce the overall uncertainty, the results are combined using the BLUE method, assuming fully correlated systematic uncertainties and uncorrelated statistical uncertainties.

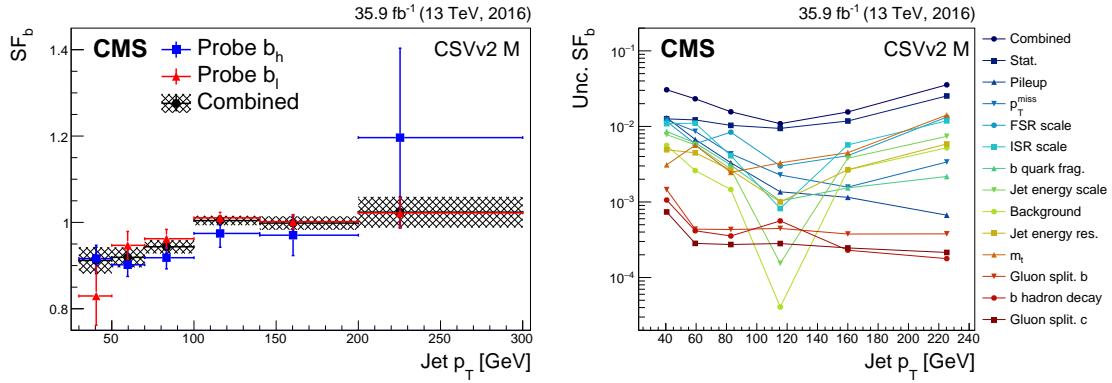


Figure 46. Data-to-simulation scale factors for b jets from the hadronic or leptonic side of the single-lepton $t\bar{t}$ decay as well as for their combination, as a function of the jet p_T for the medium working point of the CSVv2 tagger (left). The error bars represent the combined statistical and systematic uncertainty. Size of the individual uncertainties in the combined scale factors for the CSVv2 medium working point (right).

Figure 47 (left) shows the data-to-simulation scale factors for b jets for the medium working point of the c tagger as a function of the jet p_T . Since the probability to tag non-b jets is higher for the c tagger than for the b taggers, the systematic uncertainties will be larger. On the other hand, since the probability to tag b jets with the c tagger is also smaller compared to the b tagger, also the statistical uncertainty increases. This can be seen in figure 47 (right); while the statistical uncertainty on the measured scale factors still dominates, the systematic uncertainties are significantly larger compared to figure 46 (right). As a result, the total uncertainty for the scale factors for b jets is larger for the c tagger than for the b taggers.

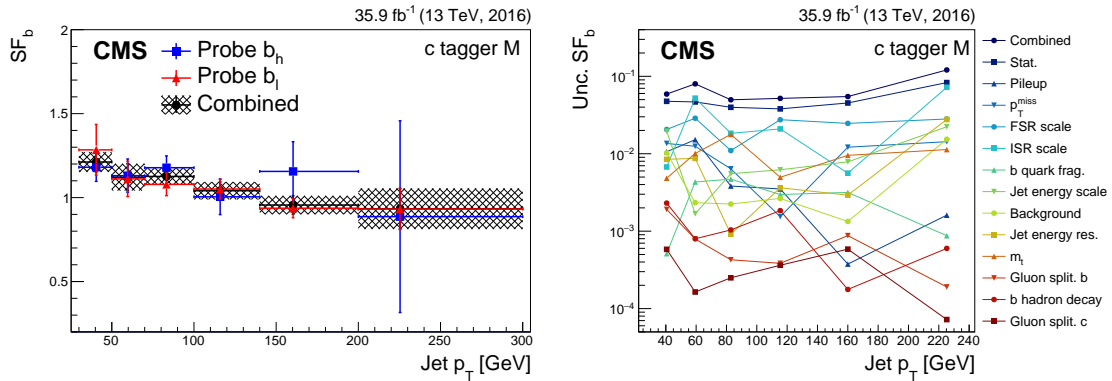


Figure 47. Data-to-simulation scale factors for b jets from the hadronic or leptonic side of the single-lepton $t\bar{t}$ decay as well as for their combination, as a function of the jet p_T for the medium working point of the c tagger (left). The error bars represent the combined statistical and systematic uncertainty. Size of the individual uncertainties in the combined scale factors for the medium working point of the c tagger (right).

8.4.4 Combination of the data-to-simulation scale factors from multijet and $t\bar{t}$ events

For the CSVv2 and DeepCSV taggers, the data-to-simulation scale factors measured with the muon-enriched multijet events are combined with the ones measured in $t\bar{t}$ events using the Kin and TnP methods. Since the c tagger and the cMVAv2 tagger rely on the information from muons from the b hadron decay, the scale factors are only measured with $t\bar{t}$ events since the muon enrichment of the multijet sample may bias the scale factor measurement. Since the Kin method relies on dilepton $t\bar{t}$ events and the TnP method on single-lepton $t\bar{t}$ events, the two scale factor measurements are statistically independent. Similarly as for the combination of the scale factors on the muon-enriched sample, the correlations between the systematic uncertainties are taken into account when combining all measurements with the BLUE method. In particular, when combining the scale factors measured with the TnP and Kin methods, the systematic uncertainty associated to final-state radiation for the TnP method is assessed in the same way as done for the Kin method.

Figure 48 shows the combination of $t\bar{t}$ measurements for the medium working point of the cMVAv2 tagger (right), and for the loose working point of the DeepCSV algorithm (left). As

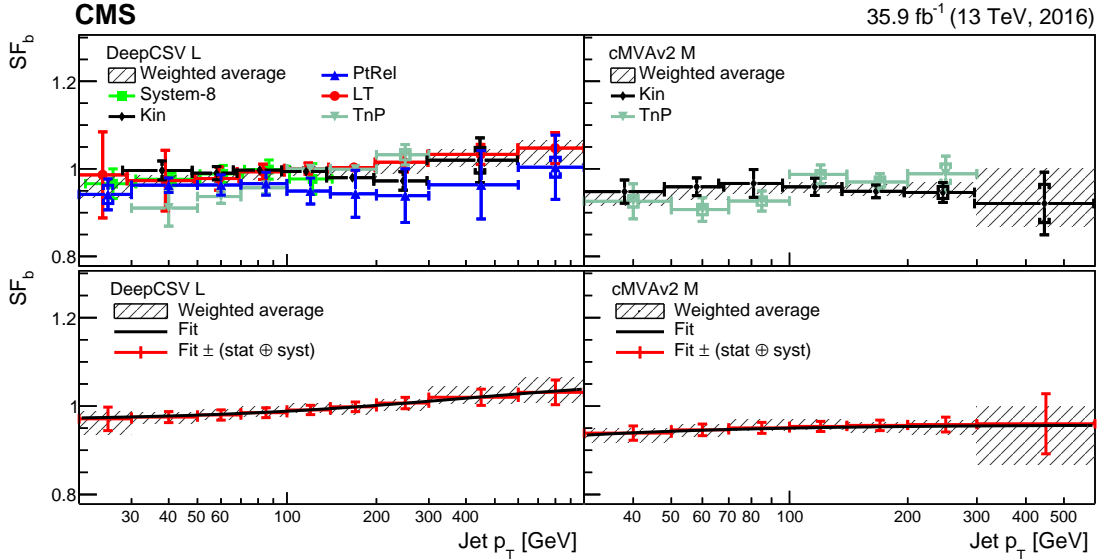


Figure 48. Data-to-simulation scale factors for b jets as a function of jet p_T for the loose DeepCSV (left) and the medium cMVAv2 (right) algorithms working points. The upper panels show the scale factors for tagging b as function of jet p_T measured with the various methods. The inner error bars represent the statistical uncertainty, and the outer error bars the combined statistical and systematic uncertainty. The combined scale factors with their overall uncertainty are displayed as a hatched area. The lower panels show the same combined scale factors with the result of a fit function (solid curve) superimposed. The combined scale factors with the overall uncertainty are centred around the fit result. To increase the visibility of the individual measurements, the scale factors obtained with various methods are slightly displaced with respect to the bin centre for which the measurement was performed. The last bin includes the overflow entries.

an illustration of the consistency between the measurements performed on $t\bar{t}$ and muon-enriched multijet events, the data-to-simulation scale factors are shown for the tight working point of the CSVv2 tagger in figure 49. Within the uncertainty, no sample dependence is observed. As

a conservative estimate to cover any residual sample dependence, a 1% systematic uncertainty is included when combining the measurements. Both in figures 48 and 49 the fit function is parameterized as described in section 8.4.1 for jets with $20 < p_T < 1000$ GeV. For jets with $p_T > 1000$ GeV the uncertainty of the scale factor is doubled. For all taggers and for an average jet

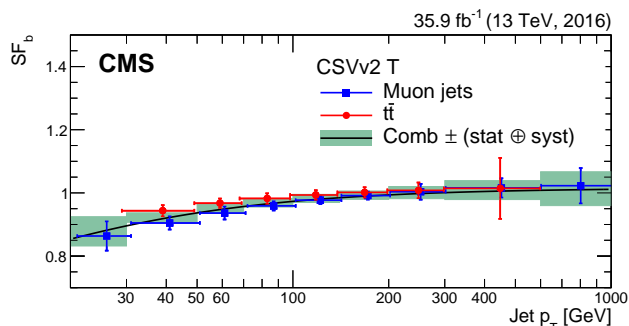


Figure 49. Data-to-simulation scale factors for b jets as a function of jet p_T measured in muon-enriched multijet and $t\bar{t}$ events for the tight working point of the CSVv2 tagger. The green area shows the combined scale factors with their overall uncertainty, including an additional 1% uncertainty to cover any residual sample dependence, fitted to the superimposed solid curve. For visibility purposes, the scale factors are slightly displaced with respect to the bin centre for which the measurement was performed. The last bin includes the overflow entries.

p_T found in $t\bar{t}$ events the data-to-simulation scale factors vary from about 0.99 for the loose working point to 0.95 for the tight working point. The achieved relative precision on the scale factor for b jets is 1 to 1.5% using jets with $70 < p_T < 100$ GeV and rises to 3–5% at the highest considered jet p_T . Overall, the statistical uncertainty is 15–30% of the total uncertainty.

In some physics analyses of precision measurements, a correlation is present between the quantity to measure and the method to derive the b tagging scale factors. An example is the measurement of the $t\bar{t}$ production cross section in an analysis requiring one or more b-tagged jets. In that case, the scale factors derived from $t\bar{t}$ events are correlated with the production cross section to be measured and the scale factor measured with muon-enriched multijet events should be used.

8.5 Measurement of the data-to-simulation scale factors as a function of the discriminator value

The last method to measure data-to-simulation scale factors is a technique of iterative fitting (IterativeFit) first described in ref. [76], which aims at correcting the full discriminator shape. This method is designed to meet the needs of analyses in which the full distribution of the b tagging discriminator values is used instead of applying a working point of the algorithm to select jets or events. If the full discriminator distribution is used, the distribution using jets in simulated events has to be corrected to match the one observed in data. Scale factors for both b and light-flavour jets are derived as a function of the discriminator value in bins of jet p_T and η . An iterative procedure is used based on a tag-and-probe technique to measure the scale factors for both b and light-flavour jets simultaneously. The scale factors are derived from events with two oppositely charged leptons (electron or muon) within the tracker acceptance and satisfying the tight identification and isolation

requirements [9, 10]. The leading (subleading) lepton is required to have $p_T > 25$ (15) GeV. Exactly two jets are required with $p_T > 20$ GeV and to lie within the tracker acceptance.

The data-to-simulation scale factors for b jets are derived from events passing the above requirements. In addition, for the events with same-flavour leptons, the dilepton invariant mass is required to be away from the Z boson mass, $|M_{\ell\ell} - M_Z| > 10$ GeV, and $p_T^{\text{miss}} > 30$ GeV. These two requirements reduce the contribution from Z + jets events. The tag jet should pass the medium working point of the algorithm for which the scale factor is to be measured. The other jet is used as probe. After these criteria have been applied, the simulated event sample is composed of 87% $t\bar{t}$, 6% single top and 7% Z + jets events. Other backgrounds are reduced to a negligible level.

The data-to-simulation scale factors for light-flavour jets are measured with Z + jets events selected among the same-flavour dilepton events with a dilepton invariant mass close to that of the Z boson, $|M_{\ell\ell} - M_Z| < 10$ GeV, and inverting the requirement on p_T^{miss} . A b jet veto is applied on the tag jet using the loose working point of the tagger for which the scale factor is to be measured. After the event selection, the sample is very pure in Z + jets events (99.9%).

After the event selection and tagging or vetoing one of the two jets, the data-to-simulation scale factors are measured using the other jet in the event as the probe. The scale factors are extracted by first normalizing the b tagging discriminator distribution of the probe jets in simulation to that observed in data. Then, when measuring the scale factor for b jets, the contribution from non-b jets is subtracted using the simulated events. Similarly, when measuring the scale factor for light-flavour jets, the expected contributions from b and c jets are subtracted. The scale factor is determined separately in exclusive bins of the b tagging discriminator distribution, p_T , and η (for light-flavour jets). Since the scale factors for light-flavour jets have an impact on the measured scale factors for b jets, an iterative procedure is performed. In the first iteration no scale factor is applied, while for the next iteration the background is subtracted using the scale factors obtained in the previous iteration. The iterative procedure stops once the scale factors obtained in the current iteration are stable with respect to those obtained in the previous iteration. Convergence is typically achieved after three iterations. When estimating the scale factor for b jets and light-flavour jets, the scale factor for c jets is set to unity with an uncertainty that is twice the uncertainty in the scale factor for b jets.

For the IterativeFit method, the following list of systematic uncertainties is considered. This list covers possible shape discrepancies between data and simulation for the tagger discriminator distribution.

- **Sample purity:** several systematic uncertainties impact the sample purity. These need to be taken into account when measuring the data-to-simulation scale factor for light-flavour or b jets. The sample purity may be affected by background processes or the modelling of the signal in the simulation, e.g. related to the production of additional jets in association with the top quark pair when measuring the scale factor for b jets. All sources of systematic uncertainties influencing the sample purity are combined in a single systematic uncertainty. For the scale factor for light-flavour jets, the expected contribution from processes other than Z + jets is negligible. However, the sample purity can be contaminated by heavy-flavour jets produced in association with the Z boson. The fraction of heavy-flavour jets in the sample is conservatively varied upwards and downwards by 20% when calculating SF_1 . For SF_b , the dominant contribution originates from $t\bar{t}$ events. The dilepton $t\bar{t}$ events are selected requiring

exactly two jets, consistent with the two b jets expected from the $t\bar{t}$ decay. However, because of ISR and FSR and the acceptance of the event selection, also non-b jets are selected. The rate of $t\bar{t}$ events produced with ≥ 2 additional partons varies within up to 20%. Therefore, the fraction of non-b jets is varied by this amount to evaluate the uncertainty in the purity of the sample.

- **Jet energy scale:** the uncertainty in the jet energy scale is assessed in the same way as described in section 8.3.1.
- **Statistical uncertainty:** an uncertainty arises due to the limited number of entries in each bin of the discriminator distribution, resulting in statistical fluctuations in certain regions, e.g. at high discriminator values for light-flavour jets and at low discriminator values for b jets. Linear and quadratic functions, $f_1(x) = 1 - 2x$ and $f_2(x) = 1 - 6x(1 - x)$, are introduced, where x corresponds to the central value of a discriminator bin. The linear function parameterizes the effect of statistical fluctuations that would tilt the discriminator distribution. In contrast, the quadratic function represents fluctuations that would increase or decrease the data-to-simulation scale factor in the centre of the discriminator distribution compared to the low and high discriminator values. To assess the size of the systematic uncertainty related to statistical fluctuations, the scale factor value is varied according to $\pm\sigma(x)f_i(x)$, where $\sigma(x)$ is the statistical uncertainty in the scale factor in that bin. The scale factors are refitted after applying these variations, resulting in two independent functions that span an envelope around the nominal scale factor function for each of the two types of statistical fluctuations.
- **Treatment of SF_c :** for c jets the data-to-simulation scale factor, SF_c , is set to unity. The uncertainty in this value is obtained by doubling the aforementioned relative uncertainties in the scale factor for b jets and adding them in quadrature to obtain a relative uncertainty in SF_c . Similarly as for the statistical uncertainty, two separate uncertainties are constructed using linear and quadratic functions $f_i(x)$. The scale factor value is then varied according to $\pm\sigma(x)f_i(x)$, where $\sigma(x)$ is the relative uncertainty in SF_c . These linear and quadratic variations of SF_c are applied independently from the other uncertainties after which the scale factors are refitted to obtain the functions corresponding to the uncertainty in SF_c .

Figures 50 and 51 show an example of the distribution for the CSVv2 tagger and the derived data-to-simulation scale factors using jets with $40 < p_T < 60$ GeV in a topology enriched in b jets and a topology enriched in light-flavour jets, respectively. The scale factors are parameterized as a function of the CSVv2 discriminator value. The scale factor for light-flavour jets as a function of the discriminator value is fitted with a sixth-order polynomial function. For the scale factor for b jets, no satisfactory parameterization was found. Therefore, a smooth function is obtained by interpolating between the scale factors measured in bins of the CSVv2 discriminator distribution. No interpolation is done between the bin below 0, which includes jets with a negative CSVv2 discriminator value, and the first bin above 0.

The data-to-simulation scale factors obtained with the IterativeFit method have been validated in various control regions. One example is the validation in a control region dominated by single-lepton $t\bar{t}$ events. The flavour composition in this control region is very different from both the dilepton $t\bar{t}$ and $Z +$ jets topologies used to derive the scale factors, thereby providing a powerful

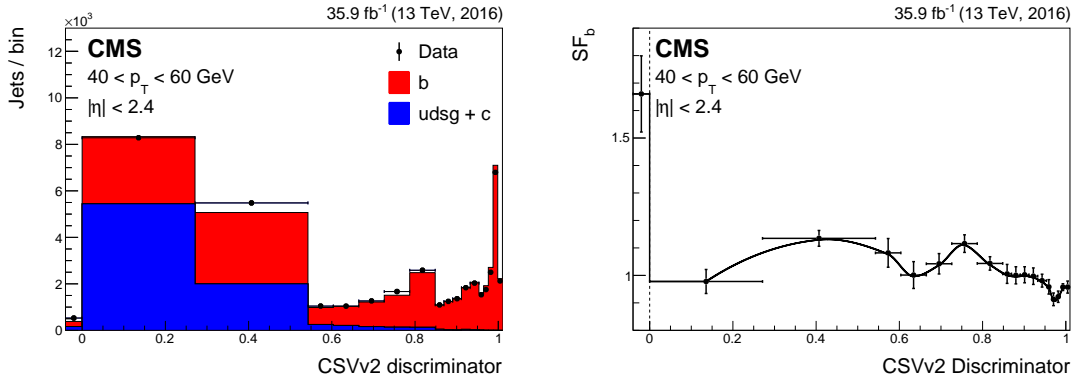


Figure 50. Distribution of the CSVv2 discriminator values for jets with $40 < p_T < 60$ GeV before the data-to-simulation scale factors are applied in the $t\bar{t}$ dilepton sample (left). The simulation is normalized to the number of entries in data. Measured scale factors for b jets as a function of the CSVv2 discriminator value (right). The line is an interpolation between the scale factors measured in each bin of the CSVv2 discriminator distribution. The bin below 0 contains the jets with a default discriminator value.

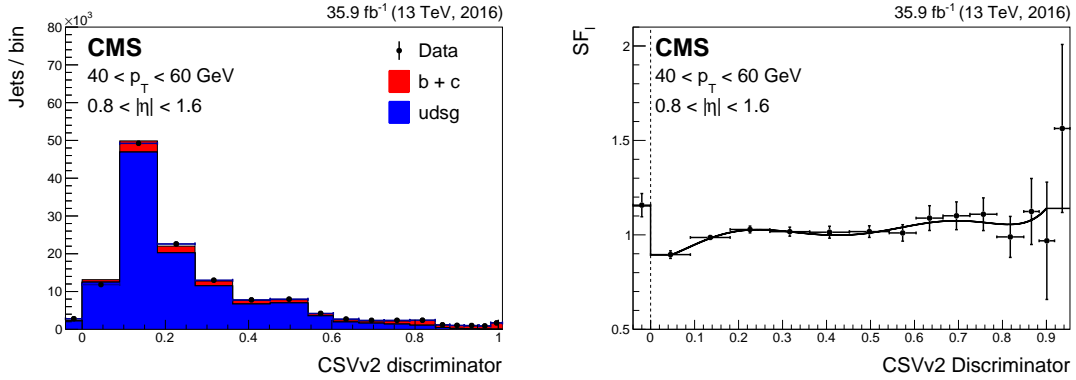


Figure 51. Distribution of the CSVv2 discriminator values for jets with $40 < p_T < 60$ GeV and $0.8 < |\eta| < 1.6$ before the data-to-simulation scale factors are applied in the Z + jets sample (left). The simulation is normalized to the number of entries for data. Measured scale factors for light-flavour jets as a function of the CSVv2 discriminator value (right). The line represents a polynomial fit to the scale factors measured in each bin of the CSVv2 discriminator distribution. The bin below 0 contains the jets with a default discriminator value.

cross check. Events are selected requiring an isolated electron or muon with $p_T > 30$ GeV and $|\eta| < 2.1$ and exactly four jets with $p_T > 30$ GeV, of which exactly two are b tagged according to the medium working point of the CSVv2 algorithm. The distribution of the CSVv2 discriminator values is shown in figure 52 for all the jets in the control region. The agreement between the data and simulation improves significantly after applying the measured scale factors, and the remaining fluctuations are covered by the systematic uncertainties.

8.6 Comparison of the measured data-to-simulation scale factors

In most cases, the measured data-to-simulation scale factors for heavy- (light-) flavour jets are smaller (larger) than unity. This is expected because the quantities of relevance for heavy-flavour

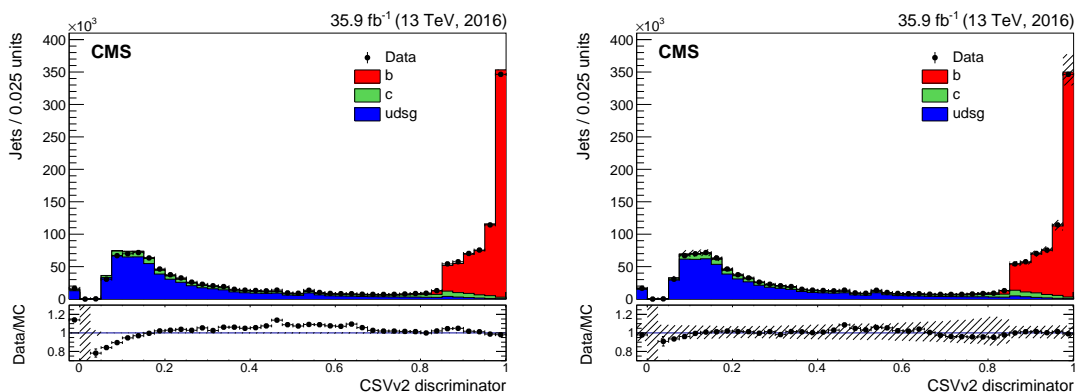


Figure 52. Distribution of the CSVv2 discriminator values for the single-lepton $t\bar{t}$ sample. Exactly four jets are required, two of which passing the medium working point of the CSVv2 algorithm. The values of the discriminator are shown before (left) and after (right) applying the data-to-simulation scale factors derived with the IterativeFit method. The hatched band around the ratios shows the statistical uncertainty (left), and the total uncertainty (right) in the measured scale factors. The simulation is normalized to the total number of data events. The bin below 0 contains the jets with a default discriminator value.

jet identification are not perfectly modelled by the simulation. The scale factors derived with the various methods are compared to each other after averaging the measured scale factor following the p_T spectrum for $t\bar{t}$ events. Figure 53 compares the measured scale factors. However, this figure should not be used to decide which method performs best, since, e.g. for the TagCount method the scale factors were remeasured inclusively over the jet p_T range, resulting in a smaller uncertainty than when the weighted average is used over the measurements in bins of jet p_T . This is because for the measurement as a function of the jet p_T the two tagged jets are required to be in the same jet p_T bin, resulting in a loss of events compared to the inclusive measurement. Moreover, to allow a comparison, the scale factors for the IterativeFit method are remeasured using only one bin above the discriminator value corresponding to the working point for which the scale factor is derived. As can be seen from figure 53, the measured scale factors are consistent within their uncertainties. Only for the tight working point of the CSVv2 and DeepCSV taggers there is a hint of tension between the TagCount method and the other methods. This is explained by the fact that the central value of the TagCount method is quite sensitive to the background subtraction and the sample purity. The scale factor for b jets for the cMVAv2 and c tagger working points is not measured with muon-enriched multijet events to avoid a bias due to the muon information used in these taggers. The right panels in figure 53 show that the precision on the scale factors for c jets for the loose and medium working points of the b taggers, is on the same level as the precision reached on the scale factors for b jets, for jets with a p_T distribution as expected in $t\bar{t}$ events. For the tight working point of the b taggers, the uncertainty in the average scale factor is relatively large because of the low number of c jets passing the tagging requirement. Similarly, as can be seen from the lower left panel in figure 53 the uncertainty in the average scale factor for b jets for the c tagger working points is larger compared to the corresponding uncertainty for the working points of the b taggers, because of two reasons. First, the uncertainty for the c tagger tight working point is large because of the low efficiency for b jets to pass this tagging requirement (section 5.2.2), resulting in a relatively large statistical uncertainty.

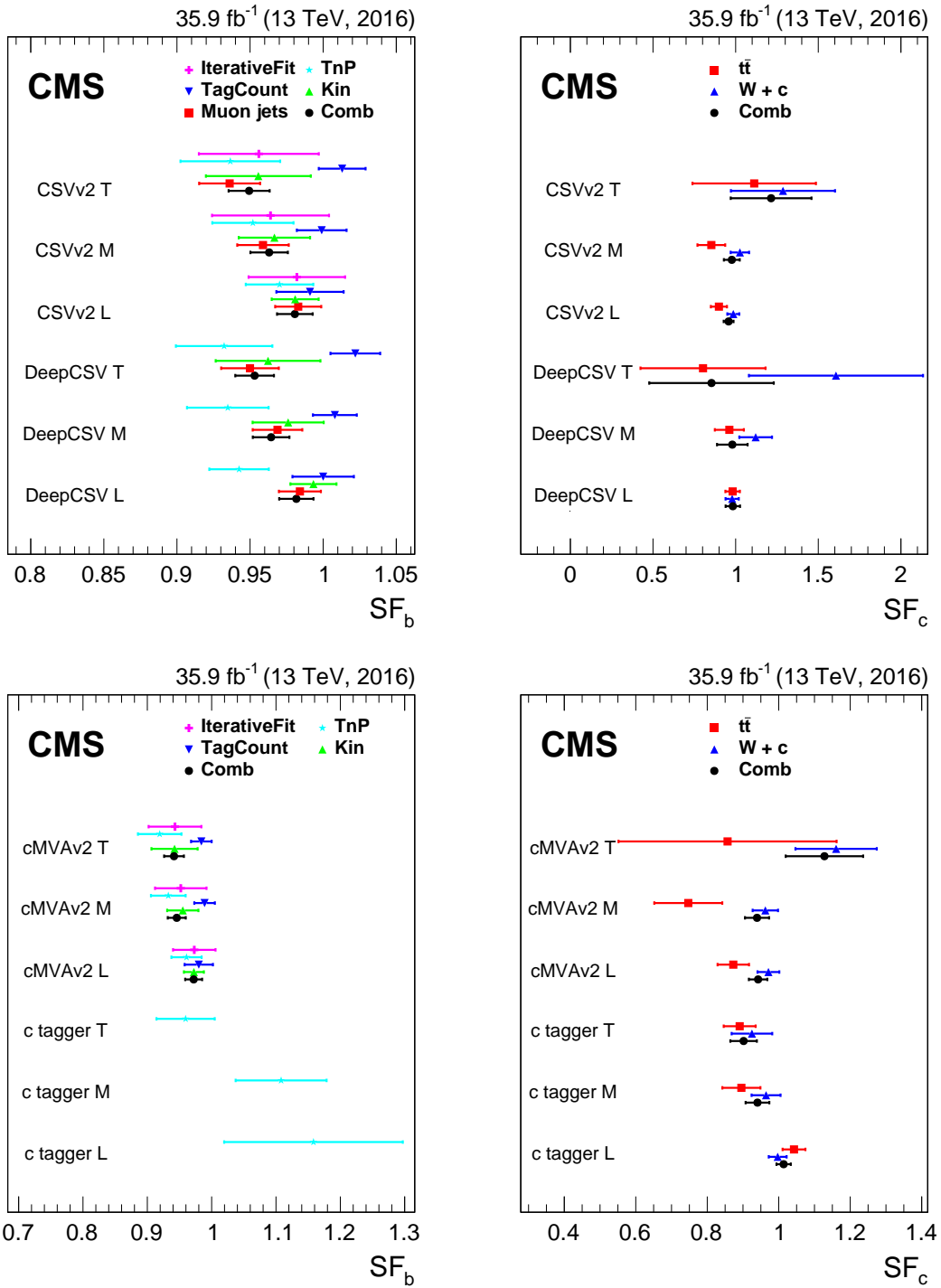


Figure 53. Comparison of the data-to-simulation scale factors derived with various methods and their combination, for b (left) and c (right) jets. The scale factors measured with the different methods agree within their uncertainties. For the left panels, the combination includes all measurements with the exception of the IterativeFit and the TagCount methods.

Second, the uncertainty for the c tagger loose and medium working points is large due to the larger contribution from light-flavour jets resulting in a larger systematic uncertainty. It was also checked that the scale factor for light-flavour jets obtained with the IterativeFit method is consistent with the one obtained using the negative tag method.

9 Measurement of the tagging efficiency for boosted topologies

In section 6, the performance of b tagging algorithms in boosted topologies was discussed and the double- b tagger was presented to identify boosted particles decaying to two b quarks. This section summarizes the efficiency measurements for b tagging in boosted topologies. In section 9.1 the data are compared to the simulation for two topologies: a sample of muon-enriched subjets of AK8 jets and a sample of double-muon-tagged AK8 jets. Section 9.2 discusses the methods to measure the efficiency for b tagging subjets with the CSVv2 tagger. The efficiency measurement of the double- b tagger is presented in section 9.3. In both cases, the data-to-simulation scale factors are measured as a function of the jet p_T . At this stage, the size of the jet sample is not yet large enough to provide also scale factors as a function of the jet $|\eta|$.

9.1 Comparison of data with simulation

The data are compared to the simulation using jets in boosted topologies. Jets are selected from events satisfying the following description:

- **Muon-enriched boosted subjets sample:** a sample of muon-enriched multijet events is obtained using a combination of single-jet (AK4 and AK8) triggers requiring a muon in the jet. The data are compared to the simulation for soft-drop subjets (section 6) of AK8 jets with $p_T > 350$ GeV and within the tracker acceptance. The subjets are required to contain at least one muon with $p_T > 7$ GeV and $\Delta R < 0.4$. In addition, to reduce the contribution from prompt muons, the ratio of the p_T of the muon to that of the jet is required to be smaller than 0.5. The subjet p_T distribution in simulation is reweighted to match the observed distribution.
- **Double-muon-tagged boosted jet sample:** a second sample of muon-enriched multijet events is obtained by combining the triggers used to select the previous sample with dijet triggers with a lower jet p_T threshold, and by requiring a muon in each of the two jets. In this way, the sample contains also AK8 jets with $250 < p_T < 350$ GeV. Each subjet is required to contain a muon with $p_T > 7$ GeV and $\Delta R < 0.4$. The sum of the p_T of the two muons with respect to the p_T of the AK8 jet is required to be less than 0.6. Some of the triggers are prescaled. The p_T distribution of the AK8 jet in the simulation is reweighted to match the observed distribution in data.

In figure 54 the data are compared to the simulation for subjets in the muon-enriched sample. The distributions of a few selected input variables are shown as well as the CSVv2 discriminator output distribution. The agreement is reasonable, with variations of up to 20%. Similarly, figure 55 shows the simulation and data for double-muon-tagged AK8 jets. Some of the input variables of the double- b tagger are shown as well as the discriminator output distribution itself.

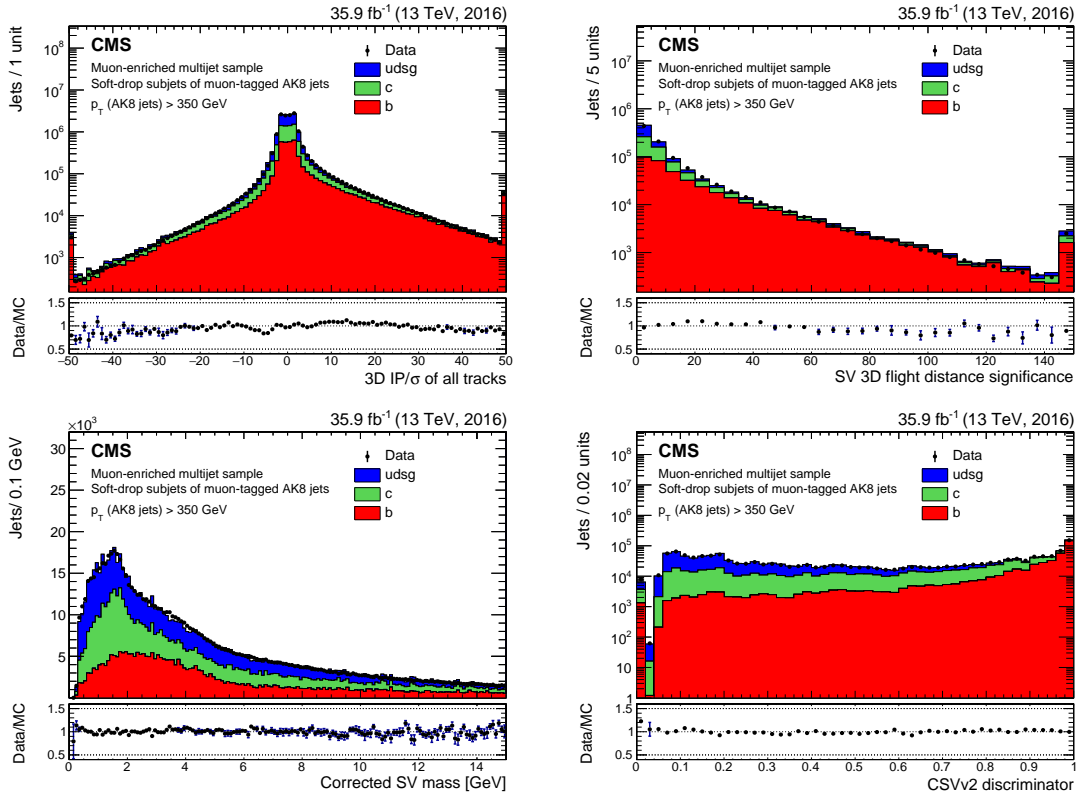


Figure 54. Distribution of the 3D impact parameter significance of the tracks (upper left), the secondary vertex 3D flight distance significance (upper right), the corrected secondary vertex mass (lower left), and the CSVv2 discriminator (lower right) for muon-tagged subjects of AK8 jets with $p_T > 350 \text{ GeV}$. The simulated contributions of each jet flavour are shown with a different colour. The total number of entries in the simulation is normalized to the number of observed entries in data. The first and last bin of each histogram contain the underflow and overflow entries, respectively.

9.2 Efficiency for subjects

9.2.1 Misidentification probability

The CSVv2 algorithm is used when applying b jet identification on subjects of AK8 jets. Data-to-simulation scale factors for light-flavour subjects from AK8 jets are derived with the negative-tag method used to measure the scale factors for light-flavour jets in section 8.2. A sample of inclusive multijet events is selected using single-jet triggers with different p_T thresholds ranging from 140 to 500 GeV. The AK8 jet is required to have an offline reconstructed soft-drop jet mass between 50 and 200 GeV, where the jet mass is obtained from the invariant mass of the two subjects. The scale factors are measured for the loose and medium working points of the CSVv2 taggers using subjects with $p_T > 20 \text{ GeV}$ within the tracker acceptance. The same sources of systematic effects are taken into account as for the scale factor measurement for AK4 light-flavour jets.

The measured data-to-simulation scale factors are shown in figure 56 for the loose and medium working points of the CSVv2 algorithm as a function of the subject p_T . The measurement is compared to the corresponding AK4 jet scale factors, and within the uncertainty both scale factors agree for

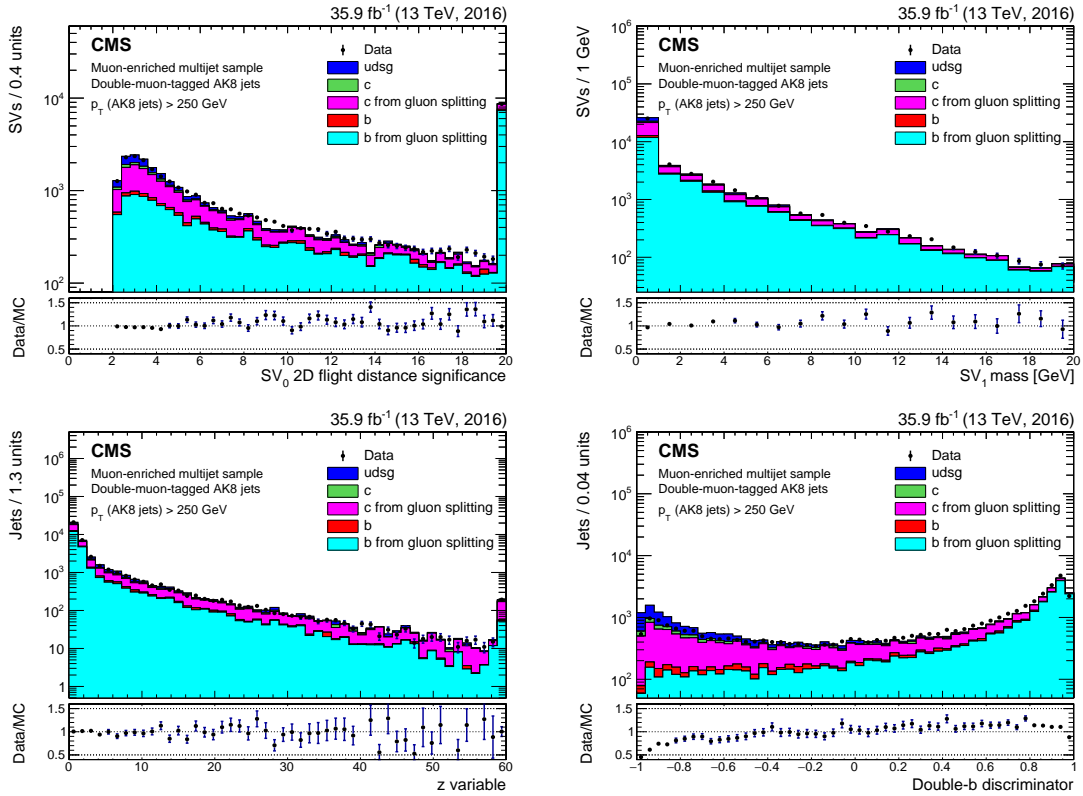


Figure 55. Distribution of the 2D flight distance significance of the secondary vertex associated with the first τ axis (upper left), the mass of the secondary vertex associated with the second τ axis (upper right), the z variable (lower left), and the double- b discriminator (lower right) for double-muon-tagged AK8 jets with $p_T > 250$ GeV. The simulated contributions of each jet flavour are shown with a different colour. The total number of entries in the simulation is normalized to the number of observed entries in data. The first and last bin of the upper and lower right histograms contain the underflow and overflow entries, respectively.

jets with $p_T > 200$ GeV. The difference for low jet p_T is because of the very different environment for low- p_T subjets in a boosted AK8 jet compared to low- p_T AK4 jets.

9.2.2 Measurement of the b tagging efficiency

The data-to-simulation scale factors for subjets originating from b quarks are measured on subjets of AK8 jets using the selection requirements described in section 9.1. The LifeTime LT method presented in section 8.4.1 is applied to measure the scale factors for the loose and medium working points of the CSVv2 algorithm. The templates of the JP distribution for the various flavours obtained from simulation are fitted to the distribution observed in the data before and after applying the tagging requirement. An example of the fitted JP distribution for subjets with $240 < p_T < 450$ GeV is shown in figure 57 for all subjets and for subjets passing the medium working point of the CSVv2 algorithm. The systematic uncertainties associated with the scale factor measurements are the same as evaluated for AK4 jets discussed in section 8.4.1. Compared to the measurements in section 8.4.1, the calibration of the track probabilities used in the resolution function of the JP algorithm (section 5.1.1) is performed differently. In particular, for the nominal scale factor values

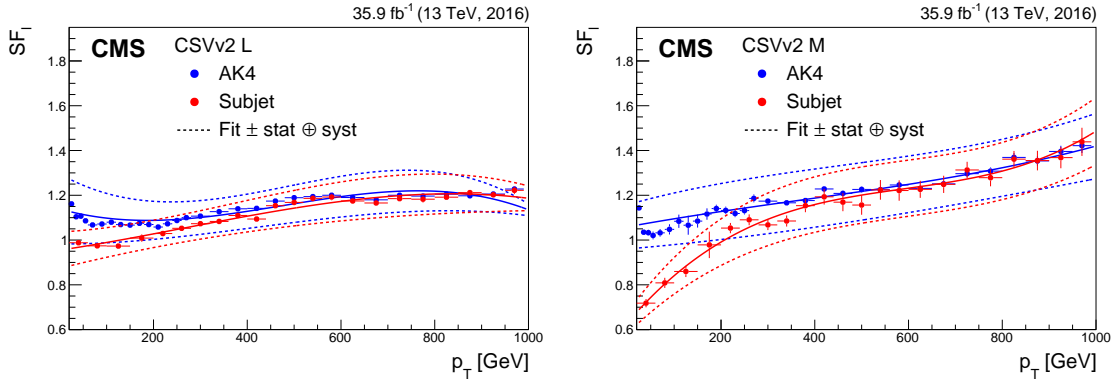


Figure 56. Data-to-simulation scale factors for light-flavour subjects of AK8 jets as a function of the subject p_T , as well as for AK4 jets as a function of jet p_T , for the loose (left) and medium (right) working points of the CSVv2 algorithm. The solid curve is the result of a fit to the scale factors, and the dashed lines represent the overall statistical and systematic uncertainty of the measurements.

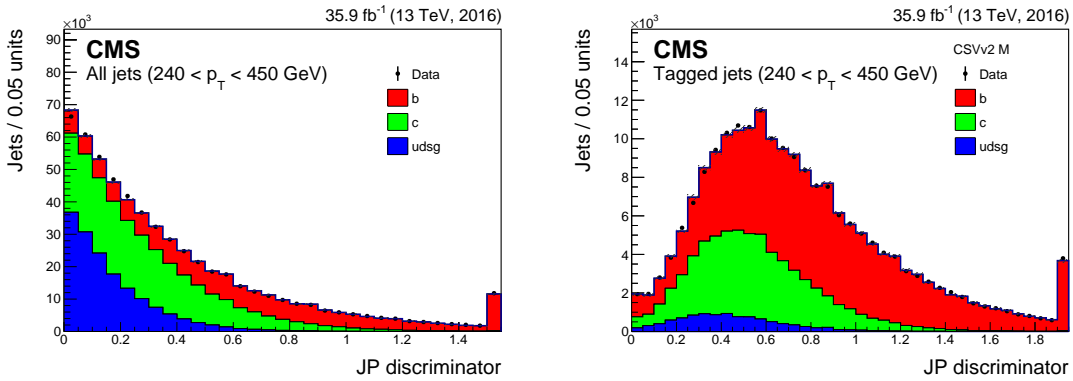


Figure 57. Fitted JP discriminator distribution for all soft-drop subjects with $240 < p_T < 450$ GeV (left) and for the subsample of those subjects passing the medium working point of the CSVv2 algorithm (right). The last bin contains the overflow entries.

considered here, the calibration of the track probabilities is derived from simulation and applied to both data and simulation. The systematic effect is evaluated from the difference between the nominal scale factor and that obtained by applying to the data the calibration of the track probabilities derived from the data. The uncertainty due to jets without a JP discriminator value is found to be negligible because of the higher jet p_T .

The measured data-to-simulation scale factors for the loose and medium working points of the CSVv2 tagger are presented as function of the subject p_T in figure 58. As a comparison, the scale factors for AK4 jets obtained with the LT method are also shown. The scale factors for AK4 jets and subjets are consistent within their uncertainties.

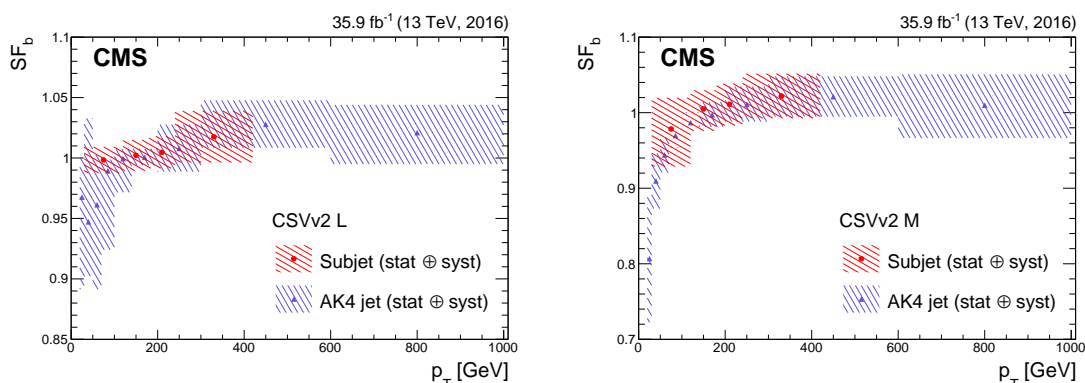


Figure 58. Data-to-simulation scale factors for b subjets of AK8 jets as a function of the subjet p_T , as well as for AK4 jets as a function of jet p_T , for the loose (left) and medium (right) working points of the CSVv2 algorithm. The hatched band around the scale factors represents the overall statistical and systematic uncertainty of the measurements.

9.3 Efficiency of the double-b tagger

9.3.1 Measurement of the double-b tagging efficiency

To measure the efficiency of the four working points of the double-b tagger defined in section 6.2, a pure sample of boosted $b\bar{b}$ jets needs to be selected from data. The measurement is performed using a sample of high- p_T jets enriched with $g \rightarrow b\bar{b}$ jets. The enrichment is achieved by requiring each AK8 jet to be double-muon tagged, as described in section 9.1. While additional systematic uncertainties arise from using $b\bar{b}$ jets from gluon splitting, the statistical uncertainty of a measurement performed on boosted $H \rightarrow b\bar{b}$ jets would be too large. Also $Z \rightarrow b\bar{b}$ events cannot be easily used because of the difficulty to obtain a pure sample of those events. Using the simulation, it has been verified that the $g \rightarrow b\bar{b}$ jets can be used as a proxy for the $H \rightarrow b\bar{b}$ jets signal. Indeed, after the selection, the distributions of the double-b tagger discriminator values and its input variables were compared for simulated $g \rightarrow b\bar{b}$ and $H \rightarrow b\bar{b}$ jets. Since a different shape was observed for the discriminator distribution, the $g \rightarrow b\bar{b}$ events were reweighted using the distribution of the z variable and the secondary vertex energy ratio, which are the variable distributions with the largest shape difference. The data-to-simulation scale factors were then computed using either the reweighted $g \rightarrow b\bar{b}$ simulation or the original $g \rightarrow b\bar{b}$ simulation. Both scale factors were found to be compatible, which confirms that the $g \rightarrow b\bar{b}$ events allow for an unbiased measurement of the efficiency.

The efficiency and the corresponding data-to-simulation scale factor $SF_{\text{double-b}}$ is measured using data for the working points of the double-b tagger defined in section 6. The measurement is performed using the LT method, presented in section 8.4.1 and also used in section 9.2.2. The expected templates of the JP discriminator after the tagging requirement consist of two contributions, one arising from $g \rightarrow b\bar{b}$ jets and one from jets not stemming from this process (background jets). These two templates are used to fit the fraction of each contribution to the JP discriminator in data. The fit is performed in three bins of jet p_T for the loose, medium-1, and medium-2 working points, and in two bins of jet p_T for the tight working point. An example of the fitted distributions is shown

in figure 59 for AK8 jets with $350 < p_T < 430$ GeV before and after applying the loose working point of the double-b algorithm. The background jets are shown separately for b and $g \rightarrow c\bar{c}$ jets and for c and light-flavour jets. However, the templates of these two components are merged for the tagged jet sample when performing the fit.

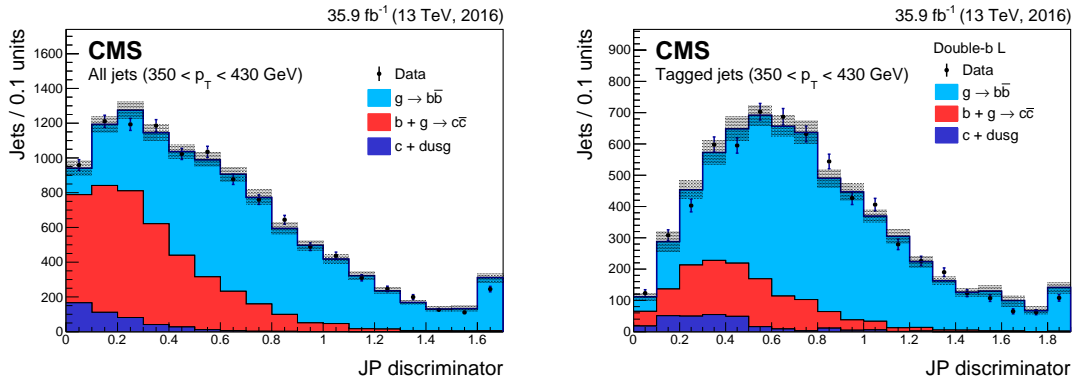


Figure 59. Fitted JP discriminator distribution for all soft-drop subjects with $350 < p_T < 430$ GeV (left) and for the subsample of those subjects passing the loose working point of the double-b algorithm (right). The shaded area represents the statistical and systematic uncertainties in the templates obtained from simulation. The last bin contains the overflow entries.

The measurement is sensitive to the flavour composition of the background sample. The uncertainty due to the flavour composition is estimated by varying by $\pm 50\%$ the normalization of each flavour in the background templates. As a cross check, the potential systematic effect of merging all background jets in a single template is assessed by remeasuring the data-to-simulation scale factor using a separate template for each flavour in the fit. The systematic uncertainty due to the template variation results in a systematic uncertainty of up to 2.3% in the measured scale factor. The uncertainty related to the track probability calibration for the resolution function used in the JP discriminator is evaluated as described in section 9.2.2, and results in an uncertainty of 2.9% in the measured scale factors. The impact of the uncertainty in the number of pileup interactions results in an uncertainty of 1.3% in the scale factors. The following systematic uncertainties were found to be negligible: bin-by-bin correlations, jet energy corrections, the number of tracks, the branching fractions for c hadrons to muons, the b fragmentation function, the fragmentation rate of a c quark to various D mesons, and the K_S^0 and Λ production fractions.

The data-to-simulation scale factor $SF_{\text{double-b}}$ is presented in figure 60 for two working points of the double-b tagger. The measurement is performed using jets with $p_T > 250$ GeV. Jets with $p_T > 840$ GeV are included in the last bin. The scale factor is positioned at the average jet p_T value of the jets populating that bin.

9.3.2 Measurement of the misidentification probability for top quarks

The probability to misidentify a boosted top quark jet corresponding to the decay $t \rightarrow bW \rightarrow bq\bar{q}$ for the four working points of the double-b tagger is estimated from the data. Semileptonic $t\bar{t}$ events are selected by requiring exactly one isolated muon with $p_T > 50$ GeV and $|\eta| < 2.1$. The muon is used to define two hemispheres in the event. The leptonic hemisphere is defined as

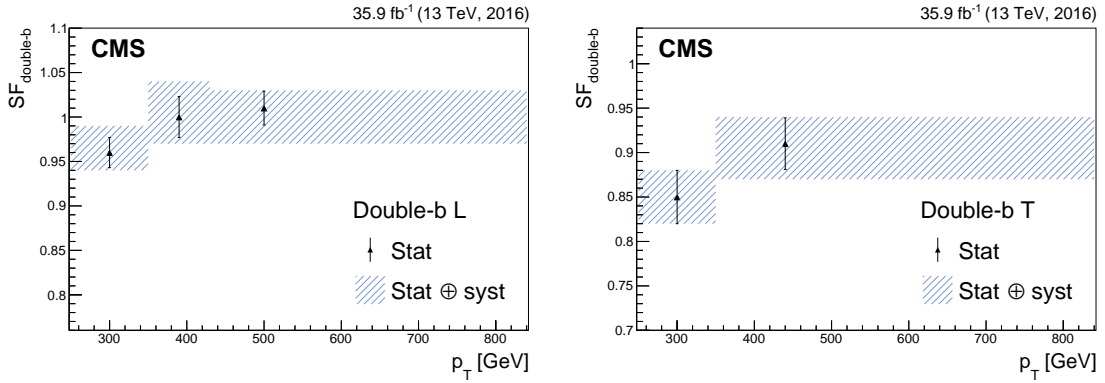


Figure 60. Data-to-simulation scale factors for correctly identifying two b jets in an AK8 jet as a function of the jet p_T for the loose (left) and tight (right) working points of the double-b tagger. The hatched band around the scale factors represents the overall statistical and systematic uncertainty in the measurement. Jets with $p_T > 840$ GeV are included in the last p_T bin.

$|\phi_{\text{jet}} - \phi_{\mu}| < \frac{2}{3}\pi$, and the hadronic hemisphere is its complement. At least one AK4 jet is required in each hemisphere, with $p_T > 30$ GeV and within the tracker acceptance. In addition, the AK4 jet in the leptonic hemisphere should pass the loose working point of the CSVv2 algorithm. At least one AK8 jet is required in the hadronic hemisphere with $p_T > 250$ GeV, $|\eta| < 2.4$, and a pruned jet mass between 50 and 200 GeV. The N-subjettiness parameters τ_1 and τ_2 (section 6) should satisfy the condition $\tau_2/\tau_1 < 0.6$. If more than one such jet is present, the one with the highest p_T is considered. The aforementioned selection is referred to as the “2-prong” selection.

After the event selection, the simulated events are normalized to the yield observed in the data. Figure 61 shows the distribution of the double-b discriminator and the pruned jet mass for the selected 2-prong events. The purity of the sample is high and the AK8 jet mass distribution is consistent with the decay of the W boson to quarks.

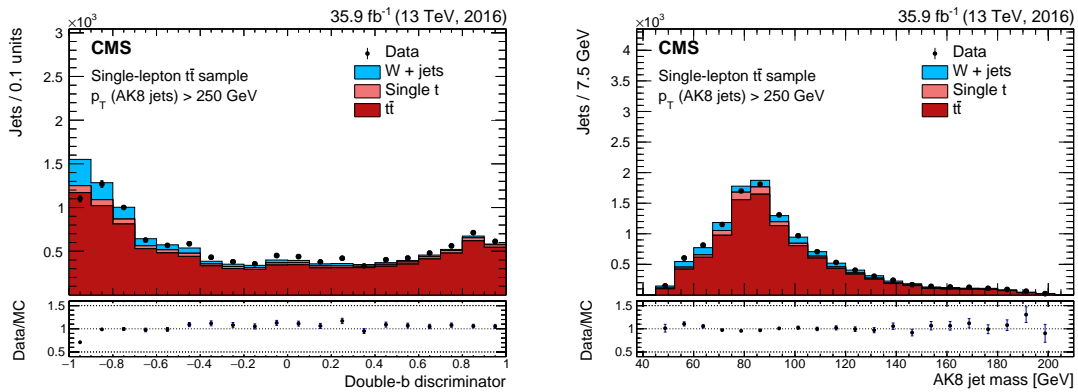


Figure 61. Distribution of the double-b tagger discriminator (left) and pruned jet mass (right) for AK8 jets passing the 2-prong event selection as described in the text. The simulation is normalized to the observed number of events.

The probability to misidentify a boosted top quark jet in data is obtained as follows:

$$\varepsilon_{\text{top}} = \frac{N_{\text{bb-tagged}}^{\text{data}} - N_{\text{bb-tagged}}^{\text{bkg,MC}}}{N^{\text{data}} - N^{\text{bkg,MC}}}, \quad (9.1)$$

where $N_{\text{bb-tagged}}^{\text{data}}$ and N^{data} are the number of events with a tagged AK8 jet in data and the total number of events in data, respectively. Similarly, $N_{\text{bb-tagged}}^{\text{bkg,MC}}$ and $N^{\text{bkg,MC}}$ are the simulated number of background events with a tagged AK8 jet and the number of simulated background events before applying the working point of the double-b tagger, respectively. The data-to-simulation scale factors are measured both inclusively and in bins of the AK8 jet p_T . The main systematic effect arises from the normalization of the background processes. An uncertainty of 30% is assigned to the cross section of each background contribution. An additional systematic uncertainty is related to the reweighting of the top quark p_T spectrum. The shape of the p_T distribution for top quarks in data is observed to be softer than in the simulation [77, 78]. For the nominal scale factor measurements, a reweighting procedure is applied to correct for the observed difference. To assess the size of any systematic effect due to the reweighting, the uncertainty is obtained as the difference between the nominal scale factor values and the scale factors obtained when repeating the measurement without applying the reweighting procedure. The systematic uncertainty is found to be 1–2%.

The data-to-simulation scale factors for the misidentification of boosted top quark jets for two of the working points of the double-b tagger are shown as a function of the jet p_T in figure 62. The scale factors are positioned at the average jet p_T value of the jets populating that bin.

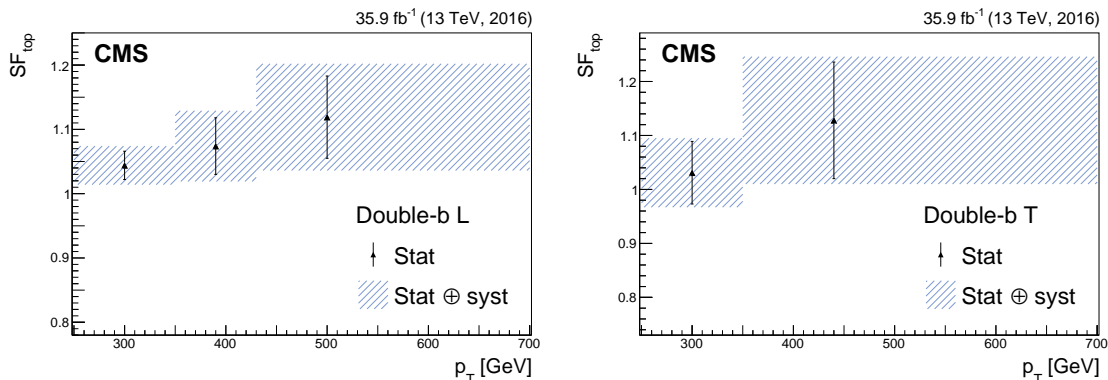


Figure 62. Data-to-simulation scale factors for misidentifying a top quark jet as a function of the jet p_T for the loose (left) and tight (right) working points of the double-b tagger. The hatched band around the scale factors represents the overall statistical and systematic uncertainty in the measurement. Jets with $p_T > 840$ GeV are included in the last p_T bin.

10 Summary

A variety of discriminating variables and algorithms used by the CMS experiment for the identification of heavy-flavour (charm and bottom) jets in proton-proton collisions at 13 TeV have been reviewed. Detailed simulation studies have allowed the reoptimization of existing b tagging algorithms and, in addition, new algorithms have been developed for the first time to identify c jets,

as well as $b\bar{b}$ jets in events with boosted topologies. The performance of these heavy-flavour jet identification algorithms has been studied with simulations of different final states with heavy- and light-flavour quarks. The efficiency to correctly identify b jets in resolved $t\bar{t}$ events is 68% at a misidentification probability for light-flavour jets of 1%, which is an improvement of 15% in relative efficiency compared to the best performing algorithm used during LHC Run 1.

The variables and discriminators have been also compared to the data collected by the CMS experiment in 2016 for various event topologies enriched in heavy- or light-flavour jets. Various methods have been presented to determine the data-to-simulation scale factors for the heavy-flavour jet identification efficiency, as well as for the probability to misidentify light-flavour jets. A precision of a few per cent is obtained in the tagging efficiency for b jets with $30 < p_T < 300$ GeV. For b jets with $p_T > 500$ GeV, the precision is of the order of 5%. For scale factors measured in boosted topologies and for c jets in resolved topologies, the total uncertainty is 5–10%, and the statistical uncertainty in the tagging efficiency dominates over the full jet p_T range.

With the increasing integrated luminosity delivered by the LHC, the precision of the data-to-simulation scale factors for the specified topologies, jet flavours, and p_T ranges will increase further. Differential studies of the heavy-flavour identification performances as a function of jet pseudorapidity, and of the number of multiple proton-proton interactions in the same bunch crossing, will also become viable.

Acknowledgments

We congratulate our colleagues in the CERN accelerator departments for the excellent performance of the LHC and thank the technical and administrative staffs at CERN and at other CMS institutes for their contributions to the success of the CMS effort. In addition, we gratefully acknowledge the computing centres and personnel of the Worldwide LHC Computing Grid for delivering so effectively the computing infrastructure essential to our analyses. Finally, we acknowledge the enduring support for the construction and operation of the LHC and the CMS detector provided by the following funding agencies: the Austrian Federal Ministry of Science, Research and Economy and the Austrian Science Fund; the Belgian Fonds de la Recherche Scientifique, and Fonds voor Wetenschappelijk Onderzoek; the Brazilian Funding Agencies (CNPq, CAPES, FAPERJ, and FAPESP); the Bulgarian Ministry of Education and Science; CERN; the Chinese Academy of Sciences, Ministry of Science and Technology, and National Natural Science Foundation of China; the Colombian Funding Agency (COLCIENCIAS); the Croatian Ministry of Science, Education and Sport, and the Croatian Science Foundation; the Research Promotion Foundation, Cyprus; the Secretariat for Higher Education, Science, Technology and Innovation, Ecuador; the Ministry of Education and Research, Estonian Research Council via IUT23-4 and IUT23-6 and European Regional Development Fund, Estonia; the Academy of Finland, Finnish Ministry of Education and Culture, and Helsinki Institute of Physics; the Institut National de Physique Nucléaire et de Physique des Particules / CNRS, and Commissariat à l'Énergie Atomique et aux Énergies Alternatives / CEA, France; the Bundesministerium für Bildung und Forschung, Deutsche Forschungsgemeinschaft, and Helmholtz-Gemeinschaft Deutscher Forschungszentren, Germany; the General Secretariat for Research and Technology, Greece; the National Scientific Research Foundation, and National Innovation Office, Hungary; the Department of Atomic Energy and the Department of Science

and Technology, India; the Institute for Studies in Theoretical Physics and Mathematics, Iran; the Science Foundation, Ireland; the Istituto Nazionale di Fisica Nucleare, Italy; the Ministry of Science, ICT and Future Planning, and National Research Foundation (NRF), Republic of Korea; the Lithuanian Academy of Sciences; the Ministry of Education, and University of Malaya (Malaysia); the Mexican Funding Agencies (BUAP, CINVESTAV, CONACYT, LNS, SEP, and UASLP-FAI); the Ministry of Business, Innovation and Employment, New Zealand; the Pakistan Atomic Energy Commission; the Ministry of Science and Higher Education and the National Science Centre, Poland; the Fundação para a Ciência e a Tecnologia, Portugal; JINR, Dubna; the Ministry of Education and Science of the Russian Federation, the Federal Agency of Atomic Energy of the Russian Federation, Russian Academy of Sciences, the Russian Foundation for Basic Research and the Russian Competitiveness Program of NRNU “MEPhI”; the Ministry of Education, Science and Technological Development of Serbia; the Secretaría de Estado de Investigación, Desarrollo e Innovación, Programa Consolider-Ingenio 2010, Plan de Ciencia, Tecnología e Innovación 2013-2017 del Principado de Asturias and Fondo Europeo de Desarrollo Regional, Spain; the Swiss Funding Agencies (ETH Board, ETH Zurich, PSI, SNF, UniZH, Canton Zurich, and SER); the Ministry of Science and Technology, Taipei; the Thailand Center of Excellence in Physics, the Institute for the Promotion of Teaching Science and Technology of Thailand, Special Task Force for Activating Research and the National Science and Technology Development Agency of Thailand; the Scientific and Technical Research Council of Turkey, and Turkish Atomic Energy Authority; the National Academy of Sciences of Ukraine, and State Fund for Fundamental Researches, Ukraine; the Science and Technology Facilities Council, UK; the US Department of Energy, and the US National Science Foundation.

Individuals have received support from the Marie-Curie programme and the European Research Council and Horizon 2020 Grant, contract No. 675440 (European Union); the Leventis Foundation; the A. P. Sloan Foundation; the Alexander von Humboldt Foundation; the Belgian Federal Science Policy Office; the Fonds pour la Formation à la Recherche dans l’Industrie et dans l’Agriculture (FRIA-Belgium); the Agentschap voor Innovatie door Wetenschap en Technologie (IWT-Belgium); the Ministry of Education, Youth and Sports (MEYS) of the Czech Republic; the Council of Scientific and Industrial Research, India; the HOMING PLUS programme of the Foundation for Polish Science, cofinanced from European Union, Regional Development Fund, the Mobility Plus programme of the Ministry of Science and Higher Education, the National Science Center (Poland), contracts Harmonia 2014/14/M/ST2/00428, Opus 2014/13/B/ST2/02543, 2014/15/B/ST2/03998, and 2015/19/B/ST2/02861, Sonata-bis 2012/07/E/ST2/01406; the National Priorities Research Program by Qatar National Research Fund; the Programa Severo Ochoa del Principado de Asturias; the Thalís and Aristeia programmes cofinanced by EU-ESF and the Greek NSRF; the Rachadapisek Sompot Fund for Postdoctoral Fellowship, Chulalongkorn University and the Chulalongkorn Academic into Its 2nd Century Project Advancement Project (Thailand); the Welch Foundation, contract C-1845; and the Weston Havens Foundation (USA).

A Parameterization of the efficiency

To facilitate phenomenological studies relying on b jet identification, we provide the b jet identification efficiency as a function of the jet p_T for the three operating points of the DeepCSV algorithm.

The efficiency is obtained using jets with $p_T > 20$ GeV in a simulated $t\bar{t}$ sample and is multiplied by the data-to-simulation scale factor to obtain the tagging efficiency expected in data. This efficiency is shown in figure 63 for the three jet flavours. Polynomial functions are used to fit the dependence of the efficiency on the jet p_T for jets with $20 < p_T < 1000$ GeV. It is worth noting that the parameterization of the fitted functions is not reliable outside this jet p_T range. The parameterizations are summarized in table 6.

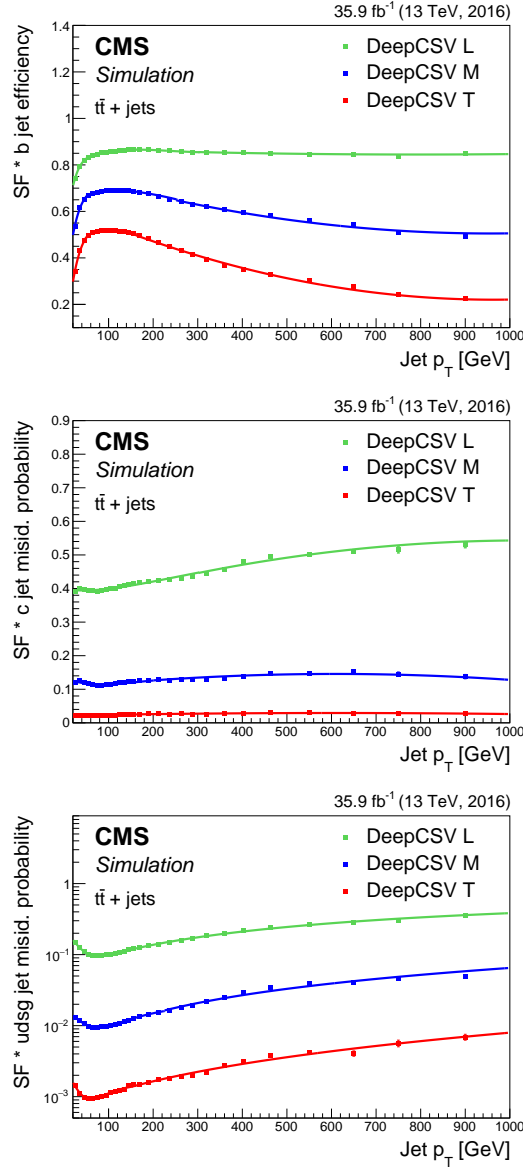


Figure 63. Efficiency for b tagging jets for the three different working points of the DeepCSV algorithm multiplied by the measured data-to-simulation scale factor. The efficiencies are shown as a function of the jet p_T using jets with $p_T > 20$ GeV in $t\bar{t}$ events for b jets (upper), c jets (middle), and light-flavour jets (lower). The solid lines represents the functions used to fit the dependence on the jet p_T . The last bin includes the overflow.

Table 6. Polynomial functions used to fit the efficiency of the three working points of the DeepCSV algorithm for the three jet flavours as a function of the jet p_T for jets with $20 < p_T < 1000$ GeV.

Flavour	Working point	p_T (GeV)	Function
b	DeepCSV L	20–160	$0.4344 + 0.02069p_T - 0.0004429p_T^2 + 5.137 \times 10^{-6}p_T^3 - 3.406 \times 10^{-8}p_T^4 + 1.285 \times 10^{-10}p_T^5 - 2.559 \times 10^{-13}p_T^6 + 2.084 \times 10^{-16}p_T^7$
		160–300	$0.714 + 0.002617p_T - 1.656 \times 10^{-5}p_T^2 + 4.767 \times 10^{-8}p_T^3 - 6.431 \times 10^{-11}p_T^4 + 3.287 \times 10^{-14}p_T^5$
		300–1000	$0.872 - 6.885 \times 10^{-5}p_T + 4.34 \times 10^{-8}p_T^2$
	DeepCSV M	20–50	$0.194 + 0.0211p_T - 0.000348p_T^2 + 2.761 \times 10^{-6}p_T^3 - 1.044 \times 10^{-8}p_T^4 + 1.499 \times 10^{-11}p_T^5$
		50–250	$0.557 + 0.003417p_T - 3.26 \times 10^{-5}p_T^2 + 1.506 \times 10^{-7}p_T^3 - 3.63 \times 10^{-10}p_T^4 + 3.522 \times 10^{-13}p_T^5$
		250–1000	$0.768 - 0.00055p_T + 2.876 \times 10^{-7}p_T^2$
	DeepCSV T	20–50	$-0.033 + 0.0225p_T - 0.00035p_T^2 + 2.586 \times 10^{-6}p_T^3 - 9.096 \times 10^{-9}p_T^4 + 1.212 \times 10^{-11}p_T^5$
		50–160	$0.169 + 0.013p_T - 0.00019p_T^2 + 1.373 \times 10^{-6}p_T^3 - 4.923 \times 10^{-9}p_T^4 + 6.87 \times 10^{-12}p_T^5$
		160–1000	$0.62 - 0.00083p_T + 4.3078 \times 10^{-7}p_T^2$
c	DeepCSV L	20–300	$0.398 - 0.000182p_T + 2.53 \times 10^{-6}p_T^2 - 6.796 \times 10^{-9}p_T^3 + 8.66 \times 10^{-12}p_T^4 - 4.42 \times 10^{-15}p_T^5$
		300–1000	$0.35 + 0.000374p_T - 1.81 \times 10^{-7}p_T^2$
	DeepCSV M	20–200	$0.136 - 0.000639p_T + 6.188 \times 10^{-6}p_T^2 - 2.26 \times 10^{-8}p_T^3 + 3.61 \times 10^{-11}p_T^4 + 2.09 \times 10^{-14}p_T^5$
		200–1000	$0.103 + 0.00014p_T - 1.15 \times 10^{-7}p_T^2$
	DeepCSV T	20–65	$0.0234 - 8.417 \times 10^{-5}p_T + 1.24 \times 10^{-6}p_T^2 - 5.5 \times 10^{-9}p_T^3 + 9.96 \times 10^{-12}p_T^4 - 6.32 \times 10^{-15}p_T^5$
		165–1000	$0.0218 + 2.46 \times 10^{-5}p_T - 2.021 \times 10^{-8}p_T^2$
udsg	DeepCSV L	20–150	$0.245 - 0.0054p_T + 6.92 \times 10^{-5}p_T^2 - 3.89 \times 10^{-7}p_T^3 + 1.021 \times 10^{-9}p_T^4 - 1.007 \times 10^{-12}p_T^5$
		150–1000	$0.0558 + 0.000428p_T - 1.0 \times 10^{-7}p_T^2$
	DeepCSV M	20–225	$0.019 - 0.00031p_T + 3.39 \times 10^{-6}p_T^2 - 1.47 \times 10^{-8}p_T^3 + 2.92 \times 10^{-11}p_T^4 - 2.12 \times 10^{-14}p_T^5$
		225–1000	$0.00328 + 5.7 \times 10^{-5}p_T + 4.7 \times 10^{-9}p_T^2$
	DeepCSV T	20–150	$0.00284 - 8.63 \times 10^{-5}p_T + 1.38 \times 10^{-6}p_T^2 - 9.69 \times 10^{-9}p_T^3 + 3.19 \times 10^{-11}p_T^4 - 3.97 \times 10^{-14}p_T^5$
		150–1000	$0.00063 + 4.51 \times 10^{-6}p_T + 2.83 \times 10^{-9}p_T^2$

References

- [1] CMS collaboration, *Identification of b-quark jets with the CMS experiment*, 2013 *JINST* **8** P04013 [[arXiv:1211.4462](#)].
- [2] CMS collaboration, *Description and performance of track and primary-vertex reconstruction with the CMS tracker*, 2014 *JINST* **9** P10009 [[arXiv:1405.6569](#)].
- [3] K. Rose, *Deterministic annealing for clustering, compression, classification, regression, and related optimization problems*, *Proc. IEEE* **86** (1998) 2210.
- [4] R. Fruhwirth, W. Waltenberger and P. Vanlaer, *Adaptive vertex fitting*, *J. Phys.* **G 34** (2007) N343.
- [5] CMS collaboration, *Particle-flow reconstruction and global event description with the CMS detector*, 2017 *JINST* **12** P10003 [[arXiv:1706.04965](#)].
- [6] M. Cacciari, G.P. Salam and G. Soyez, *The anti- k_t jet clustering algorithm*, *JHEP* **04** (2008) 063 [[arXiv:0802.1189](#)].
- [7] M. Cacciari, G.P. Salam and G. Soyez, *FastJet user manual*, *Eur. Phys. J. C* **72** (2012) 1896 [[arXiv:1111.6097](#)].
- [8] CMS collaboration, *Jet energy scale and resolution in the CMS experiment in pp collisions at 8 TeV*, 2017 *JINST* **12** P02014 [[arXiv:1607.03663](#)].
- [9] CMS collaboration, *Performance of electron reconstruction and selection with the CMS detector in proton-proton collisions at $\sqrt{s} = 8$ TeV*, 2015 *JINST* **10** P06005 [[arXiv:1502.02701](#)].
- [10] CMS collaboration, *Performance of CMS muon reconstruction in pp collision events at $\sqrt{s} = 7$ TeV*, 2012 *JINST* **7** P10002 [[arXiv:1206.4071](#)].
- [11] CMS collaboration, *The CMS trigger system*, 2017 *JINST* **12** P01020 [[arXiv:1609.02366](#)].
- [12] CMS collaboration, *The CMS experiment at the CERN LHC*, 2008 *JINST* **3** S08004.
- [13] GEANT4 collaboration, S. Agostinelli et al., *GEANT4: a simulation toolkit*, *Nucl. Instrum. Meth. A* **506** (2003) 250.
- [14] J. Allison et al., *Recent developments in GEANT4*, *Nucl. Instrum. Meth. A* **835** (2016) 186.
- [15] GEANT4 collaboration, *GEANT4 developments and applications*, *IEEE Trans. Nucl. Sci.* **53** (2006) 270.
- [16] P. Nason, *A new method for combining NLO QCD with shower Monte Carlo algorithms*, *JHEP* **11** (2004) 040 [[hep-ph/0409146](#)].
- [17] S. Frixione, P. Nason and C. Oleari, *Matching NLO QCD computations with parton shower simulations: the POWHEG method*, *JHEP* **11** (2007) 070 [[arXiv:0709.2092](#)].
- [18] S. Alioli, P. Nason, C. Oleari and E. Re, *A general framework for implementing NLO calculations in shower Monte Carlo programs: the POWHEG BOX*, *JHEP* **06** (2010) 043 [[arXiv:1002.2581](#)].
- [19] J.M. Campbell, R.K. Ellis, P. Nason and E. Re, *Top-pair production and decay at NLO matched with parton showers*, *JHEP* **04** (2015) 114 [[arXiv:1412.1828](#)].
- [20] E. Re, *Single-top Wt-channel production matched with parton showers using the POWHEG method*, *Eur. Phys. J. C* **71** (2011) 1547 [[arXiv:1009.2450](#)].
- [21] S. Alioli, P. Nason, C. Oleari and E. Re, *NLO single-top production matched with shower in POWHEG: s- and t-channel contributions*, *JHEP* **09** (2009) 111 [Erratum *ibid.* **1002** (2010) 011] [[arXiv:0907.4076](#)].

- [22] J. Alwall et al., *The automated computation of tree-level and next-to-leading order differential cross sections and their matching to parton shower simulations*, *JHEP* **07** (2014) 079 [[arXiv:1405.0301](#)].
- [23] P. Artoisenet, R. Frederix, O. Mattelaer and R. Rietkerk, *Automatic spin-entangled decays of heavy resonances in Monte Carlo simulations*, *JHEP* **03** (2013) 015 [[arXiv:1212.3460](#)].
- [24] R. Frederix and S. Frixione, *Merging meets matching in MC@NLO*, *JHEP* **12** (2012) 061 [[arXiv:1209.6215](#)].
- [25] T. Melia, P. Nason, R. Rontsch and G. Zanderighi, *W^+W^- , WZ and ZZ production in the POWHEG BOX*, *JHEP* **11** (2011) 078 [[arXiv:1107.5051](#)].
- [26] P. Nason and G. Zanderighi, *W^+W^- , WZ and ZZ production in the POWHEG-BOX-V2*, *Eur. Phys. J. C* **74** (2014) 2702 [[arXiv:1311.1365](#)].
- [27] M.L. Mangano, M. Moretti, F. Piccinini and M. Treccani, *Matching matrix elements and shower evolution for top-quark production in hadronic collisions*, *JHEP* **01** (2007) 013 [[hep-ph/0611129](#)].
- [28] L. Randall and R. Sundrum, *Large mass hierarchy from a small extra dimension*, *Phys. Rev. Lett.* **83** (1999) 3370 [[hep-ph/9905221](#)].
- [29] T. Sjöstrand et al., *An introduction to PYTHIA 8.2*, *Comput. Phys. Commun.* **191** (2015) 159 [[arXiv:1410.3012](#)].
- [30] CMS collaboration, *Event generator tunes obtained from underlying event and multiparton scattering measurements*, *Eur. Phys. J. C* **76** (2016) 155 [[arXiv:1512.00815](#)].
- [31] NNPDF collaboration, R.D. Ball et al., *Parton distributions with LHC data*, *Nucl. Phys. B* **867** (2013) 244 [[arXiv:1207.1303](#)].
- [32] CMS collaboration, *Investigations of the impact of the parton shower tuning in PYTHIA 8 in the modelling of $t\bar{t}$ at $\sqrt{s} = 8$ and 13 TeV*, *CMS-PAS-TOP-16-021* (2016).
- [33] NNPDF collaboration, R.D. Ball et al., *Parton distributions for the LHC Run II*, *JHEP* **04** (2015) 040 [[arXiv:1410.8849](#)].
- [34] M. Cacciari and G.P. Salam, *Pileup subtraction using jet areas*, *Phys. Lett. B* **659** (2008) 119 [[arXiv:0707.1378](#)].
- [35] PARTICLE DATA GROUP collaboration, C. Patrignani et al., *Review of Particle Physics*, *Chin. Phys. C* **40** (2016) 100001.
- [36] W. Waltenberger, *Adaptive Vertex Reconstruction*, *CMS-NOTE-2008-033* (2008).
- [37] CMS collaboration, *Measurement of $B\bar{B}$ Angular Correlations based on Secondary Vertex Reconstruction at $\sqrt{s} = 7$ TeV*, *JHEP* **03** (2011) 136 [[arXiv:1102.3194](#)].
- [38] D. Guest, J. Collado, P. Baldi, S.-C. Hsu, G. Urban and D. Whiteson, *Jet Flavor Classification in High-Energy Physics with Deep Neural Networks*, *Phys. Rev. D* **94** (2016) 112002 [[arXiv:1607.08633](#)].
- [39] W.S. Sarle, *Neural networks and statistical models*, in *Proceedings of the Nineteenth Annual SAS Users Group International Conference*, Strasburg France (1994).
- [40] F. Chollet, *Keras*, <https://github.com/fchollet/keras> (2015).
- [41] M. Abadi et al., *TensorFlow: Large-scale machine learning on heterogeneous systems*, software available from <http://tensorflow.org> (2015).
- [42] F. Pedregosa et al., *Scikit-learn: Machine Learning in Python*, *J. Machine Learning Res.* **12** (2011) 2825 [[arXiv:1201.0490](#)].

- [43] A. Dominguez et al., *CMS technical design report for the pixel detector upgrade*, [CERN-LHCC-2012-016](#) (2012).
- [44] M. Lehmann and N. Wermes, *Measurement of the flavour composition of dijet events in proton-proton collisions at $\sqrt{s} = 7$ TeV with the ATLAS detector at the LHC*, [CERN-THESIS-2013-050](#) (2013).
- [45] A.J. Larkoski, S. Marzani, G. Soyez and J. Thaler, *Soft drop*, *JHEP* **05** (2014) 146 [[arXiv:1402.2657](#)].
- [46] M. Dasgupta, A. Fregoso, S. Marzani and G.P. Salam, *Towards an understanding of jet substructure*, *JHEP* **09** (2013) 029 [[arXiv:1307.0007](#)].
- [47] J. Thaler and K. Van Tilburg, *Identifying boosted objects with N -subjettiness*, *JHEP* **03** (2011) 015 [[arXiv:1011.2268](#)].
- [48] CMS collaboration, *Jet algorithms performance in 13 TeV data*, [CMS-PAS-JME-16-003](#) (2017).
- [49] J.M. Butterworth, A.R. Davison, M. Rubin and G.P. Salam, *Jet substructure as a new Higgs search channel at the LHC*, in *Proceedings of 34th International Conference on High Energy Physics (ICHEP 2008)*, Philadelphia U.S.A. (2008).
- [50] D. Krohn, J. Thaler and L.-T. Wang, *Jet trimming*, *JHEP* **02** (2010) 084 [[arXiv:0912.1342](#)].
- [51] S.D. Ellis, C.K. Vermilion and J.R. Walsh, *Recombination algorithms and jet substructure: pruning as a tool for heavy particle searches*, *Phys. Rev. D* **81** (2010) 094023 [[arXiv:0912.0033](#)].
- [52] A. Hocker et al., *TMVA — toolkit for multivariate data analysis with ROOT*, [PoS\(ACAT\)040 \[physics/0703039\]](#).
- [53] CMS collaboration, *Inclusive b -jet production in pp collisions at $\sqrt{s} = 7$ TeV*, *JHEP* **04** (2012) 084 [[arXiv:1202.4617](#)].
- [54] CMS collaboration, *Measurement of the Inclusive Jet Cross Section in pp Collisions at $\sqrt{s} = 7$ TeV*, *Phys. Rev. Lett.* **107** (2011) 132001 [[arXiv:1106.0208](#)].
- [55] CMS collaboration, *CMS Tracking Performance Results from early LHC Operation*, *Eur. Phys. J. C* **70** (2010) 1165 [[arXiv:1007.1988](#)].
- [56] CMS collaboration, *Strange Particle Production in pp Collisions at $\sqrt{s} = 0.9$ and 7 TeV*, *JHEP* **05** (2011) 064 [[arXiv:1102.4282](#)].
- [57] ATLAS collaboration, *Measurement of the Inelastic Proton-Proton Cross Section at $\sqrt{s} = 13$ TeV with the ATLAS Detector at the LHC*, *Phys. Rev. Lett.* **117** (2016) 182002 [[arXiv:1606.02625](#)].
- [58] CMS collaboration, *Measurement of associated $W +$ charm production in pp collisions at $\sqrt{s} = 7$ TeV*, *JHEP* **02** (2014) 013 [[arXiv:1310.1138](#)].
- [59] L. Gladilin, *Fragmentation fractions of c and b quarks into charmed hadrons at LEP*, *Eur. Phys. J. C* **75** (2015) 19 [[arXiv:1404.3888](#)].
- [60] CMS collaboration, *Measurement of differential cross sections for top quark pair production using the lepton+jets final state in proton-proton collisions at 13 TeV*, *Phys. Rev. D* **95** (2017) 092001 [[arXiv:1610.04191](#)].
- [61] CMS collaboration, *Cross section measurement of t -channel single top quark production in pp collisions at $\sqrt{s} = 13$ TeV*, *Phys. Lett. B* **772** (2017) 752 [[arXiv:1610.00678](#)].
- [62] CMS collaboration, *Observation of the associated production of a single top quark and a W boson in pp collisions at $\sqrt{s} = 8$ TeV*, *Phys. Rev. Lett.* **112** (2014) 231802 [[arXiv:1401.2942](#)].

- [63] CMS collaboration, *Measurement of the differential cross sections for the associated production of a W boson and jets in proton-proton collisions at $\sqrt{s} = 13$ TeV*, *Phys. Rev. D* **96** (2017) 072005 [[arXiv:1707.05979](#)].
- [64] CMS collaboration, *Measurement of the production cross section of a W boson in association with two b jets in pp collisions at $\sqrt{s} = 8$ TeV*, *Eur. Phys. J. C* **77** (2017) 92 [[arXiv:1608.07561](#)].
- [65] CMS collaboration, *CMS luminosity measurements for the 2016 data taking period*, [CMS-PAS-LUM-17-001](#) (2017).
- [66] CMS collaboration, *Measurements of $t\bar{t}$ cross sections in association with b jets and inclusive jets and their ratio using dilepton final states in pp collisions at $\sqrt{s} = 13$ TeV*, *Phys. Lett. B* **776** (2018) 355 [[arXiv:1705.10141](#)].
- [67] P. Skands, S. Carrazza and J. Rojo, *Tuning PYTHIA 8.1: the Monash 2013 Tune*, *Eur. Phys. J. C* **74** (2014) 3024 [[arXiv:1404.5630](#)].
- [68] L. Lyons, D. Gibaut and P. Clifford, *How to combine correlated estimates of a single physical quantity*, *Nucl. Instrum. Meth. A* **270** (1988) 110.
- [69] A. Valassi, *Combining correlated measurements of several different physical quantities*, *Nucl. Instrum. Meth. A* **500** (2003) 391.
- [70] D0 collaboration, V.M. Abazov et al., *b -Jet Identification in the D0 Experiment*, *Nucl. Instrum. Meth. A* **620** (2010) 490 [[arXiv:1002.4224](#)].
- [71] ALEPH collaboration, R. Barate et al., *Measurement of the gluon splitting rate into $b\bar{b}$ pairs in hadronic Z decays*, *Phys. Lett. B* **434** (1998) 437.
- [72] PARTICLE DATA GROUP collaboration, C. Amsler et al., *Review of Particle Physics*, *Phys. Lett. B* **667** (2008) 1.
- [73] G. Mahlon and S.J. Parke, *Spin Correlation Effects in Top Quark Pair Production at the LHC*, *Phys. Rev. D* **81** (2010) 074024 [[arXiv:1001.3422](#)].
- [74] B.A. Betchart, R. Demina and A. Harel, *Analytic solutions for neutrino momenta in decay of top quarks*, *Nucl. Instrum. Meth. A* **736** (2014) 169 [[arXiv:1305.1878](#)].
- [75] ALEPH collaboration, A. Heister et al., *A measurement of the gluon splitting rate into $c\bar{c}$ pairs in hadronic Z decays*, *Phys. Lett. B* **561** (2003) 213 [[hep-ex/0302003](#)].
- [76] CMS collaboration, *Search for the associated production of the Higgs boson with a top-quark pair*, *JHEP* **09** (2014) 087 [Erratum *ibid.* **1410** (2014) 106] [[arXiv:1408.1682](#)].
- [77] CMS collaboration, *Measurement of the $t\bar{t}$ production cross section in the all-jets final state in pp collisions at $\sqrt{s} = 8$ TeV*, *Eur. Phys. J. C* **76** (2016) 128 [[arXiv:1509.06076](#)].
- [78] CMS collaboration, *Measurement of the differential cross section for top quark pair production in pp collisions at $\sqrt{s} = 8$ TeV*, *Eur. Phys. J. C* **75** (2015) 542 [[arXiv:1505.04480](#)].

The CMS collaboration

Yerevan Physics Institute, Yerevan, Armenia

A.M. Sirunyan, A. Tumasyan

Institut für Hochenergiephysik, Wien, Austria

W. Adam, F. Ambrogio, E. Asilar, T. Bergauer, J. Brandstetter, E. Brondolin, M. Dragicevic, J. Erö, A. Escalante Del Valle, M. Flechl, M. Friedl, R. Frühwirth¹, V.M. Ghete, J. Grossmann, J. Hrubec, M. Jeitler¹, A. König, N. Krammer, I. Krätschmer, D. Liko, T. Madlener, I. Mikulec, E. Pree, N. Rad, H. Rohringer, J. Schieck¹, R. Schöfbeck, M. Spanring, D. Spitzbart, W. Waltenberger, J. Wittmann, C.-E. Wulz¹, M. Zarucki

Institute for Nuclear Problems, Minsk, Belarus

V. Chekhovsky, V. Mossolov, J. Suarez Gonzalez

Universiteit Antwerpen, Antwerpen, Belgium

E.A. De Wolf, D. Di Croce, X. Janssen, J. Lauwers, M. Van De Klundert, H. Van Haevermaet, P. Van Mechelen, N. Van Remortel

Vrije Universiteit Brussel, Brussel, Belgium

S. Abu Zeid, F. Blekman, J. D'Hondt, I. De Bruyn, J. De Clercq, K. Deroover, G. Flouris, D. Lontkovskyi, S. Lowette, I. Marchesini, S. Moortgat, L. Moreels, Q. Python, K. Skovpen, S. Tavernier, W. Van Doninck, P. Van Mulders, I. Van Parijs

Université Libre de Bruxelles, Bruxelles, Belgium

D. Beghin, B. Bilin, H. Brun, B. Clerbaux, G. De Lentdecker, H. Delannoy, B. Dorney, G. Fasanella, L. Favart, R. Goldouzian, A. Grebenyuk, T. Lenzi, J. Luetic, T. Maerschalk, A. Marinov, T. Seva, E. Starling, C. Vander Velde, P. Vanlaer, D. Vannerom, R. Yonamine, F. Zenoni, F. Zhang²

Ghent University, Ghent, Belgium

A. Cimmino, T. Cornelis, D. Dobur, A. Fagot, M. Gul, I. Khvastunov³, D. Poyraz, C. Roskas, S. Salva, M. Tytgat, W. Verbeke, N. Zaganidis

Université Catholique de Louvain, Louvain-la-Neuve, Belgium

H. Bakhshiansohi, O. Bondu, S. Brochet, G. Bruno, C. Caputo, A. Caudron, P. David, S. De Visscher, C. Delaere, M. Delcourt, B. Francois, A. Giammanco, M. Komm, G. Krintiras, V. Lemaitre, A. Magitteri, A. Mertens, M. Musich, K. Piotrkowski, L. Quertenmont, A. Saggio, M. Vidal Marono, S. Wertz, J. Zobec

Centro Brasileiro de Pesquisas Fisicas, Rio de Janeiro, Brazil

W.L. Aldá Júnior, F.L. Alves, G.A. Alves, L. Brito, M. Correa Martins Junior, C. Hensel, A. Moraes, M.E. Pol, P. Rebello Teles

Universidade do Estado do Rio de Janeiro, Rio de Janeiro, Brazil

E. Belchior Batista Das Chagas, W. Carvalho, J. Chinellato⁴, E. Coelho, E.M. Da Costa, G.G. Da Silveira⁵, D. De Jesus Damiao, S. Fonseca De Souza, L.M. Huertas Guativa, H. Malbouisson, M. Melo De Almeida, C. Mora Herrera, L. Mundim, H. Nogima, L.J. Sanchez Rosas, A. Santoro, A. Sznajder, M. Thiel, E.J. Tonelli Manganote⁴, F. Torres Da Silva De Araujo, A. Vilela Pereira

Universidade Estadual Paulista ^a, Universidade Federal do ABC ^b, São Paulo, Brazil

S. Ahuja^a, C.A. Bernardes^a, T.R. Fernandez Perez Tomei^a, E.M. Gregores^b, P.G. Mercadante^b, S.F. Novaes^a, Sandra S. Padula^a, D. Romero Abad^b, J.C. Ruiz Vargas^a

Institute for Nuclear Research and Nuclear Energy, Bulgarian Academy of Sciences, Sofia, Bulgaria

A. Aleksandrov, R. Hadjiiska, P. Iaydjiev, M. Misheva, M. Rodozov, M. Shopova, G. Sultanov

University of Sofia, Sofia, Bulgaria

A. Dimitrov, L. Litov, B. Pavlov, P. Petkov

Beihang University, Beijing, China

W. Fang⁶, X. Gao⁶, L. Yuan

Institute of High Energy Physics, Beijing, China

M. Ahmad, G.M. Chen, H.S. Chen, M. Chen, Y. Chen, C.H. Jiang, D. Leggat, H. Liao, Z. Liu, F. Romeo, S.M. Shaheen, A. Spiezia, J. Tao, J. Thomas-wilsker, C. Wang, Z. Wang, E. Yazgan, H. Zhang, S. Zhang, J. Zhao

State Key Laboratory of Nuclear Physics and Technology, Peking University, Beijing, China

Y. Ban, G. Chen, J. Li, Q. Li, S. Liu, Y. Mao, S.J. Qian, D. Wang, Z. Xu

Tsinghua University, Beijing, China

Y. Wang

Universidad de Los Andes, Bogota, Colombia

C. Avila, A. Cabrera, C.A. Carrillo Montoya, L.F. Chaparro Sierra, C. Florez, C.F. González Hernández, J.D. Ruiz Alvarez, M.A. Segura Delgado

University of Split, Faculty of Electrical Engineering, Mechanical Engineering and Naval Architecture, Split, Croatia

B. Courbon, N. Godinovic, D. Lelas, I. Puljak, P.M. Ribeiro Cipriano, T. Sculac

University of Split, Faculty of Science, Split, Croatia

Z. Antunovic, M. Kovac

Institute Rudjer Boskovic, Zagreb, Croatia

V. Brigljevic, D. Ferencek, K. Kadija, B. Mesic, A. Starodumov⁷, T. Susa

University of Cyprus, Nicosia, Cyprus

M.W. Ather, A. Attikis, G. Mavromanolakis, J. Mousa, C. Nicolaou, F. Ptochos, P.A. Razis, H. Rykaczewski

Charles University, Prague, Czech Republic

M. Finger⁸, M. Finger Jr.⁸

Universidad San Francisco de Quito, Quito, Ecuador

E. Carrera Jarrin

Academy of Scientific Research and Technology of the Arab Republic of Egypt, Egyptian Network of High Energy Physics, Cairo, Egypt

E. El-khateeb⁹, S. Elgammal¹⁰, A. Ellithi Kamel¹¹

National Institute of Chemical Physics and Biophysics, Tallinn, Estonia

R.K. Dewanjee, M. Kadastik, L. Perrini, M. Raidal, A. Tiko, C. Veelken

Department of Physics, University of Helsinki, Helsinki, Finland

P. Eerola, H. Kirschenmann, J. Pekkanen, M. Voutilainen

Helsinki Institute of Physics, Helsinki, Finland

J. Havukainen, J.K. Heikkilä, T. Järvinen, V. Karimäki, R. Kinnunen, T. Lampén, K. Lassila-Perini, S. Laurila, S. Lehti, T. Lindén, P. Luukka, H. Siikonen, E. Tuominen, J. Tuominiemi

Lappeenranta University of Technology, Lappeenranta, Finland

T. Tuuva

IRFU, CEA, Université Paris-Saclay, Gif-sur-Yvette, France

M. Besancon, F. Couderc, M. Dejardin, D. Denegri, J.L. Faure, F. Ferri, S. Ganjour, S. Ghosh, P. Gras, G. Hamel de Monchenault, P. Jarry, I. Kucher, C. Leloup, E. Locci, M. Machet, J. Malcles, G. Negro, J. Rander, A. Rosowsky, M.Ö. Sahin, M. Titov

Laboratoire Leprince-Ringuet, Ecole polytechnique, CNRS/IN2P3, Université Paris-Saclay, Palaiseau, France

A. Abdulsalam, C. Amendola, I. Antropov, S. Baffioni, F. Beaudette, P. Busson, L. Cadamuro, C. Charlot, R. Granier de Cassagnac, M. Jo, S. Lisniak, A. Lobanov, J. Martin Blanco, M. Nguyen, C. Ochando, G. Ortona, P. Paganini, P. Pigard, R. Salerno, J.B. Sauvan, Y. Sirois, A.G. Stahl Leitton, T. Strebler, Y. Yilmaz, A. Zabi, A. Zghiche

Université de Strasbourg, CNRS, IPHC UMR 7178, F-67000 Strasbourg, France

J.-L. Agram¹², J. Andrea, D. Bloch, J.-M. Brom, M. Buttignol, E.C. Chabert, N. Chanon, C. Collard, E. Conte¹², X. Coubez, J.-C. Fontaine¹², D. Gelé, U. Goerlach, M. Jansová, A.-C. Le Bihan, N. Tonon, P. Van Hove

Centre de Calcul de l'Institut National de Physique Nucleaire et de Physique des Particules, CNRS/IN2P3, Villeurbanne, France

S. Gadrat

Université de Lyon, Université Claude Bernard Lyon 1, CNRS-IN2P3, Institut de Physique Nucléaire de Lyon, Villeurbanne, France

S. Beauceron, C. Bernet, G. Boudoul, R. Chierici, D. Contardo, P. Depasse, H. El Mamouni, J. Fay, L. Finco, S. Gascon, M. Gouzevitch, G. Grenier, B. Ille, F. Lagarde, I.B. Laktineh, M. Lethuillier, L. Mirabito, A.L. Pequegnot, S. Perries, A. Popov¹³, V. Sordini, M. Vander Donckt, S. Viret

Georgian Technical University, Tbilisi, Georgia

A. Khvedelidze⁸

Tbilisi State University, Tbilisi, Georgia

Z. Tsamalaidze⁸

RWTH Aachen University, I. Physikalisches Institut, Aachen, Germany

C. Autermann, L. Feld, M.K. Kiesel, K. Klein, M. Lipinski, M. Preuten, C. Schomakers, J. Schulz, M. Teroerde, V. Zhukov¹³

RWTH Aachen University, III. Physikalisches Institut A, Aachen, Germany

A. Albert, E. Dietz-Laursonn, D. Duchardt, M. Endres, M. Erdmann, S. Erdweg, T. Esch, R. Fischer, A. Güth, M. Hamer, T. Hebbeker, C. Heidemann, K. Hoepfner, S. Knutzen, M. Merschmeyer, A. Meyer, P. Millet, S. Mukherjee, T. Pook, M. Radziej, H. Reithler, M. Rieger, F. Scheuch, D. Teyssier, S. Thüer

RWTH Aachen University, III. Physikalisches Institut B, Aachen, Germany

G. Flügge, B. Kargoll, T. Kress, A. Künsken, T. Müller, A. Nehr Korn, A. Nowack, C. Pistone, O. Pooth, A. Stahl¹⁴

Deutsches Elektronen-Synchrotron, Hamburg, Germany

M. Aldaya Martin, T. Arndt, C. Asawatangtrakuldee, K. Beernaert, O. Behnke, U. Behrens, A. Bermúdez Martínez, A.A. Bin Anuar, K. Borras¹⁵, V. Botta, A. Campbell, P. Connor, C. Contreras-Campana, F. Costanza, M.M. Defranchis, C. Diez Pardos, G. Eckerlin, D. Eckstein, T. Eichhorn, E. Eren, E. Gallo¹⁶, J. Garay Garcia, A. Geiser, J.M. Grados Luyando, A. Grohsjean, P. Gunnellini, M. Guthoff, A. Harb, J. Hauk, M. Hempel¹⁷, H. Jung, M. Kasemann, J. Keaveney, C. Kleinwort, I. Korol, D. Krücker, W. Lange, A. Lelek, T. Lenz, J. Leonard, K. Lipka, W. Lohmann¹⁷, R. Mankel, I.-A. Melzer-Pellmann, A.B. Meyer, G. Mittag, J. Mnich, A. Mussgiller, E. Ntomari, D. Pitzl, A. Raspereza, M. Savitskyi, P. Saxena, R. Shevchenko, S. Spannagel, N. Stefaniuk, G.P. Van Onsem, R. Walsh, Y. Wen, K. Wichmann, C. Wissing, O. Zenaiev

University of Hamburg, Hamburg, Germany

R. Aggleton, S. Bein, V. Blobel, M. Centis Vignali, T. Dreyer, E. Garutti, D. Gonzalez, J. Haller, A. Hinzmann, M. Hoffmann, A. Karavdina, R. Klanner, R. Kogler, N. Kovalchuk, S. Kurz, T. Lapsien, D. Marconi, M. Meyer, M. Niedziela, D. Nowatschin, F. Pantaleo¹⁴, T. Peiffer, A. Perieanu, C. Scharf, P. Schleper, A. Schmidt, S. Schumann, J. Schwandt, J. Sonneveld, H. Stadie, G. Steinbrück, F.M. Stober, M. Stöver, H. Tholen, D. Troendle, E. Usai, A. Vanhoefer, B. Vormwald

Institut für Experimentelle Kernphysik, Karlsruhe, Germany

M. Akbiyik, C. Barth, M. Baselga, S. Baur, E. Butz, R. Caspart, T. Chwalek, F. Colombo, W. De Boer, A. Dierlamm, K. El Morabit, N. Faltermann, B. Freund, R. Friese, M. Giffels, M.A. Harrendorf, F. Hartmann¹⁴, S.M. Heindl, U. Husemann, F. Kassel¹⁴, S. Kudella, H. Mildner, M.U. Mozer, Th. Müller, M. Plagge, G. Quast, K. Rabbertz, M. Schröder, I. Shvetsov, G. Sieber, H.J. Simonis, R. Ulrich, S. Wayand, M. Weber, T. Weiler, S. Williamson, C. Wöhrmann, R. Wolf

Institute of Nuclear and Particle Physics (INPP), NCSR Demokritos, Aghia Paraskevi, Greece

G. Anagnostou, G. Daskalakis, T. Gerasis, A. Kyriakis, D. Loukas, I. Topsis-Giotis

National and Kapodistrian University of Athens, Athens, Greece

G. Karathanasis, S. Kesisoglou, A. Panagiotou, N. Saoulidou

National Technical University of Athens, Athens, Greece

K. Kousouris

University of Ioánnina, Ioánnina, Greece

I. Evangelou, C. Foudas, P. Giannelos, P. Katsoulis, P. Kokkas, S. Mallios, N. Manthos, I. Papadopoulos, E. Paradas, J. Strologas, F.A. Triantis, D. Tsitsonis

MTA-ELTE Lendület CMS Particle and Nuclear Physics Group, Eötvös Loránd University, Budapest, Hungary

M. Csanad, N. Filipovic, G. Pasztor, O. Surányi, G.I. Veres¹⁸

Wigner Research Centre for Physics, Budapest, Hungary

G. Bencze, C. Hajdu, D. Horvath¹⁹, Á. Hunyadi, F. Sikler, V. Veszpremi

Institute of Nuclear Research ATOMKI, Debrecen, Hungary

N. Beni, S. Czellar, J. Karancsi²⁰, A. Makovec, J. Molnar, Z. Szillasi

Institute of Physics, University of Debrecen, Debrecen, Hungary

M. Bartók¹⁸, P. Raics, Z.L. Trocsanyi, B. Ujvari

Indian Institute of Science (IISc), Bangalore, India

S. Choudhury, J.R. Komaragiri

National Institute of Science Education and Research, Bhubaneswar, India

S. Bahinipati²¹, S. Bhowmik, P. Mal, K. Mandal, A. Nayak²², D.K. Sahoo²¹, N. Sahoo, S.K. Swain

Panjab University, Chandigarh, India

S. Bansal, S.B. Beri, V. Bhatnagar, R. Chawla, N. Dhingra, A.K. Kalsi, A. Kaur, M. Kaur, S. Kaur, R. Kumar, P. Kumari, A. Mehta, J.B. Singh, G. Walia

University of Delhi, Delhi, India

Ashok Kumar, Aashaq Shah, A. Bhardwaj, S. Chauhan, B.C. Choudhary, R.B. Garg, S. Keshri, A. Kumar, S. Malhotra, M. Naimuddin, K. Ranjan, R. Sharma

Saha Institute of Nuclear Physics, HBNI, Kolkata, India

R. Bhardwaj, R. Bhattacharya, S. Bhattacharya, U. Bhawandeep, S. Dey, S. Dutt, S. Dutta, S. Ghosh, N. Majumdar, A. Modak, K. Mondal, S. Mukhopadhyay, S. Nandan, A. Purohit, A. Roy, S. Roy Chowdhury, S. Sarkar, M. Sharan, S. Thakur

Indian Institute of Technology Madras, Madras, India

P.K. Behera

Bhabha Atomic Research Centre, Mumbai, India

R. Chudasama, D. Dutta, V. Jha, V. Kumar, A.K. Mohanty¹⁴, P.K. Netrakanti, L.M. Pant, P. Shukla, A. Topkar

Tata Institute of Fundamental Research-A, Mumbai, India

T. Aziz, S. Dugad, B. Mahakud, S. Mitra, G.B. Mohanty, N. Sur, B. Sutar

Tata Institute of Fundamental Research-B, Mumbai, India

S. Banerjee, S. Bhattacharya, S. Chatterjee, P. Das, M. Guchait, Sa. Jain, S. Kumar, M. Maity²³, G. Majumder, K. Mazumdar, T. Sarkar²³, N. Wickramage²⁴

Indian Institute of Science Education and Research (IISER), Pune, India

S. Chauhan, S. Dube, V. Hegde, A. Kapoor, K. Kotheekar, S. Pandey, A. Rane, S. Sharma

Institute for Research in Fundamental Sciences (IPM), Tehran, Iran

S. Chenarani²⁵, E. Eskandari Tadavani, S.M. Etesami²⁵, M. Khakzad, M. Mohammadi Najafabadi, M. Naseri, S. Paktinat Mehdiabadi²⁶, F. Rezaei Hosseinabadi, B. Safarzadeh²⁷, M. Zeinali

University College Dublin, Dublin, Ireland

M. Felcini, M. Grunewald

INFN Sezione di Bari ^a, Università di Bari ^b, Politecnico di Bari ^c, Bari, Italy

M. Abbrescia^{a,b}, C. Calabria^{a,b}, A. Colaleo^a, D. Creanza^{a,c}, L. Cristella^{a,b}, N. De Filippis^{a,c}, M. De Palma^{a,b}, F. Errico^{a,b}, L. Fiore^a, G. Iaselli^{a,c}, S. Lezki^{a,b}, G. Maggi^{a,c}, M. Maggi^a, G. Miniello^{a,b}, S. My^{a,b}, S. Nuzzo^{a,b}, A. Pompili^{a,b}, G. Pugliese^{a,c}, R. Radogna^a, A. Ranieri^a, G. Selvaggi^{a,b}, A. Sharma^a, L. Silvestris^{a,14}, R. Venditti^a, P. Verwilligen^a

INFN Sezione di Bologna ^a, Università di Bologna ^b, Bologna, Italy

G. Abbiendi^a, C. Battilana^{a,b}, D. Bonacorsi^{a,b}, L. Borgonovi^{a,b}, S. Braibant-Giacomelli^{a,b}, R. Campanini^{a,b}, P. Capiluppi^{a,b}, A. Castro^{a,b}, F.R. Cavallo^a, S.S. Chhibra^a, G. Codispoti^{a,b}, M. Cuffiani^{a,b}, G.M. Dallavalle^a, F. Fabbri^a, A. Fanfani^{a,b}, D. Fasanella^{a,b}, P. Giacomelli^a, C. Grandi^a, L. Guiducci^{a,b}, S. Marcellini^a, G. Masetti^a, A. Montanari^a, F.L. Navarria^{a,b}, A. Perrotta^a, A.M. Rossi^{a,b}, T. Rovelli^{a,b}, G.P. Siroli^{a,b}, N. Tosi^a

INFN Sezione di Catania ^a, Università di Catania ^b, Catania, Italy

S. Albergo^{a,b}, S. Costa^{a,b}, A. Di Mattia^a, F. Giordano^{a,b}, R. Potenza^{a,b}, A. Tricomi^{a,b}, C. Tuve^{a,b}

INFN Sezione di Firenze ^a, Università di Firenze ^b, Firenze, Italy

G. Barbagli^a, K. Chatterjee^{a,b}, V. Ciulli^{a,b}, C. Civinini^a, R. D'Alessandro^{a,b}, E. Focardi^{a,b}, P. Lenzi^{a,b}, M. Meschini^a, S. Paoletti^a, L. Russo^{a,28}, G. Sguazzoni^a, D. Strom^a, L. Viliani^{a,b,14}

INFN Laboratori Nazionali di Frascati, Frascati, Italy

L. Benussi, S. Bianco, F. Fabbri, D. Piccolo, F. Primavera¹⁴

INFN Sezione di Genova ^a, Università di Genova ^b, Genova, Italy

V. Calvelli^{a,b}, F. Ferro^a, F. Ravera^{a,b}, E. Robutti^a, S. Tosi^{a,b}

INFN Sezione di Milano-Bicocca ^a, Università di Milano-Bicocca ^b, Milano, Italy

A. Benaglia^a, A. Beschi^b, L. Brianza^{a,b}, F. Brivio^{a,b}, V. Ciriolo^{a,b,14}, M.E. Dinardo^{a,b}, S. Fiorendi^{a,b}, S. Gennai^a, A. Ghezzi^{a,b}, P. Govoni^{a,b}, M. Malberti^{a,b}, S. Malvezzi^a, R.A. Manzoni^{a,b}, D. Menasce^a, L. Moroni^a, M. Paganoni^{a,b}, K. Pauwels^{a,b}, D. Pedrini^a, S. Pigazzini^{a,b,29}, S. Ragazzi^{a,b}, T. Tabarelli de Fatis^{a,b}

INFN Sezione di Napoli ^a, Università di Napoli 'Federico II' ^b, Napoli, Italy, Università della Basilicata ^c, Potenza, Italy, Università G. Marconi ^d, Roma, Italy

S. Buontempo^a, N. Cavallo^{a,c}, S. Di Guida^{a,d,14}, F. Fabozzi^{a,c}, F. Fienga^{a,b}, A.O.M. Iorio^{a,b}, W.A. Khan^a, L. Lista^a, S. Meola^{a,d,14}, P. Paolucci^{a,14}, C. Sciacca^{a,b}, F. Thyssen^a

INFN Sezione di Padova ^a, Università di Padova ^b, Padova, Italy, Università di Trento ^c, Trento, Italy

P. Azzi^a, N. Bacchetta^a, L. Benato^{a,b}, D. Bisello^{a,b}, A. Boletti^{a,b}, P. Checchia^a, M. Dall'Osso^{a,b}, P. De Castro Manzano^a, T. Dorigo^a, U. Dosselli^a, F. Fanzago^a, F. Gasparini^{a,b}, U. Gasparini^{a,b}, A. Gozzelino^a, S. Lacaprara^a, P. Lujan, M. Margoni^{a,b}, A.T. Meneguzzo^{a,b}, N. Pozzobon^{a,b}, P. Ronchese^{a,b}, R. Rossin^{a,b}, F. Simonetto^{a,b}, E. Torassa^a, S. Ventura^a, M. Zanetti^{a,b}, P. Zotto^{a,b}

INFN Sezione di Pavia ^a, Università di Pavia ^b, Pavia, Italy

A. Braghieri^a, A. Magnani^a, P. Montagna^{a,b}, S.P. Ratti^{a,b}, V. Re^a, M. Ressegotti^{a,b}, C. Riccardi^{a,b}, P. Salvini^a, I. Vai^{a,b}, P. Vitulo^{a,b}

INFN Sezione di Perugia ^a, Università di Perugia ^b, Perugia, Italy

L. Alunni Solestizi^{a,b}, M. Biasini^{a,b}, G.M. Bilei^a, C. Cecchi^{a,b}, D. Ciangottini^{a,b}, L. Fanò^{a,b}, R. Leonardi^{a,b}, E. Manoni^a, G. Mantovani^{a,b}, V. Mariani^{a,b}, M. Menichelli^a, A. Rossi^{a,b}, A. Santocchia^{a,b}, D. Spiga^a

INFN Sezione di Pisa ^a, Università di Pisa ^b, Scuola Normale Superiore di Pisa ^c, Pisa, Italy

K. Androsov^a, P. Azzurri^{a,14}, G. Bagliesi^a, T. Boccali^a, L. Borrello, R. Castaldi^a, M.A. Ciocci^{a,b}, R. Dell'Orso^a, G. Fedi^a, L. Giannini^{a,c}, A. Giassi^a, M.T. Grippo^{a,28}, F. Ligabue^{a,c}, T. Lomtadze^a, E. Manca^{a,c}, G. Mandorli^{a,c}, A. Messineo^{a,b}, F. Palla^a, A. Rizzi^{a,b}, A. Savoy-Navarro^{a,30}, P. Spagnolo^a, R. Tenchini^a, G. Tonelli^{a,b}, A. Venturi^a, P.G. Verdini^a

INFN Sezione di Roma ^a, Sapienza Università di Roma ^b, Rome, Italy

L. Barone^{a,b}, F. Cavallari^a, M. Cipriani^{a,b}, N. Daci^a, D. Del Re^{a,b,14}, E. Di Marco^{a,b}, M. Diemoz^a, S. Gelli^{a,b}, E. Longo^{a,b}, F. Margaroli^{a,b}, B. Marzocchi^{a,b}, P. Meridiani^a, G. Organtini^{a,b}, R. Paramatti^{a,b}, F. Preiato^{a,b}, S. Rahatlou^{a,b}, C. Rovelli^a, F. Santanastasio^{a,b}

INFN Sezione di Torino ^a, Università di Torino ^b, Torino, Italy, Università del Piemonte Orientale ^c, Novara, Italy

N. Amapane^{a,b}, R. Arcidiacono^{a,c}, S. Argiro^{a,b}, M. Arneodo^{a,c}, N. Bartosik^a, R. Bellan^{a,b}, C. Biino^a, N. Cartiglia^a, F. Cenna^{a,b}, M. Costa^{a,b}, R. Covarelli^{a,b}, A. Degano^{a,b}, N. Demaria^a, B. Kiani^{a,b}, C. Mariotti^a, S. Maselli^a, E. Migliore^{a,b}, V. Monaco^{a,b}, E. Monteil^{a,b}, M. Monteno^a, M.M. Obertino^{a,b}, L. Pacher^{a,b}, N. Pastrone^a, M. Pelliccioni^a, G.L. Pinna Angioni^{a,b}, A. Romero^{a,b}, M. Ruspa^{a,c}, R. Sacchi^{a,b}, K. Shchelina^{a,b}, V. Sola^a, A. Solano^{a,b}, A. Staiano^a, P. Traczyk^{a,b}

INFN Sezione di Trieste ^a, Università di Trieste ^b, Trieste, Italy

S. Belforte^a, M. Casarsa^a, F. Cossutti^a, G. Della Ricca^{a,b}, A. Zanetti^a

Kyungpook National University, Daegu, Korea

D.H. Kim, G.N. Kim, M.S. Kim, J. Lee, S. Lee, S.W. Lee, C.S. Moon, Y.D. Oh, S. Sekmen, D.C. Son, Y.C. Yang

Chonbuk National University, Jeonju, Korea

A. Lee

Chonnam National University, Institute for Universe and Elementary Particles, Kwangju, Korea

H. Kim, D.H. Moon, G. Oh

Hanyang University, Seoul, Korea

J.A. Brochero Cifuentes, J. Goh, T.J. Kim

Korea University, Seoul, Korea

S. Cho, S. Choi, Y. Go, D. Gyun, S. Ha, B. Hong, Y. Jo, Y. Kim, K. Lee, K.S. Lee, S. Lee, J. Lim, S.K. Park, Y. Roh

Seoul National University, Seoul, Korea

J. Almond, J. Kim, J.S. Kim, H. Lee, K. Lee, K. Nam, S.B. Oh, B.C. Radburn-Smith, S.h. Seo, U.K. Yang, H.D. Yoo, G.B. Yu

University of Seoul, Seoul, Korea

H. Kim, J.H. Kim, J.S.H. Lee, I.C. Park

Sungkyunkwan University, Suwon, Korea

Y. Choi, C. Hwang, J. Lee, I. Yu

Vilnius University, Vilnius, Lithuania

V. Dudenas, A. Juodagalvis, J. Vaitkus

National Centre for Particle Physics, Universiti Malaya, Kuala Lumpur, Malaysia

I. Ahmed, Z.A. Ibrahim, M.A.B. Md Ali³¹, F. Mohamad Idris³², W.A.T. Wan Abdullah, M.N. Yusli, Z. Zolkapli

Centro de Investigacion y de Estudios Avanzados del IPN, Mexico City, Mexico

Reyes-Almanza, R, Ramirez-Sanchez, G., Duran-Osuna, M. C., H. Castilla-Valdez, E. De La Cruz-Burelo, I. Heredia-De La Cruz³³, Rabadan-Trejo, R. I., R. Lopez-Fernandez, J. Mejia Guisao, A. Sanchez-Hernandez

Universidad Iberoamericana, Mexico City, Mexico

S. Carrillo Moreno, C. Oropeza Barrera, F. Vazquez Valencia

Benemerita Universidad Autonoma de Puebla, Puebla, Mexico

J. Eysermans, I. Pedraza, H.A. Salazar Ibarguen, C. Uribe Estrada

Universidad Autónoma de San Luis Potosí, San Luis Potosí, Mexico

A. Morelos Pineda

University of Auckland, Auckland, New Zealand

D. Krofcheck

University of Canterbury, Christchurch, New Zealand

P.H. Butler

National Centre for Physics, Quaid-I-Azam University, Islamabad, Pakistan

A. Ahmad, M. Ahmad, Q. Hassan, H.R. Hoorani, A. Saddique, M.A. Shah, M. Shoaib, M. Waqas

National Centre for Nuclear Research, Swierk, Poland

H. Bialkowska, M. Bluj, B. Boimska, T. Frueboes, M. Górski, M. Kazana, K. Nawrocki, M. Szleper, P. Zalewski

Institute of Experimental Physics, Faculty of Physics, University of Warsaw, Warsaw, Poland

K. Bunkowski, A. Byszuk³⁴, K. Doroba, A. Kalinowski, M. Konecki, J. Krolikowski, M. Misiura, M. Olszewski, A. Pyskir, M. Walczak

Laboratório de Instrumentação e Física Experimental de Partículas, Lisboa, Portugal

P. Bargassa, C. Beirão Da Cruz E Silva, A. Di Francesco, P. Faccioli, B. Galinhas, M. Gallinaro, J. Hollar, N. Leonardo, L. Lloret Iglesias, M.V. Nemallapudi, J. Seixas, G. Strong, O. Toldaiev, D. Vadrucio, J. Varela

Joint Institute for Nuclear Research, Dubna, Russia

A. Baginyan, A. Golunov, I. Golutvin, A. Kamenev, V. Karjavin, I. Kashunin, V. Korenkov, G. Kozlov, A. Lanev, A. Malakhov, V. Matveev^{35,36}, V. Palichik, V. Pereygin, S. Shmatov, V. Smirnov, V. Trofimov, B.S. Yuldashev³⁷, A. Zarubin

Petersburg Nuclear Physics Institute, Gatchina (St. Petersburg), Russia

Y. Ivanov, V. Kim³⁸, E. Kuznetsova³⁹, P. Levchenko, V. Murzin, V. Oreshkin, I. Smirnov, D. Sosnov, V. Sulimov, L. Uvarov, S. Vavilov, A. Vorobyev

Institute for Nuclear Research, Moscow, Russia

Yu. Andreev, A. Dermenev, S. Gninenko, N. Golubev, A. Karneyeu, M. Kirsanov, N. Krasnikov, A. Pashenkov, D. Tlisov, A. Toropin

Institute for Theoretical and Experimental Physics, Moscow, Russia

V. Epshteyn, V. Gavrilov, N. Lychkovskaya, V. Popov, I. Pozdnyakov, G. Safronov, A. Spiridonov, A. Stepenov, M. Toms, E. Vlasov, A. Zhokin

Moscow Institute of Physics and Technology, Moscow, Russia

T. Aushev, A. Bylinkin³⁶

National Research Nuclear University 'Moscow Engineering Physics Institute' (MEPhI), Moscow, Russia

R. Chistov⁴⁰, M. Danilov⁴⁰, P. Parygin, D. Philippov, S. Polikarpov, E. Tarkovskii

P.N. Lebedev Physical Institute, Moscow, Russia

V. Andreev, M. Azarkin³⁶, I. Dremin³⁶, M. Kirakosyan³⁶, A. Terkulov

Skobeltsyn Institute of Nuclear Physics, Lomonosov Moscow State University, Moscow, Russia

A. Baskakov, A. Belyaev, E. Boos, M. Dubinin⁴¹, L. Dudko, A. Ershov, A. Gribushin, V. Klyukhin, O. Kodolova, I. Lokhtin, I. Miagkov, S. Obraztsov, S. Petrushanko, V. Savrin, A. Snigirev

Novosibirsk State University (NSU), Novosibirsk, Russia

V. Blinov⁴², D. Shtol⁴², Y. Skovpen⁴²

State Research Center of Russian Federation, Institute for High Energy Physics, Protvino, Russia

I. Azhgirey, I. Bayshev, S. Bitioukov, D. Elumakhov, A. Godizov, V. Kachanov, A. Kalinin, D. Konstantinov, P. Mandrik, V. Petrov, R. Ryutin, A. Sobol, S. Troshin, N. Tyurin, A. Uzunian, A. Volkov

University of Belgrade, Faculty of Physics and Vinca Institute of Nuclear Sciences, Belgrade, Serbia

P. Adzic⁴³, P. Cirkovic, D. Devetak, M. Dordevic, J. Milosevic, V. Rekovic

Centro de Investigaciones Energéticas Medioambientales y Tecnológicas (CIEMAT), Madrid, Spain

J. Alcaraz Maestre, I. Bachiller, M. Barrio Luna, M. Cerrada, N. Colino, B. De La Cruz, A. Delgado Peris, C. Fernandez Bedoya, J.P. Fernández Ramos, J. Flix, M.C. Fouz, O. Gonzalez Lopez, S. Goy Lopez, J.M. Hernandez, M.I. Josa, D. Moran, A. Pérez-Calero Yzquierdo, J. Puerta Pelayo, A. Quintario Olmeda, I. Redondo, L. Romero, M.S. Soares, A. Álvarez Fernández

Universidad Autónoma de Madrid, Madrid, Spain

C. Albajar, J.F. de Trocóniz, M. Missiroli

Universidad de Oviedo, Oviedo, Spain

J. Cuevas, C. Erice, J. Fernandez Menendez, I. Gonzalez Caballero, J.R. González Fernández, E. Palencia Cortezon, S. Sanchez Cruz, P. Vischia, J.M. Vizán García

Instituto de Física de Cantabria (IFCA), CSIC-Universidad de Cantabria, Santander, Spain

I.J. Cabrillo, A. Calderon, B. Chazin Quero, E. Curras, J. Duarte Campderros, M. Fernandez, J. Garcia-Ferrero, G. Gomez, A. Lopez Virto, J. Marco, C. Martinez Rivero, P. Martinez Ruiz del Arbol, F. Matorras, J. Piedra Gomez, T. Rodrigo, A. Ruiz-Jimeno, L. Scodellaro, N. Trevisani, I. Vila, R. Vilar Cortabitarte

CERN, European Organization for Nuclear Research, Geneva, Switzerland

D. Abbaneo, B. Akgun, E. Auffray, P. Baillon, A.H. Ball, D. Barney, J. Bendavid, M. Bianco, P. Bloch, A. Bocci, C. Botta, T. Camporesi, R. Castello, M. Cepeda, G. Cerminara, E. Chapon, Y. Chen, D. d'Enterria, A. Dabrowski, V. Daponte, A. David, M. De Gruttola, A. De Roeck, N. Deelen, M. Dobson, T. du Pree, M. Dünser, N. Dupont, A. Elliott-Peisert, P. Everaerts, F. Fallavollita, G. Franzoni, J. Fulcher, W. Funk, D. Gigi, A. Gilbert, K. Gill, F. Glege, D. Gulhan, P. Harris, J. Hegeman, V. Innocente, A. Jafari, P. Janot, O. Karacheban¹⁷, J. Kieseler, V. Knünz, A. Kornmayer, M.J. Kortelainen, M. Krammer¹, C. Lange, P. Lecoq, C. Lourenço, M.T. Lucchini, L. Malgeri, M. Mannelli, A. Martelli, F. Meijers, J.A. Merlin, S. Mersi, E. Meschi, P. Milenovic⁴⁴, F. Moortgat, M. Mulders, H. Neugebauer, J. Ngadiuba, S. Orfanelli, L. Orsini, L. Pape, E. Perez, M. Peruzzi, A. Petrilli, G. Petrucciani, A. Pfeiffer, M. Pierini, D. Rabadý, A. Racz, T. Reis, G. Rolandi⁴⁵, M. Rovere, H. Sakulin, C. Schäfer, C. Schwick, M. Seidel, M. Selvaggi, A. Sharma, P. Silva, P. Sphicas⁴⁶, A. Stakia, J. Steggemann, M. Stoye, M. Tosi, D. Treille, A. Triossi, A. Tsirou, V. Veckalns⁴⁷, M. Verweij, W.D. Zeuner

Paul Scherrer Institut, Villigen, Switzerland

W. Bertl[†], L. Caminada⁴⁸, K. Deiters, W. Erdmann, R. Horisberger, Q. Ingram, H.C. Kaestli, D. Kotlinski, U. Langenegger, T. Rohe, S.A. Wiederkehr

ETH Zurich - Institute for Particle Physics and Astrophysics (IPA), Zurich, Switzerland

M. Backhaus, L. Bäni, P. Berger, L. Bianchini, B. Casal, G. Dissertori, M. Dittmar, M. Donegà, C. Dorfer, C. Grab, C. Heidegger, D. Hits, J. Hoss, G. Kasieczka, T. Klijnsma, W. Lustermann, B. Mangano, M. Marionneau, M.T. Meinhard, D. Meister, F. Micheli, P. Musella, F. Nessi-Tedaldi, F. Pandolfi, J. Pata, F. Pauss, G. Perrin, L. Perrozzi, M. Quittnat, M. Reichmann, D.A. Sanz Becerra, M. Schönenberger, L. Shchutska, V.R. Tavolaro, K. Theofilatos, M.L. Vesterbacka Olsson, R. Wallny, D.H. Zhu

Universität Zürich, Zurich, Switzerland

T.K. Aarrestad, C. AMSler⁴⁹, M.F. Canelli, A. De Cosa, R. Del Burgo, S. Donato, C. Galloni, T. Hreus, B. Kilminster, D. Pinna, G. Rauco, P. Robmann, D. Salerno, K. Schweiger, C. Seitz, Y. Takahashi, A. Zucchetta

National Central University, Chung-Li, Taiwan

V. Candelise, Y.H. Chang, K.y. Cheng, T.H. Doan, Sh. Jain, R. Khurana, C.M. Kuo, W. Lin, A. Pozdnyakov, S.S. Yu

National Taiwan University (NTU), Taipei, Taiwan

Arun Kumar, P. Chang, Y. Chao, K.F. Chen, P.H. Chen, F. Fiori, W.-S. Hou, Y. Hsiung, Y.F. Liu, R.-S. Lu, E. Paganis, A. Psallidas, A. Steen, J.f. Tsai

Chulalongkorn University, Faculty of Science, Department of Physics, Bangkok, Thailand

B. Asavapibhop, K. Kovitanggoon, G. Singh, N. Srimanobhas

Çukurova University, Physics Department, Science and Art Faculty, Adana, Turkey

A. Bat, F. Boran, S. Cerci⁵⁰, S. Damarseekin, Z.S. Demiroglu, C. Dozen, I. Dumanoglu, S. Girgis, G. Gokbulut, Y. Guler, I. Hos⁵¹, E.E. Kangal⁵², O. Kara, A. Kayis Topaksu, U. Kiminsu, M. Oglakci, G. Onengut⁵³, K. Ozdemir⁵⁴, D. Sunar Cerci⁵⁰, B. Tali⁵⁰, U.G. Tok, S. Turkcapar, I.S. Zorbakir, C. Zorbilmez

Middle East Technical University, Physics Department, Ankara, Turkey

G. Karapinar⁵⁵, K. Ocalan⁵⁶, M. Yalvac, M. Zeyrek

Bogazici University, Istanbul, Turkey

E. Gülmez, M. Kaya⁵⁷, O. Kaya⁵⁸, S. Tekten, E.A. Yetkin⁵⁹

Istanbul Technical University, Istanbul, Turkey

M.N. Agaras, S. Atay, A. Cakir, K. Cankocak, I. Köseoglu

Institute for Scintillation Materials of National Academy of Science of Ukraine, Kharkov, Ukraine

B. Grynyov

National Scientific Center, Kharkov Institute of Physics and Technology, Kharkov, Ukraine

L. Levchuk

University of Bristol, Bristol, U.K.

F. Ball, L. Beck, J.J. Brooke, D. Burns, E. Clement, D. Cussans, O. Davignon, H. Flacher, J. Goldstein, G.P. Heath, H.F. Heath, L. Kreczko, D.M. Newbold⁶⁰, S. Paramesvaran, T. Sakuma, S. Seif El Nasr-storey, D. Smith, V.J. Smith

Rutherford Appleton Laboratory, Didcot, U.K.

K.W. Bell, A. Belyaev⁶¹, C. Brew, R.M. Brown, L. Calligaris, D. Cieri, D.J.A. Cockerill, J.A. Coughlan, K. Harder, S. Harper, J. Linacre, E. Olaiya, D. Petyt, C.H. Shepherd-Themistocleous, A. Thea, I.R. Tomalin, T. Williams

Imperial College, London, U.K.

G. Auzinger, R. Bainbridge, J. Borg, S. Breeze, O. Buchmuller, A. Bundock, S. Casasso, M. Citron, D. Colling, L. Corpe, P. Dauncey, G. Davies, A. De Wit, M. Della Negra, R. Di Maria, A. Elwood, Y. Haddad, G. Hall, G. Iles, T. James, R. Lane, C. Laner, L. Lyons, A.-M. Magnan, S. Malik, L. Mastrolorenzo, T. Matsushita, J. Nash, A. Nikitenko⁷, V. Palladino, M. Pesaresi, D.M. Raymond, A. Richards, A. Rose, E. Scott, C. Seez, A. Shtipliyski, S. Summers, A. Tapper, K. Uchida, M. Vazquez Acosta⁶², T. Virdee¹⁴, N. Wardle, D. Winterbottom, J. Wright, S.C. Zenz

Brunel University, Uxbridge, U.K.

J.E. Cole, P.R. Hobson, A. Khan, P. Kyberd, I.D. Reid, L. Teodorescu, S. Zahid

Baylor University, Waco, U.S.A.

A. Borzou, K. Call, J. Dittmann, K. Hatakeyama, H. Liu, N. Pastika, C. Smith

Catholic University of America, Washington DC, U.S.A.

R. Bartek, A. Dominguez

The University of Alabama, Tuscaloosa, U.S.A.

A. Buccilli, S.I. Cooper, C. Henderson, P. Rumerio, C. West

Boston University, Boston, U.S.A.

D. Arcaro, A. Avetisyan, T. Bose, D. Gastler, D. Rankin, C. Richardson, J. Rohlf, L. Sulak, D. Zou

Brown University, Providence, U.S.A.

G. Benelli, D. Cutts, A. Garabedian, M. Hadley, J. Hakala, U. Heintz, J.M. Hogan, K.H.M. Kwok, E. Laird, G. Landsberg, J. Lee, Z. Mao, M. Narain, J. Pazzini, S. Piperov, S. Sagir, R. Syarif, D. Yu

University of California, Davis, Davis, U.S.A.

R. Band, C. Brainerd, R. Breedon, D. Burns, M. Calderon De La Barca Sanchez, M. Chertok, J. Conway, R. Conway, P.T. Cox, R. Erbacher, C. Flores, G. Funk, W. Ko, R. Lander, C. Mclean, M. Mulhearn, D. Pellett, J. Pilot, S. Shalhout, M. Shi, J. Smith, D. Stolp, K. Tos, M. Tripathi, Z. Wang

University of California, Los Angeles, U.S.A.

M. Bachtis, C. Bravo, R. Cousins, A. Dasgupta, A. Florent, J. Hauser, M. Ignatenko, N. Mccoll, S. Regnard, D. Saltzberg, C. Schnaible, V. Valuev

University of California, Riverside, Riverside, U.S.A.

E. Bouvier, K. Burt, R. Clare, J. Ellison, J.W. Gary, S.M.A. Ghiasi Shirazi, G. Hanson, J. Heilman, G. Karapostoli, E. Kennedy, F. Lacroix, O.R. Long, M. Olmedo Negrete, M.I. Paneva, W. Si, L. Wang, H. Wei, S. Wimpenny, B. R. Yates

University of California, San Diego, La Jolla, U.S.A.

J.G. Branson, S. Cittolin, M. Derdzinski, R. Gerosa, D. Gilbert, B. Hashemi, A. Holzner, D. Klein, G. Kole, V. Krutelyov, J. Letts, M. Masciovecchio, D. Olivito, S. Padhi, M. Pieri, M. Sani, V. Sharma, M. Tadel, A. Vartak, S. Wasserbaech⁶³, J. Wood, F. Würthwein, A. Yagil, G. Zevi Della Porta

University of California, Santa Barbara - Department of Physics, Santa Barbara, U.S.A.

N. Amin, R. Bhandari, J. Bradmiller-Feld, C. Campagnari, A. Dishaw, V. Dutta, M. Franco Sevilla, F. Golf, L. Gouskos, R. Heller, J. Incandela, A. Ovcharova, H. Qu, J. Richman, D. Stuart, I. Suarez, J. Yoo

California Institute of Technology, Pasadena, U.S.A.

D. Anderson, A. Bornheim, J.M. Lawhorn, H.B. Newman, T. Nguyen, C. Pena, M. Spiropulu, J.R. Vlimant, S. Xie, Z. Zhang, R.Y. Zhu

Carnegie Mellon University, Pittsburgh, U.S.A.

M.B. Andrews, T. Ferguson, T. Mudholkar, M. Paulini, J. Russ, M. Sun, H. Vogel, I. Vorobiev, M. Weinberg

University of Colorado Boulder, Boulder, U.S.A.

J.P. Cumalat, W.T. Ford, F. Jensen, A. Johnson, M. Krohn, S. Leontsinis, T. Mulholland, K. Stenson, S.R. Wagner

Cornell University, Ithaca, U.S.A.

J. Alexander, J. Chaves, J. Chu, S. Dittmer, K. McDermott, N. Mirman, J.R. Patterson, D. Quach, A. Rinkevicius, A. Ryd, L. Skinnari, L. Soffi, S.M. Tan, Z. Tao, J. Thom, J. Tucker, P. Wittich, M. Zientek

Fermi National Accelerator Laboratory, Batavia, U.S.A.

S. Abdullin, M. Albrow, M. Alyari, G. Apollinari, A. Apresyan, A. Apyan, S. Banerjee, L.A.T. Bauerdick, A. Beretvas, J. Berryhill, P.C. Bhat, G. Bolla[†], K. Burkett, J.N. Butler, A. Canepa, G.B. Cerati, H.W.K. Cheung, F. Chlebana, M. Cremonesi, J. Duarte, V.D. Elvira, J. Freeman, Z. Gecse, E. Gottschalk, L. Gray, D. Green, S. Grünendahl, O. Gutsche, R.M. Harris, S. Hasegawa, J. Hirschauer, Z. Hu, B. Jayatilaka, S. Jindariani, M. Johnson, U. Joshi, B. Klima, B. Kreis, S. Lammel, D. Lincoln, R. Lipton, M. Liu, T. Liu, R. Lopes De Sá, J. Lykken, K. Maeshima, N. Magini, J.M. Marraffino, D. Mason, P. McBride, P. Merkel, S. Mrenna, S. Nahn, V. O'Dell, K. Pedro, O. Prokofyev, G. Rakness, L. Ristori, B. Schneider, E. Sexton-Kennedy, A. Soha, W.J. Spalding, L. Spiegel, S. Stoynev, J. Strait, N. Strobbe, L. Taylor, S. Tkaczyk, N.V. Tran, L. Uplegger, E.W. Vaandering, C. Vernieri, M. Verzocchi, R. Vidal, M. Wang, H.A. Weber, A. Whitbeck

University of Florida, Gainesville, U.S.A.

D. Acosta, P. Avery, P. Bortignon, D. Bourilkov, A. Brinkerhoff, A. Carnes, M. Carver, D. Curry, R.D. Field, I.K. Furic, S.V. Gleyzer, B.M. Joshi, J. Konigsberg, A. Korytov, K. Kotov, P. Ma, K. Matchev, H. Mei, G. Mitselmakher, K. Shi, D. Sperka, N. Terentyev, L. Thomas, J. Wang, S. Wang, J. Yelton

Florida International University, Miami, U.S.A.

Y.R. Joshi, S. Linn, P. Markowitz, J.L. Rodriguez

Florida State University, Tallahassee, U.S.A.

A. Ackert, T. Adams, A. Askew, S. Hagopian, V. Hagopian, K.F. Johnson, T. Kolberg, G. Martinez, T. Perry, H. Prosper, A. Saha, A. Santra, V. Sharma, R. Yohay

Florida Institute of Technology, Melbourne, U.S.A.

M.M. Baarmand, V. Bhopatkar, S. Colafranceschi, M. Hohlmann, D. Noonan, T. Roy, F. Yumiceva

University of Illinois at Chicago (UIC), Chicago, U.S.A.

M.R. Adams, L. Apanasevich, D. Berry, R.R. Betts, R. Cavanaugh, X. Chen, O. Evdokimov, C.E. Gerber, D.A. Hangal, D.J. Hofman, K. Jung, J. Kamin, I.D. Sandoval Gonzalez, M.B. Tonjes, H. Trauger, N. Varelas, H. Wang, Z. Wu, J. Zhang

The University of Iowa, Iowa City, U.S.A.

B. Bilki⁶⁴, W. Clarida, K. Dilsiz⁶⁵, S. Durgut, R.P. Gandrajula, M. Haytmyradov, V. Khristenko, J.-P. Merlo, H. Mermerkaya⁶⁶, A. Mestvirishvili, A. Moeller, J. Nachtman, H. Ogul⁶⁷, Y. Onel, F. Ozok⁶⁸, A. Penzo, C. Snyder, E. Tiras, J. Wetzel, K. Yi

Johns Hopkins University, Baltimore, U.S.A.

B. Blumenfeld, A. Cocoros, N. Eminizer, D. Fehling, L. Feng, A.V. Gritsan, P. Maksimovic, J. Roskes, U. Sarica, M. Swartz, M. Xiao, C. You

The University of Kansas, Lawrence, U.S.A.

A. Al-bataineh, P. Baringer, A. Bean, S. Boren, J. Bowen, J. Castle, S. Khalil, A. Kropivnitskaya, D. Majumder, W. Mcbrayer, M. Murray, C. Royon, S. Sanders, E. Schmitz, J.D. Tapia Takaki, Q. Wang

Kansas State University, Manhattan, U.S.A.

A. Ivanov, K. Kaadze, Y. Maravin, A. Mohammadi, L.K. Saini, N. Skhirtladze, S. Toda

Lawrence Livermore National Laboratory, Livermore, U.S.A.

F. Rebassoo, D. Wright

University of Maryland, College Park, U.S.A.

C. Anelli, A. Baden, O. Baron, A. Belloni, S.C. Eno, Y. Feng, C. Ferraioli, N.J. Hadley, S. Jabeen, G.Y. Jeng, R.G. Kellogg, J. Kunkle, A.C. Mignerey, F. Ricci-Tam, Y.H. Shin, A. Skuja, S.C. Tonwar

Massachusetts Institute of Technology, Cambridge, U.S.A.

D. Abercrombie, B. Allen, V. Azzolini, R. Barbieri, A. Baty, R. Bi, S. Brandt, W. Busza, I.A. Cali, M. D'Alfonso, Z. Demiragli, G. Gomez Ceballos, M. Goncharov, D. Hsu, M. Hu, Y. Iiyama, G.M. Innocenti, M. Klute, D. Kovalskyi, Y.-J. Lee, A. Levin, P.D. Luckey, B. Maier, A.C. Marini,

C. McGinn, C. Mironov, S. Narayanan, X. Niu, C. Paus, C. Roland, G. Roland, J. Salfeld-Nebgen, G.S.F. Stephans, K. Tatar, D. Velicanu, J. Wang, T.W. Wang, B. Wyslouch

University of Minnesota, Minneapolis, U.S.A.

A.C. Benvenuti, R.M. Chatterjee, A. Evans, P. Hansen, J. Hiltbrand, S. Kalafut, Y. Kubota, Z. Lesko, J. Mans, S. Nourbakhsh, N. Ruckstuhl, R. Rusack, J. Turkewitz, M.A. Wadud

University of Mississippi, Oxford, U.S.A.

J.G. Acosta, S. Oliveros

University of Nebraska-Lincoln, Lincoln, U.S.A.

E. Avdeeva, K. Bloom, D.R. Claes, C. Fangmeier, R. Gonzalez Suarez, R. Kamalieddin, I. Kravchenko, J. Monroy, J.E. Siado, G.R. Snow, B. Stieger

State University of New York at Buffalo, Buffalo, U.S.A.

J. Dolen, A. Godshalk, C. Harrington, I. Iashvili, D. Nguyen, A. Parker, S. Rappoccio, B. Roozbahani

Northeastern University, Boston, U.S.A.

G. Alverson, E. Barberis, C. Freer, A. Hortiangtham, A. Massironi, D.M. Morse, T. Orimoto, R. Teixeira De Lima, D. Trocino, T. Wamorkar, B. Wang, A. Wisecarver, D. Wood

Northwestern University, Evanston, U.S.A.

S. Bhattacharya, O. Charaf, K.A. Hahn, N. Mucia, N. Odell, M.H. Schmitt, K. Sung, M. Trovato, M. Velasco

University of Notre Dame, Notre Dame, U.S.A.

R. Bucci, N. Dev, M. Hildreth, K. Hurtado Anampa, C. Jessop, D.J. Karmgard, N. Kellams, K. Lannon, W. Li, N. Loukas, N. Marinelli, F. Meng, C. Mueller, Y. Musienko³⁵, M. Planer, A. Reinsvold, R. Ruchti, P. Siddireddy, G. Smith, S. Taroni, M. Wayne, A. Wightman, M. Wolf, A. Woodard

The Ohio State University, Columbus, U.S.A.

J. Alimena, L. Antonelli, B. Bylsma, L.S. Durkin, S. Flowers, B. Francis, A. Hart, C. Hill, W. Ji, B. Liu, W. Luo, B.L. Winer, H.W. Wulsin

Princeton University, Princeton, U.S.A.

S. Cooperstein, O. Driga, P. Elmer, J. Hardenbrook, P. Hebda, S. Higginbotham, A. Kalogeropoulos, D. Lange, J. Luo, D. Marlow, K. Mei, I. Ojalvo, J. Olsen, C. Palmer, P. Piroué, D. Stickland, C. Tully

University of Puerto Rico, Mayaguez, U.S.A.

S. Malik, S. Norberg

Purdue University, West Lafayette, U.S.A.

A. Barker, V.E. Barnes, S. Das, S. Folgueras, L. Gutay, M.K. Jha, M. Jones, A.W. Jung, A. Khatiwada, D.H. Miller, N. Neumeister, C.C. Peng, H. Qiu, J.F. Schulte, J. Sun, F. Wang, R. Xiao, W. Xie

Purdue University Northwest, Hammond, U.S.A.

T. Cheng, N. Parashar, J. Stupak

Rice University, Houston, U.S.A.

Z. Chen, K.M. Ecklund, S. Freed, F.J.M. Geurts, M. Guilbaud, M. Kilpatrick, W. Li, B. Michlin, B.P. Padley, J. Roberts, J. Rorie, W. Shi, Z. Tu, J. Zabel, A. Zhang

University of Rochester, Rochester, U.S.A.

A. Bodek, P. de Barbaro, R. Demina, Y.t. Duh, T. Ferbel, M. Galanti, A. Garcia-Bellido, J. Han, O. Hindrichs, A. Khukhunaishvili, K.H. Lo, P. Tan, M. Verzetti

The Rockefeller University, New York, U.S.A.

R. Ciesielski, K. Goulianos, C. Mesropian

Rutgers, The State University of New Jersey, Piscataway, U.S.A.

A. Agapitos, J.P. Chou, Y. Gershtein, T.A. Gómez Espinosa, E. Halkiadakis, M. Heindl, E. Hughes, S. Kaplan, R. Kunnawalkam Elayavalli, S. Kyriacou, A. Lath, R. Montalvo, K. Nash, M. Osherson, H. Saka, S. Salur, S. Schnetzer, D. Sheffield, S. Somalwar, R. Stone, S. Thomas, P. Thomassen, M. Walker

University of Tennessee, Knoxville, U.S.A.

A.G. Delannoy, M. Foerster, J. Heideman, G. Riley, K. Rose, S. Spanier, K. Thapa

Texas A&M University, College Station, U.S.A.

O. Bouhali⁶⁹, A. Castaneda Hernandez⁶⁹, A. Celik, M. Dalchenko, M. De Mattia, A. Delgado, S. Dildick, R. Eusebi, J. Gilmore, T. Huang, T. Kamon⁷⁰, R. Mueller, Y. Pakhotin, R. Patel, A. Perloff, L. Perniè, D. Rathjens, A. Safonov, A. Tatarinov, K.A. Ulmer

Texas Tech University, Lubbock, U.S.A.

N. Akchurin, J. Damgov, F. De Guio, P.R. Duderov, J. Faulkner, E. Gurpinar, S. Kunori, K. Lamichhane, S.W. Lee, T. Libeiro, T. Mengke, S. Muthumuni, T. Peltola, S. Undleeb, I. Volobouev, Z. Wang

Vanderbilt University, Nashville, U.S.A.

S. Greene, A. Gurrola, R. Janjam, W. Johns, C. Maguire, A. Melo, H. Ni, K. Padeken, P. Sheldon, S. Tuo, J. Velkovska, Q. Xu

University of Virginia, Charlottesville, U.S.A.

M.W. Arenton, P. Barria, B. Cox, R. Hirosky, M. Joyce, A. Ledovskoy, H. Li, C. Neu, T. Sinthuprasith, Y. Wang, E. Wolfe, F. Xia

Wayne State University, Detroit, U.S.A.

R. Harr, P.E. Karchin, N. Poudyal, J. Sturdy, P. Thapa, S. Zaleski

University of Wisconsin - Madison, Madison, WI, U.S.A.

M. Brodski, J. Buchanan, C. Caillol, S. Dasu, L. Dodd, S. Duric, B. Gomber, M. Grothe, M. Herndon, A. Hervé, U. Hussain, P. Klabbers, A. Lanaro, A. Levine, K. Long, R. Loveless, T. Ruggles, A. Savin, N. Smith, W.H. Smith, D. Taylor, N. Woods

- †: Deceased
- 1: Also at Vienna University of Technology, Vienna, Austria
 - 2: Also at State Key Laboratory of Nuclear Physics and Technology, Peking University, Beijing, China
 - 3: Also at IRFU, CEA, Université Paris-Saclay, Gif-sur-Yvette, France
 - 4: Also at Universidade Estadual de Campinas, Campinas, Brazil
 - 5: Also at Universidade Federal de Pelotas, Pelotas, Brazil
 - 6: Also at Université Libre de Bruxelles, Bruxelles, Belgium
 - 7: Also at Institute for Theoretical and Experimental Physics, Moscow, Russia
 - 8: Also at Joint Institute for Nuclear Research, Dubna, Russia
 - 9: Now at Ain Shams University, Cairo, Egypt
 - 10: Now at British University in Egypt, Cairo, Egypt
 - 11: Now at Cairo University, Cairo, Egypt
 - 12: Also at Université de Haute Alsace, Mulhouse, France
 - 13: Also at Skobeltsyn Institute of Nuclear Physics, Lomonosov Moscow State University, Moscow, Russia
 - 14: Also at CERN, European Organization for Nuclear Research, Geneva, Switzerland
 - 15: Also at RWTH Aachen University, III. Physikalisches Institut A, Aachen, Germany
 - 16: Also at University of Hamburg, Hamburg, Germany
 - 17: Also at Brandenburg University of Technology, Cottbus, Germany
 - 18: Also at MTA-ELTE Lendület CMS Particle and Nuclear Physics Group, Eötvös Loránd University, Budapest, Hungary
 - 19: Also at Institute of Nuclear Research ATOMKI, Debrecen, Hungary
 - 20: Also at Institute of Physics, University of Debrecen, Debrecen, Hungary
 - 21: Also at Indian Institute of Technology Bhubaneswar, Bhubaneswar, India
 - 22: Also at Institute of Physics, Bhubaneswar, India
 - 23: Also at University of Visva-Bharati, Santiniketan, India
 - 24: Also at University of Ruhuna, Matara, Sri Lanka
 - 25: Also at Isfahan University of Technology, Isfahan, Iran
 - 26: Also at Yazd University, Yazd, Iran
 - 27: Also at Plasma Physics Research Center, Science and Research Branch, Islamic Azad University, Tehran, Iran
 - 28: Also at Università degli Studi di Siena, Siena, Italy
 - 29: Also at INFN Sezione di Milano-Bicocca; Università di Milano-Bicocca, Milano, Italy
 - 30: Also at Purdue University, West Lafayette, U.S.A.
 - 31: Also at International Islamic University of Malaysia, Kuala Lumpur, Malaysia
 - 32: Also at Malaysian Nuclear Agency, MOSTI, Kajang, Malaysia
 - 33: Also at Consejo Nacional de Ciencia y Tecnología, Mexico city, Mexico
 - 34: Also at Warsaw University of Technology, Institute of Electronic Systems, Warsaw, Poland
 - 35: Also at Institute for Nuclear Research, Moscow, Russia
 - 36: Now at National Research Nuclear University 'Moscow Engineering Physics Institute' (MEPhI), Moscow, Russia
 - 37: Also at Institute of Nuclear Physics of the Uzbekistan Academy of Sciences, Tashkent, Uzbekistan
 - 38: Also at St. Petersburg State Polytechnical University, St. Petersburg, Russia
 - 39: Also at University of Florida, Gainesville, U.S.A.
 - 40: Also at P.N. Lebedev Physical Institute, Moscow, Russia
 - 41: Also at California Institute of Technology, Pasadena, U.S.A.
 - 42: Also at Budker Institute of Nuclear Physics, Novosibirsk, Russia
 - 43: Also at Faculty of Physics, University of Belgrade, Belgrade, Serbia

- 44: Also at University of Belgrade, Faculty of Physics and Vinca Institute of Nuclear Sciences, Belgrade, Serbia
- 45: Also at Scuola Normale e Sezione dell'INFN, Pisa, Italy
- 46: Also at National and Kapodistrian University of Athens, Athens, Greece
- 47: Also at Riga Technical University, Riga, Latvia
- 48: Also at Universität Zürich, Zurich, Switzerland
- 49: Also at Stefan Meyer Institute for Subatomic Physics (SMI), Vienna, Austria
- 50: Also at Adiyaman University, Adiyaman, Turkey
- 51: Also at Istanbul Aydin University, Istanbul, Turkey
- 52: Also at Mersin University, Mersin, Turkey
- 53: Also at Cag University, Mersin, Turkey
- 54: Also at Piri Reis University, Istanbul, Turkey
- 55: Also at Izmir Institute of Technology, Izmir, Turkey
- 56: Also at Necmettin Erbakan University, Konya, Turkey
- 57: Also at Marmara University, Istanbul, Turkey
- 58: Also at Kafkas University, Kars, Turkey
- 59: Also at Istanbul Bilgi University, Istanbul, Turkey
- 60: Also at Rutherford Appleton Laboratory, Didcot, U.K.
- 61: Also at School of Physics and Astronomy, University of Southampton, Southampton, U.K.
- 62: Also at Instituto de Astrofísica de Canarias, La Laguna, Spain
- 63: Also at Utah Valley University, Orem, U.S.A.
- 64: Also at Beykent University, Istanbul, Turkey
- 65: Also at Bingol University, Bingol, Turkey
- 66: Also at Erzincan University, Erzincan, Turkey
- 67: Also at Sinop University, Sinop, Turkey
- 68: Also at Mimar Sinan University, Istanbul, Istanbul, Turkey
- 69: Also at Texas A&M University at Qatar, Doha, Qatar
- 70: Also at Kyungpook National University, Daegu, Korea

Publications Stijn Buitink

Reconstructing air shower parameters with LOFAR using event specific GDAS atmospheres

P. Mitra^{a,*}, A. Bonardi^{b,a}, A. Corstanje^b, S. Buitink^{a,b}, G. K Krampah^a, H. Falcke^{b,c,d,k},
B. M. Hare^e, J. R. Hörandel^{a,b,c}, T. Huege^{h,a}, K. Mulrey^a, A. Nelles^{f,i}, H. Pandya^a,
J.P. Rachen^a, L. Rossetto^b, O. Scholten^{e,g}, S. ter Veen^d, T.N.G. Trinh^{e,j}, T. Winchen^{a,k}

^a*Astrophysical Institute, Vrije Universiteit Brussel, Pleinlaan 2, 1050 Brussels, Belgium*

^b*Department of Astrophysics / IMAPP, Radboud University Nijmegen, P. O. Box 9010, 6500 GL, Nijmegen, The Netherlands*

^c*NIKHEF, Science Park Amsterdam, 1098 XG Amsterdam, The Netherlands*

^d*Netherlands Institute of Radio Astronomy (ASTRON), Postbus 2, 7990 AA Dwingeloo, The Netherlands*

^e*KVI-CART, University Groningen, P. O. Box 72, 9700 AB Groningen, The Netherlands*

^f*DESY, Platanenallee 6, 15738 Zeuthen, Germany*

^g*Interuniversity Institute for High-Energy, Vrije Universiteit Brussel, Pleinlaan 2, 1050 Brussels, Belgium*

^h*Institut für Kernphysik, Karlsruhe Institute of Technology(KIT), P. O. Box 3640, 76021, Karlsruhe, Germany*

ⁱ*Institut für Physik, Humboldt-Universität zu Berlin, 12489 Berlin, Germany*

^j*Department of Physics, School of Education, Can Tho University Campus II, 3/2 Street, Ninh Kieu District, Can Tho City, Vietnam*

^k*Max-Planck Institute for Radio Astronomy, Bonn, Germany*

Abstract

The limited knowledge of atmospheric parameters like humidity, pressure, temperature, and the index of refraction has been one of the important systematic uncertainties in reconstructing the depth of the shower maximum from the radio emission of air showers. Current air shower Monte Carlo simulation codes like CORSIKA and the radio plug-in CoREAS use various averaged parameterized atmospheres. However, time-dependent and location-specific atmospheric models are needed for the cosmic ray analysis method used for LOFAR data. There, dedicated simulation sets are used for each detected cosmic ray, to take into account the actual atmospheric conditions at the time of the measurement. Using the Global Data Assimilation System (GDAS), a global atmospheric model, we have implemented time-dependent, realistic atmospheric profiles in CORSIKA and CoREAS. We have produced realistic event-specific atmospheres for all air showers measured with LOFAR, an event set spanning several years and many different weather conditions. A complete re-analysis of our data set shows that for the majority of data, our previous correction factor performed rather well; we found only a small systematic shift of 2 g/cm^2 in the reconstructed X_{max} . However, under extreme weather conditions, for example, very low air pressure, the shift can be up to 15 g/cm^2 . We provide a correction formula to determine the shift in X_{max} resulting from a comparison of simulations done using the US-Std atmosphere and the GDAS-based atmosphere.

Keywords: LOFAR, Cosmic Ray, EAS, Radio detection technique, Atmosphere, GDAS, Index of refraction, Effects of humidity, X_{\max} reconstruction

1. Introduction

In recent years, the field of radio detection of air showers has advanced quite rapidly [1, 2]. Estimating the depth of the shower maximum, X_{\max} , with improved accuracy is of great interest for the study of the primary particle composition [3, 4]. The development of the air shower induced by a cosmic ray is governed by the interactions and decays of the secondary particles. The secondary electrons and positrons in the air shower undergo charge separation as they travel through the magnetic field of the Earth. This leads to a time-varying transverse current, producing radio emission. There is another small contribution to the radiation from the excess of negative charge accumulated at the shower front, known as the ‘Askaryan effect’ [5]. The emission reaches the ground as a short pulse on the order of 10 to 100 ns with a specific lateral intensity distribution, or footprint, that depends on X_{\max} ; X_{\max} is calculated in terms of total atmospheric matter traversed by the air shower from the top of the atmosphere to the point where the particle number reaches the maximum. It is therefore important to know the altitude-dependent air density. Another atmospheric parameter that plays a crucial role in the radio emission is the refractive index of air. If for a given emission region along the shower axis an observer is located at the corresponding Cherenkov angle, radiation emitted from all along this region arrives simultaneously. This results in a highly compressed signal in time, forming a ring-like structure on the ground [6, 7]. The refractive index determines the propagation velocity of the radio signal at different altitudes and influences the time compression [8, 9]. For observers located on the Cherenkov ring, pulses are coherent up to GHz frequencies [10]. The angle at which Cherenkov emission is emitted is inversely proportional to the refractive index. At higher frequencies pulses are more sensitive to the refractive index. In general, at all frequencies, the variations in the refractive index lead to changes in the radio intensity footprint [11]. Both the density and the refractive index of air are dependent on air temperature, humidity and pressure. Thus, having a good understanding of these atmospheric variables is crucial.

The radio detection technique can be used in combination with established techniques such as fluorescence detection and surface detection with scintillators and water Cherenkov detectors. Dense antenna arrays like the core of the LOFAR radio telescope [12] provide the opportunity to investigate the radio footprint, i.e. the lateral intensity distribution, in close detail and enable the measurement of X_{\max} up to a precision of < 20 g/cm². The precision is sensitive to the choice of an atmospheric model included in the Monte Carlo air shower simulation codes. There are several parameterized atmospheric models incorporated in the CORSIKA air shower simulation code, based on averaged profiles: U.S. standard

*Corresponding author

Email address: `pmitra@vub.be` (P. Mitra)

atmosphere parameterized according to J. Linsley [13], parameterized atmospheres for the Pierre Auger Observatory near Malargüe (Argentina) by M. Will and B. Keilhauer [14], South Pole atmospheres parameterized by P. Lipari and D. Chirkin etc. So far, the US standard atmosphere has been used in LOFAR analyses, through CORSIKA simulations [13] and the CoREAS extension [13] which is used to calculate the radio emission of the air showers.

A first order linear correction to the US standard atmosphere has been applied to account for the fact that the US-standard atmosphere does not reflect the realistic atmospheric conditions at a given time. It is preferable to integrate a realistic atmosphere directly into the simulations. In particular, the reconstruction of X_{\max} depends on the refractive index of air, and so a realistic refractive index profile needs to be included.

The effects of the refractive index, n , on the reconstructed X_{\max} have been previously reported in Ref.[15] and Ref.[11], using different simulation codes. In Ref.[11], CoREAS was used to simulate two ensembles of showers, one with a globally higher refractivity $N = (n - 1) 10^6$, another with standard values. A Monte Carlo based approach was taken to study the systematic shift in reconstructed X_{\max} by comparing the set of simulations with higher refractivity to the standard ones. The shift in the reconstructed X_{\max} from the default value was found to be proportional to the geometric distance to X_{\max} . The effect was stronger in the high frequency band of 120–250 MHz than in the 30–80 MHz band. In Ref.[15], a more realistic profile of the refractivity was constructed for one particular day using information from the Global Data Assimilation System, GDAS, a global weather database. The differences between this atmosphere and default atmospheres were studied using the SELFAS radio emission simulation code [16]. The results showed that correcting for the realistic density is the most important factor in the accurate reconstruction of X_{\max} , causing about 30 g/cm² bias in X_{\max} . And the second most important correction was through the inclusion of the high frequency refractivity formula, applicable at radio frequencies, contributing about 5 g/cm² bias in X_{\max} . The effects of the increased refractivity on the time traces and the lateral distribution function (LDF) were also reported. In the 20–80 MHz frequency band, relatively small differences in the amplitude of the electric field and LDF were found, whereas considerable differences were found studying the high frequency band between 120–250 MHz. These results were in agreement with Ref.[11]. While both works paved the way for the understanding of atmospheric effects on radio simulations, a direct application to real data using simulations with realistic atmospheric conditions was not addressed.

In this work, for the first time, GDAS-based atmospheric profiles, automatically included in CoREAS simulations are applied to LOFAR data. The effects of atmospheric parameters like pressure and humidity on the reconstructed X_{\max} are studied and compared to the results of previously used linear corrections. A new GDAS-based correction is introduced and compared to previous methods. Furthermore, a tool is developed to extract GDAS atmospheric parameters which are then interfaced with CORSIKA. The utility of this tool is not only limited to LOFAR. This code, called ‘gdastool’, has been available for public use since the release of CORSIKA version 7.6300. It is flexible and ready to be adapted by the users to obtain parameterized atmospheric profiles for user-specified time and location.

Sections 2 and 3 describe the processing of GDAS data to extract the atmospheric state variables and examples of atmospheric profiles at the LOFAR site, respectively. Section 4 covers the details of the implementation of GDAS in CORSIKA. In sections 5 and 6, LOFAR cosmic ray data are evaluated with the GDAS atmospheric profiles, the GDAS-correction factor is introduced and the explicit effects of humidity on shower parameters are discussed.

2. Extracting atmospheric variables from GDAS data

The Global Data Assimilation System (GDAS) developed at NOAA's¹ National Centers for Environmental Prediction (NCEP) is a tool used to describe the global atmosphere. It is run four times a day (0, 6, 12, and 18 UTC) and provides a 3-, 6- and 9-hour forecast based on the interpolation of meteorological measurements from all over the world including weather stations on land, ships and airplanes as well as radiosondes and weather satellites [17]. The three hourly data are available at 23 constant pressure levels, from 1000 hPa (roughly sea level) to 20 hPa (≈ 26 km) on a global 1° spaced latitude-longitude grid (180° by 360°). Each data set is complemented by data at the surface level. The data are stored in weekly files and made available online. In order to model a realistic atmosphere one needs to obtain the suitable atmospheric parameters from GDAS. Parameters like temperature (K), height (m) relative humidity (H) and pressure (hPa) can be directly extracted from the database. In the GDAS data, the altitude is in geopotential units with respect to a geoid (mean sea level). This is an adjustment to geometric height or elevation above mean sea level using the variation of gravity with latitude and elevation. To convert from geopotential height h (m) to standard geometric altitude z (m) we use the formula

$$z(h, \Phi) = (1 + 0.002644 \cdot \cos(2\Phi)) \cdot h + (1 + 0.0089 \cdot \cos(2\Phi)) \left(\frac{h^2}{6245000} \right) \quad (1)$$

where Φ is the geometric latitude [18]. To calculate the air density, the relative humidity is to be converted into water vapor pressure. The following approximation of the empirical Magnus formula is used to calculate the water vapor pressure (hPa) in terms of humidity and temperature [18]:

$$e = \frac{H}{100\%} \times 6.1064 \times \exp\left(\frac{21.88 t}{265.5 + t}\right) \quad \text{for } t \leq 0^\circ C \quad (2)$$

and

$$e = \frac{H}{100\%} \times 6.1070 \times \exp\left(\frac{17.15 t}{234.9 + t}\right) \quad \text{for } t \geq 0^\circ C. \quad (3)$$

The density can be calculated from the ideal gas law as

$$\rho = \frac{P M_{\text{air}}}{R T} \quad (4)$$

¹National Oceanic and Atmospheric Administration.

where P is the atmospheric pressure in Pa, T is temperature in K and R is the universal gas constant, having a value of $8.31451 \text{ J K}^{-1} \text{ mol}^{-1}$ and M_{air} is the molar mass of air. Moist air can be decomposed into three components to calculate its molar mass: dry air, water vapor and carbon dioxide. The molar mass of humid air is the sum of the molar masses of the components, weighted with the volume percentage ϕ_i of that component [18],

$$M_{air} = M_{dry} \cdot \phi_{dry} + M_{water} \cdot \phi_{water} + M_{CO_2} \cdot \phi_{CO_2}. \quad (5)$$

The molar masses of dry air, water vapor and CO_2 are 0.02897 , 0.04401 and $0.01802 \text{ kg-mol}^{-1}$ respectively. The volume percentage of CO_2 is taken as 385 ppmv , the percentage of water ϕ_{water} is the partial pressure of water vapor divided by the pressure P ; the dry air makes up the rest.

The refractivity, defined as $N = (n - 1) 10^6$, is a function of humidity, pressure and temperature can be expressed as

$$N = 77.6890 \text{ K hPa}^{-1} \frac{p_d}{T} + 71.2952 \text{ K hPa}^{-1} \frac{p_w}{T} + 375 463 \text{ K}^2 \text{ hPa}^{-1} \frac{p_w}{T^2} \quad (6)$$

with p_w , p_d and T being the partial water vapor pressure ($p_w = e \times 100 \text{ Pa}$), partial dry air pressure and temperature respectively [19]. The effect of humidity is important for our study as it tends to increase the refractivity in comparison to that of dry air at the radio frequencies. There are differences between the refractivities obtained in radio and the ones in the visible, near the infrared and UV ranges as described in [18]. To account for the uncertainties in GDAS data one needs to perform in situ measurements with weather balloons. Since this is beyond the scope of this work and we refer to [18], which provides a comparison between GDAS data and weather balloon measurements in Argentina. Since global atmospheric models are typically more precise in the Northern hemisphere where more weather data is available we assume that the intrinsic uncertainty of GDAS at the LOFAR site is similar to that in Argentina. Various relevant uncertainties are: $\pm 0.5 \text{ }^\circ\text{C}$ for temperature, 0.5 hPa for pressure, and 0.05 hPa for water vapor pressure and less than 1 g/cm^2 in atmospheric depth over the altitude range from 3 to 6 km . The uncertainty in water vapor pressure translates to $2 - 7\%$ uncertainty in humidity. The resulting relative uncertainty in N due to these parameters is around 0.5% at the same altitude range. The GDAS data have a resolution of 1° by 1° in latitude longitude. This can be roughly approximated as a distance of 100 km between two adjacent grid points. For highly inclined showers the distance to the region of shower development from the observation site can be larger than the distance between two grid points. For air showers coming from 70° zenith this distance is around 70 km and for zenith $> 75^\circ$ it is about 100 km . In these cases, the choice of an exact grid point becomes complicated. Also at this point, for zenith angles $> 70^\circ$ the correction due to curved atmosphere becomes important. This does not occur for LOFAR as the detected cosmic rays are limited to within a $< 55^\circ$ zenith angle due to the particle detectors used for triggering. In this regime the GDAS model works well.

3. GDAS atmospheric profiles at the LOFAR site

In this section several GDAS atmospheric profiles extracted at the LOFAR site are discussed. Fig-1 (**left**) shows humidity as a function of altitude for 5 arbitrary atmospheric profiles for different days in the year 2011, between June and November. A significant day-to-day fluctuation is seen. The red solid and blue dashed lines indicate two very different weather conditions; the red solid line having high saturating humidity between 5 – 8 km suggests higher cloud coverage and the blue dashed line with low humidity in that range indicates low cloud coverage. Fig-1 (**right**) shows the difference in atmospheric depth profile between the US standard atmosphere and the GDAS atmospheres at LOFAR for 8 profiles over the years 2011 – 2016. The GDAS atmospheres vary significantly from the US atmosphere. Atmospheric profiles with similar atmospheric depth at ground can evolve differently higher in the atmosphere. This is important for calculating the correct distance to the shower maximum. Fig-2 shows the mean profile for the relative difference in refractivity $\Delta N_{\text{relative}}$ between GDAS and the US standard atmosphere as a function of altitude for over 3 years for 100 cosmic rays recorded at LOFAR. It is defined as $\Delta N_{\text{relative}} = (N_{\text{GDAS}} - N_{\text{US}})/N_{\text{US}}$, where N_{GDAS} is calculated from Eq-6 using GDAS atmospheres at LOFAR. N_{US} is obtained from the linear relation $N_{\text{US}} = \frac{\rho_{\text{us}}}{\rho_{\text{sealevel}}} N_{\text{sealevel}}$, with $N_{\text{sealevel}} = 292$. This is the default option for calculating refractivity in CoREAS as well.

The absolute value of the mean $\Delta N_{\text{relative}}$ is around 10% near ground and around 3 – 8% between 3 to 10 km of altitude, the region important for shower development.

Approximately 75% of the atmospheric matter and 99% of the total mass of water vapor and aerosols are contained within the troposphere, the lowest layer of Earth’s atmosphere. Within the troposphere the temperature drops with altitude, reaching a constant value in the tropopause, the boundary region between troposphere and stratosphere. In the U.S standard atmosphere the troposphere ends at 11 km and tropopause extends to an altitude of 20 km. For the local GDAS atmospheres these boundaries are not sharply defined. The flat part in the mean $\Delta N_{\text{relative}} > 10$ km in Fig-2 is the result of constant temperature in the tropopause. However contribution from this region to the radio emission is minimal. To consider the effects of refractive index in the propagation time of radio signal it is important to calculate the effective N [1, 8]. This is defined as

$$N_{\text{eff}} = \frac{\int N(h)dh}{D} \quad (7)$$

where D is the distance between the line of emission and observer. The values of relative effective refractivity $\Delta N_{\text{relative}}^{\text{eff}}$ between the GDAS and US standard atmosphere are around 7 – 10 % in the range of altitude mentioned above, for observers within < 100 m of the shower axis.

4. Implementation in CORSIKA/CoREAS

To incorporate the atmospheric parameters extracted from GDAS in CORSIKA and CoREAS we have developed a program named ‘gdastool’ that downloads the required GDAS

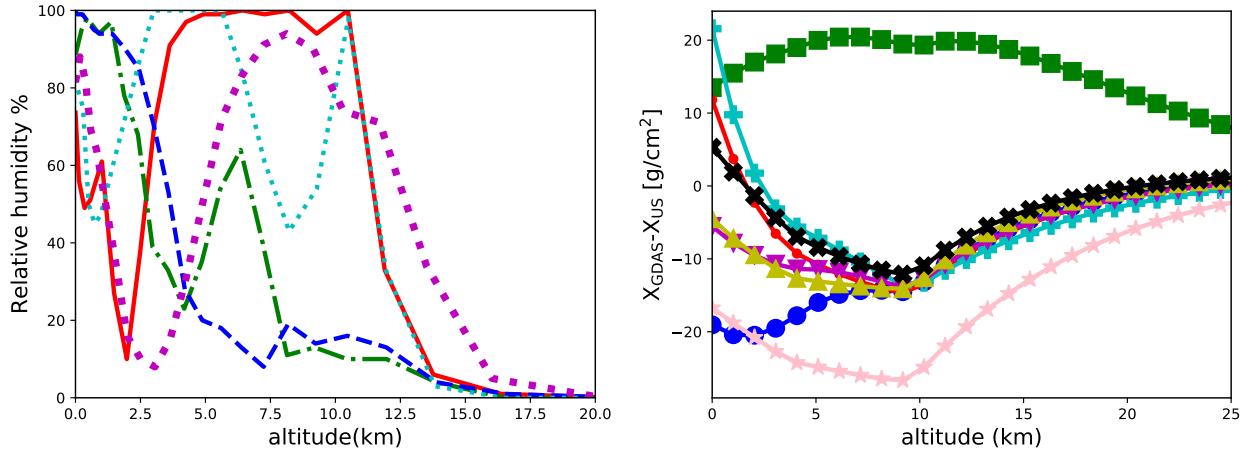


Figure 1: Atmospheric profiles at LOFAR. **Left:** Example of 5 humidity profiles between June to November during the year 2011. **Right:** 8 profiles for the difference in atmospheric depth between US standard atmosphere and GDAS atmospheres as a function of altitude between the years 2011 – 2016.

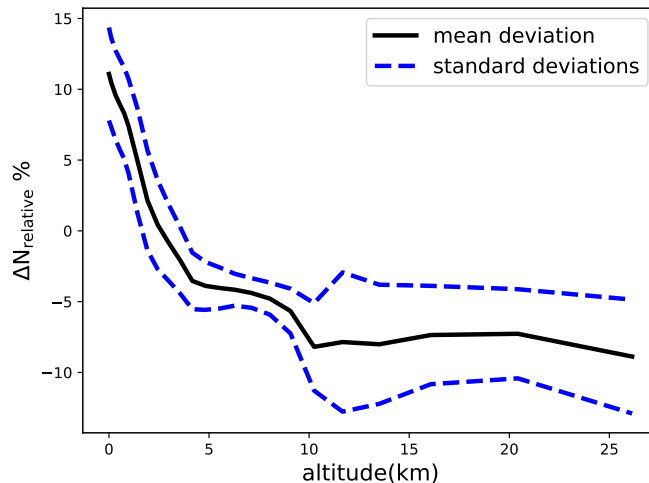


Figure 2: Mean relative refractivity, defined as $\Delta N_{\text{relative}} = \frac{N_{\text{GDAS}} - N_{\text{US}}}{N_{\text{US}}}$; profiles for 100 recorded cosmic rays at LOFAR spanning over the years 2011 to 2014. The black solid line denotes the mean profile and the blue dashed lines show the standard deviations.

file given the time and location of observation of the event and returns refractive indices between ground and the highest GDAS level. It also fits the density profile according to the standard 5 layer atmospheric model used in CORSIKA [13]. In this model the density $\rho(h)$ has an exponential dependence on the altitude leading to the functional form of mass overburden $T(h)$ which is the density integrated over height (km) as

$$T(h) = a_i + b_i e^{-10^5 h/c_i} \quad i = 1, \dots, 4. \quad (8)$$

Thus, the density is

$$\rho(h) = b_i/c_i e^{-10^5 h/c_i} \quad i = 1, \dots, 4. \quad (9)$$

In the fifth layer the overburden is assumed to decrease linearly with height. The parameters a_i , b_i and c_i are obtained in a manner such that the function $T(h)$ is continuous at the layer boundaries and can be differentiated continuously. The first three layers constitute of the 24 density points obtained from GDAS data. The first layer consists of 10 points, second layer of 7 points and the third layer of 7 points. Since GDAS provides data on constant pressure levels, not of constant heights, the layer boundaries vary slightly between different atmospheric profiles. The mean values of the boundaries for the conditions of 100 cosmic ray events are 3.56 ± 0.11 km, 9.09 ± 0.23 km, 26.27 ± 0.56 km from boundary 1 to 3, respectively.

Next, we fit the data to Eq- 9 in the following way:

For layer 1 the density profile is fitted with two free parameters. Then the density ρ_1 at boundary 1 is calculated using Eq- 9 with the obtained parameters b_1 , c_1 . The condition that the density has to be continuous at the boundaries reduces the number of free parameters to 1 which is the parameter c . Thus the parameter b_2 for second layer can be expressed as a function of ρ_1 and c_2 with c_2 being the only free parameter. The same fitting procedure is repeated for the third layer. The fourth layer ranges from the highest GDAS altitude to 100 km. At these altitudes there are no physical GDAS data. The parameter c_4 is obtained by fitting the last GDAS point and the density at 100 km from US standard atmosphere. At these altitudes the mass overburden is less than 0.1% of the value at ground. The important factor is to satisfy the boundary conditions throughout the atmosphere. Along with density the continuity of mass overburden is also preserved. For that, once a smooth profile for the density is obtained, the parameter a in Eq- 8 is solved for analytically, using the boundary conditions for the mass overburden. The parameterization for the fifth layer was adapted from the US standard atmosphere [13]. The ‘gdastool’ also returns a density profile plot with the best fit parameters as a function of altitude and the rms of the relative density difference between data and fit. The relative density is defined as $\frac{\rho_{\text{fit}} - \rho_{\text{data}}}{\rho_{\text{fit}}}$. Fig-3 (**left**) and its rms is used as a goodness of fit. Fig-3 (**left**) shows the example of a density profile between the fitted model and GDAS. The mean relative error in density for 100 profiles as a function of altitude is presented in Fig-3 (**right**). At lower altitudes the model fits the data very well; deviations $> 2\%$ start at altitudes higher than 15 km which are not so important for the shower development. A bump in the profile at 10 km is observed, this can be explained by the change in the atmosphere at the troposphere boundary as discussed in the previous section. There will be an error on the atmospheric depth introduced by the fitted model in Eq- 8. It is on the order of 2 g/cm^2 on average between the altitude range mentioned above with a variance of $4 - 5 \text{ g/cm}^2$.

The ‘gdastool’ can be executed as a stand alone script within CORSIKA. Given the coordinate and UTC time stamp as input parameters it downloads the required GDAS files and extracts atmospheric data. It then returns an output file that contains fitted mass overburden parameters and tabulated refractive indices interpolated to 1 m intervals. This output file can be invoked through the CORSIKA steering file. When called, it replaces the default atmospheric parameters in CORSIKA with the new ones and the on-the-fly refractive index calculation in CoREAS with the look-up table.

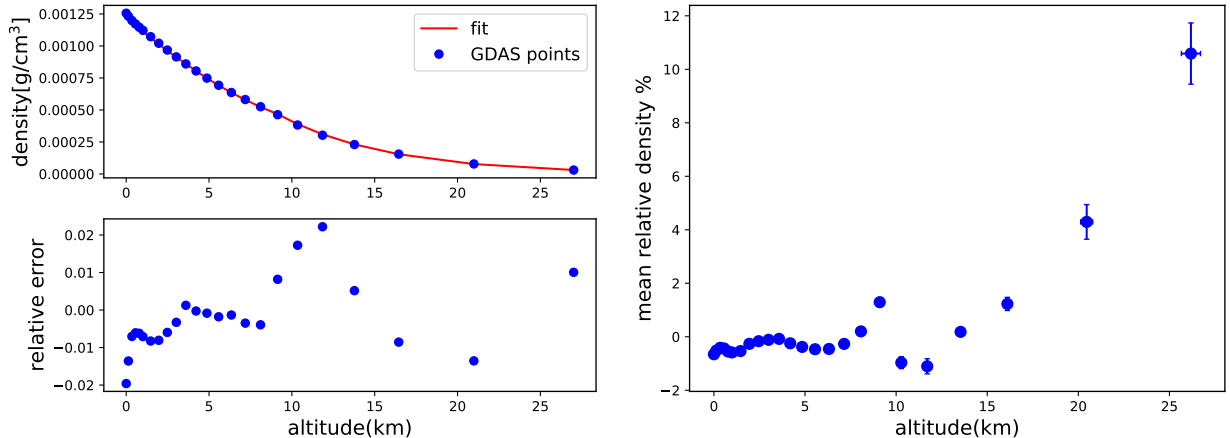


Figure 3: **Left:** Example of one density profile, GDAS and the fitted 5-layered atmospheric model. The bottom panel shows the relative error defined as $\frac{\rho_{\text{fit}} - \rho_{\text{data}}}{\rho_{\text{fit}}}$. **Right:** Mean relative error in density for 100 different atmospheric profiles. The mean is calculated at each of the 24 GDAS points for all the profiles. The error bars indicate the standard deviation.

5. Effects on the reconstruction of the depth of the shower maximum

The highest precision for the determination of X_{max} with the radio technique is currently achieved with the LOFAR radio telescope. Situated in the north of the Netherlands, the dense core of LOFAR consists of 288 low-band dipole antennas within a circle with a diameter of 320 meters, known as the Superterp. The radio emission from air showers in the frequency range 30–80 MHz is recorded by the LOFAR low-band antennas [12, 20]. An array of particle detectors installed on the Superterp provides the trigger for the detection of the air showers [21].

The X_{max} reconstruction technique used at LOFAR is based on the production of dedicated simulation sets for each detected air shower. The number of simulations needed to reconstruct the shower maximum is optimized with CONEX [22]. A set of full CORSIKA simulations with proton and iron primaries is produced for each detected cosmic ray. The radio emission is simulated in a star-shaped pattern for antenna positions in the shower plane using CoREAS. An antenna model is applied to the simulated electric fields and compared to the measured signal in the dipole antennas [23]. The time integrated pulse power is calculated in a 55 ns window centered around the pulse maximum, summed over both polarizations. Finally, a two-dimensional map of the time integrated power is created by interpolating the star-shaped pattern [24]. In the previous analysis a hybrid fitting technique was used in which both the radio and particle data were fitted to the two-dimensional radiation map and the one-dimensional particle lateral distribution function simultaneously. In this work instead of the combined fit we fit only the radio data to the radio simulation. The advantage of switching to the radio only fitting method is that it results in reduced systematic uncertainties.

Fig-4 shows the fit quality for an air shower detected with LOFAR as a function of X_{max}

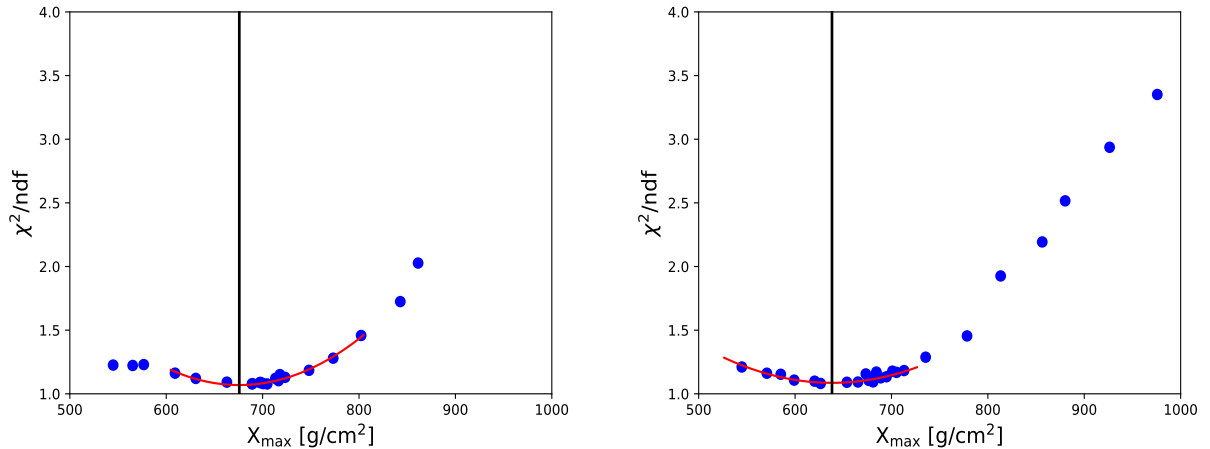


Figure 4: Quality of fit as a function of simulated X_{\max} for a LOFAR event of energy 1.4×10^8 GeV, with a zenith angle of 38° . **Left:** simulated with default US standard atmosphere, reconstructed $X_{\max} = 675.8$ g/cm 2 . Applying the linear first order atmospheric correction, the resulting $X_{\max} = 658$ g/cm 2 . **Right:** simulated with GDAS atmosphere, reconstructed $X_{\max} = 638.3$ g/cm 2 , the reconstructed X_{\max} in both the cases is indicated by solid black lines.

simulated with two different atmospheres - one with the corresponding GDAS atmosphere and the other with the US standard atmosphere. The reconstructed value of X_{\max} is found from the minimum of the fitted parabola around the best fitted points. We chose a LOFAR event for which the ground pressure was much lower than the US standard atmosphere, by 20 hPa. The atmospheric profile for this particular event is represented by the blue line with circles in Fig-1 (**right**). The reconstructed X_{\max} with the US atmosphere corresponds to a much higher mass overburden than the reconstructed X_{\max} using much thinner GDAS atmosphere. In this example this translates to a difference of around 37.5 g/cm 2 in the reconstructed X_{\max} between the two cases. This large deviation is attributed to the extreme weather condition for the shower chosen in the example. In the previous LOFAR analysis a correction factor to the US atmosphere was used to account for the real atmosphere [3, 24]. The simulations that are produced with US standard atmosphere would approximately yield the correct geometrical altitude to the shower maximum. Then the corrected X_{\max} is calculated by integrating the GDAS density profile obtained at LOFAR, from the top of the atmosphere to the geometric altitude of X_{\max} in the following way:

$$X(h) = \frac{1}{\cos \theta} \int_h^\infty \rho_{\text{gdas}}(h) dh. \quad (10)$$

The corrected X_{\max} for this particular example is 658 g/cm 2 and the difference between the corrected and new X_{\max} is about 20 g/cm 2 .

Using the same approach described above we have studied 123 air showers recorded with LOFAR with three simulation sets:

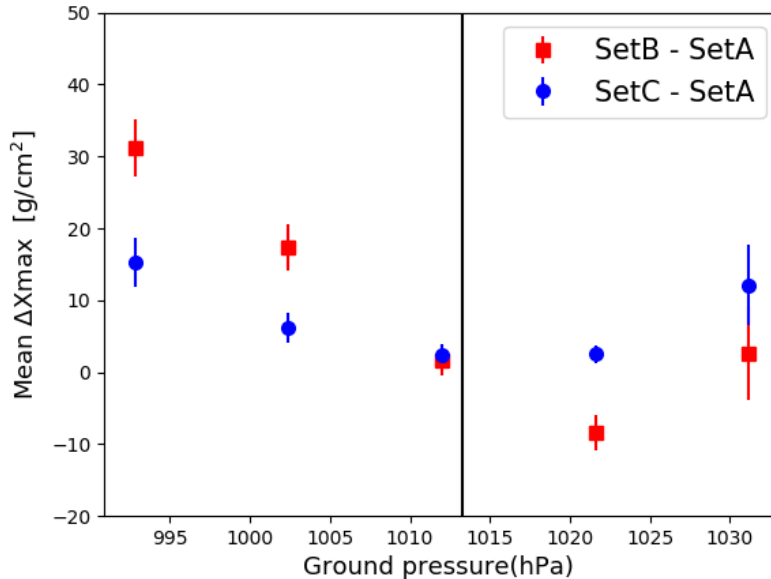


Figure 5: Difference in mean X_{\max} as a function of ground pressure. The total sample contains 123 air showers recorded at LOFAR. The black line denotes the U.S standard atmospheric pressure.

- **Set A**—the showers were simulated with CORSIKA v-7.6300 and GDAS atmosphere.
- **Set B**—the showers were simulated with CORSIKA v-7.4385 and US standard atmosphere.
- **Set C**—this set is identical to **Set B** but with the additional atmospheric correction factor to it as described above.

The effect of using different CORSIKA versions on the reconstructed X_{\max} , irrespective of the atmospheric model, was probed. The difference in X_{\max} found using CORSIKA versions 7.6300 and 7.4385 was found to be very small, around 1.4 g/cm^2 . This confirms that the differences between Set-A, Set-B and Set-C are due to different atmospheric models, not any artifact arising from different versions of CORSIKA.

In Fig-5 the difference in mean reconstructed X_{\max} between the various simulation sets mentioned above is plotted against ground pressure bins obtained from GDAS. Both the blue circles and red squares converge to zero where GDAS pressure approaches the US standard pressure at 1013 hPa. The red squares have large ΔX_{\max} in general. This is expected as there is no atmospheric correction involved in Set-B. The blue circles however show a higher deviation both at low and high pressure values. This suggests that the linear first order correction added to the standard US atmosphere implemented in Set-C is not sufficient. As the refractive index effects can not be included in the linear first order correction, one needs full GDAS-based atmospheric profiles for more extreme atmospheric conditions.

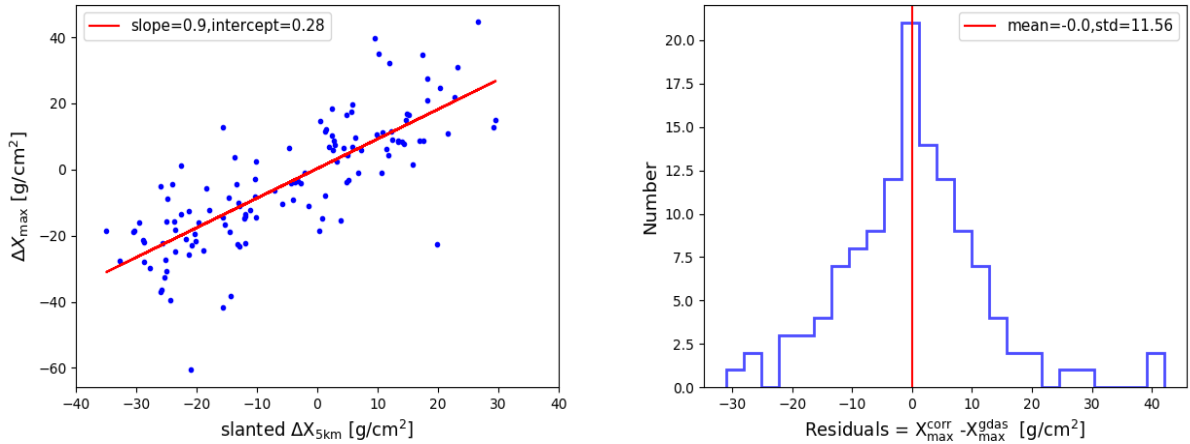


Figure 6: **Left:** scatter plot of $\Delta X_{\max} = X_{\max}^{\text{gdas}} - X_{\max}^{\text{us}}$ vs difference in slanted mass overburden $\Delta X_{5\text{km}} = X_{5\text{km}}^{\text{gdas}} - X_{5\text{km}}^{\text{us}}$. The red line is a linear fit to the profile. **Right:** Histogram shows the residual of fitted and actual X_{\max} ; residual = $X_{\max}^{\text{corr}} - X_{\max}^{\text{gdas}}$.

Here, we study the possibility to introduce a new global correction factor to the reconstructed X_{\max} with US standard atmosphere to correct for realistic atmospheres without having to run full GDAS-based CoREAS simulations. To achieve this we studied the correlation between X_{\max} , refractivity, and slanted mass overburden which is defined as the integrated density from the edge of the atmosphere to a given height at the slant of zenith angle, at different altitudes. It was seen that both the correlation between X_{\max} and refractivity and between X_{\max} and slanted mass overburden correlation are poor at ground and at lower altitudes. At the higher altitudes, between 4 - 6 km, X_{\max} and mass overburden show a higher correlation which is not prominent in X_{\max} vs refractivity profiles at these altitudes. We have found the strongest correlation at an altitude of 5 km. Fig-6 (left) shows the scatter plot of ΔX_{\max} defined as $X_{\max}^{\text{gdas}} - X_{\max}^{\text{us}}$ and difference in the slanted mass overburden $\Delta X_{5\text{km}} = X_{5\text{km}}^{\text{gdas}} - X_{5\text{km}}^{\text{us}}$. The precise correlation suggests the profile can be fit with a straight line and is used as a parameterization of global correction factor, provided by the equation:

$$X_{\max}^{\text{corr}} - X_{\max}^{\text{us}} = 0.9 \left(X_{5\text{km}}^{\text{us}} - X_{5\text{km}}^{\text{gdas}} \right) + 0.28. \quad (11)$$

The histogram in Fig-6 (right) shows the residual of the X_{\max}^{corr} from X_{\max}^{gdas} . The profile is symmetric with mean 0 g/cm^2 and standard deviation 11.56 g/cm^2 . The fluctuations are within the typical systematic uncertainty of the reconstructed X_{\max} with LOFAR, which is around 17 g/cm^2 [24]. This correction factor can be used as a rule of thumb for the estimation of reconstructed X_{\max} with the following caveats. It is specific to LOFAR, as simulations were performed involving weather conditions, observation level, and magnetic field particular to LOFAR. Corresponding correction equations for other experiments can be constructed in the same manner and can yield different results depending on atmospheric parameters.

However, while this global correction factor is very useful when a fast reconstruction is

needed, we will use the full Monte Carlo approach in a future composition analysis. Simulations with event specific GDAS atmospheres are always more accurate than the correction factor. The correction factor might also introduce biases related to the mass of the primary particles. Proton primaries on average generate showers that reach maximum lower in the atmosphere than iron; these kind of effects are not taken into account.

6. Effects of humidity

As described in section 2, in the radio frequency regime, humidity increases the refractive index. For this study, two sets of simulations were produced. In one set the showers were simulated with the respective GDAS atmosphere and in the other with a GDAS atmosphere with vanishing humidity. This was achieved by hard-coding the partial water vapor pressure in Eq-3 to negligible values. For the GDAS atmosphere an extremely humid weather condition at the LOFAR site was chosen. The same atmospheric parameters are used in both cases to ensure that the particles evolve in a similar way in the atmosphere and produce same shower maximum. In this way the inclusion of humidity only influences the simulated radio pulses. The difference in the refractive index manifests in terms of propagation effects on the pulse arrival time and power. The pulse propagating through an atmosphere with higher refractive index will have a lower velocity compared to dry air. This results in a delayed arrival time of the signal, as seen in Fig-7. The difference in peak arrival time is less than 1 ns for an observer at 150 m. The effect is found to be less prominent for observers further away from the axis. The lateral distribution of the energy fluence, the time-integrated power per unit area, for different observer positions is also studied for different frequency bands for these two cases, as shown in Fig-8. In the low frequency band of 30–80 MHz relevant for LOFAR the difference in the fluence between the two sets is small, from around 4% closer to shower axis to 2% at a distance of 100 m from the axis. In the high frequency band of 50–350 MHz the values are larger, being around 8% at 100 m from the core. In the higher frequency band the Cherenkov-like effects become stronger and the signal is compressed along the Cherenkov ring [25]. A rough estimate of the radius of the ring can be obtained from the projection of a cone with an opening angle given by the Cherenkov angle starting from the shower maximum. The opening angle is strongly dependent on the index of refraction. This explains the higher difference in power in Fig-8. Similar effects in high and low frequency bands were also reported in [15] by studying the LDF of the electric field profiles. Inside the Cherenkov radius pulses are stretched due to refractive index effects. For higher refractive indices this will lead to lower pulse power which explains the negative sign in the relative fluence for observer distances close to the core.

The radiation energy is the total energy contained in the radio signal. It scales quadratically with the cosmic ray energy, thus can be used as a cosmic ray energy estimator [26, 27]. The surface integral over the radio LDF mentioned above yields the radiation energy. The relative difference in the integrated LDF between the humid and non-humid profiles for both the low and high frequency regimes is smaller than 1%. This indicates that humidity has almost no effect on the estimated cosmic ray energy as determined from the radiation energy which was also concluded in [28].

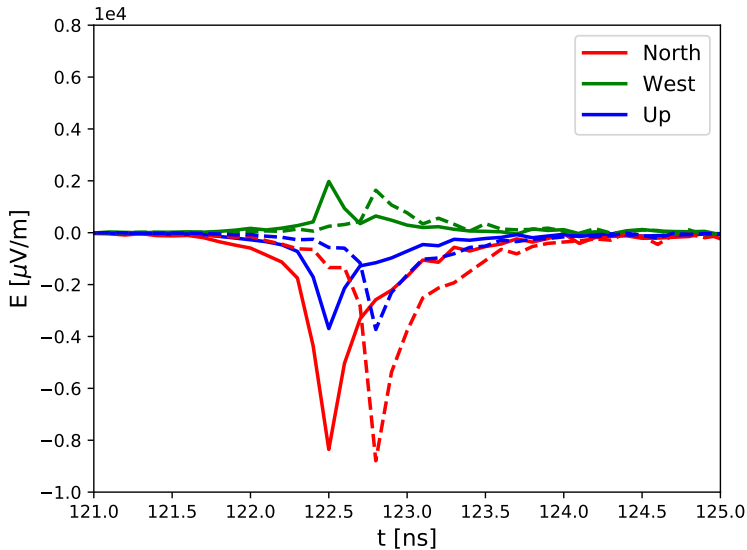


Figure 7: Unfiltered electric field components of a CoREAS pulse in time for two different refractive index profiles for a 10^{17} eV proton shower with a zenith angle of 45° coming from east for an observer at 150 m from the axis. The solid and dashed lines represent the profiles with lower and higher refractive indices respectively.

Next, to investigate the effect of humidity on X_{\max} measurements we have performed a Monte Carlo comparison study between two sets of simulations that deals with the atmospheres in a similar way as described in the beginning of this section. For each of these cases we have used a set of 40 simulated events with different energy, zenith and azimuth angles. Each of these sets consist of an ensemble of proton and iron initiated showers based on CONEX selection criteria. One shower from the set with higher humidity is taken as reference and all the simulated showers from the set with zero humidity are used to perform the reconstruction. This yields a reconstructed X_{reco} that can be compared to the actual X_{real} of the reference shower. The same method is repeated for all the showers in the set with higher humidity. Showers with extreme values of X_{\max} were not included in the fit. The range of the fit was taken as ± 50 g/cm 2 of the actual X_{\max} for the test shower.

The difference $X_{\text{reco}} - X_{\text{real}}$ estimates the effect of humidity on the reconstructed X_{\max} . We do not observe any significant shift in X_{\max} in this study. This indicates that these effects are most likely smaller than the overall resolution in reconstructed X_{\max} in the LOFAR frequency band. We also performed the same study in a higher frequency band between 50 and 350 MHz, corresponding to the SKA-low band. There, an overall shift of 6.8 g/cm 2 in the reconstructed X_{\max} was observed. These results, shown in Fig-9, are in line with the LDF studies described earlier in this section.

In Ref.[11], larger shifts of about 10 to 22 g/cm 2 in reconstructed X_{\max} in the high frequency band of 120–250 MHz for 4% higher refractivity and 3.5 to 11 g/cm 2 in the low frequency band of 30–80 MHz were reported. A toy model was used to describe the effects. The toy

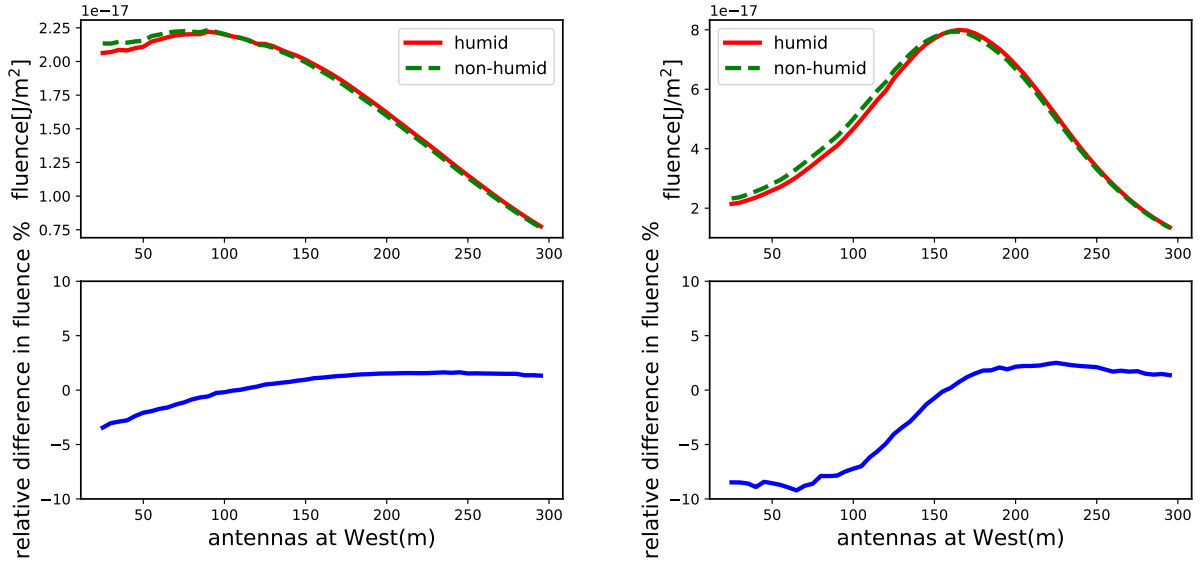


Figure 8: LDF profiles for a 10^{17} eV proton shower coming from zenith 45° with $X_{\max} = 593\text{g/cm}^2$. Observers are located to the west of the shower axis. **Left:** low frequency band between 30–80 MHz, **Right:** high frequency band between 50–350 MHz. The upper panel shows the LDF of total fluence for the humid and non-humid sets, the lower panel shows the relative difference between these two.

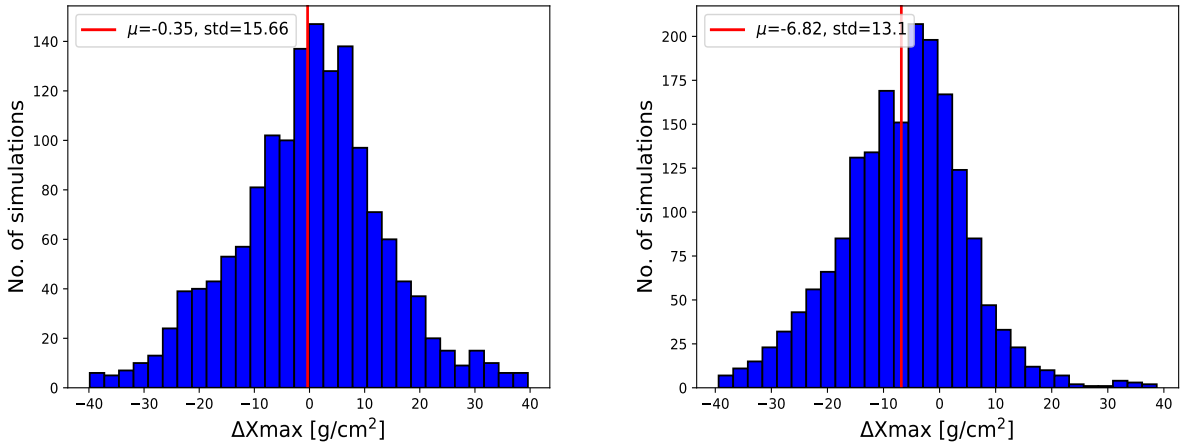


Figure 9: Histogram for the $\Delta X_{\max} = X_{\text{reco}} - X_{\text{real}}$ between the reconstructed and true value of the X_{\max} obtained from the Monte Carlo study between the humid and non-humid simulation sets. **Left:** for the low frequency band of 30–80 MHz. **Right:** for the high frequency band of 50–350 MHz. The shift in the X_{\max} is significant at 2σ level.

model was based on the assumptions that the size of the radio footprint on the ground would be proportional to the geometric distance to X_{\max} and to the Cherenkov angle at the altitude of X_{\max} . The effect of constant higher refractivity would correspond to a higher Cherenkov

angle resulting in an underestimation of X_{\max} . This then leads to a clear linear relation between shift in X_{\max} and distance to X_{\max} . Without having prior knowledge of individual atmospheric conditions, an overall scaling of the refractivity profile had to suffice. However, the realistic scenario is quite different. There are strong interplays between humidity, pressure, and temperature which are reflected in refractivity. The relative refractivity profile in Fig-2 shows that the shift is not a constant, but is altitude dependent. From near ground to higher altitudes it switches from being a higher value than US standard atmosphere to a lower value. This makes an one-to-one comparison to Ref.[11] hard. However, we can argue that qualitatively same trait in the high and low frequency band has been found in both the works.

The effects of different zenith angles, true X_{\max} and energy were probed for the shift in X_{\max} for both the frequency bins. The simulation set was divided in two groups, each group belonging to high and low values of the parameters mentioned above. No significant effect was seen.

Frequency band	Zenith	ΔX_{\max} (g/cm ²)
50–350 MHz	low < 30°	-6.24±0.30
50–350 MHz	high > 30°	-6.19± 0.37
30–80 MHz	low < 30°	0.10±0.50
30–80 MHz	high > 30°	-0.05±0.46
Frequency band	True X_{\max} (g/cm ²)	ΔX_{\max} (g/cm ²)
50–350 MHz	low < 624	-6.78±0.41
50–350 MHz	high > 624	-6.30± 0.32
30–80 MHz	low < 624	-0.61±0.51
30–80 MHz	high > 624	0.51±0.46
Frequency band	Energy(GeV)	ΔX_{\max} (g/cm ²)
50–350 MHz	low < 2.18×10^8	-6.86±0.35
50–350 MHz	high > 2.18×10^8	-6.92± 0.38
30–80 MHz	low < 2.18×10^8	-0.48±0.48
30–80 MHz	high > 2.18×10^8	0.±0.49

Table 1: Shift in X_{\max} for different zenith, energy and X_{\max} bins for different frequency bands.

7. Conclusion and discussion

Simulating air showers with realistic atmospheres is important for the precise reconstruction of X_{\max} with the radio technique. The GDAS database is a useful platform to extract atmospheric parameters for a given time and location. Atmospheric effects on radio simulations were previously studied in Refs. [11] and [15]. The studies demonstrated the role of correct description of atmospheric density and refractive index when included in the radio simulation codes. However, the application of simulations with realistic atmospheres to real data was not addressed.

We report, for the first time, the application of GDAS-based atmospheric profiles, automated in CoREAS simulation to cosmic ray data. By systematically performing GDAS-based CoREAS simulations for the LOFAR dataset, we have done comparison between GDAS-based atmospheres a linear geometrical first order correction to the US standard atmosphere on X_{\max} . While the linear correction is sufficient for the bulk of the events, it becomes indispensable to use full GDAS based atmospheres for extreme values of the air pressure. When the air pressure at ground level differs by less than 10 hPa from the US standard atmosphere value, the reconstructed X_{\max} value including the linear correction agrees with the full GDAS-based reconstruction value within 2 g/cm². However, when the ground pressure is more than 10 hPa from the US standard atmosphere, this difference grows significantly up to 15 g/cm².

We have also introduced a GDAS-based correction factor for X_{\max} reconstructed with US standard atmosphere without having to run full GDAS-based CoREAS simulations. It is specific to LOFAR, but similar relations can be worked out for other experiments as well. The uncertainty on the predicted X_{\max} using the correction factor is about 12 g/cm²; this is within the typical X_{\max} reconstruction uncertainty with LOFAR, around 17 g/cm².

We have probed the effects of humidity on the lateral distribution of radio power by comparing two profiles with high and low humidity. We performed this study for different frequency bands. In the LOFAR frequency band of 30–80 MHz the relative difference in power is small. For a higher frequency band of 50–350 MHz the same effects are comparatively larger, up to 10%. We also estimated the radiation energy from the LDF profiles to see the effects of humidity on the reconstructed energy. No significant difference was found for either frequency regime which indicates that humidity does not influence the estimated energy. A Monte Carlo study on the reconstructed X_{\max} was also done for these frequency bands. No significant effect of humidity is found on the reconstructed X_{\max} for the low frequency band relevant for LOFAR; for the higher frequency band a mean difference on the order of 7 g/cm² is observed. This could be important for the high precision X_{\max} measurements for the cosmic ray detection with the SKA experiment [29].

In the process of implementing GDAS-based parameterized density and refractive index profile in CORSIKA/CoREAS, we have developed a tool, called ‘gdastool’, which has been available for public use since the release of CORSIKA version 7.6300, and is already being used by other experiments in the community around the globe.

In the previous LOFAR analysis the effects of refractive index were included within the systematic uncertainties on the reconstructed X_{\max} . The improved atmospheric correction will lead to a reduced systematic uncertainty. An update on the mass composition results is not within the scope of this study. It will be discussed in a future publication, which involves, along with atmospheric corrections, improved calibration of the radio antennas, energy scale, and new X_{\max} reconstruction techniques.

8. Acknowledgement

The LOFAR cosmic ray key science project acknowledges funding from an Advanced Grant of the European Research Council (FP/2007-2013)/ERC Grant Agreement no 227610. The project has also received funding from the European Research Council (ERC) under the European Union's Horizon 2020 research and innovation program (grant agreement No 640130). We furthermore acknowledge financial support from FOM, (FOM-project 12PR304). AN is supported by the DFG (Emmy-Noether grant NE 2031/2-1). LOFAR, the Low Frequency Array designed and constructed by ASTRON, has facilities in several countries, that are owned by various parties (each with their own funding sources), and that are collectively operated by the International LOFAR Telescope foundation under a joint scientific policy. We sincerely thank the CORSIKA developers for their assistance regarding the implementation of our work in CORSIKA modules.

References

- [1] T. Huege. Radio detection of cosmic ray air showers in the digital era. *Physics Reports*, 620:1–52, 2016.
- [2] Frank G. Schröder. Radio detection of Cosmic-Ray Air Showers and High-Energy Neutrinos. *Prog. Part. Nucl. Phys.*, 93:1–68, 2017.
- [3] S. Buitink et al. A large light-mass component of cosmic rays at 10^{17} - $10^{17.5}$ eV from radio observations. *Nature*, 531:70, 2016.
- [4] W. D. Apel et al. Reconstruction of the energy and depth of maximum of cosmic-ray air-showers from LOPES radio measurements. *Phys. Rev.*, D90(6):062001, 2014.
- [5] G. A. Askar'yan. Excess negative charge of an electron-photon shower and its coherent radio emission. *Sov. Phys. JETP*, 14(2):441–443, 1962. [Zh. Eksp. Teor. Fiz.41,616(1961)].
- [6] A. Nelles et al. Measuring a Cherenkov ring in the radio emission from air showers at 110–190 MHz with LOFAR. *Astropart. Phys.*, 65:11–21, 2015.
- [7] H. Schoorlemmer et al. Energy and Flux Measurements of Ultra-High Energy Cosmic Rays Observed During the First ANITA Flight. *Astropart. Phys.*, 77:32–43, 2016.
- [8] Jaime Alvarez-Muniz, Washington R. Carvalho, Jr., and Enrique Zas. Monte Carlo simulations of radio pulses in atmospheric showers using ZHAireS. *Astropart. Phys.*, 35:325–341, 2012.
- [9] K. D. de Vries, A. M. van den Berg, O. Scholten, and K. Werner. Coherent Cherenkov Radiation from Cosmic-Ray-Induced Air Showers. *Phys. Rev. Lett.*, 107:061101, 2011.
- [10] R. Šmída et al. First Experimental Characterization of Microwave Emission from Cosmic Ray Air Showers. *Phys. Rev. Lett.*, 113(22):221101, 2014.
- [11] A. Corstanje et al. The effect of the atmospheric refractive index on the radio signal of extensive air showers. *Astropart. Phys.*, 89:23–29, 2017.
- [12] P. Schellart et al. Detecting cosmic rays with the LOFAR radio telescope. *Astronomy and Astrophysics*, 560(A98), 2013.
- [13] D. Heck et al. CORSIKA: A Monte Carlo code to simulate extensive air showers. *Report FZKA*, 6019, 1998.
- [14] Bianca Keilhauer, J. Blumer, R. Engel, H. O. Klages, and M. Risse. Impact of varying atmospheric profiles on extensive air shower observation: - Atmospheric density and primary mass reconstruction. *Astropart. Phys.*, 22:249–261, 2004.
- [15] F. Gaté, B. Revenu, D. García-Fernández, V. Marin, R. Dallier, A. Escudié, and L. Martin. Computing the electric field from extensive air showers using a realistic description of the atmosphere. *Astropart. Phys.*, 98:38–51, 2018.
- [16] Vincent Marin and Benoit Revenu. Simulation of radio emission from cosmic ray air shower with SELFAS2. *Astropart. Phys.*, 35:733–741, 2012.
- [17] National oceanic and atmospheric administration, global data assimilation system. <https://www.ncdc.noaa.gov/data-access/model-data/model-datasets/global-data-assimilation-system-gdas>.

- [18] P. Abreu et al. Description of Atmospheric Conditions at the Pierre Auger Observatory using the Global Data Assimilation System (GDAS). *Astropart. Phys.*, 35:591–607, 2012.
- [19] J. Rueger. Refractive index formulae for radio waves. *Proceedings of FIG XXII International Congress*, 2002.
- [20] M. P. van Haarlem et al. LOFAR: The LOw-Frequency ARray. *Astronomy and Astrophysics*, 556:56, 2013.
- [21] S. Thoudam et al. LORA: A scintillator array for LOFAR to measure extensive air showers. *Nucl.Instrum.Meth*, A767:339–346, 2014.
- [22] S. Buitink et al. Cosmic ray mass composition with LOFAR. *PoS*, ICRC2017:499, 2018.
- [23] K. Mulrey et al. Calibration of the LOFAR low-band antennas using the Galaxy and a model of the signal chain. *Astropart. Phys.*, 111:1–11, 2019.
- [24] S. Buitink et al. Method for high precision reconstruction of air shower X_{\max} using two-dimensional radio intensity profiles. *Phys. Rev. D*, 90(8), 2014.
- [25] A. Nelles et al. A parameterization for the radio emission of air showers as predicted by CoREAS simulations and applied to LOFAR measurements. *Astropart.Phys.*, 60:13–24, 2015.
- [26] Alexander Aab et al. Energy Estimation of Cosmic Rays with the Engineering Radio Array of the Pierre Auger Observatory. *Phys. Rev.*, D93(12):122005, 2016.
- [27] Alexander Aab et al. Measurement of the Radiation Energy in the Radio Signal of Extensive Air Showers as a Universal Estimator of Cosmic-Ray Energy. *Phys. Rev. Lett.*, 116(24):241101, 2016.
- [28] Christian Glaser, Martin Erdmann, Jörg R. Hörandel, Tim Huege, and Johannes Schulz. Simulation of Radiation Energy Release in Air Showers. *JCAP*, 1609(09):024, 2016.
- [29] T. Huege et al. High-precision measurements of extensive air showers with the SKA. *PoS*, ICRC2015:309, 2016.

Cosmic-ray energy spectrum and composition up to the ankle – the case for a second Galactic component

S. Thoudam^{1,2,*}, J.P. Rachen¹, A. van Vliet¹, A. Achterberg¹, S. Buitink³, H. Falcke^{1,4,5}, J.R. Hörandel^{1,4}

¹ Department of Astrophysics/IMAPP, Radboud University, P.O. Box 9010, 6500 GL Nijmegen, The Netherlands

² Now at: Department of Physics and Electrical Engineering, Linnéuniversitetet, 35195 Växjö, Sweden

³ Astronomical Institute, Vrije Universiteit Brussel, Pleinlaan 2, 1050 Brussels, Belgium

⁴ NIKHEF, Science Park Amsterdam, 1098 XG Amsterdam, The Netherlands

⁵ ASTRON, Postbus 2, 7990 AA Dwingeloo, The Netherlands

November 14, 2016

ABSTRACT

Motivated by the recent high-precision measurements of cosmic rays by several new-generation experiments, we have carried out a detailed study to understand the observed energy spectrum and composition of cosmic rays with energies up to about 10^{18} eV. Our study shows that a single Galactic component with subsequent energy cut-offs in the individual spectra of different elements, optimised to explain the observed elemental spectra below $\sim 10^{14}$ eV and the ‘knee’ in the all-particle spectrum, cannot explain the observed all-particle spectrum above $\sim 2 \times 10^{16}$ eV. We discuss two approaches for a second component of Galactic cosmic rays – re-acceleration at a Galactic wind termination shock, and supernova explosions of Wolf-Rayet stars, and show that the latter scenario can explain almost all observed features in the all-particle spectrum and the composition up to $\sim 10^{18}$ eV, when combined with a canonical extra-galactic spectrum expected from strong radio galaxies or a source population with similar cosmological evolution. In this two-component Galactic model, the knee at $\sim 3 \times 10^{15}$ eV and the ‘second knee’ at $\sim 10^{17}$ eV in the all-particle spectrum are due to the cut-offs in the first and second components, respectively. We also discuss several variations of the extra-galactic component, from a minimal contribution to scenarios with a significant component below the ‘ankle’ (at $\sim 4 \times 10^{18}$ eV), and find that extra-galactic contributions in excess of regular source evolution are neither indicated nor in conflict with the existing data. We also provide arguments that an extra-galactic contribution is unlikely to dominate at or below the second knee. Our main result is that the second Galactic component predicts a composition of Galactic cosmic rays at and above the second knee that largely consists of helium or a mixture of helium and CNO nuclei, with a weak or essentially vanishing iron fraction, in contrast to most common assumptions. This prediction is in agreement with new measurements from LOFAR and the Pierre Auger Observatory which indicate a strong light component and a rather low iron fraction between $\sim 10^{17}$ and 10^{18} eV.

Key words. Galaxy — cosmic rays — diffusion — ISM: supernova remnants — Stars: winds — Stars: Wolf-Rayet

1. Introduction

Until a decade ago, the cosmic ray spectrum from ~ 10 GeV to $\sim 10^{11}$ GeV was seen as a power law with two main features: a steepening from a spectral index $\gamma \approx -2.7$ to $\gamma \approx -3.1$ at about 3×10^6 GeV, commonly called the ‘knee’, and a flattening back to $\gamma \approx -2.7$ at about 4×10^9 GeV, consequently denoted as the ‘ankle’. Phenomenological explanations for the knee have been given due to propagation effects in the Galaxy (Ptuskin et al. 1993), progressive cut-offs in the spectra of nuclear components from hydrogen to lead (Hörandel 2003a), or re-acceleration at shocks in a Galactic wind (Völk & Zirakashvili 2004), but left open the question of the primary Galactic accelerators producing these particles. Explanations based on source physics have been mostly built on the assumption that supernova remnants, on grounds of energetics known as one of the most promising sources for cosmic rays (Baade & Zwicky 1934), accelerate cosmic rays at shocks ploughing into the interstellar medium to energies up to about 10^{5-6} GeV

(Lagage & Cesarsky 1983; Axford 1994). This may extend to $\sim 10^8$ GeV if they are propagating in fast and highly magnetised stellar winds (Völk & Biermann 1988; Biermann & Cassinelli 1993), or if non-linear effects in the acceleration process are considered (Bell & Lucek 2001). The combination of such components could eventually explain cosmic rays below and above the knee as a superposition of components of different nuclei, as shown, for example by Stanev et al. (1993). At energies above 10^9 GeV this steep component was assumed to merge into a flatter extra-galactic component (Rachen et al. 1993; Berezhinsky et al. 2004), explaining the ankle in the spectrum. For this extra-galactic component, sources on all scales have been proposed: From clusters of galaxies (Kang et al. 1996) through radio galaxies (Rachen & Biermann 1993), compact AGN jets (Mannheim et al. 2001) to gamma-ray bursts (Waxman 1995). It was commonly assumed to be dominated by protons. Eventually, at $\sim 10^{11}$ GeV the cosmic ray spectrum was believed to terminate in the so-called GZK cutoff (Greisen 1966; Zatsepin & Kuzmin 1996) due to interaction with cosmic microwave background (CMB) photons.

* E-mail: satyendra.thoudam@lnu.se

Recent measurements of cosmic rays by several new generation experiments have severely challenged this simple view. At low energies, below $\sim 10^6$ GeV, satellite and balloon-borne experiments such as ATIC-2 (Panov et al. 2007), CREAM (Yoon et al. 2011), TRACER (Obermeier et al. 2011), PAMELA (Adriani et al. 2014), AMS-02 (Aguilar et al. 2014, 2015a,b), and *Fermi*-LAT (Abdo et al. 2009) have measured the energy spectra of various elements of cosmic rays ranging from protons to heavier nuclei such as iron as well as the leptonic component of cosmic rays, and anti-particles such as positrons and anti-protons. Some of their results, for example the rise of the positron fraction above ~ 10 GeV (Aguilar et al. 2013), the harder energy spectrum of helium nuclei with respect to the proton spectrum (Adriani et al. 2011), and the spectral hardening of both the proton and helium nuclei at TeV energies (Yoon et al. 2011), are difficult to explain using standard models of cosmic-ray acceleration in supernova remnants and their subsequent propagation in the Galaxy. At high energies, that is above $\sim 10^6$ GeV, ground-based experiments such as KASCADE-Grande (Apel et al. 2013), the Tibet III array (Amenomori et al. 2008), IceTop (Aartsen et al. 2013), the Pierre Auger Observatory (Ghia et al. 2015) and the Telescope Array (Abu-Zayyad et al. 2013) have carried out detailed measurements of the all-particle energy spectrum and the composition of cosmic rays. First, they confirm a third major break in the spectrum, a steepening to $\gamma \approx -3.3$ above about 10^8 GeV, which has been suggested before both by the Fly’s Eye stereo energy spectrum (Bird et al. 1994) and theoretical arguments about the structure of the ankle (Berezinsky & Grigorieva 1988; Rachen et al. 1993). It has anatomically been named the ‘second knee’ (Hörandel 2006). While this still fits with the original view, the cosmic-ray composition measurements at these energies pose a severe challenge: Instead of gradually becoming heavier as expected, the data show that the composition reaches a maximum mean mass at energies around 6×10^7 GeV, and then becomes gradually lighter again up to the ankle. Finally, above the ankle the composition becomes heavier again. It has been shown that the observed spectrum and composition at the highest energies can be explained by a mixed-composition extra-galactic source spectrum with progressive cutoffs at $\sim Z \times 5 \times 10^9$ GeV, where Z is the nuclear charge (Aloisio et al. 2014). This would imply that there is no significant impact of the GZK effect in cosmic ray propagation except through photo-disintegration of nuclei. In addition, the measurement of an ankle-like feature in the light component of cosmic rays at $\sim 10^8$ GeV by the KASCADE-Grande experiment (Apel et al. 2013), and the new revelation of a strong light component and a very small iron component by the LOFAR measurements between $\sim (1 - 4) \times 10^8$ GeV (Buitink et al. 2016), and by the Pierre Auger Observatory above $\sim 7 \times 10^8$ GeV (Aab et al. 2014) add further challenges to the standard model.

The new data have led to a number of theoretical modifications of the standard model. The spectral hardening at TeV energies has been explained as due to the hardening in the source spectrum of cosmic rays (Biermann et al. 2010a; Ohira et al. 2011; Yuan et al. 2011; Ptuskin et al. 2013), as a propagation effect (Tomassetti 2012; Blasi et al. 2012), the effect of re-acceleration by weak shocks (Thoudam & Hörandel 2014) or the effect of nearby sources (Thoudam & Hörandel 2012, 2013;

Erlykin & Wolfendale 2012). At high energies, the increasing mean mass around the knee still fits well the idea of progressive cut-offs (Hörandel 2003a), if the nuclear species are constrained to masses up to iron and thus limited to energies below about 3×10^7 GeV. The light composition around the ankle revived interest in the so-called ‘proton dip model’, which explains the ankle feature as due to an extra-galactic propagation effect of protons producing electron-positron pairs at the CMB (Berezinsky & Grigorieva 1988; Berezinsky et al. 2006). This would imply that the cosmic ray spectrum below the ankle is, at least in part, of extra-galactic origin. While the recent measurement of $\sim 40\%$ proton fraction at the ankle by the Pierre Auger Collaboration (Aab et al. 2014) has raised problems with this approach, as the model is compatible only with more than 80% protons (Berezinsky et al. 2006), a number of new models have been suggested, involving compact sources with significant photo-disintegration of nuclei during acceleration (Globus et al. 2015a; Unger et al. 2015), or as a component with primordial element composition accelerated at clusters of galaxies and limited by pair production losses in the CMB (Rachen 2016). However, with all these new ideas, big questions remain open: How does the cosmic ray component at the knee connect to the one at the second knee to ankle regime, and where is the transition from Galactic to extra-galactic cosmic rays?

In this work, we revisit the basic models of Galactic cosmic-ray production in view of the currently available data. We start by developing a detailed model description for low-energy cosmic rays assuming them to be primarily produced inside supernova remnants (SNRs) present in the interstellar medium (hereafter, these cosmic rays will be referred to as the ‘SNR-CRs’). This model, described in Section 2, has been demonstrated to explain the observed spectral hardening of protons and helium nuclei in the TeV region and, at the same time, explains the observed composition of cosmic rays at low energies (Thoudam & Hörandel 2014). The model prediction will be extended to high energies, and compared with the observed all-particle energy spectrum. It will be shown that SNR-CRs cannot explain the observed energy spectrum above $\sim 10^7$ GeV. We then revisit two possibilities for a second Galactic component in Section 3: (a) The re-acceleration of SNR-CRs escaped into the Galactic halo by the Galactic wind termination shocks (Jokipii & Morfill 1987; Zirakashvili & Völk 2006), and (b) the contribution of cosmic rays from the explosions of Wolf-Rayet stars in the Galaxy (Biermann & Cassinelli 1993). The possibility of a second Galactic component has also been discussed in Hillas (2005) who considered Type II SNRs expanding into a dense wind of their precursor stars. For both the scenarios considered in the present work, we assume the extra-galactic proton component used by Rachen et al. (1993) to obtain proper results for total spectrum and composition at energies just below the ankle in Section 4. In Section 5 we then check the effect of other hypotheses for the extra-galactic component, using (1) a phenomenological ‘minimal model’ derived from composition results measured at the Pierre Auger Observatory (di Matteo et al. 2015), (2) the minimal model plus the ‘primordial cluster component’ introduced by Rachen (2016), and (3) the ‘extra-galactic ankle’ model by Unger et al. (2015). In Section 6, we present a discussion of our results and their implications, and other views on the cosmic rays below 10^9 GeV, followed by our conclusions in Section 7.

2. Cosmic rays from supernova remnants (SNR-CRs)

Although the exact nature of cosmic-ray sources in the Galaxy is not yet firmly established, supernova remnants are considered to be the most plausible candidates both from the theoretical and the observational points of view. It has been theoretically established that shock waves associated with supernova remnants can accelerate particles from the thermal pool to a non-thermal distribution of energetic particles. The underlying acceleration process, commonly referred to as the diffusive shock acceleration process, has been studied quite extensively, and it produces a power-law spectrum of particles with a spectral index close to 2 (Krymskii 1977; Bell 1978; Blandford & Ostriker 1978; Drury 1983; Ptuskin et al. 2010; Caprioli et al. 2011), which is in good agreement with the values inferred from radio observation of supernova remnants (Green 2009). Moreover, the total power of $\sim 10^{42}$ ergs s^{-1} injected by supernova explosions into the Galaxy, considering a supernova explosion energy of $\sim 10^{51}$ ergs and an explosion frequency of $\sim 1/30$ yr $^{-1}$, is more than sufficient to maintain the cosmic-ray energy content of the Galaxy. In addition to the radio measurements, observational evidence for the presence of high-energy particles inside supernova remnants is provided by the detection of non-thermal X-rays (Vink & Laming 2003; Parizot et al. 2006) and TeV gamma rays from a number of supernova remnants (Aharonian et al. 2006, 2008; Albert et al. 2007). For instance, the detection of TeV gamma rays up to energies close to 100 TeV from the supernova remnant RX J1713.7-3946 by the H.E.S.S. Cherenkov telescope array indicates that particles with energies up to ~ 1 PeV can be accelerated inside supernova remnants (Aharonian et al. 2007).

2.1. Transport of SNR-CRs in the Galaxy

After acceleration by strong supernova remnant shock waves, cosmic rays escape from the remnants and undergo diffusive propagation through the Galaxy. During the propagation, some fraction of cosmic rays may further get re-accelerated due to repeated encounters with expanding supernova remnant shock waves in the interstellar medium (Wandel 1988; Berezhko et al. 2003). This re-acceleration is expected to be produced mainly by older remnants, with weaker shocks, because of their bigger sizes. Therefore, the re-acceleration is expected to generate a particle spectrum which is steeper than the initial source spectrum of cosmic rays produced by strong shocks. This model has been described in detail in Thoudam & Hörandel (2014), and it has been shown that the re-accelerated cosmic rays can dominate the GeV energy region while the non-re-accelerated cosmic rays dominate at TeV energies, thereby explaining the observed spectral hardening in the TeV region. Below, we briefly summarise some key features of the model which are important for the present study.

The steady-state transport equation for cosmic-ray nuclei in the Galaxy in the re-acceleration model is described by,

$$\nabla \cdot (D\nabla N) - [\bar{n}v\sigma + \xi] \delta(z)N + \left[\xi s p^{-s} \int_{p_0}^p du N(u) u^{s-1} \right] \delta(z) = -Q\delta(z), \quad (1)$$

where we have adopted a cylindrical geometry for the propagation region described by the radial r and vertical z coordinates with $z = 0$ representing the Galactic plane. We assume the region to have a constant halo boundary at $z = \pm L$, and no boundary in the radial direction. This is a reasonable assumption for cosmic rays at the galactocentric radius of the Sun as the majority of them are produced within a radial distance $\sim L$ from the Sun (Thoudam 2008). Choosing a different (smaller) halo height for the Galactic centre region, as indicated by the observed *WMAP* haze (Biermann et al. 2010b), will not produce significant effects in our present study. $N(r, z, p)$ represents the differential number density of the cosmic-ray nuclei with momentum/nucleon p , and $Q(r, p)\delta(z)$ is the injection rate of cosmic rays per unit volume by supernova remnants in the Galaxy. The diffusive nature of the propagation is represented by the first term in Equation 1. The diffusion coefficient $D(\rho)$ is assumed to be a function of the particle rigidity ρ as, $D(\rho) = D_0\beta(\rho/\rho_0)^a$, where D_0 is the diffusion constant, $\beta = v/c$ with $v(p)$ and c representing the velocity of the particle and the velocity of light respectively, $\rho_0 = 3$ GV is a constant, and a is the diffusion index. The rigidity is defined as $\rho = Apc/Ze$, where A and Z represent the mass number and the charge number of the nuclei respectively, and e is the charge of an electron. The second term in Equation 1 represents the loss of particles during the propagation due to inelastic interaction with the interstellar matter, and also due to re-acceleration to higher energies, where \bar{n} represents the surface density of matter in the Galactic disk, $\sigma(p)$ is the inelastic interaction cross-section, and ξ corresponds to the rate of re-acceleration. We take $\xi = \eta V \bar{v}$, where $V = 4\pi\mathfrak{R}^3/3$ is the volume occupied by a supernova remnant of radius \mathfrak{R} re-accelerating the cosmic rays, η is a correction factor that is introduced to account for the actual unknown size of the remnants, and \bar{v} is the frequency of supernova explosions per unit surface area in the Galactic disk. The term containing the integral in Equation 1 represents the gain in the number of particles due to re-acceleration from lower energies. The effect of Galactic wind and ionisation losses which are important mostly at low energies, below ~ 1 GeV/nucleon, are not included explicitly in the transport equation. Instead, we introduce a low-momentum cut-off, $p_0 \sim 100$ MeV/nucleon, in the particle distribution to account for the effect on the number of low-energy particles available for re-acceleration in the presence of these processes (Wandel et al. 1987). We assume that re-acceleration instantaneously produces a power-law spectrum of particles with spectral index s . The source term $Q(r, p)$ can be expressed as $Q(r, p) = \bar{v}H[R - r]H[p - p_0]Q(p)$, where $H(m) = 1(0)$ for $m > 0(< 0)$ represents a Heaviside step function, and the source spectrum $Q(p)$ is assumed to follow a power-law in total momentum with an exponential cut-off which, in terms of momentum/nucleon, can be written as

$$Q(p) = AQ_0(Ap)^{-q} \exp\left(-\frac{Ap}{Zp_c}\right), \quad (2)$$

where Q_0 is a normalisation constant which is proportional to the amount of energy f channelled into cosmic rays by a single supernova event, q is the spectral index, and p_c is the cut-off momentum for protons. The exponential cut-off in Equation 2 represents a good approximation for particles at the shock produced by the diffusive shock accel-

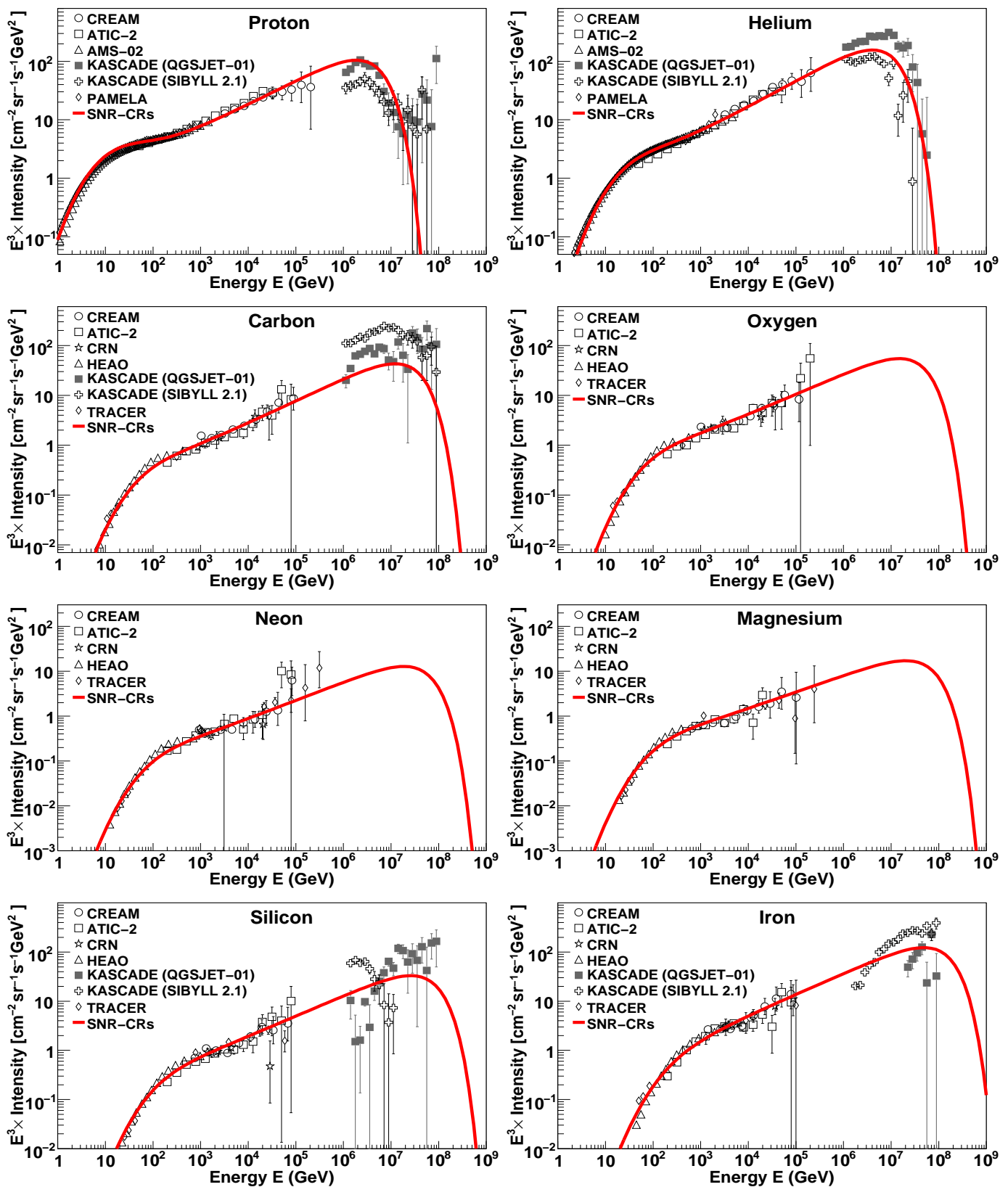


Fig. 1. Energy spectra for different cosmic-ray elements. *Solid line*: Model prediction for the SNR-CRs. *Data*: CREAM (Ahn et al. 2009; Yoon et al. 2011), ATIC-2 (Panov et al. 2007), AMS-02 (Aguilar et al. 2015a,b), PAMELA (Adriani et al. 2011), CRN (Müller et al. 1991; Swordy et al. 1990), HEAO (Engelmann et al. 1990), TRACER (Obermeier et al. 2011), and KASCADE (Antoni et al. 2005). Cosmic-ray source parameters (q, f) used in the calculation are given in Table 1. For the other model parameters (D_0, a, η, s), see text for details.

Table 1. Source spectral indices, q , and energy injected per supernova, f , for the different species of cosmic rays used in the calculation of the SNR-CRs spectra shown in Figures 1 and 2.

Particle type	q	f ($\times 10^{49}$ ergs)
Proton	2.24	6.95
Helium	2.21	0.79
Carbon	2.21	2.42×10^{-2}
Oxygen	2.25	2.52×10^{-2}
Neon	2.25	3.78×10^{-3}
Magnesium	2.29	5.17×10^{-3}
Silicon	2.25	5.01×10^{-3}
Iron	2.25	4.95×10^{-3}

ation mechanism (see e.g. Malkov & Drury 2001). We assume that the maximum energy for cosmic-ray nuclei produced by the supernova shock is Z times the maximum energy for protons. Based on the observed high concentration of supernova remnants and atomic and molecular hydrogen near the Galactic disk, in Equation 1, we assume that both cosmic-ray sources and interstellar matter are distributed in the disk (i.e. at $z = 0$). The distributions are assumed to be uniform, and extended up to a radius R .

Recalling the analytical solution of Equation 1 derived in Thoudam & Hörandel (2014), the cosmic-ray density at the position $r = 0$ for $p > p_0$ follows,

$$N(z, p) = \bar{\nu}R \int_0^\infty dk \frac{\sinh[k(L-z)]}{\sinh(kL)} \times \frac{J_1(kR)}{B(p)} \left\{ Q(p) + \xi s p^{-s} \int_{p_0}^p dp' p'^s Q(p') \mathcal{A}(p') \exp\left(\xi s \int_{p'}^p \mathcal{A}(u) du\right) \right\}, \quad (3)$$

where J_1 is a Bessel function of order 1, and the functions B and \mathcal{A} are given by,

$$B(p) = 2D(p)k \coth(kL) + \bar{n}v(p)\sigma(p) + \xi$$

$$\mathcal{A}(u) = \frac{1}{uB(u)}. \quad (4)$$

From Equation 3, the cosmic-ray density at the Earth can be obtained by taking $z = 0$ considering that our Solar system lies close to the Galactic plane.

2.2. Model prediction for the low-energy measurements

By comparing the abundance ratio of boron-to-carbon nuclei predicted by the model with the measurements, the cosmic-ray propagation parameters (D_0, a) and the re-acceleration parameters (η, s) have been obtained to be, $D_0 = 9 \times 10^{28}$ cm² s⁻¹, $a = 0.33$, $\eta = 1.02$, and $s = 4.5$ (Thoudam & Hörandel 2014). We adopt these values in our present study. The supernova remnant radius is taken to be $\mathfrak{R} = 100$ pc. The inelastic interaction cross-section for protons is taken from Kelner et al. (2006), and for heavier nuclei, the cross-sections are taken from Letaw et al. (1983). The surface matter density is taken as the averaged density in the Galactic disk within a radius equal to the size of the diffusion boundary L . We choose $L = 5$ kpc, which gives an averaged surface density of atomic hydrogen of $\bar{n} = 7.24 \times 10^{20}$ atoms cm⁻² (Thoudam & Hörandel 2013).

An extra 10% is further added to \bar{n} to account for the helium abundance in the interstellar medium. The radial extent of the source distribution is taken as $R = 20$ kpc. Each supernova explosion is assumed to release a total kinetic energy of 10^{51} ergs, and the supernova explosion frequency is taken as $\bar{\nu} = 25$ SNe Myr⁻¹ kpc⁻². The latter corresponds to a rate of ~ 3 supernova explosions per century in the Galaxy.

Using the values of various parameters mentioned above, the energy spectra of SNR-CRs for different elements are calculated. In Figure 1, results for eight elements (proton, helium, carbon, oxygen, neon, magnesium, silicon and iron, which represent the dominant species at low energies) are compared with the measured data at low energies. The source parameters (q, f) for the individual elements are kept free in the calculation, and they are optimised based on the observed individual spectra at low energies. The parameter values that best reproduce the measured data are listed in Table 1. The source spectral indices are in the range of 2.21 – 2.29, and out of the total of 8% of the supernova explosion energy channelled into SNR-CRs, the largest fraction goes into protons at the level of 6.95%, followed by helium nuclei with 0.79%. The calculated spectra reproduce the measured data quite well including the behaviour of spectral hardening at TeV energies observed for protons and helium nuclei. In our model, the absence of such a spectral hardening for heavier nuclei is explained as due to the increasing effect of inelastic collision over re-acceleration with the increase in mass (Thoudam & Hörandel 2014).

2.3. Extrapolation of the SNR-CR spectrum to high energies

In Figure 1, we also show an extrapolation of the model prediction to high energies. For protons, helium, carbon, silicon and iron nuclei, the predictions are compared with the available measurements from the KASCADE experiment above $\sim 10^6$ GeV. The calculation assumes an exponential cut-off for the proton source spectrum at $E_c = 4.5 \times 10^6$ GeV, and for the heavier nuclei at ZE_c . This value of E_c , which is obtained by comparing the predicted all-particle spectrum with the observed all-particle spectrum as shown in Figure 2, represents the maximum E_c value permitted by the measurements. While obtaining the all-particle spectrum shown in Figure 2, we also include contributions from the sub-dominant primary cosmic-ray elements ($Z < 26$), calculated using elemental abundances at 10^3 GeV given in Hörandel (2003a) and a source index of 2.25. Their total contribution amounts up to $\sim 8\%$ of the all-particle spectrum. The predicted all-particle spectrum agrees with the data up to $\sim 2 \times 10^7$ GeV, and reproduces the observed knee at the right position. Choosing E_c values larger than 4.5×10^6 GeV will produce an all-particle spectrum which is inconsistent both with the observed knee position and the intensity above the knee. Although our estimate for the best-fit E_c value does not rely on the proton measurements at high energies, it can be noticed from Figure 1 that both the predicted proton and helium spectra are in good agreement (within systematic uncertainties) with the KASCADE data. For carbon, silicon and iron nuclei, the agreement with the data is less convincing, which may be related to the larger systematic uncertainties in the shapes of the measured spectra.

From Figure 2, it can be observed that, at energies around the knee, the all-particle spectrum is predicted to be

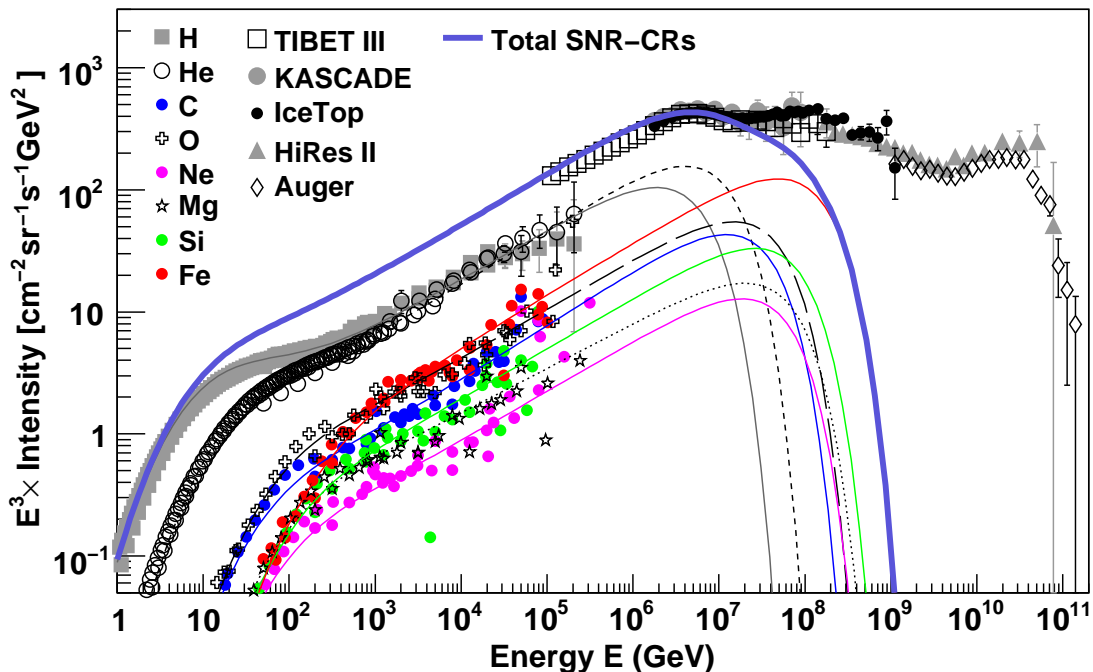


Fig. 2. Contribution of SNR-CRs to the all-particle cosmic-ray spectrum. The thin lines represent spectra for the individual elements, and the thick-solid line represents the total contribution. The calculation assumes an exponential cut-off energy for protons at $E_c = 4.5 \times 10^6$ GeV. Other model parameters, and the low-energy data are the same as in Figure 1. Error bars are shown only for the proton and helium data. High-energy data: KASCADE (Antoni et al. 2005), IceTop (Aartsen et al. 2013), Tibet III (Amenomori et al. 2008), the Pierre Auger Observatory (Schulz et al. 2013), and HiRes II (Abbasi et al. 2009).

dominated by helium nuclei, not by protons. The CREAM measurements have shown that helium nuclei become more abundant than protons at energies $\sim 10^5$ GeV. Such a trend is also consistent with the KASCADE measurements above $\sim 10^6$ GeV (see Figure 1). Based on our prediction, helium nuclei dominate the all-particle spectrum up to $\sim 1.5 \times 10^7$ GeV, while above, iron nuclei dominate. The maximum energy of SNR-CRs, which corresponds to the fall-off energy of iron nuclei, is $26 \times E_c = 1.2 \times 10^8$ GeV. Although this energy is close to the position of the second knee, the predicted intensity is not enough to explain the observed intensity around the second knee. Our result shows that SNR-CRs alone cannot account for the observed cosmic rays above $\sim 2 \times 10^7$ GeV. At 10^8 GeV, they contribute only $\sim 30\%$ of the observed data.

3. Additional component of Galactic cosmic rays

Despite numerous studies, it is not clearly understood at what energy the transition from Galactic to extra-galactic cosmic rays (EG-CRs) occurs. Although it was pointed out soon after the discovery of the CMB and the related GZK effect that it is possible to construct an all-extra-galactic spectrum of cosmic rays containing both the knee and the ankle as features of cosmological propagation (Hillas 1967), the most natural explanation was assumed to be that the transition occurs at the ankle, where a steep Galactic component is taken over by a flatter extra-galactic one. To obtain a sharp feature like the ankle in such a construction, it is necessary to assume a cut-off in the Galactic component to occur immediately below it (Rachen et al. 1993; Axford 1994), thus this scenario is naturally expecting a second knee feature. For a typical Galactic magnetic field

strength of $3 \mu\text{G}$, the Larmor radii for cosmic rays of energy $Z \times 10^8$ GeV is 36 pc, much smaller than the size of the diffusion halo of the Galaxy, which is typically considered to be a few kpc in cosmic-ray propagation studies, keeping cosmic rays around the second knee well confined in the Galaxy. This suggests that the Galactic cut-off at this energy must be intrinsic to a source population or acceleration mechanism different from the standard supernova remnants we have discussed above. In an earlier work, Hillas (2005) considered an additional Galactic component resulting from Type II supernova remnants in the Galaxy expanding into a dense slow wind of the precursor stars. In the following, we discuss two other possible scenarios. The first is the re-acceleration of SNR-CRs by Galactic wind termination shocks in the Galactic halo (Jokipii & Morfill 1987; Zirakashvili & Völk 2006), and the second is the contribution of cosmic rays from the explosions of Wolf-Rayet stars in the Galaxy (Biermann & Cassinelli 1993). Both these ideas have been explored in the past when detailed measurements of the cosmic-ray spectrum and composition at low and high energies were not available. Using new measurements of cosmic rays and astronomical data (like the Wolf-Rayet wind composition), our study can provide a more realistic estimate of the cosmic-ray contribution from these two possible mechanisms. In the following, the re-accelerated cosmic rays from Galactic wind termination shocks will be referred to as ‘GW-CRs’, and cosmic rays from Wolf-Rayet stars as ‘WR-CRs’. Some ramifications of these basic scenarios will be discussed in Section 6, after investigating the effect of different extra-galactic contributions below the ankle in Section 5.

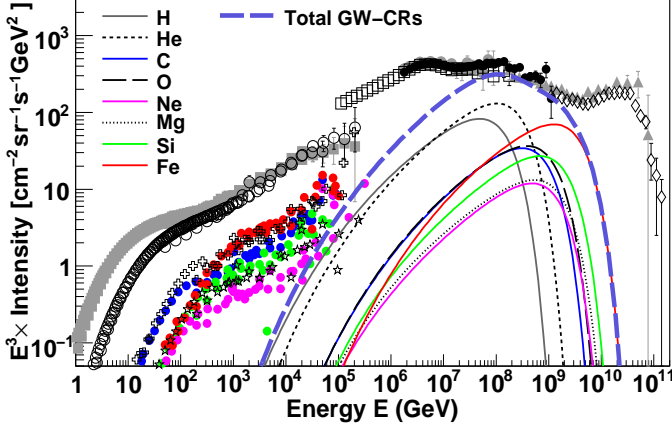


Fig. 3. Contribution of GW-CRs to the all-particle cosmic-ray spectrum. The thin lines represent spectra for the individual elements, and the thick dashed line represents the total contribution. The injection fraction, $k_w = 14.5\%$, and the exponential cut-off energy for protons, $E_{\text{sh}} = 9.5 \times 10^7$ GeV. See text for the other model parameters. Data are the same as in Figure 2.

3.1. Re-acceleration of SNR-CRs by Galactic wind termination shocks (GW-CRs)

The effect of Galactic winds on the transport of cosmic rays in the Galaxy has been discussed quite extensively (Lerche & Schlickeiser 1982a; Bloemen et al. 1993; Strong & Moskalenko 1998; Jones et al. 2001; Breitschwerdt et al. 2002). For cosmic rays produced by sources in the Galactic disk such as the SNR-CRs, the effect of winds on their transport is expected to be negligible above a few GeV as the transport is expected to be dominated mainly by the diffusion process. However, Galactic winds can lead to the production of an additional component of cosmic rays which can dominate at high energies. Galactic winds, which start at a typical velocity of about few km/s near the disk, reach supersonic speeds at distances of a few tens of kpc away from the disk. At about a hundred kpc distance or so, the wind flow terminates resulting into the formation of termination shocks. These shocks can catch the SNR-CRs escaping from the disk into the Galactic halo, and re-accelerate them via the diffusive shock acceleration process. The reaccelerated cosmic rays can return to the disk through diffusive propagation against the Galactic wind outflow. For an energy dependent diffusion process, only the high-energy particles may be effectively able to reach the disk.

To obtain the contribution of GW-CRs, we will first calculate the escape rate of SNR-CRs from the *inner* diffusion boundary, then propagate the escaped cosmic rays through the Galactic wind region, and calculate the cosmic-ray flux injected into the Galactic wind termination shocks. The escaped flux of SNR-CRs from the diffusion boundary, F_{esc} , can be calculated as,

$$F_{\text{esc}} = [D\nabla N]_{z=\pm L} = \left[D \frac{dN}{dz} \right]_{z=\pm L}, \quad (5)$$

where $N(z, p)$ is given by Equation 3. Equation 5 assumes that cosmic rays escape only through the diffusion boundaries located at $z = \pm L$. Under this assumption, the total escape rate of SNR-CRs is given by,

$$Q_{\text{esc}} = F_{\text{esc}} \times 2A_{\text{esc}}, \quad (6)$$

where $A_{\text{esc}} = \pi R^2$ is the surface area of one side of the cylindrical diffusion boundary which is assumed to have the same radius as the Galactic disk, and the factor 2 is to account for the two boundaries at $z = \pm L$. The propagation of the escaped SNR-CRs in the Galactic wind region is governed by the following transport equation:

$$\nabla \cdot (D_w \nabla N_w - \mathbf{V} N_w) + \frac{\partial}{\partial p} \left\{ \frac{\nabla \cdot \mathbf{V}}{3} p N_w \right\} = -Q_{\text{esc}} \delta(\mathbf{r}), \quad (7)$$

where we have assumed a spherically symmetric geometry characterised by the radial variable r , D_w represents the diffusion coefficient of cosmic rays in the wind region which is taken to be spatially constant, $N_w(r, p)$ is the cosmic-ray number density, $\mathbf{V} = \tilde{V} r \hat{r}$ is the wind velocity which is assumed to increase linearly with r and directed radially outwards, \tilde{V} is a constant that denotes the velocity gradient, and $Q_{\text{esc}}(p)$ is given by Equation 6. The exact nature of the Galactic wind is not known. The spatial dependence of the wind velocity considered here is based on the model of magnetohydrodynamic wind driven by cosmic rays, which shows that the wind velocity increases linearly with distance from the Galactic disk until it reaches an asymptotic value at a distance of around 100 kpc (Zirakashvili et al. 1996). The second term on the left-hand side of Equation 7 represents the loss of particles due to advection by the Galactic wind, and the third term represents momentum loss due to the adiabatic expansion of the wind flow which is assumed to be spherically symmetric. In writing Equation 7, considering that the size of the wind region is much larger than the size of the escaping region of the SNR-CRs, we neglect the size of the escaping region and consider Q_{esc} to be a point source located at $r = 0$. By solving Equation 7 analytically, the density of cosmic rays at distance r is given by (see Appendix A),

$$N_w(r, p) = \frac{\sqrt{\tilde{V}} p^2}{8\pi^{3/2}} \int_0^\infty dp' \frac{Q_{\text{esc}}(p')}{\left[\int_p^{p'} u D_w(u) du \right]^{3/2}} \times \exp \left(-\frac{r^2 \tilde{V} p^2}{4 \int_p^{p'} u D_w(u) du} \right). \quad (8)$$

From Equation 8, the cosmic-ray flux with momentum/nucleon p at the termination shock is obtained as,

$$F_w(p) = \left[-D_w \frac{\partial N_w}{\partial r} + \mathbf{V} N_w \right]_{r=R_{\text{sh}}}, \quad (9)$$

where R_{sh} represents the radius of the termination shock. The total rate of cosmic rays injected into the termination shock is given by,

$$Q_{\text{inj}}(p) = F_w(p) \times A_{\text{sh}}, \quad (10)$$

where $A_{\text{sh}} = 4\pi R_{\text{sh}}^2$ is the surface area of the termination shock. Assuming that only a certain fraction, k_{sh} , participates in the re-acceleration process, the cosmic-ray spectrum produced by the termination shock under the test particle approximation can be written as (Drury 1983),

$$Q_{\text{sh}}(p) = \gamma p^{-\gamma} \exp \left(-\frac{Ap}{Zp_{\text{sh}}} \right) \int_{p_0}^p k_{\text{sh}} Q_{\text{inj}}(u) u^{\gamma-1} du, \quad (11)$$

Table 2. Relative abundances of different cosmic-ray species with respect to helium for two different Wolf-Rayet wind compositions used in our model (Pollock et al. 2005).

Particle type	C/He = 0.1	C/He = 0.4
Proton	0	0
Helium	1.0	1.0
Carbon	0.1	0.4
Oxygen	3.19×10^{-2}	7.18×10^{-2}
Neon	0.42×10^{-2}	1.03×10^{-2}
Magnesium	2.63×10^{-4}	6.54×10^{-4}
Silicon	2.34×10^{-4}	5.85×10^{-4}
Iron	0.68×10^{-4}	1.69×10^{-4}

where we have introduced an exponential cut-off in the spectrum at momentum Zp_{sh} with p_{sh} representing the maximum momentum for protons, and γ is the spectral index. In our calculation, p_{sh} and k_{sh} will be kept as model parameters, and their values will be determined based on the measured all-particle spectrum.

After re-acceleration, the transport of cosmic-rays from the termination shock towards the Galactic disk also follows Equation 7. In the absence of adiabatic losses, the density of re-accelerated cosmic rays at the Earth (taken to be at $r = 0$) is given by,

$$N_{\text{GW-CRs}}(p) = \frac{Q_{\text{sh}}}{4\pi D_{\text{w}} R_{\text{sh}}} \exp\left[-\frac{\tilde{V} R_{\text{sh}}^2}{2D_{\text{w}}}\right] \quad (12)$$

The diffusion in the wind region is assumed to be much faster than near the Galactic disk as the level of magnetic turbulence responsible for particle scattering is expected to decrease with the distance away from the Galactic disk. We assume D_{w} to follow the same rigidity dependence as D , and take $D_{\text{w}} = 10D$. For the wind velocity, we take the velocity gradient $\tilde{V} = 15 \text{ km/s/kpc}$. This value of \tilde{V} is within the range predicted in an earlier study using an advection-diffusion propagation model (Bloemen et al. 1993), but slightly larger than the constraint given in Strong & Moskalenko (1998). It may be noted that as long as both D_{w} and \tilde{V} are within a reasonable range, it is not their individual values that is important in determining the flux of GW-CRs, but their ratio \tilde{V}/D_{w} , as can be seen from Equation 12. The larger this ratio, the more the flux will be suppressed, and vice-versa.

The distance to the termination shock can be estimated by balancing the Galactic wind ram pressure, $P_{\text{w}} = \rho V_{\text{t}}^2$, against the intergalactic pressure, P_{IGM} , at the position of the termination shock, where ρ is the mass density of the wind and $V_{\text{t}} = \tilde{V} R_{\text{sh}}$ represents the terminal velocity of the wind. The ram pressure is related to the total mechanical luminosity of the wind at the termination shock as, $L_{\text{w}} = 2\pi R_{\text{sh}}^2 P_{\text{w}} V_{\text{t}}$. Using this, we obtain,

$$R_{\text{sh}} = \left(\frac{L_{\text{w}}}{2\pi P_{\text{IGM}} \tilde{V}}\right)^{1/3}. \quad (13)$$

For Galactic wind driven by cosmic rays (Zirakashvili et al. 1996), the total mechanical luminosity of the wind cannot be larger than the total power of the cosmic rays. From Section 2.2, the total power invested in SNR-CRs (which dominates the overall cosmic-ray energy density in our model)

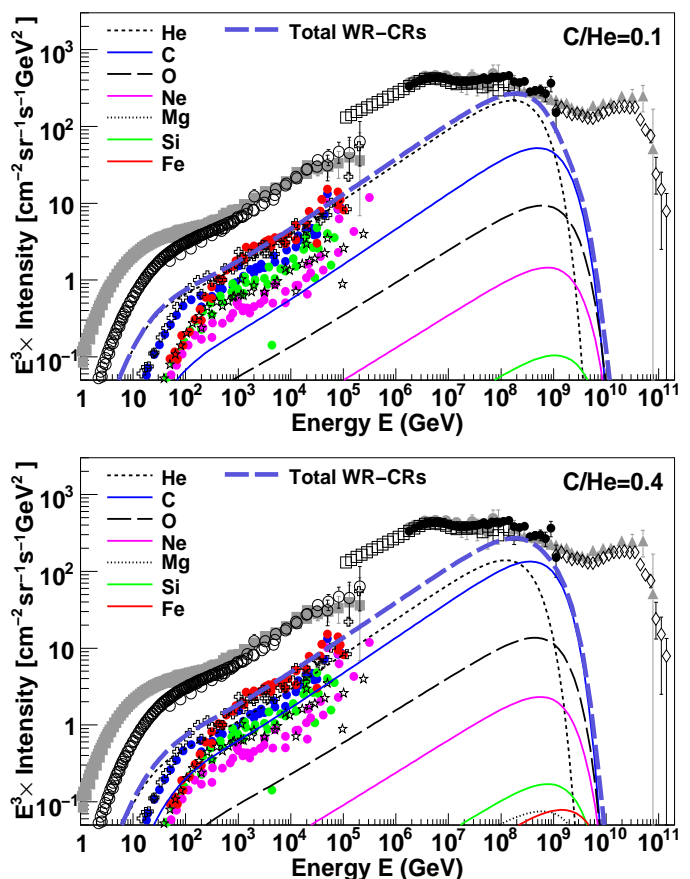


Fig. 4. Contribution of WR-CRs to the all-particle spectrum. *Top:* C/He = 0.1. *Bottom:* C/He = 0.4. The thin lines represent spectra for the individual elements, and the thick dashed line represents the total contribution. The calculation assumes an exponential energy cut-off for protons at $E_c = 1.8 \times 10^8 \text{ GeV}$ for C/He = 0.1, and $E_c = 1.3 \times 10^8 \text{ GeV}$ for C/He = 0.4. See text for the other model parameters. Data: same as in Figure 2.

is $\sim 8\%$ of the mechanical power injected by supernova explosions in the Galaxy. This corresponds to a total power of $\sim 8 \times 10^{40} \text{ ergs s}^{-1}$ injected into SNR-CRs. Using this, and taking an intergalactic pressure of $P_{\text{IGM}} = 10^{-15} \text{ ergs cm}^{-3}$ (Breitschwerdt et al. 1991), we obtain $R_{\text{sh}} = 96 \text{ kpc}$ from Equation 13. The spectral indices γ are taken to be the same as the source indices of the SNR-CRs listed in Table 1. Having fixed these parameter values, the spectra of the GW-CRs calculated using Equation 12 are shown in Figure 3. Spectra for the individual elements and also the total contribution are shown. The same particle injection fraction of $k_{\text{sh}} = 14.5\%$ is applied to all the elements, and the maximum proton energy corresponding to p_{sh} is taken as $E_{\text{sh}} = 9.5 \times 10^7 \text{ GeV}$. These values are chosen so that the total GW-CR spectrum reasonably agrees with the observed all-particle spectrum between $\sim 10^8$ and 10^9 GeV .

The GW-CRs produce a negligible contribution at low energies. This is due to the increasing effect of advection over diffusion at these energies, preventing particles from reaching the Galactic disk. Higher energy particles, which diffuse relatively faster, can overcome the advection and reach the disk more effectively. The flux suppression at low energies is more significant for heavier nuclei like iron which is due to their slower diffusion relative to lighter nuclei at the same total energy. Adding adiabatic losses to

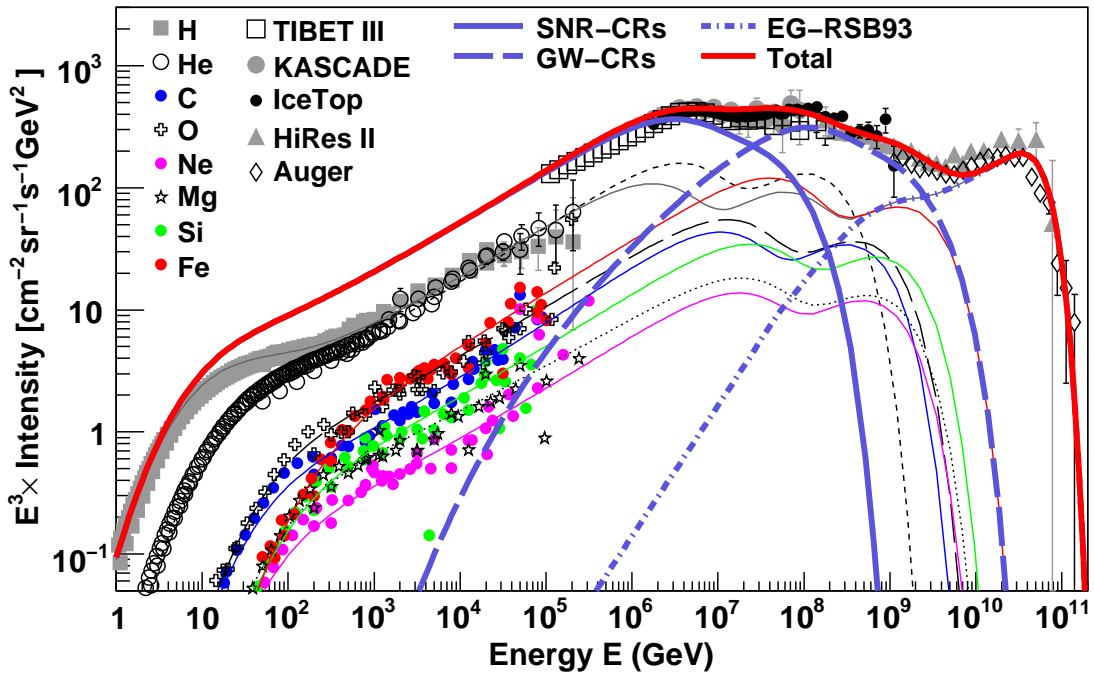


Fig. 5. Model prediction for the all-particle spectrum using the Galactic wind re-acceleration model. The thick solid blue line represents the total SNR-CRs, the thick dashed line represents GW-CRs, the thick dotted-dashed line represents extra-galactic cosmic rays (EG-RSB93) taken from Rachen et al. (1993), and the thick solid red line represents the total all-particle spectrum. The thin lines represent total spectra for the individual elements. For the SNR-CRs, an exponential energy cut-off for protons at $E_c = 3 \times 10^6$ GeV is assumed. See text for the other model parameters. Data are the same as in Figure 2.

Table 3. Injection energy of SNR-CRs used in the calculation of all-particle spectrum in the WR-CR model (Figure 6).

Particle type	C/He = 0.1 $f(\times 10^{49}$ ergs)	C/He = 0.4 $f(\times 10^{49}$ ergs)
Proton	8.11	8.11
Helium	0.67	0.78
Carbon	2.11×10^{-2}	0.73×10^{-2}
Oxygen	2.94×10^{-2}	2.94×10^{-2}
Neon	4.41×10^{-3}	4.41×10^{-3}
Magnesium	6.03×10^{-3}	6.03×10^{-3}
Silicon	5.84×10^{-3}	5.84×10^{-3}
Iron	5.77×10^{-3}	5.77×10^{-3}

Equation 12 will lead to further suppression of the flux at low energies. But, at energies of our interest, that is above $\sim 10^7$ GeV, the result will not be significantly affected as the particle diffusion time, $t_{\text{dif}} = R_{\text{sh}}^2 / (6D_w)$, is significantly less than the adiabatic energy loss time, $t_{\text{ad}} = 1/\tilde{V} = 6.52 \times 10^7$ yr. The steep spectral cut-offs at high energies are due to the exponential cut-offs introduced in the source spectra.

3.2. Cosmic rays from Wolf-Rayet star explosions (WR-CRs)

While the majority of the supernova explosions in the Galaxy occur in the interstellar medium, a small fraction is expected to occur in the winds of massive progenitors like Wolf-Rayet stars (Gal-Yam et al. 2014). Magnetic fields in the winds of Wolf-Rayet stars can reach of the order of 100 G, and it has been argued that a strong supernova

shock in such a field can lead to particle acceleration of energies up to $\sim 3 \times 10^9$ GeV (Biermann & Cassinelli 1993; Stanev et al. 1993).

Since the distribution of Wolf-Rayet stars in the Galaxy is concentrated close to the Galactic disk (see e.g. Rosslowe & Crowther (2015)), the propagation of WR-CRs can also be described by Equation 1 with the source term replaced by $Q(r, p) = \bar{\nu}_0 H[R - r] H[p - p_0] Q(p)$, where $\bar{\nu}_0$ represents the frequency of Wolf-Rayet supernova explosions per unit surface area in the Galactic disk, and the source spectrum $Q(p)$ follows Equation 2. We assume that each Wolf-Rayet supernova explosion releases a kinetic energy of 10^{51} ergs, same as the normal supernova explosion in the interstellar medium. From the estimated total number of Wolf-Rayet stars of ~ 1200 in the Galaxy and an average lifetime of ~ 0.25 Myr for these stars (Rosslowe & Crowther 2015), we estimate a frequency of ~ 1 Wolf-Rayet explosion in every 210 years. This corresponds to ~ 1 Wolf-Rayet explosion in every 7 supernova explosions occurring in the Galaxy. The source indices of the different cosmic-ray species and the propagation parameters for the WR-CRs are taken to be the same as for the SNR-CRs.

The contribution of WR-CRs to the all-particle spectrum is shown in Figure 4. The results are for two different compositions of the Wolf-Rayet winds available in the literatures: Carbon-to-helium (C/He) ratio of 0.1 (top panel) and 0.4 (bottom panel), given in Pollock et al. (2005). The abundance ratios of different elements with respect to helium for the two different wind compositions are listed in Table 2. In our calculation, these ratios are assumed to be proportional to the relative amount of supernova explosion energy injected into different elements. The overall normalization of the total WR-CR spectrum and the maximum en-

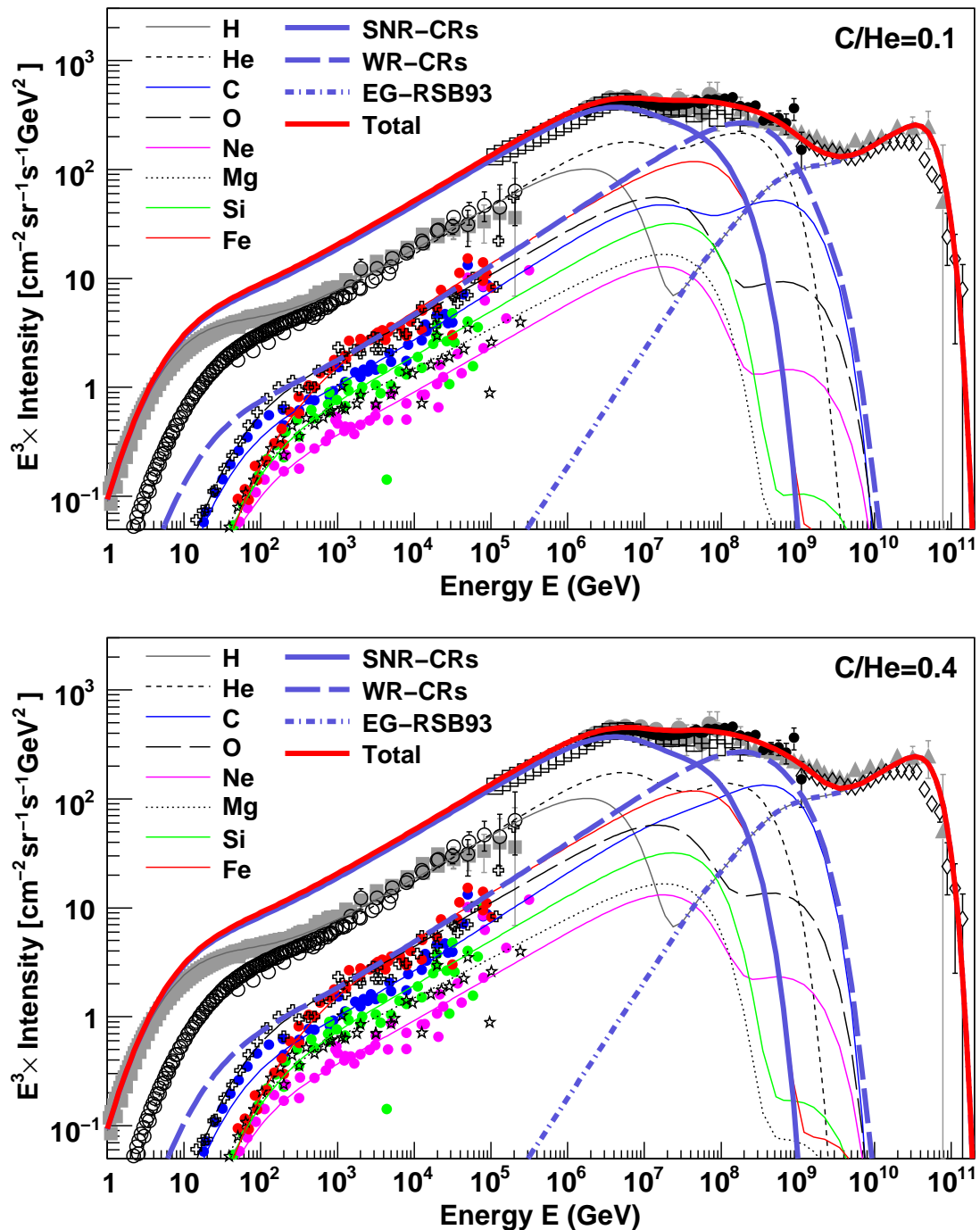


Fig. 6. Model prediction for the all-particle spectrum using the Wolf-Rayet stars model. *Top:* $C/He = 0.1$. *Bottom:* $C/He = 0.4$. The thick solid blue line represents the total SNR-CRs, the thick dashed line represents WR-CRs, the thick dotted-dashed line represents extra-galactic cosmic rays (EG-RSB93) taken from Rachen et al. (1993), and the thick solid red line represents the total all-particle spectrum. The thin lines represent total spectra for the individual elements. For the SNR-CRs, an exponential energy cut-off for protons at $E_c = 4.1 \times 10^6$ GeV is assumed. See text for the other model parameters. Data are the same as in Figure 2.

ergy of the proton source spectrum are taken as free parameters. Their values are determined based on the observed all-particle spectrum between $\sim 10^8$ and 10^9 GeV. For $C/He = 0.1$, we obtain an injection energy of 1.3×10^{49} ergs into helium nuclei from a single supernova explosion and a proton source spectrum cut-off of 1.8×10^8 GeV, while for $C/He = 0.4$, we obtain 9.4×10^{48} ergs and 1.3×10^8 GeV respectively. For both the progenitor wind compositions, the total amount of energy injected into cosmic rays by

a single supernova explosion is approximately 5 times less than the total energy injected into SNR-CRs by a supernova explosion in the Galaxy. The total WR-CR spectrum for the $C/He = 0.1$ case is dominated by helium nuclei up to $\sim 10^9$ GeV, while for the $C/He = 0.4$ case, helium nuclei dominate up to $\sim 2 \times 10^8$ GeV. At higher energies, carbon nuclei dominate. One major difference of the WR-CR spectra from the GW-CR spectrum (Figure 3) is the absence of the proton component, and a very small contribution of the

heavy elements like magnesium, silicon and iron. Another major difference is the much larger flux of WR-CRs than the GW-CRs below $\sim 10^5$ GeV. Below the knee, the total WR-CR spectrum is an order of magnitude less than the total SNR-CRs spectrum (Figure 2).

4. All-particle spectrum and composition of cosmic rays at high energies

The all-particle spectrum obtained by combining the contributions of SNR-CRs, GW-CRs and EG-CRs is compared with the measured data in Figure 5. For the SNR-CRs shown in the figure, we have slightly reduced the value of E_c from 4.5×10^6 GeV (as used in Figure 2) to 3×10^6 GeV in order to reproduce the measurements better around the knee. The extra-galactic contribution, denoted by EG-RSB93 in the figure, is taken from Rachen et al. (1993), which represents a pure proton population with a source spectrum of E^{-2} and an exponential cut-off at 10^{11} GeV as expected from strong radio galaxies or sources with a similar cosmological evolution. Also shown in the figure are the spectra of the individual elements. The model prediction reproduces the observed elemental spectra as well as the observed features in the all-particle spectrum.

The total spectra for the two WR-CR scenarios are shown in Figure 6. For the SNR-CRs, here we take $E_c = 4.1 \times 10^6$ GeV, and a slightly lower value of ν which corresponds to 6 out of every 7 supernova explosions in the Galaxy (assuming a fraction 1/7 going into Wolf-Rayet supernova explosions as deduced in the previous section). The injection energy f for the different elements of the SNR-CRs has been re-adjusted accordingly, so that the sum of SNR-CRs and WR-CRs for the individual elements agree with the measured elemental spectra at low energies. The f values are listed in Table 3. The cosmic-ray propagation parameters are the same as in Figure 2. The predicted all-particle spectra are in good agreement with the measurements. The WR-CR scenarios are found to reproduce the second knee and the ankle better than the GW-CR model.

In Figure 7, we show the elemental fraction at high energies predicted by the GW-CR and WR-CR models. In all the models, the composition consists of a large fraction of helium nuclei over a wide energy range. The maximum helium fraction is found in the case of WR-CR (C/He=0.1) scenario, where the fraction reaches up to $\sim 63\%$ at energy $\sim 2 \times 10^8$ GeV. In contrast to common perceptions, the WR-CR scenarios predict a composition of Galactic cosmic rays dominated mainly by helium (in the C/He = 0.1 case) or carbon nuclei (in the C/He = 0.4) near the transition energy region from Galactic to extra-galactic cosmic rays. The GW-CR model predicts an almost equal contribution of helium and iron nuclei at the transition region.

The cosmic-ray composition at energies above $\sim 3 \times 10^5$ GeV is not quite as well-measured as at lower energies. Above $\sim 10^6$ GeV, KASCADE has provided spectral measurements for groups of elements by measuring the electron and muon numbers of extensive air showers induced by cosmic rays in the Earth's atmosphere. Several other experiments such as LOFAR, TUNKA, and the Pierre Auger Observatory have also provide composition measurements at high energies by measuring the depth of the shower maximum (X_{\max}). Heavier nuclei interact higher in the atmosphere, resulting in smaller values of X_{\max} as compared to

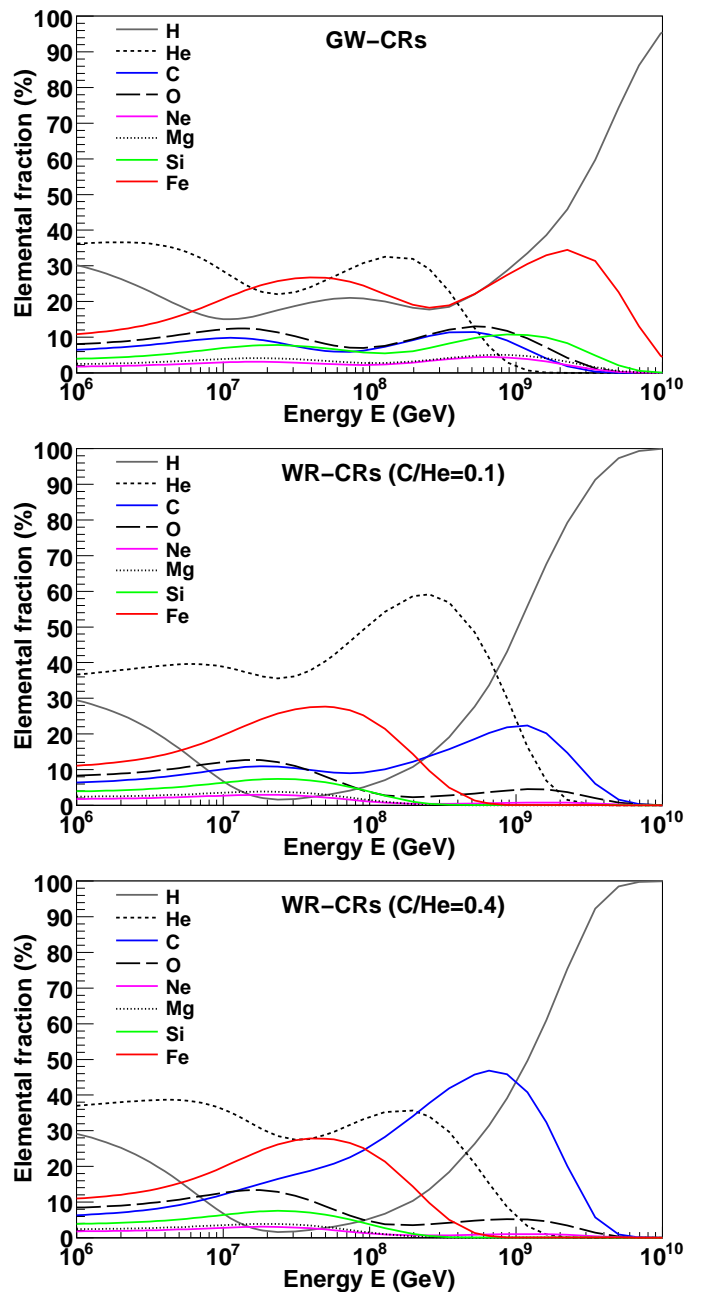


Fig. 7. Elemental fraction predicted by the different models of the additional Galactic component. *Top*: GW-CRs, *middle*: WR-CRs (C/He = 0.1), and *bottom*: WR-CRs (C/He = 0.4).

lighter nuclei. For comparison with theoretical predictions, we often use the mean logarithmic mass, $\langle \ln A \rangle$, of the measured cosmic rays which can be obtained from the measured X_{\max} values using the relation (Hörandel 2003b),

$$\langle \ln A \rangle = \left(\frac{X_{\max} - X_{\max}^{\text{P}}}{X_{\max}^{\text{Fe}} - X_{\max}^{\text{P}}} \right) \times \ln A_{\text{Fe}}, \quad (14)$$

where X_{\max}^{P} and X_{\max}^{Fe} represent the average depths of the shower maximum for protons and iron nuclei respectively given by Monte-Carlo simulations, and A_{Fe} is the mass number of iron nuclei.

In Figure 8, the $\langle \ln A \rangle$ values predicted by the different models are compared with the measurements from different experiments. Although all our model predictions are

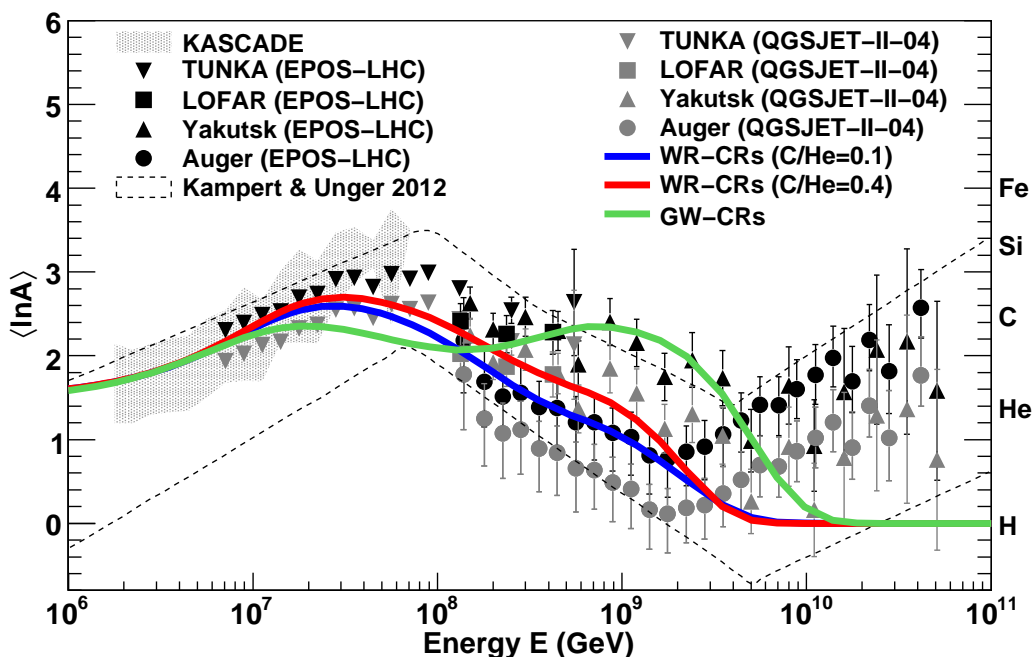


Fig. 8. Mean logarithmic mass, $\langle \ln A \rangle$, of cosmic rays predicted using the three different models of the additional Galactic component: WR-CRs ($C/He = 0.1$), WR-CRs ($C/He = 0.4$), and GW-CRs. Data: KASCADE (Antoni et al. 2005), TUNKA (Berezhnev et al. 2013), LOFAR (Buitink et al. 2016), Yakutsk (Knurenko & Sabourov 2010), the Pierre Auger Observatory (Porcelli et al. 2015), and the different optical measurements compiled in Kampert & Unger (2012). The two sets of data points correspond to two different hadronic interaction models (EPOS-LHC and QGSJET-II-04) used to convert X_{\max} values to $\langle \ln A \rangle$.

within the large systematic uncertainties of the measurements, at energies above $\sim 10^7$ GeV, the GW-CR model deviates from the general trend of the observed composition which reaches a maximum mean mass at $\sim 6 \times 10^7$ GeV, and becomes gradually lighter up to the ankle. However, in the narrow energy range of $\sim (1 - 5) \times 10^8$ GeV, the behaviour of the GW-CR model is in good agreement with the measurements from TUNKA, LOFAR and Yakutsk experiments which show a nearly constant composition that is different from the behaviour observed by the Pierre Auger Observatory at these energies. Understanding the systematic differences between the different measurements at these energies will be important for further testing of the GW-CR model. Up to around the ankle, the WR-CR models show an overall better agreement with the measurements than the GW-CR model. At around $(3 - 5) \times 10^7$ GeV, the WR-CR models seem to slightly under predict the KASCADE measurements, and they are more in agreement with the TUNKA measurements. Cosmic-ray composition measured by experiments like KASCADE, which measures the particle content of air showers on the ground, is known to have a large systematic difference from the composition measured with fluorescence and Cherenkov light detectors using X_{\max} measurements (Hörandel 2003b). The large discrepancy between the model predictions and the data above the ankle is due to the absence of heavy elements in the EG-CR model considered in our calculation. The effect of choosing other models of EG-CRs will be discussed in the next section.

5. Test with different models of extra-galactic cosmic rays

Despite of the dominance of the ankle-transition model in the general discussion, it has often been pointed out

that the essential high-energy features of the cosmic ray spectrum, that is the ankle and, in part, even the second knee, can be explained by propagation effects of extra-galactic protons in the cosmologically evolving microwave background (Hillas 1967; Berezhinsky & Grigorieva 1988; Berezhinsky et al. 2006; Hillas 2005; Aloisio et al. 2012, 2014). While the most elegant and also most radical formulation of this hypothesis, the so-called ‘proton dip model’, is meanwhile considered disfavoured by the proton fraction at the ankle measured by the Pierre Auger Observatory (Aab et al. 2014), the light composition below the ankle recently reported by the LOFAR measurement (Buitink et al. 2016) and a potential ‘light ankle’ at about 10^8 GeV found by the KASCADE-Grande experiment (Apel et al. 2013) have reinstated the interest in such models, and led to a number of ramifications, all predicting a more or less significant contribution of extra-galactic cosmic rays below the ankle. As such a component can greatly modify the model parameters, in particular the maximum energy, for the additional Galactic component – if not removing its necessity altogether – we study this effect using the WR-CR models, which show an overall best agreement with the data below the ankle, as a Galactic paradigm.

Before, however, discussing a stronger extra-galactic component below the ankle, we want to think about the *minimal* extra-galactic contribution we can have, if we assume the largely heavy spectrum above the ankle is all extra-galactic and consider their propagation over extra-galactic distances. To construct this ‘minimal model’, we follow di Matteo et al. (2015) and use the Monte-Carlo simulation code CRPropa 3.0 (Batista et al. 2016), which takes into account all important interaction processes undergone by EG-CRs while propagating through the CMB and the extra-galactic background light, and also the energy loss as-

sociated with the cosmological expansion. The effects of uncertainties in the simulations are discussed in Batista et al. (2015). We assume the sources to be uniformly distributed in a comoving volume, and they produce cosmic rays with a spectrum given by (di Matteo et al. 2015),

$$Q_{\text{EG}} = K_0 F_j \left(\frac{E}{E_0} \right)^{-\gamma}, \quad \frac{E}{Z} < R_c$$

$$= K_0 F_j \left(\frac{E}{E_0} \right)^{-\gamma} \exp \left(1 - \frac{E}{ZR_c} \right), \quad \frac{E}{Z} > R_c \quad (15)$$

where K_0 is a normalisation constant, F_j is the injection fraction which depends on the type of the nuclei j , $E_0 = 10^9$ GeV, γ is the source spectral index which is assumed to be the same for the different nuclei, and R_c is the rigidity at which the spectrum deviates from a power law. The model parameters are determined by simultaneously fitting the cosmic-ray energy spectrum, X_{max} and variance of X_{max} above the ankle observed at the Pierre Auger Observatory. We adopt the CTG¹ model for our calculation (di Matteo et al. 2015), and consider that the sources inject protons, helium, nitrogen and iron nuclei. The best-fit model parameters values are $\gamma = 0.73$, $R_c = 3.8 \times 10^9$ GV, $F_{\text{H}} = 0\%$, $F_{\text{He}} = 0\%$, $F_{\text{N}} = 98.69\%$ and $F_{\text{Fe}} = 1.31\%$. In this model, the EG-CR spectrum below $\sim 10^{10}$ GeV is dominated by protons and helium nuclei which are secondary products from the photo-disintegration of heavier nuclei during the propagation. At higher energies up to $\sim 6 \times 10^{10}$ GeV, the spectrum is dominated by the CNO group. Above $\sim 3 \times 10^{10}$ GeV, the spectrum exhibits a steep cut-off which is mostly due to the intrinsic cut-off in the injection spectrum, and not due to the GZK absorption during the propagation. This gives an overall best agreement with the measured data (di Matteo et al. 2015).

The first assumption we consider for an additional component of light particles below the ankle is based on the same physics, that is photo-disintegration of energetic nuclei in photon backgrounds, but considering this effect already in potentially densely photon loaded sources during acceleration. The physical motivation for this scenario is the acceleration of heavy nuclei at external/internal shocks in gamma ray bursts (Murase et al. 2008; Globus et al. 2015b), or in tidal disruption events (Farrar & Gruzinov 2009). Two variants of this assumptions have been recently suggested: the first, by Globus et al. (2015a), assumes that diffusion losses in the source are faster than the photo-disintegration time scale over a large range of energies, leading to a significantly steeper spectrum of the secondary protons than for the escaping residual nuclei, while in the second model by Unger et al. (2015) only the highest energy particles have an escape time which is smaller than the photo-disintegration time. While the predictions of the former model for secondary protons below the ankle are phenomenologically quite similar to the extra-galactic component of Rachen et al. (1993) at these energies, that is an approximate E^{-2} source spectrum with a cosmological evolution $\propto (1+z)^{3.5}$, the second model Unger et al. (2015, hereafter the ‘UFA model’) predicts a strong pure-proton component concentrated only about one order of magnitude in energy below the ankle. Within their fiducial model, they

consider a mix with a pure iron Galactic cosmic-ray component in Unger et al. (2015). For our study, we use results which are optimised for a pure nitrogen Galactic composition², which is closer to our predicted composition for the WR-CR model (C/He = 0.4) around the second knee.

A second assumption for an additional extra-galactic component is based on a universal scaling argument, which links the energetics of extra-galactic cosmic-ray sources on various scales and predicts that a dominant contribution to extra-galactic cosmic rays is expected from clusters of galaxies, accelerating a primordial proton-helium mix at their accretion shocks during cosmological structure formation (Rachen 2016). As it has been shown already by Kang et al. (1997) that, for canonical assumptions on the diffusion coefficient around shocks (e.g. Bohm diffusion), the particle acceleration in this scenario is limited by pair-production losses in the CMB, this extra-galactic component is rather expected not to reach ultra-high energies, except for very optimistic assumptions on the acceleration process, but to be confined to energies *below* the ankle. As so far no detailed Monte-Carlo propagation for this model has been calculated, we use here the analytical approximation developed in Rachen (2016). Assuming that both injection and acceleration of primordial protons and helium nuclei are only dependent on particle rigidity, the model predicts a succession of a proton and helium component with increasing energy, which are fixed in relative normalisation by the known primordial abundances. The more energetic helium component sharply cuts off at the ankle, merging into the cosmic-ray spectrum produced by extra-galactic sources at smaller scales, for which acceleration even in the conservative case is not limited by CMB or other photon interactions, and thus reaches the so-called Hillas limit, $E = ZeBR$, if B is the typical magnetic field, and R the typical size of the accelerator (Hillas 1984). In our treatment, we hereby keep the exact cut-off energy and the total normalisation of this primordial cluster shock component as free parameters and determine them from fitting the all-particle spectrum, where we use the minimal model derived above as the second extra-galactic component extending into ultra-high energies. This model is henceforth denoted as ‘PCS model’.

In Figure 9, we present the all-particle spectrum above 10^6 GeV obtained using the three different EG-CR models – minimal model only, UFA and PCS model. The galactic contributions are from SNR-CRs and WR-CRs (C/He = 0.4). For the SNR-CRs, all the model parameters are the same as in Figure 6 (bottom). For the WR-CRs, the cut-off energy and the normalisation of the source spectrum are re-adjusted in order to produce an overall good fit to the measured spectrum and composition. They are allowed to vary in the three different cases. For the minimal model, the best-fit proton cut-off energy of the WR-CRs is found to be 1.7×10^8 GeV. This is approximately a factor 1.3 larger than the value used in Figure 6. For the PCS and the UFA models, the proton cut-off energies are almost the same at 1.1×10^8 GeV, which are about a factor 1.5 less than that of the minimal model. This relaxation in the cut-off energy is due to the strong contribution of EG-CRs below the ankle in the two models. In the minimal model, the transition from Galactic to extra-galactic components occurs around the ankle, while in the PCS and UFA models, it occurs at

¹ CRPropa with the default TALYS photo-disintegration cross sections and the EBL model of Gilmore et al. (2012)

² Michael Unger, private communication.

$\sim 7 \times 10^8$ GeV. The variation in the injection energy of WR-CRs remain within 6% between the three models. In Figure 9, spectra of five different mass groups are also shown. The elemental fraction of these mass groups are shown in Figure 10.

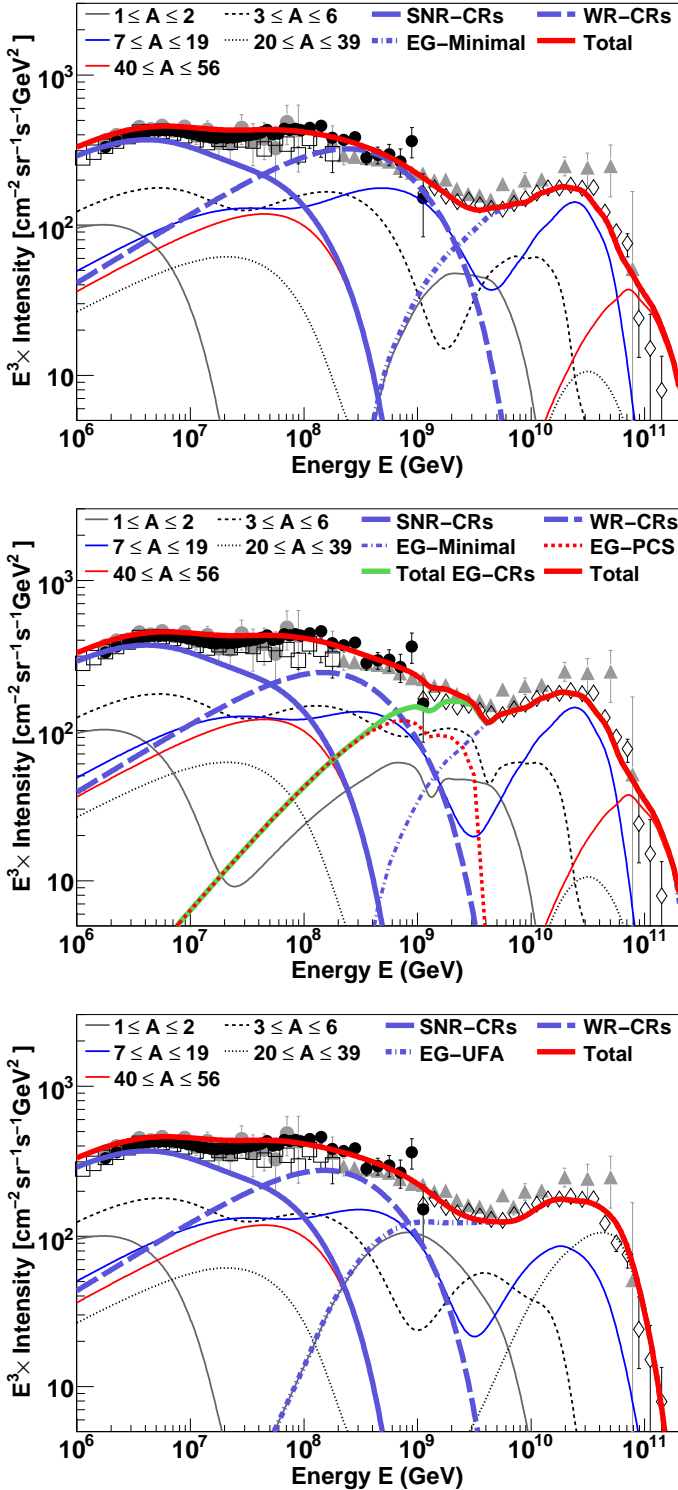


Fig. 9. All-particle spectrum for the three different models of EG-CRs – Minimal (*Top*), PCS (*middle*), and UFA (*bottom*) – combined with the WR-CR ($C/He = 0.4$) model for the additional Galactic component. SNR-CR spectra shown are the same as in Figure 6 (bottom). Data are the same as in Figure 2. For results using WR-CR ($C/He = 0.1$) model, see Appendix B.

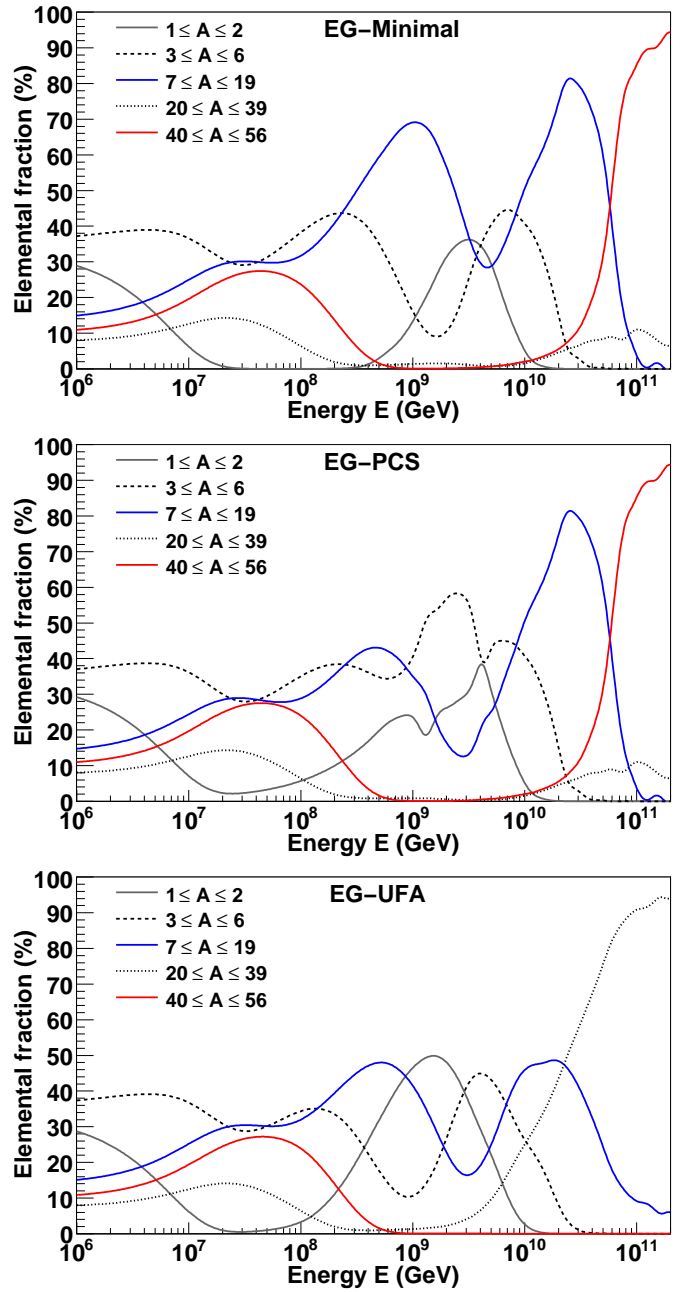


Fig. 10. Elemental fraction of the five different mass groups shown in Figure 9 for the three different EG-CR models: minimal (*top*), PCS (*middle*), and UFA (*bottom*), combined with the WR-CRs ($C/He = 0.4$) model for the additional Galactic component. Results obtained using WR-CR ($C/He = 0.1$) model are given in Appendix B.

In Figure 11, we show $\langle \ln A \rangle$ predicted by the three EG-CRs model after adding the Galactic contribution. At energies between $\sim 3 \times 10^8$ GeV and 3×10^9 GeV, the minimal model shows a bump that follows the trend of LOFAR and the data from other experiments, but contradicts the composition data from the Pierre Auger Observatory at $\sim 10^9$ GeV. The UFA model over predicts the data above the ankle as the model is also tuned to the variance of $\langle \ln A \rangle$, but it is well within the systematic uncertainties (experimental as well as theoretical) as discussed in Unger et al. (2015). The sharp feature present just above 10^9 GeV in the PCS model is due to the dip in the proton spectrum

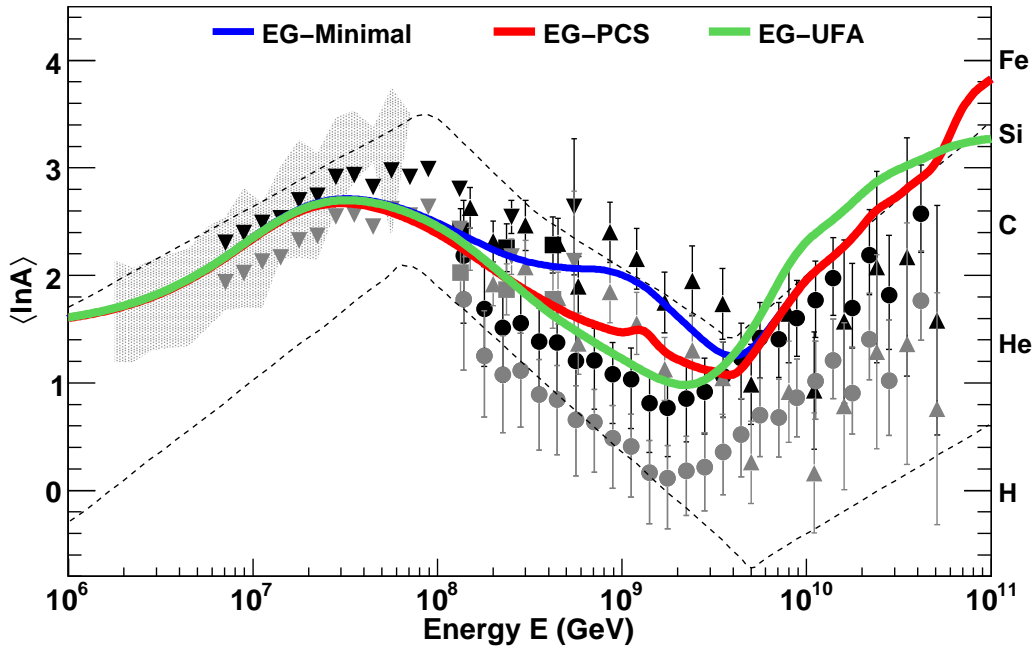


Fig. 11. Mean logarithmic mass for the three different EG-CR models combined with the WR-CR ($C/He = 0.4$) model. Data are the same as in Figure 8. Results obtained using WR-CR ($C/He = 0.1$) model are shown in Appendix B.

(Figure 9, middle panel, black-thin-solid line) that results from the intersection of the components from galaxy clusters and the minimal model, and is partially an artefact of the simplified propagation approach applied to this model. We expect it to be much smoother for realistic propagation. At energies below $\sim 10^9$ GeV, both the PCS and the UFA models produce similar results which are in better agreement with the observed trend of the composition, but do not introduce a significant improvement over the canonical extra-galactic component used in Section 4. In all the three cases for the EG-CR model, the CNO group dominates the composition of Galactic cosmic rays at the transition region from Galactic to extra-galactic cosmic rays. A clear distinction between the models would be possible from a detailed measurement of the five major mass groups shown in Figure 10, in which they all have their characteristic ‘fingerprint’: for example, around 10^9 GeV the minimal model is dominated by the CNO group, the PCS model by helium, and the UFA model by protons.

Results obtained using the WR-CR ($C/He = 0.1$) scenario are given in Appendix B. The main difference from the results of the $C/He = 0.4$ scenario is the significant dominance of helium up to the transition energy region from Galactic to extra-galactic cosmic rays (see Figures B.1 and B.2). The main results and the parameter values of the different models discussed in the present work are summarised in Table 4.

6. Discussions

Our study has demonstrated that cosmic rays below $\sim 10^9$ GeV can be predominantly of Galactic origin. Above 10^9 GeV, they are most likely to have an extra-galactic origin. We show that both the observed all-particle spectrum and the composition at high energies can be explained if the Galactic contribution consists of two components: (i) SNR-CRs which dominates the spectrum up to $\sim 10^7$ GeV, and

(ii) GW-CRs or preferably WR-CRs which dominates at higher energies up to $\sim 10^9$ GeV. When combined with an extra-galactic component expected from strong radio galaxies or a source population with similar cosmological evolution, the WR-CR scenarios predict a transition from Galactic to extra-galactic cosmic rays at around $(6-8) \times 10^8$ GeV, with a Galactic composition mainly dominated by helium or the CNO group, in contrast to most common assumptions. In the following, we discuss our results for the SNR-CRs, GW-CRs, and WR-CRs in the context of other views on the Galactic cosmic rays below 10^9 GeV, the implication of our results on the strength of magnetic fields in the Galactic halo and Wolf-Rayet stars, and also the case of a steep extra-galactic component extending below the second knee.

6.1. SNR-CRs

The maximum contribution of the SNR-CRs to the all-particle spectrum is obtained at a proton cut-off energy of $\sim 4.5 \times 10^6$ GeV (see Figure 2). Such a high energy is not readily achievable under the standard model of diffusive shock acceleration theory in supernova remnants for magnetic field values typical of that in the interstellar medium (see e.g. Lagage & Cesarsky 1983). However, numerical simulations have shown that the magnetic field near supernova shocks can be amplified considerably up to $\sim 10 - 100$ times the mean interstellar value (Lucek & Bell 2000; Reville & Bell 2012). This is also supported by observations of thin X-ray filaments in supernova remnants which can be explained as due to rapid synchrotron losses of energetic electrons in the presence of strong magnetic fields (Vink & Laming 2003; Parizot et al. 2006). Such strong fields may lead to proton acceleration up to energies close to the cut-off energy obtain in our study (Bell 2004).

The main composition of cosmic rays predicted by the SNR-CRs *alone* looks similar to the prediction of the polygonato model (Hörandel 2003a). Both show a helium domi-

Table 4. Summary of the different models for cosmic rays, and their results presented in this work. In all the models, the Galactic contribution consists of two components: the first component which is produced by regular supernova explosions in the Galaxy (SNR-CRs), and the second component which is considered to be produced either by cosmic-ray re-acceleration by Galactic wind termination shocks (GW-CRs) or by explosions of Wolf-Rayet stars in the Galaxy (WR-CRs). The source spectral indices for the second Galactic component in all the models are assumed to be the same as for the SNR-CRs (see Table 1). For the extra-galactic component, the different models considered are: (a) sources with strong cosmological evolution like strong radio galaxies (EG-RSB93) (b) extra-galactic contribution mainly above the ankle irrespective of the nature of the sources (EG-Minimal), (c) significant photo-disintegration of cosmic-rays in a source region with high photon density (EG-UFA), and (d) cosmic rays accelerated by accretion shocks in clusters of galaxies (EG-PCS). The all-particle spectra predicted by the different combinations of the Galactic and extra-galactic components are quite similar, and show good agreement with the measured spectrum. On the other hand, although the $\langle \ln A \rangle$ predicted by the different models are almost within the range of the different measurements compiled by Kampert & Unger (2012), they show distinctive differences especially in the energy range between the second knee and the ankle. For the model using GW-CRs, the predicted $\langle \ln A \rangle$ also show deviation from the prediction of other models between $\sim 10^7$ and 10^8 GeV. The comments on $\langle \ln A \rangle$ given in the table are with respect to the measurements from TUNKA (Berezhnev et al. 2013), LOFAR (Buitink et al. 2016), Yakutsk (Knurenko & Sabourov 2010), and the Pierre Auger Observatory (Porcelli et al. 2015) between the second knee and the ankle. QGSJET in the table refers to the QGSJET-II-04 model.

Model	Reference sections	Reference figures	Cut-off rigidities (GV)		Composition at: 10 ⁸ GeV, 10 ⁹ GeV (p, He, CNO, Fe)	Extra-galactic contribution at (10 ⁸ , 10 ⁹) GeV	Predicted $\langle \ln A \rangle$ between the second knee and the ankle	
			First Galactic component	Second Galactic component				
GW-CRs	EG-RSB93	3.1 & 4	5, 7 & 8	3.0×10^6	9.5×10^7	(20%, 32%, 12%, 24%), (32%, 2%, 18%, 30%)	(4%, 30%)	Good agreement with TUNKA (QGSJET) and LOFAR/Yakutsk (EPOS-LHC) data, but strong disagreement with Auger data
WR-CRs (C/He=0.1)	EG-RSB93	3.2 & 4	6, 7 & 8	4.1×10^6	1.8×10^8	(6%, 51%, 14%, 24%), (48%, 25%, 26%, 0%)	(6%, 50%)	Moderate agreement with LOFAR and Yakutsk (QGSJET) data, and excellent agreement with Auger (EPOS-LHC) data
WR-CRs (C/He=0.4)	EG-RSB93	3.2 & 4	6, 7 & 8	4.1×10^6	1.3×10^8	(6%, 34%, 30%, 24%), (44%, 6%, 49%, 0%)	(5%, 45%)	Good agreement with LOFAR (QGSJET) data, and moderate agreement with Yakutsk (QGSJET) and Auger (EPOS-LHC) data
WR-CRs (C/He=0.1)	EG-Minimal	5 & B	B.1, B.2 & B.3	4.1×10^6	2.4×10^8	(0%, 57%, 14%, 24%), (15%, 51%, 35%, 0%)	(0%, 16%)	Excellent agreement with LOFAR (QGSJET) and moderate agreement with TUNKA/Yakutsk (QGSJET) data, but strong disagreement with Auger data
WR-CRs (C/He=0.1)	EG-PCS	5 & B	B.1, B.2 & B.3	4.1×10^6	1.5×10^8	(6%, 52%, 13%, 24%), (25%, 53%, 21%, 0%)	(10%, 66%)	Moderate agreement with LOFAR and Yakutsk (QGSJET) data, and good agreement with Auger (EPOS-LHC) data
WR-CRs (C/He=0.1)	EG-UFA	5 & B	B.1, B.2 & B.3	4.1×10^6	1.6×10^8	(4%, 52%, 14%, 24%), (49%, 25%, 25%, 0%)	(3%, 58%)	Moderate agreement with LOFAR (QGSJET) data, and excellent agreement with Auger (EPOS-LHC) data
WR-CRs (C/He=0.4)	EG-Minimal	5	9, 10 & 11	4.1×10^6	1.7×10^8	(0%, 38%, 32%, 24%), (14%, 15%, 69%, 0%)	(0%, 15%)	Good agreement with TUNKA (QGSJET) and LOFAR (EPOS-LHC) data, and moderate agreement with Yakutsk data, but strong disagreement with Auger data
WR-CRs (C/He=0.4)	EG-PCS	5	9, 10 & 11	4.1×10^6	1.1×10^8	(6%, 36%, 29%, 24%), (24%, 42%, 35%, 0%)	(10%, 62%)	Moderate agreement with LOFAR/Yakutsk (QGSJET) and Auger (EPOS-LHC) data
WR-CRs (C/He=0.4)	EG-UFA	5	9, 10 & 11	4.1×10^6	1.1×10^8	(3%, 35%, 32%, 24%), (47%, 10%, 41%, 0%)	(3%, 55%)	Moderate agreement with LOFAR/Yakutsk (QGSJET) data, and good agreement with Auger (EPOS-LHC) data

nance over proton around the knee, and iron taking over at higher energies at $\sim 10^7$ GeV in the SNR-CRs, and at $\sim 6 \times 10^6$ GeV in the poly-gonato model. The helium dominance is more significant in the SNR-CRs than in the poly-gonato model which is due to the flatter spectral index required to reproduce the recent measurements from CREAM and ATIC experiments with the SNR-CRs. The main difference, however, is in the total contribution above $\sim 2 \times 10^7$ GeV. SNR-CRs alone cannot explain the observed all-particle spectrum above $\sim 2 \times 10^7$ GeV. They contribute only $\sim 30\%$ of the observed cosmic rays at $\sim 10^8$ GeV. On the other hand, in the poly-gonato model, the total contribution from elements with $1 \leq Z \leq 28$ can explain the observed spectrum up to energies close to 10^8 GeV. This difference is mainly due to the difference in the shapes of the spectral cut-offs of particles between the two models.

For the SNR-CRs, we consider a power-law with an exponential cut-off, while the poly-gonato model assumes a broken power-law with a smooth break around the cut-off (break) energy. This leads to a higher flux around the cut-off energy in the poly-gonato model. On adding GW-CRs or WR-CRs as an additional Galactic component, the composition above $\sim 10^7$ GeV in our model has a large fraction of helium or a mixture of helium and CNO group, which is quite different from the prediction of the poly-gonato model where the composition is mainly dominated by iron nuclei. Our prediction (in particular, that of the WR-CR scenario) is more in agreement with the X_{\max} measurements from fluorescence and Cherenkov light detectors, while the poly-gonato model is in agreement with data from the measurements of air shower particles on the ground.

Recently, Globus et al. (2015a) claimed that a single Galactic component with rigidity dependent cut-off is sufficient to explain the observed all-particle spectrum when combined with an extra-galactic component. Their claim that an additional Galactic component is not needed does not contradict our claim of having one. It is simply that they assume the particle spectrum as a *broken* power law with an exponential cut-off which leads to an increased flux above the break energy (knee) as in the poly-gonato model. However, we have demonstrated that if one considers a power-law spectrum with an exponential cut-off which is expected for particles produced by diffusive shock acceleration process in supernova remnants (Malkov & Drury 2001), a single component cannot explain the observed spectrum beyond the knee, and a second Galactic component is inevitable. Their single component, which they had not assigned to any specific source class, would correspond to the superposition of multiple components similar to the ones proposed in our model. Based on the physical models of the most plausible sources and the propagation of cosmic rays in the Galaxy, we show that two Galactic components are sufficient to explain the measured spectrum, but do not exclude the existence of more than two components.

6.2. GW-CRs

Assuming that the maximum energy of particles produced by the Galactic wind termination shock is limited by the condition that the particle diffusion length must be less than the size of the shock, the maximum energy under Bohm diffusion can be written as, $E_m \sim 3ZeB(V_s/c)R_s$, where B is the magnetic field, V_s is the shock velocity and R_s is the shock radius. From the GW-CR parameters obtained in our study, we can take $R_s = R_{sh} = 96$ kpc, $V_s = \dot{V}R_s = 1443$ km s⁻¹ which is the terminal wind velocity, and $E_m = 9.5 \times 10^7$ GeV which is the proton cut-off energy. Using these values, the magnetic field strength in the Galactic halo is estimated to be ~ 73 nG. This is approximately a factor 3 less than the value obtained assuming Parker's magnetic field topology for the solar wind (Equation 16).

An intrinsic issue in the case of re-acceleration by Galactic wind termination shock is the difficulty to observe the re-accelerated particles in the Galactic disk because of advection by the wind flow, except for the highest energy particles, as discussed in Section 3.1. As a consequence, the spectrum in the disk may not show a continuous transition between the SNR-CRs and GW-CRs (see e.g. Zirakashvili & Völk 2006). This effect is actually visible in the predicted spectra of the individual elements shown in Figure 5. However, we notice that the superposition of the individual spectra smears out this effect in the all-particle spectrum. Nevertheless, in order to avoid this effect, Zirakashvili & Völk (2006) considered termination shocks which are stronger near the Galactic poles and weaker towards the Galactic equator, unlike in our study where the shocks are considered to have equal strengths in all the directions. In their configuration, the maximum energy of particles decreases from the poles towards the equator, and therefore, the superposition of spectra from different colatitudes produces a continuity in the total spectrum. Another consideration is the particle re-acceleration by spiral shocks in the Galactic wind which are formed

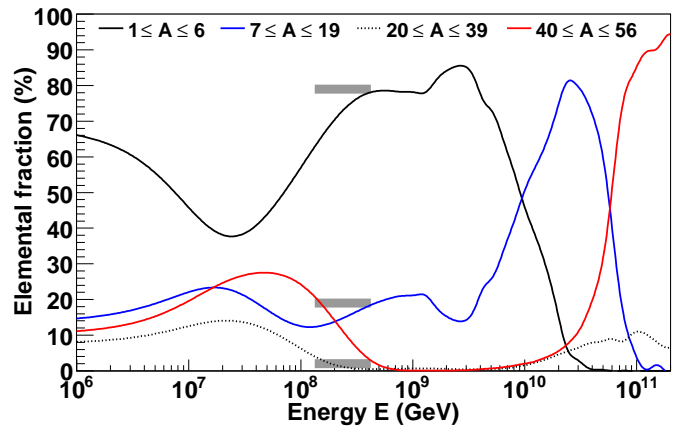


Fig. 12. Elemental fraction for four mass groups obtained using the PCS model of EG-CRs and WR-CRs ($C/He = 0.1$). The proton fraction (not shown in the figure) predicted by the model in the LOFAR energy range is $\sim 10\%$. The grey bands, from top to bottom, represent the best-fit LOFAR measurements of 79% helium, 19% nitrogen and 2% iron nuclei in the energy range of $(1.3 - 4.2) \times 10^8$ GeV (Buitink et al. 2016). At 99% confidence level, the measured proton plus helium fraction can vary in the range of (38–98)%, and the combined nitrogen and iron fraction within (2–62)%.

by the interaction between fast winds originating from the Galactic spiral arms and slow winds from the interarm regions (Völk & Zirakashvili 2004). These shocks, which can be formed at distances of $\sim 50 - 100$ kpc, can accelerate SNR-CRs up to $\sim Z \times 10^8$ GeV. An alternative possibility is the re-acceleration by multiple shock waves in the Galactic wind generated by time dependent outflows of gas from the Galactic disk (Dorfi & Breitschwerdt 2012). These shocks, which are long-lived like the termination shocks, can accelerate particles up to $\sim 10^8 - 10^9$ GeV in the lower Galactic halo. An attractive feature of this model is the advection of particles downstream of the shocks towards the Galactic disk, thereby, resolving the difficulty of observing the re-accelerated particles in the disk. Despite having different features, the cosmic-ray composition predicted by all these different models in the energy range of $\sim 10^7 - 10^9$ GeV are expected to be similar to the result presented here since they consider the same seed particles (cosmic rays from the Galactic disk) for re-acceleration as in our study. Below $\sim 10^7$ GeV where the GW-CRs are significantly suppressed in our case, the other wind models discussed above will give a different result.

6.3. WR-CRs

The prediction of a large helium fraction and a small iron fraction between around 10^8 and 10^9 GeV by the WR-CR ($C/He = 0.1$) model seems to be in agreement with new measurements from the LOFAR radio telescope (Buitink et al. 2016), and the Pierre Auger Observatory (Aab et al. 2014). These measurements have revealed a strong light component, and an almost negligible iron component above $\sim 10^8$ GeV. In Figure 12, the elemental fraction predicted by the WR-CR ($C/He = 0.1$) model combined with the PCS model for the EG-CRs is compared with the best-fit composition of the LOFAR data for four mass groups: $1 \leq A \leq 6$, $7 \leq A \leq 19$, $20 \leq A \leq 39$, and

$40 \leq A \leq 56$. The model predictions are found to show a good agreement with the data.

Using the maximum energy of particles for the WR-CRs, it is possible to estimate the strength of the magnetic field at the surface of Wolf-Rayet stars. Assuming that the magnetic field configuration in the Wolf-Rayet winds follows Parker's model (Parker 1958), the toroidal magnetic field strength near the equatorial plane of the star at the position R_w from the star follows the relation,

$$B = B_0 \frac{\omega R_*^2}{V_w R_w}, \quad (16)$$

where B_0 is the magnetic field at the surface of the star, ω is the angular rotation velocity, R_* is the radius of the star, and V_w is the wind velocity. Using the relation $E_m \sim 3ZeB(V_s/c)R_s$ for the maximum energy as in the case of the GW-CRs, and the proton cut-off energy of $E_m = 1.1 \times 10^8$ GeV for the WR-CRs ($C/He = 0.4$) obtained using the PCS/UFA model, we get $BR_s \sim 1.2 \times 10^{15}$ G cm, where we take the shock velocity $V_s = 0.1 c$ (Soderberg et al. 2012). Using this value of BR_s in Parker's magnetic field configuration (Equation 16) by taking $R_w = R_s$ and other Wolf-Rayet star parameters as $R_* = 3 \times 10^{12}$ cm, $\omega = 10^{-6} \text{ s}^{-1}$, and $V_w = 2000 \text{ km s}^{-1}$ (Berezhko & Völk 2000), we obtain the magnetic field at the surface of the star as $B_0 \sim 1.5 \times 10^4$ G. Such a strong magnetic field was also predicted in an earlier study by Biermann & Cassinelli (1993), and is found to be in agreement with recent magnetic field measurements from Wolf-Rayet stars. Based on an upper limit of 100 G in the observable parts of Wolf-Rayet winds, Chevrotière et al. (2013) estimated an upper limit for the surface magnetic field of ~ 5400 G. An even stronger field in the wind, up to ~ 2000 G, has been reported (Chevrotière et al. 2014), which indicates that the surface magnetic field of these stars can go well above the order of 10^4 G.

From the total energy of 1.4×10^{49} ergs injected into WR-CRs by a single supernova explosion, and the explosion rate of Wolf-Rayet stars in the Galaxy of $1/210 \text{ yr}^{-1}$, we estimate the total power injected into WR-CRs as $2.1 \times 10^{39} \text{ ergs s}^{-1}$. This is approximately a factor 40 less than the power injected into SNR-CRs by supernova explosions in the interstellar medium. The required amount of supernova explosion energy injected into helium nuclei for WR-CRs is about 1.2 – 1.6 times that of the SNR-CRs. This indicates that the average abundance of helium nuclei swept up by supernova shocks in the Wolf-Rayet winds must be higher than the helium abundance present in the interstellar medium if the particle injection fraction and the acceleration efficiency of the shocks are the same for the SNR-CRs and the WR-CRs.

Our results for the WR-CRs are obtained by assuming that the particle injection fraction into the shocks is the same for all the different elements. The injection fraction may depend on the type of the element, and the nature of this dependence is not quite understood. By taking the ratio of the SNR-CRs source spectra (Equation 2) at a fixed rigidity to the known Solar system elemental abundances (Lodders & Palme 2009), we estimate the relative injection fraction of particles for the different elements. Applying these relative injection fractions to the WR-CRs, we find that the composition is significantly dominated by carbon nuclei, in contrast to the results shown in Figure 4 where the composition is mainly dominated by helium or a mixture

helium and carbon nuclei. Thus, the contribution of WR-CRs in this case is strongly constrained by the measured carbon spectrum at low energies. The all-particle spectrum for this case, after adding the contributions of SNR-CRs and EG-CRs, underpredicts the measured data between the second knee and the ankle. This problem might be resolved if we consider that both GW-CRs and WR-CRs contribute at the same time. In future, we will explore the parameter space of this combined scenario.

6.4. Comparison with Hillas's 'Component B'

Bell & Lucek (2001) showed that magnetic field upstream of supernova shock fronts can be amplified non-linearly by cosmic rays up to many times the pre-shock magnetic field. They showed that these highly amplified magnetic fields can facilitate cosmic-ray acceleration up to energies $Z \times 10^8$ GeV for supernova shocks expanding in the interstellar medium, even higher by an order of magnitude for shocks expanding into pre-existing stellar winds. Based on the Bell-Lucek's version of diffusive shock acceleration, Hillas (2005) proposed a second Galactic component 'Component B', produced by Type II supernova remnants in the Galaxy expanding into dense slow winds of the preceding red supergiants, to accommodate for the observed cosmic rays above $\sim 10^7$ GeV. In the Hillas (2005) model, a Galactic component 'Component A', produced by Type Ia supernova remnants in the Galaxy, dominates the all-particle energy spectrum below $\sim 10^7$ GeV. The 'Component A' has a similar composition to the SNR-CRs in our model, but the 'Component B' has a large iron fraction in contrast to the WR-CR component in our model which is dominated mostly by helium or a mixture of helium and CNO group with a small iron fraction. Between $\sim 10^8$ and 10^9 GeV, the predicted all-particle spectrum in Hillas (2005) consists of a significant iron fraction which may be in agreement with the $\langle \ln A \rangle$ data when mixed with a strong extra-galactic proton component, but is in tension with the small iron fraction ($\sim 2 - 10\%$) preferred by the recent measurements of LO-FAR (Buitink et al. 2016) and the Pierre Auger Observatory (Aab et al. 2014). These new measurements disfavour the general view that the Galactic component above the second knee is dominated by heavy (iron) nuclei.

6.5. A steep EG-CR component extending below the second knee

An alternative model that does not require the introduction of an additional Galactic component is to assume that EG-CRs have a significant contribution down to energies below the second knee. Such a scenario would require a steep spectrum of $\sim E^{-3}$ and a strong flux suppression below $\sim 10^8$ GeV (see Hillas 2005 for a brief discussion, and also Muraishi et al. 2005 in the context of the origin of the knee). To explore this scenario, we inject an additional extra-galactic component of pure protons at the position of the Galactic wind termination shocks, and allow them to propagate diffusively towards the Galactic disk in the presence of the Galactic wind outflow. The injection spectrum is assumed to follow $E^{-\gamma} \exp(-E/E_c)$. The propagation is treated exactly the same as the propagation of GW-CRs from the termination shock towards the Galactic disk. All propagation parameters are kept the same, except for the

wind velocity constant \tilde{V} which is treated as a free parameter. The best-fit all-particle spectrum obtained after adding the contribution of SNR-CRs and EG-CRs from the minimal model is shown in Figure 13. The best-fit parameters are $\gamma = 3.3$, $E_c = 4.1 \times 10^6$ GeV for the SNR-CRs protons, $E_c = 1.5 \times 10^9$ GeV for the additional EG-CRs, and $\tilde{V} = 200.5$ km/s/kpc. This value of \tilde{V} gives a wind velocity which is about a factor 13 larger than the wind velocity used in the study of GW-CRs. Such a fast wind is required in order to generate a strong modulation for particles below the second knee so that the predicted flux does not exceed the observed data at low energies. For $\gamma < 3.3$, the required wind velocity is lower, but the model prediction does not fit the observed data very well (see e.g. the case of $\gamma = 3$ in Figure 13). Replacing the additional extra-galactic protons with heavier elements only slightly reduces the required wind velocity. Having a strong Galactic wind can have serious effects on the spectrum and distribution of low-energy cosmic rays in the Galaxy (see e.g. Bloemen et al. 1993). In the presence of a strong wind, cosmic-ray transport will be dominated by advection rather than diffusion, and will produce a cosmic-ray distribution that resembles the distribution of the sources. But, the cosmic-ray distribution inferred from the observations of diffuse gamma-ray emission from the Galaxy indicates a radial gradient weaker than the distribution of supernova remnants or pulsars in the Galaxy. These observations suggest that if supernova remnants are the main sources of cosmic rays in the Galaxy, the propagation of cosmic rays should be dominated by diffusion, not by advection. In addition, if the transport is dominated by advection, the cosmic-ray spectrum is expected to exhibit a break (steepening) at an energy where the advection boundary, $z_c \propto [D(E)/\tilde{V}]^{1/2}$, equals the halo boundary L . Such a break is not observed below the knee, except at ~ 10 GeV which is due to Solar modulation. Attributing the knee to such a break raises issues regarding the cosmic-ray injection index. Below the break, cosmic-ray transport is advection dominated and the spectrum is expected to follow $E^{-(\gamma+a/2)}$, where γ is the source index and a is the diffusion index. For the observed spectral index of ~ 2.7 and $a = 0.33$ used in our study, we get $\gamma = 2.53$. This is incompatible with the prediction of diffusive shock acceleration theory which predicts an index close to 2 for the strong shocks present in supernova remnants (Ptuskin et al. 2010; Caprioli et al. 2011). Choosing $a = 0.6$, as in pure diffusion propagation models, gives $\gamma = 2.4$. This relaxes the tension a bit, but such a high value of a is not favoured by the observed small level of cosmic-ray anisotropy. Another strong constraint on the Galactic wind velocity is provided by the abundance ratio of radioactive secondary to stable secondary. Measurement of $^{10}\text{Be}/^9\text{Be}$ ratio puts a constraint at $\tilde{V} \leq 45$ km/s/kpc (Bloemen et al. 1993). All these arguments pose a serious problem to the alternative scenario of a strong EG-CR component with a steep spectrum extending below the second knee, and modulating by Galactic wind. One possibility, but rather unrealistic, for this scenario to work is if the additional EG-CR component has a spectrum and composition almost similar to that of the GW-CRs produced at the Galactic wind termination shocks.

An alternative to the modulation of EG-CRs by the Galactic wind is the ‘magnetic horizon effect’ (Stanev et al. 2000; Lemoine 2005; Aloisio & Berezhinsky 2005), which

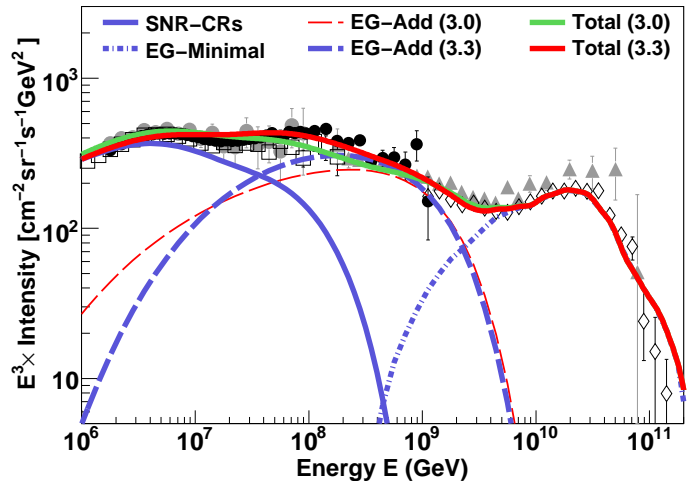


Fig. 13. All-particle energy spectrum for an additional component of EG-CR protons extended down to low energies and modulated by Galactic wind. The numbers within the parentheses denote the injection index for the additional extra-galactic component. For the SNR-CRs, an exponential cut-off energy for protons at 4.1×10^6 GeV is assumed. See text for other details. The EG-Minimal component is the same as in Figure 9 (top). Data: Same as in Figure 2.

leads to a flattening of the extra-galactic spectrum below an energy where the diffusive propagation distance in a partly turbulent extra-galactic magnetic field, over the time scale set by energy losses of the cosmic rays through interactions with ambient photon backgrounds, gets below the average distance of cosmic ray sources. Assuming a relatively strong ($\gtrsim 1$ nG) extra-galactic field with a constant coherence length extending over the entire universe, this effect could set in at around 10^9 GeV, effectively cutting off the extra-galactic component at lower energies slightly below the ankle (Aloisio et al. 2012), or even above (Mollerach & Roulet 2013). However, more detailed treatments in the context of large scale structure formation (Kotera & Lemoine 2008), have indicated that this effect is much less efficient due to the large voids in the universe which are essentially free of magnetic fields. As shown recently in detailed simulations, the magnetic horizon effect should play virtually no role above the second knee for any type of nuclei, and for protons in some extra-galactic magnetic field scenarios, not even above the knee (Batista & Sigl 2014).

We point out that neither the Galactic wind nor the magnetic horizon effects discussed above prevent a hard extra-galactic component, like the light component with $\gamma = 2.7$ as indicated by the KASCADE-Grande measurements above $\sim 10^8$ GeV (Apel et al. 2013), from contributing around the second knee as such a hard component will be already consistent with the measured data at low energies. Even if such a hard extra-galactic component is present, an additional Galactic component will still be required as the extra-galactic component will remain subdominant in the all-particle spectrum below 10^8 GeV.

An additional problem for EG-CRs with an overall spectrum steeper than $E^{-2.7}$ is that, if one assumes that they fill the extra-galactic space homogeneously with energies from ~ 1 GeV to 10^9 GeV, it contains more energy than the gravitational binding energy released in the universe during structure formation (Rachen 2016). Using realistic

cally low efficiencies for this energy – which is, besides the lower overall nuclear binding energy released in fusion by all primordial baryonic matter going into stars, the only fundamental energy budget present in the late universe – to be converted into cosmic rays, one can conclude that spectral indices as discussed here for a dominant extra-galactic component below the second knee cannot easily be reconciled with this energy budget, no matter which kind of sources one proposes. Mainly on the basis of this argument, together with the difficulties of a sufficient spectral modification at low energies discussed above, we consider a dominantly extra-galactic explanation of cosmic rays below 10^8 GeV as implausible.

7. Conclusions

We have demonstrated that a single Galactic component with progressive energy cut-offs in the individual spectra of different elements, and describing the low-energy measurements below $\sim 10^6$ GeV from balloon and satellite-borne experiments, cannot explain simultaneously the knee and the second knee observed in the all-particle spectrum. We show that a two-component Galactic model, the first component dominating up to $\sim 5 \times 10^7$ GeV and the second component dominating in the range of $\sim 5 \times 10^7 - 10^9$ GeV, can explain almost all observed features in the all-particle spectrum and composition when combined with an extra-galactic component dominating above $\sim 10^9$ GeV. Discussing two different scenarios for the second Galactic component, we find that a contribution of Wolf-Rayet supernovae explain best both the measured energy spectrum and composition. Our main result is that this component predicts a Galactic contribution at and above the second knee which is mainly dominated by helium or a mixture of helium and CNO nuclei, and is consistent with a ‘regular’ extra-galactic contribution from sources with a flat spectral index and a cosmological evolution typical for AGNs or star formation. Using re-acceleration at the Galactic wind termination shock as a second Galactic component also allows to fit the all-particle energy spectrum, but not the observed composition very well. Tests of the two-component Galactic model using different hypotheses for a significant extra-galactic cosmic-ray component below the ankle, do neither significantly improve nor deteriorate this result, mostly because *both* the Galactic and extra-galactic components have a rather light composition, and contain little or no heavy nuclei like iron, in contrast to common assumptions. In all cases, the transition from Galactic to extra-galactic cosmic rays occurs between the second knee and the ankle, and we see neither the need nor a theoretical case for an extra-galactic component significantly contributing at or below 10^8 GeV. Our findings are in agreement with recent measurements from LOFAR and the Pierre Auger Observatory, which have revealed a strong light component and a rather low iron fraction between $\sim 10^8$ and 10^9 GeV. A clear distinction of the various discussed Galactic and extra-galactic scenarios would be possible if we could separately measure the spectra of at least four major mass groups, that is protons, helium, CNO, and heavier, at energies between the second knee and the ankle.

Acknowledgements

We wish to thank Michael Unger, Glennys Farrar and Luis Anchordoqui, for their comments on the manuscript, and for providing us results for the UFA model. We also thank Peter Biermann for his insightful comments, and Torsten Enßlin and Christoph Pfrommer for helping to improve the manuscript during a discussion at the meeting of ‘International Team 323’ at the International Space Science Institute in Bern. ST wishes to thank Onno Pols for discussions on Wolf-Rayet stars. AvV acknowledges financial support from the NWO Astroparticle physics grant WARP. We furthermore acknowledge financial support from an Advanced Grant of the European Research Council (grant agreement no. 227610), European Union’s Horizon 2020 research and innovation programme (grant agreement no. 640130), the NWO TOP grant (grant agreement no. 614.001.454), and the Crafoord Foundation (grant no. 20140718).

References

- Aab, A., et al. (Pierre Auger Collaboration), 2014, PRD, 90 122006
Aartsen, M. G., et al. 2013, PRD, 88, 042004
Abbasi, R. U., et al. 2009, APh, 32, 53
Abdo, A. A., et al. 2009, PRL, 102, 181101
Abu-Zayyad, T., et al. 2013, ApJ, 768, L1
Aharonian, F. A., et al. 2006, ApJ, 636, 777
Aharonian, F. A., et al. 2007, A&A, 464, 235
Aharonian, F. A., et al. 2008, A&A, 477, 353
Adriani, O., et al. 2011, Science, 332, 69
Adriani, O., et al. 2014, Physics Reports, 544, 323
Aguilar, M., et al. 2013, PRL, 110, 141102
Aguilar, M., et al. 2014, PRL, 113, 121102
Aguilar, M., et al. 2015a, PRL, 114, 171103
Aguilar, M., et al. 2015b, PRL, 115, 211101
Ahn, H. S., Allison, P. S., Bagliesi, M. G., et al. 2009, ApJ, 707, 593
Albert, J., et al. 2007, A&A, 474, 937
Aloisio, R., & Berezhinsky, V. S., 2005, ApJ, 625, 249
Aloisio, R., Berezhinsky, V. S., & Gazizov, A., 2012, APh, 39, 129
Aloisio, R., Berezhinsky, V. S., & Blasi, P., 2014, JCAP, 10, 020
Amenomori, M., et al. 2008, ApJ, 678, 1165
Antoni, T., et al. 2005, APh, 24, 1
Apel, W. D., et al. 2013, PRD, 87, 081101
Axford, W. I., 1994, ApJS, 90, 937
Baade, W., & Zwicky, F., 1934, PNAS, 20, 259
Batista, R. A., & Sigl, G., 2014, JCAP, 1411, 031
Batista, R. A., et al. 2015, JCAP, 10, 063
Batista, R. A., et al. 2016, JCAP, 05, 038
Bell, A. R. 1978, MNRAS 182, 147
Bell, A. R., 2004, MNRAS, 353, 550
Bell, A. R., & Lucek, S. G., 2001, MNRAS, 321, 433
Berezhko, E. G., & Völk, H. J., 2000, A&A, 357, 283
Berezhko, E. G., Ksenofontov, L. T., Ptuskin, V. S., Zirakashvili, V. N., Völk, H. J., 2003, A&A, 410, 189
Berezhnev, S. F., et al. 2013, in Proc. 33rd ICRC, Paper ID 326
Berezhinsky, V. S., & Grigorieva, S. I., 1988, A&A, 199, 1
Berezhinsky, V. S., Grigorieva, S. I., & Hnatyk, B. I., 2004, APh, 21, 617
Berezhinsky, V. S., Gazizov, A., & Grigorieva, S. I., 2006, PRD, 74, 043005
Biermann, P. L., & Cassinelli, J. P., 1993, A&A, 277, 691
Biermann, P. L., Becker, J. K., Dreyer, J., Meli, A., Seo, E., & Stanev, T., 2010a, ApJ, 725, 184
Biermann, P. L., Becker, J. K., Caceres, G., Meli, A., Seo, E., & Stanev, T., 2010b, ApJ, 725, 184
Bird, D. J., et al. 1994, ApJ, 424, 491
Blandford, R., & Ostriker, J. P., 1978, ApJ, 221, L29
Blasi, P., Amato, E., & Serpico, P. D., 2012, PRL, 109, 061101
Bloemen, J. B. G. M., Dogiel, V. A., Dorman, V. L., & Ptuskin, V. S., 1993, A&A, 267, 372
Buitink, S., et al. (LOFAR Collaboration) 2016, Nature, 531, 70
Breitschwerdt, D., McKenzie, J. F., & Völk, H. J., 1991, A&A, 245, 79
Breitschwerdt, D., Dogiel, V. A., & Völk, H. J., 2002, A&A, 385, 216
Capioli, D., Blasi, P., & Amato, E., 2011, APh, 34, 447

- de la Chevrotiefe, A., St-Louis, N., & Moffat, A. F. J., (MiMeS Collaboration) 2013, *ApJ*, 764, 171
- de la Chevrotiefe, A., St-Louis, N., & Moffat, A. F. J., (MiMeS Collaboration) 2014, *ApJ*, 781, 73
- di Matteo, A. for the Pierre Auger Collaboration, *PoS (ICRC2015)*, 249; arXiv:1509.03732
- Dorfi, E. A., & Breitschwerdt, D., 2012, *A&A*, 540, A77
- Drury, L. O., 1983, *Reports on Progress in Physics*, 46, 973
- Engelmann, J. J., Ferrando, P., Soutoul, A., Goret, P., & Juliusson, E., 1990, *A&A*, 233, 96
- Erlykin, A. D. & Wolfendale, A. W., 2012, *Aph*, 35, 449
- Farrar, G. R., & Gruzinov, A., 2009, *ApJ*, 693, 329
- Gal-Yam, A., et al. 2014, *Nature*, 509, 471
- Ghia, P. L., for the Pierre Auger Collaboration, *PoS (ICRC2015)*, 034; arXiv:1509.03732
- Gilmore, R. C., et al. 2012, *MNRAS*, 422, 3189
- Globus, N., Allard, D., & Parizot, E., 2015, *PRD*, 92, 021302
- Globus, N., Allard, D., Mochkovich, R., & Parizot, E., 2015, *MNRAS*, 451, 751
- Green, D. A., 2009, *BASI*, 37, 45
- Greisen, K., 1966, *PRL*, 16, 748
- Hillas, A. M., 1967, *Physics Letters A*, 24, 677
- Hillas, A. M., 1984, *ARA&A*, 22, 425
- Hillas, A. M., 2005, *Journal of Physics G: Nuclear and Particle Physics*, 31, R95
- Hörandel, J. R., 2003a, *Aph*, 19, 193
- Hörandel, J. R., 2003b, *Journal of Physics G: Nuclear and Particle Physics*, 29, 2439
- Hörandel, J. R., 2006, *JPhCS*, 47, 41
- Jokipii, J. R., & Morfill, G., 1987, 312, 170
- Jones, F. C, Lukasiak, A., Ptuskin, V., & Webber, W., 2001, *ApJ*, 547, 264
- Kampert, K. H., & Unger, M., 2012, 35, 660
- Kang, H., Ryu, D., & Jones, T. W., 1996, *ApJ*, 456, 422
- Kang, H., Rachen, J. P., & Biermann, P. L., 1997, *MNRAS*, 286, 257
- Kelner, S. R., Aharonian, F. A., & Bugayov, V. V., 2006, *PRD* 74, 034018
- Knurenko, S., & Sabourov, A., 2010, *Proc. XVI ISVHECRI*
- Kotera, K., & Lemoine, M., 2008, *PRD*, 77, 023005
- Krymskii, G. F., 1977, *Akad. Nauk SSSR Dokl.*, 234, 1306
- Lagage P. O., & Cesarsky C. J., 1983, *A&A*, 125, 249
- Lemoine, M., 2005, *PRD*, 71, 083007
- Lerche, I., & Schlickeiser, R., 1982a, *A&A*, 116, 10
- Lerche, I., & Schlickeiser, R., 1982b, *MNRAS*, 201, 1041
- Letaw, J. R., Silberberg, R., & Tsao, C. H., 1983, *ApJS*, 51, 271
- Lucek S. G., & Bell A. R., 2000, *MNRAS*, 314, 65
- Lodders, K., & Palme, H., 2009, *Meteoritics and Planetary Science Supplement*, 72, 5154
- Malkov M. A., Drury L. O'C, 2001, *Reports on Progress in Physics*, 64, 429
- Mannheim, K., Protheroe, R. J. and Rachen, J. P., 2001, *PRD*, 63, 023003
- Mollerach, S., & Roulet, E., 2013, *JCAP*, 1310, 013
- Müller, D., Swordy, S. P., Meyer, P., L'Heureux, J., & Grunsfeld, J. M., 1991, *ApJ*, 374, 356
- Muraishi, H., Yanagita, S. & Yoshida, T., 2005, *Progress of Theoretical Physics*, 113, 721
- Murase, K., Ioka, K., Nagataki, S. & Nakamura, T., 2008, *PRD*, 78, 023005
- Obermeier, A., Ave, M., Boyle, P., et al., 2011, *ApJ*, 742, 14
- Ohira, Y., Murase, K., & Yamazaki, R., 2011, *MNRAS*, 410, 1577
- Panov, A. D., et al. 2007, *Bull. Russ. Acad. Sci.*, Vol. 71, No. 4, pp. 494
- Parizot, E., Marcowith, A., Ballet, J., & Gallant, Y. A. 2006, *A&A*, 453, 387
- Parker, E. N., 1958, *ApJ*, 128, 664
- Pollock, A. M. T., Corcoran, M. F., Stevens, I. R., & Williams, P. M., 2005, *ApJ*, 629, 482
- Porcelli, A. for the Pierre Auger Collaboration, *PoS (ICRC2015)*, 420; arXiv:1509.03732
- Ptuskin, V. S., Rogovaya, S. I., Zirakashvili, V., Chuvilgin, L. G, et al. 1993, *A&A*, 268, 726
- Ptuskin, V. S., Zirakashvili, V., & Seo, E. S., 2010, *ApJ*, 718, 31
- Ptuskin, V. S., Zirakashvili, V., & Seo, E. S., 2013, *ApJ*, 763, 47
- Rachen, J. P., & Biermann, P. L., 1993, *A&A*, 272, 161
- Rachen, J. P., Stanev, T., & Biermann, P. L., 1993, *A&A*, 273, 377
- Rachen, J. P., 2016, *Proc. 28th Texas Symposium on Relativistic Astrophysics*, Geneva, Switzerland, 13-18 December 2015, *Electronic Proceedings #230*
- Reville, B., & Bell, A. R. 2012, *MNRAS*, 419, 2433
- Rosslowe, C. K., & Crowther, P. A., 2015, arXiv:1412.0699
- Schulz, A. for the Pierre Auger Collaboration, 2013, in *Proc. 33rd ICRC*, Rio de Janeiro; arXiv:1307.5059
- Soderberg, A. M., et al. 2012, *ApJ*, 752, 78
- Stanev, T., Biermann, P. L., & Gaisser, T. K., 1993, *A&A*, 274, 902
- Stanev, T., Engel, R. Mücke, A. Protheroe, R. J., & Rachen, J. P., 2000, *PRD*, 62, 093005
- Strong, A. W., & Moskalenko, I. V., 1998, *ApJ*, 509, 212
- Swordy, S. P., Müller, D., Meyer, P., L'Heureux, J., & Grunsfeld, J. M., 1990, *ApJ*, 349, 625
- Thoudam, S., 2008, *MNRAS*, 388, 335
- Thoudam, S., & Hörandel, J. R. 2012, *MNRAS*, 421, 1209
- Thoudam, S., & Hörandel, J. R. 2013, *MNRAS*, 435, 2532
- Thoudam, S., & Hörandel, J. R. 2014, *A&A*, 567, A33
- Tomasetti, N. 2012, *ApJ*, 752, L13
- Unger, M., Farrar, G. R., & Anchordoqui, L. A. 2015, *PRD*, 92, 123001
- Vink J., & Laming J. M., 2003, *ApJ*, 584, 758
- Völk, H. J. & Biermann, P. L., 1988, *ApJ*, 333, L65
- Völk, H. J. & Zirakashvili, V. N., 2004, *A&A*, 417, 807
- Wandel, A., 1988, *A&A*, 200, 279
- Wandel, A., Eichler, D. S., Letaw, J. R., Silberberg, R., & Tsao, C. H., 1987, *ApJ*, 316, 676
- Waxman, E., 1995, *PRL*, 75, 386
- Yoon, Y. S., et al. 2011, *ApJ*, 728, 122
- Yuan, Q., Zhang, B., & Bi, X. -J, 2011, *PRD* 84, 043002
- Zatsepin, G. T., & Kuzmin V. A., 1966, *JETPh Lett.*, 4, 78
- Zirakashvili, V., Breitschwerdt, D., Ptuskin, V. S. & Völk, H. J., 1996, *A&A*, 311, 113
- Zirakashvili, V., & Völk, H. J., 2006, *AdSpR*, 37, 1923

Appendix A: Derivation of Equation 8

The Green's function, $G(\mathbf{r}, \mathbf{r}', p, p')$, of Equation 7 satisfies,

$$\nabla \cdot (D_w \nabla G - \mathbf{V}G) + \frac{\partial}{\partial p} \left\{ \frac{\nabla \cdot \mathbf{V}}{3} pG \right\} = -\delta(\mathbf{r} - \mathbf{r}')\delta(p - p'). \quad (\text{A.1})$$

In rectangular coordinates, the above equation can be written as,

$$\begin{aligned} D_w \frac{\partial^2 G}{\partial x^2} + D_w \frac{\partial^2 G}{\partial y^2} + D_w \frac{\partial^2 G}{\partial z^2} - \tilde{V} \frac{\partial}{\partial x}(xG) - \tilde{V} \frac{\partial}{\partial y}(yG) \\ - \tilde{V} \frac{\partial}{\partial z}(zG) + \frac{\partial}{\partial p}(\tilde{V}pN) = -\delta(x - x')\delta(y - y')\delta(z)\delta(p - p'), \end{aligned} \quad (\text{A.2})$$

where we have written $\mathbf{V} = \tilde{V}(x\hat{i} + y\hat{j} + z\hat{k})$ with \hat{i} , \hat{j} and \hat{k} representing the unit vectors along the x , y and z directions. Following a similar procedure adopted in Lerche & Schlickeiser (1982b), we express,

$$\begin{aligned} G(x, x', y, y', z, z', p, p') = \\ \int_{-\infty}^{\infty} dk_x \int_{-\infty}^{\infty} dk_y \int_{-\infty}^{\infty} dk_z \bar{G}(k_x, x', k_y, y', k_z, z', p, p') \\ \times e^{ik_x(x-x')} e^{ik_y(y-y')} e^{ik_z(z-z')}, \end{aligned} \quad (\text{A.3})$$

and,

$$\begin{aligned} \delta(x - x') &= \frac{1}{2\pi} \int_{-\infty}^{\infty} dk_x e^{ik_x(x-x')}, \\ \delta(y - y') &= \frac{1}{2\pi} \int_{-\infty}^{\infty} dk_y e^{ik_y(y-y')}, \\ \delta(z - z') &= \frac{1}{2\pi} \int_{-\infty}^{\infty} dk_z e^{ik_z(z-z')}. \end{aligned} \quad (\text{A.4})$$

Inserting Equations A.3 and A.4 into Equation A.2, we get,

$$\begin{aligned}
& -D_w (k_x^2 + k_y^2 + k_z^2) \bar{G} - i\tilde{V} (k_x x' + k_y y' + k_z z') \bar{G} \\
& + \tilde{V} \left(k_x \frac{\partial \bar{G}}{\partial k_x} + k_y \frac{\partial \bar{G}}{\partial k_y} + k_z \frac{\partial \bar{G}}{\partial k_z} \right) + \tilde{V} p \frac{\partial \bar{G}}{\partial p} + \tilde{V} \bar{G} \\
& = -\frac{1}{8\pi^3} \delta(p - p'). \tag{A.5}
\end{aligned}$$

We now introduce variables ψ_x , ψ_y and ψ_z such that $k_x = \psi_x F(p)$, $k_y = \psi_y F(p)$ and $k_z = \psi_z F(p)$, where

$$F(p) = \exp \left(\tilde{V} \int^p du \frac{1}{\tilde{V}u} \right). \tag{A.6}$$

This reduces Equation A.5 to

$$\tilde{V} p \frac{\partial \bar{G}}{\partial p} + B(p) \bar{G} = -\frac{1}{8\pi^3} \delta(p - p'), \tag{A.7}$$

where,

$$\begin{aligned}
B(p) = & -D_w(p) (\psi_x^2 + \psi_y^2 + \psi_z^2) F^2(p) \\
& - i (\psi_x x' + \psi_y y' + \psi_z z') F \tilde{V} + \tilde{V}. \tag{A.8}
\end{aligned}$$

The solution of Equation A.7 is given by,

$$\begin{aligned}
\bar{G}(k_x, x', k_y, y', k_z, z', p, p') = & \frac{1 - H[p - p']}{8\pi^3 \tilde{V} p'} \\
& \times \exp \left[\int_{E'}^E du \frac{B(u)}{\tilde{V}u} \right], \tag{A.9}
\end{aligned}$$

where the Heaviside step function $H[p - p'] = 1(0)$ for $p > p' (< p')$. Taking inverse Fourier transform of \bar{G} , we obtain the required Green's function as,

$$\begin{aligned}
G(x, x', y, y', z, z', p, p') = & \frac{1 - H[p - p']}{8\pi^3 \tilde{V} p} \left(\frac{\pi}{I_{p,p'}} \right)^{3/2} \\
& \times \exp \left[-\frac{(C_{x,x'}^2 + C_{y,y'}^2 + C_{z,z'}^2)}{4I_{p,p'}} \right] \tag{A.10}
\end{aligned}$$

where,

$$\begin{aligned}
C_{x,x'} = & \tilde{V} x' \int_{p'}^p du \frac{1}{\tilde{V}u} \frac{F(u)}{F(p)} - x' + x, \\
C_{y,y'} = & \tilde{V} y' \int_{p'}^p du \frac{1}{\tilde{V}u} \frac{F(u)}{F(p)} - y' + y, \\
C_{z,z'} = & \tilde{V} z' \int_{p'}^p du \frac{1}{\tilde{V}u} \frac{F(u)}{F(p)} - z' + z, \tag{A.11}
\end{aligned}$$

and,

$$I_{p,p'} = \int_p^{p'} du \frac{D_w(u)}{\tilde{V}u} \left(\frac{F(u)}{F(p)} \right)^2. \tag{A.12}$$

Then, for a given cosmic-ray source characterised by $q(x', y', z', p')$, the differential number density of particles with momentum p at a distance (x, y, z) is given by,

$$\begin{aligned}
N(x, y, z, p) = & \int_0^\infty dx' \int_0^\infty dy' \int_0^\infty dz' \int_0^\infty dp' \\
& \times G(x, x', y, y', z, z', p, p') q(x', y', z', p'). \tag{A.13}
\end{aligned}$$

For any point source located at $(0, 0, 0)$ and emitting $q(p)$ spectrum of particles, that is $q(x', y', z', p') = \delta(x') \delta(y') \delta(z') q(p')$, the solution becomes,

$$\begin{aligned}
N(x, y, z, p) = & \frac{1}{8\pi^3 \tilde{V} p} \int_p^\infty dp' q(p') \left(\frac{\pi}{I_{p,p'}} \right)^{3/2} \\
& \times \exp \left[-\frac{(x^2 + y^2 + z^2)}{4I_{p,p'}} \right]. \tag{A.14}
\end{aligned}$$

From Equation A.6, since $F(p)$ reduces to p , and so also $F(u)$ to u , by writing $(x^2 + y^2 + z^2) = r^2$ in spherical coordinates and replacing $q(p)$ by $Q_{\text{esc}}(p)$ as given by Equation 6, Equation A.14 can be reduced in the form of Equation 8:

$$\begin{aligned}
N(r, p) = & \frac{\sqrt{\tilde{V}} p^2}{8\pi^{3/2}} \int_0^\infty dp' \frac{Q_{\text{esc}}(p')}{\left[\int_p^{p'} u D_w(u) du \right]^{3/2}} \\
& \times \exp \left(-\frac{r^2 \tilde{V} p^2}{4 \int_p^{p'} u D_w(u) du} \right). \tag{A.15}
\end{aligned}$$

Appendix B: All-particle spectrum and composition of cosmic rays obtained using different EG-CR models and WR-CRs (C/He = 0.1)

The predicted all-particle spectrum, elemental fraction and $\langle \ln A \rangle$ obtained for the three different models of EG-CRs (the minimal, PCS and UFA), combined with the WR-CR (C/He = 0.1) scenario for the additional Galactic component, are shown in Figures B.1, B.2, and B.3, respectively. The proton cut-off energies for the WR-CRs required to produce a good-fit to the measured spectrum are 2.4×10^8 GeV for the minimal model, 1.5×10^8 GeV for the PCS model, and 1.6×10^8 GeV for the UFA model. These values are about a factor 1.4 larger than the cut-off energies obtained in the case of C/He = 0.4. The variation in the injection energy of WR-CRs between the three cases remain within 6% as in the C/He = 0.4 scenario.

The predicted composition is dominated by helium nuclei up to around the second knee for the minimal and the UFA models, while for the PCS model, helium dominates up to around 10^{10} GeV. The Galactic component at the transition energy region from Galactic to extra-galactic cosmic rays is dominated by helium, unlike in the case of C/He = 0.4, where it is dominated by a mixture of helium and CNO group.

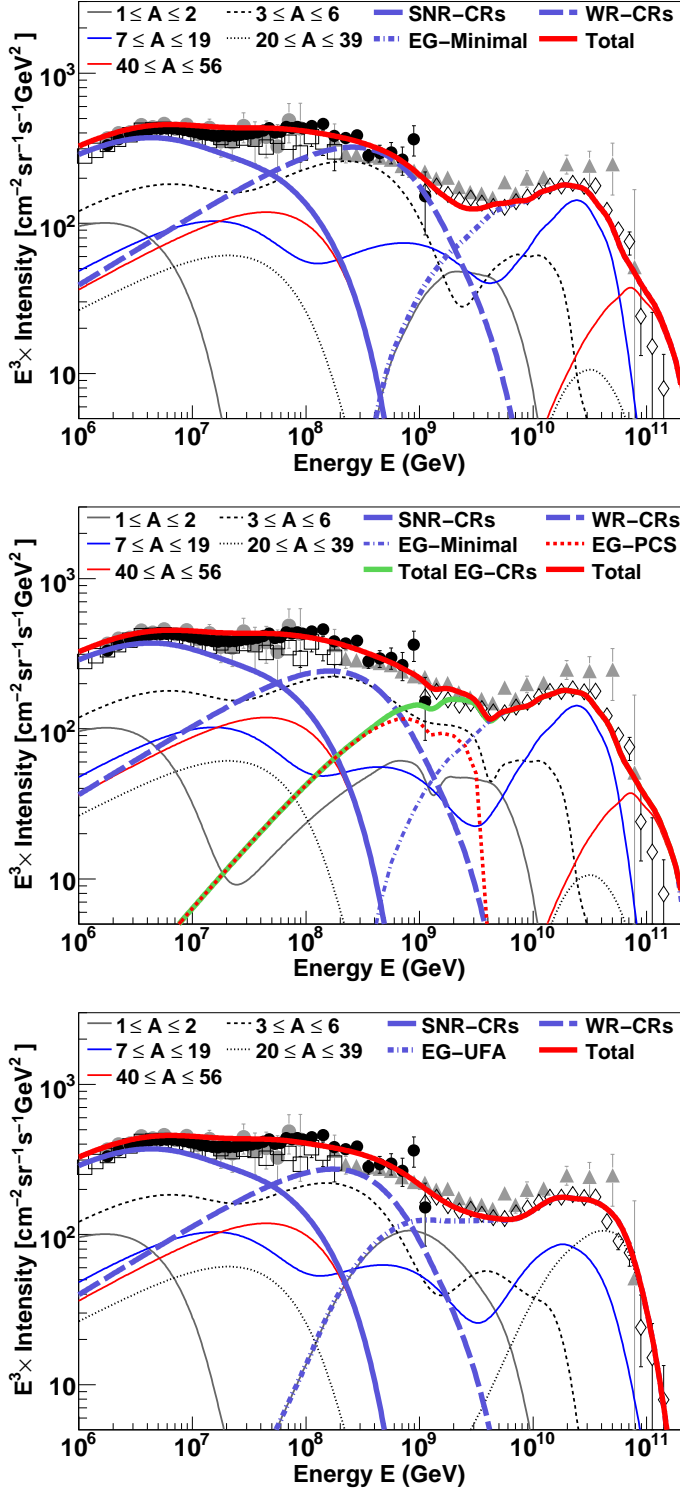


Fig. B.1. All-particle spectrum for the three different EG-CR models: minimal (*top*), PCS (*middle*), and UFA (*bottom*), obtained using WR-CRs ($C/He = 0.1$) as the additional Galactic component. The proton cut-off energies for the WR-CRs used in the calculation are 2.4×10^8 GeV for the minimal model, 1.5×10^8 GeV for the PCS model, and 1.6×10^8 GeV for the UFA model. The injection energy of the WR-CRs varies within 6% between the three models. SNR-CR spectra are the same as in Figure 6 (*top*). Data are the same as in Figure 2.

The $\langle \ln A \rangle$ predicted by the minimal model shows some deviation from the general trend of the measurements be-

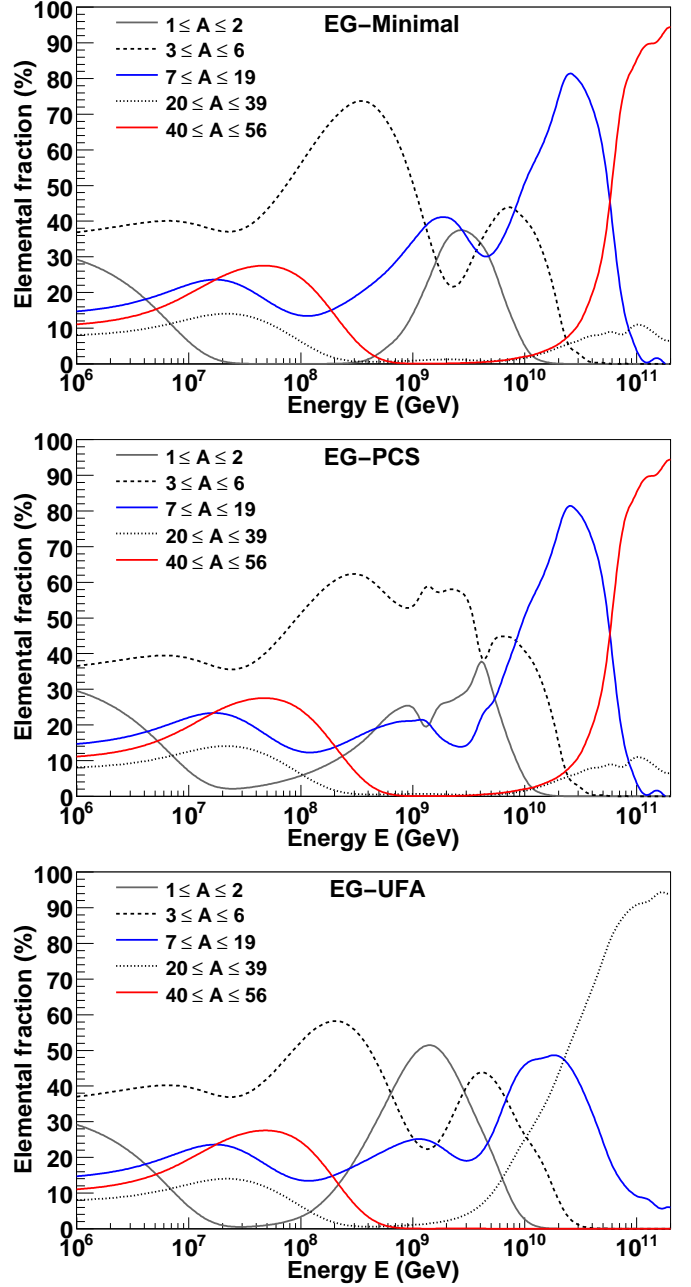


Fig. B.2. Elemental fraction of the five different mass groups shown in Figure B.1 for the three different EG-CR models: minimal (*top*), PCS (*middle*), and UFA (*bottom*), obtained using WR-CRs ($C/He = 0.1$) as the additional Galactic component.

tween $\sim 10^8$ and 5×10^9 GeV, although the discrepancy is less than that observed in the $C/He = 0.4$ scenario. The predictions of both the PCS and the UFA models show better agreement with the data below $\sim 10^9$ GeV. Between around 10^7 and 10^9 GeV, they predict a mean mass lighter than the prediction of the $C/He = 0.4$ case, and show a better agreement with the data (EPOS-LHC) from the Pierre Auger Observatory in the $10^8 - 10^9$ GeV energy range, but slightly under predict the available measurements at around $\sim 10^8$ GeV. The two WR-CR scenarios should be possible to differentiate by accurate measurements of the elemental composition between 10^7 and 10^9 GeV.

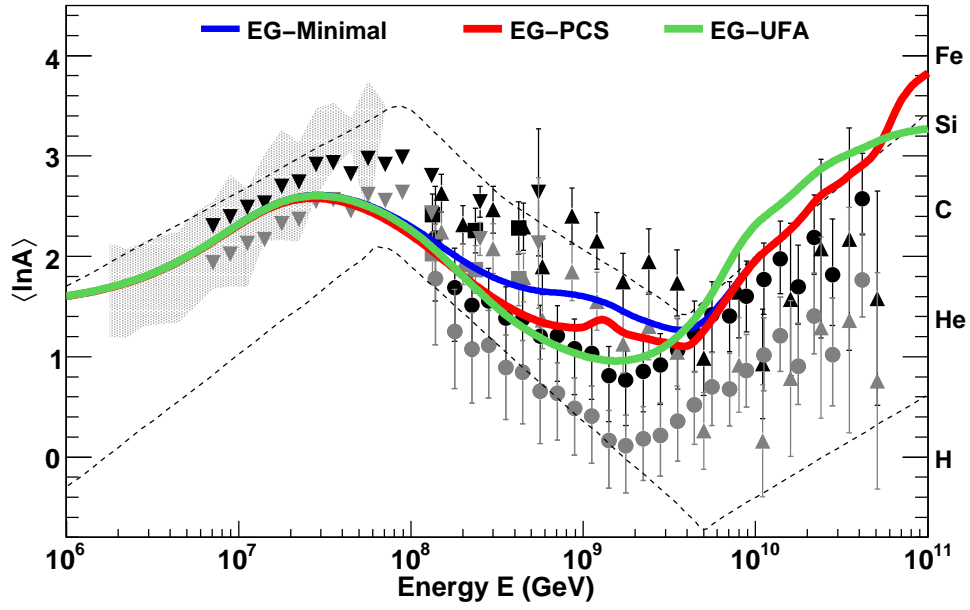


Fig. B.3. Mean logarithmic mass of cosmic rays for the minimal, PCS and UFA models of EG-CRs obtained using WR-CRs ($C/He = 0.1$) as the additional Galactic component. Data are the same as in Figure 8.

On the cosmic-ray energy scale of the LOFAR radio telescope

K. Mulrey¹ S. Buitink^{1,2} A. Corstanje^{1,2} H. Falcke^{2,3,4}
B. M. Hare⁵ J. R. Hörandel^{1,2,3} T. Huege^{1,6} G. K. Krampah¹
P. Mitra¹ A. Nelles^{7,8} H. Pandya¹ J. P. Rachen¹ O. Scholten⁹
S. ter Veen^{2,4} S. Thoudam¹⁰ T. N. G. Trinh¹¹ T. Winchen¹²

¹*Astrophysical Institute, Vrije Universiteit Brussel, Pleinlaan 2, 1050 Brussels, Belgium*

²*Department of Astrophysics/IMAPP, Radboud University, P.O. Box 9010, 6500 GL Nijmegen, The Netherlands*

³*Nikhef, Science Park 105, 1098 XG Amsterdam, The Netherlands*

⁴*Netherlands Institute of Radio Astronomy (ASTRON), Postbus 2, 7990 AA Dwingeloo, The Netherlands*

⁵*University of Groningen, Kapteyn Astronomical Institute, Groningen, 9747 AD, Netherlands*

⁶*Institut für Kernphysik, Karlsruhe Institute of Technology (KIT), P.O. Box 3640, 76021, Karlsruhe, Germany*

⁷*DESY, Platanenallee 6, 15738 Zeuthen, Germany*

⁸*ECAP, Friedrich-Alexander-University Erlangen-Nürnberg, 91058 Erlangen, Germany*

⁹*Interuniversity Institute for High-Energy, Vrije Universiteit Brussel, Pleinlaan 2, 1050 Brussels, Belgium*

¹⁰*Department of Physics, Khalifa University, PO Box 127788, Abu Dhabi, United Arab Emirates*

¹¹*Department of Physics, School of Education, Can Tho University Campus II, 3/2 Street, Ninh Kieu District, Can Tho City, Vietnam*

¹²*Max-Planck-Institut für Radioastronomie, Auf dem Hügel 69, 53121 Bonn*

E-mail: kmulrey@vub.be

Abstract. Cosmic rays are routinely measured at LOFAR, both with a dense array of antennas and with the LOFAR Radboud air shower Array (LORA) which is an array of plastic scintillators. In this paper, we present two results relating to the cosmic-ray energy scale of LOFAR. First, we present the reconstruction of cosmic-ray energy using radio and particle techniques along with a discussion of the event-by-event and absolute scale uncertainties. The resulting energies reconstructed with each method are shown to be in good agreement, and because the radio-based reconstructed energy has smaller uncertainty on an event-to-event basis, LOFAR analyses will use that technique in the future. Second, we present the radiation energy of air showers measured at LOFAR and demonstrate how radiation energy can be used to compare the energy scales of different experiments. The radiation energy scales quadratically with the electromagnetic energy in an air shower, which can in turn be related to the energy of the primary particle. Once the local magnetic field is accounted for, the radiation energy allows for a direct comparison between the LORA particle-based energy scale and that of the Pierre Auger Observatory. They are shown to agree to within $(6\pm 20)\%$ for a radiation energy of 1 MeV, where the uncertainty on the comparison is dominated by the antenna calibrations of each experiment. This study motivates the development of a portable radio array which will be used to cross-calibrate the energy scales of different experiments using radiation energy and the same antennas, thereby significantly reducing the uncertainty on the comparison.

Contents

1	Introduction	1
2	The cosmic-ray energy scale of LOFAR	3
2.1	Cosmic-ray measurements with LOFAR	3
2.2	Energy reconstruction	4
2.2.1	Radio energy reconstruction	5
2.2.2	Particle energy reconstruction	6
2.3	Comparison of energy reconstruction techniques	9
3	Using radiation energy to compare energy scales of different experiments	10
3.1	Determination of the LOFAR radiation energy	10
3.2	Comparison of the energy scales of LORA and the Pierre Auger Observatory	12
4	Conclusions	15
A	Uncertainties	15
A.1	Event-by-event Uncertainties	15
A.2	Systematic Uncertainties	18

1 Introduction

One of the main challenges in the field of cosmic-ray astrophysics is accurately determining the energy of detected cosmic rays. Experiments use different detection, calibration, and reconstruction techniques, resulting in different energy scales. Currently, it is necessary to shift the energy scales of different experiments in order to align them to produce an overall spectral fit [1, 2]. Understanding an experiment’s energy scale is critical for comparing the spectrum and composition measurements of different experiments and for building global models of cosmic-ray sources, acceleration and propagation [3, 4].

An important factor that influences an experiment’s energy scale and the associated uncertainties is the way in which cosmic rays are detected. Above roughly 100 TeV, cosmic rays are detected indirectly, via the air shower that is generated when the primary cosmic ray interacts in the atmosphere. Air shower particles that reach the Earth’s surface can be sampled with detectors on the ground and used to estimate the energy in the air shower [5, 6]. However, this method only captures a snapshot of the shower development and relies heavily on hadronic interaction models for the interpretation of data, which introduce large systematic uncertainties at high energies [7]. An alternative approach is to measure the energy deposition from the electromagnetic part of the air shower during its longitudinal development, which eliminates most of the dependency on hadronic interaction models. This can be done, for example, by measuring the fluorescence light emitted by air molecules that have been excited by the shower particles. The fluorescence detection method provides a calorimetric energy measurement, but can only be done during dark nights and requires good knowledge of atmospheric conditions [8–11].

Air showers are also detected using the broadband radio emission that is generated as the shower develops [12–16]. The dominant contribution to the radio emission comes from

the geomagnetically induced, time-varying transverse current that develops as the shower propagates [17, 18]. The strength of this emission scales with the absolute value of the geomagnetic field and the sine of the angle between the shower velocity and the geomagnetic field. A secondary contribution comes from emission that results from the development of a charge excess in the shower front [19]. Radio emission is produced primarily by the electromagnetic components of the shower, and is calculated from first principles using classical electrodynamics [20]. The measured radio signal is integrated over the whole air shower, and so measurements can be used to perform complete calorimetric energy reconstructions without having to consider absorption or scattering [21, 22]. Furthermore, the total energy radiated by the air shower in the form of radio emission, or radiation energy, of the shower can be determined by integrating the radio energy fluence (energy per unit area) footprint on the ground. Once the radiation energy is corrected for the strength of the local magnetic field and second order effects such as the effect of atmospheric density on the shower development and the relative charge excess contribution, it becomes a universal quantity. If the radiation energy from an air shower is found in conjunction with the shower energy, determined using an independent method, it can be used to compare the energy of cosmic rays detected at different locations. The radio measurement technique also allows for the precise reconstruction of the atmospheric depth of shower maximum, X_{\max} [23, 24]. The interpretation of this parameter relies on having an accurate energy determination.

The LOw Frequency ARray (LOFAR) is a distributed radio telescope with a dense antenna array in the Netherlands [25]. An in-situ particle detector array, the LOFAR Radboud Air Shower Array (LORA), is used to trigger antenna readout [26]. Each event is simultaneously sampled by the LOFAR antennas, which measure emission in the 30 – 80 MHz band, and LORA scintillators which detect particles reaching ground level. Features of the primary cosmic ray are reconstructed with high precision [14, 27]. In this paper we present two results related to the cosmic-ray energy scale of LOFAR.

First, we present energy reconstruction techniques using the radio emission measured with the LOFAR antennas and particle data measured with the LORA scintillators. The techniques are based on CoREAS and CORSIKA simulations, respectively, and provide unique energy reconstructions. We establish that the energies reconstructed with both methods are consistent. Until recently, within LOFAR, shower properties like X_{\max} and energy were reconstructed using a hybrid method that included both particle and radio data, with the particle data determining the absolute energy. In general, the event-by-event uncertainties on radio-based energy reconstructions are smaller than those of particle-based energy reconstructions, and so with this work we move to using radio measurements to set the LOFAR energy scale [28].

Second, we determine the radiation energy of each LOFAR event using a relation derived from CoREAS simulations [22, 29] and demonstrate how radiation energy can be used to compare the energy scales of different experiments. Radiation energy is measured by the Auger Engineering Radio Array (AERA) [21, 30] in conjunction with traditional cosmic-ray measurements made at the Pierre Auger Observatory. This allows us to compare the LORA and Auger energy scales via the radiation energy measured at each location.

This paper is organized as follows. In Section 2.1 the LOFAR telescope and cosmic-ray data processing techniques are introduced. In Section 2.2 both the radio-based and particle-based energy reconstruction methods and experimental uncertainties are described. In Section 2.3 a comparison is made of the energy reconstructions resulting from each method. In Section 3.1 we find the radiation energy for events measured at LOFAR. Finally, in Sec-

tion 3.2, the LORA and Auger energy scales are compared using the radiation energy, and a new technique is introduced that will be used to compare energy scales between experiments in the future.

2 The cosmic-ray energy scale of LOFAR

This section contains a discussion of the cosmic-ray measurements made at the LOFAR telescope. Radio and particle-based energy reconstruction techniques are described, and a comparison is made between the two.

2.1 Cosmic-ray measurements with LOFAR

LOFAR is a radio telescope with antenna stations distributed across northern Europe. A dense core of 24 stations is located in the North of the Netherlands [25]. At the center is the “Superterp,” consisting of six stations located within a 160 m radius. Each station consists of 96 dual-polarized Low Band Antennas (LBAs) that operate in the 30 – 80 MHz band as well as High Band Antennas which are not used in this analysis. The 96 LBAs are organized in inner and outer sets of 48 each, and at any given time one of the two sets is operational. Each antenna is digitized at 200 mega-samples per second and the data are stored in a 5 s ring buffer. Also on the Superterp is LORA, a particle detector array consisting of 20 plastic scintillators. LORA detects showers above 10^{16} eV and acts as a trigger for radio readout. When a cosmic ray is detected, the ring buffers are frozen and 2.1 ms of data are saved. Data from the LBAs are processed offline [14] where radio frequency interference (RFI) is removed and the data are calibrated [31]. The arrival direction of the event is found using the timing of arrival of the radio signal. The voltage at each antenna position is integrated over a 55 ns time window centered at the pulse peak, resulting in what will be referred to as “measured energy,” ε .

The interpretation of both radio and particle data depends on the detector calibration, or in other words, how the measured signals in analog-digital conversion (ADC) units are translated into a quantity with physical meaning. This requires comparing measured data to a known source. The LOFAR system response, including the antennas and signal chain, is calibrated using Galactic emission as a source, as it is the primary contributor to the background in the antenna signals. However, there is a secondary contribution to the signal from electronic noise introduced in the signal chain. In order to estimate this contribution, modeled Galactic emission is propagated through the antenna and signal chain component by component, including frequency dependent gains and losses in the system and electronic noise where it enters the system. The electronic noise is not known a priori, and is determined using a fitting procedure that makes use of the variation of the Galactic emission measured by the LOFAR antennas as a function of local sidereal time. The calibration can then be found by comparing measured background signals to the predicted Galactic and electronic noise signals. The resulting calibration has an uncertainty of 13%, which is dominated by the uncertainty on the underlying models used to predict the Galactic emission. Details of the LOFAR system response calibration are given in [31].

The energy deposited by the shower particles in the scintillators is determined by calibrating the scintillators using single muons [26]. The scintillators are operated in a mode with a low trigger setting, so that singly charged particles trigger the detector readout. In order to calculate the total signal produced by a single muon, which corresponds to the total energy deposit, the ADC time trace is integrated in a time window of $(-75, +875)$ ns around

the peak of the signal. By collecting many muons, we build a distribution of energy deposits from which the most probable value can be determined. This procedure can be done in the field, so that the scintillators are calibrated under realistic operating conditions. Energy deposits from single muons are also simulated with GEANT4 [32], using an all-sky $\cos^2(\theta)$ zenith angle distribution of arrival directions and a realistic description of the detector. This provides a distribution of simulated energy deposits from which we determine the most probable value. By comparing the peak of the measured muon distribution to the simulated muon distribution, we arrive at a calibration factor for the LORA scintillators. More details on the scintillator calibration are provided in Appendix A.

A preliminary radio-based energy estimate is made using a two dimensional LDF that makes use of the asymmetry in the radio footprint due to the interference of geomagnetic and charge excess components [33]. The radio fluence at the position of each antenna is determined, and the LDF is fit using a minimization procedure. This results in initial estimates for energy, X_{\max} , and core position. These values are the starting points for the final shower reconstruction which is described in the following section.

2.2 Energy reconstruction

The LOFAR energy reconstruction is based on CORSIKA [34] and CoREAS [29] simulations. CORSIKA 7.7100 is used with hadronic interaction models FLUKA [35] and QGSJETII-04 [36]. A thinning method, where only a sub-sample of particles are tracked to make large simulations more feasible, is applied at the 10^{-6} level with optimized weight limitation [37]. A GEANT4 [32] simulation of the scintillator panels is used to derive the energy deposit from the CORSIKA-simulated particles at ground level as a function of radius from shower core, which is then used to determine the simulated energy deposit at the position of the LORA scintillators. The ‘gdastool’ CORSIKA plug-in is used to simulate each event with a realistic atmosphere [38]. The CORSIKA “STEPFC” parameter, which controls the electron multiple scattering length used in the EGS4 package (which handles electromagnetic interactions), is set to its default value of 1. This value was shown to produce radiation energy 11% lower than an optimized value of STEPFC=0.05 [39]. In order to correct for this, we increase the simulated radiation energy by 11%. Details of the simulation procedure can be found in [27].

A set of simulations is generated for each shower using the initial energy estimate and the direction determined from radio signal arrival times as input parameters. The set contains both iron nuclei and protons as primaries and X_{\max} values spanning the natural range. Antenna positions are simulated in a star-shaped pattern with 8 arms of 20 antennas spaced 25 m apart. The pattern is generated in the shower plane and then projected onto the ground plane, so that two arms align with the $\mathbf{v} \times \mathbf{B}$ axis and two with the $\mathbf{v} \times \mathbf{v} \times \mathbf{B}$ axis, where \mathbf{v} is the velocity axis of the shower front and \mathbf{B} is the Earth’s magnetic field.

The simulated electric field traces are converted into voltages by applying the LBA antenna model, and bandpass filtered to 30 – 80 MHz. As is done with measured data, the simulated voltage traces are integrated over a 55 ns time window centered at the pulse peak, resulting in a simulated “measured energy,” ε_{sim} . Radio and particle-based energy reconstructions are then done using χ^2 fitting procedures, which are described in the following subsections.

2.2.1 Radio energy reconstruction

The radio-based energy reconstruction is done by comparing ε_{sim} at each LOFAR antenna position to the detected ε . For this, a two-dimensional radiation map is generated by interpolating ε_{sim} in the antennas simulated in the star-shaped pattern in the shower plane. This way, ε_{sim} at any given antenna position $(x_{\text{ant}}, y_{\text{ant}})$ can be obtained. The map is then fit to LOFAR data using a minimization procedure with free parameters for the core position of the shower and a scale factor for the energy, as

$$\chi_{\text{radio}}^2 = \sum_{\text{antennas}} \left(\frac{\varepsilon - f_r^2 \varepsilon_{\text{sim}}(x_{\text{ant}} - x_0, y_{\text{ant}} - y_0)}{\sigma_{\text{ant}}} \right)^2 \quad (2.1)$$

where σ_{ant} refers to the one sigma level of the time-integrated voltage of measured traces outside the signal window, (x_0, y_0) is the shower core position, and f_r is the energy scaling factor, allowing for deviations from the simulated cosmic-ray energy. A χ^2 fit is done for each simulation in the set. This is similar to the fit procedure that has been used for LOFAR X_{max} analyses in the past [23, 27], the difference being that here there is no particle data information included in the fit. In the case that the scale factor is greater than 2 or less than 0.5, a new set of simulations is run with a new starting energy estimate. The values of f_r , x_0 , and y_0 for the simulation with minimum χ^2 are taken as the reconstructed values for this event, and the radio-based energy is found as

$$E_{\text{radio}} = f_r \times E_{\text{sim}}. \quad (2.2)$$

An example of the best fit ε_{sim} map to measured data is shown in the left panel of Fig. 1. The background color represents the ε_{sim} that would be received by an antenna at each position, and the colors in the white circles represent ε at specific antenna positions. The white cross represents the shower core.

We consider systematic uncertainties, which affect the absolute scale of the reconstructed cosmic-ray energy, and event-by-event uncertainties, both of which are outlined in Table 1. An overview of the uncertainties is given here, and an extended discussion can be found in Appendix A. Event-by-event uncertainties on the radio-based energy include the following. The simulated antenna model predicts the antenna response as a function of direction, which is different for each event. By offsetting the direction of the incoming cosmic ray by $\pm 5^\circ$ in the zenith direction and propagating the effects through the energy reconstruction process, we conservatively estimate that the uncertainties in the antenna response have at most a 5% effect on the reconstructed energy. Change in antenna gain as a function of temperature is found to be negligible. We use realistic atmospheres on an event-by-event basis for our simulations, and so any effects arising from incorrect atmospheric conditions are also negligible. There is uncertainty which comes from the event reconstruction procedure, and is estimated using a Monte Carlo vs. Monte Carlo method. This uncertainty includes the effects of the noise levels and geometry on the reconstruction of a particular event. Values range from 4% to 18%, with a typical value being 9%. Additionally, there is an uncertainty due to the fact that the type of the primary is unknown. Given the same shower geometry and X_{max} , an air shower initiated by a proton primary yields a reconstructed energy consistently 10% lower than an air shower initiated by an iron primary. In the fitting procedure the best-fit simulation that is used to reconstruct the energy is associated either with a proton or an iron primary. Therefore, we add an asymmetric event-by-event uncertainty to each event to account for the unknown primary. The typical total event-by-event uncertainty is then 14%.

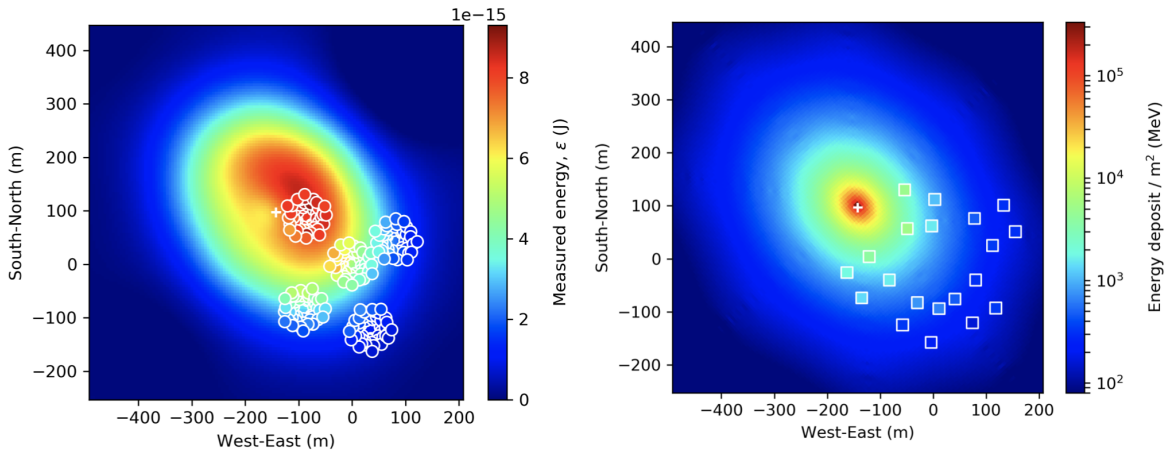


Figure 1. Left: Example radio footprint for a LOFAR event, shown in the ground plane, with energy 7.2×10^{17} eV, zenith angle 37° , azimuth angle 41° south of east, and $X_{\max} = 670$ g/cm 2 . The color scale represents measured energy, ϵ , at each position. The background map results from simulations, and the colors in the white circles represent data measured with the LOFAR antennas. Right: Map of the particle energy deposit in LORA scintillators for the same event. The color scale represents the energy deposit per square meter in MeV. The background color comes from simulations, and the filled squares represent energy deposits measured by LORA scintillators.

Systematic uncertainties which affect the absolute radio-based energy scale include the calibration of the antenna and signal chain, the effects of hadronic interaction models, and the choice of radio simulation package, namely, CoREAS [29] or ZHAireS [40]. The system calibration is the dominant factor, at 13% [31]. The choice of simulation package has a 2.6% effect on energy, and the effect of the choice of hadronic interaction model is 3% [39, 41]. Although the radio emission is primarily generated by the electromagnetic component of the air shower, the choice of hadronic interaction model influences how much of the primary particle energy goes into that component.

2.2.2 Particle energy reconstruction

The particle-based energy reconstruction uses the best fit CORSIKA simulation as determined by the radio χ^2 fit. The radio-based measurements are more sensitive to X_{\max} and shower development, and so are more reliable for determining the best simulation. Furthermore, the core position from the radio measurement is used. When the core position falls outside the footprint of the particle detectors, it is difficult to constrain. In this sense, the two reconstructions are not entirely independent, but once the shower geometry is fixed the scale set for the particle-based energy is determined entirely by the scintillator data. A diagram of the radio and particle energy reconstruction procedures is shown in Figure 2.

Because we use results from the radio reconstruction to fix the shower geometry, many of the typical uncertainties associated with particle-based reconstructions are avoided. We take this approach, and do not attempt a completely independent particle-based reconstruction for two reasons. First, in past LOFAR analyses, a hybrid method was used to reconstruct energy which combined radio and particle information. The radio information was primarily used to determine the event geometry, while the energy was set using the particle information. The particle-based method described in this section is consistent with past analyses, and therefore allows us to compare the energy set in past analyses with the new radio-based technique.

Table 1. Summary of the uncertainties in the radio-based energy scale. The \oplus symbol indicates quadratic addition. Details of how these uncertainties are derived can be found in Appendix A.

Uncertainty	Value
Event-by-event	
angular dependence of antenna model	5%
temperature dependence	negligible
reconstruction uncertainty	typically 9%
composition uncertainty	10 %
Total event-by-event	11% \oplus reconstruction uncertainty
Absolute scale	
antenna calibration and system response	13%
hadronic interaction models	3%
radio simulation method	2.6%
Total absolute scale	13.6%

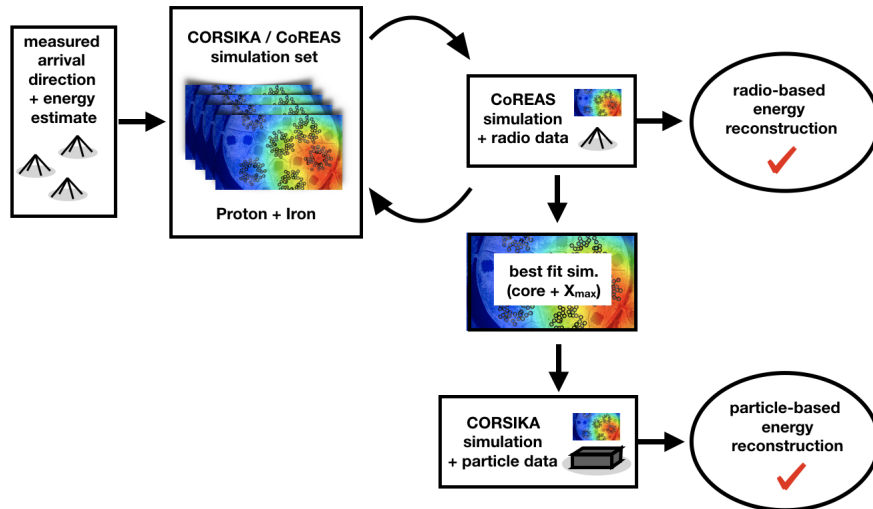


Figure 2. Diagram of the radio and particle energy reconstruction procedures. The radio-based reconstruction is done first, resulting in a best-fit simulation. This is then used in the particle-based reconstruction.

Secondly, because of the small footprint of the scintillator array, independent particle-based reconstructions would suffer from poor core reconstruction, which would severely reduce the number of usable events we have, and furthermore, the resulting uncertainties would be prohibitively large. It should be noted that LORA detects a large number of lower energy air showers that fall within the footprint of the scintillator array but do not have a strong radio signal. In this work we are interested in comparing the radio and particle reconstruction techniques, so these events aren't considered, however they were the source of an independent spectral analysis [42].

With the best simulation known, a particle χ^2 is fit, as

$$\chi_{\text{particle}}^2 = \sum_{\substack{\text{particle} \\ \text{detectors}}} \left(\frac{d_{\text{det}} - f_p d_{\text{sim}}}{\sigma_{\text{det}}} \right)^2 \quad (2.3)$$

where d_{det} is the deposited energy measured by a LORA detector with one standard deviation of background noise level σ_{det} , and d_{sim} is the GEANT4 simulated deposit. The particle scale factor f_p is needed to bring the simulated energy into agreement with the measurements. An example of the particle footprint of the best fit simulation is shown in the right panel of Fig. 1. The background color represents the simulated energy per square meter that would be deposited in a LORA scintillator at each location. On average, one muon deposits 6.5 MeV in a scintillator panel. The squares represent the locations of the scintillators with the color being the measured energy deposit. Again, the white cross represents the shower core. The particle-based energy is then found as

$$\begin{aligned} E_{\text{particle}} &= f_p \times E_{\text{sim}} \\ &= \frac{f_p}{f_r} \times E_{\text{radio}}. \end{aligned} \quad (2.4)$$

The uncertainties on the particle-based energy reconstruction are summarized in Table 2. Event-by-event uncertainties include variation in the detector response, as well as the reconstruction uncertainty for each event. Scintillators have on average a 10% fluctuation in response, but since the fluctuations are not correlated between scintillators, this propagates into a 2.5% uncertainty on the reconstructed energy. The reconstruction uncertainty on the particle-based energy, like the radio-based energy, is determined using a Monte Carlo vs. Monte Carlo method. The reconstruction uncertainty on the particle-based energy is larger than that of the radio-based energy, and extends from 10% up to 50%. The unknown composition of the measured events also contributes a significant uncertainty. Although constraining the shower geometry using information from the radio fit reduces this uncertainty, we find that for events with the same X_{max} and geometry, the reconstructed energies for showers initiated by iron primaries are lower than for proton-initiated showers. This effect is a function of zenith angle, with almost no difference in energy reconstructions for vertical showers, and up to 30% difference at zenith angles around 50° . We have parameterized this effect, and added an asymmetric event-by-event uncertainty accordingly, based on the primary of the best-fit simulation.

Systematic uncertainties include the uncertainty on the scintillator calibration and the effect of the choice of hadronic interaction model used in the simulations. Using a field calibration method, scintillator calibration can be performed at any time and the uncertainty in calibration values propagates into 3% uncertainty in energy. In order to estimate the uncertainty introduced by the choice of hadronic interaction model, we simulated a subset of events using both Sibyll 2.3c and QGSJETII-04 and found an average 7% difference in reconstructed energy between the two. More details about the uncertainties on the particle energy are given in Appendix A.

It is also known that above 10^{16} eV, there is a discrepancy between the number of simulated and measured muons in air showers [43–46], with a 50% deficit in simulated muons at $10^{17.5}$ eV reported by Auger. In order to quantify the effect this has on our reconstructed energy, we ran simulations, artificially inflating the muonic component of the signal at ground

Table 2. Summary of the uncertainties in the particle-based energy scale. The \oplus symbol indicates quadratic addition. Details of how these uncertainties are derived can be found in Appendix A. Note: this technique for reconstructing the energy based on particle information also uses information from the radio reconstruction, such as shower geometry and age, reducing the overall uncertainties.

Uncertainty	Value
Event-by-event	
scintillator response variation	2.5%
reconstruction uncertainty	10 – 50%
composition uncertainty	2 – 30%
Total event-by-event	2.5% \oplus reconstruction uncertainty \oplus composition uncertainty
Absolute scale	
scintillator calibration	3%
hadronic interaction models	7%
Total absolute scale	7.6%

level by 50%. The signal in the scintillators is dominated by the electromagnetic component of the shower, so the muon discrepancy does not have a large effect on the reconstructed energy. For the majority of our events, increasing the simulated muonic component of the air shower by 50% corresponded to a $\sim 5\%$ decrease in reconstructed energy. At zenith angles above 40° , the effects becomes larger, up to $\sim 10\%$.

2.3 Comparison of energy reconstruction techniques

In the past, LOFAR X_{\max} analyses used the scintillator measurements to set the energy scale. With an absolute antenna calibration available [31], and because the event-by-event uncertainties on the energy reconstruction using radio data are significantly lower than for the reconstruction using particle data, LOFAR analyses will move to the radio-only approach from now on [28]. Here, we compare the radio-based and particle-based energy reconstruction of each event to demonstrate the consistency of the results. Fig. 3 shows the relation between energy reconstructed with LOFAR radio data and LORA particle data. The error bars represent the event-by-event uncertainties of each event. For both radio and particle-based energies, these uncertainties are dominated by the uncertainty on the reconstruction technique, discussed in Section 2.2. The data consist of 283 events between 2011 and 2018, where we have chosen events where both radio and particle fits converge, the reconstructed core position has an uncertainty of less than 5 m, and the radio and particle reduced χ^2 of each event are less than 5. We also only consider events with particle-based energy reconstructed above 10^{16} eV. Since the radio signal scales with energy and is thus small at low energies, the detection is biased to upward fluctuations. The diagonal line represents a one-to-one correlation. The inset histogram shows the relative difference between radio-based and particle-based energy reconstructions. The mean of the distribution, found using a Gaussian fit, is -0.07, and the standard deviation is 0.35.

There is a small population of events towards the lower energies where the radio-based reconstructions are higher than the particle-based reconstructions. Some of these events have

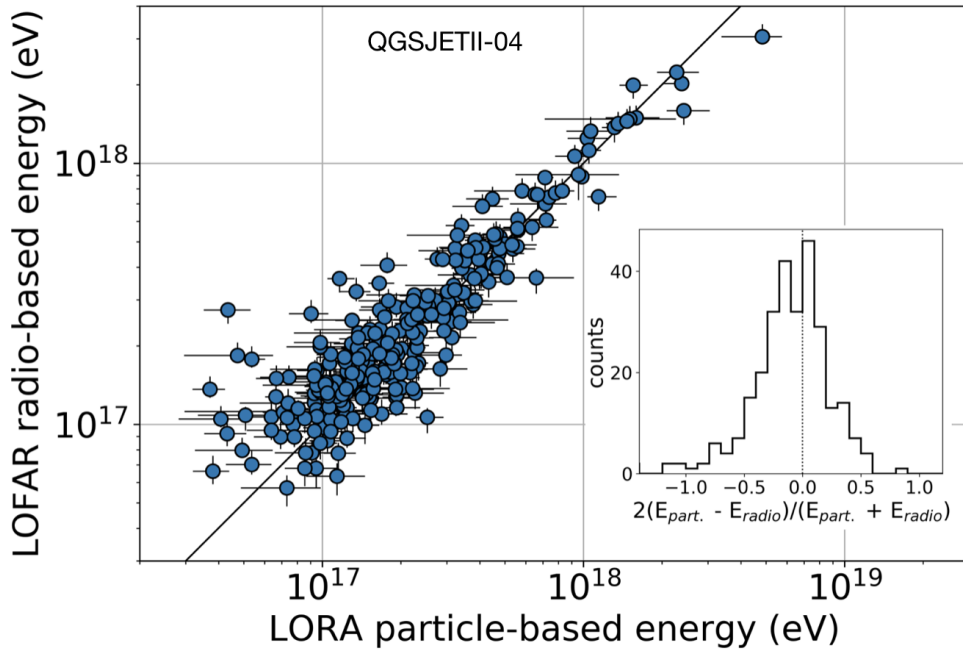


Figure 3. Comparison of energy reconstructed using radio and particle-based methods. Error bars indicate event-by-event uncertainties. Inset: Relative difference between particle-based and radio-based reconstructed energy. The mean of the distribution, found using a Gaussian fit, is -0.07 , and the standard deviation 0.35 .

relatively small event-by-event uncertainties compared to their distance from the line. Normally there would be fluctuations on either side of the mean from each method. However, since the radio signal becomes difficult to detect at low energies, it is more probable to have upwards fluctuations of radio-based energy reconstructions than downward fluctuations. This is also evident in the asymmetry of the relative energy histogram. As this effect is insignificant for our analysis, we do not correct for it. We conclude that the radio and energy based reconstructions are consistent within the resolution of the measurements.

3 Using radiation energy to compare energy scales of different experiments

In this section we will demonstrate how radiation energy, S_{RD} , which is the total amount of radio emission emitted by an air shower, can be used to compare the energy scales of different experiments when measured in conjunction with the total shower energy, determined using an independent method.

3.1 Determination of the LOFAR radiation energy

Here, we first describe radiation energy and the corrections needed to make it a universal quantity in a general way. Then, we will lay out how we use the results presented in [22], which are based on CoREAS simulations, to determine the corrected radiation energy for LOFAR events.

The radiation energy contained in an air shower can be found by integrating the energy deposit per unit area, or fluence, over the radio footprint. Since radio waves are not attenuated

in the atmosphere, the altitude of the observation site is inconsequential as long as all the radiation energy in the shower has been released before it reaches the ground. This makes radiation energy an ideal value to compare between different locations. However, it must still be corrected for various factors in order to make it a universal quantity which can be compared between different experiments and events. The corrections outlined here follow those described in [22].

The strength of the local magnetic field influences the strength of the geomagnetic emission. For example, the magnetic field at LOFAR is 0.492 G, which is twice as strong as the 0.243 G magnetic field at Auger. This means for the same event, the radiation energy detected at LOFAR would be larger. To correct for this, the radiation energy is scaled by the ratio of the magnetic field of a reference location and the local magnetic field. Furthermore, when the radiation energy is calculated, the geomagnetic contribution to the radiation energy is corrected to account for the shower geometry, in particular, the angle between the magnetic field and shower axis, α . The charge excess fraction of the radiation energy has been parameterized so that this correction can be made to only the geomagnetic contribution. The radiation energy also depends on the air density in which the air shower develops; showers that develop in a less dense atmosphere have relatively larger radiation energy. In general, one has to consider “clipping” effects when the radiation energy is not yet completely released at the observer height. For LOFAR events, this is not a concern due to the fact that the observation height is close to sea level and that most shower energies are below 10^{18} eV. Making these corrections yields the “corrected radiation energy” which can be compared between different experiments.

The work presented in [22] used CoREAS simulations to derive a relation between the corrected radiation energy in the 30–80 MHz band, $S_{RD,corr}$, and the electromagnetic energy, E_{em} , contained in the air shower. The radiation energy was found by integrating the simulated fluence in the 30–80 MHz band over the radio footprint, and making the corrections discussed above. The magnetic field strength was normalized to the magnetic field strength at Auger. This resulted in the equation

$$S_{RD,corr} = A \times 10^7 \text{eV} (E_{em}/10^{18} \text{eV})^B \quad (3.1)$$

where $A = 1.683 \pm 0.004$, and $B = 2.006 \pm 0.001$.

We use this result to directly find the corrected radiation energy of LOFAR events. In the fitting method described in Section 2.2.1, we determine the CoREAS simulation that best fits the measured radio data. Once this is known the energy contained in the electromagnetic component of the air shower, E_{em} , can be found using the longitudinal profile information provided by the associated CORSIKA simulation, scaled by the radio scale factor f_r found in Section 2.2.1. We then use Eq. 3.1 to determine the corrected radiation energy. Finding $S_{RD,corr}$ this way is only possible because we use a simulation-based reconstruction technique and identify a best fit simulation for each event. This gives us direct access to information about the (simulated) electromagnetic component of the air shower. Alternatively, one can integrate the fluence over the radio footprint of the best-fit simulation and make the corrections described above to determine the corrected radiation energy. We have confirmed that both methods yield the same result. We also note that the fraction of E_{em} to the total cosmic-ray energy depends on the choice of hadronic interaction model, where here we have used QGSJETII-04.

3.2 Comparison of the energy scales of LORA and the Pierre Auger Observatory

Equation 3.1 gives the relation between the corrected radiation energy, $S_{RD,corr}$, and the electromagnetic energy in the shower, E_{em} . In order to compare the energy scales of different experiments using the universal quantity $S_{RD,corr}$, we need a relation between it and the total cosmic-ray energy, E_{CR} . We will use a function of the same form as equation 3.1 to relate $S_{RD,corr}$ and E_{CR} , written generally as $S_{RD,corr} = A' \times 10^7 \text{eV} (E_{CR}/10^{18} \text{eV})^{B'}$. We use the notation A', B' for the parameters in this case to distinguish them from A, B in equation 3.1, and we emphasize that they should not be directly compared because here we relate $S_{RD,corr}$ and E_{CR} , whereas equation 3.1 relates $S_{RD,corr}$ and E_{em} . For reference, in the LOFAR energy range roughly 85% of the total cosmic-ray energy goes into the electromagnetic components of the air shower. The fraction of E_{CR} that goes into E_{em} differs by particle type, with protons generating showers with a higher fraction of electromagnetic particles than iron nuclei. The difference is roughly 4.5% at 10 EeV, and decreases towards higher energies [7, 47]. Since we expect the experiments we want to compare to measure a similar composition, we don't take this difference into account.

Because the radio and particle components of each LOFAR event are measured simultaneously, we can derive the relation between $S_{RD,corr}$ determined using the LOFAR antennas and the particle-based cosmic-ray energy determined using the LORA scintillators, E_{CR}^{LORA} . In order to avoid any biases in detection that occur at lower energies, only events where both the radio and particle-based energies reconstruct to greater than 1.3×10^{17} eV are used. Using an Orthogonal Distance Regression [48] method and fitting the equation

$$S_{RD,corr} = A'_{\text{LORA}} \times 10^7 \text{eV} (E_{CR}^{\text{LORA}}/10^{18} \text{eV})^{B'_{\text{LORA}}} \quad (3.2)$$

results in the parameters $A'_{\text{LORA}} = 1.57 \pm 0.12(\text{stat}) \pm 0.49(\text{sys})$, $B'_{\text{LORA}} = 2.07 \pm 0.06(\text{stat})$, where the statistical uncertainty comes from the fitting procedure. The systematic uncertainty includes both the uncertainties on the radio-based energy scale which propagate into the radiation energy, and the uncertainties on the particle-based energy scale.

Fig. 4 shows the LOFAR corrected radiation energy as a function of LORA cosmic-ray energy. Error bars indicate the event-by-event uncertainties on each point. The resulting best-fit line of the form 3.2 is also shown in purple, with the shaded region indicating the absolute scale uncertainty on the corrected radiation energy.

We compare the energy scales of LORA and Auger by making use of the relation between the corrected radiation energy measured with AERA and the total cosmic-ray energy, E_{CR}^{Auger} , as determined by the Auger surface detectors [49] which are calibrated using the calorimetric energy measurements of the fluorescence detectors [50]. We denote the AERA corrected radiation energy as $S_{RD,corr}^*$, to indicate that in this case corrections are made for the relative strength of the geomagnetic emission, but second order corrections for charge excess fraction and air density in the region of shower development are not included. Derived in [15] and [21], the total corrected radiation energy in the 30 – 80 MHz band can be related to total cosmic-ray energy using

$$S_{RD,corr}^* = \frac{S_{RD}}{\sin^2(\alpha)} = A'_{\text{Auger}} \times 10^7 \text{eV} (E_{CR}^{\text{Auger}}/10^{18} \text{eV})^{B'_{\text{Auger}}} \quad (3.3)$$

where $A'_{\text{Auger}} = 1.58 \pm 0.07(\text{stat}) \pm 0.67(\text{sys})$, $B'_{\text{Auger}} = 1.98 \pm 0.04(\text{stat})$, and α is the angle between magnetic field and shower axis. The systematic uncertainties include both the 16% uncertainty (at $10^{17.5}$ eV) on the Auger energy scale [50], and the 14% uncertainty on the

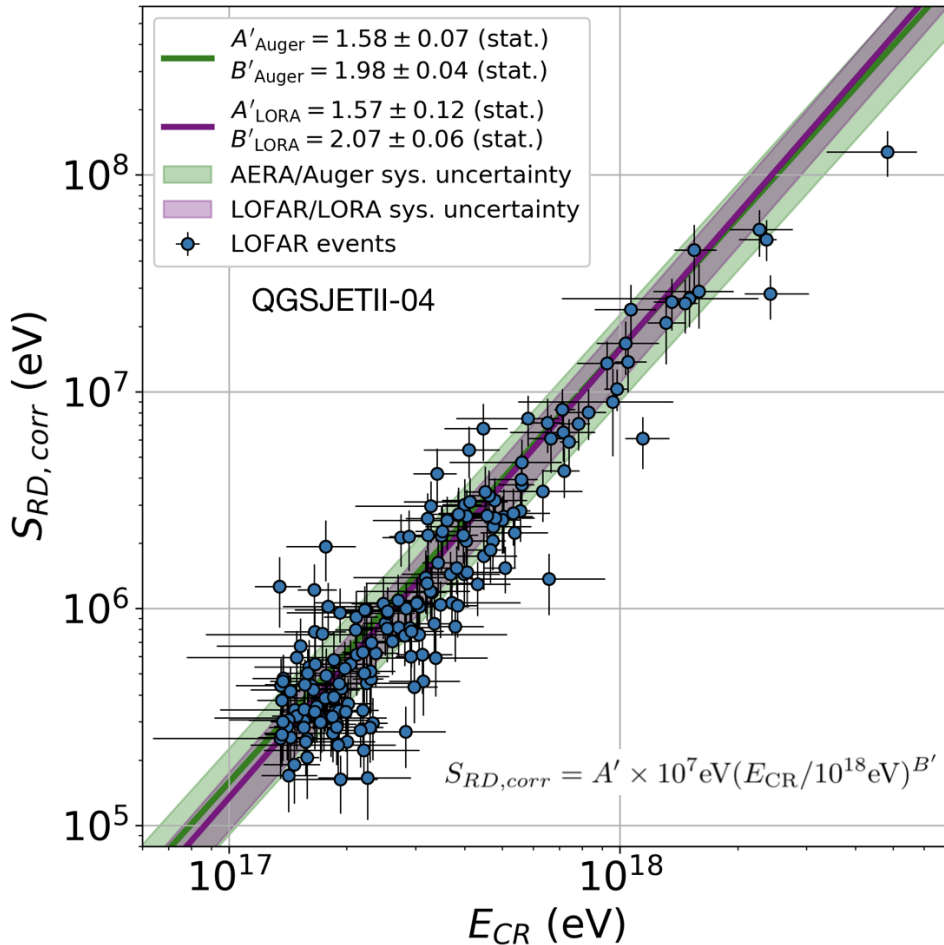


Figure 4. Relation between the corrected radiation energy measured by the LOFAR antennas and the cosmic-ray energy as determined by the LORA scintillators. The error bars represent event-by-event uncertainties. The purple line shows the best fit line for LOFAR measurements of corrected radiation energy and LORA cosmic-ray energy, and the banded region around the best fit line represents the systematic uncertainties on the corrected radiation energy. The green line shows the best fit line for AERA measurements of corrected radiation energy and Auger cosmic-ray energy [21], and the shaded green region represents the systematic uncertainties on the corrected radiation energy. QGSJETII-04 was used in the simulations on which the LOFAR and LORA energy reconstructions are based.

AERA antenna calibration [30]. Equation 3.1, used to find the corrected radiation energy for LOFAR, already includes a normalization of the local magnetic field to that of Auger. Therefore the parameters $A'_{\text{LORA}}, B'_{\text{LORA}}$ and $A'_{\text{Auger}}, B'_{\text{Auger}}$ and in equations 3.2 and 3.3 are comparable, with the caveat that second order corrections are not made for the Auger radiation energy. Equation 3.3 is also shown in Fig. 4 in green, with the shaded region indicating the absolute scale uncertainties on the radiation energy.

Using equations 3.2 and 3.3, we compare the average energies of LORA and Auger at a corrected radiation energy $S_{RD,corr} = 1$ MeV. This value of $S_{RD,corr}$ was chosen for the comparison because it is close to the average value of the LOFAR corrected radiation energy (determined in log-space). $S_{RD,corr} = 1$ MeV corresponds to a LORA energy of $(2.64 \pm 0.42(\text{sys})) \times 10^{17}$ eV and an Auger energy of $(2.48 \pm 0.52(\text{sys})) \times 10^{17}$ eV. The ratio

between the LORA and Auger energies $E_{\text{CRLORA}}/E_{\text{CRAuger}} = 1.06 \pm 0.20$, meaning that LORA energy is 6% larger, with a 20% combined uncertainty on the comparison. The uncertainty on the comparison includes only the radio-based uncertainties on the radiation energy, namely the uncertainties on the calibration of the AERA antennas and the LOFAR radio-based energy scale. We do not include the uncertainties associated with the Auger or LORA energy scales because we are not making a statement about the absolute energy scale of either experiment, only the comparison between the two. The B'_{LORA} and B'_{Auger} parameters of equations 3.2 and 3.3 are different, so the ratio between LORA and Auger energy changes with energy. At the low end of the LOFAR corrected radiation energy range, $S_{RD,corr} = 0.25$ MeV, $E_{\text{CRLORA}}/E_{\text{CRAuger}} = 1.11 \pm 0.20$. At the high end, $S_{RD,corr} = 10$ MeV, $E_{\text{CRLORA}}/E_{\text{CRAuger}} = 1.01 \pm 0.20$. For all these points, the energy scales of Auger and LORA agree within the comparison uncertainty, although it should be noted that the comparison uncertainty is larger than the absolute uncertainty on either energy scale. The LORA cosmic-ray energy is derived using an approach based on hadronic interaction models. In contrast, the Auger cosmic-ray energy comes from surface detector measurements, which are calibrated using the fluorescence detectors which make model-independent, calorimetric measurements [50]. Nevertheless, this comparison shows that the energy scales of the two experiments are compatible, albeit with a large uncertainty on the comparison.

Radio techniques have previously been used to compare the energy scales of different experiments. The energy scales of Tunka-133 [51] and KASCADE-Grande [52] have been compared using their radio extensions, Tunka-Rex [53] and LOPES [54]. This was done both by comparing the absolute amplitude of the radio measurements 100 m from the shower core at each location with the energies measured by Tunka-133 and KASCADE-Grande, and by using a simulation-based method [55]. This study benefited from the fact that the antennas at each location were calibrated using the same technique, which reduced the uncertainties on the comparison. The remaining uncertainties on the comparison were due to the LOPES antenna model and the fact that the absolute amplitude of the signal at 100 m was compared, rather than radiation energy. This value is harder to compare because it relies on knowledge of the radio footprint at a particular location, and corrections have to be made for observation level and zenith angle. In the study presented here, we have avoided these location and shower-specific uncertainties by using the universal measurement of corrected radiation energy rather than signal amplitude. However, the uncertainties associated with our comparison are large, because for each experiment, the uncertainties on the radiation energy, most notably the antenna calibration, must be included.

Having a method to compare the energy scales of different experiments with minimal uncertainty is necessary in order to make meaningful comparisons of their spectra and composition measurements, which are used to build global models of cosmic-ray sources, acceleration and propagation [1, 2]. We plan to do this by combining the techniques used here and in [55]. A portable array of antennas will be built and deployed at various experiments, measuring radiation energy in conjunction with the host experiment's traditional air shower measurements. The radiation energy can feasibly be reconstructed with only 5 antennas, as AERA has demonstrated [21]. Using radiation energy to compare the energy scales eliminates uncertainties due to measurements being made at different locations, and using the same array eliminates the uncertainties associated with the antennas and calibration. This will allow for a cross-calibration of the energy scales of different experiments with minimal uncertainty.

4 Conclusions

Cosmic-ray air showers are regularly detected at LOFAR, where simultaneous measurements are made with antennas and particle detectors. In this work we compared the reconstructed energies using radio-based and particle-based methods. The reconstruction methods are based on CoREAS and CORSIKA simulations respectively, where simulated radio and particle footprints are fit to measured data using χ^2 minimization processes. In the past, LOFAR analyses have used a hybrid approach in which both radio and particle data were fit simultaneously. The radio information was primarily used to determine the shower geometry, while the energy was set with the particle information. In this work, the energies are fit separately, yielding two unique energy reconstructions. We have shown that both methods of determining energy produce consistent results.

We discussed the uncertainties on both methods, and find a 13.6% systematic uncertainty on radio-based energy and 7.6% on particle-based energy. The event-by-event uncertainties on radio-based energies are around 14%. For particle-based energies the event-by-event uncertainties extend to more than 50%. Both are dominated by the uncertainty in the event reconstruction procedure and unknown composition. Taking into consideration the relative uncertainties, we now move from using the hybrid fitting method to using the radio-based reconstruction method to set the LOFAR energy scale.

We also used the corrected radiation energy in the 30 – 80 MHz band to compare the LORA and Auger energy scales. Radiation energy between experiments can be compared because it represents a calorimetric energy measurement that primarily depends on the local magnetic field, which is a well known quantity and which can be accounted for. Second order corrections can also be made with knowledge of the shower geometry and atmospheric conditions. Using the relations derived in equations 3.2 and 3.3, we determined that for a corrected radiation energy of 1 MeV the difference in LORA and Auger energies is 6% with an uncertainty on the comparison of 20%.

Moving forward, we will use corrected radiation energy to cross-calibrate the energy scales of different experiments. The systematic uncertainties that are relevant for the comparison of the corrected radiation energy between experiments are dominated by the uncertainties associated with antenna and system calibrations, here 14% for AERA antennas and 13% for the LOFAR antenna and system response. By using the same detection system in each location, these uncertainties can be removed from the comparison of relative energies. We plan to build a portable array of antennas which will be used to measure radio emission from air showers in situ at different experiments. The corrected radiation energy will then be used to directly compare the energy scales of the experiments with minimal systematic uncertainties, allowing for the establishment of a universal energy scale.

A Uncertainties

This appendix addresses how the uncertainties on the reconstructed energy of LOFAR events were derived.

A.1 Event-by-event Uncertainties

Radio and Particle: reconstruction uncertainties

The reconstruction uncertainty of each event is derived using a Monte Carlo vs. Monte Carlo method. The simulation set created for each event contains at least 40 showers. One shower is used as mock “data” and the time-integrated power, ε , at the position of each LOFAR antenna is found using the two dimensional ε_{sim} map. Noise is added to the “data” that reflects the noise level in the actual event data. This “event” is then reconstructed using the remaining simulations using the same procedure discussed in Section 2.2.1. The fit produces the scale factor f_r , used to convert the simulated energy E_{sim} to event energy as $E_{\text{radio}} = f_r \times E_{\text{sim}}$. Each shower in the set is simulated at the same energy, so if the fit were perfect the scale factor would always be $f_r = 1$. This procedure is repeated using every simulation in the set as the “event”, yielding a set of scale factors, f_r . The same procedure is also applied to the particle data, yielding a set of reconstructed scale factors f_p . The resulting distributions of scale factors for one event are shown in the histograms in Fig. 5, where the radio scale factors are in the left panel and particle scale factors are in the right panel. One standard deviation of the distribution is taken to be the fit uncertainty for a particular event.

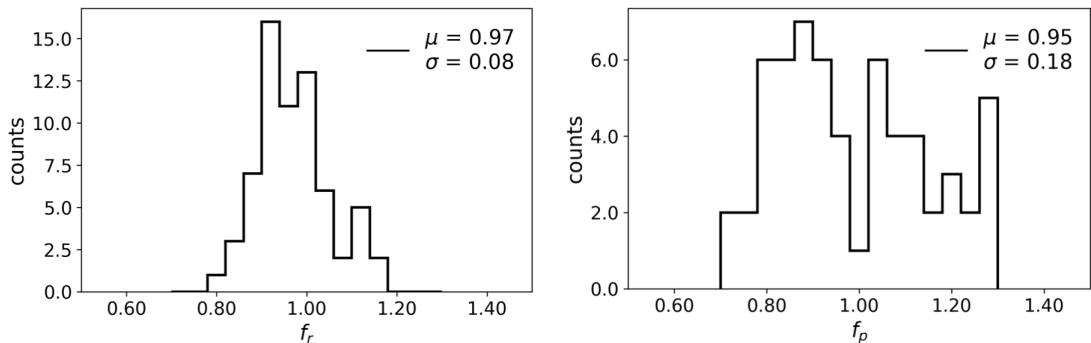


Figure 5. Reconstructed scale factors resulting from a Monte Carlo vs. Monte Carlo study for one event. Radio scale factors are shown in the left panel, and particle scale factors in the right panel. The standard deviation of each distribution is taken as the fit uncertainty for this event.

Fig. 6 shows the distribution of the standard deviation of scale factors for each event, or equivalently, the reconstruction uncertainty, for all events. Again, the radio uncertainty is shown in the left panel, and particle uncertainty in the right. We see that typical values for reconstruction uncertainties on radio-based energy are close to 9% with little spread. The most probable value (MPV) of the particle-based uncertainties is 12%, but they have a much larger spread and extend to 50%.

Radio and Particle: composition uncertainties

Although the radio reconstruction technique discussed in Section 2.2.1 reconstructs X_{max} to within 17 g/cm^2 [27], there is still uncertainty associated with the primary composition. For each event, a best fit simulation is chosen out of a set of more than 40 simulations of both proton and iron primaries. The energy of the event is then found using equations 2.1 and 2.2. The fact that the best fit simulation is associated with either a proton or an iron primary affects the reconstructed energy. In order to quantify this uncertainty, we ran simulations for a subset of events collecting a set of both 15 proton and 15 iron simulations with X_{max} values within 5 g/cm^2 of the reconstructed value of the event. We found that iron-initiated showers

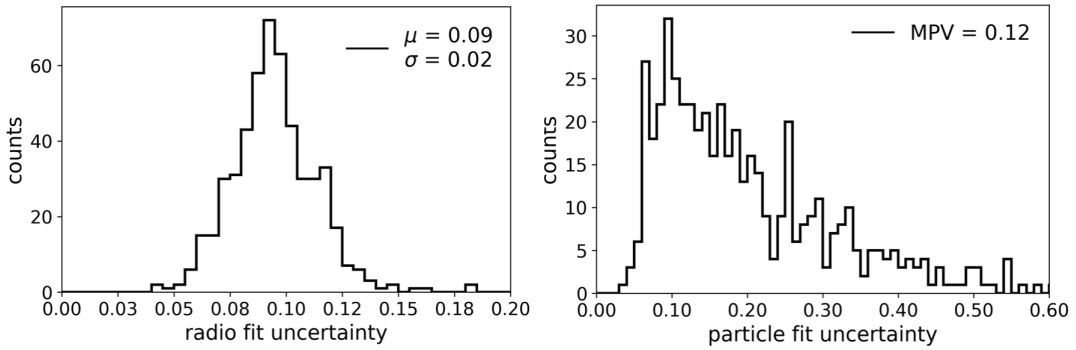


Figure 6. Distribution of fit uncertainties for radio-based energy reconstruction (left), and particle-based energy reconstruction (right).

consistently reconstruct with an radio-based energy 10% higher than proton-initiated showers. This effect is independent of X_{\max} or zenith angle. For each event, we include an asymmetric 10% uncertainty. For example, if the best fit simulation corresponds to a proton primary, the error bar is included in the positive direction. This provides a conservative estimate for the composition uncertainty on the radio-based energy reconstruction.

Likewise, there is a composition uncertainty on the particle-based energy reconstruction. Given the same X_{\max} , proton-initiated showers reconstruct with a higher energy than iron-initiated showers. This effect is amplified with increasing zenith angle. For vertical showers, proton-initiated events reconstruct a few percent higher than iron. At 50° zenith, this difference increases to 30%. We have parameterized the difference between proton and iron energy reconstruction as a function of zenith angle, and added asymmetric error bars accordingly.

Radio: angular dependence of the antenna model

We account for the uncertainty in the angular dependence of the antenna model. The overall calibration of the antenna model is handled separately [31]. Measurements have been made using a reference source attached to an octocopter that showed that the received power as a function of direction, based on the antenna model, is in general agreement with measurements [56]. In order to estimate the remaining uncertainty, we offset the antenna model by $\pm 1^\circ$ and $\pm 5^\circ$ in the zenith direction. Events are then reprocessed with the offset antenna model to determine the effect on reconstructed energy. The ratio between the energy reconstructed with the offset and without the offset for each event is shown in Fig. 7. We take an uncertainty of $\pm 5\%$, which is reflective of the distributions of the energy reconstruction ratio with the model offset 5° . This is a conservative estimate, because in practice, each antenna may have a slightly different offset in different directions, in which case the effect of the antenna model will have less impact on the final energy.

Radio: temperature dependence

There was no apparent seasonal or temperature dependence found in the antenna gain. This was determined by looking at the average power contained in the background of event traces over the course of the year. The dominant contribution to the background radio signal is Galactic noise. While the same sky is visible over 24 hours in local sidereal time, the

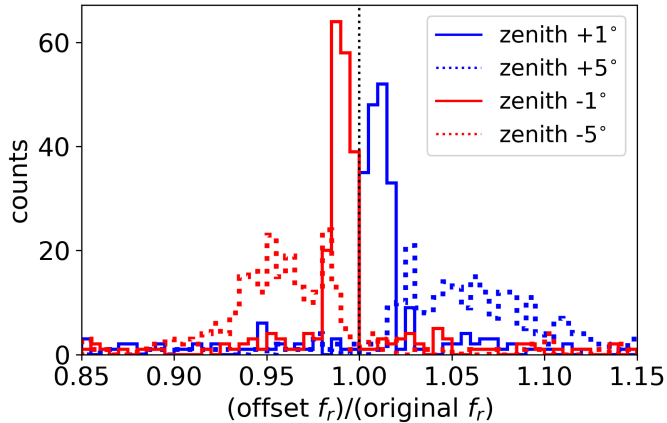


Figure 7. The ratio between energy reconstructed with antenna model offsets and the original model. Offsets of $\pm 1^\circ$ and $\pm 5^\circ$ were applied.

portion that is visible during nighttime and daytime hours changes from winter to summer; more Galactic emission is visible at night in the winter. There are more LBA observations in night hours, and so the average power increases in the winter months. The effect is that there is 10% more noise power in the traces, but this effect is simply an offset and not multiplicative, and is handled in the data processing pipeline. We also do not see any degradation in the average antenna signal over time.

Particle: scintillator response variation

The response of the scintillators varies over time. We characterize the variation of each scintillator by looking at the daily average energy deposit. The variation is then determined by taking the standard deviation of average energy deposits. There is no apparent systematic variation with temperature, degradation over time, or correlation between detectors. In order to propagate this uncertainty into the energy reconstruction, we repeat the analysis while adjusting the scintillator calibration, or equivalently, the conversion factor from deposited energy in ADC units into MeV. Since the variation in each scintillator is uncorrelated, the adjustment to each scintillator’s calibration is made by selecting a new value from a Gaussian distribution with the original conversion factor as the mean, and variation as the standard deviation. This process was repeated three times, and the maximum effect on the resulting energy scale was 2.5%.

A.2 Systematic Uncertainties

Radio: antenna calibration

The antenna and signal chain calibration is the dominant systematic uncertainty in the radio-based energy reconstruction at 13%. The calibration is based on modeling the propagation of Galactic noise through the LOFAR signal chain. Details are given in [31]. The dominant contribution to the uncertainty on the calibration is the uncertainty on the underlying models predicting the brightness temperature of the galaxy, which contribute 11%.

Radio: choice of simulation code

The simulated radio emission for this analysis was generated using CoREAS. CoREAS determines radio emission from a given particle track in the cascade by applying the endpoint formalism [29, 41]. There are other methods, including the approach taken in ZHAireS, which implements the ZHS method [57, 58]. The agreement between the two simulation codes was studied in [39], and the effect of choosing one code over the other on the energy scale was determined to be less than 2.6%.

Radio and particle: hadronic interaction model

In order to determine the effect of the choice of hadronic interaction model used in the CORSIKA simulation, ten events, with a minimum of 40 simulations each, were re-analyzed using simulations produced with the Sibyll 2.3c [59] interaction model instead of QGSJETII-04. This changed the resulting radio-based energy by 3% and particle-based energy by 7%.

Particle: scintillator calibration

In order to calibrate the scintillators, or in other words, to find the conversion between charge deposit in ADC counts and MeV, it is necessary to collect single muon events. This is done in the field by setting the trigger threshold very low, and collecting a combination of singly charged particle events (presumably dominated by muons) and noise triggers from a single scintillator. Then, the most probable muon deposit from LORA data can be compared to the most probable energy deposit based on GEANT4 simulated muon events using a realistic detector description and arrival directions following a $\cos(\theta)^2$ zenith angle distribution [32]. The resulting muon energy deposit distributions are shown in Fig. 8. The distribution shown in red comes from simulation, and the blue distribution shows events measured in the field. For the field events, the noise peak is also visible. We also measured the energy deposit of single muon events in a laboratory setting, using a muon tower to ensure the triggered events were exclusively single muons. The resulting distribution is shown in green. The field measurements have a broader distribution due to the environment being less controlled, but the peak of the distribution still represents the most probably muon energy deposit.

There is a systematic uncertainty associated with the calibration of the LORA scintillators. By repeating the field calibration process a number of times, we find the standard deviation of the calibration values for each scintillator. Then, this uncertainty is propagated through the analysis, and new energy reconstructions are obtained. The average standard deviation of the scintillator calibration value is $\pm 3\%$, which propagates into $\pm 3\%$ uncertainty in event energy. This is shown in Fig. 9. The histograms represent the ratio of energy reconstructed with the standard calibration plus 3% (in blue), and minus 3% (in orange) to the original energy reconstruction.

The spatial response of the scintillators was measured at Karlsruhe Institute of Technology (KIT) and using a muon tracking detector which was originally used for muon tracking in the KASCADE experiment [52]. The response is very uniform over the surface of the scintillator, and is now included in LORA simulations [60].

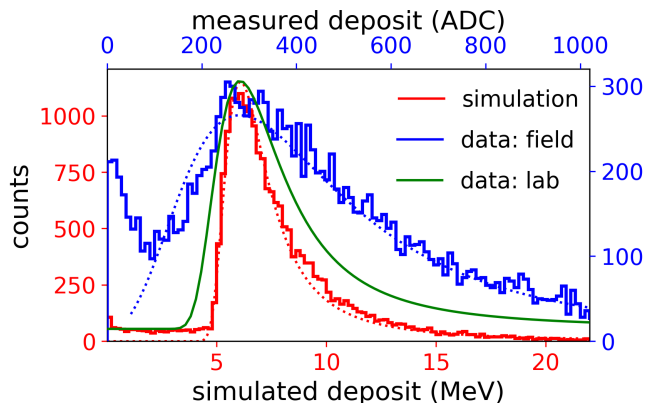


Figure 8. Distributions of energy deposits from single muons. The distribution in red shows the GEANT4 simulated deposits. The green and blue lines represent muon energy deposits measured in the lab and field, respectively.

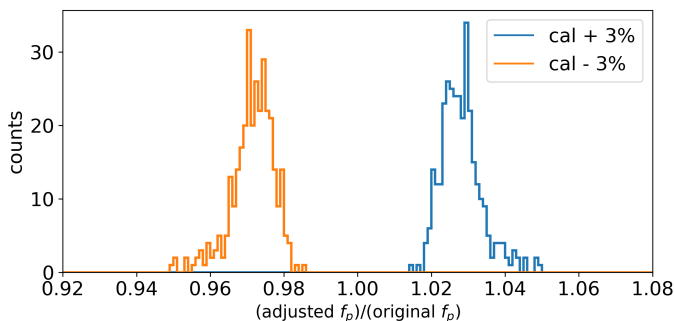


Figure 9. Ratio of energy reconstructed with the standard calibration plus 3% (in blue), and minus 3% (in orange) to the original energy reconstruction.

Acknowledgments

We thank the referee for thoughtful feedback that lead to an improved analysis. The LOFAR cosmic-ray key science project acknowledges funding from an Advanced Grant of the European Research Council (FP/2007-2013) / ERC Grant Agreement n. 227610. The project has also received funding from the European Research Council (ERC) under the European Union’s Horizon 2020 research and innovation programme (grant agreement No 640130). We furthermore acknowledge financial support from FOM, (FOM-project 12PR304). ST acknowledges funding from the Khalifa University Startup grant (project code 8474000237). BMH is supported by NWO (VI.VENI.192.071). KM is supported by FWO (FWOTM944). AN acknowledges the DFG grant NE 2031/2-1. LOFAR, the Low Frequency Array designed and constructed by ASTRON, has facilities in several countries, that are owned by various parties (each with their own funding sources), and that are collectively operated by the International LOFAR Telescope foundation under a joint scientific policy.

References

- [1] J. Hörandel, *On the knee in the energy spectrum of cosmic rays*, *Astropart. Phys.* **19** (2003) 193 [[astro-ph/0210453](#)].
- [2] H. P. Dembinski, R. Engel, A. Fedynitch, T. Gaisser, F. Riehn and T. Stanev, *Data-driven model of the cosmic-ray flux and mass composition from 10 GeV to 10^{11} GeV*, *PoS ICRC2017* (2018) 533 [[1711.11432](#)].
- [3] J. Blümer, R. Engel and J. R. Hörandel, *Cosmic Rays from the Knee to the Highest Energies*, *Prog. Part. Nucl. Phys.* **63** (2009) 293 [[0904.0725](#)].
- [4] PIERRE AUGER, TELESCOPE ARRAY collaboration, *The energy spectrum of ultra-high energy cosmic rays measured at the Pierre Auger Observatory and at the Telescope Array*, *PoS ICRC2019* (2020) 234 [[2001.08811](#)].
- [5] KASCADE, LOPES collaboration, *KASCADE extensive air shower experiment*, *Proc. SPIE Int. Soc. Opt. Eng.* **4858** (2003) 41.
- [6] ICECUBE collaboration, *IceTop: The surface component of IceCube*, *Nucl. Instrum. Meth.* **A700** (2013) 188 [[1207.6326](#)].
- [7] R. Engel, D. Heck and T. Pierog, *Extensive air showers and hadronic interactions at high energy*, *Ann. Rev. Nucl. Part. Sci.* **61** (2011) 467.
- [8] PIERRE AUGER collaboration, *The Pierre Auger Cosmic Ray Observatory*, *Nuclear Instruments and Methods in Physics Research Section A: Accelerators, Spectrometers, Detectors and Associated Equipment* **798** (2015) 172 .
- [9] PIERRE AUGER collaboration, *Atmospheric effects on extensive air showers observed with the Surface Detector of the Pierre Auger Observatory*, *Astropart. Phys.* **32** (2009) 89 [[0906.5497](#)].
- [10] TELESCOPE ARRAY collaboration, *Telescope Array Experiment*, *Nuclear Physics B - Proceedings Supplements* **175-176** (2008) 221 .
- [11] PIERRE AUGER collaboration, *The Rapid Atmospheric Monitoring System of the Pierre Auger Observatory*, *JINST* **7** (2012) P09001 [[1208.1675](#)].
- [12] LOPES collaboration, *Detection and imaging of atmospheric radio flashes from cosmic ray air showers*, *Nature* **435** (2005) 313 [[astro-ph/0505383](#)].
- [13] TUNKA-REX collaboration, *Measurement of cosmic-ray air showers with the Tunka Radio Extension (Tunka-Rex)*, *Nucl. Instrum. Meth.* **A802** (2015) 89 [[1509.08624](#)].
- [14] P. Schellart et al., *Detecting cosmic rays with the LOFAR radio telescope*, *Astronomy and Astrophysics* **560** (2013) .
- [15] PIERRE AUGER collaboration, *Energy Estimation of Cosmic Rays with the Engineering Radio Array of the Pierre Auger Observatory*, *Phys. Rev.* **D93** (2016) 122005 [[1508.04267](#)].
- [16] CODALEMA collaboration, *Radio-Detection Signature of High Energy Cosmic Rays by the CODALEMA Experiment*, *Nucl. Instrum. Meth.* **A555** (2005) 148 [[astro-ph/0504297](#)].
- [17] F. D. Kahn and I. Lerche, *Radiation from cosmic ray air showers*, *R. Soc. Lond. A* **289** (1966) .
- [18] K. Werner and O. Scholten, *Macroscopic Treatment of Radio Emission from Cosmic Ray Air Showers based on Shower Simulations*, *Astropart. Phys.* **29** (2008) 393 [[0712.2517](#)].
- [19] G. Askaryan, *Excess negative charge of an electron-photon shower and its coherent radio emission*, *JETP* **14** (1962) 441.
- [20] T. Huege, *Radio detection of cosmic ray air showers in the digital era*, *Physics Reports* **620** (2016) 1.

- [21] PIERRE AUGER collaboration, *Measurement of the Radiation Energy in the Radio Signal of Extensive Air Showers as a Universal Estimator of Cosmic-Ray Energy*, *Phys. Rev. Lett.* **116** (2016) 241101 [[1605.02564](#)].
- [22] C. Glaser, M. Erdmann, J. R. Hörandel, T. Huege and J. Schulz, *Simulation of Radiation Energy Release in Air Showers*, *JCAP* **1609** (2016) 024 [[1606.01641](#)].
- [23] S. Buitink et al., *A large light-mass component of cosmic rays at $10^{17} - 10^{17.5}$ eV from radio observations*, *Nature* **531** (2016) 70.
- [24] TUNKA-REX collaboration, *Radio measurements of the energy and the depth of the shower maximum of cosmic-ray air showers by Tunka-Rex*, *JCAP* **1601** (2016) 052 [[1509.05652](#)].
- [25] M. P. van Haarlem et al., *LOFAR: The LOw-Frequency ARray*, *Astronomy and Astrophysics* **556** (2013) 56.
- [26] S. Thoudam et al., *LORA: A scintillator array for LOFAR to measure extensive air showers*, *Nucl.Instrum.Meth* **A767** (2014) 339.
- [27] S. Buitink et al., *Method for high precision reconstruction of air shower X_{max} using two-dimensional radio intensity profiles*, *Phys. Rev. D* **90** (2014) .
- [28] A. Corstanje et al., *X_{max} reconstruction and mass composition of cosmic rays with LOFAR*, *PoS ICRC2019* (2019) .
- [29] T. Huege, M. Ludwig and C. W. James, *Simulating radio emission from air showers with CoREAS*, *AIP Conf. Proc.* **1535** (2013) 128 [[1301.2132](#)].
- [30] PIERRE AUGER collaboration, *Status and Prospects of the Auger Engineering Radio Array*, *PoS ICRC2015* (2016) 615.
- [31] K. Mulrey et al., *Calibration of the LOFAR low-band antennas using the Galaxy and a model of the signal chain*, *Astropart. Phys.* **111** (2019) 1 [[1903.05988](#)].
- [32] S. Agostinelli et al., *GEANT4 – a simulation toolkit*, *NIMPA* **506** (2003) 250.
- [33] A. Nelles et al., *A parameterization for the radio emission of air showers as predicted by CoREAS simulations and applied to LOFAR measurements*, *Astropart.Phys.* **60** (2015) 13.
- [34] D. Heck et al., *CORSIKA: A Monte Carlo code to simulate extensive air showers*, *Report FZKA* **6019** (1998) .
- [35] A. Ferrari et al., *FLUKA: a multi-particle transport code*, *CERN-2005-10 INFN/TC_05/11* (2005) .
- [36] S. Ostapchenko, *Monte Carlo treatment of hadronic interactions in enhanced Pomeron scheme: QGSJET-II model*, *Phys. Rev. D* **83** (2011) .
- [37] PIERRE AUGER collaboration, *A thinning method using weight limitation for air-shower simulations*, *Astropart. Phys.* **15** (2001) 259.
- [38] P. Mitra et al., *Reconstructing air shower parameters with LOFAR using event specific GDAS atmospheres*, *Astropart. Phys.* (submitted 2020) .
- [39] M. Gottowik, C. Glaser, T. Huege and J. Rautenberg, *Determination of the absolute energy scale of extensive air showers via radio emission: systematic uncertainty of underlying first-principle calculations*, *Astropart. Phys.* **103** (2018) 87 [[1712.07442](#)].
- [40] J. Alvarez-Muniz, J. Carvalho, Washington R. and E. Zas, *Monte Carlo simulations of radio pulses in atmospheric showers using ZHAireS*, *Astropart. Phys.* **35** (2012) 325 [[1107.1189](#)].
- [41] C. W. James, H. Falcke, T. Huege and M. Ludwig, *General description of electromagnetic radiation processes based on instantaneous charge acceleration in ‘endpoints’*, *Phys. Rev.* **E84** (2011) 056602 [[1007.4146](#)].

- [42] S. Thoudam et al., *Measurement of the cosmic-ray energy spectrum above 10^{16} eV with the LOFAR Radboud Air Shower Array*, *Astroparticle Physics* **73** (2016) 34.
- [43] PIERRE AUGER, TELESCOPE ARRAY, EAS-MSU, ICECUBE, KASCADE-GRANDE, NEVOD-DECOR, SUGAR, YAKUTSK EAS collaboration, *Working Group Report on the Combined Analysis of Muon Density Measurements from Eight Air Shower Experiments*, *PoS ICRC2019* (2020) 214 [2001.07508].
- [44] KASCADE-GRANDE collaboration, *Measurements of the muon content of EAS in KASCADE-Grande compared with SIBYLL 2.3 predictions*, *PoS ICRC2017* (2017) 316.
- [45] PIERRE AUGER collaboration, *Direct Measurement of the Muon Density in Air Showers with the Pierre Auger Observatory*, *EPJ Web of Conferences* **210** (2019) 02013.
- [46] PIERRE AUGER collaboration, *Direct measurement of the muonic content of extensive air showers between 2×10^{17} and 2×10^{18} eV at the Pierre Auger Observatory*, *Eur. Phys. J. C* **80** (2020) 751.
- [47] PIERRE AUGER collaboration, *Data-driven estimation of the invisible energy of cosmic ray showers with the Pierre Auger Observatory*, *Phys. Rev. D* **100** (2019) 082003 [1901.08040].
- [48] P. T. Boggs and J. E. Rogers, *Orthogonal Distance Regression, Contemporary Mathematics: Statistical analysis of measurement error models and applications* **112** (1990) 186.
- [49] PIERRE AUGER collaboration, *The AMIGA infill detector of the Pierre Auger Observatory: Performance and first data*, *Proceedings of the 32nd International Cosmic Ray Conference, ICRC 2011* **1** (2011) 267.
- [50] PIERRE AUGER collaboration, *The Energy Scale of the Pierre Auger Observatory*, in *Proceedings, 33rd International Cosmic Ray Conference (ICRC2013): Rio de Janeiro, Brazil, July 2-9, 2013*, p. 0928, 2013, <http://www.cbpf.br/%7Eicrc2013/papers/icrc2013-0928.pdf>.
- [51] S. Berezhnev et al., *The Tunka-133 EAS Cherenkov light array: status of 2011*, *Nucl. Instrum. Meth. A* **692** (2012) 98 [1201.2122].
- [52] KASCADE collaboration, *The cosmic-ray experiment KASCADE*, *Nuclear Instruments and Methods A* **513** (2003) 490.
- [53] TUNKA-REX collaboration, *Overview on the Tunka-Rex antenna array for cosmic-ray air showers*, *PoS ICRC2017* (2017) 459 [1708.00627].
- [54] F. G. Schröder et al., *Measuring the radio emission of cosmic ray air showers with LOPES*, *Nucl. Instrum. Meth. A* **617** (2010) 515.
- [55] TUNKA-REX, LOPES collaboration, *A comparison of the cosmic-ray energy scales of Tunka-133 and KASCADE-Grande via their radio extensions Tunka-Rex and LOPES*, *Phys. Lett. B* **763** (2016) 179 [1610.08343].
- [56] A. Nelles et al., *Calibrating the absolute amplitude scale for air showers measured at LOFAR*, *JINST* **10** (2015) P11005 [1507.08932].
- [57] E. Zas, F. Halzen and T. Stanev, *Electromagnetic pulses from high-energy showers: Implications for neutrino detection*, *Phys. Rev.* **D45** (1992) 362.
- [58] J. Alvarez-Muniz, A. Romero-Wolf and E. Zas, *Cherenkov radio pulses from electromagnetic showers in the time-domain*, *Phys. Rev.* **D81** (2010) 123009 [1002.3873].
- [59] R. S. Fletcher, T. K. Gaisser, P. Lipari and T. Stanev, *SIBYLL: An Event generator for simulation of high-energy cosmic ray cascades*, *Phys. Rev.* **D50** (1994) 5710.
- [60] LOFAR collaboration, *Extension of the LOFAR Radboud Air Shower Array*, in *Proceedings, 36th International Cosmic Ray Conference (ICRC2016): Madison, Wisconsin, July 24- August 1, 2019*, p. 363, 2019.

A large light-mass component of cosmic rays at 10^{17} - $10^{17.5}$ eV from radio observations

S. Buitink^{1,2}, A. Corstanje², H. Falcke^{2,3,4,5}, J. R. Hörandel^{2,4}, T. Huege⁶, A. Nelles^{2,7}, J. P. Rachen², L. Rossetto², P. Schellart², O. Scholten^{8,9}, S. ter Veen³, S. Thoudam², T. N. G. Trinh⁸, J. Anderson¹⁰, A. Asgekar^{3,11}, I. M. Avruch^{12,13}, M. E. Bell¹⁴, M. J. Bantum^{3,15}, G. Bernardi^{16,17}, P. Best¹⁸, A. Bonafede¹⁹, F. Breitling²⁰, J. W. Broderick²¹, W. N. Brouw^{3,13}, M. Brügger¹⁹, H. R. Butcher²², D. Carbone²³, B. Ciardi²⁴, J. E. Conway²⁵, F. de Gasperin¹⁹, E. de Geus^{3,26}, A. Deller³, R.-J. Dettmar²⁷, G. van Diepen³, S. Duscha³, J. Eislöffel²⁸, D. Engels²⁹, J. E. Enriquez², R. A. Fallows³, R. Fender³⁵, C. Ferrari³⁰, W. Frieswijk³, M. A. Garrett^{3,31}, J. M. Grießmeier^{32,33}, A. W. Gunst³, M. P. van Haarlem³, T. E. Hassall²¹, G. Heald^{3,13}, J. W. T. Hessels^{3,23}, M. Hoft²⁸, A. Horneffer⁵, M. Iacobelli³, H. Intema^{31,34}, E. Juette²⁷, A. Karastergiou³⁵, V. I. Kondratiev^{3,36}, M. Kramer^{5,44}, M. Kuniyoshi³⁷, G. Kuper³, J. van Leeuwen^{3,23}, G. M. Loose³, P. Maat³, G. Mann²⁰, S. Markoff²³, R. McFadden³, D. McKay-Bukowski^{38,39}, J. P. McKean^{3,13}, M. Mevius^{3,13}, D. D. Mulcahy²¹, H. Munk³, M. J. Norden³, E. Orru³, H. Paas⁴⁰, M. Pandey-Pommier⁴¹, V. N. Pandey³, M. Pietka³⁵, R. Pizzo³, A. G. Polatidis³, W. Reich⁵, H. J. A. Röttgering³¹, A. M. M. Scaife²¹, D. J. Schwarz⁴², M. Serylak³⁵, J. Sluman³, O. Smirnov^{43,17}, B. W. Stappers⁴⁴, M. Steinmetz²⁰, A. Stewart³⁵, J. Swinbank^{23,45}, M. Tagger³², Y. Tang³, C. Tasse^{43,46}, M. C. Toribio^{3,31}, R. Vermeulen³, C. Vocks²⁰, C. Vogt³, R. J. van Weeren¹⁶, R. A. M. J. Wijers²³, S. J. Wijnholds³, M. W. Wise^{3,23}, O. Wucknitz⁵, S. Yatawatta³, P. Zarka⁴⁷, J. A. Zensus⁵

¹*Astrophysical Institute, Vrije Universiteit Brussel, Pleinlaan 2, 1050 Brussels, Belgium*

²*Department of Astrophysics/IMAPP, Radboud University Nijmegen, P.O. Box 9010, 6500 GL*

Nijmegen, The Netherlands

³*ASTRON, Netherlands Institute for Radio Astronomy, Postbus 2, 7990 AA, Dwingeloo, The Netherlands*

⁴*Nikhef, Science Park Amsterdam, 1098 XG Amsterdam, The Netherlands*

⁵*Max-Planck-Institut für Radioastronomie, Auf dem Hügel 69, 53121 Bonn, Germany*

⁶*IKP, Karlsruhe Institute of Technology (KIT), Postfach 3640, 76021 Karlsruhe, Germany*

⁷*Department of Physics and Astronomy, University of California Irvine, Irvine, CA 92697, USA*

⁸*KVI CART, University of Groningen, 9747 AA Groningen, The Netherlands*

⁹*Vrije Universiteit Brussel, Dienst ELEM, Brussels, Belgium*

¹⁰*Helmholtz-Zentrum Potsdam, DeutschesGeoForschungsZentrum GFZ, Department 1: Geodesy and Remote Sensing, Telegrafenberg, A17, 14473 Potsdam, Germany*

¹¹*Shell Technology Center, Bangalore, India*

¹²*SRON Netherlands Insitute for Space Research, PO Box 800, 9700 AV Groningen, The Netherlands*

¹³*Kapteyn Astronomical Institute, PO Box 800, 9700 AV Groningen, The Netherlands*

¹⁴*CSIRO Australia Telescope National Facility, PO Box 76, Epping NSW 1710, Australia*

¹⁵*University of Twente, The Netherlands*

¹⁶*Harvard-Smithsonian Center for Astrophysics, 60 Garden Street, Cambridge, MA 02138, USA*

¹⁷*SKA South Africa, 3rd Floor, The Park, Park Road, Pinelands, 7405, South Africa*

¹⁸*Institute for Astronomy, University of Edinburgh, Royal Observatory of Edinburgh, Blackford Hill, Edinburgh EH9 3HJ, UK*

- ¹⁹ *University of Hamburg, Gojenbergsweg 112, 21029 Hamburg, Germany*
- ²⁰ *Leibniz-Institut für Astrophysik Potsdam (AIP), An der Sternwarte 16, 14482 Potsdam, Germany*
- ²¹ *School of Physics and Astronomy, University of Southampton, Southampton, SO17 1BJ, UK*
- ²² *Research School of Astronomy and Astrophysics, Australian National University, Canberra, ACT 2611 Australia*
- ²³ *Anton Pannekoek Institute for Astronomy, University of Amsterdam, Science Park 904, 1098 XH Amsterdam, The Netherlands*
- ²⁴ *Max Planck Institute for Astrophysics, Karl Schwarzschild Str. 1, 85741 Garching, Germany*
- ²⁵ *Onsala Space Observatory, Dept. of Earth and Space Sciences, Chalmers University of Technology, SE-43992 Onsala, Sweden*
- ²⁶ *SmarterVision BV, Oostersingel 5, 9401 JX Assen*
- ²⁷ *Astronomisches Institut der Ruhr-Universität Bochum, Universitaetsstrasse 150, 44780 Bochum, Germany*
- ²⁸ *Thüringer Landessternwarte, Sternwarte 5, D-07778 Tautenburg, Germany*
- ²⁹ *Hamburger Sternwarte, Gojenbergsweg 112, D-21029 Hamburg*
- ³⁰ *Laboratoire Lagrange, Université Côte d’Azur, Observatoire de la Côte d’Azur, CNRS, Blvd de l’Observatoire, CS 34229, 06304 Nice cedex 4, France*
- ³¹ *Leiden Observatory, Leiden University, PO Box 9513, 2300 RA Leiden, The Netherlands*
- ³² *LPC2E - Universite d’Orleans/CNRS*
- ³³ *Station de Radioastronomie de Nancy, Observatoire de Paris - CNRS/INSU, USR 704 - Univ. Orleans, OSUC , route de Souesmes, 18330 Nancy, France*

³⁴*National Radio Astronomy Observatory, 1003 Lopezville Road, Socorro, NM 87801-0387, USA*

³⁵*Astrophysics, University of Oxford, Denys Wilkinson Building, Keble Road, Oxford OX1 3RH*

³⁶*Astro Space Center of the Lebedev Physical Institute, Profsoyuznaya str. 84/32, Moscow 117997, Russia*

³⁷*National Astronomical Observatory of Japan, Japan*

³⁸*Sodankylä Geophysical Observatory, University of Oulu, Tähteläntie 62, 99600 Sodankylä, Finland*

³⁹*STFC Rutherford Appleton Laboratory, Harwell Science and Innovation Campus, Didcot OX11 0QX, UK*

⁴⁰*Center for Information Technology (CIT), University of Groningen, The Netherlands*

⁴¹*Centre de Recherche Astrophysique de Lyon, Observatoire de Lyon, 9 av Charles André, 69561 Saint Genis Laval Cedex, France*

⁴²*Fakultät für Physik, Universität Bielefeld, Postfach 100131, D-33501, Bielefeld, Germany*

⁴³*Department of Physics and Electronics, Rhodes University, PO Box 94, Grahamstown 6140, South Africa*

⁴⁴*Jodrell Bank Center for Astrophysics, School of Physics and Astronomy, The University of Manchester, Manchester M13 9PL, UK*

⁴⁵*Department of Astrophysical Sciences, Princeton University, Princeton, NJ 08544, USA*

⁴⁶*GEPI, Observatoire de Paris, CNRS, Université Paris Diderot, 5 place Jules Janssen, 92190 Meudon, France*

⁴⁷*LESIA, UMR CNRS 8109, Observatoire de Paris, 92195 Meudon, France*

Cosmic rays are the highest energy particles found in nature. Measurements of the mass composition of cosmic rays between 10^{17} eV and 10^{18} eV are essential to understand whether this energy range is dominated by Galactic or extragalactic sources. It has also been proposed that the astrophysical neutrino signal¹ comes from accelerators capable of producing cosmic rays of these energies². Cosmic rays initiate cascades of secondary particles (air showers) in the atmosphere and their masses are inferred from measurements of the atmospheric depth of the shower maximum, X_{\max} ³, or the composition of shower particles reaching the ground⁴. Current measurements⁵ suffer from either low precision, and/or a low duty cycle. Radio detection of cosmic rays⁶⁻⁸ is a rapidly developing technique⁹, suitable for determination of X_{\max} ^{10,11} with a duty cycle of in principle nearly 100%. The radiation is generated by the separation of relativistic charged particles in the geomagnetic field and a negative charge excess in the shower front^{6,12}. Here we report radio measurements of X_{\max} with a mean precision of 16 g/cm² between $10^{17} - 10^{17.5}$ eV. Because of the high resolution in X_{\max} we can determine the mass spectrum and find a mixed composition, containing a light mass fraction of $\sim 80\%$. Unless the extragalactic component becomes significant already below $10^{17.5}$ eV, our measurements indicate an additional Galactic component dominating at this energy range.

Observations were made with the Low Frequency Array (LOFAR¹³), a radio telescope consisting of thousands of crossed dipoles, with built-in air shower detection capability¹⁴. LOFAR records the radio signals from air showers continuously while running astronomical observations simultaneously. It comprises a scintillator array (LORA), that triggers the readout of buffers, stor-

ing the full waveforms received by all antennas.

We have selected air showers from the period June 2011 - January 2015 with radio pulses in at least 192 antennas. The total uptime was ~ 150 days, limited by construction and commissioning of the telescope. Showers that occurred within an hour from lightning activity, or have a polarisation pattern that is indicative of influences from atmospheric electric fields are excluded from the sample¹⁵.

Radio intensity patterns from air showers are asymmetric due to the interference between geomagnetic and charge excess radiation. They can be reproduced from first principles by summing the radio contributions of all electrons and positrons in the shower. We use the radio simulation code CoREAS¹⁶, a plug-in of CORSIKA¹⁷, which follows this approach.

It has been shown that X_{\max} can be accurately reconstructed from densely sampled radio measurements¹⁸. We use a hybrid approach, simultaneously fitting the radio and particle data. The radio component is very sensitive to X_{\max} , while the particle component is used for the energy measurement.

The fit contains four free parameters: the shower core position (x, y) , and scaling factors for the particle density f_p and the radio power f_r . If f_p deviates significantly from unity, the reconstructed energy does not match the simulation and a new set of simulations is produced. This procedure is repeated until the energies agree within uncertainties. The ratio between f_r and f_p should be the same for all showers and is used to derive the energy resolution of 32% (see Figure

1).

The radio intensity fits have reduced χ^2 -values ranging from 0.9 to 2.9. All features in the data are well reproduced by the simulation (see Extended Data Figs. 1-5), demonstrating that the radiation mechanism is now well-understood. The reduced χ^2 -values exceeding unity may indicate remaining uncertainties in the antenna response, atmospheric properties, or limitations of the simulation software.

Radio detection becomes more efficient for higher-altitude showers that have larger footprints. The particle trigger, however, becomes less efficient since the number of particles reaching the ground decreases. To avoid a bias, we require that *all* the simulations produced for a shower pass the trigger criteria. Above 10^{17} eV this cut removes 4 showers from the sample. At lower energies, this number rapidly increases, and we exclude all showers below 10^{17} eV from this analysis.

Furthermore, we evaluate the reconstructed core positions of all simulated showers. Showers with a mean reconstruction error above 5 m are rejected. This cut does not introduce a composition bias, because it is based on the sets of simulated showers, and not on the data. The final event sample contains 118 showers.

The uncertainty on X_{\max} is determined independently for all showers¹⁸, and has a mean value of 16 g/cm^2 (see Extended Data Figure 6). Figure 2 shows our measurements of the *average* X_{\max} , which are consistent with earlier experiments using different methods, within statistical un-

certainties. The high resolution for X_{\max} *per shower* allows us to derive more information on the composition of cosmic rays, by studying the complete shape of the X_{\max} distribution. For each shower, we calculate:

$$a = \frac{\langle X_{\text{proton}} \rangle - X_{\text{shower}}}{\langle X_{\text{proton}} \rangle - \langle X_{\text{iron}} \rangle} \quad (1)$$

where X_{shower} is the reconstructed X_{\max} , and $\langle X_{\text{proton}} \rangle$ and $\langle X_{\text{iron}} \rangle$ are mean values predicted by the hadronic interaction code QGSJETII.04¹⁹.

The cumulative probability density function (CDF) for all showers is plotted in Fig. 3. First, we fit a 2-component model of proton and iron nuclei, with the mixing ratio as the only free parameter. To calculate the corresponding CDFs we use a parametrisation of the X_{\max} distribution fitted to simulations based on QGSJETII.04. The best fit is found for a proton fraction of 62%, but it describes the data poorly with a p-value of 1.1×10^{-6} .

A better fit is achieved with a four-component model (p+He+N+Fe), yielding a p-value of 0.17. While the best fit is found for a Helium fraction of 80%, the fit quality deteriorates only slowly when replacing helium by protons. This is demonstrated in Figure 4 where the p-value is plotted for four-component fits where the fractions of helium and proton are fixed, and the ratio between N and Fe is left as the only free parameter. The total fraction of light elements (p+He) is in the range [0.38,0.98] at 99% confidence level, with a best fit value of 0.8. The heaviest composition that is allowed within systematic uncertainties still has a best fit p+He fraction of 0.6, and a 99% confidence level interval of [0.18, 0.82]. The online method section contains information about the systematic uncertainties and the statistical analysis.

The abundances of individual elements depend on the hadronic interaction model. The X_{\max} values predicted by EPOS-LHC²⁰ are on average 15-20 g/cm² higher than QGSJETII.04 (see Fig. 2). This coincides with the separation between, for example, protons and deuterium or between helium and beryllium. We therefore prefer to present our result as a total fraction of light elements, instead of placing too much emphasis on individual elements.

Recent results for the Pierre Auger Observatory indicate that the cosmic ray composition at 10¹⁸ eV, just below the ankle, can be fitted with a mixture of protons and either helium (QGSJET.II04) or nitrogen (EPOS-LHC)³. With decreasing energy, their proton fraction drops, while their helium (or nitrogen) fraction rises, down to the threshold energy of $7 \cdot 10^{17}$ eV. An extrapolation of this trend to our mean energy of $3 \cdot 10^{17}$ eV connects smoothly to our best fitting solution in which helium dominates.

KASCADE-Grande has reported an ankle-like feature at 10^{17.1} eV, where the spectral index for light elements changes to $\gamma = -2.79 \pm 0.08^4$. However, they find a light particle (p+He) fraction below 30% at 3×10^{17} eV (based on their Figure 4), considerably lower than our value. In contrast to LOFAR and Auger, their composition measurements are based on the muon/electron ratio. Auger has reported a muon excess compared to all commonly used hadronic interaction models²¹. Inaccurate predictions of muon production, or $\langle X_{\max} \rangle$, can be the cause of the discrepancy in the fraction of light particles between LOFAR and KASCADE-Grande.

If the knee in the all-particle spectrum near 3×10^{15} eV corresponds to the proton or helium cut-off of the main Galactic cosmic-ray population, the corresponding iron cut-off would lie at most

at an energy 26 times larger. If this population still dominates at 10^{17} eV, the mass composition should be dominated by heavy elements at that energy. Therefore, the large component of light elements observed with LOFAR must have another origin.

In principle, it is possible that we observe an extragalactic component. In that case the ankle in the cosmic-ray spectrum, slightly above 10^{18} eV, does not indicate the transition from Galactic to extragalactic origin. Instead, it can be explained as the imprint of pair production on the cosmic microwave background on an extragalactic proton spectrum²². However, since this feature only appears for a proton-dominated flux it is in tension with our data that favours a mixture of light elements.

A second Galactic component, dominating around 10^{17} eV, can be produced by a class of extremely energetic sources (Galactic exatrons), like the explosions of Wolf Rayet stars into their stellar winds²³, or past Galactic gamma-ray bursts²⁴. Alternatively, the original Galactic population could be reaccelerated by the Galactic wind termination shock²⁵. Such scenarios predict mixtures of light elements, consistent with our results.

References

1. Aartsen, M. et al. [IceCube collaboration], Evidence for High-Energy Extraterrestrial Neutrinos at the IceCube Detector, *Science* **342**, 1242856 (2013).
2. Murase, K., Ahlers, M., and Lacki, B., Testing the hadronuclear origin of PeV neutrinos observed with IceCube, *Phys. Rev. D* **88**, 121301 (2013).

3. Aab, A. et al. [Pierre Auger collaboration], Depth of maximum of air-shower profiles at the Pierre Auger Observatory. II. Composition implications, *Phys. Rev. D* **90**, 122006 (2014).
4. Apel, W. et al. [KASCADE-Grande collaboration], Ankle-like feature in the energy spectrum of light elements of cosmic rays observed with KASCADE-Grande, *Phys. Rev. D* **87**, 081101 (2013).
5. Kampert, K.-H. and Unger, M., Measurements of the cosmic ray composition with air shower experiments, *Astropart. Phys.* **35**, 660-678 (2012).
6. Allan, H. R., Radio Emission from Extensive Air Showers, *Prog. Elem. Part. Cosm. Ray Phys.* **10**, 171-302 (1971).
7. Falcke, H. & Gorham, P.W., Detecting radio emission from cosmic ray air showers and neutrinos with a digital radio telescope, *Astropart. Phys.* **19**, 477-494 (2003).
8. Falcke, H. et al. [LOPES collaboration], Detection and imaging of atmospheric radio flashes from cosmic ray air showers, *Nature* **435**, 313-316 (2005).
9. Huege, T., The Renaissance of Radio Detection of Cosmic Rays, *Brazilian Journal of Physics* **44**, 520-529 (2014).
10. Apel, W. et al. [LOPES collaboration], Reconstruction of the energy and depth of maximum of cosmic-ray air showers from LOPES radio measurements, *Phys. Rev. D* **90**, 062001 (2014).
11. Belov, K. et al. [ANITA collaboration], Towards determining the energy of the UHECRs observed by the ANITA detector, *AIP Conference Proceedings* **1535**, 209-213 (2013).

12. Werner, K. and Scholten, O., Macroscopic Treatment of Radio Emission from Cosmic Ray Air Showers based on Shower Simulations, *Astropart. Phys.* **29**, 393-411 (2008).
13. Van Haarlem, M. et al. [LOFAR collaboration], LOFAR: The LOw-Frequency ARray, *Astron. Astrophys.* **556**, A2 (2013).
14. Schellart, P. et al. [LOFAR collaboration], Detecting cosmic rays with the LOFAR radio telescope, *Astron. Astrophys.* **560** A98 (2013).
15. Schellart, P. et al. [LOFAR collaboration], Probing Atmospheric Electric Fields in Thunderstorms through Radio Emission from Cosmic-Ray-Induced Air Showers, *Phys. Rev. Lett.* **114**, 165001 (2015).
16. Huege, T., Ludwig, M. and James, C., Simulating radio emission from air showers with CoREAS, *AIP Conference Proceedings* **1535**, 128-132 (2012).
17. Heck, D. et al., CORSIKA: a Monte Carlo code to simulate extensive air showers, *Report FZKA 6019* (1998).
18. Buitink, S. et al. [LOFAR collaboration], Method for high precision reconstruction of air shower X_{max} using two-dimensional radio intensity profiles, *Phys. Rev. D* **90**, 082003 (2014).
19. Ostapchenko, S., QGSJET-II: results for extensive air showers, *Nucl. Phys. B Proc. Suppl.* **151**, 147-150 (2006).
20. Pierog, T., and Werner, K., EPOS Model and Ultra High Energy Cosmic Rays, *Nucl. Phys. B Proc. Suppl.* **196**, 102-105 (2009).

21. Aab, A. et al. [Pierre Auger collaboration], Muons in air showers at the Pierre Auger Observatory: Mean number in highly inclined events, *Phys. Rev. D* **91**, 032003 (2015).
22. Aloisio, R. et al., A dip in the UHECR spectrum and the transition from galactic to extragalactic cosmic rays, *Astropart. Phys.* **27**, 76-91 (2007).
23. Stanev, T., Biermann, P., and Gaisser, T., Cosmic rays. IV. The spectrum and chemical composition above 10 GeV, *Astron. Astrophys.* **274**, 902-915 (1993).
24. Calvez, A., Kusenko, S., and Nagataki, S., Role of Galactic sources and magnetic fields in forming the observed energy-dependent composition of ultrahigh-energy cosmic rays, *Phys. Rev. Lett.* **105**, 091101 (2010).
25. Jokipii, J.R. and Morfill, G., Ultra-high-energy cosmic rays in a galactic wind and its termination shock, *Astrophys. J.* **312**, 170-177 (1987).
26. Porcelli, A. for the Pierre Auger Collaboration, PoS (ICRC2015) 420; arXiv:1509.03732
27. Abu-Zayyad, T. et al. [HiRes/MIA collaboration], Measurement of the Cosmic-Ray Energy Spectrum and Composition from 10^{17} to $10^{18.3}$ eV Using a Hybrid Technique, *Astrophys. J.* **557** (2001) 686-699.
28. Knurenko, S. and Sabourov, A. [Yakutsk collaboration], The depth of maximum shower development and its fluctuations: cosmic ray mass composition at $E_0 \geq 10^{17}$ eV, *Proc. XVI ISVHECRI* (2010).

29. Berezhnev, S.F. et al. [Tunka collaboration.], Tunka-133: Primary Cosmic Ray Mass Composition in the Energy Range $6 \times 10^{15} - 10^{18}$ eV, *Proc. 32nd ICRC Beijing 209* (2011).

Acknowledgements We acknowledge financial support from the Netherlands Organization for Scientific Research (NWO), VENI grant 639-041-130, the Netherlands Research School for Astronomy (NOVA), the Samenwerkingsverband Noord-Nederland (SNN) and the Foundation for Fundamental Research on Matter (FOM). We acknowledge funding from the European Research Council under the European Union's Seventh Framework Program (FP/2007-2013) / ERC (grant agreement n. 227610) and under the European Union's Horizon 2020 research and innovation programme (grant agreement n. 640130). LOFAR, the Low Frequency Array designed and constructed by ASTRON, has facilities in several countries, that are owned by various parties (each with their own funding sources), and that are collectively operated by the International LOFAR Telescope (ILT) foundation under a joint scientific policy.

Author Contributions All authors are part of the LOFAR collaboration and have contributed to the design, construction, calibration, and maintenance of LOFAR and/or LORA. The first thirteen authors constitute the Cosmic Ray Key Science Project and have contributed to the acquisition, calibration, and analysis of cosmic ray radio data and LORA data. The manuscript was written by S.B. and subjected to an internal collaboration-wide review process. All authors approved the final version of the manuscript.

Author Information Reprints and permissions information is available at www.nature.com/reprints. The authors declare no competing financial interests. Correspondence and requests for materials should be addressed to Stijn Buitink (Stijn.Buitink@vub.ac.be).

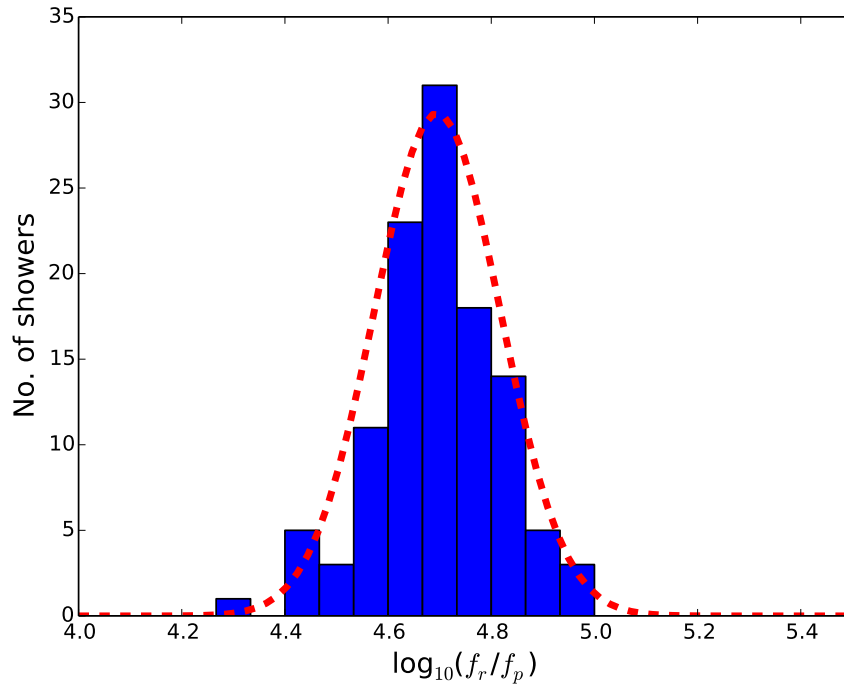


Figure 1 | Energy resolution. The distribution of f_r/f_p is fitted with a Gaussian, yielding $\sigma = 0.12$ on a logarithmic scale, corresponding to an energy resolution of 32%. This value is actually the quadratic sum of the energy resolution of the radio and particle resolutions. In this analysis, there was no absolute calibration for the received radio power yet, so f_r has an arbitrary scale.

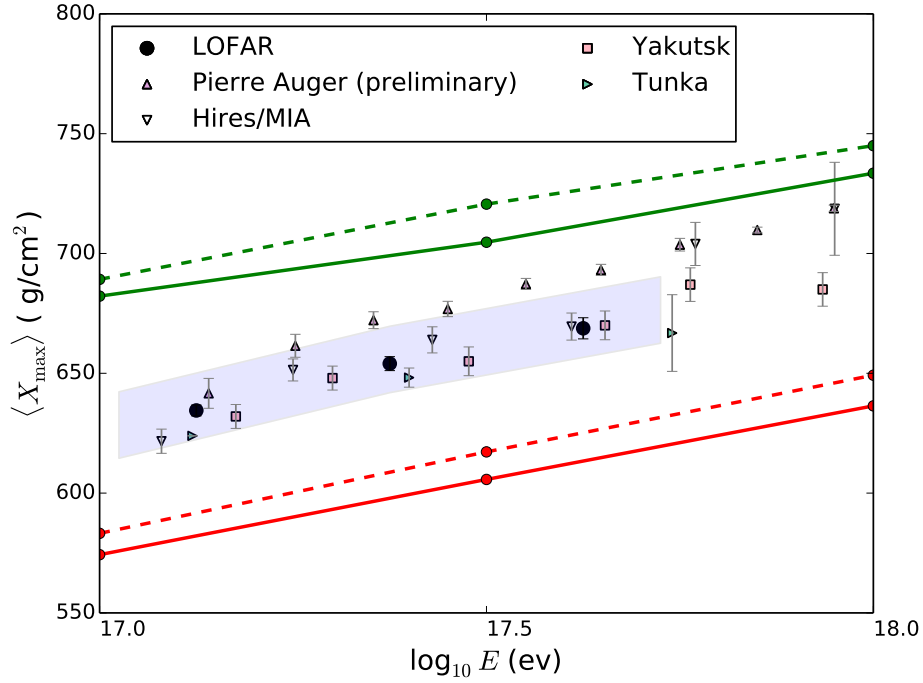


Figure 2 | Measurements of $\langle X_{\max} \rangle$. The mean depth of shower maximum as a function of energy is plotted for LOFAR and earlier experiments based on different techniques^{26–29}. Error bars indicate one-sigma uncertainties. The systematic uncertainties are +14/-10 g/cm² on $\langle X_{\max} \rangle$ and 27% on energy and are indicated with a shaded band. The Pierre Auger Observatory measures the fluorescence light emitted by atmospheric molecules excited by air shower particles. Hires/MIA used a combination of the fluorescence technique and muon detection. The Tunka and Yakutsk arrays use non-imaging Cherenkov detectors. The green (upper) lines indicate the $\langle X_{\max} \rangle$ for proton shower simulated with QGSJETII.04 (solid) and EPOS-LHC (dashed). The blue (lower) lines are for showers initiated by iron nuclei.

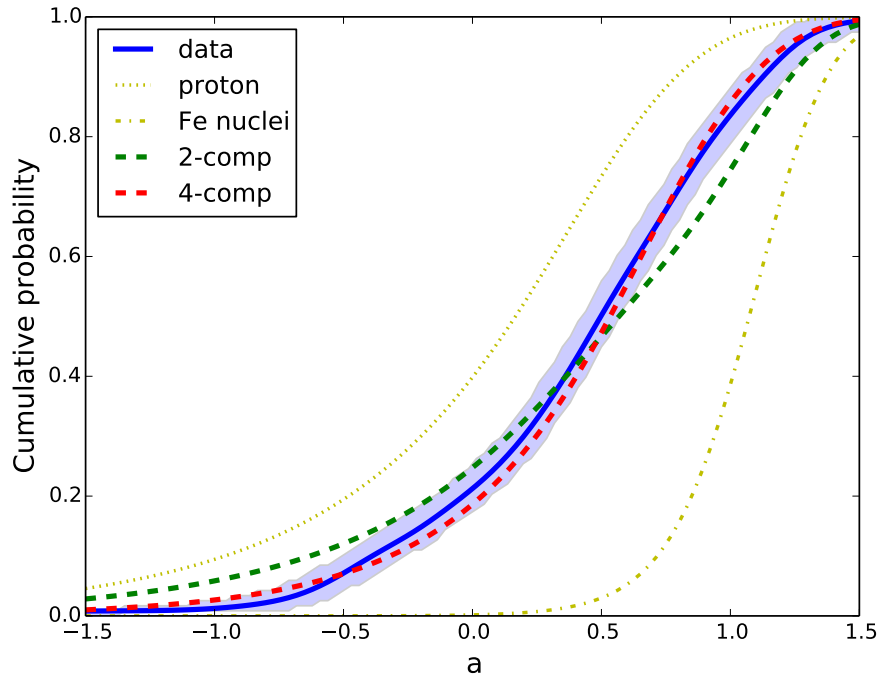


Figure 3 | Composition model fits. The cumulative probability density of the parameter a (see Eqn. 2) is plotted for the data (blue line, shading indicates the range where the p -value > 0.01) and several models, based on QGSJETII.04 simulations. A set that contains only proton showers is centered around $a = 0$ and has a large spread, while iron showers give a small spread around $a = 1$. A two-component model of proton and iron yields the best fit for a proton fraction of 62%, but does not describe the data well with a p -value of 1.1×10^{-6} . A four-component model gives the best fit at 0% proton, 79% helium, 19% nitrogen, and 2% iron, with a p -value of 0.17. The uncertainty on these values is explored in Figure 4.

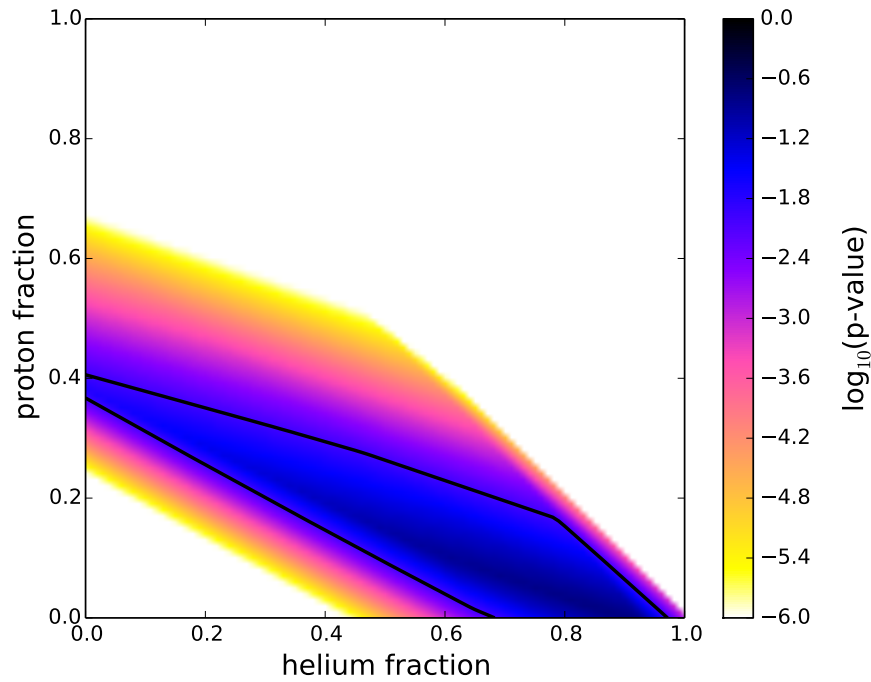
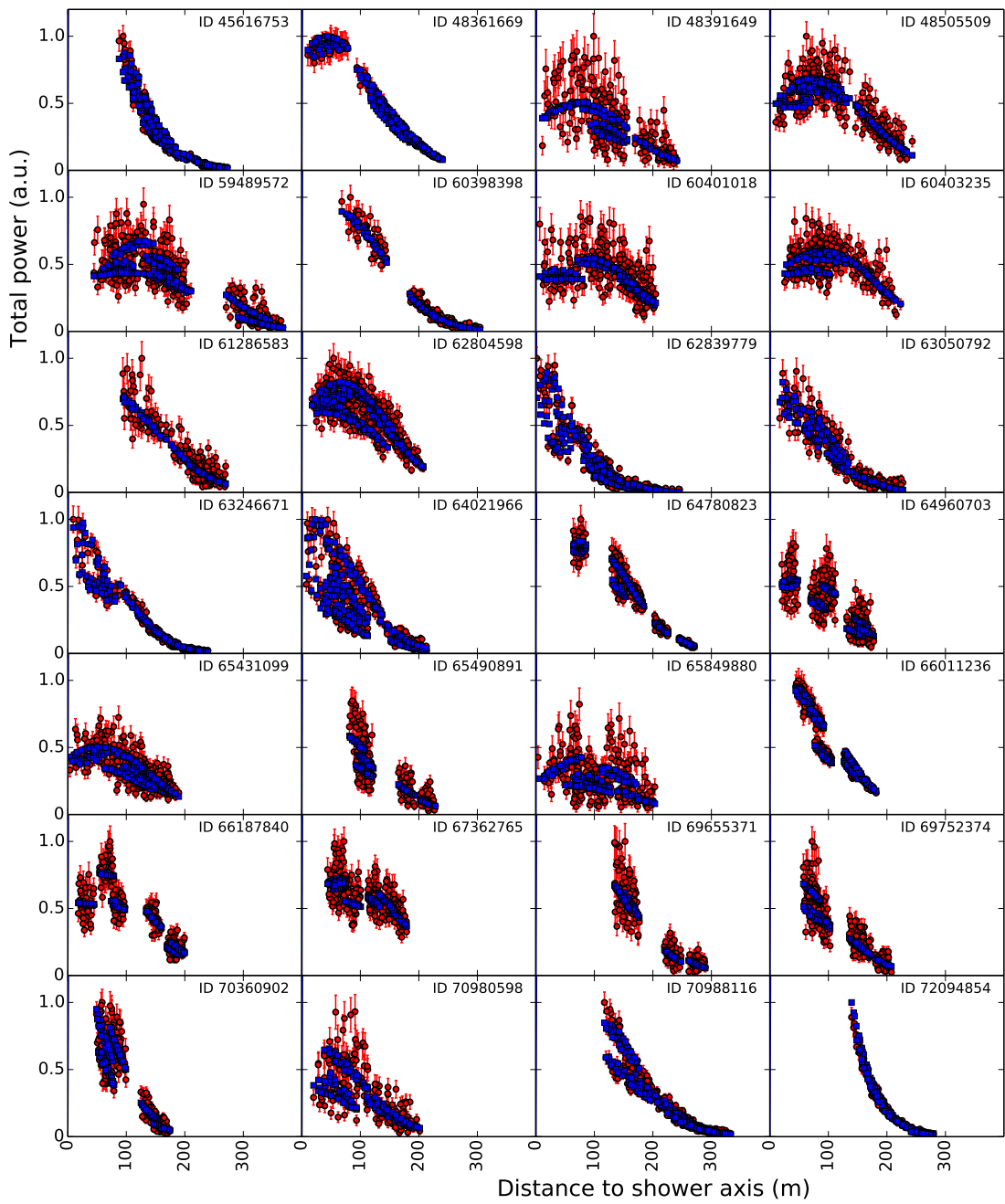
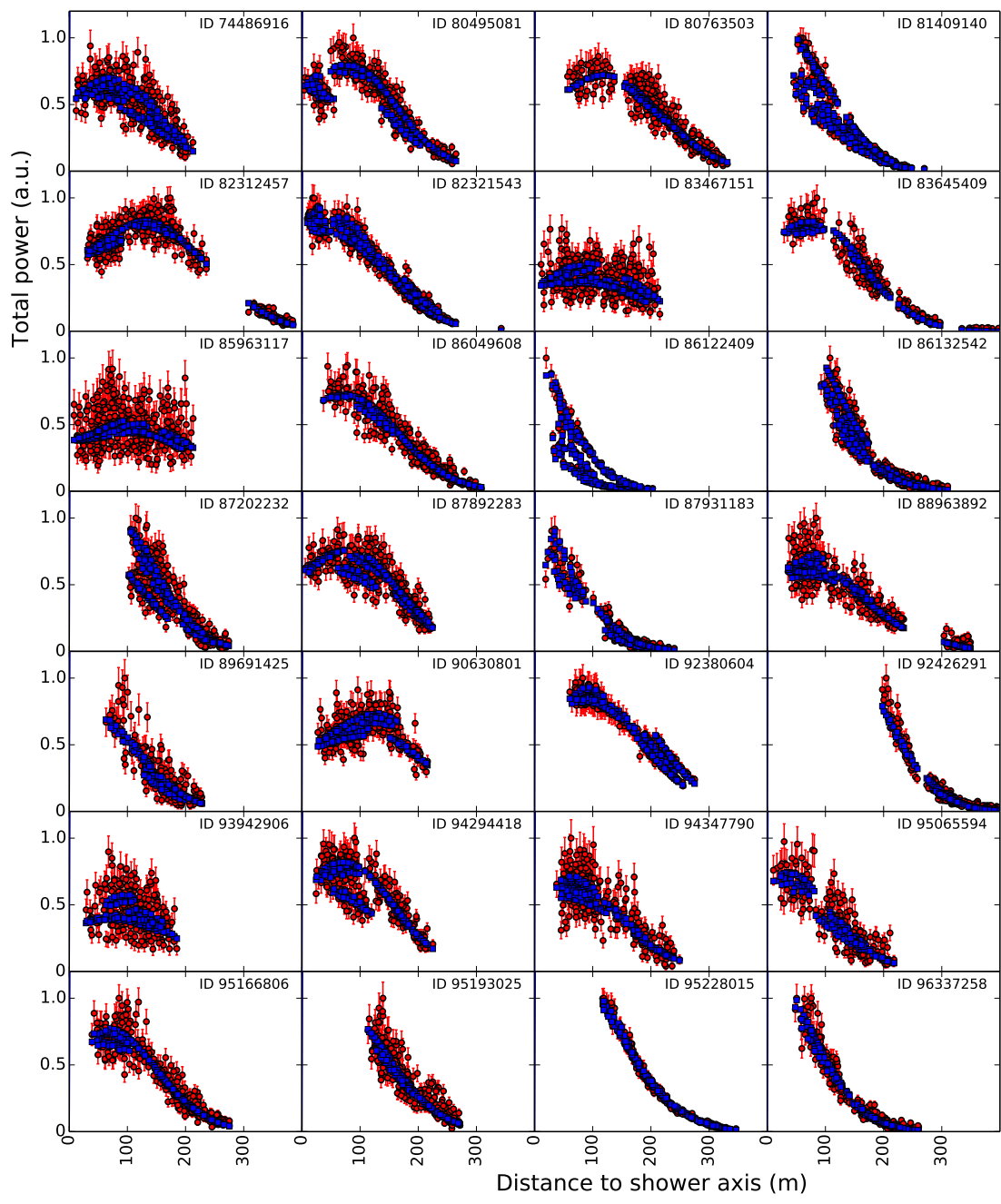


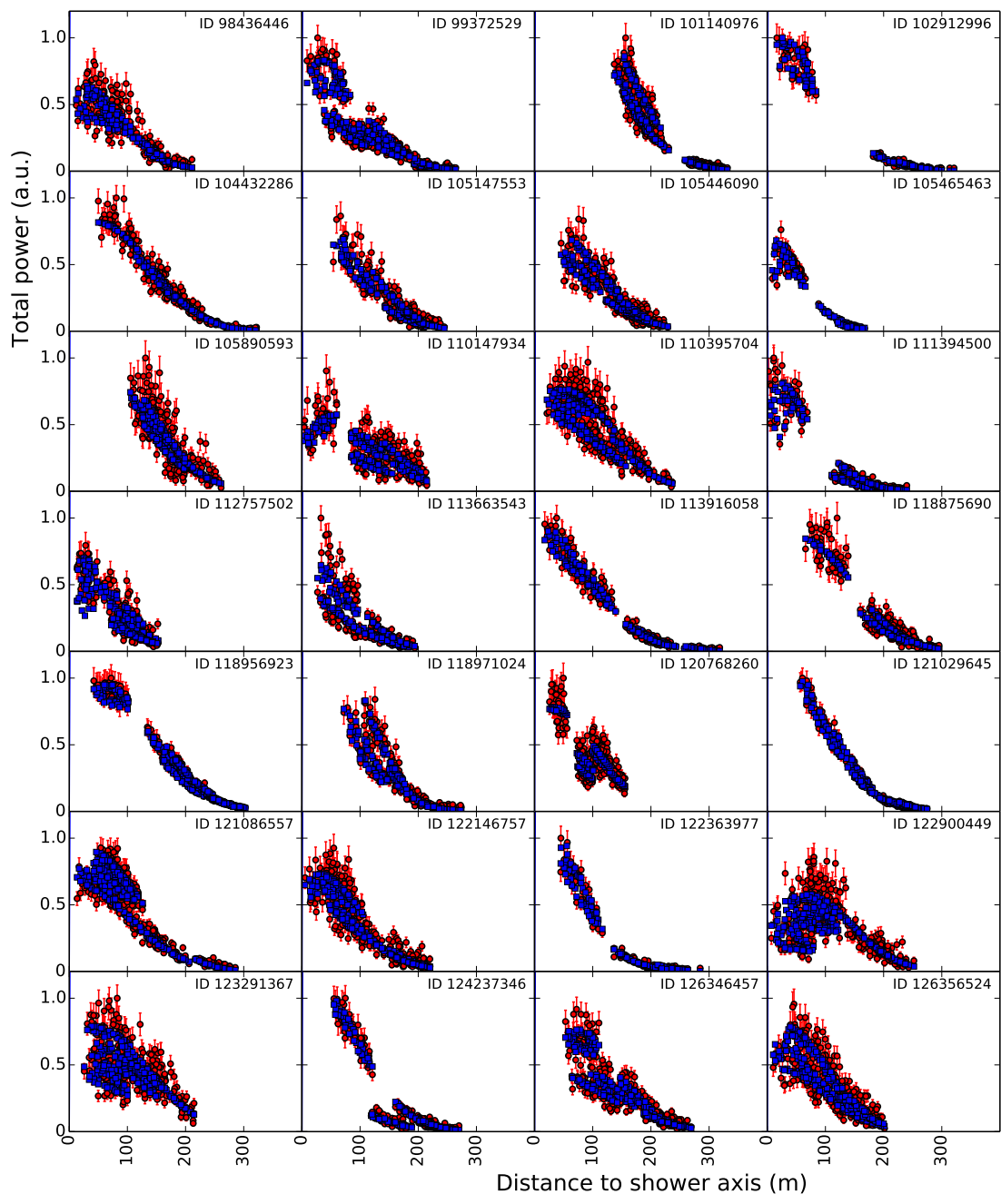
Figure 4 | p-value distribution for four-component model. The four-component model is explored further by keeping the proton and helium fractions fixed at all possible combinations, and solving for the nitrogen/iron ratio. The p-value (see Fig. 3) is plotted as a function of the proton and helium fraction. The optimal fit is found at 0% proton and 79% helium ($p=0.17$), but the deviation only deteriorates slowly when replacing helium with proton. The thick black contour line contains all combinations for which $p > 0.01$. At this significance level the total fraction of light elements (p+He) lies between 0.38 and 0.98.



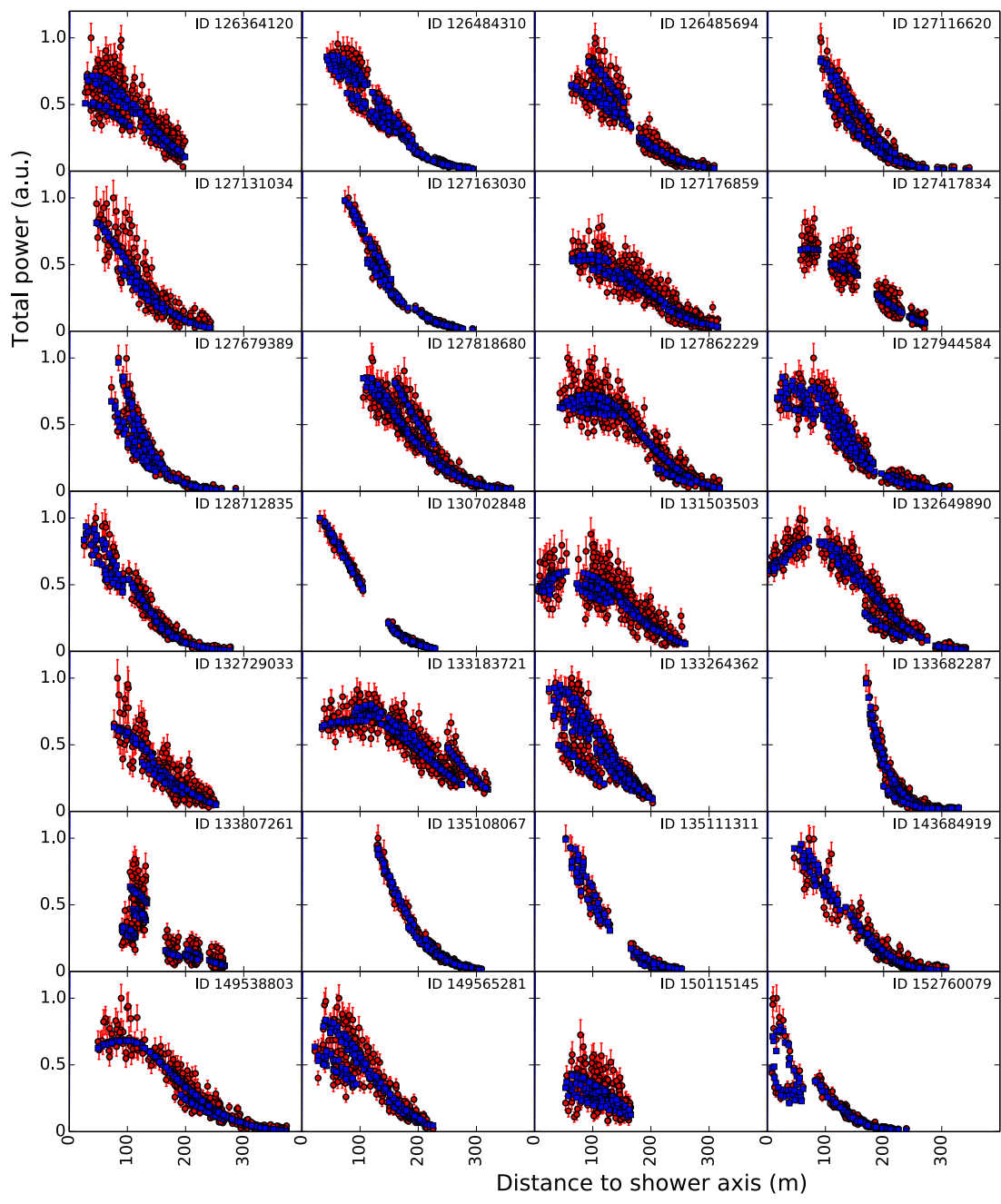
Extended Data Figure 1 | Fitted lateral distributions. Lateral distribution of radio pulse power for all 118 measured showers (red circles) and the corresponding best-fitting CoREAS simulation (blue squares).



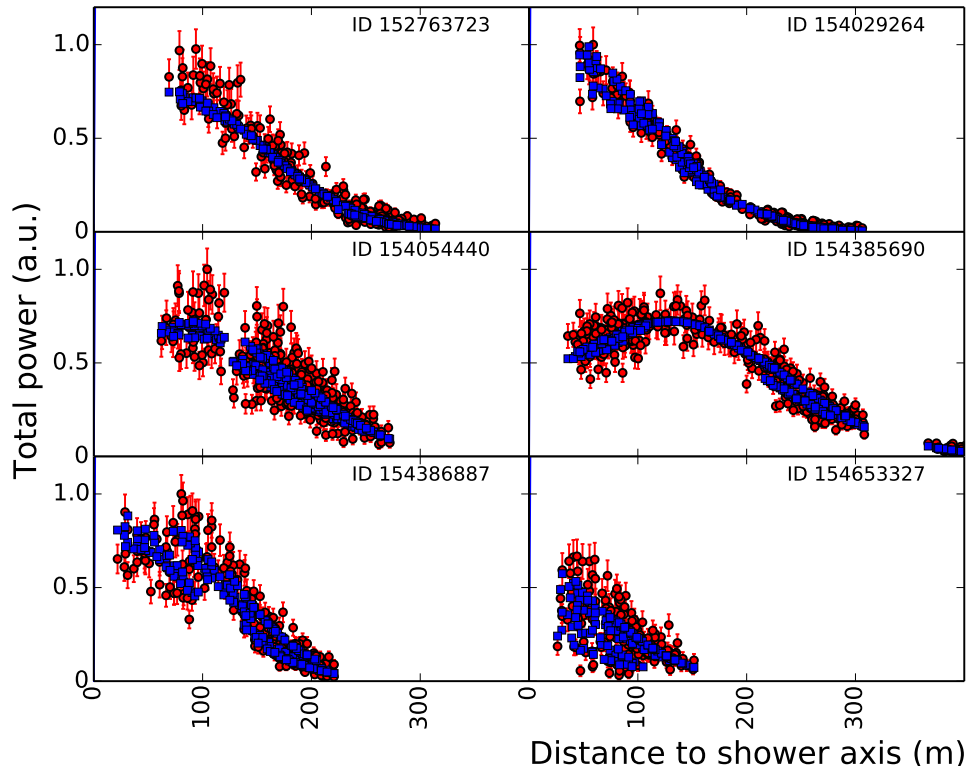
Extended Data Figure 2 | Fitted lateral distributions. Continuation of Extended Data Figure 1.



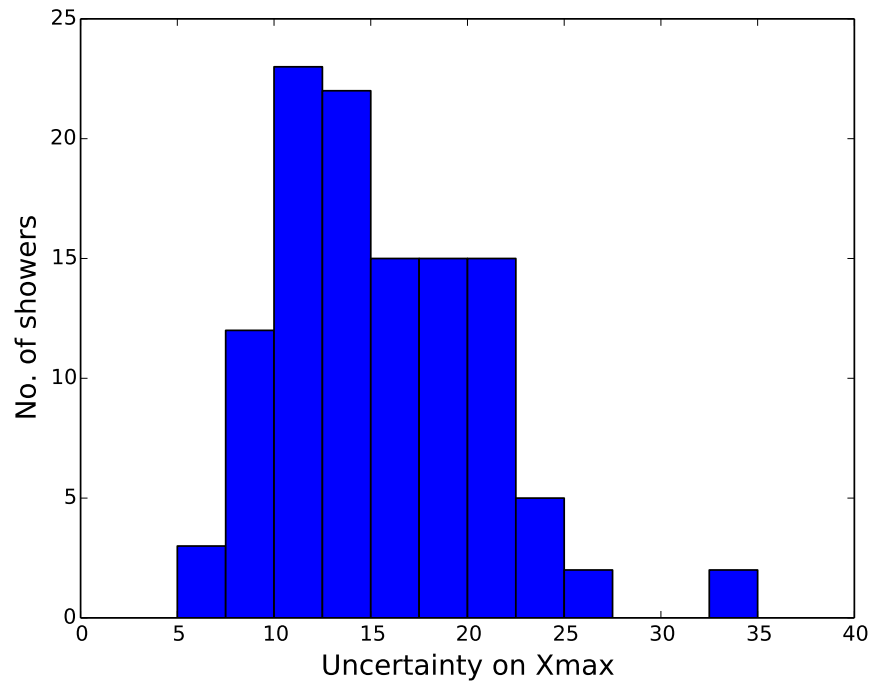
Extended Data Figure 3 | Fitted lateral distributions. Continuation of Extended Data Figure 2.



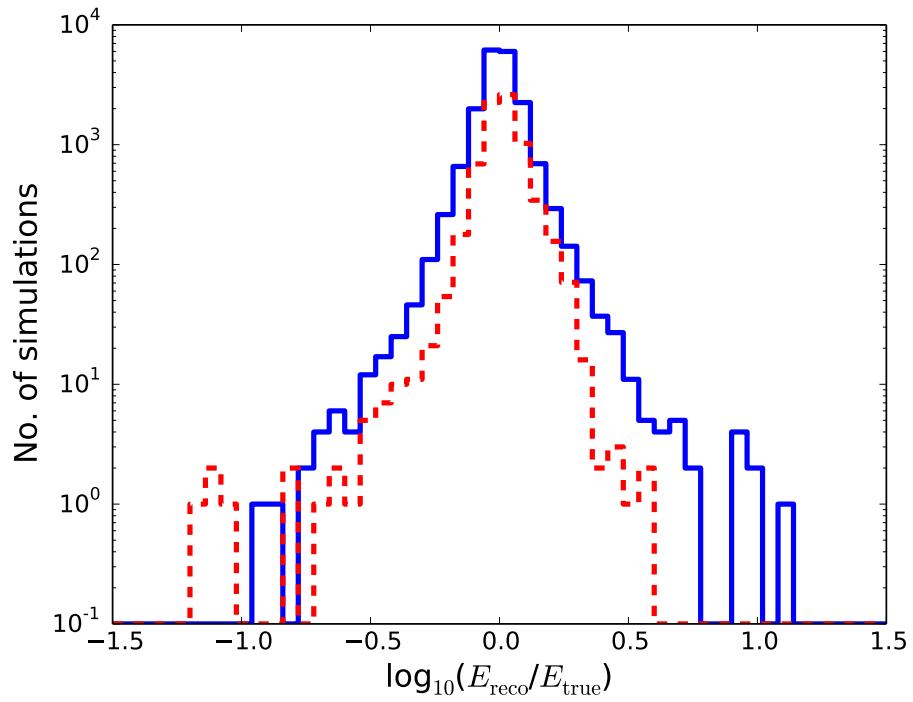
Extended Data Figure 4 | Fitted lateral distributions. Continuation of Extended Data Figure 3.



Extended Data Figure 5 | Fitted lateral distributions. Continuation of Extended Data Figure 4.



Extended Data Figure 6 | Distribution of uncertainty on X_{\max} The distribution of the uncertainty on X_{\max} for all showers used in this analysis. The mean value is 16 g/cm^2 .



Extended Data Figure 7 | Energy reconstruction Distributions of the ratio between true and reconstructed energy for proton (blue, solid) and iron showers (red, dashed). The two types of showers have a systematic offset of the order of $\sim 1\%$.

Methods

Event selection Cosmic ray detection at LOFAR continuously runs in the background during astronomical observations. When 16 out of the 20 scintillator stations of the LORA particle array detect a signal, a trigger is issued and the ring buffers of all active antennas within a ~ 1 km radius are stored for offline analysis¹⁴. Which antennas are active depends on the settings of the astronomical observation. For this analysis we have selected showers that were measured with at least 4 antenna stations (corresponding to at least 192 antennas) in the low band (30 - 80 MHz after filtering)

The trigger and selection criteria introduce a composition bias. This bias is removed with a cut based on dedicated sets of simulations that are produced for each observed shower. These sets contain 50 proton and 25 iron showers, that span the whole range of possible shower depths. A shower is only accepted when *all* simulations in its set pass the triggering and selection criteria. This anti-bias cut removes many showers below 10^{17} eV, but only 4 above that energy. In this analysis, we restrict ourselves to the higher-energy showers and impose a cut on energy $E_{\text{reco}} > 10^{17}$ eV.

The energy cut itself is another potential source of compositional bias, as the reconstructed energy might be dependent on the depth of the shower. However, in our reconstruction approach this effect is very small because energy and X_{max} are fitted simultaneously. Extended Data Figure 7 shows distributions of the ratio between true and reconstructed energy for proton and iron simulations. The systematic offset between the two particle types is of the order of $\sim 1\%$.

We used data from the Royal Netherlands Meteorological Institute to check for lightning storm conditions during our observations. When lightning strikes have been detected in the North of the Netherlands within an hour from a detection, the event is flagged and excluded from the analysis. The presence of electric fields in the clouds can severely alter the radio emission even in the absence of lightning discharges³⁰. The polarisation angle of the radio pulse is very sensitive to the nature of the emission mechanism^{15,31} and is used as an additional veto against strong field conditions.

Finally, a quality cut is imposed on the sample in order to only include showers that have a core position and arrival direction that allows accurate reconstruction. We use the dedicated sets of simulations produced for each shower to derive uncertainties on core position, energy and X_{\max} . These three values are highly correlated, so a single cut on the core uncertainty of $\sigma_{\text{core}} < 5$ m is sufficient.

The quality cut is based on the dedicated sets of simulations. These sets are produced for a specific combination of core position and arrival direction. Therefore, the quality cut is effectively a cut on position and direction, and does not introduce a composition bias.

Furthermore, we stress that there is no cut on the quality of the reconstruction of the actual data. By applying the cuts described above we obtain a sample of 118 showers that are fitted to the simulation yielding reduced χ^2 -values in the range 0.9-2.9. Deviations from unity can be ascribed to uncertainties in antenna response, atmospheric properties like the index of refraction, or limitations of the simulation software.

Reconstruction The energy and X_{\max} of the shower are reconstructed with the technique described in Buitink et al. (2014)¹⁸.

Statistical uncertainty The statistical uncertainty on the power measurements of individual antennas include three contributions. First, there is contribution from the background noise which is a combination of system noise and the Galactic background. Secondly, there is a contribution from uncertainties in the antenna response model. There can be differences between the responses of antennas, either because of antenna properties (e.g. cross-talk between nearby antennas), or because of signal properties (e.g. polarisation). Since these fluctuations are different for each shower core position and arrival direction, they are essentially random and included as a 10% statistical uncertainty on the power. A third contribution is due to the error introduced by interpolating the simulated pulse power. Strictly speaking this is not a measurement uncertainty, but it must be taken into account when fitting the data to simulation. The interpolation error is of the order of 2.5% of the maximum power¹⁸. The three contributions are added in quadrature and produce the one sigma error bars shown in Extended Data Figures 1-5.

The statistical uncertainty on X_{\max} is given by the quadratic sum of the uncertainties due to reconstruction technique and the atmospheric correction. The former is found by applying our analysis to simulated events with added Gaussian noise, where the noise level is determined from the data.

In the CORSIKA simulations the standard US atmosphere model was used. The reconstructed shower depth is corrected for variations in the atmosphere using data from the Global

Data Assimilation System (GDAS) of the NOAA National Climatic Data Center. We follow a procedure developed by the Pierre Auger collaboration³². This typically leads to adjustments of the order of 5–20 g/cm². Remaining uncertainty after correction is of the order of 1 g/cm²

The index of refraction of air is a function of temperature, air pressure, and relative humidity. Using local weather information the final data sample was split in two equal size groups corresponding to conditions with relatively high or low index of refraction. The mean reconstructed X_{\max} of these groups deviate from the mean by ± 5 g/cm², and we adopt this value as an additional statistical uncertainty. Because the refractivity used in simulation corresponds to dry air there is also an associated systematic error (see below).

The total statistical uncertainty on X_{\max} is found by adding above factors in quadrature. A distribution of the uncertainty for the showers in our final sample is shown in Extended Data Figure 6.

The energy resolution is 32% and is found by comparing energy scaling factors of the radio power and particle density fit (see Figure 1).

Systematic effects The data has been subjected to several tests to find the systematic uncertainty on the reconstructed values for X_{\max} :

- **Zenith angle dependence** The final data sample is split into two groups of equal size by selecting showers with a zenith angle below or above 32 degrees. For both groups the mean

reconstructed X_{\max} is calculated, yielding deviations from the mean value of $\pm 8 \text{ g/cm}^2$. This spread is larger than expected from random fluctuations alone and is included as a systematic uncertainty. The dependence on zenith angle may be related with atmospheric uncertainties (see below).

- **Index of refraction of air** As explained above, the index of refraction changes because of differences in atmospheric conditions. Fluctuations on X_{\max} due to changing humidity are of the order of 5 g/cm^2 with respect to the mean. However, the index of refraction that was used in the radio simulations corresponds to dry air, and is a lower bound to the actual value. Therefore, the real value of X_{\max} can be higher than the reconstructed value but not lower, and we adopt an asymmetrical systematic uncertainty of $+10 \text{ g/cm}^2$.
- **Hadronic interaction model** Since the reconstruction technique is based on full Monte Carlo simulations, it is sensitive to the choice of hadronic interaction model that is used. It has been shown with a comparison between QGSJETII.04, SYBILL 2.1, and EPOS-LHC, that the uncertainty due to model dependence is $\sim 5 \text{ g/cm}^2$. Note that the uncertainty on the *composition* due to different models (in other words: on how to interpret the measured X_{\max} values) is of course larger.
- **Radiation code** For this analysis we have used the radiation code CoREAS in which the contributions of all individual charges to radiation field are added together. The advantage of this microscopic approach is that it is completely model-independent and based on first principles. ZHAireS³⁴ is another microscopic code and gives very similar results³⁵. To calculate the emission CoREAS uses the end-point formalism³⁶, while ZHAireS is based on the

ZHS algorithm³⁷. Both formalisms are derived directly from Maxwell's equations and have been shown to be equivalent³⁸. The other difference between CoREAS and ZHAires is that they take the particle distribution from different air shower propagation codes (CORSIKA and AIRES respectively) that internally use different hadronic interaction models. Since the radiation formalisms themselves are equivalent, small differences between CoREAS and ZHAireS are most likely due to differences in the hadronic interaction models used to simulate the particle interactions. The choice of radiation code does therefore not introduce an additional systematic uncertainty on top of the uncertainty to hadronic interaction models that is already included. A comparison study with LOFAR data did also not show any evidence for a systematic offset between the codes and will be published in an upcoming paper.

The remaining small dependence of X_{\max} on zenith angle is possibly related to the index of refraction. Showers with different inclination angles have their shower maximum at different altitudes, and therefore different local air pressure and index of refraction. Therefore, increasing the index of refraction used in simulations will result in a zenith-dependent change in reconstructed X_{\max} . This possibly removes the observed dependence of the composition on zenith angle. Correctly taking into account a complete atmospheric model for the profile of the refractivity of air is subject of further study. Here, we treat the effect conservatively by adding the first two contributions to the uncertainty linearly. The other two contribution are independent and are added in quadrature, yielding a total systematic uncertainty of $+14/ - 10 \text{ g/cm}^2$.

The systematic uncertainty on the energy reconstruction with the LORA particle detector array is 27%, which includes effects due to detector calibration, hadronic interaction models, and the assumed slope of the primary cosmic-ray spectrum in the CORSIKA simulations^{33,39}

Statistical analysis For each observed shower, we calculate:

$$a = \frac{\langle X_{\text{proton}} \rangle - X_{\text{shower}}}{\langle X_{\text{proton}} \rangle - \langle X_{\text{iron}} \rangle} \quad (2)$$

where X_{shower} is the reconstructed X_{max} , and $\langle X_{\text{proton}} \rangle$ and $\langle X_{\text{iron}} \rangle$ are mean values predicted by QGSJETII.04¹⁹. Thus a is an energy-independent parameter that is mass sensitive. A pure proton composition would give a wide distribution of a centered around zero, while a pure iron composition gives a narrower distribution around unity.

From the measurements we construct a cumulative distribution function (CDF) in the following Monte Carlo approach. A realisation of the data is made by taking the measured values for the energy and X_{max} , adding random fluctuations based on the statistical uncertainty of these parameters, and calculating the a parameters and the corresponding CDF. By constructing a large number of realisations with different random fluctuation, we can calculate the mean CDF and the region that contains 99% of all realisations. These are indicated in Figure 3 as the solid blue line and the shaded region respectively.

We fit theoretical CDFs based on composition with two or four mass components to the data. The test statistic in the fit is the maximum deviation between the data and the model CDFs. The p-value is given by the probability of observing this deviation, or a larger one, assuming the fitted

composition model.

We first use a two-component model of proton and iron nuclei, where the mixing ratio is the only free parameter. The best fit is found for a proton fraction of 62%, but it describes the data poorly with a p-value of 1.1×10^{-6} .

A better fit is achieved with a four-component model (p+He+N+Fe), yielding a p-value of 0.17. While the best fit is found for a Helium fraction of 80%, the fit quality deteriorates only slowly when replacing helium by protons. This is demonstrated in Figure 4 where the p-value is plotted for four-component fits where the fractions of helium and proton are fixed, and the ratio between N and Fe is left as the only free parameter. The solid line in this Figure contains the parameter space where $p > 0.01$. We construct a 99% confidence level interval on the total fraction of light elements (p+He) by finding the two extreme values of this fraction that still lie within the $p > 0.01$ region.

The total fraction of light elements (p+He) is in the range [0.38,0.98] at 99% confidence level, with a best fit value of 0.8. The heaviest composition that is allowed within systematic uncertainties (see above) still has a best fit p+He fraction of 0.6, and a 99% confidence level interval of [0.18, 0.82].

References

30. Buitink, S. et al. [LOPES collaboration], Amplified radio emission from cosmic ray air showers in thunderstorms., *Astron. Astrophys.* **467**, 385-394 (2007).
31. Schellart, P. et al. [LOFAR collaboration], Polarized radio emission from extensive air showers measured with LOFAR, *JCAP* **10**, 14 (2014).
32. Abreu, P. et al. [Pierre Auger collaboration], Description of atmospheric conditions at the Pierre Auger Observatory using the Global Data Assimilation System (GDAS), *Astropart. Phys.* **35**, 591-607 (2012).
33. Thoudam, S. et al. [LOFAR collaboration], LORA: A scintillator array for LOFAR to measure extensive air showers, *Nucl. Instr. and Meth. in Phys. Res. A* **767**, 339-346 (2014).
34. Alvarez-Muñiz, J. et al., Monte Carlo simulations of radio pulses in atmospheric showers using ZHAireS, *Astropart. Phys.* **35**, 325-341 (2012).
35. Huege, T. et al., The convergence of EAS radio emission models and a detailed comparison of REAS3 and MGMR simulations, *NIMPA* **662**, 179-186 (2012).
36. James, C., Falcke, H., Huege, T. and Ludwig, M., General description of electromagnetic radiation processes based on instantaneous charge acceleration in “endpoints”., *Phys. Rev. E* **84**, 056602 (2011).
37. Zas, E., Halzen, F., and Stanev. T., Electromagnetic pulses from high-energy showers: Implications for neutrino detection. *Phys. Rev. D* **45**, 362-376 (1992).

38. Belov, K. et al. [SLAC T-510], Accelerator measurements of magnetically-induced radio emission from particle cascades with applications to cosmic-ray air showers [eprint arXiv:1507.07296] (2015).
39. Thoudam, S. et al. [LOFAR collaboration], Measurement of the cosmic-ray energy spectrum above 10^{16} eV with the LOFAR Radboud Air Shower Array, *Astropart. Phys.* **73**, 34-43 (2016).

Depth of shower maximum and mass composition of cosmic rays from 50 PeV to 2 EeV measured with the LOFAR radio telescope

A. Corstanje^{a,b,*}, S. Buitink^{a,b}, H. Falcke^{b,c,d}, B. M. Hare^e, J. R. Hörandel^{b,d,a}, T. Huege^{f,a}, G. K. Krampah^a, P. Mitra^a, K. Mulrey^a, A. Nelles^{g,i}, H. Pandya^a, J. P. Rachen^a, O. Scholten^h, S. ter Veen^c, S. Thoudam^j, G. Trinh^k, T. Winchen^l

^a*Astrophysical Institute, Vrije Universiteit Brussel, Pleinlaan 2, 1050 Brussels, Belgium*

^b*Department of Astrophysics/IMAPP, Radboud University Nijmegen, P.O. Box 9010, 6500 GL Nijmegen, The Netherlands*

^c*Netherlands Institute for Radio Astronomy (ASTRON), Postbus 2, 7990 AA Dwingeloo, The Netherlands*

^d*Nikhef, Science Park Amsterdam, 1098 XG Amsterdam, The Netherlands*

^e*University of Groningen, Kapteyn Astronomical Institute, Groningen, 9747 AD, Netherlands*

^f*Institut für Astroteilchenphysik, Karlsruhe Institute of Technology (KIT), P.O. Box 3640, 76021, Karlsruhe, Germany*

^g*DESY, Platanenallee 6, 15738 Zeuthen, Germany*

^h*Interuniversity Institute for High-Energy, Vrije Universiteit Brussel, Pleinlaan 2, 1050 Brussels, Belgium*

ⁱ*ECAP, Friedrich-Alexander-University Erlangen-Nürnberg, 91058 Erlangen, Germany*

^j*Department of Physics, Khalifa University, P.O. Box 127788, Abu Dhabi, United Arab Emirates*

^k*Department of Physics, School of Education, Can Tho University Campus II, 3/2 Street, Ninh Kieu District, Can Tho City, Vietnam*

^l*Max-Planck-Institut für Radioastronomie, Auf dem Hügel 69, 53121 Bonn, Germany*

Abstract

We present an updated cosmic-ray mass composition analysis in the energy range $10^{16.8}$ to $10^{18.3}$ eV from 334 air showers measured with the LOFAR radio telescope, and selected for minimal bias. In this energy range, the origin of cosmic rays is expected to shift from galactic to extragalactic sources. The analysis is based on an improved method to infer the depth of maximum X_{\max} of extensive air showers from radio measurements and air shower simulations.

We show results of the average and standard deviation of X_{\max} versus primary energy, and analyze the X_{\max} -dataset at distribution level to estimate the cosmic ray mass composition. Our approach uses an unbinned maximum likelihood analysis, making use of existing parametrizations of X_{\max} -distributions per element. The analysis has been repeated for three main models of hadronic interactions.

Results are consistent with a significant light-mass fraction, at best fit 23 to 39% protons plus helium, depending on the choice of hadronic interaction model. The fraction of intermediate-mass nuclei dominates. This confirms earlier results from LOFAR, with systematic uncertainties on X_{\max} now lowered to 7 to 9 g/cm².

We find agreement in mass composition compared to results from Pierre Auger Observatory, within statistical and systematic uncertainties. However, in line with earlier LOFAR results, we find a slightly lower average X_{\max} . The values are in tension with those found at Pierre Auger Observatory, but agree with results from other cosmic ray observatories based in the Northern hemisphere.

Keywords: Cosmic rays, radio detection, composition

1. Introduction

Cosmic rays arrive at the Earth's atmosphere in an energy range from below 10^9 to above 10^{20} eV. Upon interacting in the atmosphere, they produce a cascade of secondary particles called *extensive air shower*,

*Corresponding author

Email address: A.Corstanje@astro.ru.nl (A. Corstanje)

which is measurable in ground-based detector arrays for energies above about 10^{14} eV. At the high end of the energy spectrum, these particles have the highest energy of the known particles in the Universe. Therefore, the questions about their origin and their mass composition have raised considerable interest, and cosmic-ray air showers are measured in observatories around the world. The largest is the Pierre Auger Observatory in Argentina [1, 2], spanning an area of 3000 km^2 .

In this analysis, we study cosmic rays with a primary energy between $10^{16.8}$ and $10^{18.3}$ eV, the energy range where a transition is expected from particles originating from within the Galaxy, to an extragalactic origin. Heavy nuclei from the Galaxy are expected to reach higher energies than protons, as they are more easily magnetically contained due to their higher charge (i.e., the Hillas criterion [3]). Therefore, composition measurements in this energy region are interesting for comparison with models of cosmic-ray sources and propagation. For instance, in [4] it is argued that a secondary Galactic component may (still) dominate around 10^{17} eV. In one scenario where supernovas of Wolf-Rayet stars are the main sources, one expects a rather low proton fraction together with a higher helium and C/N/O fraction, before proton-dominated extragalactic cosmic rays take over around 10^{18} eV.

Along the track of an air shower, the number of secondary particles reaches a maximum, at a depth expressed in g/cm^2 of traversed matter, referred to as X_{max} . This maximum is reached for almost all showers in our energy range, typically at altitudes of 2 to 7 km. At a given primary energy, X_{max} depends on the mass of the primary particle. It is different for protons compared to heavy nuclei, both on average and in distribution. The shift in average X_{max} with respect to protons is approximately proportional to $\ln A$, for particles with atomic mass number A , where protons have the deepest shower maximum on average. Thus, measuring X_{max} for a collection of air showers gives information about their composition, and is the basis for the present analysis.

There are three main techniques for measuring X_{max} : (i) measuring fluorescence light along the trail of the air shower, (ii) measuring Cherenkov light, and (iii) measuring the radio signal using antennas on the ground [5, 6]. Measuring secondary particles on the ground, especially the electron/muon ratio, yields composition information without (explicitly) measuring X_{max} . The radio detection technique has shown substantial development in recent years, leading to a method to determine X_{max} with a resolution about 20 g/cm^2 [7]. The method has been demonstrated using the LOFAR radio telescope, showing that the cosmic rays around 10^{17} eV have a considerable light-mass component [8]. Here, we present a method which has been improved on several points, thus lowering the systematic uncertainties, and an extended dataset.

The method relies on air shower simulations tracking individual particles, and summing up their contributions to the radio signal measured on the ground. For this, the CORSIKA [9] simulation program has been used, with its plugin CoREAS [10] for computing the radio signal. For an ensemble of simulated air showers, their lateral intensity distribution or ‘radio footprint’ is fitted to the measurements, from which X_{max} and the energy of the measured shower are reconstructed.

The X_{max} -distributions for the different elements have substantial overlap. Achieving low systematic uncertainties on X_{max} is therefore a crucial point for composition measurements, besides a good X_{max} -resolution per shower. This is done by a fiducial sample selection based on the CoREAS simulations per shower, and lowering known contributions to systematic uncertainties where possible. For example, in [11] it was shown that accurately representing local atmospheric conditions (refractive index) at the time of the air shower, removes a systematic error of 4 to 11 g/cm^2 .

Other improvements to the analysis include a radio-only reconstruction of both X_{max} and energy, the latter using a new calibration based on Galactic emission [12] which halves the systematic energy uncertainty compared to the earlier particle-based treatment. Using a fast pre-computation of shower simulations with CONEX [13] streamlines the reconstruction, as showers can be pre-selected for their X_{max} . The selection criteria to obtain a bias-free X_{max} sample have been improved, and a refined statistical analysis has been done. All these increase the accuracy of the composition analysis, by lowering systematic and/or statistical uncertainties.

The Low Frequency Array (LOFAR) [14] is a radio telescope consisting of many separate antennas. The core region in the north of the Netherlands has a high density of antennas. The antennas are grouped in stations, each of which in the Netherlands contains 96 low-band antennas (LBA), working in the 10 to 90 MHz range, and 48 high-band antennas (HBA) operating at 110 – 240 MHz. The center of LOFAR is a circular

area of 320 m diameter, with six of those stations. In a core region of about 6 km², there are 18 more stations. LOFAR uses ring buffers to store up to 5 seconds of the raw measured signals at each antenna, which are used to measure the radio signals of air showers. For air shower measurements, we use signals from the low-band antennas, filtered to 30 to 80 MHz.

To trigger a buffer readout when an air shower arrives, a particle detector array called LORA (LOFAR Radboud Air shower Array) [15] is located inside the innermost ring of LOFAR. With 20 scintillator detectors monitored in real time, a trigger is sent to LOFAR when a threshold of 13 coincident detections is reached, a level which is optimal for our purposes.

The paper is organized as follows: in Sect. 2, we present the method of fitting air shower simulations to measured data to infer X_{\max} . Furthermore, we discuss the selection criteria used to obtain a bias-free sample of showers. In Sect. 3, the statistical analysis to infer particle composition from the X_{\max} values is explained. The results are split into two sections, Sect. 4 for the X_{\max} distribution from our dataset, and Sect. 5 for the composition results. A summary is given in Sect. 6.

2. Method

The discussion of the methods is split into five sections. After an introduction to the use of CORSIKA and CoREAS simulations, we give a brief review of the procedure to infer X_{\max} for individual measured air showers. A more detailed explanation is found in [7]; the details that have changed in this version are given below. The method to estimate the primary energy, and its uncertainties, are discussed in Sect. 2.3. We show how including the local atmospheric conditions into the simulations leads to improved accuracy. Finally, we explain our method to select showers in order to create an unbiased sample.

2.1. CORSIKA/CoREAS simulations

For the reconstruction of LOFAR-measured air showers, we use CORSIKA (version 7.7100) to simulate air showers, with its plugin CoREAS which calculates the radio emission from the particle showers. The simulation uses a ‘microscopic’ approach: it simulates individual particles and their contribution to radio emission, as they are produced along the evolution of the shower. Air showers are simulated from a Monte Carlo approach to particle interactions, and applying classical electrodynamics (Maxwell’s equations) to obtain the radio signal at the antennas. For the particle part, three main models of hadronic interactions have been considered: QGSJetII-04 [16], EPOS-LHC [17], and Sibyll-2.3d [18] [19]. Their differences represent the intrinsic (systematic) uncertainty on hadronic interactions at the high energy levels of cosmic rays in our energy range and beyond.

The radio signals are calculated from first principles, i.e., without free parameters other than those from discretization approaches, which are set to values fine enough to reach convergence in results. This is important for accuracy in reconstructing X_{\max} . Calculations are based on the ‘endpoint formalism’ presented in [20]. In particular, there is no distinction between separate emission mechanisms such as geomagnetic and charge-excess contributions (see e.g. [21]), as these are naturally included. The radio signals at ground level are a (coherent) superposition of contributions from particles along the shower track, propagated geometrically to the antennas. Therefore, one reconstructs essentially the (geometric) distance to X_{\max} from the radio signals.

When fitting simulated air showers to LOFAR measurements, close agreement is found, for pulse energy [8] as well as for detailed measurements such as circular polarization [22]. Comparisons of results from Corsika/CoREAS with another simulation program based on the same principles, ZHAireS [23], show close agreement [6, 24, 25], and remaining differences are ascribed to details in the simulation of particle interactions. The given detailed and, where possible, parameter-free approach, together with agreement between different extensively developed simulation codes, gives a solid basis for accurate air shower reconstructions.

2.2. Using CoREAS simulations to estimate X_{\max} of measured air showers

Starting point is a set of air showers measured with LOFAR. When an event is triggered by the particle detector array LORA, its radio dataset is passed through our analysis pipeline [26]. Its primary output

parameter for this analysis is pulse ‘energy’, defined as the square of the measured voltage in an antenna, integrated over a time window of 55 ns (11 samples) around the pulse maximum. When reconstruction quality criteria are passed, a dataset consists of pulse energy, including its uncertainty, per antenna in at least 3 LOFAR stations, an accurate measurement of the incoming direction, and an initial estimate of X_{\max} and primary energy from fitting a (parametrized) lateral distribution function [27]. The initial estimates are used as a starting point for the simulations. Simulations are iterated if the initial parameters are found to be inaccurate. Therefore, the final estimates do not depend on them.

For each shower measured with LOFAR, we produce an ensemble of CoREAS showers, spanning the natural range of X_{\max} for protons and for iron nuclei. We use the QGSJetII-04 hadronic interaction model [16] to produce the particle showers with CORSIKA. As simulation energy we use an estimate from fitting an analytic description of the radio footprint [27], or an estimate from the particle detectors when the fit failed to converge.

As a pre-computation stage we produce 600 showers with the fast simulation method CONEX, version 4.3700 [13], of which 150 have an iron primary while the others start from a proton. This is suitable to select those random number seeds to span the natural range of X_{\max} roughly uniformly with about 15 showers. The same random number seeds are used in the full CORSIKA (version 7.7100) simulations. The number of CONEX showers is high enough to sample into the tails of the X_{\max} -distributions at a level corresponding to the size of our final dataset ($N = 334$). The aim is twofold, to have simulated showers covering the entire range of X_{\max} , which is important for the selection criteria for a bias-free sample (see Sect. 2.5), and to have a region around the best-fitting X_{\max} with extra dense coverage, to improve precision.

Therefore, ten additional showers are simulated in a region of ± 20 g/cm² around the first X_{\max} estimate, aiming to have a high density of simulations close to the reconstructed X_{\max} . The total number of simulated showers is around 30 per measured shower. If the reconstructed X_{\max} deviates from the initial fit, extra showers are simulated to match the dense region with the reconstructed X_{\max} . An example is shown in the middle panel of Fig. 1; existing showers with $X_{\max} > 700$ fall outside the plotted vertical range.

The radio signal of each simulated shower is passed through our antenna model for the LOFAR LBA antennas [26], and through the bandpass filter used in the data analysis, to be able to compare with LOFAR data. The signal energy for each simulated shower is then matched per antenna to the LOFAR measurements. In this fit, the core position and an overall scaling factor are free parameters. This gives a chi-squared value for each shower:

$$\chi_{\text{radio}}^2 = \sum_{\text{antennas}} \left(\frac{P_{\text{ant}} - f_r^2 P_{\text{sim}}(x_{\text{ant}} - x_0, y_{\text{ant}} - y_0)}{\sigma_{\text{ant}}} \right)^2, \quad (1)$$

where P_{ant} and σ_{ant} denote the measured signal energy and its uncertainty, and P_{sim} is the simulated pulse energy. The overall scaling factor is f_r^2 , and (x_0, y_0) is the fitted shower core position. In contrast to the method in [7], we perform the fit based on the radio signals only, making the radio reconstruction self-sufficient. In the previous analysis, the fit included both radio and particle detector data. As a consequence, showers for which the reconstruction cannot be done accurately without the particle detector signals are now (automatically) discarded.

The result of the fitting procedure for one of our measured showers is shown in Fig. 1. In the left panel, the best-fitting simulated shower is shown (background color) together with the measurements (colored circles). The colored circles blend in well with the background color, indicating a good fit. This is confirmed by the middle plot, showing a reduced χ^2 of 1.3 for the best fit, and a clear minimum as a function of X_{\max} . The right panel shows a one-dimensional representation of the simulated and measured intensities per antenna.

We employ a Monte Carlo procedure, using the simulated ensemble of showers to infer the uncertainties on X_{\max} , the energy and the shower core position. For each simulated shower in our ensemble we create three mock datasets as they would have been measured, i.e., adding the noise level found in each LOFAR antenna. They represent three different realisations of the random noise, at a fixed shower core position. This simulated shower is then reconstructed through the above procedure, using the ensemble of all other simulations. Statistically comparing the reconstructions with the real X_{\max} , core position, and radio scale factor, which are known in simulations, yields their uncertainties. The uncertainties thus found are calculated

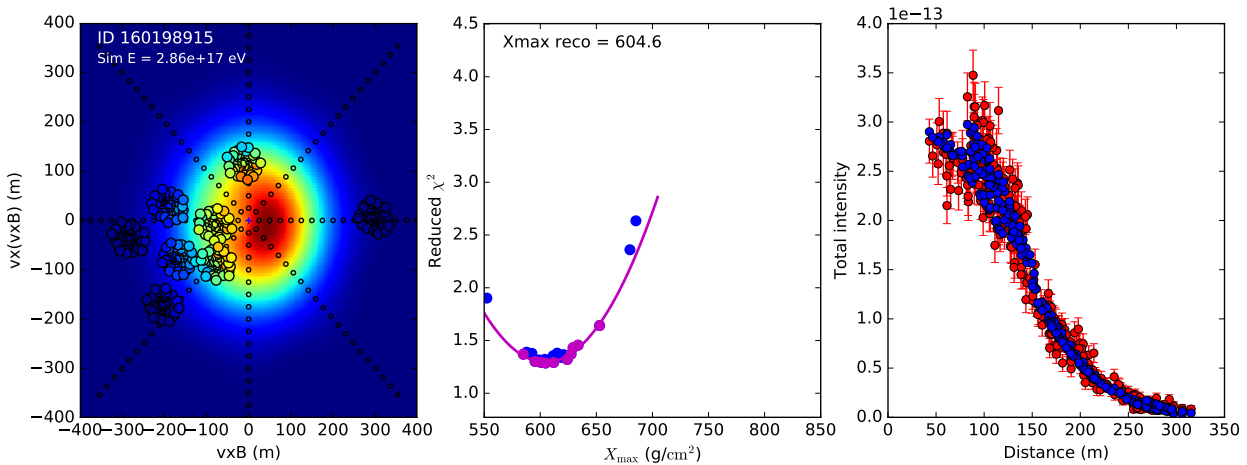


Figure 1: An example of fitted CoREAS showers to a LOFAR-measured shower. The left panel shows simulated signal energy along with the measurements, in the shower plane, for the best-fitting shower. The lateral intensity (and pulse energy) distribution is not rotationally symmetric. The middle panel shows the reduced χ^2 as a function of X_{\max} , with a parabolic fit through the lower envelope denoted by the magenta line. The right panel shows a 1-D lateral distribution function, where red points with uncertainties denote the measurements, and blue points denote the simulated intensities.

from the entire simulated ensemble, and are applicable to the measured shower as well as to each simulated shower; this is important in the bias-free sample selection procedure explained in Sect. 2.5. This procedure, relying on the reconstruction method described above, now also uses only the radio signals.

2.3. Estimate of the primary particle energy

We estimate the energy of the primary particle by comparing the pulse energy of the measured radio signal with the predicted radio signal from CoREAS, which was produced at a given simulation energy obtained from the initial fit. The intensity, and measured pulse energy, of the radio signal scale quadratically with the primary energy [28, 29, 30]. Fitting CoREAS radio signal energy to LOFAR data produces an overall scale factor. The square root of this is taken as a correction to the simulation energy, giving an estimate of the primary particle energy. Moreover, following [24] we apply a correction factor of 11% to the simulated pulse intensities. This accounts for a finite step size (electron multiple scattering length) in tracking the particle cascade in the simulation.

This procedure of matching simulated and measured pulse energy relies on an accurate absolute calibration of the radio antennas at LOFAR. The calibration has been improved with respect to the previous analysis [12]. It uses the emission from the Galaxy, which enters the measured time traces of the antenna signals as ‘noise’. The galactic emission model LFMap [31] is used to obtain the contribution of each point on the sky at a given (sidereal) time. This is integrated over the visible sky, using the antenna response as known from [26]. Apart from this, the contributions of electronic noise in multiple stages of the signal chain have been fitted, by comparing the measured variations with sidereal time to the curve from LFMap.

Uncertainties in the calibration, and in the directional dependence in the antenna model, translate into systematic uncertainties on the energy estimates. The X_{\max} -estimate is, at least to lowest order, not affected, as all signals arrive from the same direction (to within a degree) for a given air shower. Systematic uncertainties on the calibration amount to 13% in total, where the main contributor (by 11%) is the uncertainty on the sky temperature in our frequency range. The other, minor contributions are uncertainties in the electronic noise levels and from the antenna model.

In [25], a cross-check is described between the energy scales determined from radio and from the particle detectors, respectively. For the particle-based reconstruction, one compares the particle footprint from the best-fitting Corsika shower to the signals at the LORA detectors. The conversion from particles reaching

the ground to LORA signals is simulated using the GEANT4 simulation package [32], a procedure described further in Sect. 2.5.1. Agreement within 10 % was found between the resulting energy scales from radio and from particles.

Additional contributions to the systematic uncertainty on primary energy have been tested and were found to be small. These arise from the choice of simulation code, and from the choice of hadronic interaction model within the simulation code. Switching from CoREAS to ZHAireS [23] yields a difference below 3 %. Thus, importantly, two independent simulation codes aimed at detailed simulations produce very close radio energy levels. A cross-analysis of the QGSJetII-04 interaction model versus Sibyll-2.3c gives another contribution of 3 %.

The resulting systematic uncertainty is 14 %, from adding the contributions in quadrature. This is a considerable improvement from the 27 % in the previous analysis based on the particle detectors.

The statistical uncertainty on the energy estimate follows from our Monte Carlo uncertainty analysis per shower (see Sect. 2.2). The average values for the uncertainties on energy and log-energy, i.e., σ_E and $\sigma_{\log E}$, corresponds to 9 %. Again, this is a notable improvement over the 32 % uncertainty in [8], arising from the large number of radio antennas compared to the 20 particle detectors used earlier.

2.4. Including local atmospheric parameters

To improve the accuracy of the simulations and the X_{\max} reconstructions, we have co-developed an updated version of CORSIKA and CoREAS, which allows to include local atmospheric altitude profiles of density and refractive index into the simulation runs (v7.7100 includes the update).

The atmospheric parameters at the time of each air shower are taken from the Global Data Assimilation System (GDAS) [33], which gives pressure, temperature, and humidity in 24 layers in the atmosphere. These are data used, e.g., in weather models.

The important quantities for us are the altitude profiles of density and refractive index. The density profile determines the amount of matter traversed by the particles along the shower evolution, and therefore the shower geometry depends on this. Due to natural variations in air pressure and temperature, the geometric distance to X_{\max} may be under- or overestimated, leading to a systematic error per shower on the order of 15 to 20 g/cm². In the earlier analysis of [7], the GDAS density profile was used to correct to first order the X_{\max} estimate from simulations using the US Standard Atmosphere.

The refractive index n and its variations are important for the radio emission processes. The refractive index is a function of both the density and the humidity. Natural variations in n make the Cherenkov angle wider or narrower, thus affecting the intensity footprint on the ground [11]. Typical variations of $(n - 1)$ are on the order of 4 %, and introduce a systematic error on the inferred X_{\max} . From simulations, this error was found to be about 4 to 11 g/cm², depending on the zenith angle.

Residual uncertainties in $(n - 1)$ as taken from GDAS temperature, pressure, and humidity are about 0.5 %. From this, uncertainties on X_{\max} are on the order of 1 to 2 g/cm², and will vary between positive and negative from one shower to another, adding to the statistical uncertainty per shower. We have thus removed a systematic uncertainty that is important for precision measurements.

In CORSIKA, five layers are used to parametrize the atmospheric density profile as a function of altitude. In each layer (except for the top layer), the density is set to fall off exponentially with altitude, with a scale height as a free parameter. We have used least-squares curve fitting to determine the optimal parameters to match the five-layer model atmosphere to the GDAS representation [34]. The error on X_{\max} induced by the five-layer approximation was found to be about 4 g/cm², and adds to the statistical uncertainty per shower. It introduces a systematic uncertainty of 1 to 2 g/cm², depending on altitude, hence taken as 2 g/cm².

2.5. Bias-free sample selection

In this section we show how to apply fiducial cuts, i.e., to reject showers that would introduce a composition bias to the sample. Cuts are made only based on the simulated ensemble of showers, not on the measured data (for instance, through fit quality). For the composition measurement, we aim to obtain a sample which is unbiased in X_{\max} . We do not expect, however, to obtain a sample reflecting the natural cosmic-ray energy spectrum, as the effective exposure area, both on the ground and on the sky, depends strongly on energy.

A bias may arise from the particle detector trigger, which is reached more easily for showers penetrating deeper into the atmosphere (high X_{\max}). Another, opposite source of bias arises from the radio detection threshold. We require at least 3 LOFAR stations to detect significant pulses for a given shower. Showers with low X_{\max} have a larger radio footprint, and hence are more likely to trigger three LOFAR stations.

We analyze each measured shower given its energy, reconstructed shower core position, and incoming direction. The central requirement is that this shower would have produced a trigger in both the particle detectors and in the radio data, if it had any other value of X_{\max} in the natural range. Moreover, it must meet the core reconstruction quality criterion explained below. As noted in Sect. 2.2, our simulated ensemble for each measured shower is based on a pre-selection from 600 random showers simulated with CONEX. This sufficiently represents the natural range of X_{\max} , as our (final) dataset is smaller than this.

A dataset comprising all measured showers that meet this requirement is then unbiased in X_{\max} , so this requirement is a sufficient condition. Due to the irregular array layout and moderate event count, a per-shower inclusion criterion is more efficient than attempting to construct a fiducial volume in parameter space (which would also be rather irregular).

2.5.1. Removing selection bias arising from the particle trigger

For each measured shower, we use the set of all simulated showers, including their particle content, to see if each simulated shower would have triggered LORA.

For this, we use the GEANT4 simulation tool [32], which simulates the particles traversing the detectors and their deposited energy. The simulation of the LORA detectors was also used in the measurement of the cosmic-ray energy spectrum presented in [35]. Only if all showers in the ensemble are able to trigger, the measured shower is included in the sample.

From CORSIKA we obtain a list of particles reaching the ground, with their respective positions and momenta. In the GEANT4 simulation, this is converted to an energy deposit at the detector locations. We divide the energy deposit by an average value of 6.2 MeV per particle. The value of 6.2 MeV arises from the most probable energy deposit of single, high-energy muons from an all-sky distribution [35]. Although the muons vary in energy, their deposit is nearly constant with energy.

At the time of each measured shower, we note the trigger threshold of each detector, which was derived during operation from the baseline and standard deviation of its signal time trace. This can be expressed in equivalent muons. When particles hit a detector and produce enough energy deposit, it will trigger. This is subject to Poisson statistics. We evaluate the probability of having $\geq n$ particles giving an energy deposit of 6.2 MeV each, where n is the first integer above the ratio trigger threshold / 1 equivalent muon.

In our trigger setup, a number k out of 20 LORA detectors must trigger in coincidence for the radio data of the air shower to be recorded. The threshold k has been variable over the years of measurements, where $k = 13$ was the most common value. Changes have been made mainly when one or more detectors were down. For each measurement, we use the trigger setting at that time. Hence, also from all simulated showers we require that with a probability of 99%, at least k detectors would trigger (due to statistical fluctuations, the probability cannot reach exactly 100%).

This test has a tendency to remove showers from the sample which have large reconstructed X_{\max} values, i.e., at relatively low altitude in the atmosphere, and/or high inclination. In this case, the given measured shower has produced a trigger, but had its X_{\max} been lower, the number of particles would have been too small. Similarly, showers with low energy and/or a core position far from the LORA detectors are more likely to be rejected.

2.5.2. Removing bias arising from the radio detection threshold

We perform a test against bias from the finite radio detection threshold. The criterion is, similar to the particle detection bias test, that the radio signal for each simulated shower in the ensemble would have been detected above the noise in at least three LOFAR stations.

To this end, we take the core position of the shower that fits best to the LOFAR-measured shower, and position also all other simulated showers here with respect to LOFAR. From the best-fitting shower, we have a fitted scale factor relating simulated to measured pulse energy. Using this scale factor, we obtain the pulse intensities for each simulated shower and for each antenna. The noise intensities from the LOFAR-measured

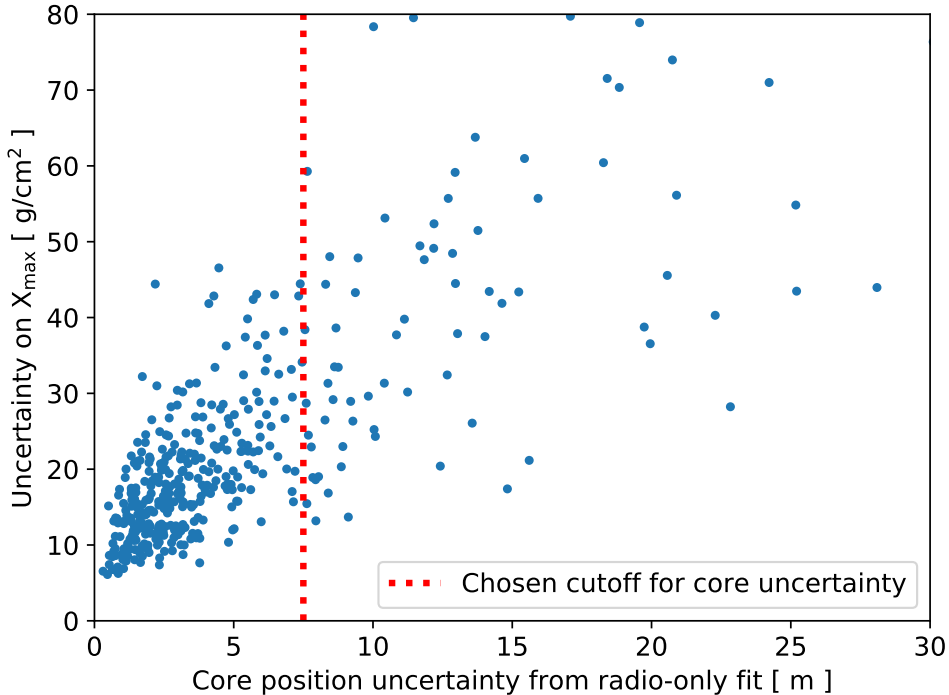


Figure 2: The uncertainty on X_{\max} versus the uncertainty on the core position, per measured shower, after cuts on energy and fiducial selection criteria. The dotted line indicates the chosen cutoff.

showers are taken as reference, and a threshold criterion is set as an energy signal-to-noise ratio of 6 in each antenna. In the data processing pipeline, we have a (somewhat arbitrary) threshold requiring half of the antennas per station to trigger to have a ‘good’ detection. Although that detection is amplitude-based, an energy signal-to-noise ratio of 6 was found to be slightly conservative, and otherwise in good agreement with the amplitude threshold detection.

This test typically rejects showers with a small reconstructed X_{\max} value, i.e., relatively high in the atmosphere, and/or zenith angle; a shower with the same parameters would then have a much smaller radio footprint at high X_{\max} , which may not be able to trigger three LOFAR stations.

2.6. Reconstruction quality cuts

The procedure described in Sect. 2.2 to infer the uncertainty on X_{\max} is also useful as a test of the reconstruction quality of the radio signal. Apart from the X_{\max} uncertainty, it also gives an uncertainty on the fitted shower core position and on the energy. These uncertainties are calculated from the entire simulated ensemble, and hence they are the same for each simulated shower being tested by the two above procedures.

From the three uncertainties, the precision of the core position reconstruction is arguably the most relevant indicator of overall shower reconstruction quality. When this precision is low, one cannot expect either X_{\max} or energy to be reconstructed accurately. Shown in Fig. 2 is the uncertainty on X_{\max} versus the core position uncertainty. They are clearly correlated, and a cut on the reconstruction uncertainty at 7.5 meters was found to be sufficient to reject the majority of poorly reconstructed showers, while retaining showers with low X_{\max} uncertainty.

The appearance of poorly reconstructed showers, despite meeting the other criteria, comes mainly from the position of some showers with respect to the LOFAR array geometry. Most notably, when the core

position is outside the array and/or only three stations have been triggered at low signal-to-noise ratio, the reconstruction precision becomes well below average. This criterion catches these cases automatically.

2.7. Systematic uncertainties

Our method to determine X_{\max} is affected by the following systematic uncertainties, which are summarized in Table 1. The choice of the hadronic interaction model used in CORSIKA, in this case QGSJetII-04, introduces a systematic uncertainty of 5 g/cm^2 [8] in the X_{\max} measurements, due to minor differences in radio footprints when changing the model, for example, to EPOS-LHC [17]. The choice of hadronic interaction model also causes another, larger uncertainty in the composition analysis, as the average X_{\max} for a given element varies by up to about 15 g/cm^2 between models. This is treated separately by repeating the composition analysis with different models.

Residual systematic uncertainties due to variations in the atmosphere, local weather etc. are about 2 g/cm^2 from the five-layer approximation of CORSIKA. This approximation also produces an additional statistical uncertainty of 4 g/cm^2 which is added in quadrature to the statistical uncertainty on X_{\max} per shower. A systematic uncertainty, or bias, in averages of X_{\max} may arise from possible residual bias after applying the above selection criteria. We test this in Sect. 4.2, obtaining a value of 3.3 g/cm^2 to be added as a systematic uncertainty on X_{\max} . Hence, a total systematic uncertainty on X_{\max} of 7 g/cm^2 follows. This is comparable to the systematic uncertainty on X_{\max} in the measurements of [36] who find a value between 7 and 10 g/cm^2 for primary energies above $10^{17.8} \text{ eV}$.

Table 1: Systematic uncertainties in the X_{\max} reconstruction

	Syst. uncertainty	Added stat. unc.
Choice of hadronic interaction model	5 g/cm^2	
Remaining atmospheric uncertainty	$\sim 1 \text{ g/cm}^2$	$\sim 2 \text{ g/cm}^2$
Five-layer atmosphere CORSIKA	2 g/cm^2	4 g/cm^2
Possible residual bias	3.3 g/cm^2	
Curve fit for χ^2 optimum	$\leq 1 \text{ g/cm}^2$	
Total, added in quadrature	7 g/cm^2	

When performing the parabolic fit to the χ^2 values per simulation, as in the middle panel of Fig. 1, a systematic error of up to 5 g/cm^2 may arise if the fit optimum is not contained in the dense region of simulations. This is removed by simulating extra showers around the optimum when needed. A Monte Carlo simulation shows no residual systematic error ($\leq 1 \text{ g/cm}^2$) if the dense region is positioned asymmetrically around the optimum but does contain it.

The systematic uncertainty in the energy estimate from the radio antennas was found to be 14%, or 0.057 in $\lg(E)$ [12]; by convention we write $\lg E \equiv \log_{10} E$.

3. Mass composition analysis

Having established the set of showers for the mass composition analysis, we perform statistical analysis on the measured data, being $(X_{\max}, \sigma_{X_{\max}}, \lg E, \sigma_{\lg E})$ for each shower. We make use of the probability density functions of X_{\max} as a function of energy and atomic mass number A , as parametrized by [37] and updated by [38]. The parametrizations follow a generalized Gumbel distribution, which is a function with 3 parameters, yielding a variable mean, spread, and tail-end asymmetry, respectively. The function has been fitted to a large sample of CONEX showers and has a precision within 2 g/cm^2 for both average and standard deviation of X_{\max} , as well as a close fit to the distribution itself; the high-end tail, which drops exponentially, was shown to be well represented. It should be noted that CONEX is a faster but less complete shower simulation method than CORSIKA. Average X_{\max} values were found to deviate by 4 to 5 g/cm^2 . This is therefore treated as an additional systematic uncertainty on X_{\max} , which for the composition analysis then amounts to 8 g/cm^2 .

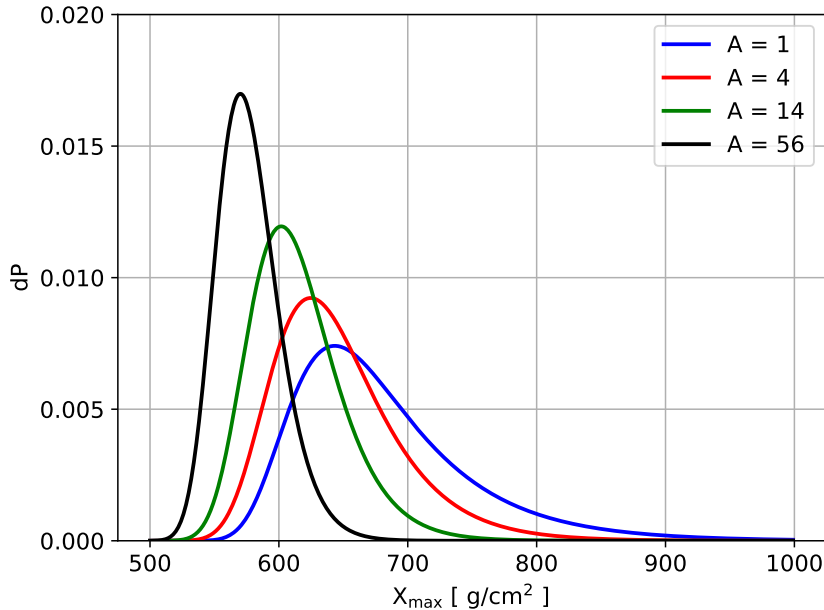


Figure 3: The probability density functions for the depth of shower maximum X_{\max} , for the elements H, He, N, and Fe, at energy 10^{17} eV and hadronic interaction model QGSJetII-04.

Example curves are shown in Fig. 3 for $E = 10^{17}$ eV for protons, helium, nitrogen, and iron nuclei. The functions overlap substantially, limiting the extent to which the individual elements can be distinguished. This is the statistical challenge in performing a composition analysis on X_{\max} data. The mean X_{\max} shifts approximately proportionally to $\ln A$. Therefore, for a 4-component model of astrophysically relevant elements, a reasonable choice is to take p, He, C/N/O, and Fe. These are roughly equally spaced in $\ln A$; as C, N, and O cannot be readily distinguished, either of them can be chosen as a proxy for all three. We choose nitrogen, as this is in between carbon and oxygen, and the best choice in terms of equal spacing in $\ln A$.

3.1. Statistical analysis

We use an unbinned maximum likelihood method to determine the best-fitting parameters for the four-component composition model. This has the advantage of treating each shower separately, instead of relying on X_{\max} -histograms and/or binning in energy. This is especially suitable when the dataset is relatively small and a narrow binning in shower energies is inappropriate.

Given a measured shower with parameters $(X_{\max}, \sigma_{X_{\max}}, \lg E, \sigma_{\lg E})$, its likelihood function for a given element is described by the curves in Fig. 3, convolved with a Gaussian for the uncertainties $\sigma_{X_{\max}}$ and $\sigma_{\lg E}$. For a mixed composition, the likelihood function is a weighted average of these; the mix fractions maximizing the likelihood is taken as the best-fitting composition.

With this method, a complementary goodness-of-fit test is needed, for which we use a Kolmogorov-Smirnov test, enhanced with Monte Carlo simulation. This is a simple, well-known method, comparing the cumulative distribution function (cdf) of the best-fit model to the empirical cumulative distribution of the data. The Kolmogorov-Smirnov test statistic is defined as the maximum difference between the model's cdf $F(X)$ and the empirical distribution $E(X)$:

$$K = \sup_X |F(X) - E(X)|. \quad (2)$$

For our case, where the best-fitting distribution has been estimated from data, standard critical values of the test statistic K do not apply. Instead, to determine the p -value corresponding to K , we use parametric bootstrap sampling from $F(X)$, counting how often the K -value is larger than the one for the dataset. This tests the null hypothesis that the dataset is a random drawing from $F(X)$.

The best-fit model X_{\max} distribution $F(X)$ is taken as the cumulative integral of the linear combination of X_{\max} -distributions $f(X_{\max}, E)$ for the best-fitting composition:

$$f_{\text{sum}}(X_{\max}) = \frac{1}{N} \sum_{k=1}^N \sum_i \alpha_i f_i(X_{\max}, E_k) * \mathcal{N}_X(X_{\max}, \sigma_{X_{\max},k}^2) * \mathcal{N}_{\lg E}(\lg E_k, \sigma_{\lg E,k}^2), \quad (3)$$

summing over all showers (index k) and over the elements in the composition model (index i). Here, $*$ denotes convolution, in this case with Gaussians corresponding to uncertainties in X_{\max} and log-energy.

For the uncertainty analysis we use a likelihood ratio test. Denoting the likelihood of the best-fitting composition as $L(\{\hat{\alpha}\})$, we fix one of the element fractions, say the proton fraction, scanning over the range from 0 to 1. We then find the maximum likelihood composition given the fixed proton fraction, $L(\alpha_p, \{\hat{\alpha}_i\})$, again optimizing over the free parameters indexed by i . This gives the test statistic D :

$$D = 2 \ln \left(\frac{L(\{\hat{\alpha}\})}{L(\alpha_p, \{\hat{\alpha}_i\})} \right). \quad (4)$$

This is nonnegative by definition, and in the large- N limit it follows a chi-squared distribution with 1 degree of freedom, when fixing 1 parameter. The confidence intervals at significance level $1 - p$ then follow directly from the critical values of the chi-squared distribution. For confidence levels of 68, 95, and 99%, these are 1.00, 3.84, and 6.64, respectively.

Confidence intervals for two elements simultaneously, such as used in the contour plot Fig. 11 in Sect. 5 are computed analogously, fixing two parameters instead of one, and noting that the test statistic D then follows a $\chi^2(2)$ -distribution.

When splitting the sample into two equal-sized bins, such as done in Sect. 5.4, one can use another likelihood ratio test to assess the significance of the difference between results in the two bins. For instance, in a model with three independent parameters such as used in this analysis, splitting into two bins adds three parameters to the (model) description of the data. As a result, the combined (log)likelihood, and test statistic D , will be higher than in a single-bin analysis. The difference follows a $\chi^2(3)$ -distribution under the null hypothesis that the data in both bins is a drawing from the same model distributions. This yields a p -value for the difference between the bin results.

4. Results: the measured X_{\max} distribution

In the following sections, we present the results regarding statistics on X_{\max} , such as the estimate of the mean and standard deviation of the X_{\max} distribution. After this, the implications for the cosmic-ray composition in our energy range are given, based on the statistical analysis presented in Sect. 3.

The results are based on a dataset of $N = 334$ cosmic rays with energies between $10^{16.8}$ and $10^{18.3}$ eV, which pass all selection criteria for a bias-free sample with accurately reconstructable showers, as explained in Sect. 2.5. It is a subset of 720 showers measured in at least three LOFAR stations, of which 469 have a core reconstruction precision better than 7.5 m. Another 135 showers did not meet the sample selection criteria; their inclusion would lead to a dataset biased in X_{\max} . The uncertainty on the X_{\max} measurement per shower is on average 19 g/cm^2 . The average fit quality of the best-fitting simulation to the measured LOFAR data is $\chi^2/\text{dof} = 1.19$, indicating a good fit.

4.1. Mean and standard deviation of X_{\max} as a function of primary energy

We have divided the dataset into energy bins of width 0.25 in $\lg(E/\text{eV})$, and computed the mean and standard deviation in each bin.

The sample averages are shown in Fig. 4. The given uncertainty is the uncertainty on the mean of the X_{\max} distribution, i.e., $\sigma/\sqrt{N_{\text{bin}}}$, with sample standard deviation σ . For positioning the points we have used the average log-energy inside each bin. Two showers above $\lg(E/\text{eV}) = 18.25$ were discarded, as no meaningful average can be taken from them.

For comparison, results are included from the Pierre Auger Observatory [39], HiRes [40], Tunka [41], and Yakutsk [42]. We also include recent results from TALE [43], noting that their method to infer a bias-corrected $\langle X_{\max} \rangle$ is different and assumes the EPOS-LHC hadronic interaction model.

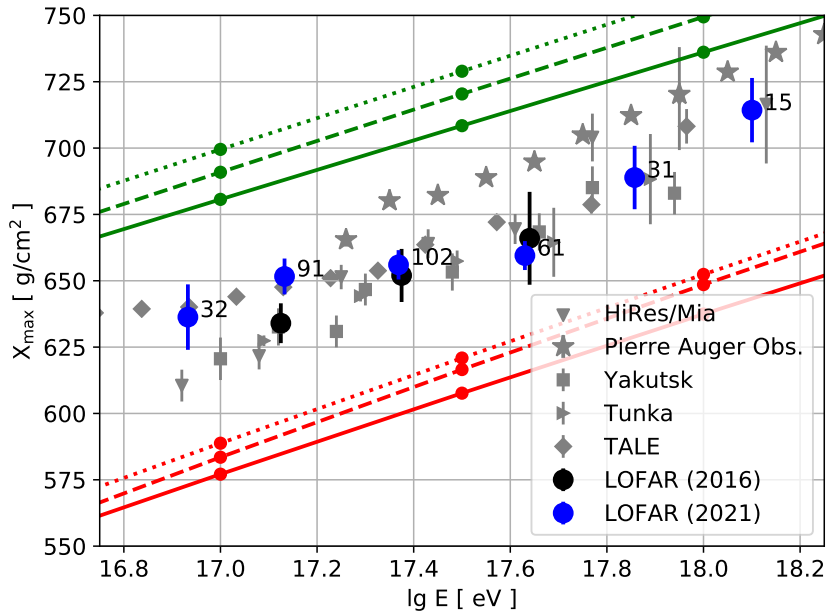


Figure 4: The average depth of shower maximum X_{\max} , as a function of primary particle energy. The annotated numbers indicate the number of showers in each bin, and the error margins indicate the uncertainty on the mean of the X_{\max} distribution. The upper lines indicate the mean values expected for protons, from simulations with QGSJetII-04 (solid), EPOS-LHC (dashed) and Sibyll-2.3d (dotted). The lower lines show the mean predicted values for iron nuclei. For comparison, results from Pierre Auger [39], Yakutsk [42], Tunka [41], HiRes/Mia [40], and TALE [43] are included.

The differences with respect to the earlier LOFAR results [8] can be explained through statistical fluctuations, and from the revised treatment of systematic effects including the atmosphere and the radio-derived energy scale. The lowest-energy data point stands out somewhat, with a difference of 17.6 g/cm^2 , at statistical uncertainties of 7.5 and 6.8 g/cm^2 for the older and newer result, respectively. Such a difference in one of three overlapping data points is not unreasonable just from statistics; it is also possible that improvements in fiducial selection criteria make some difference here, as differences are expected to appear especially at lower energies where signals are closer to trigger thresholds.

The average X_{\max} agrees reasonably well with the other experiments such as Tunka, Yakutsk, HiRes/Mia, and TALE, especially for $\lg E > 17.2$. However, the results from the Pierre Auger Observatory, which is the largest experiment, are somewhat higher starting at the bin around $\lg E = 17.325$. Their statistical uncertainty is smaller than the plotted symbols, arising from a high number of showers (1000 to 2600) per individual bin. Systematic uncertainties on X_{\max} in this energy range are about 11 g/cm^2 for Auger [44], and about 7 g/cm^2 for LOFAR. Additionally, there is a systematic uncertainty in energy, which for LOFAR as well as Auger [45] is about 0.057 in $\lg E$.

To better compare the results of LOFAR and Pierre Auger Observatory and their systematic uncertainties, we have plotted these separately in Fig. 5. The band plots are seen to have little to no overlap, although systematic uncertainties in energy could shift either result horizontally in this plot, according to the margins

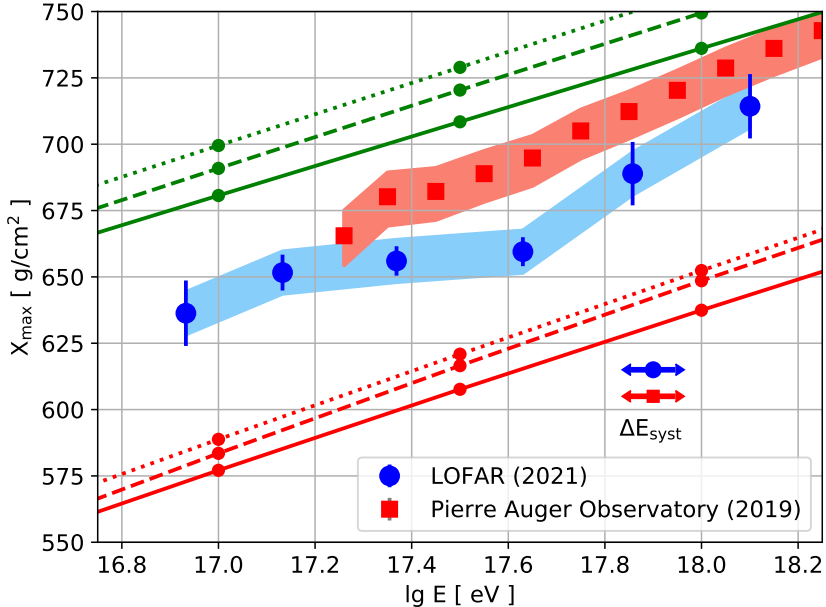


Figure 5: Average X_{\max} versus primary energy, for LOFAR and Pierre Auger Observatory, with colored bands indicating their systematic uncertainty on X_{\max} . The uncertainty margins per data point are statistical uncertainties only. The systematic uncertainty on energy is the same for both experiments, and is indicated by the arrows to the lower right.

indicated by arrows.

Thus, there is tension between these results. There is a notable difference in methodology to measure X_{\max} , being direct fluorescence detection versus radio detection with Corsika/CoREAS simulations. In both cases, considerable attention was given to estimating systematic uncertainties from different contributions. In the range where LOFAR and Auger overlap, our results are in agreement with the other shown experiments on the Northern hemisphere, including the recent results from TALE. Also, our earlier results from 2016 are consistent with the present results, while for the latter, systematic uncertainties on energy and atmospheric effects have been lowered considerably. Hence, the apparent difference is not fully explained at present.

In Fig. 6, we show the standard deviation in each bin, along with its uncertainty. To calculate these, as an estimator $\hat{\sigma}$ of the underlying X_{\max} -distribution's standard deviation, we subtract the variance caused by the X_{\max} uncertainty per measured shower:

$$\hat{\sigma} = \sqrt{\sigma^2 - \frac{1}{N_j} \sum_{i=1}^{N_j} u_i^2}, \quad (5)$$

with σ the sample standard deviation, u_i the X_{\max} uncertainty on each shower, and N_j is the number of showers in energy bin j . The uncertainty on the standard deviation of the distribution is estimated using a parametric bootstrap, taking the best-fit mass composition from Sect. 5.1. In this method one needs to assume a particular model distribution, but it is suitable for estimating uncertainties in small samples. Switching the hadronic interaction model was found to make little difference here.

The results are consistent with those from the Pierre Auger Observatory, except for one bin around $\lg E = 17.625$. However, a caveat is the relatively low number of showers per bin, and the exponential tail of the X_{\max} -distributions. The showers at the high end of X_{\max} , roughly $X_{\max} > 800 \text{ g/cm}^2$, appear in our dataset only at low-number statistics level, while their presence shifts the standard deviation considerably upward. In the energy bin from $\lg E = 17.5$ to 17.75 , there happen to be none, thus lowering the sample standard deviation.

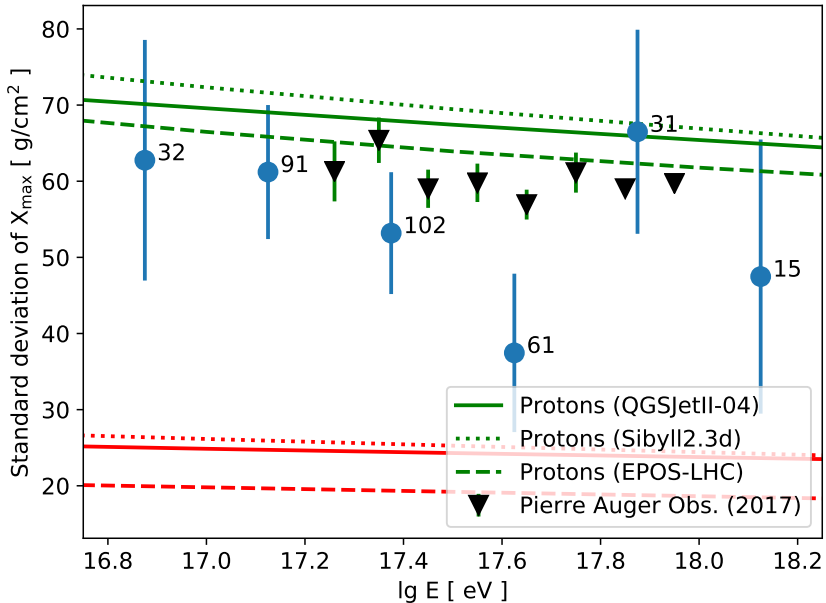


Figure 6: The standard deviation of X_{\max} as a function of primary particle energy. The margins indicate the uncertainty on the standard deviation of the X_{\max} distribution. Results from the Pierre Auger Observatory are shown, together with the values from simulations of protons and iron nuclei (high and low lines, respectively).

The results are summarized in Fig. 7, showing the histograms in each energy bin.

4.2. Tests for residual bias

In our energy range, the average X_{\max} of the measured showers is expected to be independent of shower parameters such as the zenith angle. This follows from the fact that the cosmic-ray composition in our energy range is independent of time and incoming direction, as far as is known from experiments. This allows to perform a test of our sample for a residual bias in X_{\max} due to variations in these parameters. Our sample of 334 showers has an average X_{\max} of $659 \pm 3.3 \text{ g/cm}^2$.

As discussed in Sect. 2.5, a biased sample would readily show a dependence of the average X_{\max} on zenith angle. However, the average X_{\max} also depends on the energy; its expected value is to good approximation linear in $\lg E$ over our energy range. From the parametrization using Gumbel distributions, as discussed in Sect. 3, and for the QGSJetII-04 hadronic interaction model, we find, for a factor 10 increase in energy, an average rise in X_{\max} (elongation rate) of 55.4, 57.8 and 60.3 g/cm^2 , for protons, nitrogen, and iron nuclei, respectively. This is in good agreement with the elongation rate of 58 g/cm^2 predicted, for example, by the Heitler-Matthews model [46].

The average (log-)energy of our measured showers tends to rise with zenith angle. This is no problem, as long as there is no bias in X_{\max} . A possible residual bias in X_{\max} , corrected for the influence of varying energy, is evaluated by introducing a parameter Y for each shower, as

$$Y = X_{\max} + 57 (\lg (E/\text{eV}) - 17.4) \text{ g/cm}^2, \quad (6)$$

where 17.4 is approximately the average value of log-energy in our sample.

The results are shown in the right panel of Fig. 8, together with a linear fit. The uncertainty margins are once again given by the standard error of the mean. A constant fit of $Y = 660$ as well as a linear fit are shown.

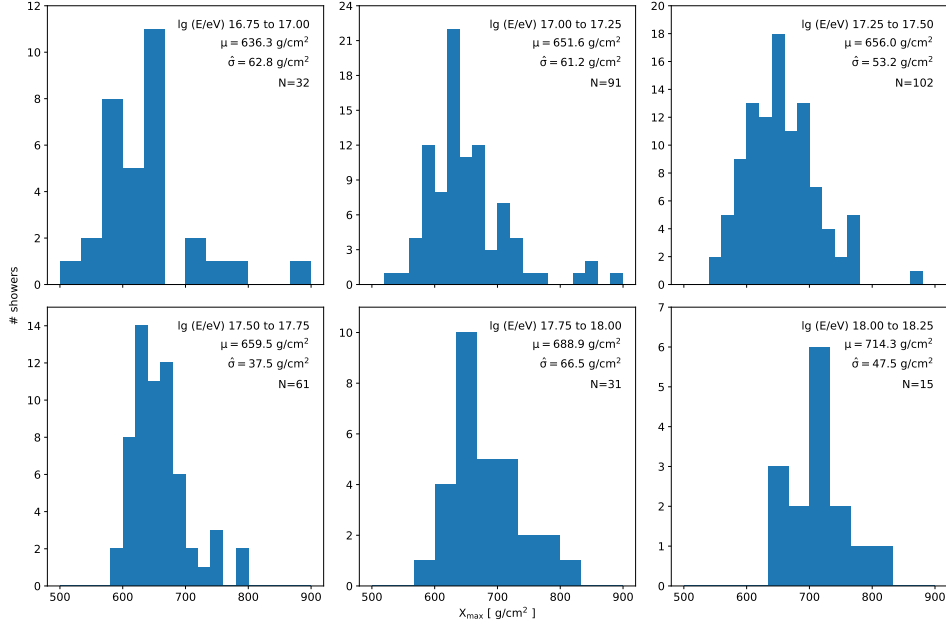


Figure 7: Histograms of X_{\max} for each energy bin. The average (μ) and standard deviation estimates ($\hat{\sigma}$) per bin are as shown in Figs. 4 and 6, respectively.

The linear fit has a slope parameter of -0.10 ± 0.30 . Hence, the slope is compatible with zero, and no residual bias is evident. The high value near 700 for the rightmost bin appears suggestive, but as it contains only eight showers and has a correspondingly large uncertainty, it is not significant. The constant fit has an uncertainty of 3.3 g/cm^2 . A bias at this level cannot be ruled out, hence this is added as a contribution to the systematic uncertainty on X_{\max} .

We also show a complete scatter plot of X_{\max} versus zenith angle, in Fig. 9. This plot shows the effect of the bias tests for the radio and particle detectors and the corresponding fiducial cuts (Sect. 2.5.1 and 2.5.2). As expected, the particle bias test flags most events at high inclination and high X_{\max} , especially above 45 degrees. The radio bias test flags mostly the opposite region, low X_{\max} and low inclination.

Consequently, we see only few showers passing the tests at $\theta < 10^\circ$, and there are only 8 in the highest zenith angle bin above 45° . The plot makes clear that the fiducial cuts from Sect. 2.5 are necessary, as there would have been a strong zenith angle dependence, and thus a biased X_{\max} -sample, had it been omitted.

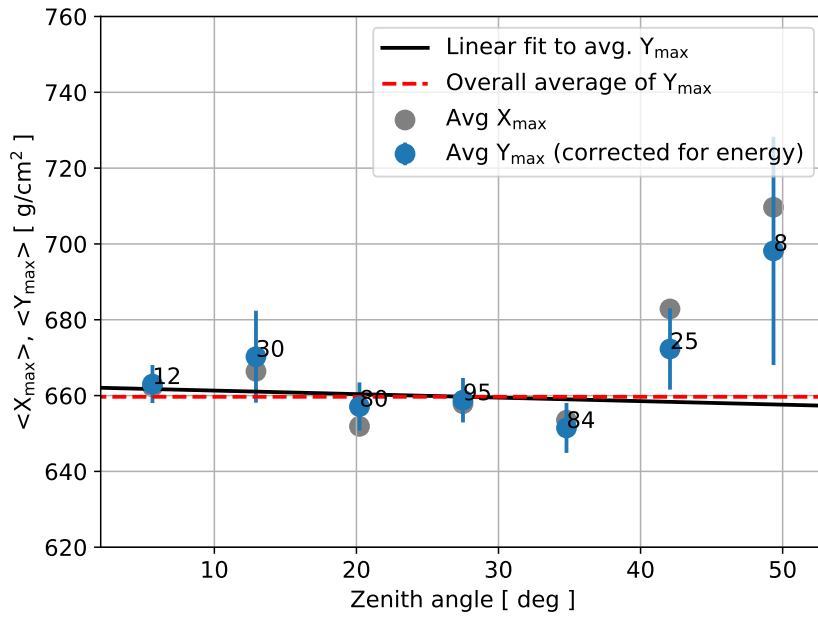


Figure 8: Average Y (from Eq. 6) versus zenith angle, together with a constant and linear fit.

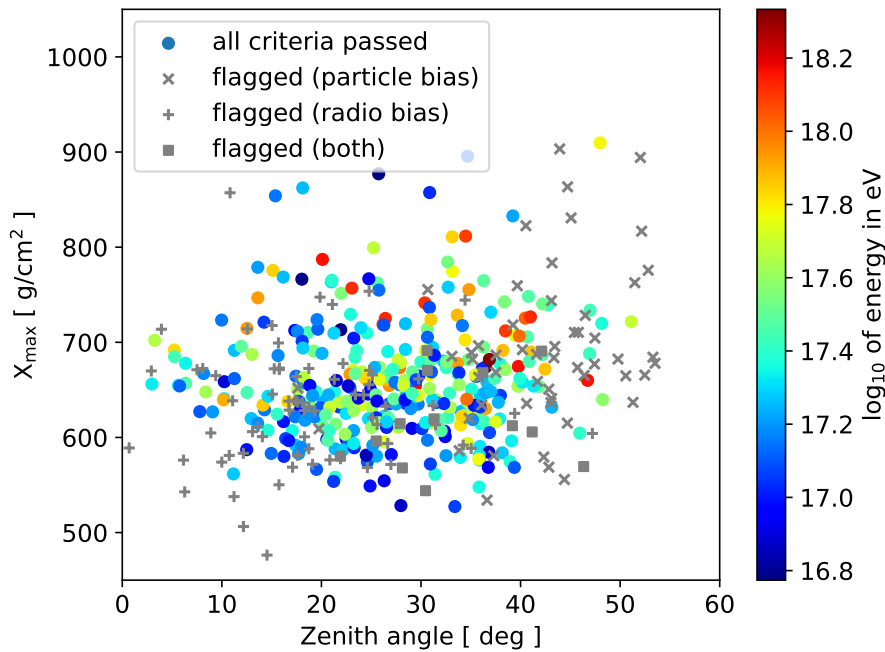


Figure 9: Scatter plot of X_{\max} versus zenith angle, for all 469 showers with core reconstruction precision better than 7.5 m. Colored circles represent the 334 showers passing all criteria, with the color denoting their energy. The showers flagged by the particle and radio bias tests are also shown.

5. Mass composition results

We have applied the statistical analysis in Sect. 3 to the set of 334 showers passing all selection criteria. Results are shown in detail for the QGSJetII-04 model, and summarized for the other two considered, which are EPOS-LHC [17] and Sibyll-2.3d [18]. We show the results for the full range, followed by a division in two equally-sized energy bins. Owing to the strong overlap in X_{\max} -distributions (see Fig. 3), an $N = 334$ dataset is modest-sized for mass composition analysis based on a multi-element model, hence further binning is not appropriate. The statistical method presented in Sect. 3.1 is well suited for analysis of a wide energy range without loss of measurement information.

5.1. Statistics for the QGSJetII-04 hadronic interaction model

The maximum likelihood estimate was found to be 28% protons, 11% helium, 60% nitrogen and 1% iron. A histogram of X_{\max} is shown in Fig. 10 (top), for the full energy range. The coverage of this energy range can be summarized by a mean log-energy of $\lg(E/\text{eV}) = 17.39$ and a standard deviation of 0.32. Hence, the ‘center of mass’ of the dataset lies between 17.07 and 17.71.

The red (solid) curve is the best-fitting distribution, found using the maximum likelihood method and Eq. 3. The distributions for the elements that make up the best-fitting distribution are also shown, scaled by their respective mix fractions.

We have tested the goodness-of-fit of the best-fitting model to our dataset, using the Kolmogorov-Smirnov distance between the cumulative and empirical distributions (Sect. 3.1) as compared to random drawings from the best-fit distribution. As shown in Fig. 10 (bottom), the model is a good fit to the data ($p = 0.96$). Switching the hadronic interaction model to EPOS-LHC or Sibyll-2.3d produces about equally good fits to the data, at $p = 0.93$ and $p = 0.90$ respectively. Hence, all three models fit the data well, at their respective best-fitting composition. It is of course possible that this would change with a larger dataset and/or smaller energy bins.

We observe that protons and helium are to a significant degree interchangeable in the statistical analysis of our model, given our dataset. This is readily seen in the contour plot in Fig. 11, showing the D -statistic for the likelihood ratio test, versus proton and helium fractions. The contours show the allowed regions with confidence levels one-sigma (68%), 95%, and 99%, respectively. Within the one-sigma region, one can exchange helium for protons in a ratio of about 3 to 1. The contour plot underlines, for example, that the dataset only allows a very low proton fraction if the helium fraction is rather large instead.

5.2. Accounting for systematic uncertainties

The systematic uncertainty in X_{\max} amounts to $\pm 8.1 \text{ g/cm}^2$ (before roundoff), including the contribution from the CONEX-based parametrizations. The energy uncertainty of 14%, or 0.057 in $\lg E$ has, to first order, the effect of an overall shift of X_{\max} in the X_{\max} -distributions (see Eq. 6), of 3.1 g/cm^2 . By adding both uncertainties in quadrature, we obtain a systematic uncertainty of 9 g/cm^2 .

Evaluating the composition results for $X_{\max} \pm 9 \text{ g/cm}^2$ for all showers, we obtain limits for the best fit, as well as the (expanded) confidence intervals that arise for a systematic shift in this range. Noteworthy is for example that when the average X_{\max} is shifted downward, the helium fraction is fitted much higher at the expense of the nitrogen fraction. Helium is then favored over nitrogen in the fit, due to the lower expected X_{\max} at lower energies, and the longer ‘tail’ of the X_{\max} distribution for helium.

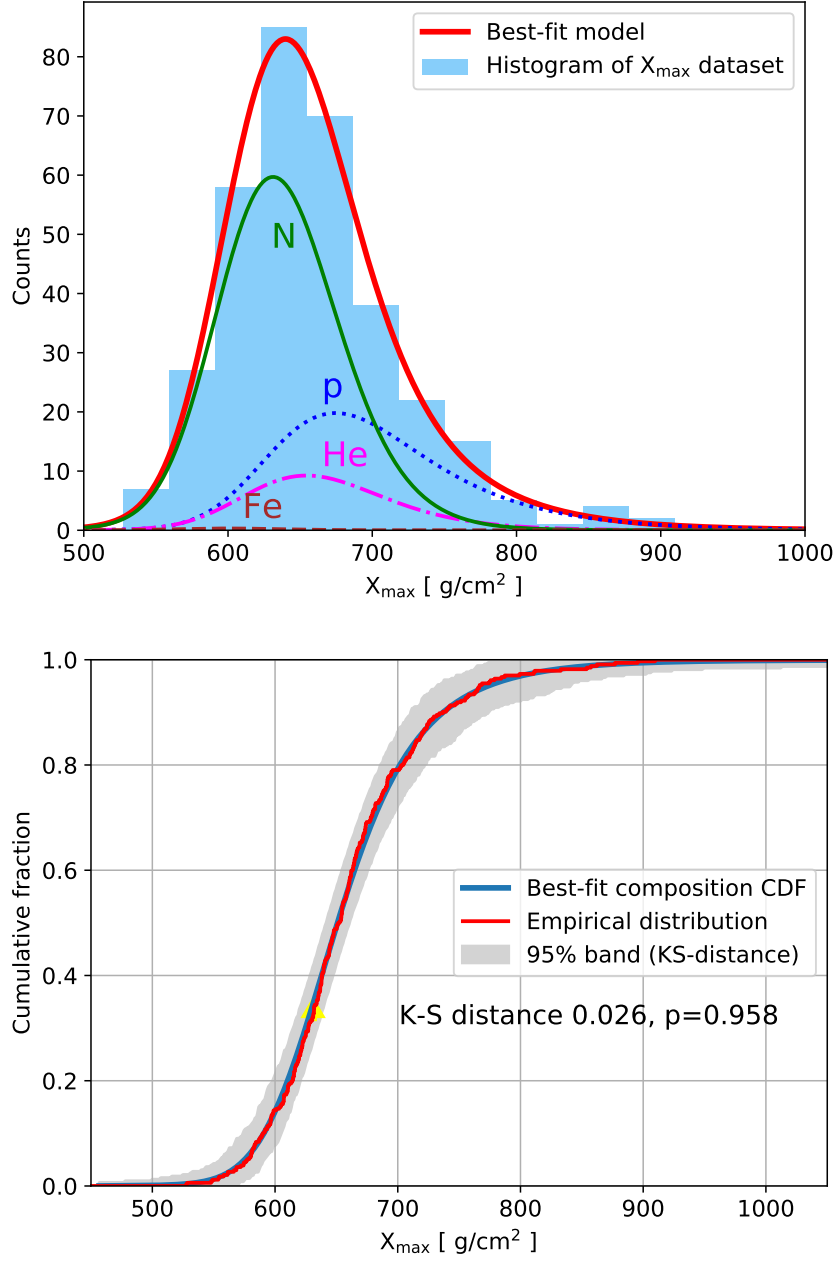


Figure 10: Top: A histogram of X_{\max} , together with the best-fitting distribution from Eq. 3. Bottom: The cumulative distribution corresponding to the best-fit composition model, together with the empirical distribution from our dataset. The yellow arrow indicates where the distance between CDF and empirical distribution is maximal. The grey band is the envelope of all simulated empirical distributions that have a K-S distance to the CDF below its 95-percentile level. Both graphs indicate a good fit.

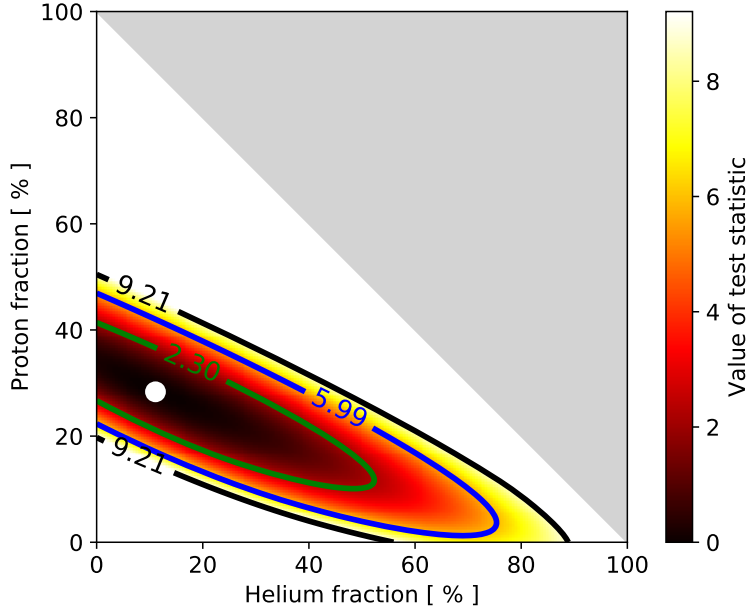


Figure 11: Contour plot of the proton and helium fraction, giving the regions consistent with a one-sigma, 95% and 99% confidence level, respectively.

5.3. Results for three hadronic interaction models

The results for the hadronic interaction models QGSJetII-04, EPOS-LHC, and Sibyll-2.3d are plotted in Fig. 12.

For EPOS-LHC, it is seen that the fit favors a more heavy composition, with more iron instead of nitrogen, and with a significant upper bound on the helium fraction. Sibyll-2.3d shows a still somewhat heavier composition, with a lower proton fraction and a higher nitrogen fraction at best fit. Otherwise, the results are very similar across these three hadronic interaction models, especially considering the uncertainty margins. The intermediate-mass elements in the C/N/O range (possibly stretching to somewhat higher mass numbers as well) are dominant, and there is a significant fraction of light elements, i.e., protons and helium, at best fit ranging from 23 to 39%, depending on the interaction model. Apart from a crossover from C/N/O to iron, the choice of hadronic interaction model has only a limited effect on the best-fit results. From the large intermediate-mass contribution it is clear that the composition cannot be described as a two-component mixture of protons and iron. This is confirmed by a likelihood ratio test with respect to the 4-component model, yielding a p-value $p < 10^{-10}$. However, a two-component mixture of protons and nitrogen would work for QGSJetII-04 ($p = 0.9$).

For this dataset, helium and nitrogen are not fully resolved in the composition model. The fitted values for the helium and nitrogen fraction are highly anti-correlated, which follows from the requirement that all mix fractions sum up to 1. Helium and nitrogen are a factor 3.5 apart in atomic mass number, whereas the other consecutive elements are a factor 4 apart; constant factors here correspond to a constant shift in $\ln A$, and the mean of the X_{\max} -distributions varies by an amount proportional to $\ln A$. Moreover, helium and nitrogen have two 'neighboring' elements in the composition model, unlike hydrogen and iron. This increases sensitivity to a systematic shift (up or down) in X_{\max} .

Importantly, when comparing the current results to the earlier LOFAR results published in [8], the results are found to be consistent, after various improvements to the analysis setup, the systematic uncertainties, and having a larger dataset.

The previous, smaller dataset allowed for a near-100% helium fraction and essentially no protons; this

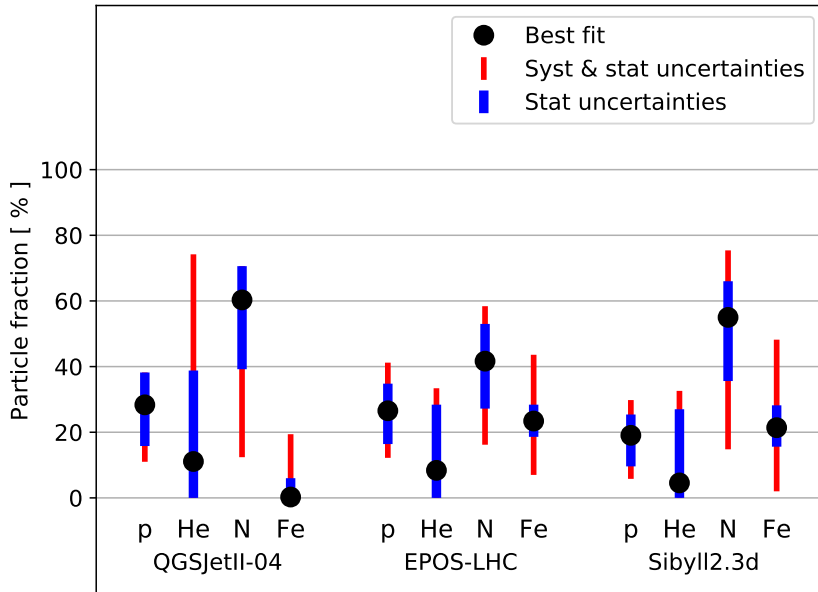


Figure 12: Composition results from our dataset, assuming each of the three hadronic interaction models shown at the bottom. The best fit is shown along with statistical and systematic uncertainties.

scenario is now very unlikely. As shown in Fig. 11, a similar but somewhat more constrained interchange between protons and helium is still possible. There are astrophysical scenarios where one would see very few protons but a large helium and carbon fraction. For example, a transition from a Galactic component dominated by Wolf-Rayet supernovae to a particularly strong extragalactic component at these energies could produce a helium fraction near 60% plus a small proton fraction of about 5% at our central energy around $2 \cdot 10^{17}$ eV [4]. This is still allowed within 95% confidence limits.

Comparing the results to those from Pierre Auger Observatory [47], starting at $\lg(E/\text{eV}) = 17.25$, agreement is found within statistical and systematic margins. At best fit, their proton fractions are higher, in line with the higher average X_{max} . The difficulty in resolving helium and nitrogen remains, at their higher level of statistics.

Generally, the statistical margins indicate that the analysis would improve with more data. This is no surprise, at a modest number of showers. However, systematic uncertainties are also important at any level of statistics, as they enlarge the margins of statistical plus systematic uncertainties together. This is especially evident in the fitted iron fraction, which is well bounded by statistics, but has substantially expanded margins when systematic uncertainties are included. Also, looking once more at the substantially overlapping X_{max} -distributions in Fig. 3, it is clear that achieving lower systematic offsets in X_{max} is still important, to improve the resolution of the composition analysis as well as the separability of the element fractions.

5.4. Analysis in two energy bins

We have divided the dataset into two bins with equal number of showers, being those below versus above the median of $\lg(E/\text{eV}) = 17.34$. This is a conservative choice with respect to statistical significance. The results for the three interaction models are shown in Fig. 13. The coverage of the energy bins, summarized as an average and standard deviation, is mainly at $\lg(E/\text{eV}) = 17.14 \pm 0.13$, and 17.65 ± 0.23 , respectively.

Notable is the best-fit proton fraction, which is lower in the high-energy bin for all three interaction models. However, from a likelihood ratio test (see Sect. 3.1, bottom) the difference between the two bins

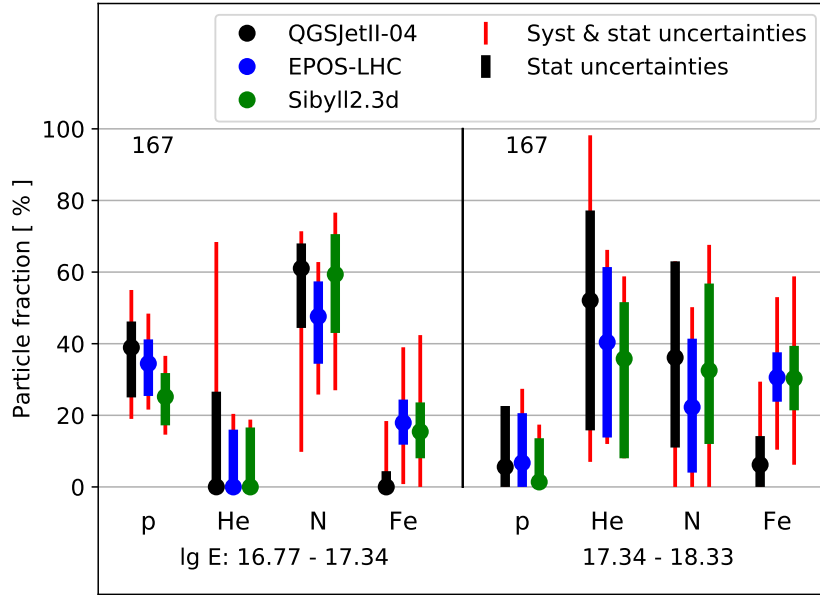


Figure 13: Mass composition results in two energy bins. The energy ranges per bin are shown; their main coverage is at 17.14 ± 0.13 , and 17.65 ± 0.23 , respectively.

was found not to be statistically significant. That is, a null hypothesis that the observed difference between the two bins would arise from a mass composition constant with energy, as in Fig. 12, is not rejected ($p = 0.58$).

A similar, simpler test is to use Eq. 6 to take out the first-order energy-dependence of X_{\max} , and split the dataset in two equal-sized bins, for lower and higher energy, respectively. This is a non-parametric test which does not depend on element-based composition models using X_{\max} -distributions. Also, the elongation rate does not have a strong dependence on the interaction model.

The difference in average Y_{\max} between the low and the high-energy bin is not significant ($p = 0.25$). Thus, it is clear that a larger dataset is needed to draw conclusions on possible variations of the element fractions with energy. Would such a trend towards lower proton fractions be confirmed, it would challenge the hypothesis of a transition from a helium and C/N/O-dominated Galactic to a proton-dominated extragalactic component at energies below 10^{18} eV.

6. Summary

We have presented an updated cosmic-ray mass composition analysis from LOFAR radio data, built on an improved method for measuring the depth of shower maximum X_{\max} of air showers. For the reconstruction of shower parameters, CORSIKA / CoREAS simulations have been used.

We have incorporated several refinements to our analysis, such as including local atmospheric parameters, the Galaxy-based radio calibration and energy measurement, and improved detector characterisation in the fiducial sampling procedure. This leads to an energy resolution of 9% and an X_{\max} -resolution of 19 g/cm² on average, and a systematic uncertainty of 14% on energy and 7 g/cm² on X_{\max} , or 9 g/cm² in the mass composition analysis.

To obtain an unbiased dataset suitable for composition studies, three selection criteria were applied to a set of 720 reconstructed showers, based on the ensemble of simulations per measured shower. Requiring a shower core precision better than 7.5 m gives a sufficient general cut on reconstruction quality. We further require that each simulated shower in the CORSIKA / CoREAS ensemble must be able to trigger the LORA particle detector array, and also pass the detection and quality criteria of the LOFAR radio analysis pipeline. This procedure leaves a sample of 334 showers for analysis of X_{\max} -statistics and (mixed) element composition.

The inferred average and standard deviation of X_{\max} have been presented in a (log-)energy range of $16.75 < \lg(E/\text{eV}) < 18.25$. The average X_{\max} was found to be in line with results from Northern hemisphere-based observatories such as Tunka, Yakutsk, HiRes/Mia, and TALE. However, the values are somewhat lower than those from the Pierre Auger Observatory, where their energy range overlaps. The origin of this tension remains unclear and requires additional research.

Apart from the first two moments, we have also analysed the X_{\max} -data at (complete) distribution level, using a four-component model of elements, about equally spaced in $\ln A$. An unbinned maximum likelihood method was found suitable to obtain the best-fitting mass composition in our energy range, together with a separate goodness-of-fit test. This relies on high-precision parametrizations of the X_{\max} -distributions of the elements, as produced by [37] and updated by [38].

From this analysis, the best-fitting mass composition for our dataset is 28% protons, 11% helium, 60% nitrogen and 1% iron, assuming the QGSJetII-04 hadronic interaction model. This is averaged over our energy range, with coverage mainly at a log-energy of $\lg(E/\text{eV}) = 17.39 \pm 0.32$. The EPOS-LHC and Sibyll-2.3d models tend towards a heavier composition, with an iron fraction just above 20% as a best fit. The light-mass elements together, protons plus helium, form a fraction of 23 to 39% at best fit. Overall, the differences in composition results between these three important hadronic interaction models are minor, apart from a shift between nitrogen and iron. For these differences to become significant, a larger dataset would be needed. A division of the dataset into two equal-sized bins, for lower and higher energy respectively, yielded no significant difference, both in the model-based composition analysis and in the difference in elongation-rate-corrected X_{\max} (Eq. 6).

The present results are consistent with the earlier LOFAR results [8], thus confirming an appreciable light-mass component in this energy range, at a lower level of systematic uncertainties and from an extended dataset. The element-based mass composition results are in agreement with those from the Pierre Auger Observatory, within systematic and statistical uncertainties. Hence, the tension in the average X_{\max} results does not translate to element-based results outside their uncertainty margins. To conclude, we have shown that our X_{\max} -analysis per air shower achieves an accuracy in line with the current state of the art, and demonstrates the value of the radio detection method for measuring air showers.

Acknowledgements

We acknowledge funding from the European Research Council under the European Union’s Horizon 2020 research and innovation programme (grant agreement n. 640130). TNGT acknowledges funding from Vietnam National Foundation for Science and Technology Development (NAFOSTED) under grant number 103.01-2019.378. ST acknowledges funding from the Khalifa University Startup grant, project code 8474000237-FSU-2020-13.

LOFAR, the Low Frequency Array designed and constructed by ASTRON, has facilities in several countries, that are owned by various parties (each with their own funding sources), and that are collectively operated by the International LOFAR Telescope (ILT) foundation under a joint scientific policy.

References

References

- [1] J. Abraham, et al., Trigger and aperture of the surface detector array of the Pierre Auger Observatory, *Nuclear Instruments and Methods in Physics Research Section A: Accelerators, Spectrometers, Detectors and Associated Equipment* 613 (1) (2010) 29 – 39. doi:10.1016/j.nima.2009.11.018.
- [2] J. Abraham, et al., Properties and performance of the prototype instrument for the Pierre Auger Observatory, *Nuclear Instruments and Methods in Physics Research Section A: Accelerators, Spectrometers, Detectors and Associated Equipment* 523 (1) (2004) 50 – 95. doi:10.1016/j.nima.2003.12.012.
- [3] A. Hillas, The origin of ultra-high energy cosmic rays, *Annual Review of Astronomy and Astrophysics* 22 (1984) 425.
- [4] Thoudam, S., et al., Cosmic-ray energy spectrum and composition up to the ankle: the case for a second Galactic component, *A&A* 595 (2016) A33. doi:10.1051/0004-6361/201628894.
- [5] K.-H. Kampert, M. Unger, Measurements of the cosmic ray composition with air shower experiments, *Astroparticle Physics* 35 (10) (2012) 660 – 678. doi:10.1016/j.astropartphys.2012.02.004.
- [6] T. Huege, Radio detection of cosmic ray air showers in the digital era, *Physics Reports* 620 (2016) 1.
- [7] S. Buitink, et al., Method for high precision reconstruction of air shower X_{\max} using two-dimensional radio intensity profiles, *Phys. Rev. D* 90 (2014) 082003. doi:10.1103/PhysRevD.90.082003.
- [8] S. Buitink, et al., A large light-mass component of cosmic rays at $10^{17} - 10^{17.5}$ electronvolts from radio observations, *Nature* (2016) 70 doi:10.1038/nature16976.
- [9] D. Heck, et al., CORSIKA: a Monte Carlo code to simulate extensive air showers., 1998.
- [10] T. Huege, M. Ludwig, C. W. James, Simulating radio emission from air showers with CoREAS, ARENA 2012, AIP Conf. Proc. 1535 (2013) 128–132doi:10.1063/1.4807534.
- [11] A. Corstanje, et al., The effect of the atmospheric refractive index on the radio signal of extensive air showers, *Astroparticle Physics* 89 (2017) 23 – 29. doi:10.1016/j.astropartphys.2017.01.009.
- [12] K. Mulrey, et al., Calibration of the LOFAR low-band antennas using the Galaxy and a model of the signal chain, *Astroparticle Physics* 111 (2019) 1–11. doi:10.1016/j.astropartphys.2019.03.004.
- [13] T. Bergmann, et al., One-dimensional hybrid approach to extensive air shower simulation, *Astroparticle Physics* 26 (6) (2007) 420 – 432. doi:10.1016/j.astropartphys.2006.08.005.
- [14] M. P. van Haarlem, et al., LOFAR: The Low Frequency Array, *Astronomy and Astrophysics* 556 (2013) A2.
- [15] S. Thoudam, et al., LORA: A scintillator array for LOFAR to measure extensive air showers, *Nuclear Instruments and Methods in Physics Research Section A: Accelerators, Spectrometers, Detectors and Associated Equipment* 767 (2014) 339 – 346. doi:10.1016/j.nima.2014.08.021.
- [16] S. Ostapchenko, QGSJET-II: physics, recent improvements, and results for air showers, *EPJ Web of Conferences* 52 (2013) 02001. doi:10.1051/epjconf/20125202001.
- [17] T. Pierog, I. Karpenko, J. M. Katzy, E. Yatsenko, K. Werner, EPOS LHC: test of collective hadronization with data measured at the CERN Large Hadron Collider, *Phys. Rev. C* 92 (2015) 034906. doi:10.1103/PhysRevC.92.034906.
- [18] F. Riehn, R. Engel, A. Fedynitch, T. K. Gaisser, T. Stanev, Hadronic interaction model sibyll 2.3d and extensive air showers, *Phys. Rev. D* 102 (2020) 063002. doi:10.1103/PhysRevD.102.063002.
- [19] E.-J. Ahn, R. Engel, T. K. Gaisser, P. Lipari, T. Stanev, Cosmic ray interaction event generator SIBYLL 2.1, *Phys. Rev. D* 80 (2009) 094003. doi:10.1103/PhysRevD.80.094003.
- [20] C. W. James, H. Falcke, T. Huege, M. Ludwig, General description of electromagnetic radiation processes based on instantaneous charge acceleration in “endpoints”, *Phys. Rev. E* 84 (2011) 056602. doi:10.1103/PhysRevE.84.056602.
- [21] O. Scholten, K. Werner, F. Ruydi, A macroscopic description of coherent geo-magnetic radiation from cosmic-ray air showers, *Astroparticle Physics* 29 (2008) 94–103. arXiv:0709.2872, doi:10.1016/j.astropartphys.2007.11.012.
- [22] O. Scholten, T. N. G. Trinh, et al., Measurement of the circular polarization in radio emission from extensive air showers confirms emission mechanisms, *Phys. Rev. D* 94 (2016) 103010. doi:10.1103/PhysRevD.94.103010.
- [23] J. Alvarez-Muñiz, et al., Monte Carlo simulations of radio pulses in atmospheric showers using ZHAireS, *Astroparticle Physics* 35 (2012) 325–341.

- [24] M. Gottowik, C. Glaser, T. Huege, J. Rautenberg, Determination of the absolute energy scale of extensive air showers via radio emission: Systematic uncertainty of underlying first-principle calculations, *Astroparticle Physics* 103 (2018) 87 – 93. doi:10.1016/j.astropartphys.2018.07.004.
- [25] K. Mulrey, et al., On the cosmic-ray energy scale of the LOFAR radio telescope, *Journal of Cosmology and Astroparticle Physics* 2020 (11) (2020) 017–017. doi:10.1088/1475-7516/2020/11/017.
- [26] P. Schellart, A. Nelles, et al., Detecting cosmic rays with the LOFAR radio telescope, *Astronomy & Astrophysics* 560 (2013) A98. arXiv:1311.1399, doi:10.1051/0004-6361/201322683.
- [27] A. Nelles, et al., The radio emission pattern of air showers as measured with LOFAR: a tool for the reconstruction of the energy and the shower maximum, *Journal of Cosmology and Astroparticle Physics* 2015 (05) (2015) 018.
- [28] Pierre Auger Collaboration, Measurement of the radiation energy in the radio signal of extensive air showers as a universal estimator of cosmic-ray energy, *Phys. Rev. Lett.* 116 (2016) 241101. doi:10.1103/PhysRevLett.116.241101.
- [29] A. Nelles, et al., A parameterization for the radio emission of air showers as predicted by CoREAS simulations and applied to LOFAR measurements, *Astroparticle Physics* 60 (2015) 13 – 24. doi:10.1016/j.astropartphys.2014.05.001.
- [30] C. Glaser, M. Erdmann, Jörg R. Hörandel, T. Huege, J. Schulz, Simulation of radiation energy release in air showers, *Journal of Cosmology and Astroparticle Physics* 2016 (09) (2016) 024–024. doi:10.1088/1475-7516/2016/09/024.
- [31] E. Polisensky, LFmap: A low frequency sky map generating program.
URL <http://www.faculty.ece.vt.edu/swe/lwa/memo/lwa0111.pdf>
- [32] S. Agostinelli, et al., Geant4: a simulation toolkit, *Nuclear Instruments and Methods in Physics Research Section A: Accelerators, Spectrometers, Detectors and Associated Equipment* 506 (3) (2003) 250 – 303. doi:10.1016/S0168-9002(03)01368-8.
- [33] National Oceanic and Atmospheric Administration, Global Data Assimilation System (GDAS), www.ncdc.noaa.gov/data-access/model-data/model-datasets/global-data-assimilation-system-gdas.
URL <https://www.ncdc.noaa.gov/data-access/model-data/model-datasets/global-data-assimilation-system-gdas>
- [34] P. Mitra, et al., Reconstructing air shower parameters with lofar using event specific gdas atmosphere, *Astroparticle Physics* 123 (2020) 102470. doi:10.1016/j.astropartphys.2020.102470.
- [35] S. Thoudam, et al., Measurement of the cosmic-ray energy spectrum above 10^{16} eV with the LOFAR Radboud Air Shower Array, *Astroparticle Physics* 73 (2016) 34 – 43. doi:10.1016/j.astropartphys.2015.06.005.
- [36] Pierre Auger Collaboration, Depth of maximum of air-shower profiles at the Pierre Auger Observatory. I. Measurements at energies above $10^{17.8}$ eV, *Phys. Rev. D* 90 (2014) 122005. doi:10.1103/PhysRevD.90.122005.
- [37] M. De Domenico, M. Settimo, S. Riggi, E. Bertin, Reinterpreting the development of extensive air showers initiated by nuclei and photons, *Journal of Cosmology and Astroparticle Physics* 2013 (07) (2013) 050.
- [38] S. Petrerá, Pers. communication.
- [39] A. Yushkov, et al., Mass composition of cosmic rays with energies above $10^{17.2}$ eV from the hybrid data of the Pierre Auger Observatory, Proceedings of the 36th International Cosmic Ray Conference, Madison, USA, PoS (2019) 482.
- [40] P. Sokolsky, Final results from the High resolution Fly’s Eye (HiRes) Experiment, *Nuclear Physics B - Proceedings Supplements* 212-213 (2011) 74 – 78, proceedings of the Cosmic Ray International Seminars (CRIS 2010). doi:10.1016/j.nuclphysbps.2011.03.010.
- [41] V. Prosin, et al., Primary CR energy spectrum and mass composition by the data of Tunka-133 array, *EPJ Web of Conferences* 99 (2015) 04002. doi:10.1051/epjconf/20159904002.
- [42] S. Knurenko, et al., Mass composition of cosmic rays in the energy region 10^{16} - 10^{18} eV by data the Small Cherenkov Array at Yakutsk. Comparison with other Arrays, Proceedings of the 34th International Cosmic Ray Conference, The Hague, The Netherlands, PoS (2015) 254.
- [43] Telescope Array Collaboration, The cosmic-ray composition between 2 PeV and 2 EeV observed with the TALE detector in monocular mode (2020). arXiv:2012.10372v1.
- [44] J. Bellido, et al., Depth of maximum of air-shower profiles at the Pierre Auger Observatory: Measurements above $10^{17.2}$ eV and Composition Implications, Proceedings of the 35th International Cosmic Ray Conference, Busan, Korea, PoS (2017) 506.
- [45] B. Dawson, et al., The Energy Scale of the Pierre Auger Observatory, Proceedings of the 36th International Cosmic Ray Conference, Madison, USA, PoS (2019) 231.
- [46] J. Matthews, A Heitler model of extensive air showers, *Astroparticle Physics* 22 (2005) 387.
- [47] S. Petrerá, Recent results from the Pierre Auger Observatory, *EPJ Web Conf.* 208 (2019) 08001. doi:10.1051/epjconf/201920808001.

Publications Nick van Eindhoven

PAPER

Design and sensitivity of the Radio Neutrino Observatory in Greenland (RNO-G)

To cite this article: J.A. Aguilar *et al* 2021 *JINST* **16** P03025

View the [article online](#) for updates and enhancements.

You may also like

- [THE INTERMEDIATE-MASS STAR-FORMING REGION LYNDS 1340. AN OPTICAL VIEW](#)
Mária Kun, Attila Moór, Elza Szegedi-Elek et al.
- [Electrochemical Reduction of 2-Nitroimidazole in Aqueous Mixed Medium](#)
J. A. Squella, L. J. Núñez-Vergara, A. Campero et al.
- [SPECTRALLY RESOLVED PURE ROTATIONAL LINES OF WATER IN PROTOPLANETARY DISKS](#)
Klaus M. Pontoppidan, Colette Salyk, Geoffrey A. Blake et al.



The Electrochemical Society
Advancing solid state & electrochemical science & technology

241st ECS Meeting

May 29 – June 2, 2022 Vancouver • BC • Canada

Abstract submission deadline: Dec 3, 2021

Connect. Engage. Champion. Empower. Accelerate.
We move science forward



Submit your abstract



Design and sensitivity of the Radio Neutrino Observatory in Greenland (RNO-G)

J.A. Aguilar,¹ P. Allison,² J.J. Beatty,² H. Bernhoff,³ D. Besson,^{4,5} N. Bingefors,⁶ O. Botner,⁶ S. Buitink,⁷ K. Carter,⁸ B.A. Clark,⁹ A. Connolly,² P. Dasgupta,¹ S. de Kockere,¹⁰ K.D. de Vries,¹⁰ C. Deaconu,¹¹ M.A. DuVernois,¹² N. Feigl,¹³ D. García-Fernández,^{13,14} C. Glaser,⁶ A. Hallgren,⁶ S. Hallmann,¹⁴ J.C. Hanson,¹⁵ B. Hendricks,¹⁷ B. Hokanson-Fasig,¹² C. Hornhuber,⁴ K. Hughes,¹¹ A. Karle,¹² J.L. Kelley,¹² S.R. Klein,¹⁶ R. Krebs,¹⁷ R. Lahmann,¹³ M. Magnuson,⁴ T. Meures,¹² Z.S. Meyers,^{13,14} A. Nelles,^{14,13,*} A. Novikov,⁴ E. Oberla,¹¹ B. Oeyen,¹⁸ H. Pandya,⁷ I. Plaisier,^{13,14} L. Pyras,^{19,14} D. Ryckbosch,¹⁸ O. Scholten,¹⁰ D. Seckel,²⁰ D. Smith,¹¹ D. Southall,¹¹ J. Torres,² S. Toscano,¹ D.J. Van Den Broeck,^{10,7} N. van Eijndhoven,¹⁰ A.G. Viereg, ¹¹ C. Welling,^{13,14} S. Wissel,^{17,8} R. Young⁴ and A. Zink¹³

¹Université Libre de Bruxelles, Science Faculty CP230, B-1050 Brussels, Belgium

²Dept. of Physics, Center for Cosmology and AstroParticle Physics, Ohio State University, Columbus, OH 43210, U.S.A.

³Uppsala University, Dept. of Engineering Sciences, Division of Electricity, Uppsala, SE-752 37, Sweden

⁴University of Kansas, Dept. of Physics and Astronomy, Lawrence, KS 66045, U.S.A.

⁵National Nuclear Research University MEPhI, Kashirskoe Shosse 31, 115409, Moscow, Russia

⁶Uppsala University, Dept. of Physics and Astronomy, Uppsala, SE-752 37, Sweden

⁷Vrije Universiteit Brussel, Astrophysical Institute, Pleinlaan 2, 1050 Brussels, Belgium

⁸Physics Dept. California Polytechnic State University, San Luis Obispo, CA 93407, U.S.A.

⁹Dept. of Physics and Astronomy, Michigan State University, East Lansing, MI 48824, U.S.A.

¹⁰Vrije Universiteit Brussel, Dienst ELEM, B-1050 Brussels, Belgium

¹¹Dept. of Physics, Enrico Fermi Inst., Kavli Inst. for Cosmological Physics, University of Chicago, Chicago, IL 60637, U.S.A.

¹²Wisconsin IceCube Particle Astrophysics Center (WIPAC) and Dept. of Physics, University of Wisconsin-Madison, Madison, WI 53703, U.S.A.

¹³Erlangen Center for Astroparticle Physics (ECAP), Friedrich-Alexander-University Erlangen-Nuremberg, 91058 Erlangen, Germany

¹⁴DESY, Platanenallee 6, 15738 Zeuthen, Germany

¹⁵Whittier College, Whittier, CA 90602, U.S.A.

¹⁶Lawrence Berkeley National Laboratory, Berkeley, CA 94720, U.S.A.

¹⁷Dept. of Physics, Dept. of Astronomy & Astrophysics, Penn State University, University Park, PA 16801, U.S.A.

*Corresponding author.

¹⁸*Ghent University, Dept. of Physics and Astronomy, B-9000 Gent, Belgium*

¹⁹*Humboldt-Universität zu Berlin, Unter den Linden 6, 10117 Berlin, Germany*

²⁰*Dept. of Physics and Astronomy, University of Delaware, Newark, DE 19716, U.S.A.*

E-mail: anna.nelles@desy.de

ABSTRACT: This article presents the design of the Radio Neutrino Observatory Greenland (RNO-G) and discusses its scientific prospects. Using an array of radio sensors, RNO-G seeks to measure neutrinos above 10 PeV by exploiting the Askaryan effect in neutrino-induced cascades in ice. We discuss the experimental considerations that drive the design of RNO-G, present first measurements of the hardware that is to be deployed and discuss the projected sensitivity of the instrument. RNO-G will be the first production-scale radio detector for in-ice neutrino signals.

KEYWORDS: Large detector systems for particle and astroparticle physics; Neutrino detectors

ARXIV EPRINT: [2010.12279](https://arxiv.org/abs/2010.12279)

Contents

1	Introduction	2
1.1	Scope of RNO-G	2
1.2	Relation to previous and current radio experiments	2
2	Science case and design requirements	4
2.1	Diffuse neutrino flux	5
2.2	Sky coverage	6
2.3	Transient sources	7
2.4	Fundamental physics	8
2.5	Radio emission from neutrino interactions in ice and consequences for site selection	9
2.6	Air showers as both a potential background and calibration signal	10
3	Experimental design considerations	12
3.1	Summit station, Greenland	14
3.2	A low-power, low-threshold trigger and data acquisition system	15
3.3	Detector geometry: an integrated approach with deep and surface components	15
3.4	High analysis efficiency and low background to enhance discovery potential	17
4	The RNO-G instrument design	20
4.1	Antennas	20
4.2	Radio-frequency front-end design	23
4.3	Triggering, digitization, and data acquisition	23
4.4	Autonomous power and wireless communications	26
5	Installation, calibration, and operations	28
5.1	Drilling and installation plan	29
5.2	Calibration requirements and strategies	29
5.3	Operations and data systems	30
6	Projected sensitivity of RNO-G	31
6.1	Sensitivity to diffuse flux	32
6.2	Energy measurement	33
6.3	Angular sensitivity	35
6.4	Sensitivity to transient events	36
6.5	Sensitivity to air shower signals	38
7	Conclusions	39

1 Introduction

This paper describes the Radio Neutrino Observatory Greenland (RNO-G) as it will be constructed at Summit Station in Greenland starting in 2021. RNO-G science targets astrophysical neutrinos of several PeV in energy up to the EeV range.

In this paper, we first motivate the science case for RNO-G, elaborate on experimental design considerations and then outline the instrument design. Awaiting in-field performance data, this article does not serve as a technical document, but describes the concept, the current hardware developments and boundary conditions behind the RNO-G approach. We conclude with a description of initial estimates of the design sensitivity of the instrument, as well as the expected resolution for such quantities as neutrino arrival direction and energy.

1.1 Scope of RNO-G

RNO-G will be constructed over three installation seasons. RNO-G will reach unprecedented yearly sensitivity to neutrino signals above 10 PeV, and will demonstrate a large-scale implementation (35 stations) of the in-ice radio neutrino detection technique. Even further scaling up of the in-ice radio technique, beyond the scale of RNO-G, is being developed as part of IceCube-Gen2 [1].

Considering both logistical constraints and also science opportunities (detailed below), RNO-G will be constructed at Summit Station in Greenland. The RNO-G collaboration consists of members of all previous radio in-ice neutrino experiments from both Europe and the United States.

1.2 Relation to previous and current radio experiments

Due to the extremely low neutrino flux at energies above 10 PeV, no neutrino has yet been detected using the radio technique. However, several experiments have shown the feasibility of this detection method and its potential. RNO-G builds heavily on the experience of previous radio neutrinos detectors, like the pioneering RICE [2, 3], the ARA [4–6] and ARIANNA [7, 8] experiments, as well as the balloon-borne ANITA [9, 10] experiment. These efforts tested different aspects of the radio technique and helped illuminate technologically important aspects of operating in remote locations in harsh polar conditions.

The first experience with in-ice radio detectors was gained with the Radio Ice Cherenkov Experiment (RICE) [2] at the South Pole. After a number of prototypes and initial measurements of the ice characteristics, the main experiment operated from 1999 until 2010. RICE provided the first neutrino limits [3] from radio detectors and valuable experience in operating radio detectors at depths of down to 200 m.

The Askaryan Radio Array (ARA) [5] has operated at South Pole since 2010 [11] and is a direct successor to RICE. While the RICE antennas were co-located with the AMANDA and IceCube experiments at South Pole, all five ARA stations operate in dedicated dry holes of depths 50 m–200 m. While different hardware has been deployed in different ARA stations, the station layout is mostly uniform. Every station consists of four receiver strings down to 200 m. Each string is equipped with two vertically-polarized birdcage dipole antennas (VPol) and two ferrite-loaded slot antennas (Hpol) to reconstruct the radio signals. In addition, one or two calibration strings as well as surface antennas (on the earlier stations) are deployed. As the narrow cylindrical borehole

geometry limits the intrinsic antenna gain, ARA pioneered the phased-array technique for radio detection of neutrinos at the most recently completed station [12].

To date, the ARA collaboration has published constraints on the diffuse ultra-high energy (UHE) neutrino flux [6], neutrinos from gamma-ray bursts (GRBs) [13], and radio emission from solar flares [14]. The performance of the instrument has been verified using transmitters lowered into the SPICE borehole [15], which also allowed for the measurement of glaciological properties of the ice — some of which can be used for improved neutrino event reconstruction [16, 17].

The Antarctic Ross Ice-Shelf ANtenna Neutrino Array (ARIANNA) began construction at the Ross Ice-Shelf in 2010, with a first hexagonal radio array being completed in 2015 [7, 8]. The ARIANNA concept is based around surface stations, i.e. the antennas are deployed just underneath the snow-surface. High-gain log-periodic dipole antennas (LPDAs) are deployed in shallow slots in the snow, where they are not restricted by the borehole geometry and exhibit broadband characteristics and dedicated polarization sensitivity, particularly to horizontally polarized signals. By placing the antennas at Moore’s Bay on the Ross Ice-Shelf, the neutrino-detection strategy utilizes the reflective surface at the bottom of the ice at the water interface, which reflects downward going neutrino signals back to the stations. Without external infrastructure, ARIANNA pioneered autonomous low-power stations, based on renewable energy sources, operated via wireless communications. Most recently wind turbines were added to the solar power-provision system [18].

ARIANNA has successfully detected the radio signal of air showers as calibration and verification signals [19] and published limits on the UHE neutrino flux [20]. The collaboration also published the effectiveness of recording signals reflected from the surface by monitoring snow accumulation [21]. Two ARIANNA stations have also been deployed at South Pole to test the robustness of the hardware under environmental circumstances differing from the Ross Ice Shelf. The same calibration source as used for ARA from the SPICE borehole was then also used to verify the reconstruction capabilities of the ARIANNA experiment with respect to arrival direction and polarization [22].

The Antarctic Impulsive Transient Antenna (ANITA) experiment has flown four separate missions over Antarctica. ANITA is a balloon-borne radio receiver array that scans the surface from afar for upcoming neutrino signals generated below the ice surface. Several components of the ANITA hardware have been incorporated into the ARA and ARIANNA designs [9, 10, 23]. While equipped with much different power and lifetime requirements, the technological challenges remain similar. A data acquisition system with high timing accuracy and thorough calibration is needed to reliably reconstruct neutrino or cosmic-ray signals. ANITA was the first radio-neutrino experiment to report the detection of air shower signals [24], which helped to verify the simulation chain and the understanding of the energy calibration [25]. The ANITA collaboration observed several events which, if neutrinos, would seem to be in tension with Standard-Model cross-sections [26–28]. Those events may also stem from unexplained systematics or ice effects [29, 30].

Operation of existing ARA stations continue in close cooperation with IceCube. In addition, proposals for an ANITA-successor ballooning effort are being discussed, as well as an extension of the ARIANNA array at Moore’s Bay.

In addition to building on experiences with dedicated radio neutrino experiments, RNO-G also profits from knowledge gained at accelerator experiments about the nature of the in-medium emission from particle showers [31–34], as well as those from mid-scale air shower arrays measuring the radio emission of cosmic ray induced showers e.g. [35–39]. First efforts at exploring the feasibility

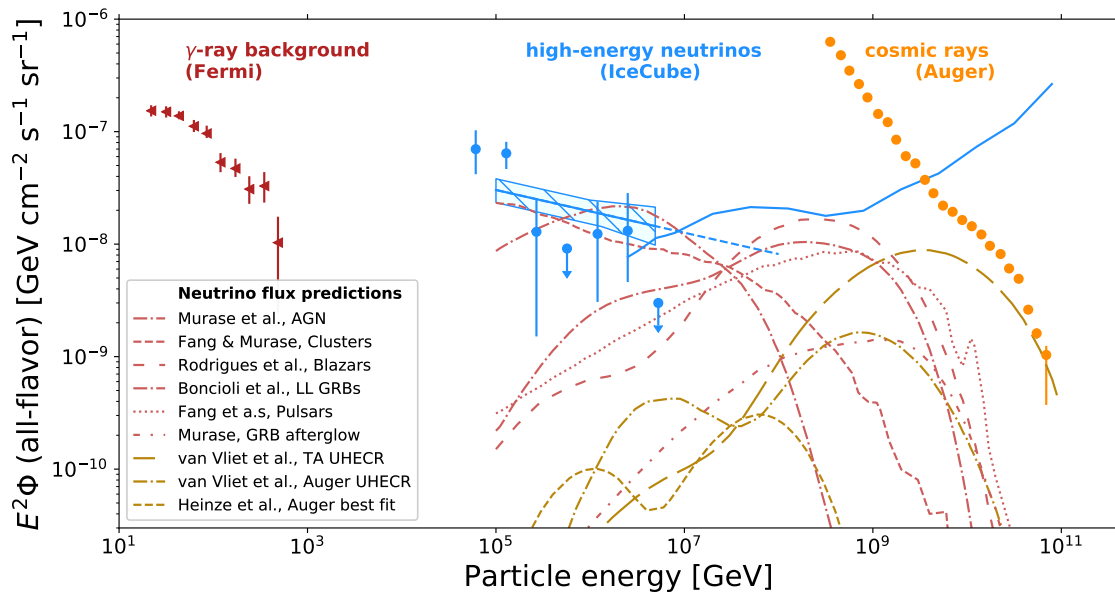


Figure 1. A multi-messenger view of the high-energy universe, inspired by [43], showing the science reach for radio detection of neutrinos. Shown are models predicting neutrinos from sources (in red lines) [44–49] and those from the interaction of the ultra-high energy cosmic rays with various photon backgrounds (in dark yellow lines). Overlaid are [50, 51] the γ -ray measurements from Fermi [52], the IceCube neutrino measurements and the fit to the muon neutrino spectrum [53–55], as well as the spectrum of ultra-high energy cosmic rays as reported by the Pierre Auger Observatory [56].

of a detector in Greenland have been conducted previously by members of the collaboration [40–42] and have encouraged the development of RNO-G.

2 Science case and design requirements

Neutrinos are ideal messengers to identify the UHE sources in the universe. Unlike cosmic rays, which are deflected by magnetic fields and interact with intervening matter and radiation, neutrinos point back to their sources and can reach Earth from the most distant corners of the universe. Furthermore, due to their low interaction cross section, neutrinos are unique messengers to convey information about the inner engine of cosmic accelerator sites. Unlike γ -rays, which can also be created by inverse Compton scattering, the observation of high-energy neutrinos from astronomical objects provides incontrovertible evidence for hadronic cosmic-ray acceleration. Identifying the sources of cosmic rays and the acceleration mechanisms requires a comprehensive multi-messenger observation program comprising cosmic rays, γ -rays, and neutrinos across many decades of energy.

In the last years, neutrinos have delivered on their promise to provide a key piece of this astronomical puzzle with the discovery of a diffuse flux of astrophysical neutrinos [57–60]. IceCube has measured the neutrino energy spectrum to above 1 PeV — the highest-energy neutrinos ever observed. Beyond the PeV scale, the limited size of IceCube prohibits observation of the steeply falling neutrino flux. Figure 1 compares the neutrino flux measured by IceCube with the diffuse flux of γ -rays measured by Fermi [52] and the cosmic-ray spectrum measured by Auger [56]. The

three spectra display tantalizingly similar energy densities, suggesting a common origin. In such a scenario, cosmic-ray collisions produce pions, where gamma-rays then stem from decays of neutral pions and neutrinos from those of charged pions. The figure also shows the gap in observations of UHE neutrinos beyond the energies reachable by IceCube.

Multi-messenger observations are even more intriguing in light of the announcement in July 2018 of the first coincident observation of a neutrino from the direction of a source (the blazar TXS 0506+056) that was flaring simultaneously in γ -rays [61, 62]. This was also the first multi-messenger observation triggered by a high-energy neutrino, demonstrating the capability to send real time alerts and establishing the field as a vital pillar of multi-messenger astronomy. To fully understand the neutrino sky, however, a larger detector must be built and observations extended to the PeV–EeV energy range.

The radio detection technique naturally targets neutrino energies beyond the reach of IceCube. Due to the kilometer scale attenuation length of radio waves in ice, very sparse radio detectors cover large volumes of material, providing huge effective volumes at 10 PeV to 100 EeV. In this energy range, several transient and diffuse sources of neutrinos are expected and an experimental measurement would strongly impact identification of the sources of ultra-high energy cosmic rays.

The general science case of neutrino astronomy has been reviewed in the context of the 2020 US decadal survey [63, 64]. This section will thus focus specifically on the science program that can be conducted by radio detectors for high-energy neutrinos.

2.1 Diffuse neutrino flux

The radio detection of neutrinos targets the energy range from 10 PeV to beyond 100 EeV. In this range, diffuse neutrino fluxes both directly from sources (*astrophysical neutrinos*), as well as from the interaction of ultra-high energy cosmic rays (UHECRs) with photon backgrounds (*cosmogenic neutrinos*) are predicted. Detecting either will enable studies of high-energy neutrino production mechanisms locally, at the still unknown sources.

Figure 1 shows different models for astrophysical (red) and cosmogenic (yellow) neutrinos that fall in the energy range of radio detectors. Cosmogenic neutrinos result from interactions of UHECRs with photon fields like the extra-galactic background light, the infra-red background, or the cosmic microwave background [65]. The flux and spectrum of these neutrinos are grounded in the UHECR mass composition, but are subject to model assumptions about the cosmological luminosity and chemical evolution of the sources, which can differ outside of the local universe probed by UHECRs [66]. For the cosmogenic neutrino predictions shown in figure 1, we compare predictions based on compositions measured by the Telescope Array (TA) [67, 68] and the Pierre Auger Observatory (Auger) [50, 69]. These are in fact only examples of the full range of possible models admitted by current constraints [51].

While the cosmogenic fluxes predicted assuming the Auger and TA compositions vary significantly, composition measurements from the two experiments are compatible within systematic uncertainties [70]. With a measurement of UHE neutrinos, radio detectors can resolve the question of a pure-proton composition, which is disfavored by Auger, but still allowed by TA data. More generally, measuring UHE neutrinos will constrain a combination of proton fraction, source evolution and highest-energy cutoffs of UHECRs well beyond local sources.

We consider ‘astrophysical’ neutrinos as those created directly in (or very close to) the sources of UHECRs. These neutrinos tend to have lower energies than cosmogenic neutrinos, but also reach the energy range of radio detectors. They will definitely trace their sources, allowing for stacking analyses to reveal them. These neutrinos are not necessarily time-coincident with explosive events (see section 2.3), but contribute to a constant diffuse flux. Potential candidates range from Active Galactic Nuclei (AGN) [47] to various types of gamma-ray bursts (GRBs) [46, 49], pulsars [45], galaxy clusters [44], Flat Spectrum Radio Quasars (FSRQs) [71], and blazars [48].

The diversity of models of astrophysical neutrinos is already large and promising, but we expect more models to become available as detectors with the necessary sensitivities are commissioned.

It remains to be explored whether astrophysical neutrinos are the source of the diffuse flux as measured by IceCube or whether the observed flux is the low energy tail of the cosmogenic neutrinos. So far, despite the multi-messenger successes, studies demonstrate that neutrinos from blazars cannot comprise the bulk of the diffuse neutrino spectrum at energies accessible by IceCube [72–77]. A radio detector will be able to measure the continuation of the IceCube flux to higher energies and thereby provide additional information on the spectral shape of the flux, which may be useful to disentangle the source contributions.

A successful search for the diffuse neutrino flux at energies beyond 10 PeV requires, above all, an adequate flux sensitivity to ensure a first observation. To subsequently discriminate putative production mechanisms, a detector must provide an adequate energy estimate for every neutrino and an angular reconstruction that allows for the correlation of arrival directions with known sources.

2.2 Sky coverage

Figure 2 demonstrates the field of view of a radio neutrino telescope sited in Greenland. When targeting point-like sources, either steady or transient (see section 2.3), the field of view of the detector becomes relevant. The Earth is opaque to neutrinos at PeV to EeV energies, such that UHE neutrino observatories are most sensitive to down-going or Earth-skimming neutrinos. As will be discussed in more detail section 2.5, a radio neutrino detector in glacial ice on bedrock will be most sensitive to an annulus above the horizon.

Combining the opacity of the Earth to neutrinos above PeV energies with the inherent radio detector sensitivity means that, for example, a follow-up of TeV-scale IceCube events at higher energies requires a Northern detector such as RNO-G. A *single event* observed by a radio detector in the Northern hemisphere will define the flux in a new energy regime, and even a non-detection will constrain the allowed flux through *multi-wavelength* neutrino observations.

The continuous sky coverage and large field-of-view will enable studies of point sources of high-energy neutrinos. The hotspot of UHECRs observed by TA [79] (red ellipse in figure 2) lies in the Northern Hemisphere. While the cosmogenic neutrino flux is expected to be diffuse, studies attributing the TA hotspot to a single source of cosmic rays like M82 predict point sources of EeV neutrinos [80]. There are additionally four intriguing point sources nearing the threshold for a high-confidence long-term detection in IceCube (shown as navy blue diamonds in figure 2), all of which lie in the Northern Hemisphere due to the sensitivity of IceCube. These include not only TXS 0506+056, but also NGC 1068, an AGN which lies near the strongest hotspot in IceCube’s all-sky scan [78].

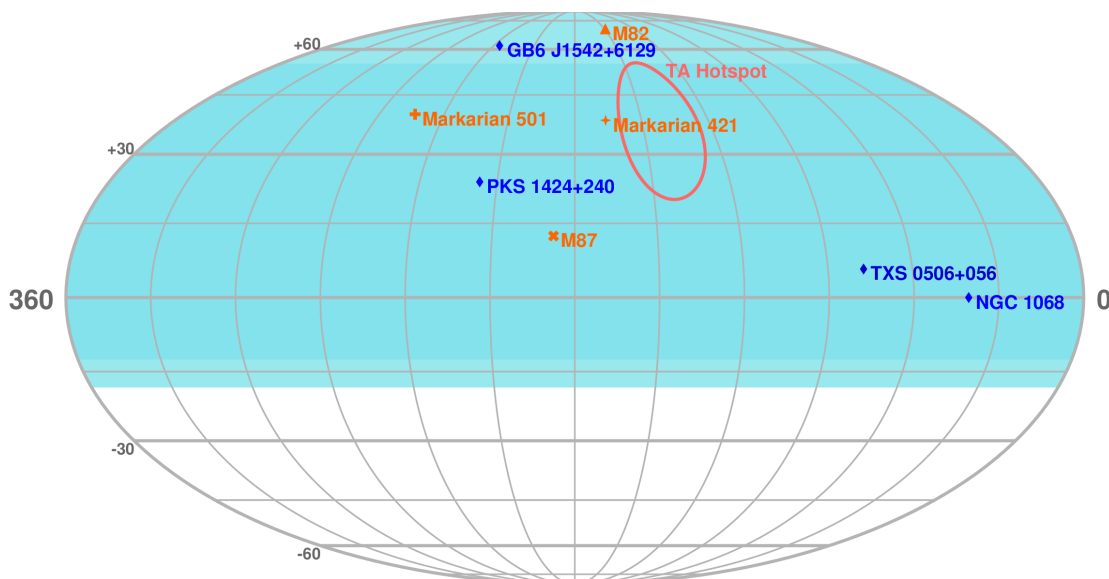


Figure 2. The field of view, in equatorial coordinates, of an in-ice radio detector for neutrinos in Greenland. The colored background represents the diurnally-averaged total field of view of the detector. Also shown are targets with interesting multi-messenger implications. The blue sources are those seen by IceCube as the most significant sources in a point-source search [78]. In orange, we show other interesting candidates, with strong γ -ray emission and/or radio emission. Furthermore, we indicate what is known as the *TA hotspot* as indicated by the anisotropy measurement in cosmic ray measured with the Telescope Array [79].

2.3 Transient sources

Detecting neutrino emission in temporal and spatial coincidence with an explosive event has shaped and will continue to shape multi-messenger astronomy [61, 62]. By uniquely identifying sources, neutrinos will help to characterize and discover the most energetic non-thermal sources on the sky. Many models of astrophysical transient phenomena predict neutrinos in the detectable energy range of radio neutrino detectors.

The overlap in sky coverage with IceCube, where IceCube has its best efficiency for directional reconstruction of astrophysical neutrinos, will enable studies of several interesting flaring, transient sources over a broad energy band. Should the first tentative extra-galactic neutrino source, the blazar TXS 0506+056, flare [61, 62] again, observations made by IceCube and RNO-G may be able to define the neutrino spectrum. Similarly, the first blazars known to flare with TeV γ -rays emission, Markarian 501 [81] and Markarian 421 [82], also lie in the Northern sky. Models of transient bursts of neutrinos due to tidally disrupted stars [83–89] and binary neutron star mergers [90, 91] also predict neutrinos in the PeV to EeV energy scale. The latter are targets for multi-messenger observations of gravitational waves and neutrinos. Figure 3 shows a fraction of the parameter space over which neutrinos are expected as transient phenomena from various source classes. In the figure, model-dependent fluence is compared to duration for varying neutrino energies around EeV. Furthermore, different populations of blazars, including low-luminosity BL Lacs, high-luminosity BL Lacs and FSRQs [48], the most powerful blazars in the γ -ray band [71], could provide intriguing candidates for multi-wavelength follow up. The energy threshold of RNO-G will allow sensitive

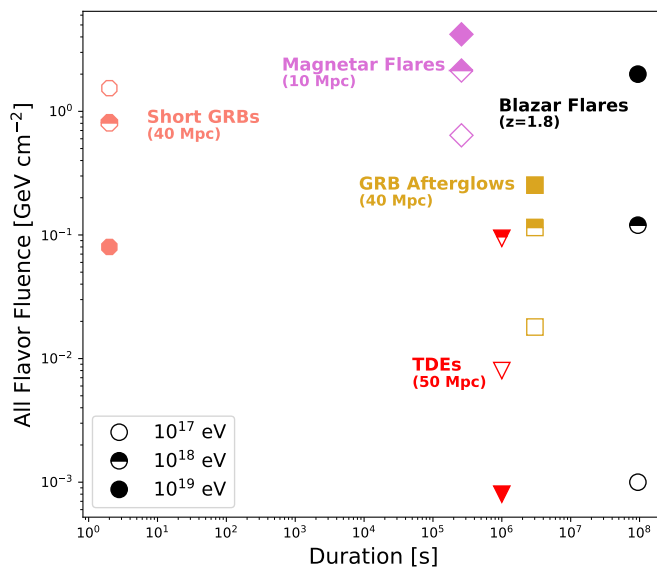


Figure 3. Expected neutrino flux at Earth integrated over transient duration from different classes of astrophysical objects placed at probable and previously studied distances. These include short GRBs (possibly associated with a Neutron Star-Neutron Star merger) [130] and GRB afterglows [49] at a distance of 40 Mpc, the high state SED of Tidal Disruption Events (TDEs) at 50 Mpc [89], and stable fast-spinning young magnetars [131] at 10 Mpc roughly 4 days post merger. Blazar flares [132] are shown based on a proton synchrotron model applied to multi-wavelength observations of PKS 1502+106, which has a redshift of $z=1.8$. The expected transient fluence for each object is plotted against duration, or flare time, for three neutrino energies: 10^{17} eV (hollow shapes), 10^{18} eV (half shapes), and 10^{19} eV (filled shapes).

searches for GRBs [46, 49, 92–113, 113–128] with lower neutrino luminosity than previously conducted with radio neutrino experiments [13, 129].

A successful radio detector for transient signals needs reliable absolute timing and good angular reconstruction. Ideally, the angular reconstruction is both sufficiently rapid and accurate to allow meaningful alerts to be quickly sent to the multi-messenger community. Absolute timing is critical to the multi-messenger mission.

2.4 Fundamental physics

High-energy cosmic neutrinos uniquely probe fundamental particles and interactions in an uncharted and otherwise unreachable energy and redshift regime, as summarized in [64].

The energy regime of neutrino radio detectors encompasses a relatively unmapped parameter space, helping to answer questions about the fundamental neutrino properties such as the behavior of neutrino cross-sections [133–140] and flavor mixing at high energies [141–147], or even whether neutrinos are stable in general [144, 148–154]. There is the chance to contribute to broader phenomenology such as the nature of dark matter [155–171], the quest for the fundamental symmetries of nature, [172–184] and/or potential hidden interactions with cosmic backgrounds [144, 185–190].

Overall, for a radio detector to provide experimental data for fundamental physics experiments, the highest priority is to detect neutrinos with adequate statistics. After this is given, the accuracy of statements regarding fundamental physics will strongly depend on the accuracy of the reconstruction.

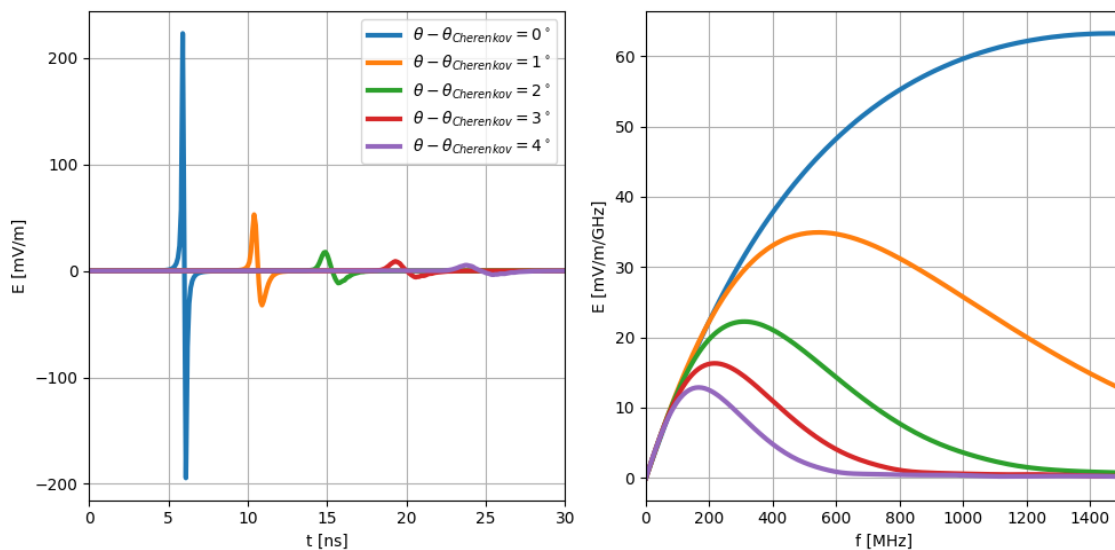


Figure 4. Electric-field waveforms (left) and spectra (right) of the radio signal emitted at different viewing angles relative to the Cherenkov angle, for a hadronic shower with energy deposition of 1 EeV. For enhanced readability, the waveforms have been offset in time. No propagation or detector effects have been included.

The obtainable energy resolution directly impacts spectral measurements and the accuracy of energy dependent quantities in fundamental physics. For studies relying on for example the amount of matter traversed, angular resolution has a direct impact. Potential flavor sensitivity of radio experiments would be interesting to answer yet another set of fundamental physics questions.

2.5 Radio emission from neutrino interactions in ice and consequences for site selection

The radio emission following a neutrino interaction stems from the *Askaryan* effect [191]. Postulated more than 50 years ago, the effect has been demonstrated in accelerator experiments in several dielectrics including ice [31–34], as well as identified as secondary emission mechanisms in air showers [192, 193].

Askaryan emission is caused by showers developing in a (dense) medium. Thus, a radio signal follows the interaction of neutrino of all flavors, as long as a particle shower is generated, both for hadronic and electromagnetic showers [194]. It is also possible to detect showers induced by catastrophic energy-losses of secondaries such as muons or taus [195]. The emission is a coherent effect, originating in the charge imbalance resulting from medium electrons either Compton scattering into the advancing shower or annihilating with shower positrons. With respect to the surrounding medium a net-negative charge is present in the shower front.

The radio signal itself is a broad-band bipolar pulse with \sim ns-duration. Coherence is given over all frequencies (typically tens of MHz to tens of GHz) close to the Cherenkov angle, where the signal is strongest as the emission at all frequencies arrives in phase. Coherence is lost off the Cherenkov angle first at high frequencies, so that the Cherenkov ring is rather narrow at high frequencies and broader at low frequencies. A discussion of a variety of models for the radio emission of neutrinos can be found in [196], they range from simplified parameterized models in the frequency domain to

more advanced semi-analytical time-domain models. In figure 4 we show typical pulses and their frequency spectra derived from [197], for an illustration of the variety and the behavior.

The energy threshold for a neutrino detection is significantly higher in radio than for optical instruments [2]. Depending on the exact instrumental parameters, the pulse amplitude at a distance of 100 m reaches the level of the typical thermal noise in low-noise radio receivers at approximately 1 PeV. Although the energy per radio photon is significantly smaller than for optical photons, signal coherence compensates as the charge imbalance grows. As a coherent effect, the amplitude scales linearly with the number of excess electrons, which itself is linear in shower energy [31, 198]. However, it should be noted that the detected signal amplitude scales with $\frac{1}{r}$, with r being the distance to the neutrino interaction vertex.

At the same observer distance r , the detected signal amplitudes linearly as function of energy. This has been confirmed in air showers since the attenuation in air is negligible [37]. The situation is different for instrumentation deployed in-ice. The kilometer-scale attenuation length in ice [5, 41, 199–201], determines the range to an observable neutrino interaction, and, therefore, the detector effective volume. The attenuation length decreases with increasing temperature, which favors cold and thick ice for deployment.

Naturally occurring ice follows a depth-dependent density profile with a gradient, from fresh snow to solid ice, resulting in a varying light velocity with depth, and therefore non-rectilinear ray trajectories. In a medium with a refractive index gradient, radio signals are bent towards the denser medium, producing bent trajectories and a limited field of view for detectors in or close to the near-surface firn layer. These bent trajectories complicate the reconstruction, particularly when there are uncertainties in the ice properties. The simplest ansatz assumes a smooth ice density gradient. Calculations demonstrate that anisotropies in the firn (or below) may support unexpected horizontal propagation, as borne out by experimental data [42, 202]. A radio detector should therefore preferably be built at a site with a small firn layer and otherwise smooth and homogeneous ice.

Starting from PeV energies, the Earth is opaque to neutrinos, such that radio detectors will be sensitive to an annulus of neutrino directions above and slightly below the horizon. The deeper the detector, the more vertically incoming neutrino directions can be detected. For a detector at a few hundred meters depth, the sensitivity does not reach far beyond 30° elevation, unless the reflective property of the bottom of a shelf-ice is used, as for the ARIANNA experiment [203].

In summary, an in-ice radio neutrino detector in glacial ice on bedrock will have the largest acceptance if installed in thick, smooth and cold ice. It will never be able to provide full sky coverage, but only be sensitive to a ring of elevations above and slightly below the local horizon.

Figure 5 provides an overview of the geometry for the detection radio signals with a detector buried in the ice. Every station monitors a large volume of ice, which means that by shear geometry a detection is most likely to show small signals as this corresponds to an interaction in the largest visible volume.

2.6 Air showers as both a potential background and calibration signal

The radio emission of air showers from the electron charge excess is similar to that for neutrino induced showers in ice. However, in air the geomagnetic emission [204, 205] dominates over the Askaryan effect. The geomagnetic emission stems from the charge separation induced by the Lorentz force in the Earth’s magnetic field. The different signatures of the two contributions

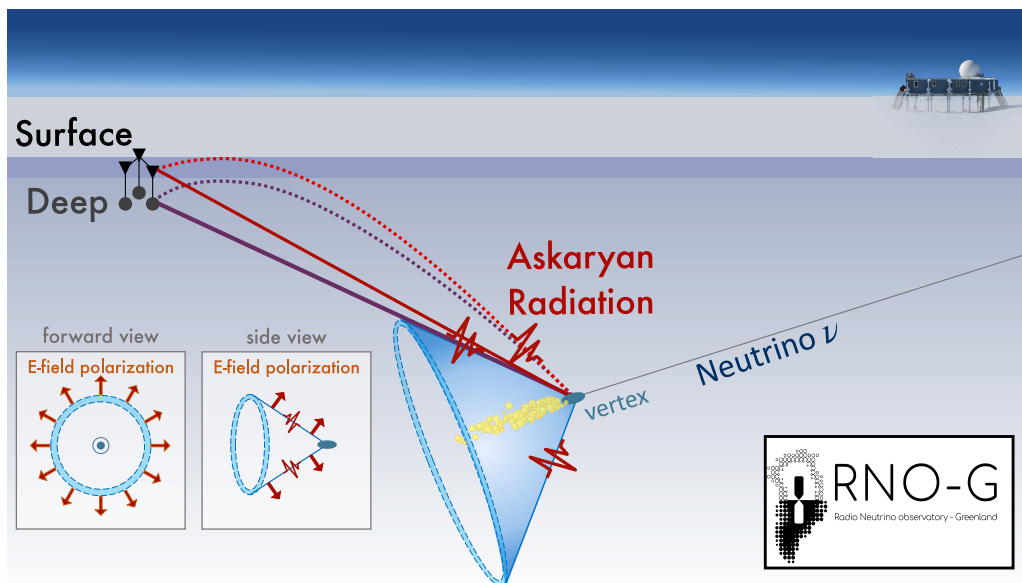


Figure 5. Schematic of the detection of the radio emission following a neutrino interaction (not to scale). The emission is strongest at the Cherenkov angle (blue cone) and can follow straight and bent trajectories to the receiving station depending on the profile of the index of refraction of the ice. The signal is usually detected at large distances and is strongly polarized as illustrated in the insets.

can be disentangled by their polarization. While still mostly linearly polarized, the main axis of the polarization from geomagnetic emission is aligned with the cross-product of shower axis and magnetic field [192, 193].

Due to their larger extent and the resulting consequences for coherence, air shower signals typically contain more low frequencies than those from showers in dense media [206]. Nevertheless, signals from air showers and denser in-ice showers are remarkably similar, which makes the much more abundant air shower signals a suitable calibration signal. Since the cosmic ray energy spectrum is well-known (e. g. [70]) and the radio energy scale understood [37, 207], measuring air showers will allow any detector to be calibrated *in-situ*, which includes checking the sensitivity simulations on an absolute scale. This will lend confidence to the signal identification and reconstruction [19].

The remarkable similarity can of course also be a reason for concern. The in-air signal will be (partly) refracted into the ice, where it may be picked-up by antennas and incorrectly identified as neutrino induced signal. While the signal will clearly be down-going, so may be signals from neutrino interactions, due to the ray bending properties of the ice [196]. It has also been argued that an incompletely developed air shower may cause transition radiation and other phenomena observable in deep detector stations [208]. In addition, stochastic energy losses by high energy muons in an air shower penetrating the ice may mimic the interaction of a neutrino [195]. Without additional detectors, the muons themselves are invisible to radio detectors, while the energy losses are detectable. Depending on the exact detector configuration and trigger, these background events may limit the analysis efficiency, albeit dropping sharply in number with energy.

Overall, this argues to equip all radio neutrino detectors with their own dedicated air shower array, for both calibration and veto purposes. Conveniently, due to the signal similarity, no additional

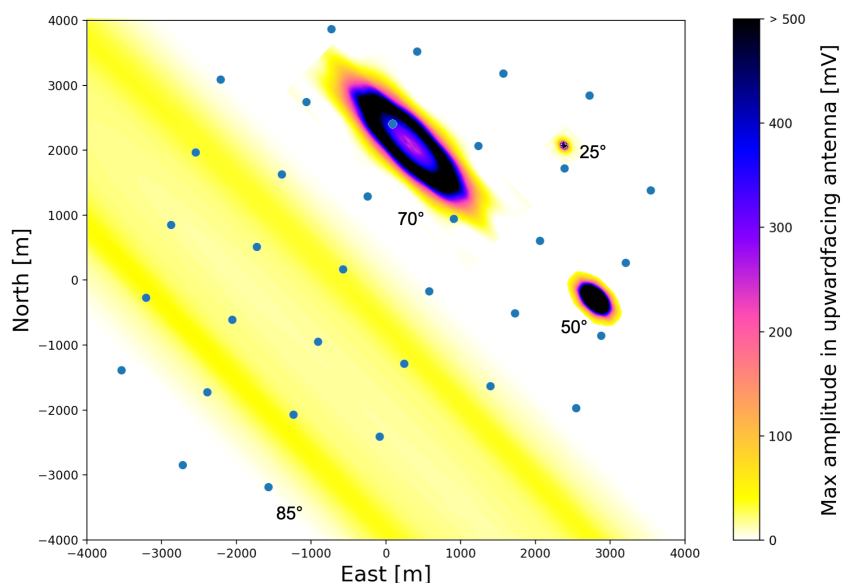


Figure 6. Simulated radio air shower footprints at 4 different incoming zenith angles. Simulations were performed using CORSIKA and the RNO-G site (magnetic field and height above sea level) in Greenland, and include the response of upward facing logarithmic periodic dipole antennas, as planned for RNO-G (see figure 7). The global maximum of the amplitudes in three antennas is shown. The air shower energy is 3.2×10^{18} eV for all showers, and the zenith angles are indicated in the figure.

technology is needed for such a detector, but does require additional surface antennas connected to the same data-acquisition system (DAQ). A dedicated air shower trigger, optimized to the lower frequency content of the air shower signals, would significantly enhance efficiency and detection rate. Due to the height of the interaction in the atmosphere and the fact that $n_{air} \approx 1.0$ co-aligns the emission with the shower axis, the detectable footprint of the radio signal from air showers is centered on the shower axis, with lateral extent distributed ellipsoidally on the ground, as shown in figure 6. The exact size is governed by the distance to shower maximum and the projection effect of the zenith angle [209]. The figure qualitatively illustrates that vetoing horizontal air showers will be relatively straightforward, while retaining high efficiency for vertical showers presents more of a challenge. The typical threshold for air shower detection is around 10 PeV, which is again similar to the threshold of in-ice detection.

3 Experimental design considerations

RNO-G is designed to demonstrate the scalability of the radio detection technology, while enabling the world's-best UHE neutrino sensitivity through low thresholds and also high efficiency. The system is designed to provide high fidelity identification of neutrino signals and reconstruction of neutrino properties. Building on these requirements, a station and array design as schematically depicted in figure 7 was developed.

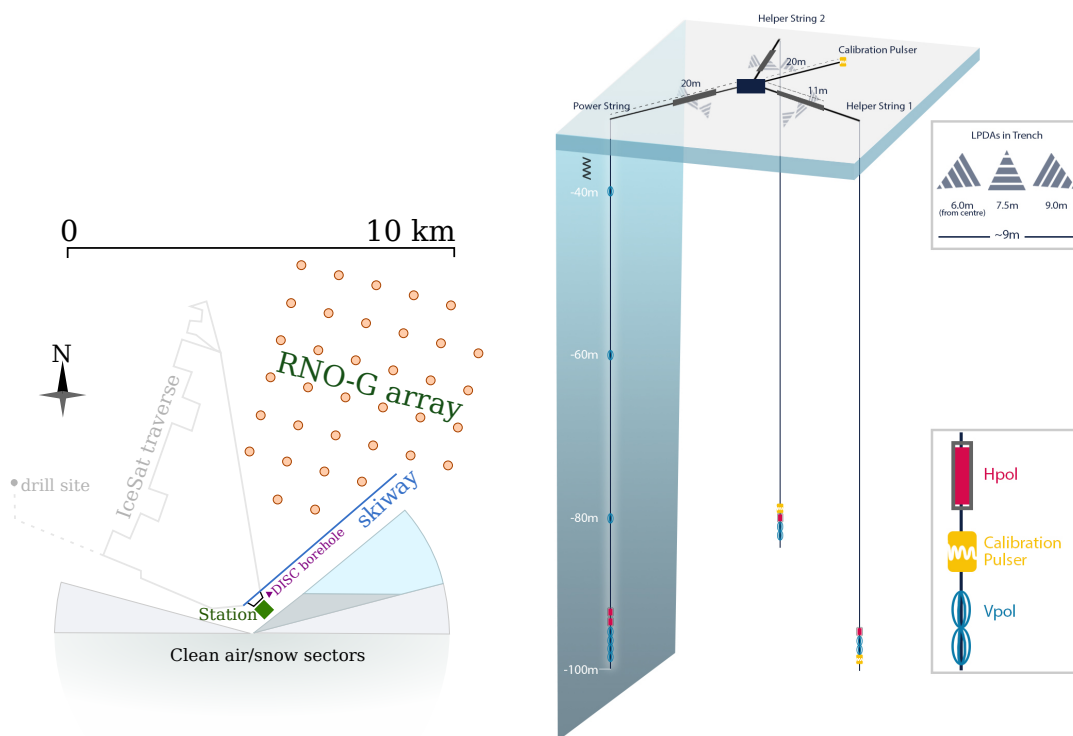


Figure 7. Left: map of the planned RNO-G array at Summit Station; grid spacing is approximately 1 km. Right: a single RNO-G station consists of three strings of antennas (Hpol and Vpol) plus surface antennas (LPDAs), as well as three calibration pulsers located both deep in the ice and also at the surface. The string containing the phased array trigger is designated as the *power string*, while the two additional strings are designated as *support strings*.

The design of RNO-G combines the experience gained with all prior in-ice radio neutrino experiments, especially ARA [5] and ARIANNA [210], and also builds on lessons learned with radio air shower arrays that have first demonstrated the experimental power of the radio detection technique, e.g. [37, 38].

As outlined above, a location is needed with thick, homogeneous and cold ice to yield the best experimental results. An additional requirement is the availability of a sufficiently developed infrastructure to allow for installation, running and maintenance of the detector. While the instrumented stations can be fully autonomous, the amount of cargo and personnel needed for installation requires accessibility by plane or large vehicle. The number of accessible research stations fitting these requirements in either Antarctica or Greenland is limited. The host institutions of the RNO-G collaboration members and their access to national infrastructure additionally excludes some obvious candidate sites (Dome A, Dome C and Vostok in Antarctica, e.g.), leaving essentially South Pole Station and Summit Station in Greenland. South Pole station already houses a premier CMB instrument (the South Pole Telescope [211]), as well as the world’s largest neutrino telescope (IceCube), which is in the process of installing the IceCube-Upgrade [212]. The logistical burden is, thus, already high at South Pole.

If RNO-G is also to be used to develop and test hardware for the radio component of IceCube-Gen2 [1], a site similar to South Pole has advantages, if South Pole station is unavailable. Interesting coastal sites, like the Ross-Ice-Shelf close to McMurdo Station, which hosts the ARIANNA experiment [213], can assist in developing other technologies, but would be unable to replicate some of the particular challenges of South Pole.

To achieve a high trigger efficiency, a cosmic-ray veto, and the ability to reconstruct events with high accuracy, the RNO-G design combines a surface with a deep array capable of operating at low threshold (see figure 7). The collaboration will develop the necessary expertise for rapid installation with a minimum of logistical impact, enabled by newer, fast drilling technology and lightweight, low-power, autonomous stations that still achieve excellent single-station effective volume.

3.1 Summit station, Greenland

Going to Greenland also has some fundamental consequences for the design decisions. The Antarctic has been host to several pioneering arrays that aim to detect in-ice radio emission from UHE neutrinos. Through previous efforts, the Arctic has been established as a parallel site for a future radio neutrino observatory [41, 42, 214]. Summit Station offers several advantages as a testbed site. It is located at $72^{\circ}35'46''$ N, $38^{\circ}25'19''$ W at the peak of the Greenland ice cap, atop more than 3 km of glacial ice that we have measured to be remarkably radio transparent [41] at ~ 100 MHz, and with a ~ 100 m deep firn layer that we have preliminarily characterized [42]. It is a year-round scientific research station sponsored by the National Science Foundation. It has a snow runway that accommodates LC-130 Hercules flights to deliver cargo and personnel, and facilities on site to support science. Compared to sites in Antarctica, Summit Station (72° N Latitude) is easier to access from the Northern hemisphere, in particular through commercial flights from Europe, and has a larger fraction of the year with daily periods of light, providing a higher livetime for autonomous solar-powered stations. This final aspect is particularly important, given the reduced electrical generator infrastructure at Summit compared to South Pole. The restriction to renewable energies, combined with battery buffering limitations and the desire for high livetime, cap the amount of power the detector can draw and ultimately drive the station design.

Logistical considerations at Summit also favor a compact geometry with fewer, more sensitive stations rather than more, less sensitive stations. Similarly, the drilling technique must be lightweight and mobile and, therefore, mechanical.

The ASIG drill, which is able to drill 5.75'' diameter boreholes to 100 m at a rate of 1 hole per day, was initially considered as the main option [215]; subsequent antenna design was adapted to that form factor. Alternatively, the British Antarctic Survey (BAS) has been developing a mechanical drill that provides larger boreholes of 11.2'', which will allow for greater flexibility in antenna design. Both drills satisfy the drilling rate, hole diameter and logistical impact specifications. See section 5.1 for an in-depth discussion of drilling and installation.

To compensate for the warmer, more attenuating ice in Greenland compared to South Pole, triggering is performed with the deeper antennas, below the firn. Since no detector has detected the radio emission following a neutrino interaction yet, the exact experimental signature is predicted by simulations only, arguing for a detector design that detects the neutrino signal in a multitude of channels to increase confidence. It can be considered to adapt and simplify the detection strategy once the first neutrino has been conclusively identified.

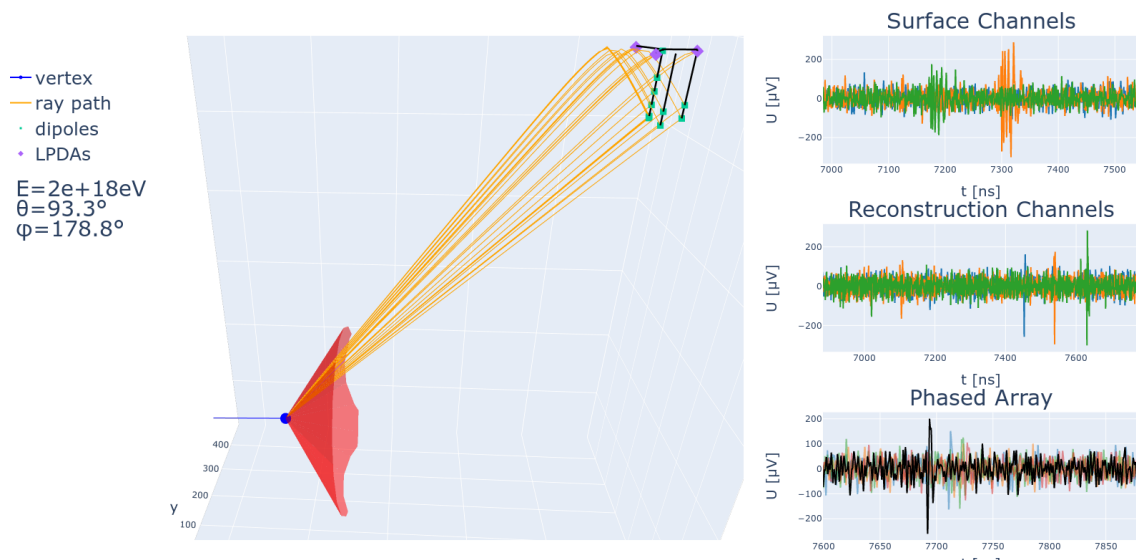


Figure 8. A simulated RNO-G neutrino event. The left side shows the event geometry illustrating both the direct and reflected ray-paths to the antennas, as well as the incoming neutrino and interaction vertex (blue) and its Cherenkov cone (red), where the strongest signals are expected. The right side shows the waveforms in selected antennas, and the improvement in signal-to-noise-ratio obtained by phasing the signals as done in the phased array trigger (shown in black, bottom row). This simulation and online event display utilize tools developed by the greater radio community [196, 216]. For better visibility, only selected channels are shown.

3.2 A low-power, low-threshold trigger and data acquisition system

The RNO-G stations are built around an interferometric phased array, similar to what has been demonstrated *in situ* at the South Pole on the ARA experiment [12, 214], achieving the lowest sustainable signal trigger threshold demonstrated in the field. Since the astrophysical neutrino flux shows a falling spectrum, improved sensitivity to lower-energy events dramatically increases the detected neutrino event rate. The phased-array technology has been adapted for RNO-G to provide similar sensitivity, albeit with a reduced power consumption.

The phased array trigger coherently sums single channel waveforms with time delays corresponding to a range of angles of incident plane waves, improving the trigger-level signal-to-noise ratio roughly linearly with the number of antennas in the array [12], as illustrated in figure 8. Projecting the performance of the existing ARA system, we expect to achieve an elevation-averaged 50% trigger efficiency point at a $2\sigma_{\text{noise}}$ threshold in voltage. This low threshold is needed to observe the largest volume of ice possible as discussed in section 2.5.

It should be noted that for the simulations, the following definition for signal-to-noise ratio (SNR) and noise is handled. SNR is defined as the amplitude of the noiseless signal over the standard deviation σ_{noise} of a pure noise waveform. A threshold of $2\sigma_{\text{noise}}$ thus means a threshold of twice the standard deviation of a trace without signal.

3.3 Detector geometry: an integrated approach with deep and surface components

After extensive trade studies, we have coalesced on a station design that integrates a deep component with a surface component, as shown in figure 7. This integrated design achieves the highest effective

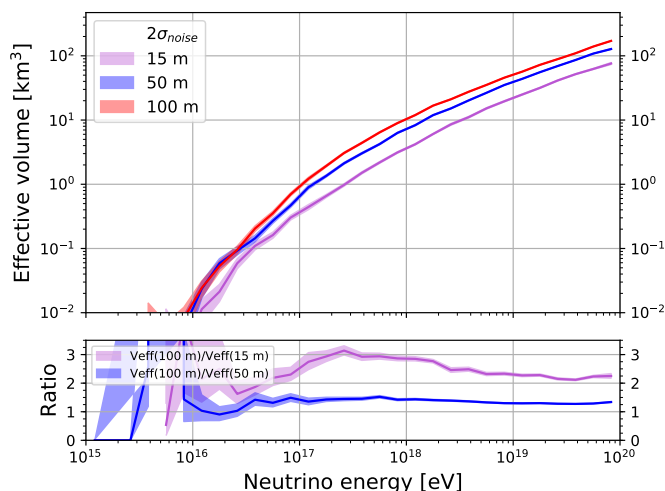


Figure 9. Scaling of the effective volume as a function of the depth of antennas used for the phased-array trigger for a single station deployed at Summit Station. 100 m was used during the design process as the technological limit due to drilling restrictions. As the trigger antennas are placed deeper into the ice, the effective volume increases, due to the number of allowed ray trajectories in the ice. The curves have been obtained using a $2\sigma_{\text{noise}}$ dipole proxy for the phased array. Shown are statistical uncertainties only. Below 10 PeV the uncertainties on the effective volume become too large to draw firm conclusions.

volume per station given the phased-array trigger and mechanical drilling technology to 100 m. As shown in figure 9, the effective volume per station increases with increasing depth, so our design places the deep component of the station as deep as is logistically feasible, given the current constraints of drilling.

In addition to maximizing effective volume, the station design has been optimized for neutrino reconstruction efficiency. The string containing the phased array trigger will feature additional Vpol antennas almost equally spaced vertically along the string allowing us to pin-point the neutrino vertex and zenith angle of the signal arrival direction, and achieving high accuracy by exploiting azimuthal symmetry. Since the down-hole Vpol antennas are typically more sensitive than the Hpol antennas and the trigger selects signals having a measurable component in the vertical polarization, the Vpol antennas dominate vertex and signal arrival direction reconstruction. Adding two Hpol antennas above the phased array will allow us to improve the reconstruction of the full electric field. Combining the four Vpol antennas of the phased array with the two Hpols in proximity, should provide sufficient information to reconstruct the polarization of the signal, as well as its frequency slope, and thereby the off-Cherenkov signal angle and neutrino arrival direction.

The radio signal from a neutrino interaction often travels along direct, refracted or reflected paths (designated DnR) to the deep array, as shown in figure 8. The characteristic double pulse would be a smoking-gun signature of an in-ice source. The difference in direct and refracted arrival times significantly improves the reconstruction of the neutrino vertex position, and thereby the shower energy, as well as arrival direction [21]. The probability to observe both a direct and a reflected signal is depth dependent. The spacing of the Vpol antennas on the main string is the result of an optimization between double pulse detection and long lever arm for good angular reconstruction.

The two additional deep boreholes are needed for a full direction reconstruction. Three independent measurements are needed for azimuthal information, which is provided by the Vpol antennas. By placing the Hpol antennas at different depths on every string, both zenith and azimuth information will be provided for those signals with a strong horizontal polarization component, as well as increasing the probability to reconstruct a signal for those events with little signal strength in the horizontal component.

The additional strings also host the calibration pulsers, which will ensure regular monitoring of the performance of the station and provide information useful for precise calibration of the antenna geometry. In addition, a surface pulser is foreseen, which will be deployed in a hand-drilled hole below the surface.

The surface component will deliver precision polarization measurements and timing information for all events detected at the surface. Also, the broad-band sensitivity of the log-periodic dipole antennas (LPDAs) will broaden the frequency coverage of the detector, which helps determine the radio detection angle with respect to the Cherenkov cone, improving energy reconstruction and pointing resolution. Events detected only in the surface components, however, only add minimally to the total neutrino effective volume.

With the planned layout, any events observed in coincidence between the surface component and the deep component are particularly valuable for event reconstruction; the fraction of these events is discussed in section 3.4. In addition, the surface channels serve as an efficient air shower veto, reducing the background for neutrino searches as will be discussed in the following section.

The stations will be deployed on a square grid with 1 km baseline. This means that at energies beyond 1×10^{18} eV the effective volumes of the stations start to overlap and coincident measurements of the same neutrino become likely. This can be seen from figure 10, where the fraction of events triggered in coincidence is shown for different neutrino energies and grid spacings. While limiting the total effective volume of the system, 1 km was chosen to restrict the logistical impact in installation and preserve the opportunity of coincident events, which will simplify event identification and provide excellent reconstructed properties. As the project advanced, one may consider spacing stations further apart.

3.4 High analysis efficiency and low background to enhance discovery potential

In addition to triggering on and extracting event parameters from neutrino events, we must be able to separate any neutrino events in our recorded data set with high efficiency from all backgrounds. The three major sources of background are incoherent thermal noise, impulsive anthropogenic noise, and radio impulses resulting from cosmic-ray air showers. A discovery experiment of this scale requires low backgrounds at the level of 0.01 per station per year (or less). RNO-G is designed to achieve this ambitious background level by building on two key measures that have been developed to ensure event purity.

- (1) Triggering from deep in the ice (at a depth of 100 m), where the backgrounds are smaller than at the surface: ARA has shown that the anthropogenic and thermal backgrounds decrease for receivers deployed deeper in the ice [217] and further from human activity at research stations, achieving a background on the most recent analysis of 0.01 events in two stations over

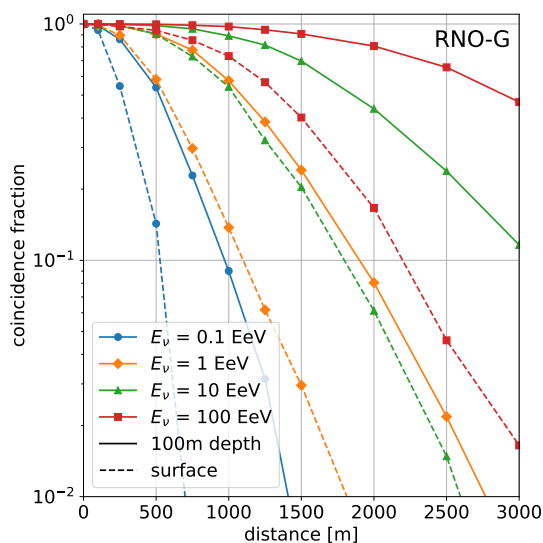


Figure 10. Fraction of coincident triggers on nearby stations as a function of the grid distance between stations for different neutrino energies. In addition to the 100 m deep power string, the coincidence fraction expected for a trigger near the surface is given for comparison.

1100 days of livetime [4]. This shows that successful background rejection can be achieved also during the summer at South Pole when anthropogenic backgrounds are more significant.

- (2) Vetoing backgrounds using a surface detector component: non-thermal backgrounds are introduced from the surface or from close to the surface by man-made sources or air shower remnants. Surface antennas will help to separate neutrino induced signals originating within the ice from those of air showers [208] and those from showers caused by catastrophic energy losses from atmospheric muons [195].

Neutrino events triggered near threshold in the phased array system carry the risk to have low SNR in antennas needed for reconstruction. The information content in different numbers of antennas is illustrated in figure 11. Three channels detecting a signal $>3\sigma_{\text{noise}}$ is taken as a simple proxy for events that can be identified and reconstructed with currently available analysis techniques such as interferometry [218], template matching [7] and signal de-dispersion [23]. With a signal in the antennas of the phased array as well as in an antenna on the support string, it is possible to reconstruct the neutrino arrival direction (see section 6.3). To reconstruct the shower energy, at least 3 of the reconstruction antennas on the *power string* need to detect a pulse so that the distance to the interaction vertex can be reconstructed (see section 6.2). In some cases, the radio signal is reflected off the ice-air interface or diffracted downwards, so that two signals from the same shower can be detected. These so-called *DnR pulses* become more likely with higher neutrino energies and can be used to greatly improve the reconstruction accuracy. More details on reconstruction and resolution is given in section 6.2 and 6.3. Foreseeable advances in analysis techniques will further improve the efficiency near threshold, both in firmware and also in off-line analysis.

An accurate knowledge of the existing background is needed in order to project what fraction of triggers are due to non-neutrino backgrounds, and also to assess whether a veto mechanism is

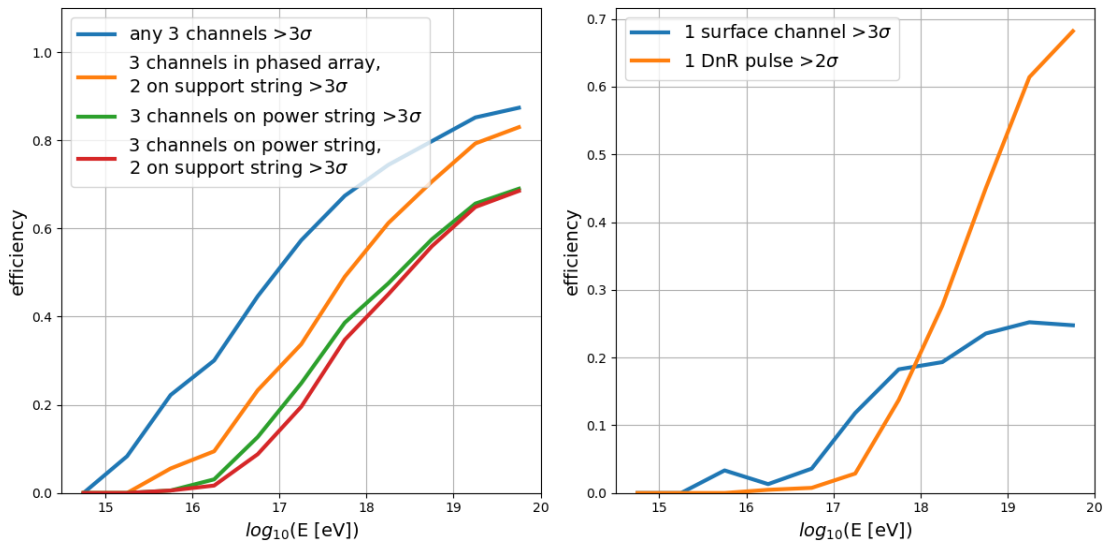


Figure 11. Estimate of anticipated analysis efficiency, defined here as the fraction of events recorded in a pre-defined number of antennas (channels) above a given threshold. The left figure illustrates detections in the deep part of the array only. A detection in the support string (see figure 7) will allow for a reconstruction of the arrival direction of the signal and three antennas on the power string are needed for a vertex reconstruction. The right figure shows the fraction of DnR signals, which are particularly valuable for the vertex reconstruction and the fraction of very valuable events measured in both the deep array and the surface antennas. For these simulations we assume a trigger at $2.0\sigma_{\text{noise}}$ trigger in the phased array.

advisable (or mandatory). An important type of background which is difficult to distinguish from actual neutrino events is the background created by the energy losses from atmospheric muons from cosmic ray showers. These muons are produced in the atmosphere, continue their propagation into the ice; their subsequent interactions (mainly bremsstrahlung, photonuclear interaction, and pair production) create hadronic and electromagnetic showers that emit radiation and are therefore detectable by an in-ice radio array [219]. These muons share shower characteristics, arrival directions and vertex positions with the sought-after neutrinos (see [195]). We have calculated the number of expected muon-initiated showers for a 35-station array at Summit Station, using a 100 m-deep dipole with an amplitude threshold between $1.5\sigma_{\text{noise}}$ and $2.5\sigma_{\text{noise}}$ as a proxy for the phased array. The effective areas have been calculated using NuRadioMC [196] and its interface to PROPOSAL [220]. Then, these effective areas are convolved with the expected muon flux at the detector, calculated by MCEq [221]. The chosen cosmic ray flux model is the Global Spline Fit from [222]. This procedure is explained more in detail in [195]. The results are presented in figure 12, where each band represents the results for a hadronic interaction model. Shown are the expected number of detected muons for the phased array proxies (from 1.5 to $2.5\sigma_{\text{noise}}$) and also the 68% CL interval for the uncertainty due to cosmic ray flux, hadronic modeling and effective area. Figure 12, left, contains the expected detected number of muons per year for 35 stations as a function of shower energy, while figure 12, right, presents the same results as a function of cosmic ray energy.

The lower and upper bounds on the number of detected atmospheric muons per year for a 35-station layout, as well as the average number for a $2.0\sigma_{\text{noise}}$ trigger, can be found in table 1. While these values are relatively benign, we remind that the neutrino event rate may be equally low,

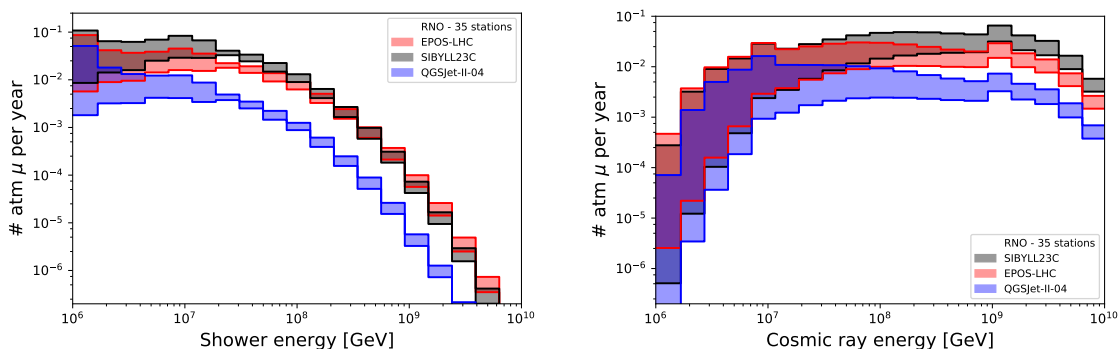


Figure 12. Number of atmospheric muons detected by a 35-station array at Summit Station. The phased array is modeled with dipoles having amplitude thresholds varying from 1.5 to $2.5\sigma_{\text{noise}}$, at 100 m of depth. Each color represents a different hadronic model, as specified in the legend. The bands include the range of expected events for the different simulated thresholds as well as the 68% CL contour corresponding to the effective area uncertainty. Left: number of detected atmospheric muons per year as a function of shower energy. Right: same results, presented as a function of cosmic ray energy. The drop off at low energies is an artifact of only simulating muons down to 1×10^6 GeV.

	$2.5\sigma_{\text{noise}}$ 68% CL LB	$2.0\sigma_{\text{noise}}$ average	$1.5\sigma_{\text{noise}}$ 68% CL UB
SIBYLL 2.3C	0.212	0.296	0.684
EPOS-LHC	0.129	0.173	0.444
QGSJet-II-04	0.031	0.044	0.180

Table 1. Number of detected atmospheric muons per year for a 35-station layout. Three hadronic models are shown. The numbers shown are the lower 68% CL lower bound for a $2.5\sigma_{\text{noise}}$ trigger (first column), the average values for a $2.0\sigma_{\text{noise}}$ trigger, and the 68% upper bound for a $1.5\sigma_{\text{noise}}$ trigger. See text for details.

at least at the threshold energy of the detector. Hence, the air shower self-vetoing on the detector deserves special attention, as well as the development of algorithms using event parameters such as arrival direction and vertex location to disentangle neutrino signals from those potential background events. Also, since the flux and composition of cosmic rays at the relevant energies is subject to large uncertainties, those same uncertainties propagate into the background prediction for radio arrays.

4 The RNO-G instrument design

RNO-G will provide high-quality science data and a robust, low trigger threshold with minimal power consumption using a station design schematically depicted in figure 13. In nominal operating mode, a station will use 25 W, including DC-DC converter losses. All equipment is rated to operate at -40° C and 3200 m altitude.

4.1 Antennas

The initial downhole antenna designs are driven by the 5.75'' diameter of the boreholes (ASIG drill [215]), with some modifications possible, if bigger boreholes are available (see section 3.1.

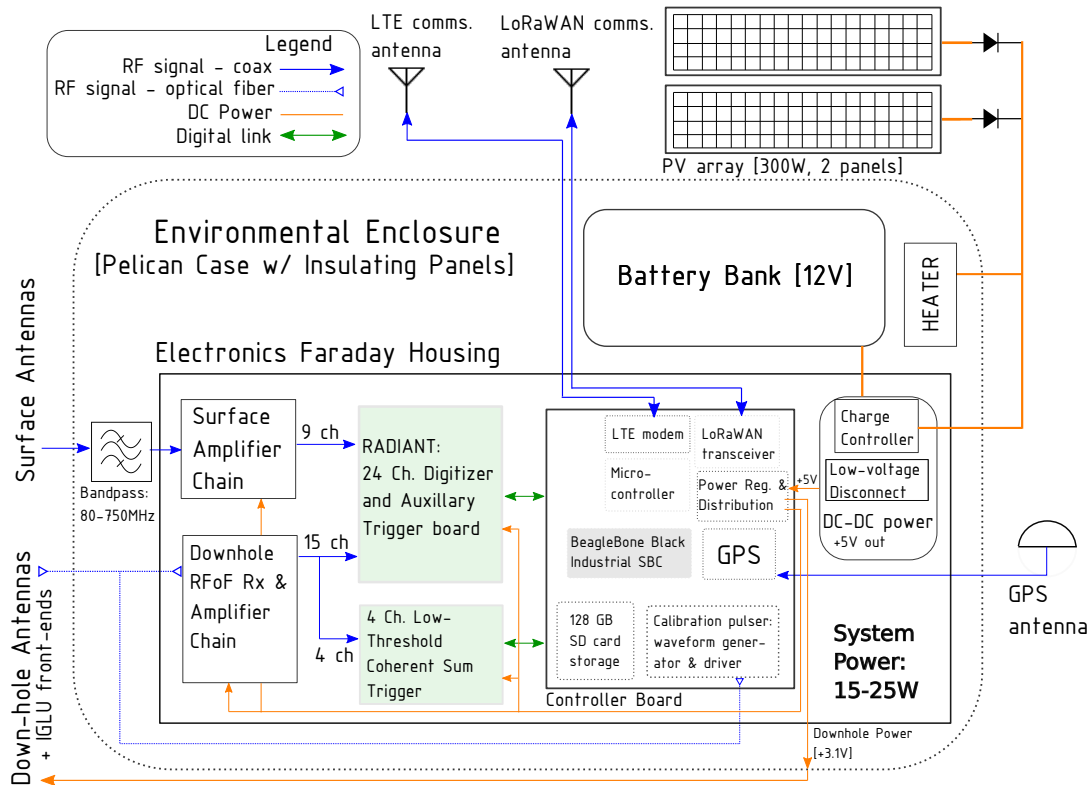


Figure 13. System diagram for an RNO-G station. See text for details.

The vertically-polarized (Vpol) antennas will be a *fat dipole* design (see figure 14) previously used in neutrino detection experiments, which have an azimuthally symmetric beam pattern and usable bandwidth ranging from 150-600 MHz [2, 214]. For horizontal polarization (Hpol), cylindrical *tri-slot antennas* are considered. They are nearly azimuthally-symmetric in gain, with differences of less than 1 dB up to 800 MHz, which corresponds to differences of less than 12% in effective length. Only Vpol antennas are used for the trigger because the Hpol antennas inherently have narrower usable bandwidth than the fat dipoles, as shown in figure 15. With the current Hpol designs, there is enough overlap with the Vpol band to combine the signals for polarization reconstruction in analysis. Larger boreholes (RAID drill) will especially help improve the broadband characteristics of the Hpol antennas. It is under consideration to exchange the tri-slot design for 8" quad-slot antennas, which will have a lower frequency turn-on and improved gain characteristics taking advantage of the larger allowed diameter.

The surface component employs commercially available log-periodic dipole antennas (LPDAs, Create CLP-5130-2N), successfully used by the ARIANNA experiment. ARIANNA's extensive in-field experience with these antennas will significantly simplify calibration. Owing to the high gain allowed without the borehole constraints, the nine LPDAs arranged in various orientations (see figure 7, right) will measure all polarization components with high-precision, and provide a clear separation of upgoing versus downgoing signals. Due to their size the LPDAs have the largest gain of all employed antennas and will provide the greatest frequency coverage for the detected signals.

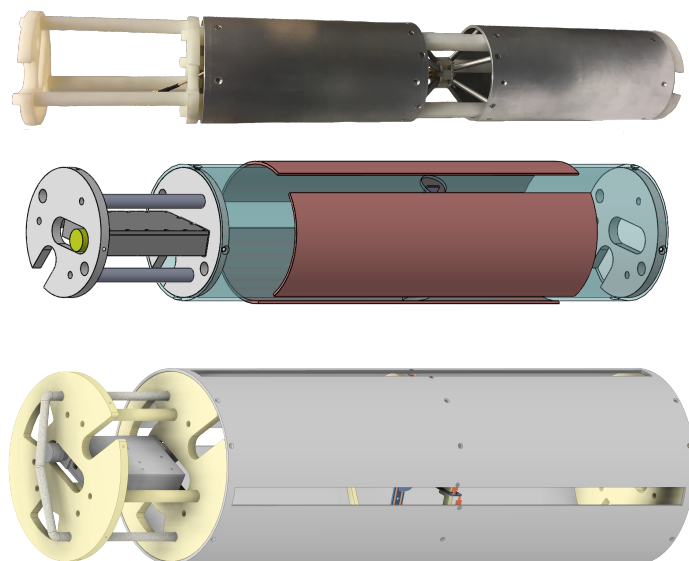


Figure 14. Photo of a Vpol prototype (top) and technical drawings of options for the Hpol antennas (trislots, middle, quadslots, bottom). The Vpol and trislots are the first iterations of the deep antennas for RNO-G, while the quadslot is being considered for use in conjunction with larger diameter boreholes.

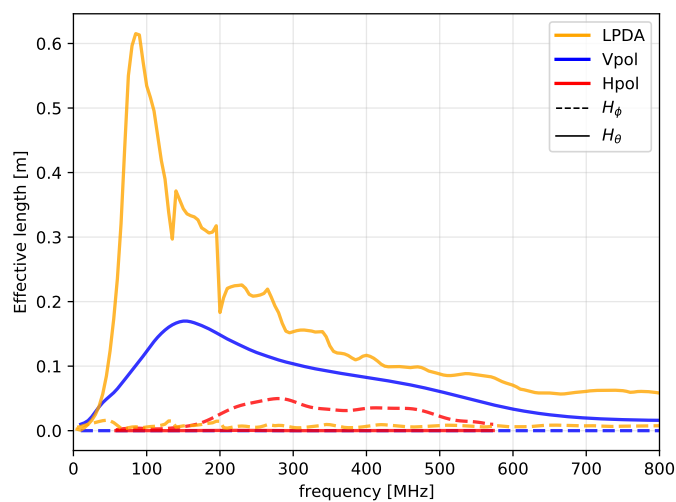


Figure 15. Antenna effective length magnitude for the LPDA, Vpol and Hpol (tri-slot) in the direction of maximum gain H_θ (V-pol and LPDA) or H_ϕ (H-pol). Results of detailed antenna simulations of the v1 iterations as shown in figure 14.

Particular care will be taken to placement and alignment of the LPDAs in the trenches at the surface, as well as surveying the position of boreholes and antenna locations to ensure good starting values for the system calibration using the *in situ* pulsers.

4.2 Radio-frequency front-end design

To minimize system noise temperature, the feed of each antenna deployed in the borehole is connected with a short coaxial cable to a downhole front-end (figure 13), where a Low-Noise Amplifier (LNA, type IGLU, see figure 16) boosts the signal strength. To prevent a significant gain slope from long lengths of copper coaxial cable, each front-end contains a Radio Frequency over Fiber (RFoF) transmitter. The RFoF link and LNA are both powered by a DC connection from the surface, which is the only through-going coaxial cable in the boreholes. The LNA and RFoF are custom designs optimized for minimal noise temperature (≤ 150 K) and low power. Each downhole channel consumes 140 mW, compared to 2.5 W in the previous installation of the phased-array in ARA. A total of 15 downhole antennas are distributed across three boreholes.

After being transmitted over fiber, the signals are received by another set of amplifiers in the DAQ box (type DRAB, see figure 16) and converted back to analog signals. At the DAQ box, the signals from the surface channels are also received and amplified. Given the relatively short run of coaxial cable from the LPDAs to the DAQ box of less than 20 m, the signals require only one amplification stage after being fed into the DAQ box (type SURFACE, see figure 16).

All amplifiers are placed in custom-designed RF-tight housings using iridized aluminium (chromate conversion coating). This significantly reduces the influence of noise on the amplifiers and protects the IGLU amplifiers in the boreholes from the environment. The amplifiers exhibit excellent uniformity in laboratory tests (see figure 17). Nevertheless, all amplifiers will be calibrated individually to reduce systematic uncertainties on the reconstructed signals.

4.3 Triggering, digitization, and data acquisition

The main trigger of RNO-G will come from a phased-array at depth of 100 m. The design of the field-proven phased-array installed at ARA [12] had to be changed to accommodate the lower power requirements of autonomous stations and was optimized with respect to the neutrino signals typically expected in Greenland and with respect to per-item cost for the scalability of the array.

The primary trigger will thus be a coherent-sum and beam-forming trigger from a compact array of four vertically-polarized antennas installed at the bottom of the main borehole string at a depth of 100 m. A commercially available 8-bit 500 MSa/s ADC is used to digitize and continuously stream data to an FPGA. This reduces the effective band to operate at the low-end of the signal bandwidth, 80 MHz–250 MHz. The lower cut-off is determined by the amplifier design that takes advantage of the full-range of low-frequency power that the antenna delivers.

Eight beams will be formed that cover the full range of expected signal arrival directions. Compared to the previous phased-array implementation in ARA there will be fewer beams, but each of them wider, thus no angular coverage loss is incurred. Overall, the power-savings total to about a factor of 10 for the trigger board, using 4 W in full operation mode.

A single-antenna voltage threshold of $2\sigma_{\text{noise}}$ can be achieved with this trigger, based on simulation studies as shown in figure 18. The smaller bandwidth reduces the SNR of on-cone

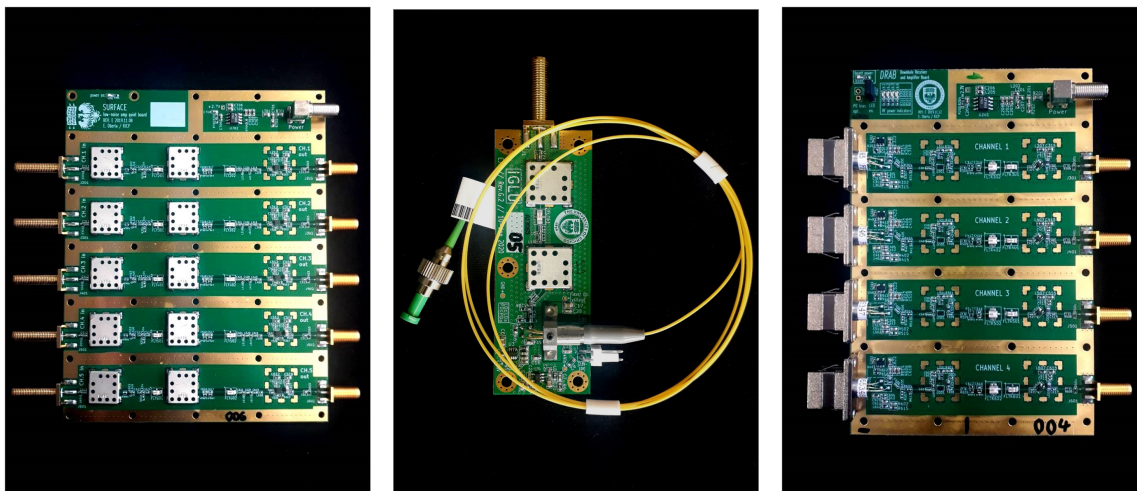


Figure 16. Amplifiers as designed for RNO-G. Left: SURFACE amplifiers for the signals coming from the LPDAs via coaxial cable. Middle: an IGLU board (In-ice Gain with Low-power Unit) used to convert signals from antennas deep in the ice to analog RF signals and then feed them into the indicated fiber. Right: DRAB board (Down-hole Receiver and Amplifier Board) located within the station housing. All amplifiers are shown without their environmental enclosures.

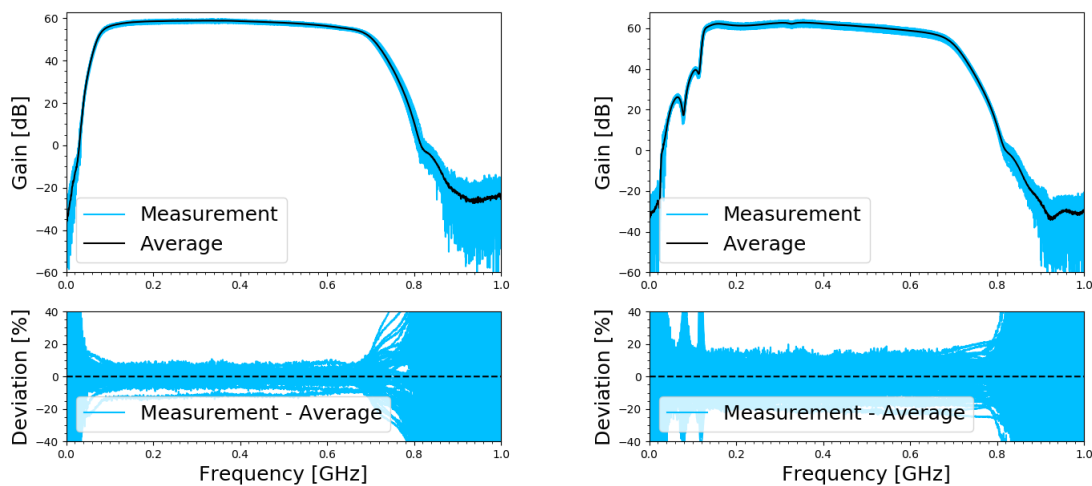


Figure 17. Gain of the RNO-G amplifiers. Left: 12 SURFACE amplifiers. Right: combination of 23 IGLU and DRAB amplifiers, including a 50 m optical fiber cable. All amplifiers are revision v1 hardware.

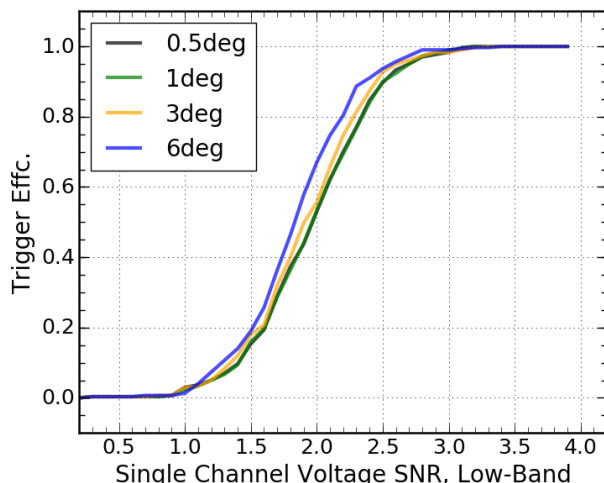


Figure 18. End-to-end simulation of the 4-antenna phased array trigger design for RNO-G. The simulated trigger efficiency for a number of neutrino signals at different off-cone viewing angles in the trigger bandwidth of 80 MHz–250 MHz.

signals (i.e. 0.5 deg in figure 18) by 10%, however, increases the SNR for off-cone events by up to 80%, thereby incurring very little loss on the absolute neutrino effective volume. This is due to the limited high-frequency content of off-cone neutrino signals (see also figure 4).

The full-band waveforms for all 24 antennas within a station will be digitized using the Radio DIgitizer and Auxiliary Neutrino Trigger (RADIANT) board (figure 19). The single-channel LAB4D switched-capacitor array sampling ASIC is used for waveform recording at a rate up to 3.0 GSa/s with an adjustable record length up to ~ 700 ns and the capability for multi-event buffering on-chip [223]. For RNO-G it is planned to operate the LAB4D in 2x 2048-sample buffers for essentially deadtime-less performance.

A trigger decision can be made using input from the primary neutrino trigger board (phased-array) or an auxiliary on-board trigger using similar Schottky diode detector circuits. The auxiliary on-board trigger is formed using a comparison between a DC voltage level and the enveloped waveform, which is fed to the on-board FPGA to build a combinatoric trigger decision. As the auxiliary trigger will have a higher overall threshold than is possible with the primary neutrino trigger board, it will predominately be used as additional trigger for the surface antennas as an air shower trigger. In periods in which the power available to the stations is low (see section 4.4) it can serve as main trigger, however, with a much weaker sensitivity to neutrino signals.

Once an event is digitized, the waveforms and metadata are transferred to a BeagleBoneBlack Industrial, an ARMv71 Linux system, over a Serial Peripheral Interface (SPI) link, which allows data transfer at up to 20 Mbps. The operating system and acquisition software are stored on robust eMMC storage, while a 128 GB industrial SD card stage data before it is transmitted wirelessly to Summit Station. The acquisition software is an evolution of field-proven ARA phased array acquisition software.

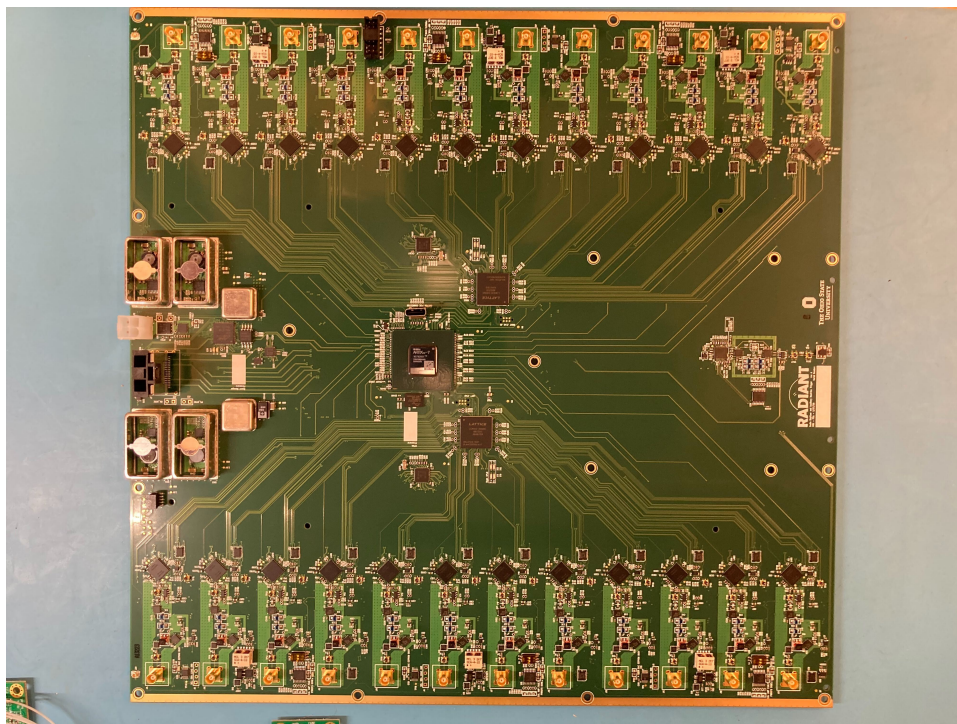


Figure 19. First iteration of the Radiant Board that will be the main DAQ of RNO-G. All 24 channels are accommodated on one board and read out by LAB-4D chips.

4.4 Autonomous power and wireless communications

Autonomous power and wireless communications simplify logistics for an experiment of this scale and become even more efficient for even larger arrays, such as IceCube-Gen2. Each station will be powered by two solar panels, with a total maximum power output of 300 W, and a 5 kWh sealed lead-acid battery bank that provides three days of full-system (24 W) running capacity during cloudy or inclement conditions, with a 60% de-rating margin. Lead-acid batteries, when lightly discharged relative to total capacity, have a proven track record in Arctic environments as demonstrated by the UNAVCO remote stations [224]. The daily solar energy delivered to a RNO-G station using a 300 W solar panel array is shown in figure 20, using realistic estimates of 70% total sun fraction (including diffuse and snow-reflected contributions) and a 90% charge-controller efficiency. A low-power microcontroller (μC) will manage the power system and turn parts of the detector on and off as necessary. The μC communicates with the Beaglebone SBC via a serial connection so that the SBC may be shut down cleanly if necessary. Enough power granularity is available to run the detector in a low-power, lower-sensitivity mode if needed.

The RNO-G station can be operated in several different modes depending on the available solar power capacity, in order to maintain constant science data during long stretches of inclement weather and during the shoulder seasons, when the sun only rises above the horizon for short periods per day. These operating modes include:

1. **Full-station mode:** power, trigger, and data acquisition on the full 24-channel station including the low-threshold trigger and full LTE data telemetry. Power: ~ 24 W.

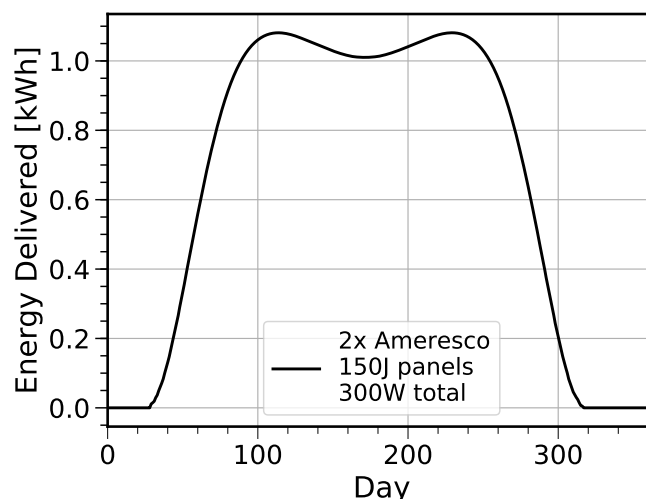


Figure 20. Predicted daily energy delivered by a 300 W photo-voltaic (PV) array to an RNO-G station at Summit Station. The PV array comprises two Ameresco 150J rugged panels mounted vertically and facing south. The total PV area is 2 m².

2. **High-threshold mode:** power, trigger, and data acquisition on the full 24-channel station without the low-threshold trigger and minimal LTE data telemetry. Power:~17 W.
3. **Surface-only mode:** power, trigger, and data acquisition only on the 9 surface LPDAs and minimal LTE data telemetry. Power:~6 W.
4. **Winter-over mode:** operating mode during the polar night. All power is turned off except to the charge-controller, LoRaWAN network, and station-control microcontroller. Only minimal housekeeping data is telemetered over LoRa. The estimated power draw is ~70 mW.

The expected uptime for an RNO-G station at Summit Camp with the 300 W PV panel array is 216 days in operating mode 1 (59%), 25 days in mode 2 (7%), and another 20 days in mode 3 (5%) for a total science livetime of ~70% averaged over the year. For the remaining 30% of the year, the station will be put in winter-over mode. These different operating modes can be engaged by the RNO-G station controller autonomously or commanded remotely over one of the wireless networks.

Options to operate further into the winter are being explored. This R&D is particularly relevant for a potential larger array at the South Pole such as IceCube-Gen2, where the polar night is longer. Although not part of the baseline RNO-G design, wind-turbines may allow to extend the full-station mode operations of RNO-G throughout the winter. Development of radio-quiet wind turbines that can survive in the polar environment is ongoing [18]. Modeling using historical wind data [225, 226] suggests that a feasible 25%-efficient turbine at a height of 10 m would produce a daily average of 1200 Wh per square meter of collection area. Due to extended periods of low wind speeds a larger battery buffer will be needed for operation on wind power.

The main data transfer link from each detector to Summit Station will use modern cellular technology. A private LTE network provides high bandwidth (up to 75 Mbps total uplink) and long range while consuming minimal power (<1 W average) at each station. A commercially-sourced



Figure 21. The station solar charge controller and high-efficiency DC-DC board for RNO-G.

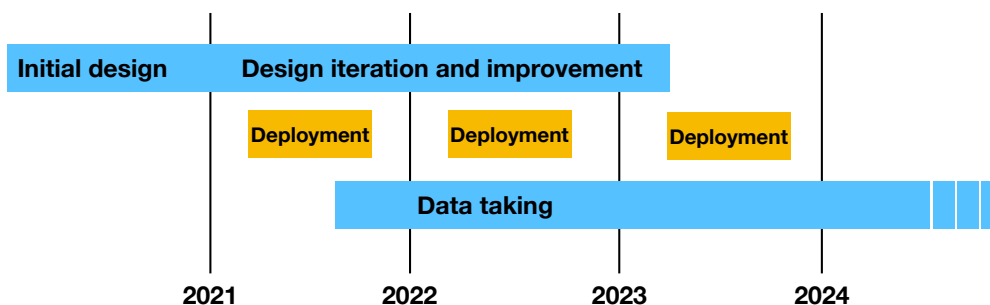


Figure 22. The anticipated timeline of RNO-G. The initial design work is ongoing. Installation will take place in the summer of 2021, 2022, and 2023, tentatively scheduling the installation of 10, 10 and 15 stations, respectively. Data taking will commence with the first deployed station.

LTE base station will be deployed with an antenna on the roof of the Science and Operations Building at Summit Station. As a compromise between range and minimizing interference with our detectors, LTE Band 8 (880-915 MHz uplink, 925-960 MHz downlink) was chosen and a permit has been acquired from the Greenlandic Radio Administration. Link modeling, including terrain shielding and a 10 dB fading margin, predicts a usable range up to 10 km.

A 34-dBi roof-top sectorial antenna at Summit can cover the azimuthal extent of the array and each station will be equipped with a 9 dBi antenna on a 3 m mast. A secondary LoRaWAN [227] network will also be deployed, providing a backup low-power but low-bandwidth connection for control and monitoring.

5 Installation, calibration, and operations

The anticipated timeline of the construction of RNO-G is shown in figure 22. The initial design work is already on-going and a first installation of stations is anticipated for 2021, provided that there are no continued restrictions due to the COVID-19 virus.

5.1 Drilling and installation plan

The main tasks for installation of each RNO-G station are:

1. drill boreholes for deep instrumentation,
2. deploy the solar panels and communications,
3. deploy detector instrumentation in boreholes and trenches,
4. confirm station operation and take calibration data.

The baseline RNO-G scenario assumed use of the ASIG mechanical drilling technology. The ASIG drill, owned and operated by the US Ice Drilling Program (IDP) is an auger with add-in drill sections. One 100 m deep hole requires a single working shift of 10 hours for three people. Therefore, the three holes required for each RNO-G station can be drilled in three days assuming one work shift per day, or one and a half days assuming two work shifts per day.

The preferred drill under consideration is the Rapid Access Isotope Drill (RAID) from the British Antarctic Survey (BAS). Holes of the diameter of 3 '' were successfully drilled to 461 m at Little Dome C. For RNO-G larger diameter holes are needed, which is why an existing proto-type development BigRAID is being considered [228]. It will provide 285 mm or 11.2 '' holes, taking about 0.85 days to reach 200 m or 0.38 days to reach 100 m, making it both faster and more versatile than the ASIG drill.

Using a mechanical drilling approach is much more scalable than previous drilling efforts for the ARA experiment at the South Pole, which used a hot water drill to reach 200 m depths. Mechanical drills are significantly lighter weight and less complex. Future development in drilling technology may enable exploring a wider range of more aggressive designs with RNO-G, which may lead to further improved sensitivity or event reconstruction capability. Drilling below the firn layer may provide significant increases in field-of-view due to fewer limitations in ray bending. However, care needs to be taken that any drill remains fast enough so as not to be the rate limiting step in installation and that personnel to operate the drill remains limited. Partly autonomous drilling operation is also under consideration.

Although subject to considerations such as firn thickness (which impacts drill depth) and ice temperature, local snow accumulation rate, average daily temperatures and the availability of solar and wind power, the station design is purposely general. This allows easy adaptation of the design for future larger in-ice arrays at other sites, such as IceCube-Gen2 at the South Pole.

The installation of both infrastructure (solar panels and communication antennas) and instrumentation is anticipated to be faster than hole-drilling. A drilling and installation team of seven people is foreseen for the first installation season, with installation beginning a week after commencing drilling. We project that an installation of up to 20 stations a year at Summit Station seems feasible. After installation, additional time will be required in the field to commission and validate station operation.

5.2 Calibration requirements and strategies

In order to optimally reconstruct events, the relative antenna positions must be known to a small fraction of the wavelength. Calibration using a local radio transmitter is necessary to achieve the

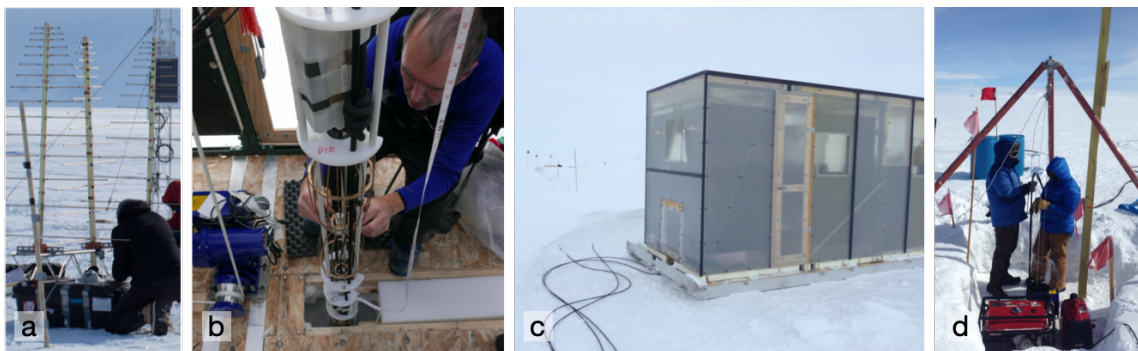


Figure 23. RNO-G installation plans are based on prior deployments of (a) surface stations at ARIANNA and (b) strings of antennas deployed in boreholes for ARA, both in compact phased arrays and reconstruction strings. A deployment shed for the drill and installation will be built on skis based on prior work done for ARA (c). Site studies conducted at Summit Station in Greenland also informed the installation plans (d).

required few-cm precision. Two deep transmitting antennas will be included with each station, as well as one at the surface. The calibration signal is generated in the surface controller board and sent downhole over RFoF. By measuring the relative time delays of the signal at each receiving antenna, the positions may be determined. After initial calibration, occasional runs of the pulser serve as a check of system stability.

An existing 740 m deep nearby borehole (DISC) [229], will also be used to send pulses to the array from various depths. This serves as a check of the antenna position and, by varying the depth of transmission, allows inversion of the radio properties of the ice. Understanding the refractive index profile of the firm is key to reconstruction and sensitivity modeling. Additional pulsing from the surface will be performed to further understand the ice.

Every station is equipped with a GPS, which will be used to synchronize event timing between stations at the 10 ns level. This is especially important for analyzing extensive air shower events, multi-station neutrino events and for absolute time difference measurements useful for ice studies. The GPS will also track the movement of station locations with the ice flow, which will provide valuable input for ice-modeling. A higher timing precision between stations can be obtained if suitable transmitters are identified at site [230] or through the usage of airplane signals [231]. This may also allow the combined reconstruction of neutrino signals detected in multiple stations [195], which would then yield improved precision.

All S-parameters of amplifiers, cables, and components will be calibrated before installation. Experience from radio air shower arrays has shown that a measurement of all individual components, including a temperature-dependent gain correction will be crucial to reduce systematic uncertainties. A continually-updated MongoDB database fully integrated with the simulation and reconstruction software [196, 216] will be used to track the parameters of all components.

5.3 Operations and data systems

The acquisition software on the Single-board computer (SBC) adjusts the trigger thresholds to maintain as fast a trigger rate as possible ($\mathcal{O}(10\text{ Hz})$) without incurring significant downtime. This high sustained rate drives system performance downstream, so second-stage filtering is applied

on the SBC to reduce the rate of saved triggers to a time-averaged 1 Hz. Additionally, 0.1 Hz of forced-trigger data will be recorded at regular intervals to help characterize the noise environment.

The on-disk compressed size of each event is an estimated 30 kB, implying an average data rate of around 260 kbps per station at 1.1 Hz. The LTE network can easily accommodate this rate with a relatively low duty-cycle at each modem, thereby saving power. This rate allows storage for six weeks on the local SD cards in the event of an unexpected network outage. If more time is needed, the station can be instructed via LoraWAN to reduce the rate. In the unlikely case of simultaneous LTE and LoraWAN failure, the software on the station will automatically throttle the rate. Once data is transmitted to Summit Station, it will be stored on a redundant disk array for collection each summer. At the estimated 1 TB/station/per year of data, full build-out requires a redundant storage capacity (with margin) of 35 TB, which can easily be achieved with a single commodity rack server (e.g. Dell PowerEdge R7515).

All instrument status data and event metadata as well as a subset of the waveform data (5 GB/day total) will be transmitted with low latency via Summit Station’s satellite link to the University of Wisconsin for monitoring and quality assurance. A small portion of available bandwidth will be reserved for remote login for any configuration changes or remote maintenance required. The JADE software [232] successfully developed and deployed for IceCube data management will be used for RNO-G. For data acquisition performance, all data is initially stored in a compressed packed-binary format resembling the in-memory format used by the data acquisition system. Converters will be maintained from the raw data format to more convenient archival formats (e.g. HDF5).

All low-latency data will be readily available to the collaboration via an interactive monitoring web site.¹ A comprehensive set of checks on the metadata and system health will be performed by the computer systems at Summit Station. Any anomalies will result in an email alert.

Monitoring duty will be apportioned to institutes on a rotating basis. While monitoring, an institution is responsible for timely investigation of all alerts and daily checks of the low-latency data for potential issues. Weekly monitoring reports will be issued to provide historical context for any issues that may arise.

Several mock stations, taking pure thermal noise data from terminated amplifiers, will be operated at collaborating institutions. These provide a testing ground for any configuration changes, assist with training, and help debug any issues that may arise. The pure thermal noise data also serves as a useful tool in developing analyses.

6 Projected sensitivity of RNO-G

In order to calculate the sensitivity of RNO-G, we have simulated the full 35-station array with a detailed modelling of the baseline hardware. Simulations for radio detectors are constantly evolving, incorporating experience from air shower simulations [38, 233–235] and previous codes for neutrino radio detectors [217, 236–238].

All simulation results presented herein have been performed with the NuRadioMC code [196]. For the same emission model, ice model and detector quantities, the results of this code have been shown to agree to the percent level with previous and independent codes, both for single event

¹Based on <https://github.com/vPhase/monutor>.

signatures as well as for the calculations of effective volumes. It has been found that the trigger-level sensitivities are in particular affected by the precise implementation of the trigger, the exact frequency band of the detector, the noise temperature of the system, the chosen emission model describing the Askaryan effect, whether a complete array is simulated or the array is scaled up from one station (impacting the number of events detected by multiple stations), and whether the interactions of secondary particles (taus and muons) are included in the sensitivity calculation. The latter three factors are most significant, with variations up to 50% in effective area depending on the energy. Since, in the design process, many of the instrument parameters are not completely fixed, we carefully quote in the following the assumptions made for the array and the hardware, bearing in mind that these design sensitivities are subject to change as the instrument design matures.

For the simulations, we use as a simplified proxy for the trigger in section 4.3, a single vertical dipole per station with an amplitude threshold. A range of thresholds was used from $1.5\sigma_{\text{noise}}$ to $2.5\sigma_{\text{noise}}$ to account for possible variations in the exact design of the phased-array. Currently, $2.0\sigma_{\text{noise}}$ is the expected to be the best proxy for the phased-array trigger using 4 dipole antennas that is in production (see figure 18). Dipoles are simulated at 100 m of depth, roughly at the same depth as the planned phased array.

We have simulated the response of a dipole of 50 cm length similar to the one in figure 14 and used it for the sensitivity calculation. The simulations performed with XFDTD [239] provide full gain and phase information as a function of incoming signal direction.

We have used NuRadioMC [196] with the *ARZ2020* parameterization given in [197, 240] as our model for signal emission. We have included triggers induced by secondary particles produced by the outgoing lepton after a charged current (CC) interaction, following the procedure outlined in [195]. The simulated station layout is that shown in figure 7, with 35 stations having 1 km spacing between them on a rectangular grid.

We first discuss the sensitivity of RNO-G to a diffuse neutrino flux and how the neutrino energy will be determined, then its angular sensitivity and lastly the sensitivity to a transient event. We will also briefly report on the expected sensitivity to air shower signals.

6.1 Sensitivity to diffuse flux

Figure 24 shows the expected 90% CL upper limit to an all-flavor flux for 5 years of operation of the full 35 station array, assuming a 67% duty cycle, as expected under only solar power. This is using effective volumes for an isotropic all-sky flux and full-decade energy bins. See [196] for more details on the V_{eff} calculation, and the inclusion of the interaction length to convert from A_{eff} to V_{eff} .

We have applied the Feldman-Cousins method [243] for no detected events and zero background. The zero background assumption is justified as a first approximation, as according to table 1, we expect ~ 0.58 detected muons over the full energy range for five years of operation time (using SIBYLL 2.3C for signal generation and a $2\sigma_{\text{noise}}$ proxy).

The expected upper limit is shown in figure 24 along with other experimental bounds and model predictions. The red band shows the expected range of 90% CL upper limits for noise levels varying from $1.5\sigma_{\text{noise}}$ -equivalent trigger (lower part of the band) to $2.5\sigma_{\text{noise}}$ -equivalent trigger (higher part), and includes 95% CL contours due to the effective volume uncertainty. The black band shows the obtained 90% CL sensitivity for a $2.0\sigma_{\text{noise}}$ -equivalent trigger, which is the most realistic assumption for the RNO-G experiment. We also show in figure 24 the sensitivity for a

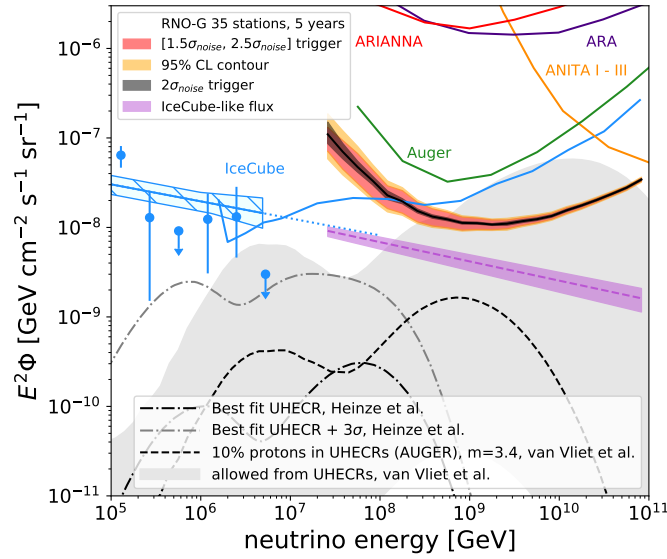


Figure 24. The five-year sensitivity (90% CL upper limits) of RNO-G to the all-flavor diffuse flux for 35 stations (assuming the stations are active two thirds of the total time), compared with existing experiments and several predicted fluxes [4, 23, 241, 242]. The red band represents the differential sensitivity band for a range of phased array proxies, spanning the interval from $1.5\sigma_{\text{noise}}$ to $2.5\sigma_{\text{noise}}$ using decade energy bins. 95% CL contours are represented by the orange band. The black band is the sensitivity expected for a $2.0\sigma_{\text{noise}}$ trigger, including 95% CL contours. The purple band depicts the expected integrated sensitivity (90% CL upper limits) for an IceCube-like flux, over the $[1.5\sigma_{\text{noise}}, 2.5\sigma_{\text{noise}}]$ trigger range.

single power law spectrum with exponents in the range indicated by the flux observed in IceCube. The purple band represents the upper limit for the IceCube flux spanned by the $[1.5\sigma_{\text{noise}}, 2.5\sigma_{\text{noise}}]$ range. The dashed line in the middle of the band is the result for the $2.0\sigma_{\text{noise}}$ trigger. These upper limits have been calculated using the expected number of events above 20 PeV for a range IceCube flux spectral indices and finding that value that yields the number of events equal to the Feldman-Cousins 90% CL upper limit under the assumption of no background. The median upper limit exponents for the plausible trigger range cover the interval $[-2.24, -2.19]$, with -2.21 being the median upper limit spectral index for a $2.0\sigma_{\text{noise}}$ trigger. If no neutrino events are detected, RNO-G will be able to exclude IceCube-like fluxes above these levels.

6.2 Energy measurement

The ability of RNO-G to measure the neutrino spectrum will depend on the accuracy at which the energy of each event can be determined. The relation between the neutrino energy E_ν and the amplitude $|\vec{E}|$ of the electric field of the radio signal at the station is given by:

$$|\vec{E}| \sim E_\nu \cdot y \cdot f(\varphi) \cdot \frac{\exp(-d/l_{\text{atten}})}{d} \quad (6.1)$$

where y is the fraction of the neutrino energy deposited into the shower, and $f(\varphi)$ a dependence on the angle under which the particle shower is observed. The last term accounts for the attenuation of the radio signal as it travels to the antenna, with d being the distance of the interaction vertex from the station and l_{atten} the attenuation length of the ice.

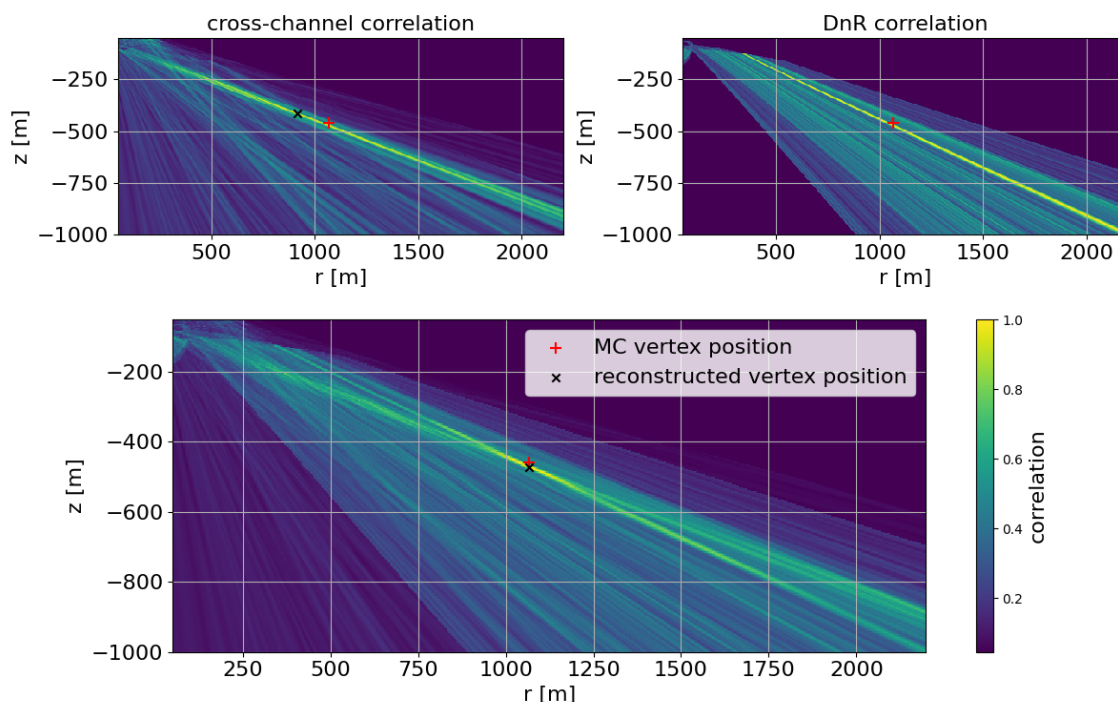


Figure 25. Neutrino interaction vertex reconstruction for one event using correlations between different channels (top left), correlations between different rays reaching the same antenna (top right) and a combination of both (bottom). Colors specify the normalized sum of correlations between channels, shifted by the difference in signal travel time expected for a given vertex position.

In general, the (*inelasticity*) fraction y of the neutrino energy that contributes to a particle shower undergoes event-by-event fluctuations and cannot be reconstructed on a single-event basis. It therefore must be estimated from theory, resulting in a statistical uncertainty of, on average, a factor of ~ 2 [21]. This restriction imposes a hard bound on the energy resolution obtainable with any neutrino detector that only observes the cascade. The goal is therefore to reconstruct the other parameters in eq. (6.1) precisely enough for the uncertainty in y to be dominant. It should be noted that in case of an electron neutrino interaction, the full amount of energy is transferred to two particle showers very close to each other, which argues against having the unknown fraction y as bound. However, these two cascades can interfere constructively or destructively and pure-electromagnetic cascades are subject to the LPM-effect [244, 245] at high energies, which changes their radio emission [246]. This makes it reasonable to treat the inelasticity for all cases as bound in a first general consideration.

The resolution on the RNO-G measurement of the full electric field $|\vec{E}|$ depends on a number of factors. Ideally, the amplitude should be obtained for all polarization components, with separate levels of noise. In general, the larger the detected amplitude of the signals (larger measured signal-to-noise ratio (SNR_m), see below), the smaller the influence of noise on the uncertainty. Similarly, noise effects are mitigated as antenna hit-multiplicities increase. As the Hpol antennas have lower gain than the Vpol antennas, the Hpol signals will typically have smaller SNR_m . Several methods such as *forward folding* [196], template matching [19], or information field theory [247] can be

used to mitigate noise effects; nevertheless, the obtainable resolution of the amplitude will vary significantly from event to event.

It should be pointed out that using SNR_m differs from the situation of simulations (as defined in section 3.2), as the true amplitude of the signal S without noise is unknown, so the measured $\text{SNR}_m = (\text{signal} + \text{noise}) / \text{noise}$. Using a definition of $\text{SNR}_m = 0.5(\max(S) - \min(S)) / \sigma_{\text{noise}}$, a typical waveform of the length of RNO-G has a roughly 50% chance of reaching $\text{SNR}_m = 3$ simply by fluctuations of noise. At $\text{SNR}_m = 3.5$ this probability is reduced to about 1%.

Due to constructive interference, the radio signal emitted by the particle shower is strongest if viewed directly at the Cherenkov angle, and diminishes (in a frequency-dependent manner) the further the observer viewing angle departs from the Cherenkov angle. As shown in figure 4, the higher frequencies lose signal coherence earliest. Therefore, the shape of the frequency spectrum of the signal can be used to reconstruct the viewing angle relative to the Cherenkov angle and, ultimately, make a correction. This method has been demonstrated for particle showers in air [206], and our first simulations indicate the same to be true for neutrino showers. Quantitatively, we anticipate that $f(\varphi)$ will be obtainable for RNO-G for signals detected with at least a measured $\text{SNR}_m = 3.5$.

The signal pathlength d (eq. (6.1)) will depend on the reconstruction of the interaction vertex, so the resolution of the vertex position is another important ingredient for energy reconstruction.

Figure 25 shows one example of vertex reconstruction for a simulated neutrino interaction detected with RNO-G. This method to obtain the vertex position is based on cross-correlating the signals detected in all antennas with each other and deriving a probability map of the vertex location. Especially for those events in which RNO-G records both the direct emission, as well as the one reflected at/refracted-below the surface, the resolution on the vertex position will be excellent, making the unknown factor y (eq. (6.1)) the dominating uncertainty. Further work will be carried out to determine the fraction of events for which a good vertex resolution will be obtainable and the SNR_m for which this will be possible. Preliminary results indicate that, conservatively, an analysis efficiency at least corresponding to the green curve in figure 11 is reachable for the vertex and thereby energy reconstruction.

The profile of the attenuation length of the ice in Greenland, which defines l_{atten} in eq. (6.1) has been measured [41] and is used for the simulations. The remaining systematic uncertainty and variations across the array will be addressed by additional calibration campaigns as discussed in section 5.2.

6.3 Angular sensitivity

The sky coverage of RNO-G is mostly determined by the geometry of its location in Greenland. In figure 26 we show the effective areas for different zenith angle bands for RNO-G, as well as their projection onto equatorial coordinates. Outside of these bands, the effective area decreases rapidly (see also [195]), making RNO-G mostly sensitive to an annulus of roughly 45° just above the horizon.

The ability of RNO-G to provide an accurate arrival direction for detected neutrinos depends on its ability to detect the signal arrival direction and the angle with respect to the Cherenkov cone, as well as the signal polarization, and is again a strong function of the number of antennas with detected signal and their SNR_m .

The signal arrival direction can be directly determined from the time difference in the captured channel-by-channel waveforms, using (for example) cross-correlation. The obtained resolution is a

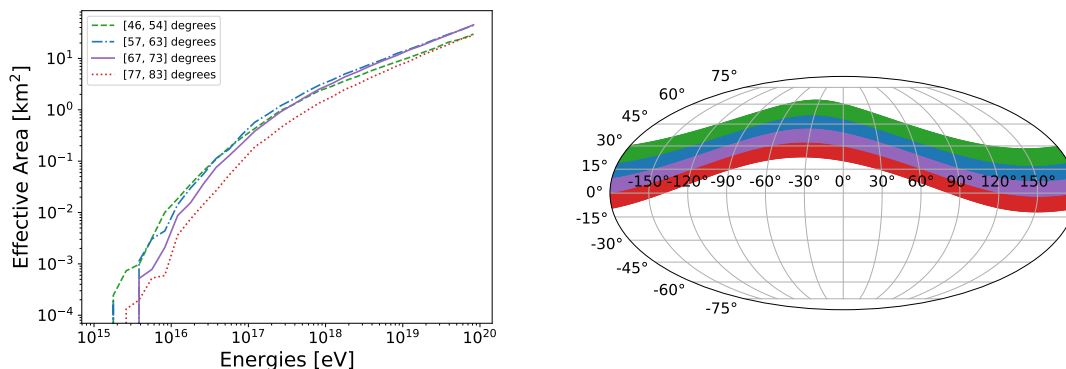


Figure 26. RNO-G instantaneous sky coverage. Left: simulated effective area as a function of neutrino energy is shown for the four most sensitive zenith bands, centered at 50° , 60° , 70° , and 80° . Simulations were performed for the full RNO-G array of 35 stations with a distance of 1 km. Right: these bands are projected in Right Ascension (RA) and Declination (Dec) for one particular time of day to illustrate the instantaneous sky coverage. Bands outside this range still show some, albeit a strongly reduced (< 0.1 fraction of maximum effective area), sensitivity for neutrino interactions.

function of the number of antennas with signal; sub-degree values have typically been obtained by previous experiments [4, 16, 21, 22]. Knowing only the arrival direction for the signal at a specific station, the neutrino arrival direction can be determined to lie on a cone, projecting to a ring on-sky as shown in figure 27. Only a fraction of the ring corresponds to a probable physical solution, as many arrival directions can be excluded by the known Earth absorption.

The radio signal is the strongest on the Cherenkov cone and then weakens once the angle to the shower axis deviates from the Cherenkov angle. Depending on the type of event, viewing angles of more than 10 degrees with respect to the Cherenkov angle may still be observable. As discussed in section 6.2, the electric-field is a function of the viewing angle, as the higher frequencies fall off further away from the Cherenkov cone, so the viewing angle is reconstructable via the frequency slope. Combining signal arrival direction and viewing angle narrows the ring of possible arrival directions.

As the radio signal is due to the Askaryan effect, the polarization of the induced electric-field points radially inwards towards the shower axis. Therefore, a measure of the polarization is needed for a unique neutrino arrival direction. As shown in figure 27, adding polarization allows reducing the entire ring to a small patch on the sky. The absolute angular resolution as function of energy, elevation and SNR_m per antenna is still under study. Thus, figure 27 has been constructed to highlight the influence of different signal parameters on the angular resolution, while using a simulated event, as detectable in RNO-G, including noise but no detector uncertainties. The event shown has an $\text{SNR}_m \approx 6$ in both Vpol and Hpol antennas, meaning that all pulses can be clearly identified.

6.4 Sensitivity to transient events

Using the same simulations as performed for section 6.1, the sensitivity of RNO-G to transient events has been obtained, as shown in figure 28. Most models predict small neutrinos fluxes in the energy range of RNO-G, as compiled in figure 3. However, given, e.g., large uncertainties in the modelling of mergers of neutron stars and that this area of multi-messenger astronomy is still in its infancy, RNO-G may make serendipitous discoveries. Its location in the Northern hemisphere

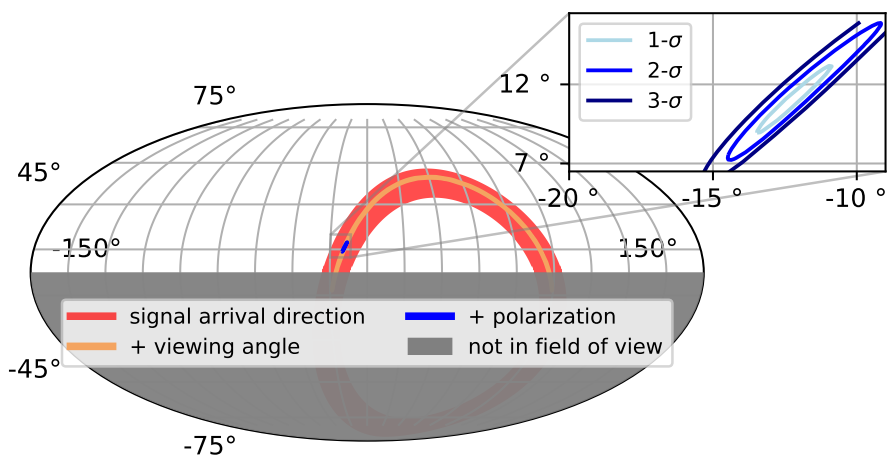


Figure 27. Radio neutrino detector arrival direction reconstruction. Given the limited field of view, the reconstructed signal arrival direction restricts the neutrino arrival direction to the red circular band shown. Adding information from the frequency content constrains the viewing angle, and reduces the width of the band. Finally, including data from both Hpol and Vpol antennas, polarization reconstruction reduces the allowed arrival direction to a small area on sky. The reconstruction and uncertainties are shown for one event simulated for RNO-G with NuRadioMC. The coordinates are local azimuth and zenith angle.

makes it uniquely sensitive, and complementary to other planned radio neutrino observatories in the Southern Hemisphere.

GRBs and other cataclysmic events are promising candidates for transient flares of UHE neutrinos. GRB afterglows are expected to produce the highest energy neutrinos over months-long time scales [49]. Short GRBs resulting from binary neutron star mergers may be detectable with RNO-G if they are nearby or connected with the production of giant flares from magnetars [248]. Similarly, magnetars resulting from binary neutron star mergers can drive UHE neutrino production [131]. As shown in figure 28, RNO-G can constrain the neutrino fluence from GRB afterglows, short GRBs, and long-lived magnetars within tens of Megaparsecs. Furthermore, Tidal Disruption Events (TDEs) are another cataclysmic source class still in the infancy of their discovery, with frequent new observations and population increases thanks to transient observatories such as the Zwicky Transient Facility (ZTF) [249]. As more is uncovered about their nature, they may also become a viable multi-messenger target for RNO-G.

Flaring blazars are particularly interesting targets for RNO-G. As an example, a model of the neutrino fluence expected from the flare of the bright gamma-ray blazar PKS 1502+106 [132] is compared to the RNO-G sensitivities in figure 28. This particular blazar is an FSRQ, which are notable for their expected high UHE neutrino fluxes [71], and spatially coincident with a “golden” event (IC190730A) seen in IceCube [250, 251]. In the model, neutrinos are produced in the two different scenarios that are consistent with multi-wavelength photon observations, but the neutrino spectrum is strongly impacted by the radiation mechanism. Stacking searches in RNO-G for flares of blazars or multi-messenger driven searches may reveal UHE neutrinos or constrain the neutrino spectrum at the highest energies. Note that while PKS 1506+106 is at a distant redshift, closer blazars will have a stronger neutrino fluence.

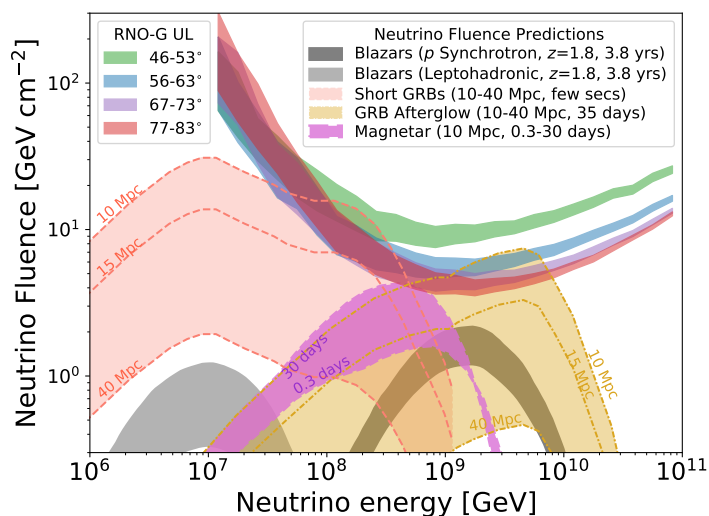


Figure 28. 95% CL fluence sensitivities between triggers at $1.5\sigma_{\text{noise}}$ and $2.5\sigma_{\text{noise}}$ are shown for four zenith bands centered at (top to bottom) 50° (green), 60° (blue), 70° (purple), and 80° (red). Sensitivities are calculated for a full decade in energy. Model-predicted fluences from several transient classes (bright gamma-ray blazars [132], short GRBs [130], magnetars [131], and GRB afterglows [49]) are also shown for direct comparison. We scale the short GRB and GRB afterglows by several luminosity distances to demonstrate the distance over which RNO-G will be sensitive to transients; a similar scaling can be applied to other source classes. For the calculation of sensitivities here we have used an integrated background expectation of no events. Note that for longer duration transients, integrated background may become non-negligible.

RNO-G has unique capabilities to process alerts in nearly real time. Summit Station’s continuous satellite link and the LTE communications strategy can permit alerts from other multi-messenger observatories to be sent to and from the RNO-G stations.

6.5 Sensitivity to air shower signals

RNO-G will be equipped with upward-facing LPDAs, sensitive to air shower signals. These will be triggered through the auxiliary trigger as described in section 4.3. First simulations indicate a turn-on of the trigger efficiency to air showers between 1×10^{16} eV and 1×10^{17} eV, with details depending on the exact system noise temperature and environmental noise conditions that will need to be confirmed during the first deployment season in-situ. The DAQ is designed to store 0.1 Hz of triggers from the surface antennas, dedicated to the detection of air showers. The passband of the envelope trigger has been optimized for the highest surface antenna trigger efficiency and will be between 80 MHz and 180 MHz. We expect the detection in the order of one air shower per day per station.

The air shower trigger at RNO-G will serve two purposes. As discussed in section 3.4, the muonic component of air showers may constitute a background for neutrino detection with RNO-G. While the flux of these background events depends strongly on the composition of the cosmic ray flux, as well as hadronic interaction models, the safest way to contain the impact of this background is to unambiguously tag air showers. RNO-G will therefore continue to be optimized to provide

its own air shower veto. In addition, air shower reconstruction will help calibrate the system and ensure an independent cross-check of up-time and efficiency.

7 Conclusions

We have presented the concept of the Radio Neutrino Observatory in Greenland (RNO-G), currently scheduled to commence installation at Summit Station in 2021. The location in Greenland both drives design considerations, such as autonomous low-power stations, and, given the unique field of view from the Northern Hemisphere, also defines the strong science case.

The RNO-G hardware builds on previous radio array experience and strives for a very low-noise system that can sustain a low trigger-threshold, but high duty-cycle operation of autonomous stations. Each of the 35 RNO-G stations will consist of log-periodic dipole antennas deployed at the surface and custom-made dipole and tri- or quad-slot antennas deployed in three mechanically drilled holes to a depth of 100 m. The stations will mainly be triggered by a phased array of four deep dipoles at the 100 m maximum depth, which will ensure the best neutrino aperture. Auxiliary envelope triggers are available for low-power operations in the seasons with less abundant solar-power and for reading out the surface antennas to detect and veto air showers.

RNO-G will be the first uniform deployment of a neutrino radio array that will demonstrate the feasibility of scaling to arbitrarily large arrays. The delivered per-year sensitivity will be the largest achieved to-date with a radio array. RNO-G with its unique view of the Northern hemisphere may provide insights into transient sources of UHE neutrinos and will bring the detection of a continuation of the astrophysical neutrinos flux to high energies as detected by IceCube within reach. Additionally, models for cosmogenic neutrinos assuming a significant proton fraction in UHE cosmic-rays will be either be conclusively ruled out or will lead, if confirmed, to a detection of neutrinos with RNO-G.

Acknowledgments

We would like to acknowledge our home institutions and funding agencies for supporting the RNO-G work; in particular the Belgian Funds for Scientific Research (FRS-FNRS and FWO) and the FWO programme for International Research Infrastructure (IRI), the German research foundation (DFG, Grant NE 2031/2-1), and the Helmholtz Association (Initiative and Networking Fund, W2/W3 Program).

References

- [1] ICECUBE GEN2 collaboration, *IceCube-Gen2: the window to the extreme universe*, [arXiv:2008.04323](#).
- [2] RICE collaboration, *Performance and simulation of the RICE detector*, *Astropart. Phys.* **19** (2003) 15 [[astro-ph/0112372](#)].
- [3] I. Kravchenko et al., *RICE limits on the diffuse ultrahigh energy neutrino flux*, *Phys. Rev. D* **73** (2006) 082002 [[astro-ph/0601148](#)].

- [4] ARA collaboration, *Performance of two Askaryan Radio Array stations and first results in the search for ultrahigh energy neutrinos*, *Phys. Rev. D* **93** (2016) 082003 [[arXiv:1507.08991](#)].
- [5] P. Allison et al., *Design and initial performance of the Askaryan Radio Array prototype EeV neutrino detector at the south pole*, *Astropart. Phys.* **35** (2012) 457 [[arXiv:1105.2854](#)].
- [6] ARA collaboration, *Constraints on the diffuse flux of ultrahigh energy neutrinos from four years of Askaryan Radio Array data in two stations*, *Phys. Rev. D* **102** (2020) 043021 [[arXiv:1912.00987](#)].
- [7] ARIANNA collaboration, *A first search for cosmogenic neutrinos with the ARIANNA hexagonal radio array*, *Astropart. Phys.* **70** (2015) 12 [[arXiv:1410.7352](#)].
- [8] S.W. Barwick et al., *Design and performance of the ARIANNA HRA-3 neutrino detector systems*, *IEEE Trans. Nucl. Sci.* **62** (2015) 2202 [[arXiv:1410.7369](#)].
- [9] ANITA collaboration, *The antarctic impulsive transient antenna ultra-high energy neutrino detector design, performance, and sensitivity for 2006–2007 balloon flight*, *Astropart. Phys.* **32** (2009) 10 [[arXiv:0812.1920](#)].
- [10] ANITA collaboration, *Observational constraints on the ultra-high energy cosmic neutrino flux from the second flight of the ANITA experiment*, *Phys. Rev. D* **82** (2010) 022004 [Erratum *ibid.* **85** (2012) 049901] [[arXiv:1003.2961](#)].
- [11] P. Allison et al., *IceRay: an IceCube-centered radio-Cherenkov GZK neutrino detector*, *Nucl. Instrum. Meth. A* **604** (2009) S64 [[arXiv:0904.1309](#)].
- [12] P. Allison et al., *Design and performance of an interferometric trigger array for radio detection of high-energy neutrinos*, *Nucl. Instrum. Meth. A* **930** (2019) 112 [[arXiv:1809.04573](#)].
- [13] P. Allison et al., *Constraints on the ultra-high energy neutrino flux from gamma-ray bursts from a prototype station of the Askaryan Radio Array*, *Astropart. Phys.* **88** (2017) 7 [[arXiv:1507.00100](#)].
- [14] P. Allison et al., *Observation of reconstructable radio emission coincident with an X-class solar flare in the Askaryan Radio Array prototype station*, [arXiv:1807.03335](#).
- [15] K. Casey, T. Fudge, T. Neumann, E. Steig, M. Cavitte and D. Blankenship, *The 1500 m south pole ice core: recovering a 40 ka environmental record*, *Annals Glaciol.* **55** (2014) 137.
- [16] P. Allison et al., *Measurement of the real dielectric permittivity ϵ_r of glacial ice*, *Astropart. Phys.* **108** (2019) 63 [[arXiv:1712.03301](#)].
- [17] P. Allison et al., *Long-baseline horizontal radio-frequency transmission through polar ice*, *JCAP* **12** (2020) 009 [[arXiv:1908.10689](#)].
- [18] A. Nelles, *A wind-turbine for autonomous stations for radio detection of neutrinos*, *PoS(ICRC2019)968* (2020).
- [19] S.W. Barwick et al., *Radio detection of air showers with the ARIANNA experiment on the Ross ice shelf*, *Astropart. Phys.* **90** (2017) 50 [[arXiv:1612.04473](#)].
- [20] A. Anker et al., *A search for cosmogenic neutrinos with the ARIANNA test bed using 4.5 years of data*, *JCAP* **03** (2020) 053 [[arXiv:1909.00840](#)].
- [21] A. Anker et al., *Neutrino vertex reconstruction with in-ice radio detectors using surface reflections and implications for the neutrino energy resolution*, *JCAP* **11** (2019) 030 [[arXiv:1909.02677](#)].
- [22] ARIANNA collaboration, *Probing the angular and polarization reconstruction of the ARIANNA detector at the south pole*, *2020 JINST* **15** P09039 [[arXiv:2006.03027](#)].

- [23] ANITA collaboration, *Constraints on the diffuse high-energy neutrino flux from the third flight of ANITA*, *Phys. Rev. D* **98** (2018) 022001 [[arXiv:1803.02719](#)].
- [24] ANITA collaboration, *Observation of ultra-high-energy cosmic rays with the ANITA balloon-borne radio interferometer*, *Phys. Rev. Lett.* **105** (2010) 151101 [[arXiv:1005.0035](#)].
- [25] H. Schoorlemmer et al., *Energy and flux measurements of ultra-high energy cosmic rays observed during the first ANITA flight*, *Astropart. Phys.* **77** (2016) 32 [[arXiv:1506.05396](#)].
- [26] ANITA collaboration, *Characteristics of four upward-pointing cosmic-ray-like events observed with ANITA*, *Phys. Rev. Lett.* **117** (2016) 071101 [[arXiv:1603.05218](#)].
- [27] ANITA collaboration, *Observation of an unusual upward-going cosmic-ray-like event in the third flight of ANITA*, *Phys. Rev. Lett.* **121** (2018) 161102 [[arXiv:1803.05088](#)].
- [28] A. Romero-Wolf et al., *Comprehensive analysis of anomalous ANITA events disfavors a diffuse tau-neutrino flux origin*, *Phys. Rev. D* **99** (2019) 063011 [[arXiv:1811.07261](#)].
- [29] K.D. de Vries and S. Prohira, *Coherent transition radiation from the geomagnetically-induced current in cosmic-ray air showers: implications for the anomalous events observed by ANITA*, *Phys. Rev. Lett.* **123** (2019) 091102 [[arXiv:1903.08750](#)].
- [30] I.M. Shoemaker, A. Kusenko, P.K. Munneke, A. Romero-Wolf, D.M. Schroeder and M.J. Siegert, *Reflections on the anomalous ANITA events: the antarctic subsurface as a possible explanation*, *Annals Glaciol.* **61** (2020) 92 [[arXiv:1905.02846](#)].
- [31] D. Saltzberg et al., *Observation of the Askaryan effect: coherent microwave Cherenkov emission from charge asymmetry in high-energy particle cascades*, *Phys. Rev. Lett.* **86** (2001) 2802 [[hep-ex/0011001](#)].
- [32] P.W. Gorham et al., *Accelerator measurements of the Askaryan effect in rock salt: a roadmap toward teraton underground neutrino detectors*, *Phys. Rev. D* **72** (2005) 023002 [[astro-ph/0412128](#)].
- [33] ANITA collaboration, *Observations of the Askaryan effect in ice*, *Phys. Rev. Lett.* **99** (2007) 171101 [[hep-ex/0611008](#)].
- [34] T-510 collaboration, *Accelerator measurements of magnetically-induced radio emission from particle cascades with applications to cosmic-ray air showers*, *Phys. Rev. Lett.* **116** (2016) 141103 [[arXiv:1507.07296](#)].
- [35] LOPES collaboration, *Detection and imaging of atmospheric radio flashes from cosmic ray air showers*, *Nature* **435** (2005) 313 [[astro-ph/0505383](#)].
- [36] D. Ardouin et al., *Geomagnetic origin of the radio emission from cosmic ray induced air showers observed by CODALEMA*, *Astropart. Phys.* **31** (2009) 192 [[arXiv:0901.4502](#)].
- [37] PIERRE AUGER collaboration, *Measurement of the radiation energy in the radio signal of extensive air showers as a universal estimator of cosmic-ray energy*, *Phys. Rev. Lett.* **116** (2016) 241101 [[arXiv:1605.02564](#)].
- [38] P. Schellart et al., *Detecting cosmic rays with the LOFAR radio telescope*, *Astron. Astrophys.* **560** (2013) A98 [[arXiv:1311.1399](#)].
- [39] TUNKA-REX collaboration, *Radio measurements of the energy and the depth of the shower maximum of cosmic-ray air showers by Tunka-Rex*, *JCAP* **01** (2016) 052 [[arXiv:1509.05652](#)].
- [40] S.A. Wissel et al., *Site characterization and detector development for the Greenland neutrino observatory*, *PoS(ICRC2015)1150* (2016).

- [41] J. Avva, J.M. Kovac, C. Miki, D. Saltzberg and A.G. Vieregg, *An in situ measurement of the radio-frequency attenuation in ice at summit station, Greenland*, *J. Glaciol.* **61** (2015) 1005 [[arXiv:1409.5413](#)].
- [42] C. Deaconu et al., *Measurements and modeling of near-surface radio propagation in glacial ice and implications for neutrino experiments*, *Phys. Rev. D* **98** (2018) 043010 [[arXiv:1805.12576](#)].
- [43] M. Ahlers, *Neutrino sources from a multi-messenger perspective*, in *Proceedings, 7th Roma International Conference on Astroparticle Physics (RICAP18)*, Rome, Italy, 4–7 September 2018 [*EPJ Web Conf.* **209** (2019) 01013] [[arXiv:1811.07633](#)].
- [44] K. Fang and K. Murase, *Linking high-energy cosmic particles by black hole jets embedded in large-scale structures*, *Nature Phys.* **14** (2018) 396 [[arXiv:1704.00015](#)].
- [45] K. Fang, K. Kotera, K. Murase and A.V. Olinto, *Testing the newborn pulsar origin of ultrahigh energy cosmic rays with EeV neutrinos*, *Phys. Rev. D* **90** (2014) 103005 [Erratum *ibid.* **92** (2015) 129901] [[arXiv:1311.2044](#)].
- [46] D. Boncioli, D. Biehl and W. Winter, *On the common origin of cosmic rays across the ankle and diffuse neutrinos at the highest energies from low-luminosity gamma-ray bursts*, *Astrophys. J.* **872** (2019) 110 [[arXiv:1808.07481](#)].
- [47] K. Murase, Y. Inoue and C.D. Dermer, *Diffuse neutrino intensity from the inner jets of active galactic nuclei: impacts of external photon fields and the blazar sequence*, *Phys. Rev. D* **90** (2014) 023007 [[arXiv:1403.4089](#)].
- [48] X. Rodrigues, J. Heinze, A. Palladino, A. van Vliet and W. Winter, *AGN jets as the origin of UHECRs and perspectives for the detection of EeV astrophysical neutrinos*, [arXiv:2003.08392](#).
- [49] K. Murase, *High energy neutrino early afterglows gamma-ray bursts revisited*, *Phys. Rev. D* **76** (2007) 123001 [[arXiv:0707.1140](#)].
- [50] J. Heinze, A. Fedynitch, D. Boncioli and W. Winter, *A new view on Auger data and cosmogenic neutrinos in light of different nuclear disintegration and air-shower models*, *Astrophys. J.* **873** (2019) 88 [[arXiv:1901.03338](#)].
- [51] A. van Vliet, R. Alves Batista and J.R. Hörandel, *Determining the fraction of cosmic-ray protons at ultrahigh energies with cosmogenic neutrinos*, *Phys. Rev. D* **100** (2019) 021302 [[arXiv:1901.01899](#)].
- [52] FERMI-LAT collaboration, *The spectrum of isotropic diffuse gamma-ray emission between 100 MeV and 820 GeV*, *Astrophys. J.* **799** (2015) 86 [[arXiv:1410.3696](#)].
- [53] ICECUBE collaboration, *A measurement of the diffuse astrophysical muon neutrino flux using eight years of IceCube data*, *PoS(ICRC2017)1005* (2018) [[arXiv:1710.01191](#)].
- [54] ICECUBE collaboration, *Observation of astrophysical neutrinos in six years of IceCube data*, *PoS(ICRC2017)981* (2018) [[arXiv:1710.01191](#)].
- [55] ICECUBE collaboration, *Differential limit on the extremely-high-energy cosmic neutrino flux in the presence of astrophysical background from nine years of IceCube data*, *Phys. Rev. D* **98** (2018) 062003 [[arXiv:1807.01820](#)].
- [56] PIERRE AUGER collaboration, *The Pierre Auger observatory: contributions to the 34th International Cosmic Ray Conference (ICRC 2015)*, in *Proceedings, 34th International Cosmic Ray Conference (ICRC 2015)*, The Hague, The Netherlands, 30 July–6 August 2015 [[arXiv:1509.03732](#)].

- [57] ICECUBE collaboration, *Evidence for high-energy extraterrestrial neutrinos at the IceCube detector*, *Science* **342** (2013) 1242856 [[arXiv:1311.5238](#)].
- [58] ICECUBE collaboration, *Observation of high-energy astrophysical neutrinos in three years of IceCube data*, *Phys. Rev. Lett.* **113** (2014) 101101 [[arXiv:1405.5303](#)].
- [59] ICECUBE collaboration, *Evidence for astrophysical muon neutrinos from the northern sky with IceCube*, *Phys. Rev. Lett.* **115** (2015) 081102 [[arXiv:1507.04005](#)].
- [60] ICECUBE collaboration, *Observation and characterization of a cosmic muon neutrino flux from the northern hemisphere using six years of IceCube data*, *Astrophys. J.* **833** (2016) 3 [[arXiv:1607.08006](#)].
- [61] ICECUBE, FERMI-LAT, MAGIC, AGILE, ASAS-SN, HAWC, H.E.S.S., INTEGRAL, KANATA, KISO, KAPTEYN, LIVERPOOL TELESCOPE, SUBARU, SWIFT NUSTAR, VERITAS and VLA/17B-403 collaborations, *Multimessenger observations of a flaring blazar coincident with high-energy neutrino IceCube-170922A*, *Science* **361** (2018) eaat1378 [[arXiv:1807.08816](#)].
- [62] ICECUBE collaboration, *Neutrino emission from the direction of the blazar TXS 0506 + 056 prior to the IceCube-170922A alert*, *Science* **361** (2018) 147 [[arXiv:1807.08794](#)].
- [63] M. Ackermann et al., *Astrophysics uniquely enabled by observations of high-energy cosmic neutrinos*, *Bull. Am. Astron. Soc.* **51** (2019) 185 [[arXiv:1903.04334](#)].
- [64] M. Ackermann et al., *Fundamental physics with high-energy cosmic neutrinos*, *Bull. Am. Astron. Soc.* **51** (2019) 215 [[arXiv:1903.04333](#)].
- [65] V.S. Berezinsky and G.T. Zatsepin, *Cosmic rays at ultrahigh-energies (neutrino?)*, *Phys. Lett. B* **28** (1969) 423.
- [66] M. Ahlers and F. Halzen, *Minimal cosmogenic neutrinos*, *Phys. Rev. D* **86** (2012) 083010 [[arXiv:1208.4181](#)].
- [67] A. van Vliet, *CRProa simulations, similar to PoS(ICRC2019) 190*, private communication, (2019).
- [68] TELESCOPE ARRAY collaboration, *Combined fit of the spectrum and composition from Telescope Array*, *PoS(ICRC2019) 190* (2020).
- [69] PIERRE AUGER collaboration, *Combined fit of spectrum and composition data as measured by the Pierre Auger observatory*, *JCAP* **04** (2017) 038 [Erratum *ibid.* **03** (2018) E02] [[arXiv:1612.07155](#)].
- [70] PIERRE AUGER and TELESCOPE ARRAY collaborations, *The energy spectrum of ultra-high energy cosmic rays measured at the Pierre Auger observatory and at the Telescope Array*, *PoS(ICRC2019) 234* (2020) [[arXiv:2001.08811](#)].
- [71] C. Righi, A. Palladino, F. Tavecchio and F. Vissani, *EeV astrophysical neutrinos from flat spectrum radio quasars*, *Astron. Astrophys.* **642** (2020) A92 [[arXiv:2003.08701](#)].
- [72] K. Murase and E. Waxman, *Constraining high-energy cosmic neutrino sources: implications and prospects*, *Phys. Rev. D* **94** (2016) 103006 [[arXiv:1607.01601](#)].
- [73] S. Ando, M.R. Feyereisen and M. Fornasa, *How bright can the brightest neutrino source be?*, *Phys. Rev. D* **95** (2017) 103003 [[arXiv:1701.02165](#)].
- [74] ICECUBE collaboration, *The contribution of Fermi-2LAC blazars to the diffuse TeV-PeV neutrino flux*, *Astrophys. J.* **835** (2017) 45 [[arXiv:1611.03874](#)].

- [75] A. Neronov, D.V. Semikoz and K. Ptitsyna, *Strong constraints on hadronic models of blazar activity from Fermi and IceCube stacking analysis*, *Astron. Astrophys.* **603** (2017) A135 [[arXiv:1611.06338](#)].
- [76] ICECUBE collaboration, *Results of IceCube searches for neutrinos from blazars using seven years of through-going muon data*, *PoS(ICRC2017)994* (2018) [[arXiv:1710.01179](#)].
- [77] D. Hooper, T. Linden and A. Vieregg, *Active galactic nuclei and the origin of IceCube's diffuse neutrino flux*, *JCAP* **02** (2019) 012 [[arXiv:1810.02823](#)].
- [78] ICECUBE collaboration, *Time-integrated neutrino source searches with 10 years of IceCube data*, *Phys. Rev. Lett.* **124** (2020) 051103 [[arXiv:1910.08488](#)].
- [79] TELESCOPE ARRAY collaboration, *Indications of intermediate-scale anisotropy of cosmic rays with energy greater than 57 EeV in the northern sky measured with the surface detector of the Telescope Array experiment*, *Astrophys. J. Lett.* **790** (2014) L21 [[arXiv:1404.5890](#)].
- [80] H.-N. He, A. Kusenko, S. Nagataki, B.-B. Zhang, R.-Z. Yang and Y.-Z. Fan, *Monte Carlo Bayesian search for the plausible source of the Telescope Array hotspot*, *Phys. Rev. D* **93** (2016) 043011 [[arXiv:1411.5273](#)].
- [81] J. Quinn et al., *Detection of gamma-rays with $E > 300$ GeV from Markarian 501*, *Astrophys. J. Lett.* **456** (1996) L83.
- [82] M. Punch et al., *Detection of TeV photons from the active galaxy Markarian 421*, *Nature* **358** (1992) 477.
- [83] X.-Y. Wang and R.-Y. Liu, *Tidal disruption jets of supermassive black holes as hidden sources of cosmic rays: explaining the IceCube TeV-PeV neutrinos*, *Phys. Rev. D* **93** (2016) 083005 [[arXiv:1512.08596](#)].
- [84] L. Dai and K. Fang, *Can tidal disruption events produce the IceCube neutrinos?*, *Mon. Not. Roy. Astron. Soc.* **469** (2017) 1354 [[arXiv:1612.00011](#)].
- [85] N. Senno, K. Murase and P. Meszaros, *High-energy neutrino flares from X-ray bright and dark tidal disruption events*, *Astrophys. J.* **838** (2017) 3 [[arXiv:1612.00918](#)].
- [86] C. Lunardini and W. Winter, *High energy neutrinos from the tidal disruption of stars*, *Phys. Rev. D* **95** (2017) 123001 [[arXiv:1612.03160](#)].
- [87] B.T. Zhang, K. Murase, F. Oikonomou and Z. Li, *High-energy cosmic ray nuclei from tidal disruption events: origin, survival, and implications*, *Phys. Rev. D* **96** (2017) 063007 [Addendum *ibid.* **96** (2017) 069902] [[arXiv:1706.00391](#)].
- [88] D. Biehl, D. Boncioli, C. Lunardini and W. Winter, *Tidally disrupted stars as a possible origin of both cosmic rays and neutrinos at the highest energies*, *Sci. Rep.* **8** (2018) 10828 [[arXiv:1711.03555](#)].
- [89] C. Guépin, K. Kotera, E. Barausse, K. Fang and K. Murase, *Ultra-high energy cosmic rays and neutrinos from tidal disruptions by massive black holes*, *Astron. Astrophys.* **616** (2018) A179 [Erratum *ibid.* **636** (2020) C3] [[arXiv:1711.11274](#)].
- [90] K. Fang and B.D. Metzger, *High-energy neutrinos from millisecond magnetars formed from the merger of binary neutron stars*, *Astrophys. J.* **849** (2017) 153 [[arXiv:1707.04263](#)].
- [91] S.S. Kimura, K. Murase, I. Bartos, K. Ioka, I.S. Heng and P. Mészáros, *Transejecta high-energy neutrino emission from binary neutron star mergers*, *Phys. Rev. D* **98** (2018) 043020 [[arXiv:1805.11613](#)].

- [92] E. Waxman and J.N. Bahcall, *High-energy neutrinos from cosmological gamma-ray burst fireballs*, *Phys. Rev. Lett.* **78** (1997) 2292 [[astro-ph/9701231](#)].
- [93] J.P. Rachen and P. Meszaros, *Photohadronic neutrinos from transients in astrophysical sources*, *Phys. Rev. D* **58** (1998) 123005 [[astro-ph/9802280](#)].
- [94] C.D. Dermer and A. Atoyan, *High energy neutrinos from gamma-ray bursts*, *Phys. Rev. Lett.* **91** (2003) 071102 [[astro-ph/0301030](#)].
- [95] D. Guetta, D. Hooper, J. Alvarez-Muniz, F. Halzen and E. Reuveni, *Neutrinos from individual gamma-ray bursts in the BATSE catalog*, *Astropart. Phys.* **20** (2004) 429 [[astro-ph/0302524](#)].
- [96] S. Razzaque, P. Meszaros and E. Waxman, *Neutrino signatures of the supernova: gamma-ray burst relationship*, *Phys. Rev. D* **69** (2004) 023001 [[astro-ph/0308239](#)].
- [97] K. Murase and S. Nagataki, *High energy neutrino emission and neutrino background from gamma-ray bursts in the internal shock model*, *Phys. Rev. D* **73** (2006) 063002 [[astro-ph/0512275](#)].
- [98] K. Murase, *Prompt high-energy neutrinos from gamma-ray bursts in the photospheric and synchrotron self-Compton scenarios*, *Phys. Rev. D* **78** (2008) 101302 [[arXiv:0807.0919](#)].
- [99] X.-Y. Wang and Z.-G. Dai, *Prompt TeV neutrinos from dissipative photospheres of gamma-ray bursts*, *Astrophys. J. Lett.* **691** (2009) L67 [[arXiv:0807.0290](#)].
- [100] P. Baerwald, S. Hummer and W. Winter, *Magnetic field and flavor effects on the gamma-ray burst neutrino flux*, *Phys. Rev. D* **83** (2011) 067303 [[arXiv:1009.4010](#)].
- [101] M. Ahlers, M.C. Gonzalez-Garcia and F. Halzen, *GRBs on probation: testing the UHE CR paradigm with IceCube*, *Astropart. Phys.* **35** (2011) 87 [[arXiv:1103.3421](#)].
- [102] K. Murase, K. Asano, T. Terasawa and P. Meszaros, *The role of stochastic acceleration in the prompt emission of gamma-ray bursts: application to hadronic injection*, *Astrophys. J.* **746** (2012) 164 [[arXiv:1107.5575](#)].
- [103] Z. Li, *Note on the normalization of predicted GRB neutrino flux*, *Phys. Rev. D* **85** (2012) 027301 [[arXiv:1112.2240](#)].
- [104] S. Hummer, P. Baerwald and W. Winter, *Neutrino emission from gamma-ray burst fireballs, revised*, *Phys. Rev. Lett.* **108** (2012) 231101 [[arXiv:1112.1076](#)].
- [105] H.-N. He, R.-Y. Liu, X.-Y. Wang, S. Nagataki, K. Murase and Z.-G. Dai, *IceCube non-detection of GRBs: constraints on the fireball properties*, *Astrophys. J.* **752** (2012) 29 [[arXiv:1204.0857](#)].
- [106] B. Zhang and P. Kumar, *Model-dependent high-energy neutrino flux from gamma-ray bursts*, *Phys. Rev. Lett.* **110** (2013) 121101 [[arXiv:1210.0647](#)].
- [107] R.-Y. Liu and X.-Y. Wang, *Diffuse PeV neutrinos from gamma-ray bursts*, *Astrophys. J.* **766** (2013) 73 [[arXiv:1212.1260](#)].
- [108] S. Gao, K. Kashiyama and P. Mészáros, *On the neutrino non-detection of GRB 130427A*, *Astrophys. J. Lett.* **772** (2013) L4 [[arXiv:1305.6055](#)].
- [109] M. Petropoulou, *The role of hadronic cascades in GRB models of efficient neutrino production*, *Mon. Not. Roy. Astron. Soc.* **442** (2014) 3026 [[arXiv:1405.7669](#)].
- [110] M. Petropoulou, D. Giannios and S. Dimitrakoudis, *Implications of a PeV neutrino spectral cutoff in GRB models*, *Mon. Not. Roy. Astron. Soc.* **445** (2014) 570 [[arXiv:1405.2091](#)].

- [111] M. Bustamante, P. Baerwald, K. Murase and W. Winter, *Neutrino and cosmic-ray emission from multiple internal shocks in gamma-ray bursts*, *Nature Commun.* **6** (2015) 6783 [[arXiv:1409.2874](#)].
- [112] X.-Y. Wang, S. Razzaque and P. Meszaros, *On the origin and survival of UHE cosmic-ray nuclei in GRBs and hypernovae*, *Astrophys. J.* **677** (2008) 432 [[arXiv:0711.2065](#)].
- [113] K. Murase, K. Ioka, S. Nagataki and T. Nakamura, *High-energy cosmic-ray nuclei from high- and low-luminosity gamma-ray bursts and implications for multi-messenger astronomy*, *Phys. Rev. D* **78** (2008) 023005 [[arXiv:0801.2861](#)].
- [114] A. Calvez, A. Kusenko and S. Nagataki, *The role of galactic sources and magnetic fields in forming the observed energy-dependent composition of ultrahigh-energy cosmic rays*, *Phys. Rev. Lett.* **105** (2010) 091101 [[arXiv:1004.2535](#)].
- [115] N. Globus, D. Allard, R. Mochkovitch and E. Parizot, *UHECR acceleration at GRB internal shocks*, *Mon. Not. Roy. Astron. Soc.* **451** (2015) 751 [[arXiv:1409.1271](#)].
- [116] D. Biehl, D. Boncioli, A. Fedynitch and W. Winter, *Cosmic-ray and neutrino emission from gamma-ray bursts with a nuclear cascade*, *Astron. Astrophys.* **611** (2018) A101 [[arXiv:1705.08909](#)].
- [117] B. Paczynski and G.H. Xu, *Neutrino bursts from gamma-ray bursts*, *Astrophys. J.* **427** (1994) 708.
- [118] I. Bartos, A.M. Beloborodov, K. Hurley and S. Márka, *Detection prospects for GeV neutrinos from collisionally heated gamma-ray bursts with IceCube/DeepCore*, *Phys. Rev. Lett.* **110** (2013) 241101 [[arXiv:1301.4232](#)].
- [119] K. Murase, K. Kashiyama and P. Mészáros, *Subphotospheric neutrinos from gamma-ray bursts: the role of neutrons*, *Phys. Rev. Lett.* **111** (2013) 131102 [[arXiv:1301.4236](#)].
- [120] K. Murase and S. Nagataki, *High energy neutrino flash from far-UV/X-ray flares of gamma-ray bursts*, *Phys. Rev. Lett.* **97** (2006) 051101 [[astro-ph/0604437](#)].
- [121] E. Waxman and J.N. Bahcall, *Neutrino afterglow from gamma-ray bursts: similar to 10^{18} eV*, *Astrophys. J.* **541** (2000) 707 [[hep-ph/9909286](#)].
- [122] C.D. Dermer, *Neutrino, neutron, and cosmic ray production in the external shock model of gamma-ray bursts*, *Astrophys. J.* **574** (2002) 65 [[astro-ph/0005440](#)].
- [123] S. Razzaque, *Long-lived PeV-EeV neutrinos from gamma-ray burst blastwave*, *Phys. Rev. D* **88** (2013) 103003 [[arXiv:1307.7596](#)].
- [124] K. Murase, K. Ioka, S. Nagataki and T. Nakamura, *High energy neutrinos and cosmic-rays from low-luminosity gamma-ray bursts?*, *Astrophys. J. Lett.* **651** (2006) L5 [[astro-ph/0607104](#)].
- [125] N. Gupta and B. Zhang, *Neutrino spectra from low and high luminosity populations of gamma ray bursts*, *Astropart. Phys.* **27** (2007) 386 [[astro-ph/0606744](#)].
- [126] N. Senno, K. Murase and P. Meszaros, *Choked jets and low-luminosity gamma-ray bursts as hidden neutrino sources*, *Phys. Rev. D* **93** (2016) 083003 [[arXiv:1512.08513](#)].
- [127] B.T. Zhang, K. Murase, S.S. Kimura, S. Horiuchi and P. Mészáros, *Low-luminosity gamma-ray bursts as the sources of ultrahigh-energy cosmic ray nuclei*, *Phys. Rev. D* **97** (2018) 083010 [[arXiv:1712.09984](#)].
- [128] B.T. Zhang and K. Murase, *Ultrahigh-energy cosmic-ray nuclei and neutrinos from engine-driven supernovae*, *Phys. Rev. D* **100** (2019) 103004 [[arXiv:1812.10289](#)].
- [129] A.G. Vieregg et al., *The first limits on the ultra-high energy neutrino fluence from gamma-ray bursts*, *Astrophys. J.* **736** (2011) 50 [[arXiv:1102.3206](#)].

- [130] S.S. Kimura, K. Murase, P. Mészáros and K. Kiuchi, *High-energy neutrino emission from short gamma-ray bursts: prospects for coincident detection with gravitational waves*, *Astrophys. J. Lett.* **848** (2017) L4 [[arXiv:1708.07075](#)].
- [131] K. Fang and B.D. Metzger, *High-energy neutrinos from millisecond magnetars formed from the merger of binary neutron stars*, *Astrophys. J.* **849** (2017) 153 [[arXiv:1707.04263](#)].
- [132] X. Rodrigues, S. Garrappa, S. Gao, V.S. Paliya, A. Franckowiak and W. Winter, *Multi-wavelength and neutrino emission from blazar PKS 1502 + 106*, [arXiv:2009.04026](#).
- [133] A. Connolly, R.S. Thorne and D. Waters, *Calculation of high energy neutrino-nucleon cross sections and uncertainties using the MSTW parton distribution functions and implications for future experiments*, *Phys. Rev. D* **83** (2011) 113009 [[arXiv:1102.0691](#)].
- [134] A. Cooper-Sarkar, P. Mertsch and S. Sarkar, *The high energy neutrino cross-section in the Standard Model and its uncertainty*, *JHEP* **08** (2011) 042 [[arXiv:1106.3723](#)].
- [135] V. Bertone, R. Gauld and J. Rojo, *Neutrino telescopes as QCD microscopes*, *JHEP* **01** (2019) 217 [[arXiv:1808.02034](#)].
- [136] I. Romero and O.A. Sampayo, *Leptoquarks signals in km³ neutrino telescopes*, *JHEP* **05** (2009) 111 [[arXiv:0906.5245](#)].
- [137] D. Hooper, *Measuring high-energy neutrino nucleon cross-sections with future neutrino telescopes*, *Phys. Rev. D* **65** (2002) 097303 [[hep-ph/0203239](#)].
- [138] S.R. Klein and A. Connolly, *Neutrino absorption in the earth, neutrino cross-sections, and new physics*, in *Community summer study 2013: Snowmass on the Mississippi*, (2013) [[arXiv:1304.4891](#)].
- [139] J. Ellis, K. Sakurai and M. Spannowsky, *Search for sphalerons: IceCube vs. LHC*, *JHEP* **05** (2016) 085 [[arXiv:1603.06573](#)].
- [140] S.R. Klein, *Probing high-energy interactions of atmospheric and astrophysical neutrinos*, in *Particle physics with neutrino telescopes*, *World Scientific*, Singapore (2020), pg. 75 [ISBN:978-981-3275-01-0] [[arXiv:1906.02221](#)].
- [141] M. Bustamante, J.F. Beacom and W. Winter, *Theoretically palatable flavor combinations of astrophysical neutrinos*, *Phys. Rev. Lett.* **115** (2015) 161302 [[arXiv:1506.02645](#)].
- [142] J.G. Learned and S. Pakvasa, *Detecting tau-neutrino oscillations at PeV energies*, *Astropart. Phys.* **3** (1995) 267 [[hep-ph/9405296](#)].
- [143] C.A. Argüelles, T. Katori and J. Salvado, *New physics in astrophysical neutrino flavor*, *Phys. Rev. Lett.* **115** (2015) 161303 [[arXiv:1506.02043](#)].
- [144] I.M. Shoemaker and K. Murase, *Probing BSM neutrino physics with flavor and spectral distortions: prospects for future high-energy neutrino telescopes*, *Phys. Rev. D* **93** (2016) 085004 [[arXiv:1512.07228](#)].
- [145] M.C. Gonzalez-Garcia, M. Maltoni, I. Martinez-Soler and N. Song, *Non-standard neutrino interactions in the earth and the flavor of astrophysical neutrinos*, *Astropart. Phys.* **84** (2016) 15 [[arXiv:1605.08055](#)].
- [146] R.W. Rasmussen, L. Lechner, M. Ackermann, M. Kowalski and W. Winter, *Astrophysical neutrinos flavored with beyond the Standard Model physics*, *Phys. Rev. D* **96** (2017) 083018 [[arXiv:1707.07684](#)].

- [147] M. Ahlers, M. Bustamante and S. Mu, *Unitarity bounds of astrophysical neutrinos*, *Phys. Rev. D* **98** (2018) 123023 [[arXiv:1810.00893](#)].
- [148] Y. Chikashige, R.N. Mohapatra and R.D. Peccei, *Spontaneously broken lepton number and cosmological constraints on the neutrino mass spectrum*, *Phys. Rev. Lett.* **45** (1980) 1926.
- [149] G.B. Gelmini, S. Nussinov and M. Roncadelli, *Bounds and prospects for the majoron model of left-handed neutrino masses*, *Nucl. Phys. B* **209** (1982) 157.
- [150] R. Tomas, H. Pas and J.W.F. Valle, *Generalized bounds on majoron-neutrino couplings*, *Phys. Rev. D* **64** (2001) 095005 [[hep-ph/0103017](#)].
- [151] J.F. Beacom, N.F. Bell, D. Hooper, S. Pakvasa and T.J. Weiler, *Decay of high-energy astrophysical neutrinos*, *Phys. Rev. Lett.* **90** (2003) 181301 [[hep-ph/0211305](#)].
- [152] P. Baerwald, M. Bustamante and W. Winter, *Neutrino decays over cosmological distances and the implications for neutrino telescopes*, *JCAP* **10** (2012) 020 [[arXiv:1208.4600](#)].
- [153] M. Bustamante, J.F. Beacom and K. Murase, *Testing decay of astrophysical neutrinos with incomplete information*, *Phys. Rev. D* **95** (2017) 063013 [[arXiv:1610.02096](#)].
- [154] P.B. Denton and I. Tamborra, *Invisible neutrino decay could resolve IceCube's track and cascade tension*, *Phys. Rev. Lett.* **121** (2018) 121802 [[arXiv:1805.05950](#)].
- [155] J.L. Feng, *Dark matter candidates from particle physics and methods of detection*, *Ann. Rev. Astron. Astrophys.* **48** (2010) 495 [[arXiv:1003.0904](#)].
- [156] J.F. Beacom, N.F. Bell and G.D. Mack, *General upper bound on the dark matter total annihilation cross section*, *Phys. Rev. Lett.* **99** (2007) 231301 [[astro-ph/0608090](#)].
- [157] H. Yuksel, S. Horiuchi, J.F. Beacom and S. Ando, *Neutrino constraints on the dark matter total annihilation cross section*, *Phys. Rev. D* **76** (2007) 123506 [[arXiv:0707.0196](#)].
- [158] K. Murase and J.F. Beacom, *Constraining very heavy dark matter using diffuse backgrounds of neutrinos and cascaded gamma rays*, *JCAP* **10** (2012) 043 [[arXiv:1206.2595](#)].
- [159] B. Feldstein, A. Kusenko, S. Matsumoto and T.T. Yanagida, *Neutrinos at IceCube from heavy decaying dark matter*, *Phys. Rev. D* **88** (2013) 015004 [[arXiv:1303.7320](#)].
- [160] A. Esmaili and P.D. Serpico, *Are IceCube neutrinos unveiling PeV-scale decaying dark matter?*, *JCAP* **11** (2013) 054 [[arXiv:1308.1105](#)].
- [161] T. Higaki, R. Kitano and R. Sato, *Neutrino universe*, *JHEP* **07** (2014) 044 [[arXiv:1405.0013](#)].
- [162] C. Rott, K. Kohri and S.C. Park, *Superheavy dark matter and IceCube neutrino signals: bounds on decaying dark matter*, *Phys. Rev. D* **92** (2015) 023529 [[arXiv:1408.4575](#)].
- [163] E. Dudas, Y. Mambrini and K.A. Olive, *Monochromatic neutrinos generated by dark matter and the seesaw mechanism*, *Phys. Rev. D* **91** (2015) 075001 [[arXiv:1412.3459](#)].
- [164] Y. Ema, R. Jinno and T. Moroi, *Cosmic-ray neutrinos from the decay of long-lived particle and the recent IceCube result*, *Phys. Lett. B* **733** (2014) 120 [[arXiv:1312.3501](#)].
- [165] J. Zavala, *Galactic PeV neutrinos from dark matter annihilation*, *Phys. Rev. D* **89** (2014) 123516 [[arXiv:1404.2932](#)].
- [166] K. Murase, R. Laha, S. Ando and M. Ahlers, *Testing the dark matter scenario for PeV neutrinos observed in IceCube*, *Phys. Rev. Lett.* **115** (2015) 071301 [[arXiv:1503.04663](#)].
- [167] L.A. Anchordoqui et al., *IceCube neutrinos, decaying dark matter, and the Hubble constant*, *Phys. Rev. D* **92** (2015) 061301 [Erratum *ibid.* **94** (2016) 069901] [[arXiv:1506.08788](#)].

- [168] S.M. Boucenna et al., *Decaying leptophilic dark matter at IceCube*, *JCAP* **12** (2015) 055 [[arXiv:1507.01000](#)].
- [169] P.S.B. Dev, D. Kazanas, R.N. Mohapatra, V.L. Teplitz and Y. Zhang, *Heavy right-handed neutrino dark matter and PeV neutrinos at IceCube*, *JCAP* **08** (2016) 034 [[arXiv:1606.04517](#)].
- [170] N. Hiroshima, R. Kitano, K. Kohri and K. Murase, *High-energy neutrinos from multibody decaying dark matter*, *Phys. Rev. D* **97** (2018) 023006 [[arXiv:1705.04419](#)].
- [171] M. Chianese, G. Miele and S. Morisi, *Interpreting IceCube 6-year HESE data as an evidence for hundred TeV decaying dark matter*, *Phys. Lett. B* **773** (2017) 591 [[arXiv:1707.05241](#)].
- [172] G. Amelino-Camelia, J.R. Ellis, N.E. Mavromatos, D.V. Nanopoulos and S. Sarkar, *Tests of quantum gravity from observations of gamma-ray bursts*, *Nature* **393** (1998) 763 [[astro-ph/9712103](#)].
- [173] D. Hooper, D. Morgan and E. Winstanley, *Lorentz and CPT invariance violation in high-energy neutrinos*, *Phys. Rev. D* **72** (2005) 065009 [[hep-ph/0506091](#)].
- [174] M.C. Gonzalez-Garcia, F. Halzen and M. Maltoni, *Physics reach of high-energy and high-statistics IceCube atmospheric neutrino data*, *Phys. Rev. D* **71** (2005) 093010 [[hep-ph/0502223](#)].
- [175] L.A. Anchordoqui et al., *Probing Planck scale physics with IceCube*, *Phys. Rev. D* **72** (2005) 065019 [[hep-ph/0506168](#)].
- [176] J.L. Bazo, M. Bustamante, A.M. Gago and O.G. Miranda, *High energy astrophysical neutrino flux and modified dispersion relations*, *Int. J. Mod. Phys. A* **24** (2009) 5819 [[arXiv:0907.1979](#)].
- [177] M. Bustamante, A.M. Gago and C. Pena-Garay, *Energy-independent new physics in the flavour ratios of high-energy astrophysical neutrinos*, *JHEP* **04** (2010) 066 [[arXiv:1001.4878](#)].
- [178] A. Kostelecky and M. Mewes, *Neutrinos with Lorentz-violating operators of arbitrary dimension*, *Phys. Rev. D* **85** (2012) 096005 [[arXiv:1112.6395](#)].
- [179] J.S. Diaz, A. Kostelecky and M. Mewes, *Testing relativity with high-energy astrophysical neutrinos*, *Phys. Rev. D* **89** (2014) 043005 [[arXiv:1308.6344](#)].
- [180] F.W. Stecker, S.T. Scully, S. Liberati and D. Mattingly, *Searching for traces of Planck-scale physics with high energy neutrinos*, *Phys. Rev. D* **91** (2015) 045009 [[arXiv:1411.5889](#)].
- [181] F.W. Stecker and S.T. Scully, *Propagation of superluminal PeV IceCube neutrinos: a high energy spectral cutoff or new constraints on Lorentz invariance violation*, *Phys. Rev. D* **90** (2014) 043012 [[arXiv:1404.7025](#)].
- [182] G. Tomar, S. Mohanty and S. Pakvasa, *Lorentz invariance violation and IceCube neutrino events*, *JHEP* **11** (2015) 022 [[arXiv:1507.03193](#)].
- [183] J. Ellis, N.E. Mavromatos, A.S. Sakharov and E.K. Sarkisyan-Grinbaum, *Limits on neutrino Lorentz violation from multimessenger observations of TXS 0506 + 056*, *Phys. Lett. B* **789** (2019) 352 [[arXiv:1807.05155](#)].
- [184] R. Laha, *Constraints on neutrino speed, weak equivalence principle violation, Lorentz invariance violation, and dual lensing from the first high-energy astrophysical neutrino source TXS 0506 + 056*, *Phys. Rev. D* **100** (2019) 103002 [[arXiv:1807.05621](#)].
- [185] J. Lykken, O. Mena and S. Razzaque, *Ultrahigh-energy neutrino flux as a probe of large extra-dimensions*, *JCAP* **12** (2007) 015 [[arXiv:0705.2029](#)].
- [186] K. Ioka and K. Murase, *IceCube PeV–EeV neutrinos and secret interactions of neutrinos*, *PTEP* **2014** (2014) 061E01 [[arXiv:1404.2279](#)].

- [187] K.C.Y. Ng and J.F. Beacom, *Cosmic neutrino cascades from secret neutrino interactions*, *Phys. Rev. D* **90** (2014) 065035 [Erratum *ibid.* **90** (2014) 089904] [[arXiv:1404.2288](#)].
- [188] K. Blum, A. Hook and K. Murase, *High energy neutrino telescopes as a probe of the neutrino mass mechanism*, [arXiv:1408.3799](#).
- [189] W. Altmannshofer, C.-Y. Chen, P.S. Bhupal Dev and A. Soni, *Lepton flavor violating Z' explanation of the muon anomalous magnetic moment*, *Phys. Lett. B* **762** (2016) 389 [[arXiv:1607.06832](#)].
- [190] G. Barenboim, P.B. Denton and I.M. Oldengott, *Constraints on inflation with an extended neutrino sector*, *Phys. Rev. D* **99** (2019) 083515 [[arXiv:1903.02036](#)].
- [191] G.A. Askar'yan, *Excess negative charge of an electron-photon shower and its coherent radio emission*, *Sov. Phys. JETP* **14** (1962) 441 [*Zh. Eksp. Teor. Fiz.* **41** (1961) 616].
- [192] PIERRE AUGER collaboration, *Probing the radio emission from air showers with polarization measurements*, *Phys. Rev. D* **89** (2014) 052002 [[arXiv:1402.3677](#)].
- [193] P. Schellart et al., *Polarized radio emission from extensive air showers measured with LOFAR*, *JCAP* **10** (2014) 014 [[arXiv:1406.1355](#)].
- [194] A.L. Connolly and A.G. Viereg, *Radio detection of high energy neutrinos*, in *Neutrino astronomy — current status, future prospects*, T. Gaisser and A. Karle eds., *World Scientific*, Singapore (2017), pg. 217 [[arXiv:1607.08232](#)].
- [195] D. García-Fernández, A. Nelles and C. Glaser, *Signatures of secondary leptons in radio-neutrino detectors in ice*, *Phys. Rev. D* **102** (2020) 083011 [[arXiv:2003.13442](#)].
- [196] C. Glaser et al., *NuRadioMC: simulating the radio emission of neutrinos from interaction to detector*, *Eur. Phys. J. C* **80** (2020) 77 [[arXiv:1906.01670](#)].
- [197] J. Alvarez-Muniz, A. Romero-Wolf and E. Zas, *Practical and accurate calculations of Askaryan radiation*, *Phys. Rev. D* **84** (2011) 103003 [[arXiv:1106.6283](#)].
- [198] E. Zas, F. Halzen and T. Stanev, *Electromagnetic pulses from high-energy showers: implications for neutrino detection*, *Phys. Rev. D* **45** (1992) 362.
- [199] T. Barrella, S. Barwick and D. Saltzberg, *Ross ice shelf in situ radio-frequency ice attenuation*, *J. Glaciol.* **57** (2011) 61 [[arXiv:1011.0477](#)].
- [200] D.Z. Besson et al., *In situ radioglaciological measurements near Taylor dome, antarctica and implications for UHE neutrino astronomy*, *Astropart. Phys.* **29** (2008) 130 [[astro-ph/0703413](#)].
- [201] S. Barwick, D. Besson, P. Gorham and D. Saltzberg, *South polar in situ radio-frequency ice attenuation*, *J. Glaciol.* **51** (2005) 231.
- [202] S.W. Barwick et al., *Observation of classically 'forbidden' electromagnetic wave propagation and implications for neutrino detection*, *JCAP* **07** (2018) 055 [[arXiv:1804.10430](#)].
- [203] ARIANNA collaboration, *Targeting ultra-high energy neutrinos with the ARIANNA experiment*, *Adv. Space Res.* **64** (2019) 2595 [[arXiv:1903.01609](#)].
- [204] F.D. Kahn and I. Lerche, *Radiation from cosmic ray air showers*, *Proc. Roy. Soc. Lond. A* **289** (1966) 206.
- [205] H.R. Allan, *Low frequency radio emission from extensive air showers*, *Nature* **237** (1972) 384.
- [206] C. Welling, C. Glaser and A. Nelles, *Reconstructing the cosmic-ray energy from the radio signal measured in one single station*, *JCAP* **10** (2019) 075 [[arXiv:1905.11185](#)].

- [207] K. Mulrey et al., *On the cosmic-ray energy scale of the LOFAR radio telescope*, *JCAP* **11** (2020) 017 [[arXiv:2005.13441](#)].
- [208] K.D. de Vries, S. Buitink, N. van Eijndhoven, T. Meures, A. Ó Murchadha and O. Scholten, *The cosmic-ray air-shower signal in Askaryan Radio Detectors*, *Astropart. Phys.* **74** (2016) 96 [[arXiv:1503.02808](#)].
- [209] A. Nelles, S. Buitink, H. Falcke, J. Hörandel, T. Huege and P. Schellart, *A parameterization for the radio emission of air showers as predicted by CoREAS simulations and applied to LOFAR measurements*, *Astropart. Phys.* **60** (2015) 13 [[arXiv:1402.2872](#)].
- [210] ARIANNA collaboration, *Performance of the ARIANNA hexagonal radio array*, *PoS(ICRC2015)1149* (2016) [[arXiv:1509.00109](#)].
- [211] J.E. Carlstrom et al., *The 10 meter south pole telescope*, *Publ. Astron. Soc. Pac.* **123** (2011) 568 [[arXiv:0907.4445](#)].
- [212] ICECUBE collaboration, *The IceCube upgrade — design and science goals*, *PoS(ICRC2019)1031* (2020) [[arXiv:1908.09441](#)].
- [213] L. Gerhardt et al., *A prototype station for ARIANNA: a detector for cosmic neutrinos*, *Nucl. Instrum. Meth. A* **624** (2010) 85 [[arXiv:1005.5193](#)].
- [214] J. Avva et al., *Development toward a ground-based interferometric phased array for radio detection of high energy neutrinos*, *Nucl. Instrum. Meth. A* **869** (2017) 46 [[arXiv:1605.03525](#)].
- [215] U.S. Ice Drilling Program, *Agile sub-ice geological drill operations and maintenance manual*, <https://icedrill.org/library/agile-sub-ice-geological-drill-operations-and-maintenance-manual>, (2019).
- [216] C. Glaser et al., *NuRadioReco: a reconstruction framework for radio neutrino detectors*, *Eur. Phys. J. C* **79** (2019) 464 [[arXiv:1903.07023](#)].
- [217] ARA collaboration, *First constraints on the ultra-high energy neutrino flux from a prototype station of the Askaryan Radio Array*, *Astropart. Phys.* **70** (2015) 62 [[arXiv:1404.5285](#)].
- [218] A. Romero-Wolf et al., *An interferometric analysis method for radio impulses from ultra-high energy particle showers*, *Astropart. Phys.* **60** (2015) 72.
- [219] S.I. Dutta, M.H. Reno, I. Sarcevic and D. Seckel, *Propagation of muons and taus at high-energies*, *Phys. Rev. D* **63** (2001) 094020 [[hep-ph/0012350](#)].
- [220] J.-H. Koehne et al., *PROPOSAL: a tool for propagation of charged leptons*, *Comput. Phys. Commun.* **184** (2013) 2070.
- [221] T.K. Gaisser, D. Soldin, A. Crossman and A. Fedynitch, *Precision of analytical approximations in calculations of atmospheric leptons*, *PoS(ICRC2019)893* (2020) [[arXiv:1910.08676](#)].
- [222] H.P. Dembinski, R. Engel, A. Fedynitch, T. Gaisser, F. Riehn and T. Stanev, *Data-driven model of the cosmic-ray flux and mass composition from 10 GeV to 10¹¹ GeV*, *PoS(ICRC2017)533* (2018) [[arXiv:1711.11432](#)].
- [223] J.M. Roberts et al., *LAB4D: a low power, multi-GSAs, transient digitizer with sampling timebase trimming capabilities*, *Nucl. Instrum. Meth. A* **925** (2019) 92 [[arXiv:1803.04600](#)].
- [224] UNAVCO, *Remote station engineering — power systems*, <https://www.unavco.org/projects/project-support/polar/remote/power/power.html>, (2014) [Accessed July 2019].

- [225] K. Steffen, J. Box and W. Abdalati, *Greenland climate network: GC-net*, CRREL special report, U.S. Army Cold Regions Reattach and Engineering (CRREL), (1996), pg. 98.
- [226] NOAA, *Global monitoring laboratory*, <https://www.esrl.noaa.gov/gmd/dv/data.html>, (2020).
- [227] LoRA alliance, *LoRaWAN specification v.1.03*, (2018).
- [228] British Antarctic Survey (BAS), private communication.
- [229] J.A. Johnson et al., *A new 122 mm electromechanical drill for Deep Ice-Sheet Coring (DISC): 5. Experience during Greenland field testing*, *Annals Glaciol.* **47** (2007) 54.
- [230] A. Corstanje et al., *Timing calibration and spectral cleaning of LOFAR time series data*, *Astron. Astrophys.* **590** (2016) A41 [[arXiv:1603.08354](https://arxiv.org/abs/1603.08354)].
- [231] PIERRE AUGER collaboration, *Nanosecond-level time synchronization of autonomous radio detector stations for extensive air showers*, 2016 *JINST* **11** P01018 [[arXiv:1512.02216](https://arxiv.org/abs/1512.02216)].
- [232] P. Meade, *jade: an end-to-end data transfer and catalog tool*, *J. Phys. Conf. Ser.* **898** (2017) 062050.
- [233] T. Huege, M. Ludwig and C.W. James, *Simulating radio emission from air showers with CoREAS*, *AIP Conf. Proc.* **1535** (2013) 128 [[arXiv:1301.2132](https://arxiv.org/abs/1301.2132)].
- [234] J. Alvarez-Muniz, W.R. Carvalho, Jr. and E. Zas, *Monte Carlo simulations of radio pulses in atmospheric showers using ZHAireS*, *Astropart. Phys.* **35** (2012) 325 [[arXiv:1107.1189](https://arxiv.org/abs/1107.1189)].
- [235] PIERRE AUGER collaboration, *Advanced functionality for radio analysis in the offline software framework of the Pierre Auger observatory*, *Nucl. Instrum. Meth. A* **635** (2011) 92 [[arXiv:1101.4473](https://arxiv.org/abs/1101.4473)].
- [236] K. Dookayka, *Characterizing the search for ultra-high energy neutrinos with the ARIANNA detector*, Ph.D. thesis, University of California, Irvine, CA, U.S.A. (2011).
- [237] ANITA collaboration, *The simulation of the sensitivity of the antarctic impulsive transient antenna (ANITA) to Askaryan radiation from cosmogenic neutrinos interacting in the antarctic ice*, 2019 *JINST* **14** P08011 [[arXiv:1903.11043](https://arxiv.org/abs/1903.11043)].
- [238] B. Hokanson-Fasig, *Design studies for the Radio Neutrino Observatory (RNO)*, *PoS(ICRC2019)913* (2020).
- [239] REMCOM, *XFDTD 3D electromagnetic simulation software*, <https://www.remcom.com/xfDTD-3d-em-simulation-software>, (2020).
- [240] J. Alvarez-Muñiz, P.M. Hansen, A. Romero-Wolf and E. Zas, *Askaryan radiation from neutrino-induced showers in ice*, *Phys. Rev. D* **101** (2020) 083005 [[arXiv:2003.09705](https://arxiv.org/abs/2003.09705)].
- [241] PIERRE AUGER collaboration, *Improved limit to the diffuse flux of ultrahigh energy neutrinos from the Pierre Auger observatory*, *Phys. Rev. D* **91** (2015) 092008 [[arXiv:1504.05397](https://arxiv.org/abs/1504.05397)].
- [242] ICECUBE collaboration, *A measurement of the diffuse astrophysical muon neutrino flux using eight years of IceCube data*, *PoS(ICRC2017)1005* (2017) [[arXiv:1710.01191](https://arxiv.org/abs/1710.01191)].
- [243] G.J. Feldman and R.D. Cousins, *A unified approach to the classical statistical analysis of small signals*, *Phys. Rev. D* **57** (1998) 3873 [[physics/9711021](https://arxiv.org/abs/hep-ph/9711021)].
- [244] L.D. Landau and I. Pomeranchuk, *Limits of applicability of the theory of bremsstrahlung electrons and pair production at high-energies*, *Dokl. Akad. Nauk Ser. Fiz.* **92** (1953) 535.
- [245] A.B. Migdal, *Bremsstrahlung and pair production in condensed media at high-energies*, *Phys. Rev.* **103** (1956) 1811.

- [246] L. Gerhardt and S.R. Klein, *Electron and photon interactions in the regime of strong LPM suppression*, *Phys. Rev. D* **82** (2010) 074017 [[arXiv:1007.0039](#)].
- [247] M. Selig et al., *NIFTY — numerical information field theory. A versatile Python library for signal inference*, *Astron. Astrophys.* **554** (2013) A26 [[arXiv:1301.4499](#)].
- [248] J. Yang et al., *GRB 200415A: a short gamma-ray burst from a magnetar giant flare?*, [arXiv:2010.05128](#).
- [249] S. van Velzen et al., *Seventeen tidal disruption events from the first half of ZTF survey observations: entering a new era of population studies*, *Astrophys. J.* **908** (2021) 4 [[arXiv:2001.01409](#)].
- [250] ICECUBE collaboration, *IceCube-190730A — IceCube observation of a high-energy neutrino candidate event*, *GRB Coord. Network* **25225** (2019) 1.
- [251] A. Franckowiak et al., *Patterns in the multiwavelength behavior of candidate neutrino blazars*, *Astrophys. J.* **893** (2020) 162 [[arXiv:2001.10232](#)].

Time-Integrated Neutrino Source Searches with 10 Years of IceCube Data

M. G. Aartsen,¹⁶ M. Ackermann,⁵⁵ J. Adams,¹⁶ J. A. Aguilar,¹² M. Ahlers,²⁰ M. Ahrens,⁴⁶ C. Alispach,²⁶ K. Andeen,³⁷ T. Anderson,⁵² I. Ansseau,¹² G. Anton,²⁴ C. Argüelles,¹⁴ J. Auffenberg,¹ S. Axani,¹⁴ P. Backes,¹ H. Bagherpour,¹⁶ X. Bai,⁴³ A. Balagopal,²⁹ A. Barbano,²⁶ S. W. Barwick,²⁸ B. Bastian,⁵⁵ V. Baum,³⁶ S. Baur,¹² R. Bay,⁸ J. J. Beatty,^{18,19} K.-H. Becker,⁵⁴ J. Becker Tjus,¹¹ S. BenZvi,⁴⁵ D. Berley,¹⁷ E. Bernardini,⁵⁵ D. Z. Besson,³⁰ G. Binder,^{8,9} D. Bindig,⁵⁴ E. Blaufuss,¹⁷ S. Blot,⁵⁵ C. Boehm,⁴⁶ M. Börner,²¹ S. Böser,³⁶ O. Botner,⁵³ J. Böttcher,¹ E. Bourbeau,²⁰ J. Bourbeau,³⁵ F. Bradascio,⁵⁵ J. Braun,³⁵ S. Bron,²⁶ J. Brostean-Kaiser,⁵⁵ A. Burgman,⁵³ J. Buscher,¹ R. S. Busse,³⁸ T. Carver,^{26,*} C. Chen,⁶ E. Cheung,¹⁷ D. Chirkin,³⁵ S. Choi,⁴⁸ K. Clark,³¹ L. Classen,³⁸ A. Coleman,³⁹ G. H. Collin,¹⁴ J. M. Conrad,¹⁴ P. Coppin,¹³ P. Correa,¹³ D. F. Cowen,^{51,52} R. Cross,⁴⁵ P. Dave,⁶ C. De Clercq,¹³ J. J. DeLaunay,⁵² H. Dembinski,³⁹ K. Deoskar,⁴⁶ S. De Ridder,²⁷ P. Desiati,³⁵ K. D. de Vries,¹³ G. de Wasseige,¹³ M. de With,¹⁰ T. DeYoung,²² A. Diaz,¹⁴ J. C. Díaz-Vélez,³⁵ H. Dujmovic,²⁹ M. Dunkman,⁵² E. Dvorak,⁴³ B. Eberhardt,³⁵ T. Ehrhardt,³⁶ P. Eller,⁵² R. Engel,²⁹ P. A. Evenson,³⁹ S. Fahey,³⁵ A. R. Fazely,⁷ J. Felde,¹⁷ K. Filimonov,⁸ C. Finley,⁴⁶ D. Fox,⁵¹ A. Franckowiak,⁵⁵ E. Friedman,¹⁷ A. Fritz,³⁶ T. K. Gaisser,³⁹ J. Gallagher,³⁴ E. Ganster,¹ S. Garrappa,⁵⁵ L. Gerhardt,⁹ K. Ghorbani,³⁵ T. Glauch,²⁵ T. Glüsenkamp,²⁴ A. Goldschmidt,⁹ J. G. Gonzalez,³⁹ D. Grant,²² Z. Griffith,³⁵ S. Griswold,⁴⁵ M. G. Günder,¹ M. Gündüz,¹¹ C. Haack,¹ A. Hallgren,⁵³ R. Halliday,²² L. Halve,¹ F. Halzen,³⁵ K. Hanson,³⁵ A. Haungs,²⁹ D. Hebecker,¹⁰ D. Heereman,¹² P. Heix,¹ K. Helbing,⁵⁴ R. Hellauer,¹⁷ F. Henningsen,²⁵ S. Hickford,⁵⁴ J. Hignight,²³ G. C. Hill,² K. D. Hoffman,¹⁷ R. Hoffmann,⁵⁴ T. Hoinka,²¹ B. Hokanson-Fasig,³⁵ K. Hoshina,³⁵ F. Huang,⁵² M. Huber,²⁵ T. Huber,^{29,55} K. Hultqvist,⁴⁶ M. Hünnefeld,²¹ R. Hussain,³⁵ S. In,⁴⁸ N. Iovine,¹² A. Ishihara,¹⁵ G. S. Japaridze,⁵ M. Jeong,⁴⁸ K. Jero,³⁵ B. J. P. Jones,⁴ F. Jonske,¹ R. Joppe,¹ D. Kang,²⁹ W. Kang,⁴⁸ A. Kappes,³⁸ D. Kappesser,³⁶ T. Karg,⁵⁵ M. Karl,²⁵ A. Karle,³⁵ U. Katz,²⁴ M. Kauer,³⁵ J. L. Kelley,³⁵ A. Kheirandish,³⁵ J. Kim,⁴⁸ T. Kintscher,⁵⁵ J. Kiryluk,⁴⁷ T. Kittler,²⁴ S. R. Klein,^{8,9} R. Koirala,³⁹ H. Kolanoski,¹⁰ L. Köpke,³⁶ C. Kopper,²² S. Kopper,⁵⁰ D. J. Koskinen,²⁰ M. Kowalski,^{10,55} K. Krings,²⁵ G. Krückl,³⁶ N. Kulacz,²³ N. Kurahashi,⁴² A. Kyriacou,² M. Labare,²⁷ J. L. Lanfranchi,⁵² M. J. Larson,¹⁷ F. Lauber,⁵⁴ J. P. Lazar,³⁵ K. Leonard,³⁵ A. Leszczyńska,²⁹ M. Leuermann,¹ Q. R. Liu,³⁵ E. Lohfink,³⁶ C. J. Lozano Mariscal,³⁸ L. Lu,¹⁵ F. Lucarelli,²⁶ J. Lünemann,¹³ W. Luszczak,³⁵ Y. Lyu,^{8,9} W. Y. Ma,⁵⁵ J. Madsen,⁴⁴ G. Maggi,¹³ K. B. M. Mahn,²² Y. Makino,¹⁵ P. Mallik,¹ K. Mallot,³⁵ S. Mancina,³⁵ I. C. Mariş,¹² R. Maruyama,⁴⁰ K. Mase,¹⁵ H. S. Matis,⁹ R. Maunu,¹⁷ F. McNally,³³ K. Meagher,³⁵ M. Medici,²⁰ A. Medina,¹⁹ M. Meier,²¹ S. Meighen-Berger,²⁵ T. Menne,²¹ G. Merino,³⁵ T. Meures,¹² J. Micallef,²² D. Mockler,¹² G. Momenté,³⁶ T. Montaruli,²⁶ R. W. Moore,²³ R. Morse,³⁵ M. Moulai,¹⁴ P. Muth,¹ R. Nagai,¹⁵ U. Naumann,⁵⁴ G. Neer,²² H. Niederhausen,²⁵ M. U. Nisa,²² S. C. Nowicki,²² D. R. Nygren,⁹ A. Obertacke Pollmann,⁵⁴ M. Oehler,²⁹ A. Olivas,¹⁷ A. O'Murchadha,¹² E. O'Sullivan,⁴⁶ T. Palczewski,^{8,9} H. Pandya,³⁹ D. V. Pankova,⁵² N. Park,³⁵ P. Peiffer,³⁶ C. Pérez de los Heros,⁵³ S. Philippen,¹ D. Pieloth,²¹ E. Pinat,¹² A. Pizzuto,³⁵ M. Plum,³⁷ A. Porcelli,²⁷ P. B. Price,⁸ G. T. Przybylski,⁹ C. Raab,¹² A. Raissi,¹⁶ M. Rameez,²⁰ L. Rauch,⁵⁵ K. Rawlins,³ I. C. Rea,²⁵ R. Reimann,¹ B. Relethford,⁴² M. Renschler,²⁹ G. Renzi,¹² E. Resconi,²⁵ W. Rhode,²¹ M. Richman,⁴² S. Robertson,⁹ M. Rongen,¹ C. Rott,⁴⁸ T. Ruhe,²¹ D. Ryckbosch,²⁷ D. Rysewyk,²² I. Safa,³⁵ S. E. Sanchez Herrera,²² A. Sandrock,²¹ J. Sandros,³⁶ M. Santander,⁵⁰ S. Sarkar,⁴¹ S. Sarkar,²³ K. Satalecka,⁵⁵ M. Schaufel,¹ H. Schieler,²⁹ P. Schlunder,²¹ T. Schmidt,¹⁷ A. Schneider,³⁵ J. Schneider,²⁴ F. G. Schröder,^{29,39} L. Schumacher,¹ S. Scalfani,⁴² D. Seckel,³⁹ S. Seunarine,⁴⁴ S. Shefali,¹ M. Silva,³⁵ R. Snihur,³⁵ J. Soedingrekso,²¹ D. Soldin,³⁹ M. Song,¹⁷ G. M. Spiczak,⁴⁴ C. Spiering,⁵⁵ J. Stachurska,⁵⁵ M. Stamatikos,¹⁹ T. Stanev,³⁹ R. Stein,⁵⁵ P. Steinmüller,²⁹ J. Stettner,¹ A. Steuer,³⁶ T. Stezelberger,⁹ R. G. Stokstad,⁹ A. Stöbl,¹⁵ N. L. Strotjohann,⁵⁵ T. Stürwald,¹ T. Stuttard,²⁰ G. W. Sullivan,¹⁷ I. Taboada,⁶ F. Tenholt,¹¹ S. Ter-Antonyan,⁷ A. Terliuk,⁵⁵ S. Tilav,³⁹ K. Tollefson,²² L. Tomankova,¹¹ C. Tönnis,⁴⁹ S. Toscano,¹² D. Tosi,³⁵ A. Trettin,⁵⁵ M. Tselengidou,²⁴ C. F. Tung,⁶ A. Turcati,²⁵ R. Turcotte,²⁹ C. F. Turley,⁵² B. Ty,³⁵ E. Unger,⁵³ M. A. Unland Elorrieta,³⁸ M. Usner,⁵⁵ J. Vandenbroucke,³⁵ W. Van Driessche,²⁷ D. van Eijk,³⁵ N. van Eijndhoven,¹³ S. Vanheule,²⁷ J. van Santen,⁵⁵ M. Vraeghe,²⁷ C. Walck,⁴⁶ A. Wallace,² M. Wallraff,¹ N. Wandkowsky,³⁵ T. B. Watson,⁴ C. Weaver,²³ A. Weindl,²⁹ M. J. Weiss,⁵² J. Weldert,³⁶ C. Wendt,³⁵ J. Werthebach,³⁵ B. J. Whelan,² N. Whitehorn,³² K. Wiebe,³⁶ C. H. Wiebusch,¹ L. Wille,³⁵ D. R. Williams,⁵⁰ L. Wills,⁴² M. Wolf,²⁵ J. Wood,³⁵ T. R. Wood,²³ K. Woschnagg,⁸ G. Wrede,²⁴ D. L. Xu,³⁵ X. W. Xu,⁷ Y. Xu,⁴⁷ J. P. Yanez,²³ G. Yodh,²⁸ S. Yoshida,¹⁵ T. Yuan,³⁵ and M. Zöcklein¹

¹III. Physikalisches Institut, RWTH Aachen University, D-52056 Aachen, Germany

²Department of Physics, University of Adelaide, Adelaide, 5005, Australia

³Department of Physics and Astronomy, University of Alaska Anchorage, 3211 Providence Dr., Anchorage, Alaska 99508, USA

⁴Department of Physics, University of Texas at Arlington, 502 Yates St., Science Hall Rm 108, Box 19059, Arlington, Texas 76019, USA

- ⁵*CTSPS, Clark-Atlanta University, Atlanta, Georgia 30314, USA*
- ⁶*School of Physics and Center for Relativistic Astrophysics, Georgia Institute of Technology, Atlanta, Georgia 30332, USA*
- ⁷*Department of Physics, Southern University, Baton Rouge, Louisiana 70813, USA*
- ⁸*Department of Physics, University of California, Berkeley, California 94720, USA*
- ⁹*Lawrence Berkeley National Laboratory, Berkeley, California 94720, USA*
- ¹⁰*Institut für Physik, Humboldt-Universität zu Berlin, D-12489 Berlin, Germany*
- ¹¹*Fakultät für Physik & Astronomie, Ruhr-Universität Bochum, D-44780 Bochum, Germany*
- ¹²*Université Libre de Bruxelles, Science Faculty CP230, B-1050 Brussels, Belgium*
- ¹³*Vrije Universiteit Brussel (VUB), Dienst ELEM, B-1050 Brussels, Belgium*
- ¹⁴*Department of Physics, Massachusetts Institute of Technology, Cambridge, Massachusetts 02139, USA*
- ¹⁵*Department of Physics and Institute for Global Prominent Research, Chiba University, Chiba 263-8522, Japan*
- ¹⁶*Department of Physics and Astronomy, University of Canterbury, Private Bag 4800, Christchurch, New Zealand*
- ¹⁷*Department of Physics, University of Maryland, College Park, Maryland 20742, USA*
- ¹⁸*Department of Astronomy, Ohio State University, Columbus, Ohio 43210, USA*
- ¹⁹*Department of Physics and Center for Cosmology and Astro-Particle Physics, Ohio State University, Columbus, Ohio 43210, USA*
- ²⁰*Niels Bohr Institute, University of Copenhagen, DK-2100 Copenhagen, Denmark*
- ²¹*Department of Physics, TU Dortmund University, D-44221 Dortmund, Germany*
- ²²*Department of Physics and Astronomy, Michigan State University, East Lansing, Michigan 48824, USA*
- ²³*Department of Physics, University of Alberta, Edmonton, Alberta, Canada T6G 2E1*
- ²⁴*Erlangen Centre for Astroparticle Physics, Friedrich-Alexander-Universität Erlangen-Nürnberg, D-91058 Erlangen, Germany*
- ²⁵*Physik-department, Technische Universität München, D-85748 Garching, Germany*
- ²⁶*Département de physique nucléaire et corpusculaire, Université de Genève, CH-1211 Genève, Switzerland*
- ²⁷*Department of Physics and Astronomy, University of Gent, B-9000 Gent, Belgium*
- ²⁸*Department of Physics and Astronomy, University of California, Irvine, California 92697, USA*
- ²⁹*Karlsruhe Institute of Technology, Institut für Kernphysik, D-76021 Karlsruhe, Germany*
- ³⁰*Department of Physics and Astronomy, University of Kansas, Lawrence, Kansas 66045, USA*
- ³¹*SNOLAB, 1039 Regional Road 24, Creighton Mine 9, Lively, Ontario, Canada P3Y 1N2*
- ³²*Department of Physics and Astronomy, UCLA, Los Angeles, California 90095, USA*
- ³³*Department of Physics, Mercer University, Macon, Georgia 31207-0001, USA*
- ³⁴*Department of Astronomy, University of Wisconsin, Madison, Wisconsin 53706, USA*
- ³⁵*Department of Physics and Wisconsin IceCube Particle Astrophysics Center, University of Wisconsin, Madison, Wisconsin 53706, USA*
- ³⁶*Institute of Physics, University of Mainz, Staudinger Weg 7, D-55099 Mainz, Germany*
- ³⁷*Department of Physics, Marquette University, Milwaukee, Wisconsin, 53201, USA*
- ³⁸*Institut für Kernphysik, Westfälische Wilhelms-Universität Münster, D-48149 Münster, Germany*
- ³⁹*Bartol Research Institute and Department of Physics and Astronomy, University of Delaware, Newark, Delaware 19716, USA*
- ⁴⁰*Department of Physics, Yale University, New Haven, Connecticut 06520, USA*
- ⁴¹*Department of Physics, University of Oxford, Parks Road, Oxford OX1 3PU, United Kingdom*
- ⁴²*Department of Physics, Drexel University, 3141 Chestnut Street, Philadelphia, Pennsylvania 19104, USA*
- ⁴³*Physics Department, South Dakota School of Mines and Technology, Rapid City, South Dakota 57701, USA*
- ⁴⁴*Department of Physics, University of Wisconsin, River Falls, Wisconsin 54022, USA*
- ⁴⁵*Department of Physics and Astronomy, University of Rochester, Rochester, New York 14627, USA*
- ⁴⁶*Oskar Klein Centre and Department of Physics, Stockholm University, SE-10691 Stockholm, Sweden*
- ⁴⁷*Department of Physics and Astronomy, Stony Brook University, Stony Brook, New York 11794-3800, USA*
- ⁴⁸*Department of Physics, Sungkyunkwan University, Suwon 16419, Korea*
- ⁴⁹*Institute of Basic Science, Sungkyunkwan University, Suwon 16419, Korea*
- ⁵⁰*Department of Physics and Astronomy, University of Alabama, Tuscaloosa, Alabama 35487, USA*
- ⁵¹*Department of Astronomy and Astrophysics, Pennsylvania State University, University Park, Pennsylvania 16802, USA*
- ⁵²*Department of Physics, Pennsylvania State University, University Park, Pennsylvania 16802, USA*
- ⁵³*Department of Physics and Astronomy, Uppsala University, Box 516, S-75120 Uppsala, Sweden*
- ⁵⁴*Department of Physics, University of Wuppertal, D-42119 Wuppertal, Germany*
- ⁵⁵*DESY, D-15738 Zeuthen, Germany*

 (Received 18 October 2019; revised manuscript received 13 December 2019; accepted 6 January 2020; published 6 February 2020)

This Letter presents the results from pointlike neutrino source searches using ten years of IceCube data collected between April 6, 2008 and July 10, 2018. We evaluate the significance of an astrophysical signal from a pointlike source looking for an excess of clustered neutrino events with energies typically above ~ 1 TeV among the background of atmospheric muons and neutrinos. We perform a full-sky scan, a search within a selected source catalog, a catalog population study, and three stacked Galactic catalog searches.

The most significant point in the northern hemisphere from scanning the sky is coincident with the Seyfert II galaxy NGC 1068, which was included in the source catalog search. The excess at the coordinates of NGC 1068 is inconsistent with background expectations at the level of 2.9σ after accounting for statistical trials from the entire catalog. The combination of this result along with excesses observed at the coordinates of three other sources, including TXS 0506 + 056, suggests that, collectively, correlations with sources in the northern catalog are inconsistent with background at 3.3σ significance. The southern catalog is consistent with background. These results, all based on searches for a cumulative neutrino signal integrated over the 10 years of available data, motivate further study of these and similar sources, including time-dependent analyses, multimessenger correlations, and the possibility of stronger evidence with coming upgrades to the detector.

DOI: [10.1103/PhysRevLett.124.051103](https://doi.org/10.1103/PhysRevLett.124.051103)

Cosmic rays (CRs) have been observed for over a hundred years [1] penetrating the entire surface of the Earth's atmosphere in the form of leptonic and hadronic charged particles with energies up to $\sim 10^{20}$ eV [2]. These particles are heavily deflected on their journey to the Earth by magnetic fields and, although at energies $\gtrsim 10^{19}$ eV this deflection could become much smaller, their origin is still largely unknown. Very-high-energy (VHE) γ rays ($E_\gamma > 100$ GeV) travel without deflection and so provide evidence for astrophysical acceleration sites. However, these photons can be produced by both leptonic and hadronic processes and are attenuated by extragalactic background light, meaning they cannot probe redshifts larger than $z \sim 1$ at energies above ~ 1 TeV. In comparison, only hadronic processes can produce an astrophysical neutrino flux which would travel unattenuated and undeflected from the source to the Earth. Thus, astrophysical neutrino observations are critical to identify CR sources, or to discover distant very-high-energy accelerators.

IceCube has discovered a flux of astrophysical neutrinos in multiple diffuse searches [3–6], which integrate observed emission over most of the sky. Notably, a potential neutrino source, TXS 0506 + 056, has been identified through a multimessenger campaign around a high-energy IceCube event in September 2017 [7]. IceCube also found evidence for neutrino emission over ~ 110 days from 2014–2015 at the location of TXS 0506 + 056 when examining over nine years of archival data [8]. Nonetheless, the estimated flux from this source alone is less than 1% of the total astrophysical neutrino flux [3] and the contribution of a catalog of blazars as a population to the best fit total astrophysical neutrino flux between 10 TeV and 2 PeV is limited to 27% [9]. In this Letter we search for various pointlike neutrino sources using 10 years of IceCube observations.

The IceCube neutrino telescope is a cubic kilometer array of digital optical modules (DOMs) each containing a 10" PMT [10] and on-board read-out electronics [11]. These DOMs are arranged in 86 strings between 1.45 and 2.45 km below the surface of the ice at the South Pole [12]. The DOMs are sensitive to Cherenkov light from energy

losses of ultrarelativistic charged particles traversing the ice. This analysis targets astrophysical muon neutrinos and antineutrinos (ν_μ), which undergo charged-current interactions in the ice to produce a muon traversing the detector. The majority of the background for this analysis originates from CRs interacting with the atmosphere to produce showers of particles including atmospheric muons and neutrinos. The atmospheric muons from the southern hemisphere are able to penetrate the ice and are detected as tracklike events in IceCube at a rate orders of magnitude higher than the corresponding atmospheric neutrinos [12]. Almost all of the atmospheric muons from the northern hemisphere are filtered out by the Earth. However, poorly reconstructed atmospheric muons from the southern sky create a significant background in the northern hemisphere. Atmospheric neutrinos also produce muons from charged-current ν_μ interactions, acting as an irreducible background in both hemispheres. Neutral-current interactions or ν_e and ν_τ charged-current interactions produce particle showers with spherical topology known as cascade events. Tracks at \sim TeV energies are reconstructed with a typical angular resolution of $\lesssim 1^\circ$, while cascades have an angular resolution of $\sim 10^\circ$ – 15° [13]. This analysis selects tracklike events because of their better angular resolution. Tracks have the additional advantage that they can be used even if the neutrino interaction vertex is located outside of the detector. This greatly increases the detection efficiency.

During the first three years of data included here, IceCube was incomplete and functioned with 40, 59, and 79 strings. For these years and also during the first year of data taking of the full detector (IC86), the event selection and reconstruction was updated until it stabilized in 2012, as detailed in Table I. Seven years of tracks were previously analyzed to search for point sources [14]. Subsequently, an eight-year sample of tracks from the northern sky used for diffuse muon neutrino searches was also analyzed looking for point sources [15]. The aim of this Letter is to introduce a selection which unifies the event filtering adopted in these two past searches. Additionally, the direction reconstruction [16,17] has been updated to use the deposited event energy in the detector. This improves

TABLE I. IceCube configuration, livetime, number of final tracklike events, start and end date and published reference in which the sample selection is described.

Data samples					
Year	Livetime (Days)	Number of events	Start day	End day	Ref.
IC40	376.4	36900	2008/04/06	2009/05/20	[19]
IC59	352.6	107011	2009/05/20	2010/05/31	[20]
IC79	316.0	93133	2010/06/01	2011/05/13	[21]
IC86-2011	332.9	136244	2011/05/13	2012/05/15	[22]
IC86-2012-18	2198.2	760923	2012/04/26 ^a	2018/07/10	This Letter

^aStart date for test runs of the new processing. The remainder of this run began 2012/05/15.

the angular resolution by more than 10% for events above 10 TeV compared to the seven-year study [14], and achieves a similar angular resolution as the eight-year northern diffuse track selection [15], which also uses deposited event energy in the direction reconstruction (see Fig. 1). The absolute pointing accuracy of IceCube by combining many events has been demonstrated to be $\lesssim 0.2^\circ$ [18] via measurements of the effect of the Moon shadow on the background CR flux.

Different criteria are applied to select track-like events from the northern and southern hemisphere (with a boundary between them at declination $\delta = -5^\circ$), because the background differs in these two regions. Almost all the atmospheric muons in the northern hemisphere can be removed by selecting high-quality tracklike events. In the southern hemisphere, the atmospheric background is reduced by strict cuts on the reconstruction quality and minimum energy deposited in the detector, since the astrophysical neutrino fluxes are expected to have a harder energy spectrum than the background of atmospheric muons and neutrinos. This effectively removes almost all

southern hemisphere events with an estimated energy below ~ 10 TeV [23].

In both hemispheres, atmospheric muons and cascade events are further filtered using multivariate boosted decision trees (BDTs). In this analysis, a single BDT is trained to recognize three classes of events in the northern hemisphere: single muon tracks from atmospheric and astrophysical neutrinos, atmospheric muons, and cascades, where neutrino-induced tracks are treated as signal. This BDT uses 11 variables related to event topology and reconstruction quality. When applied to simulated events, the northern BDT preserves $\sim 90\%$ of the atmospheric neutrinos and $\sim 0.1\%$ of the atmospheric muons from the initial selection of tracklike events, also applied in previous muon neutrino searches [14,15]. In the southern hemisphere, the BDT and selection filters are taken from Ref. [14]. The final all-sky event rate of ~ 2 mHz is dominated by muons from atmospheric neutrinos in the northern hemisphere and by high-energy, well-reconstructed muons in the southern hemisphere. This updated selection applied to the final six years of data shown in Table I. The preceding four years of data are handled exactly as in the past.

The point-source searches conducted in this paper use the existing maximum-likelihood ratio method which compares the hypothesis of pointlike signal plus diffuse background versus a background-only null hypothesis. All of the searches and source catalogs were predefined before any of the following results were obtained. This technique, described in Refs. [19,30], was also applied in the seven- and eight-year point source searches [14,15]. The all-sky scan and the selected source catalog searches look for directions which maximize the likelihood-ratio in the northern and southern hemisphere separately. Since this analysis assumes pointlike sources, it is suboptimal to those with extended neutrino emission regions. The sensitivity of this analysis to a neutrino flux with an E^{-2} spectrum, calculated according to [19], shows a $\sim 35\%$ improvement compared to the seven-year all-sky search [14] due to the longer livetime, updated event selection, and updated reconstructions. While the sensitivity in the northern hemisphere is comparable to the eight-year study for an E^{-2} spectrum [15], the analysis presented in this work achieves

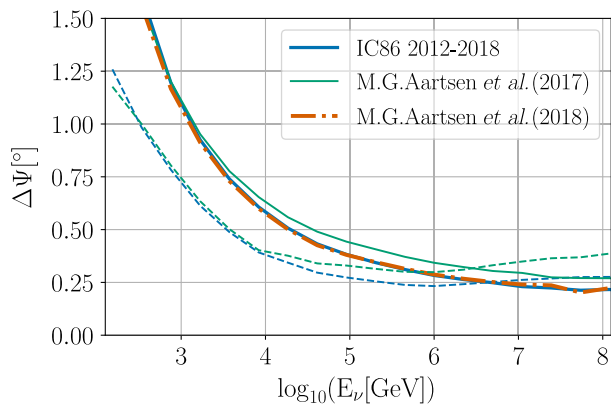


FIG. 1. The median angle between simulated neutrino and reconstructed muon directions as a function of energy for the data selection used in the latest six years compared to that in Ref. [14] (solid and dashed lines are for northern and southern hemispheres, respectively) and in Ref. [15] for the northern hemisphere. The differences between hemispheres come from the differences in the background composition and the respective selection criteria.

a $\sim 30\%$ improvement in sensitivity to sources with a softer spectrum, such as E^{-3} . This difference is due to the more general nature of this work which assumes an $E^{-\gamma}$ power-law energy spectrum, where $1 \leq \gamma \leq 4$, whereas the eight-year study targets the sources responsible for the diffuse astrophysical neutrino flux seen in [31] by applying a strict Gaussian prior on the spectral index, γ , centered at 2.19 ± 0.1 .

All-sky scan.—The brightest sources of astrophysical neutrinos may differ from the brightest sources observed in the electromagnetic (EM) spectrum. For example, cosmic accelerators can be surrounded by a dense medium which attenuates photon emission while neutrinos could be further generated by cosmic-ray interactions in the medium. For this reason, a general all-sky search for the brightest single pointlike neutrino source in each hemisphere is conducted, and is unbiased by EM observations. This involves maximizing the signal-over-background likelihood-ratio at a grid of points across the entire sky with a finer spacing ($\sim 0.1^\circ \times \sim 0.1^\circ$) than the typical event angular uncertainty. The points within 8° of the celestial poles are excluded due to poor statistics and limitations in the background estimation technique.

At each position on the grid, the likelihood-ratio function is maximized resulting in a maximum test-statistic (TS), a best fit number of astrophysical neutrino events (\hat{n}_s), and the spectral index ($\hat{\gamma}$) for an assumed power-law energy spectrum. The local pre-trial probability (p -value) of obtaining the given or larger TS value at a certain location from only background is estimated at every grid point by fitting the TS distribution from many background trials with a χ^2 function. Each background trial is obtained from the data themselves by scrambling the right ascension of each event, thereby removing any clustering of the signal. The location of the most significant p -value in each hemisphere is defined to be the hottest spot. The post-trial probability is estimated by comparing the p -value of the hottest spot in the data with a distribution of hottest spots in the corresponding hemisphere from a large number of background trials.

The most significant point in the northern hemisphere is found at equatorial coordinates (J2000) right ascension 40.9° , declination -0.3° with a local p -value of 3.5×10^{-7} . The best fit parameters at this spot are $\hat{n}_s = 61.5$ and $\hat{\gamma} = 3.4$. Considering the trials from examining the entire hemisphere increases the p -value to 9.9×10^{-2} post-trial. The probability sky map in a 3° by 3° window around the most significant point in the northern hemisphere is plotted in Fig. 2. This point is found 0.35° from the active galaxy NGC 1068, which is independently included as a source in the northern source catalog. To study whether the 0.35° offset between the all-sky hotspot and NGC 1068 is typical of the reconstruction uncertainty of a neutrino source, we inject a soft-spectrum source according to the best-fit $E^{-3.2}$ flux at the *Fermi*-LAT coordinates for NGC 1068 into our

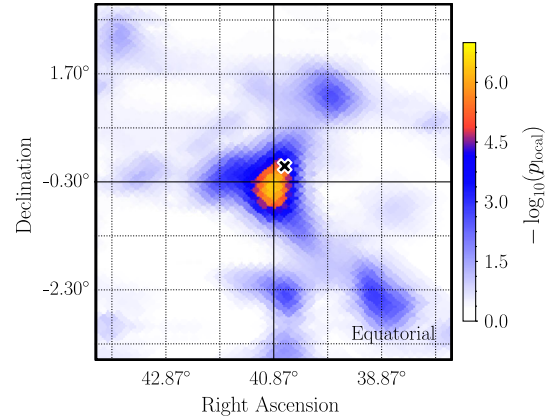


FIG. 2. Local pre-trial p -value map around the most significant point in the Northern hemisphere. The black cross marks the coordinates of the galaxy NGC 1068 taken from *Fermi*-4FGL.

background samples. Scanning in a 5° window around the injection point, we find that the median separation between the most significant hotspot and the injection point is 0.35° . Thus, if the excess is due to an astrophysical signal from NGC 1068, the offset between the all-sky hotspot and *Fermi*-LAT's coordinates is consistent with the IceCube angular resolution for such a source.

The most significant hotspot in the southern hemisphere, at right ascension 350.2° and declination -56.5° , is less significant with a pre-trial p -value of 4.3×10^{-6} and fit parameters $\hat{n}_s = 17.8$, and $\hat{\gamma} = 3.3$. The p -value of this hotspot becomes 0.75 post-trial. Both hotspots alone are consistent with a background-only hypothesis.

Source catalog searches.—The motivation of this search is to improve sensitivity to detect possible neutrino sources already observed in γ rays. A new catalog composed of 110 sources has been constructed which updates the catalog used in previous sources searches [14]. The new catalog uses the latest γ ray observations and is based on rigorous application of a few simple criteria, described below. The size of the catalog was chosen to limit the trials factor applied to the most significant source in the catalog such that a 5σ significance before trials would remain above 4σ after trials. These 110 sources are composed of Galactic and extragalactic sources, which are selected separately.

The extragalactic sources are selected from the *Fermi*-LAT 4FGL catalog [32] since it provides the highest-energy unbiased measurements of γ -ray sources over the full sky. Sources from 4FGL are weighted according to the integral *Fermi*-LAT flux above 1 GeV divided by the sensitivity flux for this analysis at the respective source declination. The 5% highest-weighted BL Lacs and flat spectrum radio quasars (FSRQs) are each selected. The minimum weighted integral flux from the combined selection of BL Lac and FSRQs is used as a flux threshold to include sources marked as unidentified blazars and AGN. Eight 4FGL sources are identified as starburst galaxies. Since these types of objects are thought to host hadronic emission

[33,34], they are all included in the final source list. The blazar TXS 0506 + 056 is selected in the top 5% of BL Lacs due to its high luminosity in γ rays and its location in the most sensitive region of the sky for IceCube.

To select Galactic sources, we consider measurements of VHE γ -ray sources from TeVCat [35,36] and gammaCat [37]. Spectra of the γ rays were converted to equivalent neutrino fluxes, assuming a purely hadronic origin of the observed γ -ray emission where $E_\gamma \simeq 2E_\nu$, and compared to the sensitivity of this analysis at the declination of the source (Fig. 3). Those Galactic objects with predicted energy fluxes $> 50\%$ of IceCube's sensitivity limit for an E^{-2} spectrum, were included in the source catalog. A total of 12 Galactic γ -ray sources survived the selection.

The final list of neutrino source candidates is a northern-sky catalog containing 97 objects (87 extragalactic and 10 Galactic) and a southern-sky catalog containing 13 sources (11 extragalactic and 2 Galactic). The large north-south difference is due to the difference in the sensitivity of IceCube in the northern and southern hemispheres. The post-trial p -value for each catalog describes the significance of the single most significant source in the catalog and is calculated as the fraction of background trials where the pre-trial p -value of the most significant fluctuation is smaller than the pre-trial p -value found in data.

The obtained pre-trial p -values are provided in the supplementary material and their associated 90% C.L. flux upper limits are shown in Fig. 3, together with the expected sensitivity and discovery potential fluxes. The most significant excess in the northern catalog of 97 sources is found in the direction of the galaxy NGC 1068, analyzed for the first time by IceCube in this analysis, with a local pre-trial p -value of 1.8×10^{-5} (4.1σ). The best

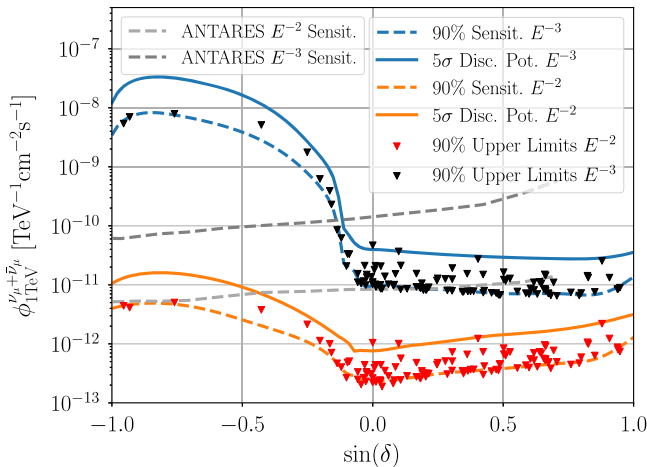


FIG. 3. 90% C.L. median sensitivity and 5σ discovery potential as a function of source declination for a neutrino source with an E^{-2} and E^{-3} spectrum. The 90% upper limits are shown excluding an E^{-2} and E^{-3} source spectrum for the sources in the source list. The grey curves show the 90% C.L. median sensitivity from 11 yrs of ANTARES data [38].

fit parameters are $\gamma = 3.2$ and $\hat{n}_s = 50.4$, consistent with the results for the all-sky northern hottest spot, 0.35° away. From Fig. 2 it can be inferred that the significance of the all-sky hotspot and the excess at NGC 1068 are dominated by the same cluster of events. The parameters of the best fit spectrum at the coordinates of NGC 1068 are shown in Fig. 4. When the significance of NGC 1068 is compared to the most significant excesses in the northern catalog from many background trials, the post-trial significance is 2.9σ .

Out of the 13 different source locations examined in the Southern catalog, the most significant excess has a pretrial p -value of 0.06 in the direction of PKS 2233-148. The associated post-trial p -value is 0.55, which is consistent with background.

Four sources in the northern catalog found a pretrial p -value < 0.01 : NGC 1068, TXS 0506 + 056, PKS 1424 + 240, and GB6 J1542 + 6129. Evidence has been presented for TXS 0506 + 056 to be a neutrino source [8] using an overlapping event selection in a time-dependent analysis. However, TXS 0506 + 056 was included in the northern catalog independently of this result due to its relatively high γ -ray flux observed by *Fermi*-LAT. In this Letter, in which we only consider the cumulative signal integrated over 10 years, we find a pretrial significance of 3.6σ at the coordinates of TXS 0506 + 056 for a best fit spectrum of $E^{-2.1}$, consistent with previous results.

In addition to the single source search, a source population study is conducted to understand if excesses from several sources, each not yet at evidence level, can cumulatively indicate a population of neutrino sources in the catalog.

The population study uses the pretrial p -values of each source in the catalog and searches for an excess in the

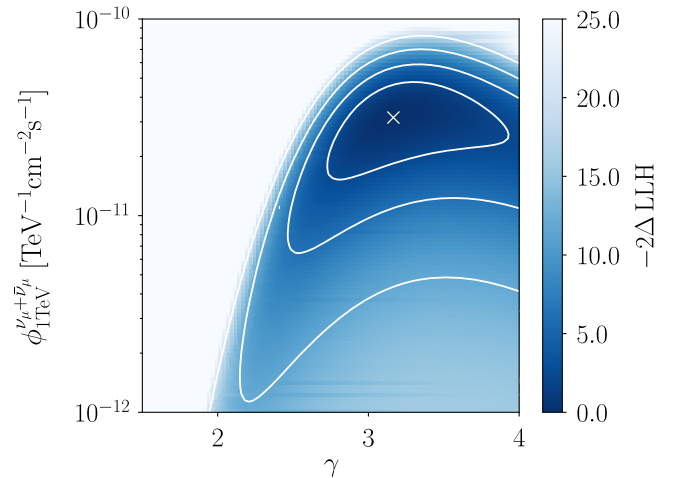


FIG. 4. Likelihood map at the position of NGC 1068 as a function of the astrophysical flux spectral index and normalization at 1 TeV. Contours show 1, 2, 3, and 4σ confidence intervals assuming Wilks' theorem with 2 degrees of freedom [39]. The best fit spectrum is point marked with "x".

number of small p -values compared to the uniform background expectation. If the number of objects in the search catalog is N , and the number of sources below a given threshold p_k is k , then the probability of background producing k or more sources with p -values smaller than p_k is given by the cumulative binomial probability:

$$p_{\text{bkg}} = \sum_{i=k}^N P_{\text{binom}}(i|p_k, N) = \sum_{i=k}^N \binom{N}{i} p_k^i (1-p_k)^{N-i}. \quad (1)$$

In order to maximize sensitivity to any possible population size of neutrino sources within the catalog, the probability threshold (p_k) is increased iteratively to vary k between 1 and N . The result of this search is the most significant p_{bkg} from N different tested values of k , then the post-trial p -value from this search must take into account a trial factor for the different tested values of k .

The most significant p_{bkg} from the northern catalog population analysis is 3.3×10^{-5} (4.0σ), which is found when $k = 4$. The four most significant sources which contribute to this excess are those with p -value < 0.01 as described above. When accounting for the fact that different signal population sizes are tested, the post-trial p -value is 4.8×10^{-4} (3.3σ). Since evidence has already been presented for TXS 0506 + 056 to be a neutrino source [8], an *a posteriori* search is conducted removing this source from the catalog. The resulting most significant excess is 2.3σ post-trial due to the remaining three most significant sources. For the southern catalog, the pretrial p -value of the most significant excess is 0.12, provided by 5 of the 13 sources. The resulting post-trial p -value is 0.36.

Stacked source searches.—In the case of catalogs of sources that produce similar fluxes, stacking searches require a lower flux per source for a discovery than considering each source individually. Three catalogs of Galactic γ -ray sources are stacked in this paper. Sources are selected from VHE γ -ray measurements and categorized into pulsar wind nebulae (PWN), supernova remnants (SNR), and unidentified objects (UNID), with the aim of grouping objects likely to have similar properties as Galactic neutrino emitters. The final groups consist of 33 PWN, 23 SNR, and 58 UNID described in the Supplemental Material. A weighting scheme is adopted to describe the relative contribution expected from each source in a single catalog based on the integral of the extrapolated γ -ray flux above 10 TeV. All three catalogs find p -values > 0.1 .

Conclusion.—This Letter presents an updated event selection optimized for pointlike neutrino source signals applied to 10 years of IceCube data taken from April 2008 to July 2018. Multiple neutrino source searches are performed: an all-sky scan, a source catalog and corresponding catalog population study for each hemisphere, and three stacked Galactic-source searches.

TABLE II. Summary of final p -values (pretrial and post-trial) for each pointlike source search implemented in this Letter.

Analysis	Category	Pretrial significance (p_{local})	Post-trial significance
All-Sky Scan	North	3.5×10^{-7}	9.9×10^{-2}
	South	4.3×10^{-6}	0.75
Source list	North	1.8×10^{-5}	2.0×10^{-3} (2.9σ)
	South	5.9×10^{-2}	0.55
Catalog	North	3.3×10^{-5}	4.8×10^{-4} (3.3σ)
	South	0.12	0.36
Stacking	SNR	...	0.11
Search	PWN	...	1.0
	UNID	...	0.4

The results of these analyses, all searching for cumulative neutrino signals integrated over the 10 years of data-taking, are summarized in Table II. The most significant source in the northern catalog, NGC 1068, is inconsistent with a background-only hypothesis at 2.9σ due to being located 0.35° from the most significant excess in the northern hemisphere and the northern source catalog provides a 3.3σ inconsistency with a background-only hypothesis for the entire catalog. This result comes from an excess of significant p -values in the directions of the Seyfert II galaxy NGC 1068, the blazar TXS 0506 + 056, and the BL Lacs PKS 1424 + 240 and GB6 J1542 + 6129. NGC 1068, at a 14.4 Mpc distance, is the most luminous Seyfert II galaxy detected by *Fermi*-LAT [24]. NGC 1068 is an observed particle accelerator, charged particles are accelerated in the jet of the AGN or in the AGN-driven molecular wind [40], producing γ rays and potentially neutrinos. Other work has previously indicated NGC 1068 as a potential CR accelerator [33,41,42]. Assuming that the observed excess is indeed of astrophysical origin and connected with NGC 1068, the best-fit neutrino spectrum inferred from this work is significantly higher than that predicted from models developed to explain the *Fermi*-LAT gamma-ray measurements [25]. However, the large uncertainty from our spectral measurement and the high x-ray and γ -ray absorption along the line of sight [26,43] prevent a straight forward connection. Time-dependent analyses and the possibility of correlating with multimessenger observations for this and other sources may provide additional evidence of neutrino emission and insights into its origin. Continued data-taking, more refined event reconstruction, and the planned upgrade of IceCube promise further improvements in sensitivity [44].

The authors gratefully acknowledge the support from the following agencies and institutions: USA: U.S. National Science Foundation-Office of Polar Programs,

U.S. National Science Foundation-Physics Division, Wisconsin Alumni Research Foundation, Center for High Throughput Computing (CHTC) at the University of Wisconsin-Madison, Open Science Grid (OSG), Extreme Science and Engineering Discovery Environment (XSEDE), U.S. Department of Energy-National Energy Research Scientific Computing Center, Particle astrophysics research computing center at the University of Maryland, Institute for Cyber-Enabled Research at Michigan State University, and Astroparticle physics computational facility at Marquette University; Belgium: Funds for Scientific Research (FRS-FNRS and FWO), FWO Odysseus and Big Science programmes, and Belgian Federal Science Policy Office (Belspo); Germany: Bundesministerium für Bildung und Forschung (BMBF), Deutsche Forschungsgemeinschaft (DFG), Helmholtz Alliance for Astroparticle Physics (HAP), Initiative and Networking Fund of the Helmholtz Association, Deutsches Elektronen Synchrotron (DESY), and High Performance Computing cluster of the RWTH Aachen; Sweden: Swedish Research Council, Swedish Polar Research Secretariat, Swedish National Infrastructure for Computing (SNIC), and Knut and Alice Wallenberg Foundation; Australia: Australian Research Council; Canada: Natural Sciences and Engineering Research Council of Canada, Calcul Québec, Compute Ontario, Canada Foundation for Innovation, WestGrid, and Compute Canada; Denmark: Villum Fonden, Danish National Research Foundation (DNRF), Carlsberg Foundation; New Zealand: Marsden Fund; Japan: Japan Society for Promotion of Science (JSPS) and Institute for Global Prominent Research (IGPR) of Chiba University; Korea: National Research Foundation of Korea (NRF); Switzerland: Swiss National Science Foundation (SNSF); United Kingdom: Department of Physics, University of Oxford.

*Corresponding author.

analysis@icecube.wisc.edu

- [1] V. F. Hess, Über Beobachtungen der durchdringenden Strahlung bei sieben Freiballonfahrten, *Phys. Z.* **13**, 1084 (1912).
- [2] D. J. Bird *et al.*, Detection of a cosmic ray with measured energy well beyond the expected spectral cutoff due to cosmic microwave radiation, *Astrophys. J.* **441**, 144 (1995).
- [3] M. G. Aartsen *et al.* (IceCube Collaboration), Observation and characterization of a cosmic muon neutrino flux from the Northern hemisphere using six years of IceCube data, *Astrophys. J.* **833**, 3 (2016).
- [4] M. G. Aartsen *et al.* (IceCube Collaboration), The IceCube neutrino observatory—Contributions to ICRC 2017 Part II: Properties of the atmospheric and astrophysical neutrino flux, *Proc. Sci. ICR2017* (2017) 981 [arXiv:1710.01191].
- [5] M. Aartsen *et al.*, Evidence for high-energy extraterrestrial neutrinos at the IceCube detector, *Science* **342**, 1242856 (2013).
- [6] M. G. Aartsen *et al.* (IceCube Collaboration), Observation of High-Energy Astrophysical Neutrinos in Three Years of IceCube Data, *Phys. Rev. Lett.* **113**, 101101 (2014).
- [7] M. G. Aartsen *et al.*, Multimessenger observations of a flaring blazar coincident with high-energy neutrino Icecube-170922a, *Science* **361**, eaat1378 (2018).
- [8] M. G. Aartsen *et al.* (IceCube Collaboration), Neutrino emission from the direction of the blazar TXS 0506 + 056 prior to the IceCube-170922A alert, *Science* **361**, 147 (2018).
- [9] M. G. Aartsen *et al.* (IceCube Collaboration), The contribution of Fermi-2LAC blazars to the diffuse TeV-PeV neutrino flux, *Astrophys. J.* **835**, 45 (2017).
- [10] R. Abbasi *et al.*, Calibration and characterization of the IceCube photomultiplier tube, *Nucl. Instrum. Methods Phys. Res., Sect. A* **618**, 139 (2010).
- [11] R. Abbasi *et al.* (IceCube Collaboration), The IceCube data acquisition system: Signal capture, digitization, and time-stamping, *Nucl. Instrum. Methods Phys. Res., Sect. A* **601**, 294 (2009).
- [12] M. G. Aartsen *et al.* (IceCube Collaboration), The IceCube Neutrino observatory: Instrumentation and online systems, *J. Instrum.* **12**, P03012 (2017).
- [13] M. G. Aartsen *et al.* (IceCube Collaboration), Search for astrophysical sources of neutrinos using cascade events in IceCube, *Astrophys. J.* **846**, 136 (2017).
- [14] M. G. Aartsen *et al.* (IceCube Collaboration), All-sky search for time-integrated neutrino emission from astrophysical sources with 7 yr of IceCube data, *Astrophys. J.* **835**, 151 (2017).
- [15] M. G. Aartsen *et al.* (IceCube Collaboration), Search for steady point-like sources in the astrophysical muon neutrino flux with 8 years of IceCube data, *Eur. Phys. J. C.* **79**, 234 (2018).
- [16] J. Ahrens *et al.* (AMANDA Collaboration), Muon track reconstruction and data selection techniques in AMANDA, *Nucl. Instrum. Methods Phys. Res., Sect. A* **524**, 169 (2004).
- [17] M. G. Aartsen *et al.*, Improvement in fast particle track reconstruction with robust statistics, *Nucl. Instrum. Methods Phys. Res., Sect. A* **736**, 143 (2014).
- [18] M. G. Aartsen *et al.* (IceCube Collaboration), Observation of the cosmic-ray shadow of the Moon with IceCube, *Phys. Rev. D* **89**, 102004 (2014).
- [19] R. Abbasi *et al.* (IceCube Collaboration), Time-integrated searches for point-like sources of neutrinos with the 40-string IceCube detector, *Astrophys. J.* **732**, 18 (2011).
- [20] M. G. Aartsen *et al.* (IceCube Collaboration), Search for time-independent neutrino emission from astrophysical sources with 3 yr of IceCube data, *Astrophys. J.* **779**, 132 (2013).
- [21] K. Schatto, Stacked searches for high-energy neutrinos from blazars with IceCube, Ph. D. thesis, Mainz U., 2014.
- [22] M. G. Aartsen *et al.* (IceCube Collaboration), Searches for extended and point-like neutrino sources with four years of IceCube data, *Astrophys. J.* **796**, 109 (2014).
- [23] See Supplemental Material at <http://link.aps.org/supplemental/10.1103/PhysRevLett.124.051103> for more details on the properties of the event selection, catalogs of investigated astrophysical sources, further context for the observations around NGC 1068. This material includes Refs. [24–29].

- [24] M. Ackermann *et al.*, GeV observations of star-forming galaxies with the Fermi Large Area Telescope, *Astrophys. J.* **755**, 164 (2012).
- [25] A. Lamastra, F. Fiore, D. Guetta, L. A. Antonelli, S. Colafrancesco, N. Menci, S. Puccetti, A. Stamerra, and L. Zappacosta, Galactic outflow driven by the active nucleus and the origin of the gamma-ray emission in NGC 1068, *Astron. Astrophys.* **596**, A68 (2016).
- [26] A. Lamastra, N. Menci, F. Fiore, L. A. Antonelli, S. Colafrancesco, D. Guetta, and A. Stamerra, Extragalactic gamma-ray background from AGN winds and star-forming galaxies in cosmological galaxy formation models, *Astron. Astrophys.* **607**, A18 (2017).
- [27] T. Neunhoffer, Estimating the angular resolution of tracks in neutrino telescopes based on a likelihood analysis, *Astropart. Phys.* **25**, 220 (2006).
- [28] V. A. Acciari *et al.* (MAGIC Collaboration), Constraints on gamma-ray and neutrino emission from NGC 1068 with the MAGIC telescopes, *Astrophys. J.* **883**, 135 (2019).
- [29] F. Aharonian *et al.* (H.E.S.S. Collaboration), Observations of selected AGN with H.E.S.S., *Astron. Astrophys.* **441**, 465 (2005).
- [30] J. Braun, J. Dumm, F. De Palma, C. Finley, A. Karle, and T. Montaruli, Methods for point source analysis in high energy neutrino telescopes, *Astropart. Phys.* **29**, 299 (2008).
- [31] C. Haack and C. Wiebusch (IceCube Collaboration), A measurement of the diffuse astrophysical muon neutrino flux using eight years of IceCube data, *Proc. Sci., ICRC2017* (2018) 1005.
- [32] The Fermi-LAT Collaboration, Fermi Large Area Telescope fourth source catalog, [arXiv:1902.10045](https://arxiv.org/abs/1902.10045).
- [33] A. Loeb and E. Waxman, The cumulative background of high energy neutrinos from starburst galaxies, *J. Cosmol. Astropart. Phys.* **05** (2006) 003.
- [34] K. Murase, M. Ahlers, and B. C. Lacki, Testing the hadronuclear origin of PeV neutrinos observed with IceCube, *Phys. Rev. D* **88**, 121301(R) (2013).
- [35] TeVCat: Online catalogue of TeV sources, <http://tevcat.uchicago.edu/> (2018).
- [36] S. P. Wakely and D. Horan, TeVCat: An online catalog for very high energy gamma-ray astronomy, *Int. Cosmic Ray Conf.* **3**, 1341 (2008).
- [37] GammaCat: Online catalogue of Gamma-ray sources, <https://gamma-cat.readthedocs.io/data/overview.html> (2018).
- [38] J. Aublin, G. Illuminati, and S. Navas (ANTARES Collaboration), Searches for point-like sources of cosmic neutrinos with 11 years of ANTARES data, [arXiv:1908.08248](https://arxiv.org/abs/1908.08248).
- [39] S. S. Wilks, The large-sample distribution of the likelihood ratio for testing composite hypotheses, *Ann. Math. Stat.* **9**, 60 (1938).
- [40] A. Lamastra, F. Fiore, D. Guetta, L. A. Antonelli, S. Colafrancesco, N. Menci, S. Puccetti, A. Stamerra, and L. Zappacosta, Galactic outflow driven by the active nucleus and the origin of the gamma-ray emission in NGC 1068, *Astron. Astrophys.* **596**, A68 (2016).
- [41] T. M. Yoast-Hull, J. S. Gallagher III, E. G. Zweibel, and J. E. Everett, Active galactic nuclei, neutrinos, and interacting cosmic rays in NGC 253 and NGC 1068, *Astrophys. J.* **780**, 137 (2014).
- [42] B. C. Lacki, T. A. Thompson, E. Quataert, A. Loeb, and E. Waxman, On the GeV & TeV detections of the Starburst galaxies M82 & NGC 253, *Astrophys. J.* **734**, 107 (2011).
- [43] R. Wojaczyński, A. Niedźwiecki, F.-G. Xie, and M. Szanecki, Gamma-ray activity of Seyfert galaxies and constraints on hot accretion flows, *Astron. Astrophys.* **584**, A20 (2015).
- [44] J. van Santen (IceCube Gen2 Collaboration), IceCube-Gen2: The next-generation neutrino observatory for the South Pole, *Proc. Sci., ICRC2017* (2018) 991.

RESEARCH ARTICLE SUMMARY

NEUTRINO ASTROPHYSICS

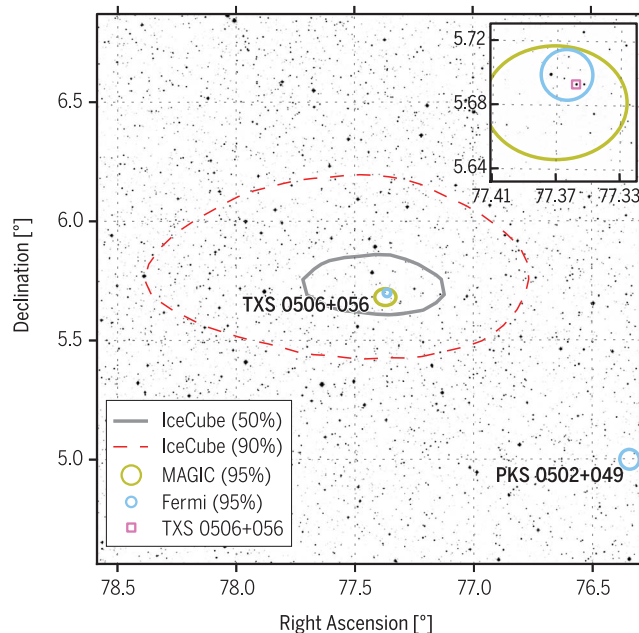
Multimessenger observations of a flaring blazar coincident with high-energy neutrino IceCube-170922A

The IceCube Collaboration, *Fermi*-LAT, MAGIC, *AGILE*, ASAS-SN, HAWC, H.E.S.S., *INTEGRAL*, Kanata, Kiso, Kapteyn, Liverpool Telescope, Subaru, *Swift*/*NuSTAR*, VERITAS, and VLA/17B-403 teams*†

INTRODUCTION: Neutrinos are tracers of cosmic-ray acceleration: electrically neutral and traveling at nearly the speed of light, they can escape the densest environments and may be traced back to their source of origin. High-energy neutrinos are expected to be produced in blazars: intense extragalactic radio, optical, x-ray, and, in some cases, γ -ray sources characterized by relativistic jets of plasma pointing close to our line of sight. Blazars are among the most powerful objects in the Universe and are widely speculated to be sources of high-energy cosmic rays. These cosmic rays generate high-energy neutrinos and γ -rays, which are produced when the cosmic rays accelerated in the jet interact with nearby gas or photons. On 22 September 2017, the cubic-kilometer IceCube Neutrino Observatory detected a ~ 290 -TeV neutrino from a direction consistent with the flaring γ -ray blazar TXS 0506+056. We report the details of this observation and the results of a multiwavelength follow-up campaign.

RATIONALE: Multimessenger astronomy aims for globally coordinated observations of cosmic rays, neutrinos, gravitational waves, and electromagnetic radiation across a broad range of wavelengths. The combination is expected to yield crucial information on the mechanisms energizing the most powerful astrophysical sources. That the production of neutrinos is accompanied by electromagnetic radiation from the source favors the chances of a multiwavelength identification. In particular, a measured association of high-energy neutrinos with a flaring source of γ -rays would elucidate the mechanisms and conditions for acceleration of the highest-energy cos-

mic rays. The discovery of an extraterrestrial diffuse flux of high-energy neutrinos, announced by IceCube in 2013, has characteristic properties that hint at contributions from extragalactic sources, although the individual sources remain as yet unidentified. Continuously monitoring the entire sky for astrophysical neu-



Multimessenger observations of blazar TXS 0506+056. The 50% and 90% containment regions for the neutrino IceCube-170922A (dashed red and solid gray contours, respectively), overlain on a V-band optical image of the sky. Gamma-ray sources in this region previously detected with the *Fermi* spacecraft are shown as blue circles, with sizes representing their 95% positional uncertainty and labeled with the source names. The IceCube neutrino is coincident with the blazar TXS 0506+056, whose optical position is shown by the pink square. The yellow circle shows the 95% positional uncertainty of very-high-energy γ -rays detected by the MAGIC telescopes during the follow-up campaign. The inset shows a magnified view of the region around TXS 0506+056 on an R-band optical image of the sky.

trinos, IceCube provides real-time triggers for observatories around the world measuring γ -rays, x-rays, optical, radio, and gravitational waves, allowing for the potential identification of even rapidly fading sources.

RESULTS: A high-energy neutrino-induced muon track was detected on 22 September 2017, automatically generating an alert that was

ON OUR WEBSITE

Read the full article at <http://dx.doi.org/10.1126/science.aat1378>

distributed worldwide within 1 min of detection and prompted follow-up searches by telescopes over a broad range of wavelengths. On 28 September 2017, the *Fermi* Large Area Telescope Collaboration reported that the direction of the neutrino was coincident with a cataloged γ -ray source, 0.1° from the neutrino direction. The source, a blazar known as TXS 0506+056 at a measured redshift of 0.34, was in a flaring state at the time with enhanced γ -ray activity in the GeV range. Follow-up observations by imaging atmospheric Cherenkov telescopes, notably the Major Atmospheric

Gamma Imaging Cherenkov (MAGIC) telescopes, revealed periods where the detected γ -ray flux from the blazar reached energies up to 400 GeV. Measurements of the source have also been completed at x-ray, optical, and radio wavelengths. We have investigated models associating neutrino and γ -ray production and find that correlation of the neutrino with the flare of TXS 0506+056 is statistically significant at the level of 3 standard deviations (σ). On the basis of the redshift of TXS 0506+056, we derive constraints for the muon-neutrino luminosity for this source and find them to be similar to the luminosity observed in γ -rays.

CONCLUSION: The energies of the γ -rays and the neutrino indicate that blazar jets may accelerate cosmic rays to at least several PeV. The observed association of a high-energy neutrino with a blazar during a period of enhanced γ -ray emission suggests that blazars may indeed be one of the long-sought sources of very-high-energy cosmic rays, and hence responsible for a sizable fraction of the cosmic neutrino flux observed by IceCube. ■

The list of author affiliations is available in the full article online.

*The full lists of participating members for each team and their affiliations are provided in the supplementary materials.

†Email: analysis@icecube.wisc.edu
 Cite this article as IceCube Collaboration et al., *Science* 361, eaat1378 (2018). DOI: 10.1126/science.aat1378

RESEARCH ARTICLE

NEUTRINO ASTROPHYSICS

Multimessenger observations of a flaring blazar coincident with high-energy neutrino IceCube-170922A

The IceCube Collaboration, *Fermi*-LAT, MAGIC, AGILE, ASAS-SN, HAWC, H.E.S.S., INTEGRAL, Kanata, Kiso, Kapteyn, Liverpool Telescope, Subaru, *Swift*/NuSTAR, VERITAS, and VLA/17B-403 teams*†

Previous detections of individual astrophysical sources of neutrinos are limited to the Sun and the supernova 1987A, whereas the origins of the diffuse flux of high-energy cosmic neutrinos remain unidentified. On 22 September 2017, we detected a high-energy neutrino, IceCube-170922A, with an energy of ~ 290 tera-electron volts. Its arrival direction was consistent with the location of a known γ -ray blazar, TXS 0506+056, observed to be in a flaring state. An extensive multiwavelength campaign followed, ranging from radio frequencies to γ -rays. These observations characterize the variability and energetics of the blazar and include the detection of TXS 0506+056 in very-high-energy γ -rays. This observation of a neutrino in spatial coincidence with a γ -ray-emitting blazar during an active phase suggests that blazars may be a source of high-energy neutrinos.

Since the discovery of a diffuse flux of high-energy astrophysical neutrinos (1, 2), IceCube has searched for its sources. The only nonterrestrial neutrino sources identified previously are the Sun and the supernova 1987A, producing neutrinos with energies millions of times lower than the high-energy diffuse flux, such that the mechanisms and the environments responsible for the high-energy cosmic neutrinos are still to be ascertained (3, 4). Many candidate source types exist, with active galactic nuclei (AGN) among the most prominent (5), in particular the small fraction of them designated as radio-loud (6). In these AGNs, the central supermassive black hole converts gravitational energy of accreting matter and/or the rotational energy of the black hole into powerful relativistic jets, within which particles can be accelerated to high energies. If a number of these particles are protons or nuclei, their interactions with the radiation fields and matter close to the source would give rise to a flux of high-energy pions that eventually decay into photons and neutrinos (7). In blazars (8)—AGNs that have one of the jets pointing close to our line of sight—the observable flux of neutrinos and radiation is expected to be greatly enhanced owing to relativistic Doppler boosting. Blazar electromagnetic (EM) emission is known to be highly variable on time scales from minutes to years (9).

Neutrinos travel largely unhindered by matter and radiation. Even if high-energy photons (TeV

and above) are unable to escape the source owing to intrinsic absorption, or are absorbed by interactions with the extragalactic background light (EBL) (10, 11), high-energy neutrinos may escape and travel unimpeded to Earth. An association of observed astrophysical neutrinos with blazars would therefore imply that high-energy protons or nuclei up to energies of at least tens of PeV are produced in blazar jets, suggesting that they may be the birthplaces of the most energetic particles observed in the Universe, the ultrahigh-energy cosmic rays (12). If neutrinos are produced in correlation with photons, the coincident observation of neutrinos with electromagnetic flares would greatly increase the chances of identifying the source(s). Neutrino detections must therefore be combined with the information from broadband observations across the electromagnetic spectrum (multimessenger observations).

To take advantage of multimessenger opportunities, the IceCube neutrino observatory (13) has established a system of real-time alerts that rapidly notify the astronomical community of the direction of astrophysical neutrino candidates (14). From the start of the program in April 2016 through October 2017, 10 public alerts have been issued for high-energy neutrino candidate events with well-reconstructed directions (15).

We report the detection of a high-energy neutrino by IceCube and the multiwavelength/multi-instrument observations of a flaring γ -ray blazar, TXS 0506+056, which was found to be positionally coincident with the neutrino direction (16). Chance coincidence of the IceCube-170922A event with the flare of TXS 0506+056 is statistically disfavored at the level of 3σ in models

evaluated below, associating neutrino and γ -ray production.

The neutrino alert

IceCube is a neutrino observatory with more than 5000 optical sensors embedded in 1 km^3 of the Antarctic ice-sheet close to the Amundsen-Scott South Pole Station. The detector consists of 86 vertical strings frozen into the ice 125 m apart, each equipped with 60 digital optical modules (DOMs) at depths between 1450 and 2450 m. When a high-energy muon-neutrino interacts with an atomic nucleus in or close to the detector array, a muon is produced moving through the ice at superluminal speed and creating Cherenkov radiation detected by the DOMs. On 22 September 2017 at 20:54:30.43 Coordinated Universal Time (UTC), a high-energy neutrino-induced muon track event was detected in an automated analysis that is part of IceCube's real-time alert system. An automated alert was distributed (17) to observers 43 s later, providing an initial estimate of the direction and energy of the event. A sequence of refined reconstruction algorithms was automatically started at the same time, using the full event information. A representation of this neutrino event with the best-fitting reconstructed direction is shown in Fig. 1. Monitoring data from IceCube indicate that the observatory was functioning normally at the time of the event.

A Gamma-ray Coordinates Network (GCN) Circular (18) was issued ~ 4 hours after the initial notice, including the refined directional information (offset 0.14° from the initial direction; see Fig. 2). Subsequently, further studies were performed to determine the uncertainty of the directional reconstruction arising from statistical and systematic effects, leading to a best-fitting right ascension (RA) $77.43^{+0.95}_{-0.65}$ and declination (Dec) $+5.72^{+0.50}_{-0.30}$ (degrees, J2000 equinox, 90% containment region). The alert was later reported to be in positional coincidence with the known γ -ray blazar TXS 0506+056 (16), which is located at RA 77.36° and Dec $+5.69^\circ$ (J2000) (19), 0.1° from the arrival direction of the high-energy neutrino.

The IceCube alert prompted a follow-up search by the Mediterranean neutrino telescope ANTARES (Astronomy with a Neutrino Telescope and Abyss environmental REsearch) (20). The sensitivity of ANTARES at the declination of IceCube-170922A is about one-tenth that of IceCube's (21), and no neutrino candidates were found in a ± 1 day period around the event time (22).

An energy of 23.7 ± 2.8 TeV was deposited in IceCube by the traversing muon. To estimate the parent neutrino energy, we performed simulations of the response of the detector array, considering that the muon-neutrino might have interacted outside the detector at an unknown distance. We assumed the best-fitting power-law energy spectrum for astrophysical high-energy muon neutrinos, $dN/dE \propto E^{-2.13}$ (2), where N is the number of neutrinos as a function of energy E . The simulations yielded a most probable neutrino energy of 290 TeV, with a 90% confidence level (CL)

*The full lists of participating members for each team and their affiliations are provided in the supplementary materials.
†Email: analysis@icecube.wisc.edu

lower limit of 183 TeV, depending only weakly on the assumed astrophysical energy spectrum (25).

The vast majority of neutrinos detected by IceCube arise from cosmic-ray interactions within Earth's atmosphere. Although atmospheric neutrinos are dominant at energies below 100 TeV, their spectrum falls steeply with energy, allowing astrophysical neutrinos to be more easily identified at higher energies. The muon-neutrino as-

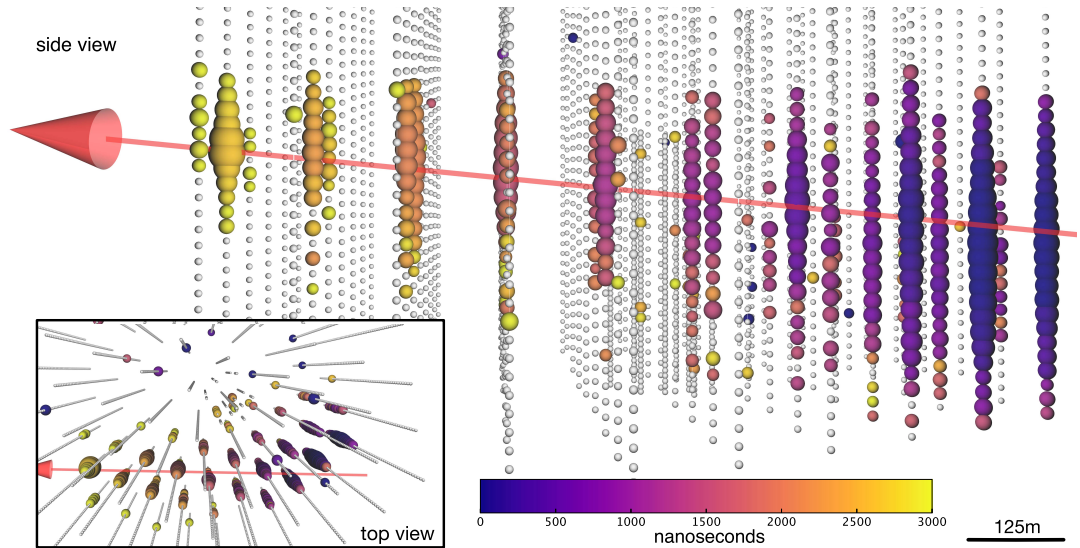
trophysical spectrum, together with simulated data, was used to calculate the probability that a neutrino at the observed track energy and zenith angle in IceCube is of astrophysical origin. This probability, the so-called signalness of the event (14), was reported to be 56.5% (17). Although IceCube can robustly identify astrophysical neutrinos at PeV energies, for individual neutrinos at several hundred TeV, an atmospheric origin

cannot be excluded. Electromagnetic observations are valuable to assess the possible association of a single neutrino to an astrophysical source.

Following the alert, IceCube performed a complete analysis of relevant data prior to 31 October 2017. Although no additional excess of neutrinos was found from the direction of TXS 0506+056 near the time of the alert, there are indications at the 3σ level of high-energy neutrino

Fig. 1. Event display for neutrino event IceCube-170922A.

The time at which a DOM observed a signal is reflected in the color of the hit, with dark blues for earliest hits and yellow for latest. Times shown are relative to the first DOM hit according to the track reconstruction, and earlier and later times are shown with the same colors as the first and last times, respectively. The total time the event took to cross the detector is ~ 3000 ns. The size of a colored sphere is proportional to the logarithm of the amount of light observed at the DOM, with larger spheres corresponding to larger signals. The total charge recorded is ~ 5800 photoelectrons. Inset is an overhead perspective view of the event. The best-fitting track direction is shown as an arrow, consistent with a zenith angle $5.7_{-0.30}^{+0.50}$ degrees below the horizon.



Downloaded from https://www.science.org at Vrije Universiteit Brussel on November 11, 2021

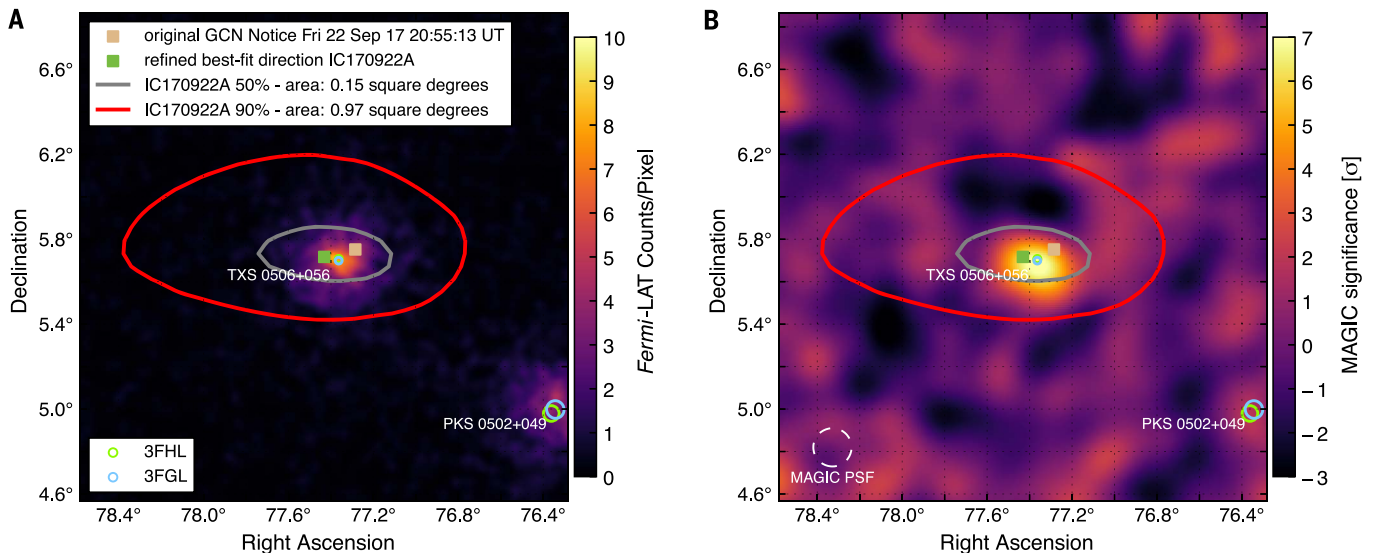


Fig. 2. Fermi-LAT and MAGIC observations of IceCube-170922A's location. Sky position of IceCube-170922A in J2000 equatorial coordinates overlaying the γ -ray counts from Fermi-LAT above 1 GeV (A) and the signal significance as observed by MAGIC (B) in this region. The tan square indicates the position reported in the initial alert, and the green square indicates the final best-fitting position from follow-up reconstructions (18). Gray and red curves show the 50% and 90% neutrino containment regions, respectively, including statistical and systematic errors. Fermi-LAT data are shown as a photon counts map in 9.5 years of data in units of counts per

pixel, using detected photons with energy of 1 to 300 GeV in a 2° by 2° region around TXS0506+056. The map has a pixel size of 0.02° and was smoothed with a 0.02° -wide Gaussian kernel. MAGIC data are shown as signal significance for γ -rays above 90 GeV. Also shown are the locations of a γ -ray source observed by Fermi-LAT as given in the Fermi-LAT Third Source Catalog (3FGL) (23) and the Third Catalog of Hard Fermi-LAT Sources (3FHL) (24) source catalogs, including the identified positionally coincident 3FGL object TXS 0506+056. For Fermi-LAT catalog objects, marker sizes indicate the 95% CL positional uncertainty of the source.

emission from that direction in data prior to 2017, as discussed in a companion paper (26).

High-energy γ -ray observations of TXS 0506+056

On 28 September 2017, the *Fermi* Large Area Telescope (LAT) Collaboration reported that the direction of origin of IceCube-170922A was consistent with a known γ -ray source in a state of enhanced emission (16). *Fermi*-LAT is a pair-conversion telescope aboard the *Fermi Gamma-ray Space Telescope* sensitive to γ -rays with energies from 20 MeV to greater than 300 GeV (27). Since August 2008, it has operated continuously, primarily in an all-sky survey mode. Its wide field of view of ~ 2.4 steradian provides coverage of the entire γ -ray sky every 3 hours. The search for possible counterparts to IceCube-170922A was part of the *Fermi*-LAT collaboration's routine multiwavelength, multimessenger program.

Inside the error region of the neutrino event, a positional coincidence was found with a previously cataloged γ -ray source, 0.1° from the best-fitting neutrino direction. TXS 0506+056 is a blazar of BL Lacertae (BL Lac) type. Its redshift of $z = 0.3365 \pm 0.0010$ was measured only recently based on the optical emission spectrum in a study triggered by the observation of IceCube-170922A (28).

TXS 0506+056 is a known *Fermi*-LAT γ -ray source, appearing in three catalogs of *Fermi* sources (23, 24, 29) at energies above 0.1, 50, and 10 GeV, respectively. An examination of the *Fermi* All-Sky Variability Analysis (FAVA) (30) photometric light curve for this object showed that TXS 0506+056 had brightened considerably in the GeV band starting in April 2017 (16). Independently, a γ -ray flare was also found by *Fermi*'s Automated Science Processing [ASP (25)]. Such flaring is not unusual for a BL Lac object and would not have been followed up as extensively if the neutrino were not detected.

Figure 3 shows the *Fermi*-LAT light curve and the detection time of the neutrino alert. The light curve of TXS 0506+056 from August 2008 to October 2017 was calculated in bins of 28 days for the energy range above 0.1 GeV. An additional light curve with 7-day bins was calculated for the period around the time of the neutrino alert. The γ -ray flux of TXS 0506+056 in each time bin was determined through a simultaneous fit of this source and the other *Fermi*-LAT sources in a 10° by 10° region of interest along with the Galactic and isotropic diffuse backgrounds, using a maximum-likelihood technique (25). The integrated γ -ray flux of TXS 0506+056 for $E > 0.1$ GeV, averaged over all *Fermi*-LAT observations spanning 9.5 years, is $(7.6 \pm 0.2) \times 10^{-8} \text{ cm}^{-2} \text{ s}^{-1}$. The

highest flux observed in a single 7-day light curve bin was $(5.3 \pm 0.6) \times 10^{-7} \text{ cm}^{-2} \text{ s}^{-1}$, measured in the week 4 to 11 July 2017. Strong flux variations were observed during the γ -ray flare, the most prominent being a flux increase from $(7.9 \pm 2.9) \times 10^{-8} \text{ cm}^{-2} \text{ s}^{-1}$ in the week 8 to 15 August 2017 to $(4.0 \pm 0.5) \times 10^{-7} \text{ cm}^{-2} \text{ s}^{-1}$ in the week 15 to 22 August 2017.

The Astro-Rivelatore Gamma a Immagini Leggero (*AGILE*) γ -ray telescope (31) confirmed the elevated level of γ -ray emission at energies above 0.1 GeV from TXS 0506+056 in a 13-day window (10 to 23 September 2017). The *AGILE* measured flux of $(5.3 \pm 2.1) \times 10^{-7} \text{ cm}^{-2} \text{ s}^{-1}$ is consistent with the *Fermi*-LAT observations in this time period.

High-energy γ -ray observations are shown in Figs. 3 and 4. Details on the *Fermi*-LAT and *AGILE* analyses can be found in (25).

Very-high-energy γ -ray observations of TXS 0506+056

Following the announcement of IceCube-170922A, TXS 0506+056 was observed by several ground-based Imaging Atmospheric Cherenkov Telescopes (IACTs). A total of 1.3 hours of observations in the direction of the blazar TXS 0506+056 were taken using the High-Energy Stereoscopic System (H.E.S.S.) (32), located in Namibia, on 23 September 2017 [Modified Julian Date (MJD)

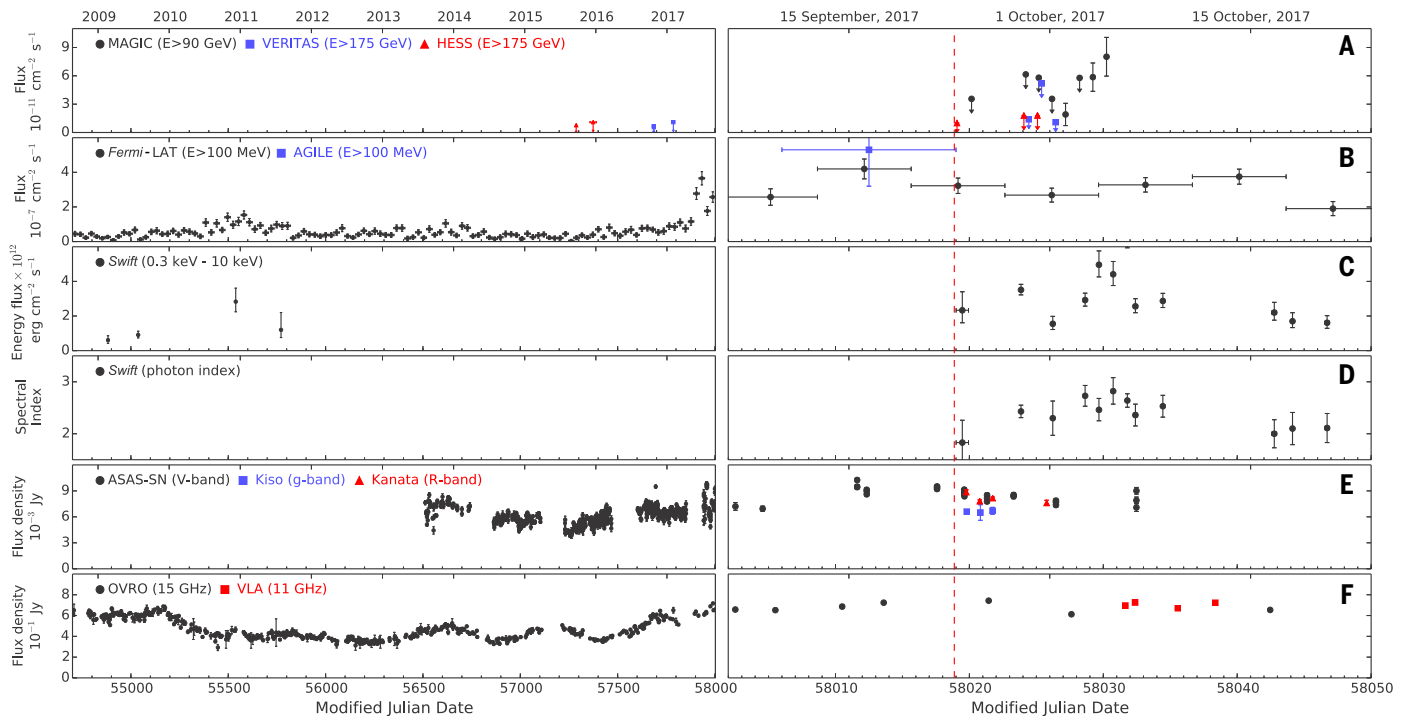


Fig. 3. Time-dependent multiwavelength observations of TXS 0506+056 before and after IceCube-170922A. Significant variability of the electromagnetic emission can be observed in all displayed energy bands, with the source being in a high-emission state around the time of the neutrino alert. From top to bottom: (A) VHE γ -ray observations by MAGIC, H.E.S.S., and VERITAS; (B) high-energy γ -ray observations by *Fermi*-LAT and *AGILE*; (C and D) x-ray observations by *Swift* XRT; (E) optical light curves from ASAS-SN, Kiso/KWFC, and Kanata/HONIR; and (F) radio observations by OVRO and VLA. The red

dashed line marks the detection time of the neutrino IceCube-170922A. The left set of panels shows measurements between MJD 54700 (22 August 2008) and MJD 58002 (6 September 2017). The set of panels on the right shows an expanded scale for time range MJD 58002 to MJD 58050 (24 October 2017). The *Fermi*-LAT light curve is binned in 28-day bins on the left panel, while finer 7-day bins are used on the expanded panel. A VERITAS limit from MJD 58019.40 (23 September 2017) of $2.1 \times 10^{-10} \text{ cm}^{-2} \text{ s}^{-1}$ is off the scale of the plot and not shown.

58019], ~4 hours after the circulation of the neutrino alert. A 1-hour follow-up observation of the neutrino alert under partial cloud coverage was performed using the Very Energetic Radiation Imaging Telescope Array System (VERITAS) γ -ray telescope array (33), located in Arizona, USA, later on the same day, ~12 hours after the IceCube detection. Both telescopes made additional observations on subsequent nights, but neither detected γ -ray emission from the source [see Fig. 3 and (25)]. Upper limits at 95% CL on the γ -ray flux were derived accordingly (assuming the measured spectrum, see below): $7.5 \times 10^{-12} \text{ cm}^{-2} \text{ s}^{-1}$ during the H.E.S.S. observation period and $1.2 \times 10^{-11} \text{ cm}^{-2} \text{ s}^{-1}$ during the VERITAS observations, both for energies $E > 175 \text{ GeV}$.

The Major Atmospheric Gamma Imaging Cherenkov (MAGIC) Telescopes (34) observed TXS 0506+056 for 2 hours on 24 September 2017 (MJD 58020) under nonoptimal weather conditions and then for a period of 13 hours from 28 September to 4 October 2017 (MJD 58024–58030) under good conditions. MAGIC consists of two 17-m telescopes, located at the Roque de los Muchachos Observatory on the Canary Island of La Palma (Spain).

No γ -ray emission from TXS 0506+056 was detected in the initial MAGIC observations on 24 September 2017, and an upper limit was derived on the flux above 90 GeV of $3.6 \times 10^{-11} \text{ cm}^{-2} \text{ s}^{-1}$

at 95% CL (assuming a spectrum $dN/dE \propto E^{-3.9}$). However, prompted by the *Fermi*-LAT detection of enhanced γ -ray emission, MAGIC performed another 13 hours of observations of the region starting 28 September 2017. Integrating the data, MAGIC detected a significant very-high-energy (VHE) γ -ray signal (35) corresponding to 374 ± 62 excess photons, with observed energies up to about 400 GeV. This represents a 6.2σ excess over expected background levels (25). The day-by-day light curve of TXS 0506+056 for energies above 90 GeV is shown in Fig. 3. The probability that a constant flux is consistent with the data is less than 1.35%. The measured differential photon spectrum (Fig. 4) can be described over the energy range of 80 to 400 GeV by a simple power law, $dN/dE \propto E^\gamma$, with a spectral index $\gamma = -3.9 \pm 0.4$ and a flux normalization of $(2.0 \pm 0.4) \times 10^{-10} \text{ TeV}^{-1} \text{ cm}^{-2} \text{ s}^{-1}$ at $E = 130 \text{ GeV}$. Uncertainties are statistical only. The estimated systematic uncertainties are <15% in the energy scale, 11 to 18% in the flux normalization, and ± 0.15 for the power-law slope of the energy spectrum (34). Further observations after 4 October 2017 were prevented by the full Moon.

An upper limit to the redshift of TXS 0506+056 can be inferred from VHE γ -ray observations using limits on the attenuation of the VHE flux due to interaction with the EBL. Details on the method are available in (25). The obtained upper

limit ranges from 0.61 to 0.98 at a 95% CL, depending on the EBL model used. These upper limits are consistent with the measured redshift of $z = 0.3365$ (28).

No γ -ray source above 1 TeV at the location of TXS 0506+056 was found in survey data of the High Altitude Water Cherenkov (HAWC) γ -ray observatory (36), either close to the time of the neutrino alert or in archival data taken since November 2014 (25).

VHE γ -ray observations are shown in Figs. 3 and 4. All measurements are consistent with the observed flux from MAGIC, considering the differences in exposure, energy range, and observation periods.

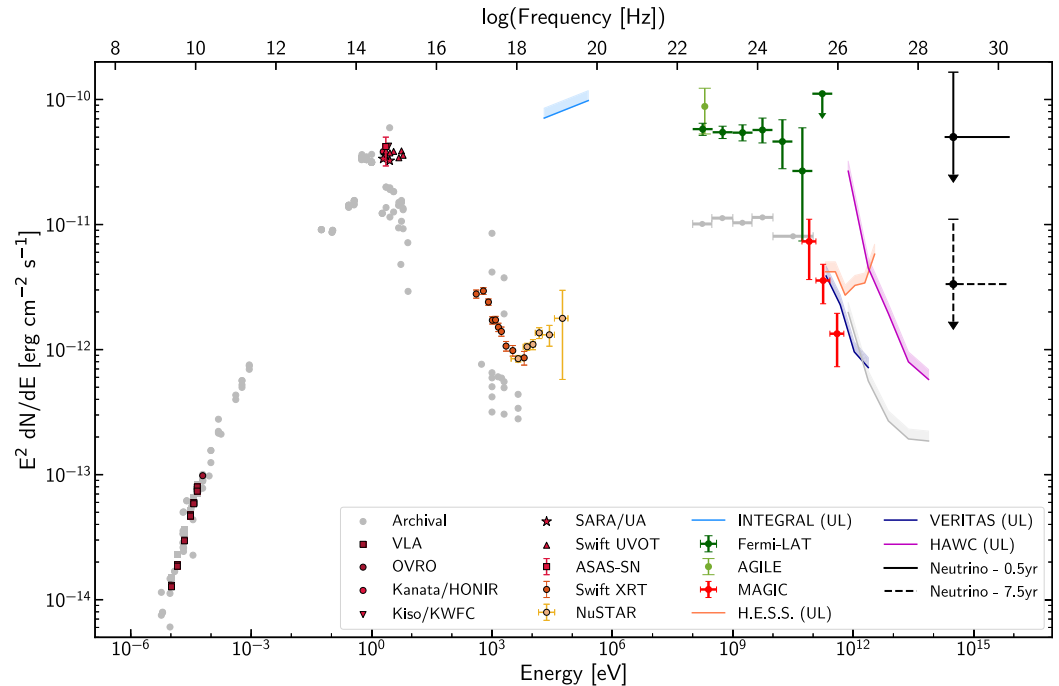
Radio, optical, and x-ray observations

The Karl G. Jansky Very Large Array (VLA) (37) observed TXS 0506+056 starting 2 weeks after the alert in several radio bands from 2 to 12 GHz (38), detecting significant radio flux variability and some spectral variability of this source. The source is also in the long-term blazar monitoring program of the Owens Valley Radio Observatory (OVRO) 40-m telescope at 15 GHz (39). The light curve shows a gradual increase in radio emission during the 18 months preceding the neutrino alert.

Optical observations were performed by the All-Sky Automated Survey for Supernovae (ASAS-SN) (40), the Liverpool Telescope (41), the

Fig. 4. Broadband spectral energy distribution for the blazar TXS 0506+056. The SED is

based on observations obtained within 14 days of the detection of the IceCube-170922A event. The $E^2 dN/dE$ vertical axis is equivalent to a vF_ν scale. Contributions are provided by the following instruments: VLA (38), OVRO (39), Kanata Hiroshima Optical and Near-Infrared camera (HONIR) (52), Kiso, and the Kiso Wide Field Camera (KWFC) (43), Southeastern Association for Research in Astronomy Observatory (SARA/UA) (53), ASAS-SN (54), *Swift* Ultraviolet and Optical Telescope (UVOT) and XRT (55), *NuSTAR* (56), *INTEGRAL* (57), *AGILE* (58), *Fermi*-LAT (16), MAGIC (35), VERITAS (59), H.E.S.S. (60), and HAWC (61). Specific observation dates and times are provided in (25). Differential flux upper limits (shown as colored bands and indicated as “UL” in the legend) are quoted at the 95% CL, while markers indicate significant detections. Archival observations are shown in gray to illustrate the historical flux level of the blazar in the radio-to-keV range as retrieved from the ASDC SED Builder (62), and in the γ -ray band as listed in the *Fermi*-LAT 3FGL catalog (23) and from an analysis of 2.5 years of HAWC data. The γ -ray observations have not been corrected for absorption owing to the EBL. SARA/UA, ASAS-SN, and Kiso/KWFC observations have not been corrected for Galactic attenuation. The electromagnetic SED displays a double-bump structure, one



peaking in the optical-ultraviolet range and the second one in the GeV range, which is characteristic of the nonthermal emission from blazars. Even within this 14-day period, there is variability observed in several of the energy bands shown (see Fig. 3), and the data are not all obtained simultaneously. Representative $v_\mu + \bar{\nu}_\mu$ neutrino flux upper limits that produce on average one detection like IceCube-170922A over a period of 0.5 (solid black line) and 7.5 years (dashed black line) are shown, assuming a spectrum of $dN/dE \propto E^{-2}$ at the most probable neutrino energy (311 TeV).

Kanata Telescope (42), the Kiso Schmidt Telescope (43), the high-resolution spectrograph (HRS) on the Southern African Large Telescope (SALT) (44), the Subaru telescope Faint Object Camera and Spectrograph (FOCAS) (45), and the X-SHOOTER instrument on the Very Large Telescope (VLT) (46). The V band flux of the source is the highest observed in recent years, and the spectral energy distribution has shifted toward blue wavelengths. Polarization was detected by Kanata in the R band at the level of 7%. Redshift determination for BL Lac objects is difficult owing to the nonthermal continuum from the nucleus outshining the spectral lines from the host galaxies. Attempts were made using optical spectra from the Liverpool, Subaru, and VLT telescopes to measure the redshift of TXS 0506+056, but only limits could be derived [see, e.g., (47)]. The redshift of TXS 0506+056 was later determined to be $z = 0.3365 \pm 0.0010$ using the Gran Telescopio Canarias (28).

X-ray observations were made by the X-Ray Telescope (XRT) on the *Neil Gehrels Swift Observatory* (0.3 to 10 keV) (48), *MAXI* Gas Slit Camera (GSC) (2 to 10 keV) (49), Nuclear Spectroscopic Telescope Array (*NuSTAR*) (3 to 79 keV) (50), and the International Gamma-Ray Astrophysics Laboratory (*INTEGRAL*) (20 to 250 keV) (51), with detections by *Swift* and *NuSTAR*. In a 2.1 square degree region around the neutrino alert, *Swift* identified nine x-ray sources, including TXS 0506+056.

Swift monitored the x-ray flux from TXS 0506+056 for 4 weeks after the alert, starting 23 September 2017 00:09:16 UT, finding clear evidence for spectral variability (see Fig. 3D). The strong increase in flux observed at VHE energies over several days up until MJD 58030 (4 October 2017) correlates well with an increase in the x-ray emission during this period of time. The spectrum of TXS 0506+056 observed in the week after the flare is compatible with the sum of two power-law spectra, a soft spectrum with index -2.8 ± 0.3 in the soft x-ray band covered by *Swift* XRT, and a hard spectrum with index -1.4 ± 0.3 in the hard x-ray band covered by *NuSTAR* (25). Extrapolated to 20 MeV, the *NuSTAR* hard-spectrum component connects smoothly to the plateau (index -2) component observed by the *Fermi*-LAT between 0.1 and 100 GeV and the soft VHE γ -ray component observed by MAGIC (compare Fig. 4). Taken together, these observations provide a mostly complete, contemporaneous picture of the source emissions from 0.3 keV to 400 GeV, more than nine orders of magnitude in photon energy.

Figures 3 and 4 summarize the multiwavelength light curves and the changes in the broadband spectral energy distribution (SED), compared to archival observations. Additional details about the radio, optical, and x-ray observations can be found in (25).

Chance coincidence probability

Data obtained from multiwavelength observations of TXS 0506+056 can be used to constrain the blazar-neutrino chance coincidence probability.

This coincidence probability is a measure of the likelihood that a neutrino alert like IceCube-170922A is correlated by chance with a flaring blazar, considering the large number of known γ -ray sources and the modest number of neutrino alerts.

Given the large number of potential neutrino source classes available, no a priori blazar-neutrino coincidence model was selected ahead of the alert. After the observation, however, several correlation scenarios were considered and tested to quantify the a posteriori significance of the observed coincidence. Testing multiple models is important as the specific assumptions about the correlation between neutrinos and γ -rays have an impact on the chance coincidence probability. In each case, the probability to obtain, by chance, a degree of correlation at least as high as that observed for IceCube-170922A was calculated using simulated neutrino alerts and the light curves of *Fermi*-LAT γ -ray sources. Given the continuous all-sky monitoring of the *Fermi*-LAT since 2008, all tests utilized 28-day binned γ -ray light curves above 1 GeV from 2257 extragalactic *Fermi*-LAT sources, derived in the same manner as used for the analysis of TXS 0506+056 γ -ray data.

To calculate the chance probabilities, a likelihood ratio test is used that allows different models of blazar-neutrino flux correlation to be evaluated in a consistent manner. All models assume that at least some of the observed γ -ray flux is produced in the same hadronic interactions that would produce high-energy neutrinos within the source. Our first model assumes that the neutrino flux is linearly correlated with the high-energy γ -ray energy flux (4). In this scenario, neutrinos are more likely to be produced during periods of bright, hard γ -ray emission. In the second model, the neutrino flux is modeled as strongly tied to variations in the observed γ -ray flux, regardless of the average flux of γ -rays. Here, a weak or a strong γ -ray source is equally likely to be a neutrino source if the neutrino is temporally correlated with variability in the γ -ray light curve. Third, we consider a correlation of the neutrino flux with the VHE γ -ray flux. Because hadronic acceleration up to a few PeV is required to explain the detected neutrino energy, VHE γ -ray sources are potential progenitors. Full details and results from these analyses are presented in (25).

The neutrino IceCube-170922A was found to arrive in a period of flaring activity in high-energy γ -rays. Prior to IceCube-170922A, nine public alerts had been issued by the IceCube real-time system. Additionally, 41 archival events have been identified among the IceCube data recorded since 2010, before the start of the real-time program in April 2016, which would have caused alerts if the real-time alert system had been in place. These events were also tested for coincidence with the γ -ray data.

Chance coincidence of the neutrino with the flare of TXS 0506+056 is disfavored at the 3σ level in any scenario where neutrino production is linearly correlated with γ -ray production or with γ -ray flux variations. This includes look-elsewhere corrections for all 10 alerts issued

previously by IceCube and the 41 archival events. One of the neutrino events that would have been sent as an alert and had a good angular resolution ($<5^\circ$) is in a spatial correlation with the γ -ray blazar 3FGL J1040.4+0615. However, this source was not in a particularly bright emission state at the detection time of the corresponding neutrino. Therefore, a substantially lower test statistic would be obtained in the chance correlation tests defined in this paper (25).

We have investigated how typical the blazar TXS 0506+056 is among those blazars that might have given rise to a coincident observation similar to the one reported here. A simulation that assumes that the neutrino flux is linearly correlated with the blazar γ -ray energy flux shows that in 14% of the signal realizations, we would find a neutrino coincident with a similarly bright γ -ray state as that observed for TXS 0506+056 (25). The detection of a single neutrino does not allow us to probe the details of neutrino production models or measure the neutrino-to- γ -ray production ratio. Further observations will be needed to unambiguously establish a correlation between high-energy neutrinos and blazars, as well as to understand the emission and acceleration mechanism in the event of a correlation.

Discussion

Blazars have often been suggested as potential sources of high-energy neutrinos. The calorimetric high-energy output of certain candidate blazars is high enough to explain individual observed IceCube events at 100-TeV to 1-PeV energies (63). Spatial coincidences between catalogs of blazars and neutrinos have been examined in (64), while (65) investigated one shower-like event with several thousand square degrees angular uncertainty observed in time coincidence with a blazar outburst. A track-like event, IceCube-160731, has been previously connected to a flaring γ -ray source (66). However, the limited evidence for a flaring source in the multiwavelength coverage did not permit an identification of the source type of the potential counterpart (66).

Owing to the precise direction of IceCube-170922A, combined with extensive multiwavelength observations, a chance correlation between a high-energy neutrino and the potential counterpart can be rejected at the 3σ level. Considering the association between IceCube-170922A and TXS 0506+056, γ -ray blazars are strong candidate sources for at least a fraction of the observed astrophysical neutrinos. Earlier studies of the cross-correlation between IceCube events and the γ -ray blazar population observed by *Fermi*-LAT demonstrated that these blazars can only produce a fraction of the observed astrophysical neutrino flux above 10 TeV (4). Although these limits constrain the contribution from blazars to the diffuse neutrino background, the potential association of one or two high-energy neutrinos to blazars over the total observing time of IceCube is fully compatible with the constraint.

Adopting standard cosmological parameters (67) $H_0 = 67.8$, $\Omega_m = 0.308$, $\Omega_\Lambda = 0.692$, where H_0 is the Hubble constant, Ω_m is the matter

density, and Ω_λ is the dark energy density, the observed redshift of $z = 0.3365$ implies an isotropic γ -ray luminosity between 0.1 and 100 GeV of 1.3×10^{47} erg s $^{-1}$ in the ± 2 weeks around the arrival time of the IceCube neutrino, and a luminosity of 2.8×10^{46} erg s $^{-1}$, averaged over all *Fermi*-LAT observations. Observations in the optical, x-ray, and VHE γ -ray bands show typical characteristics of blazar flares: strong variability on time scales of a few days and an indication of a shift of the synchrotron emission peak toward higher frequencies. VHE γ -ray emission is found to change by a factor of ~ 4 within just 3 days. Similarly, the high-energy γ -ray energy band shows flux variations up to a factor of ~ 5 from one week to the next.

No other neutrino event that would have passed the selection criteria for a high-energy alert was observed from this source since the start of IceCube observations in May 2010. The muon neutrino fluence for which we would expect to detect one high-energy alert event with IceCube in this period of time is 2.8×10^{-3} erg cm $^{-2}$. A power-law neutrino spectrum is assumed in this calculation with an index of -2 between 200 TeV and 7.5 PeV, the range between the 90% CL lower and upper limits for the energy of the observed neutrino [see (25) for details].

The fluence can be expressed as an integrated energy flux if we assume a time period during which the source was emitting neutrinos. For a source that emits neutrinos only during the ~ 6 -month period corresponding to the duration of the high-energy γ -ray flare, the corresponding average integrated muon neutrino energy flux would be 1.8×10^{-10} erg cm $^{-2}$ s $^{-1}$. Alternatively, the average integrated energy flux of a source that emits neutrinos over the whole observation period of IceCube (i.e., 7.5 years) would be 1.2×10^{-11} erg cm $^{-2}$ s $^{-1}$. These two benchmark cases are displayed in Fig. 4. In an ensemble of faint sources with a summed expectation of order 1, we would anticipate observing a neutrino even if the individual expectation value is $\ll 1$. This is expressed by the downward arrows on the neutrino flux points in Fig. 4.

The two cases discussed above correspond to average isotropic muon neutrino luminosities of 7.2×10^{46} erg s $^{-1}$ for a source that was emitting neutrinos in the ~ 6 -month period of the high-energy γ -ray flare, and 4.8×10^{45} erg s $^{-1}$ for a source that emitted neutrinos throughout the whole observation period. This is similar to the luminosity observed in γ -rays and thus broadly consistent with hadronic source scenarios (68).

A neutrino flux that produces a high-energy alert event can, over time, produce many lower-energy neutrino-induced muons in IceCube. A study of neutrino emission from TXS 0506+056 prior to the high-energy γ -ray flare, based on the investigation of these lower-energy events, is reported in a companion paper (26).

REFERENCES AND NOTES

- M. G. Aartsen et al., Evidence for high-energy extraterrestrial neutrinos at the IceCube detector. *Science* **342**, 1242856 (2013). doi: [10.1126/science.1242856](https://doi.org/10.1126/science.1242856); PMID: 24264993
- M. G. Aartsen et al., Observation and characterization of a cosmic muon neutrino flux from the Northern Hemisphere using six years of IceCube data. *Astrophys. J.* **833**, 3 (2016). doi: [10.3847/0004-637X/833/1/3](https://doi.org/10.3847/0004-637X/833/1/3)
- M. G. Aartsen et al., All-sky search for time-integrated neutrino emission from astrophysical sources with 7 yr of IceCube data. *Astrophys. J.* **835**, 151 (2017). doi: [10.3847/1538-4357/835/2/151](https://doi.org/10.3847/1538-4357/835/2/151)
- M. G. Aartsen et al., the contribution of *FERMI*-2LAC blazars to diffuse TeV–PeV neutrino flux. *Astrophys. J.* **835**, 45 (2017). doi: [10.3847/1538-4357/835/1/45](https://doi.org/10.3847/1538-4357/835/1/45)
- F. W. Stecker, C. Done, M. H. Salamon, P. Sommers, High-energy neutrinos from active galactic nuclei. *Phys. Rev. Lett.* **66**, 2697–2700 (1991). doi: [10.1103/PhysRevLett.66.2697](https://doi.org/10.1103/PhysRevLett.66.2697); PMID: 10043593
- K. Mannheim, High-energy neutrinos from extragalactic jets. *Astropart. Phys.* **3**, 295–302 (1995). doi: [10.1016/0927-6505\(94\)00044-4](https://doi.org/10.1016/0927-6505(94)00044-4)
- M. Petropoulos, S. Dimitrakoudis, P. Padovani, A. Mastichiadis, E. Resconi, Photohadronic origin of γ -ray BL Lac emission: Implications for IceCube neutrinos. *Mon. Not. R. Astron. Soc.* **448**, 2412–2429 (2015). doi: [10.1093/mnras/stv179](https://doi.org/10.1093/mnras/stv179)
- C. M. Urry, P. Padovani, Unified schemes for radio-loud active galactic nuclei. *Publ. Astron. Soc. Pac.* **107**, 803 (1995). doi: [10.1086/133630](https://doi.org/10.1086/133630)
- M.-H. Ulrich, L. Maraschi, C. M. Urry, Variability of active galactic nuclei. *Annu. Rev. Astron. Astrophys.* **35**, 445–502 (1997). doi: [10.1146/annurev.astro.35.1.445](https://doi.org/10.1146/annurev.astro.35.1.445)
- M. G. Hauser, E. Dwek, The cosmic infrared background: Measurements and implications. *Annu. Rev. Astron. Astrophys.* **39**, 249–307 (2001). doi: [10.1146/annurev.astro.39.1.249](https://doi.org/10.1146/annurev.astro.39.1.249)
- F. W. Stecker, O. C. de Jager, M. H. Salamon, TeV gamma rays from 3C 279 - A possible probe of origin and intergalactic infrared radiation fields. *Astrophys. J.* **390**, L49 (1992). doi: [10.1086/186369](https://doi.org/10.1086/186369)
- K. A. Olive et al., Review of particle physics. *Chin. Phys. (Beijing)* **C 38**, 090001 (2014). doi: [10.1088/1674-1137/38/9/090001](https://doi.org/10.1088/1674-1137/38/9/090001)
- M. G. Aartsen et al., The IceCube Neutrino Observatory: Instrumentation and online systems. *J. Instrum.* **12**, P03012 (2017). doi: [10.1088/1748-0221/12/03/P03012](https://doi.org/10.1088/1748-0221/12/03/P03012)
- M. G. Aartsen et al., The IceCube realtime alert system. *Astropart. Phys.* **92**, 30–41 (2017). doi: [10.1016/j.astropartphys.2017.05.002](https://doi.org/10.1016/j.astropartphys.2017.05.002)
- GCN/AMON Notices, <https://gcn.gsfc.nasa.gov/amon.html>; accessed: 26 April 2018.
- Y. T. Tanaka, S. Buson, D. Kocovski, *The Astronomer's Telegram* **10791** (2017).
- IceCube Collaboration, *GRB Coordinates Network/AMON Notices* 50579430_130033 (2017).
- IceCube Collaboration, *GRB Coordinates Network, Circular Service* **21916** (2017).
- G. E. Lanyi et al., The celestial reference frame at 24 and 43 GHz. I. *Astronomy. Astron. J.* **139**, 1695–1712 (2010). doi: [10.1088/0004-6256/139/5/1695](https://doi.org/10.1088/0004-6256/139/5/1695)
- M. Ageron et al., ANTARES: The first undersea neutrino telescope. *Nucl. Instrum. Methods Phys. Res. A* **656**, 11–38 (2011). doi: [10.1016/j.nima.2011.06.103](https://doi.org/10.1016/j.nima.2011.06.103)
- A. Albert et al., First all-flavor neutrino pointlike source search with the ANTARES neutrino telescope. *Phys. Rev. D* **96**, 082001 (2017). doi: [10.1103/PhysRevD.96.082001](https://doi.org/10.1103/PhysRevD.96.082001)
- D. Dornic, A. Coleiro, *The Astronomer's Telegram* **10773** (2017).
- F. Acero et al., *FERMI* Large Area Telescope Third Source Catalog. *Astrophys. J.* **218** (suppl.), 23 (2015). doi: [10.1088/0067-0049/218/2/23](https://doi.org/10.1088/0067-0049/218/2/23)
- M. Ajello et al., 3FHL: The Third Catalog of Hard *Fermi* -LAT Sources. *Astrophys. J.* **232** (suppl.), 18 (2017). doi: [10.3847/1538-4357/aa8221](https://doi.org/10.3847/1538-4357/aa8221)
- Materials and methods are available as supplementary materials.
- IceCube Collaboration, Neutrino emission from the direction of the blazar TXS 0506+056 prior to the IceCube-170922A alert. *Science* **361**, 147–151 (2018).
- W. B. Atwood et al., The Large Area Telescope on the *FERMI* Gamma-Ray Space Telescope mission. *Astrophys. J.* **697**, 1071–1102 (2009). doi: [10.1088/0004-637X/697/2/1071](https://doi.org/10.1088/0004-637X/697/2/1071)
- S. Paiano, R. Falomo, A. Treves, R. Scarpa, The redshift of the BL Lac object TXS 0506+056. *Astrophys. J.* **854**, L32 (2018). doi: [10.3847/2041-8213/aaad5e](https://doi.org/10.3847/2041-8213/aaad5e)
- M. Ackermann et al., 2FHL: The second catalog of hard *FERMI* -LAT sources. *Astrophys. J.* **222** (suppl.), 5 (2016). doi: [10.3847/0067-0049/222/1/5](https://doi.org/10.3847/0067-0049/222/1/5)
- S. Abdollahi et al., The second catalog of flaring gamma-ray sources from the Fermi All-sky Variability Analysis. *Astrophys. J.* **846**, 34 (2017). doi: [10.3847/1538-4357/aa8092](https://doi.org/10.3847/1538-4357/aa8092)
- M. Tavani et al., The *AGILE* mission. *Astron. Astrophys.* **502**, 995–1013 (2009). doi: [10.1051/0004-6361/200810527](https://doi.org/10.1051/0004-6361/200810527)
- F. Aharonian et al., Observations of the Crab Nebula with HESS. *Astron. Astrophys.* **457**, 899–915 (2006). doi: [10.1051/0004-6361:20065351](https://doi.org/10.1051/0004-6361:20065351)
- J. Holder et al., The first VERITAS telescope. *Astropart. Phys.* **25**, 391–401 (2006). doi: [10.1016/j.astropartphys.2006.04.002](https://doi.org/10.1016/j.astropartphys.2006.04.002)
- J. Aleksić et al., The major upgrade of the MAGIC telescopes. Part II: A performance study using observations of the Crab Nebula. *Astropart. Phys.* **72**, 76–94 (2016). doi: [10.1016/j.astropartphys.2015.02.005](https://doi.org/10.1016/j.astropartphys.2015.02.005)
- R. Mirzoyan, *The Astronomer's Telegram* **10817** (2017).
- A. U. Abeysekara et al., Observation of the Crab Nebula with the HAWC Gamma-Ray Observatory. *Astrophys. J.* **843**, 39 (2017). doi: [10.3847/1538-4357/aa7555](https://doi.org/10.3847/1538-4357/aa7555)
- R. A. Perley, C. J. Chandler, B. J. Butler, J. M. Wrobel, The expanded Very Large Array: A new telescope for new science. *Astrophys. J.* **739**, L1 (2011). doi: [10.1088/2041-8205/739/1/L1](https://doi.org/10.1088/2041-8205/739/1/L1)
- A. J. Tetarenko, G. R. Sivakoff, A. E. Kimball, J. C. A. Miller-Jones, *The Astronomer's Telegram* **10861** (2017).
- J. L. Richards et al., Blazars in the *FERMI* Era: The OVRO 40 m telescope monitoring program. *Astrophys. J.* **194** (suppl.), 29 (2011). doi: [10.1088/0067-0049/194/2/29](https://doi.org/10.1088/0067-0049/194/2/29)
- C. S. Kochanek et al., The All-Sky Automated Survey for Supernovae (ASAS-SN) Light Curve Server v1.0. *Publ. Astron. Soc. Pac.* **129**, 104502 (2017). doi: [10.1088/1538-3873/aa80d9](https://doi.org/10.1088/1538-3873/aa80d9)
- I. A. Steele et al., *Ground-based Telescopes*, J. M. Oschmann Jr., Ed. (2004), vol. 5489 of Proc. SPIE, pp. 679–692.
- H. Akitaya et al., *Ground-based and Airborne Instrumentation for Astronomy V* (2014), vol. 9147 of Proc. SPIE, p. 914740.
- S. Sako et al., *Ground-based and Airborne Instrumentation for Astronomy IV* (2012), vol. 8446 of Proc. SPIE, p. 84466L.
- L. A. Crause et al., *Ground-based and Airborne Instrumentation for Astronomy V* (2014), vol. 9147 of Proc. SPIE, p. 91476T.
- N. Kashikawa et al., FOCAS: The Faint Object Camera and Spectrograph for the Subaru Telescope. *Publ. Astron. Soc. Jpn.* **54**, 819–832 (2002). doi: [10.1093/pasj/54.6.819](https://doi.org/10.1093/pasj/54.6.819)
- J. Vernet et al., X-shooter, the new wide band intermediate resolution spectrograph at the ESO Very Large Telescope. *Astron. Astrophys.* **536**, A105 (2011). doi: [10.1051/0004-6361/201117752](https://doi.org/10.1051/0004-6361/201117752)
- A. Coleiro, S. Chaty, *The Astronomer's Telegram* **10840** (2017).
- D. N. Burrows et al., The Swift X-Ray Telescope. *Space Sci. Rev.* **120**, 165–195 (2005). doi: [10.1007/s11214-005-5097-2](https://doi.org/10.1007/s11214-005-5097-2)
- M. Matsuoka et al., The MAXI mission on the ISS: Science and instruments for monitoring All-Sky X-Ray Images. *Publ. Astron. Soc. Jpn.* **61**, 999–1010 (2009). doi: [10.1093/pasj/61.5.999](https://doi.org/10.1093/pasj/61.5.999)
- F. A. Harrison et al., The Nuclear Spectroscopic Telescope Array (*nuSTAR*) high-energy x-ray mission. *Astrophys. J.* **770**, 103 (2013). doi: [10.1088/0004-637X/770/2/103](https://doi.org/10.1088/0004-637X/770/2/103)
- C. Winkler et al., The INTEGRAL mission. *Astron. Astrophys.* **411**, L1–L6 (2003). doi: [10.1051/0004-6361:20031288](https://doi.org/10.1051/0004-6361:20031288)
- M. Yamanaka, et al., *The Astronomer's Telegram* **10844** (2017).
- W. Keel, M. Santander, *The Astronomer's Telegram* **10831** (2017).
- A. Franckowiak, et al., *The Astronomer's Telegram* **10794** (2017).
- A. Keivani, et al., *The Astronomer's Telegram* **10792** (2017).
- D. B. Fox, et al., *The Astronomer's Telegram* **10845** (2017).
- V. Savchenko et al., *GRB Coordinates Network, Circular Service* **21917** (2017).
- F. Lucarelli, et al., *The Astronomer's Telegram* **10801** (2017).
- R. Mukherjee, *The Astronomer's Telegram* **10833** (2017).
- M. de Naurois, H.E.S.S. Collaboration, *The Astronomer's Telegram* **10787** (2017).
- I. Martínez, I. Tobaoda, M. Hui, R. Lauer, *The Astronomer's Telegram* **10802** (2017).
- G. Stratta et al., The ASDC SED Builder Tool description and tutorial. [arXiv:1103.0749](https://arxiv.org/abs/1103.0749) [astro-ph.IM] (3 March 2011).
- F. Krauß et al., TANAMI blazars in the IceCube PeV-neutrino fields. *Astron. Astrophys.* **566**, L7 (2014). doi: [10.1051/0004-6361/201424219](https://doi.org/10.1051/0004-6361/201424219)
- P. Padovani, E. Resconi, P. Giommi, B. Arsioli, Y. L. Chang, Extreme blazars as counterparts of IceCube astrophysical neutrinos. *Mon. Not. R. Astron. Soc.* **457**, 3582–3592 (2016). doi: [10.1093/mnras/stw228](https://doi.org/10.1093/mnras/stw228)

65. M. Kadler *et al.*, Coincidence of a high-fluence blazar outburst with a PeV-energy neutrino event. *Nat. Phys.* **12**, 807–814 (2016). doi: [10.1038/nphys3715](https://doi.org/10.1038/nphys3715)
66. F. Lucarelli *et al.*, *AGILE* detection of a candidate gamma-ray precursor to the ICECUBE-160731 neutrino event. *Astrophys. J.* **846**, 121 (2017). doi: [10.3847/1538-4357/aa81c8](https://doi.org/10.3847/1538-4357/aa81c8)
67. P. A. R. Ade *et al.*, *Planck* 2015 results. *Astron. Astrophys.* **594**, A13 (2016). doi: [10.1051/0004-6361/201525830](https://doi.org/10.1051/0004-6361/201525830)
68. T. K. Gaisser, F. Halzen, T. Stanev, Particle astrophysics with high energy neutrinos. *Phys. Rep.* **258**, 173–236 (1995). doi: [10.1016/0370-1573\(95\)00003-Y](https://doi.org/10.1016/0370-1573(95)00003-Y)

ACKNOWLEDGMENTS

MAGIC: We thank the Instituto de Astrofísica de Canarias for the excellent working conditions at the Observatorio del Roque de los Muchachos in La Palma. **AGILE:** We thank ASI personnel involved in the operations and data center of the *AGILE* mission. **ASAS-SN:** We thank Las Cumbres Observatory and its staff for their continued support of ASAS-SN. **HAWC:** Thanks to S. Delay, L. Daz, and E. Murrieta for technical support. **H.E.S.S.:** We appreciate the excellent work of the technical support staff in Berlin, Zeuthen, Heidelberg, Palaiseau, Paris, Saclay, Tübingen and in Namibia in the construction and operation of the equipment. **VERITAS:** We acknowledge the excellent work of the technical support staff at the Fred Lawrence Whipple Observatory and at the collaborating institutions in the construction and operation of the instrument. **VLA/17B-403 team:** We thank the NRAO for granting us DDT VLA time to observe this source and the NRAO staff for rapidly executing the observations.

Funding

IceCube Collaboration: The IceCube collaboration gratefully acknowledge the support from the following agencies and institutions: USA—U.S. National Science Foundation—Office of Polar Programs, U.S. National Science Foundation—Physics Division, Wisconsin Alumni Research Foundation, Center for High Throughput Computing (CHTC) at the University of Wisconsin—Madison, Open Science Grid (OSG), Extreme Science and Engineering Discovery Environment (XSEDE), U.S. Department of Energy National Energy Research Scientific Computing Center, Particle astrophysics research computing center at the University of Maryland, Institute for Cyber-Enabled Research at Michigan State University, and Astroparticle physics computational facility at Marquette University; Belgium—Funds for Scientific Research (FRS-FNRS and FWO), FWO Odysseus and Big Science programmes, and Belgian Federal Science Policy Office (Belspo); Germany—Bundesministerium für Bildung und Forschung (BMBF), Deutsche Forschungsgemeinschaft (DFG), Helmholtz Alliance for Astroparticle Physics (HAP), Initiative and Networking Fund of the Helmholtz Association, Deutsches Elektronen Synchrotron (DESY), and High Performance Computing cluster of the RWTH Aachen; Sweden—Swedish Research Council, Swedish Polar Research Secretariat, Swedish National Infrastructure for Computing (SNIC), and Knut and Alice Wallenberg Foundation; Australia—Australian Research Council; Canada—Natural Sciences and Engineering Research Council of Canada, Calcul Québec, Compute Ontario, Canada Foundation for Innovation, WestGrid, and Compute Canada; Denmark—Villum Fonden, Danish National Research Foundation (DNRF); New Zealand—Marsden Fund; Japan—Japan Society for Promotion of Science (JSPS) and Institute for Global Prominent Research (IGPR) of Chiba University; Korea—National Research Foundation of Korea (NRF); Switzerland—Swiss National Science Foundation (SNSF). **Fermi-LAT collaboration:** The *Fermi-LAT* Collaboration acknowledges generous ongoing support from a number of agencies and institutes that have supported both the development and the operation of the LAT as well as scientific data analysis. These include the National Aeronautics and Space Administration and the Department of Energy in the United States, the Commissariat à l’Énergie Atomique and the Centre National de la Recherche Scientifique /Institut National de Physique Nucléaire et de Physique des Particules in France, the Agenzia Spaziale Italiana and the Istituto Nazionale di Fisica Nucleare in Italy, the Ministry of Education, Culture, Sports, Science and Technology (MEXT), High Energy Accelerator Research Organization (KEK) and Japan Aerospace Exploration Agency (JAXA) in Japan, and the K. A. Wallenberg Foundation, the Swedish Research Council and the Swedish National Space Board in Sweden. Additional support for science analysis during the operations phase is gratefully acknowledged from the Istituto Nazionale di Astrofisica in Italy and the Centre National d’Études Spatiales in France. This work performed in part under DOE Contract DE-AC02-76SF00515.

MAGIC collaboration: The financial support of the German BMBF and MPG, the Italian INFN and INAF, the Swiss National Fund SNF,

the ERDF under the Spanish MINECO (FPA2015-69818-P, FPA2012-36668, FPA2015-68378-P, FPA2015-69210-C6-2-R, FPA2015-69210-C6-4-R, FPA2015-69210-C6-6-R, AYA2015-71042-P, AYA2016-76012-C3-1-P, ESP2015-71662-C2-2-P, CSD2009-00064), and the Japanese JSPS and MEXT is gratefully acknowledged. This work was also supported by the Spanish Centro de Excelencia “Severo Ochoa” SEV-2012-0234 and SEV-2015-0548, and Unidad de Excelencia “Mara de Maetzu” MDM-2014-0369, by the Croatian Science Foundation (HrZZ) Project IP-2016-06-9782 and the University of Rijeka Project 13.12.1.3.02, by the DFG Collaborative Research Centers SFB823/C4 and SFB876/C3, the Polish National Research Centre grant UMO-2016/22/M/ST9/00382 and by the Brazilian MCTIC, CNPq and FAPERJ. **AGILE:** *AGILE* is an ASI space mission developed with scientific and programmatic support from INAF and INFN. Research partially supported through the ASI grant no. I/028/I/2.2. Part of this work is based on archival data, software or online services provided by the ASI Space Science Data Center (SSDC, previously known as ASDC). **ASAS-SN:** ASAS-SN is funded in part by the Gordon and Betty Moore Foundation through grant GBMF5490 to the Ohio State University, NSF grant AST-1515927, the Mt. Cuba Astronomical Foundation, the Center for Cosmology and AstroParticle Physics (CCAPP) at OSU, and the Chinese Academy of Sciences South America Center for Astronomy (CASSACA). A.F. was supported by the Initiative and Networking Fund of the Helmholtz Association. J.F.B. is supported by NSF grant PHY-1714479. S.D. acknowledges Project IC120009 supported by NSF. J.L.P. is supported by FONDECYT grant 1151445 and by the Ministry of Economy, Development, and Tourism’s Millennium Science Initiative through grant IC120009, awarded to The Millennium Institute of Astrophysics (MAS). This research was made possible through the use of the AAVSO Photometric All-Sky Survey (APASS), funded by the Robert Martin Ayers Sciences Fund. **HAWC:** HAWC acknowledges the support from: the US National Science Foundation (NSF) the US Department of Energy Office of High-Energy Physics; the Laboratory Directed Research and Development (LDRD) program of Los Alamos National Laboratory; Consejo Nacional de Ciencia y Tecnología (CONACyT), México (grants 271051, 232656, 260378, 179588, 239762, 254964, 271737, 258865, 243290, 132197, 281653) (Cátedras 873, 1563), Laboratorio Nacional HAWC de rayos gamma; L’OREAL Fellowship for Women in Science 2014; Red HAWC, México; DGAPA-UNAM (grants IG100317, IN111315, IN111716-3, IA102715, 109916, IA102917, IN112218); VIEP-BUAP; PIFI 2012, 2013, PROFOCIE 2014, 2015; Royal Society grant Newton Advanced Fellowship 180385; the University of Wisconsin Alumni Research Foundation; the Institute of Geophysics, Planetary Physics, and Signatures at Los Alamos National Laboratory; Polish Science Centre grant DEC-2014/13/B/ST9/945; Coordinación de la Investigación Científica de la Universidad Michoacana. **H.E.S.S.:** The support of the Namibian authorities and of the University of Namibia in facilitating the construction and operation of H.E.S.S. is gratefully acknowledged, as is the support by the German Ministry for Education and Research (BMBF), the Max Planck Society, the German Research Foundation (DFG), the Helmholtz Association, the Alexander von Humboldt Foundation, the French Ministry of Higher Education, Research and Innovation, the Centre National de la Recherche Scientifique (CNRS/IN2P3 and CNRS/INSU), the Commissariat à l’Énergie atomique et aux énergies alternatives (CEA), the UK Science and Technology Facilities Council (STFC), the Knut and Alice Wallenberg Foundation, the National Science Centre, Poland grant no. 2016/22/M/ST9/00382, the South African Department of Science and Technology and National Research Foundation, the University of Namibia, the National Commission on Research, Science & Technology of Namibia (NCRST), the Austrian Federal Ministry of Education, Science and Research and the Austrian Science Fund (FWF), the Australian Research Council (ARC), the Japan Society for the Promotion of Science and by the University of Amsterdam. This work benefited from services provided by the H.E.S.S. Virtual Organisation, supported by the national resource providers of the EGI Federation. **INTEGRAL:** *INTEGRAL* is an ESA space mission, with its instruments and science data center funded by the ESA member states (specifically the PI countries: Denmark, France, Germany, Italy, Switzerland, Spain), and with additional participation of Russia and the USA. The *INTEGRAL* SPI instrument was provided through Co-PI institutes IRAP (Toulouse/France) and MPE (Garching/Germany), the SPI project was coordinated and managed by CNES (Toulouse/France). The *INTEGRAL* IBIS instrument was provided through Co-PI institutes IAPS (Rome/Italy) and CEA (Saclay/France). The SPI-ACS detector system has been provided by MPE Garching/Germany. The SPI team is grateful to ASI, CEA, CNES, DLR, ESA, INTA, NASA, and OSTC for

their support. The Italian *INTEGRAL* team acknowledges the support of ASI/INAF agreement n. 2013-025-R.1. J.R. acknowledges support from the European Union’s Horizon 2020 Programme under the AHEAD project (grant no. 654215). R.D. acknowledges the German *INTEGRAL* support through DLR grants 50 OG 1101 and 1601. **Kanata, Kiso and Subaru observing teams:** Observations with the Kanata and Kiso Schmidt telescopes were supported by the Optical and Near-infrared Astronomy Inter-University Cooperation Program and the Grants-in-Aid of the Ministry of Education, Science, Culture, and Sport JP23740143, JP25800103, JP16H02158, JP17K14253, JP17H04830, JP26800103, JP24103003. This work was also based in part on data collected at Subaru Telescope, which is operated by the National Astronomical Observatory of Japan. **Kapteyn:** The Jacobus Kapteyn telescope is operated at the Observatorio del Roque de los Muchachos on the Spanish island of La Palma by the SARA consortium, whose member institutions (listed at <http://saraobservatory.org>) fund its operation. Refitting for remote operations and instrumentation were funded by the National Science Foundation under grant 1337566 to Texas A&M University–Commerce. **Liverpool Telescope:** The Liverpool Telescope is operated on the island of La Palma by Liverpool John Moores University in the Spanish Observatorio del Roque de los Muchachos of the Instituto de Astrofísica de Canarias with financial support from the UK Science and Technology Facilities Council. **Swift/NuSTAR:** A.K. and D.F.C. acknowledge support from the National Aeronautics and Space Administration *Swift* Guest Investigator Program under grant NNX17AI95G. The *Swift* team at the Mission Operations Center (MOC) at Penn State acknowledges support from NASA contract NAS5-00136. *Swift* is supported at the University of Leicester by the UK Space Agency. **VERITAS:** This research is supported by grants from the U.S. Department of Energy Office of Science, the U.S. National Science Foundation and the Smithsonian Institution, and by NSERC in Canada. **VLA/17B-403** The National Radio Astronomy Observatory (NRAO) is a facility of the National Science Foundation operated under cooperative agreement by Associated Universities, Inc. A.J.T. is supported by a Natural Sciences and Engineering Research Council of Canada (NSERC) Post-Graduate Doctoral Scholarship (PGSD2-490318-2016). A.J.T. and G.R.S. are supported by NSERC Discovery Grants (RGPIN-402752-2011 and RGPIN-06569-2016). J.C.A.M.J. is the recipient of an Australian Research Council Future Fellowship (FT140101082). **Author contributions:** All authors meet the journal’s authorship criteria. **IceCube:** The IceCube Collaboration designed, constructed and now operates the IceCube Neutrino Observatory. Data processing and calibration, Monte Carlo simulations of the detector and of theoretical models, and data analyses were performed by a large number of collaboration members, who also discussed and approved the scientific results presented here. The paper was reviewed by the entire collaboration before publication, and all authors approved the final version of the manuscript. **Fermi-LAT:** The *Fermi-LAT* contact authors and internal reviewers are S.B., A.F., Y.T., K.B., E.C., and M.W. **MAGIC:** E.B. is the MAGIC multimessenger contact and PI of the neutrino follow-up program. K.S. is co-converter of the MAGIC transient working group. L.F. and M.P. are the main analysts of the MAGIC data. A.M. and E.P. derived an upper limit to the redshift inferred from MAGIC data. **AGILE:** All coauthors contributed to the scientific results presented in the paper. F.L. and M.T. wrote the part of the manuscript related to the *AGILE* results. **ASAS-SN:** A.F., B.J.S., and S.H. installed an automatic follow up to IceCube triggers which provided additional early data on this event. K.Z.S., C.S.K., J.F.B., T.A.T., T.W.S.H., S.D., J.L.P., and B.J.S. built the telescopes and developed the data processing pipelines. **HAWC:** T.W. is convener of the HAWC extragalactic working group. M.H. is the HAWC multimessenger contact. I.T., R.L., and I.M.C. were the main analysts of the HAWC data. **H.E.S.S.:** A.T. is convener of the H.E.S.S. extragalactic working group. F.S. is the H.E.S.S. multimessenger contact and PI of the neutrino follow-up program. C.H. is the main analyzer of the H.E.S.S. data presented here. S.O. provided a cross-check of the presented analysis. **INTEGRAL:** V.S. performed the *INTEGRAL* analysis. C.F. is the PI of *INTEGRAL* Science Data Center. R.D. is the co-PI of the SPI instrument. E.K. is *INTEGRAL* Project Scientist. P.L. and P.U. are co-PIs of *INTEGRAL*/IBIS instrument. S.M. is responsible for the *INTEGRAL*/IBAS. All of the collaborators provided contribution to the text. **Kanata, Kiso and Subaru observing teams:** Y.T.T., Y.U., and K.O. developed the follow-up strategy to search for IceCube counterparts. T.N. and M.K. conducted the near-infrared imaging and polarimetric observations of the TXS 0506+056 using the HONIR instrument on the Kanata telescope, which were processed by the data reduction system developed by R.I. The reduced

images were mainly examined by H.M. and H.N. M.Y. reduced the polarimetric data. K.S.K. supervised all of the above. T.M. conducted the optical imaging observations of TXS 0506+056 with the KWFC instrument on the Kiso Schmidt telescope and reduced the data. Y.M. conducted optical spectroscopic observations of the TXS 0506+056 with the FOCAS spectrograph on the 8.2 m Subaru telescope. The data are reduced and examined by M.Y. and T.M. **Kapteyn:** W.C.K. obtained and reduced the optical observations at the Kapteyn telescope. **Liverpool Telescope:** I.S. and C.C. obtained, reduced, and analyzed the Liverpool Telescope spectra. **Swift/NuSTAR:** A.K. led reduction of *Swift* XRT data, and J.J.D. led reduction of *NuSTAR* data. D.B.F. carried out the joint *Swift* XRT + *NuSTAR* analysis, and A.K. managed author contributions to this section. **VERITAS:** The construction, operation, and maintenance of the VERITAS telescopes, as well as the tools to analyze the VERITAS data, are the work of the the VERITAS Collaboration as a whole. The VERITAS Collaboration contacts for this paper are M.S. and D.A.W. **VLA/17B-403:** GRS wrote the Director's Discretionary Time proposal for the VLA observations. A.J.T. performed the VLA data reduction and analyses in consultation with the rest of the team. A.J.T. and G.R.S. wrote the VLA-related text in consultation with the rest of the team. G.R.S. contributed to writing the entire paper. **Competing interests:** All collaborations declare no competing interests.

Data and materials availability: IceCube: All IceCube data related to the the results presented in this paper are provided in the supplementary materials (25). **Fermi-LAT:** The *Fermi*-LAT data are available from the *Fermi* Science Support Center <http://fermi.gsfc.nasa.gov/ssc> and https://www.glast.stanford.edu/pub_data/1483/. **MAGIC:** The MAGIC data and analysis results are accessible at <https://magic.mpp.mpg.de/public/public-data/>. **AGILE:** The *AGILE* data are available at www.ssdsc.asi.it/mmia/index.php?mission=agilemmia. Data analysis software and calibrations are available at <http://agile.ssdsc.asi.it/publicsoftware.html>. **ASAS-SN:** The ASAS-SN light curves are available at <https://asas-sn.osu.edu>. **HAWC:** The HAWC data are available at <https://data.hawc-observatory.org/datasets/ic170922/index.php>. **H.E.S.S.:** The H.E.S.S. data are available at https://www.mpi-hd.mpg.de/hfm/HESS/pages/publications/auxiliary/auxinfo_TXS0506.html. **INTEGRAL:** The *INTEGRAL* data and analysis software are available at www.isdc.unige.ch/. **Kanata, Kiso and Subaru observing teams:** Data taken with the Kiso, Kanata, and Subaru telescopes are available in the archive SMOKA <https://smoka.nao.ac.jp/>, operated by the Astronomy Data Center, National Astronomical Observatory of Japan. The Subaru data were taken in the open-use program S16B-0711. **Kapteyn:** The Kapteyn data were taken from (53). **Liverpool Telescope:** The Liverpool Telescope data are available in the telescope archive at <http://telescope.livjm.ac.uk/cgi-bin/>

It_search. Swift/NuSTAR: The *Swift* data are available at www.swift.ac.uk/archive/obs.php. The initial tiling observations, shortly after the IceCube trigger, are targetIDs 10308-10326. The monitoring ObsIDs observed from 23 September to 23 October are 00010308001, 00083368001-006, 00010308008-013. The *NuSTAR* data are available at <https://heasarc.gsfc.nasa.gov/FTP/nustar/data/obs/03/9//90301618002/> under ObsID 90301618002. **VERITAS:** The VERITAS data are available at <https://veritas.sao.arizona.edu/veritas-science/veritas-results-mainmenu-72/490-ic-result-VLA/17B-403> team: The VLA data are available through the NRAO Science Data Archive <https://archive.nrao.edu/archive/advquery.jsp> under Project Code 17B-403.

SUPPLEMENTARY MATERIALS

www.sciencemag.org/content/361/6398/eaati378/suppl/DC1
Full Author List
Materials and Methods
Tables S1 to S10
Figs. S1 to S7
References (69–116)

9 February 2018; accepted 8 June 2018
10.1126/science.aati378

Multimessenger observations of a flaring blazar coincident with high-energy neutrino IceCube-170922A

Mark AartsenMarkus AckermannJenni AdamsJuan Antonio AguilarMarkus AhlersMaryon AhrensImen Al SamaraiDavid AltmannKaren AndeenTyler AndersonIsabelle AnseauGisela AntonCarlos ArgüellesJan AuffenbergSpencer AxaniHadis BagherpourXinhua BaiJared BarronSteve BarwickVolker BaumRyan BayJames BeattyKarl Heinz BeckerJulia TjusSegev BenZviDavid BerleyElisa BernardiniDavid BessonGary BinderDaniel BindigErik BlaufussSummer BlotChristian BoehmMathis BoernerFabian BosSebastian BoeserOlga BotnerEtienne BourbeauJames BourbeauFederica BradascioJim BraunMartin BrenzkeHans-Peter BretzStephanie BronJannes Brostean-KaiserAlexander BurgmanRaffaella BusseTessa CarverEdward ChengDmitry ChirkinAsen ChristovKen ClarkLew ClassenS. CoendersGabriel CollinJanet ConradPaul CoppinPablo CorreaDoug CowenRobert CrossPranav DaveMelanie DayJoao Pedro A M de AndreCatherine De ClercqJames DelaunayHans DembinskiSam DeRidderPaolo DesiatiKrijn de VriesGwenhael DeWasseigeMeike DeWithTy DeYoungJuan Carlos Díaz-VélezVincenzo Di LorenzoHrvoje DujmovicJonathan DummMatt DunkmanEmily DvorakBenjamin EberhardtThomas EhrhardtBjorn EichmannPhilipp EllerPaul EvensonSam FaheyAli FazelyJohn FeldeKirill FilimonovChad FinleySamuel FlisAnna FranckowiakElizabeth FriedmanAlexander FritzTom GaisserJay GallagherLisa GerhardtKevin GhorbaniTheo GlauchThorsten GluesenkampAzriel GoldschmidtJavier GonzalezDarren GrantZachary GriffithChristian HaackAllan HallgrenFrancis HalzenKael HansonDustin HebeckerDavid HeeremanKlaus HelbingRobert HellauerStephanie HickfordJoshua HignightGary HillKara HoffmanRuth HoffmannTobias HoinkaBenjamin Hokanson-FasigKotoyo HoshinaFeifei HuangMatthias HuberKlas HultqvistMirco HuenefeldRaamis HussainSeongjin InNadège IovineAya IshiharaEmanuel JacobiGeorge JaparidzeMinjin JeongKyle JeroBenjamin JonesPiotr KalaczynskiWoosik KangAlexander KappesDavid KappesserTimo KargAlbrecht KarleUli KatzMatt KauerAzadeh KeivaniJohn KelleyAli KheirandishJongHyun KimMyoungchul KimThomas KintscherJoanna KirylukThomas KittlerSpencer KleinRamesh KoiralaHermann KolanoskiLutz KoepkeClaudio KopperSandro KopperJan Paul KoschinskyJason KoskinenMarek KowalskiKai KringsMike KrollGerald KrueckiSamridha KunwarNaoko Kurahashi NeilsonTakao KuwabaraAlexander KyriacouMathieu LabareJustin LanfranchiMichael LarsonFrederik LauberKayla LeonardMariola Lesiak-BzdakMartin LeuermannQinrui LiuCristian Jesús Lozano MariscalLu LuJan LuenemannWilliam LuszcakJames MadsenGiuliano MaggiKendall MahnSarah MancinaReina MaruyamaKeiichi MaseRyan MaunuKevin MeagherMorten MediciMaximilian MeierThorben MenneGonzalo MerinoThomas MeuresSandy MiareckiJessie MicallefGiulio MomenteTeresa MontaruliRoger MooreRobert MorseMarjon MoulaiRolf NahnauerPrabandha NakarmiUwe NaumannGarrett NeerHans NiederhausenSarah NowickiDave NygrenAnna PollmannAlex OlivasAongus Ó MurchadhaErin O'SullivanTomasz PalczewskiHershal PandyaDaria PankovaPeter PeifferJames PepperCarlos de los HerosDamian PielothElisa PinatMatthias PlumBuford PriceGerald PrzybylskiChristoph RaabLeif RaedeiMohamed RameezLudwig RauchKatherine RawlinsImmacolata Carmen ReaRene ReimannBen RelethfordMatt RelichElisa ResconiWolfgang RhodeMike RichmanSally RobertsonMartin RongenCarsten RottTim RuheDirk RyckboschDevyn RysewykIbrahim SafaTobias SaelzerSebastian SanchezAlexander SandrockJoakim SandroosMarcos SantanderSourav SarkarSubir SarkarKonstancja SataleckaPhilipp SchlunderTorsten SchmidtAustin SchneiderSebastian SchoenenSebastian SchonebergLisa SchumacherStephen SclanfaniDave SeckelSuruj SeunarineJan SoedingreksoDennis SoldinMing SongGlenn SpiczakChristian SpieringJuliana StachurskaMichael StamatikosTodor StanevAlexander StasikRobert SteinJoeran StettnerAnna SteuerThorsten StetzelbergerRobert StokstadAchim StoessINora Linn StrotjohannThomas StuttardGreg SullivanMichael SutherlandIgnacio TabaodaJoulien TatarFrederik TenholtSamvel Ter-AntonyanAndrii TerliukSerap TilavPat ToaleMoriah TobinChristoph ToennisSimona ToscanoDelia TosiMaria TselengidouChunFai TungAndrea TurcatiColin TurleyBunheng TyLisa UngerMarcel UsnerWard Van DriesscheDaan Van EijkNick van EijndhovenJustin VandenbrouckeSander VanheuleJakob van SantenEric VogelMatthias VraegheChristian WalckAlexander WallaceMarius WallraffFrank WandlerNancy WandkowskyAatif WazaChris WeaverMatthew WeissChris WendtJohannes WerthebachStefan WesterhoffBen WhelanNathan WhitehornKlaus WiebeChristopher WiebuschLogan WilleDawn WilliamsLizz WillsMartin WolfJoshua WoodTania WoodKurt WoschnaggDonglian XuXianwu XuYiqian XuJuan Pablo YanezGaurang YodhShigeru YoshidaTianlu YuanSoheila AbdollahiMarco AjelloRoberto AngioniLuca BaldiniJean BalletGuido BarbielliniDenis BastieriKeith BechtolRonaldo BellazziniBijan BerenjiElisabetta BissaldiRoger BlandfordRaffaella BoninoEugenio BottaciniJohan BregeonPhilippe BruelRolf BuehlerToby BurnettEric BurnsSara BusonRob CameronRegina CaputoPatrizia A. CaraveoElisabetta CavazzutiEric CharlesSina ChenTeddy CheungJames ChiangGraziano ChiaroStefano CipriniJohann Cohen-TanugiJan ConradDenise CostantinSara CutiniFilippo D'AmmandoFrancesco de PalmaSeth DigelNiccolò Di LallaMattia Di MauroLeonardo Di VenereAlberto DominguezCecilia FavuzziAnna FranckowiakYasushi FukazawaStefan FunkPiergiorgio FuscoFabio GarganoDario GasparriniNico GigliettoMatteo GiomiPaolo GiommiFrancesco GiordanoMarcello GirolettiThomas GlanzmanDavid

Use of think article is subject to the [Terms of service](#)

Science (ISSN 1095-9203) is published by the American Association for the Advancement of Science, 1200 New York Avenue NW, Washington, DC 20005. The title *Science* is a registered trademark of AAAS.

Copyright © 2018 The Authors, some rights reserved; exclusive licensee American Association for the Advancement of Science. No claim to original U.S. Government Works

GreenIsabelle GrenierMarie-Hélène GrondinSylvain GuiriecAlice HardingMasaaki HayashidaLiz HaysJohn HewittDeirdre HoranGuðlaugur JóhannessonMatthias KadlerShiki KenseiDaniel KocevskiFelicia KraussMichael KreterMichael KussGiovanni La MuraStefan LarssonLuca LatronicoMarianne Lemoine-GoumardJian LiFrancesco LongoFrancesco LoparcoMichael LovellettePasquale LubranoJeffrey MagillSimone MalderaDmitry MalyshevAlberto ManfredaMario Nicola MazziottaJulie McEneryManuel MeyerPeter MichelsonTsunefumi MizunoMaria Elena MonzaniAldo MorselliGor MoskalenkoMichela NegroEric NussRoopesh OjhaNicola OmodeiMonica OrientiElena OrlandoMichele PalatielloVaidehi PaliyaJeremy PerkinsMassimo PersicMelissa Pesce-RollinsFrederic PironTroy PorterGiacomo PrincipeSilvia RainòRiccardo RandoBindu RaniMassimiliano RazzanoSoebur RazzaqueAnita ReimerOlaf ReimerNicolas Renault-TinacciSteve RitzLeon RochesterPablo Saz ParkinsonCarmelo SgròEric J. SiskindGloria SpandrePaolo SpinelliDan SusonHiro TajimaMitsunari TakahashiYasuyuki TanakaJana ThayerDavid J. ThompsonLuigi TibaldoDiego F. TorresEleonora TorresiGino TostiEleonora TrojaJaneth Verónica ValverdeGiacomo VianelloMatthew VogelKent WoodMatthew WoodGabriela ZaharijasMax Ludwig AhnenStefano AnsoldiLucio Angelo AntonelliCornelia ArcaroDominik BaackAna Babi#Biswajit BanerjeePriyadarshini BangaleUlisses Barres de AlmeidaJuan Abel BarrioJosefa Becerra GonzálezWlodek BednarekElisa BernardiniAlessio BertiWrijupan BhattacharyyaAdrian BilandOscar BlanchGiacomo BonnoliRoberto CarosiAlessandro CarosiGiovanni CeribellaAnshu ChatterjeeSidika Merve ColakPierre ColinEduardo ColomboJose Luis ContrerasJuan CortinaStefano CovinoPaolo CumaniPaolo Da VelaFrancesco DazziAlessandro De AngelisBarbara De LottoManuel DelfinoJordi DelgadoFederico Di PieroAlberto DominguezDijana Dominis PresterDaniela DörnerMichele DoroSabrina EineckeDominik ElsaesserVandad Fallah RamazaniAlba Fernández-BarralDavid FidalgoLuca FoffanoKonstantin PfrangMaria Victoria FonsecaLluis FontChristian FruckDaniel GalindoStefano GallozziRamon J. García LópezMarkus GarczarczykMarkus GaugPaola GiammariaNikola Godinovi#Dariusz GoraDaniel GubermanDaniela HadaschAlexander HahnTarek HassanMasaaki HayashidaJavier HerreraJuergen HoseDario HrupecSusumu InoueKazuma IshioYusuke KonnoHidetoshi KuboJunko KushidaDamira LelasElina LindforsSaverio LombardiFrancesco LongoMarcos LópezCamilla MaggioPratik MajumdarMartin MakarievGalina ManevaMarina ManganaroKarl MannheimLaura MaraschiMosé MariottiManel MartínezShu MasudaDaniel MazinMilen MinevJose Miguel MirandaRazmik MirzoyanAbelardo MoralejoVictoria MorenoElena MorettiTsutomu NagayoshiVitaly NeustroevAndrzej NiedzwieckiMireia Nieves RosilloCosimo NigroKari NilssonDaniele NinciKyoshi NishijimaKoji NodaLeyre NoguésSimona PaianoJoaquim PalacioDavid PanequeRiccardo PaolettiJosep M. ParedesGiovanna PedalettiMichele PeresanoMassimo PersicPier Giorgio Prada MoroniElisa Prandinilvica PuljakJezabel RodriguezIgnasi ReichardtWolfgang RhodeMarc RibóJavier RicoChiara RighiAndrea RugliancichTakayuki SaitoKonstancja SataleckaThomas SchweizerJulian SitarekIva Šnidari#Dorota SobczynskaAntonio StamerraMarcel StrzysTihomir Suri#Mitsunari TakahashiFabrizio TavecchioPetar TemnikovTomislav Terzi#Masahiro TeshimaNuria Torres-AlbàAldo TrevesShimpei TsujimotoGaia VanzoMonica Vazquez Acostalevgen VovkJohn E. WardMartin WillDarko Zari#Alberto FranceschiniFabrizio LucarelliMarco TavaniGiovanni Pianolma DonnarummaCarlotta PittoriFrancesco VerrecchiaGuido BarbielliniAndrea BulgarelliPatrizia CaraveoPaolo Walter CattaneoSergio ColafrancescoEnrico CostaGuido Di CoccoAttilio FerrariFulvio GianottiAndrea GiulianiPaolo LipariSandro MereghettiAldo MorselliLuigi PaccianiFranco PaolettiNicolò ParmiggianiAlberto PellizzoniPiergiorgio PicozzaMaura PiliaAndrea RappoldiAlessio TroisStefano VercelloneValerio VittoriniAndrea AlbertRuben AlfaroCésar ÁlvarezRoberto ArceoJuan Carlos Arteaga VelázquezDaniel Omar Avila RojasHugo Alberto Ayala SolaresAna Delia BecerrilErnesto Belmont-MorenoAbel BernalKaren S. Caballero MoraTomás Capistrán RojasAlberto CarramiñanaSabrina CasanovaMario Alberto Castillo MaldonadoUmberto CottiJorge CotzomiSara Coutiño de LeónCederik León De León AcuñaEduardo De la FuenteRaquel Diaz HernandezSimone Dichiarabrenda DingusMichael DuVernoisJuan Carlos Díaz VelezRobert EllsworthKristi EngelDaniel W. FiorinoHenrike FleischhackNissim Illich FraijaJosé Andrés García GonzálezFernando GarfiasMaria Magdalena GonzálezAdiv González MuñozJordan A. GoodmanZigfried Hampel-AriasJ. Patrick HardingSergio Hernandez CadenaBinita HonaFiliberto Hueyotl-ZahuantitlaMichelle HuiPetra HüntemeyerArturo IriarteArmelle Jardin-BlicqVikas JoshiSarah KaufmannGerd J. KundeAlejandro LaraRobert LauerWilliam LeeDirk LennarzHermes León VargasJim LinnemannAnna Lia LonginottiGilgamesh Luis-RayaRene Luna-GarcíaKelly MaloneSamuel Stephens MarinelliOscar MartinezIsrael Martinez CastellanosHumberto Martínez HuertaJesús Martínez CastroJohn MatthewsPedro Miranda-RomagnoliEduardo Moreno BarbosaMiguel MostafaAmid NayerhodaLukas NellenMichael NewboldMehr Un NisaRoberto Noriega-PapaquiRodrigo PelayoJohn PretzEucario Gonzalo Pérez PérezZhixiang RenChang Dong RhoColas RivièreDaniel Rosa GonzálezMatthew RosenbergEdna Ruiz-VelascoEnrique Ruiz-VelascoFrancisco Salesa GreusAndres SandovalMichael SchneiderHarm SchoorlemmerGus SinnisAndrew James SmithWayne SpringerPooja SurajbaliOmar TibollaKirsten TollefsonIbrahim TorresLuis VillaseñorThomas WeisgarberFelix WernerTolga YapiciGaurang YodhArnulfo ZepedaHao ZhouJuan de Dios Álvarez RomeroH. AbdallaE. O. AngünerC. ArmandM. BackesY. BecheriniD. BergeM. BöttcherC. BoissonJ. BolmontS. BonnefoyP. BordasF. BrunM. BüchleT. BulikS. CaroffA. CarosiS. CasanovaM. CerrutiN. ChakrabortyS. ChandraA. ChenS. ColafrancescoL. D.

Use of think article is subject to the [Terms of service](#)

Science (ISSN 1095-9203) is published by the American Association for the Advancement of Science, 1200 New York Avenue NW, Washington, DC 20005. The title *Science* is a registered trademark of AAAS.

Copyright © 2018 The Authors, some rights reserved; exclusive licensee American Association for the Advancement of Science. No claim to original U.S. Government Works

DavidsC. DeilJ. DevinA. Djannati-AtaïK. EgbertsG. EmeryS. EschbachA. FiassonG. FontaineS. FunkM. FüßlingY. A. GallantF. GatéG. GiavittoD. GlawionJ. F. GlicensteinD. GottschallM.-H. GrondinM. HauptG. HenriJ. A. HintonC. HoischenT. L. HolchD. HuberM. JamroznyD. JankowskyF. JankowskyL. JouvinI. Jung-RichardtD. KerszbergB. KhélifiJ. KingS. KlepserW. Klu#niakNu. KominM. KrausJ. LefaucheurA. LemièrM. Lemoine-GoumardJ.-P. LenainE. LeserT. LohseR. López-CotoM. LorentzI. LypovaV. MarandonG. Guillem Martí-DevesaG. MaurinA.M.W. MitchellR. ModerskiM. MohamedL. MohrmannE. MoulinT. MurachM. de NauroisF. NiederwangerJ. NiemiecL. OakesP. O'BrienS. OhmM. OstrowskiI. OyaM. PanterR. D. ParsonsC. PerennesQ. PielS. PitaV. PoireauA. Priyana NoelH. ProkophG. PühlhoferA. QuirrenbachS. RaabR. RauthM. RenaudF. RiegerL. RinchiusoC. RomoliG. RowellB. RudakD. A. SanchezM. SasakiR. SchlickeiserF. SchüsslerA. SchulzJ. SchwankeM. Seglar-ArroyoN. ShafiR. SimoniH. SolC. StegmannC. SteppaT. TavernierA. M. TaylorD. TizianiC. TrichardM. TsirouC. van EldikC. van RensburgB. van SoelenJ. VehP. VincentF. VoisinS. J. WagnerR. M. WagnerA. WierzcholskaR. ZaninA. A. ZdziarskiA. ZechA. ZieglerJ. ZornN. ZywucaV. SavchenkoC. FerrignoA. BazzanoR. DiehlE. KuulkersP. LaurentS. MereghettiL. NatalucciF. PanessaJ. RodiP. UbertiniTomoki MorokumaKouji OhtaYasuyuki T. TanakaHiroki MoriMasayuki YamanakaKoji S. KawabataYousuke UtsumiTatsuya NakaokaMiho KawabataHiroki NagashimaMichitoshi YoshidaYoshiki MatsuokaRyosuke ItohWilliam KeelChristopher CopperwheatIain SteeleS. Bradley CenkoPhilip EvansDerek FoxJamie KenneaFrancis MarshallJulian OsborneAaron TohuvavohuColin TurleyDouglas CowenJames DeLaunayAzadeh KeivaniMarcos SantanderAnushka AbeysekeraAvery ArcherWystan BenbowRalph BirdAryeh BrillRobert BroseMatthew BuchoveckyJames BuckleyViatcheslav BugaevJodi ChristiansenMichael ConnollyWei CuiMichael DanielManel ErrandoAbraham FalconeQi FengJohn FinleyLucy FortsonAmy FurnissOrel GuetaMoritz HüttenOlivier HervetGareth HughesThomas HumenskyCaitlin JohnsonPhilip KaaretPayel KarNathan Kelley-HoskinsMary KertzmanDavid KiedaMaria KrauseFrank KrennrichSajan KumarMark LangTony LinGernot MaierSteven McArthurPatrick MoriartyReshmi MukherjeeDaniel NietoStephen O'BrienRene OngAdam OtteNahee ParkAndriy PetrashykhMartin PohlAlexis PopkowElisa PueschelJohn QuinnKenneth RaganPaul ReynoldsGregory RichardsEmmet RoacheCameron RultenIftach SadehMarcos SantanderSkyler ScottGlenn SembroskiKarlen ShahinyanLurii SushchSamuel TrépanierJonathan TylerVladimir VassilievScott WakelyAmanda WeinsteinRita WellsPatrick WilcoxAlina WilhelmDavid WilliamsBenjamin ZitzerAlexandra TetarenkoAmy KimballJames Miller-JonesGregory Sivakoff

Science, 361 (6398), eaat1378. • DOI: 10.1126/science.aat1378

Neutrino emission from a flaring blazar

Neutrinos interact only very weakly with matter, but giant detectors have succeeded in detecting small numbers of astrophysical neutrinos. Aside from a diffuse background, only two individual sources have been identified: the Sun and a nearby supernova in 1987. A multiteam collaboration detected a high-energy neutrino event whose arrival direction was consistent with a known blazar—a type of quasar with a relativistic jet oriented directly along our line of sight. The blazar, TXS 0506+056, was found to be undergoing a gamma-ray flare, prompting an extensive multiwavelength campaign. Motivated by this discovery, the IceCube collaboration examined lower-energy neutrinos detected over the previous several years, finding an excess emission at the location of the blazar. Thus, blazars are a source of astrophysical neutrinos.

Science, this issue p. 147, p. eaat1378

View the article online

<https://www.science.org/doi/10.1126/science.aat1378>

Permissions

<https://www.science.org/help/reprints-and-permissions>

Use of think article is subject to the [Terms of service](#)

Science (ISSN 1095-9203) is published by the American Association for the Advancement of Science, 1200 New York Avenue NW, Washington, DC 20005. The title *Science* is a registered trademark of AAAS.

Copyright © 2018 The Authors, some rights reserved; exclusive licensee American Association for the Advancement of Science. No claim to original U.S. Government Works



Multi-messenger Observations of a Binary Neutron Star Merger*

LIGO Scientific Collaboration and Virgo Collaboration, Fermi GBM, INTEGRAL, IceCube Collaboration, AstroSat Cadmium Zinc Telluride Imager Team, IPN Collaboration, The Insight-HXMT Collaboration, ANTARES Collaboration, The Swift Collaboration, AGILE Team, The 1M2H Team, The Dark Energy Camera GW-EM Collaboration and the DES Collaboration, The DLT40 Collaboration, GRAWITA: GRAvitational Wave Inaf TeAm, The Fermi Large Area Telescope Collaboration, ATCA: Australia Telescope Compact Array, ASKAP: Australian SKA Pathfinder, Las Cumbres Observatory Group, OzGrav, DWF (Deeper, Wider, Faster Program), AST3, and CAASTRO Collaborations, The VINROUGE Collaboration, MASTER Collaboration, J-GEM, GROWTH, JAGWAR, Caltech-NRAO, TTU-NRAO, and NuSTAR Collaborations, Pan-STARRS, The MAXI Team, TZAC Consortium, KU Collaboration, Nordic Optical Telescope, ePESSTO, GROND, Texas Tech University, SALT Group, TOROS: Transient Robotic Observatory of the South Collaboration, The BOOTES Collaboration, MWA: Murchison Widefield Array, The CALET Collaboration, IKI-GW Follow-up Collaboration, H.E.S.S. Collaboration, LOFAR Collaboration, LWA: Long Wavelength Array, HAWC Collaboration, The Pierre Auger Collaboration, ALMA Collaboration, Euro VLBI Team, Pi of the Sky Collaboration, The Chandra Team at McGill University, DFN: Desert Fireball Network, ATLAS, High Time Resolution Universe Survey, RIMAS and RATIR, and SKA South Africa/MeerKAT (See the end matter for the full list of authors.)

Received 2017 October 3; revised 2017 October 6; accepted 2017 October 6; published 2017 October 16

Abstract

On 2017 August 17 a binary neutron star coalescence candidate (later designated GW170817) with merger time 12:41:04 UTC was observed through gravitational waves by the Advanced LIGO and Advanced Virgo detectors. The *Fermi* Gamma-ray Burst Monitor independently detected a gamma-ray burst (GRB 170817A) with a time delay of ~ 1.7 s with respect to the merger time. From the gravitational-wave signal, the source was initially localized to a sky region of 31 deg^2 at a luminosity distance of 40_{-8}^{+8} Mpc and with component masses consistent with neutron stars. The component masses were later measured to be in the range 0.86 to $2.26 M_{\odot}$. An extensive observing campaign was launched across the electromagnetic spectrum leading to the discovery of a bright optical transient (SSS17a, now with the IAU identification of AT 2017gfo) in NGC 4993 (at ~ 40 Mpc) less than 11 hours after the merger by the One-Meter, Two Hemisphere (1M2H) team using the 1 m Swope Telescope. The optical transient was independently detected by multiple teams within an hour. Subsequent observations targeted the object and its environment. Early ultraviolet observations revealed a blue transient that faded within 48 hours. Optical and infrared observations showed a redward evolution over ~ 10 days. Following early non-detections, X-ray and radio emission were discovered at the transient's position ~ 9 and ~ 16 days, respectively, after the merger. Both the X-ray and radio emission likely arise from a physical process that is distinct from the one that generates the UV/optical/near-infrared emission. No ultra-high-energy gamma-rays and no neutrino candidates consistent with the source were found in follow-up searches. These observations support the hypothesis that GW170817 was produced by the merger of two neutron stars in NGC 4993 followed by a short gamma-ray burst (GRB 170817A) and a kilonova/macronova powered by the radioactive decay of *r*-process nuclei synthesized in the ejecta.

Key words: gravitational waves – stars: neutron

1. Introduction

Over 80 years ago Baade & Zwicky (1934) proposed the idea of neutron stars, and soon after, Oppenheimer & Volkoff (1939) carried out the first calculations of neutron star models. Neutron stars entered the realm of observational astronomy in the 1960s by providing a physical interpretation of X-ray emission from Scorpius X-1 (Giacconi et al. 1962; Shklovsky 1967) and of radio pulsars (Gold 1968; Hewish et al. 1968; Gold 1969).

The discovery of a radio pulsar in a double neutron star system by Hulse & Taylor (1975) led to a renewed interest in binary stars and compact-object astrophysics, including the

development of a scenario for the formation of double neutron stars and the first population studies (Flannery & van den Heuvel 1975; Masevitch et al. 1976; Clark 1979; Clark et al. 1979; Dewey & Cordes 1987; Lipunov et al. 1987; for reviews see Kalogera et al. 2007; Postnov & Yungelson 2014). The Hulse-Taylor pulsar provided the first firm evidence (Taylor & Weisberg 1982) of the existence of gravitational waves (Einstein 1916, 1918) and sparked a renaissance of observational tests of general relativity (Damour & Taylor 1991, 1992; Taylor et al. 1992; Wex 2014). Merging binary neutron stars (BNSs) were quickly recognized to be promising sources of detectable gravitational waves, making them a primary target for ground-based interferometric detectors (see Abadie et al. 2010 for an overview). This motivated the development of accurate models for the two-body, general-relativistic dynamics (Blanchet et al. 1995; Buonanno & Damour 1999; Pretorius 2005; Baker et al. 2006; Campanelli et al. 2006; Blanchet 2014) that are critical for detecting and interpreting gravitational waves (Abbott et al. 2016c, 2016d, 2016e, 2017a, 2017c, 2017d).

* Any correspondence should be addressed to lvc.publications@ligo.org.



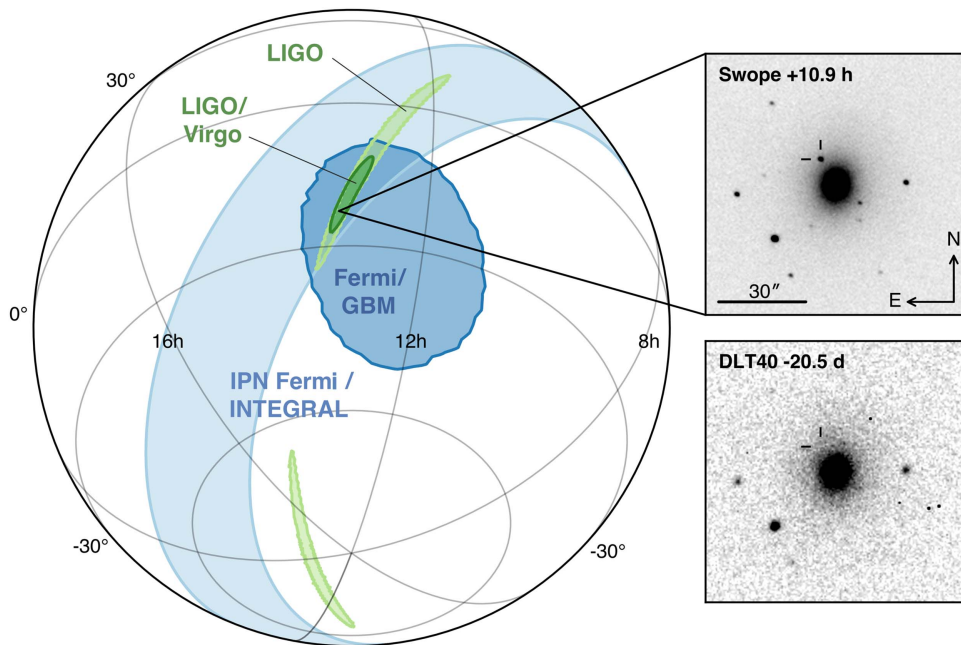


Figure 1. Localization of the gravitational-wave, gamma-ray, and optical signals. The left panel shows an orthographic projection of the 90% credible regions from LIGO (190 deg²; light green), the initial LIGO-Virgo localization (31 deg²; dark green), IPN triangulation from the time delay between *Fermi* and *INTEGRAL* (light blue), and *Fermi*-GBM (dark blue). The inset shows the location of the apparent host galaxy NGC 4993 in the Swope optical discovery image at 10.9 hr after the merger (top right) and the DLT40 pre-discovery image from 20.5 days prior to merger (bottom right). The reticle marks the position of the transient in both images.

In the mid-1960s, gamma-ray bursts (GRBs) were discovered by the Vela satellites, and their cosmic origin was first established by Klebesadel et al. (1973). GRBs are classified as *long* or *short*, based on their duration and spectral hardness (Dezalay et al. 1992; Kouveliotou et al. 1993). Uncovering the progenitors of GRBs has been one of the key challenges in high-energy astrophysics ever since (Lee & Ramirez-Ruiz 2007). It has long been suggested that short GRBs might be related to neutron star mergers (Goodman 1986; Paczynski 1986; Eichler et al. 1989; Narayan et al. 1992).

In 2005, the field of short gamma-ray burst (sGRB) studies experienced a breakthrough (for reviews see Nakar 2007; Berger 2014) with the identification of the first host galaxies of sGRBs and multi-wavelength observation (from X-ray to optical and radio) of their afterglows (Berger et al. 2005; Fox et al. 2005; Gehrels et al. 2005; Hjorth et al. 2005b; Villasenor et al. 2005). These observations provided strong hints that sGRBs might be associated with mergers of neutron stars with other neutron stars or with black holes. These hints included: (i) their association with both elliptical and star-forming galaxies (Barthelmy et al. 2005; Prochaska et al. 2006; Berger et al. 2007; Ofek et al. 2007; Troja et al. 2008; D’Avanzo et al. 2009; Fong et al. 2013), due to a very wide range of delay times, as predicted theoretically (Bagot et al. 1998; Fryer et al. 1999; Belczynski et al. 2002); (ii) a broad distribution of spatial offsets from host-galaxy centers (Berger 2010; Fong & Berger 2013; Tunnicliffe et al. 2014), which was predicted to arise from supernova kicks (Narayan et al. 1992; Bloom et al. 1999); and (iii) the absence of associated supernovae (Fox et al. 2005; Hjorth et al. 2005c, 2005a; Soderberg et al. 2006; Kocevski et al. 2010; Berger et al. 2013a). Despite these strong hints, proof that sGRBs were powered by neutron star mergers remained elusive, and interest intensified in following up gravitational-wave detections electromagnetically (Metzger & Berger 2012; Nissanke et al. 2013).

Evidence of beaming in some sGRBs was initially found by Soderberg et al. (2006) and Burrows et al. (2006) and confirmed

by subsequent sGRB discoveries (see the compilation and analysis by Fong et al. 2015 and also Troja et al. 2016). Neutron star binary mergers are also expected, however, to produce isotropic electromagnetic signals, which include (i) early optical and infrared emission, a so-called kilonova/macronova (hereafter kilonova; Li & Paczyński 1998; Kulkarni 2005; Rosswog 2005; Metzger et al. 2010; Roberts et al. 2011; Barnes & Kasen 2013; Kasen et al. 2013; Tanaka & Hotokezaka 2013; Grossman et al. 2014; Barnes et al. 2016; Tanaka 2016; Metzger 2017) due to radioactive decay of rapid neutron-capture process (*r*-process) nuclei (Lattimer & Schramm 1974, 1976) synthesized in dynamical and accretion-disk-wind ejecta during the merger; and (ii) delayed radio emission from the interaction of the merger ejecta with the ambient medium (Nakar & Piran 2011; Piran et al. 2013; Hotokezaka & Piran 2015; Hotokezaka et al. 2016). The late-time infrared excess associated with GRB 130603B was interpreted as the signature of *r*-process nucleosynthesis (Berger et al. 2013b; Tanvir et al. 2013), and more candidates were identified later (for a compilation see Jin et al. 2016).

Here, we report on the global effort⁹⁵⁸ that led to the first joint detection of gravitational and electromagnetic radiation from a single source. An ~ 100 s long gravitational-wave signal (GW170817) was followed by an sGRB (GRB 170817A) and an optical transient (SSS17a/AT 2017gfo) found in the host galaxy NGC 4993. The source was detected across the electromagnetic spectrum—in the X-ray, ultraviolet, optical, infrared, and radio bands—over hours, days, and weeks. These observations support the hypothesis that GW170817 was produced by the merger of two neutron stars in NGC 4993, followed by an sGRB and a kilonova powered by the radioactive decay of *r*-process nuclei synthesized in the ejecta.

⁹⁵⁸ A follow-up program established during initial LIGO-Virgo observations (Abadie et al. 2012) was greatly expanded in preparation for Advanced LIGO-Virgo observations. Partners have followed up binary black hole detections, starting with GW150914 (Abbott et al. 2016a), but have discovered no firm electromagnetic counterparts to those events.

2. A Multi-messenger Transient

On 2017 August 17 12:41:06 UTC the *Fermi* Gamma-ray Burst Monitor (GBM; Meegan et al. 2009) onboard flight software triggered on, classified, and localized a GRB. A Gamma-ray Coordinates Network (GCN) Notice (Fermi-GBM 2017) was issued at 12:41:20 UTC announcing the detection of the GRB, which was later designated GRB 170817A (von Kienlin et al. 2017). Approximately 6 minutes later, a gravitational-wave candidate (later designated GW170817) was registered in low latency (Cannon et al. 2012; Messick et al. 2017) based on a single-detector analysis of the Laser Interferometer Gravitational-wave Observatory (LIGO) Hanford data. The signal was consistent with a BNS coalescence with merger time, t_c , 12:41:04 UTC, less than 2 s before GRB 170817A. A GCN Notice was issued at 13:08:16 UTC. Single-detector gravitational-wave triggers had never been disseminated before in low latency. Given the temporal coincidence with the *Fermi*-GBM GRB, however, a GCN Circular was issued at 13:21:42 UTC (LIGO Scientific Collaboration & Virgo Collaboration et al. 2017a) reporting that a highly significant candidate event consistent with a BNS coalescence was associated with the time of the GRB⁹⁵⁹. An extensive observing campaign was launched across the electromagnetic spectrum in response to the *Fermi*-GBM and LIGO–Virgo detections, and especially the subsequent well-constrained, three-dimensional LIGO–Virgo localization. A bright optical transient (SSS17a, now with the IAU identification of AT 2017gfo) was discovered in NGC 4993 (at ~ 40 Mpc) by the 1M2H team (August 18 01:05 UTC; Coulter et al. 2017a) less than 11 hr after the merger.

2.1. Gravitational-wave Observation

GW170817 was first detected online (Cannon et al. 2012; Messick et al. 2017) as a single-detector trigger and disseminated through a GCN Notice at 13:08:16 UTC and a GCN Circular at 13:21:42 UTC (LIGO Scientific Collaboration & Virgo Collaboration et al. 2017a). A rapid re-analysis (Nitz et al. 2017a, 2017b) of data from LIGO-Hanford, LIGO-Livingston, and Virgo confirmed a highly significant, coincident signal. These data were then combined to produce the first three-instrument skymap (Singer & Price 2016; Singer et al. 2016) at 17:54:51 UTC (LIGO Scientific Collaboration & Virgo Collaboration et al. 2017b), placing the source nearby, at a luminosity distance *initially* estimated to be 40_{-8}^{+8} Mpc in an elongated region of ≈ 31 deg² (90% credibility), centered around R.A. $\alpha(\text{J2000.0}) = 12^{\text{h}}57^{\text{m}}$ and decl. $\delta(\text{J2000.0}) = -17^{\circ}51'$. Soon after, a coherent analysis (Veitch et al. 2015) of the data from the detector network produced a skymap that was distributed at 23:54:40 UTC (LIGO Scientific Collaboration & Virgo Collaboration et al. 2017c), consistent with the initial one: a ≈ 34 deg² sky region at 90% credibility centered around $\alpha(\text{J2000.0}) = 13^{\text{h}}09^{\text{m}}$ and $\delta(\text{J2000.0}) = -25^{\circ}37'$.

The offline gravitational-wave analysis of the LIGO-Hanford and LIGO-Livingston data identified GW170817 with a false-alarm rate of less than one per 8.0×10^4 (Abbott et al. 2017c). This analysis uses post-Newtonian waveform models (Blanchet et al. 1995, 2004, 2006; Bohé et al. 2013) to construct a matched-filter search (Sathyaprakash & Dhurandhar 1991; Cutler et al. 1993; Allen et al. 2012) for gravitational waves from the coalescence of compact-object binary systems in the (detector frame) total mass range 2–500 M_{\odot} . GW170817 lasted for ~ 100 s in the detector sensitivity band. The signal reached Virgo first,

then LIGO-Livingston 22 ms later, and after 3 ms more, it arrived at LIGO-Hanford. GW170817 was detected with a combined signal-to-noise ratio across the three-instrument network of 32.4. For comparison, GW150914 was observed with a signal-to-noise ratio of 24 (Abbott et al. 2016c).

The properties of the source that generated GW170817 (see Abbott et al. 2017c for full details; here, we report parameter ranges that span the 90% credible interval) were derived by employing a coherent Bayesian analysis (Veitch et al. 2015; Abbott et al. 2016b) of the three-instrument data, including marginalization over calibration uncertainties and assuming that the signal is described by waveform models of a binary system of compact objects in quasi-circular orbits (see Abbott et al. 2017c and references therein). The waveform models include the effects introduced by the objects' intrinsic rotation (spin) and tides. The source is located in a region of 28 deg² at a distance of 40_{-14}^{+8} Mpc, see Figure 1, consistent with the early estimates disseminated through GCN Circulares (LIGO Scientific Collaboration & Virgo Collaboration et al. 2017b, 2017c). The misalignment between the total angular momentum axis and the line of sight is $\leq 56^{\circ}$.

The (source-frame⁹⁶⁰) masses of the primary and secondary components, m_1 and m_2 , respectively, are in the range $m_1 \in (1.36\text{--}2.26)M_{\odot}$ and $m_2 \in (0.86\text{--}1.36)M_{\odot}$. The chirp mass,⁹⁶¹ \mathcal{M} , is the mass parameter that, at the leading order, drives the frequency evolution of gravitational radiation in the inspiral phase. This dominates the portion of GW170817 in the instruments' sensitivity band. As a consequence, it is the best measured mass parameter, $\mathcal{M} = 1.188_{-0.002}^{+0.004} M_{\odot}$. The total mass is $2.82_{-0.09}^{+0.47} M_{\odot}$, and the mass ratio m_2/m_1 is bound to the range 0.4–1.0. These results are consistent with a binary whose components are neutron stars. White dwarfs are ruled out since the gravitational-wave signal sweeps through 200 Hz in the instruments' sensitivity band, implying an orbit of size ~ 100 km, which is smaller than the typical radius of a white dwarf by an order of magnitude (Shapiro & Teukolsky 1983). However, for this event gravitational-wave data *alone* cannot rule out objects more compact than neutron stars such as quark stars or black holes (Abbott et al. 2017c).

2.2. Prompt Gamma-Ray Burst Detection

The first announcement of GRB 170817A came from the GCN Notice (Fermi-GBM 2017) automatically generated by *Fermi*-GBM at 12:41:20 UTC, just 14 s after the detection of the GRB at $T_0 = 12:41:06$ UTC. GRB 170817A was detected by the *International Gamma-Ray Astrophysics Laboratory* (*INTEGRAL*) spacecraft using the Anti-Coincidence Shield (von Kienlin et al. 2003) of the spectrometer on board *INTEGRAL* (SPI), through an offline search initiated by the LIGO–Virgo and *Fermi*-GBM reports. The final *Fermi*-GBM localization constrained GRB 170817A to a region with highest probability at $\alpha(\text{J2000.0}) = 12^{\text{h}}28^{\text{m}}$ and $\delta(\text{J2000.0}) = -30^{\circ}$ and 90% probability region covering ~ 1100 deg² (Goldstein et al. 2017a). The difference between the binary merger and the

⁹⁵⁹ The trigger was recorded with LIGO–Virgo ID G298048, by which it is referred throughout the GCN Circulares.

⁹⁶⁰ Any mass parameter $m^{(\text{det})}$ derived from the observed signal is measured in the detector frame. It is related to the mass parameter, m , in the source frame by $m^{(\text{det})} = (1+z)m$, where z is the source's redshift. Here, we always report source-frame mass parameters, assuming standard cosmology (Ade et al. 2016) and correcting for the motion of the solar System barycenter with respect to the cosmic microwave background (Fixsen 2009). From the gravitational-wave luminosity distance measurement, the redshift is determined to be $z = 0.008_{-0.003}^{+0.002}$. For full details see Abbott et al. (2016b, 2017c, 2017e).

⁹⁶¹ The binary's chirp mass is defined as $\mathcal{M} = (m_1 m_2)^{3/5} / (m_1 + m_2)^{1/5}$.

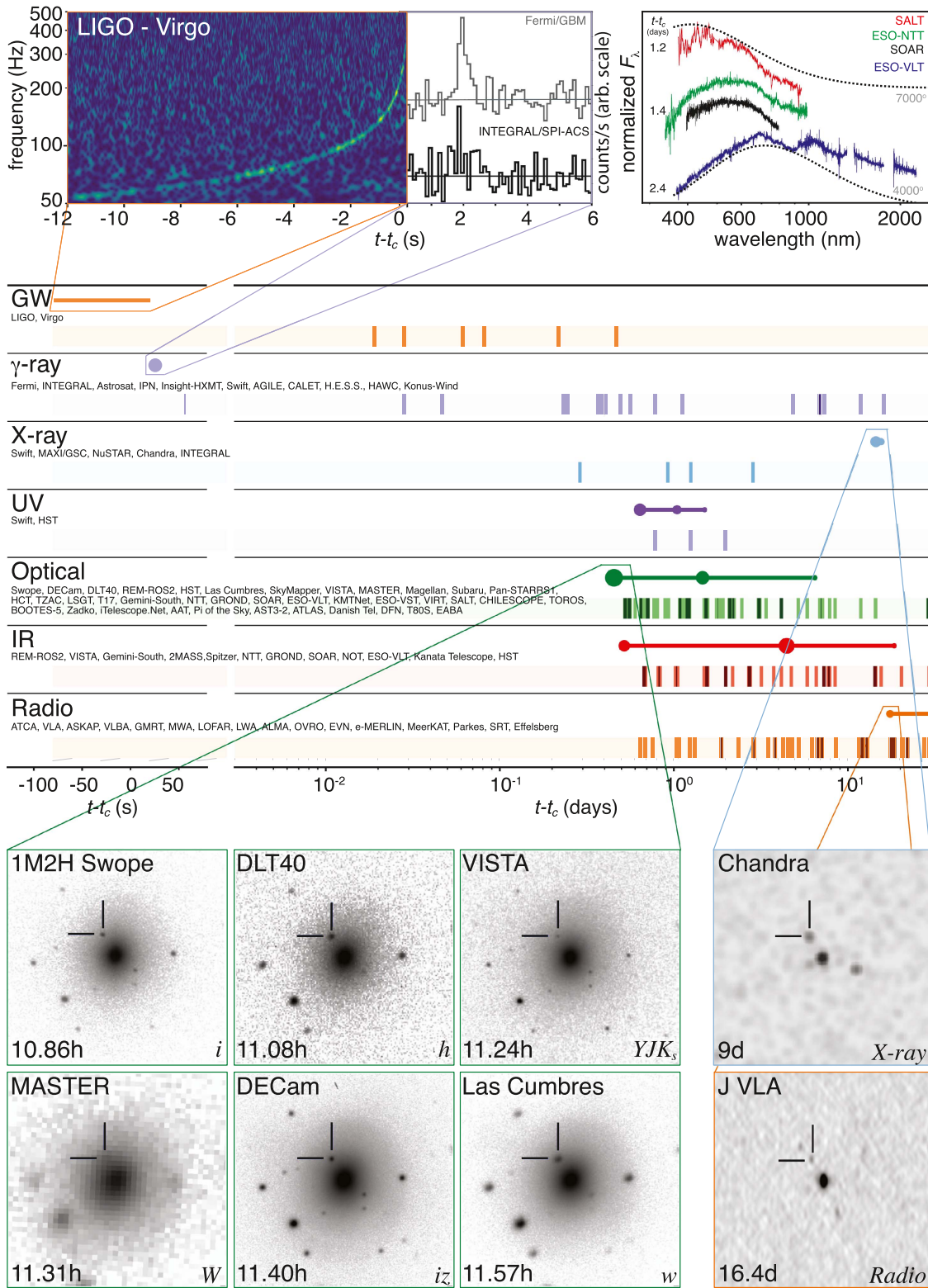


Figure 2. Timeline of the discovery of GW170817, GRB 170817A, SSS17a/AT 2017gfo, and the follow-up observations are shown by messenger and wavelength relative to the time t_c of the gravitational-wave event. Two types of information are shown for each band/messenger. First, the shaded dashes represent the times when information was reported in a GCN Circular. The names of the relevant instruments, facilities, or observing teams are collected at the beginning of the row. Second, representative observations (see Table 1) in each band are shown as solid circles with their areas approximately scaled by brightness; the solid lines indicate when the source was detectable by at least one telescope. Magnification insets give a picture of the first detections in the gravitational-wave, gamma-ray, optical, X-ray, and radio bands. They are respectively illustrated by the combined spectrogram of the signals received by LIGO-Hanford and LIGO-Livingston (see Section 2.1), the *Fermi*-GBM and *INTEGRAL*/SPI-ACS lightcurves matched in time resolution and phase (see Section 2.2), 1.5×1.5 postage stamps extracted from the initial six observations of SSS17a/AT 2017gfo and four early spectra taken with the SALT (at $t_c + 1.2$ days; Buckley et al. 2017; McCully et al. 2017b), ESO-NTT (at $t_c + 1.4$ days; Smartt et al. 2017), the SOAR 4 m telescope (at $t_c + 1.4$ days; Nicholl et al. 2017d), and ESO-VLT-XShooter (at $t_c + 2.4$ days; Smartt et al. 2017) as described in Section 2.3, and the first X-ray and radio detections of the same source by *Chandra* (see Section 3.3) and JVLA (see Section 3.4). In order to show representative spectral energy distributions, each spectrum is normalized to its maximum and shifted arbitrarily along the linear y-axis (no absolute scale). The high background in the SALT spectrum below 4500 Å prevents the identification of spectral features in this band (for details McCully et al. 2017b).

GRB is $T_0 - t_c = 1.734 \pm 0.054$ s (Abbott et al. 2017g). Exploiting the difference in the arrival time of the gamma-ray signals at *Fermi*-GBM and *INTEGRAL* SPI-ACS (Svinkin et al. 2017c) provides additional significant constraints on the gamma-ray localization area (see Figure 1). The IPN localization capability will be especially important in the case of future gravitational-wave events that might be less well-localized by LIGO-Virgo.

Standard follow-up analyses (Goldstein et al. 2012; Paciesas et al. 2012; Gruber et al. 2014) of the *Fermi*-GBM trigger determined the burst duration to be $T_{90} = 2.0 \pm 0.5$ s, where T_{90} is defined as the duration over which 90% of the burst fluence is accumulated in the energy range of 50–300 keV. From the *Fermi*-GBM T_{90} measurement, GRB 170817A was classified as an sGRB with 3:1 odds over being a long GRB. The classification of GRB 170817A as an sGRB is further supported by incorporating the hardness ratio of the burst and comparing it to the *Fermi*-GBM catalog (Goldstein et al. 2017a). The SPI-ACS duration for GRB 170817A of 100 ms is consistent with an sGRB classification within the instrument’s historic sample (Savchenko et al. 2012).

The GRB had a peak photon flux measured on a 64 ms timescale of 3.7 ± 0.9 photons $s^{-1} cm^{-2}$ and a fluence over the T_{90} interval of $(2.8 \pm 0.2) \times 10^{-7}$ erg cm^{-2} (10–1000 keV; (Goldstein et al. 2017a). GRB 170817A is the closest sGRB with measured redshift. By usual measures, GRB 170817A is sub-luminous, a tantalizing observational result that is explored in Abbott et al. (2017g) and Goldstein et al. (2017a).

Detailed analysis of the *Fermi*-GBM data for GRB 170817A revealed two components to the burst: a main pulse encompassing the GRB trigger time from $T_0 - 0.320$ s to $T_0 + 0.256$ s followed by a weak tail starting at $T_0 + 0.832$ s and extending to $T_0 + 1.984$ s. The spectrum of the main pulse of GRB 170817A is best fit with a Comptonized function (a power law with an exponential cutoff) with a power-law photon index of -0.62 ± 0.40 , peak energy $E_{\text{peak}} = 185 \pm 62$ keV, and time-averaged flux of $(3.1 \pm 0.7) \times 10^{-7}$ erg $cm^{-2} s^{-1}$. The weak tail that follows the main pulse, when analyzed independently, has a localization consistent with both the main pulse and the gravitational-wave position. The weak tail, at 34% the fluence of the main pulse, extends the T_{90} beyond the main pulse and has a softer, blackbody spectrum with $kT = 10.3 \pm 1.5$ keV (Goldstein et al. 2017a).

Using the *Fermi*-GBM spectral parameters of the main peak and T_{90} interval, the integrated fluence measured by *INTEGRAL* SPI-ACS is $(1.4 \pm 0.4) \times 10^{-7}$ erg cm^{-2} (75–2000 keV), compatible with the *Fermi*-GBM spectrum. Because SPI-ACS is most sensitive above 100 keV, it detects only the highest-energy part of the main peak near the start of the longer *Fermi*-GBM signal (Abbott et al. 2017f).

2.3. Discovery of the Optical Counterpart and Host Galaxy

The announcements of the *Fermi*-GBM and LIGO-Virgo detections, and especially the well-constrained, three-dimensional LIGO-Virgo localization, triggered a broadband observing campaign in search of electromagnetic counterparts. A large number of teams across the world were mobilized using ground- and space-based telescopes that could observe the region identified by the gravitational-wave detection. GW170817 was localized to the southern sky, setting in the early evening for the northern hemisphere

telescopes, thus making it inaccessible to the majority of them. The LIGO-Virgo localization region (LIGO Scientific Collaboration & Virgo Collaboration et al. 2017b, 2017c) became observable to telescopes in Chile about 10 hr after the merger with an altitude above the horizon of about 45° .

The One-Meter, Two-Hemisphere (1M2H) team was the first to discover and announce (August 18 01:05 UTC; Coulter et al. 2017a) a bright optical transient in an *i*-band image acquired on August 17 at 23:33 UTC ($t_c + 10.87$ hr) with the 1 m Swope telescope at Las Campanas Observatory in Chile. The team used an observing strategy (Gehrels et al. 2016) that targeted known galaxies (from White et al. 2011b) in the three-dimensional LIGO-Virgo localization taking into account the galaxy stellar mass and star formation rate (Coulter et al. 2017). The transient, designated Swope Supernova Survey 2017a (SSS17a), was $i = 17.057 \pm 0.018$ mag⁹⁶² (August 17 23:33 UTC, $t_c + 10.87$ hr) and did not match any known asteroid or supernova. SSS17a (now with the IAU designation AT 2017gfo) was located at $\alpha(J2000.0) = 13^h09^m48^s.085 \pm 0.018$, $\delta(J2000.0) = -23^\circ22'53''343 \pm 0.218$ at a projected distance of $10''6$ from the center of NGC 4993, an early-type galaxy in the ESO 508 group at a distance of $\simeq 40$ Mpc (Tully–Fisher distance from Freedman et al. 2001), consistent with the gravitational-wave luminosity distance (LIGO Scientific Collaboration & Virgo Collaboration et al. 2017b).

Five other teams took images of the transient within an hour of the 1M2H image (and before the SSS17a announcement) using different observational strategies to search the LIGO-Virgo sky localization region. They reported their discovery of the same optical transient in a sequence of GCNs: the Dark Energy Camera (01:15 UTC; Allam et al. 2017), the Distance Less Than 40 Mpc survey (01:41 UTC; Yang et al. 2017a), Las Cumbres Observatory (LCO; 04:07 UTC; Arcavi et al. 2017a), the Visible and Infrared Survey Telescope for Astronomy (VISTA; 05:04 UTC; Tanvir et al. 2017a), and MASTER (05:38 UTC; Lipunov et al. 2017d). Independent searches were also carried out by the Rapid Eye Mount (REM-GRAWITA, optical, 02:00 UTC; Melandri et al. 2017a), *Swift* UVOT/XRT (ultraviolet, 07:24 UTC; Evans et al. 2017a), and Gemini-South (infrared, 08:00 UT; Singer et al. 2017a).

The Distance Less Than 40 Mpc survey (DLT40; L. Tartaglia et al. 2017, in preparation) team independently detected SSS17a/AT 2017gfo, automatically designated DLT17ck (Yang et al. 2017a) in an image taken on August 17 23:50 UTC while carrying out high-priority observations of 51 galaxies (20 within the LIGO-Virgo localization and 31 within the wider *Fermi*-GBM localization region; Valenti et al. 2017, accepted). A confirmation image was taken on August 18 00:41 UTC after the observing program had cycled through all of the high-priority targets and found no other transients. The updated magnitudes for these two epochs are $r = 17.18 \pm 0.03$ and 17.28 ± 0.04 mag, respectively.

SSS17a/AT 2017gfo was also observed by the VISTA in the second of two 1.5 deg^2 fields targeted. The fields were chosen to be within the high-likelihood localization region of GW170817 and to contain a high density of potential host galaxies (32 of the 54 entries in the list of Cook et al. 2017a). Observations began during evening twilight and were repeated twice to give a short temporal baseline over which to search for

⁹⁶² All apparent magnitudes are AB and corrected for the Galactic extinction in the direction of SSS17a ($E(B - V) = 0.109$ mag; Schlafly & Finkbeiner 2011).

variability (or proper motion of any candidates). The magnitudes of the transient source in the earliest images taken in the near-infrared were measured to be $K_s = 18.63 \pm 0.05$, $J = 17.88 \pm 0.03$, and $Y = 17.51 \pm 0.02$ mag.

On August 17 23:59 UTC, the MASTER-OAFA robotic telescope (Lipunov et al. 2010), covering the sky location of GW170817, recorded an image that included NGC 4993. The autodetection software identified MASTER OT J130948.10-232253.3, the bright optical transient with the unfiltered magnitude $W = 17.5 \pm 0.2$ mag, as part of an automated search performed by the MASTER Global Robotic Net (Lipunov et al. 2017a, 2017d).

The Dark Energy Camera (DECam; Flaugher et al. 2015) Survey team started observations of the GW170817 localization region on August 17 23:13 UTC. DECam covered 95% of the probability in the GW170817 localization area with a sensitivity sufficient to detect a source up to 100 times fainter than the observed optical transient. The transient was observed on 2017 August 18 at 00:05 UTC and independently detected at 00:42 UTC (Allam et al. 2017). The measured magnitudes of the transient source in the first images were $i = 17.30 \pm 0.02$, $z = 17.45 \pm 0.03$. A complete analysis of DECam data is presented in Soares-Santos et al. (2017).

Las Cumbres Observatory (LCO; Brown et al. 2013) surveys started their observations of individual galaxies with their global network of 1 and 2 m telescopes upon receipt of the initial *Fermi*-GBM localization. Approximately five hours later, when the LIGO-Virgo localization map was issued, the observations were switched to a prioritized list of galaxies (from Dalya et al. 2016) ranked by distance and luminosity (Arcavi et al. 2017, in preparation). In a 300 s w -band exposure beginning on August 18 00:15 UTC, a new transient, corresponding to AT 2017gfo/SSS17a/DLT17ck, was detected near NGC 4993 (Arcavi et al. 2017a). The transient was determined to have $w = 17.49 \pm 0.04$ mag (Arcavi et al. 2017e).

These early photometric measurements, from the optical to near-infrared, gave the first broadband spectral energy distribution of AT 2017gfo/SSS17a/DLT17ck. They do not distinguish the transient from a young supernova, but they serve as reference values for subsequent observations that reveal the nature of the optical counterpart as described in Section 3.1. Images from the six earliest observations are shown in the inset of Figure 2.

3. Broadband Follow-up

While some of the first observations aimed to tile the error region of the GW170817 and GRB 170817A localization areas, including the use of galaxy targeting (White et al. 2011a; Dalya et al. 2016; D. Cook & M. Kasliwal 2017, in preparation; S. R. Kulkarni et al. 2017, in preparation), most groups focused their effort on the optical transient reported by Coulter et al. (2017) to define its nature and to rule out that it was a chance coincidence of an unrelated transient. The multi-wavelength evolution within the first 12–24 hr, and the subsequent discoveries of the X-ray and radio counterparts, proved key to scientific interpretation. This section summarizes the plethora of key observations that occurred in different wavebands, as well as searches for neutrino counterparts.

3.1. Ultraviolet, Optical, and Infrared

The quick discovery in the first few hours of Chilean darkness, and the possibility of fast evolution, prompted the need for the ultraviolet–optical–infrared follow-up community to have access to both space-based and longitudinally separated ground-based facilities. Over the next two weeks, a network of ground-based telescopes, from 40 cm to 10 m, and space-based observatories spanning the ultraviolet (UV), optical (O), and near-infrared (IR) wavelengths followed up GW170817. These observations revealed an exceptional electromagnetic counterpart through careful monitoring of its spectral energy distribution. Here, we first consider photometric and then spectroscopic observations of the source.

Regarding photometric observations, at $t_c + 11.6$ hr, the *Magellan*-Clay and *Magellan*-Baade telescopes (Drout et al. 2017a; Simon et al. 2017) initiated follow-up observations of the transient discovered by the Swope Supernova Survey from the optical (g band) to NIR (K_s band). At $t_c + 12.7$ hr and $t_c + 12.8$ hr, the Rapid Eye Mount (REM)/ROS2 (Melandri et al. 2017b) detected the optical transient and the Gemini-South FLAMINGO2 instrument first detected near-infrared K_s -band emission constraining the early optical to infrared color (Kasliwal et al. 2017; Singer et al. 2017a), respectively. At $t_c + 15.3$ hr, the *Swift* satellite (Gehrels 2004) detected bright, ultraviolet emission, further constraining the effective temperature (Evans et al. 2017a, 2017b). The ultraviolet evolution continued to be monitored with the *Swift* satellite (Evans et al. 2017b) and the *Hubble Space Telescope* (*HST*; Adams et al. 2017; Cowperthwaite et al. 2017b; Kasliwal et al. 2017).

Over the course of the next two days, an extensive photometric campaign showed a rapid dimming of this initial UV–blue emission and an unusual brightening of the near-infrared emission. After roughly a week, the redder optical and near-infrared bands began to fade as well. Ground- and space-based facilities participating in this photometric monitoring effort include (in alphabetic order): CTIO1.3 m, DECam (Cowperthwaite et al. 2017b; Nicholl et al. 2017a, 2017d), IRSF, the Gemini-South FLAMINGO2 (Singer et al. 2017a, 2017b; Chornock et al. 2017b; Troja et al. 2017b, 2017d), Gemini-South GMOS (Troja et al. 2017b), GROND (Chen et al. 2017; Wiseman et al. 2017), *HST* (Cowperthwaite et al. 2017b; Levan & Tanvir 2017; Levan et al. 2017a; Tanvir & Levan 2017; Troja et al. 2017a), *i*Telescope.Net telescopes (Im et al. 2017a, 2017b), the Korea Microlensing Telescope Network (KMTNet; Im et al. 2017c, 2017d), LCO (Arcavi et al. 2017b, 2017c, 2017e), the Lee Sang Gak Telescope (LSGT)/SNUCAM-II, the *Magellan*-Baade and *Magellan*-Clay 6.5 m telescopes (Drout et al. 2017a; Simon et al. 2017), the Nordic Optical Telescope (Malesani et al. 2017a), Pan-STARRS1 (Chambers et al. 2017a, 2017b, 2017c, 2017d), REM/ROS2 and REM/REMIR (Melandri et al. 2017a, 2017c), SkyMapper (Wolf et al. 2017), Subaru Hyper Suprime-Cam (Yoshida et al. 2017a, 2017b, 2017c, 2017d; Tominaga et al. 2017), ESO-VISTA (Tanvir et al. 2017a), ESO-VST/OmegaCAM (Grado et al. 2017a, 2017b), and ESO-VLT/FORS2 (D’Avanzo et al. 2017).

One of the key properties of the transient that alerted the worldwide community to its unusual nature was the rapid luminosity decline. In bluer optical bands (i.e., in the g band), the transient showed a fast decay between daily photometric measurements (Cowperthwaite et al. 2017b; Melandri et al. 2017c). Pan-STARRS (Chambers et al. 2017c) reported

photometric measurements in the optical/infrared *izy* bands with the same cadence, showing fading by 0.6 mag per day, with reliable photometry from difference imaging using already existing sky images (Chambers et al. 2016; Cowperthwaite et al. 2017b). Observations taken every 8 hr by LCO showed an initial rise in the *w* band, followed by rapid fading in all optical bands (more than 1 mag per day in the blue) and reddening with time (Arcavi et al. 2017e). Accurate measurements from Subaru (Tominaga et al. 2017), LSGT/SNUCAM-II and KMTNet (Im et al. 2017c), ESO-VLT/FORS2 (D’Avanzo et al. 2017), and DECam (Cowperthwaite et al. 2017b; Nicholl et al. 2017b) indicated a similar rate of fading. On the contrary, the near-infrared monitoring reports by GROND and Gemini-South showed that the source faded more slowly in the infrared (Chornock et al. 2017b; Wiseman et al. 2017) and even showed a late-time plateau in the Ks band (Singer et al. 2017b). This evolution was recognized by the community as quite unprecedented for transients in the nearby (within 100 Mpc) universe (e.g., Siebert et al. 2017).

Table 1 reports a summary of the imaging observations, which include coverage of the entire gravitational-wave sky localization and follow-up of SSS17a/AT2017gfo. Figure 2 shows these observations in graphical form.

Concerning spectroscopic observations, immediately after discovery of SSS17a/AT2017gfo on the Swope 1 m telescope, the same team obtained the first spectroscopic observations of the optical transient with the LDSS-3 spectrograph on the 6.5 m *Magellan*-Clay telescope and the MagE spectrograph on the 6.5 m *Magellan*-Baade telescope at Las Campanas Observatory. The spectra, just 30 minutes after the first image, showed a blue and featureless continuum between 4000 and 10000 Å, consistent with a power law (Drout et al. 2017a; Shappee et al. 2017). The lack of features and blue continuum during the first few hours implied an unusual, but not unprecedented transient since such characteristics are common in cataclysmic-variable stars and young core-collapse supernovae (see, e.g., Li et al. 2011a, 2011b).

The next 24 hr of observation were critical in decreasing the likelihood of a chance coincidence between SSS17a/AT2017gfo, GW170817, and GRB 170817A. The SALT-RSS spectrograph in South Africa (Buckley et al. 2017; McCully et al. 2017b; Shara et al. 2017), ePESSTO with the EFOSC2 instrument in spectroscopic mode at the ESO New Technology Telescope (NTT, in La Silla, Chile; Lyman et al. 2017), the X-shooter spectrograph on the ESO Very Large Telescope (Pian et al. 2017b) in Paranal, and the Goodman Spectrograph on the 4 m SOAR telescope (Nicholl et al. 2017c) obtained additional spectra. These groups reported a rapid fall off in the blue spectrum without any individual features identifiable with line absorption common in supernova-like transients (see, e.g., Lyman et al. 2017). This ruled out a young supernova of any type in NGC 4993, showing an exceptionally fast spectral evolution (Drout et al. 2017; Nicholl et al. 2017d). Figure 2 shows some representative early spectra (SALT spectrum is from Buckley et al. 2017; McCully et al. 2017b; ESO spectra from Smartt et al. 2017; SOAR spectrum from Nicholl et al. 2017d). These show rapid cooling, and the lack of commonly observed ions from elements abundant in supernova ejecta, indicating this object was unprecedented in its optical and near-infrared emission. Combined with the rapid fading, this was broadly indicative of a possible kilonova (e.g., Arcavi et al. 2017e; Cowperthwaite et al. 2017b; McCully et al. 2017b;

Kasen et al. 2017; Kasliwal et al. 2017; Kilpatrick et al. 2017b; Nicholl et al. 2017d; Smartt et al. 2017). This was confirmed by spectra taken at later times, such as with the Gemini Multi-Object Spectrograph (GMOS; Kasliwal et al. 2017; McCully et al. 2017b; Troja et al. 2017a, 2017b), the LDSS-3 spectrograph on the 6.5 m *Magellan*-Clay telescope at Las Campanas Observatory (Drout et al. 2017; Shappee et al. 2017), the LCO FLOYDS spectrograph at Faulkes Telescope South (McCully et al. 2017a, 2017b), and the AAOmega spectrograph on the 3.9 m Anglo-Australian Telescope (Andreoni et al. 2017), which did not show any significant emission or absorption lines over the red featureless continuum. The optical and near-infrared spectra over these few days provided convincing arguments that this transient was unlike any other discovered in extensive optical wide-field surveys over the past decade (see, e.g., Siebert et al. 2017).

The evolution of the spectral energy distribution, rapid fading, and emergence of broad spectral features indicated that the source had physical properties similar to models of kilonovae (e.g., Metzger et al. 2010; Kasen et al. 2013; Barnes & Kasen 2013; Tanaka & Hotokezaka 2013; Grossman et al. 2014; Metzger & Fernández 2014; Barnes et al. 2016; Tanaka 2016; Kasen et al. 2017; Kilpatrick et al. 2017b; Metzger 2017). These show a very rapid shift of the spectral energy distribution from the optical to the near-infrared. The FLAMINGOS2 near-infrared spectrograph at Gemini-South (Chornock et al. 2017c; Kasliwal et al. 2017) shows the emergence of very broad features in qualitative agreement with kilonova models. The ESO-VLT/X-shooter spectra, which simultaneously cover the wavelength range 3200–24800 Å, were taken over 2 weeks with a close to daily sampling (Pian et al. 2017a; Smartt et al. 2017) and revealed signatures of the radioactive decay of *r*-process nucleosynthesis elements (Pian et al. 2017a). Three epochs of infrared grism spectroscopy with the *HST* (Cowperthwaite et al. 2017b; Levan & Tanvir 2017; Levan et al. 2017a; Tanvir & Levan 2017; Troja et al. 2017a)⁹⁶³ identified features consistent with the production of lanthanides within the ejecta (Levan & Tanvir 2017; Tanvir & Levan 2017; Troja et al. 2017a).

The optical follow-up campaign also includes linear polarimetry measurements of SSS17a/AT2017gfo by ESO-VLT/FORS2, showing no evidence of an asymmetric geometry of the emitting region and lanthanide-rich late kilonova emission (Covino et al. 2017). In addition, the study of the galaxy with the MUSE Integral Field Spectrograph on the ESO-VLT (Levan et al. 2017b) provides simultaneous spectra of the counterpart and the host galaxy, which show broad absorption features in the transient spectrum, combined with emission lines from the spiral arms of the host galaxy (Levan & Tanvir 2017; Tanvir & Levan 2017).

Table 2 reports the spectroscopic observations that have led to the conclusion that the source broadly matches kilonovae theoretical predictions.

3.2. Gamma-Rays

The fleet of ground- and space-based gamma-ray observatories provided broad temporal and spectral coverage of the source location. Observations spanned ~ 10 orders of magnitude in energy and covered the position of SSS17a/AT2017gfo from a few hundred seconds before the GRB 170817A trigger time (T_0) to days afterward. Table 3 lists, in chronological order, the results reporting observation

⁹⁶³ *HST* Program GO 14804 Levan, GO 14771 Tanvir, and GO 14850 Troja.

Table 1

A Partial Summary of Photometric Observations up to 2017 September 5 UTC with at Most Three Observations per Filter per Telescope/Group, i.e., the Earliest, the Peak, and the Latest in Each Case

Telescope/Instrument	UT Date	Band	References
DFN/–	2017 Aug 17 12:41:04	visible	Hancock et al. (2017),
MASTER/–	2017 Aug 17 17:06:47	Clear	Lipunov et al. (2017a, 2017b)
PioftheSky/PioftheSkyNorth	2017 Aug 17 21:46:28	visible wide band	Cwiek et al. (2017); Batsch et al. (2017); Zdrozny et al. (2017)
MASTER/–	2017 Aug 17 22:54:18	Visible	Lipunov et al. (2017b, 2017a)
Swope/DirectCCD	2017 Aug 17 23:33:17	i	Coulter et al. (2017a, 2017b, 2017)
PROMPT5(DLT40)/–	2017 Aug 17 23:49:00	r	Yang et al. (2017a), Valenti et al. (submitted)
VISTA/VIRCAM	2017 Aug 17 23:55:00	K	Tanvir & Levan (2017)
MASTER/–	2017 Aug 17 23:59:54	Clear	Lipunov et al. (2017d, 2017a)
Blanco/DECam/–	2017 Aug 18 00:04:24	i	Cowperthwaite et al. (2017b); Soares-Santos et al. (2017)
Blanco/DECam/–	2017 Aug 18 00:05:23	z	Cowperthwaite et al. (2017b); Soares-Santos et al. (2017)
VISTA/VIRCAM	2017 Aug 18 00:07:00	J	Tanvir & Levan (2017)
Magellan-Clay/LDSS3-C	2017 Aug 18 00:08:13	g	Simon et al. (2017); Drout et al. (2017b)
Magellan-Baade/FourStar	2017 Aug 18 00:12:19	H	Drout et al. (2017b)
LasCumbres 1-m/Sinistro	2017 Aug 18 00:15:50	w	Arcavi et al. (2017a, 2017e)
VISTA/VIRCAM	2017 Aug 18 00:17:00	Y	Tanvir & Levan (2017)
MASTER/–	2017 Aug 18 00:19:05	Clear	Lipunov et al. (2017d, 2017a)
Magellan-Baade/FourStar	2017 Aug 18 00:25:51	J	Drout et al. (2017b)
Magellan-Baade/FourStar	2017 Aug 18 00:35:19	Ks	Drout et al. (2017b)
PROMPT5(DLT40)/–	2017 Aug 18 00:40:00	r	Yang et al. (2017a), Valenti et al. (submitted)
REM/ROS2	2017 Aug 18 01:24:56	g	Melandri et al. (2017a); Pian et al. (2017a)
REM/ROS2	2017 Aug 18 01:24:56	i	Melandri et al. (2017a); Pian et al. (2017a)
REM/ROS2	2017 Aug 18 01:24:56	z	Melandri et al. (2017a); Pian et al. (2017a)
REM/ROS2	2017 Aug 18 01:24:56	r	Melandri et al. (2017a); Pian et al. (2017a)
Gemini-South/Flamingos-2	2017 Aug 18 01:30:00	Ks	Singer et al. (2017a); Kasliwal et al. (2017)
PioftheSky/PioftheSkyNorth	2017 Aug 18 03:01:39	visible wide band	Cwiek et al. (2017); Batsch et al. (2017),
Swift/UVOT	2017 Aug 18 03:37:00	uvm2	Evans et al. (2017a, 2017b)
Swift/UVOT	2017 Aug 18 03:50:00	uvw1	Evans et al. (2017a, 2017b)
Swift/UVOT	2017 Aug 18 03:58:00	u	Evans et al. (2017a, 2017b)
Swift/UVOT	2017 Aug 18 04:02:00	uvw2	Evans et al. (2017a, 2017b)
Subaru/HyperSuprime-Cam	2017 Aug 18 05:31:00	z	Yoshida et al. (2017a, 2017b), Y. Utsumi et al. (2017, in preparation)
Pan-STARRS1/GPC1	2017 Aug 18 05:33:00	y	Chambers et al. (2017a); Smartt et al. (2017)
Pan-STARRS1/GPC1	2017 Aug 18 05:34:00	z	Chambers et al. (2017a); Smartt et al. (2017)
Pan-STARRS1/GPC1	2017 Aug 18 05:35:00	i	Chambers et al. (2017a); Smartt et al. (2017)
Pan-STARRS1/GPC1	2017 Aug 18 05:36:00	y	Chambers et al. (2017a); Smartt et al. (2017)
Pan-STARRS1/GPC1	2017 Aug 18 05:37:00	z	Chambers et al. (2017a); Smartt et al. (2017)
Pan-STARRS1/GPC1	2017 Aug 18 05:38:00	i	Chambers et al. (2017a); Smartt et al. (2017)
LasCumbres 1-m/Sinistro	2017 Aug 18 09:10:04	w	Arcavi et al. (2017b, 2017e)
SkyMapper/–	2017 Aug 18 09:14:00	i	...
SkyMapper/–	2017 Aug 18 09:35:00	z	...
LasCumbres 1-m/Sinistro	2017 Aug 18 09:37:26	g	Arcavi et al. (2017e)
SkyMapper/–	2017 Aug 18 09:39:00	r	...
SkyMapper/–	2017 Aug 18 09:41:00	g	...
LasCumbres 1-m/Sinistro	2017 Aug 18 09:43:11	r	Arcavi et al. (2017e)
T17/–	2017 Aug 18 09:47:13	g	Im et al. (2017a, 2017b), Im et al. (2017, in preparation)
SkyMapper/–	2017 Aug 18 09:50:00	v	...
T17/–	2017 Aug 18 09:56:46	r	Im et al. (2017a, 2017b), Im et al. (2017, in preparation)
SkyMapper/–	2017 Aug 18 10:01:00	i	Wolf et al. (2017),
SkyMapper/–	2017 Aug 18 10:03:00	r	Wolf et al. (2017),
SkyMapper/–	2017 Aug 18 10:05:00	g	Wolf et al. (2017),
T17/–	2017 Aug 18 10:06:18	i	Im et al. (2017a, 2017b), Im et al. (2017, in preparation)
SkyMapper/–	2017 Aug 18 10:07:00	v	Wolf et al. (2017),
LSGT/SNUCAM-II	2017 Aug 18 10:08:01	m425	Im et al. (2017a, 2017b), Im et al. (2017, in preparation)
SkyMapper/–	2017 Aug 18 10:09:00	u	Wolf et al. (2017),
LSGT/SNUCAM-II	2017 Aug 18 10:12:48	m475	Im et al. (2017a, 2017b), Im et al. (2017, in preparation)
LSGT/SNUCAM-II	2017 Aug 18 10:15:16	m525	Im et al. (2017a, 2017b), Im et al. (2017, in preparation)
T17/–	2017 Aug 18 10:15:49	z	Im et al. (2017a, 2017b), Im et al. (2017, in preparation)
LSGT/SNUCAM-II	2017 Aug 18 10:21:14	m575	Im et al. (2017a, 2017b), Im et al. (2017, in preparation)
LSGT/SNUCAM-II	2017 Aug 18 10:22:33	m625	Im et al. (2017a, 2017b), Im et al. (2017, in preparation)
AST3-2/wide-fieldcamera	2017 Aug 18 13:11:49	g	Hu et al. (2017),
Swift/UVOT	2017 Aug 18 13:30:00	uvm2	Cenko et al. (2017); Evans et al. (2017b)
Swift/UVOT	2017 Aug 18 13:37:00	uvw1	Cenko et al. (2017); Evans et al. (2017b)

Table 1
(Continued)

Telescope/Instrument	UT Date	Band	References
<i>Swift</i> /UVOT	2017 Aug 18 13:41:00	u	Cenko et al. (2017); Evans et al. (2017b)
IRSF/SIRIUS	2017 Aug 18 16:34:00	Ks	Utsumi et al. (2017, in press)
IRSF/SIRIUS	2017 Aug 18 16:34:00	H	Utsumi et al. (2017, in press)
IRSF/SIRIUS	2017 Aug 18 16:48:00	J	Utsumi et al. (2017, in press)
KMTNet-SAAO/wide-fieldcamera	2017 Aug 18 17:00:36	B	Im et al. (2017d, 2017c); Troja et al. (2017a)
KMTNet-SAAO/wide-fieldcamera	2017 Aug 18 17:02:55	V	Im et al. (2017d, 2017c); Troja et al. (2017a)
KMTNet-SAAO/wide-fieldcamera	2017 Aug 18 17:04:54	R	Im et al. (2017d, 2017c); Troja et al. (2017a)
MASTER/–	2017 Aug 18 17:06:55	Clear	Lipunov et al. (2017e, 2017a)
KMTNet-SAAO/wide-fieldcamera	2017 Aug 18 17:07:12	I	Im et al. (2017d, 2017c); Troja et al. (2017a)
MASTER/–	2017 Aug 18 17:17:33	R	Lipunov et al. (2017c, 2017b, 2017a)
MASTER/–	2017 Aug 18 17:34:02	B	Lipunov et al. (2017b, 2017a)
1.5 m Boyden/–	2017 Aug 18 18:12:00	r	Smartt et al. (2017)
MPG2.2 m/GROND	2017 Aug 18 18:12:00	g	Smartt et al. (2017)
NOT/NOTCam	2017 Aug 18 20:24:08	Ks	Malesani et al. (2017a); Tanvir & Levan (2017)
NOT/NOTCam	2017 Aug 18 20:37:46	J	Malesani et al. (2017a); Tanvir & Levan (2017)
PioftheSky/PioftheSkyNorth	2017 Aug 18 21:44:44	visible wide band	Cwiek et al. (2017); Batsch et al. (2017),
LasCumbres1-m/Sinistro	2017 Aug 18 23:19:40	i	Arcavi et al. (2017e)
Blanco/DECam/–	2017 Aug 18 23:25:56	Y	Cowperthwaite et al. (2017b); Soares-Santos et al. (2017)
<i>Magellan</i> -Clay/LDSS3-C	2017 Aug 18 23:26:33	z	Drout et al. (2017b)
Blanco/DECam/–	2017 Aug 18 23:26:55	z	Cowperthwaite et al. (2017b); Soares-Santos et al. (2017)
Blanco/DECam/–	2017 Aug 18 23:27:54	i	Cowperthwaite et al. (2017b); Soares-Santos et al. (2017)
KMTNet-CTIO/wide-fieldcamera	2017 Aug 18 23:28:35	B	Im et al. (2017d, 2017c); Troja et al. (2017a)
Blanco/DECam/–	2017 Aug 18 23:28:53	r	Cowperthwaite et al. (2017b); Soares-Santos et al. (2017)
Blanco/DECam/–	2017 Aug 18 23:29:52	g	Cowperthwaite et al. (2017b); Soares-Santos et al. (2017)
KMTNet-CTIO/wide-fieldcamera	2017 Aug 18 23:30:31	V	Im et al. (2017d, 2017c); Troja et al. (2017a)
Blanco/DECam/–	2017 Aug 18 23:30:50	u	Cowperthwaite et al. (2017b); Soares-Santos et al. (2017)
<i>Magellan</i> -Clay/LDSS3-C	2017 Aug 18 23:30:55	i	Drout et al. (2017b)
REM/ROS2	2017 Aug 18 23:31:02	z	Melandri et al. (2017c); Pian et al. (2017a)
<i>Magellan</i> -Clay/LDSS3-C	2017 Aug 18 23:32:02	r	Drout et al. (2017b)
KMTNet-CTIO/wide-fieldcamera	2017 Aug 18 23:32:36	R	Im et al. (2017d, 2017c); Troja et al. (2017a)
<i>Magellan</i> -Baade/FourStar	2017 Aug 18 23:32:58	J	Drout et al. (2017b)
KMTNet-CTIO/wide-fieldcamera	2017 Aug 18 23:34:48	I	Im et al. (2017d, 2017c); Troja et al. (2017a)
<i>Magellan</i> -Clay/LDSS3-C	2017 Aug 18 23:35:20	B	Drout et al. (2017b)
VISTA/VIRCAM	2017 Aug 18 23:44:00	J	Tanvir & Levan (2017)
<i>Magellan</i> -Baade/FourStar	2017 Aug 18 23:45:49	H	Drout et al. (2017b)
PROMPT5(DLT40)/–	2017 Aug 18 23:47:00	r	Yang et al. (2017b), Valenti et al. (submitted)
VLT/FORS2	2017 Aug 18 23:47:02	Rspecial	Wiersema et al. (2017); Covino et al. (2017)
Swope/DirectCCD	2017 Aug 18 23:52:29	V	Kilpatrick et al. (2017a); Coulter et al. (2017)
VISTA/VIRCAM	2017 Aug 18 23:53:00	Y	Tanvir & Levan (2017)
TOROS/T8OS	2017 Aug 18 23:53:00	g	Diaz et al. (2017a, 2017b), Diaz et al. (2017, in preparation)
TOROS/T8OS	2017 Aug 18 23:53:00	r	Diaz et al. (2017a, 2017b), Diaz et al. (2017, in preparation)
TOROS/T8OS	2017 Aug 18 23:53:00	i	Diaz et al. (2017a, 2017b), Diaz et al. (2017, in preparation)
MPG2.2 m/GROND	2017 Aug 18 23:56:00	i	Smartt et al. (2017)
MPG2.2 m/GROND	2017 Aug 18 23:56:00	z	Smartt et al. (2017)
MPG2.2 m/GROND	2017 Aug 18 23:56:00	J	Smartt et al. (2017)
MPG2.2 m/GROND	2017 Aug 18 23:56:00	r	Smartt et al. (2017)
MPG2.2 m/GROND	2017 Aug 18 23:56:00	H	Smartt et al. (2017)
MPG2.2 m/GROND	2017 Aug 18 23:56:00	Ks	Smartt et al. (2017)
Gemini-South/Flamingos-2	2017 Aug 19 00:00:19	H	Cowperthwaite et al. (2017b)
<i>Magellan</i> -Baade/FourStar	2017 Aug 19 00:02:53	J1	Drout et al. (2017b)
VLT/X-shooter	2017 Aug 19 00:08:58	r	Pian et al. (2017a, 2017a)
VLT/X-shooter	2017 Aug 19 00:10:46	z	Pian et al. (2017b, 2017b)
VLT/X-shooter	2017 Aug 19 00:14:01	g	Pian et al. (2017, 2017)
<i>Swift</i> /UVOT	2017 Aug 19 00:41:00	u	Evans et al. (2017b)
Swope/DirectCCD	2017 Aug 19 00:49:15	B	Kilpatrick et al. (2017a); Coulter et al. (2017)
Swope/DirectCCD	2017 Aug 19 01:08:00	r	Coulter et al. (2017)
NTT/–	2017 Aug 19 01:09:00	U	Smartt et al. (2017)
Swope/DirectCCD	2017 Aug 19 01:18:57	g	Coulter et al. (2017)
BOOTES-5/JGT/–	2017 Aug 19 03:08:14	clear	Castro-Tirado et al. (2017), Zhang et al. (2017, in preparation)
Pan-STARRS1/GPC1	2017 Aug 19 05:42:00	y	Chambers et al. (2017b); Smartt et al. (2017)
Pan-STARRS1/GPC1	2017 Aug 19 05:44:00	z	Chambers et al. (2017b); Smartt et al. (2017)

Table 1
(Continued)

Telescope/Instrument	UT Date	Band	References
Pan-STARRS1/GPC1	2017 Aug 19 05:46:00	i	Chambers et al. (2017b); Smartt et al. (2017)
MOA-II/MOA-cam3	2017 Aug 19 07:26:00	R	Utsumi et al. (2017, in press)
B&C61cm/Tripole5	2017 Aug 19 07:26:00	g	Utsumi et al. (2017, in press)
KMTNet-SSO/wide-fieldcamera	2017 Aug 19 08:32:48	B	Im et al. (2017d, 2017c); Troja et al. (2017a)
KMTNet-SSO/wide-fieldcamera	2017 Aug 19 08:34:43	V	Im et al. (2017d, 2017c); Troja et al. (2017a)
KMTNet-SSO/wide-fieldcamera	2017 Aug 19 08:36:39	R	Im et al. (2017d, 2017c); Troja et al. (2017a)
KMTNet-SSO/wide-fieldcamera	2017 Aug 19 08:38:42	I	Im et al. (2017d, 2017c); Troja et al. (2017a)
T27/-	2017 Aug 19 09:01:31	V	Im et al. (2017a, 2017b), Im et al. (2017, in preparation)
T30/-	2017 Aug 19 09:02:27	V	Im et al. (2017a, 2017b), Im et al. (2017, in preparation)
T27/-	2017 Aug 19 09:02:27	R	Im et al. (2017a, 2017b), Im et al. (2017, in preparation)
T31/-	2017 Aug 19 09:02:34	R	Im et al. (2017a, 2017b), Im et al. (2017, in preparation)
T27/-	2017 Aug 19 09:11:30	I	Im et al. (2017a, 2017b), Im et al. (2017, in preparation)
Zadko/CCDimager	2017 Aug 19 10:57:00	r	Coward et al. (2017a),
MASTER/-	2017 Aug 19 17:06:57	Clear	Lipunov et al. (2017b, 2017a)
MASTER/-	2017 Aug 19 17:53:34	R	Lipunov et al. (2017b, 2017a)
LasCumbres 1-m/Sinistro	2017 Aug 19 18:01:26	V	Arcavi et al. (2017e)
LasCumbres 1-m/Sinistro	2017 Aug 19 18:01:26	z	Arcavi et al. (2017e)
MASTER/-	2017 Aug 19 18:04:32	B	Lipunov et al. (2017b, 2017a)
1.5 m Boyden/-	2017 Aug 19 18:16:00	r	Smartt et al. (2017)
REM/ROS2	2017 Aug 19 23:12:59	r	Melandri et al. (2017c); Pian et al. (2017)
REM/ROS2	2017 Aug 19 23:12:59	i	Melandri et al. (2017c); Pian et al. (2017)
REM/ROS2	2017 Aug 19 23:12:59	g	Melandri et al. (2017c); Pian et al. (2017)
MASTER/-	2017 Aug 19 23:13:20	Clear	Lipunov et al. (2017b, 2017a)
Gemini-South/Flamingos-2	2017 Aug 19 23:13:34	H	Cowperthwaite et al. (2017b)
MPG2.2 m/GROND	2017 Aug 19 23:15:00	r	Smartt et al. (2017)
MPG2.2 m/GROND	2017 Aug 19 23:15:00	z	Smartt et al. (2017)
MPG2.2 m/GROND	2017 Aug 19 23:15:00	H	Smartt et al. (2017)
MPG2.2 m/GROND	2017 Aug 19 23:15:00	i	Smartt et al. (2017)
MPG2.2 m/GROND	2017 Aug 19 23:15:00	J	Smartt et al. (2017)
TOROS/EABA	2017 Aug 19 23:18:38	r	Diaz et al. (2017b), Diaz et al. (2017, in preparation)
Magellan-Baade/FourStar	2017 Aug 19 23:18:50	H	Drout et al. (2017b)
Etelman/VIRT/CCDimager	2017 Aug 19 23:19:00	R	Gendre et al. (2017), Andreoni et al. (2017, in preparation)
Blanco/DECam/-	2017 Aug 19 23:23:29	Y	Cowperthwaite et al. (2017b); Soares-Santos et al. (2017)
Blanco/DECam/-	2017 Aug 19 23:26:59	r	Cowperthwaite et al. (2017b); Soares-Santos et al. (2017)
Blanco/DECam/-	2017 Aug 19 23:27:59	g	Cowperthwaite et al. (2017b); Soares-Santos et al. (2017)
ChilescopeRC-1000/-	2017 Aug 19 23:30:33	clear	Pozanenko et al. (2017a, 2017b), Pozanenko et al. (2017, in preparation)
Magellan-Baade/FourStar	2017 Aug 19 23:31:06	J1	Drout et al. (2017b)
Blanco/DECam/-	2017 Aug 19 23:31:13	u	Cowperthwaite et al. (2017b); Soares-Santos et al. (2017)
Magellan-Baade/FourStar	2017 Aug 19 23:41:59	Ks	Drout et al. (2017b)
Magellan-Baade/IMACS	2017 Aug 20 00:13:32	r	Drout et al. (2017b)
Gemini-South/Flamingos-2	2017 Aug 20 00:19:00	Ks	Kasliwal et al. (2017)
LasCumbres 1-m/Sinistro	2017 Aug 20 00:24:28	g	Arcavi et al. (2017e)
Gemini-South/Flamingos-2	2017 Aug 20 00:27:00	J	Kasliwal et al. (2017)
NTT/-	2017 Aug 20 01:19:00	U	Smartt et al. (2017)
Pan-STARRS1/GPC1	2017 Aug 20 05:38:00	y	Chambers et al. (2017c); Smartt et al. (2017)
Pan-STARRS1/GPC1	2017 Aug 20 05:41:00	z	Chambers et al. (2017c); Smartt et al. (2017)
Pan-STARRS1/GPC1	2017 Aug 20 05:45:00	i	Chambers et al. (2017c); Smartt et al. (2017)
T31/-	2017 Aug 20 09:20:38	R	Im et al. (2017a, 2017b), Im et al. (2017, in preparation)
MASTER/-	2017 Aug 20 17:04:36	Clear	Lipunov et al. (2017b, 2017a)
MASTER/-	2017 Aug 20 17:25:56	R	Lipunov et al. (2017b, 2017a)
MASTER/-	2017 Aug 20 17:36:32	B	Lipunov et al. (2017b, 2017a)
LasCumbres 1-m/Sinistro	2017 Aug 20 17:39:50	i	Arcavi et al. (2017e)
LasCumbres 1-m/Sinistro	2017 Aug 20 17:45:36	z	Arcavi et al. (2017e)
LasCumbres 1-m/Sinistro	2017 Aug 20 17:49:55	V	Arcavi et al. (2017e)
MPG2.2 m/GROND	2017 Aug 20 23:15:00	g	Smartt et al. (2017)
Magellan-Baade/FourStar	2017 Aug 20 23:20:42	J	Drout et al. (2017b)
ChilescopeRC-1000/-	2017 Aug 20 23:21:09	clear	Pozanenko et al. (2017a)
VISTA/VIRCAM	2017 Aug 20 23:24:00	K	Tanvir & Levan (2017)
Blanco/DECam/-	2017 Aug 20 23:37:06	u	Cowperthwaite et al. (2017b); Soares-Santos et al. (2017)
Swope/DirectCCD	2017 Aug 20 23:44:36	V	Coulter et al. (2017)
Swope/DirectCCD	2017 Aug 20 23:53:00	B	Coulter et al. (2017)

Table 1
(Continued)

Telescope/Instrument	UT Date	Band	References
MASTER/–	2017 Aug 21 00:26:31	Clear	Lipunov et al. (2017b, 2017a)
Gemini-South/Flamingos-2	2017 Aug 21 00:38:00	H	Kasliwal et al. (2017); Troja et al. (2017a)
Pan-STARRS1/GPC1	2017 Aug 21 05:37:00	y	Chambers et al. (2017d); Smartt et al. (2017)
Pan-STARRS1/GPC1	2017 Aug 21 05:39:00	z	Chambers et al. (2017d); Smartt et al. (2017)
Pan-STARRS1/GPC1	2017 Aug 21 05:42:00	i	Chambers et al. (2017d); Smartt et al. (2017)
AST3-2/wide-fieldcamera	2017 Aug 21 15:36:50	g	...
MASTER/–	2017 Aug 21 17:08:14	Clear	Lipunov et al. (2017b, 2017a)
MASTER/–	2017 Aug 21 18:06:12	R	Lipunov et al. (2017b, 2017a)
MASTER/–	2017 Aug 21 19:20:23	B	Lipunov et al. (2017b, 2017a)
duPont/RetroCam	2017 Aug 21 23:17:19	Y	Drout et al. (2017b)
Etelman/VIRT/CCDimager	2017 Aug 21 23:19:00	Clear	Gendre et al. (2017); Andreoni et al. (2017, in preparation)
MPG2.2 m/GROND	2017 Aug 21 23:22:00	Ks	Smartt et al. (2017)
VLT/FORS2	2017 Aug 21 23:23:11	R	D’Avanzo et al. (2017); Pian et al. (2017)
ChileScopeRC-1000/–	2017 Aug 21 23:32:09	clear	Pozanenko et al. (2017c)
duPont/RetroCam	2017 Aug 21 23:34:34	H	Drout et al. (2017b)
LasCumbres 1-m/Sinistro	2017 Aug 21 23:48:28	w	Arcavi et al. (2017e)
Swope/DirectCCD	2017 Aug 21 23:54:57	r	Coulter et al. (2017)
duPont/RetroCam	2017 Aug 21 23:57:41	J	Drout et al. (2017b)
Swope/DirectCCD	2017 Aug 22 00:06:17	g	Coulter et al. (2017)
VLT/FORS2	2017 Aug 22 00:09:09	z	D’Avanzo et al. (2017); Pian et al. (2017)
VLT/FORS2	2017 Aug 22 00:18:49	I	D’Avanzo et al. (2017); Pian et al. (2017)
Magellan-Clay/LDSS3-C	2017 Aug 22 00:27:40	g	Drout et al. (2017b)
VLT/FORS2	2017 Aug 22 00:28:18	B	D’Avanzo et al. (2017); Pian et al. (2017)
VLT/FORS2	2017 Aug 22 00:38:20	V	D’Avanzo et al. (2017); Pian et al. (2017)
HST/WFC3/IR	2017 Aug 22 07:34:00	F110W	Tanvir & Levan (2017); Troja et al. (2017a)
LasCumbres 1-m/Sinistro	2017 Aug 22 08:35:31	r	Arcavi et al. (2017e)
HST/WFC3/IR	2017 Aug 22 10:45:00	F160W	Tanvir & Levan (2017); Troja et al. (2017a)
HubbleSpaceTelescope/WFC3	2017 Aug 22 20:19:00	F336W	Adams et al. (2017); Kasliwal et al. (2017)
Etelman/VIRT/CCDimager	2017 Aug 22 23:19:00	Clear	Gendre et al. (2017); Andreoni et al. (2017, in preparation)
VLT/VIMOS	2017 Aug 22 23:30:00	z	Tanvir & Levan (2017)
duPont/RetroCam	2017 Aug 22 23:33:54	Y	Drout et al. (2017b)
VLT/VIMOS	2017 Aug 22 23:42:00	R	Tanvir & Levan (2017)
VLT/VIMOS	2017 Aug 22 23:53:00	u	Evans et al. (2017b)
VLT/FORS2	2017 Aug 22 23:53:31	Rspecial	Covino et al. (2017)
VST/OmegaCam	2017 Aug 22 23:58:32	g	Grado et al. (2017a); Pian et al. (2017)
VLT/X-shooter	2017 Aug 23 00:35:20	r	Pian et al. (2017)
VLT/X-shooter	2017 Aug 23 00:37:08	z	Pian et al. (2017)
VLT/X-shooter	2017 Aug 23 00:40:24	g	Pian et al. (2017)
Zadko/CCDimager	2017 Aug 23 11:32:00	r	Coward et al. (2017a),
IRSF/SIRIUS	2017 Aug 23 17:22:00	Ks	Kasliwal et al. (2017)
IRSF/SIRIUS	2017 Aug 23 17:22:00	J	Kasliwal et al. (2017)
IRSF/SIRIUS	2017 Aug 23 17:22:00	H	Kasliwal et al. (2017)
VST/OmegaCam	2017 Aug 23 23:26:51	i	Grado et al. (2017a); Pian et al. (2017)
VLT/VISIR	2017 Aug 23 23:35:00	8.6um	Kasliwal et al. (2017)
VST/OmegaCam	2017 Aug 23 23:42:49	r	Grado et al. (2017a); Pian et al. (2017)
CTIO1.3 m/ANDICAM	2017 Aug 24 23:20:00	Ks	Kasliwal et al. (2017)
Swope/DirectCCD	2017 Aug 24 23:45:07	i	Coulter et al. (2017)
ChileScopeRC-1000/–	2017 Aug 24 23:53:39	clear	Pozanenko et al. (2017b),
Blanco/DECam/–	2017 Aug 24 23:56:22	g	Cowperthwaite et al. (2017b); Soares-Santos et al. (2017)
Magellan-Clay/LDSS3-C	2017 Aug 25 00:43:27	B	Drout et al. (2017b)
HST/WFC3/UVIS	2017 Aug 25 13:55:00	F606W	Tanvir & Levan (2017); Troja et al. (2017a)
HST/WFC3/UVIS	2017 Aug 25 15:28:00	F475W	Tanvir & Levan (2017); Troja et al. (2017a)
HST/WFC3/UVIS	2017 Aug 25 15:36:00	F275W	Levan & Tanvir (2017); Tanvir & Levan (2017),
Magellan-Clay/LDSS3-C	2017 Aug 25 23:19:41	z	Drout et al. (2017b)
Blanco/DECam/–	2017 Aug 25 23:56:05	r	Cowperthwaite et al. (2017b); Soares-Santos et al. (2017)
VLT/FORS2	2017 Aug 26 00:13:40	z	Covino et al. (2017)
duPont/RetroCam	2017 Aug 26 00:14:28	J	Drout et al. (2017b)
VLT/FORS2	2017 Aug 26 00:27:16	B	Pian et al. (2017)
IRSF/SIRIUS	2017 Aug 26 16:57:00	J	Kasliwal et al. (2017)
IRSF/SIRIUS	2017 Aug 26 16:57:00	Ks	Kasliwal et al. (2017)
IRSF/SIRIUS	2017 Aug 26 16:57:00	H	Kasliwal et al. (2017)

Table 1
(Continued)

Telescope/Instrument	UT Date	Band	References
VISTA/VIRCAM	2017 Aug 26 23:38:00	Y	Tanvir & Levan (2017)
ApachePointObservatory/NICFPs	2017 Aug 27 02:15:00	Ks	Kasliwal et al. (2017)
Palomar200inch/WIRC	2017 Aug 27 02:49:00	Ks	Kasliwal et al. (2017)
HST/WFC3/IR	2017 Aug 27 06:45:56	F110W	Cowperthwaite et al. (2017b)
HST/WFC3/IR	2017 Aug 27 07:06:57	F160W	Cowperthwaite et al. (2017b)
HST/WFC3/UVIS	2017 Aug 27 08:20:49	F336W	Cowperthwaite et al. (2017b)
HST/ACS/WFC	2017 Aug 27 10:24:14	F475W	Cowperthwaite et al. (2017b)
HST/ACS/WFC	2017 Aug 27 11:57:07	F625W	Cowperthwaite et al. (2017b)
HST/ACS/WFC	2017 Aug 27 13:27:15	F775W	Cowperthwaite et al. (2017b)
HST/ACS/WFC	2017 Aug 27 13:45:24	F850LP	Cowperthwaite et al. (2017b)
Gemini-South/Flamingos-2	2017 Aug 27 23:16:00	J	Kasliwal et al. (2017)
CTIO1.3 m/ANDICAM	2017 Aug 27 23:18:00	Ks	Kasliwal et al. (2017)
Blanco/DECam/–	2017 Aug 27 23:23:33	Y	Cowperthwaite et al. (2017b); Soares-Santos et al. (2017)
MPG2.2 m/GROND	2017 Aug 27 23:24:00	J	Smartt et al. (2017)
Gemini-South/Flamingos-2	2017 Aug 27 23:28:10	K_s	Cowperthwaite et al. (2017b)
Gemini-South/Flamingos-2	2017 Aug 27 23:33:07	H	Cowperthwaite et al. (2017b)
duPont/RetroCam	2017 Aug 27 23:36:25	H	Drout et al. (2017b)
Blanco/DECam/–	2017 Aug 27 23:40:57	z	Cowperthwaite et al. (2017b); Soares-Santos et al. (2017)
Blanco/DECam/–	2017 Aug 28 00:00:01	i	Cowperthwaite et al. (2017b); Soares-Santos et al. (2017)
VLT/FORS2	2017 Aug 28 00:07:31	R	Pian et al. (2017a)
VLT/FORS2	2017 Aug 28 00:15:56	V	Pian et al. (2017a)
MPG2.2 m/GROND	2017 Aug 28 00:22:00	H	Smartt et al. (2017)
HST/WFC3/IR	2017 Aug 28 01:50:00	F110W	Tanvir & Levan (2017); Troja et al. (2017a)
HST/WFC3/IR	2017 Aug 28 03:25:00	F160W	Tanvir & Levan (2017); Troja et al. (2017a)
HST/WFC3/UVIS	2017 Aug 28 20:56:00	F275W	Levan & Tanvir (2017); Tanvir & Levan (2017),
HST/WFC3/UVIS	2017 Aug 28 22:29:00	F475W	Tanvir & Levan (2017); Troja et al. (2017a)
HST/WFC3/UVIS	2017 Aug 28 23:02:00	F814W	Tanvir & Levan (2017); Troja et al. (2017a)
NTT/–	2017 Aug 28 23:03:00	H	Smartt et al. (2017)
HST/WFC3/UVIS	2017 Aug 28 23:08:00	F606W	Tanvir & Levan (2017); Troja et al. (2017a)
MPG2.2 m/GROND	2017 Aug 28 23:22:00	Ks	Smartt et al. (2017)
VISTA/VIRCAM	2017 Aug 28 23:33:00	J	Tanvir & Levan (2017)
Gemini-South/Flamingos-2	2017 Aug 28 23:36:01	K_s	Cowperthwaite et al. (2017b)
VLT/FORS2	2017 Aug 29 00:00:13	I	Pian et al. (2017a)
HubbleSpaceTelescope/WFC3/UVIS	2017 Aug 29 00:36:00	F275W	Kasliwal et al. (2017)
HubbleSpaceTelescope/WFC3/UVIS	2017 Aug 29 00:36:00	F225W	Kasliwal et al. (2017)
NTT/–	2017 Aug 29 22:56:00	Ks	Smartt et al. (2017)
VLT/VIMOS	2017 Aug 29 23:16:00	R	Tanvir & Levan (2017)
SkyMapper/–	2017 Aug 30 09:26:00	u	...
SkyMapper/–	2017 Aug 30 09:32:00	v	...
NTT/–	2017 Aug 30 23:03:00	Ks	Smartt et al. (2017)
VLT/FORS2	2017 Aug 31 23:34:46	z	Pian et al. (2017a)
VISTA/VIRCAM	2017 Aug 31 23:42:00	K	Tanvir & Levan (2017)
Gemini-South/Flamingos-2	2017 Aug 31 23:50:00	H	Singer et al. (2017b); Kasliwal et al. (2017)
SkyMapper/–	2017 Sep 01 09:12:00	i	...
SkyMapper/–	2017 Sep 01 09:14:00	z	...
SkyMapper/–	2017 Sep 03 09:21:00	g	...
SkyMapper/–	2017 Sep 03 09:23:00	r	...
NTT/–	2017 Sep 04 23:12:00	Ks	Smartt et al. (2017)
Gemini-South/Flamingos-2	2017 Sep 04 23:28:45	K_s	Cowperthwaite et al. (2017b)
VLT/VIMOS	2017 Sep 05 23:23:00	z	Tanvir & Levan (2017)
Gemini-South/Flamingos-2	2017 Sep 05 23:48:00	Ks	Kasliwal et al. (2017)
Magellan-Baade/FourStar	2017 Sep 06 23:24:28	Ks	Drout et al. (2017b)
VLT/HAWKI	2017 Sep 07 23:11:00	K	Tanvir & Levan (2017)
VLT/HAWKI	2017 Sep 11 23:21:00	K	Tanvir & Levan (2017)

Note. This is a subset of all the observations made in order to give a sense of the substantial coverage of this event.

time, flux upper limits, and the energy range of the observations, which are summarized here.

At the time of GRB 170817A, three out of six spacecraft of the Inter Planetary Network (Hurley et al. 2013) had a

favorable orientation to observe the LIGO-Virgo skymap. However, based on the *Fermi*-GBM (Goldstein et al. 2017b) and *INTEGRAL* analyses, GRB 170817A was too weak to be detected by *Konus-Wind* (Svinkin et al. 2017a). Using the

Table 2
Record of Spectroscopic Observations

Telescope/Instrument	UT Date	Wavelengths (Å)	Resolution (R)	References
<i>Magellan</i> -Clay/LDSS-3	2017 Aug 18 00:26:17	3780–10200	860	Drout et al. (2017); Shappee et al. (2017)
<i>Magellan</i> -Clay/LDSS-3	2017 Aug 18 00:40:09	3800–6200	1900	Shappee et al. (2017)
<i>Magellan</i> -Clay/LDSS-3	2017 Aug 18 00:52:09	6450–10000	1810	Shappee et al. (2017)
<i>Magellan</i> -Baade/MagE	2017 Aug 18 01:26:22	3650–10100	5800	Shappee et al. (2017)
ANU2.3/WiFeS	2017 Aug 18 09:24:00	3200–9800	B/R 3000	...
SALT/RSS	2017 Aug 18 17:07:00	3600–8000	300	Shara et al. (2017),
NTT/EFOSC2Gr#11+16	2017 Aug 18 23:19:12	3330–9970	260/400	Smartt et al. (2017)
VLT/X-shooter	2017 Aug 18 23:22:25	3000–24800	4290/8150/5750	Pian et al. (2017b, 2017b)
SOAR/GHTS	2017 Aug 18 23:22:39	4000–8000	830	Nicholl et al. (2017d)
<i>Magellan</i> -Clay/LDSS-3	2017 Aug 18 23:47:37	3820–9120	860	Shappee et al. (2017)
VLT/MUSE	2017 Aug 18 23:49:00	4650–9300	3000	Levan & Tanvir (2017); Tanvir & Levan (2017)
<i>Magellan</i> -Clay/MIKE	2017 Aug 19 00:18:11	3900–9400	30000	Shappee et al. (2017)
<i>Magellan</i> -Baade/MagE	2017 Aug 19 00:35:25	3800–10300	4100	Shappee et al. (2017)
Gemini-South/FLAMINGOS2	2017 Aug 19 00:42:27	9100–18000	500	Chornock et al. (2017a)
LCOFaulkesTelescopeSouth/FLOYDS	2017 Aug 19 08:36:22	5500–9250	700	GC21908, McCully et al. (2017b)
ANU2.3/WiFeS	2017 Aug 19 09:26:12	3200–9800	B/R 3000	...
SALT/RSS	2017 Aug 19 16:58:00	3600–8000	300	Shara et al. (2017)
SALT/RSS	2017 Aug 19 16:58:32	3600–8000	300	Shara et al. (2017); Shara et al. 2017, McCully et al. (2017b)
NTT/EFOSC2Gr#11+16	2017 Aug 19 23:25:41	3330–9970	260/400	Smartt et al. (2017)
SOAR/GHTS	2017 Aug 19 23:28:32	4000–8000	830	Nicholl et al. (2017d)
VLT/Xshooterfixed	2017 Aug 19 23:28:46	3700–22790	4290/3330/5450	Smartt et al. (2017)
Gemini-South/FLAMINGOS2	2017 Aug 19 23:42:56	9100–18000	500	Chornock et al. (2017a)
<i>Magellan</i> -Baade/IMACS	2017 Aug 20 00:26:28	4355–8750	1000	Shappee et al. (2017)
GeminiSouth/GMOS	2017 Aug 20 01:01:54	4000–9500	400	McCully et al. (2017a, 2017b)
Gemini-South/GMOS	2017 Aug 20 01:08:00	6000–9000	1900	Kasliwal et al. (2017)
ANU2.3/WiFeS	2017 Aug 20 09:21:33	3200–9800	B/R 3000	...
NTT/EFOSC2Gr#11+16	2017 Aug 20 23:21:13	3330–9970	390/600	Smartt et al. (2017)
SOAR/GHTS	2017 Aug 20 23:23:17	5000–9000	830	Nicholl et al. (2017d)
VLT/X-shooter	2017 Aug 20 23:25:28	3000–24800	4290/8150/5750	Pian et al. (2017a)
<i>Magellan</i> -Clay/LDSS-3	2017 Aug 20 23:45:53	4450–10400	860	Shappee et al. (2017)
Gemini-South/GMOS	2017 Aug 21 00:15:00	3800–9200	1700	Troja et al. (2017b); Kasliwal et al. (2017); Troja et al. (2017a)
GeminiSouth/GMOS	2017 Aug 21 00:16:09	4000–9500	400	Troja et al. (2017b); McCully et al. (2017b); Troja et al. (2017a)
VLT/FORS2	2017 Aug 21 00:43:12	3500–8600	800–1000	Pian et al. (2017a)
ANU2.3/WiFeS	2017 Aug 21 09:13:00	3200–7060	B 3000 R 7000	...
NTT/SOFIBlueGrism	2017 Aug 21 23:11:37	9380–16460	550	Smartt et al. (2017)
SOAR/GHTS	2017 Aug 21 23:24:49	4000–8000	830	Nicholl et al. (2017d)
VLT/Xshooterfixed	2017 Aug 21 23:25:38	3700–22790	4290/3330/5450	Smartt et al. (2017)
VLT/FORS2	2017 Aug 21 23:31:12	3500–8600	800–1000	Pian et al. (2017a)
Gemini-South/FLAMINGOS2	2017 Aug 21 23:40:09	9100–18000	500	Chornock et al. (2017a)
Gemini-South/Flamingos-2	2017 Aug 22 00:21:00	12980–25070	600	Kasliwal et al. (2017)
Gemini-South/Flamingos-2	2017 Aug 22 00:47:00	9840–18020	600	Kasliwal et al. (2017)
<i>Magellan</i> -Clay/LDSS-3	2017 Aug 22 00:50:34	5010–10200	860	Shappee et al. (2017)
<i>HST</i> /WFC3/IR-G102	2017 Aug 22 09:07:00	8000–11150	210	Tanvir & Levan (2017); Troja et al. (2017a)
<i>HST</i> /WFC3/IR-G141	2017 Aug 22 10:53:00	10750–17000	130	Tanvir & Levan (2017); Troja et al. (2017a)
<i>Magellan</i> -Clay/LDSS-3	2017 Aug 22 23:34:00	5000–10200	860	Shappee et al. (2017)
<i>HST</i> /STIS	2017 Aug 23 02:51:54	1600–3200	700	Nicholl et al. (2017d)

Table 2
(Continued)

Telescope/Instrument	UT Date	Wavelengths (\AA)	Resolution (R)	References
AAT/AAOmega2DF	2017 Aug 24 08:55:00	3750–8900	1700	Andreoni et al. (2017),
<i>HST</i> /WFC3/IR-G102	2017 Aug 24 18:58:00	8000–11150	210	Tanvir & Levan (2017); Troja et al. (2017a)
<i>Magellan</i> -Clay/LDSS-3	2017 Aug 24 23:33:51	6380–10500	1810	Shappee et al. (2017)
SOAR/GHTS	2017 Aug 24 23:34:31	5000–9000	830	Nicholl et al. (2017d)
Gemini-South/FLAMINGOS2	2017 Aug 24 23:56:32	9100–18000	500	Chornock et al. (2017a)
KeckI/LRIS	2017 Aug 25 05:45:00	2000–10300	1000	Kasliwal et al. (2017)
<i>Magellan</i> /Baade/IMACS	2017 Aug 25 23:37:59	4300–9300	1100	Nicholl et al. (2017d)
<i>Magellan</i> -Clay/LDSS-3	2017 Aug 25 23:39:18	6380–10500	1810	Shappee et al. (2017)
Gemini-South/FLAMINGOS2	2017 Aug 26 00:21:24	9100–18000	500	Chornock et al. (2017a)
<i>HST</i> /WFC3/IR-G141	2017 Aug 26 22:57:00	10750–17000	130	Tanvir & Levan (2017); Troja et al. (2017a)
<i>Magellan</i> /Baade/IMACS	2017 Aug 26 23:20:54	4300–9300	1100	Nicholl et al. (2017d)
Gemini-South/FLAMINGOS2	2017 Aug 27 00:12:20	9100–18000	500	Chornock et al. (2017a)
Gemini-South/FLAMINGOS2	2017 Aug 28 00:16:28	9100–18000	500	Chornock et al. (2017a)
<i>HST</i> /WFC3/IR-G102	2017 Aug 28 01:58:00	8000–11150	210	Tanvir & Levan (2017); Troja et al. (2017a)
<i>HST</i> /WFC3/IR-G141	2017 Aug 28 03:33:00	10750–17000	130	Tanvir & Levan (2017); Troja et al. (2017a)
Gemini-South/Flamingos-2	2017 Aug 29 00:23:00	12980–25070	600	Kasliwal et al. (2017)

Table 3
Gamma-Ray Monitoring and Evolution of GW170817

Observatory	UT Date	Time since GW Trigger	90% Flux Upper Limit ($\text{erg cm}^{-2} \text{s}^{-1}$)	Energy Band	GCN/Reference
<i>Insight</i> -HXMT/HE	Aug 17 12:34:24 UTC	−400 s	3.7×10^{-7}	0.2–5 MeV	Li et al. (2017)
CALET CGBM	Aug 17 12:41:04 UTC	0.0	1.3×10^{-7a}	10–1000 keV	Nakahira et al. (2017)
<i>Konus-Wind</i>	Aug 17 12:41:04.446 UTC	0.0	3.0×10^{-7} [erg cm^{-2}]	10 keV–10 MeV	Svinkin et al. (2017a)
<i>Insight</i> -HXMT/HE	Aug 17 12:41:04.446 UTC	0.0	3.7×10^{-7}	0.2–5 MeV	Li et al. (2017)
<i>Insight</i> -HXMT/HE	Aug 17 12:41:06.30 UTC	1.85 s	6.6×10^{-7}	0.2–5 MeV	Li et al. (2017)
<i>Insight</i> -HXMT/HE	Aug 17 12:46:04 UTC	300 s	1.5×10^{-7}	0.2–5 MeV	Li et al. (2017)
AGILE-GRID	Aug 17 12:56:41 UTC	0.011 days	3.9×10^{-9}	0.03–3 GeV	V. Verrecchia et al. (2017, in preparation)
<i>Fermi</i> -LAT	Aug 17 13:00:14 UTC	0.013 days	4.0×10^{-10}	0.1–1 GeV	Kocevski et al. (2017)
H.E.S.S.	Aug 17 17:59 UTC	0.22 days	3.9×10^{-12}	0.28–2.31 TeV	H. Abdalla et al. (H.E.S.S. Collaboration) (2017, in preparation)
HAWC	Aug 17 20:53:14—Aug 17 22:55:00 UTC	0.342 days + 0.425 days	1.7×10^{-10}	4–100 TeV	Martinez-Castellanos et al. (2017)
<i>Fermi</i> -GBM	Aug 16 12:41:06—Aug 18 12:41:06 UTC	± 1.0 days	$(8.0\text{--}9.9) \times 10^{-10}$	20–100 keV	Goldstein et al. (2017a)
NTEGRAL IBIS/ISGRI	Aug 18 12:45:10—Aug 23 03:22:34 UTC	1–5.7 days	2.0×10^{-11}	20–80 keV	Savchenko et al. (2017)
INTEGRAL IBIS/ISGRI	Aug 18 12:45:10—Aug 23 03:22:34 UTC	1–5.7 days	3.6×10^{-11}	80–300 keV	Savchenko et al. (2017)
INTEGRAL IBIS/PICsIT	Aug 18 12:45:10—Aug 23 03:22:34 UTC	1–5.7 days	0.9×10^{-10}	468–572 keV	Savchenko et al. (2017)
INTEGRAL IBIS/PICsIT	Aug 18 12:45:10—Aug 23 03:22:34 UTC	1–5.7 days	4.4×10^{-10}	572–1196 keV	Savchenko et al. (2017)
INTEGRAL SPI	Aug 18 12:45:10—Aug 23 03:22:34 UTC	1–5.7 days	2.4×10^{-10}	300–500 keV	Savchenko et al. (2017)
INTEGRAL SPI	Aug 18 12:45:10—Aug 23 03:22:34 UTC	1–5.7 days	7.0×10^{-10}	500–1000 keV	Savchenko et al. (2017)
INTEGRAL SPI	Aug 18 12:45:10—Aug 23 03:22:34 UTC	1–5.7 days	1.5×10^{-9}	1000–2000 keV	Savchenko et al. (2017)
INTEGRAL SPI	Aug 18 12:45:10—Aug 23 03:22:34 UTC	1–5.7 days	2.9×10^{-9}	2000–4000 keV	Savchenko et al. (2017)
H.E.S.S.	Aug 18 17:55 UTC	1.22 days	3.3×10^{-12}	0.27–3.27 TeV	H. Abdalla et al. (H.E.S.S. Collaboration) (2017, in preparation)
H.E.S.S.	Aug 19 17:56 UTC	2.22 days	1.0×10^{-12}	0.31–2.88 TeV	H. Abdalla et al. (H.E.S.S. Collaboration) (2017, in preparation)
H.E.S.S.	Aug 21 + Aug 22 18:15 UTC	4.23 days + 5.23 days	2.9×10^{-12}	0.50–5.96 TeV	H. Abdalla et al. (H.E.S.S. Collaboration) (2017, in preparation)

Note.

^a Assuming no shielding by the structures of ISS.

Earth Occultation technique (Wilson-Hodge et al. 2012), *Fermi*-GBM placed limits on persistent emission for the 48 hr period centered at the *Fermi*-GBM trigger time over the 90% credible region of the GW170817 localization. Using the offline targeted search for transient signals (Blackburn et al. 2015), *Fermi*-GBM also set constraining upper limits on precursor and extended emission associated with GRB 170817A (Goldstein et al. 2017b). *INTEGRAL* (Winkler et al. 2003) continued uninterrupted observations after GRB 170817A for 10 hr. Using the PiCSIT (Labanti et al. 2003) and SPI-ACS detectors, the presence of a steady source 10 times weaker than the prompt emission was excluded (Savchenko et al. 2017).

The High Energy telescope on board *Insight*-HXMT monitored the entire GW170817 skymap from $T_0 - 650$ s to $T_0 + 450$ s but, due to the weak and soft nature of GRB 170817A, did not detect any significant excess at T_0 (Liao et al. 2017). Upper limits from 0.2–5 MeV for GRB 170817A and other emission episodes are reported in Li et al. (2017).

The Calorimetric Electron Telescope (CALET) Gamma-ray Burst Monitor (CGBM) found no significant excess around T_0 . Upper limits may be affected due to the location of SSS17a/AT2017gfo being covered by the large structure of the International Space Station at the time of GRB 170817A (Nakahira et al. 2017). *AstroSat* CZTI (Singh et al. 2014; Bhalerao et al. 2017) reported upper limits for the 100 s interval centered on T_0 (Balasubramanian et al. 2017); the position of SSS17a/AT2017gfo was occulted by the Earth, however, at the time of the trigger.

For the AstroRivelatore Gamma a Immagini Leggero (AGILE) satellite (Tavani et al. 2009) the first exposure of the GW170817 localization region by the Gamma Ray Imaging Detector (GRID), which was occulted by the Earth at the time of GRB 170817A, started at $T_0 + 935$ s. The GRID observed the field before and after T_0 , typically with 150 s exposures. No gamma-ray source was detected above 3σ in the energy range 30 MeV–30 GeV (V. Verrecchia et al. 2017, in preparation).

At the time of the trigger, *Fermi* was entering the South Atlantic Anomaly (SAA) and the Large Area Telescope (LAT) was not collecting science data (*Fermi*-GBM uses different SAA boundaries and was still observing). *Fermi*-LAT resumed data taking at roughly $T_0 + 1153$ s, when 100% of the low-latency GW170817 skymap (LIGO Scientific Collaboration & Virgo Collaboration et al. 2017b) was in the field of view for ~ 1000 s. No significant source of high-energy emission was detected. Additional searches over different timescales were performed for the entire time span of LAT data, and no significant excess was detected at the position of SSS17a/AT2017gfo (Kocevski et al. 2017).

The High Energy Stereoscopic System (H.E.S.S.) array of imaging atmospheric Cherenkov telescopes observed from August 17 18:00 UTC with three pointing positions. The first, at $T_0 + 5.3$ hr, covered SSS17a/AT2017gfo. Observations repeated the following nights until the location moved outside the visibility window, with the last pointing performed on August 22 18:15 UTC. A preliminary analysis with an energy threshold of ~ 500 GeV revealed no significant gamma-ray emission (de Naurois et al. 2017), confirmed by the final, offline analysis (see H. Abdalla et al. (H.E.S.S. Collaboration) 2017, in preparation, for more results).

For the High-Altitude Water Cherenkov (HAWC) Observatory (Abeysekara et al. 2017) the LIGO-Virgo localization

region first became visible on August 17 between 19:57 and 23:25 UTC. SSS17a/AT2017gfo was observed for 2.03 hr starting at 20:53 UTC. Upper limits from HAWC for energies > 40 TeV assuming an $E^{-2.5}$ spectrum are reported in Martinez-Castellanos et al. (2017).

INTEGRAL (3 keV–8 MeV) carried out follow-up observations of the LIGO-Virgo localization region, centered on the optical counterpart, starting 24 hr after the event and spanning 4.7 days. Hard X-ray emission is mostly constrained by IBIS (Ubertini et al. 2003), while above 500 keV SPI (Vedrenne et al. 2003) is more sensitive. Besides the steady flux limits reported in Table 3, these observations exclude delayed bursting activity at the level of giant magnetar flares. No gamma-ray lines from a kilonova or $e^{+/-}$ pair plasma annihilation were detected (see Savchenko et al. 2017).

3.3. Discovery of the X-Ray Counterpart

While the UV, optical, and IR observations mapped the emission from the sub-relativistic ejecta, X-ray observations probed a different physical regime. X-ray observations of GRB afterglows are important to constrain the geometry of the outflow, its energy output, and the orientation of the system with respect to the observers' line of sight.

The earliest limits at X-ray wavelengths were provided by the Gas Slit Camera (GSC) of the *Monitor of All-Sky X-ray Image* (*MAXI*; Matsuoka et al. 2009). Due to an unfavorable sky position, the location of GW170817 was not observed by *MAXI* until August 17 17:21 UTC ($T_0 + 0.19$ days). No X-ray emission was detected at this time to a limiting flux of 8.6×10^{-9} erg cm $^{-2}$ s $^{-1}$ (2–10 keV; Sugita et al. 2017; S. Sugita 2017, in preparation). *MAXI* obtained three more scans over the location with no detections before the more sensitive pointed observations began.

In addition, the Super-*AGILE* detector (Feroci et al. 2007) on board the *AGILE* mission (Tavani et al. 2009) observed the location of GW170817 starting at August 18 01:16:34.84 UTC ($T_0 + 0.53$ days). No X-ray source was detected at the location of GW170817, with a 3σ upper limit of 3.0×10^{-9} erg cm $^{-2}$ s $^{-1}$ (18–60 keV; V. Verrecchia et al. 2017, in preparation).

The first pointed X-ray observations of GW170817 were obtained by the X-Ray Telescope (Burrows et al. 2005) on the *Swift* satellite (Gehrels 2004) and the *Nuclear Spectroscopic Telescope ARray* (*NuSTAR*; Harrison et al. 2013), beginning at $T_0 + 0.62$ days and $T_0 + 0.70$ days, respectively. No X-ray emission was detected at the location of GW170817 to limiting fluxes of 2.7×10^{-13} erg cm $^{-2}$ s $^{-1}$ (0.3–10.0 keV; Evans et al. 2017a, 2017b) and 2.6×10^{-14} erg cm $^{-2}$ s $^{-1}$ (3.0–10.0 keV; Evans et al. 2017a, 2017b). *Swift* continued to monitor the field, and after stacking several epochs of observations, a weak X-ray source was detected near the location of GW170817 at a flux of 2.6×10^{-14} erg cm $^{-2}$ s $^{-1}$ (Evans et al. 2017c).

INTEGRAL (see Section 3.2) performed pointed follow-up observations from one to about six days after the trigger. The X-ray monitor JEM-X (Lund et al. 2003) constrained the average X-ray luminosity at the location of the optical transient to be $< 2 \times 10^{-11}$ erg cm $^{-2}$ s $^{-1}$ (3–10.0 keV) and $< 7 \times 10^{-12}$ erg cm $^{-2}$ s $^{-1}$ (10–25 keV; Savchenko et al. 2017).

Chandra obtained a series of observations of GW170817 beginning at August 19 17:10 UTC ($T_0 + 2.2$ days) and continuing until the emission from NGC 4993 became unobservable because of SSS17a/AT2017gfo's proximity to

the Sun (Fong et al. 2017; Haggard et al. 2017b; Margutti et al. 2017a; Troja et al. 2017c, 2017e). Two days post-trigger, Margutti et al. (2017a) reported an X-ray non-detection for SSS17a/AT 2017gfo in a $\simeq 25$ ks *Chandra* exposure,⁹⁶⁴ along with the detection of an extended X-ray source whose position was consistent with the host NGC 4993 (Margutti et al. 2017b). Refined astrometry from subsequent *Swift* observations confirmed that the previously reported candidate was indeed associated with the host nucleus (Evans et al. 2017a, 2017b).

Nine days post-trigger, Troja et al. (2017c) reported the discovery of the X-ray counterpart with *Chandra*. In a 50 ks exposure observation, they detected significant X-ray emission at the same position of the optical/IR counterpart (Troja et al. 2017a; top right panel in Figure 2)⁹⁶⁵. Fifteen days post-trigger, two additional 50 ks *Chandra* observations were made, which confirmed the continued presence of X-ray emission. Based on the first of these two observations^{966,967}: Fong et al. (2017) reported the detection of the X-ray counterpart and the presence of an additional X-ray point source in the near vicinity (Margutti et al. 2017b), and Troja et al. (2017e) reported a flux of 4.5×10^{-15} erg cm⁻² s⁻¹ for the X-ray counterpart. One day later, Haggard et al. (2017b) reported another deep observation showing continued distinct X-ray emission coincident with SSS17a/AT 2017gfo, NGC 4993, and the additional point source (Haggard et al. 2017a, 2017b).¹⁰

Neither *Swift* nor *Chandra* can currently observe GW170817 because it is too close to the Sun ($<47^\circ$ for *Swift*, $<46^\circ$ for *Chandra*). Hence, until early 2017 December, *NuSTAR* is the only sensitive X-ray observatory that can continue to observe the location of GW170817.

All X-ray observations of GW170817 are summarized in Table 4.

3.4. Discovery of the Radio Counterpart

Radio emission traces fast-moving ejecta from a neutron star coalescence, providing information on the energetics of the explosion, the geometry of the ejecta, as well as the environment of the merger. The spectral and temporal evolution of such emission, coupled with X-ray observations, are likely to constrain several proposed models (see, e.g., Nakar & Piran 2011; Piran et al. 2013; Hotokezaka & Piran 2015; Hotokezaka et al. 2016; Gottlieb et al. 2017).

Prior to detection of SSS17a/AT 2017gfo, a blind radio survey of cataloged galaxies in the gravitational-wave localization volume commenced with the Australia Telescope Compact Array (ATCA; Wilson et al. 2011), and observed the merger events' location on 2017 August 18 at 01:46 UTC (Kaplan et al. 2017a). In addition, the Long Wavelength Array 1 (LWA1; Ellingson et al. 2013) followed up the gravitational-wave localization with observations at $t_c + 6.5$ hr, then on 2017 August 23 and 30 (Callister et al. 2017a; Callister et al. 2017b) using four beams (one centered on NGC 4993, one off-center, and two off NGC 4993). These observations set 3σ upper limits for the appearance of a radio source in the beam centered on NGC 4993, about 8 hours after the GW event, as ~ 200 Jy at 25 MHz and ~ 100 Jy at 45 MHz.

The first reported radio observations of the optical transient SSS17a/AT 2017gfo's location occurred on August 18 at 02:09:00 UTC (T0+13.5 hr) with the Karl G. Jansky Very Large Array (VLA) by Alexander et al. (2017d).⁹⁶⁸ Initially attributed to the optical transient, this radio source was later established to be an AGN in the nucleus of the host galaxy, NGC 4993 (Alexander et al. 2017e, 2017c). Subsequent observations with several radio facilities spanning a wide range of radio and millimeter frequencies continued to detect the AGN, but did not reveal radio emission at the position of the transient (Alexander et al. 2017f; Bannister et al. 2017b; Corsi et al. 2017a, 2017b, 2017c; De et al. 2017a, 2017b; Kaplan et al. 2017a; Lynch et al. 2017a, 2017b, 2017c; Mooley et al. 2017a; Resmi et al. 2017).

The first radio counterpart detection consistent with the *HST* position (refined by *Gaia* astrometry) of SSS17a/AT 2017gfo (Adams et al. 2017) was obtained with the VLA on 2017 September 2 and 3 at two different frequencies (≈ 3 GHz and ≈ 6 GHz) via two independent observations: the Jansky VLA mapping of Gravitational Wave bursts as Afterglows in Radio (JAGWAR⁹⁶⁹; Mooley et al. 2017b) and VLA/16A-206⁹⁷⁰ (Corsi et al. 2017d). Marginal evidence for radio excess emission at the location of SSS17a/AT 2017gfo was also confirmed in ATCA images taken on September 5 at similar radio frequencies (≈ 7.25 GHz; Murphy et al. 2017). Subsequent repeated detections spanning multiple frequencies have confirmed an evolving transient (Hallinan et al. 2017a, 2017b; Corsi et al. 2017d; Mooley et al. 2017b). Independent observations carried out on 2017 September 5 with the same frequency and exposure time used by Corsi et al. (2017d) did not detect any emission to a 5σ limit⁹⁷¹ (Alexander et al. 2017a), but this group also subsequently detected the radio counterpart on 2017 September 25 (Alexander et al. 2017b, 2017c).

SSS17a/AT 2017gfo, as well as other parts of the initial gravitational-wave localization area, were and are also being continuously monitored at a multitude of different frequencies with the Atacama Large Millimeter/submillimeter Array (ALMA; Wootten & Thompson 2009; Schulze et al. 2017; Kim et al. 2017, in preparation; Alexander et al. 2017c; Williams et al. 2017a), the Australian Square Kilometre Array Pathfinder (ASKAP; Johnston et al. 2007), ASKAP-Fast Radio Burst (Bannister et al. 2017a, 2017c), ATCA, Effelsberg-100 m (Barr et al. 2013), the Giant Metrewave Radio Telescope (GMRT; Swarup et al. 1991), the Low-Frequency Array (LOFAR; van Haarlem et al. 2013), the Long Wavelength Array (LWA1), MeerKAT (Goedhart et al. 2017a), the Murchison Widefield Array (MWA; Tingay et al. 2013), Parkes-64 m (SUPERB; Bailes et al. 2017a; Keane et al. 2017), Sardinia Radio Telescope (SRT; Prandoni et al. 2017), VLA, VLA Low Band Ionosphere and Transient Experiment (VLITE; Clarke & Kassim 2016), and also using the very long baseline interferometry (VLBI) technique with e-MERLIN (Moldon et al. 2017a, 2017b), the European VLBI Network (Paragi et al. 2017a, 2017b), and the Very Long Baseline Array (VLBA; Deller et al. 2017a, 2017b). The latter have the potential to resolve (mildly) relativistic ejecta on a timescale of months.

Table 5 summarizes the radio observations of GW170817.

⁹⁶⁴ *Chandra* OBSID-18955, PI: Fong.

⁹⁶⁵ *Chandra* OBSID-19294, PI: Troja.

⁹⁶⁶ *Chandra* OBSID-20728, PI: Troja (Director's Discretionary Time observation distributed also to Haggard, Fong, and Margutti).

⁹⁶⁷ *Chandra* OBSID-18988, PI: Haggard.

⁹⁶⁸ VLA/17A-218, PI: Fong.

⁹⁶⁹ VLA/17A-374, PI: Mooley.

⁹⁷⁰ VLA/16A-206, PI: Corsi.

⁹⁷¹ VLA/17A-231, PI: Alexander.

Table 4
X-Ray Monitoring and Evolution of GW170817

Observatory	UT Date (Start)	Time since GW trigger (days)	f_x (erg cm ⁻² s ⁻¹)	L_x (erg s ⁻¹)	Energy (keV)	GCN/Reference
<i>MAXI</i>	Aug 17 17:21:54 UTC	0.19	$<8.6 \times 10^{-9}$	$<1.65 \times 10^{45}$	2–10	S. Sugita et al. (2017, in preparation)
<i>MAXI</i>	Aug 17 18:54:27 UTC	0.26	$<7.7 \times 10^{-8}$	$<1.47 \times 10^{46}$	2–10	S. Sugita et al. (2017, in preparation)
<i>MAXI</i>	Aug 18 00:44:59 UTC	0.50	$<4.2 \times 10^{-9}$	$<8.0 \times 10^{44}$	2–10	S. Sugita et al. (2017, in preparation)
<i>Super-AGILE</i>	Aug 18 01:16:34 UTC	0.53	$<3.0 \times 10^{-9}$	$<5.4 \times 10^{44}$	18–60	V. Verrecchia et al. (2017, in preparation)
<i>MAXI</i>	Aug 18 02:18:08 UTC	0.57	$<2.2 \times 10^{-9}$	$<4.2 \times 10^{44}$	2–10	S. Sugita et al. (2017, in preparation)
<i>Swift-XRT</i>	Aug 18 03:34:33 UTC	0.62	$<2.74 \times 10^{-13}$	$<5.25 \times 10^{40}$	0.3–10	Evans et al. (2017b)
<i>NuSTAR</i>	Aug 18 05:25 UTC	0.7	$<2.62 \times 10^{-14}$	$<5.01 \times 10^{39}$	3–10	Evans et al. (2017b)
<i>Swift-XRT</i>	Aug 18 12:11:49 UTC	0.98	$<2.62 \times 10^{-12}$	$<5.01 \times 10^{41}$	0.3–10	Evans et al. (2017b)
<i>INTEGRAL JEM-X</i>	Aug 18 12:45:10 UTC	1–5.7	$<1.9 \times 10^{-11}$	$<3.6 \times 10^{42}$	3–10	Savchenko et al. (2017)
<i>INTEGRAL JEM-X</i>	Aug 18 12:45:10 UTC	1–5.7	$<7.0 \times 10^{-12}$	$<1.3 \times 10^{42}$	10–25	Savchenko et al. (2017)
<i>Swift-XRT</i>	Aug 18 13:29:43 UTC	1.03	$<1.77 \times 10^{-13}$	$<3.39 \times 10^{40}$	0.3–10	Evans et al. (2017b)
<i>Swift-XRT</i>	Aug 19 00:18:22 UTC	1.48	$<1.31 \times 10^{-13}$	$<2.51 \times 10^{40}$	0.3–10	Evans et al. (2017b)
<i>Chandra</i>	Aug 19 17:10:09 UTC	2.20	non-detection	...	0.3–10	Margutti et al. (2017a)
<i>Swift-XRT</i>	Aug 19 13:24:05 UTC	2.03	$<1.02 \times 10^{-13}$	$<1.95 \times 10^{40}$	0.3–10	Evans et al. (2017b)
<i>Swift-XRT</i>	Aug 19 18:30:52 UTC	2.24	$<1.34 \times 10^{-13}$	$<2.57 \times 10^{40}$	0.3–10	Evans et al. (2017b)
<i>Swift-XRT</i>	Aug 20 03:24:44 UTC	2.61	$<1.41 \times 10^{-13}$	$<2.69 \times 10^{40}$	0.3–10	Evans et al. (2017b)
<i>Swift-XRT</i>	Aug 20 08:28:05 UTC	2.82	$<3.87 \times 10^{-14}$	$<7.41 \times 10^{39}$	0.3–10	Evans et al. (2017b)
<i>Swift-XRT</i>	Aug 21 01:43:44 UTC	3.54	$<6.73 \times 10^{-14}$	$<1.29 \times 10^{40}$	0.3–10	Evans et al. (2017b)
<i>NuSTAR</i>	Aug 21 20:45:00 UTC	4.3	$<2.08 \times 10^{-14}$	$<3.98 \times 10^{39}$	3–10	Evans et al. (2017b)
<i>Swift-XRT</i>	Aug 22 00:05:57 UTC	4.48	$<6.28 \times 10^{-14}$	$<1.20 \times 10^{40}$	0.3–10	Evans et al. (2017b)
<i>Swift-XRT</i>	Aug 23 06:22:57 UTC	5.74	$<6.89 \times 10^{-14}$	$<1.32 \times 10^{40}$	0.3–10	Evans et al. (2017b)
<i>Swift-XRT</i>	Aug 23 23:59:57 UTC	6.47	$<7.21 \times 10^{-14}$	$<1.38 \times 10^{40}$	0.3–10	Evans et al. (2017b)
<i>Chandra</i>	Aug 26 10:33:50 UTC	8.9	Detection	...	0.5–8.0	Troja et al. (2017c, 2017a)
<i>Swift-XRT</i>	Aug 26 23:59:57 UTC	9.47	$<8.67 \times 10^{-14}$	$<1.66 \times 10^{40}$	0.3–10	Evans et al. (2017b)
<i>Swift-XRT</i>	Aug 28 10:46:17 UTC	10.92	$<1.41 \times 10^{-13}$	$<2.69 \times 10^{40}$	0.3–10	Evans et al. (2017b)
<i>Swift-XRT</i>	Aug 29 01:04:57 UTC	11.52	$<6.00 \times 10^{-14}$	$<1.15 \times 10^{40}$	0.3–10	Evans et al. (2017b)
<i>Swift-XRT</i>	Aug 30 01:00:57 UTC	12.51	$<5.47 \times 10^{-14}$	$<1.05 \times 10^{40}$	0.3–10	Evans et al. (2017b)
<i>Swift-XRT</i>	Aug 31 02:27:52 UTC	13.57	$<3.87 \times 10^{-14}$	$<7.41 \times 10^{39}$	0.3–10	Evans et al. (2017b)
<i>Swift-XRT</i>	Sep 01 05:53:04 UTC	14.72	$<4.45 \times 10^{-14}$	$<8.51 \times 10^{39}$	0.3–10	Evans et al. (2017b)
<i>Chandra</i>	Sep 01 15:22:22 UTC	15.1	Fong et al. (2017); Margutti et al. (2017b)
<i>Chandra</i>	Sep 01 15:22:22 UTC	15.1	4.5×10^{-15}	9×10^{38}	0.5–8.0	Troja et al. (2017e, 2017a)
<i>Chandra</i>	Sep 02 15:22:22 UTC	15.1	3.5×10^{-15}	2.7×10^{38}	0.3–10	Haggard et al. (2017b, 2017a)
<i>Chandra</i>	Sep 02 00:00:00 UTC	16.1	3.8×10^{-15}	3.0×10^{38}	0.3–10	Haggard et al. (2017b, 2017a)
<i>Swift-XRT</i>	Sep 02 08:40:56 UTC	15.83	$<1.51 \times 10^{-13}$	$<2.88 \times 10^{40}$	0.3–10	Evans et al. (2017b)
<i>NuSTAR</i>	Sep 04 17:56 UTC	18.2	$<6.58 \times 10^{-14}$	$<1.26 \times 10^{40}$	3–10	Evans et al. (2017b)
<i>NuSTAR</i>	Sep 05 14:51 UTC	19.1	$<4.15 \times 10^{-14}$	$<7.94 \times 10^{39}$	3–10	Evans et al. (2017b)
<i>NuSTAR</i>	Sep 06 17:56 UTC	20.1	$<3.30 \times 10^{-14}$	$<6.31 \times 10^{39}$	3–10	Evans et al. (2017b)
<i>NuSTAR</i>	Sep 21 11:10 UTC	34.9	$<1.65 \times 10^{-14}$	$<3.16 \times 10^{39}$	3–10	Evans et al. (2017b)

Table 5
Radio Monitoring and Evolution of GW170817

Telescope	UT Date	Time since GW Trigger (days)	Central Frequency (GHz)	Bandwidth (GHz)	Flux (μ Jy), 3σ	GCN/Reference
LWA1	Aug 17 13:09:51 UTC	0.02	0.02585	0.020	...	Callister et al. (2017a)
LWA1	Aug 17 13:09:51 UTC	0.02	0.04545	0.020	...	Callister et al. (2017a)
LWA1	Aug 17 19:15:00 UTC	0.27	0.02585	0.020	$<2 \times 10^8$	Callister et al. (2017a)
LWA1	Aug 17 19:15:00 UTC	0.27	0.04545	0.020	$<1 \times 10^8$	Callister et al. (2017a)
VLBA	Aug 17 19:58:00 UTC	0.30	8.7	0.26		Deller et al. (2017a)
VLA	Aug 18 02:18:00 UTC	0.57	10.0	...		Alexander et al. (2017d, 2017e)
ATCA	Aug 18 01:00:00 UTC	1	8.5	2.049	<120	Bannister et al. (2017d)
						Kaplan et al. (2017a)
						Hallinan et al. (2017a)
ATCA	Aug 18 01:00:00 UTC	1	10.5	2.049	<150	Bannister et al. (2017d)
						Kaplan et al. (2017a)
						Hallinan et al. (2017a)
ATCA	Aug 18 01:00:00 UTC	1	16.7	2.049	<130	Kaplan et al. (2017a)
						Hallinan et al. (2017a)
ATCA	Aug 18 01:00:00 UTC	1	21.2	2.049	<140	Kaplan et al. (2017a)
						Hallinan et al. (2017a)
VLITE	Aug 18 22:23:31 UTC	1.44	0.3387	0.034	<34800	Hallinan et al. (2017a)
ASKAP	Aug 18 04:05:35 UTC	0.67	1.34	0.19		Bannister et al. (2017e, 2017c)
MWA	Aug 18 07:07:50 UTC	1	0.185	0.03	$<51\ 000$	Kaplan et al. (2017b)
ASKAP	Aug 18 08:57:33 UTC	0.86	1.34	0.19		Bannister et al. (2017e, 2017c)
VLA	Aug 18 22:04:57 UTC	1	10.0	3.8	<17.0	Alexander et al. (2017f)
ALMA	Aug 18 22:50:40 UTC	1.4	338.5	7.5	...	Schulze et al. (2017)
GMRT	Aug 18 11:00:00 UTC	1	10.0	0.032	<195	De et al. (2017a)
						Hallinan et al. (2017a)
Parkes	Aug 18 00:00:00 UTC	1.38	1.34	0.34	$<1.4 \times 10^6$	Bailes et al. (2017a)
Parkes	Aug 18 00:00:00 UTC	1.46	1.34	0.34	$<1.4 \times 10^6$	Bailes et al. (2017a)
ASKAP	Aug 19 02:08:00 UTC	1.58	1.34	0.19		Bannister et al. (2017e)
ASKAP	Aug 19 05:34:33 UTC	2	1.345	...	<900	Dobie et al. (2017a)
VLA	Aug 19 22:01:48 UTC	2	6.0	4	<22	Corsi et al. (2017a)
VLA	Aug 19 22:01:48 UTC	2	6.0	4	<22	Corsi et al. (2017a)
VLITE	Aug 19 22:29:29 UTC	2.44	0.3387	0.034	<28800	Hallinan et al. (2017a)
VLA	Aug 19 22:30:10 UTC	2.42	15.0	6	<22	Corsi et al. (2017e)
						Hallinan et al. (2017a)
VLA	Aug 19 23:04:06 UTC	2.44	10.0	4	<17	Corsi et al. (2017b)
						Hallinan et al. (2017a)
VLA	Aug 19 23:33:30 UTC	2.46	6.0	...	<20	Corsi et al. (2017a)
						Hallinan et al. (2017a)
ALMA	Aug 19 22:31:43 UTC	2	97.5	...	<50	Williams et al. (2017a)
Parkes	Aug 20 00:00:00 UTC	3.17	1.34	0.34	$<1.4 \times 10^6$	Bailes et al. (2017a)
Parkes	Aug 20 00:00:00 UTC	3.21	1.34	0.34	$<1.4 \times 10^6$	Bailes et al. (2017a)
VLITE	Aug 20 20:49:36 UTC	3.34	0.3387	0.034	<44700	Hallinan et al. (2017a)
VLA	Aug 20 00:01:24 UTC	3	9.7	4	<18	Corsi et al. (2017b)
GMRT	Aug 20 08:00:00 UTC	3	0.4	0.2	<780	De et al. (2017b)
GMRT	Aug 20 08:00:00 UTC	3	1.2	0.4	<98	De et al. (2017b)
VLA	Aug 20 21:07:00 UTC	3	6.2	4	<19	Corsi et al. (2017c)
VLA/JAGWAR	Aug 20 22:20:00 UTC	3	3.0	...	<32	Mooley et al. (2017a)
ATCA	Aug 20 23:31:03 UTC	3	8.5	2.049	<20	Lynch et al. (2017a)

Table 5
(Continued)

Telescope	UT Date	Time since GW Trigger (days)	Central Frequency (GHz)	Bandwidth (GHz)	Flux (μ Jy), 3σ	GCN/Reference
ATCA	Aug 20 23:31:03 UTC	3	10.5	2.049	<135	Lynch et al. (2017a)
ALMA	Aug 20 22:40:16 UTC	3	338.5	7.5	...	Schulze et al. (2017)
VLBA	Aug 20 21:36:00 UTC	3	8.7	...	<48	Deller et al. (2017b)
ALMA	Aug 21 20:58:51 UTC	4.3	338.5	7.5	...	Schulze et al. (2017)
VLA	Aug 22 23:50:18 UTC	5.48	10.0	Alexander et al. (2017c)
e-MERLIN	Aug 23 12:00:00 UTC	6	5.0	0.512	<108	Moldon et al. (2017a)
e-MERLIN	Aug 24 12:00:00 UTC	7	5.0	0.512	<96	Moldon et al. (2017a)
LWA1	Aug 24 19:50:00 UTC	7	0.02585	0.016	...	Callister et al. (2017b)
LWA1	Aug 24 19:50:00 UTC	7	0.04545	0.016	...	Callister et al. (2017b)
e-MERLIN	Aug 25 12:00:00 UTC	8	5.0	512	<96	Moldon et al. (2017a)
VLITE	Aug 25 20:38:22 UTC	8.37	0.3387	0.034	<37500	Hallinan et al. (2017a)
GMRT	Aug 25 09:30:00 UTC	7.9	1.39	0.032	<130	Resmi et al. (2017)
VLA	Aug 25 19:15:12 UTC	8.29	10.0	Alexander et al. (2017c)
ALMA	Aug 25 22:35:17 UTC	8.4	338.5	7.5	...	Schulze et al. (2017)
MeerKAT	Aug 26 08:43:00 UTC	10	1.48	0.22	<70	Goedhart et al. (2017a)
ALMA	Aug 26 22:49:25 UTC	9.43	97.5	Williams et al. (2017a)
ALMA	Aug 26 22:58:41 UTC	9.4	338.5	7.5	...	Schulze et al. (2017); S. Kim et al. (2017, in preparation)
EVN	Aug 26 12:15:00 UTC	9	5.0	0.256	<96	Paragi et al. (2017a)
e-MERLIN	Aug 26 12:00:00 UTC	9	5.0	0.512	<114	Moldon et al. (2017a)
e-MERLIN	Aug 27 12:00:00 UTC	10	5.0	0.512	<90	Moldon et al. (2017a)
ATCA	Aug 27 23:26:25 UTC	10	8.5	2.049	<54	Lynch et al. (2017b)
ATCA	Aug 27 23:26:25 UTC	10	10.5	2.049	<39	Lynch et al. (2017b)
e-MERLIN	Aug 28 12:00:00 UTC	11	5.0	0.512	<90	Moldon et al. (2017a)
VLITE	Aug 30 23:10:28 UTC	13.45	0.3387	0.034	<20400	Hallinan et al. (2017a)
LWA1	Aug 30 19:50:00 UTC	13	0.02585	0.016	...	Callister et al. (2017)
LWA1	Aug 30 19:50:00 UTC	13	0.04545	0.016	...	Callister et al. (2017)
VLA	Aug 30 22:09:24 UTC	13.41	10.0	Alexander et al. (2017c)
e-MERLIN	Aug 31 13:00:00 UTC	14	5.0	0.512	<109	Moldon et al. (2017b)
VLITE	Sep 1 20:44:59 UTC	15.37	0.3387	0.034	<11400	Hallinan et al. (2017a)
ATCA	Sep 1 12:00:00 UTC	15	16.7	...	<50	Troja et al. (2017f)
ATCA	Sep 1 12:00:00 UTC	15	21.2	...	<50	Troja et al. (2017f)
ATCA	Sep 1 12:00:00 UTC	15	43.0	...	<90	Troja et al. (2017f)
ATCA	Sep 1 12:00:00 UTC	15	45.0	...	<90	Troja et al. (2017f)
e-MERLIN	Sep 1 13:00:00 UTC	15	5.0	0.512	<114	Moldon et al. (2017b)
ALMA	Sep 120:22:05 UTC	15.33	97.5	Alexander et al. (2017c)
VLA/JAGWAR	Sep 2 00:00:00 UTC	16	3.0	...	Detection	Mooley et al. (2017b); Hallinan et al. (2017a)
e-MERLIN	Sep 2 13:00:00 UTC	16	5.0	0.512	<144	Moldon et al. (2017b)
VLITE	Sep 2 18:51:34 UTC	16.36	0.3387	0.034	<11700	Hallinan et al. (2017a)
e-MERLIN	Sep 3 13:00:00 UTC	17	5.0	0.512	<166	Moldon et al. (2017b)
VLA	Sep 3 23:30:00 UTC	17	6.0	...	Detection	Corsi et al. (2017d); Hallinan et al. (2017a)
VLITE	Sep 3 20:08:05 UTC	17.40	0.3387	0.034	<6900	Hallinan et al. (2017a)
e-MERLIN	Sep 4 13:00:00 UTC	18	5.0	0.512	<147	Moldon et al. (2017b)
ATCA	Sep 5 10:03:04 UTC	19	7.25	...	Detection	Murphy et al. (2017)
e-MERLIN	Sep 5 13:00:00 UTC	19	5.0	0.512	<162	Moldon et al. (2017b)
VLA	Sep 5 22:12:00 UTC	19.47	6.0	Alexander et al. (2017a)
VLA	Sep 5 23:26:06 UTC	19.43	10.0	Alexander et al. (2017c)
MeerKAT	Sep 6 03:22:00 UTC	20	1.48	0.22	<75	Goedhart et al. (2017a)

Table 5
(Continued)

Telescope	UT Date	Time since GW Trigger (days)	Central Frequency (GHz)	Bandwidth (GHz)	Flux (μ Jy), 3σ	GCN/Reference
VLITE	Sep 7 19:09:43 UTC	21.36	0.3387	0.034	<8100	Hallinan et al. (2017a)
SRT	Sep 7 10:41:00 UTC	20.92	7.2	0.68	<1200	Aresu et al. (2017)
ATCA	Sep 8 12:00:00 UTC	22	17.0	...	<35	Wieringa et al. (2017)
ATCA	Sep 8 12:00:00 UTC	22	21.0	...	<35	Wieringa et al. (2017)
SRT	Sep 8 11:00:00 UTC	21.93	7.2	0.68	<1500	Aresu et al. (2017)
VLITE	Sep 8 19:05:35 UTC	22.37	0.3387	0.034	<6300	Hallinan et al. (2017a)
SRT	Sep 9 10:37:00 UTC	22.92	7.2	0.68	<1800	Aresu et al. (2017)
VLITE	Sep 9 18:52:45 UTC	23.36	0.3387	0.034	<4800	Hallinan et al. (2017a)
GMRT	Sep 9 11:30:00 UTC	23.0	1.39	0.032	...	Resmi et al. (2017), S. Kim et al. (2017, in preparation)
e-MERLIN	Sep 10 13:00:00 UTC	24	5.0	0.512	<126	Moldon et al. (2017b)
Effelsberg	Sep 10 13:10 UTC	24	5	2	<30000	Kramer et al. (2017)
Effelsberg	Sep 10 13:35 UTC	24	32	2	<90000	Kramer et al. (2017)
VLITE	Sep 10 18:36:48 UTC	24.35	0.3387	0.034	<6600	Hallinan et al. (2017a)
e-MERLIN	Sep 11 13:00:00 UTC	25	5.0	0.512	<151	Moldon et al. (2017b)
e-MERLIN	Sep 12 13:00:00 UTC	26	5.0	0.512	<113	Moldon et al. (2017b)
e-MERLIN	Sep 14 13:00:00 UTC	28	5.0	0.512	<147	Moldon et al. (2017b)
e-MERLIN	Sep 15 13:00:00 UTC	29	5.0	0.512	<106	Moldon et al. (2017b)
GMRT	Sep 16 07:30:00 UTC	29.8	1.39	0.032	...	Resmi et al. (2017); S. Kim et al. (2017, in preparation)
e-MERLIN	Sep 16 13:00:00 UTC	30	5.0	0.512	<118	Moldon et al. (2017b)
ALMA	Sep 16 20:36:21 UTC	30.34	97.5	Alexander et al. (2017c)
MeerKAT	Sep 17 07:16:00 UTC	31	1.48	0.22	<60	Goedhart et al. (2017a)
e-MERLIN	Sep 17 13:00:00 UTC	31	5.0	0.512	<111	Moldon et al. (2017b)
e-MERLIN	Sep 18 13:00:00 UTC	32	5.0	0.512	111	Moldon et al. (2017b)
SRT	Sep 19 11:38:00 UTC	32.96	7.2	0.68	<1200	Aresu et al. (2017)
EVN	Sep 20 10:00:00 UTC	34	5.0	0.256	<84	Paragi et al. (2017b)
e-MERLIN	Sep 21 13:00:00 UTC	35	5.0	0.512	<132	Moldon et al. (2017b)
e-MERLIN	Sep 22 13:00:00 UTC	36	5.0	0.512	<121	Paragi et al. (2017b)
VLA	Sep 25 16:51:45 UTC	39.2	6.0 GHz		Detection	Alexander et al. (2017b)

Table 6
Gamma-ray Coordinates Network (GCN) Notices and Circulars related to GW170817 until 2017 October 1 UTC

Telescope	UT Date	Δt (days)	Obs. Wavelength	References
Fermi/GBM	2017 Aug 17 12:41:20	0.0	gamma-ray	GCN Notice 524666471, Fermi-GBM (2017)
LIGO-Virgo/-	2017 Aug 17 13:21:42	0.03	gw	GCN 21505, LIGO Scientific Collaboration & Virgo Collaboration et al. (2017a)
Fermi/GBM	2017 Aug 17 13:47:37	0.05	gamma-ray	GCN 21506, Connaughton et al. (2017)
INTEGRAL/SPI-ACS	2017 Aug 17 13:57:47	0.05	gamma-ray	GCN 21507, Savchenko et al. (2017a)
IceCube/-	2017 Aug 17 14:05:11	0.06	neutrino	GCN 21508, Bartos et al. (2017a)
LIGO-Virgo/-	2017 Aug 17 14:09:25	0.06	gw	GCN 21509, LIGO Scientific Collaboration & Virgo Collaboration et al. (2017d)
LIGO-Virgo/-	2017 Aug 17 14:38:46	0.08	gw	GCN 21510, LIGO Scientific Collaboration & Virgo Collaboration et al. (2017e)
IceCube/-	2017 Aug 17 14:54:58	0.09	neutrino	GCN 21511, Bartos et al. (2017c)
LIGO-Virgo/-	2017 Aug 17 17:54:51	0.22	gw	GCN 21513, LIGO Scientific Collaboration & Virgo Collaboration et al. (2017b)
Astrosat/CZTI	2017 Aug 17 18:16:42	0.23	gamma-ray	GCN 21514, Balasubramanian et al. (2017)
IPN/-	2017 Aug 17 18:35:12	0.25	gamma-ray	GCN 21515, Svinikin et al. (2017b)
-/-	2017 Aug 17 18:55:12	0.26		GCN 21516, Dalya et al. (2016)
Insight-HXMT/HE	2017 Aug 17 19:35:28	0.29	gamma-ray	GCN 21518, Liao et al. (2017)
-/-	2017 Aug 17 20:00:07	0.3		GCN 21519, Cook et al. (2017a)
Fermi/GBM	2017 Aug 17 20:00:07	0.3	gamma-ray	GCN 21520, von Kienlin et al. (2017)
-/-	2017 Aug 17 20:12:41	0.31		GCN 21521, Cook et al. (2017b)
ANTARES/-	2017 Aug 17 20:35:31	0.33	neutrino	GCN 21522, Ageron et al. (2017a)
Swift/BAT	2017 Aug 17 21:34:36	0.37	gamma-ray	GCN 21524, Barthelmy et al. (2017)
AGILE/MCAL	2017 Aug 17 22:01:26	0.39	gamma-ray	GCN 21525, Pilia et al. (2017)
AGILE/GRID	2017 Aug 17 22:22:43	0.4	gamma-ray	GCN 21526, Piano et al. (2017)
LIGO-Virgo/-	2017 Aug 17 23:54:40	0.47	gw	GCN 21527, LIGO Scientific Collaboration & Virgo Collaboration et al. (2017c)
Fermi/GBM	2017 Aug 18 00:36:12	0.5	gamma-ray	GCN 21528, Goldstein et al. (2017b)
Swope/-	2017 Aug 18 01:05:23	0.52	optical	GCN 21529, Coulter et al. (2017a)
DECam/-	2017 Aug 18 01:15:01	0.52	optical	GCN 21530, Allam et al. (2017)
DLT40/-	2017 Aug 18 01:41:13	0.54	optical	GCN 21531, Yang et al. (2017a)
REM-ROS2/-	2017 Aug 18 02:00:40	0.56	optical, IR	GCN 21532, Melandri et al. (2017a)
ASAS-SN/-	2017 Aug 18 02:06:30	0.56	optical	GCN 21533, Cowperthwaite et al. (2017a)
Fermi/LAT	2017 Aug 18 02:09:53	0.56	gamma-ray	GCN 21534, Kocevski et al. (2017)
-/-	2017 Aug 18 02:48:50	0.59		GCN 21535, Cook et al. (2017c)
HST/-	2017 Aug 18 03:01:20	0.6	optical	GCN 21536, Foley et al. (2017a)
ATCA/-	2017 Aug 18 04:04:00	0.64	radio	GCN 21537, Bannister et al. (2017d)
LasCumbres/-	2017 Aug 18 04:06:31	0.64	optical	GCN 21538, Arcavi et al. (2017a)
DLT40/-	2017 Aug 18 04:11:35	0.65	optical	GCN 21539, Yang et al. (2017c)
DECam/-	2017 Aug 18 04:44:32	0.67	optical	GCN 21541, Nicholl et al. (2017a)
SkyMapper/-	2017 Aug 18 04:46:27	0.67	optical	GCN 21542, Moller et al. (2017)
LasCumbres/-	2017 Aug 18 04:54:23	0.68	optical	GCN 21543, Arcavi et al. (2017d)
VISTA/VIRCAM	2017 Aug 18 05:03:48	0.68	optical, IR	GCN 21544, Tanvir et al. (2017a)
VLA/-	2017 Aug 18 05:07:58	0.69	radio	GCN 21545, Alexander et al. (2017d)
MASTER/-	2017 Aug 18 05:37:59	0.71	optical	GCN 21546, Lipunov et al. (2017d)
Magellan/-	2017 Aug 18 05:46:33	0.71	optical	GCN 21547, Drout et al. (2017)
VLA/-	2017 Aug 18 06:56:44	0.76	radio	GCN 21548, Alexander et al. (2017e)
Subaru/HSC	2017 Aug 18 07:07:07	0.77	optical	GCN 21549, Yoshida et al. (2017a)
Swift/UVOT,XRT	2017 Aug 18 07:24:04	0.78	x-ray, uv	GCN 21550, Evans et al. (2017a)
Magellan/LDSS-3	2017 Aug 18 07:54:23	0.8	optical	GCN 21551, Simon et al. (2017)
Gemini-South/Flamingos-2	2017 Aug 18 08:00:58	0.81	IR	GCN 21552, Singer et al. (2017a)
Pan-STARRS/-	2017 Aug 18 08:37:20	0.83	optical	GCN 21553, Chambers et al. (2017a)

Table 6
(Continued)

Telescope	UT Date	Δt (days)	Obs. Wavelength	References
HCT/HFOSC	2017 Aug 18 09:54:21	0.88	optical	GCN 21554, Pavana et al. (2017)
MAXI/GSC/-	2017 Aug 18 10:43:45	0.92	x-ray	GCN 21555, Sugita et al. (2017)
REM-ROS2/-	2017 Aug 18 10:54:42	0.93	optical	GCN 21556, Melandri et al. (2017b)
-/-	2017 Aug 18 12:15:23	0.98		GCN 21557, Foley et al. (2017b)
TZAC/TAROT-Reunion	2017 Aug 18 13:04:25	1.02	optical	GCN 21558, Klotz et al. (2017)
ATCA/-	2017 Aug 18 13:27:25	1.03	radio	GCN 21559, Bannister et al. (2017b)
SkyMapper/-	2017 Aug 18 13:54:11	1.05	optical	GCN 21560, Wolf et al. (2017)
Subaru/HSC	2017 Aug 18 14:27:26	1.07	optical	GCN 21561, Yoshida et al. (2017b)
ASKAP/-	2017 Aug 18 14:36:00	1.08	radio	GCN 21562, Bannister et al. (2017e)
LSGT,T17/SNUCAM-II	2017 Aug 18 14:45:33	1.09	optical	GCN 21563, Im et al. (2017a)
AGILE/GRID	2017 Aug 18 15:22:43	1.11	gamma-ray	GCN 21564, Bulgarelli et al. (2017)
LasCumbres/-	2017 Aug 18 15:58:41	1.14	optical	GCN 21565, Arcavi et al. (2017b)
LSGT,T17/SNUCAM-II	2017 Aug 18 17:15:43	1.19	optical	GCN 21566, Im et al. (2017b)
Swope/-	2017 Aug 18 17:19:22	1.19	optical	GCN 21567, Coulter et al. (2017b)
IceCube/-	2017 Aug 18 17:27:25	1.2	neutrino	GCN 21568, Bartos et al. (2017b)
Gemini-South/-	2017 Aug 18 17:44:26	1.21	optical, IR	GCN 21569, Singer et al. (2017c)
MASTER/-	2017 Aug 18 18:06:51	1.23	optical	GCN 21570, Lipunov et al. (2017e)
VLA/-	2017 Aug 18 18:16:30	1.23	radio	GCN 21571, Williams et al. (2017b)
Swift/UVOT,XRT	2017 Aug 18 18:32:37	1.24	x-ray, uv	GCN 21572, Cenko et al. (2017)
ATCA/-	2017 Aug 18 20:19:00	1.32	radio	GCN 21574, Kaplan et al. (2017a)
2MASS,Spitzer/-	2017 Aug 18 20:23:05	1.32	IR	GCN 21575, Eikenberry et al. (2017)
VISTA/VIRCam	2017 Aug 18 21:16:32	1.36	IR	GCN 21576, Tanvir et al. (2017b)
-/-	2017 Aug 18 23:00:31	1.43		GCN 21577, Malesani et al. (2017b)
-/-	2017 Aug 18 23:11:30	1.44		GCN 21578, Cowperthwaite et al. (2017c)
PROMPT5/-	2017 Aug 19 00:18:04	1.48	optical	GCN 21579, Yang et al. (2017b)
DECam/-	2017 Aug 19 00:22:23	1.49	optical	GCN 21580, Nicholl et al. (2017b)
LasCumbres/-	2017 Aug 19 01:26:07	1.53	optical	GCN 21581, Arcavi et al. (2017c)
NTT/-	2017 Aug 19 01:46:26	1.55	optical, IR	GCN 21582, Lyman et al. (2017)
Swope/-	2017 Aug 19 01:54:36	1.55	optical	GCN 21583, Kilpatrick et al. (2017a)
GROND/-	2017 Aug 19 01:58:14	1.55	optical, IR	GCN 21584, Wiseman et al. (2017)
SOAR/GoodmanSpectrograph	2017 Aug 19 03:10:19	1.6	IR, optical	GCN 21585, Nicholl et al. (2017c)
Subaru/HSC	2017 Aug 19 06:52:33	1.76	optical	GCN 21586, Yoshida et al. (2017c)
MASTER/-	2017 Aug 19 08:10:30	1.81	optical	GCN 21587, Lipunov et al. (2017c)
VLBA/-	2017 Aug 19 09:36:26	1.87	radio	GCN 21588, Deller et al. (2017a)
VLA/-	2017 Aug 19 09:51:33	1.88	radio	GCN 21589, Alexander et al. (2017f)
Pan-STARRS/-	2017 Aug 19 10:14:53	1.9	optical	GCN 21590, Chambers et al. (2017b)
NOT/NOTCam	2017 Aug 19 12:00:05	1.97	IR	GCN 21591, Malesani et al. (2017a)
ESO-VLT/X-shooter	2017 Aug 19 12:16:37	1.98	IR, optical	GCN 21592, Pian et al. (2017b)
ESO-VLT/FORS2	2017 Aug 19 14:13:15	2.06	optical	GCN 21594, Wiersema et al. (2017)
Subaru/HSC	2017 Aug 19 14:46:41	2.09	optical	GCN 21595, Tominaga et al. (2017)
REM-ROS2/-	2017 Aug 19 16:38:19	2.16	optical	GCN 21596, Melandri et al. (2017c)
KMTNet/wide-fieldcamera	2017 Aug 19 16:55:08	2.18	optical	GCN 21597, Im et al. (2017d)
ESO-VST/OmegaCam	2017 Aug 19 17:37:19	2.21	optical	GCN 21598, Grado et al. (2017c)
LaSilla-QUEST/-	2017 Aug 19 18:04:05	2.22	optical	GCN 21599, Rabinowitz et al. (2017)
GMRT/-	2017 Aug 19 21:18:21	2.36	radio	GCN 21603, De et al. (2017a)
PROMPT5/-	2017 Aug 19 23:31:25	2.45	optical	GCN 21606, Valenti et al. (2017)

Table 6
(Continued)

Telescope	UT Date	Δt (days)	Obs. Wavelength	References
GROND/–	2017 Aug 20 04:49:21	2.67	optical, IR	GCN 21608, Chen et al. (2017)
VIRT/–	2017 Aug 20 05:27:49	2.7	optical	GCN 21609, Gendre et al. (2017)
SALT/–	2017 Aug 20 06:14:37	2.73	optical	GCN 21610, Shara et al. (2017)
<i>Swift</i> /XRT	2017 Aug 20 08:42:40	2.83	x-ray	GCN 21612, Evans et al. (2017c)
VLA/–	2017 Aug 20 09:17:57	2.86	radio	GCN 21613, Corsi et al. (2017b)
VLA/–	2017 Aug 20 10:26:01	2.91	radio	GCN 21614, Corsi et al. (2017a)
Pan-STARRS/–	2017 Aug 20 13:59:50	3.05	optical	GCN 21617, Chambers et al. (2017c)
ChilescopeRC-1000/–	2017 Aug 20 14:24:47	3.07	optical	GCN 21618, Pozanenko et al. (2017d)
TOROS/–	2017 Aug 20 14:48:49	3.09	optical	GCN 21619, Diaz et al. (2017a)
TOROS/–	2017 Aug 20 15:03:42	3.1	optical	GCN 21620, Diaz et al. (2017c)
–/–	2017 Aug 20 15:40:35	3.12	...	GCN 21621, Lipunov (2017)
Kanata/HONIR	2017 Aug 20 16:37:38	3.16	IR	GCN 21623, Nakaoka et al. (2017)
BOOTES-5/–	2017 Aug 20 21:59:59	3.39	optical	GCN 21624, Castro-Tirado et al. (2017)
ASKAP/–	2017 Aug 21 00:58:33	3.51	radio	GCN 21625, Dobie et al. (2017b)
<i>NuSTAR</i> /–	2017 Aug 21 04:33:27	3.66	x-ray	GCN 21626, Harrison et al. (2017)
Zadko/–	2017 Aug 21 05:57:23	3.72	optical	GCN 21627, Coward et al. (2017b)
ATCA/–	2017 Aug 21 07:45:30	3.79	radio	GCN 21628, Lynch et al. (2017c)
ATCA/–	2017 Aug 21 09:02:12	3.85	radio	GCN 21629, Lynch et al. (2017d)
ANTARES/–	2017 Aug 21 15:08:00	4.1	neutrino	GCN 21631, Ageron et al. (2017b)
KMTNet,iTelescope.NET/–	2017 Aug 21 15:49:41	4.13	optical	GCN 21632, Im et al. (2017c)
Pan-STARRS/–	2017 Aug 21 16:03:52	4.14	optical	GCN 21633, Chambers et al. (2017d)
TOROS/CASLEO	2017 Aug 21 16:05:22	4.14	optical	GCN 21634, Diaz et al. (2017d)
ChilescopeRC-1000/–	2017 Aug 21 16:11:53	4.15	optical	GCN 21635, Pozanenko et al. (2017a)
VLA/–	2017 Aug 21 18:40:08	4.25	radio	GCN 21636, Corsi et al. (2017e)
MWA/–	2017 Aug 22 00:59:36	4.51	radio	GCN 21637, Kaplan et al. (2017c)
Gemini-South/Flamingos-2	2017 Aug 22 05:20:11	4.69	IR	GCN 21638, Chornock et al. (2017c)
ASKAP/–	2017 Aug 22 07:23:04	4.78	radio	GCN 21639, Dobie et al. (2017a)
CALET/CGBM	2017 Aug 22 09:36:51	4.87	gamma-ray	GCN 21641, Nakahira et al. (2017)
ChilescopeRC-1000/–	2017 Aug 22 15:23:04	5.11	optical	GCN 21644, Pozanenko et al. (2017c)
6dFGS/–	2017 Aug 22 16:55:17	5.18	optical	GCN 21645, Sadler et al. (2017)
<i>Chandra</i> /CXO	2017 Aug 22 18:06:23	5.23	x-ray	GCN 21648, Margutti et al. (2017b)
VLA/JAGWAR	2017 Aug 22 19:13:38	5.27	radio	GCN 21650, Mooley et al. (2017a)
ESO-VLT/FORS2	2017 Aug 23 07:52:38	5.8	optical	GCN 21653, D’Avanzo et al. (2017)
VLA/–	2017 Aug 23 18:25:07	6.24	radio	GCN 21664, Corsi et al. (2017c)
<i>HST</i> /Pan-STARRS1/GPC1	2017 Aug 24 01:39:20	6.54	optical	GCN 21669, Yu et al. (2017)
ATCA/–	2017 Aug 24 04:30:05	6.66	radio	GCN 21670, Lynch et al. (2017a)
ASKAP/–	2017 Aug 24 06:10:24	6.73	radio	GCN 21671, Bannister et al. (2017c)
<i>INTEGRAL</i> /SPI,IBIS,JEM-X,OMC	2017 Aug 24 09:03:02	6.85	gamma-ray, x-ray, optical	GCN 21672, Savchenko et al. (2017b)
H.E.S.S./–	2017 Aug 24 10:35:02	6.91	gamma-ray	GCN 21674, de Naurois et al. (2017)
LOFAR/ILT	2017 Aug 24 13:35:06	7.04	radio	GCN 21676, Broderick et al. (2017)
AAT/AAO	2017 Aug 24 15:31:25	7.12	optical	GCN 21677, Andreoni et al. (2017)
LWA/LWA1	2017 Aug 24 16:08:17	7.14	radio	GCN 21680, Callister et al. (2017a)
ESO-VLT/MUSEIntegralFieldUnit	2017 Aug 24 19:28:30	7.28	optical	GCN 21681, Levan et al. (2017b)
Gemini-South/Flamingos-2,GMOS	2017 Aug 24 19:31:19	7.28	optical, IR	GCN 21682, Troja et al. (2017b)
HAWC/–	2017 Aug 24 19:35:19	7.29	gamma-ray	GCN 21683, Martinez-Castellanos et al. (2017)
Gemini-South/Flamingos-2	2017 Aug 25 04:04:17	7.64	IR	GCN 21684, Chornock et al. (2017b)

Table 6
(Continued)

Telescope	UT Date	Δt (days)	Obs. Wavelength	References
Subaru/HSC	2017 Aug 25 07:38:17	7.79	optical	GCN 21685, Yoshida et al. (2017d)
Auger/SurfaceDetector	2017 Aug 25 08:13:23	7.81	neutrino	GCN 21686, Alvarez-Muniz et al. (2017)
MASTER/MASTER-II	2017 Aug 25 08:48:24	7.84	optical	GCN 21687, Lipunov et al. (2017b)
ESO-VST/OmegaCAM	2017 Aug 25 22:15:33	8.4	optical	GCN 21703, Grado et al. (2017a)
GMRT/–	2017 Aug 26 01:23:58	8.53	radio	GCN 21708, De et al. (2017b)
ATCA/–	2017 Aug 29 03:49:22	11.63	radio	GCN 21740, Lynch et al. (2017b)
Zadko/–	2017 Aug 29 08:29:39	11.83	optical	GCN 21744, Coward et al. (2017a)
Konus-Wind/–	2017 Aug 29 10:55:08	11.93	gamma-ray	GCN 21746, Svinkin et al. (2017a)
ALMA/–	2017 Aug 29 12:37:56	12.0	radio	GCN 21747, Schulze et al. (2017)
ALMA/–	2017 Aug 29 14:55:15	12.09	radio	GCN 21750, Williams et al. (2017a)
OVRO/–	2017 Aug 30 03:23:28	12.61	radio	GCN 21760, Pearson et al. (2017)
EVN/VLBI	2017 Aug 30 09:48:26	12.88	radio	GCN 21763, Paragi et al. (2017a)
Chandra/CXO	2017 Aug 30 12:07:12	12.98	x ray	GCN 21765, Troja et al. (2017c)
GMRT/–	2017 Aug 30 16:06:24	13.14	radio	GCN 21768, Resmi et al. (2017)
Gemini-South/–	2017 Aug 31 18:28:50	14.24	IR	GCN 21778, Troja et al. (2017d)
Gemini-South/Flamingos-2	2017 Aug 31 18:32:01	14.24	IR	GCN 21779, Singer et al. (2017b)
HST/–	2017 Aug 31 20:33:24	14.33	optical, IR	GCN 21781, Levan et al. (2017a)
PioftheSky/PioftheSkyNorth	2017 Sep 01 21:54:25	15.38	optical	GCN 21783, Cwiek et al. (2017)
AGILE/GRID	2017 Sep 02 16:54:59	16.18	gamma-ray	GCN 21785, Verrecchia et al. (2017)
Chandra/CXO	2017 Sep 02 16:57:54	16.18	x ray	GCN 21786, Fong et al. (2017)
Chandra/CXO	2017 Sep 02 17:06:21	16.18	x ray	GCN 21787, Troja et al. (2017e)
Chandra/CXO	2017 Sep 03 20:24:16	17.32	x ray	GCN 21798, Haggard et al. (2017b)
ATCA/–	2017 Sep 04 02:26:14	17.57	radio	GCN 21803, Troja et al. (2017f)
e-MERLIN/–	2017 Sep 04 07:48:43	17.8	radio	GCN 21804, Moldon et al. (2017a)
VLA/–	2017 Sep 04 22:14:55	18.4	radio	GCN 21814, Mooley et al. (2017b)
VLA/–	2017 Sep 04 22:14:59	18.4	radio	GCN 21815, Corsi et al. (2017d)
HST/HST,Gaia	2017 Sep 05 00:30:09	18.49	optical, IR, uv	GCN 21816, Adams et al. (2017)
ESO-VST/OMEGACam	2017 Sep 06 15:07:27	20.1	optical	GCN 21833, Grado et al. (2017b)
ATCA/–	2017 Sep 07 02:31:55	20.58	radio	GCN 21842, Murphy et al. (2017)
LWA/LWA1	2017 Sep 08 02:47:01	21.59	radio	GCN 21848, Callister et al. (2017b)
VLBA/–	2017 Sep 08 11:16:27	21.94	radio	GCN 21850, Deller et al. (2017b)
VLA/–	2017 Sep 08 13:23:16	22.03	radio	GCN 21851, Alexander et al. (2017a)
ATCA/–	2017 Sep 14 05:25:42	27.7	radio	GCN 21882, Wieringa et al. (2017)
AST3-2/–	2017 Sep 15 03:45:21	28.63	optical	GCN 21883, Hu et al. (2017)
ATLAS/–	2017 Sep 15 11:24:15	28.95	optical	GCN 21886, Tonry et al. (2017)
DanishTel/–	2017 Sep 15 16:40:07	29.17	optical	GCN 21889, Cano et al. (2017)
MeerKAT/–	2017 Sep 15 20:16:29	29.32	radio	GCN 21891, Goedhart et al. (2017b)
DFN/–	2017 Sep 18 13:45:29	32.04	optical	GCN 21894, Hancock et al. (2017)
T80S,EABA/–	2017 Sep 18 16:22:27	32.15	optical	GCN 21895, Diaz et al. (2017b)
VLBA/–	2017 Sep 19 07:51:22	32.8	radio	GCN 21897, Deller et al. (2017c)
ChilescopeRC-1000/–	2017 Sep 19 18:09:03	33.23	optical	GCN 21898, Pozanenko et al. (2017b)
Parkes/–	2017 Sep 21 02:38:29	34.58	radio	GCN 21899, Bailes et al. (2017a)
ATCA/–	2017 Sep 21 06:42:36	34.75	radio	GCN 21900, Ricci et al. (2017)
LasCumbres/FLOYDS,Gemini	2017 Sep 22 03:24:44	35.61	optical	GCN 21908, McCully et al. (2017a)
SRT/–	2017 Sep 22 19:06:44	36.27	radio	GCN 21914, Aresu et al. (2017)
Effelsberg/–	2017 Sep 23 20:34:41	37.33	radio	GCN 21920, Kramer et al. (2017)

Table 6
(Continued)

Telescope	UT Date	Δt (days)	Obs. Wavelength	References
MWA/-	2017 Sep 25 22:30:34	39.41	radio	GCN 21927, Kaplan et al. (2017b)
Parkes/-	2017 Sep 26 02:00:59	39.56	radio	GCN 21928, Bailes et al. (2017b)
VLA/-	2017 Sep 26 05:14:16	39.69	radio	GCN 21929, Hallinan et al. (2017b)
PioftheSky/PioftheSkyNorth	2017 Sep 26 21:17:49	40.36	optical	GCN 21931, Batsch et al. (2017)
MeerKAT/-	2017 Sep 27 13:19:14	41.03	radio	GCN 21933, Goedhart et al. (2017a)
VLA/-	2017 Sep 27 19:03:46	41.27	radio	GCN 21935, Alexander et al. (2017b)
EVN/-	2017 Sep 28 10:35:27	41.91	radio	GCN 21939, Paragi et al. (2017b)
e-MERLIN/-	2017 Sep 28 11:12:37	41.94	radio	GCN 21940, Moldon et al. (2017b)

3.5. Neutrinos

The detection of GW170817 was rapidly followed up by the IceCube (Aartsen et al. 2017) and ANTARES (Ageron et al. 2011) neutrino observatories and the Pierre Auger Observatory (Aab et al. 2015a) to search for coincident, high-energy (GeV–EeV) neutrinos emitted in the relativistic outflow produced by the BNS merger. The results from these observations, described briefly below, can be used to constrain the properties of relativistic outflows driven by the merger (A. Albert et al. 2017, in preparation).

In a search for muon–neutrino track candidates (Aartsen et al. 2016), and contained neutrino events of any flavor (Aartsen et al. 2015), IceCube identified no neutrinos that were directionally coincident with the final localization of GW170817 at 90% credible level, within ± 500 s of the merger (Bartos et al. 2017a, 2017b). Additionally, no MeV supernova neutrino burst signal was detected coincident with the merger. Following the identification via electromagnetic observations of the host galaxy of the event, IceCube also carried out an extended search in the direction of NGC 4993 for neutrinos within the 14 day period following the merger, but found no significant neutrino emission (A. Albert et al. 2017, in preparation).

A neutrino search for upgoing high-energy muon neutrinos was carried out using the online ANTARES data stream (Ageron et al. 2017a). No upgoing neutrino candidates were found over a $t_c \pm 500$ s time window. The final localization of GW170817 (LIGO Scientific Collaboration & Virgo Collaboration et al. 2017c) was above the ANTARES horizon at the time of the GW event. A search for downgoing muon neutrinos was thus performed, and no neutrinos were found over $t_c \pm 500$ s (Ageron et al. 2017b). A search for neutrinos originating from below the ANTARES horizon, over an extended period of 14 days after the merger, was also performed, without yielding significant detection (A. Albert et al. 2017, in preparation).

The Pierre Auger Observatory carried out a search for ultra-high-energy (UHE) neutrinos above $\sim 10^{17}$ eV using its Surface Detector (Aab et al. 2015a). UHE neutrino-induced extensive air showers produced either by interactions of downward-going neutrinos in the atmosphere or by decays of tau leptons originating from tau neutrino interactions in the Earth’s crust can be efficiently identified above the background of the more numerous ultra-high-energy cosmic rays (Aab et al. 2015b). Remarkably, the position of the transient in NGC 4993 was just between $0^\circ.3$ and $3^\circ.2$ below the horizon during $t_c \pm 500$ s. This region corresponds to the most efficient geometry for Earth-skimming tau neutrino detection at 10^{18} eV energies. No neutrino candidates were found in $t_c \pm 500$ s (Alvarez-Muniz et al. 2017) nor in the 14 day period after it (A. Albert et al. 2017, in preparation).

4. Conclusion

For the first time, gravitational and electromagnetic waves from a single source have been observed. The gravitational-wave observation of a binary neutron star merger is the first of its kind. The electromagnetic observations further support the interpretation of the nature of the binary, and comprise three components at different wavelengths: (i) a prompt sGRB that demonstrates that BNS mergers are the progenitor of at least a fraction of such bursts; (ii) an ultraviolet, optical, and infrared transient (kilonova), which allows for the identification of the host galaxy and is associated with the aftermath of the BNS

merger; and (iii) delayed X-ray and radio counterparts that provide information on the environment of the binary. These observations, described in detail in the companion articles cited above, offer a comprehensive, sequential description of the physical processes related to the merger of a binary neutron star. Table 6 collects all of the Gamma-ray Coordinates Network (GCN) notices and circulars related to GW170817 through 2017 October 1 UTC. The results of this campaign demonstrate the importance of collaborative gravitational-wave, electromagnetic, and neutrino observations and mark a new era in multi-messenger, time-domain astronomy.

(*IM2H*) We thank J. McIver for alerting us to the LVC circular. We thank J. Mulchaey (Carnegie Observatories director), L. Infante (Las Campanas Observatory director), and the entire Las Campanas staff for their extreme dedication, professionalism, and excitement, all of which were critical in the discovery of the first gravitational-wave optical counterpart and its host galaxy as well as the observations used in this study. We thank I. Thompson and the Carnegie Observatory Time Allocation Committee for approving the Swope Supernova Survey and scheduling our program. We thank the University of Copenhagen, DARK Cosmology Centre, and the Niels Bohr International Academy for hosting D.A.C., R.J.F., A.M.B., E.R., and M.R.S. during the discovery of GW170817/SSS17a. R.J.F., A.M.B., and E.R. were participating in the Kavli Summer Program in Astrophysics, “Astrophysics with gravitational wave detections.” This program was supported by the the Kavli Foundation, Danish National Research Foundation, the Niels Bohr International Academy, and the DARK Cosmology Centre. The UCSC group is supported in part by NSF grant AST–1518052, the Gordon & Betty Moore Foundation, the Heising-Simons Foundation, generous donations from many individuals through a UCSC Giving Day grant, and from fellowships from the Alfred P. Sloan Foundation (R.J.F.), the David and Lucile Packard Foundation (R.J.F. and E.R.) and the Niels Bohr Professorship from the DNRF (E.R.). A.M.B. acknowledges support from a UCMEXUS-CONACYT Doctoral Fellowship. Support for this work was provided by NASA through Hubble Fellowship grants HST–HF–51348.001 (B.J.S.) and HST–HF–51373.001 (M.R.D.) awarded by the Space Telescope Science Institute, which is operated by the Association of Universities for Research in Astronomy, Inc., for NASA, under contract NAS5–26555. This paper includes data gathered with the 1 meter Swope and 6.5 meter Magellan Telescopes located at Las Campanas Observatory, Chile.

(*AGILE*) The AGILE Team thanks the ASI management, the technical staff at the ASI Malindi ground station, the technical support team at the ASI Space Science Data Center, and the Fucino AGILE Mission Operation Center. AGILE is an ASI space mission developed with programmatic support by INAF and INFN. We acknowledge partial support through the ASI grant No. I/028/12/2. We also thank INAF, Italian Institute of Astrophysics, and ASI, Italian Space Agency.

(*ANTARES*) The ANTARES Collaboration acknowledges the financial support of: Centre National de la Recherche Scientifique (CNRS), Commissariat à l’énergie atomique et aux énergies alternatives (CEA), Commission Européenne (FEDER fund and Marie Curie Program), Institut Universitaire de France (IUF), IdEx program and UnivEarthS Labex program at Sorbonne Paris Cité (ANR-10-LABX-0023 and ANR-11-IDEX-0005-02), Labex OCEVU (ANR-11-LABX-0060) and the A*MIDEX project (ANR-11-IDEX-0001-02), Région

Île-de-France (DIM-ACAV), Région Alsace (contrat CPER), Région Provence-Alpes-Côte d'Azur, Département du Var and Ville de La Seyne-sur-Mer, France; Bundesministerium für Bildung und Forschung (BMBF), Germany; Istituto Nazionale di Fisica Nucleare (INFN), Italy; Nederlandse organisatie voor Wetenschappelijk Onderzoek (NWO), the Netherlands; Council of the President of the Russian Federation for young scientists and leading scientific schools supporting grants, Russia; National Authority for Scientific Research (ANCS), Romania; Ministerio de Economía y Competitividad (MINECO): Plan Estatal de Investigación (refs. FPA2015-65150-C3-1-P, -2-P and -3-P; MINECO/FEDER), Severo Ochoa Centre of Excellence and MultiDark Consolider (MINECO), and Prometeo and Grisolia programs (Generalitat Valenciana), Spain; Ministry of Higher Education, Scientific Research and Professional Training, Morocco. We also acknowledge the technical support of Ifremer, AIM and Foselev Marine for the sea operation and the CC-IN2P3 for the computing facilities.

(AST3) The AST3 project is supported by the National Basic Research Program (973 Program) of China (Grant Nos. 2013CB834901, 2013CB834900, 2013CB834903), and the Chinese Polar Environment Comprehensive Investigation & Assessment Program (grant No. CHINARE2016-02-03-05). The construction of the AST3 telescopes has received fundings from Tsinghua University, Nanjing University, Beijing Normal University, University of New South Wales, and Texas A&M University, the Australian Antarctic Division, and the National Collaborative Research Infrastructure Strategy (NCRIS) of Australia. It has also received funding from Chinese Academy of Sciences through the Center for Astronomical Mega-Science and National Astronomical Observatory of China (NAOC).

(Auger) The successful installation, commissioning, and operation of the Pierre Auger Observatory would not have been possible without the strong commitment and effort from the technical and administrative staff in Malargüe. We are very grateful to the following agencies and organizations for financial support: Argentina—Comisión Nacional de Energía Atómica; Agencia Nacional de Promoción Científica y Tecnológica (ANPCyT); Consejo Nacional de Investigaciones Científicas y Técnicas (CONICET); Gobierno de la Provincia de Mendoza; Municipalidad de Malargüe; NDM Holdings and Valle Las Leñas; in gratitude for their continuing cooperation over land access; Australia—the Australian Research Council; Brazil—Conselho Nacional de Desenvolvimento Científico e Tecnológico (CNPq); Financiadora de Estudos e Projetos (FINEP); Fundação de Amparo à Pesquisa do Estado de Rio de Janeiro (FAPERJ); São Paulo Research Foundation (FAPESP) grant Nos. 2010/07359-6 and 1999/05404-3; Ministério da Ciência, Tecnologia, Inovações e Comunicações (MCTIC); Czech Republic—grant Nos. MSMT CR LG15014, LO1305, LM2015038 and CZ.02.1.01/0.0/0.0/16_013/0001402; France—Centre de Calcul IN2P3/CNRS; Centre National de la Recherche Scientifique (CNRS); Conseil Régional Ile-de-France; Département Physique Nucléaire et Corpusculaire (PNC-IN2P3/CNRS); Département Sciences de l'Univers (SDU-INSU/CNRS); Institut Lagrange de Paris (ILP) grant No. LABEX ANR-10-LABX-63 within the Investissements d'Avenir Programme Grant No. ANR-11-IDEX-0004-02; Germany—Bundesministerium für Bildung und Forschung (BMBF); Deutsche Forschungsgemeinschaft (DFG); Finanzministerium Baden-Württemberg; Helmholtz Alliance for Astroparticle Physics (HAP); Helmholtz-Gemeinschaft Deutscher Forschungszentren (HGF); Ministerium für Innovation,

Wissenschaft und Forschung des Landes Nordrhein-Westfalen; Ministerium für Wissenschaft, Forschung und Kunst des Landes Baden-Württemberg; Italy—Istituto Nazionale di Fisica Nucleare (INFN); Istituto Nazionale di Astrofisica (INAF); Ministero dell'Istruzione, dell'Università e della Ricerca (MIUR); CETEMPS Center of Excellence; Ministero degli Affari Esteri (MAE); Mexico—Consejo Nacional de Ciencia y Tecnología (CONACYT) No. 167733; Universidad Nacional Autónoma de México (UNAM); PAPIIT DGAPA-UNAM; The Netherlands – Ministerie van Onderwijs, Cultuur en Wetenschap; Nederlandse Organisatie voor Wetenschappelijk Onderzoek (NWO); Stichting voor Fundamenteel Onderzoek der Materie (FOM); Poland—National Centre for Research and Development, grant Nos. ERA-NET-ASPERA/01/11 and ERA-NET-ASPERA/02/11; National Science Centre, grant Nos. 2013/08/M/ST9/00322, 2013/08/M/ST9/00728, and HARMONIA 5–2013/10/M/ST9/00062, UMO-2016/22/M/ST9/00198; Portugal—Portuguese national funds and FEDER funds within Programa Operacional Factores de Competitividade through Fundação para a Ciência e a Tecnologia (COMPETE); Romania—Romanian Authority for Scientific Research ANCS; CNDI-UEFISCDI partnership projects grant Nos. 20/2012 and 194/2012 and PN 16 42 01 02; Slovenia—Slovenian Research Agency; Spain—Comunidad de Madrid; Fondo Europeo de Desarrollo Regional (FEDER) funds; Ministerio de Economía y Competitividad; Xunta de Galicia; European Community 7th Framework Program grant No. FP7-PEOPLE-2012-IEF-328826; USA—Department of Energy, Contract Nos. DE-AC02-07CH11359, DE-FR02-04ER41300, DE-FG02-99ER41107, and DE-SC0011689; National Science Foundation, grant No. 0450696; The Grainger Foundation; Marie Curie-IRSES/EPLANET; European Particle Physics Latin American Network; European Union 7th Framework Program, grant No. PIRSES-2009-GA-246806; European Union's Horizon 2020 research and innovation programme (grant No. 646623); and UNESCO.

(Australian Radio) T.M. acknowledges the support of the Australian Research Council through grant FT150100099. S.O. acknowledges the Australian Research Council grant Laureate Fellowship FL15010014. D.L.K. and I.S.B. are additionally supported by NSF grant AST-141242. P.A.B. and the DFN team acknowledge the Australian Research Council for support under their Australian Laureate Fellowship scheme. The Australia Telescope Compact Array is part of the Australia Telescope National Facility, which is funded by the Australian Government for operation as a National Facility managed by CSIRO. This scientific work makes use of the Murchison Radio-astronomy Observatory, operated by CSIRO. We acknowledge the Wajarri Yamatji people as the traditional owners of the Observatory site. Support for the operation of the MWA is provided by the Australian Government (NCRIS), under a contract to Curtin University administered by Astronomy Australia Limited. We acknowledge the Pawsey Supercomputing Centre, which is supported by the Western Australian and Australian Governments. The Australian SKA Pathfinder is part of the Australia Telescope National Facility, which is managed by CSIRO. Operation of ASKAP is funded by the Australian Government with support from the National Collaborative Research Infrastructure Strategy. ASKAP uses the resources of the Pawsey Supercomputing Centre. Establishment of ASKAP, the Murchison Radio-astronomy Observatory and the Pawsey Supercomputing Centre are initiatives of the Australian Government, with support from

the Government of Western Australia and the Science and Industry Endowment Fund. Parts of this research were conducted by the Australian Research Council Centre of Excellence for All-sky Astrophysics in 3D (ASTRO 3D) through project number CE170100013.

(*Berger Time-Domain Group*) The Berger Time-Domain Group at Harvard is supported in part by the NSF through grants AST-1411763 and AST-1714498, and by NASA through grants NNX15AE50G and NNX16AC22G.

(*Bootes*) A.J.C.T. acknowledges support from the Spanish Ministry Project AYA 2015-71718-R (including FEDER funds) and Junta de Andalucía Proyecto de Excelencia TIC-2839. I.H.P. acknowledges the support of the National Research Foundation (NRF-2015R1A2A1A01006870). S.J. acknowledges the support of Korea Basic Science Research Program (NRF2014R1A6A3A03057484 and NRF-2015R1D1A4A01020961). The BOOTES-5/JGT observations were carried out at Observatorio Astronómico Nacional in San Pedro Mártir (OAN-SPM, México), operated by Instituto de Astronomía, UNAM and with support from Consejo Nacional de Ciencia y Tecnología (México) through the Laboratorios Nacionales Program (México), Instituto de Astrofísica de Andalucía (IAA-CSIC, Spain) and Sungkyunkwan University (SKKU, South Korea). We also thank the staff of OAN-SPM for their support in carrying out the observations.

(*CAASTRO*) Parts of this research were conducted by the Australian Research Council Centre of Excellence for All-sky Astrophysics (CAASTRO), through project number CE110001020. The national facility capability for SkyMapper has been funded through ARC LIEF grant LE130100104 from the Australian Research Council, awarded to the University of Sydney, the Australian National University, Swinburne University of Technology, the University of Queensland, the University of Western Australia, the University of Melbourne, Curtin University of Technology, Monash University, and the Australian Astronomical Observatory. SkyMapper is owned and operated by The Australian National University's Research School of Astronomy and Astrophysics.

(*CALET*) The CALET team gratefully acknowledges support from NASA, ASI, JAXA, and MEXT KAKENHI grant numbers JP 17H06362, JP26220708, and JP17H02901.

(*Chandra/McGill*) This work was supported in part by Chandra Award Number GO7-18033X, issued by the Chandra X-ray Observatory Center, which is operated by the Smithsonian Astrophysical Observatory for and on behalf of the National Aeronautics Space Administration (NASA) under contract NAS8-03060. D.H., M.N., and J.J.R. acknowledge support from a Natural Sciences and Engineering Research Council of Canada (NSERC) Discovery Grant and a Fonds de recherche du Québec–Nature et Technologies (FRQNT) Nouveaux Chercheurs Grant. P.A.E. acknowledges UKSA support. J.A.K. acknowledges the support of NASA grant NAS5-00136. D.H. also acknowledges support from the Canadian Institute for Advanced Research (CIFAR).

(*CZTI/AstroSat*) CZTI is built by a TIFR-led consortium of institutes across India, including VSSC, ISAC, IUCAA, SAC, and PRL. The Indian Space Research Organisation funded, managed, and facilitated the project.

(*DLT40*) D.J.S. acknowledges support for the DLT40 program from NSF grant AST-1517649.

(*EuroVLBI*) The European VLBI Network is a joint facility of independent European, African, Asian, and North American

radio astronomy institutes. Scientific results from data presented in this publication are derived from the following EVN project code: RP029. e-MERLIN is a National Facility operated by the University of Manchester at Jodrell Bank Observatory on behalf of STFC. The collaboration between LIGO/Virgo and EVN/e-MERLIN is part of a project that has received funding from the European Unions Horizon 2020 research and innovation programme under grant agreement No. 653477.

(*ePESSTO*) We acknowledge ESO programs 199.D-0143 and 099.D-0376. PS1 and ATLAS are supported by NASA grants NNX08AR22G, NNX12AR65G, NNX14AM74G, and NNX12AR55G. We acknowledge the Leibniz-Prize to Prof. G. Hasinger (DFG grant HA 1850/28-1), EU/FP7-ERC grants 291222, 615929, 647208, 725161, STFC grants ST/P000312/1 and ERF ST/M005348/1, ST/P000495/1. Marie Skłodowska-Curie grant No 702538. Polish NCN grant OPUS 2015/17/B/ST9/03167, Knut and Alice Wallenberg Foundation. PRIN-INAF 2014. David and Ellen Lee Prize Postdoctoral Fellowship at the California Institute of Technology. Alexander von Humboldt Sofja Kovalevskaja Award. Royal Society—Science Foundation Ireland Vilho, Yrjö and Kalle Väisälä Foundation. FONDECYT grant number 3160504. US NSF grant AST-1311862. Swedish Research Council and the Swedish Space Board. The Quantum Universe I-Core program, the ISF, BSF, and Kimmel award. IRC grant GOIPG/2017/1525. Australian Research Council CAASTRO CE110001020 and grant FT160100028. We acknowledge Millennium Science Initiative grant IC120009.

(*Fermi-GBM*) B.C., V.C., A.G., and W.S.P. gratefully acknowledge NASA funding through contract NNM13AA43C. M.S.B., R.H., P.J., C.A.M., S.P., R.D.P., M.S., and P.V. gratefully acknowledge NASA funding from cooperative agreement NNM11AA01A. E.B. is supported by an appointment to the NASA Postdoctoral Program at the Goddard Space Flight Center, administered by Universities Space Research Association under contract with NASA. D.K., C.A.W.H., C.M. H., and J.R. gratefully acknowledge NASA funding through the *Fermi*-GBM project. Support for the German contribution to GBM was provided by the Bundesministerium für Bildung und Forschung (BMBF) via the Deutsches Zentrum für Luft und Raumfahrt (DLR) under contract number 50 QV 0301. A. v.K. was supported by the Bundesministeriums für Wirtschaft und Technologie (BMWi) through DLR grant 50 OG 1101. S. M.B. acknowledges support from Science Foundation Ireland under grant 12/IP/1288.

(*Fermi-LAT*) The *Fermi*-LAT Collaboration acknowledges support for LAT development, operation, and data analysis from NASA and DOE (United States), CEA/Irfu and IN2P3/CNRS (France), ASI and INFN (Italy), MEXT, KEK, and JAXA (Japan), and the K.A. Wallenberg Foundation, the Swedish Research Council and the National Space Board (Sweden). Science analysis support in the operations phase from INAF (Italy) and CNES (France) is also gratefully acknowledged. This work performed in part under DOE Contract DE-AC02-76SF00515.

(*FRBSG*) S.L.L. is supported by NSF grant PHY-1607291 (LIU). Construction of the LWA has been supported by the Office of Naval Research under Contract N00014-07-C-0147. Support for operations and continuing development of the LWA1 is provided by the National Science Foundation

under grants AST-1139963 and AST-1139974 of the University Radio Observatory program.

(*GRAWITA*) We acknowledge INAF for supporting the project “Gravitational Wave Astronomy with the first detections of adLIGO and adVIRGO experiments—GRAWITA” PI: E. Brocato. Observations are made with ESO Telescopes at the Paranal Observatory under programmes ID 099.D-0382 (PI: E. Pian), 099.D-0622 (PI: P. D’Avanzo), 099.D-0191 (PI: A. Grado), 099.D-0116 (PI: S. Covino) and with the REM telescope at the ESO La Silla Observatory under program ID 35020 (PI: S. Campana). We thank the ESO operation staff for excellent support of this program. The Sardinia Radio Telescope (SRT) is funded by the Department of University and Research (MIUR), the Italian Space Agency (ASI), and the Autonomous Region of Sardinia (RAS) and is operated as National Facility by the National Institute for Astrophysics (INAF). Z.J. is supported by the External Cooperation Program of BIC (number 114332KYSB20160007). J.M. is supported by the Hundred Talent Program, the Major Program of the Chinese Academy of Sciences (KJZD-EW-M06), the National Natural Science Foundation of China 11673062, and the Oversea Talent Program of Yunnan Province. R.L.C. Starling, K.W., A.B.H., N.R.T., and C.G.M. are supported by the STFC (Science and Technology Facilities Council). D.K., acknowledges the financial support from the Slovenian Research Agency (P1-0188). S.K. and A.N.G. acknowledge support by grant DFG Kl 766/16-3. D.G. acknowledges the financial support of the UnivEarthS Labex program at Sorbonne Paris Cité (ANR-10-LABX-0023 and ANR-11-IDEX-0005-02). K.T. was supported by JSPS grant 15H05437 and by a JST Consortia grant.

(*GROND*) Part of the funding for GROND was generously granted from the Leibniz-Prize to Prof. G. Hasinger (DFG grant HA 1850/28-1). “We acknowledge the excellent help in obtaining GROND data from Angela Hempel, Markus Rabus and Régis Lachaume on La Silla.”

(*GROWTH*, *JAGWAR*, *Caltech-NRAO*, *TTU-NRAO*, and *NuSTAR*) This work was supported by the GROWTH (Global Relay of Observatories Watching Transients Happen) project funded by the National Science Foundation under PIRE grant No. 1545949. GROWTH is a collaborative project among California Institute of Technology (USA), University of Maryland College Park (USA), University of Wisconsin–Milwaukee (USA), Texas Tech University (USA), San Diego State University (USA), Los Alamos National Laboratory (USA), Tokyo Institute of Technology (Japan), National Central University (Taiwan), Indian Institute of Astrophysics (India), Inter-University Center for Astronomy and Astrophysics (India), Weizmann Institute of Science (Israel), The Oskar Klein Centre at Stockholm University (Sweden), Humboldt University (Germany), Liverpool John Moores University (UK). A.H. acknowledges support by the I-Core Program of the Planning and Budgeting Committee and the Israel Science Foundation. T.M. acknowledges the support of the Australian Research Council through grant FT150100099. Parts of this research were conducted by the Australian Research Council Centre of Excellence for All-sky Astrophysics (CAASTRO), through project number CE110001020. The Australia Telescope Compact Array is part of the Australia Telescope National Facility which is funded by the Australian Government for operation as a National Facility managed by CSIRO. D.L.K. is additionally supported by NSF grant AST-1412421.

A.A.M. is funded by the Large Synoptic Survey Telescope Corporation in support of the Data Science Fellowship Program. P.C.Y., C.C.N., and W.H.I. thank the support from grants MOST104-2923-M-008-004-MY5 and MOST106-2112-M-008-007. A.C. acknowledges support from the National Science Foundation CAREER award 1455090, “CAREER: Radio and gravitational-wave emission from the largest explosions since the Big Bang.” T.P. acknowledges the support of Advanced ERC grant TReX. B.E.C. thanks SMARTS 1.3 m Queue Manager Bryndis Cruz for prompt scheduling of the SMARTS observations. Basic research in radio astronomy at the Naval Research Laboratory (NRL) is funded by 6.1 Base funding. Construction and installation of VLITE was supported by NRL Sustainment Restoration and Maintenance funding. K.P.M.’s research is supported by the Oxford Centre for Astrophysical Surveys, which is funded through the Hintze Family Charitable Foundation. J.S. and A. G. are grateful for support from the Knut and Alice Wallenberg Foundation. GREAT is funded by the Swedish Research Council (V.R.). E.O.O. is grateful for the support by grants from the Israel Science Foundation, Minerva, Israeli ministry of Science, the US-Israel Binational Science Foundation, and the I-CORE Program of the Planning and Budgeting Committee and The Israel Science Foundation. We thank the staff of the GMRT that made these observations possible. The GMRT is run by the National Centre for Radio Astrophysics of the Tata Institute of Fundamental Research. AYQH was supported by a National Science Foundation Graduate Research Fellowship under grant No. DGE-1144469. S.R. has been supported by the Swedish Research Council (VR) under grant number 2016 03657 3, by the Swedish National Space Board under grant number Dnr. 107/16 and by the research environment grant “Gravitational Radiation and Electromagnetic Astrophysical Transients (GREAT)” funded by the Swedish Research council (V.R.) under Dnr. 2016-06012. We acknowledge the support of the Science and Engineering Research Board, Department of Science and Technology, India and the Indo-US Science and Technology Foundation for the GROWTH-India project.

(*HAWC*) We acknowledge the support from: the US National Science Foundation (NSF); the US Department of Energy Office of High-Energy Physics; the Laboratory Directed Research and Development (LDRD) program of Los Alamos National Laboratory; Consejo Nacional de Ciencia y Tecnología (CONACyT), Mexico (grants 271051, 232656, 167281, 260378, 179588, 239762, 254964, 271737, 258865, 243290); Red HAWC, Mexico; DGAPA-UNAM (grants RG100414, IN111315, IN111716-3, IA102715, 109916); VIEP-BUAP; the University of Wisconsin Alumni Research Foundation; the Institute of Geophysics, Planetary Physics, and Signatures at Los Alamos National Laboratory; Polish Science Centre grant DEC-2014/13/B/ST9/945. We acknowledge the support of the Science and Engineering Research Board, Department of Science and Technology, India and the Indo-US Science and Technology Foundation for the GROWTH-India project.

(*H.E.S.S.*) The support of the Namibian authorities and of the University of Namibia in facilitating the construction and operation of H.E.S.S. is gratefully acknowledged, as is the support by the German Ministry for Education and Research (BMBF), the Max Planck Society, the German Research Foundation (DFG), the Alexander von Humboldt Foundation, the Deutsche Forschungsgemeinschaft, the French Ministry for Research, the CNRS-IN2P3 and the Astroparticle

Interdisciplinary Programme of the CNRS, the U.K. Science and Technology Facilities Council (STFC), the INPN of the Charles University, the Czech Science Foundation, the Polish National Science Centre, the South African Department of Science and Technology and National Research Foundation, the University of Namibia, the National Commission on Research, Science and Technology of Namibia (NCRST), the Innsbruck University, the Austrian Science Fund (FWF), and the Austrian Federal Ministry for Science, Research and Economy, the University of Adelaide and the Australian Research Council, the Japan Society for the Promotion of Science and by the University of Amsterdam. We appreciate the excellent work of the technical support staff in Berlin, Durham, Hamburg, Heidelberg, Palaiseau, Paris, Saclay, and in Namibia in the construction and operation of the equipment. This work benefited from services provided by the H.E.S.S. Virtual Organisation, supported by the national resource providers of the EGI Federation.

(Insight-HXMT) The *Insight-HXMT* team acknowledges the support from the China National Space Administration (CNSA), the Chinese Academy of Sciences (CAS; grant No. XDB23040400), and the Ministry of Science and Technology of China (MOST; grant No. 2016YFA0400800).

(IceCube) We acknowledge the support from the following agencies: U.S. National Science Foundation-Office of Polar Programs, U.S. National Science Foundation-Physics Division, University of Wisconsin Alumni Research Foundation, the Grid Laboratory of Wisconsin (GLOW) grid infrastructure at the University of Wisconsin—Madison, the Open Science Grid (OSG) grid infrastructure; U.S. Department of Energy, and National Energy Research Scientific Computing Center, the Louisiana Optical Network Initiative (LONI) grid computing resources; Natural Sciences and Engineering Research Council of Canada, WestGrid and Compute/Calcul Canada; Swedish Research Council, Swedish Polar Research Secretariat, Swedish National Infrastructure for Computing (SNIC), and Knut and Alice Wallenberg Foundation, Sweden; German Ministry for Education and Research (BMBF), Deutsche Forschungsgemeinschaft (DFG), Helmholtz Alliance for Astroparticle Physics (HAP), Initiative and Networking Fund of the Helmholtz Association, Germany; Fund for Scientific Research (FNRS-FWO), FWO Odysseus programme, Flanders Institute to encourage scientific and technological research in industry (IWT), Belgian Federal Science Policy Office (Belspo); Marsden Fund, New Zealand; Australian Research Council; Japan Society for Promotion of Science (JSPS); the Swiss National Science Foundation (SNSF), Switzerland; National Research Foundation of Korea (NRF); Villum Fonden, Danish National Research Foundation (DNRF), Denmark.

(IKI-GW) A.S.P., A.A.V., E.D.M., and P.Y.u.M. acknowledge the support from the Russian Science Foundation (grant 15-12-30015). V.A.K., A.V.K., and I.V.R. acknowledge the Science and Education Ministry of Kazakhstan (grant No. 0075/GF4). R.I. is grateful to the grant RUSTAVELI FR/379/6-300/14 for partial support. We acknowledge the excellent help in obtaining Chilescope data from Sergei Pogrebsskiy and Ivan Rubzov.

(INTEGRAL) This work is based on observations with INTEGRAL, an ESA project with instruments and science data center funded by ESA member states (especially the PI countries: Denmark, France, Germany, Italy, Switzerland, Spain), and with the participation of Russia and the USA. The INTEGRAL SPI project has been completed under the responsibility and leadership of CNES. The SPI-ACS detector

system has been provided by MPE Garching/Germany. The SPI team is grateful to ASI, CEA, CNES, DLR, ESA, INTA, NASA, and OSTC for their support. The Italian INTEGRAL team acknowledges the support of ASI/INAF agreement No. 2013-025-R.1. R.D. and A.v.K. acknowledge the German INTEGRAL support through DLR grant 50 OG 1101. A.L. and R.S. acknowledge the support from the Russian Science Foundation (grant 14-22-00271). A.D. is funded by Spanish MINECO/FEDER grant ESP2015-65712-C5-1-R.

(IPN) K.H. is grateful for support under NASA grant NNX15AE60G. R.L.A. and D.D.F. are grateful for support under RFBF grant 16-29-13009-ofi-m.

(J-GEM) MEXT KAKENHI (JP17H06363, JP15H00788, JP24103003, JP10147214, JP10147207), JSPS KAKENHI (JP16H02183, JP15H02075, JP15H02069, JP26800103, JP25800103), Inter-University Cooperation Program of the MEXT, the NINS program for cross-disciplinary science study, the Toyota Foundation (D11-R-0830), the Mitsubishi Foundation, the Yamada Science Foundation, Inoue Foundation for Science, the National Research Foundation of South Africa.

(KU) The Korea-Uzbekistan Consortium team acknowledges the support from the NRF grant No. 2017R1A3A3001362, and the KASI grant 2017-1-830-03. This research has made use of the KMTNet system operated by KASI.

(Las Cumbres) Support for I.A. and J.B. was provided by NASA through the Einstein Fellowship Program, grants PF6-170148 and PF7-180162, respectively. D.A.H., C.M., and G.H. are supported by NSF grant AST-1313484. D.P. and D.M. acknowledge support by Israel Science Foundation grant 541/17. This work makes use of observations from the LCO network.

(LIGO and Virgo) The authors gratefully acknowledge the support of the United States National Science Foundation (NSF) for the construction and operation of the LIGO Laboratory and Advanced LIGO as well as the Science and Technology Facilities Council (STFC) of the United Kingdom, the Max-Planck-Society (MPS), and the State of Niedersachsen/Germany for support of the construction of Advanced LIGO and construction and operation of the GEO600 detector. Additional support for advanced LIGO was provided by the Australian Research Council. The authors gratefully acknowledge the Italian Istituto Nazionale di Fisica Nucleare (INFN), the French Centre National de la Recherche Scientifique (CNRS) and the Foundation for Fundamental Research on Matter supported by the Netherlands Organisation for Scientific Research, for the construction and operation of the Virgo detector and the creation and support of the EGO consortium. The authors also gratefully acknowledge research support from these agencies as well as by the Council of Scientific and Industrial Research of India, the Department of Science and Technology, India, the Science & Engineering Research Board (SERB), India, the Ministry of Human Resource Development, India, the Spanish Agencia Estatal de Investigación, the Vicepresidència i Conselleria d'Innovació Recerca i Turisme and the Conselleria d'Educació i Universitat del Govern de les Illes Balears, the Conselleria d'Educació Investigació Cultura i Esport de la Generalitat Valenciana, the National Science Centre of Poland, the Swiss National Science Foundation (SNSF), the Russian Foundation for Basic Research, the Russian Science Foundation, the European Commission, the European Regional Development Funds (ERDF), the Royal Society, the Scottish Funding Council, the Scottish Universities Physics Alliance, the Hungarian Scientific Research Fund (OTKA), the Lyon Institute of Origins

(LIO), the National Research, Development and Innovation Office Hungary (NKFI), the National Research Foundation of Korea, Industry Canada and the Province of Ontario through the Ministry of Economic Development and Innovation, the Natural Science and Engineering Research Council Canada, the Canadian Institute for Advanced Research, the Brazilian Ministry of Science, Technology, Innovations, and Communications, the International Center for Theoretical Physics South American Institute for Fundamental Research (ICTP-SAIFR), the Research Grants Council of Hong Kong, the National Natural Science Foundation of China (NSFC), the China National Space Administration (CNSA) and the Chinese Academy of Sciences (CAS), the Ministry of Science and Technology of China (MOST), the Leverhulme Trust, the Research Corporation, the Ministry of Science and Technology (MOST), Taiwan and the Kavli Foundation. The authors gratefully acknowledge the support of the NSF, STFC, MPS, INFN, CNRS, and the State of Niedersachsen/Germany for provision of computational resources. The *MAXI* team acknowledges the support by JAXA, RIKEN, and MEXT KAKENHI grant number JP 17H06362. The National Radio Astronomy Observatory is a facility of the National Science Foundation operated under cooperative agreement by Associated Universities, Inc. The European VLBI Network is a joint facility of independent European, African, Asian, and North American radio astronomy institutes. Scientific results from data presented in this publication are derived from the following EVN project code: RP029. e-MERLIN is a National Facility operated by the University of Manchester at Jodrell Bank Observatory on behalf of STFC. The collaboration between LIGO/Virgo and EVN/e-MERLIN is part of a project that has received funding from the European Union's Horizon 2020 research and innovation programme under grant agreement No. 653477. We thank Britt Griswold (NASA/GSFC) for graphic arts. P.G.J. acknowledges ERC-Consolidator grant No. 647208. We thank the GMRT staff for prompt scheduling of these observations. The GMRT is run by the National Center for Radio Astrophysics of the Tata Institute of Fundamental Research. INAF, Italian Institute of Astrophysics ASI, Italian Space Agency. This work is part of the research program Innovational Research Incentives Scheme (Vernieuwingsimpuls), which is financed by the Netherlands Organization for Scientific Research through the NWO VIDI grant No. 639.042.612-Nissanke and NWO TOP grant No. 62002444-Nissanke. We thank ESO for granting full access to all the LVC MoU partners of the observations of GW170817 obtained with NACO and VISIR under the Observatory program 60.A-9392.

(*LOFAR*) LOFAR, the Low-Frequency Array designed and constructed by ASTRON, has facilities in several countries that are owned by various parties (each with their own funding sources) and that are collectively operated by the International LOFAR Telescope (ILT) foundation under a joint scientific policy. P.G.J. acknowledges support from ERC grant number 647208. R.F. was partially funded by ERC Advanced Investigator Grant 267607 “4 PI SKY.”

(*MASTER*) Development Programme of Lomonosov Moscow State University, Sergey Bodrov of Moscow Union OPTICA, Russian Scientific Foundation 16-12-00085, National Research Foundation of South Africa, Russian Federation Ministry of Education and Science (14.B25.31.0010, 14.593.21.0005, 3.10131.2017/NM), RFBR 17-52-80133

(*MAXI*) The *MAXI* team acknowledges support by JAXA, RIKEN, and MEXT KAKENHI grant number JP 17H06362.

(*Nordic Optical Telescope*) J.P.U.F. acknowledges the Carlsberg foundation for funding for the NTE project. D.X. acknowledges the support by the One-Hundred-Talent Program of the Chinese Academy of Sciences (CAS) and by the Strategic Priority Research Program “Multi-wavelength Gravitational Wave Universe” of the CAS (No. XDB23000000). Based on observations made with the Nordic Optical Telescope (program 55-013), operated by the Nordic Optical Telescope Scientific Association.

(*OzGrav*) Part of this research was funded by the Australian Research Council Centre of Excellence for Gravitational Wave Discovery (OzGrav), CE170100004 and the Australian Research Council Centre of Excellence for All-sky Astrophysics (CAASTRO), CE110001020. J.C. acknowledges the Australian Research Council Future Fellowship grant FT130101219. Research support to I.A. is provided by the Australian Astronomical Observatory (AAO). A.T.D. acknowledges the support of an Australian Research Council Future Fellowship (FT150100415). Based in part on data acquired through the Australian Astronomical Observatory. We acknowledge the traditional owners of the land on which the AAT stands, the Gamilaraay people, and pay our respects to elders past and present. The Etelman/VIRT team acknowledge NASA grant NNX13AD28A.

(*Pan-STARRS*) The Pan-STARRS1 observations were supported in part by NASA grant No. NNX14AM74G issued through the SSO Near Earth Object Observations Program and the Queen's University Belfast. The Pan-STARRS1 Surveys were made possible through contributions by the Institute for Astronomy, the University of Hawaii, the Pan-STARRS Project Office, the Max-Planck Society and its participating institutes, the Max Planck Institute for Astronomy, Heidelberg and the Max Planck Institute for Extraterrestrial Physics, Garching, The Johns Hopkins University, Durham University, the University of Edinburgh, the Queen's University Belfast, the Harvard-Smithsonian Center for Astrophysics, the LCO Global Telescope Network Incorporated, the National Central University of Taiwan, the Space Telescope Science Institute, and the National Aeronautics and Space Administration under grant No. NNX08AR22G issued through the Planetary Science Division of the NASA Science Mission Directorate, the National Science Foundation grant No. AST-1238877, the University of Maryland, Eotvos Lorand University (ELTE), and the Los Alamos National Laboratory. The Pan-STARRS1 Surveys are archived at the Space Telescope Science Institute (STScI) and can be accessed through MAST, the Mikulski Archive for Space Telescopes. Additional support for the Pan-STARRS1 public science archive is provided by the Gordon and Betty Moore Foundation.

(*Pi of the Sky*) The Pi of the Sky team is grateful for the support of the ESAt/INTA-CEDEA personnel in Mazagón, Huelva (Spain). Analysis of the Pi of the Sky data was based on the LUIZA software developed within the GLORIA project, funded from the European Union Seventh Framework Programme (FP7/2007-2013) under grant 283783.

(*SALT*) D.B., S.M.C., E.R.C., S.B.P., P.V., and T.W. acknowledge support from the South African National Research Foundation. M.M.S. gratefully acknowledges the support of the late Paul Newman and the Newmans Own Foundation. We are most grateful for the DDT allocation for the SALT observations.

(*SKA*) R.F. was partially funded by ERC Advanced Investigator Grant 267607 “4 PI SKY.”

(*Swift*) Funding for the *Swift* mission in the UK is provided by the UK Space Agency. The *Swift* team at the MOC at Penn State acknowledges support from NASA contract NAS5-00136. The Italian *Swift* team acknowledge support from ASI-INAF grant I/004/11/3.

(*TOROS*) We thank support from the USA Air Force Office of International Scientific Research (AFOSR/IO), the Dirección de Investigación de la Universidad de La Serena, the Consejo Nacional de Investigaciones Científicas y Técnicas de Argentina, the FAPESP, and the Observatorio Nacional-MCT of Brasil.

(*TTU Group*) A.C. and N.T.P. acknowledge support from the NSF CAREER Award 1455090: “CAREER: Radio and gravitational-wave emission from the largest explosions since the Big Bang.” The National Radio Astronomy Observatory is a facility of the National Science Foundation operated under cooperative agreement by Associated Universities, Inc.

(*VINROUGE*) Based on observations made with ESO telescopes at the La Silla Paranal Observatory under programmes ID 099.D-0668, 099.D-0116, 099.D-0622, 179.A-2010, and 198.D-2010; and with the NASA/ESA *Hubble Space Telescope* observations under programs GO 14771, GO 14804, GO 14850. The VISTA observations were processed by C.G.F. at the Cambridge Astronomy Survey Unit (CASU), which is funded by the UK Science and Technology Research Council under grant ST/N005805/1. This research used resources provided by the Los Alamos National Laboratory Institutional Computing Program, which is supported by the U.S. Department of Energy National Nuclear Security Administration under Contract No. DE-AC52-06NA25396. We acknowledge support to the following bodies: the ERC (grant No. 725246); STFC via grant ST/P000495/1; VILLUM FONDEN (investigator grant project number 16599); the Spanish project AYA 2014-58381-P; the Juan de la Cierva Incorporación fellowship IJCI-2014-21669; the Juan de la Cierva Incorporación fellowship IJCI-2015-26153; the NRFK grant No. 2017R1A3A3001362; grants GO718062A and HSTG014850001A; the Swedish Research Council (VR) under grant number 2016-03657-3; the Swedish National Space Board under grant number Dnr. 107/16; the research environment grant “Gravitational Radiation and Electromagnetic Astrophysical Transients (GREAT)” under Dnr 2016-06012; UKSA.

(*Zadko*) The Zadko Telescope was made possible by a philanthropic donation by James Zadko to the University of Western Australia (UWA). Zadko Telescope operations are supported by UWA and the Australian Research Council Centre of Excellence OzGrav CE170100004. The TAROT network of telescopes is supported by the French Centre National de la Recherche Scientifique (CNRS), the Observatoire de la Côte d’Azur (OCA), and we thank the expertise and support of the Observatoire des Sciences de l’Univers, Institut Pythéas, Aix-Marseille University. The FIGARONet network is supported under the Agence Nationale de la Recherche (ANR) grant 14-CE33. The paper-writing team would like to thank Britt Griswold (NASA/GSFC) and Aaron Geller (Northwestern/NUIT/CIERA) for assistance with graphics.

References

Aab, A., Abreu, P., Aglietta, M., et al. 2015a, *NIMPA*, 798, 172
 Aab, A., Abreu, P., Aglietta, M., et al. 2015b, *PhRvD*, 91, 092008
 Aartsen, M. G., Ackermann, M., Adams, J., et al. 2015, *PhRvD*, 91, 022001
 Aartsen, M. G., Ackermann, M., Adams, J., et al. 2017, *JInst*, 12, P03012

Aartsen, M. G., Abraham, K., Ackermann, M., et al. 2016, *JInst*, 11, P11009
 Abadie, J., Abbott, B. P., Abbott, R., et al. 2010, *CQGra*, 27, 173001
 Abadie, J., Abbott, B. P., Abbott, R., et al. 2012, *A&A*, 541, A155
 Abbott, B. P., Abbott, R., Abbott, T. D., et al. 2016a, *ApJL*, 826, L13
 Abbott, B. P., Abbott, R., Abbott, T. D., et al. 2016b, *PhRvL*, 116, 241102
 Abbott, B. P., Abbott, R., Abbott, T. D., et al. 2016c, *PhRvL*, 116, 061102
 Abbott, B. P., Abbott, R., Abbott, T. D., et al. 2016d, *PhRvL*, 116, 241103
 Abbott, B. P., Abbott, R., Abbott, T. D., et al. 2016e, *PhRvX*, 6, 041015
 Abbott, B. P., Abbott, R., Abbott, T. D., et al. 2017a, *PhRvL*, 118, 221101
 Abbott, B. P., Abbott, R., Abbott, T. D., et al. 2017b, *PhRvL*, 118, 221101
 Abbott, B. P., Abbott, R., Abbott, T. D., et al. 2017c, *PhRvL*, 119, 161101
 Abbott, B. P., Abbott, R., Abbott, T. D., et al. 2017d, *PhRvL*, 119, 141101
 Abbott, B. P., Abbott, R., Abbott, T. D., et al. 2017e, *Natur*, <https://doi.org/10.1038/nature24471>
 Abbott, B. P., Abbott, R., Abbott, T. D., et al. 2017f, *ApJL*, <https://doi.org/10.3847/2041-8213/aa920c>
 Abbott, B. P., Abbott, R., Abbott, T. D., et al. 2017g, *ApJL*, <https://doi.org/10.3847/2041-8213/aa91c9>
 Abeyssekara, A. U., Albert, A., Alfaro, R., et al. 2017, *ApJ*, 843, 39
 Adams, S. M., Kasliwal, M. M., Blagorodnova, N., et al. 2017, GCN, 21816
 Ade, P. A. R., Aghanim, N., Arnaud, M., et al. 2016, *A&A*, 594, A13
 Ageron, M., Aguilar, J. A., Al Samara, I., et al. 2011, *NIMPA*, 656, 11
 Ageron, M., Baret, B., Coleiro, A., et al. 2017a, GCN, 21522
 Ageron, M., Baret, B., Coleiro, A., et al. 2017b, GCN, 21631
 Alexander, K. D., Berger, E., Eftekhari, T., et al. 2017a, GCN, 21851
 Alexander, K., Berger, E., Fong, W., et al. 2017c, *ApJL*, <https://doi.org/10.3847/2041-8213/aa905d>
 Alexander, K. D., Fong, W., Berger, E., et al. 2017d, GCN, 21545
 Alexander, K. D., Fong, W., Berger, E., et al. 2017e, GCN, 21548
 Alexander, K. D., Fong, W., Berger, E., et al. 2017f, GCN, 21589
 Alexander, K. D., Fong, W., Williams, P. K. G., et al. 2017b, GCN, 21935
 Allam, S., Annis, J., Berger, E., et al. 2017, GCN, 21530
 Allen, B., Anderson, W. G., Brady, P. R., Brown, D. A., & Creighton, J. D. E. 2012, *PhRvD*, 85, 122006
 Alvarez-Muniz, J., Pedreira, F., Zas, E., et al. 2017, GCN, 21686
 Andreoni, I., Cooke, J., Lidman, C., et al. 2017, GCN, 21677
 Arcavi, I., Howell, D. A., McCully, C., et al. 2017a, GCN, 21538
 Arcavi, I., Howell, D. A., McCully, C., et al. 2017b, GCN, 21565
 Arcavi, I., Howell, D. A., McCully, C., et al. 2017c, GCN, 21581
 Arcavi, I., Howell, D. A., McCully, C., et al. 2017d, GCN, 21543
 Arcavi, I., Hosseinzadeh, G., Howell, D., et al. 2017e, *Natur*, <https://doi.org/10.1038/nature24291>
 Aresu, G., Bachetti, M., Buffa, F., et al. 2017, GCN, 21914
 Baade, W., & Zwicky, F. 1934, *PhRv*, 46, 76
 Bagot, P., Portegies Zwart, S. F., & Yungelson, L. R. 1998, *A&A*, 332, L57
 Bailes, M., Andreoni, I., et al. 2017a, GCN, 21899
 Bailes, M., Andreoni, I., et al. 2017b, GCN, 21928
 Baker, J. G., Centrella, J., Choi, D., Koppitz, M., & van Meter, J. 2006, *PhRvL*, 96, 111102
 Balasubramanian, A., Mate, S., Bhalariao, V., et al. 2017, GCN, 21514
 Bannister, K., Lynch, C., Kaplan, D., et al. 2017b, GCN, 21559
 Bannister, K., Lynch, C., Kaplan, D., et al. 2017d, GCN, 21537
 Bannister, K., Shannon, R., Hotan, A., et al. 2017c, GCN, 21671
 Bannister, K., Shannon, R., Hotan, A., et al. 2017e, GCN, 21562
 Bannister, K. W., Shannon, R. M., Macquart, J.-P., et al. 2017a, *ApJL*, 841, L12
 Barnes, J., & Kasen, D. 2013, *ApJ*, 775, 18
 Barnes, J., Kasen, D., Wu, M.-R., & Martínez-Pinedo, G. 2016, arXiv:1605.07218
 Barr, E. D., Guillemot, L., Champion, D. J., et al. 2013, *MNRAS*, 429, 1633
 Barthelmy, S. D., Chincarini, G., Burrows, D. N., et al. 2005, *Natur*, 438, 994
 Barthelmy, S. D., Lien, A. Y., Palmer, D. M., et al. 2017, GCN, 21524
 Bartos, I., Countryman, S., Finley, C., et al. 2017a, GCN, 21508
 Bartos, I., Countryman, S., Finley, C., et al. 2017b, GCN, 21568
 Bartos, I., Countryman, S., Finley, C., et al. 2017c, GCN, 21511
 Batsch, T., Castro-Tirado, A. J., Czyrkowski, H., et al. 2017, GCN, 21931
 Belczynski, K., Kalogera, V., & Bulik, T. 2002, *ApJ*, 572, 407
 Berger, E. 2010, *ApJ*, 722, 1946
 Berger, E. 2014, *ARA&A*, 52, 43
 Berger, E., Fong, W., & Chornock, R. 2013a, *ApJL*, 774, L23
 Berger, E., Fong, W., & Chornock, R. 2013b, *ApJL*, 774, L23
 Berger, E., Fox, D. B., Price, P. A., et al. 2007, *ApJ*, 664, 1000
 Berger, E., Price, P. A., Cenko, S. B., et al. 2005, *Natur*, 438, 988
 Bhalariao, V., Bhattacharya, D., Vibhute, A., et al. 2017, *JApA*, 38, 31
 Blackburn, L., Briggs, M. S., Camp, J., et al. 2015, *ApJS*, 217, 8
 Blanchet, L. 2014, *LRR*, 17, 2

- Blanchet, L., Buonanno, A., & Faye, G. 2006, *PhRvD*, **74**, 104034 (Erratum: 2007, *PhRvD*, **75**, 049903; Erratum: 2010, *PhRvD*, **81**, 089901)
- Blanchet, L., Damour, T., Esposito-Farèse, G., & Iyer, B. R. 2004, *PhRvL*, **93**, 091101
- Blanchet, L., Damour, T., Iyer, B. R., Will, C. M., & Wiseman, A. G. 1995, *PhRvL*, **74**, 3515
- Bloom, J. S., Sigurdsson, S., & Pols, O. R. 1999, *MNRAS*, **305**, 763
- Bohé, A., Marsat, S., & Blanchet, L. 2013, *CQGra*, **30**, 135009
- Broderick, J. W., Rowlinson, A., Jonker, P. G., et al. 2017, *GCN*, 21676
- Brown, T. M., Baliber, N., Bianco, F. B., et al. 2013, *PASP*, **125**, 1031
- Buckley, D. A. H., Andreoni, I., Barway, S., et al. 2017, *MNRAS*, submitted
- Bulgarelli, A., Tavani, M., Verrecchia, F., et al. 2017, *GCN*, 21564
- Buonanno, A., & Damour, T. 1999, *PhRvD*, **59**, 084006
- Burrows, D. N., Grupe, D., Capalbi, M., et al. 2006, *ApJ*, **653**, 468
- Burrows, D. N., Hill, J. E., Nousek, J. A., et al. 2005, *SSRv*, **120**, 165
- Callister, T., Dowell, J., Kanner, J., et al. 2017a, *GCN*, 21680
- Callister, T., Dowell, J., Kanner, J., et al. 2017b, *GCN*, 21848
- Campanelli, M., Lousto, C. O., Marronetti, & Zlochower, Y. 2006, *PhRvL*, **96**, 111101
- Cannon, K., Cariou, R., Chapman, A., et al. 2012, *ApJ*, **748**, 136
- Cano, Z., Jorgensen, U. G., Hodosan, G., et al. 2017, *GCN*, 21889
- Castro-Tirado, A. J., Tello, J. C., Hu, Y., et al. 2017, *GCN*, 21624
- Cenko, S. B., Emery, S. W. K., Campana, S., et al. 2017, *GCN*, 21572
- Chambers, K. C., Huber, M. E., Smartt, S. J., et al. 2017a, *GCN*, 21553
- Chambers, K. C., Huber, M. E., Smitch, K. W., et al. 2017c, *GCN*, 21617
- Chambers, K. C., Huber, M. E., Smitch, K. W., et al. 2017d, *GCN*, 21633
- Chambers, K. C., Magnier, E. A., Metcalfe, N., et al. 2016, arXiv:1612.05560
- Chambers, K. C., Smartt, S. J., Huber, M. E., et al. 2017b, *GCN*, 21590
- Chen, T. W., Wiseman, P., Greiner, J., et al. 2017, *GCN*, 21608
- Chornock, R., Berger, E., et al. 2017b, *GCN*, 21684
- Chornock, R., Berger, E., et al. 2017c, *GCN*, 21638
- Chornock, R., Berger, E., Kasen, D., et al. 2017a, *ApJL*, <https://doi.org/10.3847/2041-8213/aa905c>
- Clark, J. P. A. 1979, in *Sources of Gravitational Radiation*, ed. L. L. Smarr (Cambridge: Cambridge Univ. Press), 447
- Clark, J. P. A., van den Heuvel, E. P. J., & Sutantyo, W. 1979, *A&A*, **72**, 120
- Clarke, T. E., Kassim, N. E., Brisken, W., et al. 2016, in *Ground-based and Airborne Telescopes VI*, Vol. 990699065B
- Connaughton, V., Blackburn, L., Briggs, M. S., et al. 2017, *GCN*, 21506
- Cook, D. O., Van Sistine, A., Singer, L., et al. 2017a, *GCN*, 21519
- Cook, D. O., Van Sistine, A., Singer, L., et al. 2017b, *GCN*, 21521
- Cook, D. O., Van Sistine, A., Singer, L., et al. 2017c, *GCN*, 21535
- Corsi, A., Hallinan, G., Mooley, K., et al. 2017d, *GCN*, 21815
- Corsi, A., Kasliwal, M. M., et al. 2017a, *GCN*, 21614
- Corsi, A., Kasliwal, M. M., et al. 2017b, *GCN*, 21613
- Corsi, A., Kasliwal, M. M., Frail, D., et al. 2017c, *GCN*, 21664
- Corsi, A., Kasliwal, M. M., et al. 2017e, *GCN*, 21636
- Coulter, D. A., Kilpatrick, C. D., Siebert, M. R., et al. 2017, *Sci*, <https://doi.org/10.1126/science.aap9811>
- Coulter, D. A., Kilpatrick, C. D., Siebert, M. R., et al. 2017a, *GCN*, 21529
- Coulter, D. A., Kilpatrick, C. D., Siebert, M. R., et al. 2017b, *GCN*, 21567
- Covino, S., Wiersema, K., Fan, Y., & Toma, K. 2017, *Natur*, doi:10.1038/s41550-017-0285-z
- Coward, D., Howell, E., Laugier, R., et al. 2017a, *GCN*, 21744
- Coward, D., Howell, E., Laugier, R., et al. 2017b, *GCN*, 21627
- Cowperthwaite, P. S., Berger, E., Villar, V. A., et al. 2017b, *ApJL*, <https://doi.org/10.3847/2041-8213/aa8fc7>
- Cowperthwaite, P. S., Foley, R. J., & Berger, E. 2017a, *GCN*, 21533
- Cowperthwaite, P. S., Nicholl, M., & Berger, E. 2017c, *GCN*, 21578
- Cutler, C., Apostolos, T. A., Bildsten, L., et al. 1993, *PhRvL*, **70**, 2984
- Cwiek, A., Zarnecki, A. F., Mankiewicz, A., et al. 2017, *GCN*, 21783
- Dalya, G., Frei, Z., Galgoczi, G., Raffai, P., & de Souza, R. 2016, *yCat*, 7275
- Damour, T., & Taylor, J. H. 1991, *ApJ*, **366**, 501
- Damour, T., & Taylor, J. H. 1992, *PhRvD*, **45**, 1840
- D'Avanzo, P., Malesani, D., Covino, S., et al. 2009, *A&A*, **498**, 711
- D'Avanzo, P., Melandri, A., Covino, S., et al. 2017, *GCN*, 21653
- De, K., Kasliwal, M. M., Bhalerao, V., et al. 2017a, *GCN*, 21603
- De, K., Mooley, K. P., Chandra, P., et al. 2017b, *GCN*, 21708
- de Naurois, M., Schussler, F., et al. 2017, *GCN*, 21674
- Deller, A., Bailes, M., Andreoni, I., et al. 2017a, *GCN*, 21588
- Deller, A., Bailes, M., Andreoni, I., et al. 2017b, *GCN*, 21850
- Deller, A., Bailes, M., Andreoni, I., et al. 2017c, *GCN*, 21897
- Dewey, R. J., & Cordes, J. M. 1987, *ApJ*, **321**, 780
- Dezalay, J.-P., Barat, C., Talon, R., et al. 1992, in *AIP Conf. Proc.* 265, *Gamma-Ray Bursts*, ed. W. S. Paciesas & G. J. Fishman (Melville, NY: AIP), 304
- Diaz, M., Garcia Lambas, D., Macri, L., Nilo Castellon, J. L., & Bernoiz, M. 2017a, *GCN*, 21619
- Diaz, M., Garcia Lambas, D., Macri, L., Nilo Castellon, J. L., & Bernoiz, M. 2017c, *GCN*, 21620
- Diaz, M., Garcia Lambas, D., Macri, L., Nilo Castellon, J. L., & Bernoiz, M. 2017d, *GCN*, 21634
- Diaz, M., Macri, L., Nilo Castellon, J. L., et al. 2017b, *GCN*, 21895
- Dobie, D., Hotan, A., Bannister, K., et al. 2017a, *GCN*, 21639
- Dobie, D., Hotan, A., Bannister, K., et al. 2017b, *GCN*, 21625
- Drout, M. R., et al. 2017b, *Sci*, <https://doi.org/10.1126/science.aaq0049>
- Drout, M. R., Simon, J. D., Shappee, B. J., et al. 2017a, *GCN*, 21547
- Eichler, D., Livio, M., Piran, T., & Schramm, D. N. 1989, *Natur*, **340**, 126
- Eikenberry, S., Ackley, K., & Klimentko, S. 2017, *GCN*, 21575
- Einstein, A. 1916, *Sitzungsberichte der Königlich Preußischen Akademie der Wissenschaften (Berlin)*, **1**, 688
- Einstein, A. 1918, *Sitzungsberichte der Königlich Preußischen Akademie der Wissenschaften (Berlin)*, **1**, 154
- Ellingson, S. W., Taylor, G. B., Craig, J., et al. 2013, *ITAP*, **61**, 2540
- Evans, P., Cenko, S., Kennea, J. A., et al. 2017a, *Sci*, <https://doi.org/10.1126/science.aap9580>
- Evans, P., Kennea, J. A., Breeveld, A. A., et al. 2017b, *GCN*, 21550
- Evans, P., Kennea, J. A., Cenko, S. B., et al. 2017c, *GCN*, 21612
- Fermi-GBM 2017, *GCN*, 524666471
- Feroci, M., Costa, E., Soffitta, P., et al. 2007, *NIMPA*, **581**, 728
- Fixsen, D. J. 2009, *ApJ*, **707**, 916
- Flannery, B. P., & van den Heuvel, E. P. J. 1975, *A&A*, **39**, 61
- Flaugher, B., Diehl, H. T., Honscheid, K., et al. 2015, *AJ*, **150**, 150
- Foley, R. J. 2017b, *GCN*, 21557
- Foley, R. J., Kilpatrick, C. D., Nicholl, M., & Berger, E. 2017a, *GCN*, 21536
- Fong, W., Berger, E., Chornock, R., et al. 2013, *ApJ*, **769**, 56
- Fong, W., Berger, E., Margutti, R., & Zauderer, B. A. 2015, *ApJ*, **815**, 102
- Fong, W., Margutti, R., Haggard, D., et al. 2017, *GCN*, 21786
- Fong, W., Margutti, R., Haggard, D., et al. 2013, *ApJ*, **776**, 18
- Fox, D. B., Frail, D. A., Price, P. A., et al. 2005, *Natur*, **437**, 845
- Freedman, W. L., Madore, B. F., Gibson, B. K., et al. 2001, *ApJ*, **553**, 47
- Fryer, C. L., Woosley, S. E., & Hartmann, D. H. 1999, *ApJ*, **526**, 152
- Gehrels, N. 2004, in *AIP Conf. Ser.* 727, *Gamma-Ray Bursts: 30 Years of Discovery*, ed. E. Fenimore & M. Galassi (Melville, NY: AIP), 637
- Gehrels, N., Cannizzo, J. K., Kanner, J., et al. 2016, *ApJ*, **820**, 136
- Gehrels, N., Sarazin, C. L., O'Brien, P. T., et al. 2005, *Natur*, **437**, 851
- Gendre, B., Cucchiara, A., Morris, D., et al. 2017, *GCN*, 21609
- Giacconi, R., Gursky, H., Paolini, F. R., & Rossi, B. B. 1962, *PhRvL*, **9**, 439
- Goedhart, S., Mooley, K., et al. 2017a, *GCN*, 21933
- Goedhart, S., Mooley, K., et al. 2017b, *GCN*, 21891
- Gold, T. 1968, *Natur*, **218**, 731
- Gold, T. 1969, *Natur*, **221**, 25
- Goldstein, A., Burgess, J. M., Preece, R. D., et al. 2012, *ApJS*, **199**, 19
- Goldstein, A., Veres, P., Burns, E., et al. 2017a, *ApJL*, <https://doi.org/10.3847/2041-8213/aa8f41>
- Goldstein, A., Veres, P., von Kienlin, A., et al. 2017b, *GCN*, 21528
- Goodman, J. 1986, *ApJL*, **308**, L47
- Gottlieb, O., Nakar, E., & Piran, T. 2017, arXiv:1705.10797
- Grado, A., Cappellaro, E., Greco, G., et al. 2017c, *GCN*, 21598
- Grado, A., Getman, F., Limatola, L., et al. 2017a, *GCN*, 21703
- Grado, A., Getman, F., Limatola, L., et al. 2017b, *GCN*, 21833
- Grossman, D., Korobkin, O., Rosswog, S., & Piran, T. 2014, *MNRAS*, **439**, 757
- Gruber, D., Goldstein, A., Weller von Ahlefeld, V., et al. 2014, *ApJS*, **211**, 12
- Haggard, D., Nynka, M., Ruan, J. J., et al. 2017a, *ApJL*, <https://doi.org/10.3847/2041-8213/aa8ede>
- Haggard, D., Nynka, M., Kalogera, V., et al. 2017b, *GCN*, 21798
- Hallinan, G., et al. 2017a, *Sci*, <https://doi.org/10.1126/science.aap9855>
- Hallinan, G., Corsi, A., Mooley, K., et al. 2017b, *GCN*, 21929
- Hancock, P. J., Tingay, S. J., de Gois, J. S., et al. 2017, *GCN*, 21894
- Harrison, F. A., Craig, W. W., Christensen, F. E., et al. 2013, *ApJ*, **770**, 103
- Harrison, F. A., Forster, K., Garcia, J., et al. 2017, *GCN*, 21626
- Hewish, A., Bell, S. J., Pilkington, J. D. H., Scott, P. F., & Collins, R. A. 1968, *Natur*, **217**, 709
- Hjorth, J., Sollerman, J., Gorosabel, J., et al. 2005a, *ApJL*, **630**, L117
- Hjorth, J., Watson, D., Fynbo, J. P. U., et al. 2005b, *Natur*, **437**, 859
- Hjorth, J., Watson, D., Fynbo, J. P. U., et al. 2005c, *Natur*, **437**, 859
- Hotkezaka, K., Nissanke, S., Hallinan, G., et al. 2016, *ApJ*, **831**, 190
- Hotkezaka, K., & Piran, T. 2015, *MNRAS*, **450**, 1430
- Hu, L., Wang, L., Sun, T., et al. 2017, *GCN*, 21883

- Hulse, R. A., & Taylor, J. H. 1975, *ApJL*, **195**, L51
- Hurley, K., Mitrofanov, I. G., Golovin, D., et al. 2013, in EAS Publications Ser. 61, *Gamma-ray Bursts: 15 Years of GRB Afterglows – Progenitors, Environments and Host Galaxies from the Nearby to the Early Universe*, ed. A. J. Castro-Tirado, J. Gorosabel, & I. H. Park (Les Ulis: EDP Sciences), 459
- Im, M., Choi, C., Kim, J., et al. 2017a, GCN, 21563
- Im, M., Choi, C., Kim, J., et al. 2017b, GCN, 21566
- Im, M., Choi, C., Kim, J., et al. 2017c, GCN, 21632
- Im, M., Choi, C., Kim, J., et al. 2017d, GCN, 21597
- Jin, Z.-P., Hotokezaka, K., Li, X., et al. 2016, *NatCo*, **7**, 12898
- Johnston, S., Bailes, M., Bartel, N., et al. 2007, *PASA*, **24**, 174
- Kalogera, V., Belczynski, K., Kim, C., O’Shaughnessy, R., & Willems, B. 2007, *PhR*, **442**, 75
- Kaplan, D., Brown, I., Sokolowski, M., et al. 2017b, GCN, 21927
- Kaplan, D., Murphy, T., Bannister, K., et al. 2017a, GCN, 21574
- Kaplan, D., Sokolowski, M., Wayth, R., et al. 2017c, GCN, 21637
- Kasen, D., Badnell, N. R., & Barnes, J. 2013, *ApJ*, **774**, 25
- Kasen, D., Metzger, B., Barnes, J., Quataert, E., & Ramirez-Ruiz, E. 2017, *Natur*, <https://doi.org/10.1038/nature24453>
- Kasliwal, M., Nakar, E., Singer, L. P., & Kaplan, D. E. A. 2017, *Sci*, <https://doi.org/10.1126/science.aap9455>
- Kilpatrick, C. D., Coulter, D. A., Siebert, M. R., et al. 2017a, GCN, 21583
- Kilpatrick, C. D., Foley, R. J., Kasen, D., et al. 2017b, *Science*, <https://doi.org/10.1126/science.aag0073>
- Klebesadel, R. W., Strong, I. B., & Olson, R. A. 1973, *ApJL*, **182**, L85
- Klotz, A., Laugier, R., Boer, M., et al. 2017, GCN, 21558
- Kocevski, D., Omodei, N., Buson, S., et al. 2017, GCN, 21534
- Kocevski, D., Thöne, C. C., Ramirez-Ruiz, E., et al. 2010, *MNRAS*, **404**, 963
- Kouveliotou, C., Meegan, C. A., Fishman, G. J., et al. 1993, *ApJL*, **413**, L101
- Kramer, M., Kraus, A., Eatough, R., & Nissanke, S. 2017, GCN, 21920
- Kulkarni, S. R. 2005, arXiv:[astro-ph/0510256](https://arxiv.org/abs/astro-ph/0510256)
- Labanti, C., Di Cocco, G., Ferro, G., et al. 2003, *A&A*, **411**, L149
- Lattimer, J. M., & Schramm, D. N. 1974, *ApJL*, **192**, L145
- Lattimer, J. M., & Schramm, D. N. 1976, *ApJ*, **210**, 549
- Lee, W. H., & Ramirez-Ruiz, E. 2007, *NJPh*, **9**, 17
- Levan, A. J., Lyman, J. D., Tanvir, N. R., et al. 2017, *ApJL*, <https://doi.org/10.3847/2041-8213/aa905f>
- Levan, A., Lyman, J. D., Steeghs, D. T. H., et al. 2017b, GCN, 21681
- Levan, A., Troja, E., Tanvir, N. R., et al. 2017a, GCN, 21781
- Li, L.-X., & Paczyński, B. 1998, *ApJL*, **507**, L59
- Li, T. P., Xiong, S. L., Zhang, S. N., et al. 2017, *Science China Physics, Mechanics & Astronomy*, <https://doi.org/10.1007/s11433-017-9107-5>
- Li, W., Chornock, R., Leaman, J., et al. 2011a, *MNRAS*, **412**, 1473
- Li, W., Leaman, J., Chornock, R., et al. 2011b, *MNRAS*, **412**, 1441
- Liao, J. Y., Li, C. K., Ge, M. Y., et al. 2017, GCN, 21518
- LIGO Scientific Collaboration & Virgo Collaboration et al. 2017a, GCN, 21505
- LIGO Scientific Collaboration & Virgo Collaboration et al. 2017b, GCN, 21513
- LIGO Scientific Collaboration & Virgo Collaboration et al. 2017c, GCN, 21527
- LIGO Scientific Collaboration & Virgo Collaboration et al. 2017d, GCN, 21509
- LIGO Scientific Collaboration & Virgo Collaboration et al. 2017e, GCN, 21510
- Lipunov, V., Gorbvskoy, E., Kornilov, V., et al. 2017a, *ApJL*, <https://doi.org/10.3847/2041-8213/aa92c0>
- Lipunov, V., Kornilov, V., Gorbvskoy, E., et al. 2010, *AdAst*, **2010**, 349171
- Lipunov, V. M. 2017, GCN, 21621
- Lipunov, V. M., Gorbvskoy, E., Kornilov, V. G., et al. 2017b, GCN, 21687
- Lipunov, V. M., Gorbvskoy, E., Kornilov, V. G., et al. 2017c, GCN, 21587
- Lipunov, V. M., Gorbvskoy, E., Kornilov, V. G., et al. 2017d, GCN, 21546
- Lipunov, V. M., Gorbvskoy, E., Kornilov, V. G., et al. 2017e, GCN, 21570
- Lipunov, V. M., Postnov, K. A., & Prokhorov, M. E. 1987, *A&A*, **176**, L1
- Lund, N., Budtz-Jørgensen, C., Westergaard, N. J., et al. 2003, *A&A*, **411**, L231
- Lyman, J., Homan, D., Maguire, K., et al. 2017, GCN, 21582
- Lynch, C., Murphy, T., Kaplan, D., et al. 2017a, GCN, 21670
- Lynch, C., Murphy, T., Kaplan, D., et al. 2017b, GCN, 21740
- Lynch, C., Murphy, T., Kaplan, D., et al. 2017c, GCN, 21628
- Lynch, C., Murphy, T., Kaplan, D., et al. 2017d, GCN, 21629
- Malesani, D., Pian, E., Hjorth, J., et al. 2017a, GCN, 21591
- Malesani, D., Watson, D., & Hjorth, J. 2017b, GCN, 21577
- Margutti, R., Berger, E., Fong, W., et al. 2017b, *ApJL*, <https://doi.org/10.3847/2041-8213/aa9057>
- Margutti, R., Fong, W., Berger, E., et al. 2017a, GCN, 21648
- Martínez-Castellanos, I., Smith, A. J., et al. 2017, GCN, 21683
- Massevitch, A. G., Tutukov, A. V., & Jungelson, L. R. 1976, *Ap&SS*, **40**, 115
- Matsuoka, M., Kawasaki, K., Ueno, S., et al. 2009, *PASJ*, **61**, 999
- McCully, C., Hiramatsu, D., Howell, D. A., et al. 2017b, *ApJL*, <https://doi.org/10.3847/2041-8213/aa9111>
- McCully, C., Howell, D. A., & Hosseinzadeh 2017a, GCN, 21908
- Meegan, C., Lichti, G., Bhat, P. N., et al. 2009, *ApJ*, **702**, 791
- Melandri, A., Campana, S., Covino, S., et al. 2017a, GCN, 21532
- Melandri, A., D’Avanzo, P., Campana, S., et al. 2017b, GCN, 21556
- Melandri, A., D’Avanzo, P., Campana, S., et al. 2017c, GCN, 21596
- Messick, C., Blackburn, K., Brady, P., et al. 2017, *PhRvD*, **95**, 042001
- Metzger, B. D. 2017, *LRR*, **20**, 3
- Metzger, B. D., & Berger, E. 2012, *ApJ*, **746**, 48
- Metzger, B. D., & Fernández, R. 2014, *MNRAS*, **441**, 3444
- Metzger, B. D., Martínez-Pinedo, G., Darbha, S., et al. 2010, *MNRAS*, **406**, 2650
- Moldon, J., Beswick, R., Paragi, Z., et al. 2017a, GCN, 21804
- Moldon, J., Beswick, R., Paragi, Z., et al. 2017b, GCN, 21940
- Möller, A., Chang, & Wolf, C. 2017, GCN, 21542
- Mooley, K. P., Hallinan, G., et al. 2017a, GCN, 21650
- Mooley, K. P., Hallinan, G., Corsi, A., et al. 2017b, GCN, 21814
- Murphy, T., Lenc, E., Lynch, C., et al. 2017, GCN, 21842
- Nakahira, S., Yoshida, A., Sakamoto, T., et al. 2017, GCN, 21641
- Nakaoka, T., Kawabata, K. S., Kawabata, M., et al. 2017, GCN, 21623
- Nakar, E. 2007, *PhR*, **442**, 166
- Nakar, E., & Piran, T. 2011, *Natur*, **478**, 82
- Narayan, R., Paczynski, B., & Piran, T. 1992, *ApJL*, **395**, L83
- Nicholl, M., Berger, E., Kasen, D., et al. 2017d, *ApJL*, <https://doi.org/10.3847/2041-8213/aa9029>
- Nicholl, M., Briceno, C., & Cowperthwaite 2017c, GCN, 21585
- Nicholl, M., Cowperthwaite, P. S., Allam, S., et al. 2017a, GCN, 21541
- Nicholl, M., Cowperthwaite, P. S., Berger, E., et al. 2017b, GCN, 21580
- Nissanke, S., Kasliwal, M., & Georgieva, A. 2013, *ApJ*, **767**, 124
- Nitz, A. H., Dent, T., Dal Canton, T., Fairhurst, S., & Brown, D. A. 2017a, arXiv:[1705.01513](https://arxiv.org/abs/1705.01513)
- Nitz, A., Harry, I., Brown, D., et al. 2017b, ligo-cbc/pycbc: O2 Production Release 20, doi:[10.5281/zenodo.883086](https://doi.org/10.5281/zenodo.883086)
- Ofek, E. O., Cenko, S. B., Gal-Yam, A., et al. 2007, *ApJ*, **662**, 1129
- Oppenheimer, J. R., & Volkoff, G. M. 1939, *PhRv*, **55**, 374
- Paciesas, W. S., Meegan, C. A., von Kienlin, A., et al. 2012, *ApJS*, **199**, 18
- Paczynski, B. 1986, *ApJL*, **308**, L43
- Paragi, Z., Agudo, I., An, T., et al. 2017a, GCN, 21763
- Paragi, Z., Yang, J., Marcote, B., et al. 2017b, GCN, 21939
- Pavana, M., Kiran, B. S., Anupama, G. C., et al. 2017, GCN, 21554
- Pearson, T. J., Readhead, A. C. S., et al. 2017, GCN, 21760
- Pian, E., D’Avanzo, P., Bennetti, S., et al. 2017a, *Natur*, <https://doi.org/10.1038/nature24298>
- Pian, E., D’Elia, V., Piranomonte, S., et al. 2017b, GCN, 21592
- Piano, G., Verrecchia, F., Pilia, M., et al. 2017, GCN, 21526
- Pilia, M., Cardillo, M., Piano, G., et al. 2017, GCN, 21525
- Piran, T., Nakar, E., & Rosswog, S. 2013, *MNRAS*, **430**, 2121
- Postnov, K. A., & Yungelson, L. R. 2014, *LRR*, **17**, 3
- Pozanenko, A., Volnova, A., Mazaeva, E., et al. 2017a, GCN, 21635
- Pozanenko, A., Volnova, A., Mazaeva, E., et al. 2017b, GCN, 21898
- Pozanenko, A., Volnova, A., Mazaeva, E., et al. 2017c, GCN, 21644
- Pozanenko, A., Volnova, A., Mazaeva, E., et al. 2017d, GCN, 21618
- Prandoni, I., Murgia, M., Tarchi, A., et al. 2017, arXiv:[1703.09673](https://arxiv.org/abs/1703.09673)
- Pretorius, F. 2005, *PhRvL*, **95**, 121101
- Prochaska, J. X., Bloom, J. S., Chen, H.-W., et al. 2006, *ApJ*, **642**, 989
- Rabinowitz, D., Baltay, C., et al. 2017, GCN, 21599
- Resmi, L., Misra, K., Tanvir, N. R., et al. 2017, GCN, 21768
- Ricci, R., Wieringa, M., Piro, L., & Troja, E. 2017, GCN, 21900
- Roberts, L. F., Kasen, D., Lee, W. H., & Ramirez-Ruiz, E. 2011, *ApJL*, **736**, L21
- Rosswog, S. 2005, *ApJ*, **634**, 1202
- Sadler, E. M., Allison, J. R., Kaplan, D. L., et al. 2017, GCN, 21645
- Sathyaprakash, B. S., & Dhurandhar, S. V. 1991, *PhRvD*, **44**, 3819
- Savchenko, V., Ferrigno, C., Kuulkers, E., et al. 2017, *ApJL*, <https://doi.org/10.3847/2041-8213/aa8f94>
- Savchenko, V., Ferrigno, C., Kuulkers, E., et al. 2017b, GCN, 21672
- Savchenko, V., Neronov, A., & Courvoisier, T. J.-L. 2012, *A&A*, **541**, A122
- Savchenko, V., Mereghetti, S., Ferrigno, C., et al. 2017a, GCN, 21507
- Schlaflly, E. F., & Finkbeiner, D. P. 2011, *ApJ*, **737**, 103
- Schulze, S., Kim, S., Martin, S., et al. 2017, GCN, 21747
- Shapiro, S. L., & Teukolsky, S. A. 1983, *Black Holes, White Dwarfs, and Neutron Stars: The Physics of Compact Objects* (New York: Wiley)
- Shappee, B. J., Simon, J. D., Drout, M. R., et al. 2017, *Sci*, <https://doi.org/10.1126/science.aag0186>
- Shara, M., Williams, T., Vaisanen, et al. 2017, GCN, 21610
- Shklovsky, I. S. 1967, *ApJL*, **148**, L1
- Siebert, M. R., Foley, R. J., Drout, M. R., et al. 2017, *ApJL*, <https://doi.org/10.3847/2041-8213/aa905e>

- Simon, J. D., Shappee, B. J., Drout, M. R., et al. 2017, *GCN*, 21551
- Singer, L. P., et al. 2017c, *GCN*, 21569
- Singer, L. P., Chen, H.-Y., Holz, D. E., et al. 2016, *ApJL*, 829, L15
- Singer, L. P., Lau, R., Kasliwal, M. M., et al. 2017a, *GCN*, 21552
- Singer, L. P., Lau, R., Kasliwal, M. M., et al. 2017b, *GCN*, 21779
- Singer, L. P., & Price, L. 2016, *PhRvD*, 93, 024013
- Singh, K. P., Tandon, S. N., Agrawal, P. C., et al. 2014, *ASTROSAT Mission*, doi:[10.1117/12.2062667](https://doi.org/10.1117/12.2062667)
- Smartt, S. J., et al. 2017, *Natur*, <https://doi.org/10.1038/nature24303>
- Soares-Santos, M., Holz, D., Annis, J., et al. 2017, *ApJL*, <https://doi.org/10.3847/2041-8213/aa9059>
- Soderberg, A. M., Berger, E., Kasliwal, M., et al. 2006, *ApJ*, 650, 261
- Sugita, S., Kawai, N., Serino, M., et al. 2017, *GCN*, 21555
- Svinkin, D., Golenetskii, S., Aptekar, R., et al. 2017a, *GCN*, 21746
- Svinkin, D., Hurley, K., von Kienlin, A., et al. 2017b, *GCN*, 21515
- Svinkin, D., Hurley, K., von, K. A., et al. 2017c, *GCN*, 21515
- Swarup, G., Ananthakrishnan, S., Kapahi, V. K., et al. 1991, *CSci*, 60, 95
- Tanaka, M. 2016, *AdAst*, 2016, 634197
- Tanaka, M., & Hotokezaka, K. 2013, *ApJ*, 775, 113
- Tanvir, N. R., Levan, A. J., et al. 2017a, *GCN*, 21544
- Tanvir, N. R., Levan, A. J., Fruchter, A. S., et al. 2013, *Natur*, 500, 547
- Tanvir, N. R., Levan, A. J., González-Fernández, C., et al. 2017, *ApJL*, <https://doi.org/10.3847/2041-8213/aa90b6>
- Tanvir, N. R., Levan, A. J., & Steeghs, D. 2017b, *GCN*, 21576
- Tavani, M., Barbiellini, G., Argan, A., et al. 2009, *A&A*, 502, 995
- Taylor, J. H., & Weisberg, J. M. 1982, *ApJ*, 253, 908
- Taylor, J. H., Wolszczan, A., Damour, T., & Weisberg, J. M. 1992, *Natur*, 355, 132
- Tingay, S. J., Goeke, R., Bowman, J. D., et al. 2013, *PASA*, 30, e007
- Tominaga, N., Yoshida, M., Tanaka, M., et al. 2017, *GCN*, 21595
- Tonry, J., Smith, K. W., Denneau, L., et al. 2017, *GCN*, 21886
- Troja, E., Butler, N., Watson, A., et al. 2017d, *GCN*, 21778
- Troja, E., King, A. R., O'Brien, P. T., Lyons, N., & Cusumano, G. 2008, *MNRAS*, 385, L10
- Troja, E., Piro, L., Sakamoto, T., et al. 2017c, *GCN*, 21765
- Troja, E., Piro, L., Sakamoto, T., et al. 2017e, *GCN*, 21787
- Troja, E., Piro, L., van Eerten, H., et al. 2017a, *Natur*, doi:[10.1038/nature24290](https://doi.org/10.1038/nature24290)
- Troja, E., Sakamoto, T., Cenko, S. B., et al. 2016, *ApJ*, 827, 102
- Troja, E., Watson, A., Covina, S., et al. 2017b, *GCN*, 21682
- Troja, E., Ricci, R., Wieringa, M. L., & Piro, L. 2017f, *GCN*, 21803
- Tunncliffe, R. L., Levan, A. J., Tanvir, N. R., et al. 2014, *MNRAS*, 437, 1495
- Ubertini, P., Lebrun, F., di Cocco, G., et al. 2003, *A&A*, 411, L131
- Valenti, S., Yang, S., Sand, D., et al. 2017, *GCN*, 21606
- van Haarlem, M. P., Wise, M. W., Gunst, A. W., et al. 2013, *A&A*, 556, A2
- Vedrenne, G., Roques, J.-P., Schönfelder, V., et al. 2003, *A&A*, 411, L63
- Veitch, J., Raymond, V., Farr, B., et al. 2015, *PhRvD*, 91, 042003
- Verrecchia, F., Cardillo, M., Bulgarelli, A., et al. 2017, *GCN*, 21785
- Villasenor, J. S., Lamb, D. Q., Ricker, G. R., et al. 2005, *Natur*, 437, 855
- von Kienlin, A., Beckmann, V., Rau, A., et al. 2003, *A&A*, 411, L299
- von Kienlin, A., Meegan, C., Goldstein, A., et al. 2017, *GCN*, 21520
- Wex, N. 2014, arXiv:1402.5594
- White, D. J., Daw, E., & Dhillon, V. 2011a, *CQGra*, 28, 085016
- White, D. J., Daw, E. J., & Dhillon, V. S. 2011b, *CQGra*, 28, 085016
- Wieringa, M., Ricci, R., & Piro Troja, E. 2017, *GCN*, 21882
- Wiersema, K., Covino, S., Melandri, A., et al. 2017, *GCN*, 21594
- Williams, P. K. G., Alexander, K. D., Berger, E., et al. 2017a, *GCN*, 21750
- Williams, P. K. G., Alexander, K. D., Berger, E., et al. 2017b, *GCN*, 21571
- Wilson, W. E., Ferris, R. H., Axtens, P., et al. 2011, *MNRAS*, 416, 832
- Wilson-Hodge, C. A., Case, G. L., Cherry, M. L., et al. 2012, *ApJS*, 201, 33
- Winkler, C., Courvoisier, T. J.-L., Di Cocco, G., et al. 2003, *A&A*, 411, L1
- Wiseman, P., Chen, T. W., Greiner, J., et al. 2017, *GCN*, 21584
- Wolf, C., Chang, S. W., & Möller, A. 2017, *GCN*, 21560
- Wootten, A., & Thompson, A. R. 2009, *IEEEP*, 97, 1463
- Yang, S., Valenti, S., Sand, D., et al. 2017a, *GCN*, 21531
- Yang, S., Valenti, S., Sand, D., et al. 2017b, *GCN*, 21579
- Yang, S., Valenti, S., Sand, D., et al. 2017c, *GCN*, 21539
- Yoshida, M., Tanaka, M., Terai, T., et al. 2017a, *GCN*, 21549
- Yoshida, M., Tanaka, M., Terai, T., et al. 2017b, *GCN*, 21561
- Yoshida, M., Tanaka, M., Terai, T., et al. 2017c, *GCN*, 21586
- Yoshida, M., Tanaka, M., Utsumi, Y., et al. 2017d, *GCN*, 21685
- Yu, P.-C., Ngeow, C.-C., Ip, W.-H., et al. 2017, *GCN*, 21669
- Zadrożny, A., Sokolowski, M., Mankiewicz, L., & Żarnęcki, A. F. 2017, Pi of the Sky in LSC-Virgo's EM follow-up in O1 science, doi:[10.1117/12.2281024](https://doi.org/10.1117/12.2281024)

- B. P. Abbott¹, R. Abbott¹, T. D. Abbott², F. Acernese^{3,4}, K. Ackley^{5,6}, C. Adams⁷, T. Adams⁸, P. Addesso⁹, R. X. Adhikari¹, V. B. Adya¹⁰, C. Affeldt¹⁰, M. Afrough¹¹, B. Agarwal¹², M. Agathos¹³, K. Agatsuma¹⁴, N. Aggarwal¹⁵, O. D. Aguiar¹⁶, L. Aiello^{17,18}, A. Ain¹⁹, P. Ajith²⁰, B. Allen^{10,21,22}, G. Allen¹², A. Allocca^{23,24}, P. A. Altin²⁵, A. Amato²⁶, A. Ananyeva¹, S. B. Anderson¹, W. G. Anderson²¹, S. V. Angelova²⁷, S. Antier²⁸, S. Appert¹, K. Arai¹, M. C. Araya¹, J. S. Areeda²⁹, N. Arnaud^{28,30}, K. G. Arun³¹, S. Ascenzi^{32,33}, G. Ashton¹⁰, M. Ast³⁴, S. M. Aston⁷, P. Astone³⁵, D. V. Atallah³⁶, P. Aufmuth²², C. Aulbert¹⁰, K. AultO'Neal³⁷, C. Austin², A. Avila-Alvarez²⁹, S. Babak³⁸, P. Bacon³⁹, M. K. M. Bader¹⁴, S. Bae⁴⁰, P. T. Baker⁴¹, F. Baldaccini^{42,43}, G. Ballardín³⁰, S. W. Ballmer⁴⁴, S. Banagiri⁴⁵, J. C. Barayoga¹, S. E. Barclay⁴⁶, B. C. Barish¹, D. Barker⁴⁷, K. Barkett⁴⁸, F. Barone^{3,4}, B. Barr⁴⁶, L. Barsotti¹⁵, M. Barsuglia³⁹, D. Barta⁴⁹, S. D. Barthelmy⁵⁰, J. Bartlett⁴⁷, I. Bartos^{51,5}, R. Bassiri⁵², A. Basti^{23,24}, J. C. Batch⁴⁷, M. Bawaj^{53,43}, J. C. Bayley⁴⁶, M. Bazzan^{54,55}, B. Bécsy⁵⁶, C. Beer¹⁰, M. Bejger⁵⁷, I. Belahcene²⁸, A. S. Bell⁴⁶, B. K. Berger¹, G. Bergmann¹⁰, J. J. Bero⁵⁸, C. P. L. Berry⁵⁹, D. Bersanetti⁶⁰, A. Bertolini¹⁴, J. Betzwieser⁷, S. Bhagwat⁴⁴, R. Bhandare⁶¹, I. A. Bilenko⁶², G. Billingsley¹, C. R. Billman⁵, J. Birch⁷, R. Birney⁶³, O. Birmholtz¹⁰, S. Biscans^{1,15}, S. Biscoveanu^{64,6}, A. Bisht²², M. Bitossi^{30,24}, C. Biwer⁴⁴, M. A. Bizouard²⁸, J. K. Blackburn¹, J. Blackman⁴⁸, C. D. Blair^{1,65}, D. G. Blair⁶⁵, R. M. Blair⁴⁷, S. Bloemen⁶⁶, O. Bock¹⁰, N. Bode¹⁰, M. Boer⁶⁷, G. Bogaert⁶⁷, A. Bohe³⁸, F. Bondu⁶⁸, E. Bonilla⁵², R. Bonnand⁸, B. A. Boom¹⁴, R. Bork¹, V. Boschi^{30,24}, S. Bose^{69,19}, K. Bossie⁷, Y. Bouffanais³⁹, A. Bozzi³⁰, C. Bradaschia²⁴, P. R. Brady²¹, M. Branchesi^{17,18}, J. E. Brau⁷⁰, T. Briant⁷¹, A. Brillet⁶⁷, M. Brinkmann¹⁰, V. Brisson²⁸, P. Brockill²¹, J. E. Broida⁷², A. F. Brooks¹, D. A. Brown⁴⁴, D. D. Brown⁷³, S. Brunett¹, C. C. Buchanan², A. Buikema¹⁵, T. Bulik⁷⁴, H. J. Bulten^{75,14}, A. Buonanno^{38,76}, D. Buskulic⁸, C. Buy³⁹, R. L. Byer⁵², M. Cabero¹⁰, L. Cadonati⁷⁷, G. Cagnoli^{26,78}, C. Cahillane¹, J. Calderón Bustillo⁷⁷, T. A. Callister¹, E. Calloni^{79,4}, J. B. Camp⁵⁰, M. Canepa^{60,80}, P. Canizares⁶⁶, K. C. Cannon⁸¹, H. Cao⁷³, J. Cao⁸², C. D. Capano¹⁰, E. Capocasa³⁹, F. Carbognani³⁰, S. Caride⁸³, M. F. Carney⁸⁴, J. Casanueva Diaz²⁸, C. Casentini^{32,33}, S. Caudill^{14,21}, M. Cavaglia¹¹, F. Cavalier²⁸, R. Cavalieri³⁰, G. Cella²⁴, C. B. Cepeda¹, P. Cerdá-Durán⁸⁵, G. Cerretani^{23,24}, E. Cesarini^{33,86}, S. J. Chamberlin⁶⁴, M. Chan⁴⁶, S. Chao⁸⁷, P. Charlton⁸⁸, E. Chase⁸⁹, E. Chassande-Mottin³⁹, D. Chatterjee²¹, K. Chatziioannou⁹⁰, B. D. Cheeseboro⁴¹, H. Y. Chen⁹¹, X. Chen⁶⁵, Y. Chen⁴⁸, H.-P. Cheng⁵, H. Chia⁵, A. Chincarini⁶⁰, A. Chiummo³⁰, T. Chmiel⁸⁴, H. S. Cho⁹², M. Cho⁷⁶, J. H. Chow²⁵, N. Christensen^{72,67}, Q. Chu⁶⁵, A. J. K. Chua¹³, S. Chua⁷¹, A. K. W. Chung⁹³, S. Chung⁶⁵, G. Ciani^{5,54,55}, R. Ciolfi^{94,95}, C. E. Cirelli⁵², A. Cirone^{60,80}, F. Clara⁴⁷, J. A. Clark⁷⁷, P. Clearwater⁹⁶, F. Cleva⁶⁷, C. Cocchieri¹¹, E. Coccia^{17,18}, P.-F. Cohadon⁷¹, D. Cohen²⁸, A. Colla^{97,35}, C. G. Collette⁹⁸,

L. R. Cominsky⁹⁹, M. Constanancio Jr.¹⁶, L. Conti⁵⁵, S. J. Cooper⁵⁹, P. Corban⁷, T. R. Corbitt², I. Cordero-Carrión¹⁰⁰, K. R. Corley⁵¹, N. Cornish¹⁰¹, A. Corsi⁸³, S. Cortese³⁰, C. A. Costa¹⁶, M. W. Coughlin^{72,1}, S. B. Coughlin⁸⁹, J.-P. Coulon⁶⁷, S. T. Countryman⁵¹, P. Couvares¹, P. B. Covas¹⁰², E. E. Cowan⁷⁷, D. M. Coward⁶⁵, M. J. Cowart⁷, D. C. Coyne¹, R. Coyne⁸³, J. D. E. Creighton²¹, T. D. Creighton¹⁰³, J. Cripe², S. G. Crowder¹⁰⁴, T. J. Cullen^{29,2}, A. Cumming⁴⁶, L. Cunningham⁴⁶, E. Cuoco³⁰, T. Dal Canton⁵⁰, G. Dálya⁵⁶, S. L. Danilishin^{22,10}, S. D'Antonio³³, K. Danzmann^{22,10}, A. Dasgupta¹⁰⁵, C. F. Da Silva Costa⁵, V. Dattilo³⁰, I. Dave⁶¹, M. Davies²⁸, D. Davis⁴⁴, E. J. Daw¹⁰⁶, B. Day⁷⁷, S. De⁴⁴, D. DeBra⁵², J. Degallaix²⁶, M. De Laurentis^{17,4}, S. Deléglise⁷¹, W. Del Pozzo^{59,23,24}, N. Demos¹⁵, T. Denker¹⁰, T. Dent¹⁰, R. De Pietri^{107,108}, V. Dergachev³⁸, R. De Rosa^{79,4}, R. T. DeRosa⁷, C. De Rossi^{26,30}, R. DeSalvo¹⁰⁹, O. de Varona¹⁰, J. Devenson²⁷, S. Dhurandhar¹⁹, M. C. Díaz¹⁰³, L. Di Fiore⁴, M. Di Giovanni^{110,95}, T. Di Girolamo^{51,79,4}, A. Di Lieto^{23,24}, S. Di Pace^{97,35}, I. Di Palma^{97,35}, F. Di Renzo^{23,24}, Z. Doctor⁹¹, V. Dolique²⁶, F. Donovan¹⁵, K. L. Dooley¹¹, S. Doravari¹⁰, I. Dorrington³⁶, R. Douglas⁴⁶, M. Dovalé Álvarez⁵⁹, T. P. Downes²¹, M. Drago¹⁰, C. Dreissigacker¹⁰, J. C. Driggers⁴⁷, Z. Du⁸², M. Ducrot⁸, P. Dujpej⁴⁶, S. E. Dwyer⁴⁷, T. B. Edo¹⁰⁶, M. C. Edwards⁷², A. Effler⁷, P. Ehrens¹, J. Eichholz¹, S. S. Eikenberry⁵, R. A. Eisenstein¹⁵, R. C. Essick¹⁵, D. Estevez⁸, Z. B. Etienne⁴¹, T. Etzel¹, M. Evans¹⁵, T. M. Evans⁷, M. Factourovich⁵¹, V. Fafone^{32,33,17}, H. Fair⁴⁴, S. Fairhurst³⁶, X. Fan⁸², S. Farinon⁶⁰, B. Farr⁹¹, W. M. Farr⁵⁹, E. J. Fauchon-Jones³⁶, M. Favata¹¹¹, M. Fays³⁶, C. Fee⁸⁴, H. Fehrmann¹⁰, J. Feicht¹, M. M. Fejer⁵², A. Fernandez-Galiana¹⁵, I. Ferrante^{23,24}, E. C. Ferreira¹⁶, F. Ferrini³⁰, F. Fiducaro^{23,24}, D. Finstad⁴⁴, I. Fiori³⁰, D. Fiorucci³⁹, M. Fishbach⁹¹, R. P. Fisher⁴⁴, M. Fitz-Axen⁴⁵, R. Flaminio^{26,112}, M. Fletcher⁴⁶, H. Fong⁹⁰, J. A. Font^{85,113}, P. W. F. Forsyth²⁵, S. S. Forsyth⁷⁷, J.-D. Fournier⁶⁷, S. Frasca^{97,35}, F. Frasconi²⁴, Z. Frei⁵⁶, A. Freise⁵⁹, R. Frey⁷⁰, V. Frey²⁸, E. M. Fries¹, P. Fritschel¹⁵, V. V. Frolov⁷, P. Fulda⁵, M. Fyffe⁷, H. Gabbard⁴⁶, B. U. Gadre¹⁹, S. M. Gaebel⁵⁹, J. R. Gair¹¹⁴, L. Gammaitoni⁴², M. R. Ganija⁷³, S. G. Gaonkar¹⁹, C. Garcia-Quiros¹⁰², F. Garufi^{79,4}, B. Gateley⁴⁷, S. Gaudio³⁷, G. Gaur¹¹⁵, V. Gayathri¹¹⁶, N. Gehrels^{50,95,4}, G. Gemme⁶⁰, E. Genin³⁰, A. Gennai²⁴, D. George¹², J. George⁶¹, L. Gergely¹¹⁷, V. Germain⁸, S. Ghonge⁷⁷, Abhirup Ghosh²⁰, Archisman Ghosh^{20,14}, S. Ghosh^{66,14,21}, J. A. Giaime^{2,7}, K. D. Giardino⁷, A. Giazotto²⁴, K. Gill³⁷, L. Glover¹⁰⁹, E. Goetz¹¹⁸, R. Goetz⁵, S. Gomes³⁶, B. Goncharov⁶, G. González², J. M. Gonzalez Castro^{23,24}, A. Gopakumar¹¹⁹, M. L. Gorodetsky⁶², S. E. Gossan¹, M. Gosselin³⁰, R. Gouaty⁸, A. Grado^{120,4}, C. Graef⁴⁶, M. Granata²⁶, A. Grant⁴⁶, S. Gras¹⁵, C. Gray⁴⁷, G. Greco^{121,122}, A. C. Green⁵⁹, E. M. Gretarsson³⁷, B. Griswold⁷⁰, P. Groot⁶⁶, H. Grote¹⁰, S. Grunewald³⁸, P. Gruning²⁸, G. M. Guidi^{121,122}, X. Guo⁸², A. Gupta⁶⁴, M. K. Gupta¹⁰⁵, K. E. Gushwa¹, E. K. Gustafson¹, R. Gustafson¹¹⁸, O. Halim^{18,17}, B. R. Hall⁶⁹, E. D. Hall¹⁵, E. Z. Hamilton³⁶, G. Hammond⁴⁶, M. Haney¹²³, M. M. Hanke¹⁰, J. Hanks⁴⁷, C. Hanna⁶⁴, M. D. Hannam³⁶, O. A. Hannuksela⁹³, J. Hanson⁷, T. Hardwick², J. Harms^{17,18}, G. M. Harry¹²⁴, I. W. Harry³⁸, M. J. Hart⁴⁶, C.-J. Haster⁹⁰, K. Haughian⁴⁶, J. Healy⁵⁸, A. Heidmann⁷¹, M. C. Heintze⁷, H. Heitmann⁶⁷, P. Hello²⁸, G. Hemming³⁰, M. Hendry⁴⁶, I. S. Heng⁴⁶, J. Hennig⁴⁶, A. W. Heptonstall¹, M. Heurs^{10,22}, S. Hild⁴⁶, T. Hinderer⁶⁶, D. Hoak³⁰, D. Hofman²⁶, K. Holt⁷, D. E. Holz⁹¹, P. Hopkins³⁶, C. Horst²¹, J. Hough⁴⁶, E. A. Houston⁴⁶, E. J. Howell⁶⁵, A. Hreibi⁶⁷, Y. M. Hu¹⁰, E. A. Huerta¹², D. Huet²⁸, B. Hughey³⁷, S. Husa¹⁰², S. H. Huttner⁴⁶, T. Huynh-Dinh⁷, N. Indik¹⁰, R. Inta⁸³, G. Intini^{97,35}, H. N. Isa⁴⁶, J.-M. Isac⁷¹, M. Isi¹, B. R. Iyer²⁰, K. Izumi⁴⁷, T. Jacqmin⁷¹, K. Jani⁷⁷, P. Jaranowski¹²⁵, S. Jawahar⁶³, F. Jiménez-Forteza¹⁰², W. W. Johnson², D. I. Jones¹²⁶, R. Jones⁴⁶, R. J. G. Jonker¹⁴, L. Ju⁶⁵, J. Junker¹⁰, C. V. Kalaghatgi³⁶, V. Kalogera⁸⁹, B. Kamai¹, S. Kandhasamy⁷, G. Kang⁴⁰, J. B. Kanner¹, S. J. Kapadia²¹, S. Karki⁷⁰, K. S. Karvinen¹⁰, M. Kasprzak², M. Katolik¹², E. Katsavounidis¹⁵, W. Katzman⁷, S. Kaufer²², K. Kawabe⁴⁷, F. Kéfélian⁶⁷, D. Keitel⁴⁶, A. J. Kembal¹², R. Kennedy¹⁰⁶, C. Kent³⁶, J. S. Key¹²⁷, F. Y. Khalili⁶², I. Khan^{17,33}, S. Khan¹⁰, Z. Khan¹⁰⁵, E. A. Khazanov¹²⁸, N. Kijbunchoo²⁵, Chunglee Kim¹²⁹, J. C. Kim¹³⁰, K. Kim⁹³, W. Kim⁷³, W. S. Kim¹³¹, Y.-M. Kim⁹², S. J. Kimbrell⁷⁷, E. J. King⁷³, P. J. King⁴⁷, M. Kinley-Hanlon¹²⁴, R. Kirchhoff¹⁰, J. S. Kissel⁴⁷, L. Kleybolte³⁴, S. Klimenko⁵, T. D. Knowles⁴¹, P. Koch¹⁰, S. M. Koehlenbeck¹⁰, S. Koley¹⁴, V. Kondrashov¹, A. Kontos¹⁵, M. Korobko³⁴, W. Z. Korth¹, I. Kowalska⁷⁴, D. B. Kozak¹, C. Krämer¹⁰, V. Kringel¹⁰, B. Krishnan¹⁰, A. Królak^{132,133}, G. Kuehn¹⁰, P. Kumar⁹⁰, R. Kumar¹⁰⁵, S. Kumar²⁰, L. Kuo⁸⁷, A. Kutynia¹³², S. Kwang²¹, B. D. Lackey³⁸, K. H. Lai⁹³, M. Landry⁴⁷, R. N. Lang¹³⁴, J. Lange⁵⁸, B. Lantz⁵², R. K. Lanza¹⁵, S. L. Larson⁸⁹, A. Lartaux-Vollard²⁸, P. D. Lasky⁶, M. Laxen⁷, A. Lazzarini¹, C. Lazzaro⁵⁵, P. Leaci^{97,35}, S. Leavey⁴⁶, C. H. Lee⁹², H. K. Lee¹³⁵, H. M. Lee¹³⁶, H. W. Lee¹³⁰, K. Lee⁴⁶, J. Lehmann¹⁰, A. Lenon⁴¹, M. Leonardi^{110,95}, N. Leroy²⁸, N. Letendre⁸, Y. Levin⁶, T. G. F. Li⁹³, S. D. Linker¹⁰⁹, T. B. Littenberg¹³⁷, J. Liu⁶⁵, R. K. L. Lo⁹³, N. A. Lockerbie⁶³, L. T. London³⁶, J. E. Lord⁴⁴, M. Lorenzini^{17,18}, V. Lorette¹³⁸, M. Lormand⁷, G. Losurdo²⁴, J. D. Lough¹⁰, C. O. Lousto⁵⁸, G. Lovelace²⁹, H. Lück^{22,10}, D. Lumaca^{32,33}, A. P. Lundgren¹⁰, R. Lynch¹⁵, Y. Ma⁴⁸, R. Macas³⁶, S. Macfoy²⁷, B. Machenschalk¹⁰, M. MacInnis¹⁵, D. M. Macleod³⁶, I. Magaña Hernandez²¹, F. Magaña-Sandoval⁴⁴, L. Magaña Zertuche⁴⁴, R. M. Magee⁶⁴, E. Majorana³⁵, I. Maksimovic¹³⁸, N. Man⁶⁷, V. Mandic⁴⁵, V. Mangano⁴⁶, G. L. Mansell²⁵, M. Manske^{21,25}, M. Mantovani³⁰, F. Marchesoni^{53,43}, F. Marion⁸, S. Márka⁵¹, Z. Márka⁵¹, C. Markakis¹², A. S. Markosyan⁵², A. Markowitz¹, E. Maros¹, A. Marquina¹⁰⁰, P. Marsh¹²⁷, F. Martelli^{121,122}, L. Martellini⁶⁷, I. W. Martin⁴⁶, R. M. Martin¹¹¹, D. V. Martynov¹⁵, K. Mason¹⁵, E. Massera¹⁰⁶, A. Maserot⁸, T. J. Massinger¹, M. Masso-Reid⁴⁶, S. Mastrogiovanni^{97,35}, A. Matas⁴⁵, F. Matichard^{1,15}, L. Matone⁵¹, N. Mavalvala¹⁵, N. Mazumder⁶⁹, R. McCarthy⁴⁷, D. E. McClelland²⁵, S. McCormick⁷, L. McCuller¹⁵, S. C. McGuire¹³⁹, G. McIntyre¹, J. McIver¹, D. J. McManus²⁵, L. McNeill⁶, T. McRae²⁵, S. T. McWilliams⁴¹, D. Meacher⁶⁴, G. D. Meadors^{38,10}, M. Mehmet¹⁰,

J. Meidam¹⁴, E. Mejuto-Villa⁹, A. Melatos⁹⁶, G. Mendell⁴⁷, R. A. Mercer²¹, E. L. Merilh⁴⁷, M. Merzougui⁶⁷, S. Meshkov¹, C. Messenger⁴⁶, C. Messick⁶⁴, R. Metzdrorff⁷¹, P. M. Meyers⁴⁵, H. Miao⁵⁹, C. Michel²⁶, H. Middleton⁵⁹, E. E. Mikhailov¹⁴⁰, L. Milano^{79,4}, A. L. Miller^{5,97,35}, B. B. Miller⁸⁹, J. Miller¹⁵, M. Millhouse¹⁰¹, M. C. Milovich-Goff¹⁰⁹, O. Minazzoli^{67,141}, Y. Minenkov³³, J. Ming³⁸, C. Mishra¹⁴², S. Mitra¹⁹, V. P. Mitrofanov⁶², G. Mitselmakher⁵, R. Mittleman¹⁵, D. Moffa⁸⁴, A. Moggi²⁴, K. Mogushi¹¹, M. Mohan³⁰, S. R. P. Mohapatra¹⁵, M. Montani^{121,122}, C. J. Moore¹³, D. Moraru⁴⁷, G. Moreno⁴⁷, S. R. Morris¹⁰³, B. Mours⁸, C. M. Mow-Lowry⁵⁹, G. Mueller⁵, A. W. Muir³⁶, Arunava Mukherjee¹⁰, D. Mukherjee²¹, S. Mukherjee¹⁰³, N. Mukund¹⁹, A. Mullavey⁷, J. Munch⁷³, E. A. Muñiz⁴⁴, M. Muratore³⁷, P. G. Murray⁴⁶, K. Napier⁷⁷, I. Nardecchia^{32,33}, L. Naticchioni^{97,35}, R. K. Nayak¹⁴³, J. Neilson¹⁰⁹, G. Nelemans^{66,14}, T. J. N. Nelson⁷, M. Nery¹⁰, A. Neunzert¹¹⁸, L. Nevin¹, J. M. Newport¹²⁴, G. Newton^{46,955}, K. K. Y. Ng⁹³, P. Nguyen⁷⁰, T. T. Nguyen²⁵, D. Nichols⁶⁶, A. B. Nielsen¹⁰, S. Nisanke^{66,14}, A. Nitz¹⁰, A. Noack¹⁰, F. Nocera³⁰, D. Nolting⁷, C. North³⁶, L. K. Nuttall³⁶, J. Oberling⁴⁷, G. D. O'Dea¹⁰⁹, G. H. Ogil¹⁴⁴, J. J. Oh¹³¹, S. H. Oh¹³¹, F. Ohme¹⁰, M. A. Okada¹⁶, M. Oliver¹⁰², P. Oppermann¹⁰, Richard J. Oram⁷, B. O'Reilly⁷, R. Ormiston⁴⁵, L. F. Ortega⁵, R. O'Shaughnessy⁵⁸, S. Ossokine³⁸, D. J. Ottaway⁷³, H. Overmier⁷, B. J. Owen⁸³, A. E. Pace⁶⁴, J. Page¹³⁷, M. A. Page⁶⁵, A. Pai^{116,145}, S. A. Pai⁶¹, J. R. Palamos⁷⁰, O. Palashov¹²⁸, C. Palomba³⁵, A. Pal-Singh³⁴, Howard Pan⁸⁷, Huang-Wei Pan⁸⁷, B. Pang⁴⁸, P. T. H. Pang⁹³, C. Pankow⁸⁹, F. Pannarale³⁶, B. C. Pant⁶¹, F. Paoletti²⁴, A. Paoli³⁰, M. A. Papa^{38,21,10}, A. Parida¹⁹, W. Parker⁷, D. Pascucci⁴⁶, A. Pasqualetti³⁰, R. Passaquietti^{23,24}, D. Passuello²⁴, M. Patil¹³³, B. Patricelli^{146,24}, B. L. Pearlstone⁴⁶, M. Pedraza¹, R. Pedurand^{26,147}, L. Pekowsky⁴⁴, A. Pele⁷, S. Penn¹⁴⁸, C. J. Perez⁴⁷, A. Perreca^{1,110,95}, L. M. Perri⁸⁹, H. P. Pfeiffer^{90,38}, M. Phelps⁴⁶, O. J. Piccinni^{97,35}, M. Pichot⁶⁷, F. Piergiovanni^{121,122}, V. Pierro⁹, G. Pillant³⁰, L. Pinard²⁶, I. M. Pinto⁹, M. Pirello⁴⁷, M. Pitkin⁴⁶, M. Poe²¹, R. Poggiani^{23,24}, P. Popolizio³⁰, E. K. Porter³⁹, A. Post¹⁰, J. Powell^{46,149}, J. Prasad¹⁹, J. W. W. Pratt³⁷, G. Pratten¹⁰², V. Predoi³⁶, T. Prestegard²¹, L. R. Price¹, M. Prijatelj¹⁰, M. Principe⁹, S. Privitera³⁸, G. A. Prodi^{110,95}, L. G. Prokhorov⁶², O. Puncken¹⁰, M. Punturo⁴³, P. Puppo³⁵, M. Pürerer³⁸, H. Qi²¹, V. Quetschke¹⁰³, E. A. Quintero¹, R. Quitzow-James⁷⁰, F. J. Raab⁴⁷, D. S. Rabeling²⁵, H. Radkins⁴⁷, P. Raffai⁵⁶, S. Raja⁶¹, C. Rajan⁶¹, B. Rajbhandari⁸³, M. Rakhmanov¹⁰³, K. E. Ramirez¹⁰³, A. Ramos-Buades¹⁰², P. Rapagnani^{97,35}, V. Raymond³⁸, M. Razzano^{23,24}, J. Read²⁹, T. Regimbau⁶⁷, L. Rei⁶⁰, S. Reid⁶³, D. H. Reitze^{1,5}, W. Ren¹², S. D. Reyes⁴⁴, F. Ricci^{97,35}, P. M. Ricker¹², S. Rieger¹⁰, K. Riles¹¹⁸, M. Rizzo⁵⁸, N. A. Robertson^{1,46}, R. Robie⁴⁶, F. Robinet²⁸, A. Rocchi³³, L. Rolland⁸, J. G. Rollins¹, V. J. Roma⁷⁰, R. Romano^{3,4}, C. L. Romel⁴⁷, J. H. Romie⁷, D. Rosińska^{150,57}, M. P. Ross¹⁵¹, S. Rowan⁴⁶, A. Rüdiger¹⁰, P. Ruggi³⁰, G. Rutins²⁷, K. Ryan⁴⁷, S. Sachdev¹, T. Sadecki⁴⁷, L. Sadeghian²¹, M. Sakellariadou¹⁵², L. Salconi³⁰, M. Saleem¹¹⁶, F. Salemi¹⁰, A. Samajdar¹⁴³, L. Sammut⁶, L. M. Sampson⁸⁹, E. J. Sanchez¹, L. E. Sanchez¹, N. Sanchis-Gual⁸⁵, V. Sandberg⁴⁷, J. R. Sanders⁴⁴, B. Sassolas²⁶, B. S. Sathyaprakash^{64,36}, P. R. Saulson⁴⁴, O. Sauter¹¹⁸, R. L. Savage⁴⁷, A. Sawadsky³⁴, P. Schale⁷⁰, M. Scheel⁴⁸, J. Scheuer⁸⁹, J. Schmidt²⁰⁵, P. Schmidt^{1,66}, R. Schnabel³⁴, R. M. S. Schofield⁷⁰, A. Schönbeck³⁴, E. Schreiber¹⁰, D. Schuette^{10,22}, B. W. Schulte¹⁰, B. F. Schutz^{36,10}, S. G. Schwalbe³⁷, J. Scott⁴⁶, S. M. Scott²⁵, E. Seidel¹², D. Sellers⁷, A. S. Sengupta¹⁵³, D. Sentenac³⁰, V. Sequino^{32,33,17}, A. Sergeev¹²⁸, D. A. Shaddock²⁵, T. J. Shaffer⁴⁷, A. A. Shah¹³⁷, M. S. Shahriar⁸⁹, M. B. Shaner¹⁰⁹, L. Shao³⁸, B. Shapiro⁵², P. Shawhan⁷⁶, A. Sheperd²¹, D. H. Shoemaker¹⁵, D. M. Shoemaker⁷⁷, K. Siellez⁷⁷, X. Siemens²¹, M. Sieniawska⁵⁷, D. Sigg⁴⁷, A. D. Silva¹⁶, L. P. Singer⁵⁰, A. Singh^{38,10,22}, A. Singhal^{17,35}, A. M. Sintes¹⁰², B. J. J. Slagmolen²⁵, B. Smith⁷, J. R. Smith²⁹, R. J. E. Smith^{1,6}, S. Somala¹⁵⁴, E. J. Son¹³¹, J. A. Sonnenberg²¹, B. Sorazu⁴⁶, F. Sorrentino⁶⁰, T. Souradeep¹⁹, A. P. Spencer⁴⁶, A. K. Srivastava¹⁰⁵, K. Staats³⁷, A. Staley⁵¹, M. Steinke¹⁰, J. Steinlechner^{34,46}, S. Steinlechner³⁴, D. Steinmeyer¹⁰, S. P. Stevenson^{59,149}, R. Stone¹⁰³, D. J. Stops⁵⁹, K. A. Strain⁴⁶, G. Stratta^{121,122}, S. E. Strigin⁶², A. Strunk⁴⁷, R. Sturani¹⁵⁵, A. L. Stuver⁷, T. Z. Summerscales¹⁵⁶, L. Sun⁶, S. Sunil¹⁰⁵, J. Suresh¹⁹, P. J. Sutton³⁶, B. L. Swinkels³⁰, M. J. Szczepańczyk³⁷, M. Tacca¹⁴, S. C. Tait⁴⁶, C. Talbot¹⁴⁸, D. Talukder⁷⁰, D. B. Tanner⁵, M. Tápai¹¹⁷, A. Taracchini³⁸, J. D. Tasson⁷², J. A. Taylor¹³⁷, R. Taylor¹, S. V. Tewari¹⁴⁸, T. Theeg¹⁰, F. Thies¹⁰, E. G. Thomas⁵⁹, M. Thomas⁷, P. Thomas⁴⁷, K. A. Thorne⁷, K. S. Thorne⁴⁸, E. Thrane⁶, S. Tiwari^{17,95}, V. Tiwari³⁶, K. V. Tokmakov⁶³, K. Toland⁴⁶, M. Tonelli^{23,24}, Z. Tornasi⁴⁶, A. Torres-Forné⁸⁵, C. I. Torrie¹, D. Töyrä⁵⁹, F. Travasso^{30,43}, G. Traylor⁷, J. Trinastic⁵, M. C. Tringali^{110,95}, L. Trozzo^{157,24}, K. W. Tsang¹⁴, M. Tse¹⁵, R. Tso¹, L. Tsukada⁸¹, D. Tsuna⁸¹, D. Tuyenbayev¹⁰³, K. Ueno²¹, D. Ugolini¹⁵⁸, C. S. Unnikrishnan¹¹⁹, A. L. Urban¹, S. A. Usman³⁶, H. Vahlbruch²², G. Vajente¹, G. Valdes², N. van Bakel¹⁴, M. van Beuzekom¹⁴, J. F. J. van den Brand^{75,14}, C. Van Den Broeck¹⁴, D. C. Vander-Hyde⁴⁴, L. van der Schaaf¹⁴, J. V. van Heijningen¹⁴, A. A. van Veggel⁴⁶, M. Vardaro^{54,55}, V. Varma⁴⁸, S. Vass¹, M. Vasúth⁴⁹, A. Vecchio⁵⁹, G. Vedovato⁵⁵, J. Veitch⁴⁶, P. J. Veitch⁷³, K. Venkateswara¹⁵¹, G. Venugopalan¹, D. Verkindt⁸, F. Vetrano^{121,122}, A. Vicere^{121,122}, A. D. Viets²¹, S. Vinciguerra⁵⁹, D. J. Vine²⁷, J.-Y. Vinet⁶⁷, S. Vitale¹⁵, T. Vo⁴⁴, H. Vocca^{42,43}, C. Vorvick⁴⁷, S. P. Vyatchanin⁶², A. R. Wade¹, L. E. Wade⁸⁴, M. Wade⁸⁴, R. Walet¹⁴, M. Walker²⁹, L. Wallace¹, S. Walsh^{38,10,21}, G. Wang^{17,122}, H. Wang⁵⁹, J. Z. Wang⁶⁴, W. H. Wang¹⁰³, Y. F. Wang⁹³, R. L. Ward²⁵, J. Warner⁴⁷, M. Was⁸, J. Watchi⁹⁸, B. Weaver⁴⁷, L.-W. Wei^{10,22}, M. Weinert¹⁰, A. J. Weinstein¹, R. Weiss¹⁵, L. Wen⁶⁵, E. K. Wessel¹², P. Wessels¹⁰, J. Westerweck¹⁰, T. Westphal¹⁰, K. Wette²⁵, J. T. Whelan⁵⁸, S. E. Whitcomb¹, B. F. Whiting⁵, C. Whittle⁶, D. Wilken¹⁰, D. Williams⁴⁶, R. D. Williams¹, A. R. Williamson⁶⁶, J. L. Willis^{1,159}, B. Willke^{22,10}, M. H. Wimmer¹⁰, W. Winkler¹⁰, C. C. Wipf¹, H. Wittel^{10,22}, G. Woan⁴⁶, J. Woehler¹⁰, J. Wofford⁵⁸, K. W. K. Wong⁹³, J. Worden⁴⁷, J. L. Wright⁴⁶, D. S. Wu¹⁰, D. M. Wysocki⁵⁸, S. Xiao¹, H. Yamamoto¹, C. C. Yancey⁷⁶, L. Yang¹⁶⁰, M. J. Yap²⁵

M. Yazback⁵, Hang Yu¹⁵, Haocun Yu¹⁵, M. Yvert⁸, A. Zdrozny¹³², M. Zanolin³⁷, T. Zelenova³⁰, J.-P. Zendri⁵⁵, M. Zevin⁸⁹,
L. Zhang¹, M. Zhang¹⁴⁰, T. Zhang⁴⁶, Y.-H. Zhang⁵⁸, C. Zhao⁶⁵, M. Zhou⁸⁹, Z. Zhou⁸⁹, S. J. Zhu^{38,10}, X. J. Zhu⁶,
A. B. Zimmerman⁹⁰, M. E. Zucker^{1,15}, J. Zweizig¹,
(LIGO Scientific Collaboration and Virgo Collaboration),
C. A. Wilson-Hodge¹³⁷, E. Bissaldi^{161,162}, L. Blackburn^{163,15}, M. S. Briggs¹⁶⁴, E. Burns⁵⁰, W. H. Cleveland¹⁶⁵,
V. Connaughton¹⁶⁵, M. H. Gibby¹⁶⁶, M. M. Giles¹⁶⁶, A. Goldstein¹⁶⁵, R. Hamburg¹⁶⁴, P. Jenke¹⁶⁴, C. M. Hui¹³⁷,
R. M. Kippen¹⁶⁷, D. Kocevski¹³⁷, S. McBreen¹⁶⁸, C. A. Meegan¹⁶⁴, W. S. Paciesas¹⁶⁵, S. Poolakkil¹⁶⁴, R. D. Preece¹⁶⁴,
J. Racusin⁵⁰, O. J. Roberts¹⁶⁵, M. Stanbro¹⁶⁴, P. Veres¹⁶⁴, A. von Kienlin¹⁶⁹,
(Fermi GBM),
V. Savchenko¹⁷⁰, C. Ferrigno¹⁷⁰, E. Kuulkers¹⁷¹, A. Bazzano¹⁷², E. Bozzo¹⁷⁰, S. Brandt¹⁷³, J. Chenevez¹⁷³, T. J.-L. Courvoisier¹⁷⁰,
R. Diehl¹⁶⁹, A. Domingo¹⁷⁴, L. Hanlon¹⁶⁸, E. Jourdain¹⁷⁵, P. Laurent^{176,177}, F. Lebrun¹⁷⁶, A. Lutovinov^{178,179},
A. Martin-Carrillo¹⁶⁸, S. Mereghetti¹⁸⁰, L. Natalucci¹⁷², J. Rodi¹⁷², J.-P. Roques¹⁷⁵, R. Sunyaev^{178,181}, P. Ubertini¹⁷²,
(INTEGRAL),
M. G. Aartsen¹⁸², M. Ackermann¹⁸³, J. Adams¹⁸⁴, J. A. Aguilar¹⁸⁵, M. Ahlers¹⁸⁶, M. Ahrens¹⁸⁷, I. Al Samarai¹⁸⁸,
D. Altmann¹⁸⁹, K. Andeen¹⁹⁰, T. Anderson¹⁹¹, I. Anseau¹⁸⁵, G. Anton¹⁸⁹, C. Argüelles¹⁹², J. Auffenberg¹⁹³, S. Axani¹⁹²,
H. Bagherpour¹⁸⁴, X. Bai¹⁹⁴, J. P. Barron¹⁹⁵, S. W. Barwick¹⁹⁶, V. Baum¹⁹⁷, R. Bay¹⁹⁸, J. J. Beatty^{199,200}, J. Becker Tjus²⁰¹,
E. Bernardini¹⁸³, D. Z. Besson²⁰², G. Binder^{198,203}, D. Bindig²⁰⁴, E. Blaufuss²⁰⁵, S. Blot¹⁸³, C. Bohm¹⁸⁷, M. Börner²⁰⁶,
F. Bos²⁰¹, D. Bose²⁰⁷, S. Böser¹⁹⁷, O. Botner²⁰⁸, E. Bourbeau¹⁸⁶, J. Bourbeau²⁰⁹, F. Bradascio¹⁸³, J. Braun²¹⁰, L. Brayeur²¹⁰,
M. Brenzke¹⁹³, H.-P. Bretz¹⁸³, S. Bron¹⁸⁸, J. Brostean-Kaiser¹⁸³, A. Burgman²⁰⁸, T. Carver¹⁸⁸, J. Casey²⁰⁹, M. Casier²¹⁰,
E. Cheung²⁰⁵, D. Chirkin²⁰⁹, A. Christov¹⁸⁸, K. Clark²¹¹, L. Classen²¹², S. Coenders²¹³, G. H. Collin¹⁹², J. M. Conrad¹⁹²,
D. F. Cowen^{191,214}, R. Cross²⁰², M. Day²⁰⁹, J. P. A. M. de André²¹⁶, C. De Clercq²¹⁰, J. J. DeLaunay¹⁹¹, H. Dembinski²¹⁷,
S. De Ridder²¹⁸, P. Desiati²⁰⁹, K. D. de Vries²¹⁰, G. de Wasseige²¹⁰, M. de With²¹⁹, T. DeYoung²¹⁶, J. C. Díaz-Vélez²⁰⁹,
V. di Lorenzo¹⁹⁷, H. Dujmovic²⁰⁷, J. P. Dumm¹⁸⁷, M. Dunkman¹⁹¹, E. Dvorak¹⁹⁴, B. Eberhardt¹⁹⁷, T. Ehrhardt¹⁹⁷,
B. Eichmann²⁰¹, P. Eller¹⁹¹, P. A. Evenson²¹⁷, S. Fahey²⁰⁹, A. R. Fazely²²⁰, J. Felde²⁰⁵, K. Filimonov¹⁹⁸, C. Finley¹⁸⁷,
S. Flis¹⁸⁷, A. Franckowiak¹⁸³, E. Friedman²⁰⁵, T. Fuchs²⁰⁶, T. K. Gaisser²¹⁷, J. Gallagher²²¹, L. Gerhardt²⁰⁵, K. Ghorbani²⁰⁹,
W. Giang¹⁹⁵, T. Glauch¹⁹³, T. Glusenkamp¹⁸⁹, A. Goldschmidt²⁰⁵, J. G. Gonzalez²¹⁷, D. Grant¹⁹⁵, Z. Griffith²⁰⁹, C. Haack¹⁹³,
A. Hallgren²⁰⁸, F. Halzen²⁰⁹, K. Hanson²⁰⁹, D. Hebecker²¹⁹, D. Heereman¹⁸⁵, K. Helbing²⁰⁴, R. Hellauer²⁰⁵, S. Hickford²⁰⁴,
J. Hignight²¹⁶, G. C. Hill¹⁸², K. D. Hoffman²⁰⁵, R. Hoffmann²⁰⁴, B. Hokanson-Fasig²⁰⁹, K. Hoshina^{209,222}, F. Huang¹⁹¹,
M. Huber²¹³, K. Hultqvist¹⁸⁷, M. Hünnefeld²⁰⁶, S. In²⁰⁷, A. Ishihara²²³, E. Jacobi¹⁸³, G. S. Japaridze²²⁴, M. Jeong²⁰⁷,
K. Jero²⁰⁹, B. J. P. Jones²²⁵, P. Kalaczynski¹⁹³, W. Kang²⁰⁷, A. Kappes²¹², T. Karg¹⁸³, A. Karle²⁰⁹, M. Kauer²⁰⁹,
A. Keivani¹⁹¹, J. L. Kelley²⁰⁹, A. Kheirandish²⁰⁹, J. Kim²⁰⁷, M. Kim²²³, T. Kintscher¹⁸³, J. Kiryluk²²⁶, T. Kittler¹⁸⁹,
S. R. Klein^{205,198}, G. Kohlen²²⁷, R. Koirala²¹⁷, H. Kolanoski²¹⁹, L. Köpke¹⁹⁷, C. Kopper¹⁹⁵, S. Kopper²²⁸, J. P. Koschinsky¹⁹³,
D. J. Koskinen¹⁸⁶, M. Kowalski^{219,183}, K. Krings²¹³, M. Kroll²⁰¹, G. Krückl¹⁹⁷, J. Kunnen²¹⁰, S. Kunwar¹⁸³, N. Kurahashi²²⁹,
T. Kuwabara²²³, A. Kyriacou¹⁸², M. Labare²¹⁸, J. L. Lanfranchi¹⁹¹, M. J. Larson¹⁸⁶, F. Lauber²⁰⁴, M. Lesiak-Bzdak²²⁶,
M. Leuermann¹⁹³, Q. R. Liu²⁰⁹, L. Lu²²³, J. Lünemann²¹⁰, W. Luszczak²⁰⁹, J. Madsen²³⁰, G. Maggi²¹⁰, K. B. M. Mahn²¹⁶,
S. Mancina²⁰⁹, R. Maruyama²³¹, K. Mase²²³, R. Maunu²⁰⁵, F. McNally²⁰⁹, K. Meagher¹⁸⁵, M. Medici¹⁸⁶, M. Meier²⁰⁶,
T. Menne²⁰⁶, G. Merino²⁰⁹, T. Meures¹⁸⁵, S. Miarecki^{205,198}, J. Micallef²¹⁶, G. Momenté¹⁹⁷, T. Montaruli¹⁸⁸, R. W. Moore¹⁹⁵,
M. Moulai¹⁹², R. Nahnauer¹⁸³, P. Nakarmi²²⁸, U. Naumann²⁰⁴, G. Neer²¹⁶, H. Niederhausen²²⁶, S. C. Nowicki¹⁹⁵,
D. R. Nygren²⁰³, A. Obertacke Pollmann²⁰⁴, A. Olivás²⁰⁵, A. O'Murchadha¹⁸⁵, T. Palczewski^{203,198}, H. Pandya²¹⁷,
D. V. Pankova¹⁹¹, P. Peiffer¹⁹⁷, J. A. Pepper²²⁸, C. Pérez de los Heros²⁰⁸, D. Pieloth²⁰⁶, E. Pinat¹⁸⁵, P. B. Price¹⁹⁸,
G. T. Przybylski²⁰³, C. Raab¹⁸⁵, L. Rädcl¹⁹³, M. Rameez¹⁸⁶, K. Rawlins²³², I. C. Rea²¹³, R. Reimann¹⁹³, B. Relethford²²⁹,
M. Relich²²³, E. Resconi²¹³, W. Rhode²⁰⁶, M. Richman²²⁹, S. Robertson¹⁸², M. Rongen¹⁹³, C. Rott²⁰⁷, T. Ruhe²⁰⁶,
D. Ryckbosch²¹⁸, D. Rysewyk²¹⁶, T. Sälzer¹⁹³, S. E. Sanchez Herrera¹⁹⁵, A. Sandrock²⁰⁶, J. Sandroos¹⁹⁷, M. Santander²²⁸,
S. Sarkar^{186,233}, S. Sarkar¹⁹⁵, K. Satalecka¹⁸³, P. Schlunder²⁰⁶, T. Schmidt²⁰³, A. Schneider²⁰⁹, S. Schoenen¹⁹³,
S. Schöneberg²⁰¹, L. Schumacher¹⁹³, D. Seckel²¹⁷, S. Seunarine²³⁰, J. Soedingrekso²⁰⁶, D. Soldin²⁰⁴, M. Song²⁰⁵,
G. M. Spiczak²³⁰, C. Spiering¹⁸³, J. Stachurska¹⁸³, M. Stamatikos¹⁹⁹, T. Stanev²¹⁷, A. Stasik¹⁸³, J. Stettner¹⁹³, A. Steuer¹⁹⁷,
T. Stezelberger²⁰³, R. G. Stokstad²⁰³, A. Stössl²²³, N. L. Strotjohann¹⁸³, T. Stuttard¹⁸⁶, G. W. Sullivan²⁰⁵, M. Sutherland¹⁹⁹,
I. Taboada²³⁴, J. Tatar^{203,198}, F. Tenholt²⁰¹, S. Ter-Antonyan²²⁰, A. Terliuk¹⁸³, G. Tešić¹⁹¹, S. Tilav²¹⁷, P. A. Toale²²⁸,
M. N. Tobin²⁰⁹, S. Toscano²¹⁰, D. Tosi²⁰⁹, M. Tselengidou¹⁸⁹, C. F. Tung²³⁴, A. Turcati²¹³, C. F. Turley¹⁹¹, B. Ty²⁰⁹,
E. Unger²⁰⁸, M. Usner¹⁸³, J. Vandenbroucke²⁰⁹, W. Van Driessche²¹⁸, N. van Eijndhoven²¹⁰, S. Vanheule²¹⁸, J. van Santen¹⁸³,
M. Vehrings¹⁹³, E. Vogel¹⁹³, M. Vraeghe²¹⁸, C. Walck¹⁸⁷, A. Wallace¹⁸², M. Wallraff¹⁹³, F. D. Wandler¹⁹⁵,
N. Wandkowsky²⁰⁹, A. Waza¹⁹³, C. Weaver¹⁹⁵, M. J. Weiss¹⁹¹, C. Wendt²⁰⁹, J. Werthebach²⁰⁶, B. J. Whelan¹⁸², K. Wiebe¹⁹⁷,
C. H. Wiebusch¹⁹³, L. Wille²⁰⁹, D. R. Williams²²⁸, L. Wills²²⁹, M. Wolf²⁰⁹, T. R. Wood¹⁹⁵, E. Woolsey¹⁹⁵, K. Woschnagg¹⁹⁸,
D. L. Xu²⁰⁹, X. W. Xu²²⁰, Y. Xu²²⁶, J. P. Yanez¹⁹⁵, G. Yodh¹⁹⁶, S. Yoshida²²³, T. Yuan²⁰⁹, M. Zoll¹⁸⁷,
(IceCube Collaboration),

- A. Balasubramanian^{235,236}, S. Mate²³⁶, V. Bhalerao²³⁶, D. Bhattacharya¹⁹, A. Vibhute¹⁹, G. C. Dewangan¹⁹, A. R. Rao¹¹⁹,
S. V. Vadawale²³⁷,
(AstroSat Cadmium Zinc Telluride Imager Team),
D. S. Svinkin²³⁸, K. Hurley²³⁹, R. L. Apte²³⁸, D. D. Frederiks²³⁸, S. V. Golenetskii²³⁸, A. V. Kozlova²³⁸, A. L. Lysenko²³⁸,
Ph. P. Oleynik²³⁸, A. E. Tsvetkova²³⁸, M. V. Ulanov²³⁸, T. Cline²⁴⁰,
(IPN Collaboration),
T. P. Li^{241,82,242}, S. L. Xiong²⁴¹, S. N. Zhang^{241,242}, F. J. Lu²⁴¹, L. M. Song²⁴¹, X. L. Cao²⁴¹, Z. Chang²⁴¹, G. Chen²⁴¹,
L. Chen²⁴³, T. X. Chen²⁴¹, Y. Chen²⁴¹, Y. B. Chen⁸², Y. P. Chen²⁴¹, W. Cui^{241,82}, W. W. Cui²⁴¹, J. K. Deng⁸²,
Y. W. Dong²⁴¹, Y. Y. Du²⁴¹, M. X. Fu⁸², G. H. Gao^{241,242}, H. Gao^{241,242}, M. Gao²⁴¹, M. Y. Ge²⁴¹, Y. D. Gu²⁴¹, J. Guan²⁴¹,
C. C. Guo^{241,242}, D. W. Han²⁴¹, W. Hu²⁴¹, Y. Huang²⁴¹, J. Huo²⁴¹, S. M. Jia²⁴¹, L. H. Jiang²⁴¹, W. C. Jiang²⁴¹, J. Jin²⁴¹,
Y. J. Jin⁸², B. Li²⁴¹, C. K. Li²⁴¹, G. Li²⁴¹, M. S. Li²⁴¹, W. Li²⁴¹, X. Li²⁴¹, X. B. Li²⁴¹, X. F. Li²⁴¹, Y. G. Li²⁴¹, Z. J. Li^{241,242},
Z. W. Li²⁴¹, X. H. Liang²⁴¹, J. Y. Liao²⁴¹, C. Z. Liu²⁴¹, G. Q. Liu⁸², H. W. Liu²⁴¹, S. Z. Liu²⁴¹, X. J. Liu²⁴¹, Y. Liu²⁴¹,
Y. N. Liu⁸², B. Lu²⁴¹, X. F. Lu²⁴¹, T. Luo²⁴¹, X. Ma²⁴¹, B. Meng²⁴¹, Y. Nang^{241,242}, J. Y. Nie²⁴¹, G. Ou²⁴¹, J. L. Qu²⁴¹,
N. Sai^{241,242}, L. Sun²⁴¹, Y. Tan²⁴¹, L. Tao²⁴¹, W. H. Tao²⁴¹, Y. L. Tuo^{241,242}, G. F. Wang²⁴¹, H. Y. Wang²⁴¹, J. Wang²⁴¹,
W. S. Wang²⁴¹, Y. S. Wang²⁴¹, X. Y. Wen²⁴¹, B. B. Wu²⁴¹, M. Wu²⁴¹, G. C. Xiao^{241,242}, H. Xu²⁴¹, Y. P. Xu²⁴¹,
L. L. Yan^{241,242}, J. W. Yang²⁴¹, S. Yang²⁴¹, Y. J. Yang²⁴¹, A. M. Zhang²⁴¹, C. L. Zhang²⁴¹, C. M. Zhang²⁴¹, F. Zhang²⁴¹,
H. M. Zhang²⁴¹, J. Zhang²⁴¹, Q. Zhang²⁴¹, S. Zhang²⁴¹, T. Zhang²⁴¹, W. Zhang^{241,242}, W. C. Zhang²⁴¹, W. Z. Zhang²⁴³,
Y. Zhang²⁴¹, Y. Zhang^{241,242}, Y. F. Zhang²⁴¹, Y. J. Zhang²⁴¹, Z. Zhang⁸², Z. L. Zhang²⁴¹, H. S. Zhao²⁴¹, J. L. Zhao²⁴¹,
X. F. Zhao^{241,242}, S. J. Zheng²⁴¹, Y. Zhu²⁴¹, Y. X. Zhu²⁴¹, C. L. Zou²⁴¹,
(The Insight-HXMT Collaboration),
A. Albert²⁴⁴, M. André²⁴⁵, M. Anghinolfi^{246,247}, M. Ardid²⁴⁷, J.-J. Aubert²⁴⁸, J. Aublin²⁴⁹, T. Avgitas²⁴⁹, B. Baret²⁴⁹,
J. Barrios-Martí²⁵⁰, S. Basa²⁵¹, B. Belhorma²⁵², V. Bertin²⁴⁸, S. Biagi²⁵³, R. Bormuth^{14,254}, S. Bourret²⁴⁹, M. C. Bouwhuis¹⁴,
H. Brânzaș²⁵⁵, R. Bruijn^{14,256}, J. Brunner²⁴⁸, J. Bustó²⁴⁸, A. Capone^{257,258}, L. Caramete²⁵⁵, J. Carr²⁴⁸, S. Celli^{257,258,259},
R. Cherkaoui El Moursli²⁶⁰, T. Chiarusi²⁶¹, M. Circella²⁶², J. A. B. Coelho²⁴⁹, A. Coleiro^{249,250}, R. Coniglione²⁵³,
H. Costantini²⁴⁸, P. Coyle²⁴⁸, A. Creusot²⁴⁹, A. F. Díaz²⁶³, A. Deschamps²⁶⁴, G. De Bonis²⁵⁸, C. Distefano²⁵³,
I. Di Palma^{257,258}, A. Domi^{246,265}, C. Donzaud^{249,266}, D. Dornic²⁴⁸, D. Drouhin²⁴⁴, T. Eberl^{189,260,267}, I. El Bojaddaini²⁶⁷,
N. El Khayati²⁶⁰, D. Elsässer²⁶⁸, A. Enzenhöfer²⁴⁸, A. Ettahiri²⁶⁰, F. Fassi²⁶⁰, I. Felis²⁴⁷, L. A. Fusco^{261,269}, P. Gay^{270,249},
V. Giordano²⁷¹, H. Glotin^{272,273}, T. Grégoire²⁴⁹, R. Gracia Ruiz²⁴⁹, K. Graf¹⁸⁹, S. Hallmann¹⁸⁹, H. van Haren²⁷⁴,
A. J. Heijboer¹⁴, Y. Hello²⁶⁴, J. J. Hernández-Rey²⁵⁰, J. Hössl¹⁸⁹, J. Hofestädt¹⁸⁹, C. Hugon^{246,265}, G. Illuminati²⁵⁰,
C. W. James¹⁸⁹, M. de Jong^{14,254}, M. Jongen¹⁴, M. Kadler²⁶⁸, O. Kalekin¹⁸⁹, U. Katz¹⁸⁹, D. Kiessling¹⁸⁹, A. Kouchner^{249,273},
M. Kreter²⁶⁸, I. Kreykenbohm²⁷⁵, V. Kulikovskiy^{248,276}, C. Lachaud²⁴⁹, R. Lahmann¹⁸⁹, D. Lefèvre²⁷⁷, E. Leonora^{271,278},
M. Lotze²⁵⁰, S. Loucatos^{279,249}, M. Marcellin²⁵¹, A. Margiotta^{261,269}, A. Marinelli^{280,281}, J. A. Martínez-Mora²⁴⁷,
R. Mele^{282,283}, K. Melis^{14,256}, T. Michael¹⁴, P. Migliozzi²⁸², A. Moussa²⁸⁴, S. Navas²⁸⁴, E. Nezri²⁵¹, M. Organokov²⁸⁵,
G. E. Pávlaš²⁵⁵, C. Pellegrino^{261,269}, C. Perrina^{257,258}, P. Piattelli²⁵³, V. Popa²⁵⁵, T. Pradier²⁸⁵, L. Quinn²⁴⁸, C. Racca²⁴⁴,
G. Riccobene²⁵³, A. Sánchez-Losa²⁶², M. Saldaña²⁴⁷, I. Salvadori²⁴⁸, D. F. E. Samtleben^{14,254}, M. Sanguineti^{246,265},
P. Sapienza²⁵³, C. Sieger¹⁸⁹, M. Spurio^{261,269}, Th. Stolarczyk²⁷⁹, M. Taiuti^{246,265}, Y. Tayalati²⁶⁰, A. Trovato²⁵³, D. Turpin²⁴⁸,
C. Tönnis²⁵⁰, B. Vallage^{279,249}, V. Van Elewyck^{249,273}, F. Versari^{261,269}, D. Vivolo^{282,283}, A. Vizzoca^{257,258}, J. Wilms²⁷⁵,
J. D. Zornoza²⁵⁰, J. Zúñiga²⁵⁰,
(ANTARES Collaboration),
A. P. Beardmore²⁸⁶, A. A. Breeveld²⁸⁷, D. N. Burrows²⁸⁸, S. B. Cenko^{289,290}, G. Cusumano²⁹¹, A. D’Ai²⁹¹, M. de Pasquale²⁹²,
S. W. K. Emery²⁸⁷, P. A. Evans²⁸⁶, P. Giommi²⁹³, C. Gronwall^{288,294}, J. A. Kennea²⁸⁸, H. A. Krimm^{295,296}, N. P. M. Kuin²⁸⁷,
A. Lien^{297,298}, F. E. Marshall²⁸⁷, A. Melandri²⁹⁹, J. A. Nousek²⁸⁸, S. R. Oates³⁰⁰, J. P. Osborne²⁸⁶, C. Pagani²⁸⁶, K. L. Page²⁸⁶,
D. M. Palmer³⁰¹, M. Perri^{302,293}, M. H. Siegel²⁸⁸, B. Sbarufatti²⁸⁸, G. Tagliaferri²⁹⁹, A. Tohuvavohu^{288,303},
(The Swift Collaboration),
M. Tavani^{304,305,306}, F. Verrecchia^{307,308}, A. Bulgarelli³⁰⁹, Y. Evangelista³⁰⁴, L. Pacciani³⁰⁴, M. Feroci³⁰⁴, C. Pittori^{307,308},
A. Giuliani³¹⁰, E. Del Monte³⁰⁴, I. Donnarumma³¹¹, A. Argan³⁰⁴, A. Trois³¹², A. Ursi³⁰⁴, M. Cardillo³⁰⁴, G. Piano³⁰⁴,
F. Longo³¹³, F. Lucarelli^{307,308}, P. Munar-Adrover³¹⁴, F. Fuschino³⁰⁹, C. Labanti³⁰⁹, M. Marisaldi³¹⁵, G. Minervini³⁰⁴,
V. Fioretti³⁰⁹, N. Parmiggiani³⁰⁹, F. Gianotti³⁰⁹, M. Trifoglio³⁰⁹, G. Di Persio³⁰⁴, L. A. Antonelli³¹¹, G. Barbiellini³¹³,
P. Caraveo³¹⁰, P. W. Cattaneo³¹⁶, E. Costa³⁰⁴, S. Colafrancesco³¹⁷, F. D’Amico³¹¹, A. Ferrari³¹⁸, A. Morselli³¹⁹, F. Paoletti³²⁰,
P. Picozza³¹⁹, M. Pilia³¹², A. Rappoldi³¹⁶, P. Soffitta³⁰⁴, S. Vercellone³²¹,
(AGILE Team),
R. J. Foley³²², D. A. Coulter³²², C. D. Kilpatrick³²², M. R. Drout³²³, A. L. Piro³²³, B. J. Shappee^{323,324}, M. R. Siebert³²²,
J. D. Simon³²³, N. Ulloa³²⁵, D. Kasen^{326,327}, B. F. Madore³²³, A. Murguía-Berthier³²², Y.-C. Pan³²², J. X. Prochaska³²²,
E. Ramirez-Ruiz^{322,328}, A. Rest^{329,330}, C. Rojas-Bravo³²²,
(The 1M2H Team),

E. Berger¹⁶³, M. Soares-Santos^{331,332}, J. Annis³³², K. D. Alexander¹⁶³, S. Allam³³², E. Balbinot³³³, P. Blanchard¹⁶³, D. Brout³³⁴, R. E. Butler^{335,332}, R. Chornock³³⁶, E. R. Cook^{337,338}, P. Cowperthwaite¹⁶³, H. T. Diehl³³², A. Drlica-Wagner³³², M. R. Drout³³⁹, F. Durret³⁴⁰, T. Eftekhari¹⁶³, D. A. Finley³³², W. Fong³⁴¹, J. A. Frieman³³², C. L. Fryer³⁴², J. García-Bellido³⁴³, R. A. Gruendl³⁴⁴, W. Hartley^{345,346}, K. Herner³³², R. Kessler³⁴⁷, H. Lin³³², P. A. A. Lopes³⁴⁸, A. C. C. Lourenço³⁴⁸, R. Margutti³⁴⁹, J. L. Marshall³³⁷, T. Matheson³⁵⁰, G. E. Medina³⁵¹, B. D. Metzger³⁵², R. R. Muñoz³⁵¹, J. Muir³⁵³, M. Nicholl¹⁶³, P. Nugent³⁵⁴, A. Palmese³⁴⁵, F. Paz-Chinchón³⁴⁴, E. Quataert³⁵⁵, M. Sako³³⁴, M. Sauseda³³⁷, D. J. Schlegel³⁵⁶, D. Scolnic³⁴⁷, L. F. Secco³³⁴, N. Smith³⁵⁷, F. Sobreira^{358,359}, V. A. Villar¹⁶³, A. K. Vivas³⁶⁰, W. Wester³³², P. K. G. Williams¹⁶³, B. Yanny³³², A. Zenteno³⁶⁰, Y. Zhang³³², T. M. C. Abbott³⁶⁰, M. Banerji^{361,362}, K. Bechtol³³⁸, A. Benoit-Lévy^{363,345,364}, E. Bertin^{363,364}, D. Brooks³⁴⁵, E. Buckley-Geer³³², D. L. Burke^{365,366}, D. Capozzi³⁶⁷, A. Carnero Rosell^{359,368}, M. Carrasco Kind^{369,344}, F. J. Castander³⁷⁰, M. Crocce³⁷⁰, C. E. Cunha³⁶⁵, C. B. D'Andrea³³⁴, L. N. da Costa^{359,368}, C. Davis³⁶⁵, D. L. DePoy³⁷¹, S. Desai³⁷², J. P. Dietrich^{373,374}, T. F. Eifler^{375,376}, E. Fernandez³⁷⁷, B. Flaugher³³², P. Fosalba³⁷⁰, E. Gaztanaga³⁷⁰, D. W. Gerdes^{378,379}, T. Giannantonio^{361,362,380}, D. A. Goldstein^{381,354}, D. Gruen^{365,366}, J. Gschwend^{359,368}, G. Gutierrez³³², K. Honscheid^{382,383}, D. J. James³⁸⁴, T. Jeltema³⁸⁵, M. W. G. Johnson³⁴⁴, M. D. Johnson³⁴⁴, S. Kent^{332,347}, E. Krause³⁶⁵, R. Kron^{332,347}, K. Kuehn³⁸⁶, O. Lahav³⁴⁵, M. Lima^{387,359}, M. A. G. Maia^{359,368}, M. March³³⁴, P. Martini^{382,388}, R. G. McMahon^{361,362}, F. Menanteau^{369,344}, C. J. Miller^{378,379}, R. Miquel^{389,377}, J. J. Mohr^{373,374,390}, R. C. Nichol³⁶⁷, R. L. C. Ogando^{359,368}, A. A. Plazas³⁷⁶, A. K. Romer³⁹¹, A. Roodman^{365,366}, E. S. Rykoff^{365,366}, E. Sanchez³⁹², V. Scarpine³³², R. Schindler³⁶⁶, M. Schubnell³⁷⁹, I. Sevilla-Noarbe³⁹², E. Sheldon³⁹³, M. Smith³⁹⁴, R. C. Smith³⁶⁰, A. Stebbins³³², E. Suchyta³⁹⁵, M. E. C. Swanson³⁴⁴, G. Tarle³⁷⁹, R. C. Thomas³⁵⁴, M. A. Troxel^{382,383}, D. L. Tucker³³², V. Vikram³⁹⁶, A. R. Walker³⁶⁰, R. H. Wechsler^{397,365,366}, J. Weller^{373,390,380}, J. L. Carlin³³⁸, M. S. S. Gill³⁶⁶, T. S. Li³³², J. Marriner³³², E. Neilsen³³²,
 (The Dark Energy Camera GW-EM Collaboration and the DES Collaboration),
 J. B. Haislip³⁹⁸, V. V. Kouprianov³⁹⁸, D. E. Reichart³⁹⁸, D. J. Sand³⁹⁹, L. Tartaglia^{399,400}, S. Valenti⁴⁰⁰, S. Yang^{400,401,402},
 (The DLT40 Collaboration),
 S. Benetti⁴⁰³, E. Brocato⁴⁰⁴, S. Campana⁴⁰⁵, E. Cappellaro⁴⁰³, S. Covino⁴⁰⁵, P. D'Avanzo⁴⁰⁵, V. D'Elia^{404,406}, F. Getman⁴⁰⁷, G. Ghirlanda⁴⁰⁵, G. Ghisellini⁴⁰⁵, L. Limatola⁴⁰⁷, L. Nicastro⁴⁰⁸, E. Palazzi⁴⁰⁸, E. Pian⁴⁰⁸, S. Piranomonte⁴⁰⁴, A. Possenti³¹², A. Rossi⁴⁰⁸, O. S. Salafia^{409,405}, L. Tomasella⁴⁰³, L. Amati⁴⁰⁸, L. A. Antonelli⁴⁰⁴, M. G. Bernardini^{410,405}, F. Bufano⁴¹¹, M. Capaccioli^{407,412}, P. Casella⁴⁰⁴, M. Dadina⁴⁰⁸, G. De Cesare⁴⁰⁸, A. Di Paola⁴⁰⁴, G. Giuffrida⁴⁰⁴, A. Giunta⁴⁰⁴, G. L. Israel⁴⁰⁴, M. Lisi⁴⁰⁴, E. Maiorano⁴⁰⁸, M. Mapelli^{403,413}, N. Masetti^{408,414}, A. Pescalli^{415,405}, L. Pulone⁴⁰⁴, R. Salvaterra⁴¹⁶, P. Schipani⁴⁰⁷, M. Spera⁴⁰³, A. Stameria^{146,417}, L. Stella⁴⁰⁴, V. Testa⁴⁰⁴, M. Turatto⁴⁰³, D. Vergani⁴⁰⁸, G. Aresu³¹², M. Bachetti³¹², F. Buffa³¹², M. Burgay³¹², M. Buttu³¹², T. Caria³¹², E. Carretti³¹², V. Casasola⁴¹⁸, P. Castangia³¹², G. Carboni³¹², S. Casu³¹², R. Concu³¹², A. Corongiu³¹², G. L. Deiana³¹², E. Egron³¹², A. Fara³¹², F. Gaudiomonte³¹², V. Gusai³¹², A. Ladu³¹², S. Loru³¹², S. Leurini³¹², L. Marongiu³¹², A. Melis³¹², G. Melis³¹², Carlo Migoni³¹², Sabrina Milia³¹², Alessandro Navarrini³¹², A. Orlati³¹², P. Ortu³¹², S. Palmas³¹², A. Pellizzoni³¹², D. Perrodin³¹², T. Pisanu³¹², S. Poppi³¹², S. Righini⁴¹⁹, A. Saba³¹², G. Serra³¹², M. Serrau³¹², M. Stagni⁴¹⁹, G. Surcis³¹², V. Vacca³¹², G. P. Vargiu³¹², L. K. Hunt⁴¹⁸, Z. P. Jin⁴²⁰, S. Klose⁴²¹, C. Kouveliotou^{422,423}, P. A. Mazzali^{424,425}, P. Möller⁴²⁶, L. Nava^{405,427}, T. Piran⁴²⁸, J. Selsing³²⁸, S. D. Vergani^{429,405}, K. Wiersema⁴³⁰, K. Toma^{431,432}, A. B. Higgins⁴³⁰, C. G. Mundell⁴³³, S. di Serego Alighieri⁴¹⁸, D. Gótz⁴³⁴, W. Gao⁴³⁵, A. Gomboc⁴³⁶, L. Kaper⁴³⁷, S. Kobayashi⁴³⁸, D. Kopac⁴³⁹, J. Mao⁴⁴⁰, R. L. C. Starling⁴³⁰, I. Steele⁴⁴¹, A. J. van der Horst^{442,423},
 (GRAWITA: GRAVitational Wave Inaf TeAm),
 F. Acero⁴⁴³, W. B. Atwood⁴⁴⁴, L. Baldini⁴⁴⁵, G. Barbiellini^{446,447}, D. Bastieri^{448,449}, B. Berenji⁴⁵⁰, R. Bellazzini⁴⁵¹, E. Bissaldi^{452,453}, R. D. Blandford⁴⁵⁴, E. D. Bloom⁴⁵⁴, R. Bonino^{455,456}, E. Bottacini⁴⁵⁴, J. Bregoni⁴⁵⁷, R. Buehler⁴⁶⁹, S. Buson⁵⁰, R. A. Cameron⁴⁵⁴, R. Caputo⁴⁵⁹, P. A. Caraveo¹⁸⁰, E. Cavazzuti⁴⁶⁰, A. Chekhtman⁴⁶¹, C. C. Cheung⁴⁶², J. Chiang⁴⁵⁴, S. Ciprini^{462,463}, J. Cohen-Tanugi⁴⁵⁷, L. R. Cominsky⁴⁶⁵, D. Costantini⁴⁴⁹, A. Cuoco^{466,455}, F. D'Ammando^{466,467}, F. de Palma^{453,468}, S. W. Digel⁴⁵⁴, N. Di Lalla⁴⁴⁵, M. Di Mauro⁴⁵⁴, L. Di Venere^{452,453}, R. Dubois⁴⁵⁴, S. J. Fegan⁴⁵⁸, W. B. Focke⁴⁵⁴, A. Franckowiak⁴⁵⁸, Y. Fukazawa⁴⁷¹, S. Funk¹⁸⁹, P. Fusco^{452,453}, F. Gargano⁴⁵³, D. Gasparrini^{462,464}, N. Giglietto^{452,453}, F. Giordano^{452,453}, M. Giroletti⁴⁶⁶, T. Glanzman⁴⁵⁴, D. Green^{472,50}, M.-H. Grondin⁴⁷³, L. Guillemot^{474,475}, S. Guiriec^{50,422}, A. K. Harding⁵⁰, D. Horan⁴⁵⁸, G. Jóhannesson^{476,477}, T. Kamae⁴⁷⁸, S. Kensei⁴⁷¹, M. Kuss⁴⁵¹, G. La Mura⁴⁴⁹, L. Latronico⁴⁵⁵, M. Lemoine-Goumard⁴⁷³, F. Longo^{446,447}, F. Loparco^{452,453}, M. N. Lovellette⁴⁶², P. Lubrano⁴⁶³, J. D. Magill⁴⁷², S. Maldera⁴⁵⁵, A. Manfreda⁴⁴⁵, M. N. Mazziotta⁴⁵³, J. E. McEnery^{50,472}, M. Meyer⁴⁵⁴, P. F. Michelson⁴⁵⁴, N. Mirabal⁵⁰, M. E. Monzani⁴⁵⁴, E. Moretti⁴⁸¹, A. Morselli⁴⁷⁹, I. V. Moskalenko⁴⁵⁴, M. Negro^{455,456}, E. Nuss⁴⁵⁷, R. Ojha⁵⁰, N. Omodei⁴⁵⁴, M. Orienti⁴⁶⁷, E. Orlando⁴⁵⁴, M. Palatiello^{446,446}, V. S. Paliya⁴⁸⁰, D. Paneque⁴⁸¹, M. Pesce-Rollins⁴⁵¹, F. Piron⁴⁵⁷, T. A. Porter⁴⁵⁴, G. Principe¹⁸⁹, S. Rainò^{452,453}, R. Rando^{448,449}, M. Razzano⁴⁵¹, S. Razzaque⁴⁸², A. Reimer^{483,454}, O. Reimer^{483,454}, T. Reposeur⁴⁷³, L. S. Rochester⁴⁵⁴, P. M. Saz Parkinson^{444,484,485}, C. Sgrò⁴⁵¹, E. J. Siskind⁴⁸⁶, F. Spada⁴⁵¹, G. Spandre⁴⁵¹, D. J. Suson⁴⁸⁷, M. Takahashi⁴⁸¹, Y. Tanaka⁴⁸⁸, J. G. Thayer⁴⁵⁴, J. B. Thayer⁴⁵⁴, D. J. Thompson⁵⁰, L. Tibaldo^{489,490}, D. F. Torres^{491,492}, E. Torresi⁴⁹³, E. Troja^{50,472}, T. M. Venters⁵⁰,

- G. Vianello⁴⁵⁴, G. Zaharijas^{446,447,494},
 (The Fermi Large Area Telescope Collaboration),
 J. R. Allison^{495,496}, K. W. Bannister⁴⁹⁷, D. Dobie^{495,497,498}, D. L. Kaplan⁴⁹⁹, E. Lenc^{495,498}, C. Lynch^{495,498}, T. Murphy^{495,498},
 E. M. Sadler^{495,498},
 (ATCA: Australia Telescope Compact Array),
 A. Hotan⁵⁰⁰, C. W. James⁵⁰¹, S. Osłowski⁵⁰², W. Raja⁴⁹⁷, R. M. Shannon^{497,501}, M. Whiting⁴⁹⁷,
 (ASKAP: Australian SKA Pathfinder),
 I. Arcavi^{503,504}, D. A. Howell^{503,504}, C. McCully^{503,504}, G. Hosseinzadeh^{503,504}, D. Hiramatsu^{503,504}, D. Poznanski⁵⁰⁵,
 J. Barnes⁵⁰⁶, M. Zaltzman⁵⁰⁵, S. Vasylyev^{503,504}, D. Maoz⁵⁰⁵,
 (Las Cumbres Observatory Group),
 J. Cooke^{507,508,509}, M. Bailes^{507,508}, C. Wolf^{510,509,508}, A. T. Deller^{507,508,509}, C. Lidman^{511,509}, L. Wang^{512,513,514},
 B. Gendre⁵¹⁵, I. Andreoni^{507,508,511,509}, K. Ackley⁵¹⁶, T. A. Pritchard⁵⁰⁷, M. S. Bessell⁵¹⁰, S.-W. Chang^{510,509},
 A. Möller^{510,509}, C. A. Onken^{510,509}, R. A. Scalzo^{510,509,517}, R. Ridden-Harper⁵¹⁰, R. G. Sharp⁵¹⁰, B. E. Tucker^{510,509},
 T. J. Farrell⁵¹¹, E. Elmer⁵¹⁸, S. Johnston^{519,509}, V. Venkatraman Krishnan^{507,509}, E. F. Keane^{520,509}, J. A. Green⁵¹⁹,
 A. Jameson^{507,509}, L. Hu^{513,514}, B. Ma^{521,514}, T. Sun^{513,514}, X. Wu^{513,514}, X. Wang⁵²², Z. Shang^{521,523,514}, Y. Hu^{521,514},
 M. C. B. Ashley⁵²⁴, X. Yuan^{525,514}, X. Li^{525,514}, C. Tao⁵²², Z. Zhu⁵²⁶, H. Zhang⁵²⁷, N. B. Suntzeff⁵¹², J. Zhou⁵²⁷, J. Yang⁵¹³,
 B. Orange⁵²⁸, D. Morris⁵¹⁵, A. Cucchiara⁵¹⁵, T. Giblin⁵²⁹, A. Klotz⁵³⁰, J. Staff⁵¹⁵, P. Thierry⁵³¹, B. P. Schmidt^{532,509},
 (OzGrav, DWF (Deeper, Wider, Faster program), AST3, and CAASTRO Collaborations),
 N. R. Tanvir⁵³³, A. J. Levan³⁰⁰, Z. Cano^{52,534}, A. de Ugarte-Postigo^{527,534}, C. González-Fernández⁵³⁵, J. Greiner⁵³⁶,
 J. Hjorth³²⁸, M. Irwin⁵³⁵, T. Krühler⁵³⁶, I. Mandel⁵³⁷, B. Milvang-Jensen³²⁸, P. O'Brien⁵³³, E. Rol⁵³⁸, S. Rosetti⁵³³,
 S. Rosswog⁵³⁹, A. Rowlinson^{540,541}, D. T. H. Steeghs³⁰⁰, C. C. Thöne⁵³⁴, K. Ulaczyk³⁰⁰, D. Watson³²⁸, S. H. Bruun³²⁸,
 R. Cutter³⁰⁰, R. Figuera Jaimes⁵⁴², Y. I. Fujii^{543,544}, A. S. Fruchter⁵⁴⁵, B. Gompertz³⁰⁰, P. Jakobsson⁵⁴⁶, G. Hodosan⁵³⁴,
 U. G. Jørgensen⁵⁴³, T. Kangas⁵⁴⁵, D. A. Kann⁵³⁴, M. Rabus^{547,548}, S. L. Schröder³²⁸, E. R. Stanway³⁰⁰, R. A. M. J. Wijers⁵⁴⁰,
 (The VINROUGE Collaboration),
 V. M. Lipunov^{549,550}, E. S. Gorbvskoy⁵⁵⁰, V. G. Kornilov^{549,550}, N. V. Tyurina⁵⁵⁰, P. V. Balanutsa⁵⁵⁰, A. S. Kuznetsov⁵⁵⁰,
 D. M. Vlasenko^{549,550}, R. C. Podesta⁵⁵¹, C. Lopez⁵⁵¹, F. Podesta⁵⁵¹, H. O. Levato⁵⁵², C. Saffe⁵⁵², C. C. Malmacci⁵⁵³,
 N. M. Budnev⁵⁵⁴, O. A. Gress^{554,550}, D. A. Kuvshinov^{549,550}, I. A. Gorbunov^{549,550}, V. V. Vladimirov⁵⁵⁰,
 D. S. Zimnukhov^{549,550}, A. V. Gabovich⁵⁵⁵, V. V. Yurkov⁵⁵⁵, Yu. P. Sergienko⁵⁵⁵, R. Reboló⁵⁵⁶, M. Serra-Ricart⁵⁵⁶,
 A. G. Tlatov⁵⁵⁷, Yu. V. Ishmuhametova⁵⁵⁴,
 (MASTER Collaboration),
 F. Abe⁵⁵⁸, K. Aoki⁵⁵⁹, W. Aoki⁵⁶⁰, Y. Asakura^{558,956}, S. Baar⁵⁶¹, S. Barway⁵⁶², I. A. Bond⁵⁶³, M. Doi⁵⁶⁴, F. Finet⁵⁵⁹,
 T. Fujiyoshi⁵⁵⁹, H. Furusawa⁵⁶⁰, S. Honda⁵⁶¹, R. Itoh⁵⁶⁵, N. Kanda⁵⁶⁶, K. S. Kawabata⁵⁶⁷, M. Kawabata⁵⁶⁸, J. H. Kim⁵⁵⁹,
 S. Koshida⁵⁵⁹, D. Kuroda⁵⁶⁹, C.-H. Lee⁵⁵⁹, W. Liu^{567,570}, K. Matsubayashi⁵⁶⁹, S. Miyazaki⁵⁷¹, K. Morihana⁵⁷²,
 T. Morokuma⁵⁶⁴, K. Motohara⁵⁶⁴, K. L. Murata⁵⁶⁵, H. Nagai⁵⁶⁰, H. Nagashima⁵⁶⁸, T. Nagayama⁵⁷³, T. Nakaoka⁵⁶⁸,
 F. Nakata⁵⁵⁹, R. Ohsawa⁵⁶⁴, T. Ohshima⁵⁶¹, K. Ohta⁵⁷⁴, H. Okita⁵⁵⁹, T. Saito⁵⁶¹, Y. Saito⁵⁶⁵, S. Sako^{564,575}, Y. Sekiguchi⁵⁷⁶,
 T. Sumi⁵⁷¹, A. Tajitsu⁵⁵⁹, J. Takahashi⁵⁶¹, M. Takayama⁵⁶¹, Y. Tamura⁵⁷², I. Tanaka⁵⁵⁹, M. Tanaka⁵⁶⁰,
 T. Terai⁵⁵⁹, N. Tominaga^{577,578}, P. J. Tristram⁵⁷⁹, M. Uemura⁵⁶⁷, Y. Utsumi⁵⁶⁷, M. S. Yamaguchi⁵⁶⁴, N. Yasuda⁵⁷⁸,
 M. Yoshida⁵⁵⁹, T. Zenko⁵⁷⁴,
 (J-GEM),
 S. M. Adams⁵⁸⁰, G. C. Anupama⁵⁸¹, J. Bally⁵⁸², S. Barway⁵⁸³, E. Bellm⁵⁸⁴, N. Blagorodnova⁵⁸⁰, C. Cannella⁵⁸⁰,
 P. Chandra⁵⁸⁵, D. Chatterjee⁵⁸⁶, T. E. Clarke⁵⁸⁷, B. E. Cobb⁵⁸⁸, D. O. Cook⁵⁸⁰, C. Copperwheat⁴⁴¹, K. De⁵⁸⁰,
 S. W. K. Emery⁵⁸⁹, U. Feindt⁵⁹¹, K. Foster⁵⁸⁰, O. D. Fox⁵⁹², D. A. Frail⁵⁹³, C. Fremling⁵⁸⁰, C. Frohmaier^{594,595},
 J. A. Garcia⁵⁸⁰, S. Ghosh⁵⁸⁶, S. Giacintucci⁵⁸⁷, A. Goobar⁵⁹¹, O. Gottlieb⁵⁹⁶, B. W. Grefenstette⁵⁸⁰, G. Hallinan⁵⁸⁰,
 F. Harrison⁵⁸⁰, M. Heida⁵⁸⁰, G. Helou⁵⁹⁷, A. Y. Q. Ho⁵⁸⁰, A. Horesh⁵⁹⁸, K. Hotokezaka⁵⁹⁹, W.-H. Ip⁶⁰⁰, R. Itoh⁶⁰¹,
 Bob Jacobs⁶⁶, J. E. Jencson⁵⁸⁰, D. Kasen^{602,603}, M. M. Kasliwal⁵⁸⁰, N. E. Kassim⁵⁸⁷, H. Kim⁶⁰⁴, B. S. Kiran⁵⁸¹,
 N. P. M. Kuin⁵⁸⁹, S. R. Kulkarni⁵⁸⁰, T. Kupfer⁵⁸⁰, R. M. Lau⁵⁸⁰, K. Madsen⁵⁸⁰, P. A. Mazzali^{441,605}, A. A. Miller^{606,607},
 H. Miyasaka⁵⁸⁰, K. Mooley⁶⁰⁸, S. T. Myers⁵⁹³, E. Nakar⁵⁹⁶, C.-C. Ngeow⁶⁰⁰, P. Nugent^{602,354}, E. O. Ofek⁶⁰⁹,
 N. Palliyaguru⁶¹⁰, M. Pavana⁵⁸¹, D. A. Perley⁶¹¹, W. M. Peters⁵⁸⁷, S. Pike⁵⁸⁰, T. Piran⁵⁹⁸, H. Qi⁵⁸⁶, R. M. Quimby^{612,613},
 J. Rana¹⁹, S. Rosswog⁶¹⁴, F. Rusu⁶¹⁵, E. M. Sadler^{495,616}, A. Van Sistine⁵⁸⁶, J. Sollerman⁶¹⁴, Y. Xu⁵⁸⁰, L. Yan^{580,597},
 Y. Yatsu⁶⁰¹, P.-C. Yu⁶⁰⁰, C. Zhang⁵⁸⁶, W. Zhao⁶¹⁵,
 (GROWTH, JAGWAR, Caltech-NRAO, TTU-NRAO, and NuSTAR Collaborations),
 K. C. Chambers⁶¹⁷, M. E. Huber⁶¹⁷, A. S. B. Schultz⁶¹⁷, J. Bulger⁶¹⁷, H. Flewelling⁶¹⁷, E. A. Magnier⁶¹⁷, T. B. Lowe⁶¹⁷,
 R. J. Wainscoat⁶¹⁷, C. Waters⁶¹⁷, M. Willman⁶¹⁷,
 (Pan-STARRS),

- K. Ebisawa⁶¹⁸, C. Hanyu⁶¹⁹, S. Harita⁶²⁰, T. Hashimoto⁶²¹, K. Hidaka⁶¹⁹, T. Hori⁶²², M. Ishikawa⁶²³, N. Isobe⁶¹⁸,
W. Iwakiri⁶²⁴, H. Kawai⁶²⁵, N. Kawai^{620,624}, T. Kawamuro⁶²⁶, T. Kawase⁶²⁷, Y. Kitaoka⁶²¹, K. Makishima⁶²⁴,
M. Matsuoka⁶²⁴, T. Mihara⁶²⁴, T. Morita⁶²², K. Morita⁶²⁰, S. Nakahira⁶²⁴, M. Nakajima⁶²⁷, Y. Nakamura⁶²⁵, H. Negoro⁶²⁷,
S. Oda⁶²², A. Sakamaki⁶²⁷, R. Sasaki⁶²⁵, M. Serino⁶²¹, M. Shidatsu⁶²⁴, R. Shimomukai⁶¹⁸, Y. Sugawara⁶¹⁸, S. Sugita⁶²⁰,
M. Sugizaki⁶²⁴, Y. Tachibana⁶²⁰, Y. Takao⁶²⁴, A. Tanimoto⁶²², H. Tomida⁶¹⁸, Y. Tsuboi⁶²⁵, H. Tsunemi⁶²⁸, Y. Ueda⁶²²,
S. Ueno⁶¹⁸, S. Yamada⁶²², K. Yamaoka⁶²⁹, M. Yamauchi⁶¹⁹, F. Yatabe⁶²⁴, T. Yoneyama⁶²⁸, T. Yoshii⁶²⁰,
(The MAXI Team),
D. M. Coward⁶³⁰, H. Crisp⁶³⁰, D. Macpherson⁶³⁰, I. Andreoni⁶³¹, R. Laugier⁶³², K. Noysena^{632,633}, A. Klotz⁶³³,
B. Gendre^{632,634}, P. Thierry⁶³⁵, D. Turpin⁶³⁰,
(TZAC Consortium),
M. Im⁶³⁶, C. Choi⁶³⁶, J. Kim⁶³⁶, Y. Yoon⁶³⁶, G. Lim⁶³⁶, S.-K. Lee⁶³⁶, C.-U. Lee⁶³⁷, S.-L. Kim⁶³⁷, S.-W. Ko⁶³⁷, J. Joe⁶³⁷,
M.-K. Kwon⁶³⁷, P.-J. Kim⁶³⁷, S.-K. Lim⁶³⁷, J.-S. Choi⁶³⁷,
(KU Collaboration),
J. P. U. Fynbo³²⁸, D. Malesani³²⁸, D. Xu⁶³⁸,
(Nordic Optical Telescope),
S. J. Smartt⁶³⁹, A. Jerkstrand⁴²⁵, E. Kankare⁶³⁹, S. A. Sim⁶³⁹, M. Fraser¹⁶⁸, C. Inserra⁶⁴⁰, K. Maguire⁶³⁹, G. Leloudas³²⁸,
M. Magee⁶³⁹, L. J. Shingles⁶³⁹, K. W. Smith⁶³⁹, D. R. Young⁶³⁹, R. Kotak⁶³⁹, A. Gal-Yam⁶⁴¹, J. D. Lyman⁶⁴²,
D. S. Homan⁶⁴³, C. Agliozzo^{644,645}, J. P. Anderson⁶⁴⁶, C. R. Angus⁶⁴⁰, C. Ashall⁶¹¹, C. Barbarino⁶⁴⁷, F. E. Bauer^{648,645,649},
M. Berton^{650,651}, M. T. Botticella⁶⁵², M. Bulla⁶⁵³, G. Cannizzaro⁶⁵⁴, R. Cartier⁶⁴⁰, A. Cikota⁶⁵⁵, P. Clark⁶³⁹, A. De Cia⁶⁵⁵,
M. Della Valle^{652,656}, M. Dennefeld⁶⁵⁷, L. Dessart⁶⁵⁸, G. Dimitriadis⁶⁴⁰, N. Elias-Rosa⁶⁵⁹, R. E. Firth⁶⁴⁰, A. Flörs^{655,425},
C. Frohmaier⁶⁶⁰, L. Galbany⁶⁶¹, S. González-Gaitán⁶⁶², M. Gromadzki⁶⁶³, C. P. Gutiérrez⁶⁴⁰, A. Hamanowicz^{655,663},
J. Harmanen⁶⁶⁴, K. E. Heintz^{546,328}, M.-S. Hernandez⁶⁶⁵, S. T. Hodgkin⁶⁶⁶, I. M. Hook⁶⁶⁷, L. Izzo⁶⁶⁸, P. A. James⁶¹¹,
P. G. Jonker^{654,66}, W. E. Kerzendorfer⁶⁵⁵, Z. Kostrzewa-Rutkowska^{654,66}, M. Kromer^{669,670}, H. Kuncarayakti^{671,664},
A. Lawrence⁶⁴³, I. Manulis⁶⁴¹, S. Mattila⁶⁶⁴, O. McBrien⁶³⁹, A. Müller⁶⁷², J. Nordin⁶⁷³, D. O'Neill⁶³⁹, F. Onori⁶⁵⁴,
J. T. Palmerio⁶⁷⁴, A. Pastorello⁶⁷⁵, F. Patat⁶⁵⁵, G. Pignata^{644,645}, P. Podsiadlowski⁶⁷⁶, A. Razza^{646,677}, T. Reynolds⁶⁶⁴,
R. Roy⁶⁴⁷, A. J. Ruiter^{678,532,679}, K. A. Rybicki⁶⁶³, L. Salmon¹⁶⁸, M. L. Pumo^{680,675,681}, S. J. Prentice⁶¹¹,
I. R. Seitzzahl^{678,532}, M. Smith⁶⁴⁰, J. Sollerman⁶⁴⁷, M. Sullivan⁶⁴⁰, H. Szegedi⁶⁸², F. Taddia⁶⁴⁷, S. Taubenberger^{655,425},
G. Terreran^{349,675}, B. Van Soelen⁶⁸², J. Vos⁶⁶⁵, N. A. Walton⁶⁶⁶, D. E. Wright⁶⁸³, Ł. Wyrzykowski⁶⁶³, O. Yaron⁶⁴¹,
(ePESSTO),
T.-W. Chen⁶⁸⁴, T. Krühler⁶⁸⁴, P. Schady⁶⁸⁴, P. Wiseman⁶⁸⁴, J. Greiner⁶⁸⁴, A. Rau⁶⁸⁴, T. Schweyer⁶⁸⁴, S. Klose⁶⁸⁵,
A. Nicuesa Guelbenzu⁶⁸⁵,
(GROND),
N. T. Palliyaguru⁶⁸⁶,
(Texas Tech University),
M. M. Shara^{687,361}, T. Williams⁶⁸⁸, P. Vaisanen^{688,689}, S. B. Potter⁶⁸⁸, E. Romero Colmenero^{688,689}, S. Crawford^{688,689},
D. A. H. Buckley⁶⁸⁸, J. Mao⁴⁴⁰,
(SALT Group),
M. C. Díaz⁶⁹⁰, L. M. Macri⁶⁹¹, D. García Lambas⁶⁹², C. Mendes de Oliveira⁶⁹³, J. L. Nilo Castellón^{694,695}, T. Ribeiro⁶⁹⁶,
B. Sánchez⁶⁹², W. Schoenell^{693,697}, L. R. Abramo⁶⁹⁸, S. Akras⁶⁹⁹, J. S. Alcaniz⁶⁹⁹, R. Artola⁶⁹², M. Beroiz⁶⁹⁰, S. Bonoli⁷⁰⁰,
J. Cabral⁶⁹², R. Camuccio⁶⁹⁰, V. Chavushyan⁷⁰¹, P. Coelho⁶⁹³, C. Colazo⁶⁹², M. V. Costa-Duarte⁶⁹³, H. Cuevas Larenas⁶⁹⁵,
M. Domínguez Romero⁶⁹², D. Dultzin⁷⁰², D. Fernández⁷⁰³, J. García⁶⁹⁰, C. Girardini⁶⁹², D. R. Gonçalves⁷⁰⁴,
T. S. Gonçalves⁷⁰⁴, S. Gurovich⁶⁹², Y. Jiménez-Teja⁶⁹⁹, A. Kanaan⁶⁹⁷, M. Lares⁶⁹², R. Lopes de Oliveira^{696,705},
O. López-Cruz⁷⁰¹, R. Melia⁶⁹², A. Molino⁶⁹³, N. Padilla⁷⁰³, T. Peñuela^{690,706}, V. M. Placco^{707,708}, C. Quiñones⁶⁹²,
A. Ramírez Rivera⁶⁹⁵, V. Renzi⁶⁹², L. Riguccini⁷⁰⁴, E. Ríos-López⁷⁰¹, H. Rodríguez⁶⁹², L. Sampedro⁶⁹³, M. Schneider⁶⁹²,
L. Sodre⁶⁹³, M. Starck⁶⁹², S. Torres-Flores⁶⁹⁵, M. Tornatore⁶⁹², A. Zdrożny⁶⁹⁰, M. Castillo⁶⁹⁰,
(TOROS: Transient Robotic Observatory of the South Collaboration),
A. J. Castro-Tirado^{709,710}, J. C. Tello⁷⁰⁹, Y.-D. Hu⁷⁰⁹, B.-B. Zhang⁷⁰⁹, R. Cunniffe⁷⁰⁹, A. Castellón⁷¹¹, D. Hiriart⁷¹²,
M. D. Caballero-García⁷¹³, M. Jelínek⁷¹⁴, P. Kubánek⁷¹⁵, C. Pérez del Pulgar⁷¹⁰, I. H. Park⁷¹⁶, S. Jeong⁷¹⁶,
J. M. Castro Cerón⁷¹⁷, S. B. Pandey⁷¹⁸, P. C. Yock⁷¹⁹, R. Querel⁷²⁰, Y. Fan⁷²¹, C. Wang⁷²¹,
(The BOOTES Collaboration),
A Beardsley⁷²², I. S. Brown⁴⁹⁹, B. Crosse⁵⁰¹, D. Emrich⁵⁰¹, T. Franzen⁵⁰¹, B. M. Gaensler⁷²³, L. Horsley⁵⁰¹,
M. Johnston-Hollitt⁷²⁴, D. Kenney⁵⁰¹, M. F. Morales⁷²⁵, D. Pallot⁷²⁶, M. Sokolowski^{501,498,727}, K. Steele⁵⁰¹,
S. J. Tingay^{501,498}, C. M. Trott^{501,498}, M. Walker⁵⁰¹, R. Wayth^{501,498}, A. Williams⁵⁰¹, C. Wu⁷²⁶,
(MWA: Murchison Widefield Array),

- A. Yoshida⁷²⁸, T. Sakamoto⁷²⁸, Y. Kawakubo⁷²⁸, K. Yamaoka⁷²⁹, I. Takahashi⁷³⁰, Y. Asaoka⁷³¹, S. Ozawa⁷³¹, S. Torii⁷³¹, Y. Shimizu⁷³², T. Tamura⁷³², W. Ishizaki⁷³³, M. L. Cherry⁷³⁴, S. Ricciarini⁷³⁴, A. V. Penacchioni⁷³⁵, P. S. Marrochiesi⁷³⁵,
(The CALET Collaboration),
A. S. Pozanenko^{736,737,738}, A. A. Volnova⁷³⁶, E. D. Mazaeva⁷³⁶, P. Yu. Minaev⁷³⁶, M. A. Krugov⁷³⁹, A. V. Kusakin⁷³⁹,
I. V. Reva⁷³⁹, A. S. Moskvitin⁷⁴⁰, V. V. Rumyantsev⁷⁴¹, R. Inasaridze⁷⁴², E. V. Klunko⁷⁴³, N. Tungalag⁷⁴⁴,
S. E. Schmalz⁷⁴⁵, O. Burhonov⁷⁴⁶,
(IKI-GW Follow-up Collaboration),
H. Abdalla⁷⁴⁷, A. Abramowski⁷⁴⁸, F. Aharonian^{749,750,751}, F. Ait Benkhali⁷⁴⁹, E. O. Angüner⁷⁵², M. Arakawa⁷⁵³, M. Arrieta⁷⁵⁴,
P. Aubert⁷⁵⁵, M. Backes⁷⁵⁶, A. Balzer⁷⁵⁷, M. Barnard⁷⁴⁷, Y. Becherini⁷⁵⁸, J. Becker Tjus⁷⁵⁹, D. Berge⁷⁶⁰, S. Bernhard⁷⁶¹,
K. Bernlöhr⁷⁴⁹, R. Blackwell⁷⁶², M. Böttcher⁷⁴⁷, C. Boisson⁷⁵⁴, J. Bolmont⁷⁶³, S. Bonnefoy¹⁸³, P. Bordas⁷⁴⁹, J. Bregeon⁷⁶⁴,
F. Brun⁷⁶⁵, P. Brun⁷⁶⁶, M. Bryan⁷⁵⁷, M. Büchele¹⁸⁹, T. Bulik⁷⁶⁷, M. Capasso⁷⁶⁸, S. Caroff⁴⁷⁰, A. Carosi⁷⁵⁵,
S. Casanova^{752,746}, M. Cerruti⁷⁶³, N. Chakraborty⁷⁴⁶, R. C. G. Chaves⁷⁶⁴, A. Chen⁷⁶⁹, J. Chevalier⁷⁵⁵, S. Colafrancesco⁷⁶⁹,
B. Condon⁷⁶⁵, J. Conrad⁷⁷⁰, I. D. Davids⁷⁵⁶, J. Decock⁷⁶⁶, C. Deil⁷⁴⁶, J. Devin⁷⁶⁴, P. deWilt⁷⁶², L. Dirson⁷⁴⁵,
A. Djannati-Atai⁷⁷¹, A. Donath⁷⁴⁶, L. O'C. Drury⁷⁵⁰, K. Dutson⁷⁷², J. Dyks⁷⁷³, T. Edwards⁷⁴⁶, K. Egberts⁷⁷⁴, G. Emery⁷⁶³,
J.-P. Ernenwein⁷⁷⁵, S. Eschbach¹⁸⁹, C. Farnier^{770,758}, S. Fegan⁴⁷⁰, M. V. Fernandes⁷⁴⁵, A. Fiasson⁷⁵⁵, G. Fontaine⁴⁷⁰,
S. Funk¹⁸⁹, M. Füssling¹⁸³, S. Gabici⁷⁷¹, Y. A. Gallant⁷⁶⁴, T. Garrigoux⁷⁴⁴, F. Gaté⁷⁵⁵, G. Giavitto¹⁸³, B. Giebels⁴⁷⁰,
D. Glawion⁷⁷⁶, J. F. Glicenstein⁷⁶⁶, D. Gottschall⁷⁶⁸, M.-H. Grondin⁷⁶⁵, J. Hahn⁷⁴⁶, M. Haupt¹⁸³, J. Hawkes⁷⁶²,
G. Heinzlmann⁷⁴⁵, G. Henri⁷⁷⁷, G. Hermann⁷⁴⁶, J. A. Hinton⁷⁴⁶, W. Hofmann⁷⁴⁶, C. Hoischen⁷⁷⁴, T. L. Holch⁷⁷⁸,
M. Holler⁷⁶¹, D. Horns⁷⁴⁵, A. Ivascenko⁷⁴⁴, H. Iwasaki⁷⁵³, A. Jacholkowska⁷⁶³, M. Jamroz⁷⁷⁹, D. Jankowsky¹⁸⁹,
F. Jankowsky⁷⁷⁶, M. Jingo⁷⁶⁹, L. Jouvin⁷⁷¹, I. Jung-Richardt¹⁸⁹, M. A. Kastendieck⁷⁴⁵, K. Katarzyński⁷⁸⁰,
M. Katsuragawa^{781,763}, D. Kerszberg⁷⁶³, D. Khangulyan⁷⁵³, B. Khélifi⁷⁷¹, J. King⁷⁴⁶, S. Klepser¹⁸³, D. Klochkov⁷⁶⁸,
W. Kluźniak⁷⁷³, Nu. Komin⁷⁶⁹, K. Kosack⁷⁶⁶, S. Krakau⁷⁵⁹, M. Kraus¹⁸⁹, P. P. Krüger⁷⁴⁴, H. Laffon⁷⁶⁵, G. Lamanna⁷⁵⁵,
J. Lau⁷⁶², J.-P. Lees⁷⁵⁵, J. Lefaucheur⁷⁵⁴, A. Lemièrre⁷⁷¹, M. Lemoine-Goumard⁷⁶⁵, J.-P. Lenain⁷⁶³, E. Leser⁷⁷⁴, T. Lohse⁷⁷⁸,
M. Lorentz⁷⁶⁶, R. Liu⁷⁴⁶, I. Lypova¹⁸³, D. Malyshev⁷⁶⁸, V. Marandon⁷⁴⁶, A. Marcowith⁷⁶⁴, C. Mariaud⁴⁷⁰, R. Marx⁷⁴⁶,
G. Maurin⁷⁵⁵, N. Maxted⁷⁶², M. Mayer⁷⁷⁸, P. J. Meintjes⁷⁸², M. Meyer⁷⁷⁰, A. M. W. Mitchell⁷⁴⁶, R. Moderski⁷⁷³,
M. Mohamed⁷⁷⁶, L. Mohrmann¹⁸⁹, K. Morā⁷⁷⁰, E. Moulin⁷⁶⁶, T. Murach¹⁸³, S. Nakashima⁷⁸¹, M. de Naurois⁴⁷⁰,
H. Ndiyavala⁷⁴⁴, F. Niederwanger⁷⁶¹, J. Niemiec⁷⁵², L. Oakes⁷⁷⁸, P. O'Brien⁷⁷², H. Odaka⁷⁸¹, S. Ohm¹⁸³, M. Ostrowski⁷⁷⁹,
I. Oya¹⁸³, M. Padovani⁷⁶⁴, M. Panter⁷⁴⁶, R. D. Parsons⁷⁴⁶, N. W. Pekeur⁷⁴⁴, G. Pelletier⁷⁷⁷, C. Perennes⁷⁶³, P.-O. Petrucci⁷⁷⁷,
B. Peyaud⁷⁶⁶, Q. Piel⁷⁵⁵, S. Pita⁷⁷¹, V. Poireau⁷⁵⁵, H. Poon⁷⁴⁶, D. Prokhorov⁷⁵⁸, H. Prokoph⁷⁶⁰, G. Pühlhofer⁷⁶⁸,
M. Punch^{771,758}, A. Quirrenbach⁷⁷⁶, S. Raab¹⁸⁹, R. Rauth⁷⁶¹, A. Reimer⁷⁶¹, O. Reimer⁷⁶¹, M. Renaud⁷⁶⁴, R. de los Reyes⁷⁴⁶,
F. Rieger^{746,783}, L. Rinchuso⁷⁶⁶, C. Romoli⁷⁵⁰, G. Rowell⁷⁶², B. Rudak⁷⁷³, C. B. Rulten⁷⁵⁴, V. Sahakian^{784,751}, S. Saito⁷⁵³,
D. A. Sanchez⁷⁵⁵, A. Santangelo⁷⁶⁸, M. Sasaki¹⁸⁹, R. Schlickeiser⁷⁵⁹, F. Schüssler⁷⁶⁶, A. Schulz¹⁸³, U. Schwanke⁷⁷⁸,
S. Schwemmer⁷⁷⁶, M. Seglar-Arroyo⁷⁶⁶, M. Settimo⁷⁶³, A. S. Seyffert⁷⁴⁴, N. Shafi⁷⁶⁹, I. Shilon¹⁸⁹, K. Shiningayamwe⁷⁵⁶,
R. Simoni⁷⁵⁷, H. Sol⁷⁵⁴, F. Spanier⁷⁴⁴, M. Spir-Jacob⁷⁷¹, Ł. Stawarz⁷⁷⁹, R. Steenkamp⁷⁵⁶, C. Stegmann^{774,183}, C. Steppa⁷⁷⁴,
I. Sushch⁷⁴⁴, T. Takahashi⁷⁸¹, J.-P. Tavernet⁷⁶³, T. Tavernier⁷⁷¹, A. M. Taylor¹⁸³, R. Terrier⁷⁷¹, L. Tibaldo⁷⁴⁶, D. Tiziani¹⁸⁹,
M. Tluczykont⁷⁴⁵, C. Trichard⁷⁷⁵, M. Tsirou⁷⁶⁴, N. Tsuji⁷⁵³, R. Tuffs⁷⁴⁶, Y. Uchiyama⁷⁵³, D. J. van der Walt⁷⁴⁴,
C. van Eldik¹⁸⁹, C. van Rensburg⁷⁴⁴, B. van Soelen⁷⁸², G. Vasileiadis⁷⁶⁴, J. Veh¹⁸⁹, C. Venter⁷⁴⁴, A. Viana⁷⁴⁶, P. Vincent⁷⁶³,
J. Vink⁷⁵⁷, F. Voisin⁷⁶², H. J. Völk⁷⁴⁶, T. Vuillaume⁷⁵⁵, Z. Wadiasingh⁷⁴⁴, S. J. Wagner⁷⁷⁶, P. Wagner⁷⁷⁸, R. M. Wagner⁷⁷⁰,
R. White⁷⁴⁶, A. Wierzcholska⁷⁵², P. Willmann¹⁸⁹, A. Wörnlein¹⁸⁹, D. Wouters⁷⁶⁶, R. Yang⁷⁴⁶, D. Zaborov⁴⁷⁰, M. Zacharias⁷⁴⁴,
R. Zanin⁷⁴⁶, A. A. Zdziarski⁷⁷³, A. Zech⁷⁵⁴, F. Zefi⁴⁷⁰, A. Ziegler¹⁸⁹, J. Zorn⁷⁴⁶, N. Żywucka⁷⁷⁹,
(H.E.S.S. Collaboration),
R. P. Fender⁷⁸⁵, J. W. Broderick⁵⁴¹, A. Rowlinson^{786,541}, R. A. M. J. Wijers⁷⁸⁶, A. J. Stewart⁷⁸⁵, S. ter Veen⁵⁴¹,
A. Shulevski⁵⁴¹,
(LOFAR Collaboration),
M. Kavic⁷⁸⁷, J. H. Simonetti⁷⁸⁸, C. League⁷⁸⁷, J. Tsai⁷⁸⁸, K. S. Obenberger⁷⁸⁹, K. Nathaniel⁷⁸⁸, G. B. Taylor⁷⁹⁰,
J. D. Dowell⁷⁹⁰, S. L. Liebling⁷⁹¹, J. A. Estes⁷⁸⁷, M. Lippert⁷⁸⁷, I. Sharma⁷⁸⁷, P. Vincent⁷⁸⁷, B. Farella⁷⁸⁷,
(LWA: Long Wavelength Array),
A. U. Abeysekara⁷⁹², A. Albert⁷⁹³, R. Alfaro⁷⁹⁴, C. Alvarez⁷⁹⁵, R. Arceo⁷⁹⁵, J. C. Arteaga-Velázquez⁷⁹⁶, D. Avila Rojas⁷⁹⁴,
H. A. Ayala Solares⁷⁹⁷, A. S. Barber⁷⁹², J. Becerra Gonzalez⁵⁰, A. Becerril⁷⁹⁴, E. Belmont-Moreno⁷⁹⁴, S. Y. BenZvi⁷⁹⁸,
D. Berley⁷⁹⁹, A. Bernal⁸⁰⁰, J. Braun⁸⁰¹, C. Brisbois⁷⁹⁷, K. S. Caballero-Mora⁷⁹⁵, T. Capistrán⁸⁰², A. Carramiñana⁸⁰²,
S. Casanova⁸⁰³, M. Castillo⁷⁹⁶, U. Cotti⁷⁹⁶, J. Cotzomi⁸⁰⁴, S. Coutiño de León⁸⁰², C. De León⁸⁰⁴, E. De la Fuente⁸⁰⁵,
R. Diaz Hernandez⁸⁰², S. Dichiarā⁸⁰⁰, B. L. Dingus⁷⁹³, M. A. DuVernois⁸⁰¹, J. C. Díaz-Vélez^{805,801}, R. W. Ellsworth⁸⁰⁶,
K. Engel⁷⁹⁹, O. Enríquez-Rivera⁸⁰⁷, D. W. Fiorino⁷⁹⁹, H. Fleischhack⁷⁹⁷, N. Fraija⁸⁰⁰, J. A. García-González⁷⁹⁴, F. Garfias⁸⁰⁰,
M. Gerhardt⁷⁹⁷, A. González Muñoz⁷⁹⁴, M. M. González⁸⁰⁰, J. A. Goodman⁷⁹⁹, Z. Hampel-Arias⁸⁰¹, J. P. Harding⁷⁹³,
S. Hernandez⁷⁹⁴, A. Hernandez-Almada⁷⁹⁴, B. Hona⁷⁹⁷, P. Hüntemeyer⁷⁹⁷, A. Iriarte⁸⁰⁰, A. Jardin-Blicq⁸⁰⁸, V. Joshi⁸⁰⁸,

- S. Kaufmann⁷⁹⁵, D. Kieda⁷⁹², A. Lara⁸⁰⁷, R. J. Lauer⁸⁰⁹, D. Lennarz⁸¹⁰, H. León Vargas⁷⁹⁴, J. T. Linnemann⁸¹¹, A. L. Longinotti⁸⁰², G. Luis Raya⁸¹², R. Luna-García⁸¹³, R. López-Coto⁸⁰⁸, K. Malone⁸¹⁴, S. S. Marinelli⁸¹¹, O. Martínez⁸⁰⁴, I. Martínez-Castellanos⁷⁹⁹, J. Martínez-Castro⁸¹³, H. Martínez-Huerta⁸¹⁵, J. A. Matthews⁸⁰⁹, P. Miranda-Romagnoli⁸¹⁶, E. Moreno⁸⁰⁴, M. Mostafá⁸¹⁴, L. Nellen⁸¹⁷, M. Newbold⁷⁹², M. U. Nisa⁷⁹⁸, R. Noriega-Papaqui⁸¹⁶, R. Pelayo⁸¹³, J. Pretz⁸¹⁴, E. G. Pérez-Pérez⁸¹², Z. Ren⁸⁰⁹, C. D. Rho⁷⁹⁸, C. Rivière⁷⁹⁹, D. Rosa-González⁸⁰², M. Rosenberg⁸¹⁴, E. Ruiz-Velasco⁷⁹⁴, H. Salazar⁸⁰⁴, F. Salesa Greus⁸⁰³, A. Sandoval⁷⁹⁴, M. Schneider⁸¹⁸, H. Schoorlemmer⁸⁰⁸, G. Sinnis⁷⁹³, A. J. Smith⁷⁹⁹, R. W. Springer⁷⁹², P. Surajbali⁸⁰⁸, O. Tibolla⁷⁹⁵, K. Tollefson⁸¹¹, I. Torres⁸⁰², T. N. Ukwatta⁷⁹³, T. Weisgarber⁸⁰¹, S. Westerhoff⁸⁰¹, I. G. Wisher⁸⁰¹, J. Wood⁸⁰¹, T. Yapici⁸¹¹, G. B. Yodh⁸¹⁹, P. W. Younk⁷⁹³, H. Zhou⁷⁹³, J. D. Álvarez⁷⁹⁶
- (HAWC Collaboration),
- A. Aab⁶⁶, P. Abreu⁸²⁰, M. Aglietta^{821,822}, I. F. M. Albuquerque⁸²³, J. M. Albury⁸²⁴, I. Allekotte⁸²⁵, A. Almela^{826,827}, J. Alvarez Castillo⁸²⁸, J. Alvarez-Muñiz⁸²⁹, G. A. Anastasi^{830,831}, L. Anchordoqui⁸³², B. Andrada⁸²⁶, S. Andringa⁸²⁰, C. Aramo⁸³³, N. Arsene⁸³⁴, H. Asorey^{825,835}, P. Assis⁸²⁰, G. Avila^{836,837}, A. M. Badescu⁸³⁸, A. Balaceanu⁸³⁹, F. Barbato^{840,820}, R. J. Barreira Luz⁸²⁰, K. H. Becker²⁰⁴, J. A. Bellido⁸²⁴, C. Berat⁸⁴¹, M. E. Bertaina^{822,842}, X. Bertou⁸²⁵, P. L. Biermann⁸⁴³, J. Biteau⁸⁴⁴, S. G. Blaess⁸²⁴, A. Blanco⁸²⁰, J. Blazek⁸⁴⁵, C. Bleve^{846,847}, M. Boháčová⁸⁴⁵, C. Bonifazi⁸⁴⁸, N. Borodai⁸⁴⁹, A. M. Botti^{826,850}, J. Brack⁸⁵¹, I. Brancus⁸³⁹, T. Bretz⁸⁵², A. Bridgeman⁸⁵³, F. L. Briechele⁸⁵², P. Buchholz⁸⁵⁴, A. Bueno⁸⁵⁵, S. Buitink⁶⁶, M. Buscemi^{856,857}, K. S. Caballero-Mora⁷⁹⁵, L. Caccianiga⁸⁵⁸, A. Cancio^{827,826}, F. Canfora^{14,66}, R. Caruso^{856,857}, A. Castellina^{821,822}, F. Catalani⁸⁵⁹, G. Cataldi⁸⁴⁷, L. Cazon⁸²⁰, A. G. Chavez⁸⁶⁰, J. A. Chinellato⁸⁶¹, J. Chudoba⁸⁴⁵, R. W. Clay⁸²⁴, A. C. Cobos Cerutti⁸⁶², R. Colalillo^{840,833}, A. Coleman⁸⁶³, L. Collica⁸⁶⁴, M. R. Coluccia^{846,847}, R. Conceição⁸²⁰, G. Consolati^{864,865}, F. Contreras^{836,837}, M. J. Cooper⁸²⁴, S. Coutu⁸⁶³, C. E. Covault⁸⁶⁶, J. Cronin^{867,957}, S. D'Amico^{868,847}, B. Daniel⁸⁶¹, S. Dasso^{869,870}, K. Daumiller⁸⁵⁰, B. R. Dawson⁸²⁴, J. A. Day⁸²⁴, R. M. de Almeida⁸⁷¹, S. J. de Jong^{14,66}, G. De Mauro^{14,66}, J. R. T. de Mello Neto^{848,872}, I. De Mitri^{846,847}, J. de Oliveira⁸⁷¹, V. de Souza⁸⁷³, J. Debatin⁸⁵³, O. Deligny⁸⁴⁴, M. L. Díaz Castro⁸⁶¹, F. Diogo⁸²⁰, C. Dobrigkeit⁸⁶¹, J. C. D'Olivo⁸²⁸, Q. Dorosti⁸⁵⁴, R. C. Dos Anjos⁸⁷⁴, M. T. Dova⁸⁷⁵, A. Dundovic⁸⁷⁶, J. Ebr⁸⁴⁵, R. Engel⁸⁵⁰, M. Erdmann⁸⁵², M. Erfani⁸⁵⁴, C. O. Escobar⁸⁷⁷, J. Espadanal⁸²⁰, A. Etchegoyen^{826,827}, H. Falcke^{14,66,878}, J. Farmer⁸⁶⁷, G. Farrar⁸⁷⁹, A. C. Fauth⁸⁶¹, N. Fazzini⁸⁷⁷, F. Feldbusch⁸⁸⁰, F. Fenu^{822,842}, B. Fick⁸⁸¹, J. M. Figueira⁸²⁶, A. Filipčić^{494,882}, M. M. Freire⁸⁸³, T. Fujii⁸⁶⁷, A. Fuster^{826,827}, R. Gaïor⁸⁸⁴, B. García⁸⁶², F. Gate⁸⁸⁵, H. Gemmeke⁸⁸⁰, A. Gherghel-Lascu⁸³⁹, P. L. Ghia⁸⁴⁴, U. Giaccari^{848,886}, M. Giammarchi⁸⁶⁴, M. Giller⁸⁸⁷, D. Głás⁸⁸⁸, C. Glaser⁸⁵², G. Golup⁸²⁵, M. Gómez Berisso⁸²⁵, P. F. Gómez Vitale^{836,837}, N. González^{826,850}, A. Gorgi^{821,822}, M. Gottowik²⁰⁴, A. F. Grillo^{831,954}, T. D. Grubb⁸²⁴, F. Guarino^{840,833}, G. P. Guedes⁸⁸⁹, R. Halliday⁸⁶⁶, M. R. Hampel⁸²⁶, P. Hansen⁸⁷⁵, D. Harari⁸²⁵, T. A. Harrison⁸²⁴, V. M. Harvey⁸²⁴, A. Haungs⁸⁵⁰, T. Hebbeker⁸⁵², D. Heck⁸⁵⁰, P. Heimann⁸⁵⁴, A. E. Herve⁸⁵³, G. C. Hill⁸²⁴, C. Hojvat⁸⁷⁷, E. Holt^{850,826}, P. Homola⁸⁴⁹, J. R. Hörandel^{14,66}, P. Horvath⁸⁹⁰, M. Hrabovský⁸⁹⁰, T. Huege⁸⁵⁰, J. Hulsman^{826,850}, A. Insolia^{856,857}, P. G. Isar⁸³⁴, I. Jandt²⁰⁴, J. A. Johnsen⁸⁹¹, M. Josebachuili⁸²⁶, J. Jurysek⁸⁴⁵, A. Kääpä²⁰⁴, K. H. Kampert²⁰⁴, B. Keilhauer⁸⁵⁰, N. Kemmerich⁸²³, J. Kemp⁸⁵², R. M. Kieckhafer⁸⁸¹, H. O. Klages⁸⁵⁰, M. Kleifges⁸⁸⁰, J. Kleinfeller⁸³⁶, R. Krause⁸⁵², N. Krohm²⁰⁴, D. Kuempel²⁰⁴, G. Kukec Mezek⁴⁹⁴, N. Kunka⁸⁸⁰, A. Kuotb Awad⁸⁵³, B. L. Lago⁸⁹², D. LaHurd⁸⁶⁶, R. G. Lang⁸⁷³, M. Lauscher⁸⁵², R. Legumina⁸⁸⁷, M. A. Leigui de Oliveira⁸⁹³, A. Letessier-Selvon⁸⁸⁴, I. Lhenry-Yvon⁸⁴⁴, K. Link⁸⁵³, D. Lo Presti^{856,857}, L. Lopes⁸²⁰, R. López⁸⁹⁴, A. López Casado⁸²⁹, R. Lorek⁸⁶⁶, Q. Luce⁸⁴⁴, A. Lucero⁸²⁶, M. Malacari⁸⁶⁷, M. Mallamaci^{858,864}, D. Mandat⁸⁴⁵, P. Mantsch⁸⁷⁷, A. G. Mariazzi⁸⁷⁵, I. C. Maris⁸⁹⁵, G. Marsella^{846,847}, D. Martello^{846,847}, H. Martinez⁸⁹⁶, O. Martínez Bravo⁸⁹⁴, J. J. Masías Meza⁸⁷⁰, H. J. Mathes⁸⁵⁰, S. Mathys²⁰⁴, J. Matthews², G. Matthiae^{897,898}, E. Mayotte²⁰⁴, P. O. Mazur⁸⁷⁷, C. Medina⁸⁹¹, G. Medina-Tanco⁸²⁸, D. Melo⁸²⁶, A. Meshikov⁸⁸⁰, K.-D. Merenda⁸⁹¹, S. Michal⁸⁹⁰, M. I. Micheletti⁸⁸³, L. Middendorf⁸⁵², L. Miramonti^{858,864}, B. Mitrica⁸³⁹, D. Mockler⁸⁵³, S. Mollerach⁸²⁵, F. Montanet⁸⁴¹, C. Morello^{821,822}, G. Morlino^{830,831}, A. L. Müller^{826,850}, G. Müller⁸⁵², M. A. Muller^{861,899}, S. Müller^{853,826}, R. Mussa⁸²², I. Naranjo⁸²⁵, P. H. Nguyen⁸²⁴, M. Niculescu-Oglinzanu⁸³⁹, M. Niechciol⁸⁵⁴, L. Niemiets²⁰⁴, T. Niggemann⁸⁵², D. Nitz⁸⁸¹, D. Nosek⁹⁰⁰, V. Novotny⁹⁰⁰, L. Nožka⁸⁹⁰, L. A. Núñez⁸³⁵, F. Oikonomou⁸⁶³, A. Olinto⁸⁶⁷, M. Palatka⁸⁴⁵, J. Pallotta⁹⁰¹, P. Papenbreer²⁰⁴, G. Parente⁸²⁹, A. Parra⁸⁹⁴, T. Paul⁸³², M. Pech⁸⁴⁵, F. Pedreira⁸²⁹, J. Pękala⁸⁴⁹, J. Peña-Rodríguez⁸³⁵, L. A. S. Pereira⁸⁶¹, M. Perlin⁸²⁶, L. Perrone^{846,847}, C. Peters⁸⁵², S. Petrera^{830,831}, J. Phuntsok⁸⁶³, T. Pierog⁸⁵⁰, M. Pimenta⁸²⁰, V. Pirronello^{856,857}, M. Platino⁸²⁶, M. Plum⁸⁵², J. Poh⁸⁶⁷, C. Porowski⁸⁴⁹, R. R. Prado⁸⁷³, P. Privitera⁸⁶⁷, M. Prouza⁸⁴⁵, E. J. Quel⁹⁰¹, S. Querschfeld²⁰⁴, S. Quinn⁸⁶⁶, R. Ramos-Pollan⁸³⁵, J. Rautenberg²⁰⁴, D. Ravnigani⁸²⁶, J. Ridky⁸⁴⁵, F. Riehn⁸²⁰, M. Risse⁸⁵⁴, P. Ristori⁹⁰¹, V. Rizi^{831,902}, W. Rodrigues de Carvalho⁸²³, G. Rodríguez Fernandez^{897,898}, J. Rodríguez Rojo⁸³⁶, M. J. Roncoroni⁸²⁶, M. Roth⁸⁵⁰, E. Roulet⁸²⁵, A. C. Rovero⁸⁶⁹, P. Ruehl⁸⁵⁴, S. J. Saffi⁸²⁴, A. Saftoiu⁸³⁹, F. Salamida^{902,831}, H. Salazar⁸⁹⁴, A. Saleh⁴⁹⁴, G. Salina⁸⁹⁸, F. Sánchez⁸²⁶, P. Sanchez-Lucas⁸⁵⁵, E. M. Santos⁸²³, E. Santos⁸⁴⁵, F. Sarazin⁸⁹¹, R. Sarmento⁸²⁰, C. Sarmiento-Cano⁸²⁶, R. Sato⁸³⁶, M. Schauer²⁰⁴, V. Scherini⁸⁴⁷, H. Schieler⁸⁵⁰, M. Schimp²⁰⁴, D. Schmidt^{850,826}, O. Scholten^{903,904}, P. Schovánek⁸⁴⁵, F. G. Schröder⁸⁵⁰, S. Schröder²⁰⁴, A. Schulz⁸⁵⁰, J. Schumacher⁸⁵², S. J. Sciutto⁸⁷⁵, A. Segreto^{857,905}, A. Shadkam², R. C. Shellard⁸⁸⁶, G. Sigl⁸⁷⁶, G. Silli^{826,850}, R. Šmída⁸⁵⁰, G. R. Snow⁹⁰⁶, P. Sommers⁸⁶³, S. Sonntag⁸⁵⁴, J. F. Soriano⁸³², R. Squartini⁸³⁶, D. Stanca⁸³⁹, S. Stanić⁴⁹⁴, J. Stasielak⁸⁴⁹, P. Stassi⁸⁴¹, M. Stolpovskiy⁸⁴¹, F. Strafella^{846,847}, A. Streich⁸⁵³

F. Suarez^{826,827}, M. Suarez-Durán⁸³⁵, T. Sudholz⁸²⁴, T. Suomijärvi⁸⁴⁴, A. D. Supanitsky⁸⁶⁹, J. Šupík⁸⁹⁰, J. Swain⁹⁰⁷, Z. Szadkowski⁸⁸⁸, A. Taboada⁸⁵⁰, O. A. Taborda⁸²⁵, C. Timmermans^{14,66}, C. J. Todero Peixoto⁸⁵⁹, L. Tomankova⁸⁵⁰, B. Tomé⁸²⁰, G. Torralba Elipse⁸²⁹, P. Travnicek⁸⁴⁵, M. Trini⁴⁹⁴, M. Tueros⁸⁷⁵, R. Ulrich⁸⁵⁰, M. Unger⁸⁵⁰, M. Urban⁸⁵², J. F. Valdés Galicia⁸²⁸, I. Valiño⁸²⁹, L. Valore^{840,833}, G. van Aar⁶⁶, P. van Bodegom⁸²⁴, A. M. van den Berg⁹⁰³, A. van Vliet⁶⁶, E. Varela⁸⁹⁴, B. Vargas Cárdenas⁸²⁸, R. A. Vázquez⁸²⁹, D. Veberič⁸⁵⁰, C. Ventura⁸⁷², I. D. Vergara Quispe⁸⁷⁵, V. Verzi⁸⁹⁸, J. Vicha⁸⁴⁵, L. Villaseñor⁸⁶⁰, S. Vorobiov⁴⁹⁴, H. Wahlberg⁸⁷⁵, O. Wainberg^{826,827}, D. Walz⁸⁵², A. A. Watson⁹⁰⁸, M. Weber⁸⁸⁰, A. Weindl⁸⁵⁰, M. Wiedeński⁸⁸⁸, L. Wiencke⁸⁹¹, H. Wilczyński⁸⁴⁹, M. Wirtz⁸⁵², D. Wittkowski²⁰⁴, B. Wundheiler⁸²⁶, L. Yang⁴⁹⁴, A. Yushkov⁸⁴⁵, E. Zas⁸²⁹, D. Zavrtanik^{494,882}, M. Zavrtanik^{494,882}, A. Zepeda⁸⁹⁶, B. Zimmermann⁸⁸⁰, M. Ziolkowski⁸⁵⁴, Z. Zong⁸⁴⁴, F. Zuccarello^{909,857},
 (The Pierre Auger Collaboration),
 S. Kim^{548,910}, S. Schulze⁹¹¹, F. E. Bauer^{649,910,912}, J. M. Corral-Santana⁹¹³, I. de Gregorio-Monsalvo^{913,914}, J. González-López⁹¹⁰, D. H. Hartmann⁹¹⁵, C. H. Ishwara-Chandra⁹¹⁶, S. Martín^{913,914}, A. Mehner⁹¹³, K. Misra⁹¹⁷, M. J. Michałowski⁹¹⁸, L. Resmi⁹¹⁹,
 (ALMA Collaboration),
 Z. Paragi⁹²⁰, I. Agudo⁹²¹, T. An^{922,923}, R. Beswick⁹²⁴, C. Casadio⁹²⁵, S. Frey⁹²⁶, P. Jonker^{66,927}, M. Kettenis⁹²⁰, B. Marcote⁹²⁰, J. Moldon⁹²⁴, A. Szomoru⁹²⁰, H. J. van Langevelde^{920,928}, J. Yang⁹²⁹,
 (Euro VLBI Team),
 A. Cwiek⁷²⁷, M. Cwiok⁹³⁰, H. Czyrkowski⁹³⁰, R. Dabrowski⁹³⁰, G. Kasprócz⁹³¹, L. Mankiewicz⁹³², K. Nawrocki⁷²⁷, R. Opiela⁹³², L. W. Piotrowski⁹³³, G. Wrochna⁷²⁷, M. Zaremba⁹³⁰, A. F. Żarnęcki⁹³⁰,
 (Pi of the Sky Collaboration),
 D. Haggard⁹³⁴, M. Nynka⁹³⁴, J. J. Ruan⁹³⁴,
 (The Chandra Team at McGill University),
 P. A. Bland⁹³⁵, T. Boller⁵⁰¹, H. A. R. Devillepoix⁹³⁵, J. S. de Gois⁵⁰¹, P. J. Hancock⁵⁰¹, R. M. Howie⁹³⁶, J. Paxman⁹³⁶, E. K. Sansom⁹³⁵, M. C. Towner⁹³⁵,
 (DFN: Desert Fireball Network),
 J. Tonry⁶¹⁷, M. Coughlin⁹³⁷, C. W. Stubbs⁹³⁸, L. Denneau⁶¹⁷, A. Heinze⁶¹⁷, B. Stalder⁹³⁹, H. Weiland⁶¹⁷,
 (ATLAS),
 R. P. Eatough⁹⁴⁰, M. Kramer⁹⁴⁰, A. Kraus⁹⁴⁰,
 (High Time Resolution Universe Survey),
 E. Troja^{941,942}, L. Piro¹⁷², J. Becerra González^{943,944}, N. R. Butler⁷²², O. D. Fox⁹⁴⁵, H. G. Khandrika⁹⁴⁵, A. Kutyrev^{941,942}, W. H. Lee^{946,298}, R. Ricci⁹⁴⁷, R. E. Ryan Jr.⁹⁴⁵, R. Sánchez-Ramírez¹⁷², S. Veilleux^{942,290}, A. M. Watson⁹⁴⁶, M. H. Wieringa⁹⁴⁸, J. M. Burgess⁹⁴⁹, H. van Eerten⁹⁵⁰, C. J. Fontes⁹⁵¹, C. L. Fryer⁹⁵¹, O. Korobkin⁹⁵¹, R. T. Wollaeger⁹⁵¹,
 (RIMAS and RATIR),
 and
 F. Camilo⁹⁵², A. R. Foley⁹⁵², S. Goedhart⁹⁵², S. Makhathini⁹⁵², N. Oozeer⁹⁵², O. M. Smirnov⁹⁵², R. P. Fender⁶⁶, and P. A. Woudt⁹⁵³
 (SKA South Africa/MeerKAT)

¹ LIGO, California Institute of Technology, Pasadena, CA 91125, USA² Louisiana State University, Baton Rouge, LA 70803, USA³ Università di Salerno, Fisciano, I-84084 Salerno, Italy⁴ INFN, Sezione di Napoli, Complesso Universitario di Monte S. Angelo, I-80126 Napoli, Italy⁵ University of Florida, Gainesville, FL 32611, USA⁶ OzGrav, School of Physics & Astronomy, Monash University, Clayton, VIC 3800, Australia⁷ LIGO Livingston Observatory, Livingston, LA 70754, USA⁸ Laboratoire d'Annecy-le-Vieux de Physique des Particules (LAPP), Université Savoie Mont Blanc, CNRS/IN2P3, F-74941 Annecy, France⁹ University of Sannio at Benevento, I-82100 Benevento, Italy and INFN, Sezione di Napoli, I-80100 Napoli, Italy¹⁰ Albert-Einstein-Institut, Max-Planck-Institut für Gravitationsphysik, D-30167 Hannover, Germany¹¹ The University of Mississippi, University, MS 38677, USA¹² NCSA, University of Illinois at Urbana-Champaign, Urbana, IL 61801, USA¹³ University of Cambridge, Cambridge CB2 1TN, UK¹⁴ Nikhef, Science Park, 1098 XG Amsterdam, The Netherlands¹⁵ LIGO, Massachusetts Institute of Technology, Cambridge, MA 02139, USA¹⁶ Instituto Nacional de Pesquisas Espaciais, 12227-010 São José dos Campos, São Paulo, Brazil¹⁷ Gran Sasso Science Institute (GSSI), I-67100 L'Aquila, Italy¹⁸ INFN, Laboratori Nazionali del Gran Sasso, I-67100 Assergi, Italy¹⁹ Inter-University Centre for Astronomy and Astrophysics, Pune 411007, India²⁰ International Centre for Theoretical Sciences, Tata Institute of Fundamental Research, Bengaluru 560089, India²¹ University of Wisconsin-Milwaukee, Milwaukee, WI 53201, USA²² Leibniz Universität Hannover, D-30167 Hannover, Germany²³ Università di Pisa, I-56127 Pisa, Italy

- ²⁴ INFN, Sezione di Pisa, I-56127 Pisa, Italy
- ²⁵ OzGrav, Australian National University, Canberra, ACT 0200, Australia
- ²⁶ Laboratoire des Matériaux Avancés (LMA), CNRS/IN2P3, F-69622 Villeurbanne, France
- ²⁷ SUPA, University of the West of Scotland, Paisley PA1 2BE, UK
- ²⁸ LAL, Univ. Paris-Sud, CNRS/IN2P3, Université Paris-Saclay, F-91898 Orsay, France
- ²⁹ California State University Fullerton, Fullerton, CA 92831, USA
- ³⁰ European Gravitational Observatory (EGO), I-56021 Cascina, Pisa, Italy
- ³¹ Chennai Mathematical Institute, Chennai 603103, India
- ³² Università di Roma Tor Vergata, I-00133 Roma, Italy
- ³³ INFN, Sezione di Roma Tor Vergata, I-00133 Roma, Italy
- ³⁴ Universität Hamburg, D-22761 Hamburg, Germany
- ³⁵ INFN, Sezione di Roma, I-00185 Roma, Italy
- ³⁶ Cardiff University, Cardiff CF24 3AA, UK
- ³⁷ Embry-Riddle Aeronautical University, Prescott, AZ 86301, USA
- ³⁸ Albert-Einstein-Institut, Max-Planck-Institut für Gravitationsphysik, D-14476 Potsdam-Golm, Germany
- ³⁹ APC, AstroParticule et Cosmologie, Université Paris Diderot, CNRS/IN2P3, CEA/Irfu, Observatoire de Paris, Sorbonne Paris Cité, F-75205 Paris Cedex 13, France
- ⁴⁰ Korea Institute of Science and Technology Information, Daejeon 34141, Korea
- ⁴¹ West Virginia University, Morgantown, WV 26506, USA
- ⁴² Università di Perugia, I-06123 Perugia, Italy
- ⁴³ INFN, Sezione di Perugia, I-06123 Perugia, Italy
- ⁴⁴ Syracuse University, Syracuse, NY 13244, USA
- ⁴⁵ University of Minnesota, Minneapolis, MN 55455, USA
- ⁴⁶ SUPA, University of Glasgow, Glasgow G12 8QQ, UK
- ⁴⁷ LIGO Hanford Observatory, Richland, WA 99352, USA
- ⁴⁸ Caltech CaRT, Pasadena, CA 91125, USA
- ⁴⁹ Wigner RCP, RMKI, Konkoly Thege Miklós út 29-33, H-1121 Budapest, Hungary
- ⁵⁰ NASA Goddard Space Flight Center, Greenbelt, MD 20771, USA
- ⁵¹ Columbia University, New York, NY 10027, USA
- ⁵² Stanford University, Stanford, CA 94305, USA
- ⁵³ Università di Camerino, Dipartimento di Fisica, I-62032 Camerino, Italy
- ⁵⁴ Università di Padova, Dipartimento di Fisica e Astronomia, I-35131 Padova, Italy
- ⁵⁵ INFN, Sezione di Padova, I-35131 Padova, Italy
- ⁵⁶ Institute of Physics, Eötvös University, Pázmány P. s. 1/A, H-1117 Budapest, Hungary
- ⁵⁷ Nicolaus Copernicus Astronomical Center, Polish Academy of Sciences, 00-716, Warsaw, Poland
- ⁵⁸ Rochester Institute of Technology, Rochester, NY 14623, USA
- ⁵⁹ University of Birmingham, Birmingham B15 2TT, UK
- ⁶⁰ INFN, Sezione di Genova, I-16146 Genova, Italy
- ⁶¹ RRCAT, Indore MP 452013, India
- ⁶² Faculty of Physics, Lomonosov Moscow State University, Moscow 119991, Russia
- ⁶³ SUPA, University of Strathclyde, Glasgow G1 1XQ, UK
- ⁶⁴ The Pennsylvania State University, University Park, PA 16802, USA
- ⁶⁵ OzGrav, University of Western Australia, Crawley, WA 6009, Australia
- ⁶⁶ Institute of Mathematics, Astrophysics and Particle Physics, Radboud University, 6525 AJ Nijmegen, The Netherlands
- ⁶⁷ Artemis, Université Côte d'Azur, Observatoire Côte d'Azur, CNRS, CS 34229, F-06304 Nice Cedex 4, France
- ⁶⁸ Institut FOTON, CNRS, Université de Rennes 1, F-35042 Rennes, France
- ⁶⁹ Washington State University, Pullman, WA 99164, USA
- ⁷⁰ University of Oregon, Eugene, OR 97403, USA
- ⁷¹ Laboratoire Kastler Brossel, UPMC-Sorbonne Universités, CNRS, ENS-PSL Research University, Collège de France, F-75005 Paris, France
- ⁷² Carleton College, Northfield, MN 55057, USA
- ⁷³ OzGrav, University of Adelaide, Adelaide, SA 5005, Australia
- ⁷⁴ Astronomical Observatory Warsaw University, 00-478 Warsaw, Poland
- ⁷⁵ VU University Amsterdam, 1081 HV Amsterdam, The Netherlands
- ⁷⁶ University of Maryland, College Park, MD 20742, USA
- ⁷⁷ Center for Relativistic Astrophysics, Georgia Institute of Technology, Atlanta, GA 30332, USA
- ⁷⁸ Université Claude Bernard Lyon 1, F-69622 Villeurbanne, France
- ⁷⁹ Università di Napoli "Federico II," Complesso Universitario di Monte S. Angelo, I-80126 Napoli, Italy
- ⁸⁰ Dipartimento di Fisica, Università degli Studi di Genova, I-16146 Genova, Italy
- ⁸¹ RESCEU, University of Tokyo, Tokyo, 113-0033, Japan
- ⁸² Tsinghua University, Beijing 100084, China
- ⁸³ Texas Tech University, Lubbock, TX 79409, USA
- ⁸⁴ Kenyon College, Gambier, OH 43022, USA
- ⁸⁵ Departamento de Astronomía y Astrofísica, Universitat de València, E-46100 Burjassot, València, Spain
- ⁸⁶ Museo Storico della Fisica e Centro Studi e Ricerche Enrico Fermi, I-00184 Roma, Italy
- ⁸⁷ National Tsing Hua University, Hsinchu City, 30013 Taiwan, Republic of China
- ⁸⁸ Charles Sturt University, Wagga Wagga, NSW 2678, Australia
- ⁸⁹ Center for Interdisciplinary Exploration & Research in Astrophysics (CIERA), Northwestern University, Evanston, IL 60208, USA
- ⁹⁰ Canadian Institute for Theoretical Astrophysics, University of Toronto, Toronto, ON M5S 3H8, Canada
- ⁹¹ University of Chicago, Chicago, IL 60637, USA
- ⁹² Pusan National University, Busan 46241, Korea
- ⁹³ The Chinese University of Hong Kong, Shatin, NT, Hong Kong
- ⁹⁴ INAF, Osservatorio Astronomico di Padova, I-35122 Padova, Italy
- ⁹⁵ INFN, Trento Institute for Fundamental Physics and Applications, I-38123 Povo, Trento, Italy
- ⁹⁶ OzGrav, University of Melbourne, Parkville, VIC 3010, Australia
- ⁹⁷ Università di Roma "La Sapienza," I-00185 Roma, Italy

- ⁹⁸ Université Libre de Bruxelles, Brussels 1050, Belgium
- ⁹⁹ Sonoma State University, Rohnert Park, CA 94928, USA
- ¹⁰⁰ Departamento de Matemáticas, Universitat de València, E-46100 Burjassot, València, Spain
- ¹⁰¹ Montana State University, Bozeman, MT 59717, USA
- ¹⁰² Universitat de les Illes Balears, IAC3—IEEC, E-07122 Palma de Mallorca, Spain
- ¹⁰³ The University of Texas Rio Grande Valley, Brownsville, TX 78520, USA
- ¹⁰⁴ Bellevue College, Bellevue, WA 98007, USA
- ¹⁰⁵ Institute for Plasma Research, Bhat, Gandhinagar 382428, India
- ¹⁰⁶ The University of Sheffield, Sheffield S10 2TN, UK
- ¹⁰⁷ Dipartimento di Scienze Matematiche, Fisiche e Informatiche, Università di Parma, I-43124 Parma, Italy
- ¹⁰⁸ INFN, Sezione di Milano Bicocca, Gruppo Collegato di Parma, I-43124 Parma, Italy
- ¹⁰⁹ California State University, Los Angeles, 5151 State University Drive, Los Angeles, CA 90032, USA
- ¹¹⁰ Università di Trento, Dipartimento di Fisica, I-38123 Povo, Trento, Italy
- ¹¹¹ Montclair State University, Montclair, NJ 07043, USA
- ¹¹² National Astronomical Observatory of Japan, 2-21-1 Osawa, Mitaka, Tokyo 181-8588, Japan
- ¹¹³ Observatori Astronòmic, Universitat de València, E-46980 Paterna, València, Spain
- ¹¹⁴ School of Mathematics, University of Edinburgh, Edinburgh EH9 3FD, UK
- ¹¹⁵ University and Institute of Advanced Research, Koba Institutional Area, Gandhinagar Gujarat 382007, India
- ¹¹⁶ IISER-TVM, CET Campus, Trivandrum Kerala 695016, India
- ¹¹⁷ University of Szeged, Dóm tér 9, H-6720 Szeged, Hungary
- ¹¹⁸ University of Michigan, Ann Arbor, MI 48109, USA
- ¹¹⁹ Tata Institute of Fundamental Research, Mumbai 400005, India
- ¹²⁰ INAF, Osservatorio Astronomico di Capodimonte, I-80131, Napoli, Italy
- ¹²¹ Università degli Studi di Urbino “Carlo Bo,” I-61029 Urbino, Italy
- ¹²² INFN, Sezione di Firenze, I-50019 Sesto Fiorentino, Firenze, Italy
- ¹²³ Physik-Institut, University of Zurich, Winterthurerstrasse 190, CH-8057 Zurich, Switzerland
- ¹²⁴ American University, Washington, DC 20016, USA
- ¹²⁵ University of Białystok, 15-424 Białystok, Poland
- ¹²⁶ University of Southampton, Southampton SO17 1BJ, UK
- ¹²⁷ University of Washington Bothell, 18115 Campus Way NE, Bothell, WA 98011, USA
- ¹²⁸ Institute of Applied Physics, Nizhny Novgorod, 603950, Russia
- ¹²⁹ Korea Astronomy and Space Science Institute, Daejeon 34055, Korea
- ¹³⁰ Inje University Gimhae, South Gyeongsang 50834, Korea
- ¹³¹ National Institute for Mathematical Sciences, Daejeon 34047, Korea
- ¹³² NCBJ, 05-400 Świerk-Otwock, Poland
- ¹³³ Institute of Mathematics, Polish Academy of Sciences, 00656 Warsaw, Poland
- ¹³⁴ Hillsdale College, Hillsdale, MI 49242, USA
- ¹³⁵ Hanyang University, Seoul 04763, Korea
- ¹³⁶ Seoul National University, Seoul 08826, Korea
- ¹³⁷ NASA Marshall Space Flight Center, Huntsville, AL 35812, USA
- ¹³⁸ ESPCI, CNRS, F-75005 Paris, France
- ¹³⁹ Southern University and A&M College, Baton Rouge, LA 70813, USA
- ¹⁴⁰ College of William and Mary, Williamsburg, VA 23187, USA
- ¹⁴¹ Centre Scientifique de Monaco, 8 quai Antoine 1er, MC-98000, Monaco
- ¹⁴² Indian Institute of Technology Madras, Chennai 600036, India
- ¹⁴³ IISER-Kolkata, Mohanpur, West Bengal 741252, India
- ¹⁴⁴ Whitman College, 345 Boyer Avenue, Walla Walla, WA 99362 USA
- ¹⁴⁵ Indian Institute of Technology Bombay, Powai, Mumbai, Maharashtra 400076, India
- ¹⁴⁶ Scuola Normale Superiore, Piazza dei Cavalieri 7, I-56126 Pisa, Italy
- ¹⁴⁷ Université de Lyon, F-69361 Lyon, France
- ¹⁴⁸ Hobart and William Smith Colleges, Geneva, NY 14456, USA
- ¹⁴⁹ OzGrav, Swinburne University of Technology, Hawthorn, VIC 3122, Australia
- ¹⁵⁰ Janusz Gil Institute of Astronomy, University of Zielona Góra, 65-265 Zielona Góra, Poland
- ¹⁵¹ University of Washington, Seattle, WA 98195, USA
- ¹⁵² King’s College London, University of London, London WC2R 2LS, UK
- ¹⁵³ Indian Institute of Technology, Gandhinagar Ahmedabad Gujarat 382424, India
- ¹⁵⁴ Indian Institute of Technology Hyderabad, Sangareddy, Khandi, Telangana 502285, India
- ¹⁵⁵ International Institute of Physics, Universidade Federal do Rio Grande do Norte, Natal RN 59078-970, Brazil
- ¹⁵⁶ Andrews University, Berrien Springs, MI 49104, USA
- ¹⁵⁷ Università di Siena, I-53100 Siena, Italy
- ¹⁵⁸ Trinity University, San Antonio, TX 78212, USA
- ¹⁵⁹ Abilene Christian University, Abilene, TX 79699, USA
- ¹⁶⁰ Colorado State University, Fort Collins, CO 80523, USA
- ¹⁶¹ INFN Sezione di Bari, I-70126 Bari, Italy
- ¹⁶² Politecnico di Bari, I-70126 Bari BA, Italy
- ¹⁶³ Harvard-Smithsonian Center for Astrophysics, 60 Garden Street, Cambridge, MA 02138, USA
- ¹⁶⁴ University of Alabama in Huntsville, Huntsville, AL 35899, USA
- ¹⁶⁵ Universities Space Research Association, Huntsville, AL 35805, USA
- ¹⁶⁶ Jacobs Technology, Inc., Huntsville, AL 35806, USA
- ¹⁶⁷ Los Alamos National Laboratory, Los Alamos, NM 87545, USA
- ¹⁶⁸ School of Physics, O’Brien Centre for Science North, University College Dublin, Belfield, Dublin 4, Ireland
- ¹⁶⁹ Max-Planck-Institut für extraterrestrische Physik, D-85748 Garching, Germany
- ¹⁷⁰ ISDC, Department of Astronomy, University of Geneva, Chemin d’Écogia, 16 CH-1290 Versoix, Switzerland
- ¹⁷¹ European Space Research and Technology Centre (ESA/ESTEC), Keplerlaan 1, 2201 AZ Noordwijk, The Netherlands
- ¹⁷² INAF, Istituto di Astrofisica e Planetologia Spaziali, via Fosso del Cavaliere 100, I-00133 Rome, Italy

- ¹⁷³ DTU Space, National Space Institute Elektrovej, Building 327 DK-2800 Kongens Lyngby Denmark
- ¹⁷⁴ Centro de Astrobiología (CAB-CSIC/INTA, ESAC Campus), Camino bajo del Castillo S/N, E-28692 Villanueva de la Cañada, Madrid, Spain
- ¹⁷⁵ IRAP, Université de Toulouse, CNRS, UPS, CNES, 9 Av. Roche, F-31028 Toulouse, France
- ¹⁷⁶ APC, AstroParticule et Cosmologie, Université Paris Diderot, CNRS/IN2P3, CEA/Irfu, Observatoire de Paris Sorbonne Paris Cité, 10 rue Alice Domont et Léonie Duquet, F-75205 Paris Cedex 13, France.
- ¹⁷⁷ DSM/Irfu/Service d'Astrophysique, Bat. 709 Orme des Merisiers CEA Saclay, F-91191 Gif-sur-Yvette Cedex, France
- ¹⁷⁸ Space Research Institute of Russian Academy of Sciences, Profsoyuznaya 84/32, Moscow, 117997, Russia
- ¹⁷⁹ Moscow Institute of Physics and Technology, Institutskiy per. 9, Dolgoprudny, Moscow Region, 141700, Russia
- ¹⁸⁰ INFN-Istituto di Astrofisica Spaziale e Fisica Cosmica Milano, via E. Bassini 15, I-20133 Milano, Italy
- ¹⁸¹ Max Planck Institute for Astrophysics, Karl-Schwarzschild-Str. 1, Garching b. Munchen D-85741, Germany
- ¹⁸² Department of Physics, University of Adelaide, Adelaide, 5005, Australia
- ¹⁸³ DESY, D-15738 Zeuthen, Germany
- ¹⁸⁴ Dept. of Physics and Astronomy, University of Canterbury, Private Bag 4800, Christchurch, New Zealand
- ¹⁸⁵ Université Libre de Bruxelles, Science Faculty CP230, B-1050 Brussels, Belgium
- ¹⁸⁶ Niels Bohr Institute, University of Copenhagen, DK-2100 Copenhagen, Denmark
- ¹⁸⁷ Oskar Klein Centre and Dept. of Physics, Stockholm University, SE-10691 Stockholm, Sweden
- ¹⁸⁸ Département de physique nucléaire et corpusculaire, Université de Genève, CH-1211 Genève, Switzerland
- ¹⁸⁹ Friedrich-Alexander-Universität Erlangen-Nürnberg, Erlangen Centre for Astroparticle Physics, Erwin-Rommel-Str. 1, D-91058 Erlangen, Germany
- ¹⁹⁰ Department of Physics, Marquette University, Milwaukee, WI, 53201, USA
- ¹⁹¹ Dept. of Physics, Pennsylvania State University, University Park, PA 16802, USA
- ¹⁹² Dept. of Physics, Massachusetts Institute of Technology, Cambridge, MA 02139, USA
- ¹⁹³ III. Physikalisches Institut, RWTH Aachen University, D-52056 Aachen, Germany
- ¹⁹⁴ Physics Department, South Dakota School of Mines and Technology, Rapid City, SD 57701, USA
- ¹⁹⁵ Dept. of Physics, University of Alberta, Edmonton, AB T6G 2E1, Canada
- ¹⁹⁶ Dept. of Physics and Astronomy, University of California, Irvine, CA 92697, USA
- ¹⁹⁷ Institute of Physics, University of Mainz, Staudinger Weg 7, D-55099 Mainz, Germany
- ¹⁹⁸ Dept. of Physics, University of California, Berkeley, CA 94720, USA
- ¹⁹⁹ Dept. of Physics and Center for Cosmology and Astro-Particle Physics, Ohio State University, Columbus, OH 43210, USA
- ²⁰⁰ Dept. of Astronomy, Ohio State University, Columbus, OH 43210, USA
- ²⁰¹ Fakultät für Physik & Astronomie, Ruhr-Universität Bochum, D-44780 Bochum, Germany
- ²⁰² Dept. of Physics and Astronomy, University of Kansas, Lawrence, KS 66045, USA
- ²⁰³ Lawrence Berkeley National Laboratory, Berkeley, CA 94720, USA
- ²⁰⁴ Bergische Universität Wuppertal, Department of Physics, Wuppertal, Germany
- ²⁰⁵ Dept. of Physics, University of Maryland, College Park, MD 20742, USA
- ²⁰⁶ Dept. of Physics, TU Dortmund University, D-44221 Dortmund, Germany
- ²⁰⁷ Dept. of Physics, Sungkyunkwan University, Suwon 440-746, Korea
- ²⁰⁸ Dept. of Physics and Astronomy, Uppsala University, Box 516, S-75120 Uppsala, Sweden
- ²⁰⁹ Dept. of Physics and Wisconsin IceCube Particle Astrophysics Center, University of Wisconsin, Madison, WI 53706, USA
- ²¹⁰ Vrije Universiteit Brussel (VUB), Dienst ELEM, B-1050 Brussels, Belgium
- ²¹¹ SNOLAB, 1039 Regional Road 24, Creighton Mine 9, Lively, ON P3Y 1N2, Canada
- ²¹² Institut für Kernphysik, Westfälische Wilhelms-Universität Münster, D-48149 Münster, Germany
- ²¹³ Physik-department, Technische Universität München, D-85748 Garching, Germany
- ²¹⁴ Dept. of Astronomy and Astrophysics, Pennsylvania State University, University Park, PA 16802, USA
- ²¹⁵ Dept. of Physics and Astronomy, University of Rochester, Rochester, NY 14627, USA
- ²¹⁶ Dept. of Physics and Astronomy, Michigan State University, East Lansing, MI 48824, USA
- ²¹⁷ Bartol Research Institute and Dept. of Physics and Astronomy, University of Delaware, Newark, DE 19716, USA
- ²¹⁸ Dept. of Physics and Astronomy, University of Gent, B-9000 Gent, Belgium
- ²¹⁹ Institut für Physik, Humboldt-Universität zu Berlin, D-12489 Berlin, Germany
- ²²⁰ Dept. of Physics, Southern University, Baton Rouge, LA 70813, USA
- ²²¹ Dept. of Astronomy, University of Wisconsin, Madison, WI 53706, USA
- ²²² Earthquake Research Institute, University of Tokyo, Bunkyo, Tokyo 113-0032, Japan
- ²²³ Dept. of Physics and Institute for Global Prominent Research, Chiba University, Chiba 263-8522, Japan
- ²²⁴ CTSPS, Clark-Atlanta University, Atlanta, GA 30314, USA
- ²²⁵ Dept. of Physics, University of Texas at Arlington, 502 Yates Street, Science Hall Room 108, Box 19059, Arlington, TX 76019, USA
- ²²⁶ Dept. of Physics and Astronomy, Stony Brook University, Stony Brook, NY 11794-3800, USA
- ²²⁷ Université de Mons, B-7000 Mons, Belgium
- ²²⁸ Dept. of Physics and Astronomy, University of Alabama, Tuscaloosa, AL 35487, USA
- ²²⁹ Dept. of Physics, Drexel University, 3141 Chestnut Street, Philadelphia, PA 19104, USA
- ²³⁰ Dept. of Physics, University of Wisconsin, River Falls, WI 54022, USA
- ²³¹ Dept. of Physics, Yale University, New Haven, CT 06520, USA
- ²³² Dept. of Physics and Astronomy, University of Alaska Anchorage, 3211 Providence Drive, Anchorage, AK 99508, USA
- ²³³ Dept. of Physics, University of Oxford, 1 Keble Road, Oxford OX1 3NP, UK
- ²³⁴ School of Physics and Center for Relativistic Astrophysics, Georgia Institute of Technology, Atlanta, GA 30332, USA
- ²³⁵ Indian Institute of Science Education and Research, Dr. Homi Bhabha Road, Pashan, Pune 411008, India
- ²³⁶ Department of Physics, Indian Institute of Technology Bombay, Mumbai 400076, India
- ²³⁷ Physical Research Laboratory, Ahmedabad, India
- ²³⁸ Ioffe Institute, Politekhnicheskaya 26, St. Petersburg 194021, Russia
- ²³⁹ University of California-Berkeley, Space Sciences Lab, 7 Gauss Way, Berkeley, CA 94720, USA
- ²⁴⁰ Emeritus, NASA Goddard Space Flight Center, Greenbelt, MD 20771, USA
- ²⁴¹ Key Laboratory Of Particle Astrophysics, Institute Of High Energy Physics, Chinese Academy Of Sciences, Beijing 100049, China
- ²⁴² University Of Chinese Academy Of Sciences, Chinese Academy Of Sciences, Beijing 100049, China
- ²⁴³ Beijing Normal University, Beijing 100088, China
- ²⁴⁴ GRPHE, Université de Haute Alsace, Institut universitaire de technologie de Colmar, 34 rue du Grillenbreit BP 50568, F-68008 Colmar, France
- ²⁴⁵ Technical University of Catalonia, Laboratory of Applied Bioacoustics, Rambla Exposició, E-08800 Vilanova i la Geltrú, Barcelona, Spain
- ²⁴⁶ INFN—Sezione di Genova, Via Dodecaneso 33, I-16146 Genova, Italy

- ²⁴⁷ Institut d'Investigació per a la Gestió Integrada de les Zones Costaneres (IGIC), Universitat Politècnica de València. C/ Paranimf 1, E-46730 Gandia, Spain
- ²⁴⁸ Aix Marseille Univ, CNRS/IN2P3, CPPM, Marseille, France
- ²⁴⁹ APC, Univ Paris Diderot, CNRS/IN2P3, CEA/Irfu, Obs de Paris, Sorbonne Paris Cité, France
- ²⁵⁰ IFIC, Instituto de Física Corpuscular (CSIC—Universitat de València), c/ Catedrático José Beltrán, 2 E-46980 Paterna, Valencia, Spain
- ²⁵¹ LAM—Laboratoire d'Astrophysique de Marseille, Pôle de l'Étoile Site de Château-Gombert, rue Frédéric Joliot-Curie 38, F-13388 Marseille Cedex 13, France
- ²⁵² National Center for Energy Sciences and Nuclear Techniques, B.P. 1382, R. P. 10001 Rabat, Morocco
- ²⁵³ INFN—Laboratori Nazionali del Sud (LNS), Via S. Sofia 62, I-95123 Catania, Italy
- ²⁵⁴ Huygens-Kamerlingh Onnes Laboratorium, Universiteit Leiden, The Netherlands
- ²⁵⁵ Institute for Space Science, RO-077125 Bucharest, Măgurele, Romania
- ²⁵⁶ Universiteit van Amsterdam, Instituut voor Hoge-Energie Fysica, Science Park 105, 1098 XG Amsterdam, The Netherlands
- ²⁵⁷ INFN—Sezione di Roma, P.le Aldo Moro 2, I-00185 Roma, Italy
- ²⁵⁸ Dipartimento di Fisica dell'Università La Sapienza, P.le Aldo Moro 2, I-00185 Roma, Italy
- ²⁵⁹ Gran Sasso Science Institute, Viale Francesco Crispi 7, I-00167 L'Aquila, Italy
- ²⁶⁰ University Mohammed V in Rabat, Faculty of Sciences, 4 av. Ibn Battouta, B.P. 1014, 10000, Rabat, Morocco
- ²⁶¹ INFN—Sezione di Bologna, Viale Berti-Pichat 6/2, I-40127 Bologna, Italy
- ²⁶² INFN—Sezione di Bari, Via E. Orabona 4, I-70126 Bari, Italy
- ²⁶³ Department of Computer Architecture and Technology/CITIC, University of Granada, E-18071 Granada, Spain
- ²⁶⁴ Géoazur, UCA, CNRS, IRD, Observatoire de la Côte d'Azur, Sophia Antipolis, France
- ²⁶⁵ Dipartimento di Fisica dell'Università, Via Dodecaneso 33, I-16146 Genova, Italy
- ²⁶⁶ Université Paris-Sud, F-91405 Orsay Cedex, France
- ²⁶⁷ University Mohammed I, Laboratory of Physics of Matter and Radiations, B.P. 717, Oujda 6000, Morocco
- ²⁶⁸ Institut für Theoretische Physik und Astrophysik, Universität Würzburg, Emil-Fischer Str. 31, D-97074 Würzburg, Germany
- ²⁶⁹ Dipartimento di Fisica e Astronomia dell'Università, Viale Berti Pichat 6/2, I-40127 Bologna, Italy
- ²⁷⁰ Laboratoire de Physique Corpusculaire, Clermont Université, Université Blaise Pascal, CNRS/IN2P3, BP 10448, F-63000 Clermont-Ferrand, France
- ²⁷¹ INFN—Sezione di Catania, Viale Andrea Doria 6, I-95125 Catania, Italy
- ²⁷² LSIS, Aix Marseille Université CNRS ENSAM LSIS UMR 7296 F-13397 Marseille, France; Université de Toulon CNRS LSIS UMR 7296, F-83957 La Garde, France
- ²⁷³ Institut Universitaire de France, F-75005 Paris, France
- ²⁷⁴ Royal Netherlands Institute for Sea Research (NIOZ) and Utrecht University, Landsdiep 4, 1797 SZ 't Horntje (Texel), The Netherlands
- ²⁷⁵ Dr. Remeis-Sternwarte and ECAP, Universität Erlangen-Nürnberg, Sternwartstr. 7, D-96049 Bamberg, Germany
- ²⁷⁶ Moscow State University, Skobel'syn Institute of Nuclear Physics, Leninskie gory, 119991 Moscow, Russia
- ²⁷⁷ Mediterranean Institute of Oceanography (MIO), Aix-Marseille University, F-13288, Marseille, Cedex 9, France; Université du Sud Toulon-Var, CNRS-INSU/IRD UM 110, 83957, La Garde Cedex, France
- ²⁷⁸ Dipartimento di Fisica ed Astronomia dell'Università, Viale Andrea Doria 6, I-95125 Catania, Italy
- ²⁷⁹ Direction des Sciences de la Matière, Institut de recherche sur les lois fondamentales de l'Univers, Service de Physique des Particules, CEA Saclay, F-91191 Gif-sur-Yvette Cedex, France
- ²⁸⁰ INFN—Sezione di Pisa, Largo B. Pontecorvo 3, I-56127 Pisa, Italy
- ²⁸¹ Dipartimento di Fisica dell'Università, Largo B. Pontecorvo 3, I-56127 Pisa, Italy
- ²⁸² INFN—Sezione di Napoli, Via Cintia I-80126 Napoli, Italy
- ²⁸³ Dipartimento di Fisica dell'Università Federico II di Napoli, Via Cintia I-80126, Napoli, Italy
- ²⁸⁴ Dpto. de Física Teórica y del Cosmos & C.A.F.P.E., University of Granada, E-18071 Granada, Spain
- ²⁸⁵ Université de Strasbourg, CNRS, IPHC UMR 7178, F-67000 Strasbourg, France
- ²⁸⁶ University of Leicester, X-ray and Observational Astronomy Research Group, Leicester Institute for Space and Earth Observation, Department of Physics & Astronomy, University Road, Leicester, LE1 7RH, UK
- ²⁸⁷ University College London, Mullard Space Science Laboratory, Holmbury St. Mary, Dorking, RH5 6NT, UK
- ²⁸⁸ Department of Astronomy and Astrophysics, The Pennsylvania State University, University Park, PA 16802, USA
- ²⁸⁹ Astrophysics Science Division, NASA Goddard Space Flight Center, Greenbelt, MD 20771 USA
- ²⁹⁰ Joint Space-Science Institute, University of Maryland, College Park, MD 20742, USA
- ²⁹¹ Istituto Nazionale di Astrofisica – Istituto di Astrofisica Spaziale e Fisica Cosmica Palermo, Via Ugo La Malfa 153, I-90146, Palermo, Italy
- ²⁹² Department of Astronomy and Space Sciences, University of Istanbul, Beyzıt 34119, Istanbul, Turkey
- ²⁹³ Space Science Data Center—Agenzia Spaziale Italiana, I-00133 Roma, Italy
- ²⁹⁴ Institute for Gravitation and the Cosmos, The Pennsylvania State University, University Park, PA 16802, USA
- ²⁹⁵ Universities Space Research Association, 7178 Columbia Gateway Drive, Columbia, MD 21046, USA
- ²⁹⁶ National Science Foundation, 2415 Eisenhower Avenue, Alexandria, VA 22314, USA
- ²⁹⁷ Center for Research and Exploration in Space Science and Technology (CRESST) and NASA Goddard Space Flight Center, Greenbelt MD, 20771 USA
- ²⁹⁸ Department of Physics, University of Maryland, Baltimore County, 1000 Hilltop Circle, Baltimore, MD 21250, USA
- ²⁹⁹ Istituto Nazionale di Astrofisica – Osservatorio Astronomico di Brera, Via Bianchi 46, I-23807 Merate, Italy
- ³⁰⁰ Department of Physics, University of Warwick, Coventry CV4 7AL, UK
- ³⁰¹ Los Alamos National Laboratory, B244, Los Alamos, NM, 87545, USA
- ³⁰² Istituto Nazionale di Astrofisica – Osservatorio Astronomico di Roma, Via Frascati 33, I-00040 Monteporzio Catone, Italy
- ³⁰³ Department of Physics and Astronomy, University of Maryland, College Park, MD 20742-4111, USA
- ³⁰⁴ INAF-IAPS, via del Fosso del Cavaliere 100, I-00133 Roma, Italy
- ³⁰⁵ Dip. di Fisica, Univ. di Roma “Tor Vergata,” via della Ricerca Scientifica 1, I-00133 Roma, Italy
- ³⁰⁶ Gran Sasso Science Institute, viale Francesco Crispi 7, I-67100 L'Aquila, Italy
- ³⁰⁷ INAF-OAR, via Frascati 33, I-00078 Monte Porzio Catone (Roma), Italy
- ³⁰⁸ ASI Space Science Data Center (SSDC), via del Politecnico, I-00133 Roma, Italy
- ³⁰⁹ INAF-IASF-Bologna, via Gobetti 101, I-40129 Bologna, Italy
- ³¹⁰ INAF-IASF Milano, via E. Bassini 15, I-20133 Milano, Italy
- ³¹¹ Agenzia Spaziale Italiana, via del Politecnico, I-00133 Roma, Italy
- ³¹² INAF, Osservatorio Astronomico di Cagliari, Via della Scienza 5, I-09047 Selargius (CA), Italy
- ³¹³ Dip. di Fisica, Università di Trieste and INFN, via Valerio 2, I-34127 Trieste, Italy
- ³¹⁴ Unitat de Física de les Radiacions, Departament de Física, and CERES-IEEC, Universitat Autònoma de Barcelona, E-08193 Bellaterra, Spain
- ³¹⁵ Birkeland Centre for Space Science, Department of Physics and Technology, University of Bergen, Bergen, Norway
- ³¹⁶ INFN-Pavia, via Bassi 6, I-27100 Pavia, Italy
- ³¹⁷ University of Witwatersrand, Johannesburg, South Africa

- ³¹⁸ CIFS, c/o Physics Department, University of Turin, via P. Giuria 1, I-10125, Torino, Italy
- ³¹⁹ INFN Roma Tor Vergata, via della Ricerca Scientifica 1, I-00133 Roma, Italy
- ³²⁰ East Windsor RSD, 25A Leshin Lane, Hightstown, NJ 08520, USA
- ³²¹ Osservatorio Astronomico di Brera, via Emilio Bianchi 46, I-23807 Merate (LC), Italy
- ³²² Department of Astronomy and Astrophysics, University of California, Santa Cruz, CA 95064, USA
- ³²³ The Observatories of the Carnegie Institution for Science, 813 Santa Barbara Street, Pasadena, CA 91101, USA
- ³²⁴ Institute for Astronomy, University of Hawai'i, 2680 Woodlawn Drive, Honolulu, HI 96822, USA
- ³²⁵ Departamento de Física y Astronomía, Universidad de La Serena, La Serena, Chile
- ³²⁶ Nuclear Science Division, Lawrence Berkeley National Laboratory, Berkeley, CA 94720, USA
- ³²⁷ Departments of Physics and Astronomy, University of California, Berkeley, CA 94720, USA
- ³²⁸ Dark Cosmology Centre, Niels Bohr Institute, University of Copenhagen, Juliane Maries Vej 30, DK-2100 Copenhagen Ø, Denmark
- ³²⁹ Space Telescope Science Institute, 3700 San Martin Drive, Baltimore, MD 21218, USA
- ³³⁰ Department of Physics and Astronomy, The Johns Hopkins University, 3400 North Charles Street, Baltimore, MD 21218, USA
- ³³¹ Department of Physics, Brandeis University, Waltham, MA, USA
- ³³² Fermi National Accelerator Laboratory, P. O. Box 500, Batavia, IL 60510, USA
- ³³³ Department of Physics, University of Surrey, Guildford GU2 7XH, UK
- ³³⁴ Department of Physics and Astronomy, University of Pennsylvania, Philadelphia, PA 19104, USA
- ³³⁵ Department of Astronomy, Indiana University, 727 E. Third Street, Bloomington, IN 47405, USA
- ³³⁶ Astrophysical Institute, Department of Physics and Astronomy, 251B Clippinger Lab, Ohio University, Athens, OH 45701, USA
- ³³⁷ George P. and Cynthia Woods Mitchell Institute for Fundamental Physics and Astronomy, and Department of Physics and Astronomy, Texas A&M University, College Station, TX 77843, USA
- ³³⁸ LSST, 933 North Cherry Avenue, Tucson, AZ 85721, USA
- ³³⁹ The Observatories of the Carnegie Institution for Science, 813 Santa Barbara St., Pasadena, CA 91101, USA
- ³⁴⁰ Institut d'Astrophysique de Paris (UMR7095: CNRS & UPMC), 98 bis Bd Arago, F-75014, Paris, France
- ³⁴¹ Center for Interdisciplinary Exploration and Research in Astrophysics (CIERA) and Department of Physics and Astronomy, Northwestern University, Evanston, IL 60208, USA
- ³⁴² Center for Theoretical Astrophysics, Los Alamos National Laboratory, Los Alamos, NM 87544, USA
- ³⁴³ Instituto de Física Teórica UAM/CSIC, Universidad Autónoma de Madrid, E-28049 Madrid, Spain
- ³⁴⁴ National Center for Supercomputing Applications, 1205 West Clark Street, Urbana, IL 61801, USA
- ³⁴⁵ Department of Physics & Astronomy, University College London, Gower Street, London WC1E 6BT, UK
- ³⁴⁶ Department of Physics, ETH Zurich, Wolfgang-Pauli-Strasse 16, CH-8093 Zurich, Switzerland
- ³⁴⁷ Kavli Institute for Cosmological Physics, University of Chicago, Chicago, IL 60637, USA
- ³⁴⁸ Observatório do Valongo, Universidade Federal do Rio de Janeiro, Ladeira do Pedro Antônio 43, Rio de Janeiro, RJ, 20080-090, Brazil
- ³⁴⁹ Center for Interdisciplinary Exploration and Research in Astrophysics (CIERA) and Department of Physics and Astronomy, Northwestern University, Evanston, IL 60208, USA
- ³⁵⁰ National Optical Astronomy Observatory, 950 North Cherry Avenue, Tucson, AZ 85719, USA
- ³⁵¹ Departamento de Astronomía, Universidad de Chile, Camino del Observatorio 1515, Las Condes, Santiago, Chile
- ³⁵² Department of Physics and Columbia Astrophysics Laboratory, Columbia University, New York, NY 10027, USA
- ³⁵³ Department of Physics, University of Michigan, 450 Church Street, Ann Arbor, MI 48109-1040, USA
- ³⁵⁴ Lawrence Berkeley National Laboratory, 1 Cyclotron Road, Berkeley, CA 94720, USA
- ³⁵⁵ Department of Astronomy & Theoretical Astrophysics Center, University of California, Berkeley, CA 94720-3411, USA
- ³⁵⁶ Physics Division, Lawrence Berkeley National Laboratory, Berkeley, CA 94720-8160, USA
- ³⁵⁷ Steward Observatory, University of Arizona, 933 N. Cherry Avenue, Tucson, AZ 85721, USA
- ³⁵⁸ Instituto de Física Gleb Wataghin, Universidade Estadual de Campinas, Campinas, SP—13083-859, Brazil
- ³⁵⁹ Laboratório Interinstitucional de e-Astronomia—LIneA, Rua Gal. José Cristino 77, Rio de Janeiro, RJ—20921-400, Brazil
- ³⁶⁰ Cerro Tololo Inter-American Observatory, National Optical Astronomy Observatory, Casilla 603, La Serena, Chile
- ³⁶¹ Institute of Astronomy, University of Cambridge, Madingley Road, Cambridge CB3 0HA, UK
- ³⁶² Kavli Institute for Cosmology, University of Cambridge, Madingley Road, Cambridge CB3 0HA, UK
- ³⁶³ CNRS, UMR 7095, Institut d'Astrophysique de Paris, F-75014, Paris, France
- ³⁶⁴ Sorbonne Universités, UPMC Univ Paris 06, UMR 7095, Institut d'Astrophysique de Paris, F-75014, Paris, France
- ³⁶⁵ Kavli Institute for Particle Astrophysics & Cosmology, P. O. Box 2450, Stanford University, Stanford, CA 94305, USA
- ³⁶⁶ SLAC National Accelerator Laboratory, Menlo Park, CA 94025, USA
- ³⁶⁷ Institute of Cosmology & Gravitation, University of Portsmouth, Portsmouth PO1 3FX, UK
- ³⁶⁸ Observatório Nacional, Rua Gal. José Cristino 77, Rio de Janeiro, RJ—20921-400, Brazil
- ³⁶⁹ Department of Astronomy, University of Illinois, 1002 W. Green Street, Urbana, IL 61801, USA
- ³⁷⁰ Institute of Space Sciences, IEEC-CSIC, Campus UAB, Carrer de Can Magrans, s/n, E-08193 Barcelona, Spain
- ³⁷¹ George P. and Cynthia Woods Mitchell Institute for Fundamental Physics and Astronomy, and Department of Physics and Astronomy, Texas A&M University, College Station, TX 77843, USA
- ³⁷² Department of Physics, IIT Hyderabad, Kandi, Telangana 502285, India
- ³⁷³ Excellence Cluster Universe, Boltzmannstr. 2, D-85748 Garching, Germany
- ³⁷⁴ Faculty of Physics, Ludwig-Maximilians-Universität, Scheinerstr. 1, D-81679 Munich, Germany
- ³⁷⁵ Department of Physics, California Institute of Technology, Pasadena, CA 91125, USA
- ³⁷⁶ Jet Propulsion Laboratory, California Institute of Technology, 4800 Oak Grove Drive, Pasadena, CA 91109, USA
- ³⁷⁷ Institut de Física d'Altes Energies (IFAE), The Barcelona Institute of Science and Technology, Campus UAB, 08193 Bellaterra (Barcelona), Spain
- ³⁷⁸ Department of Astronomy, University of Michigan, Ann Arbor, MI 48109, USA
- ³⁷⁹ Department of Physics, University of Michigan, Ann Arbor, MI 48109, USA
- ³⁸⁰ Universitäts-Sternwarte, Fakultät für Physik, Ludwig-Maximilians-Universität München, Scheinerstr. 1, D-81679 München, Germany
- ³⁸¹ Department of Astronomy, University of California, Berkeley, 501 Campbell Hall, Berkeley, CA 94720, USA
- ³⁸² Center for Cosmology and Astro-Particle Physics, The Ohio State University, Columbus, OH 43210, USA
- ³⁸³ Department of Physics, The Ohio State University, Columbus, OH 43210, USA
- ³⁸⁴ Astronomy Department, University of Washington, Box 351580, Seattle, WA 98195, USA
- ³⁸⁵ Santa Cruz Institute for Particle Physics, Santa Cruz, CA 95064, USA
- ³⁸⁶ Australian Astronomical Observatory, North Ryde, NSW 2113, Australia
- ³⁸⁷ Departamento de Física Matemática, Instituto de Física, Universidade de São Paulo, CP 66318, São Paulo, SP—05314-970, Brazil
- ³⁸⁸ Department of Astronomy, The Ohio State University, Columbus, OH 43210, USA

- ³⁸⁹ Institutió Catalana de Recerca i Estudis Avançats, E-08010 Barcelona, Spain
- ³⁹⁰ Max Planck Institute for Extraterrestrial Physics, Giessenbachstrasse, D-85748 Garching, Germany
- ³⁹¹ Department of Physics and Astronomy, Pevensey Building, University of Sussex, Brighton BN1 9QH, UK
- ³⁹² Centro de Investigaciones Energéticas, Medioambientales y Tecnológicas (CIEMAT), Madrid, Spain
- ³⁹³ Brookhaven National Laboratory, Building 510, Upton, NY 11973, USA
- ³⁹⁴ School of Physics and Astronomy, University of Southampton, Southampton SO17 1BJ, UK
- ³⁹⁵ Computer Science and Mathematics Division, Oak Ridge National Laboratory, Oak Ridge, TN 37831, USA
- ³⁹⁶ Argonne National Laboratory, 9700 South Cass Avenue, Lemont, IL 60439, USA
- ³⁹⁷ Department of Physics, Stanford University, 382 Via Pueblo Mall, Stanford, CA 94305, USA
- ³⁹⁸ Department of Physics and Astronomy, University of North Carolina at Chapel Hill, Chapel Hill, NC 27599, USA
- ³⁹⁹ Department of Astronomy and Steward Observatory, University of Arizona, 933 N Cherry Avenue, Tucson, AZ 85719, USA
- ⁴⁰⁰ Department of Physics, University of California, 1 Shields Avenue, Davis, CA 95616-5270, USA
- ⁴⁰¹ Department of Physics and Astronomy, University of Padova, Via 8 Febbraio, I-35122 Padova, Italy
- ⁴⁰² INAF—Osservatorio Astronomico di Padova, Vicolo della Osservatorio 5, I-35122 Padova, Italy
- ⁴⁰³ INAF—Osservatorio Astronomico di Padova, Vicolo dell'Osservatorio 5, I-35122 Padova, Italy
- ⁴⁰⁴ INAF—Osservatorio Astronomico di Roma, Via di Frascati, 33, I-00078 Monteporzio Catone, Italy
- ⁴⁰⁵ INAF—Osservatorio Astronomico di Brera, Via E. Bianchi 46, I-23807 Merate (LC), Italy
- ⁴⁰⁶ Space Science Data Center, ASI, Via del Politecnico, s.n.c., I-00133, Roma, Italy
- ⁴⁰⁷ INAF—Osservatorio Astronomico di Capodimonte, salita Moiariello 16, I-80131, Napoli, Italy
- ⁴⁰⁸ INAF—Istituto di Astrofisica Spaziale e Fisica Cosmica di Bologna, Via Gobetti 101, I-40129 Bologna, Italy
- ⁴⁰⁹ Dipartimento di Fisica “G. Occhialini,” Università degli Studi di Milano-Bicocca, P.za della Scienza 3, I-20126 Milano, Italy
- ⁴¹⁰ Laboratoire Univers et Particules de Montpellier, Université Montpellier 2, 34095, Montpellier, France
- ⁴¹¹ INAF—Osservatorio Astronomico di Catania, Via S. Sofia 78, I-95123, Catania, Italy
- ⁴¹² Department of physics, University of Naples Federico II, Corso Umberto I, 40, I-80138 Napoli, Italy
- ⁴¹³ Institute for Astrophysics and Particle Physics, University of Innsbruck, Technikerstrasse 25/8, A-6020 Innsbruck, Austria
- ⁴¹⁴ Departamento de Ciencias Físicas, Universidad Andrés Bello, Fernández Concha 700, Las Condes, Santiago, Chile
- ⁴¹⁵ Università degli Studi dell'Insubria, via Valleggio 11, I-22100, Como, Italy
- ⁴¹⁶ INAF—Istituto di Astrofisica Spaziale e Fisica Cosmica di Milano, via E. Bassini 15, I-20133 Milano, Italy
- ⁴¹⁷ INAF—Osservatorio Astrofisico di Torino, Pino Torinese, Italy
- ⁴¹⁸ INAF—Osservatorio Astrofisico di Arcetri, Largo Enrico Fermi 5, I-50125, Florence, Italy
- ⁴¹⁹ INAF—Istituto di Radioastronomia di Bologna, Bologna, Italy
- ⁴²⁰ Key Laboratory of dark Matter and Space Astronomy, Purple Mountain Observatory, Chinese Academy of Science, Nanjing 210008, China
- ⁴²¹ Thüringer Landessternwarte Tautenburg, Sternwarte 5, D-07778 Tautenburg, Germany
- ⁴²² Department of Physics, The George Washington University, Corcoran Hall, Washington, DC 20052, USA
- ⁴²³ Astronomy, Physics, and Statistics Institute of Sciences (APSI)
- ⁴²⁴ Astrophysics Research Institute, Liverpool John Moores University, Liverpool Science Park, IC2, 146 Brownlow Hill, Liverpool L3 5RF, UK
- ⁴²⁵ Max-Planck-Institut für Astrophysik, Karl-Schwarzschild-Str. 1, D-85748 Garching bei München, Germany
- ⁴²⁶ European Southern Observatory, Karl-Schwarzschild-Strasse 2, D-85748 Garching bei München, Germany
- ⁴²⁷ INAF—Osservatorio Astronomico di Trieste, Via G.B. Tiepolo 11, I-34143 Trieste, Italy
- ⁴²⁸ Racah Institute of Physics, The Hebrew University of Jerusalem, Jerusalem 91904, Israel
- ⁴²⁹ GEPI, Observatoire de Paris, PSL Research University, CNRS, Place Jules Janssen, F-92190, Meudon, France
- ⁴³⁰ Department of Physics and Astronomy, University of Leicester, Leicester LE1 7RH, UK
- ⁴³¹ Frontier Research Institute for Interdisciplinary Sciences, Tohoku University, Sendai 980-8578, Japan
- ⁴³² Astronomical Institute, Tohoku University, Sendai 980-8578, Japan
- ⁴³³ Department of Physics, University of Bath Claverton Down, Bath, BA2 7AY, UK
- ⁴³⁴ CEA Saclay—DRF/Irfu/Département d'Astrophysique, F-91191 Gif-sur-Yvette, France
- ⁴³⁵ Department of Physics and Institute of Theoretical Physics, Nanjing Normal University, Nanjing 210046, China
- ⁴³⁶ Center for Astrophysics and Cosmology (CAC), University of Nova Gorica, Nova Gorica, Slovenia
- ⁴³⁷ Anton Pannekoek Institute, University of Amsterdam, Science Park 904, 1098XH Amsterdam, The Netherlands
- ⁴³⁸ Astrophysics Research Institute, Liverpool John Moores University, ic2, Liverpool Science Park, 146 Brownlow Hill, Liverpool L3 5RF, UK
- ⁴³⁹ Faculty of Mathematics and Physics, University of Ljubljana, Jadranska 19, 1000 Ljubljana, Slovenia
- ⁴⁴⁰ Yunnan Observatories, Chinese Academy of Sciences, 650011 Kunming, Yunnan Province, China
- ⁴⁴¹ Astrophysics Research Institute, Liverpool John Moores University, Liverpool, L3 5RF, UK
- ⁴⁴² Department of Physics, The George Washington University, 725 21st Street NW, Washington, DC 20052, USA
- ⁴⁴³ Laboratoire AIM, CEA-IRFU/CNRS/Université Paris Diderot, Service d'Astrophysique, CEA Saclay, F-91191 Gif-sur-Yvette, France
- ⁴⁴⁴ Santa Cruz Institute for Particle Physics, Department of Physics and Department of Astronomy and Astrophysics, University of California at Santa Cruz, Santa Cruz, CA 95064, USA
- ⁴⁴⁵ Università di Pisa and Istituto Nazionale di Fisica Nucleare, Sezione di Pisa, I-56127 Pisa, Italy
- ⁴⁴⁶ Istituto Nazionale di Fisica Nucleare, Sezione di Trieste, and Università di Trieste, I-34127 Trieste, Italy
- ⁴⁴⁷ Dipartimento di Fisica, Università di Trieste, I-34127 Trieste, Italy
- ⁴⁴⁸ Istituto Nazionale di Fisica Nucleare, Sezione di Padova, I-35131 Padova, Italy
- ⁴⁴⁹ Dipartimento di Fisica e Astronomia “G. Galilei,” Università di Padova, I-35131 Padova, Italy
- ⁴⁵⁰ California State University, Los Angeles, Department of Physics and Astronomy, Los Angeles, CA 90032, USA
- ⁴⁵¹ Istituto Nazionale di Fisica Nucleare, Sezione di Pisa, I-56127 Pisa, Italy
- ⁴⁵² Dipartimento di Fisica “M. Merlin” dell'Università e del Politecnico di Bari, I-70126 Bari, Italy
- ⁴⁵³ Istituto Nazionale di Fisica Nucleare, Sezione di Bari, I-70126 Bari, Italy
- ⁴⁵⁴ W. W. Hansen Experimental Physics Laboratory, Kavli Institute for Particle Astrophysics and Cosmology, Department of Physics and SLAC National Accelerator Laboratory, Stanford University, Stanford, CA 94305, USA
- ⁴⁵⁵ Istituto Nazionale di Fisica Nucleare, Sezione di Torino, I-10125 Torino, Italy
- ⁴⁵⁶ Dipartimento di Fisica, Università degli Studi di Torino, I-10125 Torino, Italy
- ⁴⁵⁷ Laboratoire Univers et Particules de Montpellier, Université Montpellier, CNRS/IN2P3, F-34095 Montpellier, France
- ⁴⁵⁸ Deutsches Elektronen Synchrotron DESY, D-15738 Zeuthen, Germany
- ⁴⁵⁹ Center for Research and Exploration in Space Science and Technology (CRESTT) and NASA Goddard Space Flight Center, Greenbelt, MD 20771, USA
- ⁴⁶⁰ Italian Space Agency, Via del Politecnico, snc, I-00133 Roma, Italy
- ⁴⁶¹ College of Science, George Mason University, Fairfax, VA 22030; Resident at Naval Research Laboratory, Washington, DC 20375, USA

- ⁴⁶² Space Science Division, Naval Research Laboratory, Washington, DC 20375-5352, USA
- ⁴⁶³ Space Science Data Center—Agenzia Spaziale Italiana, Via del Politecnico, snc, I-00133, Roma, Italy
- ⁴⁶⁴ Istituto Nazionale di Fisica Nucleare, Sezione di Perugia, I-06123 Perugia, Italy
- ⁴⁶⁵ Department of Physics and Astronomy, Sonoma State University, Rohnert Park, CA 94928-3609, USA
- ⁴⁶⁶ RWTH Aachen University, Institute for Theoretical Particle Physics and Cosmology (TTK), D-52056 Aachen, Germany
- ⁴⁶⁷ INAF Istituto di Radioastronomia, I-40129 Bologna, Italy
- ⁴⁶⁸ Dipartimento di Astronomia, Università di Bologna, I-40127 Bologna, Italy
- ⁴⁶⁹ Università Telematica Pegaso, Piazza Trieste e Trento, 48, I-80132 Napoli, Italy
- ⁴⁷⁰ Laboratoire Leprince-Ringuet, École polytechnique, CNRS/IN2P3, F-91128 Palaiseau, France
- ⁴⁷¹ Department of Physical Sciences, Hiroshima University, Higashi-Hiroshima, Hiroshima 739-8526, Japan
- ⁴⁷² Department of Physics and Department of Astronomy, University of Maryland, College Park, MD 20742, USA
- ⁴⁷³ Centre d'Études Nucléaires de Bordeaux Gradignan, IN2P3/CNRS, Université Bordeaux 1, BP120, F-33175 Gradignan Cedex, France
- ⁴⁷⁴ Laboratoire de Physique et Chimie de l'Environnement et de l'Espace, Université d'Orléans/CNRS, F-45071 Orléans Cedex 02, France
- ⁴⁷⁵ Station de radioastronomie de Nançay, Observatoire de Paris, CNRS/INSU, F-18330 Nançay, France
- ⁴⁷⁶ Science Institute, University of Iceland, IS-107 Reykjavik, Iceland
- ⁴⁷⁷ Nordita, Roslagstullsbacken 23, 106 91 Stockholm, Sweden
- ⁴⁷⁸ Department of Physics, Graduate School of Science, University of Tokyo, 7-3-1 Hongo, Bunkyo-ku, Tokyo 113-0033, Japan
- ⁴⁷⁹ Istituto Nazionale di Fisica Nucleare, Sezione di Roma "Tor Vergata," I-00133 Roma, Italy
- ⁴⁸⁰ Department of Physics and Astronomy, Clemson University, Kinard Lab of Physics, Clemson, SC 29634-0978, USA
- ⁴⁸¹ Max-Planck-Institut für Physik, D-80805 München, Germany
- ⁴⁸² Department of Physics, University of Johannesburg, PO Box 524, Auckland Park 2006, South Africa
- ⁴⁸³ Institut für Astro- und Teilchenphysik and Institut für Theoretische Physik, Leopold-Franzens-Universität Innsbruck, A-6020 Innsbruck, Austria
- ⁴⁸⁴ Department of Physics, The University of Hong Kong, Pokfulam Road, Hong Kong, China
- ⁴⁸⁵ Laboratory for Space Research, The University of Hong Kong, Hong Kong, China
- ⁴⁸⁶ NYCB Real-Time Computing Inc., Lattingtown, NY 11560-1025, USA
- ⁴⁸⁷ Purdue University Northwest, Hammond, IN 46323, USA
- ⁴⁸⁸ Hiroshima Astrophysical Science Center, Hiroshima University, Higashi-Hiroshima, Hiroshima 739-8526, Japan
- ⁴⁸⁹ CNRS, IRAP, F-31028 Toulouse cedex 4, France
- ⁴⁹⁰ GAHEC, Université de Toulouse, UPS-OMP, IRAP, F-31400 Toulouse, France
- ⁴⁹¹ Institute of Space Sciences (CSICIEEC), Campus UAB, Carrer de Magrans s/n, E-08193 Barcelona, Spain
- ⁴⁹² Institutíó Catalana de Recerca i Estudis Avançats (ICREA), E-08010 Barcelona, Spain
- ⁴⁹³ INAF-Istituto di Astrofisica Spaziale e Fisica Cosmica Bologna, via P. Gobetti 101, I-40129 Bologna, Italy
- ⁴⁹⁴ Centre for Astrophysics and Cosmology, University of Nova Gorica, Vipavska 11c, 5270 Ajdovščina, Slovenia
- ⁴⁹⁵ Sydney Institute for Astronomy, School of Physics, The University of Sydney, Sydney, NSW 2006, Australia
- ⁴⁹⁶ ARC Centre of Excellence for All-sky Astrophysics in 3 Dimensions (ASTRO 3D)
- ⁴⁹⁷ ATNF, CSIRO Astronomy and Space Science, PO Box 76, Epping, NSW 1710, Australia
- ⁴⁹⁸ ARC Centre of Excellence for All-sky Astrophysics (CAASTRO)
- ⁴⁹⁹ University of Wisconsin–Milwaukee, Milwaukee, WI 53201, USA
- ⁵⁰⁰ ATNF, CSIRO Astronomy and Space Science, 26 Dick Perry Avenue, Kensington, WA 6152, Australia
- ⁵⁰¹ International Centre for Radio Astronomy Research, Curtin University, Bentley, WA 6102, Australia
- ⁵⁰² Centre for Astrophysics and Supercomputing, Swinburne University of Technology, Mail H30, PO Box 218, VIC 3122, Australia
- ⁵⁰³ Department of Physics, University of California, Santa Barbara, CA 93106-9530, USA
- ⁵⁰⁴ Las Cumbres Observatory, 6740 Cortona Drive, Suite 102, Goleta, CA 93117-5575, USA
- ⁵⁰⁵ School of Physics and Astronomy, Tel Aviv University, Tel Aviv 69978, Israel
- ⁵⁰⁶ Columbia Astrophysics Laboratory, Columbia University, New York, NY, 10027, USA
- ⁵⁰⁷ Centre for Astrophysics and Supercomputing, Swinburne University of Technology, PO Box 218, H29, Hawthorn, VIC 3122, Australia
- ⁵⁰⁸ The Australian Research Council Centre of Excellence for Gravitational Wave Discovery (OzGrav), Australia
- ⁵⁰⁹ The Australian Research Council Centre of Excellence for All-Sky Astrophysics (CAASTRO), Australia
- ⁵¹⁰ Research School of Astronomy and Astrophysics, The Australian National University, Canberra, ACT 2611, Australia
- ⁵¹¹ Australian Astronomical Observatory, 105 Delhi Road, North Ryde, NSW 2113, Australia
- ⁵¹² George P. and Cynthia Woods Mitchell Institute for Fundamental Physics & Astronomy, Texas A. & M. University, Department of Physics and Astronomy, 4242 TAMU, College Station, TX 77843, USA
- ⁵¹³ Purple Mountain Observatory, Chinese Academy of Sciences, Nanjing 210008, China
- ⁵¹⁴ Chinese Center for Antarctic Astronomy, Nanjing 210008, China
- ⁵¹⁵ The University of the Virgin Islands, 2 John Brewer's Bay, St. Thomas 00802, USVI
- ⁵¹⁶ Monash Centre for Astrophysics, Monash University, VIC 3800, Australia
- ⁵¹⁷ Centre for Translational Data Science, University of Sydney, Sydney, NSW 2006, Australia
- ⁵¹⁸ School of Physics and Astronomy, University of Nottingham, Nottingham, UK
- ⁵¹⁹ CSIRO Astronomy & Space Science, Australia Telescope National Facility, P.O. Box 76, Epping, NSW 1710, Australia
- ⁵²⁰ SKA Organisation, Jodrell Bank Observatory, SK11 9DL, UK
- ⁵²¹ National Astronomical Observatories, Chinese Academy of Sciences, Beijing 100012, China
- ⁵²² Physics Department and Tsinghua Center for Astrophysics (THCA), Tsinghua University, Beijing, 100084, China
- ⁵²³ Tianjin Normal University, Tianjin 300074, China
- ⁵²⁴ School of Physics, University of New South Wales, NSW 2052, Australia
- ⁵²⁵ Nanjing Institute of Astronomical Optics and Technology, Nanjing 210042, China
- ⁵²⁶ Department of Astronomy, Beijing Normal University, Beijing 100875, China
- ⁵²⁷ School of Astronomy and Space Science and Key Laboratory of Modern Astronomy and Astrophysics in Ministry of Education, Nanjing University, Nanjing 210093, China
- ⁵²⁸ Orangewave Innovation Science, 2113 Old Highway 52, Moncks Corner, SC 29461, USA
- ⁵²⁹ Department of Physics, 2354 Fairchild Drive, U.S. Air Force Academy, CO 80840, USA
- ⁵³⁰ Université de Toulouse, IRAP 14 Av. Edouard Belin, F-31000 Toulouse France
- ⁵³¹ Auragne Observatory, France
- ⁵³² Research School of Astronomy and Astrophysics, The Australian National University, Canberra, ACT 2611, Australia
- ⁵³³ Department of Physics and Astronomy, University of Leicester, University Road, Leicester, LE1 7RH, UK
- ⁵³⁴ Instituto de Astrofísica de Andalucía (IAA-CSIC), Glorieta de la Astronomía s/n, E-18008 Granada, Spain

- ⁵³⁵ Institute of Astronomy, University of Cambridge, Madingley Road, Cambridge, CB3 0HA, UK
- ⁵³⁶ Max-Planck-Institut für extraterrestrische Physik, Giessenbachstr. 1, D-85740 Garching, Germany
- ⁵³⁷ Birmingham Institute for Gravitational Wave Astronomy and School of Physics and Astronomy, University of Birmingham, Birmingham B15 2TT, UK
- ⁵³⁸ School of Physics and Astronomy and Monash Centre for Astrophysics, Monash University, VIC 3800, Australia
- ⁵³⁹ The Oskar Klein Centre, Department of Astronomy, AlbaNova, Stockholm University, SE-106 91 Stockholm, Sweden
- ⁵⁴⁰ Anton Pannekoek Institute, University of Amsterdam, Science Park 904, 1098 XH Amsterdam, the Netherlands
- ⁵⁴¹ ASTRON, the Netherlands Institute for Radio Astronomy, Postbus 2, 7990 AA Dwingeloo, the Netherlands
- ⁵⁴² SUPA, School of Physics & Astronomy, University of St Andrews, North Haugh, St Andrews KY16 9SS, UK
- ⁵⁴³ Niels Bohr Institute & Centre for Star and Planet Formation, University of Copenhagen Øster Voldgade 5, DK-1350—Copenhagen, Denmark
- ⁵⁴⁴ Institute for Advanced Research, Nagoya University, Furo-cho, Chikusa-ku, Nagoya 464-8601, Japan
- ⁵⁴⁵ Space Telescope Science Institute, 3700 San Martin Drive, Baltimore, MD 21218, USA
- ⁵⁴⁶ Centre for Astrophysics and Cosmology, Science Institute, University of Iceland, Dunhagi 5, 107 Reykjavík, Iceland
- ⁵⁴⁷ Instituto de Astrofísica, Pontificia Universidad Católica de Chile, Av. Vicuña Mackenna 4860, 7820436 Macul, Santiago, Chile
- ⁵⁴⁸ Max-Planck-Institut für Astronomie Königstuhl 17, D-69117 Heidelberg, Germany
- ⁵⁴⁹ Lomonosov Moscow State University, Physics Department, Vorobievsky gory, 1 Moscow, 119991, Russia
- ⁵⁵⁰ Lomonosov Moscow State University, SAI, Universitetsky prospekt, 13 Moscow, 119234, Russia
- ⁵⁵¹ Observatorio Astronómico Félix Aguilar (OFA), Avda Benavides s/n, Rivadavia, El Leonsito, Argentina
- ⁵⁵² Instituto de Ciencias Astronómicas de la Tierra y del Espacio, Casilla de Correo 49, 5400 San Juan, Argentina
- ⁵⁵³ Universidad Nacional de San Juan, Av. Ignacio de la Roza 391, San Juan, 5400, Argentina
- ⁵⁵⁴ Irkutsk State University Applied Physics Institute, 20, Boulevard, 664003, Irkutsk, Russia
- ⁵⁵⁵ Blagoveschensk State Pedagogical University, Lenin str., 104, Blagoveschensk, 675000, Russia
- ⁵⁵⁶ Instituto de Astrofísica de Canarias, C/Vía Lctea, s/n E-38205, La Laguna, Tenerife, Spain
- ⁵⁵⁷ Kislovodsk Solar Station, Pulkovo Observatory RAS, Gagarina str. 100, Kislovodsk, 357700, Russia
- ⁵⁵⁸ Institute for Space-Earth Environmental Research, Nagoya, 464-8601, Japan
- ⁵⁵⁹ Subaru Telescope, Hilo, HI 96720, USA
- ⁵⁶⁰ National Astronomical Observatory of Japan, Mitaka, Tokyo 181-8588, Japan
- ⁵⁶¹ University of Hyogo, Sayo 679-5313, Japan
- ⁵⁶² South African Astronomical Observatory, Cape Town, South Africa
- ⁵⁶³ Massey University, Auckland 0745, New Zealand
- ⁵⁶⁴ Institute of Astronomy, Graduate School of Science, Mitaka 181-0015, Japan
- ⁵⁶⁵ Tokyo Institute of Technology, Tokyo 152-8551, Japan
- ⁵⁶⁶ Osaka City University, Osaka 558-8585, Japan
- ⁵⁶⁷ Hiroshima Astrophysical Science Center, Higashi-Hiroshima 739-8526, Japan
- ⁵⁶⁸ Hiroshima University, Higashi-Hiroshima, 739-8526, Japan
- ⁵⁶⁹ Okayama Astrophysical Observatory, Asakuchi 719-0232, Japan
- ⁵⁷⁰ Purple Mountain Observatory, Nanjing 210008, China
- ⁵⁷¹ Osaka University, Toyonaka 560-0043, Japan
- ⁵⁷² Nagoya University, Nagoya 464-8602, Japan
- ⁵⁷³ Kagoshima University, Kagoshima 890-0065, Japan
- ⁵⁷⁴ Kyoto University, Kyoto 606-8502, Japan
- ⁵⁷⁵ Precursory Research for Embryonic Science and Technology, Mitaka, Tokyo 181-0015, Japan
- ⁵⁷⁶ Toho University, Funabashi 274-8510, Japan
- ⁵⁷⁷ Konan University, Kobe 658-8501, Japan
- ⁵⁷⁸ Kavli Institute for the Physics and Mathematics of the Universe (WPI), Kashiwa 277-8583, Japan
- ⁵⁷⁹ University of Canterbury, Mt John Observatory, Lake Tekapo 7945, New Zealand
- ⁵⁸⁰ Division of Physics, Math and Astronomy, California Institute of Technology, Pasadena, CA 91125, USA
- ⁵⁸¹ Indian Institute of Astrophysics, Bangalore-560034, India
- ⁵⁸² University of Colorado, Boulder, CO 80309, USA
- ⁵⁸³ South African Astronomical Observatory (SAAO), Cape Town 7935, South Africa
- ⁵⁸⁴ Department of Astronomy, University of Washington, Seattle, WA 98195, USA
- ⁵⁸⁵ National Center for Radio Astrophysics, Tata Institute of Fundamental Research, Pune University Campus, Ganeshkhind Pune 411007, India
- ⁵⁸⁶ Department of Physics, University of Wisconsin, Milwaukee, WI 53201, USA
- ⁵⁸⁷ Remote Sensing Division, Naval Research Laboratory, Code 7213, Washington, DC 20375, USA
- ⁵⁸⁸ Department of Physics, George Washington University, Washington, DC 20052, USA
- ⁵⁸⁹ University College London, Mullard Space Science Laboratory, RH5 6NT, UK
- ⁵⁹⁰ X-ray and Observational Astronomy Research Group, Leicester Institute for Space and Earth Observation, Department of Physics & Astronomy, University of Leicester, Leicester LE1 7RH, UK
- ⁵⁹¹ The Oskar Klein Centre, Department of Physics, Stockholm, University, AlbaNova, SE-106 91 Stockholm, Sweden
- ⁵⁹² Space Telescope Science Institute, Baltimore, MD 21218, USA
- ⁵⁹³ National Radio Astronomy Observatory, Socorro, NM, USA
- ⁵⁹⁴ Department of Physics and Astronomy, University of Southampton, Southampton, Hampshire SO17 1BJ, UK
- ⁵⁹⁵ Institute of Cosmology and Gravitation, University of Portsmouth, Portsmouth PO1 3FX, UK
- ⁵⁹⁶ The Raymond and Beverly Sackler School of Physics and Astronomy, Tel Aviv University, Tel Aviv 69978, Israel
- ⁵⁹⁷ Infrared Processing and Analysis Center, California Institute of Technology, Pasadena, CA 91125, USA
- ⁵⁹⁸ Racah Institute of Physics, The Hebrew University of Jerusalem, Jerusalem, 91904, Israel
- ⁵⁹⁹ Center for Computational Astrophysics, Simons Foundation, New York, NY 10010, USA
- ⁶⁰⁰ Graduate Institute of Astronomy, National Central University, Taoyuan City 32001, Taiwan
- ⁶⁰¹ Department of Physics, Tokyo Institute of Technology, Tokyo 152-8551, Japan
- ⁶⁰² Department of Astronomy, University of California, Berkeley, CA 94720-3411, USA
- ⁶⁰³ Department of Physics, University of California, Berkeley, CA 94720, USA
- ⁶⁰⁴ Gemini Observatory, Casilla 603, La Serena, Chile
- ⁶⁰⁵ Max-Planck Institute for Astrophysics, Garching, Germany
- ⁶⁰⁶ Center for Interdisciplinary Exploration and Research in Astrophysics (CIERA), Department of Physics and Astronomy, Northwestern University, Evanston, IL 60208, USA
- ⁶⁰⁷ The Adler Planetarium, Chicago, IL 60605, USA

- ⁶⁰⁸ Astrophysics, Department of Physics, University of Oxford, Oxford OX1 3RH, UK
- ⁶⁰⁹ Department of Particle Physics & Astrophysics, Weizmann Institute of Science, Rehovot 7610001, Israel
- ⁶¹⁰ Department of Physics and Astronomy, Texas Tech University, Lubbock, TX 79409-1051, USA
- ⁶¹¹ Astrophysics Research Institute, Liverpool John Moores University, IC2, Liverpool Science Park, 146 Brownlow Hill, Liverpool L3 5RF, UK
- ⁶¹² Department of Astronomy, San Diego State University, CA 92182, USA
- ⁶¹³ Kavli Institute for the Physics and Mathematics of the Universe (WPI), The University of Tokyo Institutes for Advanced Study, The University of Tokyo, Kashiwa, Chiba 277-8583, Japan
- ⁶¹⁴ The Oskar Klein Centre, Department of Astronomy, Stockholm University, AlbaNova, SE-106 91 Stockholm, Sweden
- ⁶¹⁵ University of California Merced, Merced, CA, USA
- ⁶¹⁶ Australian Research Council Centre of Excellence for All-sky Astrophysics (CAASTRO), Sydney Institute for Astronomy, School of Physics, The University of Sydney, Sydney, NSW 2006, Australia
- ⁶¹⁷ Institute for Astronomy, University of Hawaii, 2680 Woodlawn Drive, Honolulu, Hawaii 96822, USA
- ⁶¹⁸ ISAS/JAXA, Sagamihara, Kanagawa 229-8510, Japan
- ⁶¹⁹ University of Miyazaki, Miyazaki, Miyazaki 889-2192, Japan
- ⁶²⁰ Tokyo Institute of Technology, Meguro-ku, Tokyo 152-8551, Japan
- ⁶²¹ Aoyama Gakuin University, Sagamihara, Kanagawa 229-8558, Japan
- ⁶²² Kyoto University, Kyoto, Kyoto, 606-8502, Japan
- ⁶²³ JAXA, Tsukuba, Ibaraki 305-8505, Japan
- ⁶²⁴ RIKEN, Wako, Saitama, 351-0198, Japan
- ⁶²⁵ Chuo University, Bunkyo-ku, Tokyo 112-8551, Japan
- ⁶²⁶ National Astronomical Observatory of Japan, Mitaka, Tokyo 181-8588, Japan
- ⁶²⁷ Nihon University, Chiyoda-ku, Tokyo 101-8308, Japan
- ⁶²⁸ Osaka University, Toyonaka, Osaka 560-0043, Japan
- ⁶²⁹ Nagoya University, Nagoya, Aichi 464-8601, Japan
- ⁶³⁰ The University of Western Australia, 35, Stirling Highway, Perth, WA 6009, Australia
- ⁶³¹ Swinburne University, John Street, Hawthorn, VIC 3122, Australia
- ⁶³² ARTEMIS (UCA, CNRS, OCA), boulevard de l'Observatoire, CS 34229, F-06304 Nice, France
- ⁶³³ IRAP (CNRS, UPS), 14 avenue Edouard Belin, F-31029 Toulouse, France
- ⁶³⁴ The University of the Virgin Islands, 2 John Brewer's Bay, St Thomas 00802, USVI
- ⁶³⁵ The Auragne Observatory, F-31190 Auragne, France
- ⁶³⁶ Center of the Exploration of the Origin of the Universe, Astronomy Program, Dept. of Physics & Astronomy, Seoul National University, 1 Gwanak-rho, Gwanak-gu, Seoul 08826, Korea
- ⁶³⁷ Korea Astronomy and Space Science Institute, 776 Daedeokdae-ro, Yuseong-gu, Daejeon 34055, Korea
- ⁶³⁸ CAS Key Laboratory of Space Astronomy and Technology, National Astronomical Observatories, Chinese Academy of Sciences, Beijing 100012, China
- ⁶³⁹ Astrophysics Research Centre, School of Mathematics and Physics, Queens University Belfast, Belfast BT7 1NN, UK
- ⁶⁴⁰ Department of Physics and Astronomy, University of Southampton, Southampton SO17 1BJ, UK
- ⁶⁴¹ Department of Particle Physics and Astrophysics, Weizmann Institute of Science, Rehovot 76100, Israel
- ⁶⁴² Department of Physics, University of Warwick, Coventry CV4 7AL, UK
- ⁶⁴³ Institute for Astronomy, SUPA (Scottish Universities Physics Alliance), University of Edinburgh, Royal Observatory, Blackford Hill, Edinburgh EH9 3HJ, UK
- ⁶⁴⁴ Departamento de Ciencias Físicas, Universidad Andres Bello, Avda. Republica 252, Santiago, 8320000, Chile
- ⁶⁴⁵ Millennium Institute of Astrophysics (MAS), Nuncio Monseñor Sótero Sanz 100, Providencia, Santiago, Chile
- ⁶⁴⁶ European Southern Observatory, Alonso de Córdova 3107, Casilla 19, Santiago, Chile
- ⁶⁴⁷ The Oskar Klein Centre, Department of Astronomy, Stockholm University, AlbaNova, SE-10691 Stockholm, Sweden
- ⁶⁴⁸ Instituto de Astrofísica and Centro de Astroingeniería, Facultad de Física, Pontificia Universidad Católica de Chile, Casilla 306, Santiago 22, Chile
- ⁶⁴⁹ Space Science Institute, 4750 Walnut Street, Suite 205, Boulder, CO 80301, USA
- ⁶⁵⁰ Dipartimento di Fisica e Astronomia "G. Galilei," Università di Padova, Vicolo dell'Osservatorio 3, I-35122, Padova, Italy
- ⁶⁵¹ INAF—Osservatorio Astronomico di Brera, via E. Bianchi 46, I-23807 Merate (LC), Italy
- ⁶⁵² INAF—Osservatorio Astronomico di Capodimonte, via Salita Moiariello 16, I-80131 Napoli, Italy
- ⁶⁵³ The Oskar Klein Centre, Department of Physics, Stockholm University, AlbaNova, SE-10691 Stockholm, Sweden
- ⁶⁵⁴ SRON, Netherlands Institute for Space Research, Sorbonnelaan 2, NL-3584 CA Utrecht, The Netherlands
- ⁶⁵⁵ European Southern Observatory, Karl-Schwarzschild-Str. 2, D-85748 Garching b. München, Germany
- ⁶⁵⁶ ICRANet-Pescara, Piazza della Repubblica 10, I-65122 Pescara, Italy
- ⁶⁵⁷ IAP/CNRS and Université Pierre et Marie Curie, Paris, France
- ⁶⁵⁸ Unidad Mixta Internacional Franco-Chilena de Astronomía (CNRS UMI 3386), Departamento de Astronomía, Universidad de Chile, Camino El Observatorio 1515, Las Condes, Santiago, Chile
- ⁶⁵⁹ Istituto Nazionale di Astrofisica, Viale del Parco Mellini 84, I-00136 Roma, Italy
- ⁶⁶⁰ Institute of Cosmology and Gravitation, Dennis Sciama Building, University of Portsmouth, Burnaby Road, Portsmouth PO1 3FX, UK
- ⁶⁶¹ PITT PACC, Department of Physics and Astronomy, University of Pittsburgh, Pittsburgh, PA 15260, USA
- ⁶⁶² CENTRA, Instituto Superior Técnico, Universidade de Lisboa, Portugal
- ⁶⁶³ Warsaw University Astronomical Observatory, Al. Ujazdowskie 4, 00-478 Warszawa, Poland
- ⁶⁶⁴ Tuorla Observatory, Department of Physics and Astronomy, University of Turku, Väisälantie 20, FI-21500 Piikkiö, Finland
- ⁶⁶⁵ Instituto de Física y Astronomía, Universidad de Valparaíso, Gran Bretaña 1111, Playa Ancha, Valparaíso 2360102, Chile
- ⁶⁶⁶ Institute of Astronomy, University of Cambridge, Madingley Road, Cambridge, CB3 0HA, UK
- ⁶⁶⁷ Department of Physics, Lancaster University, Lancaster LA1 4YB, UK
- ⁶⁶⁸ Instituto de Astrofísica de Andalucía (IAA-CSIC), Glorieta de la Astronomía s/n, E-18008, Granada, Spain
- ⁶⁶⁹ Zentrum für Astronomie der Universität Heidelberg, Institut für Theoretische Astrophysik, Philosophenweg 12, D-69120 Heidelberg, Germany
- ⁶⁷⁰ Heidelberger Institut für Theoretische Studien, Schloss-Wolfsbrunnengasse 35, D-69118 Heidelberg, Germany
- ⁶⁷¹ Finnish Centre for Astronomy with ESO (FINCA), University of Turku, Väisälantie 20, 21500 Piikkiö, Finland
- ⁶⁷² Max Planck Institute for Astronomy, Königstuhl 17, D-69117 Heidelberg, Germany
- ⁶⁷³ Institut für Physik, Humboldt-Universität zu Berlin, Newtonstr. 15, D-12489 Berlin, Germany
- ⁶⁷⁴ Sorbonne Universités, UPMC Univ. Paris 6 and CNRS, UMR 7095, Institut d'Astrophysique de Paris, 98 bis bd Arago, F-75014 Paris, France
- ⁶⁷⁵ INAF-Osservatorio Astronomico di Padova, Vicolo dell'Osservatorio 5, I-35122 Padova, Italy
- ⁶⁷⁶ Department of Astrophysics, University of Oxford, Oxford OX1 3RH, UK
- ⁶⁷⁷ Department of Astronomy, Universidad de Chile, Camino El Observatorio 1515, Las Condes, Santiago de Chile, Chile

- ⁶⁷⁸ School of Physical, Environmental, and Mathematical Sciences, University of New South Wales, Australian Defence Force Academy, Canberra, ACT 2600, Australia
- ⁶⁷⁹ ARC Centre of Excellence for All-sky Astrophysics (CAASTRO), Canberra, ACT 2611, Australia
- ⁶⁸⁰ Università degli studi di Catania, DFA & DIEEI, Via Santa Sofia 64, I-95123 Catania, Italy
- ⁶⁸¹ INFN—Laboratori Nazionali del Sud, Via Santa Sofia 62, I-95123 Catania, Italy
- ⁶⁸² Department of Physics, University of the Free State, Bloemfontein, 9300 South Africa
- ⁶⁸³ School of Physics and Astronomy, University of Minnesota, 116 Church Street SE, Minneapolis, MN 55455-0149, USA
- ⁶⁸⁴ Max-Planck-Institut für Extraterrestrische Physik, Giessenbachstraße 1, D-85748, Garching, Germany
- ⁶⁸⁵ Thüringer Landessternwarte Tautenburg, Sternwarte 5, D-07778 Tautenburg, Germany
- ⁶⁸⁶ Texas Tech University, Lubbock, TX 79409, USA
- ⁶⁸⁷ Department of Astrophysics, American Museum of Natural History, Central Park West and 79th Street, New York, NY 10024, USA
- ⁶⁸⁸ South African Astronomical Observatory, PO Box 9, 7935 Observatory, South Africa
- ⁶⁸⁹ Southern African Large Telescope Foundation, P.O. Box 9, 7935 Observatory, South Africa.
- ⁶⁹⁰ Center for Gravitational Wave Astronomy and Department of Physics & Astronomy, University of Texas—Río Grande Valley, Brownsville, TX, USA
- ⁶⁹¹ George P. and Cynthia W. Mitchell Institute for Fundamental Physics & Astronomy, Department of Physics & Astronomy, Texas A&M University, College Station, TX, USA
- ⁶⁹² IATE-OAC, Universidad Nacional de Córdoba-CONICET, Córdoba, Argentina
- ⁶⁹³ Instituto de Astronomia, Geofísica e Ciências Atmosféricas da U. de São Paulo, São Paulo, SP, Brazil
- ⁶⁹⁴ Instituto de Investigación Multidisciplinario en Ciencia y Tecnología, Universidad de La Serena, La Serena, Chile
- ⁶⁹⁵ Departamento de Física y Astronomía, Universidad de La Serena, La Serena, Chile
- ⁶⁹⁶ Departamento de Física, Universidade Federal de Sergipe, São Cristóvão, SE, Brazil
- ⁶⁹⁷ Departamento de Física, Universidade Federal de Santa Catarina, Florianópolis, SC, Brazil
- ⁶⁹⁸ Departamento de Física Matemática, Instituto de Física, Universidade de São Paulo, São Paulo, SP, Brazil
- ⁶⁹⁹ Departamento de Astronomia, Observatório Nacional, Rio de Janeiro, RJ, Brazil
- ⁷⁰⁰ Centro de Estudios de Física del Cosmos de Aragón, E-44001 Teruel, Spain
- ⁷⁰¹ Instituto Nacional de Astrofísica, Óptica y Electrónica, Tonantzintla, Puebla, México
- ⁷⁰² Instituto de Astronomía, Universidad Nacional Autónoma de México, Ciudad de México, México
- ⁷⁰³ Instituto de Astrofísica, Pontificia Universidad Católica de Chile, Santiago, Chile
- ⁷⁰⁴ Observatorio do Valongo, Universidade Federal do Rio de Janeiro, Rio de Janeiro, RJ, Brazil
- ⁷⁰⁵ X-ray Astrophysics Laboratory and CRESST, NASA Goddard Space Flight Center, Greenbelt, MD, USA
- ⁷⁰⁶ Ludwig Maximilian Universität Munich, Faculty of Physics, Munich, Germany
- ⁷⁰⁷ Department of Physics, University of Notre Dame, Notre Dame, IN, USA
- ⁷⁰⁸ Joint Institute for Nuclear Astrophysics—Center for the Evolution of the Elements, USA
- ⁷⁰⁹ Instituto de Astrofísica de Andalucía del Consejo Superior de Investigaciones Científicas (IAA-CSIC), Granada, Apdo. 03004, E-18080 Granada, Spain
- ⁷¹⁰ Departamento de Ingeniería de Sistemas y Automática, Escuela de Ingenierías (Unidad Asociada al IAA-CSIC), Universidad de Málaga, Dr. Pedro Ortiz Ramos, E-29071 Málaga, Spain
- ⁷¹¹ Departamento de Álgebra, Geometría y Topología, Facultad de Ciencias, Universidad de Málaga, Málaga, Campus de Teatinos, E-29071 sn, Málaga, Spain
- ⁷¹² Instituto de Astronomía, Universidad Nacional Autónoma de México, Apdo. Postal 870, 2800 Ensenada, Baja California, México
- ⁷¹³ Astronomical Institute, Academy of Sciences of the Czech Republic, Boční II 1401, CZ-141 00 Prague, Czech Republic
- ⁷¹⁴ Astronomical Institute, Academy of Sciences of the Czech Republic, 251 65 Ondřejov, Czech Republic
- ⁷¹⁵ Institute of Physics of the Czech Academy of Sciences, Na Slovance 1999/2, 182 21 Praha 8, Czech Republic
- ⁷¹⁶ Department of Physics, Sungkyunkwan University, 2066, Seobu-ro, Jangan-gu, Suwon, Gyeonggi-do, 16419, Korea
- ⁷¹⁷ ISDEFE for ESA, ESAC, E-28692 Villanueva de la Cañada (Madrid), Spain
- ⁷¹⁸ Aryabhata Research Institute of Observational Sciences, Manora Peak, Nainital 263 002, India
- ⁷¹⁹ Department of Physics, University of Auckland, Private Bag 92019, Auckland, New Zealand
- ⁷²⁰ National Institute of Water and Atmospheric Research (NIWA), Lauder, New Zealand
- ⁷²¹ Yunnan Astronomical Observatory, CAS, Kunming 650011, Yunnan, China
- ⁷²² School of Earth and Space Exploration, Arizona State University, Tempe, AZ 85287, USA
- ⁷²³ Dunlap Institute for Astronomy and Astrophysics, University of Toronto, Toronto, ON M5S 3H4, Canada
- ⁷²⁴ Peripety Scientific Ltd., PO Box 11355 Manners Street, Wellington, 6142, New Zealand
- ⁷²⁵ Department of Physics, University of Washington, Seattle, WA 98195, USA
- ⁷²⁶ International Centre for Radio Astronomy Research, University of Western Australia, Crawley, WA 6009, Australia
- ⁷²⁷ National Centre for Nuclear Research, 00-681 Warsaw, Poland
- ⁷²⁸ Aoyama Gakuin University, 5-10-1 Fuchinobe, Chuo, Sagami-hara, Kanagawa 252-5258, Japan
- ⁷²⁹ Nagoya University, Furo, Chikusa, Nagoya 464-8601, Japan
- ⁷³⁰ Kavli Institute for the Physics and Mathematics of the Universe, The University of Tokyo, 5-1-5 Kashiwanoha, Kashiwa 277-8583, Japan
- ⁷³¹ Waseda University, 3-4-1 Okubo, Shinjuku, Tokyo 169-8555, Japan
- ⁷³² Kanagawa University, 3-27-1 Rokkakubashi, Kanagawa, Yokohama, Kanagawa 221-8686, Japan
- ⁷³³ Institute for Cosmic Ray Research, The University of Tokyo, 5-1-5 Kashiwa-no-Ha, Kashiwa, Chiba 277-8582, Japan
- ⁷³⁴ Institute of Applied Physics (IFAC), National Research Council (CNR), Via Madonna del Piano, 10, I-50019 Sesto, Fiorentino, Italy
- ⁷³⁵ University of Siena, Rettorato, via Banchi di Sotto 55, I-53100 Siena, Italy
- ⁷³⁶ Space Research Institute, Moscow, 117997, Russia
- ⁷³⁷ National Research University Higher School of Economics, Moscow, 101000, Russia
- ⁷³⁸ National Research Nuclear University MEPhI, Moscow, 115409, Russia
- ⁷³⁹ Fesenkov Astrophysical Institute, Almaty, 050020, Kazakhstan
- ⁷⁴⁰ Special Astrophysical Observatory of Russian Academy of Sciences, Nizhniy Arkhyz, 369167, Russia
- ⁷⁴¹ Crimean Astrophysical Observatory, Nauchny, Crimea 298409
- ⁷⁴² Kharadze Abastumani Astrophysical Observatory, Ilia State University, Tbilisi, 0162, Georgia
- ⁷⁴³ Institute of Solar Terrestrial Physics, Irkutsk, 664033 Russia
- ⁷⁴⁴ Institute of Astronomy and Geophysics, Mongolian Academy of Sciences, 13343, Ulaanbaatar, Mongolia
- ⁷⁴⁵ Keldysh Institute of Applied Mathematics, Russian Academy of Sciences, Miusskaya 4, 125047, Moscow, Russia
- ⁷⁴⁶ Ulugh Beg Astronomical Institute, Astronomicheskaya st., 33, Tashkent, 100052, Uzbekistan
- ⁷⁴⁷ Centre for Space Research, North-West University, Potchefstroom 2520, South Africa
- ⁷⁴⁸ Universität Hamburg, Institut für Experimentalphysik, Luruper Chaussee 149, D 22761 Hamburg, Germany
- ⁷⁴⁹ Max-Planck-Institut für Kernphysik, P.O. Box 103980, D-69029 Heidelberg, Germany

- ⁷⁵⁰ Dublin Institute for Advanced Studies, 31 Fitzwilliam Place, Dublin 2, Ireland
- ⁷⁵¹ National Academy of Sciences of the Republic of Armenia, Marshall Baghramian Avenue, 24, 0019 Yerevan, Republic of Armenia
- ⁷⁵² Instytut Fizyki Jądrowej PAN, ul. Radzikowskiego 152, 31-342 Kraków, Poland
- ⁷⁵³ Department of Physics, Rikkyo University, 3-34-1 Nishi-Ikebukuro, Toshima-ku, Tokyo 171-8501, Japan
- ⁷⁵⁴ LUTH, Observatoire de Paris, PSL Research University, CNRS, Université Paris Diderot, 5 Place Jules Janssen, F-92190 Meudon, France
- ⁷⁵⁵ Laboratoire d'Annecy-le-Vieux de Physique des Particules, Université Savoie Mont-Blanc, CNRS/IN2P3, F-74941 Annecy-le-Vieux, France
- ⁷⁵⁶ University of Namibia, Department of Physics, Private Bag 13301, Windhoek, Namibia
- ⁷⁵⁷ GRAPPA, Anton Pannekoek Institute for Astronomy, University of Amsterdam, Science Park 904, 1098 XH Amsterdam, The Netherlands
- ⁷⁵⁸ Department of Physics and Electrical Engineering, Linnaeus University, 351 95 Växjö, Sweden
- ⁷⁵⁹ Institut für Theoretische Physik, Lehrstuhl IV: Weltraum und Astrophysik, Ruhr-Universität Bochum, D 44780 Bochum, Germany
- ⁷⁶⁰ GRAPPA, Anton Pannekoek Institute for Astronomy and Institute of High-Energy Physics, University of Amsterdam, Science Park 904, 1098 XH Amsterdam, The Netherlands
- ⁷⁶¹ Institut für Astro- und Teilchenphysik, Leopold-Franzens-Universität Innsbruck, A-6020 Innsbruck, Austria
- ⁷⁶² School of Physical Sciences, University of Adelaide, Adelaide 5005, Australia
- ⁷⁶³ Sorbonne Universités, UPMC Université Paris 06, Université Paris Diderot, Sorbonne Paris Cité, CNRS, Laboratoire de Physique Nucléaire et de Hautes Energies (LPNHE), 4 place Jussieu, F-75252, Paris Cedex 5, France
- ⁷⁶⁴ Laboratoire Univers et Particules de Montpellier, CNRS/IN2P3, Centre d'Études Nucléaires de Bordeaux Gradignan, F-33175 Gradignan, France
- ⁷⁶⁵ Université Bordeaux, CNRS/IN2P3, Centre d'Études Nucléaires de Bordeaux Gradignan, F-33175 Gradignan, France
- ⁷⁶⁶ IRFU, CEA, Université Paris-Saclay, F-91191 Gif-sur-Yvette, France
- ⁷⁶⁷ Astronomical Observatory, The University of Warsaw, Al. Ujazdowskie 4, 00-478 Warsaw, Poland
- ⁷⁶⁸ Institut für Astronomie und Astrophysik, Universität Tübingen, Sand 1, D 72076 Tübingen, Germany
- ⁷⁶⁹ School of Physics, University of the Witwatersrand, 1 Jan Smuts Avenue, Braamfontein, Johannesburg 2050, South Africa
- ⁷⁷⁰ Oskar Klein Centre, Department of Physics, Stockholm University, Albanova University Center, SE-10691 Stockholm, Sweden
- ⁷⁷¹ APC, AstroParticule et Cosmologie, Université Paris Diderot, CNRS/IN2P3, CEA/Irfu, Observatoire de Paris, Sorbonne Paris Cité, 10, rue Alice Domon et Léonie Duquet, 75205 Paris Cedex 13, France
- ⁷⁷² Department of Physics and Astronomy, The University of Leicester, University Road, Leicester LE1 7RH, UK
- ⁷⁷³ Nicolaus Copernicus Astronomical Center, Polish Academy of Sciences, ul. Bartycka 18, 00-716 Warsaw, Poland
- ⁷⁷⁴ Institut für Physik und Astronomie, Universität Potsdam, Karl-Liebknecht-Strasse 24/25, D 14476 Potsdam, Germany
- ⁷⁷⁵ Aix Marseille Université, CNRS/IN2P3, CPPM, Marseille, France
- ⁷⁷⁶ Landessternwarte, Universität Heidelberg, Königstuhl, D 69117 Heidelberg, Germany
- ⁷⁷⁷ Univ. Grenoble Alpes, CNRS, IPAG, F-38000 Grenoble, France
- ⁷⁷⁸ Institut für Physik, Humboldt-Universität zu Berlin, Newtonstr. 15, D 12489 Berlin, Germany
- ⁷⁷⁹ Obserwatorium Astronomiczne, Uniwersytet Jagielloński, ul. Orla 171, 30-244 Kraków, Poland
- ⁷⁸⁰ Centre for Astronomy, Faculty of Physics, Astronomy and Informatics, Nicolaus Copernicus University, Grudziadzka 5, 87-100 Torun, Poland
- ⁷⁸¹ Japan Aerospace Exploration Agency (JAXA), Institute of Space and Astronautical Science (ISAS), 3-1-1 Yoshinodai, Chuo-ku, Sagami-hara, Kanagawa 229-8510, Japan
- ⁷⁸² Department of Physics, University of the Free State, PO Box 339, Bloemfontein 9300, South Africa
- ⁷⁸³ Heisenberg Fellow (DFG), ITA Universität Heidelberg, Germany
- ⁷⁸⁴ Yerevan Physics Institute, 2 Alikhanian Brothers Street, 375036 Yerevan, Armenia
- ⁷⁸⁵ Astrophysics, Department of Physics, University of Oxford, Keble Road, Oxford OX1 3RH, UK
- ⁷⁸⁶ Anton Pannekoek Institute, University of Amsterdam, Science Park 904, 1098 XH Amsterdam, The Netherlands
- ⁷⁸⁷ Long Island University, New York, NY 11201, USA
- ⁷⁸⁸ Virginia Tech, Blacksburg, VA 24061, USA
- ⁷⁸⁹ Air Force Research Laboratory, NM 87117, USA
- ⁷⁹⁰ University of New Mexico, Albuquerque, NM 87131, USA
- ⁷⁹¹ Long Island University, Brookville, NY 11548, USA
- ⁷⁹² Department of Physics and Astronomy, University of Utah, Salt Lake City, UT, USA
- ⁷⁹³ Physics Division, Los Alamos National Laboratory, Los Alamos, NM, USA
- ⁷⁹⁴ Instituto de Física, Universidad Nacional Autónoma de México, Ciudad de México, México
- ⁷⁹⁵ Universidad Autónoma de Chiapas, Tuxtla Gutiérrez, Chiapas, México
- ⁷⁹⁶ Universidad Michoacana de San Nicolás de Hidalgo, Morelia, México
- ⁷⁹⁷ Department of Physics, Michigan Technological University, Houghton, MI, USA
- ⁷⁹⁸ Department of Physics & Astronomy, University of Rochester, Rochester, NY, USA
- ⁷⁹⁹ Department of Physics, University of Maryland, College Park, MD, USA
- ⁸⁰⁰ Instituto de Astronomía, Universidad Nacional Autónoma de México, Ciudad de México, México
- ⁸⁰¹ Department of Physics, University of Wisconsin-Madison, Madison, WI, USA
- ⁸⁰² Instituto Nacional de Astrofísica, Óptica y Electrónica, Puebla, Mexico
- ⁸⁰³ Instytut Fizyki Jądrowej im Henryka Niewodniczanskiego Polskiej Akademii Nauk, IFJ-PAN, Krakow, Poland
- ⁸⁰⁴ Facultad de Ciencias Físico Matemáticas, Benemérita Universidad Autónoma de Puebla, Puebla, Mexico
- ⁸⁰⁵ Departamento de Física, Centro Universitario de Ciencias Exactas e Ingenierías, Universidad de Guadalajara, Guadalajara, Mexico
- ⁸⁰⁶ School of Physics, Astronomy, and Computational Sciences, George Mason University, Fairfax, VA, USA
- ⁸⁰⁷ Instituto de Geofísica, Universidad Nacional Autónoma de México, Ciudad de México, México
- ⁸⁰⁸ Max-Planck Institute for Nuclear Physics, 69117 Heidelberg, Germany
- ⁸⁰⁹ Department of Physics and Astronomy, University of New Mexico, Albuquerque, NM, USA
- ⁸¹⁰ School of Physics and Center for Relativistic Astrophysics—Georgia Institute of Technology, Atlanta, GA, USA 30332
- ⁸¹¹ Department of Physics and Astronomy, Michigan State University, East Lansing, MI, USA
- ⁸¹² Universidad Politécnica de Pachuca, Pachuca, Hgo, Mexico
- ⁸¹³ Centro de Investigación en Computación, Instituto Politécnico Nacional, México City, México.
- ⁸¹⁴ Department of Physics, Pennsylvania State University, University Park, PA, USA
- ⁸¹⁵ Physics Department, Centro de Investigación y de Estudios Avanzados del IPN, México City, DF, México
- ⁸¹⁶ Universidad Autónoma del Estado de Hidalgo, Pachuca, Mexico
- ⁸¹⁷ Instituto de Ciencias Nucleares, Universidad Nacional Autónoma de México, Ciudad de México, México
- ⁸¹⁸ Santa Cruz Institute for Particle Physics, University of California, Santa Cruz, Santa Cruz, CA, USA
- ⁸¹⁹ Department of Physics and Astronomy, University of California, Irvine, Irvine, CA, USA

- ⁸²⁰ Laboratório de Instrumentação e Física Experimental de Partículas – LIP and Instituto Superior Técnico – IST, Universidade de Lisboa – UL, Lisboa, Portugal
- ⁸²¹ Osservatorio Astrofisico di Torino (INAF), Torino, Italy
- ⁸²² INFN, Sezione di Torino, Torino, Italy
- ⁸²³ Universidade de São Paulo, Instituto de Física, São Paulo, SP, Brazil
- ⁸²⁴ University of Adelaide, Adelaide, SA, Australia
- ⁸²⁵ Centro Atómico Bariloche and Instituto Balseiro (CNEA-UNCuyo-CONICET), San Carlos de Bariloche, Argentina
- ⁸²⁶ Instituto de Tecnologías en Detección y Astropartículas (CNEA, CONICET, UNSAM), Buenos Aires, Argentina
- ⁸²⁷ Universidad Tecnológica Nacional, Facultad Regional Buenos Aires, Buenos Aires, Argentina
- ⁸²⁸ Universidad Nacional Autónoma de México, México, D.F., México
- ⁸²⁹ Universidad de Santiago de Compostela, Santiago de Compostela, Spain
- ⁸³⁰ Gran Sasso Science Institute (INFN), L'Aquila, Italy
- ⁸³¹ INFN Laboratori Nazionali del Gran Sasso, Assergi (L'Aquila), Italy
- ⁸³² Department of Physics and Astronomy, Lehman College, City University of New York, New York, NY, USA
- ⁸³³ INFN, Sezione di Napoli, Napoli, Italy
- ⁸³⁴ Institute of Space Science, Bucharest-Magurele, Romania
- ⁸³⁵ Universidad Industrial de Santander, Bucaramanga, Colombia
- ⁸³⁶ Observatorio Pierre Auger, Malargüe, Argentina
- ⁸³⁷ Observatorio Pierre Auger and Comisión Nacional de Energía Atómica, Malargüe, Argentina
- ⁸³⁸ University Politehnica of Bucharest, Bucharest, Romania
- ⁸³⁹ “Horia Hulubei” National Institute for Physics and Nuclear Engineering, Bucharest-Magurele, Romania
- ⁸⁴⁰ Università di Napoli “Federico II”, Dipartimento di Fisica “Ettore Pancini,” Napoli, Italy
- ⁸⁴¹ Laboratoire de Physique Subatomique et de Cosmologie (LPSC), Université Grenoble-Alpes, CNRS/IN2P3, Grenoble, France
- ⁸⁴² Università Torino, Dipartimento di Fisica, Torino, Italy
- ⁸⁴³ Max-Planck-Institut für Radioastronomie, Bonn, Germany
- ⁸⁴⁴ Institut de Physique Nucléaire d'Orsay (IPNO), Université Paris-Sud, Univ. Paris/Saclay, CNRS-IN2P3, Orsay, France
- ⁸⁴⁵ Institute of Physics of the Czech Academy of Sciences, Prague, Czech Republic
- ⁸⁴⁶ Università del Salento, Dipartimento di Matematica e Fisica “E. De Giorgi,” Lecce, Italy
- ⁸⁴⁷ INFN, Sezione di Lecce, Lecce, Italy
- ⁸⁴⁸ Universidade Federal do Rio de Janeiro, Instituto de Física, Rio de Janeiro, RJ, Brazil
- ⁸⁴⁹ Institute of Nuclear Physics PAN, Krakow, Poland
- ⁸⁵⁰ Karlsruhe Institute of Technology, Institut für Kernphysik, Karlsruhe, Germany
- ⁸⁵¹ Colorado State University, Fort Collins, CO 80523
- ⁸⁵² RWTH Aachen University, III. Physikalisches Institut A, Aachen, Germany
- ⁸⁵³ Karlsruhe Institute of Technology, Institut für Experimentelle Kernphysik (IEKP), Karlsruhe, Germany
- ⁸⁵⁴ Universität Siegen, Fachbereich 7 Physik – Experimentelle Teilchenphysik, Siegen, Germany
- ⁸⁵⁵ Universidad de Granada and C.A.F.P.E., Granada, Spain
- ⁸⁵⁶ Università di Catania, Dipartimento di Fisica e Astronomia, Catania, Italy
- ⁸⁵⁷ INFN, Sezione di Catania, Catania, Italy
- ⁸⁵⁸ Università di Milano, Dipartimento di Fisica, Milano, Italy
- ⁸⁵⁹ Universidade de São Paulo, Escola de Engenharia de Lorena, Lorena, SP, Brazil
- ⁸⁶⁰ Universidad Michoacana de San Nicolás de Hidalgo, Morelia, Michoacán, México
- ⁸⁶¹ Universidade Estadual de Campinas, IFGW, Campinas, SP, Brazil
- ⁸⁶² Instituto de Tecnologías en Detección y Astropartículas (CNEA, CONICET, UNSAM), and Universidad Tecnológica Nacional – Facultad Regional Mendoza (CONICET/CNEA), Mendoza, Argentina
- ⁸⁶³ Pennsylvania State University, University Park, PA, USA
- ⁸⁶⁴ INFN, Sezione di Milano, Milano, Italy
- ⁸⁶⁵ Politecnico di Milano, Dipartimento di Scienze e Tecnologie Aerospaziali, Milano, Italy
- ⁸⁶⁶ Case Western Reserve University, Cleveland, OH, USA
- ⁸⁶⁷ University of Chicago, Enrico Fermi Institute, Chicago, IL, USA
- ⁸⁶⁸ Università del Salento, Dipartimento di Ingegneria, Lecce, Italy
- ⁸⁶⁹ Instituto de Astronomía y Física del Espacio (IAFE, CONICET-UBA), Buenos Aires, Argentina
- ⁸⁷⁰ Departamento de Física and Departamento de Ciencias de la Atmósfera y los Océanos, FCEyN, Universidad de Buenos Aires and CONICET, Buenos Aires, Argentina
- ⁸⁷¹ Universidade Federal Fluminense, EEIMVR, Volta Redonda, RJ, Brazil
- ⁸⁷² Universidade Federal do Rio de Janeiro (UFRJ), Observatório do Valongo, Rio de Janeiro, RJ, Brazil
- ⁸⁷³ Universidade de São Paulo, Instituto de Física de São Carlos, São Carlos, SP, Brazil
- ⁸⁷⁴ Universidade Federal do Paraná, Setor Palotina, Palotina, Brazil
- ⁸⁷⁵ IFLP, Universidad Nacional de La Plata and CONICET, La Plata, Argentina
- ⁸⁷⁶ Universität Hamburg, II. Institut für Theoretische Physik, Hamburg, Germany
- ⁸⁷⁷ Fermi National Accelerator Laboratory, USA
- ⁸⁷⁸ Stichting Astronomisch Onderzoek in Nederland (ASTRON), Dwingeloo, The Netherlands
- ⁸⁷⁹ New York University, New York, NY, USA
- ⁸⁸⁰ Karlsruhe Institute of Technology, Institut für Prozessdatenverarbeitung und Elektronik, Karlsruhe, Germany
- ⁸⁸¹ Michigan Technological University, Houghton, MI, USA
- ⁸⁸² Experimental Particle Physics Department, J. Stefan Institute, Ljubljana, Slovenia
- ⁸⁸³ Instituto de Física de Rosario (IFIR) – CONICET/U.N.R. and Facultad de Ciencias Bioquímicas y Farmacéuticas U.N.R., Rosario, Argentina
- ⁸⁸⁴ Laboratoire de Physique Nucléaire et de Hautes Energies (LPNHE), Universités Paris 6 et Paris 7, CNRS-IN2P3, Paris, France
- ⁸⁸⁵ SUBATECH, École des Mines de Nantes, CNRS-IN2P3, Université de Nantes, France
- ⁸⁸⁶ Centro Brasileiro de Pesquisas Físicas, Rio de Janeiro, RJ, Brazil
- ⁸⁸⁷ University of Łódź, Faculty of Astrophysics, Łódź, Poland
- ⁸⁸⁸ University of Łódź, Faculty of High-Energy Astrophysics, Łódź, Poland
- ⁸⁸⁹ Universidade Estadual de Feira de Santana, Feira de Santana, Brazil
- ⁸⁹⁰ Palacky University, RCPTM, Olomouc, Czech Republic
- ⁸⁹¹ Colorado School of Mines, Golden, CO, USA
- ⁸⁹² Centro Federal de Educação Tecnológica Celso Suckow da Fonseca, Nova Friburgo, Brazil

- ⁸⁹³ Universidade Federal do ABC, Santo André, SP, Brazil
- ⁸⁹⁴ Benemérita Universidad Autónoma de Puebla, Puebla, México
- ⁸⁹⁵ Université Libre de Bruxelles (ULB), Brussels, Belgium
- ⁸⁹⁶ Centro de Investigación y de Estudios Avanzados del IPN (CINVESTAV), México, D.F., México
- ⁸⁹⁷ Università di Roma "Tor Vergata," Dipartimento di Fisica, Roma, Italy
- ⁸⁹⁸ INFN, Sezione di Roma "Tor Vergata", Roma, Italy
- ⁸⁹⁹ Also at Universidade Federal de Alfenas, Brasília, Brazil
- ⁹⁰⁰ Charles University, Faculty of Mathematics and Physics, Institute of Particle and Nuclear Physics, Prague, Czech Republic
- ⁹⁰¹ Centro de Investigaciones en Láseres y Aplicaciones, CITEDEF and CONICET, Villa Martelli, Argentina
- ⁹⁰² Università dell'Aquila, Dipartimento di Scienze Fisiche e Chimiche, L'Aquila, Italy
- ⁹⁰³ KVI – Center for Advanced Radiation Technology, University of Groningen, Groningen, The Netherlands
- ⁹⁰⁴ Also at Vrije Universiteit Brussels, Brussels, Belgium
- ⁹⁰⁵ INAF – Istituto di Astrofisica Spaziale e Fisica Cosmica di Palermo, Palermo, Italy
- ⁹⁰⁶ University of Nebraska, Lincoln, NE, USA
- ⁹⁰⁷ Northeastern University, Boston, MA, USA
- ⁹⁰⁸ School of Physics and Astronomy, University of Leeds, Leeds, UK
- ⁹⁰⁹ Università di Catania, Dipartimento di Fisica e Astronomia, Catania, Italy
- ⁹¹⁰ Instituto de Astrofísica and Centro de Astroingeniería, Facultad de Física, Pontificia Universidad Católica de Chile, Casilla 306, Santiago 22, Chile
- ⁹¹¹ Department of Particle Physics and Astrophysics, Weizmann Institute of Science, Rehovot 761000, Israel
- ⁹¹² Millennium Institute of Astrophysics (MAS), Nuncio Monseñor Sótero Sanz 100, Providencia, Santiago, Chile
- ⁹¹³ European Southern Observatory, Alonso de Córdova 3107, Vitacura, Santiago 763-0355, Chile
- ⁹¹⁴ Joint ALMA Observatory, Alonso de Córdova 3107, Vitacura, Santiago 763-0355, Chile
- ⁹¹⁵ Department of Physics & Astronomy, Clemson University, Clemson, SC 29634, USA
- ⁹¹⁶ National Center for Radio Astrophysics, Pune 411007, India
- ⁹¹⁷ ARIES, Manora Peak, Nainital 263 001, India
- ⁹¹⁸ Astronomical Observatory Institute, Faculty of Physics, Adam Mickiewicz University, ul. Stoleczna 36, 60-286 Poznań, Poland
- ⁹¹⁹ Indian Institute of Space Science & Technology, Trivandrum 695547, India
- ⁹²⁰ Joint Institute for VLBI ERIC (JIVE), 7991 PD Dwingeloo, The Netherlands
- ⁹²¹ Instituto de Astrofísica de Andalucía-CSIC, Granada, Spain
- ⁹²² Shanghai Astronomical Observatory (ShAO), Key Laboratory of Radio Astronomy, CAS, Shanghai 200030 China
- ⁹²³ Guilin University of Electronic Technology (GUET), Guilin 541004, China
- ⁹²⁴ JBCA, The University of Manchester, Manchester M13 9PL, UK
- ⁹²⁵ Max Planck Institut für Radioastronomie, D-53121, Bonn, Germany
- ⁹²⁶ Konkoly Observatory, MTA CSFK, H-1121 Budapest, Hungary
- ⁹²⁷ SRON Netherlands Institute for Space Research, 3584 CA Utrecht, The Netherlands
- ⁹²⁸ Leiden Observatory, Leiden University, 2300 RA Leiden, The Netherlands.
- ⁹²⁹ Onsala Space Observatory, 439 92 Onsala, Sweden
- ⁹³⁰ University of Warsaw, Faculty of Physics, 02-093 Warsaw, Poland
- ⁹³¹ Warsaw University of Technology, Institute of Electronic Systems, 00-665 Warsaw, Poland
- ⁹³² Center for Theoretical Physics, Polish Academy of Sciences, 02-668 Warsaw, Poland
- ⁹³³ RIKEN, Wako, 351-0198 Saitama, Japan
- ⁹³⁴ McGill Space Institute and Department of Physics, McGill University, 3600 rue University, Montreal, QC H3A 2T8, Canada
- ⁹³⁵ Department of Applied Geology, Curtin University, GPO Box U1987, Perth, WA 6845, Australia
- ⁹³⁶ Department of Mechanical Engineering, Curtin University, GPO Box U1987, Perth, WA 6845, Australia
- ⁹³⁷ LIGO Laboratory West Bridge, California Institute of Technology, MC 100-36, Room 257, Pasadena, CA 91125
- ⁹³⁸ Department of Physics, Harvard University, Cambridge, MA 02138, USA
- ⁹³⁹ LSST, 950 N. Cherry Avenue, Tucson, AZ 85719, USA
- ⁹⁴⁰ Max-Planck-Institut für Radioastronomie, Auf dem Hügel 69, D-53177 Bonn, Germany
- ⁹⁴¹ NASA Goddard Space Flight Center, 8800 Greenbelt Road, Greenbelt, MD 20771, USA
- ⁹⁴² Department of Astronomy, University of Maryland, College Park, MD 20742-4111, USA
- ⁹⁴³ Inst. de Astrofísica de Canarias, E-38200 La Laguna, Tenerife, Spain
- ⁹⁴⁴ Universidad de La Laguna, Dpto. Astrofísica, E-38206 La Laguna, Tenerife, Spain
- ⁹⁴⁵ Space Telescope Science Institute, Baltimore MD, 21218
- ⁹⁴⁶ Instituto de Astronomía, Universidad Nacional Autónoma de México, Apartado Postal 70-264, 04510 México, CDMX, Mexico
- ⁹⁴⁷ INFN—Istituto di Radioastronomia, Via Gobetti 101, I-40129, Italy
- ⁹⁴⁸ CSIRO Astronomy and Space Science, P.O. Box 76, Epping, NSW 1710, Australia
- ⁹⁴⁹ Max-Planck-Institut für extraterrestrische Physik, Giessenbachstrasse, D-85748 Garching, Germany
- ⁹⁵⁰ Department of Physics, University of Bath, Claverton Down, Bath BA2 7AY, UK
- ⁹⁵¹ Center for Theoretical Astrophysics, Los Alamos National Laboratory, Los Alamos, NM 87545, USA
- ⁹⁵² SKA South Africa, Pinelands, 7405, South Africa
- ⁹⁵³ Department of Astronomy, Astrophysics, Cosmology and Gravity Centre, University of Cape Town, Private Bag X3 Rondebosch, 7701 South Africa
- ⁹⁵⁴ Deceased 2017 February.
- ⁹⁵⁵ Deceased 2016 December.
- ⁹⁵⁶ Deceased 2017 August 18.
- ⁹⁵⁷ Deceased 2016 August.



OBSERVATION AND CHARACTERIZATION OF A COSMIC MUON NEUTRINO FLUX FROM THE NORTHERN HEMISPHERE USING SIX YEARS OF ICECUBE DATA

M. G. AARTSEN¹, K. ABRAHAM², M. ACKERMANN³, J. ADAMS⁴, J. A. AGUILAR⁵, M. AHLERS⁶, M. AHRENS⁷, D. ALTMANN⁸, K. ANDEEN⁹, T. ANDERSON¹⁰, I. ANSSEAU⁵, G. ANTON⁸, M. ARCHINGER¹¹, C. ARGÜELLES¹², J. AUFFENBERG¹³, S. AXANI¹², X. BAI¹⁴, S. W. BARWICK¹⁵, V. BAUM¹¹, R. BAY¹⁶, J. J. BEATTY^{17,18}, J. BECKER TJUS¹⁹, K.-H. BECKER²⁰, S. BENZVI²¹, P. BERGHAUS²², D. BERLEY²³, E. BERNARDINI³, A. BERNHARD², D. Z. BESSON²⁴, G. BINDER^{16,25}, D. BINDIG²⁰, M. BISSOK¹³, E. BLAUFUSS²³, S. BLOT³, C. BOHM⁷, M. BÖRNER²⁶, F. BOS¹⁹, D. BOSE²⁷, S. BÖSER¹¹, O. BOTNER²⁸, J. BRAUN⁶, L. BRAYEUR²⁹, H.-P. BRETZ³, A. BURGMAN²⁸, T. CARVER³⁰, M. CASIER²⁹, E. CHEUNG²³, D. CHIRKIN⁶, A. CHRISTOV³⁰, K. CLARK³¹, L. CLASSEN³², S. COENDERS², G. H. COLLIN¹², J. M. CONRAD¹², D. F. COWEN^{10,33}, R. CROSS²¹, M. DAY⁶, J. P. A. M. DE ANDRÉ³⁴, C. DE CLERCQ²⁹, E. DEL PINO ROSENDO¹¹, H. DEMBINSKI³⁵, S. DE RIDDER³⁶, P. DESIATI⁶, K. D. DE VRIES²⁹, G. DE WASSEIGE²⁹, M. DE WITH³⁷, T. DEYOUNG³⁴, J. C. DÍAZ-VÉLEZ⁶, V. DI LORENZO¹¹, H. DUJMOVIC²⁷, J. P. DUMM⁷, M. DUNKMAN¹⁰, B. EBERHARDT¹¹, T. EHRHARDT¹¹, B. EICHMANN¹⁹, P. ELLER¹⁰, S. EULER²⁸, P. A. EVENSON³⁵, S. FAHEY⁶, A. R. FAZELY³⁸, J. FEINTZEIG⁶, J. FELDE²³, K. FILIMONOV¹⁶, C. FINLEY⁷, S. FLIS⁷, C.-C. FÖSIG¹¹, A. FRANCKOWIAK³, E. FRIEDMAN²³, T. FUCHS²⁶, T. K. GAISSER³⁵, J. GALLAGHER³⁹, L. GERHARDT^{16,25}, K. GHORBANI⁶, W. GIANG⁴⁰, L. GLADSTONE⁶, M. GLAGLA¹³, T. GLÜSENKAMP³, A. GOLDSCHMIDT²⁵, G. GOLUP²⁹, J. G. GONZALEZ³⁵, D. GRANT⁴⁰, Z. GRIFFITH⁶, C. HAACK¹³, A. HAJ ISMAIL³⁶, A. HALLGREN²⁸, F. HALZEN⁶, E. HANSEN⁴¹, B. HANSMANN¹³, T. HANSMANN¹³, K. HANSON⁶, D. HEBECKER³⁷, D. HEEREMAN⁵, K. HELBING²⁰, R. HELLAUER²³, S. HICKFORD²⁰, J. HIGNIGHT³⁴, G. C. HILL¹, K. D. HOFFMAN²³, R. HOFFMANN²⁰, K. HOLZAPFEL², K. HOSHINA^{6,42}, F. HUANG¹⁰, M. HUBER², K. HULTOVIST⁷, S. IN²⁷, A. ISHIHARA⁴³, E. JACOBI³, G. S. JAPARIDZE⁴⁴, M. JEONG²⁷, K. JERO⁶, B. J. P. JONES¹², M. JURKOVIC², A. KAPPES³², T. KARG³, A. KARLE⁶, U. KATZ⁸, M. KAUER⁶, A. KEIVANI¹⁰, J. L. KELLEY⁶, J. KEMP¹³, A. KHEIRANDISH⁶, M. KIM²⁷, T. KINTSCHER³, J. KIRYLUK⁴⁵, T. KITTLER⁸, S. R. KLEIN^{16,25}, G. KOHNEN⁴⁶, R. KOIRALA³⁵, H. KOLANOSKI³⁷, R. KONIETZ¹³, L. KÖPKE¹¹, C. KOPPER⁴⁰, S. KOPPER²⁰, D. J. KOSKINEN⁴¹, M. KOWALSKI^{3,37}, K. KRINGS², M. KROLL¹⁹, G. KRÜCKL¹¹, C. KRÜGER⁶, J. KUNNEN²⁹, S. KUNWAR³, N. KURAHASHI⁴⁷, T. KUWABARA⁴³, M. LABARE³⁶, J. L. LANFRANCHI¹⁰, M. J. LARSON⁴¹, F. LAUBER²⁰, D. LENNARZ³⁴, M. LESIAK-BZDAK⁴⁵, M. LEUERMANN¹³, J. LEUNER¹³, L. LU⁴³, J. LÜNEMANN²⁹, J. MADSEN⁴⁸, G. MAGGI²⁹, K. B. M. MAHN³⁴, S. MANCINA⁶, M. MANDELARTZ¹⁹, R. MARUYAMA⁴⁹, K. MASE⁴³, R. MAUNU²³, F. MCNALLY⁶, K. MEAGHER⁵, M. MEDICI⁴¹, M. MEIER²⁶, A. MELI³⁶, T. MENNE²⁶, G. MERINO⁶, T. MEURES⁵, S. MIARECKI^{16,25}, L. MOHRMANN³, T. MONTARULI³⁰, M. MOULAI¹², R. NAHNHAUER³, U. NAUMANN²⁰, G. NEER³⁴, H. NIEDERHAUSEN⁴⁵, S. C. NOWICKI⁴⁰, D. R. NYGREN²⁵, A. OBERTACKE POLLMANN²⁰, A. OLIVAS²³, A. O'MURCHADHA⁵, T. PALCZEWSKI⁵⁰, H. PANDYA³⁵, D. V. PANKOVA¹⁰, P. PEIFFER¹¹, Ö. PENEK¹³, J. A. PEPPER⁵⁰, C. PÉREZ DE LOS HEROS²⁸, D. PIELOTH²⁶, E. PINAT⁵, P. B. PRICE¹⁶, G. T. PRZYBYLSKI²⁵, M. QUINNAN¹⁰, C. RAAB⁵, L. RÄDEL¹³, M. RAMEEZ⁴¹, K. RAWLINS⁵¹, R. REIMANN¹³, B. RELETHFORD⁴⁷, M. RELICH⁴³, E. RESCONI², W. RHODE²⁶, M. RICHMAN⁴⁷, B. RIEDEL⁴⁰, S. ROBERTSON¹, M. RONGEN¹³, C. ROTT²⁷, T. RUHE²⁶, D. RYCKBOSCH³⁶, D. RYSEWYK³⁴, L. SABBATINI⁶, S. E. SANCHEZ HERRERA⁴⁰, A. SANDROCK²⁶, J. SANDROOS¹¹, S. SARKAR^{41,52}, K. SATALECKA³, M. SCHIMP¹³, P. SCHLUNDER²⁶, T. SCHMIDT²³, S. SCHOENEN¹³, S. SCHÖNEBERG¹⁹, L. SCHUMACHER¹³, D. SECKEL³⁵, S. SEUNARINE⁴⁸, D. SOLDIN²⁰, M. SONG²³, G. M. SPICZAK⁴⁸, C. SPIERING³, M. STAHLBERG¹³, T. STANEV³⁵, A. STASIK³, A. STEUER¹¹, T. STEZELBERGER²⁵, R. G. STOKSTAD²⁵, A. STÖBL³, R. STRÖM²⁸, N. L. STROTJOHANN³, G. W. SULLIVAN²³, M. SUTHERLAND¹⁷, H. TAAVOLA²⁸, I. TABOADA⁵³, J. TATAR^{16,25}, F. TENHOLT¹⁹, S. TER-ANTONYAN³⁸, A. TERLIUK³, G. TEŠIĆ¹⁰, S. TILAV³⁵, P. A. TOALE⁵⁰, M. N. TOBIN⁶, S. TOSCANO²⁹, D. TOSI⁶, M. TSELENGIDOU⁸, A. TURCATI², E. UNGER²⁸, M. USNER³, J. VANDENBROUCKE⁶, N. VAN EIJNDHOVEN²⁹, S. VANHEULE³⁶, M. VAN ROSSEM⁶, J. VAN SANTEN³, J. VEENKAMP², M. VEHRING¹³, M. VOGÉ⁵⁴, M. VRAEGHE³⁶, C. WALCK⁷, A. WALLACE¹, M. WALLRAFF¹³, N. WANDKOWSKY⁶, CH. WEAVER⁴⁰, M. J. WEISS¹⁰, C. WENDT⁶, S. WESTERHOFF⁶, B. J. WHELAN¹, S. WICKMANN¹³, K. WIEBE¹¹, C. H. WIEBUSCH¹³, L. WILLE⁶, D. R. WILLIAMS⁵⁰, L. WILLS⁴⁷, M. WOLF⁷, T. R. WOOD⁴⁰, E. WOOLSEY⁴⁰, K. WOSCHNAGG¹⁶, D. L. XU⁶, X. W. XU³⁸, Y. XU⁴⁵, J. P. YANEZ³, G. YODH¹⁵, S. YOSHIDA⁴³, AND M. ZOLL⁷

(ICECUBE COLLABORATION)

¹ Department of Physics, University of Adelaide, Adelaide, 5005, Australia

² Physik-department, Technische Universität München, D-85748 Garching, Germany

³ DESY, D-15735 Zeuthen, Germany

⁴ Dept. of Physics and Astronomy, University of Canterbury, Private Bag 4800, Christchurch, New Zealand

⁵ Université Libre de Bruxelles, Science Faculty CP230, B-1050 Brussels, Belgium

⁶ Dept. of Physics and Wisconsin IceCube Particle Astrophysics Center, University of Wisconsin, Madison, WI 53706, USA

⁷ Oskar Klein Centre And Dept. Of Physics, Stockholm University, SE-10691 Stockholm, Sweden

⁸ Erlangen Centre for Astroparticle Physics, Friedrich-Alexander-Universität Erlangen-Nürnberg, D-91058 Erlangen, Germany

⁹ Department of Physics, Marquette University, Milwaukee, WI, 53201, USA

¹⁰ Dept. of Physics, Pennsylvania State University, University Park, PA 16802, USA

¹¹ Institute of Physics, University of Mainz, Staudinger Weg 7, D-55099 Mainz, Germany

¹² Dept. of Physics, Massachusetts Institute of Technology, Cambridge, MA 02139, USA

¹³ III. Physikalisches Institut, RWTH Aachen University, D-52056 Aachen, Germany

¹⁴ Physics Department, South Dakota School of Mines and Technology, Rapid City, SD 57701, USA

¹⁵ Dept. of Physics and Astronomy, University of California, Irvine, CA 92697, USA

¹⁶ Dept. of Physics, University of California, Berkeley, CA 94720, USA

¹⁷ Dept. of Physics and Center for Cosmology and Astro-Particle Physics, Ohio State University, Columbus, OH 43210, USA

- ¹⁸ Dept. of Astronomy, Ohio State University, Columbus, OH 43210, USA
¹⁹ Fakultät für Physik & Astronomie, Ruhr-Universität Bochum, D-44780 Bochum, Germany
²⁰ Dept. of Physics, University of Wuppertal, D-42119 Wuppertal, Germany
²¹ Dept. of Physics and Astronomy, University of Rochester, Rochester, NY 14627, USA
²² National Research Nuclear University MEPhI (Moscow Engineering Physics Institute), Moscow, Russia
²³ Dept. of Physics, University of Maryland, College Park, MD 20742, USA
²⁴ Dept. of Physics and Astronomy, University of Kansas, Lawrence, KS 66045, USA
²⁵ Lawrence Berkeley National Laboratory, Berkeley, CA 94720, USA
²⁶ Dept. of Physics, TU Dortmund University, D-44221 Dortmund, Germany
²⁷ Dept. of Physics, Sungkyunkwan University, Suwon 440-746, Korea
²⁸ Dept. of Physics and Astronomy, Uppsala University, Box 516, S-75120 Uppsala, Sweden
²⁹ Vrije Universiteit Brussel, Dienst ELEM, B-1050 Brussels, Belgium
³⁰ Département de physique nucléaire et corpusculaire, Université de Genève, CH-1211 Genève, Switzerland
³¹ Dept. of Physics, University of Toronto, Toronto, Ontario, M5S 1A7, Canada
³² Institut für Kernphysik, Westfälische Wilhelms-Universität Münster, D-48149 Münster, Germany
³³ Dept. of Astronomy and Astrophysics, Pennsylvania State University, University Park, PA 16802, USA
³⁴ Dept. of Physics and Astronomy, Michigan State University, East Lansing, MI 48824, USA
³⁵ Bartol Research Institute and Dept. of Physics and Astronomy, University of Delaware, Newark, DE 19716, USA
³⁶ Dept. of Physics and Astronomy, University of Gent, B-9000 Gent, Belgium
³⁷ Institut für Physik, Humboldt-Universität zu Berlin, D-12489 Berlin, Germany
³⁸ Dept. of Physics, Southern University, Baton Rouge, LA 70813, USA
³⁹ Dept. of Astronomy, University of Wisconsin, Madison, WI 53706, USA
⁴⁰ Dept. of Physics, University of Alberta, Edmonton, Alberta, T6G 2E1, Canada
⁴¹ Niels Bohr Institute, University of Copenhagen, DK-2100 Copenhagen, Denmark
⁴² Earthquake Research Institute, University of Tokyo, Bunkyo, Tokyo 113-0032, Japan
⁴³ Dept. of Physics and Institute for Global Prominent Research, Chiba University, Chiba 263-8522, Japan
⁴⁴ CTSPS, Clark-Atlanta University, Atlanta, GA 30314, USA
⁴⁵ Dept. of Physics and Astronomy, Stony Brook University, Stony Brook, NY 11794-3800, USA
⁴⁶ Université de Mons, 7000 Mons, Belgium
⁴⁷ Dept. of Physics, Drexel University, 3141 Chestnut Street, Philadelphia, PA 19104, USA
⁴⁸ Dept. of Physics, University of Wisconsin, River Falls, WI 54022, USA
⁴⁹ Dept. of Physics, Yale University, New Haven, CT 06520, USA
⁵⁰ Dept. of Physics and Astronomy, University of Alabama, Tuscaloosa, AL 35487, USA
⁵¹ Dept. of Physics and Astronomy, University of Alaska Anchorage, 3211 Providence Dr., Anchorage, AK 99508, USA
⁵² Dept. of Physics, University of Oxford, 1 Keble Road, Oxford OX1 3NP, UK
⁵³ School of Physics and Center for Relativistic Astrophysics, Georgia Institute of Technology, Atlanta, GA 30332, USA
⁵⁴ Physikalisches Institut, Universität Bonn, Nussallee 12, D-53115 Bonn, Germany
- Received 2016 July 26; revised 2016 August 31; accepted 2016 August 31; published 2016 December 1*

ABSTRACT

The IceCube Collaboration has previously discovered a high-energy astrophysical neutrino flux using neutrino events with interaction vertices contained within the instrumented volume of the IceCube detector. We present a complementary measurement using charged current muon neutrino events where the interaction vertex can be outside this volume. As a consequence of the large muon range the effective area is significantly larger but the field of view is restricted to the Northern Hemisphere. IceCube data from 2009 through 2015 have been analyzed using a likelihood approach based on the reconstructed muon energy and zenith angle. At the highest neutrino energies between 194 TeV and 7.8 PeV a significant astrophysical contribution is observed, excluding a purely atmospheric origin of these events at 5.6σ significance. The data are well described by an isotropic, unbroken power-law flux with a normalization at 100 TeV neutrino energy of $(0.90_{-0.27}^{+0.30}) \times 10^{-18} \text{ GeV}^{-1} \text{ cm}^{-2} \text{ s}^{-1} \text{ sr}^{-1}$ and a hard spectral index of $\gamma = 2.13 \pm 0.13$. The observed spectrum is harder in comparison to previous IceCube analyses with lower energy thresholds which may indicate a break in the astrophysical neutrino spectrum of unknown origin. The highest-energy event observed has a reconstructed muon energy of (4.5 ± 1.2) PeV which implies a probability of less than 0.005% for this event to be of atmospheric origin. Analyzing the arrival directions of all events with reconstructed muon energies above 200 TeV no correlation with known γ -ray sources was found. Using the high statistics of atmospheric neutrinos we report the current best constraints on a prompt atmospheric muon neutrino flux originating from charmed meson decays which is below 1.06 in units of the flux normalization of the model in Enberg et al.

Key words: astroparticle physics – methods: data analysis – neutrinos

1. INTRODUCTION

The detection of high-energy cosmic neutrinos as cosmic messengers has been an important goal of astroparticle physics. Being stable, electrically neutral particles, high-energy neutrinos are able to propagate almost undisturbed through the universe from their production sites to Earth keeping their directional and energy information. Hence, they constitute excellent cosmic messenger particles, particularly at the highest

energies. They arise from weak decays of hadrons, mostly pions and kaons, which are expected to be produced by hadronic interactions of cosmic rays in the surrounding matter of the cosmic-ray accelerator. Their observation will help to elucidate the unknown sources of high-energy cosmic rays (Gaisser et al. 1995; Learned & Mannheim 2000; Becker 2008).

Already in the 1960s the observation of high-energy neutrinos had been discussed by Greisen (1960), Markov

(1960), and Reines (1960), shortly after the discovery of the neutrino by Reines & Cowan (1956). The proposed method was the detection of up-going muons as a signature of a charged-current (CC) muon neutrino interaction below the detector. Soon it was realized that the expected astrophysical fluxes are small and cubic-kilometer-sized detectors would be needed to accomplish the goal, see e.g., Roberts (1992). The construction of large Cherenkov detectors by instrumenting optically transparent natural media, i.e., deep oceans, lakes, and glaciers with photo-sensors (Belolaptikov et al. 1997; Andres et al. 2000; Ageron et al. 2011) proved to be a key concept. The largest instrument to date is the IceCube Neutrino Observatory at the geographic South Pole (Achterberg et al. 2006).

Main backgrounds to the search for astrophysical neutrinos are high-energy atmospheric neutrinos and muons produced by cosmic-ray interactions in the Earth’s atmosphere.

In 2013, a diffuse all-flavor flux of high-energy astrophysical neutrinos was discovered (Aartsen et al. 2013a, 2014b). The analysis selected events due to high-energy neutrinos which interact within the detector by using its outer layers as a veto. This strategy enables a full-sky sensitivity for all neutrino flavors. The veto not only rejects atmospheric muons entering the detector from the outside extremely efficiently, but also atmospheric neutrinos from above the detector which are produced together with muons.

In this analysis we focus on up-going muons which arise from charged-current interactions of muon neutrinos both inside and outside the detector. By allowing neutrinos to interact outside the instrumented volume a larger effective area is achieved. However, at the same time it is necessary to restrict the analysis to the Northern Hemisphere where the Earth filters atmospheric muons efficiently. Furthermore, the analysis is mainly sensitive to a muon neutrino flux because of the large muon range. Nevertheless this strategy will impose further constraints on possible models (Cholis & Hooper 2013; He et al. 2013; Kalashev et al. 2013; Laha et al. 2013; Razzaque 2013; Roulet et al. 2013; Stecker 2013; Anchordoqui et al. 2014; Gonzalez-Garcia et al. 2014; Murase et al. 2014; Tamborra et al. 2014; Bechtol et al. 2015; Senno et al. 2016) that have been proposed to explain the observed astrophysical neutrino flux.

This analysis is based on a high-purity and high-statistics selection of about 350,000 well-reconstructed up-going muon events from six years of IceCube operation, improving the statistics compared to previous analyses (Aartsen et al. 2014c, 2015c) by almost an order of magnitude.

Even when individual astrophysical neutrino sources cannot be identified because they are too weak, their cumulative flux can be measured as a diffuse flux. The signature of an astrophysical neutrino signal with respect to the background of atmospheric neutrinos is illustrated in Figure 1. Astrophysical neutrinos from cosmic accelerators are generically expected to have a hard energy spectrum as originally predicted by Fermi: $dN_\nu/dE \simeq \phi_0 \cdot E^{-2}$. However, the spectral index depends in detail on the source properties and the acceleration mechanism (Bell 2013; Kashti & Waxman 2005; Klein et al. 2013). Recent IceCube analyses (Kopper et al. 2015; Aartsen et al. 2015a, 2015b; Lesiak-Bzdak et al. 2015) yielded a softer spectrum with a spectral index between 2.5 and 2.7.

The energy spectrum of the atmospheric neutrino background is about one power steeper than the primary cosmic-ray spectrum ($dN_{CR}/dE \propto E^{-2.7..3.1}$), with the exception of prompt

neutrinos from heavy meson decays, which follow the primary spectrum more closely. The astrophysical signal appears as an excess above energies of about 100 TeV. As shown, the zenith distribution differs for signal and backgrounds which themselves depend on the energy. At the highest energies the Earth becomes increasingly opaque to neutrinos and the signal is dominated by events near the horizon.

The identification of an astrophysical signal is based on a two-dimensional likelihood fit in zenith and energy. It follows the methods of the previous analyses (Aartsen et al. 2014c, 2015c) which are improved with respect to the treatment of systematic uncertainties.

The data selection is described in Section 2. The method is described in Section 3. The results of the analysis with respect to the astrophysical signal are presented in Section 4, where we discuss the fit results, tests of alternative hypotheses and investigations on the most energetic event (Schoenen & Raedel 2015). In Section 5 we present investigations on the directions of recorded events and the attempt to correlate these directions with astrophysical objects. In Section 6 we discuss implications of this analysis for the expected flux of high-energy prompt atmospheric neutrinos from the decay of charmed mesons and obtain the currently most constraining exclusion limit.

2. DATA SAMPLE

2.1. IceCube Detector

The IceCube Neutrino Observatory is a cubic-kilometer-sized Cherenkov detector embedded in the ice at the geographic South Pole (Achterberg et al. 2006). It has been designed to detect neutrinos above TeV energies by measuring the Cherenkov light produced by charged particles produced in neutrino interactions. A total of 5160 optical photomultiplier tubes (PMTs) instrument 86 cable strings with a vertical spacing of 17 m at depths between 1450 and 2450 m beneath the surface of the glacial ice sheet (Abbasi et al. 2010). Each PMT is housed in a digital optical module (DOM), consisting of a pressure-resistant sphere, digitization/calibration electronics, and calibration LEDs (Abbasi et al. 2009).

The strings are deployed in a hexagonal pattern with an inter-string spacing of about 125 m except for the central eight strings which have a smaller spacing of about 60 m and also a smaller vertical DOM spacing.

The detector was completed in 2010 December; prior to that, data were recorded with partially installed detector configurations. In the remainder of the paper we differentiate the partial detector configurations by the number of strings, e.g., IC59 for the 59-string configuration. The complete detector with 86 strings is referred to by the year the data taking started, e.g., IC2011. The analysis presented here uses data taken from 2009 May until 2015 May which includes the partial detector configurations IC59, IC79 and the seasons IC2011–2014 of the completed detector.

2.2. Event Selection

The events that trigger IceCube are predominantly down-going atmospheric muons produced in cosmic-ray air showers. The standard trigger condition for high-energy neutrino analyses in IceCube requires a minimum of eight DOMs recording light within a time window of 5 μ s, which results in a rate above 2 kHz. The triggering DOMs must be in a local

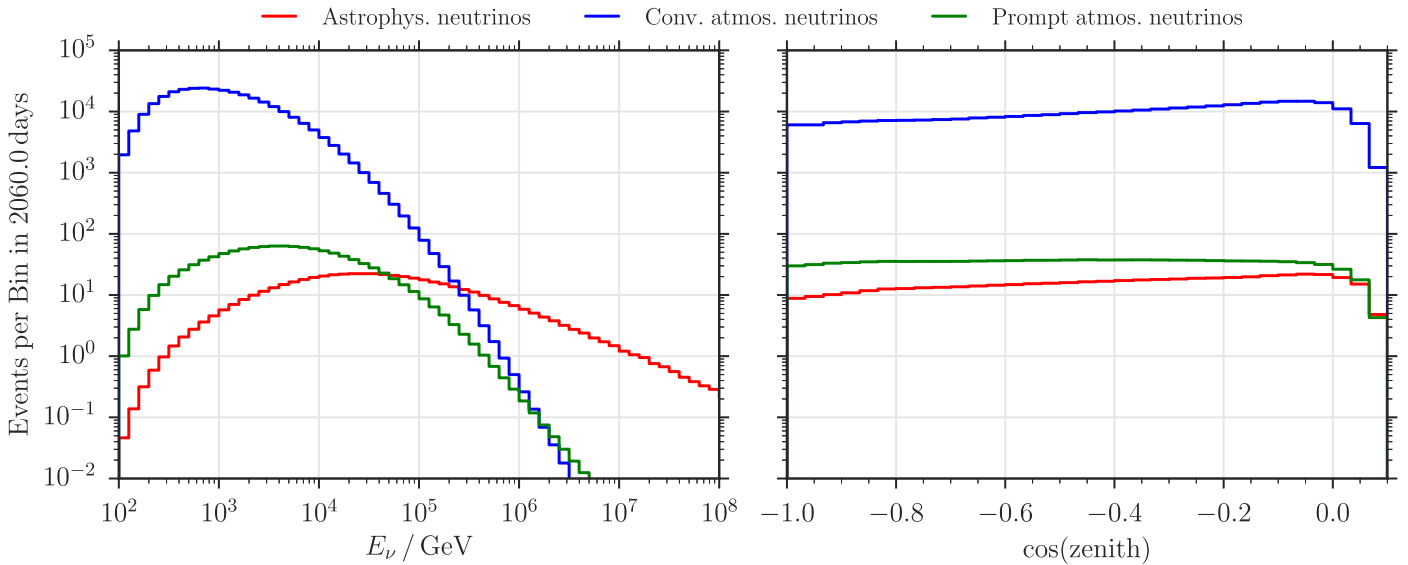


Figure 1. Distribution of the expected neutrino energy (left) and zenith angle (right) for the data selection of this analysis. Shown are the distributions of conventional atmospheric neutrinos (Honda et al. 2007), prompt atmospheric neutrinos (Enberg et al. 2008) where both are corrected for the cosmic-ray spectrum in Gaisser (2012), and a benchmark astrophysical signal $10^{-18} \text{ GeV}^{-1} \text{ cm}^{-2} \text{ sr}^{-1} \text{ s}^{-1} (E_\nu/100 \text{ TeV})^{-2}$.

coincidence with either their neighboring or next-to-nearest neighboring DOMs.

For each trigger the digitized PMT waveforms of the detected Cherenkov-light signals are sent to the surface where the number of photons as well as their arrival times are extracted. This information is used to reconstruct the energy and geometry of the event (Ahrens et al. 2004; Abbasi et al. 2013; Aartsen et al. 2014a).

The data processing schemes were improved during the construction of IceCube and the event selection has been optimized for each detector configuration. Data are processed and reconstructed at the South Pole in real time. A filter criterion, optimized for high-energy track-like signatures, requires a minimum amount of detected total charge and a good quality of the track reconstruction. This reduces the data stream to about 34 Hz that is sent off-site via satellite for further data processing. These events are still dominated by down-going atmospheric muon events. In order to select high-energy up-going muons with high purity and high efficiency, more sophisticated reconstruction algorithms are applied and high-quality events are selected.

The neutrino event selections are based on Monte Carlo (MC) generated neutrinos and atmospheric muons. Note that there are differences in the MC used for the different seasons due to improving simulation code and models which is accounted for in the likelihood fit (see Section 3.2). The simulation of neutrinos is performed by injecting a neutrino at the Earth’s surface and propagating it through the Earth. The neutrino interaction in ice or rock is simulated (Gazizov & Kowalski 2005) with the deep inelastic scattering cross section calculated using the CTEQ5 parton distribution functions (Lai et al. 2000) or the updated HERA1.5 PDFs (Cooper-Sarkar et al. 2011). At the energies of interest the cross sections differ by less than 5%. Each simulated neutrino is forced to interact in the vicinity of the instrumented volume. The volume is scaled as a function of the neutrino energy to include the maximum range of the muon produced in the interaction. The muon is propagated through the detector taking into account energy losses and decay (Chirkin & Rhode 2004; Koehne et al. 2013).

The Cherenkov light from charged particles is tracked through the ice to the DOMs (Lundberg et al. 2007; Chirkin 2013c, and from work by C. Kopper in 2011⁵⁵) taking into account the Antarctic ice properties (Ackermann et al. 2006; Aartsen et al. 2013b; Chirkin 2013a). Finally, the detector response and data acquisition are simulated. The same simulation chain is used for atmospheric muons which are simulated with CORSIKA (Heck et al. 1998). Both neutrino simulation and atmospheric muon simulation can be weighted to different fluxes.

The event selection for IC59 is identical to Aartsen et al. (2014c) and covers the up-going zenith range 90° – 180° . For the later seasons the zenith range has been enlarged to additionally cover angles between 85° and 90° as in Aartsen et al. (2015c) where the overburden by the Antarctic ice sheet is still more than 12 km of water equivalent. Additionally, the separation of mis-reconstructed atmospheric muons and well reconstructed neutrino-induced muons has been improved by using boosted decision trees (BDTs). For IC2011 and later, the AdaBoost algorithm (Freund & Schapire 1997) implemented in Pedregosa et al. (2011) has been used. Due to filter and processing changes after the first complete detector season a separate BDT has been trained for IC2011 and the data are treated separately as for the seasons IC59 and IC79.

For the optimization of the BDT we use simulations of up-going muon neutrinos following an E^{-2} spectrum which produce a muon via a charged-current interaction. In addition, to define the signal for the BDT, only simulated events with directions reconstructed to better than 5° are used. The background is defined by atmospheric muons from cosmic-ray air showers that have been mis-reconstructed as up-going. The simulation is weighted to the cosmic-ray model in Gaisser (2012). The features used in the training of the BDT are characteristics of the event topology and parameters evaluating the quality of the reconstructions. These parameters have been selected requiring good agreement between experimental and

⁵⁵ <https://github.com/claudiok/clsim>

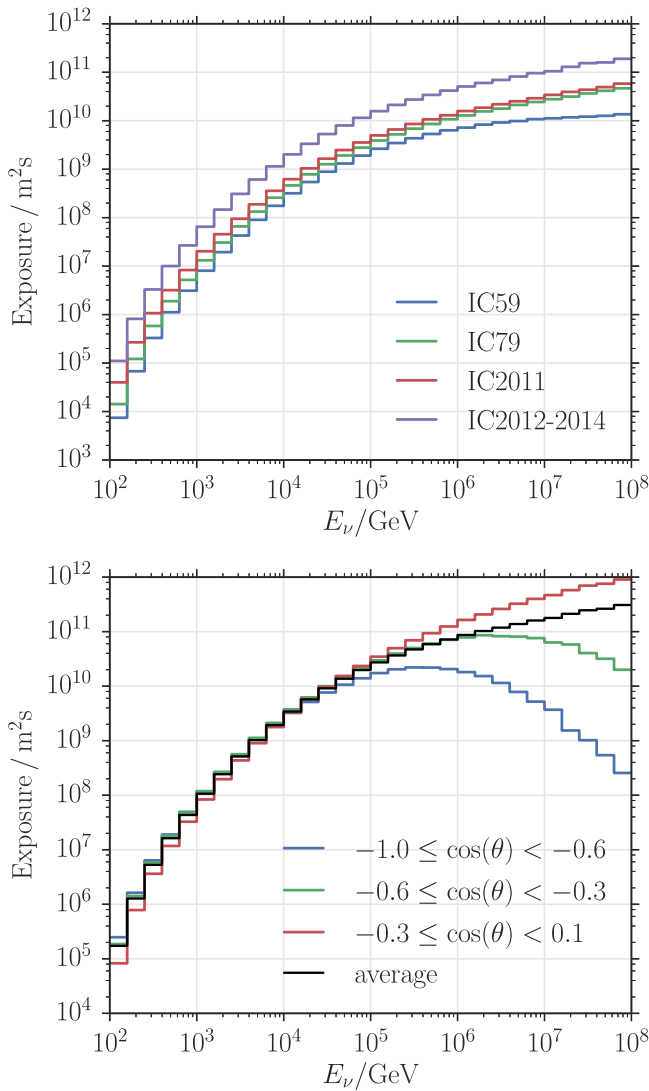


Figure 2. Exposure. Top: individual contributions to the total exposure from the different detector configurations. Bottom: total exposure for different zenith regions for the combined data set. Note that the exposure is based on the sum of the effective areas of ν_μ and $\bar{\nu}_\mu$. Therefore, the total number of events is obtained by integrating the product of exposure and averaged neutrino flux $\Phi_{(\nu_\mu + \bar{\nu}_\mu)/2}$ over the neutrino energy and solid angle.

simulated data. The threshold of the BDT classifier is chosen by considering the neutrino selection efficiency and the purity. In order to model the atmospheric background using simulation a high purity is required, rejecting nearly all atmospheric muons. The chosen threshold results in a purity which is better than 99.7%. The remaining background clusters at low energies and is strongly dominated by atmospheric neutrinos. Thus, it cannot affect the analysis and therefore does not have to be taken into account as a separate template in the likelihood fit. The performance estimates are based on 10-fold cross validation (Narsky & Porter 2013) and a separate validation set. Additionally, a fit of the data has been performed excluding events from above the horizon between 85° and 90° . Since the fit results remain nearly unaffected we conclude that the fit is not biased by any unaccounted high-energy muons.

Figure 2 shows the total exposure for the different detector configurations and for the full data set for different ranges in cosine zenith. The total number of events as well as the total

Table 1
Summary of the Data Selection

Season	$\theta_{\min} - \theta_{\max}$ (deg)	t_{live} (days)	N_{event}
IC59	90–180	348.1	21, 411
IC79	85–180	310.0	36, 880
IC2011	85–180	342.1	71, 191
IC2012–2014	85–180	1059.8	222, 812

Note. The table gives the number of events and the effective live time for each data set used.

live time categorized by season are summarized in Table 1. For the best-fit astrophysical flux (see Section 4.2) the expected number of astrophysical muon neutrinos included in these data is approximately 500.

3. ANALYSIS METHOD

3.1. Likelihood Method

The experimental and simulated data are binned in two observables sensitive to distinguish between signal and background: reconstructed muon energy and cosine of the zenith angle. These bins are analyzed by a maximum likelihood approach. The expectation in each bin is a function of the signal and nuisance parameters. The likelihood used in this analysis is given by Chirkin (2013b) and is the same as used in Aartsen et al. (2014c). The likelihood per bin is

$$\mathcal{L}_i = \left(\frac{\mu_i}{s_i/n_s} \right)^{s_i} \cdot \left(\frac{\mu_i}{d_i} \right)^{d_i}, \quad (1)$$

where n_s defines the ratio of the live times for simulation and experimental data, d_i is the number of events in the data, s_i the number of simulated events, and μ_i the expectation in bin i . With this likelihood the expectation μ_i is optimized based on the knowledge of the statistics of the simulated and experimental data set. Unlike a Poisson likelihood, we account for the finite statistics of simulated data which becomes relevant for small bin contents in a multi-dimensional parameter space. In the limit of infinite statistics of simulated data this likelihood converges to a saturated Poisson likelihood. A version of Equation (1), modified for weighted events according to Chirkin (2013b), is used in the analysis.

The per-bin expectation is given by

$$\begin{aligned} \mu_i(\boldsymbol{\theta}; \boldsymbol{\xi}) = & \mu_i^{\text{conv.}}(\boldsymbol{\xi}) \\ & + \mu_i^{\text{prompt}}(\Phi_{\text{prompt}}; \Delta\gamma_{\text{CR}}, \lambda_{\text{CR}}, \boldsymbol{\xi}_{\text{det}}) \\ & + \mu_i^{\text{astro.}}(\Phi_{\text{astro}}, \gamma_{\text{astro}}; \boldsymbol{\xi}_{\text{det}}), \end{aligned}$$

which depends on the signal $\boldsymbol{\theta}$ and nuisance parameters $\boldsymbol{\xi}$ (see Table 2). Here, $\boldsymbol{\xi}_{\text{det}}$ corresponds to the parameters taking into account the neutrino detection uncertainties (see Section 3.2.1). In this analysis, the signal parameters consist of the astrophysical flux parameters and the prompt flux parameter. The astrophysical flux model used here is a single power-law flux described by two parameters: the normalization Φ_{astro} at 100 TeV neutrino energy and the spectral index γ_{astro} :

$$\Phi_{\nu+\bar{\nu}} = \Phi_{\text{astro}} \cdot \left(\frac{E}{100 \text{ TeV}} \right)^{-\gamma_{\text{astro}}}. \quad (2)$$

Table 2
Nuisance Parameters

	IC59	IC79	IC2011	IC2012-2014	scaling	Best Fit (68% C.L.)
<i>Flux properties:</i>						
Conventional flux Φ_{conv}	1.028	1.047	1.184	1.194	relative	0.998 ± 0.003
Kaon-pion ratio K/π	1.310	1.514	1.002	1.032	relative	0.977 ± 0.027
Cosmic-ray spectral index $\Delta_{\gamma_{\text{CR}}}$	-0.049	-0.049	-0.061	0.012	absolute	$0.008^{+0.004}_{-0.023}$
Cosmic-ray model λ_{CR}	1.0 (H3p)	1.0 (H3p)	1.0 (H3p)	1.0 (H3p)	absolute	0.0–0.5
Optical efficiency ϵ_{opt}	1.011	0.974	1.042	1.056	relative	1.002 ± 0.002
<i>Optical ice properties:</i>						
Scattering length λ_{scat}	1.027	1.014	relative	0.999 ± 0.005
Absorption length λ_{abs}	1.000	1.047	relative	1.001 ± 0.004
Absorption/scattering length $\lambda_{\text{abs/scat}}$...	0.991	relative	1.000 ± 0.004
Ice model λ_{ice1} [SpiceMie,WHAM]	0. (SpiceMie)	SpiceMie (fixed)	absolute	$0.000 + 0.014$
Ice model λ_{ice2} [SpiceMie,SpiceLea]	0.551	SpiceLea (fixed)	absolute	0.006 ± 0.057

Note. Columns two to five show the best-fit values for each data sample individually where the fit was performed on data within a predefined background region. The background regions were defined as follows: for IC59 the muon energy loss proxy must be less than 1 GeV m^{-1} and for IC79, IC2011 and IC2012-2014 the muon energy proxy must be less than 10 TeV. These best-fit values are used as default values to define a common baseline. In the combined likelihood fit the default values are then scaled by global nuisance parameters where the best-fit values including the 68% C.L. error determined by the profile likelihood technique are shown in the last column. Column six shows if the scaling is an absolute or relative change with respect to the default values. Note that the nuisance parameters quoted here are allowed to change for each data set to absorb differences in the simulations which are caused by improvements in the simulation code and models. Thus, they do not have to reflect their real physical quantities.

The prompt neutrino flux is described by the prediction taken from Enberg et al. (2008) (ERS) where the absolute normalization Φ_{prompt} is taken as free parameter. In addition, nuisance parameters are introduced to take into account systematic uncertainties, e.g., the conventional atmospheric neutrino flux is described by the prediction taken from Honda et al. (2007) and the flux normalization Φ_{conv} is taken as a nuisance parameter. Note that the conventional and prompt neutrino flux predictions have been corrected for the knee in the cosmic-ray spectrum based on the cosmic-ray models in Hoerandel (2003) and Gaisser (2012) (see Section 3.2). The implementation of nuisance parameters is described in Section 3.2 in more detail.

The global likelihood, which is maximized, is the product of all per-bin-likelihoods $\mathcal{L} = \prod_i \mathcal{L}_i$. The significances and parameter uncertainties in this analysis are derived using the profile likelihood technique and Wilks’ theorem (Wilks 1938). The applicability of Wilks’ theorem has been tested and verified by ensemble studies.

3.2. Systematic Uncertainties

In order to account for systematic uncertainties, resulting from the imperfect background and signal modeling, continuous nuisance parameters valid for the entire energy and zenith range are introduced. The systematic uncertainties can be divided into two categories: neutrino detection uncertainties and atmospheric flux uncertainties. The former include the optical efficiency of the detector, the neutrino–nucleon cross section, the muon energy loss cross section and the optical properties of the Antarctic ice. The latter include the flux normalizations, the spectral shape and composition of the cosmic-ray spectrum in the “knee” region, the spectral index of the primary cosmic-ray spectrum, and the relative production yield of pions and kaons in the atmosphere. The implementation of these uncertainties as nuisance parameters in the likelihood function is done similar to Aartsen et al. (2014c). Main improvements with respect to previous analyses are the

parameterizations of the systematic detector effects as unbinned functions of both fit observables (S. Schoenen 2016, in preparation) using adaptive kernel density estimation and the interpolations between specific models to account for the model uncertainties. The systematic detector effects are studied by simulated data sets where the default parameters are changed within their uncertainties. In cases where no interpolation between specific models is used, the nuisance parameters are implemented by using independent correction factors $f_k(\xi_k)$. These factors scale the default per-bin expectation μ_i^0 for each flux contribution with respect to the individual nuisance parameter ξ_k :

$$\mu_i^0 \mapsto \mu_i^0 \cdot \prod_k f_k(\xi_k).$$

3.2.1. Neutrino Detection Uncertainties

Optical efficiency of the detector. The optical efficiency ϵ_{opt} takes into account all uncertainties related to the light production and detection in the detector, e.g., the number of produced Cherenkov photons, the overall optical transparency of the ice, the photon detection efficiency of the DOMs, and the shadowing of photons by detector components. Since the optical efficiency is directly connected to the brightness of an event as observed with the detector, its uncertainty results in an uncertainty on the reconstructed energy scale. The effect has been parameterized as a function of the muon energy proxy and the cosine zenith angle and is implemented as a nuisance parameter. The uncertainty on the optical efficiency is estimated to be less than 15%. Since the ice properties of the refrozen water within the drill holes differ from the bulk ice properties they are taken into account as a modification of the angular acceptance (Aartsen et al. 2013b).

Optical properties of the Antarctic ice. The probability of a Cherenkov photon to be detected by a DOM depends not only on the optical efficiency of the detector but also on the optical transparency of the Antarctic ice. The main processes are

scattering and absorption of photons on their path to the DOM. For the Antarctic ice this is modeled by depth-dependent scattering and absorption lengths. The modeling is done using measured data from calibration light sources that are integrated into the DOMs. Different models of the ice have been developed during the operation of IceCube. For this analysis the following ice models are used: *WHAM* for IC59 (based on a measurement of the optical properties of the glacial ice at the South Pole presented in Ackermann et al. 2006), *SpiceMie* for IC59, IC79 and IC2011 (Aartsen et al. 2013b), and *SpiceLea* for IC2011-2014 (Chirkin 2013a). For all available simulation data sets, the effects of the optical ice properties as a function of reconstructed energy proxy and cosine zenith are parameterized and implemented as a nuisance parameter. This is done for different ice models and each detector configuration. The parameterization is done by introducing a parameter λ_{ice} that describes a linear combination ($\lambda_{\text{ice}} \cdot M_1 + (1 - \lambda_{\text{ice}}) \cdot M_2$) between two ice models where M_1 and M_2 are the expectations per bin corresponding to the two ice models. In addition, for a given ice model the effects of different scattering lengths λ_{scat} and absorption lengths λ_{abs} on the muon energy proxy and the cosine zenith angle have been parameterized. Owing to missing simulations this could not be done for IC59. For IC79 the scattering and absorption lengths have been varied simultaneously resulting in only one effective nuisance parameter $\lambda_{\text{abs/scat}}$. From IC2011 on the scattering and absorption lengths have been varied separately. For more information see Table 2. The individual uncertainty for both quantities is estimated to be less than 10%. The scattering length mainly influences the angular resolution of the neutrino arrival direction and therefore the reconstructed zenith angle. Since the cosine zenith bin width of the analysis is relatively coarse, the effect of this uncertainty on the observable distribution is small. The absorption length mainly influences the flux normalization and the shape of the energy distribution. This effect is much larger, compared to the scattering length effect.

3.2.2. Atmospheric Flux Uncertainties

Flux normalization. The uncertainty on the normalization of the conventional atmospheric neutrino flux is implemented as a nuisance parameter Φ_{conv} that scales the flux normalization of the model by Honda et al. (2007). This model has been extrapolated to higher energy based on the method in taking into account a more realistic spectrum of cosmic rays and their composition (Illana et al. 2011; Schukraft 2013). Note that the uncertainty of this parameter is relatively large, on the order of 30%. Thus, it absorbs any kind of uncertainty which influences the global flux normalization in the fit.

Cosmic-ray model and spectral index. The composition of the cosmic rays is uncertain, in particular above the knee at an energy of about 3 PeV. Models are based on the superposition of Galactic cosmic-rays with rigidity-dependent cut-offs and an emerging extragalactic component. Since conventional and prompt atmospheric neutrinos are produced by cosmic-ray interactions within the atmosphere, the uncertainty on the cosmic-ray spectrum also affects the expectation of these neutrinos. The effect of different cosmic-ray models is parameterized by λ_{CR} as a function of the muon energy proxy and the cosine zenith angle similar to the discrete ice models. Here, a linear combination between Hoerandel (2003) and Gaisser (2012), which are the extreme cases, is used. In addition to the effects between different cosmic-ray models an

overall change in the cosmic-ray spectral index affects the expectation of atmospheric neutrinos. Therefore, a shift of the cosmic-ray spectral index $\Delta\gamma_{\text{CR}}$ is implemented as a nuisance parameter representing the uncertainty on the cosmic-ray spectral index. The uncertainty is estimated to be of the order of 4% based on differences between the aforementioned cosmic-ray models. A positive $\Delta\gamma_{\text{CR}}$ corresponds to a softer energy spectrum.

Kaon-to-pion ratio. Conventional atmospheric neutrinos are produced by decays of pions and kaons which are themselves produced in air showers. The relative contribution of kaons and pions K/π to the production of conventional atmospheric neutrinos affects their zenith angle distribution. In this analysis it is defined by the ratio of the integrated neutrino fluxes from kaon and pion decays. Using the neutrino flux parameterization from Gaisser (1990) fitted to the conventional atmospheric neutrino prediction from Honda et al. (2007) between 1 and 10 TeV, the kaon-to-pion ratio is implemented as a nuisance parameter where the uncertainty is estimated to be of the order of 10%.

Atmospheric temperature effects. The expected number of conventional atmospheric neutrinos is directly connected to the number of pion and kaon decays in the atmosphere. A denser atmosphere will increase the interaction probability for pions and kaons relative to the decay probability, which reduces the overall neutrino flux. Thus, annual temperature fluctuations influence the expectation of conventional atmospheric neutrinos. Since the prediction of conventional atmospheric neutrinos from Honda et al. (2007) is based on the standard US atmosphere, the expectation is corrected for annual temperature fluctuations. This is done using the formalism reported in Desiati et al. (2014) and data measured by the instrument AIRS installed on the *AQUA* satellite (AIRS Science Team/Joao Texeira 2013). The effect of this correction is estimated to be of the order of 2% with an uncertainty of about 0.1%.

With the goal of achieving an unbiased result for the signal parameters, we note that many nuisance parameters were deliberately chosen correlated (see Figure 3). For example, the optical detector efficiency is correlated to the Cherenkov light yield uncertainty and to the effects of the uncertainties in the muon energy loss cross sections. In cases where the effects of one uncertainty are fully absorbed by other nuisance parameters only one parameter has been implemented for better numerical stability of the fit. A list of the implemented parameters is given in Table 2. In order to obtain an unbiased result the nuisance parameters are implemented without priors which is tested to have no effect on the sensitivity for an astrophysical or prompt flux.

The fit procedure was tested by generating pseudo experiments where the input parameters were varied. The fit of the signal parameters was found to be robust and unbiased against the choice of nuisance parameters.

Since IceCube's MC simulations have evolved and improved from year to year, the default expectations for each nuisance parameter have changed for simulated data sets year by year. In order to avoid a tension in the fitted nuisance parameters induced purely by the differences of the simulations, two methods were tested: the implementation of individual nuisance parameters for each year, and the alignment of all nuisance parameters to a common baseline. We found that the two methods give similar sensitivities both for the astrophysical and the prompt flux parameters, and the

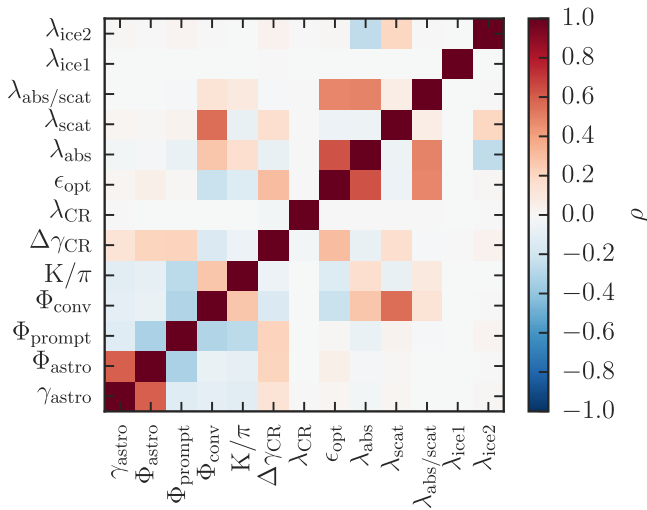


Figure 3. Correlation matrix of signal and nuisance parameters. λ_{ice1} describes the linear combination between SpiceMie (Aartsen et al. 2013b) and WHAM (Ackermann et al. 2006) for IC59, λ_{ice2} describes the linear combination between SpiceMie (Aartsen et al. 2013b) and SpiceLea (Chirkin 2013a) for IC2011. $\lambda_{\text{abs/scat}}$ describes the relative change of the ice properties for IC79 and λ_{abs} , λ_{scat} describes the relative change of the ice properties for IC2011-14.

alignment method is chosen since the time consumption for the fit is much lower. The alignment is done by fitting the nuisance parameters in a predefined background region for each year individually. The resulting best-fit values for the nuisance parameters, summarized in Table 2, define the default values for each year. In the combined likelihood fit of all six years these default values are then scaled by global nuisance parameters. The scaling can be either an absolute or relative change with respect to the aligned default values.

The flavor composition at Earth is not identical to the flavor composition at an astrophysical source due to neutrino oscillations. For a source dominated by $p\gamma/pp$ -interactions, the initial flavor ratio of 1:2:0 ($\nu_e:\nu_\mu:\nu_\tau$) is transformed to be approximately equally partitioned among the flavors (Learned & Pakvasa 1995; Athar et al. 2006). Therefore, it is necessary to take into account the muonic decay of taus originating from charged current ν_τ interactions by combining it with the astrophysical muon neutrino flux. A fit of the data with and without this contribution shows that accounting for it leads to a decrease in the astrophysical normalization of about 5% and has no effect on the spectral index. In the rest of the paper we account for the contribution of ν_τ assuming equal partitioning. The astrophysical normalization for other expected flavor compositions of astrophysical neutrino sources can be obtained by rescaling.

3.3. Parametric Unfolding

The best-fit result for the neutrino energy spectrum measured by this analysis can be used to determine for each event a neutrino energy probability density function $P(E_\nu|E_{\text{reco}}^i)$ with respect to its muon energy proxy E_{reco}^i . These functions depend on the assumption for the neutrino energy spectrum and are therefore model-dependent. In particular, for the astrophysical neutrino flux an unbroken, single power law is assumed. For the full six-year data sample the neutrino energy distribution is given by the sum over the probability density function of all events $\sum_i P(E_\nu|E_{\text{reco}}^i)$ where each function is normalized to an

event count of one. Since this approach is model-dependent it is called *parametric unfolding* in the following. Note that this method cannot replace a model-independent unfolding as done in Boerner et al. (2015) for different IceCube data samples.

4. RESULTS OF THE SPECTRAL LIKELIHOOD FIT

4.1. Fit Result

The result of the fit is presented as a set of one-dimensional projections of energy and zenith in Figure 4 separately for each contributing data sample. The experimental data are shown as black crosses, and the best-fit expectations for astrophysical and conventional atmospheric neutrinos are shown as red and blue bands, respectively. An excess of high-energy events consistent with an astrophysical signal above the atmospheric background is visible for each data sample. The overall agreement between the data and the MC of the full data set is good for all energies and zenith angles. We have tested quality of the fit based on the two-dimensional distributions using the ratio between the likelihood (Equation (1)) and the saturated likelihood as test-statistic (Olive et al. 2014). The test-statistic distribution was generated via pseudo experiments based on the best fit. The resulting p -value is 95.4%, indicating a very good agreement between data and MC. All nuisance parameters are fitted to values consistent with their uncertainty (Table 2).

Note that the data sample taken with the 79-string configuration contains roughly twice as many high-energy events above a reconstructed muon energy of 100 TeV than other years (see Figure 4). Nevertheless, the result of the fit for all years is consistent with the fits for individual years. Visual inspection and other cross checks of these events revealed no indication of any time-dependent detector effects. A dedicated analysis searching for time-dependent neutrino sources (Aartsen et al. 2015e) has found no indication of a signal. Therefore, the observations are consistent with a statistical fluctuation.

4.2. Astrophysical Flux

The best fit for the unbroken power-law model of the astrophysical flux results in

$$\Phi_{\nu+\bar{\nu}} = (0.90^{+0.30}_{-0.27}) \cdot (E_\nu/100 \text{ TeV})^{-(2.13 \pm 0.13)} \quad (3)$$

in units of $10^{-18} \text{ GeV}^{-1} \text{ cm}^{-2} \text{ sr}^{-1} \text{ s}^{-1}$. The statistical significance of this flux with respect to the atmospheric-only hypothesis is 5.6 standard deviations. The fit results are shown in Figure 5 and summarized in Table 3. The quoted errors are based on the profile likelihood using Wilks' theorem (Wilks 1938) and include both statistical and systematic uncertainties. No contribution from prompt atmospheric neutrinos is preferred by the best-fit spectrum, and an upper limit, based on the profile likelihood, is shown in Figure 5. For more information about the upper limit for prompt atmospheric neutrinos see Section 6.

The two-dimensional contours of the profile likelihood as a function of the signal parameters are shown in Figure 6. While the fitted astrophysical flux normalization is strongly correlated with the astrophysical spectral index, these astrophysical signal parameters are found to be largely independent of the prompt flux normalization.

The model assumes an unbroken power law for the astrophysical signal. We estimate that neutrinos in the

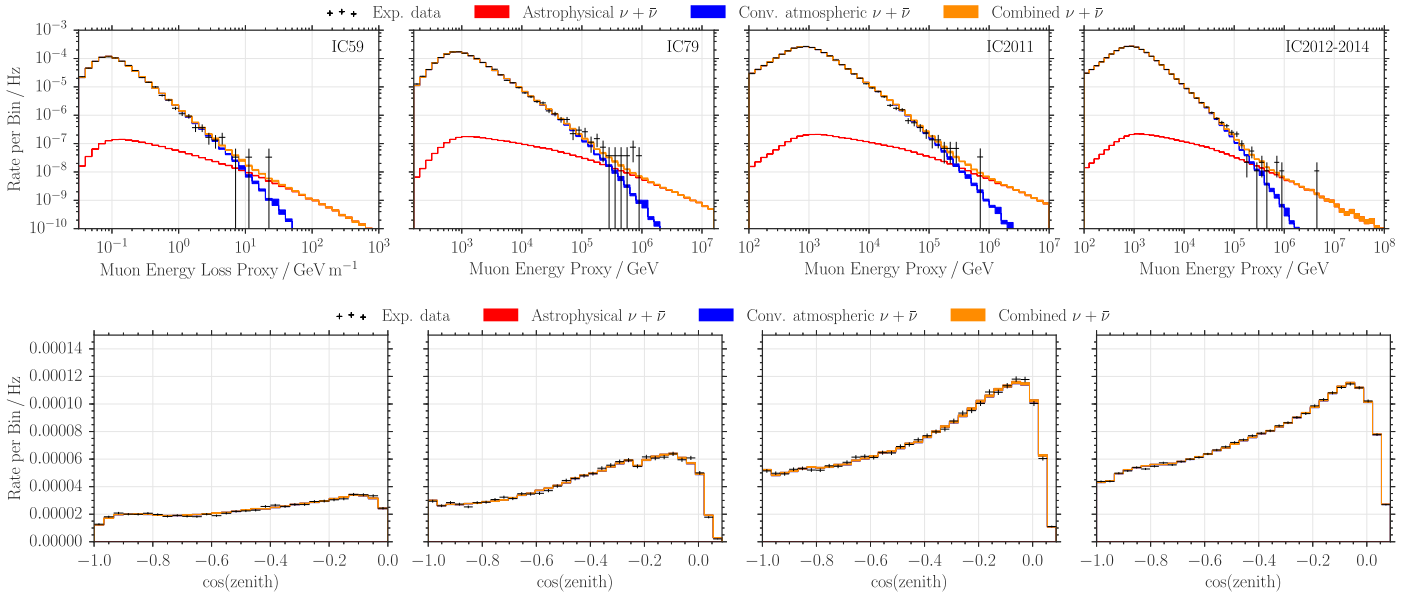


Figure 4. Distributions of the experimental data for the muon energy proxy (top) and reconstructed zenith (bottom) for each contributing data sample (left: 59-string, center-left: 79-string, center-right: 86-string (2011–2012), right: 86-string (2012–2015)). Note that IC2011 is different from the later years due to changes in the data processing. The best-fit model for astrophysical and atmospheric neutrinos is superimposed. Only statistical errors are shown.

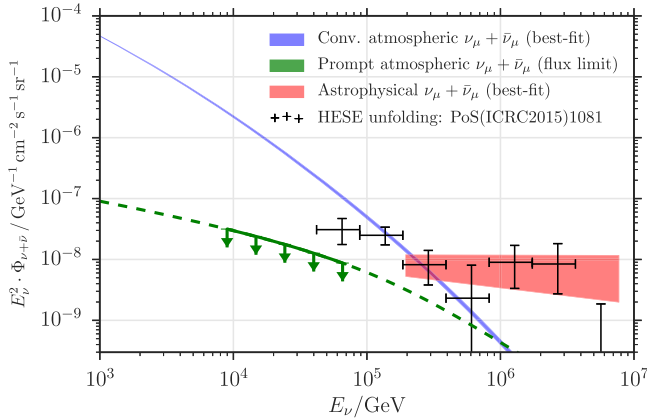


Figure 5. Best-fit neutrino spectra for the unbroken power-law model. The width of the line corresponding to conventional atmospheric neutrinos (blue) represents the one-sigma error on the measured spectrum. The width of the line corresponding to astrophysical neutrinos (red) shows the effect of varying both of the astrophysical parameters within one-sigma of the best fit values, without accounting for correlation. The green line represents the upper limit on the prompt model (Enberg et al. 2008). The horizontal width of the red band denotes the energy range of neutrino energies which contribute 90% to the total likelihood ratio between the best-fit and the conventional atmospheric-only hypothesis. The black crosses show the unfolded spectrum published in Kopper et al. (2015).

experimental data sample with energies mainly between 194 TeV and 7.8 PeV contribute to this observation. This energy range is shown in Figure 5. It defines the central range of neutrino energies that contribute 90% to the total observed likelihood ratio between the best fit and the conventional atmospheric-only hypothesis. Note that this definition is different from Aartsen et al. (2015b, 2015c).

4.3. Multi-PeV Track-like Event

The selected data include one exceptionally high-energy muon event that is shown in Figure 7 (Schoenen & Raelde 2015). The deposited energy has been measured to (2.6 ± 0.3)

Table 3
Best-fit Parameter Values for the Unbroken Power-law Model

Parameter	Best-Fit	68% C.L.
Φ_{astro}	0.90	0.62–1.20
γ_{astro}	2.13	2.00–2.26
Φ_{prompt}	0.00	0.00–0.19

Note. Φ_{astro} is the normalization of the astrophysical neutrino flux at 100 TeV and is given in units of $10^{-18} \text{ GeV}^{-1} \text{ s}^{-1} \text{ sr}^{-1} \text{ cm}^{-2}$. Φ_{prompt} is given in units of the model in Enberg et al. (2008). The normalizations correspond to the sum of neutrinos and antineutrinos.

PeV of equivalent electromagnetic energy Aartsen et al. (2014a). Assuming the best-fit atmospheric energy spectrum from this analysis (see Figure 5) the p -value of this event being of atmospheric origin has been estimated to be less than 0.005%, strongly suggesting an astrophysical origin.

The segmented energy loss reconstruction described in Aartsen et al. (2014a) can be used to reconstruct the direction of through-going muons. This includes the timing of not only the first photon but all photons as well as the total number of photons. The reconstructed direction of the event is given in Table 4 and discussed in Section 5.1.

In order to estimate the angular uncertainty and the most likely muon and neutrino energy we have simulated events with energies according to our best-fit energy spectrum with directions varying by 1° around the best-fit direction. Additionally, the position where the muon enters the instrumented volume has been varied within 10 m. Systematic uncertainties due to the lack of knowledge of the optical ice properties are taken into account by varying the ice model parameters within their uncertainties during the simulation.

Based on these simulations we evaluate the muon energy at the point of entrance into the instrumented volume, that results in the observed deposited energy. The obtained median muon energy is (4.5 ± 1.2) PeV where the error range corresponds to 68% C.L.

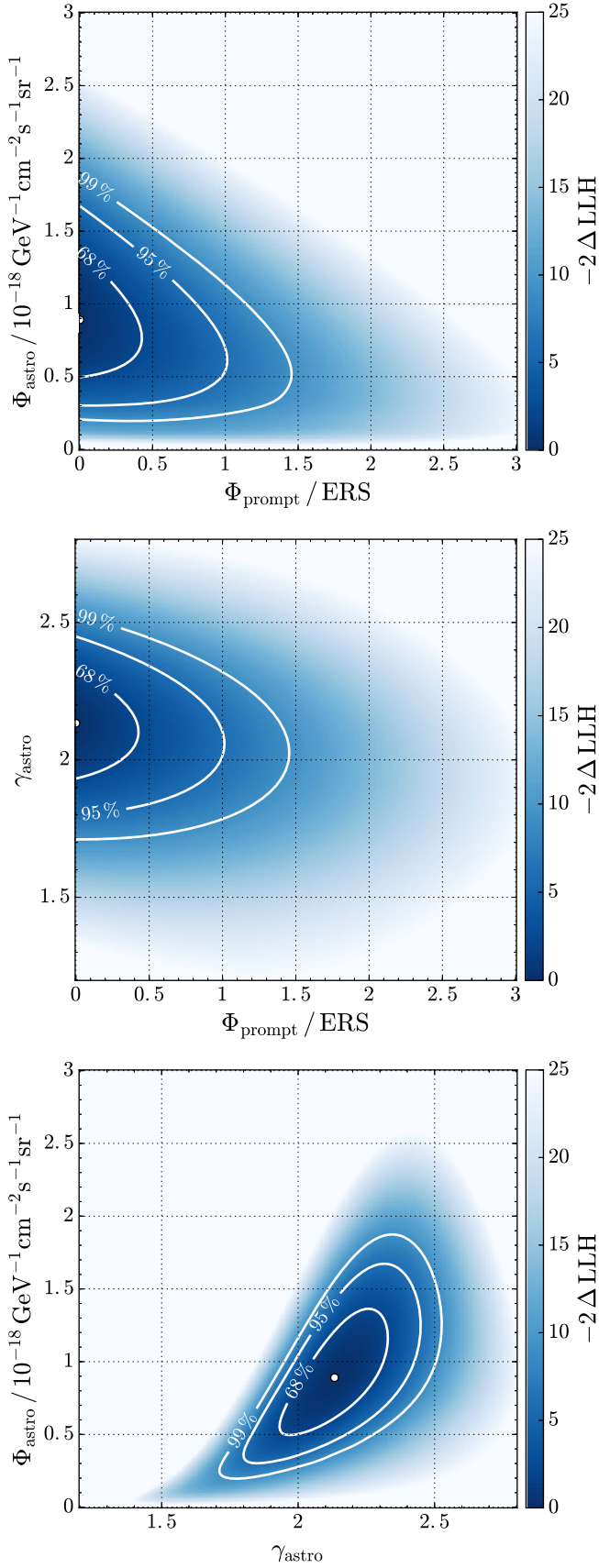


Figure 6. Two-dimensional profile likelihood scans of the astrophysical parameter Φ_{astro} , γ_{astro} and the prompt normalization Φ_{prompt} in units of the model in Enberg et al. (2008). The contours at 68%, 95%, and 99% CL assuming Wilks' theorem are shown.

For the estimation of the median expected neutrino energy we have taken into account that high-energy muons arise not only from ν_{μ} charged-current interactions but also from muonic decay of charged-current ν_{τ} interactions and muonic W^{-} decays in $\bar{\nu}_e + e^{-} \rightarrow W^{-}$ interactions. Here, we assume the best-fit astrophysical spectrum and an equal flux of all flavors but include the effects of the Earth's absorption for the specific decl. of the event. Under these assumptions, we find 87.7% probability of a primary ν_{μ} , 10.9% for a primary ν_{τ} and 1.4% for a primary $\bar{\nu}_e$. The respective probability distributions of primary neutrino energy are shown in Figure 8. The expected neutrino energy depends on the primary flavor. The median expected muon neutrino energy is 8.7 PeV for the above assumptions.

The angular reconstruction uncertainty including systematic uncertainties of the Antarctic ice (see Section 3.2) can be estimated from the aforementioned dedicated simulation. Figure 9 shows the angular reconstruction uncertainty for an ensemble of events with similar deposited energy, direction and entry point into the fiducial volume. The angular reconstruction uncertainty is given by the angular distance between the true and the reconstructed muon direction. The median angular uncertainty is 0.23° and the 99% containment is 0.9° . Details of the studies of the multi-PeV track-like event are shown in L. Rädcl (2016, in preparation).

4.4. Test for a Spectral Cut-off

The default hypothesis of an unbroken power law is tested against the hypothesis of a spectral cut-off. For this, an exponential energy cut-off $E_{\nu}^{\text{cut-off}}$ is added to the astrophysical neutrino flux:

$$\Phi_{\nu+\bar{\nu}} = \Phi_{\text{astro}} \cdot \exp\left(-\frac{E_{\nu}}{E_{\nu}^{\text{cut-off}}}\right) \cdot \left(\frac{E_{\nu}}{100 \text{ TeV}}\right)^{-\gamma_{\text{astro}}}. \quad (4)$$

In the fit the spectral index γ_{astro} is highly degenerate with an exponential energy cut-off $E_{\nu}^{\text{cut-off}}$, therefore two scenarios with fixed spectral indices have been tested. For the spectral indices the benchmark model with $\gamma_{\text{astro}} = 2$ and the best-fit value $\gamma_{\text{astro}} = 2.13$ are chosen. Figure 10 shows the two-dimensional contours of the profile likelihood as a function of the signal parameters Φ_{astro} , $E_{\nu}^{\text{cut-off}}$ and Φ_{prompt} . For the benchmark model a cut-off is slightly preferred at the level of one standard deviation. This is an expected behavior as the actual best-fit spectral index is softer. Thus, fixing the spectral index to a harder spectrum will result in a slight deficit at the highest neutrino energies. When fixing the spectral index to the best-fit value for an unbroken power law, this slight preference for an exponential cut-off disappears. These results are nearly independent of the prompt flux normalization.

4.5. Unfolded Astrophysical Spectrum

The best-fit results for the neutrino energy spectrum as quoted in Table 3 and the knowledge of the connection between the reconstructed muon and true neutrino energy can be used to unfold a neutrino energy distribution for the six-year sample (see Section 3.3). The results of this parametric unfolding are shown in Figure 11 as a cumulative energy distribution of the number of neutrinos with energies greater than E_{ν} . The statistical error band is given by the square root of this number. The error band that corresponds to the uncertainty

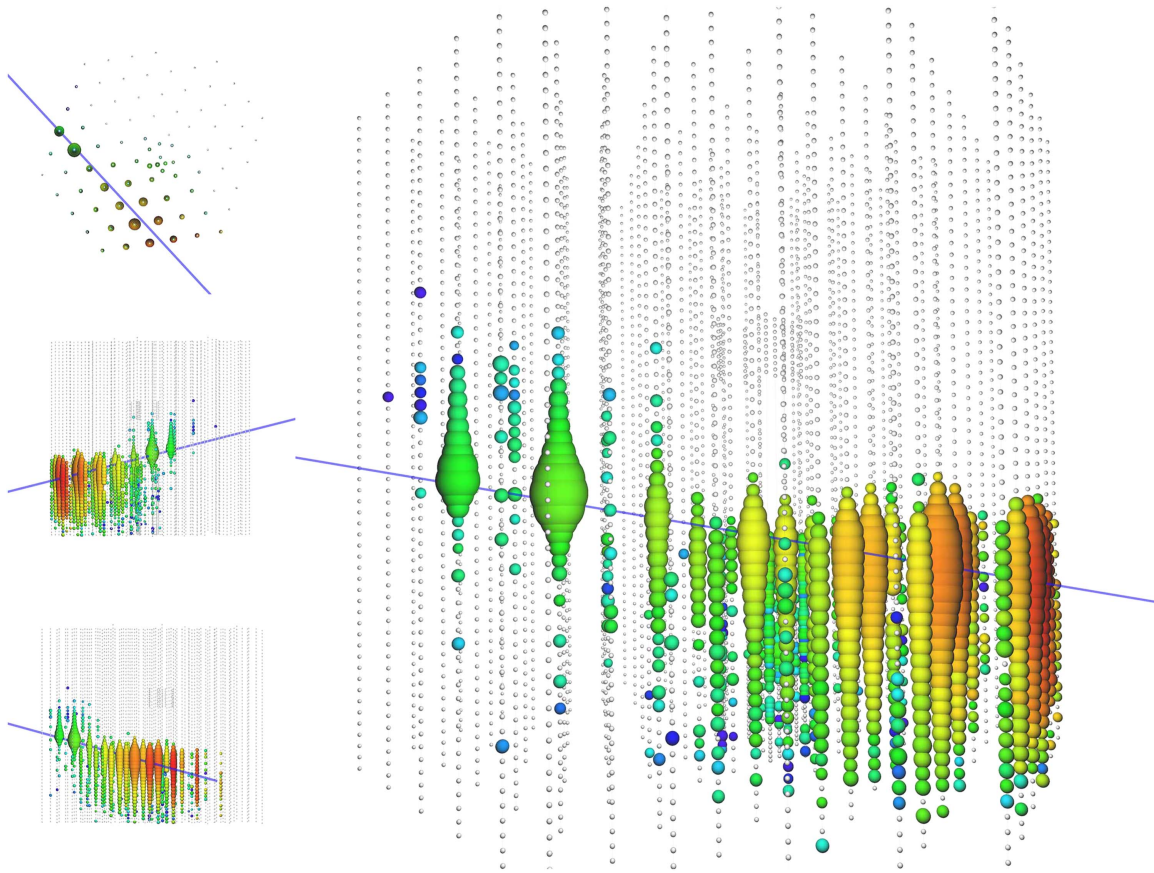


Figure 7. Event view of the PeV track-like event recorded by IceCube on 2014 June 11. Left: top and two side views. Right: perspective view. Shown are the IceCube DOMs as black dots. The colors indicate the photon arrival time from red (early) to green (late) and the size of the sphere the amount of measured charge. Note that the scaling is nonlinear and a doubling in sphere size corresponds to one hundred times the measured charge. The blue line shows the reconstructed particle track. The reconstructed equatorial coordinates of this event are decl.=11°42' and R.A.=110°63'. This event deposited an energy of 2.6 ± 0.3 PeV within the detection volume.

on the astrophysical flux is determined by varying the astrophysical spectrum within the measured uncertainties on the astrophysical flux parameters. Based on the per-event probability density function $P(E_\nu | E_{\text{reco}}^i)$ the median neutrino energy for each event can also be calculated. Figure 12 shows the distribution of the median neutrino energies for the six-year sample.

In both distributions a clear excess above approximately 100 TeV in neutrino energy is visible, and is not compatible with the atmospheric background expectation. Although only a single event with energy greater than a PeV has been observed, we can infer from our fit and from the relation between muon energy and energy of the parent neutrino that there are most likely several neutrinos with energies above a PeV in the six-year sample.

4.6. Discussion

This analysis found an astrophysical spectral index of $\gamma = 2.13 \pm 0.13$, which is harder than previously reported measurements, see e.g., Kopper et al. (2015), Neiderhausen et al. (2015) and Aartsen et al. (2015f). We refer to these analyses in the rest of the section as starting event analysis, cascade analysis and combined analysis, respectively. Figure 13 compares the measured astrophysical neutrino flux normalization and spectral index with these results and the previous measurement using through-going muons Aartsen et al. (2015c).

While the sample used in the cascade analysis is completely statistically independent, the starting event analysis and global fit have an overlap in events. The combined fit includes three years of muon data from 2009 to 2012 based on Aartsen et al. (2014c, 2015c). The starting event analysis includes a small fraction (6%) of up-going muons that start within the detector, that are also included here. However, these three analyses are strongly dominated by independent cascade-like events of which a large fraction originates from the Southern Hemisphere. For the starting event analysis 73% of the events above 100 TeV are down-going and 93% of these are cascade-like. For the investigation of the tension in the observed energy spectrum of astrophysical neutrinos, the assumption of statistical independence is reasonably well justified but will result in a lower limit on the tension.

The combined analysis finds the smallest confidence region of the three aforementioned results. The p -value for obtaining the combined fit result and the result reported here from an unbroken powerlaw flux is 3.3σ , and is therefore in significant tension. For the discussion, it is important to highlight the systematic differences between these measurements. The threshold for the up-going muon signal is a few hundred TeV while astrophysical starting events are detected above a few times 10 TeV. It should be noted that for the overlapping energy region >200 TeV the measured fluxes for the cascade-dominated channels are in good agreement with the results reported here, as shown in Figure 5. As a conclusion, we

Table 4
Summary of Highest Energy Events above 200 TeV in All Years

ID	MJD	Signalness	Energy Proxy (TeV)	Decl. (deg)	50% C.L.	90% C.L.	R.A. (deg)	50% C.L.	90% C.L.
1	55056.70 ^a	0.78	480	1.23	+0.08 -0.08	+0.18 -0.22	29.51	+0.15 -0.17	+0.40 -0.38
2	55141.13 ^a	0.52	250	11.74	+0.10 -0.18	+0.32 -0.38	298.21	+0.17 -0.22	+0.53 -0.57
3	55355.49 ^b	0.65	340	23.58	+0.91 -1.18	+2.31 -4.13	344.93	+1.14 -1.04	+3.39 -2.90
4	55370.74 ^b	0.54	260	47.80	+0.25 -0.22	+0.56 -0.48	141.25	+0.23 -0.16	+0.46 -0.45
5	55387.54 ^b	0.49	230	21.00	+0.57 -0.59	+2.25 -1.56	306.96	+0.94 -1.12	+2.70 -2.28
6	55421.51 ^b	0.89	770	15.21	+3.02 -3.10	+9.35 -7.41	252.00	+4.63 -6.48	+9.56 -16.65
7	55464.90 ^b	0.77	460	13.40	+0.24 -0.15	+0.52 -0.45	266.29	+0.22 -0.23	+0.58 -0.62
8	55478.38 ^b	0.86	660	11.09	+0.18 -0.19	+0.41 -0.49	331.08	+0.18 -0.35	+0.49 -0.80
9	55497.30 ^b	0.92	950	0.50	+0.10 -0.10	+0.25 -0.21	88.95	+0.18 -0.25	+0.48 -0.53
10	55513.60 ^b	0.80	520	3.15	+0.33 -0.25	+0.70 -0.63	285.95	+0.58 -0.42	+1.29 -1.50
11	55589.56 ^b	0.52	240	1.03	+0.07 -0.08	+0.19 -0.21	307.71	+0.08 -0.08	+0.52 -0.44
12	55702.77 ^b	0.60	300	20.30	+0.44 -0.62	+1.00 -1.43	235.13	+0.89 -0.55	+2.70 -1.76
13	55722.43 ^b	0.47	210	35.55	+0.28 -0.29	+0.69 -0.69	272.22	+0.50 -0.38	+1.23 -1.19
14	55764.22 ^b	0.46	210	5.29	+1.87 -1.96	+4.85 -4.72	315.66	+2.37 -1.39	+5.91 -5.35
15	55896.86 ^b	0.59	300	1.87	+0.57 -0.37	+1.25 -1.18	222.87	+0.90 -1.14	+1.95 -1.73
16	55911.28 ^b	0.86	660	19.10	+0.54 -0.77	+2.21 -2.21	36.65	+0.61 -0.56	+1.85 -1.71
17	56062.96	0.45	200	31.96	+0.30 -0.37	+0.81 -0.85	198.74	+0.49 -0.18	+1.44 -1.09
18	56146.21	0.55	260	1.57	+0.22 -0.18	+0.46 -0.42	330.10	+0.24 -0.36	+0.65 -0.82
19	56211.77	0.46	210	-2.39	+0.18 -0.19	+0.42 -0.51	205.11	+0.17 -0.24	+0.54 -0.66
20	56226.60	0.88	750	28.04	+0.31 -0.23	+0.67 -0.66	169.61	+0.45 -0.48	+1.16 -1.11
21	56470.11 ^c	0.87	670	14.46	+0.40 -0.39	+0.86 -0.94	93.38	+0.33 -0.34	+0.83 -0.90
22	56521.83	0.71	400	-4.44	+0.42 -0.39	+1.21 -0.94	224.89	+0.33 -0.32	+0.87 -1.19
23	56579.91	0.49	390	10.20	+0.15 -0.15	+0.34 -0.49	32.94	+0.20 -0.27	+0.63 -0.62
24	56666.50	0.90	850	32.82	+0.16 -0.14	+0.39 -0.41	293.29	+0.18 -0.40	+0.55 -1.08
25	56799.96	0.73	400	18.05	+0.75 -0.63	+1.94 -1.80	349.39	+1.13 -1.75	+2.89 -4.12
26	56817.64	0.66	340	1.29	+0.33 -0.29	+0.83 -0.74	106.26	+0.86 -0.74	+2.27 -1.90
27	56819.20	0.995	4450	11.42	+0.07 -0.08	+0.17 -0.17	110.63	+0.16 -0.28	+0.46 -0.55
28	57049.48	0.46	210	4.56	+0.19 -0.12	+0.68 -0.50	100.48	+0.23 -0.34	+0.95 -1.87
29	57157.94	0.52	240	12.18	+0.19 -0.18	+0.37 -0.35	91.60	+0.10 -0.37	+0.16 -0.74

Notes. The horizontal lines separate the different data sets IC59, IC79, IC2011 and IC2012-2014. The signalness is defined as the ratio of the astrophysical expectation over the sum of the atmospheric and astrophysical expectations for a given energy proxy and the best-fit spectrum. The signalness decreases up to about 10% when taking into account a prompt flux at the conservative upper limit of $1.06 \times \text{ERS}$ (see Section 6). The angular errors are statistical errors only and do not include systematics.

^a These events were included in Aartsen et al. (2014c).

^b These events were included in Aartsen et al. (2015c).

^c This event is identical to Event 38 in Kopper et al. (2015).

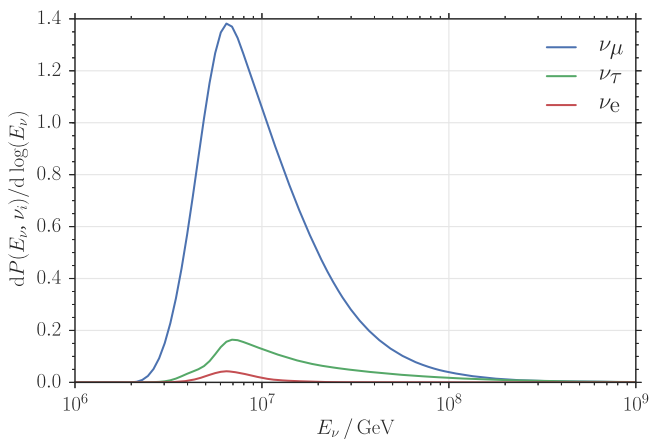


Figure 8. Probability distribution of primary neutrino energies that could result in the observed multi-PeV track-like event. The total probabilities for the different flavors are 87.7%, 10.9% and 1.4% for ν_μ , ν_τ , and $\bar{\nu}_e$, respectively.

confirm for the Northern Hemisphere a flux of muon neutrinos that is generally consistent with the observed all flavor flux in the Southern Hemisphere, but which is in tension with the assumption of a single power law describing this and previous observations with a lower energy threshold at the same time.

It is expected that for a Galactic origin the neutrino flux should be correlated with the Galactic plane. It is generally assumed that the contribution from the Galactic plane and Galactic sources is stronger in the Southern Hemisphere, which e.g., includes the Galactic center. The measured astrophysical flux is not strongly affected by a split in right ascension (see Section 5.2), where one region includes the part of the Galactic plane which is visible in the northern sky and the other does not. This can be interpreted as an indication that the flux observed here is mostly of extragalactic origin.

The observed tension may arise either from a spectral break at lower energies for the same sources or from an additional flux component, e.g., expected from Galactic sources or the

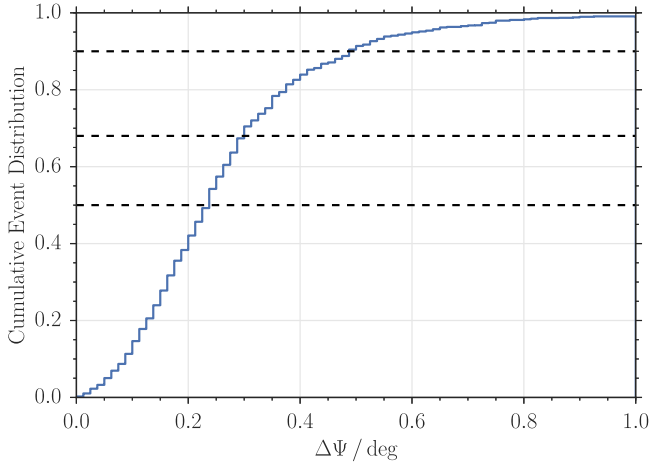


Figure 9. Angular reconstruction uncertainty of the multi-PeV track-like event. The estimate is based on an ensemble of simulated events with similar deposited energy, direction and entry point into the fiducial volume. The simulation takes into account the ice uncertainties (see Section 3.2). Including statistical and systematic uncertainties, 50% (99%) of the events are reconstructed better than $0^\circ.23$ ($0^\circ.90$).

Galactic plane, that is sub-dominant at the high energies to which this analysis is sensitive.

Figure 14 compares the measured diffuse astrophysical muon neutrino flux to theoretical flux predictions corresponding to different source types. The measured flux is within its uncertainties slightly below the Waxman–Bahcall upper bound (Waxman 2013). Senno et al. (2016) predict a diffuse neutrino flux originating from gamma-ray bursts, which is currently not ruled out (Aartsen et al. 2015d, 2016). A flux of cosmogenic neutrinos as predicted by Kotera et al. (2010) would only contribute subdominantly to the measured astrophysical neutrino flux. Neutrino fluxes from blazars and star-forming galaxies are predicted by e.g., Murase et al. (2014) and Bechtol et al. (2015), respectively. Glüsenskamp (2016) already constrains this blazar model. These fluxes are of the same order of magnitude as the measured flux within the given uncertainty band. However, due to the small statistics at high energies we cannot differentiate if the measured astrophysical neutrino flux corresponds to a neutrino flux originating from a specific source type or if it is a combination of different source types.

5. ANALYSIS OF ARRIVAL DIRECTIONS AND SEARCH FOR ANISOTROPIES

5.1. Arrival Directions of Highest-energy Events

The multi-PeV event discussed in Section 4.3 has a high probability of being astrophysical. Therefore, it is particularly interesting to correlate such an event with potential sources.

Figure 15 shows the direction of the event with its angular uncertainty and nearby high-energy gamma-ray sources from Nolan et al. (2012), Acero et al. (2015), Wakely & Horan (2007) in a window centered around the arrival direction. The closest source is multiple degrees away which is much larger than the angular error estimate.

For events that have a muon energy proxy above 200 TeV we expect roughly twice as many events with an astrophysical origin than with an atmospheric origin, assuming the best-fit

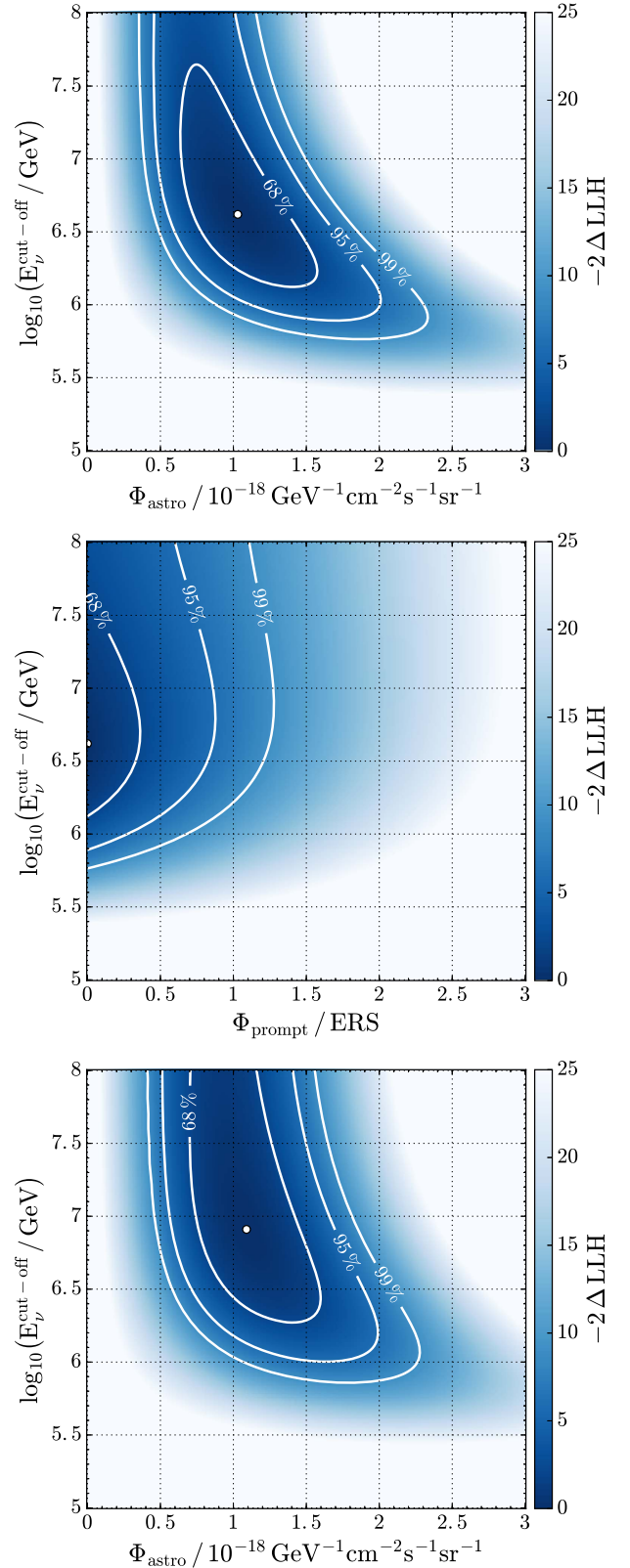


Figure 10. Two-dimensional profile likelihood scans of the astrophysical parameters Φ_{astro} , $E_{\nu}^{\text{cut-off}}$ and the prompt normalization Φ_{prompt} in units of the model in Enberg et al. (2008). The contour lines at 68%, 90% and 95% CL assume Wilks’ theorem. For the top and middle figure the spectral index is fixed to $\gamma_{\text{astro}} = 2$, while in the bottom figure it is fixed to the best-fit value $\gamma_{\text{astro}} = 2.13$. The white dots indicate the best-fit values.

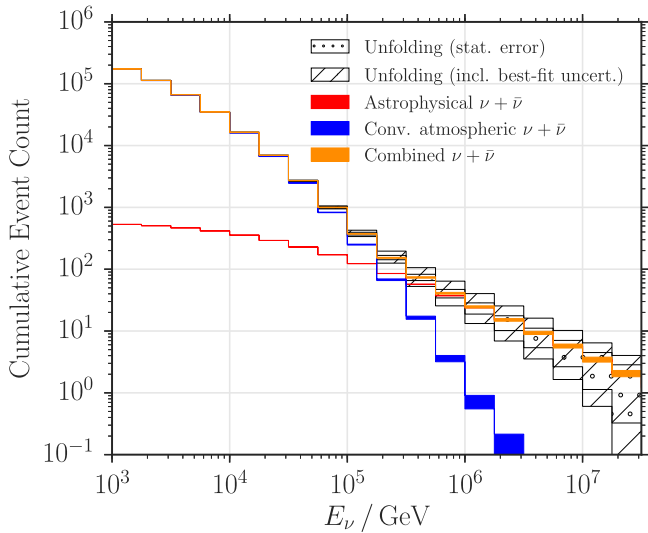


Figure 11. Cumulative distribution of the parametric unfolded neutrino energy spectrum for the six-year data sample assuming the best-fit spectrum as given by this analysis. Blue/red corresponds to the conventional atmospheric/astrophysical expectation weighted to the best-fit spectrum. Orange represents the sum of both expectations. The parametric unfolded data are shown as a hatched band where the gray band shows the statistical uncertainty and the white band additionally the effect of the uncertainties on the fitted astrophysical flux parameters.

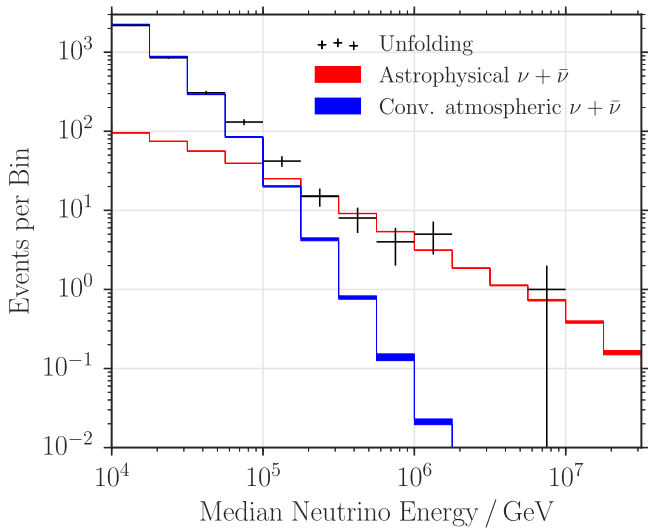


Figure 12. Distribution of the median expected neutrino energy assuming the best-fit spectrum as given by this analysis. The black crosses corresponds to experimental data and blue/red to the conventional atmospheric/astrophysical expectation weighted to the best-fit spectrum.

spectrum. Figure 16 shows the arrival direction of these events. Most events are located relatively close to the horizon where the Earth is not yet opaque to high energy neutrinos. Table 4 summarizes the per-event information. No obvious correlation with gamma-ray sources in the catalogs of Nolan et al. (2012), Acero et al. (2015), or Wakely & Horan (2007) were found. However, event 10 is close to the extended TeV source HESS J1857+026 (Wakely & Horan 2007).

A dedicated analysis searching for clusters in the neutrino arrival directions has been performed and found no evidence for a neutrino point source (M. G. Aartsen et al. 2016, in preparation).

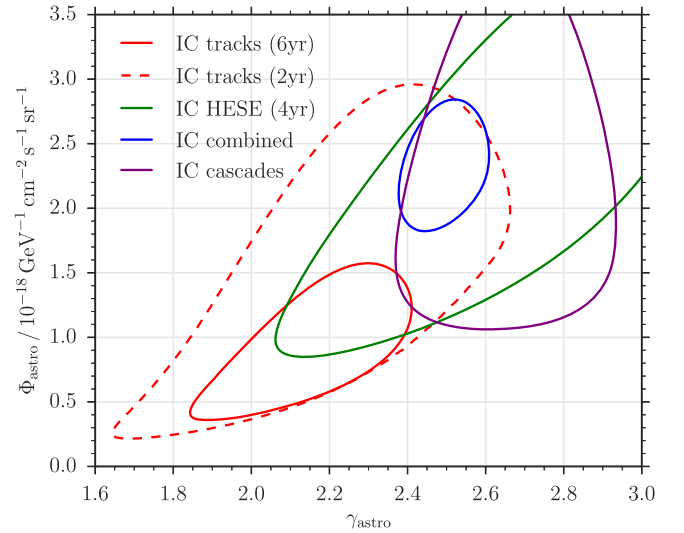


Figure 13. Results of different IceCube analyses measuring the astrophysical flux parameters Φ_{astro} and γ_{astro} . The contour lines show the 90% CL. The result of this analysis (IC tracks, 6yr) is shown by the red solid contour line. The contour obtained by the previous measurement using through-going muons (Aartsen et al. 2015c) (IC tracks, 2yr) is the red dashed line. In addition, the results for the most recent analysis of starting events (Kopper et al. 2015) (IC HESE, 4yr), the complementary cascade channel (Niederhausen et al. 2015) (IC cascades) and an analysis combining different IceCube results (IC combined, Aartsen et al. 2015f) are shown. The result of this analysis (red, solid) and IC combined are incompatible at 3.3σ (two-sided significance).

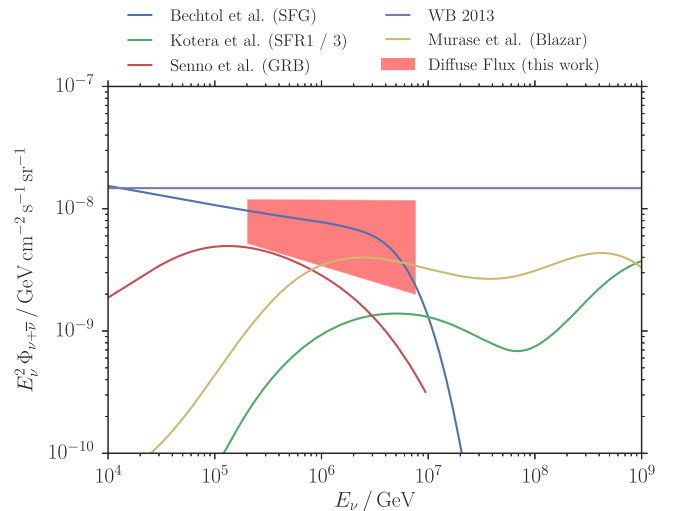


Figure 14. Comparison of the measured diffuse astrophysical muon neutrino flux (see Figure 5) with theoretical neutrino flux predictions corresponding to different source types (Kotera et al. 2010; Murase et al. 2014; Bechtol et al. 2015; Senno et al. 2016). Since Murase et al. 2014 predicts a lower and upper flux bound for neutrinos originating from blazars the central line between both bounds is shown. The purple line shows the Waxman–Bahcall upper bound (Waxman 2013).

5.2. Test for Anisotropies Related to the Galactic Plane

As discussed in Section 4.6 the measurement in this paper confirms the observation of an all-sky diffuse high-energy astrophysical neutrino flux. However, a tension exists between the measured spectral index of this analysis with the starting event data which originate mostly from the Southern Hemisphere. Furthermore, Neronov & Semikoz (2016) claim inconsistency of the previously published starting event data

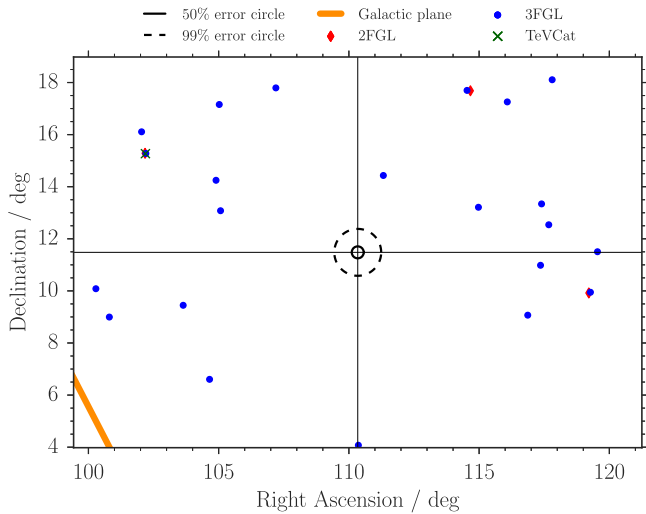


Figure 15. Window centered around the arrival direction of the multi-PeV track-like event. The solid (dashed) black line shows the 50% (99%) error circle for the angular reconstruction. The orange line indicates the Galactic plane. Additionally, the gamma-ray sources of the catalogs Wakely & Horan (2007), Acero et al. (2015), Nolan et al. (2012) within the window are shown.

with an isotropic signal with a preference of a Galactic latitude dependency. As the comparison to the Southern Hemisphere is subject to different energy thresholds and detector systematics, we perform a simple, self-consistent test for a dominant signal from the Galactic plane.

We split the sample into two right ascension regions, one containing the main parts of the Galactic plane: $\alpha \in [0^\circ:0, 108^\circ:9) \cup [275^\circ:0, 360^\circ:0)$ and one excluding it: $\alpha \in [108^\circ:9, 275^\circ:0)$. These intervals are chosen such that the two split samples are of similar statistics, resulting in 162363 and 189931 events respectively. Both samples are fitted independently and the aforementioned systematics can be considered identical as they are equalized by the daily Earth rotation.

The fit result, shown in Figure 17, is a small but not statistically significant larger flux and softer spectrum from the region including the Galactic plane. The p -value for both results being compatible is at about 43%. In conclusion, the observed flux is not dominated by the Galactic plane. However a small, sub-dominant contribution cannot be excluded.

6. SEARCH FOR A SIGNATURE OF PROMPT ATMOSPHERIC NEUTRINOS

The expected prompt neutrino flux provides a background for the measurement of the astrophysical flux. However, a flux of prompt neutrinos is interesting by itself and can be constrained by the present analysis.

The prompt flux predicted by Enberg et al. (2008) is sub-dominant to the conventional flux at low energies and the astrophysical flux at high energies. Nevertheless, the correlation of the energy spectrum and arrival directions of neutrinos at the detector lead to a clear signature. Figure 18 shows the pulls for simulated data corresponding to six years of live time and based on the IC2012-2014 event selection. Here, signal is defined as the prompt expectation and background is the sum of the conventional and astrophysical flux. The main effect of a prompt neutrino flux on the two observables will be visible for muon energy proxy values between 1 and 100 TeV in the fairly

up-going directions. However, a large part of this signature is absorbed within the uncertainties represented by the implemented nuisance parameters (see Section 3.2).

The overall best-fit prompt normalization is zero. Figure 19 shows the best-fit prompt normalization as a function of the astrophysical normalization and spectral index. Additionally, the two-dimensional confidence contours for the astrophysical parameters are shown. In the region where our experimental data are compatible with our single power-law model, the best-fit prompt normalization does not deviate from zero. Only for strong deviations from the best-fit astrophysical spectrum is a non-zero prompt normalization fitted, but this is strongly disfavored with respect to the best fit. Such behavior is expected. If the astrophysical flux decreases, the measured high-energy events need to be explained by another component. Assuming an unbroken power-law model for the astrophysical flux, the sensitivity for the prompt neutrino flux, taking into account the systematic uncertainties, is estimated to be $1.5 \times \text{ERS}$. Note that the sensitivity (median expected upper limit in the absence of a prompt neutrino flux) on a prompt neutrino flux depends on the chosen input values for the astrophysical flux.

In the absence of an indication of a non-zero prompt contribution an upper limit is calculated. Based on the profile likelihood for the prompt normalization, the upper limit at 90% confidence level is $0.50 \times \text{ERS}$. The more stringent limit compared to the sensitivity is caused by an under-fluctuation of the conventional atmospheric and astrophysical background by about one standard deviation.

For this reason we scan the resulting limit on the prompt flux as a function of the astrophysical signal parameters.

Figure 20 shows the joint three-dimensional 90% confidence region for the prompt flux and the astrophysical parameters. It was obtained using Wilks' theorem, and is bound by the surface for which $-2\Delta \log L$ is 6.25 higher than the best-fit value. The maximum prompt flux in the three-dimensional confidence region is $1.06 \times \text{ERS}$. We take this as a conservative upper limit on the prompt flux. Further tests have shown that reasonable changes to the astrophysical hypothesis, such as the introduction of a high-energy cut-off, have only small effects on this limit.

Several more recent calculations of the prompt flux have been published: GMS (H3p) (Garzelli et al. 2015), BERSS (H3p) (Bhattacharya et al. 2015) and GRRST (H3p) (Gauld et al. 2016). Figure 21 shows multiple predictions for the prompt flux as well as the upper limit calculated here using the prediction from Enberg et al. (2008) and taking into account a more realistic cosmic-ray model (Gaisser 2012). Since nuisance parameters describing the uncertainties of the cosmic-ray model, e.g., the cosmic-ray spectral index, are implemented, the upper limit curve slightly deviates from the ERS prediction including the knee. The energy range has been calculated such that the limit increases by 10% if only neutrinos with energies in that range are taken into account. For the sensitive region which is between 9 and 69 TeV the effect of the prompt predictions is only a change in normalization and it is therefore appropriate to convert the limit obtained with the ERS prediction to the other predictions. Also, the cosmic-ray composition only changes the normalization in this energy range. The values are summarized in Table 5.

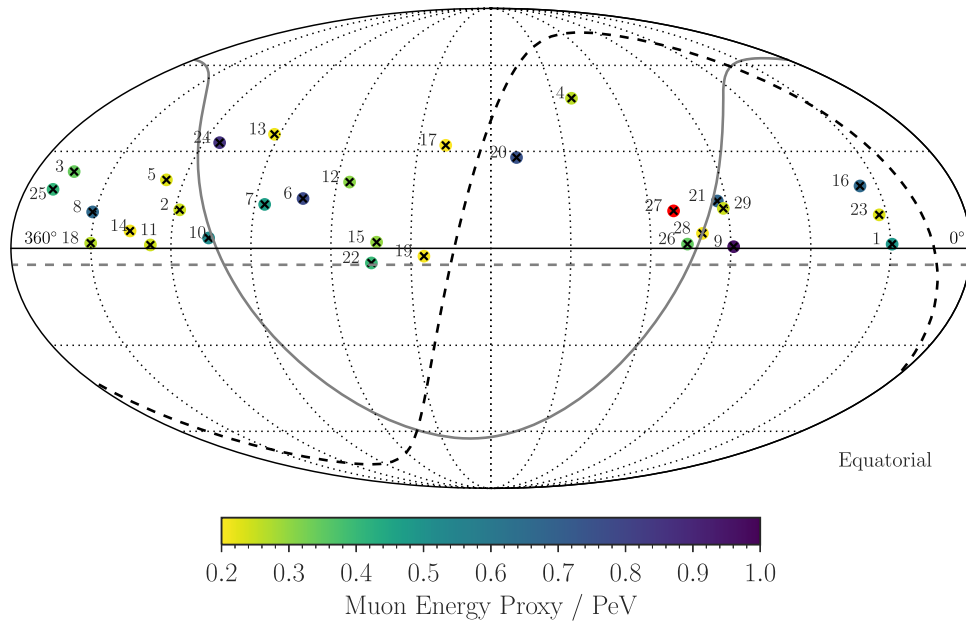


Figure 16. Arrival directions of events with a muon energy proxy above 200 TeV. Given the best-fit spectrum the ratio of astrophysical to atmospheric events is about two to one. The horizontal dashed gray line shows the applied zenith angle cut of 85° . The curved gray line indicates the Galactic plane and the dashed black line the supergalactic plane (Lahav et al. 2000). The multi-PeV track event is shown as a red dot and the energy proxy value listed in Table 4.

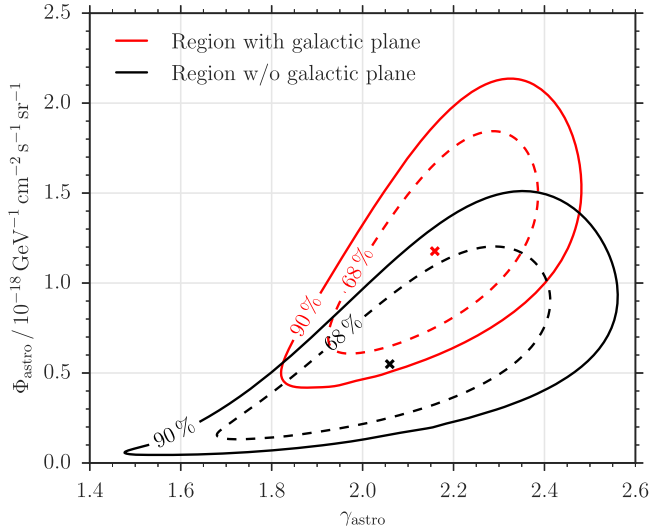


Figure 17. Two-dimensional profile likelihood scans of the astrophysical parameters Φ_{astro} and γ_{astro} for the two disjoint right ascension regions, one containing the Northern Hemisphere part of the Galactic plane (red) and the other not (black). The contour lines at 68% and 90% CL assume Wilks' theorem.

7. SUMMARY AND CONCLUSIONS

In this paper we have presented the result of analyzing six years of up-going muon data measured with the IceCube neutrino telescope. We measure an astrophysical flux of $\Phi_{\nu+\bar{\nu}} = (0.90^{+0.30}_{-0.27}) 10^{-18} \text{ GeV}^{-1} \text{ cm}^{-2} \text{ sr}^{-1} \text{ s}^{-1}$. $(E_\nu/100 \text{ TeV})^{-(2.13 \pm 0.13)}$ with a statistical significance of 5.6 standard deviations with respect to only being of atmospheric origin. With this result we have further established the observation of an astrophysical neutrino signal (Aartsen et al. 2013a, 2014b, 2015c) in a second, largely independent detection channel. The detection channel used here is of great interest because of the good directional reconstruction of

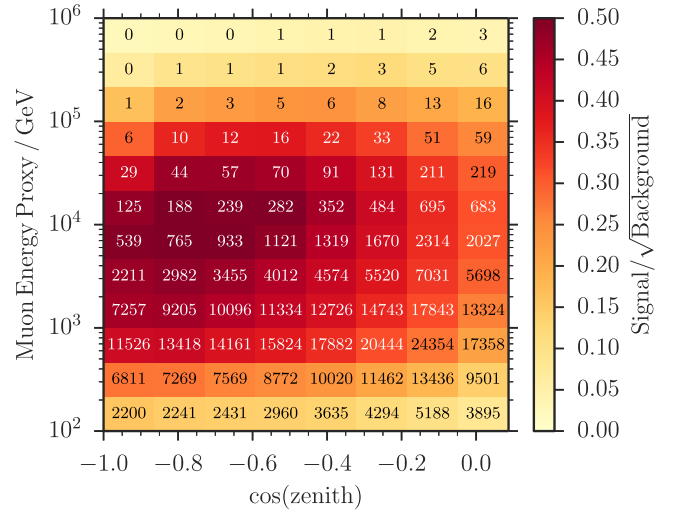


Figure 18. Signal over square root of background for the reconstructed muon energy vs. zenith angle corresponding to six years of IceCube data after applying the event selection for the 86-string configuration (IC2012-2014). Here, background is defined as the sum of the conventional atmospheric (Honda et al. 2007) and astrophysical ($10^{-8} \times E^{-2}$) $\nu_\mu + \bar{\nu}_\mu$ flux. The prompt atmospheric (Enberg et al. 2008) $\nu_\mu + \bar{\nu}_\mu$ flux is defined as the signal. The numbers in each bin correspond to the expected number of background events in six years.

detected muons and a large signal efficiency with an estimated number of about 500 astrophysical neutrinos included in this data sample.

The data include an exceptionally high-energy muon with $(2.6 \pm 0.3) \text{ PeV}$ deposited energy, which is the highest-energy lepton that has been reported to date.

A parametric unfolding of neutrino energies shows that the spectrum extends to about 10 PeV in neutrino energy with no significant spectral break or cut-off.

The measured hard spectral index of $\gamma = 2.13 \pm 0.13$ is in tension with complementary measurements of IceCube, which

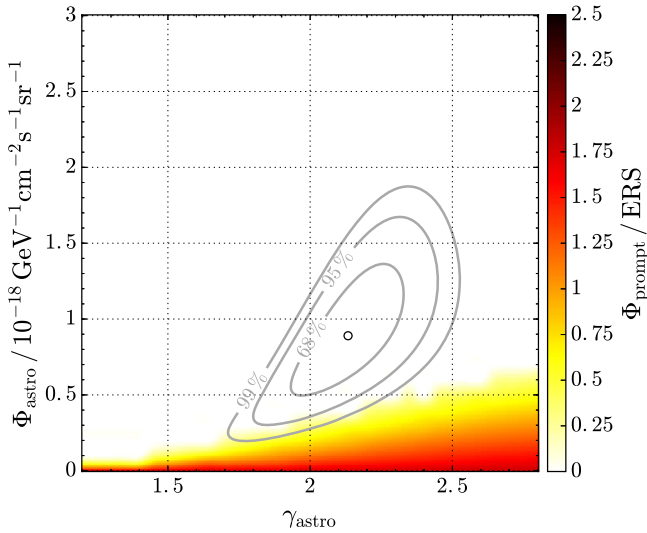


Figure 19. Best-fit prompt normalization Φ_{prompt} in units of the model of Enberg et al. (2008) for each scan point $\Phi_{\text{astro}}, \gamma_{\text{astro}}$. Additionally, the two-dimensional contours for $\Phi_{\text{astro}}, \gamma_{\text{astro}}$ are shown.

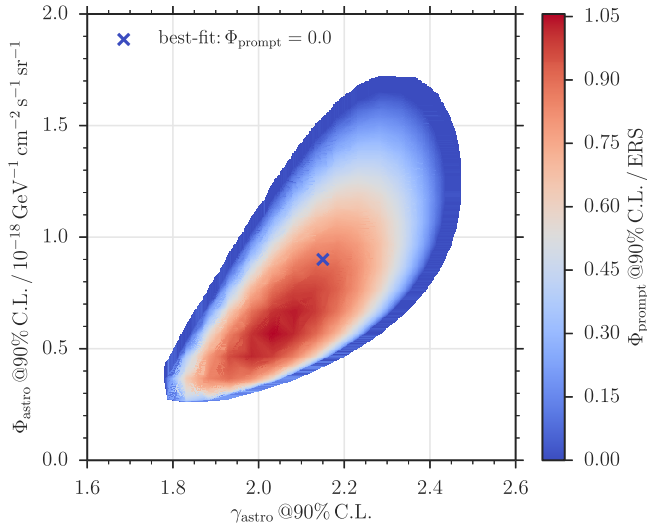


Figure 20. 90% CL contour assuming Wilks' theorem based on a three-dimensional profile likelihood scans of the astrophysical parameters $\Phi_{\text{astro}}, \gamma_{\text{astro}}$ and the prompt normalization Φ_{prompt} in units of the model of Enberg et al. (2008).

have a lower energy threshold by about one order of magnitude and are predominantly sensitive to the Southern Hemisphere. However, the consistency of the observed fluxes at high energies may be interpreted as indication of a spectral break or additional astrophysical component at lower energy to which this analysis is not sensitive.

For the highest-energy events no correlation with known high-energy gamma-ray sources or other astrophysical objects could be identified.

By splitting the data in right ascension, we find no significant correlation with the orientation of the Galactic plane and conclude that the dominant fraction of the flux is largely all-sky and isotropic.

The present analysis is also sensitive to a flux of prompt neutrinos which are expected from the decay of heavy mesons in the atmosphere. We find no indications for such a signal. However, because the prompt flux is subdominant to the

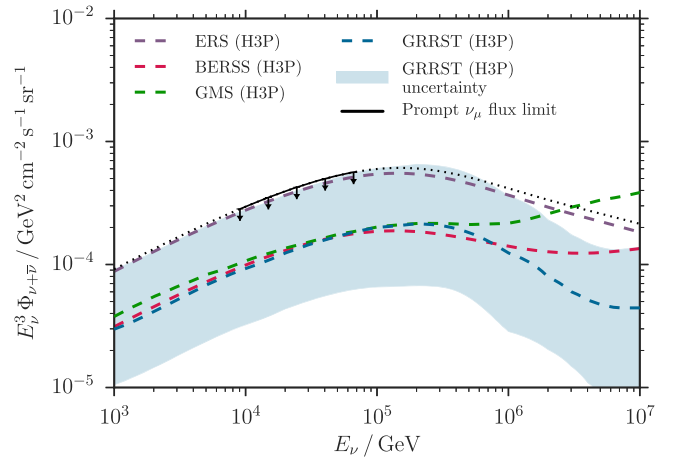


Figure 21. Prompt atmospheric muon neutrino flux predictions shown as dashed lines (Enberg et al. 2008; Bhattacharya et al. 2015; Garzelli et al. 2015; Gauld et al. 2016) in comparison to the constraint on the prompt flux given by this analysis. The shaded area shows the uncertainty band corresponding to the prediction in Gauld et al. (2016). Besides the ERS (H3p) prediction this is the closest band to the prompt flux constraint. For better readability the uncertainty bands of the other models are not shown. The black solid line shows the neutrino energy region where the prompt neutrino flux based on the model in Enberg et al. (2008) is constrained. The black dotted line indicates the model behavior including the best-fit nuisance parameters beyond the sensitive energy range. All flux predictions are based on the cosmic-ray model from Gaisser (2012).

Table 5
Limits for Fluxes of Prompt Neutrinos for Different Predictions

Model	Flux limit
ERS (H3p)	1.06
GMS (H3p)	≈ 2.9
BERSS (H3p)	≈ 3.0
GRRST (H3p)	≈ 3.1

Note. The limits for GMS (H3p) (Garzelli et al. 2015), BERSS (H3p) (Bhattacharya et al. 2015) and GRRST (H3p) (Gauld et al. 2016) are determined by rescaling the ERS (H3p) limit with the corresponding flux ratio at 30 TeV which is well within the sensitive energy range. All flux predictions are based on the cosmic ray model from Gaisser (2012).

astrophysical and conventional atmospheric neutrino flux, the exclusion depends on the assumed astrophysical model parameters. Variations of the astrophysical flux uncertainties lead to a conservative exclusion limit of approximately at the level of the mean expected flux normalization from Enberg et al. (2008). For the first time, it is possible to constrain such a flux in this range of theoretical predictions. However, recent perturbative QCD calculations from Garzelli et al. (2015), Bhattacharya et al. (2015) and (Gauld et al. 2016) predict lower prompt neutrino fluxes which are not yet constrained by the upper limit.

We acknowledge the support from the following agencies: U.S. National Science Foundation-Office of Polar Programs, U.S. National Science Foundation-Physics Division, University of Wisconsin Alumni Research Foundation, the Grid Laboratory Of Wisconsin (GLOW) grid infrastructure at the University of Wisconsin-Madison, the Open Science Grid (OSG) grid infrastructure; U.S. Department of Energy, and

National Energy Research Scientific Computing Center, the Louisiana Optical Network Initiative (LONI) grid computing resources; Natural Sciences and Engineering Research Council of Canada, WestGrid and Compute/Calcul Canada; Swedish Research Council, Swedish Polar Research Secretariat, Swedish National Infrastructure for Computing (SNIC), and Knut and Alice Wallenberg Foundation, Sweden; German Ministry for Education and Research (BMBF), Deutsche Forschungsgemeinschaft (DFG), Helmholtz Alliance for Astroparticle Physics (HAP), Research Department of Plasmas with Complex Interactions (Bochum), Germany; Fund for Scientific Research (FNRS-FWO), FWO Odysseus programme, Flanders Institute to encourage scientific and technological research in industry (IWT), Belgian Federal Science Policy Office (Belspo); University of Oxford, United Kingdom; Marsden Fund, New Zealand; Australian Research Council; Japan Society for Promotion of Science (JSPS); the Swiss National Science Foundation (SNSF), Switzerland; National Research Foundation of Korea (NRF); and Villum Fonden, Danish National Research Foundation (DNRF), Denmark.

REFERENCES

- Aartsen, M. G., Abbasi, R., Abdou, Y., Ackermann, M., & Adams, J. 2013a, *Sci*, 342, 1242856
- Aartsen, M. G., Abbasi, R., Abdou, Y., et al. 2013b, *NIMPA*, 711, 73
- Aartsen, M. G., Abbasi, R., Ackermann, M., et al. 2014a, *JInst*, 9, P03009
- Aartsen, M. G., Abbasi, R., Ackermann, M., et al. 2014c, *PhRvD*, 89, 062007
- Aartsen, M. G., Abraham, K., Ackermann, M., et al. 2015a, *ApJ*, 809, 98
- Aartsen, M. G., Abraham, K., Ackermann, M., et al. 2015f, in Proc. 34th ICRC, 21
- Aartsen, M. G., Abraham, K., Ackermann, M., et al. 2015c, *PhRvL*, 115, 081102
- Aartsen, M. G., Abraham, K., Ackermann, M., et al. 2016, *ApJ*, submitted (arXiv:1601.06484)
- Aartsen, M. G., Ackermann, M., Adams, J., et al. 2014b, *PhRvL*, 113, 101101
- Aartsen, M. G., Ackermann, M., Adams, J., et al. 2015b, *PhRvD*, 91, 022001
- Aartsen, M. G., Ackermann, M., Adams, J., et al. 2015d, *ApJL*, 805, L5
- Aartsen, M. G., Ackermann, M., Adams, J., et al. 2015e, *ApJ*, 807, 46
- Abbasi, R., Abdou, Y., Abu-Zayyad, T., et al. 2010, *NIMPA*, 618, 139
- Abbasi, R., Abdou, Y., Ackermann, M., et al. 2013, *NIMPA*, 703, 190
- Abbasi, R., Ackermann, M., Adams, J., et al. 2009, *NIMPA*, 601, 294
- Ajero, F., Ackermann, M., Ajello, M., et al. 2015, *ApJS*, in press (arXiv:1501.02003)
- Achterberg, A., Ackermann, M., Adams, J., et al. 2006, *Aph*, 26, 155
- Ackermann, M., Ahrens, J., Bai, X., et al. 2006, *JGRD*, 111, D13
- Ageron, M., Aguilar, J. A., Al Samarai, I., et al. 2011, *NIMPA*, 656, 11
- Ahrens, J., Bai, X., Bay, R., et al. 2004, *NIMPA*, 524, 169
- AIRS Science Team/Joao Teixeira, 2013, Aqua AIRS Level 3 Daily Standard Physical Retrieval (AIRS+AMSU), version 006, Tech. Rep. (Washington, DC: NASA)
- Anchordoqui, L. A., Goldberg, H., Lynch, M. H., et al. 2014, *PhRvD*, 89, 083003
- Andres, E., Askebjerg, P., Barwick, S., et al. 2000, *Aph*, 13, 1
- Athar, H., Kim, C. S., & Lee, J. 2006, *MPLA*, 21, 1049
- Bechtol, K., Ahlers, M., Di Mauro, M., Ajello, M., & Vandenbroucke, J. 2015, *ApJ*, submitted (arXiv:1511.00688)
- Becker, J. K. 2008, *PhR*, 458, 173
- Bell, A. 2013, *Aph*, 43, 56
- Belolaptikov, I. A., Bezrukov, L. B., Borisovets, B. A., et al. 1997, *Aph*, 7, 263
- Bhattacharya, A., Enberg, R., Reno, M. H., Sarcevic, I., & Stasto, A. 2015, *JHEP*, 2015, 110
- Boerner, M., Ruhe, T., Scheriau, F., & Schmitz, M. 2015, in Proc. 34th ICRC, 53
- Chirkin, D. 2013a, in Proc. 33rd ICRC, 17
- Chirkin, D. 2013b, arXiv:1304.0735
- Chirkin, D. 2013c, *NIMPA*, 725, 141
- Chirkin, D., & Rhode, W. 2004, arXiv:hep-ph/0407075
- Cholis, I., & Hooper, D. 2013, *JCAP*, 2013, 030
- Cooper-Sarkar, A., Mertsch, P., & Sarkar, S. 2011, *JHEP*, 08, 042
- Desiati, P., et al. 2014, in Proc. 33rd ICRC, 0492
- Enberg, R., Reno, M. H., & Sarcevic, I. 2008, *PhRvD*, 78, 043005
- Freund, Y., & Schapire, R. E. 1997, *J. Comput. Syst. Sci.*, 55, 119
- Gaisser, T. K. 1990, *Cosmic Rays and Particle Physics* (Cambridge: Cambridge Univ. Press)
- Gaisser, T. K. 2012, *Aph*, 35, 801
- Gaisser, T. K., Halzen, F., & Stanev, T. 1995, *PhR*, 258, 173
- Garzelli, M. V., Moch, S., & Sigl, G. 2015, *JHEP*, 2015, 115
- Gauld, R., Rojo, J., Rottoli, L., Sarkar, S., & Talbert, J. 2016, *JHEP*, 02, 130
- Gazizov, A., & Kowalski, M. P. 2005, *CoPhC*, 172, 203
- Glüsenkamp, T. 2016, *EPJ*, 121, 05006
- Gonzalez-Garcia, M., Halzen, F., & Niro, V. 2014, *Aph*, 57-58, 39
- Greisen, K. 1960, *ARNPS*, 10, 63
- He, H.-N., Wang, T., Fan, Y.-Z., Liu, S.-M., & Wei, D.-M. 2013, *PhRvD*, 87, 063011
- Heck, D., Schatz, G., Thouw, T., Knapp, J., & Capdevielle, J. 1998, CORSIKA: A Monte Carlo Code to Simulate Extensive Air Showers, Tech. Rep. (Karlsruhe: KIT)
- Hoerandel, J. R. 2003, *Aph*, 19, 193
- Honda, M., Kajita, T., Kasahara, K., Midorikawa, S., & Sanuki, T. 2007, *PhRvD*, 75, 043006
- Illana, J. I., Lipari, P., Masip, M., & Meloni, D. 2011, *Aph*, 34, 663
- Kalashov, O. E., Kusenkov, A., & Essey, W. 2013, *PhRvL*, 111, 041103
- Kashti, T., & Waxman, E. 2005, *PhRvL*, 95, 181101
- Klein, S. R., Mikkelsen, R. E., & Becker Tjus, J. 2013, *ApJ*, 779, 106
- Koehne, J. H., Frantzen, K., Schmitz, M., et al. 2013, *CoPhC*, 184, 2070
- Kopper, C., Kurahashi, N., et al. 2015, in Proc. 34th ICRC, 45
- Kotera, K., Allard, D., & Olinto, A. V. 2010, *JCAP*, 1010, 013
- Laha, R., Beacom, J. F., Dasgupta, B., Horiuchi, S., & Murase, K. 2013, *PhRvD*, 88, 043009
- Lahav, O., Santiago, B., Webster, A., et al. 2000, *MNRAS*, 312, 166
- Lai, H. L., Huston, J., Kuhlmann, S., et al. 2000, *EPJC*, 12, 375
- Learned, J., & Mannheim, K. 2000, *ARNPS*, 50, 679
- Learned, J. G., & Pakvasa, S. 1995, *Aph*, 3, 267
- Lundberg, J., Miocinovic, P., Burgess, T., et al. 2007, *NIMPA*, 581, 619
- Markov, M. 1960, in Proc. 10th Int. Conf. on High-Energy Physics, ed. E. C. G. Sudarshan, J. H. Tinlot, & A. C. Melissinos (Rochester, NY: Rochester Univ. Press), 578
- Murase, K., Inoue, Y., & Dermer, C. D. 2014, *PhRvD*, 90, 023007
- Narsky, I., & Porter, F. C. 2013, *Statistical Analysis Techniques in Particle Physics: Fits, Density Estimation and Supervised Learning* (New York: Wiley)
- Neronov, A., & Semikoz, D. V. 2016, *Aph*, 75, 60
- Niederhausen, H., Lesiak-Bzdak, M., Stössl, A., et al. 2015, in Proc. 34th ICRC, 59
- Nolan, P. L., Abdo, A. A., Ackermann, M., et al. 2012, *ApJS*, 199, 31
- Olive, K. A., et al. 2014, *ChPhC*, 38, 090001
- Pedregosa, F., Varoquaux, G., Gramfort, A., et al. 2011, *J. Mach. Learn. Res.*, 12, 2825
- Razzaque, S. 2013, *PhRvD*, 88, 081302
- Reines, F. 1960, *ARNPS*, 10, 1
- Reines, F., & Cowan, C. L. 1956, *Natur*, 178, 446
- Roberts, A. 1992, *RvMP*, 64, 259
- Roulet, E., Sigl, G., van Vliet, A., & Mollerach, S. 2013, *JCAP*, 01, 028
- Schoenen, S., & Raedel, L. 2015, *ATel*, 7856, 1
- Schukraft, A. 2013, PhD thesis, RWTH Aachen Univ.
- Senno, N., Murase, K., & Meszaros, P. 2016, *PhRvD*, 93, 083003
- Stecker, F. W. 2013, *PhRvD*, 88, 047301
- Tamborra, I., Ando, S., & Murase, K. 2014, *JCAP*, 1409, 043
- Wakely, S. P., & Horan, D. 2007, Proc. 30th ICRC, 3, 1341
- Waxman, E. 2013, in Proc. 9th Rencontres du Vietnam: Windows on the Universe, ed. J. Dumarchez et al. (Quy Nhon: ICISE), 161
- Wilks, S. S. 1938, *Ann. Math. Statist.*, 9, 60

Publications Alberto Mariotti

New axion searches at flavor factories

Xabier Cid Vidal,^a Alberto Mariotti,^b Diego Redigolo,^{c,d,e} Filippo Sala^f
and Kohsaku Tobioka^{g,h}

^a*Instituto Galego de Física de Altas Enerxías (IGFAE),
Santiago de Compostela, Spain*

^b*Theoretische Natuurkunde and IIHE/ELEM,
Vrije Universiteit Brussel, and International Solvay Institutes,
Pleinlaan 2, B-1050 Brussels, Belgium*

^c*Raymond and Beverly Sackler School of Physics and Astronomy, Tel-Aviv University,
Tel-Aviv 69978, Israel*

^d*School of Natural Sciences, Institute for Advanced Study,
Einstein Drive, Princeton, NJ 08540, U.S.A.*

^e*Department of Particle Physics and Astrophysics, Weizmann Institute of Science,
Rehovot 7610001, Israel*

^f*DESY,
Notkestraße 85, D-22607 Hamburg, Germany*

^g*Department of Physics, Florida State University,
Tallahassee, FL 32306, U.S.A.*

^h*Theory Center, High Energy Accelerator Research Organization (KEK),
Tsukuba 305-0801, Japan*

*E-mail: xabier.cid.vidal@cern.ch, alberto.mariotti@vub.ac.be,
d.redigolo@gmail.com, filippo.sala@desy.de, ktobioka@fsu.edu*

ABSTRACT: We assess the impact of searches at flavor factories for new neutral resonances that couple to both photons and gluons. These are well motivated by “heavy axion” solutions of the strong CP problem and by frameworks addressing both Dark Matter and the Higgs hierarchy problem. We use LHCb public diphoton data around the B_s mass to derive the current best limit on these resonances for masses between 4.9 and 6.3 GeV. We estimate that a future LHCb dedicated search would test an axion decay constant of $O(\text{TeV})$ for axion masses in the few-to-tens of GeV, being fully complementary to the low mass ATLAS and CMS searches. We also derive the impact of BABAR searches based on Υ decays and the future Belle-II reach.

KEYWORDS: Beyond Standard Model, Particle and resonance production, Hadron-Hadron scattering (experiments), Flavor physics, B physics

ARXIV EPRINT: [1810.09452](https://arxiv.org/abs/1810.09452)

Contents

1	Introduction	1
2	Results	3
3	Physics cases	7
3.1	Heavy axions	7
3.2	ALP-mediated dark matter	9
3.3	R-axion in supersymmetry	10
4	Diphoton searches at LHCb	10
5	Conclusions	13
A	More on the signal	14
B	$m_{\gamma\gamma}$ distribution of the 0CV category	15
C	Details on the LHCb calorimeter	16
D	Signal acceptance and efficiency	18

1 Introduction

The lack of new physics at the Large Hadron Collider (LHC) and the lack of direct detection signal of dark matter (DM) at present experiments make it necessary to rethink the theoretical questions in the SM from a wider viewpoint and trigger broader experimental searches for new physics (NP). In this paper we make a step in this direction by presenting a NP case for flavor factories at the intensity frontier. These are light resonances below the EW scale which are neutral under the SM gauge group and couple to both gluons and photons. We show that flavor experiments have an unexploited potential to probe these states in a complementary mass range to previously proposed low-mass resonance searches at ATLAS and CMS [1]. Pointing out these gaps in the search program at flavor facilities is now a particularly important question in view of the upcoming LHCb upgrade and the Belle II data taking.

The possibility we consider here is that the new physics scale M_{NP} lies beyond the reach of the LHC. If that is the case, NP signals might still arise from pseudo-Nambu-Goldstone bosons (pNGBs) associated to spontaneously broken approximate symmetries. These are often called axion-like particle (ALP) in the literature, they can be sensibly lighter than the NP scale ($m_a \ll M_{\text{NP}}$) and their couplings to the SM are controlled by the inverse of

the decay constant $1/f$. Generically, one has $M_{\text{NP}} = g_* f$ with g_* being the typical size of the couplings in the NP sector, so that probing weak enough couplings of the pNGB gives an indirect probe of the scale of new physics.

The focus of this paper will be on pNGBs with m_a between 2 and 20 GeV, a mass window within the reach of flavor experiments. The driving question is *whether flavor experiments can be sensitive to couplings of pNGBs small enough to probe new physics beyond the LHC reach*. This question has been partially addressed for ALPs which couple to the SM by mixing with the Higgs sector [2, 3] but it is surprisingly unexplored for ALPs with only gluon and photon couplings.

In the large theory space of all the possible couplings of the ALP to the SM, having a non-zero coupling to gluons is particularly well motivated from the theory perspective. In this paper we will discuss in detail two particularly compelling examples: “heavy” QCD axions [4–16] and the R -axion [17–19] in low energy SUSY-breaking. As we will show, in these two classes of models the gluon coupling is unavoidable, the photon coupling generic, the mass range of interest for this paper can be easily achieved. A TeV decay constant is theoretically favoured by ensuring the quality of the axion potential [20–23] or by explaining the DM relic abundance via thermal freeze out. Besides these two examples, ALPs with both gluon and photons couplings arise for instance as new pions in Composite Higgs models [24–26], in theories with vector-like confinement [27] or in models of EW baryogenesis [28].

The first observation of this paper is that many existing search strategies for light resonances in the 2–20 GeV range [29–35] lose sensitivity as soon as the gluon coupling is switched on. The main reason is that the decay width into gluons dominates over the one into photons unless a non-generic hierarchy of couplings is assumed, therefore strongly suppressing the signals expected in the existing strategies.

The dominant di-jet final states are much more difficult to distinguish from the SM background than diphotons.¹ As a way to overcome this issue, we show that the large production rate in pp collisions induced by the non-zero gluon coupling can be exploited at LHCb, which already has a low mass diphoton trigger designed to look for the rare decay $B_s \rightarrow \gamma\gamma$. To substantiate this point, we use 80 pb^{-1} of public LHCb diphoton data [38] around the B_s mass to derive a limit of $\mathcal{O}(100) \text{ pb}$ on the signal strength of new diphoton resonances. This limit already constitutes the strongest existing probe for ALPs in the mass range between 4.9 and 6.3 GeV and motivates a dedicated LHCb search for diphoton resonances in a broader mass range. We estimate the sensitivity of such a search and show that decay constants at around the TeV scale are within reach of the high-luminosity phase of LHCb. This extends the coverage of low-mass resonance searches down to masses as low as 2 GeV and constitutes a new probe of multi-TeV scale NP which could be difficult to produce directly at the LHC. A similar point was made in ref. [1] with ATLAS, CMS, and Tevatron diphoton searches, that are however limited by trigger issues to masses roughly above 10 GeV.

¹As an example the LEP limit on $\text{BR}(Z \rightarrow \gamma a)$ is $1.7 \cdot 10^{-5}$ from 36.9 pb^{-1} of data if a is a diphoton resonance [36] and $4.7 \cdot 10^{-4}$ from 5.5 pb^{-1} of data if a is a dijet resonance [37].

We finally discuss bounds on light resonances produced from SM meson decays. We estimate the BABAR constraint on $\Upsilon(1, 2, 3S) \rightarrow \gamma a(jj)$ and assess the future Belle-II sensitivity. This production channel currently constitutes the best probe of ALPs below ~ 3 GeV.

2 Results

We consider a spontaneously broken approximate U(1) symmetry in the UV. Integrating out the new physics sector at the scale M_{NP} , we write down the effective interactions between the pNGBs and the SM

$$\mathcal{L}_{\text{eff}} = \frac{1}{2}(\partial_\mu a)^2 - \frac{1}{2}m_a^2 a^2 + \frac{a}{f} \sum_{i=1}^3 c_i \frac{\alpha_i}{4\pi} F_{i,\mu\nu} \tilde{F}_i^{\mu\nu}, \quad (2.1)$$

where i runs over the hypercharge, weak and strong gauge groups, $\tilde{F}_i^{\mu\nu} = \epsilon^{\mu\nu\rho\sigma} F_{i,\rho\sigma}/2$, $\alpha_i = g_i^2/4\pi$ and α_1 is GUT-normalised ($\alpha_1 = 5\alpha_y/3$). The constants c_i are anomaly coefficients which depend on the number of degrees of freedom chiral under the U(1) symmetry and carrying a non-zero charge under the SM gauge group.²

In the NP sector, the strength of the interaction g_* generically limits the maximal number of degrees of freedom to be below $\approx (4\pi)^2/g_*^2$. Therefore, a lower g_* allows for large couplings of the ALP to the SM but at the same time it lowers the scale of new physics $M_{\text{NP}} \simeq g_* f$.

For $m_a \lesssim M_Z$, we can write the ALP couplings to photons and gluons below EWSB using the same notation of the QCD axion

$$\mathcal{L}_{\text{eff}} \supset \frac{N\alpha_3}{4\pi} \frac{a}{f} G_{\mu\nu} \tilde{G}^{\mu\nu} + \frac{E\alpha_{\text{em}}}{4\pi} \frac{a}{f} F_{\mu\nu} \tilde{F}^{\mu\nu}, \quad (2.2)$$

where we have

$$N = c_3 \quad , \quad E = c_2 + 5c_1/3 \quad , \quad g_{a\gamma\gamma} = \frac{\alpha_{\text{em}}}{\pi f} E, \quad (2.3)$$

where $g_{a\gamma\gamma}$ agrees with the standard formula for the QCD axion after normalizing the decay constant with respect to the QCD coupling $f = 2N f_{\text{PQ}}$. The relevant decay widths of the pNGB are

$$\Gamma_{\gamma\gamma} = \frac{\alpha_{\text{em}}^2 E^2}{64\pi^3} \frac{m_a^3}{f^2}, \quad \Gamma_{gg} = K_{gg} \frac{\alpha_s^2 N^2}{8\pi^3} \frac{m_a^3}{f^2}, \quad (2.4)$$

where we include NNLO corrections to the gluon width [42] in K_{gg} (see appendix A for more details). Note that $(0.1 \text{ mm})^{-1} \ll \Gamma_{\text{tot}} = \Gamma_{gg} + \Gamma_{\gamma\gamma} \ll m_{\gamma\gamma}^{\text{bin}}$ over the mass range of our interest. The new resonance decays promptly and has a very narrow width compared to its mass.

The LHCb constraint and sensitivities derived in section 4 are displayed on the ALP parameter space in figure 1, for the benchmark $c_1 = c_2 = c_3 = 10$. We compute $\sigma(pp \rightarrow a)$ with ggHiggs v4 [43–46] using the mstw2008nn1o pdf set. We compare it with that obtained

²If the SM fermions and the Higgs doublet are uncharged under the U(1) symmetry, the couplings of the pNGB to them arise only from loops of SM gauge bosons and can safely be neglected.

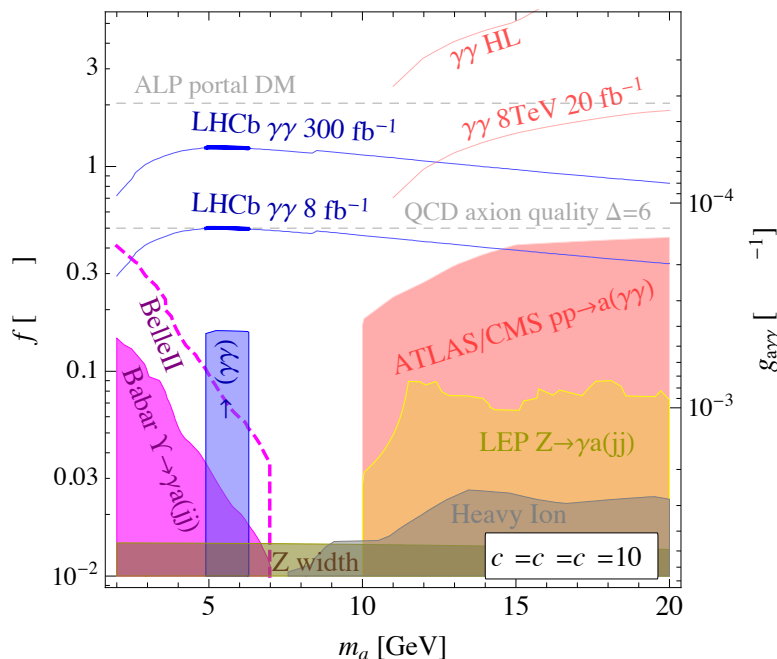


Figure 1. Limits (shaded regions) and sensitivities (colored lines) on the ALP parameter space described in eq. (2.1). The bounds from Babar and LHCb are first derived here from data in [31, 38], projections are given for Belle II and future LHC stages. Details are given in section 4. The other bounds are derived from Z width measurements [29, 39], heavy ion collisions [40, 41], $Z \rightarrow \gamma a(jj)$ decays at LEP I [30] and diphoton cross section measurements at CDF (relevant only for $m_a \simeq 10$ GeV), CMS and ATLAS [1]. For the latter we also give sensitivities up to the HL stage as derived in ref. [1]. The thin dashed lines indicate theory benchmarks motivated by heavy QCD axion models and by ALP-portal Dark Matter described in section 3. New coloured and EW states are expected to have masses of order $g_* f$, where $g_* = 4\pi/\sqrt{N_{\text{mess}}} = 4\pi/\sqrt{2}c_i$.

by the use of different pdf sets and of MadgraphLO_v2.6 [47, 48] upon implementing the ALP model in FeynRules [49], finding differences from 20% at $m_a = 20$ GeV to a factor of 2 or larger for $m_a < 5$ GeV. As detailed in appendix A, a more precise determination of the signal would be needed, especially for $m_a \lesssim 5$ GeV.

In figure 1 we also show

- i) the 2σ constraint $\Gamma_Z - \Gamma_Z^{\text{SM}} < 5.8$ MeV [29, 39];
- ii) the LEP limit $\text{BR}(Z \rightarrow \gamma a(jj)) < 1\text{--}5 \times 10^{-4}$ [30];
- iii) the constraint derived in [1] from the ATLAS [50, 51], CMS [52], and CDF [53] inclusive diphoton cross section measurements, corresponding to $\sigma(pp/p\bar{p} \rightarrow X a(\gamma\gamma)) < 10\text{--}100$ pb;
- iv) the sensitivities derived in [1] from inclusive diphoton cross section measurements at ATLAS and CMS. The HL-LHC reach assumes minimal photon p_T cuts of 25 and 22 GeV and minimal photon separation of $\Delta R = 0.4$. These numbers correspond to the 7 TeV measurement in ref. [50]. Higher p_T cuts would increase the minimal value of the invariant mass within the reach of HL-LHC.

v) the BABAR constraint $\text{BR}(\Upsilon_{2S,3S} \rightarrow \gamma a(jj)) < 10^{-4} - 10^{-6}$ [31], where we compute

$$\frac{\text{BR}(\Upsilon \rightarrow \gamma a)}{\text{BR}(\Upsilon \rightarrow \mu\bar{\mu})} \simeq 8 E^2 \frac{\alpha_{\text{em}}}{4\pi} \left(\frac{m_\Upsilon}{4\pi f}\right)^2 \left(1 - \frac{m_a^2}{m_\Upsilon^2}\right)^3, \quad (2.5)$$

where $\text{BR}(\Upsilon_{2S,3S} \rightarrow \mu\bar{\mu}) = 1.92\%, 2.18\%$. The above expression corrects a factor of 4 in the result of ref. [54].

- vi) the Belle-II sensitivity in the same channel, that we determine simply by rescaling the expected sensitivities in [31] by a factor of 10. This assumes that the Belle-II reach will be statistics-dominated, and that it will be based on a factor of 100 more $\Upsilon(3S)$ than the BABAR one (i.e. on $\simeq 1.2 \times 10^{10}$ $\Upsilon(3S)$ in total). The current Belle-II run plan for the first years assumes only a factor of 10 for the above ratio [55, 56], corresponding to a few weeks of dedicated run at the $\Upsilon(3S)$ threshold. An extra factor of 10 could be obtained in a comparable time with dedicated later runs, because a higher instantaneous luminosity is foreseen [56]. An analogous search could be effectively performed, at Belle-II, also analysing the decays of $\Upsilon(1S, 2S)$.
- vii) limits from the diphoton final state from heavy ion collisions are extracted from the recent CMS analysis in ref. [41] and the reinterpretation of the ATLAS light by light scattering data [40] of ref. [57]. The lower reach of these measurements is set to $m_a \gtrsim 5$ GeV as a consequence of the minimal cuts on the two photons transverse momenta.

ATLAS limits from $Z \rightarrow \gamma a(\gamma\gamma)$ [58] are not displayed in figure 1. They imply $\text{BR}(Z \rightarrow \gamma a(\gamma\gamma)) < 2.2 \cdot 10^{-6}$ and turn out to be comparable to the heavy ions bound for our benchmark in figure 1. Similar constraints can be derived from the ATLAS inclusive search in $pp \rightarrow \gamma a(\gamma\gamma)$ [58]. The lower invariant mass reach of these ATLAS searches is set by the diphoton isolation requirement of [58], $\Delta R_{\gamma\gamma} = 0.15$. This corresponds to an ALP mass of 4 GeV as discussed in ref. [59]. Notice that LEP searches for $Z \rightarrow \gamma a(\gamma\gamma)$ [32] are weaker than the ATLAS bound. Future sensitivities from $e^+e^- \rightarrow \gamma a(\gamma\gamma)$ [34, 35] do not reach values of f larger than $\simeq 50$ GeV and are not shown. Finally, the proposed search in $B \rightarrow K^{(*)} a(\gamma\gamma)$ [34] at Belle-II has some sensitivity in a very limited portion of our mass range and it is not shown to avoid clutter.

In figure 2 we fix the ALP masses to two representative values $m_a = 5, 15$ GeV and show the impact of the various searches in the plane $(N/f, E/f)$ which control the ALP's gluon and photon coupling respectively. As one can see from figure 2, diphoton searches for a ALP produced in gluon fusion both at ATLAS/CMS (see ref. [1]) and at LHCb (see section 4) can be sensitive to N/f as small as 10^{-4} GeV $^{-1}$ as long as the coupling to the photons is large enough. Moreover they can cover significant portion of the parameter space where the couplings are of their natural size.

Searches taking advantage of uniquely the photon coupling such as the ones in refs. [33, 35, 58] become relevant only in the upper left corner of the plane where $E/N \gtrsim 50$. Such a hierarchy can be realized in clockwork constructions where the photon coupling is enhanced with respect to the gluon one (see for example ref. [60]).

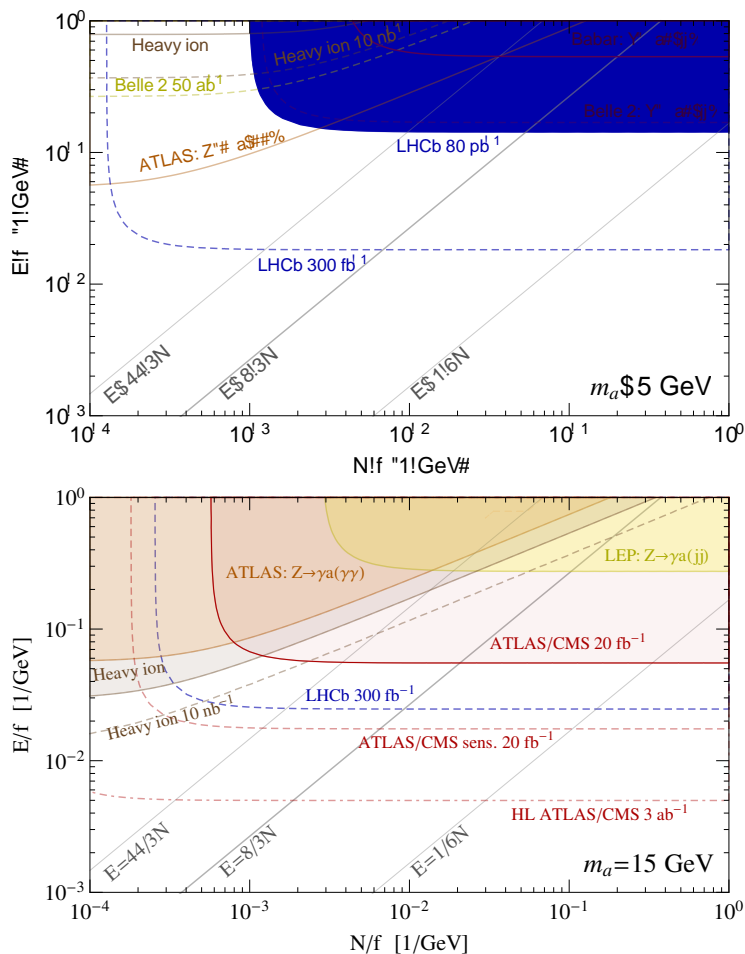


Figure 2. Constraints on the ALP parameter space for fixed masses $m_a = 5, 15$ GeV in the up, down panel respectively. We fix $c_1 = c_2$ so that E in eq. (2.3) controls both the $Z\gamma$ and the $\gamma\gamma$ coupling. The bounds are shown as shaded regions while the projections as dashed lines. The three grey lines show the “axion window” obtained by integrating out fermions in different representations of the SM gauge group, the central one $E = 8N/3$ corresponds to the choice of figure 1.

The ATLAS, CMS and LHCb limits and sensitivities shown in figure 2 are derived assuming gluon fusion as the ALP production process, so they sharply stop at a given small gluon coupling. If other production processes like vector-boson-fusion are taken into account, the limits and sensitivities would be slightly improved in the upper left corner of figure 2. Practically, the Heavy Ion results that we are including will always lead to stronger constraint because of the enhanced photon-fusion production and the loop suppressed background from light-by-light scattering.

The bottom right corner where the new resonance mostly couples to gluons is challenging to constrain in this mass range, even though boosted dijet searches at the LHC were recently able to go down to invariant masses of 50 GeV (see refs. [1, 61, 62]). Of course for $N/f \gtrsim (100\text{GeV})^{-1}$ one expects color states generating the ALP coupling to be within the reach of the LHC.

3 Physics cases

In this section we expand on the two theory lines displayed in figure 1. We would like to motivate: 1) the coupling of the axion to gluons and photons, 2) the TeV decay constant, 3) the mass range considered here.

3.1 Heavy axions

As a first example, we consider a particular class of axion solutions to the strong CP problem in the SM. First of all, introducing a spontaneously broken Peccei-Quinn symmetry $U(1)_{\text{PQ}}$ which is anomalous under QCD [63, 64] leads unavoidably to a light axion with non-zero couplings to gluons [65, 66]. In this sense, the axion coupling to gluons is deeply connected to its role in solving the strong CP problem. Taking the SM fields to be uncharged under the $U(1)_{\text{PQ}}$, the QCD anomaly is generated by heavy vector-like fermions like in KSVZ type of models [67, 68]

$$\mathcal{L}_{\text{PQ}} \supset g_* \Phi \psi \tilde{\psi} + \text{h.c.}, \quad \Phi = \frac{f}{\sqrt{2}} e^{ia/f}, \quad (3.1)$$

where the fermion charges should satisfy $|q_\psi^{\text{PQ}} - q_{\tilde{\psi}}^{\text{PQ}}| = q_\Phi^{\text{PQ}}$ and by writing eq. (3.1) we take $q_\Phi^{\text{PQ}} = 1$. After $U(1)_{\text{PQ}}$ gets spontaneously broken by the VEV of Φ , the fermion mass is at $M_{\text{NP}} = g_* f / \sqrt{2}$. Below the PQ breaking scale we can integrate out the heavy fermions and match to the effective Lagrangian in eq. (2.2):

$$N = q_\Phi^{\text{PQ}} \sum_\psi C_3(R_\psi) \quad E = q_\Phi^{\text{PQ}} \sum_\psi Q_{\text{em}}^2(R_\psi). \quad (3.2)$$

The vector-like fermions are often assumed to carry a non-zero hypercharge in order to allow a non-zero mixing with the SM quarks, to make them decay avoiding cosmological problems. This induces an anomaly of $U(1)_{\text{PQ}}$ with respect to the hypercharge, which leads to a non-zero coupling of the axion to photons: $E \neq 0$. To fix a benchmark, we add N_{mess} complete $SU(5)$ fundamental representations, that lead to $N = N_{\text{mess}}/2$ and $E = 4/3 N_{\text{mess}}$. This is the scaling assumed in figure 1, where we also take $N_{\text{mess}} = (4\pi/g_*)^2$ to ensure calculability below M_{NP} . In figure 2 we go beyond this benchmark and show how E/N can be modified changing the SM representation of the fermions in eq. (3.1) (see ref. [69] for a discussion).

Operators breaking $U(1)_{\text{PQ}}$ other than the QCD anomaly would in general spoil the axion solution of the strong CP problem [20–23]. We can parametrize these contributions as new terms in the potential for the scalar Φ :

$$\Delta V_{\text{PQ}} = \lambda_\Delta \frac{\Phi^\Delta}{\Lambda_{\text{UV}}^{\Delta-4}} + \text{h.c.}, \quad \lambda_\Delta = |\lambda_\Delta| e^{i\alpha_\Delta}. \quad (3.3)$$

In the presence of these new contributions the axion potential below the QCD phase transition is

$$V_a \simeq -\Lambda_{\text{QCD}}^4 \cos \frac{Na}{f} + \frac{1}{2^{\frac{\Delta}{2}-1}} \frac{|\lambda_\Delta| f^\Delta}{\Lambda_{\text{UV}}^{\Delta-4}} \cos \left(\alpha_\Delta + \Delta \frac{a}{f} \right). \quad (3.4)$$

Since the new phase α_Δ is in general not aligned with the contribution given by the QCD anomaly, the presence of the UV operator shifts the axion VEV away from the origin, jeopardizing the solution to the strong CP problem. Note that this holds even if the NP sector inducing eq. (3.3) preserves CP, because a new phase $\alpha_\Delta \sim O(1)$ is induced by rotating away the phase in the quark mass matrices. Requiring $2\langle Na/f \rangle \lesssim 10^{-10}$ to satisfy the present bound on the neutron dipole moment [70, 71] gives an upper bound on the axion decay constant

$$f \lesssim \Lambda_{UV} \left[10^{-10} \cdot \frac{N}{\Delta} \cdot \left(\frac{\Lambda_{QCD}}{\Lambda_{UV}} \right)^4 \right]^{1/\Delta}, \quad (3.5)$$

where we have assumed $|\lambda_\Delta| \sim \alpha_\Delta \sim O(1)$ and neglected other $O(1)$ factors for simplicity. The upper bound on f depends on the scale of the UV completion $\Lambda_{UV} \gtrsim g_* f$ and on the “quality” of the $U(1)_{PQ}$, i.e. the dimension Δ of the lowest dimension operator breaking the symmetry.

In the best case scenario, first discussed in refs. [20–23], the $U(1)_{PQ}$ is only broken by Planck suppressed operators³ but, more generally, one might argue that all the global symmetries should be an accidental consequence of the gauge and matter content of the theory, exactly like in the SM. In the latter case the Λ_{UV} in eq. (3.5) will be below M_{Pl} . Taking eq. (3.5) at face value, the most dangerous contribution comes from $\Delta = 5$ operators, that would require $f \lesssim O(10)$ GeV even for $\Lambda_{UV} = M_{Pl}$. However, if operators of dimension five are forbidden (for example by a discrete Z_2 -symmetry) then $\Delta = 6$ contributions give $f \lesssim O(10)$ TeV for $\Lambda_{UV} = M_{Pl}$ and $f \lesssim O(1)$ TeV for $\Lambda_{UV} = M_{GUT}$, motivating the ranges of decay constant of interest for this paper. Having f around the TeV scale would lead to axion solutions relying on $U(1)_{PQ}$ with the same quality of the baryon number in the SM.

In the usual QCD axion where $m_a \simeq 6 \text{ keV} \cdot \text{TeV}/f$ (see e.g. [74]), values of the decay constant motivated by the axion quality problem are abundantly excluded by star cooling bounds [75] and $K \rightarrow \pi a$ transitions [3, 76]. A common solution to this problem is to go to higher values of f and require a $U(1)_{PQ}$ with higher quality. Such a $U(1)_{PQ}$ can be made accidental in extra-dimensions or with more complicated UV completions in 4 dimensions (we refer to refs. [77–80] for an illustration of the challenges involved in constructing gauge theories with a $U(1)_{PQ}$ with arbitrarily high quality).

Alternatively, one can construct QCD axion models where the axion mass is heavier than its QCD value. The idea is to introduce new contributions to the axion potential which are aligned to the QCD one, so that the axion mass gets larger without spoiling the solution to the strong CP problem. A larger m_a then relaxes the experimental constraints on f , potentially allowing to satisfy eq. (3.5). There are several classes of models of this type which differ from the way the alignment is achieved: mirror axion models with one

³Gravity is expected to break global symmetries at the non perturbative level via wormhole solutions swallowing the PQ charge [72]. In this case the Wilson coefficient of the operators in eq. (3.3) can be very suppressed for a large enough wormhole action: $|\lambda_\Delta| \sim e^{-S_{Euc1}}$. The latter has been shown in ref. [73] to be too small in the Einstein theory of gravity but large enough in theories where the Einstein theory is suitably modified at Planckian distances.

axion and two mirror QCD's [4–8], models where the QCD running is modified at high energies [9–14], and a more recent proposals [15] where the QCD group is embedded in $SU(3)^N$ with N axions relaxing each one of the allowed θ -angles.

All the solutions of the strong CP problem mentioned above can easily achieve the 2–20 GeV mass range, and result in an axion which generically couples to both gluons and photons with a decay constant at the TeV scale or lower. These are a perfect benchmark for the collider searches discussed here. For illustrative purposes we show in figure 1 the value of f corresponding to a $U(1)_{PQ}$ broken by $\Delta = 6$ operators generated at $M_{GUT} = 10^{15}$ GeV.

3.2 ALP-mediated dark matter

The second example of ALP with coupling and masses of interest for this study comes from demanding it to be the mediator that couples the SM to fermion DM, singlet under the SM gauge group. This possibility has particular interest for colliders because direct detection constraints are totally irrelevant, see e.g. [81].

We write the ALP coupling to DM as in equation (3.1) and identify the DM as the Dirac fermion $(\psi, \tilde{\psi}^\dagger)$, so that $m_\psi = g_* f / \sqrt{2}$. The DM annihilation cross section into SM particles, mediated by the ALP, is dominated by final state gluon pairs and reads

$$(\sigma v)_{gg} = \frac{2}{\pi} \left(\frac{c_3 \alpha_s}{4\pi} \right)^2 \frac{g_*^2}{f^2}, \tag{3.6}$$

where α_s is evaluated at the scale $\mu = 2 m_\psi$. The cross section for t -channel annihilation into a pair of mediators is p -wave and reads [82]

$$(\sigma v_{\text{rel}})_{aa} = \frac{v_{\text{rel}}^2}{384\pi} \frac{g_*^4}{m_\psi^2}, \tag{3.7}$$

therefore it is negligible with respect to the annihilation into gluons for the parameter values we are interested in, even for relativistic v_{rel} . Requiring eq. (3.6) to match 4.8×10^{-26} cm^3/sec , which is the value needed for heavy Dirac DM to reproduce the correct DM abundance via thermal freeze-out [83], we find

$$m_\psi \simeq 4.6 \text{ TeV} \frac{c_3}{10} \left(\frac{g_*}{3} \right)^2 \Rightarrow f \simeq 1.9 \text{ TeV} \frac{3}{g_*}, \tag{3.8}$$

where in the second equality we have assumed the scaling $c_3 \simeq 8\pi^2/g_*^2$. This is the benchmark value we display in figure 1. It is interesting to note that indirect detection is still far from probing thermal values of the annihilation cross section for DM in this mass range (see e.g. [84–86]), thus adding further motivation to test this scenario with colliders.

Note that we have neglected the possible Sommerfeld enhancement from exchange of the ALP in the initial state. The precise computation of this effect is still the object of some debate, see e.g. [87] for a recent study with references, so that for simplicity we do not include it here. Its inclusion would result in an $O(1)$ change in the favoured value of f , but would not affect our physics point that pseudoscalar mediated DM motivates ALP searches at flavor factories.

3.3 R-axion in supersymmetry

We finally notice that the simplified DM model presented above arises naturally in theories of low-scale SUSY breaking. These predict that the lightest supersymmetric particle (LSP) is the Gravitino, whose mass $m_{3/2}$ is generically too small to account for the observed DM abundance. Indeed, using the power counting described in [19], one gets $m_{3/2} = F/(\sqrt{3}M_{\text{Pl}}) \simeq 11 \text{ meV} \cdot (g_*/3) \cdot (f/4 \text{ TeV})^2$. While not reproducing the observed value of DM, Gravitino masses in this ballpark are safe both from collider [88–90] and cosmological [91] constraints.

In the absence of stable superpartners, the natural DM candidate in these SUSY theories are particles belonging to the messenger or SUSY breaking sectors, see [92] for a first study of this possibility. In this case, as first noted in [93] (see [94] for further model building), the DM phenomenology may be dominated by its interactions with a pseudoscalar that is naturally present in the theory, the R -axion.

This arises as the pNGB of the $U(1)_R$ symmetry, defined as the only abelian global symmetry which does not commute with the SUSY generators. The spontaneous breaking of the $U(1)_R$ is intimately related to SUSY-breaking according to the general results of [17, 95]. The R -axion couplings to gluons and photons are unavoidably generated by loops of gauginos, whose Majorana masses are chiral under the $U(1)_R$, and possibly by UV messengers. Couplings to fermions and to the Higgs are less generic and can be suppressed by suitable charge assignment (see [19] for more details). Under these circumstances, the R -axion matches perfectly the Lagrangian in eq. (2.1).

For $f = O(\text{TeV})$, motivated here not only by DM but also by the naturalness of the Fermi scale, i) its mass is expected to lie in the MeV range [96] or above [19, 95], thus motivating searches at flavor factories, ii) superpartners can be taken outside the LHC reach, thus making it potentially the first sign of SUSY at colliders [19].

4 Diphoton searches at LHCb

LHCb detects photons either as “unconverted”, i.e. they reach the electromagnetic calorimeter (ECAL), or as “converted”, i.e. they convert to an e^+e^- pair upon interacting with the detector material before reaching the ECAL. The public LHCb note [38] presents the trigger and cut strategy that will be used to look for $B_s \rightarrow \gamma\gamma$, and classifies diphoton events into two unconverted (0CV), one unconverted and one converted (1CV LL and DD, corresponding to conversions occurring in the Vertex Locator region or after it) and two converted (2CV) samples.

Searches for $B_s \rightarrow \gamma\gamma$ benefit from requiring the $\gamma\gamma$ vertex to be displaced from the pp interaction point, while the resonances we are interested in typically have a lifetime much shorter than the B_s one. A displaced $\gamma\gamma$ vertex is however not imposed on the 0CV sample, because the resolution on the directions of the photons does not allow for a precise enough vertex reconstruction. Therefore this sample can be used to derive a bound on prompt diphoton resonances.

Measured diphoton events that pass the cuts are reported in [38] for $L = 80 \text{ pb}^{-1}$ of data, for each conversion category, in a diphoton invariant mass interval $4.9 \text{ GeV} <$

$m_{\gamma\gamma} < 6.3$ GeV and in bins of 14.5 MeV. No known QCD or SM resonance is expected to give a signal within the LHCb reach, explaining why the event distributions in $m_{\gamma\gamma}$ are very smooth in all categories, so that they constitute an ideal avenue to look for BSM resonances. Therefore, we place an upper limit on the signal cross section of a resonance a decaying to diphotons as

$$N_{\text{sig}}(m_a) < 2\sqrt{N_{\text{bkg}} \frac{m_{\gamma\gamma}^{\text{bin}}}{14.5 \text{ MeV}}}, \quad (4.1)$$

where

$$N_{\text{sig}} = \epsilon \times \sigma_{\text{fid}} \times L, \quad \sigma_{\text{fid}} = A \times \sigma(pp \rightarrow Xa(\gamma\gamma)), \quad (4.2)$$

with A the geometrical acceptance of the signal in the LHCb detector and ϵ the total efficiency of the cuts plus detector effects in a given diphoton category. We use

$$A = 0.15, \quad \epsilon_{0\text{CV}} = 0.142, \quad (4.3)$$

where the latter is given in [38] for the SM “signal” $B_s \rightarrow \gamma\gamma$, and we determine the former by simulating the signal (see appendix D for details) and imposing $2 < \eta < 5$ at truth level.

Coming to the right-hand side of eq. (4.1), N_{bkg} is the number of background events in the 14.5 MeV bin reported in [38], which we take constant as the distribution in $m_{\gamma\gamma}$ is actually flat well within its statistical uncertainties.⁴ $m_{\gamma\gamma}^{\text{bin}}$ is the size of the bin centered on $m_{\gamma\gamma} = m_a$ that we expect to contain most of the signal from the resonance, which we assume to be narrow. In practice we use

$$N_{\text{bkg}} = 8000 \times \frac{L}{80 \text{ pb}^{-1}}, \quad m_{\gamma\gamma}^{\text{bin}} = 4\delta m_{\gamma\gamma}, \quad (4.4)$$

where $\delta m_{\gamma\gamma}$ is the invariant mass resolution for the 0CV category which can be derived from the energy resolution and the granularity of the LHCb ECAL (see appendix C). Fixing for definiteness $m_{\gamma\gamma}^{\text{bin}}/m_{\gamma\gamma} = 13\%$, we obtain

$$\sigma_{\text{fid}}^{0\text{CV}} \lesssim 106 \text{ pb} \cdot \sqrt{\frac{m_a}{5 \text{ GeV}}} \cdot \sqrt{\frac{80 \text{ pb}^{-1}}{L}}. \quad (4.5)$$

The sensitivities that could be achieved by the current full dataset of $\simeq 8 \text{ fb}^{-1}$ and by the High Luminosity phase of LHCb with $\simeq 300 \text{ fb}^{-1}$ of data can be easily obtained from the above equation.⁵

We also extend the mass range of the search to $3 < m_{\gamma\gamma}/\text{GeV} < 20$, where the lower bound is chosen to make the computation of the signal strength reliable (see also

⁴While this holds for the 1CV and 2CV categories, the distribution in the 0CV category is flat up to $m_{\gamma\gamma} \simeq 5.7 \text{ GeV}$, and then drops smoothly. A possible origin of this drop is the use of 2×2 ECAL cells to measure the photon energy deposition at the first level of the software trigger (HLT1) [38]. In appendix B we verified that imposing invariant mass cuts at HLT1 can cause a flat background at HLT1 to develop a dropping shape at higher level, where the invariant mass is defined using 3×3 cells.

⁵Actually only $\simeq 2 \text{ fb}^{-1}$ have been recorded outside the B_s mass window, we neglect this drop in luminosity for simplicity.

appendix A) and the upper bound is chosen somehow arbitrarily at 20 GeV, where the reach of the current ATLAS/CMS inclusive diphoton dataset [1] is already stronger than the projections of LHCb. For simplicity we take the signal acceptance and the efficiency to be constant and equal to the ones in eq. (4.3). We discuss in appendix D the motivations for this simplified assumption. Moreover we assume that the background is also constant in the extended mass range and equal to the one in eq. (4.4). This simple procedure sets a useful benchmark for the actual search, which is good enough for the purpose of this paper. The resulting reach in the ALP parameter space is shown in figure 1.

We finally speculate about the limit and reach obtainable if the 1CV photon categories could be used. To set an optimistic reach, we do not take into account the signal loss because of the requirement of vertex displacement in present LHCb search. With this assumption, we repeat the procedure described above, with constant background $N_{\text{bkg}}^{1\text{CV},\text{DD}} = 1600$ and $N_{\text{bkg}}^{1\text{CV},\text{LL}} = 1300$ and constant efficiencies $\epsilon_{1\text{CV},\text{DD}} = 1.35\%$ and $\epsilon_{1\text{CV},\text{LL}} = 1.32\%$ as reported in ref. [38]. Concerning the mass resolution, we take the one of the 0CV category divided by $\sqrt{2}$ to roughly account for the much better energy resolution of the converted photon. With all these assumptions we combine in quadrature the exclusions from the LL and DD single-converted categories and get

$$\sigma_{\text{fid}}^{1\text{CV}} \lesssim 283 \text{ pb} \cdot \sqrt{\frac{m_a}{5 \text{ GeV}}} \cdot \sqrt{\frac{80 \text{ pb}^{-1}}{L}}, \quad (4.6)$$

which is almost a factor of 3 weaker than the 0CV bound. In more realistic conditions we expect a sensible loss of signal from the requirement of displacement, although better background discrimination might be also achieved thanks to the converted photon. We do not even study the 2CV photon category because it is plagued by a very small signal efficiency.

As a useful input for future more detailed studies, we collect here some considerations about the LHCb reach outside the interval $4.9 \text{ GeV} < m_{\gamma\gamma} < 6.3 \text{ GeV}$:

- ◊ As far as the signal is concerned, we do not expect a significant drop in the efficiency going at higher invariant masses. As detailed in appendix D at higher invariant masses the diphoton final state will be less forward, reducing the geometric acceptance. However, the decreasing boost of the produced particle is more than compensated by the higher efficiency of the photon p_T cuts. Practically, the ultimate high mass reach of LHCb is not very relevant for the purposes of discovering new physics, since above 10–20 GeV it is likely to be superseded by the ATLAS/CMS diphoton searches (see [1] for details).
- ◊ The most stringent limitation for scanning masses above $\sim 12 \text{ GeV}$ at LHCb is the current dynamic range of the ECAL. This range, which depends on the electronics and not on the actual configuration of the detector, limits at the moment reconstructing photons with E_T above $\sim 10 \text{ GeV}$ ($\sim 6 \text{ GeV}$ at the level of the first level of the software trigger HLT1). Therefore, a potential increase in the dynamic range of the ECAL after the LHCb Upgrade would be very beneficial to increase LHCb's sensitivity to higher masses. For instance, modifying the electronics to increase the

range to 15–20 GeV would be enough to cover all the mass range for which ATLAS and CMS have a poor sensitivity.

- ◊ As already mentioned, the invariant mass distribution in the 0CV category from the data in ref. [38] displays a drop for masses larger than approximately $m_{\gamma\gamma} \simeq 5.7$ GeV. In appendix B, we argue that such drop is a consequence of the use of 2×2 ECAL cells to measure the photon energy deposition at HLT1. If our guess is correct there should be another drop of the background at low invariant masses in a region not showed by the plot of ref. [38].
- ◊ Understanding the composition of the diphoton background given in ref. [38] would require a detailed MC simulation, including detector effects, which is beyond the scope of this paper. In appendix C we provide a simple kinematical argument which shows that the background from boosted π^0 faking photons is likely to dominate over the one from real photons. A categorization of the data in different η regions would help suppressing this background at small η . This could be used to maximize the reach. A quantitative assessment of this is left for future studies.
- ◊ The precise assessment of the 1CV limit and sensitivities would require a dedicated search for promptly decaying resonances *without* the requirement of a displaced vertex. In this case one could get an even better reach than the one presented here by combining the 0CV and the 1CV category.

We hope that this work could provide enough motivation to explore further the open issues described above and in general the possibility of performing bump hunts on the top of the diphoton background at such low invariant masses.

5 Conclusions

The LHC has pushed the energy scale of many motivated SM extensions beyond the TeV range. How to experimentally test NP models at and beyond those scales? A possibility is to look for low energy remnants of such theories, like pseudo-Goldstone bosons (aka ALPs) from an approximate global symmetry.

In section 3 we showed that ALPs with masses and decay constants of interest for flavor factories arise as a solution to the strong CP problem (“heavy QCD axions”) and in frameworks motivated by Dark Matter freeze-out and the Higgs hierarchy problem (e.g. the SUSY R -axion as mediator of DM interactions). These scenarios share the prediction of ALP couplings to gluons and photons, that are currently tested in a particularly poor way for masses below $O(10)$ GeV.

In section 4, we have used 80 pb^{-1} of public LHCb data to set a bound on diphoton resonances of $\sigma(pp \rightarrow Xa(\gamma\gamma)) \lesssim 100 \text{ pb}$, and we have performed a first study to assess future LHCb sensitivities. This bound is already the strongest existing one on the ALPs discussed above, and shows that LHCb has a very promising potential to test unexplored territory of well-motivated BSM extensions. Technical results that might be useful for future LHCb studies are provided in appendices C and D. We have also recasted BABAR

limits on $\Upsilon \rightarrow \gamma a(jj)$ on this model, and estimated the associated future capabilities of Belle-II, finding they would be particularly relevant for masses below ≈ 3 GeV. These results are summarised in figure 1.

Our findings provide a strong motivation to pursue the phenomenological and experimental program of testing this class of ALPs at LHCb and Belle-II, thus enriching the physics case of both machines.

Acknowledgments

We thank Sean Benson and Albert Puig Navarro for many useful discussions, in particular about the LHCb note [38], and Marco Bonvini for clarifications about ggHiggs. D.R. thanks Simon Knapen for discussion and clarifications on ref. [57]. D.R. thanks CERN and the Galileo Galilei Institute for theoretical physics (GGI) for kind hospitality during the completion of this work. F.S. is grateful to the Mainz Institute for Theoretical Physics (MITP), CERN and GGI for kind hospitality at various stages of this work. K.T. thanks MITP for kind hospitality during the completion of this work.

Funding and research infrastructure acknowledgements:

- * X.C.V. is supported by MINECO through the Ramón y Cajal program RYC-2016-20073;
- * A.M. is supported by the SRP High Energy Physics and the Research Council of the Vrije Universiteit Brussel; A.M. is also supported by FWO under the EOS-BE.H project n. 30820817
- * D.R. is supported in part by the National Science Foundation under Grant No. NSF PHY17-48958;
- * F.S. is supported in part by a PIER Seed Project funding (Project ID PIF-2017-72);
- * K.T. is supported by his start-up funding at Florida State University.

A More on the signal

We compute the gluon fusion production cross section at N3LO using ggHiggs v4 [43–46] and at LO using MadGraphLO. We compare the two predictions in figure 3 left, for different choices of the pdf sets, and rescaling the ggHiggs cross section using that $c_3/f = 1/(\sqrt{2}v)$ with $v \simeq 246$ GeV (anomaly coefficient coming from a top loop). The agreement between these determinations goes from the 20% level at $m_a = 20$ GeV, down to a factor of 2 and worse for $m_a \leq 4$ GeV. We mention that at such low values the ggHiggs output should be taken with extra care, as it also yields some negative LO and NLO cross sections. This comparison underlines the need for a more precise determination of the production cross section, especially for ALP masses below 5 GeV or so. This task goes however beyond the purpose of this paper. We use the ggHiggs prediction with the `mstw2008nnlo` pdf set for all the LHC phenomenology in section 2.

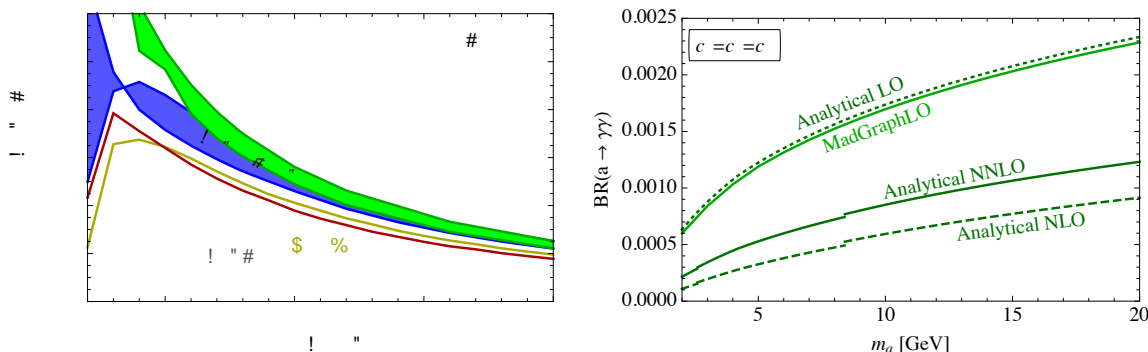


Figure 3. Left: production cross section of an ALP coupled to $G\tilde{G}$, as determined with MadGraphLO and with ggHiggs at N3LO, for various choices of the pdf sets, fixing $f = 1$ TeV and $c_3 = 1$. For ggHiggs we display the band enclosed by $\mu_f = \mu_r = m_a/2$ and $\mu_f = \mu_r = 2m_a$. Right: ALP branching ratio into diphoton at LO, NLO and NNLO, and from MadGraphLO.

Coming now to the ALP branching ratios, we use the NNLO QCD correction to the width of a pseudoscalar into gluons from [42]. In the notation of eq. (2.4), it reads $K_{gg} = 1 + \frac{\alpha_s^{(5)}}{\pi} E_A + \left(\frac{\alpha_s^{(5)}}{\pi}\right)^2 E_A \left(\frac{3}{4} E_A + \frac{\beta_1}{\beta_0}\right)$, where $E_A = \frac{97}{4} - \frac{7}{6} N_f$, $\beta_0 = \frac{11}{4} - \frac{N_f}{6}$, $\beta_1 = \frac{51}{8} - \frac{19}{24} N_f$. In figure 3 right we plot the resulting diphoton branching ratio together with its NLO and LO value and with the one given by Madgraph. NNLO corrections to the diphoton branching ratio reduce its LO value by a factor of $\simeq 2$, over the whole mass range we consider. We use the NNLO expression for all the limits and sensitivities described in section 2.

B $m_{\gamma\gamma}$ distribution of the 0CV category

In our analysis, we assume the background yield to be roughly constant with respect to the diphoton invariant mass even outside the mass range reported in ref. [38]. This is to provide an order-of-magnitude estimate of the background for the LHCb sensitivities to ALPs. The flatness of the data is actually seen in the 1CV and 2CV categories of figure 4(b–c) of ref. [38]. However, in the 0CV category (figure 4(a)), a kink is observed at large invariant masses. In what follows, we argue that this is an artifact due to the trigger level invariant mass cut.

In the invariant mass calculation at the trigger level of the 0CV category, two approximations are employed to speed up the calculation: 1) the photon energy is calculated from the energy deposition in 2×2 ECAL cells, 2) the mass formula takes into account only the leading order of the diphoton opening angle, $m_{\gamma\gamma}^{\text{trigger}} = \sqrt{E_{\gamma_1}^{(2 \times 2)} E_{\gamma_2}^{(2 \times 2)}} \Delta\theta_{\gamma_1\gamma_2}$. We examined these two approximation and concluded that 1) could be the reason for the kink.

It is easy to show that the approximate mass formula is equivalent to the full mass formula with $\mathcal{O}(0.01)$ accuracy. This comes from the fact that the diphoton events within the LHCb fiducial volume have a small opening angle $\Delta\theta_{\gamma_1\gamma_2} = \mathcal{O}(0.1)$, after the E_T trigger cuts are imposed. On the other hand one needs to use 3×3 cells to capture full energy deposit of a photon, so the information based on 2×2 cells underestimates the photon energy, which leads to the lower invariant mass, $m_{\gamma\gamma}^{\text{trigger}} < m_{\gamma\gamma}^{\text{full}}$. Because the first

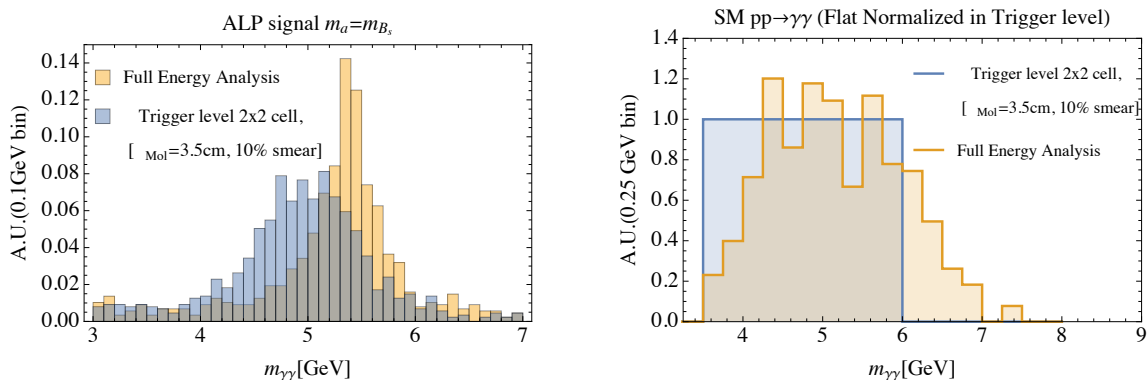


Figure 4. Left: ALP signal event with $m_a = m_{B_s}$ in diphoton invariant mass $m_{\gamma\gamma}^{\text{full}}$ (yellow) and trigger level diphoton invariant mass $m_{\gamma\gamma}^{\text{trigger}}$ (blue). Fraction of energy, $E_{\gamma}^{(2 \times 2)} = E_{\gamma}^{\text{full}} \min[1, \mathcal{P}_{\text{normal}}(\mu = 0.95, \sigma = 0.1)]$, is used for the calculation of trigger level invariant mass. Right: SM diphoton event with a cut, $3.5 \text{ GeV} < m_{\gamma\gamma}^{\text{trigger}} < 6 \text{ GeV}$, in $m_{\gamma\gamma}^{\text{full}}$ (yellow) and in $m_{\gamma\gamma}^{\text{trigger}}$ (blue). To demonstrate bin migration effect, the distribution in $m_{\gamma\gamma}^{\text{trigger}}$ is flat normalized.

invariant mass cut is made at the trigger level, $3.5 \text{ GeV} < m_{\gamma\gamma}^{\text{trigger}} < 6 \text{ GeV}$, bins with a given $m_{\gamma\gamma}^{\text{trigger}}$ migrate to bins with $m_{\gamma\gamma}^{\text{full}} > m_{\gamma\gamma}^{\text{trigger}}$. This could explain why the reduction of the yield appears above $m_{\gamma\gamma}^{\text{full}} \sim 6 \text{ GeV}$. This argument is confirmed by figure 1 bottom of [38], that shows how the trigger level mass distribution of the B_s signal shifts to higher values of off-line invariant mass.

We further validate the argument modelling the energy smearing of the LHCb ECAL. For simplicity, we focus on the inner ECAL and approximate 2×2 cells as a circle of radius 4 cm. Because the Molière radius of a photon in the LHCb ECAL is 3.5cm,⁶ the energy deposit inside the 2×2 cells is expected to be 95% of the total energy deposit on average. In order to model a realistic environment we include a stochastic gaussian smearing from the average value. We choose a standard deviation of 10%⁷ such that the shift of the signal at $m_a = m_{B_s}$ reproduces figure 1 bottom of [38]. This result is shown in figure 4 left. Then, we use the same prescription for the background-like events. The result is shown in figure 4 right. The invariant mass distribution in terms of $m_{\gamma\gamma}^{\text{trigger}}$ is normalized to be rectangular after the invariant mass cut. When the same dataset is plotted in terms of $m_{\gamma\gamma}^{\text{full}}$ we can see that a kink is induced.

C Details on the LHCb calorimeter

The Electromagnetic Calorimeter (ECAL) of LHCb has three layers with different granularities and is placed vertically with respect to the beam axis at $z_{\text{Ecal}} = 12.52 \text{ m}$ away from the collision point. The ECAL square cells have side lengths of $\Delta x_{\text{cell}} = 4.04, 6.06 \text{ cm}$, 12.12cm for inner, middle, and outer layer, respectively [97]. The photon reconstruction

⁶Inside the Molière radius, the energy deposit into the corresponding area is 90% of the total energy on average.

⁷ $E_{\gamma}^{(2 \times 2)} = E_{\gamma}^{\text{full}} \min[1, \mathcal{P}_{\text{normal}}(\mu = 0.95, \sigma = 0.1)]$.

algorithm uses patterns of 3×3 cells in each layer. Therefore, the inner layer, where most of the energy is expected to be deposited, has the best angular resolution.

Invariant mass resolution. The invariant mass can be written as

$$m_{\gamma\gamma}^2 = 2E_{\gamma_1}E_{\gamma_2}(1 - \cos \theta_{\gamma\gamma}), \quad (\text{C.1})$$

where $E_{\gamma_{1,2}}$ are the energies of the two photons and $\theta_{\gamma\gamma}$ is the angular separation between them. Using the above formula, we can relate the invariant mass smearing to the photon energy smearing and the ECAL granularity

$$\begin{aligned} \frac{\delta m_{\gamma\gamma}}{m_{\gamma\gamma}} &\simeq \frac{1}{2} \frac{\delta m_{\gamma\gamma}^2}{m_{\gamma\gamma}^2} = \frac{1}{2} \left(\frac{\delta E_{\gamma_1}}{E_{\gamma_1}} \oplus \frac{\delta E_{\gamma_2}}{E_{\gamma_2}} \oplus \frac{\sin \theta_{\gamma\gamma} \delta \theta}{1 - \cos \theta_{\gamma\gamma}} \right) \\ &\simeq \frac{1}{\sqrt{2}} \frac{\delta E_{\gamma}}{E_{\gamma}} \oplus \frac{\delta \theta}{\theta_{\gamma\gamma}} = 6.4\% \sqrt{\frac{\text{GeV}}{E_{\gamma}}} \oplus 0.6\% \oplus 0.3\% \frac{E_{\gamma}}{m_{\gamma\gamma}}. \end{aligned} \quad (\text{C.2})$$

In the second line we assumed for simplicity $E_{\gamma_1} \simeq E_{\gamma_2} \simeq E_{\gamma}$ and approximated our result at the first order in $\theta \ll 1$. To obtain the second expression in the second line, we used the LHCb ECAL energy resolution $\delta E/E \simeq 9\% \sqrt{\text{GeV}/E} \oplus 0.8\%$ reported in ref. [98] and the granularity of the inner layer of the ECAL $\delta \theta = \Delta x_{\text{cell}}/z_{\text{Ecal}} \simeq 0.003$. Moreover, we have approximated $\theta_{\gamma\gamma} \simeq m_{\gamma\gamma}/E_{\gamma}$ to get an expression of the typical energy smearing as a function of the typical photon energy. In computing the invariant mass resolution in the text, we take $E_{\gamma} = 50\text{GeV}$. We believe this is a realistic benchmark value for this analysis because $E_{\gamma} = E_{T\gamma} \cosh \eta$ and the LHCb analysis in ref. [38] imposes $E_{T\gamma} > 3.5\text{GeV}$ and $E_{T\gamma_1} + E_{T\gamma_2} > 8\text{GeV}$ on 2×2 cell clusters.

Background from π^0 faking single photon. One of the advantages to study low mass diphoton resonances at LHCb is that low energy fake photons from QCD can be distinguished from real photon candidates. Here we focus on fake photons from π^0 decays whose collimated diphoton decay can mimic a single photon candidate.

Photon pairs from π^0 decay have angular separation $\theta_{\gamma\gamma}^{\pi^0} \simeq m_{\pi^0}/E_{\gamma} \simeq 2m_{\pi^0}/E_{\pi^0}$. The corresponding separation on a given ECAL layer is then

$$\Delta r_{\gamma\gamma}^{\pi^0} \simeq z_{\text{Ecal}} \theta_{\gamma\gamma}^{\pi^0} \simeq \frac{2z_{\text{Ecal}} m_{\pi^0}}{E_{\pi^0}}. \quad (\text{C.3})$$

If the π^0 is very energetic, the diphoton separation $\Delta r_{\gamma\gamma}^{\pi^0}$ is smaller than a single cell size and the object is mostly misidentified as a single photon candidate of energy E_{π^0} . Viceversa, when a pion is less energetic and the diphoton separation is large, $\Delta r_{\gamma\gamma}^{\pi^0} > \mathcal{O}(2)\Delta x_{\text{cell}}$, two photon clusters are separately formed and a pion is *resolved*. In a regime where $1.8\Delta x_{\text{cell}} > \Delta r_{\gamma\gamma}^{\pi^0} \gtrsim 0.5x_{\text{cell}}$, the shower shape information makes a single energy cluster identified as a π^0 , which is called *merged* π^0 [99]. The identification efficiency using both *resolved* and *merged* π^0 is $\mathcal{O}(50\%)$ for $p_{T\pi^0} \lesssim 10\text{GeV}$ (figure 21 left of ref. [99]). As shown in figure 5, the final energy thresholds vary depending on the ECAL layer. For example, in the inner ECAL diphotons with $E_{\pi^0} < 28\text{GeV}$ corresponding to a large separation of $\Delta r_{\gamma\gamma}^{\pi^0} > 3\Delta x_{\text{cell}}$

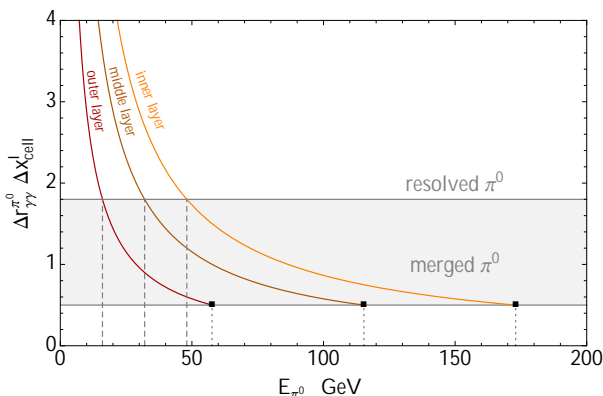


Figure 5. Separation of photon pairs from π^0 decay as a function of the pion total energy E_{π^0} . If this photon pair is misidentified as a single (fake) photon, E_{π^0} is the energy of the fake photon. Cases of inner, middle, and outer layers are plotted in blue, red and magenta respectively.

can be reconstructed as resolved π^0 s, while the ones with $46 \text{ GeV} < E_{\pi^0} \lesssim 160 \text{ GeV}$ could be seen as merged π^0 s.

The planned LHCb $B_s \rightarrow \gamma\gamma$ analysis uses a photon energy threshold of $E_{T\gamma} > 3.5 \text{ GeV}$ which corresponds to $E_\gamma = 13(260) \text{ GeV}$ at $\eta = 2(5)$. Comparing with the threshold determined above for the pions to be detected as fake photons, one learns that i) the background to the current search contains a non-negligible amount of fake photons; ii) a categorization in η of the data could help in reducing photon fakes.

D Signal acceptance and efficiency

In this appendix we discuss the strategy that we adopted to estimate the acceptance and efficiency of the signal. As mentioned in the main text, we eventually consider a constant value for the product of acceptance times efficiency on the mass range of interest for this paper. As reference value, we have chosen the one at the invariant mass of 5 GeV , corresponding to the B_s signal considered in the LHCb note [38].

In order to estimate the acceptance and efficiency of the signal at LHCb, we implement the axion model in FeynRules [49], we generate events with MadgraphLO_v2.6 [47, 48] and shower them with Pythia 8.1 [100, 101], matching up to 1 extra jets [102]. We then perform a simple analysis of the resulting samples using MadAnalysis5 [103]. Note that the signal events which are inside the acceptance of LHCb contain topologies where the axion has acquired a significant longitudinal boost, without the need of extra hard radiation. As a consequence the signal efficiency is essentially not changed by including extra jets (the minimal E_T cuts of the LHCb selection can be satisfied with just a small transverse boost). This has to be contrasted with the low invariant mass searches at ATLAS/CMS where the recoil of the resonance against the extra jet increases the signal efficiency of the p_T cuts significantly, as it was shown in ref. [1].

$m_a[\text{GeV}]$	5	7	9	11	13	15
\mathcal{A}	0.15	0.15	0.14	0.13	0.12	0.12
ϵ	0.26	0.36	0.46	0.64	0.72	0.81

Table 1. Acceptance (D.1) and efficiency (D.2) for the axion signal in the LHCb analysis, for different mass values.

In table 1 we report the acceptance and the efficiency that we find in the mass range 5–15 GeV by following the selection cuts of ref. [38], that is

$$\mathcal{A} : 2 < \eta(\gamma) < 5 \tag{D.1}$$

$$\epsilon : \begin{cases} E_T(\gamma) > 3.5 \text{ GeV}, \\ E_T^{\gamma_1} + E_T^{\gamma_2} > 8 \text{ GeV} \\ p_T(\gamma_1\gamma_2) > 2 \text{ GeV} \end{cases} \tag{D.2}$$

We first observe that the value we find for the product $\mathcal{A} \times \epsilon$, though in the same ballpark than the number reported by the LHCb note (see eq. (4.3)), differs by around a factor of 2 on the case of $m_a = 5 \text{ GeV}$. In order to check wheter the discrepancy could be caused by detector effects, we also processed the same samples using Delphes as fast LHCb detector simulator, but we did not find a substantial improvement in the agreement.

However, besides the discrepancy on the benchmark of 5 GeV, our simple analysis provides indications on what could be the expected product of $\mathcal{A} \times \epsilon$ for the selection cuts (D.2) for different mass values. As one can observe from table 1, increasing the mass of the axion the acceptance generically decreases. This is due to the fact that a heavier resonance will more likely be produced with less boost on the longitudinal axis, and hence the resulting photons will be less into the forward region which is covered by the LHCb detector. On the other hand, for larger values of the axion mass the outgoing photons will be more energetic and will more likely pass the energy and p_T cuts, hence resulting in an increase in the signal efficiency. The combination of these two effects result in a product of acceptance times efficiency which actually slightly grows along the mass interval 5–15 GeV, but does not changes significantly. This justifies the simplified choice that we have adopted in the main part of the paper.

Open Access. This article is distributed under the terms of the Creative Commons Attribution License ([CC-BY 4.0](https://creativecommons.org/licenses/by/4.0/)), which permits any use, distribution and reproduction in any medium, provided the original author(s) and source are credited.

References

- [1] A. Mariotti, D. Redigolo, F. Sala and K. Tobioka, *New LHC bound on low-mass diphoton resonances*, *Phys. Lett. B* **783** (2018) 13 [[arXiv:1710.01743](https://arxiv.org/abs/1710.01743)] [[INSPIRE](#)].
- [2] F. Wilczek, *Decays of Heavy Vector Mesons Into Higgs Particles*, *Phys. Rev. Lett.* **39** (1977) 1304 [[INSPIRE](#)].
- [3] M. Freytsis, Z. Ligeti and J. Thaler, *Constraining the Axion Portal with $B \rightarrow Kl^{+l^{-}}$* , *Phys. Rev. D* **81** (2010) 034001 [[arXiv:0911.5355](https://arxiv.org/abs/0911.5355)] [[INSPIRE](#)].
- [4] V.A. Rubakov, *Grand unification and heavy axion*, *JETP Lett.* **65** (1997) 621 [[hep-ph/9703409](https://arxiv.org/abs/hep-ph/9703409)] [[INSPIRE](#)].
- [5] Z. Berezhiani, L. Gianfagna and M. Giannotti, *Strong CP problem and mirror world: The Weinberg-Wilczek axion revisited*, *Phys. Lett. B* **500** (2001) 286 [[hep-ph/0009290](https://arxiv.org/abs/hep-ph/0009290)] [[INSPIRE](#)].
- [6] A. Hook, *Anomalous solutions to the strong CP problem*, *Phys. Rev. Lett.* **114** (2015) 141801 [[arXiv:1411.3325](https://arxiv.org/abs/1411.3325)] [[INSPIRE](#)].
- [7] H. Fukuda, K. Harigaya, M. Ibe and T.T. Yanagida, *Model of visible QCD axion*, *Phys. Rev. D* **92** (2015) 015021 [[arXiv:1504.06084](https://arxiv.org/abs/1504.06084)] [[INSPIRE](#)].
- [8] S. Dimopoulos, A. Hook, J. Huang and G. Marques-Tavares, *A collider observable QCD axion*, *JHEP* **11** (2016) 052 [[arXiv:1606.03097](https://arxiv.org/abs/1606.03097)] [[INSPIRE](#)].
- [9] B. Holdom and M.E. Peskin, *Raising the Axion Mass*, *Nucl. Phys. B* **208** (1982) 397 [[INSPIRE](#)].
- [10] K. Choi, C.W. Kim and W.K. Sze, *Mass Renormalization by Instantons and the Strong CP Problem*, *Phys. Rev. Lett.* **61** (1988) 794 [[INSPIRE](#)].
- [11] B. Holdom, *Strong QCD at High-energies and a Heavy Axion*, *Phys. Lett. B* **154** (1985) 316 [*Erratum ibid.* **B 156** (1985) 452] [[INSPIRE](#)].
- [12] M. Dine and N. Seiberg, *String Theory and the Strong CP Problem*, *Nucl. Phys. B* **273** (1986) 109 [[INSPIRE](#)].
- [13] J.M. Flynn and L. Randall, *A Computation of the Small Instanton Contribution to the Axion Potential*, *Nucl. Phys. B* **293** (1987) 731 [[INSPIRE](#)].
- [14] K. Choi and H.D. Kim, *Small instanton contribution to the axion potential in supersymmetric models*, *Phys. Rev. D* **59** (1999) 072001 [[hep-ph/9809286](https://arxiv.org/abs/hep-ph/9809286)] [[INSPIRE](#)].
- [15] P. Agrawal and K. Howe, *Factoring the Strong CP Problem*, *JHEP* **12** (2018) 029 [[arXiv:1710.04213](https://arxiv.org/abs/1710.04213)] [[INSPIRE](#)].
- [16] M.K. Gaillard, M.B. Gavela, R. Houtz, P. Quilez and R. Del Rey, *Color unified dynamical axion*, *Eur. Phys. J. C* **78** (2018) 972 [[arXiv:1805.06465](https://arxiv.org/abs/1805.06465)] [[INSPIRE](#)].
- [17] A.E. Nelson and N. Seiberg, *R symmetry breaking versus supersymmetry breaking*, *Nucl. Phys. B* **416** (1994) 46 [[hep-ph/9309299](https://arxiv.org/abs/hep-ph/9309299)] [[INSPIRE](#)].
- [18] H.-S. Goh and M. Ibe, *R-axion detection at LHC*, *JHEP* **03** (2009) 049 [[arXiv:0810.5773](https://arxiv.org/abs/0810.5773)] [[INSPIRE](#)].

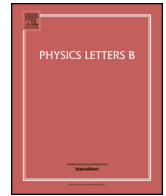
- [19] B. Bellazzini, A. Mariotti, D. Redigolo, F. Sala and J. Serra, *R-axion at colliders*, *Phys. Rev. Lett.* **119** (2017) 141804 [[arXiv:1702.02152](#)] [[INSPIRE](#)].
- [20] M. Kamionkowski and J. March-Russell, *Planck scale physics and the Peccei-Quinn mechanism*, *Phys. Lett. B* **282** (1992) 137 [[hep-th/9202003](#)] [[INSPIRE](#)].
- [21] R. Holman, S.D.H. Hsu, T.W. Kephart, E.W. Kolb, R. Watkins and L.M. Widrow, *Solutions to the strong CP problem in a world with gravity*, *Phys. Lett. B* **282** (1992) 132 [[hep-ph/9203206](#)] [[INSPIRE](#)].
- [22] S.M. Barr and D. Seckel, *Planck scale corrections to axion models*, *Phys. Rev. D* **46** (1992) 539 [[INSPIRE](#)].
- [23] S. Ghigna, M. Lusignoli and M. Roncadelli, *Instability of the invisible axion*, *Phys. Lett. B* **283** (1992) 278.
- [24] G. Ferretti and D. Karateev, *Fermionic UV completions of Composite Higgs models*, *JHEP* **03** (2014) 077 [[arXiv:1312.5330](#)] [[INSPIRE](#)].
- [25] A. Belyaev, G. Cacciapaglia, H. Cai, T. Flacke, A. Parolini and H. Serôdio, *Singlets in composite Higgs models in light of the LHC 750 GeV diphoton excess*, *Phys. Rev. D* **94** (2016) 015004 [[arXiv:1512.07242](#)] [[INSPIRE](#)].
- [26] G. Ferretti, *Gauge theories of Partial Compositeness: Scenarios for Run-II of the LHC*, *JHEP* **06** (2016) 107 [[arXiv:1604.06467](#)] [[INSPIRE](#)].
- [27] C. Kilic, T. Okui and R. Sundrum, *Vectorlike Confinement at the LHC*, *JHEP* **02** (2010) 018 [[arXiv:0906.0577](#)] [[INSPIRE](#)].
- [28] K.S. Jeong, T.H. Jung and C.S. Shin, *Axionic Electroweak Baryogenesis*, [arXiv:1806.02591](#) [[INSPIRE](#)].
- [29] ALEPH, DELPHI, L3, OPAL, SLD collaborations, LEP Electroweak Working Group, SLD Electroweak Group, SLD Heavy Flavour Group, *Precision electroweak measurements on the Z resonance*, *Phys. Rept.* **427** (2006) 257 [[hep-ex/0509008](#)] [[INSPIRE](#)].
- [30] L3 collaboration, *Isolated hard photon emission in hadronic Z0 decays*, *Phys. Lett. B* **292** (1992) 472 [[INSPIRE](#)].
- [31] BABAR collaboration, *Search for hadronic decays of a light Higgs boson in the radiative decay $\Upsilon \rightarrow \gamma A^0$* , *Phys. Rev. Lett.* **107** (2011) 221803 [[arXiv:1108.3549](#)] [[INSPIRE](#)].
- [32] L3 collaboration, *Search for anomalous $Z \rightarrow \gamma\gamma\gamma$ events at LEP*, *Phys. Lett. B* **345** (1995) 609 [[INSPIRE](#)].
- [33] S. Knapen, T. Lin, H.K. Lou and T. Melia, *Searching for Axionlike Particles with Ultrapерipheral Heavy-Ion Collisions*, *Phys. Rev. Lett.* **118** (2017) 171801 [[arXiv:1607.06083](#)] [[INSPIRE](#)].
- [34] E. Izaguirre, T. Lin and B. Shuve, *Searching for Axionlike Particles in Flavor-Changing Neutral Current Processes*, *Phys. Rev. Lett.* **118** (2017) 111802 [[arXiv:1611.09355](#)] [[INSPIRE](#)].
- [35] M.J. Dolan, T. Ferber, C. Hearty, F. Kahlhoefer and K. Schmidt-Hoberg, *Revised constraints and Belle II sensitivity for visible and invisible axion-like particles*, *JHEP* **12** (2017) 094 [[arXiv:1709.00009](#)] [[INSPIRE](#)].
- [36] DELPHI collaboration, *Measurement of the $e^+e^- \rightarrow \gamma\gamma(\gamma)$ cross-section at LEP energies*, *Phys. Lett. B* **327** (1994) 386 [[INSPIRE](#)].

- [37] L3 collaboration, *Search for narrow high mass resonances in radiative decays of the Z0*, *Phys. Lett. B* **262** (1991) 155 [INSPIRE].
- [38] S. Benson and A. Puig Navarro, *Triggering $B_s^0 \rightarrow \gamma\gamma$ at LHCb*, LHCb-PUB-2018-006.
- [39] J. de Blas et al., *Electroweak precision observables and Higgs-boson signal strengths in the Standard Model and beyond: present and future*, *JHEP* **12** (2016) 135 [arXiv:1608.01509] [INSPIRE].
- [40] ATLAS collaboration, *Evidence for light-by-light scattering in heavy-ion collisions with the ATLAS detector at the LHC*, *Nature Phys.* **13** (2017) 852 [arXiv:1702.01625] [INSPIRE].
- [41] CMS collaboration, *Evidence for light-by-light scattering and searches for axion-like particles in ultraperipheral PbPb collisions at $\sqrt{s_{NN}} = 5.02$ TeV*, arXiv:1810.04602 [INSPIRE].
- [42] K.G. Chetyrkin, B.A. Kniehl, M. Steinhauser and W.A. Bardeen, *Effective QCD interactions of CP odd Higgs bosons at three loops*, *Nucl. Phys. B* **535** (1998) 3 [hep-ph/9807241] [INSPIRE].
- [43] R.D. Ball, M. Bonvini, S. Forte, S. Marzani and G. Ridolfi, *Higgs production in gluon fusion beyond NNLO*, *Nucl. Phys. B* **874** (2013) 746 [arXiv:1303.3590] [INSPIRE].
- [44] M. Bonvini, R.D. Ball, S. Forte, S. Marzani and G. Ridolfi, *Updated Higgs cross section at approximate N^3LO* , *J. Phys. G* **41** (2014) 095002 [arXiv:1404.3204] [INSPIRE].
- [45] M. Bonvini, S. Marzani, C. Muselli and L. Rottoli, *On the Higgs cross section at N^3LO+N^3LL and its uncertainty*, *JHEP* **08** (2016) 105 [arXiv:1603.08000] [INSPIRE].
- [46] T. Ahmed et al., *Pseudo-scalar Higgs boson production at $N^3LO_A + N^3LL'$* , *Eur. Phys. J. C* **76** (2016) 663 [arXiv:1606.00837] [INSPIRE].
- [47] J. Alwall, M. Herquet, F. Maltoni, O. Mattelaer and T. Stelzer, *MadGraph 5: Going Beyond*, *JHEP* **06** (2011) 128 [arXiv:1106.0522] [INSPIRE].
- [48] J. Alwall et al., *The automated computation of tree-level and next-to-leading order differential cross sections and their matching to parton shower simulations*, *JHEP* **07** (2014) 079 [arXiv:1405.0301] [INSPIRE].
- [49] A. Alloul, N.D. Christensen, C. Degrande, C. Duhr and B. Fuks, *FeynRules 2.0 — A complete toolbox for tree-level phenomenology*, *Comput. Phys. Commun.* **185** (2014) 2250 [arXiv:1310.1921] [INSPIRE].
- [50] ATLAS collaboration, *Measurement of isolated-photon pair production in pp collisions at $\sqrt{s} = 7$ TeV with the ATLAS detector*, *JHEP* **01** (2013) 086 [arXiv:1211.1913] [INSPIRE].
- [51] ATLAS collaboration, *Measurements of integrated and differential cross sections for isolated photon pair production in pp collisions at $\sqrt{s} = 8$ TeV with the ATLAS detector*, *Phys. Rev. D* **95** (2017) 112005 [arXiv:1704.03839] [INSPIRE].
- [52] CMS collaboration, *Measurement of differential cross sections for the production of a pair of isolated photons in pp collisions at $\sqrt{s} = 7$ TeV*, *Eur. Phys. J. C* **74** (2014) 3129 [arXiv:1405.7225] [INSPIRE].
- [53] CDF collaboration, *Measurement of the Cross Section for Prompt Isolated Diphoton Production in $p\bar{p}$ Collisions at $\sqrt{s} = 1.96$ TeV*, *Phys. Rev. D* **84** (2011) 052006 [arXiv:1106.5131] [INSPIRE].
- [54] E. Masso and R. Toldra, *On a light spinless particle coupled to photons*, *Phys. Rev. D* **52** (1995) 1755 [hep-ph/9503293] [INSPIRE].

- [55] I. Komarov, *Status and prospects of belle ii at superkekb*, in *Moriond QCD 2018*, (2018).
- [56] BELLE II collaboration, *The Belle II Physics Book*, [arXiv:1808.10567](#) [INSPIRE].
- [57] S. Knapen, T. Lin, H.K. Lou and T. Melia, *LHC limits on axion-like particles from heavy-ion collisions*, in *Photon 2017: International Conference on the Structure and the Interactions of the Photon and 22th International Workshop on Photon-Photon Collisions and the International Workshop on High Energy Photon Colliders*, CERN, Geneva, Switzerland, May 22–26, 2017 (2017) [[arXiv:1709.07110](#)] [INSPIRE].
- [58] ATLAS collaboration, *Search for new phenomena in events with at least three photons collected in pp collisions at $\sqrt{s} = 8$ TeV with the ATLAS detector*, *Eur. Phys. J. C* **76** (2016) 210 [[arXiv:1509.05051](#)] [INSPIRE].
- [59] J. Jaeckel and M. Spannowsky, *Probing MeV to 90 GeV axion-like particles with LEP and LHC*, *Phys. Lett. B* **753** (2016) 482 [[arXiv:1509.00476](#)] [INSPIRE].
- [60] M. Farina, D. Pappadopulo, F. Rompineve and A. Tesi, *The photo-philic QCD axion*, *JHEP* **01** (2017) 095 [[arXiv:1611.09855](#)] [INSPIRE].
- [61] CMS collaboration, *Search for low mass vector resonances decaying into quark-antiquark pairs in proton-proton collisions at $\sqrt{s} = 13$ TeV*, *JHEP* **01** (2018) 097 [[arXiv:1710.00159](#)] [INSPIRE].
- [62] E. Arganda, A.D. Medina, N.I. Mileo, R.A. Morales and A. Szykman, *Constraining R-axion models through dijet searches at the LHC*, [arXiv:1808.01292](#) [INSPIRE].
- [63] R.D. Peccei and H.R. Quinn, *Constraints Imposed by CP Conservation in the Presence of Instantons*, *Phys. Rev. D* **16** (1977) 1791 [INSPIRE].
- [64] R.D. Peccei and H.R. Quinn, *CP Conservation in the Presence of Instantons*, *Phys. Rev. Lett.* **38** (1977) 1440 [INSPIRE].
- [65] S. Weinberg, *A New Light Boson?*, *Phys. Rev. Lett.* **40** (1978) 223 [INSPIRE].
- [66] F. Wilczek, *Problem of Strong P and T Invariance in the Presence of Instantons*, *Phys. Rev. Lett.* **40** (1978) 279 [INSPIRE].
- [67] J.E. Kim, *Weak Interaction Singlet and Strong CP Invariance*, *Phys. Rev. Lett.* **43** (1979) 103 [INSPIRE].
- [68] M.A. Shifman, A.I. Vainshtein and V.I. Zakharov, *Can Confinement Ensure Natural CP Invariance of Strong Interactions?*, *Nucl. Phys. B* **166** (1980) 493 [INSPIRE].
- [69] L. Di Luzio, F. Mescia and E. Nardi, *Redefining the Axion Window*, *Phys. Rev. Lett.* **118** (2017) 031801 [[arXiv:1610.07593](#)] [INSPIRE].
- [70] J.M. Pendlebury et al., *Revised experimental upper limit on the electric dipole moment of the neutron*, *Phys. Rev. D* **92** (2015) 092003 [[arXiv:1509.04411](#)] [INSPIRE].
- [71] M. Pospelov and A. Ritz, *Electric dipole moments as probes of new physics*, *Annals Phys.* **318** (2005) 119 [[hep-ph/0504231](#)] [INSPIRE].
- [72] S.B. Giddings and A. Strominger, *Axion Induced Topology Change in Quantum Gravity and String Theory*, *Nucl. Phys. B* **306** (1988) 890 [INSPIRE].
- [73] R. Kallosh, A.D. Linde, D.A. Linde and L. Susskind, *Gravity and global symmetries*, *Phys. Rev. D* **52** (1995) 912 [[hep-th/9502069](#)] [INSPIRE].
- [74] G. Grilli di Cortona, E. Hardy, J. Pardo Vega and G. Villadoro, *The QCD axion, precisely*, *JHEP* **01** (2016) 034 [[arXiv:1511.02867](#)] [INSPIRE].

- [75] G.G. Raffelt, *Stars as laboratories for fundamental physics*, (1996) [INSPIRE].
- [76] H. Georgi, D.B. Kaplan and L. Randall, *Manifesting the Invisible Axion at Low-energies*, *Phys. Lett. B* **169** (1986) 73 [INSPIRE].
- [77] L. Randall, *Composite axion models and Planck scale physics*, *Phys. Lett. B* **284** (1992) 77 [INSPIRE].
- [78] M. Redi and R. Sato, *Composite Accidental Axions*, *JHEP* **05** (2016) 104 [arXiv:1602.05427] [INSPIRE].
- [79] L. Di Luzio, E. Nardi and L. Ubaldi, *Accidental Peccei-Quinn symmetry protected to arbitrary order*, *Phys. Rev. Lett.* **119** (2017) 011801 [arXiv:1704.01122] [INSPIRE].
- [80] M. Duerr, K. Schmidt-Hoberg and J. Unwin, *Protecting the Axion with Local Baryon Number*, *Phys. Lett. B* **780** (2018) 553 [arXiv:1712.01841] [INSPIRE].
- [81] F. Bishara, J. Brod, B. Grinstein and J. Zupan, *From quarks to nucleons in dark matter direct detection*, *JHEP* **11** (2017) 059 [arXiv:1707.06998] [INSPIRE].
- [82] F. D’Eramo, J. de Vries and P. Panci, *A 750 GeV Portal: LHC Phenomenology and Dark Matter Candidates*, *JHEP* **05** (2016) 089 [arXiv:1601.01571] [INSPIRE].
- [83] G. Steigman, B. Dasgupta and J.F. Beacom, *Precise Relic WIMP Abundance and its Impact on Searches for Dark Matter Annihilation*, *Phys. Rev. D* **86** (2012) 023506 [arXiv:1204.3622] [INSPIRE].
- [84] FERMI-LAT collaboration, *Searching for Dark Matter Annihilation from Milky Way Dwarf Spheroidal Galaxies with Six Years of Fermi Large Area Telescope Data*, *Phys. Rev. Lett.* **115** (2015) 231301 [arXiv:1503.02641] [INSPIRE].
- [85] G. Giesen et al., *AMS-02 antiprotons, at last! Secondary astrophysical component and immediate implications for Dark Matter*, *JCAP* **09** (2015) 023 [arXiv:1504.04276] [INSPIRE].
- [86] H.E.S.S. collaboration, *Search for dark matter annihilations towards the inner Galactic halo from 10 years of observations with H.E.S.S.*, *Phys. Rev. Lett.* **117** (2016) 111301 [arXiv:1607.08142] [INSPIRE].
- [87] B. Bellazzini, M. Cliche and P. Tanedo, *Effective theory of self-interacting dark matter*, *Phys. Rev. D* **88** (2013) 083506 [arXiv:1307.1129] [INSPIRE].
- [88] A. Brignole, F. Feruglio and F. Zwirner, *Signals of a superlight gravitino at e^+e^- colliders when the other superparticles are heavy*, *Nucl. Phys. B* **516** (1998) 13 [Erratum *ibid.* **B 555** (1999) 653] [hep-ph/9711516] [INSPIRE].
- [89] A. Brignole, F. Feruglio, M.L. Mangano and F. Zwirner, *Signals of a superlight gravitino at hadron colliders when the other superparticles are heavy*, *Nucl. Phys. B* **526** (1998) 136 [Erratum *ibid.* **B 582** (2000) 759] [hep-ph/9801329] [INSPIRE].
- [90] F. Maltoni, A. Martini, K. Mawatari and B. Oehl, *Signals of a superlight gravitino at the LHC*, *JHEP* **04** (2015) 021 [arXiv:1502.01637] [INSPIRE].
- [91] K. Osato, T. Sekiguchi, M. Shirasaki, A. Kamada and N. Yoshida, *Cosmological Constraint on the Light Gravitino Mass from CMB Lensing and Cosmic Shear*, *JCAP* **06** (2016) 004 [arXiv:1601.07386] [INSPIRE].
- [92] S. Dimopoulos, G.F. Giudice and A. Pomarol, *Dark matter in theories of gauge mediated supersymmetry breaking*, *Phys. Lett. B* **389** (1996) 37 [hep-ph/9607225] [INSPIRE].

- [93] J. Mardon, Y. Nomura and J. Thaler, *Cosmic Signals from the Hidden Sector*, *Phys. Rev. D* **80** (2009) 035013 [[arXiv:0905.3749](#)] [[INSPIRE](#)].
- [94] J. Fan, J. Thaler and L.-T. Wang, *Dark matter from dynamical SUSY breaking*, *JHEP* **06** (2010) 045 [[arXiv:1004.0008](#)] [[INSPIRE](#)].
- [95] K.A. Intriligator, N. Seiberg and D. Shih, *Supersymmetry breaking, R-symmetry breaking and metastable vacua*, *JHEP* **07** (2007) 017 [[hep-th/0703281](#)] [[INSPIRE](#)].
- [96] J. Bagger, E. Poppitz and L. Randall, *The R axion from dynamical supersymmetry breaking*, *Nucl. Phys. B* **426** (1994) 3 [[hep-ph/9405345](#)] [[INSPIRE](#)].
- [97] LHCb collaboration, *LHCb Detector Performance*, *Int. J. Mod. Phys. A* **30** (2015) 1530022 [[arXiv:1412.6352](#)] [[INSPIRE](#)].
- [98] LHCb collaboration, *First Years of Running for the LHCb Calorimeter System*, *PoS(TIPP2014)030* (2014) [[arXiv:1407.4289](#)] [[INSPIRE](#)].
- [99] O. Deschamps, F.P. Machefert, M.H. Schune, G. Pakhlova and I. Belyaev, *Photon and neutral pion reconstruction*, *LHCb-2003-091*.
- [100] T. Sjöstrand, S. Mrenna and P.Z. Skands, *PYTHIA 6.4 Physics and Manual*, *JHEP* **05** (2006) 026 [[hep-ph/0603175](#)] [[INSPIRE](#)].
- [101] T. Sjöstrand, S. Mrenna and P.Z. Skands, *A Brief Introduction to PYTHIA 8.1*, *Comput. Phys. Commun.* **178** (2008) 852 [[arXiv:0710.3820](#)] [[INSPIRE](#)].
- [102] J. Alwall et al., *Comparative study of various algorithms for the merging of parton showers and matrix elements in hadronic collisions*, *Eur. Phys. J. C* **53** (2008) 473 [[arXiv:0706.2569](#)] [[INSPIRE](#)].
- [103] E. Conte, B. Fuks and G. Serret, *MadAnalysis 5, A User-Friendly Framework for Collider Phenomenology*, *Comput. Phys. Commun.* **184** (2013) 222 [[arXiv:1206.1599](#)] [[INSPIRE](#)].



New LHC bound on low-mass diphoton resonances

Alberto Mariotti^a, Diego Redigolo^{b,c}, Filippo Sala^{d,e,*}, Kohsaku Tobioka^{b,c,f}

^a Theoretische Natuurkunde and IIHE/ELEM, Vrije Universiteit Brussel, and International Solvay Institutes, Pleinlaan 2, B-1050 Brussels, Belgium

^b Raymond and Beverly Sackler School of Physics and Astronomy, Tel-Aviv University, Tel-Aviv 69978, Israel

^c Department of Particle Physics and Astrophysics, Weizmann Institute of Science, Rehovot 7610001, Israel

^d DESY, Notkestraße 85, D-22607 Hamburg, Germany

^e LPTHE, UMR 7589 CNRS, 4 Place Jussieu, F-75252, Paris, France

^f C.N. Yang Institute for Theoretical Physics, Stony Brook University, Stony Brook, NY 11794-3800, United States of America

ARTICLE INFO

Article history:

Received 25 May 2018

Received in revised form 14 June 2018

Accepted 16 June 2018

Available online 22 June 2018

Editor: G.F. Giudice

ABSTRACT

We derive a new bound on diphoton resonances using inclusive diphoton cross section measurements at the LHC, in the so-far poorly constrained mass range between the Υ and the SM Higgs. This bound sets the current best limit on axion-like particles that couple to gluons and photons, for masses between 10 and 65 GeV. We also estimate indicative sensitivities of a dedicated diphoton LHC search in the same mass region, at 7, 8 and 14 TeV. As a byproduct of our analysis, we comment on the axion-like particle interpretation of the CMS excesses in low-mass dijet and diphoton searches.

© 2018 The Authors. Published by Elsevier B.V. This is an open access article under the CC BY license (<http://creativecommons.org/licenses/by/4.0/>). Funded by SCOAP³.

1. Introduction

Searches for two body decays of heavy resonances led to fundamental discoveries in the history of particle physics such as the J/ψ [1,2], the Υ [3] and the Z boson [4]. An extensive program is currently looking for higher mass resonances at the LHC in various final states (see [5] for a complete list).

Despite the high background rates, advances in data-driven background estimates guarantee good sensitivities to discover/exclude such peak signals. A marvelous proof of the high performance of resonance searches at the LHC is the recent discovery of the Standard Model (SM) Higgs boson in the diphoton channel [6,7].

As a matter of fact, the current LHC search program is mostly tailored to probe new resonances of mass higher than roughly 100 GeV. This is the result of a general theoretical bias towards heavy new physics (NP) and of the common belief that either previous collider experiments (UA1, UA2, LEP and Tevatron) and/or Higgs coupling fits (through the decay of the Higgs into two new particles) put constraints on lighter resonances that are stronger than the LHC capabilities. On the experimental side, going to low masses poses the challenge of looking for resonances with a mass below the sum of the cuts on the transverse momentum (p_T) of the decay products.

The aim of this letter is to go beyond these common beliefs and to motivate the LHC collaborations to look for resonances down to the smallest possible mass. We first derive a new bound (of 10–100 pb) on the diphoton signal strength of a new resonance in the mass range between the Υ and the SM Higgs. This new bound comes from inclusive diphoton cross section measurements at ATLAS [8,9] and CMS [10]. Assuming zero knowledge about the background, we simply impose that the NP events are less than the total measured events plus twice their uncertainty.

We show how this conservative procedure sets already the strongest existing constraint on axion-like particles (ALPs) with mass between 10 and 65 GeV. We finally estimate the indicative reaches on the diphoton signal strengths that could be attainable by proper searches at the LHC, up to its high luminosity (HL) phase, and interpret their impact on the ALP parameter space.

2. Axion-like particles in diphotons

When a $U(1)$ global symmetry (which can be the subgroup of some larger global symmetry \mathcal{G}) is spontaneously broken in the vacuum, then a massless Nambu–Goldstone boson (NGB) arises in the low energy spectrum. If the $U(1)$ symmetry is only approximate, the NGB gets a mass m_a and it becomes a pseudo-Nambu–Goldstone boson (pNGB), often called axion-like particle (ALP). The mass m_a of the pNGB is a technically natural parameter which depends on the explicit breaking of the $U(1)$ global symmetry, and is smaller than the associated NP scale $M_{\text{NP}} \sim 4\pi f_a$, where f_a is

* Corresponding author.

E-mail address: filippo.sala@desy.de (F. Sala).

the scale of spontaneous breaking. In particular m_a can be smaller than the SM Higgs mass without any fine-tuning price.

The axial couplings of the pNGB to SM gauge bosons can be written as

$$\mathcal{L}_{\text{int}} = \frac{a}{4\pi f_a} \left[\alpha_s c_3 G\tilde{G} + \alpha_2 c_2 W\tilde{W} + \alpha_1 c_1 B\tilde{B} \right], \quad (1)$$

where $\alpha_1 = 5/3\alpha'$ is the GUT normalized $U(1)_Y$ coupling constant, a is the canonically normalized pNGB field, and the coefficients c_i encode the Adler–Bell–Jackiw (ABJ) anomalies of the global $U(1)$ with $SU(3)$ and $SU(2) \times U(1)_Y$. Further couplings of the pNGB with the SM Higgs and/or with the SM fermions can be set to zero if these fields are not charged (or very weakly charged) under the global $U(1)$.

As one can see from Eq. (1), the strength of the couplings of the pNGB is controlled by its decay constant f_a . As we will show, the phenomenology of the pNGB becomes of interest for this study, and more in general for present colliders, for $f_a \sim 0.1$ –10 TeV. Decay constants in this range are ubiquitous in popular theoretical frameworks addressing the naturalness of the EW scale, like low-scale Supersymmetry (SUSY) and Compositeness.¹ Note that generically we expect that other fields associated to the $U(1)$ spontaneous breaking (e.g. the radial mode) should have a mass $\lesssim 4\pi f_a$. Hence in the lower extreme of the range for f_a other signatures associated to the BSM theory could be accessible at the LHC.

Supersymmetry (SUSY) and its breaking predict on general grounds the existence of an R -axion [20], pNGB of the $U(1)_R$ symmetry, potentially accessible at the LHC if the SUSY scale is sufficiently low [21]. In this context the couplings to gauge bosons of Eq. (1) are realized naturally from ABJ anomalies between $U(1)_R$ and the SM gauge group, while the couplings to SM fermions and Higgses can be set to zero with a well-defined R -charge assignment ($R_H = 0$ in the notation of [21]). In composite Higgs models, attempts of fermionic UV completions point to the need of non-minimal cosets (see e.g. [22–24]), which in turn imply the existence of pNGBs lighter than the new confinement scale. See [25] for recent work about these pNGBs, and [26] for a systematic classification of the cosets structures that give rise to pNGBs that couple to both gluons and EW gauge bosons.

A common feature of both SUSY and Composite Higgs models is that the QCD anomaly receives an irreducible contribution from loops of colored states, like gluinos and/or tops, which are generically chiral under the spontaneously broken $U(1)$. As a consequence one typically expects $c_3 \neq 0$, unless model dependent cancellations occur. In conclusion, $f_a \sim 0.1$ –10 TeV and $c_3 \neq 0$ in a broad class of SUSY and Composite Higgs models, so that a is copiously produced in pp collisions at the LHC. For this reason we believe that our study applies to a wide range of theoretically motivated ALP models.

From a phenomenological point of view, ALPs of interest for this study have received much attention as mediators of simplified Dark Matter models (see for example the recent [27]). Finally, ALPs can exist if Strong Dynamics is present at some scale [28]. In such a case, having $f_a \sim 0.1$ –10 TeV would be a phenomenological assumption not motivated by any naturalness consideration.

For $m_a \lesssim m_h$, the relevant two body decays of a are in diphotons and dijets, with widths

$$\Gamma_{gg} = K_g \frac{\alpha_s^2 c_3^2 m_a^3}{8\pi^3 f_a^2}, \quad \Gamma_{\gamma\gamma} = \frac{\alpha_{\text{em}}^2 c_\gamma^2 m_a^3}{64\pi^3 f_a^2}, \quad (2)$$

where $c_\gamma = c_2 + 5c_1/3$, and where both α_s and α_{em} are computed at the mass of m_a . We encode the higher-order QCD corrections in $K_g = 2.1$ [29]. Unless $c_{1,2} \gtrsim 10^2 c_3$, the width into gluons is the dominant one. The total width Γ_{tot} is typically very narrow, for example for $f_a \gtrsim 100$ GeV and $c_i \sim O(1)$ one obtains $\Gamma_{\text{tot}}/m_a \lesssim 10^{-3}$.

For simplicity, we do not study the phenomenology associated to the $Z\gamma$ decay channel, which is anyhow open only for $m_a > m_Z$, and phenomenologically more relevant than $\gamma\gamma$ only for specific values of c_1 and c_2 .

3. Current searches

A new resonance decaying in two jets or two photons is probed at colliders by looking at the related invariant mass distributions, possibly in addition with extra objects, either SM or BSM (see e.g. [30,31]) depending on the production mechanism. We summarize and discuss here the most relevant searches for light resonances at the LHC, and refer to the supplementary material for a more complete list and a discussion of the existing searches and of diphoton cross section measurements, at the LHC, Tevatron, LEP and Sp \bar{p} S.

- ◇ Dijet resonances down to 50 GeV have been recently looked for by CMS [32]. In order to overcome the trigger on the jet p_T 's, CMS has a strong cut on the total hadronic activity H_T . Recoiling against the hard jet, the resonance is boosted and its decay products collimated. For this reason advanced jet substructure techniques were essential to reconstruct the dijet resonance inside a single “fat” jet [33,34]. The CMS low-mass dijet limits are given on the inclusive dijet signal strength of a $q\bar{q}$ -initiated resonance $\sigma_{q\bar{q}}^{\text{CMS}}$. We recast them for a gluon initiated resonance as

$$\sigma_{gg}^{\text{our}} = \sigma_{q\bar{q}}^{\text{CMS}} \cdot \frac{\epsilon_{H_T}^{q\bar{q}}}{\epsilon_{H_T}^{gg}}, \quad (3)$$

where $\epsilon_{H_T}^{q\bar{q}}$ and $\epsilon_{H_T}^{gg}$ are the efficiencies of the cut in hadronic activity $H_T > 650$ GeV.² These are estimated from simulations³ of a gg and a $q\bar{q}$ initiated scalar signals (including matching up to 2 jets and detector simulation). We take the efficiency ratio in Eq. (3) to be constant and equal to 0.08, which is the value that we find at $m_a = 80$ GeV. Accounting for the m_a dependence introduces variations up to 20% within the mass range 50–125 GeV. The fact that the efficiency ratio is roughly constant in m_a can be understood observing that \sqrt{s} is always dominated by the cut of $H_T > 650$ GeV, which is much larger than any of the values of m_a of our interest.

- ◇ Existing diphoton searches are inclusive and extend to a lower invariant mass of 65 GeV [43–46], where the two photons satisfy standard isolation and identification requirements. The ATLAS diphoton search at 8 TeV [43] is the one extending down to 65 GeV. The bound is given in term of the diphoton “fiducial” cross-section $\sigma^{\text{fid}} = \sigma^{\text{th}} \cdot \epsilon_5 / C_X$. C_X is a model independent number that we take from [43] and encodes the

¹ String theory constructions could provide an extra motivation for ALPs. However, the expected values of f_a in string models like [11–13] are order of magnitudes too high for being phenomenologically interesting at colliders. Similarly, solutions of the strong CP problem based on a QCD axion [14–17] with a decay constant f_a at the TeV scale are hard to conceive (see however [18,19]).

² We thank Phil Harris for private communications on [32].

³ Throughout this paper we use FeynRules 2.0 [35], MadGraph 5 v2 LO [36,37] with the default pdf set, Pythia 8.1 [38,39], DELPHES 3 [40] and MadAnalysis 5 [41]. The MLM matching [42] is performed to include matrix element correction to ISR's.

Table 1

Signal efficiencies for the 7 TeV and 8 TeV cross-section measurements at the LHC [8–10] and at the Tevatron [8,9] for a resonance produced in gluon fusion.

m_a in GeV	10	20	30	40	50	60	70	80	90	100	110	120
ϵ_S for $\sigma_{7\text{ TeV}}$ ATLAS [8]	0	0.008	0.022	0.040	0.137	0.293	0.409	0.465	0.486	0.533	0.619	0.637
ϵ_S for $\sigma_{7\text{ TeV}}$ CMS [10]	0	0.002	0.010	0.020	0.030	0.058	0.156	0.319	0.424	0.499	0.532	0.570
ϵ_S for $\sigma_{8\text{ TeV}}$ ATLAS [9]	0	0.0007	0.008	0.014	0.024	0.037	0.071	0.233	0.347	0.419	0.452	0.484
ϵ_S for $\sigma_{2\text{ TeV}}$ CDF [48,49]	0.001	0.007	0.026	0.143	0.212	0.241	0.276	0.275	0.283	0.3	0.319	0.327
ϵ_S for $\sigma_{2\text{ TeV}}$ DO [50]	0	0.002	0.008	0.018	0.114	0.169	0.208	0.21	0.217	0.234	0.244	0.252

detector acceptance once the kinematical cuts are already imposed ($C_X \simeq 0.6$ in the mass range of our interest).⁴ To extract the efficiency ϵ_S we simulated the signal for the ALP model in Eq. (1) accounting for all the cuts of [43].

The CMS searches at 8 and 13 TeV [44,46] provide the bound on the theoretical signal strength for a resonance with the same couplings of the SM Higgs but lighter mass. Since gluon fusion is the dominant production mechanism for a SM Higgs in the low mass range [47], we take the CMS result as a bound on the theoretical diphoton signal strength of our ALP.

4. New bound and LHC sensitivities from $\gamma\gamma$ cross-section measurements

Here we extract a new bound on diphoton resonances from inclusive diphoton measurements at the LHC and at Tevatron, and we present the projected LHC sensitivities.

New bound from measurements The papers [8–10,49] provide tables of the measured differential diphoton cross sections per invariant mass bin, $d\sigma_{\gamma\gamma}/dm_{\gamma\gamma}$, together with their relative statistical (Δ_{stat}) and systematical (Δ_{sys}) uncertainties. We derive a conservative bound on the theoretical signal strength $\sigma_{\gamma\gamma}^{\text{th}}$ of a diphoton resonance by imposing

$$\sigma_{\gamma\gamma}^{\text{th}}(m_a) \lesssim \left[m_{\gamma\gamma}^{\text{Bin}} \cdot \frac{d\sigma_{\gamma\gamma}}{dm_{\gamma\gamma}} (1 + 2\Delta_{\text{tot}}) \right] \cdot \frac{1}{\epsilon_S(m_a)}, \quad (4)$$

where $\Delta_{\text{tot}} = \sqrt{\Delta_{\text{sys}}^2 + \Delta_{\text{stat}}^2}$, $m_{\gamma\gamma}^{\text{Bin}}$ is the size of the bin containing m_a , and ϵ_S is the signal efficiency accounting for the kinematical and the isolation cuts of the photons.

At a given center of mass energy s , we derive ϵ_S as

$$\epsilon_S(m_a) = \frac{\sigma_{\gamma\gamma}^{\text{MCcuts}}(m_a, s)}{C_s \sigma_{\gamma\gamma}^{\text{LO}}(m_a, s)}. \quad (5)$$

$\sigma_{\gamma\gamma}^{\text{LO}}(m_a, s)$ is the LO gluon fusion cross section, derived using the gluon pdf from [51], multiplied by the LO branching ratio into $\gamma\gamma$ computed from Eq. (1). We also compute a total “simulated” diphoton signal strength $\sigma_{\gamma\gamma}^{\text{MCTot}}$, which includes matching up to 2 jets, by a Monte Carlo (MC) simulation of the signal for the ALP model in Eq. (1). We find that $\sigma_{\gamma\gamma}^{\text{LO}}$ reproduces up to a constant factor C_s the shape of $\sigma_{\gamma\gamma}^{\text{MCTot}}$ for $m_{\gamma\gamma} \gtrsim 60$ GeV (i.e. sufficiently far from the sum of the minimal detector p_T cuts on the photons). A constant factor $C_s \equiv \sigma_{\gamma\gamma}^{\text{MCTot}}(s)/\sigma_{\gamma\gamma}^{\text{LO}}(s)$ is hence included in Eq. (5) and we obtain $C_{7\text{ TeV}} \simeq C_{8\text{ TeV}} \simeq 0.85$ while $C_{2\text{ TeV}} \simeq 1$ at the Tevatron center of mass energy. The signal strength after cuts $\sigma_{\gamma\gamma}^{\text{MCcuts}}$ is obtained by the MC simulations imposing on the events samples the relevant cuts for each of the experimental search.

To validate our procedure with a measured quantity, we simulate the SM diphoton background and verify that it reproduces well the experimental diphoton cross section measurements of [8,9].

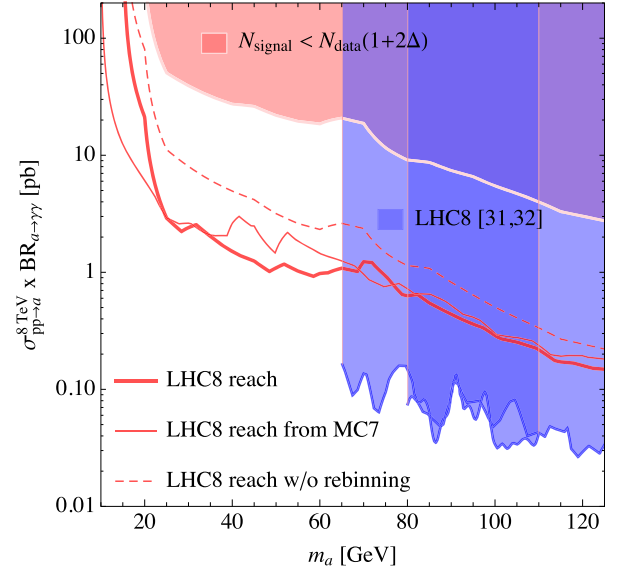


Fig. 1. Bounds (shaded) and expected sensitivities (lines) on the diphoton signal strength of a resonance produced in gluon fusion, at 8 TeV. More details in the text.

We refer the reader to the supplementary material for more details on our derivation of $\epsilon_S(m_a)$, including validations. We list in Table 1 the efficiencies as a function of m_a for the various cross section measurements.

We stress that, for very light mass values, a NP resonance can pass the cuts on the photon p_T 's by recoiling against a jet, which is not vetoed since the cross section measurements are inclusive. This is reflected in the efficiencies of the signal which are non vanishing (though small) also in the region of very low resonance mass.

Our final results are shown in Fig. 1, where the conservative bound extracted from 8 TeV ATLAS data [9] using Eq. (4) is compared against the existing 8 TeV searches at ATLAS [43] and CMS [44].

Sensitivities from measurements An expected sensitivity $\sigma_{\gamma\gamma}^{\text{sens}}$ can be derived by assuming the measured cross section to be dominated by the SM diphoton background, and requiring the signal to be within the $2\Delta_{\text{tot}}$ variation of the background:

$$\sigma_{\gamma\gamma}^{\text{sens}}(m_a) = \left[m_{\gamma\gamma}^{\text{Bin}} \cdot \frac{d\sigma_{\gamma\gamma}}{dm_{\gamma\gamma}} \cdot 2\Delta_{\text{tot}} \right] \cdot \frac{1}{\epsilon_S(m_a)}. \quad (6)$$

The sensitivities we present in Fig. 1 as thick continuous and dashed lines correspond to two different choices of $m_{\gamma\gamma}^{\text{Bin}}$, and both correspond to 8 TeV data with integrated luminosity 20.2 fb^{-1} [9].

The most conservative sensitivity between the two corresponds to the binning given directly in the ATLAS 8 TeV cross section measurement [9], where the mass bins have a size of 30 to 10 GeV in the region of our interest. A better sensitivity is obtained by reducing the bin size $m_{\gamma\gamma}^{\text{Bin}}$ down to the invariant mass resolution obtained from the ATLAS and CMS ECAL energy resolution on a single photon, that we extract from [52] and [40], and which leads

⁴ We thank Liron Barak for private communications on [43].

to mass bins of size $\simeq 3$ GeV for values of m_a below the sum of the minimal p_T cuts of the photons (see the supplementary material for more details). Since the signal is narrow, the number of signal events in the bin is not affected. The number of background N_{bkg} events is instead reduced and the sensitivity increased assuming that the errors scale as $\sqrt{N_{\text{bkg}}}$.⁵ This scaling holds for statistical errors and we assume the same scaling for systematic ones. The assumption is motivated by the scaling of some of the systematics (e.g. those associated to poor statistics in control regions) and by the fact that the CMS cross section measurements [10] do not separate statistical from systematical uncertainties.

Sensitivities adding MC input, up to 14 TeV Now we discuss how to rescale the sensitivities from lower energies \sqrt{s}_{low} to higher energies \sqrt{s}_{high} . To rescale the diphoton background we first obtain, from MC simulations, $\sigma_{\text{low}}^{\text{MC}}$ and $\sigma_{\text{high}}^{\text{MC}}$. These are the SM diphoton cross sections at \sqrt{s}_{low} and \sqrt{s}_{high} after the cuts of the cross section measurements at \sqrt{s}_{low} are imposed. We then take $\sigma_{\gamma\gamma,\text{high}}^{\text{bkg}} = \sigma_{\gamma\gamma,\text{low}}^{\text{bkg}} \sigma_{\text{high}}^{\text{MC}} / \sigma_{\text{low}}^{\text{MC}}$, where $\sigma_{\gamma\gamma,\text{low}}^{\text{bkg}}$ is extracted from the experimental measurements. The total relative uncertainties for the background are rescaled as the squared root of the total number of events so that $\Delta_{\text{high}} = \sqrt{L_{\text{low}}/L_{\text{high}}} \sqrt{\sigma_{\text{low}}^{\text{MC}}/\sigma_{\text{high}}^{\text{MC}}} \Delta_{\text{low}}$. Finally we also account for the different efficiencies for the signal going from \sqrt{s}_{low} to \sqrt{s}_{high} . All in all, starting from Eq. (6) we get

$$\sigma_{\gamma\gamma,\text{high}}^{\text{sens}}(m_a) = \sqrt{\frac{L_{\text{low}}}{L_{\text{high}}} \cdot \frac{\sigma_{\text{high}}^{\text{MC}}}{\sigma_{\text{low}}^{\text{MC}}} \cdot \frac{\epsilon_S^{\text{low}}}{\epsilon_S^{\text{high}}}} \cdot \sigma_{\gamma\gamma,\text{low}}^{\text{sens}}(m_a). \quad (7)$$

We show it in Fig. 1 for the extrapolation of the ATLAS reach from $\sqrt{s}_{\text{low}} = 7$ TeV and 4.9 fb^{-1} of data to $\sqrt{s}_{\text{high}} = 8$ TeV and 20.2 fb^{-1} of data (thus with the cuts of the ATLAS7 measurement [8]). The overlap (in the region where the difference in the cuts matters less) between the 8 TeV sensitivities and the rescaled ones from 7 TeV is a nice consistency check of our procedure. We find an analogous agreement between the two 14 TeV sensitivities derived from 7 and 8 TeV data, as shown in the supplementary material.

5. Discussion

Our sensitivities assume the uncertainties from MC modeling to be subdominant with respect to the ones associated to the measurement. However, this might not be the case in the entire mass range (see e.g. [8–10]) and a better control on the MC modeling might be necessary. The current MC uncertainty can be read off e.g. [9], and can be as large as 40% for $m_{\gamma\gamma}$ below the minimal p_T cuts of the photons (see also [53] for a discussion of the challenges of background modeling in the context of high mass diphoton resonances). While the relatively good agreement of the MC modeling with the observed data would in principle make a discovery possible for large enough signal cross sections, the large MC uncertainties are a limiting factor to the discovery potential of a resonance search below the minimal p_T cuts for the photons.

On the theory side this motivates an improvement in the diphoton MC's, while on the analysis side it pushes to extend the data-driven estimates of the background to lower $m_{\gamma\gamma}$, reducing further

the associated uncertainties and thus improving the limits. Data-driven estimates of the SM background were indeed used in the ATLAS 8 TeV analysis [43], and we believe their effectiveness is at the origin of the discrepancy between our 8 TeV sensitivities and the actual ATLAS limits. As shown in Fig. (1) the discrepancy amounts to a factor of ~ 5 .⁶

The experimental challenge of going to lower invariant masses is ultimately related to lowering the minimal cuts $p_{T1,2}^{\text{min}}$ on the two photon p_T 's and/or relax the photon isolation requirement $\Delta R \gtrsim 0.4$, where $\Delta R \equiv \sqrt{\Delta\phi^2 + \Delta\eta^2}$ is the photon separation. Indeed by simple kinematics we get the strict lower bound on $m_{\gamma\gamma}$

$$m_{\gamma\gamma} > \Delta R \cdot \sqrt{p_{T1}^{\text{min}} p_{T2}^{\text{min}}}, \quad (8)$$

where we used $m_{\gamma\gamma}^2 = 2p_{T1}p_{T2}(\cosh\Delta\eta - \cos\Delta\phi)$ that for small $\Delta\phi$ and $\Delta\eta$ is $m_{\gamma\gamma}^2 \simeq \Delta R^2 \cdot p_{T1}p_{T2}$. This absolute lower bound on $m_{\gamma\gamma}$ explains why in Fig. 1 the 8 TeV reach derived from ATLAS7, which has the lowest $p_{T1,2}^{\text{min}}$, can reach lower $m_{\gamma\gamma}$ than the ones derived from ATLAS8 measurements.

From Eq. (8) we conclude that in order to extend the diphoton resonant searches to lower invariant masses one would have to lower either $p_{T1,2}^{\text{min}}$ or ΔR . Both these possibilities deserve further experimental study.

A first possible strategy would be to require a hard ISR jet in the diphoton analysis, along the way of what was done in the recent CMS search for low-mass dijet resonances [32]. The hard jet requirement would raise the p_T of the resonance recoiling against it, collimating the two photons and hence posing the challenge of going to smaller ΔR . In this kinematical regime, the two photons would look like a single photon-jet [54,55] and it would be interesting to study if substructure techniques similar to those used in [32] for dijet resonances can be applied to such an object.

A second strategy would be to lower the photon $p_{T1,2}^{\text{min}}$. This, however, poses well-known problems with the SM background, like the larger backgrounds from QCD processes (see e.g. [56]) and the challenge of recording, storing, and processing so many events.⁷ One might handle the high data-rate and long-term storage challenge with the data scouting/Trigger-object Level Analysis methods [57–61] where, rather than storing the full detector data for a given event, one stores only a necessary subset. Alternatively, one could accommodate lower trigger thresholds by recording full events for only a fixed fraction of the data [61,62], with *prescaled* triggers, and/or setting aside these data for processing and analysis later [57,63] (data parking/delayed stream). Such techniques have already been used in searches for dijet signals [58–60,63], where one is similarly interested in localized deviations from smooth, data-driven background estimates.

The quantitative comparison of the reach of these different possibilities for low-mass diphoton resonances goes beyond the scope of this paper, but we do encourage the ATLAS and CMS collaborations to take steps in these directions.

6. Impact on ALP parameter space

To determine the diphoton signal strength $\sigma_{\gamma\gamma}^{\text{th}}$ that enters the bound in Eq. (4) and that should be compared with the sensitivities in Eqs. (6) and (7), we multiply the tree level pp cross section by a constant K -factor $K_\sigma = 3.7$ (see the supplementary material for more details) and we use the widths of Eq. (2).

⁵ The CMS sensitivities using different binning in Fig. 1 are very close in the 75–100 GeV range. This is because in this mass range CMS reports its measurement in 5 GeV bins, comparable to the ECAL mass resolution of ~ 2.5 GeV, while in other mass ranges (and in the ATLAS measurements) the bin sizes vary between 10 and 40 GeV.

⁶ We checked further differences between Ref. [43] and the procedure used here, such as a finer categorisation of the diphoton final states as in [6], and a fully unbinned analysis. We find that they can affect the sensitivity at most by 20–40%.

⁷ We thank Antonio Boveia and Caterina Doglioni for many clarifications on these matters.

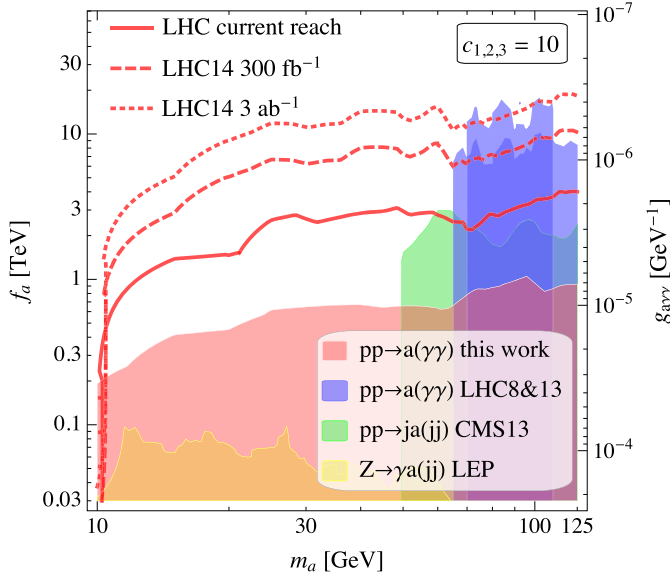


Fig. 2. Shaded: constraints on the ALP parameter space from existing collider searches at LEP [64] and the LHC [32,43,44,46] (see text for our rescaling of the CMS dijet bound [32]), and from the bound derived in this work using the data in [8–10]. Lines: our LHC sensitivities at 8 and 14 TeV.

In Fig. 2 we show how the different searches at the LHC, at Tevatron and at LEP constrain the ALP decay constant f_a for a given value of the ALP mass m_a . We fix for reference the anomalies to their GUT inspired value $c_1 = c_2 = c_3 = 10$. On the right y-axes, we write the pNGB coupling to photons in a notation inspired by the QCD axion, as $g_{a\gamma\gamma} = \frac{\alpha_{em}}{\pi f_a} \frac{c_\gamma}{c_3}$.

Our conservative bound extracted from Eq. (4) by combining 8 TeV and 7 TeV LHC data together with Tevatron data sets the strongest existing limit on ALPs between 10 and 50 GeV: $f_a \gtrsim 500$ GeV, corresponding to $g_{a\gamma\gamma} \lesssim 10^{-5}$ GeV. This is a major improvement with respect to the strongest existing bound in that range, which comes from measurements of $Z \rightarrow \gamma a(jj)$ at LEP I [64] giving $\text{BR}(Z \rightarrow \gamma + jj) < 1 - 5 \cdot 10^{-4}$. We checked that the other LEP limits in [65–67] are not relevant for our choice of the anomalies. The limit from the boosted dijet search of CMS [32] is the strongest one between 50 and 65 GeV, while above 65 GeV the ATLAS [43] and CMS [46] diphoton searches take over.

The LHC has the potential to probe values of f_a much larger than 1 TeV, as shown by the sensitivities lines in Fig. 2. The solid line is obtained from Eq. (6) combining both 8 TeV and 7 TeV data with the finer possible binning. The dashed and dotted lines are the projected sensitivities respectively at LHC14 and HL-LHC, from 8 TeV and 7 TeV data, based on Eq. (7). Notice that the HL-LHC projection is stronger than the future ILC [68] and FCC-ee [69] reaches. The latter is expected to probe $\text{BR}(Z \rightarrow \gamma + jj) \lesssim 1 - 5 \cdot 10^{-7}$, which correspond to $f_a \sim 1 - 3$ TeV if $\mathcal{O}(10^{12})$ Z's will be produced.

The relative importance of low-mass diphoton bounds and sensitivities with respect to the other existing searches is robust with respect to choosing different values of the anomalies $c_{1,2,3}$, as long as $c_3 \neq 0$. For $c_{1,2} \gtrsim 4c_3$, our conservative low-mass diphoton limit even overcomes the dijet exclusions between 50 and 65 GeV, while still doing largely better than LEP.

Other processes that could be relevant for an ALP with couplings as in Eq. (1) and mass above 10 GeV, like $Z \rightarrow 3\gamma$ at LEP (see e.g. [56,70] for recent studies of this and other signatures), set limits that are too weak to even appear on the parameter space presented in Fig. 2. Analogously, the sensitivity of ALP searches in heavy ion collisions estimated in [71] is sizeably weaker than our conservative bounds. The obvious reason is the generic suppres-

sion of the photon width compared to the gluon one by $(\alpha_{em}/\alpha_s)^2$. If Higgs decays to ALP pairs were allowed by the UV charge assignments, then the related constraints [72–74] would apply. Their relative importance would be model dependent but in any case they would typically not probe f_a values beyond a TeV, see [21] for more details.

As an exercise to conclude this section, we comment on the ALP interpretation of the excesses recently reported (both at 2.9σ local) by CMS in diphoton [46] and dijet [32] searches, at invariant masses of 95 and 115 GeV respectively. The ALP parameters that would fit each of them are

$$\frac{f_a}{c_\gamma} \simeq 470 \text{ GeV} \sqrt{\frac{50 \text{ fb}}{\sigma_{\gamma\gamma}^{\text{sign}}}}, \quad c_3 \lesssim 2 \cdot c_\gamma, \quad (9)$$

for the 95 GeV $\gamma\gamma$ excess, and

$$\frac{f_a}{c_3} \simeq 310 \text{ GeV} \sqrt{\frac{300 \text{ pb}}{\sigma_{gg}^{\text{sign}}}}, \quad c_\gamma \lesssim 0.8 \cdot c_3, \quad (10)$$

for the 115 GeV jj one. $\sigma_{\gamma\gamma,gg}^{\text{sign}}$ are the theoretical signal cross sections of the excesses, whose normalization is chosen as follows. For the 95 GeV $\gamma\gamma$ excess we use the expected sensitivity at that mass as reported in Ref. [46], for the 115 GeV jj we use the analogous sensitivity reported in [32] for a Z' , and rescale it to an ALP produced in gluon fusion using Eq. (3). Dijet bounds [32] on the 95 GeV $\gamma\gamma$ excess [46], and diphoton bounds [43] on the 115 GeV jj excess [32], give the second inequalities in Eqs. (9) and (10) respectively.

Eqs. (9) and (10) allow to conclude that either of the two excesses, if coming from an ALP, could be interpreted in terms of reasonable values of f_a and of the ABJ anomalies. Such an ALP could be the first sign of a NP scale not too far from a TeV, still allowing the rest of the new states to be at $M_{\text{NP}} \sim 4\pi f_a$ and hence out of the current LHC reach.

7. Conclusions

Theoretical frameworks such as Supersymmetry and Compositeness predict, on general grounds, the existence of pNGBs (ALPs) with couplings of relevance for colliders. Similar ALPs have also received much attention as mediators of Dark Matter interactions with the SM. The current experimental searches for these particles, however, still contain holes. In particular huge ($> 10^4$ pb) gluon fusion cross sections at the LHC, for ALP masses below 65 GeV, are allowed by all existing constraints.

In this paper, we used public data from inclusive diphoton cross section measurements at the LHC [8–10] to put a new bound on diphoton resonances between 10 and 65 GeV. We showed how this bound sets the by-far strongest existing constraint on the parameter space of ALPs that couple to both gluon and EW boson field strengths, see Fig. 2. We have also derived indicative sensitivities that would be achievable by a proper LHC analysis, both with already existing 8 TeV data and at higher energies.

We hope that this work will motivate the LHC collaborations to extend the mass range of their diphoton resonant searches to lower values. Similar ideas could in principle be applied to probe light resonances decaying into other final states than diphotons. A great example is the current CMS search of boosted dijet resonances [32]. Going to lower invariant masses in dijet—and perhaps in other—final states would certainly deserve further experimental effort.

Acknowledgements

We thank Liron Barak, Sophia Borowka, Antonio Boveia, Marco Bonvini, Caterina Doglioni, Gabriele Ferretti, Mark Goodsell, Phil Harris, Bradley J. Kavanagh, Greg Landsberg, Giovanni Marchiori, Pier Francesco Monni, Ian Moulton, Kostantinos Vellidis and Andi Weiler for useful discussions. A special thank goes to Giovanni Marchiori, that first pointed us to [8]. We also thank Antonio Boveia, Caterina Doglioni, Gabriele Ferretti, Ian Moulton, David Shih, Lorenzo Ubaldi and Andreas Weiler for comments on the draft. D.R. thanks the LPthe for kind hospitality during the completion of this work. F.S. is grateful to the Weizmann institute of Science, the Mainz Institute for Theoretical Physics (MITP), the Galileo Galilei Institute (GGI), and the Institut d'Astrophysique de Paris (IAP) for kind hospitality at various stages of this work.

Funding and research infrastructure acknowledgments:

* A.M. is supported by the Strategic Research Program High Energy Physics and the Research Council of the Vrije Universiteit Brussel;

* F.S. is partly supported by the European Research Council (ERC) under the EU Seventh Framework Programme (FP7/2007–2013)/ERC Starting Grant (agreement n. 278234—NEWDARK' project), by MITP, and by a PRER Seed Project funding (Project ID PIF-2017-72);

* K.T. is supported in part by the NSF award 1620628.

Appendix A. Supplementary material

Supplementary material related to this article can be found online at <https://doi.org/10.1016/j.physletb.2018.06.039>.

References

- [1] J.J. Aubert, et al., *Phys. Rev. Lett.* 33 (1974) 1404, <https://link.aps.org/doi/10.1103/PhysRevLett.33.1404>.
- [2] J. Augustin, et al., *Phys. Rev. Lett.* 33 (1974) 1406, <https://link.aps.org/doi/10.1103/PhysRevLett.33.1406>.
- [3] S.W. Herb, et al., *Phys. Rev. Lett.* 39 (1977) 252, <https://link.aps.org/doi/10.1103/PhysRevLett.39.252>.
- [4] G. Arnison, et al., *UA1, Phys. Lett. B* 126 (1983) 398.
- [5] N. Craig, P. Draper, K. Kong, Y. Ng, D. Whiteson, [arXiv:1610.09392](https://arxiv.org/abs/1610.09392), 2016.
- [6] G. Aad, et al., *ATLAS, Phys. Lett. B* 716 (2012) 1, [arXiv:1207.7214](https://arxiv.org/abs/1207.7214).
- [7] S. Chatrchyan, et al., *CMS, Phys. Lett. B* 716 (2012) 30, [arXiv:1207.7235](https://arxiv.org/abs/1207.7235).
- [8] G. Aad, et al., *ATLAS, J. High Energy Phys.* 01 (2013) 086, [arXiv:1211.1913](https://arxiv.org/abs/1211.1913).
- [9] M. Aaboud, et al., *ATLAS, Phys. Rev. D* 95 (2017) 112005, [arXiv:1704.03839](https://arxiv.org/abs/1704.03839).
- [10] S. Chatrchyan, et al., *CMS, Eur. Phys. J. C* 74 (2014) 3129, [arXiv:1405.7225](https://arxiv.org/abs/1405.7225).
- [11] P. Srvcck, E. Witten, *J. High Energy Phys.* 06 (2006) 051, [arXiv:hep-th/0605206](https://arxiv.org/abs/hep-th/0605206).
- [12] A. Arvanitaki, S. Dimopoulos, S. Dubovsky, N. Kaloper, J. March-Russell, *Phys. Rev. D* 81 (2010) 123530, [arXiv:0905.4720](https://arxiv.org/abs/0905.4720).
- [13] M. Cicoli, M. Goodsell, A. Ringwald, *J. High Energy Phys.* 10 (2012) 146, [arXiv:1206.0819](https://arxiv.org/abs/1206.0819).
- [14] R.D. Peccei, H.R. Quinn, *Phys. Rev. Lett.* 38 (1977) 1440.
- [15] R.D. Peccei, H.R. Quinn, *Phys. Rev. D* 16 (1977) 1791.
- [16] S. Weinberg, *Phys. Rev. Lett.* 40 (1978) 223.
- [17] F. Wilczek, *Phys. Rev. Lett.* 40 (1978) 279.
- [18] H. Fukuda, K. Harigaya, M. Ibe, T.T. Yanagida, *Phys. Rev. D* 92 (2015) 015021, [arXiv:1504.06084](https://arxiv.org/abs/1504.06084).
- [19] S. Dimopoulos, A. Hook, J. Huang, G. Marques-Tavares, *J. High Energy Phys.* 11 (2016) 052, [arXiv:1606.03097](https://arxiv.org/abs/1606.03097).
- [20] A.E. Nelson, N. Seiberg, *Nucl. Phys. B* 416 (1994) 46, [arXiv:hep-ph/9309299](https://arxiv.org/abs/hep-ph/9309299).
- [21] B. Bellazzini, A. Mariotti, D. Redigolo, F. Sala, J. Serra, *Phys. Rev. Lett.* 119 (2017) 141804, [arXiv:1702.02152](https://arxiv.org/abs/1702.02152).
- [22] J. Barnard, T. Gherghetta, T.S. Ray, *J. High Energy Phys.* 02 (2014) 002, [arXiv:1311.6562](https://arxiv.org/abs/1311.6562).
- [23] G. Ferretti, D. Karateev, *J. High Energy Phys.* 03 (2014) 077, [arXiv:1312.5330](https://arxiv.org/abs/1312.5330).
- [24] G. Ferretti, *J. High Energy Phys.* 06 (2014) 142, [arXiv:1404.7137](https://arxiv.org/abs/1404.7137).
- [25] G. Ferretti, *J. High Energy Phys.* 06 (2016) 107, [arXiv:1604.06467](https://arxiv.org/abs/1604.06467).
- [26] A. Belyaev, G. Cacciapaglia, H. Cai, T. Flacke, A. Parolini, H. Seródio, *Phys. Rev. D* 94 (2016) 015004, [arXiv:1512.07242](https://arxiv.org/abs/1512.07242).
- [27] S. Banerjee, D. Barducci, G. Bélanger, B. Fuks, A. Goudelis, B. Zaldivar, *J. High Energy Phys.* 07 (2017) 080, [arXiv:1705.02327](https://arxiv.org/abs/1705.02327).
- [28] C. Kilic, T. Okui, R. Sundrum, *J. High Energy Phys.* 02 (2010) 018, [arXiv:0906.0577](https://arxiv.org/abs/0906.0577).
- [29] A. Djouadi, *Phys. Rep.* 459 (2008) 1, [arXiv:hep-ph/0503173](https://arxiv.org/abs/hep-ph/0503173).
- [30] A. Delgado, M. Garcia-Pepin, M. Quiros, J. Santiago, R. Vega-Morales, *J. High Energy Phys.* 06 (2016) 042, [arXiv:1603.00962](https://arxiv.org/abs/1603.00962).
- [31] U. Ellwanger, M. Rodriguez-Vazquez, *J. High Energy Phys.* 11 (2017) 008, [arXiv:1707.08522](https://arxiv.org/abs/1707.08522).
- [32] A.M. Sirunyan, et al., *CMS, J. High Energy Phys.* 01 (2018) 097, [arXiv:1710.00159](https://arxiv.org/abs/1710.00159).
- [33] J. Dolen, P. Harris, S. Marzani, S. Rappoccio, N. Tran, *J. High Energy Phys.* 05 (2016) 156, [arXiv:1603.00027](https://arxiv.org/abs/1603.00027).
- [34] I. Moulton, L. Necib, J. Thaler, *J. High Energy Phys.* 12 (2016) 153, [arXiv:1609.07483](https://arxiv.org/abs/1609.07483).
- [35] A. Alloul, N.D. Christensen, C. Degrande, C. Duhr, B. Fuks, *Comput. Phys. Commun.* 185 (2014) 2250, [arXiv:1310.1921](https://arxiv.org/abs/1310.1921).
- [36] J. Alwall, M. Herquet, F. Maltoni, O. Mattelaer, T. Stelzer, *J. High Energy Phys.* 06 (2011) 128, [arXiv:1106.0522](https://arxiv.org/abs/1106.0522).
- [37] J. Alwall, R. Frederix, S. Frixione, V. Hirschi, F. Maltoni, O. Mattelaer, H.S. Shao, T. Stelzer, P. Torrielli, M. Zaro, *J. High Energy Phys.* 07 (2014) 079, [arXiv:1405.0301](https://arxiv.org/abs/1405.0301).
- [38] T. Sjostrand, S. Mrenna, P.Z. Skands, *J. High Energy Phys.* 05 (2006) 026, [arXiv:hep-ph/0603175](https://arxiv.org/abs/hep-ph/0603175).
- [39] T. Sjostrand, S. Mrenna, P.Z. Skands, *Comput. Phys. Commun.* 178 (2008) 852, [arXiv:0710.3820](https://arxiv.org/abs/0710.3820).
- [40] J. de Favereau, C. Delaere, P. Demin, A. Giammanco, V. Lemaître, A. Mertens, M. Selvaggi, *DELPHES 3, J. High Energy Phys.* 02 (2014) 057, [arXiv:1307.6346](https://arxiv.org/abs/1307.6346).
- [41] E. Conte, B. Fuks, G. Serret, *Comput. Phys. Commun.* 184 (2013) 222, [arXiv:1206.1599](https://arxiv.org/abs/1206.1599).
- [42] J. Alwall, et al., *Eur. Phys. J. C* 53 (2008) 473, [arXiv:0706.2569](https://arxiv.org/abs/0706.2569).
- [43] G. Aad, et al., *ATLAS, Phys. Rev. Lett.* 113 (2014) 171801, [arXiv:1407.6583](https://arxiv.org/abs/1407.6583).
- [44] Tech. Rep. CMS-PAS-HIG-14-037. CERN, Geneva, 2015, <https://cds.cern.ch/record/2063739>.
- [45] V. Khachatryan, et al., *CMS, Phys. Lett. B* 750 (2015) 494, [arXiv:1506.02301](https://arxiv.org/abs/1506.02301).
- [46] Tech. Rep. CMS-PAS-HIG-17-013. CERN, Geneva, 2017, <http://cds.cern.ch/record/2285326>.
- [47] J.R. Andersen, et al., LHC Higgs Cross Section Working Group, [arXiv:1307.1347](https://arxiv.org/abs/1307.1347), 2013.
- [48] T. Aaltonen, et al., *CDF, Phys. Rev. D* 84 (2011) 052006, [arXiv:1106.5131](https://arxiv.org/abs/1106.5131).
- [49] T. Aaltonen, et al., *CDF Collaboration, Phys. Rev. Lett.* 110 (2013) 101801, <https://link.aps.org/doi/10.1103/PhysRevLett.110.101801>.
- [50] V.M. Abazov, et al., *D0, Phys. Lett. B* 690 (2010) 108, [arXiv:1002.4917](https://arxiv.org/abs/1002.4917).
- [51] A.D. Martin, W.J. Stirling, R.S. Thorne, G. Watt, *Eur. Phys. J. C* 63 (2009) 189, [arXiv:0901.0002](https://arxiv.org/abs/0901.0002).
- [52] M. Aharrouché, et al., *Nucl. Instrum. Methods Phys. Res., Sect. A* 568 (2006) 601, [arXiv:physics/0608012](https://arxiv.org/abs/physics/0608012).
- [53] J.F. Kamenik, G. Perez, M. Schlaffer, A. Weiler, *Eur. Phys. J. C* 77 (2017) 126, [arXiv:1607.06440](https://arxiv.org/abs/1607.06440).
- [54] S.D. Ellis, T.S. Roy, J. Scholtz, *Phys. Rev. Lett.* 110 (2013) 122003, [arXiv:1210.1855](https://arxiv.org/abs/1210.1855).
- [55] S.D. Ellis, T.S. Roy, J. Scholtz, *Phys. Rev. D* 87 (2013) 014015, [arXiv:1210.3657](https://arxiv.org/abs/1210.3657).
- [56] J. Jaeckel, M. Spannowsky, *Phys. Lett. B* 753 (2016) 482, [arXiv:1509.00476](https://arxiv.org/abs/1509.00476).
- [57] <http://cds.cern.ch/record/1480607>, 2012.
- [58] V. Khachatryan, et al., *CMS, Phys. Rev. Lett.* 117 (2016) 031802, [arXiv:1604.08907](https://arxiv.org/abs/1604.08907).
- [59] Tech. Rep. ATLAS-CONF-2016-030. CERN, Geneva, 2016, <http://cds.cern.ch/record/2161135>.
- [60] A.M. Sirunyan, et al., *CMS, Phys. Lett. B* 769 (2017) 520; Erratum: *Phys. Lett. B* 772 (2017) 882, [arXiv:1611.03568](https://arxiv.org/abs/1611.03568).
- [61] M. Aaboud, et al., *ATLAS, Eur. Phys. J. C* 77 (2017) 317, [arXiv:1611.09661](https://arxiv.org/abs/1611.09661).
- [62] V. Khachatryan, et al., *CMS, J. Instrum.* 12 (2017) P01020, [arXiv:1609.02366](https://arxiv.org/abs/1609.02366).
- [63] G. Aad, et al., *ATLAS, Phys. Rev. D* 91 (2015) 052007, [arXiv:1407.1376](https://arxiv.org/abs/1407.1376).
- [64] O. Adriani, et al., *L3, Phys. Lett. B* 292 (1992) 472.
- [65] M. Acciarri, et al., *L3, Phys. Lett. B* 345 (1995) 609.
- [66] P. Abreu, et al., *DELPHI Collaboration, Phys. Lett. B* 458 (1999) 431, 20 pp. <http://cds.cern.ch/record/393660>.
- [67] P. Abreu, et al., *DELPHI, Phys. Lett. B* 433 (1998) 429.
- [68] K. Fujii, et al., [arXiv:1702.05333](https://arxiv.org/abs/1702.05333), 2017.
- [69] D. d'Enterria, in: *Proceedings, 17th Lomonosov Conference on Elementary Particle Physics, Moscow, Russia, August 20–26, 2015, 2017*, pp. 182–191, <https://inspirehep.net/record/1421932/files/arXiv:1602.05043.pdf>.
- [70] K. Mimasu, V. Sanz, *J. High Energy Phys.* 06 (2015) 173, [arXiv:1409.4792](https://arxiv.org/abs/1409.4792).
- [71] S. Knapen, T. Lin, H.K. Lou, T. Melia, *Phys. Rev. Lett.* 118 (2017) 171801, [arXiv:1607.06083](https://arxiv.org/abs/1607.06083).
- [72] G. Aad, et al., *ATLAS, CMS, J. High Energy Phys.* 08 (2016) 045, [arXiv:1606.02266](https://arxiv.org/abs/1606.02266).
- [73] V. Khachatryan, et al., *CMS, J. High Energy Phys.* 10 (2017) 076, [arXiv:1701.02032](https://arxiv.org/abs/1701.02032).
- [74] G. Aad, et al., *ATLAS, Phys. Rev. D* 92 (2015) 052002, [arXiv:1505.01609](https://arxiv.org/abs/1505.01609).

R-Axion at Colliders

Brando Bellazzini,^{1,2} Alberto Mariotti,³ Diego Redigolo,^{4,5} Filippo Sala,⁶ and Javi Serra⁷¹*Institut de Physique Théorique, Université Paris Saclay, CEA, CNRS, F-91191 Gif-sur-Yvette, France*²*Dipartimento di Fisica e Astronomia, Università di Padova, Via Marzolo 8, I-35131 Padova, Italy*³*Theoretische Natuurkunde and IIHE/ELEM, Vrije Universiteit Brussel, and International Solvay Institutes, Pleinlaan 2, B-1050 Brussels, Belgium*⁴*Raymond and Beverly Sackler School of Physics and Astronomy, Tel-Aviv University, Tel-Aviv 69978, Israel*⁵*Department of Particle Physics and Astrophysics, Weizmann Institute of Science, Rehovot 7610001, Israel*⁶*LPTHE, UMR 7589 CNRS, 4 Place Jussieu, F-75252 Paris, France*⁷*Theory Division, CERN, CH-1211 Geneva 23, Switzerland*

(Received 12 April 2017; published 5 October 2017)

We study the effective theory of a generic class of hidden sectors where supersymmetry is broken together with an approximate R -symmetry at low energy. The light spectrum contains the gravitino and the pseudo-Nambu-Goldstone boson of the R -symmetry, the R -axion. We derive new model-independent constraints on the R -axion decay constant for R -axion masses ranging from GeV to TeV, which are of relevance for hadron colliders, lepton colliders, and B factories. The current bounds allow for the exciting possibility that the first sign of supersymmetry will be the R -axion. We point out its most distinctive signals, providing a new experimental handle on the properties of the hidden sector and a solid motivation for searches of axionlike particles.

DOI: 10.1103/PhysRevLett.119.141804

In this Letter we argue that there are generic signs of supersymmetry (SUSY) to be looked for at colliders that have not yet been satisfactorily explored: those associated with the R -axion, the pseudo-Nambu-Goldstone boson (PNGB) of a spontaneously broken R -symmetry.

Although it is well known that supersymmetry must be broken in a “hidden sector,” its dynamics is left unspecified in the vast majority of phenomenological studies, which instead focus on the “visible sector,” e.g., the minimal supersymmetric standard model (MSSM). Here we point out that in an extensive class of models the hidden sector leaves its footprints in observables accessible to the current experimental program. In particular, we perform a thorough phenomenological study of the R -axion at high- and low-energy hadron and lepton colliders.

The $\mathcal{N} = 1$ SUSY algebra contains a single $U(1)_R$ (“ R -symmetry”) under which supercharges transform, $[R, Q_\alpha] = -Q_\alpha$, such that components of a given supermultiplet have R charges r differing by one unit (e.g., gauge fields carry no R charge while gauginos have $r_\lambda = 1$). R -symmetry plays a crucial role in models of low-energy dynamical SUSY breaking. According to the general result of Nelson and Seiberg, an R -symmetry must exist in any generic, calculable model which breaks SUSY with F

terms, and if the R -symmetry is spontaneously broken then SUSY is also broken [1]. Spontaneous R -symmetry breaking often occurs also in incalculable models like in [2,3]. If the SUSY-breaking vacuum is metastable, like in Intriligator-Seiberg-Shih (ISS) constructions [4], then an analogue of the Nelson-Seiberg result holds for an approximate R -symmetry [5]. When $U(1)_R$ is explicitly broken by a suitable deformation of the hidden sector, the R -axion gets a mass in addition to the irreducible contribution from supergravity [6] but can remain naturally lighter than the other hidden-sector resonances.

In light of the above observations, and contrary to what previously explored in the literature, we treat the R -axion mass m_a as a free parameter, together with its decay constant f_a . Our analysis shows that such a particle could well be the first sign of SUSY to show up in experiments. We also derive model-independent bounds on the scale of spontaneous R -symmetry breaking, opening a new observational window on the properties of the SUSY-breaking hidden sector.

Setup.—We parametrize with m_* the SUSY mass gap of the hidden sector and with g_* the coupling strength between hidden-sector states at m_* . The generic size of the SUSY-breaking vacuum expectation value (VEV) is then $F \sim m_*^2/g_*$, an outcome of naive dimensional analysis (NDA) with a single scale and coupling [7,8]. The R -axion decay constant is $f_a \sim m_*/g_*$, while the R -axion mass should satisfy $m_a \ll m_*$ in order for the R -symmetry axion to be a PNGB.

As a generic consequence of spontaneous SUSY breaking, a light gravitino is also present in the low-energy

Published by the American Physical Society under the terms of the Creative Commons Attribution 4.0 International license. Further distribution of this work must maintain attribution to the author(s) and the published article's title, journal citation, and DOI.

spectrum. In the rigid limit (i.e., $M_{\text{Pl}} \rightarrow \infty$) the transverse degrees of freedom of the gravitino decouple, leaving a massless Goldstino in the spectrum. The effective action of the Goldstino and the R -axion can be written using the nonlinear superfield formalism of [9] and reads

$$\begin{aligned} \mathcal{L}_{\text{hid}} = & \int d^4\theta \left(X^\dagger X + \frac{f_a^2}{2} \mathcal{R}^\dagger \mathcal{R} \right) \\ & + \int d^2\theta (FX + w_R \mathcal{R}^2) + \text{c.c.} \\ \supset & -F^2 + i\bar{G}\bar{\sigma}^\mu \partial_\mu G + \frac{f_a^2}{2} (\partial_\mu a)^2 \\ & - \frac{w_R}{F^2} (iG^2 e^{-2ia} \square a + \text{c.c.}), \end{aligned} \quad (1)$$

where X and $\mathcal{R} = e^{iA}$ carry R charge 2 and 1, respectively (the R charge of a supermultiplet is identified with that of its bottom component) and satisfy the nonlinear constraints $X^2 = 0$ and $X(\mathcal{R}^\dagger \mathcal{R} - 1) = 0$. The above constraints, in combination with (1), give $X = G^2/2F^2 + \sqrt{2}G\theta - F\theta^2$, $A = a + O(aG)$; see the Supplemental Material for more details [10].

Since the R charge of \mathcal{R} is 1, its effective action differs from the one of a SUSY axion in that a superpotential term is allowed. This is controlled by the dimension-three parameter w_R , which is related to the VEV of the superpotential and satisfies the inequality $w_R < f_a F/2\sqrt{2}$, under the assumption of no extra light degrees of freedom other than the R -axion and the Goldstino [11,12]. The superpotential term induces cubic interactions between the R -axion and two Goldstini, proportional to m_a^2 , that lead to an invisible decay channel for the R -axion. The corresponding decay rate of the R -axion into two Goldstini is

$$\Gamma(a \rightarrow GG) = \frac{1}{4\pi} \left(\frac{m_a^5 w_R^2}{f_a^2 F^4} \right) < \frac{1}{32\pi} \frac{m_a^5}{F^2} \quad (2)$$

and it is bounded from above as a consequence of the upper bound on w_R , saturated only in free theories. Our power counting gives $w_R \sim F f_a$, making the width within an $O(1)$ factor of the upper limit in Eq. (2). For ordinary axions, w_R would instead break explicitly the associated global symmetry, resulting in a suppression of the decay width into Goldstini by extra powers of m_a^2/m_*^2 . Hence, a sizable invisible decay width is a distinctive feature of the R -axion compared to other axionlike particles.

The R -axion mass is generated by sources of explicit R -symmetry breaking and can be parametrized as

$$m_a^2 \sim \frac{\epsilon_{\mathcal{R}} F}{f_a^2} r_\epsilon^2 \ll m_*^2 \quad \text{from } \mathcal{L}_{\mathcal{R}} = \int d^2\theta \frac{1}{2} \epsilon_{\mathcal{R}} X R^{-r_\epsilon}, \quad (3)$$

where r_ϵ is the R charge of the explicit-breaking spurion $\epsilon_{\mathcal{R}}$, with $\epsilon_{\mathcal{R}}/F \ll 1$ technically natural. Explicit examples of this mass hierarchy arise by adding suitable R -symmetry

breaking deformations in calculable models of dynamical SUSY breaking like the 3-2 model [1,13,14] or in SUSY QCD at large N once the hidden gauginos and squarks get soft masses [15,16]. Moreover, in SUSY-breaking models like the one in [5], the explicit breaking of the R -symmetry is generically bounded from above ($\epsilon_{\mathcal{R}}/F \ll 1$) by requiring the SUSY-breaking vacuum to be metastable.

The R -symmetry breaking contribution (3) can well be expected to dominate over the unavoidable supergravity (SUGRA) contribution arising from the tuning of the cosmological constant [6], which gives rise to $m_a^2 \sim (10 \text{ MeV})^2 \times m_*/10 \text{ TeV} \times m_{3/2}/\text{eV}$ (we refer to the Supplemental Material for its derivation [10]).

We now study the couplings of the R -axion with the visible-sector fields, which we take to be the MSSM (with matter or R parity). The superpartners get SUSY-breaking masses m_{soft} from their interactions with the hidden sector, which are controlled by a perturbative coupling g . This coupling is a proxy for the SM gauge coupling constants in gauge mediation models [17,18] or for Yukawa-type interactions in extended gauge mediation; see [19] for a review. The scaling of m_{soft} strongly depends on the type of mediation mechanism. We can estimate it as

$$m_{\text{soft}} \sim \left(\frac{g}{g_*} \right)^n \times g \frac{F}{m_*} = \left(\frac{g}{g_*} \right)^{n+1} \times m_*. \quad (4)$$

In this Letter we assume that gauginos get a mass via their coupling to the hidden-sector global current, so that $m_{\text{soft}} \sim (g/g_*)^2 m_*$. Notice that if $g_* = 4\pi/\sqrt{N_{\text{mess}}}$ we recover the ordinary gauge mediation scaling where N_{mess} is the number of messengers. Other scaling, e.g., the one of [20] for Dirac gauginos ($n=0$), will be discussed elsewhere. Besides, whatever the scaling in Eq. (4), there is always a large portion of parameter space where the R -symmetry axion is lighter than the superpartners, which correspond to $r_\epsilon \sqrt{g_* \epsilon_{\mathcal{R}}}/m_* \lesssim (g/g_*)^{n+1}$. It would also be interesting to depart from the NDA expectation for the scales F and f_a and explore models where a large separation between the two is realized.

We consider in the following a small SUSY-breaking scale \sqrt{F} in the range from 1 to a few 100s of TeV. This regime is welcome for fine-tuning and Higgs mass considerations. The resulting gravitino mass lies in the window $10^{-4} \text{ eV} \lesssim m_{3/2} \lesssim 5 \text{ eV}$, where the upper limit comes from cosmological and astrophysical bounds on gravitino abundance [21–23], while the lower limit comes from LEP [24] and LHC [25,26] bounds.

Since the visible sector feels the SUSY breaking only through g/g_* effects, we can treat the MSSM superfields linearly and “dress” the R -charged operators with appropriate powers of the R -axion. We also neglect subleading effects from explicit R -breaking terms, suppressed by powers of $\sim m_a/m_*$. The interactions of the R -axion with the MSSM gauge sector are then

$$\begin{aligned} \mathcal{L}_{\text{gauge}} &= \int d^2\theta \left(-ig_i^2 \frac{c_i^{\text{hid}}}{16\pi^2} \mathcal{A} - \frac{m_{\lambda_i}}{2F} X \mathcal{R}^{-2} \right) \mathcal{W}_i^2 + \text{c.c.} \\ &\supset \frac{g_i^2 c_i^{\text{hid}}}{16\pi^2} \frac{a}{f_a} F^i \tilde{F}^i - \frac{m_{\lambda_i}}{2} \lambda_i \lambda_i \left(e^{-2ia/f_a} + \frac{g_i^2 c_i^{\text{hid}}}{4\pi^2} i \frac{a}{f_a} \right) \\ &\quad + \text{c.c.}, \end{aligned} \quad (5)$$

where \mathcal{W} is the field strength superfield ($r_{\mathcal{W}} = 1$) and i labels the SM gauge group, where we defined $g_1 = \sqrt{5/3}g_Y$ and $\tilde{F}^{i,\mu\nu} = 1/2\epsilon^{\mu\nu\rho\sigma} F_{\rho\sigma}^i$. The Majorana gaugino masses are of order $m_{\lambda_i} \approx m_{\text{soft}}$ by assumption. The coefficients c_i^{hid} encode the hidden-sector contributions to the mixed anomalies of the $U(1)_R$ with the SM gauge groups. For example, we get $c_i^{\text{hid}} = -N_{\text{mess}}$ for $i = 1, 2, 3$, for N_{mess} messengers chiral under $U(1)_R$ and in the $5 + \bar{5}$ of $SU(5)$ with zero R charge [in our NDA, $N_{\text{mess}} \sim (4\pi/g_*)^2$]. We encode the contributions to the anomalies from the MSSM fields in the full loop functions.

The interactions in the Higgs sector can be written as

$$\begin{aligned} \mathcal{L}_{\text{Higgs}} &= \int d^4\theta \left(\frac{\mu}{F} X^\dagger \mathcal{R}^{2-r_H} - \frac{B_\mu}{F^2} |X|^2 \mathcal{R}^{-r_H} \right) H_u H_d + \text{c.c.} \\ &\supset \mu \tilde{h}_u \tilde{h}_d e^{i(2-r_H)a/f_a} - B_\mu h_u h_d e^{-ir_H a/f_a} + \text{c.c.}, \end{aligned} \quad (6)$$

where $\tilde{h}_{u,d}$ are the Higgsinos and $h_{u,d}$ the Higgs doublets. We have assumed the μ term, in addition to B_μ , is generated by the hidden dynamics. The actual value of $r_H = r_{H_u} + r_{H_d}$ thus depends on the charge assignments in the hidden sector. The charge assignment of the visible sector fields is modified by higher-dimensional operators in the Kahler potential like $|H_{u,d}|^2 |\mathcal{R}|^2$, etc., which lead to g/g_* suppressed effects that will be neglected in what follows.

The coupling to the MSSM Higgses proportional to B_μ induces, after electroweak symmetry breaking, a small mixing between a and the MSSM Higgs boson A [27]

$$\delta = r_H \frac{v}{f_a} \frac{s_{2\beta}}{2} \frac{1}{1 - m_a^2/m_A^2} \simeq r_H \frac{v}{f_a} \frac{s_{2\beta}}{2}. \quad (7)$$

If we assume the Yukawa interactions in the superpotential are allowed in the limit of exact $U(1)_R$ ($r_{H_u} + r_Q + r_U = 2$, etc.), the mixing δ is the only source of couplings between a and the SM fermions and we get

$$\mathcal{L}_f = ir_H \frac{a}{f_a} [c_\beta^2 m_u \bar{u} \gamma_5 u + s_\beta^2 m_d \bar{d} \gamma_5 d + s_\beta^2 m_\ell \bar{\ell} \gamma_5 \ell]. \quad (8)$$

The same mixing induces

$$\mathcal{L}_{ahh} = \frac{\delta^2}{v} h (\partial_\mu a)^2, \quad (9)$$

where h is the SM-like Higgs, as well as extra interactions with the MSSM Higgses, whose phenomenological consequences we leave for future work [14]. Finally, the a couplings to sfermions also arise from its mixing with A and are proportional to the A terms. Since we assume all the sfermions to be

heavy and the A terms to be small, these couplings do not play any role in the R -axion phenomenology discussed here.

Phenomenology.—We focus on R -axion masses in the range between 2 GeV and 2 TeV, and we refer to [28] for a LHC study for masses of $O(100)$ MeV. For definiteness we fix $r_H = 2$, which allows for an R -symmetric μ term and a B_μ term from spontaneous $U(1)_R$ breaking. We will comment on the phenomenological differences of the $r_H = 0$ case, where the role of μ and B_μ is reversed. The Majorana gaugino masses cannot be arbitrarily larger than the scale of spontaneous R breaking, so we take $f_a \gtrsim 0.3$ TeV and fix for illustrative purposes the gaugino masses to the grand unified theory (GUT) universal values $m_{\lambda_{1,2,3}} = 0.7, 1.4, 3.6$ TeV (different values do not change the R -axion phenomenology as long as $m_{\lambda_i} > m_a/2$). For $f_a \lesssim 1$ TeV, obtaining such heavy gauginos present model building challenges which are beyond the scope of this Letter.

We now discuss the different production modes of the R -axion. For the purposes of this Letter we ignore R -axion production from SUSY decay chains. As for any axionlike particle, the single production modes scale with $1/f_a^2$ and double production ones with $1/f_a^4$.

(i) At the LHC, the resonant a (+SM) production is dominated by gluon fusion, which we determine using the leading-order prediction multiplied by a constant K factor of 2.4 [29] (see the Supplemental Material for details [10]).

(ii) Also at the LHC, we have double a production from Higgs decays driven by the coupling in Eq. (9).

(iii) At lepton colliders the R -axion can be single produced via its coupling to the Z , which is dominated by the anomaly in Eq. (5).

(iv) At flavor factories we consider R -axion production via $B \rightarrow K^{(*)} a$ and $\Upsilon \rightarrow \gamma a$ decays. The $\text{BR}(B \rightarrow K^{(*)} a)$ are computed from the general result of [30], accounting for the mixing of the R -axion with the CP -odd Higgs (7) [31], and choosing for reference $m_{H^\pm} = 1$ TeV (we take the form factor relevant for K^* from [32]). The $\text{BR}(\Upsilon \rightarrow \gamma a)/\text{BR}(\Upsilon \rightarrow ll)$ is computed using the standard Wilczek formula [33].

The R -axion decays to pairs of gauge bosons and of SM fermions, to Goldstini (invisible) and, if kinematically allowed, to supersymmetric particles. We refer the reader to the Supplemental Material for quantitative details [10].

In Fig. 1 we summarize the present constraints on the R -axion in the m_a - f_a plane as well as the most promising processes to search for it at future experiments. For $m_a \gtrsim m_h/2$, the most important bounds come from resonant a production at the LHC. The most distinctive feature of the R -axion is the invisible signal strength of Eq. (2), which is important for large m_a . This results in constraints from monojet searches at 8 and 13 TeV [34,35]. To draw them, we have determined the ratio of the a and $a + \text{jet(s)}$ production cross sections via a MADGRAPH [56,57] simulation, for the different missing energy cuts for which the bounds are given in [34,35] (we believe this approximation to be sufficient for our purposes).

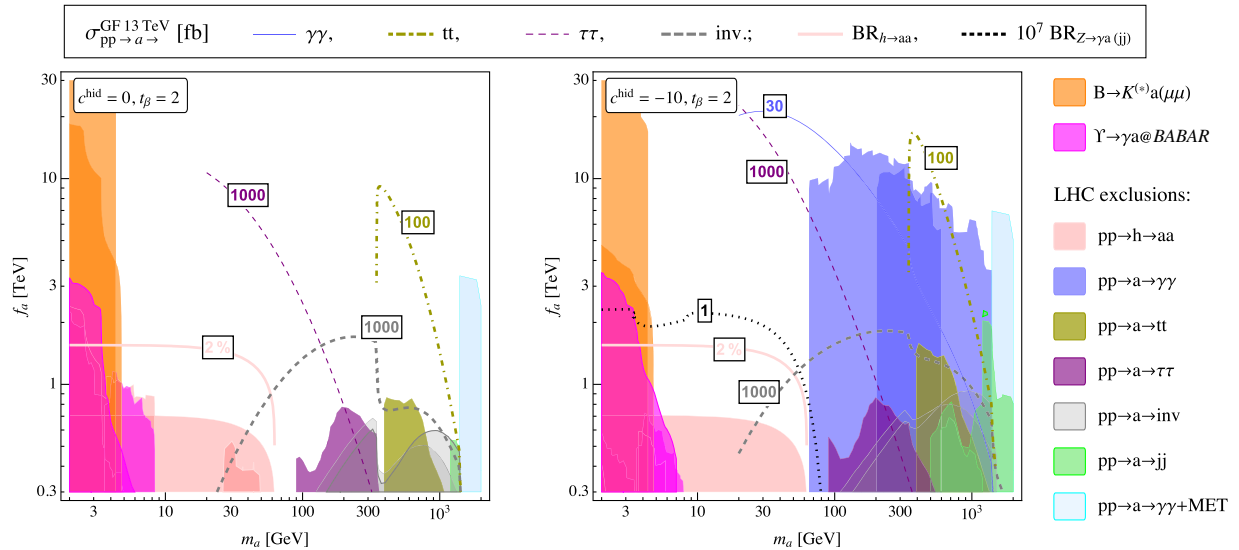


FIG. 1. Shaded areas show LHC8 and LHC13 [34–49], LHCb [50,51], BABAR [52–54], and Belle [55] exclusions. Contours show signal strengths at the LHC13 and Higgs and Z boson branching ratios. The tiny area in the lower right corner where $m_a \approx 4\pi f_a$ lies beyond the regime of validity of our effective description.

At $m_a > 1.4$ TeV the decay into bino pairs opens up, resulting in a $\gamma\gamma + \text{MET}$ final state via the prompt bino decay to $\gamma + G$. This is constrained by inclusive $\gamma\gamma + \text{MET}$ searches [36], which we translate in a bound $\sigma_{gg \rightarrow a \rightarrow \lambda_1 \lambda_1}^{8\text{TeV}} < 0.3$ fb.

For large anomalies, diphoton resonant searches [37–39] at 8 and 13 TeV dominate the collider phenomenology for $m_a > 60$ GeV [58]. Searches for a resonance decaying into dijet [40–42], into $t\bar{t}$ at 8 TeV [43,44], and into ditau at 13 TeV [45,46] give complementary bounds for $m_a > 500$ GeV, $m_a > 2m_t$, and $100 \text{ GeV} \lesssim m_a < 2m_t$, respectively.

For small anomalies the LHC constraints are sensibly weakened by the reduced production cross section and by the suppressed branching ratio in diphotons. A lower bound on f_a can still be derived from a combination of $t\bar{t}$, ditau, and monojet searches.

For $m_a \lesssim 2m_h$, the major constraint comes from the upper bound on $\text{BR}(h \rightarrow \text{untagged}) < 32\%$ [47]. This bound depends only on the mixing in Eq. (7) and applies to both cases with $N_{\text{mess}} = 10$ and $N_{\text{mess}} = 0$. We also include constraints arising from exclusive Higgs decays (e.g., $h \rightarrow aa \rightarrow 4\mu$ or $h \rightarrow aa \rightarrow 2\tau 2\mu$) [48,49]. Finally, LEP constraints [59–64] are not relevant for the f_a considered in this study.

For $m_a \lesssim 9$ GeV, stringent constraints on f_a come from BABAR searches of $\Upsilon \rightarrow a\gamma$, with a decaying into tau or muon pairs [52,53] or hadrons [54]. For $m_a \lesssim 4$ GeV, we consider LHCb [50,51] and Belle [55] bounds from $B \rightarrow K^* \mu\mu$. In particular, the recent LHCb limit $\text{BR}(B \rightarrow K^* \mu\mu) \lesssim 2 \times 10^{-9}$ [50] puts the strongest bound on f_a , among all the searches we considered, reaching $f_a \gtrsim 200$ TeV for $N_{\text{mess}} = 0$.

At large t_β , δ becomes smaller [see Eq. (7)], reducing the bounds from Higgs branching ratio measurements and $B \rightarrow K$ transitions. The couplings to quarks and leptons are also t_β dependent; most importantly, the $t\bar{t}$ signal strength is

reduced at large t_β . For $r_H = 0$ (and within our previous assumptions) the R -axion does not couple to SM fermions at the linear level. This makes it generically very difficult to be constrained for $m_a < m_h/2$. For larger values of m_a and irrespective of the values of t_β and r_H , diphoton constraints give $f_a \gtrsim 10$ TeV for large anomalies, while for small anomalies a milder bound on f_a is anyway given by monojet and dijet searches.

Promising signatures for future experimental programs are also shown in Fig. 1. The most distinctive one is the decay into two Goldstini, which gives a large invisible signal strength. This will be probed by monojet searches at the LHC (multijet + MET searches could also be relevant [65]) and constitutes a very good motivation for the high-luminosity LHC program. For large anomalies, the diphoton final state will be the most promising one at the LHC, while for small anomalies ditau and $t\bar{t}$ will be more important. For $m_a < m_h/2$ we show how an improvement of the Higgs coupling measurements down to 1%–2% (which is within the reach of ILC [66]) would probe f_a up to 1.5 TeV. Even bigger values of f_a are within the reach of machines like CLIC, CEPC, and FCC-ee, which plan to probe Higgs coupling with a precision of roughly 10^{-3} [66]. For large anomalies, an important probe of a light R -axion would be $Z \rightarrow \gamma a$ measurements at future lepton colliders. A naive rescaling of the LEP I analysis [62] indicates that $Z \rightarrow \gamma a(jj)$ branching ratios in the ballpark of 10^{-7} could be probed at the FCC-ee, if $O(10^{12})$ Z s will be produced. We notice that the mass window $10 \lesssim m_a \lesssim 65$ GeV is less constrained by the searches we considered. This could be improved by extending the coverage of resonance searches, in particular $\gamma\gamma$, to lower invariant masses.

To distinguish the R -axion from other scalar resonances, a jet + MET signal would certainly help in combination with

a pattern along the lines discussed above. Of course, to reinforce the R -axion interpretation of a possible signal, one would eventually need to find evidence for superpartners.

Conclusions.—The possibility that the R -axion could be the first sign of SUSY at colliders is well motivated from theoretical and phenomenological considerations, *a fortiori* given the strong LHC bounds on sparticles.

In this Letter we have investigated the low-energy dynamics of SUSY-breaking sectors with a light R -axion (and gravitino) coupled to the MSSM. Our results are summarized in Fig. 1, where we show how current and future colliders probe the space of R -axion masses and decay constants. We have also identified some promising signatures to cover the currently unconstrained part of the parameter space.

The R -axion constitutes a very interesting prototype of axionlike particles, with couplings that follow from well-defined selection rules of the theory, and whose mass can be safely considered a free parameter.

The rich phenomenology of the R -axion certainly deserves further investigation. The R -axion can give rise to nonstandard heavy Higgs decays or SUSY decay chains, it can be a further motivation for high-intensity experiments (in its light-mass window), and it could impact cosmological and astrophysical processes.

Finally, we wish to point out that other appealing features of SUSY, such as unification and dark matter, might find an interesting interplay with a light R -axion, opening new model-building avenues. We leave the exploration of this exciting physics for the future.

We thank Lorenzo Di Pietro, Zohar Komargodski, David Shih, Riccardo Torre, and Lorenzo Ubaldi for useful discussions. The authors thank CERN and the LPTHE for kind hospitality during the completion of this work. F. S. is grateful to the Institut d’Astrophysique de Paris (IAP) for hospitality. B. B. is supported in part by the MIUR-FIRB Grant No. RBFR12H1MW, “A New Strong Force, the Origin of Masses and the LHC.” A. M. is supported by the Strategic Research Program High Energy Physics and the Research Council of the Vrije Universiteit Brussel. F. S. is supported by the European Research Council (ERC) under the EU Seventh Framework Programme (FP7/2007-2013)/ERC Starting Grant No. 278234, “NewDark” project.

-
- [1] A. E. Nelson and N. Seiberg, *Nucl. Phys.* **B416**, 46 (1994).
 - [2] I. Affleck, M. Dine, and N. Seiberg, *Phys. Lett.* **137B**, 187 (1984).
 - [3] I. Affleck, M. Dine, and N. Seiberg, *Phys. Lett.* **140B**, 59 (1984).
 - [4] K. A. Intriligator, N. Seiberg, and D. Shih, *J. High Energy Phys.* **04** (2006) 021.
 - [5] K. A. Intriligator, N. Seiberg, and D. Shih, *J. High Energy Phys.* **07** (2007) 017.
 - [6] J. Bagger, E. Poppitz, and L. Randall, *Nucl. Phys.* **B426**, 3 (1994).

- [7] A. G. Cohen, D. B. Kaplan, and A. E. Nelson, *Phys. Lett. B* **412**, 301 (1997).
- [8] M. A. Luty, *Phys. Rev. D* **57**, 1531 (1998).
- [9] Z. Komargodski and N. Seiberg, *J. High Energy Phys.* **09** (2009) 066.
- [10] See Supplemental Material at <http://link.aps.org/supplemental/10.1103/PhysRevLett.119.141804> for more details on the constrained superfield formalism and on our conventions, and for more quantitative considerations on the R -axion mass and its phenomenology.
- [11] M. Dine, G. Festuccia, and Z. Komargodski, *J. High Energy Phys.* **03** (2010) 011.
- [12] B. Bellazzini, *J. High Energy Phys.* **02** (2017) 034.
- [13] I. Affleck, M. Dine, and N. Seiberg, *Nucl. Phys.* **B256**, 557 (1985).
- [14] B. Bellazzini, A. Mariotti, D. Redigolo, F. Sala, and J. Serra (to be published).
- [15] S. P. Martin and J. D. Wells, *Phys. Rev. D* **58**, 115013 (1998).
- [16] M. Dine, P. Draper, L. Stephenson-Haskins, and D. Xu, *J. High Energy Phys.* **05** (2017) 122.
- [17] G. F. Giudice and R. Rattazzi, *Phys. Rep.* **322**, 419 (1999).
- [18] P. Meade, N. Seiberg, and D. Shih, *Prog. Theor. Phys. Suppl.* **177**, 143 (2009).
- [19] J. A. Evans and D. Shih, *J. High Energy Phys.* **08** (2013) 093.
- [20] T. Gherghetta and A. Pomarol, *J. High Energy Phys.* **12** (2011) 069.
- [21] E. Pierpaoli, S. Borgani, A. Masiero, and M. Yamaguchi, *Phys. Rev. D* **57**, 2089 (1998).
- [22] M. Viel, J. Lesgourgues, M. G. Haehnelt, S. Matarrese, and A. Riotto, *Phys. Rev. D* **71**, 063534 (2005).
- [23] K. Osato, T. Sekiguchi, M. Shirasaki, A. Kamada, and N. Yoshida, *J. Cosmol. Astropart. Phys.* **06** (2016) 004.
- [24] A. Brignole, F. Feruglio, and F. Zwirner, *Nucl. Phys.* **B516**, 13 (1998); **B555**, 653(E) (1999).
- [25] A. Brignole, F. Feruglio, M. L. Mangano, and F. Zwirner, *Nucl. Phys.* **B526**, 136 (1998); **B582**, 759(E) (2000).
- [26] F. Maltoni, A. Martini, K. Mawatari, and B. Oehl, *J. High Energy Phys.* **04** (2015) 021.
- [27] Equation (7) accounts for both mass and kinetic mixing between A and a . In fact, in the limit $m_a \rightarrow 0$, δ parametrizes the misidentification of a as the R -axion after electroweak symmetry breaking (given that for $r_H \neq 0$ the Higgs is R charged, $f_a^2 \rightarrow f_a^2 + r_H v^2 s_{2\beta}^2$).
- [28] H.-S. Goh and M. Ibe, *J. High Energy Phys.* **03** (2009) 049.
- [29] T. Ahmed, M. C. Kumar, P. Mathews, N. Rana, and V. Ravindran, *Eur. Phys. J. C* **76**, 355 (2016).
- [30] L. J. Hall and M. B. Wise, *Nucl. Phys.* **B187**, 397 (1981).
- [31] M. Freytsis, Z. Ligeti, and J. Thaler, *Phys. Rev. D* **81**, 034001 (2010).
- [32] P. Ball and R. Zwicky, *Phys. Rev. D* **71**, 014029 (2005).
- [33] F. Wilczek, *Phys. Rev. Lett.* **39**, 1304 (1977).
- [34] G. Aad *et al.* (ATLAS Collaboration), *Eur. Phys. J. C* **75**, 299 (2015); **75**, 408(E) (2015).
- [35] M. Aaboud *et al.* (ATLAS Collaboration), *Phys. Rev. D* **94**, 032005 (2016).
- [36] G. Aad *et al.* (ATLAS Collaboration), *Phys. Rev. D* **92**, 072001 (2015).
- [37] G. Aad *et al.* (ATLAS Collaboration), *Phys. Rev. Lett.* **113**, 171801 (2014).

- [38] CERN Report No. ATLAS-CONF-2016-059, 2016, <http://cds.cern.ch/record/2206154>.
- [39] V. Khachatryan *et al.* (CMS Collaboration), *Phys. Lett. B* **767**, 147 (2017).
- [40] V. Khachatryan *et al.* (CMS Collaboration), *Phys. Rev. Lett.* **117**, 031802 (2016).
- [41] A. M. Sirunyan *et al.* (CMS Collaboration), *Phys. Lett. B* **769**, 520 (2017).
- [42] CERN Report No. ATLAS-CONF-2016-069, 2016, <http://cds.cern.ch/record/2206212>.
- [43] G. Aad *et al.* (ATLAS Collaboration), *J. High Energy Phys.* **08** (2015) 148.
- [44] S. Chatrchyan *et al.* (CMS Collaboration), *Phys. Rev. Lett.* **111**, 211804 (2013); **112**, 119903(E) (2014).
- [45] CERN Report No. ATLAS-CONF-2016-085, 2016, <http://cds.cern.ch/record/2206278>.
- [46] CMS Collaboration, Report No. CMS-PAS-HIG-16-037, CERN, 2016.
- [47] G. Aad *et al.* (ATLAS and CMS Collaborations), *J. High Energy Phys.* **08** (2016) 045.
- [48] V. Khachatryan *et al.* (CMS Collaboration), arXiv: 1701.02032.
- [49] G. Aad *et al.* (ATLAS Collaboration), *Phys. Rev. D* **92**, 052002 (2015).
- [50] R. Aaij *et al.* (LHCb Collaboration), *Phys. Rev. Lett.* **115**, 161802 (2015).
- [51] R. Aaij *et al.* (LHCb Collaboration), *J. High Energy Phys.* **02** (2013) 105.
- [52] J. P. Lees *et al.* (BABAR Collaboration), *Phys. Rev. D* **88**, 071102 (2013).
- [53] J. P. Lees *et al.* (BABAR Collaboration), *Phys. Rev. D* **87**, 031102 (2013); **87**, 059903(E) (2013).
- [54] J. P. Lees *et al.* (BABAR Collaboration), *Phys. Rev. Lett.* **107**, 221803 (2011).
- [55] H. J. Hyun *et al.* (Belle Collaboration), *Phys. Rev. Lett.* **105**, 091801 (2010).
- [56] J. Alwall, M. Herquet, F. Maltoni, O. Mattelaer, and T. Stelzer, *J. High Energy Phys.* **06** (2011) 128.
- [57] J. Alwall, R. Frederix, S. Frixione, V. Hirschi, F. Maltoni, O. Mattelaer, H. S. Shao, T. Stelzer, P. Torrielli, and M. Zaro, *J. High Energy Phys.* **07** (2014) 079.
- [58] Decays into dibosons and $Z\gamma$ have a poorer reach for our choice of the anomalies.
- [59] P. Abreu *et al.* (DELPHI Collaboration), *Phys. Lett. B* **327**, 386 (1994).
- [60] M. Acciarri *et al.* (L3 Collaboration), *Phys. Lett. B* **345**, 609 (1995).
- [61] G. Rupak and E. H. Simmons, *Phys. Lett. B* **362**, 155 (1995).
- [62] O. Adriani *et al.* (L3 Collaboration), *Phys. Lett. B* **292**, 472 (1992).
- [63] M. Acciarri *et al.* (L3 Collaboration), *Phys. Lett. B* **346**, 190 (1995).
- [64] E. Anashkin *et al.* (DELPHI Collaboration), in *Proceedings of the International Europhysics Conference on High Energy Physics (EPS-HEP 1999), Tampere, Finland, 1999*, <http://cdsweb.cern.ch/search.py?sysno=000339520cer>.
- [65] O. Buchmueller, S. A. Malik, C. McCabe, and B. Penning, *Phys. Rev. Lett.* **115**, 181802 (2015).
- [66] S. Dawson *et al.*, in *Proceedings of the 2013 Community Summer Study on the Future of U.S. Particle Physics: Snowmass on the Mississippi (CSS2013), Minneapolis, MN, USA, 2013* (2013), <https://inspirehep.net/record/1262795/files/arXiv:1310.8361.pdf>.

Ripples in spacetime from broken supersymmetry

Nathaniel Craig,^a Noam Levi,^b Alberto Mariotti^c and Diego Redigolo^{d,e}

^a*Department of Physics, University of California,
Santa Barbara, CA 93106, U.S.A.*

^b*Raymond and Beverly Sackler School of Physics and Astronomy, Tel-Aviv University,
Tel-Aviv 69978, Israel*

^c*Theoretische Natuurkunde and IIHE/ELEM, Vrije Universiteit Brussel and
International Solvay Institutes,
Pleinlaan 2, B-1050 Brussels, Belgium*

^d*CERN, Theoretical Physics Department,
Geneva, Switzerland*

^e*INFN Sezione di Firenze,
Via G. Sansone 1, I-50019 Sesto Fiorentino, Italy*

*E-mail: d.redigolo@gmail.com, noam@mail.tau.ac.il,
amariotti.vub@gmail.com, ncraig@physics.ucsb.edu*

ABSTRACT: We initiate the study of gravitational wave (GW) signals from first-order phase transitions in supersymmetry-breaking hidden sectors. Such phase transitions often occur along a pseudo-flat direction universally related to supersymmetry (SUSY) breaking in hidden sectors that spontaneously break R -symmetry. The potential along this pseudo-flat direction imbues the phase transition with a number of novel properties, including a nucleation temperature well below the scale of heavy states (such that the temperature dependence is captured by the low-temperature expansion) and significant friction induced by the same heavy states as they pass through bubble walls. In low-energy SUSY-breaking hidden sectors, the frequency of the GW signal arising from such a phase transition is guaranteed to lie within the reach of future interferometers given existing cosmological constraints on the gravitino abundance. Once a mediation scheme is specified, the frequency of the GW peak correlates with the superpartner spectrum. Current bounds on supersymmetry are compatible with GW signals at future interferometers, while the observation of a GW signal from a SUSY-breaking hidden sector would imply superpartners within reach of future colliders.

KEYWORDS: Cosmology of Theories beyond the SM, Supersymmetry Breaking, Supersymmetric Effective Theories, Thermal Field Theory

ARXIV EPRINT: [2011.13949](https://arxiv.org/abs/2011.13949)

Contents

1	Introduction	2
2	Detectable GW signals in low energy SUSY-breaking	6
2.1	Low-energy SUSY-breaking	6
2.2	First order phase transitions and SGWB	10
2.3	LESB in the future: GW interferometers vs. colliders	15
3	Anatomy of the SUSY-breaking phase transition	16
3.1	The SUSY-breaking pseudomodulus	17
3.2	First order phase transitions in the low- T expansion	19
3.3	α, β_H and fine-tuning	22
3.4	A toy example: fine-tuning vs. single SUSY-breaking scale	23
4	Explicit models	24
4.1	Warm up: the O’Raifeartaigh model at finite temperature	25
4.2	O’Raifeartaigh model with explicit R -symmetry breaking	29
4.2.1	First order phase transition dynamics	30
4.2.2	Phenomenological challenges	32
4.3	O’Raifeartaigh model with gauge interactions	33
4.3.1	First order phase transition dynamics	37
4.3.2	Gravitational wave spectrum and phenomenology	38
5	Phenomenology	40
5.1	Gravitino cosmology vs future colliders	41
5.2	A complete model of gauge mediation	44
6	Conclusions	45
A	The effective potential	47
B	Bounce action computation schemes	48
B.1	Triangular barrier approximation of the bounce action	49
B.1.1	Optimized triangular bounce	51
B.1.2	Triangular bounce for the O’Raifeartaigh model with gauge interactions	52
B.2	Single field approximation of the multi-field bounce action	54
C	Sensitivity of GW interferometers	55
C.1	PLI curves	56
C.1.1	Experimental parameters	57

1 Introduction

If supersymmetry is a property of our universe, how will it be discovered? Conventionally, searches for evidence of supersymmetry (SUSY) have focused on the Standard Model, looking for supersymmetric partners of Standard Model particles in direct production at colliders, scattering in dark matter experiments, and virtual effects in precision measurements. Thus far, no evidence has emerged of supersymmetry as it relates to the Standard Model, raising the prospect that it may lie outside the reach of the existing experimental program. Although this would pose a challenge to supersymmetry as a fully natural explanation for the scale of electroweak symmetry breaking, the abundance of remaining motivation (e.g. gauge coupling unification, dark matter, and straightforward string-theoretic embedding) favors continuing the search to shorter and shorter distances. While the LHC and proposed future colliders are promising tools in this search, the immense technical challenges of exploring energies far above the TeV scale in terrestrial experiments suggests casting a broader net. It invites identifying both new ways of accessing shorter distances and new sectors in which supersymmetry may be manifest.

A compelling avenue to shorter distances is to make use of the incredible energies of the Big Bang, searching for the imprint of supersymmetric phenomena on the early universe. In some sense, this is already the path taken by dark matter searches looking for the population of stable superpartners produced in the early universe, but it is not the only cosmological avenue for discovering SUSY. For example, spontaneous breaking of supersymmetry during inflation raises the prospect of observing signals in the three-point function of primordial curvature perturbations [1, 2], although the size of the signal depends on the strength of couplings between SUSY multiplets and the inflaton.

As for new sectors, at least one is *guaranteed* to exist in a supersymmetric universe: the sector responsible for breaking supersymmetry. Although there are many dynamical mechanisms for breaking supersymmetry, they typically possess a number of generic or universal features which can provide new ways of searching for supersymmetry even when superpartners of the Standard Model are decoupled. These include the goldstino, a goldstone fermion of spontaneous supersymmetry breaking (which becomes the longitudinal mode of the gravitino, the supersymmetric partner of the graviton, once gravity is accounted for), as well as a novel abelian global symmetry called the R -symmetry. The R -symmetry is generically spontaneously broken by the same dynamics that breaks supersymmetry, giving rise to a goldstone boson (the R -axion) and its scalar partner, a pseudo-modulus whose flat potential is protected by supersymmetry. In theories with low-energy supersymmetry breaking (LESB), in which the effects of SUSY breaking are communicated to the Standard Model by forces stronger than gravitation, these states may be accessible on their own. For example, the goldstino couples directly to Standard Model particles and may be produced at colliders, although the current reach of the LHC makes these searches less promising than continuing to look for Standard Model superpartners.

In this paper, we explore a new avenue for discovering supersymmetry in the physics of the early universe: using the stochastic gravitational wave background (SGWB) produced by a first-order phase transition to directly probe the sector responsible for breaking super-

symmetry [3]. This makes use of the extraordinary opportunities afforded by the detection of gravitational waves (GW) by the LIGO-Virgo collaboration [4], which has opened a new era in the exploration of the early universe. Sensitivity of current and proposed GW interferometers to stochastic gravitational wave backgrounds broadly motivates identifying beyond-the-Standard Model (BSM) scenarios whose first-order phase transitions may generate such a signal and exploring the complementarity of GW interferometry with other probes of new physics such as present and future colliders.¹

Among the most compelling scenarios for SGWB are those in which a first order phase transition (FOPT) is associated with the breaking of a global or gauge symmetry in the early universe [7–13]. As we will show, the supersymmetry-breaking sector is a natural candidate for such a phase transition because it generically possesses at least one pseudo-flat complex scalar direction, the pseudomodulus. In our constructions, the phase of this complex scalar direction is associated to the R -symmetry, which is in turn tied to the SUSY-breaking dynamics by many known theorems about SUSY quantum field theories [14–16]. This complex scalar direction is lifted by quantum corrections and the resulting potential is likely to possess a metastable minimum at the origin (where R -symmetry is preserved), which will then decay to the true minimum through a FOPT in the early universe. At the true minimum the R -symmetry is broken, consistently with a realistic SUSY spectrum featuring Majorana masses for the fermionic partners of Standard Model gauge bosons.

In our framework, the SUSY-breaking scale \sqrt{F} correlates directly with the frequency range of the SGWB, such that theories of low-energy SUSY breaking feature a peak frequency accessible at LIGO-Virgo or proposed GW interferometers such as the Laser Interferometer Space Antenna (LISA), Einstein Telescope (ET), Cosmic Explorer (CE), DECI-hertz Interferometer Gravitational wave Observatory (DECIGO), and the Big Bang Observatory (BBO). In fact, a consistent cosmological history (in which the production of gravitinos in the early universe is consistent with the present dark matter abundance and small-scale structure constraints) guarantees that low-energy supersymmetry-breaking phase transitions produce a peak frequency in the range accessible to current and future interferometers [17–20].

Once a mechanism is specified to mediate supersymmetry breaking to the Standard Model, the scale \sqrt{F} is also correlated with the spectrum of Standard Model superpartners, allowing the possibility of cross-correlating GW and collider signals. As we will see, the non-observation of SUSY particles at the LHC leaves open the opportunity for seeing SGWB signatures from low-energy SUSY breaking, making this a leading avenue for the discovery of supersymmetry. In return, the observation of a SGWB signal from a low-energy supersymmetry breaking phase transition would imply the SUSY spectrum to be within the reach of future colliders such as FCC-hh, SPPC, or a high-energy muon collider, highlighting the strong complementarity between such SGWB signals and proposed colliders.

Along the way, we identify a qualitatively new class of natural potentials capable of generating large GW signals from a first-order phase transition, corresponding to the scalar

¹Note that the LIGO-Virgo collaboration already places direct constraints on SGWB [5, 6] beyond existing indirect limits.

potential along the pseudo-flat direction associated with SUSY breaking. The size of the vacuum energy gap between the metastable and the true vacuum is set by the SUSY-breaking scale \sqrt{F} , which is necessarily smaller than the SUSY masses of other heavy fields in the sector in order to avoid tachyonic directions. As a consequence, the thermal corrections to the potential along the pseudomodulus direction are well described by a low- T expansion. Another distinctive feature of the pseudomodulus potential is the flatness at large field values, which is ensured by SUSY cancellations independently of the nature of SUSY-breaking deformations around the origin. These features combine to give strong first-order phase transitions, with the strongest transitions arising most naturally in models with two distinct SUSY-breaking scales. As we will discuss, a large amount of tuning would be necessary to realize a similar situation in non-SUSY scenarios, which explains why this possibility has not been explored so far in the literature (see for instance [21] for a collection of potentials giving rise to FOPT for the SM Higgs).

The organization of our paper is intended to highlight the qualitative connections between low-energy supersymmetry breaking, first-order phase transitions, and stochastic gravitational wave signals before progressing into explicit examples, and does not presume deep familiarity with spontaneous supersymmetry breaking. We begin in section 2 by giving a broad overview of the phenomenology of low-energy SUSY breaking, the parametrics of gravitational wave signals from first-order phase transitions, and the relationship between the frequency of the SGWB signal and spectrum of SUSY particles. In section 3 we discuss the general features of the pseudomodulus potential and the properties of a first-order phase transition along this direction, highlighting their novelty compared to commonly-studied potentials for FOPT. We present a simple toy model that captures the main features of concrete SUSY potentials, showing how a promising GW signal from FOPT requires multiple SUSY-breaking scales.

We then proceed to develop a series of increasingly realistic SUSY-breaking hidden sectors featuring FOPT in section 4. In section 4.1, we derive the phase diagram of the simple O’Raifeartaigh model. In section 4.2 we present the simplest single scale model featuring a FOPT, which is a simple deformation of the O’Raifeartaigh model with explicit R -symmetry breaking. Here, the FOPT takes place between the SUSY-breaking vacuum at the origin (which enjoys an unbroken R -symmetry) and the R -symmetry breaking minimum far away from the origin, where SUSY is restored unless coupled to an additional source of SUSY-breaking. In section 4.3, we develop a fully realistic model by introducing gauge interactions to the O’Raifeartaigh model, such that SUSY is broken in both the metastable vacuum at the origin and true vacuum. The presence of both F -term and D -term SUSY-breaking naturally gives rise to strong GW signals.

In section 5 we further comment on the phenomenology of our setup and the complementarity between GW observatories and colliders, highlighting the sense in which the observation of a SGWB signal in our models would ensure further evidence for SUSY at future colliders. We summarize our qualitative conclusions and future directions in section 6. Technical details are reserved for a series of appendices, including a review of the one-loop thermal effective potential in appendix A, approaches to the calculation of the bounce action in appendix B and inputs to our projections for GW interferometers in appendix C.

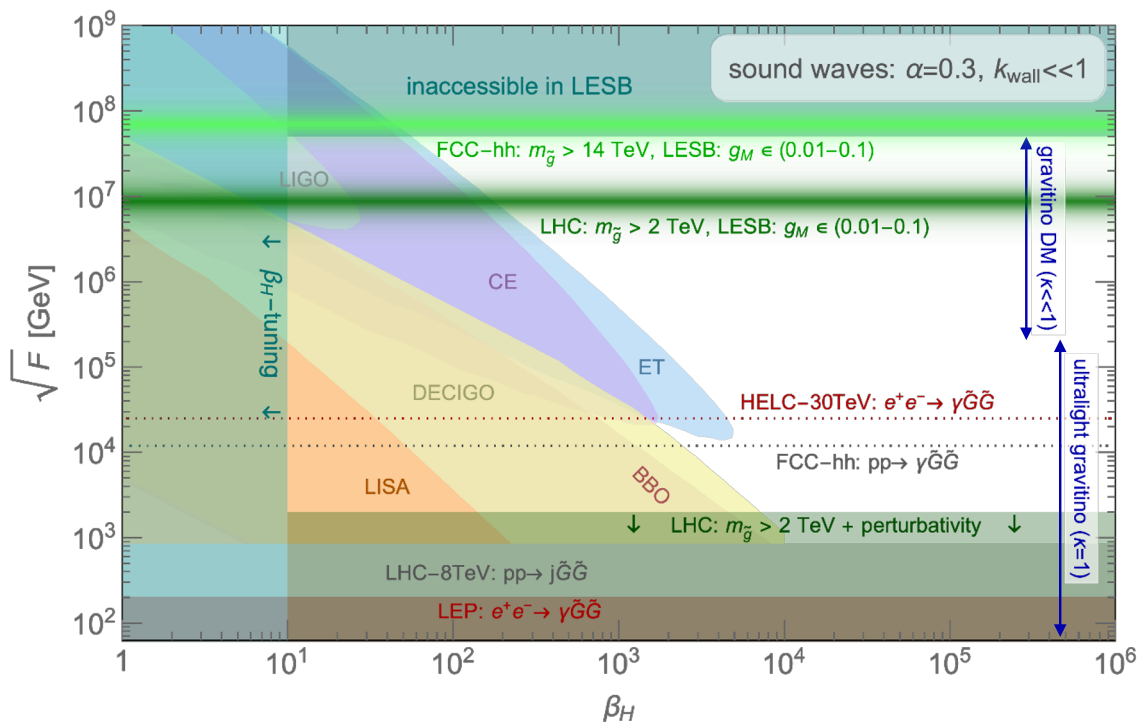


Figure 1. Parameter space of low energy SUSY-breaking models in the (\sqrt{F}, β_H) plane, with $\alpha = 0.3$ and $T_{r.h.} = \sqrt{F}$ (see section (2.2) for definitions). The GW reach is computed by requiring the strength of the SGBW signal at the peak frequency to intersect with the PLI curve of a given GW interferometer (see appendix C.1 for details). The *colored regions* show the reach for a signal generated from plasma waves which is generically the dominant one in our scenarios (see section 2.2). The *cyan region* with $\beta_H < 10$ implies a large fine-tuning in our setups (see discussion around eq. (2.18), the parametric discussion in section 3 and the explicit evaluation in the models of section 4). In the *red shaded region* gravitino pair production is excluded by a $\gamma + \text{MET}$ search at LEP with $\mathcal{L} = 0.24 \text{ fb}^{-1}$ [22], the gray region is excluded by ATLAS bounds $j + \text{MET}$ at $\sqrt{s} = 8 \text{ TeV}$ and $\mathcal{L} = 10.5 \text{ fb}^{-1}$ [23, 24]. The *dotted gray* and *dotted red* lines are the projection of the $\gamma + \text{MET}$ reach at FCC-hh with $\sqrt{s} = 100 \text{ TeV}$ and $\mathcal{L} = 30 \text{ ab}^{-1}$ and a future high energy lepton collider (HELIC) with $\sqrt{s} = 30 \text{ TeV}$ and $\mathcal{L} = 100 \text{ ab}^{-1}$. The *dark green shaded region* with *dark green arrows* indicates the bound on the SUSY-breaking scale derived from the LHC bound on gluinos $m_{\tilde{g}} > 2 \text{ TeV}$, requiring the messenger sector to be perturbative. The two *dark green* and *light green* bands show the impact of the present LHC bounds [25–28] and the future FCC-hh reach on gluinos [29] for perturbative messenger sectors with $g_M \in (0.01, 0.1)$ (see eq. (2.10) for a definition of g_M). The region between these two lines will be naturally populated by the model discussed in section 4.3 and section 5.2. The *dark blue arrows* on the right hand side shows the *ultralight gravitino window* where $m_{3/2} \leq 16 \text{ eV}$ and the gravitino does not poses any cosmological challenge with $\kappa = 1$ (see eq. (2.2) for a definition) and the *gravitino dark matter window* where $\kappa \ll 1$ and the full gravitino mass is heavier than the gravitino mass contribution set by \sqrt{F} . The *dark cyan region* marked as *inaccessible in LESB* is always excluded by a combination of gravitino overabundance [30] and BBN constraints [31] (see section 5 for details).

2 Detectable GW signals in low energy SUSY-breaking

In this section we illustrate the correlation between possible signals at present and future GW interferometers and the phenomenology of low energy SUSY-breaking (LESB). The underlying assumption is that the SGWB is produced through a first-order phase transition controlled by the SUSY-breaking hidden sector. As we will show, this connection is relatively insensitive to the details of the dynamics in the hidden sector. In section 2.1 we summarize the structure and the parametric predictions of LESB theories, while in section 2.2 we go through the field theory inputs that are necessary to compute the spectrum of GWs from a FOPT. In section 2.3 we combine the results of the preceding sections to delineate the parameter space of possible gravitational wave signals from low-energy supersymmetry breaking, illustrated in figure 1.

2.1 Low-energy SUSY-breaking

Here we briefly review the structure of LESB and its broad parametric predictions, remaining agnostic as to the particular model realization. This general discussion is buttressed by section 5, where we will present the predictions of a simple, explicit model which gives rise to GW signals. For the purposes of this paper, we adopt a phenomenological definition of low-energy SUSY breaking: LESB models are those in which *the gravitino is the lightest supersymmetric particle (LSP)*. This requirement has deep implications for collider searches, precision observables, and cosmology, which we summarize in turn.

The first ingredient in low energy SUSY-breaking scenarios is a hidden sector at a high scale m_* , which breaks supersymmetry (and R -symmetry) spontaneously. At energies much below m_* , the spontaneous breaking of both supersymmetry and the R -symmetry can be encoded in a model-independent manner through the F - and scalar components of a single chiral superfield

$$\langle X \rangle = \frac{f_a}{\sqrt{2}} e^{2ia/f_a} + \sqrt{2}\theta\tilde{G} + \theta^2 F, \quad (2.1)$$

where f_a is the order parameter for the R -symmetry breaking while \sqrt{F} is the SUSY breaking scale, corresponding to an R -charge $R_X = 2$ for the superfield X . The parameter θ is a constant, complex anti-commuting two-component spinor enabling component fields of different spin to be united into a single superfield. The Majorana fermion in the multiplet is the Goldstino \tilde{G} , the goldstone fermion associated with spontaneous SUSY-breaking, while the compact scalar field a is the R -axion, the goldstone boson associated with spontaneous R -symmetry breaking.

Switching on gravity, the Goldstino becomes the longitudinal component of the gravitino via the super-Higgs mechanism [32] while the R -axion is lifted by an unavoidable explicit symmetry-breaking contribution arising from the fine-tuning of the cosmological

constant [33, 34]. The gravitino and R -axion masses can be written as

$$m_{3/2} = \frac{F_0}{\sqrt{3}M_{\text{Pl}}} \simeq 24 \text{ keV} \left(\frac{1}{\kappa}\right) \left(\frac{\sqrt{F}}{10^7 \text{ GeV}}\right)^2, \quad (2.2)$$

$$m_a^{\text{grav.}} = m_{3/2} \left[\frac{6^{3/2}M_{\text{Pl}}}{f_a}\right]^{1/2} \simeq 5.2 \text{ GeV} \left(\frac{m_{3/2}}{24 \text{ keV}}\right) \left(\frac{10^7 \text{ GeV}}{\sqrt{F}}\right) \left(\frac{\sqrt{\epsilon_R}}{1}\right), \quad (2.3)$$

where $M_{\text{Pl}} = 2.4 \cdot 10^{18} \text{ GeV}$ is the reduced Planck scale and we have defined

$$\kappa \stackrel{\text{def}}{=} F/F_0, \quad \epsilon_R \stackrel{\text{def}}{=} 2F/f_a^2. \quad (2.4)$$

This reflects the fact that the gravitino mass is set by the sum of supersymmetry-breaking contributions from all sectors, corresponding to a total SUSY-breaking scale $\sqrt{F_0}$ that may be larger than the scale \sqrt{F} in the LESB sector under consideration (i.e. $\kappa \lesssim 1$). Similarly, the R -symmetry breaking scale f_a may exceed the scale of supersymmetry breaking \sqrt{F} (i.e. $\epsilon_R \lesssim 1$), as is often the case in calculable hidden sectors. In writing the gravity contribution to the R -axion mass in eq. (2.3) we saturated the upper bound on the superpotential vacuum expectation value (VEV) [35]. In the presence of a possible explicit R -symmetry breaking term in the hidden sector $\epsilon_{\mathcal{R}}$, the R -axion mass will receive an extra contribution

$$m_a^{\mathcal{R}} = \sqrt{\epsilon_{\mathcal{R}} F} \simeq 10^3 \text{ TeV} \left(\frac{\epsilon_{\mathcal{R}}}{0.01}\right)^{1/2} \left(\frac{\sqrt{F}}{10^7 \text{ GeV}}\right), \quad (2.5)$$

making the R -axion heavier than the superpartners of Standard Model fields and hence phenomenologically irrelevant.

Most of the universal phenomenological predictions of low-energy SUSY breaking follow from the gravitino's role as the LSP [36]. First, the gravitino is the endpoint of every superpartner decay. In particular, the lifetime of the next-to-lightest supersymmetric particle (NLSP) is determined by its decay into the gravitino plus a Standard Model state,

$$\tau_{\text{NLSP}} = \frac{48\pi}{c_{\text{NLSP}}} \frac{M_{\text{Pl}}^2 m_{3/2}^2}{m_{\text{NLSP}}^5} \simeq 10^2 \text{ sec} \left(\frac{1}{c_{\text{NLSP}}}\right) \left(\frac{m_{3/2}}{24 \text{ keV}}\right)^2 \left(\frac{500 \text{ GeV}}{m_{\text{NLSP}}}\right)^5, \quad (2.6)$$

where c_{NLSP} is an $\mathcal{O}(1)$ coefficient which depends on the particulars of the NLSP. Second, the gravitino may be directly produced in pairs with a rate controlled by dimension-eight contact operators suppressed by $1/F^2$ in the $m_{\text{soft}} \gg m_{3/2}$ limit [22, 37]. These operators lead to a total cross section at lepton colliders for pair production in association with a photon of the form

$$\sigma(e^+e^- \rightarrow \tilde{G}\tilde{G}\gamma) \simeq \frac{\alpha_{\text{em}} s^3}{160\pi^2 F^4} \left[\frac{247}{60} + \log\left(\frac{4E_{\text{min}}^2}{s}\right)\right] \log\left(\frac{1 - \cos\theta_{\text{min}}}{1 + \cos\theta_{\text{min}}}\right), \quad (2.7)$$

where \sqrt{s} is the beam energy, E_{min} is the minimal photon energy, and θ_{min} is the minimal photon angle with respect to the beam direction. Here we have expanded in $E_{\text{min}} \ll \sqrt{s}$ (see ref. [22] for the full formula). A similar formula can be derived for $\sigma(pp \rightarrow \tilde{G}\tilde{G}j)$ as shown in ref. [23]. Using these formulas and rescaling the Standard Model backgrounds to higher

energies and luminosities, we may determine the sensitivity of missing energy searches at future colliders gravitino pair production; see section 5 for details. These searches lead to projected direct constraints on the SUSY-breaking scale \sqrt{F} as shown in figure 1.

Finally, the stability of the gravitino LSP typically results in a cosmological hazard. This is the well known “gravitino problem” of LESB theories [38–40]. For sufficiently high reheating temperature (i.e. $T_{\text{r.h.}} > 45m_{3/2}^2 M_{\text{Pl}}/M_3^2$, where M_3 is the soft mass of the gluino), the gravitino is in thermal equilibrium with the Standard Model bath. At freeze-out, the gravitino is still relativistic and its abundance is bounded from above by small-scale cosmological observables [41, 42]. The latter imply $m_{3/2} \lesssim 16$ eV, which corresponds to $\sqrt{F} < 260$ TeV. Alternately, if the reheating temperature is low enough, the gravitino is never in equilibrium with the Standard Model bath but is typically overproduced by a combination of UV scattering contributions [43–47], freeze-in from the decays of superpartners [48], and decay of the NLSP relic abundance after freeze-out [49, 50].

In order for SUSY-breaking sectors to generate sizable GW signals, the hidden sector needs to be reheated after inflation. Fixing the reheating temperature $T_{\text{r.h.}} = \sqrt{F}$ and requiring the gravitino to not overclose the universe implies

$$C_{\text{UV}} \frac{M_3^2 T_{\text{r.h.}}}{m_{3/2}} + C_{\text{F.O.}} \frac{m_{3/2} m_{\text{NLSP}}}{\alpha_{\text{eff}}^2} \lesssim 0.27 T_{\text{eq}} M_{\text{Pl}}, \quad (2.8)$$

where $C_{\text{UV}} = 45\sqrt{5}f_3/(8\pi^{13/2}g_*^{3/2}) \simeq 4 \cdot 10^{-5}$, $g_* \simeq 230$, and $f_3 \simeq 18$ encodes the thermal corrections as computed in ref. [46]; $C_{\text{F.O.}} = x_{\text{F.O.}}/(4\pi\sqrt{g_*}) = 0.12$ for $x_{\text{F.O.}} = 23$, and $\alpha_{\text{eff}} \simeq 0.01$ is chosen to match the correct dark matter relic abundance in the pure Higgsino case [51]. Eq. (2.8) reflects a similar expression in ref. [30], although here we have dropped the freeze-in contribution from superpartner decays because it is always subdominant compared to UV scattering contributions.

For $\kappa = 1$, the only region where the gravitino is not overabundant for $T_{\text{r.h.}} = \sqrt{F}$ corresponds to $\sqrt{F} < 260$ TeV, while for $\kappa \ll 1$ one can decouple the gravitino mass and push the SUSY-breaking scale to be as high as $\sqrt{F} \simeq 5 \cdot 10^7$ GeV. In this case, the upper bound is obtained by combining the overclosure bound, LHC bounds on Standard Model superpartner masses, and the BBN bounds on NLSP decays into the gravitino through the universal two-body decay in eq. (2.6) as derived in ref. [31]. This bound could slightly vary depending on the NLSP type and the detailed features of the spectrum, but this does not alter the primary message: requiring a reheating temperature $T_{\text{r.h.}} = \sqrt{F}$ to obtain sufficiently strong gravitational wave signals implies a quite stringent upper bound on \sqrt{F} as long as the gravitino is required to be the LSP.

Thus far, our discussion has not correlated the scale \sqrt{F} of supersymmetry breaking with the mass spectrum of Standard Model superpartners. Supersymmetry breaking in the hidden sector is transmitted to the visible sector (which we will take to be the minimal supersymmetric Standard Model, or MSSM, in this paper) through a mediation mechanism. The simplest possibility is to assume that a certain number of messengers N_{mess} in a given representation of the SM gauge group are coupled to the SUSY-breaking field X via the superpotential $W_{\text{mess}} = y_{\text{mess}} X \Phi \tilde{\Phi}$. Given this coupling, the R -symmetry breaking scale f_a controls the masses of the fermionic messengers, while the SUSY-breaking scale \sqrt{F} gives

an off-diagonal mass to the scalar messengers. The non-supersymmetric splitting between scalar and fermionic messengers is then transmitted to MSSM superfields via Standard Model gauge interactions. The resulting gaugino and squark masses are those of standard gauge mediation [36],

$$M_I = \frac{\alpha_I N_{\text{mess}} s_M}{4\pi} \left(\frac{\sqrt{2}F}{f_a} \right), \quad m_{\tilde{f}}^2 = \sum_I C_{\tilde{f}}(I) \left(\frac{\alpha_I N_{\text{mess}}}{4\pi} \right)^2 \left(\frac{\sqrt{2}F}{f_a} \right)^2, \quad (2.9)$$

where $C_{\tilde{f}}(I)$ is the quadratic Casimir of the representation of the MSSM sfermion \tilde{f} under the I th Standard Model gauge group and for simplicity we have considered messengers in the $5 + \bar{5}$ representation of $SU(5)$. The additional coefficient $s_M \lesssim 1$ appearing in the gaugino masses accounts for the phenomenon of “gaugino screening” [16, 52, 53]. In the simple scenarios discussed here, the ratio between the gluino and squark soft masses $M_3/m_{\tilde{q}} \simeq \sqrt{N_{\text{mess}}} s_M \lesssim 1$, so that the most relevant collider bounds at current and future colliders can be framed purely in terms of the gluino mass, assuming the squarks to be decoupled and the lightest gaugino to be the next-to-lightest SUSY particle (NLSP).

Writing the R -symmetry breaking VEV as in eq. (2.4), the final gluino mass can be simply written in terms of underlying parameters as

$$m_{\tilde{g}} \simeq 7 \text{ TeV} \left(\frac{g_M}{0.1} \right) \frac{\sqrt{F}}{10^7 \text{ GeV}}, \quad g_M \stackrel{\text{def}}{=} N_{\text{mess}} \sqrt{\epsilon_R} s_M \left[1 + \frac{\alpha_3}{4\pi} \left(9 + 6 \log \frac{Q}{M_3} \right) \right], \quad (2.10)$$

where we have collected various coefficients into a model-dependent prefactor g_M which encodes i) the suppression of the gaugino masses due to $f_a \gg \sqrt{F}$ (i.e. $\sqrt{\epsilon_R} \ll 1$), ii) the enhancement for $N_{\text{mess}} \gg 1$, iii) the gaugino screening controlled by $s_M \lesssim 1$, and iv) the relation of the gluino soft mass to its pole mass, correctly accounting for the one loop running of the gluino soft mass at low energies in the limit of heavy squarks [54, 55].

Broadly speaking, eq. (2.10) establishes an interesting relation between the SUSY-breaking scale and the present and future collider bounds on the gluino. Given the current LHC bound on gluino masses, which ranges between $m_{\tilde{g}} \gtrsim 2 - 2.5 \text{ TeV}$ [25–28], eq. (2.10) indicates the lowest values of the SUSY-breaking scale \sqrt{F} consistent with data.

Depending on the model, g_M can span many orders of magnitude, but there are three parametric regimes of interest:

- $1 \ll g_M \lesssim 160$, which is realized in strongly-coupled messenger sectors that are at the boundary of perturbativity. The upper bound on g_M is indeed obtained by requiring the SM gauge couplings and y_{mess} to be perturbative at the scale of the hidden sector.
- $g_M \simeq 1$, which is realized in weakly-coupled messenger sectors if $M_{\text{mess}} \simeq \sqrt{F}$ and the gaugino masses are not screened. The latter requirement requires non-trivial dynamics in the hidden sector, as shown in ref. [16].
- $g_M \ll 1$, which is typical of models where the soft masses are suppressed compared to the SUSY-breaking scale because $f_a \gg \sqrt{F}$ and the gaugino masses may be further screened compared to the squark masses. As we will show in section 5, this is the typical situation in simple, explicit setups featuring SGWB signals.

One of the most appealing features of LESB mediated via gauge interactions is the flavor-preserving nature of the MSSM superpartner spectrum. This is because the flavor-blind contributions to superpartner masses transmitted by gauge interactions vastly exceeds the omnipresent, flavor-violating “gravity-mediated” contributions. However, these gravity-mediated contributions reflect *all* contributions to SUSY breaking, while the gauge-mediated contributions reflect only the SUSY-breaking in the sector of interest. Thus when the gravitino mass is enhanced by $\kappa \ll 1$, the contribution from gravity mediation increases relative to the contribution from gauge mediation, and may eventually run afoul of bounds on flavor violation. In particular, this implies that κ is bounded from below by bounds from flavor-changing neutral currents (FCNCs). For instance, considering the slepton contributions to $\mu \rightarrow e\gamma$ [56, 57] and the squark contributions to Δm_K [58, 59] leads to the bounds

$$\kappa|_{\mu \rightarrow e\gamma} \gtrsim 10^{-9} \cdot \left(\frac{1}{\epsilon_R}\right), \quad \kappa|_{\Delta m_K} \gtrsim 10^{-9} \cdot \left(\frac{\sqrt{F}}{10^7 \text{ GeV}}\right) \cdot \left(\frac{1}{\epsilon_R}\right)^{3/4}, \quad (2.11)$$

where κ and ϵ_R are defined in eq. (2.4) and we set $\text{BR}(\mu \rightarrow e\gamma) < 4.2 \cdot 10^{-13}$ and $\Delta m_K = (3.479 \pm 0.001) \cdot 10^{-12}$ MeV, asking for the squark contribution to be less than present experimental uncertainty. These constraints give a robust upper bound on the gravitino mass in our framework. Finally, even in the absence of flavor violating effects, the electric dipole moments arising from the relative phase between gaugino and higgsino masses can be probed in precision experiments such as ACME [60, 61]. The current limits are already challenging a CP-violating phase of order 10^{-2} with gauginos below the TeV scale and the future experimental program will sensibly improve this reach making it one of the most interesting indirect probes of LESB [62, 63].

2.2 First order phase transitions and SGWB

Phase transitions in field theory are triggered by the nucleation of vacuum bubbles and their subsequent percolation in the space-time volume. The vacuum bubbles can be found in Euclidean signature as the stationary minimum-energy bounce solutions interpolating between the false and true vacuum [64, 65]. In all cases we consider here, the thermal fluctuations will dominate so that the total decay rate per unit volume can be approximated as

$$\Gamma(T) \simeq T^4 \left(\frac{S_3}{2\pi T}\right)^{\frac{3}{2}} \exp(-S_3/T), \quad (2.12)$$

where S_3 is the 3 dimensional Euclidean action for the $O(3)$ -symmetric bounce [66, 67]. The decay rate encodes the probability of true vacuum bubbles to be nucleated in a spacetime region where the false vacuum dominates.

The time evolution of the phase transition can be described in terms of different temperatures. First of all, a necessary condition for nucleation is that the universe reaches temperatures below the critical temperature T_c , where the false and true vacuum are degenerate. At the nucleation temperature $T_n < T_c$, one bubble will nucleate per Hubble

volume, corresponding to²

$$\frac{\Gamma(T_n)}{H(T_n)^4} = 1 \quad \Rightarrow \quad \frac{S_3(T_n)}{T_n} \simeq -9.2 \log \frac{g_*}{230} + 4 \log \frac{M_{\text{Pl}}}{T_n} + \frac{3}{2} \log \frac{S_3(T_n)}{T_n}, \quad (2.13)$$

where we assumed that the phase transition happens during radiation domination so that $H^2(T) = \frac{\pi^2 g_* T^4}{90 M_{\text{Pl}}^2}$ and normalized g_* to the number of the degrees of freedom in the MSSM. In all the cases we will consider, the last term in eq. (2.13) can be neglected together with the constant term, so that solving

$$\frac{S_3(T_n)}{T_n} \simeq \mathcal{C}(T_n), \quad \mathcal{C}(T_n) \stackrel{\text{def}}{=} 104 \log \left(\frac{10^7 \text{ GeV}}{T_n} \right) \quad (2.14)$$

is always a good approximation. Since $\mathcal{C}(T)$ is a slowly-varying function of T , we can further simplify this equation assuming $\mathcal{C}(T_n) \simeq \mathcal{C}(T_c)$; this number is always going to be $\mathcal{O}(10^2)$ in the temperature range of interest.

After one bubble per volume has been nucleated at T_n , the bubbles expand to fill the space-time volume. The phase transition is considered to be completed at the percolation temperature T_p , when a small fraction of the total volume remains in the false vacuum. For fast phase transitions like the ones discussed here, one can show that $T_p \simeq T_n$ so that we can neglect this difference and take T_n as the temperature at which the phase transition completes. This sets the relevant dimensionful scale controlling the frequency range of the SGWB spectrum.

The shape and amplitude of the SGWB spectrum strongly depends on the amount of energy released into GWs during the FOPT, the duration of the phase transition, and the behavior of the bubbles in the cosmic fluid. The two first ingredients can be easily quantified in terms of field theory data via the quantities

$$\alpha(T_n) = \frac{30}{\pi^2 g_* T_n^4} \left(\Delta V(T_n) - T_n \left. \frac{d\Delta V(T)}{dT} \right|_{T=T_n} \right), \quad (2.15)$$

$$\beta_H(T_n) \stackrel{\text{def}}{=} \frac{\beta(T_n)}{H(T_n)} = T_n \frac{d}{dT} \left(\frac{S_3}{T} \right) \Big|_{T=T_n}, \quad (2.16)$$

where $\Delta V(T_n)$ is the potential energy difference between the true and the false vacuum at T_n . The amount of energy released into GWs is quantified by α , the latent heat relative to the radiation energy density $\rho_R = \frac{\pi^2 g_* T^4}{30}$ [68]. The duration of the phase transition is quantified by β_H , the inverse of the typical timescale of the transition normalized with respect to Hubble; it is defined under the assumption that the nucleation rate rises exponentially [66, 67] as $S(t) = e^{\beta_H H(t)(t-t_n)}$. Using the approximate nucleation condition in eq. (2.14) we can write

$$\beta_H(T_n) \simeq S'(T_n) - \mathcal{C}, \quad (2.17)$$

where $S'(T_n) \gtrsim \mathcal{C}$ in order for the nucleation rate to rise as a function of time, and $\beta_H \gtrsim \mathcal{C} \sim 100$ unless there is some measure of fine-tuning between the first and the second

²The nucleation temperature is formally defined by the integral $1 = \int_{T_n}^{T_c} \frac{dT}{T} \frac{\Gamma(T)}{H(T)^4}$, which is well approximated by eq. (2.13) since $\Gamma(T)$ depends exponentially on the temperature.

terms of the above expression. To evaluate the fine-tuning associated with β_H in explicit models, we define

$$\Delta_{\beta_H} \stackrel{\text{def}}{=} \text{Max}_{\{p_i\}} \Delta_{\beta_H}^{p_i} = \text{Max}_{\{p_i\}} \left| \frac{d \log \beta_H}{d \log p_i} \right|, \quad (2.18)$$

where $\Delta_{\beta_H}^{p_i}$ are the individual tunings with respect to the underlying parameters of the theory p_i . As we will discuss in section 3, the parametric dependence of the fine-tuning can be derived for our general class of models and then computed explicitly in the models of section 4. As a result, obtaining $\beta_H < 10$ would imply a large amount of fine tuning (in the sense of being a non-generic prediction of a given model). This is illustrated in figure 1, where it provides a meaningful bound on the parameter space of GW signals in LESB. The dominant production mechanism of gravity waves during the first-order phase transition depends on the dynamics of the bubbles in the cosmic fluid. If the mean free path of the particles is much longer than the width of the bubble wall, the velocity of the wall v_w can be determined by equilibrating the pressure on the bubble wall induced by the difference in potential energy ΔV with the friction forces exerted by the surrounding plasma [69–71]. The latter are induced by states whose mass changes in passing from the false to the true vacuum. For $v_w \rightarrow 1$, the total pressure can be derived in a quasi-classical approximation [71–73] and reads

$$p = \Delta V - \Delta P_{\text{LO}} - \Delta P_{\text{NLO}}, \quad \Delta P_{\text{LO}} = \frac{\Delta m^2 T^2}{24}, \quad \Delta P_{\text{NLO}} \simeq \frac{1}{16\pi^2} \gamma g^2 \Delta m_V T^3, \quad (2.19)$$

where the Lorentz gamma factor is $\gamma = 1/\sqrt{1 - v_w^2}$ and the leading-order plasma friction P_{LO} depends on the change in the masses-squared Δm^2 of all the states in the thermal bath [72]. Since $\Delta m^2 = m_{\text{true}}^2 - m_{\text{false}}^2$, the approximate expression in eq. (2.19) is only valid when both $\gamma T \gtrsim m_{\text{true}}$ and $T \gtrsim m_{\text{false}}$. The first condition ensures that particles in the false vacuum have enough energy to pass through the wall, while the second forestalls Boltzmann suppression of the pressure [71]. The next-to-leading order radiation pressure P_{NLO} is instead induced by the change in mass of the vector bosons and it is γ -enhanced for $v_w \rightarrow 1$, as first derived in [73].

The pressure in eq. (2.19) determines both how much the bubble wall accelerates as a function of the bubble radius [74, 75], and the fraction of the FOPT energy which is in the bubble wall at the time of collision T_* (traditionally called k_{coll}). Since we will be dealing with fast phase transitions, we take $T_* \simeq T_p \simeq T_n$.

In the absence of friction, the acceleration of the bubble wall grows linearly with the bubble radius until the gamma factor reaches a terminal value

$$\gamma_* \simeq \frac{2 R_*}{3 R_0} \simeq 2.6 \cdot 10^8 \sqrt{\frac{230}{g_*(T_n)}} \left(\frac{100}{\beta_H} \right) \left(\frac{10^7 \text{ GeV}}{T_n} \right) \left(\frac{\Delta V(T_n)}{T_n^4} \right)^{1/3}, \quad (2.20)$$

where we took the initial radius to be $R_0 \simeq R_c = \left(\frac{3}{2\pi} \frac{S_3(T_n)}{\Delta V(T_n)} \right)^{1/3}$ estimated in the thin wall approximation [64], estimated R_* as in ref. [76], and assumed radiation domination. The last term is $\mathcal{O}(1)$ in phase transitions which do not have a supercooling phase since $\Delta V(T_n)/T_n^4 < 75.6(g_*/230)$.

In the FOPTs discussed here, the bubble growth is generically stopped by plasma effects from heavy states. This is due to a novel effect in which the relevant energy scale for particles interacting with the wall reaches values $\sim \gamma T_n$ much larger than the intrinsic scales associated with the bubble. This is particularly relevant for SUSY-breaking hidden sectors, where there is a large separation of scales that can be spanned by these ultra-relativistic effects. In particular, the bubbles expand and accelerate linearly with the radius until the boost factor is large enough to allow heavy states of mass $m_{\text{true}} \gg T_n$ to cross the bubble wall. The significant mass change of these states induces a new source of LO friction,

$$\Delta P_{\text{LO}}^{\text{heavy}} \simeq \frac{1}{24} (m_{\text{true}}^2 - m_{\text{false}}^2)^2 T_n^2 e^{-m_{\text{false}}/T_n}. \quad (2.21)$$

If $\Delta V - \Delta P_{\text{NLO}}^{\text{heavy}} \leq 0$, the gamma factor of the bubble wall and the bubble radius at equilibrium are approximately

$$\gamma_{\text{eq}}^{\text{heavy}} \simeq \frac{m_{\text{true}}}{T_n}, \quad R_{\text{eq}}^{\text{heavy}} \simeq \frac{3}{2} \gamma_{\text{eq}}^{\text{heavy}} R_c. \quad (2.22)$$

This effect is very similar to the pressure term from mixing discussed in ref. [77], but here we typically pay the Boltzmann suppression of m_{false} .

The resulting fraction of the energy in the bubble wall at the time of collisions is generically very suppressed,

$$k_{\text{coll}} \simeq \frac{R_{\text{eq}}}{R_*} \left(1 - \frac{\Delta P_{\text{LO}}}{\Delta V}\right) \simeq 4 \cdot 10^{-9} \gamma_{\text{eq}}^{\text{heavy}} \left(\frac{2.6 \times 10^8}{\gamma_*}\right) \left(1 - \frac{\Delta P_{\text{LO}}}{\Delta V}\right). \quad (2.23)$$

As such, most of the energy released in the FOPT goes into the plasma, giving rise to sound waves propagating through the cosmic fluid. These sound waves source gravitational waves from the motion of the plasma with an efficiency determined by

$$k_{\text{sw}} \simeq \frac{\alpha}{0.73 + 0.083\sqrt{\alpha} + \alpha}, \quad (2.24)$$

where we have expanded the general formula of refs. [78, 79] for $k_{\text{coll}} \ll 1$. The resulting GW spectral density is

$$\Omega_{\text{sw}}^* = 3.8 \left(\frac{1}{\beta_H^2}\right) \left(\frac{\kappa_{\text{sw}} \alpha}{1 + \alpha}\right)^{3/2} \left(\frac{f}{f_{\text{sw}}^*}\right)^3 \left[1 + \frac{3}{4} \left(\frac{f}{f_{\text{sw}}^*}\right)^2\right]^{-7/2}, \quad f_{\text{sw}}^* = 1.2 \beta_H^* H_*, \quad (2.25)$$

where $H_*^2 = \frac{\pi^2 g_*(T_*)}{90} \frac{T_*^4}{M_{\text{Pl}}^2} (1 + \alpha)$ to account for the reheating of the plasma and β_H^* is normalized accordingly following eq. (2.16). The sound wave spectrum is a broken power law which drops like $\Omega_{\text{sw}}^* \sim f^3$ for $f \ll f_{\text{sw}}^*$, as expected from causality in a radiation dominated universe, and as $\Omega_{\text{sw}}^* \sim f^{-4}$ for $f \gg f_{\text{sw}}^*$. The high frequency behavior of the spectrum is likely to be affected by the turbulence contribution, whose size is still subject to large theoretical uncertainties [11, 80]. Here, we include for simplicity only the sound waves contribution to the GW spectrum in eq. (2.25), which will mainly determine the

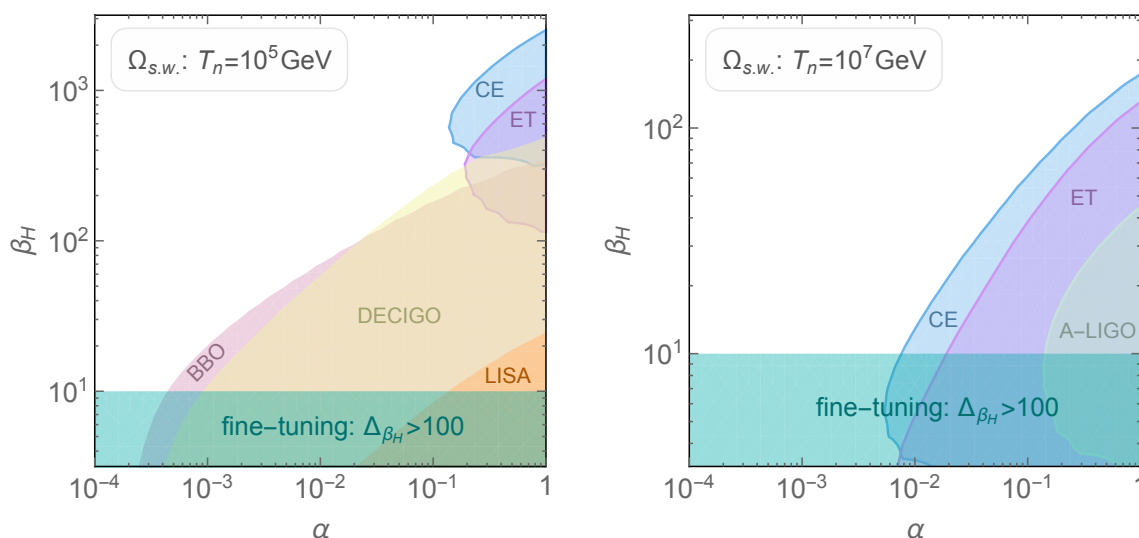


Figure 2. The reach of future GW interferometers in the (α, β_H) plane for two different scales of FOPTs, assuming the signal is dominated by sound waves given by eq. 2.25. The shaded regions are obtained by requiring the signal at the peak in eq. (2.28) to be inside the PLI curve of a given experiment. *Left:* $T_n = 10^5$ GeV corresponds to LESB scenarios with an ultralight gravitino LSP and $\kappa = 1$. *Right:* $T_n = 10^7$ GeV corresponds to LESB scenarios with gravitino DM and $\kappa \ll 1$. We will exhibit calculable scenarios of this type in section 4.

detectability of a given GW signal. After redshift is taken into account, assuming that the entropy per comoving volume remains constant [68], the GW spectrum today reads

$$\Omega_{\text{sw}}^0 h^2 = \left(\frac{a_*}{a_0}\right)^4 \left(\frac{H_*}{H_0}\right)^2 \Omega_{\text{sw}}^* = 2.8 \cdot 10^{-5} \left(\frac{230}{g_*}\right)^{1/3} \Omega_{\text{sw}}^*, \quad (2.26)$$

where the peak frequency and the power at the peak frequency scale as

$$f_{\text{sw}}^0 = f_{\text{sw}}^* \left(\frac{a_*}{a_0}\right) = 1.1 \times 10^2 \text{ Hz} \left(\frac{g_*}{230}\right)^{1/6} \left(\frac{\beta_H}{50}\right) \left(\frac{T_n}{10^7 \text{ GeV}}\right) \left(\frac{1.3}{1+\alpha}\right)^{1/4}, \quad (2.27)$$

$$\Omega_{\text{GW}}^{\text{sw},0} h^2 \simeq 10^{-10} \left(\frac{230}{g_*}\right)^{1/3} \left(\frac{50}{\beta_H}\right)^2 \left(\frac{\kappa_{\text{sw}} \alpha}{0.08}\right)^{3/2} \left(\frac{1.3}{1+\alpha}\right)^{3/2}. \quad (2.28)$$

Here we have taken $T_* \simeq T_n$ and normalized the scalings for $\alpha = 0.3$, $\beta_H = 100$ and $T_n = 10^7$ GeV, which will be the typical values for FOPTs related to fully calculable SUSY-breaking hidden sectors explored in the following sections.

Having derived the expected GW spectrum, we can determine the region in the (α, β_H) plane where we expect the SBGW to be detectable at future interferometers. Given the fraction of energy density in GWs today in eq. (2.26), the sensitivity of a given interferometer is controlled by the time integrated signal-to-noise ratio

$$\rho^2 = t_{\text{obs}} \int_{f_{\text{min}}}^{f_{\text{max}}} \left[\frac{\Omega_{\text{GW}}(f, \alpha, \beta, v_w)}{\Omega_{\text{noise}}(f)} \right]^2, \quad (2.29)$$

where $\Omega_{\text{noise}}(f)$ is the effective noise of the interferometer within a given frequency band ($f_{\text{min}}, f_{\text{max}}$) and t_{obs} is the observation time. A detectable stochastic GW background is defined to have $\rho > 10$. The Power Law Integrated (PLI) curves are generated by considering a power law function of the frequency f for the GW signal shape in eq. (2.29). The PLI curves for each GW interferometer considered here are given in appendix C for completeness.

In figure 2 we show the regions in the (α, β_H) plane where the power at the peak frequency in eq. (2.28) lies within the reach of future interferometers for two different nucleation temperatures. Low nucleation temperatures such as $T_n = 10^5$ GeV can be probed over a wide frequency range depending on β_H (i.e. the duration of the FOPT) while high nucleation temperatures such as $T_n = 10^7$ GeV will be accessible only at future high frequency interferometers such as Advanced LIGO (A-LIGO) [17], the Einstein Telescope (ET) [18] and the Cosmic Explorer (CE) [19, 20]. In the next section we show that $T_n \sim \sqrt{F}$ in our LESB scenarios, so that high nucleation temperatures in fully calculable SUSY-breaking scenarios correspond to superpartners lying out of the reach of the LHC.

2.3 LESB in the future: GW interferometers vs. colliders

We are now ready to establish a connection between the SGWB signals and SUSY-breaking phenomenology described in the previous two sections. The first step is to relate the nucleation temperature relevant for the SGWB signal to the scales in a SUSY-breaking hidden sector. As we will see, the nucleation temperature is essentially set by the SUSY-breaking scale \sqrt{F} in our scenarios.

Focusing on FOPT where the barrier between the false and the true vacuum is present at $T = 0$, S_3 is bounded from below by a constant and we can define T_{min} as the temperature where

$$\beta_H|_{T=T_{\text{min}}} = 0 \quad \Rightarrow \quad T_{\text{min}} < T_n < T_c. \quad (2.30)$$

If $S_3(T)$ is monotonic for $T > T_{\text{min}}$, the solution of the equation above is unique. The nucleation temperature is then bounded from above by T_c , where $\beta_H \rightarrow \infty$ and α in eq. (2.15) is suppressed and dominated by $\frac{d\Delta V(T_n)}{dT}$. It is further bounded from below by T_{min} where $\beta_H \rightarrow 0$ and α is dominated by $\Delta V(T_n)$.

More importantly, T_n can be directly related to the SUSY-breaking scale \sqrt{F} which sets the size of the $O(3)$ -symmetric bounce action. A simple way of seeing this is to note that the bounce action at T_n is itself set by the scale of relevant features in the potential,

$$S_3(T_n) \simeq c_3 \sqrt{F} \quad \Rightarrow \quad T_n = \frac{c_3}{\mathcal{C}} \sqrt{F}, \quad (2.31)$$

where c_3 is a model-dependent function of the parameters controlling the shape of the potential which we assume to be temperature independent for simplicity (an approximation that is certainly justified if T_n is close enough to T_{min}). Here we assume that $c_3/\mathcal{C} \sim \mathcal{O}(1)$, an assumption that will turn out to be justified analytically in section 3 and numerically in the explicit models of section 4.

Having established a relation between T_n and the SUSY-breaking scale \sqrt{F} , we identify two different viable regions of the LESB parameter space satisfying the following simple requirements:

- the gravitino is the lightest supersymmetric particle (LSP) as required by LESB, and
- the reheating temperature $T_{\text{r.h.}}$ is as high as \sqrt{F} to generate GW signals from the hidden sector. We take $T_{\text{r.h.}} = \sqrt{F}$ in figure 2.11 to maximize the allowed parameter space.

The two viable regions satisfying the above requirements are

Gravitino dark matter window: where $260 \text{ TeV} < \sqrt{F} \lesssim 50 \text{ PeV}$ and $\kappa \ll 1$ so that the gravitino mass is larger than the nominal value set by the F -term in Eq (2.1). The upper bound on the SUSY-breaking scale is obtained by combining the constraints on gravitino overabundance in eq. (2.8), BBN constraints on NLSP decays, and the LHC bound on the gluino mass $m_{\tilde{g}} > 2 \text{ TeV}$. The precise upper bound is potentially dependent on further model-building epicycles; the value here is meant to be indicative. In this window, the gravitino abundance can match the observed dark matter relic abundance today, while the soft masses are still dominated by the gauge mediation contributions in eq. (2.9) so that flavor constraints are under control when eq. (2.11) is satisfied. Perturbative gauge mediation models with $f_a \gtrsim \sqrt{F}$ and gaugino screening will naturally live in the upper end of this window for $\sqrt{F} \simeq 1 - 50 \text{ PeV}$. As shown in figure 1, the future reach on gluinos at FCC-hh [29] could provide a further direct test of these models. Future interferometers in the LIGO frequency band such as A-LIGO [17], ET [18] and CE [19, 20] have the unique opportunity to probe these scenarios as long as the thermal transition to the SUSY-breaking vacuum is associated with a sufficiently strong FOPT (see figure 2). In the rest of the paper, we discuss explicit scenarios of this type.

Ultralight gravitino window: where $m_{3/2} < 16 \text{ eV}$ and $\sqrt{F} < 260 \text{ TeV}$. This region has no cosmological issues for $\kappa = 1$, but it requires $g_M \gtrsim 1$ to satisfy the LHC bound on the gluino mass given the low SUSY-breaking scale (see eq. (2.10) for definition and comments). A lower bound on the gravitino mass can be derived from direct searches for gravitino pair production at LEP in $\gamma + \text{MET}$ and at the LHC in $j + \text{MET}$. As shown in figure 1, present direct bounds on the gravitino are not competitive with the bound on \sqrt{F} obtained by requiring $m_{\tilde{g}} > 2 \text{ TeV}$ and perturbativity in the messenger sector. The HL-LHC will not improve much on that. Future colliders — in particular, high energy lepton colliders (HELCS) — can drastically improve the reach on gravitino pair production and meaningfully probe this window even if MSSM superpartners remain inaccessible. As shown in figure 2, these scenarios can be probed across a wide frequency range by future GW interferometers depending on the strength and the duration of the FOPT. Building explicit calculable models in this window presents challenges [81, 82], and we leave a study of possible GW signals for a future work.

3 Anatomy of the SUSY-breaking phase transition

In this section we describe the generic features of FOPT occurring in calculable SUSY-breaking hidden sectors. First, we discuss how a large class of perturbative hidden sectors can be encoded in the effective field theory of the *universal pseudomodulus*, which is the scalar component x of the chiral superfield X in eq. (2.1), universally related to the spontaneous breaking of supersymmetry [14–16].

Second, we show how the flatness of the pseudomodulus potential gives rise to a new class of FOPTs with a very distinctive feature: the nucleation temperature is generically small compared to the SUSY mass scale, $T_n \leq m_*$, so that the thermal potential is well approximated in the low- T expansion. As we will discuss, non-supersymmetric realizations of this class of FOPT typically entail a large amount of fine-tuning.

Finally, we derive parametric estimates for T_n , α and β_H for this new class of FOPTs using the triangular barrier approximation [83, 84] and comment on a universal feature of bubble dynamics in our FOPTs. The observations of this section will find a concrete realization in the working examples of section 4.

3.1 The SUSY-breaking pseudomodulus

The existence of flat directions is a trademark of hidden sectors with spontaneous SUSY breaking. Here we focus on a large class of SUSY breaking sectors where the dynamics of both SUSY and R -symmetry breaking can be embedded in a single chiral superfield X parametrized as in eq. (2.1)

$$X = \frac{x}{\sqrt{2}} e^{2ia/f_a} + \sqrt{2}\theta\tilde{G} + \theta^2 F, \tag{3.1}$$

where the R -charges of the components are respectively $R[x] = 2, R[\tilde{G}] = 1, R[F] = 0$. The scalar component x (the *universal pseudomodulus*) tracks the breaking of the R -symmetry, while $\langle F \rangle$ sets the SUSY breaking scale.³ The phase transition occurs along x from a local minimum at the origin $x = 0$ (where R -symmetry is preserved) to the $T = 0$ vacuum of the theory where $\langle x \rangle = f_a$ and R -symmetry is broken. Hence $\langle x \rangle = f_a$ is the order parameter of the phase transitions of interest here, parameterizing the spontaneous breaking of the R -symmetry.

In hidden sectors which admit a weakly coupled description, the phase transition can be fully described by studying the effective potential of the pseudomodulus x , whose mass is typically well below the mass m_* of the heavy SUSY states in the hidden sector. As we will see, the unique features of the pseudomodulus potential leave a strong imprint on the properties of the phase transition. The full effective potential for the pseudomodulus can be written as

$$V_{\text{eff}}(x) = V_0(x) + V_T(x), \tag{3.2}$$

where $V_0(x)$ encodes the zero-temperature quantum corrections and $V_T(x)$ the thermal ones.

The zero-temperature part of the effective potential $V_0(x)$ is flat at tree level, up to explicit R -symmetry breaking effects. Along this so-called F -flat direction, the size of the potential energy is set by supersymmetry breaking, $V \sim F^2$. Interactions that explicitly violate the R -symmetry typically destabilize the origin and give a slope to the pseudomodulus potential at tree level, but these features are usually small compared to the scale \sqrt{F} . At one loop, quantum corrections lift the pseudomodulus potential; these corrections are

³In more general scenarios there could be multiple different field directions associated to SUSY-breaking and R -symmetry breaking [16] or even multiple pseudo-flat directions from multiple sources of F -term SUSY breaking [85].

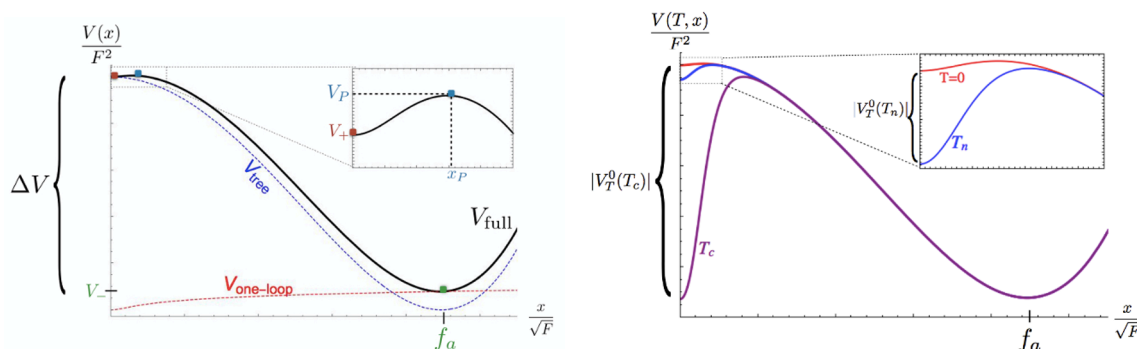


Figure 3. Qualitative features of the pseudomodulus potential relevant to the FOPT in SUSY-breaking hidden sectors. *Left:* sketch of the zero-temperature potential as described in section 3.1, exhibiting the following features: i) the distance between the two minima is larger than their potential difference, $f_a^4 \gtrsim \Delta V$, and ii) the height of the peak between the two minima is loop-suppressed compared to the potential difference, $V_P \ll \Delta V$. An explicit realization of this potential is presented in section 3.4. The tree level potential (*dashed blue*) generated by explicit R -symmetry breaking destabilizes the origin, giving rise to a minimum at $\langle x \rangle = f_a$ where the R -symmetry is further spontaneously broken by the VEV of x . Quantum corrections (*dashed red*) generate a local minimum at origin. *Right:* behavior of the temperature corrections described in eq. (3.5) at $T = 0$, $T = T_c$, and $T = T_n$. The thermal corrections give a contribution to the potential at the origin which at T_n is typically much smaller than F^2 . The barrier and the true vacuum are essentially unchanged. The approximations in section 3.2 are then justified.

present even in the absence of explicit R -symmetry breaking. The combination of tree-level explicit R -symmetry breaking and one-loop quantum corrections give rise to the schematic zero-temperature potential shown in figure 3. Assuming the quantum corrections exceed the R -symmetry breaking effects, at zero temperature this creates a metastable vacuum at the origin that is separated by a barrier from the true vacuum at $\langle x \rangle_{\text{true}} = f_a$. The energy difference between the two vacua ΔV is proportional to the SUSY-breaking scale. The barrier is located at a distance x_P from the origin; at this point, the barrier height is V_P . The essential features characterizing the zero temperature potential are:

- *The potential is flat.* This means that the distance f_a in field space between the false vacuum and the true vacuum is larger than the size of the potential energy difference ΔV :

$$f_a^4 > \Delta V, \quad (3.3)$$

where this hierarchy assumes that R -symmetry breaking effects are parametrically smaller than the loop corrections. This will be manifest in the toy model of section 3.4. Under this assumption, the flatness of the potential is a direct consequence of the fact that SUSY loop corrections asymptote to a logarithm at large field values (see for instance [86]). Obtaining similar quantum corrections in non-supersymmetric theories with a field-independent mass gap is notoriously difficult without fine-tuning.⁴

⁴A well studied example of a flat potential is that of the dilaton of spontaneously broken conformal symmetry. Here, however, the mass gap is field-dependent and as a consequence the theory becomes strongly coupled at the origin [87]. The features of the dilaton phase transition are consequently very different from the one described here.

- *The barrier between the two vacua is small.* Given that the potential is generated by loop effects (and subleading R -symmetry breaking effects), the size of the barrier V_P is one-loop suppressed with respect to the energy difference between the true and the false vacuum ΔV :

$$\frac{V_P}{\Delta V} = \frac{\lambda_{\text{eff}}^2}{16\pi^2}, \tag{3.4}$$

where $\lambda_{\text{eff}} \sim \mathcal{O}(1)$ should be thought of as the effective coupling determining the height of the barrier. The position of the barrier x_P is model-dependent, but will not play a critical role in the determination of the bounce action as long as eq. (3.3) is satisfied.

We now turn to the finite temperature corrections. First, as it is well known, finite temperature effects break SUSY and thus significantly modify the pseudo-modulus potential. The thermal effects are dominated by the loops of heavy fields in the SUSY hidden sector coupled to x , whose mass is of order m_* . Since m_* is by construction larger than the SUSY-breaking scale \sqrt{F} setting the zero-temperature potential, the relevant temperatures for the phase transition are smaller than the mass scale m_* of the particles running in thermal loops. This implies that the correct approximation of the thermal potential is the *low temperature expansion* (see appendix A for explicit formulas). This makes the finite-temperature potential of the pseudomodulus qualitatively different from ordinary non-SUSY models, where the high temperature approximation applies since the typical scalar potential curvature is of the same order of the highest mass scale in the theory.

The effect of thermal corrections on the pseudomodulus potential takes the schematic form

$$V_T(x) \simeq -N T^4 \left(\frac{\lambda^2 x^2 + m_*^2}{(2\pi T)^2} \right)^{3/4} e^{-\sqrt{\frac{\lambda^2 x^2 + m_*^2}{T^2}}}, \tag{3.5}$$

where we assumed the presence of N degrees of freedom with masses-squared $\sim \lambda^2 x^2 + m_*^2$. Notice that N counts all the heavy degrees of freedom, both bosonic and fermionic, which contribute with the same sign to the thermal potential. This enhances the importance of thermal effects compared to zero-temperature loops, where cancellations occur between states of different statistics.

The thermal correction constitutes a negative contribution to the potential which is maximal (in absolute value) at the origin of the pseudomodulus, when $x \sim 0$ and the Boltzmann suppression factor is minimized. As a consequence, thermal corrections in our scenarios have an exponentially larger impact at the origin relative to the true vacuum or the barrier. This behavior is explicitly shown in the right panel of figure 3. As we will show in section 4 small deviations from this generic feature can be induced by heavy states becoming lighter at large field values of the pseudomodulus.

3.2 First order phase transitions in the low- T expansion

Given the shape of our potential as shown in figure 3, we can approximate the bounce action in the triangular barrier approximation [83, 84]. Within this approximation, we will be able to capture the parametric behavior of the FOPTs analytically and in section 4 we

will show how the full analytical solution in explicit models reflects the general features explored here. A more in-depth discussion about the computation of the bounce action in the various cases can be found in appendix B.

Taking the false vacuum to be at the origin of field space, we can write the bounce action in the triangular barrier approximation as

$$\frac{S_3}{T} = \frac{144\sqrt{2}\pi}{5} \frac{(V_P - V_+)^{5/2}}{(V_P - V_-)^3} \frac{f_a^3}{T} f(r_\lambda), \quad \text{for } \frac{f_a}{x_P} > g(r_\lambda), \quad (3.6)$$

where we have defined the variables

$$r_\lambda \stackrel{\text{def}}{=} \frac{\lambda_-}{\lambda_+}, \quad \lambda_- \stackrel{\text{def}}{=} \frac{V_P - V_-}{f_a - x_P}, \quad \lambda_+ \stackrel{\text{def}}{=} \frac{V_P - V_+}{x_P}, \quad (3.7)$$

and the functions

$$f(r_\lambda) = \frac{r_\lambda^3(1+r_\lambda)}{3\sqrt{3}(3+2r_\lambda-3(1+r_\lambda)^2/3)^{3/2}} \underset{r_\lambda \rightarrow 0}{\simeq} 1 + \frac{5}{3}r_\lambda, \quad (3.8)$$

$$g(r_\lambda) = 1 + \frac{r_\lambda}{3+2r_\lambda-3(1+r_\lambda)^{2/3}} \underset{r_\lambda \rightarrow 0}{\simeq} \frac{3}{r_\lambda} + \frac{7}{3}. \quad (3.9)$$

The expansion for $r_\lambda \rightarrow 0$ is justified as long as both eq. (3.3) and eq. (3.4) are satisfied and the true vacuum VEV f_a sets the largest scale in the pseudomodulus potential. The triangular barrier approximation can be extended beyond the region set by $f_a/x_P > g(r_\lambda)$, but the range of validity of eq. (3.6) is sufficient to capture the parametrics of the phase transitions of interest. We give the full expression of the triangular barrier approximation in appendix B.

The triangular barrier approximation depends in general on only five parameters characterizing the potential: the three values of the potential at the critical points, V_\pm, V_P , and the position of the two critical points, f_a, x_P . For a given theory we can compute these temperature-dependent quantities explicitly, and find that the bounce action in eq. (3.6) is an excellent match to the full numerical result.⁵

At the leading order in the $r_\lambda \rightarrow 0$ expansion, the bounce action is independent of x_P ; our analytical estimates will assume that this holds. To further simplify our analytical treatment, we approximate the thermal potential in eq. (3.5) by only including thermal corrections at $x = 0$, where the exponential suppression is minimized, and neglecting the temperature dependence of V_- and V_P . Within this approximation we obtain

$$V_+ = V_T^0, \quad V_T^0 \stackrel{\text{def}}{=} V_T(x=0), \quad V_- = -\Delta V, \quad (3.10)$$

where we set V_+ to be exactly zero at zero temperature so that its (strictly negative) value is purely controlled by the thermal corrections at the origin. The value of the potential at the true vacuum is $-\Delta V$, and independent of temperature in this approximation.

With these approximations, the bounce action becomes simply

$$\frac{S_3}{T} \simeq \frac{144\sqrt{2}\pi}{5T} \frac{(V_P - V_T^0)^{5/2} f_a^3}{(\Delta V)^3}, \quad \frac{3V_T^0}{\Delta V} + 1 > 0, \quad (3.11)$$

⁵Throughout this paper we make use of the Mathematica package FindBounce [88] for our numerical analysis, which we further validate using CosmoTransitions [89].

and we are now ready to describe the shape of S_3/T as a function of T . First we define the critical temperature T_c , where the thermal corrections at the origin balance the zero-temperature potential difference between the two minima:

$$|V_{T_c}^0| \simeq \Delta V \quad \Rightarrow \quad T_c \simeq \frac{2}{5} \frac{m_*}{\mathcal{W}\left(0.13 \left(N \frac{m_*^4}{F^2}\right)^{2/5}\right)}, \quad (3.12)$$

where $\mathcal{W}(x)$ is the Lambert function, defined as the solution to the equation $\mathcal{W}(x)e^{\mathcal{W}(x)} = x$. At large x the function $\mathcal{W}(x)$ behaves approximately like $3/4 \log(1+x)$, and this simple approximation can be used for all practical purposes here (see appendix A for a short summary of the properties of the Lambert function). Using this, the low- T expansion will apply in regions of parameter space where

$$T_c \lesssim m_* \quad \Rightarrow \quad \sqrt{F} \lesssim 0.8 \left(\frac{N}{10}\right)^{5/8} m_*, \quad (3.13)$$

where we have normalized the number of degrees of freedom in the thermal loops to the typical order of magnitude we will find in the explicit examples of section 4. The low- T approximation is then valid whenever eq. (3.13) is satisfied, making it a generic feature of the pseudomodulus potential where the vacuum energy is protected from quantum corrections induced by heavy SUSY states.

From the definition of T_c in eq. (3.12), we can immediately see that the triangular approximation in eq. (3.11) breaks down in this regime and should be extended (see appendix B). However, the nucleation temperature in our setup is generically very far from T_c , so that eq. (3.11) is always a good approximation at the temperatures relevant for the FOPT. As the temperature decreases below $T < T_c$, S_3/T decreases as long as $|V_T^0| > V_P$, since $|V_T^0|$ decreases exponentially with the temperature. When the temperature approaches T_{\min} defined in eq. (2.30), then $|V_T^0| \simeq V_P$ and S_3/T attains a minimum value. As the temperature decreases further below T_{\min} , S_3/T grows as $1/T$.

Plugging the simplified bounce action in eq. (3.11) into the T_{\min} definition in eq. (2.30), we can easily obtain an analytic expression for T_{\min} which reads

$$T_{\min} = \frac{2m_*}{3} \frac{1}{\mathcal{W}\left(\frac{5^{2/3}}{3\pi} \left(N \frac{m_*^4}{V_P}\right)^{2/3}\right)} \quad \Rightarrow \quad \frac{T_{\min}}{T_c} \lesssim 0.2, \quad (3.14)$$

where to obtain the first expression we assumed $T_{\min} \lesssim 0.48m_*$ and the second inequality follows from approximating the Lambert function $\mathcal{W}(x) \simeq 3/4 \log(x+1)$, assuming $N \sim \mathcal{O}(10)$ and using the eq. (3.4) for the scaling of V_P with $\lambda_{\text{eff}} \sim \mathcal{O}(1)$ and $\Delta V \sim F^2$. Higher values of λ_{eff} or a suppressed value of ΔV will lead to a reduction of the hierarchy between T_{\min} and T_c . The latter cases are less interesting from the point of view of the expected GW signal.

We are now ready to verify that there exists a nucleation temperature T_n where S_3/T satisfies the nucleation condition eq. (2.14). As discussed in eq. (2.30), the nucleation temperature is always within the interval (T_{\min}, T_c) . Scenarios where T_n is closer to T_{\min}

have a larger α (see eq. (2.15)) and a smaller β_H (see eq. (2.16)), favorable for generating an observable GW signal. Understanding the scaling of T_n with respect to T_{\min} and T_c thus provides valuable information about the strength of the FOPT.

Even approximating the nucleation condition in eq. (2.14) with a constant \mathcal{C} , solving the equation analytically with respect to T using S_3/T given by eq. (3.11) is not possible. We may, however, expand in $V_P/|V_T^0| \ll 1$ and solve for T_n order by order in this expansion. This is always a good approximation as long as T_n does not approach T_{\min} too closely. At first order, writing $T_n = T_n^0(1 + \delta T_n^1)$ we find

$$T_n \simeq T_n^0 \left(1 - \frac{7}{\mathcal{C}^{2/5}} \frac{V_P}{m_*^4} \left(\frac{T_n^0}{m_*} \right)^{3/5} \left(\frac{f_a m_*^3}{\Delta V} \right)^{6/5} \right), \quad (3.15)$$

where

$$T_n^0 = 0.48 m_* \frac{1}{\mathcal{W} \left(0.32 \left(\frac{N^5}{\mathcal{C}^2} \right)^{2/21} \left(\frac{f_a m_*^3}{\Delta V} \right)^{4/7} \right)}, \quad (3.16)$$

and we have again assumed $T_n^0 < 0.48 m_*$. Given that the argument of the Lambert function is much larger than one, T_n^0 depends only logarithmically on the parameters $N, \mathcal{C}, f_a, \Delta V$, and can be taken proportional to m_* for simplicity.

The leading scaling of T_n with respect to the parameters shaping the potential is captured by the leading corrections proportional to V_P in (3.15). Indeed, we observe that by increasing V_P (i.e. the height of the barrier), or by increasing f_a , the nucleation temperature decreases, approaching the region of parameter space where nucleation does not occur. The border between the nucleation and the non-nucleation areas is the portion of parameter space which is optimal for gravitational waves, since it is where β_H is minimal. This behavior is in good agreement with the numerical results of section 4, and one can verify that eq. (3.15) reproduces the behavior of the full numerical result when properly matched to the models in section 4 up to an overall scaling of the bounce action.

3.3 α , β_H and fine-tuning

Now we can use our prediction for T_n to compute the parameters characterizing the FOPT:

- Within our analytical approximation, the temperature corrections only affect the potential at the origin of field space and are exponentially suppressed for $T < m_*$. Therefore, we approximate α as

$$\alpha \simeq \frac{30}{g_*(T_n) \pi^2} \frac{\Delta V}{T_n^4}, \quad (3.17)$$

where the scaling of T_n can be obtained by using (3.15). Within this approximation, ΔV is temperature-independent and the largest values of α correspond to T_n closer to T_{\min} .

- The inverse time scale of the phase transition can be computed explicitly from (3.11), giving

$$\beta_H \simeq \mathcal{C} \left(\frac{1.1N}{\mathcal{C}^{2/5}} e^{-\frac{m_*}{T_n}} \left(\frac{T_n}{m_*} \right)^{11/10} \left(\frac{f_a m_*^3}{\Delta V} \right)^{6/5} - 1 \right). \quad (3.18)$$

One can easily verify that if $T_n = T_{\min}$, then $\beta_H \simeq 1$ within the small V_P expansion. Moreover, the exponential dependence on T_n makes β_H very sensitive to the underlying parameters.

We now use the approximate β_H formula in eq. (3.18) to estimate the β_H -tuning defined in eq. (2.18). We compute first the tuning with respect to V_P , which is encoded in eq. (3.18) through the dependence of T_n on V_P . At leading order in $V_P/m_*^4 \ll 1$ we obtain

$$\left| \frac{d \log \beta_H}{d \log V_P} \right| = \left| \left(1 - \frac{\beta_0}{\beta_H} \right) \right| \gtrsim \left| 4 \frac{\mathcal{C}}{\beta_H} \right| \quad (3.19)$$

where in the last step we used the fact that

$$\beta_0 \simeq \mathcal{C} \left(-1 + \frac{5 m_*}{2 T_n^0} \right) \gtrsim 4\mathcal{C} \quad (3.20)$$

since $T_n^0 < \frac{10}{21} m_*$ and $\beta_H \lesssim \mathcal{C}$ in the interesting region of parameter space. The tuning associated with the barrier height is the dominant one, given that the tuning with respect to vacuum distance f_a is suppressed by an extra factor of T_n^0/m_* . As in eq. (2.17), we see that the natural value of β_H is $\beta_H \simeq \mathcal{C}(T_n) \simeq 100$ for the scales of interest in this study. Smaller values of β_H can be obtained at the price of fine-tuning the barrier height at the percent level. This might imply an even larger tuning with respect to the fundamental parameters of a given model, as we will show in a concrete example in section 4.2.

3.4 A toy example: fine-tuning vs. single SUSY-breaking scale

We now present a simple toy model which captures most of the features of the pseudomodulus potential in the explicit SUSY-breaking hidden sectors we will encounter in section 4. We take the zero-temperature potential to be

$$V_0(x) = \kappa_D^2 \left(F - \epsilon_{\mathbb{R}} x^2 \right)^2 + \frac{\lambda^2}{32\pi^2} |F|^2 \log \left(\frac{\lambda^2 x^2 + m_*^2}{m_*^2} \right), \quad (3.21)$$

which reproduces the shape of the potential sketched in figure 3. The first term captures tree-level effects, while the second term captures one-loop quantum corrections. The x potential is flat at tree-level up to R -symmetry breaking operators parametrized by $\epsilon_{\mathbb{R}}$.⁶ SUSY-breaking corrections induced by heavy fields lift the x potential around the origin, giving a mass to the pseudomodulus, but ultimately become subdominant for $x \gg \sqrt{F}$ where SUSY is restored in the direction associated to the F -term. This large-field behavior is a unique characteristic of SUSY models.

As long as the explicit R -symmetry breaking is parametrically small, the position of the true vacuum and the zero temperature difference energy between the true vacuum and false vacuum are

$$\langle x \rangle_{\text{true}} = f_a = \sqrt{\frac{F}{\epsilon_{\mathbb{R}}}}, \quad \Delta V = (\kappa_D F)^2, \quad (3.22)$$

⁶As shown in section 4.2, the potential controlled by $\epsilon_{\mathbb{R}}$ can be obtained from a marginal operator breaking R -symmetry in the superpotential. Similarly, one could study explicit R -breaking operators of arbitrary dimension in the superpotential $\mathcal{W}_{\mathbb{R}} = \frac{\epsilon_{\mathbb{R}} X^n}{n \Lambda^{n-3}}$ which correspond to tree level potentials of the form $V(x) = \left(F - \frac{\epsilon_{\mathbb{R}} x^{n-1}}{\Lambda^{n-3}} \right)^2$. These types of operators would naturally be generated by UV dynamics as in ref. [90].

where we have introduced the parameter κ_D to allow the scale controlling the difference in vacuum energy to vary relative to the scale controlling the loop corrections along the pseudomodulus potential. We will exhibit a concrete realization of such a model in section 4.3. Requiring the potential to be flat as in eq. (3.3) requires $\epsilon_{\mathcal{R}} < 1/\sqrt{\kappa_D}$.

Following the triangular barrier prescription, we need to find the position of the barrier and the value of the potential at the barrier; for the toy model these take the form

$$x_P \simeq \frac{\lambda}{8\pi\kappa_D} f_a, \tag{3.23}$$

$$V_P \simeq \frac{\lambda^2 F^2}{32\pi^2} \left(2 \log \left(\frac{\lambda^2 f_a}{8\pi\kappa_D m_*} \right) - 1 \right). \tag{3.24}$$

From the last equation we see that the loop suppression of the zero-temperature barrier V_P , as assumed in Eq (3.4), is here an automatic consequence of the fact that the pseudomodulus direction is lifted by quantum corrections. For a single-scale model (i.e. $\kappa_D = 1$) the position of the peak x_P is fixed in terms of the one of the true vacuum f_a , while for a two-scale model, $\kappa_D \gg 1$ can enhance the hierarchy between x_P and f_a .

We are now ready to use the triangular barrier approximation in eq. (3.6) to compute the bounce action and the features of the FOPT between the origin and the true vacuum. For $\epsilon_{\mathcal{R}} < 1/\sqrt{\kappa_D}$, f_a is the largest scale in the problem and the approximation in eq. (3.11) is justified. If the general features of the bounce action characterize the FOPT in the low- T expansion discussed above, this simple toy model allows us to say something more precise about the scaling of the energy released during the FOPT. From eq. (3.17) we have

$$\alpha = \frac{30}{g_*(T_n)\pi^2} \left(\frac{\kappa_D F}{T_n^2} \right)^2 \sim 10^{-2} \kappa_D^2 \left(\frac{F}{m_*^2} \right)^2 \left(\frac{230}{g_*(T_n)} \right), \tag{3.25}$$

where we normalized the number of relativistic degrees of freedom at T_n to be close to the MSSM value and we substituted $T_n \sim T_n^0 \sim 0.5m_*$, which is the natural value of the nucleation temperature unless either V_P or f_a are tuned to suppress it (see eq. (3.15)). In a single-scale model where $\kappa_D = 1$, tuning $T_n \ll \sqrt{F}$ is the only way to enhance the strength of the FOPT. The same tuning will allow β_H to be small. Conversely, in a two-scale model of SUSY-breaking, having $\kappa_D \gg 1$ can compensate the suppression in eq. (3.25) without any tuning. We will show an explicit example of this class of hidden sectors in section 4.3. These are clearly the best candidates to be probed by future GW interferometers.

4 Explicit models

In this section we provide two working examples of the general idea described in the previous sections. Both models are straightforward deformations of the minimal O’Raifeartaigh model, which is the simplest theory of chiral superfields that breaks SUSY spontaneously [91]. The O’Raifeartaigh model involves three chiral superfields, namely the SUSY-breaking field X containing the pseudomodulus and two messenger fields $\Phi_{1,2}$. The dynamics are determined by three parameters: the SUSY-breaking scale \sqrt{F} , the SUSY-preserving mass m of the messengers, and the coupling λ between the three fields. To set the stage

for our analysis, we begin in section 4.1 by determining the phase diagram of the minimal O’Raifeartaigh model which can be described as a function of the dimensionless parameter

$$y_F \stackrel{\text{def}}{=} \frac{\lambda F}{m^2}. \tag{4.1}$$

The model exhibits a rich phase structure as a function of temperature and the underlying parameters; for $y_F \sim 1$ the origin of the pseudomodulus is the global minimum at all T and no interesting phase transitions occur, while for $y_F \ll 1$ a second minimum develops away from the origin that may become the global minimum at intermediate temperatures, leading to a variety of phase transitions. Unfortunately, as we will see, none of these phase transitions are sufficiently strongly first-order to generate an observable GW signal. However, this minimal O’Raifeartaigh model serves as the foundation for SUSY-breaking hidden sectors that *do* generate observable GW signals.

In section 4.2, we present the simplest SUSY-breaking hidden sector featuring a strong FOPT like the ones describe in section 3. This hidden sector involves a marginal deformation in the superpotential of the minimal O’Raifeartaigh model, breaking the R -symmetry explicitly and obtaining a pseudomodulus potential very similar to the one described in the toy model in section 3.4. We show that in such a simple single-scale model, α will be generically suppressed as predicted in eq. (3.25), and discuss quantitatively the fine-tuning of β_H defined in eq. (2.18). Phenomenologically, this model is unsatisfactory since the global minimum restores SUSY, although this may be remedied by the introduction of external SUSY-breaking effects.

In section 4.3, we show how both the shortcomings of the simple model of section 4.2 are resolved in hidden sectors with two SUSY-breaking scales, in keeping with our expectations from section 3.4. We make this concrete by gauging a $U(1)$ flavor symmetry of the messengers in the minimal O’Raifeartaigh model, which admits an additional source of SUSY breaking via the Fayet-Iliopoulos term. This additional “ D -term” supersymmetry breaking provides a second SUSY-breaking scale, which both ensures that supersymmetry is broken everywhere on the pseudomoduli space and increases α , leading to observable GW signals.

4.1 Warm up: the O’Raifeartaigh model at finite temperature

In the minimal O’Raifeartaigh model, the pseudo-modulus is stabilized at the origin by quantum corrections. Since the R -symmetry is unbroken in the global minimum at $T = 0$, one would expect that including finite temperature corrections will not induce any phase transitions. Instead, the dynamics of the O’Raifeartaigh model at finite temperature presents rich features that we discuss here in detail (see refs. [92, 93] for earlier works on related issues).

Having in mind applications to gauge mediated SUSY breaking, we consider the vector-like version of the minimal O’Raifeartaigh model, which is described by the superpotential

$$W = -FX + \lambda X \Phi_1 \tilde{\Phi}_2 + m(\Phi_1 \tilde{\Phi}_1 + \Phi_2 \tilde{\Phi}_2), \tag{4.2}$$

encoding the interactions of the SUSY-breaking chiral superfield X and two vector-like sets of messenger superfields $\Phi_i, \tilde{\Phi}_i$ ($i = 1, 2$). The first term is a tadpole ensuring that supersymmetry is broken at the scale \sqrt{F} , while the second term encodes interactions among the

fields with strength λ . We take the masses of the two pairs of messengers to be equal for simplicity. The superpotential above enjoys an unbroken R -symmetry under which X carries $R[X] = +2$, as well as a $U(1)_D$ flavor symmetry under which the messengers Φ and $\tilde{\Phi}$ have opposite charges (see figure 4 right for a summary table with the full charge assignment).

The potential for the scalar components of the chiral superfields is

$$V = |F - \lambda\phi_1\tilde{\phi}_2|^2 + |\lambda X\tilde{\phi}_2 + m\tilde{\phi}_1|^2 + |\lambda X\phi_1 + m\phi_2|^2 + |m\phi_1|^2 + |m\tilde{\phi}_2|^2, \quad (4.3)$$

where $X = \frac{x}{\sqrt{2}}$ denotes the scalar component of the pseudomodulus in the notation of eq. (3.1). For $\lambda F \leq m^2$, the tree level vacuum of the theory is at $\phi_i = \tilde{\phi}_i = 0$ with x undetermined, and SUSY is broken at a scale \sqrt{F} . Radiative corrections from loops of the messenger fields ϕ and $\tilde{\phi}$ generate a potential for x that stabilizes it at the origin, and thus the global vacuum at zero temperature lies at $\phi_i = \tilde{\phi}_i = 0$ and $\langle x \rangle = 0$. Note that the one-loop corrections have the shape described in section 3, being polynomial close to the origin of the pseudomodulus potential and logarithmic for large field values. Expanding for $y_F \equiv \frac{\lambda F}{m^2} \sim 1$ we obtain

$$V_{x \rightarrow 0}^{1\text{-loop}} \simeq \frac{\lambda^3 F}{16\pi^2} (\log 4 - 1) x^2 - \frac{\lambda^4}{384\pi^2} (12 \log 2 - 7) x^4 + O(x^6), \quad (4.4)$$

$$V_{x \rightarrow \infty}^{1\text{-loop}} \simeq \frac{\lambda^2 F^2}{16\pi^2} \log\left(\frac{x^2}{m^2}\right), \quad (4.5)$$

where we have fixed the renormalization scale to the messenger mass m . The thermal corrections to the x potential can be added with standard formulas that we review in the appendix A.

The shape of the thermal corrections is set by the x dependence of the mass eigenvalues for the scalar and fermionic components of the messengers. From (4.2) we can distinguish two classes of mass-squared eigenvalues: i) the ones growing quadratically with x , and ii) the ones decreasing as $1/x^2$ and asymptotically going to zero in the large- x region. Specifically, the fermionic eigenvalues scale as

$$m_{\pm}^2 = m^2 + \frac{\lambda^2 x^2}{4} \left(1 \pm \sqrt{1 + \frac{8m^2}{\lambda^2 x^2}} \right) = \begin{cases} m & \text{for } x \rightarrow 0 \\ \sim x^{\pm 2} & \text{for } x \rightarrow \infty \end{cases}, \quad (4.6)$$

and the bosonic eigenvalues are split in pairs around the fermionic ones, e.g. at the origin the bosonic eigenvalues are $\{m^2, m^2, m^2 + \lambda F, m^2 - \lambda F\}$. The behavior of the full spectrum as a function of x is shown in figure 4 (right). We also observe that at large x , the spectrum asymptotes to a supersymmetric one.

For low temperatures (i.e. $T < m$), the induced thermal corrections are a decreasing function of x , since they are mainly controlled by the lightest eigenstates. These corrections are mildly Boltzmann suppressed at large x and modify the pseudo-modulus potential as soon as $T^4 \sim \frac{\lambda^2 F^2}{16\pi^2}$. For larger temperatures, the contribution from the other mass eigenstates and in particular from the ones growing with x become relevant, and the thermal potential is a growing function of x . Hence at temperatures $T \sim m$ we expect the global minimum to be at the origin of the field space. However, for intermediate temperatures

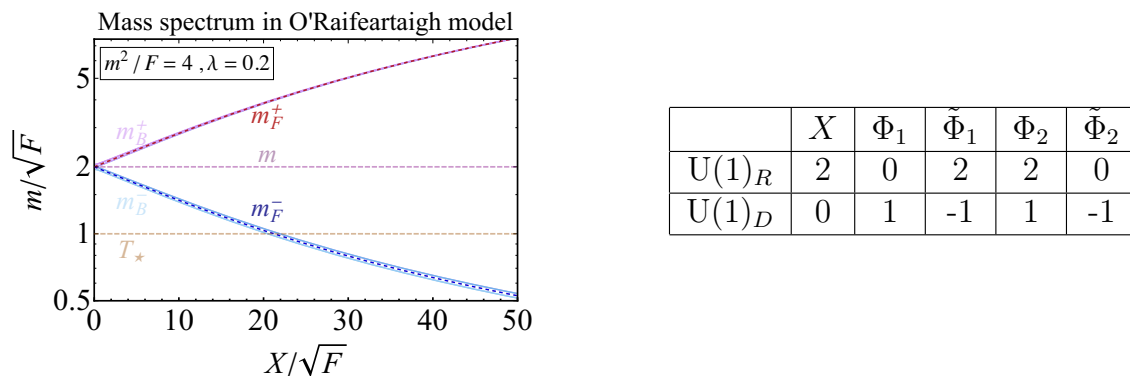


Figure 4. *Left:* behavior of the hidden sector spectrum in the simple O’Raifeartaigh model as a function of the pseudomodulus direction x . The *dashed dark red/blue* line indicates the fermionic eigenvalues growing/going to zero like $x^{\pm 2}$ (see eq. (4.6)). The two *pink* and *light blue* solid lines indicate the scalar mass states splitted in pairs around the fermionic ones. The *dashed light magenta* line indicates the states that remain independent on x . The *dashed peach* line shows T_\star for this particular benchmark, where the new vacuum induced by thermal corrections becomes degenerate with the origin (see eq. (4.7)). *Right:* unbroken symmetries of the chiral superfields in the O’Raifeartaigh model superpotential in eq. (4.2). The model enjoys a $U(1)_R$ symmetry and an extra $U(1)_D$ flavor symmetry. The first will be explicitly broken in the model in section 4.2 while the second one will be gauged in the model in section 4.3.

the thermal corrections can make the origin of the field space unstable, leading to a very rich evolution of the potential with temperature.

The thermal corrections compete with the loop corrections in the large x region (see eq. (4.5)), eventually leading to a minimum of the potential at

$$x_\star \simeq \frac{2\sqrt{2}\pi T}{\lambda y_F}, \quad T_\star \sim 0.23\sqrt{y_F}m, \quad (4.7)$$

where x_\star is obtained using the high- T expansion for the thermal potential up to T^2 , assuming 2 bosons and 2 fermions with masses-squared $\simeq \frac{2m^4}{\lambda^2 x^2}$, and T_\star is an estimate of the temperature where the new minimum can be the global one. The latter is estimated by requiring the temperature corrections at x_\star to be comparable to the height of the one loop potential. If T_\star is close to m , then the neglected contributions from the states whose masses grow with x^2 lifts again the minimum at x_\star , which will then never be the global minimum at any temperature. In conclusion, we expect that depending on the hierarchy between λF and m^2 , the minimum at x_\star could become the global minimum in a certain temperature range around T_\star . This complicated phase diagram is well summarized in figure 5, where we have fixed the ratio $\frac{F}{m^2}$ to a representative value and explore the dynamics of the model as a function of the temperature and coupling λ .

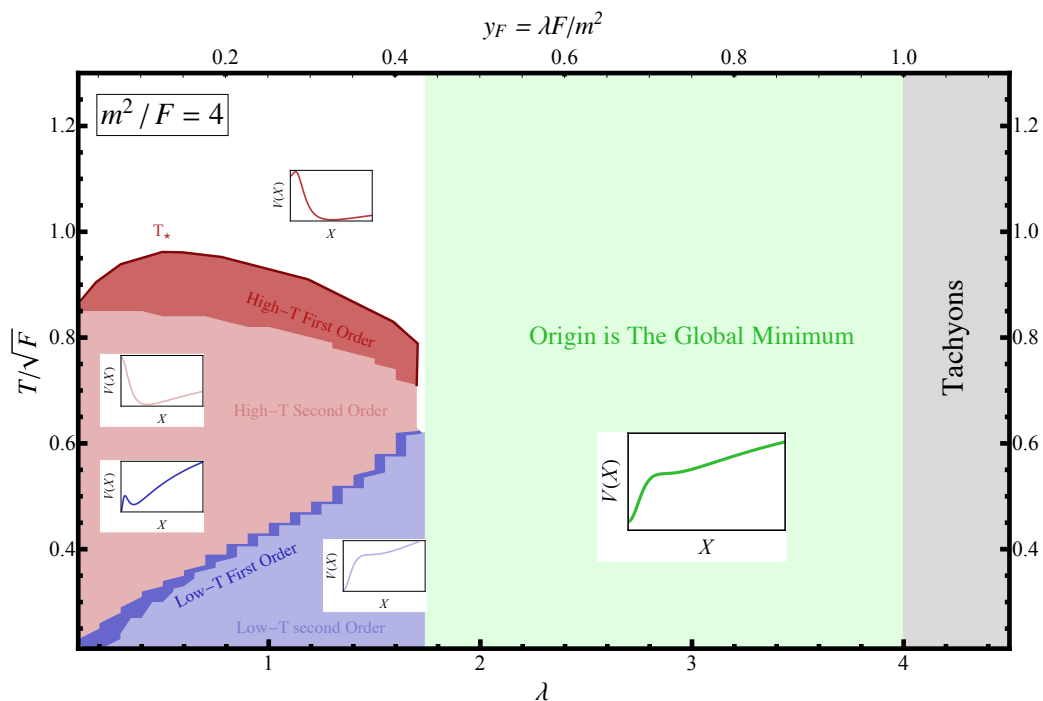


Figure 5. Phase diagram of the O’Raifeartaigh model at fixed $F/m^2 = 4$. For *large* λ the quantum corrections dominate and the origin is the global minimum at all temperatures. For *small* λ , at $T = T_*$ a new vacuum develops as a consequence of the interplay between the thermal and the loop corrections as shown in eq. (4.7). In *dark red* we show the range of temperatures where a barrier is present between the origin and the true minimum, in *light red* we show the range of temperatures where the barrier disappears. At lower temperatures, the origin again becomes the global minimum, and the second minimum decays back into the origin. In *blue* we show the range of temperatures where a barrier separates the two minima and in *light blue* the region when the barrier disappears.

For large λ , corresponding to $y_F \sim 1$, the minimum at X_* is never the global minimum of the scalar potential (green region in the plot). For small λ , i.e. $y_F \ll 1$ two phase transitions occur while lowering the temperature. Specifically, at very high temperature the global minimum is at the origin, as explained above. At intermediate temperatures the global minimum is at X_* , and finally at zero temperature the global vacuum is again at the origin. The corresponding two phase transitions can be first or second order. We have explored the parameter space of the model for different values of y_F and λ , and found that these phase transitions are never strongly first order (i.e. small β_H and large α) in the regime of perturbative λ .

Although the minimal O’Raifeartaigh model is itself not a good candidate for a strong FOPT, it nonetheless provides the foundation for simple variations that are. We explore these variations in the following subsections, restricting our attention to the region of parameter space in which the minimal O’Raifeartaigh model exhibits a simple thermal history corresponding to the green region in figure 5. Deformations of the minimal O’Raifeartaigh model will endow this region with phase transitions as a function of temperature, while avoiding the complications of new minima arising from the interplay of thermal and loop corrections shown in the red and blue regions.

4.2 O’Raifeartaigh model with explicit R -symmetry breaking

Now we turn to a simple, concrete realization of a SUSY-breaking hidden sector whose pseudomodulus potential exhibits the properties explored in section 3. This model simply amounts to deforming the minimal O’Raifeartaigh model studied in the previous section with the following marginal, R -symmetry-breaking term in the superpotential:

$$W_{\mathcal{R}}(X) = \frac{1}{3}\epsilon X^3. \quad (4.8)$$

The complete tree-level scalar potential of the model is

$$V = |-F + \epsilon X^2 + \lambda\phi_1\tilde{\phi}_2|^2 + |\lambda X\tilde{\phi}_2 + m\tilde{\phi}_1|^2 + |\lambda X\phi_1 + m\phi_2|^2 + |m\phi_1|^2 + |m\tilde{\phi}_2|^2 \quad (4.9)$$

and assuming $y_F \leq 1$, the global minimum sits at $\langle x \rangle_{\text{true}} = \sqrt{\frac{2F}{\epsilon}}$ and $\phi_i = \tilde{\phi}_i = 0$. In contrast to the minimal O’Raifeartaigh model, the R -symmetry-breaking deformation destabilizes the origin at tree level and restores supersymmetry in the true vacuum.

The radiative corrections are identical to the ones in the O’Raifeartaigh at zeroth order in ϵ , and they tend to stabilize the pseudo-modulus at $x = 0$, competing with the tree-level contributions induced by the ϵ deformation. Close to the origin, the effective potential for the pseudomodulus obtained by integrating out the ϕ_i and $\tilde{\phi}_i$ fields reads (up to quartic order)

$$V_0(x) \underset{x \rightarrow 0}{\simeq} F^2 + \frac{m_{\text{eff}}^2}{2}x^2 - \frac{\lambda_{\text{eff}}}{4}x^4, \quad \begin{cases} m_{\text{eff}}^2 = \left(\frac{\lambda^3}{8\pi^2}(\log 4 - 1) - 2\epsilon\right)F \\ \lambda_{\text{eff}} = \frac{\lambda^4}{96\pi^2}(12\log 2 - 7) - \epsilon^2 \end{cases}, \quad (4.10)$$

where again we have approximated the loop corrections in the leading order in $y_F = \frac{\lambda F}{m^2} \sim 1$. For $\epsilon < \frac{\lambda^3}{16\pi^2}(\log 4 - 1)$, the radiative corrections are sufficient to create a metastable vacuum at the origin of x . In this regime, the ϵ contribution to the quartic is always negligible. Along the pseudomodulus direction, there is now a true vacuum created by the R -symmetry-breaking deformation and a false vacuum created by radiative corrections. The height and location of the barrier between these two vacua may be approximated as

$$V_P - V_+ \simeq \frac{m_{\text{eff}}^4}{4\lambda_{\text{eff}}} \sim \frac{24\pi^2}{\lambda^4} \left(\frac{\lambda^3}{8\pi^2}(\log 4 - 1) - 2\epsilon\right)^2 F^2 \quad x_P \simeq \frac{m_{\text{eff}}}{\sqrt{\lambda_{\text{eff}}}}, \quad (4.11)$$

This approximation is valid if $x_P \lesssim \frac{m}{\lambda}$, that is if there is a cancellation between the two terms in m_{eff}^2 such that $m_{\text{eff}}^2 \lesssim \frac{\lambda^3}{96\pi^2}F$. The global minimum far away from the origin is not modified by the quantum corrections since SUSY is effectively restored there (we will come back to this point in section 4.2.2) and stays at $\langle x \rangle_{\text{true}} = \sqrt{\frac{2F}{\epsilon}}$, so that $\Delta V = F^2$.

In summary, this hidden sector provides a concrete realization of the toy model discussed in section 3.4. A direct consequence of having a single SUSY-breaking scale \sqrt{F} is that the potential difference ΔV and the quantum corrections determining the barrier are both controlled by the same scale. This corresponds to $\kappa_D = 1$ in the toy model of section 3.4, and typically leads to suppressed α as we will show below. The formulae above allow straightforward matching of the model parameters onto the variables entering in the triangular barrier bounce action of section 3.2. In the following, we will compare our analytical expectations with the full numerical analysis of the FOPT from the origin to the $\langle x \rangle_{\text{true}}$ vacuum.

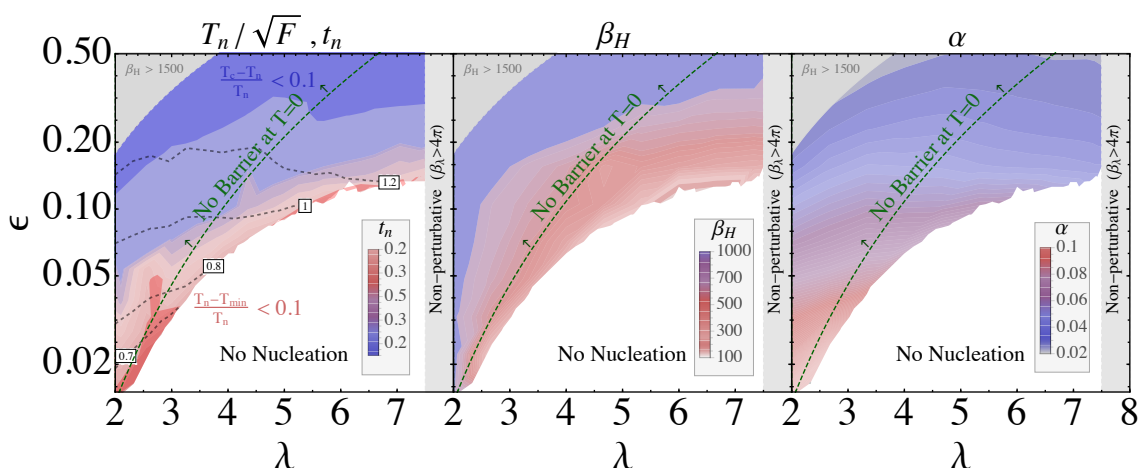


Figure 6. From the left to the right, we show the behavior of T_n/\sqrt{F} , β_H and α in the O’Raifeartaigh model with explicit R -symmetry breaking described in eq. (4.8). We fix $y_F = 3/4$ and $F = 30$ PeV so that the entire parameter space of the model can be shown in the (λ, ϵ) plane. The *black dashed contours* in the left plot show T_n/\sqrt{F} . The *red-to-blue* gradients show contours of t_n as defined in eq. (4.12) (left), of β_H as defined in eq. (2.16) (center) and of α as defined in eq. (2.15) (right). The GW signal weakens going from red to blue. Above the *green dashed* line, the barrier separating the false and true vacua disappears at zero temperature. The *grey* regions are not considered in our numerical scan because β_H is too large (top left) or λ is non-perturbative. In the *white* region the nucleation condition in eq. (2.13) cannot be satisfied.

4.2.1 First order phase transition dynamics

We now study the model at finite temperature with an eye towards the dynamics of the phase transition associated to R -symmetry breaking. The thermal corrections to the X potential are equivalent to the ones that we studied in the simplest O’Raifeartaigh model, up to small corrections proportional to ϵ . The main difference is that the thermal effects are added on top of a zero-temperature potential described in the previous section, where the global minimum is far away from the origin. If we restrict to the parameter space where $\lambda F/m^2 \sim 1$ (the green region of figure 5), the role of the thermal corrections is to stabilize the origin at high temperature. Lowering the temperature, the thermal history is very similar to the one described in section 3: the negative thermal contributions at the origin decrease in absolute value until we reach T_c , where the minimum at $x = 0$ is degenerate with the minimum at x_{true} . An analytic estimate of this temperature can be obtained following eq. (3.12). By further lowering the temperature, the thermal corrections become more and more negligible and one recovers the zero-temperature potential with a local minimum at the origin separated from the true vacuum by a loop-induced barrier.

Bounce action and nucleation temperature. The next step in determining the phase transition dynamics is to compute the bounce action and the nucleation temperature. In the left panel of figure 6, we show the numerical result for the nucleation temperature T_n as a function of the two dimensionless couplings of the model, having fixed $y_F \equiv \lambda F/m^2 = 3/4$

and the scale of SUSY breaking to $\sqrt{F} = 30$ PeV for concreteness. Numerically we see that $T_n \sim \sqrt{F}$ as assumed in the general discussion around eq. 2.31. As can be seen from the explicit formula in eq. 3.15, this feature is a consequence of the fact that F cannot be arbitrarily decoupled from m^2 if we require $y_F \sim 1$ and perturbativity of λ .

Keeping ϵ fixed, we see that the nucleation temperature T_n decreases when λ increases, up until reaching the no-nucleation zone. Indeed, increasing λ makes the barrier between the two vacua higher, and the bounce action larger, decreasing the likelihood that the phase transition completes. When the bounce action increases, the nucleation temperature lowers, approaching T_{\min} at the border of the no-nucleation region. Conversely, decreasing λ at fixed ϵ shifts the nucleation temperature towards T_c . In figure 6 we plot the quantity

$$t_n \stackrel{\text{def}}{=} \min\left(\frac{T_c - T_n}{T_c}, \frac{T_n - T_{\min}}{T_{\min}}\right), \quad (4.12)$$

which indicates whether T_n is closer to T_c or T_{\min} . As we will see this quantity is strongly correlated with the strength of the signal.

The main effect of ϵ on the pseudomodulus potential is to set the distance in field space between the origin and the true vacuum. The barrier is also ϵ -dependent, but away from the region where the effective mass in eq. (4.10) changes sign, the effect of varying ϵ is negligible. Decreasing ϵ makes $x_{\text{true}} = f_a$ larger. From eq. (3.11) we see that the bounce action grows, making it more difficult for the phase transition to occur. This explains why lowering ϵ at fixed λ causes the nucleation temperature to decrease until the no-nucleation region is reached.

The interesting area of the parameter space is the sliver between the no-nucleation region and the region where there is not a barrier at $T = 0$. Within this sliver, $\frac{\lambda^3}{16\pi^2} \sim \epsilon$ and the effective mass of the pseudomodulus in eq. (4.10) is small and positive (in units of $\sqrt{F} \sim \Delta V^{1/4}$). The whole region shrinks for small ϵ because the true vacuum is pushed to large field values, and there is no nucleation unless the effective mass at the origin is tuned to be small.

The scaling of T_n/\sqrt{F} with the Lagrangian parameters can be captured by the analytic approximations presented in section 3. We match the generic parameterization of section 3 using the expressions in (4.10) and (4.11), giving

$$T_n \sim \frac{40\sqrt{\lambda F}}{63} \frac{1}{\log\left(1 + 0.76 \frac{\lambda^{6/7}}{\mathcal{C}^{4/21} \epsilon^{2/7}}\right)} \left(1 - 0.015 \left(\frac{\lambda^9}{\mathcal{C}^2 \epsilon^3}\right)^{1/5}\right), \quad (4.13)$$

where we have approximated the radiative corrections for $y_F \sim 1$. This expression qualitatively reproduces the left panel of figure 6, up to an overall normalization of the bounce action (corresponding to a shift in \mathcal{C}).

For large ϵ , the rightmost term in parentheses in (4.13) is always $\mathcal{O}(1)$, and hence the variation of T_n is largely controlled by the prefactor. The $\sim \sqrt{\lambda}$ scaling of the numerator is balanced by the $\log \lambda$ scaling in the denominator, and the resulting prefactor of T_n is essentially flat in λ and only decreases with decreasing ϵ . In the small ϵ region, the rightmost term in parentheses in (4.13) becomes smaller than 1 and controls the shapes of the T_n contours, in agreement with the left panel of figure 6.

α , β_H and fine-tuning. The microscopic properties of the FOPT dynamics are encoded in the two parameters α and β_H , which correspond to the energy release and the duration of the phase transition. In the central and rightmost panels of figure 6, we show the behavior of β_H and α in the (λ, ϵ) plane. Here the scaling of α is essentially dictated by the scaling of T_n/\sqrt{F} , since $\alpha \sim \frac{30}{g_*\pi^2} \frac{\Delta V}{T_n^4}$ and $\Delta V \sim F^2$. We see that in the parameter space explored here, we cannot reach large values of α except in the thin sliver towards small ϵ and λ where $T_n \sim T_{\min}$ and T_{\min} is minimized with respect to \sqrt{F} . This unfortunate feature is a generic prediction of a single-scale SUSY-breaking hidden sector, as discussed in section 3.4.

As shown in figure 6, β_H is small in the regions of the parameter space at the border of the no-nucleation zone where $T_n \sim T_{\min}$. Getting closer and closer to this boundary, one can achieve $\beta_H \lesssim 100$ at the price of a large tuning of the model parameters as discussed in section 2.2. The fine-tuning is dominated by the tuning of the barrier V_P between the two minima. Substituting the dependence of V_P on the Lagrangian parameters, we can estimate the tuning of β_H with respect to λ as

$$\frac{\partial \log \beta_H}{\partial \log \lambda} \gtrsim 8 \left(\frac{\mathcal{C}(T_n)}{\beta_H} \right). \tag{4.14}$$

The same fine-tuning can be computed numerically using the prescription of eq. (3.19). We show the results in figure 7, where we see that $\beta_H \lesssim 100$ corresponds to $\Delta_{\beta_H} \sim 10^3$, which is larger than the estimate derived above. The numerical results also confirm our expectation that the tuning associated with the λ parameter (setting the height of the barrier) dominates relative to the tuning associated with the ϵ parameter (setting the location of the true vacuum). Comparing the left and right panels in figure 7, it is apparent that the tuning grows in the region of small ϵ , where α is larger.

4.2.2 Phenomenological challenges

As discussed in the previous section, the model presented here is not optimal for generating a sizable SGWB signal. Indeed, by comparing the resulting values of α and β_H in figure 6 to the values displayed in figure 2, it is clear that the typical value of α is too small to lead to a detectable signal. Of course, this issue can be resolved by going in a tuned region of the parameter space where a very small ϵ and an appropriately fine-tuned λ give $T \sim T_{\min}$ and a suppressed T_{\min} compared to \sqrt{F} . However, it is fair to say that, in general, a perturbative single-scale SUSY-breaking hidden sector cannot lead to strong SGWB signals. For this reason, we do not display the SGWB for this model, although it may easily be inferred from the α, β_H, T_n plots in figure 6.

As shown in the simple toy model of section 3.4, the suppression of α is a consequence of the fact that in a single-scale SUSY-breaking hidden sector one cannot significantly separate ΔV from T_n^4 . Notice that this conclusion hinges on requiring $y_F \sim 1$, which is necessary to avoid the region shown in figure 5 where thermal corrections at high temperatures induce new minima. A more careful study of the dynamics of single scale models for $y_F \ll 1$ is left for future work.

In addition to the α suppression, the true vacuum in this model restores SUSY, so that the phase transition is not genuinely a ‘‘SUSY-breaking phase transition’’; this sector,

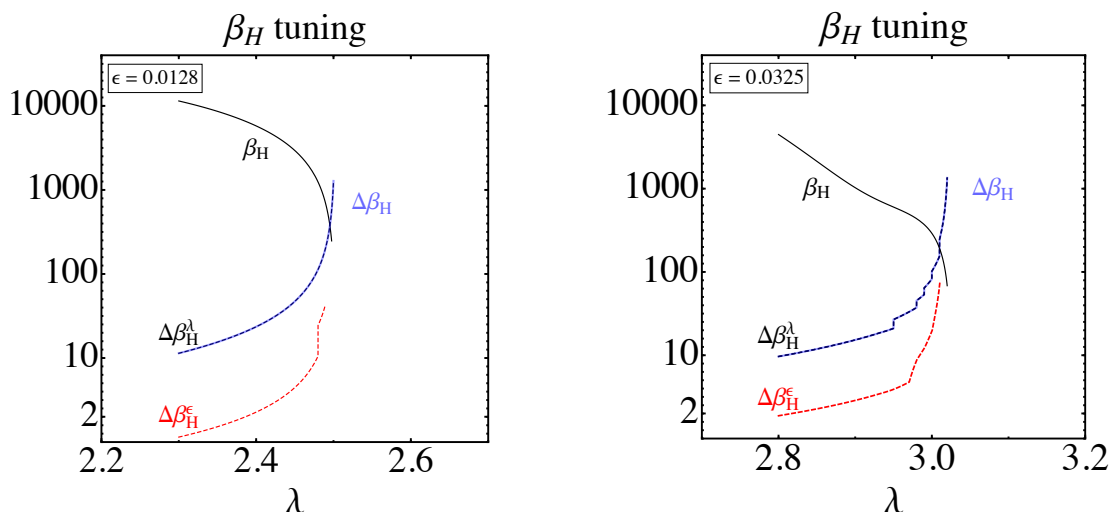


Figure 7. Behavior of β_H (black solid curve) and the associated fine-tunings defined in eq. (2.18) as a function of λ for $m^2/F = 4$ and $\sqrt{F} = 30$ PeV. The left and right plots correspond to two different values of ϵ . The black dashed curve shows the fine tuning w.r.t. λ , which dominates over the fine tuning w.r.t. ϵ shown as a red dashed curve. The λ fine-tuning corresponds to the total fine-tuning $\Delta\beta_H$ shown as a light blue solid line.

as presented, cannot be responsible for the SUSY breaking transmitted to the MSSM. However, this is not a fatal obstruction, as the vacuum energy in the true vacuum far from the origin can be easily lifted by coupling to another source of SUSY breaking, very much in the spirit of [94]. If we require the new source of SUSY-breaking to not significantly affect the dynamics of the phase transition, the parametrics of the model will not significantly deviate from those presented here and the resulting α will be still suppressed. Interestingly, our analysis seems to point towards SUSY-breaking hidden sectors with multiple dynamical field directions and scales. In the next section, we will exhibit the simplest model of this type, leaving a more thorough exploration of the different possibilities for future study.

4.3 O’Raifeartaigh model with gauge interactions

In the previous subsection we analyzed a simple model displaying a first order phase transition associated with the breaking of the R -symmetry. However, there were two aspects that were not completely satisfactory: i) SUSY breaking in the global minimum had to be added as a further deformation, and ii) the phase transition was generically not strong enough to generate a sizable signal. Both issues were related to the fact that there was only one SUSY breaking scale in the problem. In this subsection we resolve these issues in a hidden sector where the global minimum breaks both SUSY and R -symmetry spontaneously and the presence of two SUSY breaking scales leads to a strong FOPT from the origin to the true minimum.

It is well-known that adding gauge interactions to SUSY breaking models with chiral superfields modifies the potential and typically leads to a new SUSY- and R -symmetry-breaking vacuum at large field values (see e.g. [15]). As a prototype of this class of models

we consider the simplest realization, which consists of the vector-like O’Raifeartaigh model of the previous sections where the anomaly-free $U(1)_D$ flavor symmetry defined in the right panel of figure 4 is gauged. The model we consider has been studied at zero temperature in [95]. The qualitative features that we find here are generic to models where SUSY is broken through the interplay of F - and D -term effects.

The field content and superpotential are the same as those introduced in (4.2). The gauging of the $U(1)_D$ symmetry contributes new terms in the scalar potential from the D -term contribution. The F - and D -term contributions to the potential together give

$$V_F + V_D = |F - \lambda\phi_1\tilde{\phi}_2|^2 + |\lambda X\tilde{\phi}_2 + m\tilde{\phi}_1|^2 + |\lambda X\phi_1 + m\phi_2|^2 + |m\phi_1|^2 + |m\tilde{\phi}_2|^2 + \frac{g^2}{2} \left(\frac{D}{g} + |\phi_1|^2 - |\tilde{\phi}_1|^2 + |\phi_2|^2 - |\tilde{\phi}_2|^2 \right)^2, \quad (4.15)$$

where g is the gauge coupling of the $U(1)_D$ symmetry and we have also included a UV Fayet-Iliopoulos (FI) term D/g . This FI term contributes a second source of SUSY breaking that will strengthen the GW signal. Note that the model contains, in addition to the O’Raifeartaigh degrees of freedom, a gauge boson and gaugino associated with the $U(1)_D$ vector multiplet. We focus on the regime where $y_F \lesssim 1$ and we do not discuss the origin of the FI term here.⁷

The scalar potential at zero temperature. As a first step, we analyze the zero-temperature vacuum structure and map it onto the parameterization of section 3. Neglecting the gauge dynamics, the tree-level potential has a minimum at $\phi_i = \tilde{\phi}_i = 0$ where SUSY is broken everywhere along the F -flat pseudomoduli space parameterized by X . Including the gauge interactions, the minimization of the D -term part of potential favors configurations where the $\tilde{\phi}_i$ fields acquire a VEV to compensate for the FI term D/g . This results in a tension between the minimization of the F -term and D -term contributions to the potential. While the F -term can never be set to zero, one can find a runaway direction in field space which leads, asymptotically, to the vanishing of the D -term.

First, we can solve for the F -terms of Φ_1 and $\tilde{\Phi}_2$ by taking

$$\tilde{\phi}_1 = -\frac{\lambda}{m} X \tilde{\phi}_2, \quad \phi_2 = -\frac{\lambda}{m} X \phi_1. \quad (4.16)$$

On this solution the scalar potential simplifies to

$$V = |F^2 - \lambda\phi_1\tilde{\phi}_2|^2 + |m\phi_1|^2 + |m\tilde{\phi}_2|^2 \quad (4.17)$$

$$+ \frac{g^2}{2} \left[|\phi_1|^2 \left(\frac{\lambda^2 |X|^2}{m^2} + 1 \right) - |\tilde{\phi}_2|^2 \left(\frac{\lambda^2 |X|^2}{m^2} + 1 \right) + \frac{D}{g} \right]^2. \quad (4.18)$$

Note that $\phi_1, \tilde{\phi}_2$ have vanishing R -charge, so the only direction where the R -symmetry is spontaneously broken is along x . In order to visualize the shape of the scalar potential

⁷The inclusion of a fundamental FI term is not strictly required to obtain a strong FOPT. A very similar potential for the pseudomodule can be obtained by considering two different masses for the messengers and working in the regime where $\lambda F > m_1 m_2$. Models with multiple F -terms would also lead to similar conclusions.

and the approach to the runaway, we show in figure 8 the tree level scalar potential as a function of x , as well as the values of ϕ_1 and $\tilde{\phi}_2$ as a function of x .

The scalar potential is flat around the origin and then turns to the runaway direction along which the D -term diminishes. The turning point along x is where the fields ϕ_1 and $\tilde{\phi}_2$ acquire a non-vanishing VEV. The VEV of ϕ_1 is different from zero since the potential energy is most efficiently minimized if ϕ_1 partially cancels the first term in (4.18) as well as minimizing the D -term. The VEV of ϕ_1 is suppressed by a factor $\sim \frac{gF}{\lambda D}$ with respect to the VEV of $\tilde{\phi}_2$. An analytic estimate of the scalar potential can then be captured by working at zeroth order in the VEV of ϕ_1 . In this approximation, and focusing on the parameter region where $gD/m^2 < 1$, the effective mass-squared for the $\tilde{\phi}_2$ field is X -dependent,

$$m_{\tilde{\phi}_2}^2 = m^2 - gD - \frac{\lambda^2 gD}{2m^2} x^2 \quad \Rightarrow \quad x_{\text{trans}}^2 \simeq \frac{2m^2(m^2 - gD)}{\lambda^2 gD} \quad (4.19)$$

and turns negative at the transition point x_{trans} where the field $\tilde{\phi}_2$ develops a VEV.

The potential for x is flat for $x \leq x_{\text{trans}}$, while for $x \geq x_{\text{trans}}$ it can be obtained by integrating out $\tilde{\phi}_2$,

$$V_{\text{tree}}(x) \simeq \begin{cases} F^2 + \frac{1}{2}D^2 = V_+ & x < x_{\text{trans}} \\ F^2 + \frac{1}{2}D^2 - \frac{\lambda^4 D^2 (x^2 - x_{\text{trans}}^2)^2}{2(2m^2 + \lambda^2 x^2)^2} & x > x_{\text{trans}} \end{cases} . \quad (4.20)$$

Since we work in the small- g regime, radiative corrections from the gauge sector may be neglected, such that the 1-loop corrections are the same as the ones discussed in the previous sections (see eq.s (4.4) and (4.5)). They have two effects, namely i) they create a local minimum at the origin, and ii) they generate a global minimum at large x values along the D -flat direction.

The barrier between the two vacua is approximately at $x \simeq x_{\text{trans}}$ where we can estimate the one-loop potential simply by the large field behaviour in (4.5), giving

$$V_P - V_+ \simeq \frac{\lambda^2 F^2}{16\pi^2} \log \left(\frac{x_{\text{trans}}^2}{m^2} \right), \quad x_P \simeq x_{\text{trans}} . \quad (4.21)$$

Combining the approximate tree level potential in (4.20) with the loop corrections in (4.5), we find that the true vacuum at large field values lies at

$$\langle x \rangle_{\text{true}} = f_a \simeq \frac{4\sqrt{2}\pi}{\lambda y_F} \sqrt{\frac{D}{g}}, \quad \Delta V \simeq \frac{1}{2}D^2, \quad (4.22)$$

where the difference in potential energy between the two minima is dominated by the D -term contribution. This completes the matching of the potential of this model to the general discussion of section 3. Note that here the SUSY-breaking F -term controls the height of the barrier in eq. (4.21), while the SUSY-breaking D -term sets the potential energy difference as in eq. (4.22). This implies that the phase transition can have sizable values of α , as we will see in the numerical analysis.

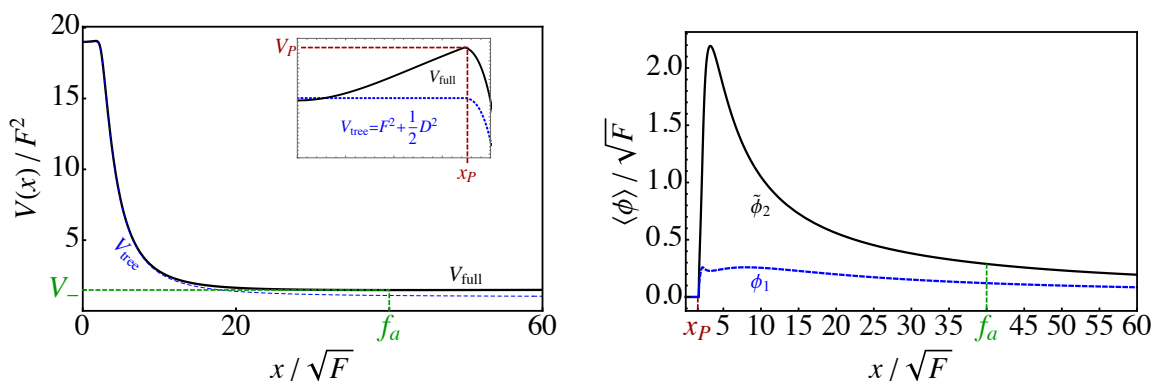


Figure 8. *Left:* tree level and one-loop scalar potential as a function of the pseudomodulus direction x minimizing the directions ϕ_1 and $\tilde{\phi}_2$. The *dashed blue* line shows the tree level potential which is flat around the origin and develops a runaway at $x_P \simeq x_{\text{trans}}$ (see Eq. (4.19)). Quantum corrections generate a local minimum at the origin as shown by the *black solid* line in the small quadrant and a global minimum far away in field space indicated with a *green dashed* line. The difference in energy density is $\Delta V \simeq \frac{1}{2}D^2$. *Right:* the VEVs of the fields ϕ_1 and $\tilde{\phi}_2$ while moving along the x -direction. Interestingly, both VEVs increase only at the barrier and they are otherwise quite small compared to \sqrt{F} . For reference, the benchmark used in both plots has $(F = 1, m = 2, D = 6, \lambda = 2.9, g = 1)$.

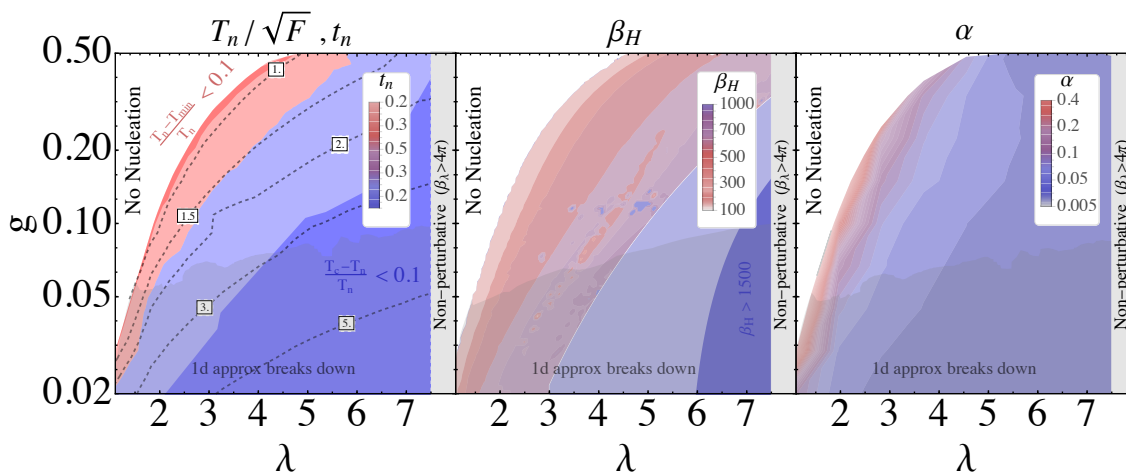


Figure 9. From the left to the right we show the behavior of T_n/\sqrt{F} , β_H and α in the O’Raifeartaigh model with gauge interactions described in eq. (4.18). We fix $F = 30$ PeV, $y_F = 3/4$ and $y_D = 1/5$ so that the entire parameter space of the model can be shown in the (λ, g) plane. The *black dashed contours* in the left plot show T_n/\sqrt{F} . The *red-to-blue* gradients show contours of t_n as defined in eq. (4.12) (left), of β_H as defined in eq. (2.16) (center) and of α as defined in eq. (2.15) (right). The GW signal weakens going from red to blue. In the *gray shaded* region at the bottom $R_{1d/3d} > 0.5$ and as described in eq. (4.23) our *1d* approximation is expected to break down. The *gray* region on the left is excluded by the perturbativity of λ below m . In the *white* region the nucleation condition in eq. (2.13) cannot be satisfied.

4.3.1 First order phase transition dynamics

We now turn to the finite-temperature corrections and compute the parameters associated with the phase transition. Note that the spectrum is similar to the O’Raifeartaigh model with the addition of the gauge boson and the gaugino of the $U(1)_D$ symmetry. These additional states are massless in the false vacuum and massive in the true vacuum, so they contribute to making the origin the global minimum at high temperatures.

We numerically evaluate the one-loop and the thermal corrections to the scalar potential, and then compute the bounce action for tunneling from the false vacuum to the true vacuum. In appendix B.1.2 we present the triangular barrier approximation for this model and compare it with the full numerics. Even though the bounce profile in field space involves three different fields, i.e. $(x, \phi_1, \tilde{\phi}_2)$, in our numerical scan, we approximate the bounce as one-dimensional, neglecting the contribution from the $\phi_1, \tilde{\phi}_2$ directions. As detailed in appendix B.2, we checked the single field approximation against the full $3d$ bounce action computed numerically with both FindBounce [88] and CosmoTransitions [89]. As a result, the single field approximation gives a good description of the bounce as long as $\phi_1, \tilde{\phi}_2$ are smaller than X at the bounce release point (defined as the starting point of the tunneling set at $r = 0$, where the kinetic terms of all the fields are exactly zero). In order to estimate where we expect sizable deviations from the multidimensional contribution, we borrow some intuition from the triangular barrier approximation, where S_3/T scales as $\sim X^3$, and define

$$R_{1d/3d} \stackrel{\text{def}}{=} \frac{X^3(r)}{\left(X^2(r) + \phi_1^2(r) + \tilde{\phi}_2^2(r)\right)^{3/2}} \Bigg|_{r=0}, \quad (4.23)$$

where $X(0)$, $\phi_1(0)$ and $\tilde{\phi}_2(0)$ are the field distances from the origin computed at the release point $r = 0$. In figure 9 we show the region where $R_{1d/3d} > 0.5$ and we expect deviations of 50% or more from our one-dimensional estimate of the bounce action. As we can see, this region is not phenomenologically relevant since it is quite far from the interesting region for GW signals.

The parameter space of this model can be explored at fixed F , after fixing the two ratios

$$y_F \stackrel{\text{def}}{=} \frac{\lambda F}{m^2}, \quad y_D \stackrel{\text{def}}{=} \frac{gD}{m^2}. \quad (4.24)$$

In figure 9 we show the behavior of T_n , α , and β_H in the (λ, g) plane, having fixed $\sqrt{F} = 30$ PeV and $y_F = 3/4$ as in the previous model and set $y_D = 1/5$. Keeping fixed the ratios in eq. (4.24), the triangular barrier parameters scale as

$$f_a \sim \frac{1}{g\sqrt{\lambda}}, \quad \frac{\Delta V}{F^2} \sim \frac{\lambda^2}{g^2}, \quad \frac{V_P}{F^2} \sim \lambda^2, \quad \frac{m_*}{\sqrt{F}} \sim \sqrt{\lambda}. \quad (4.25)$$

As a consequence of these scalings, using eq. (3.11) it is straightforward to see that for fixed λ the boundary of the nucleation region is reached for large g , while for fixed g the boundary lies at small λ . The shape of the nucleation temperature T_n can be captured by

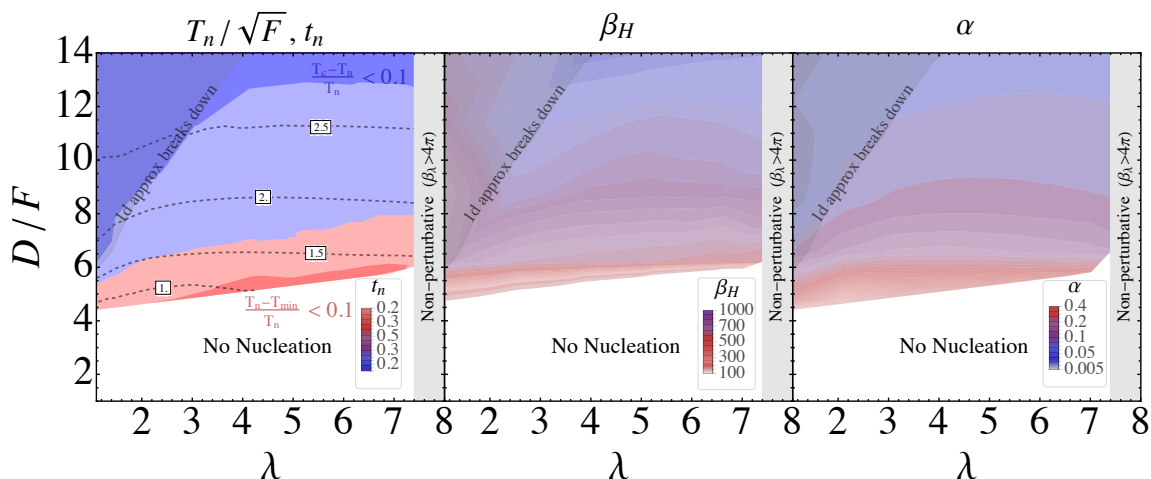


Figure 10. Same as in figure 9 but in the $(\lambda, D/F)$ plane, fixing $F = 30$ PeV, $y_F = 3/4$ and $g = 0.1$.

a simple analytic formula after rewriting eq. (3.15) in terms of the theory parameters:

$$T_n \sim 0.73\sqrt{\lambda F} \frac{1}{\log\left(1 + \frac{22.5}{c^{4/21}} \left(\frac{g}{\lambda}\right)^{4/7}\right)} \left(1 - 20.5 \left(\frac{g^6}{c^2 \lambda^6}\right)^{1/5}\right). \quad (4.26)$$

This expression reproduces the contours in figure 9 (left) up to overall normalization.

In the middle and right panels of figure 9 we show the contours for β_H and α , respectively. The main difference compared to the model in section 4.2 is that even if $T_n \sim \sqrt{F}$, it is possible to obtain sizable values of α because ΔV is here controlled by the D -term. Approaching the boundary of the nucleation zone without fine-tuning the theory parameters by more than $\mathcal{O}(1)$ we can reach $\beta_H \sim 100$ and $\alpha \sim 0.3 - 0.4$, which we use as a benchmark for our summary plot in figure 1.

The interplay of the two SUSY-breaking scales \sqrt{F} and \sqrt{D} is an essential ingredient for a strong FOPT. This is illustrated in figure 10, where we show the behavior of T_n , α , and β_H in the $(\lambda, D/F)$ plane, having again set $\sqrt{F} = 30$ PeV and $y_F = 3/4$, and now fixing $g = 0.1$. In this scaling the FOPT is essentially independent of λ , and one can see clearly that the separation of D from F is the crucial ingredient for a sufficiently strong phase transition. Notice that the required separation is $\mathcal{O}(1)$ and therefore not obviously in tension with theoretical bounds on large D -terms [96]. Strictly speaking, these bounds do not apply to our simple model, where a tree level Fayet-Iliopoulos term makes the Ferrara-Zumino multiplet not gauge invariant [97]. However they would have applied if we were to UV complete this model to a full-fledged model of dynamical SUSY-breaking or for instance if we were to explore the second branch of the model with two different messengers masses and $\lambda F > m_1 m_2$.

4.3.2 Gravitational wave spectrum and phenomenology

Having shown that a strong FOPT can be achieved without fine-tuning in a SUSY-breaking hidden sector with at least two SUSY-breaking scales, we now turn to the gravitational

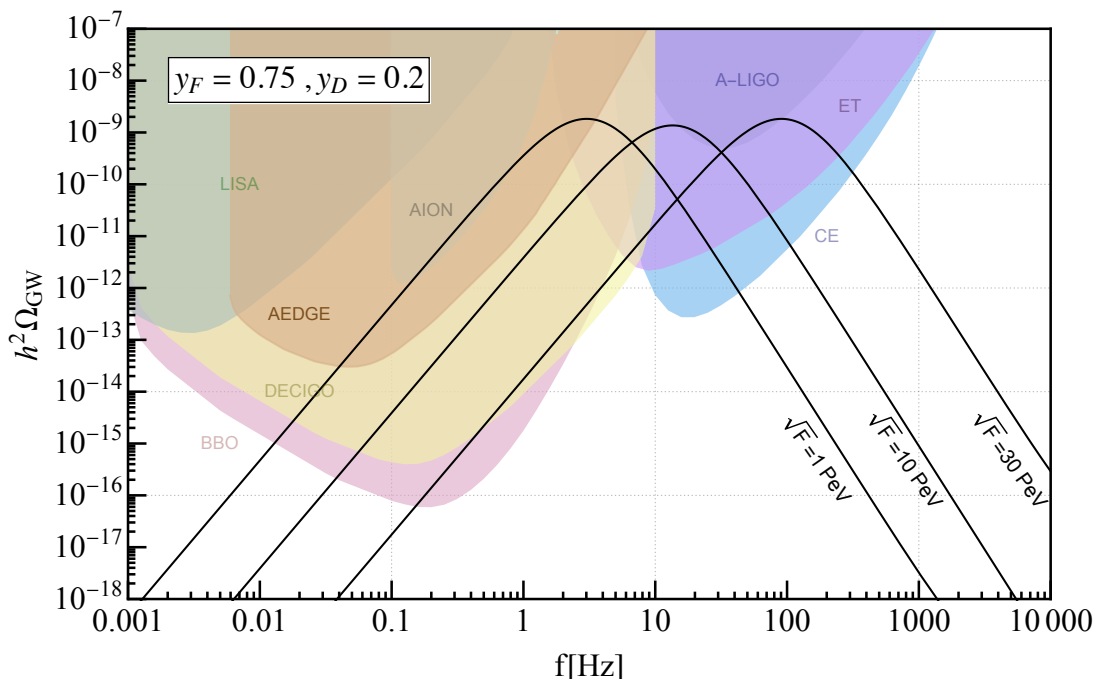


Figure 11. Predicted SGWB in the O’Raifeartaigh model with gauge interactions. We show the prediction for various values of the SUSY-breaking scale $\sqrt{F} = 1, 10, 30$ PeV and choose the theory parameters such that $\alpha \simeq 0.3$ and $\beta_H \simeq 50$. As discussed in the text, achieving these values does not require any tuning in this model. The SUSY-breaking scale correlates with the peak frequency of the GW spectrum, which is always dominated by sound waves as shown in eq. (4.28).

wave signal itself, again using the simple model presented in the previous section as a benchmark. As discussed in section 2.2, computing the SGWB signal requires understanding the macroscopic dynamics of the vacuum bubbles expanding in the plasma. This is essentially determined by the balance of the energy ΔV released in the FOPT and the pressure effects from the plasma (see eq. (2.19)). If pressure effects stop the bubbles before they collide, most of the SGWB signal will be sourced by the energy released in the plasma.

In section 2.2 we described a quite unique friction mechanism at work in our class of models. This mechanism is a direct consequence of two peculiar features of the pseudomodulus potential: i) the nucleation temperature $T_n \sim \sqrt{F}$ is set by exponentially suppressed temperature corrections to be smaller than the typical scale of the heavy states in the theory m , and ii) the true vacuum VEV is typically the larger scale in the problem and controls the mass variation $\Delta m^2/m^2 \sim \lambda^2 f_a^2/m^2 \gg 1$ of the heavy states from the false to the true vacuum. These two properties together imply that when the vacuum bubbles accelerate enough, $\gamma T_n > m_{\text{true}}$ and the heavy states can cross the bubble wall. Their crossing switches on a new pressure effect which is generically larger than ΔV and immediately stops the bubble runaway.

This last statement can be checked explicitly with the parametric dependence of the simple model described here. The heavy state pressure term in eq. (2.21) scales as

$$\Delta P_{\text{LO}}^{\text{heavy}} \sim \frac{4\pi^2}{3y_F^2 g} F D e^{-m_{\text{false}}/\sqrt{F}}, \quad (4.27)$$

where we used the scaling of the true vacuum as a function of the theory parameters in eq. (4.22) and approximated $T_n \simeq \sqrt{F}$ for simplicity (this approximation is numerically correct up to an $\mathcal{O}(1)$ factor as shown by the dashed contours in figure 9). Inside the exponential, we should take the lightest heavy states in the plasma $m_{\text{false}} \sim \sqrt{m^2 - \lambda F}$ which are of course less Boltzmann suppressed and dominate the friction. Comparing this quantity with the energy released in the phase transition $\Delta V = D^2/2$ we can get the range of the gauge coupling g such that this friction prevents the bubble runaway,

$$g \lesssim \frac{8\pi^2 F}{3y_F D} e^{-m_{\text{false}}/\sqrt{F}}. \quad (4.28)$$

Plugging in the typical numbers for our phase transition ($F/D \sim 1/5$, $y_F \sim 3/4$ and $m_{\text{false}}/\sqrt{F} \lesssim \sqrt{\lambda} \lesssim 2.5$) indicates that the vacuum bubbles are always stopped in the range of interest for the gauge coupling g for perturbative values of λ . The predicted boost factor at equilibrium in this case is

$$\gamma_{\text{eq}}^{\text{heavy}} = \frac{m_{\text{true}}}{T_n} \sim \frac{\lambda f_a}{\sqrt{F}}, \quad (4.29)$$

where again f_a is defined in this model by eq. (4.22). As a final remark, we notice that the NLO friction induced by gauge degrees of freedom radiated through the wall never dominates over the one from heavy states in the interesting range of the gauge coupling g .

Given that the bubble runaway is always prevented, the dominant SGWB comes from sound waves in the plasma. The predicted energy fraction as a function of frequency at GW interferometers has been discussed in eq. (2.25) and below. Putting everything together, in figure 11 we compare our model predictions with the PLI curves for future GW interferometers derived in appendix C.1. This clearly demonstrates that SUSY-breaking hidden sectors with multiple SUSY-breaking scales can generate stochastic signals detectable at future GW interferometers. Moreover, it makes explicit the expected correlation between the SUSY-breaking scale and the peak frequency of the resulting SGBW. All that remains is to explore the full range of viable SUSY-breaking scales (and hence signal frequencies), as well as the correlation between signals at GW interferometers and other experiments. In the next section, we will bound the SUSY-breaking scale from above around \sim few tens of PeV by computing the gravitino cosmological abundance. By specifying a mediation mechanism, we will also use the explicit hidden sector presented here to show how the SUSY-breaking scale determines the spectrum of MSSM superpartners, thereby correlating signals at GW interferometers and future colliders.

5 Phenomenology

Having demonstrated that the first-order phase transition in a SUSY-breaking hidden sector can generate an observable GW signal, we now turn to complementary aspects of hidden

sector phenomenology that shape the motivated parameter space and suggest additional experimental tests in the event of a signal at GW interferometers. We begin with universal features that are intrinsic to the hidden sector itself and independent of the mediation mechanism that connects the hidden sector to the MSSM. This includes key aspects of gravitino cosmology, where we will see that the requirement $T_{\text{r.h.}} = \sqrt{F}$ implies an upper bound on \sqrt{F} even if $m_{3/2}$ receives extra contribution from other SUSY-breaking sectors as in eq. (2.2). We also explore the prospects for collider searches for the gravitino (independent of the MSSM spectrum), finding that future high energy lepton colliders could probe almost the entirety of the light gravitino window (i.e. $m_{3/2} < 16$ eV) by directly producing gravitino pairs. We then relate the parameters of the hidden sector to the spectrum of the MSSM, which requires specifying details of the mediation mechanism. Here we consider the prototypical example of gauge mediation via vector-like messengers, where the parameter space for observable GW signals generates a superpartner spectrum within reach of future proton-proton colliders such as FCC-hh.

5.1 Gravitino cosmology vs future colliders

The gravitino overabundance is a well known problem of LESB scenarios [38–40]. This problem is exacerbated in our setup, because having sizeable GW signals from the SUSY-breaking hidden sector requires the reheating temperature $T_{\text{r.h.}}$ to be at least as high as the SUSY-breaking scale, enhancing the gravitino production from scattering as detailed in eq. (2.8). In light of this tension, here we delve into further detail about the two viable scenarios sketched section 2.3. Since $T_{\text{r.h.}} \sim \sqrt{F}$, which is much larger than the scale of the soft masses, the main player in determining the final gravitino abundance is the production from UV scattering computed in [43–46]. The final yield can be written as

$$Y_{3/2}^{\text{UV}} = C_{\text{UV}} \frac{M_3^2 \sqrt{F}}{m_{3/2}^2 M_{\text{Pl}}}, \quad C_{\text{UV}} = \frac{45\sqrt{5}f_3}{8\pi^{13/2}g_*^{3/2}} \simeq 4 \times 10^{-5}, \quad (5.1)$$

where the production through gluon-gluino scattering dominates over the other channels and we have substituted $T_{\text{r.h.}} \simeq \sqrt{F}$, which is the lowest reheating temperature compatible with our scenario. Following eq. (2.2), we assume that the gravitino mass $m_{3/2}$ is set by an independent SUSY-breaking scale $F_0 = F/\kappa$, possibly higher than the one setting the soft spectrum (i.e. $\kappa \ll 1$).

Ultralight gravitino window vs. pair production at future colliders. If the gravitino mass and the soft spectrum are set by the same SUSY-breaking scale \sqrt{F} , the yield scales as $Y_{3/2}^{\text{UV}} \sim M_{\text{Pl}}/\sqrt{F}$. For sufficiently low SUSY-breaking scales, the yield becomes just the equilibrium one, $Y_{3/2}^{\text{UV}} > Y_{\text{eq}}$, where $Y_{\text{eq}} = n_{3/2}^{\text{eq}}/s = 1.8 \times 10^{-3}$. The gravitino is a thermal relic as long as $\sqrt{F} \lesssim \left(\frac{3}{45}M_{\text{Pl}}M_3^2\right)^{1/3}$, which corresponds to $\sqrt{F} \lesssim 8.6 \times 10^7$ GeV for $M_3 = 2$ TeV. Moreover, since $\sqrt{F} \gg m_{3/2}$, the gravitino is relativistic at freeze-out and its abundance today is constrained by measurements of the matter power spectrum at short scales [41, 42]. The current bounds imply

$$m_{3/2} \lesssim 16 \text{ eV}, \quad F \lesssim 260 \text{ TeV}. \quad (5.2)$$

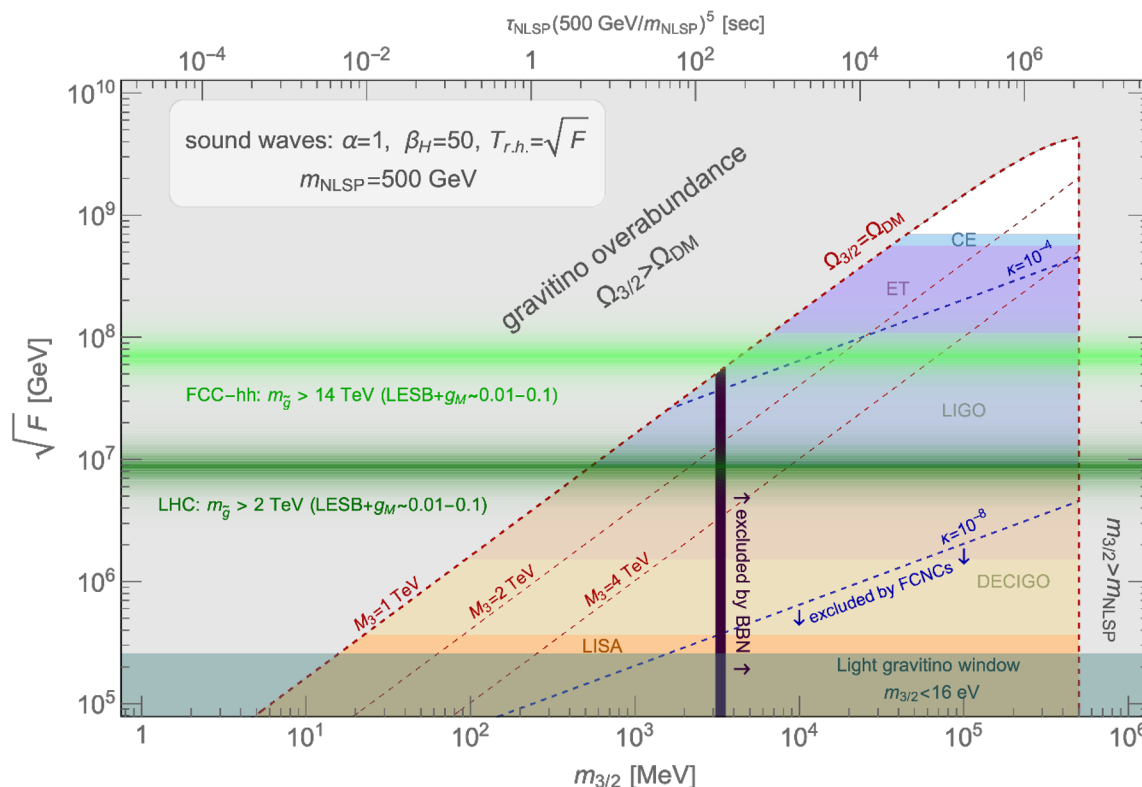


Figure 12. Parameter space of low energy SUSY-breaking in the $(m_{3/2}, \sqrt{F})$ plane. The *gray shaded* region is excluded by gravitino overabundance and the requirement $m_{3/2} < m_{\text{NLSP}}$, having fixed $m_{\text{NLSP}} = 500$ GeV. The red dashed line shows the region where $\Omega_{3/2} = \Omega_{\text{DM}}$ for different values of the gluino soft mass. The colored regions show the sensitivities of different GW interferometers to signals with fixed $\alpha = 1$ and $\beta_H = 50$. The two *dark green* and *light green* bands show the impact of the present LHC bounds [25–28] and the future FCC-hh reach on gluinos [29] for perturbative messenger sectors with $g_M \in (0.01, 0.1)$ (see eq. (2.10) for a definition of g_M). The *dark blue dashed* lines show the values of $\kappa = F/F_0$, the ratio between the total SUSY-breaking scale F_0 and one controlling the soft masses (see eq. (2.2)). As discussed in eq. (2.11), we expect constraints on flavor changing neutral currents to exclude $\kappa \lesssim 10^{-8}$ as indicated by the *dark blue arrows*. The *dark magenta thick* line indicates the BBN bound on the higgsino NLSP decaying to gravitino plus hadrons as obtained in [31].

The above requirement identifies the *ultralight gravitino window*. Although it is unquestionably challenging to decouple the soft spectrum from the LHC in this window (see [81, 82] for attempts in this direction), it is interesting to ask whether future colliders can test this window in a model-independent fashion through direct pair production of the longitudinal component of the gravitino, the goldstino. This production rate depends directly on \sqrt{F} even when the MSSM superpartners are decoupled, and so provides a direct experimental test of the SUSY-breaking sector.

The projected sensitivity to gravitino pair production at both hadron and lepton colliders is displayed in figure 1. For the bound at future lepton colliders, we consider a high energy lepton collider operating at $\sqrt{s} = 30$ TeV. Assuming minimal cuts on the photon

kinematics ($E_\gamma > 50 \text{ GeV}$, $|\eta_\gamma| < 2.4$), the signal cross section from eq. (2.7) is

$$\sigma_{30\text{TeV}}(\ell^+\ell^- \rightarrow \tilde{G}\tilde{G}\gamma) \simeq 487 \text{ fb} \left(\frac{10 \text{ TeV}}{\sqrt{F}} \right)^8. \quad (5.3)$$

Applying the same minimal cuts on the photon, the SM background (estimated with MadGraph5 [98, 99]) is $\sigma_{SM} \simeq 2\text{pb}$. In contrast to LEP, at high energy lepton colliders the SM background is dominated by WW fusion while the Drell-Yan process with an ISR photon is negligible. We can then derive a lower bound on the scale of SUSY breaking as displayed in figure 1 given an assumed integrated luminosity, namely

$$\sqrt{F} \gtrsim 25 \text{ TeV} \left(\frac{\mathcal{L}}{100 \text{ ab}^{-1}} \right)^{1/16}, \quad (5.4)$$

which is still an order of magnitude away from entirely closing the ultralight gravitino window. However, improved analyses and new cosmological data could strengthen the gravitino mass bound by an order of magnitude, potentially closing the ultralight gravitino window completely. For instance, ref. [100] already claims a bound on the gravitino mass of $m_{3/2} < 4.7 \text{ eV}$; although the robustness of this bound is subject to interpretation, improved limits from Planck data are likely to be comparable.

In order to estimate the reach of future hadron colliders, we perform a rescaling of the limits discussed in [24], based on the mono-photon search of ATLAS [101], which constrain $\sqrt{F} \gtrsim 850\text{GeV}$ with 20.3fb^{-1} at $\sqrt{s} = 8 \text{ TeV}$.⁸ As at lepton colliders, the signal cross section for gravitino pair production in association with a photon $\sigma(pp \rightarrow \tilde{G}\tilde{G}\gamma)$ scales as s^3/F^4 at hadron colliders [23]. To estimate the limit attainable at $\sqrt{s} = 100 \text{ TeV}$, we first compute the ratio of the signal cross sections at $\sqrt{s} = 100 \text{ TeV}$ and $\sqrt{s} = 8 \text{ TeV}$, taking the partonic signal cross section to scale as $\sigma_{\text{sig}} \sim \hat{s}^3/F^4$ and assuming that the $p_{T,\gamma} \geq 125 \text{ GeV}$ cut at $\sqrt{s} = 8 \text{ TeV}$ is increased to $p_{T,\gamma} \geq 1 \text{ TeV}$ at $\sqrt{s} = 100 \text{ TeV}$. We additionally compute the ratio of background cross sections, assuming the partonic background cross section scales as $\sigma_{\text{bkg}} \sim 1/\hat{s}$. Using the $\sqrt{s} = 8 \text{ TeV}$ signal and background predictions in [101] and the above ratios, we find the expected limit at $\sqrt{s} = 100 \text{ TeV}$ to be

$$\sqrt{F} \gtrsim 12 \text{ TeV} \left(\frac{\sqrt{s}}{100 \text{ TeV}} \right)^{3/4} \left(\frac{\mathcal{L}}{30 \text{ ab}^{-1}} \right)^{1/16}, \quad (5.5)$$

which is the one displayed in figure 1. Even with this aggressive estimate, the reach of high energy hadron colliders is limited compared to the reach of high energy lepton colliders because the signal cross section at the former only grows with \hat{s}^3 , while at the latter it grows as s^3 .

Gravitino dark matter window. If the SUSY-breaking scale $\sqrt{F_0}$ setting the gravitino mass exceeds the scale \sqrt{F} of the hidden sector, we can treat $m_{3/2}$ as a free parameter and access an interesting region where the gravitino is never in thermal equilibrium with the SM.

⁸The bounds from mono-jet searches are comparable [24], but involve backgrounds from a mix of both quark- and gluon-initiated processes that are less amenable to simple rescaling. Thus we focus on the mono-photon signal for simplicity.

This could arise naturally from additional sequestered sectors that break supersymmetry at higher scales. As shown in figure 12, we also require this new source of SUSY-breaking to not spoil the defining phenomenological features of LESB, namely i) the gravitino is still the LSP, and ii) the soft masses are dominated by the flavor-diagonal contribution from gauge mediation.

Requiring the gravitino avoid thermalization, $Y_{3/2}^{\text{UV}} < Y_{\text{eq}}$, we obtain an upper bound on \sqrt{F} at fixed gravitino mass which can be cast as an upper bound on the ratio between the two SUSY-breaking scales, $\kappa = F/F_0$:

$$Y_{3/2}^{\text{UV}} < Y_{\text{eq}} \quad \Rightarrow \quad \kappa < 0.02 \left(\frac{F}{10^7 \text{ GeV}} \right)^{1/4} \left(\frac{0.1}{g_M} \right), \quad (5.6)$$

Here we have used the expression for the gravitino mass in eq. (2.2) and the one for the gluinos in eq. (2.10), where the parameter g_M encodes the model-dependence of the latter. If the gravitino is never in thermal equilibrium, we can assume (as usual in freeze-in scenarios) that the gravitino sector is not directly reheated after inflation and the gravitino abundance is frozen-in through scattering of SM states with their superpartners. Setting the gravitino abundance to explain the DM abundance today, we can predict the gluino mass in the $(m_{3/2}, \sqrt{F})$ plane,

$$M_3 \simeq 2 \text{ TeV} \left(\frac{10^7 \text{ GeV}}{\sqrt{F}} \right)^{1/2} \left(\frac{m_{3/2}}{2.5 \text{ GeV}} \right)^{1/2} \simeq 2 \text{ TeV} \left(\frac{\sqrt{F}}{10^7 \text{ GeV}} \right)^{1/2} \left(\frac{10^{-5}}{\kappa} \right), \quad (5.7)$$

which corresponds to the red lines of figure 12 where the gravitino accounts for the total DM abundance today at fixed gluino mass. The current LHC bounds on the gluino mass set a boundary of our parameter space, which is shown in figure 12.⁹ The second scaling in eq. (5.7) shows the value of κ required to achieve a given gluino mass. As shown in figure 12, the parameter space of interest has κ between $(10^{-8}, 10^{-4})$, where smaller values of κ would not open up more parameter space and in any event would be in tension with FCNC constraints as discussed in eq. (2.11).

The bound at larger gravitino masses (the gray band on the r.h.s. on figure 12) is given by the requirement that the gravitino be the LSP. A stronger bound is derived from BBN constraints on the freeze-out abundance of the NLSP decaying into gravitinos. We have computed the NLSP freeze-out abundance assuming the NLSP is a pure higgsino NLSP and applied the BBN bound of ref. [31] given the NLSP lifetime in eq. (2.6). The triangular-shaped region where the gravitino could be DM can be probed by both GW interferometers and future colliders, as shown in figure 12. This highlights the potential for future colliders to determine whether a SUSY-breaking phase transition is the source of a SGWB signal observed at GW interferometers.

5.2 A complete model of gauge mediation

Finally, we can correlate the GW signals of the SUSY-breaking hidden sector with the superpartner spectrum of the MSSM by specifying a mediation mechanism. In order to

⁹Strictly speaking, the gluino mass here is the soft mass at computed at the high scale; since the low-scale pole mass will be larger, we generously show the parameter space up to $M_3 = 1 \text{ TeV}$.

embed the model of section 4.3 into a successful model of gauge mediation, we work in terms of a simple generalization of the gauged O’Raifeartaigh model which allows a natural embedding of both the gauged $U(1)_D$ symmetry and the SM gauge group into the flavor symmetry of the messengers. This requires M copies of the vector-like messengers Φ and $\tilde{\Phi}$ coupled to the singlet X , so that the superpotential is identical to the one of the O’Raifeartaigh model in eq. (4.2), but where now the fields are intended as vectors with M components. The minimal setup requires $M = 6$ so that the superpotential enjoys an $SU(6)$ symmetry, where a $U(1)$ subgroup of the $SU(6)$ is the gauged $U(1)_D$ with a non vanishing Fayet-Iliopoulos term, while the SM gauge group lies inside the remaining global $SU(5)$ such that the messengers can be taken to transform in the $5 + \bar{5}$ representation of $SU(5)$ as in standard gauge mediation scenarios [36].

The mass matrix of the messenger fields is

$$\mathcal{M}_{\text{mess}} = \begin{pmatrix} \frac{\lambda f_a}{\sqrt{2}} & m \\ m & 0 \end{pmatrix}, \tag{5.8}$$

where f_a is the VEV of the pseudomodulus given in eq. (4.22). Integrating out the messengers, one can compute the soft masses for the MSSM following the general formulas in [102]. The scalar masses follow the standard gauge mediation scaling discussed in eq. (2.9), while it is worth explicitly writing the parametric dependence of the gluino soft mass in the notation of eq. (2.9):

$$M_3 = \frac{\alpha_3}{4\pi} \frac{\sqrt{2}F}{f_a} s_M, \quad s_M = \frac{y_F^2}{6}. \tag{5.9}$$

Here we have expanded in $\lambda f_a \gg m \gtrsim F$ and identified the gaugino screening factor s_M in this model. Since we typically have $y_F \sim 1$ in our scenarios (in order to remain in the green region of figure 5) the gaugino screening factor does not provide significant suppression, but interestingly it is generic for models like ours where the messengers mass matrix is never singular along the pseudomodulus direction [16, 53]. Abandoning this requirement, one could avoid gaugino screening at the price of opening up messenger field directions where the SM gauge group is spontaneously broken in the UV [103].

Substituting the value of f_a in eq. (4.22) and taking as benchmark values a typical point with $\alpha \sim 0.3$ and $\beta_H \sim 100$ from figure 9, the gaugino pole mass is

$$m_{\tilde{g}} \simeq 2 \text{ TeV} \left(\frac{F}{30 \text{ PeV}} \right)^{1/2} \left(\frac{y_F}{0.75} \right)^3 \left(\frac{F}{2.5D} \right)^{1/2} \left(\frac{\lambda}{4} \right) \left(\frac{g}{0.4} \right). \tag{5.10}$$

This shows that the band between the present exclusion at the LHC and the future reach of FCC-hh can be populated with simple, concrete models featuring strong SGWB signals within the reach of future high-frequency interferometers such as A-LIGO, ET and CE.

6 Conclusions

We began by asking if future gravity wave detectors could provide a new window into supersymmetry by probing SUSY-breaking hidden sectors in a region not yet excluded by

LHC searches. The answer to this question is well summarized in figure 1, which shows the complementarity of future gravitational wave interferometers and colliders in probing scenarios of low-energy supersymmetry breaking (LESB). Fortuitously, the cosmological history of the gravitino — a key degree of freedom in LESB scenarios — bounds the SUSY-breaking scale from above, so that the viable parameter space lies within reach of both high-frequency GW interferometers and high-energy colliders.

The underlying assumption in figure 1 is that the SUSY-breaking hidden sector actually undergoes a strong first-order phase transition. The remainder of the paper has been devoted to demonstrating, on general grounds, the circumstances under which strong FOPTs can be produced in SUSY-breaking hidden sectors. We have focused on phase transitions along the pseudomodulus direction, which as a universal feature of spontaneous SUSY-breaking is guaranteed to exist in a vast class of SUSY-breaking hidden sectors. Remarkably, the generic features of the pseudomodulus potential gave rise to a parametrically new way of realizing strong first-order phase transitions in field theory.

The novelty of the pseudomodulus FOPT is a consequence of the flatness of the tree-level potential accompanied by the presence of a mass gap for the heavy states, which makes the theory calculable everywhere in field space. Since the mass gap is supersymmetric, it does not destroy the flatness of the potential at large field values. The two resulting features of this setup are that i) the nucleation temperature is well below the scale of the heavy states, so that the low- T expansion applies, and ii) the pressure from Boltzmann-suppressed heavy states in the plasma is responsible for stopping the vacuum bubble runaway. The dominant GW signal then comes from the energy released in the plasma during the phase transition.

The strength of the GW signal depends on finer details of the hidden sector dynamics. However, we found that multiple SUSY-breaking scales in the hidden sector are a necessary condition for generating strong GW signals without fine tuning of the theory parameters. This result is quite general and can be obtained analytically without reference to a specific model. For the sake of concreteness, we presented an explicit model for a hidden sector generating a strong GW signal, where SUSY is broken by both an F -term and a D -term. Detailed predictions for the GW signal and superpartner spectrum in this model substantiate the general phenomenological observations of figure 1.

Acknowledgments

We thank Tomer Volansky for collaboration at the initial stage of this project. We thank Andrea Tesi for asking if there was a non-SUSY realization of our phase transitions. In trying to answer this question we realized how special these SUSY-breaking phase-transitions were. We also thank Daniele Barducci, Toby Opferkuch for interesting discussions. We thank Victor Guada for assistance with the FindBounce package. DR would like to thank the Galileo Galilei Institute for Theoretical Physics (GGI) for its hospitality, and Patrick Fox for useful discussions therein.

AM is supported by the Strategic Research Program High-Energy Physics and the Research Council of the Vrije Universiteit Brussel, and by the “Excellence of Science —

EOS” — be.h project n.30820817. NC is supported in part by the Department of Energy under the award DE-SC0011702. NL would like to thank the Milner Foundation for the award of a Milner Fellowship.

A The effective potential

The effective scalar potential is given by a sum of quantum and thermal contributions

$$V_{\text{eff}}(x, T) = V_0(x) + V_T(x, T). \quad (\text{A.1})$$

The temperature independent potential can be written as $V_0(x) = V_{\text{tree}}(x) + V_{\text{CW}}(x)$, where $V_{\text{CW}}(x)$ is the one loop Coleman-Weinberg potential at zero temperature which in the $\overline{\text{MS}}$ scheme is given by

$$V_{\text{CW}}(x) = \sum_i (-1)^F \frac{g_i m_i^4(x)}{64\pi^2} \left(\log \frac{m_i^2(x)}{m_0^2} - c_i \right), \quad (\text{A.2})$$

where $F = 1$ (0) for fermions (bosons), the number of degrees of freedom associated with the particle i is $g_i = 1/2/3$ for real scalars, fermions and vectors, respectively, and $c_i = \frac{3}{2}$ ($\frac{5}{2}$) for scalars/fermions (vectors). The thermal one-loop potential is given by

$$V_T(x, T) = \frac{T^4}{2\pi^2} \sum_i (-1)^F g_i J_{\text{B/F}} \left(\frac{m_i^2(x)}{T^2} \right), \quad (\text{A.3})$$

where the thermal functions for both species are

$$J_{\text{B/F}}(z^2) = \int_0^\infty dx x^2 \log[1 \mp \exp(-\sqrt{x^2 + z^2})], \quad (\text{A.4})$$

with $z_i \equiv m_i/T$. These functions can only be fully evaluated numerically, but admit analytical approximations for large and small $|z^2|$. In the high-temperature limit, $|z^2| \ll 1$ and the thermal functions are

$$\begin{aligned} J_B(z^2) &\approx J_B^{\text{high-}T}(z^2) = -\frac{\pi^4}{45} + \frac{\pi^2}{12} z^2 - \frac{\pi}{6} z^3 - \frac{1}{32} z^4 \log\left(\frac{z^2}{a_b}\right), \\ J_F(z^2) &\approx J_F^{\text{high-}T}(z^2) = \frac{7\pi^4}{360} - \frac{\pi^2}{24} z^2 - \frac{1}{32} z^4 \log\left(\frac{z^2}{a_f}\right), \quad \text{for } |z^2| \ll 1, \end{aligned} \quad (\text{A.5})$$

where $a_b = \pi^2 \exp(3/2 - 2\gamma_E)$ and $a_f = 16\pi^2 \exp(3/2 - 2\gamma_E)$. The low temperature limit (i.e. $|z^2| \gg 1$) can be approximated in terms of modified Bessel functions of the second kind

$$\begin{aligned} J_B(z^2) &= \tilde{J}_B^{(m)}(z^2) = -\sum_{n=1}^m \frac{1}{n^2} z^2 K_2(zn), \\ J_F(z^2) &= \tilde{J}_F^{(m)}(z^2) = -\sum_{n=1}^m \frac{(-1)^n}{n^2} z^2 K_2(zn), \quad \text{for } |z^2| \gg 1, \end{aligned} \quad (\text{A.6})$$

where m is high enough such that the series converge. For T low enough, we can take only the first term in the series and further expand the modified Bessel function to the leading order $K_\nu(z) \underset{z \rightarrow \infty}{\simeq} \sqrt{\frac{\pi}{2z}} e^{-z}$ to get

$$J_B(z^2) = -J_F(z^2) \underset{z \rightarrow \infty}{\simeq} - \left(\frac{\pi z^3}{2} \right)^{1/2} e^{-z}. \tag{A.7}$$

Within this approximation we can obtain a simple expression for $V_{\text{th}}(x, T)$ which is valid at the leading order in the low- T expansion:

$$V_T(x, T) \simeq -T^4 \sum_{\text{B/F}} g_i \left(\frac{m_i(x)}{2\pi T} \right)^{3/2} e^{-m_i(x)/T}, \tag{A.8}$$

where it is important to notice that bosons and fermions contribute with the same (negative) sign to the effective potential. The approximation above is used in section 3 to derive an analytical scaling of the dynamics of FOPTs.

Lambert function. As a consequence of the low- T expansion the equations we will be dealing with have the typical form

$$Az^{-a} e^{-z} - B = 0, \quad z = a\mathcal{W} \left[\frac{1}{a} \left(\frac{A}{B} \right)^{1/a} \right], \tag{A.9}$$

where $\mathcal{W}(z)$ is the Lambert function, which is defined such that $\mathcal{W}(z)e^{\mathcal{W}(z)} = z$. Without entering into the details of the interesting properties of this function, we restrict our interest to finding a good approximation for it using simpler functions. First, we will consider $\mathcal{W}(z)$ for strictly positive arguments. Second, we note that $\mathcal{W} \rightarrow 0$ for $z \rightarrow 0$ and that $\mathcal{W}(z) \sim \log z$ for $z \rightarrow \infty$. By inspection one finds that a good approximation of $\mathcal{W}(z)$ is given simply by

$$\mathcal{W}(z) \simeq \frac{3}{4} \log(1+z). \tag{A.10}$$

The relative difference between the Lambert function and the approximation with the logarithm in (A.10) is at most $\sim 1/4$ (for $z \rightarrow 0$ and $z \rightarrow \infty$) and smaller (in absolute value) in intermediate regions. For practical purposes in analytic estimations of relevant quantities, we will hence often consider the approximation in (A.10).

B Bounce action computation schemes

The transition of a quantum system from a meta-stable vacuum state to the true vacuum can be driven either by quantum tunneling or by thermal fluctuations. In the FOPTs describe in this paper the latter are always dominant. The probability of thermal tunnelling is described semi-classically by eq. 2.12 and it is exponentially dependent on the classical $O(3)$ -symmetric bounce solution [66, 67]. In this appendix we review both the analytical and the numerical approaches we used to study the behavior of the $O(3)$ -symmetric bounce in our FOPTs.

First, in section B.1, we describe in detail the triangular barrier approximation introduced in ref. [83] and its generalization to the $O(3)$ -symmetric case [84]. We compare this approximation with the behavior of the full bounce action computed numerically with the FindBounce package [88, 104] and the CosmoTransitions code [89]. In section B.1.1 we discuss an optimization of the triangular barrier approximation which leads to excellent agreement with the full numerical computation. In section B.1.2 we consider the O’Raifeartaigh model with gauge interactions of section 4.3 as our main case study.

Second, in section B.2 we discuss the single field approximation of the bounce action in the model of section 4.3. We study numerically the behavior of the bounce action in the full three-dimensional field space and compare it with the single field approximation, deriving where we expect the latter to deviate sensibly from the full solution.

B.1 Triangular barrier approximation of the bounce action

The d -dimensional Euclidean action for n scalar fields ϕ_i is

$$S_d = \Omega_d \sum_i \int_0^\infty r^{d-1} dr \left[\frac{1}{2} \dot{\phi}_i^2 + V(\phi_i) \right], \tag{B.1}$$

where $\Omega_d = 2\pi^{d/2}/\Gamma(d/2)$ and the equations of motion for ϕ_i are

$$\ddot{\phi}_i + \frac{(d-1)}{r} \dot{\phi}_i = V'(\phi_i). \tag{B.2}$$

The boundary conditions defining the bounce solution are

$$\dot{\phi}_i(r=0) = 0, \quad \phi_i(r \rightarrow \infty) = \phi_{i_f} \quad \text{and} \quad \dot{\phi}_i(r \rightarrow \infty) = 0, \tag{B.3}$$

where the conditions at $r \rightarrow \infty$ ensures that the solution starts with zero kinetic energy from the false vacuum and stops at $r = 0$ with zero kinetic energy. Here, we are interested in solving this equation for a single field ($n = 1$) and in $d = 3$.

The idea behind the triangular barrier approximation is to approximate the potential as a piecewise linear function anchored at three points: the false vacuum, the top of the barrier and the true vacuum. In the following, we review in some details the derivation of the 3d bounce action in the triangular barrier approximation, and we refer to the original paper [83] for more details and to [105] for the derivation in arbitrary dimensions.

Following the notation of [83], we define the false vacuum to be at the field position ϕ_+ with potential V_+ ; the peak of the triangular barrier to be at ϕ_P with potential V_P ; and the true vacuum to be at ϕ_- with potential V_- . It is then convenient to define the magnitudes of the gradients of the potential by

$$\lambda_\pm \stackrel{\text{def}}{=} \frac{\Delta V_\pm}{\Delta \phi_\pm}, \tag{B.4}$$

so that $V'(\phi) = \pm \lambda_\pm$ on either side of the barrier, precisely

$$V(\phi) = \begin{cases} V_+ + \lambda_+(\phi - \phi_+) & \text{for } \phi < \phi_P \\ V_- + \lambda_-(\phi - \phi_-) & \text{for } \phi > \phi_P \end{cases} \tag{B.5}$$

In order to solve the equation of motions we have to specify the boundary conditions. At a large radius R_+ the field attains the false vacuum, so we have

$$\phi(R_+) = \phi_+ \quad \dot{\phi}(R_+) = 0, \quad (\text{B.6})$$

Then, we have to specify the boundary conditions at the start of the tunneling. There are two possibilities:

1. The field immediately start to roll at $r = 0$ and hence we impose

$$\phi(0) = \phi_0 \quad \dot{\phi}(0) = 0, \quad (\text{B.7})$$

where the initial field value ϕ_0 is the undetermined release point. This is the valid regime if one finds that $\phi_0 \leq \phi_-$.

2. Otherwise, the field sits in the true vacuum for $r < R_0$ and then starts rolling. In this second case the boundary conditions are

$$\phi(r) = \phi_- \quad 0 < r < R_0 \quad (\text{B.8})$$

$$\phi(R_0) = \phi_- \quad \dot{\phi}(R_0) = 0, \quad (\text{B.9})$$

We begin with the analysis of the first case. Imposing the previous boundary conditions one finds the following solutions for the equations of motion in the different radius intervals

$$\phi(r) = \begin{cases} \phi_R(r) = \phi_0 - \frac{\lambda_-}{6} r^2 & 0 < r < R_P \\ \phi_L(r) = \phi_+ + \frac{\lambda_+}{6} \left(r^2 - 3R_+^2 + 2\frac{R_+^3}{r} \right) & R_P < r < R_+ \end{cases} \quad (\text{B.10})$$

Then we impose that the two solutions match at R_P and also that their first derivatives match at R_P , obtaining the following conditions

$$\phi_0 = \phi_P + \frac{\lambda_+ R_P^2}{6} \quad (\text{B.11})$$

$$R_P^3 = (1 + r_\lambda) R_+^3 \quad (\text{B.12})$$

$$R_P^2 = \frac{6\Delta\phi_+^2}{\left[3 + 2r_\lambda - 3(1 + r_\lambda)^{2/3} \right] \Delta V_+} \quad (\text{B.13})$$

where we have introduced $r_\lambda \equiv \frac{\lambda_-}{\lambda_+}$. Then we insert into the action the solutions (B.10) and we integrate from $r = 0$ to $r = R_+$ with the appropriate potential (see (B.5)). From this computation we have to subtract the action for the case in which the field sits at the false vacuum from $r = 0$ to $r = R_+$, that is we compute all in all

$$S_3^{TBA} = S_3[\phi(r)] - S_3[\phi_+] \quad (\text{B.14})$$

Using the equations in (B.13) we can rewrite the result as a function of the parameters of the potential to obtain

$$\left(\frac{S_3}{T} \right)_{\text{TBA}} = \frac{16\sqrt{6}\pi}{5} \frac{1}{T} \frac{(1 + r_\lambda)}{\left[3 + 2r_\lambda - 3(1 + r_\lambda)^{2/3} \right]^{3/2}} \left(\frac{\Delta\phi_+^3}{\sqrt{\Delta V_+}} \right), \quad (\text{B.15})$$

The condition to select the first case (i.e. $\phi_0 > \phi_-$) can also be rewritten by employing again formula (B.13) as

$$\frac{\Delta\phi_-}{\Delta\phi_+} \geq \frac{r_\lambda}{3 + 2r_\lambda - 3(1 + r_\lambda)^{2/3}}. \quad (\text{B.16})$$

We then analyse the second case. Imposing the boundary conditions we get the solutions

$$\phi(r) = \begin{cases} \phi_R(r) = \phi_- & 0 < r < R_0 \\ \phi_R(r) = \phi_- - \frac{\lambda_-}{6} \left(r^2 - 3R_0^2 + 2\frac{R_0^3}{r} \right) & R_0 < r < R_P \\ \phi_L(r) = \phi_+ + \frac{\lambda_+}{6} \left(r^2 - 3R_+^2 + 2\frac{R_+^3}{r} \right) & R_P < r < R_+ \end{cases} \quad (\text{B.17})$$

By imposing matching of the fields and the derivative at $R = R_P$ we get the following equations for the unknown parameters R_0, R_P, R_+

$$R_P^3 = \frac{r_\lambda R_0^3 + R_+^3}{1 + r_\lambda} \quad (\text{B.18})$$

$$\Delta\phi_- = \frac{r_\lambda \lambda_+ (R_0 - R_P)^2 (2R_0 + R_P)}{6R_P} \quad (\text{B.19})$$

$$\Delta\phi_+ = \frac{\lambda_+ (R_+ - R_P)^2 (2R_+ + R_P)}{6R_P} \quad (\text{B.20})$$

We then compute the bounce action by inserting the solutions and integrating from r to R_+ , and after some rearrangements we get

$$\left(\frac{S_3}{T} \right)_{\text{TBA}} = \frac{8\pi}{15} \frac{1}{T} \left(R_+^3 \Delta\phi_+ - r_\lambda R_0^3 \Delta\phi_- \right) \frac{\Delta V_+}{\Delta\phi_+} \quad (\text{B.21})$$

where R_+ and R_0 are functions of parameters of the scalar potential through the implicit equations (B.20).

So we conclude that in both possible cases, the computation of the bounce action in the TBA approximation only needs to specify the *critical* points of the potential, that is the metastable vacuum, the peak of the barrier and the true vacuum. For the scenarios studied in this paper the first case (B.15) is the relevant one, and the validity condition is reported also in (3.6) (note that in the conventions in the main text we always choose the metastable vacuum to be at the origin of the field space). In this appendix we have nevertheless reviewed both cases for completeness.

In the following we will compute the TBA bounce action by both evaluating the potential numerically and approximating it analytically. These approximations can be compared with the results of the full-fledged numerical bounce action computation.

B.1.1 Optimized triangular bounce

Studying the evolution of the bubble profiles for the actions computed numerically we note that the release point ϕ_0 is typically closer to the potential barrier than to the true vacuum at ϕ_- in our setups. Therefore, we introduce here a modified version of the TBA that takes into account this feature, leading to a better agreement with the full numerics than

the analytic formulas presented above. The idea is to allow the minimum of the potential to be a free parameter rather than to fix it at the true vacuum, allowing the TBA to more closely represent the shape of the potential, where the slope is closer to linear.

The TBA bounce action is computed by replacing $\phi_- \rightarrow \phi_0$ and $V_-(\phi_-) \rightarrow V_-(\phi_0)$, where ϕ_0 is now an arbitrary point along the potential in the interval $\phi_{\text{eq}} < \phi_0 < \phi_-$ (here $\phi_{\text{eq}} > \phi_P$ is the point after the potential barrier where $V(\phi_{\text{eq}}) = V_+$). This procedure defines a function $S_3/T(\phi_0)$ that we can minimize over ϕ_0 in the allowed interval. The resulting minimum is the sought bounce action, that we have dubbed the optimal TBA.

B.1.2 Triangular bounce for the O’Raifeartaigh model with gauge interactions

In this section, we specify the discussion to the triangular barrier approximation for the model of section 4.3 and compute the inputs needed for the TBA bounce action. We denote the usual combination of parameters as $y_F \equiv \frac{\lambda F}{m^2}$ and $y_D \equiv \frac{gD}{m^2}$.

The local minimum at the origin is approximated as

$$\phi_+ = 0, \tag{B.22}$$

$$V_+(T) = F^2 + \frac{1}{2}D^2 - \frac{3T^{5/2}e^{-\frac{m}{T}}(128m^2 + 240mT)}{128\sqrt{2}\pi^{3/2}\sqrt{m}} + \frac{m^4}{32\pi^2} \left[(1 + y_F)^2 \log(1 + y_F) + (1 - y_F)^2 \log(1 - y_F) - 3y_F^2 \right], \tag{B.23}$$

The peak of the barrier is located at

$$\phi_P \simeq \frac{F}{m} \frac{\sqrt{2 - 2y_D}}{y_F \sqrt{y_D}}, \tag{B.24}$$

$$V_P(T) \simeq F^2 + \frac{1}{2}D^2 + \frac{m^4}{16\pi^2} y_F^2 \log\left(\frac{1 - y_D}{y_D}\right) - \frac{T^{5/2}e^{-\frac{m}{T}}(128m^2 + 240mT)}{32\sqrt{2}\pi^{3/2}\sqrt{m}}, \tag{B.25}$$

Finally, the true vacuum location and energy are given by

$$\phi_- \simeq \frac{F}{m} \frac{4\pi}{g} \frac{\sqrt{2y_D}}{y_F^2}, \tag{B.26}$$

$$V_- \simeq F^2 + \frac{m^4}{16\pi^2} y_F^2 \log\left(\frac{16\pi^2}{g^2} \frac{y_D}{y_F^2}\right), \tag{B.27}$$

where we set the renormalization scale $\mu = m$. Within our approximation the thermal effects only enter at the origin, and at the top of the barrier, where they act to lower the potential relative to the true vacuum, and the potential difference between the top of the barrier and origin, respectively.

In figure 13 we consider two benchmarks with very different r_λ at T_n and show the bounce action S_3/T as a function of the temperature, computed in different approximations. The black line is computed using the fully numerical thermal effective potential and the mathematica package “FindBounce” [88]. The blue line is obtained with the TBA evaluated on the full-numerical scalar potential and optimized with the procedure explained above. The red line is the TBA (as computed in appendix B.1) evaluated on the full-numerical

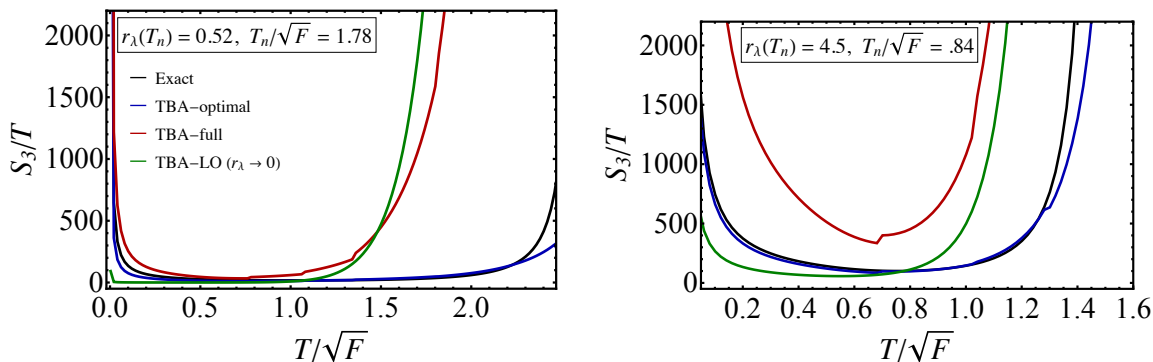


Figure 13. Bounce action computed using different approximations in the O’Raifeartaigh model with gauge interactions of section 4.3. The benchmarks on the left and on the right are distinguished by the size of r_λ . The *black lines* are the full numerical computation of the bounce action. In *blue* we show the TBA computed using the numerical scalar potential and optimized with the procedures explained in the text. The *red lines* are the standard TBA approximations as described in appendix B.1. The *green line* is the standard TBA evaluated on the analytic approximation of the scalar potential (as detailed in the text) and taking only the zeroth order term in the expansion for small r_λ (as in eq. (3.6)). This last approximation is the one used in section 3 to derive analytic estimates.

scalar potential. Finally, the green is the TBA evaluated on the analytical approximation of the critical points of the scalar potential as explained above, and moreover keeping only the leading order term in the small r_λ expansion in eq. (3.6). This is the approximation used to derive the analytic formulas in section 3.

First, we see that the optimal TBA reproduces almost perfectly the numerical bounce computation. The standard TBA can predict well the location of T_{\min} but the overall normalization can be off up by a factor of \sim few, and in particular it does not agree with the numerical result in the vicinity of T_c . However, the different trend in the overall shape of the bounce action in the two benchmarks (e.g. very flat around T_{\min} in the left one) is also captured in the standard TBA approximation.

Then, we note that the simplest approximation of the standard TBA reproduces very well the TBA when r_λ is small. This was not obvious a priori since, besides expanding the TBA at leading order in small r_λ , we have: i) assumed that the only temperature dependence is in the height of the potential at the origin; ii) employed the low- T approximation of the scalar potential to estimate it. The agreement between the red and green curve in the left panel of figure 13 hence confirms the fact that low- T is the correct approximation to employ, as discussed at length in section 3. When r_λ is larger (right plot) the simplest approximation (green line) clearly deviates from the standard TBA (red line), but nevertheless capture approximately the location of T_{\min} and the shape of the numerical results. It is important to observe that even if the normalization of the bounce action and its raising towards T_c are not exactly reproduced by the approximations employed, they can still track the changes of the bounce action (shape deformations and overall size) as a function of the fundamental parameters of the model. This elucidates why the analytic estimates obtained in section 3 can capture the scaling of T_n in the different models as discussed in section 4.2 and 4.3.

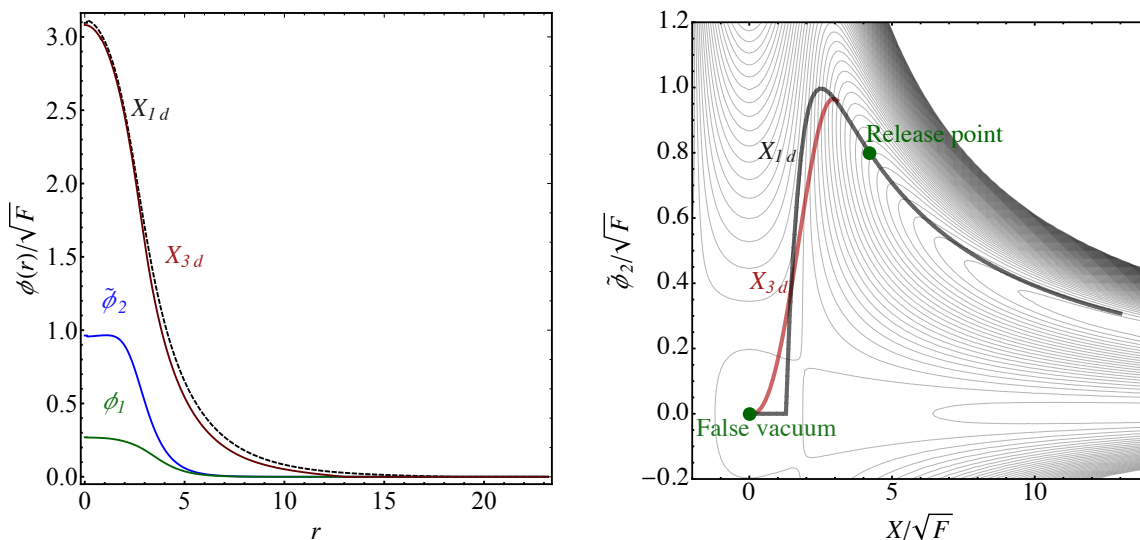


Figure 14. *Left:* bubble profiles for the single field and three field bounce actions as a function of the bubble radii. The release point for the single field (pseudo flat) direction is practically identical in both schemes, while the contribution coming from motion along the other field directions is generally small, but non-zero. *Right:* the bubble trajectory in field space for the single field and three field bounce action. The x-axis represents motion along the pseudo flat direction while the y-axis represents motion along the larger of the other two field directions ($\tilde{\phi}_2$). It is clear from both plots that the motion along the pseudo flat direction is mostly unaffected by the motion along the other directions, and therefore the single field path approximation is viable.

B.2 Single field approximation of the multi-field bounce action

As discussed previously, the model presented in section 4.3, contains more than one dynamical degree of freedom that actually enters into the bounce action computation. Namely, the fields X , ϕ_1 and $\tilde{\phi}_2$ vary along the minimal potential energy trajectory in field space which connects the two minima of the potential. This implies that the full bounce solution is that of a three field problem, which is in general only solvable numerically. In this appendix we explain why in the model under study the bounce action can be effectively approximated with a one field problem and what is the regime of validity of such approximation.

The bounce action involving the three fields is

$$\begin{aligned}
 S_3 &= \frac{2\pi^{3/2}}{\Gamma(3/2)} \sum_i \int_0^\infty r^2 (T_i + V(\phi_i)) \\
 &= \frac{2\pi^{3/2}}{\Gamma(3/2)} \int_0^\infty r^2 \left(\frac{1}{2} \dot{X}^2 + \frac{1}{2} \dot{\phi}_1^2 + \frac{1}{2} \dot{\tilde{\phi}}_2^2 + V(X, \phi_1, \tilde{\phi}_2) \right),
 \end{aligned}
 \tag{B.28}$$

where T_i is the kinetic energy associated with each field, which is an additive quantity. In our analysis we approximate this action by minimizing $V(X, \phi_1, \tilde{\phi}_2)$ along all three directions and by solving the bounce equation only for X . This corresponds to neglect the contribution from the kinetic energy of the other two fields ϕ_1 and $\tilde{\phi}_2$. Since the kinetic energy of these fields is related to the potential energy along the same directions by the equation

of motion, we expect that the kinetic energy contributions of ϕ_1 and $\tilde{\phi}_2$ can be consistently neglected if their VEVs along the bounce trajectory are small compared to the one of X .

This is typically what happens in this model as we show in the left panel of figure 14, where we plot the bubble profiles of the full three field problem computed using FindBounce (red, blue and green line). We also show for comparison (in dashed black) the bubble profile that we obtain for the single-field bounce solution for X , which is essentially identical to the one in the three-field solution. In the right panel of figure 14 we show a two dimensional slice of the field path along the bounce solution, in the $X, \tilde{\phi}_2$ plane (we show $\tilde{\phi}_2$ since the ϕ_1 vev is smaller and hence it has even a smaller impact on the value of the bounce action). We see that the X trajectory is almost unchanged by the addition of the second field. We hence conclude that it is typically a robust approximation in this model to neglect the kinetic contribution of the fields ϕ_1 and $\tilde{\phi}_2$ and to solve the one-field problem.

Nevertheless, we would like to estimate the range of validity of our approximation. As mentioned, we expect the difference to come from the kinetic terms of ϕ_1 and $\tilde{\phi}_2$, which will be non negligible if the size of the ϕ_1 and $\tilde{\phi}_2$ VEV's compared to the one of X is not negligible. In particular, we would like to estimate the impact of this approximation in the overall bounce action. We hence use intuition from the TBA where the size of the bounce action is proportional to the cubic power of the field displacement. We define the following ratio

$$R_{1d/3d} \stackrel{\text{def}}{=} \frac{X^3(r)}{\left(X^2(r) + \phi_1^2(r) + \tilde{\phi}_2^2(r)\right)^{3/2}} \Bigg|_{r=0}, \quad (\text{B.29})$$

where $X(0)$, $\phi_1(0)$ and $\tilde{\phi}_2(0)$ are the field distances from the origin computed at the release point $r = 0$. The ratio $R_{1d/3d}$ provides a measure of the relative error of the single-field bounce action computation against the full three-field one. Indeed, we have also cross-checked numerically in several benchmarks that the difference in the values of the bounce action is negligible when $R_{1d/3d}$ is small. In the main body of the paper, we will define the region where the 1-field approximation breaks down as when the quantity $R_{1d/3d} > 0.5$, corresponding approximately to a relative error of $\sim 50\%$ of the single field approximation compared to the full three field solution.

C Sensitivity of GW interferometers

In this section we briefly discuss the interpretation and generation of the sensitivity curves used to define detection of a GW signal. We follow standard definitions and conclusions obtained in [106–109], see also [110] and references therein. The detection sensitivity for GW background for a given experimental setup, is given by the integrated signal-to-noise ratio (SNR) over an observation time interval t_{obs} as

$$\rho = \frac{\langle S \rangle}{\langle N^{1/2} \rangle} = \left[n_{\text{det}} t_{\text{obs}} \int_{f_{\text{min}}}^{f_{\text{max}}} df \left(\frac{S_S(f)}{S_N^{\text{eff}}(f)} \right)^2 \right]^{1/2}, \quad S_N^{\text{eff}}(f) = \frac{D_N(f)}{\mathcal{R}(f)}, \quad (\text{C.1})$$

where $\langle S \rangle$ is the mean signal, $\langle N^{1/2} \rangle = \sqrt{\langle S_{IJ}^2 \rangle - \langle S_{IJ} \rangle^2}$ is the average noise, $I, J = 1, 2$ indicate coupled detectors, n_{det} distinguishes between experiments that aim at detecting

the signal by means of an auto-correlation of a single detector ($n_{det} = 1$) or a cross-correlation of a couple of detectors ($n_{det} = 2$) measurement. The effective noise strain can be written in terms of the noise strain power spectrum $D_N(f)$ and the frequency dependent detector response function $\mathcal{R}(f)$. The latter quantities are the ones typically reported by the experimental collaborations. The detector response becomes more intricate in the case of correlated detectors [109], where an overlap detection function must be computed. We perform the appropriate procedure when computing the relevant SNR. The signal/noise strains can be rewritten in terms of the signal/noise spectrum density as

$$\Omega_{S/N}(f) = \frac{2\pi^2 f^3}{3H_0^2} S_{S/N}(f), \tag{C.2}$$

so that eq. (C.1) becomes

$$\rho = \left[n_{det} t_{obs} \int_{f_{min}}^{f_{max}} df \left(\frac{\Omega_S(f)}{\Omega_N(f)} \right)^2 \right]^{1/2}, \tag{C.3}$$

where in this paper $\Omega_S(f)$ will be the energy density of a SGWB produced by the SUSY-breaking FOPT in the early universe redshifted till today (see eq. (2.26)). The frequency interval (f_{min}, f_{max}) is determined by the bandwidth of each experiment, typically related to the length scale of each detector. This integrated quantity will imply detection if it surpasses a predefined threshold value $\rho^2 \geq \rho_{thr}^2$ set by bayesian probabilistic measures [106], usually taken between 3 and 10.

By defining a frequency dependent shape function which models the expected signal one can define the sensitivity of a given experiment even though this procedure does not provide a precise statistical indication of the expected sensitivity as the signal to noise ratio in eq. (C.3). Depending on how well the signal shape is approximated, sensitivity curve based on the shape function approximation can provide an instructive visual tool for estimating detection in a frequency dependent way. In the following section we discuss the most common method of generating sensitivity curves for 1OPT GW signal detection.

C.1 PLI curves

Power Law Integrated (PLI) curves are generated by considering a power law function of the frequency f for the GW signal shape. The most common assumption, is a power law of the form

$$h^2 \Omega_S(f) = h^2 \tilde{\Omega}_{S,b}(\tilde{f}) \left(\frac{f}{\tilde{f}} \right)^b, \tag{C.4}$$

where b is known as the spectral index. Taking this assumption we obtain the integrated SNR as [111, 112]

$$h^2 \tilde{\Omega}_{S,b}(\tilde{f}) > h^2 \tilde{\Omega}_{GW,b}^{thr}(\tilde{f}) \equiv \frac{\rho_{thr}}{\sqrt{t_{obs} n_{det}}} \left[\int_{f_{min}}^{f_{max}} df \left(\frac{(f/\tilde{f})^b}{h^2 \Omega_N(f)} \right)^2 \right]^{-1/2}. \tag{C.5}$$

Finally, we can define the PLI sensitivity curve by maximizing the integrated SNR over the spectral index b , that is

$$h^2 \Omega_{PLI}(\tilde{f}) \equiv h^2 \max_b \left[\tilde{\Omega}_{S,b}^{thr}(\tilde{f}) \right], \tag{C.6}$$

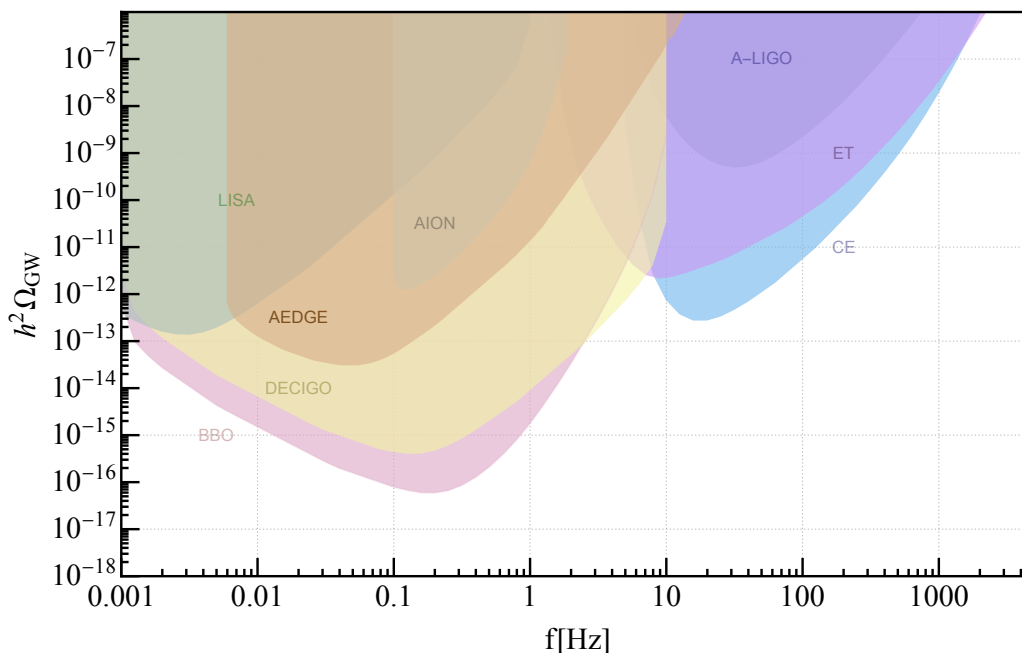


Figure 15. PLI curves for the different experiments considered here with the threshold value for the signal to noise ratio is conservatively fixed to $\rho_{\text{thr}} = 10$. The required data to derive a PLI curve for every experiment are collected in table 1.

which gives the threshold value for the signal at each frequency. A curve which crosses the threshold value at a given frequency will therefore represent a detectable signal, assuming an approximate power law behavior. Given that GW signals from FOPTs have a broken power law shape, the method described here is typically appropriate to visualize the sensitivity of a given experiment. In figure 15 we summarize the PLI curves for the different GW interferometers considered here.

C.1.1 Experimental parameters

For completeness we recompute here the PLI curves as described in the previous section for ground based interferometers such as The Laser Interferometer Gravitational Wave Observatory (LIGO) [17], the Einstein Telescope (ET) [18], the Cosmic Explorer (CE) [19, 20] and the Atom Interferometer Observatory and Network (AION) [121], as well as for space based detectors such as The Laser Interferometer Space Antenna (LISA) [113], the Big Bang Observer (BBO) [116], the Deci-Hertz Interferometer Gravitational-Wave Observatory (DECIGO) [122–124] and the Atomic Experiment for Dark Matter and Gravity Exploration (AEDGE) [120]. While many more experiments are planned in the future, such as AIGSO [125, 126], AMIGO [127], Taiji [128], TianGO [129], TianQin [130, 131] and more, we focus on the ones cited above as representatives of the potential detection range in coming years.

In order to determine the reach of a given experiment, we need to know the frequency band, the response function of the detector $\mathcal{R}(f)$ within this band, the measured noise

	n_{det}	t_{obs} (months)	Δf (Hz)	$\mathcal{R}(f), \Gamma_{IJ}(f), D_{\text{noise}}(f), S_{\text{noise}}(f)$
LISA	1	48	$[10^{-5}, 1]$	[11, 80, 113]
DECIGO	2	48	$[10^{-3}, 10]$	[114, 115]
BBO	2	48	$[10^{-3}, 10]$	[112, 116]
CE	1	60	[4.98, 5000]	[19]
ET	2	60	[1.12, 7066.72]	[18]
LIGO	2	20	[4.98, 4978]	[17, 112, 117–119]
AEDGE	2	60	[0.006, 14.83]	[120]
AION	1	60	[0.1, 1.84]	[121]

Table 1. Summary of the experimental parameters used in generating PLI curves for GW detection in this work. Auto/cross-correlation measurement is indicated by $n_{\text{det}} = 1(2)$, the observation time and bandwidth for each experiment are presented above. The detector response $\mathcal{R}(f)$, multiple detector overlap function $\Gamma_{IJ}(f)$ and noise strain spectrum $D_{\text{noise}}(f), S_{\text{noise}}(f)$ are extracted from the references herein.

at every accessible frequency $D_{\text{noise}}^I(f)$, the time of observation t_{obs} and the number of coupled detectors n_{det} . We report the extracted parameters for the various experiments in the table 1.

Open Access. This article is distributed under the terms of the Creative Commons Attribution License ([CC-BY 4.0](https://creativecommons.org/licenses/by/4.0/)), which permits any use, distribution and reproduction in any medium, provided the original author(s) and source are credited.

References

- [1] D. Baumann and D. Green, *Signatures of supersymmetry from the early universe*, *Phys. Rev. D* **85** (2012) 103520 [[arXiv:1109.0292](https://arxiv.org/abs/1109.0292)] [[INSPIRE](#)].
- [2] N. Craig and D. Green, *Testing split supersymmetry with inflation*, *JHEP* **07** (2014) 102 [[arXiv:1403.7193](https://arxiv.org/abs/1403.7193)] [[INSPIRE](#)].
- [3] N.J. Craig, *Gravitational waves from supersymmetry breaking*, [arXiv:0902.1990](https://arxiv.org/abs/0902.1990) [[INSPIRE](#)].
- [4] LIGO SCIENTIFIC and VIRGO collaborations, *Observation of gravitational waves from a binary black hole merger*, *Phys. Rev. Lett.* **116** (2016) 061102 [[arXiv:1602.03837](https://arxiv.org/abs/1602.03837)] [[INSPIRE](#)].
- [5] LIGO SCIENTIFIC and VIRGO collaborations, *Constraints on cosmic strings using data from the first advanced LIGO observing run*, *Phys. Rev. D* **97** (2018) 102002 [[arXiv:1712.01168](https://arxiv.org/abs/1712.01168)] [[INSPIRE](#)].
- [6] LIGO SCIENTIFIC and VIRGO collaborations, *Search for the isotropic stochastic background using data from advanced LIGO’s second observing run*, *Phys. Rev. D* **100** (2019) 061101 [[arXiv:1903.02886](https://arxiv.org/abs/1903.02886)] [[INSPIRE](#)].
- [7] E. Witten, *Cosmic separation of phases*, *Phys. Rev. D* **30** (1984) 272 [[INSPIRE](#)].

- [8] C.J. Hogan, *Nucleation of cosmological phase transitions*, *Phys. Lett. B* **133** (1983) 172 [[INSPIRE](#)].
- [9] C.J. Hogan, *Gravitational radiation from cosmological phase transitions*, *Mon. Not. Roy. Astron. Soc.* **218** (1986) 629 [[INSPIRE](#)].
- [10] M.S. Turner and F. Wilczek, *Relic gravitational waves and extended inflation*, *Phys. Rev. Lett.* **65** (1990) 3080 [[INSPIRE](#)].
- [11] C. Caprini et al., *Science with the space-based interferometer eLISA. II: gravitational waves from cosmological phase transitions*, *JCAP* **04** (2016) 001 [[arXiv:1512.06239](#)] [[INSPIRE](#)].
- [12] M. Chala, V.V. Khoze, M. Spannowsky and P. Waite, *Mapping the shape of the scalar potential with gravitational waves*, *Int. J. Mod. Phys. A* **34** (2019) 1950223 [[arXiv:1905.00911](#)] [[INSPIRE](#)].
- [13] A. Mazumdar and G. White, *Review of cosmic phase transitions: their significance and experimental signatures*, *Rept. Prog. Phys.* **82** (2019) 076901 [[arXiv:1811.01948](#)] [[INSPIRE](#)].
- [14] A.E. Nelson and N. Seiberg, *R symmetry breaking versus supersymmetry breaking*, *Nucl. Phys. B* **416** (1994) 46 [[hep-ph/9309299](#)] [[INSPIRE](#)].
- [15] K.A. Intriligator, N. Seiberg and D. Shih, *Supersymmetry breaking, R-symmetry breaking and metastable vacua*, *JHEP* **07** (2007) 017 [[hep-th/0703281](#)] [[INSPIRE](#)].
- [16] Z. Komargodski and D. Shih, *Notes on SUSY and R-symmetry breaking in Wess-Zumino models*, *JHEP* **04** (2009) 093 [[arXiv:0902.0030](#)] [[INSPIRE](#)].
- [17] LIGO SCIENTIFIC collaboration, *Advanced LIGO*, *Class. Quant. Grav.* **32** (2015) 074001 [[arXiv:1411.4547](#)] [[INSPIRE](#)].
- [18] B. Sathyaprakash et al., *Scientific objectives of Einstein telescope*, *Class. Quant. Grav.* **29** (2012) 124013 [*Erratum ibid.* **30** (2013) 079501] [[arXiv:1206.0331](#)] [[INSPIRE](#)].
- [19] LIGO SCIENTIFIC collaboration, *Exploring the sensitivity of next generation gravitational wave detectors*, *Class. Quant. Grav.* **34** (2017) 044001 [[arXiv:1607.08697](#)] [[INSPIRE](#)].
- [20] D. Reitze et al., *Cosmic explorer: the U.S. contribution to gravitational-wave astronomy beyond LIGO*, *Bull. Am. Astron. Soc.* **51** (2019) 035 [[arXiv:1907.04833](#)] [[INSPIRE](#)].
- [21] D.J.H. Chung, A.J. Long and L.-T. Wang, *125 GeV Higgs boson and electroweak phase transition model classes*, *Phys. Rev. D* **87** (2013) 023509 [[arXiv:1209.1819](#)] [[INSPIRE](#)].
- [22] A. Brignole, F. Feruglio and F. Zwirner, *Signals of a superlight gravitino at e^+e^- colliders when the other superparticles are heavy*, *Nucl. Phys. B* **516** (1998) 13 [*Erratum ibid.* **555** (1999) 653] [[hep-ph/9711516](#)] [[INSPIRE](#)].
- [23] A. Brignole, F. Feruglio, M.L. Mangano and F. Zwirner, *Signals of a superlight gravitino at hadron colliders when the other superparticles are heavy*, *Nucl. Phys. B* **526** (1998) 136 [*Erratum ibid.* **582** (2000) 759] [[hep-ph/9801329](#)] [[INSPIRE](#)].
- [24] F. Maltoni, A. Martini, K. Mawatari and B. Oehl, *Signals of a superlight gravitino at the LHC*, *JHEP* **04** (2015) 021 [[arXiv:1502.01637](#)] [[INSPIRE](#)].
- [25] ATLAS collaboration, *Search for photonic signatures of gauge-mediated supersymmetry in 13 TeV pp collisions with the ATLAS detector*, *Phys. Rev. D* **97** (2018) 092006 [[arXiv:1802.03158](#)] [[INSPIRE](#)].
- [26] ATLAS collaboration, *Search for squarks and gluinos in final states with hadronically decaying τ -leptons, jets, and missing transverse momentum using pp collisions at $\sqrt{s} = 13$ TeV with the ATLAS detector*, *Phys. Rev. D* **99** (2019) 012009 [[arXiv:1808.06358](#)] [[INSPIRE](#)].

- [27] ATLAS collaboration, *Search for squarks and gluinos in final states with jets and missing transverse momentum using 139 fb^{-1} of $\sqrt{s} = 13\text{ TeV}$ pp collision data with the ATLAS detector*, [PoS\(EPS-HEP2019\)605](#) (2020) [[arXiv:2010.14293](#)] [[INSPIRE](#)].
- [28] ATLAS collaboration, *Search for squarks and gluinos in final states with an isolated lepton, jets, and missing transverse momentum at $\sqrt{s} = 13\text{ TeV}$ with the ATLAS detector*, Tech. Rep. [ATLAS-CONF-2020-047](#), CERN, Geneva, Switzerland (2020).
- [29] N. Arkani-Hamed, T. Han, M. Mangano and L.-T. Wang, *Physics opportunities of a 100 TeV proton-proton collider*, *Phys. Rept.* **652** (2016) 1 [[arXiv:1511.06495](#)] [[INSPIRE](#)].
- [30] L.J. Hall, J.T. Ruderman and T. Volansky, *A cosmological upper bound on superpartner masses*, *JHEP* **02** (2015) 094 [[arXiv:1302.2620](#)] [[INSPIRE](#)].
- [31] K. Jedamzik, *Big bang nucleosynthesis constraints on hadronically and electromagnetically decaying relic neutral particles*, *Phys. Rev. D* **74** (2006) 103509 [[hep-ph/0604251](#)] [[INSPIRE](#)].
- [32] S. Deser and B. Zumino, *Broken supersymmetry and supergravity*, *Phys. Rev. Lett.* **38** (1977) 1433 [[INSPIRE](#)].
- [33] J. Bagger, E. Poppitz and L. Randall, *The R axion from dynamical supersymmetry breaking*, *Nucl. Phys. B* **426** (1994) 3 [[hep-ph/9405345](#)] [[INSPIRE](#)].
- [34] B. Bellazzini, A. Mariotti, D. Redigolo, F. Sala and J. Serra, *R-axion at colliders*, *Phys. Rev. Lett.* **119** (2017) 141804 [[arXiv:1702.02152](#)] [[INSPIRE](#)].
- [35] M. Dine, G. Festuccia and Z. Komargodski, *A bound on the superpotential*, *JHEP* **03** (2010) 011 [[arXiv:0910.2527](#)] [[INSPIRE](#)].
- [36] G.F. Giudice and R. Rattazzi, *Theories with gauge mediated supersymmetry breaking*, *Phys. Rept.* **322** (1999) 419 [[hep-ph/9801271](#)] [[INSPIRE](#)].
- [37] A. Brignole, F. Feruglio and F. Zwirner, *On the effective interactions of a light gravitino with matter fermions*, *JHEP* **11** (1997) 001 [[hep-th/9709111](#)] [[INSPIRE](#)].
- [38] T. Moroi, H. Murayama and M. Yamaguchi, *Cosmological constraints on the light stable gravitino*, *Phys. Lett. B* **303** (1993) 289 [[INSPIRE](#)].
- [39] M. Kawasaki and T. Moroi, *Gravitino production in the inflationary universe and the effects on big bang nucleosynthesis*, *Prog. Theor. Phys.* **93** (1995) 879 [[hep-ph/9403364](#)] [[INSPIRE](#)].
- [40] T. Moroi, *Effects of the gravitino on the inflationary universe*, Ph.D. thesis, Tohoku University, Sendai, Japan (1995) [[hep-ph/9503210](#)] [[INSPIRE](#)].
- [41] E. Pierpaoli, S. Borgani, A. Masiero and M. Yamaguchi, *The formation of cosmic structures in a light gravitino dominated universe*, *Phys. Rev. D* **57** (1998) 2089 [[astro-ph/9709047](#)] [[INSPIRE](#)].
- [42] M. Viel, J. Lesgourgues, M.G. Haehnelt, S. Matarrese and A. Riotto, *Constraining warm dark matter candidates including sterile neutrinos and light gravitinos with WMAP and the Lyman- α forest*, *Phys. Rev. D* **71** (2005) 063534 [[astro-ph/0501562](#)] [[INSPIRE](#)].
- [43] M. Bolz, A. Brandenburg and W. Buchmüller, *Thermal production of gravitinos*, *Nucl. Phys. B* **606** (2001) 518 [*Erratum* *ibid.* **790** (2008) 336] [[hep-ph/0012052](#)] [[INSPIRE](#)].
- [44] J. Pradler and F.D. Steffen, *Thermal gravitino production and collider tests of leptogenesis*, *Phys. Rev. D* **75** (2007) 023509 [[hep-ph/0608344](#)] [[INSPIRE](#)].
- [45] J. Pradler and F.D. Steffen, *Constraints on the reheating temperature in gravitino dark matter scenarios*, *Phys. Lett. B* **648** (2007) 224 [[hep-ph/0612291](#)] [[INSPIRE](#)].

- [46] V.S. Rychkov and A. Strumia, *Thermal production of gravitinos*, *Phys. Rev. D* **75** (2007) 075011 [[hep-ph/0701104](#)] [[INSPIRE](#)].
- [47] H. Eberl, I.D. Gialamas and V.C. Spanos, *Gravitino thermal production revisited*, [arXiv:2010.14621](#) [[INSPIRE](#)].
- [48] C. Cheung, G. Elor and L. Hall, *Gravitino freeze-in*, *Phys. Rev. D* **84** (2011) 115021 [[arXiv:1103.4394](#)] [[INSPIRE](#)].
- [49] J.L. Feng, A. Rajaraman and F. Takayama, *Superweakly interacting massive particles*, *Phys. Rev. Lett.* **91** (2003) 011302 [[hep-ph/0302215](#)] [[INSPIRE](#)].
- [50] J.L. Feng, A. Rajaraman and F. Takayama, *SuperWIMP dark matter signals from the early universe*, *Phys. Rev. D* **68** (2003) 063504 [[hep-ph/0306024](#)] [[INSPIRE](#)].
- [51] N. Arkani-Hamed, A. Delgado and G.F. Giudice, *The well-tempered neutralino*, *Nucl. Phys. B* **741** (2006) 108 [[hep-ph/0601041](#)] [[INSPIRE](#)].
- [52] N. Arkani-Hamed, G.F. Giudice, M.A. Luty and R. Rattazzi, *Supersymmetry breaking loops from analytic continuation into superspace*, *Phys. Rev. D* **58** (1998) 115005 [[hep-ph/9803290](#)] [[INSPIRE](#)].
- [53] T. Cohen, A. Hook and B. Wecht, *Comments on gaugino screening*, *Phys. Rev. D* **85** (2012) 115004 [[arXiv:1112.1699](#)] [[INSPIRE](#)].
- [54] S.P. Martin and M.T. Vaughn, *Regularization dependence of running couplings in softly broken supersymmetry*, *Phys. Lett. B* **318** (1993) 331 [[hep-ph/9308222](#)] [[INSPIRE](#)].
- [55] S.P. Martin, *A supersymmetry primer*, *Adv. Ser. Direct. High Energy Phys.* **18** (1998) 1 [*Adv. Ser. Direct. High Energy Phys.* **21** (2010) 1] [[hep-ph/9709356](#)] [[INSPIRE](#)].
- [56] R. Barbieri, L.J. Hall and A. Strumia, *Violations of lepton flavor and CP in supersymmetric unified theories*, *Nucl. Phys. B* **445** (1995) 219 [[hep-ph/9501334](#)] [[INSPIRE](#)].
- [57] J. Hisano, T. Moroi, K. Tobe, M. Yamaguchi and T. Yanagida, *Lepton flavor violation in the supersymmetric standard model with seesaw induced neutrino masses*, *Phys. Lett. B* **357** (1995) 579 [[hep-ph/9501407](#)] [[INSPIRE](#)].
- [58] F. Gabbiani, E. Gabrielli, A. Masiero and L. Silvestrini, *A complete analysis of FCNC and CP constraints in general SUSY extensions of the standard model*, *Nucl. Phys. B* **477** (1996) 321 [[hep-ph/9604387](#)] [[INSPIRE](#)].
- [59] M. Ciuchini et al., ΔM_K and ϵ_K in SUSY at the next-to-leading order, *JHEP* **10** (1998) 008 [[hep-ph/9808328](#)] [[INSPIRE](#)].
- [60] ACME collaboration, *Order of magnitude smaller limit on the electric dipole moment of the electron*, *Science* **343** (2014) 269 [[arXiv:1310.7534](#)] [[INSPIRE](#)].
- [61] ACME collaboration, *Improved limit on the electric dipole moment of the electron*, *Nature* **562** (2018) 355 [[INSPIRE](#)].
- [62] Y. Nakai and M. Reece, *Electric dipole moments in natural supersymmetry*, *JHEP* **08** (2017) 031 [[arXiv:1612.08090](#)] [[INSPIRE](#)].
- [63] C. Cesarotti, Q. Lu, Y. Nakai, A. Parikh and M. Reece, *Interpreting the electron EDM constraint*, *JHEP* **05** (2019) 059 [[arXiv:1810.07736](#)] [[INSPIRE](#)].
- [64] S.R. Coleman, *The fate of the false vacuum. 1. Semiclassical theory*, *Phys. Rev. D* **15** (1977) 2929 [*Erratum ibid.* **16** (1977) 1248] [[INSPIRE](#)].

- [65] C.G. Callan Jr. and S.R. Coleman, *The fate of the false vacuum. 2. First quantum corrections*, *Phys. Rev. D* **16** (1977) 1762 [INSPIRE].
- [66] A.D. Linde, *Fate of the false vacuum at finite temperature: theory and applications*, *Phys. Lett. B* **100** (1981) 37 [INSPIRE].
- [67] A.D. Linde, *Decay of the false vacuum at finite temperature*, *Nucl. Phys. B* **216** (1983) 421 [Erratum *ibid.* **223** (1983) 544] [INSPIRE].
- [68] M. Kamionkowski, A. Kosowsky and M.S. Turner, *Gravitational radiation from first order phase transitions*, *Phys. Rev. D* **49** (1994) 2837 [astro-ph/9310044] [INSPIRE].
- [69] P.B. Arnold, *One loop fluctuation — dissipation formula for bubble wall velocity*, *Phys. Rev. D* **48** (1993) 1539 [hep-ph/9302258] [INSPIRE].
- [70] S. Balaji, M. Spannowsky and C. Tamarit, *Cosmological bubble friction in local equilibrium*, [arXiv:2010.08013](https://arxiv.org/abs/2010.08013) [INSPIRE].
- [71] M. Barroso Mancha, T. Prokopec and B. Swiezewska, *Field-theoretic derivation of bubble-wall force*, *JHEP* **01** (2021) 070 [[arXiv:2005.10875](https://arxiv.org/abs/2005.10875)] [INSPIRE].
- [72] D. Bödeker and G.D. Moore, *Can electroweak bubble walls run away?*, *JCAP* **05** (2009) 009 [[arXiv:0903.4099](https://arxiv.org/abs/0903.4099)] [INSPIRE].
- [73] D. Bödeker and G.D. Moore, *Electroweak bubble wall speed limit*, *JCAP* **05** (2017) 025 [[arXiv:1703.08215](https://arxiv.org/abs/1703.08215)] [INSPIRE].
- [74] L. Darmé, J. Jaeckel and M. Lewicki, *Towards the fate of the oscillating false vacuum*, *Phys. Rev. D* **96** (2017) 056001 [[arXiv:1704.06445](https://arxiv.org/abs/1704.06445)] [INSPIRE].
- [75] J. Ellis, M. Lewicki, J.M. No and V. Vaskonen, *Gravitational wave energy budget in strongly supercooled phase transitions*, *JCAP* **06** (2019) 024 [[arXiv:1903.09642](https://arxiv.org/abs/1903.09642)] [INSPIRE].
- [76] K. Enqvist, J. Ignatius, K. Kajantie and K. Rummukainen, *Nucleation and bubble growth in a first order cosmological electroweak phase transition*, *Phys. Rev. D* **45** (1992) 3415 [INSPIRE].
- [77] A. Azatov and M. Vanvlasselaer, *Bubble wall velocity: heavy physics effects*, *JCAP* **01** (2021) 058 [[arXiv:2010.02590](https://arxiv.org/abs/2010.02590)] [INSPIRE].
- [78] M. Hindmarsh, S.J. Huber, K. Rummukainen and D.J. Weir, *Gravitational waves from the sound of a first order phase transition*, *Phys. Rev. Lett.* **112** (2014) 041301 [[arXiv:1304.2433](https://arxiv.org/abs/1304.2433)] [INSPIRE].
- [79] M. Hindmarsh, S.J. Huber, K. Rummukainen and D.J. Weir, *Numerical simulations of acoustically generated gravitational waves at a first order phase transition*, *Phys. Rev. D* **92** (2015) 123009 [[arXiv:1504.03291](https://arxiv.org/abs/1504.03291)] [INSPIRE].
- [80] C. Caprini et al., *Detecting gravitational waves from cosmological phase transitions with LISA: an update*, *JCAP* **03** (2020) 024 [[arXiv:1910.13125](https://arxiv.org/abs/1910.13125)] [INSPIRE].
- [81] A. Hook and H. Murayama, *Low-energy supersymmetry breaking without the gravitino problem*, *Phys. Rev. D* **92** (2015) 015004 [[arXiv:1503.04880](https://arxiv.org/abs/1503.04880)] [INSPIRE].
- [82] A. Hook, R. McGehee and H. Murayama, *Cosmologically viable low-energy supersymmetry breaking*, *Phys. Rev. D* **98** (2018) 115036 [[arXiv:1801.10160](https://arxiv.org/abs/1801.10160)] [INSPIRE].
- [83] M.J. Duncan and L.G. Jensen, *Exact tunneling solutions in scalar field theory*, *Phys. Lett. B* **291** (1992) 109 [INSPIRE].

- [84] A. Amariti and M. Siani, *R-symmetry and supersymmetry breaking in 3D WZ models*, *JHEP* **08** (2009) 055 [[arXiv:0905.4725](#)] [[INSPIRE](#)].
- [85] D. Curtin, Z. Komargodski, D. Shih and Y. Tsai, *Spontaneous R-symmetry breaking with multiple pseudomoduli*, *Phys. Rev. D* **85** (2012) 125031 [[arXiv:1202.5331](#)] [[INSPIRE](#)].
- [86] E. Witten, *Mass hierarchies in supersymmetric theories*, *Phys. Lett. B* **105** (1981) 267 [[INSPIRE](#)].
- [87] R. Rattazzi and A. Zaffaroni, *Comments on the holographic picture of the Randall-Sundrum model*, *JHEP* **04** (2001) 021 [[hep-th/0012248](#)] [[INSPIRE](#)].
- [88] V. Guada, M. Nemevšek and M. Pintar, *FindBounce: package for multi-field bounce actions*, *Comput. Phys. Commun.* **256** (2020) 107480 [[arXiv:2002.00881](#)] [[INSPIRE](#)].
- [89] C.L. Wainwright, *CosmoTransitions: computing cosmological phase transition temperatures and bubble profiles with multiple fields*, *Comput. Phys. Commun.* **183** (2012) 2006 [[arXiv:1109.4189](#)] [[INSPIRE](#)].
- [90] K.A. Intriligator, N. Seiberg and D. Shih, *Dynamical SUSY breaking in meta-stable vacua*, *JHEP* **04** (2006) 021 [[hep-th/0602239](#)] [[INSPIRE](#)].
- [91] L. O’Raifeartaigh, *Spontaneous symmetry breaking for chiral scalar superfields*, *Nucl. Phys. B* **96** (1975) 331 [[INSPIRE](#)].
- [92] N.J. Craig, P.J. Fox and J.G. Wacker, *Reheating metastable O’Raifeartaigh models*, *Phys. Rev. D* **75** (2007) 085006 [[hep-th/0611006](#)] [[INSPIRE](#)].
- [93] A. Katz, *On the thermal history of calculable gauge mediation*, *JHEP* **10** (2009) 054 [[arXiv:0907.3930](#)] [[INSPIRE](#)].
- [94] M. McCullough, *Stimulated supersymmetry breaking*, *Phys. Rev. D* **82** (2010) 115016 [[arXiv:1010.3203](#)] [[INSPIRE](#)].
- [95] T. Vakinin, *New phases in O’Raifeartaigh-like models and R-symmetry breaking*, *JHEP* **09** (2014) 004 [[arXiv:1402.5851](#)] [[INSPIRE](#)].
- [96] T.T. Dumitrescu, Z. Komargodski and M. Sudano, *Global symmetries and D-terms in supersymmetric field theories*, *JHEP* **11** (2010) 052 [[arXiv:1007.5352](#)] [[INSPIRE](#)].
- [97] Z. Komargodski and N. Seiberg, *Comments on the Fayet-Iliopoulos term in field theory and supergravity*, *JHEP* **06** (2009) 007 [[arXiv:0904.1159](#)] [[INSPIRE](#)].
- [98] J. Alwall, M. Herquet, F. Maltoni, O. Mattelaer and T. Stelzer, *MadGraph 5: going beyond*, *JHEP* **06** (2011) 128 [[arXiv:1106.0522](#)] [[INSPIRE](#)].
- [99] J. Alwall et al., *The automated computation of tree-level and next-to-leading order differential cross sections, and their matching to parton shower simulations*, *JHEP* **07** (2014) 079 [[arXiv:1405.0301](#)] [[INSPIRE](#)].
- [100] K. Osato, T. Sekiguchi, M. Shirasaki, A. Kamada and N. Yoshida, *Cosmological constraint on the light gravitino mass from CMB lensing and cosmic shear*, *JCAP* **06** (2016) 004 [[arXiv:1601.07386](#)] [[INSPIRE](#)].
- [101] ATLAS collaboration, *Search for new phenomena in events with a photon and missing transverse momentum in pp collisions at $\sqrt{s} = 8$ TeV with the ATLAS detector*, *Phys. Rev. D* **91** (2015) 012008 [Erratum *ibid.* **92** (2015) 059903] [[arXiv:1411.1559](#)] [[INSPIRE](#)].
- [102] S.P. Martin, *Generalized messengers of supersymmetry breaking and the sparticle mass spectrum*, *Phys. Rev. D* **55** (1997) 3177 [[hep-ph/9608224](#)] [[INSPIRE](#)].

- [103] A. Riotto and E. Roulet, *Vacuum decay along supersymmetric flat directions*, *Phys. Lett. B* **377** (1996) 60 [[hep-ph/9512401](#)] [[INSPIRE](#)].
- [104] V. Guada, A. Maiezza and M. Nemevšek, *Multifield polygonal bounces*, *Phys. Rev. D* **99** (2019) 056020 [[arXiv:1803.02227](#)] [[INSPIRE](#)].
- [105] A. Amariti, *Analytic bounces in d dimensions*, [arXiv:2009.14102](#) [[INSPIRE](#)].
- [106] B. Allen, *The stochastic gravity wave background: sources and detection*, in *Les Houches school of physics: astrophysical sources of gravitational radiation*, (1996), pg. 373 [[gr-qc/9604033](#)] [[INSPIRE](#)].
- [107] B. Allen and J.D. Romano, *Detecting a stochastic background of gravitational radiation: signal processing strategies and sensitivities*, *Phys. Rev. D* **59** (1999) 102001 [[gr-qc/9710117](#)] [[INSPIRE](#)].
- [108] M. Maggiore, *Gravitational wave experiments and early universe cosmology*, *Phys. Rept.* **331** (2000) 283 [[gr-qc/9909001](#)] [[INSPIRE](#)].
- [109] J.D. Romano and N.J. Cornish, *Detection methods for stochastic gravitational-wave backgrounds: a unified treatment*, *Living Rev. Rel.* **20** (2017) 2 [[arXiv:1608.06889](#)] [[INSPIRE](#)].
- [110] K. Schmitz, *New sensitivity curves for gravitational-wave signals from cosmological phase transitions*, *JHEP* **01** (2021) 097 [[arXiv:2002.04615](#)] [[INSPIRE](#)].
- [111] N.J. Cornish, *Detecting a stochastic gravitational wave background with the Laser Interferometer Space Antenna*, *Phys. Rev. D* **65** (2002) 022004 [[gr-qc/0106058](#)] [[INSPIRE](#)].
- [112] E. Thrane and J.D. Romano, *Sensitivity curves for searches for gravitational-wave backgrounds*, *Phys. Rev. D* **88** (2013) 124032 [[arXiv:1310.5300](#)] [[INSPIRE](#)].
- [113] T. Robson, N.J. Cornish and C. Liu, *The construction and use of LISA sensitivity curves*, *Class. Quant. Grav.* **36** (2019) 105011 [[arXiv:1803.01944](#)] [[INSPIRE](#)].
- [114] K. Yagi, *Scientific potential of DECIGO pathfinder and testing GR with space-borne gravitational wave interferometers*, *Int. J. Mod. Phys. D* **22** (2013) 1341013 [[arXiv:1302.2388](#)] [[INSPIRE](#)].
- [115] S. Kuroyanagi, K. Nakayama and J. Yokoyama, *Prospects of determination of reheating temperature after inflation by DECIGO*, *PTEP* **2015** (2015) 013E02 [[arXiv:1410.6618](#)] [[INSPIRE](#)].
- [116] K. Yagi, N. Tanahashi and T. Tanaka, *Probing the size of extra dimension with gravitational wave astronomy*, *Phys. Rev. D* **83** (2011) 084036 [[arXiv:1101.4997](#)] [[INSPIRE](#)].
- [117] KAGRA, LIGO SCIENTIFIC and VIRGO collaborations, *Prospects for observing and localizing gravitational-wave transients with advanced LIGO, advanced Virgo and KAGRA*, *Living Rev. Rel.* **21** (2018) 3 [[arXiv:1304.0670](#)] [[INSPIRE](#)].
- [118] A. Nishizawa, A. Taruya, K. Hayama, S. Kawamura and M.-A. Sakagami, *Probing non-tensorial polarizations of stochastic gravitational-wave backgrounds with ground-based laser interferometers*, *Phys. Rev. D* **79** (2009) 082002 [[arXiv:0903.0528](#)] [[INSPIRE](#)].
- [119] Y. Himemoto and A. Taruya, *Impact of correlated magnetic noise on the detection of stochastic gravitational waves: estimation based on a simple analytical model*, *Phys. Rev. D* **96** (2017) 022004 [[arXiv:1704.07084](#)] [[INSPIRE](#)].

- [120] AEDGE collaboration, *AEDGE: Atomic Experiment for Dark matter and Gravity Exploration in space*, *EPJ Quant. Technol.* **7** (2020) 6 [[arXiv:1908.00802](#)] [[INSPIRE](#)].
- [121] L. Badurina et al., *AION: an Atom Interferometer Observatory and Network*, *JCAP* **05** (2020) 011 [[arXiv:1911.11755](#)] [[INSPIRE](#)].
- [122] N. Seto, S. Kawamura and T. Nakamura, *Possibility of direct measurement of the acceleration of the universe using 0.1 Hz band laser interferometer gravitational wave antenna in space*, *Phys. Rev. Lett.* **87** (2001) 221103 [[astro-ph/0108011](#)] [[INSPIRE](#)].
- [123] K. Yagi and N. Seto, *Detector configuration of DECIGO/BBO and identification of cosmological neutron-star binaries*, *Phys. Rev. D* **83** (2011) 044011 [Erratum *ibid.* **95** (2017) 109901] [[arXiv:1101.3940](#)] [[INSPIRE](#)].
- [124] S. Isoyama, H. Nakano and T. Nakamura, *Multiband gravitational-wave astronomy: observing binary inspirals with a decihertz detector, B-DECIGO*, *PTEP* **2018** (2018) 073E01 [[arXiv:1802.06977](#)] [[INSPIRE](#)].
- [125] D. Gao, J. Wang and M. Zhan, *Atomic Interferometric Gravitational-wave Space Observatory (AIGSO)*, *Commun. Theor. Phys.* **69** (2018) 37 [[arXiv:1711.03690](#)] [[INSPIRE](#)].
- [126] G. Wang, D. Gao, W.-T. Ni, J. Wang and M. Zhan, *Orbit design for space atom-interferometer AIGSO*, *Int. J. Mod. Phys. D* **29** (2020) 1940004 [[arXiv:1905.00600](#)] [[INSPIRE](#)].
- [127] W.-T. Ni, G. Wang and A.-M. Wu, *Astrodynamical middle-frequency interferometric gravitational wave observatory AMIGO: mission concept and orbit design*, *Int. J. Mod. Phys. D* **29** (2020) 1940007 [[arXiv:1909.04995](#)] [[INSPIRE](#)].
- [128] W.-R. Hu and Y.-L. Wu, *The Taiji program in space for gravitational wave physics and the nature of gravity*, *Natl. Sci. Rev.* **4** (2017) 685 [[INSPIRE](#)].
- [129] K.A. Kuns, H. Yu, Y. Chen and R.X. Adhikari, *Astrophysics and cosmology with a decihertz gravitational-wave detector: TianGO*, *Phys. Rev. D* **102** (2020) 043001 [[arXiv:1908.06004](#)] [[INSPIRE](#)].
- [130] TIANQIN collaboration, *TianQin: a space-borne gravitational wave detector*, *Class. Quant. Grav.* **33** (2016) 035010 [[arXiv:1512.02076](#)] [[INSPIRE](#)].
- [131] X.-C. Hu et al., *Fundamentals of the orbit and response for TianQin*, *Class. Quant. Grav.* **35** (2018) 095008 [[arXiv:1803.03368](#)] [[INSPIRE](#)].

Singlet-Doublet dark matter freeze-in: LHC displaced signatures versus cosmology

Lorenzo Calibbi,^a Laura Lopez-Honorez,^{b,c} Steven Lowette^d and Alberto Mariotti^{c,d}

^a*CAS Key Laboratory of Theoretical Physics, Institute of Theoretical Physics, Chinese Academy of Sciences, Beijing 100190, P.R. China*

^b*Service de Physique Théorique, Université Libre de Bruxelles, C.P. 225, B-1050 Brussels, Belgium*

^c*Theoretische Natuurkunde, Vrije Universiteit Brussel, Pleinlaan 2, B-1050 Brussels, Belgium*

^d*Inter-University Institute for High Energies, Vrije Universiteit Brussel, Pleinlaan 2, B-1050 Brussels, Belgium*

E-mail: calibbi@itp.ac.cn, llopezho@ulb.ac.be, steven.lowette@vub.be, alberto.mariotti@vub.be

ABSTRACT: We study the Singlet-Doublet dark matter model in the regime of feeble couplings, where the dark matter abundance is obtained via the freeze-in mechanism. As a consequence of the small couplings, the heavier particles in the model are long-lived with decay length at typical scales of collider experiments. We analyse the collider signatures of the model, characterised by displaced h and Z bosons plus missing momentum, employing current LHC searches for displaced vertices and missing energy to significantly constrain the parameter space of the model. We also take into account the cosmological bounds relevant for our light dark matter candidate arising from Lyman- α forest constraints. Our analysis emphasises the interplay between displaced signatures at the LHC and cosmology for dark matter candidates whose relic abundance is obtained through the freeze-in mechanism.

KEYWORDS: Beyond Standard Model, Cosmology of Theories beyond the SM

ARXIV EPRINT: [1805.04423](https://arxiv.org/abs/1805.04423)

Contents

1	Introduction	1
2	The feebly-coupled Singlet-Doublet DM model	3
2.1	The spectrum	4
2.2	Decay modes and decay lengths	5
3	Dark matter abundance from Freeze-in	7
3.1	Freeze-in: collider and cosmology interplay	9
3.2	The viable dark matter parameter space	10
4	Cosmology probe of light dark matter	11
5	Signatures at the LHC	13
5.1	Recasting strategy for displaced h and $Z + \cancel{E}_T$	18
5.2	DV + \cancel{E}_T constraints on the Singlet-Doublet model	21
6	Displaced vertices vs cosmology for freeze-in DM	24
7	Summary and conclusions	25
A	Yukawa interactions and mixing matrix	27
A.1	Yukawa interactions	27
A.2	Approximate expression of the rotation matrix	27
B	Recasting of the ATLAS search	27

1 Introduction

Compelling observational evidence supports the existence of dark matter (DM), the most abundant form of matter in the Universe [1]. Yet, at present, the nature of the dark sector, possibly including dark matter particle(s) and new mediators driving the interactions between dark matter and the Standard Model (SM), is still unknown. In the last decades most of the attention has been devoted to the weakly interacting massive particle (WIMP) paradigm, in which dark matter is a new type of elementary particle with weak-type interactions with the SM. In WIMP models the abundance of the dark matter is obtained through the freeze-out mechanism. The weak couplings involved typically imply a viable — i.e. giving rise to the observed relic abundance — dark matter particle with mass of the order of the electroweak (EW) scale. This remarkable coincidence — the so-called *WIMP miracle* — has motivated a large effort in the study of WIMP dark matter scenarios both

in top-down approaches, triggered by supersymmetry, and bottom-up approaches focusing on effective theories and simplified models. In the latter framework, an important effort has been deployed in the last years to characterise dark matter simplified model parameter space, to search for the dark matter particle and the associated mediators at colliders, and to explore the complementarity between the LHC, the direct and indirect detection experiments, see e.g. [2–4]. The recurrent null results in the search for WIMPs (both at the LHC and in direct/indirect detection experiments) provide good motivations though to take a step back and to investigate alternative dark matter paradigms and to study thoroughly their phenomenology.

Here we focus on the so-called *freeze-in* mechanism for producing a *feebly* coupled dark matter candidate, i.e. particles that were not in thermal equilibrium with the SM in the early universe, see e.g. [5–7]. Because of the very small coupling involved, these models can give rise to displaced signatures at the LHC in terms of long-lived mediators decaying into dark matter plus SM fields, as it has already been underlined in a number of works [5, 8–11]. Long-lived particles and displaced signatures at colliders in relation to dark matter simplified models have been discussed also in [12–18]. The requirement of a viable frozen-in dark matter scenario giving rise to displacement at colliders of detector size points directly towards light dark matter candidates, with a mass of the order of the keV [5]. This is typically the mass scale currently tested by cosmology and astrophysics probes in the framework of warm dark matter scenarios, see e.g. [19–21], that lead to the suppression of the small scale structure formation and, by the same token, can help to alleviate the small scale crisis [22–27] in the Λ CDM (the Standard Cosmological scenario) see e.g. the discussion in [28–35]. On the other hand, due to the feeble coupling involved, direct and indirect detection dark matter searches are challenging, see however e.g. [36–39].

In this paper we will study how the combination of collider and cosmological constraints can probe a significant portion of the parameter space of frozen-in dark matter models. First, note that the long-lived mediators typically possess sizeable couplings with the SM particles that keep them in thermal equilibrium with the SM bath, and thus they can copiously be produced at the LHC. Second, the reach of displaced vertex signatures at the LHC can actually extend beyond the regime where the mean decay length of the heavy mediator, $c\tau$, is within the tracking detector with typical radius $\simeq 1$ m. This is because of the background-free nature of displaced signatures and because of the exponential decay distribution.¹ In general, the study of displaced signatures with missing energy at the LHC is thus a powerful probe of frozen-in dark matter in the small mass regime (keV to a few MeV), complementing the existing constraints from astro-physics and cosmology on light free-streaming DM candidates.

For concreteness, we focus here on the Singlet-Doublet dark matter model [41–52]. In the Singlet-Doublet model, the SM is augmented with a pair of electroweak doublet Weyl fermions and one Majorana singlet, interacting with the SM Higgs via Yukawa couplings. The dark sector contains thus a charged fermion and three neutral fermions, whose lightest

¹The latter is indeed such that a substantial fraction of the mediators produced at LHC would decay within the detector even for $c\tau > 1$ m, see e.g. [40].

state constitutes a stable dark matter candidate. Within the freeze-in regime of such model, the Yukawa couplings are feeble and thus the dark matter particle is mostly singlet while the role of the long-lived mediators is played by the components of the electroweak doublets. Two of them are neutral and hence a smoking-gun signature of this scenario at the LHC consists of displaced Higgs bosons or Z -bosons plus missing momentum. We analyse the LHC sensitivity on such interesting final states by recasting an existing ATLAS search for displaced vertices and missing energy [53]. Making use of the large statistics already collected, we show that the proper decay length that can be (will be) tested is actually significantly larger than the detector size, reaching more than 10 (100) meters. In the corresponding parts of the parameter space with the correct dark matter abundance, this currently constrains the dark matter mass to be as large as 500 keV and could reach a few MeV with 300 fb^{-1} , hence well beyond the warm dark matter regime.

The rest of the paper is organised as follows. In section 2, we discuss the model in the feeble-coupling regime and analyse the decay modes of the dark sector particles. Section 3 is devoted to the calculation of the abundance of dark matter produced through the freeze-in mechanism. We then study the constraints on light dark matter from cosmology in section 4. In section 5, we analyse in detail the main collider signatures — disappearing charged tracks, as well as displaced Higgs or Z plus missing transverse momentum (\cancel{E}_T) — of our scenario and we present the recasting of the ATLAS search [53]. In section 6, we combine the results of the previous sections and show the interplay between collider and cosmological signatures in probing our model of freeze-in dark matter. We summarise and conclude in section 7, while we present some technical details in the appendices.

2 The feebly-coupled Singlet-Doublet DM model

We perform our analysis within the Singlet-Doublet dark matter model [41], which consists in adding to the SM a pair of Weyl doublet fermions, ψ_u and ψ_d , with opposite hypercharges and one fermionic singlet, ψ_s :

$$(\psi_u)_{2, \frac{1}{2}} = \begin{pmatrix} \psi^+ \\ \psi_u^0 \end{pmatrix}, \quad (\psi_d)_{2, -\frac{1}{2}} = \begin{pmatrix} \psi_d^0 \\ \psi^- \end{pmatrix}, \quad (\psi_s)_{1, 0}. \quad (2.1)$$

The subscripts indicate the $SU(2)_L \times U(1)_Y$ quantum numbers and these new fields are assumed to be odd under an unbroken Z_2 symmetry, under which the SM fields are even, so as to guarantee the stability of dark matter.

The mass terms and Yukawa interactions of the model read

$$-\mathcal{L} \supset \mu \psi_d \cdot \psi_u + y_d \psi_d \cdot H \psi_s + y_u H^\dagger \psi_u \psi_s + \frac{1}{2} m_s \psi_s \psi_s + h.c., \quad (2.2)$$

where H is the Higgs doublet (with hypercharge 1/2) and \cdot indicates a contraction of the $SU(2)_L$ indices through the antisymmetric tensor ϵ_{ab} , see appendix A for more details. For later convenience, we also define the following alternative parameterisation of the two Yukawa couplings:

$$y_u \equiv y \sin \theta, \quad y_d \equiv y \cos \theta. \quad (2.3)$$

As is apparent from the field content, the model is a generalisation of the “Bino-Higgsino” system of supersymmetric models with free couplings y_u and y_d (whereas supersymmetry would relate them to the SM gauge couplings).

2.1 The spectrum

Upon EW-symmetry breaking, the Lagrangian in eq. (2.2) leads to mixing among the neutral components $(\psi_s, \psi_d^0, \psi_u^0)$ of the Z_2 -odd fermions. The resulting mass matrix reads

$$\mathcal{M} = \begin{pmatrix} m_s & \frac{y_d v}{\sqrt{2}} & \frac{y_u v}{\sqrt{2}} \\ \frac{y_d v}{\sqrt{2}} & 0 & \mu \\ \frac{y_u v}{\sqrt{2}} & \mu & 0 \end{pmatrix}, \quad (2.4)$$

where $v \simeq 246$ GeV is the vev of the Higgs field. The above matrix is diagonalised by a rotation matrix U , $UMU^T = \hat{\mathcal{M}}$. The mass eigenstates are then given by

$$(\chi_1, \chi_2, \chi_3)^T = U (\psi_s, \psi_d^0, \psi_u^0)^T. \quad (2.5)$$

We employ the convention $|m_{\chi_1}| < |m_{\chi_2}| < |m_{\chi_3}|$, thus our dark matter candidate is χ_1 .

The model has already been extensively investigated within the framework of the freeze-out mechanism of dark matter production [41–52]. The latter requires the couplings y_u and y_d to be of the order of $10^{-2} - 1$ for the Yukawa interactions to drive the relic abundance to the observed one. In that case the model is constrained by direct and indirect detection experiments and also features interesting collider signatures, typically resembling the Bino-Higgsino system of supersymmetric models (but with arbitrary Yukawa couplings). In contrast, in this work, we focus on the freeze-in mechanism of dark matter production associated to very feeble Singlet-Doublet interactions. As it will become clear from the discussion in section 3, the typical Yukawa couplings of interest for our analysis range from 10^{-9} to 10^{-6} and a large mass difference between the singlet and the doublet mass-scales will have to be considered: $|m_s| \ll |\mu|$. As a result, the model features suppressed mixing between the singlet and doublet and the singlet fermion $\psi_s \simeq \chi_1$ is the lightest of the neutral fermions.

In the limit

$$|y_u|, |y_d| \ll 1, \quad |m_s| \ll |\mu|, \quad (2.6)$$

we can expand the mass eigenvalues at the first order in $y_{u,d}^2$ and get²

$$\begin{aligned} m_{\chi_1} &= m_s + \frac{v^2 (y_u - y_d)^2}{4 (\mu + m_s)} - \frac{v^2 (y_u + y_d)^2}{4 (\mu - m_s)}, \\ m_{\chi_2} &= -\mu - \frac{v^2 (y_u - y_d)^2}{4 (\mu + m_s)}, \\ m_{\chi_3} &= \mu + \frac{v^2 (y_u + y_d)^2}{4 (\mu - m_s)}. \end{aligned} \quad (2.7)$$

From these expressions, we see that, in the feebly-coupled regime, there is one neutral state of mass approximately m_s (corresponding to $\chi_1 \sim \psi_s$), two neutral fermions $\chi_{2,3}$

²An approximate expression of the corresponding rotation matrix U is given in appendix A.

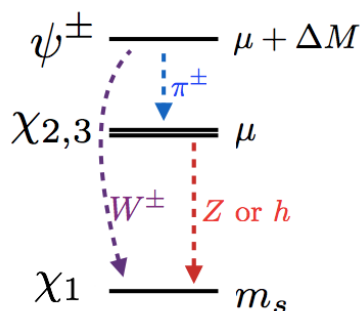


Figure 1. Mass spectrum of the Singlet-Doublet model considered here and possible decay modes.

with mass approximately μ (equal mixture of ψ_u^0 and ψ_d^0), and one charged fermion with mass $m_\psi = \mu$, that we denote with ψ^\pm .

The set of states with tree-level mass μ is further split by quantum corrections at one loop, which increases the mass of the charged state. Using the results of [54], one finds that the splitting between the charged and the neutral states is

$$\Delta M = |m_\psi| - |m_{\chi_{2,3}}| = \frac{\alpha_2 \mu}{4\pi} \sin^2 \theta_W f\left(\frac{m_Z}{\mu}\right), \quad (2.8)$$

$$f(x) = \frac{x}{2} \left(2x^3 \log x - 2x + \sqrt{x^2 - 4}(x^2 + 2) \log \left[\frac{1}{2}(x^2 - 2 - x\sqrt{x^2 - 4}) \right] \right),$$

where $\alpha_2 = g^2/(4\pi)$ (with g being the $SU(2)_L$ gauge coupling) and θ_W is the weak mixing angle. Considering $|\mu| > 100$ GeV, ΔM spans the following range

$$250 \text{ MeV} \lesssim \Delta M \lesssim 350 \text{ MeV}. \quad (2.9)$$

A sketch of the spectrum of the model and the possible decay modes, described in the next section, is shown in figure 1.

2.2 Decay modes and decay lengths

In this subsection we study the decay modes of the fermion mass eigenstates in the feeble coupling regime that control the phenomenology of the model. General expressions for the decay widths through the model’s Yukawa interactions can be found in the appendix of ref. [47], while here we specialise to the regime of (2.6) making use of the expression for the mixing matrix reported in appendix A.

Throughout this work, we consider $|\mu| > m_W$ as a doublet mass lower than about 90 GeV is excluded by searches for charged fermions performed at LEP (see [55], for a recent reassessment). In this regime, the heavy charged states ψ^\pm can decay directly into the lightest mass eigenstate, $\psi^\pm \rightarrow W^\pm \chi_1$, via the suppressed Singlet-Doublet mixing, or to the heavier neutral states (\sim neutral components of the doublet) and a soft pion, $\psi^\pm \rightarrow \pi^\pm \chi_{2,3}$, via gauge interactions. The latter decay mode occurs via an off-shell W and, for the range of charged-neutral state mass splitting reported in eq. (2.9), it dominates over possible leptonic modes involving $\ell^\pm \nu$ instead of π^\pm . Half of the decays into pions

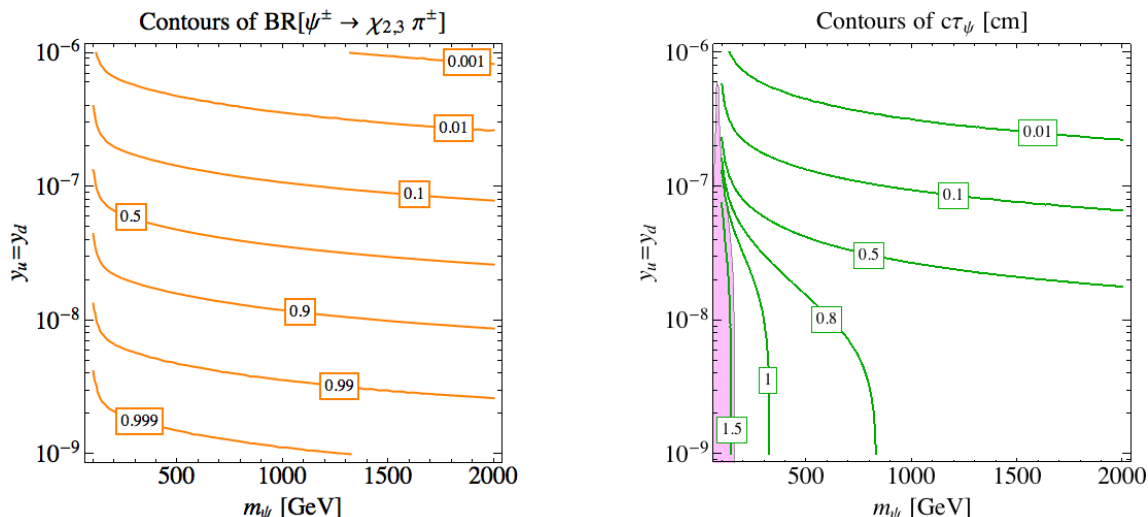


Figure 2. Left: branching ratios of the decay of the charged fermion into $\chi_{2,3}$ plus a pion. Right: decay length (in cm) of the charged fermion; the shaded region is excluded by the ATLAS search for disappearing tracks [57, 58]. The mass of the lightest neutral fermion is fixed to $m_{\chi_1} = 10$ keV.

plus neutral states go to $\pi^\pm \chi_2$ and the other half to $\pi^\pm \chi_3$, with the partial decay widths given by [56]:

$$\Gamma[\psi^\pm \rightarrow \pi^\pm \chi_{2,3}] = \frac{G_F^2}{2\pi} \cos^2 \theta_c f_\pi^2 \Delta M^3 \sqrt{1 - \left(\frac{m_\pi}{\Delta M}\right)^2}, \quad (2.10)$$

where $f_\pi \simeq 130$ MeV, G_F is the Fermi constant and θ_c the Cabibbo angle. As mentioned above, this decay mode competes with the decay into the lightest fermion eigenstate $W^\pm \chi_1$ induced by the small Singlet-Doublet mixing. At leading order in the Yukawa couplings, taking $\tan \theta = 1$ (i.e. $y_u = y_d = \frac{y}{\sqrt{2}}$), the decay width reads (for $\mu \geq 0$):

$$\Gamma[\psi^\pm \rightarrow W^\pm \chi_1] = \frac{\alpha y^2 v^2}{32 s_W^2} \sqrt{\lambda(m_\psi^2, m_{\chi_1}^2, m_W^2)} \times \frac{((m_\psi \pm m_{\chi_1})^2 + 2m_W^2) ((m_\psi \mp m_{\chi_1})^2 - m_W^2)}{m_\psi^3 m_W^2 (\mu - m_s)^2}, \quad (2.11)$$

where

$$\lambda(a, b, c) = a^2 + b^2 + c^2 - 2ab - 2ac - 2bc,$$

α is the electromagnetic constant, and $s_W \equiv \sin \theta_W$. It can be shown that $\Gamma[\psi^\pm \rightarrow W^\pm \chi_1]$ has a negligible dependence on $\tan \theta$ in the limit (2.6), and hence the formula (2.11) will suffice to our purposes.

Making use of eqs. (2.10) and (2.11), we show in figure 2 the branching ratios for the decay process $\psi^\pm \rightarrow \pi^\pm \chi_{2,3}$ (left panel) and the contours for fixed values of the charged fermion decay length $c\tau_\psi$ (right panel) on the (m_ψ, y) plane in the custodial symmetry limit $y_u = y_d$ for $m_{\chi_1} = 10$ keV. We can see that for $y \leq 10^{-8}$ the decay mode into $\pi^\pm \chi_{2,3}$ is the dominant one. Moreover, comparing the two panels of figure 2, we can see that, when ψ^\pm decays preferably into pions plus heavy neutral state, the decay length is about 1 cm

that is approximately the minimal length, to which LHC searches for disappearing charged tracks have sensitivity. For illustrative purposes, we thus also show, in the right panel of figure 2, a purple region excluded by a recent ATLAS analysis [57, 58]. We will address the collider constraints in more details in section 5. Let us mention that the overall picture depends neither on m_{χ_1} nor on $\tan\theta$ in the limit (2.6) that we are interested in here.

The two neutral states χ_2 and χ_3 can decay either into $Z\chi_1$ or into $h\chi_1$ through the Yukawa interactions. At leading order in y_u and y_d , the decay widths read (for $\mu \gtrsim 0$):

$$\Gamma[\chi_2 \rightarrow Z\chi_1] = \frac{\alpha(y_u + y_d)^2}{64s_W^2 c_W^2} \sqrt{\lambda(m_{\chi_2}^2, m_{\chi_1}^2, m_Z^2)} \times \frac{v^2((m_{\chi_2} \pm m_{\chi_1})^2 + 2m_Z^2)((m_{\chi_2} \mp m_{\chi_1})^2 - m_Z^2)}{m_{\chi_2}^3 m_Z^2 (\mu - m_s)^2}, \quad (2.12)$$

$$\Gamma[\chi_3 \rightarrow Z\chi_1] = \frac{\alpha(y_u - y_d)^2}{64s_W^2 c_W^2} \sqrt{\lambda(m_{\chi_3}^2, m_{\chi_1}^2, m_Z^2)} \times \frac{v^2((m_{\chi_3} \mp m_{\chi_1})^2 + 2m_Z^2)((m_{\chi_3} \pm m_{\chi_1})^2 - m_Z^2)}{m_{\chi_3}^3 m_Z^2 (\mu + m_s)^2}, \quad (2.13)$$

$$\Gamma[\chi_2 \rightarrow h\chi_1] = \frac{(y_u - y_d)^2}{64\pi} \frac{(m_{\chi_2} \mp m_{\chi_1})^2 - m_h^2}{m_{\chi_2}^3} \sqrt{\lambda(m_{\chi_2}^2, m_{\chi_1}^2, m_h^2)}, \quad (2.14)$$

$$\Gamma[\chi_3 \rightarrow h\chi_1] = \frac{(y_u + y_d)^2}{64\pi} \frac{(m_{\chi_3} \pm m_{\chi_1})^2 - m_h^2}{m_{\chi_3}^3} \sqrt{\lambda(m_{\chi_3}^2, m_{\chi_1}^2, m_h^2)}, \quad (2.15)$$

after having redefined the fermionic fields in order for m_{χ_i} to be positive. Notice that, in practice, in the regime of (2.6), the above decay widths are not affected by the sign of μ . The typical decay lengths of χ_2 (solid line) and χ_3 (dashed line) are shown as a function of their mass in figure 3 for two values of $\tan\theta$ and $m_s = 10$ keV. As can be seen, for a y coupling of the order 10^{-7} , the decay length is around 1 cm, while it exceeds 10 m for $y \sim 10^{-9}$. In addition, the decay lengths of χ_2 and χ_3 appear to be essentially equal for $m_{\chi_{1,2}} \gtrsim 300$ GeV or for $\tan\theta \gg 1$. Let us also emphasize that, in the limit of eq. (2.6), the decays $\chi_3 \rightarrow \chi_2$ are not allowed due to the tiny mass splittings, as it can be verified by inspecting the expressions in eq. (2.7).

3 Dark matter abundance from Freeze-in

In the feeble Yukawa coupling regime that we are considering, the dark matter candidate $\chi_1 \sim \psi_s$ has strongly suppressed interactions with the SM particles. Hence it is not in thermal equilibrium with the SM bath at the time of production. In contrast, the components of the electroweak doublet are in thermal equilibrium because of their unsuppressed gauge interactions. Assuming zero initial abundance of χ_1 , the dominant production mechanism for the dark matter particle is through the decay of the heavy mediators (ψ^\pm and $\chi_{2,3}$) along the cosmological evolution.³ This production “freezes-in” when the abundance of

³In our model, the scattering processes with χ_1 in the final state give definitely subdominant contributions with respect to mediators’ decays, such as in e.g. [5]. Moreover, decays of SM particles into DM, such as $Z \rightarrow \chi_1\chi_1$ and $h \rightarrow \chi_1\chi_1$, also give negligible contributions, because doubly suppressed by the tiny Singlet-Doublet mixing.

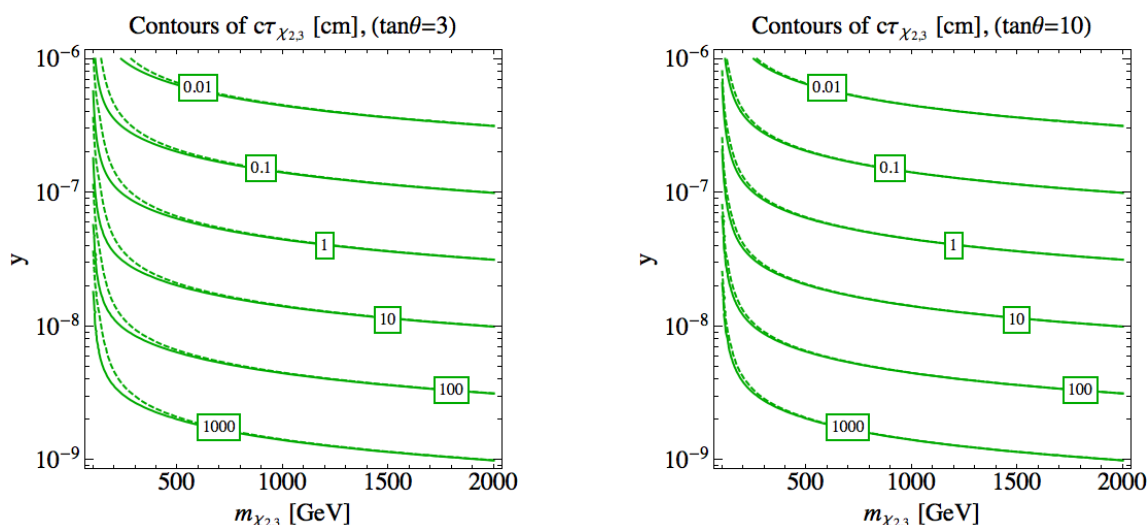


Figure 3. Decay length of the two heavy neutral fermions, χ_2 (solid lines) and χ_3 (dashed lines) for two different choices of $\tan \theta = y_u/y_d$. The mass of the lightest neutral fermion is set to $m_{\chi_1} = 10$ keV.

the heavy mediators is Boltzmann suppressed, that is approximately when the temperature drops below their mass. This is the framework in which we carry out our analysis; see e.g. [5–9, 11, 59, 60] for some previous examples. The DM comoving number density induced through the decay of $A \rightarrow B \chi_{\text{DM}}$ simply reduces to [5]

$$Y_{\chi_{\text{DM}}} = \frac{135g_A}{(1.66)8\pi^3g_*^{3/2}} \frac{M_{\text{Pl}}\Gamma_A}{m_A^2}, \tag{3.1}$$

where g_A counts the spin degrees of freedom of the mother particle A , g_* is the number of degrees of freedom at the freeze-in temperature $T \sim m_A$, and $M_{\text{Pl}} = 1.22 \times 10^{19}$ GeV is the Planck mass. This result is obtained making the following simplifying assumptions: (i) the mother particle A and the daughter particle B are in thermal equilibrium with the SM thermal bath; (ii) A follows a Maxwell-Boltzmann distribution function; (iii) we can neglect the Pauli-blocking/stimulated emission effects associated to B . See also the discussion in [61].

Let us notice that the freeze-in mechanism considered here — taking place through the decay of a mediator that is in thermal equilibrium with the Standard Model sector in the early universe — shares some similarities with the so-called superWIMP mechanism [62]. In the latter case, the late decay of the WIMP mother particle — occurring considerably after its freeze-out — give rise to the dark matter abundance. The main difference between the two mechanisms is the life-time of the mother particle in thermal contact with the Standard Model. In the superWIMP case, the life-time is typically much longer ($\tau \sim 10^5 - 10^8$ s) and the scenario is subject to constraints from big bang nucleosynthesis [62, 63].

3.1 Freeze-in: collider and cosmology interplay

In the context of the Singlet-Doublet model, three mass degenerate heavy states can decay into dark matter, namely the charged fermion ψ^\pm and the two neutral fermions $\chi_{2,3}$, giving rise to the DM yield:

$$Y_{\chi_1} = \frac{270M_{\text{Pl}}}{(1.66)8\pi^3 g_*^{3/2}} \left(\sum_{B=Z,h} \frac{\Gamma[\chi_3 \rightarrow B\chi_1]}{m_{\chi_3}^2} + \sum_{B=Z,h} \frac{\Gamma[\chi_2 \rightarrow B\chi_1]}{m_{\chi_2}^2} + g_\psi \frac{\Gamma[\psi^+ \rightarrow W^+\chi_1]}{m_\psi^2} \right), \quad (3.2)$$

where $g_\psi = 2$ takes into account the number of degrees of freedom of the charged fermion. Notice that the contributions of the heavy neutral fermions $\chi_{2,3}$ directly depend on the total decay widths of $\chi_{2,3}$, which we will denote $\Gamma_{\chi_{2,3}}$ in the following, as the decays into χ_1 are the only available decay modes. On the other hand, for the charged fermion, only the partial decay width into the $W^+\chi_1$ final state appears since the ψ^\pm decays into $\chi_{2,3}$ are already accounted for by the two first contributions associated to the thermal equilibrium abundances of $\chi_{2,3}$. We can now compute the DM relic density in terms of Y_{χ_1} :

$$\Omega_{\chi_1} h^2 = m_{\chi_1} \frac{s_0 h^2}{\rho_c} Y_{\chi_1}, \quad (3.3)$$

where the present entropy density and critical density are respectively $s_0 = 2.8912 \times 10^9 \text{ m}^{-3}$ and $\rho_c = 10.537 h^2 \text{ GeV}/\text{m}^3$. Considering that, in our scenario, we have $m_{\chi_{2,3}} \simeq m_\psi \simeq \mu$, we obtain as a result

$$\Omega_{\chi_1} h^2 = 0.1 \left(\frac{105}{g_*} \right)^{3/2} \left(\frac{m_{\chi_1}}{10 \text{ keV}} \right) \left(\frac{1 \text{ TeV}}{\mu} \right)^2 \left(\frac{\sum_{ij} g_{A_i} \Gamma_{ij}}{5 \times 10^{-15} \text{ GeV}} \right), \quad (3.4)$$

where g_{A_i} is the number of degrees of freedom of the mother particle A_i , Γ_{ij} denotes the decay width $\Gamma[A_i \rightarrow B_j \chi_1]$, with $A_i = \chi_{2,3}^0$ or ψ^\pm decaying into χ_1 plus a SM boson, $B_j = Z, h$ or W^\pm .

Obtaining the dark matter yield on more general grounds, starting from Maxwell-Boltzmann statistics, requires a fully numerical treatment of the evolution equations, which makes the computation and the interpretation of the freeze-in mechanism less straightforward. The authors of ref. [61] have however recently delivered the public code `micrOMEGAs5.0` that allows to easily handle such computations. We have explicitly checked that the analytical results presented here are in excellent agreement with the ones obtained with `micrOMEGAs5.0` (employing the Singlet-Doublet model files from our implementation in `FeynRules` [64]) in the Maxwell-Boltzmann limit.⁴ Beyond this simplifying assumption, the full numerical treatment of the evolution equations gives rise to a moderate positive correction to $\Omega_{\chi_1} h^2$ with respect to our analytical result (about 25%). In this paper, we choose to discuss the results of our analysis with the Maxwell-Boltzmann approximation, thus neglecting the above small correction, in order to have a fully analytical understanding of the parameter space of the model yielding the observed DM abundance.

⁴See ref. [61] for a discussion on the relevance of the statistics in different dark matter scenarios.

The result of eq. (3.4) is rather generic for the freeze-in scenarios, independently of the underlying dark matter model, and indicates the typical order of magnitude of the physical quantities involved, that is the dark matter mass, the mediator(s) mass, and the mediator(s) widths. Note that the decay length of a particle is related to the total decay width through

$$c\tau_A = \frac{10^{-15} \text{ GeV}}{\Gamma_A} \times 19 \text{ cm}. \quad (3.5)$$

Hence mother particles or equivalently mediators, A , with a total decay width allowing for the dark matter density to be in agreement with the observed abundance $\Omega h^2 \simeq 0.12$, are in the right ballpark to give rise to macroscopically long displacements at colliders. In order for the mediators to be produced at the LHC, their mass cannot typically exceed the TeV scale. For such mass scale, a DM mass in the heavy range $1 \text{ MeV} \lesssim m_{\chi_1} \lesssim 1 \text{ GeV}$ corresponds to mediators escaping the detectors, while for light dark matter, $1 \text{ keV} \lesssim m_{\chi_1} \lesssim 1 \text{ MeV}$, the signature will be characterised by displaced vertices visible inside the detectors. This highlights the natural interplay among LHC long-lived or displaced signatures, the freeze-in mechanism, and cosmological or astrophysical probes of light ($\simeq \text{keV}$) dark matter. An important remark is that these considerations and correlations are strictly correct for mediators that can decay into dark matter only, which is the case of $\chi_{2,3}$ here. We study this complementarity in further detail in sections 5 and 6.

3.2 The viable dark matter parameter space

We can now employ the decay widths that we computed in section 2.2 to derive the predicted value of the dark matter relic abundance on the parameter space of the Singlet-Doublet model. Expanding the expressions of the decay widths in the limit of small m_{χ_1} one finds at leading order:

$$\sum_{i=2,3} \Gamma[\chi_i \rightarrow Z\chi_1] = \frac{y^2}{32\pi} \frac{(m_Z^2 - \mu^2)^2 (2m_Z^2 + \mu^2)}{\mu^5} \quad (3.6)$$

$$\sum_{i=2,3} \Gamma[\chi_i \rightarrow h\chi_1] = \frac{y^2}{32\pi} \frac{(m_h^2 - \mu^2)^2}{\mu^3} \quad (3.7)$$

$$\Gamma[\psi^\pm \rightarrow W^\pm\chi_1] = \frac{y^2}{32\pi} \frac{(m_W^2 - \mu^2)^2 (2m_W^2 + \mu^2)}{\mu^5}. \quad (3.8)$$

These expressions show that the combinations of the decay widths entering in the computation of the relic abundance do not depend on $\tan\theta$ at zeroth order in m_{χ_1} . Plugging these expressions into eq. (3.3), we find the following approximate expression

$$\Omega_{\chi_1} h^2 \simeq 0.11 \left(\frac{105}{g_*}\right)^{3/2} \left(\frac{y}{10^{-8}}\right)^2 \left(\frac{m_{\chi_1}}{10 \text{ keV}}\right) \left(\frac{700 \text{ GeV}}{\mu}\right), \quad (3.9)$$

which accounts for the correct relic abundance up to a few percent level error when $\mu \gtrsim 400 \text{ GeV}$. Eq. (3.9) shows how the dark matter relic abundance via freeze-in scales with the different parameters of the model. The results of the dark matter calculations presented in what follows always make use of the full expressions of eqs. (3.2), (3.3) with $g_* = 105$.

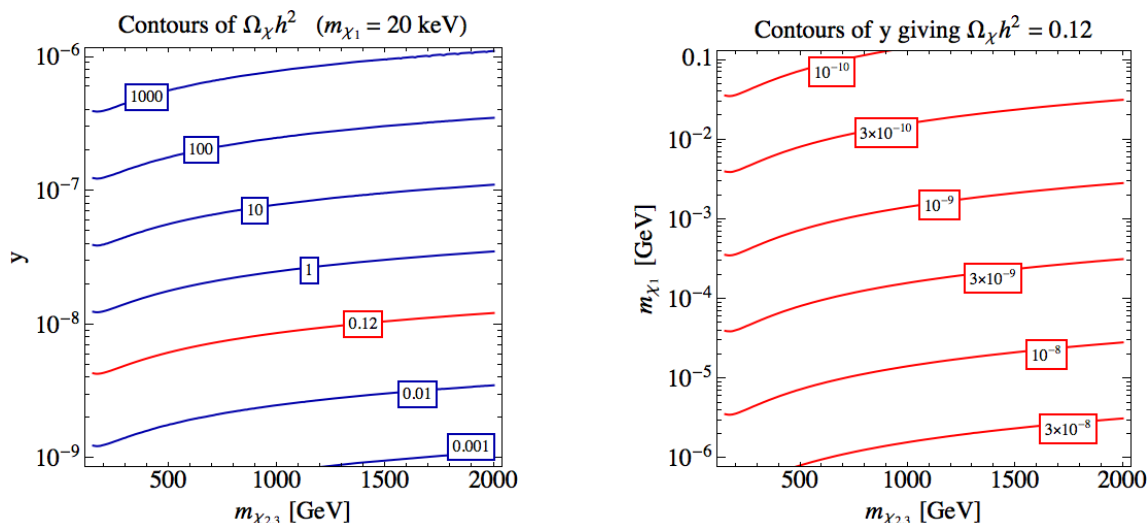


Figure 4. Left: contours of Ωh^2 for $m_{\chi_1} = m_s = 20$ keV. Right: contours of the values of y on the $(m_{\chi_{2,3}}, m_{\chi_1})$ plane required to get the observed DM relic abundance.

In the left panel of figure 4, we show the dependence of the dark matter abundance through the freeze-in mechanism on the parameters of the model for a fixed DM mass $m_{\chi_1} = 20$ keV on the $(m_{\chi_{2,3}}, y)$ plane, or equivalently (μ, y) plane. It appears that, for $m_{\chi_1} \sim$ few tens of keV, the coupling should be $y = \mathcal{O}(10^{-8})$ in order to reproduce the observed dark matter density. In the right panel of figure 4 instead, we show on the $(m_{\chi_{2,3}}, m_{\chi_1})$ plane contours of the values of the coupling y that yield $\Omega_{\chi_1} h^2 = 0.12$. We can see that, for m_{χ_1} in the [100 MeV, 1 keV] mass range and a μ scale of relevance for colliders, the required size of the Yukawa coupling is in the range

$$10^{-8} \lesssim y \lesssim 10^{-10}. \quad (3.10)$$

The largest values of the coupling $y \sim 10^{-8}$ allow for very light dark matter candidates (few keV) to account for all the dark matter while heavier particles of hundreds of MeV requires even more suppressed Yukawa interactions with $y \sim 10^{-10}$. This observation will be relevant when comparing the reach of collider experiments to the one of cosmology probes on the frozen-in Singlet-Doublet dark matter parameter space.

4 Cosmology probe of light dark matter

Dark matter candidates with non negligible velocity dispersion deep in the radiation dominated era can leave a distinctive imprint in cosmology and astrophysics observations due to their free-streaming that delays the structure growth. Overdensities are suppressed below the comoving free-streaming horizon given by

$$\lambda_{fs} = \int_0^1 \frac{\langle v \rangle}{a^2 H} da \quad (4.1)$$

where a is the scale factor and H is the Hubble rate and $\langle v \rangle$ is the velocity dispersion of the dark matter ($\langle v \rangle$ is given by the velocity of light for relativistic dark matter). For example,

thermal warm dark matter (WDM), which was in thermal equilibrium and relativistic until decoupling at temperature T_D , has a free-streaming length of $\lambda_{fs} \simeq \text{Mpc} (\text{keV}/m_X) T_D/T_\nu$ where T_ν is the temperature of active neutrinos and m_X is the WDM mass.⁵ Such a WDM scenario has served as a benchmark for non-cold dark matter cosmology. In this work we exploit the results of Lyman- α forest studies that have been used to set a lower bound on the thermal WDM mass of

$$m_{\text{WDM}} > 4.65 \text{ keV} \quad [\text{thermal WDM}] \quad (4.2)$$

at 95% confidence level (CL) [20]. Notice that the above constraint can e.g. relax to $m_{\text{WDM}} > 3.2 \text{ keV}$ at 95% CL when the WDM makes only part ($> 80\%$) of the total DM content [65]. It has also been argued that considering a different thermal history in the treatment of the Lyman- α forest data (especially the ones associated to high redshift quasars), a few keV DM candidate could even provide a good fit to the data, see [19, 65, 66], a possibility that is strongly challenged by X-ray constraints in the context of sterile neutrinos [65].

Thermal warm dark matter is not the only relic that would suppress small scale structure formation. Other DM candidates with non negligible velocity at the time of production will give rise to similar effect.⁶ Among them, one finds (non-)resonantly produced sterile neutrinos [78–82], sterile neutrinos from frozen-in scalars [83, 84], mixed dark matter scenarios [85] and — of interest for this paper — other frozen-in particles [5, 86–89]. The different mechanisms of production involved can typically give rise to distribution functions that can differ from the (thermal) Fermi-Dirac distribution. As a result, the imprint on the linear matter power spectrum should a priori be recomputed making use of the relevant Boltzmann codes. Dedicated hydrodynamical simulations should then be performed so as to extract the non-linear evolution of a baryon+DM population and properly compute the observables relevant to estimate the Lyman- α flux power spectra within a given DM scenario and compare with data. All this procedure is however beyond the scope of this paper.

Here we use the constraints that have been derived in refs. [86, 88] on keV dark matter produced through the freeze-in from the decay(s) of some thermalised mother particle A into the DM and another daughter particle B . In ref. [88], the suppression of the linear matter power spectrum in the freeze-in scenario has been computed and compared to the one of thermal WDM with a mass of 4.65 keV.⁷ This provided a constraint on the mass of

⁵The thermal abundance of WDM is given by $\Omega_X h^2 \simeq (T_D/T_\nu)^3 m_X / 94 \text{ eV}$ where $T_D/T_\nu = (g_*(T_\nu)/g_*(T_D))^{1/3}$ for entropy conservation with $g_*(T)$ the effective number of relativistic degrees of freedom and $g_*(T_\nu) = 10.75$. All together, an injection of large number of relativistic degrees ($> 10^4$) of freedom is needed, compared to the available ones in the SM $g_*(T > T_{EW}) = 106.75$, so as to be able to get a thermal WDM of a still allowed few keV WDM [19–21].

⁶Notice that collisional or Silk damping (in contrast with free streaming \equiv collision-less damping) can also give rise to a similar imprint in small scale structures. This would be typically the case of dark matter interacting with relativistic species, see e.g. [67–77].

⁷In ref. [88], the transfer function of DM (associated to the ratio of cold DM and freeze-in DM linear matter power spectra) produced through freeze-in from the decays of some thermalised mother particle $A \rightarrow B + \text{DM}$ always appear to have the very same spectral form as the one of thermal WDM. For other references, estimating the range of viable non-cold dark matter candidates based on the derivation of the linear matter power spectrum, see e.g. [71, 85, 87, 90–92].

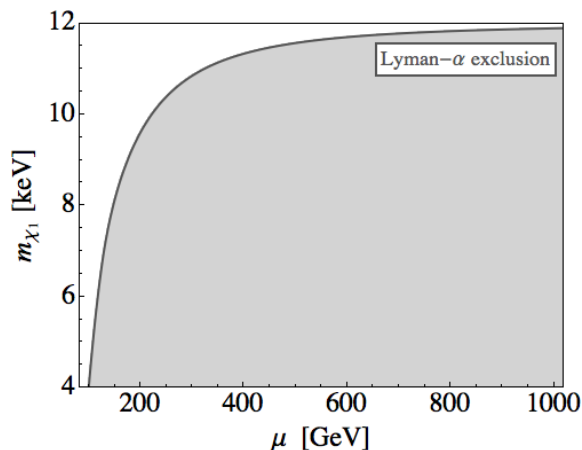


Figure 5. Bound on the DM mass from Lyman- α ; the area below the curve is excluded.

the frozen-in dark matter particle that shows a dependence on the mass splitting between A and B for compressed spectra. Within our framework, the resulting constraint on the dark matter mass reads:

$$m_{\text{DM}} > 12 \text{ keV} \left(\frac{\sum_{ij} g_{A_i} \Gamma_{ij} \Delta_{ij}^\eta}{\sum_{ij} g_{A_i} \Gamma_{ij}} \right)^{1/\eta}. \quad (4.3)$$

where $\eta = 1.9$ (as obtained in ref. [88] from a numerical fit), and Γ_{ij} is the decay width $\Gamma(A_i \rightarrow B_j \chi_1)$, $\Delta_{ij} = (m_{A_i}^2 - m_{B_j}^2)/m_{A_i}^2$ with $A_i = \chi_{2,3}^0$ and ψ^\pm denoting the mediators that decay into the dark matter fermion χ_1 and another SM final state $B_j = Z, h$ or W^\pm . The results of ref. [88] imply thus that, in general, frozen-in DM, resulting from the decay of a thermalised mother particle with $m_{\text{DM}} > 12 \text{ keV}$, evades the constraints from the Lyman- α forest data derived in [20]. Lower DM masses can become allowed when Δ_{ij} is small, i.e. for small mass splittings between A_i and B_j (as pointed out in [86]). Our bound is shown in figure 5 as a function of the doublet mass μ . As we can see, the lower bound on the DM mass becomes weaker than $m_{\chi_1} > 12 \text{ keV}$ only for values of the doublet mass μ approaching the mass of the decay products $B_j = Z, h, W^\pm$.

Notice that astrophysics and cosmology already provide other complementary probes of dark matter scenarios suppressing structure formation on small scales. Among them one finds CMB fluctuations, galaxy clustering, galaxy satellite number count, etc., see e.g. refs. [35, 71, 73, 76, 77, 93–97]; and also e.g. refs. [76, 77, 98–100] for future probes. Currently, most (combinations of) probes tend to exclude a few keV thermal warm dark matter scenarios, on a par with the results of the Lyman- α forest analysis considered here.

5 Signatures at the LHC

In the feebly-coupled regime of the Singlet-Doublet dark matter model, the mediators ψ^\pm and $\chi_{2,3}$ are essentially the charged and neutral components of the extra $\text{SU}(2)_L$ doublets. As a result, they can be produced at the LHC through electroweak processes. These

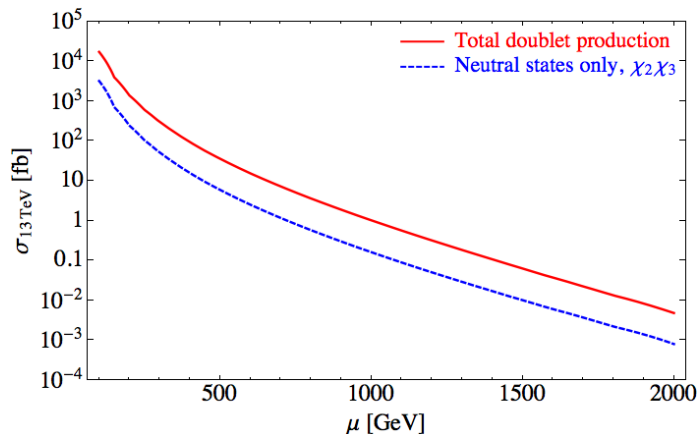


Figure 6. NLO production cross section of the states belonging to the fermion doublet pair at the LHC with $\sqrt{s}=13$ TeV as computed by `Prospino2` [101]. The solid red line indicates the sum over all possible production modes, while the dashed blue line shows the production cross section of the neutral states $\chi_2\chi_3$ only.

production processes are induced by gauge couplings only and thus the cross sections are independent of the couplings y_u and y_d . They are actually equal to those of a pure Higgsino in supersymmetry (SUSY) that can be computed using public tools such as `Prospino2` [101]. Referring to the SUSY nomenclature, the relevant production modes include neutralino pair production, chargino pair production, and associated production of neutralino and chargino:

$$pp \rightarrow \chi_2\chi_3 + X, \quad pp \rightarrow \psi^+\psi^- + X, \quad pp \rightarrow \chi_{2,3}\psi^\pm + X. \quad (5.1)$$

Being substantially decoupled from the SM sector, the singlet dark matter χ_1 can only be produced at the last step of the decay chain, with the possible decay modes as illustrated in figure 1. We report in figure 6 the total production cross section (obtained by summing over all mediator pair and associated production modes) with a continuous red line, and the production cross section of a $\chi_2\chi_3$ pair with a dashed blue line, as a function of the doublet mass scale μ . The cross sections were computed by means of `Prospino2` for pp collisions with $\sqrt{s} = 13$ TeV at next-to-leading order (NLO).

In order to obtain the collider constraints, we first have to compute the typical decay length of the heavy mediators in the viable dark matter parameter space, i.e. where $\Omega_{\chi_1} h^2 = 0.12$. In figure 7, we present the decay length of the mediators for the model parameters accounting for the whole observed dark matter abundance. In the left panel, we show contours for the decay length of the heavy neutral fermions, $c\tau_{\chi_{2,3}}$. On general grounds, the results depend on $\tan\theta$ but, as already noticed in figure 3, the $\tan\theta$ dependence is negligible as long as $\mu \gtrsim 300$ GeV or $\tan\theta \gg 1$. Also, as expected from the discussion in section 3, the figure shows that decay lengths leading to displaced signatures within the volume of LHC detectors correspond to the light dark matter regime, $m_{\chi_1} \lesssim 1$ MeV. On the right panel of figure 7, the dashed orange contours indicate the branching fraction of the ψ^\pm decay into pions and $\chi_{2,3}$. We see that this decay mode is dominant except in a small corner of the parameter space where $m_{\chi_1} = \mathcal{O}(1)$ keV and $m_\psi = \mu$ is larger

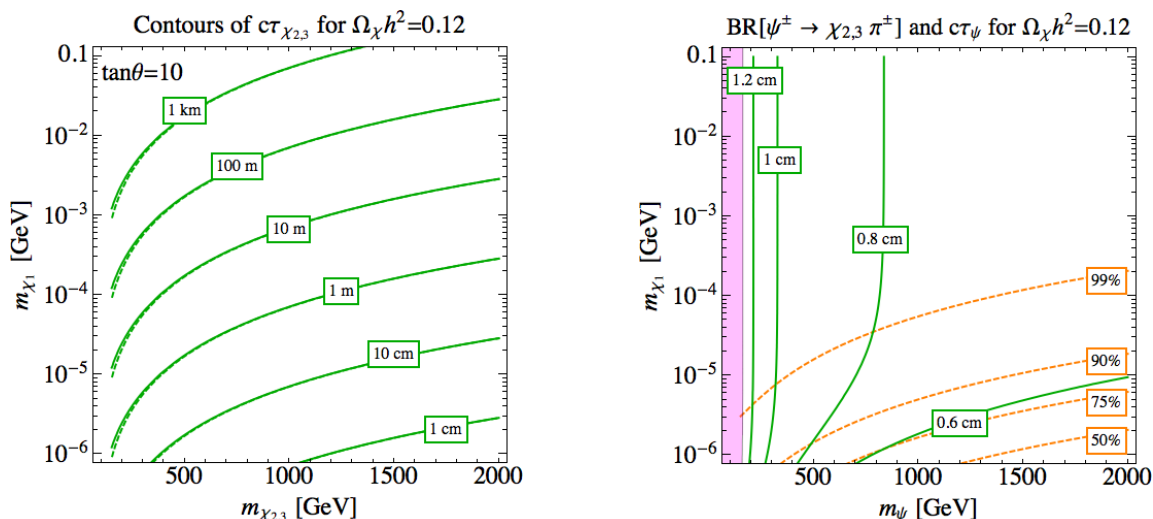


Figure 7. Left: decay length of the neutral fermions χ_2 (solid lines) and χ_3 (dashed lines). Right: branching ratio (orange dashed lines) and decay length (green solid lines) of $\psi^\pm \rightarrow \chi_{2,3} \pi^\pm$; the shaded region is excluded by searches for disappearing tracks [57, 58]. The coupling y is set in both plots by requiring $\Omega h^2 = 0.12$.

than about 1 TeV. The ψ^\pm decay mode into $W^\pm \chi_1$, driven by the Yukawa interactions and contributing to the dark matter relic abundance, is typically subdominant, due to the feeble couplings involved. As a consequence, the decay length of ψ^\pm is always of the order of 1 cm in the parameter region relevant for the freeze-in mechanism as shown by the green solid lines in the right panel of figure 7.

We can now discuss the LHC signatures of our freeze-in Singlet-Doublet model.

- Disappearing tracks:** independently of the final steps of the decay chain, the charged fermions ψ^\pm decay with a small displacement (of the order 1 cm at most, cf. figure 7) leading to ‘disappearing’ charged tracks that can be searched for at the LHC. In fact, a recent ATLAS analysis [57] (see also the similar search [102] from the CMS Collaboration), reinterpreted in [58] in terms of pure Higgsino production (which is exactly our case), excludes the regions shaded in purple in the right panels of figures 2 and 7. This search constrains the mass of the charged fermions to be larger than about 150 GeV in the regime in which $\psi^\pm \rightarrow \pi^\pm \chi_{2,3}$ dominates. For future prospects of searches for disappearing tracks and possible strategies to increase their sensitivity, see [103, 104], where Higgsino masses up to approximately 400 – 500 GeV are foreseen to be accessible at the future high-luminosity run of the LHC (HL-LHC).

- Displaced h and/or $Z + \cancel{E}_T$:** most of the mediator production modes will eventually produce a pair of heavy neutral fermions ($\chi_2 \chi_2$, $\chi_2 \chi_3$ or $\chi_3 \chi_3$), possibly with extra soft objects that will go undetected. Indeed, as shown above, the relic abundance requirement implies that the charged fermions decay dominantly into the heavy neutral ones, $\chi_{2,3}$, plus soft pions. Given the possible decay modes of $\chi_{2,3}$, our key collider signature is thus characterised by a final state with displaced ZZ , hh or Zh , plus missing momentum,

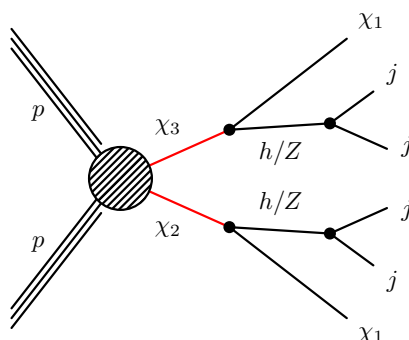


Figure 8. Schematic representation of one of the processes leading to displaced Z or h bosons plus missing energy at the LHC. The red lines denote long-lived particles. Similar final states arise from χ_2 or χ_3 pair production. Note that we do not specify the production mechanism of the pair of neutral heavy fermions since it could be produced directly through electroweak processes or through the decay of the charged fermion.

as illustrated in figure 8. By summing all the possible production modes, the process is symmetric in the $\chi_2 \leftrightarrow \chi_3$ exchange, since ψ^\pm decays democratically into $\chi_{2,3}$, cf. eq. (2.10). Hence, the precise signal yield in each of the three channels ZZ , hh and hZ is determined by the branching fractions of the two neutral fermions $\chi_{2,3}$. In figure 9, we show the branching fractions of the $\chi_{2,3}$ decays into $h\chi_1$ (dashed line) and $Z\chi_1$ (continuous line) as a function of $\tan\theta$ and for several benchmark masses. As we can see, for $\tan\theta \approx 1$, i.e. $y_u \approx y_d$, one of the two heavy fermions decays predominantly into $Z + \chi_1$ and the other one into $h + \chi_1$, independently of their mass. This leads to final states with a balanced sample of hh (25%), ZZ (25%) and hZ (50%). The same is true for $\tan\theta \gg 1$ or $\tan\theta \ll 1$ and when the mass of the neutral fermions is much larger than the Higgs mass (where effectively one has $\text{BR}[\chi_{2,3} \rightarrow Z\chi_1] = \text{BR}[\chi_{2,3} \rightarrow h\chi_1] = 50\%$). The only configuration where there is not a balance in h and Z is when the mass of the neutral fermions is close to the Higgs mass. In this latter case, kinematics favor the decays into $Z + \chi_1$, and hence final states with $ZZ + \cancel{E}_T$ are more probable.

In the next subsection, we will estimate the constraints on the three final states with displaced $ZZ + \cancel{E}_T$, $hh + \cancel{E}_T$ or $hZ + \cancel{E}_T$ that can be obtained from existing LHC searches at 13 TeV for displaced signatures, and we will subsequently study the impact on the parameter space of our model. Notice that searches performed at the LHC with $\sqrt{s} = 8$ TeV can also be sensitive to the main signatures of our model, $ZZ + \cancel{E}_T$, $hh + \cancel{E}_T$ or $hZ + \cancel{E}_T$. A number of such searches have been considered in ref. [105] and reinterpreted in terms of supersymmetric models. In particular, our scenario is similar to the case of Higgsinos decaying into gravitino in gauge-mediated SUSY models considered in [105], which is constrained mainly by a search for displaced dileptons [106] and a search for displaced jet pairs [107, 108], both performed by CMS. In the next subsection, we show a comparison of the sensitivity of these searches with the 13 TeV analysis we are going to recast. Note that our model and the Higgsino-gravitino scenario considered in [105]

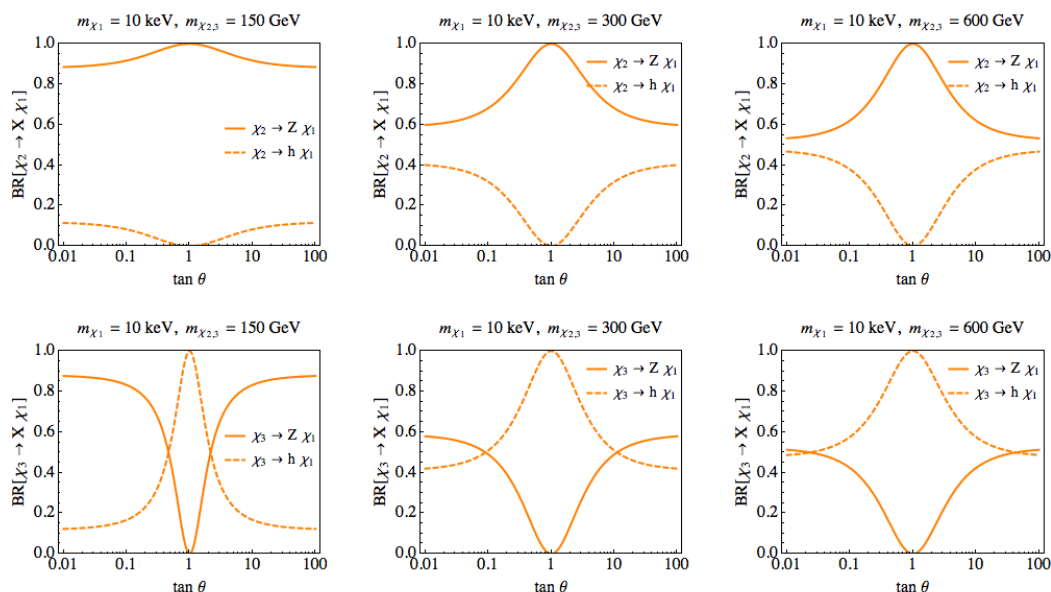


Figure 9. Branching ratios of χ_2 (first row) and χ_3 (second row) as a function of $\tan \theta \equiv y_u/y_d$, for different choices of their mass. If $\tan \theta < 0$, χ_2 and χ_3 simply exchange role.

differ in an important aspect. The main difference is that the mass splitting between the neutral components of the Higgsino multiplets in SUSY scenarios is typically sizeable ($\gtrsim \mathcal{O}(1)$ GeV) due to mixing with gauginos, even if such particles are substantially heavier than the Higgsino (up to $\mathcal{O}(10)$ TeV). As a consequence, the heaviest neutral component of the Higgsino decays mostly in the lightest component plus soft SM particles and the balance among the hh , hZ , and ZZ final states only depends on the branching ratios of the lightest neutral component of the Higgsino into the gravitino plus h or Z . In contrast, in the Singlet-Doublet freeze-in model, the mass splitting between the heavy neutral components is so small — as shown by the expressions in eq. (2.7) — that the two neutral fermions always decay directly to $\chi_1 Z$ or $\chi_1 h$ with branching ratios as illustrated in figure 9.

• **Searches for prompt decays:** for small values of the decay length of the mediators (corresponding to moderate/large values of y), we expect that limits from standard prompt searches can be effective. A combination of recent searches at the LHC with $\sqrt{s} = 13$ TeV for production of supersymmetric charginos and neutralinos can be found in ref. [109]. Possible final states are $hh + \cancel{E}_T$, $ZZ + \cancel{E}_T$ and $hZ + \cancel{E}_T$, which are typical signatures of searches targeting Higgsino-like neutralinos in gauge mediated supersymmetry breaking [110], or Higgsinos decaying into light Bino, see e.g. [111]. In these final states, limits to the Higgsino mass up to 600–700 GeV were obtained.⁸ A second type of relevant final states are $WZ + \cancel{E}_T$ and $Wh + \cancel{E}_T$, which are possible in our model for moderate/large values of y , such that the charged fermions ψ^\pm decay promptly into $W^\pm \chi_1$, cf. figure 2.

⁸Searches performed with the dataset of the 8 TeV run of the LHC are comparatively much less sensitive, constraining Higgsino masses up to around 250 GeV [111], so that we are not going to consider them here.

Experiment	Final state	\mathcal{L}, \sqrt{s}	Ref.
ATLAS	DV+ \cancel{E}_T	32.8 fb ⁻¹ , 13 TeV	[53]
ATLAS	lepton-jets	3.4 fb ⁻¹ , 13 TeV	[118]
ATLAS	jets	3.2 fb ⁻¹ , 13 TeV	[119]
CMS	jets	2.6 fb ⁻¹ , 13 TeV	[120]
CMS	μ, e	2.6 fb ⁻¹ , 13 TeV	[121]

Table 1. Summary of 13 TeV ATLAS and CMS searches for displaced signatures possibly relevant for the final state under study.

Note that the configurations of the model giving rise to the observed relic abundance through freeze-in considered in section 3 never give rise to prompt decays, i.e. the decay length is always larger than about 1 mm. We discuss thus these prompt decay searches briefly. For more detailed discussions of the prompt signatures of the Singlet-Doublet model, see refs. [43, 47].

- **Mono-X searches:** in the region with very large decay length, where the neutral fermions escape the detectors, mono-X searches could be the only strategy to look for this model at the LHC (besides the disappearing charged tracks associated to the charged fermion). In this regime the collider signature of our model is very similar to an Higgsino dark matter scenario in which the mass splitting among the Higgsino components is tiny, as already mentioned. There have been several investigations on this scenario and the corresponding mono-X signatures, e.g. in [112–117]. Some of these investigations have exploited the soft leptons that would be present for a mass splitting of the order of few GeV, which is however not the case of our model. Instead, the case of a pure mono-jet signal has been shown to be not promising, with an estimated reach on the Higgsino mass of order 200 GeV at HL-LHC with 3000 fb⁻¹ [115]. Hence we decide not to include these signatures in our analysis.

5.1 Recasting strategy for displaced h and $Z + \cancel{E}_T$

The aim of this subsection is to estimate the current LHC limit on displaced ZZ , Zh and $hh + \cancel{E}_T$ using public information from ATLAS and CMS searches. In table 1, we report on the relevant ATLAS and CMS searches for displaced signatures, focussing on the most recent analyses at 13 TeV. Among these searches, we identify the recent ATLAS analysis on displaced vertices (DV) with jets and \cancel{E}_T [53] as the most promising for our scenario. The motivation is manifold: (i) this analysis exploits the largest available dataset among those listed in table 1; (ii) the large hadronic branching fractions of h and Z imply that our model yields a sizeable production cross section in this channel; (iii) our final states contain a relevant source of \cancel{E}_T , and the analysis of ref. [53] is the only one targeting it with a dedicated selection; (iv) and finally, detailed auxiliary material is provided with the information needed for a recasting [122].

The ATLAS DV+ \cancel{E}_T analysis [53] targets final states with at least one displaced vertex with jets and large missing transverse momentum. The results are interpreted in a model with long-lived gluinos decaying into jets and the lightest neutralino. In the auxiliary material [122], the efficiencies for the missing momentum and the displaced vertex reconstruction are provided. In particular, the efficiencies of the displaced vertex reconstruction are given prior to detector simulation, as a function of the invariant mass of the vertex, of the number of tracks and of the displacement.

In order to estimate the sensitivity of this search on our final states, we have first implemented the model in `FeynRules` [64], and then simulated the relevant samples with `MadGraph5` [123], combined with `Pythia8` [124] for the parton showering and the underlying pp collision, and `Delphes3` [125] (with the standard ATLAS card) for the detector simulation. The displacement is applied to the simulated events a posteriori, taking into account the four momenta of the long-lived particle in order to properly compute the displacement,⁹ which is obtained by sampling an exponential distribution with mean decay length $c\tau_{\chi_{2,3}}$. In appendix B, we discuss the details of the selection and the validation of our implementation. The latter was performed by reproducing the exclusion limits set by the ATLAS search on the simplified model they considered with long-lived gluino.

After this validation, we can now estimate the efficiency of the ATLAS DV+ \cancel{E}_T analysis in the final states we are interested in, which are $ZZ + \cancel{E}_T$, $hh + \cancel{E}_T$ or $hZ + \cancel{E}_T$.¹⁰ We do this as a function of the lifetime $\tau_{\chi_{2,3}}$ and of the mass of the long-lived particles, which are simply the two neutral fermions χ_2 and χ_3 produced in pairs (cf. appendix B for plots displaying the resulting efficiencies). The mass is important in order to determine the boost factor in the displacement, as well as to get the correct p_T distribution of the displaced tracks. We can now use the obtained selection efficiencies to evaluate the reach of the ATLAS analysis in three simplified models with fixed branching fractions, that serve for illustrative purposes:

- i) $\text{BR}[\chi_{2,3} \rightarrow h\chi_1] = 100\%$;
- ii) $\text{BR}[\chi_{2,3} \rightarrow Z\chi_1] = \text{BR}[\chi_{2,3} \rightarrow h\chi_1] = 50\%$;
- iii) $\text{BR}[\chi_{2,3} \rightarrow Z\chi_1] = 100\%$.

In order to constrain the above simplified models, we consider the total production cross section of the doublet fermions states, computed at NLO by `Prospino2` [101], summing all production modes shown in (5.1), corresponding to the solid red line in figure 6. With no background in the signal region, the parameter configuration of a model is excluded at 95% confidence level (CL) or more if it yields a number of selected events ≥ 3.0 . The resulting estimated exclusion is depicted in figure 10 by the three solid lines. As we can see, the difference in the efficiencies among the three simplified models results in only a

⁹In this approach we neglected distortions of the kinematic distributions of the final state charged tracks due to the displacement.

¹⁰If Z or h decay into $b\bar{b}$, (some of) the resulting tracks may have an additional displacement, which makes the reconstruction of the DV more involved, as discussed in more detail in appendix B. In the following, we neglect possible issues related to this for the reasons discussed in the appendix.

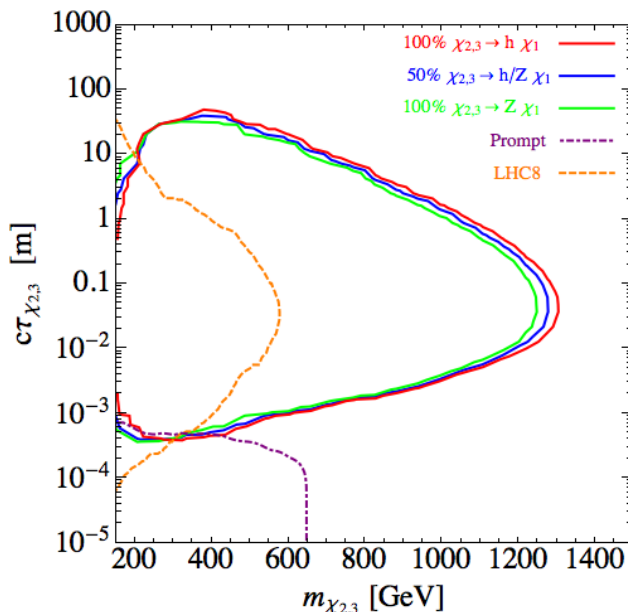


Figure 10. Estimated exclusion curves from collider searches in the plane of the decay length versus the mass of the heavy neutral fermions. Our recasting of the ATLAS DV+ \cancel{E}_T search, associated to the final states of $hh + \cancel{E}_T$, $hZ + \cancel{E}_T$ or $ZZ + \cancel{E}_T$, for the simplified models i), ii) and iii) (see the text for details) are shown with red, blue and green solid lines respectively. The orange dashed line is the exclusion of displaced searches at 8 TeV LHC, as estimated in [105]. The purple dashed-dotted line is our estimate of the impact of the prompt searches at 13 TeV performed by CMS [109].

small impact on the sensitivity. Moreover, the largest doublet mass (about 1.3 TeV) is probed for a decay length around $c\tau \approx 5$ cm. Also, the exclusion curves are not symmetric in $c\tau$ with respect to this maximal reach. This is due to the fact that the exponential distribution determining the displacement is falling very rapidly for a displacement larger than a given $c\tau$, while it goes to zero less steeply for displacement smaller than $c\tau$. This also explains why the reach of the analysis extends to regions with very large decay lengths, up to $c\tau \approx 50$ m.

In figure 10, we also show for comparison the exclusion from the 8 TeV searches, as reported by ref. [105]. This is depicted as a dashed orange line and includes both searches targeting displaced leptons [106] and displaced di-jets [107, 108]. The displayed 8 TeV limit has been obtained in ref. [105] in a simplified model with an Higgsino-like neutralino undergoing displaced decays into gravitino plus Z or h in the large $\tan\beta$ regime, which roughly corresponds to our simplified model ii).¹¹ As we can see, in the region of low doublet mass, the sensitivity of the ATLAS DV+ \cancel{E}_T analysis is diminished because the spectrum is compressed and jet/ \cancel{E}_T cuts become more severe. This is where the 8 TeV searches, in particular the one targeting displaced dileptons, become instead more efficient,

¹¹The other simplified models considered in ref. [105], corresponding to our cases i) and iii), give very similar exclusion power.

despite the small leptonic branching fractions of the bosons.¹² Finally, we also display on the same plot an estimate of the reach of the prompt searches (as a purple dot-dashed line), considering the $\text{BR}[\chi_{2,3} \rightarrow Z\chi_1] = \text{BR}[\chi_{2,3} \rightarrow h\chi_1] = 50\%$ case reported in [109]. We stress that this limit will never be relevant in the parameter region leading to the correct freeze-in dark matter abundance, but we report it here for illustrative purposes. In order to draw this line, we have compared the cross section limits reported in ref. [109] to the total production cross section of the doublets multiplied by the probability that both produced particles decay promptly given a certain mean decay length $c\tau_{\chi_{2,3}}$.¹³

5.2 DV + \cancel{E}_T constraints on the Singlet-Doublet model

We can now use the recasting presented above to provide estimates for the ATLAS exclusion on the parameter space of the Singlet-Doublet freeze-in model. For this purpose, at each point of the parameter space, we sum the production cross sections over the production channels weighted by the appropriate branching fraction in order to determine the signal strength for each of the possible final states. For instance, the signal cross section in $hh + \cancel{E}_T$ is given by

$$\begin{aligned} \sigma(pp \rightarrow hh\chi_1\chi_1) &= \sigma(pp \rightarrow \psi^+\psi^-) \times \text{BR}[\psi^\pm \rightarrow \pi^\pm\chi_{2,3}]^2 \times \text{BR}[\chi_{2,3} \rightarrow h\chi_1]^2 + \\ &\quad \sigma(pp \rightarrow \psi^\pm\chi_{2,3}) \times \text{BR}[\psi^\pm \rightarrow \pi^\pm\chi_{2,3}] \times \text{BR}[\chi_{2,3} \rightarrow h\chi_1]^2 + \\ &\quad \sigma(pp \rightarrow \chi_2\chi_3) \times \text{BR}[\chi_2 \rightarrow h\chi_1] \times \text{BR}[\chi_3 \rightarrow h\chi_1], \end{aligned} \quad (5.2)$$

and analogous expressions can be written for the $hZ + \cancel{E}_T$ and $ZZ + \cancel{E}_T$. The production cross section in each channel is hence a function of the parameter space of the model through the branching fraction dependence on (y_u, y_d, μ, m_s) . We multiply these three type of signal cross sections with the corresponding efficiencies (derived in appendix B) to obtain the final estimate on the number of expected events. Each efficiency is also a function of the parameters (y_u, y_d, μ, m_s) , since it depends on the mass of the long-lived particle, which is simply μ , and on the decay lengths that follow from eqs. (2.12)–(2.15). For simplicity, we take the average of the decay length of χ_2 and χ_3 as the mean decay length setting the displacement. As we have discussed above, this is an excellent approximation as long as $\tan\theta \gg 1$ or $\mu \gtrsim 300$ GeV (see figure 3). We neglect the extra displacement induced by the decay of the charged fermion. Note that this is indeed typically a small fraction of the overall displacement in the relevant portion of the parameter space, as illustrated by the green contours in the right panel of figure 7. In our estimate we also consider the same efficiency in the case in which the neutral heavy fermions are directly pair produced as in the case in which the neutral fermions are produced through the decay of the charged fermion. We checked this hypothesis on a few benchmark points and it induces an effect of at most 20%, which is largely negligible for the purpose of our recasting. As for the

¹²We also remark that, as discussed in detail in the appendix B, our implementation of the ATLAS DV+ \cancel{E}_T analysis tends to overestimate the exclusion in the compressed region (for mass splittings $\lesssim 100$ GeV). The complementarity with the 8 TeV searches is thus welcome.

¹³As a rough estimate, we consider to be prompt the events with a total displacement ≤ 0.5 mm that we compute based on $c\tau$ only, without taking into account the boost factor.

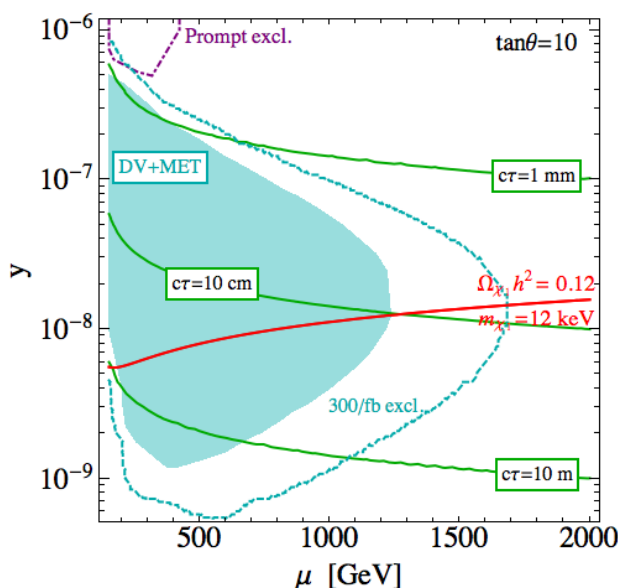


Figure 11. Exclusion capability of the 13 TeV ATLAS search for displaced jets + \cancel{E}_T for the Singlet-Doublet freeze-in model (cyan region labelled as “DV+MET”) on the plane (μ, y) with $m_{\chi_{2,3}} = m_{\psi} = \mu$. The dashed cyan line represents the prospected bound with 300 fb^{-1} . The dot-dashed purple line is our estimate of the limit set by LHC searches for the prompt signature $WZ + \cancel{E}_T$ (see the text for details). The green contours indicate the average decay length of χ_2 and χ_3 . The red line corresponds to the correct relic abundance for $m_{\chi_1} = 12 \text{ keV}$.

case of the simplified models considered in section 5.1, we employ the NLO cross sections computed by Prospino2 [101] and we calculate 95% CL cross section upper exclusion limits assuming no background.

Under the above assumptions, we can assess the current limits on the Singlet-Doublet parameter space from the ATLAS DV+ \cancel{E}_T search. The region excluded according to our recasting is shown with filled cyan colour in figure 11. Its shape follows from combining the excluded regions for the simplified models reported in figure 10 with the iso-contours of the average $c\tau_{\chi_{2,3}}$ (denoted as $c\tau$). The latter are shown with green continuous lines in figure 11 while the dashed cyan curve gives the estimated reach of an analogous DV+ \cancel{E}_T search with a dataset of 300 fb^{-1} .¹⁴ The red continuous curve shows the (y, μ) combinations that account for all the DM for a 12 keV DM candidate. Going above the red line, i.e. to larger values of the coupling y , induces an overabundant dark matter population, while below the red line it is underabundant; see eq. (3.9). Finally, the dot-dashed line delimits the region excluded by LHC searches for the prompt signature $WZ + \cancel{E}_T$.

¹⁴The estimated curve for the DV+ \cancel{E}_T search with a dataset of 300 fb^{-1} results from simply rescaling the luminosity and assuming the signal to remain background free. While this is an optimistic assumption, it may not be unthinkable that backgrounds can continue to be suppressed at the cost of only a small signal inefficiency.

It is remarkable that the sensitivity of the ATLAS DV+ \cancel{E}_T search extends to heavy electroweak states and to quite large values of the decay lengths. This is related to the almost background-free nature of displaced vertices signatures which renders the search very efficient even for small signal cross section. Note that the largest excluded mediator mass is about 1.2 TeV, somewhat smaller than for the simplified model analysis of figure 10. The reason is as follows. In the high mass region, when the lifetime, or equivalently the coupling y , maximises the experimental sensitivity ($y \approx 10^{-8}$) the branching fraction of the process $\psi^\pm \rightarrow \chi_1 W^\pm$ is not completely negligible (up to about 10%, see figure 2 left), and hence the signal yield into long-lived neutral fermion pairs is slightly diminished. In the case of the DV+ \cancel{E}_T analysis extrapolation to 300 fb^{-1} , we expect to probe masses of the neutral fermions up to 1.7 TeV and decay lengths as large as 100 m.

Let us add here a remark on the uncertainties on our recasting and their effects on the estimated limits in figure 11. Given the steep fall of the production cross section as a function of the mediators' mass (see figure 6), we expect that even $\mathcal{O}(1)$ modifications of our estimated efficiencies would have a small impact on the mass reach (for instance a 50% change in the efficiency would only correspond to a change of around 10% in the mediators' mass limits).¹⁵

Let us stress that the collider bounds presented in figure 11 are expected to be independent of the dark matter mass for m_{χ_1} below the GeV scale. The only curve that is affected by the m_{χ_1} parameter is the relic abundance continuous red contour. Considering larger values of the dark matter mass the red line would be shifted to lower values of y . As a result, the dark matter candidates with $m_\chi > 12 \text{ keV}$ (i.e. compatible with the Lyman- α bound discussed in section 4) are concerned with the excluded region below the red curve of figure 11. For instance, from the right panel of figure 4, one can deduce that for e.g. $m_{\chi_1} \approx 1 \text{ MeV}$ the $\Omega h^2 = 0.12$ contour should appear at $y \approx 10^{-9}$ in figure 11. This corresponds to larger values of $c\tau$ where the DV+ \cancel{E}_T search loses sensitivity in such a way that no constraint can be set at present.

For completeness, let us briefly discuss the prompt decay constraints. In the upper part of figure 11, the size of the coupling y is such that the mediators decays are prompt. In particular, the charged fermion ψ^\pm predominantly decays into $W^\pm \chi_1$.¹⁶ In order to estimate the corresponding constraint, we have computed the $WZ + \cancel{E}_T$ production cross section in the Singlet-Doublet model multiplied by the probability that both heavy particles decay promptly, using the same approximations as for the prompt exclusion in figure 10. Comparing the latter results with the limits on the cross section given in ref. [109] we exclude the region delimited by the dot dashed purple line of figure 11. As discussed above, such constraint lies however in a zone of the parameter space where the frozen-in dark matter scenarios with masses above the Lyman- α bound give an overabundant dark matter relic density.

¹⁵Note in particular that this applies to the possible issues associated with b -jets, discussed at the end of appendix B, that would at most reduce the signal strength by $\approx 25\%$.

¹⁶The other prompt signatures discussed above are less sensitive as the production cross section is sensibly lower for χ_2, χ_3 production only. The latter is indeed almost one order of magnitude smaller than the total doublet production as seen in figure 6.

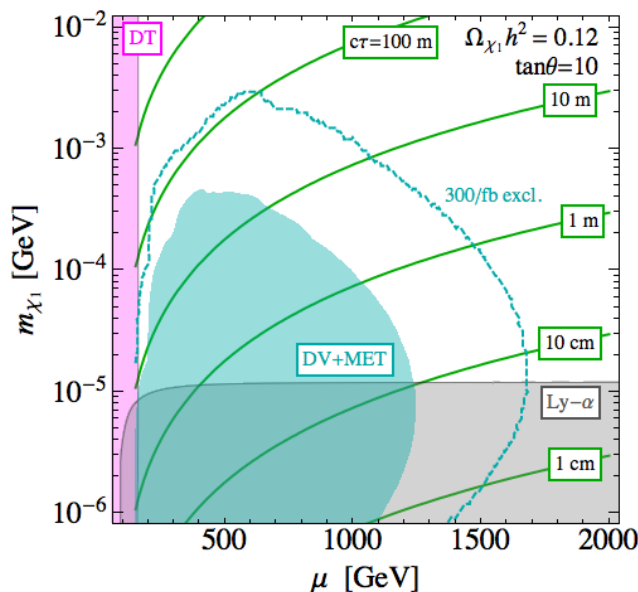


Figure 12. Combined constraints on the mediator mass vs DM mass plane ($m_{\chi_{2,3}} = m_\psi = \mu$). Our estimate of the ATLAS DV + \cancel{E}_T exclusion is shaded in cyan (“DV+MET”), the magenta region is excluded by disappearing tracks (“DT”), the Lyman- α bound is shown in gray (“Ly- α ”). Green contours correspond to the average $\chi_{2,3}$ decay length. The cyan dashed line is the estimated exclusion of LHC with 300 fb^{-1} . The coupling y is fixed such that $\Omega_{\chi_1} h^2 = 0.12$ everywhere.

6 Displaced vertices vs cosmology for freeze-in DM

We can now combine the LHC limits and the cosmological bound derived in the previous sections, in order to characterise the experimental sensitivity on the viable parameter space of the freeze-in Singlet-Doublet model. As at the end of section 3, we present our results in the DM mass vs mediator mass plane fixing in each point the coupling y to the value that accounts for the observed relic abundance through the freeze-in mechanism. On the same two dimensional plane, we can show the combination of the existing (and future) constraints on the model. Our summary plot is shown in figure 12. As before, the green lines indicate contours of fixed average decay length of the neutral fermions, which controls the phenomenology at colliders. The magenta shading at low mediator masses represents the region excluded by searches for disappearing charged tracks (DT) [57, 58]. It does not depend on the DM mass (or equivalently on the value of the y coupling) since, in this region, the decay length of the charged fermion is independent of m_{χ_1} , as can be seen in the right panel of figure 7. The cyan region and the dashed cyan line are the estimated exclusion and future prospect of the ATLAS DV+ \cancel{E}_T search, discussed in section 5. The gray region, finally, is excluded by the Lyman- α forest data, as discussed in section 4.

Figure 12 summarises the findings of this paper, as it nicely shows the interplay between collider searches for displaced signatures and cosmological constraints in our freeze-in dark matter model. On the one side, the observed DM abundance implies a relation among the parameters of the theory, leaving only two free parameters (plus a third one, $\tan\theta$, that affects the phenomenology of the model very mildly in our limit, as we discussed in

the previous sections). On the other side, for the range of decay lengths that are a priori optimal for studying displaced signatures at the LHC ($\mathcal{O}(10)$ cm) and μ scales within the reach of the collider ($\mu \lesssim \mathcal{O}(1)$ TeV), our dark matter model can leave a testable imprint on small scale structures. In such a region, we have a complementary constraint from the Lyman- α forest observations, which is essentially independent of the mediator mass. In contrast, the reach of LHC searches is intrinsically limited by the production cross section of the mediators, hence by their mass, and by the size of the detector. Due to the very low background of the recast search and the large dataset available, the current LHC limit actually extends to rather large values of the mediators' lifetime and, likewise, it can probe DM masses larger than those tested by cosmology, reaching up to $m_{\chi_1} = \mathcal{O}(1)$ MeV.

7 Summary and conclusions

Despite many experimental and theoretical efforts, the nature of dark matter remains a mystery. It is thus timely to look for DM beyond the most popular paradigms. In this work, we considered the case of a dark matter candidate with such a tiny coupling that it never reaches thermal equilibrium with the SM in the early universe. It is well known that, despite such suppressed interactions, the observed dark matter density can be accounted for by the freeze-in mechanism, with the dark matter being produced, for instance, via the decay of thermalised mediators. Within this context, we studied the case of the Singlet-Doublet dark matter model that consists in extending the SM with a pair of Weyl electroweak doublet fermions and a singlet Majorana fermion. The new fermions interact with the SM through gauge interactions and/or the Higgs portal induced by Yukawa interaction terms that couple the doublet and the singlet fermions to the Higgs particle. The Singlet-Doublet model rests thus on 4 free parameters only: 2 new mass scales (the doublet mass scale μ and the singlet mass scale m_s), and two Yukawa couplings (y_u and y_d). We have shown that, considering these couplings in the range $[10^{-8}, 10^{-10}]$ together with a doublet mass scale μ larger than the Higgs mass, the lightest neutral fermion, which is essentially the singlet Majorana fermion, can account for the whole dark matter abundance via the freeze-in mechanism. In this regime, the DM is light with a mass between a few keV up to hundreds of MeV.

Such a dark matter scenario could seem hopelessly beyond the reach of any dark matter experimental search. We show instead that the range of model parameters required for a successful freeze-in naturally gives rise to long-lived/displaced collider signatures that are already strongly bounded by the present LHC data. In addition, it is well known that thermal warm dark matter candidates of a few keV are also constrained by cosmology due to their free-streaming suppressing the growth of small scale structure. Even though frozen-in dark matter was never in thermal equilibrium in the early universe, Lyman- α bounds turn out to constrain the dark matter to be always heavier than 12 keV. In the low dark matter mass region, the model features thus both exotic LHC signals and a testable imprint on cosmology providing two complementary handles to probe the same scenario.

Concerning the collider searches, the relevant signatures of this model consist of disappearing charged tracks, related to the production of the charged component of the doublet

ψ^\pm , and displaced h and/or $Z + \cancel{E}_T$, associated to the decay of the two neutral fermions $\chi_{2,3}$. In the first case, ψ^\pm decays with a small displacement (about 1 cm) and our scenario is essentially the case of pure Higgsino DM in supersymmetric models. Current searches for disappearing tracks thus constrain the doublet mass scale μ to be larger than 150 GeV. In the second case, the $\chi_{2,3}$ fermions decay with displacements in a wide range, from centimetres to kilometres, depending on the point of the viable parameter space of interest (i.e. for y_u, y_d giving rise to the right relic abundance through freeze-in). We have argued that, at present, the most constraining search was provided by ATLAS in ref. [53] and we have reinterpreted its results in the framework of the Singlet-Doublet dark matter model. According to our recasting, this analysis can exclude scenarios with a decay length of the heavy neutral mediators as large as ~ 50 m, mediator masses as large as 1.2 TeV, and dark matter candidates with masses as large as 500 keV.

In figure 12, we have brought together all the experimental signatures which can probe the viable parameter space where the freeze-in production mechanism gives rise to the correct dark matter abundance. This nicely illustrates the interplay between collider searches and cosmology for frozen-in dark matter.

An interesting extension of our work is to enlarge the experimental reach on the parameter space of the model. The LHC sensitivity, shown in figure 12, could be improved towards large mediator masses, or towards small or large decay lengths. This is possible on all these three fronts by exploiting the presence of a displaced Z or h resonance, both in hadronic and leptonic decay channels, such that some of the event selection requirements that currently limit selection efficiencies can be relaxed, while keeping backgrounds to a negligible level. Also, at higher luminosities a dedicated event selection would help to suppress the increasing backgrounds. As a result of our study, we thus advocate dedicated experimental searches for displaced $Z + \cancel{E}_T$ or $h + \cancel{E}_T$ signatures, potentially in association with an extra identified Z or h boson. On the other hand, it would be interesting to also probe the case with large/moderate dark matter mass and very long-lived mediators (upper part of figure 12). For this purpose, one could for instance estimate the reach of the proposed detector MATHUSLA [126] on this scenario.

Finally, we stress again that interplay between exotic collider signatures and cosmology constraints go beyond the Singlet-Doublet model and apply to a large class of simplified models of freeze-in dark matter where the production occurs through decays of heavy mediators in thermal equilibrium with the SM bath. From the model building perspective, it would be interesting to investigate such complementarity in other models, also including those where the freeze-in is not realised through the decays of heavy mediators, but via scattering processes and/or via non-renormalisable interactions [127]. We leave these interesting possibilities for future works.

Acknowledgments

We are grateful to Francesco D’Eramo, Michele Frigerio, Julian Heeck, Lawrence Lee, Daniele Teresi, Pantelis Tziveloglou, and Bryan Zaldivar for useful discussions. LLH is supported by the Fonds National de la Recherche Scientifique. AM and LLH are supported

by the Strategic Research Program *High-Energy Physics* and the Research Council of the Vrije Universiteit Brussel. AM and SL are supported by FWO under the “Excellence of Science - EOS” - be.h project n.30820817.

A Yukawa interactions and mixing matrix

A.1 Yukawa interactions

For the contraction of the indices in the Lagrangian of eq. (2.2), we follow the conventions of refs. [47, 50]. In particular, the Yukawa interactions

$$- y_d \psi_d \cdot H \psi_s - y_u H^\dagger \psi_u \psi_s + h.c. \tag{A.1}$$

can be explicitly written as

$$- y_d \psi_{di} H_j \epsilon^{ij} \psi_s - y_u \psi_{ui} H^{*i} \psi_s + h.c., \tag{A.2}$$

where i and j are $SU(2)_L$ indices.

A.2 Approximate expression of the rotation matrix

In the limit (2.6), the mass eigenvalues at the first order in the couplings $y_{u,d}^2$ result as shown in eq. (2.7). We report here the rotation matrix, defined as in eq. (2.5), at leading order in y_u and y_d :

$$U = \begin{pmatrix} 1 & -\frac{v}{2\sqrt{2}} \left(\frac{y_u - y_d}{\mu + m_s} + \frac{y_u + y_d}{\mu - m_s} \right) & \frac{v}{2\sqrt{2}} \left(\frac{y_u - y_d}{\mu + m_s} - \frac{y_u + y_d}{\mu - m_s} \right) \\ \frac{v}{2} \frac{y_u - y_d}{\mu + m_s} & -\frac{1}{\sqrt{2}} & \frac{1}{\sqrt{2}} \\ -\frac{v}{2} \frac{y_u + y_d}{\mu - m_s} & -\frac{1}{\sqrt{2}} & -\frac{1}{\sqrt{2}} \end{pmatrix}. \tag{A.3}$$

We omit the $\mathcal{O}(y_{u,d}^2)$ terms that are needed in order to diagonalise correctly the mass matrix \mathcal{M} obtaining the eigenvalues shown in eq. (2.7). In fact, in our parameter regime, the above expression suffices to reproduce the rotations resulting from numerical diagonalisation to high accuracy. Hence, we employ it to derive the expressions for the decay widths of the heavy particles reported in section 2.2.

B Recasting of the ATLAS search

In this appendix, we provide details about the recasting of the ATLAS search of ref. [53] that we employed in order to set limits on the Singlet-Doublet model and in particular on displaced neutral bosons + \cancel{E}_T final states.

The signature that we consider both in the validation (gluino-neutralino simplified model) and in the Singlet-Doublet model is constituted by a pair of heavy long-lived particles decaying into charged tracks plus missing energy. For the case of two neutral heavy fermions, the process is depicted in figure 8, with the long-lived particle highlighted in red.

We first review the selection cuts of the search, we then validate our simulation with the simplified model studied in the ATLAS analysis, and then we apply the same recasting to our dark matter model.

Selection criteria of the ATLAS DV+ \cancel{E}_T search [53]. The ATLAS analysis [53] is explained in detail in the auxiliary material in [122]. The search targets displaced vertices and missing transverse momentum.

The displaced vertices are identified by analysing the associated displaced tracks. First, a selected displaced track should satisfy the following requirements:

- The track is associated to a stable particle;
- The particle has a transverse momenta $p_T > 1$ GeV;
- The transverse impact parameter $d_0 \equiv R_{\text{decay}} \sin \Delta\phi > 2$ mm, where R_{decay} is the transverse decay length and $\Delta\phi$ is the azimuthal angle between the heavy decaying particle momentum and the track momentum.

With the following selected tracks, one can construct a candidate displaced vertex which should satisfy the following criteria:

- The transverse displacement R_{decay} should be within 4 and 300 mm;
- The longitudinal displacement should be smaller than $|z_{\text{decay}}| < 300$ mm;
- The number of associated charged tracks should be $n_{\text{tracks}} \geq 5$;
- The invariant mass of the vertex should be larger than 10 GeV (a pion mass for the tracks is assumed).

Given the previous strategy to select displaced tracks and displaced vertices, events are hence required to satisfy the following conditions.

1. $\cancel{E}_T^{\text{truth}} > 200$ GeV where $\cancel{E}_T^{\text{truth}}$ is the missing energy at truth level, here interpreted as the magnitude of the transverse component of the vector sum of the dark matter momenta.
2. On 3/4 of the events, the ATLAS analysis also demands the presence of either
 - One jet with $p_T > 70$ GeV
 - Two jets with $p_T > 25$ GeV

These jets should satisfy the requirement that the scalar sum of the p_T of the charged particles that are not displaced (according to the previous selection) should not exceed 5 GeV.

3. The events must contain at least one displaced vertex which has passed the selection.

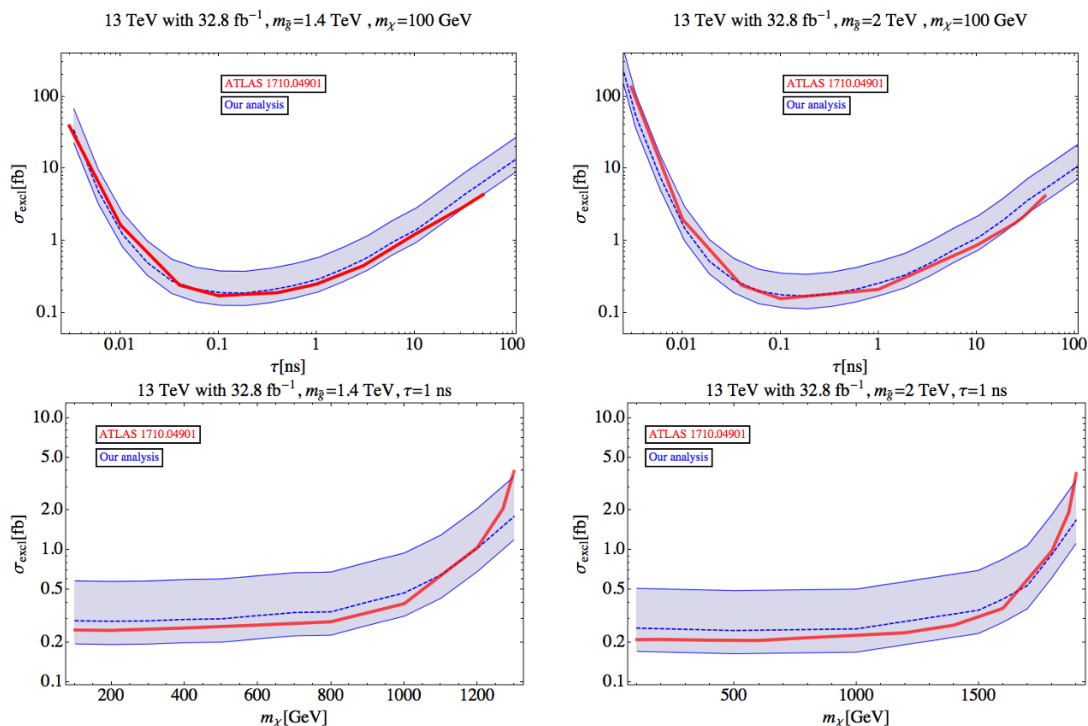


Figure 13. Comparison between the result of our simulation and the excluded cross section reported in the ATLAS paper [53] for a long-lived gluino simplified model. The ATLAS results are shown as red lines, while our analysis corresponds to the blue bands. In order to draw our bands, we considered variation of the efficiency of $\pm 50\%$. The upper plots show the excluded cross section as a function of $c\tau$ for a fixed neutralino mass $m_\chi = 100$ GeV and two benchmark values for the gluino mass, $m_{\tilde{g}} = 1400, 2000$ GeV. The lower plots show the excluded cross section as a function of m_χ fixing $\tau = 1$ ns and the same two benchmarks for $m_{\tilde{g}}$.

Recasting and validation. On the selected events, one can then apply the efficiency as reported in the auxiliary material. Indeed, the ATLAS collaboration provides the efficiency for reconstructing the displaced vertices as a function of the number of displaced tracks and of their invariant mass. They also provides the efficiency tables as a function of the missing energy at truth level.

In order to recast this analysis, we have simulated LO events of the new physics process with `MadGraph5 + Pythia8 + Delphes3` with standard minimal cuts, default parameters for MC and detector simulator (we used the default ATLAS card), assuming prompt decays of the heavy pair-produced particles. We employed generator level information in order to extract the momenta of the two heavy particles and of their associated tracks and in order to introduce the displacement by hand, including the boost factor of the heavy decaying particle. The decay time was generated through an exponential distribution with a mean lifetime τ . With this information we derived the impact parameter of each track and the other relevant geometrical properties. Then we processed the output following the ATLAS selection cuts strategy, including the reconstruction efficiencies. We first applied this procedure to a simplified model analogous to the one considered in the ATLAS paper, by considering gluino pair production followed by displaced decays into $q\bar{q}$ plus neutralino.

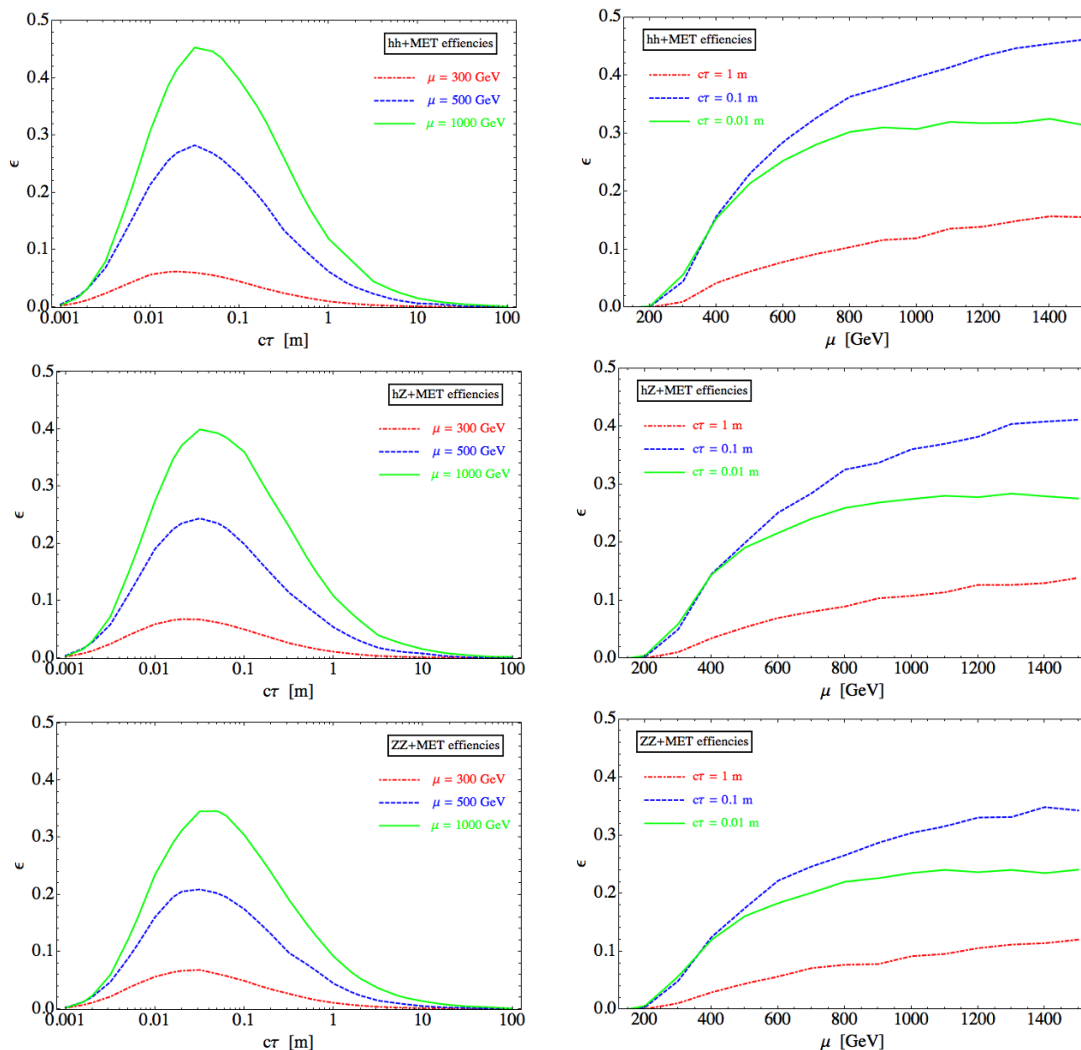


Figure 14. Efficiencies for the simplified final states with $hh + \cancel{E}_T$, $hZ + \cancel{E}_T$, $ZZ + \cancel{E}_T$. Left: efficiencies as a function of $c\tau$ for $m_{\chi_2} = m_{\chi_3} = 300, 500, 1000$ GeV. Right: efficiencies as a function of the mass $m_{\chi_2} = m_{\chi_3}$ for $c\tau = 1, 10, 100$ cm.

In figure 13 we show our estimated cross section exclusion compared to the ATLAS results. We find a good agreement in the region of un-compressed spectrum, while our simulation overestimate the exclusion power in the compressed spectrum case. We argue that this is due to our implementation of the jet cut (number 2. in the list above), for which we have only a limited amount of information provided by the ATLAS documentation. The plots of figure 13 shows that, on the other hand, our simulation consistently reproduces the ATLAS analysis for a mass difference between the heavy particle and its decay products larger than ≈ 100 GeV, taking into account an uncertainty of $\pm 50\%$ on the efficiency.

In figure 14 we display the result of our recasting: the efficiency curves for the final states characterising the Singlet-Doublet model. The samples have been generated at LO with MadGraph5 + Pythia3 + Delphes3 after implementing the model in FeynRules. We

simulated the following three cases

$$pp \rightarrow \chi_2\chi_3 \rightarrow ZZ\chi_1\chi_1, \quad pp \rightarrow \chi_2\chi_3 \rightarrow hh\chi_1\chi_1, \quad pp \rightarrow \chi_2\chi_3 \rightarrow hZ\chi_1\chi_1,$$

where the decay of the bosons is performed in `Pythia`. We then processed the output with the selection procedures explained above to extract the efficiencies as a function of the mean lifetime $c\tau$ and the mass of the decaying heavy particles $m_{\chi_2} = m_{\chi_3}$.

As a final remark, let us notice that the efficiencies displayed in figure 14 have been obtained by treating displaced heavy flavour jets like light-flavour ones. However, the case of Z or h decaying into $b\bar{b}$ pairs requires in principle additional care, since the recast DV+ \cancel{E}_T search associates tracks to a displaced vertex based on track-vertex compatibility requirements, and merges displaced vertices if within 1 mm. For displaced b jets, these requirements are difficult to recast. As we mentioned, we choose to neglect this possible issue (an interesting discussion of which can be found in ref. [128]). We argue that this simplification has a limited impact on our estimated exclusions (shown in figures 11 and 12) for the following reasons: (i) Only one DV is enough to satisfy the analysis' requirements, thus there is no loss of sensitivity if at least one of the pair-produced heavy particles decays into a Z decaying into light flavours (and the DV is reconstructed); (ii) Due to the gluons radiated by the b quarks, a DV can still be formed on the tracks not coming from the b -decay vertex; (iii) Part of the b decays will still happen within the required 1 mm.

Open Access. This article is distributed under the terms of the Creative Commons Attribution License ([CC-BY 4.0](https://creativecommons.org/licenses/by/4.0/)), which permits any use, distribution and reproduction in any medium, provided the original author(s) and source are credited.

References

- [1] PLANCK collaboration, P.A.R. Ade et al., *Planck 2015 results. XIII. Cosmological parameters*, *Astron. Astrophys.* **594** (2016) A13 [[arXiv:1502.01589](https://arxiv.org/abs/1502.01589)] [[INSPIRE](#)].
- [2] J. Abdallah et al., *Simplified Models for Dark Matter Searches at the LHC*, *Phys. Dark Univ.* **9-10** (2015) 8 [[arXiv:1506.03116](https://arxiv.org/abs/1506.03116)] [[INSPIRE](#)].
- [3] D. Abercrombie et al., *Dark Matter Benchmark Models for Early LHC Run-2 Searches: Report of the ATLAS/CMS Dark Matter Forum*, [arXiv:1507.00966](https://arxiv.org/abs/1507.00966) [[INSPIRE](#)].
- [4] A. Albert et al., *Recommendations of the LHC Dark Matter Working Group: Comparing LHC searches for heavy mediators of dark matter production in visible and invisible decay channels*, [arXiv:1703.05703](https://arxiv.org/abs/1703.05703) [[INSPIRE](#)].
- [5] L.J. Hall, K. Jedamzik, J. March-Russell and S.M. West, *Freeze-In Production of FIMP Dark Matter*, *JHEP* **03** (2010) 080 [[arXiv:0911.1120](https://arxiv.org/abs/0911.1120)] [[INSPIRE](#)].
- [6] X. Chu, T. Hambye and M.H.G. Tytgat, *The Four Basic Ways of Creating Dark Matter Through a Portal*, *JCAP* **05** (2012) 034 [[arXiv:1112.0493](https://arxiv.org/abs/1112.0493)] [[INSPIRE](#)].
- [7] N. Bernal, M. Heikinheimo, T. Tenkanen, K. Tuominen and V. Vaskonen, *The Dawn of FIMP Dark Matter: A Review of Models and Constraints*, *Int. J. Mod. Phys. A* **32** (2017) 1730023 [[arXiv:1706.07442](https://arxiv.org/abs/1706.07442)] [[INSPIRE](#)].

- [8] R.T. Co, F. D’Eramo, L.J. Hall and D. Pappadopulo, *Freeze-In Dark Matter with Displaced Signatures at Colliders*, *JCAP* **12** (2015) 024 [[arXiv:1506.07532](#)] [[INSPIRE](#)].
- [9] A.G. Hessler, A. Ibarra, E. Molinaro and S. Vogl, *Probing the scotogenic FIMP at the LHC*, *JHEP* **01** (2017) 100 [[arXiv:1611.09540](#)] [[INSPIRE](#)].
- [10] F. D’Eramo, N. Fernandez and S. Profumo, *Dark Matter Freeze-in Production in Fast-Expanding Universes*, *JCAP* **02** (2018) 046 [[arXiv:1712.07453](#)] [[INSPIRE](#)].
- [11] G. Brooijmans et al., *Les Houches 2017: Physics at TeV Colliders New Physics Working Group Report*, in *10th Les Houches Workshop of Physics at TeV Colliders (PhysTeV 2017)*, Les Houches France (2017) [[arXiv:1803.10379](#)] [[INSPIRE](#)].
- [12] S. Chang and M.A. Luty, *Displaced Dark Matter at Colliders*, [arXiv:0906.5013](#) [[INSPIRE](#)].
- [13] A. Davoli, A. De Simone, T. Jacques and V. Sanz, *Displaced Vertices from Pseudo-Dirac Dark Matter*, *JHEP* **11** (2017) 025 [[arXiv:1706.08985](#)] [[INSPIRE](#)].
- [14] O. Buchmueller et al., *Simplified Models for Displaced Dark Matter Signatures*, *JHEP* **09** (2017) 076 [[arXiv:1704.06515](#)] [[INSPIRE](#)].
- [15] M. Garny, J. Heisig, B. LülF and S. Vogl, *Coannihilation without chemical equilibrium*, *Phys. Rev. D* **96** (2017) 103521 [[arXiv:1705.09292](#)] [[INSPIRE](#)].
- [16] A. Ghosh, T. Mondal and B. Mukhopadhyaya, *Heavy stable charged tracks as signatures of non-thermal dark matter at the LHC: a study in some non-supersymmetric scenarios*, *JHEP* **12** (2017) 136 [[arXiv:1706.06815](#)] [[INSPIRE](#)].
- [17] M. Garny, J. Heisig, M. Hufnagel and B. LülF, *Top-philic dark matter within and beyond the WIMP paradigm*, *Phys. Rev. D* **97** (2018) 075002 [[arXiv:1802.00814](#)] [[INSPIRE](#)].
- [18] A. Davoli, A. De Simone, T. Jacques and A. Morandini, *LHC Phenomenology of Dark Matter with a Color-Octet Partner*, *JHEP* **07** (2018) 054 [[arXiv:1803.02861](#)] [[INSPIRE](#)].
- [19] M. Viel, G.D. Becker, J.S. Bolton and M.G. Haehnelt, *Warm dark matter as a solution to the small scale crisis: New constraints from high redshift Lyman- α forest data*, *Phys. Rev. D* **88** (2013) 043502 [[arXiv:1306.2314](#)] [[INSPIRE](#)].
- [20] C. Yèche, N. Palanque-Delabrouille, J. Baur and H. du Mas des Bourboux, *Constraints on neutrino masses from Lyman-alpha forest power spectrum with BOSS and XQ-100*, *JCAP* **06** (2017) 047 [[arXiv:1702.03314](#)] [[INSPIRE](#)].
- [21] V. Iršič et al., *New Constraints on the free-streaming of warm dark matter from intermediate and small scale Lyman- α forest data*, *Phys. Rev. D* **96** (2017) 023522 [[arXiv:1702.01764](#)] [[INSPIRE](#)].
- [22] J.S. Bullock and M. Boylan-Kolchin, *Small-Scale Challenges to the Λ CDM Paradigm*, *Ann. Rev. Astron. Astrophys.* **55** (2017) 343 [[arXiv:1707.04256](#)] [[INSPIRE](#)].
- [23] A.A. Klypin, A.V. Kravtsov, O. Valenzuela and F. Prada, *Where are the missing Galactic satellites?*, *Astrophys. J.* **522** (1999) 82 [[astro-ph/9901240](#)] [[INSPIRE](#)].
- [24] B. Moore et al., *Dark matter substructure within galactic halos*, *Astrophys. J.* **524** (1999) L19 [[astro-ph/9907411](#)] [[INSPIRE](#)].
- [25] M. Boylan-Kolchin, J.S. Bullock and M. Kaplinghat, *The Milky Way’s bright satellites as an apparent failure of LCDM*, *Mon. Not. Roy. Astron. Soc.* **422** (2012) 1203 [[arXiv:1111.2048](#)].

- [26] B. Moore, T.R. Quinn, F. Governato, J. Stadel and G. Lake, *Cold collapse and the core catastrophe*, *Mon. Not. Roy. Astron. Soc.* **310** (1999) 1147 [[astro-ph/9903164](#)].
- [27] V. Springel et al., *The Aquarius Project: the subhalos of galactic halos*, *Mon. Not. Roy. Astron. Soc.* **391** (2008) 1685 [[arXiv:0809.0898](#)].
- [28] P. Bode, J.P. Ostriker and N. Turok, *Halo formation in warm dark matter models*, *Astrophys. J.* **556** (2001) 93 [[astro-ph/0010389](#)] [[INSPIRE](#)].
- [29] J. Zavala et al., *The velocity function in the local environment from LCDM and LWDM constrained simulations*, *Astrophys. J.* **700** (2009) 1779 [[arXiv:0906.0585](#)] [[INSPIRE](#)].
- [30] M.R. Lovell et al., *The Haloes of Bright Satellite Galaxies in a Warm Dark Matter Universe*, *Mon. Not. Roy. Astron. Soc.* **420** (2012) 2318 [[arXiv:1104.2929](#)].
- [31] A. Schneider, R.E. Smith, A.V. Macciò and B. Moore, *Nonlinear Evolution of Cosmological Structures in Warm Dark Matter Models*, *Mon. Not. Roy. Astron. Soc.* **424** (2012) 684 [[arXiv:1112.0330](#)].
- [32] M.R. Lovell, C.S. Frenk, V.R. Eke, A. Jenkins, L. Gao and T. Theuns, *The properties of warm dark matter haloes*, *Mon. Not. Roy. Astron. Soc.* **439** (2014) 300 [[arXiv:1308.1399](#)] [[INSPIRE](#)].
- [33] R. Kennedy, C. Frenk, S. Cole and A. Benson, *Constraining the warm dark matter particle mass with Milky Way satellites*, *Mon. Not. Roy. Astron. Soc.* **442** (2014) 2487 [[arXiv:1310.7739](#)] [[INSPIRE](#)].
- [34] M.R. Lovell et al., *Addressing the too big to fail problem with baryon physics and sterile neutrino dark matter*, *Mon. Not. Roy. Astron. Soc.* **468** (2017) 2836 [[arXiv:1611.00005](#)] [[INSPIRE](#)].
- [35] L. Lopez-Honorez, O. Mena, S. Palomares-Ruiz and P. Villanueva-Domingo, *Warm dark matter and the ionization history of the Universe*, *Phys. Rev. D* **96** (2017) 103539 [[arXiv:1703.02302](#)] [[INSPIRE](#)].
- [36] Y. Hochberg et al., *Detection of sub-MeV Dark Matter with Three-Dimensional Dirac Materials*, *Phys. Rev. D* **97** (2018) 015004 [[arXiv:1708.08929](#)] [[INSPIRE](#)].
- [37] S. Knapen, T. Lin, M. Pyle and K.M. Zurek, *Detection of Light Dark Matter With Optical Phonons in Polar Materials*, [arXiv:1712.06598](#) [[INSPIRE](#)].
- [38] M. Heikinheimo, T. Tenkanen and K. Tuominen, *Prospects for indirect detection of frozen-in dark matter*, *Phys. Rev. D* **97** (2018) 063002 [[arXiv:1801.03089](#)] [[INSPIRE](#)].
- [39] N. Bernal, C. Cosme and T. Tenkanen, *Phenomenology of Self-Interacting Dark Matter in a Matter-Dominated Universe*, [arXiv:1803.08064](#) [[INSPIRE](#)].
- [40] K. Ishiwata, T. Ito and T. Moroi, *Long-Lived Unstable Superparticles at the LHC*, *Phys. Lett. B* **669** (2008) 28 [[arXiv:0807.0975](#)] [[INSPIRE](#)].
- [41] R. Mahbubani and L. Senatore, *The Minimal model for dark matter and unification*, *Phys. Rev. D* **73** (2006) 043510 [[hep-ph/0510064](#)] [[INSPIRE](#)].
- [42] F. D’Eramo, *Dark matter and Higgs boson physics*, *Phys. Rev. D* **76** (2007) 083522 [[arXiv:0705.4493](#)] [[INSPIRE](#)].
- [43] R. Enberg, P.J. Fox, L.J. Hall, A.Y. Papaioannou and M. Papucci, *LHC and dark matter signals of improved naturalness*, *JHEP* **11** (2007) 014 [[arXiv:0706.0918](#)] [[INSPIRE](#)].

- [44] T. Cohen, J. Kearney, A. Pierce and D. Tucker-Smith, *Singlet-Doublet Dark Matter*, *Phys. Rev. D* **85** (2012) 075003 [[arXiv:1109.2604](#)] [[INSPIRE](#)].
- [45] C. Cheung and D. Sanford, *Simplified Models of Mixed Dark Matter*, *JCAP* **02** (2014) 011 [[arXiv:1311.5896](#)] [[INSPIRE](#)].
- [46] T. Abe, R. Kitano and R. Sato, *Discrimination of dark matter models in future experiments*, *Phys. Rev. D* **91** (2015) 095004 [[arXiv:1411.1335](#)] [[INSPIRE](#)].
- [47] L. Calibbi, A. Mariotti and P. Tziveloglou, *Singlet-Doublet Model: Dark matter searches and LHC constraints*, *JHEP* **10** (2015) 116 [[arXiv:1505.03867](#)] [[INSPIRE](#)].
- [48] A. Freitas, S. Westhoff and J. Zupan, *Integrating in the Higgs Portal to Fermion Dark Matter*, *JHEP* **09** (2015) 015 [[arXiv:1506.04149](#)] [[INSPIRE](#)].
- [49] D. Egana-Ugrinovic, *The minimal fermionic model of electroweak baryogenesis*, *JHEP* **12** (2017) 064 [[arXiv:1707.02306](#)] [[INSPIRE](#)].
- [50] L. Lopez-Honorez, M.H.G. Tytgat, P. Tziveloglou and B. Zaldivar, *On Minimal Dark Matter coupled to the Higgs*, *JHEP* **04** (2018) 011 [[arXiv:1711.08619](#)] [[INSPIRE](#)].
- [51] S. Esch, M. Klasen and C.E. Yaguna, *A singlet doublet dark matter model with radiative neutrino masses*, [arXiv:1804.03384](#) [[INSPIRE](#)].
- [52] G. Arcadi, *2HDM portal for Singlet-Doublet Dark Matter*, [arXiv:1804.04930](#) [[INSPIRE](#)].
- [53] ATLAS collaboration, *Search for long-lived, massive particles in events with displaced vertices and missing transverse momentum in $\sqrt{s} = 13$ TeV pp collisions with the ATLAS detector*, *Phys. Rev. D* **97** (2018) 052012 [[arXiv:1710.04901](#)] [[INSPIRE](#)].
- [54] M. Cirelli and A. Strumia, *Minimal Dark Matter: Model and results*, *New J. Phys.* **11** (2009) 105005 [[arXiv:0903.3381](#)] [[INSPIRE](#)].
- [55] D. Egana-Ugrinovic, M. Low and J.T. Ruderman, *Charged Fermions Below 100 GeV*, *JHEP* **05** (2018) 012 [[arXiv:1801.05432](#)] [[INSPIRE](#)].
- [56] S.D. Thomas and J.D. Wells, *Phenomenology of Massive Vectorlike Doublet Leptons*, *Phys. Rev. Lett.* **81** (1998) 34 [[hep-ph/9804359](#)] [[INSPIRE](#)].
- [57] ATLAS collaboration, *Search for long-lived charginos based on a disappearing-track signature in pp collisions at $\sqrt{s} = 13$ TeV with the ATLAS detector*, *JHEP* **06** (2018) 022 [[arXiv:1712.02118](#)] [[INSPIRE](#)].
- [58] ATLAS collaboration, *Search for direct pair production of higgsinos by the reinterpretation of the disappearing track analysis with 36.1 fb^{-1} of $\sqrt{s} = 13$ TeV data collected with the ATLAS experiment*, *ATL-PHYS-PUB-2017-019* (2017).
- [59] M. Frigerio, T. Hambye and E. Masso, *Sub-GeV dark matter as pseudo-Goldstone from the seesaw scale*, *Phys. Rev. X* **1** (2011) 021026 [[arXiv:1107.4564](#)] [[INSPIRE](#)].
- [60] J.M. Frère, F.S. Ling, L. Lopez-Honorez, E. Nezri, Q. Swillens and G. Vertongen, *MeV right-handed neutrinos and dark matter*, *Phys. Rev. D* **75** (2007) 085017 [[hep-ph/0610240](#)] [[INSPIRE](#)].
- [61] G. Bélanger, F. Boudjema, A. Goudelis, A. Pukhov and B. Zaldivar, *MicrOMEGAs5.0: Freeze-in*, *Comput. Phys. Commun.* **231** (2018) 173 [[arXiv:1801.03509](#)] [[INSPIRE](#)].
- [62] J.L. Feng, A. Rajaraman and F. Takayama, *Superweakly interacting massive particles*, *Phys. Rev. Lett.* **91** (2003) 011302 [[hep-ph/0302215](#)] [[INSPIRE](#)].

- [63] J.L. Feng, A. Rajaraman and F. Takayama, *SuperWIMP dark matter signals from the early universe*, *Phys. Rev. D* **68** (2003) 063504 [[hep-ph/0306024](#)] [[INSPIRE](#)].
- [64] A. Alloul, N.D. Christensen, C. Degrande, C. Duhr and B. Fuks, *FeynRules 2.0 — A complete toolbox for tree-level phenomenology*, *Comput. Phys. Commun.* **185** (2014) 2250 [[arXiv:1310.1921](#)] [[INSPIRE](#)].
- [65] J. Baur et al., *Constraints from Ly- α forests on non-thermal dark matter including resonantly-produced sterile neutrinos*, *JCAP* **12** (2017) 013 [[arXiv:1706.03118](#)] [[INSPIRE](#)].
- [66] A. Garzilli, A. Boyarsky and O. Ruchayskiy, *Cutoff in the Lyman α forest power spectrum: warm IGM or warm dark matter?*, *Phys. Lett. B* **773** (2017) 258 [[arXiv:1510.07006](#)] [[INSPIRE](#)].
- [67] A. Molin e, J.A. Schewtschenko, S. Palomares-Ruiz, C. Boehm and C.M. Baugh, *Isotropic extragalactic flux from dark matter annihilations: lessons from interacting dark matter scenarios*, *JCAP* **08** (2016) 069 [[arXiv:1602.07282](#)] [[INSPIRE](#)].
- [68] J.A. Schewtschenko, C.M. Baugh, R.J. Wilkinson, C. Boehm, S. Pascoli and T. Sawala, *Dark matter-radiation interactions: the structure of Milky Way satellite galaxies*, *Mon. Not. Roy. Astron. Soc.* **461** (2016) 2282 [[arXiv:1512.06774](#)] [[INSPIRE](#)].
- [69] J.A. Schewtschenko, R.J. Wilkinson, C.M. Baugh, C. Boehm and S. Pascoli, *Dark matter-radiation interactions: the impact on dark matter haloes*, *Mon. Not. Roy. Astron. Soc.* **449** (2015) 3587 [[arXiv:1412.4905](#)] [[INSPIRE](#)].
- [70] R.J. Wilkinson, C. Boehm and J. Lesgourgues, *Constraining Dark Matter-Neutrino Interactions using the CMB and Large-Scale Structure*, *JCAP* **05** (2014) 011 [[arXiv:1401.7597](#)] [[INSPIRE](#)].
- [71] R. Murgia, A. Merle, M. Viel, M. Totzauer and A. Schneider, *“Non-cold” dark matter at small scales: a general approach*, *JCAP* **11** (2017) 046 [[arXiv:1704.07838](#)] [[INSPIRE](#)].
- [72] M.R. Buckley, J. Zavala, F.-Y. Cyr-Racine, K. Sigurdson and M. Vogelsberger, *Scattering, Damping and Acoustic Oscillations: Simulating the Structure of Dark Matter Halos with Relativistic Force Carriers*, *Phys. Rev. D* **90** (2014) 043524 [[arXiv:1405.2075](#)] [[INSPIRE](#)].
- [73] M. Vogelsberger, J. Zavala, F.-Y. Cyr-Racine, C. Pfrommer, T. Bringmann and K. Sigurdson, *ETHOS — an effective theory of structure formation: dark matter physics as a possible explanation of the small-scale CDM problems*, *Mon. Not. Roy. Astron. Soc.* **460** (2016) 1399 [[arXiv:1512.05349](#)] [[INSPIRE](#)].
- [74] F.-Y. Cyr-Racine, K. Sigurdson, J. Zavala, T. Bringmann, M. Vogelsberger and C. Pfrommer, *ETHOS — an effective theory of structure formation: From dark particle physics to the matter distribution of the Universe*, *Phys. Rev. D* **93** (2016) 123527 [[arXiv:1512.05344](#)] [[INSPIRE](#)].
- [75] F.-Y. Cyr-Racine, R. de Putter, A. Raccanelli and K. Sigurdson, *Constraints on Large-Scale Dark Acoustic Oscillations from Cosmology*, *Phys. Rev. D* **89** (2014) 063517 [[arXiv:1310.3278](#)] [[INSPIRE](#)].
- [76] M.R. Lovell et al., *ETHOS — an effective theory of structure formation: Predictions for the high-redshift Universe — abundance of galaxies and reionization*, [arXiv:1711.10497](#) [[INSPIRE](#)].

- [77] M. Escudero, L. Lopez-Honorez, O. Mena, S. Palomares-Ruiz and P. Villanueva-Domingo, *A fresh look into the interacting dark matter scenario*, *JCAP* **06** (2018) 007 [[arXiv:1803.08427](#)] [[INSPIRE](#)].
- [78] S. Dodelson and L.M. Widrow, *Sterile-neutrinos as dark matter*, *Phys. Rev. Lett.* **72** (1994) 17 [[hep-ph/9303287](#)] [[INSPIRE](#)].
- [79] X.-D. Shi and G.M. Fuller, *A New dark matter candidate: Nonthermal sterile neutrinos*, *Phys. Rev. Lett.* **82** (1999) 2832 [[astro-ph/9810076](#)] [[INSPIRE](#)].
- [80] A.D. Dolgov and S.H. Hansen, *Massive sterile neutrinos as warm dark matter*, *Astropart. Phys.* **16** (2002) 339 [[hep-ph/0009083](#)] [[INSPIRE](#)].
- [81] K. Abazajian, G.M. Fuller and M. Patel, *Sterile neutrino hot, warm and cold dark matter*, *Phys. Rev. D* **64** (2001) 023501 [[astro-ph/0101524](#)] [[INSPIRE](#)].
- [82] T. Asaka, M. Shaposhnikov and M. Laine, *Lightest sterile neutrino abundance within the ν MSM*, *JHEP* **01** (2007) 091 [[hep-ph/0612182](#)].
- [83] A. Merle, V. Niro and D. Schmidt, *New Production Mechanism for keV Sterile Neutrino Dark Matter by Decays of Frozen-In Scalars*, *JCAP* **03** (2014) 028 [[arXiv:1306.3996](#)] [[INSPIRE](#)].
- [84] Z. Kang, *Upgrading sterile neutrino dark matter to FIMP using scale invariance*, *Eur. Phys. J. C* **75** (2015) 471 [[arXiv:1411.2773](#)] [[INSPIRE](#)].
- [85] A. Boyarsky, J. Lesgourgues, O. Ruchayskiy and M. Viel, *Lyman- α constraints on warm and on warm-plus-cold dark matter models*, *JCAP* **05** (2009) 012 [[arXiv:0812.0010](#)] [[INSPIRE](#)].
- [86] J. Heeck and D. Teresi, *Cold keV dark matter from decays and scatterings*, *Phys. Rev. D* **96** (2017) 035018 [[arXiv:1706.09909](#)] [[INSPIRE](#)].
- [87] K.J. Bae, A. Kamada, S.P. Liew and K. Yanagi, *Light axinos from freeze-in: production processes, phase space distributions and Ly- α forest constraints*, *JCAP* **01** (2018) 054 [[arXiv:1707.06418](#)] [[INSPIRE](#)].
- [88] S. Boulebnane, J. Heeck, A. Nguyen and D. Teresi, *Cold light dark matter in extended seesaw models*, *JCAP* **04** (2018) 006 [[arXiv:1709.07283](#)] [[INSPIRE](#)].
- [89] V. Brdar, J. Kopp, J. Liu and X.-P. Wang, *X-Ray Lines from Dark Matter Annihilation at the keV Scale*, *Phys. Rev. Lett.* **120** (2018) 061301 [[arXiv:1710.02146](#)] [[INSPIRE](#)].
- [90] A. Merle, A. Schneider and M. Totzauer, *Dodelson-Widrow Production of Sterile Neutrino Dark Matter with Non-Trivial Initial Abundance*, *JCAP* **04** (2016) 003 [[arXiv:1512.05369](#)] [[INSPIRE](#)].
- [91] A. Merle and M. Totzauer, *keV Sterile Neutrino Dark Matter from Singlet Scalar Decays: Basic Concepts and Subtle Features*, *JCAP* **06** (2015) 011 [[arXiv:1502.01011](#)] [[INSPIRE](#)].
- [92] J. König, A. Merle and M. Totzauer, *keV Sterile Neutrino Dark Matter from Singlet Scalar Decays: The Most General Case*, *JCAP* **11** (2016) 038 [[arXiv:1609.01289](#)] [[INSPIRE](#)].
- [93] M. Viel, J. Lesgourgues, M.G. Haehnelt, S. Matarrese and A. Riotto, *Constraining warm dark matter candidates including sterile neutrinos and light gravitinos with WMAP and the Lyman-alpha forest*, *Phys. Rev. D* **71** (2005) 063534 [[astro-ph/0501562](#)] [[INSPIRE](#)].
- [94] U. Seljak, A. Makarov, P. McDonald and H. Trac, *Can sterile neutrinos be the dark matter?*, *Phys. Rev. Lett.* **97** (2006) 191303 [[astro-ph/0602430](#)] [[INSPIRE](#)].

- [95] M. Viel, J. Lesgourgues, M.G. Haehnelt, S. Matarrese and A. Riotto, *Can sterile neutrinos be ruled out as warm dark matter candidates?*, *Phys. Rev. Lett.* **97** (2006) 071301 [[astro-ph/0605706](#)] [[INSPIRE](#)].
- [96] P. Jethwa, D. Erkal and V. Belokurov, *The upper bound on the lowest mass halo*, *Mon. Not. Roy. Astron. Soc.* **473** (2018) 2060 [[arXiv:1612.07834](#)] [[INSPIRE](#)].
- [97] P. Villanueva-Domingo, N.Y. Gnedin and O. Mena, *Warm Dark Matter and Cosmic Reionization*, *Astrophys. J.* **852** (2018) 139 [[arXiv:1708.08277](#)] [[INSPIRE](#)].
- [98] M. Sitwell, A. Mesinger, Y.-Z. Ma and K. Sigurdson, *The Imprint of Warm Dark Matter on the Cosmological 21-cm Signal*, *Mon. Not. Roy. Astron. Soc.* **438** (2014) 2664 [[arXiv:1310.0029](#)] [[INSPIRE](#)].
- [99] I.P. Carucci, F. Villaescusa-Navarro, M. Viel and A. Lapi, *Warm dark matter signatures on the 21cm power spectrum: Intensity mapping forecasts for SKA*, *JCAP* **07** (2015) 047 [[arXiv:1502.06961](#)] [[INSPIRE](#)].
- [100] I.P. Carucci, F. Villaescusa-Navarro and M. Viel, *The cross-correlation between 21 cm intensity mapping maps and the Ly α forest in the post-reionization era*, *JCAP* **04** (2017) 001 [[arXiv:1611.07527](#)] [[INSPIRE](#)].
- [101] W. Beenakker, M. Klasen, M. Krämer, T. Plehn, M. Spira and P.M. Zerwas, *The Production of charginos/neutralinos and sleptons at hadron colliders*, *Phys. Rev. Lett.* **83** (1999) 3780 [*Erratum ibid.* **100** (2008) 029901] [[hep-ph/9906298](#)] [[INSPIRE](#)].
- [102] CMS collaboration, *Search for disappearing tracks as a signature of new long-lived particles in proton-proton collisions at $\sqrt{s} = 13$ TeV*, *JHEP* **08** (2018) 016 [[arXiv:1804.07321](#)] [[INSPIRE](#)].
- [103] R. Mahbubani, P. Schwaller and J. Zurita, *Closing the window for compressed Dark Sectors with disappearing charged tracks*, *JHEP* **06** (2017) 119 [*Erratum ibid.* **1710** (2017) 061] [[arXiv:1703.05327](#)] [[INSPIRE](#)].
- [104] H. Fukuda, N. Nagata, H. Otono and S. Shirai, *Higgsino Dark Matter or Not: Role of Disappearing Track Searches at the LHC and Future Colliders*, *Phys. Lett. B* **781** (2018) 306 [[arXiv:1703.09675](#)] [[INSPIRE](#)].
- [105] Z. Liu and B. Tweedie, *The Fate of Long-Lived Superparticles with Hadronic Decays after LHC Run 1*, *JHEP* **06** (2015) 042 [[arXiv:1503.05923](#)] [[INSPIRE](#)].
- [106] CMS collaboration, *Search for long-lived particles that decay into final states containing two electrons or two muons in proton-proton collisions at $\sqrt{s} = 8$ TeV*, *Phys. Rev. D* **91** (2015) 052012 [[arXiv:1411.6977](#)] [[INSPIRE](#)].
- [107] CMS collaboration, *Search for long-lived neutral particles decaying to dijets*, *CMS-PAS-EXO-12-038* (2013).
- [108] CMS collaboration, *Search for Long-Lived Neutral Particles Decaying to Quark-Antiquark Pairs in Proton-Proton Collisions at $\sqrt{s} = 8$ TeV*, *Phys. Rev. D* **91** (2015) 012007 [[arXiv:1411.6530](#)] [[INSPIRE](#)].
- [109] CMS collaboration, *Combined search for electroweak production of charginos and neutralinos in proton-proton collisions at $\sqrt{s} = 13$ TeV*, *JHEP* **03** (2018) 160 [[arXiv:1801.03957](#)] [[INSPIRE](#)].
- [110] K.T. Matchev and S.D. Thomas, *Higgs and Z boson signatures of supersymmetry*, *Phys. Rev. D* **62** (2000) 077702 [[hep-ph/9908482](#)] [[INSPIRE](#)].

- [111] L. Calibbi, J.M. Lindert, T. Ota and Y. Takanishi, *LHC Tests of Light Neutralino Dark Matter without Light Sfermions*, *JHEP* **11** (2014) 106 [[arXiv:1410.5730](#)] [[INSPIRE](#)].
- [112] P. Schwaller and J. Zurita, *Compressed electroweakino spectra at the LHC*, *JHEP* **03** (2014) 060 [[arXiv:1312.7350](#)] [[INSPIRE](#)].
- [113] H. Baer, A. Mustafayev and X. Tata, *Monojets and mono-photons from light higgsino pair production at LHC14*, *Phys. Rev. D* **89** (2014) 055007 [[arXiv:1401.1162](#)] [[INSPIRE](#)].
- [114] Z. Han, G.D. Kribs, A. Martin and A. Menon, *Hunting quasidegenerate Higgsinos*, *Phys. Rev. D* **89** (2014) 075007 [[arXiv:1401.1235](#)] [[INSPIRE](#)].
- [115] M. Low and L.-T. Wang, *Neutralino dark matter at 14 TeV and 100 TeV*, *JHEP* **08** (2014) 161 [[arXiv:1404.0682](#)] [[INSPIRE](#)].
- [116] A. Arbey, M. Battaglia and F. Mahmoudi, *Monojet Searches for MSSM Simplified Models*, *Phys. Rev. D* **94** (2016) 055015 [[arXiv:1506.02148](#)] [[INSPIRE](#)].
- [117] A. Nelson, P. Tanedo and D. Whiteson, *Limiting SUSY compressed spectra scenarios*, *Phys. Rev. D* **93** (2016) 115029 [[arXiv:1509.08485](#)] [[INSPIRE](#)].
- [118] ATLAS collaboration, *Search for long-lived neutral particles decaying into displaced lepton jets in proton–proton collisions at $\sqrt{s} = 13$ TeV with the ATLAS detector*, *ATLAS-CONF-2016-042* (2016).
- [119] ATLAS collaboration, *Search for long-lived neutral particles decaying in the hadronic calorimeter of ATLAS at $\sqrt{s} = 13$ TeV in 3.2 fb^{-1} of data*, *ATLAS-CONF-2016-103* (2016).
- [120] CMS collaboration, *Search for new long-lived particles at $\sqrt{s} = 13$ TeV*, *Phys. Lett. B* **780** (2018) 432 [[arXiv:1711.09120](#)] [[INSPIRE](#)].
- [121] CMS collaboration, *Search for displaced leptons in the e-mu channel*, *CMS-PAS-EXO-16-022* (2016).
- [122] <https://atlas.web.cern.ch/Atlas/GROUPS/PHYSICS/PAPERS/SUSY-2016-08/#auxstuff>.
- [123] J. Alwall et al., *The automated computation of tree-level and next-to-leading order differential cross sections and their matching to parton shower simulations*, *JHEP* **07** (2014) 079 [[arXiv:1405.0301](#)] [[INSPIRE](#)].
- [124] T. Sjöstrand et al., *An Introduction to PYTHIA 8.2*, *Comput. Phys. Commun.* **191** (2015) 159 [[arXiv:1410.3012](#)] [[INSPIRE](#)].
- [125] DELPHES 3 collaboration, J. de Favereau et al., *DELPHES 3, A modular framework for fast simulation of a generic collider experiment*, *JHEP* **02** (2014) 057 [[arXiv:1307.6346](#)] [[INSPIRE](#)].
- [126] D. Curtin and M.E. Peskin, *Analysis of Long Lived Particle Decays with the MATHUSLA Detector*, *Phys. Rev. D* **97** (2018) 015006 [[arXiv:1705.06327](#)] [[INSPIRE](#)].
- [127] F. Elahi, C. Kolda and J. Unwin, *Ultra Violet Freeze-in*, *JHEP* **03** (2015) 048 [[arXiv:1410.6157](#)] [[INSPIRE](#)].
- [128] B.C. Allanach, M. Badziak, G. Cottin, N. Desai, C. Hugonie and R. Ziegler, *Prompt Signals and Displaced Vertices in Sparticle Searches for Next-to-Minimal Gauge Mediated Supersymmetric Models*, *Eur. Phys. J. C* **76** (2016) 482 [[arXiv:1606.03099](#)] [[INSPIRE](#)].

Publications Steven Lowette

Search for millicharged particles in proton-proton collisions at $\sqrt{s} = 13$ TeV

A. Ball,¹ G. Beauregard,² J. Brooke,³ C. Campagnari,⁴ M. Carrigan,⁵ M. Citron,⁴ J. De La Haye,¹ A. De Roeck,¹ Y. Elskens,⁶ R. Escobar Franco,⁴ M. Ezeldine,⁷ B. Francis,⁵ M. Gastal,¹ M. Ghimire,² J. Goldstein,³ F. Golf,⁸ J. Guiang,^{4,*} A. Haas,² R. Heller,^{4,†} C. S. Hill,⁵ L. Lavezzo,⁵ R. Loos,¹ S. Lowette,⁶ G. Magill,^{9,10} B. Manley,⁵ B. Marsh,⁴ D. W. Miller,¹¹ B. Odegard,⁴ F. R. Saab,⁷ J. Sahili,⁷ R. Schmitz,⁴ F. Setti,⁴ H. Shakeshaft,¹ D. Stuart,⁴ M. Swiatlowski,^{11,‡} J. Yoo,^{4,§} H. Zaraket,⁷ and H. Zheng¹¹

¹CERN, Geneva 1211, Switzerland

²New York University, New York, New York 10012, USA

³University of Bristol, Bristol BS8 1TH, United Kingdom

⁴University of California, Santa Barbara, California 93106, USA

⁵The Ohio State University, Columbus, Ohio 43218, USA

⁶Vrije Universiteit Brussel, Brussel 1050, Belgium


⁷Lebanese University, Hadeth-Beirut, Lebanon

⁸University of Nebraska, Lincoln, Nebraska 68588, USA

⁹McMaster University, Hamilton L8S 4L8, Canada

¹⁰Perimeter Institute for Theoretical Physics, Waterloo N2L 2Y5, Canada

¹¹University of Chicago, Chicago, Illinois 60637, USA

 (Received 13 May 2020; accepted 17 July 2020; published 6 August 2020)

We report on a search for elementary particles with charges much smaller than the electron charge using a data sample of proton-proton collisions provided by the CERN Large Hadron Collider in 2018, corresponding to an integrated luminosity of 37.5 fb^{-1} at a center-of-mass energy of 13 TeV. A prototype scintillator-based detector is deployed to conduct the first search at a hadron collider sensitive to particles with charges $\leq 0.1e$. The existence of new particles with masses between 20 and 4700 MeV is excluded at 95% confidence level for charges between $0.006e$ and $0.3e$, depending on their mass. New sensitivity is achieved for masses larger than 700 MeV.

DOI: [10.1103/PhysRevD.102.032002](https://doi.org/10.1103/PhysRevD.102.032002)

I. INTRODUCTION

Over a quarter of the mass energy of the Universe is widely thought to be some kind of nonluminous “dark” matter (DM), however, all experiments to date have failed to confirm its existence as a particle, much less its properties. The possibility that DM is not a single particle, but rather a diverse set of particles with as complex a structure in their sector as normal matter, has grown in prominence in the past decade, beginning with attempts to explain observations in high-energy astrophysics experiments [1,2].

Many experimental efforts have been launched to look for signs of a dark sector, including searches at high-energy colliders, explorations at low-energy colliders, precision tests, and effects in DM direct detection experiments (for recent reviews see Refs. [3–5]). Most of these experiments target the dark sector via a massive dark photon, in what we refer to as the “Okun phase” [6,7]. An alternative assumption, which we call the “Holdom phase” [7,8], results in massless dark photons. In these models the principal physical effect is that new dark sector particles that couple to the dark photon will have a small effective electric charge. These are generically called millicharged particles since a natural value for their electric charge of $Q \sim \alpha e / \pi$ arises from one-loop effects [9]. In this paper we use the symbol χ to denote a millicharged particle. For a given mass and charge, the pair production of millicharged particles at the CERN Large Hadron Collider (LHC) is almost model independent. Every standard model (SM) process that results in dilepton pairs through a virtual photon would, if kinematically allowed, also produce $\chi^+ \chi^-$ pairs with a cross section reduced by a factor of $(Q/e)^2$ and by mass-dependent factors that are well understood.

*Present address: University of California, San Diego, California 92093, USA.

†Present address: Fermi National Accelerator Laboratory, Batavia, Illinois 60510, USA.

‡Present address: TRIUMF, Vancouver V6T 2A3, Canada.

§Present address: Korea University, Seoul 02841, South Korea.

Published by the American Physical Society under the terms of the [Creative Commons Attribution 4.0 International license](https://creativecommons.org/licenses/by/4.0/). Further distribution of this work must maintain attribution to the author(s) and the published article’s title, journal citation, and DOI. Funded by SCOAP³.

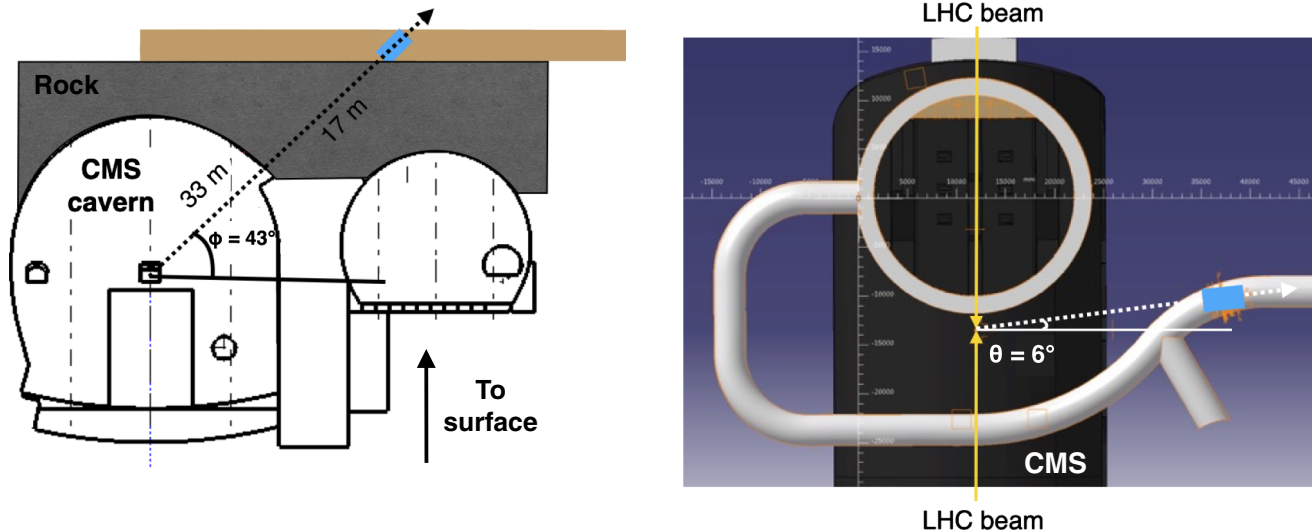


FIG. 1. The position of the detector, shown as a blue rectangular volume, in an elevation view (left) and plan view (right). The dashed lines represent the projection of the center of the detector to the CMS IP.

Millicharged particles can also be produced through Z boson couplings that depend on their hypercharge [7].

Previous experiments have searched for millicharged particles [10–17]. The parameter space spanned by the mass and charge of χ is also constrained by indirect observations from astrophysical systems [9,15,18–24], terrestrial matter [25], the cosmic microwave background (CMB) [26], big-bang nucleosynthesis [27], and universe overclosure bounds [18]. While direct searches robustly constrain the parameter space of millicharged particles, indirect observations can be evaded by adding extra degrees of freedom, which can readily occur in minimally extended dark sector models [7]. In particular, the parameter space $1 < m_\chi < 100$ GeV, an ideal mass range for production at the LHC, is largely unexplored by direct (or indirect) searches. Such a signature would not be detectable by the CMS and ATLAS experiments at the LHC [28,29], as all detector elements rely on the electromagnetic (EM) interaction of the millicharged particle with ordinary matter. For a millicharged particle the interaction strength is reduced by a factor of $(Q/e)^2$ with respect to that of a particle of the same mass that has charge e . The detector signal is also reduced by the same factor, and is typically too small to be recorded by detectors designed for particles of charge e . The production of millicharged particles in collider experiments would result in events with missing transverse momentum, however, SM processes with neutrinos as well as instrumental effects tend to overwhelm their signatures. No searches for particles with $Q \lesssim 0.1e$ have been performed at hadron colliders.

It is then clear that dedicated detectors are needed to search for millicharged particles at a hadron collider. In 2016, we discussed the possibility to build such a detector at the LHC, which we called milliQan [30], at the CMS experimental site and aligned with the CMS interaction

point (IP). Since then we have installed and operated a small fraction of such a detector (“milliQan demonstrator”) to measure backgrounds and provide a proof of principle and feedback for the full detector design. In 2018, the demonstrator collected a dataset of proton-proton (pp) interactions corresponding to an integrated luminosity of 37.5 fb^{-1} , at a center-of-mass energy of 13 TeV. This corresponds to 86% of the total luminosity delivered by the LHC in the period the demonstrator was operational. While the demonstrator is only $\sim 1\%$ of the full milliQan, the data collected already provides competitive constraints on the existence of millicharged particles of mass $20\text{--}4700 \text{ MeV}/c^2$ and $Q/e \sim 0.01\text{--}0.3$.

II. DETECTOR

A thick sensitive volume is required to be capable of observing the small energy deposition of a particle with $Q \lesssim 0.1e$. The milliQan demonstrator is, therefore, composed of three layers of $80 \times 5 \times 5$ cm scintillator bar arrays pointing to the CMS IP, with each array consisting of three pairs of bars, stacked on a 3.6 m long rectangular aluminum tube, for a total of 18 bars. We label the closest, middle and furthest layer from the CMS IP as layer 1, layer 2 and layer 3, respectively.

The milliQan demonstrator is located in an underground tunnel at a distance of 33 m from the CMS IP, with 17 m of rock between the CMS IP and the demonstrator that provides shielding from most particles produced in LHC collisions. In the CMS coordinate system [29], the detector is positioned at an azimuthal angle (ϕ) of 43° and pseudorapidity (η) of 0.1. Diagrams of the detector’s position are shown in Fig. 1. Located 70 m underground, the muon flux from cosmic rays is reduced by a factor of ~ 100 compared to the surface. The detector is aligned

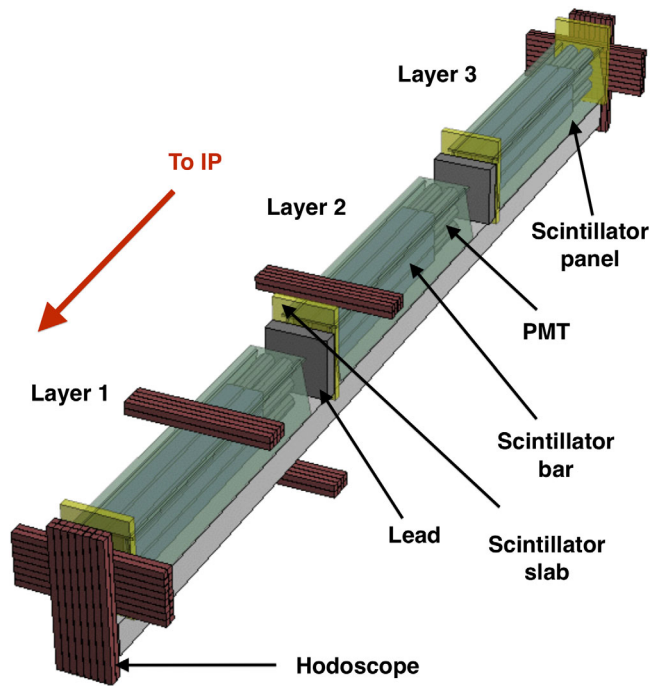


FIG. 2. A diagram of the detector components. The PMTs are not shown for the slabs or panels. All components are installed on an aluminum tube.

using standard laser-based survey techniques such that the center of the scintillator array projects a line to within 1 cm of the CMS IP. This alignment is validated using muons produced at the CMS IP, as discussed in Sec. IV C.

In addition to the scintillator bars, additional components were installed to reduce or characterize certain types of backgrounds. Lead bricks are placed between the layers to prevent low-energy secondary particles from one layer from entering another layer. Four scintillator slabs are located along the length of the detector to tag throughgoing particles, provide time information, and shield the bars from neutron radiation. Thin scintillator panels cover the top and sides, providing the ability to reject cosmic muons. Lastly, hodoscopes consisting of $2 \times 2 \times 45$ cm scintillator volumes are used to identify the tracks of beam and cosmic muons. A diagram of the detector components is shown in Fig. 2, and a photograph of the installed detector is shown in Fig. 3. All scintillator volumes are comprised of Eljen EJ-200 [31].

Scintillator light in the bars, panels, and slabs is detected by photomultiplier tubes (PMTs) coupled to the scintillator volumes. Three types of PMTs are used in order to test different manufacturers and gains: the Hamamatsu R878, Hamamatsu R7725 [32], and Electron Tube 9814B [33]. Analog signals from each PMT are sent to two 16-channel CAEN V1743 digitizers [34], operating at 1.6×10^9 samples per second with 12-bit resolution, providing 1024 samples within a 640 ns acquisition window. Each scintillator volume with a PMT attached is referred to as a

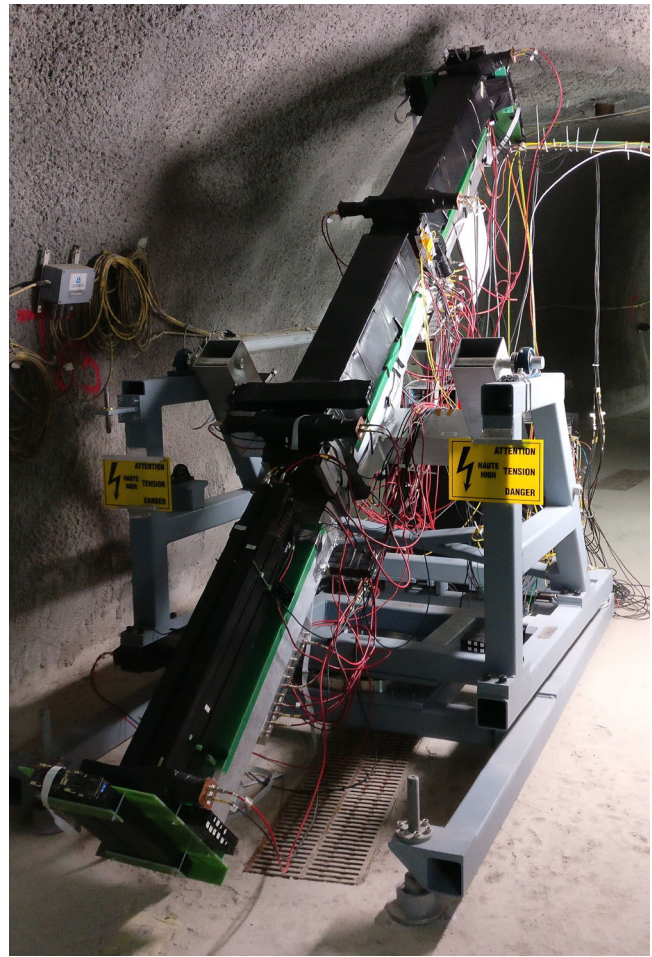


FIG. 3. A photograph of the detector, with the panels removed from layer 1 so that the bars may be seen.

“channel.” Since millicharged particles produced at the CMS IP would traverse the full length of the detector in $\mathcal{O}(10)$ ns, tight timing requirements allow for a significant reduction in combinatoric backgrounds by requiring the coincidence of in time signals in all layers, as described in Sec. V. The PMTs are powered by a CAEN SY5527 power supply system [35]. The hodoscopes are readout with silicon photomultipliers. Their data are triggered and stored independently from the main data stream.

The dataset analyzed for this search was collected during 2018, including periods with the LHC beam providing pp collisions (the “beam-on” dataset) and periods with no collisions (the “beam-off” dataset). The beam-off dataset provides a statistically independent sample to study background processes. The detector is located in an area in the far fringe field of the CMS superconducting magnet, and both beam-on and beam-off datasets were recorded with the magnet at its nominal strength of 3.8 T. The actual magnetic field in the milliQan cavern is measured by magnetic field sensors installed in various positions around the detector. We find this magnetic field to be under 2 mT when the CMS

magnet is at 3.8 T. Additional data samples were recorded with the field at 0 T for PMT calibration.

Data is collected by triggering on the coincidence of at least three channels (triple coincidence) within a window of 100 ns. A bar contributes to this coincidence if it has a rising edge consistent with a single photoelectron threshold, and the panels and slabs contribute to the coincidence with more stringent thresholds appropriate for identification of muons from cosmic rays (“cosmic muons”) and muons from pp interactions (“beam muons”). The total trigger live times were 1106 and 1042 hours for the beam-on and beam-off datasets, respectively. The average trigger rate was 14.4 Hz. Outside of the beam time, additional specialized runs were taken using single-channel and double-coincidence triggers, with different thresholds and operating voltage settings, in order to collect data samples for calibrations and validation studies.

III. CALIBRATION

We first calibrate the size of the generated pulses in each channel, which requires a measurement of the average size of a pulse from a single photoelectron (SPE) in each PMT, as well as the mean number of photoelectrons $\langle N_{\text{PE}} \rangle$ generated in each channel by a throughgoing muon. The former is strictly a property of each PMT, while the latter depends on each scintillator, its wrapping, its coupling to the PMT, and the PMT quantum efficiency.

The SPE calibration is performed *in situ* by isolating pulses from late-arriving scintillation photons, which largely produce SPEs in the PMTs. The mean SPE area is then found by locating the peak of the resulting pulse area distribution. These measurements are cross-checked by bench measurements of SPE waveforms generated by a flashing LED, following the method outlined in Ref. [36]. In the following, the n_{pe} of a given pulse is defined as the pulse area divided by this per-channel SPE calibration, and represents an estimate of the true number of photoelectrons that generated the pulse.

For panels and slabs, the $\langle N_{\text{PE}} \rangle$ calibration is performed directly based on throughgoing beam muons (slabs) and cosmic muons (panels). The measured average pulse area is scaled by the per-channel SPE measurement to calculate the mean number of photoelectrons generated by a beam or cosmic muon.

For the bars, we use cosmic ray muons for calibration. Direct calibration with radioactive sources was not possible because the detector could not be accessed during LHC running. Since cosmic ray muons saturate the readout, we take an indirect approach, using the fact that the PMT response scales as a power law over a wide range of operating voltages. First, the mean areas of cosmic muon pulses are measured at 5–6 operating voltages, which are low enough to ensure that the PMT signals do not saturate. A power law function is then fit to these points, and extrapolated to the nominal operating voltage. Finally, this

number is scaled by the per-channel SPE measurement to arrive at an estimate of the number of photoelectrons generated by a cosmic muon. The validity of the power law assumption is confirmed by separately fitting a power law function to the mean areas of SPE pulses over a range of voltages near the nominal operating voltage. The fitted exponent is found to be consistent with that from the fit to the cosmic muon pulse areas for all bars. The calibrated value of $\langle N_{\text{PE}} \rangle$ for a beam muon traversing the full 80 cm length of a bar varies from 22 000 to 82 000; this means that $\langle N_{\text{PE}} \rangle = 1$ is expected in the bars for particles of charge $Q/e \sim 0.004\text{--}0.007$.

The dominant source of uncertainty in each bar’s $\langle N_{\text{PE}} \rangle$ measurement is the statistical uncertainty from the power law fit and extrapolation, which is 10%–20% depending on the channel, and is uncorrelated between channels. Smaller uncertainties, generally on the order of a few percent, come from differences in the residual magnetic field between calibration runs and data-taking runs; the effect of a low-pass filter applied to the waveforms; and differences between the *in situ* and lab-based SPE measurements. These are correlated between bars with PMTs of the same type. Time dependent drifts in the response, inferred from variations in the dark count rate, are subdominant.

The timing of the PMTs must also be calibrated. The calibration procedure is designed such that a particle traveling near the speed of light through the detector from the CMS IP should have the same time value in every bar, panel and slab. This calibration is performed using both beam and cosmic muons. Figure 4 shows the time difference between a muon pulse in layer 3 compared to a muon pulse in layer 1, where the events have been categorized as either beam or cosmic muons based on the timing of the pulses in the slabs. The resolution in the time difference between layers is approximately 4 ns for beam muons which travel through the detector from the CMS IP. An additional correction is applied to account for the dependence of the timing of the pulses on their size. This correction is derived using secondary particles that result from the interactions of beam muons with the detector as they traverse it. The timing resolution degrades as the size of the pulses gets smaller; the resolution of the lowest n_{pe} pulses passing the selection outlined in Sec. V is ~ 15 ns. The modeling of the timing of these secondaries is used to derive a systematic uncertainty in the timing in simulation.

The trigger efficiency is measured as a function of n_{pe} for each channel by comparing the rate between dedicated triple-coincidence runs and double-coincidence runs. For the triple-coincidence runs, the trigger decision is based on coincident signals in two “tag-channels” and one “probe channel,” whose trigger efficiency is to be measured. For the double coincidence runs, the trigger decision involves only the two tag channels. The trigger efficiency for each channel is given by the ratio of the pulse rate when the

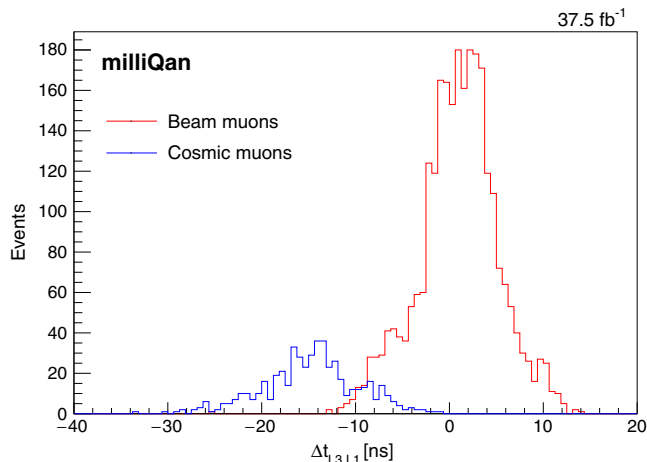


FIG. 4. Time difference, measured in a combination of the beam-on and beam-off datasets, between layer 3 and layer 1 for beam (red) and cosmic (blue) muons that travel through the detector.

probe channel is required in the trigger over the pulse rate when the probe channel is not required in the trigger. This efficiency is used to reweight the simulated samples of signals from millicharged particles described in Sec. IV B. The trigger efficiency is measured to reach 100% for $n_{pe} \gtrsim 2$ for all channels.

IV. SIMULATION

A. Event generation

We generate pair production of millicharged particles in 13 TeV pp collisions through the Drell-Yan process, as well as from Υ , J/ψ , $\psi(2S)$, ϕ , ρ , and ω decays into $\chi^+\chi^-$, and from Dalitz decays of π^0 , η , η' , and ω .

Drell-Yan events are generated assuming that χ s are isospin singlet fermions, using the Lagrangian of Ref. [37] implemented in the MADGRAPH5_aMC@NLO [38] event generator, with a minimum invariant mass requirement on the millicharged pair of $2 \text{ GeV}/c^2$. Because of the limited integrated luminosity and the small size of the demonstrator, there is essentially no sensitivity to Drell-Yan production of millicharged particles in the dataset discussed in this paper.

The production cross section and transverse momentum p_T distribution of J/ψ and $\psi(2S)$ in the central rapidity y region is taken from calculations of charmonium production from direct processes [39–41] and from bottom hadron decays [42–44], including theoretical uncertainties. Theoretical calculations of bottomonium production [45] are not reliable at low transverse momentum ($p_T < 15 \text{ GeV}$) [46], where most of the cross section lies. As a result, for $p_T > 20 \text{ GeV}$ we use the cross sections and p_T spectra measured at a center-of-mass energy of 13 TeV [47]; at lower p_T we use measurements from 7 TeV data

[48,49], rescaled using the measured ratio of 13 to 7 TeV cross sections at slightly higher rapidity ($2 < y < 2.5$) [50].

All relevant light flavor mesons except ϕ mesons are generated with the minimum bias PYTHIA8 generator [51] with the Monash 2013 tune [52]. This is the tune that gives the best agreement with several measurements of light meson rates and p_T spectra at the LHC, albeit in most cases at center-of-mass energies lower than 13 TeV [53–56]. The Monte Carlo spectra for $\eta(\rho, \omega)$ with $p_T < 3$ (1) GeV are scaled down by factors as large as 2, based on the experimental results cited above. On the other hand, the production of ϕ mesons is modeled with the minimum bias PYTHIA6 generator [57] with the DW tune [58], since this Monte Carlo setup best reproduces ϕ meson data [59]. All PYTHIA Monte Carlo generations are normalized to a minimum bias cross section of $80 \pm 10 \text{ mb}$ based on a measurement by ATLAS [60], with an uncertainty taken to cover the difference with respect to a similar CMS measurement [61]. We assess an additional 30% uncertainty in the overall rate of each process to account for remaining differences between experimental measurements and PYTHIA predictions of the rates of light mesons per minimum bias event, based on the references cited above.

The branching fractions for all vector meson decays, $V \rightarrow \chi^+\chi^-$, as a function of the χ mass are calculated using the Van Royen-Weisskopf formula [62], normalized to the PDG value of the branching fraction for $V \rightarrow e^+e^-$ [63], and rescaled appropriately for the assumed charge of the χ . The branching fractions for meson Dalitz decays, e.g., $\eta' \rightarrow \chi^+\chi^-\gamma$ or $\omega \rightarrow \chi^+\chi^-\pi^0$, as well as the $\chi^+\chi^-$ invariant mass distributions in these decays are modeled as a function of the χ mass and charge using the partial width for decays into photons, e.g., $\eta' \rightarrow \gamma\gamma$ or $\omega \rightarrow \pi^0\gamma$ [64], assuming a vector dominance model for the form factors.

Production cross sections of millicharged particles from different processes are summarized in Fig. 5. The possible contribution from millicharged particle production in EM showers in the CMS calorimeters generated by particles from pp collisions is not considered in this analysis.

We also generate inclusive muon events ($pp \rightarrow X \rightarrow \mu$) that are used for calibration and background studies. The same theoretical calculation used to obtain the differential cross sections of J/ψ and $\psi(2S)$ from bottom hadron decays is also used to generate muons from bottom and charm hadron decays, while muons from decays in flight of pions and kaons are generated with PYTHIA8 using the Monash 2013 tune. Muons from W and Z decays are taken from MADGRAPH5, though these electroweak processes contribute only $\sim 3\%$ of the total muon flux. Finally, muons are generated using an appropriate angular distribution to simulate cosmic ray events. This angular distribution is derived by assuming a $\cos^2(\theta_{\text{zenith}})$ distribution at the surface and propagating the muons to the demonstrator using the method described in Sec. IV B.

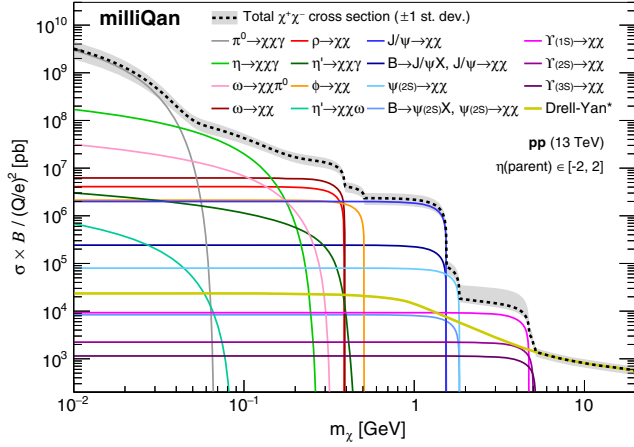


FIG. 5. Cross section times branching ratios for production of different particles with $|\eta| < 2$ decaying into $\chi^+\chi^-$ pairs, as a function of χ mass. For Drell-Yan the plotted cross section requires at least one of the χ s to have $|\eta| < 1$.

B. Detector response

Generated particles are propagated through a simplified model of the material in the CMS detector, including the magnetic field, and the 17 m of rock between the CMS cavern and the demonstrator.

Propagation is performed with fourth-order Runge-Kutta integration, incorporating the effects of the magnetic field, multiple scattering, and energy loss. Particles are propagated until 2 m before the face of the demonstrator, after which they are fed into a full GEANT4 [65] simulation of the remaining rock, the drainage gallery where the demonstrator is located, and the demonstrator itself. Similarly, muons from cosmic ray showers are propagated from the surface of the earth to a plane 1 m above the top of the cavern. Muon interactions in the cavern walls generate showers of gamma rays and electrons that significantly contribute to the cosmic ray background. A simulated cosmic ray shower event is shown in Fig. 6.

The simulation parameters are nominally configured to be consistent with EJ-200 scintillator and existing measurements for Tyvek reflectivity and each PMT species' quantum efficiency [66]. Overall photon propagation is handled using GEANT4's UNIFIED optical model [67]. Photon propagation is further calibrated by measuring the effects of scintillator roughness and wrapping quality on light attenuation in the scintillator bars and matching the effect in simulation. These measurements indicated a wrapping reflectivity $R = 0.97$ and scintillator roughness $\sigma = 1\%$, typical values for Tyvek and EJ-200 [68]. A per-channel calibration is applied to each PMT quantum efficiency so that the measured $\langle N_{PE} \rangle$ values agree between data and simulation.

The electronic response is simulated using SPE waveform templates measured on a test bench with an LED. SPE templates for each GEANT4 photoelectron are added

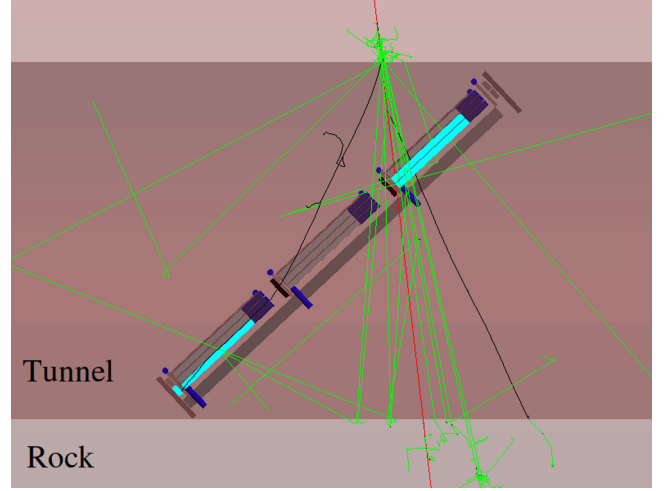


FIG. 6. Simulation of the milliQan demonstrator response to a simulated cosmic ray shower event. The incident muon (red) interacts with the cavern walls to produce a shower. Electrons (black) and gamma rays (green) generated in the rock are a significant background source. The interactions of muons and shower particles with detector material produce scintillation photons (cyan).

together, with appropriate arrival times, and including the individual PMT calibration described in Sec. III. The resulting waveform is then added to a randomly selected zero-bias data waveform to properly account for electronic noise.

C. Validation

The simulation is validated by studying beam muons as well as cosmic ray events. The absolute rate of beam muons passing through all four slabs is compared with the rate predicted from a simulated sample of muon production from heavy-flavor and electroweak decays, as well as meson decays in flight, as described in Sec. IV B. We measure a rate of 0.20 ± 0.01 muons/pb $^{-1}$, based on a sample of 7363 muons, in agreement with the prediction of 0.25 ± 0.08 muons/pb $^{-1}$. The dominant uncertainties in this prediction arise from the uncertainty in the $b\bar{b}$ cross section (21%) and from the modeling of the material between the CMS IP and milliQan (25%). This last uncertainty is derived from a 7% variation in the total amount of intervening material, which is in turn due primarily to uncertainties in both the thickness and density of the rock layer. This 7% variation corresponds to a 25% uncertainty in the muon rate because of the steeply falling muon momentum distribution. This same variation is used to derive a systematic uncertainty in the predicted signal yields, though in that case the effect is much smaller because of the smaller charge of the χ .

We additionally perform a comparison of the angular distribution of beam muon trajectories, in order to probe the scattering and magnetic field modeling in simulation and

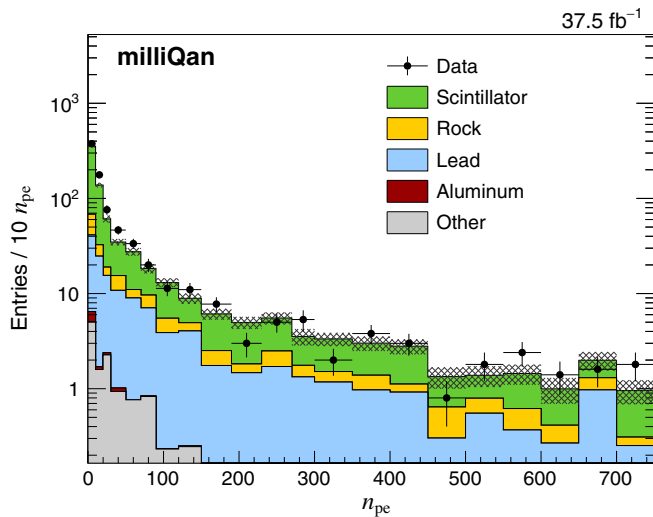


FIG. 7. Comparison of data and simulation n_{pe} distributions in events with a tagged throughgoing beam muon, for bars that do not contain a pulse consistent with originating from a muon, and are not neighboring any such bars. Note that only 783 out of 7363 tagged muons produced detectable showers entering this figure. Simulation events are categorized based on the material in which the particle(s) that produced the pulse originated.

validate the alignment of the detector. We compare rates of muons passing through various subsets of bars that trace a range of angles through the detector. The rates of these paths in both the horizontal and vertical directions are measured to be consistent within statistical uncertainties between data and simulation.

Finally, the GEANT4 modeling is validated by comparing distributions of photoelectron counts in bars near either beam or cosmic muon trajectories. Hits are expected from electrons and gamma rays produced as the muon travels through the rock or nearby detector material. An example comparison is shown in Fig. 7. Here we show n_{pe} distributions in data and simulation in events with a tagged beam muon, for bars that do not contain a pulse consistent with originating from a muon ($n_{pe} < 750$), and are not neighboring any such bars. Contributions come primarily from electrons and gamma rays produced in scintillator material, rock, or the lead bricks. Good agreement is seen across a wide range of n_{pe} levels.

V. SEARCH FOR MILLICHARGED PARTICLES

The search for millicharged particles looks for a signal with the signature of a pulse in each of the three layers of the demonstrator. A number of sources can produce such a signature:

- (i) Each PMT has a dark current arising from effects such as the thermal emission of electrons from the cathode. The simplest background source comes from random overlap of three such dark rate pulses.

In addition, dark rate counts may overlap with two correlated pulses from another source.

- (ii) Cosmic muon showers may generate a large number of gamma rays and electrons from an interaction of one or more cosmic ray muons with the rock in the milliQan cavern. This may cause a pulse in each layer of the demonstrator. Such a background could also be expected from a beam muon that travels close to the demonstrator.
- (iii) Radiation in the cavern, scintillator bars or surrounding material can cause correlated deposits in several bars. The lead blocks placed between layers should reduce the probability of deposit in multiple layers arising from photons or electrons while the slabs provide shielding of neutrons.
- (iv) Afterpulses, which are small pulses caused by positive ions generated by the ionization of residual gases in the PMT, can appear several hundred nanoseconds to over a few microseconds after the initial pulse. The afterpulses from correlated deposits in several PMTs may overlap and produce a signal-like signature in the demonstrator. For this to occur, the interaction event that gives rise to the afterpulses must not be triggered because, in this case, the afterpulses will fall in the $125 \mu s$ readout deadtime that follows each triggered event, and will not be recorded.

Selections are applied in order to reject contributions from these background sources. If there is a pulse within the acquisition time window in any panel, or in more than one bar in each layer, the event is rejected. These requirements reject backgrounds due to cosmic muon showers, which are expected to cause deposits across the detector. In addition, if there is a pulse in any slab within the acquisition time window consistent with originating from a muon ($n_{pe} > 250$) the event is vetoed. This requirement rejects deposits due to beam and cosmic muons passing close to the bars. The bars with reconstructed pulses are required to be pointing to the CMS IP. This reduces the backgrounds from neutrons, cosmic muon showers and random overlap, while being efficient for signal, which typically has a small angular spread. To mitigate backgrounds from afterpulses, in each channel a requirement is made to reject the event if a pulse occurs before the window in which the pulse may be involved in the trigger decision. In addition, the first pulse in each channel must have the largest n_{pe} value. Events that contain initial pulses in the bars with a large spread in n_{pe} (maximum $n_{pe}/\text{minimum } n_{pe} > 10$) are vetoed to reject events containing contributions from different sources, such as dark rate overlap with shower deposits or deposits from two or more shower particles traveling through the demonstrator. Finally, the maximum calibrated time difference between the first bar pulse in each layer (Δt_{max}) is required to be less than 15 ns, which is efficient for signals traveling through the detector from the CMS IP and forms a

TABLE I. Sequential impact of each requirement on the number of events passing the selection criteria.

Selection	Data	Data	Signal	Signal	Signal	
	beam-on $t = 1106$ h	beam-off $t = 1042$ h	$m_\chi = 0.05$ GeV $Q/e = 0.007$	$m_\chi = 1.0$ GeV $Q/e = 0.02$	$m_\chi = 3.0$ GeV $Q/e = 0.1$	
Common	≥ 1 hit per layer	2 003 170	1 939 900	136.4	34.2	5.7
Selections	Exactly one hit per layer	714 991	698 349	123.1	31.0	5.0
	Panel veto	647 936	632 494	122.5	30.8	4.9
	First pulse is max	418 711	409 296	114.3	30.6	4.8
	Veto early pulses	301 979	295 040	113.9	30.6	4.8
	$\max n_{pe} / \min n_{pe} < 10$	154 203	150 949	104.2	29.6	4.7
	$\Delta t_{\max} < 15$ ns	5 284	5 161	72.8	28.4	4.4
	Slab muon veto	5 224	5 153	72.8	28.4	4.4
	Straight path	350	361	68.4	28.1	4.2
	$N_{\text{slab}} = 0$	332	339	64.8	16.9	0.0
	$N_{\text{slab}} \geq 1$	18	22	3.6	11.2	4.2
SR 1	$N_{\text{slab}} = 0$ and $\min n_{pe} \in [2, 20]$	129	131	47.4	0.4	0.0
SR 2	$N_{\text{slab}} = 0$ and $\min n_{pe} > 20$	52	45	0.0	16.5	0.0
SR 3	$N_{\text{slab}} = 1$ and $\min n_{pe} \in [5, 30]$	8	9	1.1	0.5	0.0
SR 4	$N_{\text{slab}} = 1$ and $\min n_{pe} > 30$	4	4	0.0	8.7	0.0
SR 5	$N_{\text{slab}} \geq 2$	1	1	0.0	2.0	4.2

powerful rejection of backgrounds that have different paths through the detector, such as cosmic muon showers, or that have deposits in each layer that are uncorrelated in their timing, such as dark rate overlap.

Selected events are subsequently categorized into five signal regions (SRs) through requirements on both the number of slabs that contain a pulse and the minimum n_{pe} of the pulses in the three bars. This categorization allows for sensitivity to a wide range of charge values in the signal parameter space. The definitions of the five SRs are summarized in Table I. For events with a pulse in each of the three layers the selection criteria provide high efficiency for the targeted models while rejecting the background by more than 5 orders of magnitude.

Residual background passing selection is estimated for each signal region by measuring the pass/fail ratio of the timing requirement in events with a hit in each layer, consistent with signal requirements except that the bars do not form a pointing path towards the CMS IP, and then multiplying it by the number of events failing the timing selection that form a pointing path towards the CMS IP. This prediction method relies on the independence of the dominant backgrounds on the pointing path requirement. This method is used rather than taking the prediction from the beam-off dataset as it is robust against time dependent drifts in the background rate. However, the beam-off dataset provides a statistically independent sample to validate the prediction without contamination from signal. The results of the beam-off prediction for the SR are summarized in Table II. The uncertainty in the prediction

reflects the limited statistics in the regions used to make the prediction. The prediction is shown to be in agreement with the observation for all validation regions. The level of agreement between prediction and observation in each validation region is used to derive a systematic uncertainty in the prediction.

Given the validation of the background prediction method with the beam-off dataset, the SR prediction is made using the beam-on dataset. The background contribution from beam processes is estimated from simulation to be less than 2% for all regions. Results are given in Table III. The predictions are seen to be consistent with those from the beam-off dataset (taking the 6% difference in collection time into account), which provides additional confidence that the beam-based backgrounds are negligible. The uncertainty in the prediction reflects both the limited statistical power of the regions used for the

TABLE II. Summary of the results of the validation using the beam-off dataset. The systematic values are derived from the level of agreement between the prediction and observation.

Region	N_{slab}	$\min n_{pe}$	Prediction	Observation	Systematic
1	0	[2,20]	$121.2^{+6.0}_{-5.9}$	131	8%
2	0	>20	$47.4^{+5.2}_{-4.8}$	45	5%
3	1	[5,30]	$7.8^{+2.5}_{-1.8}$	9	15%
4	1	>30	$2.7^{+2.1}_{-1.1}$	4	48%
5	≥ 2	...	$0.8^{+1.4}_{-0.4}$	1	25%

TABLE III. Summary of the results of the signal region prediction.

Region	N_{slab}	min n_{pe}	Prediction	Observation
1	0	[2,20]	124^{+11}_{-11}	129
2	0	> 20	$49.9^{+6.0}_{-5.4}$	52
3	1	[5,30]	$10.7^{+3.6}_{-2.6}$	8
4	1	>30	$2.4^{+2.1}_{-1.1}$	4
5	≥ 2	...	$0.0^{+0.9}_{-0.0}$	1

prediction as well as the systematic uncertainty derived from the validation using the beam-off dataset. The predictions are found to be consistent with the observations in all SRs.

VI. INTERPRETATION

The search is interpreted using the signal model described in Sec. IV. The full set of selection criteria described in Sec. V is applied to each event. The efficiency to pass these criteria for three benchmark χ masses and charges is shown in Table I.

There are several sources of systematic uncertainty in the number of signal events entering the SRs. These are evaluated independently for each model point and are summarized below:

- (i) Signal cross section (described in Sec. IV A): typically 15%–30% depending on the mass of the χ .
- (ii) Material interactions (described in Sec. IV C): typically 1%–5% depending on the charge and mass of the χ .
- (iii) Pulse timing (described in Sec. III): typically 1%–40% depending on the charge of the χ .
- (iv) $\langle N_{\text{PE}} \rangle$ calibration (described in Sec. III): 1%–50% depending on the SR populated by the χ .
- (v) Limited simulated sample size: up to 30%.

Under the signal plus background hypothesis, a modified frequentist approach is used to determine observed upper limits at 95% confidence level on the cross section (σ) to produce a pair of χ s, as a function of mass and charge. The approach uses the LHC-style profile likelihood ratio as the test statistic [69] and the criterion of the C.L. [70,71]. The observed upper limits are evaluated through the use of asymptotic formulas [72]. Figure 8 shows the exclusion at 95% confidence level in mass and charge of the χ . The exclusion is compared to existing constraints, showing new sensitivity for χ masses above 700 MeV.

VII. FUTURE PLANS

In Refs. [30,37] we assumed the largest irreducible background to the signal would come from dark-current pulses in the PMTs. From experience gained by operating the demonstrator, we now know that an equally important background comes from correlated effects caused by

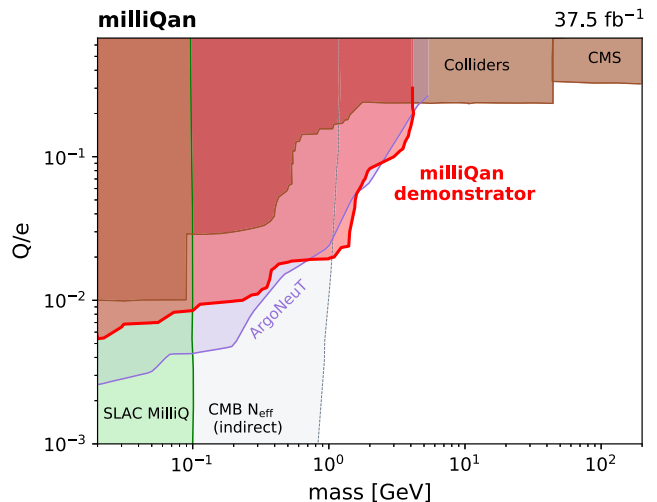


FIG. 8. Exclusion at 95% confidence level compared to existing constraints from colliders, CMS, ArgoNeuT and SLAC MilliQ [10–16,27] as well as the indirect constraint from the CMB relativistic degrees of freedom [26].

activity in the scintillator (from effects such as environmental radiation or cosmic muon showers). This realization prompted us to revisit the milliQan design, adding a fourth layer in order to mitigate the contribution from these correlated backgrounds.

We have studied the effect of adding a fourth layer with the demonstrator. The demonstrator has three rather than four layers so backgrounds are determined for threefold coincidence and then extended to fourfold using an additional pulse in a slab. The results of this study indicate that the contribution from pure dark-current overlap drops to a negligible level for the case of fourfold coincidence, even with the somewhat high-noise PMTs that are used in the demonstrator. The calculations presented in Refs. [30,37] remain a conservative estimate of the milliQan discovery potential since the background with four layers as measured with the demonstrator is significantly smaller than the estimate used in those simulations.

Given the experience obtained from the demonstrator, we are confident that the proposed full-scale detector will perform as expected provided sufficient funding becomes available.

VIII. CONCLUSIONS

We have deployed a prototype dedicated detector at the LHC to conduct the first search for elementary particles with charges much smaller than the electron charge at a hadron collider. We analyzed a data sample of proton-proton collisions collected at $\sqrt{s} = 13$ TeV provided by the LHC, corresponding to an integrated luminosity of 37.5 fb^{-1} . The existence of new particles with masses between 20 and 4700 MeV is excluded at 95% confidence level for charges varying between $0.006e$ and $0.3e$,

depending on mass. New sensitivity is achieved for masses larger than 700 MeV. The successful operation of the milliQan demonstrator and search carried out have shown the feasibility of a dedicated detector for millicharged particles at the LHC and provided important lessons for the design of the full detector.

ACKNOWLEDGMENTS

We congratulate our colleagues in the CERN accelerator departments for the excellent performance of the LHC and thank the technical and administrative staffs at CERN.

In addition, we gratefully acknowledge the CMS collaboration for supporting this endeavor by providing invaluable logistical and technical assistance. We also thank Eder Izaguirre and Itay Yavin for their enduring contributions to this idea. Finally, we acknowledge the following funding agencies who support the investigators that carried out this research in various capacities: FWO (Belgium) under the Excellence of Science EOS be.h Project No. 30820817; DFG and HGF (Germany); Swiss Funding Agencies (Switzerland); STFC (United Kingdom); DOE and NSF (USA); Lebanese University (Lebanon).

-
- [1] N. Arkani-Hamed, D. P. Finkbeiner, T. R. Slatyer, and N. Weiner, A theory of dark matter, *Phys. Rev. D* **79**, 015014 (2009).
- [2] M. Pospelov and A. Ritz, Astrophysical signatures of secluded dark matter, *Phys. Lett. B* **671**, 391 (2009).
- [3] M. Battaglieri, A. Belloni, A. Chou *et al.*, U.S. cosmic visions: New ideas in dark matter 2017: Community report, in *U.S. Cosmic Visions: New Ideas in Dark Matter* (Fermilab, Batavia, 2017), Vol. 7.
- [4] J. Beacham, C. Burrage, D. Curtin *et al.*, Physics beyond colliders at CERN: Beyond the standard model working group report, *J. Phys. G* **47**, 010501 (2020).
- [5] European Strategy for Particle Physics Preparatory Group, *Physics Briefing Book* (CERN, Geneva, 2019).
- [6] L. B. Okun, Limits of electrodynamics: Paraphotons?, *Zh. Eksp. Teor. Fiz.* **83**, 892 (1982) [*Sov. Phys. JETP* **56**, 502 (1982)], <https://inspirehep.net/literature/177918>.
- [7] E. Izaguirre and I. Yavin, New window to millicharged particles at the LHC, *Phys. Rev. D* **92**, 035014 (2015).
- [8] B. Holdom, Two $U(1)$'s and epsilon charge shifts, *Phys. Lett. B* **166**, 196 (1986).
- [9] S. Davidson and M. E. Peskin, Astrophysical bounds on millicharged particles in models with a paraphoton, *Phys. Rev. D* **49**, 2114 (1994).
- [10] A. Prinz, R. Baggs, J. Ballam *et al.*, Search for Millicharged Particles at SLAC, *Phys. Rev. Lett.* **81**, 1175 (1998).
- [11] R. Essig, J. A. Jaros, W. Wester *et al.*, Working group report: New light weakly coupled particles, in *Community Summer Study 2013: Snowmass on the Mississippi* (Fermilab, Batavia, 2013), Vol. 10.
- [12] S. Chatrchyan (CMS Collaboration), Search for fractionally charged particles in pp collisions at $\sqrt{s} = 7$ TeV, *Phys. Rev. D* **87**, 092008 (2013).
- [13] S. Chatrchyan (CMS Collaboration), Searches for long-lived charged particles in pp collisions at $\sqrt{s} = 7$ and 8 TeV, *J. High Energy Phys.* **07** (2013) 122.
- [14] R. Acciarri, C. Adams, J. Asaadi *et al.*, Improved Limits on Millicharged Particles Using the ArgoNeUT Experiment at Fermilab, *Phys. Rev. Lett.* **124**, 131801 (2020).
- [15] S. Davidson, S. Hannestad, and G. Raffelt, Updated bounds on millicharged particles, *J. High Energy Phys.* **05** (2000) 003.
- [16] A. Badertscher, P. Crivelli, W. Fetscher, U. Gendotti, S. N. Gninenko, V. Postoev, A. Rubbia, V. Samoylenko, and D. Sillou, An improved limit on invisible decays of positronium, *Phys. Rev. D* **75**, 032004 (2007).
- [17] G. Magill, R. Plestid, M. Pospelov, and Y.-D. Tsai, Millicharged Particles in Neutrino Experiments, *Phys. Rev. Lett.* **122**, 071801 (2019).
- [18] S. Davidson, B. Campbell, and D. C. Bailey, Limits on particles of small electric charge, *Phys. Rev. D* **43**, 2314 (1991).
- [19] R. Mohapatra and I. Rothstein, Astrophysical constraints on minicharged particles, *Phys. Lett. B* **247**, 593 (1990).
- [20] R. Agnese, A. Anderson, D. Balakishiyeva *et al.*, First Direct Limits on Lightly Ionizing Particles with Electric Charge Less than $e/6$, *Phys. Rev. Lett.* **114**, 111302 (2015).
- [21] T. Emken, R. Essig, C. Kouvaris, and M. Sholapurkar, Direct detection of strongly interacting sub-gev dark matter via electron recoils, *J. Cosmol. Astropart. Phys.* **09** (2019) 070.
- [22] L. Singh (TEXONO Collaboration), Constraints on millicharged particles with low-threshold germanium detectors at Kuo-Sheng Reactor Neutrino Laboratory, *Phys. Rev. D* **99**, 032009 (2019).
- [23] S. I. Alvis (Majorana Collaboration), First Limit on the Direct Detection of Lightly Ionizing Particles for Electric Charge as Low as $e/1000$ with the Majorana Demonstrator, *Phys. Rev. Lett.* **120**, 211804 (2018).
- [24] P. C. Kim, E. R. Lee, I. T. Lee, M. L. Perl, V. Halyo, and D. Loomba, Search for Fractional-Charge Particles in Meteoritic Material, *Phys. Rev. Lett.* **99**, 161804 (2007).
- [25] D. C. Moore, A. D. Rider, and G. Gratta, Search for Millicharged Particles Using Optically Levitated Microspheres, *Phys. Rev. Lett.* **113**, 251801 (2014).
- [26] C. Brust, D. E. Kaplan, and M. T. Walters, New light species and the CMB, *J. High Energy Phys.* **12** (2013) 058.
- [27] H. Vogel and J. Redondo, Dark radiation constraints on minicharged particles in models with a hidden photon, *J. Cosmol. Astropart. Phys.* **02** (2014) 029.
- [28] G. Aad (ATLAS Collaboration), The ATLAS experiment at the CERN large hadron collider, *J. Instrum.* **3**, S08003 (2008).

- [29] S. Chatrchyan (CMS Collaboration), The CMS experiment at the CERN LHC, *J. Instrum.* **3**, S08004 (2008).
- [30] A. Ball, J. Brooke, C. Campagnari *et al.*, A letter of intent to install a millicharged particle detector at LHC P5, [arXiv:1607.04669](https://arxiv.org/abs/1607.04669).
- [31] Eljen Technology, <https://eljentechnology.com/products/plastic-scintillators/ej-200-ej-204-ej-208-ej-212>.
- [32] Hamamatsu Photonics K.K., <https://www.hamamatsu.com/>.
- [33] ET Enterprises, Ltd., <http://et-enterprises.com/>.
- [34] CAEN S.p.A, <https://www.caen.it/products/v1743/>.
- [35] CAEN S.p.A, <https://www.caen.it/products/sy5527/>.
- [36] R. Saldanha, L. Grandi, Y. Guardincerri, and T. Wester, Model independent approach to the single photoelectron calibration of photomultiplier tubes, *Nucl. Instrum. Methods Phys. Res., Sect. A* **863**, 35 (2017).
- [37] A. Haas, C. S. Hill, E. Izaguirre, and I. Yavin, Looking for millicharged particles with a new experiment at the LHC, *Phys. Lett. B* **746**, 117 (2015).
- [38] J. Alwall, R. Frederix, S. Frixione, V. Hirschi, F. Maltoni, O. Mattelaer, H.-S. Shao, T. Stelzer, P. Torrielli, and M. Zaro, The automated computation of tree-level and next-to-leading order differential cross sections, and their matching to parton shower simulations, *J. High Energy Phys.* **07** (2014) 079.
- [39] Y.-Q. Ma, K. Wang, and K.-T. Chao, A complete NLO calculation of the J/ψ and ψ' production at hadron colliders, *Phys. Rev. D* **84**, 114001 (2011).
- [40] Y.-Q. Ma, K. Wang, and K.-T. Chao, $J/\psi(\psi')$ Production at the Tevatron and LHC at $\mathcal{O}(\alpha_s^4 v^4)$ in Nonrelativistic QCD, *Phys. Rev. Lett.* **106**, 042002 (2011).
- [41] Y.-Q. Ma and R. Venugopalan, Comprehensive Description of J/ψ Production in Proton-Proton Collisions at Collider Energies, *Phys. Rev. Lett.* **113**, 192301 (2014).
- [42] M. Cacciari, M. L. Mangano, and P. Nason, Gluon PDF constraints from the ratio of forward heavy-quark production at the LHC at $\sqrt{s} = 7$ and 13 TeV, *Eur. Phys. J. C* **75**, 610 (2015).
- [43] M. Cacciari, S. Frixione, N. Houdeau, M. L. Mangano, P. Nason, and G. Ridolfi, Theoretical predictions for charm and bottom production at the LHC, *J. High Energy Phys.* **10** (2012) 137.
- [44] M. Cacciari, S. Frixione, and P. Nason, The p_T spectrum in heavy flavor photoproduction, *J. High Energy Phys.* **03** (2001) 006.
- [45] H. Han, Y.-Q. Ma, C. Meng, H.-S. Shao, Y.-J. Zhang, and K.-T. Chao, $\Upsilon(nS)$ and $\chi_b(nP)$ production at hadron colliders in nonrelativistic QCD, *Phys. Rev. D* **94**, 014028 (2016).
- [46] Y.-Q. Ma (private communication).
- [47] S. Chatrchyan (CMS Collaboration), Measurement of quarkonium production cross sections in pp collisions at $\sqrt{s} = 13$ TeV, *Phys. Lett. B* **780**, 251 (2018).
- [48] G. Aad (ATLAS Collaboration), Measurement of the $\Upsilon(1S)$ production cross section in pp collisions at $\sqrt{s} = 7$ TeV in ATLAS, *Phys. Lett. B* **705**, 9 (2011).
- [49] G. Aad (ATLAS Collaboration), Measurement of Upsilon production in 7 TeV pp collisions at ATLAS, *Phys. Rev. D* **87**, 052004 (2013).
- [50] R. Aaij (LHCb Collaboration), Measurement of Υ production in pp collisions at $\sqrt{s} = 13$ TeV, *J. High Energy Phys.* **07** (2018) 134; Erratum, *J. High Energy Phys.* **05** (2019) 076.
- [51] T. Sjöstrand, S. Mrenna, and P. Skands, A brief introduction to PYTHIA8.1, *Comput. Phys. Commun.* **178**, 852 (2008).
- [52] P. Skands, S. Carrazza, and J. Rojo, Tuning PYTHIA8.1: The Monash 2013 Tune, *Eur. Phys. J. C* **74**, 3024 (2014).
- [53] S. Acharya (ALICE Collaboration), π^0 and η meson production in proton-proton collisions at $\sqrt{s} = 8$ TeV, *Eur. Phys. J. C* **78**, 263 (2018).
- [54] S. Acharya (ALICE Collaboration), Production of the $\rho(770)^0$ meson in pp and Pb-Pb collisions at $\sqrt{s_{NN}} = 2.76$ TeV, *Phys. Rev. C* **99**, 064901 (2019).
- [55] S. Acharya (ALICE Collaboration), Production of $\omega(782)$ in pp collisions at $\sqrt{s} = 7$ TeV, CERN Technical Report No. ALICE-PUBLIC-2018-004, 2018.
- [56] S. Chatrchyan (CMS Collaboration), Measurement of charged pion, kaon, and proton production in proton-proton collisions at $\sqrt{s} = 13$ TeV, *Phys. Rev. D* **96**, 112003 (2017).
- [57] T. Sjöstrand, S. Mrenna, and P. Skands, PYTHIA6.4 physics and manual, *J. High Energy Phys.* **05** (2006) 026.
- [58] M. G. Albrow, M. Begel, D. Bourilkov *et al.*, Tevatron-for-LHC report of the QCD working group, [arXiv:hep-ph/0610012](https://arxiv.org/abs/hep-ph/0610012).
- [59] G. Aad (ATLAS Collaboration), The differential production cross section of the $\phi(1020)$ meson in $\sqrt{s} = 7$ TeV pp collisions measured with the ATLAS detector, *Eur. Phys. J. C* **74**, 2895 (2014).
- [60] G. Aad (ATLAS Collaboration), Measurement of the Inelastic Proton-Proton Cross Section at $\sqrt{s} = 13$ TeV with the ATLAS Detector at the LHC, *Phys. Rev. Lett.* **117**, 182002 (2016).
- [61] S. Chatrchyan (CMS Collaboration), Measurement of the inelastic proton-proton cross section at $\sqrt{s} = 13$ TeV, CERN Technical Report No. CMS-PAS-FSQ-15-005, 2016.
- [62] R. Van Royen and V. F. Weisskopf, Hadron decay processes and the quark model, *Nuovo Cimento A* **50**, 617 (1967); Erratum, *Nuovo Cimento A* **51**, 583 (1967).
- [63] M. Tanabashi *et al.* (Particle Data Group), Review of particle physics, *Phys. Rev. D* **98**, 030001 (2018).
- [64] L. G. Landsberg, Electromagnetic decays of light mesons, *Phys. Rep.* **128**, 301 (1985).
- [65] S. Agostinelli, J. Allison, K. Amako *et al.*, GEANT4A simulation toolkit, *Nucl. Instrum. Methods Phys. Res., Sect. A* **506**, 250 (2003).
- [66] M. Janecek and W. W. Moses, Optical reflectance measurements for commonly used reflectors, *IEEE Trans. Nucl. Sci.* **55**, 2432 (2008).
- [67] A. Levin and C. Moisan, A more physical approach to model the surface treatment of scintillation counters and

- its implementation into DETECT, in *1996 IEEE Nuclear Science Symposium. Conference Record* (IEEE, Anaheim, CA, 1996), Vol. 2, p. 702.
- [68] P. Papacz, Optimization of the particle detection efficiency for scintillation detectors with SiPM readout, Master's thesis, RWTH Aachen University, 2010.
- [69] G. Aad (ATLAS and CMS Collaborations), Procedure for the LHC Higgs boson search combination in Summer 2011, CERN Technical Reports No. CMS-NOTE-2011-005 and No. ATL-PHYS-PUB-2011-11, 2011.
- [70] T. Junk, Confidence level computation for combining searches with small statistics, *Nucl. Instrum. Methods Phys. Res., Sect. A* **434**, 435 (1999).
- [71] A. L. Read, Presentation of search results: The CLs technique, *J. Phys. G* **28**, 2693 (2002).
- [72] G. Cowan, K. Cranmer, E. Gross, and O. Vitells, Asymptotic formulas for likelihood-based tests of new physics, *Eur. Phys. J. C* **71**, 1554 (2011); Erratum, *Eur. Phys. J. C* **73**, 2501 (2013).

Search for a Narrow Resonance Lighter than 200 GeV Decaying to a Pair of Muons in Proton-Proton Collisions at $\sqrt{s} = 13$ TeV

A. M. Sirunyan *et al.**
(CMS Collaboration)

 (Received 10 December 2019; accepted 24 February 2020; published 3 April 2020)

A search is presented for a narrow resonance decaying to a pair of oppositely charged muons using $\sqrt{s} = 13$ TeV proton-proton collision data recorded at the LHC. In the 45–75 and 110–200 GeV resonance mass ranges, the search is based on conventional triggering and event reconstruction techniques. In the 11.5–45 GeV mass range, the search uses data collected with dimuon triggers with low transverse momentum thresholds, recorded at high rate by storing a reduced amount of trigger-level information. The data correspond to integrated luminosities of 137 and 96.6 fb⁻¹ for conventional and high-rate triggering, respectively. No significant resonant peaks are observed in the probed mass ranges. The search sets the most stringent constraints to date on a dark photon in the ~ 30 –75 and 110–200 GeV mass ranges.

DOI: [10.1103/PhysRevLett.124.131802](https://doi.org/10.1103/PhysRevLett.124.131802)

A large body of cosmological evidence points to the existence of dark matter [1–4]. Unraveling its origin remains one of the outstanding problems of particle physics and cosmology. Dark matter is expected to interact very weakly, if at all, with standard model (SM) particles. This raises the possibility of a hidden, dark sector of particles whose interaction with SM particles may be mediated by a hypothetical dark photon (Z_D) [5].

We present a search for a narrow resonance decaying to a pair of oppositely charged muons using $\sqrt{s} = 13$ TeV proton-proton (pp) collision data recorded by the CMS experiment at the CERN LHC. The search looks for a narrow resonance in the 11.5–200 GeV mass range, omitting the 75–110 GeV range where Z boson production dominates. The results of this search are interpreted in the context of a Z_D that interacts with SM particles through the kinetic mixing of its $U(1)_D$ gauge field with the $U(1)_Y$ hypercharge field of the SM [6–8]. The degree of mixing and the strength of the coupling of Z_D to SM particles is determined by the kinetic mixing coefficient ϵ . A discussion of the theory of kinetic mixing and its impact on electroweak symmetry breaking and on the electroweak precision variables can be found in Ref. [9]. Constraints have been placed on visible Z_D decays in direct searches by beam dump [10], fixed-target [11], rare meson decay [12], and collider [13–16] experiments.

The central feature of the CMS apparatus is a superconducting solenoid of 6 m internal diameter, providing a magnetic field of 3.8 T. Within the solenoid volume are a silicon pixel and strip tracker, a lead tungstate crystal electromagnetic calorimeter, and a brass and scintillator hadron calorimeter, each composed of a barrel and two end cap sections. Forward calorimeters extend the pseudorapidity (η) coverage provided by the barrel and end cap detectors. Muons are detected in gas-ionization chambers embedded in the steel flux-return yoke outside the solenoid. A detailed description of the CMS detector, together with a definition of the coordinate system used and the relevant kinematic variables, can be found in Ref. [17].

Events of interest are selected using a two-tiered trigger system [18]. The first level (L1), composed of custom hardware processors, uses information from the calorimeters and muon detectors to select events at a rate of around 100 kHz within a time interval of 4 μ s. The second level, known as the high-level trigger (HLT), consists of a farm of processors running a version of the full event reconstruction software optimized for fast processing. A set of triggers in the HLT system reduces the event rate to around 1 kHz, allowing data containing all the information necessary for complete event reconstruction, ~ 1 MB/event, to be transferred to storage. These triggers are termed “standard triggers” in this Letter. The standard dimuon triggers have transverse momentum (p_T) requirements of 12–15 GeV on the highest p_T muon, and 5–7 GeV on the second-highest p_T muon reconstructed at L1. Requirements of $p_T > 17$ and 8 GeV are imposed at the HLT on the highest and second-highest p_T muons, respectively. The standard dimuon triggers collect data at a rate of around 30 Hz at the peak instantaneous luminosity of 2×10^{34} cm⁻² s⁻¹. These data are then fully reconstructed and used in the

*Full author list given at the end of the article.

Published by the American Physical Society under the terms of the [Creative Commons Attribution 4.0 International license](https://creativecommons.org/licenses/by/4.0/). Further distribution of this work must maintain attribution to the author(s) and the published article's title, journal citation, and DOI. Funded by SCOAP³.

search for dimuon resonance masses greater than 45 GeV. Dimuon events that do not pass the standard dimuon triggers, but are selected by certain single-muon triggers are also included. These required $p_T > 24$ GeV in the 2016 and 2018 data taking periods, and $p_T > 27$ GeV in 2017. The data collected during the years 2016–2018 correspond to an integrated luminosity of 137 fb^{-1} .

For dimuon resonance masses below ~ 40 GeV, the p_T thresholds in the standard dimuon triggers significantly reduce the signal acceptance, thereby adversely affecting the search sensitivity. Therefore, a dedicated set of triggers with significantly lower muon p_T thresholds were implemented. Events selected with these triggers contain a very limited amount of information about muons reconstructed at the HLT. This includes the muon four momenta, the number of hits left by each muon track in the tracking system, the normalized χ^2 of the muon track, and the isolation around the muon computed as the scalar sum of the p_T of all additional tracks in a $R = \sqrt{(\eta)^2 + (\phi)^2} = 0.3$ cone around the muon. The resulting event size is $\sim 4(8)$ kB for data taken in 2017 (2018). Consequently, these triggers can operate at significantly higher rates compared to the standard triggers. We refer to this approach as “data scouting” [19], and the high-rate triggers are termed “scouting triggers.”

The scouting triggers include an L1 trigger requiring two muons with opposite charge and $p_T > 4(4.5)$ GeV for data collected in 2017 (2018). An additional requirement of

$R < 1.2$ is imposed on the two muons to reduce the trigger rate. Furthermore, an L1 trigger requiring a pair of oppositely charged muons with $p_T > 4.5$ GeV and $|\eta| < 2.0$, forming an invariant mass between 7 and 18 GeV, is added. These two L1 triggers collect most of the events of interest in the dimuon mass range below ~ 20 GeV. Events passing the standard L1 dimuon triggers are also included, and collect a large fraction of events in the dimuon mass range above ~ 20 GeV. The two muons are required to have $p_T > 3$ GeV at the HLT. Lower muon thresholds are used for the HLT to maximize efficiency for events accepted by the L1 Trigger. The scouting dimuon triggers were fully commissioned for 2017 and recorded events at a rate of ~ 2 kHz at the peak instantaneous luminosity of $2 \times 10^{34} \text{ cm}^{-2} \text{ s}^{-1}$. Data corresponding to an integrated luminosity of 96.6 fb^{-1} were collected with these triggers in 2017 and 2018.

The Z_D signal is simulated at leading order (LO) using the hidden Abelian Higgs model (HAHM v3) [9,20] implemented with the MadGraph5_aMC@NLO2.2.2 (2.4.2) generator [21] for the 2016 (2017, 2018) data period. The width and cross section of the signal process are directly proportional to e^2 . The analysis does not rely on simulation for background estimation. However, simulations of certain SM processes are used to evaluate data-to-simulation corrections and corresponding uncertainties in the signal prediction. The process involving the production of the

$\Upsilon(1S)$ resonance and its decay to a pair of muons is simulated at LO with PYTHIA8.230 [22]. The Drell-Yan (DY) background is simulated at LO and next-to-LO (NLO) using MadGraph5_aMC@NLO, with up to four and two additional partons in the matrix element calculations, respectively.

Events simulated at the matrix element level for the signal and background processes are then interfaced with PYTHIA in order to simulate the fragmentation, parton shower, and hadronization of partons in the initial and final states, along with the underlying event. This is done using the CUETP8M1 (CP5) tune [23,24] in the simulation for the 2016 (2017, 2018) data period. Jets from LO (NLO) simulations obtained with MadGraph5_aMC@NLO are matched to the parton shower produced by PYTHIA following the MLM [25] (FxFx [26]) prescription. The 2016 (2017, 2018) era simulations use the NNPDF 3.0 (3.1) parton distribution functions (PDFs) [27,28]. The interactions of all final-state particles with the CMS detector are simulated using GEANT4 [29]. Simulated events include the contribution of particles from additional pp interactions within the same or nearby bunch crossings (pileup), with the multiplicity of reconstructed primary vertices adjusted to match that in data.

Events selected with the standard muon triggers are reconstructed using a particle-flow (PF) algorithm [30] that aims to reconstruct and identify individual particles in an event, with an optimized combination of information from the various elements of the CMS detector. Muons are reconstructed by associating a track reconstructed in the tracking detectors with a track in the muon system. The muon momentum is obtained from the curvature of the corresponding track. The candidate vertex with the largest value of summed physics-object p_T^2 is taken to be the primary pp interaction vertex (PV). The physics objects in this case are the jets, clustered using the jet finding algorithm [31,32] with a distance parameter of 0.4, with the tracks assigned to the candidate vertices as inputs, and the associated missing transverse momentum, taken as the negative vector sum of the p_T of those jets. Jets arising from b quark hadronization and decay (b jets) are identified using a deep neural network algorithm termed “deepCSV,” which takes as input tracks that are displaced from the PV, secondary vertices, and jet kinematic variables [33]. A working point on the output of the deepCSV algorithm is chosen such that the efficiency of identifying a b jet is ~ 65 – 75% and the probability of misidentifying a light-flavor jet as a b jet is about 1%.

In the search performed using the standard triggers, events are required to contain at least one well-reconstructed PV and two oppositely charged muons that are geometrically matched to the HLT muon candidates within a cone of $R = 0.1$. The highest and second-highest p_T muons are required to have $p_T > 20$ and 10 GeV, respectively, and $|\eta| < 1.9$. The restriction on η is imposed

to ensure optimal dimuon mass resolution without incurring a significant loss in acceptance. In events selected with the single-muon triggers, the muon p_T threshold is set to 26 (29) GeV for data collected in 2016 (2017, 2018). The muons are required to pass certain selection requirements based on the quality of their reconstructed tracks. The absolute values of the transverse and longitudinal impact parameters of the muon tracks are required to be less than 0.2 and 0.5 cm, respectively. The muon isolation, computed as the scalar sum of the p_T of PF candidates (photons, charged hadrons, neutral hadrons) within a cone $R = 0.4$ around the direction of the muon momentum, is required to be less than 15% of the muon p_T . Charged PF hadrons not associated with the PV are ignored in this sum. The contribution of neutral particles from pileup, estimated to be one half of the scalar sum of the p_T of charged PF hadrons from pileup in the cone, is subtracted from this sum. Events containing one or more b jets with $p_T > 30$ GeV and $|\eta| < 2.4$ are rejected to suppress most of the background from single and pair-produced top quarks.

In the search performed using the scouting triggers, events are required to contain two muons of opposite charge, with $p_T > 4$ GeV and $|\eta| < 1.9$, that are consistent with originating from the same vertex. The muons are required to pass selection requirements based on the track quality information available in the event. The muon isolation is required to be less than 15% of the muon p_T . In order to suppress the background involving muons from heavy flavor decays that typically have low p_T , the (second-) highest p_T muon is required to have $p_T > m_{\mu\mu}/(4) \cdot 3$, where $m_{\mu\mu}$ is the dimuon invariant mass.

Figure 1 shows the $m_{\mu\mu}$ distributions obtained with data collected using the standard and scouting triggers. The $m_{\mu\mu}$ distribution of fully reconstructed events collected using the standard triggers suffers from a significant acceptance loss resulting in the structure visible for $m_{\mu\mu} \lesssim 40$ GeV. The loss of acceptance is due to the p_T thresholds of 20 and 10 GeV on the two muons. The $m_{\mu\mu}$ distribution of events collected using the scouting triggers, however, continues to rise steadily for masses lower than 40 GeV. For masses lower than 20 GeV, an even steeper rise is observed. This is the region where the L1 trigger with a requirement for $m_{\mu\mu}$ to be in the range 7–18 GeV contributes significantly.

The $m_{\mu\mu}$ resolution depends strongly on the $|\eta|$ of the two muons. The p_T resolution of muons with $p_T < 50$ GeV is $\sim 1\%$ in the central barrel region of the detector ($|\eta| < 0.9$), and $\sim 3\%$ in the end caps of the muon system ($|\eta| > 1.2$) [34]. Therefore, events are divided in two categories. The barrel category consists of events in which both muons have $|\eta| < 0.9$, and the forward category contains events in which at least one of the two muons has $0.9 < |\eta| < 1.9$.

The intrinsic width of the signal resonance considered in this search is assumed to be much narrower than the detector resolution. The signal line shape is modeled using a parametric shape called the double-sided crystal ball

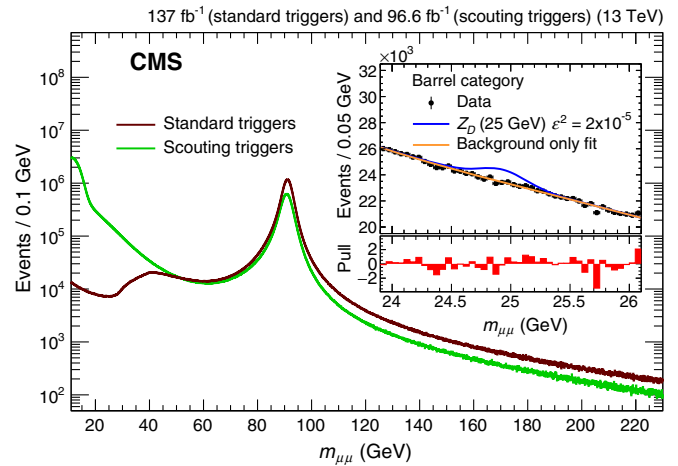


FIG. 1. The $m_{\mu\mu}$ distributions of events selected with the standard muon triggers (maroon, darker), and the scouting dimuon triggers (green, lighter). Events are required to pass all the selection requirements. The inset is restricted to events in the barrel category in the mass range 23.9–26.1 GeV. A function describing the background is fit to these data, and a 25 GeV Z_D signal corresponding to $\epsilon^2 = 2 \times 10^{-5}$ is added. The bottom panel of the inset shows the bin-by-bin difference between the number of events in data and the prediction from the background fit, divided by the statistical uncertainty.

(DCB) function [35]. The core of this function consists of a Gaussian distribution of mean s and standard deviation σ . The s and σ parameters represent the peak position and resolution of the resonance, and are allowed to vary using constrained nuisance parameters corresponding to the muon momentum scale and resolution uncertainties. The uncertainty in the $m_{\mu\mu}$ resolution is estimated to be 10% of σ . The uncertainty in the mass scale is 0.1% of the resonance mass in the search performed using data from standard triggers, while it varies in the range 0.06–0.1% for the search performed using data from the scouting triggers.

There are several experimental sources of systematic uncertainty in the estimation of the signal yield. The measured integrated luminosity has an uncertainty of 2.3 (2.5)% for data collected in 2017 (2016, 2018) [36–38]. In the search performed using the standard muon triggers, uncertainties of 0.2 and 1.5–3.0% are ascribed to the measurement of the trigger and muon selection efficiencies, respectively. The uncertainty in the inefficiency caused by the b jet rejection is 1%. In the search performed using scouting data, the uncertainty in the muon selection efficiency varies in the range 3–10%. The efficiency of the scouting triggers is measured with respect to fully reconstructed muons using events selected with independent standard triggers. The average uncertainty in the trigger efficiency is of order 5%, a value that takes into account a small uncertainty associated with the requirement that the muons be fully reconstructed, and a potential effect arising from background contamination.

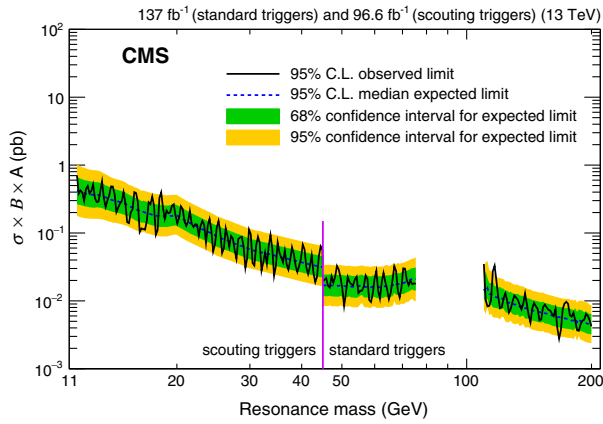


FIG. 2. Expected and observed upper limits at 95% C.L. on the product of the signal cross section (σ) for a narrow resonance, branching fraction to a pair of muons (B), and acceptance (A) as a function of the mass of a narrow resonance. Results obtained using the scouting (standard) triggers are to the left (right) of the vertical purple line.

In order to extract the signal from data, a simultaneous binned maximum likelihood fit is performed to the $m_{\mu\mu}$ distributions in the barrel and forward event categories. A parametric function is used to model the shape of the background. The parameters of this function and the background yield are allowed to float freely in the fit, and are uncorrelated between the two event categories. In the search using the standard triggers, the fit is performed in a range of $\pm 7\sigma$ around the probed resonance mass, where σ is the mass resolution parameter of the DCB function used to model the signal. The background, which is dominated by DY events, is modeled in both event categories using the product of a modified form of the Breit-Wigner function [39] and a second-order Bernstein polynomial. In the search using the scouting triggers, the fit is performed in a range of $\pm 5\sigma$ around the probed resonance mass. The background mass distribution is modeled using a fourth-order Bernstein polynomial. The chosen background functions, and the sizes of the mass windows maximize the expected sensitivity while introducing only a small bias in the measured signal yield. Figure 1 (inset) shows, as an example, the $m_{\mu\mu}$ distribution of events in the barrel category in the 23.9–26.1 GeV window that is used to search for a 25 GeV resonance. A fit performed to these data assuming no signal is also shown along with the expected signal contribution for a 25 GeV Z_D with $\epsilon^2 = 2 \times 10^{-5}$.

In order to assess the possible bias in the measurement of a signal due to the choice of the function used to model the background distribution, we consider several alternative functions to model the shape of the background. An alternative test function is fit to the data in each event category, and is then used to generate 2000 sets of pseudodata. A certain amount of signal is injected in each of the pseudodata sets. A signal-plus-background fit is

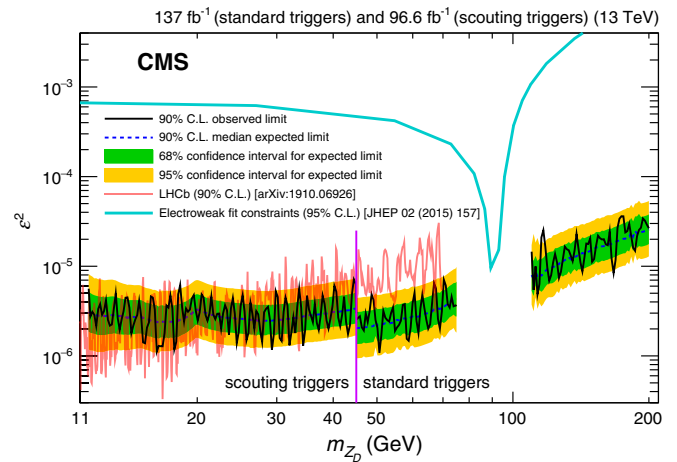


FIG. 3. Expected and observed upper limits at 90% C.L. on ϵ^2 , the square of the kinetic mixing coefficient, as a function of the Z_D mass. Results obtained using the scouting (standard) triggers are to the left (right) of the vertical purple line. Limits at 90% C.L. from the search performed by the LHCb Collaboration [16] are shown in red, and constraints at 95% C.L. from the measurements of the electroweak observables are shown in light blue [9].

performed using the chosen background function to each of the pseudodata sets with the signal yield allowed to float freely. The bias is quantified as the ratio of the difference between the measured and injected signals, and the statistical uncertainty in the measured signal yield. The bias is found to be less than 10% of the statistical uncertainty in the measured signal yield for resonance masses greater than 20 GeV, in both event categories. For masses below 20 GeV, the bias is estimated to be less than 20(30)% of the statistical uncertainty for the barrel (forward) category. In order to account for this uncertainty, we introduce an additional background in the fit. The shape of the background is taken to be the same as that of the signal, and its normalization is treated as a nuisance parameter with mean value zero, whose variations are constrained by a Gaussian distribution with standard deviation equal to the bias found in the tests.

The statistical analysis is performed using a profile likelihood ratio test statistic in which systematic uncertainties are modeled as constrained nuisance parameters. The nuisance parameters for the $m_{\mu\mu}$ scale and resolution uncertainties, and the bias due to the choice of the background fit function are modeled using the Gaussian probability density function. All other sources of systematic uncertainty affect the signal yield, and are modeled with nuisance parameters that are constrained using the log-normal probability density function.

The data are found to be consistent with the background expectation. Figure 2 shows the upper limits at 95% confidence level (C.L.) on the product of the signal cross section, branching fraction to a pair of muons, and the kinematic and geometrical acceptance for a narrow resonance using an asymptotic CL_s criterion [40–42].

The results of this search are interpreted in the context of a dark photon model. The signal is kinematically similar to the SM DY process. Therefore, an NLO K factor has been computed for the LO signal simulation by comparing the NLO and LO DY cross sections, and is found to be 1.09 over the entire mass range under consideration. Uncertainties due to the choice of the renormalization and factorization scales (4.5%), and the modeling of the PDFs (1%) are ascribed to the signal cross section. We set upper limits at 90% C.L. on ϵ^2 as a function of the Z_D mass, as shown in Fig. 3. These are compared with recent results from the LHCb Collaboration [16,43] and indirect constraints at 95% C.L. from measurements of the electroweak observables [9]. This search sets the most stringent limits to date in the $\sim 30\text{--}75$ and $110\text{--}200$ GeV mass ranges. Furthermore, limits from this search are competitive with those obtained in Ref. [16] at lower masses.

In summary, a search has been presented for a narrow resonance decaying to a pair of muons using proton-proton collision data recorded by the CMS experiment at $\sqrt{s} = 13$ TeV. The search in the $45\text{--}75$ and $110\text{--}200$ GeV resonance mass ranges uses fully reconstructed data containing a pair of muons with transverse momenta greater than 20 and 10 GeV, corresponding to an integrated luminosity of 137 fb^{-1} . The search in the resonance mass range of $11.5\text{--}45.0$ GeV is performed using data collected with high-rate dimuon triggers, corresponding to an integrated luminosity of 96.6 fb^{-1} . This is the first search that uses data with reduced trigger-level muon information, collected with dimuon triggers that have transverse momentum thresholds of 3 GeV. The data are found to be consistent with the background prediction. The search sets the lowest upper limits to date on the kinetic mixing coefficient of a dark photon in the $\sim 30\text{--}75$ and $110\text{--}200$ GeV mass ranges.

We congratulate our colleagues in the CERN accelerator departments for the excellent performance of the LHC and thank the technical and administrative staffs at CERN and at other CMS institutes for their contributions to the success of the CMS effort. In addition, we gratefully acknowledge the computing centers and personnel of the Worldwide LHC Computing Grid for delivering so effectively the computing infrastructure essential to our analyses. Finally, we acknowledge the enduring support for the construction and operation of the LHC and the CMS detector provided by the following funding agencies: BMBWF and FWF (Austria); FNRS and FWO (Belgium); CNPq, CAPES, FAPERJ, FAPERGS, and FAPESP (Brazil); MES (Bulgaria); CERN; CAS, MoST, and NSFC (China); COLCIENCIAS (Colombia); MSES and CSF (Croatia); RPF (Cyprus); SENESCYT (Ecuador); MoER, ERC IUT, PUT and ERDF (Estonia); Academy of Finland, MEC, and HIP (Finland); CEA and CNRS/IN2P3 (France); BMBF, DFG, and HGF (Germany); GSRT (Greece); NKFI

(Hungary); DAE and DST (India); IPM (Iran); SFI (Ireland); INFN (Italy); MSIP and NRF (Republic of Korea); MES (Latvia); LAS (Lithuania); MOE and UM (Malaysia); BUAP, CINVESTAV, CONACYT, LNS, SEP, and UASLP-FAI (Mexico); MOS (Montenegro); MBIE (New Zealand); PAEC (Pakistan); MSHE and NSC (Poland); FCT (Portugal); JINR (Dubna); MON, RosAtom, RAS, RFBR, and NRC KI (Russia); MESTD (Serbia); SEIDI, CPAN, PCTI, and FEDER (Spain); MOSTR (Sri Lanka); Swiss Funding Agencies (Switzerland); MST (Taipei); ThEPCenter, IPST, STAR, and NSTDA (Thailand); TUBITAK and TAEK (Turkey); NASU (Ukraine); STFC (United Kingdom); DOE and NSF (USA).

-
- [1] G. Bertone and J. Silk, *Particle Dark Matter: Observations, Models and Searches* (Cambridge University Press, Cambridge, England, 2010).
 - [2] J. L. Feng, Dark matter candidates from particle physics and methods of detection, *Annu. Rev. Astron. Astrophys.* **48**, 495 (2010).
 - [3] T. A. Porter, R. P. Johnson, and P. W. Graham, Dark matter searches with astroparticle data, *Annu. Rev. Astron. Astrophys.* **49**, 155 (2011).
 - [4] P. A. R. Ade *et al.* (Planck Collaboration), Planck 2015 results. XIII. Cosmological parameters, *Astron. Astrophys.* **594**, A13 (2016).
 - [5] R. Essig *et al.*, Dark sectors and new, light weakly-coupled particles, in *Planning the Future of U.S. Particle Physics: The Snowmass 2013 Proceedings*, edited by R. H. Bernstein *et al.* (Minneapolis, MN, USA, 2013).
 - [6] P. Galison and A. Manohar, Two Z 's or not two Z 's?, *Phys. Lett.* **136B**, 279 (1984).
 - [7] B. Holdom, Two $U(1)$'s and ϵ charge shifts, *Phys. Lett.* **166B**, 196 (1986).
 - [8] K. R. Dienes, C. F. Kolda, and J. March-Russell, Kinetic mixing and the supersymmetric gauge hierarchy, *Nucl. Phys.* **B492**, 104 (1997).
 - [9] D. Curtin, R. Essig, S. Gori, and J. Shelton, Illuminating dark photons with high-energy colliders, *J. High Energy Phys.* **02** (2015) 157.
 - [10] A. Konaka *et al.*, Search for Neutral Particles in Electron-Beam-Dump Experiment, *Phys. Rev. Lett.* **57**, 659 (1986).
 - [11] S. Abrahamyan *et al.* (APEX Collaboration), Search for a New Gauge Boson in Electron-Nucleus Fixed-Target Scattering by the APEX Experiment, *Phys. Rev. Lett.* **107**, 191804 (2011).
 - [12] R. M. Drees *et al.* (SINDRUM I Collaboration), Search for Weakly Interacting Neutral Bosons Produced in $\pi^- p$ Interactions at Rest and Decaying Into e^+e^- Pairs, *Phys. Rev. Lett.* **68**, 3845 (1992).
 - [13] J. P. Lees *et al.* (BABAR Collaboration), Search for a Dark Photon in e^+e^- Collisions at BABAR, *Phys. Rev. Lett.* **113**, 201801 (2014).
 - [14] P. Ilten, Y. Soreq, J. Thaler, M. Williams, and W. Xue, Proposed Inclusive Dark Photon Search at LHCb, *Phys. Rev. Lett.* **116**, 251803 (2016).

- [15] LHCb Collaboration, Search for Dark Photons Produced in 13 TeV pp Collisions, *Phys. Rev. Lett.* **120**, 061801 (2018).
- [16] LHCb Collaboration, Search for $A' \rightarrow \mu^+\mu^-$ Decays, *Phys. Rev. Lett.* **124**, 041801 (2020).
- [17] CMS Collaboration, The CMS experiment at the CERN LHC, *J. Instrum.* **3**, S08004 (2008).
- [18] CMS Collaboration, The CMS trigger system, *J. Instrum.* **12**, P01020 (2017).
- [19] CMS Collaboration, Search for Narrow Resonances in Dijet Final States at $\sqrt{s} = 8$ TeV With the Novel CMS Technique of Data Scouting, *Phys. Rev. Lett.* **117**, 031802 (2016).
- [20] S. Gopalakrishna, S. Jung, and J. D. Wells, Higgs boson decays to four fermions through an Abelian hidden sector, *Phys. Rev. D* **78**, 055002 (2008).
- [21] J. Alwall, R. Frederix, S. Frixione, V. Hirschi, F. Maltoni, O. Mattelaer, H. S. Shao, T. Stelzer, P. Torrielli, and M. Zaro, The automated computation of tree-level and next-to-leading order differential cross sections, and their matching to parton shower simulations, *J. High Energy Phys.* **07** (2014) 079.
- [22] T. Sjöstrand, S. Ask, J. R. Christiansen, R. Corke, N. Desai, P. Ilten, S. Mrenna, S. Prestel, C. O. Rasmussen, and P. Z. Skands, An introduction to PYTHIA8.2, *Comput. Phys. Commun.* **191**, 159 (2015).
- [23] CMS Collaboration, Event generator tunes obtained from underlying event and multiparton scattering measurements, *Eur. Phys. J. C* **76**, 155 (2016).
- [24] CMS Collaboration, Extraction and validation of a new set of CMS PYTHIA8 tunes from underlying-event measurements, *Eur. Phys. J. C* **80**, 4 (2020).
- [25] M. L. Mangano, M. Moretti, F. Piccinini, and M. Treccani, Matching matrix elements and shower evolution for top-pair production in hadronic collisions, *J. High Energy Phys.* **01** (2007) 013.
- [26] R. Frederix and S. Frixione, Merging meets matching in MC@NLO, *J. High Energy Phys.* **12** (2012) 061.
- [27] R. D. Ball *et al.* (NNPDF Collaboration), Parton distributions for the LHC Run II, *J. High Energy Phys.* **04** (2015) 040.
- [28] R. D. Ball *et al.* (NNPDF Collaboration), Parton distributions from high-precision collider data, *Eur. Phys. J. C* **77**, 663 (2017).
- [29] S. Agostinelli *et al.* (GEANT4 Collaboration), GEANT4—A simulation toolkit, *Nucl. Instrum. Methods Phys. Res., Sect. A* **506**, 250 (2003).
- [30] CMS Collaboration, Particle-flow reconstruction and global event description with the CMS detector, *J. Instrum.* **12**, P10003 (2017).
- [31] M. Cacciari, G. P. Salam, and G. Soyez, The anti- k_T jet clustering algorithm, *J. High Energy Phys.* **04** (2008) 063.
- [32] M. Cacciari, G. P. Salam, and G. Soyez, FastJet user manual, *Eur. Phys. J. C* **72**, 1896 (2012).
- [33] CMS Collaboration, Identification of heavy-flavour jets with the CMS detector in pp collisions at 13 TeV, *J. Instrum.* **13**, P05011 (2018).
- [34] CMS Collaboration, Performance of the CMS muon detector and muon reconstruction with proton-proton collisions at $\sqrt{s} = 13$ TeV, *J. Instrum.* **13**, P06015 (2018).
- [35] J. E. Gaiser, Charmonium spectroscopy from radiative decays of the J/ψ and ψ' , Ph.D. thesis, Stanford University, 1982, SLAC Report No. SLAC-R-255, <https://www-public.slac.stanford.edu/sciDoc/docMeta.aspx?slacPubNumber=slac-r-255>.
- [36] CMS Collaboration, CMS luminosity measurements for the 2016 data taking period, Technical Report No. CMS-PAS-LUM-17-001, CERN, Geneva, 2017, <https://cds.cern.ch/record/2257069>.
- [37] CMS Collaboration, CMS luminosity measurement for the 2017 data-taking period at $\sqrt{s} = 13$ TeV, Technical Report No. CMS-PAS-LUM-17-004, CERN, Geneva, 2018, <https://cds.cern.ch/record/2621960>.
- [38] CMS Collaboration, CMS luminosity measurement for the 2018 data-taking period at $\sqrt{s} = 13$ TeV, Technical Report No. CMS-PAS-LUM-18-002, CERN, Geneva, 2019, <https://cds.cern.ch/record/2676164>.
- [39] CMS Collaboration, Search for the Higgs Boson Decaying to Two Muons in Proton-Proton Collisions at $\sqrt{s} = 13$ TeV, *Phys. Rev. Lett.* **122**, 021801 (2019).
- [40] A. L. Read, Presentation of search results: The CL_s technique, *J. Phys. G* **28**, 2693 (2002).
- [41] T. Junk, Confidence level computation for combining searches with small statistics, *Nucl. Instrum. Methods Phys. Res., Sect. A* **434**, 435 (1999).
- [42] G. Cowan, K. Cranmer, E. Gross, and O. Vitells, Asymptotic formulae for likelihood-based tests of new physics, *Eur. Phys. J. C* **71**, 1554 (2011).
- [43] P. Ilten, Y. Soreq, M. Williams, and W. Xue, Serendipity in dark photon searches, *J. High Energy Phys.* **06** (2018) 004.

A. M. Sirunyan,^{1,a} A. Tumasyan,¹ W. Adam,² F. Ambrogio,² T. Bergauer,² M. Dragicevic,² J. Erö,² A. Escalante Del Valle,² M. Flechl,² R. Frühwirth,^{2,b} M. Jeitler,^{2,b} N. Krammer,² I. Krätschmer,² D. Liko,² T. Madlener,² I. Mikulec,² N. Rad,² J. Schieck,^{2,b} R. Schöfbeck,² M. Spanring,² D. Spitzbart,² W. Waltenberger,² C.-E. Wulz,^{2,b} M. Zarucki,² V. Drugakov,³ V. Mossolov,³ J. Suarez Gonzalez,³ M. R. Darwish,⁴ E. A. De Wolf,⁴ D. Di Croce,⁴ X. Janssen,⁴ A. Lelek,⁴ M. Pieters,⁴ H. Rejeb Sfar,⁴ H. Van Haevermaet,⁴ P. Van Mechelen,⁴ S. Van Putte,⁴ N. Van Remortel,⁴ F. Blekman,⁵ E. S. Bols,⁵ S. S. Chhibra,⁵ J. D'Hondt,⁵ J. De Clercq,⁵ D. Lontkovskiy,⁵ S. Lowette,⁵ I. Marchesini,⁵ S. Moortgat,⁵ Q. Python,⁵ K. Skovpen,⁵ S. Tavernier,⁵ W. Van Doninck,⁵ P. Van Mulders,⁵ D. Beghin,⁶ B. Bilin,⁶ B. Clerbaux,⁶ G. De Lentdecker,⁶ H. Delannoy,⁶ B. Dorney,⁶ L. Favart,⁶ A. Grebenyuk,⁶ A. K. Kalsi,⁶ A. Popov,⁶ N. Postiau,⁶ E. Starling,⁶ L. Thomas,⁶ C. Vander Velde,⁶ P. Vanlaer,⁶ D. Vannerom,⁶ T. Cornelis,⁷ D. Dobur,⁷ I. Khvastunov,^{7,c} M. Niedziela,⁷ C. Roskas,⁷

M. Tytgat,⁷ W. Verbeke,⁷ B. Vermassen,⁷ M. Vit,⁷ O. Bondu,⁸ G. Bruno,⁸ C. Caputo,⁸ P. David,⁸ C. Delaere,⁸ M. Delcourt,⁸ A. Giammanco,⁸ V. Lemaître,⁸ J. Prisciandaro,⁸ A. Saggio,⁸ M. Vidal Marono,⁸ P. Vischia,⁸ J. Zobec,⁸ F. L. Alves,⁹ G. A. Alves,⁹ G. Correia Silva,⁹ C. Hensel,⁹ A. Moraes,⁹ P. Rebello Teles,⁹ E. Belchior Batista Das Chagas,¹⁰ W. Carvalho,¹⁰ J. Chinellato,^{10,d} E. Coelho,¹⁰ E. M. Da Costa,¹⁰ G. G. Da Silveira,^{10,e} D. De Jesus Damiao,¹⁰ C. De Oliveira Martins,¹⁰ S. Fonseca De Souza,¹⁰ L. M. Huertas Guativa,¹⁰ H. Malbouisson,¹⁰ J. Martins,^{10,f} D. Matos Figueiredo,¹⁰ M. Medina Jaime,^{10,g} M. Melo De Almeida,¹⁰ C. Mora Herrera,¹⁰ L. Mundim,¹⁰ H. Nogima,¹⁰ W. L. Prado Da Silva,¹⁰ L. J. Sanchez Rosas,¹⁰ A. Santoro,¹⁰ A. Sznajder,¹⁰ M. Thiel,¹⁰ E. J. Tonelli Manganote,^{10,d} F. Torres Da Silva De Araujo,¹⁰ A. Vilela Pereira,¹⁰ C. A. Bernardes,^{11a} L. Calligaris,^{11a} T. R. Fernandez Perez Tomei,^{11a} E. M. Gregores,^{11a,11b} D. S. Lemos,^{11a} P. G. Mercadante,^{11a,11b} S. F. Novaes,^{11a} Sandra S. Padula,^{11a} A. Aleksandrov,¹² G. Antchev,¹² R. Hadjiiska,¹² P. Iaydjiev,¹² M. Misheva,¹² M. Rodozov,¹² M. Shopova,¹² G. Sultanov,¹² M. Bonchev,¹³ A. Dimitrov,¹³ T. Ivanov,¹³ L. Litov,¹³ B. Pavlov,¹³ P. Petkov,¹³ W. Fang,^{14,h} X. Gao,^{14,h} L. Yuan,¹⁴ M. Ahmad,¹⁵ Z. Hu,¹⁵ Y. Wang,¹⁵ G. M. Chen,¹⁶ H. S. Chen,¹⁶ M. Chen,¹⁶ C. H. Jiang,¹⁶ D. Leggat,¹⁶ H. Liao,¹⁶ Z. Liu,¹⁶ A. Spiezia,¹⁶ J. Tao,¹⁶ E. Yazgan,¹⁶ H. Zhang,¹⁶ S. Zhang,^{16,i} J. Zhao,¹⁶ A. Agapitos,¹⁷ Y. Ban,¹⁷ G. Chen,¹⁷ A. Levin,¹⁷ J. Li,¹⁷ L. Li,¹⁷ Q. Li,¹⁷ Y. Mao,¹⁷ S. J. Qian,¹⁷ D. Wang,¹⁷ Q. Wang,¹⁷ M. Xiao,¹⁸ C. Avila,¹⁹ A. Cabrera,¹⁹ C. Florez,¹⁹ C. F. González Hernández,¹⁹ M. A. Segura Delgado,¹⁹ J. Mejia Guisao,²⁰ J. D. Ruiz Alvarez,²⁰ C. A. Salazar González,²⁰ N. Vanegas Arbelaez,²⁰ D. Giljanović,²¹ N. Godinovic,²¹ D. Lelas,²¹ I. Puljak,²¹ T. Sculac,²¹ Z. Antunovic,²² M. Kovac,²² V. Brigljevic,²³ D. Ferencek,²³ K. Kadija,²³ B. Mesic,²³ M. Roguljic,²³ A. Starodumov,^{23,j} T. Susa,²³ M. W. Ather,²⁴ A. Attikis,²⁴ E. Erodotou,²⁴ A. Ioannou,²⁴ M. Kolosova,²⁴ S. Konstantinou,²⁴ G. Mavromanolakis,²⁴ J. Mousa,²⁴ C. Nicolaou,²⁴ F. Ptochos,²⁴ P. A. Razis,²⁴ H. Rykaczewski,²⁴ D. Tsiakkouri,²⁴ M. Finger,^{25,k} M. Finger Jr.,^{25,k} A. Kveton,²⁵ J. Tomsa,²⁵ E. Ayala,²⁶ E. Carrera Jarrin,²⁷ Y. Assran,^{28,l,m} S. Elgammal,^{28,l} S. Bhowmik,²⁹ A. Carvalho Antunes De Oliveira,²⁹ R. K. Dewanjee,²⁹ K. Ehattaht,²⁹ M. Kadastik,²⁹ M. Raidal,²⁹ C. Veelken,²⁹ P. Eerola,³⁰ L. Forthomme,³⁰ H. Kirschenmann,³⁰ K. Osterberg,³⁰ M. Voutilainen,³⁰ F. Garcia,³¹ J. Havukainen,³¹ J. K. Heikkilä,³¹ V. Karimäki,³¹ M. S. Kim,³¹ R. Kinnunen,³¹ T. Lampén,³¹ K. Lassila-Perini,³¹ S. Laurila,³¹ S. Lehti,³¹ T. Lindén,³¹ P. Luukka,³¹ T. Mäenpää,³¹ H. Siikonen,³¹ E. Tuominen,³¹ J. Tuominiemi,³¹ T. Tuuva,³² M. Besancon,³³ F. Couderc,³³ M. Dejardin,³³ D. Denegri,³³ B. Fabbro,³³ J. L. Faure,³³ F. Ferri,³³ S. Ganjour,³³ A. Givernaud,³³ P. Gras,³³ G. Hamel de Monchenault,³³ P. Jarry,³³ C. Leloup,³³ B. Lenzi,³³ E. Locci,³³ J. Malcles,³³ J. Rander,³³ A. Rosowsky,³³ M. Ö. Sahin,³³ A. Savoy-Navarro,^{33,n} M. Titov,³³ G. B. Yu,³³ S. Ahuja,³⁴ C. Amendola,³⁴ F. Beaudette,³⁴ P. Busson,³⁴ C. Charlot,³⁴ B. Diab,³⁴ G. Falmagne,³⁴ R. Granier de Cassagnac,³⁴ I. Kucher,³⁴ A. Lobanov,³⁴ C. Martin Perez,³⁴ M. Nguyen,³⁴ C. Ochando,³⁴ P. Paganini,³⁴ J. Rembser,³⁴ R. Salerno,³⁴ J. B. Sauvan,³⁴ Y. Sirois,³⁴ A. Zabi,³⁴ A. Zghiche,³⁴ J.-L. Agram,^{35,o} J. Andrea,³⁵ D. Bloch,³⁵ G. Bourgatte,³⁵ J.-M. Brom,³⁵ E. C. Chabert,³⁵ C. Collard,³⁵ E. Conte,^{35,o} J.-C. Fontaine,^{35,o} D. Gelé,³⁵ U. Goerlach,³⁵ M. Jansová,³⁵ A.-C. Le Bihan,³⁵ N. Tonon,³⁵ P. Van Hove,³⁵ S. Gadrat,³⁶ S. Beauceron,³⁷ C. Bernet,³⁷ G. Boudoul,³⁷ C. Camen,³⁷ A. Carle,³⁷ N. Chanon,³⁷ R. Chierici,³⁷ D. Contardo,³⁷ P. Depasse,³⁷ H. El Mamouni,³⁷ J. Fay,³⁷ S. Gascon,³⁷ M. Gouzevitch,³⁷ B. Ille,³⁷ Sa. Jain,³⁷ F. Lagarde,³⁷ I. B. Laktineh,³⁷ H. Lattaud,³⁷ A. Lesauvage,³⁷ M. Lethuillier,³⁷ L. Mirabito,³⁷ S. Perries,³⁷ V. Sordini,³⁷ L. Torterotot,³⁷ G. Touquet,³⁷ M. Vander Donckt,³⁷ S. Viret,³⁷ A. Khvedelidze,^{38,k} Z. Tsamalaidze,^{39,k} C. Autermann,⁴⁰ L. Feld,⁴⁰ K. Klein,⁴⁰ M. Lipinski,⁴⁰ D. Meuser,⁴⁰ A. Pauls,⁴⁰ M. Preuten,⁴⁰ M. P. Rauch,⁴⁰ J. Schulz,⁴⁰ M. Teroerde,⁴⁰ B. Wittmer,⁴⁰ M. Erdmann,⁴¹ B. Fischer,⁴¹ S. Ghosh,⁴¹ T. Hebbeker,⁴¹ K. Hoepfner,⁴¹ H. Keller,⁴¹ L. Mastrolorenzo,⁴¹ M. Merschmeyer,⁴¹ A. Meyer,⁴¹ P. Millet,⁴¹ G. Mocellin,⁴¹ S. Mondal,⁴¹ S. Mukherjee,⁴¹ D. Noll,⁴¹ A. Novak,⁴¹ T. Pook,⁴¹ A. Pozdnyakov,⁴¹ T. Quast,⁴¹ M. Radziej,⁴¹ Y. Rath,⁴¹ H. Reithler,⁴¹ J. Roemer,⁴¹ A. Schmidt,⁴¹ S. C. Schuler,⁴¹ A. Sharma,⁴¹ S. Wiedenbeck,⁴¹ S. Zaleski,⁴¹ G. Flügge,⁴² W. Haj Ahmad,^{42,p} O. Hlushchenko,⁴² T. Kress,⁴² T. Müller,⁴² A. Nowack,⁴² C. Pistone,⁴² O. Pooth,⁴² D. Roy,⁴² H. Sert,⁴² A. Stahl,^{42,q} M. Aldaya Martin,⁴³ P. Asmuss,⁴³ I. Babounikau,⁴³ H. Bakhshiansohi,⁴³ K. Beernaert,⁴³ O. Behnke,⁴³ A. Bermúdez Martínez,⁴³ D. Bertsche,⁴³ A. A. Bin Anuar,⁴³ K. Borras,^{43,r} V. Botta,⁴³ A. Campbell,⁴³ A. Cardini,⁴³ P. Connor,⁴³ S. Consuegra Rodríguez,⁴³ C. Contreras-Campana,⁴³ V. Danilov,⁴³ A. De Wit,⁴³ M. M. Defranchis,⁴³ C. Diez Pardos,⁴³ D. Domínguez Damiani,⁴³ G. Eckerlin,⁴³ D. Eckstein,⁴³ T. Eichhorn,⁴³ A. Elwood,⁴³ E. Eren,⁴³ E. Gallo,^{43,s} A. Geiser,⁴³ A. Grohsjean,⁴³ M. Guthoff,⁴³ M. Haranko,⁴³ A. Harb,⁴³ A. Jafari,⁴³ N. Z. Jomhari,⁴³ H. Jung,⁴³ A. Kasem,^{43,r} M. Kasemann,⁴³ H. Kaveh,⁴³ J. Keaveney,⁴³ C. Kleinwort,⁴³ J. Knolle,⁴³ D. Krücker,⁴³ W. Lange,⁴³ T. Lenz,⁴³ J. Lidrych,⁴³ K. Lipka,⁴³ W. Lohmann,^{43,t} R. Mankel,⁴³ I.-A. Melzer-Pellmann,⁴³ A. B. Meyer,⁴³ M. Meyer,⁴³ M. Missiroli,⁴³ J. Mnich,⁴³ A. Mussgiller,⁴³ V. Myronenko,⁴³ D. Pérez Adán,⁴³ S. K. Pflitsch,⁴³ D. Pitzl,⁴³ A. Raspereza,⁴³ A. Saibel,⁴³ M. Savitskiy,⁴³ V. Scheurer,⁴³ P. Schütze,⁴³ C. Schwanenberger,⁴³ R. Shevchenko,⁴³ A. Singh,⁴³ H. Tholen,⁴³ O. Turkot,⁴³

A. Vagnerini,⁴³ M. Van De Klundert,⁴³ R. Walsh,⁴³ Y. Wen,⁴³ K. Wichmann,⁴³ C. Wissing,⁴³ O. Zenaiev,⁴³ R. Zlebick,⁴³
R. Aggleton,⁴⁴ S. Bein,⁴⁴ L. Benato,⁴⁴ A. Benecke,⁴⁴ V. Blobel,⁴⁴ T. Dreyer,⁴⁴ A. Ebrahimi,⁴⁴ F. Feindt,⁴⁴ A. Fröhlich,⁴⁴
C. Garbers,⁴⁴ E. Garutti,⁴⁴ D. Gonzalez,⁴⁴ P. Gunnellini,⁴⁴ J. Haller,⁴⁴ A. Hinzmann,⁴⁴ A. Karavdina,⁴⁴ G. Kasieczka,⁴⁴
R. Klanner,⁴⁴ R. Kogler,⁴⁴ N. Kovalchuk,⁴⁴ S. Kurz,⁴⁴ V. Kutzner,⁴⁴ J. Lange,⁴⁴ T. Lange,⁴⁴ A. Malara,⁴⁴ J. Multhaupt,⁴⁴
C. E. N. Niemeyer,⁴⁴ A. Perieanu,⁴⁴ A. Reimers,⁴⁴ O. Rieger,⁴⁴ C. Scharf,⁴⁴ P. Schlexer,⁴⁴ S. Schumann,⁴⁴ J. Schwandt,⁴⁴
J. Sonneveld,⁴⁴ H. Stadie,⁴⁴ G. Steinbrück,⁴⁴ F. M. Stober,⁴⁴ B. Vormwald,⁴⁴ I. Zoi,⁴⁴ M. Akbiyik,⁴⁵ C. Barth,⁴⁵
M. Baselga,⁴⁵ S. Baur,⁴⁵ T. Berger,⁴⁵ E. Butz,⁴⁵ R. Caspart,⁴⁵ T. Chwalek,⁴⁵ W. De Boer,⁴⁵ A. Dierlamm,⁴⁵ K. El Morabit,⁴⁵
N. Faltermann,⁴⁵ M. Giffels,⁴⁵ P. Goldenzweig,⁴⁵ A. Gottmann,⁴⁵ M. A. Harrendorf,⁴⁵ F. Hartmann,^{45,q} U. Husemann,⁴⁵
S. Kudella,⁴⁵ S. Mitra,⁴⁵ M. U. Mozer,⁴⁵ D. Müller,⁴⁵ Th. Müller,⁴⁵ M. Musich,⁴⁵ A. Nürnberg,⁴⁵ G. Quast,⁴⁵ K. Rabbertz,⁴⁵
M. Schröder,⁴⁵ I. Shvetsov,⁴⁵ H. J. Simonis,⁴⁵ R. Ulrich,⁴⁵ M. Wassmer,⁴⁵ M. Weber,⁴⁵ C. Wöhrmann,⁴⁵ R. Wolf,⁴⁵
G. Anagnostou,⁴⁶ P. Asenov,⁴⁶ G. Daskalakis,⁴⁶ T. Geralis,⁴⁶ A. Kyriakis,⁴⁶ D. Loukas,⁴⁶ G. Paspalaki,⁴⁶
M. Diamantopoulou,⁴⁷ G. Karathanasis,⁴⁷ P. Kontaxakis,⁴⁷ A. Manousakis-katsikakis,⁴⁷ A. Panagiotou,⁴⁷ I. Papavergou,⁴⁷
N. Saoulidou,⁴⁷ A. Stakia,⁴⁷ K. Theofilatos,⁴⁷ K. Vellidis,⁴⁷ E. Vourliotis,⁴⁷ G. Bakas,⁴⁸ K. Kousouris,⁴⁸
I. Papakrivopoulos,⁴⁸ G. Tsipolitis,⁴⁸ I. Evangelou,⁴⁹ C. Foudas,⁴⁹ P. Gianneios,⁴⁹ P. Katsoulis,⁴⁹ P. Kokkas,⁴⁹ S. Mallios,⁴⁹
K. Manitaras,⁴⁹ N. Manthos,⁴⁹ I. Papadopoulos,⁴⁹ J. Strogas,⁴⁹ F. A. Triantis,⁴⁹ D. Tsitsonis,⁴⁹ M. Bartók,^{50,u}
R. Chudasama,⁵⁰ M. Csanad,⁵⁰ P. Major,⁵⁰ K. Mandal,⁵⁰ A. Mehta,⁵⁰ M. I. Nagy,⁵⁰ G. Pasztor,⁵⁰ O. Surányi,⁵⁰ G. I. Veres,⁵⁰
G. Bencze,⁵¹ C. Hajdu,⁵¹ D. Horvath,^{51,v} F. Sikler,⁵¹ T. Á. Vámi,⁵¹ V. Veszpremi,⁵¹ G. Vesztergombi,^{51,a,w} N. Beni,⁵²
S. Czellar,⁵² J. Karancsi,^{52,u} J. Molnar,⁵² Z. Szillasi,⁵² P. Raics,⁵³ D. Teyssier,⁵³ Z. L. Trocsanyi,⁵³ B. Ujvari,⁵³ T. Csorgo,⁵⁴
W. J. Metzger,⁵⁴ F. Nemes,⁵⁴ T. Novak,⁵⁴ S. Choudhury,⁵⁵ J. R. Komaragiri,⁵⁵ P. C. Tiwari,⁵⁵ S. Bahinipati,^{56,x} C. Kar,⁵⁶
G. Kole,⁵⁶ P. Mal,⁵⁶ V. K. Muraleedharan Nair Bindhu,⁵⁶ A. Nayak,^{56,y} D. K. Sahoo,^{56,x} S. K. Swain,⁵⁶ S. Bansal,⁵⁷
S. B. Beri,⁵⁷ V. Bhatnagar,⁵⁷ S. Chauhan,⁵⁷ R. Chawla,⁵⁷ N. Dhingra,⁵⁷ R. Gupta,⁵⁷ A. Kaur,⁵⁷ M. Kaur,⁵⁷ S. Kaur,⁵⁷
P. Kumari,⁵⁷ M. Lohan,⁵⁷ M. Meena,⁵⁷ K. Sandeep,⁵⁷ S. Sharma,⁵⁷ J. B. Singh,⁵⁷ A. K. Viridi,⁵⁷ G. Walia,⁵⁷ A. Bhardwaj,⁵⁸
B. C. Choudhary,⁵⁸ R. B. Garg,⁵⁸ M. Gola,⁵⁸ S. Keshri,⁵⁸ Ashok Kumar,⁵⁸ M. Naimuddin,⁵⁸ P. Priyanka,⁵⁸ K. Ranjan,⁵⁸
Aashaq Shah,⁵⁸ R. Sharma,⁵⁸ R. Bhardwaj,^{59,z} M. Bharti,^{59,z} R. Bhattacharya,⁵⁹ S. Bhattacharya,⁵⁹ U. Bhawandeep,^{59,z}
D. Bhowmik,⁵⁹ S. Dutta,⁵⁹ S. Ghosh,⁵⁹ B. Gomber,^{59,aa} M. Maity,^{59,bb} K. Mondal,⁵⁹ S. Nandan,⁵⁹ A. Purohit,⁵⁹ P. K. Rout,⁵⁹
G. Saha,⁵⁹ S. Sarkar,⁵⁹ T. Sarkar,^{59,bb} M. Sharan,⁵⁹ B. Singh,^{59,z} S. Thakur,^{59,z} P. K. Behera,⁶⁰ P. Kalbhor,⁶⁰ A. Muhammad,⁶⁰
P. R. Pujahari,⁶⁰ A. Sharma,⁶⁰ A. K. Sikdar,⁶⁰ D. Dutta,⁶¹ V. Jha,⁶¹ V. Kumar,⁶¹ D. K. Mishra,⁶¹ P. K. Netrakanti,⁶¹
L. M. Pant,⁶¹ P. Shukla,⁶¹ T. Aziz,⁶² M. A. Bhat,⁶² S. Dugad,⁶² G. B. Mohanty,⁶² N. Sur,⁶² Ravindra Kumar Verma,⁶²
S. Banerjee,⁶³ S. Bhattacharya,⁶³ S. Chatterjee,⁶³ P. Das,⁶³ M. Guchait,⁶³ S. Karmakar,⁶³ S. Kumar,⁶³ G. Majumder,⁶³
K. Mazumdar,⁶³ N. Sahoo,⁶³ S. Sawant,⁶³ S. Dube,⁶⁴ B. Kansal,⁶⁴ A. Kapoor,⁶⁴ K. Kothekar,⁶⁴ S. Pandey,⁶⁴ A. Rane,⁶⁴
A. Rastogi,⁶⁴ S. Sharma,⁶⁴ S. Chenarani,^{65,cc} E. Eskandari Tadavani,⁶⁵ S. M. Etesami,^{65,cc} M. Khakzad,⁶⁵
M. Mohammadi Najafabadi,⁶⁵ M. Naseri,⁶⁵ F. Rezaei Hosseinabadi,⁶⁵ M. Felcini,⁶⁶ M. Grunewald,⁶⁶ M. Abbrescia,^{67a,67b}
R. Aly,^{67a,67b,dd} C. Calabria,^{67a,67b} A. Colaleo,^{67a} D. Creanza,^{67a,67c} L. Cristella,^{67a,67b} N. De Filippis,^{67a,67c} M. De Palma,^{67a,67b}
A. Di Florio,^{67a,67b} W. Elmetenawee,^{67a,67b} L. Fiore,^{67a} A. Gelmi,^{67a,67b} G. Iaselli,^{67a,67c} M. Ince,^{67a,67b} S. Lezki,^{67a,67b}
G. Maggi,^{67a,67c} M. Maggi,^{67a} J. A. Merlin,^{67a} G. Miniello,^{67a,67b} S. My,^{67a,67b} S. Nuzzo,^{67a,67b} A. Pompili,^{67a,67b}
G. Pugliese,^{67a,67c} R. Radogna,^{67a} A. Ranieri,^{67a} G. Selvaggi,^{67a,67b} L. Silvestris,^{67a} F. M. Simone,^{67a,67b} R. Venditti,^{67a}
P. Verwilligen,^{67a} G. Abbiendi,^{68a} C. Battilana,^{68a,68b} D. Bonacorsi,^{68a,68b} L. Borgonovi,^{68a,68b} S. Braibant-Giacomelli,^{68a,68b}
R. Campanini,^{68a,68b} P. Capiluppi,^{68a,68b} A. Castro,^{68a,68b} F. R. Cavallo,^{68a} C. Ciocca,^{68a} G. Codispoti,^{68a,68b} M. Cuffiani,^{68a,68b}
G. M. Dallavalle,^{68a} F. Fabbri,^{68a} A. Fanfani,^{68a,68b} E. Fontanesi,^{68a,68b} P. Giacomelli,^{68a} C. Grandi,^{68a} L. Guiducci,^{68a,68b}
F. Iemmi,^{68a,68b} S. Lo Meo,^{68a,ee} S. Marcellini,^{68a} G. Masetti,^{68a} F. L. Navarra,^{68a,68b} A. Perrotta,^{68a} F. Primavera,^{68a,68b}
A. M. Rossi,^{68a,68b} T. Rovelli,^{68a,68b} G. P. Siroli,^{68a,68b} N. Tosi,^{68a} S. Albergo,^{69a,69b,ff} S. Costa,^{69a,69b} A. Di Mattia,^{69a}
R. Potenza,^{69a,69b} A. Tricomi,^{69a,69b,ff} C. Tuve,^{69a,69b} G. Barbagli,^{70a} A. Cassese,^{70a} R. Ceccarelli,^{70a} V. Ciulli,^{70a,70b}
C. Civinini,^{70a} R. D'Alessandro,^{70a,70b} F. Fiori,^{70a,70b} E. Focardi,^{70a,70b} G. Latino,^{70a,70b} P. Lenzi,^{70a,70b} M. Meschini,^{70a}
S. Paoletti,^{70a} G. Sguazzoni,^{70a} L. Viliani,^{70a} L. Benussi,⁷¹ S. Bianco,⁷¹ D. Piccolo,⁷¹ M. Bozzo,^{72a,72b} F. Ferro,^{72a}
R. Mulargia,^{72a,72b} E. Robutti,^{72a} S. Tosi,^{72a,72b} A. Benaglia,^{73a} A. Beschi,^{73a,73b} F. Brivio,^{73a,73b} V. Ciriolo,^{73a,73b,q}
M. E. Dinardo,^{73a,73b} P. Dini,^{73a} S. Gennai,^{73a} A. Ghezzi,^{73a,73b} P. Govoni,^{73a,73b} L. Guzzi,^{73a,73b} M. Malberti,^{73a}
S. Malvezzi,^{73a} D. Menasce,^{73a} F. Monti,^{73a,73b} L. Moroni,^{73a} M. Paganoni,^{73a,73b} D. Pedrini,^{73a} S. Ragazzi,^{73a,73b}
T. Tabarelli de Fatis,^{73a,73b} D. Valsecchi,^{73a,73b} D. Zuolo,^{73a,73b} S. Buontempo,^{74a} N. Cavallo,^{74a,74c} A. De Iorio,^{74a,74b}
A. Di Crescenzo,^{74a,74b} F. Fabozzi,^{74a,74c} F. Fienga,^{74a} G. Galati,^{74a} A. O. M. Iorio,^{74a,74b} L. Lista,^{74a,74b} S. Meola,^{74a,74d,q}

P. Paolucci,^{74a,q} B. Rossi,^{74a} C. Sciacca,^{74a,74b} E. Voevodina,^{74a,74b} P. Azzi,^{75a} N. Bacchetta,^{75a} D. Bisello,^{75a,75b}
 A. Boletti,^{75a,75b} A. Bragagnolo,^{75a,75b} R. Carlin,^{75a,75b} P. Checchia,^{75a} P. De Castro Manzano,^{75a} T. Dorigo,^{75a} U. Dosselli,^{75a}
 F. Gasparini,^{75a,75b} U. Gasparini,^{75a,75b} A. Gozzelino,^{75a} S. Y. Hoh,^{75a,75b} P. Lujan,^{75a} M. Margoni,^{75a,75b}
 A. T. Meneguzzo,^{75a,75b} J. Pazzini,^{75a,75b} M. Presilla,^{75a,75b} P. Ronchese,^{75a,75b} R. Rossin,^{75a,75b} F. Simonetto,^{75a,75b} A. Tiko,^{75a}
 M. Tosi,^{75a,75b} M. Zanetti,^{75a,75b} P. Zotto,^{75a,75b} G. Zumerle,^{75a,75b} A. Braghieri,^{76a} D. Fiorina,^{76a,76b} P. Montagna,^{76a,76b}
 S. P. Ratti,^{76a,76b} V. Re,^{76a} M. Ressegotti,^{76a,76b} C. Riccardi,^{76a,76b} P. Salvini,^{76a} I. Vai,^{76a} P. Vitulo,^{76a,76b} M. Biasini,^{77a,77b}
 G. M. Bilei,^{77a} D. Ciangottini,^{77a,77b} L. Fanò,^{77a,77b} P. Lariccia,^{77a,77b} R. Leonardi,^{77a,77b} E. Manoni,^{77a} G. Mantovani,^{77a,77b}
 V. Mariani,^{77a,77b} M. Menichelli,^{77a} A. Rossi,^{77a,77b} A. Santocchia,^{77a,77b} D. Spiga,^{77a} K. Androsov,^{78a} P. Azzurri,^{78a}
 G. Bagliesi,^{78a} V. Bertacchi,^{78a,78c} L. Bianchini,^{78a} T. Boccali,^{78a} R. Castaldi,^{78a} M. A. Ciocci,^{78a,78b} R. Dell'Orso,^{78a}
 S. Donato,^{78a} G. Fedi,^{78a} L. Giannini,^{78a,78c} A. Giassi,^{78a} M. T. Grippo,^{78a} F. Ligabue,^{78a,78c} E. Manca,^{78a,78c}
 G. Mandorli,^{78a,78c} A. Messineo,^{78a,78b} F. Palla,^{78a} A. Rizzi,^{78a,78b} G. Rolandi,^{78a,gg} S. Roy Chowdhury,^{78a} A. Scribano,^{78a}
 P. Spagnolo,^{78a} R. Tenchini,^{78a} G. Tonelli,^{78a,78b} N. Turini,^{78a} A. Venturi,^{78a} P. G. Verdini,^{78a} F. Cavallari,^{79a}
 M. Cipriani,^{79a,79b} D. Del Re,^{79a,79b} E. Di Marco,^{79a} M. Diemoz,^{79a} E. Longo,^{79a,79b} P. Meridiani,^{79a} G. Organtini,^{79a,79b}
 F. Pandolfi,^{79a} R. Paramatti,^{79a,79b} C. Quaranta,^{79a,79b} S. Rahatlou,^{79a,79b} C. Rovelli,^{79a} F. Santanastasio,^{79a,79b} L. Soffi,^{79a,79b}
 N. Amapane,^{80a,80b} R. Arcidiacono,^{80a,80c} S. Argiro,^{80a,80b} M. Arneodo,^{80a,80c} N. Bartosik,^{80a} R. Bellan,^{80a,80b} A. Bellora,^{80a}
 C. Biino,^{80a} A. Cappati,^{80a,80b} N. Cartiglia,^{80a} S. Cometti,^{80a} M. Costa,^{80a,80b} R. Covarelli,^{80a,80b} N. Demaria,^{80a}
 B. Kiani,^{80a,80b} F. Legger,^{80a} C. Mariotti,^{80a} S. Maselli,^{80a} E. Migliore,^{80a,80b} V. Monaco,^{80a,80b} E. Monteil,^{80a,80b}
 M. Monteno,^{80a} M. M. Obertino,^{80a,80b} G. Ortona,^{80a,80b} L. Pacher,^{80a,80b} N. Pastrone,^{80a} M. Pelliccioni,^{80a}
 G. L. Pinna Angioni,^{80a,80b} A. Romero,^{80a,80b} M. Ruspa,^{80a,80c} R. Salvatico,^{80a,80b} V. Sola,^{80a} A. Solano,^{80a,80b} D. Soldi,^{80a,80b}
 A. Staiano,^{80a} D. Trocino,^{80a,80b} S. Belforte,^{81a} V. Candelise,^{81a,81b} M. Casarsa,^{81a} F. Cossutti,^{81a} A. Da Rold,^{81a,81b}
 G. Della Ricca,^{81a,81b} F. Vazzoler,^{81a,81b} A. Zanetti,^{81a} B. Kim,⁸² D. H. Kim,⁸² G. N. Kim,⁸² J. Lee,⁸² S. W. Lee,⁸²
 C. S. Moon,⁸² Y. D. Oh,⁸² S. I. Pak,⁸² S. Sekmen,⁸² D. C. Son,⁸² Y. C. Yang,⁸² H. Kim,⁸³ D. H. Moon,⁸³ G. Oh,⁸³
 B. Francois,⁸⁴ T. J. Kim,⁸⁴ J. Park,⁸⁴ S. Cho,⁸⁵ S. Choi,⁸⁵ Y. Go,⁸⁵ S. Ha,⁸⁵ B. Hong,⁸⁵ K. Lee,⁸⁵ K. S. Lee,⁸⁵ J. Lim,⁸⁵
 J. Park,⁸⁵ S. K. Park,⁸⁵ Y. Roh,⁸⁵ J. Yoo,⁸⁵ J. Goh,⁸⁶ H. S. Kim,⁸⁷ J. Almond,⁸⁸ J. H. Bhyun,⁸⁸ J. Choi,⁸⁸ S. Jeon,⁸⁸ J. Kim,⁸⁸
 J. S. Kim,⁸⁸ H. Lee,⁸⁸ K. Lee,⁸⁸ S. Lee,⁸⁸ K. Nam,⁸⁸ M. Oh,⁸⁸ S. B. Oh,⁸⁸ B. C. Radburn-Smith,⁸⁸ U. K. Yang,⁸⁸ H. D. Yoo,⁸⁸
 I. Yoon,⁸⁸ D. Jeon,⁸⁹ J. H. Kim,⁸⁹ J. S. H. Lee,⁸⁹ I. C. Park,⁸⁹ I. J. Watson,⁸⁹ Y. Choi,⁹⁰ C. Hwang,⁹⁰ Y. Jeong,⁹⁰ J. Lee,⁹⁰
 Y. Lee,⁹⁰ I. Yu,⁹⁰ V. Veckalns,^{91,hh} V. Dudenas,⁹² A. Juodagalvis,⁹² A. Rinkevicius,⁹² G. Tamulaitis,⁹² J. Vaitkus,⁹²
 Z. A. Ibrahim,⁹³ F. Mohamad Idris,^{93,ii} W. A. T. Wan Abdullah,⁹³ M. N. Yusli,⁹³ Z. Zolkapli,⁹³ J. F. Benitez,⁹⁴
 A. Castaneda Hernandez,⁹⁴ J. A. Murillo Quijada,⁹⁴ L. Valencia Palomo,⁹⁴ H. Castilla-Valdez,⁹⁵ E. De La Cruz-Burelo,⁹⁵
 I. Heredia-De La Cruz,^{95,ji} R. Lopez-Fernandez,⁹⁵ A. Sanchez-Hernandez,⁹⁵ S. Carrillo Moreno,⁹⁶ C. Oropeza Barrera,⁹⁶
 M. Ramirez-Garcia,⁹⁶ F. Vazquez Valencia,⁹⁶ J. Eysermans,⁹⁷ I. Pedraza,⁹⁷ H. A. Salazar Ibarquen,⁹⁷ C. Uribe Estrada,⁹⁷
 A. Morelos Pineda,⁹⁸ J. Mijuskovic,^{99,c} N. Raicevic,⁹⁹ D. Krofcheck,¹⁰⁰ S. Bheesette,¹⁰¹ P. H. Butler,¹⁰¹ A. Ahmad,¹⁰²
 M. Ahmad,¹⁰² Q. Hassan,¹⁰² H. R. Hoorani,¹⁰² W. A. Khan,¹⁰² M. A. Shah,¹⁰² M. Shoaib,¹⁰² M. Waqas,¹⁰² V. Avati,¹⁰³
 L. Grzanka,¹⁰³ M. Malawski,¹⁰³ H. Bialkowska,¹⁰⁴ M. Bluj,¹⁰⁴ B. Boimska,¹⁰⁴ M. Górski,¹⁰⁴ M. Kazana,¹⁰⁴ M. Szeleper,¹⁰⁴
 P. Zalewski,¹⁰⁴ K. Bunkowski,¹⁰⁵ A. Byszuk,^{105,kk} K. Doroba,¹⁰⁵ A. Kalinowski,¹⁰⁵ M. Konecki,¹⁰⁵ J. Krolikowski,¹⁰⁵
 M. Olszewski,¹⁰⁵ M. Walczak,¹⁰⁵ M. Araujo,¹⁰⁶ P. Bargassa,¹⁰⁶ D. Bastos,¹⁰⁶ A. Di Francesco,¹⁰⁶ P. Faccioli,¹⁰⁶
 B. Galinhas,¹⁰⁶ M. Gallinaro,¹⁰⁶ J. Hollar,¹⁰⁶ N. Leonardo,¹⁰⁶ T. Niknejad,¹⁰⁶ J. Seixas,¹⁰⁶ K. Shchelina,¹⁰⁶ G. Strong,¹⁰⁶
 O. Toldaiev,¹⁰⁶ J. Varela,¹⁰⁶ S. Afanasiev,¹⁰⁷ P. Bunin,¹⁰⁷ M. Gavrilenko,¹⁰⁷ I. Golutvin,¹⁰⁷ I. Gorbunov,¹⁰⁷ A. Kamenev,¹⁰⁷
 V. Karjavine,¹⁰⁷ A. Lanev,¹⁰⁷ A. Malakhov,¹⁰⁷ V. Matveev,^{107,ll,mmm} P. Moisezenz,¹⁰⁷ V. Palichik,¹⁰⁷ V. Perelygin,¹⁰⁷
 M. Savina,¹⁰⁷ S. Shmatov,¹⁰⁷ S. Shulha,¹⁰⁷ N. Skatchkov,¹⁰⁷ V. Smirnov,¹⁰⁷ N. Voytishin,¹⁰⁷ A. Zarubin,¹⁰⁷
 L. Chtchipounov,¹⁰⁸ V. Golovtsov,¹⁰⁸ Y. Ivanov,¹⁰⁸ V. Kim,^{108,nn} E. Kuznetsova,^{108,oo} P. Levchenko,¹⁰⁸ V. Murzin,¹⁰⁸
 V. Oreshkin,¹⁰⁸ I. Smirnov,¹⁰⁸ D. Sosnov,¹⁰⁸ V. Sulimov,¹⁰⁸ L. Uvarov,¹⁰⁸ A. Vorobyev,¹⁰⁸ Yu. Andreev,¹⁰⁹ A. Dermenev,¹⁰⁹
 S. Gninenko,¹⁰⁹ N. Golubev,¹⁰⁹ A. Karneyeu,¹⁰⁹ M. Kirsanov,¹⁰⁹ N. Krasnikov,¹⁰⁹ A. Pashenkov,¹⁰⁹ D. Tlisov,¹⁰⁹
 A. Toropin,¹⁰⁹ V. Epshteyn,¹¹⁰ V. Gavrilo,¹¹⁰ N. Lychkovskaya,¹¹⁰ A. Nikitenko,^{110,pp} V. Popov,¹¹⁰ I. Pozdnyakov,¹¹⁰
 G. Safronov,¹¹⁰ A. Spiridonov,¹¹⁰ A. Stepenov,¹¹⁰ M. Toms,¹¹⁰ E. Vlasov,¹¹⁰ A. Zhokin,¹¹⁰ T. Aushev,¹¹¹ O. Bychkova,¹¹²
 R. Chistov,^{112,qq} M. Danilov,^{112,qq} S. Polikarpov,^{112,qq} E. Tarkovskii,¹¹² V. Andreev,¹¹³ M. Azarkin,¹¹³ I. Dremin,¹¹³
 M. Kirakosyan,¹¹³ A. Terkulov,¹¹³ A. Baskakov,¹¹⁴ A. Belyaev,¹¹⁴ E. Boos,¹¹⁴ V. Bunichev,¹¹⁴ M. Dubinin,^{114,rr} L. Dudko,¹¹⁴
 A. Ershov,¹¹⁴ A. Gribushin,¹¹⁴ V. Klyukhin,¹¹⁴ I. Lokhtin,¹¹⁴ S. Obraztsov,¹¹⁴ S. Petrushanko,¹¹⁴ V. Savrin,¹¹⁴
 A. Barnyakov,^{115,ss} V. Blinov,^{115,ss} T. Dimova,^{115,ss} L. Kardapoltsev,^{115,ss} Y. Skovpen,^{115,ss} I. Azhgirey,¹¹⁶ I. Bayshev,¹¹⁶

S. Bitioukov,¹¹⁶ V. Kachanov,¹¹⁶ D. Konstantinov,¹¹⁶ P. Mandrik,¹¹⁶ V. Petrov,¹¹⁶ R. Ryutin,¹¹⁶ S. Slabospitskii,¹¹⁶
A. Sobol,¹¹⁶ S. Troshin,¹¹⁶ N. Tyurin,¹¹⁶ A. Uzunian,¹¹⁶ A. Volkov,¹¹⁶ A. Babaev,¹¹⁷ A. Iuzhakov,¹¹⁷ V. Okhotnikov,¹¹⁷
V. Borchsh,¹¹⁸ V. Ivanchenko,¹¹⁸ E. Tchernaiev,¹¹⁸ P. Adzic,^{119,tt} P. Cirkovic,¹¹⁹ M. Dordevic,¹¹⁹ P. Milenovic,¹¹⁹
J. Milosevic,¹¹⁹ M. Stojanovic,¹¹⁹ M. Aguilar-Benitez,¹²⁰ J. Alcaraz Maestre,¹²⁰ A. Álvarez Fernández,¹²⁰ I. Bachiller,¹²⁰
M. Barrio Luna,¹²⁰ Cristina F. Bedoya,¹²⁰ J. A. Brochero Cifuentes,¹²⁰ C. A. Carrillo Montoya,¹²⁰ M. Cepeda,¹²⁰
M. Cerrada,¹²⁰ N. Colino,¹²⁰ B. De La Cruz,¹²⁰ A. Delgado Peris,¹²⁰ J. P. Fernández Ramos,¹²⁰ J. Flix,¹²⁰ M. C. Fouz,¹²⁰
O. Gonzalez Lopez,¹²⁰ S. Goy Lopez,¹²⁰ J. M. Hernandez,¹²⁰ M. I. Josa,¹²⁰ D. Moran,¹²⁰ Á. Navarro Tobar,¹²⁰
A. Pérez-Calero Yzquierdo,¹²⁰ J. Puerta Pelayo,¹²⁰ I. Redondo,¹²⁰ L. Romero,¹²⁰ S. Sánchez Navas,¹²⁰ M. S. Soares,¹²⁰
A. Triossi,¹²⁰ C. Willmott,¹²⁰ C. Albajar,¹²¹ J. F. de Trocóniz,¹²¹ R. Reyes-Almanza,¹²¹ B. Alvarez Gonzalez,¹²² J. Cuevas,¹²²
C. Erice,¹²² J. Fernandez Menendez,¹²² S. Folgueras,¹²² I. Gonzalez Caballero,¹²² J. R. González Fernández,¹²²
E. Palencia Cortezon,¹²² V. Rodríguez Bouza,¹²² S. Sanchez Cruz,¹²² I. J. Cabrillo,¹²³ A. Calderon,¹²³ B. Chazin Quero,¹²³
J. Duarte Campderros,¹²³ M. Fernandez,¹²³ P. J. Fernández Manteca,¹²³ A. García Alonso,¹²³ G. Gomez,¹²³
C. Martinez Rivero,¹²³ P. Martinez Ruiz del Arbol,¹²³ F. Matorras,¹²³ J. Piedra Gomez,¹²³ C. Prieels,¹²³ T. Rodrigo,¹²³
A. Ruiz-Jimeno,¹²³ L. Russo,^{123,uu} L. Scodellaro,¹²³ I. Vila,¹²³ J. M. Vizan Garcia,¹²³ K. Malagalage,¹²⁴
W. G. D. Dharmaratna,¹²⁵ N. Wickramage,¹²⁵ D. Abbaneo,¹²⁶ B. Akgun,¹²⁶ E. Auffray,¹²⁶ G. Auzinger,¹²⁶ J. Baechler,¹²⁶
P. Baillon,¹²⁶ A. H. Ball,¹²⁶ D. Barney,¹²⁶ J. Bendavid,¹²⁶ M. Bianco,¹²⁶ A. Bocci,¹²⁶ P. Bortignon,¹²⁶ E. Bossini,¹²⁶
C. Botta,¹²⁶ E. Brondolin,¹²⁶ T. Camporesi,¹²⁶ A. Caratelli,¹²⁶ G. Cerminara,¹²⁶ E. Chapon,¹²⁶ G. Cucciati,¹²⁶
D. d'Enterria,¹²⁶ A. Dabrowski,¹²⁶ N. Daci,¹²⁶ V. Daponte,¹²⁶ A. David,¹²⁶ O. Davignon,¹²⁶ A. De Roeck,¹²⁶ M. Deile,¹²⁶
M. Dobson,¹²⁶ M. Dünser,¹²⁶ N. Dupont,¹²⁶ A. Elliott-Peisert,¹²⁶ N. Emrskova,¹²⁶ F. Fallavollita,^{126,vv} D. Fasanella,¹²⁶
S. Fiorendi,¹²⁶ G. Franzoni,¹²⁶ J. Fulcher,¹²⁶ W. Funk,¹²⁶ S. Giani,¹²⁶ D. Gigi,¹²⁶ K. Gill,¹²⁶ F. Glege,¹²⁶ L. Gouskos,¹²⁶
M. Gruchala,¹²⁶ M. Guilbaud,¹²⁶ D. Gulhan,¹²⁶ J. Hegeman,¹²⁶ C. Heidegger,¹²⁶ Y. Iiyama,¹²⁶ V. Innocente,¹²⁶ T. James,¹²⁶
P. Janot,¹²⁶ O. Karacheban,^{126,t} J. Kaspar,¹²⁶ J. Kieseler,¹²⁶ M. Krammer,^{126,b} N. Kratochwil,¹²⁶ C. Lange,¹²⁶ P. Lecoq,¹²⁶
C. Lourenço,¹²⁶ L. Malgeri,¹²⁶ M. Mannelli,¹²⁶ A. Massironi,¹²⁶ F. Meijers,¹²⁶ S. Mersi,¹²⁶ E. Meschi,¹²⁶ F. Moortgat,¹²⁶
M. Mulders,¹²⁶ J. Ngadiuba,¹²⁶ J. Niedziela,¹²⁶ S. Nourbakhsh,¹²⁶ S. Orfanelli,¹²⁶ L. Orsini,¹²⁶ F. Pantaleo,^{126,q} L. Pape,¹²⁶
E. Perez,¹²⁶ M. Peruzzi,¹²⁶ A. Petrilli,¹²⁶ G. Petrucciani,¹²⁶ A. Pfeiffer,¹²⁶ M. Pierini,¹²⁶ F. M. Pitters,¹²⁶ D. Rabady,¹²⁶
A. Racz,¹²⁶ M. Rieger,¹²⁶ M. Rovere,¹²⁶ H. Sakulin,¹²⁶ J. Salfeld-Nebgen,¹²⁶ C. Schäfer,¹²⁶ C. Schwick,¹²⁶ M. Selvaggi,¹²⁶
A. Sharma,¹²⁶ P. Silva,¹²⁶ W. Snoeys,¹²⁶ P. Sphicas,^{126,ww} J. Steggemann,¹²⁶ S. Summers,¹²⁶ V. R. Tavolaro,¹²⁶ D. Treille,¹²⁶
A. Tsirou,¹²⁶ G. P. Van Onsem,¹²⁶ A. Vartak,¹²⁶ M. Verzetti,¹²⁶ W. D. Zeuner,¹²⁶ L. Caminada,^{127,xx} K. Deiters,¹²⁷
W. Erdmann,¹²⁷ R. Horisberger,¹²⁷ Q. Ingram,¹²⁷ H. C. Kaestli,¹²⁷ D. Kotlinski,¹²⁷ U. Langenegger,¹²⁷ T. Rohe,¹²⁷
S. A. Wiederkehr,¹²⁷ M. Backhaus,¹²⁸ P. Berger,¹²⁸ N. Chernyavskaya,¹²⁸ G. Dissertori,¹²⁸ M. Dittmar,¹²⁸ M. Donegà,¹²⁸
C. Dorfer,¹²⁸ T. A. Gómez Espinosa,¹²⁸ C. Grab,¹²⁸ D. Hits,¹²⁸ W. Lustermann,¹²⁸ R. A. Manzoni,¹²⁸ M. T. Meinhard,¹²⁸
F. Micheli,¹²⁸ P. Musella,¹²⁸ F. Nessi-Tedaldi,¹²⁸ F. Pauss,¹²⁸ G. Perrin,¹²⁸ L. Perrozzi,¹²⁸ S. Pigazzini,¹²⁸ M. G. Ratti,¹²⁸
M. Reichmann,¹²⁸ C. Reissel,¹²⁸ T. Reitenspiess,¹²⁸ B. Ristic,¹²⁸ D. Ruini,¹²⁸ D. A. Sanz Becerra,¹²⁸ M. Schönenberger,¹²⁸
L. Shchutska,¹²⁸ M. L. Vesterbacka Olsson,¹²⁸ R. Wallny,¹²⁸ D. H. Zhu,¹²⁸ T. K. Aarrestad,¹²⁹ C. Amsler,^{129,yy}
D. Brzhechko,¹²⁹ M. F. Canelli,¹²⁹ A. De Cosa,¹²⁹ R. Del Burgo,¹²⁹ B. Kilminster,¹²⁹ S. Leontsinis,¹²⁹ V. M. Mikuni,¹²⁹
I. Neutelings,¹²⁹ G. Raucó,¹²⁹ P. Robmann,¹²⁹ K. Schweiger,¹²⁹ C. Seitz,¹²⁹ Y. Takahashi,¹²⁹ S. Wertz,¹²⁹ A. Zucchetta,¹²⁹
T. H. Doan,¹³⁰ C. M. Kuo,¹³⁰ W. Lin,¹³⁰ A. Roy,¹³⁰ S. S. Yu,¹³⁰ P. Chang,¹³¹ Y. Chao,¹³¹ K. F. Chen,¹³¹ P. H. Chen,¹³¹
W.-S. Hou,¹³¹ Y. y. Li,¹³¹ R.-S. Lu,¹³¹ E. Paganis,¹³¹ A. Psallidas,¹³¹ A. Steen,¹³¹ B. Asavapibhop,¹³²
C. Asawatangtrakuldee,¹³² N. Srimanobhas,¹³² N. Suwonjandee,¹³² A. Bat,¹³³ F. Boran,¹³³ A. Celik,^{133,zz}
S. Damarseckin,^{133,aaa} Z. S. Demiroglu,¹³³ F. Dolek,¹³³ C. Dozen,^{133,bbb} I. Dumanoglu,¹³³ E. Eskut,¹³³ G. Gokbulut,¹³³
Emine Gurpinar Guler,^{133,ccc} Y. Guler,¹³³ I. Hos,^{133,ddd} C. Isik,¹³³ E. E. Kangal,^{133,eee} O. Kara,¹³³ A. Kayis Topaksu,¹³³
U. Kiminsu,¹³³ G. Onengut,¹³³ K. Ozdemir,^{133,fff} S. Ozturk,^{133,ggg} A. E. Simsek,¹³³ B. Tali,^{133,hhh} U. G. Tok,¹³³
S. Turkcapar,¹³³ I. S. Zorbakir,¹³³ C. Zorbilmez,¹³³ B. Isildak,^{134,iii} G. Karapinar,^{134,iii} M. Yalvac,¹³⁴ I. O. Atakisi,¹³⁵
E. Gülmez,¹³⁵ M. Kaya,^{135,kkk} O. Kaya,^{135,iii} Ö. Özçelik,¹³⁵ S. Tekten,¹³⁵ E. A. Yetkin,^{135,mmm} A. Cakir,¹³⁶ K. Cankocak,¹³⁶
Y. Komurcu,¹³⁶ S. Sen,^{136,nnn} B. Kaynak,¹³⁷ S. Ozkorucuklu,¹³⁷ B. Grynyov,¹³⁸ L. Levchuk,¹³⁹ E. Bhal,¹⁴⁰ S. Bologna,¹⁴⁰
J. J. Brooke,¹⁴⁰ D. Burns,^{140,ooo} E. Clement,¹⁴⁰ D. Cussans,¹⁴⁰ H. Flacher,¹⁴⁰ J. Goldstein,¹⁴⁰ G. P. Heath,¹⁴⁰ H. F. Heath,¹⁴⁰
L. Kreczko,¹⁴⁰ B. Krikler,¹⁴⁰ S. Paramesvaran,¹⁴⁰ B. Penning,¹⁴⁰ T. Sakuma,¹⁴⁰ S. Seif El Nasr-Storey,¹⁴⁰ V. J. Smith,¹⁴⁰
J. Taylor,¹⁴⁰ A. Titterton,¹⁴⁰ K. W. Bell,¹⁴¹ A. Belyaev,^{141,ppp} C. Brew,¹⁴¹ R. M. Brown,¹⁴¹ D. J. A. Cockerill,¹⁴¹
J. A. Coughlan,¹⁴¹ K. Harder,¹⁴¹ S. Harper,¹⁴¹ J. Linacre,¹⁴¹ K. Manolopoulos,¹⁴¹ D. M. Newbold,¹⁴¹ E. Olaiya,¹⁴¹

D. Petyt,¹⁴¹ T. Reis,¹⁴¹ T. Schuh,¹⁴¹ C. H. Shepherd-Themistocleous,¹⁴¹ A. Thea,¹⁴¹ I. R. Tomalin,¹⁴¹ T. Williams,¹⁴¹ R. Bainbridge,¹⁴² P. Bloch,¹⁴² J. Borg,¹⁴² S. Breeze,¹⁴² O. Buchmuller,¹⁴² A. Bundock,¹⁴² Gurpreet Singh CHAHAL,^{142,qqq} D. Colling,¹⁴² P. Dauncey,¹⁴² G. Davies,¹⁴² M. Della Negra,¹⁴² R. Di Maria,¹⁴² P. Everaerts,¹⁴² G. Hall,¹⁴² G. Iles,¹⁴² M. Komm,¹⁴² L. Lyons,¹⁴² A.-M. Magnan,¹⁴² S. Malik,¹⁴² A. Martelli,¹⁴² V. Milosevic,¹⁴² A. Morton,¹⁴² J. Nash,^{142,rrr} V. Palladino,¹⁴² M. Pesaresi,¹⁴² D. M. Raymond,¹⁴² A. Richards,¹⁴² A. Rose,¹⁴² E. Scott,¹⁴² C. Seez,¹⁴² A. Shtipliyski,¹⁴² M. Stoye,¹⁴² T. Strebler,¹⁴² A. Tapper,¹⁴² K. Uchida,¹⁴² T. Virdee,^{142,q} N. Wardle,¹⁴² D. Winterbottom,¹⁴² A. G. Zecchinelli,¹⁴² S. C. Zenz,¹⁴² J. E. Cole,¹⁴³ P. R. Hobson,¹⁴³ A. Khan,¹⁴³ P. Kyberd,¹⁴³ C. K. Mackay,¹⁴³ I. D. Reid,¹⁴³ L. Teodorescu,¹⁴³ S. Zahid,¹⁴³ K. Call,¹⁴⁴ B. Caraway,¹⁴⁴ J. Dittmann,¹⁴⁴ K. Hatakeyama,¹⁴⁴ C. Madrid,¹⁴⁴ B. McMaster,¹⁴⁴ N. Pastika,¹⁴⁴ C. Smith,¹⁴⁴ R. Bartek,¹⁴⁵ A. Dominguez,¹⁴⁵ R. Uniyal,¹⁴⁵ A. M. Vargas Hernandez,¹⁴⁵ A. Buccilli,¹⁴⁶ S. I. Cooper,¹⁴⁶ C. Henderson,¹⁴⁶ P. Rumerio,¹⁴⁶ C. West,¹⁴⁶ A. Albert,¹⁴⁷ D. Arcaro,¹⁴⁷ Z. Demiragli,¹⁴⁷ D. Gastler,¹⁴⁷ C. Richardson,¹⁴⁷ J. Rohlf,¹⁴⁷ D. Sperka,¹⁴⁷ I. Suarez,¹⁴⁷ L. Sulak,¹⁴⁷ D. Zou,¹⁴⁷ G. Benelli,¹⁴⁸ B. Burkley,¹⁴⁸ X. Coubez,^{148,r} D. Cutts,¹⁴⁸ Y. t. Duh,¹⁴⁸ M. Hadley,¹⁴⁸ U. Heintz,¹⁴⁸ J. M. Hogan,^{148,sss} K. H. M. Kwok,¹⁴⁸ E. Laird,¹⁴⁸ G. Landsberg,¹⁴⁸ K. T. Lau,¹⁴⁸ J. Lee,¹⁴⁸ M. Narain,¹⁴⁸ S. Sagir,^{148,ttt} R. Syarif,¹⁴⁸ E. Usai,¹⁴⁸ W. Y. Wong,¹⁴⁸ D. Yu,¹⁴⁸ W. Zhang,¹⁴⁸ R. Band,¹⁴⁹ C. Brainerd,¹⁴⁹ R. Breedon,¹⁴⁹ M. Calderon De La Barca Sanchez,¹⁴⁹ M. Chertok,¹⁴⁹ J. Conway,¹⁴⁹ R. Conway,¹⁴⁹ P. T. Cox,¹⁴⁹ R. Erbacher,¹⁴⁹ C. Flores,¹⁴⁹ G. Funk,¹⁴⁹ F. Jensen,¹⁴⁹ W. Ko,^{149,a} O. Kukral,¹⁴⁹ R. Lander,¹⁴⁹ M. Mulhearn,¹⁴⁹ D. Pellett,¹⁴⁹ J. Pilot,¹⁴⁹ M. Shi,¹⁴⁹ D. Taylor,¹⁴⁹ K. Tos,¹⁴⁹ M. Tripathi,¹⁴⁹ Z. Wang,¹⁴⁹ F. Zhang,¹⁴⁹ M. Bachtis,¹⁵⁰ C. Bravo,¹⁵⁰ R. Cousins,¹⁵⁰ A. Dasgupta,¹⁵⁰ A. Florent,¹⁵⁰ J. Hauser,¹⁵⁰ M. Ignatenko,¹⁵⁰ N. Mccoll,¹⁵⁰ W. A. Nash,¹⁵⁰ S. Regnard,¹⁵⁰ D. Saltzberg,¹⁵⁰ C. Schnaible,¹⁵⁰ B. Stone,¹⁵⁰ V. Valuev,¹⁵⁰ K. Burt,¹⁵¹ Y. Chen,¹⁵¹ R. Clare,¹⁵¹ J. W. Gary,¹⁵¹ S. M. A. Ghiasi Shirazi,¹⁵¹ G. Hanson,¹⁵¹ G. Karapostoli,¹⁵¹ O. R. Long,¹⁵¹ M. Olmedo Negrete,¹⁵¹ M. I. Paneva,¹⁵¹ W. Si,¹⁵¹ L. Wang,¹⁵¹ S. Wimpenny,¹⁵¹ B. R. Yates,¹⁵¹ Y. Zhang,¹⁵¹ J. G. Branson,¹⁵² P. Chang,¹⁵² S. Cittolin,¹⁵² S. Cooperstein,¹⁵² N. Deelen,¹⁵² M. Derdzinski,¹⁵² R. Gerosa,¹⁵² D. Gilbert,¹⁵² B. Hashemi,¹⁵² D. Klein,¹⁵² V. Krutelyov,¹⁵² J. Letts,¹⁵² M. Masciovecchio,¹⁵² S. May,¹⁵² S. Padhi,¹⁵² M. Pieri,¹⁵² V. Sharma,¹⁵² M. Tadel,¹⁵² F. Würthwein,¹⁵² A. Yagil,¹⁵² G. Zevi Della Porta,¹⁵² N. Amin,¹⁵³ R. Bhandari,¹⁵³ C. Campagnari,¹⁵³ M. Citron,¹⁵³ V. Dutta,¹⁵³ M. Franco Sevilla,¹⁵³ J. Incandela,¹⁵³ B. Marsh,¹⁵³ H. Mei,¹⁵³ A. Ovcharova,¹⁵³ H. Qu,¹⁵³ J. Richman,¹⁵³ U. Sarica,¹⁵³ D. Stuart,¹⁵³ S. Wang,¹⁵³ D. Anderson,¹⁵⁴ A. Bornheim,¹⁵⁴ O. Cerri,¹⁵⁴ I. Dutta,¹⁵⁴ J. M. Lawhorn,¹⁵⁴ N. Lu,¹⁵⁴ J. Mao,¹⁵⁴ H. B. Newman,¹⁵⁴ T. Q. Nguyen,¹⁵⁴ J. Pata,¹⁵⁴ M. Spiropulu,¹⁵⁴ J. R. Vlimant,¹⁵⁴ S. Xie,¹⁵⁴ Z. Zhang,¹⁵⁴ R. Y. Zhu,¹⁵⁴ M. B. Andrews,¹⁵⁵ T. Ferguson,¹⁵⁵ T. Mudholkar,¹⁵⁵ M. Paulini,¹⁵⁵ M. Sun,¹⁵⁵ I. Vorobiev,¹⁵⁵ M. Weinberg,¹⁵⁵ J. P. Cumalat,¹⁵⁶ W. T. Ford,¹⁵⁶ E. MacDonald,¹⁵⁶ T. Mulholland,¹⁵⁶ R. Patel,¹⁵⁶ A. Perloff,¹⁵⁶ K. Stenson,¹⁵⁶ K. A. Ulmer,¹⁵⁶ S. R. Wagner,¹⁵⁶ J. Alexander,¹⁵⁷ Y. Cheng,¹⁵⁷ J. Chu,¹⁵⁷ A. Datta,¹⁵⁷ A. Frankenthal,¹⁵⁷ K. Mcdermott,¹⁵⁷ J. R. Patterson,¹⁵⁷ D. Quach,¹⁵⁷ A. Ryd,¹⁵⁷ S. M. Tan,¹⁵⁷ Z. Tao,¹⁵⁷ J. Thom,¹⁵⁷ P. Wittich,¹⁵⁷ M. Zientek,¹⁵⁷ S. Abdullin,¹⁵⁸ M. Albrow,¹⁵⁸ M. Alyari,¹⁵⁸ G. Apollinari,¹⁵⁸ A. Apresyan,¹⁵⁸ A. Apyan,¹⁵⁸ S. Banerjee,¹⁵⁸ L. A. T. Bauerdick,¹⁵⁸ A. Beretvas,¹⁵⁸ D. Berry,¹⁵⁸ J. Berryhill,¹⁵⁸ P. C. Bhat,¹⁵⁸ K. Burkett,¹⁵⁸ J. N. Butler,¹⁵⁸ A. Canepa,¹⁵⁸ G. B. Cerati,¹⁵⁸ H. W. K. Cheung,¹⁵⁸ F. Chlebana,¹⁵⁸ M. Cremonesi,¹⁵⁸ J. Duarte,¹⁵⁸ V. D. Elvira,¹⁵⁸ J. Freeman,¹⁵⁸ Z. Gecse,¹⁵⁸ E. Gottschalk,¹⁵⁸ L. Gray,¹⁵⁸ D. Green,¹⁵⁸ S. Grünendahl,¹⁵⁸ O. Gutsche,¹⁵⁸ Allison Reinsvold Hall,¹⁵⁸ J. Hanlon,¹⁵⁸ R. M. Harris,¹⁵⁸ S. Hasegawa,¹⁵⁸ R. Heller,¹⁵⁸ J. Hirschauer,¹⁵⁸ B. Jayatilaka,¹⁵⁸ S. Jindariani,¹⁵⁸ M. Johnson,¹⁵⁸ U. Joshi,¹⁵⁸ T. Klijnsma,¹⁵⁸ B. Klima,¹⁵⁸ M. J. Kortelainen,¹⁵⁸ B. Kreis,¹⁵⁸ S. Lammel,¹⁵⁸ J. Lewis,¹⁵⁸ D. Lincoln,¹⁵⁸ R. Lipton,¹⁵⁸ M. Liu,¹⁵⁸ T. Liu,¹⁵⁸ J. Lykken,¹⁵⁸ K. Maeshima,¹⁵⁸ J. M. Marraffino,¹⁵⁸ D. Mason,¹⁵⁸ P. McBride,¹⁵⁸ P. Merkel,¹⁵⁸ S. Mrenna,¹⁵⁸ S. Nahn,¹⁵⁸ V. O'Dell,¹⁵⁸ V. Papadimitriou,¹⁵⁸ K. Pedro,¹⁵⁸ C. Pena,¹⁵⁸ G. Rakness,¹⁵⁸ F. Ravera,¹⁵⁸ L. Ristori,¹⁵⁸ B. Schneider,¹⁵⁸ E. Sexton-Kennedy,¹⁵⁸ N. Smith,¹⁵⁸ A. Soha,¹⁵⁸ W. J. Spalding,¹⁵⁸ L. Spiegel,¹⁵⁸ S. Stoynev,¹⁵⁸ J. Strait,¹⁵⁸ N. Strobbe,¹⁵⁸ L. Taylor,¹⁵⁸ S. Tkaczyk,¹⁵⁸ N. V. Tran,¹⁵⁸ L. Uplegger,¹⁵⁸ E. W. Vaandering,¹⁵⁸ C. Vernieri,¹⁵⁸ R. Vidal,¹⁵⁸ M. Wang,¹⁵⁸ H. A. Weber,¹⁵⁸ D. Acosta,¹⁵⁹ P. Avery,¹⁵⁹ D. Bourilkov,¹⁵⁹ A. Brinkerhoff,¹⁵⁹ L. Cadamuro,¹⁵⁹ V. Cherepanov,¹⁵⁹ F. Errico,¹⁵⁹ R. D. Field,¹⁵⁹ S. V. Gleyzer,¹⁵⁹ D. Guerrero,¹⁵⁹ B. M. Joshi,¹⁵⁹ M. Kim,¹⁵⁹ J. Konigsberg,¹⁵⁹ A. Korytov,¹⁵⁹ K. H. Lo,¹⁵⁹ K. Matchev,¹⁵⁹ N. Menendez,¹⁵⁹ G. Mitselmakher,¹⁵⁹ D. Rosenzweig,¹⁵⁹ K. Shi,¹⁵⁹ J. Wang,¹⁵⁹ S. Wang,¹⁵⁹ X. Zuo,¹⁵⁹ Y. R. Joshi,¹⁶⁰ T. Adams,¹⁶¹ A. Askew,¹⁶¹ S. Hagopian,¹⁶¹ V. Hagopian,¹⁶¹ K. F. Johnson,¹⁶¹ R. Khurana,¹⁶¹ T. Kolberg,¹⁶¹ G. Martinez,¹⁶¹ T. Perry,¹⁶¹ H. Prosper,¹⁶¹ C. Schiber,¹⁶¹ R. Yohay,¹⁶¹ J. Zhang,¹⁶¹ M. M. Baarmand,¹⁶² M. Hohmann,¹⁶² D. Noonan,¹⁶² M. Rahmani,¹⁶² M. Saunders,¹⁶² F. Yumiceva,¹⁶² M. R. Adams,¹⁶³ L. Apanasevich,¹⁶³ R. R. Betts,¹⁶³ R. Cavanaugh,¹⁶³ X. Chen,¹⁶³ S. Dittmer,¹⁶³ O. Evdokimov,¹⁶³ C. E. Gerber,¹⁶³ D. A. Hangal,¹⁶³ D. J. Hofman,¹⁶³ C. Mills,¹⁶³ T. Roy,¹⁶³ M. B. Tonjes,¹⁶³ N. Varelas,¹⁶³ J. Viinikainen,¹⁶³ H. Wang,¹⁶³ X. Wang,¹⁶³ Z. Wu,¹⁶³ M. Alhusseini,¹⁶⁴ B. Bilki,^{164,ccc} K. Dilsiz,^{164,uuu} S. Durgut,¹⁶⁴ R. P. Gandrajula,¹⁶⁴ M. Haytmyradov,¹⁶⁴ V. Khristenko,¹⁶⁴

O. K. Köseyan,¹⁶⁴ J.-P. Merlo,¹⁶⁴ A. Mestvirishvili,^{164,vvv} A. Moeller,¹⁶⁴ J. Nachtman,¹⁶⁴ H. Ogul,^{164,www} Y. Onel,¹⁶⁴ F. Ozok,^{164,xxx} A. Penzo,¹⁶⁴ C. Snyder,¹⁶⁴ E. Tiras,¹⁶⁴ J. Wetzel,¹⁶⁴ B. Blumenfeld,¹⁶⁵ A. Cocoros,¹⁶⁵ N. Eminizer,¹⁶⁵ A. V. Gritsan,¹⁶⁵ W. T. Hung,¹⁶⁵ S. Kyriacou,¹⁶⁵ P. Maksimovic,¹⁶⁵ J. Roskes,¹⁶⁵ M. Swartz,¹⁶⁵ C. Baldenegro Barrera,¹⁶⁶ P. Baringer,¹⁶⁶ A. Bean,¹⁶⁶ S. Boren,¹⁶⁶ J. Bowen,¹⁶⁶ A. Bylinkin,¹⁶⁶ T. Isidori,¹⁶⁶ S. Khalil,¹⁶⁶ J. King,¹⁶⁶ G. Krintiras,¹⁶⁶ A. Kropivnitskaya,¹⁶⁶ C. Lindsey,¹⁶⁶ D. Majumder,¹⁶⁶ W. Mcbrayer,¹⁶⁶ N. Minafra,¹⁶⁶ M. Murray,¹⁶⁶ C. Rogan,¹⁶⁶ C. Royon,¹⁶⁶ S. Sanders,¹⁶⁶ E. Schmitz,¹⁶⁶ J. D. Tapia Takaki,¹⁶⁶ Q. Wang,¹⁶⁶ J. Williams,¹⁶⁶ G. Wilson,¹⁶⁶ S. Duric,¹⁶⁷ A. Ivanov,¹⁶⁷ K. Kaadze,¹⁶⁷ D. Kim,¹⁶⁷ Y. Maravin,¹⁶⁷ D. R. Mendis,¹⁶⁷ T. Mitchell,¹⁶⁷ A. Modak,¹⁶⁷ A. Mohammadi,¹⁶⁷ F. Rebassoo,¹⁶⁸ D. Wright,¹⁶⁸ A. Baden,¹⁶⁹ O. Baron,¹⁶⁹ A. Belloni,¹⁶⁹ S. C. Eno,¹⁶⁹ Y. Feng,¹⁶⁹ N. J. Hadley,¹⁶⁹ S. Jabeen,¹⁶⁹ G. Y. Jeng,¹⁶⁹ R. G. Kellogg,¹⁶⁹ A. C. Mignerey,¹⁶⁹ S. Nabili,¹⁶⁹ F. Ricci-Tam,¹⁶⁹ M. Seidel,¹⁶⁹ Y. H. Shin,¹⁶⁹ A. Skuja,¹⁶⁹ S. C. Tonwar,¹⁶⁹ K. Wong,¹⁶⁹ D. Abercrombie,¹⁷⁰ B. Allen,¹⁷⁰ A. Baty,¹⁷⁰ R. Bi,¹⁷⁰ S. Brandt,¹⁷⁰ W. Busza,¹⁷⁰ I. A. Cali,¹⁷⁰ M. D'Alfonso,¹⁷⁰ G. Gomez Ceballos,¹⁷⁰ M. Goncharov,¹⁷⁰ P. Harris,¹⁷⁰ D. Hsu,¹⁷⁰ M. Hu,¹⁷⁰ M. Klute,¹⁷⁰ D. Kovalskyi,¹⁷⁰ Y.-J. Lee,¹⁷⁰ P. D. Luckey,¹⁷⁰ B. Maier,¹⁷⁰ A. C. Marini,¹⁷⁰ C. MCGinn,¹⁷⁰ C. Mironov,¹⁷⁰ S. Narayanan,¹⁷⁰ X. Niu,¹⁷⁰ C. Paus,¹⁷⁰ D. Rankin,¹⁷⁰ C. Roland,¹⁷⁰ G. Roland,¹⁷⁰ Z. Shi,¹⁷⁰ G. S. F. Stephans,¹⁷⁰ K. Sumorok,¹⁷⁰ K. Tatar,¹⁷⁰ D. Velicanu,¹⁷⁰ J. Wang,¹⁷⁰ T. W. Wang,¹⁷⁰ B. Wyslouch,¹⁷⁰ R. M. Chatterjee,¹⁷¹ A. Evans,¹⁷¹ S. Guts,^{171,a} P. Hansen,¹⁷¹ J. Hiltbrand,¹⁷¹ Sh. Jain,¹⁷¹ Y. Kubota,¹⁷¹ Z. Lesko,¹⁷¹ J. Mans,¹⁷¹ M. Revering,¹⁷¹ R. Rusack,¹⁷¹ R. Saradhy,¹⁷¹ N. Schroeder,¹⁷¹ M. A. Wadud,¹⁷¹ J. G. Acosta,¹⁷² S. Oliveros,¹⁷² K. Bloom,¹⁷³ S. Chauhan,¹⁷³ D. R. Claes,¹⁷³ C. Fangmeier,¹⁷³ L. Finco,¹⁷³ F. Golf,¹⁷³ R. Kamalieddin,¹⁷³ I. Kravchenko,¹⁷³ J. E. Siado,¹⁷³ G. R. Snow,^{173,a} B. Stieger,¹⁷³ W. Tabb,¹⁷³ G. Agarwal,¹⁷⁴ C. Harrington,¹⁷⁴ I. Iashvili,¹⁷⁴ A. Kharchilava,¹⁷⁴ C. McLean,¹⁷⁴ D. Nguyen,¹⁷⁴ A. Parker,¹⁷⁴ J. Pekkanen,¹⁷⁴ S. Rappoccio,¹⁷⁴ B. Roozbahani,¹⁷⁴ G. Alverson,¹⁷⁵ E. Barberis,¹⁷⁵ C. Freer,¹⁷⁵ Y. Haddad,¹⁷⁵ A. Hortiangtham,¹⁷⁵ G. Madigan,¹⁷⁵ B. Marzocchi,¹⁷⁵ D. M. Morse,¹⁷⁵ T. Orimoto,¹⁷⁵ L. Skinnari,¹⁷⁵ A. Tishelman-Charny,¹⁷⁵ T. Wamorkar,¹⁷⁵ B. Wang,¹⁷⁵ A. Wisecarver,¹⁷⁵ D. Wood,¹⁷⁵ S. Bhattacharya,¹⁷⁶ J. Bueghly,¹⁷⁶ A. Gilbert,¹⁷⁶ T. Gunter,¹⁷⁶ K. A. Hahn,¹⁷⁶ N. Odell,¹⁷⁶ M. H. Schmitt,¹⁷⁶ K. Sung,¹⁷⁶ M. Trovato,¹⁷⁶ M. Velasco,¹⁷⁶ R. Bucci,¹⁷⁷ N. Dev,¹⁷⁷ R. Goldouzian,¹⁷⁷ M. Hildreth,¹⁷⁷ K. Hurtado Anampa,¹⁷⁷ C. Jessop,¹⁷⁷ D. J. Karmgard,¹⁷⁷ K. Lannon,¹⁷⁷ W. Li,¹⁷⁷ N. Loukas,¹⁷⁷ N. Marinelli,¹⁷⁷ I. Mcalister,¹⁷⁷ F. Meng,¹⁷⁷ Y. Musienko,^{177,II} R. Ruchti,¹⁷⁷ P. Siddireddy,¹⁷⁷ G. Smith,¹⁷⁷ S. Taroni,¹⁷⁷ M. Wayne,¹⁷⁷ A. Wightman,¹⁷⁷ M. Wolf,¹⁷⁷ A. Woodard,¹⁷⁷ J. Alimena,¹⁷⁸ B. Bylsma,¹⁷⁸ L. S. Durkin,¹⁷⁸ B. Francis,¹⁷⁸ C. Hill,¹⁷⁸ W. Ji,¹⁷⁸ A. Lefeld,¹⁷⁸ T. Y. Ling,¹⁷⁸ B. L. Winer,¹⁷⁸ G. Dezoort,¹⁷⁹ P. Elmer,¹⁷⁹ J. Hardenbrook,¹⁷⁹ N. Haubrich,¹⁷⁹ S. Higginbotham,¹⁷⁹ A. Kalogeropoulos,¹⁷⁹ S. Kwan,¹⁷⁹ D. Lange,¹⁷⁹ M. T. Lucchini,¹⁷⁹ J. Luo,¹⁷⁹ D. Marlow,¹⁷⁹ K. Mei,¹⁷⁹ I. Ojalvo,¹⁷⁹ J. Olsen,¹⁷⁹ C. Palmer,¹⁷⁹ P. Piroué,¹⁷⁹ D. Stickland,¹⁷⁹ C. Tully,¹⁷⁹ S. Malik,¹⁸⁰ S. Norberg,¹⁸⁰ A. Barker,¹⁸¹ V. E. Barnes,¹⁸¹ S. Das,¹⁸¹ L. Gutay,¹⁸¹ M. Jones,¹⁸¹ A. W. Jung,¹⁸¹ A. Khatiwada,¹⁸¹ B. Mahakud,¹⁸¹ D. H. Miller,¹⁸¹ G. Negro,¹⁸¹ N. Neumeister,¹⁸¹ C. C. Peng,¹⁸¹ S. Piperov,¹⁸¹ H. Qiu,¹⁸¹ J. F. Schulte,¹⁸¹ N. Trevisani,¹⁸¹ F. Wang,¹⁸¹ R. Xiao,¹⁸¹ W. Xie,¹⁸¹ T. Cheng,¹⁸² J. Dolen,¹⁸² N. Parashar,¹⁸² U. Behrens,¹⁸³ K. M. Ecklund,¹⁸³ S. Freed,¹⁸³ F. J. M. Geurts,¹⁸³ M. Kilpatrick,¹⁸³ Arun Kumar,¹⁸³ W. Li,¹⁸³ B. P. Padley,¹⁸³ R. Redjimi,¹⁸³ J. Roberts,¹⁸³ J. Rorie,¹⁸³ W. Shi,¹⁸³ A. G. Stahl Leiton,¹⁸³ Z. Tu,¹⁸³ A. Zhang,¹⁸³ A. Bodek,¹⁸⁴ P. de Barbaro,¹⁸⁴ R. Demina,¹⁸⁴ J. L. Dulemba,¹⁸⁴ C. Fallon,¹⁸⁴ T. Ferbel,¹⁸⁴ M. Galanti,¹⁸⁴ A. Garcia-Bellido,¹⁸⁴ O. Hindrichs,¹⁸⁴ A. Khukhunaishvili,¹⁸⁴ E. Ranken,¹⁸⁴ R. Taus,¹⁸⁴ B. Chiarito,¹⁸⁵ J. P. Chou,¹⁸⁵ A. Gandrakota,¹⁸⁵ Y. Gershtein,¹⁸⁵ E. Halkiadakis,¹⁸⁵ A. Hart,¹⁸⁵ M. Heindl,¹⁸⁵ E. Hughes,¹⁸⁵ S. Kaplan,¹⁸⁵ I. Laflotte,¹⁸⁵ A. Lath,¹⁸⁵ R. Montalvo,¹⁸⁵ K. Nash,¹⁸⁵ M. Osherson,¹⁸⁵ H. Saka,¹⁸⁵ S. Salur,¹⁸⁵ S. Schnetzer,¹⁸⁵ S. Somalwar,¹⁸⁵ R. Stone,¹⁸⁵ S. Thomas,¹⁸⁵ H. Acharya,¹⁸⁶ A. G. Delannoy,¹⁸⁶ S. Spanier,¹⁸⁶ O. Bouhali,^{187,yyy} M. Dalchenko,¹⁸⁷ M. De Mattia,¹⁸⁷ A. Delgado,¹⁸⁷ S. Dildick,¹⁸⁷ R. Eusebi,¹⁸⁷ J. Gilmore,¹⁸⁷ T. Huang,¹⁸⁷ T. Kamon,^{187,zzz} H. Kim,¹⁸⁷ S. Luo,¹⁸⁷ S. Malhotra,¹⁸⁷ D. Marley,¹⁸⁷ R. Mueller,¹⁸⁷ D. Overton,¹⁸⁷ L. Perniè,¹⁸⁷ D. Rathjens,¹⁸⁷ A. Safonov,¹⁸⁷ N. Akchurin,¹⁸⁸ J. Damgov,¹⁸⁸ F. De Guio,¹⁸⁸ V. Hegde,¹⁸⁸ S. Kunori,¹⁸⁸ K. Lamichhane,¹⁸⁸ S. W. Lee,¹⁸⁸ T. Mengke,¹⁸⁸ S. Muthumuni,¹⁸⁸ T. Peltola,¹⁸⁸ S. Undleeb,¹⁸⁸ I. Volobouev,¹⁸⁸ Z. Wang,¹⁸⁸ A. Whitbeck,¹⁸⁸ S. Greene,¹⁸⁹ A. Gurrola,¹⁸⁹ R. Janjam,¹⁸⁹ W. Johns,¹⁸⁹ C. Maguire,¹⁸⁹ A. Melo,¹⁸⁹ H. Ni,¹⁸⁹ K. Padeken,¹⁸⁹ F. Romeo,¹⁸⁹ P. Sheldon,¹⁸⁹ S. Tuo,¹⁸⁹ J. Velkovska,¹⁸⁹ M. Verweij,¹⁸⁹ M. W. Arenton,¹⁹⁰ P. Barria,¹⁹⁰ B. Cox,¹⁹⁰ G. Cummings,¹⁹⁰ J. Hakala,¹⁹⁰ R. Hirosky,¹⁹⁰ M. Joyce,¹⁹⁰ A. Ledovskoy,¹⁹⁰ C. Neu,¹⁹⁰ B. Tannenwald,¹⁹⁰ Y. Wang,¹⁹⁰ E. Wolfe,¹⁹⁰ F. Xia,¹⁹⁰ R. Harr,¹⁹¹ P. E. Karchin,¹⁹¹ N. Poudyal,¹⁹¹ J. Sturdy,¹⁹¹ P. Thapa,¹⁹¹ T. Bose,¹⁹² J. Buchanan,¹⁹² C. Caillol,¹⁹² D. Carlsmith,¹⁹² S. Dasu,¹⁹² I. De Bruyn,¹⁹² L. Dodd,¹⁹² C. Galloni,¹⁹² H. He,¹⁹² M. Herndon,¹⁹² A. Hervé,¹⁹² U. Hussain,¹⁹² A. Lanaro,¹⁹² A. Loeliger,¹⁹² K. Long,¹⁹² R. Loveless,¹⁹²

J. Madhusudanan Sreekala,¹⁹² D. Pinna,¹⁹² T. Ruggles,¹⁹² A. Savin,¹⁹² V. Sharma,¹⁹² W. H. Smith,¹⁹²
D. Teague,¹⁹² and S. Trembath-reichert¹⁹²

(CMS Collaboration)

¹*Yerevan Physics Institute, Yerevan, Armenia*

²*Institut für Hochenergiephysik, Wien, Austria*

³*Institute for Nuclear Problems, Minsk, Belarus*

⁴*Universiteit Antwerpen, Antwerpen, Belgium*

⁵*Vrije Universiteit Brussel, Brussel, Belgium*

⁶*Université Libre de Bruxelles, Bruxelles, Belgium*

⁷*Ghent University, Ghent, Belgium*

⁸*Université Catholique de Louvain, Louvain-la-Neuve, Belgium*

⁹*Centro Brasileiro de Pesquisas Físicas, Rio de Janeiro, Brazil*

¹⁰*Universidade do Estado do Rio de Janeiro, Rio de Janeiro, Brazil*

^{11a}*Universidade Estadual Paulista, São Paulo, Brazil*

^{11b}*Universidade Federal do ABC, São Paulo, Brazil*

¹²*Institute for Nuclear Research and Nuclear Energy, Bulgarian Academy of Sciences, Sofia, Bulgaria*

¹³*University of Sofia, Sofia, Bulgaria*

¹⁴*Beihang University, Beijing, China*

¹⁵*Department of Physics, Tsinghua University, Beijing, China*

¹⁶*Institute of High Energy Physics, Beijing, China*

¹⁷*State Key Laboratory of Nuclear Physics and Technology, Peking University, Beijing, China*

¹⁸*Zhejiang University, Hangzhou, China*

¹⁹*Universidad de Los Andes, Bogota, Colombia*

²⁰*Universidad de Antioquia, Medellin, Colombia*

²¹*University of Split, Faculty of Electrical Engineering, Mechanical Engineering and Naval Architecture, Split, Croatia*

²²*University of Split, Faculty of Science, Split, Croatia*

²³*Institute Rudjer Boskovic, Zagreb, Croatia*

²⁴*University of Cyprus, Nicosia, Cyprus*

²⁵*Charles University, Prague, Czech Republic*

²⁶*Escuela Politecnica Nacional, Quito, Ecuador*

²⁷*Universidad San Francisco de Quito, Quito, Ecuador*

²⁸*Academy of Scientific Research and Technology of the Arab Republic of Egypt,
Egyptian Network of High Energy Physics, Cairo, Egypt*

²⁹*National Institute of Chemical Physics and Biophysics, Tallinn, Estonia*

³⁰*Department of Physics, University of Helsinki, Helsinki, Finland*

³¹*Helsinki Institute of Physics, Helsinki, Finland*

³²*Lappeenranta University of Technology, Lappeenranta, Finland*

³³*IRFU, CEA, Université Paris-Saclay, Gif-sur-Yvette, France*

³⁴*Laboratoire Leprince-Ringuet, CNRS/IN2P3, Ecole Polytechnique, Institut Polytechnique de Paris*

³⁵*Université de Strasbourg, CNRS, IPHC UMR 7178, Strasbourg, France*

³⁶*Centre de Calcul de l'Institut National de Physique Nucléaire et de Physique des Particules, CNRS/IN2P3, Villeurbanne, France*

³⁷*Université de Lyon, Université Claude Bernard Lyon 1, CNRS-IN2P3, Institut de Physique Nucléaire de Lyon, Villeurbanne, France*

³⁸*Georgian Technical University, Tbilisi, Georgia*

³⁹*Tbilisi State University, Tbilisi, Georgia*

⁴⁰*RWTH Aachen University, I. Physikalisches Institut, Aachen, Germany*

⁴¹*RWTH Aachen University, III. Physikalisches Institut A, Aachen, Germany*

⁴²*RWTH Aachen University, III. Physikalisches Institut B, Aachen, Germany*

⁴³*Deutsches Elektronen-Synchrotron, Hamburg, Germany*

⁴⁴*University of Hamburg, Hamburg, Germany*

⁴⁵*Karlsruher Institut fuer Technologie, Karlsruhe, Germany*

⁴⁶*Institute of Nuclear and Particle Physics (INPP), NCSR Demokritos, Aghia Paraskevi, Greece*

⁴⁷*National and Kapodistrian University of Athens, Athens, Greece*

⁴⁸*National Technical University of Athens, Athens, Greece*

⁴⁹*University of Ioánnina, Ioánnina, Greece*

⁵⁰*MTA-ELTE Lendület CMS Particle and Nuclear Physics Group, Eötvös Loránd University, Budapest, Hungary*

⁵¹*Wigner Research Centre for Physics, Budapest, Hungary*

- ⁵²*Institute of Nuclear Research ATOMKI, Debrecen, Hungary*
⁵³*Institute of Physics, University of Debrecen, Debrecen, Hungary*
⁵⁴*Eszterhazy Karoly University, Karoly Robert Campus, Gyongyos, Hungary*
⁵⁵*Indian Institute of Science (IISc), Bangalore, India*
⁵⁶*National Institute of Science Education and Research, HBNI, Bhubaneswar, India*
⁵⁷*Panjab University, Chandigarh, India*
⁵⁸*University of Delhi, Delhi, India*
⁵⁹*Saha Institute of Nuclear Physics, HBNI, Kolkata, India*
⁶⁰*Indian Institute of Technology Madras, Madras, India*
⁶¹*Bhabha Atomic Research Centre, Mumbai, India*
⁶²*Tata Institute of Fundamental Research-A, Mumbai, India*
⁶³*Tata Institute of Fundamental Research-B, Mumbai, India*
⁶⁴*Indian Institute of Science Education and Research (IISER), Pune, India*
⁶⁵*Institute for Research in Fundamental Sciences (IPM), Tehran, Iran*
⁶⁶*University College Dublin, Dublin, Ireland*
^{67a}*INFN Sezione di Bari*
^{67b}*Università di Bari*
^{67c}*Politecnico di Bari*
^{68a}*INFN Sezione di Bologna, Bologna, Italy*
^{68b}*Università di Bologna, Bologna, Italy*
^{69a}*INFN Sezione di Catania, Catania, Italy*
^{69b}*Università di Catania, Catania, Italy*
^{70a}*INFN Sezione di Firenze, Firenze, Italy*
^{70b}*Università di Firenze, Firenze, Italy*
⁷¹*INFN Laboratori Nazionali di Frascati, Frascati, Italy*
^{72a}*INFN Sezione di Genova, Genova, Italy*
^{72b}*Università di Genova, Genova, Italy*
^{73a}*INFN Sezione di Milano-Bicocca, Milano, Italy*
^{73b}*Università di Milano-Bicocca, Milano, Italy*
^{74a}*INFN Sezione di Napoli, Napoli, Italy*
^{74b}*Università di Napoli 'Federico II', Napoli, Italy*
^{74c}*Università della Basilicata, Potenza, Italy*
^{74d}*Università G. Marconi, Roma, Italy*
^{75a}*INFN Sezione di Padova, Padova, Italy*
^{75b}*Università di Padova, Padova, Italy*
^{75c}*Università di Trento, Trento, Italy*
^{76a}*INFN Sezione di Pavia*
^{76b}*Università di Pavia*
^{77a}*INFN Sezione di Perugia, Perugia, Italy*
^{77b}*Università di Perugia, Perugia, Italy*
^{78a}*INFN Sezione di Pisa, Pisa, Italy*
^{78b}*Università di Pisa, Pisa, Italy*
^{78c}*Scuola Normale Superiore di Pisa, Pisa, Italy*
^{79a}*INFN Sezione di Roma, Rome, Italy*
^{79b}*Sapienza Università di Roma, Rome, Italy*
^{80a}*INFN Sezione di Torino, Torino, Italy*
^{80b}*Università di Torino, Torino, Italy*
^{80c}*Università del Piemonte Orientale, Novara, Italy*
^{81a}*INFN Sezione di Trieste, Trieste, Italy*
^{81b}*Università di Trieste, Trieste, Italy*
⁸²*Kyungpook National University, Daegu, Korea*
⁸³*Chonnam National University, Institute for Universe and Elementary Particles, Kwangju, Korea*
⁸⁴*Hanyang University, Seoul, Korea*
⁸⁵*Korea University, Seoul, Korea*
⁸⁶*Kyung Hee University, Department of Physics*
⁸⁷*Sejong University, Seoul, Korea*
⁸⁸*Seoul National University, Seoul, Korea*
⁸⁹*University of Seoul, Seoul, Korea*
⁹⁰*Sungkyunkwan University, Suwon, Korea*
⁹¹*Riga Technical University, Riga, Latvia*

- ⁹²Vilnius University, Vilnius, Lithuania
- ⁹³National Centre for Particle Physics, Universiti Malaya, Kuala Lumpur, Malaysia
- ⁹⁴Universidad de Sonora (UNISON), Hermosillo, Mexico
- ⁹⁵Centro de Investigacion y de Estudios Avanzados del IPN, Mexico City, Mexico
- ⁹⁶Universidad Iberoamericana, Mexico City, Mexico
- ⁹⁷Benemerita Universidad Autonoma de Puebla, Puebla, Mexico
- ⁹⁸Universidad Autónoma de San Luis Potosí, San Luis Potosí, Mexico
- ⁹⁹University of Montenegro, Podgorica, Montenegro
- ¹⁰⁰University of Auckland, Auckland, New Zealand
- ¹⁰¹University of Canterbury, Christchurch, New Zealand
- ¹⁰²National Centre for Physics, Quaid-I-Azam University, Islamabad, Pakistan
- ¹⁰³AGH University of Science and Technology Faculty of Computer Science, Electronics and Telecommunications, Krakow, Poland
- ¹⁰⁴National Centre for Nuclear Research, Swierk, Poland
- ¹⁰⁵Institute of Experimental Physics, Faculty of Physics, University of Warsaw, Warsaw, Poland
- ¹⁰⁶Laboratório de Instrumentação e Física Experimental de Partículas, Lisboa, Portugal
- ¹⁰⁷Joint Institute for Nuclear Research, Dubna, Russia
- ¹⁰⁸Petersburg Nuclear Physics Institute, Gatchina (St. Petersburg), Russia
- ¹⁰⁹Institute for Nuclear Research, Moscow, Russia
- ¹¹⁰Institute for Theoretical and Experimental Physics named by A.I. Alikhanov of NRC ‘Kurchatov Institute’, Moscow, Russia
- ¹¹¹Moscow Institute of Physics and Technology, Moscow, Russia
- ¹¹²National Research Nuclear University ‘Moscow Engineering Physics Institute’ (MEPhI), Moscow, Russia
- ¹¹³P.N. Lebedev Physical Institute, Moscow, Russia
- ¹¹⁴Skobeltsyn Institute of Nuclear Physics, Lomonosov Moscow State University, Moscow, Russia
- ¹¹⁵Novosibirsk State University (NSU), Novosibirsk, Russia
- ¹¹⁶Institute for High Energy Physics of National Research Centre ‘Kurchatov Institute’, Protvino, Russia
- ¹¹⁷National Research Tomsk Polytechnic University, Tomsk, Russia
- ¹¹⁸Tomsk State University, Tomsk, Russia
- ¹¹⁹University of Belgrade: Faculty of Physics and VINCA Institute of Nuclear Sciences
- ¹²⁰Centro de Investigaciones Energéticas Medioambientales y Tecnológicas (CIEMAT), Madrid, Spain
- ¹²¹Universidad Autónoma de Madrid, Madrid, Spain
- ¹²²Universidad de Oviedo, Instituto Universitario de Ciencias y Tecnologías Espaciales de Asturias (ICTEA), Oviedo, Spain
- ¹²³Instituto de Física de Cantabria (IFCA), CSIC-Universidad de Cantabria, Santander, Spain
- ¹²⁴University of Colombo, Colombo, Sri Lanka
- ¹²⁵University of Ruhuna, Department of Physics, Matara, Sri Lanka
- ¹²⁶CERN, European Organization for Nuclear Research, Geneva, Switzerland
- ¹²⁷Paul Scherrer Institut, Villigen, Switzerland
- ¹²⁸ETH Zurich—Institute for Particle Physics and Astrophysics (IPA), Zurich, Switzerland
- ¹²⁹Universität Zürich, Zurich, Switzerland
- ¹³⁰National Central University, Chung-Li, Taiwan
- ¹³¹National Taiwan University (NTU), Taipei, Taiwan
- ¹³²Chulalongkorn University, Faculty of Science, Department of Physics, Bangkok, Thailand
- ¹³³Çukurova University, Physics Department, Science and Art Faculty, Adana, Turkey
- ¹³⁴Middle East Technical University, Physics Department, Ankara, Turkey
- ¹³⁵Bogazici University, Istanbul, Turkey
- ¹³⁶Istanbul Technical University, Istanbul, Turkey
- ¹³⁷Istanbul University, Istanbul, Turkey
- ¹³⁸Institute for Scintillation Materials of National Academy of Science of Ukraine, Kharkov, Ukraine
- ¹³⁹National Scientific Center, Kharkov Institute of Physics and Technology, Kharkov, Ukraine
- ¹⁴⁰University of Bristol, Bristol, United Kingdom
- ¹⁴¹Rutherford Appleton Laboratory, Didcot, United Kingdom
- ¹⁴²Imperial College, London, United Kingdom
- ¹⁴³Brunel University, Uxbridge, United Kingdom
- ¹⁴⁴Baylor University, Waco, Texas, USA
- ¹⁴⁵Catholic University of America, Washington, DC, USA
- ¹⁴⁶The University of Alabama, Tuscaloosa, Alabama, USA
- ¹⁴⁷Boston University, Boston, Massachusetts, USA
- ¹⁴⁸Brown University, Providence, Rhode Island, USA
- ¹⁴⁹University of California, Davis, Davis, California, USA
- ¹⁵⁰University of California, Los Angeles, California, USA
- ¹⁵¹University of California, Riverside, Riverside, California, USA

- ¹⁵²University of California, San Diego, La Jolla, California, USA
¹⁵³University of California, Santa Barbara—Department of Physics, Santa Barbara, California, USA
¹⁵⁴California Institute of Technology, Pasadena, California, USA
¹⁵⁵Carnegie Mellon University, Pittsburgh, Pennsylvania, USA
¹⁵⁶University of Colorado Boulder, Boulder, Colorado, USA
¹⁵⁷Cornell University, Ithaca, New York, USA
¹⁵⁸Fermi National Accelerator Laboratory, Batavia, Illinois, USA
¹⁵⁹University of Florida, Gainesville, Florida, USA
¹⁶⁰Florida International University, Miami, Florida, USA
¹⁶¹Florida State University, Tallahassee, Florida, USA
¹⁶²Florida Institute of Technology, Melbourne, Florida, USA
¹⁶³University of Illinois at Chicago (UIC), Chicago, Illinois, USA
¹⁶⁴The University of Iowa, Iowa City, Iowa, USA
¹⁶⁵Johns Hopkins University, Baltimore, Maryland, USA
¹⁶⁶The University of Kansas, Lawrence, Kansas, USA
¹⁶⁷Kansas State University, Manhattan, Kansas, USA
¹⁶⁸Lawrence Livermore National Laboratory, Livermore, California, USA
¹⁶⁹University of Maryland, College Park, Maryland, USA
¹⁷⁰Massachusetts Institute of Technology, Cambridge, Massachusetts, USA
¹⁷¹University of Minnesota, Minneapolis, Minnesota, USA
¹⁷²University of Mississippi, Oxford, Mississippi, USA
¹⁷³University of Nebraska-Lincoln, Lincoln, Nebraska, USA
¹⁷⁴State University of New York at Buffalo, Buffalo, New York, USA
¹⁷⁵Northeastern University, Boston, Massachusetts, USA
¹⁷⁶Northwestern University, Evanston, Illinois, USA
¹⁷⁷University of Notre Dame, Notre Dame, Indiana, USA
¹⁷⁸The Ohio State University, Columbus, Ohio, USA
¹⁷⁹Princeton University, Princeton, New Jersey, USA
¹⁸⁰University of Puerto Rico, Mayaguez, Puerto Rico, USA
¹⁸¹Purdue University, West Lafayette, Indiana, USA
¹⁸²Purdue University Northwest, Hammond, Indiana, USA
¹⁸³Rice University, Houston, Texas, USA
¹⁸⁴University of Rochester, Rochester, New York, USA
¹⁸⁵Rutgers, The State University of New Jersey, Piscataway, New Jersey, USA
¹⁸⁶University of Tennessee, Knoxville, Tennessee, USA
¹⁸⁷Texas A&M University, College Station, Texas, USA
¹⁸⁸Texas Tech University, Lubbock, Texas, USA
¹⁸⁹Vanderbilt University, Nashville, Tennessee, USA
¹⁹⁰University of Virginia, Charlottesville, Virginia, USA
¹⁹¹Wayne State University, Detroit, Michigan, USA
¹⁹²University of Wisconsin—Madison, Madison, WI, Wisconsin, USA

^aDeceased.

^bAlso at Vienna University of Technology, Vienna, Austria.

^cAlso at IRFU, CEA, Université Paris-Saclay, Gif-sur-Yvette, France.

^dAlso at Universidade Estadual de Campinas, Campinas, Brazil.

^eAlso at Federal University of Rio Grande do Sul, Porto Alegre, Brazil.

^fAlso at UFMS.

^gAlso at Universidade Federal de Pelotas, Pelotas, Brazil.

^hAlso at Université Libre de Bruxelles, Bruxelles, Belgium.

ⁱAlso at University of Chinese Academy of Sciences.

^jAlso at Institute for Theoretical and Experimental Physics named by A.I. Alikhanov of NRC ‘Kurchatov Institute’, Moscow, Russia.

^kAlso at Joint Institute for Nuclear Research, Dubna, Russia.

^lAlso at British University in Egypt, Cairo, Egypt.

^mAlso at Suez University, Suez, Egypt.

ⁿAlso at Purdue University, West Lafayette, Indiana, USA.

^oAlso at Université de Haute Alsace, Mulhouse, France.

^pAlso at Erzincan Binali Yildirim University, Erzincan, Turkey.

^qAlso at CERN, European Organization for Nuclear Research, Geneva, Switzerland.

^rAlso at RWTH Aachen University, III. Physikalisches Institut A, Aachen, Germany.

- ^s Also at University of Hamburg, Hamburg, Germany.
- ^t Also at Brandenburg University of Technology, Cottbus, Germany.
- ^u Also at Institute of Physics, University of Debrecen, Debrecen, Hungary.
- ^v Also at Institute of Nuclear Research ATOMKI, Debrecen, Hungary.
- ^w Also at MTA-ELTE Lendület CMS Particle and Nuclear Physics Group, Eötvös Loránd University, Budapest, Hungary.
- ^x Also at IIT Bhubaneswar, Bhubaneswar, India.
- ^y Also at Institute of Physics, Bhubaneswar, India.
- ^z Also at Shoolini University, Solan, India.
- ^{aa} Also at University of Hyderabad, Hyderabad, India.
- ^{bb} Also at University of Visva-Bharati, Santiniketan, India.
- ^{cc} Also at Isfahan University of Technology.
- ^{dd} Also at INFN Sezione di Bari, Università di Bari, Politecnico di Bari, Bari, Italy.
- ^{ee} Also at Italian National Agency for New Technologies, Energy and Sustainable Economic Development.
- ^{ff} Also at Centro Siciliano di Fisica Nucleare e di Struttura Della Materia.
- ^{gg} Also at Scuola Normale e Sezione dell'INFN, Pisa, Italy.
- ^{hh} Also at Riga Technical University, Riga, Latvia.
- ⁱⁱ Also at Malaysian Nuclear Agency, MOSTI, Kajang, Malaysia.
- ^{jj} Also at Consejo Nacional de Ciencia y Tecnología, Mexico City, Mexico.
- ^{kk} Also at Warsaw University of Technology, Institute of Electronic Systems, Warsaw, Poland.
- ^{ll} Also at Institute for Nuclear Research, Moscow, Russia.
- ^{mmm} Also at National Research Nuclear University 'Moscow Engineering Physics Institute' (MEPhI), Moscow, Russia.
- ⁿⁿ Also at St. Petersburg State Polytechnical University, St. Petersburg, Russia.
- ^{oo} Also at University of Florida, Gainesville, Florida, USA.
- ^{pp} Also at Imperial College, London, United Kingdom.
- ^{qq} Also at P.N. Lebedev Physical Institute, Moscow, Russia.
- ^{rr} Also at California Institute of Technology, Pasadena, California, USA.
- ^{ss} Also at Budker Institute of Nuclear Physics, Novosibirsk, Russia.
- ^{tt} Also at Faculty of Physics, University of Belgrade, Belgrade, Serbia.
- ^{uu} Also at Università degli Studi di Siena, Siena, Italy.
- ^{vv} Also at INFN Sezione di Pavia, Università di Pavia, Pavia, Italy.
- ^{ww} Also at National and Kapodistrian University of Athens, Athens, Greece.
- ^{xx} Also at Universität Zürich, Zurich, Switzerland.
- ^{yy} Also at Stefan Meyer Institute for Subatomic Physics, Vienna, Austria.
- ^{zz} Also at Burdur Mehmet Akif Ersoy University.
- ^{aaa} Also at Şırnak University.
- ^{bbb} Also at Department of Physics, Tsinghua University, Beijing, China.
- ^{ccc} Also at Beykent University, Istanbul, Turkey.
- ^{ddd} Also at Istanbul Aydin University, Application and Research Center for Advanced Studies (App. & Res. Cent. for Advanced Studies).
- ^{eee} Also at Mersin University, Mersin, Turkey.
- ^{fff} Also at Piri Reis University, Istanbul, Turkey.
- ^{ggg} Also at Gaziosmanpasa University, Tokat, Turkey.
- ^{hhh} Also at Adiyaman University, Adiyaman, Turkey.
- ⁱⁱⁱ Also at Ozyegin University, Istanbul, Turkey.
- ^{jjj} Also at Izmir Institute of Technology, Izmir, Turkey.
- ^{kkk} Also at Marmara University, Istanbul, Turkey.
- ^{lll} Also at Kafkas University, Kars, Turkey.
- ^{mmm} Also at Istanbul Bilgi University, Istanbul, Turkey.
- ⁿⁿⁿ Also at Hacettepe University, Ankara, Turkey.
- ^{ooo} Also at Vrije Universiteit Brussel, Brussel, Belgium.
- ^{ppp} Also at School of Physics and Astronomy, University of Southampton, Southampton, United Kingdom.
- ^{qqq} Also at IPPP Durham University.
- ^{rrr} Also at Monash University, Faculty of Science, Clayton, Australia.
- ^{sss} Also at Bethel University, St. Paul, Minneapolis, USA.
- ^{ttt} Also at Karamanoğlu Mehmetbey University, Karaman, Turkey.
- ^{uuu} Also at Bingol University, Bingol, Turkey.
- ^{vvv} Also at Georgian Technical University, Tbilisi, Georgia.
- ^{www} Also at Sinop University, Sinop, Turkey.
- ^{xxx} Also at Mimar Sinan University, Istanbul, Istanbul, Turkey.
- ^{yyy} Also at Texas A&M University at Qatar, Doha, Qatar.
- ^{zzz} Also at Kyungpook National University, Daegu, Korea.

MAJOR REPORT • OPEN ACCESS

Searching for long-lived particles beyond the Standard Model at the Large Hadron Collider

To cite this article: Juliette Alimena *et al* 2020 *J. Phys. G: Nucl. Part. Phys.* **47** 090501

View the [article online](#) for updates and enhancements.

You may also like

- [Electron and photon reconstruction and identification with the CMS experiment at the CERN LHC](#)
The CMS collaboration, A.M. Sirunyan, A. Tumasyan *et al.*
- [Performance of the ATLAS RPC detector and Level-1 muon barrel trigger at \(s\)=13 TeV](#)
The ATLAS collaboration, G. Aad, B. Abbott *et al.*
- [The ATLAS Fast Tracker system](#)
The ATLAS collaboration, G. Aad, B. Abbott *et al.*

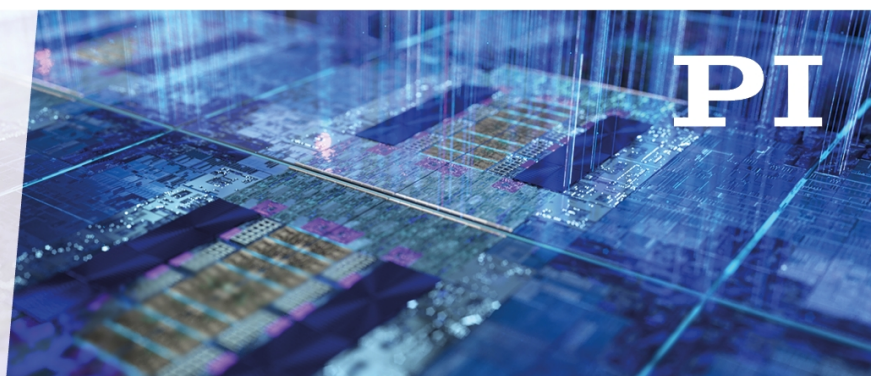
Recent citations

- [Hunting wino and higgsino dark matter at the muon collider with disappearing tracks](#)
Rodolfo Capdevilla *et al*
- [Searching for elusive dark sectors with terrestrial and celestial observations](#)
Roberto Contino *et al*
- [Supernova constraints on dark flavored sectors](#)
Jorge Martin Camalich *et al*

ENABLING THE
TECHNOLOGIES
FOR SEMICON

It's Possible Sessions

November 30, 2021



Searching for long-lived particles beyond the Standard Model at the Large Hadron Collider

Juliette Alimena

(Experimental Coverage, Backgrounds, Upgrades)¹ 

James Beacham


(Document Editor, Simplified Models)² 

(Backgrounds, Upgrades)³ 


(Upgrades)⁴, Xabier Cid Vidal

(Experimental Coverage)⁵ 

(Simplified Models, Reinterpretations)^{6,7,8} 

(Simplified Models)⁹ 


(Experimental Coverage)¹⁰ 

(Reinterpretations)¹¹ 

(Simplified Models, Experimental Coverage)¹² 

Simon Knapen

(Dark Showers)¹³ 


(Reinterpretations)¹⁴ 

(Reinterpretations)¹⁵, Zhen Liu

(Simplified Models, Backgrounds, Reinterpretations)¹⁶ 

Sascha Mehlhase

(Backgrounds)¹⁷ 

(Simplified Models)^{18,19} 

(Experimental Coverage)²⁰ 

(Simplified Models, Dark Showers)²¹ 

(Document Editor, Simplified Models, Simplified Models

Library)^{22,23} 

(Upgrades)²⁴ 

(Experimental Coverage)^{25,26} 

Contributors & Endorsers:
Todd Adams²⁷, Michael Adersberger²⁸, Cristiano Alpigiani²⁹,

Artur Apresyan³⁰, Robert John Bainbridge³¹,

Varvara Batozskaya³², Hugues Beauchesne³³, Lisa Benato³⁴,

S Berlendis³⁵, Eshwen Bhal³⁶, Freya Blekman³⁷,

Christina Borovilou³⁸, Jamie Boyd¹⁰, Benjamin P Brau³⁹,

Lene Bryngemark⁴⁰, Oliver Buchmueller³¹,

Malte Buschmann⁴¹, William Buttinger¹⁰,

Mario Campanelli⁴², Cari Cesarotti⁴³, Chunhui Chen⁴⁴,

Hsin-Chia Cheng⁴⁵, Sanha Cheong^{46,47}, Matthew Citron⁴⁸,
 Andrea Coccaro⁴⁹, V Coco¹⁰, Eric Conte⁵⁰, Félix Cormier⁵¹,
 Louie D Corpe⁴², Nathaniel Craig⁴⁸, Yanou Cui²³,
 Elena Dall’Occo⁵², C Dallapiccola³⁹, M R Darwish⁵³,
 Alessandro Davoli^{54,55}, Annapaola de Cosa⁵⁶,
 Andrea De Simone^{54,55}, Luigi Delle Rose^{57,58},
 Frank F Deppisch⁴², Biplab Dey⁵⁹, Miriam D Diamond⁹,
 Keith R Dienes^{35,60}, Sven Dildick⁶¹, Babette Döbrich¹⁰,
 Marco Drewes⁶², Melanie Eich³⁴, M ElSawy^{63,64},
 Alberto Escalante del Valle⁶⁵, Gabriel Facini⁴²,
 Marco Farina⁶⁶, Jonathan L Feng⁶⁷, Oliver Fischer²⁵,
 H U Flaecher³⁶, Patrick Foldenauer⁶⁸, Marat Freytsis^{13,69,70},
 Benjamin Fuks^{71,72}, Iftah Galon⁷³, Yuri Gershtein⁷⁴,
 Stefano Giagu⁷⁵, Andrea Giammanco⁶²,
 Vladimir V Gligorov⁷⁶, Tobias Golling⁷⁷,
 Sergio Grancagnolo⁷⁸, Giuliano Gustavino⁷⁹,
 Andrew Haas⁸⁰, Kristian Hahn⁸¹, Jan Hajer⁶²,
 Ahmed Hammad⁸², Lukas Heinrich¹⁰, Jan Heisig⁶²,
 J C Helo⁸³, Gavin Hesketh⁴², Christopher S Hill¹,
 Martin Hirsch⁸⁴, M Hohlmann⁸⁵, Tova Holmes⁸⁶,
 W Hulsbergen⁵², John Huth⁴³, Philip Ilten⁸⁷,
 Thomas Jacques⁵⁴, Bodhitha Jayatilaka³⁰,
 Geng-Yuan Jeng⁶⁰, K A Johns³⁵, Toshiaki Kaji⁸⁸,
 Gregor Kasieczka³⁴, Yevgeny Kats³³, Malgorzata Kazana⁸⁹,
 Henning Keller⁹⁰, Maxim Yu Khlopov^{91,92}, Felix Kling⁶⁷,
 Ted R Kolberg²⁷, Igor Kostiuik^{52,93}, Emma Sian Kuwertz¹⁰,
 Audrey Kvam²⁹, Greg Landsberg⁹⁴, Gaia Lanfranchi^{10,95},
 Iñaki Lara⁹⁶, Alexander Ledovskoy⁹⁷, Dylan Linthorne⁹⁸,
 Jia Liu⁸⁶, Iacopo Longarini⁹⁹, Steven Lowette³⁷,
 Henry Lubatti²⁹, Margaret Lutz³⁹, Jingyu Luo¹⁰⁰,
 Judita Mamučić⁸⁴, Matthieu Marinangeli¹⁰¹,
 Alberto Mariotti³⁷, Daniel Marlow¹⁰⁰, Matthew McCullough¹⁰,
 Kevin McDermott⁴, P Mermoud⁷⁷, David Milstead¹⁰²,
 Siddharth Mishra-Sharma⁸⁰, Vasiliki A Mitsou⁸⁴,
 Javier Montejo Berlingen¹⁰, Filip Moortgat^{10,103},
 Alessandro Morandini^{54,55}, Alice Polyxeni Morris⁴²,
 David Michael Morse¹⁰⁴, Stephen Mrenna³⁰,
 Benjamin Nachman¹⁰⁵, Miha Nemevšek¹⁰⁶, Fabrizio Nesti¹⁰⁷,
 Christian Ohm^{108,109}, Silvia Pascoli¹¹⁰, Kevin Pedro³⁰,
 Cristián Peña^{30,111}, Karla Josefina Pena Rodriguez³⁴,
 Jónatan Piedra¹¹², James L Pinfold¹¹², Antonio Policicchio⁷⁵,
 Goran Popara¹¹³, Jessica Prisciandaro⁶², Mason Proffitt²⁹,
 Giorgia Rauco⁵⁶, Federico Redi¹⁰¹, Matthew Reece⁴³,
 Allison Reinsvold Hall³⁰, H Rejeb Sfar⁵³, Sophie Renner¹¹⁴,
 Dean Robinson^{105,115}, Amber Roepe⁷⁹, Manfredi Ronzani⁸⁰,

Ennio Salvioni¹¹⁶, Arka Santra⁸⁴, Ryu Sawada¹¹⁷,
 Jakub Scholtz¹¹⁰, Philip Schuster⁴⁶, Pedro Schwaller¹¹⁴,
 Cristiano Sebastiani⁷⁵, Sezen Sekmen¹¹⁸,
 Michele Selvaggi¹⁰, Weinan Si²³, Livia Soffi⁷⁵,
 Daniel Stolarski⁹⁸, David Stuart⁴⁸, John Stupak III⁷⁹,
 Kevin Sung⁸¹, Wendy Taylor¹¹⁹, Sebastian Tempel⁶⁵,
 Brooks Thomas¹²⁰, Emma Torró-Pastor²⁹,
 Daniele Trocino¹⁰³, Sebastian Trojanowski¹²¹,
 Marco Trovato¹²², Yuhsin Tsai¹⁶, C G Tully¹⁰⁰,
 Tamás Álmos Vámi¹²³, Juan Carlos Vasquez¹²⁴,
 Carlos Vázquez Sierra⁵², K Vellidis³⁸, Basile Vermassen¹⁰³,
 Martina Vit¹⁰³, Devin G E Walker¹²⁵, Xiao-Ping Wang¹²²,
 Gordon Watts²⁹, Si Xie¹¹¹, Melissa Yexley¹²⁶,
 Charles Young⁴⁶, Jiang-Hao Yu^{18,127}, Piotr Zalewski⁸⁹ and
 Yongchao Zhang¹²⁸

¹ Department of Physics, The Ohio State University, 191 W. Woodruff Ave., Columbus, OH 43210-1117, United States of America

² Department of Physics, Duke University, 120 Science Drive, Durham, NC 27710, United States of America

³ Physikalisches Institut, Ruprecht-Karls-Universität Heidelberg, Im Neuenheimer Feld 226, D-69120, Heidelberg, Germany

⁴ Cornell University, 245 East Avenue, Ithaca, NY 14853, United States of America

⁵ Instituto Galego de Física de Altas Enerxías, U. Santiago de Compostela, IGFAE, Rúa de Xoaquín Díaz de Rábago, s/n, E-15782 Santiago de Compostela, Spain

⁶ Departamento de Ciencias, Facultad de Artes Liberales, Universidad Adolfo Ibáñez, Diagonal Las Torres 2640, Santiago, Chile

⁷ Department of Physics, National Taiwan University, Taipei 10617, Taiwan

⁸ Instituto de Física, Pontificia Universidad Católica de Chile, Avenida Vicuña Mackenna 4860, Santiago, Chile

⁹ Department of Physics, University of Toronto, 60 St. George Street, Toronto, ON M5S 1A7, Canada

¹⁰ CERN, Esplanade des particules 1, Geneva, Switzerland

¹¹ Department of Theoretical Physics, Tata Institute of Fundamental Physics, Homi Bhabha Road, Mumbai 400005, India

¹² Department of Physics, University of Cincinnati, 400 Geology/Physics Bldg., Cincinnati, OH 45221, United States of America

¹³ School of Natural Sciences, Institute for Advanced Study, 1 Einstein Drive, Princeton, NJ 08540, United States of America

¹⁴ Laboratoire de Physique Subatomique et de Cosmologie, Université Grenoble-Alpes, CNRS/IN2P3, 53 Avenue des Martyrs, F-38026 Grenoble, France

¹⁵ Universidade Federal do ABC, Av. dos Estados, 5001, Santo Andre, 09210-580 SP, Brazil

¹⁶ Maryland Center for Fundamental Physics, Department of Physics, University of Maryland, College Park, MD 20742, United States of America

¹⁷ Faculty of Physics, Ludwig-Maximilians-Universität München, Schellingstraße 4, D-80799 Munich, Germany

¹⁸ Amherst Center for Fundamental Interactions, Department of Physics, University of Massachusetts Amherst, Lederle Graduate Research Center 416, Amherst, MA 01003 United States of America

- ¹⁹T.-D. Lee Institute and School of Physics and Astronomy, Shanghai Jiao Tong University, 800 Dongchuan Road, Shanghai, 200240, People's Republic of China
- ²⁰Department of Physics, McGill University, Montreal, QC H3A 2T8, Canada
- ²¹University of Illinois at Urbana-Champaign, 1110 W. Green St., Urbana, IL 61801, United States of America
- ²²Harvey Mudd College, 301 Platt Blvd., Claremont, CA 91711, United States of America
- ²³University of California, Riverside, 900 University Avenue, Riverside, CA 92521, United States of America
- ²⁴Universita' di Roma Tre and INFN, via della Vasca Navale 84, I-00146 Roma, Italy
- ²⁵Institute for Nuclear Physics, Karlsruhe Inst. of Technology, Hermann-von-Helmholtz-Platz 1, D-76344 Eggenstein-Leopoldshafen, Germany
- ²⁶Institute for Theoretical Particle Physics (TTP), Karlsruhe Institute of Technology, Engesserstraße 7, D-76128 Karlsruhe, Germany
- ²⁷Florida State University, 77 Chieftan Way, Tallahassee, FL 32306, United States of America
- ²⁸Faculty of Physics, Ludwig-Maximilians Universität München, Schellingstrasse 4, D-80799 Munich, Germany
- ²⁹University of Washington, Seattle, 1410 NE Campus Parkway Seattle, WA 98195, United States of America
- ³⁰Fermi National Accelerator Laboratory, PO Box 500, Batavia, IL 60510, United States of America
- ³¹High Energy Physics Group, Blackett Laboratory, Imperial College, Prince Consort Road, London SW7 2AZ, United Kingdom
- ³²National Centre for Nuclear Research (NCBJ), Hoża 69, 00-681 Warsaw, Poland
- ³³Department of Physics, Ben-Gurion University, 1 Ben-Gurion Boulevard Beer-Sheva, Beer-Sheva 8410501, Israel
- ³⁴Institut für Experimentalphysik, Universität Hamburg, Luruper Chaussee 149, D-22761 Hamburg, Germany
- ³⁵University of Arizona, 118 E. 4th St., Tucson AZ 85721, United States of America
- ³⁶University of Bristol, HH Wills Physics Laboratory, Tyndall Avenue, Bristol, BS8 1TL, United Kingdom
- ³⁷IIHE, Vrije Universiteit Brussel, Pleinlaan 2, B-1050 Brussels, Belgium
- ³⁸Physics Department, National and Kapodistrian University of Athens, Panepistimioupoli, Zografou, 15784, Greece
- ³⁹University of Massachusetts, Amherst, 1126 LGRT, University of Massachusetts, Amherst, MA 01003-9337, United States of America
- ⁴⁰Department of Physics, Division of Particle Physics, Lund University, Box 118, SE-221 00 Lund, Sweden
- ⁴¹Leinweber Center for Theoretical Physics, University of Michigan, 450 Church Street, Ann Arbor MI-48109, United States of America
- ⁴²University College London, Gower Street WC1E 6BT London, United Kingdom
- ⁴³Department of Physics, Harvard University, 17 Oxford Street, Cambridge, MA, 02138
- ⁴⁴Department of Physics and Astronomy, Iowa State University, 2323 Osborn Drive, Physics 0012, Ames, IA 50011-3160, United States of America
- ⁴⁵Department of Physics, University of California, Davis, One Shields Avenue, Davis, CA 95616, United States of America
- ⁴⁶SLAC National Accelerator Laboratory, 2575 Sand Hill Rd, Menlo Park, CA 94025, United States of America
- ⁴⁷Physics Department, Stanford University, 450 Serra Mall, Stanford, CA 94305, United States of America
- ⁴⁸Department of Physics, Broida Hall, University of California, Santa Barbara, CA 93106, United States of America
- ⁴⁹INFN Sezione di Genova, Via Dodecaneso, 33, I-16146—Genova, Italy

- ⁵⁰ Institut Pluridisciplinaire Hubert Curien (IPHC), Département Recherches Subatomiques, Université de Strasbourg/CNRS-IN2P3, 23 Rue du Loess, F-67037 Strasbourg, France
- ⁵¹ Department of Physics & Astronomy, The University of British Columbia, 2329 West Mall, Vancouver, BC V6T 1Z4, Canada
- ⁵² Nikhef National Institute for Subatomic Physics, Science Park 105, 1098 XG Amsterdam, The Netherlands
- ⁵³ Antwerp University, Prinsstraat 13, B-2000 Antwerpen, Belgium
- ⁵⁴ SISSA, Via Bonomea 265, Trieste, I-34136, Italy
- ⁵⁵ INFN Sezione di Trieste, via Bonomea 265, I-34136 Trieste, Italy
- ⁵⁶ University of Zürich, Winterthurerstrasse 190, 8057 Zurich, Switzerland
- ⁵⁷ Department of Physics and Astronomy, University of Florence, Via G. Sansone 1, 50019 Sesto Fiorentino, Italy
- ⁵⁸ University of Southampton, Highfield, Southampton SO17 1BJ, United Kingdom
- ⁵⁹ Institute of Particle Physics, Central China Normal University, Wuhan, Hubei, People's Republic of China
- ⁶⁰ Department of Physics, University of Maryland, 4296 Stadium Drive, College Park, MD 20742, United States of America
- ⁶¹ Texas A&M University, 4242 TAMU College Station, TX 77843-4242, United States of America
- ⁶² Centre for Cosmology, Particle Physics and Phenomenology (CP3), Université catholique de Louvain, Chemin du Cyclotron 2, B-1348, Louvain-la-Neuve, Belgium
- ⁶³ Basic Science Department, Faculty of Engineering, The British University in Egypt, El Sherouk City, Misr-Ismaïlia Road, Postal No 11837, PO Box 43, Cairo, Egypt
- ⁶⁴ Physics Department, Faculty of Science, Beni Suef University, Qism Bani Sweif, Bani Sweif, Beni Suef Governorate, Egypt
- ⁶⁵ Institute of High Energy Physics, Austrian Academy of Sciences, Nikolsdorfer Gasse 18, A-1050 Vienna, Austria
- ⁶⁶ Stony Brook University, Stony Brook, NY 11794-3840, United States of America
- ⁶⁷ Department of Physics and Astronomy, University of California, Irvine, CA 92697-4575, United States of America
- ⁶⁸ Institut für Theoretische Physik, Universität Heidelberg, Philosophenweg 16, D-69120 Heidelberg, Germany
- ⁶⁹ Raymond and Beverly Sackler School of Physics and Astronomy, Tel Aviv University, Tel-Aviv 69978, Israel
- ⁷⁰ Institute of Theoretical Science, University of Oregon, Eugene, OR 97403, United States of America
- ⁷¹ LPTHE, UMR 7589, Sorbonne Université et CNRS, 4 Place Jussieu, F-75252 Paris Cedex 05, France
- ⁷² Institut Universitaire de France, 103 boulevard Saint-Michel, F-75005 Paris, France
- ⁷³ New High Energy Theory Center, Rutgers, The State University of New Jersey, Piscataway, NJ 08854-8019, United States of America
- ⁷⁴ Rutgers University, 136 Frelinghuysen Rd, Piscataway, NJ 08854 United States of America
- ⁷⁵ Sapienza Università di Roma and INFN Roma1, P.le A. Moro 5, Roma, I-00185, Italy
- ⁷⁶ LPNHE, Sorbonne Université, Paris Diderot Sorbonne Paris Cité, CNRS/IN2P3, Barre 12-22, 4 Place Jussieu, F-75252 Paris Cedex 05, France
- ⁷⁷ Département de Physique Nucléaire et Corpusculaire, Université de Genève, 24, quai Ernest-Ansermet CH-1211 Genève 4, Switzerland
- ⁷⁸ Humboldt-Universität, Newtonstraße 15, D-12489 Berlin, Germany
- ⁷⁹ The University of Oklahoma, 440 W. Brooks St. Norman, OK 73019, United States of America
- ⁸⁰ New York University, 726 Broadway, New York, NY 10003, United States of America

- ⁸¹ Northwestern University, 2145 Sheridan Rd, Evanston, IL 60208, United States of America
- ⁸² Departement of Physics, University of Basel, Klingelbergstrasse 82, 4056, Basel, Switzerland
- ⁸³ Departamento de Física y Astronomía, Facultad de Ciencias, Universidad de La Serena, Avenida Cisternas 1200, La Serena, Chile
- ⁸⁴ Instituto de Física Corpuscular/Consejo Superior de Investigaciones Científicas—University of Valencia (IFIC/CSIC—UV), Carrer del Catedratic José Beltrán Martínez, 2, E-46980 Paterna, València, Spain
- ⁸⁵ Dept. of Aerospace, Physics & Space Sciences, Florida Institute of Technology, 150 W. University Blvd., Melbourne, FL 32901, United States of America
- ⁸⁶ Enrico Fermi Institute, University of Chicago, 5640 S. Ellis Avenue, RI-183, Chicago, IL 60637, United States of America
- ⁸⁷ University of Birmingham, Edgbaston, Birmingham B15 2TT, United Kingdom
- ⁸⁸ Waseda University, Ookubo 3-4-1, Shinjuku-ku, Tokyo 169-8555, Japan
- ⁸⁹ National Centre for Nuclear Research (NCBJ), Andrzeja Sołtana 7, 05-400 Otwock-Świerk, Poland
- ⁹⁰ RWTH Aachen University, Otto-Blumenthal-Straße, D-52074 Aachen, Germany
- ⁹¹ National Research Nuclear University MEPhI, Kashirskoe chaussee 31, Moscow 115409, Russia
- ⁹² APC Laboratory, 10, rue Alice Domon et Léonie Duquet, F-75205, Paris Cedex 13, France
- ⁹³ Institute for Nuclear Research of the National Academy of Sciences (KINR), 47 Nauky Avenue, 03680, Kyiv, Ukraine
- ⁹⁴ Brown University, 182 Hope St, Providence, RI 02912, United States of America
- ⁹⁵ Laboratori Nazionali di Frascati, INFN, via E. Fermi 40, I-00044 Frascati RM, Italy
- ⁹⁶ Instituto de Física Teórica (UAM-CSIC), C/Nicolás Cabrera 13-15 Campus de Cantoblanco, E-28049 Madrid, Spain
- ⁹⁷ Physics Department, University of Virginia, PO Box 400714, 382 McCormick Rd , Charlottesville, VA, 22904-4714, United States of America
- ⁹⁸ Carleton University, 1125 Colonel By Dr, Ottawa, ON K1S 5B6, Canada
- ⁹⁹ Università degli studi di Roma 'La Sapienza' and INFN Roma, Dipartimento di Fisica G. Marconi. Piazzale Aldo Moro 5, I-00185, Roma, Italy
- ¹⁰⁰ Physics Department, Washington Road, Princeton University, Princeton, NJ 08544, United States of America
- ¹⁰¹ École Polytechnique Fédérale de Lausanne, Route Cantonale, 1015 Lausanne, Switzerland
- ¹⁰² Fysikum, Stockholms Universitet, Roslagstullsbacken 21, SE-114 21 Stockholm, Sweden
- ¹⁰³ Department of Physics and Astronomy, University of Ghent, Proeftuinstraat 86, B-9000 Ghent, Belgium
- ¹⁰⁴ Northeastern University, 360 Huntington Ave., Boston, MA 02115, United States of America
- ¹⁰⁵ Physics Division, Lawrence Berkeley National Laboratory, Berkeley, 1 Cyclotron Road, CA 94720, United States of America
- ¹⁰⁶ Jožef Stefan Institute, Jamova 39, Ljubljana 1000, Slovenia
- ¹⁰⁷ Università dell'Aquila, via Vetoio, L'Aquila, I-67100, Italy
- ¹⁰⁸ KTH Royal Institute of Technology, AlbaNova Universitetscentrum, KTH, Physics Department, SE-106 91 Stockholm, Sweden
- ¹⁰⁹ Oskar Klein Centre for Cosmoparticle Physics, Stockholm University, SE-106 91 Stockholm, Sweden
- ¹¹⁰ IPPP, Department of Physics, Durham University, South Road, Durham, DH1 3LE, United Kingdom

- ¹¹¹ California Institute of Technology, 1200 E California Blvd, MC 256-48, Pasadena, CA, 91125, United States of America
- ¹¹² Physics Department, University of Alberta, Edmonton, AB T6G 2E1, Canada
- ¹¹³ Ruder Bošković Institute, Bijenička cesta 54, 10000 Zagreb, Croatia
- ¹¹⁴ PRISMA Cluster of Excellence & Mainz Inst. for Theoretical Physics, Johannes Gutenberg Univ., Staudingerweg 7, D-55128 Mainz, Germany
- ¹¹⁵ Santa Cruz Institute for Particle Physics and Department of Physics, University of California Santa Cruz, Santa Cruz, CA 95064, United States of America
- ¹¹⁶ Technical University of Munich, Physics Department, James-Franck-Strasse 1, D-85748 Garching, Germany
- ¹¹⁷ International Center for Elementary Particle Physics, The University of Tokyo, Hongo 7-3-1, Bunkyo-ku, Tokyo 113-0033, Japan
- ¹¹⁸ Department of Physics, Kyungpook National University, 80 Daehakro, Bukgu, Daegu 41566, Republic of Korea
- ¹¹⁹ York University, 4700 Keele St, Toronto, ON M3J 1P3, Canada
- ¹²⁰ Lafayette College, 730 High St. Easton, PA 18042, United States of America
- ¹²¹ Consortium for Fundamental Physics, School of Mathematics and Statistics, University of Sheffield, Hounsfield Road, Sheffield S3 7RH, United Kingdom
- ¹²² Argonne National Laboratory, 9700 Cass Avenue, Lemont, IL 60439, United States of America
- ¹²³ Wigner Research Centre for Physics, Konkoly-Thege Miklós út 29-33, Budapest 1121, Hungary
- ¹²⁴ Universidad Técnica Federico Santa María, Avenida España 1680, Valparaiso, 2340000, Chile
- ¹²⁵ Department of Physics and Astronomy, Dartmouth College, Hanover, NH 03755 United States of America
- ¹²⁶ Lancaster University, Lancaster LA1 4YW, United Kingdom
- ¹²⁷ CAS Key Laboratory of Theoretical Physics, Institute of Theoretical Physics, Chinese Academy of Sciences, Beijing 100190, People's Republic of China
- ¹²⁸ Department of Physics and McDonnell Center for the Space Sciences, Washington University, St. Louis, MO 63130, United States of America

E-mail: juliette.alimena@cern.ch, j.beacham@cern.ch, martino.borsato@cern.ch, yangyang.cheng@cornell.edu, xabier.cid.vidal@cern.ch, gcottin@phys.ntu.edu.tw, dcurtin@physics.utoronto.ca, deroeck@mail.cern.ch, desai@theory.tifr.res.in, jaredaevans@gmail.com, knapien@ias.edu, sabine.kraml@lpsc.in2p3.fr, andre.lessa@ufabc.edu.br, zliuphys@umd.edu, sascha.mehlhase@cern.ch, mjrm@physics.umass.edu, hrussell@cern.ch, sheltonj@illinois.edu, bshuve@g.hmc.edu, monica.verducci@cern.ch, jose.zurita@kit.edu, tadams@hep.fsu.edu, michael.adersberger@cern.ch, Cristiano.Alpigiani@cern.ch, apresyan@fnal.gov, robert.bainbridge@cern.ch, varvara.batozskaya@cern.ch, beauches@post.bgu.ac.il, lisa.benato@cern.ch, simon.berlendis@cern.ch, eshwen.bhal@cern.ch, freya.blekman@cern.ch, Christiclip@Hotmail.Com, Jamie.Boyd@cern.ch, bbrau@physics.umass.edu, lene.bryngemark@cern.ch, oliver.buchmueller@cern.ch, buschman@umich.edu, william.buttinger@cern.ch, mario.campanelli@cern.ch, ccesarotti@g.harvard.edu, cchen23@iastate.edu, cheng@physics.ucdavis.edu, sanha@slac.stanford.edu, mcitron@cern.ch, andrea.coccaro@cern.ch, victor.coco@cern.ch, eric.conte@iphe.cnrs.fr, fcormier@cern.ch, l.corpe@cern.ch, nraig@physics.ucsb.edu, yanou.cui@ucr.edu, elena.dall'occo@cern.ch, carlod@physics.umass.edu, mohamed.anwar@cern.ch, alessandro.davoli@sissa.it, decosa@cern.ch, andrea.desimone@sissa.it, luigi.dellerose@fi.infn.it, f.deppisch@ucl.ac.uk, biplab.dey@cern.ch, mdiamond@physics.utoronto.ca, dienes@email.arizona.edu, sven.dildick@cern.ch, babette.dobrich@cern.ch, marco.drewes@uclouvain.be, melanie.eich@desy.de, mai.el.sawy@cern.ch, a.escalante.del.valle@cern.ch, [7](mailto:gabriel.</p></div><div data-bbox=)

facini@cern.ch, farina.phys@gmail.com, jlf@uci.edu, oliver.fischer@kit.edu, henning.flacher@cern.ch, foldenauer@thphys.uni-heidelberg.de, freytsis@ias.edu, fuks@lpthe.jussieu.fr, iftah.galon@physics.rutgers.edu, gershtein@physics.rutgers.edu, stefano.giagu@cern.ch, andrea.giammanco@cern.ch, vgligoro@lpnhe.in2p3.fr, Tobias.Golling@unige.ch, sergio.grancagnolo@cern.ch, sergio.giuliano.gustavino@cern.ch, andy.haas@nyu.edu, kristian.hahn@northwestern.edu, jan.hajer@uclouvain.be, ahmed.hammad@unibas.ch, lukas.heinrich@cern.ch, jan.heisig@uclouvain.be, jchelo@userena.cl, gavin.hesketh@ucl.ac.uk, chill@physics.osu.edu, mahirsch@ific.uv.es, hohlmann@fit.edu, wouterh@nikhef.nl, huth@physics.harvard.edu, philten@cern.ch, t.d.jacques@gmail.com, boj@fnal.gov, geng-yuan.jeng@cern.ch, johns@physics.arizona.edu, toshiaki.kaji@cern.ch, gregor.kasieczka@cern.ch, katsye@bgu.ac.il, malgorzata.kazana@cern.ch, henning.keller@cern.ch, khlopov@apc.in2p3.fr, fkling@uci.edu, tkolberg@hep.fsu.edu, igor.kostiuk@cern.ch, emma.sian.kuwertz@cern.ch, akvam@cern.ch, landsberg@hep.brown.edu, Gaia.Lanfranchi@Inf.infn.it, inaki.lara@csic.es, alexander.ledovskoy@cern.ch, dylan.linthorne@carleton.ca, liuj1@uchicago.edu, iacopo.longarini@cern.ch, steven.lowette@cern.ch, lubatti@u.washington.edu, margaret.susan.lutz@cern.ch, jingyu@princeton.edu, judita.mamuzic@cern.ch, matthieu.marinangeli@cern.ch, alberto.mariotti@vub.be, marlow@princeton.edu, matthew.mccullough@cern.ch, kpm82@cornell.edu, philippe.mermoud@cern.ch, milstead@fysik.su.se, sm8383@nyu.edu, vasiliki.mitsou@cern.ch, jmontejo@cern.ch, filip.moortgat@cern.ch, amorandi@sissa.it, alice.morris@cern.ch, david.michael.morse@cern.ch, mrenna@fnal.gov, bpnachman@lbl.gov, miha.nemevsek@ijs.si, nesti@aquila.infn.it, ohm@cern.ch, silvia.pascoli@durham.ac.uk, pedrok@cern.ch, cmorgoth@fnal.gov, karla.pena@cern.ch, piedra@cern.ch, jpinfold@ualberta.ca, antonio.policicchio@cern.ch, gpopara@irb.hr, jessica.prisciandaro@cern.ch, mproffit@cern.ch, giorgia.rauco@cern.ch, federico.redi@cern.ch, mreecce@g.harvard.edu, ahall@fnal.gov, haifa.rejeb.sfar@cern.ch, soerenner@uni-mainz.de, drobinson@lbl.gov, amber.rebecca.roepe@cern.ch, manfredi.ronzani@cern.ch, ennio.salvioni@tum.de, arka.santra@cern.ch, sawada@icepp.s.u-tokyo.ac.jp, jakubscholtz@gmail.com, schuster@slac.stanford.edu, pedro.schwaller@uni-mainz.de, cristiano.sebastiani@cern.ch, ssekmen@cern.ch, michele.selvaggi@cern.ch, weinan.si@cern.ch, livia.soffi@cern.ch, stolar@physics.carleton.ca, stuart@physics.ucsb.edu, john.stupak@ou.edu, Kevin.Kai.Hong.Sung@cern.ch, taylorw@yorku.ca, sebastian.templ@cern.ch, thomasbd@lafayette.edu, Emma.Torro.Pastor@cern.ch, daniele.trocino@cern.ch, Sebastian.Trojanowski@ncbj.gov.pl, marco.trovato@cern.ch, yhtsai@umd.edu, cgtully@princeton.edu, tamas.almos.vami@cern.ch, juan.vasquezcar@usm.cl, carlos.vazquez@cern.ch, konstantinos.vellidis@cern.ch, basile.vermassen@cern.ch, martina.vit@cern.ch, devin.g.walker@dartmouth.edu, xia.wang@anl.gov, gwatts@uw.edu, sixie@caltech.edu, m.yexley@cern.ch, young@slac.stanford.edu, jhyu@itp.ac.cn, piotr.zalewski@ncbj.gov.pl and yongchao2228@gmail.com

Received 23 May 2019

Accepted for publication 17 September 2019

Published 2 September 2020



CrossMark



Original content from this work may be used under the terms of the [Creative Commons Attribution 3.0 licence](https://creativecommons.org/licenses/by/3.0/). Any further distribution of this work must maintain attribution to the author(s) and the title of the work, journal citation and DOI.

Abstract

Particles beyond the Standard Model (SM) can generically have lifetimes that are long compared to SM particles at the weak scale. When produced at experiments such as the Large Hadron Collider (LHC) at CERN, these long-lived particles (LLPs) can decay far from the interaction vertex of the primary proton–proton collision. Such LLP signatures are distinct from those of promptly decaying particles that are targeted by the majority of searches for new physics at the LHC, often requiring customized techniques to identify, for example, significantly displaced decay vertices, tracks with atypical properties, and short track segments. Given their non-standard nature, a comprehensive overview of LLP signatures at the LHC is beneficial to ensure that possible avenues of the discovery of new physics are not overlooked. Here we report on the joint work of a community of theorists and experimentalists with the ATLAS, CMS, and LHCb experiments—as well as those working on dedicated experiments such as MoEDAL, milliQan, MATHUSLA, CODEX-b, and FASER—to survey the current state of LLP searches at the LHC, and to chart a path for the development of LLP searches into the future, both in the upcoming Run 3 and at the high-luminosity LHC. The work is organized around the current and future potential capabilities of LHC experiments to generally discover new LLPs, and takes a signature-based approach to surveying classes of models that give rise to LLPs rather than emphasizing any particular theory motivation. We develop a set of simplified models; assess the coverage of current searches; document known, often unexpected backgrounds; explore the capabilities of proposed detector upgrades; provide recommendations for the presentation of search results; and look towards the newest frontiers, namely high-multiplicity ‘dark showers’, highlighting opportunities for expanding the LHC reach for these signals.

Keywords: beyond the Standard Model, long-lived particles, Large Hadron Collider, high-luminosity LHC, collider phenomenology, high-energy collider experiments

1. Introduction

Document editors: James Beacham, Brian Shuve

Particles in the Standard Model (SM) have lifetimes spanning an enormous range of magnitudes, from the Z boson ($\tau \sim 2 \times 10^{-25}$ s) through to the proton ($\tau \sim 10^{34}$ years) and electron (stable), as shown in figure 1.

Similarly, models beyond the SM (BSM) typically predict new particles with a variety of lifetimes. In particular, new weak-scale particles can easily have long lifetimes for several reasons, including approximate symmetries that stabilize the long-lived particle (LLP), small couplings between the LLP and lighter states, and suppressed phase space available for decays. For particles moving close to the speed of light, this can lead to macroscopic,

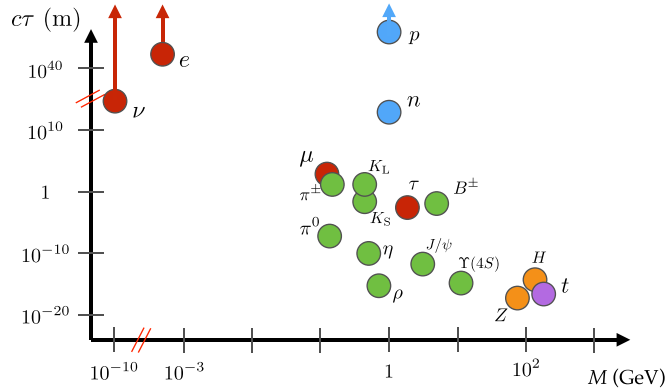


Figure 1. Particle lifetime $c\tau$, expressed in meters, as a function of particle mass, expressed in GeV, for a variety of particles in the Standard Model [1].

detectable displacements between the production and decay points of an unstable particle for $c\tau \sim 10 \mu\text{m}$ ¹²⁹.

The experimental signatures of LLPs at the Large Hadron Collider (LHC) are varied and, by nature, are often very different from signals of SM processes. For example, LLP signatures can include tracks with unusual ionization and propagation properties; small, localized deposits of energy inside of the calorimeters without associated tracks; stopped particles (SPs) that decay out of time with collisions; displaced vertices (DV) in the inner detector (ID) or muon spectrometer (MS); and disappearing, appearing, and kinked tracks. A schematic of a sampling of the variety of LLP signatures that are different from both SM signatures and the majority of BSM searches at the LHC is shown in figure 2.

Because the LLPs of the SM have masses $< 5 \text{ GeV}$ and have well-understood experimental signatures, the unusual signatures of BSM LLPs offer excellent prospects for the discovery of new physics at particle colliders. At the same time, standard reconstruction algorithms may reject events or objects containing LLPs precisely because of their unusual nature, and dedicated searches are needed to uncover LLP signals. These atypical signatures can also resemble noise, pile-up (PU), or mis-reconstructed objects in the detector; due to the rarity of such mis-reconstructions, Monte Carlo (MC) simulations may not accurately model backgrounds for LLP searches, and dedicated methods are needed to do so.

Although small compared to the large number of searches for prompt decays of new particles, many searches for LLPs at the ATLAS, CMS, and LHCb experiments at the LHC have already been performed; we refer the reader to chapter 3 for descriptions of and references to these searches. Existing LLP searches have necessitated the development of novel methods for identifying signals of LLPs, and measuring and suppressing the relevant backgrounds. Indeed, in several scenarios searches for LLPs have sensitivities that greatly

¹²⁹ Recently, a comprehensive collection of the vast array of theoretical frameworks within which LLPs naturally arise has been assembled as part of the physics case document for the proposed MATHUSLA experiment [2]. Because the focus of the current document is on the experimental signatures of LLPs and explicitly not the theories that predict them, the combination of the MATHUSLA physics case document (and the large number of references therein) and the present document can be considered, together, a comprehensive view of the present status of theoretical motivation and experimental possibilities for the potential discovery of LLPs produced at the interaction points (IPs) of the LHC.

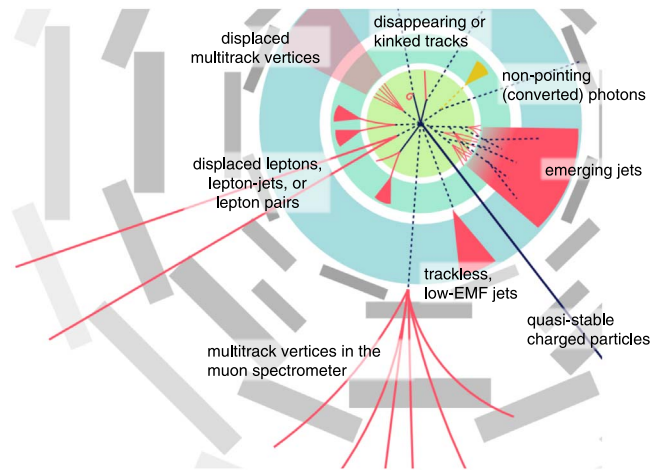


Figure 2. Schematic of the variety of challenging, atypical experimental signatures that can result from BSM LLPs in the detectors at the LHC. Shown is a cross-sectional plane in azimuthal angle, ϕ , of a general purpose detector such as ATLAS or CMS. From [3].

exceed the search for similar, promptly decaying new particles (as is true, for example, for directly produced staus in supersymmetry [4]). The excellent sensitivity of these searches, together with the lack of a definitive signal in any prompt channels at the LHC, have focused attention on other types of LLP signatures that are not currently covered. These include low-mass LLPs that do not pass trigger or selection thresholds of current searches, high multiplicities of LLPs produced in dark-sector showers, or unusual LLP production and decay modes that are not covered by current methods. Given the excellent sensitivity of LHC detectors to LLPs, along with the potentially large production cross sections of LLPs and the enormous amount of data expected to be collected when the LHC switches to high-luminosity running in the 2020s, it is imperative that the space of LLP signatures be explored as thoroughly as possible to ensure that no signals are missed. This is particularly important now, with the recent conclusion of LHC Run 2, as new triggering strategies for LLP signatures in the upcoming Run 3 can be investigated with urgency. Moreover, decisions are currently being made about detector upgrades for Phase 2 of the LHC, and design choices should be made to ensure that sensitivity to LLPs is retained or possibly improved through high-luminosity running, as may indeed be the case for many of the plans under consideration by the main experiments.

The increased interest in LLP signatures at the LHC is naturally complementary to the recognition that there are several BSM scenarios that give rise to particles difficult to optimally detect at the LHC—either promptly decaying particles or those with naturally long lifetimes—and that are searched for or planned to be searched for in fixed-target experiments, B-factories, and beam dump experiments [5–7].

The growing theoretical and experimental interest in LLPs has been mirrored by an increased activity in proposals for searches for LLPs produced at the main LHC IPs—either within the existing ATLAS, CMS, and LHCb collaborations or with new, dedicated detectors—new experimental analyses, and meetings to communicate results and discuss new ideas.

Workshops focused on LLPs at the University of Massachusetts, Amherst¹³⁰, in November of 2015; Fermilab; and KITP (UCSB)¹³¹ in May of 2016, among others, highlighted the need for a community-wide effort to map the current space of both theoretical models for LLPs and the atypical experimental signatures that could be evidence of LLPs, assess the coverage of current experimental methods to these models, and identify areas where new searches are required. Additionally, the work presented in these meetings underscored the importance of presenting the results of experimental searches in a manner that allows for their application to different models, and generated new ideas for designing analyses with the goal of minimizing model dependence. Such largely model-independent presentation makes current searches more powerful by increasing their applicability to new scenarios, while reducing redundancies in searches and ensuring that gaps in coverage are identified and addressed. This task extends beyond the purview of any particular theoretical model or experiment, and requires an effort across collaborations to address the needs of the LLP community and illuminate a path forward.

This flurry of activity eventually coalesced in the establishment of a more central and regular platform—the LHC LLP Community—for experimentalists at the LHC and those in the theoretical and phenomenological communities to exchange ideas about LLP searches to ensure the full discovery potential of the LHC. This began with a mini-workshop at CERN in May of 2016¹³² and has continued with workshops in April of 2017 at CERN¹³³, October of 2017 at ICTP Trieste¹³⁴, May of 2018 again at CERN¹³⁵, at Nikhef, in Amsterdam, in October of 2018¹³⁶, May of 2019 at CERN¹³⁷ and November of 2019 at Ghent University¹³⁸

This is the work undertaken by the LHC LLP Community and presented in this document. Based on the most pressing needs identified by the community, we organize the work of this initiative into a few key realms:

- *Simplified models:* We seek to identify a minimal (but expandable) set of simplified models that capture, with a very limited number of free parameters, the most important LLP signatures motivated by theory and accessible at the LHC. The simplified models approach has been successfully applied to models such as supersymmetry (SUSY) and dark matter (DM), and proposals exist for LLP simplified models in particular contexts. We aim to provide a basis of models that serves as a focal point for the other studies performed by the community, as well as a library that can be used in simulating LLP signal events, to allow for a common grammar to better understand how current and future searches cover LLP signature space.

¹³⁰ ‘LHC Searches for Long-Lived BSM Particles: Theory Meets Experiment’, <https://physics.umass.edu/acfi/seminars-and-workshops/lhc-searches-for-long-lived-bsm%2Dparticles-theory-meets-experiment>.

¹³¹ ‘Experimental Challenges for the LHC Run II’, <http://online.kitp.ucsb.edu/online/experlhc16/>.

¹³² ‘LHC Long-Lived Particle Mini-Workshop’, https://indico.cern.ch/e/LHC_LL2016.

¹³³ ‘Searches for LLPs at the LHC: First workshop of the LHC LLP Community’, https://indico.cern.ch/e/LHC_LL2017.

¹³⁴ ‘Searches for LLPs at the LHC: Second workshop of the LHC LLP Community’, https://indico.cern.ch/e/LHC_LL2017.

¹³⁵ ‘Searching for LLPs at the LHC: Third workshop of the LHC LLP Community’, https://indico.cern.ch/e/LHC_LL2018.

¹³⁶ ‘Searching for LLPs at the LHC: Fourth workshop of the LHC LLP Community’, https://indico.cern.ch/e/LHC_LL2018.

¹³⁷ ‘Searching for LLPs at the LHC: Fifth Workshop of the LHC LLP Community’, https://indico.cern.ch/e/LHC_LL2019.

¹³⁸ ‘Searching for LLPs at the LHC: Sixth Workshop of the LHC LLP Community’, https://indico.cern.ch/e/LHC_LL2019.

- *Experimental coverage:* In spite of the many successful LLP searches undertaken by the ATLAS, CMS, and LHCb experiments, there remains a need for a systematic study of the complementary coverage of LLP searches to the parameter spaces of LLP models. Having developed a simplified model basis, we provide a comprehensive overview of the sensitivity of existing searches, highlighting gaps in coverage and high-priority searches to be undertaken in the future.
- *Backgrounds to LLP searches:* We provide a summary and analysis of backgrounds for LLP signals at the LHC, sources of which can be rare, unexpected, and largely irrelevant for searches for prompt BSM particles, and thus not fully well understood. We assemble the collected knowledge and experience of backgrounds to prior searches with the intention of providing insight into the opportunities and challenges of searching for LLP signatures.
- *Upgrades and triggering strategies:* We discuss the prospects for LLP searches with upgraded detectors for Phase 2 of LHC running, with a focus on how upgrades can offer new sensitivity to LLPs as well as mitigate the effects of PU. New opportunities for improving sensitivity of triggers and searches to LLPs are additionally presented for the upgrades planned for Run 3. This is tied to the crucial question of triggers for LLPs; we discuss the performance of current triggers for LLPs, as well as the effects of future upgrades to the trigger system. Most importantly, we identify a few concrete upgrade studies that should be performed by the experiments that are of prime interest to the community.
- *Reinterpretation of LLP searches:* Due to the non-standard nature of the objects used in analyses, LLP searches are notoriously hard to reinterpret for models beyond those considered by the experimental collaborations. Designing searches and presenting search results in a way that is broadly applicable to current and yet-to-be-developed LLP models is crucial to the impact and legacy of the LLP search program. We discuss the reinterpretation of the LLP searches by means of concrete examples to illustrate specific challenges and, based on the lessons learned from this procedure, we provide recommendations on the presentation of LLP experimental search results.
- *Dark showers:* Current LLP search strategies have limited sensitivity to models where the LLPs are very soft, highly collimated, and come in large multiplicities, as can occur in models of dark-sector showers. We report on recent progress in theoretically parameterizing the space of dark-shower models and signatures, as well as experimental searches to uncover these signals.

Finally, we provide information about current and proposed experiments to search for LLPs at the LHC via dedicated detectors. These include the MoEDAL monopole search, the milliQan milli-charged particle (mCP) experiment, the MATHUSLA surface detector for ultra-LLPs, the CODEX-b proposal for a new detector near LHCb, and the FASER proposal for a long, narrow detector located in the forward direction well downstream one of the collision points.

This is the first report of the LHC LLP Community initiative, and is expected to be followed by future reports as our collective understanding of these signatures as a means of discovering new physics at the LHC evolves.

2. Simplified models yielding LLPs

Chapter editors: James Beacham, Giovanna Cottin, David Curtin, Jared Evans, Zhen Liu, Michael Ramsey-Musolf, Jessie Shelton, Brian Shuve

Contributors: Oliver Buchmueller, Alessandro Davoli, Andrea De Simone, Kristian Hahn, Jan Heisig, Thomas Jacques, Matthew McCullough, Stephen Mrenna, Marco Trovato, Jiang-Hao Yu

Long-lived particles (LLPs) arise in many well-motivated theories of physics BSM, ranging from heavily studied scenarios such as the minimal supersymmetric SM (MSSM) [8–12] to newer theoretical frameworks such as neutral naturalness [13–15] and hidden sector DM [16–21]. Macroscopic decay lengths of new particles naturally arise from the presence and breaking of symmetries, which can be motivated by cosmology (such as DM and baryogenesis) [22–35], neutrino masses [36–52], as well as solutions to the hierarchy problem [13–15, 53–61] or in asymptotically safe completions of the SM [62]; indeed, LLPs are generically a prediction of new hidden sectors at and below the weak scale [63–71]. An extensive and encyclopedic compilation of theoretical motivations for LLPs has already been performed for the physics case of the proposed MATHUSLA experiment [2], and we refer the reader to this document and the references therein for an in-depth discussion of theoretical motivations for LLPs. Given the large number of theories predicting LLPs, however, it is clear that a comprehensive search program for LLPs is critical to fully leverage the LHC’s immense capability to illuminate the physics of the weak scale and beyond.

The simplified model framework has proven to be a highly successful approach to characterizing signals of BSM physics. Simplified models have driven the development of searches for new signatures at the LHC and allowed existing searches to be reinterpreted for many models beyond the one(s) initially targeted in the analysis. Comprehensive simplified model programs exist for scenarios featuring prompt decays of new particles [72–78] or DM produced at colliders [79–90]. Simplified models are so successful because the majority of search sensitivity is driven by only a few broad aspects of a given BSM signature, such as the production process, overall production rate, and decay topology. Meanwhile, the sensitivity of searches is typically insensitive to other properties such as the spin of the particles involved [91–94].

To extend the simplified model approach to LLP signatures in a systematic way, we develop a proposal for a set of simplified models which aims to ensure that experimental results can be characterized as follows: (i) *powerful*, covering as much territory in model space as possible; (ii) *efficient*, reducing unnecessary redundancy among searches; (iii) *flexible*, so that they are broadly applicable to different types of models; and (iv) *durable*, providing a common framework for MC simulation of signals and facilitating the communication of results of LLP searches so that they may be applied to new models for years to come. We elaborate on these goals in section 2.1. This framework helps illuminate gaps in coverage and highlight areas where new searches are needed, and we undertake such a study in chapter 3. Our efforts build on earlier work proposing simplified model programs for LLPs motivated by particular considerations such as SUSY or DM [95–100].

In our work, we concentrate on establishing an initial basis of simplified models representative of theories giving rise to final states with one or two LLPs¹³⁹. The simplified model approach is very powerful for LLP signatures: the typically lower backgrounds for displaced signatures allow searches to be highly inclusive with respect to other objects in the

¹³⁹ Some models predict moderately higher LLP multiplicities, but the coverage of such signatures from 1-2 LLP searches is good provided the LLPs do not overlap in the detector. Our proposed simplified models are not, however, representative of high-multiplicity signatures such as dark showers (see section 2.6 and chapter 7).

event or the identification of objects originating from the decay of an LLP. This enables a single analysis to have sensitivity to a wide variety of models for LLP production and decay.

We organize our simplified models in terms of LLP channels characterized by a combination of a particular LLP production mode with a particular decay mode. Because the production and decay positions of LLPs are physically distinct¹⁴⁰, it is often possible to factorize and consider separately their production and decay¹⁴¹. For each LLP channel, the lifetime of the LLP is taken to be a free parameter. We emphasize that the LLP channel defined here is *not* the same as an experimental signature that manifests in the detector: a single channel can give rise to many different signatures depending on where (or whether)¹⁴² the LLP decays occur inside the detector, while a single experimental search for a particular signature could potentially cover many simplified model channels. In this chapter, we focus on the construction and simulation of a concrete basis of LLP simplified model channels; a partial mapping of existing searches into our basis of simplified models is discussed in chapter 3, along with the highest-priority gaps in current coverage and proposals for new searches.

As discussed in the existing simplified model literature, simplified models have their own limited range of applicability [78, 86–88, 106]. For example, the presentation of search results in terms of simplified models often assume 100% branching fractions into particular final states. In a UV model where the LLP decays in a very large number of ways, none of the individual simplified model searches may be sufficient to constrain it. Similarly, if the LLP is produced in a UV model with other associated objects that spoil the signal efficiency (for example, the production of energetic, prompt objects collimated with the LLP such that the signal fails isolation or displacement criteria; this is particularly important for high-multiplicity or dark-shower scenarios, as discussed in chapter 7), then the simplified model result does not apply and a more targeted analysis is required to cover the model. Nevertheless, the simplified models framework allows us to organize possible production modes and signatures in a systematic way and identify if there are any interesting signals or parts of parameter space that are missed by current searches. Therefore, we present a proposal for simplified models here with the understanding that there exist scenarios where UV models remain important for developing searches and presenting results.

The basis of simplified models presented here is a starting point, rather than a final statement. The present goal is to provide a set of simplified models that covers the majority of the best-motivated and simplest UV models predicting LLPs, which we outline in section 2.2. Many of these contain singly and doubly produced LLPs (or in some cases, three-to-four relatively isolated LLPs, which are typically covered well by searches for 1–2 LLPs) and so we restrict our simplified model proposal to cover these multiplicities. By design, simplified models do not include all of the specific details and subtle features that may be found in a given complete model. Therefore, the provided list is meant to be

¹⁴⁰ Indeed, the decay position may be so far from the collision point that external detectors can also be used to search for ultra-long-lived neutral or mCPs [101–105].

¹⁴¹ In addition to production and decay, a third consideration is the propagation of particles through the detector. While neutral LLPs undergo straightforward propagation, states with electric or color charge (e.g. SUSY R -hadrons), or particles with exotic charges such as magnetic monopoles or quirks, typically engage in a more complicated and often very uncertain traverse through the detector. This spoils the factorization of LLP production and decay. The subtleties related to LLPs with electric or color charge is discussed more in section 2.4.3. A trickier question is how to best simulate such states: since LLPs with electric or color charge interact with the detector material, there must be an interface between the detector simulation software and the program implementing decay. This is discussed further in section 2.5.2.

¹⁴² The case of detector-stable particles is understood to be included in the simplified models by setting $c\tau \rightarrow \infty$. In this case there is manifestly no dependence on the decay mode. See section 2.3.2 for further details.

expanded to cover new or more refined models as the LLP-search program develops. For instance, extending the simplified model framework to separately treat final states with heavy-flavor particles is of great interest (in analogy with the prompt case [107–109]); see section 2.6 for a discussion of this and other limitations of the current framework along with future opportunities for expansion. High-multiplicity signatures such as dark showers or emerging jets present different experimental and theoretical issues, which are discussed in chapter 7. Finally, a broader set of simplified models may be needed to present the results of experimental searches and to allow ready application of experimental results to UV models of interest (see chapter 6).

2.1. Goals of the present simplified model framework

The purpose of the simplified model framework is to provide a simple, common language that experimentalists and theorists can use to describe theories of LLPs and the corresponding mapping between models and experimental signatures. We therefore want our simplified model space to:

1. Use a minimal but sufficient set of models to cover a wide range of the best-motivated theories of LLPs.
2. Furnish a simple map between models and signatures to enable a clear assessment of existing search coverage and possible gaps.
3. Expand flexibly when needed to incorporate theories and signatures not yet proposed.
4. Provide a concrete MC signal event generation framework for signals.
5. Facilitate the reinterpretation of searches by supplying a sufficiently varied set of standard benchmark models for which experimental efficiencies can be provided for validation purposes.

Note that points #1 and #5 are somewhat in tension with one another: we wish to have a compact set of models that can be the subject of systematic study in terms of experimental signatures, but expressing experimental results in terms of only this set of simplified models may make it challenging to reinterpret experimental searches for UV models that are not precisely described by one of the simplified models. In this section, we prioritize having a minimal set of simplified models for the purpose of studying experimental coverages and generating new search ideas, while we defer a discussion of simplified models in the presentation and reinterpretation of search results to chapter 6¹⁴³.

In the remainder of this chapter, we construct a proposal for a minimal basis of simplified models for events with one or two LLPs. We begin with a discussion of the well-motivated UV theories that predict the existence of LLPs, and identify a set of umbrella models that yield LLPs in section 2.2. We next identify the relevant (simplified) production and decay modes for LLPs in section 2.3, emphasizing that each channel for production and decay has a characteristic set of predictions for the number and nature of *prompt* accompanying objects (AOs) producing along with the LLP. In section 2.4, we combine these production and decay modes into our simplified model basis set and highlight how different umbrella models naturally populate the various LLP channels. Section 2.5 and the appendix present a framework and instructions for how the best-motivated simplified model channels can be

¹⁴³ We note that, in general, more benchmark models may be needed for enabling reliable reinterpretation than the minimal set discussed here. An example where an extended set of simplified models is used can be seen in the heavy stable charged particle (HSCP) reinterpretation in section 6.3.2 (table 5).

simulated in MC using a new model library provided in the [appendix](#). Finally, limitations of the existing framework, along with opportunities for its further development are outlined in section 2.6.

2.2. Existing well-motivated theories for LLPs

Here we provide a brief distillation of many of the best-motivated theories with LLPs into five over-arching categories, focusing in particular on those that give rise to single and double production of LLPs at colliders. We emphasize that each of these categories is a broad umbrella containing many different individual models containing LLPs; in many cases, the motivations and model details among theories within a particular category may be very different, but tend to predict similar types of LLPs. Additionally, the categories are not mutually exclusive, with several examples of UV models falling into one or more category. In all cases, long lifetimes typically arise from some combination of hierarchies of scales in interactions that mediate decays; small couplings; and phase space considerations (such as small mass splittings between particles or large multiplicities of final-state particles in a decay). Many of the broad theoretical motivations for LLPs have recently been summarized in the literature [2].

The UV umbrella models we consider are:

- *Supersymmetry-like theories (SUSY)*. This category contains models with multiple new particles carrying SM gauge charges and a variety of allowed cascade decays. Here LLPs can arise as a result of approximate symmetries (such as R -parity [55, 110, 111] or indeed SUSY itself in the case of gauge mediation [112]) or through a hierarchy of mass scales (such as highly off-shell intermediaries in split SUSY [113], or nearly-degenerate multiplets [63, 64, 114], as in anomaly-mediated SUSY breaking [65]). Finally, models of SUSY hidden sectors such as stealth SUSY [54] generically lead to LLPs. Our terminology classifies any non-SUSY models with new SM gauge-charged particles, such as composite Higgs or extra-dimensional models, under the SUSY-like umbrella because of the prediction of new particles above the weak scale with SM gauge charges. In this category, LLP production is typically dominated by SM gauge interactions, whether of the LLP itself or of a heavy parent (HP) particle that decays to LLPs.
- *Higgs-portal theories (Higgs)*. In this category, LLPs couple predominantly to the SM-like Higgs boson. This possibility is well motivated because the SM Higgs field provides one of the leading renormalizable portals for new gauge-singlet particles to couple to the SM, and the experimental characterization of the Higgs boson leaves much scope for couplings of the Higgs to BSM physics [115, 116]. The most striking signatures here are exotic Higgs decays to low-mass particles [117] (as in many Hidden Valley (HV) scenarios [66, 67]), which can arise in models of neutral naturalness [13, 14, 118] and DM [119], as well as in more exotic scenarios such as relaxion models [120]. The Higgs is also special in that it comes with a rich set of associated production modes in addition to the dominant gluon-fusion process, with vector-boson fusion (VBF) and Higgs-strahlung (VH) production modes allowing novel opportunities for triggering on and suppressing backgrounds to Higgs-portal LLP signatures. Indeed, in many scenarios where LLPs are produced in exotic Higgs decays, associated-production modes can be the only way of triggering on the event.
- *Gauge-portal theories (ZP)*. This category contains scenarios where new vector mediators can produce LLPs. These are similar to Higgs models, although here the vector mediator is predominantly produced from $q\bar{q}$ initial states without other associated

objects except for gluon initial-state radiation (ISR). Examples include models where both SM fermions and LLPs carry a charge associated with a new Z' (for a review, see [121]), as well as either Abelian or non-Abelian dark photon or dark Z models [122] in which the couplings of new vector bosons to the SM are mediated by kinetic mixing. Scenarios with LLPs coupled to new gauge bosons are well motivated by theories of DM, particularly models with significant self-interactions [123–125] and/or sub-weak mass scales [17, 18, 20, 126, 127].

- *DM theories.* Non-SUSY and hidden-sector DM scenarios are collected in this category, which encompasses models where the cosmological DM is produced as a final state in the collider process. Examples of multi-component DM theories include models of new electroweak multiplets [64, 128–130], strongly interacting massive particles (SIMPs) [131], iDM [132–135], models with DM coannihilation partners [98, 136–141] (including scenarios where the coannihilation partners are out of chemical equilibrium, giving distinctly predictions for the relic abundance [142–145]), and non-thermal ‘freeze-in’ scenarios [146–153]. In many of these models, the collider phenomenology and LLP lifetime can be tied to the DM relic abundance [135, 146, 154]. For LLPs decaying inside the detector, an important feature distinguishing this category from the Higgs and gauge scenarios above is that an explicit detector-level signature of a DM candidate, i.e. missing energy (\cancel{E}_T), is a necessary and irreducible component [30, 66, 67, 100, 133, 135, 155–157].
- *Heavy neutrino theories (RH ν).* The see-saw mechanism of SM neutrino mass generation predicts new right-handed neutrino (RHN) states [158–162]. If the RHNs have masses in the GeV to TeV range, they typically have a long lifetime and can be probed at the LHC [38, 43–45, 48, 49, 163–174]. Examples of well-motivated, UV-complete models with RHNs include the neutrino minimal SM (ν MSM) [175, 176] and the left–right symmetric model [177–180]. Characteristic features of models in this category are LLPs produced singly via SM neutral- and charged-current (CC) interactions, and lepton-rich signatures in terms of prompt and displaced objects (often in association with quarks). For example, in extended scenarios like left–right symmetric models, production through new right-handed W and Z bosons can result in between one and four LLPs, and cascade decays between RHNs can lead to phenomena such as doubly displaced decays. Additionally, RHNs can be produced via Higgs decays [40, 41, 44, 170, 172, 181].

It is possible for a given model to fit into two or more of the umbrella UV model categories. For example, a SUSY theory with a stable lightest SUSY particle (LSP) could have the LSP serve as a DM candidate, while alternatively DM could be a new electroweak multiplet, giving rise to SUSY-like signatures [64, 128–130]. In other models featuring particles charged under a confining gauge group (such as ‘quirks’ [182]), there can exist many production possibilities for the LLPs, including via the Higgs portal and the annihilation of new TeV-scale states (see, for example, [183]). Thus, the umbrella models should not be considered as exclusive categories, but rather as over-arching scenarios that motivate particular classes of signatures (such as new SM gauge-charged particles in the SUSY-like category, or presence of \cancel{E}_T in DM models).

In developing our simplified model framework below, we construct maps between these UV model categories and the simplified model channels to illuminate some of the best-motivated combinations of production and decay modes for LLPs. This allows us to focus on the most interesting channels and assess their coverage in chapter 3.

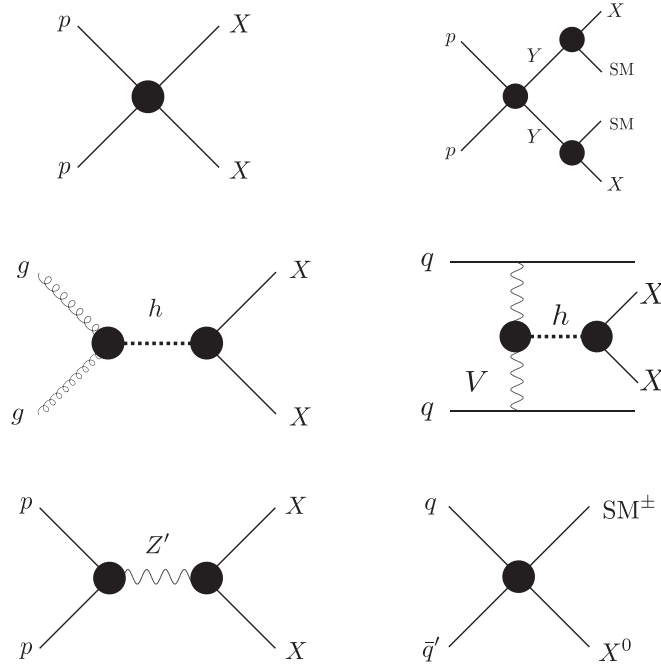


Figure 3. Schematic illustrations of LLP production modes in our simplified model framework. From top to bottom and left to right: direct pair production (DPP); HP; Higgs modes (HIG), including gluon fusion and VBF production (not shown here is VH production); heavy resonance (RES); charged current (CC).

2.3. The simplified model building blocks

As discussed above, production and decay can largely be factorized in LLP searches¹⁴⁴. This allows us to specify the relevant production and decay modes for LLP models separately; we then put them together and map the space of models into the umbrella categories of motivated theories.

2.3.1. Production modes. Motivated by our over-arching UV frameworks, we can identify a minimal set of interesting production modes for LLPs. Schematic diagrams for each production mode are shown in figure 3. These production modes determine LLP signal rates both by relating the LLP production cross section to meaningful theory parameters such as gauge charges or Higgs couplings, and by determining the kinematic distribution of the LLP. Additionally, a given production mechanism also makes clear predictions for the number and type of *prompt* objects accompanying the LLP(s). These prompt AOs can be important for both triggering on events with LLPs and for background rejection, particularly when the LLP has a low mass or decays purely hadronically, and they can be either SM states (leptons, \cancel{E}_T , tagging jets) or BSM objects such as Z' or dark photons [157, 184, 185].

¹⁴⁴ Once again, we comment that non-factorization of production and decay due to LLP interaction with the detector material and non-trivial propagation effects arise in models with LLPs with electric or color charge, and we discuss these subtleties further in section 2.5.2.

- *Direct-pair production (DPP)*: Here the LLP is dominantly pair-produced non-resonantly from SM initial states. This is most straightforwardly obtained when the LLP is charged under a SM gauge interaction. In this case, an irreducible production cross section is then specified by the LLP gauge charge and mass. Such continuum DPP can also occur in the presence of a (heavy, virtual) mediator (e.g. an initial quark–antiquark pair may exchange a virtual squark to pair produce bino-like neutralinos); in this case the production cross section is essentially a free parameter, as it is determined by the unknown heavy mediator masses and couplings.
- *Heavy parent (HP)*: The LLP is produced in the decays of on-shell HP particles that are themselves pair produced from the pp initial state. The production cross section is essentially a free parameter, and is indirectly specified by the gauge charges and masses of the HP particles. Heavy-parent production gives very different kinematics for the LLP than DPP, and often produces additional prompt AOs in the rapid cascade decays of the parents.
- *Higgs (HIG)*: Here the LLP is produced through its couplings to the SM-like Higgs boson. This case has an interesting interplay of possible production modes. The dominant production is via gluon fusion, which features no AOs beyond gluon ISR. Owing to its role in electroweak symmetry breaking, however, the Higgs has associated production modes (VBF, VH), each with its own characteristic features. The best prospects for discovery are for LLP masses below $m_h/2$, in which case the LLPs can be in decays of the on-shell SM-like Higgs boson. Higher-mass LLPs can still be produced via an off-shell Higgs, albeit at substantially lower rates [26, 186]. The LLP can be pair produced or singly produced through the Higgs portal depending on the model; an LLP X can also be produced in association with \cancel{E}_T via $h \rightarrow XX + \cancel{E}_T$ or $h \rightarrow X + \cancel{E}_T$. The cross section (or, equivalently, the Higgs branching fraction into the LLP) is a free parameter of the model. The Higgs mass can also be taken as a free parameter: there exist many theories that predict new exotic scalar states (such as the singlet-scalar extension to the SM [119]), and these new scalars can be produced in the same manner as the SM Higgs.
- *Heavy resonance (RES)*: Here the LLP is produced in the decay of an on-shell resonance, such as a heavy Z' gauge boson initiated by $q\bar{q}$ initial state. Note that production via an off-shell resonance is kinematically similar to the DPP mode. As with HIG, the LLP can be pair produced or singly produced (potentially in association with \cancel{E}_T). In RES models, ISR is the dominant source of prompt AOs. Models with new heavy scalars could conceivably fall into either RES or HIG; the main determining factor according to our organizational scheme is whether the scalar possesses Higgs-like production modes such as VBF and VH. Note that heavy resonance decays to SM particles also occur in these models, and searches for such resonances [187–193] may complement the sensitivity for decays to LLPs.
- *Charged current*: In models with weak-scale RHNs, the LLP can be produced in the leptonic decays of W/W' . Single production is favored. Prompt charged leptons from the CC interaction are typical prompt AOs.

It is important to note that each of the above production mechanisms has its own ‘natural’ set of triggers to record the signal. For example, HIG production can be accompanied by forward jets or leptons that are characteristic of VBF or VH production. Similarly, CC production often results in prompt charged leptons, while HP production comes with AOs from the HP decay. However, the reader should be cautioned that this does not necessarily mean that the ‘natural’ trigger is *optimal* for a particular signal. For example, the HIG modes suggest the use of VBF- or VH-based triggers, but if the LLP decays leptonically, it might be

more efficient to trigger on the lepton from the LLP decay. Thus, the final word on which trigger is most effective for a given simplified model depends on the production mode as well as the nature and kinematics of the LLP decay. The prompt AOs of each production mode could still, however, be used to extend sensitivity to the model (see section 6.3).

We also comment that some models may span several production modes. For example, a charged LLP that is part of an electroweak multiplet and nearly degenerate with a stable, neutral component [63–65, 99, 128–130, 194, 195] gives both DPP signatures (via $pp \rightarrow \chi^+ \chi^-$) and CC production (via associated production $pp \rightarrow \chi^\pm \chi^0$). Comprehensive coverage of each of the above production modes will allow for a conservative determination of sensitivity for models that span many production modes.

2.3.2. Decay modes. We now list a characteristic set of LLP decay modes. As we attempt to construct a minimal, manageable set of decay-mode building blocks, it is important to bear in mind that a given experimental search for LLPs can frequently be sensitive to a variety of possible LLP decay modes. As a result, it is not always necessary to perform separate searches for each possible decay mode as might otherwise be needed for prompt signatures.

The fact that LLP searches can be sensitive to many LLP decay modes is, in part, because LLPs that decay far from the collision point offer fewer avenues for particle identification. For example, for an LLP decaying inside of the calorimeter, most decay products are reconstructed as missing energy, or an energy deposition in the calorimeter. Consequently, particle identification criteria are typically relaxed in comparison to requirements on searches without displaced objects. Indeed, these ‘loose’ collider objects can differ significantly from the corresponding ‘tight’ prompt objects. This leads to more inclusive analyses that can cover a wider range of signatures with a single search.

Additionally, backgrounds for LLP searches are often small; for a comprehensive discussion of backgrounds to LLP searches, see chapter 4. As a result, tight identification and/or reconstruction criteria typically found in exclusive prompt analyses are no longer needed to suppress backgrounds. For example, ATLAS has a displaced vertex (DV) search sensitive to di-lepton and multi-track vertices that is relatively inclusive with respect to other objects originating from near the DV [196]. Similarly, CMS has an analysis sensitive to events with one each of a high-impact-parameter muon and electron without reconstructing a vertex or any other objects [197]. For these examples, the backgrounds are sufficiently low that other requirements may be relaxed and the specific decay mode of the LLP may not be too important so long as certain objects (such as muons) are present or the decay occurs in a specific location. An even more extreme example in this regard is the search for highly-ionizing tracks sensitive to electrically and color-charged LLPs. While the searches are primarily targeted to detector-stable particles (HSCPs or R -hadrons) they can also be used to probe intermediate lifetimes for which only a certain fraction of LLPs traverse the tracker before decaying (see e.g. [142]). Both because of low backgrounds as well as modified particle identification criteria compared to prompt searches, LLP searches can often be inclusive and therefore covered by a more limited range of simplified models.

In some cases, however, the topology of a decay does matter. One potentially important factor that influences the sensitivity of a search to a particular model is whether the LLP decays into two SM objects versus three, because the kinematics of multi-body decay are distinct from two-body decay and this may affect the acceptance of particular search strategies. An additional simplified model featuring a three-body decay of the LLP may consequently be needed to span the space of signatures.

Below, we describe an irreducible set of decay modes that can be used to characterize LLP signatures for various LLP charges (including neutral, electrically charged, and color

charged). For each, we also provide an explicit example for how the decay would appear in a particular UV model. We emphasize that the following decay modes are loosely defined with the understanding that their signatures are also representative of similar, related decay modes; for example $2j$ or $2j + \cancel{E}_T$ can also be proxies for $3j$ because searches for multi-body hadronic LLP decays can be sensitive to both and typically do not require reconstruction of a third jet. It should also be noted that we are not recommending searches to be optimized to the exact, exclusive decay mode because that could suppress sensitivity to related but slightly more complicated LLP decays.

- *Di-photon decays:* The LLP can decay resonantly to $\gamma\gamma$ (like in Higgs-portal models or left–right symmetric models [198]) or to $\gamma\gamma + \text{invisible}$ (in DM models). This latter mode stands as a proxy for other $\gamma\gamma + X$ decays where the third object is not explicitly reconstructed, although whether X is truly invisible can influence the triggers used. *Example: a singlino decaying to a singlet (which decays to $\gamma\gamma$) and a gravitino in Stealth SUSY [54].*
- *Single-photon decays:* The LLP decays to $\gamma + \text{invisible}$ (like in SUSY models). The SUSY model mandates a near-massless invisible particle, while other models (such as DM theories [134, 156]) allow for a heavy invisible particle. *Example: a bino decaying to photon plus gravitino in gauge-mediated models of SUSY breaking [199].*
- *Hadronic decays:* The LLP can decay into two jets (jj) (like in Higgs and gauge-portal models, or RPV SUSY), $jj + \text{invisible}$ (SUSY, DM, or neutrino models), or $j + \text{invisible}$ (SUSY). Here, ‘jet’ (j) means either a light-quark parton, gluon, or b -quark. This category also encompasses decays directly into hadrons (for example, LLP decay into π^+ plus an invisible particle [63–65]). *Example: a scalar LLP decaying to $b\bar{b}$ due to mixing with the SM Higgs boson, as in models of neutral naturalness [13, 14, 118].*
- *Semi-leptonic decays:* The LLP can decay into a lepton + 1 jet (such as in leptoquark (LQs) models) or 2 jets (like in SUSY or neutrino models). *Example: a RHN decaying to a left-handed lepton and an on- or off-shell hadronically decaying W boson (or W' boson in a left–right symmetric model) [163].*
- *Leptonic decays:* The LLP can decay into $\ell^+\ell^- (+\text{invisible})$, or $\ell^\pm + \text{invisible}$ (as in Higgs-portal, gauge-portal, SUSY, or neutrino models). Here the symbol ℓ may be any flavor of charged lepton, but the decays are lepton flavor-universal and (for $\ell^+\ell^-$ decays) flavor-conserving. *Example: a wino decaying to a neutralino and an on- or off-shell leptonic Z boson in SUSY [55].*
- *Flavored leptonic decays:* The LLP can decay into $\ell_\alpha + \text{invisible}$, $\ell_\alpha^+\ell_\beta^-$ or $\ell_\alpha^+\ell_\beta^- + \text{invisible}$ where flavors $\alpha \neq \beta$ (as in SUSY or neutrino models). *Example: a neutralino decaying to two leptons and a neutrino in R -parity-violating SUSY [55]; or a RHN decaying to two leptons and a neutrino [200].*

In all cases, both the LLP mass and proper lifetime are free parameters. Therefore, the case of detector-stable particles is automatically included by taking any of the above decay modes and taking the lifetime to infinity¹⁴⁵. We emphasize that, depending on the location of the LLP within the detector, these decay modes may or may not be individually distinguishable: a displaced di-jet decay will look very different from a displaced di-photon decay in the tracker, but nearly identical if the decay occurs in the calorimeter. The goal here is to identify promising channels (as distinct from detector signatures).

¹⁴⁵ As mentioned earlier, in the $c\tau \rightarrow \infty$ limit the decay mode becomes irrelevant. However, an exception is the search for particles that are stopped inside the detector material and decay out of time, which are discussed in section 3.5.3.

As an example of how the above-listed decay modes cover the most important experimental signatures, we consider a scenario of an LLP decaying to top quarks. This scenario is very well motivated (for instance, with long-lived stops in SUSY) and might appear to merit its own decay category of an LLP decaying to one or more top quarks. However, the top quark immediately decays to final states that *are* covered in the above list, giving an effective semileptonic decay mode ($t \rightarrow b\ell^+\nu$) and a hadronic decay mode ($t \rightarrow bj\bar{j}$) of the LLP. Similarly, LLP decays to four or more final states are typically covered by the above inclusive definitions of decay modes; this provides motivation not to over-optimize experimental searches to the specific, exclusive features of a particular decay mode.

While it would be ideal to have separate experimental searches for each of the above decay modes (when distinguishable), it is rare for specific models to allow the LLP to decay in only one manner; as in the example of an LLP decaying to a top quark, a number of decay modes typically occur with specific predictions for the branching fractions. As another example, if the LLP couples to the SM via mixing with the SM Higgs boson, then the LLP decays via mass-proportional couplings giving rise to b - and τ -rich signatures. If, instead, the LLP decays through a kinetic mixing as in the case of dark photons or Z bosons, then the LLP can decay to any particle charged under the weak interactions, giving rise to a relatively large leptonic branching fraction in addition to hadronic decay modes. This allows some level of prioritization of decay modes based on motivated UV-complete models; for example, the Higgs-portal model prioritizes searches for heavy-flavor quarks and leptons in LLP decay, while the gauge-portal model prioritizes searches for electrons and muons in LLP decay. Ultimately, however, it is desirable to retain independent sensitivity to each individual decay mode as much as possible. Indeed, for each decay mode listed above, models exist for which the given decay mode would be the main discovery channel.

Invisible final-state particles: Where invisible particles appear as products of LLP decays, additional model dependence arises from the unknown mass of the invisible particle. The invisible particle could be a SM neutrino, DM, an LSP in SUSY, or another BSM particle. The phenomenology depends strongly on the mass splitting, $\Delta \equiv M_{\text{LLP}} - M_{\text{invisible}}$. If $\Delta \ll M_{\text{LLP}}$ (i.e. $M_{\text{LLP}} \sim M_{\text{invisible}}$), the spectrum is compressed and the visible decay products of the LLP are soft. This could, for instance, lead to signatures such as disappearing tracks (DTs) or necessitate the use of ISR jets to trigger on the LLP signature. If the mass splitting is large, $M_{\text{invisible}} \ll M_{\text{LLP}}$, then the signatures lose their dependence on the invisible particle mass.

We suggest three possible benchmarks: a compressed spectrum with $\Delta \ll M_{\text{LLP}}$ (example: a nearly degenerate chargino-neutralino pair, giving rise to soft leptons or DTs [63–65, 99, 128–130, 194, 195]); a massless invisible state, $\Delta = M_{\text{LLP}}$ (example: a next-to-lightest SUSY particle (NLSP) decaying to SM particles and a massless gravitino in gauge-mediated SUSY breaking (GMSB) [112, 201–206]); and an intermediate splitting corresponding to a democratic mass hierarchy, $\Delta \approx M_{\text{LLP}}/2$ (example: NLSPs in mini-split SUSY [57, 58, 96]).

2.4. A simplified model proposal

In this section, we present a compact set of simplified model channels that, broadly speaking, covers the space of theoretical models in order to motivate new experimental searches. Such a minimal, compact set may not be optimal for reinterpretation of results (where variations on our listed production and decay modes may influence signal efficiencies and cross section sensitivities), but rather provides a convenient characterization of possible signals to ensure that no major discovery mode is missed. These models may therefore serve as a starting point

for systematically understanding experimental coverage of LLP signatures and devising new searches, but may need to be extended in future for the purposes of facilitating reinterpretation. We undertake an in-depth discussion of these topics in section 6.

We classify LLPs according to their SM gauge charges, as these dictate the dominant or allowed LLP production and decay modes, and can give rise to different signatures (for example, DTs and hadronized LLPs). We separately consider LLPs that are: (a) neutral; (b) electrically charged but color neutral; and (c) color charged. In the latter case, it is important to distinguish between the long-lived parton (which carries a charge under quantum chromodynamics, QCD) that hadronizes prior to decay, and the physical LLP, which is a color-singlet ‘ R -hadron’ (using the standard nomenclature inspired by SUSY). The decays of the R -hadron are still dominated by the parton-level processes.

All of the following models have the LLP mass and lifetime as free parameters. For HP production, the parent mass is an additional parameter, while for invisible decays, several different benchmarks for mass splittings between LLP and invisible final state may have to be separately considered as described in section 2.3.2. The cross section may have a theoretically well-motivated target value depending on UV-model parameters, but phenomenologically can generally be taken as a free parameter.

We emphasize that in spite of the many simplified model channels proposed below, a small number of experimental LLP searches can have excellent coverage over a wide range of channels (at least for certain lifetime ranges). The list is intended to be comprehensive in order to identify whether there are new searches that could have a similarly high impact on the space of simplified models, and identify where the gaps in coverage are.

2.4.1. Neutral LLPs. The simplified model channels for neutral LLPs are shown in table 1, where X indicates the LLP.

In our initial proposal, which is the first iteration of the simplified model framework, it is sufficient to consider as ‘jets’ all of the following: $j = u, d, s, c, b, g$. It is worth commenting that b -quarks pose unique challenges and opportunities. Since b -quarks are themselves LLPs, they appear with an additional displacement relative to the LLP decay location. They also often give rise to soft muons in their decays, which could in principle lead to additional trigger or selection possibilities. However, these subtleties can be addressed in further refinements of the simplified models; we discuss this further in section 2.6. Similarly, we consider e, μ, τ to be included in the broad category of ‘leptons’, with the proviso that searches should be designed where possible with sensitivity to each.

When multiple production modes are specified in one row of the table, this means that multiple especially well-motivated production channels give rise to similar signatures. Typically only one of these simplified model production modes will actually need to be included when developing and assessing sensitivity of an experimental search, but we sometimes include multiple different production modes as individuals may variously prefer one over the other.

In each entry of the table, we indicate which umbrella category of well-motivated UV models (section 2.2) can predict a particular (production) \times (decay) mode. An asterisk (*) on the umbrella model indicates that \cancel{E}_T is required in the decay. A dagger (†) indicates that this particle production \times decay scenario is not present in the *simplest and most minimal* implementations or spectra of the umbrella model, but could be present in extensions of the minimal models. While the HIG production signatures are best-motivated for the SM-like 125 GeV Higgs, exotic Higgses of other masses can still have the same production modes and so m_H can be taken as a free parameter.

Table 1. Simplified model channels for neutral LLPs. The LLP is indicated by X . Each row shows a separate production mode and each column shows a separate possible decay mode, and therefore every cell in the table corresponds to a different simplified model channel of (production) \times (decay). We have cross-referenced the UV models from section 2.2 with cells in the table to show how the most common signatures of complete models populate the simplified model space. The asterisk (*) shows that the model definitively predicts missing energy in the LLP decay. A dagger (\dagger) indicates that this particle production \times decay scenario is not present in the *simplest and most minimal* implementations or spectra of the umbrella model, but could be present in extensions of the minimal models. When two production modes are provided (with an ‘or’), either simplified model can be used to simulate the same simplified model channel.

Production	Decay					
	$\gamma\gamma(+\text{inv.})$	$\gamma + \text{inv.}$	$jj(+\text{inv.})$	$jj\ell$	$\ell^+\ell^- (+\text{inv.})$	$\ell_\alpha^+\ell_{\beta\neq\alpha}^- (+\text{inv.})$
DPP: sneutrino pair or neutralino pair	\dagger	SUSY	SUSY	SUSY	SUSY	SUSY
HP: squark pair, $\tilde{q} \rightarrow jX$ or gluino pair $\tilde{g} \rightarrow jjX$	\dagger	SUSY	SUSY	SUSY	SUSY	SUSY
HP: slepton pair, $\tilde{\ell} \rightarrow \ell X$ or chargino pair, $\tilde{\chi} \rightarrow WX$	\dagger	SUSY	SUSY	SUSY	SUSY	SUSY
HIG: $h \rightarrow XX$ or $\rightarrow XX + \text{inv.}$	Higgs, DM*	\dagger	Higgs, DM*	RH ν	Higgs, DM* RH ν^*	RH ν^*
HIG: $h \rightarrow X + \text{inv.}$	DM*, RH ν	\dagger	DM*	RH ν	DM*	\dagger
RES: $Z(Z') \rightarrow XX$ or $\rightarrow XX + \text{inv.}$	Z', DM^*	\dagger	Z', DM^*	RH ν	Z', DM^*	\dagger
RES: $Z(Z') \rightarrow X + \text{inv.}$	DM	\dagger	DM	RH ν	DM	\dagger
CC: $W(W') \rightarrow \ell X$	\dagger	\dagger	RH ν^*	RH ν	RH ν^*	RH ν^*

We remind the reader that the production modes listed in table 1 encompass also the associated production of characteristic prompt objects. For example, the Higgs production modes not only proceed through gluon fusion, but also through VBF and VH production, each of which results in associated prompt objects such as forward jets in VBF, and leptons or \cancel{E}_T in VH. All of the production modes listed in table 1 could be accompanied by ISR jets that aid in triggering or identifying signal events. It is therefore important that searches are designed to exploit such prompt AOs whenever they can improve signal sensitivity, especially with regard to triggering.

To demonstrate how to map full models onto the list of simplified models (and vice-versa), we consider a few concrete cases. For instance, if we consider a model of neutral naturalness where X is a long-lived scalar that decays via Higgs mixing (for instance, X could be the lightest quasi-stable glueball), then the process where the SM Higgs h decays via $h \rightarrow XX$, $X \rightarrow b\bar{b}$ would be covered with the HIG production mechanism and a di-jet decay. Entirely unrelated models, such as the case where X is a bino-like neutralino with RPV decays $h \rightarrow XX$, $X \rightarrow jjj$ could be covered with the same simplified model because most hadronic LLP searches do not have exclusive requirements on jet multiplicity. Similarly, a hidden-sector model with a dark photon, A' , produced in $h \rightarrow A'A'$, $A' \rightarrow f\bar{f}$ would also give rise to the di-jet signature when f is a quark, whereas it would populate the $\ell^+\ell^-$ column if f is a lepton. Finally, a scenario with multiple hidden-sector states X_1 and X_2 , in which X_2 is an LLP and X_1 is a stable, invisible particle, could give rise to signatures like $h \rightarrow X_2X_2$, $X_2 \rightarrow X_1jj$ that would be covered by the same HIG production, hadronic-decay simplified model; however, we see how \cancel{E}_T can easily appear in the final state, and that the LLP decay products may not be entirely hadronic. Therefore, the simplified models in table 1 can cover an incredibly broad range of signatures, but only if searches are not overly optimized to particular features such as \cancel{E}_T and LLPs decaying entirely visibly (which would allow reconstruction of the LLP mass)¹⁴⁶.

2.4.2. Electrically charged LLPs: $|Q| = 1$. For an electrically charged LLP, we need to consider far fewer production modes because of the irreducible gauge production associated with the electric charge. We still consider the additional possibility of a HP scenario where the parent has a QCD charge, as this could potentially dominate the production cross section, see e.g. [95]. We summarize our proposals in table 2.

Note that we group all resonant production into the Z' simplified model. The reason is that the SM Higgs cannot decay into two on-shell charged particles due to the model-independent limits from LEP on charged particle masses, $M \gtrsim 75\text{--}90$ GeV (see, for example, [207]); because of this lower limit on the LLP mass, it is less important to use AOs for triggering and reconstructing charged LLP signatures than for neutral LLPs. Additionally, there are fewer allowed decay modes because of the requirement of charge conservation.

For concreteness, we recommend using $|Q| = 1$ as a benchmark for charged LLPs for the purpose of determining allowed decay modes. Although other values of Q are possible, these often result in cosmologically stable charged relics or necessitate different decay modes than those listed here. Additionally, LLPs with $|Q| = 1$ are motivated within SUSY [63–65, 208–210] and within Type-III seesaw models of neutrino masses [211–214]. We note that there exist already dedicated searches for heavy quasi-stable charged particles with non-

¹⁴⁶ This should not, of course, be interpreted as saying that searches shouldn't be done that exploit these features. Instead, our position is that experiments should bear in mind the range of topologies and models covered by each cell in table 1 when designing searches, and that some more inclusive signal regions should be established where possible.

Table 2. Simplified model channels for electrically charged LLPs such that $|Q| = 1$. The LLP is indicated by X . Each row shows a separate production mode and each column shows a separate possible decay mode, and therefore every cell in the table corresponds to a different simplified model channel of (production) \times (decay). We have cross-referenced the UV models from section 2.2 with cells in the table to show how the most common signatures of complete models populate the simplified model space. The asterisk (*) shows that the model definitively predicts missing energy in the LLP decay. A dagger (\dagger) indicates that this particle production \times decay scenario is not present in the *simplest and most minimal* implementations or spectra of the umbrella model, but could be present in extensions of the minimal models. When two production modes are provided (with an ‘or’), both production simplified models can be used to cover the same experimental signatures.

Production	Decay			
	$\ell + \text{inv.}$	$jj(+\text{inv.})$	$jj\ell$	$\ell\gamma$
DPP: chargino pair or slepton pair	SUSY DM*	SUSY DM*	SUSY	\dagger
HP: $\tilde{q} \rightarrow jX$	SUSY DM*	SUSY DM*	SUSY	\dagger
RES: $Z' \rightarrow XX$	Z', DM^*	Z', DM^*	Z'	\dagger
CC: $W' \rightarrow X + \text{inv.}$	DM*	DM*	$\text{RH}\nu$	\dagger

standard charges [215, 216]. Because such searches are by construction not intended to be sensitive to the decays of the LLP, the existing models are sufficient for characterizing these signatures and they do not need to be additionally included in our framework.

For massive particles with $|Q| = 1$ with intermediate or large lifetimes such that the LLP traverses a significant part (or all) of the tracker, the highly ionizing track of the LLP provides a prominent signature. This can be exploited for an efficient suppression of backgrounds while keeping identification and/or reconstruction criteria as loose and, hence, as inclusive as possible. In particular, for decay-lengths of the order of or larger than the detector size, the signature of highly ionizing tracks and anomalous time of flight (TOF) (i.e. searches for HSCPs; see sections 3.5 and 6.4.1) constitute an important search strategy covering a large range of lifetimes present in the parameter space of theoretically motivated models. While the searches for HSCPs are largely inclusive with respect to additional objects in the event, they depend strongly on the velocity of the LLP. For $\beta \rightarrow 1$ one loses the discriminating power against minimally ionizing particles, while for small velocities, $\beta \approx 0.5$, the reconstruction becomes increasingly difficult due to timing issues. It is therefore important to include the HP production scenario which covers a much larger kinematic range than direct production alone and which may feature a much wider range of signal efficiencies than the DPP scenario [97].

While the signatures in table 2 form a minimal set, they also encompass some scenarios that merit special comment. One of these is the DT signature [63–65, 99, 128–130, 194, 195], in which a charged LLP decays to a nearly degenerate neutral particle. The lifetime is long in this scenario due to the tiny mass splitting between the two states. Formally, these are included in the chargino or slepton DPP modes in table 2 with decays to $\ell + \text{inv.}$ or $q\bar{q}' + \text{inv.}$ taken in the limit where the splitting between the charged LLP and the invisible final state is of $\mathcal{O}(200 \text{ MeV})$. In the case of a hadronic decay, X decays to a soft pion that is very challenging to reconstruct and so the track simply disappears. This is an important scenario that is already the topic of existing searches [217, 218]. As the degeneracy between

Table 3. Simplified model channels for LLPs with color charge. The LLP is indicated by X . Each row shows a separate production mode and each column shows a separate possible decay mode, and therefore every cell in the table corresponds to a different simplified model channel of (production) \times (decay). We have cross-referenced the UV models from section 2.2 with cells in the table to show how the most common signatures of complete models populate the simplified model space. A dagger (\dagger) indicates that this particle production \times decay scenario is not present in the *simplest and most minimal* implementations or spectra of the umbrella model, but could be present in extensions of the minimal models. When two production modes are provided (with an ‘or’), both production simplified models can be used to cover the same experimental signatures.

Production	Decay			
	$j + \text{inv.}$	$jj(+\text{inv.})$	$j\ell$	$j\gamma$
DPP: squark pair or gluino pair	SUSY	SUSY	SUSY	\dagger

the charged LLP and the neutral state is relaxed, other signatures are possible; this parameter range is well motivated both by SUSY and DM models with coannihilation [98, 136, 137].

Finally, we comment on the challenges of simulating the charged LLP simplified models. Because the LLP bends and interacts with detector material prior to its decay, the simulation of the LLP propagation is important in correctly modeling the experimental signature. The subsequent decay of the LLP must either be hard-coded into the detector simulation, or allow for an interface with programs such as Pythia 8 to implement the decays. We discuss the challenges of simulating signals for LLPs with electric or color charge in section 2.5.2.

2.4.3. LLPs with color charge. An LLP charged under QCD is more constrained than even electrically charged LLPs. Because of the non-Abelian nature of the strong interactions, the gauge pair-production cross section of the LLP is specified by the LLP mass and its representation under the color group, $SU(3)_C$. We do not consider LLP production via a HP particle because that cross section is unlikely to dominate the total production rate at the LHC relative to DPP. The simplified model channels are provided in table 3.

A complication of the QCD-charged LLP is that the LLP hadronizes prior to its decay, forming an R -hadron bound state. The modeling of hadronization and subsequent propagation is directly related to many properties of the long-lived parton, such as electric charge, flavor, and spin. Event generators such as Pythia 8 have routines [219, 220] to simulate LLP hadronization, although it is unclear how precise these predictions are. For a point of comparison, using the default settings of Pythia 8 yields an estimate of the neutral R -hadron fraction from a gluino (color-octet fermion, \tilde{g}) of approximately 54%, while the neutral R -hadron fraction for a stop (scalar top partner) is estimated to be 44% [96]. After hadronization, the charge of the R -hadron may change as it passes through the detector. For instance, some estimates [221, 222] suggest that heavy, color-octet gluinos \tilde{g} would predominantly form mesons (e.g. $(u\tilde{g}\bar{d})$) at first. They eventually drop to the lower-energy neutral singlet baryon $\tilde{\Lambda} = (\tilde{g}uds)$ state when interacting with the protons and neutrons within the calorimeters.

The modeling of LLP hadronization and propagation is crucial to designing searches for color-charged LLPs and assessing their sensitivity. For example, only the charged R -hadrons can be found in HSCP search; if the LLP charge changes as it passes through the detector, HSCP searches may have limited sensitivity. To take this into account, the experimental searches include both tracker-only or tracker + calorimeter signal regions [4, 223], which

enhances sensitivity to the scenario in which R -hadrons lose their charge by the time they reach the calorimeters.

Because no R -hadrons have been discovered to date and hence their properties cannot be directly measured, R -hadron modeling in detector simulations is challenging. We discuss the challenges of simulating the propagation and decays of LLPs with color charge in section 2.5.2.

2.5. Proposal for a simplified model library

The simplified models outlined in the above sections provide a common language for theorists and experimentalists to study the sensitivity of existing searches, propose new search ideas, and interpret results in terms of UV models. Each of these activities demands a simple framework for the simulation of signal events that can be used to evaluate signal efficiencies of different search strategies and map these back onto model parameters. Requiring individual users to create their own MC models for each simplified model is impractical, redundant, and invites the introduction of errors into the analysis process.

In this section, we propose and provide a draft version of a *simplified model library* consisting of model files and MC generator cards that can be used to generate events for various simplified models in a straightforward fashion. Because each experiment uses slightly different MC generators and settings, this allows each collaboration (as well as theorists) to generate events for each simplified model based on the provided files. Depending on how the LLP program expands and develops over the next few years, it may become expedient to expand the simplified model library to include sets of events in a standard format (such as the Les Houches format [224]) that can be directly fed into event-generator and detector-simulation programs. Given the factorization of production and decay of LLPs that is valid for neutral LLPs, this could involve two mini-libraries: a set of production events for LLPs and a set of decay events for LLPs, along with a protocol for ‘stitching’ the events together.

The current version of the library is available at the LHC LLP Community website¹⁴⁷, hosted at CERN. In [appendix](#), we also provide tables that list how to simulate each LLP simplified model channel with one of the specified base models. These proposals are based on the models outlined in section 2.5.1 and often match the best-motivated simplified models from section 2.4, and also building on the DM-inspired LLP simplified models proposed and detailed in [100]. The library currently focuses on models of neutral LLPs; simulating the propagation of charged LLPs along with the full range of decays listed in sections 2.4.2–2.4.3 requires more careful collaboration with detector simulation and other MC programs to ensure that they can practically be used in experimental studies.

We provide model files in the popular universal Feynrules output (UFO) format [225], which is designed to interface easily with parton-level simulation programs such as Mad-Graph5_aMC@NLO [226]. The goal is to cover as many of the simplified models of section 2.4 with as few UFO models as possible; this limits the amount of upkeep needed to maintain the library and develops familiarity with the few UFO models needed to simulate the LLP simplified models. We provide specific instructions for how to simulate each simplified LLP channel along with the UFO models.

2.5.1. Base models for library. In order to reproduce the simplified model channels of section 2.3, we need a collection of models that:

¹⁴⁷ <http://cern.ch/longlivedparticles>

- Includes additional gauge bosons and scalars to allow vector- and scalar-portal production of LLPs (RES and HIG).
- Includes new gauge-charged fermions and scalars to cover direct and simple cascade production modes of LLPs (DPP and HP).
- Includes a RHN-like state with couplings to SM neutrinos and leptons (CC).
- *Recommended, but optional*: Allows for the decays of the LLP particle through all of the decay modes listed in section 2.3, either through renormalizable or higher-dimensional couplings. If couplings that allow LLP decay are included in the UFO model, then the decays can be performed directly at the matrix-element level in programs such as MadGraph5_aMC@NLO [226] and accompanying packages such as MadSpin [227]. Alternatively, it is possible for neutral LLPs to simulate the production and decay as a single process; in such cases, numerical instabilities sometimes arise, for which dedicated event generators are needed [49]. If the couplings needed for LLP are not in the UFO model, then LLPs can be left stable at the matrix-element level and decays implemented via Pythia 8 [219, 220], which allows for the straightforward implementation of decays according to a phase-space model, but does not correctly model the angular distribution of decay products. Instructions for implementing decays in Pythia are included with the model library files.

Fortunately, an extensive set of UFO models is already available for simulating the production of BSM particles. We note that extensions or generalizations of only three already-available UFO models are needed at the present time; the SUSY models in particular can cover many of the simplified models since they contain an enormous collection of new fermions and scalars. We also provide an optional fourth model, the Hidden Abelian Higgs Model, that can be helpful to simulate HIG and ZP theories.

1. *The MSSM*: The use of this model is motivated by and allows for the simulation of SUSY-like theories. The model contains a whole host of new particles with various gauge charges and spins. Therefore, an MSSM-based model allows for the simulation of many of the simplified model channels. In particular, we note that existing UFO variants of the MSSM that include gauge-mediated supersymmetry breaking (GMSB) couplings (including decays to light gravitinos), R -parity violation (making unstable the otherwise stable LSPs [55, 110, 111]), and the phenomenological MSSM (pMSSM) [228, 229] already cover most of the SUSY-motivated LLP scenarios. In some cases, the model is modified to give direct couplings between the Higgs states and gluons/photons.
2. *The left–right symmetric model (LRSM)*: This UFO model is best for simulating UV theories with right-handed neutrinos ($\text{RH}\nu$). The UFO model supplements the SM by an additional $\text{SU}(2)_R$ symmetry, which gives additional charged and neutral gauge bosons. The model is available in the simplified models library and contains a RHN which is the typical LLP candidate. The LLP can be produced via SM W , Z , or via the new gauge and Higgs bosons (both charged and neutral) present in the theory¹⁴⁸. The LRSM therefore contains many of the charged and neutral current LLP production processes outlined in section 2.4.1.
3. *Dark-matter simplified models (DMSM)*: These UFO models are best for simulating UV theories in the DM class. These UFO models have been created by the LHC DM working group [86]. They typically consist of a new BSM mediator particle (such as a scalar of a Z') coupled to invisible DM particles. The UFO models can either be modified to include an unstable LLP, or else the otherwise stable ‘DM’ particle can be decayed via Pythia.

¹⁴⁸ Additional LRSM tools are available at <https://sites.google.com/site/leftrighthep/>.

The utility and applicability of the DM simplified model framework to LLPs has already been demonstrated with a detailed proposal and study of classes of DM simplified models for LLPs [100]. These models are particularly good for simulating LLP production via a heavy resonance (RES), and can also simulate continuum production of LLPs in the limit where the mediator is taken to be light and off-shell (DPP).

4. (Optional) *The hidden abelian Higgs model (HAHM)*: This UFO model contains new scalars and gauge bosons and so can be used to simulate both Higgs-portal and gauge-portal (ZP) theories. The model consists of the SM supplemented by a ‘hidden sector’ consisting of a new U(1) gauge boson and a corresponding Higgs field. The physical gauge and Higgs bosons couple to the SM via kinetic and mass mixing, respectively. The HAHM allows for straightforward simulation of Higgs-portal production of LLPs, as well as Z' models and many hidden sector scenarios. The UFO implementation is from [230].

If additional decay modes are needed beyond those in the specified simplified models, then the library can be updated to include the new couplings mediating the decay. Alternatively, the LLPs can be left stable at parton level and decayed in event generators such as Pythia.

A detailed list of processes that can be used to simulate each simplified model channel is provided in the [appendix](#). The primary purpose of the library is to be used to simulate events for determining acceptances, and, as a result, the signal cross section is not important. Thus, for example, SM gauge interactions can be used as proxies for much weaker exotic interactions. Similarly, the spins of the particles are generally of subdominant importance: replacing the direct production of a fermion with the direct production of a scalar will not fundamentally alter the signature. As long as results are expressed in terms of sensitivity to cross sections and not couplings, the results can be qualitatively (and in many cases, quantitatively) applied to any similar production mode regardless of spin. However, we caution the reader that changing the spin of the LLP (or its parent) can change the angular distribution, and since in some cases LLP searches are typically more sensitive to aspects of event geometry than prompt searches, the second-order effects of spin could have more of an effect than for prompt simplified models.

2.5.2. LLP propagation and interaction with detector material. Long-lived particles with electric or QCD charges interact with the detector material prior to decay, and their propagation through the detector must be correctly modeled. The propagation of both LLPs with color charge (in the form of R -hadrons) and electrically charged LLPs can be implemented in the Geant4 (G4) toolkit [231]. For example, routines exist to simulate the propagation of color-charged LLPs [232, 233]. G4 also includes routines that can implement N -body decays of LLPs using a phase-space model. This works fine for decays of LLPs to leptons, photons, invisible particles such as neutrinos, as well as exclusive hadronic decays.

However, G4 cannot implement decays to partons that subsequently shower and hadronize. One solution to this limitation is employed by CMS [234, 235] and ATLAS [236] in their searches for stopped LLPs. In these analyses, the signal simulation proceeds in two stages. During the first stage, the production of the LLP and its subsequent interactions with the detector are simulated. Once the stopping point of the LLP is determined, a new event is simulated including the LLP decay; the LLP decay products are then manually moved to the stopping point from the first stage. G4 is then run a second time to determine the efficiency for reconstructing the LLP decay signal.

It would be preferable to fully automate the simulation of decays of charged LLPs after propagation in G4. There exists in G4 a class called G4ExtDecayer, which can be used to

implement decays by interfacing with an external generator. This class has been used to interface G4 with Pythia 6¹⁴⁹. The interface with Pythia 6 has been used most recently to model LLP gluino propagation and decay in a search for DV and missing energy in ATLAS [237]. Work is ongoing to extend this functionality to Pythia 8 and to simplify the interface.

An additional challenge of simulating LLP decays is that, if the LLP undergoes a multi-body decay, generators such as Pythia use a phase-space model to implement the decays. If more accuracy is required, it may be preferable to use the full matrix element via generators such as MadGraph5 [226, 238]. If the matrix element is important for computing the decay of the LLP, then either an interface with MadGraph is needed to implement the decay prior to passing the vertex back to Pythia 8 for showering and hadronization, or matrix-element-based methods within the event generator itself must be used.

Because of the need to interface with G4 in simulating the decays of LLPs with electric or color charges, we do not at this point include such decay modes in our simplified model library. The decays of such LLPs will be most easily simulated via an interface with Pythia 8 once it is finalized.

Finally, we comment that LLPs can have even stranger propagation properties than LLPs with electric or color charges. For example, quirks are LLPs that are charged under a hidden-sector gauge interaction that confines at macroscopic scales [182]. Because the confinement scale can be just about any distance, quirks can have very unusual properties; as a specific example, if electrically charged quirk–anti-quirk pairs are bound on the millimeter or centimeter level, they behave as an electric dipole and therefore do not leave conventional tracks that bend in the magnetic field. Other confinement scales give rise to different behaviors, such as meta-stable heavy charged particles and non-helical tracks [239, 240]. In scenarios where the quirks carry color charge, the quirks hadronize and can undergo charge-flipping interactions as they move through the detector. These quirk scenarios can be challenging to model, and no public code exists that allows for the propagation and interaction of quirks with the detector material; we encourage the collaborations to validate and release any internal software they may have to study the propagation of quirks (for more discussion, see the discussion of quirks in section 3.5)¹⁵⁰.

2.6. Limitations of simplified models and future opportunities

We conclude our discussion of simplified models with a more extensive discussion of the limitations of the current simplified model proposal in its application to models of various types, along with opportunities for future development. The presented framework is only the first step of a simplified model program that is comprehensive in terms of generating LHC signatures and allowing straightforward reinterpretation of experimental results for UV models. The framework we have developed with separate, modular components for LLP production and decay is amenable to expansion, and we encourage members of the theory and experimental communities to continue to do so over the coming years to ensure maximal utility of the simplified models framework.

One significant simplification we have undertaken in our framework is to define a ‘jet’ as any of $j = u, c, d, s, b, g$. In reality, different partons give rise to different signatures, especially when one of the ‘jets’ is a heavy-flavor quark. Jets initiated by b and c quarks have some useful distinguishing features, such as the fact that the underlying heavy-flavor meson

¹⁴⁹ See http://geant4-userdoc.web.cern.ch/geant4-userdoc/Doxygen/examples_doc/html/Exampledecayer6.html

¹⁵⁰ Ideally, this software would be well-documented to facilitate sharing between experiments. A successful example of readily shareable software between experiments is the G4 package for R -hadrons and other particles’ interaction with matter, found at <http://r-hadrons.web.cern.ch/r-hadrons/>.

decays at a distance slightly displaced from the proton interaction vertex and that there are often associated soft leptons resulting from meson decays. In particular, it is possible that the soft muons associated with B -meson decays could be used to enhance trigger and reconstruction prospects for LLPs decaying to b -jets [241]. However, heavy quarks also constitute an important background for LLP searches, and so LLPs decaying to b - and c -jets may necessitate dedicated treatment in future. Similarly, LLP decays to τ leptons may merit further specialized studies.

Another property of the current framework is that it is restricted to LLP signatures of low multiplicity. By ‘low multiplicity’, we mean collider signatures with one or two LLPs. Searches inspired by these models are also suitable for many scenarios with three or four LLPs per event (which include models with dark-Higgs decays into lepton-jets (LJs) [155], or left–right symmetric models [169]), since the LLP signatures are generally extremely rare and so only one or two typically need to be identified in a given event to greatly suppress backgrounds. Thus, as long as the search is inclusive with respect to possible additional displaced objects, the signature can be covered with low-multiplicity strategies. As the LLP multiplicity grows, however, the simplified model space we have presented requires modification. This is both because the individual LLPs grow softer, making them harder to reconstruct on an individual level, and they become less separated in the detector, which makes isolation and identification of signal a challenge. On the other hand, the high LLP multiplicity may allow for new handles for further rejecting backgrounds, and the kinematics can vary widely based on the model (for example, in some ‘quirky’ scenarios, LLPs can be produced in a variety of ways with different kinematic distributions [120]). In extreme cases, signals can even mimic PU [242]. High-multiplicity signatures therefore require dedicated modeling, and we defer the study of these signatures to chapter 7.

Finally, we conclude by noting that simplified models are intended to provide a general framework to cover a broad swath of models. Any simplified model set-up, however, cannot cover every single UV model without becoming as complex as the UV model space itself. As with the case of promptly decaying new particles, care must also be taken in the interpretation of simplified models [78, 86–88, 106]: for example, constraints on simplified models assuming 100% branching fractions of LLPs to a particular final state may not accurately represent the constraint on a full model due to the large multiplicity of possible decay modes. There will additionally always be very well-motivated models that predict specific signatures that are challenging to incorporate into the simplified model framework outlined here. Experimental searches for these signatures should still be done where possible, but we encourage theorists and experimentalists alike to think carefully about how to design such searches so as to retain maximal sensitivity to simplified models that may give rise to similar signatures.

3. Experimental coverage of LLP signatures

Chapter editors: Juliette Alimena, Xabier Cid Vidal, Albert de Roeck, Jared Evans, Heather Russell, Jose Zurita

Contributors: David Curtin, Alberto Escalante del Valle, Philippe Mermod, Antonio Policicchio, Brian Shuve

A critical component of any discussion of LLP searches at the LHC is the comprehensive review of the existing searches from ATLAS, CMS, and LHCb, and an assessment of their coverage and any gaps therein. This is an inherently challenging task, given the varied and atypical objects often defined and utilized in LLP analyses and the differences among the

experiments. As such, the following discussion assumes little-to-no background on LLP search strategies and includes a high level of detail regarding the current analyses. The focus of the discussion is on the existing studies, while acknowledging that the landscape for new physics models and LLP signatures can be broader than the ones described here.

Backgrounds to most of these studies are typically small, as most LLP signatures are not naturally mimicked by any irreducible SM processes. Backgrounds for LLP searches typically include peripheral or machine effects, those rarely important for searches for prompt physics, including cosmic muons, beam halo, detector noise, and cavern backgrounds. Such backgrounds are discussed in detail in chapter 4. As rare as these backgrounds typically are, their rates are not completely negligible, and particular, model-dependent selection requirements (based on, for instance, the LLP mass range or specific decay modes) must be made to reduce backgrounds as much as possible and, in some cases, make the searches ‘background-free’. Additionally, many default object reconstruction algorithms are not designed to detect particles originating from decays of LLPs, and so dedicated reconstruction of tracks, jets, leptons, or other objects may be required for LLP searches. Taken altogether, these factors make LLP searches very different from searches for prompt objects, and the following discussion additionally aims to collate and summarize the current techniques for LLP reconstruction at the LHC.

A particular challenge for many LLP signatures is the trigger. With the exception of certain dedicated ATLAS triggers in the calorimeters or MS, there are no Level-1 (L1) triggers that directly exploit the displaced nature of LLP decays, and L1 trigger thresholds must be surpassed by standard objects (such as leptons or high-energy jets) for the event to be recorded¹⁵¹. Throughout this chapter, we highlight the role and limitations of the trigger(s) employed in current searches, and the design of customized LLP triggers is to be encouraged to probe new and otherwise inaccessible regions of parameter space.

A detailed review of all existing searches is presented in sections 3.1 through section 3.5. This survey of the current experimental coverage aims to highlight the highest-priority searches still yet to be performed, which we summarize in section 3.6. In all cases, we focus on the latest version of each analysis. Notably we will typically present searches based on data taken at a center-of-mass energy $\sqrt{s} = 13$ TeV, and discuss searches using Run 1 data only when the newer version is not yet available, or when there are conceptual differences between two versions of the same analysis.

Because LLPs travel macroscopic distances in the detectors, many of the search strategies rely on the identification of displaced objects, namely SM particles (charged leptons, photons, hadrons, jets) that are produced at a location away from the primary vertex (PV) where the hard pp collision takes place. The secondary vertex at which the decay of the LLP occurs is referred to as a DV. As far as possible, our classification of searches is linked to the parton-level objects produced in LLP decays, which allows a relatively straightforward linkage to LLP models (as well as simplified models; see chapter 2). Borrowing the terminology from prompt searches, we consider the following categories for the analogous displaced objects produced in LLP decays: all-hadronic (jets), leptonic, semi-leptonic, and photonic. However, we caution the reader that these ‘jets’ or ‘photons’ may not be of the standard type, and so other objects may pass the selections of these analyses. The remaining searches fall in the ‘other long-lived exotics’ category, mostly consisting of non-standard tracks (DTs, HSCPs, quirks, etc), but also including some trackless signals, such as SPs and SIMPs. These

¹⁵¹ It is true that, depending on the signature, some of these caveats can be circumvented by a sensible use of existing prompt triggers. For example, photon triggers will collect displaced electrons, calorimeter/jet triggers will record displaced hadronic vertices, etc.

categories are not to be interpreted as exclusive; many models and searches could fit into several categories¹⁵². For example, [243–245] show how searches for different signatures and LLP lifetimes can be combined to cover large parts of the parameter spaces of particular UV models.

3.1. All-hadronic decays

ATLAS has several searches for displaced decays with hadronic objects, including searches for two objects decaying in the hadronic calorimeter (HCAL) [246, 247]; decays within the muon system (MS) or ID [248]; ID decays in association with large \cancel{E}_T [237]; and ID decays in association with large \cancel{E}_T , jets, or leptons [196]. CMS has inclusive searches for displaced jets using 13 (8) TeV data [249, 250] [251]. Moreover, the CMS displaced jets searches are relatively inclusive and so also cover LLPs with semi-leptonic decays despite having no specific lepton requirements. CMS also has a search for DV in multijet events [252]. LHCb has searches for both one [253] and two [254] all-hadronic DVs in their detector. Here the discussion is restricted to summarizing the hadronic channels, while those studies including leptons [196, 249] will be revisited in sections 3.2 and 3.3 for the fully-leptonic and semi-leptonic cases, respectively.

3.1.1. ATLAS searches. The reconstruction of displaced tracks in the ATLAS ID [255] follows a two-step procedure. In the first iteration, the default track identification algorithm is applied, which uses hits in the pixel system, semiconductor tracker, and transition radiation tracker (TRT) to reconstruct tracks with a small impact parameter. The hits not associated to a track during the first pass are used in a second run of the track finder, with loose requirements on the transverse and longitudinal impact parameters (d_0 and z_0) and the number of silicon hits that are shared (or not shared) with another track. This two-step procedure is referred to as the *large radius tracking* (LRT) algorithm by the ATLAS collaboration. Applying the LRT procedure is CPU-intensive, and thus it is only run once per data-processing campaign, on a subset of specially-requested events [255].

In searches where the LLPs decay exclusively in the ID, standard triggers are used to select events with high- p_T jets, \cancel{E}_T , or high- p_T leptons [196, 237]. An ATLAS 13 TeV search [237] uses a standard \cancel{E}_T trigger and an offline requirement of $\cancel{E}_T > 250$ GeV. The 8 TeV search [196] covers a larger range of topologies, and the event must have either $\cancel{E}_T > 180$ GeV or contain four, five, or six jets with $p_T > 90, 65, \text{ or } 55$ GeV to pass the trigger. In both searches, the ID vertex is required to have at least 5 tracks and the invariant mass of the DV tracks to fulfill $m_{DV} > 10$ GeV. These searches are interpreted in the context of various SUSY scenarios involving gluinos or squarks decaying into leptons, jets and missing energy, namely R -parity-violating (RPV), general gauge mediation, and split SUSY. In the latter case R -hadrons¹⁵³ are considered. The particular LLP decay topology determines which trigger and analysis mode (specified by jet and lepton multiplicity, small/large \cancel{E}_T , etc) has the best sensitivity. The LLPs covered by these searches are typically high mass (~ 100 GeV), and correspond to the direct-pair-production and HP production modes with hadronic decays (in the language of the simplified models presented in section 2). However,

¹⁵² Another important ingredient of the LLP searches is the possibility to reinterpret their results to a large variety of models, namely be able to *recast* them. While we refer the interested reader to chapter 6 it is worth mentioning here that many existing searches publicly provide useful recasting information, such as efficiency maps or model-independent bounds on production cross sections.

¹⁵³ R -hadrons form when BSM colored particles hadronize due to a lifetime larger than the hadronization scale. In split SUSY the R -hadrons are typically long-lived due to their decays being mediated by heavy squarks.

these searches do not have sensitivity to low-mass LLPs, especially those resulting from the Higgs, Z' , or CC production portals and then decaying hadronically.

For LLPs decaying in the HCAL or MS, dedicated *CalRatio* and *MuonRoI* triggers are employed [246–248, 256], allowing the searches to place limited requirements on the non-displaced portion of the event. We describe these triggers in more detail shortly. The efficiency of these triggers is 50%–70% for decays within the relevant geometric detector region, and negligible outside of them (see figure 3 of [248]). The results of these analyses are interpreted in terms of a $\Phi \rightarrow ss$ model, where Φ is a heavy scalar boson with $100 \text{ GeV} < m_\Phi < 1000 \text{ GeV}$ and s is a long-lived, neutral scalar decaying to hadrons with branching fractions dictated by the Yukawa coupling. This can map to Higgs or Z' production modes and hadronic decay mode in the simplified models.

The CalRatio trigger selects events with at least one trackless jet that has a very low fraction of energy deposited in the ECAL¹⁵⁴. These CalRatio jets are characteristic of an LLP that decays within or just before the HCAL. The 13 TeV analysis [246] requires two CalRatio jets, where the exact CalRatio criteria are determined using a series of machine learning techniques to optimally discriminate the displaced decay signature from QCD jets and beam-induced background. Using the simplified $\Phi \rightarrow ss$ model with $125 \text{ GeV} < m_\Phi < 1000 \text{ GeV}$ and $5 \text{ GeV} < m_s < 400 \text{ GeV}$, good sensitivity is observed for $c\tau$ between 0.05 and 35 m, depending on the Φ and LLP masses. Notably, SM-like Higgs boson decays to LLP pairs are constrained below 10% branching ratio in the most sensitive lifetime ranges, with exact limits dependent on the LLP mass [246]. The 8 TeV result also requires two CalRatio jets, and shows sensitivity for $100 \text{ GeV} < m_\Phi < 900 \text{ GeV}$ and $10 \text{ GeV} < m_s < 150 \text{ GeV}$ [247].

The MuonRoI trigger selects events with clusters of L1 regions of interest (RoIs) in the MS that are isolated from activity in the ID and calorimeters. It is efficient for LLPs that decay between 3 and 7 m transversely or 5–13 m longitudinally from the PV, for LLP masses greater than 10 GeV. After trigger selection, the ATLAS analysis in question requires either two reconstructed DVs in the MS [257] or one ID vertex and one MS vertex [248]. This ID–MS combination provides increased sensitivity to shorter lifetimes than an analysis only considering MS vertices, and shows good sensitivity to $100 \text{ GeV} < m_\Phi < 900 \text{ GeV}$ and $10 \text{ GeV} < m_s < 150 \text{ GeV}$. Decays of a SM-like Higgs boson to LLP pairs are constrained below 1% in the most sensitive $c\tau$ regions (with cross section limits as low as 50 fb). The efficiency degrades for benchmarks with higher LLP boosts or very low mass LLPs, as fewer tracks are reconstructed. Another ATLAS search includes signal regions with only 1 DV in the MS, with sensitivity to SM-like Higgs decays to LLPs extending down to branching fractions of 0.1% [258]; this search also presents constraints on a wide range of models that helps facilitate reinterpretation for other BSM scenarios. In addition, a combination of the results from this search with the results from the 13 TeV CalRatio search was performed in [246] for the models common to both, and provides a summary of the ATLAS results for pair-produced neutral LLPs.

Recently, ATLAS presented a new study for hadronically decaying LLPs produced in association with a leptonically decaying Z boson [259]. In this analysis, the LLP decays inside of the HCAL. The use of lepton triggers on the associated Z decay products gives sensitivity to production of a *single* low-mass LLP, whereas other searches typically require 2 DVs; it is therefore an excellent example of the utility of prompt associated objects in obtaining

¹⁵⁴ The variable used to discriminate between CalRatio jets and standard jets is $\log_{10}(E_{\text{HAD}}/E_{\text{EM}})$, where E_{HAD} and E_{EM} are the fractions of the measured energies of the jets appearing in the HCAL and ECAL, respectively. The trigger selects trackless jets with $\log_{10}(E_{\text{HAD}}/E_{\text{EM}}) > 1.2$, which corresponds to an electromagnetic fraction of 0.067.

sensitivity to low-mass LLPs. The model constraints are expressed in terms of a Higgs portal model where the SM-like Higgs decays to a bosonic LLP.

With the exceptions of [196, 237, 259], which require prompt activity in addition to the DV and have comparatively high trigger thresholds, the ATLAS all-hadronic analyses require two DVs, and thus are insensitive to models that produce a single DV inside the detector¹⁵⁵.

3.1.2. CMS searches. The CMS analyses [249–251] are based on a dedicated offline *displaced jet tagging* algorithm using tracker information to identify pairs of displaced jets. The triggers used here are based on large values of $H_T = \sum |p_{T,j}| = 350(500)$ GeV for 8 (13) TeV, where the H_T sum runs over all jets with $p_{T,j} > 40$ GeV and $|\eta_j| < 3.0$. The trigger for the 13 TeV analysis based on 2015 data additionally requires either two jets with $p_T > 40$ GeV and no more than two associated prompt tracks ($d_0 < 1$ mm) and the H_T threshold is lowered to 350 GeV if the two jets each have at least one track that originates far from the PV¹⁵⁶. Only events with two or more displaced jets are kept in the analysis, while those with only one are used as a control sample to estimate the prompt jet misidentification rate. For $c\tau < 3$ mm¹⁵⁷, the algorithm is inefficient as more than two tracks tend to have impact parameters less than 1 mm; for $c\tau > 1$ m the search is inefficient as most decays occur too far from the PV to form reconstructable tracks. A key difference among these searches is that the 8 TeV [251] and 13 TeV (2016 data) [250] analyses explicitly reconstruct the DV, while the 13 TeV (2015 data) [249] analysis does not.

CMS interprets the signal in several benchmark models that can be mapped to the direct pair production simplified model production mode, including a neutral LLP decaying hadronically and a color-charged LLP decaying into a jet plus a lepton. For neutral LLP pair production decaying democratically into light jets, the trigger efficiencies for $c\tau = 30$ mm are reported to be 2%, 41%, 81%, and 92% for 50, 100, 300, 1000 GeV masses, respectively. It is evident that the requirements on H_T and on $p_{T,j}$ make the search inefficient for low LLP masses. Indeed, a phenomenological recast of the 8 TeV analysis [251] in terms of rare decays of a SM-like Higgs boson with a mass of 125 GeV Higgs sets very mild bounds for LLP masses below $m_h/2$ [260]. Thus, the CMS search has limited sensitivity to low-mass, hadronically decaying LLPs through the Higgs, Z' , or CC simplified production modes.

As mentioned above, CMS also has a search for DV in multijet events [252], which was released near the time of the final editing of this manuscript.

3.1.3. LHCb search. The LHCb searches [253, 254] trigger directly on DVs with a transverse distance of $L_{xy} > 4$ mm) with four or more tracks, vetoing dense material regions in which hadronic interactions with the detector can mimic LLP decays. The trigger thresholds are, however, low. For example, the invariant mass of particles associated with the vertex must exceed 2 GeV and the scalar sum p_T of tracks at the vertex must exceed 3 GeV. Jet reconstruction is then performed offline with standard algorithms. The benchmark model used by these searches is a scalar particle decaying to two neutral LLPs, π_v (dark or ‘valley’ pions), which corresponds to the Higgs simplified model with hadronic decay modes. The parent particle can be either a SM-like 125 GeV Higgs [253] or a Higgs-like scalar with mass in the 80–140 GeV range [254]. The search is performed for π_v masses between 25 and

¹⁵⁵ This may be the result of a signal that produces two DVs, but the lifetime is sufficiently long that only one DV appears inside the detector.

¹⁵⁶ In this case this is defined by requiring that the transverse impact parameter significance $|d_0|/\sigma_{d_0}$ have a value greater than 5.

¹⁵⁷ Note that in principle the low $c\tau$ regime can be covered with standard triggers, however they require higher H_T thresholds.

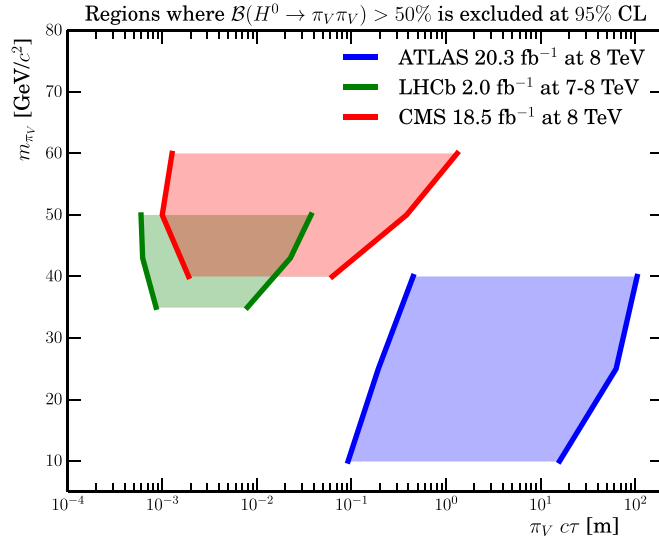


Figure 4. Comparison of the ATLAS [196], CMS [251] and LHCb [253] reaches for dark pions π_V decaying into jets. The CMS result is taken from the recast done in [260] of the 8 TeV analysis [251]. In the shaded regions $B(H \rightarrow \pi_V \pi_V)$ is constrained to be below 50%. Note that the ATLAS reach extends to higher masses as well; the plot was produced using the benchmark scenarios presented in [196], hence the meaningful bound is on the lifetimes. Taken from [253].

50 GeV and decay lengths between 0.6 and 15 mm. It is expected that LHCb will extend their coverage to shorter lifetimes by improving the understanding of the material and to lower masses by using fat-jets and jet-substructure to access larger boosts [261]. In principle, the search is also sensitive to direct pair production of LLPs.

Because of the low thresholds, the LHCb search focuses on low-mass LLPs with short lifetimes, for which it has excellent sensitivity. However, its sensitivity for other signatures is limited by the geometry of the detector and the LHCb luminosity compared to ATLAS and CMS. A model-dependent direct comparison among the LHCb, ATLAS and CMS reaches for the Higgs production mode decaying into dark pion LLPs can be seen in figure 4.

3.1.4. Summary. Searches in hadronic final states do not currently cover LLP parent masses below ~ 100 GeV in a comprehensive way. This is typically due to the large $p_{T,j}$ requirements at the trigger level, with an exception being the DV reconstruction at LHCb. Additionally, the powerful ATLAS searches for LLPs decaying in the HCAL or MS require two LLP decays in the detector, meaning that as of this writing there is no sensitivity to singly produced long-lifetime LLPs with hadronic decays¹⁵⁸. While the existing searches are typically sensitive to both direct pair production and HP production of LLPs, not all of the searches provide benchmarks with a variety of LLP production kinematics and boost.

A potential way to extend the sensitivity of current analyses is to use other existing triggers exploiting such things as VBF production modes, leptons, \cancel{E}_T , etc, to trigger on associated *prompt* objects and perform the hadronic DV reconstruction offline. The ATLAS 8 TeV study [196] does employ multiple triggers (such as lepton triggers), but in each case the

¹⁵⁸ Highly-inclusive searches for single LLPs decaying in the ATLAS MS have been proposed [262], finding that backgrounds are appreciable and need to be controlled using data-driven methods.

triggered object must be associated with the DV (for a lepton trigger, the lepton must originate from the DV). If, instead, a prompt lepton or VBF trigger were used with the offline reconstruction of a separate displaced object, sensitivity could be recovered to low-mass hadronic DVs in a variety of simplified models, including Higgs production (via VBF or VH associated production modes) [260, 263] or CC production (in association with a prompt lepton) [264]. In particular, triggering on associated prompt objects would improve the efficiency of reconstructing low-mass hadronic LLPs produced in the decays of a SM-like 125 GeV Higgs. As there is no theoretical lower limit on the masses of light neutral LLPs, it is imperative to lower the LLP mass coverage as much as possible. If at all possible, a dedicated *online* reconstruction of DVs would allow for a further reduction on the p_T threshold, giving sensitivity to light LLP masses.

3.2. Leptonic decays

All three experiments have searches for a pair of leptons coming from a DV [196, 265–269]. CMS also has a search requiring exactly one isolated muon and one isolated electron (i.e. events with additional isolated leptons are discarded) with large transverse impact parameters ($0.2 \text{ cm} < |d_0| < 10 \text{ cm}$), but without any other additional requirement including, for example, that the reconstructed tracks do not need to point to a common vertex [197]. This loose selection makes the search sensitive to a variety of new physics scenarios. Light and boosted LLPs can decay into collimated light leptons, dubbed *LJs* [127], which are searched for at both CMS [270, 271] and ATLAS. ATLAS has searches for both displaced [272, 273] and prompt LJs [274]. The LHCb collaboration also looks for light, neutral LLPs decaying into $\mu^+\mu^-$ pairs by studying B -meson decays to kaons, for exclusive decay channels for both neutral [267] and charged [268] B -mesons, as well as dark photons that decay into muon pairs [269].

3.2.1. CMS searches. The CMS searches trigger on leptons reconstructed using information from either the tracker [265] or the muon chambers [266], where the latter search uses only muons. In the tracker-based analysis, the LLP is reconstructed by forming pairs of charged leptons (where muons are required to have opposite signs), with p_T cuts of 26 GeV for muons, and 36 (21) GeV for the leading (subleading) electron. This yields slightly larger efficiencies in the muon channel. The transverse impact parameter $|d_0|$ needs to be 12 times larger than its uncertainty σ_d (approximately corresponding to a distance $\sim 200 \mu\text{m}$) to reject prompt backgrounds. In the MS-based analysis, muon candidates are reconstructed using hits in the muon chambers, and no information from the silicon tracker is used. In order to avoid biases from a loose beamspot constraint in the seeding step, these muons undergo an additional refit step. These candidates are referred to as *re-fitted stand-alone* muons, and they need to fulfill $p_T > 26 \text{ GeV}$, $|\eta| < 2$, and to be separated by $\Delta R > 0.2$. More importantly, these candidates are rejected if they can be matched to a $p_T > 10 \text{ GeV}$ track in the inner tracker, which efficiently excludes prompt muons and also renders this study fully complementary to the tracker-based one. Both these searches are interpreted in terms of decays of an SM-like Higgs H ($H \rightarrow XX$, $X \rightarrow l^+l^-$) and RPV squarks, covering proper lifetimes of $0.01\text{--}10^5 \text{ cm}$ for the Higgs scenario, and $0.1\text{--}10^4 \text{ cm}$ for the SUSY case. The difference in the lower reach of $c\tau$ is due to the larger boost factor of the Higgs. These benchmarks map to the direct pair production, HP and Higgs production simplified models, with flavor-conserving leptonic decays of the LLP. There is good sensitivity down to relatively low masses (LLPs of masses $\sim 20 \text{ GeV}$ produced in Higgs decays) due to the low lepton trigger thresholds.

Additionally, CMS has a search for one electron and one muon, each with large transverse impact parameter ($200 \mu\text{m} < |d_0| < 10 \text{ cm}$) [197]. Events are selected using a dedicated trigger for $e\mu$ pairs that applies a p_T cut on the leptons (42 GeV for electrons, 40 GeV for muons) but, unlike standard triggers, places no restriction on the maximum d_0 or distance from the PV. Events with exactly one muon and exactly one electron are kept, and then separated into ‘prompt’, ‘displaced control’ and ‘signal’ regions, defined as $|d_0| < 100 \mu\text{m}$, $100 \mu\text{m} < |d_0| < 200 \mu\text{m}$, and $|d_0| > 200 \mu\text{m}$, respectively. This selection makes the signal region almost free of leptons coming from SM processes, with rare tau-leptons, B -mesons or D -mesons as the largest remaining background.

Although in the original search the results are interpreted in the context of long-lived RPV stops (excluding masses below 870 GeV for $c\tau = 2 \text{ cm}$)¹⁵⁹, this search has been shown to be sensitive to many scenarios, including long-lived staus in gauge mediated SUSY breaking [205] and RHNs [45]. Indeed, this search has sensitivity to LLPs produced via any of the simplified model production modes and (semi)-leptonic decays that give exactly one electron and one muon. On the other hand, models where LLPs decay only to *either* muons *or* electrons (e.g. $\tilde{\mu} \rightarrow \mu\tilde{G}$) are unconstrained by this search. Furthermore, same-sign lepton signatures and signatures with additional leptons are not constrained by the current search but could be covered by extensions of the search [45, 205]. Due to the generality of tau-specific models, searches for hadronic tau channels is also desirable. This search has sensitivity to relatively low-mass LLPs; however, the 8 TeV analysis [275] has lower thresholds ($p_T > 22 \text{ GeV}$ on both leptons) albeit with a requirement for shorter decay distances ($|d_0| < 2 \text{ cm}$), and so has superior sensitivity to very low- p_T displaced signals. Maintaining low trigger thresholds is necessary to obtain sensitivity to the lowest-mass leptonic LLP signals.

3.2.2. ATLAS searches. The primary ATLAS search for displaced leptons [196] triggers on muons without an ID track, electrons, or photons¹⁶⁰. The trigger and offline p_T criteria are relatively high, requiring one of the following: one muon of at least 50 GeV; one electron of at least 110 GeV; one photon of at least 130 GeV; or two electrons, photons, or an electron and a photon with minimum p_T requirements for both objects in the 38–48 GeV range. The DV is formed from opposite-sign leptons, irrespective of flavor, and needs to be located more than 4 mm away from the PV in the transverse plane. DVs in regions with dense detector material are vetoed to suppression backgrounds from converted photons (e.g. $\gamma p \rightarrow e^+e^-p$). This search is in principle sensitive to events with a reconstructed DV mass $m_{\text{DV}} > 10 \text{ GeV}$, but the high p_T requirements for the leptons restrict the sensitivity to low-mass LLPs.

ATLAS has also recently released a search for pairs of muons that correspond to a DV [276]. This search is sensitive to LLP decays that occur sufficiently far from the IP that the muons are reconstructed only in the MS. The analysis has four separate trigger pathways: $\cancel{E}_T > 110 \text{ GeV}$; one muon with $p_T > 60 \text{ GeV}$ and $|\eta| < 1.05$; two muons with $p_T > 15 \text{ GeV}$ and $\Delta R_{\mu\mu} < 0.5$; or three muons with $p_T > 6 \text{ GeV}$. Thus, the search has sensitivity to final states with high and low masses (down to $m_{\mu\mu} = 15 \text{ GeV}$), as well as with various lepton multiplicities. Offline selections require the muons to have $p_T > 10 \text{ GeV}$ and opposite charge, and the search is efficient at reconstructing muons

¹⁵⁹ We note that a CMS prompt search for LQs has been recasted using the same model, finding stringent constraints for lifetimes below a few millimeters. This reinterpretation is discussed in detail in section 6.7.

¹⁶⁰ Electrons with large transverse impact parameters d_0 tend to be missing a track at trigger level and are reconstructed as photons.

for transverse impact parameters up to $|d_0| = 200$ cm. Muons are also required to satisfy isolation requirements from jets as well as from nearby tracks. The search puts constraints on a SUSY model and a model of dark photon production in Higgs decays; this can be used to determine sensitivity to all of the simplified production modes from chapter 2 in the $\mu\mu$ decay mode (or $\mu\mu$ in association with other objects). It also demonstrates how combining many trigger pathways and loose selection requirements can enhance sensitivity to a wide range of LLP models.

3.2.3. LHCb searches. LHCb has a search that looks for the direct production of both promptly decaying and long-lived dark photons [269]. As a result of the direct production, dark photons do not tend to be highly boosted in the transverse direction. Events¹⁶¹ are required to have a single muon with $p_T > 1.8$ GeV, or two muons with a product of transverse momenta $(1.5 \text{ GeV})^2$. The displaced search constrains previously uncovered dark photon parameter space around masses of ~ 300 MeV.

The LHCb searches for displaced leptons in rare B meson decays [267, 268] rely on standard techniques to identify the B^\pm decay vertex and the kaons and pions in the event, and the di-muon invariant mass $m(\mu^+\mu^-)$ variable is scanned for excesses. The $X \rightarrow \mu^+\mu^-$ vertex is not required to be displaced from the B^\pm vertex, and thus the constraints apply to both prompt and LLPs. The analysis probes LLP masses of 214 (250) MeV $< m_X < 4350$ (4700) MeV for the $B^0 \rightarrow K^*\mu^+\mu^-$ ($B^+ \rightarrow K^+X$, $X \rightarrow \mu^+\mu^-$) process, with the mass range being limited by kinematics.

3.2.4. Lepton-jet searches. Searches for LJs are focused on $\mathcal{O}(\text{GeV})$ LLP masses and distinctly boosted signatures, and thus we treat them separately.

The ATLAS 8 TeV search [272] considers three types of LJs: those containing only muons, only electrons/pions, or a mixture of the two. The muon and electron/pion LJs can contain either two or four leptons, while the mixed LJ must contain two muons and a jet consistent with a displaced electron/pion pair. As these signatures contain relatively soft leptons, the ATLAS 8 TeV analysis uses a trigger that requires three muon tracks in the MS with $p_T > 6$ GeV. There is a built-in limitation to this trigger, which is that the L1 requirement of three separate muon RoIs makes it only sensitive to topologies with two LJs in which one LJ has a wide enough opening angle between two muons to create two level-one RoIs. For the electron LJs, when the electrons are produced in the HCAL they are indistinguishable from a hadronic decay and thus the CalRatio trigger is used.

In the 13 TeV ATLAS analysis [273], a *narrow-scan* muon trigger is additionally used. This trigger starts off by selecting events with one muon with $p_T > 20$ GeV, then requires a second muon with $p_T > 6$ GeV within $\Delta R = 0.5$ of the leading muon.

Both the 8 and 13 TeV ATLAS searches are interpreted for Higgs-like scalar particles (with masses of 125 and 800 GeV) that decay effectively into either two or four lepton pairs, with each lepton pair assumed to come from a low-mass ‘dark’ photon, γ_D . The ATLAS result excludes exotic Higgs branching ratios below 10% for dark photon lifetimes $2 < c\tau < 100$ mm. Note that here γ_D is also allowed to decay to pions and so the results can also be interpreted for hadronically and semi-leptonically decaying LLPs. This corresponds to

¹⁶¹ For the prompt dark photon search, events are reconstructed at trigger level so that all online reconstructed particles are recorded, while the rest of event information is discarded [277]. The prompt search constrains entirely new territory above 10 GeV.

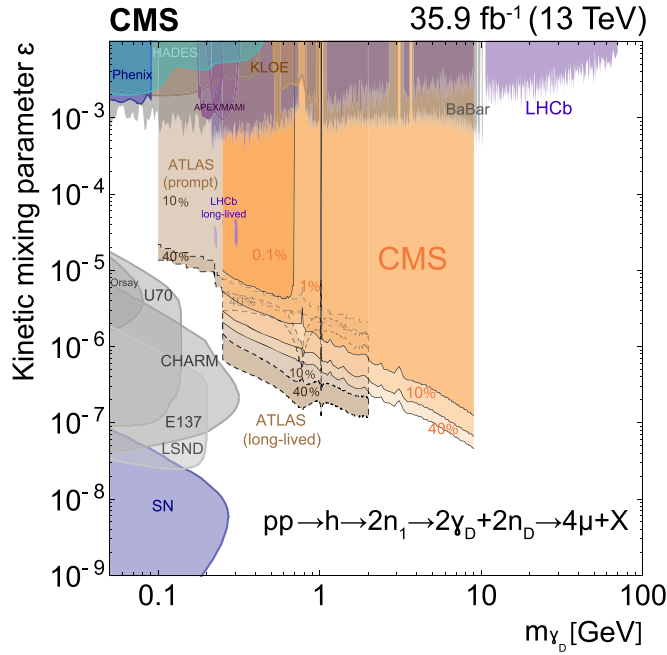


Figure 5. Comparison of the lepton-jet searches at ATLAS [272] and CMS [271] with respect to a dark photon scenario [155] vis-a-vis dark photon limits coming from low-energy experiments. Figure taken from [271].

the Higgs production mode in the simplified models proposal with an admixture of flavor-conserving leptonic and hadronic LLP decays.

The CMS LJ search focuses on fully muonic LJs and has been performed with both the 8 TeV dataset [270] and part of the 13 TeV dataset [271]. The 13 TeV search is sensitive to di-muon parent particle masses up to 8.5 GeV. Events are selected with a di-muon trigger with standard isolation requirements. Further selection requires at least four muons, forming a minimum of two opposite-charged pairs. CMS uses a benchmark model with scalars decaying into either lighter scalars or dark photons, with varying scalar and dark photon mass. For the case of a 125 GeV Higgs they can exclude an exotic branching ratio of below 0.1% for some parameter points. The CMS search can be compared with the ATLAS results, as can be seen in figure 5. We note that this study includes sensitivity to both prompt and displaced muonic lepton jets.

3.2.5. Summary. To summarize, the lepton searches rely on fairly standard lepton identification, with vertex reconstruction being performed mostly offline. Searches for leptonically decaying LLPs typically enjoy low trigger thresholds and good sensitivity to LLP production rates. Extending the success of the leptonic LLP program to future LHC running will necessitate maintaining low-threshold triggers for displaced leptons in a high-luminosity environment; this is a major challenge but one that must be overcome. Another outstanding challenge is coverage of LLP decays to τ leptons, which lie at the interface between hadronic and leptonic searches. Such decays are very well motivated from the theoretical point of view, as a Higgs-like scalar can typically decay about 300 times more often into $\tau^+\tau^-$ if

kinematically allowed, and also one could have large rates into mixed decay modes such as $\tau^+\mu^-$. A displaced hadronic τ is a striking object, and most likely will have few backgrounds. Hence, limits on exclusive displaced τ s would be of utmost importance¹⁶².

As the leptonic searches explicitly require opposite-sign leptons, the same-sign lepton signature (motivated from Majorana neutrinos; see the LHCb search in section 3.3, or heavy, doubly-charged LLPs) is currently neglected. Furthermore, the sensitivity of the CMS search for two high- $|d_0|$ leptons is currently only sensitive to opposite sign $e\mu$ pairs, with a veto on additional leptons. Relaxing these requirements would greatly enhance sensitivity to certain scenarios, especially the simplified models with flavor-conserving leptonic LLP decays.

Lepton-jet searches currently cover only final states with at least two LLPs and some muons in the final state¹⁶³, and the same statement currently applies to both the LHCb searches for dark photons [269, 277] and for LLPs produced in B -meson decays. The existing ATLAS LJ studies express their results in terms of specific dark photon models¹⁶⁴, which makes it complicated to apply the results to other models. We refer the reader to section 6 for a further discussion of this topic. In extending LJ searches, it would be beneficial to have additional searches with a single LJ or low-mass, leptonically-decaying LLP (which are motivated in models with hidden sectors and Majorana neutrinos, for example in [43, 135]). In addition, the status of coverage in the intermediate mass-transition region between ‘standard’ displaced lepton pairs and LJs is unclear, and may potentially harbor a gap; adopting the simplified model approach for leptonic LLP decays with masses varying between the GeV and weak scale would ensure comprehensive coverage of low-mass leptonically decaying LLPs.

Finally, we comment on gaps in sensitivity to very low-mass leptonically decaying LLPs. A benchmark LLP model is the heavy neutral lepton (HNL), which corresponds to the CC production mode with (semi-)leptonic LLP decays in our simplified model framework. HNLs constitute an important physics case that leads to multi-lepton displaced signatures from W decays, with nice prospects at ATLAS and CMS (see, e.g. [43, 48, 49]). While previous searches were not sensitive to this scenario due to either high- p_T requirements or the requirement of two DVs in the same event, the presence of a prompt lepton from the W allows the relaxation of these requirements in a dedicated analysis. Moreover, the prospects of triggering on a prompt lepton in such searches was studied recently in [48] and demonstrated in a prompt search in [278]¹⁶⁵. The identification of two leptons from the vertex is a powerful discriminant against backgrounds from meta-stable particle decays and hadronic interactions in material. This permits a potentially cleaner exploration of the lower HNL mass range (3–6 GeV) than in the semi-leptonic channel (see section 3.3) despite the lower branching ratio. It should be noted that HNL models can predict LLP decays to all three lepton flavors (either democratically or hierarchically), necessitating the capability to reconstruct displaced leptons of all flavors, including taus.

¹⁶² We note that if the τ originates from outside the tracker, the hadronically decaying taus are indistinguishable from other displaced hadrons. For instance, in the ATLAS search utilizing muon RoIs [248] the results are interpreted for a model with a scalar particle with Higgs-like couplings to SM fermions, which includes a branching fraction into $\tau^+\tau^-$. However, if the τ originates from the ID, the low number of tracks associated to it (one to three) will not fulfill the requirements of the ATLAS study of five or more tracks associated to a DV.

¹⁶³ The ATLAS 8 TeV search [272] included a search channel with two electron-only LJs, but the performance was poor and it was excluded from the final result.

¹⁶⁴ Recall that the LJ studies also consider the $\gamma_D \rightarrow \pi^+\pi^-$ decay mode.

¹⁶⁵ Note that the displaced large transverse impact parameter $e\mu$ CMS search [197] fails to cover this scenario due to the aforementioned lepton veto, which eliminates sensitivity to the tri-lepton signals discussed in [43], as well as relatively high lepton p_T trigger thresholds compared to the kinematics of 4-body W decay.

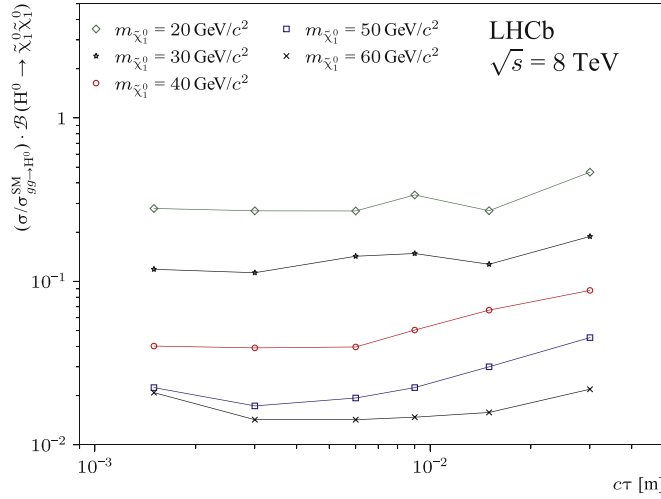


Figure 6. LHCb reach for displaced semi-leptonic decays. Taken from [279].

3.3. Semi-leptonic decays

As semi-leptonic signatures include aspects of both hadronic and leptonic LLP decays, many of the previously discussed searches can partially cover these cases, and some do so explicitly. For instance, the ATLAS search for electrons and muons accompanied by tracks [196], the inclusive CMS search for DVs [249] (which contains a specific model interpretation called ‘*B*-lepton’ addressing precisely this channel), and the search for a large impact parameter $e\mu$ pair by CMS [197] are all inclusive with respect to other hadrons produced in the LLP decay, provided the leptons are sufficiently isolated¹⁶⁶. In addition, LHCb has dedicated searches for semi-leptonically decaying LLPs [279] and semi-leptonic decays of long-lived Majorana neutrinos coming from B^- mesons [280]. The two CMS searches [197, 249] need no further explanation for how they cover semi-leptonic LLPs because of their very inclusive nature (see section 3.2.1), but we now describe the rest of these searches in some detail.

3.3.1. LHCb searches. The LHCb search for semi-leptonic LLP decays selects events with a muon trigger, then reconstructs a DV offline [279]. The results are interpreted in terms of four distinctive topologies: single LLP production in association with a new particle (in this case a gluino), double LLP pair production via direct pair production, Higgs decay, or via squark pair production (HP). The LLP then decays to two quarks and a muon (which maps to the $jj\ell$ simplified model decay). Material regions are vetoed for the DV, which results in the dominant background arising from heavy flavor production either directly or from W/Z decays. The signal discrimination is obtained from a multivariate analysis based on the muon p_T and impact parameter, and subsequently the search is optimized based on the LLP reconstructed mass and the muon isolation. This study is sensitive to low-mass LLPs with lifetimes between 1.5 and 30 mm, as can be seen in figure 6.

The LHCb search for Majorana neutrinos [280], N , probes Majorana neutrinos produced in leptonic B decays, $B^\pm \rightarrow \mu^\pm N$. The Majorana neutrino subsequently decays exclusively to

¹⁶⁶ Note that the lepton isolation affects most of the semi-leptonic searches.

$N \rightarrow \mu^\pm \pi^\mp$; both prompt and displaced decays are considered¹⁶⁷. A same-sign muon requirement, along with the reconstruction of the N and B meson masses, greatly reduces backgrounds to the search. The sensitivity of the search is limited by the restriction to muons in the final state (so models that predominantly decay to e or τ are not constrained), and the same-sign lepton requirement gives sensitivity only to lepton-number-violating processes. More inclusive searches looking for additional N production modes [282], decays with opposite-sign leptons, or searches targeting decays of heavier mesons like B_c [283] could also improve the sensitivity to semi-leptonically decaying LLPs.

3.3.2. ATLAS search. The ATLAS search for semi-leptonic LLP decays [196] looks for a vertex with a lepton accompanied by tracks. This search uses the same trigger as the dilepton vertex search described in section 3.2. The DV is required to have a lepton as well as at least four additional associated displaced tracks, and the invariant mass of the tracks must exceed 10 GeV. Thus, the search in principle can have sensitivity down to masses ~ 10 GeV, although the high p_T threshold for the displaced electron/muon typically limits sensitivity to low-mass LLPs; the vertex must contain a muon with $p_T > 55$ GeV or an electron with $p_T > 125$ GeV.

3.3.3. Summary. When considering the application of inclusive hadronic or leptonic searches to semi-leptonic LLP decays, it is important to understand how the simultaneous presence of leptons and jets in the signal can degrade the sensitivity. For instance, prompt jet searches explicitly can remove non-standard jets through jet cleaning cuts. Lepton isolation criteria can severely reduce the signal acceptance for a highly-boosted LLP decaying into a lepton and a jet, and they might also veto extra tracks in the events. Thus, boosted semi-leptonic decays (as might be found in the displaced decay of a low-mass, RHN produced via W decay) may not be covered by existing searches.

One of the major gaps in semi-leptonic LLP searches is at the smallest LLP masses. In this case, it can be challenging for the leptons from LLP decays to pass trigger thresholds and/or isolation criteria; backgrounds from heavy-flavor and other processes are also higher for semi-leptonic processes than fully leptonic ones. However, there are very good motivations for low-mass semi-leptonic LLPs from the HNL benchmark model¹⁸ introduced in section 3.2.5, which predicts LLPs for HNLs of masses below 30 GeV. The signature of HNLs from W decays with displaced semi-leptonic HNL decays is an important item on the search agenda of ATLAS, CMS and LHCb [38, 43, 48, 49, 284, 285]. Recently, there has also been a proposal to search for low-mass HNLs in heavy ion collisions [286]. The semi-leptonic channel has the highest branching ratio (about 50% in the relevant mass range [287]) and can therefore offer the best discovery prospects at LHC experiments for HNL masses up to 30 GeV as long as a DV mass cut of around 6 GeV is made to mitigate backgrounds from B-mesons, $m_B \sim 5$ GeV, and backgrounds from random-crossings can be suppressed. The lower end of the 6–30 GeV mass range corresponds to a non-perturbative regime for the hadronization of the HNL decay products. As the number of charged hadrons significantly affects the DV reconstruction efficiency, the validation of event generator outputs for this process is an important issue currently being addressed by the community (see e.g. [48]). The ability of LHCb to trigger directly on the HNL decay products and better reconstruct

¹⁶⁷ Some care is required in interpreting the results of the search on a model with a Majorana neutrino, as the original theory interpretation is problematic [281].

¹⁶⁸ In the language of simplified models, this corresponds to the CC production mode, where the HNL LLP is produced in association with a prompt lepton. The HNL then decays semi-leptonically via the $jj\ell$ channel.

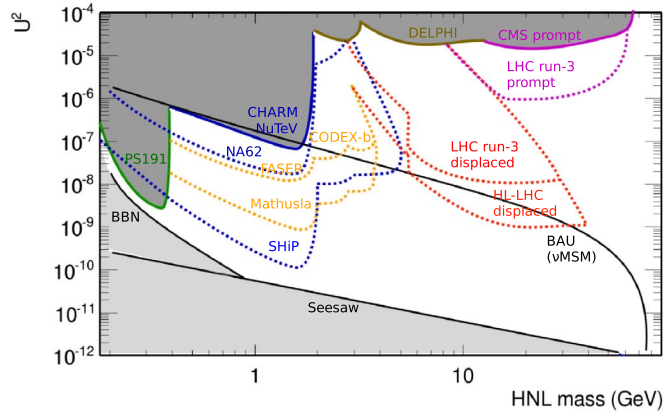


Figure 7. Summary of projected experimental sensitivities to HNLs in various experiments, in the coupling strength (U^2 for dominant mixing to ν_μ) versus mass plane. The projections labelled ‘LHC Run 3’ and ‘HL-LHC’ are for HNLs in W decays in general-purpose experiments, and the one labelled ‘MATHUSLA’ assumes the full HL-LHC MATHUSLA dataset. We also show the recent CMS result for the prompt tripton signature [278]. Prospects at proton beam-dump experiments are also shown for an already existing experiment, NA62 [288], and for the planned experiment SHiP [289]. Existing constraints from direct searches are indicated as coloured solid lines [290–294]. The lines labelled ‘Seesaw’ and ‘BBN’ show lower theoretical constraints from the observed neutrino masses (assuming a normal hierarchy) and primordial nucleosynthesis, respectively [295]. The line labelled ‘BAU’ is an upper theoretical constraint in the ν MSM model for accounting for baryon asymmetry in the Universe while the lightest HNL is a dark-matter candidate [295].

displaced tracks can in some cases compensate for its lower acceptance and luminosity, as exemplified by a recent search for DVs composed of one muon and several tracks [279, 285]; similar arguments can be made in the case of heavy ion collisions [286]. This possibly enables LHCb to better probe the more challenging tau channel. Figure 7 shows the overall expected reach of LHC searches in the HNL coupling strength (for the muon channel) versus mass plane, using assumptions detailed in [284], similar to those in [38, 43].

The sensitivity of LHC experiments to HNLs is complementary to that of fixed-target experiments which can probe lower couplings thanks to high-intensity beams albeit at lower mass ranges (i.e. targeting HNLs from c and b decays). The CERN SPS provides great opportunities with the running NA62 experiment [296] and the planned SHiP experiment [289], which comprise a vacuum decay vessel and spectrometer tracker downstream of the target to reconstruct vertices of long-lived neutral particles¹⁶⁹. These provide the best sensitivity to HNL masses up to 2 GeV, where they probe a region of the parameter space favored in models which simultaneously explain neutrino masses, matter–antimatter asymmetry and DM [295, 298–300] (see figure 7).

3.4. Photonic decays

There are two ways in which photons coming from LLP decays do not resemble standard photons. First, they cannot be traced back to the PV, thus giving rise to *non-pointing* photons. Second, they can arrive at the ECAL at a time slightly later than expected because the LLP

¹⁶⁹ The proposed detector FASER would also have the capability to reconstruct such vertices [297].

moves slower than the speed of light; these are referred to as *delayed* photons. We note that both kinds of unusual photons can be vetoed in searches for photons that originate from the PV, and thus prompt searches typically provide weaker bounds on LLP scenarios than for promptly decaying signals. ATLAS has a search for non-pointing and delayed photons [301] using the full 8 TeV dataset, which supersedes the 7 TeV analysis [302]. In CMS there are studies for delayed photons in the ECAL [303] and for non-pointing photons detected via their conversion to e^+e^- pairs [304]. The underlying topology in all these models is the neutralino decay into a gravitino and a photon ($\chi_1^0 \rightarrow \gamma\tilde{G}$), ubiquitous in GMSB scenarios [53, 305]. Hence all these studies require large \cancel{E}_T in the final state. This corresponds to HP production of LLPs with decays to a single photon and \cancel{E}_T in the simplified model framework; all searches described below use the Snowmass Slopes Point 8 benchmark, which is not straightforward to map to a physical spectrum of HP masses.

3.4.1. ATLAS search. The ATLAS study [301] benefits from the capability of the liquid-argon electromagnetic calorimeters (ECALs) to measure the flight direction and the photons' TOF. Resolutions on Δz_γ , the separation between the PV of the event and the extrapolated origin of the photon, and $|\Delta t_\gamma|$, difference of the arrival time of the photon with respect to the prompt case, are as low as 15 mm and 0.25 ns, respectively. The trigger demands two photons within $|\eta| < 2.5$, with transverse energies E_T of 35 and 25 GeV. In addition, to guarantee the event comes from a proton-proton collision, a PV with five or more tracks with $p_T > 0.4$ GeV is required. The offline selection requires two photons with $E_T > 50$ GeV and $|\eta| < 2.3$, not in the barrel-endcap transition region ($1.37 < |\eta| < 1.52$), at least one of them in the barrel ($|\eta| < 1.37$) and with less than 4 GeV of energy deposited in the calorimeter in a cone of $\Delta R = 0.4$ around them (constituting the *isolation* criterion). In addition, the events are binned in \cancel{E}_T : the $\cancel{E}_T < 20$ GeV bin contains the prompt backgrounds, the $25 \text{ GeV} < \cancel{E}_T < 75 \text{ GeV}$ bin is used as the control region, and finally the signal analysis is performed in the $\cancel{E}_T > 75 \text{ GeV}$ bin. This study covers lifetimes from 0.25 to 100 ns in the GMSB framework, the lower limit being a hard cut-off imposed experimentally, as the similarity between background and signal samples in that region makes discrimination rather difficult. The excluded signal rates in this range of lifetimes vary between 0.8 and 150 fb, with the best-constrained value obtained for $\tau \sim 2$ ns.

3.4.2. CMS searches. The CMS study of delayed photons [303] follows a similar approach to ATLAS. The main difference is that it demands only one photon with $p_T > 80$ GeV, but in addition two jets are required. Furthermore, the vector sum of \cancel{E}_T and E_T^γ , which is denoted $\cancel{E}_{T \text{ no } \gamma}$, is additionally used for background discrimination. Collisional backgrounds have small \cancel{E}_T and large $\cancel{E}_{T \text{ no } \gamma}$, while the non-collisional backgrounds are characterised by large \cancel{E}_T and small $\cancel{E}_{T \text{ no } \gamma}$. For the signal events the two variables are large, hence they are both requested to be larger than 60 GeV. The time resolution is 0.372 ns, slightly worse than in the optimal scenario of the ATLAS search. Their reach in lifetimes lies in the 2–30 ns range, excluding signal rates of 10–30 fb.

The CMS study of non-pointing photons [304] relies on the photon converting to e^+e^- pairs. It requires two photons, two additional jets, and $\cancel{E}_T > 60$ GeV. The photon trajectory is obtained from the conversion vertex as the line segment along the momenta of the e^+e^- track pair, and the impact parameter, $|d_{XY}|$, is defined as the closest distance between the photon and the beam axis, which can be determined within approximately 1 mm. A comparison of the reach of these 8 TeV studies, as well as those using the 7 TeV dataset, can be found in figure 8.

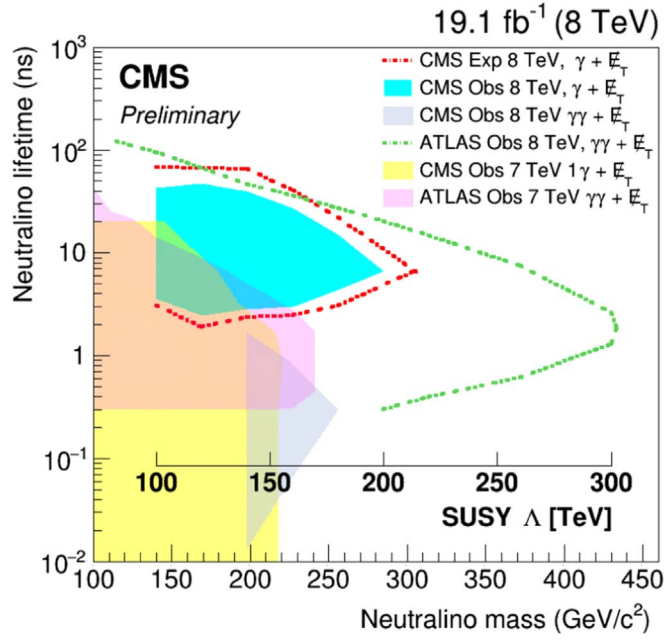


Figure 8. Summary of the $\gamma + \cancel{E}_T$ searches from ATLAS and CMS, displayed assuming the same GMSB model. Taken from [303].

3.4.3. Summary. The gaps in these studies are straightforward to identify. The requirement of large \cancel{E}_T is due to the fact that all of these studies have an underlying theoretical picture of neutralinos decaying into gravitinos and photons, motivated from GMSB scenarios. Hence, these searches do not cover cases without the presence of missing energy, including LLPs that decay to $\gamma\gamma$, $l\gamma$ or $j\gamma$. It may be possible to extract a constraint on such LLP decay modes due to mis-measurement of jets or the photon decay geometry which could mimic large missing energy; however, this would be sub-optimal compared to a dedicated search. With the exception of the CMS study [303] which requires two additional hard jets, all of these analyses require two displaced photons. A single displaced photon signature can occur in motivated models: it can easily arise, for example, from a very slightly mixed electroweak triplet and singlet as in SUSY theories (see the UV models in section 2). Furthermore, as discussed in section 3.1, a single LLP in the detector can also arise for very large lifetimes of neutral LLPs, which limits the reach of current searches at longer lifetimes. In such scenarios, it is possible that the photons from LLP decay can be quite soft, and obtaining sensitivity to models with single photons from LLP decay and/or low momenta may require triggering on associated prompt objects, similar to the recommendations in section 3.1.4.

3.5. Other exotic long-lived signatures

In the preceding sections, we presented analyses sensitive to LLPs decaying into objects such as jets, leptons, and photons. In many cases, however, LLPs give rise to signatures that are completely distinct from more conventional prompt signatures. In this section, we present analyses that exploit properties of other exotic long-lived signatures, such as non-standard tracks. We summarize in detail the existing searches for HSCPs; DTs; SPs and monopoles, and describe existing ideas on how to look for quirks and SIMPs.

Note that the terminology employed in some of these searches can be confusing, with occasional conflation of signatures with the underlying model. We provide a detailed explanation of each search, and we attempt a classification here based strictly on signature. We distinguish between three classes of signals: *tracks with anomalous ionization*, *tracks with anomalous geometry*, and finally *out-of-time* decays.

3.5.1. Tracks with anomalous ionization. In this category, we collect all searches for charged-particle tracks with anomalous ionization, i.e. those that are inconsistent with a charge $|Q| = e$. Here we include (i) the so-called HSCPs, which apply to stable, electrically charged particles but also charged particles that decay in the calorimeters and/or MS; and (ii) magnetic monopoles.

3.5.1.1. Heavy stable charged particles. The searches for HSCPs at CMS [4, 306] and ATLAS [223, 307, 308] rely on two key properties. First, particles that are massive and/or electrically charged with $|Q| \neq e$ have a characteristic ionization loss (dE/dx) distinctively different than SM particles. This property can be measured in the tracker. Second, HSCPs are typically heavy and move with a speed less than the speed of light, $\beta = v/c < 1$. Thus, compared to a particle with $\beta \approx 1$, they require a longer TOF to reach the outermost components of the detector (calorimeters and muon chambers). As decays or interactions of the HSCP with the material in the detector can change the electric charge of the HSCP, both CMS and ATLAS perform separate *tracker-only* and *tracker + TOF* studies in the language of CMS¹⁷⁰. The event selection relies on standard single-muon or large-missing-energy triggers. The offline selection relies on identifying the signal events from quality requirements on the tracks using discriminator variables built from track observables.

The HSCP search conducted by LHCb [309] is slightly different. Instead of exploiting dE/dx and TOF, they use the lack of radiation in the ring imaging Cherenkov detector (RICH). Events are required to pass a high- p_T single muon trigger ($p_T(\mu) > 15$ GeV). Two opposite sign ‘muons’ are then required, each with p_T above 50 GeV and an invariant di-muon mass above 100 GeV, to suppress muons coming from DY production, the main background for this search. In addition, particles must have $\beta > 0.8$, set by the efficiency of the muon chambers to reconstruct slow particles. As electrons and hadrons interact more with the calorimeter than an HSCP, a deposit in the calorimeter of less than 1% of the momentum of the particle is required.

The theoretical interpretation of a signal or limit depends on whether the HSCP carries both color and electroweak charges. If it carries a color charge, the default benchmarks correspond to R -hadrons, namely HSCPs that hadronize with SM particles via the strong force, e.g. gluino-gluon or quark-squark states. In the absence of a color charge, the signal is exemplified by long-lived sleptons in the context of gauge-mediated SUSY. Both ATLAS [307] and CMS [4] studies employ these two scenarios, while LHCb [309] uses a stau benchmark model¹⁷¹. Finally, CMS also looks for HSCPs coupling only to hypercharge (and hence possessing only couplings to γ and Z), while ATLAS has a search inspired by electroweakinos in SUSY: it considers the associated production of a neutral and an electrically charged LLP (chargino-neutralino), and thus only one HSCP plus missing energy are required. These scenarios correspond, in our simplified model framework, to the direct

¹⁷⁰ ATLAS measures $\beta\gamma$ from dE/dx and β from TOF and extracts an independent mass, m_β and $m_{\beta\gamma}$, from each measurement.

¹⁷¹ The ATLAS R -hadron searches using the 13 TeV dataset have recently been presented in [223].

production of LLPs with electric or color charges and that do not decay, or decay at very large distances compared to the tracking volume.

To summarize, these searches present no obvious weak points. Standard triggers and tracking algorithms are used, and the analysis methods are well-understood and have been extensively validated against data. HSCP signatures do not suffer from the low-mass gap of many neutral LLPs due to constraints from LEP and other low-energy experiments. However, mCPs are not covered by these searches and require dedicated detectors (see section 5.3.3). While the HSCP search strategies are generally robust, we encourage the experimental collaborations to continue pursuing improvements for these searches. The small number of signal events that would be produced for HSCPs above current limits render the sensitivity highly dependent on the understanding of the background and control of the systematics.

3.5.1.2. Magnetic monopoles. ATLAS [215] has a dedicated search for highly ionizing particles (HIPs), which encompass a variety of new physics scenarios, such as magnetic monopoles, dyons (particles with both magnetic and electric charge), stable microscopic black holes, etc. For the sake of concreteness, we focus on magnetic monopoles but the interpretation in terms of other models is straightforward¹⁷².

The main phenomenological feature is that magnetic charge is quantized in units of $g_D = 2\pi/e \approx 68.5$. Hence, a magnetic monopole behaves as a particle with at least 68.5 electron charges, leading to an unusually large ionization power in matter, so that they would quickly stop in the detector because HIPs lose energy at spectacular rates. Because of the large QED coupling of magnetic monopoles, a perturbative calculation of the cross section is invalid and there is no accurate determination of the production rate, but a naïve Drell–Yan production cross section is provided for the purposes of comparison. The specifics of the detector restrict the sensitivity of this search to magnetic charges $g < 2g_D$ because a large fraction of the monopoles stop in the material upstream of the ECAL, as the latter is used for the L1 trigger [310]. We note that larger magnetic charges can be tested by the MoEDAL experiment [311], which is described in detail in section 5.3.2. Additionally, theories with monopoles can also be tested in heavy ion collisions [312].

ATLAS [215] has a dedicated trigger for HIPs based on identifying relevant RoIs in the ECAL and subsequently counting the number of hits in the TRT. As well, the fraction of TRT hits that are high-threshold (HT), meaning that they have an ionization larger than ~ 3 times that expected from a SM particle, is used as a discriminant. The analysis selects events based on the fraction of TRT-HT hits matched to an EM cluster deposit, and how the energy deposits are distributed in the different layers of the ECAL. It is important to note that due to the lack of a consistent theory, the signal simulation is performed by re-scaling Drell–Yan production at leading order and assuming no coupling to the Z boson. The HIPs are assumed to have either spin-0 or $1/2$. The spin does not affect the interaction with the material, but the angular distributions are different according to angular momentum conservation (keeping in mind that there is, of course, no perturbative theoretical prediction for the angular distribution). Cross section limits for $0.5 < |g|/g_D < 2$ are set for masses in the 890–1050 (1180–1340) GeV range for the spin-0 ($1/2$) case.

The coverage in LHC Run 2 of magnetic monopoles in the g_D – σ plane is displayed in figure 9.

¹⁷² At the time of writing there was no public result on a monopole search from CMS.

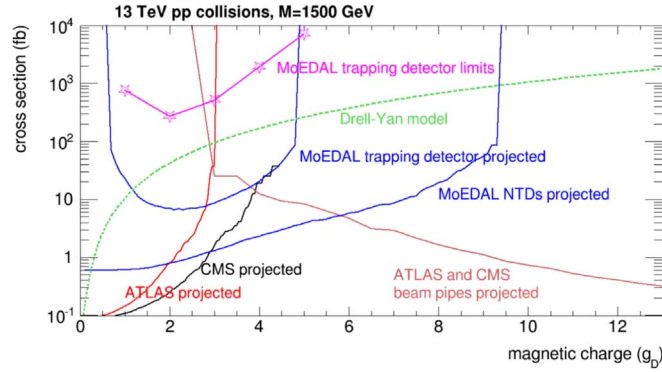


Figure 9. Comparison of the MoEDAL, ATLAS and CMS reaches for magnetic monopoles. The curves assume three signal events and a total integrated luminosity of 50 fb^{-1} for 13 TeV collisions. Updated version of existing figure in [310]. Note that the CMS curve relies on the expected performance of their detector.

3.5.2. Tracks with anomalous geometry. In this category we group searches where the tracks have an anomalous geometry, namely they disappear (track \rightarrow nothing), or follow non-standard trajectories (such as quirks). There are additional anomalous track signatures that we do not cover such as kinked tracks, where a charged LLP decays to another charged particle that travels at a non-zero angle with respect to the LLP direction [112, 313–315]; however, there are currently no dedicated searches for such signatures.

Within this category we also have the emerging jets signature that has been recently studied by CMS [316]. Since emerging jets arise from dark sector radiation, they are described in detail in chapter 7 in conjunction with the theoretical and phenomenological aspects of dark showers.

3.5.2.1. Disappearing tracks. Massive charged particles traveling in the detector can decay to a lighter, almost mass-degenerate neutral state, emitting a soft SM charged particle (typically a pion or a muon). While at first glance a small mass gap naïvely seems like a hallmark of tuning, near degeneracies often occur naturally as a result of a symmetry. In fact, electroweak symmetry generically leads to small mass splittings between components of a single electroweak multiplet. For example, $\mathcal{O}(100 \text{ MeV})$ splittings arise between the different components of an electroweak multiplet [64, 128] due to EW gauge boson loops¹⁷³. If the SM particle is sufficiently soft it cannot be reconstructed, and then a charged track seems to vanish: this is thus referred to as a DT¹⁷⁴. The actual lifetime of the charged particle is highly sensitive to the precise value of the mass splitting. For instance, the well studied cases of a fermionic doublet with $Y = 1/2$ and a fermionic triplet with $Y = 0$, reminiscent of a Higgsino and Wino in supersymmetry, respectively, have mass splittings of $\Delta = 355$ and 166 MeV , up to small corrections, but the corresponding $c\tau$ values differ by almost an order

¹⁷³ For a single fermion multiplet, the splitting can only be altered by higher-dimensional operators, and thus it is harder to vary Δ from the 1-loop EW value. For other cases, such as mixing with additional particles, the actual splitting can differ more substantially from this 1-loop EW value.

¹⁷⁴ If the charged particle could be reconstructed this case is often referred to as a *kinked track*. However, as the kinked portion has a very large impact parameter, without a serious attempt to capture the kink these tracks, too, simply disappear.

of magnitude: 6.6 mm versus 5.5 cm¹⁷⁵. This is because the lifetime, $c\tau$, depends on the third power of the mass splitting in these scenarios when the charged LLP decays to a charged pion [64, 128].

Before 2017, both ATLAS [317] and CMS [217] required a track to travel about 30 cm in order to be reconstructed, giving good coverage of the Wino scenario. This 30 cm value corresponds to four hits at ATLAS, three in the pixel layers plus one in the silicon tracker, and to seven hits in the pixel and trackers of CMS. The search employs a trigger requiring an ISR jet against which the charged particle recoils, along with the presence of large \cancel{E}_T . The DT is reconstructed offline and needs to fulfill quality criteria (isolation, p_T threshold, etc). A phenomenological study [99] has shown that reducing the distance from 30 to 10 cm would give coverage to the elusive Higgsino scenario, moving the expected reach up to 400 GeV, surpassing the expected mono-jet reach of 250 GeV [318–320]. Later, ATLAS presented a study [218, 321] using 13 TeV data and exploiting the presence of a new innermost pixel layer (IBL). This addition allows for all four hits to be in the pixel, with the outermost pixel layer now at 12.25 cm, enhancing sensitivity to lower values of $c\tau$. The summary for DTs at ATLAS for the Wino case can be seen in the left panel of figure 10, while in the right panel we show the constraints for Higgsinos from [99]. CMS also has a DTs search using 2015 and 2016 data at a center-of-mass energy of 13 TeV [322].

At LHCb the prospects for a DT analysis with the present detector are poor. Currently, the momentum of the track can only be measured if the particle passes through the tracking station (TT), which is about 3 m away from the IP. Particles decaying in the vertex locator (VELO) or RICH1 system will not leave a fully-measurable track and will be swamped in a background of SM processes such as kaon decays, which would give a similar signature in the detector components before the magnet. Detector improvements (additional magnets, better PID at low momentum, additional layers) might lead to some sensitivity for $\mathcal{O}(\text{cm})$ lived tracks, a golden opportunity for potential LLP discoveries at LHCb in the HL-LHC era.

To summarize, the search for DTs presents a few challenges. Using an ISR jet trigger means a price is paid in terms of signal efficiency. For example, [99] has shown that significantly lowering the p_T threshold of the jet or directly triggering on the momentum of the DT¹⁷⁶ would lead to a factor of two increase in the number of signal events. It is also clear that better access to lower lifetimes is needed; this may only be possible, for instance, by adding new tracking layers as close as possible to the beampipe (and/or having double layers instead of single ones).

3.5.2.2. Strongly interacting massive particles. SIMPs can be motivated by astrophysical observations of DM that do not fully agree with the WIMP paradigm (e.g. missing satellites, the core versus cusp problem; see, e.g. [327–330] for further discussion). These particles are assumed to interact strongly with baryons. Consequently, the experimental signature is little to no signal in the tracker and the ECAL, and large energy deposits in the HCAL. Such a final state with trackless jets also arises in the context of emerging jets [331], and ATLAS has a trigger for trackless jets in association with a soft muon (where the muon is required to fire L1 of the trigger) [256]. Additionally, the CalRatio trigger and associated search for displaced

¹⁷⁵ While these values set a concrete physics target, we stress again that the mass splitting can be arbitrary in other corners of the BSM parameter space (even within SUSY). For instance, $\tilde{\tau} \rightarrow \tau \tilde{\nu}$ (where the stau and sneutrino masses are free independent parameters) or for scalar particles (e.g. $H^+ \rightarrow \mu^+ H^0$), where the mass splitting and the overall mass scale are set by arbitrary quartic couplings.

¹⁷⁶ While currently there are some proposals to trigger on tracks [324], those predominantly apply to standard tracks. In particular, the new fast track reconstruction (FTK) system at ATLAS requires 10 hits in ID silicon, which corresponds to a decay radius of less than 9 cm. However, pattern banks for hits including high- $|d_0|$ tracks are currently being considered out to $d_0 \sim 2$ cm [325, 326].

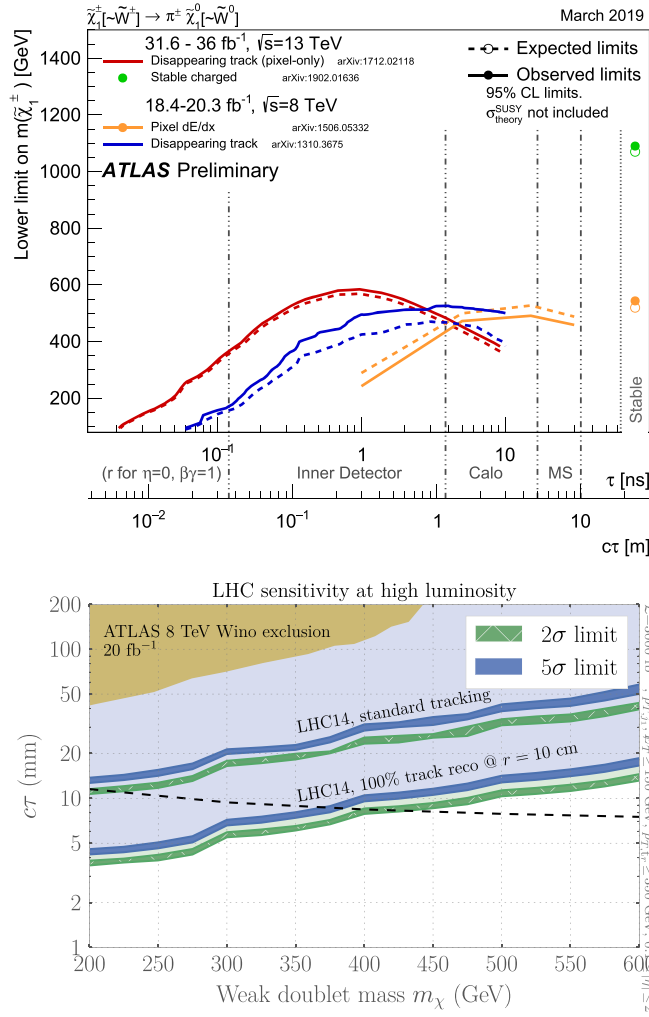


Figure 10. Top: summary of ATLAS disappearing-track searches as applied to a Wino (electroweak triplet) benchmark scenario [323]. Bottom: HL-LHC projected constraints on the Higgsino scenario [99].

hadronic decays (addressed in section 3.1) is designed to be sensitive to a similar signature and could provide some coverage of this signature as well. Strictly speaking, SIMPs are not a track-based signature, but we include them here because the interactions of the SIMPs with the tracker are different from usual hadrons in jets, while the calorimeter signatures are similar.

An LHC phenomenological study of SIMPs was carried out in [332]. We summarize the main points of the study here. In their setup, SIMPs interact with the SM via an attractive potential (either scalar or vector mediator) coupling SIMP pairs to $q\bar{q}$ pairs. The proposed analysis selects events with high- p_T , back-to-back jets within the tracker, exploiting the charged energy fraction within a jet to discriminate signal from background. The astrophysical experimental constraints on this scenario are compared with the expected

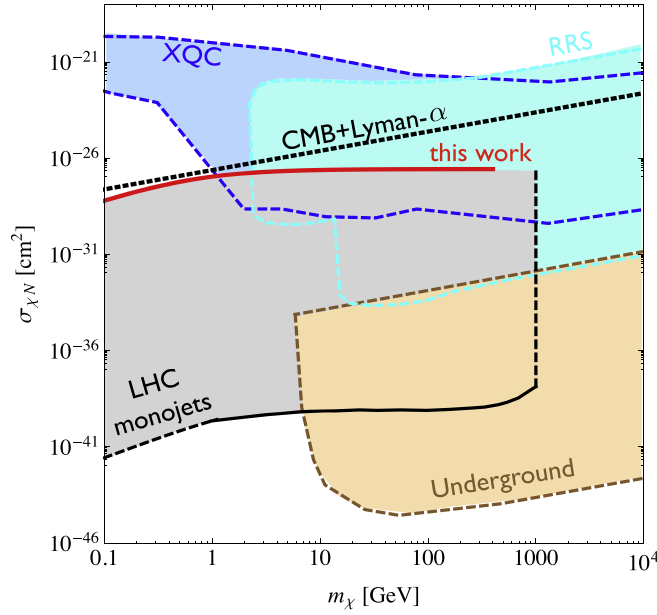


Figure 11. Astrophysical and collider constraints on a simple SIMP setup. Note that the relevance of the astrophysical constraints depends on the contribution of the SIMPs to the relic density. Taken from [332].

reach of this search and that of mono-jets in figure 11. Currently there is an ongoing analysis in CMS pursuing this strategy.

3.5.2.3. Quirks. Quirks are particles charged under both the SM and a new confining gauge group [182], referred to here as ‘infracolor’ (IC). The defining property of quirks is that the tree-level quirk masses m_Q are above the confinement scale Λ_{IC} (and thus similar to QCD but with no light-flavored quarks), so that there is never enough local energy density to create new quirks out of the vacuum. A pair consisting of a quirk and an anti-quirk can live in a quantum-mechanical bound state where the constituents are separated by macroscopic distances $\ell \sim \frac{m_Q}{\Lambda_{IC}^2}$, remaining connected by an IC flux tube. The IC flux tube exerts a force on each quirk that causes its trajectory to differ from the expected helicoidal ones for SM particles.

The collider phenomenology depends greatly on the size of ℓ . If ℓ is much less than an \AA , the rapid emission of IC glueballs results in the quirks annihilating before ever reaching the beampipe. For large enough confinement scales, the IC glueballs can decay back into SM particles on sufficiently long time scales that they can be distinguished from prompt signatures. While in this specific case, quirks produce hidden valley [66] or emerging jet [331] signatures due to these long-lived IC glueballs (see chapter 7), we stress that elsewhere in parameter space quirks exhibit their own distinct phenomenology and are not merely a subset of hidden valleys, contrary to popular lore.

If ℓ is larger than an \AA but below the mm scale, the individual quirks are not distinguished from one another. However, the pair (which is overall neutral, and therefore does not bend in the magnetic field of the tracker) appears as a single, highly ionizing straight track with missing energy aligned with it, the latter arising from mis-measurement of the track

momentum. The *D0* collaboration has searched for precisely this signature [333], requiring an additional jet for trigger purposes. This search obtained lower bounds on quirk masses of 107, 119 and 133 GeV for SU(2), SU(3) and SU(5) gauge groups, respectively. However, no extensions of this search to higher mass have been performed at the LHC, and the existing HSCP searches require low uncertainties on the track momentum that a straight quirk track would not satisfy.

Conversely, if ℓ is very large then the existence of the confining force has no effect on the quirk motions, and HSCP searches apply directly to the quirk case, with quirks charged under QCD yielding *R*-hadrons and uncolored quirks leading to slepton-like signatures. We refer the reader to the section 3.5.1.1 for more information.

For intermediate values of ℓ , there are interesting phenomenological prospects at the LHC that have been recently studied theoretically [239, 240, 334], but for which there are no current public searches by the LHC collaborations. The first study [239] has recast mono-jet and HSCP searches, finding bounds up to 1.7 TeV for colored quirk masses. In addition, it has also proposed using the CMS dataset taken with zero magnetic field. In this dataset, all SM particles are expected to follow a straight trajectory, but the quirks would still bend due to the string tension. The second study [240] has proposed a new algorithm to search for quirks, exploiting the fact that the quirk and anti-quirk pair should lie in the same plane with the highest sensitivity in the $\ell \sim 1\text{--}10$ mm range. This avoids the necessity of fitting non-helicoidal trajectories, and has the potential to extend the sensitivity to quirks well beyond the current mono-jet and HSCP limits. The third study [334] considers quirks that lose energy through material interactions with the detector. A charged or colored quirk pair can come to a stop within the detector, and annihilate out-of-time with active *pp* collisions, allowing for sensitivity from SP searches across a wide range of characteristic length scales, $\ell \sim \text{\AA}$ km range. We refer the reader to the section 3.5.3 for more information on SP searches.

Because of the non-standard nature of the tracks, quirk phenomenology poses substantial challenges in their experimental reconstruction, and the lack of constraints on quirks have already attracted the attention of the ATLAS, CMS and LHCb experiments. It would be desirable to test how the phenomenological proposals in [239, 240, 334], among others, can perform in a realistic detector simulation of one of the LHC experiments.

3.5.3. Out-of-time decays of SPs. This category is unique because LLP decays occur out-of-time with the collision. Indeed, decays can even occur when the LHC is not running! The only member of this class is the search for SPs, which we describe below.

If an HSCP is produced with very low kinetic energy, it can come to rest in the detector due to interactions with the detector materials. This most likely occurs in the calorimeters or the steel yoke in the MS as a result of their high material densities. The HSCP can then decay at a later time when no collision is taking place (known as an out-of-time decay). This experimental restriction reduces the types of background processes affecting the search, with the dominant backgrounds coming from cosmic rays (CRs), beam halo, and instrumental noise.

In the Run 1 analyses from ATLAS [236] and CMS [234], events are selected with a dedicated trigger selecting bunch crossings which are empty and have no bunches of protons nearby. The analyses require a jet with $p_T(E)$ above 30 (50) GeV at ATLAS (CMS). ATLAS further supplements the hardware trigger by requiring $p_T(j) > 50$ GeV, $|\eta| < 1.3$ and $E_T > 50$ GeV, rejecting instrumental noise. In addition, CMS has updated the jet search in Run 2 and also provided a search that triggers on out-of-time muons, both of which use the 13 TeV dataset [235]. The latter also employs the displaced stand-alone (DSA) muon reconstruction algorithm [335].

An offline selection procedure is aimed at reducing the main backgrounds. Muons coming from CRs can be identified due to their distinctive topology. The ‘beam halo’ background is the result of protons interacting with residual gas in the beampipe, the beampipe itself, or collimators upstream from the IP. Most particles will not travel far before being absorbed by various structures, but muons will travel parallel to the beam and can leave calorimeter deposits out of time with a proton–proton collision. However, these deposits will often be accompanied by corresponding horizontal tracks in the MSs and can thus be efficiently vetoed. Instrumental noise is rejected in CMS by exploiting the anomalous response in the HCAL.

Stopped particle searches provide an alternative way of probing charged particles besides more conventional HSCP searches. HSCP searches are typically more sensitive to any signature with a charged particle, so SP searches are not often expected to be a discovery mode for most simple new physics scenarios with charged LLPs¹⁷⁷. The typical added value of SP searches is that they can help identify and characterise positive signals in HSCPs, for instance by providing a cleaner extraction of the lifetime and also to properly identify the decay products. However, in some cases (such as for quirks, where HSCP searches are insensitive in much of parameter space), it has been argued that an SP search could actually be a discovery mode if modifications are made to the search strategy to improve sensitivity to quirks [334]. These modifications that would increase quirk acceptance or lower backgrounds include expanding the η range, implementing higher energy thresholds, using the timing information, and considering shower evolution in the new CMS endcap calorimeter [336].

3.6. Discovery opportunities: overview of gaps in coverage

In the preceding sections 3.1–3.5.3, we have examined the so-called ‘coverage’ of existing searches for LLPs at the LHC with the explicit and express purpose of identifying uncovered realms and places where discoveries could be hiding. Here, we summarize these gaps and potential opportunities for LLP discovery in bullet form, as a to-do list for the experimental community.

1. All-hadronic LLP decays

- Associated-object triggers (especially motivated by Higgs-like VBF and VH production modes) need to be more comprehensively used to improve sensitivity to low- p_T objects.
- Improvements are needed in sensitivity at lower masses and lifetimes (e.g. for LLPs produced in Higgs decays).
- Single hadronic DVs need to be looked for in searches that currently use two (such as decays in ATLAS HCAL and MS).
- Possibilities need to be explored for ATLAS and CMS for online reconstruction of hadronic displaced objects, as the inclusive H_T triggers used by the two collaborations miss these objects unless they have a large p_T . (By contrast, LHCb can trigger on a displaced hadronic vertex [253, 254].)
- Low-mass hadronically decaying LLPs can look somewhat like tau leptons, so the question remains as to whether there is any possibility of using, for example, L1 tau triggers to seed displaced jet triggers at HLT and improve trigger efficiency; studies need to be performed by the experimental collaborations.

¹⁷⁷ The reason why the SP searches are less efficient than the HSCP ones is twofold. On one hand, only a fraction of LLPs stop in the detector, while the HSCP search only requires that the LLP crosses the detector. On the other hand, the SP is only looked for in a specific time-window that might fail to catch a large fraction of them.

- The prospects for dedicated searches for displaced hadronic taus need to be investigated, since no dedicated searches currently exist.
 - The potential for flavor-tagging displaced jets (b-displaced jets, c-displaced jets, etc) needs to be explored.
2. Leptonic
- Coverage needs to be provided for the intermediate region between boosted, low-mass LLPs (lepton jets) and high-mass, resolved LLPs (resolved ATLAS/CMS searches).
 - Improvements need to be made to extend coverage to lower masses and to lower p_T thresholds. Currently no prescription or plan for this exists, and so dedicated studies need to be done.
 - Searches need to be done for different combinations of charge and flavor of displaced leptons (e.g. same-sign versus opposite-sign, opposite-flavor versus same-flavor).
 - Searches need to be done for tau leptons in LLP decays, in particular if they come from the ID; an unanswered question remains as to whether displaced-jet triggers can be used for this purpose.
3. Semi-leptonic
- Searches do not exist and need to be done for LLP masses below about 30 GeV; this mass range is theoretically well motivated by Majorana neutrinos.
 - Searches need to be performed for all flavor combinations (for example, one CMS search only covers $e^\pm\mu^\mp$), as well as same-sign versus opposite-sign leptons.
 - Currently unknown improvements need to be made to relax or modify isolation criteria wherever possible to recover sensitivity to boosted semi-leptonic decays.
 - Searches need to be done that better exploit triggering on associated objects for improved sensitivity to low-mass objects, or to employ high-multiplicity lepton triggers if there are multiple LLPs.
4. Photonic
- There is currently no coverage for LLPs decaying into $l\gamma$, $j\gamma$, or without \cancel{E}_T , and searches urgently need to be performed for this decay topology.
 - There is currently poor coverage (i.e. there exists no dedicated search) for single- γ topologies. The only searches with sensitivity require two jets to be present in addition to \cancel{E}_T [303]. Studies are needed to assess the sensitivity of this search to signals with only one delayed photon and different jet multiplicities.
 - There is currently no coverage for softer non-pointing or delayed photons, and searches need to be performed for these kinematic realms.
 - Studies need to be performed to determine if triggers on associated objects may improve sensitivity to signals with a single photon, without \cancel{E}_T , or for lower- p_T photons
5. Other exotic long-lived signatures
- Disappearing tracks with $c\tau \sim \text{mm}$ are very hard to probe, and new ideas and detector components are needed to extend sensitivity to this potential discovery regime. It is unclear if the ATLAS insertable B-layer will be present in HL-LHC run and how sensitivity to the DT topology will improve with the replacement of the current ID with the new inner tracker (ITk), or whether new tracking layers very close to the beam line can be added. It is an open question as to what is the lowest distance at which new layers (or double layers) can be inserted. Another open question that needs to be answered is whether there are any prospects for DTs at LHCb with an upgraded detector.

- No dedicated searches for quirks exist at the LHC, a huge, open discovery possibility for ATLAS, CMS, and LHCb. Some LHC constraints exist by reinterpreting HSCP searches, but dedicated searches need to be performed. There are significant challenges in modeling the propagation and interaction of quirks with the detector, as well as in fitting tracks to their trajectories, but new ideas have been proposed that need to be explored by the experimental collaborations that might allow improved sensitivity to quirks with less ambitious analysis methods.

4. Common sources of backgrounds for LLP searches

Chapter editors: Juliette Alimena, Martino Borsato, Zhen Liu, Sascha Mehlhase

4.1. Introduction

For many searches for LLPs, the main backgrounds do not stem from irreducible SM processes, but arise instead from *external sources*. Indeed, there can even be backgrounds of instrumental and/or algorithmic nature. Often, LLP searches are designed to have a very small number of background events, sometimes even zero events, that pass the full selection criteria. This chapter gives an overview of common LLP search backgrounds and the means to estimate or control them.

4.2. Long-lived particles in the SM

Weak decays of SM particles can naturally give rise to DV at the boosts typically encountered at the LHC. Searches for LLP signatures at sufficiently low LLP mass and lifetime suffer from large backgrounds due to displaced SM decays. One simple example is found in the search for long-lived dark photons decaying to $\mu^+\mu^-$ at LHCb [269], which drastically loses sensitivity when the dark photon mass gets too close to the $K_S \rightarrow \pi^+\pi^-$ invariant mass, despite the very low $\pi \rightarrow \mu$ misidentification rate.

Moreover, b -hadrons can decay at displacements of a few mm and can be challenging to distinguish from LLPs with masses of a few tens of GeV that decay to a pair of jets. Requiring a large track multiplicity of the DV and performing a mass fit to the dijet invariant mass can help to significantly reduce the effect of this background (see, for example, [251, 253]). Backgrounds from heavy flavors are typically more abundant in the forward region, as arises, for example, if the signature under study is an LLP from the decay of a SM-like Higgs boson. However, the LHCb forward detector, which was designed to study these SM decays, is, in most cases, capable of rejecting heavy flavor backgrounds more effectively than can be done in ATLAS or CMS. Furthermore, displaced tracks from b -mesons, which usually have impact parameters (d_0) of less than 2 mm, can be rejected by using a larger criterion for the minimum track d_0 .

4.3. Real particles produced via interactions with the detector

Particles produced in the pp collision can interact with nuclei of the detector material, giving rise to DV, and can mimic LLP signals. Vertices from these interactions will be positioned in regions of the detector containing high densities of detector material and are therefore effectively vetoed by using detailed material maps.

The LHC detectors have developed tools internal to the collaborations to define a material volume to be vetoed. As the detector configurations changed slightly from Run 1 to Run

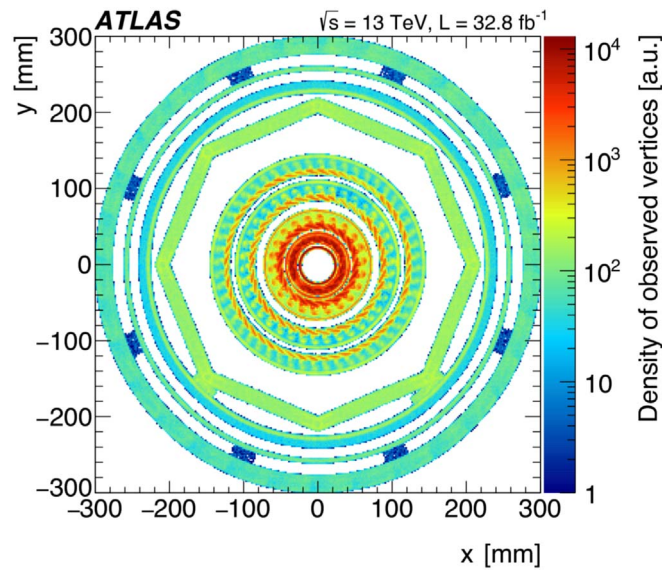


Figure 12. An example of a material map from ATLAS [237].

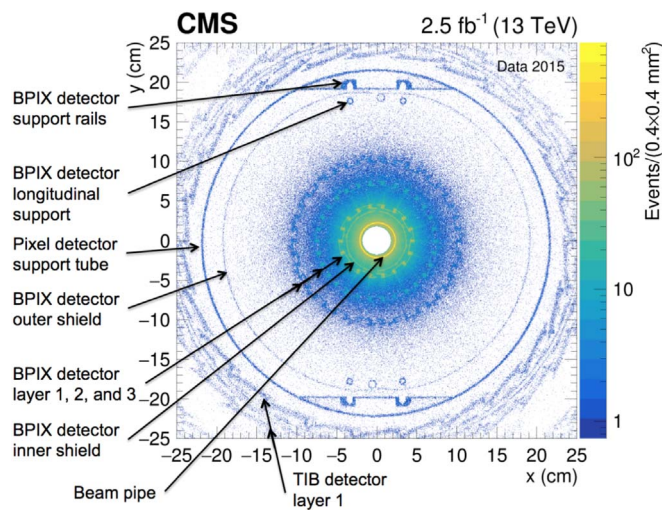


Figure 13. An example of a material map from CMS [339].

2, material maps have been determined separately for each data-taking period for both the ATLAS and CMS collaborations, using collision data. Maps can be found for ATLAS for Run 1 in [337], CMS for Run 1 in [338], ATLAS for Run 2 in [237], and CMS for Run 2 in [339]. Additionally, the Run 2 maps for both are shown here in figures 12 and 13 for ATLAS and CMS, respectively.

LHCb recently developed a precise material map of the VELO using beam-gas collisions [340], shown in figure 14. Beam-gas collisions can be distinguished from long-lived heavy flavor backgrounds and their utilization allows the map to cover precisely the whole VELO

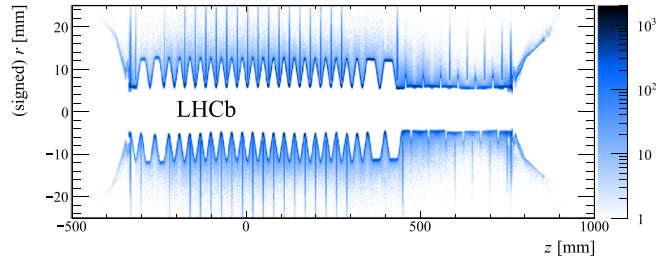


Figure 14. Reconstructed secondary vertices in the LHCb VELO from beam-gas collisions in the zr plane integrated over ϕ . These vertices are used to build the material map [340] to veto backgrounds from material interactions.

geometry, not only the region close to the IP. This map was used to veto photon conversions to di-muons, which is the main background affecting displaced dark-photon searches at low mass [269]. In analyses, this material map, together with properties of a reconstructed secondary vertex and its constituent tracks, is used to construct a p -value that is assigned to the hypothesis that the secondary vertex originates from a material interaction. As a rule of thumb, LHCb material interaction background is dominant for vertices at a distance from the beam axis larger than 6 mm (where the VELO material begins). Below 6 mm the background is dominated by heavy flavor decays [341].

Because accurate material maps are essential to performing fully reliable sensitivity studies to signatures with DV, making them publicly available to the broader LLP community is of the highest priority. The availability of such tools in fast parametric simulations such as Delphes [342] would be very useful to reinterpret LLP search results. In section 6.4.6.2, an example of a reinterpretation of an LLP search is presented, where a rough material veto was performed because these material maps were not publicly available, highlighting the shortcomings of such approaches in the absence of accurate material maps and emphasizing the benefits of making them available.

High-energy collision muons originating mainly from W decays and creating secondary interactions in the tracker, calorimeters or MS can be an additional source for DV mimicking LLP signals. This mostly minor background arises as vetoing these DV is based on a not 100% efficient detection of the high- p_T track in the tracker.

Another important background, mainly for analyses targeting the reconstruction of decay vertices of LLPs reaching the MSs, is hadronic or electromagnetic showers not contained in the calorimeter volume, so-called punch-through jets [248]. These punch-through jets occur especially in regions of reduced total interaction length in the calorimeters (e.g. transition regions between the barrel and the end-caps) and can be suppressed by either rejecting these $|\eta|$ regions or requiring a minimal number of hits in the MS and isolating the DV from calorimeter jets as well as high-energy tracks and significant track activity in the inner tracking system. In order to not reject true vertices from displaced decays that occur near the end of the calorimeters, the calorimeter-jets veto should only consider jets with a minimum total energy deposit and, e.g. a minimum electromagnetic fraction of the total energy. The track isolation requirement aims at regions with a poor calorimeter measurement (again, transition regions in the calorimeters), where a single high-energy track or the sum of the track activity in a small cone around the DV could indicate a (punch-through) jet. On the other hand, punch-through jets, given their similarity to signal signatures, can also be used to evaluate systematic uncertainties due to imperfect modeling in the muon-system simulation.

4.4. Real particles originating from outside the detector

There are several types of real particles generated outside the detector that could be sources of background in an LLP search.

4.4.1. Cosmic muons. Cosmic rays from the atmosphere can enter the detector as cosmic-ray muons. These cosmic-ray muons can be reconstructed as displaced muons in the MS or as displaced jets in the calorimeters. If cosmic-ray muons are reconstructed in the MSs, they will typically appear as two back-to-back muons with ϕ values near $\pm\pi/2$. The rate of cosmic muons in the detector is about 500 Hz at L1, but depending on the HLT path and the offline selection used, the rate of cosmic-ray muons entering a given LLP analysis is generally much less.

Cosmic-ray muons are typically an important background source to consider for displaced signatures, especially those with large displacements [234, 236, 343–345]. Cosmic-ray muons are generally only an issue for LLP analyses in CMS and ATLAS since LHCb has coverage only in the forward direction.

For many analyses, cosmic-ray muons can be rejected with a simple veto on back-to-back dimuons. However, in some LLP analyses, this veto is not optimal for the signal acceptance or it is insufficient to suppress cosmic-ray backgrounds. Another often-used way to minimize the contribution from cosmic-ray muons is requiring high-momentum muons and/or high-energy jets, since cosmic-ray muons have a rapidly falling p_T spectrum. In addition, if a search primarily looks for inner-tracker or calorimeter objects, cosmic-ray-muon events can be rejected by requiring little MS activity [234, 343, 344].

If the cosmic-ray muon background is significant for an analysis, it can be estimated using data from dedicated cosmic data-taking runs or from empty bunches in pp collision runs [234, 343, 344]. Cosmic ray muon simulations can be made, but in many LLP analyses, a data-driven approach is favoured if the simulation modeling is found to be insufficient. Timing information in the calorimeters or the MSs can be used to discriminate the signal from cosmic-ray muons, sometimes in conjunction with impact parameter variables.

4.4.2. Beam halo. Another type of real particle generated outside the detector that could be a significant source of background for LLP searches is beam halo. Beam halo is produced when protons from the LHC beam scatter off the LHC collimators and produce debris, which can appear in the detector. Beam halo can create energy deposits in the calorimeters or hits in the MS, both of which would be largely in the beam direction. These energy deposits or MS hits would appear earlier than if they had been made from particles coming from the collision (see figure 15). Beam halo is usually not modelled in MC simulation, since it is highly dependent on the beam parameters.

Beam halo is most relevant for searches for displaced signatures without tracks in the inner tracker and for searches for decays in non-collision bunches (e.g. from SPs) [234, 343, 344], which are described in section 3.5.

The contribution from beam halo can often be reduced by requiring high-momentum or high-energy reconstructed objects. One can also decrease the number of beam halo events by requiring central objects or vetoing forward MS activity, since beam halo is usually in the very forward direction [234, 343, 344]. For inner tracker-based signatures, events from beam halo are rejected by requiring a minimum number of early hits; in this way beam halo is rejected due to its anomalous timing.

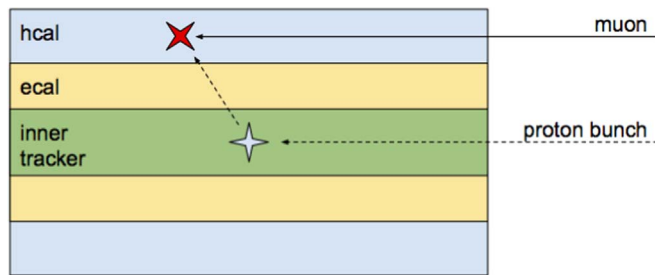


Figure 15. A sketch illustrating the timing differences due to the shorter, more direct path to the calorimeter cells between a beam-halo muon and a particle originating from the collision. The beam-halo muon is detected earlier than the particle from the collision.

Beam halo background can be estimated using data control regions near $\phi = 0$ and π . One could also identify cells with a low number of (or zero) tracks that are assigned an early time.

4.4.3. Cavern radiation. Diffuse backgrounds can also arise from proton–proton collisions filling the LHC caverns, consisting mostly of neutral, low-energy, and long-lived SM particles (i.e. neutrons and photons), leading to an overall increase in occupancy, especially in the MSs. This so-called ‘cavern background’ or ‘cavern radiation’ can constitute a significant background in a LLP search. As simulations are resource-intensive, it is usually not at all modelled in MC simulation samples.

Cavern radiation is most relevant for searches looking in non-collision data, that is, stopped-particle searches, and for searches using MS information to form tracks and vertices. It can be estimated from data by collecting events triggered by random triggers when there are no collisions, as was done in [236]¹⁷⁸. Cavern radiation can also be estimated by overlaying a cavern radiation simulation with minimum-bias events from data.

4.5. Fake-particle signatures

Another type of background for LLP searches is that from signatures that mimic real particles in the detector, but are in fact fake. Fake particles can originate from spurious detector noise. Noise appears differently for each detector, but in general, it is characterized by a single and concentrated energy deposit or hit that does not correspond in time or space to any other energy deposits or hits in the detector. Noise is usually difficult to model with MC simulation.

Calorimeter detector noise is most relevant for searches looking in non-collision bunches and low-energy collisions [234, 343, 344]. Muon system noise is most relevant for searches that are also highly affected by cosmic-ray muons.

Calorimeter noise can be rejected by vetoing single and concentrated energy deposits [234, 343, 344]. Muon system noise can be rejected by requiring high-quality muon tracks.

Noise in both the calorimeters and the MSs could be estimated by looking at dedicated cosmic data-taking runs and then applying some selection criteria to reject cosmic-ray muons. The remaining events would most likely be noise.

¹⁷⁸ Note that these triggers are unlike those used to collect the search data for stopped-particle searches, which instead select events with physics objects during empty bunch crossings.

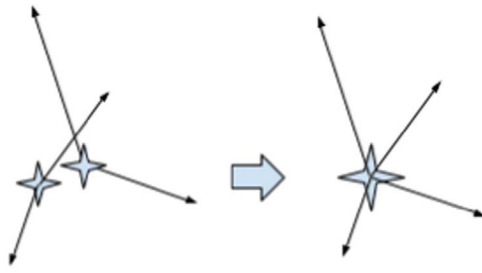


Figure 16. Illustration of two close-by, low-mass vertices being reconstructed as one high-mass vertex.

4.6. Algorithmically induced fakes

For searches that aim to reconstruct the decay vertex of an LLP, and especially for LLPs decaying in the proximity of the interaction region, algorithmically induced fakes and/or instrumental backgrounds can be of importance. Algorithmic fakes can still be a significant background to LLP searches, even if a given detector is noise-free.

4.6.1. Random/Merged vertices. This type of background, illustrated in figure 16, is especially important in the environment close to the interaction region that experiences a high track density, and arises from two main sources. First, two or more individual tracks can cross each other and can be reconstructed as a DV. Second, two close-by, low-mass vertices can be reconstructed as one high-mass DV; such a final merging/cleaning step is often part of vertexing algorithms to reduce fakes in standard vertexing.

The former source is mostly suppressed by requirements originally targeting the removal of meta-stable SM particles: a minimum transverse impact parameter, $|d_0|$, for tracks and a minimum distance between the PV and a given DV.

The latter source is harder to suppress, though can be estimated by randomly merging vertices from distinct events. By studying the number of reconstructed ‘merged’ high-mass vertices as a function of distance between the two low-multiplicity low-mass vertices that were ‘merged’—both with vertices from the same event, as well as from different events and scaling them accordingly—an estimate for this background can be derived. This method has been successfully used in the ATLAS search for DV [237] and the ATLAS multitrack analysis [196].

4.6.2. Randomly crossing tracks. A background that is typically more relevant than merged vertices is the background stemming from low-mass DV crossed by unrelated tracks, resulting in the reconstruction of a high-mass vertex, as illustrated in figure 17. The mass of the reconstructed DV is especially increased when the random track crosses the vertex in a direction that is perpendicular to the distance vector pointing from the PV to the displaced one.

As demonstrated in detail in [196, 237], this background can be estimated by constructing vertices (n -track) from lower-multiplicity ones ($n - 1$ -track) by adding pseudo-tracks, drawn randomly from data-driven track templates derived for various radial detector regions. The normalization of the prediction is performed by comparing the $n - 1$ -track-based constructed vertices with the actual n -track vertices in all radial detector regions. One

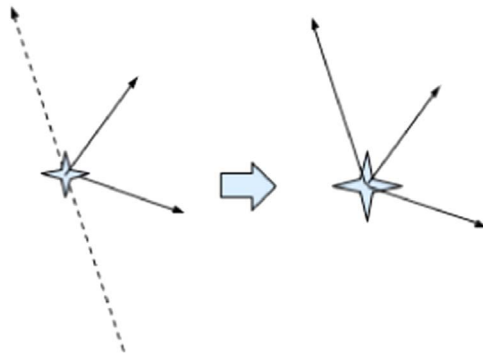


Figure 17. Illustration of a low-mass vertex crossed by an unrelated track and being reconstructed as a high-mass vertex instead.

potential method for suppressing such backgrounds is to veto vertices where removing one track substantially decreases the mass of tracks associated with the vertex.

4.7. Summary

LLP searches often have very low backgrounds, as opposed to searches for prompt particles. This makes LLP searches highly sensitive to signals of new physics.

There are, however, a few common sources of background that arise in different LLP searches: other, known, LLPs such as b -hadrons; real particles produced in the detector, such as particles produced in collisions that interact with the nuclei of the detector material; real particles produced outside the detector, such as cosmic muons or beam halo; fake particles, such as detector noise; and algorithmically induced fakes, such as two tracks that cross and are reconstructed as a DV, as described above. These backgrounds are generally atypical, difficult to model in simulation, and challenging to estimate. Thus, the possible appearance of unexpected background sources should be taken into account in any new LLP search, and the development of novel techniques and methods to estimate them is encouraged.

5. Detector upgrades

Chapter editors: Juliette Alimena, Martino Borsato, Yangyang Cheng, Monica Verducci

Contributors: Cristiano Alpigiani, Xabier Cid Vidal, David Curtin, Elena Dall’Occo, Sven Dildick, Jonathan L Feng, Iftah Galon, Christopher Hill, Henning Keller, Felix Kling, Simon Knapen, Zhen Liu, Henry Lubatti, Philippe Mermod, Vasiliki A Mitsou, James L Pinfold, Jessica Prisciandaro, Dean Robinson, Livia Soffi, Sebastian Trojanowski, Carlos Vázquez Sierra, Si Xie, Charlie Young

The experimental searches for LLPs outlined in chapter 3 are limited by the abilities of the ATLAS, CMS, and LHCb experiments to trigger on and reconstruct the objects that are associated with each signature. In the Phase 2 high-luminosity upgrade of the LHC (HL-LHC), the extremely high PU conditions necessitate the upgrade of all three detectors to maintain triggers at thresholds needed for sensitivity to electroweak, Higgs, and BSM physics (see [346, 347] for an overview); to reject particles originating from PU vertices; and to maintain object reconstruction in the high-luminosity environment. These upgrades include the addition of tracking layers to the forward regions of ATLAS and CMS, improvements to

timing reconstruction in events, and the inclusion of tracking information at earlier stages of the trigger (or, in the case of LHCb, the full online reconstruction of every event).

While these upgrades are crucial to the success of the HL-LHC physics goals for conventional searches (such as for electroweak, Higgs, or SUSY signatures), they have the opportunity to be transformative for searches for LLPs. Signatures involving LLPs are often subject to small-to-negligible irreducible backgrounds, and improvements to the reconstruction, timing, and vertexing of displaced objects can typically suppress any instrumental or fake backgrounds. (See chapter 4 for a discussion of sources of backgrounds for LLP searches.) At the same time, the introduction of tracking information to earlier stages of the trigger could be used to trigger on events that may contain hadronically decaying LLPs that must otherwise pass jet triggers, leading to an improvement in sensitivity to low-mass LLPs. Indeed, many of the gaps in coverage from current searches identified in section 3.6 can be closed or reduced using the new technology from detector upgrades. Even more uniquely, LLP signatures may themselves motivate the introduction of new detector elements that are dedicated to exploring new lifetime frontiers in particle physics.

This chapter summarizes current and proposed plans for detector upgrades for the HL-LHC, paying special attention to those features of the detector upgrades that are most relevant for LLP searches. Where available, we show the results of projections for the sensitivity to various LLP scenarios of different improvements to the detector. We also highlight LLP studies for the Phase 2 upgrades that are not yet publicly available that should be done in order to assess (and, where possible, improve) the sensitivity of planned upgrades to LLP signatures. Finally, we include contributions from a number of existing and proposed experimental collaborations whose primary purposes are to search for LLPs produced at LHC IPs using additional, dedicated detectors. These detectors complement the capabilities of ATLAS, CMS, and LHCb, allowing sensitivity to signatures that are otherwise not possible to reconstruct at the main detectors.

In section 5.1, we combine the discussions of the planned ATLAS and CMS upgrades, facilitating for each detector component a direct comparison between the features of the upgraded detectors of both ATLAS and CMS. Since LHCb has a very different geometry and physics program from ATLAS and CMS, we have a separate discussion of planned LHCb upgrades in section 5.2. Finally, we present the contributions of the dedicated LLP experiments in section 5.3.

5.1. The ATLAS and CMS experiments

The planned upgrades to the ATLAS and CMS experiments for the HL-LHC will give the detectors increased coverage in the forward regions, better spatial and timing resolutions, and other new features including track triggers. The improved hardware capabilities, combined with software developments, give rise to exciting new prospects for future LLP searches. This section gives an overview of the upgrade scope (section 5.1.1), discusses their physics potential (sections 5.1.2 and 5.1.3), and presents new ideas for detector upgrade and LLP searches (section 5.1.4).

Unless specified otherwise, the subsequent CMS experimental results are from its Technical Design Reports for the different sub-detector upgrades at HL-LHC, namely tracker [348], barrel calorimeter [349], endcap calorimeter [336], muon detectors [350], timing detector (Technical Proposal, [351]), and Level-1 Trigger (Interim Technical Design Report, [352]). ATLAS results are from the Technical Design Reports for the inner tracker pixel detector [353], the TDAQ system [354], the tile calorimeter [355], LAr calorimeter [356], MS [357], and inner tracker strip detector [358].

5.1.1. Detector and trigger upgrades for high-luminosity LHC. The high luminosity LHC (HL-LHC) will begin with the third long shutdown (LS3) of the LHC in the coming decade (as of this writing estimated to begin at the end of 2023), where the machine and detectors will be upgraded to allow for pp running at a luminosity of $5 \times 10^{34} \text{ cm}^{-2} \text{ s}^{-1}$ in the nominal scenario, or potentially $7.5 \times 10^{34} \text{ cm}^{-2} \text{ s}^{-1}$ in the ultimate performance scenario. This will allow the ATLAS and CMS experiments to collect integrated luminosities ten times that of the current operations, which amounts to around 300 fb^{-1} per year and 3000 fb^{-1} during the projected HL-LHC lifetime of ten years (up to 4000 fb^{-1} if the ultimate instantaneous luminosity can be achieved).

The HL-LHC conditions create unique challenges in terms of high PU levels and high radiation dosage. About 140 PU events per bunch crossing, on average, are expected in the nominal scenario, and up to 200 PU events in the ultimate luminosity scenario. The radiation levels will be unprecedented: for the design integrated luminosity of 3000 fb^{-1} , a 1 MeV neutron equivalent fluence of $2.3 \times 10^{16} n_{\text{eq}} \text{ cm}^{-2}$ and a total ionizing dose of 12 MGy (1.2 Grad) is expected at the centre of the detectors, where the innermost silicon pixel tracking layers will be installed.

To meet the challenges of the HL-LHC operating conditions, and to fully profit from its physics capabilities, comprehensive upgrade programmes are planned for both the ATLAS and CMS experiments. This section summarizes the main detector and trigger upgrade plans for each sub-detector component of both experiments.

5.1.1.1. Tracker. By the start of the HL-LHC, the inner trackers of both experiments must be replaced due to the significant radiation damage and performance degradation they have suffered. To maintain tracking performance in the high-density environment, and to cope with the increase of approximately a factor of ten in the integrated radiation dose, both the ATLAS and CMS experiments will entirely replace their inner tracking detectors.

CMS upgrade. The CMS tracker is composed of the inner pixel detector and the outer tracker. At the HL-LHC, the CMS inner pixel detector will include four cylindrical barrel layers covering the region of $|z| < 200 \text{ mm}$, and forward extensions of up to twelve endcap disks on both sides (compared to the current configuration with three disks), which will extend its $|\eta|$ coverage from the current value of 2.4 to approximately 4. To maintain radiation hardness and reasonable occupancy, as well as to improve resolution, small, thin pixels will be used. For the studies in the CMS tracker TDR [348], pixels with a thickness of $150 \mu\text{m}$ and $25 \times 100 \mu\text{m}^2$ in size are used in the simulation¹⁷⁹. The first layer of the barrel inner pixel detector will be positioned at a radius of 28 mm.

The CMS outer tracker is composed of six cylindrical barrel layers in the central region, covering the region of $|z| < 1200 \text{ mm}$, complemented on each side by five endcap double-disks, in the region of $1200 < |z| < 2700 \text{ mm}$. Modules are installed between $r \sim 21 \text{ cm}$ and $r \sim 112 \text{ cm}$. Three sub-detectors are distinguished: the Tracker Barrel with pixel-strip modules (TBPS), the Tracker Barrel with strip-strip modules, and the tracker endcap double-disks (TEDD). The inner rings of the TEDD disks use pixel-strip (PS) modules up to $r \sim 60 \text{ cm}$, and the rest use strip-strip modules. The outer tracker modules, called p_{T} modules, are composed of two single-sided, closely-spaced (1–4 mm separation) small pitch sensors read out by a set of front-end ASICs that correlate the signals in the two sensors and select the hit pairs (referred to as ‘stubs’) compatible with particles above the chosen p_{T}

¹⁷⁹ An alternative option being considered is that of $50 \times 50 \mu\text{m}^2$. Larger pixel sizes of $50 \times 200 \mu\text{m}^2$ or $100 \times 100 \mu\text{m}^2$ are being considered in outer barrel layers and outer rings of the endcap as a potential option to reduce power consumption.

threshold. A p_T threshold of 2 GeV corresponds to a data volume reduction of roughly one order of magnitude, which is sufficient to enable transmission of the stubs at 40 MHz. The ‘stubs’ are used as input to the hardware trigger at Level-1 (L1), which enables track-finding at L1 for all tracks with a p_T of 2 GeV or above. To improve the ‘stub’-finding efficiency and also to reduce material, the inner three outer tracker barrel layers, the TBPS, are made with flat modules in the center and tilted modules in the regions with larger z .

ATLAS upgrade The ATLAS collaboration will replace its ID with a new, all-silicon tracker to maintain tracking performance in HL-LHC conditions.

The new ATLAS ITk will consist of a greatly enlarged pixel system extending to roughly twice the radius and four times the length of the current pixel array, coupled with a much more finely-segmented strip detector. In total, the coverage of the full radius of the inner solenoid requires over three times the silicon area of the current detector.

The new system will consist of silicon barrel layers and disks (strips) or rings (pixels) with the possibility of inclined pixel modules to better cover the transition from the barrel to the end-cap regions. In detail, the strip detector has four barrel layers and six end-cap petal-design disks, both having double modules each with a small stereo angle. The strip detector, covering $|\eta| < 2.7$, is complemented by a five-layer pixel detector extending the coverage to $|\eta| < 4$. The combined strip-plus-pixel detectors provide a total of 13 hits for $|\eta| < 2.6$, with the exception of the barrel/end-cap transition of the strip detector, where the hit count is 11.

5.1.1.2. Calorimetry. Both the ATLAS and CMS calorimetry consist of ECALs and HCALs. Different materials and designs are used for the two experiments.

CMS upgrade. For the CMS detector, the existing scintillating crystals in its ECAL (ECAL) barrel (EB) will be kept for the duration of LHC. On the other hand, both front-end and back-end electronics will be replaced [349], which allows for higher transfer rates and more precise timing. The target timing resolution for the upgraded ECAL electronics is ~ 30 ps for particles with $p_T \approx 30$ GeV, which is the fundamental limit allowed by hardware and an order of magnitude smaller than the current limit. Current studies on the CMS HCAL barrel radiation damage suggest there is no need for replacement at HL-LHC.

The CMS endcap calorimeter, including both the electromagnetic (EE) and the hadronic sections, will be replaced with a high-granularity, silicon-based calorimeter (HGCAL). The HGCAL, with fine granularity in both the lateral and longitudinal directions, enables 3D imaging in reconstructing energy clusters. The intrinsic high-precision timing capabilities of the silicon sensors will add an extra dimension to event reconstruction. The HGCAL is expected to provide a timing resolution of ~ 10 s of ps for high-energy particles with p_T of tens of GeV.

ATLAS upgrade. The ATLAS liquid argon (LAr) calorimeter will be improved in Phase 2 with an electronics upgrade that will provide optimized super cells and full-granularity data to the trigger system by means of a new pre-processor. A similar upgrade of the ATLAS Tile calorimeter readout will use on-detector digitization and a new back end pre-processor. Both the LAr and Tile calorimeters expect to implement a 40 MHz readout system for Phase 2. The transmission of high-granularity calorimeter data (all cells with a transverse energy of two times the noise threshold) drives the bandwidth requirement for the upgraded trigger and data acquisition (TDAQ) system.

In addition, the outermost Tile calorimeter layer can be used to identify muons in the range $|\eta| < 1.3$ by better identifying particle energy depositions above the minimum ionizing particle (MIP) threshold.

5.1.1.3. Muon system. The MS will be upgraded at both experiments to meet HL-LHC conditions, extend geometric coverage, and improve detector performance and trigger capabilities.

CMS upgrade. For the CMS detector, its current MS consists of three different types of muon detectors. In the barrel region, drift tubes (DTs) are installed along with resistive plate chambers (RPCs). In the endcaps, there are cathode strip chambers (CSCs) together with RPCs. At the HL-LHC, the existing muon detectors will be improved with upgraded electronics to enable 40 MHz readout, as well as improve the timing resolution from the current 12.5–1 ns [350]. New muon detectors, namely gas electron multipliers and a new version of RPCs, will be added to the endcaps, covering the regions of $1.6 < |\eta| < 2.4$. Additional muon chambers, labeled ME0, will cover the very forward regions of $2.4 < |\eta| < 2.8$, a region also covered by the upgraded inner tracker. This will be used for the muon trigger at L1. The additional muon detectors are essential to achieve a high trigger efficiency with an acceptable rate, especially in the forward region. The additional hits in the new endcap muon stations, combined with improved algorithms, permit efficient triggering on displaced muon tracks even in the harsh environment of the HL-LHC.

ATLAS upgrade. Most of the front-end and detector readout of the ATLAS MS, including the trigger electronics for the RPC, thin gap chambers (TGCs), and monitored drift tube (MDT) chambers, will be replaced to face the higher trigger rates and longer latencies necessary for the new Level-0 (L0) trigger required by the HL-LHC conditions. The MDT chambers will be integrated into the L0 trigger in order to sharpen the momentum threshold. Some of the MDT chambers in the inner barrel layer will be replaced with new, small-diameter MDTs. Additional RPC chambers will be installed in the inner barrel layer to increase the acceptance and robustness of the trigger, and some chambers in high-rate regions will be refurbished. New TGC triplet chambers in the barrel–endcap transition region will replace the current TGC doublets to suppress the high trigger rate from random coincidences in this region. The electronics of all the sub-detectors will need to be replaced due to obsolescence, aging, and radiation damage. During the Phase 1 upgrade (to take place from 2019 to 2021) the new small wheel chambers will replace the CSC and the MDT chambers of the innermost endcap wheel by micromegas and small-strip TGCs. The replacement of the MDT front-end readout will address the trigger rate and latency requirements of the TDAQ system in Phase 2 and allow the use of MDT hit information to improve the muon p_T resolution in the L0 trigger. Additionally, in the upgraded detector all data from the barrel and endcap detectors will be transmitted to FPGAs at L0, which can be used to implement more advanced and flexible algorithms for muon reconstruction, including the use of neural networks and/or dedicated tracking for non-pointing muons [354].

Some LLP scenarios (e.g. HV models [66]) predict muon-jet final states, which result in collimated muons that are not identified with high efficiency by the current triggers (see section 3.2). In figure 18, the opening angle between muons in a HV model is shown, for a particular combination of particle masses and parameters. The di-muon separation is much smaller than the current system can resolve (approximately 0.2 in $\Delta\phi(\mu, \mu)$). In the no-upgrade scenario, these can only be recorded by the single muon trigger. In the upgraded scenario, a dedicated trigger is under development for a dimuon trigger with a p_T threshold of ≈ 10 GeV.

5.1.1.4. Timing detector. Precision timing can be provided by the aforementioned calorimetry upgrades. However, the tens of ps timing resolution in the upgraded calorimeters is only achievable for particles with energy above tens of GeV. Moreover, timing information for delayed objects from calorimetry alone will be affected by the

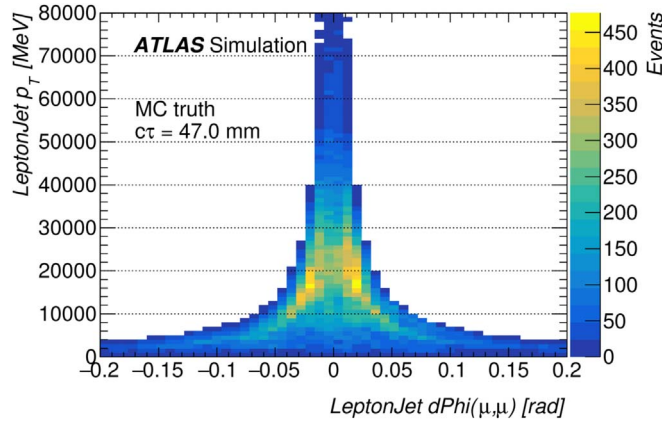


Figure 18. Opening angle between muons in a Hidden Valley model, where a sub-GeV-mass particle decays to $\mu^+\mu^-$. The opening angle is well below the resolution of the current system. From [359].

beamspot smearing, which corresponds to about 180 ps of uncertainty. Therefore, global event timing with the ability to reconstruct the vertex time and exploit time information in charged particle reconstruction requires a dedicated fast timing detector.

CMS upgrade. For the CMS experiment, the proposed MIP timing detector (MTD) will comprise a barrel and an endcap region made up of a single layer device between the tracker and calorimeters, and cover $|\eta|$ up to ~ 3 . In the barrel, the proposal is to adapt the present Tracker Support Tube (TST) design by instrumenting the current location of the thermal screen with a thin, actively-cooled, stand-alone (SA) detector, based on lutetium–yttrium orthosilicate crystals activated with cerium (LYSO:Ce) and read-out with silicon photomultipliers. The endcap region can be instrumented with a hermetic, single layer of MIP-sensitive silicon devices with high timing resolution, with a pseudorapidity acceptance from about $|\eta| = 1.6$ to $|\eta| = 2.9$. The MTD is designed to provide timing resolution of a few tens of ps for charged tracks throughout the detector lifetime. The performance projection in section 5.1.3 is evaluated with a 30 ps resolution for a p_T threshold of 0.7 GeV in the barrel and a p threshold of 0.7 GeV in the endcap, and covering the expected MTD fiducial region of $|\eta| < 3$.

ATLAS upgrade. The high-granularity timing detector (HGTD) is intended to distinguish between collisions occurring very close in space but well-separated in time. Currently there is not yet a TDR for this project. The current proposed detector design is based on low-gain avalanche detector technology that will cover the $|\eta|$ region between 2.4 and 4, with a timing resolution of 30 ps for MIPs. High-precision timing will improve the track-to-vertex association in the forward region, impacting jet and lepton reconstruction, as well as offering unique capabilities for online and offline luminosity determination.

5.1.1.5. Trigger. The ATLAS and CMS experiments adopt a two-level trigger system: the hardware-based Level-1 trigger (L1) and the software-based high-level trigger (HLT).

CMS upgrade. For the CMS experiment, the L1 trigger currently only uses calorimeter and muon information. At the HL-LHC, with the aforementioned outer tracker upgrade of p_T modules and stub-finding capabilities, tracking information will be included at L1 [352]. The

L1 track trigger uses parallel processing and pattern recognition on stub information to achieve track finding at an output rate of 750 kHz.

The L1 tracking capability will be further complemented by the calorimeter and muon upgrades, which provide more precise position and momentum resolution, calorimeter shower shape, and more muon hits in the forward region. In the L1 trigger, the electron and photon trigger algorithms for HL-LHC will use information from the ECAL as well as from the outer tracking detectors. The algorithm should preserve the ability to reconstruct electromagnetic clusters with p_T above a few GeV with high efficiency (95% or greater above 10 GeV) as well as achieve high spatial resolution which should be as close as possible to the offline reconstruction. Following the upgrade of both on-detector and off-detector electronics for the barrel calorimeters at the HL-LHC, the EB will provide energy measurements with a granularity of (0.0174, 0.0174) in (η, ϕ) , as opposed to the current input to the L1 trigger consisting of trigger towers with a granularity of (0.087, 0.087). The much finer granularity and resulting improvement in position resolution of the electromagnetic trigger algorithms is critical in improving electron/photon trigger efficiency and suppressing background at high PU.

The L1 global trigger (GT) will be upgraded with more sophisticated and effective global trigger calculations based on topology, plus an additional intermediate correlator trigger to fully exploit the increased information in the trigger objects, such as matching tracking info with finely-grained calorimeter information, or a combination of muon and track information. The upgraded detector readout and DAQ systems will allow 12.5 μ s latency and a L1 rate of 750 kHz; the latter may be substantially reduced by adding L1 tracking information matched to improved L1 trigger objects from the calorimeters and MS. At the HLT, the processing power is expected to scale up by PU and L1 rate, with an output rate of 7.5 kHz and up to 10 kHz.

ATLAS Upgrade. The ATLAS trigger and the data acquisition system are being planned with the intention of fully exploiting the physics potential of the HL-LHC. A baseline architecture has been proposed and documented in [354].

The hardware-based Level-0 Trigger system will be composed of separate calorimeter and muon triggers, as well as a GT and Central Trigger sub-systems. The result of the Level-0 trigger decision is transmitted to the data acquisition system at 1 MHz, and is followed by an upgraded Event Filter system to achieve a maximum stored event rate of 10 kHz.

The upgraded trigger system will take advantage of increased granularity provided by the calorimeters, will improve efficiency for muon-based triggers and perform hardware-based tracking profiting from the extended coverage of the planned silicon ITk. Options exist to further develop a hardware-based track trigger for quicker and less CPU-intensive rejection of the expected large increase in PU at the HL-LHC, to take full advantage of extended coverage provided by the ITk. Such a hardware track trigger (HTT) would be an evolution of the current ATLAS FTK reconstruction system.

5.1.2. Object performance: tracking and vertexing. The ability of the detectors to reconstruct tracks and find vertices with high precision and efficiency in a high-density environment underlies the experimental reach for displaced objects. This section reviews the ATLAS and CMS experiments' projected tracking performance at the HL-LHC, highlighting improvements and new features with the upgrades.

5.1.2.1. CMS performance. L1 tracking. With the aforementioned tracker and L1 track trigger upgrades, the CMS experiment will be able to do track finding at L1 as well as offline at HL-LHC. Both L1 and offline tracking performance are discussed here.

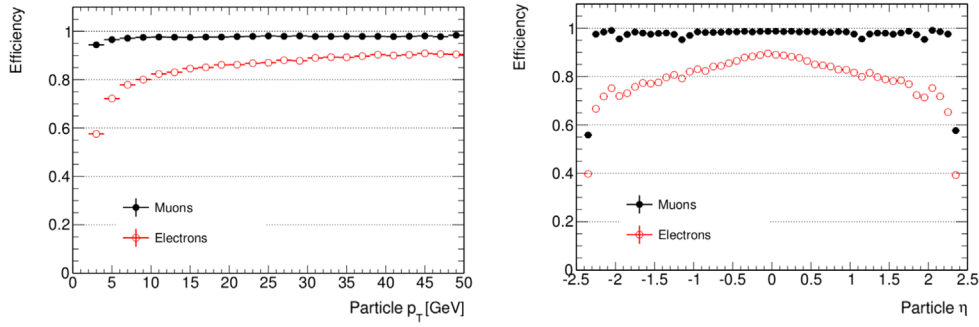


Figure 19. Left: L1 tracking efficiency versus generated particle p_T for $|\eta| < 2.4$. Right: L1 tracking efficiency versus η for $p_T > 3$ GeV. Results for muons (electrons) are shown as filled black (open red) circles, and are produced with $t\bar{t}$ events in a scenario with 200 pile-up events per bunch crossing, on average [348].

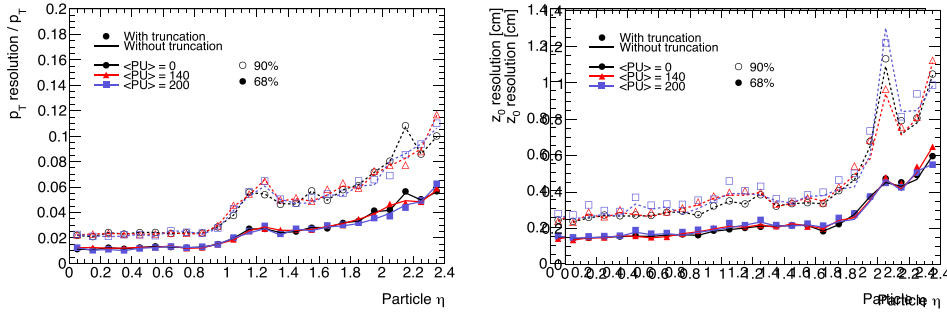


Figure 20. Relative p_T (left) and z_0 resolution versus pseudorapidity for muons in $t\bar{t}$ events with zero (black dots), 140 (red triangles), and 200 (blue squares) pile-up events per bunch crossing, on average. Results are shown for scenarios in which truncation effects are (markers) or are not (lines) considered in the emulation of L1 track processing. The resolutions correspond to intervals in the track parameter distributions that encompass 68% (filled markers and solid lines) or 90% (open markers and dashed lines) of all tracks with $p_T > 3$ GeV [348].

All L1 tracking studies have been performed assuming 3 GeV stub p_T thresholds. In figure 19, the L1 tracking efficiency for prompt muons and electrons for $t\bar{t}$ events in a scenario with 200 PU interactions per bunch crossing, on average, is presented. The tracking efficiency for muons exhibits a sharp turn-on at the 3 GeV stub p_T threshold, and saturates at approximately 98%. The tracking efficiency for electrons turns on more slowly and flattens out at 90%, mostly due to interaction with the detector material.

In figure 20, the L1 tracking resolutions of the p_T and z_0 parameters of muons with $p_T > 10$ GeV in $t\bar{t}$ events is shown for various average PU scenarios. The resolutions are defined in terms of an interval centered on the residual distribution that contains 68% or 90% of the tracks. Loss in tracking efficiency due to truncation effects (where there is insufficient time to transfer all the stub data) is determined from hardware and emulation to be at the level of 10^{-3} when considering $t\bar{t}$ samples with a PU rate of 200. As expected, resolutions degrade at forward pseudorapidity due to a corresponding increase in multiple scattering. In general,

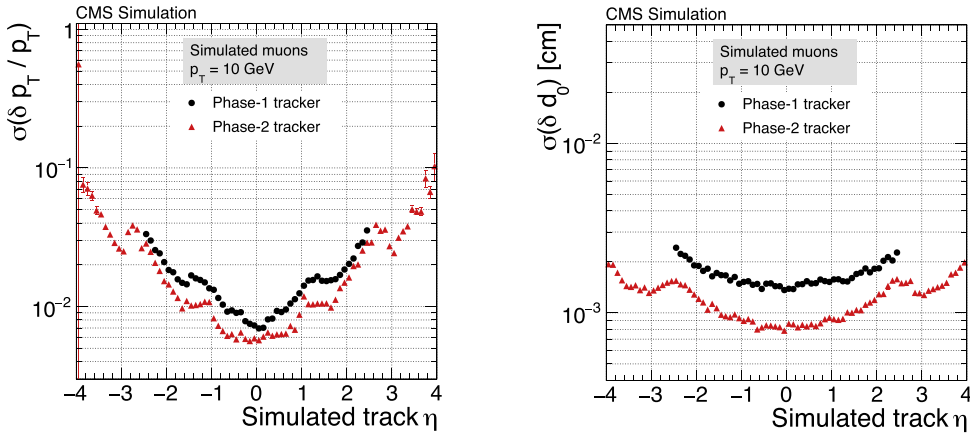


Figure 21. Relative resolution of the transverse momentum (left) and transverse impact parameter (right) as a function of the pseudorapidity for the current (black dots) and the upgraded (red triangles) CMS tracker, using single isolated muons with a transverse momentum of 10 GeV [348].

L1 parameter resolutions are excellent, which will provide for robust trigger object matching and charged particle reconstruction in the L1 trigger.

Offline tracking. Preliminary results on the offline tracking performance over the full acceptance of the CMS tracker are excellent, with further improvements expected as the detector design and simulation algorithms are optimized. In figure 21, the resolution of the transverse momentum and the transverse impact parameter for single muons with $p_T = 10$ GeV as a function of the pseudorapidity, both with the current detector and after the implementation of the HL-LHC upgrades, is shown. The better hit resolution of the HL-LHC tracker and the reduction of the material budget result in a significantly improved p_T resolution. The transverse impact parameter resolution is also improved with respect to the current detector, ranging from below $10 \mu\text{m}$ in the central region to about $20 \mu\text{m}$ at the edge of the acceptance.

For $t\bar{t}$ events, the efficiency to identify the PV correctly is $\sim 95\%$ at an average PU level of 140, and $\sim 93\%$ at an average PU level of 200. The vertex algorithm used is the same as the one used in Run 2 for a PU of about 35, therefore it is not yet optimized for vertex reconstruction at very high PU. In figure 22 the resolution of the vertex position in the x , y , and z coordinates is shown as a function of the number of tracks associated to the vertex. The vertex position resolution is almost independent of the amount of PU in the event and the longitudinal resolution is only 50% worse than the transverse one, as expected given the pixel dimensions of the inner tracker modules.

Given that the CMS HLT tracking is based on the offline tracking code, a similar level of performance is expected. Because of HLT time constraints, a parallelization of the algorithms is already under development and will be applied also in the HLT track reconstruction at HL-LHC.

5.1.2.2. ATLAS performance. Excellent tracking performance is also expected with the ITk upgrade of the ATLAS experiment for the HL-LHC era. The left panel of figure 23 shows the track reconstruction efficiency for jets in $Z' \rightarrow t\bar{t}$ events with 200 PU for different η ranges. The right panel of figure 23 shows the fake rate for reconstructed tracks in $t\bar{t}$ events, and there

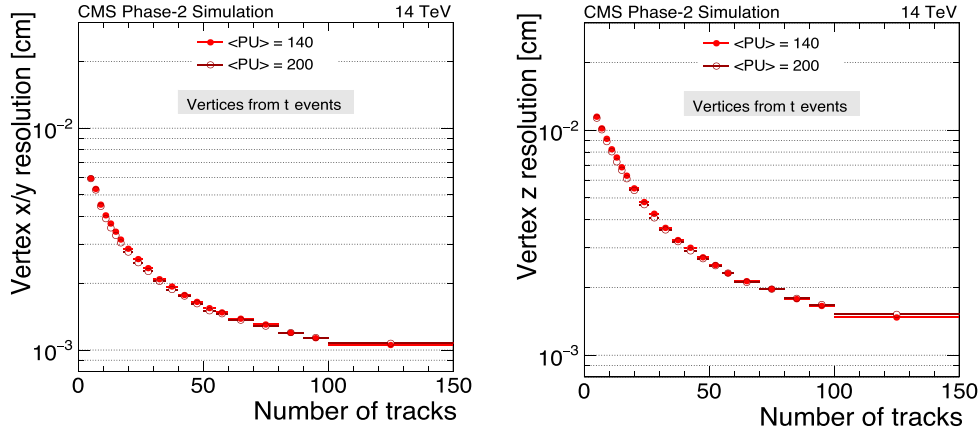


Figure 22. Vertex position resolution in x and y (left) and z (right) as a function of the number of tracks associated to the vertex, for $t\bar{t}$ events with an average of 140 (full circles) and 200 (open circles) pile-up interactions per bunch crossing [348].

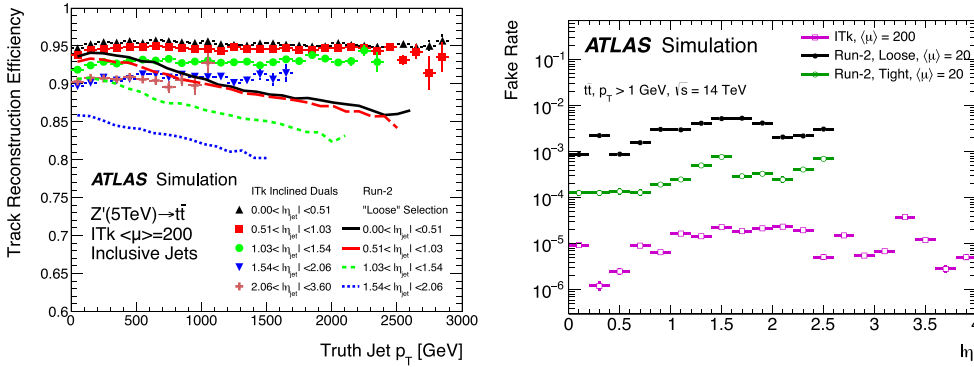


Figure 23. Left: track reconstruction efficiency for tracks in jets from $Z' \rightarrow t\bar{t}$ with 200 average pile-up events. The efficiency is shown as a function of jet p_T for different η ranges, and $M_{Z'} = 5$ TeV. Right: fake rate for tracks in $t\bar{t}$ events with 200 average pile-up events using ITk; Run 2 detector results are shown for comparison. Both figures are from [353].

is clearly substantial improvement over the Run 2 detector performance along with the improved coverage in the forward region.

In figure 24, the resolution of the transverse momentum and the longitudinal impact parameter for single muons with various p_T values is shown as a function of the pseudorapidity both with the current detector and projections for after the HL-LHC upgrade using digital clustering to find the tracks. The improvement is even more marked with analogue clustering: the transverse and longitudinal impact parameter resolutions are shown for different pixel pitches in figure 25.

5.1.3. Upgrade projection: LLP searches. Searches for LLPs are well motivated by various classes of extensions of the SM, discussed at length in chapter 2.2. Often, the production cross section for such processes is expected to be very small. The HL-LHC will allow for the

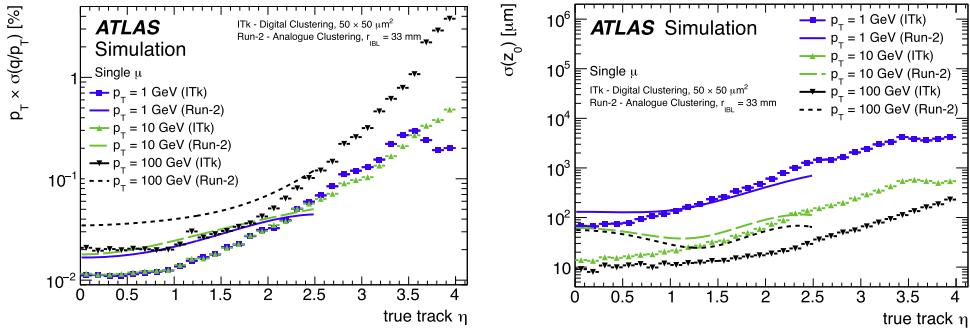


Figure 24. Resolution of the transverse momentum (left) and longitudinal impact parameter (right) as a function of the pseudorapidity for the current (solid line) and the upgraded (points) ATLAS tracker [353].

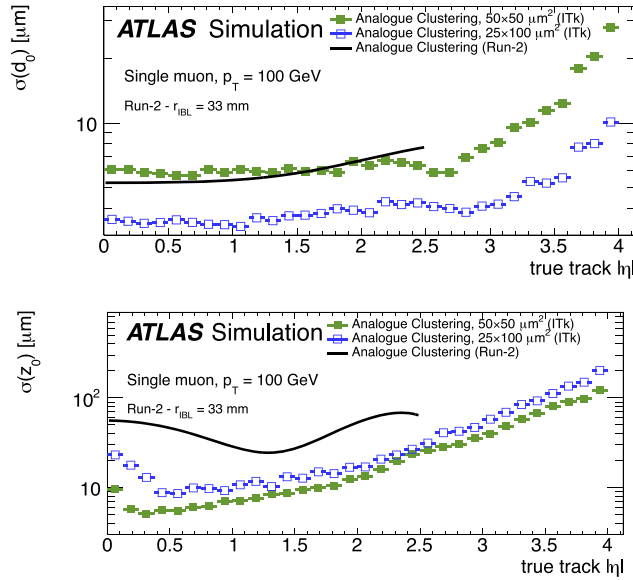


Figure 25. Track parameter resolutions using analogue clustering for (left) transverse impact parameter; (right) longitudinal impact parameter. The resolutions are shown for single muons with $p_T = 100$ GeV. The results of ITk are shown for $25 \times 100 \mu\text{m}^2$ and $50 \times 50 \mu\text{m}^2$ pixels, along with the current Run 2 detector performance [353].

collection of much larger data sets needed to reach better sensitivity to such BSM scenarios. The prospects are further strengthened with detector and trigger upgrades. This section discusses these potential improvements, and presents sensitivity projections on a number of benchmark LLP search channels with the aforementioned upgrades at the HL-LHC.

5.1.3.1. Heavy stable charged particles in CMS. A number of new physics scenarios give rise to HSCPs with long lifetimes that move with subrelativistic speed through the detector, heavily ionizing the sensor material as they pass through. In split SUSY models, the

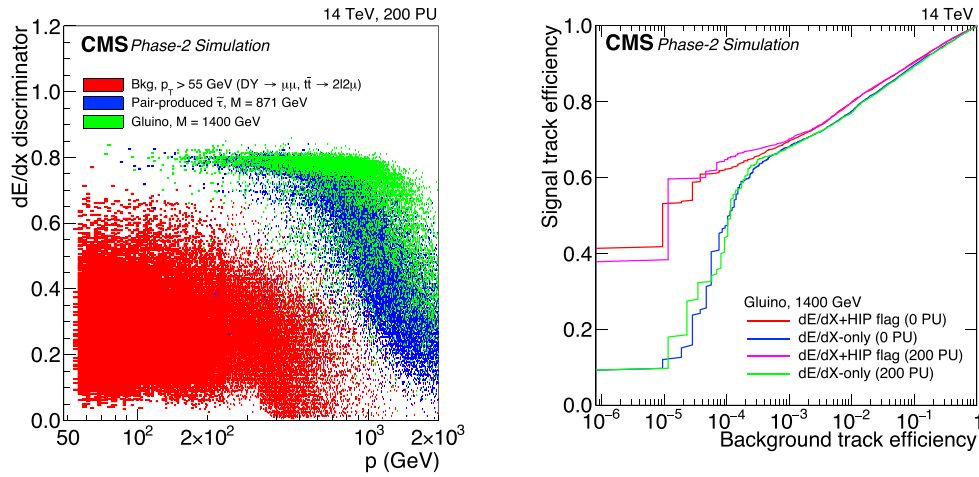


Figure 26. Left: distribution in CMS of the dE/dx discriminator versus track momentum (p) for tracks with high momentum ($p_T > 55$ GeV) in background events (red) and for candidate signal particles. Pair produced $\tilde{\tau}_5$ with a mass of 871 GeV (blue), and a gluino with a mass of 1400 GeV (green), are shown. Right: the performance of the dE/dx discriminator for selecting gluinos in events at rates of 0 pile-up (PU) and 200 PU. The signal versus background efficiency performance curves for a discriminator making use of both the pixel information and the outer tracker HIP flag (red and magenta) demonstrate a better performance compared to a discriminator trained to exploit only the dE/dx information from the pixel modules (blue and green), for a background rejection of 10^{-6} [348].

supersymmetric particles known as the stau ($\tilde{\tau}$) and the gluino (\tilde{g}) can have such characteristic signatures. The relevant simplified models are described in sections 2.4.2–2.4.3, and current searches are described in section 3.5.1.1.

Sensitivity projection with tracker upgrade. Depending on the mass and charge of the new particles, HSCPs experience anomalously high energy losses through ionization (dE/dx) in the silicon sensors with respect to the typical energy losses of SM particles, as can be seen in figure 26 (left). At the CMS experiment, the current strip tracker features analog readout. Furthermore, the pixel detector featured analog readout during Phase 0 in 2016 and before, and currently features digital readout during Phase 1, which started at the beginning of the 2017 LHC run. Therefore, these detectors allow for excellent dE/dx measurements.

At the HL-LHC, the upgraded CMS inner pixel detector will continue providing dE/dx measurements, enabled by its time-over-threshold readout, while the outer tracker cannot provide such information, given that the readout is binary. To increase the sensitivity for signatures with anomalously high ionization loss, a second, programmable, threshold has been implemented in the short strip ASICs of the PS modules of the outer tracker, and a dedicated readout bit signals if a hit is above this second threshold.

Searches for HSCPs can thus be performed by measuring the energy loss in the inner pixel detector and by discriminating HSCPs from minimum ionizing particles based on the ‘HIP flag’ in the outer tracker. The threshold of the minimum ionization needed to set the HIP flag is an adjustable parameter in each PS module independently. A threshold corresponding to the charge per unit length of 1.4 MIPs, resulting from preliminary optimization studies, is used in the simulation, and the gain in sensitivity obtained by using the HIP flag is studied.

An estimator of the degree of compatibility of the track with the MIP hypothesis is defined to separate candidate HSCPs from tracks from SM background sources. The high resolution dE/dx measurements provided by the inner pixel modules are used for the computation of the dE/dx discriminator. The tracks in background events have a low number of HT clusters with HIP flag, compared to those observed for tracks in HSCP signal events and slow-moving protons and kaons in minimum bias events.

In figure 26 (right), the performance of the discriminator is shown by evaluating the signal versus background efficiency curves to identify tracks from signal events and reject those originating from backgrounds. The performance curves are evaluated for two different strategies for the discriminator: the dE/dx discriminator, which relies solely on the inner pixel modules (dE/dx -only, ignoring the HIP flags), and a recomputed discriminator which includes the HIP flags from the outer tracker PS modules ($dE/dx + \text{HIP flags}$). The signal versus background efficiency performance curves demonstrate that for a background efficiency of 10^{-6} , analogous to the current analysis performance, the $dE/dx + \text{HIP}$ -based discriminator leads to an expected signal efficiency of 40%, around 4–8 times better than the dE/dx -only discriminator. In the dE/dx -only scenario, the efficiency for the HSCP signal is about 8 times smaller than that obtained in current data. The inclusion of the HIP flag for the PS modules of the Outer Tracker restores much of the efficiency, so that the same sensitivity as in Phase 1 will be realized with about four times the luminosity of Phase 1. The Phase 1 sensitivity will be surpassed with the full expected integrated luminosity of the HL-LHC. This study demonstrates the critical impact of the HIP flag in restoring the sensitivity of the CMS tracker for searches for HIPs in the HL-LHC era.

Additionally, the current CMS inner pixel detector provides measurements of charge deposits in each pixel up to 9600 electrons over a range of 4 bits in the digitizer. While it may be difficult to increase the number of bits used to store the charge information due to data rate constraints, it is possible to adopt a dual-slope mapping from charge deposit to ADC counts in the digitizer, which will preserve the granularity for lower charge deposits, while giving more information for HIPs such as HSCPs. This option is currently being studied to evaluate the potential improvement to dE/dx measurements. Furthermore, tuning of the HIP flag threshold may bring additional improvements.

HSCP trigger with muon detector upgrade. The upgrade of the RPC system will allow the trigger and identification of slowly moving particles by measuring their TOF to each RPC station with a resolution of $\mathcal{O}(1)$ ns. The new RPC detectors have a two-end strip readout, which provides precise measurements of the hit position in the local y or the global η coordinate. The speed of muon-like particles and the time (bunch crossing) of their origin will be computed with a fast algorithm to be implemented in the Level-1 trigger at the HL-LHC.

The RPC detectors are synchronized to register muons moving at the speed of light with a local time equal to zero with respect to the collision event that produced the trigger. Slow-moving particles, as HSCPs, will arrive with a delay depending on their speed as shown in figure 27. This time delay, measured by each RPC layer crossed by the HSCP, is exploited in order to trigger on and reconstruct such particles.

The principles of the proposed HSCP trigger algorithm are illustrated in figure 28. In this figure, the vertical axis is the time of signals measured in RPC chambers, as synchronized so that muons moving nearly at the speed of light from a particular collision are measured at the time of the collision. The horizontal axis is the distance from the collision point to the position of the RPC at which the time is measured. The diagram shows three successive bunch crossings, two of which contain muons represented at horizontal lines. The diagram also shows the RPC time measurements from two HSCPs having slopes different from zero due to their traveling significantly slower than the speed of light. The time delay Δt is related to the

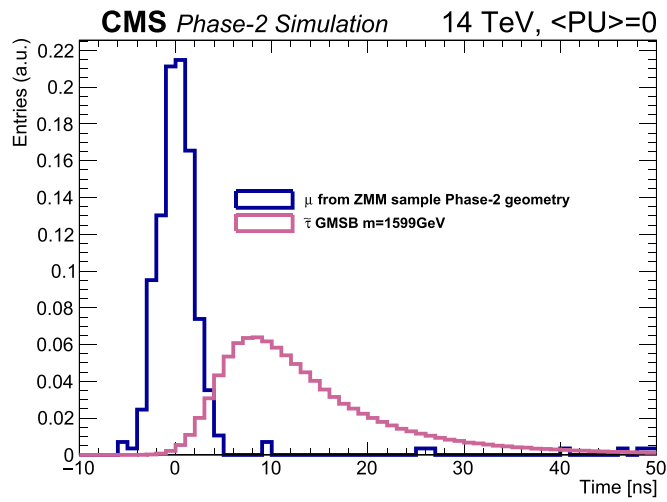


Figure 27. RPC hit time measurement distribution in CMS for muons from $Z \rightarrow \mu\mu$ events and for semi-stable $\tilde{\tau}$ particles with $m \approx 1600\text{ GeV}$, produced in $pp \rightarrow \tilde{\tau}\tilde{\tau}$ processes [350].

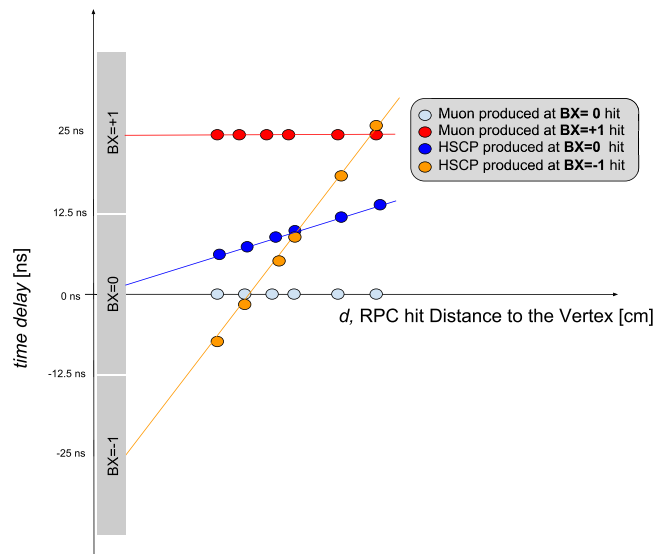


Figure 28. Diagram showing times measured at different RPC stations for particles originating at different bunch crossings and with different velocities in CMS. The x -axis represents the distances from IP to RPC detectors, while the y -axis corresponds to time. The clock at each RPC station is tuned so that particles moving with the speed of light are registered with the exact same ‘local’ times. Hence, relativistic particles are represented by horizontal lines on this diagram [350].

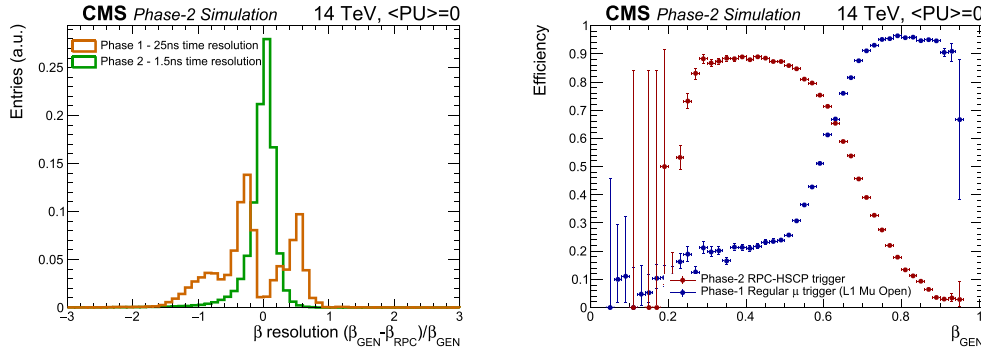


Figure 29. Left: resolution of a particle-speed measurement at L1 trigger with Phase 1 and upgraded RPC Link Board System. Right: the efficiency as a function of β of the standard L1 muon trigger without any p_T threshold, and the RPC-HSCP Phase 2 trigger with 1.56 ns sampling time. For both plots, an HSCP signal is shown [350].

speed v of an HSCP via the following equation:

$$\Delta t = d \left(\frac{1}{v} - \frac{1}{c} \right). \quad (5.1)$$

Here d is the distance between the IP and the point where an HSCP crosses an RPC. For RE4/1 chambers and $\beta = v/c = 0.2$, the delay time is > 6 bunch crossings, comparable to 150 ns.

A penetrating charged particle leaves a trail of hits in RPC chambers along its trajectory. The TOF can be computed in each RPC station with respect to a number of bunch crossing hypotheses. Should there be a common velocity solution, derived from equation (5.1), with $\beta < 0.6$, a trigger is formed. For $\beta > 0.6$, the delays are small and can be handled by the Phase 1 trigger. The performance of this algorithm has been studied with the CMS full simulation. All the detector effects (e.g. electronics jitter, signal time propagation along strips) are considered. A particle-speed measurement resolution is shown in figure 29 (right) for the case of 25 ns signal sampling time (Phase 1) and 1.56 ns sampling time provided with the upgraded RPC Link Board System. For both plots, an HSCP signal is shown.

The efficiency of the RPC-HSCP algorithm as a function of β is studied and compared with the standard L1 muon trigger. The results are shown in figure 29 (right). The current CMS-HSCP Phase 1 trigger performs well down to $\beta \approx 0.75$. The upgraded RPC Link Board System will allow for the triggering, at the correct bunch crossing, on possible HSCPs with velocities as low as $\beta \sim 0.25$.

Possible improvements for this trigger proposal in the β measurement could be achieved by matching tracks in the track trigger to the HSCP muon trigger.

5.1.3.2. Displaced muons in CMS. Many BSM theories predict particle decays with displaced muon or muon pairs in its final state, such as dark SUSY and GMSB with smuons. In order to demonstrate the physics potential of displaced muons at the HL-LHC with the CMS detector, a particular SUSY model is selected where the displaced signature consists of a dimuon final state emerging from the decay of heavy sparticles (smuons). Searches for the direct production of heavy sparticles with long lifetimes are difficult in the present LHC runs, owing to small cross sections and limited integrated luminosity, and will only become possible at the HL-LHC.

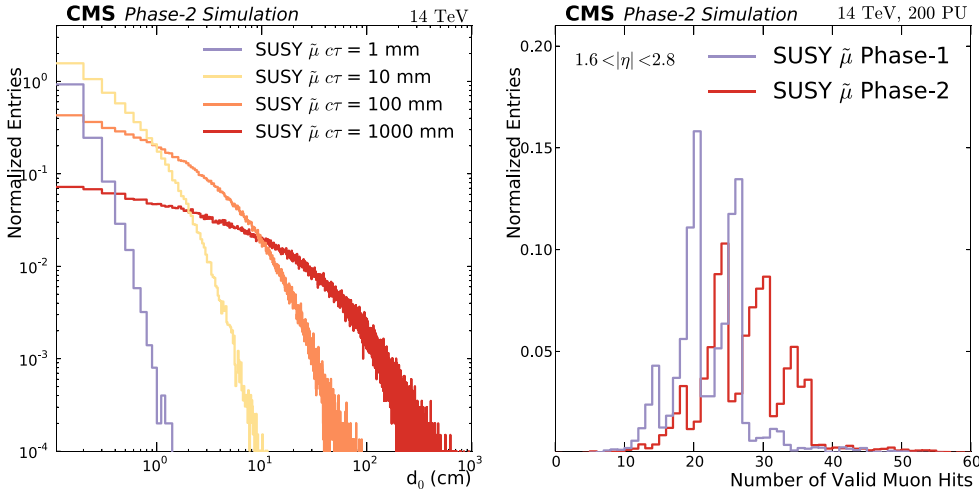


Figure 30. Left: the muon transverse impact parameter, $|d_0|$, for several simulated smuon decay lengths, $c\tau$, at the generator level. Right: distribution of the minimum number of valid hits in the CMS Phase 2 muon system for a SUSY $\tilde{\mu}$ with $m_{\tilde{\mu}} = 500$ GeV and $\tau = 1000$ mm for the Run 2 (blue) and Phase 2 (red) detectors [350].

In GMSB models, smuons can be (co-)NLSPs (next to lightest supersymmetric particles) and decay to a muon and a gravitino [360]. When the slepton is long lived, the final state signature is two displaced oppositely charged muons and significant missing transverse energy. The smuon pair production has the advantage that it can be characterized by a very clean final state topology, and we will therefore focus on the process $q\bar{q} \rightarrow \tilde{\mu}\tilde{\mu}$, where the two smuons decay far from the primary interaction vertex. For this process, the muon $|d_0|$ can reach up to approximately one meter (or longer) for sufficiently large lifetimes, as shown in figure 30 (left). Figure 30 (right) compares the number of hits created by these displaced muons in the CMS MS in Phase 2 and the current CMS detector. The hits plotted here are those associated with the DSA muon tracks, which is a muon track reconstruction algorithm specifically designed for displaced muons that can only be reconstructed in the MS [335].

Standard triggers and reconstruction algorithms that use the position of the PV will not efficiently reconstruct tracks with large impact parameters. Consequently, triggering on and reconstructing muons produced far from the IP is challenging and requires dedicated triggers and reconstruction algorithms. The upgrades to the MS in CMS, as well as the L1 tracking capabilities, significantly improve the experiment's ability to search for displaced muons at the HL-LHC.

Triggering on displaced muons. The momentum resolution of the L1 muon trigger for muons coming from the PV will be greatly improved by adding information from the L1 track trigger, discussed previously. The L1 track trigger can also be directly combined with trigger primitives at the first stage of the muon track-finder electronics; this would mirror the offline reconstruction of ‘Tracker Muons’ which improve the efficiency for very low- p_T muons, especially in the barrel region.

To trigger on both prompt and non-prompt muons effectively at L1, a SA L1 muon generates two p_T measurements for each muon, prompt and non-prompt, which are matched with L1 tracks. If the track match is successful, the L1 track trigger p_T is used and a prompt

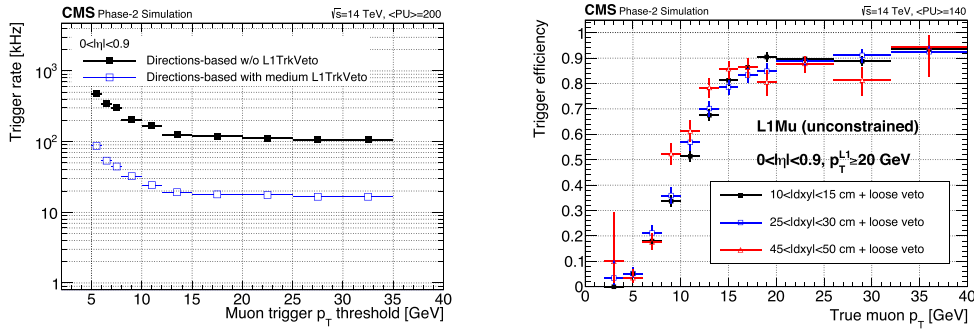


Figure 31. L1 Muon trigger rate (left) and efficiency (right) versus muon p_T threshold for the barrel displaced muon algorithm [350].

candidate is formed. If the match is unsuccessful and the muon is not vetoed by L1 tracks, the non-prompt L1 muon p_T is used to form a displaced muon candidate. Figure 31 shows good performance for displaced muons with this method, i.e. there is a reasonably high efficiency and a trigger rate for a single muon trigger of around 10 kHz under HL-LHC conditions. Further improvements to the algorithm are underway to accommodate high PU conditions. The upgrade of the RPC system will allow slowly-moving particles to pass the trigger and be identified by measuring their TOF to each RPC station with a resolution of $\mathcal{O}(1)$ ns. The speed of muon-like particles and the time (bunch crossing) of their origin will be computed with a fast algorithm to be implemented in the L1 trigger for the HL-LHC.

Reconstruction. A dedicated muon reconstruction algorithm was designed for non-prompt muons that leave hits only in the MS. This DSA algorithm is seeded by groups of track segments in the muon chambers. For each seed, a muon track is reconstructed with the same Kalman-filter technique as for the standard SA muon reconstruction algorithm, but without constraining the IP. Figure 30 (right) shows the distribution of the number of hits in the Run 2 and HL-LHC detectors for displaced muons. The impact of the new stations is clearly visible. The charge mis-identification probability is expected to further decrease with the additional hits.

Sensitivity projection with a GMSB model. To study the impact on physics sensitivity, a particular GMSB model is selected where the displaced signature consists of a dimuon final state plus gravitinos, emerging from the decay of heavy long-lived sparticles (smuons), where the gravitinos escape detection. This maps to the direct pair production simplified model with neutral LLP decays to muon + invisible in section 2.4. This signal can serve as a proxy for other models with two LLPs decaying into muons. The final-state signature is then given by two displaced, oppositely-charged muons and significant \cancel{E}_T . Example LLPs with $c\tau = 10, 100, 1000$ mm and several mass hypotheses (0.2, 0.5, 1 TeV) are simulated.

The main background for this search comes from multi-jet production (QCD), $t\bar{t}$ production, and $Z/\text{DY} \rightarrow \ell\ell$ events where large impact parameters are (mis)reconstructed. Cosmic-ray muons have been studied in Run 2 and these studies can be directly applied to Phase 2 running. In the barrel, they are efficiently rejected by the timing of the hits in the upper leg. Cosmic-ray muons do not originate at the vertex and therefore pass the upper-barrel sectors in reverse direction from outside in. The fraction of cosmic-ray muons in the endcaps is negligible.

Given the very low cross section of the signal process, it is essential to reduce the background efficiently. The best background discriminator is the impact parameter

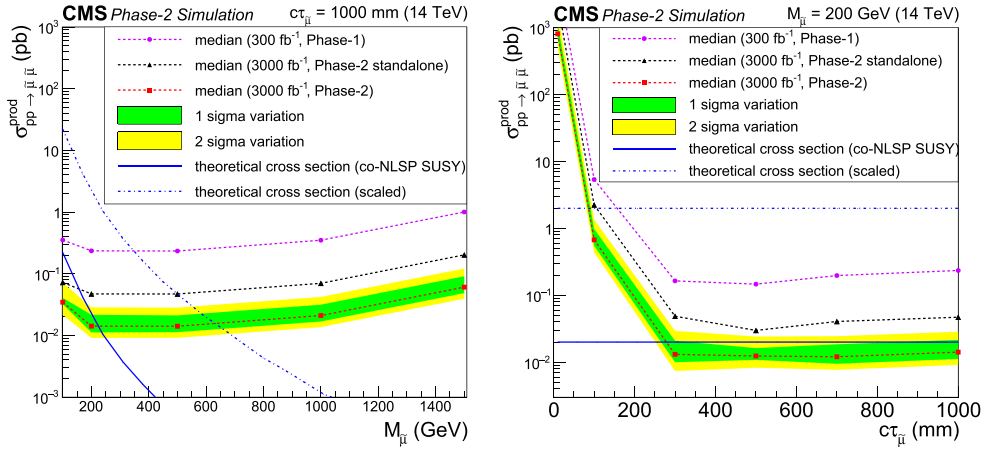


Figure 32. The 95% C.L. projected upper limits at CMS for $q\bar{q} \rightarrow \tilde{\mu}\tilde{\mu}$, $\tilde{\mu} \rightarrow \mu\tilde{G}$ for various mass hypotheses for $c\tau = 1$ m (left), and as a function of the decay length for $m_{\tilde{\mu}} = 200$ GeV (right). In both panels, the theoretical cross section for the specific model is represented by the blue solid line. For different SUSY breaking scales, $\tan\beta$ or otherwise modified parameters, the cross sections may be 100 times larger, reflected by the blue dashed–dotted line. Green (yellow) shaded bands show the one (two) sigma range of variation of the expected 95% C.L. limits. Phase 2 results with an average of 200 pile-up collisions per bunch crossing and an integrated luminosity of 300 fb^{-1} are compared to results obtained with 3000 fb^{-1} . The black line shows the sensitivity without the DSA algorithm, which reduces the reconstruction efficiency by a factor three [350].

significance $d_0/\sigma(d_0) \approx 5$. Given the signal kinematics, the muons from a signal process are expected to move in roughly opposite directions and E_T can be expected to be larger than 50 GeV. After this selection the signal efficiency is about 4%–5% for $c\tau \approx 1000$ mm, nearly independent of the smuon mass, and 10^{-5} – 10^{-4} for QCD, $t\bar{t}$, and DY backgrounds.

In figure 32, the expected exclusion limits are shown for the GMSB model in which the smuon is a (co-)next-to-lightest supersymmetric particle (NLSP, where ‘LSP’ indicates the lightest supersymmetric particle), for the predicted cross section as well as for a factor 100 larger cross section. The exclusion limits are shown as functions of smuon mass in figure 32 (left) and decay length in figure 32 (right).

The sensitivity depends on $c\tau$ because shorter decay lengths shift the signal closer to background. In figure 32 (right), the resulting physics sensitivities in terms of production cross section for the HL-LHC, normalized to 3000 fb^{-1} , are shown for the dedicated reconstruction of displaced muons and for the standard reconstruction. Also shown is the expected sensitivity at the end of Phase 1. Systematic uncertainties for the Phase 1 scenario are taken from current Run 2 analyses and adapted for expected HL-LHC conditions based on the assumptions of reduced systematics described in [361]. Clearly, only the HL-LHC will allow this process to be studied. The expected exclusion limit is around 200 GeV for $c\tau = 1000$ mm with 3000 fb^{-1} . This also illustrates the importance of keeping lepton trigger thresholds at several tens of GeV, even in the environment of 200 PU interactions per bunch crossing. Similarly, the discovery sensitivity is assessed assuming that a signal is present in data, and is shown as a function of smuon decay length in figure 33.

Sensitivity projection with a dark SUSY model. The analysis presented above was reinterpreted using a Dark SUSY model [30, 155], in which an additional dark $U_D(1)$

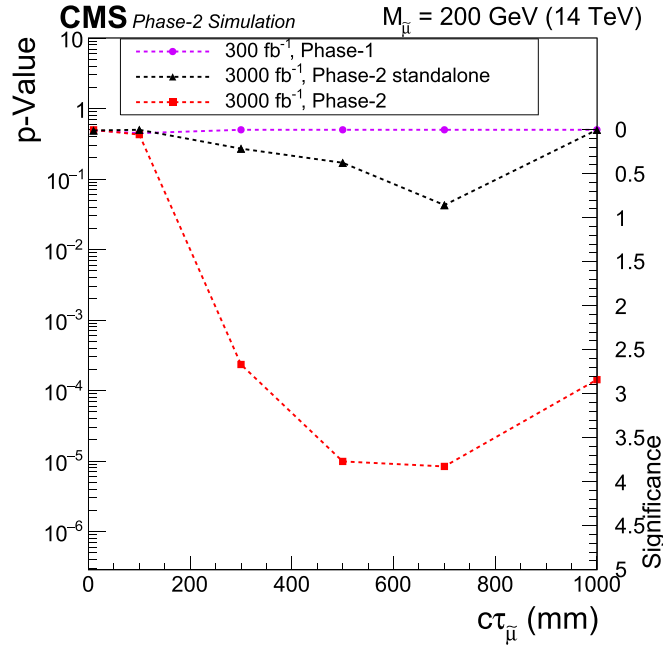


Figure 33. The projected discovery sensitivity at CMS for $q\bar{q} \rightarrow \tilde{\mu}\tilde{\mu}$, $\tilde{\mu} \rightarrow \mu\tilde{G}$ as a function of the decay length for $m_{\tilde{\mu}} = 200$ GeV. Together with the discovery sensitivity the corresponding p -value is shown. Phase 2 results with an average of 200 pile-up interactions per bunch crossing and an integrated luminosity of 3000 fb^{-1} are compared to results obtained with 300 fb^{-1} . The black line shows the sensitivity without the DSA algorithm, which reduces the reconstruction efficiency by a factor three [362].

symmetry is added as a supersymmetric SM extension. Breaking this symmetry gives rise to an additional massive boson, the so-called dark photon (γ_D), which couples to SM particles via a small kinetic mixing parameter ϵ . If ϵ is very weak, the lifetime of the dark photon can range from a few millimeters up to several meters. The lower ϵ , the longer is the dark photon lifetime which then decays displaced from the PV. A golden channel for such searches is the decay to displaced muons.

In the model studied here [362], dark photons are produced in cascade decays of the SM Higgs boson that would first decay to a pair of MSSM-like lightest neutralinos (n_1), each of which can decay further to a dark sector neutralino (n_D) and the dark photon.

For the branching fraction $\text{BR}(H \rightarrow 2\gamma_D + X)$, where X denotes the particles produced in the decay of the SM Higgs boson apart from the dark photons, 20% is used. Neutralino masses $m(n_1) = 50$ GeV and $m(n_D) = 1$ GeV are assumed. Final states with two and four muons are included in the analysis. In the former case, one dark photon decays to a pair of muons while the other dark photon decays to some other fermions (2-muon final state). In the latter case, both dark photons decay to muon pairs (4-muon final state).

The main background for this search comes from multi-jet production (QCD), $t\bar{t}$ production, and $Z/\text{DY} \rightarrow \ell\ell$ events where large impact parameters are (mis)reconstructed. Cosmic ray muons can travel through the detector far away from the PV and mimic the signature of displaced muons. However, thanks to their striking detector signature, muons from CRs can be suppressed by rejecting back-to-back kinematics.

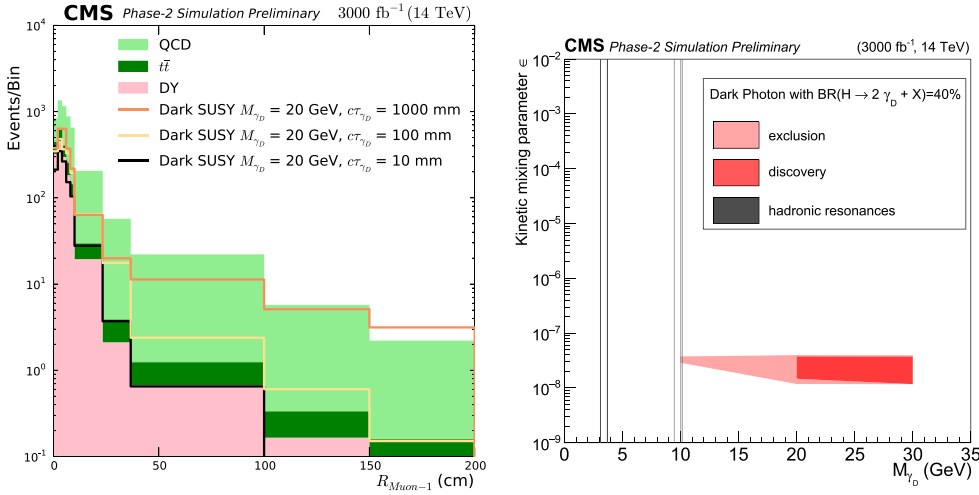


Figure 34. Left: distance of the closest approach of the displaced muon track with maximum p_T to the primary interaction vertex, $R_{\text{Muon}-1}$, for signal and background after the final event selection. Right: parameter scan in the $\epsilon - m_{\gamma_D}$ plane. The grey lines indicate the regions of narrow hadronic resonances where the analysis does not claim any sensitivity [362].

For each event, at least two DSA muons are required. If more than two, the ones with the highest p_T are chosen. The two muons must have opposite charge ($q_{\mu,1} \cdot q_{\mu,2} = -1$) and must be separated by $\Delta R = \sqrt{\Delta\phi^2 + \Delta\eta^2} > 0.05$. The three-dimensional angle between the two displaced muons is required to be less than $\pi - 0.05$ (not back-to-back) in order to suppress CR backgrounds. Additionally, $E_T > 50$ GeV is imposed to account for the dark neutralinos escaping the detector without leaving any signal.

In order to discriminate between background and signal, the three-dimensional distance from the PV to the point of closest approach of the extrapolated displaced muon track, called R_{Muon} , is used. The event yield after full event selection of both selected muons as a function of $R_{\text{Muon}-1}$ and $R_{\text{Muon}-2}$ is used to search for the signal. The left panel of figure 34 shows $R_{\text{Muon}-1}$ of the first selected muon for signal and background samples.

The search is performed using a simple counting experiment approach. In presence of the expected signal, significance of the corresponding event excess over the expected background is assessed using the likelihood method. In order to evaluate the discovery sensitivity the same input is used as in the limit calculation, now with the assumption that one would have such a signal in the data. The discovery sensitivity is shown in the two-dimensional $m_{\gamma_D} - c\tau$ plane in the right panel of figure 34. This search is sensitive to large decay length of the dark photon.

In absence of a signal, upper limits at 95% C.L. are obtained on a signal event yield with respect to the one expected for the considered model. A Bayesian method with a uniform prior for the signal event rate is used and the nuisance parameters associated with the systematic uncertainties are modeled with log-normal distributions. The resulting limits for the Dark SUSY models are depicted in figure 35. While the results shown in the left panel of figure 35 are for a dark photon with a decay length of 1 m as a function of the dark photon mass, the right panel of figure 35 shows the results for a dark photon mass of 20 GeV as a function of the decay length [362].

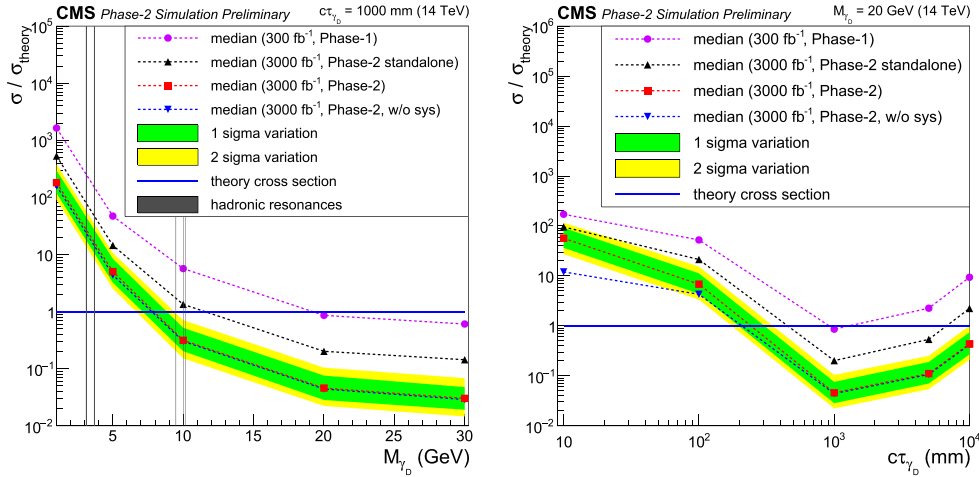


Figure 35. Upper limits at 95% C.L. on production cross section $\sigma/\sigma_{\text{theory}}$ for various dark photon mass hypotheses and a fixed decay length of $c\tau = 1000$ mm (left) and a fixed mass of $M_{\gamma_D} = 20$ GeV (right). Green and yellow shaded bands show the one and two sigma range of variation of the expected 95% C.L. limits, respectively. The grey lines indicate the regions of narrow hadronic resonances where the analysis does not claim any sensitivity [362].

5.1.3.3. Displaced photons at CMS. A number of new physics scenarios predict new particles that, upon decay, result in displaced photons in the final state (see sections 2.4 and 3.4). At the CMS experiment, with the scintillating crystal design of the ECAL that provides excellent resolution but lacks pointing capability, the photon arrival time in the ECAL is the main observable used to distinguish signal from background in displaced photon searches.

One benchmark model for displaced photon searches is the GMSB model where the lightest neutralino ($\tilde{\chi}_0^1$) is the NLSP, can be long-lived, and decays to a photon and a gravitino (\tilde{G}), which is the LSP, as illustrated in figure 36 (left). For a long-lived neutralino, the photon from the $\tilde{\chi}_0^1 \rightarrow \tilde{G} + \gamma$ decay is produced at the $\tilde{\chi}_0^1$ decay vertex, at some distance from the beam line, and reaches the detector at a time later than that of prompt, relativistic particles produced at the IP. The time of arrival of the photon at the detector can be used to discriminate the signal from the background. The aforementioned upgrade to the ECAL electronics in the barrel region, and the HGCal upgrade in the endcaps, will improve photon timing resolution at HL-LHC by an order of magnitude to as little as ~ 30 ps for photons with p_T of tens of GeV or above, hence significantly improve the experimental reach of displaced photon searches.

Moreover, the proposed MTD will be able to provide another dimension of information to reconstruct LLP decays. The TOF of the photon inside the detector is the sum of the TOF of the neutralino before its decay and the TOF of the photon itself, until it reaches the detector. Since the neutralino is a massive particle the latter is clearly negligible with respect to the former. In order to be sensitive to short neutralino lifetimes of order 1 cm, the performance of the measurement of the photon TOF is a crucial ingredient of the analysis. Therefore, the excellent resolution of the MTD apparatus can be exploited to determine with high accuracy the TOF of the neutralino, and similarly the photon, also in case of a short lifetime.

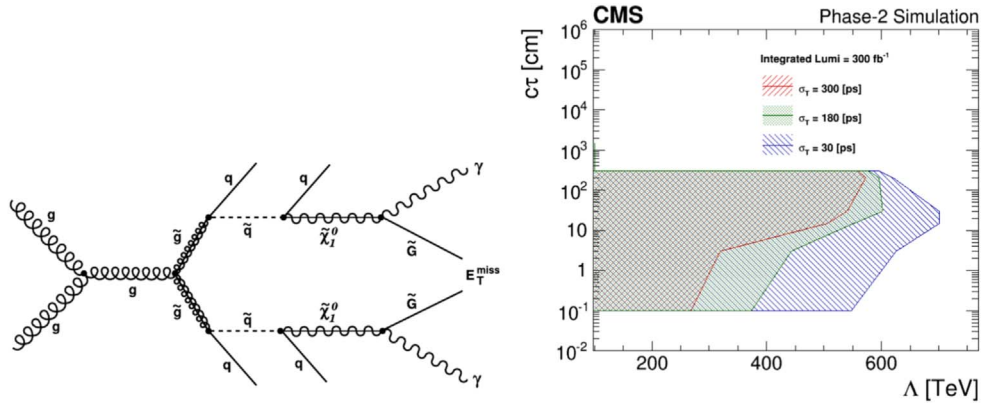


Figure 36. Left: diagrams for a SUSY process that results in a diphoton final state through gluino production at the LHC. Right: sensitivity to GMSB $\tilde{\chi}_0^1 \rightarrow \tilde{G} + \gamma$ signals expressed in terms of neutralino lifetimes for 300, 180 and 30 ps resolution, corresponding to the current detector, the HL-LHC detector with photon timing without MTD and with MTD, respectively [351].

An analysis has been performed at generator level in order to evaluate the sensitivity power of a search for displaced photons at CMS in the scenario where a 30 ps timing resolution is available from the MTD [351]. The events were generated with Pythia 8 [219], exploring neutralino lifetimes ($c\tau$) in the range 0.1–300 cm. The values of the Λ scale parameter were considered in the range 100–500 TeV, which is relevant for this model to be consistent with the observation of a 125 GeV Higgs boson. After requiring the neutralino to decay within the CMS ECAL acceptance and the photon energy being above a ‘trigger-like’ threshold, the generator-level photon TOF was smeared according to the expected experimental resolutions. A cutoff at a photon time greater than 3σ of the timing resolution is applied and the ‘signal region’ is assumed to be background free to estimate the sensitivity. The signal efficiency of such a requirement is computed and translated, assuming the theoretical cross sections provided in [66], to an upper limit, at 95% C.L., on the production cross section of the $\tilde{\chi}_0^1 \rightarrow \tilde{G} + \gamma$ process.

In figure 36 (right), the analysis sensitivity in terms of the Λ scale (and therefore of the neutralino mass) and lifetime is shown for three different assumptions on the timing resolution. The 300 ps resolution is representative of the TOF resolution consistent with current CMS detector performance. The 180 ps resolution is representative of the TOF resolution of the upgraded CMS detector without the MTD, in which case the TOF measurement will be dominated by the time spread of the luminous region. The vertex timing provided by the MTD detector will bring the TOF resolution to about 30 ps. As visible in the figure, a full-scope upgrade of the CMS detector with photon and track timing will provide a dramatic increase in sensitivity at short lifetimes and high masses, even with the first 300 fb^{-1} of integrated luminosity.

5.1.3.4. Displaced jets in ATLAS. Neutral LLPs that can decay into jets displaced from the proton–proton IP arise in many BSM theories (see chapter 2 for an extensive discussion). For example, in hidden sector models a new set of particles and forces is proposed that is weakly coupled to the SM via a communicator particle. The hidden sector is otherwise invisible to the SM sector, but its particles (some of which can be long-lived) may decay to SM particles via

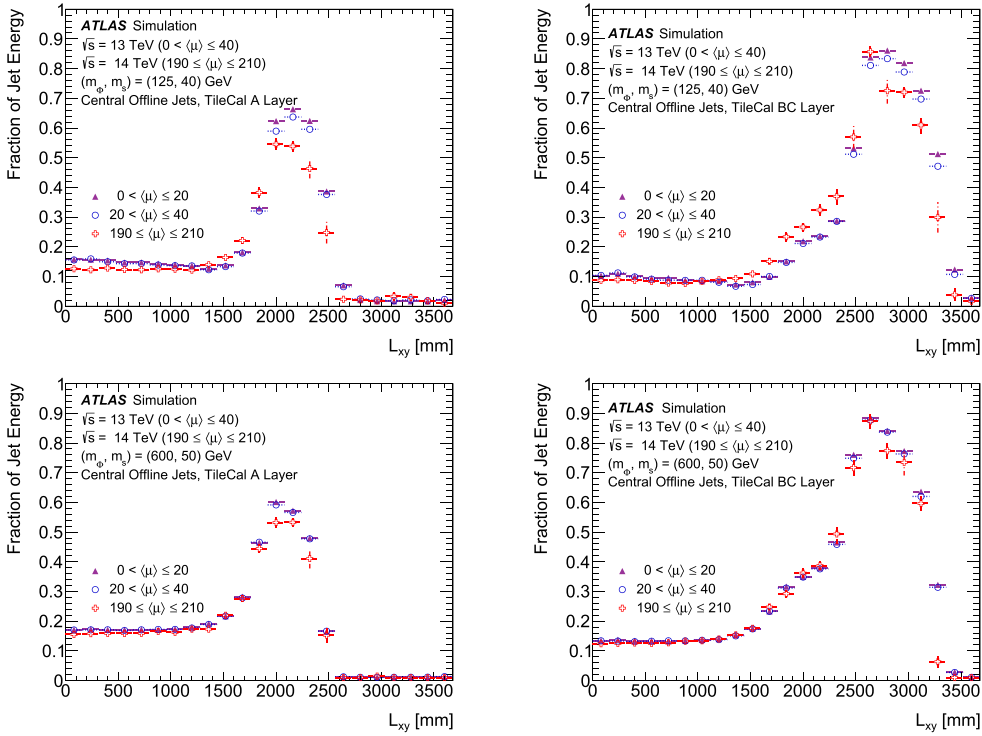


Figure 37. Simulation projections of the sensitivity of the ATLAS experiment upgrade plans to neutral LLPs. Top: the fraction of the jet energy deposited in the A-layer (left) and BC-layers (right) of the ATLAS tile calorimeter as a function of the transverse decay position of the LLP in events with a 125 GeV Higgs-like boson decaying to two 40 GeV LLPs. Bottom: the same for events with a 600 GeV Higgs-like boson decaying to two 50 GeV LLPs.

the communicator. The lifetimes of these LLPs are typically unconstrained and could be long enough for the LLPs to decay inside the ATLAS detector volume. Such particles produce unique signatures which may have been overlooked by more traditional searches for new physics. One ATLAS search for such displaced jet signatures focuses on LLPs which decay in the ATLAS HCal and consequently deposit most of their energy there and very little or none in the ECAL, and also have few or no charged tracks pointing at the hadronic energy deposits. A signature-driven trigger that optimizes the acceptance for this class of events is required for the online selection.

The existing ATLAS analysis described in section 3.1 can likely be improved by planned upgrades by using HCal information splitting the B-C layers in the calorimeter to identify the LLP decay position. The splitting between B-C layers will provide more information on the longitudinal shower profile, see figure 37.

This analysis uses a hidden sector benchmark model and considers the decay of a heavy boson to two long-lived neutral scalars; this maps to the simplified model with Higgs boson production of hadronically decaying LLPs in section 2.4. The heavy scalar bosons decaying into LLPs have masses ranging from 125 to 1000 GeV, and the LLP scalars have masses ranging between 5 and 400 GeV. Background processes, dominated by QCD dijet production,

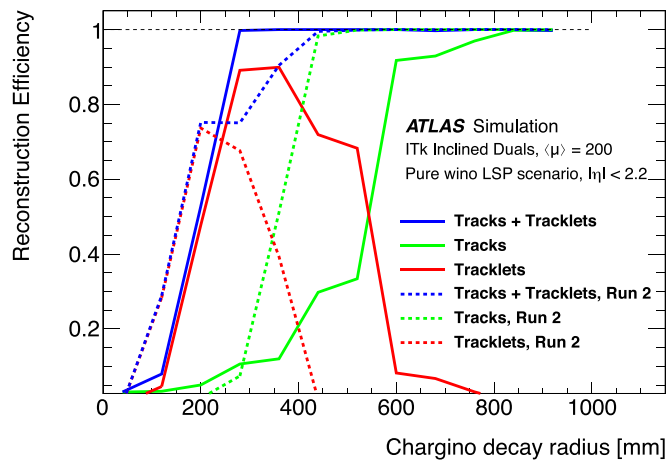


Figure 38. Reconstruction efficiency of the disappearing chargino as a function of decay radius using two track reconstruction techniques: ‘tracklets’ refers to the short tracks mentioned in the text, while ‘tracks’ refers to standard track reconstruction. The corresponding reconstruction efficiencies for Run 2 are also shown [353].

are suppressed in this analysis by requiring both scalars to decay in the calorimeter. Final results of the sensitivity projections are pending.

5.1.3.5. Disappearing tracks. In the ATLAS experiment, the planned ITk upgrade of the tracking volume for the HL-LHC can be exploited to improve the existing searches for BSM particles with a DT [353].

Such particles are predicted by many well-motivated supersymmetric models such as anomaly-mediated SUSY-breaking scenarios, where the supersymmetric partners of the SM W bosons, the wino fermions, are the lightest SUSY state. In such models, the lightest neutralino and chargino can be nearly mass-degenerate, with a mass splitting around 160 MeV, and the chargino is consequently long lived. The combination of long lifetime and boost when produced in a high-energy collider allows the chargino to leave multiple hits in the traversed tracking layers before decaying. When performing searches for such signatures in ATLAS, selected events are typically required to contain at least one short track, hereafter called a tracklet. To study how such searches can be improved with the ITk upgrade, some assumptions have been made for simulating events and projected detector response. The detector response is parametrised by using response functions based on studies performed with Geant4 simulations of the upgraded detector in high-luminosity PU conditions.

The tracklet reconstruction efficiency for signal charginos as a function of the decay radius inside the detector is shown in figure 38. A 30% systematic uncertainty on the background yields is assumed, as observed for the Run 2 analysis. The expected background is largely dominated by fake tracklets due to random crossings.

Expected limits at 95% C.L. are shown in figure 39 as a function of the chargino mass and lifetime for a pure wino and a pure Higgsino LSP scenario. For comparison, the current Run 2 limit for 36.1 fb^{-1} in the wino LSP scenario is also shown. The HL-LHC dataset of 3000 fb^{-1} extends the sensitivity of neutrinos and charginos up to 250 GeV, assuming a pure Higgsino scenario.

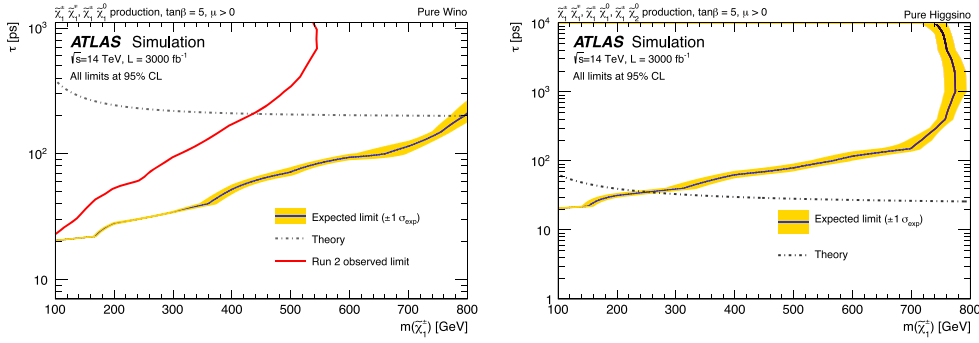


Figure 39. Projected 95% C.L. limits on a degenerate chargino-neutralino scenario assuming the chargino is a (left) pure wino; (right) pure neutralino. The limits include both pair production $\tilde{\chi}_1^+\tilde{\chi}_1^-$ and associated production $\tilde{\chi}_1^\pm\tilde{\chi}_1^0$ (the Higgsino model also includes the $\tilde{\chi}_1^\pm\tilde{\chi}_2^0$ mode) [353].

5.1.3.6. Displaced vertices in ATLAS. Massive, LLPs with lifetimes of the order of $O(10)$ ps to $O(10)$ ns can decay inside the inner tracker into charged and stable particles. The products of these decays are reconstructed as tracks with measurably distant impact parameters with respect to the IP. The reconstruction of such displaced tracks is very challenging compared to the track reconstruction of prompt particles, due to fewer hits along the track and a larger parameter phase space for track finding. In order to identify a DV, one must first identify the tracks from the decaying LLP.

Several physics models predict the existence of long-lived, massive particles. For example, a standard SUSY scenario can contain a gluino with a mass of 2 TeV and a lifetime of 1 ns. The long-lived gluino hadronises into an R -hadron, which then decays into a 100 GeV neutralino and hadrons.

In ATLAS, this topology has been investigated in Run 2 by using a dedicated algorithm for reconstructing DV [255]. The performance expected to be achieved for the ITk upgrade for this signal has been tested with a simplified simulation which has a description of the ITk active sensors and a modeling of the magnetic field. The kinematics and location of the decay products of the R -hadron are injected into the simulation and their trajectories are extrapolated through the detector model. The probability of producing at least seven silicon hits in the ITk geometry is shown in figure 40 for a 2 TeV R -hadron with $\tau = 1$ ns. The increased volume and number of ITk layers leads to improved efficiency for the reconstruction of tracks from DV (and hence the vertices themselves) out to radial distances of up to 550 mm. The increased number of silicon layers also gives more room to veto tracks with missing hits, further suppressing backgrounds.

5.1.3.7. LLP searches with precision timing at CMS. The CMS MTD will provide new, powerful information in searches for LLPs. In addition to the aforementioned displaced photon search, the additional timing information can be used to provide full kinematic reconstruction of LLP decays, and can be a powerful tool in background suppression.

Possible improvements in the ability to reconstruct LLP mass. A precision MTD allows each reconstructed vertex to be assigned a time and therefore to measure the TOF of LLPs between primary and secondary vertices. Using the measured displacement between primary and secondary vertices in space and time, the velocity of an LLP in the laboratory frame, $\vec{\beta}_{\text{LAB}}^p$ (or, equivalently, the boost γ^p), can be measured. In such scenarios, the LLP can decay to

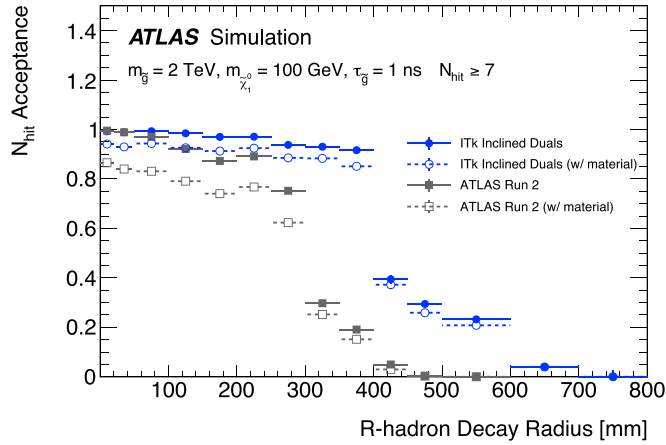


Figure 40. Probability that tracks with $p_T > 1 \text{ GeV}$ will traverse at least seven silicon ITk layers if they are produced in the decay of an R -hadron with mass 2 TeV and $\tau = 1 \text{ ns}$. The probability is also shown for at least seven hits with the Run 2 layout [353].

fully visible or partially invisible systems. Using the measured energy and momentum of the visible portion of the decay, one can calculate its energy in the LLP rest frame and reconstruct the mass of the LLP, assuming that the mass of the invisible system is known.

This capability can be demonstrated in scenarios where the LLP decay produces a Z boson, which then decays to an electron–positron pair. For example, in the GMSB model where the $\tilde{\chi}_0^1$ couples to the gravitino \tilde{G} via higher-dimension operators sensitive to the SUSY breaking scale, the $\tilde{\chi}_0^1$ may have a long lifetime, and can be produced in top-squark pair production with $\tilde{t} \rightarrow t + \tilde{\chi}_0^1$, $\tilde{\chi}_0^1 \rightarrow Z + \tilde{G}$, $Z \rightarrow ee$.

Studies with simulated event samples have been performed to estimate the possible improved sensitivity of the search with the CMS MTD upgrade. The events are generated with Pythia 8, and the masses of the top-squark and neutralino are set to 1000 GeV and 700 GeV , respectively. Generator-level quantities are smeared according to the expected experimental resolutions. A position resolution of $12 \mu\text{m}$ in each of the three spatial directions is assumed for the PV. The secondary vertex position for the electron–positron pair is reconstructed assuming $30 \mu\text{m}$ position resolution in the transverse direction. The momentum resolution for electrons is assumed to be 2% . Finally, the time resolution of charged tracks at the DV is assumed to be 30 ps .

The mass of the LLP is reconstructed assuming that the gravitino is massless. The fraction of events with separation between primary and secondary vertices exceeding 3σ in both space and time as a function of the MTD resolution is shown in figure 41 (left). The mass resolution, defined as half of the shortest mass interval that contains 68% of events with 3σ displacement is shown in figure 41 (right), as a function of the MTD resolution.

A similar study has been performed with another SUSY scenario where the two lightest neutralinos and light chargino are Higgsino-like. The light charginos and neutralinos are nearly mass degenerate and may become long-lived as a consequence of the heavy higgsinos. Figure 42 shows the mass resolution as a function of the MTD resolution in this SUSY scenario. In both studies, the additional timing information from the MTD facilitates the reconstruction of the LLP mass, the resolution and efficiency of which are further improved with the excellent timing resolution of the MTD.

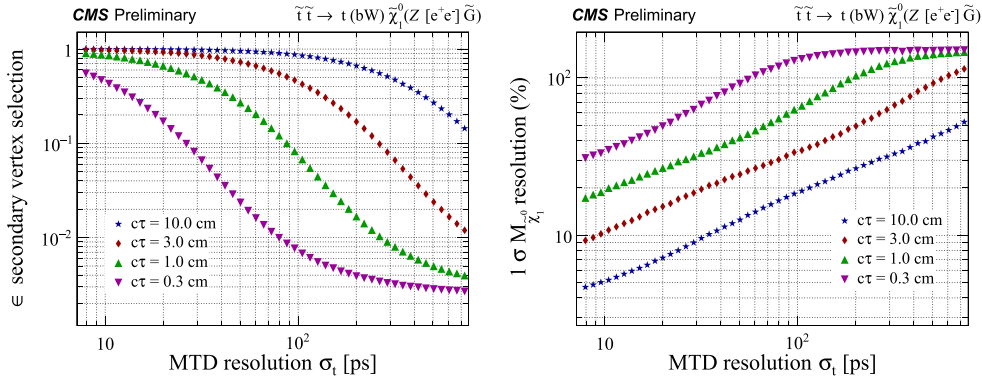


Figure 41. Efficiency (left) and mass resolution (right) as a function of the timing resolution of the MTD for reconstruction of the $\tilde{\chi}_0^1$ mass in the SUSY GMSB example of $\tilde{\chi}_0^1 \rightarrow \tilde{G}e^+e^-$, with mass of $\tilde{\chi}_0^1 = 700$ GeV, considering events with a separation of primary and secondary vertices by more than 3σ in both space and time [351].

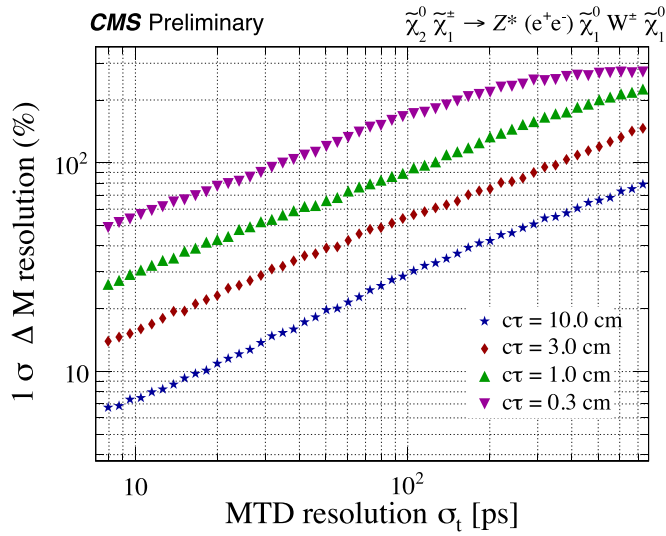


Figure 42. Resolution for the reconstruction of the LLP mass in the Higgsino scenario outlined in this section. The LLP mass resolution is shown as a function of lifetime and the MTD resolution [351].

Possible improvement to LLPs searches in general using timing information. Precision timing at CMS will provide a new tool to suppress the background and enhance the reach for LLPs in the HL-LHC era.

A schematic of a typical signal event containing an LLP is shown in figure 43. An LLP, denoted as X , travels a distance ℓ_X into a detector volume and decays into two light SM particles a and b , which then reach a timing layer at a transverse distance L_{T_2} away from the beam axis. In a typical hard collision, the SM particles generally travel very close to the speed of light. Hence, the decay products of X (using particle a as an example) arrives at the timing layer with a time delay of

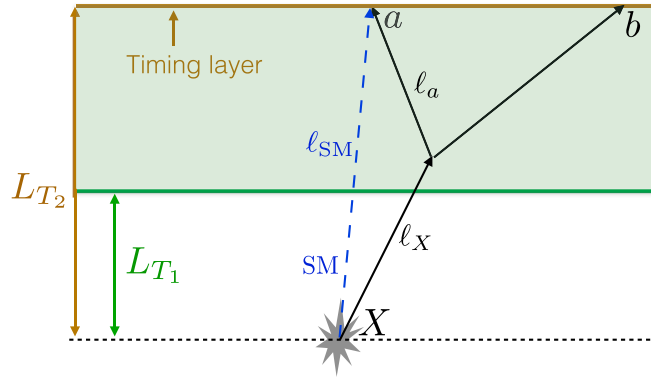


Figure 43. An event topology with an LLP X decaying to two light SM particles a and b . A timing layer, at a transverse distance L_{T_2} away from the beam axis (horizontal gray dotted line), is placed at the end of the detector volume (shaded region). The trajectory of a potential SM background particle is also shown (blue dashed line). The gray polygon indicates the primary vertex. Taken from [363].

$$\Delta t = \frac{\ell_X}{\beta_X} + \frac{\ell_a}{\beta_a} - \frac{\ell_{SM}}{\beta_{SM}}, \quad (5.2)$$

with $\beta_a \simeq \beta_{SM} \simeq 1$. An ISR jet could easily be present for all processes, and can be used to ‘timestamp’, i.e. to derive the time of the hard collision at the PV.

For the CMS MTD located just outside the tracker volume, ℓ_{SM}/β_{SM} is about $O(1 \text{ ns})$. As a result, with tens of picosecond (ps) timing resolution, a sensitivity to percent-level time delay caused by slow LLP motion, e.g. $1 - \beta_X > 0.01$ with boost factor $\gamma < 7$, is expected to be achieved.

A theory study has been done in [363] examining potential gains in sensitivity for hadronic DV reconstruction using timing information. A new trigger strategy for a delayed jet is studied by comparing the prompt jet with $p_T > 30 \text{ GeV}$ that reconstructs the four-dimensional primary vertex (PV4d) with the arrival time of another jet at the timing layer. The delayed and displaced jet signal, after requiring a minimal decay transverse distance of 0.2 m (L_{T_1}), will typically not have good tracks associated with it. Consequently, the major SM background is from trackless jets. The origins of this background can be classified into two categories: hard collision from a same vertex (SV), and PU from different vertices. Other types of background such as CRs, beam halo, material interactions, etc, are out-of-time and will become important after most of the hard collision background is removed using selections based on reconstructing vertices and timing delay. Out-of-time backgrounds may have other distinctive features that would allow their effective suppression. While the study in [363] can serve as an optimistic inspiration for increasing LLP sensitivity with timing information, detailed experimental studies are needed to determine the actual sensitivity gain.

The jet faking a displaced signal, behaving as a trackless jet, has an intrinsic time delay $\Delta t = 0$. However, due to the limited timing resolution in reconstructing the PV4d, it can have a time spread. The background differential distribution with respect to apparent delay time (Δt) can be estimated as

$$\frac{\partial N_{\text{bkg}}(t)^{\text{SV}}}{\partial \Delta t} = N_{\text{bkg}}^{\text{SV}} \mathcal{P}(\Delta t; \delta_t^{\text{SV}}). \quad (5.3)$$

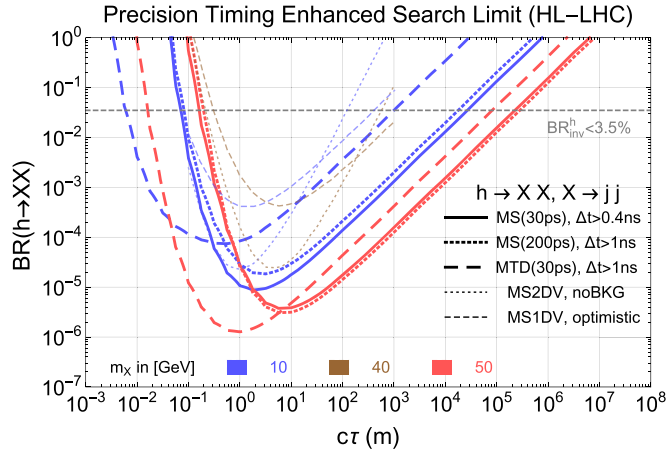


Figure 44. Theory projection from [363] of the 95% C.L. limit on $BR(h \rightarrow XX)$, where X is an LLP, for the production of $pp \rightarrow jh$ with the subsequent decay of $h \rightarrow XX$ and $X \rightarrow jj$ subject to assumptions in the text (one ISR jet with $p_{T,j} = 30$ GeV and $|\eta_j| < 2.5$, and at least one LLP inside the detector). Different colors indicate different masses of the particle X . The thick, long-dashed lines indicate searches with the CMS MTD plus the timing requirements. The thick solid and dotted lines indicate searches with a hypothetical timing layer outside the ATLAS muon spectrometer plus timing requirements. The numbers in parentheses are the assumed timing resolutions. This provides motivation to see whether these gains can be realized by studies from within the collaborations.

The time delay selection on Δt reduces such a background through a very small factor of $\mathcal{P}(\Delta t; \delta_t^{SV})$ for large $\Delta t/\delta_t^{SV}$, where δ_t^{SV} is the timing resolution for the SV background, dominant by the timing detector resolution. The LLP signal pays a much smaller penalty factor than the background due to its intrinsic delay.

The background from the PU requires the coincidence of a triggered hard event and objects from a PU (hard) collision whose PV4d fails to be reconstructed and that can mimic a signal. The differential background from PU can be estimated as

$$\frac{\partial N_{\text{bkg}}^{\text{PU}}(\Delta t)}{\partial \Delta t} \simeq N_{\text{bkg}}^{\text{PU}} \mathcal{P}(\Delta t; \delta_t^{\text{PU}}). \quad (5.4)$$

Similar to equation (5.3), δ_t^{PU} is the timing resolution for the PU background, dominated by the beam spread. The key difference between the background from the PU and the background from the same hard collision is that the typical time spread is determined by the beam property for the former, and by the timing resolution for the latter. They typically differ by a factor of a few, e.g. 190 versus 30 ps for CMS with the current upgrade plan.

Using this estimation, a sensitivity projection is presented with an example signal of a Higgs boson decaying to LLPs with the subsequent decay of the LLPs into $b\bar{b}$ pairs, with only minimal requirements of one low- p_T ISR jet, with $p_{T,j} > 30$ GeV and $|\eta_j| < 2.5$, and at least one LLP decay inside the detector. Timing information is used to suppress backgrounds. The 95% C.L. sensitivity is shown in figure 44. The decay branching ratio of the LLP $X \rightarrow jj$ is assumed to be 100%. The projection with 30 ps timing resolution of the CMS MTD is plotted with thick dashed lines. Compared to other 13 TeV HL-LHC projections (with 3 ab^{-1} of integrated luminosity) without the timing information (shown in thinner, dotted and dashed

lines), it is suggested that the addition of a selection on timing, under the set of assumptions described above, greatly reduces background and improves sensitivity. The possibility of such a significant improvement is enticing; this projection is determined from theoretical studies [363], however, and it remains to be seen whether it is possible to realize these gains in the experiment. For example, the low threshold of the single jet would require timing information at early levels of the trigger, and out-of-time backgrounds could also reduce the gains from timing information. Nevertheless, this high-level theory analysis provides an inspiration to the experimental collaborations to perform more detailed, internal studies that will ultimately determine how realistic the projections are.

In general, the prospect of improvements in LLP searches at the HL-LHC due to precision timing upgrades for CMS (and ATLAS) remains understudied, and deserves more comprehensive experimental and phenomenological studies, including understanding and reducing out-of-time backgrounds.

5.1.3.8. LLP searches with a level-1 track trigger in CMS. As discussed in section 5.1.1, a central feature of the CMS upgrade at the HL-LHC will be a new silicon outer tracker which allows track reconstruction for every LHC bunch crossing (at a rate of 40 MHz). The p_T selection for stubs (hit pairs in the p_T modules of the outer tracker) to be read out is determined by the bandwidth from the detector to the back end electronics, and is fixed at about 2 GeV. On the other hand, the choice of track finding algorithm and hardware is still being finalized, and there could be significant benefits to extending the L1 track trigger capabilities to trigger on off-pointing tracks.

To illustrate the case, a simple toy simulation to study rare Higgs boson decays into new particles with lifetimes of order of a few mm has been performed [364]. This study considers all-hadronic final states with low H_T , taking SM Higgs boson decays into four jets as an example. Theoretical motivation to look for such decays is very strong; see section 2.2 for a detailed discussion. In particular, there is currently a blind spot for lifetimes of order 1 cm in searches for new long-lived scalars in Higgs decays, i.e. $h \rightarrow \phi\phi$. The goal is to probe very small branching fractions of the Higgs boson, so for this study, $BR[h \rightarrow \phi\phi \rightarrow 4q] = 10^{-5}$ is assumed. For prompt decays, the background is overwhelming, but if the ϕ has $c\tau$ of a few mm, the offline analysis has very low backgrounds. The problem is getting such events on tape, in particular through L1. This toy study estimates how an off-pointing track reconstruction at L1 can help. To estimate the efficacy of the approach, the resulting projections are compared with the best alternatives in the absence of an off-pointing track trigger, by using associated Higgs boson production with a W boson that decays leptonically to pass a lepton trigger, or considering L1 calorimeter jets with no associated prompt tracks.

Once these positive results were obtained, a more detailed study using the full Phase 2 simulation of the CMS detector was performed [365]. The more mature exploration found that a plausible extension of the L1 track trigger to tracks with an impact parameter of a few centimeters results in dramatic gains in the trigger efficiency. The gains are even larger for additional heavy SM-like Higgs bosons with the same decay. These results are in agreement with the toy study described above. A few details of the mature study will be described below.

The study focuses on small or moderate decay lengths of the new particles, 1–50 mm, and assumes that the offline selection can remove all SM backgrounds with only a moderate loss of efficiency. While this study focuses on the specific Higgs boson decay to light scalars, the results and the proposed triggers are relevant for a broad spectrum of new physics searches, with or without macroscopic decay lengths.

The authors propose a simple jet clustering algorithm implementable in firmware, and compare it with anti- k_r jets [366] with a size parameter of $R = 0.3$, as produced by FASTJET

[367]. This simple algorithm produces a similar performance, in both L1 trigger efficiency and rate, to the full jet clustering using the anti- k_t algorithm.

Then, the performance of an algorithm for reconstruction of tracks with non-zero impact parameter is presented. This approach extends the baseline CMS L1 Track Trigger design to handle tracks with non-zero impact parameter and to include the impact parameter in the track fit. This enhanced design is feasible without greatly altering the track finding approach, but will require more FPGA computational power than the current proposal, which only considers only prompt tracks. Tracks passing the selection are clustered using the same algorithm as described above, and clusters containing tracks with high impact parameters are flagged as displaced jets. Though the baseline design of the L1 Track Trigger currently is optimized to find prompt tracks, these studies show that an enhanced L1 Track Trigger can extend the L1 trigger acceptance to include new BSM physics signals.

For now, the extended L1 track reconstruction is limited to the barrel region. In order to compare the results with prompt and extended track reconstruction, one needs to make a correction for the rapidity coverage: prompt tracks are found in $|\eta| < 2.4$, while the extended track algorithm currently only reconstructs tracks in $|\eta| < 1.0$. To scale the efficiency for finding track jets to the full $|\eta| < 2.4$ range, a scale factor based on efficiency in the full η range and the central η range was used. The scale factor was comparable to the increase in L1 rate.

Figure 45 shows the expected trigger rate as a function of efficiency for the SM and the heavy SM-like Higgs bosons.

The available bandwidth for the triggers described above, if implemented, will be decided as a part of the full trigger menu optimization. Here, two cases are considered: 5 and 25 kHz. The expected event yield for triggers using extended and prompt tracking are shown in figure 46, assuming branching fraction $\mathcal{B}[h \rightarrow \phi\phi] = 10^{-5}$ for the SM Higgs boson. For the heavy Higgs boson, the expected number of produced signal events is set to be the same as for the SM Higgs by requiring $\sigma_{pp \rightarrow h(250)} \mathcal{B}[\Phi \rightarrow \phi\phi] = 10^{-5} \sigma_{pp \rightarrow h(125)}$.

For the exotic Higgs decays considered, given the expected total dataset for the HL-LHC of 3 ab^{-1} , and assuming a branching fraction of 10^{-5} , CMS would collect $\mathcal{O}(10)$ events, which should be sufficient for discovery. A plausible extension of the L1 track finder was considered, to select tracks with impact parameters of a few cm. That approach improves the yield by more than an order of magnitude. The gains for the extended L1 track finding are even larger for the events with larger H_T , as demonstrated by the simulations of heavy Higgs boson decays.

5.1.4. Open questions and new ideas. The higher data rate and more powerful machinery in the high-luminosity era bring new prospects to LLP searches. Searches that are too challenging for the current machine may become feasible with the HL-LHC upgrades, and it is important to explore such possibilities to the full extent. Existing search methods, triggering, and reconstruction algorithms should also be updated to take full advantage of the new hardware capabilities. As the upgrade scope is being defined and finalized in the near future, it is of particular importance to evaluate the physics cases, which will also motivate the upgrade and inform its designs.

5.1.4.1. New studies for the HL-LHC. In section 5.1.3, various analyses with displaced signatures are presented in the context of how detector and trigger upgrades at the ATLAS and CMS experiments for the HL-LHC can improve their sensitivity. As was shown in section 5.1.1, while the upgrades for both experiments differ in detail, they are similar in concept and scope. It is therefore important to perform the same LLP search projections for

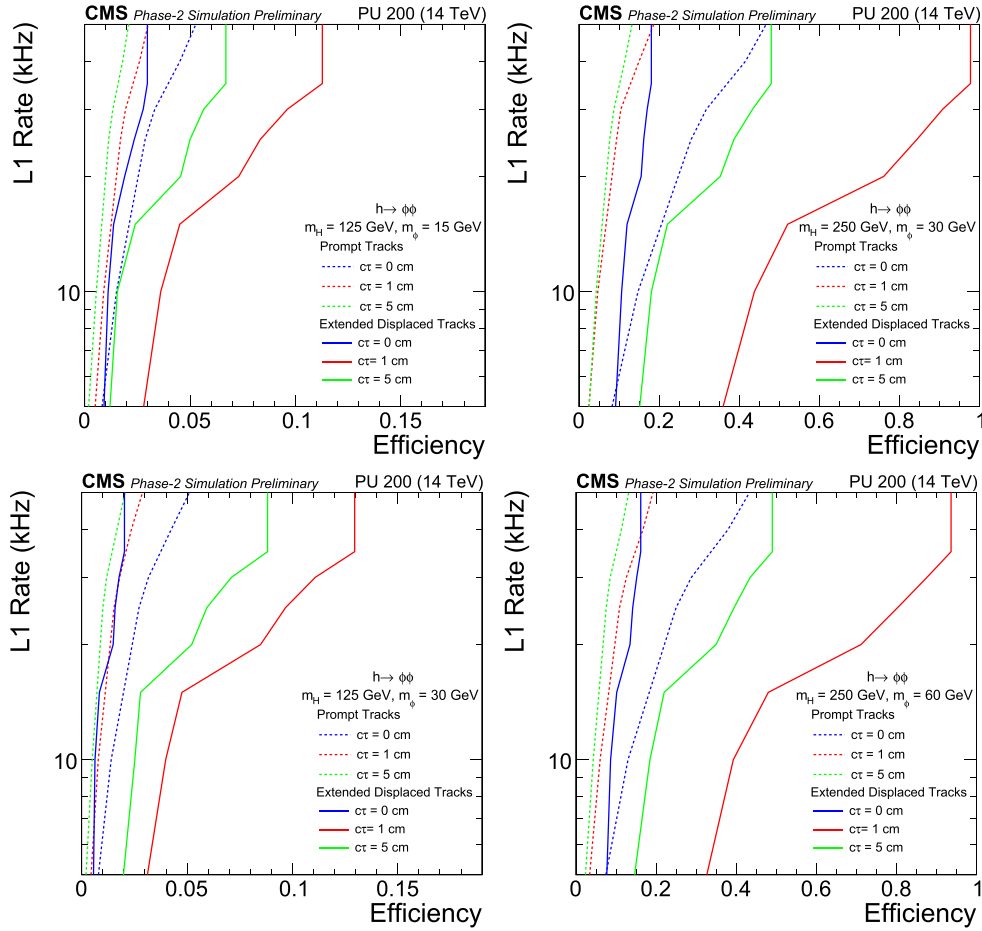


Figure 45. The rate of the track jet H_T trigger as a function of signal efficiency using extended track finding for the SM Higgs (left) and the heavy SM-like Higgs (right). The extended track finding performance is extrapolated to the full outer tracker acceptance as described in the text and in [365].

both experiments to compare performance and evaluate the complementarity of the two experiments.

For example, both experiments explore the idea of a fast timing detector at HL-LHC. The CMS MTD aims for full-coverage of a barrel layer plus endcap disks, while the ATLAS HGTD plans for multiple layers of endcaps. How the different η coverage of the timing layer might impact LLP searches will be an interesting question to answer. In the case of calorimetry, the ATLAS LAr ECAL is segmented in z , providing the additional pointing capability to find displaced photons. On the other hand, the CMS ECAL electronics upgrade in the barrel, and HGCAL upgrade in the endcaps, will considerably improve its timing resolution to identify photons that are out-of-time. A sensitivity comparison of both experiments will provide helpful information in understanding photon reconstruction and the combined reach of both experiments.

Additional opportunities exist for improving LLP sensitivity in Run 3 or at the HL-LHC, such as the ability to perform an analysis using physics objects at the trigger level, rather than

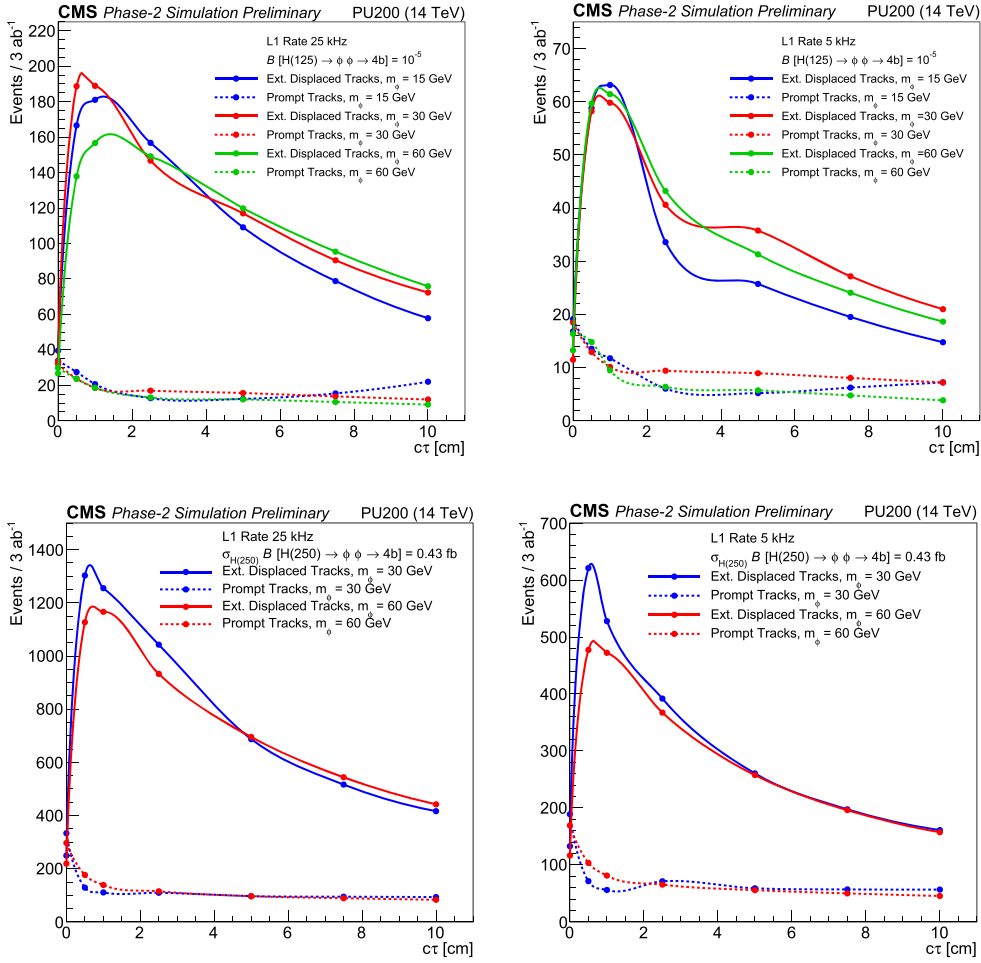


Figure 46. The number of triggered Higgs events (assuming $\mathcal{B}[h \rightarrow \phi\phi] = 10^{-5}$, corresponding to 1700 events) as a function of $c\tau$ for two choices for the trigger rates: 25 kHz (left), 5 kHz (right). Two triggers are compared: one based on prompt track finding (dotted lines) and another that is based on extended track finding with a displaced jet tag (solid lines) [365].

their more complex, offline counterparts. This analysis method—sometimes referred to as *trigger-level analysis* or *data-scouting*—has been used in searches for di-jet resonances using data from Runs 1 and 2 by the CMS Collaboration [368, 369], data from Run 2 by the ATLAS Collaboration [370] and by the LHCb Collaboration for the searches for dark photons [269]. Such data-scouting methods can be used, for example, to reduce the p_T thresholds of jets and muons used in dark photon or hidden particle searches. Such possibilities could potentially assist searches for LLPs by, for example, allowing changes in the L1 muon patterns in order to trigger on non-pointing muons.

Moreover, the applications of machine learning techniques to LLP searches is a currently under-studied realm. Such techniques could be used in the context of LLPs in particle identification, reconstruction, or generation, in addition to analysis or reinterpretation. Further studies to supplement those that already exist are of high priority for the community.

Furthermore, as new models are being proposed and new channels open up in the realm of LLP searches, many with final states challenging for the current detector conditions, it is important to evaluate their sensitivities in the HL era. Here are a few such interesting searches that are on the agenda.

- *Inelastic DM (iDM)*. While stringent limits are currently placed on WIMP-type DM from direct detection, indirect detection, and collider searches, DM particles can exist in a hidden sector with additional particles and forces. A representative example of a hidden sector consists of a DM particle which is charged under a hidden gauge or global symmetry. The DM can have both a symmetry-preserving mass and, if the symmetry is spontaneously broken, also a symmetry-violating mass, which splits the mass eigenstates. This iDM scenario [132, 133, 135] consists of two DM states that couple only off-diagonally to one another. Such iDM can be probed at colliders with the production of $DM + DM^*$ (where DM^* denotes the heavier DM state) in association with a hard SM object X , followed by the subsequent decay of $DM^* \rightarrow DM + Y$ for some potentially different SM states Y . The production is summarized as

$$\begin{aligned} pp &\rightarrow X + DM + DM^* \\ &\rightarrow X + DM + (DM^* \rightarrow DM + Y) \equiv X + \cancel{E}_T + Y, \end{aligned}$$

where X is any state that can be used to trigger on the event and reconstruct \cancel{E}_T , such as an ISR jet, and Y depends on the mode by which DM couples inelastically to the SM. One concrete, representative version of such models can be realized when the mediator is a dark photon and Y is a pair of leptons. The weak coupling between the SM and the hidden sector suggest the heavy eigenstate is meta-stable, creating a displaced signature. Because the mass splitting is small between the two eigenstates, the lepton pair is also typically softer compared with GMSB models, with p_T values of a few to tens of GeV for a $O(10 \text{ GeV})$ DM. The displaced muon trigger and reconstruction strategy with the MS upgrade at CMS can likely improve searches for this scenario. The soft p_T spectrum in this case particularly motivates the lowering of the p_T threshold in the displaced muon trigger turn-on. Moreover, the additional timing information from the fast-timing detector opens up the possibility of reconstructing the mass splitting, while taking advantage of the good resolution of the timing detector for even low- p_T particles. Sensitivity studies for iDM with a dark photon mediator are planned for the CMS MTD upgrade. The projections will also be of value to searches for other types of dark sector models, such as self-interacting DM [371], that give rise to soft displaced lepton pairs.

- *Dark showers*. If the hidden sector has a QCD-like structure with dark quarks and hidden forces, a mediator between the SM and the hidden sector, such as a Z' or heavy Higgs boson, can decay into some number of dark quarks that subsequently shower and hadronize into dark mesons, some of which are meta-stable and decay back into SM particles after a macroscopic distance from the proton–proton IP. A showering dark sector can yield a particularly rich collider phenomenology that may give rise to a high multiplicity of displaced objects often low in p_T . Depending on the final state, searches for a hadronic shower with emerging [331] or semi-visible [372] jets can be improved with the increased acceptance and enhanced resolution due to the tracker upgrades at both ATLAS and CMS, as well as the finer granularity endcap calorimeter (HGCAL) at CMS. A dark shower with displaced photon pairs can benefit from the improved timing resolution with the ECAL electronics upgrade, as well as the new timing detectors. A dark shower with displaced lepton pairs, similar to the aforementioned case of iDM, can

be probed with better sensitivity with the MS upgrades, as well as the fast timing information. For more details on dark showers, see chapter 7.

5.1.4.2. New detectors at future collider. If we are only limited by our imagination, what new detectors may exist at a future collider that can open up new capabilities for LLP searches? Regardless of practical constraints, studies for such bold new proposals also help us understand our current experimental reach and optimize our search strategies.

- *Four-dimensional tracker with timing.* Extending from the ‘timing layer’ approach for HL-LHC upgrades, it is clear more time measurements on the track are favorable. In particular, the TOF between layers is a powerful discriminant for choosing hits on a track. A future tracker that provides four-dimensional information, including precise timing information for every layer, can significantly improve track reconstruction by reducing combinatorics, providing purer track seeds, and remove fake stubs. Assuming high- p_T particles, each layer’s time measurement is advanced by 30 ps and so preserves the differences in vertex times. Low p_T particles will have even more discrimination power since their paths leave longer times between hits in consecutive layers of the tracker. Major technical advances will need to happen to achieve such an implementation, including development of fine-pitch sensors with good timing resolution, improvements in scaling and power consumption, electronics upgrade, and alterations to present pattern recognition methods in track finding.
- *Timing detector outside ATLAS muon system.* As discussed in section 5.1.3, by using a prompt object, such as an ISR jet, to ‘timestamp’ an event, and requiring a timing delay from the LLP, the new timing layer (MTD) at CMS can help significantly reduce the background and improve LLP search sensitivity. The CMS MTD is located between the tracker and the ECAL with a distance to the beamline of about 1.2 m. If one imagines a fast timing layer outside the ATLAS MS with a distance of approximately 10 m [363], timing information at such distances could provide additional discriminating power for particles with longer lifetimes. In figure 44, the projection with a 30 ps timing resolution of such a hypothetical detector outside the ATLAS MS is plotted in a thick solid line. A less-precise timing resolution (150 ps) has been also considered with a selection $\Delta t > 1$ ns to suppress background. While this study is optimistic in assuming that selections on timing can eliminate all backgrounds to the LLP search, it nevertheless serves as important inspiration for more detailed experimental studies to understand the actual extent of the sensitivity gain. The LLP efficiency is largely unaffected by this change, while low-mass LLPs lose sensitivity by a factor of a few. The CMS MTD timing upgrade for the HL-LHC already provides significant improvement [363]. The timing detector outside the ATLAS MS has the notable benefits of lower background, a larger volume for the LLP to decay and more substantial time delay for the LLP signal due to longer travel distance. Moreover, due to the extended time delay of the LLPs in the volume of the MS, less-precise timing can still achieve similar physics goals. As a result, with the above caveats it can serve as an estimate of the best achievable sensitivity using timing information in LLP searches.
- *New double-sided tracking layer very close to the beamline.* Inspired by the L1 track trigger design at CMS for the HL-LHC, a scenario may be imagined where an additional tracking layer close to the beamline is added, mechanics and radiation hardness permitting. This would allow a track veto close to the IP to be implemented, and extend the LLP sensitivity to even smaller displacements. Moreover, if such a layer can be designed with double-sided modules, similar to the CMS outer tracker approach for the

HL-LHC, hit pairs (stubs) from this layer can be used in a L1 track trigger for displaced tracks or DTs. The feasibility of such an approach would depend on the ability to store and process data at a rate not allowed by current technology. On the other hand, it is helpful to consider more innovative data-scouting methods at trigger level to store and select information, or introduce additional discriminating factors to reduce the rate for particular data streams, for the potential of exploring such signatures.

5.2. LHCb upgrade

The LHCb experiment is designed to detect decays of LLPs in the SM, namely bottom and charmed hadrons. As such, it is naturally suited for the search of BSM LLPs in a mass and lifetime range comparable to these hadrons. It is the only LHC experiment to be fully instrumented in the forward region $2 < \eta < 5$, where b - and c -hadrons are abundantly produced and their decay length is enhanced due to the large longitudinal boost. In this region, detector occupancy is extremely high and thus the LHCb experiment has been run at reduced luminosity compared to ATLAS and CMS during Runs 1 and 2. However, an upgrade of the detector is planned to allow running at a luminosity of $2 \times 10^{33} \text{ cm}^{-2} \text{ s}^{-1}$ in LHC Run 3 (starting in 2020) while maintaining or improving the current physics performance [373]. This is five times larger than the luminosity during Runs 1 and 2. This first upgrade phase (Phase 1a) will entail a novel trigger paradigm where all sub-detectors are fast enough to be read out in real time and the first trigger decisions are done in software. This trigger scheme is flexible and offers a great opportunity for searches of striking signatures like those of BSM LLPs. This upgrade comes earlier than the planned ATLAS and CMS upgrades for the HL-LHC phase which are planned to be installed during LHC long shutdown 3 (by 2025). In this shutdown, LHCb plans to consolidate and modestly enhance the Phase 1a upgrade detector (Phase 1b), while a Phase 2 upgrade to run at an even higher luminosity up to $\sim 2 \times 10^{34} \text{ cm}^{-2} \text{ s}^{-1}$ is planned to be installed later, during long shutdown 4 (by 2030) [374].

Section 5.2.1 gives a brief overview of the Phase 1 upgraded-LHCb detector design and the expected performance of the LHCb sub-detectors. An overview of the upgraded LHCb capabilities in the context of LLP searches is given in section 5.2.2 with a few example signatures. Finally, an overview of the plans for the Phase 2 upgrade and some thoughts on the opportunities given by putative additional detector features are reported in section 5.2.3.

5.2.1. LHCb detector and trigger upgrade for run 3 (Phase 1a). In LHC Run 3, LHCb plans to take data at an instantaneous luminosity of $2 \times 10^{33} \text{ cm}^{-2} \text{ s}^{-1}$, a factor of five larger than the current luminosity. The LHCb detector needs to be upgraded to cope with the higher radiation dose and, most importantly, to avoid the saturation of the trigger rate and exploit the higher luminosity. The main bottleneck in the current trigger is in the first stage, which reduces the accepted rate from 30 to 1 MHz at hardware level. For the upgrade, the hardware trigger will be removed and the full event will be read out at the bunch crossing rate of the LHC (40 MHz), with a flexible software-based trigger.

In table 4 the current and upgraded conditions of the detector are summarised. To cope with the larger occupancy and higher rate of the upgraded detector, the electronics of all of the sub-detectors must be upgraded, and some sub-detectors must be fully replaced. For example, the tracking system, which plays a crucial role in LLP searches, must be replaced.

The upgraded tracking system consists of the VELO, surrounding the IP, the Upstream Tracker, a TT placed before the magnet, and the scintillating fibers tracker (SciFi), three

Table 4. LHCb current and upgraded operating conditions [374]. Instantaneous luminosity \mathcal{L} , integrated luminosity $\int \mathcal{L}$ (including previous runs), pp collision energy \sqrt{s} and average number of visible proton interactions μ are listed.

	Current	Upgrade 1a	Upgrade 1b	Upgrade 2
$\mathcal{L}/(\text{cm}^{-2} \text{s}^{-1})$	4×10^{32}	2×10^{33}	2×10^{33}	2×10^{34}
$\int \mathcal{L}$	8 fb ⁻¹	23 fb ⁻¹	50 fb ⁻¹	300 fb ⁻¹
\sqrt{s}	7, 8, 13 TeV	14 TeV	14 TeV	14 TeV
μ	~ 1	~ 5	~ 5	~ 50

stations after the magnet. In the VELO [375], the current strips will be replaced by pixel detectors, with a custom developed ASIC (VeloPix) able to cope with a maximum hit rate of 900 Mhits/s/ASIC. The Upstream Tracker [376] is composed of four silicon micro-strip planes, with finer granularity and larger acceptance compared to the current tracker. Each station of the SciFi has four planes of 2.5 m long scintillating fibres read out by silicon photo-multipliers.

The upgrade components most important for LLP searches are the VELO, the tracking and the software trigger. In the following subsections a brief description of the design and capabilities is given for each.

5.2.1.1. VELO upgrade. The VELO plays a fundamental role in LLP searches at LHCb: due to the large boost particles typically experience in the forward direction, a precise measurement of the LLP vertex position allows LHCb to efficiently reject tracks that belong to a different b or c vertex (see section 4.2).

In upgrade conditions, the number of tracks and primary vertices will increase by about a factor of five, making it much more difficult to identify DV close to the beam-line; it is an additional challenge to accomplish this in real time. The VELO was thus completely redesigned [375] to cope with the new expected high-luminosity conditions, maintaining high physics performance and allowing real-time readout for the software trigger. The new VELO has a pixel rather than strip geometry and its distance from the LHC beams is reduced from 8 to 5 mm. This leads to an improvement in the vertex resolution (see figure 47) and reduces the rate of unphysical (ghost) tracks.

The pattern recognition efficiency for track reconstruction is superior to the one of the current VELO when evaluated in high-luminosity conditions. Particularly important for LLP searches is the efficiency of track reconstruction as a function of the displacement from the origin along the beam axis. As shown in figure 48, for the upgraded VELO the efficiency approaches 100% and is uniform in a window of 20 cm around the IP, thanks to the new configuration of the modules in the z direction and the shorter distance from the beam. The VELO acceptance degrades quickly after 20 cm in z , giving an upper limit for LLP decay lengths with vertices reconstructible in the VELO. A display of the upgraded VELO geometry and its acceptance in both the forward and backward directions is shown in figure 49.

Another important metric of detector performance is impact parameter resolution, especially in LLP searches where it can be exploited to reduce the background due to fake tracks. With the upgrade, the impact parameter resolution significantly improves for low- p_T tracks. For example, the impact parameter resolution along x for tracks with p_T of 0.5 GeV is 40 μm in the upgrade versus 70 μm in the current VELO. The replacement of strips with pixel sensors also makes the pattern recognition faster for the same multiplicity. This can be used in

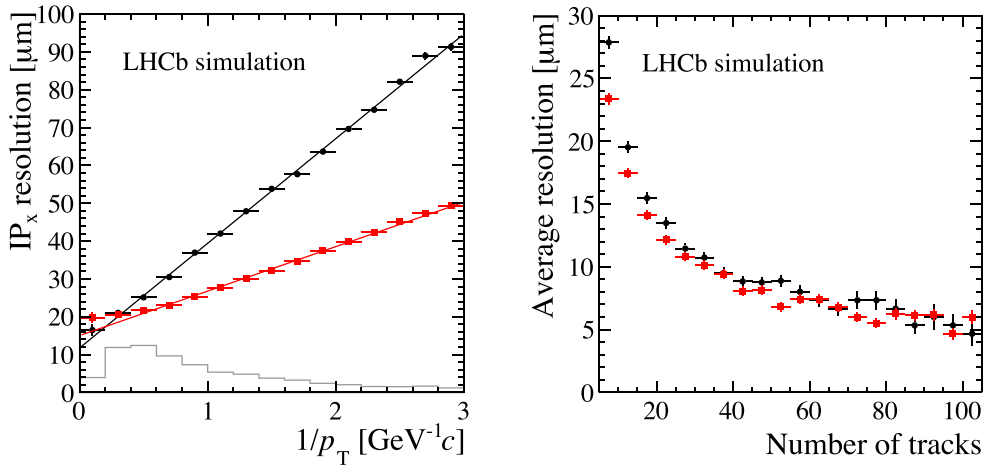


Figure 47. Left: the impact parameter resolution (in the x direction) as a function of the inverse p_T . Right: the resolution on a vertex as a function of number of tracks. The current LHCb VELO performance is shown in black points while the one of the upgraded VELO in red points [375].

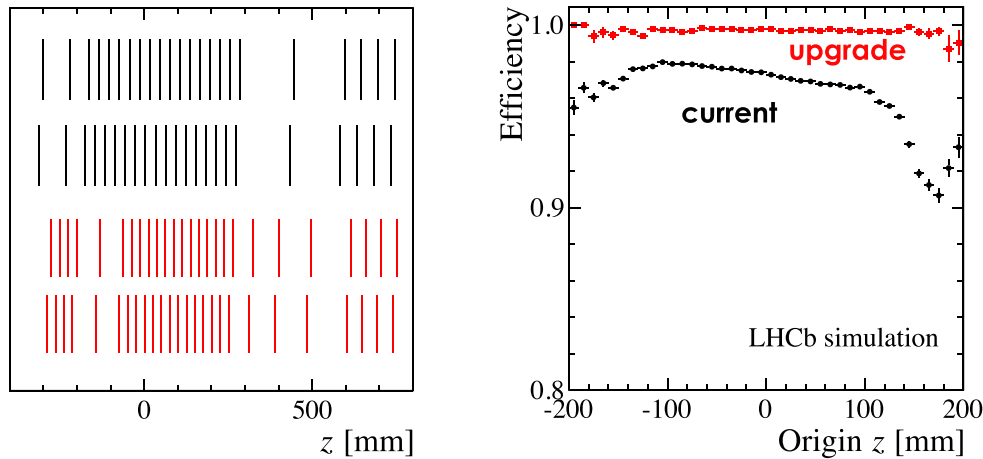


Figure 48. Left: a comparison of the current and upgrade VELO z -layouts for LHCb. The top layout (black) is the current VELO while the bottom layout (red) is the upgrade VELO. Right: the track reconstruction efficiency as a function of the origin in z for the current (black) and upgrade (black) VELO in upgrade conditions [375].

the trigger to find tracks and identify DV in the trigger, making it possible to soften or remove inefficient p_T requirements.

Real displaced tracks created by interactions in the VELO material can be a significant background to LLP searches (further details are discussed in chapter 4). The total material budget of the upgraded VELO is similar to that of the current detector (with a radiation length of about 20%) and is dominated by interactions in the radio-frequency foil separating the beam vacuum from the vacuum of the sensors. However, the average percentage of radiation length before the first measured point is significantly reduced in the upgrade VELO, passing

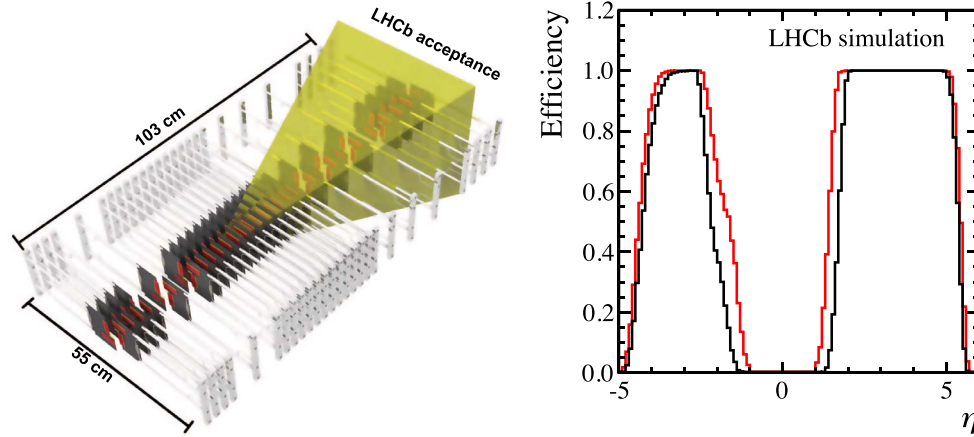


Figure 49. Left: a display of the upgrade VELO geometry and a comparison with the LHCb spectrometer acceptance which is shaded in yellow. Right: the η acceptance of the upgrade VELO geometry both for forward and backward tracks. The fraction of tracks crossing three and four modules is given in red and black, respectively [375].

from $4.6\%X_0$ in the current design to $1.7\%X_0$ in the upgraded VELO (where X_0 is the radiation length).

5.2.1.2. Upgraded trigger. The online event selection in the LHCb experiment during the 2010–2018 running period has been performed by a trigger composed of a hardware level (L0), and two software levels: High Level Trigger 1 (HLT1) and High Level Trigger 2 (HLT2). The L0 reduces the rate from 40 MHz (the LHC bunch-crossing rate) to 1 MHz using information from the calorimeter and MSs. Typical requirements in the L0 are $p_T > 1.4$ GeV for muons and $E > 2.5$ GeV for electrons. The software trigger performs a partial event reconstruction at HLT1, reconstructing tracks and primary vertices for any particle down to $p_T = 500$ MeV, followed by a complete event reconstruction at HLT2, reducing further the rate to 12.5 kHz (in LHC Run 2).

In the Phase 1 upgrade, LHCb foresees to run at a luminosity of $2 \times 10^{33} \text{ cm}^{-2} \text{ s}^{-1}$, about a factor of five larger than that experienced during LHC Run 2. For this reason, a new trigger system, able to fully exploit the LHC potential, has been designed [377, 378]. The upgraded LHCb trigger is based on two paradigms: a triggerless readout and a full software trigger. In addition, as already tested in Run 2, a real-time alignment and calibration will achieve offline-quality reconstruction already in the trigger, allowing a higher signal purity of interesting decay channels. Figure 50 shows the current and the upgraded trigger schemes.

Triggerless readout and full-software trigger. With the LHCb trigger upgrade, the 1 MHz readout limitation will be removed, allowing the full event rate to be processed in software. This will increase the efficiency for several channels which otherwise would not benefit from the higher luminosity because they would saturate the L0 trigger rate. Figure 51 shows how the rate for non-muonic B decays saturates the L0 trigger with increasing luminosity. Most of these channels saturate the L0 trigger already at the Run 2 luminosity ($4 \times 10^{32} \text{ cm}^{-2} \text{ s}^{-1}$). Moreover, a purely software trigger will not be subject to the p_T requirements currently applied at the hardware trigger level. Several physics programs involving low- p_T particles, currently prohibited by of the low L0 efficiency, will therefore become possible.

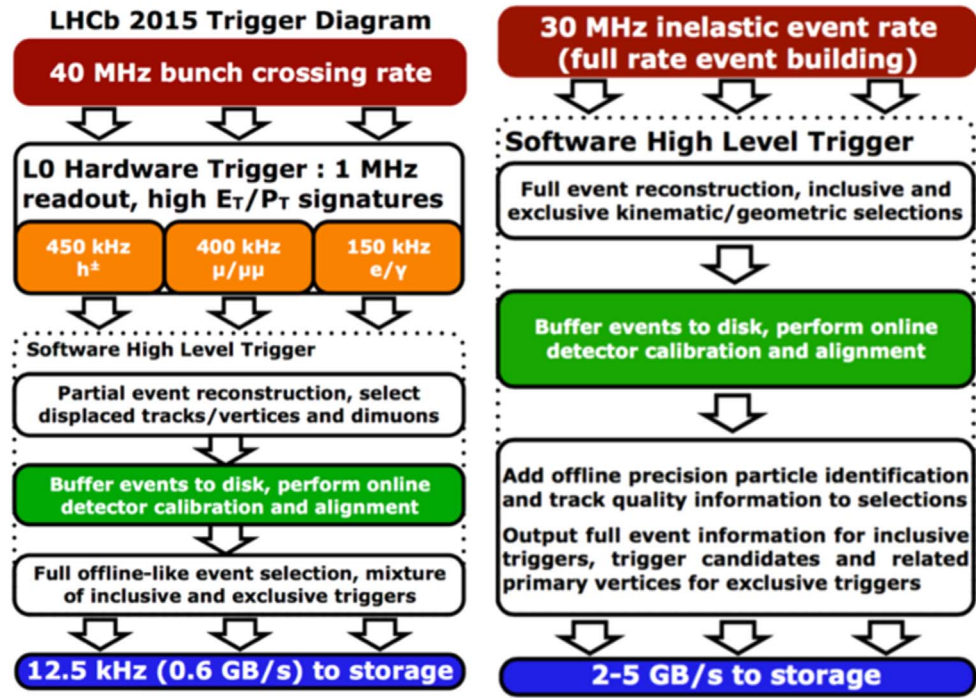


Figure 50. Scheme of the current LHCb trigger (left), and of the upgraded trigger (right) [379].

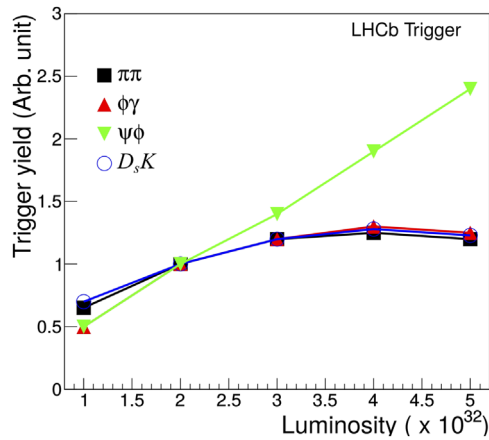


Figure 51. Trigger yields for $B \rightarrow \pi^+\pi^-$, $B_s \rightarrow \phi(K^+K^-)\gamma$, $B_s \rightarrow J/\psi(\mu^+\mu^-)\phi(K^+K^-)$ and $B_s \rightarrow D_s^-(K^+K^-\pi^-)K^+$ as a function of the luminosity with the current LHCb trigger scheme. For non-muonic channels, the saturation effect due to the L0 trigger can be observed [380].

Turbo stream. Starting from Run 2, offline-quality alignment and calibration has been applied between the HLT1 and the HLT2 levels. This was made possible by the design of a new dedicated trigger output called Turbo Stream. The event record is written directly from

the trigger and processed so that it can be used for physics analysis without the need for offline reconstruction [277]. Several variations of Turbo have been introduced in the last several years. For 2015 data taking, the first version of Turbo allowed only the triggered signal candidate objects to be saved, without keeping the rest of the event and thereby discarding all sub-detector information. While the event size was an order of magnitude smaller than for full stream data, any analysis relying on additional information from the surrounding event could not use Turbo Stream data.

For this reason, full event reconstruction was implemented as Turbo++ in 2016. Finally, a new intermediate solution between Turbo and Turbo++ called Turbo SP (Selective Persistence) was implemented in 2017. With Turbo SP, both the trigger candidate objects and a subset of the other objects in the event are saved. This flexible solution allows the analyzer to choose which objects to save, minimizing the size of the stored event. Once the trigger is upgraded to run purely at the software level, the large majority of LHCb analyses will be moved to Turbo. The reduced event size allows the storage of particle candidates at a high rate, fully exploiting the reduction in p_T thresholds due to the removal of the LO hardware trigger.

Triggers on downstream tracks. Most of the LLP searches at the LHCb experiment use so-called ‘long tracks’ to reconstruct the candidates, which are tracks where inputs from both the VELO and the TTs are considered. These tracks have an excellent spatial and momentum resolution, and result from an LLP decaying within the VELO region. This is the reason why most of the LLP searches done by LHCb correspond to long-lived candidates with displacements typically up to $\mathcal{O}(10)$ cm, with the VELO tracking algorithm optimized for displacements of up to 20 cm. However, for long-lived candidates with displacements larger than 2 cm, a different type of track which considers information only from the TTs, ‘downstream tracks’, has to be used instead of the ‘long track’ type. Unfortunately, these tracks have worse vertex and momentum resolution, limiting the capabilities of LHCb for this displacement range. In order to improve the detector sensitivity in the displacement ranges between 20 and 200 cm, a proposal to develop new trigger lines to select ‘downstream tracks’ is being studied [378]. An interesting idea which can help to achieve this task and to significantly reduce the CPU computing time is the implementation of a system of specialized processors used to rapidly find the downstream tracks through look-up tables, and present these tracks to the software trigger in parallel with all the raw detector information in the event. This system, named ‘retina’, is being studied and has its own R&D programme [381].

The much higher luminosity and improved capabilities of the upgraded LHCb detector are expected to significantly improve the capabilities for LLP searches in LHC Run 3. In the following sections, the projected sensitivities to several benchmark LLP signatures are shown to illustrate the potential of the upgraded detector. However, the potential of the upgraded triggerless readout has not been completely explored yet and its great flexibility could be exploited in several ways beyond those shown here.

5.2.2. LHCb upgrade phase 1a projections for LLP signatures

5.2.2.1. Displaced di-leptons. The upgraded LHCb experiment is expected to have exceptional sensitivity to low-mass, displaced dilepton signatures thanks to the mass resolution, excellent vertexing, and the online selection allowed by the triggerless readout.

The upgrade LHCb sensitivity to dileptons has been explored in the literature in the context of dark photon searches. Two complementary signatures have been considered: an inclusive search for BSM gauge bosons (dark photons) in $A' \rightarrow \mu^+\mu^-$, and a search for A' using radiative charm decays $D^{*0} \rightarrow D^0A'$, $A' \rightarrow e^+e^-$. The inclusive search [341] scans a

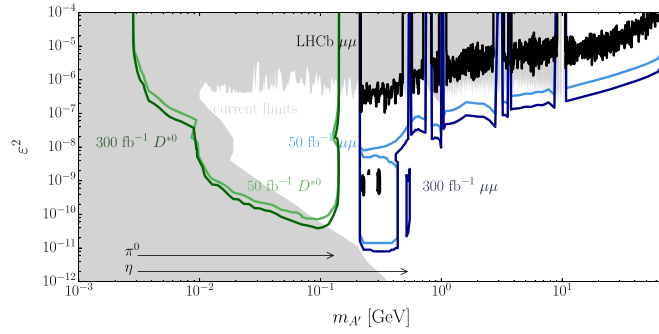


Figure 52. Current and expected limits in the dark photon parameter space mixing ϵ^2 versus A' mass [374]. The black line represents current LHCb limits from [269], while grey-shaded regions are existing limits from other experiments. Expected limits from the proposed inclusive search with 50 and 300 fb^{-1} are shown in shades of blue. The expected sensitivity of $D^{*0} \rightarrow D^0 A'(ee)$ at low mass is shown in shades of green. The arrows indicate the available mass range from light meson decays into $e^+e^-\gamma$.

large region from the dimuon threshold $2m_\mu$ all the way up to the Z pole. The second proposed signature [382] exploits a tag of the radiative decay of the D^{*0} using its reconstructed invariant mass and a di-electron dark photon final state to probe a much lower mass range allowed by the decay kinematics, $[2m_e, 142 \text{ MeV}]$. For both signatures, searches for both a prompt and a displaced dark photon vertex are carried out. The prompt search is expected to probe mixing parameters ϵ^2 below 10^{-7} despite the large irreducible background from Drell–Yan and QCD¹⁸⁰. Since the dark photons with masses above the η mass decay promptly for couplings that are accessible within LHCb, no attempt is made to probe displaced dark photons in that region.

An inclusive search for dark photons has already been performed with LHCb data collected in 2016 [269]. This was possible due to the high reconstruction and identification efficiency of soft di-muons at LHCb. These results demonstrated the unique sensitivity that can be reached at LHCb. The planned increase in luminosity and removal of the hardware-trigger stage in Run 3 should increase the number of expected $A' \rightarrow \mu\mu$ decays in the low-mass region by a factor of $\mathcal{O}(100\text{--}1000)$ compared to the 2016 data sample. The limits placed by the current data and the sensitivity expected with future LHC runs is shown in figure 52.

The exclusive search for $D^{*0} \rightarrow D^0 A', A' \rightarrow e^+e^-$ is much more challenging and not feasible prior to the upgrade, since the hardware trigger and the higher material budget degrade the sensitivity. This search highly relies on the online identification of e^+e^- pairs, since over 5 trillion of these D^{*0} decays are expected in Run 3. The expected sensitivity probes unexplored regions of phase space at low A' mass and mixing ϵ^2 that is usually in the realm of beam-dump experiments.

A displaced di-muon signature also appears in some HV scenarios [66], in which a hidden sector with strong dynamics showers and hadronizes into dark mesons that can have an appreciable decay rate to leptons. (For more information on dark showers, see chapter 7.) The upgraded LHCb prospects for this type of signature have been explored in [383] and are very promising. In the scenario explored therein, dark mesons are produced with large multiplicities of between 10 and 30. Selection criteria inspired by the proposed dark photon search [341] in the region after the first VELO module are applied. The expected reach for the

¹⁸⁰ In the limit $m_{A'} \ll m_Z$, the coupling of the dark photon to SM particles with charge Q is approximately $Qe\epsilon$.

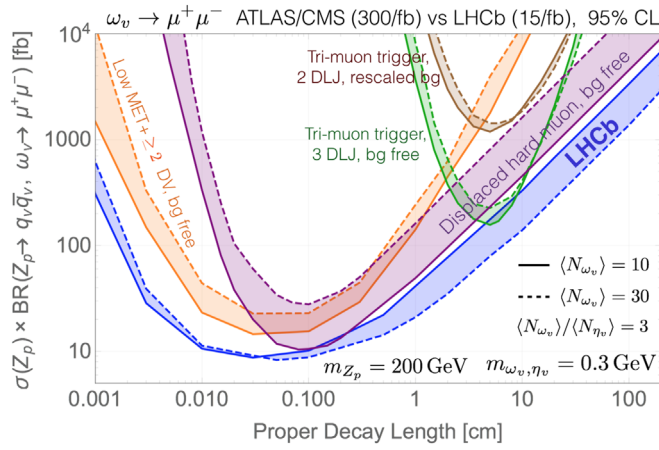


Figure 53. Projected bounds from various ATLAS/CMS searches and the LHCb search for hidden valley-like models with a Z_p decaying to a $q_{HV} q_{HV}$ pair which then undergo hadronization in the dark sector, eventually leading to dark meson decays to di-muon final states [383].

proposed searches using Run 3 data from LHCb (15 fb^{-1}) and from ATLAS/CMS (300 fb^{-1}) are shown in figure 53. The model studied involves a 200 GeV $U(1)'$ gauge boson Z_p decaying to a HV quark pair; showering and hadronization in the dark sector leads to a large multiplicity of hidden hadrons ω_V (with $m_{\omega_V} = 0.3 \text{ GeV}/c^2$) that can decay to di-muons. In this context, the upgraded LHCb detector could have better sensitivity than other proposed searches at ATLAS and CMS.

5.2.2.2. Displaced jets. Signatures with displaced jets are common in the context of LLP searches. As summarised in section 3.1.3, LHCb has started to explore its sensitivity to displaced jets by using the data collected during Run 1. In LHCb Upgrade Ia, the background rejection for displaced jet searches is expected to improve thanks to the improved VELO resolution. The selection efficiency should also be significantly higher due to the prospects for online DV identification. The main focus of LHCb will be to probe the region at small lifetime where it has already proven to be the most competitive (see discussion in section 3). The background from QCD and material interactions is the main limiting factor, and the improved vertex resolution of the upgraded VELO together with the lower material budget and the use of a detailed material map are expected to bring large improvements in the upgraded detector.

In some dark sector models, the number of hadronic DV can be large, even in the limited LHCb acceptance (see, for example, [331] and the discussion in chapter 7). An inclusive DV search would likely include a requirement on the isolation of the DV from other tracks in the event (such as the one used for the dark photon analysis [269]). This requirement could be very inefficient in the context of a dark shower and so a dedicated search strategy would be needed. Furthermore, a dedicated software trigger looking for a large number of DV in the VELO and soft p_T requirements could in principle improve the sensitivity to this kind of models, but studies are needed to fully understand its potential and compare LHCb to other experiments.

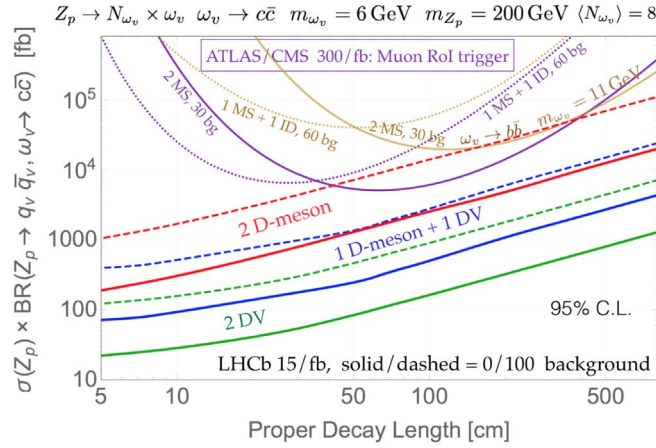


Figure 54. Projected bounds from various proposed searches for confining hidden valley models exploiting $c\bar{c}$ decays of hidden valley mesons ω_v (taken from [383]). The sensitivities with various signatures at LHCb are shown: two displaced vertices (green), one reconstructed D meson and one DV (blue) and two reconstructed D mesons (red). Searches for this same particular model at ATLAS/CMS are shown not to be competitive (more details can be found in [383]).

5.2.2.3. Displaced mesons. Quark–antiquark pairs from the decay of a low mass particle in the SM often hadronize into SM mesons that subsequently decay with known branching ratios. For example, a dark sector meson with a displaced decay to $c\bar{c}$ often produces two D mesons which in turn have non-negligible lifetimes. In this scenario, the authors of [383] have investigated the prospects of using more or less inclusive reconstruction of the two D meson decays at the upgraded LHCb. A similar approach could be used to target decays to $b\bar{b}$ that hadronize to B mesons since the latter is likely to produce D mesons in its decay. Since LHCb is designed to reconstruct heavy flavor decays, it can be competitive in this kind of search [383] (see figure 54). Furthermore, searches for displaced mesons will greatly profit from the software trigger, which is mainly designed to improve the efficiency of similar-looking hadronic decays of heavy flavor mesons.

5.2.3. After phase 1a upgrade: phase 1b and phase 2. After a consolidation phase (Phase 1b) during long shutdown (LS) 3 aiming to run in the same conditions as in Phase 1a, the LHCb detector plans a Phase 2 upgrade during LS 4 (by 2030). The Phase 2 upgrade is needed to face even more challenging conditions than during previous runs. For example, particle multiplicity, PU, and radiation damage are expected to be ten times higher than those experienced in Phase 1. The LHCb experiment expects to collect at least 300 fb^{-1} by the end of Upgrade 2 [374].

Major improvements to the LHCb detector during Phases 1b and 2 that are relevant for LLP searches are described in the following, as well as some naïve projections of Run 1 results to an an integrated luminosity of 300 fb^{-1} .

Magnet stations. Along with the ‘long’ and ‘downstream’ track types, ‘upstream’ tracks are also considered useful for LLP searches. These tracks correspond to soft charged particles bending out of the detector acceptance, produced from LLP candidates which decay within the VELO region. Aside from the installation of a new tracker during LS2, the Upstream Tracker, a proposal to add magnet stations inside the LHCb magnet to improve low

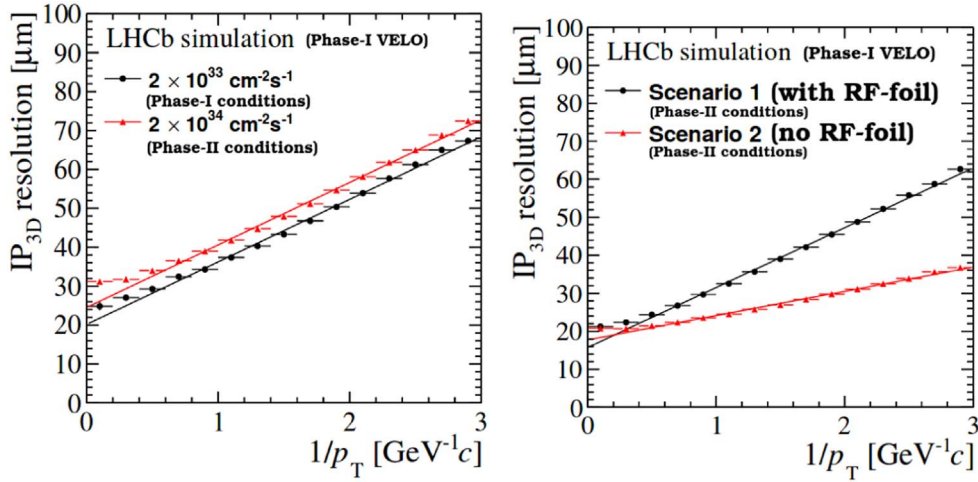


Figure 55. Impact parameter resolution estimations from simulation using the Phase 1 VELO model for the LHCb experiment: (left) a comparison if considering Phase 1 or Phase 2 conditions; (right) the effect of the RF-foil removal under Phase 2 conditions [384].

momentum resolution is considered [384]. These magnet stations have been proposed to be installed for Phase 1b, and are foreseen to highly improve the tracking of low momentum particles produced from certain kind of LLP candidates, such as for example soft pions from ‘disappearing’ chargino tracks.

Material interactions. The presence of a VELO envelope at approximately 5 mm from the beam line in order to separate the VELO and the LHC vacuums, named ‘RF-foil’, strongly affects the background composition of LLP searches in the LHCb experiment. Namely, for LLP candidates decaying below 5 mm from the beam line, the main source of background is due to heavy flavour decays, while material interactions with the RF-foil compose the main background contribution for LLPs decaying above 5 mm from the beam line. While the former is purely due to QCD processes and hence not reducible, the latter is kept under control by the use of a detailed veto map (see [269]). However, the ideal case would be to completely remove the RF-foil during the Phase 2 upgrade [384], which would result in a large reduction of the background component due to material interactions. The improvements foreseen to the Phase 2 VELO (probably based on an updated version of the Phase 1 VELO), are expected to increase the sensitivity to shorter lifetimes and better PV and impact parameter resolution (see figure 55). Unfortunately, the removal of the RF-foil requires the development of new techniques to isolate the sensors from the beam radio frequency and is not necessarily seen as a viable option. Therefore, improving the material veto maps as much as possible by accurately modeling the material interactions would be desirable as a more realistic option for the HL-LHC era.

Naïve Projections of Run 1 Results to the HL-LHC Era. By taking the published Run 1 results from the single displaced dijet search [253] at LHCb, a naïve extrapolation to the integrated luminosity foreseen to be recorded by LHCb during Phase 2, 300 fb^{-1} , is presented in figure 56. These numbers have been obtained by simply scaling signal and background with the expected increase in cross section and luminosity, neglecting PU effects and expected detector improvements. The removal of neutral objects from jet reconstruction, and the use of machine-learning techniques are expected to assist in the required suppression of

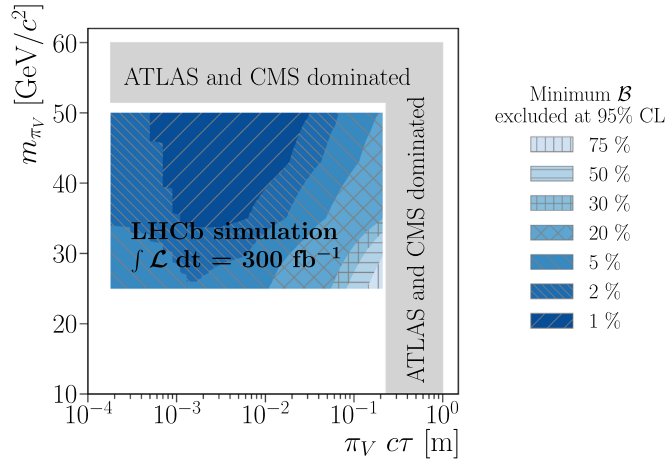


Figure 56. Naive sensitivity projections for searches of displaced dijet vertices at LHCb for the expected luminosity to be collected with the Phase 2 upgraded detector (300 fb^{-1}) [385]. The projected limit is on Higgs boson decays to dark pions π_V with branching fraction \mathcal{B} , and the dark pions each in turn decay to a pair of jets.

PU. Furthermore, jet substructure techniques are foreseen to improve the quality of di-jet object with lower mass.

5.3. Dedicated detectors for LLPs

5.3.1. Introduction. Despite a wide and seemingly comprehensive research program—both existing and, in this document, proposed to be expanded—for LLPs at the LHC, in cases of ultra-low-mass particles, ultra-long lifetimes, or unusual LLP charges, it is hard or impossible to trigger on and/or reconstruct such events in the main ATLAS, CMS, and LHCb detectors. This has led to new proposals for dedicated experiments to look for LLPs in new regimes that are otherwise inaccessible at the LHC. These experiments provide the best sensitivity to new millicharged LLPs, magnetic monopoles, and other LLPs arising from models such as those containing Higgs-portal hidden sectors, dark photons, and Majorana neutrinos.

As discussed in section 2.2, LLPs BSM are theoretically well motivated and come in wide range of masses and lifetimes. ATLAS and CMS have excellent sensitivity for fairly high mass LLPs, regardless of their lifetime (see, e.g. [4, 246, 386, 249]). Low mass and/or softer final states are more challenging due to both background and triggering limitations. In the short-lifetime regime, for $c\tau$ of the scale of the VELO, LHCb has sensitivity to somewhat lower masses and can trigger on softer muonic final states, generating complementary reach provided the LLP has a significant branching ratio to muons [253, 254, 279, 309, 387]. Finally, the low-mass/soft final states with rather long lifetimes are challenging for all three experiments. These signatures can be covered partially by NA62 [388] operating in beam dump mode, or by SHiP [389], or by dedicated LHC experiments like CODEX-b [104] (see section 5.3.5), FASER [105] (see section 5.3.6), or MATHUSLA [103] (see section 5.3.4). Each of these dedicated experiments is sensitive to different LLP lifetimes, masses, and production modes based on their position and orientation and thus each can be considered a necessary component of a comprehensive, coordinated search program for very long-lived particles at the LHC.

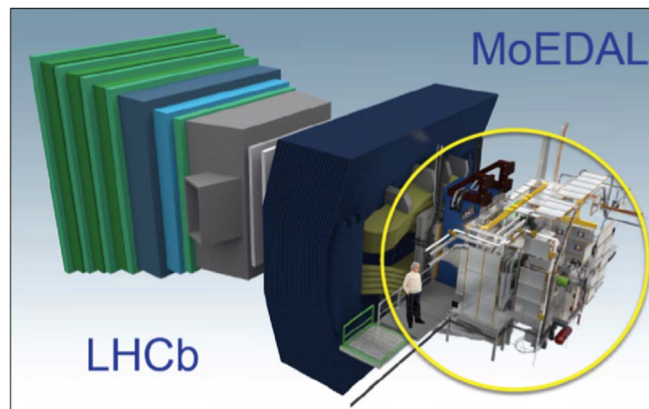


Figure 57. A three-dimensional schematic view of the MoEDAL detector (in the yellow circle) around the LHCb VELO region at Point 8 of the LHC.

5.3.2. MoEDAL experiment and future developments. Monopole and exotics detector at the LHCb (MoEDAL) [101]¹⁸⁰ is designed to search for manifestations of new physics through highly-ionising (HI) particles in a manner complementary to ATLAS and CMS [310]. The main motivation for the MoEDAL experiment is to pursue the quest for magnetic monopoles at LHC energies. Nonetheless the detector is also designed to search for any massive, long-lived, slow-moving particle [390, 391] with single or multiple electric charges arising in many scenarios of physics BSM [392].

The MoEDAL detector [311] is deployed around the intersection region at LHC Point 8 (IP8) in the LHCb VELO cavern. A schematic view of the MoEDAL experiment is shown in figure 57. It is a unique and largely passive detector comprising different detector technologies.

The main sub-detector system is made of a large array of CR-39, Makrofol® and Lexan™ nuclear track detector (NTD) stacks surrounding the intersection area. The passage of a HI particle through the plastic detector is marked by an invisible damage zone along the trajectory. The damage zone is revealed as a cone-shaped etch-pit when the plastic detector is chemically etched. Then the sheets of plastics are scanned looking for aligned etch pits in multiple sheets. The MoEDAL NTDs have a threshold of $z/\beta \sim 5$, where z is the charge and $\beta = v/c$ the velocity of the incident particle.

Another type of NTD installed is the very high charge catcher ($z/\beta \sim 50$). It consists of two flexible low-mass stacks of Makrofol®, deployed in the LHCb acceptance between RICH1 and the Trigger Tracker. It is the only NTD (partly) covering the forward region, adding only $\sim 0.5\%$ to the LHCb material budget while enhancing considerably the overall geometrical coverage of MoEDAL.

A unique feature of the MoEDAL detector is the use of paramagnetic magnetic-monopole trappers (MMTs) to capture magnetically-charged HI particles. The high magnetic charge of a monopole—being at least one Dirac charge $g_D = 68.5e$ —implies a strong magnetic dipole moment, which may result in strong binding of the monopole with the nuclei of the aluminium MMTs. In such a case, the presence of a trapped monopole would be detected through the induction technique by measuring the *persistent current*, defined as the

¹⁸⁰ For general information on the MoEDAL experiment, see: <http://moedal.web.cern.ch/>.

difference between the superconducting magnetometer currents before and after the passage of the MMT bar through the sensing coil [393, 394].

The only non-passive MoEDAL sub-detector is an array of TimePix pixel devices distributed throughout the MoEDAL cavern, forming a real-time radiation monitoring system of HI beam-related backgrounds. The operation in time-over-threshold mode allows a 3D mapping of the charge spreading in the volume of the silicon sensor, thus differentiating between various particles species from mixed radiation fields and measuring their energy deposition.

The MoEDAL detector is designed to fully exploit the energy-loss mechanisms of magnetically charged particles [395–398] in order to optimise its potential to discover these messengers of new physics. Multiple theoretical scenarios have been proposed over the years in which magnetic charge would be produced at the LHC [392], resulting in such possible new particles as light γ Hooft–Polyakov monopoles [397–399], electroweak monopoles [400–404], global monopoles [405–410], and monopolium [396, 411–413]. Magnetic monopoles that carry a non-zero magnetic charge and dyons possessing both magnetic and electric charge are predicted by many theories including grand-unified and superstring theories [414–416].

A possible explanation for the non-observation of monopoles so far is Dirac’s proposal [395, 396, 411] that monopoles are not seen freely because they form a bound state called *monopolium* [412, 413, 417, 418] being confined by strong magnetic forces. Monopolium is a neutral state, difficult to detect directly at a collider detector, although its decay into two photons would give a rather clear signal for ATLAS and CMS [419]. Nevertheless the LHC radiation detector systems can be used to detect final-state protons $pp \rightarrow pXp$ exiting the LHC beam vacuum chamber at locations determined by their fractional momentum losses [420]. Such a technique would be appealing for detecting monopolia.

The MoEDAL detector is also designed to search for any massive, long-lived, slow-moving particles [390, 391] with single or multiple electric charges arising in many scenarios of physics BSM. Supersymmetric LLPs [421], quirks, strangelets, Q-balls, and many others fall into this category [392]. A generic search for high-electric-charge objects is currently underway.

For the 2016 run at 13 TeV, the MMT included 672 aluminium rods (for a total mass of 222 kg) that were placed 1.62 m from the IP8 LHC IP under the beam pipe on the side opposite to the LHCb detector. The MMT bars were analysed and no magnetic charge $> 0.5g_D$ was detected in any of the exposed samples when passed through the ETH Zurich SQUID, which is a DC SQUID long-core magnetometer [422]. Hence cross section limits are obtained for Drell–Yan pair production of spin-1, spin-1/2 and spin-0 monopoles for $1g_D \leq |g| \leq 5g_D$ at 13 TeV [422] improving previous bounds set by MoEDAL at 8 TeV [311] and 13 TeV [423]. Monopole production via photon fusion is also now considered in MoEDAL monopole search analyses [424] following recent studies [425]. However, the large monopole-photon coupling invalidates any perturbative treatment of the cross section calculation and hence any result based on the latter is only indicative. This situation may be resolved if thermal production in heavy-ion collisions—that does not rely on perturbation theory—is considered [426], or by including a magnetic-moment term in monopoles with spin [425].

To recapitulate, under the assumption of Drell–Yan cross sections, MoEDAL has derived mass limits for $1g_D \leq |g| \leq 5g_D$, complementing ATLAS results [215, 427], which placed limits for monopoles with magnetic charge $|g| \leq 1.5g_D$, as shown in figure 58. The ATLAS bounds are better than the MoEDAL ones for $|g| = 1g_D$ due to the higher luminosity delivered in ATLAS and the loss of acceptance in MoEDAL for small magnetic charges. On the other

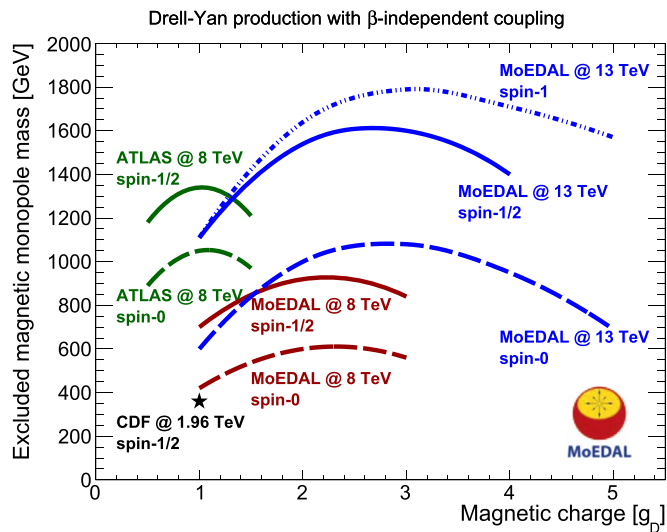


Figure 58. Magnetic monopole mass limits from CDF [429], ATLAS [215] and MoEDAL searches [311, 422] as a function of magnetic charge for various spins, assuming a Drell–Yan pair-production mechanism.

hand, higher charges are difficult to be probed in ATLAS due to the limitations of the level-1 trigger deployed for such searches. Limits on production cross sections of singly-charged magnetic monopoles set by various colliders are presented in [414, 415], while general limits including searches in cosmic radiation are reviewed in [428].

MoEDAL is proposing to deploy the MoEDAL apparatus for detecting penetrating particles (MAPP) in a tunnel shielded by some 30–50 m of rock and concrete from the IP8 [430, 431]. A prototype of the MAPP detector was installed in 2017. It is envisaged that the full detector will be installed in LS2 to take data in LHC Run 3. The purpose of the detector is to search for particles with fractional charge as small as one-thousandth the charge of an electron. This detector would also be sensitive to neutral particles from new physics scenarios via their interaction or decay in flight in the ~ 10 m decay zone in front of the detector or in the detector itself. The isolation of the detector means that the huge background from SM processes in the main detectors is largely absent. Also, the detector can be placed at various angles to the beam axis (from 5° to 25°). The ability to vary depth and angle enhances MoEDAL to be able to distinguish between theoretical scenarios in the event a signal is observed.

The first apparatus specifically designed to detect mini-charged particles was the Stanford Linear Accelerator Centre (SLAC) ‘beam dump’-type detector, comprising scintillator bars read out by photomultiplier tubes [432]. MoEDAL’s new detector, shown in figure 59, and milliQan (discussed above in section 5.3.3) proposed for deployment near to the CMS detector [102] also designed to search for mCPs, both have a design that harks back to the original SLAC detector. In order to reduce backgrounds from natural radiation the photomultiplier tubes and scintillator detectors of the MoEDAL apparatus will be constructed from materials with low natural backgrounds currently utilised in the astroparticle-physics arena. Its calibration system utilises neutral density filters to reduce the received light of high incident muons that manage to penetrate to the sheltered detector from the IP, in order to mimic the much lower light levels expected from particles with fractional charges.

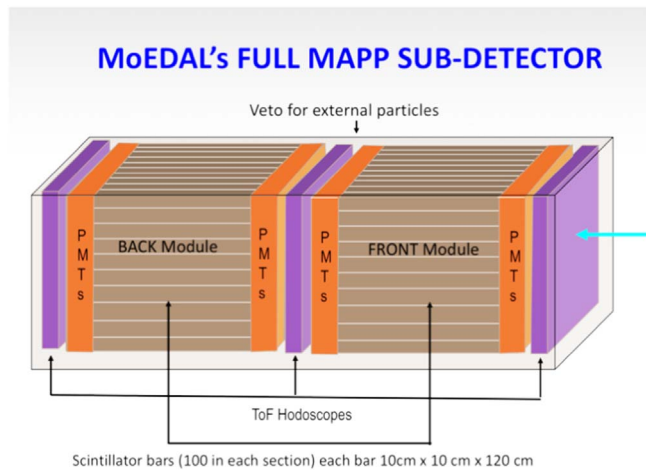


Figure 59. A depiction of the MoEDAL’s MAPP sub-detector [431].

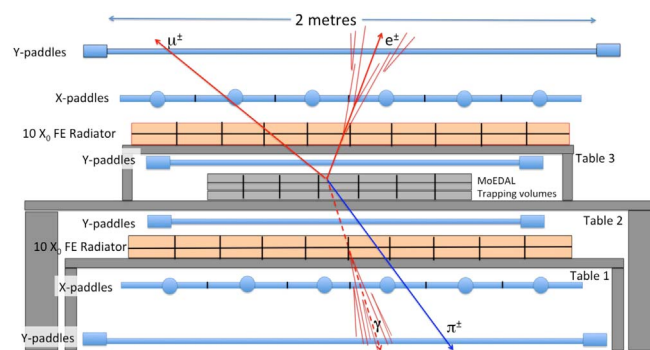


Figure 60. The MALL sub-detector designed to monitor MoEDAL trapping volumes for the decays of trapped electrically charged particles with lifetimes as long as 10 years [431].

MoEDAL is also planning another new sub-detector called MALL (MoEDAL apparatus for detecting extremely long lived particles) [431]. In this case MoEDAL trapping volumes, after they have been scanned through the ETH Zurich SQUID facility to identify any trapped monopole will be shipped to a remote underground facility to be monitored for the decay of pseudo-stable massive charged particles that may also have become trapped. MALL is the detector that monitors MoEDAL trapping volumes for decays of captured particles. It is envisaged that MALL will be installed deep underground at SNOLAB in Canada where cosmic backgrounds are minimised to one muon per $0.27 \text{ m}^2 \text{ d}^{-1}$. Background is further reduced by the ability to determine if a detected track originated within the monitored volume and also by energy cuts on deposited signals. A schematic view of the detector is shown in figure 60. Initial estimates indicate that lifetimes up to around 10 years can be probed. The MALL detector is designed to be sensitive to charged particles and to photons, with energy as small as 1 GeV. It is envisaged that construction of the detector will begin after the MAPP detector is full deployed.

The possibility of analysing decommissioned parts of the LHC beam-pipe system at the ATLAS, CMS and LHCb/MoEDAL sites with a SQUID to search for trapped magnetic monopoles has been proposed [433]. In this context the MoEDAL experiment may serve as a formal platform for coordinating machining, scanning and analysis work, in collaboration with interested ATLAS, CMS and LHCb members.

The induction technique has been successfully employed at the LHC with the dedicated MoEDAL trapping detector. Additional searches for trapped monopoles in beam pipe material would access wide windows of magnetic charges and production cross sections to which other LHC experiments are insensitive. The decommissioned central beryllium beam pipe sections of ATLAS and CMS, with a 4π coverage and exposure to the highest rates of 7 and 8 TeV pp collisions, are by far the most attractive samples to be analysed. The analysis on the CMS beam pipe is expected to be carried out in 2019.

5.3.3. The milliQan experiment. MilliQan is a dedicated experiment at the LHC to search for mCP [102, 434]. The milliQan experiment is part of a general program to search for hidden sectors [435] and other BSM scenarios [436]. As an illustrative example, we show the sensitivity of milliQan to an extra Abelian gauge field coupled to a massive Dirac fermion ('dark QED') that mixes with hypercharge through the kinetic term [122]. The result is that the new matter field is charged under hypercharge with a fractional electric charge of ϵ , where $\epsilon \ll 1$. The milliQan experiment targets an unexplored part of the parameter space, namely mCP masses $0.1 \leq M_{\text{mCP}} \leq 100$ GeV, for charges Q at the $10^{-3} e - 10^{-1} e$ level.

The experimental apparatus consists of three scintillator detector layers of roughly 1 m^3 each, positioned near one of the high-luminosity IPs of the LHC. The experimental signature consists of a few photo-electrons (PE) arising from the small ionization produced by the mCPs that travel unimpeded through material after escaping the LHC detectors.

The milliQan experiment is planned to be sited in the PX56 Observation and Drainage gallery above the CMS underground experimental cavern. The proposed gallery is limited in space. The detector will be located in this tunnel at an optimized location that is 33 m from the CMS IP, behind 17 m of rock, and at an angle of 43.1 degrees from the horizontal plane. The selected location in a 3D model is shown in figure 61.

The milliQan detector is a $1 \text{ m} \times 1 \text{ m} \times 3 \text{ m}$ plastic scintillator array. The array will be oriented such that the long axis points at the nominal CMS IP. The array is subdivided into 3 sections each containing $400 \text{ cm} \times 5 \text{ cm} \times 80 \text{ cm}$ scintillator bars optically coupled to high-gain photomultiplier tubes (PMTs). The detector will be shielded from other background sources such as activity in the scintillator and environmental radiation. With an estimated detection efficiency of about 10%, milliQan expects an average of $\mathcal{O}(1)$ PE from each attached phototube for each mCP with $Q = \mathcal{O}(10^{-3}) e$ that traverses 80 cm of plastic scintillator. The signal is a longitudinal triple-incidence of hits with one or more PEs; a triple-incidence within a 15 ns time window along longitudinally contiguous bars in each of the three sections is required to reduce the background from dark-current noise. Requiring triple-incidence is expected to control background to $\mathcal{O}(10)$ events per year with $N_{\text{PE}} \geq 1$. The milliQan detector will self-trigger to a dedicated readout with no dead time from readout, up to rates of ~ 1 kHz. Energy calibration will be done *in situ* using an ^{241}Am source.

The dominant background is expected to come from dark-current pulses in the PMTs. Pulses from background radiation, including cosmic muons, will consist of 1000s of PEs that can be easily vetoed offline. Assuming a total background rate per PMT of $\nu_B = 500$ Hz, with a time window of $(\Delta t)_{\text{online}} = 100$ ns, milliQan expects a double coincident trigger rate per board of 1.5 Hz. The entire detector will be read out if one board triggers and there will be 50 such boards in total. Therefore, the full background trigger rate is expected to be 75 Hz.

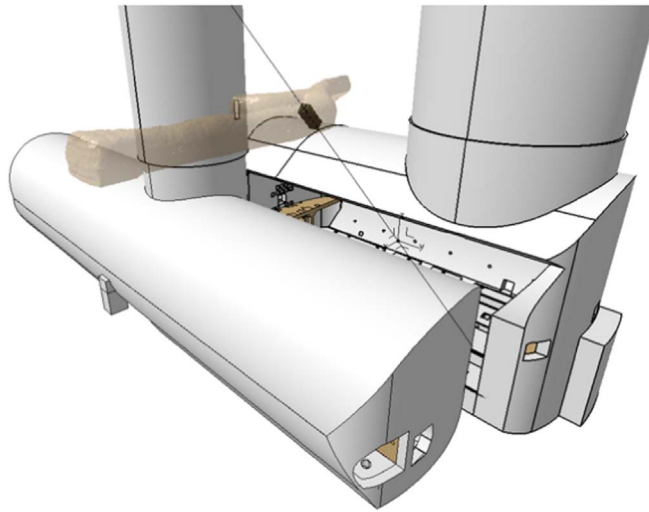


Figure 61. A 3D model showing the optimal position of milliQan within the PX56 Drainage and Observation gallery located above CMS UXC.

Offline, the time window will be tightened to $(\Delta t)_{\text{offline}} = 15$ ns, yielding an offline background rate for a triple coincidence of 2.8×10^{-8} Hz. Since there are 400 such sets, the total offline background rate is estimated to be 1.1×10^{-5} Hz. With these background rates, milliQan estimates a total of 165 (330) background events in 300 (3000) fb^{-1} of integrated luminosity.

The milliQan collaboration has performed a full simulation of the experiment to evaluate the projected sensitivity to various mCP electric charges and masses. The simulation is performed in two stages. In the first, the production of mCP particles via Drell–Yan, J/Ψ , Υ (1S), Υ (2S), and Υ (3S) channels at a center-of-mass energy of 14 TeV is performed. Particles produced at the IP are propagated to the proposed experimental site described above using a map of the CMS magnetic field. The effects of multiple scattering and energy loss are included using a simplified model of the CMS detector material budget and a region of rock spanning 17 m between the CMS experimental cavern and the proposed experimental site. The number of expected mCP particles per fb^{-1} of integrated luminosity incident at the detector is computed as a function of the mass of the mCP. The signal efficiency is then estimated after processing the calculated particles as they would emerge from the IP through a full GEANT4 simulation of the detector; this is necessary because the small charge regime is sensitive to details such as the reflectivity, the light attenuation length, and the shape of the scintillator. These details, as well as the quantum efficiency, light-emission spectrum and the fast-time constants were modeled in GEANT4 using the specifications provided by the manufacturers for the scintillator and PMTs. Combining the estimated background rates discussed above with the cross sections, acceptances and efficiencies calculated for all masses and electric charges, the sensitivity projections of the milliQan experiment for LHC and HL-LHC are shown in figure 62.

A 1/100 scale ‘demonstrator’ of milliQan to validate the detector concept was installed in the PX56 location at CERN during Technical Stop 2 of 2017 and was upgraded during the 2017–2018 year-end technical stop. This demonstrator, shown in figure 63, has been recording data since its installation, and expects to have first results later this year. If funding

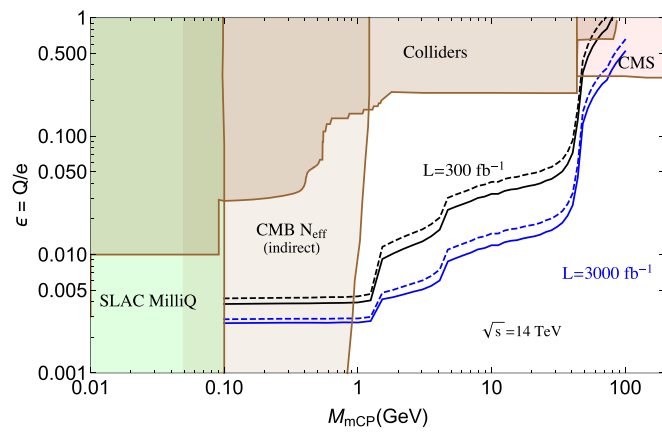


Figure 62. The expected sensitivity of the milliQan experiment for different LHC luminosity scenarios. The black line shows the expected 95% C.L. exclusion (solid) and 3σ sensitivity (dashed), assuming 300 fb^{-1} of integrated luminosity. In blue is shown the corresponding expectations for 3000 fb^{-1} .



Figure 63. The 1/100 scale ‘demonstrator’ of milliQan installed in the PX56 drainage gallery 33 m from the CMS IP.

is secured, construction of the full milliQan apparatus is planned for 2019, with installation in the tunnel in 2020.

5.3.4. The MATHUSLA experiment. The basic motivation for the MASSive Timing Hodoscope for Ultra-Stable neutral pArticles (MATHUSLA) detector [103] is the search

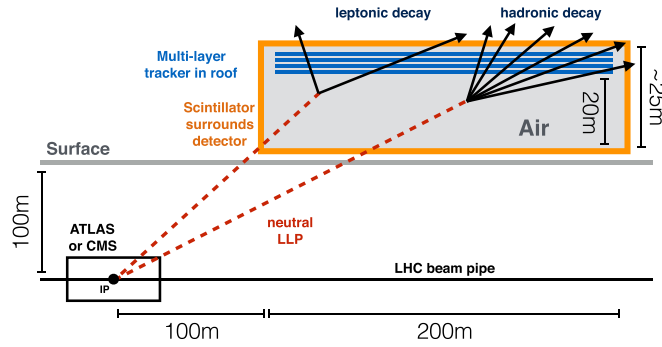


Figure 64. Simplified MATHUSLA detector layout showing the position of the $200\text{ m} \times 200\text{ m} \times 20\text{ m}$ LLP decay volume.

for LLPs with lifetimes much greater than the size of the LHC main detectors, $c\tau \gg 100\text{ m}$. Any detector that can be reasonably constructed could only catch a small fraction of such LLPs decaying inside of its volume. Even with potentially large LLP production rates at the LHC, suppression of backgrounds is therefore crucial for discovery.

For LLP searches with high-energy or lepton-containing final states, the spectacular nature of displaced-vertex (DV) signals leads to very low backgrounds in searches at LHC detectors such as ATLAS or CMS. Any other class of LLP signature suffers from backgrounds and triggering limitations that can be significant. This greatly curtails the main detectors' ability to discover LLPs with very long lifetimes.

To address this broad blind spot of existing detectors, MATHUSLA is proposed to be a large, relatively simple surface detector that can robustly reconstruct DVs with good timing resolution. This gives MATHUSLA a similar geometric acceptance to LLP decays in the long-lifetime limit as the main detectors, while providing shielding from QCD backgrounds and sufficient tracking to reject ubiquitous CRs. As a result, MATHUSLA is able to detect LLPs produced with $\sim 1\text{ pb}$ cross sections at the HL-LHC with lifetimes near lifetimes of $\sim 0.1\text{ s}$, which is generally the limit imposed by big-bang nucleosynthesis (BBN).

The simplified detector design for MATHUSLA is shown in figure 64. The main component of the detector is a tracker array situated above an air-filled decay volume that is 20 m tall and $200\text{ m} \times 200\text{ m}$ in area. The tracker should have on the order of five planes to provide robust tracking with $\sim\text{ns}$ timing and $\sim\text{cm}$ spatial resolution. The current MATHUSLA design employs proven and relatively cheap technologies to allow for MATHUSLA's construction in time for the HL-LHC upgrade. Therefore, the trackers are envisioned to be implemented with resistive plate chambers (RPCs), which have been used for very large area experiments in the past [437, 438], while plastic scintillators provide the surrounding veto.

This minimal design has been shown to be capable of measuring the LLP boost on an event-by-event basis [439] using the geometry of the LLP visible decay products. Final-state multiplicity provides a straightforward discriminant between hadronic and electromagnetic decays. Additional particle identification capability, as well as detection of final-state photons, might be possible by inserting an additional material layer between tracking layers to induce an electromagnetic shower that can be used to distinguish electrons, photons and muons.

As argued in [103], MATHUSLA could search for LLPs decaying into charged particles with little or no backgrounds. In figure 64 is shown, schematically, the two main MATHUSLA signals, LLPs decaying into at least two charged leptons, or into jets that

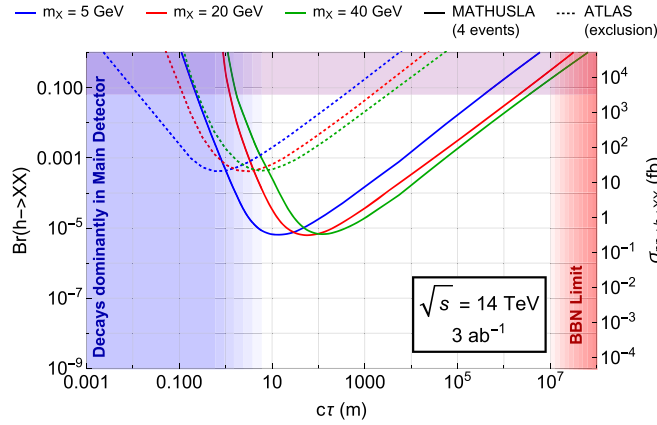


Figure 65. Sensitivity of MATHUSLA to hadronically decaying LLPs produced in exotic Higgs decays, where the solid lines correspond to four decays in the detector [103]. The dotted lines are the most optimistic ATLAS projection, using a very inclusive search for a single DV in the muon chamber [262].

contain $\mathcal{O}(10)$ charged hadrons [439]. In 50%–90% of leptonic decays and practically 100% of hadronic decays [439], two or more charged particles hit the ceiling due to the LLP boost and are recorded by the tracker. The charged particle trajectories can be fitted to reconstruct a DV. Unlike most analyses in the main detectors, these DVs must satisfy the additional stringent requirement that all trajectories coincide in time at the DV. The scintillator is used as a veto to ensure that the charged particles originate at the DV: there can be no hits along the line between the vertex and the LHC main IP, nor along the lines obtained by extrapolating the individual charged particle trajectories backwards. These exhaustive geometric and timing requirements make it extremely difficult for backgrounds to fake the LLP signal. Cosmic rays can be rejected since they travel in the wrong direction (as well as occurring mostly in CR showers with extremely highly correlated particle multiplicity in the detector). Muons from the LHC collision do not satisfy the DV signal requirement. The rare occasions in which muons scatter inside the decay volume can be vetoed with the scintillators. Finally, neutrinos from CRs and LHC collisions can scatter in the decay volume and produce DV, but those can also be rejected with geometric and timing requirements. We refer the reader to [103] for more details. More comprehensive studies of these backgrounds and their rejection strategies, including full simulations, are currently in progress.

An important general class of signals are LLPs with masses ~ 100 GeV that decay hadronically and are produced without other highly visible signals like high MET or high-energy leptons. MATHUSLA can improve the sensitivity to these LLP production cross sections by a factor of $\sim 10^3$ compared to searches with the main detectors alone. This is illustrated in figure 65, which shows MATHUSLA’s sensitivity to hadronically decaying LLPs produced in exotic Higgs decays [103] compared to an optimistic projection for searches for a single DV in the ATLAS MS [262]. For branching ratios of $\sim 10\%$, the BBN lifetime limit [440] can be probed.

Apart from reaching the BBN upper limit or ceiling of LLP parameter space, MATHUSLA extends the power of other LHC measurements. If a $\sim 10\%$ invisible branching ratio for the Higgs was detected via coupling measurements at the HL-LHC, the absence of a MATHUSLA signal would lend strong support to the interpretation that the Higgs decayed to a stable component of DM.

Beyond LLPs produced in rare Higgs decays, MATHUSLA is a general-purpose LLP detector that is sensitive to a wide range of other models. Its reach for other BSM scenarios has been explored in [172, 174, 198, 441–447]. The general physics case for MATHUSLA’s construction is made systematically in the recently released whitepaper [2].

It is important to point out that MATHUSLA is a very flexible detector concept that is completely scalable. The sensitivity of MATHUSLA is roughly proportional to the decay volume (which scales with surface area) and roughly independent of the precise geometry or location of the detector, as long as it is $\mathcal{O}(100\text{ m})$ horizontally displaced from the IP. Therefore, a detector with smaller or larger volume than the benchmark in figure 64 may be implemented, depending on available space and budget. Furthermore, the detector volume can be divided into smaller, independent modules (which cooperate for triggering purposes). These can be mass-produced economically and arranged according to the requirements of the experimental site. Such a modular construction also allows for a natural way to improve or extend the physics program of the experiment in an efficient way, by eventually upgrading, for example, one or a few modules with additional capabilities, such as higher tracking resolution for reconstruction of very low-mass LLPs below 10 MeV, or an additional material layer between the trackers for particle ID.

The MATHUSLA collaboration is currently studying such a modular design with the aim of producing a Letter-of-Intent in 2018. Crucial to this endeavor is the data from the MATHUSLA test stand, a $\sim 3 \times 3 \times 5\text{ m}$ MATHUSLA-type detector that took a few days of data in the ATLAS instrument hall in 2017 and will take data for a few months in 2018. This allows local CR backgrounds to be measured, background rejection and signal reconstruction strategies to be tested, and simulation frameworks to be calibrated.

In conclusion, the MATHUSLA detector concept calls for a dedicated LLP surface detector above ATLAS or CMS. A detector volume of $\sim 10^6\text{ m}^3$ gives sensitivity to LLPs near the BBN lifetime limit if they are produced with $\sim\text{pb}$ cross section. This improves LLP sensitivity, compared to the main detectors alone, by several orders of magnitude for many LLP scenarios. The detector is simple and relies on proven technology, making its construction in time for the HL-LHC upgrade feasible. Once constructed, MATHUSLA could function without modification as a detector for the HE-LHC (with increased sensitivity). A small-scale test stand detector is already taking data at CERN, and studies are underway to finalize a detailed design for the full-scale detector.

5.3.5. A COmpact Detector for EXotics at LHCb (CODEX-b). The CODEX-b proposal involves housing a small detector in the LHCb cavern—external to the LHCb detector itself—in a space approximately 25 m from the interaction point (IP8), behind the 3 m thick concrete UXA shield wall. This space is presently occupied by the LHCb data acquisition (DAQ) system, but will become available before Run 3 once the DAQ system is relocated to the surface. The layout of the cavern is shown in figure 66, with the location of CODEX-b overlaid. The nominal CODEX-b configuration features a $10 \times 10 \times 10\text{ m}$ volume instrumented with RPC tracking layers or other off-the-shelf tracking technology, as well as roughly 25 interaction lengths of shielding near IP8—e.g. 4.5 m of Pb—to suppress primary and secondary K_L , neutron, and other hadronic backgrounds. This shield requires an active muon veto with an efficiency of $\mathcal{O}(10^{-5})$, in order to reject backgrounds induced by muons or other charged particles in the downstream parts of the shield. The veto is located several metres within the shield such that backgrounds induced by neutral particles remain suppressed. See [104] for a study of a proof-of-concept example detector layout and corresponding tracking efficiency, as well as a detailed study of the backgrounds. More

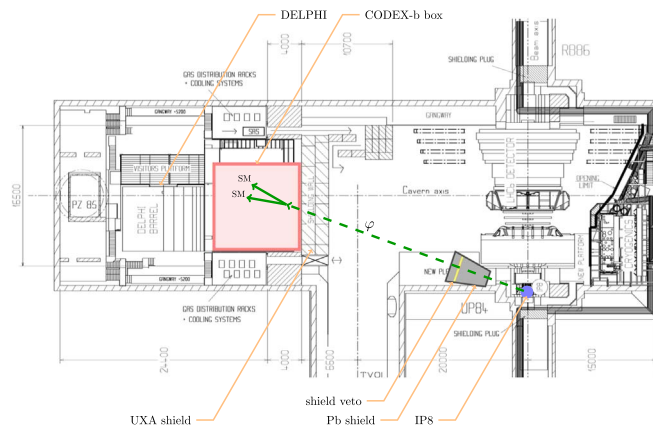


Figure 66. Layout of the LHCb experimental cavern UX85 at point 8 of the LHC [448], overlaid with the proposed CODEX-b location. From [104].

ambitious technologies, including calorimetry, precision TOF measurements, or integration into the LHCb readout may also be feasible.

For the current discussion, the reach of CODEX-b for two benchmark models is quantified: first, a light scalar field, φ , that mixes with the SM Higgs boson is considered. If $m_\varphi \lesssim 5$ GeV, the production mode is primarily through inclusive $b \rightarrow s\varphi$ decays [449–451]. The LLP φ subsequently decays back to SM fermions through the same Higgs portal. The reach in terms of m_φ and the mixing angle s_θ is shown in the left-hand panel of figure 67. CODEX-b significantly extends the projected reach of LHCb using only VELO-based DV reconstruction, and covers part of the parameter space to which SHiP [452] and MATHUSLA [443] are projected to be sensitive. Studies of the potential LHCb reach to longer lifetimes using downstream tracking are ongoing [378, 453]. The right-hand panel of figure 67 indicates the reach for more general models, where the lifetime and production rate of φ are unrelated.

For the second benchmark, a dark boson, γ_d , produced through the exotic Higgs decay $h \rightarrow \gamma_d \gamma_d$ is considered. For concreteness the γ_d is taken to be a spin-1 field which can decay through mixing with the SM photon [70, 230, 456, 457]. In this benchmark, the production and decay are therefore controlled by different portals. The projected reach is shown in figure 68, overlaid with the reach of ATLAS [262, 273] and MATHUSLA [103]. In particular, at low γ_d masses, CODEX-b complements and significantly extends the reach of ATLAS and CMS.

Finally, it might be possible to install a larger version of the CODEX-b detector at IP2, after the ALICE collaboration concludes its heavy ion program. This option is named ‘A Laboratory for Long-Lived eXotics’ (AL3X) [459], and can make use of the existing ALICE TPC, supplemented with a thick hadron absorber. The B-field from the L3 magnet would provide a good momentum measurement of the tracks, something which is absent in MATHUSLA and CODEX-b. The feasibility of this proposal is however contingent upon a luminosity upgrade of IP2, as well as the possible continuation of the ALICE physics during Run 5.

5.3.6. The forward search experiment (FASER). If new LLPs are light compared to the weak scale and very weakly coupled, the focus at the LHC on searches for new particles at high p_T

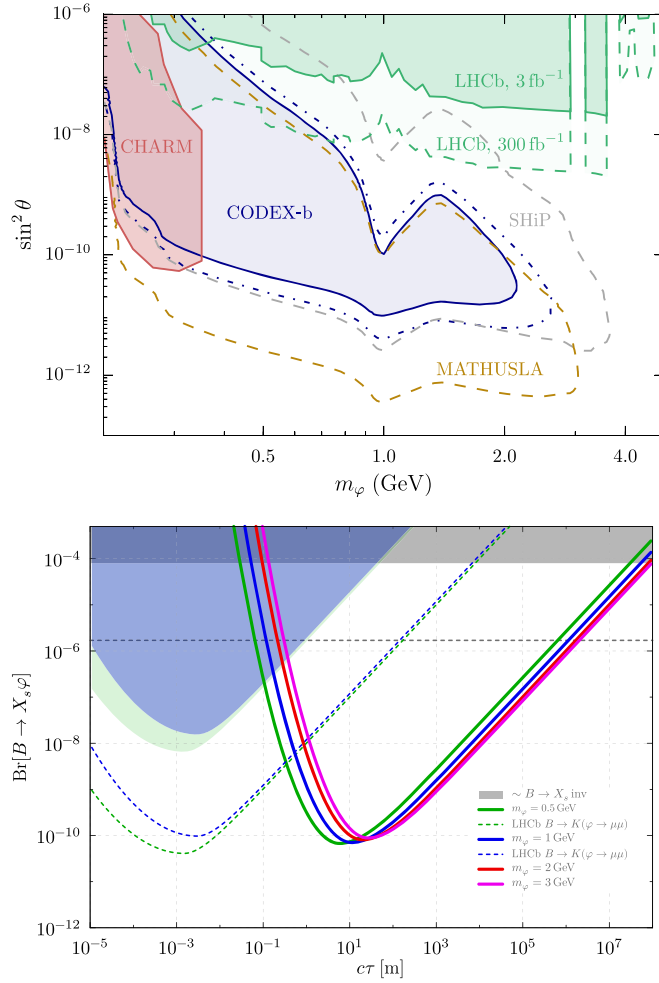


Figure 67. Top: CODEX-b reach for $B \rightarrow X_s \varphi$ in the $s_\theta^2 - m_\varphi$ plane. Solid (dotted-dashed) line assumes $\mathcal{L} = 300 \text{ fb}^{-1}$ ($\mathcal{L} = 1 \text{ ab}^{-1}$). Bottom: inclusive CODEX-b $B \rightarrow X_s \varphi$ reach (solid lines). The shaded regions (dashed lines) indicate current LHCb limits (300 fb^{-1} projection) from $B \rightarrow K(\varphi \rightarrow \mu\mu)$, rescaled to the inclusive process and assuming $\text{Br}[\varphi \rightarrow \mu\mu] \simeq 30\%$ and 10% for $m_\varphi = 0.5 \text{ GeV}$ and 1 GeV , respectively. The gray shaded area and the dashed line indicate the approximate current [454] and projected [455] limits, respectively, for Belle II, from $B \rightarrow K^{(*)} \nu \bar{\nu}$ precision measurements. From [104].

may be completely misguided. In contrast to TeV-scale particles, which are produced more or less isotropically, light particles with masses in the MeV–GeV range are dominantly produced at low p_T . In addition, because the new particles are extremely weakly coupled, very large SM event rates are required to discover the rare new physics events. These rates are not available at high p_T , but they are available at low p_T : at the 13 TeV LHC, the total inelastic pp scattering cross section is $\sigma_{\text{inel}}(13 \text{ TeV}) \approx 75 \text{ mb}$ [460, 461], with most of it in the very forward direction. This implies

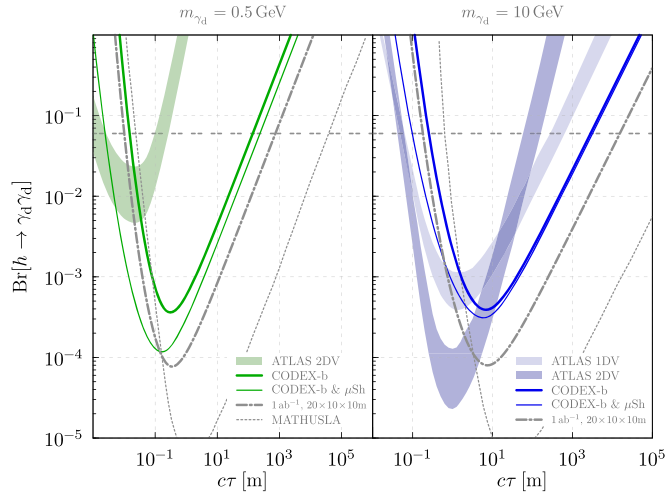


Figure 68. Comparison of experimental sensitivity to the BSM decay of an SM-like Higgs to dark photons with and without the muon shadow (μSh) for a few different existing and proposed detectors. The $\gamma_d \rightarrow \mu\mu$ branching ratio is taken from e^+e^- data [458]. The CODEX-b sensitivity here is the so-called ‘optimistic’ reach, with $\mathcal{L} = 1 \text{ ab}^{-1}$ and a larger volume, assuming DELPHI is removed. From [104].

$$N_{\text{inel}} \approx 2.3 \times 10^{16} (2.3 \times 10^{17}) \tag{5.5}$$

inelastic pp scattering events for an integrated luminosity of 300 fb^{-1} at the LHC (3 ab^{-1} at the HL-LHC). Even extremely weakly-coupled new particles may therefore be produced in sufficient numbers in the very forward region. Due to their weak coupling to the SM, such particles are typically long lived and travel a macroscopic distance before decaying back into SM particles. Moreover, such particles may be highly collimated. For example, new particles that are produced in pion (B -meson) decays are typically produced within angles of $\theta \sim \Lambda_{\text{QCD}}/E$ (m_B/E) off the beam-collision axis, where E is the energy of the particle. For $E \sim \text{TeV}$, this implies that even $\sim 500 \text{ m}$ downstream, such particles will have only spread out $\sim 10 \text{ cm} - 1 \text{ m}$ in the transverse plane. A small and inexpensive detector placed in the very forward region may therefore be capable of extremely sensitive searches to LLPs, provided a suitable location can be found and the signal can be differentiated from the SM background.

Forward search experiment (FASER) [105, 462–465], the is an experiment designed to take advantage of this opportunity. It is a small detector, with volume $\sim 1 \text{ m}^3$, that is proposed to be placed along the beam-collision axis, several hundreds of meters downstream from the ATLAS or CMS IP. In the following, we present a promising location of FASER, discuss the properties of the signal and the required detector design, and present the new physics reach for representative models.

As shown in figure 69, FASER will be placed along the beam collision axis, several hundreds of meters downstream from the ATLAS or CMS IP after the LHC tunnel starts to curve. A particularly promising location is a few meters outside the main LHC tunnel, 480 m downstream from the ATLAS IP, in service tunnel TI12, as shown in the bottom panels of figure 69. (A symmetric location on the other side of ATLAS in tunnel TI18 is also possible.) This tunnel was formerly used to connect the SPS to the LEP tunnel, but is currently empty and unused. As shown on the tunnel map in the lower left panel of figure 69, the beam collision axis passes through TI12 close to where it merges with the main LHC tunnel. A

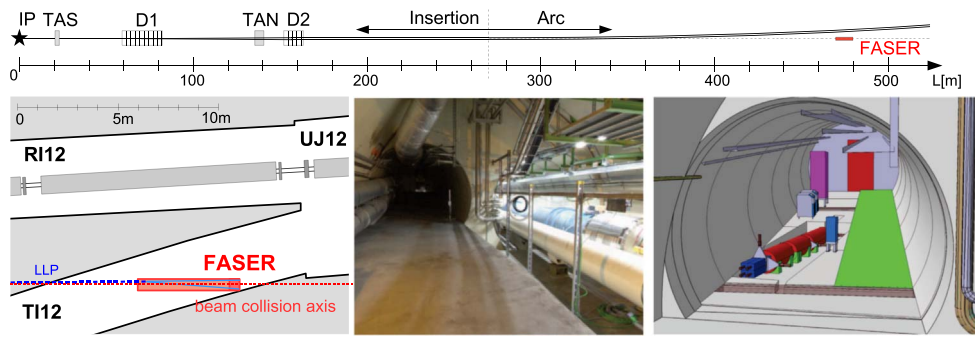


Figure 69. Proposed location for FASER in TI12. Top panel: a schematic drawing of the LHC and the very forward infrastructure downstream from the ATLAS and CMS interaction points; FASER is to be located 480 m from the IP, after the LHC ring starts to curve. Bottom panels: a map of the tunnel TI12 including the beam collision axis (left), a photo of this location (center), and a model of the experiment integrated in the TI12 tunnel (right).

more detailed study of the intersection between the beam collision axis and TI12 verifies that there exists space for FASER in the tunnel, as shown in the lower-right panel of figure 69.

In this location, FASER harnesses the enormous, previously completely unused and unexamined cross section for very forward physics ($\sigma \sim 100$ mb). This cross section implies that even very weakly coupled new particles can be produced in large numbers at the LHC. In addition, the production of LLPs at high center-of-mass energy results in long average propagation distances ($\bar{d} \sim \mathcal{O}(100)$ m) and decays that are far beyond the main LHC infrastructure in regions where the backgrounds are expected to be negligible.

FASER will search for LLPs that are produced at or close to the ATLAS IP in the very-forward direction, travel approximately 480 m, and then decay via $\text{LLP} \rightarrow \text{charged tracks} + X$. When LLPs are produced in the very-forward region of the beam collision axis, they typically have very high energies $E \sim \text{TeV}$. Although the identity of the LLP decay products depends on the mass of the LLP and the concrete new-physics model, some of the standard, characteristic LLP decay signatures are generically expected, such as two or more stable charged particles, such as electrons, muons or pions. This leads to a striking signature at FASER: two oppositely charged tracks with very high energy that emanate from a vertex inside the detector and which have a combined momentum that points back to the IP. A measurement of individual tracks with sufficient resolution and an identification of their charges is therefore imperative if the apparatus is to make use of kinematic features to distinguish signal from background. A tracking-based technology, supplemented by a magnet and a calorimeter to allow for energy measurements, will be the key components of FASER. Details of the detector design can be found in the Letter of Intent [462] and Technical Proposal [464].

The FASER signals consist of two extremely energetic ($\sim \text{TeV}$) coincident tracks or photons starting at a common vertex and pointing back to the ATLAS IP. Muons and neutrinos are the only known particles that can transport such energies through 100 m of rock and concrete between the IP and FASER. The CERN Sources, Targets, and Interactions group has computed the fluxes of muons and neutrinos at the FASER location using a FLUKA simulation [466–468]. These muon fluxes then allow one to estimate the rate and energy spectrum of muon-associated radiative processes near the detector. Preliminary estimates

show that muon-associated radiative processes and neutrino-induced backgrounds may be reduced to negligible levels [464, 464].

Emulsion detectors and battery-operated radiation monitors were installed in both TI12 and TI18 during Technical Stops in 2018. The results from these *in situ* measurements have validated the estimates of the FLUKA simulation, confirming that the high-energy particle background is highly suppressed and radiation levels are also very low and not expected to be problematic for detector electronics. Additional work is ongoing to refine background estimates, evaluate signal efficiencies, and optimize the detector.

In its first stage, FASER is an extremely compact detector, sensitive to decays in a cylindrical region of radius $R = 10$ cm and length $L = 1.5$ m. FASER is planned to be constructed and installed in LS 2 and will collect data during Run 3 of the 14 TeV LHC (2021–23). After FASER’s successful operation, FASER 2, a much larger successor with roughly $R \sim 1$ m and $L \sim 5$ m, could be constructed in LS 3 and collect data during the HL-LHC era (2026–35). More details on the FASER timeline can be found in the Letter of Intent [462] and Technical Proposal [464].

The sensitivity of FASER to detect LLPs has been studied in a plethora of new physics models, including dark photons [105], dark Higgs bosons [469], HNLs [297], axion-like particles (ALPs) [470], iDM [471], flavor-specific scalar mediators [472], $U(1)_{B-L}$ -gauge bosons [473], R -parity violating supersymmetry [60, 174] and SIMPs [474]. A summary on FASER’s physics reach for LLP can be found in [463]. Combined, these studies establish FASER’s significant impact on the LHC’s discovery reach for LLPs. The physics reach at FASER and FASER 2 for these models is shown in figure 70. Here we assume that backgrounds can be reduced to negligible levels. The gray-shaded regions of parameter space have already been excluded by previous experiments. For comparison we also show the projected reaches of other proposed experiments that search for LLPs.

Dark photons and ALPs (upper panels) are mainly produced in the decay of light mesons, via dark bremsstrahlung, or through the Primakoff process, and they are therefore very collimated around the beam collision axis. Already a very small detector is able to probe large and unconstrained regions of parameter space, making dark photons an ideal short-term goal for FASER. In contrast, dark Higgs bosons and HNLs (lower panels) define good long-term physics goals. They are both mainly produced in heavy meson decays, leading to a larger spread around the beam collision axis. A larger, but still relatively small, detector with $R \sim 1$ m is then required to exploit the full potential of FASER.

6. Reinterpretation and recommendations for the presentation of search results

Chapter editors: Giovanna Cottin, Nishita Desai, Sabine Kraml, Andre Lessa, Zhen Liu

Contributors: Juliette Alimena, Will Buttinger, Eric Conte, Yanou Cui, Jared Evans, Benjamin Fuks, Lukas Heinrich, Jan Heisig, Gavin Hesketh, David Michael Morse, Michael Ramsey-Musolf, Ennio Salvioni, Michele Selvaggi, Brian Shuve, Yuhsin Tsai

6.1. Introduction

Models and scenarios with LLPs have seen an enormous rise in interest in recent years. They include supersymmetric scenarios with almost mass-degenerate lightest states [63, 65], highly split spectra [113, 475], very weakly interacting LSPs like gravitinos or axinos [476, 477], or R -parity violation [55, 110, 111], as well as equivalent scenarios in other SM extensions (e.g. extra-dimensional models) with new SM gauge-charged particles. More recent ideas include models with feebly interacting DM [146] (supersymmetric or not), asymmetric DM [478],

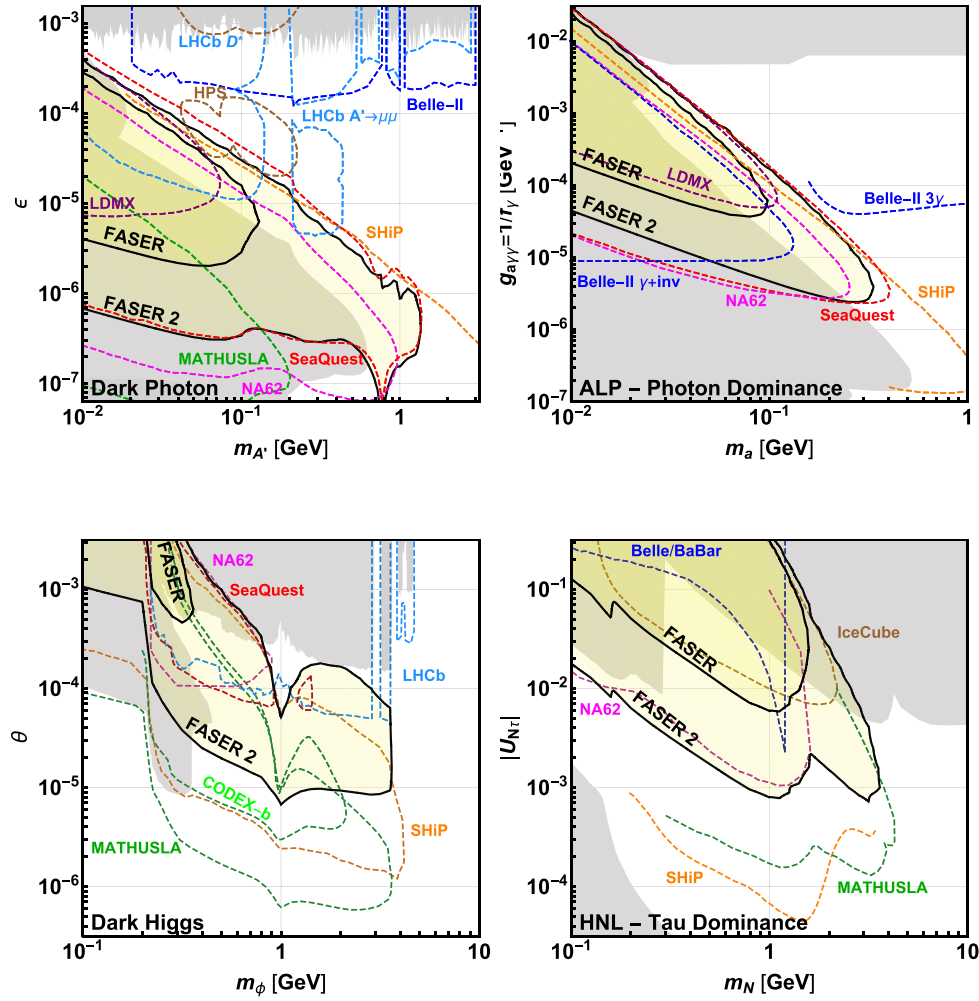


Figure 70. Projected FASER exclusion reach for benchmark new-physics scenarios containing dark photons (top left), ALPs with dominantly photon couplings (top right), dark Higgs bosons (bottom left), and HNLs with dominantly τ -mixing (bottom right) in the corresponding coupling versus mass planes. The gray shaded regions are excluded by current experimental bounds, and the colored contours represent projected future sensitivities of other proposed experiments that search for LLPs. See [463] for details.

HV models [66], and other dark-sector models; for a comprehensive discussion, see the classification of existing well-motivated theories with LLPs in chapter 2.

All of these models can feature a large variety of possible LLP signatures. In HV models [66], for instance, new particles can either decay into invisible dark particles or back to the SM, thus possibly leading to a mix of long-lived and prompt signatures, with or without missing transverse energy (\cancel{E}_T). Furthermore, new theoretical frameworks are constantly emerging, often motivated by new approaches to the hierarchy problem or DM. It is therefore

of great interest to our community to be able to reinterpret the LLP experimental results for new models which may be developed in the future¹⁸².

The reinterpretation of experimental results can generically be done in two ways: by applying appropriate simplified-model results to more complete models, or by reproducing the experimental analysis in a MC simulation. Clearly, the former is easier and faster, while the latter is more generally applicable but also more difficult and much more time consuming¹⁸³.

In the context of searches for prompt signatures with \cancel{E}_T , the use of simplified models has been shown to be a fruitful approach for both the experimental and theoretical communities [74, 76, 78, 87, 88, 480, 481]. Dedicated tools, notably SMOBELS [482–484] and FASTLIM [485], are publicly available and allow the user to reinterpret SUSY simplified-model results within the context of a full model. The coverage of a full model can, however, be severely limited by the kind of simplified-model results available, as discussed recently in [106] for the case of the phenomenological MSSM. Indeed, for some models the large number of relevant simplified-model topologies and their complexity can make the simplified-model approach inexpedient. In this case, a more complete and robust recasting procedure is necessary.

Again, for prompt signatures, a general recasting approach is available through several public tools, notably CHECKMATE [486, 487], MADANALYSIS5 [488, 489], RIVET [490] (v2.5 onwards) and Gambit’s COLLIDERBIT [491]. These tools allow the user to reproduce experimental analyses by means of MC event simulation coupled to an approximate emulation of detector effects¹⁸⁴. For the latter, CHECKMATE and MADANALYSIS5 rely on DELPHES [342], in some cases supplemented with appropriate tuning, while RIVET and COLLIDERBIT employ object smearing and analysis-specific reconstruction efficiencies. The ATLAS and CMS collaborations are helping these recasting efforts by providing more and more detailed information about their analyses and results. As an example, covariance matrices for the background correlations in the framework of simplified likelihoods were provided for the analysis of [492].

The situation is, so far, quite different for LLP searches. First, the presentation of results in terms of simplified models is still limited to a few topologies and does not always include all of the parameters required for a general purpose reinterpretation. It is worth noting that, compared with simplified models for prompt searches, simplified models for LLP searches always have at least one additional free model parameter: the lifetime of the LLP. Second, recasting LLP searches outside of the experimental collaborations is a difficult task since the searches are very sensitive to the detector response, which in most cases cannot be easily emulated by a fast detector simulation (and many backgrounds are also challenging to simulate due to their non-standard nature; see chapter 4 for a full discussion of backgrounds to LLP searches). As a result, while first steps towards the treatment of LLPs were achieved in SMOBELS [493] and MADANALYSIS5 [494], the implementation of LLP searches in public recasting tools is still in its infancy, thus limiting the applicability of the experimental results.

¹⁸² In this context we refer the reader also to the activities of the ‘Forum on the Interpretation of the LHC Results for BSM studies’ [479].

¹⁸³ When no new backgrounds need to be considered and the hypothesized signal does not affect control regions, one can simply determine the event counts in the signal regions and compare them to the 95% C.L. observed limits, or take the numbers of observed events and expected backgrounds to compute a likelihood.

¹⁸⁴ For completeness it should be noted that, while all of these tools include a more-or-less extensive set of SUSY searches, many of the searches for other, ‘exotic’ types of new physics cannot yet be reproduced outside the experimental collaborations. This concerns in particular searches relying on multivariate techniques such as boosted decision trees.

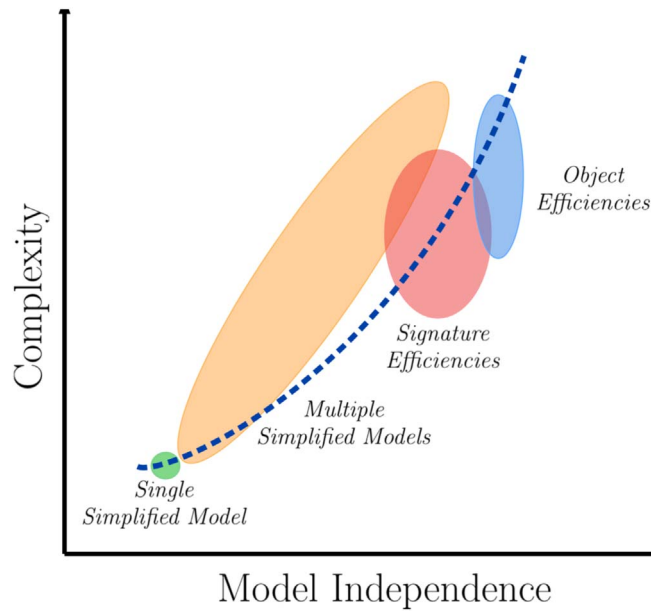


Figure 71. A qualitative overview of the possibilities for the presentation of results discussed in this chapter. The axes represent the complexity of information required by each format and the corresponding level of model independence.

In order to allow for a more extensive reinterpretation or recasting of the experimental analyses, detailed information concerning the detector performance and object reconstruction is needed. These can in principle be provided in the format of efficiencies¹⁸⁵ for selection and reconstruction of relevant objects, as demonstrated already by some pioneering experimental publications [237, 495]. One difficulty in this respect is that the information needed for recasting LLP searches is clearly analysis dependent, which means an additional workload for the analysis groups to provide this information on a case-by-case basis.

The objective of this chapter is to discuss the presentation of LLP search results with the aim that they can be re-used for interpretations beyond the models considered in the experimental publications. To this end, we first discuss in section 6.2 the various options for presenting the LLP results (and for a summary, see figure 71), and compare their advantages and shortcomings. In section 6.3, we discuss in more details how the simplified models defined in section 2 can be used to reinterpret LLP searches. In section 6.4, we present several attempts at recasting LLP searches, according to the LLP signature, focusing on HSCPs and various displaced objects. For each case, we elaborate on the lessons learned from the reinterpretation effort. Section 6.5 presents a first attempt to extend the public detector simulator DELPHES to deal with LLP searches, while section 6.6 focuses on reinterpretations performed within the experiments themselves, including the RECAST framework [496]. In section 6.7, we discuss complementary constraints on LLPs from reinterpreting prompt searches. We conclude in section 6.8 with our recommendations for the presentation of LLP results.

¹⁸⁵ We employ the term ‘efficiency’ in a broad sense. It can refer to reconstruction efficiencies, selection efficiencies, overall signal efficiencies, etc, which will be further specified below.

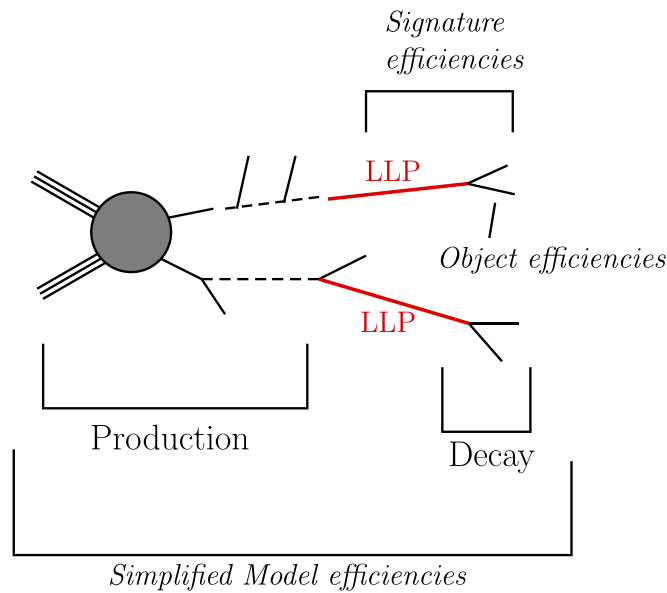


Figure 72. Possibilities for the presentation of results: simplified-model efficiencies assuming a specific topology of LLP production and decay, signature efficiencies assuming only a specific LLP decay, and final-state object efficiencies which are independent of the specific decay mode.

6.2. Options for presenting experimental results

A qualitative view of the various possibilities for presentation of search results is illustrated in figure 71. We broadly classify these possibilities according to the type of information provided for reinterpretation (in other words, the type of efficiency). Each type refers to distinct signal objects, as illustrated in figure 72. As we can see, each possibility relies on distinct assumptions about the signal, resulting in different levels of model dependence. Below, we provide a brief discussion of the advantages and limitations of the various possibilities of presentation of LLP search results. We gradually progress from the simplest case towards more complexity but also better re-usability.

Simplified models. In most cases, the simplified-model topology corresponds to single or pair production of the LLPs, though in principle simplified models for production through cascade decay of heavier states can also be envisaged. In any case, the simplified model incorporates important assumptions on the LLP production mode, decay mode and quantum numbers. Simplified-model results can be presented at different levels of sophistication and re-usability:

- exclusion curves in, e.g. a mass-versus-mass or mass-versus-lifetime plane, are highly model dependent and can rarely be used for reinterpretation without significant effort;
- cross section upper limits¹⁸⁶ can be applied to a larger variety of models in which the same LLP production and decay mode occurs through a rescaling of the cross section times branching ratio factor;

¹⁸⁶ For the sake of re-usability, cross section upper limits in absolute terms are much preferred over limits on the signal strength.

- simplified-model efficiencies go one step further: they make it possible to combine different topology contributions to the same signal region and compute an approximate likelihood using the number of expected and observed events.

The main advantages of simplified models are a parametrization of the signal sensitivity in terms of few physical parameters and a unified language and format applicable to a wide range of searches. Also, when re-using simplified-model results one avoids detector simulation uncertainties. The disadvantages are that the simplified-model result cannot be applied to other LLP production or decay modes, resulting in overly conservative limits if the LLP signal is composed from multiple topologies. This can be important if the LLP is a color singlet, but there are several heavier color-charged states which can be produced and decay to the LLP. In principle this can be overcome if efficiencies are provided for a sufficiently large number of simplified models (including cascade decays), as a function of the simplified-model parameters, which should include the LLP lifetime. These efficiencies can then be combined in order to compute the corresponding constraints to complex models, where multiple topologies are present¹⁸⁷. We stress, however, that in order for this combination to be possible, signal efficiencies and not cross section upper limits must be provided. The major drawback of this approach is that in order for the results to be applicable to a broad class of models, the number of required simplified models and their complexity can easily become very large. For achieving a high level of model independence, it is therefore desirable that the experimental analysis can be recast with MC event simulation. Two ways of presenting results are useful to this end: *signature efficiencies* and *object efficiencies*.

Signature efficiencies. Signature efficiencies are efficiencies for the reconstruction of the main LLP signature treated as a single ‘object’ (single charged track, DV, DT, etc) as a function of the LLP kinematic parameters and the lifetime. Signal efficiencies require the assumption of a specific LLP decay mode, but are otherwise highly model independent since they make no assumption on the LLP production mode. In addition, they are fully model independent for stable particles (within the detector volume), since in this case no assumptions about the LLP decay mode are required at all. In many cases, however, the reconstruction efficiencies depend on multiple kinematic variables, such as the LLP p_T , its transverse decay position, impact parameter, etc. As illustrated in section 6.4.6, these efficiencies can be very useful for recasting LLP searches, but they are not often provided by the experimental collaborations. Many recasting efforts consist of extracting these efficiencies from the provided information, but this procedure can result in large uncertainties.

Object efficiencies. Object efficiencies are efficiencies for the reconstruction of the physics objects relevant for building the LLP signature; for example, if an analysis reconstructs DV out of tracks, the associated object efficiencies would be the efficiency of reconstructing each displaced track that is later combined to form the vertex. They can clearly be applied to a wide range of LLP decay and production modes, since no specific assumptions about either is required. For instance, a displaced lepton reconstruction efficiency can be provided as a function of the lepton p_T and its transverse impact parameter d_0 . As discussed in section 6.4.2, these efficiencies can be used to recast LLP searches to an acceptable accuracy ($\sim 20\%$). Furthermore, as illustrated in section 6.4.6, knowledge of object efficiencies are essential for a general purpose recasting of the search. Within this approach the model dependence is minimal and can be restricted to a few general assumptions about the nature of the LLP. Also, object efficiencies could be included in fast-detector simulators, thus

¹⁸⁷ These points are illustrated by the reinterpretation of the CMS search for HSCPs [495] discussed in section 6.3: for the specific model considered in [97], constraints obtained using only a single simplified model (direct production of $\tilde{\tau}$ s in this case) can underestimate the bounds on the LLP mass by almost a factor of two.

providing a way of recasting LLP searches on a similar footing as prompt searches. The main difficulty with providing such object efficiencies is the potentially large number of parameters required for their parametrization.

6.3. Reinterpretation using simplified models

One of the possibilities for extending the experimental results from LLP searches to a large variety of scenarios is through the use of simplified-model topologies. Simplified models (or simplified-model spectra, SMS) have been widely used for the interpretation of prompt and LLP searches. As discussed in chapter 2, a large number of SMS topologies are possible for the distinct LLP signatures, which can be grouped by the LLP production mode, decay and lifetime. These SMS topologies aim to capture the main physical properties of the LLP signal and can then be used to constraint other scenarios containing similar topologies. The use of simplified-model results to constrain full models has been shown to be possible [93, 106, 482, 485, 497, 498], even though it has its shortcomings [106]. Also within the context of LLP searches, the use of simplified model results for reinterpretation can be a good alternative, e.g. when a recasting based on a MC simulation is difficult or is too computationally expensive. In this section, we briefly review how SMS results can be used to reinterpret searches for full models as well as the particular challenges presented by LLP searches. A concrete example of reinterpretation using simplified models is given in section 6.3.2, based on the results of [97].

6.3.1. From simplified to full models. The interpretation of experimental results using simplified models typically corresponds to producing upper limits on the production cross section or signal efficiencies for a specific SMS topology (production and decay channel). These results are provided as a function of the simplified model parameters, which have been largely taken to be the masses of the BSM particles appearing in the topology. For LLP topologies, however, a new parameter must be considered: the LLP lifetime (see chapter 2). With the exception of searches for stable particles, the lifetime is one of the main parameters affecting the topology efficiency and upper limit.

Once signal efficiencies¹⁸⁸ (ϵ) are provided for one or more SMS topologies, these can be used, under some approximations, to quickly compute the number of expected signal events (S) for a full model:

$$S = \mathcal{L} \times \left(\sum_{\text{SMS}} \sigma_{\text{SMS}} \times \text{BR}_{\text{SMS}} \times \epsilon_{\text{SMS}} \right), \quad (6.1)$$

where \mathcal{L} is the luminosity for the respective search and the sum runs over simplified model topologies. Since the production cross section (σ_{SMS}) and branching ratios (BR_{SMS}) for each topology can be quickly computed for any full model, the simplified model signal efficiencies (ϵ_{SMS}) can be directly used to obtain the signal yield. This procedure does not rely on any MC simulation or recasting of LLP searches and can be easily applied to a wide variety of models, provided ϵ_{SMS} is known. The main limitation of this approach comes from the limited (although growing) number of SMS results available. Since ϵ_{SMS} is typically known only for very few simplified models, the sum in equation (6.1) is limited to the number of available topologies, resulting in an under-estimation of S .

¹⁸⁸ For simplicity we will refer to the signal acceptance times efficiency as ‘signal efficiency’. This efficiency is a function of the simplified model parameters, including the LLP lifetime.

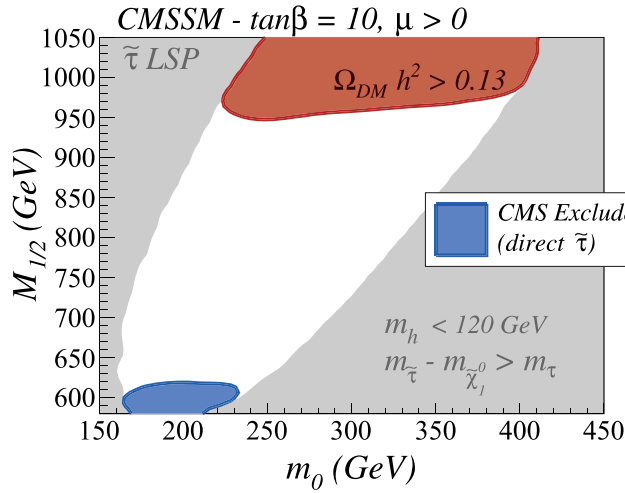


Figure 73. Region of the CMSSM parameter space with long-lived NLSP staus. The light gray regions are excluded by the requirements $m_{\tilde{\tau}} - m_{\tilde{\chi}_1^0} > m_{\tau}$ and $m_h < 120$ GeV. The top red region is excluded by the upper limit on the neutralino relic density, while the lower blue region is excluded by the CMS constraints on direct production of long-lived staus. For more details see [97].

For prompt SUSY searches, a systematic approach for reinterpreting simplified model results based on the procedure outlined above has been developed in [482, 485]. Furthermore, using the large number of available SUSY SMS results, public tools are available for constraining full models using these results [483, 485]. The same procedure can also be applied to LLP SMS results, as shown in [97] for the case of HSCPs and implemented recently in SMOBELS [493]. In the next section we review some of the results found in [97]. Although these have been obtained within the context of HSCPs, the main results can be generalized to other LLP signatures, and demonstrate some of the advantages and shortcomings of reinterpretations using LLP simplified models.

6.3.2. Reinterpretation using HSCP simplified models. The CMS search for HSCPs in [495] provided signal efficiencies for the simplified model topology $pp \rightarrow \tilde{\tau}\tilde{\tau}$ as a function of the stau mass. In the language of the simplified models of section 2.4.2, this is the direct pair production mode of a charged LLP. The stau is assumed to be stable (at detector scales), thus producing a highly ionizing track, which can be used to search for this scenario (see section 3.5). Since the stau lifetime (τ) is assumed to be $\gg 10$ ns, the signal efficiencies do not depend on τ , thus simplifying the SMS parameter space, which reduces to the stau mass¹⁸⁹. The relevant selection efficiencies required for a general purpose MC recasting of the HSCP search have also been provided by the CMS analysis; see section 6.4.1 for details.

The efficiencies for the stau simplified model can be used to constrain a full BSM scenario which contains HSCPs. In [97], the region of the CMSSM parameter space with $m_{\tilde{\tau}} - m_{\tilde{\chi}_1^0} < m_{\tau}$ has been considered, since it provides a possible solution to the Lithium problem [499, 500]. Due to the small mass difference, the stau is long-lived and decays outside the detector, thus generating a HSCP signal. In figure 73, we show the constraint on

¹⁸⁹ We point out that it is still possible to apply these simplified model results to models with smaller LLP lifetimes if we include the suppression factor from the LLP decay length distribution, as discussed in section 6.4.1.2.

Table 5. Definitions of the HSCP simplified models considered in this section. The symbol X represents the HSCP, Y_i represents intermediate BSM particles, SM represents any Standard Model particle and inv represents an invisible final state, such as the neutralino. The correspondance with the simplified models language of chapter 2 (section 2.3.1) is also given.

SMS topology	Notation in chapter 2
$pp \rightarrow X X$	DPP
$pp \rightarrow Y_1 Y_1, Y_1 \rightarrow SM X$	HP
$pp \rightarrow Y_1 Y_1, Y_1 \rightarrow SM Y_2, Y_2 \rightarrow SM X$	—
$pp \rightarrow Y_1 Y_2, Y_1 \rightarrow SM Y_2, Y_2 \rightarrow SM X$	—
$pp \rightarrow Y Y, Y \rightarrow SM SM X$	HP
$pp \rightarrow inv X$	CC
$pp \rightarrow Y_1 Y_2, Y_1 \rightarrow SM inv, Y_2 \rightarrow SM X$	—
$pp \rightarrow Y_1 Y_2, Y_1 \rightarrow SM inv, Y_2 \rightarrow Y_3 SM, Y_3 \rightarrow SM X$	—

the CMSSM parameter space obtained using only the simplified model provided by CMS (direct stau production). Since the simplified model only contains one parameter, it translates to a limit on the stau mass ($m_{\tilde{\tau}} < 260$ GeV), as shown by the blue region in figure 73. In this CMSSM scenario, however, direct production of staus only contributes to a small fraction of the total HSCP signal, since staus are typically produced from cascade decays of heavier SUSY states, such as charginos, squarks and gluinos. (Note that these correspond to the HP modes of section 2.4.2.) Furthermore, there are several possible topologies which contain a stau and the LSP ($\tilde{\chi}_1^0$) in the final state, thus resulting in a mixed missing energy-HSCP signature. Therefore using only the CMS constraints for the direct stau production simplified model largely underestimates the sensitivity of the CMS search.

In order to improve the constraints shown in figure 73, one must have efficiencies for several SMS topologies. Fortunately, a MC recasting of the 8 TeV CMS search is possible (see section 6.4.1 for details) and can be used to compute simplified model efficiencies. In [97], seven additional simplified models containing cascade decays were considered and their efficiencies computed as a function of the masses appearing in the topology. A summary of the topologies considered are shown in table 5. It is important to point out that it is not necessary to specify the SM final states appearing in the simplified models, since the HSCP search is inclusive and the efficiencies do not depend on the additional event activity. Using this extended database of simplified model efficiencies and equation (6.1), we can compute a more inclusive signal yield for each point of the CMSSM parameter space and improve the constraints on the model. The results are shown in figure 74, where we see a drastic improvement in the region excluded by the constraints on HSCPs, as expected. For this specific scenario (with $\tan \beta = 10$), all the parameter space is excluded either by the CMS or DM constraints [97].

Figure 74 illustrates the feasibility of using simplified model efficiencies to constrain full models. This approach has the advantage of being computationally inexpensive (once the efficiencies are known) and can be used to quickly test a large number of model points. However the approach relies on a few approximations and is never fully inclusive, since the number of SMS topologies with published efficiencies is always limited. Hence, it is important to verify how close the simplified model reinterpretation comes to the full recasting using a MC simulation. In [97] it was shown that, within the CMSSM scenario discussed above and using eight simplified model topologies, the SMS results reproduce the full

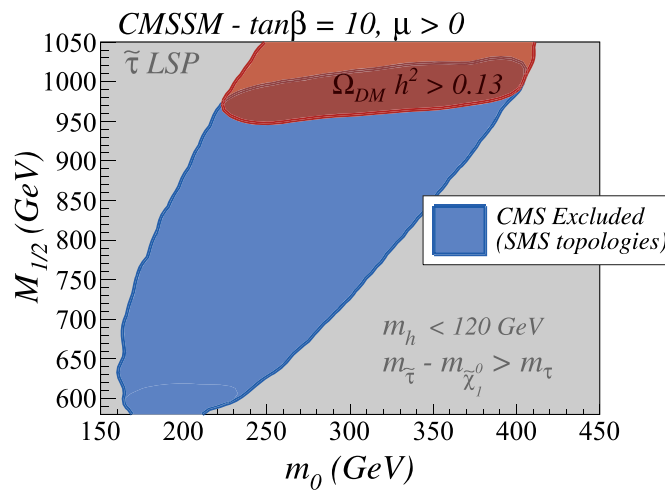


Figure 74. Region of the CMSSM parameter space with long-lived NLSP staus, as in figure 73, but here additionally using all the simplified models listed in table 5.

simulation within 20% or better. Since this error is of the order of the uncertainties in recasting, the use of simplified models becomes a viable alternative to full recasting. The SMS reinterpretation is even more relevant for the cases where a straightforward MC recasting is not possible.

Lessons learned. The example discussed in section 6.3.2 illustrates how simplified models for LLPs can be used as a reinterpretation tool. One important point which becomes clear once we compare figures 73 and 74 is the importance of a sufficiently inclusive database of simplified model efficiencies. In particular, depending on the full BSM scenario considered, the minimal set of simplified models proposed in chapter 2 and the appendix may not be sufficient to allow for a reinterpretation based on simplified model results alone. The reason is that this set was derived as the minimal set to generate a collection of relatively inclusive signatures, but may not correctly model the efficiency of every UV theory leading to that signature. In these cases, results for additional simplified model topologies are necessary and can be provided by the experimental collaborations or generated by theory groups if a full recasting is available. Furthermore, since LLP searches can be very inclusive, the simplified models considered can also be defined inclusively, as discussed above. In this way a limited number of simplified models can cover a large number of event topologies, thus increasing the SMS coverage of full models.

6.4. Recasting examples for specific searches

Here we provide examples of recasting specific experimental searches for several LLP signatures: searches for HSCPs, displaced leptons, displaced jets, displaced LJs, non-pointing photons, and DV. These recasting attempts have been made outside the experimental collaborations, making use of the public information provided by the experimental note or publication. The aim here is to highlight the challenges faced when recasting LLP searches and also to highlight the cases where the experimental information provided is straightforward and useful for recasting.

6.4.1. Heavy stable charged particles. Searches for HSCPs are based on the signature of highly ionizing tracks and/or an anomalous TOF between the particle's production at the IP and its arrival in the muon detector [390] (see section 3.5.1.1 for more details). Both signatures are sensitive to the particle's velocity and exploit the production of HSCPs outside of the ultra-relativistic regime, allowing for a powerful discrimination against the highly boosted SM backgrounds. HSCP searches assume particles are sufficiently long-lived to traverse the entire detector. They have been interpreted for HSCPs that are purely electrically charged or carry color charge, the latter of which hadronize to form R -hadrons as they propagate through the detector [10]. Typically, the HSCP signature yields high sensitivities providing a very strong background rejection while still allowing for large signal efficiencies. As a consequence, search strategies for new physics models with HSCPs typically do not benefit from more model-dependent selection criteria, like requiring additional particles in the event [95]. The corresponding searches can, hence, be performed in a mostly inclusive manner concentrating on the HSCP candidate itself. This fact opens up the possibility of providing a widely applicable recasting based on signature efficiencies. This approach has been followed by the CMS Collaboration [495], which has provided probabilities for HSCP candidates to pass the on- and off-line selection criteria for Run 1 as a function of the relevant kinematical parameters.

In this section we describe the recasting of the 8 TeV CMS search for HSCPs and discuss its validation and applicability. Furthermore, we comment on the attempt to extrapolate the 8 TeV signature efficiencies to the corresponding 13 TeV analysis, for which the corresponding efficiencies have not been provided by CMS.

6.4.1.1. Recasting using signature efficiencies. Reference [495] provides efficiencies for the reconstruction and selection of HSCP candidates with $|Q| = 1$ in the form of on- and off-line probabilities, $P_{\text{on}}(\mathbf{k})$ and $P_{\text{off}}(\mathbf{k})$. These are given as a function of the truth-level kinematic variables velocity (β), pseudo-rapidity (η) and transverse momentum (p_{T}) of isolated HSCP candidates, so the vector \mathbf{k} is defined as: $\mathbf{k} = (\beta, \eta, p_{\text{T}})$. The on- and off-line probabilities must be applied to isolated HSCP candidates, which are required to fulfill

$$\left(\sum_i^{\text{charged}} p_{\text{T}}^i \right) < 50 \text{ GeV}, \quad \left(\sum_i^{\text{visible}} \frac{E^i}{|\mathbf{p}|} \right) < 0.3, \quad (6.2)$$

where the sums include all charged and visible particles, respectively, within a radius of $\Delta R = \sqrt{\Delta\eta^2 + \Delta\phi^2} < 0.3$ around the HSCP candidate track, p_{T}^i denotes their transverse momenta and E^i their energy. Muons are not counted as visible particles and the HSCP itself is not included in either sum.

If an event contains one or more HSCPs satisfying the above isolation criteria, the efficiency for the event to pass the analysis selection is given by:

$$\epsilon = \epsilon_{\text{on}} \times \epsilon_{\text{off}}. \quad (6.3)$$

For an event with one HSCP candidate $\epsilon_{\text{on/off}}$ is directly given by the signature efficiencies $P_{\text{on/off}}(\mathbf{k})$. For an event with two candidates, the efficiency reads [495]

$$\epsilon_{\text{on/off}} = P_{\text{on/off}}(\mathbf{k}^1) + P_{\text{on/off}}(\mathbf{k}^2) - P_{\text{on/off}}(\mathbf{k}^1)P_{\text{on/off}}(\mathbf{k}^2), \quad (6.4)$$

where $\mathbf{k}^{1,2}$ are the kinematical vectors of the two HSCPs in the given event. Therefore the on- and off-line probabilities combined with the isolation criteria allow for the complete recasting of the HSCP search using only truth-level events generated in MC.

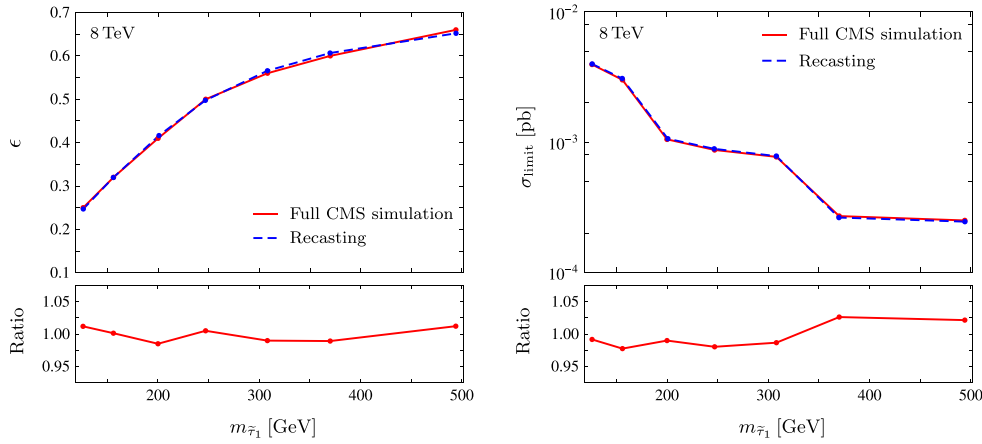


Figure 75. Left: signal efficiency ϵ of the HSCP search. Right: 95% C.L. cross section upper limit for the GMSB model as the function of the stau mass. We compare the CMS analysis [495] from the full detector simulation (red solid lines) with the recasting using signature efficiencies (blue dashed lines). In the lower frames we show the respective ratios $\epsilon^{\text{Full}}/\epsilon^{\text{Recast}}$, $\sigma_{\text{limit}}^{\text{Full}}/\sigma_{\text{limit}}^{\text{Recast}}$. Taken from [97].

The recasting of the 8 TeV search was performed in [97] using the procedure described above. Events were simulated using PYTHIA 6 [501] and the total signal efficiency for a given model was then computed using:

$$\epsilon = \frac{1}{N} \sum_{i=1}^N \epsilon_i,$$

where the sum runs over all the (N) generated events and ϵ_i is the efficiency for each event computed using equation (6.3). Since the probabilities $P_{\text{on/off}}(\mathbf{k})$ are given for four distinct cuts on the reconstructed HSCP mass (m_{rec}), these were considered as four different signal regions. The number of observed events and the expected background for which of these cuts are reported in [495].

6.4.1.2. Validation and applicability. A validation of the method described above was done in [97] using the same GMSB model considered by CMS [495]. This supersymmetric model features a gravitino and a long-lived stau as the lightest and NLSP, respectively. Since the stau only decays outside the detector volume, all cascade decays of the produced sparticles terminate in the lightest stau, which provides the HSCP signature. The left pane of figure 75 compares the resulting signal efficiency obtained by the recasting and the full CMS detector simulation. The signal efficiencies agree within 3%, demonstrating that the recast is an excellent approximation to the full CMS simulation. The differences are of the order of the statistical uncertainties from the MC simulation of the signal. In the right pane of figure 75, we show the 95% C.L. upper limits on the inclusive production cross sections, which, again, agree (within $\sim 3\%$) with the ones obtained by the full simulation in [495]. Note that both limits are based on the discrete mass cuts on m_{rec} mentioned above. In the full CMS analysis [306], an event-based mass cut is used, resulting in slightly stronger constraints for some HSCP masses.

Due to the inclusive nature of the search, the above recasting provides a widely applicable and highly reliable way to reinterpret the HSCP search for arbitrary models

containing detector-stable HSCPs. Accordingly it has been used in a variety of phenomenological studies. For instance, it has been used for reinterpretations of supersymmetric models [96, 205, 502, 503] and non-supersymmetric models of very weakly interacting DM [142, 148]. In [96, 142], the recasting has been used to reinterpret the HSCP search for finite lifetimes by convolving the signature efficiency with the fraction of HSCPs that decay after traversing the relevant parts of the detector. The recasting has also been used for a reinterpretation in terms of simplified models, as discussed in section 6.3.2.

6.4.1.3. Extrapolation to 13 TeV. While the CMS search for HSCPs at 8 TeV has provided the signature efficiencies discussed above, the same is not true for the 13 TeV analysis [4]. Therefore a straightforward recasting of the Run 2 search is not possible. Nonetheless, since the 8 TeV CMS search has proven to be extremely useful in constraining models with long-lived charged particles, it would be desirable to recast the 13 TeV analysis as well. In the following we discuss an attempt [504] to obtain a similar recasting for the corresponding HSCP search at 13 TeV. Our aim is to extrapolate the public 8 TeV efficiencies to Run 2 by introducing a correction function F that accounts for the differences between both runs:

$$P_{\text{off}}^{13 \text{ TeV}}(\mathbf{k}) = F(\beta) \times P_{\text{off}}^{8 \text{ TeV}}(\mathbf{k}), \quad (6.5)$$

where we have assumed that the correction function is mainly dependent on the HSCP velocity. If $F(\beta)$ is sufficient to account for the difference between both runs and can be computed, we can directly obtain $P_{\text{off}}^{13 \text{ TeV}}$ and, using the procedure described in section 6.4.1.1, recast the 13 TeV analysis.

In order to compute the correction function $F(\beta)$, we use the total signal efficiencies reported by the 13 TeV CMS analysis [4] for direct production of long-lived staus. Since the signal efficiencies have been provided for six distinct values of the stau mass, we perform a fit of F to the efficiencies reported. We chose to parametrize the correction function $F(\beta)$ by eight parameters (C_i). Using MADGRAPH5_AMC@NLO [226] and PYTHIA 6 [501], we obtain generator-level events for each of the stau mass points at 13 TeV. Then, comparing the total signal efficiencies obtained for a given set C_i to the efficiencies reported in [4], we can determine the best-fit values for the C_i parameters and consequently the best-fit for the correction function ($F_{\text{best-fit}}$). The result of the best-fit function and its 1σ uncertainty is shown in figure 76. The deviation of F from 1 implies a decrease or increase of the respective detector and signal efficiency between the 8 and 13 TeV analyses. Figure 76 also shows that the function is loosely constrained for low values of β .

In order to verify the validity of the extrapolation to 13 TeV, we use $F_{\text{best-fit}}$ and equation (6.5) to compute the total signal efficiencies for the same six benchmark points used in the fit. A comparison between the results obtained through recasting and the efficiencies reported by CMS is shown by the second and third columns in table 6. The results reproduce the CMS values well within the expected uncertainties, thus validating the fitting procedure. Furthermore, the inclusion of the correction function significantly improves the agreement with respect to the direct extrapolation of the 8 TeV efficiencies ($F = 1$), as shown by the fourth column in table 6.

The high level of agreement obtained with $F_{\text{best-fit}}$ for the direct stau benchmark points is expected, since these points were used in order to fit the correction function. Therefore an independent test of the above fit must be performed in order to properly validate the recasting of the 13 TeV analysis. Fortunately CMS has also reported efficiencies for a second scenario, the GMSB model with long lived staus. This scenario not only contains direct stau production, but also includes production through cascade decays of heavier sparticles. Since

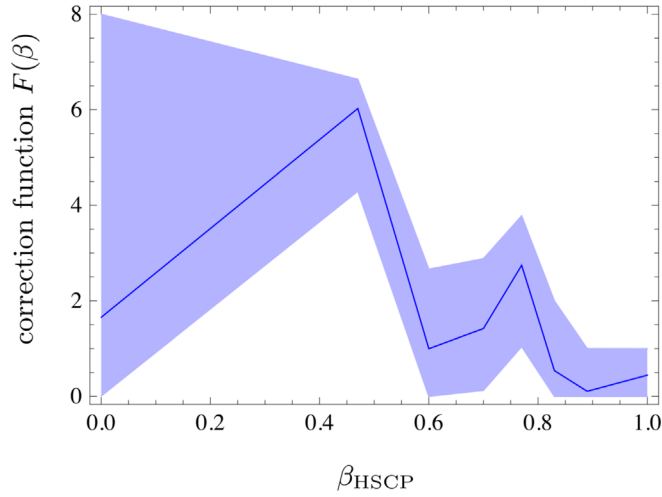


Figure 76. Best-fit correction function $F(\beta)$, used for recasting the CMS HSCP search (described in the text), and its $\pm 1\sigma$ band.

Table 6. Efficiencies for the 13 TeV LHC for the six benchmark masses in the direct stau production scenario reported by CMS (second column) and obtained through recasting using $F_{\text{best-fit}}$ and without the inclusion of the correction function ($F = 1$).

m_{HSCP} (GeV)	Direct production		
	$\epsilon(\text{CMS})$	$\epsilon(F_{\text{best-fit}})$	$\epsilon(F = 1)$
200	0.235	0.232	0.259
308	0.294	0.298	0.346
494	0.387	0.384	0.452
651	0.450	0.448	0.503
1029	0.497	0.501	0.466
1599	0.428	0.429	0.225

the GMSB model produces distinct event topologies, it provides a good test for the validity of the recasting procedure.

The results for the six GMSB benchmark points considered in [4] are shown in table 7. As we can see, they deviate from the CMS values by up to 20% for large stau masses, where our estimate undershoots the CMS efficiencies. Although the overall agreement is improved by the correction function, the result is not entirely satisfactory, given that the uncertainties for the 8 TeV recasting were under 5% (see figure 75). The observed difference might arise from several shortcomings in our description.

In particular, we assume F to only depend on β whereas the full probability maps are parametrized in the three kinematic variables β , η and p_T . However, assuming a dependence of all three kinematic variables is clearly not feasible given the very limited amount of information provided by the 13 TeV CMS analysis. Therefore we conclude that it is not possible to extrapolate the 8 TeV efficiencies in a straightforward way without additional information from the experimental collaboration.

Table 7. Efficiencies for the 13 TeV LHC for the six GMSB model benchmark points reported by CMS (second column) and obtained through recasting using $F_{\text{best-fit}}$ and without the inclusion of the correction function ($F = 1$).

m_{HSCP} (GeV)	GMSB		
	$\epsilon(\text{CMS})$	$\epsilon(F_{\text{best-fit}})$	$\epsilon(F = 1)$
200	0.276	0.297	0.279
308	0.429	0.401	0.423
494	0.569	0.494	0.556
651	0.628	0.524	0.580
1029	0.665	0.538	0.493
1599	0.481	0.442	0.228

Lessons learned. The prominent signature of HSCPs allows for a mostly inclusive search strategy concentrating on the HSCP track itself. Hence, searches for HSCPs can be reinterpreted using signature efficiencies in a widely applicable and highly reliable way. This possibility has been followed by the CMS Collaboration providing signature efficiency maps for the 8 TeV LHC. The validation reveals an excellent performance. The recast has been successfully used in the literature.

The signature efficiencies for 8 TeV can also be used to estimate the ones for Run 2 by applying a multiplicative correction function. While such an extrapolation introduces some level of approximation, a better knowledge of the underlying changes between both runs might reduce the uncertainties.

6.4.2. Displaced leptons. Searching for displaced leptons by requiring the leptons to have large impact parameters with respect to the PV is a very clean strategy due to the low backgrounds, and such searches are usually very straightforward to recast. The CMS displaced $e\mu$ search [275] demands two oppositely charged, different flavour (e, μ) leptons with large impact parameters (see also section 3.2). The recast is fairly straightforward to do, and the biggest difficulty in doing so is locating all of the relevant information as it is not all provided within the main document. The ‘standard’ isolation requirements used in the search can be found in an earlier version of the search [505]. The necessary cuts on the displaced decay position (v_T, v_Z) as well as the selection (as a function of p_T), reconstruction (as a function of impact parameter, d_0) and trigger efficiencies can be found on an additional website [506] containing auxiliary information for recasting. Although all of this information is excellent and greatly facilitates recasting the search, it is a challenge to collect the relevant information due to the fact that the additional material is not referenced in the document.

The benchmark model used in this search is the direct pair production of stops that decay through small lepton-flavor-universal RPV $\lambda'_{ijk} L_i Q_j D_k^c$ couplings ($\lambda'_{133} = \lambda'_{233} = \lambda'_{333}$) to yield displaced $\tilde{t} \rightarrow eb, \mu b$, and τb decays. The signal is simple to generate, where the only challenge is in handling the displacement properly. The most identifying pre-selection requirement of this search is that the transverse impact parameter, $|d_0|$, is required to be larger than $100 \mu\text{m}$ for both the electron and muon. The impact parameter is not the point where the parent object (e.g. τ or b) decays, i.e. the v mentioned above, but rather the distance to the point of closest approach of the lepton’s track relative to the center of the beampipe in the transverse plane. Backgrounds in this search from $Z \rightarrow \tau\tau$ or heavy flavor tend to result in leptons that are nearly collinear with the parent due to the small mass-to-momentum ratio, and yield a small impact parameter even for decays well on the lifetime tail of the parent. Events

Table 8. Left: preselection cuts in [275] (see also [506]). Right: the transverse impact parameter bins that define the exclusive signal regions. Table and figure taken from [205].

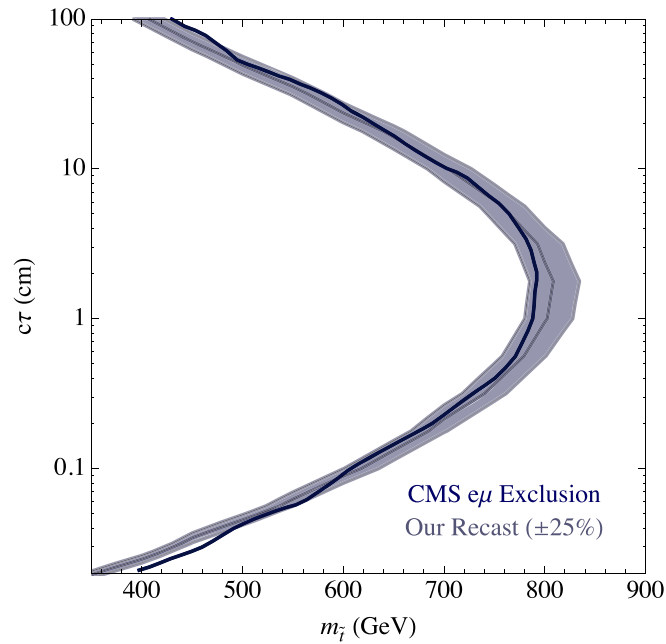
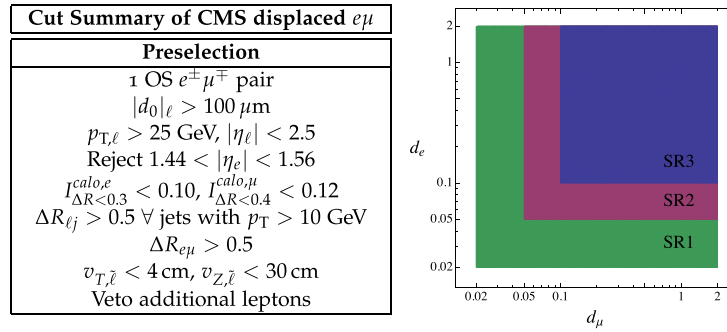


Figure 77. Validation of the CMS displaced $e\mu$ search [275] for the displaced supersymmetry benchmark model [507]. Figure taken from [205].

are binned across three exclusive signal regions: SR3, where both leptons have transverse impact parameters $|d_0|$ between 0.1 and 2.0 cm; SR2, with $|d_0|$ of both leptons between 0.05 and 2.0 cm, but not satisfying the requirement of SR3; and SR1, with $|d_0|$ between 0.02 and 2.0 cm, but not within SR2 or SR3. All selection requirements are summarized in table 8.

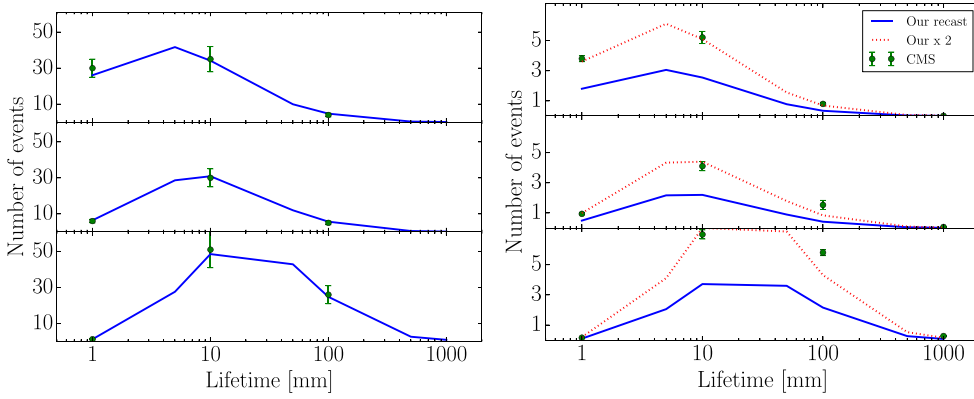


Figure 78. Number of expected events in the signal regions defined based on $|d_0|$ for the CMS displaced $e\mu$ search. The green points refer to the expected signal published by the analysis. Left: validation for 8 TeV analysis. Production cross section assumed NLO+NLL value 85.6 fb for $M_{\tilde{t}_1} = 500$ GeV, BR = 0.33 in each ℓ -channel. Right: validation for 13 TeV analysis. Production cross section assumed NLO+NLL value 67.0 fb for $M_{\tilde{t}_1} = 700$ GeV. The 13 TeV numbers are made using efficiency maps published for the 8 TeV search, as the 13 TeV maps are not yet public. Figures taken from [504].

In figure 77, we present the validation of the CMS displaced $e\mu$ search [275] from the study performed in [205]. For this search, we show the recommended 25% modeling uncertainty¹⁹⁰. The recast agrees very well with the results from the CMS displaced $e\mu$ search in the region of highest sensitivity, $300 \mu\text{m} < c\tau < 50$ cm, but exhibits a moderate deviation on the tails. As this extremely low efficiency region is overly sensitive to the tails of kinematic distributions, it may be the case that the sensitivity is slightly under-estimated for lifetimes near 1 m or $100 \mu\text{m}$, but this discrepancy typically has no qualitative impact on any application of the results.

6.4.2.1. Extrapolation to 13 TeV. We now show another reinterpretation example of the CMS displaced $e\mu$ in order to highlight the comparison between 8 TeV [275] and 13 TeV [197] analyses. We compare in figure 78 our reproduction of expected signal events with the published validation material for the 8 TeV version, and the partially-available validation material for the 13 TeV search. Information on efficiency maps from the 8 TeV analysis was needed to obtain an extrapolation to 13 TeV, as the 13 TeV efficiency maps are not yet public. As we can see, the 8 TeV recast for the CMS displaced lepton search [275] agrees very well in the region of highest sensitivity. The 13 TeV recasting, however, under-estimates the CMS values by a factor of two or more. This is likely due to the fact that the lepton efficiencies can not be directly extrapolated from 8 to 13 TeV, as assumed in making figure 78. Also, with the absence of a cut-flow table, it is impossible to verify where the mis-match arises, whether it is due to mis-modeling of the signal region cuts or due to genuine changes in the efficiencies.

Lessons learned. The selection and trigger efficiencies provided by CMS are very useful for recasting the 8 TeV CMS search for displaced leptons [275] and allow for a very good level of agreement. The main challenge, however, consisted in collecting all the available

¹⁹⁰ A similar validation was done in [96] with details provided in its appendix D. After applying a flat 80% efficiency, a 20% modeling uncertainty is found to be appropriate, as shown in figure 14 of the reference.

information, which was not provided by the main document in [275]. Furthermore, the corresponding information for the 13 TeV search is not publicly available and an extrapolation of the 8 TeV efficiencies was shown to be inadequate.

6.4.3. Displaced jets. Searches for displaced jets are less straightforward to reinterpret than displaced leptons. Interest in accurate reinterpretation is increasing, as many new physics models give rise to this particular signature. The CMS search for displaced di-jets [508] was reinterpreted in [26] to explore LLP signatures for certain weak-scale models of baryogenesis [24, 26, 509], as well as a study [96] to understand current limits on long-lived signatures in supersymmetry.

The CMS search [26] uses a multivariate discriminant composed of observables that are challenging to model in MC, such as the track-multiplicity of the vertex and the root mean square of a cluster track-multiplicity variable. The reinterpretation approach in [26, 96] was to construct track information at truth level based on the output of a parton shower program (such as PYTHIA 8), and then use the truth-level information to construct the various vertex, cluster, and track-level observables for each event. As it is difficult to adequately account for inefficiencies of track and vertex reconstruction, the efficiency of passing the cuts with truth-level observables was considered and then it was normalized to the results from CMS. To do so, the authors of [26] simulated identical signal models to those with efficiencies reported by the CMS collaboration, assumed that the MC truth-level reconstruction gave an adequate description of kinematics but *not* track and vertex reconstruction, and so computed a ratio of truth-level efficiencies to those reported by CMS. The resulting efficiency ratios were used to re-scale the truth-level results of other models, leading to a reinterpretation of the CMS search for different models beyond the ones they considered. The details can be found in [26]; a more sophisticated approach in which object efficiencies were estimated and applied to tracks and DV in [96].

To validate this approach, truth-level quantities for the models constrained in [508] were computed and compared to the numbers and distributions reported. For example, comparisons of the distributions of the observables going into the multivariate reinterpretation discriminant, as well as the output of the multivariate discriminant itself, could be performed. While the truth-level distributions disagreed with those of CMS for individual observables, the actual multivariate discriminant output agreed with that of CMS at better than 25%. The ratio of truth-level efficiencies to CMS efficiencies are also compared for different LLP masses and kinematics, and these typically agree with one another at the factor-of-two level [26]. This suggests that this reinterpretation of the CMS results in terms of cross-section limits is likely accurate to the factor-of-two level.

Lessons learned. We find that a rather naïve truth-level reconstruction of the event could give a reinterpretation of cross-section limits to agree within a factor of two, provided the efficiencies were normalized to the experimental values using an overlapping set of signal models. One of the major obstructions to improving the accuracy of the estimate was the model dependence observed among the ratios of efficiencies between truth-level information and CMS. For instance, it was found that highly boosted models showed a much lower relative reconstruction rate in data versus truth-level MC than less-boosted LLPs. Since pair production of LLPs was considered near threshold in [26], this degradation in the performance of highly boosted LLPs does not greatly affect the confidence in the final result. However, it does suggest that characterizing the effects of the particle boost are important for reinterpretation.

In addition, with a larger and more diverse set of signal benchmarks available, the prospects for the reinterpretation of search results are better. The reasons are twofold:

- Increasing the number of presented signal models by the collaboration allows for more cross-checks between MC and the results in data. This allows for more sophisticated tuning of efficiencies as applied to truth-level events.
- Having a more diverse set of benchmark signal models means that it is easier to disentangle various kinematic effects on the efficiency (such as the LLP mass, boost, etc) and find a signal benchmark that most closely matches the model for which one wants to derive sensitivity.

6.4.4. Displaced LJs. A variety of scenarios predict the existence of LLPs decaying to a pair of highly collimated leptons, also known as LJs [127]. Models giving rise to LJ signatures include heavy RHNs, exotic Higgs decays, and dark gauge bosons. The relevant signature is one or more LJs emerging from a DV. In many cases, there can also be associated prompt objects, such as a prompt lepton produced in conjunction with the RHN (corresponding to CC production in the simplified model framework of section 2.4).

Existing searches. Current search results are outlined in section 3.2. The search in [273] was interpreted in the framework of the Falkowski–Ruderman–Volanksy–Zupan (FRVZ) model [155] for the Higgs boson interacting with a hidden sector containing a massive dark photon (γ_d), massive neutralinos, and three hidden scalars. Displaced LJs are produced at the end of Higgs cascade decay that also yields two hidden light stable particles (HLSPs). Depending on the hidden-sector spectrum, the cascade decay may yield two or more γ_d that each decay to pairs of SM charged particles via kinetic mixing with the hypercharge gauge boson. The γ_d decay products are highly collimated. For $m_{\gamma_d} < 500$ MeV, LJs are the dominant decay mode, while for larger dark photon masses, displaced hadronic jets can also be significant.

Results are presented as limits on $\sigma \times \text{BR}(H \rightarrow n\gamma_d + X)$ ($n = 2, 4$) as a function of the $\gamma_d c\tau$. The strongest limits from the 8 TeV dataset arise from events that require at least one LJ with muons. For $n = 2$, $a\sigma \times \text{BR}(H \rightarrow 2\gamma_d + X)$ of 1 pb is excluded for $c\tau \sim 50$ mm.

Recast: dark photon with non-abelian kinetic mixing. The FRVZ model on which the ATLAS analysis was based implies the presence of at least two displaced LJs in the final state as well as two additional unobserved HLSPs that correspond to missing energy. The ATLAS analysis did not impose any \cancel{E}_T cuts. The presence of the two HLSPs affects the kinematics and topology of the signal event but does not explicitly enter the event selection or reconstruction. Thus, one should be able to reinterpret the ATLAS analysis in terms of any other model containing two or more displaced LJ, along with potentially additional, unobserved objects.

We consider a scenario for a dark photon X_μ that mixes with the neutral SM $SU(2)_L$ gauge boson W_μ^3 via a higher dimensional operator. Two possibilities have recently been considered: a dimension six operator involving the SM Higgs doublet, the $SU(2)_L$ field strength $W_{\mu\nu}^a$ and the corresponding $U(1)'$ field strength $X_{\mu\nu}$ [511]; and a dimension five operator involving $W_{\mu\nu}^a$, $X_{\mu\nu}$, and a real scalar triplet $\Sigma \sim (1, 3, 0)$ [512]. We consider the latter since it can yield an event topology similar to that of the FRVZ model and since it is the leading operator that may generate non-abelian kinetic mixing (NAKM) of the $U(1)'$ gauge boson with the SM. We will henceforth refer to this model as the NAKM5 scenario. The corresponding operator is

$$\mathcal{O}_{WX}^{(5)} = -\frac{\beta}{\Lambda} \text{Tr}(W_{\mu\nu}\Sigma)X^{\mu\nu}, \quad (6.6)$$

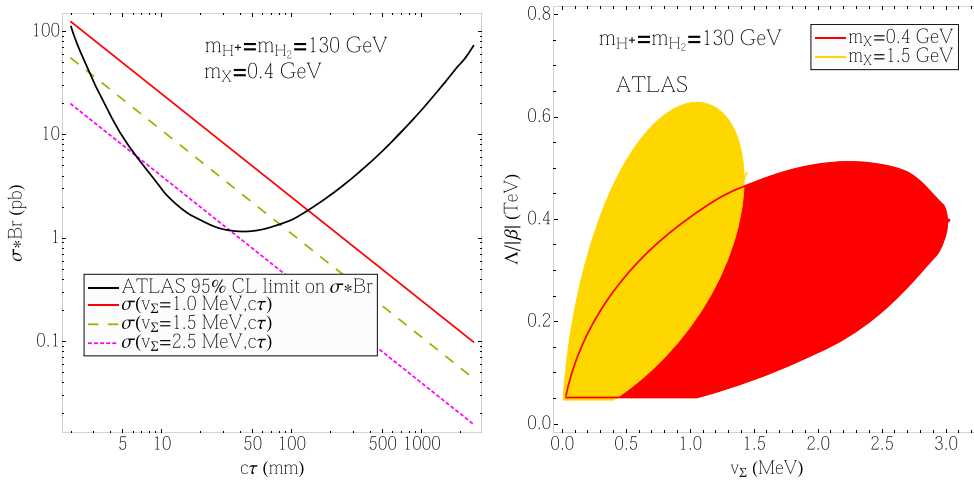


Figure 79. Constraints on the NAKM5 scenario, recast from the ATLAS search reported in [272]. The left panel gives the exclusion in the $(c\tau, \sigma \times \text{BR})$ plane, where the region above the parabola is excluded. The diagonal lines indicate the dependence of $\sigma \times \text{BR}$ on $c\tau$ for different representative choices of v_Σ . The right panel gives the exclusion region in the $(v_\Sigma, \Lambda/\beta)$ plane for $m_X = 0.4$ GeV (red region) and $m_X = 1.5$ GeV (yellow region).

where Λ is the associated effective field theory mass scale and β is a dimensionless coupling that is nominally $\mathcal{O}(1)$. When the neutral component of the Σ obtains a vacuum expectation value (vev) v_Σ , one has the ratio of the dark photon and SM photon couplings

$$\epsilon = \beta \sin \theta_W \left(\frac{v_\Sigma}{\Lambda} \right). \tag{6.7}$$

Note that the ρ -parameter constrains v_Σ to be smaller than about 4 GeV. Consequently, for Λ of order one TeV, ϵ is small (and consistent with present experimental constraints) without requiring the presence of a suppressed coupling in the Lagrangian. This feature distinguishes the dimension-five non-abelian kinetic mixing from the dimension-four kinetic mixing between X_μ and the SM hypercharge gauge boson.

The final state with two γ_d (resulting from the $X_\mu - W_\mu^3$ mixing) can be produced in one of two ways: (a) electroweak Drell–Yan pair production of triplet scalars that subsequently decay to a γ_d and SM gauge boson via the operator in equation (6.6); (b) production of the γ_d and a triplet scalar via $\mathcal{O}_{WX}^{(5)}$ with a subsequent decay of the triplet to a second γ_d plus a SM gauge boson via the same operator. In each case, one would expect the presence of two γ_d plus one or more unobserved massive prompt bosons in the final state. The ATLAS DV plus LJ analysis can be recast in a straightforward way for these event topologies, as no information about the unobserved prompt object has been used. It is worth emphasizing that both the production processes as well as the Σ decay rate are independent of the triplet vev, v_Σ . The latter only enters ϵ and, thus, only affects the dark photon $c\tau$.

The corresponding implications of the ATLAS 8 TeV results are indicated in figure 79. The first panel shows the limits on the $\sigma \times \text{BR}$ as a function of $c\tau$. The corresponding model sensitivity is shown for different choices of v_Σ by the diagonal lines. Note that for fixed v_Σ both the $\sigma \times \text{BR}$ and $c\tau$ depend on the operator coefficient β/Λ , leading to a non-trivial relationship between the two experimental quantities. This situation differs from the FRVZ

model, where $\sigma \times \text{Br}$ is independent of $c\tau$ since the mixing parameter ϵ does not depend on the parameters governing production of the hidden sector particles or their cascade decays. The intersections of the model lines with the ATLAS limits can then be translated into bounds on Λ/β as a function of v_Σ for different choices of the dark photon mass (denoted here as m_χ), as shown in the second panel of figure 79. For a 1.5 GeV dark photon, the excluded region reaches 600 GeV for $v_\Sigma = 1$ MeV.

The aforementioned recast does not require detailed information on event topology, other than the dark photon decay length. Consequently, the 13 TeV limits [273] translate rather straightforwardly into stronger bounds on the model parameter space, reaching to somewhat larger Λ/β .

Lessons learned. The triggering requirements used in the ATLAS analysis thus far limit the reach of displaced LJ searches. For models having a signal with only the displaced LJ and no other observable objects, such as the FRVZ model, triggering solely on MS tracks not associated with ID tracks is appropriate, though even here the 3mu6 trigger may not be sufficiently inclusive, as it requires at least three ROIs in the MS (see section 3.2.1). Events with LJ pairs for which neither LJ can be resolved into two separate ROIs will be missed.

It is clear that triggering on associated prompt objects, such as the lepton from one of the final state vector bosons in the NAKM5 scenario or from the W boson in heavy RHN models (CC LLP production), could significantly enhance the triggering efficiency and extend the reach of displaced LJ searches to a wider class of models and to a broader range of model parameter space. Inclusion of an associated prompt object in triggering may also enhance background rejection and relax the requirement on $\Delta\phi$ between LJs.

In addition, the implications of the mass scale of the intermediate BSM particles and the number of final state prompt objects remains to be investigated. The ATLAS 8 TeV search assumed the hidden sector particles are light compared to the mass of the SM Higgs boson, whose decay chain leads to the final states involving multiple γ_d and HLSPs. For the NAKM5 scenario and models with heavy RHNs, these assumptions about mass hierarchy may not apply. It is also not clear what impact the DV LJ isolation requirements have when there is an associated prompt lepton in the signal event.

6.4.5. Non-pointing photons. The search for non-pointing photons produced in association with missing transverse energy (\cancel{E}_T) [301] plays an important role in probing BSM particles that decay to a SM photon and an invisible particle through a highly suppressed coupling. Besides the GMSB models [513], which were the main motivation for the non-pointing photon search, this type of signal can also appear in many hidden-sector models. For example, in the dipole-mediated DM model (the ‘Dark Penguin’) [156], the production of two heavier dark fermions $pp \rightarrow Z^*/\gamma^* \rightarrow \chi_h \bar{\chi}_h$ is followed by the decays $\chi_h \rightarrow \chi_l + \gamma$. If the flavor structures of the DM mass and coupling are aligned, χ_h can be long-lived and give rise to non-pointing photons. Another example is provided by the dark-shower scenario [514, 515] that explains the galactic center gamma-ray excess. In this model, many hidden pions can be produced in the same LHC event. Some of these have displaced decays to a pair of SM photons, while others decay outside of the detector, yielding \cancel{E}_T . Notice that in this case the topology of the events is different from the previous examples, as the non-pointing photons and \cancel{E}_T originate from separate particles (and for more discussion on dark showers, see chapter 7).

Here, we describe a method used to recast the bounds of [301] to a BSM scenario that is different from the GMSB model, using the Dark Penguin signal [156] as an example.

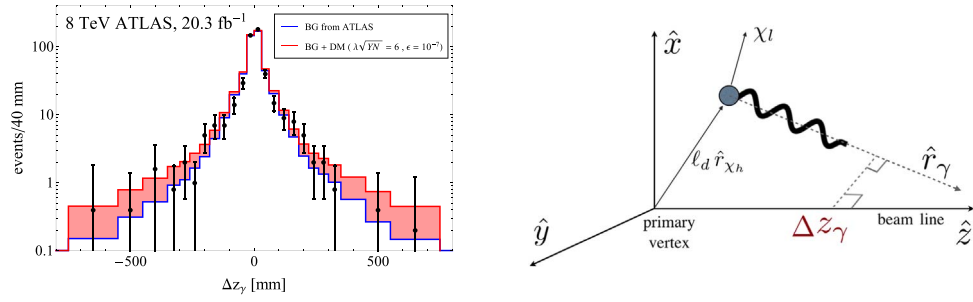


Figure 80. Left: the Δz_γ distribution of the non-pointing photon signals measured by ATLAS. The background reported by ATLAS (blue histogram) was obtained from a data-driven analysis, using diphoton events with $E_T < 20$ GeV. Also shown, stacked on top of the background (red histogram), is the signal distribution from the dipole-mediated DM scenario with $(m_{\chi_h}, m_{\chi_l}, M) = (300, 10, 300)$ GeV, $\lambda\sqrt{NY} = 6$, and $\varepsilon = 10^{-7}$. See [156] for more details. Right: the geometry of the displaced signals.

6.4.5.1. Calculation of the signal efficiency for the non-pointing photon search. We follow the non-pointing photon analysis in [301], performed by the ATLAS collaboration on about 20 fb^{-1} of 8 TeV data. In [301] delayed photons were also considered, but here we focus only on the measurement of the Δz_γ of non-pointing photons (see figure 80). For DM signals given by the long-lived $\chi_h \rightarrow \chi_l \gamma$ decay, Δz_γ can be related to the χ_h decay length ℓ_d in the lab frame:

$$\begin{aligned} \Delta z_\gamma &= \ell_d \left(\hat{f}_{\chi_h, z} - \frac{\hat{f}_{\chi_h, T} \cdot \hat{f}_{\gamma, T}}{1 - (\hat{f}_{\gamma, z})^2} \hat{f}_{\gamma, z} \right) \\ &= \ell_d [\cos \theta_{\chi_h} - \cos(\phi_{\chi_h} - \phi_\gamma) \cot \theta_\gamma \sin \theta_{\chi_h}], \end{aligned} \quad (6.8)$$

where $\hat{f}_{T, z}$ represent the transverse and longitudinal components of the unit vector \hat{f} , respectively, as shown in the right panel of figure 80. To obtain the Δz_γ distribution of the DM decay, we first simulate the prompt process, $p p \rightarrow \chi_h \bar{\chi}_h$, $\chi_h \rightarrow \chi_l \gamma$, $\bar{\chi}_h \rightarrow \bar{\chi}_l \gamma$ in MadGraph5, then we apply the cuts performed in the ATLAS analysis, and finally reweight the events using the dark penguin form factors. Then we calculate the proper lifetime of χ_h and boost it to the lab frame using the momenta of each parton-level event. The angular information of the photon and χ_h allow us to calculate Δz_γ in equation (6.8) as a function of the decay length. Using this, each simulated MC event contributes to the differential cross section in Δz_γ as

$$\frac{d\sigma_{\text{displaced}}}{d\Delta z_\gamma} = \sigma_{\text{prompt}} \frac{dP}{d\Delta z_\gamma} = \sigma_{\text{prompt}} \frac{|\mu|}{2} e^{-\mu \Delta z_\gamma}, \quad (6.9)$$

where the μ characterizing the probability distribution $dP/d\Delta z_\gamma$ of the decay is defined as

$$\mu \equiv \frac{\Gamma_{\chi_h} m_{\chi_h}}{P_{\chi_h}} \left(\hat{f}_{\chi_h, z} - \frac{\hat{f}_{\chi_h, T} \cdot \hat{f}_{\gamma, T}}{1 - (\hat{f}_{\gamma, z})^2} \hat{f}_{\gamma, z} \right)^{-1}. \quad (6.10)$$

Summing the distributions derived from all the simulated events we obtain the differential cross section in Δz_γ shown in figure 80.

The ATLAS search requires at least two loose photons with $|\eta| < 2.37$ and $E_T > 50$ GeV. At least one photon is required to be in the barrel region $|\eta| < 1.37$. To

avoid collisions due to satellite bunches, both photons are required to have an arrival time at the ECAL t_γ smaller than 4 ns, with zero defined as the expected time of arrival for a prompt photon from the PV. We approximate t_γ with the TOF of the χ_h , requiring it to be smaller than 4 ns. In our sensitivity estimate, we do not include the detailed isolation cuts on the photon. We also neglect the effect of the displaced decay on the angular acceptance of the photons, simply imposing the requirements on $|\eta|$ at the level of the prompt event. The signal region also requires $\cancel{E}_T > 75$ GeV.

Finally, to simplify the discussion we assume that every event has a reconstructed PV in the geometrical center of the detector.

For events where only one photon satisfies $|\eta| < 1.37$ (i.e. it is in the barrel calorimeter), this photon is used for the measurement of Δz_γ . For events where both photons are in the barrel, the photon with larger t_γ is used. We approximate this timing condition by taking the photon emitted by the more boosted χ_h , in which case the average decay is more delayed. In figure 80 the generated Δz_γ signal distribution is shown on top of the expected background. The latter is taken from figure 4 of the ATLAS paper [301]. Because we are focusing on the non-pointing photon signals, to set constraints on the DM couplings in [156] we remove events with $|\Delta z_\gamma| < 30$ mm. In our exploratory analysis we only consider the statistical uncertainty on the background, neglecting the effect of systematics.

Lessons learned. The ATLAS paper gives detailed descriptions of the cuts and background analysis, which makes an approximate estimation of the signal efficiency quite straightforward.

The background analysis in [301] is based on a data-driven study, for which events passing the diphoton selection with $\cancel{E}_T < 20$ GeV are used as control region sample. It is challenging for theorists to simulate the background for different energy cuts. This is particularly true for the \cancel{E}_T cut that plays a vital role in the DM and HV searches.

To obtain a more precise result, it would be useful if the ATLAS collaboration could provide the reconstruction efficiency of non-pointing photons as function of Δz_γ , or of the angle between the photon and the surface of the ECAL, a variable that may be relevant to the efficiency. The paper does provide a table of signal acceptance times efficiency for the GMSB model used therein. However, the numbers depend on details of the particular model used, and it is hard to extract the efficiency that is associated to the non-pointing photon reconstruction. Therefore, when estimating the signal efficiency, we only consider efficiency from the selection cuts and do not include possible suppressions from photon reconstruction.

It would also be very useful to have a table of background events for different cuts on \cancel{E}_T . For instance, the Dark Penguin signature has \cancel{E}_T from the decay of $\chi_h \bar{\chi}_h$ with electroweak-scale m_{χ_h} , and \cancel{E}_T can easily be higher than 100 GeV. By contrast, in the dark shower scenario where soft hidden pions decay to two SM photons, the \cancel{E}_T originating from additional late-decaying pions can be much lower than the 75 GeV cut used in the ATLAS analysis. Knowing the background and systematic uncertainty for different \cancel{E}_T cuts would be very important to constrain different models with potentially very different kinematics.

6.4.6. Displaced vertices. Displaced-vertex searches differ from displaced jets and displaced leptons due to the requirement of an actual secondary vertex from the displaced objects. These searches are sensitive to LLP lifetimes that allow it to decay in the inner trackers or MS of the LHC detectors, where vertexing is possible [196, 237, 248, 251, 253, 265, 279]. These searches have extremely low backgrounds as there are no irreducible contributions from the SM, making them sensitive to very small signals of new physics (for more information, see

chapter 4). Moreover, the identification of displaced decays can be used to extract kinematical information in a decay, such as (invisible) particle masses [516, 517].

In this section we review some reinterpretations of DV searches, differentiating between reinterpretations making use of only truth-level information to identify displaced decays and reinterpretations in which an attempt is made to reconstruct DV from displaced tracks (with an approximate detector response).

6.4.6.1. Truth level DV. The work in [26] reinterpreted the 8 TeV ATLAS search for a displaced muon and a multi-track vertex (DV+ μ) [518], where LLP signatures for certain weak-scale models of baryogenesis [24, 26, 509] were explored. For reinterpreting this search, a similar procedure described in section 6.4.3, on displaced jets, of constructing ratios of truth-level versus ATLAS efficiencies for the ATLAS multi-track vertex analysis [518] was performed, with similar results for the validation being correct within approximately a factor of two.

This DV+ μ analysis has since been superseded by [196], in which a DV is searched for at 8 TeV in association with either a muon, electrons, jets, or missing transverse momenta. Recently, an updated ATLAS analysis [237], which looks for multi-track DV at 13 TeV in association with large \cancel{E}_T , was made public. This search now includes a prescription using parametrized efficiencies as a function of vertex radial distance, number of tracks and mass. Their prescription can be applied to vertices and events passing certain particle level acceptance requirements using the truth MC event record.

Here we validate the prescription with parametrized selection efficiencies in [237]¹⁹¹. The results of this search are interpreted by ATLAS in a split-SUSY simplified model with a long-lived gluino that hadronizes, forming an R -hadron before decaying as $\tilde{g} \rightarrow q\bar{q}\tilde{\chi}_1^0$. Event samples are generated with PYTHIA 8.2 [220]. We use truth-level \cancel{E}_T and we identify the truth R -hadron decay position and decay products, as the ATLAS collaboration provides selection efficiencies that can be directly applied to these truth-level quantities. These efficiencies can be found in the auxiliary material in [519], and are given at the event-level as a function of the truth \cancel{E}_T and DV radial distance, and at the vertex level parametrized as functions of vertex invariant mass and number of tracks. The efficiencies are given for different detector regions, encapsulating also the effect of the material veto cut.

The selection of events used for the signal region requires:

- truth level $\cancel{E}_T > 200$ GeV;
- one trackless jet with $p_T > 70$ GeV, or two trackless jets with $p_T > 25$ GeV. A trackless jet is defined as a jet with $\sum_{\text{tracks}} p_T < 5$ GeV.

In addition, events must have at least one DV with:

- transverse distance between the IP and the decay position > 4 mm;
- the decay position must lie in the fiducial region $r_{\text{DV}} < 300$ mm and $|z_{\text{DV}}| < 300$ mm;
- the number of selected decay products must be at least 5, where selected decay products are charged and stable, with $p_T > 1$ GeV and $|d_0| > 2$ mm;
- the invariant mass of the truth vertex must be larger than 10 GeV, and is constructed assuming all decay products have the mass of the pion.

Applying these cuts and efficiencies, we get event-level efficiencies for two of the benchmarks (with gluino masses of 1400 GeV or 2000 TeV, and the neutralino mass is fixed to 100 GeV). Based on the efficiencies obtained and the estimated number of background

¹⁹¹ This prescription is also validated in [504].

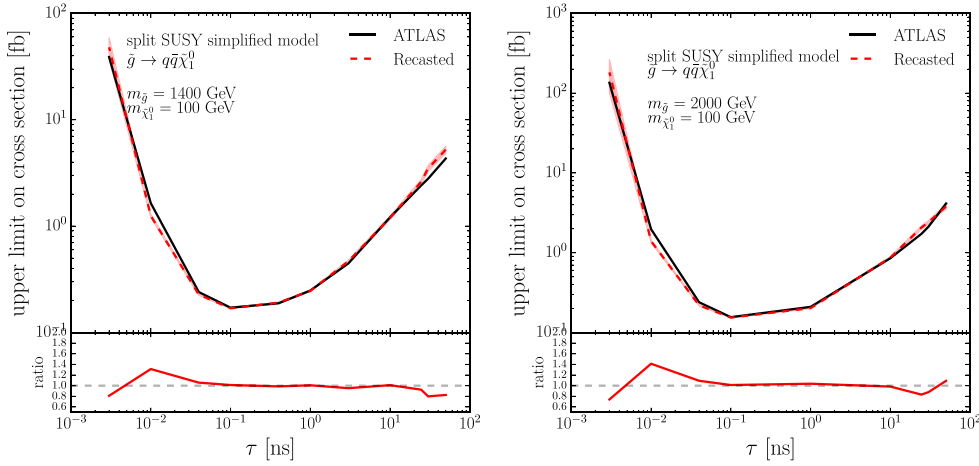


Figure 81. Comparison of our recast and ATLAS [237] on the upper limit on the gluino production cross section versus its proper lifetime [504].

vertices, we can extract 95% C.L. upper limits on the total visible cross section for the two gluino masses. For reference, assuming 100% efficiency, we get an upper limit of 0.091 fb. The curves in figure 81 show our recasting results compared to ATLAS. The level of agreement is very good, within 20% for most of the lifetime values. We also point out that the recasting limits agree well even for regions where the efficiency is very low ($\tau > 10$ ns and $\tau < 10^{-2}$ ns). This 13 TeV ATLAS multitrack analysis [237] has also been reinterpreted in the context of long-lived sterile neutrinos [48, 264].

6.4.6.2. Displaced-vertex reconstruction. Before parametrized efficiencies applicable for truth-level DV were made public, attempts to recast DV searches were made by performing their reconstruction from charged tracks only, with an approximate detector response. In [206] the ATLAS DV+jets multitrack analysis [196] was recast. Reinterpretation was performed using generator-level events and the detector fiducial region was reproduced as well as possible. A description of the criteria from the ATLAS analysis that were implemented in the recast is shown in table 9. The jets are clustered according to the anti- k_T prescription [366] in the analysis with momentum smearing, validated by reproducing the jets+ \cancel{E}_T exclusion curve of prompt searches. The selection of events used for the signal region (and the approximations to real detector simulation) were as follows:

A tracking efficiency of the form

$$\begin{aligned} \varepsilon_{\text{trk}} = & 0.5 \times \left(1 - \exp\left(\frac{-p_T}{4.0 \text{ GeV}}\right) \right) \times \exp\left(\frac{-z_{\text{DV}}}{270 \text{ mm}}\right) \\ & \times \max\left(-0.0022 \times \frac{r_{\text{DV}}}{1 \text{ mm}} + 0.8, 0\right), \end{aligned} \quad (6.11)$$

is used, where r_{DV} and z_{DV} are the transverse and longitudinal distance of the track’s production vertex (which is the same as the DV origin when using truth-level generator information). This functional form is designed to take into account the size of the detector (i.e. it imposes a linear dependence on r_{DV} , and an exponential dependence on z_{DV}), as well as a turn-on like feature dependent on the p_T of the track. It reproduces the overall behavior of efficiency falling off with vertex displacement. The parameters were determined by fitting the

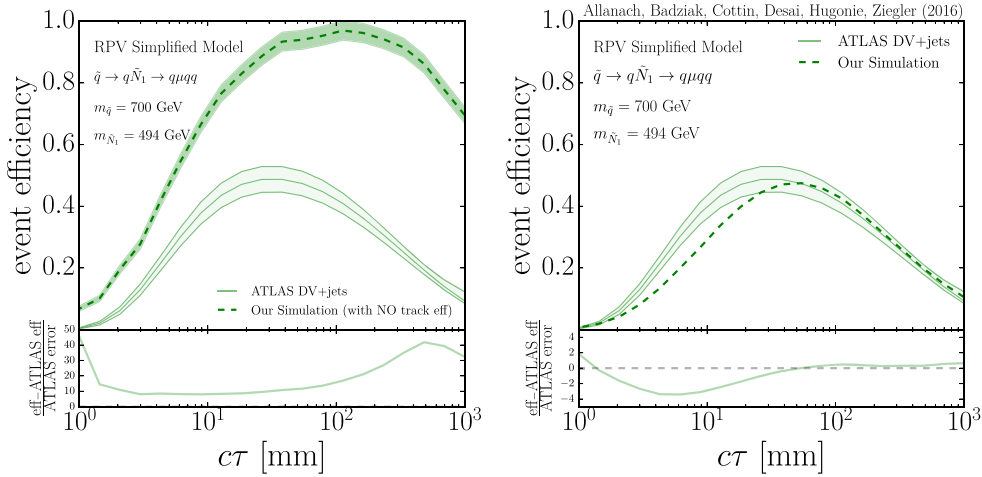


Figure 82. Validation of the DV + jets search for the ATLAS benchmark of a simplified RPV model with a 700 GeV squark decaying to a neutralino, $\tilde{q} \rightarrow q\tilde{N}_1 \rightarrow q\mu qq$. Left: without any tracking efficiency. Right: with a tracking efficiency function given by equation (6.11), taken from [206].

Table 9. Implementation of cuts applied in the ATLAS multitrack DV + jets search, from [196]. Cuts denoted by an asterisk (*) are approximations to the experimental analysis in the absence of the full detector simulation.

DV jets	4 or 5 or 6 jets with $ \eta < 2.8$ and $p_T > 90, 65, 55$ GeV, each
DV reconstruction*	DV made from tracks with $p_T > 1$ GeV, $ \eta < 2.5$ and $ d_0 > 2$ mm. Vertices within 1 mm are merged. Note: a tracking efficiency needed here; we assume a functional form given by equation (6.11)
DV fiducial	DV within 4 mm $< r_{DV} < 300$ mm and $ z_{DV} < 300$ mm
DV material*	No DV in regions near beampipe or within pixel layers. Discard tracks with $r_{DV}/\text{mm} \in \{[25, 38], [45, 60], [85, 95], [120, 130]\}$.
N_{trk}	DV track multiplicity 5
m_{DV}	DV mass > 10 GeV

efficiency curve (with lifetime dependence), for three benchmarks in the analyses. We find that fitting only one benchmark does not correctly reproduce the efficiency curve for any of the others. This is most likely due to insufficient dimensionality of the efficiency map. We expect that a full tracking-efficiency parametrization depends not only on r_{DV} , z_{DV} and p_T , but also on transverse and longitudinal impact parameters (d_0 , z_0), and on the charge and pseudorapidity of the track. Furthermore, we expect a vertex efficiency that depends on the topology of the event and the nature of the particles forming the vertex. The fit for the event efficiencies from this tracking function can be seen in figure 82.

Lessons learned. With a larger and more diverse set of signal benchmarks, the prospects for reinterpretation are better. For example, the ATLAS analysis examined in [518] only showed limits for three signal model benchmark points for which efficiencies were shown,

making it challenging to find a benchmark whose kinematics matched the desired signal models for the reinterpretations of other models (for example, in [26]). Because the efficiencies and limits were shown for either a high-mass, low-boost LLP or a low-mass, high-boost LLP, this made it more challenging to reinterpret the results for other types of kinematics.

The new parametrized efficiencies presented by ATLAS in [519] are extremely useful. They constitute an optimal efficiency map for recasting these type of analyses, as they can be applied in a straightforward way to truth-level quantities. Before this information was made public, efficiency tables (for vertex-level efficiency) in terms of r_{DV} were only available for few channels and for a single benchmark. It was not clear how to translate this information to other channels, or to parent particles of a different mass. In this case, a functional parametrization for track efficiency was needed (as derived in [206]) to be able to reproduce the experimental results. Finding this kind of parametrization is not easy, as it needs to be validated across different benchmarks. For example, [206] found that fitting only one benchmark did not correctly reproduce the event-level efficiency curve for any of the others.

6.5. Handling LLPs in DELPHES-based detector simulations

6.5.1. Long-lived particle simulation in DELPHES 3.4.1. The DELPHES package [342] allows for the generic simulation of the response of a typical detector used in high-energy physics experiments. It is widely used for simulating the effects of the ATLAS and CMS detectors or the hypothetical detectors that could be used for the future FCC and CLIC projects. The architecture of DELPHES is composed of distinct and specialized modules that interact with each other. The detector is described by the user through an input card, where the modules to be used in the simulation are sequentially enumerated and their input parameters are specified.

The detector simulation relies on a mix of parametric and algorithmic modules. More precisely, tracking is simulated through efficiency and smearing functions that are applied to the properties of the electrically-charged stable particles. The particles are then propagated to the calorimeters and dedicated modules simulate the energy deposits in the electromagnetic and HCALs. The output of such a step consists of a list of calorimetric towers. Moreover, DELPHES includes a particle-flow-like algorithm that combines tracking and calorimetric data in order to improve the identification of the final-state objects and the resolution on their reconstructed momenta.

Jet clustering is performed via an internal call to the FASTJET package [367], which takes as input the list of calorimeter towers or, alternatively, the particle-flow candidates, and outputs jet objects. Lepton and photon isolation is then handled through a specific isolation module. Finally, DELPHES takes care of removing the double-counting of objects that could be simultaneously identified as elements of different collections. The final output is stored in a ROOT file.

In addition, DELPHES allows for the simulation of PU effects by superimposing minimum-bias events attached to displaced interaction vertices along the beam direction to the hard scattering event. Procedures mimicking PU removal can then be configured in the input card. The subtraction of the charged particles belonging to PU vertices is performed at the tracker level. Neutral particles are removed by applying the jet area method [520] supplied within the FASTJET package. More advanced methods are also available in DELPHES, such as the PUPPI [521] or SOFTKILLER [522] techniques, and they can easily be added to the input card. The loss of performance originating from PU, in particular relative to the isolation, is automatically accounted for.

The official DELPHES package (version 3.4.1) with the default detector cards needs to be adapted for the proper handling of LLPs. By default, the decay products of a LLP enter the simulation as if the corresponding decay would have occurred within the tracker volume. However, the user has the possibility to define a volume in which the particle can decay and still be detected outside the tracker volume. This is achieved in practice by making use of the `RadiusMax` parameter of the `ParticlePropagator` module, that is by default set to the tracker radius stored in the `Radius` parameter. When setting the `Radius` and `RadiusMax` parameters to different values, the particles decaying outside the tracker volume, but inside the ‘decay volume’ of radius `RadiusMax`, are included in the collection of stable particles stored in the output ROOT file. They can in this way be used for an offline, more correct, treatment.

Moreover, several modules that are not used in the default ATLAS and CMS cards could serve for a better simulation of the LLPs in DELPHES. For instance, the `TrackSmearing` module allows the user to smear the track momentum according to the impact parameter in the transverse plane (i.e. the d_0 parameter) and in the longitudinal plane (i.e. the d_z parameter).

By default, the detector simulation in DELPHES totally ignores the presence of any LLP. While this is convenient for neutral particles like a neutralino which could be considered as invisible from the detector standpoint, a charged particle leaves tracks in the tracker and would interact with the calorimeters if its lifetime is large enough. In this case, if the LLP decays inside the tracker, its trajectory is properly propagated to the calorimeters and the DV is correctly accounted for. However, if the LLP decays outside the tracker, its decay products are ignored in DELPHES, unless the `RadiusMax` parameter has been specified to be larger than the tracker `Radius` parameter. In this case the decay products can be found in the `Delphes/stableParticles` output collection and treated with adequate smearing functions and efficiency directly from the DELPHES output.

Finally, DTs are simply treated as missing energy in DELPHES. Emerging tracks or tracks containing kinks are not treated appropriately, in the sense that the parameterizations required for a proper description of such signatures has not been implemented yet. Also, DELPHES does not include any trigger simulation, and the latter is in general complex in the case of LLPs.

6.5.2. Displaced tracks with the MADANALYSIS 5 tune of DELPHES. The DELPHES-LLP package can be installed from the version v1.6 of MADANALYSIS 5 [488, 523] and contains improvements of DELPHES specific to LLPs. It leads to new possibilities for phenomenological investigations of LLPs and the recasting of related LHC analyses¹⁹².

This new package was designed to handle neutral LLPs that decay into leptons within the tracker volume. Realistic efficiencies are applied to the displaced tracks and several parameters specific to this kind of analysis have been made available within MADANALYSIS 5. An extension to the case of neutral LLPs decaying into muons outside the tracker volume can be easily implemented, the muons being thus reconstructed only through their hits in the muon chambers. The simulation of the displaced leptons is performed through efficiencies and resolution functions to be specified by the user. Furthermore, another extension allowing the user to handle long-lived charged particles that decay into leptons could be implemented. A similar dedicated tune of DELPHES and MADANALYSIS was devised for the studies of neutral particles decaying to displaced leptons and jets in [44, 49, 169]¹⁹³.

¹⁹² More information is available at the following website: <https://madanalysis.irmp.ucl.ac.be/wiki/MA5LongLivedParticle>.

¹⁹³ The code is available to download at <https://sites.google.com/site/leftrighthep/>.

The DELPHES-LLP package contains a new module called `MA5EfficiencyD0` that allows for the definition of a track reconstruction efficiency parameterized as a function of the $|d_0|$ and d_z parameters (named `d0` and `dz` in the DELPHES input card). The default efficiency function, specified via a `DelphesFormula` is taken from the 8 TeV tracking performance of CMS [275]¹⁹⁴,

```
setEfficiencyFormula
{ (d0 <= 20) * (-5.061 07e - 7 * d0**6
+ 0.000 027 275 6 * d0**5 - 0.000 493 21 * d0**4
+ 0.002 871 89 * d0**3 + 0.005 220 07 * d0**2
- 0.091 795 7 * d0 + 0.924 921)
+(d0 > 20) * (0.00)}
```

In addition, the data-format of DELPHES has been extended so that the `Muon` and `Electron` classes now include the transverse ($|d_0|$) and longitudinal (d_z) impact parameters relative to the closest approach point (encoded in the `d0` and `dz` variables), the coordinates of the closest approach point (x_d, y_d, z_d) (encoded in the `xd`, `yd` and `zd` variables), and the four-vector of the vertex from which the lepton is originating from (t_p, x_p, y_p, z_p) (encoded within the `tp`, `xp`, `yp` and `zp` variables), the latter quantity being evaluated from MC information.

Consequently, the data-format of MADANALYSIS 5 has been extended, so that the `Muon` and `Electron` classes now contain the `d0()` and `dz()` methods allowing to access the value of the $|d_0|$ and d_z parameters, the `closestPoint()` method that returns the coordinates of the closest approach point (through the `X()`, `Y()` and `Z()` daughter methods) and the `vertexProd()` method that returns coordinates of the DV from which the lepton originates (through the `X()`, `Y()` and `Z()` daughter methods). An analysis example [494] can be found in the public analysis database of MADANALYSIS 5¹⁹⁵, where information about the re-implementation in MADANALYSIS 5 of [197], an analysis of 2.6 fb^{-1} of 13 TeV LHC data, is available. This is a search for LLPs decaying into electrons and muons, where signal events are selected by requiring the presence of either an electron or a muon whose transverse impact parameter lies between $200 \mu\text{m}$ and 10 cm . For a given benchmark signal where a pair of long-lived stops is produced through QCD interactions and where each stop further decays into a displaced b -jet and a displaced lepton. In table 10, we present the number of events surviving the selection of the three different signal regions of the CMS analysis. Our event generation has been performed with PYTHIA 8 [219] and for the benchmark scenario used. We observe that a good agreement is obtained, except in the case of long stop lifetimes, $c\tau = 1 \text{ m}$. This is however the region in which no public information on the CMS reconstruction efficiencies is available.

The MADANALYSIS 5 tune of DELPHES has neither been designed for disappearing (or appearing) tracks nor for track kinks. Concerning the disappearing (or appearing) tracks, the only missing experimental ingredients are the track reconstruction efficiency and resolution as a function of the number of missing hits in the (inner) outer layers of the tracker. There is to this date no public material on the tracking performance description related to track kinks.

6.5.3. What about other LLP signatures? In this section, we briefly discuss how DELPHES could be improved for a better handling of LLP signatures.

¹⁹⁴ <https://twiki.cern.ch/twiki/bin/view/CMSPublic/DisplacedSusyParametrisationStudyForUser>

¹⁹⁵ <http://madanalysis.irmp.ucl.ac.be/wiki/PublicAnalysisDatabase>

Table 10. Number of events populating the three signal regions (SR-1, SR-2 and SR-3) of [197] for different stop decay lengths ($c\tau_{\bar{t}}$). We compare the CMS and MADANALYSIS 5 (MA5) results in the second and third column of the table, respectively, and the difference taken relatively to CMS is shown in the last column.

Region	$c\tau_{\bar{t}}$ (cm)	MA5	CMS	Difference (%)
SR-1	0.1	3.89	3.8	2
	1	4.44	5.2	15
	10	0.697	0.8	15
	100	0.0610	0.009	>100%
SR-2	0.1	0.924	0.94	2
	1	3.87	4.1	5
	10	0.854	1.0	15
	100	0.0662	0.03	~100%
SR-3	0.1	0.139	0.16	15
	1	6.19	7.0	10
	10	4.45	5.8	25
	100	0.497	0.27	85

6.5.3.1. Displaced jets. Displaced jets are jets that are reconstructed either from SA calorimeter information, or from the particle-flow input with a minimum requirement on the multiplicity of tracks with high transverse displacement (see [251]). Conceptually, such jets can be handled in DELPHES provided that the displaced tracks are properly parametrized. As described above, a module designed to smear the full set of track properties, including their transverse and longitudinal displacement, exists (i.e. the `TrackSmearing` module). In addition, efficiencies based on displacement parameters have already been implemented in MADANALYSIS 5 (see above) and a module that performs the matching of an existing jet collection with a track collection based on track displacements is very similar to the already existing `TrackCountingBTagging` module. Minor modifications to this module are hence needed to be able to select tracks based on an absolute displacement instead of the impact parameter significance. Finally, in order to be able to perform a displaced jet selection, one would need a (not yet existing) module that performs jet clustering on the basis of the secondary vertices and the displaced tracks matched with these jets. Alternatively, a module that includes a vertex reconstruction efficiency and a module including a vertex position smearing could be implemented.

6.5.3.2. Displaced vertices. The missing modules described in section 6.5.3.1 could perfectly serve the purpose of a DV analysis. Provided that tracking efficiencies and resolutions are available as a function of the full set of tracking parameters (d_0 , d_z , p_T , ϕ , and θ) and, eventually, of the MC truth vertex position, a simple vertexing algorithm can be implemented in DELPHES.

6.5.3.3. Discussion: DELPHES versus a specific parametric simulation. In a fully parametric simulation of the detector, the detector effects are encoded in terms of efficiencies and resolution functions. Such a simulation is typically very fast, but is likely to suffer from a lack of accuracy in the modeling of complex observables such as jet properties and missing energy. The DELPHES simulation is an admixture of such a parametric simulation and of an algorithmic one. This is slower, but has the clear advantage of correctly treating in particular the reconstruction of the jets and the missing energy.

In order to be able to answer whether DELPHES should be used in place of a fully parametric simulation in recasting LLP analyses, further studies are needed. In the meantime, the following guidelines could be used. If the signal selection is based only on displaced tracks, a simple parametric simulation should in principle be sufficient. This simulation could encapsulate the track reconstruction efficiency and resolution, including PU effects. DELPHES could then optionally be used to mix the resulting ‘reconstructed’ tracks with the additional tracks originating from the PU vertices. On the other hand, if the analysis under consideration additionally uses calorimetric information (i.e. jets or missing energy), DELPHES should be preferred to a fully parametric framework. However, a precise quantification of these effects cannot be assessed without detailed comparative studies between the two approaches. Finally, it should be pointed out that neither of these techniques can be used to correctly simulate the instrumental background, which is challenging to simulate and is discussed in chapter 4.

6.6. Recasting inside the experimental collaborations

Reinterpretations performed within the experiments themselves present unique advantages and disadvantages. They allow for thorough and consistent treatment of detector effects and geometry, object reconstruction, and systematic uncertainties in a way which is impossible through external recasting. Groups can share resources and easily communicate all necessary details. On the other hand, they are of course limited to the model(s) chosen for reinterpretation. In the ideal situation, reinterpretations which provide meaningful results can be performed with minimal overhead to a given analysis.

As the LHC enters an era of decelerating luminosity growth and analysis techniques are becoming more sophisticated, the LHC analyses become harder to re-implement with sufficient accuracy outside of the experiments compared to cut-based analyses. Analyses increasingly utilize machine-learning algorithms that transform a large number of event-level and particle-level observables into higher-level discriminants which are not easily characterized by low-dimensional efficiency tables and may require inputs that third-party detector simulations are not able to reproduce. In particular non-prompt searches may depend on non-traditional reconstruction objects and details of the detector simulation and geometry in ways that require a more detailed simulation than is achievable by, e.g. third-party simulators. Hence, experiments are investigating approaches that enable internal reinterpretation using the full set of available information.

Full-fidelity reinterpretations are especially relevant for LLPs, since the signal simulation may depend more heavily on details not well captured by third-party simulation tools. For example, for sufficiently high lifetime, the decays must be handled by a full detector simulation such as GEANT (or some complex interaction between GEANT and MC packages such as Pythia). Such decays are not well-covered by tools like Delphes as the response of such in-detector decays may require access to a more detailed geometry description.

6.6.1. The RECAST framework. The RECAST Framework [496] is a developing platform for experiments as well as researchers external to the collaborations who wish to reinterpret LHC analyses. RECAST enables cloud-based analysis execution and common presentation of reinterpretation results. The framework consists of two components:

The RECAST front end. This is a web-based service in which reinterpretation of analyses can be suggested by interested authors that provide necessary inputs such as UFO model files [225], process and parameter card templates, or suggested scan grids. Responses to such requests, possibly by more than one analysis implementation, can then be uploaded. Such a

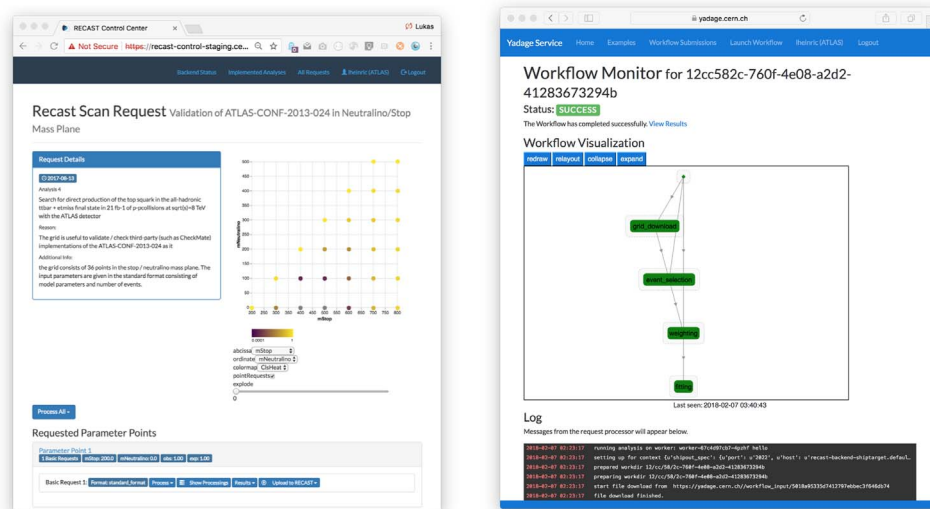


Figure 83. Left: web-based interface for the RECAST back end for an experiment that presents the requested parameter points and color-coded results. Right: an experiment-internal reinterperation executing on the distributed infrastructure built by CAP and RECAST.

web service, interfaced with services such as HepData, may then serve as a resource for the LHC community to organize and share reinterperation results obtained by the various analysis implementations.

The RECAST back end. An important objective of the framework is to enable a full-fidelity reinterperation of an LHC analysis using the original analysis code developed within the experiment that can be approved by the collaboration and be placed on an equal footing with the original publication. In contrast to third-party recasting tools, in which multiple analyses are implemented using a single, common framework that is executed on a single computing element, such an exact analysis re-execution often necessitates a distributed data analysis using a number of different frameworks in use within the experiments. Therefore, RECAST has developed a flexible graph-based analysis description and execution back end [524] that enables a faithful re-execution of nearly arbitrary analysis code on cloud platforms such as those offered by CERN¹⁹⁶. The back-end provides experiments with an access-controlled interface to view reinterperation requests, retrieve the necessary analysis description from repositories such as the CERN analysis preservation portal (CAP) [525], execute the analysis on datasets for the new model and—if approved—upload the results to the public front-end. Figure 84 shows a screenshot of the current prototype user interface, giving collaboration members an overview over requested points as well as controls to steer processing and submission.

These services are being developed in close collaboration with the CERN Analysis Preservation project, which is a common project supported by the four major LHC experiments. While this integration work is on-going, the computing back end for RECAST

¹⁹⁶ Thanks to this flexibility, the popular third-party recasting tools can be easily integrated into this back-end as well, with current integrations being available for CheckMate and Rivet.

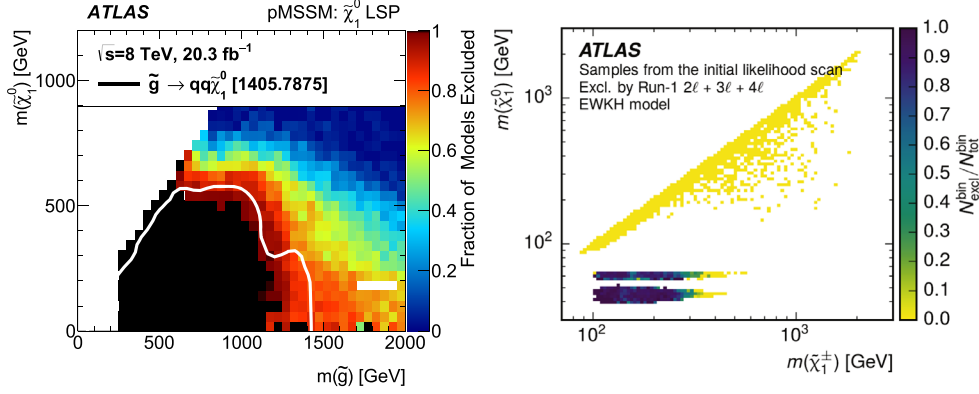


Figure 84. Left: pMSSM exclusion in the gluino-neutralino mass-plane. Results partially provided by RECAST. From [528]. Right: follow-up dark-matter reinterpretation. Exclusions presented in chargino-neutralino mass-plane. From [530].

has been successfully used for a number of Runs 1 and 2 reinterpretations published by the ATLAS Experiment.

6.6.2. Analysis preservation as a driver for reinterpretation. Within the LHC experiments, the ability to reinterpret analyses is, perhaps unintuitively, mostly limited by the internal availability of the analysis routines to the wider collaboration as opposed to, e.g. availability of computing resource constraints. The large number of measurements and searches, the heterogeneity and complexity of the analysis software, as well the size of the collaboration, all lead to a situation in which very often only a small number of analyzers of the original analysis team is able to execute any given analysis. Furthermore, due to the collaborative development model, analyzers are typically responsible for only a subset of the analysis, which results in knowledge fragmentation. Therefore, both ATLAS and CMS are now designing an interface to store analysis-relevant information (the CAP [525]) to mitigate this problem. In the context of RECAST, the software and analysis-workflow preservation aspects of this effort are most relevant. The former is mainly implemented through archiving of source-code repositories and the archival Linux Containers, which now enjoy wide-spread industry support, while internal structure of the analysis workflow is archived in CAP in the form of declarative workflow specifications such as yadage [526], which has been developed for RECAST, and the common workflow language [527]. It is planned that CAP and RECAST will utilize a common computing back-end in order to re-execute the analyses that have been preserved in the portal. As the preservation is enabled by recent technological advances and the process of archival is increasingly streamlined, it is expected that a higher number of experiment-internal analysis codes will be available for RECAST.

6.6.3. RECAST examples. ATLAS-internal analysis examples and results: A number of reinterpretation publications have been supported by the back end underpinning RECAST. After Run 1, ATLAS has conducted a thorough reinterpretation of the SUSY landscape in the context of the phenomenological pMSSM [528], a study involving 20 SUSY analyses and 50 000 fully simulated pMSSM parameter points. While at that time, most analyses had to be reinterpreted manually, the 2L electroweak analysis [529] included in that paper served as a prototype analysis and provided results using the highly automated RECAST back-ends.

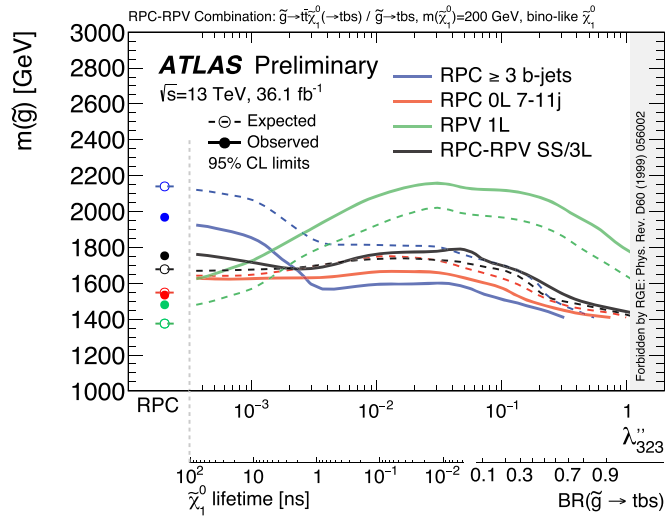


Figure 85. Exclusion limits as a function of λ''_{323} and $m(\tilde{g})$ as a result of an internal reinterpretation of several ATLAS SUSY results. Expected limits are shown with dashed lines, and observed as solid. Taken from [243].

The analysis was then later re-used with minimal additional effort in two further publications that focused on more domain-specific SUSY realizations: a five-dimensional DM reinterpretation of electroweak seaches [530], as well as a reinterpretations in the context of general gauge-mediated models [531].

Recently ATLAS has reinterpreted ten analyses [243] in terms of models of supersymmetry with non-vanishing baryon number-violating coupling strength λ'' partly through the use of the new analysis preservation infrastructure. In such models the lightest neutralino is unstable with a decay length of

$$L(\text{cm}) = \frac{0.9\beta\gamma}{\lambda''^2} \left(\frac{m(\tilde{q})}{100 \text{ GeV}} \right)^4 \left(\frac{1 \text{ GeV}}{m(\tilde{\chi}_1^0)} \right)^5. \quad (6.12)$$

This reinterpretation required a joint re-execution of a mix of analyses originally designed for R -parity-conserving and RPV models and special systematics have been added into the statistical analyses to account for the detector response and flavor-tagging rate of displaced jets. Results were presented in a two-dimensional parameter space of gluino mass and neutralino lifetime (or analogously the λ'' coupling) as shown in figure 85. Such reinterpretations are difficult to perform outside of the experiments, as the publicly available information lack details of the detector and analyses.

Third-party tool integration. Both the CheckMate [486, 487] and the Rivet [490] analysis catalogues have been implemented in the analysis execution framework. Both are configured to analyze events that are provided in the HepMC format [532]. Due to the modular approach of the analysis back end, a number of MC generation workflows, such as Herwig [533], SHERPA [534] or MadGraph [238], can be used depending on their ability to correctly model the desired signal.

For analyses where multiple implementations exists, e.g. from multiple third-party tools such as Rivet BSM, CheckMate or MadAnalysis [488, 489] as well as from multiple

experiment-internal configurations (fast simulation, full simulation), RECAST will allow the community to compare and contrast reinterpretation results.

6.6.4. Outlook. Thanks to industry-backed technological advances, a realistic technical solution to the problem of analysis preservation for the LHC experiments and the original RECAST proposal has come into view. The initial use of such infrastructure for the reinterpretation for prompt SUSY searches is generalized easily for LLP searches as the tools used for signal simulation, analysis preservation, and execution do not make simplifying assumptions on the nature of the BSM signal or analysis structure. As such, RECAST may cover reinterpretation use cases, where either third-party reinterpretations are impossible due to missing public information or limitations of third-party tools or accurate, experiment-approved results are desired.

6.7. Reinterpretation with prompt analyses

Since the decay time probability of an unstable particle follows an exponential decay law (dependent upon the mean lifetime), some percentage of the decays of the LLP will occur outside the detector, leading to an \cancel{E}_T signature if the LLP is electrically and color neutral. Likewise, some part of the LLP decays can appear ‘promptly’. Prompt searches with and without \cancel{E}_T can therefore provide additional, corroborating constraints on models with LLPs, especially for short lifetimes. Therefore, it is important to understand the sensitivity of prompt searches to displaced objects.

Reinterpreting prompt searches in the context of LLPs is, however, quite nontrivial, because (a) prompt searches may or may not make explicit requirements on the PV and (b) it is currently not documented how reconstruction efficiencies drop as a function of small displacement. Thus, the reinterpretation of prompt searches in the context of LLPs is currently best done within the collaborations themselves.

An example of such an experiment-internal reinterpretation can be found in a CMS search for an RPV SUSY model where pair-production of stops each proceed through an RPV decay to a b quark and a lepton. A dedicated long-lived search for this model exists in the $e\mu$ channel [197]. This search includes selection criteria which require the transverse impact parameter to the IP be greater than $10 \mu\text{m}$. This maximizes sensitivity to the long-lived model and greatly reduces SM backgrounds. It also necessarily highly reduces the sensitivity of the search at low stop lifetime. The exclusion curve in the stop lifetime ($c\tau$) versus top squark mass is shown in the left frame of figure 86.

A reinterpretation was performed of a search for pair-production of second generation LQs [535, 536]. In this model, massive LQs are pair-produced. Each of these bosons then decays to a muon and c quark, leading to a final state with two muons and two jets from c quarks. In the prompt limit of the RPV SUSY model with a final state of two muons and two jets from b quarks, the kinematics of the LQs are nearly identical. In the LQ search, no selection is made on jet flavor. The LQ search uses final selections which are optimized to the event kinematics for each LQ mass hypothesis, but the search in general strives to remain as model-independent as possible. In this case, the reinterpretation was simply performed using the original LQ analysis, and replacing the signal samples with the long-lived RPV samples, only taking into account the reduced branching fraction to the final state with two muons and two jets. The expected and observed exclusion curves of the reinterpretation are shown in the right frame of figure 86.

The reinterpretation gives large improvements for lifetimes $\sim 1 \text{ mm}$, and as expected, contributes little in the large lifetime limit. This type of reinterpretation is valuable not only

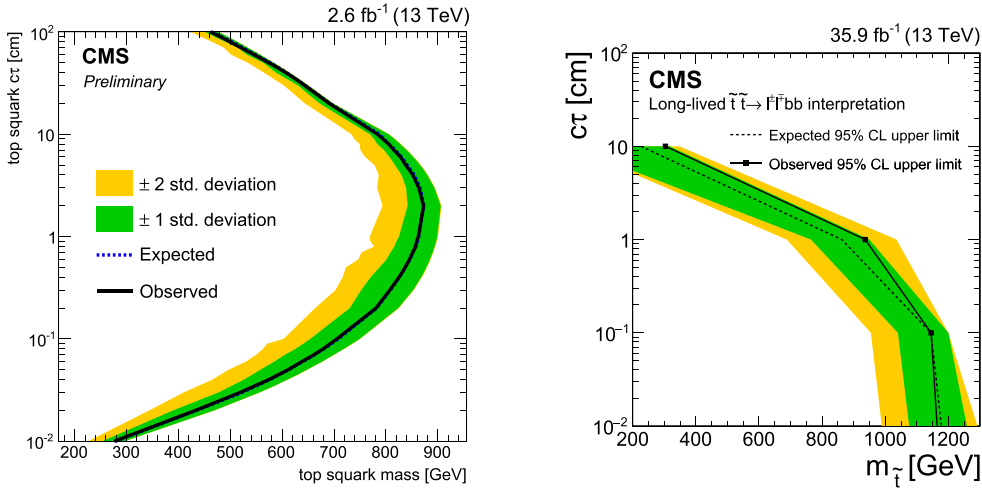


Figure 86. Left: expected and observed 95% confidence level limits in the $c\tau$ - $M_{\tilde{t}}$ plane from the displaced lepton search [197] for pair-production of long-lived stops decaying to b quarks and leptons. Right: exclusion on the pair-production of long-lived stops decaying to b quarks and leptons in the $c\tau$ - $M_{\tilde{t}}$ plane, from the prompt reinterpretation of the second generation LQ search [536].

because it extends coverage of a given model, but also because it helps guide the analysts performing the dedicated search to focus their efforts in areas which are truly uncovered.

Reinterpretations like this one, which provide meaningful results without placing a large burden on analysis teams, should be highly encouraged. Other reinterpretations along these lines can be found in [537–539]. Another relatively simple reinterpretation is [243], although in this case, it should be noted that the original analysis was modified in a simple way, that is, the reliance on tracking information to identify jets and suppress non-collision background was removed, in order to be sensitive to long-lived gluinos.

6.8. Our proposals for the presentation of results

Here we summarize the recommendations for the presentation of searches involving LLPs. These recommendations follow from the detailed examples presented in sections 6.3 and 6.4.

Our primary recommendation is that the experiments provide as detailed information as possible to make a general recasting feasible. We therefore encourage the experiments to:

- A.1. Provide LLP reconstruction and selection efficiencies at the signature or object level. Although the parametrization of efficiencies is strongly analysis dependent, it is advantageous if they are given as a function of model-independent variables (such as functions of DV d_0 , p_T , η , etc), so they do not rely on a specific LLP decay or production mode.
- A.2. Present results for at least two distinct benchmark models, with different event topologies, since it greatly helps to validate the recasting. For clarity, the input cards for the benchmark points should also be provided.
- A.3. Present cut-flow tables, for both the signal benchmarks and the background, since these are very useful for validating the recasting.

- A.4. When an analysis is superseded, differences and commonalities with previous versions of the same analysis should be made clear, especially if the amount of information presented in both analyses differs. The understanding as the extent to which the information presented in an old version can be used directly in a later version greatly helps the recasting procedure, and also highlights ways in which the new search gains or loses sensitivity relative to the superseded analysis.
- A.5. Provide all this material in numerical form, preferably on HEPdata, or on the collaboration wiki page. A very useful resource we also highly encourage is a truth-code snippet illustrating the event and object selections, such as the one from the ATLAS disappearing-track search [218] provided in HEPdata under ‘Common Resources’.

We realize that implementing the above recommendations requires an enormous amount of time and effort by the collaborations and may not always be feasible to the full extent. However, good examples of presentations are already available, such as the parametrized efficiencies provided by the ATLAS 13 TeV DV [237] (see the auxiliary material to [519]) and the CMS 8 TeV HSCP [495] analyses.

When the object- or signature-level efficiency maps are not feasible, providing efficiencies for an extensive, diverse array of simplified models can be useful for reinterpretation. Concerning simplified-model results, we recommend that the experiments:

- B.1. Provide signal efficiencies (acceptance times efficiency) for simplified models and not only upper limits or exclusion curves. Note that efficiencies for *all signal regions*, not only the best one, are necessary for reinterpretation.
- B.2. Present efficiency maps as a function of the relevant simplified-model parameters, such as the LLP mass and lifetime, with sufficient coverage of the simplified-model parameter space. While for direct production of LLPs the parameter space is two-dimensional (LLP mass and lifetime), simplified models with cascade decays have a higher-dimensional parameter space. In these cases we strongly recommend efficiencies to be provided for a significant range of *all* the parameters.
- B.3. Release the efficiencies in digital format (on HEPdata or the collaboration wiki page), going beyond the two-dimensional parameterization suitable for paper plots whenever necessary. In particular, for auxiliary material, we recommend multidimensional data tables instead of a proliferation of two-dimensional projections of the parameter space;
- B.4. Consider in each analysis a range of simplified models which aim to encompass:
 - (a) Different decay modes, including distinct final-state particles and multiplicities.
 - (b) Different LLP boosts (for example, provide efficiencies and limits for distinct parent particle masses, which decay to the LLP).

Although extensive, the above recommendations for the choice of simplified models allow for a thorough comparison between the range of validity of the LLP analyses and a detailed test of recasting methods. Furthermore, when an MC-based recasting is not available, one can use the ‘nearest’ simplified model or a combination of them to estimate the constraints on a theory of interest. Finally, if a sufficiently broad spectrum of simplified models is covered, this can be useful for quickly testing complex models which feature a large variety of signatures, and rapidly finding the interesting region in a model scan before going to more precise but computationally more expensive MC simulation.

We hope that our recommendations, in particular, points A.1–A.5, will serve as a guide for best practices and help establish a reliable and robust reinterpretation of LLP searches. The added value for the experiments and the whole HEP community will be the immediate

and more precise feedback on the implications of the LLP results for a broad range of theoretical scenarios, including gaps in coverage.

7. New frontiers: dark showers

Chapter editors: Simon Knapen, Jessie Shelton

Contributors: Michael Adersberger, James Beacham, Malte Buschmann, Cari Cesarotti, Marat Freytsis, Gregor Kasieczka, Dylan Linthorne, Sascha Mehlhase, Siddharth Mishra-Sharma, Matt Reece, Sophie Renner, Jakub Scholtz, Pedro Schwaller, Daniel Stolarski, Yuhsin Tsai

7.1. Introduction: the anatomy of a dark shower

Hidden sectors are increasingly common features in many models that address mysteries of particle physics such as the hierarchy problem, the origins of DM, baryogenesis, and neutrino masses, in addition to being a generic possibility for physics BSM; ‘hidden valleys’ are one such broad class of hidden-sector scenarios [66, 69]. Given the complexity of the SM, such hidden sectors may very well have rich dynamics of their own, with numerous far-reaching implications for their phenomenology [67, 68, 70, 71, 540]. The main LHC signatures predicted by such hidden valley models are characterized by an injection of a large amount of energy into a hidden sector, which is then shared among a large number of relatively soft particles [70]. We will refer to this class of signatures, where rich dynamics internal to the hidden sector yields a high multiplicity of dark states, as ‘dark showers’. Given that the particles emerging at the end of this process are necessarily both comparatively light and secluded from the SM, their lifetimes can easily become long, thus giving rise to displaced signatures at the LHC.

Long-lived particles are especially generic predictions of hidden valleys with confining gauge groups, similar to QCD in the SM [66]. It is worth noting that QCD already provides many familiar examples of LLPs, realizing macroscopic lifetimes through a hierarchy of scales (Λ_{QCD}/m_W) combined with approximately preserved symmetries (K_L , B and D hadrons) or restricted phase space (n). Also provided by QCD are numerous examples of particles that have a hierarchy of lifetimes. For instance, charged pions experience a slow decay through a very off-shell W boson, while neutral pions can decay much faster through their anomalous coupling to photons. The neutral pion lifetime is thus orders of magnitude shorter than the lifetime for charged pions. Both long-lived species and a hierarchy of lifetimes between species are generic predictions and nearly unavoidable consequences of confining theories which produce dark showers. However, LLPs with a hierarchy of lifetimes also arise naturally in non-confining hidden sectors, especially in theories with multiple species. A familiar example from the literature is theories with dark photons. Here, a small kinetic mixing can make the dark photon long-lived, but a simple, well-motivated extension of the model by a dark Higgs boson introduces additional dark species and production mechanisms for dark states that are independent of the small coupling controlling the macroscopic lifetime. This naturally yields high-multiplicity events featuring particles with a hierarchy of lifetimes [32, 230, 456].

More generally, a dark shower topology can be broken down in three components (see figure 87), each of which allows for a large degree of variation between models:

1. *Production.* A dark shower event begins with the production of one or more heavy states which decay into the dark sector. These heavy states could be part of the SM, most

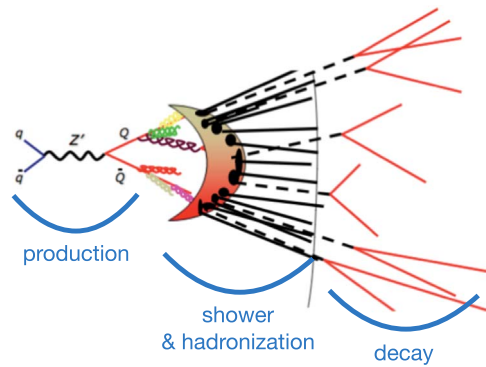


Figure 87. Schematic representation of a dark shower event, in this case from hidden valley model with a Z' production portal. Figure adapted from [71].

notably the Higgs boson, or could be a new particle from the menu of BSM states we have become accustomed to (Z' s, color triplets/octets, electroweak doublets/triplets, etc). In some cases the production mechanism provides an important trigger handle (e.g. VH production for the Higgs), but this is not universal (e.g. Z' production). The options for production are laid out in section 7.2.

2. *Showering and hadronization.* If the dark sector contains an asymptotically free gauge group, the originally produced particles will shower and possibly hadronize within the dark sector. This yields a final state with a potentially large number of dark states, similarly to how quarks and gluons undergo showering and hadronization to yield a jet of hadrons. The shape of the shower and the p_T spectrum depends on the coupling of the dark gauge group: the shower may be pencil-like, as in QCD, completely spherically symmetric, or something in between. Alternatively, it is possible that the hidden sector does not contain a gauge sector but instead features a perturbative cascade decay over a large number of states. Indeed, in certain cases the perturbative picture is dual to the strongly coupled showers. In general, showering and hadronization are the sources of greatest uncertainty from a theory perspective; the current status and some new results are discussed in section 7.3.
3. *Decay.* After the dark degrees of freedom hadronize (or reach the bottom of the cascade in perturbative models), they can decay back to the SM. The decay may occur through the same (off-shell) portal as the production, but this is not essential, and one may expect multiple species with a range of lifetimes. The specifics of the decay step (e.g. muon multiplicity) are particularly important if there is no good trigger handle from the production topology. Decays are frequently interconnected with showering and especially hadronization, however, and it is not tractable to enumerate all possibilities without making simplifying assumptions and/or inserting additional theory prejudice. For this reason it is often useful to focus on the species with the largest multiplicity and/or shortest (macroscopic) lifetime; this frequently provides a reasonable guide to the overall signatures, just as one may obtain a reasonable $O(1)$ picture of QCD jets by considering only their pions. We survey a (non-exhaustive) list of popular decay portals in section 7.4.

A priori it is typically possible to construct a model by choosing an ingredient from the menu of options for each of the three components outlined above. This is an enormous model space, and it may appear daunting to construct searches capable of capturing all possibilities.

On the other hand, the signatures of these models are often so striking that they enable powerful, inclusive searches, sensitive to a very large portion of this overall model space, provided that triggers allow the event to be recorded. Toward this end, it is useful to observe that dark shower events have the following generic features:

1. Events have a *variable and potentially large multiplicity of LLPs*. The number of produced particles of various dark species depends on the details of the parton shower and/or hadronization, as in QCD, and varies from event to event. Typically there are more than two LLPs per event.
2. The BSM species produced in dark showers exhibit a *hierarchy of proper lifetimes*. This could result in production of, e.g. mostly prompt particles with a few displaced decays; mostly invisible detector-stable particles with a few displaced decays within the detector; or anything in between.
3. *LLPs are not generically isolated*, i.e. they often appear within $\Delta R \sim 0.4$ of other LLPs and/or prompt objects (such as the decay products of short-lived species originating from the same shower).
4. The *energy flow in the event reflects the evolution of the BSM parton shower and hadronization*, and thus looks non-SM-like. For instance, hidden sector jets may be either narrower or broader than QCD jets, depending on the hidden sector gauge group, gauge coupling, and particle spectrum. Additionally, SM particle multiplicity—i.e. the relative fractions of pions, kaons, etc, produced in a jet—differs from QCD. While energy flow can be a powerful discriminant to separate dark showers from the SM at any stage from the trigger level forward, it is model dependent and must be assessed on a case-by-case basis. Note that this also implies that traditional (displaced) jet triggers do not suffice to cover the general model space, and alternative trigger strategies (e.g. track or muon multiplicity) are needed as well.

The existence of ~ 2 LLPs per event, and indeed frequently $N_{\text{LLP}} \gg 2$, generally ensures that these events can be easily distinguished from background if they can be recorded on tape and subsequently reconstructed. However, the unique features of events with dark showers require new strategies to ensure that this class of theories is actually captured by the trigger. In particular, non-isolation and the hierarchy of proper lifetimes can result in qualitatively novel collider signatures that require new triggering approaches. Meanwhile, event-level observables such as non-SM-like energy flow or particle multiplicity are potentially powerful but highly model-dependent discriminants, and must be considered on a case-by-case basis. We discuss the strengths and shortcomings of existing triggers and off-line strategies in sections 7.5 and 7.6, as well as a number of new ideas. An executive summary of our main points and recommendations is provided in section 7.7. The chapter concludes with a collection of example models for which MC event samples are currently available (see section 7.8).

7.2. Production

Events with dark showers generically begin with the pair production of dark partons Q_D . In most cases the two produced partons are of the same species, but this does not necessarily need to be true. For clarity and simplicity, we confine ourselves to the case where Q_D is a SM singlet. Then the production modes for Q_D can be simply related to the production modes discussed for neutral LLPs in section 2.4, in the chapter on Simplified Models. In particular, the most relevant production modes are:

- *Heavy parent*: Pair production of a SM-charged HP X_D , which subsequently decays via $X_D \rightarrow Q_D + (\text{SM})$. The SM quantum numbers of the parent X_D , together with its mass, control both the overall production cross section and the typical prompt AOs in the event. Depending on the lifetime of X_D , showering can begin before or after its decay. The model of [331] features this production mechanism, where the parent X_D is a heavy scalar carrying both color and dark color charges. After QCD pair-production, the mediators each decay into a visible jet and a dark shower.
- *Higgs (HIG)*: Production in exotic Higgs decays, $h \rightarrow Q_D \bar{Q}_D$. As the Higgs boson provides an especially sensitive window into low-mass dark sectors, this production mechanism is one of the best-motivated at the LHC [67, 117]. In particular, Higgs portal production is the dominant production mechanism in many Twin Higgs and related models of neutral naturalness [118, 263, 541]. The Higgs boson determines the overall mass scale of the event, often awkwardly low for LHC triggers, while the branching fraction remains a free parameter. As discussed in section 2.3.1, the SM Higgs has a characteristic set of accompanying prompt objects, which can extend trigger options. As also emphasized in section 2.3.1, this category additionally encompasses production through parent Higgs-portal scalars, which may be either heavier or lighter than the SM Higgs.
- *Z' (ZP)*: Here a new Z' boson couples to both SM and hidden sector states, allowing for production through $q\bar{q} \rightarrow Z' \rightarrow Q_D \bar{Q}_D$. This scenario was developed in the original hidden valley models [66, 69], and considered again recently in [372]. The Z' mass determines the overall mass scale, while production cross sections depend on its couplings to both SM and hidden sector states. The only typical AOs are ISR radiation.
- *Charged current*: Here the parent dark states couple to the SM through the neutrino portal, $\mathcal{O}_{\text{int}} = HL\mathcal{O}_{\text{dark}}$. When the dark states carry charge under a dark gauge group, this coupling requires (at least) two dark states, one fermionic and one bosonic. For instance, if the dark sector contains both scalar and fermionic fundamentals, ϕ and ψ , respectively, then one can construct the dimension five interaction $\mathcal{O}_{\text{int}} = HL\phi^*\psi$. This production mode has not been well studied in the literature. It is worth noting that given this dark field content, it is generically possible to also construct Higgs portal couplings, $\mathcal{O}_H = |H|^2|\phi|^2$, $|H|^2\bar{\psi}\psi$, which can generally include lower dimensional operators.

As we have taken Q_D to be SM singlets, the first process discussed in section 2.4, direct pair production, is typically negligible. Of course, if BSM mediators connecting the dark sector to the SM, like the X_D and Z' in the examples discussed above, are heavy enough to be integrated out at LHC scales, then the resulting higher-dimension operators can mediate direct pair production of Q_D . Single production of Q_D is generally suppressed, and in many cases impossible, in particular when Q_D transforms nontrivially under an unbroken gauge group. In Abelian theories, single production of a dark gauge boson is possible, e.g. through a loop of heavy bi-charged matter; this gauge boson can then subsequently shower. In perturbative cascades, a single BSM state Q_D may certainly be produced, but whether Q_D goes on to produce one or more ‘showers’ is highly dependent on the detailed kinematics of the event.

In contrast with most of the simplified models in section 2.4, after a parton Q_D is produced it undergoes extensive evolution in the hidden sector, so that there is no one-to-one connection between the initial Q_D and relevant detector objects. Thus, an event that begins with two partons may result in a final state that contains two pencil-like jets, each containing more than one displaced object; a spherical distribution of displaced objects; or anything in between.

The most important consequences of production modes for our purposes are twofold. First and most importantly, the production mode informs the types of prompt AOs in an event, as well as determining overall event rate and energy scale. These AOs can be useful levers to distinguish signals from SM background, beginning at the trigger level. Secondly, production modes rely on a mediator that couples the dark sector to the SM, which may be a BSM particle like a bifundamental X_D or a Z' , or a SM particle like the Higgs boson. In many models, this mediator-SM coupling also ultimately governs the decay of the dark sector states back into the SM. This is the case for the examples of [66, 67, 69, 118, 263, 331, 372, 541, 542], and is certainly the minimal possibility. It is worth mentioning, however, that decays may be governed by a different interaction than production. As a simple perturbative example, consider the hidden abelian Higgs model. This theory can realize dark showers in a variety of ways; consider for concreteness the perturbative cascade decay chain $h \rightarrow ss, s \rightarrow Z_D Z_D$, which can yield collimated pairs of dark photons when $m_s \ll m_h$ (see, e.g. [543]). In this case a Higgs portal interaction governs production, but the long-lived Z_D decays back to the SM through a separate vector portal interaction.

7.3. Shower

7.3.1. Motivation. A familiar feature of QCD is the formation of jets, sprays of approximately collinear hadrons arising from a parton emitted in a hard scattering process. The physics of jet formation is independent of hadronization or confinement, originating in the singularities of the weakly coupled theory at short distances [544], where the 't Hooft coupling is $\lambda \equiv g_s^2 N_c \ll 1$. In perturbation theory, the differential probability for a quark to radiate a gluon carrying a small energy fraction z at small angle θ is

$$P(z, \theta) dz d\theta \sim \frac{\lambda}{4\pi^2} \frac{dz d\theta}{z \theta}, \tag{7.1}$$

independent of the underlying hard process. The logarithmic divergences at $z, \theta \rightarrow 0$ indicate that perturbative theories favor radiation that is *soft* (low energy) and *collinear*. This enhanced emission of collinear radiation is the source of jets, even in theories that do not confine at all, such as the perturbative, conformal Banks–Zaks gauge theories [545]¹⁹⁷. The large logarithms appearing in these calculations can be numerically resummed through Markov Chain algorithms, leading to the *parton showers* widely used to model jets in MC simulations.

In the limit of strong 't Hooft coupling¹⁹⁸ ($\lambda \gg 1$) perturbation theory breaks down; soft and collinear radiation are no longer enhanced over more general radiation at wide angles. In QCD, the coupling gradually runs strong in the infrared, but other gauge theories (which could be realized in nature as hidden valleys [66]) exist that have an intrinsically large 't Hooft coupling persisting over a wide energy range. Such theories can be understood with the use of gauge/gravity duality. Examples may be conformal, e.g. strongly coupled $\mathcal{N} = 4$ super-Yang–Mills, or confining, e.g. those detailed in [547, 548]. Such large- λ theories were conjectured to lead to spherical event shapes [70], a result that has been directly proven for strongly-coupled large- N_c CFTs [549]. At colliders, these spherical events would lead to

¹⁹⁷ See [546] for a brief and clear recent introduction to jet physics emphasizing the role of scale invariance.

¹⁹⁸ When making this and similar statements below, we always implicitly mean the coupling at the energy scales being probed by a given measurement. For example, while QCD does become strongly coupled near its confinement scale, treating the theory as weakly coupled is justified provided one only ever talks about jet masses and energies at much larger scales.

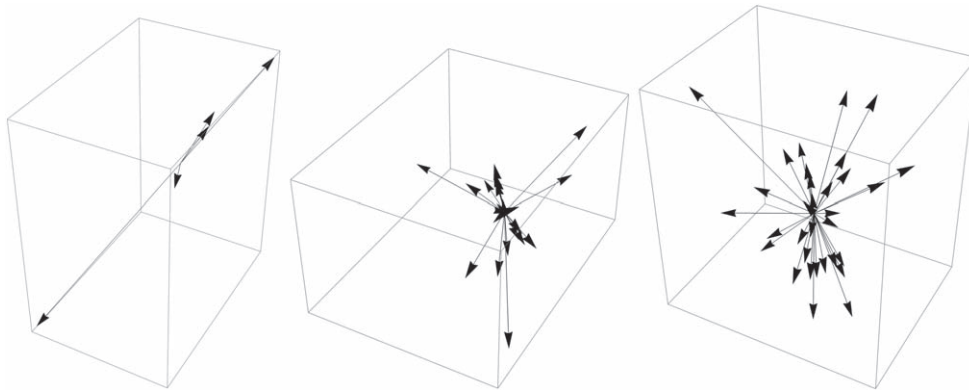


Figure 88. Illustrations of event shapes, from jetty (left) to spherical (right) with an intermediate event in the middle. The values of Sphericity and Thrust are: (left) Sphericity = 0.006 36, Thrust = 0.991; (center) Sphericity = 0.530, Thrust = 0.706; (right) Sphericity = 0.940, Thrust = 0.521.

characteristic soft unclustered energy patterns (SUEPs) [182, 242, 550]. An illustration of the range of event shapes from jets to SUEPs is shown in figure 88.

Thus we have two well-understood regimes, jets at $\lambda \ll 1$ and SUEPs at $\lambda \gg 1$. There is a gap in the middle when $\lambda \sim 1$ over a wide range of energies. Both perturbative QCD and gravitational duals approach strong coupling in this regime (from different sides) and cannot be trusted to give accurate predictions; for some questions, the predictions may not even be qualitatively accurate.

This regime is of interest because we want to ensure that LHC experiments do not miss a hidden valley signal simply because it looks different than expected. We should aim to be able to trigger on and analyze these events. While sufficiently long lifetimes may provide useful trigger handles, theories at intermediate 't Hooft coupling could also occur with prompt decays while still failing to provide the types of trigger handles typically associated with prompt hard production and decay. Given our inability to reliably calculate the predictions of this scenario, in this section we will take a pragmatic approach: we push the two tools we have, perturbation theory and gauge/gravity duality, into a regime where we do not fully trust them. To the extent that their predictions overlap, one could gain confidence in the qualitative picture we obtain. Where they differ, one would hope that experimental strategies broad enough to encompass the range of possibilities would also be sensitive to poorly modeled scenarios. In the following we present some initial results, which we aim to improve and expand upon in future published work.

7.3.2. Phenomenological models

7.3.2.1. Parton showers and their limits. One can approach the intermediate regime from the direction of weak 't Hooft coupling using parton shower methods. The coupling is then a direct parameter of the model whose value is easy to vary. However, naïvely setting the coupling to large values would quickly lead to unphysical results. The reason is that the simplest derivation of parton shower evolution equations assume that the final state can be organized as a series of splittings where $z, \theta \ll 1$ at each iteration. Since the full matrix element for a given final state has no uniquely-defined splitting history associated with it, this soft, collinear condition needs to hold as a function of the final-state kinematics alone. As the

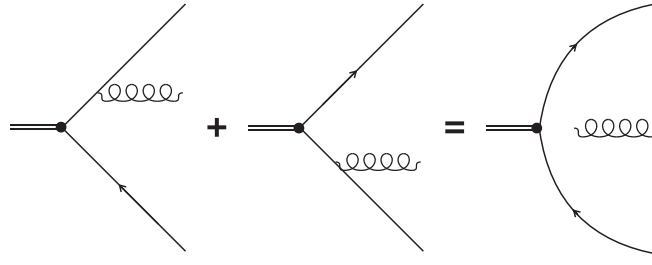


Figure 89. Schematic view of a $2 \rightarrow 3$ branching process, with the initial two-particle state approximated as a localized dipole. For more details and further discussion see [551].

coupling is increased, the increased showering probability means that there is an increased chance of populating the phase space while violating these conditions. Regions of phase space without nominal soft-collinear enhancements (but in truth populated with comparable probability) will end up under-populated, leading to more jet-like events than the underlying theory actually predicts.

Things can be somewhat improved by a more careful consideration of parton-shower methods. It is currently known how to implement iterated corrections allowing one to relax one, but not both, of the inequalities given above. Implementations which allow for the correct inclusion of finite- z (but small- θ) effects can be accomplished by extending the approximation of equation (7.1) with terms non-singular in z .

If we have reason to believe that the wide-angle structure of dark showers will be more critical to detecting models in the transition region, sacrificing finite- z corrections for a better understanding of the finite- θ region is preferable. This requires going beyond the $1 \rightarrow 2$ splitting picture of equation (7.1) as information about multiple particles in the event must be encoded. A known solution is to phrase the shower in the language of $2 \rightarrow 3$ evolution kernels [552], where radiation is treated as coming from dipoles rather than individual charges, as in figure 89. Necessarily more complicated, in this approach the splitting function describing the emission of a gluon with momentum p^μ is then expressed as

$$P(p_r^\mu) d\Phi_r \sim \frac{\lambda}{s_{ij}} \left[\left(1 - \frac{s_{ir}}{s_{ij}} - \frac{s_{rj}}{s_{ij}} \right) \left(\frac{2s_{ij}^2}{s_{ir}s_{rj}} + \frac{s_{ir}}{s_{rj}} + \frac{s_{rj}}{s_{ir}} \right) \right] \quad (7.2)$$

$$+ \text{non-singular}] d\Phi_r, \quad (7.3)$$

$$s_{ij} = (p_i + p_j)^2. \quad (7.4)$$

for the process $a + b \rightarrow a + r + b$. Features related to the expected broadening of jets at larger coupling will be well-modeled deeper into the transition region with a dipole shower. Angular structure will be correctly reproduced even at larger couplings while final-state energy sharing of collinear particles becomes increasingly untrustworthy. When some sort of angular localization of energy flow can be expected (i.e. soft-collinear enhancements are still present) the corrections at finite splitting angle may still provide a good approximation.

7.3.2.2. Gauge/gravity duality: spheres to jets. Gauge/gravity duality allows calculation in $\lambda \gg 1$ theories with spherical events, from which we extrapolate toward the $\lambda \sim 1$ regime. The

simplest case is Anti-de Sitter (AdS)/CFT duality, where events are perfectly spherical [549]. AdS space is a warped product of a $(3 + 1)$ D Minkowski space with an infinite fifth dimension. To obtain a theory with a discrete spectrum, we cut off the fifth dimension of AdS space at a hard wall or *IR brane* as in Randall–Sundrum (RS) models [553]. 5D fields then decompose into a tower of 4D Kaluza–Klein (KK) modes (dual to hadrons in the gauge theory), each with an associated wave function in the fifth dimension. This wave function, as well as the 4D mass, is calculated by solving the equations of motion up to quadratic order. The couplings between 4D mass eigenstates are proportional to the overlap of their wave functions in the fifth dimension.

Heavy KK modes decay to lighter modes, which decay to still lighter modes, populating a cascade of particles. The case of a flat (unwarped) extra dimension yields sinusoidal wave functions and modes with linearly spaced masses. In this case, the *KK number* is a conserved discrete momentum in the fifth dimension, and KK modes decay only to daughters at threshold. The RS model breaks translation invariance in the fifth dimension, so KK number is no longer exactly conserved and a variety of decays are possible. Nonetheless, for the simple model of a bulk cubic coupling, KK number is still approximately conserved, as illustrated in figure 90, top panel, and the sum of the two daughter modes is approximately equal to the KK mode of the parent. At each step of the cascade, daughter particles have small momentum. This results in spherical event shapes, with no highly boosted daughters [554]. Here we have studied a scalar field with a Φ^3 interaction for simplicity, with the expectation that qualitative features of the event shapes persist in more realistic models.

To push our toy model into the jetty regime, we introduce interactions that explicitly break KK number themselves. We continue to study the simple case of a scalar field, but now, to move toward jettier events, we include the Φ^3 interaction as a boundary term, restricted to the IR brane. As shown in figure 90, right panel, this opens up a much wider range of possible decays with greater phase space, which lead to more variety in the resulting event shapes. We emphasize that moving the Φ^3 term to the boundary is a simple toy model for the purpose of this section that accomplishes the goal of altering event shapes. However, it is not expected to be a good approximation of the dual of an actual confining gauge theory with smaller λ .

Although the IR brane interaction is used here as an ad hoc tool for generating less spherical events, we expect that similar results can be achieved in a more principled way. As λ decreases toward $O(1)$ values, the expectation from gauge/gravity duality is that more bulk fields, dual to the many single-trace operators in the gauge theory, become light. This suggests that models with several interacting bulk fields are a more faithful toy model of the physics of the dual gauge theories at intermediate λ . Such models could be of interest for a wider set of questions than event shapes, as they move the AdS/QCD toolkit—always a toy model at best—somewhat qualitatively closer to QCD. Such models and their consequences will be studied in a forthcoming publication.

7.3.3. Results. We wish to characterize to what extent our available methods allow us to model the range of behaviors we might expect from new showering sectors. Since we do not expect collimated sprays of final-state particles to be a sensible way of organizing information in the event in all cases, for our purposes here we focus on observables that can be defined globally. In particular, we study a pair of event-shape variables that have proven useful to both establish and provide precision data on the non-abelian nature of QCD.

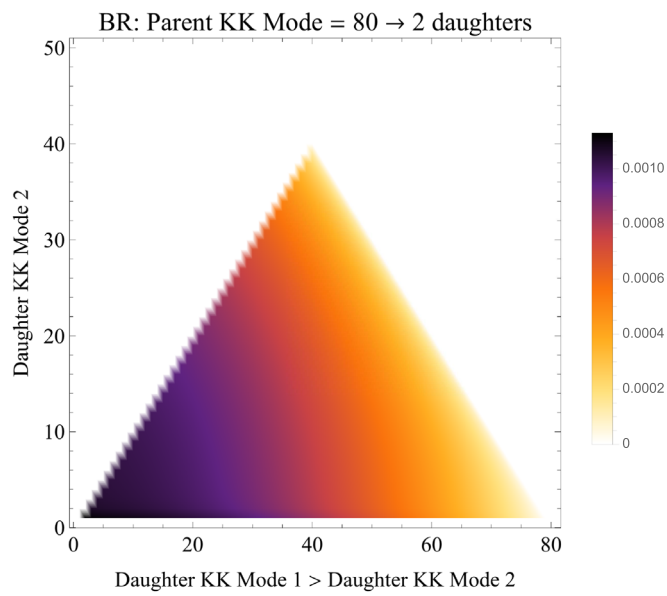
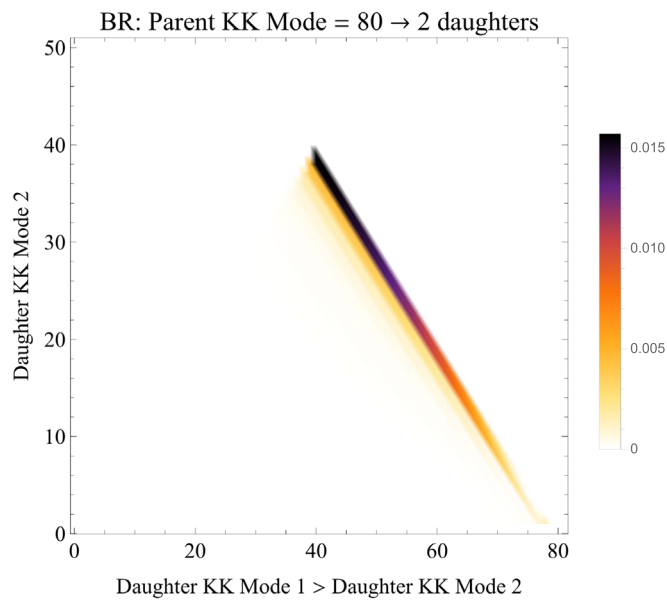


Figure 90. The branching ratio from a parent with KK-number 80 into two daughters for a cubic interaction on the bulk (top) or on the boundary (bottom). The nonzero probabilities occur along the line where KK-number is conserved for the bulk interaction, whereas the boundary interaction has non-zero probability to decay with large jumps in phase space.

Sphericity is defined as the scalar sum of the two smaller eigenvalues of the sphericity tensor

$$S^{ab} = \frac{\sum_i p_i^a p_i^b}{\sum_i |\mathbf{p}_i|^2}, \quad (7.5)$$

where the sum is over all final-state particles in the event [555]. With the eigenvalues λ_i defined in decreasing order, we have $S = \frac{3}{2}(\lambda_2 + \lambda_3)$, which can take on the values $0 \leq S \leq 1$. Thrust is instead defined via a maximization procedure with respect to all possible axes in the event [556],

$$T = \max_{|\mathbf{n}|=1} \frac{\sum_i |\mathbf{n} \cdot \mathbf{p}_i|}{\sum_i |\mathbf{p}_i|}. \quad (7.6)$$

Both observables essentially measure the divergence of an event from the pencil-like final-state structure of a $2 \rightarrow 2$ scattering process without making any direct reference to jets.

Historically, thrust had the advantage of being infrared and collinear safe. In a given event, the change in the thrust due to an additional radiated parton vanishes as the parton becomes soft or collinear to the thrust axis. Singular regions of phase space thus do not contribute to finite values of the thrust, and its measured distribution in QCD is well described by a perturbative calculation up to corrections that scale as $O(\Lambda_{\text{QCD}}/Q)^2$, where Q is a high-energy scale associated with the total system being probed by the thrust. This is not the case for sphericity—specifically a perfectly collinear splitting still changes the value of the sphericity tensor. A perturbative calculation of the sphericity is then divergent for finite values of sphericity, a divergence which can be tamed by either an explicit cutoff at the hadronization scale supplemented by a phenomenological hadronization model (the approach taken by MC generators) or by absorbing it into a form factor (as done in analytic calculations). In either case $O(1)$ sensitivity is induced to the region of phase space dominated by non-perturbative hadronization effects. For our concerns, this difference can be turned into an advantage, as any apparent difference between the two observables can act as a diagnostic of the sensitivity of our predictions to the non-perturbative parameters in the parton shower.

We generated events from models expected to yield a range of behaviors. We considered extra-dimensional models with both bulk and boundary interactions, with the former expected to yield very isotropic events. For the parton shower, we used a modified version of the VINCIA dipole-antenna parton shower [557] in which an $SU(N)$ gauge theory with only light quarks showers and hadronizes into light mesons with masses $m_{\pi_v}/\Lambda_v \sim m_{\pi}/\Lambda_{\text{QCD}}$. We then varied the Coupling boundary conditions and one-loop running while adjusting shower cutoffs to ensure that couplings remain perturbative throughout the parton shower.

We summarize the results in figure 91, with the uncertainty in the parton shower distributions coming from considering both transverse-momentum and dipole-virtuality shower ordering. The similar behavior of the two distributions indicates that sensitivity to non-perturbative effects from hadronization are not large. The lowest sphericity/highest thrust distribution is fairly close to that expected from QCD, but a wide range of non-QCD-like behaviors is observable. A significant fraction of the allowed range for these observables is populated by a combination of the extra-dimensional and the parton shower approaches, and the boundary interaction KK model and parton shower models give similar results.

Examining the behavior of observables that are perturbatively incalculable in the weakly coupled theory indicates that a degree of caution is warranted, however, with the two approaches giving qualitatively different results to certain questions. As an example, we look at the correlation between sphericity and total event multiplicity for the two closest parton

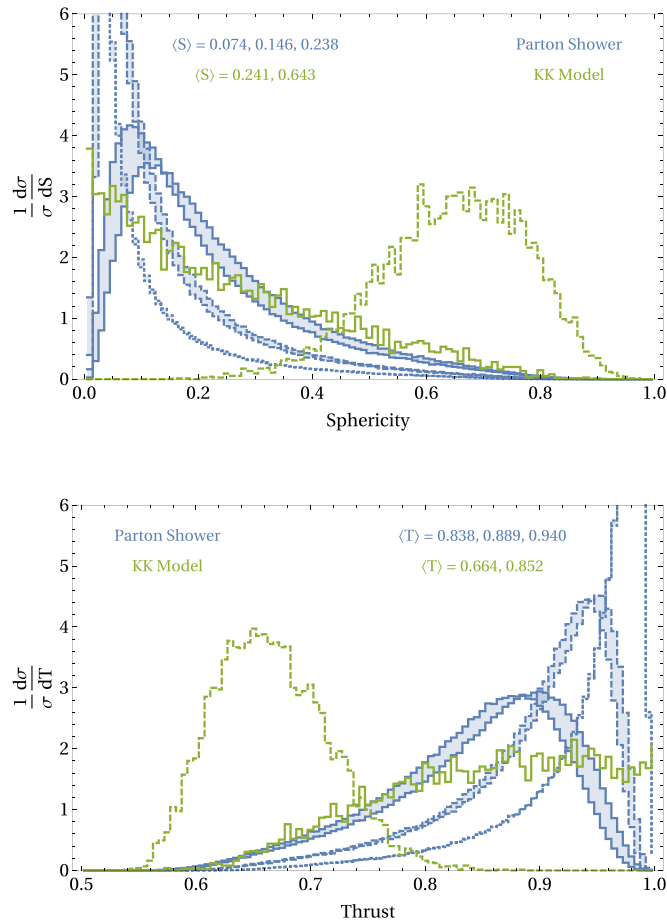


Figure 91. Comparison between accessible ranges of parton shower and AdS/CFT-inspired models (labeled ‘KK model’) for sphericity and thrust. In the parton shower, the curves correspond to events produced at $\sqrt{s} = 100\Lambda$, with confinement scale Λ ; the shading indicates the uncertainty resulting from comparing transverse momentum and dipole virtuality shower ordering. The β functions of the theories are tuned such that $g^2(100\Lambda)/4\pi$ is 0.06, 0.12, 0.24 for the 3 distributions. In the KK model case, the dashed curve corresponds to a bulk interaction while the solid curve corresponds to a boundary interaction. We also show expectation values for all distributions.

shower and extra-dimensional models. Displayed in figure 92, we see that multiplicity is broadly correlated with sphericity in the parton shower, while being nearly sphericity independent for the KK model. Such qualitative differences between the parton shower and the extra-dimensional models warrant more detailed study of event behavior in the transition region, while both approaches would benefit from further consideration of how jet-level observables, whether physically well-justified or not, vary over their accessible ranges.

7.4. Decay

In general, the mass spectrum of confining hidden sectors is poorly known, with the exception of a few special cases, like pure glue confining theories [558] and the SM QCD sector. The

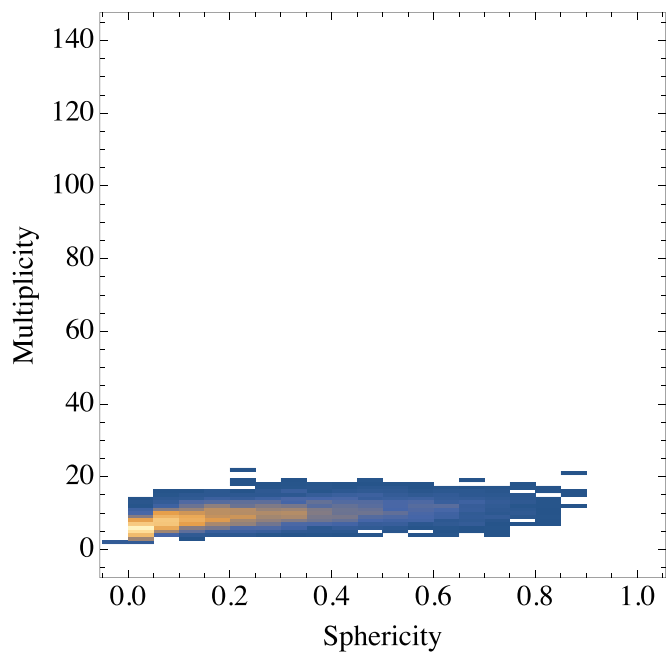
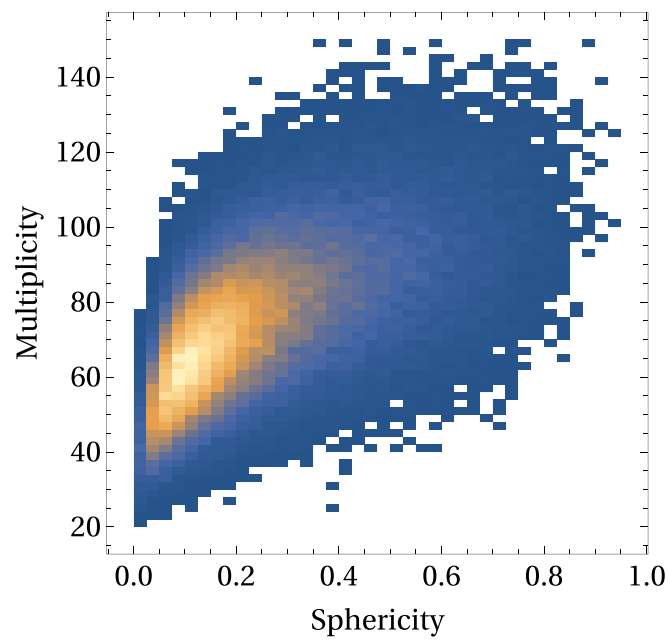


Figure 92. Correlation between sphericity and hadron multiplicity for events generated with parton shower (top) and AdS/CFT-inspired models with boundary interaction (bottom).

dynamical process of hadronization is even less well understood, and one must typically resort to uncontrolled extrapolations from the measured fragmentation functions in the SM. Moreover, states with different CP and spin quantum numbers can have greatly different lifetimes even in well-understood examples [66, 540, 559], a problem that is further exacerbated if the hidden sector contains one or more approximate flavor symmetries. For concreteness we here primarily focus on the case where only one dark species has a detector-scale lifetime; other dark states may either decay promptly to the SM or appear as MET. A useful special case realizing this scenario is one in which all internal hidden sector decays are sufficiently rapid for heavier hidden states to promptly decay down to the lightest state in the spectrum, which in turn decays to the SM. The discussion below is focused on the possible properties of this lightest hidden state which decays to the SM. We refer to it as ‘the’ LLP, keeping in mind that in complete models there may very well be multiple species of LLPs. It is therefore important to emphasize that *experimental strategies should not be overly optimized* towards the naïve assumption of a single LLP giving rise to all visible decays, as it may not be generically true. In particular, an inclusive experimental strategy should avoid making detailed assumptions about the distributions of proper lifetimes of long-lived states in the event.

7.4.1. Portals and branching ratios. The available decay channels and branching ratios of the LLP are critical both for the trigger strategy and the off-line analysis. In particular, various (multi-)muon triggers can be very effective for models where the LLP branching ratio to muons is not too small. At the same time, displaced hadronic decays tend to give more discriminating power in the off-line analysis, since they produce a larger number of tracks as compared to the leptonic modes. Since each event contains multiple LLPs, a single event can contain *both* leptonic and hadronic vertices, where one uses the former for the trigger and the latter for off-line background rejection. For this reason it is not straightforward to interpolate sensitivity between lepton-rich and hadron-rich hidden showers, since the optimal search strategy for the intermediate cases is qualitatively different from the strategies for the two extremes.

As a starting point for our exploration, we therefore recommend a small number of theoretically motivated decay portals, which cover the fully leptonic and fully hadronic cases, as well as two other intermediate scenarios. We focus our attention on operators of dimension four or five which do not induce additional flavor violation in the quark sector:

- *Neutrino portal:* If the LLP is a neutral, possibly composite, fermion X , it may decay through a small mixing with the SM neutrinos. This state predominantly decays through the $X \rightarrow \ell^+ W^{-(*)}$ and $X \rightarrow \nu Z^{(*)}$ channels and its decays tend to be rich in leptons. The muon fraction in the final states depends on the mixing angle of the X with the muon neutrino, which is model dependent. However, even if this angle is accidentally small as compared to the mixing angles with electron and tau neutrinos, one still expects a muon in roughly $\sim 10\%$ of all decays through the $W^{(*)}$ channel. In τ -rich scenarios, muons also originate from leptonic τ decays.
- *Hypercharge portal:* It is plausible for a dark sector to contain a vector particle, whether it is an elementary $U(1)$ gauge boson or a composite (the analogue of the ρ in the SM). An elementary vector boson can be copiously produced through decays of a hidden sector meson through a chiral anomaly, analogous to π^0 decay in the SM. Whether elementary or composite, such a vector state generically mixes with SM hypercharge through the kinetic mixing operator $\epsilon B^{\mu\nu} F'_{\mu\nu}$, where $F'_{\mu\nu}$ is the dark vector boson field strength. The

Table 11. Probability of finding exactly one muon/two muons in one LLP decay through the photon and Higgs portals. For the lowest mass points, the branching ratios for the photon and Higgs portals were taken from [458, 440], respectively. For the 8 and 15 GeV benchmark the hadronization was performed with Pythia 8 [219, 501].

Mass (GeV)	Photon	Higgs
0.5	0/0.4	0/0.09
1.2	0/0.35	/
8	0.08/0.16	0.25/0.02
15	0.1/0.15	0.3/0.05

branching ratios of such a state then depend on its mass and can be extracted from data, as shown in table 11 (see, e.g. [230, 458]).

- *Higgs portal:* In the same spirit, it is possible that a hidden sector scalar S mixes with the SM Higgs boson through the $SH^\dagger H$ operator. In this case, its branching ratios to SM fermions are proportional to m_f^2 , with the caveat that non-perturbative effects modify the story substantially for $m_S \lesssim 5$ GeV. For $m_S \gtrsim 1$ GeV, hadronic branching ratios can be obtained through chiral perturbation theory; however, in the intermediate range $1 \text{ GeV} \lesssim m_S \lesssim 5 \text{ GeV}$, the theory uncertainties are substantial and we do not attempt to make any quantitative statements in this regime (see [560] and references therein). As shown in table 11, the muon branching fraction predicted by Higgs-portal decays is smaller than for the previous two portals, but it can still be relevant if the (non-isolated) muons from B -meson decays are taken into account.
- *Gluon portal:* The hidden scalar (S) or pseudoscalar (a) could also decay to the SM through a coupling to gluons of the form $S \text{Tr} G^{\mu\nu} G_{\mu\nu}$ or $a \text{Tr} G^{\mu\nu} \tilde{G}_{\mu\nu}$. In this case the direct leptonic branching ratio is zero, although a small number of muons may still be produced in the hadronization process of the gluons.
- *Photon portal:* Similar to the gluon portal, the LLP could decay to two photons through the $S F^{\mu\nu} F_{\mu\nu}$ or $a F^{\mu\nu} \tilde{F}_{\mu\nu}$ operators. The signature for this case is qualitatively different from the previous four, since there are many fewer tracks. In particular, tracks only originate from photon conversions in the detector and suppressed Dalitz decays to $e^+e^-\gamma$. The signal is therefore a trackless jet with a high rate of energy depositions in the ECAL relative to the HCAL.

If the lifetime of the LLP is $\mathcal{O}(50)$ m, dark showers generically give rise to multiple decays within the detector volume. In table 12 we show the probability for the Higgs and hypercharge portals to produce an event which contains at least three or four muons, as a function of the number of decaying LLPs in the event. Assuming the event has at least four LLP decays, a multi-muon trigger has good efficiency for the Higgs portal above the $b\bar{b}$ threshold¹⁹⁹ and for all masses for the hypercharge portal²⁰⁰. This trigger strategy should also have good efficiency for neutrino-portal decays, although this scenario is more model dependent. For the gluon and photon portals a different set of triggers is needed, as discussed below. The lesson is that multi-muon triggers do not suffice to cover all possible options, but could provide a reasonably generic trigger path for an important subset of the relevant models.

¹⁹⁹ The importance of muons in decays which are rich in heavy flavor was emphasized in [71].

²⁰⁰ Again, this statement is LLP-lifetime dependent, and for sufficiently long-lived LLPs this strategy will break down as the probability of getting sufficiently large numbers of LLP decays within the detector becomes small.

Table 12. Probability of finding at least 3 muons/at least 4 muons in an event for the photon and Higgs portals, as a function of the number of LLP decays. Branching ratios and hadronization were determined as in table 11.

	Mass (GeV)	3 decays	4 decays	5 decays	6 decays	7 decays
Photon	0.5	0.36/0.36	0.53/0.53	0.67/0.67	0.77/0.77	0.85/0.85
	1.2	0.29/0.29	0.44/0.44	0.57/0.57	0.68/0.68	0.77/0.77
	8	0.13/0.07	0.23/0.13	0.33/0.21	0.42/0.28	0.5 /0.35
	15	0.14/0.07	0.23/0.13	0.33/0.2	0.42/0.27	0.51/0.35
Higgs	0.5	0.02/0.02	0.04/0.04	0.07/0.07	0.1/0.1	0.13/0.13
	8	0.04/0.0	0.09/0.02	0.15/0.04	0.23/0.07	0.31/0.12
	15	0.11/0.02	0.21/0.07	0.33/0.13	0.44/0.21	0.55/0.31

7.4.2. Lifetime. Without additional model assumptions, the theory prior on the lifetime of the LLP is rather weak. We can, however, extract some insight from the generic scaling of the width of the LLP as a function of its mass (m): for the Higgs and hypercharge portals, $\Gamma \sim m$; for the photon and gluon portals, $\Gamma \sim m^3/f^2$ with f the decay constant of the LLP (in this case, the LLP behaves similar to an axion-like particle, or ALP); for the neutrino portal, $\Gamma \sim m^5/m_W^4$. The obvious trend in all cases is that the lifetime rises as the mass decreases, steeply so for the case of the neutrino portal. It is furthermore important to note that the above scalings are lower bounds, and in many models the leading decay portal involves a higher-dimensional operator, leading to a stronger scaling with mass. This is especially relevant in confining models where the hidden states are composite particles. For example, in a pure-gluon hidden valley coupled through the Higgs portal [559], the lightest glueball can decay through its mixing with the Higgs, but as the portal coupling contains the dimension-four combination of dark gluon field strengths $G_{\mu\nu}^a G^{a\mu\nu}$, its width scales as $\Gamma \sim m^7 \times (v_h/M^2 m_h^2)^2$, where we have taken $m \sim \Lambda_D$, the scale of dark QCD, and M is the suppression scale of the portal operator.

An additional consideration is that the LLP can be discovered directly in (low energy) collider or beam-dump experiments. Since the LLP has an irreducible production cross section through the same coupling that governs its decay, collider experiments effectively impose a lower bound on the lifetime of these states. Beam-dump and supernova constraints on the other hand rely on a displaced signal and constrain the lifetime from above. These bounds are, however, not typically applicable for masses above a few hundreds of MeV (and for a summary of some of the latest constraints on the hypercharge, photon and gluon portals see, e.g. [561, 562]). However, particles that can be produced in sizable numbers at the LHC are in general coupled sufficiently strongly to the SM that they face upper limits on their lifetimes from BBN. In most cases, this upper bound is essentially mass independent and requires $\tau \gtrsim 1$ s, but this upper bound can be much weaker for lighter particles and/or particles that decay to hadron-poor final states. For the photon, gluon and hypercharge portals, prompt decays are currently allowed for masses all the way down to the electron threshold, though for the hypercharge portal LHCb is expected to completely close this window below ~ 100 MeV [341, 382]. For the Higgs portal, current LHCb results from b to s transitions [267, 268] already require $c\tau \gtrsim 0.5$ mm for masses below 4 GeV. For the neutrino portal, lifetimes $c\tau \gtrsim 10$ m are excluded if the mass is below 1 GeV and the mixing is predominantly with the electron and muon neutrino [563].

As argued above, if the mass of the LLP is larger than a few hundred MeV, their lifetime is only constrained from above by BBN. In the context of a dark-shower topology, there is, however, a much more stringent upper bound to lifetimes that can be probed at the LHC. In particular, to observe at least a handful of decays in the detector volume, the lifetime in the lab frame should satisfy

$$c\tau_{\text{lab}} \lesssim 10 \text{ m} \times \frac{N_{\text{LLP}}}{N_{\text{decays}}} \quad (7.7)$$

with N_{LLP} the typical LLP multiplicity and N_{decays} the number of observed decays in the detector²⁰¹. For instance, for $N_{\text{decays}} \sim \text{few}$ and $N_{\text{LLP}} \sim \mathcal{O}(10)$ this implies $c\tau_{\text{lab}} \lesssim 50 \text{ m}$.

Near this heuristic upper limit in the LHC's sensitivity to lifetime, the shower effectively gets stretched out over the detector elements, and it is useful to study how the decays are distributed over the different detector elements. We can use a toy MC to make some simple estimates of this effect by making the following simplifying assumptions: (1) the number of LLPs is Poisson distributed; (2) their decay lengths follow the usual exponential distribution with uniform average lifetime in the lab frame $c\tau_{\text{lab}}$; (3) the angular distribution of the vertices is approximately spherical in the lab frame. Figure 93 shows the distribution of the number of decays occurring in the tracker, calorimeter and muon chamber for two benchmark points. We hereby assume for concreteness the approximate CMS geometry with the 'tracker', 'calorimeter' and 'muon chambers' defined by $r < 100 \text{ cm}$, $100 \text{ cm} < r < 200 \text{ cm}$ and $400 \text{ cm} < r < 700 \text{ cm}$, respectively. We find that the number of decays in all detector components is roughly equal, with slightly more decays in the muon chamber for a higher number of LLP decays in the shower. The latter result is easily understood from the larger size of the MS as compared to the tracker and the calorimeter. The qualitative conclusion is that tracker-based searches for multiple DV are likely to have reasonable sensitivity over the whole relevant lifetime range. For the longer lifetimes, the sensitivity necessarily degrades although it can be partially recovered by incorporating the muon chamber in the analysis. On the other hand, searches relying exclusively on the muon chamber or the calorimeter are less sensitive to a wide range of lifetimes. To quantify this effect more accurately, detailed simulations for specific benchmark models accounting for more realistic boost and η distributions are needed, although the relative importance of the tracker is likely to continue to hold. The displaced SUEP scenario is an interesting exception, as discussed in section 7.6.2.2.

7.5. Trigger strategies

7.5.1. General considerations. Due to the immense diversity of hidden sector models, there is no trigger strategy which can comprehensively cover all options, nor is it straightforward to compile a list of such strategies. This problem is further compounded by the lack of available MC simulations, except in a handful of special cases. Many of the considerations informing the trigger strategies discussed for singly and doubly produced LLPs in chapters 3 and 5 apply to dark shower events as well. However, the four characteristic features of dark showers laid out in section 7.1 can pose both additional opportunities and challenges:

1. *The particle multiplicity can range from high to very high.* This in itself can provide a very powerful trigger strategy, especially when the muon fraction in final states is appreciable, as discussed in section 7.4.1. For models where this is not the case or where the muons are too soft to fire the trigger, triggers relying on a large multiplicity of tracks

²⁰¹ If only one or two LLPs are expected in the detector, then the dark shower maps onto the topologies with one or two DV discussed earlier in this document.

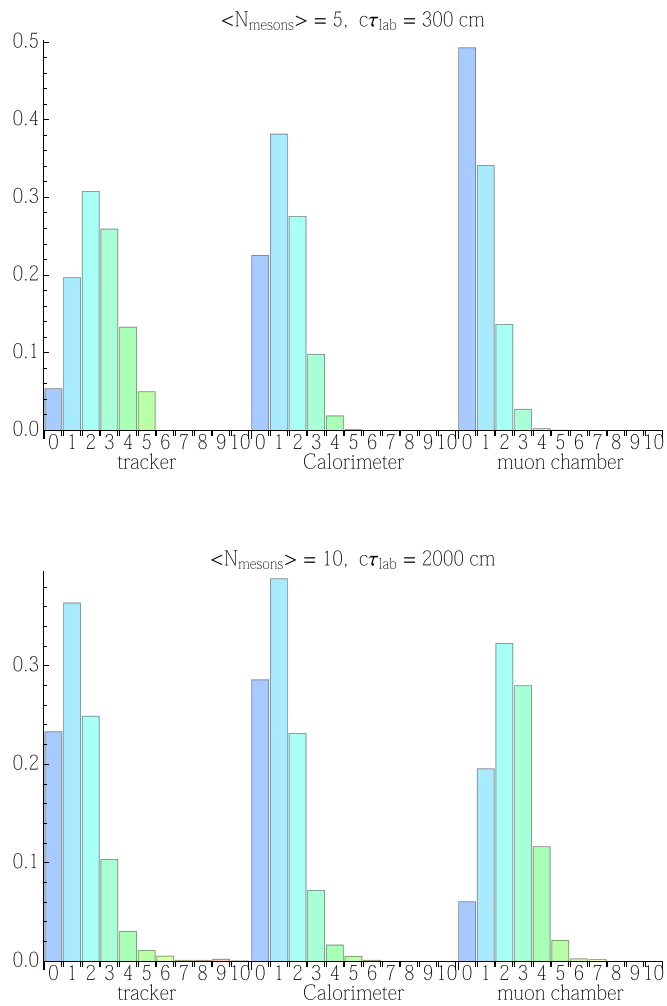


Figure 93. Distribution of decays occurring in the various detector elements, for those events with more than three decays occurring in the fiducial volume.

or an over-density of pixel hits could provide an alternative strategy. We will return to this discussion later in this section.

2. *The hidden sector may contain states with vastly different lifetimes.* While this makes it challenging to get a comprehensive grasp on the full space of possible event topologies, this feature provides interesting opportunities from the point of view of the trigger. For instance, often the most striking off-line signature is a set of DV in the tracker, which are notoriously challenging targets for the trigger. It is completely plausible that these vertices would originate from the decay of one species of hidden sector particles, while a second species decays either promptly or very displaced. This means that the event may very well come with prompt leptons, H_T , an appreciable amount of E_T , and/or activity in the muon chamber.
3. *The decay products may not be isolated.* Combining the first two features, we should prepare for the possibility that the objects we aim to use as trigger handles may not be

isolated. Especially for triggers on muons and (displaced) tracks, it is advisable to relax isolation criteria as much as possible and instead rely on the presence of one or more additional objects to reduce rates as necessary. For example, one would expect that a trigger on two isolated muons would be less effective than a trigger on three or four non-isolated muons or a trigger with two non-isolated muons and a moderate amount of \cancel{E}_T . Non-isolation is likely to be a limiting factor for the acceptance of dark shower events in specialized triggers designed for singly- or doubly-produced LLPs.

4. *The energy flow in the dark shower may be non-standard.* This implies that a dark shower may be broader or narrower than SM QCD jets, and the momentum distribution of the particles in the shower may also differ substantially from QCD predictions. This means that triggers for (trackless) jets could be effective for some models, but would by no means capture the full range of possibilities. Since such p_T distributions are very model dependent, it is moreover sensible to keep object p_T thresholds as low as possible, and instead rely on the high multiplicity by requiring multiple low p_T objects, rather than a few high p_T objects.

In summary, while some dark shower models will be very challenging to trigger on, this is not true for the entire class of models. For example, some (although certainly not all) models can readily be captured on the traditional \cancel{E}_T , H_T or lepton triggers. This means that these traditional triggers *are an excellent place to start, but a bad place to stop*. Indeed, in the context of limited resources, it makes sense to first pursue the scenarios where the trigger is not a major challenge and use these scenarios to develop off-line reconstruction techniques. It is, however, crucial to follow up with more innovative trigger strategies. While this is largely still a topic of study, we can identify two categories of non-traditional triggers:

1. *Triggers on displaced objects:* This type of trigger is notoriously challenging due to bandwidth and online computing limitations, but nevertheless a lot of progress has been made in the last few years. This is discussed in chapters 3 and 5. For our purposes here, it suffices to note that high multiplicity of LLPs in dark shower events can help provide excellent acceptance in such triggers, provided that any isolation criteria in the trigger are not spoiled by shorter-lived objects in the event.
2. *Specialized triggers for dark showers:* There are a number of (speculative) ideas for triggers which exploit the high multiplicity and/or energy features of a dark shower, as described above, although this area is much less developed than the triggers on displaced objects. We will discuss these ideas for specialized triggers briefly in the remainder of this section, and comment on the unique capabilities of LHCb when it comes to triggering on dark showers.

7.5.2. Specialized trigger ideas. In this subsection we briefly highlight some proposals for specialized trigger strategies that inherently depend on the unique features of dark shower events.

7.5.2.1. Multiplicity triggers. As emphasized throughout this chapter, dark shower models can produce a high multiplicity of dark particles, ranging from several tens up to thousands of particles in the most extreme case. This motivates triggers that aim to minimize p_T thresholds and instead exploit high particle multiplicity. The most obvious option is a suitable multi-muon trigger (three, four, or more muons), where the priority should be to avoid tight isolation criteria, if needed at the expense of increasing the muon multiplicity and/or p_T thresholds. Prompt multi-muon triggers would, however, only capture (nearly) prompt

decays, and it is critical to pursue the design and implementation of a trigger with good efficiency for displaced muons; see section 5.1.3 for more on planned displaced muon triggers.

Another way of exploiting the particle multiplicity is to trigger on an anomalously large number of tracks originating from the PV. This would likely only work for prompt or nearly prompt decays, in models which produce a rather low muon fraction and/or a very soft p_T spectrum. For this strategy to work, one must first pass the L1 trigger with MET, which can be provided by the shower itself or by initial state radiation (ISR). At the HLT it may be possible to count the number of tracks with the planned ATLAS HTT system or the future CMS HTTs. Alternatively, if the tracks are too soft and the multiplicity high enough, it is possible to pass the HLT by looking for an over-density of hits in the innermost tracking layer, centered around the z -coordinate of the PV [242].

7.5.2.2. Substructure triggers. Substructure triggers may open up the possibility of using substructure techniques to distinguish between QCD jets and other types of showers already at the trigger level. CMS currently uses jet trimming at HLT level to enhance acceptance for jets with hard splittings, optimized for boosted electroweak gauge bosons, (see, e.g. [564, 565]), and we are aware of an effort within ATLAS to investigate the inclusion of substructure routines at the HLT level. This strategy could be helpful in cases such as photon-jets (dark showers that decay into SM photons), which can otherwise pose significant trigger challenges: substructure variables such as n -subjettiness [566] and energy-energy correlations can be very effective at separating QCD jets, photons and photon-jets [567, 568]. In practical terms, this means that one may be able to use the relatively low threshold jet/tau trigger for the L1 trigger. This could be followed by a HLT trigger that uses, for instance, the ratio of the energy deposited in the ECAL/HCAL or substructure variables.

An advantage of substructure methods is that they are fairly robust with respect to the lifetime of the dark shower final states, provided the lifetime is not too long compared to the size of the relevant detector sub-system. As long as the showering process itself happens quickly (and provided that hadronization represents a small correction to the typical particle momenta), the separation between energy depositions in the calorimeter is already pre-determined. In particular, under these assumptions it does not matter if the SM decay products of the lightest dark states are themselves collimated. A clear difficulty with substructure triggers is that the actual dark showering and hadronization process, and therefore the substructure, is theoretically only understood in a handful of example models as discussed in section 7.3. While such a trigger is clearly valuable for a number of models, it is at the moment difficult to evaluate how broadly applicable it could be to different shower shapes.

7.5.2.3. Non-isolated DV trigger in the ATLAS MS. For sufficiently LLPs, fallback trigger strategies can be provided by existing ATLAS triggers that require a cluster of hits in the MS [241, 257]. As these triggers look directly for the presence of displaced objects and do not rely on any features of the rest of the event, they offer potential sensitivity to signals dominantly produced at low mass scales. The existing MS DV trigger requires at least three (barrel) or four (endcap) tracks in the MS [257]; a dedicated vertex-finding algorithm is run on these events at the analysis level. Thus this trigger option offers good sensitivity to hadronic decays of particles with mass $\lesssim 5$ GeV, but cannot provide sensitivity to individual di-leptonic or photophilic decays, nor to decays of LLPs with GeV-scale masses.

In Run 1, LLP searches with DV in the MS relied on a trigger that recorded events where the DV additionally passed isolation requirements. Specifically, events were required to have no tracks with $p_T > 5$ GeV in the ID within $\Delta R < 0.4$ of the DV, and the distance to the

nearest jet (with $E_T > 30$ GeV) was required to be $\Delta R_j > 0.7$. However, this isolation cut was not imposed for jets with anomalously large energy deposition in the HCAL, $\log_{10}(E_{\text{had}}/E_{\text{EM}}) > 0.5$ in order to improve acceptance for LLPs decaying in the outer edges of the HCAL [241]. This isolation requirement can limit acceptance for models with dark showers where multiple BSM species can spoil each other's isolation, especially in cases where the shower contains both short-lived as well as long-lived dark particles. It is an open question whether tracks from sufficiently DV in the ID would contribute to the track veto, but particles that decay within the ID would be likely to spoil the isolation requirements through calorimeter deposits alone, unless their decays involved only muons.

New in Run 2 is a trigger on *non-isolated* clusters of hits in the MS [258], which uses the same triggering algorithm for the MS hits but does not impose isolation criteria. The primary aim of this trigger is to enable background estimation for single DV searches [262], but it would also efficiently record dark shower signal events, regardless of event shape or event energy scale, provided at least one particle species in the shower has $m \gtrsim 5$ GeV, decays to final states with at least three charged particles, and has reasonable probability to decay in the MS. This trigger may be especially useful for high-multiplicity signals, where the probability for getting one particle to decay in the MS can become appreciable even for shorter-lived LLPs.

7.5.2.4. Capabilities at LHCb. The LHCb detector is designed for studying displaced decays of SM mesons. This provides a good environment to search for dark shower events containing LLPs with lifetimes below the meter scale [68]. Although LHCb does not yet have a dedicated trigger for dark shower events, many of the trigger strategies used for SM meson searches may be applied to dark shower signals. The LHCb detector is a single-arm forward spectrometer covering the pseudorapidity range $2 < \eta < 5$, which means the signals for which it is optimal have typical p_T that is much lower than the signals targeted by ATLAS and CMS. Hence, the LHCb signal trigger usually has much weaker p_T requirements compared to an ATLAS or CMS search. This allows for better observation of dark shower events that come from the decay of light parent particles boosted in the forward direction, such as dark mesons from the decay of a light Z' .

For example, [387] searches for a pair of LLPs decaying into jet pairs. Although the signal is different from a dark shower, the trigger strategy in the search can be useful for dark shower events. The hardware trigger (L0) requires a single hadron, electron, muon, or photon with object-dependent p_T thresholds. For muons (hadrons), the thresholds are $p_T > 1.48$ (3.5) GeV, and given the rapidity range of the signal, this corresponds to momenta $p > 6$ (13) GeV for muons (hadrons). These low p_T requirements can thus keep soft and low-mass dark meson decays that can be hard to trigger on at ATLAS and CMS. The software trigger contains algorithms that run a simplified version of track reconstruction and an identification of displaced tracks and vertices, and the first software stage (HLT1) requires a high-quality displaced track satisfying the above p_T requirement. In [387], the final trigger stage (HLT2) further requires a DV with ≥ 4 charged tracks, and either a > 2 mm decay length in the transverse direction or the reconstructed vertex mass > 10 GeV. Since the search focuses on b -quark final states, the HLT2 trigger also contains a multivariate algorithm to identify b -hadron decays. Although the trigger is designed for LLPs heavier than 10 GeV scale, it is important for LHCb to determine if the same strategy can be applied to even lighter particles or different decay final states.

For specific decay channels of dark mesons, we can also adapt triggers from existing SM hadron searches that look for the same final states [383]. For example, if dark mesons decay into muon pairs or c -quarks, we can use similar triggers as in the $K_s \rightarrow \mu^+\mu^-$ [569] or

$B^0 \rightarrow D^+D^-$ [570] searches to study the signal. A more recent muon trigger is used for the 13 TeV dark photon $A' \rightarrow \mu^+\mu^-$ search [269], where a muon with $p_T > 1.8$ GeV is required at the hardware trigger level, and further quality cuts on the DV and muon identification are required. This search can be useful for dark mesons that decay through a kinetic mixing, in which muon final states have a sizable branching ratio.

Planned upgrades at LHCb are further discussed in section 5.2. These upgrades will make LHCb an even more powerful facility for studying LLPs, particularly in the low-mass and short-lifetime regime, and further study of LHCb's capabilities for dark showers is well warranted.

7.5.2.5. Low PU data. While Run 2 of the LHC has brought unprecedented opportunities for discovery of new physics with a large $\sim 150 \text{ fb}^{-1}$ dataset of 13 TeV pp collisions, the ability to explore the energy frontier comes at a cost: high trigger thresholds and challenging experimental conditions may limit the sensitivity of LHC experiments to BSM models such as SUEPs with soft and diffuse signatures. During Run 2 data-taking, the typical $\langle \mu \rangle$ value has already reached ~ 60 interactions per bunch crossing.

The low PU datasets provided by the LHC during Run 2 therefore present an interesting opportunity for dark showers. There are two such data sets: one with 0.5 fb^{-1} at 13 TeV and $\langle \mu \rangle = 2$ and one with 0.3 fb^{-1} at 4 TeV and $\langle \mu \rangle = 5$. While the size of these datasets is much lower than the 13 TeV high- μ pp dataset, the change in data-taking conditions is amenable to searches for BSM scenarios which would normally be difficult to distinguish from PU noise, and low-background searches may be performed under circumstances that would otherwise be impossible.

In low PU data, object-multiplicity (track- or cluster-based) triggers (section 7.5.2.1) are typically run with lower thresholds and higher rates than otherwise may be possible. The ability to cleanly reconstruct low- p_T tracks and vertices or soft calorimeter clusters could provide the only way to experimentally access some low-mass LLP scenarios. Simple analyses in this modest dataset may provide the first limits on some models, and these results could help direct the more advanced developments discussed throughout this report.

7.5.2.6. Zero bias strategy. If all other strategies fail to capture the signal, the zero bias strategy is an ultimate fallback [571]. In this case one would simply rely on passing the L1 trigger due to an object in an unrelated PU event. The effective dataset one can ultimately obtain this way is only $\sim 0.5 \text{ fb}^{-1}$, though it might increase to $\sim 50 \text{ fb}^{-1}$ if a specialized selection could be made at the high level trigger.

7.6. Off-line analysis

In this section we discuss aspects of the off-line analyses needed to discover dark showers. As has been a primary theme throughout this chapter, hidden sector states with displaced decays are generic, but prompt decays are possible as well. Naturally cases with and without promptly decaying species require different strategies. Though the main focus of this document is on long-lived phenomena, showers where *all* species are short-lived are closely related to the signals of our main interest and provide valuable illustrations of tools and techniques that can ultimately shed light on the underlying hidden sector dynamics itself, and we accordingly provide a discussion of prompt showers as well.

7.6.1. Prompt decays. We begin by discussing dark showers with promptly decaying BSM states, i.e. with no reconstructable displaced decays in the event. Promptly-decaying dark

showers are substantially more challenging to separate from backgrounds than showers containing LLPs, as the presence of multiple displaced objects is a very powerful background-suppression tool. However, the techniques that have been proposed and/or used for prompt showers are important for several reasons. First, they provide a useful illustration of how the unique properties of showering events have been approached in analyses to date without introducing the separate complication of displacement. Second, dark showers that produce prompt SM particles may very well also produce LLPs, thanks to the hierarchies of lifetimes that are generic in confining theories. Such events can thereby produce *semi-visible jets* [372], which contain detector-stable invisible states as well as promptly-decaying states. These semi-visible jets pose some specific challenges in analysis and reconstruction, as we briefly review below.

If SM particles resulting from the dark shower are produced promptly, there are two possible experimental handles: the portal through which the hidden sector couples to the SM, and the structure of the dark shower itself. The former case depends on the operators mediating the production and decay of showering states, as described in sections 7.2 and 7.4. For example, for decays governed by the Higgs, photon, and neutrino portals, one may expect an unusually muon-rich jet (section 7.4). Similarly, the jet may be semi-visible (section 7.6.1.1) if some of the states do not decay in the detector volume. On the other hand, if the SM final states are almost purely hadronic, as when decays are governed by the gluon portal, no such obvious handles are available and one must look at the substructure of the jets themselves to find differences from those in typical QCD events. The discussion below is organized according to the typical size of the dark shower, going from narrow QCD-like jets to large-radius jets and finally to fully spherical topologies (SUEPs).

7.6.1.1. QCD-like jets ($R \approx 0.4$). The case of LJs, originally motivated by DM considerations, provides an example of showering with noticeably different particle content than a QCD shower. Here, visible decays of the dark states are primarily to leptons [155, 572], which can occur either due to other decays being kinematically inaccessible or due to selection rules. The most striking signature of the model is the presence of collimated sprays of leptons rather than hadrons in the final state. Reconstructing these objects requires the elimination of lepton isolation criteria typically imposed on leptonic final states, together with variables such as layer-specific cuts on energy deposited in the ECAL, and a fraction of HT TRT hits and/or activity in the muon chambers, selecting for electromagnetically dominated radiation. Searches for prompt lepton jets have been performed by the ATLAS and CMS collaborations [274, 573].

A more elaborate prompt scenario is the case of *semi-visible jets* [372]. Here, the visible final states are hadrons, as in typical QCD jets, but missing energy is interleaved with the visible final states as only some fraction of the states produced in the dark shower decay back to SM particles, while others escape the detector. Semi-visible jets fail to provide the dramatic handles of the lepton jet scenario. However, by considering combinations of large amounts of \cancel{E}_T and differing cuts on $\Delta\phi$, the angular separation between the \cancel{E}_T and the closest jet, control of both SM backgrounds and discrimination from more typical SUSY-like high \cancel{E}_T scenarios can be achieved. Bounds on showers with a fraction of between 0.2 and 0.9 of produced dark hadrons decaying invisibly should allow for bounds comparable to conventional resonance searches [574].

If event-level handles like lepton (or heavy flavor) multiplicity or \cancel{E}_T are not present, sensitivity might still be achieved by looking toward the internal structure of the jets themselves. While this topic is presently relatively uncovered, with only a few exploratory results available [575], similar techniques to those that have proven useful for quark/gluon

discrimination seem promising. In both cases the lack of a perturbatively-generated hard scale means that parametric separation of signal and background is challenging. Infrared and collinear (IRC) safe observables related to jet mass, such as girth and two-point energy correlations are reasonably well studied in QCD, with results readily generalizable to other gauge theories [576–578]. For quark/gluon discrimination, observables characterized by Poisson-like distributions such as particle/track multiplicities or production ratios of particular SM particles tend to yield better discrimination, but suffer from being IRC unsafe and thus subject to large non-perturbative modeling uncertainties [579], a significant point of concern when extending their use beyond QCD. Here, some recently developed IRC-safe generalizations of multiplicity [580] may prove useful. Another approach might be to explore machine-learning techniques that do not require fully labelled data for training (so-called weak supervision) [581–583]. These can be trained directly on data, here at least in the case of the QCD background, so that modeling concerns about the shower can be partially alleviated. While achieving a sizable signal-to-background ratio is likely to be the major challenge in using such jet observables to separate dark showers from QCD, it is vital to note that if signal/background separation can be achieved through other means, e.g. by reconstructing DV, these same tools offer an enormously powerful window onto the underlying dynamics of the dark shower.

7.6.1.2. Large- R jets ($R = 1.0$). As discussed in section 7.3, dark showers at larger couplings are currently poorly understood. If couplings controlling the shower can no longer be treated as small at any scale, the QCD-inspired picture of pencil-like jets starts to break down, and we might expect that showers radiate more copiously at ever larger angles, so that large- R jets can become necessary to adequately capture the underlying hard process. This is first and foremost a triggering challenge, since it is no longer clear that triggers designed for local hard depositions can maintain their sensitivity. It is likely that a viable trigger path either needs to rely on a prompt associated object from the production mechanism (ISR jet, lepton, etc) or on a high multiplicity of leptons in the shower itself. Of course, H_T triggers continue to be useful for those models with sufficiently high event energy scales, provided that a sufficient amount of the radiation in the event clusters into trigger objects of sufficiently high p_T ($\sim \text{few} \times 10 \text{ GeV}$) to be counted in the H_T trigger. As long as the event can be triggered on, observables similar to those at the end of section 7.6.1.1 should still prove useful to separate signal from background, possibly even more so, since the radiation pattern in the dark shower can now be expected to be substantially different from QCD.

7.6.1.3. Spherical showers. In the large- α Hooft coupling regime, in which we expect much more showering at large angles than in QCD (see section 7.3), the final states are soft and spherically distributed in the rest frame of the shower. This leads to so-called SUEPs in the detector. In the rest frame of the event, the momenta of the final-state SM particles are on the order of the hadronization scale of the dark strong dynamics. If this scale is much lower than 100 MeV, the decay products are too soft to be reconstructed as tracks and the entire shower is effectively invisible. In this case existing jets+MET searches can apply. For a hadronization scale around $\mathcal{O}(100 \text{ MeV})$, some amount of ISR can be needed to boost the particles enough to render a fraction of them reconstructable. Finally, if the decay products are on average harder than $\mathcal{O}(100 \text{ MeV})$, the tracks associated to the SUEP vertex can typically be reconstructed off-line, subject to momentum-dependent reconstruction efficiencies. The main parameters of interest are accordingly the number of charged particles produced and the corresponding p_T spectrum. Also important are the fraction of invisible particles and the composition of SM particles in the final state. In particular, since the momenta of the invisible

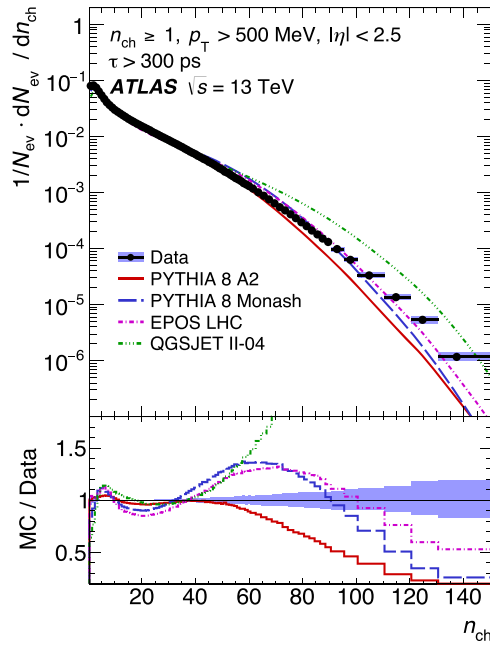


Figure 94. Charged particle multiplicities measured in minimum bias events with the ATLAS detector for events with at least one track with a minimum p_T of 500 MeV and $|\eta| < 2.5$ [584].

particles balance on average, they are not likely to give rise to a substantial \cancel{E}_T signal unless the dark shower is recoiling against a relatively hard ISR jet. A large fraction of invisible particles will instead degrade the sensitivity of a strategy relying on track multiplicity. The muon fraction, on the other hand, can be a powerful handle: even though the average muon p_T may be very low, due to the high particle multiplicity a handful of muons may still be hard enough to pass the trigger and reconstruction thresholds of the MSs.

A major background to SUEP-like signals comes from PU, which also yields a large number of isotropically distributed soft tracks, though in contrast to SUEP signatures, PU tracks arise from multiple vertices. Studies on the multiplicity of charged tracks from minimum-bias interactions like single, double or non-diffractive collisions are described in [584]. As shown in figure 94, the fraction of 13 TeV pp collisions having 80 or more associated charged tracks is $O(10^{-3})$, as measured in a PU-free environment. Some benchmark SUEP models are described in [242], one with a low-mass Higgs-mediator and two higher-mass scalar models, and charged particle multiplicities for these benchmarks are shown in figure 95; for these models, it is assumed that SUEP particles decay only to electrons and muons. Reference [242] demonstrates that counting tracks associated to the PV should provide a very powerful discriminant against PU background during off-line reconstruction for high-mass mediators, while discrimination for the Higgs-mediator model is extremely challenging. The crucial discriminating factor is the number of particle tracks that can actually be reconstructed, and both ATLAS and CMS can reconstruct tracks with a minimum momentum of roughly 400 MeV [585]. The multiplicity of tracks fulfilling this minimum- p_T requirement is shown in figure 95(c) for the three SUEP benchmark models. It was shown in [242] that, even for the highest-mass mediator, no significant losses of the

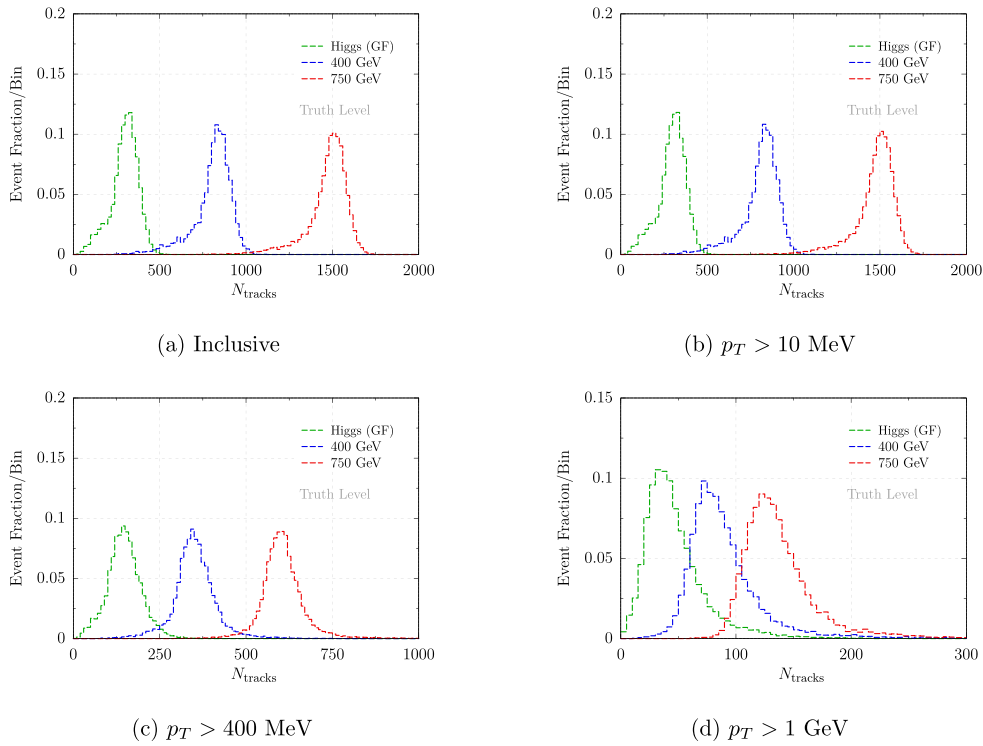


Figure 95. Event multiplicities of charged particle tracks fulfilling the respective indicated p_T requirements for three benchmark SUEP models. Figure from [242].

tracking efficiency are expected in spite of the hundreds of tracks present per event. It is moreover worth noting that, while the track multiplicity is large compared to what is generated by SM proton–proton collisions, it is still relatively small compared to the multiplicities that can be reconstructed in heavy ion collisions.

A large fraction of electrically neutral hadrons produced in the SUEP can further lower the number of associated tracks, which makes signal/background discrimination very difficult for the lowest-mass-mediator signals. A possible additional discriminant for those cases can be the hemisphere mass. This mass is estimated by dividing the event into a hemisphere associated to the ISR jet and one associated to the SUEP, while calculating the ‘jet’ mass, as in section 7.6.1.1, from the tracks in the SUEP hemisphere. This variable should be significantly higher for the SUEP events, where the heavy mediators are decaying, than for PU events.

Another possible background to SUEP signals is QCD multi-jet events. As described in section 7.5.2.1, triggering SUEP events based on \cancel{E}_T relies on the emission of an ISR jet recoiling against the system. QCD scenarios similar to SUEP signatures could arise when one hard jet is recoiling against a system of multiple soft jets. The mean number of charged tracks per jet is less than ten for jets $O(100 \text{ GeV})$ [586]. To get to $O(100)$ charged tracks, as expected from a SUEP signature, a very high number of jets is needed, hence the perturbative cross section is heavily suppressed by many orders in α_s . This background can nevertheless play a significant role for the low-mass mediator models, where significantly fewer tracks are

expected. A veto against large calorimeter deposits can be a powerful handle to reject those events, as rather hard jets are needed to get many associated charged tracks.

7.6.2. Displaced decays. Outside the prompt regime, the lifetimes of the various dark states and the composition of SM final states produced in their decays drive the phenomenology. LLPs result when there are one or more species of dark states in the hidden sector spectrum that would be stable in the absence of couplings to the SM. In particular, different species naturally come with vastly different lifetimes, as is the case for the SM π^0 and π^\pm mesons. In what follows, we consider the single-species case in most detail, and treat the case of primarily leptonic decays (LJs) separately from the cases with substantial branching fractions to hadrons (emerging jets). We finally comment on the multi-species case, and relate it to the semi-visible jet scenario mentioned in the previous section.

Even in high multiplicity events, the isolation of displaced decays from each other is not likely to pose difficulties in reconstructing DVs in the inner tracker. Two nearby DVs can be separately resolved down to separations of \sim mm. Even in the case where two DVs are closer than 1 mm, all of the tracks associated to both vertices will simply be reconstructed as a single DV with larger track multiplicity.

7.6.2.1. Single species leptonic dark showers (displaced LJs). One signature predicted by dark shower models is LJs [155, 572], whose prompt decays are discussed in section 7.6.1. Depending on the lifetime of the decaying state, these leptons can easily be produced with a measurable displacement. Explicit searches for this signature have been performed by the ATLAS Collaboration at both 8 and 13 TeV [272, 273], as detailed in section 3.2. It is worth remarking that the experimental signature of a displaced decay to electrons can be very similar to the signature of a displaced decay to a pair of charged pions, and thus searches for LJs frequently cover pionic final states as well. Searches to date have targeted LJs containing up to two lepton (pion) pairs.

To further extend coverage into low-mass regimes, it may be of interest here to investigate the samples stored through data scouting for, e.g. di-muon resonances, although the limited information retained in scouted events likely makes this a promising avenue only for sufficiently short lifetimes that dedicated displaced track reconstruction is not necessary.

7.6.2.2. Single species hadronic dark showers (emerging jets). The ATLAS, CMS, and LHCb collaborations have developed powerful searches for pairs of DVs in the trackers, typically in association with missing energy or large H_T , as described in section 3.1. These searches are nearly background-free and inclusive in the number of vertices, and thus have good sensitivity for any model of dark showers that has a large enough signal acceptance in such searches, regardless of the detailed features of the shower shape.

While these searches demonstrate the power and flexibility of inclusive low-background searches, it is unfortunately very easy for signal acceptances in existing DV searches to be prohibitively small. Primary drivers for the loss of acceptance are the requirement of associated objects (leptons, MET, sizable visible H_T , etc), and/or cuts on the invariant mass of or number of tracks belonging to the DV. Given that a hidden shower tends to produce a multitude of LLPs, it should be possible to maintain very low background levels—and therefore the power and inclusivity of the search—by relaxing many of these requirements and demanding a larger number of DV or even displaced tracks instead.

When the lightest decaying dark state has mass \gtrsim 10 GeV, backgrounds to DV searches do become more important, since the background DV rate rises rapidly as the number of tracks associated to the vertex falls; also, irreducible heavy-flavor backgrounds are important

in this mass range. The number of associated tracks is also crucial for the vertex reconstruction in both the ID and the MS. Hence, the composition of hadronic and leptonic particles in the final states may have a significant impact on the ability to reconstruct the associated vertices and/or the size of the expected backgrounds. Moreover, as the track momentum and multiplicity in the vertices drop, the odds increase that one or more tracks belonging to a particular vertex are not reconstructed. The efficiency of reconstructing displaced tracks in the inner tracker falls off substantially with displacement, as particles traverse fewer layers of the tracker: for particles produced at $r = 30$ cm from the IP, this efficiency is ~ 0.35 at ATLAS [255] and ~ 0.25 at CMS [587]. Explicitly requiring vertex reconstruction can thus come at a large cost in signal acceptance, especially for LLP decays that produce only two tracks per vertex. However, a large number of unassociated tracks with a large impact parameter is still a striking signature, despite the larger backgrounds that come with relaxing requirements on vertex reconstruction. This is the idea behind a recent CMS search [316], based on the model of [331] (see below). Whether or not explicit DV reconstruction is helpful depends on relative signal and background rates, and can be model dependent.

Backgrounds also increase as the lifetime of the decaying dark state becomes shorter; as track reconstruction efficiencies are very good for particles at small production radii, explicit vertex reconstruction is likely to be useful here to help keep backgrounds under control. Even in the short lifetime regime, a dark shower offers many additional handles for signal/background discrimination beyond the number of vertices, such as a common mass scale for reconstructed vertices and non-SM-like particle multiplicity distributions.

Given the striking nature of these high multiplicity signal events, it is typically not challenging to separate them from backgrounds once the event is on tape, provided that sufficiently many displaced tracks (and possibly vertices) can be reconstructed. At ATLAS, reconstructing displaced tracks can require running dedicated re-tracking algorithms in order to identify highly displaced tracks. This re-tracking can be computationally expensive, and necessitates the preselection of at most $\sim 5\%$ of the total event sample on tape. In this case, the preselection criteria are likely to be the limiting factor in signal acceptance at the analysis level. At CMS, the standard tracking algorithm is iterative and automatically reconstructs highly-displaced tracks, so preselection is not necessary.

Dark showers produced through mediators carrying SM charges, such as the scenario of [331], generally provide ample preselection criteria through associated objects and relatively high overall event H_T scales. For instance, typical events for the model in [331] contain two emerging jets and two QCD jets, though the additional two QCD jets can be absent in other models. The emerging jets can be reconstructed using default anti- k_t [366] $R = 0.4$ jets. A baseline preselection requires each jet to have $p_T > 200$ GeV, $|\eta| < 2.5$ and H_T exceeding 1000 GeV. These criteria assume that jets can be reconstructed using the calorimeters, which should be very efficient for the considered lifetimes in the model. CMS has recently published a search for this model [316], finding excellent sensitivity for the benchmark model developed in [331]; this analysis is an excellent demonstration that searches of this type are feasible despite the challenging nature of the signal.

When dark showers originate from a SM singlet, such as the Higgs boson or a Z' , the problem of preselection becomes more acute. The overall mass scale of signal events can easily be small, making event H_T useless for signal separation. Here perhaps one of the most robust avenues for preselection is muon multiplicity: as discussed in section 7.4, many of the operators governing LLP decays tend to predict muon-rich final states. With $\gg 2$ LLPs in an event, muon number becomes a useful and inclusive preselection criterion that places no demands on the possible presence of associated objects, event H_T , or detailed shower shape.

For muon-poor, low-mass dark shower events, pre-selection criteria become more model dependent. When such dark showers originate from an exotic Higgs decay, SM Higgs production provides a suite of associated prompt objects that offer pre-selection handles at some acceptance cost; see section 2.3.1. However it is also important to study to what extent features reflecting the presence of (multiple) LLPs in the event itself could be used as pre-selection criteria, e.g. anomalously track-poor jets, unusual ECAL/HCAL ratios (as realized by, for instance, LLPs with $c\tau \sim \text{m}$ decaying dominantly to electrons and/or photons), anomalously large numbers of poorly reconstructed or high impact parameter tracks, etc.

Off-line reconstruction for events with low-mass and/or very soft vertices, as occurs in SUEP-style models, poses additional challenges. For the reconstruction of secondary vertices in the ID in ATLAS and CMS, currently a minimum track p_T of 1 GeV is required [237, 588]. Having vertices with several tracks fulfilling this minimum p_T requirement might be rare if the hidden sector hadronization scale is low, and this is particularly true for low mediator masses. In this case, dedicated search strategies might be needed (particularly for short lifetimes). For example, it may be possible to look for increased multiplicity of hits in the outer layers of the ID compared to the inner parts, though unassociated hits from secondaries may be a significant background. A subtraction of hits from tracks stemming from vertices close to the beam pipe might be helpful, but dedicated studies are needed to assess the viability of this approach. In addition, the calorimeter may be another handle on this type of event: a large collection of soft particles could collectively contribute a non-standard energy pattern in the calorimeters provided the LLP lifetime is sufficiently long and if the calorimeter segmentation in radial direction is exploited. However, if the LLPs can reach the calorimeter, their decays typically take place over a distance longer than or comparable to the size of the calorimeter itself. This effect could wash out the signal to the extent that it may be difficult to observe above background, though a full truth-level simulation of this effect is certainly warranted.

Finally, one of the great advantages of an inclusive, low-background search strategy is that it enables a single search to apply robustly to a vast class of models. To fully realize the power and impact of such searches, it will be critical to make it possible to reinterpret searches with publicly available material. In searches for DVs in a particular detector element, it may be advantageous to bin signal and background in terms of the number of reconstructed vertices with very loose η and ϕ requirements. While more difficult experimentally, it would also be highly valuable to eventually supply the transverse distance of each vertex from the IP on an event-by-event basis, combining the different detector elements. This would allow for straightforward reinterpretation of searches to models with different shower shapes, lifetimes and p_T spectra, allowing a single search to transparently apply to a very broad model space. If possible, it would also be useful to provide the distribution of background vertices as a function of the number of tracks, as this would help theorists estimate the sensitivity to models with different masses and LLP decay modes.

For searches that rely directly on displaced tracks, it is especially important to publish information on displaced track reconstruction that allows for reliable recasting since this is challenging to model accurately using only public data. For instance, the analysis of [316] relies on the transverse impact parameter significance of a track to construct discriminating variables, but theorists cannot reconstruct impact parameter significance without clear examples of the detector response. For these searches, it would again be useful to bin signal and background in terms of the number of reconstructed objects and their geometric location within the detector, as well as their p_T .

We conclude by reiterating that, while inclusive searches are naturally desirable, there are substantial practical obstacles for such a program, some of which have been discussed above.

In reality, it is likely that a number of different semi-inclusive searches with partially overlapping acceptance are necessary. To that end, further theoretical studies are needed to map out which selection cuts are most robust against the varying of the specifics of particular models.

7.6.2.3. Multi-species dark showers. If there are multiple species in the dark shower that decay to SM final states, the lifetimes of these species will in general be very different. The intermediate case where most LLP species decay with a macroscopic lifetime produces similar phenomenology to the single-species models discussed above. Another regime occurs when at least one species decays promptly, while the others are either stable or decay outside of the detector, which gives rise to a semi-visible jet [372] (see section 7.6.1.1 above). The intermediate scenario, where some dark states decay promptly while others have macroscopic detector-scale lifetimes, is equally generic. A combination of semi-visible techniques with DV reconstruction can be used to boost sensitivity in this case. It is especially important to pay attention to potential isolation criteria on DVs, as the presence of potentially large numbers of promptly decaying dark particles may necessitate their relaxation.

7.7. Executive summary

Dark showers are a common prediction of a wide range of hidden sector theories. Although the model space is dauntingly enormous, it is possible to make some very general statements about the *signature* space of interest: dark shower events can be characterized by (1) a variable and frequently large multiplicity of particles per event; (2) BSM states with a hierarchy of proper lifetimes, making the existence of at least one LLP species generic; (3) frequently, non-isolation of LLPs from other objects in the event; and (4) non-SM-like energy flow and particle multiplicity. These features typically ensure that dark shower events are very distinctive signatures in the generic regime where at least one species has a detector-scale lifetime. Thus, it should be possible to design powerful and inclusive searches which would be sensitive to a very large portion of the vast model space without needing to rely on poorly predicted (and model-dependent) properties such as shower shape. Toward this end we have identified several promising directions for future study for both theory and experiment, and provide some recommendations here.

As always, one of the primary challenges in searches for dark showers is ensuring the events are recorded on tape. In some models, dark showers may be accompanied by E_T , H_T , or a number of associated leptons that can be triggered on, but there are many scenarios where this is not the case, or where these handles come at the expense of a large reduction in signal rate. The foremost example of this is when the dark shower is initiated by an exotic Higgs decay. It is thus critical to pursue dedicated trigger strategies, and we present a few ideas here. We expect that displaced triggers designed for singly- or doubly-produced LLPs will typically have reasonable acceptance for dark shower events, though we caution that in some cases the non-isolation of LLPs in dark shower events may limit their acceptance. Another promising avenue for triggering on dark showers exploits the high particle multiplicity typical of such events, and we recommend study of triggers on (displaced) multi-muons in particular.

The off-line analysis of dark shower events poses several challenges as well. At this time, only the limiting cases of pencil-like or fully spherical showers are under good theoretical control, and hadronization can introduce significant additional uncertainties, especially for models with a spectrum substantially different from QCD. New studies of showering in the intermediate regime were performed for the purpose of this document (presented in section 7.3), which revealed that different approaches can yield qualitatively different

phenomenology. On the one hand, this provides interesting opportunities for searches to make use of event shape and/or jet substructure variables, in particular if the decays of hidden sector states occur promptly or with small displacements. On the other hand, for larger displacements it implies that one should be careful not to heavily bias the selection choices of a search towards a particular shower shape, and rely instead on the displaced LLP decays to separate signal from background. We expect that the most inclusive, most broadly applicable, and most readily reinterpreted searches will be those in which the data is binned in terms of the number of reconstructed displaced objects and their locations within the detector. For recasting purposes, and to assist with unraveling the underlying physics in the event of a discovery, it would moreover be important to supply information concerning distributions of the number of tracks per vertex and/or the vertex mass whenever possible.

The presence of $N_{DV} \gg 2$ DV in an event will be enormously powerful for background suppression, provided those vertices can be reconstructed. To identify highly displaced tracks, it may be necessary to run dedicated and computationally expensive re-tracking algorithms, requiring the imposition of some pre-selection criteria to identify events of interest. As these pre-selection criteria are likely to be the limiting factor controlling post-trigger signal acceptance in many models, we recommend developing criteria for dark showers that rely on particle multiplicity and, if possible, the presence of multiple LLPs in the event, while keeping p_T thresholds as low as possible.

7.8. Appendix: example models

In this appendix we survey the models for which MC simulations are currently available. Please also see the [appendix](#) as some of the models are included in simplified model library.

7.8.1. Lepton-jets from radiating DM. One of the simplest and most widely discussed types of low-mass hidden sector particle is a dark photon A' , i.e. a new gauge boson associated with a local $U(1)$ symmetry in the dark sector. By kinetically mixing with the SM hypercharge gauge boson, a dark photon can act as the mediator of DM–SM interactions, in addition to being responsible for DM self-interactions. The range of dark photon masses of relevance to dark showers is between MeV and GeV. The dark sector Lagrangian in such a scenario reads

$$\mathcal{L}_{\text{dark}} \equiv \bar{\chi}(i\not{\partial} - m_\chi + ig_{A'}\not{A}')\chi - \frac{1}{4}F'_{\mu\nu}F'^{\mu\nu} + \frac{1}{2}m_{A'}^2 A'_\mu A'^\mu - \frac{\epsilon}{2}F'_{\mu\nu}F^{\mu\nu}. \quad (7.8)$$

Here, χ is the fermionic DM particle with mass m_χ , and $g_{A'} = \sqrt{4\pi\alpha'}$ is the $U(1)'$ gauge coupling. From the point of view of dark showers, interesting values for the coupling strength are $\alpha' \sim 0.01$. If α' is much smaller, there is too little radiation to form a dark shower. The dark photon mass is denoted by $m_{A'}$, and the kinetic mixing parameter by ϵ . Typically, ϵ is constrained by current limits to be $\sim 10^{-3}$. The particular mechanism by which the dark photon mass arises is not important in this context—it could originate from a dark sector Higgs mechanism or from the Stückelberg mechanism.

If $m_\chi \ll 100$ GeV, DM particles may be produced at the LHC with a large boost. This entails a large probability for radiating additional collinear A' bosons (see figure 96). A detailed analytical and numerical description of such dark photon showers is presented in [589]. The A' bosons eventually decay to observable SM particles through the kinetic mixing term in equation (7.8). Depending on the value of ϵ , the decays can be either prompt or displaced. Phenomenologically, the final state of the process $pp \rightarrow \bar{\chi}\chi + nA'$ thus consists of two ‘jets’ of collimated A' decay products, plus missing energy.

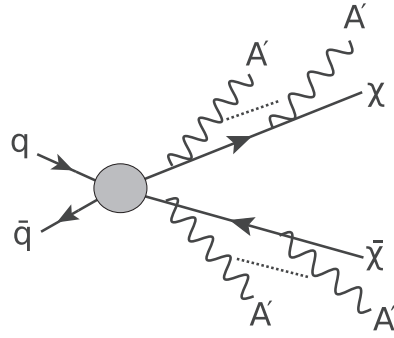


Figure 96. The process that gives radiating dark matter its name: production of two DM particles χ , followed by the emission of several soft or collinear dark photons A' [589].

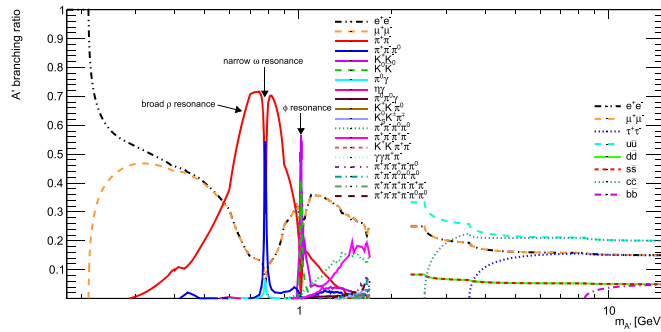


Figure 97. Branching ratios of a kinetically mixed dark photon A' as a function of $m_{A'}$ [589].

The A' branching ratios into different SM final states depend sensitively on $m_{A'}$ (see figure 97). At $m_{A'} \approx 400$ MeV, the dominant decay modes are $A' \rightarrow e^+e^-$ and $A' \rightarrow \mu^+\mu^-$. The decay rate into each lepton flavor ℓ is

$$\Gamma(A' \rightarrow \ell^+\ell^-) = \frac{1}{3}\alpha\epsilon^2m_{A'} = \frac{1}{8} \times \frac{1}{10^{-6} \text{ cm}} \left(\frac{\epsilon}{10^{-3}}\right)^2 \left(\frac{m_{A'}}{\text{GeV}}\right), \quad (7.9)$$

where $m_\ell \ll m_{A'}$ has been assumed for simplicity. For purely leptonic decays, the A' shower thus corresponds to a ‘LJ’, i.e. a set of collimated leptons. This signature has been previously discussed, for instance, in [30, 32, 117, 127, 184, 572, 590–593]. Experimental searches for LJs have been presented in [270, 272, 273, 274], where [272, 510] focus on LJs with DV.

Lepton-jet searches may also be sensitive to dark photons with masses ≈ 400 MeV, even though the leptonic branching ratio is reduced to between 20% and 70% in this regime. The mix of leptons and hadrons expected from A' decays at $m_{A'} \approx 400$ MeV implies, however, that most leptons will not be isolated, but occur in conjunction with hadronic activity in the same detector region. In view of this, dedicated trigger and analysis strategies may significantly boost the sensitivity (see section 7.6.2.1).

In certain parameter regions, the decays of radiated A' bosons may closely resemble a purely hadronic QCD jet. This will happen in particular when $m_{A'}$ is close to a QCD resonance, or when the average A' multiplicity in each shower is low, and the hadronic

branching ratio is sizeable. In this case, separation of the signal from the QCD background will most likely be possible only if ϵ is so small that A' decays are displaced.

Let us summarize several important considerations to take into account when devising a search for dark sector radiation:

- *There may or may not be a signal in the tracking detector.* Prompt A' decays will typically lead to such signals, except for specific A' decay modes to neutral particles, for instance $A' \rightarrow K^0 \bar{K}^0$ and $A' \rightarrow \pi^0 \gamma$. Displaced A' decays can also leave a signal in the tracker, however if the lifetime is sufficiently long more decays will occur in the muon chamber (see section 7.4.2).
- *There may or may not be a signal in the calorimeters.* Most A' decay modes will be visible to the calorimeters. However, it is important to realize that a signal in the HCAL can arise not only from hadronic activity, but also from displaced decays to leptons occurring inside the calorimeter.
- *There will be missing energy contained within the LJ.* As the decaying A' bosons are aligned with the DM particle from which they were radiated, the corresponding missing momentum vector points in the same direction. However, unless there is significant ISR, the missing momentum will typically be balanced between the two showers shown in figure 96, and may therefore be small.

In figure 98, we show for illustration the exclusion limits that past LHC searches place on the dark photon parameters.

7.8.2. Emerging and semi-visible jets. Hidden valley models [66] with QCD-like hidden sectors allow for interesting collider signatures. Thus we consider a confined dark gauge group $SU(N_d)$, where $N_d \geq 2$, with confinement scale Λ_d which sets the mass of the dark hadrons. There are also n_f flavors of dark quarks whose bare masses are lighter than Λ_d . The hidden valley comes equipped with a portal that couples the dark sector to the SM, and the mass is usually taken to be $M \gg \Lambda_d$. The portal can be an s -channel vector mediator, Z_d , which couples to SM quarks and dark quarks:

$$\mathcal{L} \supset - Z_{d,\mu} \sum_{i,a} (g_q \bar{q}_i \gamma^\mu q_i + g_{q_d} \bar{q}_{d,a} \gamma^\mu q_{d,a}). \quad (7.10)$$

Here g_{q/q_d} are coupling constants and i, a are flavor indices. One can also have a t -channel scalar bifundamental mediator, X , which carries color and dark color and can decay to a quark and a dark quark. In the case of the scalar mediator, the only allowable coupling is of the form

$$\mathcal{L} \supset \kappa_{ij} \bar{q}_i q_{d,j} X + \text{h.c.}, \quad (7.11)$$

where κ_{ij} is a $3 \times n_f$ matrix of Yukawa couplings. One could also add multiple flavors of X mediators, something that has also been implemented [542].

When dark quarks are produced, they shower and hadronize and the same tools that are familiar for QCD can be used to simulate these processes. Because of the large gap between the mediator mass and the confining scale, there will be large particle multiplicity and the dark hadrons will typically form into jet-like structures. In the large N_d limit, the fraction of dark baryons produced is suppressed, and in the case of QCD this fraction is $\mathcal{O}(0.1)$. Therefore the hadronization in these simulations is typically dominated by dark mesons. The lightest hadronic states are the dark pions π_d , acting as goldstone bosons of the $U(n_f) \times U(n_f)$ dark flavor symmetry. When a heavier mesonic state is produced it will promptly decay into dark pions if kinematically allowed, making the dark pions the dominant component of the dark showering process.

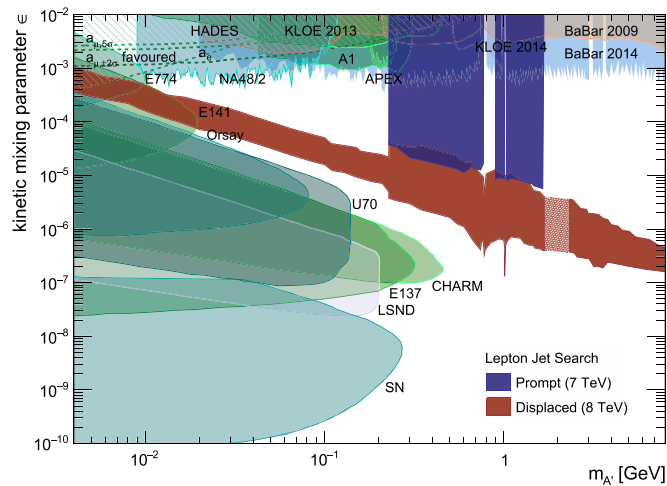


Figure 98. Limits, at the 95% C.L., on the dark photon mass $m_{A'}$ and the kinetic mixing parameter ϵ , for $m_\chi = 4$ GeV, $\alpha_{A'} = 0.2$. We have assumed χ production through a Z' portal with a mass of 1 TeV, with a production cross section of 0.58 pb at $\sqrt{s} = 7$ TeV and 0.85 pb at 8 TeV. We show exclusion limits from the ATLAS search for prompt lepton-jets in 5 fb^{-1} of 7 TeV data [594] (blue shaded region) and from the ATLAS displaced lepton-jet search in 20.3 fb^{-1} of 8 TeV data [272] (red shaded region). The lighter colored region around $m_{A'} = 2$ GeV corresponds to the transition region in terms of quark final states and an analysis based on interpolation. The computation was carried out in Pythia 8 [220, 595, 596]; see [589] for details. We also show the existing 90% C.L. exclusion limits from the electron and muon anomalous magnetic moment [19, 597, 598], HADES [599], KLOE 2013 [600] and 2014 [601], the test run results from APEX [602], BaBar 2009 [603] and 2014 [604], beam dump experiments E137, E141, and E774 [605–607], A1 [608], Orsay [609], U70 [610], CHARM [611], LSND [612], as well as constraints from astrophysical observations [613, 614] and π^0 decays [615]. Figure based on [589].

These events can be simulated with the HV [595] module/package that appears in Pythia8 [220]. Pythia8 hosts a hidden valley class which incorporates the $SU(N_d)$ model, allowing the user to vary the masses of the spectrum (π_d, ρ_d , etc), number of flavors n_f and parameters of the running coupling (Version 8.226). Pair production of X and resonant production of Z_d are implemented at tree level, and the decay of dark mesons to SM states is also present.

In [574], production of the heavy mediators with ISR/FSR was considered. This was done by interfacing with Madgraph5_aMC@NLO [226] using a modified version of the spin-1 DMSimp model²⁰² implemented through FeynRules [616]. The models are located in the repository²⁰³ folder DMSimp_s_spin1. The generation files for the t -channel exchange of the scalar X are located in the folder DMSimp_tchannel. The bi-fundamentals are denoted with $su11, su12, su21, su22\dots$, where u explicitly specifies the QCD flavor index and the numbers are the explicit dark non-abelian group indices. Similarly, the dark quarks are labeled as $qv11, qv12, qv21, qv22$. A FeynRules model file (DMSimp_tchannel.fr) as well as the Mathematica notebook (DMSimp_tchannel.nb) used to generate the

²⁰² <http://feynrules.irmp.ucl.ac.be/wiki/DMSimp>

²⁰³ <https://github.com/smsharma/SemivisibleJets>

UFO output are also provided. The showering and hadronization in the dark sector can still be performed in `Pythia8`.

7.8.2.1. Semi-visible jets. Generically, some of the dark pions could decay promptly while some could be long-lived or even collider-stable, analogous to the appearance of neutral versus charged pions in the SM. If both stable and unstable hadrons are produced in a collision, the missing energy could be aligned along one of the jets, resulting in low acceptance for traditional monojet-style searches. This is the *semi-visible jet* scenario, and [372, 574, 617] introduce a simplified model-like parameterization to map the complicated dynamics of the underlying dark sector onto a limited number of physically-motivated variables—in particular, the fraction of stable versus decaying pions, the characteristic mass scale of dark pions and the dark coupling strength. The MC production described here along with the `Pythia8` HV module allows the user to vary these parameters for the *s*- and *t*-channel UV completions. See [372, 574, 617] for further details. Emerging jets By contrast, the dark pions can be taken to have detector-scale lifetimes in the *emerging jets* scenario [331]. The expected lifetime of the dark pion can be quantified using equation (7.11). Under the assumption of universal couplings $\kappa_{ij} = \kappa$ and $m_q > \Lambda_d$, we can calculate the proper lifetime of the dark pions:

$$c\tau_0 \approx 80 \text{ mm} \times \frac{1}{\kappa} \times \left(\frac{2 \text{ GeV}}{f_{\pi_d}} \right)^2 \left(\frac{100 \text{ MeV}}{m_q} \right) \left(\frac{2 \text{ GeV}}{m_{\pi_d}} \right) \left(\frac{M_X}{1 \text{ TeV}} \right)^4. \quad (7.12)$$

Here f_{π_d} is the dark pion decay constant, and m_q is the mass of the SM quark in the final state. A similar formula applies for the Z_d mediator. Therefore a jet of dark hadrons will be created as dominantly invisible particles, but at long distance, the dark pions will decay back to SM particles and appear in shape like an ordinary jet, although it contains a large number of DV. The jet emerges as it travels through the detectors. In the case of purely *t*-channel interactions, having a non-trivial κ_{ij} in equation (7.11) will break the $U(n_f) \times U(n_f)$ dark flavor symmetry. With an appropriate n_f , the dark quark flavors can be exactly aligned with the SM down quark flavors. It is immediately clear that such alignment leads to dark pions with lifetimes that differ significantly from one another. In return, the flavor composition of the emerging jets will vary throughout the detector volume. This differs from the *s*-channel interaction, in which no breaking occurs, and n_f -stable versus $n_f(n_f - 1)$ -unstable dark pions exist.

7.8.3. SUEPs. In the strongly coupled regime, dark showers can be become spherical and almost arbitrarily soft, leading to soft, unclustered energy patterns, or SUEPs, discussed earlier in this chapter. In this case the sheer multiplicity of the final states becomes the most important experimental handle. It has been shown through the AdS/CFT correspondence that their spectrum should follow an approximately thermal distribution [618], which is what was assumed in the phenomenological study in [242]. The production mechanism for these studies was the Higgs or a heavy Higgs-like scalar. The MC code that was written for this study is currently not available publicly, though events in `hepmc` format can be obtained by contacting the authors. At this time only leptonic decays of the hidden mesons are implemented.

8. Conclusions

The research program carried out over the first nine years of the LHC at CERN has been an unqualified success. The discovery, in 2012, at a center-of-mass energy of 7 and 8 TeV, of a new particle thus far consistent with the SM Higgs boson has opened numerous new research

directions and has begun to shed light upon the source of electroweak symmetry breaking, vector boson scattering amplitudes, and the origin of particle masses. And the establishment of a wide range of searches for new physics at 7, 8, and 13 TeV with the ATLAS, CMS, and LHCb detectors—searches thus far consistent with SM expectations—has inspired new ideas and thinking about the most prominent open issues of physics, such as the nature of DM, the hierarchy problem, neutrino masses, and the possible existence of supersymmetry.

The overwhelming majority of searches for new physics have been performed under the assumption that the new particles decay promptly, i.e. very close to the proton–proton IP, leading to well-defined objects such as jets, leptons, photons, and missing transverse momentum. Such objects are constructed requiring information from all parts of the detector including hits close to the IP, calorimeter deposits known to be signatures of particles originating from the IP, and muons with tracks that traverse the entirety of the detector, moving out from the IP. However, given the large range of particle lifetimes in the SM—resulting from general concepts such as approximately preserved symmetries, scale hierarchies, or phase space restrictions—and the lack of clear, objective motivation related to any particular model or theory BSM, the lifetime of hypothetical new particles is best treated as a free parameter. This leads to a wide variety of spectacular signatures in the LHC detectors that would evade prompt searches, and which have received modest attention compared to searches for promptly decaying new particles. Because such signatures require significantly customized analysis techniques and are usually performed by a smaller number of physicists working on the experimental collaborations, a comprehensive overview and critical review of BSM LLPs at the LHC has been performed by a community of experimentalists, theorists, and phenomenologists. This effort ensures that such avenues of the possible discovery of new physics at the LHC are not overlooked. The results of this initiative have been presented in the current document.

We developed a set of simplified models and tools, in chapter 2, that can be used to parametrize the space of LLP signatures. The simplified models were organized around generic ways that various BSM LLPs can be produced and decay to displaced or non-standard objects in the LHC detectors, rather than emphasizing any one particular theory or physics motivation. These can serve as a useful grammar by which to compare coverage of LLP signature space and model classes among current and future experiments.

To that end, in chapter 3, we utilized these models and tools to assess the coverage of current LLP searches and we identified multiple avenues for improving and extending the existing LLP search program. Opportunities for new and improved triggering strategies, searches, and open questions for the experimental collaborations to explore centrally were presented as a list at the end of the chapter.

Moreover, due to the non-standard nature of LLP searches, many of them are performed under very low-background conditions. As a result, sources of backgrounds largely irrelevant to searches for promptly decaying BSM particles are important for LLP analyses and can be surprising and unexpected. In chapter 4 we discussed several sources of backgrounds for LLP searches, collecting the knowledge gained, often by trial-and-error, by experimentalists over many years of searches.

Also with an eye to the future, in chapter 5 we explored the potential for the expanded capabilities of proposed detector upgrades at ATLAS, CMS, LHCb, and related dedicated detectors, highlighting areas where new technologies can have a large impact on sensitivity to LLP signatures and suggesting several studies to be performed by the collaborations to ensure new physics potential is not missed for the upcoming era of the HL LHC.

Additionally, to ensure that current and future searches can be maximally useful in the future, in chapter 6 we explored how current searches can apply to new models and performed

a comprehensive overview of some of the challenges and pitfalls inherent in attempting to recast existing LLP analyses, leading to recommendations for the presentation of search results in the future.

Finally, in chapter 7, we looked toward the newest frontiers of LLP searches, namely high-multiplicity or ‘dark shower’ LLP signals that can, for example, be signatures of complex hidden sectors with strong dynamics and internal hadronization. In this chapter, we elaborated on the theoretical and experimental challenges and opportunities in expanding the LHC reach of these signals. Such dark shower signatures have a high potential for being overlooked with existing triggering strategies and analysis techniques. Moreover, the dark-QCD-like theoretical models from which they can arise are currently being explored in depth and the resulting LHC phenomenology is in the process of being understood. We discussed the current state of this work and we anticipate exciting independent developments in the near future.

This document is incomplete by design, since it is a record of the critical thinking and examination of the state of LLP signatures by a large number of independently organized members of the LHC LLP Community as it has evolved from 2016 to 2019, and a major component of the work has been the identification of several open questions and opportunities for discovery in such signatures. As these questions are addressed and new searches emerge from the experimental collaborations, so, too, will new ideas emerge and evolve from the community. We expect this document to be followed by future papers to record, review, and summarize the evolution of LLP signatures and searches, always with the intention of more effectively facilitating the discovery of new particles at the LHC and beyond.

Acknowledgments

We are very grateful to Andreas Albert, Tao Huang, Laura Jeanty, Joachim Kopp, Matt LeBlanc, Larry Lee, Haolin Li, Simone Pagan Griso, Michele Papucci, Matt Strassler, and Tien-Tien Yu for helpful conversations and comments on the draft.

Editors:

J Beacham acknowledges support from the US Department of Energy (DOE) and the US National Science Foundation (NSF). G Cottin acknowledges support from the Ministry of Science and Technology of Taiwan (MOST) under Grant No. MOST-107-2811-M-002-3120 and CONICYT-Chile FONDECYT Grant No. 3190051. N Desai was supported in part by the OCEVU Labex (ANR-11-LABX-0060) and the A *MIDEX project (ANR-11-IDEX-0001-02) funded by the ‘Investissements d’Avenir’ French government program managed by the ANR. J A Evans is supported by DOE grant DE-SC0011784. S Knapen is supported by DOE grant DE-SC0009988. A Lessa is supported by the Sao Paulo Research Foundation (FAPESP), project 2015/20570-1. Z Liu is supported in part by the NSF under Grant No. PHY-1620074, and by the Maryland Center for Fundamental Physics. S Mehlhase is supported by the BMBF, Germany. M J Ramsey-Musolf is supported by DOE grant DE-SC0011095. The work of P Schwaller has been supported by the Cluster of Excellence ‘Precision Physics, Fundamental Interactions, and Structure of Matter’ (PRISMA+ EXC 2118/1) funded by the German Research Foundation (DFG) within the German Excellence Strategy (Project ID 39083149). The work of J Shelton is supported in part by DOE under grant DE-SC0017840. The work of B Shuve is supported by NSF under grant PHY-1820770. X C Vidal is supported by MINECO through the Ramón y Cajal program RYC-2016-20073 and by XuntaGal under the ED431F 2018/01 project.

Contributors:

M Adersberger is supported by the BMBF, Germany. The work of C Alpigiani, A Kvam, E Torro-Pastor, M Profit, and G Watts is supported in part by the NSF. Y Cui is supported in part by DOE Grant DE-SC0008541. J L Feng is supported in part by Simons Investigator Award #376204 and by NSF Grant No. PHY-1620638. I. Galon is supported by DOE Grant DE-SC0010008. K Hahn is supported by DOE Grant DE-SC0015973. J Heisig acknowledges support from the F R S-FNRS, of which he is a postdoctoral researcher. The work of F Kling was supported by NSF under Grant No. PHY-1620638. H. Lubatti thanks the NSF for support. P Mermod was supported by Grant PP00P2_150583 of the Swiss National Science Foundation. S Mishra-Sharma is partially supported by the NSF CAREER Grant PHY-1554858 and NSF Grant PHY-1620727. V Mitsou acknowledges support by the Generalitat Valenciana (GV) through MoEDAL-supporting agreements and the GV Excellence Project PROMETEO-II/2017/033, by the Spanish MINECO under the project FPA2015-65652-C4-1-R, by the Severo Ochoa Excellence Centre Project SEV-2014-0398 and by a 2017 Leonardo Grant for Researchers and Cultural Creators, BBVA Foundation. J Prisciandaro is supported by funding from FNRS. M Reece is supported by DOE Grant DE-SC0013607. D Robinson is supported in part by NSF grant PHY-1720252. D Stolarski is supported in part by the Natural Sciences and Engineering Research Council of Canada (NSERC). S Trojanowski is supported by Lancaster-Manchester-Sheffield Consortium for Fundamental Physics under STFC grant ST/L000520/1. S Xie is supported by the California Institute of Technology High Energy Physics Contract DE-SC0011925 with the DOE. This manuscript has been partially authored by Fermi Research Alliance, LLC under Contract No. DE-AC02-07CH11359 with the US Department of Energy, Office of Science, Office of High Energy Physics.

Appendix. Simplified model library

Chapter Editor: Brian Shuve

Contributors: Eshwen Bhal, David Curtin, Alessandro Davoli, Andrea De Simone, Jared Evans, Thomas Jacques, Zhen Liu, Siddharth Mishra-Sharma, Alessandro Morandini, Michael Ramsey-Musolf, Jessie Shelton, Jiang-Hao Yu.

A.1. Instructions for the Simplified Model Library

The simplified model library is available at the LHC LLP Community website²⁰⁴, hosted at CERN. We refer here extensively to the simplified models in tables 1–3. Because it is already quite an extensive task to come up with simplified models for so many (production)×(decay) modes, we for now restrict ourselves predominantly to the ‘filled’ entries in tables 1–3. If you are interested in performing an experimental search or developing a simplified model library entry for one of the ‘unfilled’ entries, please contact the chapter editor.

There are essentially two possible pipelines to simulate LLP events with the library:

1. *LLP decay as part of matrix-element calculation:* Using UFO models in the library, it is possible to generate the production and decay of LLPs at the parton level using calculations of the matrix element for production and decay. As a concrete example, we provide cards that allow the production and decay of LLPs using MadGraph5_aMC@NLO [226] and the accompanying MadSpin [227] package. This employs the narrow-width approximation, but otherwise gives rise to the correct angular

²⁰⁴ <http://cern.ch/longlivedparticles>

distribution of LLP decay products. The downside is that if a particular decay is not allowed from the interactions in the UFO model file, the UFO must be modified to include the new coupling. The output of `MadGraph5_aMC@NLO` is then fed into programs such as `Pythia 8` [219, 220] for showering, implementation of underlying event and other particle-level processes.

2. *Phenomenological LLP decays*: Using UFO models in the library, it is possible to generate the production of LLPs, leaving them stable as outputs of the matrix-element-level calculation recorded in LHE format [224]. The LLP can then be subsequently decayed in programs such as `Pythia 8`, which allows a particle to decay into any final state, albeit without correctly modeling the angular distribution. This could be convenient for models where the interactions leading to LLP decay are not included in the UFO, or where computational time is a concern and the angular distribution of LLP decays is irrelevant. We provide detailed instructions in the library files for how to implement decays of LHE files via `Pythia`.

In the final version of the library, we aim to provide example cards to direct the production and decay of LLPs in both pipelines. Note that in all of the simplified model proposals below, any particles *not* present in the production or decay chain should have their masses set to a very large value ($M = 5 \text{ TeV}$) to ensure they are sufficiently decoupled from direct production at the LHC.

Currently, we only provide simplified model libraries for neutral LLPs. The simplified models for LLPs with electric or color charges are equally compelling, but their simulation is more subtle. In particular, the simulation of the propagation and decay of the LLPs are more challenging if the LLP carries a SM gauge charge. Such effects can be included in detector simulations using `GEANT4` [231], but decay processes typically need to be hard-coded into `GEANT` or otherwise interfaced with other MC programs. This is an important issue for the community to address, as discussed in sections 2.4.2 and 2.4.3. Without implementing the decays, it is straightforward to use the SUSY model to simulate the production of any of the electrically or color charged LLPs.

Finally, we note that there is not currently a set of minimal simplified models to cover dark showers. However, we are collecting models used in studies of dark showers that could potentially be helpful for experimentalists and theorists alike. The existing models are included in the library, along with a very brief description in section A.1.2.

A.1.1. Neutral LLPs. The instructions for simulating the simplified model channels for neutral LLPs are given below. Note that it is often true that the same simplified model production and decay channel can be simulated using several simplified models. However, the philosophy of the simplified model approach is that the UV model used to simulate the process is not important when sensitivity is expressed in terms of physical masses and cross sections. As a result, we typically provide only one set of instructions for simulating each simplified model channel.

We begin by presenting the simplified model library instructions for double pair production (DPP) in table A1, Heavy Parent (HP, QCD-charged parent) in table A2, and Heavy Parent (HP, EW-charged parent) in table A3. We then proceed to the Higgs (HIG) production modes in tables A4–A6. For the Z' (ZP) production modes, we use a set of simplified models described in tables A7–A9. A relatively simple model file is provided for each table. In addition, a more adjustable ‘advanced’ model file is provided which includes all ZP production and decay modes, and allows for features such as individual couplings to each generation of quarks. This comes at the cost of a greatly increased set of parameters, and the

Table A1. Simplified model library process proposals for double pair production (DPP) production mode. Where a ‘wino’ LSP is specified, an admixture of Higgsino is required to lead to direct pair production of the neutral wino component. As an alternative, one could have $pp \rightarrow \tilde{\chi}^\pm \tilde{\chi}^0$, $\tilde{\chi}^\pm \rightarrow W^{\pm*} \tilde{\chi}^0$ promptly, and take the $\tilde{\chi}^\pm$ to be degenerate with $\tilde{\chi}^0$ such that the additional charged decay products are essentially unobservable.

Decay mode	Simplified model library process
$X \rightarrow \gamma + \text{inv.}$	MSSM+GMSB. LLP is a bino ($\tilde{\chi}^0$) produced due to $pp \rightarrow \tilde{\chi}^0 \tilde{\chi}^0$ via t -channel squark exchange ($M_{\tilde{q}} > 5 \text{ TeV}$). Bino decays to photon + gravitino, $\tilde{\chi}^0 \rightarrow \gamma + \tilde{G}$
$X \rightarrow jj$	MSSM+RPV. LLP is sneutrino LSP ($\tilde{\nu}$) that is pair-produced via weak gauge interactions. $\tilde{\nu} \rightarrow q\bar{q}$ via the QLd^c operator
$X \rightarrow jj + \text{inv.}$	MSSM. LLP is second neutralino (wino) LSP $\tilde{\chi}_2^0$ that is pair-produced via weak gauge interactions. $\tilde{\chi}_2^0 \rightarrow q\bar{q}\tilde{\chi}_1^0$ via an off-shell sfermion, and the $\tilde{\chi}_1^0$ is invisible with arbitrary mass
$X \rightarrow jjj$	MSSM+RPV. While this is partially covered by $jj + \text{inv.}$ in the case where the additional quark is not reconstructed, we include it here for completeness. LLP is wino LSP ($\tilde{\chi}^0$) that is pair-produced via weak interactions. $\tilde{\chi}^0 \rightarrow q_\alpha q_\alpha q_\beta$ via an off-shell sfermion and the $u_\alpha^c d_\alpha^c d_\beta^c$ operator
$X \rightarrow jj\ell_\alpha$	MSSM+RPV. LLP is wino LSP ($\tilde{\chi}^0$) that is pair-produced via weak interactions $\tilde{\chi}^0 \rightarrow \ell_\alpha q\bar{q}$ via an off-shell sfermion and $L_\alpha Qd^c$ operator.
$X \rightarrow \ell_\alpha^+ \ell_\alpha^-$	MSSM+RPV. LLP is sneutrino $\tilde{\nu}_\beta$ of flavor β that is pair-produced via weak interactions $\tilde{\nu}_\beta \rightarrow \ell_\alpha^+ \ell_\alpha^-$ via the $L_\alpha L_\beta E_\alpha^c$ operator
$X \rightarrow \ell_\alpha^+ \ell_\alpha^- (+\text{inv.})$	MSSM. LLP is second neutralino $\tilde{\chi}_2^0$ that is pair-produced via weak interactions $\tilde{\chi}_2^0 \rightarrow \tilde{\chi}_1^0 \ell_\alpha^+ \ell_\alpha^-$ via an off-shell slepton
$X \rightarrow \ell_\alpha^+ \ell_\beta^- (+\text{inv.})$	MSSM+RPV. LLP is sneutrino $\tilde{\nu}_\alpha$ of flavor α that is pair-produced via weak interactions $\tilde{\nu}_\alpha \rightarrow \ell_\alpha^+ \ell_\beta^-$ via the $L_\alpha L_\beta E_\alpha^c$ operator. An additional massless invisible final state can be obtained with a wino LLP decaying into $\ell_\alpha^+ \ell_\beta^- \nu_\alpha$ through the same operator and an off-shell slepton. The massive invisible case is less motivated for $\alpha \neq \beta$

possibility of including unwanted diagrams if the process is not carefully specified. A simple python script is provided to generate the processes and set unwanted parameters to zero for those users wishing to use the advanced model files.

Finally, we provide instructions for the CC production modes in table A10. This production mode is most easily simulated using a left–right symmetric model or other right-handed-neutrino model.

A.1.2. Dark shower models. In the repository, we also include two models of dark showers. These are not meant to be representative in the same way that the simplified models are;

Table A2. Simplified model library process proposals for heavy parent (HP) production mode where the parent particle carries a QCD charge. In most of the above cases, a squark parent can be replaced by a gluino parent with an additional jet in its decay.

Decay mode	Simplified model library process
$X \rightarrow \gamma + \text{inv.}$	MSSM+GMSB. LLP is a bino ($\tilde{\chi}$) produced via $pp \rightarrow \tilde{q}\tilde{q}^*$, $\tilde{q} \rightarrow \tilde{\chi} + q$. Bino decays to photon+ gravitino, $\tilde{\chi} \rightarrow \gamma + \tilde{G}$
$X \rightarrow jj + \text{inv.}$	MSSM. LLP is wino LSP $\tilde{\chi}_2^0$ that is produced via $pp \rightarrow \tilde{q}\tilde{q}^*$, $\tilde{q} \rightarrow q\tilde{\chi}_2^0$. Then, $\tilde{\chi}_2^0 \rightarrow q\tilde{q}\tilde{\chi}_1^0$ via an off-shell quark
$X \rightarrow jjj$	MSSM+RPV. LLP is bino LSP $\tilde{\chi}$ that is produced via $pp \rightarrow \tilde{q}\tilde{q}^*$, $\tilde{q} \rightarrow q\tilde{\chi}$. Then, $\tilde{\chi} \rightarrow q_\alpha q_\alpha q_\beta$ via the $u_\alpha^c d_\alpha^c d_\beta^c$ operator
$X \rightarrow jj\ell_\alpha$	MSSM+RPV. LLP is bino LSP ($\tilde{\chi}$) that is produced via $pp \rightarrow \tilde{q}\tilde{q}^*$, $\tilde{q} \rightarrow q\tilde{\chi}$. $\tilde{\chi} \rightarrow \ell_\alpha q\tilde{q}$ via an off-shell sfermion and $L_\alpha Q d^c$ operator
$X \rightarrow \ell_\alpha^+ \ell_\alpha^-$ or $\ell_\alpha^+ \ell_\beta^-$	MSSM+RPV. LLP is sneutrino ($\tilde{\nu}$) that is produced via $pp \rightarrow \tilde{g}\tilde{g}$, $\tilde{g} \rightarrow jj\tilde{\chi}$, $\tilde{\chi} \rightarrow \tilde{\nu}\tilde{\nu}$. Then, $\tilde{\nu}_\alpha \rightarrow \ell_\alpha^+ \ell_\beta^-$ or $\tilde{\nu}_\beta \rightarrow \ell_\alpha^+ \ell_\alpha^-$ via the $L_\alpha L_\beta E_\alpha^c$ operator
$X \rightarrow \ell_\alpha^+ \ell_\alpha^- + \text{inv.}$	MSSM. LLP is second neutralino ($\tilde{\chi}_2^0$) that is produced via $pp \rightarrow \tilde{q}\tilde{q}^*$, $\tilde{q} \rightarrow q\tilde{\chi}_2^0$. Then, $\tilde{\chi}_2^0 \rightarrow \ell_\alpha^+ \ell_\alpha^- \tilde{\chi}_1^0$
$X \rightarrow \ell_\alpha^+ \ell_\beta^- + \text{inv.}$	MSSM+RPV. LLP is bino ($\tilde{\chi}^0$) that is produced via $pp \rightarrow \tilde{q}\tilde{q}^*$, $\tilde{q} \rightarrow q\tilde{\chi}^0$. Then, $\tilde{\chi}^0 \rightarrow \ell_\alpha^+ \ell_\beta^- \nu_\alpha$ via $L_\alpha L_\beta E_\alpha^c$ operator and off-shell slepton (massless invisible only)

Table A3. Simplified model library process proposals for heavy parent (HP) production mode where the parent particle carries electroweak charge.

Decay mode	Simplified model library process
$X \rightarrow \gamma + \text{inv.}$	MSSM+GMSB. LLP is a bino ($\tilde{\chi}^0$) produced via $pp \rightarrow \tilde{\chi}^+ \tilde{\chi}^-$, $\tilde{\chi}^+ \rightarrow W^+ \tilde{\chi}^0$ ($\tilde{\chi}^+$ is a wino). Bino decays to photon+ gravitino, $\tilde{\chi} \rightarrow \gamma + \tilde{G}$
$X \rightarrow jj$	MSSM+RPV. LLP is sneutrino LSP ($\tilde{\nu}$) produced via $pp \rightarrow \tilde{\chi}^+ \tilde{\chi}^-$, $\tilde{\chi}^+ \rightarrow \tilde{\nu} \ell^+$. The sneutrino decays via $\tilde{\nu} \rightarrow q\tilde{q}$ via the $u_\alpha^c d_\alpha^c d_\beta^c$ operator
$X \rightarrow jj + \text{inv.}$	MSSM. LLP is wino $\tilde{\chi}_2^0$ that is produced via $pp \rightarrow \tilde{\chi}^+ \tilde{\chi}^-$, $\tilde{\chi}_2^+ \rightarrow W^+ \tilde{\chi}_2^0$. Then, $\tilde{\chi}_2^0 \rightarrow q\tilde{q}\tilde{\chi}_1^0$ via an off-shell squark
$X \rightarrow jjj$	MSSM+RPV. LLP is bino LSP ($\tilde{\chi}^0$) that is produced via $pp \rightarrow \tilde{\chi}^+ \tilde{\chi}^-$, $\tilde{\chi}^+ \rightarrow W^+ \tilde{\chi}^0$. Then, $\tilde{\chi}^0 \rightarrow qq\tilde{q}$ via an off-shell sfermion and the $u^c d^c d^c$ operator
$X \rightarrow jj\ell_\alpha$	MSSM+RPV. LLP is bino LSP ($\tilde{\chi}^0$) that is produced via $pp \rightarrow \tilde{\chi}^+ \tilde{\chi}^-$, $\tilde{\chi}^+ \rightarrow W^+ \tilde{\chi}^0$. Then, $\tilde{\chi}^0 \rightarrow qq\ell_\alpha$ via an off-shell sfermion and the $Q d^c L_\alpha$ operator
$X \rightarrow \ell_\alpha^+ \ell_\alpha^-$ or $\ell_\alpha^+ \ell_\beta^-$	MSSM+RPV. LLP is sneutrino ($\tilde{\nu}$) that is produced via $pp \rightarrow \tilde{\chi}^+ \tilde{\chi}^-$, $\tilde{\chi}^+ \rightarrow \ell^+ \tilde{\nu}$. Then, $\tilde{\nu}_\alpha \rightarrow \ell_\alpha^+ \ell_\beta^-$ or $\tilde{\nu}_\beta \rightarrow \ell_\alpha^+ \ell_\alpha^-$ via the $L_\alpha L_\beta E_\alpha^c$ operator
$X \rightarrow \ell_\alpha^+ \ell_\alpha^- + \text{inv.}$	MSSM. LLP is second neutralino ($\tilde{\chi}_2^0$) that is produced via $pp \rightarrow \tilde{\chi}^+ \tilde{\chi}^-$, $\tilde{\chi}^+ \rightarrow W^+ \tilde{\chi}_2^0$. Then, $\tilde{\chi}_2^0 \rightarrow \ell_\alpha^+ \ell_\alpha^- \tilde{\chi}_1^0$ via an off-shell slepton and the $L_\alpha L_\beta E_\alpha^c$ operator
$X \rightarrow \ell_\alpha^+ \ell_\beta^- + \text{inv.}$	MSSM+RPV. LLP is bino ($\tilde{\chi}^0$) that is produced via $pp \rightarrow \tilde{\chi}^+ \tilde{\chi}^-$, $\tilde{\chi}^+ \rightarrow W^+ \tilde{\chi}^0$. Then, $\tilde{\chi}^0 \rightarrow \ell_\alpha^+ \ell_\beta^- \nu_\alpha$ or $\tilde{\chi}^0 \rightarrow \ell_\alpha^+ \ell_\beta^- \nu_\alpha$ via an off-shell slepton and the $L_\alpha L_\beta E_\alpha^c$ operator

Table A4. Simplified model library process proposals for Higgs (HIG) production mode where the Higgs decays to two LLPs. These modes are particularly important because they can come in association with forward jets (VBF) or leptons and \cancel{E}_T (VH). Note that, in cases of $M_X > M_h/2$, the same production modes could still occur if the Higgs is taken to be off-shell.

Decay mode	Simplified model library process
$X \rightarrow \gamma\gamma$	(N)MSSM. LLP is the lightest pseudoscalar Higgs (a) produced via $pp \rightarrow h, h \rightarrow aa$ Then, $a \rightarrow \gamma\gamma$.
$X \rightarrow \gamma\gamma + \text{inv.}$	MSSM. LLP is the second neutralino ($\tilde{\chi}_2^0$) produced via $pp \rightarrow h, h \rightarrow \tilde{\chi}_2^0 \tilde{\chi}_2^0$. Then, $\tilde{\chi}_2^0 \rightarrow \tilde{\chi}_1^0 \gamma\gamma$ via an off-shell SM Higgs
$X \rightarrow jj$	(N)MSSM. LLP is the lightest pseudoscalar Higgs (a) produced via $pp \rightarrow h, h \rightarrow aa$. Then, $a \rightarrow jj$.
$X \rightarrow jj + \text{inv.}$	MSSM. LLP is the second neutralino ($\tilde{\chi}_2^0$) that is produced via $pp \rightarrow h, h \rightarrow \tilde{\chi}_2^0 \tilde{\chi}_2^0$. Then, $\tilde{\chi}_2^0 \rightarrow jj \tilde{\chi}_1^0$ via an off-shell squark
$X \rightarrow \ell_\alpha^+ \ell_\alpha^-$	(N)MSSM. LLP is the lightest pseudoscalar Higgs (a) produced via $pp \rightarrow h, h \rightarrow aa$. Then, $a \rightarrow \ell_\alpha^+ \ell_\alpha^-$.
$X \rightarrow \ell_\alpha^+ \ell_\alpha^- + \text{inv.}$	MSSM. LLP is the second neutralino ($\tilde{\chi}_2^0$) produced via $pp \rightarrow h, h \rightarrow \tilde{\chi}_2^0 \tilde{\chi}_2^0$. Then, $\tilde{\chi}_2^0 \rightarrow \ell_\alpha^+ \ell_\alpha^- \tilde{\chi}_1^0$ via an off-shell slepton
$X \rightarrow \ell_\alpha^+ \ell_\beta^- + \text{inv.}$	MSSM+RPV. LLP is the second neutralino ($\tilde{\chi}_2^0$) produced via $pp \rightarrow h, h \rightarrow \tilde{\chi}_2^0 \tilde{\chi}_2^0$. Then, $\tilde{\chi}_2^0 \rightarrow \ell_\alpha^+ \ell_\beta^- \nu$ via an off-shell slepton and RPV couplings
$X \rightarrow \ell_\alpha^+ jj$	MSSM+RPV. LLP is the second neutralino ($\tilde{\chi}_2^0$) produced via $pp \rightarrow h, h \rightarrow \tilde{\chi}_2^0 \tilde{\chi}_2^0$. Then, $\tilde{\chi}_2^0 \rightarrow \ell_\alpha^+ jj$ via an off-shell slepton and RPV couplings

however, it does allow theorists and experimentalists to simulate these particular dark showers. The currently-included models are:

1. *Radiating lepton jets*: This is a model where DM is charged under a dark $U(1)'$ gauge interaction. The dark photon can be produced via final-state radiation from DM produced in a collider. Due to the collinear enhancement radiation of the dark photon, this can lead to a perturbative dark shower [589].
2. *Semi-visible jets*: This is a model in which hidden-sector states are charged under a new confining gauge group, leading to QCD-like showers. The showers produce both stable, invisible DM, as well as unstable states that decay back to the SM. This produces ‘semi-visible’ jets [372, 574].

Table A5. Simplified model library process proposals for Higgs (HIG) production mode where the Higgs decays to two LLPs plus invisible. These modes are particularly important because they can come in association with forward jets (VBF) or leptons and E_T (VH). Note that, in cases of $M_X > M_h/2$, the same production modes could still occur if the Higgs is taken to be off-shell.

Decay mode	Simplified model library process
$X \rightarrow \gamma\gamma$	(N)MSSM. LLP is a pseudoscalar or singlino (a) produced via $pp \rightarrow h, h \rightarrow \tilde{\chi}_2^0 \tilde{\chi}_2^0$, $\tilde{\chi}_2^0 \rightarrow \tilde{\chi}_1^0 a$. Finally, $a \rightarrow \gamma\gamma$
$X \rightarrow \gamma\gamma + \text{inv.}$	MSSM. LLP is the second neutralino ($\tilde{\chi}_2^0$) produced via $pp \rightarrow h, h \rightarrow \tilde{\nu}\tilde{\nu}^*$, $\tilde{\nu} \rightarrow \tilde{\chi}_2^0 \nu$. Then, $\tilde{\chi}_2^0 \rightarrow \tilde{\chi}_1^0 \gamma\gamma$ via an off-shell SM Higgs
$X \rightarrow jj$	MSSM+RPV. LLP is a sneutrino ($\tilde{\nu}$) produced via $pp \rightarrow h$, $h \rightarrow \tilde{\chi}_1^0 \tilde{\chi}_1^0, \tilde{\chi}_1^0 \rightarrow \tilde{\nu}\tilde{\nu}$. Then, $\tilde{\nu} \rightarrow jj$ via the RPV operator LQd^c
$X \rightarrow jj + \text{inv.}$	MSSM. LLP is the second neutralino ($\tilde{\chi}_2^0$) that is produced via $pp \rightarrow h$, $h \rightarrow \tilde{\nu}\tilde{\nu}^*, \tilde{\nu} \rightarrow \nu\tilde{\chi}_2^0$. Then, $\tilde{\chi}_2^0 \rightarrow jj\tilde{\chi}_1^0$ via an off-shell squark
$X \rightarrow \ell_\alpha^+ \ell_\alpha^-$	MSSM+RPV. LLP is a sneutrino ($\tilde{\nu}_\beta$) produced via $pp \rightarrow h$, $h \rightarrow \tilde{\chi}_1^0 \tilde{\chi}_1^0, \tilde{\chi}_1^0 \rightarrow \tilde{\nu}_\beta \bar{\nu}_\beta$. Then, $\tilde{\nu}_\beta \rightarrow \ell_\alpha^+ \ell_\alpha^-$ via the RPV operator $L_\alpha L_\beta E_\alpha^c$
$X \rightarrow \ell_\alpha^+ \ell_\alpha^- + \text{inv.}$	MSSM. LLP is the second neutralino ($\tilde{\chi}_2^0$) that is produced via $pp \rightarrow h$, $h \rightarrow \tilde{\nu}\tilde{\nu}^*, \tilde{\nu} \rightarrow \nu\tilde{\chi}_2^0$. Then, $\tilde{\chi}_2^0 \rightarrow \ell_\alpha^+ \ell_\alpha^- \tilde{\chi}_1^0$ via an off-shell slepton

Table A6. Simplified model library process proposals for Higgs (HIG) production mode where the Higgs decays to single LLP plus invisible. These modes are particularly important because they can come in association with forward jets (VBF) or leptons and E_T (VH). Note that, in cases of $M_X > M_h/2$, the same production modes could still occur if the Higgs is taken to be off-shell.

Decay mode	Simplified model library process
$X \rightarrow \gamma\gamma + \text{inv.}$	MSSM. LLP is the second neutralino ($\tilde{\chi}_2^0$) produced via $pp \rightarrow h$, $h \rightarrow \tilde{\chi}_2^0 \tilde{\chi}_1^0$. Then, $\tilde{\chi}_2^0 \rightarrow \tilde{\chi}_1^0 \gamma\gamma$ via an off-shell SM Higgs
$X \rightarrow jj + \text{inv.}$	MSSM. LLP is the second neutralino ($\tilde{\chi}_2^0$) that is produced via $pp \rightarrow h$, $h \rightarrow \tilde{\chi}_2^0 \tilde{\chi}_1^0$. Then, $\tilde{\chi}_2^0 \rightarrow jj\tilde{\chi}_1^0$ via an off-shell squark
$X \rightarrow \ell_\alpha^+ \ell_\alpha^- + \text{inv.}$	MSSM. LLP is the second neutralino ($\tilde{\chi}_2^0$) that is produced via $pp \rightarrow h$, $h \rightarrow \tilde{\chi}_2^0 \tilde{\chi}_1^0$. Then, $\tilde{\chi}_2^0 \rightarrow \ell_\alpha^+ \ell_\alpha^- \tilde{\chi}_1^0$ via an off-shell slepton
$X \rightarrow \ell_\alpha^+ jj$	MSSM+RPV. LLP is the second neutralino ($\tilde{\chi}_2^0$) that is produced via $pp \rightarrow h$, $h \rightarrow \tilde{\chi}_2^0 \tilde{\chi}_1^0$. Then, $\tilde{\chi}_2^0 \rightarrow \ell_\alpha^+ jj$ via the RPV operator QLd^c
$X \rightarrow \ell_\alpha^+ \ell_\beta^- + \text{inv.}$	MSSM+RPV. LLP is the second neutralino ($\tilde{\chi}_2^0$) that is produced via $pp \rightarrow h$, $h \rightarrow \tilde{\chi}_2^0 \tilde{\chi}_1^0$. Then, $\tilde{\chi}_2^0 \rightarrow \ell_\alpha^+ \ell_\beta^- \nu_\sigma$ via the RPV operator $L_\beta L_\sigma E_\alpha^c$

Table A7. Simplified model library process proposals for Z/Z' (ZP) production mode where the Z' decays to two LLPs. For this section, we mostly use a DM simplified model, where fermion x_2 is the LLP for $X \rightarrow SM + \text{inv}$ modes and scalar s_2 is the LLP for $X \rightarrow SM$ modes. The same models can also be used for off-shell Z/Z' where $M_X > M_{Z'}/2$. The model file includes all processes in the table; the undesired couplings can be set to zero and energy scales to be very large. The final entry uses a left–right symmetric model; the mass of the intermediate $Z/Z'/h$ can be changed to simulate the desired decay kinematics.

Decay mode	Simplified model library process
$X \rightarrow \gamma\gamma$	DMSM. LLP is scalar s_2 , produced via $pp \rightarrow Z' \rightarrow s_2 s_2$, then $s_2 \rightarrow \gamma\gamma$
$X \rightarrow \gamma\gamma + \text{inv.}$	DMSM. LLP is fermion x_2 , produced via $pp \rightarrow Z' \rightarrow x_2 x_2$, then $x_2 \rightarrow \gamma\gamma x_1$.
$X \rightarrow jj$	DMSM. LLP is scalar s_2 , produced via $pp \rightarrow Z' \rightarrow s_2 s_2$, then $s_2 \rightarrow q\bar{q}$ $s_2 \rightarrow \ell_\alpha^+ \ell_\alpha^-$ couplings are proportional to SM Yukawacouplings.
$X \rightarrow jj + \text{inv.}$	DMSM. LLP is fermion x_2 , produced via $pp \rightarrow Z' \rightarrow x_2 x_2$, then $x_2 \rightarrow q\bar{q} x_1$
$X \rightarrow \ell_\alpha^+ \ell_\alpha^-$	DMSM. LLP is scalar s_2 , produced via $pp \rightarrow Z' \rightarrow s_2 s_2$, then $s_2 \rightarrow \ell_\alpha^+ \ell_\alpha^-$. $s_2 \rightarrow \ell_\alpha^+ \ell_\alpha^-$ couplings are proportional to SM Yukawa couplings
$X \rightarrow \ell_\alpha^+ \ell_\alpha^- + \text{inv.}$	DMSM. LLP is fermion x_2 , produced via $pp \rightarrow Z' \rightarrow x_2 x_2$, then $x_2 \rightarrow \ell_\alpha^+ \ell_\alpha^- x_1$
$X \rightarrow \ell_\alpha^+ jj$.	LRSM. LLP is fermion ν_R , produced via $pp \rightarrow Z/Z'/h \rightarrow \nu_R \nu_R$, then $\nu_R \rightarrow \ell_\alpha^+ jj$ via off-shell W/W'

Table A8. Simplified model library process proposals for Z/Z' (ZP) production mode where the Z/Z' decays to two LLPs plus invisible. For this section, we use a DM simplified model, where the Z' decays into $x_3 x_3$, and x_3 then decays into the LLP (fermion x_2 for SM+inv decay mode or scalar s_2 for SM decay mode), plus invisible (scalar s_1 or fermion x_1 , respectively). The same models can also be used for off-shell Z/Z' where $M_X > M_{Z'}/2$. One model file (DMSM) includes all processes in the table.

Decay mode	Simplified model library process
$X \rightarrow \gamma\gamma$	DMSM. LLP is scalar s_2 , produced via $pp \rightarrow Z' \rightarrow x_3 x_3$, $x_3 \rightarrow s_2 x_1$, then $s_2 \rightarrow \gamma\gamma$
$X \rightarrow \gamma\gamma + \text{inv.}$	DMSM. LLP is fermion x_2 , produced via $pp \rightarrow Z' \rightarrow x_3 x_3$, $x_3 \rightarrow x_2 s_1$, then $x_2 \rightarrow \gamma\gamma x_1$
$X \rightarrow jj$	DMSM. LLP is scalar s_2 , produced via $pp \rightarrow Z' \rightarrow x_3 x_3$, $x_3 \rightarrow s_2 x_1$, then $s_2 \rightarrow q\bar{q}$ $s_2 \rightarrow \ell_\alpha^+ \ell_\alpha^-$ couplings are proportional to SM Yukawa couplings
$X \rightarrow jj + \text{inv.}$	DMSM. LLP is fermion x_2 , produced via $pp \rightarrow Z' \rightarrow x_3 x_3$, $x_3 \rightarrow x_2 s_1$, then $x_2 \rightarrow q\bar{q} x_1$
$X \rightarrow \ell_\alpha^+ \ell_\alpha^-$	DMSM. LLP is scalar s_2 , produced via $pp \rightarrow Z' \rightarrow x_3 x_3$, $x_3 \rightarrow s_2 x_1$, then $s_2 \rightarrow \ell_\alpha^+ \ell_\alpha^-$ $s_2 \rightarrow \ell_\alpha^+ \ell_\alpha^-$ couplings are proportional to SM Yukawa couplings
$X \rightarrow \ell_\alpha^+ \ell_\alpha^- + \text{inv.}$	DMSM. LLP is fermion x_2 , produced via $pp \rightarrow Z' \rightarrow x_3 x_3$, $x_3 \rightarrow x_2 s_1$, then $x_2 \rightarrow \ell_\alpha^+ \ell_\alpha^- x_1$

Table A9. Simplified model library process proposals for Z/Z' (ZP) production mode where the Z/Z' decays to single LLP plus invisible. For this section, we use a DM simplified model, where the Z' couples to an $x_1 x_2$ or $s_1 s_2$ pair. x_1 and s_1 behave as DM, the LLP x_2 decays into $x_1 + \text{SM}$, and the LLP s_2 decays into SM. The DMSM model file again includes all processes in the table except for the last, which is LRSM.

Decay mode	Simplified model library process
$X \rightarrow \gamma\gamma + \text{inv.}$	DMSM. LLP is fermion x_2 , produced via $pp \rightarrow Z' \rightarrow x_1 x_2$, then $x_2 \rightarrow \gamma\gamma x_1$; or a scalar s_2 , produced via $pp \rightarrow Z' \rightarrow s_1 s_2$, then $s_2 \rightarrow \gamma\gamma$
$X \rightarrow jj + \text{inv.}$	DMSM. LLP is fermion x_2 , produced via $pp \rightarrow Z' \rightarrow x_1 x_2$, then $x_2 \rightarrow jj x_1$; or a scalar s_2 , produced via $pp \rightarrow Z' \rightarrow s_1 s_2$, then $s_2 \rightarrow jj$
$X \rightarrow \ell_\alpha^+ \ell_\alpha^- + \text{inv.}$	DMSM. LLP is fermion x_2 , produced via $pp \rightarrow Z' \rightarrow x_1 x_2$, then $x_2 \rightarrow \ell^+ \ell^- x_1$; or a scalar s_2 , produced via $pp \rightarrow Z' \rightarrow s_1 s_2$, then $s_2 \rightarrow \ell^+ \ell^-$
$X \rightarrow \ell_\alpha^+ jj$	LRSM. LLP is fermion ν_R , produced via $pp \rightarrow Z/Z'/h \rightarrow \bar{\nu}_L \nu_R$, then $\nu_R \rightarrow \ell^+ jj$

Table A10. Simplified model library process proposals for charged current (CC) production mode, $W_{\text{SM}}^\pm/W'^\pm \rightarrow X + \ell^\pm$; these can be simulated using left–right symmetric models using either the W or W' (for simplicity, in the table above we only state explicitly W). Right-handed neutrino lifetimes are most naturally long for sub-weak-scale masses.

Decay mode	Simplified model library process
$X \rightarrow jj + \text{inv.}$	LRSM. LLP is the right-handed neutrino (ν_R) produced via $pp \rightarrow W^\pm, W^\pm \rightarrow \ell^\pm \nu_R$. Then, $\nu_R \rightarrow q\bar{q}\nu$ via an off-shell Z . For massive invisible state, it may be possible to use a cascade $\nu_{R2} \rightarrow q\bar{q}\nu_{R1}$ treating the lightest right-handed neutrino as stable
$X \rightarrow jj\ell^\pm$	LRSM. LLP is the right-handed neutrino (ν_R) produced via $pp \rightarrow W^\pm, W^\pm \rightarrow \ell^\pm \nu_R$. Then, $\nu_R \rightarrow q\bar{q}'\ell^\pm$ via an off-shell W . Alternately, production and decay can be mediated by W_R .
$X \rightarrow \ell_\alpha^+ \ell_\alpha^- + \text{inv.}$	LRSM. LLP is the right-handed neutrino (ν_R) produced via $pp \rightarrow W^\pm, W^\pm \rightarrow \ell^\pm \nu_R$
or $X \rightarrow \ell_\alpha^+ \ell_\beta^- + \text{inv.}$	Then, $\nu_R \rightarrow \ell_\alpha^+ \ell_\alpha^- \nu_\beta$ or $\nu_R \rightarrow \ell_\alpha^+ \ell_\beta^- \nu_\alpha$ via an off-shell W/Z

ORCID iDs

Juliette Alimena

 <https://orcid.org/0000-0001-6030-3191>

James Beacham

 <https://orcid.org/0000-0003-3623-3335>

Martino Borsato

 <https://orcid.org/0000-0001-5760-2924>

Xabier Cid Vidal

 <https://orcid.org/0000-0002-0468-541X>

Giovanna Cottin

<https://orcid.org/0000-0002-5308-5808>

David Curtin

<https://orcid.org/0000-0003-0263-6195>

Albert De Roeck

<https://orcid.org/0000-0002-9228-5271>

Nishita Desai

<https://orcid.org/0000-0001-7942-1649>

Jared A Evans

<https://orcid.org/0000-0001-9871-6557>

Simon Knapen

<https://orcid.org/0000-0002-6733-9231>

Sabine Kraml

<https://orcid.org/0000-0002-2613-7000>

Zhen Liu

<https://orcid.org/0000-0002-3143-1976>

Sascha Mehlhase

<https://orcid.org/0000-0002-1281-2060>

Michael J Ramsey-Musolf

<https://orcid.org/0000-0001-8110-2479>

Heather Russell

<https://orcid.org/0000-0003-4181-0678>

Jessie Shelton

<https://orcid.org/0000-0002-0959-6360>

Brian Shuve

<https://orcid.org/0000-0002-3524-2021>

Monica Verducci

<https://orcid.org/0000-0001-8209-4757>

Jose Zurita

<https://orcid.org/0000-0001-5710-3965>

References

- [1] Shuve B 2017 Theory overview of long-lived particles at the LHC https://indico.cern.ch/event/607314/contributions/2542308/attachments/1447888/2231430/LHC-LLP_Shuve.pdf
- [2] Curtin D *et al* 2019 Long-lived particles at the energy frontier: the MATHUSLA physics case *Rep. Prog. Phys.* **82** 116201
- [3] Russell H 2017 An experimental introduction to long-lived particle searches at the LHC https://indico.cern.ch/event/607314/contributions/2542309/attachments/1447873/2231444/20170424_LLPS.pdf
- [4] CMS Collaboration 2016 Search for heavy stable charged particles with 12.9 fb^{-1} of 2016 data CMS-PAS-EXO-16-036 <https://cds.cern.ch/record/2205281>
- [5] Alexander J *et al* 2016 Dark sectors 2016 workshop: community report arXiv:1608.08632 [hep-ph]
- [6] Battaglieri M *et al* 2017 *US Cosmic Visions: New Ideas in Dark Matter 2017: Community Report. U.S. Cosmic Visions: New Ideas in Dark Matter (23–25, March 2017) (College Park, MD, USA)* arXiv:1707.04591 [hep-ph]
- [7] Beacham J *et al* 2020 Physics beyond colliders at CERN: beyond the Standard Model working group report *J. Phys. G: Nucl. Part. Phys.* **47** 010501
- [8] Fayet P 1976 Supersymmetry and weak, electromagnetic and strong interactions *Phys. Lett. B* **64** 159

- [9] Fayet P 1977 Spontaneously broken supersymmetric theories of weak, electromagnetic and strong interactions *Phys. Lett. B* **69** 489
- [10] Farrar G R and Fayet P 1978 Phenomenology of the production, decay, and detection of new hadronic states associated with supersymmetry *Phys. Lett. B* **76** 575–9
- [11] Fayet P 1979 Relations between the masses of the superpartners of leptons and quarks, the goldstino couplings and the neutral currents *Phys. Lett. B* **84** 416
- [12] Dimopoulos S and Georgi H 1981 Softly broken supersymmetry and SU(5) *Nucl. Phys. B* **193** 150–62
- [13] Chacko Z, Goh H-S and Harnik R 2006 The twin Higgs: natural electroweak breaking from mirror symmetry *Phys. Rev. Lett.* **96** 231802
- [14] Burdman G *et al* 2007 Folded supersymmetry and the LEP paradox *J. High Energy Phys.* **JHEP02(2007)009**
- [15] Cai H, Cheng H-C and Terning J 2009 A quirky little Higgs model *J. High Energy Phys.* **JHEP05(2009)045**
- [16] Boehm C, Ensslin T A and Silk J 2004 Can annihilating dark matter be lighter than a few GeVs? *J. Phys. G: Nucl. Part. Phys.* **30** 279–86
- [17] Boehm C, Fayet P and Silk J 2004 Light and heavy dark matter particles *Phys. Rev. D* **69** 101302
- [18] Pospelov M, Ritz A and Voloshin M B 2008 Secluded WIMP dark matter *Phys. Lett. B* **662** 53–61
- [19] Pospelov M 2009 Secluded U(1) below the weak scale *Phys. Rev. D* **80** 095002
- [20] Arkani-Hamed N *et al* 2009 A theory of dark matter *Phys. Rev. D* **79** 015014
- [21] Pospelov M and Ritz A 2009 Astrophysical signatures of secluded dark matter *Phys. Lett. B* **671** 391–7
- [22] Bouquet A and Salati P R 1987 Parity breaking and cosmological consequences *Nucl. Phys. B* **284** 557
- [23] Campbell B A *et al* 1991 Cosmological baryon asymmetry constraints on extensions of the Standard Model *Phys. Lett. B* **256** 484–90
- [24] Cui Y and Sundrum R 2013 Baryogenesis for weakly interacting massive particles *Phys. Rev. D* **87** 116013
- [25] Barry K, Graham P W and Rajendran S 2014 Displaced vertices from R -parity violation and baryogenesis *Phys. Rev. D* **89** 054003
- [26] Cui Y and Shuve B 2015 Probing baryogenesis with displaced vertices at the LHC *J. High Energy Phys.* **JHEP02(2015)049**
- [27] Cui Y 2015 A review of WIMP baryogenesis mechanisms *Mod. Phys. Lett. A* **30** 1530028
- [28] Ipek S and March-Russell J 2016 Baryogenesis via particle-antiparticle oscillations *Phys. Rev. D* **93** 123528
- [29] Feng J L and Kumar J 2008 The WIMPlless miracle: dark-matter particles without weak-scale masses or weak interactions *Phys. Rev. Lett.* **101** 231301
- [30] Baumgart M *et al* 2009 Non-Abelian dark sectors and their collider signatures *J. High Energy Phys.* **JHEP04(2009)014**
- [31] Kaplan D E, Luty M A and Zurek K M 2009 Asymmetric dark matter *Phys. Rev. D* **79** 115016
- [32] Chan Y F *et al* 2012 LHC signatures of a minimal supersymmetric hidden valley *J. High Energy Phys.* **JHEP05(2012)155**
- [33] Dienes K R and Thomas B 2012 Dynamical dark matter: I. Theoretical overview *Phys. Rev. D* **85** 083523
- [34] Dienes K R, Su S and Thomas B 2012 Distinguishing dynamical dark matter at the LHC *Phys. Rev. D* **86** 054008
- [35] Kim I-W and Zurek K M 2014 Flavor and collider signatures of asymmetric dark matter *Phys. Rev. D* **89** 035008
- [36] Fidalgo J *et al* 2009 Neutrino physics and spontaneous CP violation in the $\mu\nu$ SSM *J. High Energy Phys.* **JHEP08(2009)105**
- [37] Ghosh P *et al* 2013 Probing the μ -from- ν supersymmetric Standard Model with displaced multileptons from the decay of a Higgs boson at the LHC *Phys. Rev. D* **88** 015009
- [38] Helo J C, Hirsch M and Kovalenko S 2014 Heavy neutrino searches at the LHC with displaced vertices *Phys. Rev. D* **89** 073005
- Helo J C, Hirsch M and Kovalenko S 2016 *Phys. Rev. D* **93** 099902 (erratum)
- [39] Antusch S, Cazzato E and Fischer O 2016 Displaced vertex searches for sterile neutrinos at future lepton colliders *J. High Energy Phys.* **JHEP12(2016)007**

- [40] Graesser M L 2007 Broadening the Higgs boson with right-handed neutrinos and a higher dimension operator at the electroweak scale *Phys. Rev. D* **76** 075006
- [41] Graesser M L 2007 Experimental constraints on Higgs Boson decays to TeV-scale right-handed neutrinos arXiv:0705.2190 [hep-ph]
- [42] Ghosh P *et al* 2015 Hunting physics beyond the Standard Model with unusual W^\pm and Z decays *Phys. Rev. D* **91** 035020
- [43] Izaguirre E and Shuve B 2015 Multilepton and lepton jet probes of sub-weak-scale right-handed neutrinos *Phys. Rev. D* **91** 093010
- [44] Maiezza A, Nemevšek M and Nesti F 2015 Lepton number violation in Higgs decay at LHC *Phys. Rev. Lett.* **115** 081802
- [45] Batell B, Pospelov M and Shuve B 2016 Shedding light on neutrino masses with dark forces *J. High Energy Phys.* **JHEP08(2016)052**
- [46] Das A, Dev P S B and Kim C S 2017 Constraining sterile neutrinos from precision Higgs data *Phys. Rev. D* **95** 115013
- [47] Lara I *et al* 2018 Looking for the left sneutrino LSP with displaced-vertex searches *Phys. Rev. D* **98** 075004
- [48] Cottin G, Helo J C and Hirsch M 2018 Searches for light sterile neutrinos with multitrack displaced vertices *Phys. Rev. D* **97** 055025
- [49] Nemevšek M, Nesti F and Popara G 2018 Keung–Senjanović process at LHC: from LNV to displaced vertices to invisible decays *Phys. Rev. D* **97** 115018
- [50] Curtin D, Dienes K R and Thomas B 2018 Dynamical dark matter, MATHUSLA, and the lifetime frontier *Phys. Rev. D* **98** 115005
- [51] Das A 2018 Searching for the minimal Seesaw models at the LHC and beyond *Adv. High Energy Phys.* **2018** 9785318
- [52] Cvetič G, Das A and Zamora-Saá J 2019 Probing heavy neutrino oscillations in rare W boson decays *J. Phys. G: Nucl. Part. Phys.* **46** 075002
- [53] Giudice G F and Rattazzi R 1999 Theories with gauge mediated supersymmetry breaking *Phys. Rep.* **322** 419–99
- [54] Fan J, Reece M and Ruderman J T 2011 Stealth supersymmetry *J. High Energy Phys.* **JHEP11(2011)012**
- [55] Barbier R *et al* 2005 R-parity violating supersymmetry *Phys. Rep.* **420** 1–202
- [56] Csaki C, Kuflik E and Volansky T 2014 Dynamical R-parity violation *Phys. Rev. Lett.* **112** 131801
- [57] Arvanitaki A *et al* 2013 Mini-split *J. High Energy Phys.* **JHEP02(2013)126**
- [58] Arkani-Hamed N *et al* 2012 Simply unnatural supersymmetry arXiv:1212.6971 [hep-ph].
- [59] de Vries J, Dreiner H K and Schmeier D 2016 R-parity violation and light neutralinos at SHiP and the LHC *Phys. Rev. D* **94** 035006
- [60] Dercks D *et al* 2019 R-parity violation and light neutralinos at CODEX-b, FASER, and MATHUSLA *Phys. Rev. D* **99** 055039
- [61] Dercks D *et al* 2019 Long-lived fermions at AL3X *Phys. Rev. D* **99** 055020
- [62] Bond A D *et al* 2017 Directions for model building from asymptotic safety *J. High Energy Phys.* **JHEP08(2017)004**
- [63] Chen C H, Drees M and Gunion J F 1996 Searching for invisible and almost invisible particles at e^+e^- colliders *Phys. Rev. Lett.* **76** 2002–5
- [64] Thomas S D and Wells J D 1998 Phenomenology of massive vectorlike doublet leptons *Phys. Rev. Lett.* **81** 34–7
- [65] Feng J L *et al* 1999 Discovering supersymmetry at the Tevatron in wino LSP scenarios *Phys. Rev. Lett.* **83** 1731–4
- [66] Strassler M J and Zurek K M 2007 Echoes of a hidden valley at hadron colliders *Phys. Lett. B* **651** 374–9
- [67] Strassler M J and Zurek K M 2008 Discovering the Higgs through highly-displaced vertices *Phys. Lett. B* **661** 263–7
- [68] Strassler M J 2006 Possible effects of a hidden valley on supersymmetric phenomenology arXiv:hep-ph/0607160 [hep-ph]
- [69] Han T *et al* 2008 Phenomenology of hidden valleys at hadron colliders *J. High Energy Phys.* **JHEP07(2008)008**
- [70] Strassler M J 2008 Why unparticle models with mass gaps are examples of hidden valleys arXiv:0801.0629 [hep-ph]

- [71] Strassler M J 2008 On the phenomenology of hidden valleys with heavy flavor arXiv:0806.2385 [hep-ph]
- [72] Arkani-Hamed N *et al* 2006 Supersymmetry and the LHC inverse problem *J. High Energy Phys.* **JHEP08(2006)070**
- [73] Knuteson B and Mrenna S 2006 BARD: interpreting new frontier energy collider physics arXiv:hep-ph/0602101 [hep-ph]
- [74] Arkani-Hamed N *et al* 2007 MARMOSSET: the path from LHC data to the new Standard Model via on-shell effective theories arXiv:hep-ph/0703088 [hep-ph]
- [75] Aaltonen T *et al* 2008 Model-independent and quasi-model-independent search for new physics at CDF *Phys. Rev. D* **78** 012002
- [76] Alwall J, Schuster P and Toro N 2009 Simplified models for a first characterization of new physics at the LHC *Phys. Rev. D* **79** 075020
- [77] Alwall J *et al* 2009 Model-independent jets plus missing energy searches *Phys. Rev. D* **79** 015005
- [78] Alves D 2012 Simplified models for LHC new physics searches *J. Phys. G: Nucl. Part. Phys.* **39** 105005
- [79] Petriello F J, Quackenbush S and Zurek K M 2008 The invisible Z' at the CERN LHC *Phys. Rev. D* **77** 115020
- [80] Dudas E *et al* 2009 (In)visible Z -prime and dark matter *J. High Energy Phys.* **JHEP08(2009)014**
- [81] Goodman J and Shepherd J 2011 LHC bounds on UV-complete models of dark matter arXiv:1111.2359 [hep-ph]
- [82] An H, Ji X and Wang L-T 2012 Light dark matter and Z' dark force at colliders *J. High Energy Phys.* **JHEP07(2012)182**
- [83] Frandsen M T *et al* 2012 LHC and tevatron bounds on the dark matter direct detection cross-section for vector mediators *J. High Energy Phys.* **JHEP07(2012)123**
- [84] Dreiner H, Schmeier D and Tattersall J 2013 Contact interactions probe effective dark matter models at the LHC *EPL* **102** 51001
- [85] Cotta R C *et al* 2014 Particle physics implications and constraints on dark matter interpretations of the CDMS signal *Phys. Rev. D* **90** 013020
- [86] Abdallah J *et al* 2015 Simplified models for dark matter searches at the LHC *Phys. Dark Univ.* **9–10** 8–23
- [87] Abercrombie D *et al* 2019 Dark matter benchmark models for early LHC Run-2 searches: report of the ATLAS/CMS dark matter forum *Phys. Dark Univ.* **26** 100371
- [88] Busoni G *et al* 2016 Recommendations on presenting LHC searches for missing transverse energy signals using simplified s -channel models of dark matter 2020 *Phys. Dark Univ.* **27** 100365
- [89] Arina C *et al* 2016 A comprehensive approach to dark matter studies: exploration of simplified top-philic models *J. High Energy Phys.* **JHEP11(2016)111**
- [90] Abe T *et al* (LHC Dark Matter Working Group) 2020 LHC dark matter working group: next-generation spin-0 dark matter models *Phys. Dark Univ.* **27** 100351
- [91] Edelhäuser L, Krämer M and Sonneveld J 2015 Simplified models for same-spin new physics scenarios *J. High Energy Phys.* **JHEP04(2015)146**
- [92] Edelhäuser L *et al* 2014 Constraining supersymmetry at the LHC with simplified models for squark production *J. High Energy Phys.* **JHEP12(2014)022**
- [93] Arina C *et al* 2015 Constraints on sneutrino dark matter from LHC Run 1 *J. High Energy Phys.* **JHEP05(2015)142**
- [94] Kraml S *et al* 2016 Scalar versus fermionic top partner interpretations of $t\bar{t} + E_T^{\text{miss}}$ searches at the LHC *J. High Energy Phys.* **JHEP11(2016)107**
- [95] Heisig J and Kersten J 2012 Long-lived staus from strong production in a simplified model approach *Phys. Rev. D* **86** 055020
- [96] Liu Z and Tweedie B 2015 The fate of long-lived superparticles with hadronic decays after LHC Run 1 *J. High Energy Phys.* **JHEP06(2015)042**
- [97] Heisig J, Lessa A and Quertenmont L 2015 Simplified models for exotic BSM searches *J. High Energy Phys.* **JHEP12(2015)087**
- [98] Khoze V V, Plascencia A D and Sakurai K 2017 Simplified models of dark matter with a long-lived co-annihilation partner *J. High Energy Phys.* **JHEP06(2017)041**
- [99] Mahbubani R, Schwaller P and Zurita J 2017 Closing the window for compressed Dark Sectors with disappearing charged tracks *J. High Energy Phys.* **JHEP06(2017)119**

- [100] Buchmueller O *et al* 2017 Simplified models for displaced dark matter signatures *J. High Energy Phys.* **JHEP09(2017)076**
- [101] Pinfold J *et al* 2009 Technical design report of the MoEDAL experiment *Technical Report CERN-LHCC-2009-006. MoEDAL-TDR-001* CERN <https://cds.cern.ch/record/1181486>
- [102] Haas A *et al* 2015 Looking for milli-charged particles with a new experiment at the LHC *Phys. Lett. B* **746** 117–20
- [103] Chou J P, Curtin D and Lubatti H J 2017 New detectors to explore the lifetime frontier *Phys. Lett. B* **767** 29–36
- [104] Gligorov V V *et al* 2018 Searching for long-lived particles: a compact detector for exotics at LHCb *Phys. Rev. D* **97** 015023
- [105] Feng J L *et al* 2018 ForwArD search ExpeRiment at the LHC *Phys. Rev. D* **97** 035001
- [106] Ambrogio F *et al* 2018 On the coverage of the pMSSM by simplified model results *Eur. Phys. J. C* **78** 215
- [107] Essig R *et al* 2012 Heavy flavor simplified models at the LHC *J. High Energy Phys.* **JHEP01(2012)074**
- [108] Brust C *et al* 2012 SUSY, the third generation and the LHC *J. High Energy Phys.* **JHEP03(2012)103**
- [109] Papucci M, Ruderman J T and Weiler A 2012 Natural SUSY endures *J. High Energy Phys.* **JHEP09(2012)035**
- [110] Lopez-Fogliani D E and Munoz C 2006 Proposal for a supersymmetric Standard Model *Phys. Rev. Lett.* **97** 041801
- [111] Ghosh P *et al* 2018 Searching for left sneutrino LSP at the LHC *Int. J. Mod. Phys. A* **33** 1850110
- [112] Dimopoulos S *et al* 1996 Experimental signatures of low-energy gauge mediated supersymmetry breaking *Phys. Rev. Lett.* **76** 3494–7
- [113] Arkani-Hamed N and Dimopoulos S 2005 Supersymmetric unification without low energy supersymmetry and signatures for fine-tuning at the LHC *J. High Energy Phys.* **JHEP06(2005)073**
- [114] Byrne M 2004 Universal extra dimensions and charged LKPs *Phys. Lett. B* **583** 309–14
- [115] Khachatryan V *et al* (CMS Collaboration) 2015 Precise determination of the mass of the Higgs boson and tests of compatibility of its couplings with the Standard Model predictions using proton collisions at 7 and 8 TeV *Eur. Phys. J. C* **75** 212
- [116] Aad G *et al* (ATLAS Collaboration) 2015 Constraints on new phenomena via Higgs boson couplings and invisible decays with the ATLAS detector *J. High Energy Phys.* **JHEP11(2015)206**
- [117] Curtin D *et al* 2014 Exotic decays of the 125 GeV Higgs boson *Phys. Rev. D* **90** 075004
- [118] Craig N *et al* 2015 Naturalness in the dark at the LHC *J. High Energy Phys.* **JHEP07(2015)105**
- [119] Silveira V and Zee A 1985 Scalar phantoms *Phys. Lett. B* **161** 136–40
- [120] Beauchesne H, Bertuzzo E and Grilli di Cortona G 2017 Constraints on the relaxion mechanism with strongly interacting vector-fermions *J. High Energy Phys.* **JHEP08(2017)093**
- [121] Langacker P 2009 The physics of heavy Z' Gauge bosons *Rev. Mod. Phys.* **81** 1199–228
- [122] Holdom B 1986 Two $U(1)$'s and epsilon charge shifts *Phys. Lett. B* **166** 196–8
- [123] Feng J L, Kaplinghat M and Yu H-B 2010 Halo shape and relic density exclusions of sommerfeld-enhanced dark matter explanations of cosmic ray excesses *Phys. Rev. Lett.* **104** 151301
- [124] Buckley M R and Fox P J 2010 Dark matter self-interactions and light force carriers *Phys. Rev. D* **81** 083522
- [125] Tulin S, Yu H-B and Zurek K M 2013 Resonant dark forces and small scale structure *Phys. Rev. Lett.* **110** 111301
- [126] Boehm C and Fayet P 2004 Scalar dark matter candidates *Nucl. Phys. B* **683** 219–63
- [127] Arkani-Hamed N and Weiner N 2008 LHC signals for a SuperUnified theory of dark matter *J. High Energy Phys.* **JHEP12(2008)104**
- [128] Cirelli M, Fornengo N and Strumia A 2006 Minimal dark matter *Nucl. Phys. B* **753** 178–94
- [129] Cirelli M and Strumia A 2009 Minimal dark matter: model and results *New J. Phys.* **11** 105005
- [130] Fileviez Perez P *et al* 2009 Triplet scalars and dark matter at the LHC *Phys. Rev. D* **79** 055024
- [131] Hochberg Y, Kuflik E and Murayama H 2016 SIMP spectroscopy *J. High Energy Phys.* **JHEP05(2016)090**
- [132] Tucker-Smith D and Weiner N 2001 Inelastic dark matter *Phys. Rev. D* **64** 043502
- [133] Bai Y and Tait T M P 2012 Inelastic dark matter at the LHC *Phys. Lett. B* **710** 335–8

- [134] Weiner N and Yavin I 2012 How dark are Majorana WIMPs? Signals from MiDM and Rayleigh dark matter *Phys. Rev. D* **86** 075021
- [135] Izaguirre E, Krnjaic G and Shuve B 2016 Discovering inelastic thermal-relic dark matter at colliders *Phys. Rev. D* **93** 063523
- [136] Griest K and Seckel D 1991 Three exceptions in the calculation of relic abundances *Phys. Rev. D* **43** 3191–203
- [137] Baker M J *et al* 2015 The coannihilation codex *J. High Energy Phys.* [JHEP12\(2015\)120](#)
- [138] De Simone A, Sanz V and Sato H P 2010 Pseudo-Dirac dark matter leaves a trace *Phys. Rev. Lett.* **105** 121802
- [139] Davoli A *et al* 2017 Displaced vertices from pseudo-dirac dark matter *J. High Energy Phys.* [JHEP11\(2017\)025](#)
- [140] El Hedri S *et al* 2017 Simplified phenomenology for colored dark sectors *J. High Energy Phys.* [JHEP04\(2017\)118](#)
- [141] Davoli A *et al* 2018 LHC phenomenology of dark matter with a color-octet partner *J. High Energy Phys.* [JHEP07\(2018\)054](#)
- [142] Garny M *et al* 2017 Coannihilation without chemical equilibrium *Phys. Rev. D* **96** 103521
- [143] D’Agnolo R T, Pappadopulo D and Ruderman J T 2017 Fourth exception in the calculation of relic abundances *Phys. Rev. Lett.* **119** 061102
- [144] Garny M *et al* 2018 Top-philic dark matter within and beyond the WIMP paradigm *Phys. Rev. D* **97** 075002
- [145] Cheng H-C, Li L and Zheng R 2018 Coscattering/coannihilation dark matter in a fraternal twin Higgs model *J. High Energy Phys.* [JHEP09\(2018\)098](#)
- [146] Hall L J *et al* 2010 Freeze-in production of FIMP dark matter *J. High Energy Phys.* [JHEP03\(2010\)080](#)
- [147] Co R T *et al* 2015 Freeze-in dark matter with displaced signatures at colliders *J. Cosmol. Astropart. Phys.* [JCAP12\(2015\)024](#)
- [148] Hessler A G *et al* 2017 Probing the scotogenic FIMP at the LHC *J. High Energy Phys.* [JHEP01\(2017\)100](#)
- [149] Ghosh A, Mondal T and Mukhopadhyaya B 2017 Heavy stable charged tracks as signatures of non-thermal dark matter at the LHC : a study in some non-supersymmetric scenarios *J. High Energy Phys.* [JHEP12\(2017\)136](#)
- [150] D’Eramo F, Fernandez N and Profumo S 2018 Dark matter freeze-in production in fast-expanding universes *J. Cosmol. Astropart. Phys.* [JCAP02\(2018\)046](#)
- [151] Calibbi L *et al* 2018 Singlet-doublet dark matter freeze-in: LHC displaced signatures versus cosmology *J. High Energy Phys.* [JHEP09\(2018\)037](#)
- [152] Garny M and Heisig J 2018 SuperWIMP meets freeze-in *Phys. Rev. D* **98** 095031
- [153] Bélanger G *et al* 2019 LHC-friendly minimal freeze-in models *J. High Energ. Phys.* [JHEP02\(2019\)186](#)
- [154] Heisig J 2018 Dark matter and long-lived particles at the LHC *53rd Rencontres de Moriond on Electroweak Interactions and Unified Theories (Moriond EW 2018) La Thuile 10–17, March 2018 (Italy, 10–17 March)* [arXiv:1805.07361 \[hep-ph\]](#)
- [155] Falkowski A *et al* 2010 Hidden Higgs decaying to lepton jets *J. High Energy Phys.* [JHEP05\(2010\)077](#)
- [156] Primulando R, Salvioni E and Tsai Y 2015 The dark penguin shines light at colliders *J. High Energy Phys.* [JHEP07\(2015\)031](#)
- [157] Bai Y, Bourbeau J and Lin T 2015 Dark matter searches with a mono- Z' jet *J. High Energy Phys.* [JHEP06\(2015\)205](#)
- [158] Minkowski P 1977 $\mu \rightarrow e\gamma$ at a rate of one out of 10^9 Muon decays? *Phys. Lett.* **67B** 421–8
- [159] Yanagida T 1979 *Horizontal Symmetry and Masses of Neutrinos Conf. Proc. C7902131* pp 95–9
- [160] Mohapatra R N and Senjanovic G 1980 Neutrino mass and spontaneous parity violation *Phys. Rev. Lett.* **44** 912
- [161] Glashow S L 1980 The future of elementary particle physics *NATO Sci. Ser. B* **61** 687
- [162] Mohapatra R N and Valle J W F 1986 Neutrino mass and baryon number nonconservation in superstring models *Phys. Rev. D* **34** 1642
- [163] Keung W-Y and Senjanovic G 1983 Majorana neutrinos and the production of the right-handed charged Gauge boson *Phys. Rev. Lett.* **50** 1427
- [164] Ferrari A *et al* 2000 Sensitivity study for new gauge bosons and right-handed Majorana neutrinos in pp collisions at $s = 14$ TeV *Phys. Rev. D* **62** 013001

- [165] Basso L *et al* 2009 Phenomenology of the minimal B-L extension of the Standard model: Z' and neutrinos *Phys. Rev. D* **80** 055030
- [166] Atre A *et al* 2009 The search for heavy Majorana neutrinos *J. High Energy Phys.* **JHEP05(2009)030**
- [167] Fileviez Perez P, Han T and Li T 2009 Testability of type I seesaw at the CERN LHC: revealing the existence of the B-L symmetry *Phys. Rev. D* **80** 073015
- [168] Nemevsek M *et al* 2011 First limits on left–right symmetry scale from LHC data *Phys. Rev. D* **83** 115014
- [169] Nemevsek M, Nesti F and Vasquez J C 2017 Majorana Higgses at colliders *J. High Energy Phys.* **JHEP04(2017)114**
- [170] Accomando E *et al* 2017 Novel SM-like Higgs decay into displaced heavy neutrino pairs in $U(1)'$ models *J. High Energy Phys.* **JHEP04(2017)081**
- [171] Accomando E *et al* 2016 Higgses and heavy neutrinos in $U(1)'$ models: from the LHC to the GUT scale *J. High Energy Phys.* **JHEP07(2016)086**
- [172] Caputo A *et al* 2017 The seesaw portal in testable models of neutrino masses *J. High Energy Phys.* **JHEP06(2017)112**
- [173] Accomando E *et al* 2018 Extra Higgs boson and Z' as portals to signatures of heavy neutrinos at the LHC *J. High Energy Phys.* **JHEP02(2018)109**
- [174] Helo J C, Hirsch M and Wang Z S 2018 Heavy neutral fermions at the high-luminosity LHC *J. High Energy Phys.* **JHEP07(2018)056**
- [175] Asaka T, Blanchet S and Shaposhnikov M 2005 The nuMSM, dark matter and neutrino masses *Phys. Lett. B* **631** 151–6
- [176] Asaka T and Shaposhnikov M 2005 The nuMSM, dark matter and baryon asymmetry of the Universe *Phys. Lett. B* **620** 17–26
- [177] Pati J C and Salam A 1974 Lepton number as the fourth color *Phys. Rev. D* **10** 275–89
Pati J C and Salam A 1975 *Phys. Rev. D* **11** 703 (erratum)
- [178] Mohapatra R N and Pati J C 1975 A natural left–right symmetry *Phys. Rev. D* **11** 2558
- [179] Senjanovic G and Mohapatra R N 1975 Exact left–right symmetry and spontaneous violation of parity *Phys. Rev. D* **12** 1502
- [180] Senjanovic G 1979 Spontaneous breakdown of parity in a class of Gauge theories *Nucl. Phys. B* **153** 334–64
- [181] Das A, Gao Y and Kamon T 2019 Heavy neutrino search via semileptonic Higgs decay at the LHC *Eur. Phys. J. C* **79** 424
- [182] Kang J and Luty M A 2009 Macroscopic strings and ‘Quirks’ at colliders *J. High Energy Phys.* **JHEP11(2009)065**
- [183] Chacko Z, Curtin D and Verhaaren C B 2016 A quirky probe of neutral naturalness *Phys. Rev. D* **94** 011504
- [184] Autran M *et al* 2015 Searches for dark matter in events with a resonance and missing transverse energy *Phys. Rev. D* **92** 035007
- [185] Blinov N, Izaguirre E and Shuve B 2018 Rare Z Boson decays to a hidden sector *Phys. Rev. D* **97** 015009
- [186] Craig N *et al* 2016 The Higgs portal above threshold *J. High Energy Phys.* **JHEP02(2016)127**
- [187] Khachatryan V *et al* (CMS Collaboration) 2017 Search for narrow resonances in dilepton mass spectra in proton–proton collisions at $\sqrt{s} = 13$ TeV and combination with 8 TeV data *Phys. Lett. B* **768** 57–80
- [188] Sirunyan A M *et al* (CMS Collaboration) 2017 Search for dijet resonances in proton–proton collisions at $\sqrt{s} = 13$ TeV and constraints on dark matter and other models *Phys. Lett. B* **769** 520–42
Sirunyan A M *et al* (CMS Collaboration) 2017 *Phys. Lett. B* **772** 882 (erratum)
- [189] Aaboud M *et al* (ATLAS Collaboration) 2017 Search for new phenomena in dijet events using 37 fb^{-1} of pp collision data collected at $\sqrt{s} = 13$ TeV with the ATLAS detector *Phys. Rev. D* **96** 052004
- [190] Sirunyan A M *et al* (CMS Collaboration) 2017 Search for low mass vector resonances decaying to quark–antiquark pairs in proton–proton collisions at $\sqrt{s} = 13$ TeV *Phys. Rev. Lett.* **119** 111802
- [191] Aaboud M *et al* (ATLAS Collaboration) 2017 Search for new high-mass phenomena in the dilepton final state using 36 fb^{-1} of proton–proton collision data at $\sqrt{s} = 13$ TeV with the ATLAS detector *J. High Energy Phys.* **JHEP10(2017)182**

- [192] Aaboud M *et al* (ATLAS Collaboration) 2018 Search for $W' \rightarrow tb$ decays in the hadronic final state using pp collisions at $\sqrt{s} = 13$ TeV with the ATLAS detector *Phys. Lett. B* **781** 327–48
- [193] Aaboud M *et al* (ATLAS Collaboration) 2019 Search for light resonances decaying to boosted quark pairs and produced in association with a photon or a jet in proton–proton collisions at $\sqrt{s} = 13$ TeV with the ATLAS detector *Phys. Lett. B* **788** 316–35
- [194] Ibe M, Moroi T and Yanagida T T 2007 Possible signals of wino LSP at the Large Hadron Collider *Phys. Lett. B* **644** 355–60
- [195] Buckley M R, Randall L and Shuve B 2011 LHC searches for non-chiral weakly charged multiplets *J. High Energy Phys.* **JHEP05(2011)097**
- [196] Aad G *et al* (ATLAS Collaboration) 2015 Search for massive, long-lived particles using multitrack displaced vertices or displaced lepton pairs in pp collisions at $\sqrt{s} = 8$ TeV with the ATLAS detector *Phys. Rev. D* **92** 072004
- [197] CMS Collaboration 2016 Search for displaced leptons in the e-mu channel *CMS-PAS-EXO-16-022* <https://cds.cern.ch/record/2205146>
- [198] Bhupal Dev P, Mohapatra R N and Zhang Y 2017 Displaced photon signal from a possible light scalar in minimal left–right seesaw model *Phys. Rev. D* **95** 115001
- [199] Dimopoulos S, Thomas S D and Wells J D 1997 Sparticle spectroscopy and electroweak symmetry breaking with gauge mediated supersymmetry breaking *Nucl. Phys. B* **488** 39–91
- [200] del Aguila F and Aguilar-Saavedra J A 2009 Distinguishing seesaw models at LHC with multi-lepton signals *Nucl. Phys. B* **813** 22–90
- [201] Ambrosanio S, Kribs G D and Martin S P 1997 Signals for gauge mediated supersymmetry breaking models at the CERN LEP-2 collider *Phys. Rev. D* **56** 1761–77
- [202] Delgado A, Giudice G F and Slavich P 2007 Dynamical mu term in gauge mediation *Phys. Lett. B* **653** 424–33
- [203] Meade P, Reece M and Shih D 2010 Long-lived neutralino NLSPs *J. High Energy Phys.* **JHEP10(2010)067**
- [204] Allanach B *et al* 2015 Light sparticles from a light singlet in Gauge mediation *Phys. Rev. D* **92** 015006
- [205] Evans J A and Shelton J 2016 Long-lived staus and displaced leptons at the LHC *J. High Energy Phys.* **JHEP04(2016)056**
- [206] Allanach B C *et al* 2016 Prompt signals and displaced vertices in sparticle searches for next-to-minimal Gauge mediated supersymmetric models *Eur. Phys. J. C* **76** 482
- [207] Abbiendi G *et al* 2003 Search for stable and longlived massive charged particles in $e + e -$ collisions at $s^{*}(1/2) = 130 - 209$ GeV *Phys. Lett. B* **572** 8–20
- [208] Jittoh T *et al* 2006 Long life stau in the minimal supersymmetric Standard Model *Phys. Rev. D* **73** 055009
- Jittoh T *et al* 2013 *Phys. Rev. D* **87** 019901 (erratum)
- [209] Brandenburg A *et al* 2005 Signatures of axinos and gravitinos at colliders *Phys. Lett. B* **617** 99–111
- [210] Heisig J *et al* 2014 A survey for low stau yields in the MSSM *J. High Energy Phys.* **JHEP04(2014)053**
- [211] Bajc B and Senjanovic G 2007 Seesaw at LHC *J. High Energy Phys.* **JHEP08(2007)014**
- [212] Bajc B, Nemevsek M and Senjanovic G 2007 Probing seesaw at LHC *Phys. Rev. D* **76** 055011
- [213] Franceschini R, Hambye T and Strumia A 2008 Type-III see-saw at LHC *Phys. Rev. D* **78** 033002
- [214] Arhrib A *et al* 2010 Collider signatures for heavy lepton triplet in type I+III seesaw *Phys. Rev. D* **82** 053004
- [215] Aad G *et al* (ATLAS Collaboration) 2016 Search for magnetic monopoles and stable particles with high electric charges in 8 TeV pp collisions with the ATLAS detector *Phys. Rev. D* **93** 052009
- [216] Khachatryan V *et al* (CMS Collaboration) 2016 Search for long-lived charged particles in proton–proton collisions at $\sqrt{s} = 13$ TeV *Phys. Rev. D* **94** 112004
- [217] Khachatryan V *et al* (CMS Collaboration) 2015 Search for disappearing tracks in proton–proton collisions at $\sqrt{s} = 8$ TeV *J. High Energy Phys.* **JHEP01(2015)096**
- [218] Aaboud M *et al* (ATLAS Collaboration) 2018 *J. High Energy Phys.* **JHEP06(2018)022**
- [219] Sjostrand T, Mrenna S and Skands P Z 2008 A brief introduction to PYTHIA 8.1 *Comput. Phys. Commun.* **178** 852–67
- [220] Sjostrand T *et al* 2015 An introduction to PYTHIA 8.2 *Comput. Phys. Commun.* **191** 159–77

- [221] Buccella F, Farrar G R and Pugliese A 1985 R Baryon masses *Phys. Lett.* **153B** 311–4
- [222] Farrar G R *et al* 2011 Limit on the mass of a long-lived or stable gluino *J. High Energy Phys.* **JHEP02(2011)018**
- [223] Aaboud *et al* (ATLAS Collaboration) 2019 Search for heavy charged long-lived particles in the ATLAS detector in 36.1 fb^{-1} of proton–proton collision data at $\sqrt{s} = 13 \text{ TeV}$ *Phys. Rev. D* **99** 092007
- [224] Alwall J *et al* 2007 A standard format for Les Houches event files *Comput. Phys. Commun.* **176** 300–4
- [225] Degrande C *et al* 2012 UFO—the universal FeynRules output *Comput. Phys. Commun.* **183** 1201–14
- [226] Alwall J *et al* 2014 The automated computation of tree-level and next-to-leading order differential cross sections, and their matching to parton shower simulations *J. High Energy Phys.* **JHEP07(2014)079**
- [227] Artoisenet P *et al* 2013 Automatic spin-entangled decays of heavy resonances in Monte Carlo simulations *J. High Energy Phys.* **JHEP03(2013)015**
- [228] Djouadi A *et al* 1998 The Minimal supersymmetric Standard Model: group summary report *GDR (Groupement De Recherche)—Supersymetrie Montpellier* 15–17 April, 1998 (*FrancearXiv: hep-ph/9901246*)
- [229] Berger C F *et al* 2009 Supersymmetry without prejudice *J. High Energy Phys.* **JHEP02(2009)023**
- [230] Curtin D *et al* 2015 Illuminating dark photons with high-energy colliders *J. High Energy Phys.* **JHEP02(2015)157**
- [231] Agostinelli S *et al* 2003 GEANT4: a simulation toolkit *Nucl. Instrum. Methods A* **506** 250–303
- [232] Mackeprang R and Rizzi A 2007 Interactions of coloured heavy stable particles in matter *Eur. Phys. J. C* **50** 353–62
- [233] Mackeprang R and Milstead D 2010 An updated description of heavy-hadron interactions in GEANT-4 *Eur. Phys. J. C* **66** 493–501
- [234] Khachatryan V *et al* (CMS Collaboration) 2015 Search for decays of stopped long-lived particles produced in proton–proton collisions at $\sqrt{s} = 8 \text{ TeV}$ *Eur. Phys. J. C* **75** 151
- [235] Sirunyan A M *et al* (CMS Collaboration) 2018 Search for decays of stopped exotic long-lived particles produced in proton–proton collisions at $\sqrt{s} = 13 \text{ TeV}$ *J. High Energy Phys.* **JHEP05(2018)127**
- [236] Aad G *et al* (ATLAS Collaboration) 2013 Search for long-lived stopped R-hadrons decaying out-of-time with pp collisions using the ATLAS detector *Phys. Rev. D* **88** 112003
- [237] Aaboud M *et al* (ATLAS Collaboration) 2018 Search for long-lived, massive particles in events with displaced vertices and missing transverse momentum in $\sqrt{s} = 13 \text{ TeV}$ pp collisions with the ATLAS detector *Phys. Rev. D* **97** 052012
- [238] Alwall J *et al* 2011 MadGraph 5: going beyond *J. High Energy Phys.* **JHEP06(2011)128**
- [239] Farina M and Low M 2017 Constraining quirky tracks with conventional searches *Phys. Rev. Lett.* **119** 111801
- [240] Knapen S *et al* 2017 Tracking down quirks at the Large Hadron Collider *Phys. Rev. D* **96** 115015
- [241] Aad G *et al* (ATLAS Collaboration) 2013 Triggers for displaced decays of long-lived neutral particles in the ATLAS detector *J. Instrum.* **8** P07015
- [242] Knapen S *et al* 2017 Triggering soft bombs at the LHC *J. High Energy Phys.* **JHEP08(2017)076**
- [243] ATLAS Collaboration 2018 Reinterpretation of searches for supersymmetry in models with variable R-parity-violating coupling strength and long-lived R-hadrons *ATLAS-CONF-2018-003* <http://cds.cern.ch/record/2308391>
- [244] Lee L, Ohm C, Soffer A and Yu T T 2018 Collider searches for long-lived particles beyond the Standard Model *Prog. Part. Nucl. Phys.* **106** 210–55
- [245] Fanti M 2017 Search for long-lived particles at LEP https://indico.cern.ch/event/517268/contributions/2041301/attachments/1272370/1886064/fanti_160512_LLPworkshop_LEP.pdf
- [246] Aaboud M *et al* (ATLAS Collaboration) 2019 Search for long-lived neutral particles in pp collisions at $\sqrt{s} = 13 \text{ TeV}$ that decay into displaced hadronic jets in the ATLAS calorimeter *Eur. Phys. J. C* **79** 481
- [247] Aad G *et al* (ATLAS Collaboration) 2015 Search for pair-produced long-lived neutral particles decaying in the ATLAS hadronic calorimeter in pp collisions at $\sqrt{s} = 8 \text{ TeV}$ *Phys. Lett. B* **743** 15–34

- [248] Aad G *et al* (ATLAS Collaboration) 2015 Search for long-lived, weakly interacting particles that decay to displaced hadronic jets in proton–proton collisions at $\sqrt{s} = 8$ TeV with the ATLAS detector *Phys. Rev. D* **92** 012010
- [249] Sirunyan A M *et al* (CMS Collaboration) 2018 Search for new long-lived particles at $\sqrt{s} = 13$ TeV *Phys. Lett. B* **780** 432–54
- [250] Sirunyan A M *et al* (CMS Collaboration) 2019 Search for long-lived particles decaying into displaced jets in proton–proton collisions at $\sqrt{s} = 13$ TeV *Phys. Rev. D* **99** 032011
- [251] Khachatryan V *et al* (CMS Collaboration) 2015 Search for long-lived neutral particles decaying to quark–antiquark pairs in proton–proton collisions at $\sqrt{s} = 8$ TeV *Phys. Rev. D* **91** 012007
- [252] Sirunyan A M *et al* (CMS Collaboration) 2018 Search for long-lived particles with displaced vertices in multijet events in proton–proton collisions at $\sqrt{s} = 13$ TeV *Phys. Rev. D* **98** 092011
- [253] Aaij R *et al* 2017 Updated search for long-lived particles decaying to jet pairs *Eur. Phys. J. C* **77** 812
- [254] Aaij R *et al* (LHCb Collaboration) 2016 Search for Higgs-like bosons decaying into long-lived exotic particles *Eur. Phys. J. C* **76** 664
- [255] ATLAS Collaboration 2017 Performance of the reconstruction of large impact parameter tracks in the ATLAS inner detector *ATLPHYS-PUB-2017-014* <https://cds.cern.ch/record/2275635>
- [256] Aad G *et al* (ATLAS Collaboration) 2013 Triggers for displaced decays of long-lived neutral particles in the ATLAS detector *J. Instrum.* **8** P07015
- [257] Aad G *et al* (ATLAS Collaboration) 2014 Standalone vertex finding in the ATLAS muon spectrometer *J. Instrum.* **9** P02001
- [258] Aaboud M *et al* (ATLAS Collaboration) 2018 Search for long-lived particles produced in pp collisions at $\sqrt{s} = 13$ TeV that decay into displaced hadronic jets in the ATLAS muon spectrometer *Phys. Rev. D* **99** 052005
- [259] Aaboud M *et al* (ATLAS Collaboration) 2019 Search for the production of a long-lived neutral particle decaying within the ATLAS hadronic calorimeter in association with a Z boson from pp collisions at $\sqrt{s} = 13$ TeV *Phys. Rev. Lett.* **122** 151801
- [260] Csaki C *et al* 2015 Searching for displaced Higgs boson decays *Phys. Rev. D* **92** 073008
- [261] Vasquez Sierra C 2017 Snapshot of current long-lived particle results at LHCb https://indico.cern.ch/event/649760/contributions/2689322/attachments/1542518/2419630/LHCb_LLPCVS.pdf
- [262] Coccaro A *et al* 2016 Data-driven model-independent searches for long-lived particles at the LHC *Phys. Rev. D* **94** 113003
- [263] Curtin D and Verhaaren C B 2015 Discovering uncolored naturalness in exotic Higgs decays *J. High Energy Phys.* **JHEP12(2015)072**
- [264] Cottin G, Helo J C and Hirsch M 2018 Displaced vertices as probes of sterile neutrino mixing at the LHC *Phys. Rev. D* **98** 035012
- [265] Khachatryan V *et al* (CMS Collaboration) 2015 Search for long-lived particles that decay into final states containing two electrons or two muons in proton–proton collisions at $\sqrt{s} = 8$ TeV *Phys. Rev. D* **91** 052012
- [266] CMS Collaboration 2015 Search for long-lived particles that decay into final states containing two muons, reconstructed using only the CMS muon chambers *CMS-PAS-EXO-14-012* <https://cds.cern.ch/record/2005761>
- [267] Aaij R *et al* (LHCb Collaboration) 2015 Search for hidden-sector bosons in $B^0 \rightarrow K^*0\mu^+\mu^-$ decays *Phys. Rev. Lett.* **115** 161802
- [268] Aaij R *et al* (LHCb Collaboration) 2017 Search for long-lived scalar particles in $B^+ \rightarrow K^+\chi(\mu^+\mu^-)$ decays *Phys. Rev. D* **95** 071101
- [269] Aaij R *et al* (LHCb Collaboration) 2018 Search for dark photons produced in 13 TeV pp collisions *Phys. Rev. Lett.* **120** 061801
- [270] Khachatryan V *et al* (CMS Collaboration) 2016 A search for pair production of new light bosons decaying into muons *Phys. Lett. B* **752** 146–68
- [271] Sirunyan A M *et al* (CMS Collaboration) 2019 A search for pair production of new light bosons decaying into muons in proton–proton collisions at 13 TeV *Phys. Lett. B* **796** 131–54
- [272] Aad G *et al* (ATLAS Collaboration) 2014 Search for long-lived neutral particles decaying into lepton jets in proton–proton collisions at $\sqrt{s} = 8$ TeV with the ATLAS detector *J. High Energy Phys.* **JHEP11(2014)088**

- [273] Aad G *et al* 2019 Search for light long-lived neutral particles produced in pp collisions at $\sqrt{s} = 13$ TeV and decaying into collimated leptons or light hadrons with the ATLAS detector *ATLAS-CONF-2016-042* arXiv:1909.01246 [hep-ex]
- [274] Aad G *et al* (ATLAS Collaboration) 2016 A search for prompt lepton-jets in pp collisions at $\sqrt{s} = 8$ TeV with the ATLAS detector *J. High Energy Phys.* **JHEP02(2016)062**
- [275] Khachatryan V *et al* (CMS Collaboration) 2015 Search for displaced supersymmetry in events with an electron and a muon with large impact parameters *Phys. Rev. Lett.* **114** 061801
- [276] Aaboud M *et al* (ATLAS Collaboration) 2019 Search for long-lived particles in final states with displaced dimuon vertices in pp collisions at $\sqrt{s} = 13$ TeV with the ATLAS detector *Phys. Rev. D* **99** 012001
- [277] Aaij R *et al* (LHCb Collaboration) 2016 Tesla: an application for real-time data analysis in high energy physics *Comput. Phys. Commun.* **208** 35–42
- [278] Sirunyan A M *et al* (CMS Collaboration) 2018 Search for heavy neutral leptons in events with three charged leptons in proton–proton collisions at $\sqrt{s} = 13$ TeV *Phys. Rev. Lett.* **120** 221801
- [279] Aaij R *et al* (LHCb Collaboration) 2017 Search for massive long-lived particles decaying semileptonically in the LHCb detector *Eur. Phys. J. C* **77** 224
- [280] Aaij R *et al* (LHCb Collaboration) 2014 Search for Majorana neutrinos in $B^- \rightarrow \pi^+ \mu^- \mu^-$ decays *Phys. Rev. Lett.* **112** 131802
- [281] Shuve B and Peskin M E 2016 Revision of the LHCb limit on Majorana neutrinos *Phys. Rev. D* **94** 113007
- [282] Gorbunov D and Shaposhnikov M 2007 How to find neutral leptons of the ν MSM? *J. High Energy Phys.* **JHEP10(2007)015**
Gorbunov D and Shaposhnikov M 2013 *J. High Energy Phys.* **JHEP11(2013)101** (erratum)
- [283] Milanes D, Quintero N and Vera C E 2016 Sensitivity to Majorana neutrinos in $\Delta L = 2$ decays of B_c meson at LHCb *Phys. Rev. D* **93** 094026
- [284] Mermoud P 2017 Right-handed neutrinos: the hunt is on! *Proc. of Prospects in Neutrino Physics (NuPhys2016)* (arXiv:1704.08635NuPhys2016-Mermoud)
- [285] Antusch S, Cazzato E and Fischer O 2017 Sterile neutrino searches via displaced vertices at LHCb *Phys. Lett. B* **774** 114
- [286] Drewes M *et al* 2020 A heavy metal path to new physics *Phys. Rev. Lett.* **124** 081801
- [287] Gronau M, Leung C N and Rosner J L 1984 Extending limits on neutral heavy leptons *Phys. Rev. D* **29** 2539
- [288] Lanfranchi G 2017 Search for hidden sector particles at NA62 *Report PoS EPS-HEP2017 (2017) 301* NA62 Collaboration DOI:10.22323/1.314.0301
- [289] SHiP Collaboration 2015 A facility to Search for Hidden Particles (SHiP) at the CERN SPS *CERN-SPSC-2015-016* arXiv:1504.04956 [physics.ins-det]
- [290] Bernardi G *et al* 1988 Further limits on heavy neutrino couplings *Phys. Lett. B* **203** 332
- [291] CHARM Collaboration 1986 A search for decays of heavy neutrinos in the mass range 0.5–2.8 GeV *Phys. Lett. B* **166** 473
- [292] NuTeV Collaboration 1999 Search for neutral heavy leptons in a high-energy neutrino beam *Phys. Rev. Lett.* **83** 4943
- [293] DELPHI Collaboration 1997 Search for neutral heavy leptons produced in Z decays *Z. Phys. C* **74** 57
- [294] Khachatryan V *et al* (CMS Collaboration) 2015 Search for heavy Majorana neutrinos in $\mu^\pm \mu^\pm +$ jets events in proton–proton collisions at $\sqrt{s} = 8$ TeV *Phys. Lett. B* **748** 144–66
- [295] Canetti L *et al* 2013 Dark matter, baryogenesis and neutrino oscillations from right handed neutrinos *Phys. Rev. D* **87** 093006
- [296] NA62 Collaboration 2017 The beam and detector of the NA62 experiment at CERN *J. Instrum.* **12** P05025
- [297] Kling F and Trojanowski S 2018 Heavy neutral leptons at FASER *Phys. Rev. D* **97** 095016
- [298] Asaka T and Shaposhnikov M 2005 The ν MSM, dark matter and baryon asymmetry of the Universe *Phys. Lett. B* **620** 17
- [299] Mermoud P 2017 Hidden sector searches with SHiP and NA62 *Proc. Int. Workshop on Neutrinos from Accelerators (NuFact2017)* arXiv:1712.01768 [hep-ex]
- [300] Drewes M *et al* 2018 ARS leptogenesis *Int. J. Mod. Phys. A* **33** 1842002
- [301] Aad G *et al* (ATLAS Collaboration) 2014 Search for nonpointing and delayed photons in the diphoton and missing transverse momentum final state in 8 TeV pp collisions at the LHC using the ATLAS detector *Phys. Rev. D* **90** 112005

- [302] Aad G *et al* (ATLAS Collaboration) 2013 Search for nonpointing photons in the diphoton and E_T^{miss} final state in $\sqrt{s} = 7$ TeV proton–proton collisions using the ATLAS detector *Phys. Rev. D* **88** 012001
- [303] CMS Collaboration 2015 Search for long-lived neutral particles in the final state of delayed photons and missing energy in proton–proton collisions at $\sqrt{s} = 8$ TeV *CMS-PAS-EXO-12-035* <https://cds.cern.ch/record/2063495>
- [304] CMS Collaboration 2015 Search for displaced photons using conversions at 8 TeV *CMS-PAS-EXO-14-017* <https://cds.cern.ch/record/2019862>
- [305] Dine M, Nelson A E and Shirman Y 1995 Low-energy dynamical supersymmetry breaking simplified *Phys. Rev. D* **51** 1362–70
- [306] Chatrchyan S *et al* (CMS Collaboration) 2013 Searches for long-lived charged particles in pp collisions at $\sqrt{s} = 7$ and 8 TeV *J. High Energy Phys.* **JHEP07(2013)122**
- [307] Aad G *et al* (ATLAS Collaboration) 2015 Searches for heavy long-lived charged particles with the ATLAS detector in proton–proton collisions at $\sqrt{s} = 8$ TeV *J. High Energy Phys.* **JHEP01(2015)068**
- [308] Aaboud M *et al* (ATLAS Collaboration) 2019 Search for heavy charged long-lived particles in proton–proton collisions at $\sqrt{s} = 13$ TeV using an ionisation measurement with the ATLAS detector *Phys. Lett. B* **788** 96–116
- [309] Aaij R *et al* (LHCb Collaboration) 2015 Search for long-lived heavy charged particles using a ring imaging Cherenkov technique at LHCb *Eur. Phys. J. C* **75** 595
- [310] De Roeck A *et al* 2012 Sensitivity of LHC experiments to exotic highly ionising particles *Eur. Phys. J. C* **72** 1985
- [311] Acharya B *et al* 2016 Search for magnetic monopoles with the MoEDAL prototype trapping detector in 8 TeV proton–proton collisions at the LHC *J. High Energy Phys.* **JHEP08(2016)067**
- [312] Bruce R *et al* 2020 New physics searches with heavy-ion collisions at the LHC *J. Phys. G: Nucl. Part. Phys.* **47** 060501
- [313] Hamaguchi K *et al* 2004 A Study of late decaying charged particles at future colliders *Phys. Rev. D* **70** 115007
- [314] Asai S *et al* 2011 Stau Kinks at the LHC *J. High Energy Phys.* **JHEP12(2011)041**
- [315] Jung S and Lee H-S 2017 Constraining Higgsino Kink tracks from existing LHC searches *Int. J. Mod. Phys. A* **32** 1750070
- [316] Sirunyan A M *et al* (CMS Collaboration) 2019 Search for new particles decaying to a jet and an emerging jet *J. High Energy Phys.* **JHEP02(2019)179**
- [317] Aad G *et al* (ATLAS Collaboration) 2013 Search for charginos nearly mass degenerate with the lightest neutralino based on a disappearing-track signature in pp collisions at $\sqrt{s} = 8$ TeV with the ATLAS detector *Phys. Rev. D* **88** 112006
- [318] Schwaller P and Zurita J 2014 Compressed electroweakino spectra at the LHC *J. High Energy Phys.* **JHEP03(2014)060**
- [319] Low M and Wang L-T 2014 Neutralino dark matter at 14 TeV and 100 TeV *J. High Energy Phys.* **JHEP08(2014)161**
- [320] Barducci D *et al* 2015 Uncovering natural supersymmetry via the interplay between the LHC and direct dark matter detection *J. High Energy Phys.* **JHEP07(2015)066**
- [321] ATLAS Collaboration 2017 Search for direct pair production of Higgsinos by the reinterpretation of the disappearing track analysis with 36.1 fb^{-1} of $\sqrt{s} = 13$ TeV data collected with the ATLAS experiment <https://cds.cern.ch/record/2297480>
- [322] Sirunyan A M *et al* (CMS Collaboration) 2018 Search for disappearing tracks as a signature of new long-lived particles in proton–proton collisions at $\sqrt{s} = 13$ TeV *J. High Energy Phys.* **JHEP08(2018)016**
- [323] ATLAS Collaboration 2019 July 2019 Summary Plot Update Tech. Rep. ATL-PHYS-PUB-2019-022 CERN Geneva <https://cds.cern.ch/record/2682063>
- [324] Gershtein Y 2017 CMS hardware track triggers and LLPs at the HL-LHC <https://indico.cern.ch/event/649760/contributions/2748968/subcontributions/239747/attachments/1544494/2423617/Trieste-2017.pdf>
- [325] Ray Holmes T 2017 ATLAS fast tracker (FTK)-Info, status, and prospects <https://indico.cern.ch/event/649760/contributions/2748920/attachments/1542791/2420193/17-10-13-LLPWorkshop.pdf>

- [326] Horyn L 2017 ATLAS Fast TracKer (FTK)-Overview of triggering constraints https://indico.cern.ch/event/649760/contributions/2748921/attachments/1542873/2420596/Horyn_LLP_FTK.pdf
- [327] Bullock J S 2010 Notes on the missing satellites problem arXiv:1009.4505 [astro-ph.CO]
- [328] Boylan-Kolchin M, Bullock J S and Kaplinghat M 2011 Too big to fail? The puzzling darkness of massive Milky Way subhaloes *Mon. Not. R. Astron. Soc.* **415** L40–4
- [329] Weinberg D H *et al* 2014 Cold dark matter: controversies on small scales *Proc. Natl Acad. Sci.* **112** 12249–55
Weinberg D H *et al* 2015 Cold dark matter: controversies on small scales *Proc. Natl Acad. Sci.* **112** 2249
- [330] Famaey B and McGaugh S 2013 Challenges for Λ CDM and MOND *J. Phys.: Conf. Ser.* **437** 012001
- [331] Schwaller P, Stolarski D and Weiler A 2015 Emerging jets *J. High Energy Phys.* **JHEP05(2015)059**
- [332] Daci N *et al* 2015 Simplified SIMPs and the LHC *J. High Energy Phys.* **JHEP11(2015)108**
- [333] Abazov V M *et al* 2010 Search for new fermions ('Quirks') at the fermilab tevatron collider *Phys. Rev. Lett.* **105** 211803
- [334] Evans J A and Luty M A 2019 Stopping quirks at the LHC *J. High Energy Phys.* **JHEP06(2019)090**
- [335] CMS Collaboration 2015 Muon reconstruction and identification improvements for run-2 and first results with 2015 run data *CMS-DP-2015-015* <http://cds.cern.ch/record/2037372>
- [336] Seez C *et al* (CMS Collaboration) 2017 The phase-2 upgrade of the CMS endcap calorimeter *CERN-LHCC-2017-023. CMS-TDR-019* <https://cds.cern.ch/record/2293646>
- [337] Aaboud M *et al* (ATLAS Collaboration) 2016 A measurement of material in the ATLAS tracker using secondary hadronic interactions in 7 TeV pp collisions *J. Instrum.* **11** P11020
- [338] CMS Collaboration 2010 Studies of tracker material *CMS-PASTRK-10-003* <https://cds.cern.ch/record/1279138>
- [339] Sirunyan A M *et al* 2018 Precision measurement of the structure of the CMS inner tracking system using nuclear interactions *J. Instrum.* **13** P10034
- [340] Alexander M *et al* 2018 Mapping the material in the LHCb vertex locator using secondary hadronic interactions *J. Instrum.* **13** P06008
- [341] Ilten P *et al* 2016 Proposed inclusive dark photon search at LHCb *Phys. Rev. Lett.* **116** 251803
- [342] de Favereau J *et al* 2014 DELPHES 3, A modular framework for fast simulation of a generic collider experiment *J. High Energy Phys.* **JHEP02(2014)057**
- [343] Chatrchyan S *et al* (CMS Collaboration) 2012 Search for stopped long-lived particles produced in pp collisions at $\sqrt{s} = 7$ TeV *J. High Energy Phys.* **JHEP08(2012)026**
- [344] Khachatryan V *et al* (CMS Collaboration) 2011 Search for stopped gluinos in pp collisions at $\sqrt{s} = 7$ TeV *Phys. Rev. Lett.* **106** 011801
- [345] Aad G *et al* (ATLAS Collaboration) 2012 Search for decays of stopped, long-lived particles from 7 TeV pp collisions with the ATLAS detector *Eur. Phys. J. C* **72** 1965
- [346] Schmidt B 2016 The high-luminosity upgrade of the LHC: physics and technology challenges for the accelerator and the experiments *J. Phys.: Conf. Ser.* **706** 022002
- [347] Apollinari G *et al* 2015 High-luminosity Large Hadron Collider (HL-LHC) : preliminary design report *CERN-2015-005* <https://cds.cern.ch/record/2116337>
- [348] CMS Collaboration 2017 The phase-2 upgrade of the CMS tracker *CMS-TDR-014* <https://cds.cern.ch/record/2272264>
- [349] CMS Collaboration 2017 The phase-2 upgrade of the CMS barrel calorimeters *CERN-LHCC-2017-011. CMS-TDR-015* <https://cds.cern.ch/record/2283187>
- [350] CMS Collaboration 2017 The phase-2 upgrade of the CMS muon detectors *CERN-LHCC-2017-012. CMS-TDR-016* <https://cds.cern.ch/record/2283189>
- [351] CMS Collaboration 2017 Technical proposal for a MIP timing detector in the CMS experiment phase-2 upgrade *CERN-LHCC-2017-027. LHCC-P-009* <https://cds.cern.ch/record/2296612>
- [352] CMS Collaboration 2017 The phase-2 upgrade of the CMS L1 trigger interim technical design report *CERN-LHCC-2017-013. CMS-TDR-017* <https://cds.cern.ch/record/2283192>
- [353] ATLAS Collaboration 2017 Technical design report for the ATLAS inner tracker pixel detector *CERN-LHCC-2017-021. ATLASTDR-030* <http://cds.cern.ch/record/2285585>

- [354] ATLAS Collaboration 2017 Technical design report for the Phase-II upgrade of the ATLAS TDAQ system *CERN-LHCC-2017-020. ATLAS-TDR-029* <https://cds.cern.ch/record/2285584>
- [355] ATLAS Collaboration 2017 Technical design report for the Phase-II Upgrade of the ATLAS tile calorimeter *CERN-LHCC-2017- 019. ATLAS-TDR-028* <https://cds.cern.ch/record/2285583>
- [356] ATLAS Collaboration 2017 Technical design report for the Phase-II upgrade of the ATLAS LAr calorimeter *CERN-LHCC-2017- 018. ATLAS-TDR-027* <https://cds.cern.ch/record/2285582>
- [357] ATLAS Collaboration 2017 Technical design report for the Phase-II upgrade of the ATLAS muon spectrometer *CERN-LHCC-2017- 017. ATLAS-TDR-026* <https://cds.cern.ch/record/2285580>
- [358] ATLAS Collaboration 2017 Technical design report for the ATLAS inner tracker strip detector *CERN-LHCC-2017-005. ATLASTDR-025* <https://cds.cern.ch/record/2257755>
- [359] ATLAS Collaboration 2019 Search prospects for dark-photons decaying to displaced collimated jets of muons at HL-LHC *ATLPHYS-PUB-2019-002* <https://cds.cern.ch/record/2257755>
- [360] Ruderman J T and Shih D 2010 Slepton co-NLSPs at the tevatron *J. High Energy Phys.* **JHEP11 (2010)046**
- [361] CMS Collaboration 2017 Estimated sensitivity for new particle searches at the HL-LHC *CMS-PAS-FTR-16-005* <http://cds.cern.ch/record/2274436>
- [362] CMS Collaboration 2018 Search sensitivity for dark photons decaying to displaced muons with CMS at the high-luminosity LHC *CMSPAS-FTR-18-002* <http://cds.cern.ch/record/2644533>
- [363] Liu J, Liu Z and Wang L-T 2019 Enhancing long-lived particles searches at the LHC with precision timing information *Phys. Rev. Lett.* **122 131801**
- [364] Gershtein Y 2017 CMS hardware track trigger: new opportunities for long-lived particle searches at the HL-LHC *Phys. Rev. D* **96 035027**
- [365] CMS Collaboration 2018 First level track jet trigger for displaced jets at high luminosity LHC *CMS-PAS-FTR-18-018* <http://cds.cern.ch/record/2647987>
- [366] Cacciari M, Salam G P and Soyez G 2008 The anti- k_r jet clustering algorithm *J. High Energy Phys.* **JHEP04(2008)063**
- [367] Cacciari M, Salam G P and Soyez G 2012 Fastjet user manual *Eur. Phys. J. C* **72 1896**
- [368] Khachatryan V *et al* (CMS Collaboration) 2016 Search for narrow resonances in dijet final states at $\sqrt{s} = 8$ TeV with the novel CMS technique of data scouting *Phys. Rev. Lett.* **117 031802**
- [369] Sirunyan A M *et al* (CMS Collaboration) 2018 Search for narrow and broad dijet resonances in proton–proton collisions at $\sqrt{s} = 13$ TeV and constraints on dark matter mediators and other new particles *J. High Energy Phys.* **JHEP08(2018)130**
- [370] Aaboud M *et al* (ATLAS Collaboration) 2018 Search for low-mass dijet resonances using trigger-level jets with the ATLAS detector in pp collisions at $\sqrt{s} = 13$ TeV *Phys. Rev. Lett.* **121 081801**
- [371] Hochberg Y *et al* 2014 Mechanism for thermal relic dark matter of strongly interacting massive particles *Phys. Rev. Lett.* **113 171301**
- [372] Cohen T, Lisanti M and Lou H K 2015 Semivisible jets: dark matter undercover at the LHC *Phys. Rev. Lett.* **115 171804**
- [373] Bediaga I *et al* (LHCb Collaboration) 2012 Framework TDR for the LHCb upgrade: technical design report *CERN-LHCC- 2012-007. LHCb-TDR-12* <https://cds.cern.ch/record/1443882>
- [374] Bediaga I *et al* (LHCb Collaboration) 2018 Physics case for an LHCb upgrade II—Opportunities in flavour physics, and beyond, in the HL-LHC era *Technical Report CERN-LHCC-2018-027 LHCb-PUB-2018-009 CERN* arXiv:1808.08865
- [375] LHCb Collaboration 2013 LHCb VELO upgrade technical design report *CERN-LHCC-2013-021* <https://cds.cern.ch/record/1624070>
- [376] LHCb Collaboration 2014 LHCb tracker upgrade technical design report *CERN-LHCC-2014-001* <https://cds.cern.ch/record/1647400>
- [377] LHCb Collaboration 2014 LHCb trigger and online upgrade technical design report *CERN-LHCC-2014-016* <https://cds.cern.ch/record/1701361>
- [378] LHCb Collaboration 2017 Upgrade trigger: biannual performance update *LHCb-PUB-2017-005. CERN-LHCb-PUB-2017-005* <https://cds.cern.ch/record/2244312>
- [379] LHCb Collaboration 2020 Trigger schemes <http://lhcb.web.cern.ch/lhcb/speakersbureau/html/TriggerScheme.html>
- [380] Albrecht J *et al* 2014 The upgrade of the LHCb trigger system *J. Instrum.* **9 C10026**

- [381] Abba A *et al* 2015 Simulation and performance of an artificial retina for 40 MHz track reconstruction *J. Instrum.* **10** C03008
- [382] Ilten P *et al* 2015 Dark photons from charm mesons at LHCb *Phys. Rev. D* **92** 115017
- [383] Pierce A *et al* 2018 Searching for confining hidden valleys at LHCb, ATLAS, and CMS *Phys. Rev. D* **97** 095033
- [384] Aaij R *et al* LHCb Collaboration 2017 Expression of interest for a Phase-II LHCb upgrade: opportunities in flavour physics, and beyond, in the HL-LHC era *CERN-LHCC-2017-003* <https://cds.cern.ch/record/2244311>
- [385] LHCb Collaboration 2018 Prospects for searches for long-lived particles after the LHCb detector upgrades *LHCb-CONF-2018-006*. *CERN-LHCb-CONF-2018-006* <http://cds.cern.ch/record/2649825>
- [386] Aaboud M *et al* (ATLAS Collaboration) 2016 Search for metastable heavy charged particles with large ionization energy loss in pp collisions at $\sqrt{s} = 13$ TeV using the ATLAS experiment *Phys. Rev. D* **93** 112015
- [387] Aaij R *et al* (LHCb Collaboration) 2015 Search for long-lived particles decaying to jet pairs *Eur. Phys. J. C* **75** 152
- [388] NA62 Collaboration 2017 The Beam and detector of the NA62 experiment at CERN *J. Instrum.* **12** P05025
- [389] Alekhin S *et al* 2016 A facility to search for hidden particles at the CERN SPS: the SHiP physics case *Rep. Prog. Phys.* **79** 124201
- [390] Fairbairn M *et al* 2007 Stable massive particles at colliders *Phys. Rep.* **438** 1–63
- [391] Burdin S *et al* 2015 Non-collider searches for stable massive particles *Phys. Rep.* **582** 1–52
- [392] Acharya B *et al* 2014 The physics programme of the MoEDAL experiment at the LHC *Int. J. Mod. Phys. A* **29** 1430050
- [393] Joergensen M D *et al* 2012 Searching for magnetic monopoles trapped in accelerator material at the Large Hadron Collider arXiv:1206.6793 [physics.ins-det]
- [394] De Roeck A *et al* 2012 Development of a magnetometer-based search strategy for stopped monopoles at the Large Hadron Collider *Eur. Phys. J. C* **72** 2212
- [395] Dirac P A M 1931 Quantized singularities in the electromagnetic field *Proc. R. Soc. A* **133** 60–72
- [396] Dirac P A M 1948 The theory of magnetic poles *Phys. Rev.* **74** 817–30
- [397] 't Hooft G 1974 Magnetic monopoles in unified gauge theories *Nucl. Phys. B* **79** 276–84
- [398] Polyakov A M 1974 Particle spectrum in the quantum field theory *JETP Lett.* **20** 194–5
Polyakov A M 1974 Particle spectrum in the quantum field theory *Pisma Zh. Eksp. Teor. Fiz.* **20** 430
- [399] Vento V and Sari Mantovani V 2013 On the magnetic monopole mass arXiv:1306.4213 [hep-ph]
- [400] Cho Y M and Maison D 1997 Monopoles in Weinberg–Salam model *Phys. Lett. B* **391** 360–5
- [401] Bae W S and Cho Y M 2005 Finite energy electroweak dyon *J. Korean Phys. Soc.* **46** 791–804 arXiv:hep-th/0210299
- [402] Cho Y M, Kimm K and Yoon J H 2016 Mass of the electroweak monopole *Mod. Phys. Lett. A* **31** 1650053
- [403] Cho Y M, Kimm K and Yoon J H 2016 Gravitationally coupled electroweak monopole *Phys. Lett. B* **761** 203–6
- [404] Ellis J, Mavromatos N E and You T 2016 The price of an electroweak monopole *Phys. Lett. B* **756** 29–35
- [405] Barriola M and Vilenkin A 1989 Gravitational field of a global monopole *Phys. Rev. Lett.* **63** 341
- [406] Drukier A K and Nussinov S 1982 Monopole pair creation in energetic collisions: is it possible? *Phys. Rev. Lett.* **49** 102
- [407] Mazur P O and Papavassiliou J 1991 Gravitational scattering on a global monopole *Phys. Rev. D* **44** 1317–20
- [408] Mavromatos N E and Papavassiliou J 2018 Singular lensing from the scattering on special space–time defects *Eur. Phys. J. C* **78** 68
- [409] Mavromatos N E and Sarkar S 2017 Magnetic monopoles from global monopoles in the presence of a Kalb–Ramond field *Phys. Rev. D* **95** 104025
- [410] Mavromatos N E and Sarkar S 2018 Regularized Kalb–Ramond magnetic monopole with finite energy *Phys. Rev. D* **97** 125010
- [411] Zeldovich Y B and Khlopov M Y 1978 On the concentration of relic magnetic monopoles in the Universe *Phys. Lett.* **79B** 239–41
- [412] Hill C T 1983 Monopolonium *Nucl. Phys. B* **224** 469–90

- [413] Dubrovich V K 2002 Association of magnetic monopoles and antimonopoles in the early universe *5th Int. Conf. COSMION 2001 (Moscow, Russia, May 21–27, 2001)* **8N1** 122–5 <https://inspirehep.net/literature/606767>
- [414] Rajantie A 2012 Introduction to magnetic monopoles *Contemp. Phys.* **53** 195–211
- [415] Rajantie A 2016 The search for magnetic monopoles *Phys. Today* **69** 40–6
- [416] Kephart T W, Leontaris G K and Shafi Q 2017 Magnetic monopoles and free fractionally charged states at accelerators and in cosmic rays *J. High Energy Phys.* **JHEP10(2017)176**
- [417] Epele L N *et al* 2008 Monopolium: the key to monopoles *Eur. Phys. J. C* **56** 87–95
- [418] Epele L N *et al* 2009 Monopolium production from photon fusion at the Large Hadron Collider *Eur. Phys. J. C* **62** 587–92
- [419] Epele L N *et al* 2016 Can the 750 GeV enhancement be a signal of light magnetic monopoles? arXiv:1607.05592 [hep-ph]
- [420] Kalliokoski M *et al* 2016 Turning the LHC ring into a new physics search machine arXiv:1604.05778 [hep-ex]
- [421] Felea D, Mamuzic J, Maselek R *et al* 2020 Prospects for discovering supersymmetric long-lived particles with MoEDAL *Eur. Phys. J. C* **80** 431
- [422] Acharya B *et al* 2018 Search for magnetic monopoles with the MoEDAL forward trapping detector in 2.11 fb⁻¹ of 13 TeV proton–proton collisions at the LHC *Phys. Lett. B* **782** 510–6
- [423] Acharya B *et al* 2017 Search for magnetic monopoles with the MoEDAL forward trapping detector in 13 TeV proton–proton collisions at the LHC *Phys. Rev. Lett.* **118** 061801
- [424] Acharya B *et al* (MoEDAL) 2019 Magnetic monopole search with the full MoEDAL trapping detector in 13 TeV pp collisions interpreted in Photon-Fusion and Drell-Yan production *Phys. Rev. Lett.* **123** 021802
- [425] Baines S *et al* 2018 Monopole production via photon fusion and Drell–Yan processes: MadGraph implementation and perturbativity via velocity-dependent coupling and magnetic moment as novel features *Eur. Phys. J. C* **78** 966
- [426] Gould O and Rajantie A 2017 Magnetic monopole mass bounds from heavy ion collisions and neutron stars *Phys. Rev. Lett.* **119** 241601
- [427] Aad G *et al* (ATLAS Collaboration) 2012 Search for magnetic monopoles in $\sqrt{s} = 7$ TeV pp collisions with the ATLAS detector *Phys. Rev. Lett.* **109** 261803
- [428] Patrizii L and Spurio M 2015 Status of searches for magnetic monopoles *Annu. Rev. Nucl. Part. Sci.* **65** 279–302
- [429] Abulencia A *et al* 2006 Direct search for Dirac magnetic monopoles in $p\bar{p}$ collisions at $\sqrt{s} = 1.96$ TeV *Phys. Rev. Lett.* **96** 201801
- [430] Pinfold J 2017 The MoEDAL experiment at the LHC *EPJ Web Conf.* **145** 12002
- [431] Pinfold J L 2018 Contribution to 4th lhc-llp workshop 2018 https://indico.cern.ch/event/744951/contributions/3171317/attachments/1739901/2816344/4th_LLIP_Workshop_2018.pdf
- [432] Prinz A A *et al* 1998 Search for millicharged particles at SLAC *Phys. Rev. Lett.* **81** 1175–8
- [433] De Roeck A *et al* 2017 Searching for trapped magnetic monopoles in LHC accelerator material https://indico.cern.ch/event/623746/attachments/1427507/2190853/expression_of_interest_beam_pipe.pdf
- [434] Ball A *et al* 2016 A letter of intent to install a milli-charged particle detector at LHC P5 arXiv:1607.04669 [physics.ins-det]
- [435] Izaguirre E and Yavin I 2015 New window to millicharged particles at the LHC *Phys. Rev. D* **92** 035014
- [436] Sher M and Stevens J 2018 Detecting a heavy neutrino electric dipole moment at the LHC *Phys. Lett. B* **777** 246–9
- [437] Aielli G *et al* 2006 Layout and performance of RPCs used in the Argo-YBJ experiment *Nucl. Instrum. Methods A* **562** 92–6
- [438] Iuppa R 2015 Potential of RPCs in cosmic ray experiments for the next decade *J. Instrum.* **10** C04044
- [439] Curtin D and Peskin M E 2018 Analysis of long lived particle decays with the MATHUSLA detector *Phys. Rev. D* **97** 015006
- [440] Fradette A and Pospelov M 2017 BBN for the LHC: constraints on lifetimes of the Higgs portal scalars *Phys. Rev. D* **96** 075033
- [441] Co R T, D’Eramo F and Hall L J 2017 Gravitino or axino dark matter with reheat temperature as high as 10¹⁶ GeV *J. High Energy Phys.* **JHEP03(2017)005**

- [442] Dev P S B, Mohapatra R N and Zhang Y 2017 Long lived light scalars as probe of low scale seesaw models *Nucl. Phys. B* **923** 179–221
- [443] Evans J A 2018 Detecting hidden particles with MATHUSLA *Phys. Rev. D* **97** 055046
- [444] Evans J A, Gori S and Shelton J 2018 Looking for the WIMP next door *J. High Energy Phys. JHEP02(2018)100*
- [445] D’Agnolo R T *et al* 2018 Exponentially light dark matter from coannihilation *J. High Energy Phys. JHEP08(2018)079*
- [446] Deppisch F F, Liu W and Mitra M 2018 Long-lived heavy neutrinos from Higgs decays *J. High Energy Phys. JHEP08(2018)181*
- [447] Jana S, Okada N and Raut D 2018 Displaced vertex signature of type-I seesaw model *Phys. Rev. D* **98** 035023
- [448] Lindner R 2017 private communication
- [449] Willey R S and Yu H L 1982 Decays k to π ℓ ℓ and limits on the mass of the neutral Higgs boson *Phys. Rev. D* **26** 3287–9
- [450] Chivukula R and Manohar A V 1988 Limits on a light Higgs boson *Phys. Lett. B* **207** 86–90
- [451] Grinstein B, Hall L J and Randall L 1988 Do B meson decays exclude a light Higgs? *Phys. Lett. B* **211** 363–9
- [452] Lanfranchi G 2017 Sensitivity of the SHiP experiment to a light scalar particle mixing with the Higgs <https://cds.cern.ch/record/2243034>
- [453] Sierra C 2017 Searches for Long-lived particles at LHCb *Talk at Workshop on the physics of HL-LHC, and perspectives at HE-LHC* https://indico.cern.ch/event/647676/contributions/2757734/attachments/1549579/2435644/HLLHC_LL_P_CVS.pdf
- [454] Patrignani C *et al* 2016 Review of particle physics *Chin. Phys. C* **40** 100001
- [455] Altmannshofer W *et al* 2018 *The Belle II Physics Book* ed E Kou and P Urquijo arXiv:1808.10567 [hep-ex].
- [456] Schabinger R M and Wells J D 2005 A minimal spontaneously broken hidden sector and its impact on Higgs boson physics at the Large Hadron Collider *Phys. Rev. D* **72** 093007
- [457] Gopalakrishna S, Jung S and Wells J D 2008 Higgs boson decays to four fermions through an abelian hidden sector *Phys. Rev. D* **78** 055002
- [458] Meade P, Papucci M and Volansky T 2009 Dark matter sees the light *J. High Energy Phys.* **12** 052
- [459] Gligorov V V *et al* 2019 Leveraging the ALICE/L3 cavern for long-lived particle searches *Phys. Rev. D* **99** 015023
- [460] Aaboud M *et al* (ATLAS Collaboration) 2016 Measurement of the Inelastic proton–proton cross section at $\sqrt{s} = 13$ TeV with the ATLAS detector at the LHC *Phys. Rev. Lett.* **117** 182002
- [461] Van Haevermaet H 2016 Measurement of the inelastic proton–proton cross section at $\sqrt{s} = 13$ TeV *PoS DIS2016* 198 arXiv:1607.02033 [hep-ex]
- [462] Ariga A *et al* 2018 Letter of intent for FASER: forward search experiment at the LHC arXiv:1811.10243
- [463] Ariga A *et al* 2019 FASER’s physics reach for long-lived particles *Phys. Rev. D* **99** 095011
- [464] Ariga A *et al* 2018 Technical proposal for FASER: forward search experiment at the LHC arXiv:1812.09139
- [465] Ariga A *et al* 2019 FASER: forward search experiment at the LHC arXiv:1901.04468
- [466] Ferrari A *et al* 2005 FLUKA: a multi-particle transport code (program version 2005) *CERN Yellow Reports: Monographs, CERN-2005-010; INFN-TC-2005-11; SLAC-R-773; CERN-2005-10* CERN, Geneva doi:10.5170/CERN-2005-010
- [467] Böhlen T T *et al* 2014 The FLUKA code: developments and challenges for high energy and medical applications *Nucl. Data Sheets* **120** 211–4
- [468] CERN Sources, Targets, and Interactions Group, *et al* 2018 Characterization of the radiation field for the FASER experiment
- [469] Feng J L *et al* 2018 Dark Higgs bosons at the forward search experiment *Phys. Rev. D* **97** 055034
- [470] Feng J L *et al* 2018 Axionlike particles at FASER: The LHC as a photon beam dump *Phys. Rev. D* **98** 055021
- [471] Berlin A and Kling F 2019 Inelastic dark matter at the LHC lifetime frontier: ATLAS, CMS, LHCb, CODEX-b, FASER, and MATHUSLA *Phys. Rev. D* **99** 015021
- [472] Batell B *et al* 2018 Flavor-specific scalar mediators *Phys. Rev. D* **98** 055026
- [473] Bauer M, Foldenauer P and Jaeckel J 2018 Hunting all the hidden photons *J. High Energy Phys.* **07** 094

- [474] Hochberg Y *et al* 2018 Strongly interacting massive particles through the axion portal *Phys. Rev. D* **98** 115031
- [475] Giudice G F and Romanino A 2004 Split supersymmetry *Nucl. Phys. B* **699** 65–89
Giudice G F and Romanino A 2005 Split supersymmetry *Nucl. Phys. B* **706** 487
- [476] Pagels H and Primack J R 1982 Supersymmetry, cosmology and new TeV physics *Phys. Rev. Lett.* **48** 223
- [477] Covi L, Kim J E and Roszkowski L 1999 Axinos as cold dark matter *Phys. Rev. Lett.* **82** 4180–3
- [478] Zurek K M 2014 Asymmetric dark matter: theories, signatures, and constraints *Phys. Rep.* **537** 91–121
- [479] CERN 2020 Forum on the Interpretation of the LHC Results for BSM studies, <https://twiki.cern.ch/twiki/bin/view/LHCPhysics/InterpretingLHCresults>
- [480] Okawa H 2011 Interpretations of SUSY searches in ATLAS with simplified models. in particles and fields, particles and fields *Proc., Meeting of the Division of the American Physical Society, DPF 2011* (9–13, August 2011) (Providence, USA arXiv:1110.0282)
- [481] Chatrchyan S and (CMS Collaboration) 2013 Interpretation of searches for supersymmetry with simplified models *Phys. Rev. D* **88** 052017
- [482] Kraml S *et al* 2014 SModelS: a tool for interpreting simplified-model results from the LHC and its application to supersymmetry *Eur. Phys. J. C* **74** 2868
- [483] Ambrogi F *et al* 2018 SModelS v1.1 user manual: Improving simplified model constraints with efficiency maps *Comput. Phys. Commun.* **227** 72–98
- [484] Ambrogi F *et al* 2020 SModelS v1.2: long-lived particles, combination of signal regions, and other novelties *Comput. Phys. Commun.* **251** 106848
- [485] Papucci M *et al* 2014 Fastlim: a fast LHC limit calculator *Eur. Phys. J. C* **74** 3163
- [486] Drees M *et al* 2015 CheckMATE: confronting your favourite new physics model with LHC data *Comput. Phys. Commun.* **187** 227–65
- [487] Dercks D *et al* 2017 Check MATE 2: from the model to the limit *Comput. Phys. Commun.* **221** 383–418
- [488] Conte E *et al* 2014 Designing and recasting LHC analyses with madanalysis 5 *Eur. Phys. J. C* **74** 3103
- [489] Dumont B *et al* 2015 Toward a public analysis database for LHC new physics searches using MADANALYSIS 5 *Eur. Phys. J. C* **75** 56
- [490] Buckley A *et al* 2013 Rivet user manual *Comput. Phys. Commun.* **184** 2803–19
- [491] Balázs C *et al* 2017 ColliderBit: a GAMBIT module for the calculation of high-energy collider observables and likelihoods *Eur. Phys. J. C* **77** 795
- [492] CMS Collaboration 2017 Simplified likelihood for the re-interpretation of public CMS results *CMS-NOTE-2017-001* <https://cds.cern.ch/record/2242860>
- [493] Heisig J, Kraml S and Lessa A 2019 Constraining new physics with searches for long-lived particles: Implementation into SModelS *Phys. Lett. B* **788** 87–95
- [494] Chang J 2018 Madanalysis5 implementation of CMS-EXO-16-022 doi:10.7484/INSPIREHEP.DATA.UFU4.99E3
- [495] Khachatryan V and (CMS Collaboration) 2015 Constraints on the pMSSM, AMSB model and on other models from the search for long-lived charged particles in proton–proton collisions at $\sqrt{s} = 8$ TeV. *Eur. Phys. J. C* **75** 325
- [496] Cranmer K and Yavin I 2011 RECAST: extending the impact of existing analyses *J. High Energy Phys.* **04** 038
- [497] Belanger G *et al* 2015 Probing U(1) extensions of the MSSM at the LHC Run I and in dark matter searches *J. High Energy Phys.* **09** 151
- [498] Barducci D *et al* 2016 Status and prospects of the nMSSM after LHC Run-1 *J. High Energy Phys.* **01** 050
- [499] Spite F and Spite M 1982 Abundance of lithium in unevolved halo stars and old disk stars: interpretation and consequences *Astron. Astrophys.* **115** 357–66 <http://adsabs.harvard.edu/full/1982A&A...115..357S>
- [500] Cyburt R H, Fields B D and Olive K A 2008 An Update on the big bang nucleosynthesis prediction for Li-7: The problem worsens *J. Cosmol. Astropart. Phys.* **JCAP11(2008)012**
- [501] Sjöstrand T, Mrenna S and Skands P 2006 PYTHIA 6.4 physics and manual *J. High Energy Phys.* **JHEP05(2006)026**
- [502] Bagnaschi E *et al* 2017 Likelihood analysis of supersymmetric SU(5) GUTs *Eur. Phys. J. C* **77** 104

- [503] Heisig J *et al* 2017 Trilinear-Augmented gaugino mediation *J. High Energy Phys.* **JHEP05(2017)003**
- [504] Brooijmans G *et al* 2017 Les Houches 2017: physics at TeV colliders new physics working group report arXiv:1803.10379
- [505] CMS Collaboration 2014 Search for displaced SUSY in dilepton final states *Report CMS-PAS-B2G-12-024 CERN* <http://cds.cern.ch/record/1706154>
- [506] Displaced SUSY Parametrisation Study For User (2014). <https://twiki.cern.ch/twiki/bin/view/CMSPublic/DisplacedSusyParametrisationStudyForUser>
- [507] Graham P W *et al* 2012 Displaced supersymmetry *J. High Energy Phys.* **JHEP07(2012)149**
- [508] CMS Collaboration 2013 Search for long-lived neutral particles decaying to dijets *CMS-PAS-EXO-12-038* <https://cds.cern.ch/record/1563591>
- [509] Cui Y 2013 Natural baryogenesis from unnatural supersymmetry *J. High Energy Phys.* **JHEP12(2013)067**
- [510] ATLAS Collaboration 2016 Search for long-lived neutral particles decaying into displaced lepton jets in proton–proton collisions at $\sqrt{s} = 13$ TeV with the ATLAS detector *ATLAS-CONF-2016-042* **94** <http://cds.cern.ch/record/2206083>
- [511] Barello G, Chang S and Newby C A 2016 Correlated signals at the energy and intensity frontiers from non-Abelian kinetic mixing *Phys. Rev. D* **94** 055018
- [512] Argüelles C A *et al* 2017 Dark gauge bosons: LHC signatures of non-abelian kinetic mixing *Phys. Lett. B* **770** 101–7
- [513] Dine M and Fischler W 1982 A phenomenological model of particle physics based on supersymmetry *Phys. Lett.* **110B** 227–31
- [514] Freytsis M, Robinson D J and Tsai Y 2015 Galactic center gamma-ray excess through a dark shower *Phys. Rev. D* **91** 035028
- [515] Freytsis M *et al* 2016 Gamma-rays from dark showers with twin Higgs models *J. High Energy Phys.* **JHEP05(2016)018**
- [516] Cottin G 2018 Reconstructing particle masses in events with displaced vertices *J. High Energy Phys.* **JHEP03(2018)137**
- [517] Park M and Zhao Y 2011 Recovering particle masses from missing energy signatures with displaced tracks arXiv:1110.1403
- [518] ATLAS Collaboration 2013 Search for long-lived, heavy particles in final states with a muon and a multi-track displaced vertex in proton–proton collisions at $\sqrt{s} = 8$ TeV *ATLAS-CONF-2013-092* <http://cds.cern.ch/record/1595755>
- [519] ATLAS Collaboration 2017 Search for long-lived, massive particles in events with displaced vertices and missing transverse momentum in $\sqrt{s} = 13$ TeV pp collisions with the ATLAS detector, Auxiliary Information *Report SUSY-2016-08* https://atlas.web.cern.ch/Atlas/GROUPS/PHYSICS/PAPERS/SUSY-2016-08/hepdata_info.pdf (2017)
- [520] Cacciari M and Salam G P 2008 Pileup subtraction using jet areas *Phys. Lett. B* **659** 119–26
- [521] Bertolini D *et al* 2014 Pileup per particle identification *J. High Energy Phys.* **JHEP10(2014)059**
- [522] Cacciari M, Salam G P and Soyez G 2015 SoftKiller a particle-level pileup removal method *Eur. Phys. J. C* **75** 59
- [523] Conte E, Fuks B and Serret G 2013 MadAnalysis 5, A user-friendly framework for collider phenomenology *Comput. Phys. Commun.* **184** 222–56
- [524] Cranmer K, Heinrich L and (ATLAS Collaboration) 2018 Analysis preservation and systematic reinterpretation within the ATLAS experiment *J. Phys. Conf. Ser.* **1085** 042011
- [525] Chen X *et al* 2016 *CERN Analysis Preservation: A Novel Digital Library Service to Enable Reusable and Reproducible Research and Advanced Technology for Digital Libraries: 20th International Conf. on Theory and Practice of Digital Libraries, TPDL 2016, (5–9 September, 2016, Hannover, Germany)* ed N Fuhr *et al* (Cham: Springer International Publishing) pp 347–56 DOI:10.1007/978-3-319-43997-6_27
- [526] Cranmer K and Heinrich L 2017 Yadage and Packtivity—analysis preservation using parametrized workflows *J. Phys.: Conf. Ser.* **898** 102019
- [527] Amstutz P *et al* 2016 Common workflow language v1.0, https://figshare.com/articles/Common_Workflow_Language_draft_3/3115156/2
- [528] Aad G and (ATLAS Collaboration) 2015 Summary of the ATLAS experiment's sensitivity to supersymmetry after LHC Run 1—interpreted in the phenomenological MSSM *J. High Energy Phys.* **JHEP10(2015)134**

- [529] Aad G and (ATLAS Collaboration) 2014 Search for direct production of charginos, neutralinos and sleptons in final states with two leptons and missing transverse momentum in pp collisions at $\sqrt{s} = 8$ TeV with the ATLAS detector *J. High Energy Phys.* **JHEP05(2014)071**
- [530] Aaboud M and (ATLAS Collaboration) 2016 Dark matter interpretations of ATLAS searches for the electroweak production of supersymmetric particles in $\sqrt{s} = 8$ TeV proton–proton collisions *J. High Energy Phys.* **JHEP09(2016)175**
- [531] ATLAS Collaboration 2016 A re-interpretation of $\sqrt{s} = 8$ TeV ATLAS results on electroweak supersymmetry production to explore general gauge mediated models *ATLAS-CONF-2016-033* <https://cds.cern.ch/record/2198316>
- [532] Dobbs M and Hansen J B 2001 The HepMC C++ Monte Carlo event record for high energy physics *Comput. Phys. Commun.* **134** 41–6
- [533] Marchesini G et al 1992 HERWIG: A Monte Carlo event generator for simulating hadron emission reactions with interfering gluons. Version 5.1-April 1991 *Comput. Phys. Commun.* **67** 465–508
- [534] Gleisberg T et al 2009 Event generation with SHERPA 1.1 *J. High Energy Phys.* **JHEP02(2009)007**
- [535] CMS Collaboration 2016 Search for pair-production of second-generation scalar leptoquarks in pp collisions at $\sqrt{s} = 13$ TeV with the CMS detector *CMS-PAS-EXO-16-007* <http://cds.cern.ch/record/2139349>
- [536] Sirunyan A M et al 2019 Search for pair production of second-generation leptoquarks at $\sqrt{s} = 13$ TeV *Phys. Rev. D* **99** 032014
- [537] ATLAS Collaboration 2014 Limits on metastable gluinos from ATLAS SUSY searches at 8 TeV *ATLAS-CONF-2014-037* <http://cds.cern.ch/record/1735199>
- [538] Sirunyan A M and (CMS Collaboration) 2018 Search for natural and split supersymmetry in proton–proton collisions at $\sqrt{s} = 13$ TeV in final states with jets and missing transverse momentum *J. High Energy Phys.* **JHEP05(2018)025**
- [539] Aaboud M and (ATLAS Collaboration) 2018 Search for the Higgs boson produced in association with a vector boson and decaying into two spin-zero particles in the $H \rightarrow aa \rightarrow 4b$ channel in pp collisions at $\sqrt{s} = 13$ TeV with the ATLAS detector *J. High Energy Phys.* **JHEP10(2018)031**
- [540] Juknevich J E, Melnikov D and Strassler M J 2009 A pure-gluon hidden valley I states and decays *J. High Energy Phys.* **JHEP07(2009)055**
- [541] Craig N et al 2016 The vector-like twin Higgs *J. High Energy Phys.* **JHEP07(2016)002**
- [542] Renner S and Schwaller P 2018 A flavoured dark sector *J. High Energy Phys.* **JHEP08(2018)052**
- [543] Izaguirre E and Stolarski D 2018 The platinum channel: Higgs decays to as many as 8 leptons *Phys. Rev. Lett.* **121** 221803
- [544] Serman G F and Weinberg S 1977 Jets from quantum chromodynamics *Phys. Rev. Lett.* **39** 1436
- [545] Banks T and Zaks A 1982 On the phase structure of vector-like gauge theories with massless fermions *Nucl. Phys. B* **196** 189–204
- [546] Larkoski A J 2017 An unorthodox introduction to QCD arXiv:1709.06195
- [547] Polchinski J and Strassler M J 2000 The string dual of a confining four-dimensional gauge theory arXiv:hep-th/0003136
- [548] Klebanov I R and Strassler M J 2000 Supergravity and a confining gauge theory: duality cascades and χ SB-resolution of naked singularities *J. High Energy Phys.* **JHEP08(2000)052**
- [549] Hofman D M and Maldacena J 2008 Conformal collider physics: energy and charge correlations *J. High Energy Phys.* **JHEP05(2008)012**
- [550] Harnik R and Wizansky T 2009 Signals of new physics in the underlying event *Phys. Rev. D* **80** 075015
- [551] Ellis R K, Stirling W J and Webber B R 1996 QCD and collider physics *Cambridge Monographs on Particle Physics, Nuclear Physics and Cosmology* vol 8 (Cambridge: Cambridge University Press) <https://doi.org/10.1017/CBO9780511628788>
- [552] Giele W T, Kosower D A and Skands P Z 2008 A simple shower and matching algorithm *Phys. Rev. D* **78** 014026
- [553] Randall L and Sundrum R 1999 A large mass hierarchy from a small extra dimension *Phys. Lett.* **83** 3370–3
- [554] Csaki C, Reece M and Terning J 2009 The AdS/QCD correspondence: still undelivered *J. High Energy Phys.* **JHEP05(2009)067**
- [555] Bjorken J D and Brodsky S J 1970 Statistical model for electron–positron annihilation into hadrons *Phys. Rev. D* **1** 1416–20

- [556] Farhi E A 1977 QCD test for jets *Phys. Rev. Lett.* **39** 1587–8
- [557] Fischer N *et al* 2016 Vincia for hadron colliders *Eur. Phys. J. C* **76** 589
- [558] Morningstar C J and Peardon M J 1999 The Glueball spectrum from an anisotropic lattice study *Phys. Rev. D* **60** 034509
- [559] Juknevich J E 2010 Pure-gluon hidden valleys through the Higgs portal *J. High Energy Phys.* **JHEP08(2010)121**
- [560] Clarke J D, Foot R and Volkas R R 2014 Phenomenology of a very light scalar ($100 \text{ MeV} < m_h < 10 \text{ GeV}$) mixing with the SM Higgs *J. High Energy Phys.* **JHEP02(2014)123**
- [561] Ilten P *et al* 2018 Serendipity in dark photon searches *J. High Energy Phys.* **JHEP06(2018)004**
- [562] Bauer M, Neubert M and Thamm A 2017 Collider probes of axion-like particles *J. High Energy Phys.* **JHEP12(2017)044**
- [563] Deppeisch F F, Bhupal Dev P S and Pilaftsis A 2015 Neutrinos and collider physics *New J. Phys.* **17** 075019
- [564] Sirunyan A M and (CMS Collaboration) 2017 Search for heavy resonances that decay into a vector boson and a Higgs boson in hadronic final states at $\sqrt{s} = 13 \text{ TeV}$ *Eur. Phys. J. C* **77** 636
- [565] Sirunyan A M and (CMS Collaboration) 2018 Search for massive resonances decaying into WW, WZ, ZZ, qW, and qZ with dijet final states at $\sqrt{s} = 13 \text{ TeV}$ *Phys. Rev. D* **97** 072006
- [566] Thaler J and Van Tilburg K 2011 Identifying boosted objects with N-subjettiness *J. High Energy Phys.* **JHEP03(2011)015**
- [567] Ellis S D, Roy T S and Scholtz J 2013 Jets and photons *Phys. Rev. Lett.* **110** 122003
- [568] Ellis S D, Roy T S and Scholtz J 2013 Phenomenology of photon-jets *Phys. Rev. D* **87** 014015
- [569] Aaij R *et al* (LHCb Collaboration) 2013 Search for the rare decay $K_S \rightarrow \mu^+ \mu^-$ *J. High Energy Phys.* **JHEP01(2013)090**
- [570] Aaij R and (LHCb Collaboration) 2016 Measurement of CP violation in $B^0 \rightarrow D^+ D^-$ decays *Phys. Rev. Lett.* **117** 261801
- [571] Nachman B and Rubbo F 2018 Search strategy using LHC pileup interactions as a zero bias sample *Phys. Rev. D* **97** 092002
- [572] Falkowski A *et al* 2010 Discovering Higgs decays to lepton jets at hadron colliders *Phys. Rev. Lett.* **105** 241801
- [573] Chatrchyan S and (CMS Collaboration) 2011 Search for light resonances decaying into pairs of muons as a signal of new physics *J. High Energy Phys.* **JHEP07(2011)098**
- [574] Cohen T *et al* 2017 LHC searches for dark sector showers *J. High Energy Phys.* **JHEP11(2017)196**
- [575] Park M and Zhang M 2017 Tagging a jet from a dark sector with jet-substructures at colliders arXiv:1712.09279
- [576] Gallicchio J *et al* 2011 Multivariate discrimination and the Higgs +W/Z search *J. High Energy Phys.* **JHEP04(2011)069**
- [577] Larkoski A J, Salam G P and Thaler J 2013 Energy correlation functions for jet substructure *J. High Energy Phys.* **JHEP06(2013)108**
- [578] Larkoski A J, Moult I and Neill D 2014 Power counting to better jet observables *J. High Energy Phys.* **JHEP12(2014)009**
- [579] Gras P *et al* 2017 Systematics of quark/gluon tagging *J. High Energy Phys.* **JHEP07(2017)091**
- [580] Frye C *et al* 2017 Casimir meets poisson: improved quark/gluon discrimination with counting observables *J. High Energy Phys.* **JHEP09(2017)083**
- [581] Dery L M *et al* 2017 Weakly supervised classification in high energy physics *J. High Energy Phys.* **JHEP05(2017)145**
- [582] Cohen T, Freytsis M and Ostdiek B 2018 (Machine) learning to do more with less *J. High Energy Phys.* **JHEP02(2018)034**
- [583] Metodiev E M, Nachman B and Thaler J 2017 Classification without labels: learning from mixed samples in high energy physics *J. High Energy Phys.* **JHEP10(2017)174**
- [584] Aad G and (ATLAS Collaboration) 2016 Charged-particle distributions in $\sqrt{s} = 13 \text{ TeV}$ pp interactions measured with the ATLAS detector at the LHC *Phys. Lett. B* **758** 67–88
- [585] Sirunyan A M and (CMS Collaboration) 2017 Particle-flow reconstruction and global event description with the CMS detector *J. Instrum.* **12** P10003
- [586] Aad G and (ATLAS Collaboration) 2016 Measurement of the charged-particle multiplicity inside jets from $\sqrt{s} = 8 \text{ TeV}$ pp collisions with the ATLAS detector *Eur. Phys. J. C* **76** 322
- [587] Rovere M 2015 CMS reconstruction improvements for the tracking in large pileup events *J. Phys.: Conf. Ser.* **664** 8

- [588] Chatrchyan S and (CMS Collaboration) 2013 Identification of b-quark jets with the CMS experiment *J. Instrum.* **8** P04013
- [589] Buschmann M *et al* 2015 Lepton jets from radiating dark matter *J. High Energy Phys.* **JHEP07(2015)045**
- [590] Cheung C *et al* 2010 Lepton jets in (supersymmetric) electroweak processes *J. High Energy Phys.* **JHEP04(2010)116**
- [591] Katz A and Sundrum R 2009 Breaking the dark force *J. High Energy Phys.* **JHEP06(2009)003**
- [592] Bai Y and Han Z 2009 Measuring the dark force at the LHC *Phys. Rev. Lett.* **103** 051801
- [593] Gupta A, Primulando R and Saraswat P 2015 A new probe of dark sector dynamics at the LHC *J. High Energy Phys.* **JHEP09(2015)079**
- [594] Aad G and (ATLAS Collaboration) 2013 A search for prompt lepton-jets in *pp* collisions at $\sqrt{s} = 7$ TeV with the ATLAS detector *Phys. Lett. B* **719** 299–317
- [595] Carloni L and Sjostrand T 2010 Visible effects of invisible hidden valley radiation *J. High Energy Phys.* **JHEP09(2010)105**
- [596] Carloni L, Rathsman J and Sjostrand T 2011 Discerning secluded sector gauge structures *J. High Energy Phys.* **JHEP04(2011)091**
- [597] Davoudiasl H, Lee H-S and Marciano W J 2012 Dark side of Higgs diphoton decays and muon $g-2$ *Phys. Rev. D* **86** 095009
- [598] Endo M, Hamaguchi K and Mishima G 2012 Constraints on hidden photon models from electron $g-2$ and hydrogen spectroscopy *Phys. Rev. D* **86** 095029
- [599] Agakishiev G *et al* 2014 Searching a dark photon with HADES *Phys. Lett. B* **731** 265–71
- [600] Babusci D *et al* 2013 Limit on the production of a light vector gauge boson in phi meson decays with the KLOE detector *Phys. Lett. B* **720** 111–5
- [601] Babusci D *et al* 2014 Search for light vector boson production in $e^+e^- \rightarrow \mu^+\mu^-\gamma$ interactions with the KLOE experiment *Phys. Lett. B* **736** 459–64
- [602] Abrahamyan S *et al* 2011 Search for a new gauge boson in electron-nucleus fixed-target scattering by the APEX experiment *Phys. Rev. Lett.* **107** 191804
- [603] Aubert B *et al* 2009 Search for dimuon decays of a light scalar boson in radiative transitions $\text{upsilon} \rightarrow \text{gamma} A_0$ *Phys. Rev. Lett.* **103** 081803
- [604] Lees J *et al* 2014 Search for a dark photon in e^+e^- collisions at BaBar *Phys. Rev. Lett.* **113** 201801
- [605] Blümlein J and Brunner J 2011 New exclusion limits for dark gauge forces from beam-dump data *Phys. Lett. B* **701** 155–9
- [606] Bjorken J D *et al* 2009 New fixed-target experiments to search for dark gauge forces *Phys. Rev. D* **80** 075018
- [607] Bross A *et al* 1991 A search for shortlived particles produced in an electron beam dump *Phys. Rev. Lett.* **67** 2942–5
- [608] Merkel H *et al* 2011 Search for light gauge bosons of the dark sector at the mainz microtron *Phys. Rev. Lett.* **106** 251802
- [609] Davier M and Nguyen Ngoc H 1989 An unambiguous search for a light Higgs boson *Phys. Lett. B* **229** 150
- [610] Blümlein J and Brunner J 2014 New exclusion limits on dark gauge forces from proton bremsstrahlung in beam-dump data *Phys. Lett. B* **731** 320–6
- [611] Gninenko S 2012 Constraints on sub-GeV hidden sector gauge bosons from a search for heavy neutrino decays *Phys. Lett. B* **713** 244–8
- [612] Essig R *et al* 2010 Discovering new light states at neutrino experiments *Phys. Rev. D* **82** 113008
- [613] Dent J B, Ferrer F and Krauss L M 2012 Constraints on light hidden sector gauge bosons from supernova cooling arXiv:1201.2683
- [614] Dreiner H K *et al* 2014 Supernova constraints on MeV dark sectors from e^+e^- annihilations *Phys. Rev. D* **89** 105015
- [615] Batley J R *et al* 2015 Search for the dark photon in π^0 decays *Phys. Lett. B* **746** 178–85
- [616] Alloul A *et al* 2014 FeynRules 2.0–A complete toolbox for tree-level phenomenology *Comput. Phys. Commun.* **185** 2250–300
- [617] Beauchesne H *et al* 2018 Collider phenomenology of hidden valley mediators of spin 0 or 1/2 with semivisible jets *J. High Energy Phys.* **JHEP08(2018)030**
- [618] Hatta Y and Matsuo T 2009 Thermal hadron spectrum in e^+e^- annihilation from gauge/string duality *Phys. Rev. Lett.* **102** 062001

OPEN ACCESS

Beam test performance of prototype silicon detectors for the Outer Tracker for the Phase-2 Upgrade of CMS

To cite this article: W. Adam *et al* 2020 *JINST* **15** P03014

View the [article online](#) for updates and enhancements.

You may also like

- [Experimental study of different silicon sensor options for the upgrade of the CMS Outer Tracker](#)
W. Adam, T. Bergauer, D. Blöchl et al.
- [Pileup mitigation at CMS in 13 TeV data](#)
A.M. Sirunyan, A. Tumasyan, W. Adam et al.
- [Test beam demonstration of silicon microstrip modules with transverse momentum discrimination for the future CMS tracking detector](#)
W. Adam, T. Bergauer, E. Brondolin et al.

Recent citations

- [The Phase-2 Upgrade of the CMS Outer Tracker](#)
Suvankar Roy Chowdhury



The Electrochemical Society
Advancing solid state & electrochemical science & technology

241st ECS Meeting

May 29 – June 2, 2022 Vancouver • BC • Canada

Abstract submission deadline: Dec 3, 2021

Connect. Engage. Champion. Empower. Accelerate.
We move science forward



Submit your abstract



Beam test performance of prototype silicon detectors for the Outer Tracker for the Phase-2 Upgrade of CMS



Tracker group of the CMS collaboration

E-mail: suvankar.roy.chowdhury@cern.ch

ABSTRACT: A new CMS tracker detector will be installed for operation at the High Luminosity LHC (HL-LHC). This detector comprises modules with two closely spaced parallel sensor plates and front-end ASICs capable of transmitting tracking information to the CMS Level-1 (L1) trigger at the 40 MHz beam crossing rate. The inclusion of tracking information in the L1 trigger decision will be essential for selecting events of interest efficiently at the HL-LHC. The CMS Binary Chip (CBC) has been designed to read out and correlate hits from pairs of tracker sensors, forming so-called track stubs. For the first time, a prototype irradiated module and a full-sized module, both equipped with the version 2 of the CBC, have been operated in test beam facilities. The efficiency of the stub finding logic of the modules for various angles of incidence has been studied. The ability of the modules to reject tracks with transverse momentum less than 2 GeV has been demonstrated. For modules built with irradiated sensors, no significant drop in the stub finding performance has been observed. Results from the beam tests are described in this paper.

KEYWORDS: Front-end electronics for detector readout; Particle tracking detectors; Performance of High Energy Physics Detectors

Contents

1	Introduction	1
2	CMS tracker for HL-LHC	2
2.1	The concept of p_T discrimination	3
2.2	Prototype detectors	4
3	Beam test infrastructure	6
3.1	Beam test setup	6
3.2	Data acquisition system	8
4	Preparations for data-taking	9
4.1	Pedestal and noise	9
4.2	Latency scans	9
5	Reconstruction	10
5.1	DUT reconstruction	11
5.2	Tracking	13
5.3	DUT alignment	14
6	Results	14
6.1	Performance of mini-modules	15
6.2	Performance of the full-size module	20
7	Summary	22
	Tracker group of the CMS collaboration	26

1 Introduction

The Large Hadron Collider (LHC) at CERN will undergo major upgrades by 2025 to be able to deliver peak instantaneous luminosities of $5 - 7.5 \times 10^{34} \text{cm}^{-2}\text{s}^{-1}$. This High Luminosity upgrade of the LHC (HL-LHC) will allow the CMS (Compact Muon Solenoid) [1] experiment to collect data corresponding to integrated luminosities of the order of 300fb^{-1} per year. Eventually, a total of 3000fb^{-1} will be collected during ten years of operation. At the nominal instantaneous luminosity of the HL-LHC, a single bunch crossing will produce 140-200 proton-proton collisions. The vast majority of these collisions are “pileup” interactions with low momentum transfer that are of little physics interest.

In order to fully exploit the increased luminosity and to cope with the very high pileup environment, the detector and the trigger system of the CMS experiment need to be upgraded

significantly [2]. The present CMS tracker was designed to operate up to an integrated luminosity of 500 fb^{-1} [2, 3], beyond which radiation damage will lead to degradation of its performance. The CMS experiment will replace the current tracker with a new silicon tracker. The upgraded tracker [3] will feature increased radiation hardness, higher granularity, compatibility with higher data rates, and a longer trigger latency. In addition, the tracker will provide tracking information to the Level-1 trigger, allowing trigger rates to be kept at a sustainable level without sacrificing physics potential [3].

The CMS tracker for the HL-LHC period will consist of modules with two “stacked” silicon sensors, read out by front-end ASICs with the capability to discriminate tracks based on their transverse momentum (p_T). The concept of p_T discrimination by means of very short track segments called stubs, in so-called p_T modules, will be discussed in the following section.

A number of module prototypes described in the following section, each with two stacked strip sensors, also known as 2S modules, were subjected to particle beams at CERN, Fermilab, and DESY beam test facilities to measure the performance of the stub finding mechanism, the uniformity of the stub finding efficiency in the entire detector, the potential to reject low p_T tracks ($< 2 \text{ GeV}$), and the ability to work efficiently up to the expected overall HL-LHC radiation level. In this paper, results from beam tests carried out at CERN are reported and, where possible, compared to those obtained at Fermilab and DESY. The results from previous beam test are reported in ref. [4].

2 CMS tracker for HL-LHC

The layout of the new tracker is shown in figure 1. The new tracker will consist of two parts: an Inner Tracker (IT) and an Outer Tracker (OT). Both the IT and the OT will have a barrel section, made out of coaxial cylindrical layers, and two endcaps, one on each side of the barrel, made out of discs. The IT barrel will feature four layers of pixel detectors, providing three-dimensional hit coordinates, resulting in excellent vertex resolution. Each IT endcap will consist of 12 pixel discs on each side of the barrel. The OT barrel will comprise six layers of detector modules each having two silicon sensors separated by a small distance and read out by the same front-end electronics. The separation between the sensors of a module, defined by the distance between the sensor mid planes, will vary between 1.6 mm and 4 mm [3]. Of the six layers of the OT barrel, the three inner layers will be equipped with modules made of one macro-pixel sensor and one strip sensor (PS p_T module). The three outer layers will be equipped with modules with two strip sensors (2S p_T module). The OT endcaps will feature six discs and will be equipped with PS and 2S modules, as shown in figure 1. The main specifications of the PS and 2S modules for the OT are listed in table 1.

Table 1. Main parameters of the 2S and PS modules of the proposed CMS Phase-2 tracker [3].

2S module			PS module		
$\sim 2 \times 90 \text{ cm}^2$ active area			$\sim 2 \times 45 \text{ cm}^2$ active area		
No. of strips/sensor plane	Strip length	Pitch	No. of strips/macro-pixels	Strip/macro-pixel length	Pitch
2×1016	$\sim 5 \text{ cm}$	$90 \mu\text{m}$	$2 \times 960/32 \times 960$	$\sim 2.4 \text{ cm}/\sim 1.5 \text{ mm}$	$100 \mu\text{m}$

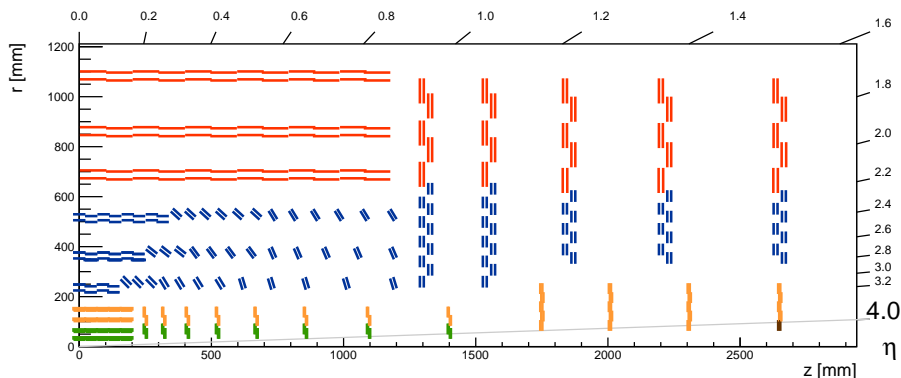


Figure 1. Sketch of one quarter of the tracker layout in $r-z$ view. The radial region below 200 mm is referred to as Inner Tracker and will be instrumented with pixel modules. In the Outer Tracker, the radial region between 200 and 600 mm is equipped with PS modules (blue lines), while the region beyond 600 mm will be populated with 2S modules (red lines). The CMS coordinate system is defined in ref. [1].

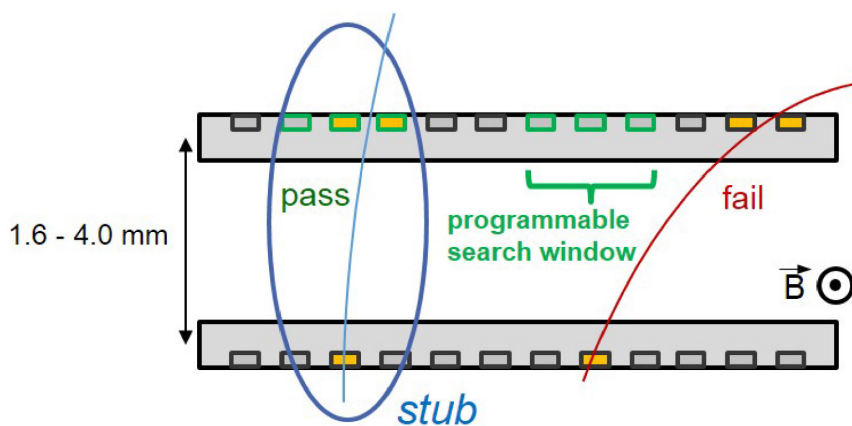


Figure 2. Illustration of the p_T module concept [3]. Correlation of signals in closely spaced sensors enables rejection of low- p_T particles. The channels shown in green represent the selection window to define an accepted stub; a low- p_T rejected track is shown in red.

2.1 The concept of p_T discrimination

In the presence of the 3.8 T solenoidal magnetic field inside the CMS detector, the trajectories of charged particles produced in a collision will bend in a plane transverse to the direction of the beam. The radius of the curvature of the trajectory of these particles depends on the particle p_T . The concept of p_T discrimination is shown in figure 2. As a charged particle passes through the module, it generates signals (hits) in the bottom and top sensors of the module. A hit in the bottom sensor is then matched to the one in the top sensor and if they are within a predefined window, these two hits are combined to form a short track segment or stub. These stubs will be used in the Level-1 (L1) track trigger.

The readout chips will provide the p_T discrimination logic described above. The window for hit matching can be set within the readout chip according to the p_T threshold to be used. For the 2S module, the readout chip is called the CMS Binary Chip (CBC) [5–9]. Each CBC has 254 readout

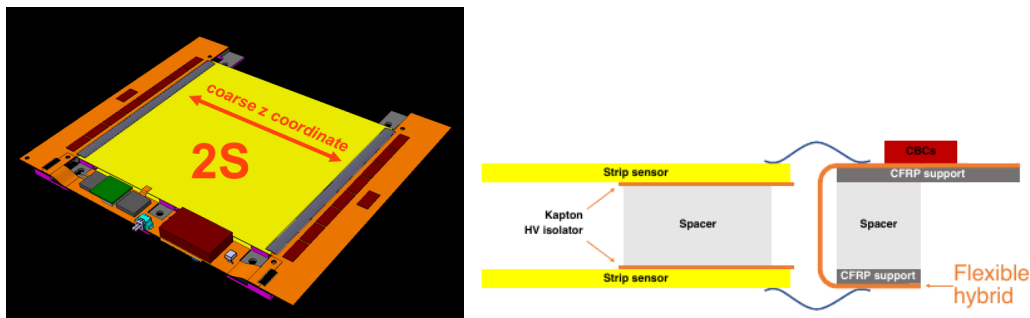


Figure 3. Left: sketch of the full-size 2S module. Right: cross section of the 2S module. The connection of the front-end chips to strips of both the top and the bottom sensor via routing lines in the flexible hybrid (flex kapton circuit), which is bent around a stiffener/spacer sandwich [3], is visible.

channels with alternate channels connected to the top and bottom sensors in a module, as shown in figure 3 (right), so that coincidences between channels of the two sensors can be obtained.

The 2S module, shown in figure 3, consists of two sensors (n-type strips in p-type silicon substrate), support structures made from Al-CF (carbon fibre reinforced aluminium), two front-end hybrids [10], each with eight CBCs and one concentrator integrated circuit (CIC) that aggregates data from the CBCs, and a service hybrid for powering and output data serialization followed by opto-electrical conversion.

All prototype modules discussed in this paper use the second prototype of the CMS Binary Chip, the CBC2 [7–9]. The block diagram of the analogue front-end (FE) of the CBC2 ASIC is shown in figure 4. Three I²C registers are used to control the main settings of the analogue FE: V_{plus} , which controls the global DC baseline of the post-amplifier output, V_{offset} (labelled “Offset” in figure 4) for fine control of the baseline of the post-amplifier output for individual channels on the CBC2, and V_{cTH} , which controls the comparator threshold. The readout for the CBC2 chip is binary, thus it does not measure the amount of charge induced on each strip. If the charge on a strip exceeds the comparator threshold, a hit is registered.

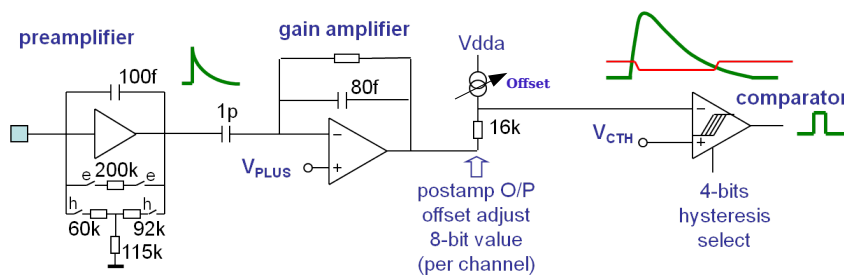


Figure 4. Block diagram of the analogue front-end (FE) of the CBC2 ASIC [7–9]. Three registers are used to control the analogue FE.

2.2 Prototype detectors

Prototypes of the 2S module have been investigated at different test beam facilities (table 2). For the beam tests described in section 3, two small prototype modules and one full-size module have

Table 2. Details of modules used in various beam tests.

Module type	No. of CBC2s	Sensor active thickness	Sensor separation	Bias voltage	Beam Test facility
Non-irradiated mini-module	2	270 μm	2.75 mm	250 V	CERN, DESY, Fermilab
Irradiated mini-module	2	240 μm	3.05 mm	600 V	CERN
Full-size module	16	240 μm	1.80 mm	240 V	CERN, Fermilab

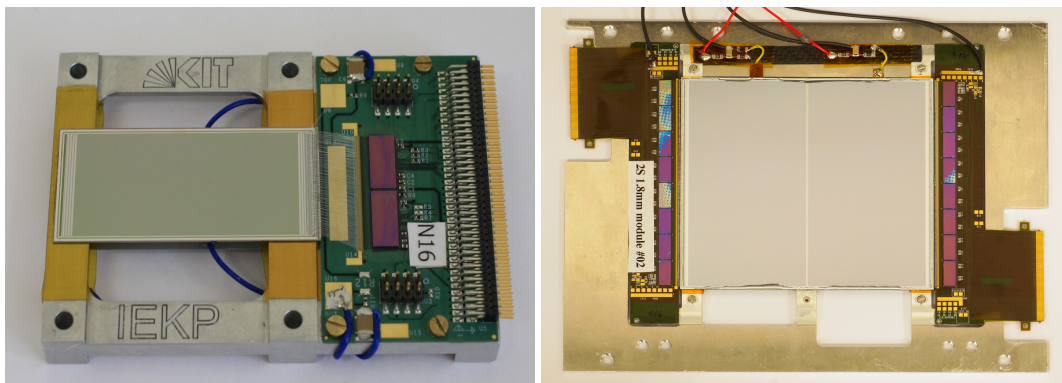


Figure 5. Left: the irradiated 2S mini-module assembled from a small prototype hybrid comprising two CBC2 readout chips and two silicon sensors with 254 strips of 5 cm length. Right: the full-size 2S module comprising two hybrids with eight CBC2 readout chips each and two full-size 2S sensors.

been studied. The strip sensors of the modules have 5 cm long n-type strips at 90 μm pitch on about 300 μm thick silicon sensors with p-type bulk. A negative voltage is applied to bias the sensors at the sensor backplane but in the following the absolute values of the bias voltage applied are quoted.

The small prototype modules, called mini-modules, consist of a version of the front-end hybrid housing two CBC2s. The hybrid is made of a rigid material with bond-pads on both sides and the sensors are wire-bonded to the top and bottom sides of it. This contrasts with the flex-kapton design used for full-sized modules that folds over the CF spacer to provide bond-pads for the bottom sensor [3, 11]. The sensors have been glued on a small frame made of aluminium. One mini-module was left unirradiated. The sensors of this module have an active thickness of 270 μm and their separation is 2.75 mm. The second mini-module, shown in figure 5 (left), with an active sensor thickness of 240 μm and a sensor separation of 3.05 mm, was irradiated with 23 MeV protons at Irradiation Center Karlsruhe [12] to a fluence of 6×10^{14} $n_{\text{eq}}/\text{cm}^2$ with an annealing of approximately two weeks at room temperature. The maximum expected fluence for the innermost layer of the 2S modules of the OT is 3×10^{14} $n_{\text{eq}}/\text{cm}^2$ [3]. This value corresponds to 3000 fb^{-1} of proton-proton (pp) collisions at $\sqrt{s} = 14 \text{ TeV}$ assuming a total inelastic cross section, σ_{pp} , of 80 mb.

The current-voltage characteristic of the sensors before and after irradiation can be seen in figure 6. The effect of irradiation is reflected by an increase of the leakage current by three orders of magnitude.

The full-size module consists of two sensors of about $10 \text{ cm} \times 10 \text{ cm}$, with two columns of 1016 strips each. The active thickness of each sensor is 240 μm and the sensors are separated by 1.8 mm. Each of the front-end hybrids on both ends of the module houses eight CBC2s. A flex hybrid is used to provide bond-pads for the top and bottom sensors (figure 3). The module is built

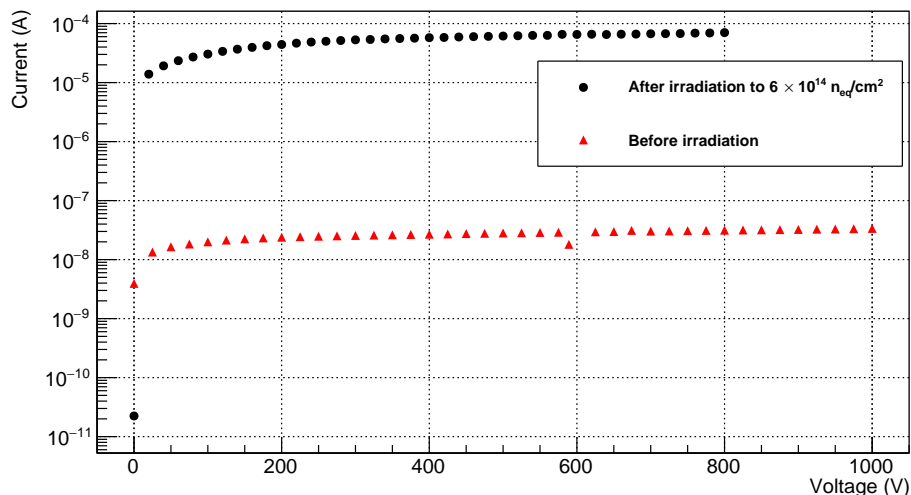


Figure 6. The current-voltage characteristic of a sensor of the mini-module before (red) and after (black) irradiation to $6 \times 10^{14} \text{ n}_{\text{eq}}/\text{cm}^2$, showing the increased current after irradiation. The measurements were taken at -20°C and 20°C for the irradiated and non-irradiated sensors, respectively.

with a rotation angle between the strips of both sensors of below $400 \mu\text{rad}$. This module is shown in figure 5 (right).

3 Beam test infrastructure

The prototype modules have been studied at beam test facilities at CERN, Fermilab and DESY. In all of the facilities, the detector under test (DUT) is placed within a tracking detector, referred to as ‘telescope’ in the following. The telescope provides a reference to reconstruct the tracks of the incident particles. The beam test facility at CERN is described in detail in the following section, and the key features of the DESY and Fermilab test beam facilities are highlighted. The data acquisition systems (DAQ) of the three facilities are also described.

3.1 Beam test setup

A schematic diagram of the setup at CERN is shown in figure 7. Data were collected using a 120 GeV pion beam. The EUDET telescope [13] used in the CERN beam test of the 2S prototype modules is a tabletop tracking detector composed of six planes of MIMOSA-26 [14] silicon pixel sensors for accurate track reconstruction, a fast-timing reference plane (FE-I4) [15] for accurate timing resolution, and a pair of crossed scintillators with photomultiplier tubes (PMTs) located at either end of the telescope for trigger generation. The six MIMOSA-26 sensor planes, each covering an active area of $10.6 \times 21.1 \text{ mm}^2$, consist of $50 \mu\text{m}$ thick $18.4 \mu\text{m} \times 18.4 \mu\text{m}$ square pixels arranged in 576 rows and 1152 columns. The fast-timing plane covers an active area of $16.8 \times 20.0 \text{ mm}^2$ and consists of $200 \mu\text{m}$ thick pixels arranged in 336 rows and 80 columns read out by the FE-I4 chip, which was designed for the innermost layer of the upgraded pixel detector of the ATLAS

experiment. Each sensor plane is mounted inside a 20 mm thick aluminium jig, and two sets of three jigs are attached via rail systems to the upstream/downstream arms of the telescope. The minimum distance between sensor planes is defined by the thickness of the aluminium jig (and is therefore 20 mm), and the maximum distance between sensor planes is defined by the length of each arm (150 mm for equidistant spacing between the sensor planes). The resolution of the telescope system over the six sensors used is $3.24\ \mu\text{m}$ [16]. The jigs are cooled to a constant temperature of 16°C to increase the stability of operation.

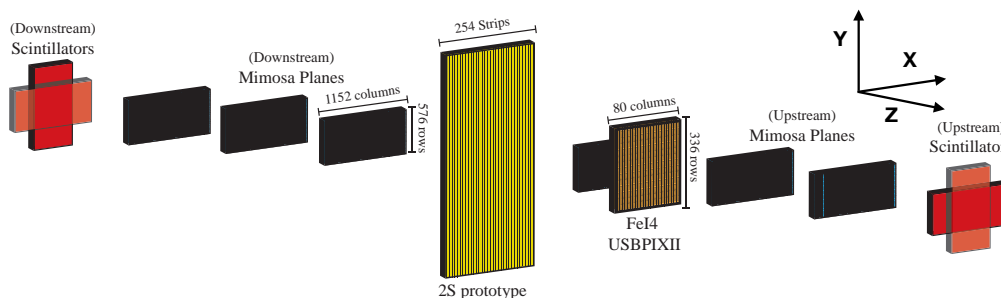


Figure 7. Schematic drawing of the beam test setup at CERN showing the three detector systems used to characterize the performance of the 2S prototype module: the 6 MIMOSA planes, the ATLAS FE-I4 plane and the four scintillators used to generate the NIM trigger. The DUT is placed within the telescope system as shown.

The synchronization of the data streams from the three detector systems (the 2S prototype, the MIMOSA-26 sensor planes, and the FE-I4 plane) is performed by an FPGA-based Trigger Logic Unit (TLU) [17, 18]. During the beam tests, dedicated NIM logic is used to generate a trigger signal using the output signals from the two pairs of crossed scintillators at either extremity of the EUDET telescope. This trigger signal is provided as input to the TLU, which distributes this signal to the DUT and to the telescope’s sensor planes.

A simple handshake protocol is used by the DAQ system to maintain synchronization among the different detector systems. The detector systems assert busy signals on separate lines, which inhibit triggers from the TLU until all of the lines are cleared. No new triggers are sent by the TLU until all detectors drop their busy-lines. This ensures that detectors with different dead-times can be triggered and read out synchronously. In addition, the TLU can send a timestamp for each trigger via a dedicated clock-data line, or it can receive a back-pressure (veto) signal from the DUTs on the same line.

The additional ATLAS FE-I4 plane is used to improve the timing resolution of the telescope by associating the FE-I4 hits with the individual hits in the $115.2\ \mu\text{s}$ rolling-shutter frame of the telescope during event building. This allows the multiple tracks in a telescope frame to be correlated to individual triggers. Because the FE-I4 readout has no dead-time and runs on an internal 40 MHz clock, the required time resolution of 25 ns for the CBC DAQ is achieved. The data streams from the telescope and the FE-I4 are sent to the EUDAQ [13] online software via the TCP/IP protocol [19]. The two streams are stored together in the same format in a file, which makes the reconstruction easier in the EUDET [20] framework.

The beam test at DESY uses the EUDET based telescope called DURANTA [13], similar to the one used during the CERN beam test. It also uses six MIMOSA-26 pixel sensors with four crossed scintillators for triggering and a TLU, however it was equipped with a CMS Phase-1 pixel [21]

module as a timing reference plane instead of the FE-I4. The data were collected with a positron beam of 5 GeV energy.

The Fermilab Test Beam Facility, or FTBF [22], is equipped with two silicon telescopes aligned along the beam line and configured to operate synchronously. It has a pixel telescope assembled from eight planes and a telescope with strip modules made up of 14 detector planes. The strip telescope increases the coverage of the pixel telescope and improves its tracking performance. The trigger is generated by a coincidence signal of three scintillation counters, one placed in front and two placed behind the telescopes. The synchronization of the data streams from the two telescopes and the 2S module is performed by a Fermilab-designed FPGA-based trigger board. The data are taken with a 120 GeV proton beam.

3.2 Data acquisition system

The DAQ system for the CBC2 modules at CERN and Fermilab test beams is based on the CERN Gigabit Link Interface Board (GLIB) [23] μ TCA Advanced Mezzanine Card (AMC). Different firmware versions are used to read data from the 2 and 16 CBC2s on the tested modules. Control signals and readout data are exchanged between the GLIB and the control PC via the IPBus [24] protocol, whereas trigger, busy and veto signals are interfaced to the TLU/Fermilab equivalent via a dedicated five-channel I/O FPGA Mezzanine Card (FMC). A simple block diagram of the different components of the DAQ system is shown in figure 8.

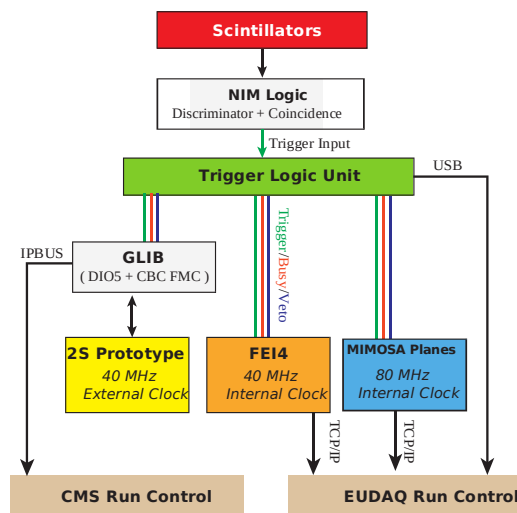


Figure 8. Block diagram of the DAQ system used in the CERN and Fermilab beam test setups. The correlation of the data from the two DAQ chains is described later in section 5.

An external high-precision clock generator was used to provide the clock signals to the GLIB via the same FMC that connects to the TLU. The CBC2 data are processed and formatted by the firmware and then sent to a XDAQ [25] application that formats events in a CMS compatible format and stores the data for later processing within the standard CMS reconstruction software, CMSSW [26]. The binary raw data stream is also stored and can be used for online data quality monitoring.

The beam test at DESY used a novel DAQ system, based on the FC7 [27] card. The FC7 hosts a Kintex-7 FPGA and comes with a system firmware allowing for communication with other devices

on the FC7 card and IPBus communication. A DIO5 FMC is used to send trigger and busy signals via LEMO connectors. These are fed into a custom-built LVDS converter box and sent to the TLU via a standard RJ45 connector.

4 Preparations for data-taking

4.1 Pedestal and noise

The pedestal and noise values of an individual channel in a system with binary readout can be inferred from a channel's S-curve. An S-curve is obtained by measuring the noise occupancy as a function of the comparator threshold (V_{CTH} in figure 4). The comparator threshold has been measured in V_{CTH} DAC units. One V_{CTH} DAC unit corresponds to 375 electrons, as measured using an X-ray source. The noise occupancy is given by the fraction of triggers for which a given channel registers a hit. Higher numerical values of V_{CTH} correspond to lower thresholds in the CBC2. Figure 4 also shows the per-channel 8-bit DAC used to control the offset of the output voltage of the second amplification stage to compensate for any channel-to-channel variations.

The pedestal value and the channel noise are extracted directly from the S-curve either by fitting the curve with a sigmoid of the form

$$f(x, \mu, \sigma) = \frac{1}{2} \left[1 + \operatorname{erf} \left(\frac{x - \mu}{\sqrt{2}\sigma} \right) \right], \quad (4.1)$$

or by numerically differentiating it. The mean parameter, μ , in eq. (4.1) (or the mean of a Gaussian fitted to the differential histogram) then corresponds to the pedestal and σ (or the RMS of a Gaussian fitted to the differential histogram) corresponds to the noise. An example of an S-curve recorded for a CBC2 on a non-irradiated prototype module and the corresponding differential histogram are shown in figure 9. Both methods return similar (i.e. consistent within 3σ) values for the pedestal and noise. The pedestal value, obtained from fitting the left plot of figure 9 with a sigmoid function, is $120.0 \pm 0.1 V_{\text{CTH}}$ DAC units. A pedestal value of $119.3 \pm 0.2 V_{\text{CTH}}$ DAC units has been obtained by fitting the distribution shown in figure 9, right, with a Gaussian function. For the noise, $2.12 \pm 0.06 V_{\text{CTH}}$ DAC units and $2.14 \pm 0.15 V_{\text{CTH}}$ DAC units are obtained, respectively.

Figure 10 shows the uniformity of the front-end response after adjustment of the individual channels' offsets. The pedestal and noise values were extracted from the fits to the individual channels' S-curves using eq. (4.1). The channel-to-channel variation in the pedestal, defined as the RMS of the measured distribution, is measured to be 0.30 ± 0.01 and $0.37 \pm 0.02 V_{\text{CTH}}$ DAC units for the first and second CBC2, respectively. The mean noise was found to be 1.36 ± 0.06 and $2.38 \pm 0.60 V_{\text{CTH}}$ DAC units for the first and second CBC2, respectively. The same figure also clearly shows that 11 of the strips connected to the second CBC2 on the hybrid are significantly noisier than the rest. These 11 strips are included in the noise figure quoted for the second CBC2. The strips exhibiting a value of noise larger than $3 V_{\text{CTH}}$ DAC units (1125 electrons) are not considered for analysis.

4.2 Latency scans

After the pedestal and noise scans, two latency scans, one for data and one for stubs, were carried out. The data latency, measured in units of 40 MHz clock cycles and set using an on-chip configuration

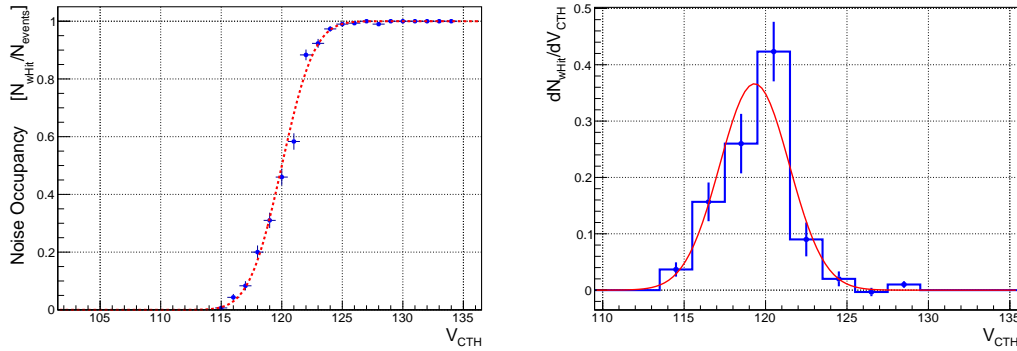


Figure 9. S-curve measured for a single input channel on one of the two CBC2s on a non-irradiated prototype module at room temperature with the sensor biased at 250 V. On the left the measured data are shown along with a fit to the measured data performed using eq. (4.1), while on the right the differential histogram is shown with the corresponding Gaussian fit.

register, defines the position in the on-chip RAM from which the data are read upon reception of a trigger. The stub latency, also measured in units of 40 MHz clock cycles and set by a configuration register in the back-end FPGA, defines the delay between hit and stub data arriving at the back-end of the data acquisition system and is required to assemble the data at the back-end.

The resolution of the data latency measurement was improved using a high-resolution time-to-digital converter (TDC) in the back-end FPGA. The TDC measures the time of arrival of the trigger signal at the back-end with respect to the 40 MHz clock edge in time slices of 3.125 ns, using a 3 bit counter operating at 320 MHz. The results of the latency scans performed in the CERN beam test are shown in figure 11. These scans were used to identify the stub and data latencies to use during data taking by counting the number of stubs and hits contained in the data stream for a fixed number of triggers and selecting values for the data and stub latency that maximize the fraction of events containing stubs and hits, respectively. Both scans were performed at a threshold of 113 DAC units (3σ away from the pedestal). For further data taking, the data latency and stub latency were fixed at 13 and 4, respectively, as shown by the dashed lines in figure 11.

5 Reconstruction

Dedicated software is used to reconstruct the data collected from the telescope system and the DUT. Initially, the reconstruction of tracks of the incident particle is carried out using the hits in the telescope system. The reconstruction of data from the DUT involves the formation of clusters and stubs using the hits from the individual channels. The reconstructed tracks are then extrapolated to the DUT, and the estimated position of the track on the DUT is computed. Using this information, an alignment is performed to correct for the relative offset in position of the DUT with respect to the telescope system. The reconstruction of tracks from the telescope data, clusters and stubs from the DUT data, and alignment procedures are described in the following sections.

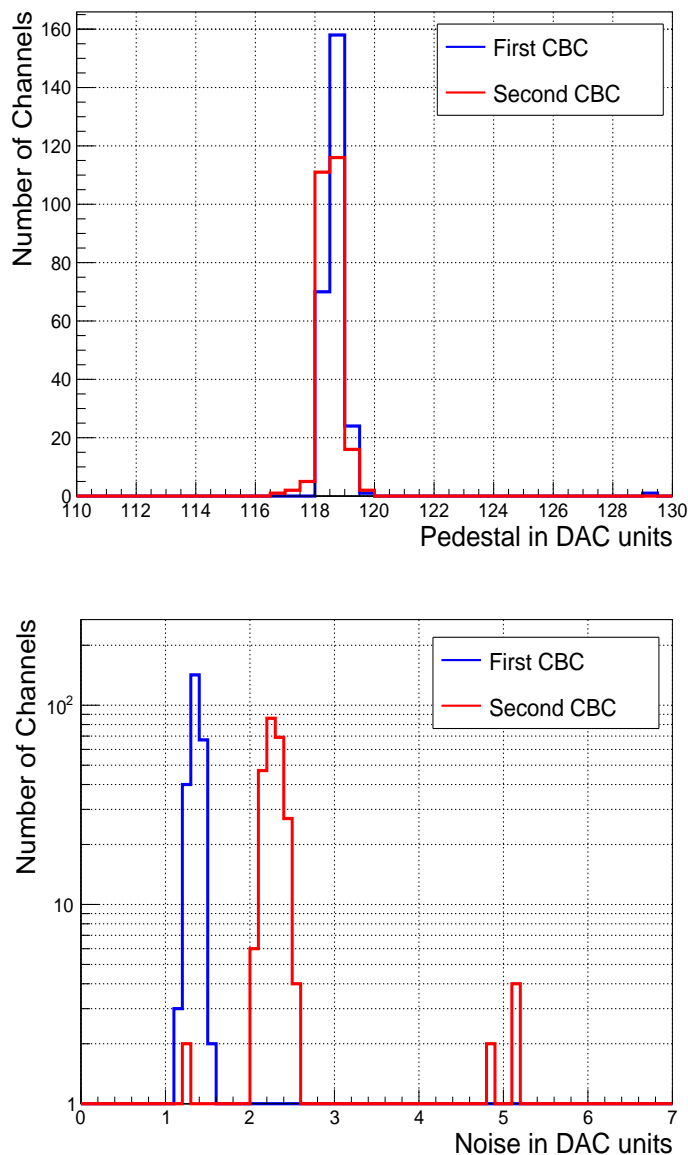


Figure 10. Pedestal (top) and noise (bottom) for both CBC2s on a prototype module.

5.1 DUT reconstruction

The schematic diagram for the processing of the DUT data is shown in figure 12. The raw data received from the 2S modules by the FPGA are converted to the CBC2 event format by the DAQ software and served to the online Data Quality Monitoring (DQM) system. The raw data are also sent to the CMS event builder (EVB) [28] which provides data in the Event Data Model (EDM) format [29, 30]. The EDM data are then processed by the CMS offline software, CMSSW [26], to produce clusters and stubs used in the offline analysis. Hits in adjacent strips of the DUT are combined to form a cluster. The number of strips included in a cluster is called the cluster width. The cluster position is defined by the center of the cluster rounded down to an integer strip number.

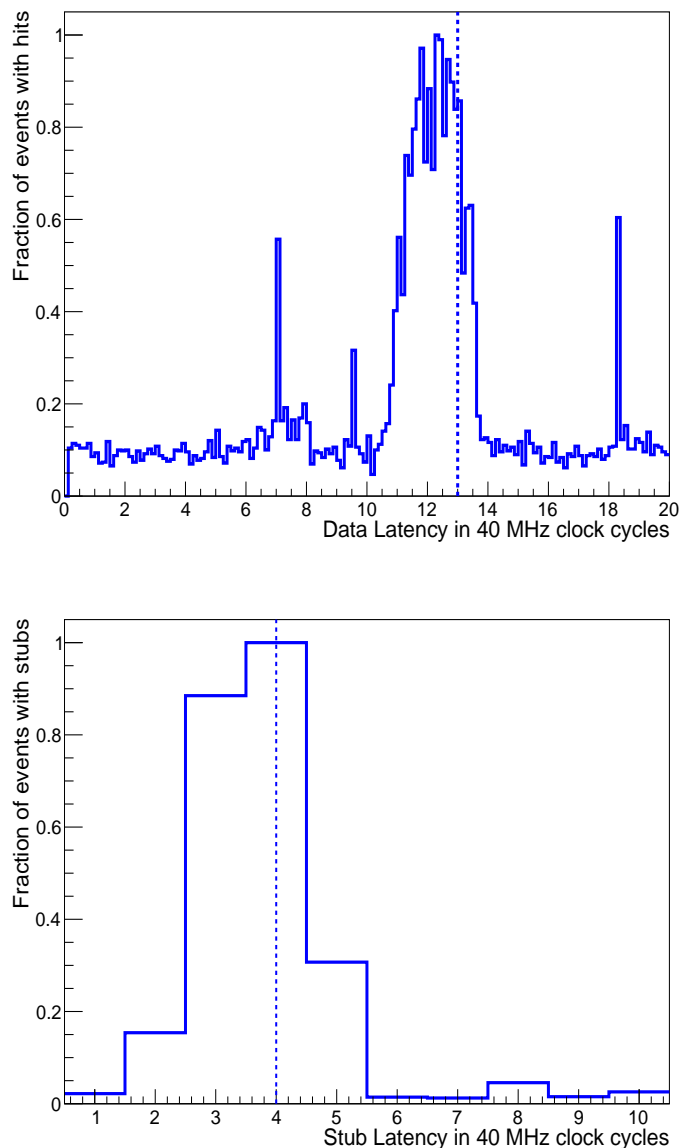


Figure 11. Results from data (top) and stub (bottom) latency scans. The TDC phase gives fine resolution within a 40 MHz clock cycle ($1/8$). The dashed lines indicate the chosen values.

The CBC2 reconstructs stubs, by calculating the cluster positions in integer strip numbers. However, it outputs only the information that a stub was present, not its position (in contrast to later versions of the chip, which include this functionality). Therefore the stub reconstruction is done offline, by emulating the logic in the CBC2. Clusters with cluster width greater than 3 are excluded from stub formation. The difference in position (in number of strips) of the clusters in the bottom sensor is calculated with respect to clusters in the top sensor. If this difference is less than the predefined window, an offline stub is formed. The position of the stub is defined as the position of the cluster in the bottom sensor seeding the stub. As the DAQ systems for the telescope and for the DUT are different, an

additional processing step is needed to synchronize the events coming from telescope and DUT data streams by matching the individual trigger numbers using the ROOT data analysis framework [31].

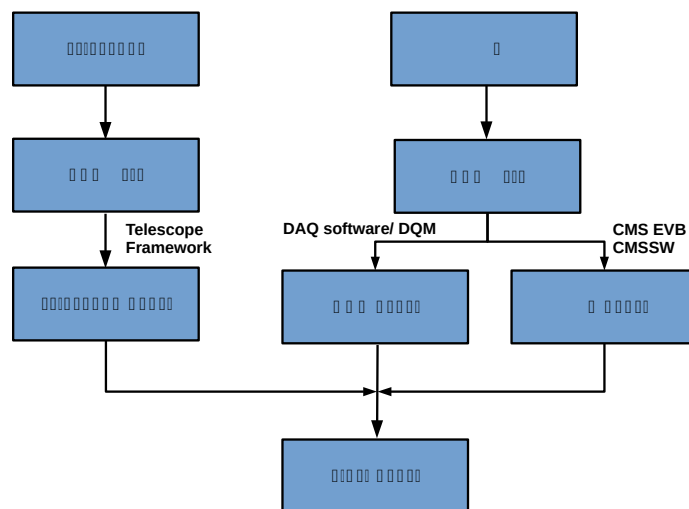


Figure 12. A schematic representation of the data processing for the beam tests at CERN. The Telescope event contains information about the incident track parameters. The DUT event contains the information of the hits as read from the DUT and also the clusters and stubs reconstructed using offline software. The CBC event contains the information about CBC errors. Data from all three sources are merged and stored into a single file for offline analysis.

5.2 Tracking

Tracks from the EUDET telescope are reconstructed in the EU Telescope [13] framework using MIMOSA-26 planes. A database of noisy pixels (pixels with exceptionally high occupancy), is built and used to exclude such pixels from subsequent steps of the analysis. Clusters are built according to the nearest neighbour search algorithm, which iteratively joins adjacent pixels with hits to form a cluster. A “*pre-alignment*” is performed in the telescope global frame, correcting only for the misalignment in X and Y directions (as shown in figure 7). The output of this step is used to constrain the alignment step itself, based on solving exact matrix equations with the Millipede II framework [32]. Shifts in X, Y and Z coordinates and 3 Euler rotation angles for each Mimosa plane are corrected for. Tracks are then reconstructed with a Deterministic Annealing Filter (DAF) algorithm [33, 34], where all hits within a given radius are used for the track reconstruction. Tracks reconstructed with the DAF are further cleaned to remove any duplicates, defined as two or more tracks with X and Y coordinates at the FE-I4 plane less than $1\ \mu\text{m}$ apart.

While Mimosa planes are read out with a rolling shutter having a window of $115\ \mu\text{s}$, the maximum acquisition rate for the DUT and the FE-I4 plane is 40 MHz. The presence of a hit in the FE-I4 plane that can be matched to the track is used as a timestamp, which largely reduces track combinatorics. Residuals at the FE-I4 plane are used to determine a nominal distance between

the track impact point and the FE–I4 hit. The residuals are fitted with a step rectangular function convolved with a Gaussian smearing. The maximum distance to accept a track is set to half the width of the step function, compatible with the FE–I4 pitch, plus two times the width of the Gaussian, compatible with the track pointing resolution.

Track reconstruction and telescope alignment at the Fermilab test beam facility are performed using a single dedicated software package [22] that provides a graphical interface to execute the various steps. An iterative algorithm implements a least-squares minimization to compute 1st-order roto-translational corrections using tracks reconstructed with a preliminary description of the geometry.

The reconstruction of beam test data at DESY follows a similar procedure to that used for beam tests at CERN. The main difference is that the entire reconstruction is performed within the EU Telescope framework and that the General Broken Lines (GBL) [35] algorithm for alignment is used. The GBL algorithm is required to account for the increased multiple scattering of the comparatively low-energy particles available at the DESY beam test facility.

5.3 DUT alignment

The DUT alignment procedure consists of minimizing the residuals at the DUT plane to constrain the degrees of freedom of the system:

$$\chi^2 = \frac{1}{N} \sum_{i=0}^N \left(\frac{x_{\text{DUT}} - x_{\text{TkAtDUT}}}{\sigma_{\text{tkres}}} \right)^2,$$

where x_{DUT} is the hit position in X and x_{TkAtDUT} the position of the hit as derived from the track extrapolation to the DUT location, while σ_{tkres} is the telescope pointing resolution. The sum runs over all events in which at least one cluster in the DUT and one track are reconstructed. For each event the closest pair is selected. To remove outliers, the sum is further restricted to events where the residual $|x_{\text{DUT}} - x_{\text{TkAtDUT}}|$ is less than $3\sigma_{\text{tkres}}$ away from the mean value of a Gaussian fit of the residual distribution.

The track impact point on the FE–I4 plane is propagated to the first sensor plane of the DUT, which corresponds to the plane of the sensor facing the beam direction, including degrees of freedom for the X position of the first plane, Z position of the first plane, θ angle around the Y-axis, and the distance between the two sensor planes of the DUT. This procedure eliminates the sign degeneracy of the θ angle. For efficiency studies reported in section 6, a track is matched to a hit, cluster or stub on the DUT if the residual, $|x_{\text{DUT}} - x_{\text{TkAtDUT}}|$, is less than $3\sigma_{\text{tkres}}$.

6 Results

After calibration, the threshold (V_{CTH}) and the angle of rotation of the DUT with respect to the beam were varied in suitable step sizes and the properties of hits, clusters and stubs were studied. The axis of rotation of the DUT was the Y axis, as shown in figure 7.

A scan of V_{CTH} was performed at vertical beam incidence and measurements of the cluster and stub efficiencies were carried out as a function of a number of functional parameters to fully characterize the mini-modules (section 6.1) and the full-size module (section 6.2).

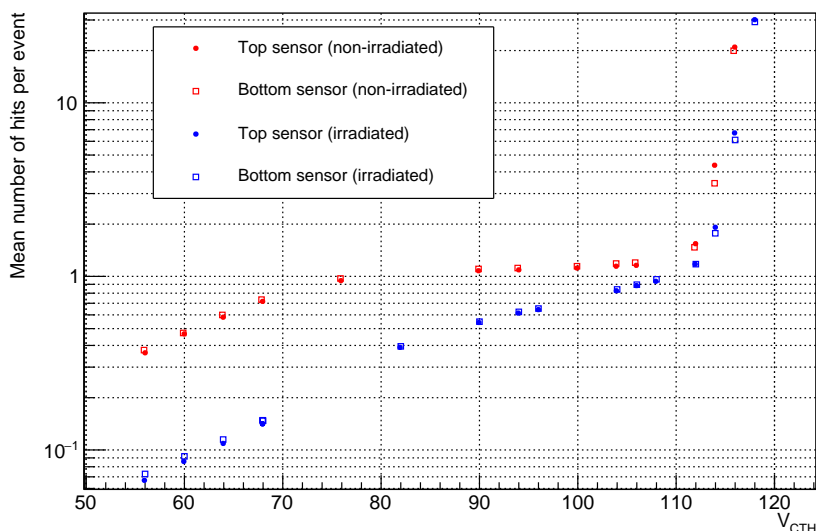


Figure 13. Average number of hits per event on non-irradiated and irradiated sensors as a function of V_{CTH} . A bias voltage of 250 V (600 V) was applied to the non-irradiated (irradiated) mini-module.

6.1 Performance of mini-modules

Figures 13 and 14 show the average number of hits and clusters on the non-irradiated and irradiated mini-modules, respectively. Lower numerical values of V_{CTH} mean a higher signal threshold, as mentioned in section 4.1. For the non-irradiated mini-module, the average number of hits/clusters increases as V_{CTH} is increased and a plateau with a value close to 1 is visible, up to V_{CTH} values of about 110. However, for the irradiated module, the average number of hits/clusters is mostly less than 1 as V_{CTH} is increased. This indicates that, for a given value of V_{CTH} , we see a lower number of hits/clusters in the irradiated mini-module as compared to the non-irradiated one. As the V_{CTH} setting is increased further ($\gtrsim 110$), the noise increases in both mini-modules, leading to a sharp rise in the average number of hits/clusters. Differential histograms of cluster occupancy as a function of V_{CTH} , derived by numerically differentiating the distributions of the cluster occupancy as shown in figure 14, are shown in figure 15. The differential distributions show an inverted Landau distribution, caused by the actual signal generated from the incident particle, and a noise peak. Comparing the differential distributions, it can again be seen that the total number of clusters is lower in the irradiated mini-module. The loss in the number of clusters for the irradiated mini-module as seen in figure 14 and figure 15 indicates that the charge collection in the irradiated mini-module is worsened due to radiation induced effects. Along with radiation induced effects, the lower sensor active thickness of $240\ \mu\text{m}$ for the irradiated module, compared to $270\ \mu\text{m}$ of the non-irradiated module, also leads to lower charge collection. By choosing appropriate V_{CTH} values of 106 and 110 DAC units for the non-irradiated and irradiated module, respectively, signals from incident particles can be collected preferentially.

The cluster efficiency, defined as the ratio between the number of events with a cluster matched to a track in a single track event and the total number of events with a single track, is then measured as

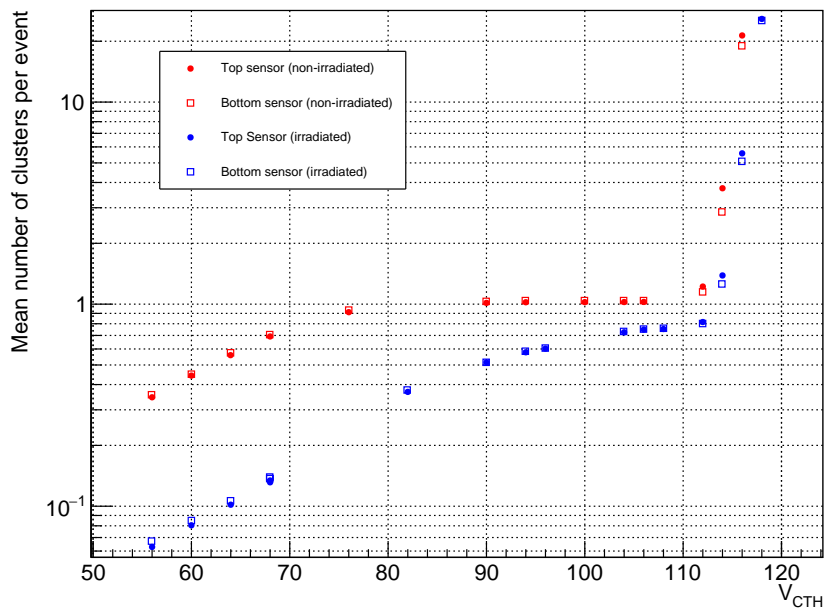


Figure 14. Average number of clusters per event for non-irradiated and irradiated sensors as a function of V_{CTH} . A bias voltage of 250 V (600 V) was applied to the non-irradiated (irradiated) mini-module.

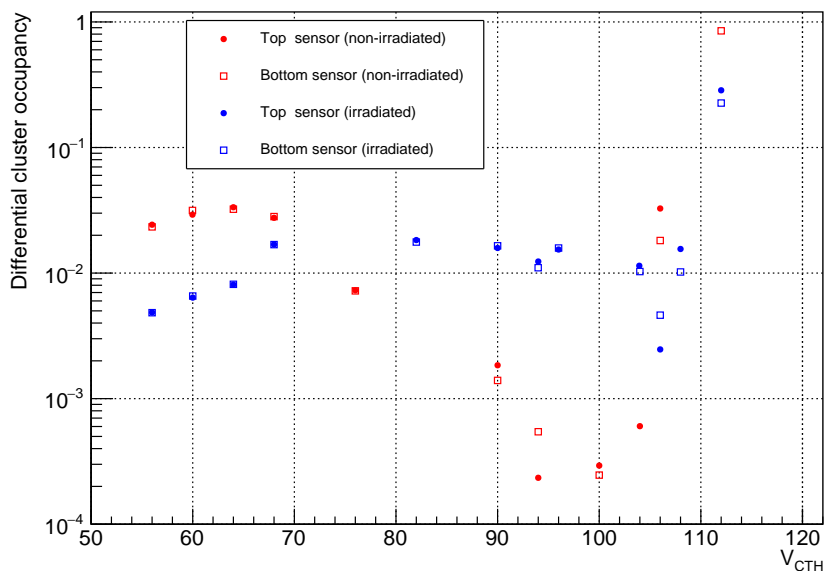


Figure 15. Differential cluster occupancy for non-irradiated and irradiated sensors as a function of V_{CTH} . A bias voltage of 250 V (600 V) was applied to the non-irradiated (irradiated) mini-module.

a function of V_{CTH} for different values of the trigger phase (TDC), to check for a potential dependency. The cluster efficiencies for one of the sensors of the non-irradiated and irradiated mini-modules are shown in figure 16. The lower charge collection in the irradiated module results in a smaller efficiency plateau (figure 16, bottom) compared to the non-irradiated module (figure 16, top). As the V_{CTH} increases further (> 110), the efficiency starts to degrade for both the mini-modules due to increase of noise. Due to the higher noise occupancy, the probability of a neighbouring strip to fire increases, resulting in larger cluster width. This shifts the position of the actual cluster away from the track causing the track matching to fail. A small dependency on the trigger phase is present for both sensors and is more evident at lower V_{CTH} . A trigger phase is present in the CERN beam test because the trigger signal is asynchronous with respect to the 40 MHz clock that drives the readout electronics.

Because there is no magnetic field, the dependence of the mini-module performance on the transverse momentum of tracks is emulated by rotating the DUT with respect to the beam direction. As the incident angle (referred to as α) of the particles increases, the charge deposited is shared by multiple strips and hence the cluster width is expected to increase, which is shown in figure 17. This effect is less evident on the irradiated module due to the radiation induced defects both in the sensor bulk and on the surface, that change the electric field inside the sensor. This leads to a modification of the charge sharing and further to a higher average cluster size at normal incidence. The same effect is also evident from the distribution of the fraction of clusters with different strip multiplicities, as shown in figure 18. The non-irradiated module shows a correlation between the cluster fractions and the angle. This dependence is much less significant for the irradiated module.

In figure 19 the cluster efficiencies for different TDC values as a function of the DUT rotation angle for the two modules are shown. The dependency on the trigger phase is negligible and the mean cluster efficiency for the full range of the angular scan is $99.56 \pm 0.01\%$ and $98.21 \pm 0.02\%$ for the non-irradiated and irradiated module, respectively.

For the CMS field strength of $B = 3.8$ T, the relationship between the beam incident angle (α) and the emulated transverse momentum p_{T} of the traversing particle for a radial position of the module (R) is given by $p_{\text{T}} [\text{GeV}] \approx \frac{0.57 \cdot R[\text{m}]}{\sin(\alpha)}$. The stub efficiency, defined as the ratio of the number of events with stubs matched to a track in single track events to the number of events with a single track, was measured for each incident angle. Tracks and stubs must match within 4σ of the spatial resolution. The stub efficiency of the two mini-modules as a function of effective p_{T} (beam-incident angle) is shown in figure 20. For larger angles of incidence the relative shift in cluster position in the two sensors of a module is larger, which leads to lower probability of correlating them as stubs. The stub efficiency drops for larger angles for this reason. A stub correlation window of 5 strips is used. A radius of 60 cm was used for the calculation of the effective p_{T} from the beam incident angle. The turn-on curve is different for the two modules due to different sensor spacing.

The turn-on curve was fitted with an error function of the form

$$f(p_{\text{T}}) = 0.5A \left(1 + \text{erf} \left(\frac{p_{\text{T}} - p_{\text{T}\mu}}{\sigma_{p_{\text{T}}}} \right) \right),$$

where A is the efficiency at the plateau, $p_{\text{T}\mu}$ is the turn-on threshold for which the efficiency is 50%, and $\sigma_{p_{\text{T}}}$ is the width of the Gaussian in the error function. The p_{T} resolution is defined as the ratio of the width of the Gaussian to the p_{T} value at 50% of the plateau height, or $\sigma_{p_{\text{T}}}/p_{\text{T}\mu}$. For the

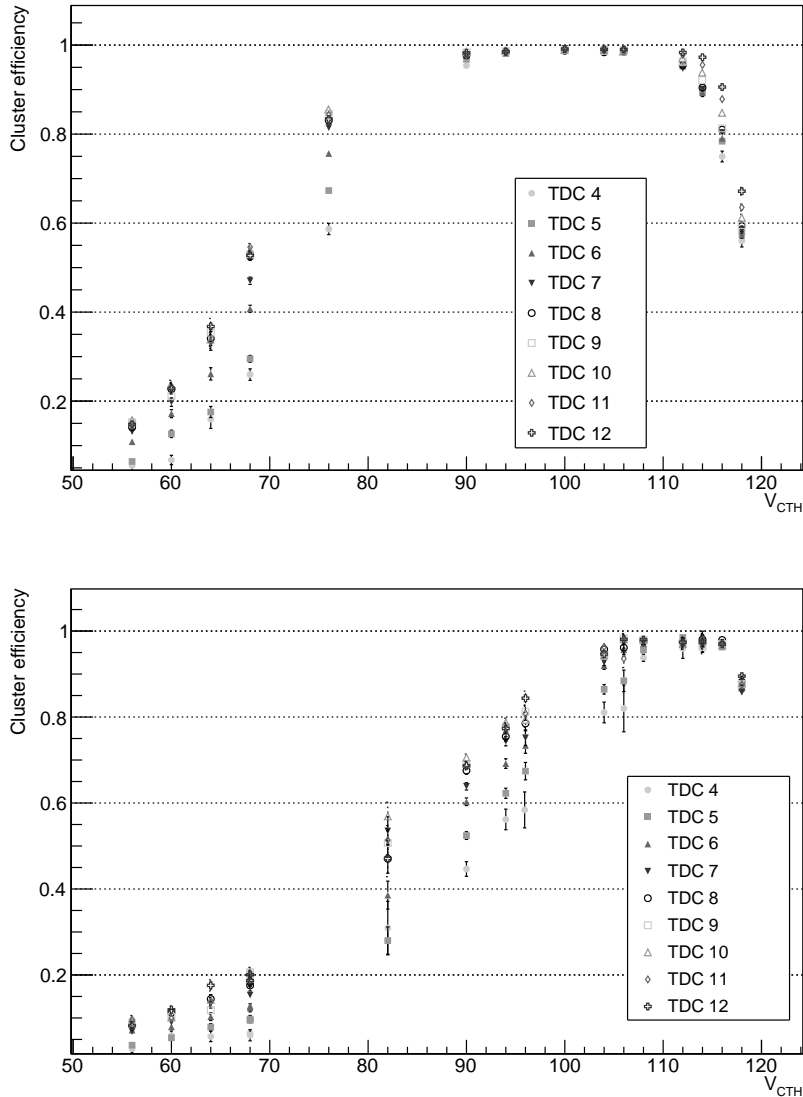


Figure 16. Cluster efficiency of the non-irradiated (top) and irradiated (bottom) 2S mini-modules presented as a function of V_{CTH} for different phase differences between trigger and readout clocks. A bias voltage of 250 V (600 V) was applied to the non-irradiated (irradiated) mini-module.

non-irradiated module, the turn-on threshold is 1.88 GeV with a p_T resolution of 5%, whereas the expected turn-on threshold is 2 GeV. The plateau efficiency for the non-irradiated module is 99%. The high plateau efficiency with sharp turn-on demonstrates that the module can reject tracks with $p_T < 2$ GeV efficiently. For the irradiated mini-module, the plateau efficiency reaches 97% with a p_T resolution of 6%. This shows that the stub finding logic of the 2S modules will work even after being irradiated to a fluence of 6×10^{14} n_{eq}/cm^2 , which is twice the expected fluence for the first layer of 2S modules. The stub efficiency measured using data collected at the DESY test beam facility with the non-irradiated mini module is found to be 99%.

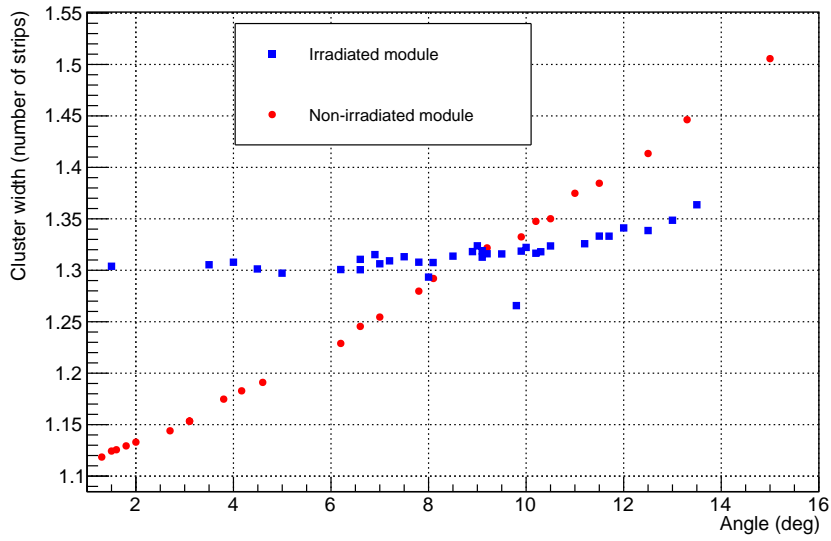


Figure 17. Mean cluster width of non-irradiated and irradiated 2S mini-modules as a function of the beam incident angle. Due to radiation induced defects, charge sharing is higher in the irradiated module, leading to a larger mean cluster size. A bias voltage of 250 V (600 V) was applied to the non-irradiated (irradiated) mini-module. A V_{CTH} value of 106 (110) DAC units was used for the non-irradiated (irradiated) mini-module.

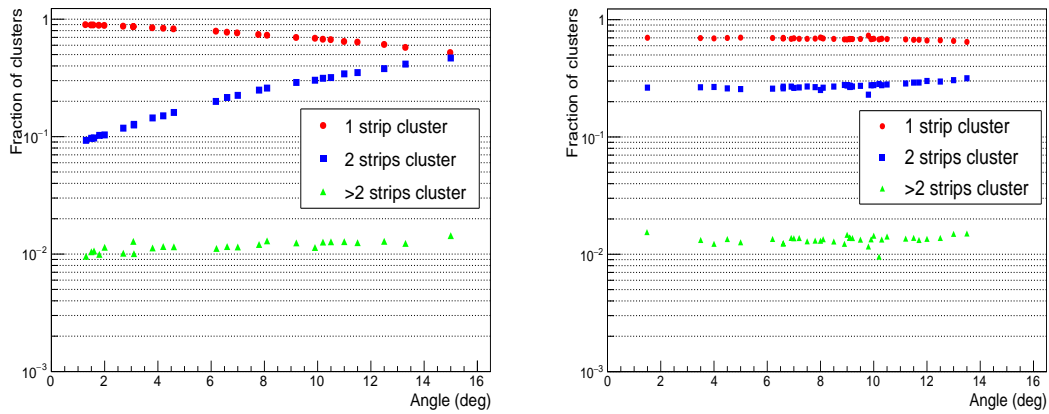


Figure 18. Fraction of clusters with different strip multiplicity; (left) non-irradiated module; (right) irradiated module. A bias voltage of 250 V (600 V) was applied to the non-irradiated (irradiated) mini-module. A V_{CTH} value of 106 (110) DAC units was used for the non-irradiated (irradiated) mini-module.

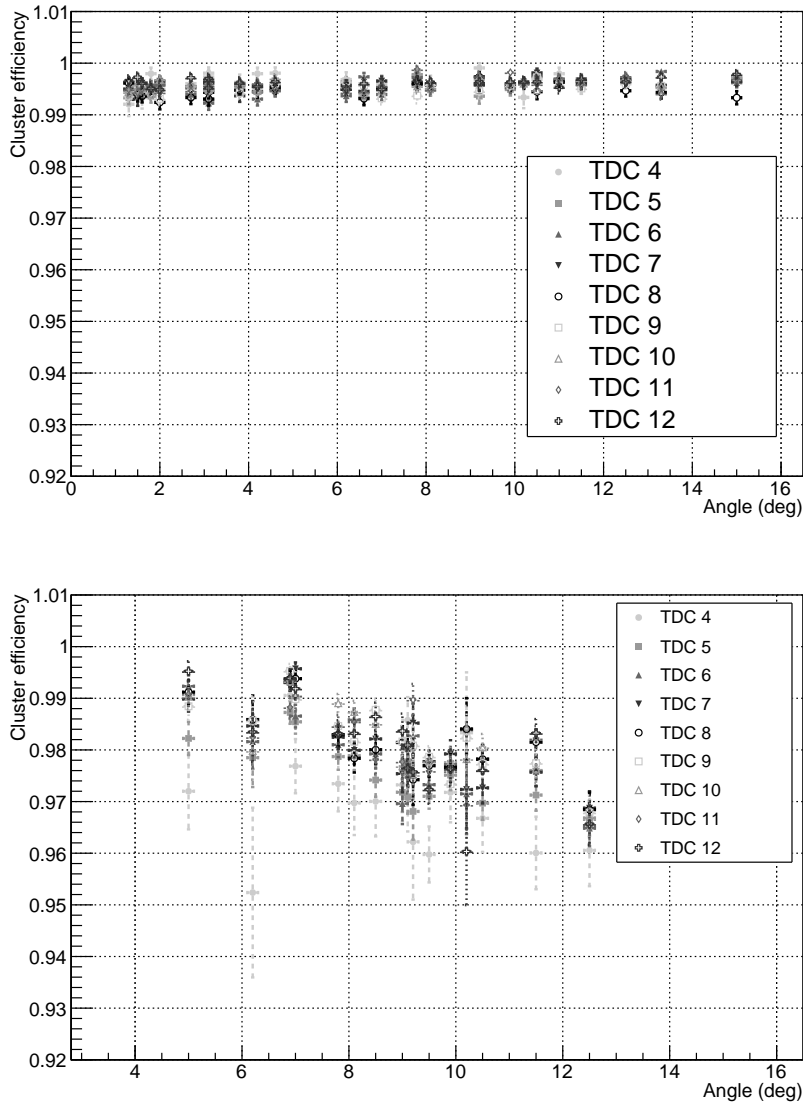


Figure 19. Cluster efficiency of the non-irradiated (top) and irradiated (bottom) 2S mini-modules as a function of the beam incident angle for different TDC phases. A bias voltage of 250 V (600 V) was applied to the non-irradiated (irradiated) mini-module. A V_{CTH} value of 106 (110) DAC units was used for the non-irradiated (irradiated) mini-module.

For the irradiated module three angular scans were performed, each with different stub correlation windows. As shown in figure 21, the turn-on curve of the efficiency depends on the selected correlation window, while the efficiency plateau does not.

6.2 Performance of the full-size module

For the full-size 2S module, the primary goal was to check the uniformity of the response across all strips. Figure 22 (top) shows the stub efficiency per strip for the full-size 2S module. The module

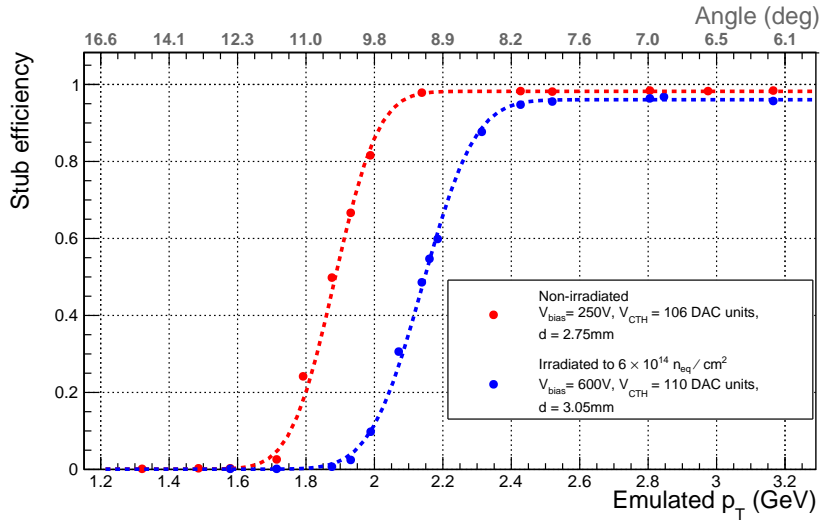


Figure 20. Stub efficiency for the irradiated (blue) and non-irradiated (red) modules as a function of the beam incident angle. As expected, for larger angles of incidence, which corresponds to smaller effective p_T , the stub efficiency drops. A radius of 60 cm was used for the calculation of p_T from the beam incident angle which is approximately the radius at which the first layer of 2S modules will be installed. The stub correlation window is set to 5 strips.

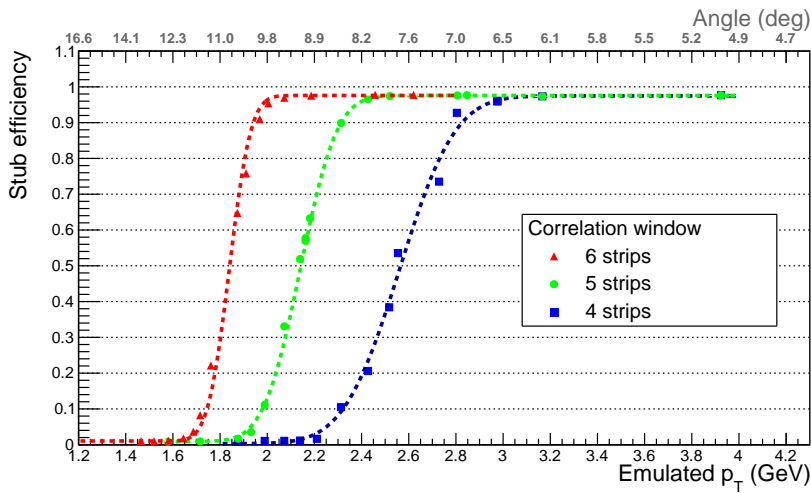


Figure 21. Stub efficiency comparison of different angular scans with different correlation windows for the irradiated module. The choice of window size leads to a shift in the turn-on p_T , but the efficiency at the plateau remains the same. A bias voltage of 600 V was applied to the irradiated mini-module.

was operated at a bias voltage of 250 V and V_{CTH} was set to 115 DAC units. The analysis techniques used are the same as reported for the mini-modules. The region between strips 185 and 239 has no data because it was not scanned by the beam. The large statistical uncertainty in efficiency at the edges is due to the limited data collected for the scans performed at the module edges. The mean stub efficiency extracted from a linear fit, where the asymmetric errors on each measurement are taken into account, is 97.4%, and the strip-to-strip variation of the stub efficiency was found to be 1.3%. The efficiency is approximately 2% lower than that measured in the 2S mini-module. The difference is due to a different operational configuration of the modules and a possible remaining contamination of events for which the module was not synchronized with the telescope. The stub efficiency per chip is shown in figure 22 (bottom). The results demonstrate that the response of the full-size 2S module is uniform across strips. The stub efficiency as a function of effective p_{T} for the full-size 2S module measured with data collected at the Fermilab test beam facility is shown in figure 23. The correlation window used for stub formation was set to 5 strips. The figure shows that the behaviour of the full-size module is similar to that of the mini-modules. From the fit, a turn-on threshold of 1.2 GeV is obtained with a p_{T} resolution of 7.9%. The turn-on threshold is lower compared to the non-irradiated mini-module since the sensor separation is smaller. The efficiency at the plateau is 99%.

7 Summary

A new silicon strip tracker will be installed in CMS for the HL-LHC period. The new Outer Tracker will comprise novel detector modules with two closely spaced sensors and a new front-end ASIC that is capable of correlating hits between the sensor layers. The performance of 2S prototype modules has been characterized at three test beam facilities. The presence of tracking detectors at these facilities has allowed for spatial matching of the tracks of the incident beam and the hits on the 2S modules. This has provided the first measurements of the absolute efficiency of these prototype detectors.

Cluster efficiencies of approximately 99.5% and 98% have been measured for non-irradiated and irradiated modules, respectively. These results are robust with respect to variations in particle arrival times relative to the trigger. For the non-irradiated module, an increase in the mean cluster width is observed as the beam incident angle increases. For the irradiated module, the average cluster size is higher in general and thus the variation of cluster width with angle is less evident.

The stub efficiency across all the strips of the sensors shows a uniform response. The stub efficiencies of both the non-irradiated mini-module and the full-size module are found to be around 99%. The stub efficiencies obtained from the analysis of data from the three test beam facilities are in agreement with each other. For the irradiated module, the stub efficiency was found to be 97%. All of the modules demonstrate the ability to reject tracks with $p_{\text{T}} < 2$ GeV. The high efficiency of the irradiated module provides evidence that the modules will be able to operate throughout the lifetime of the HL-LHC without much loss of efficiency.

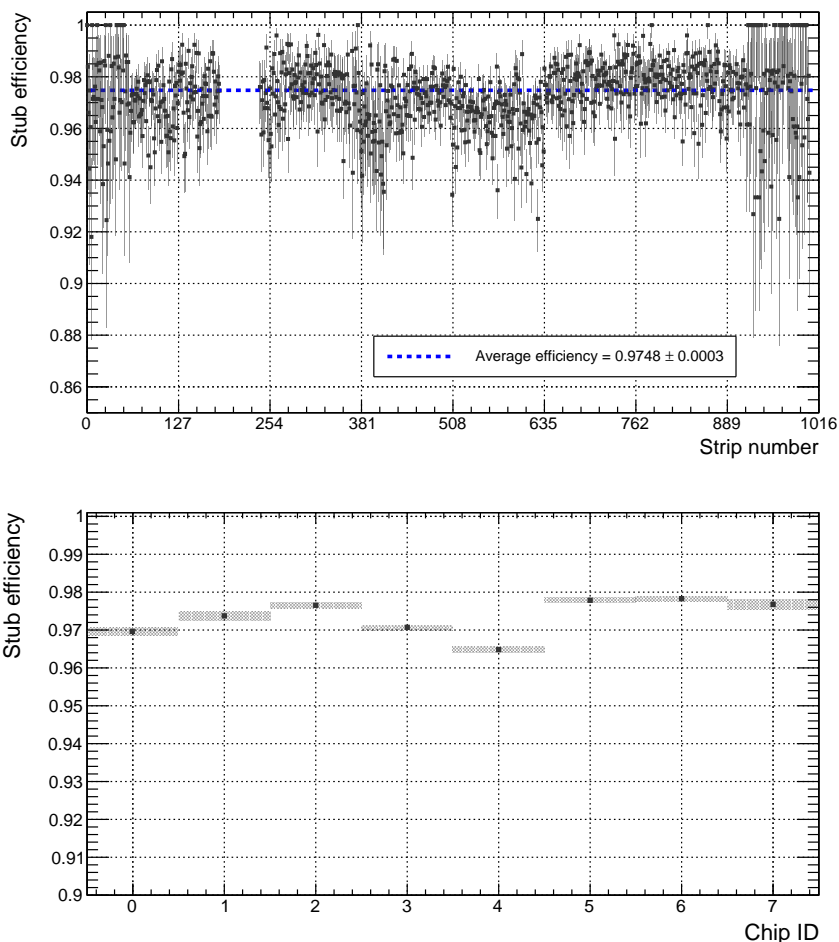


Figure 22. Stub efficiency of a full-size 2S module measured at the CERN beam test facility. The module was operated at a bias voltage of 250V and the V_{CTH} value was set to 115 DAC units. Top: stub efficiency per strip, bottom: stub efficiency per chip computed using data from strips scanned by the beam.

Acknowledgments

The tracker groups gratefully acknowledge financial support from the following funding agencies: BMWFW and FWF (Austria); FNRS and FWO (Belgium); CERN; MSE and CSF (Croatia); Academy of Finland, MEC, and HIP (Finland); CEA and CNRS/IN2P3 (France); BMBF, DFG, and HGF (Germany); GSRT (Greece); NKfIA K124850, and Bolyai Fellowship of the Hungarian Academy of Sciences (Hungary); DAE and DST (India); IPM (Iran); INFN (Italy); PAEC (Pakistan); SEIDI, CPAN, PCTI and FEDER (Spain); Swiss Funding Agencies (Switzerland); MST (Taipei); STFC (United Kingdom); DOE and NSF (U.S.A.). Individuals have received support from HFRI (Greece).

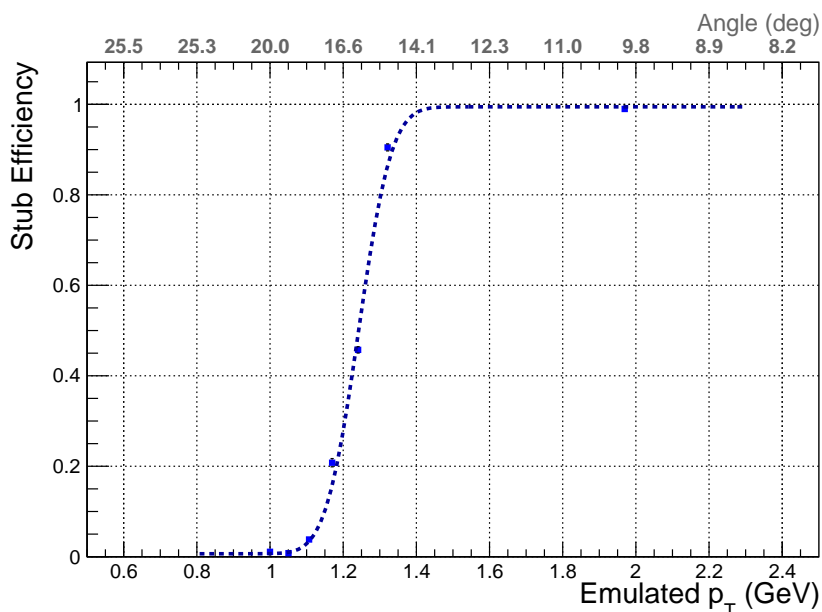


Figure 23. Stub efficiency of the full-size 2S module as a function of particle p_T measured at the Fermilab beam test facility during the angular scan. The module was operated at a bias voltage of 250 V and the V_{CTH} value was set to 92. A radius of 60 cm is used to convert the beam incident angle to effective p_T .

References

- [1] CMS collaboration, *The CMS experiment at the CERN LHC*, 2008 [JINST 3 S08004](#).
- [2] CMS collaboration, *Technical proposal for the phase-II upgrade of the CMS detector*, [CERN-LHCC-2015-010](#), CERN, Geneva, Switzerland (2015).
- [3] CMS collaboration, *The phase-2 upgrade of the CMS tracker*, [CERN-LHCC-2017-009](#), CERN, Geneva, Switzerland (2017).
- [4] CMS Tracker collaboration, *Test beam demonstration of silicon microstrip modules with transverse momentum discrimination for the future CMS tracking detector*, 2018 [JINST 13 P03003](#).
- [5] M. Raymond et al., *The CMS binary chip for microstrip tracker readout at the SLHC*, 2012 [JINST 7 C01033](#).
- [6] W. Ferguson et al., *The CBC microstrip readout chip for CMS at the high luminosity LHC*, 2012 [JINST 7 C08006](#).
- [7] D. Braga et al., *Characterization of the CBC2 readout ASIC for the CMS strip-tracker high-luminosity upgrade*, 2014 [JINST 9 C03001](#).
- [8] G. Hall et al., *CBC2: a CMS microstrip readout ASIC with logic for track-trigger modules at HL-LHC*, *Nucl. Instrum. Meth. A* **765** (2014) 214.
- [9] D. Braga et al., *CBC2: a microstrip readout ASIC with coincidence logic for trigger primitives at HL-LHC*, 2012 [JINST 7 C10003](#).
- [10] K. Klein et al., *Service hybrids for the silicon strip modules of the CMS phase-2 outer tracker upgrade*, [PoS\(TWEPP2018\)127](#) (2019).
- [11] T. Gadek, G. Blanchot, R. Gajanec, A. Honma and M.I. Kovacs, *Front-end hybrids for the strip-strip modules of the CMS outer tracker upgrade*, [PoS\(TWEPP2018\)019](#) (2019).

- [12] Irradiation center Karlsruhe, https://www.etp.kit.edu/english/irradiation_center.php.
- [13] H. Jansen et al., *Performance of the EUDET-type beam telescopes*, *EPJ Tech. Instrum.* **3** (2016) 7.
- [14] C. Hu-Guo et al., *First reticule size MAPS with digital output and integrated zero suppression for the EUDET-JRA1 beam telescope*, *Nucl. Instrum. Meth. A* **623** (2010) 480.
- [15] T. Obermann et al., *Implementation of a configurable FE-I4 trigger plane for the AIDA telescope*, 2014 *JINST* **9** C03035.
- [16] H. Jansen et al., *Performance of the EUDET-type beam telescopes*, *EPJ Tech. Instrum.* **3** (2016) 7 [[arXiv:1603.09669](https://arxiv.org/abs/1603.09669)].
- [17] D. Cussans, *A trigger/timing logic unit for ILC test-beams*, CERN-2007-007, CERN, Geneva, Switzerland (2007).
- [18] D. Cussans, *Description of the JRA1 Trigger Logic Unit (TLU)*, v0.2c, EUDET-Memo-2009-4, (2009).
- [19] V. Cerf and R. Kahn, *A protocol for packet network intercommunication*, *IEEE Trans. Commun.* **22** (1974) 637.
- [20] A. Bulgheroni, T. Klimkovich, P. Roloff and A. Zarnecki, *EUTelescope: tracking software*, Tech. Rep. EUDET-Memo-2007-20, (2007).
- [21] CMS collaboration, *CMS technical design report for the pixel detector upgrade*, CERN-LHCC-2012-016, CERN, Geneva, Switzerland (2012) [CMS-TDR-011] [FERMILAB-DESIGN-2012-02].
- [22] S. Kwan et al., *The pixel tracking telescope at the Fermilab test beam facility*, *Nucl. Instrum. Meth. A* **811** (2016) 162.
- [23] P. Vichoudis et al., *The Gigabit Link Interface Board (GLIB), a flexible system for the evaluation and use of GBT-based optical links*, 2010 *JINST* **5** C11007.
- [24] C. Ghabrous Larrea et al., *IPbus: a flexible Ethernet-based control system for xTCA hardware*, 2015 *JINST* **10** C02019.
- [25] M. Kozlovsky, *A TCP/IP transport layer for the DAQ of the CMS experiment*, *Nucl. Instrum. Meth. A* **534** (2004) 125.
- [26] C.D. Jones, M. Paterno, J. Kowalkowski, L. Sexton-Kennedy and W. Tanenbaum, *The new CMS event data model and framework*, Macmillan, India (2006).
- [27] M. Pesaresi et al., *The FC7 AMC for generic DAQ & control applications in CMS*, 2015 *JINST* **10** C03036.
- [28] G. Bauer et al., *The CMS event builder and storage system*, *J. Phys. Conf. Ser.* **219** (2010) 022038.
- [29] CMS collaboration, *CMS computing: technical design report*, CERN-LHCC-2005-023, CERN, Geneva, Switzerland (2005).
- [30] C. Grandi, D. Stickland, L. Taylor, A. Petrilli and A. Hervé, *CMS computing model: the “cms computing model RTAG”*, CMS-NOTE-2004-031, CERN, Geneva, Switzerland (2004).
- [31] R. Brun and F. Rademakers, *ROOT: an object oriented data analysis framework*, *Nucl. Instrum. Meth. A* **389** (1997) 81.
- [32] V. Blobel, *Software alignment for tracking detectors*, *Nucl. Instrum. Meth. A* **566** (2006) 5.
- [33] K. Rose, *Deterministic annealing for clustering, compression, classification, regression, and related optimization problems*, *Proc. IEEE* **86** (1998) 2210.
- [34] F. Didierjean, G. Duchêne and A. Lopez-Martens, *The deterministic annealing filter: a new clustering method for γ -ray tracking algorithms*, *Nucl. Instrum. Meth. A* **615** (2010) 188.
- [35] C. Kleinwort, *General broken lines as advanced track fitting method*, *Nucl. Instrum. Meth. A* **673** (2012) 107 [[arXiv:1201.4320](https://arxiv.org/abs/1201.4320)].

Tracker group of the CMS collaboration

Institut für Hochenergiephysik, Wien, Austria

W. Adam, T. Bergauer, D. Blöch, E. Brondolin¹, M. Dragicevic, R. Frühwirth², V. Hinger, H. Steininger

Universiteit Antwerpen, Antwerpen, Belgium

W. Beaumont, D. Di Croce, X. Janssen, J. Lauwers, P. Van Mechelen, N. Van Remortel

Vrije Universiteit Brussel, Brussel, Belgium

F. Blekman, S.S. Chhibra, J. De Clercq, J. D'Hondt, S. Lowette, I. Marchesini, S. Moortgat, Q. Python, K. Skovpen, E. Sørensen Bols, P. Van Mulders

Université Libre de Bruxelles, Bruxelles, Belgium

Y. Allard, D. Beghin, B. Bilin, H. Brun, B. Clerbaux, G. De Lentdecker, H. Delannoy, W. Deng, L. Favart, R. Goldouzian, A. Grebenyuk, A. Kalsi, J. Luetic, I. Makarenko, L. Moureaux, A. Popov, N. Postiau, F. Robert, Z. Song, L. Thomas, P. Vanlaer, D. Vannerom, Q. Wang, H. Wang, Y. Yang

Université Catholique de Louvain, Louvain-la-Neuve, Belgium

O. Bondu, G. Bruno, C. Caputo, P. David, C. Delaere, M. Delcourt, A. Giammanco, G. Krintiras, V. Lemaitre, A. Magitteri, K. Piotrkowski, A. Saggio, N. Szilasi, M. Vidal Marono, P. Vischia, J. Zobec

Institut Ruđer Bošković, Zagreb, Croatia

V. Brigljević, S. Ceci, D. Ferencsek, M. Roguljić, A. Starodumov³, T. Šuša

Department of Physics, University of Helsinki, Helsinki, Finland

P. Eerola, J. Heikkilä

Helsinki Institute of Physics, Helsinki, Finland

E. Brücken, T. Lampén, P. Luukka, L. Martikainen, E. Tuominen

Lappeenranta University of Technology, Lappeenranta, Finland

T. Tuuva

Université de Strasbourg, CNRS, IPHC UMR 7178, Strasbourg, France

J.-L. Agram⁴, J. Andrea, D. Bloch, C. Bonnin, G. Bourgatte, J.-M. Brom, E. Chabert, L. Charles, V. Cherepanov, E. Dangelser, D. Gelé, U. Goerlach, L. Gross, M. Krauth, N. Tonon

Université de Lyon, Université Claude Bernard Lyon 1, CNRS-IN2P3, Institut de Physique Nucléaire de Lyon, Villeurbanne, France

G. Baulieu, G. Boudoul, L. Caponetto, N. Chanon, D. Contardo, P. Dené, T. Dupasquier, G. Galbit, N. Lumb, L. Mirabito, B. Nodari, S. Perries, M. Vander Donckt, S. Viret

RWTH Aachen University, I. Physikalisches Institut, Aachen, Germany

C. Autermann, L. Feld, W. Karpinski, M.K. Kiesel, K. Klein, M. Lipinski, D. Meuser, A. Ostapchuk, A. Pauls, G. Pierschel, M. Preuten, M. Rauch, N. Röwert, S. Schael, J. Schulz, G. Schwering, M. Teroerde, M. Wlochal, V. Zhukov

RWTH Aachen University, III. Physikalisches Institut B, Aachen, Germany

C. Dziwok, G. Fluegge, T. Müller, O. Pooth, A. Stahl, T. Ziemons

Deutsches Elektronen-Synchrotron, Hamburg, Germany

M. Aldaya, C. Asawatrangkuldee, G. Eckerlin, D. Eckstein, T. Eichhorn, E. Gallo, M. Guthoff, M. Haranko, A. Harb, J. Keaveney, C. Kleinwort, R. Mankel, H. Maser, M. Meyer, M. Missiroli, C. Muhl, A. Mussgiller, D. Pitzl, O. Reichelt, M. Savitskyi, P. Schuetze, R. Stever, R. Walsh, A. Zuber

University of Hamburg, Hamburg, Germany

A. Benecke, H. Biskop, P. Buhmann, A. Ebrahimi, M. Eich, F. Feindt, A. Froehlich, E. Garutti, P. Gunnellini, J. Haller, A. Hinzmann, G. Kasieczka, R. Klanner, V. Kutzner, T. Lange, M. Matysek, M. Mrowietz, C. Niemeyer, Y. Nissan, K. Pena, A. Perieanu, O. Rieger, P. Schleper, J. Schwandt, D. Schwarz, J. Sonneveld, G. Steinbrück, A. Tews, B. Vormwald, J. Wellhausen, I. Zoi

Institut für Experimentelle Teilchenphysik, Karlsruhe, Germany

M. Abbas, L. Ardila, M. Balzer, C. Barth, T. Barvich, M. Baselga, T. Blank, F. Bögelspacher, E. Butz, M. Caselle, W. De Boer, A. Dierlamm, K. El Morabit, J.-O. Gosewisch, F. Hartmann, U. Husemann, R. Koppenhöfer, S. Kudella, S. Maier, S. Mallows, M. Metzler, Th. Muller, M. Neufeld, A. Nürnberg, O. Sander, D. Schell, M. Schröder, T. Schuh, I. Shvetsov, H.-J. Simonis, P. Steck, M. Wassmer, M. Weber, A. Weddigen

Institute of Nuclear and Particle Physics (INPP), NCSR Demokritos, Aghia Paraskevi, Greece

G. Anagnostou, P. Asenov, P. Assiouras, G. Daskalakis, A. Kyriakis, D. Loukas, L. Paspalaki

Wigner Research Centre for Physics, Budapest, Hungary

T. Balázs, F. Siklér, T. Vámi, V. Veszprémi

University of Delhi, Delhi, India

A. Bhardwaj, C. Jain, G. Jain, K. Ranjan

Saha Institute of Nuclear Physics, Kolkata, India

R. Bhattacharya, S. Dutta, S. Roy Chowdhury, G. Saha, S. Sarkar

INFN Sezione di Bari^a, Università di Bari^b, Politecnico di Bari^c, Bari, Italy

P. Cariola^a, D. Creanza^{a,c}, M. de Palma^{a,b}, G. De Robertis^a, L. Fiore^a, M. Ince^{a,b}, F. Loddo^a, G. Maggi^{a,c}, S. Martiradonna^a, M. Mongelli^a, S. My^{a,b}, G. Selvaggi^{a,b}, L. Silvestris^a

INFN Sezione di Catania^a, Università di Catania^b, Catania, Italy

S. Albergo^{a,b}, S. Costa^{a,b}, A. Di Mattia^a, R. Potenza^{a,b}, M.A. Saizu^{a,5}, A. Tricomi^{a,b}, C. Tuve^{a,b}

INFN Sezione di Firenze^a, Università di Firenze^b, Firenze, Italy

G. Barbagli^a, M. Brianzi^a, A. Cassese^a, R. Ceccarelli^{a,b}, R. Ciaranfi^a, V. Ciulli^{a,b}, C. Civinini^a, R. D'Alessandro^{a,b}, E. Focardi^{a,b}, G. Latino^{a,b}, P. Lenzi^{a,b}, M. Meschini^a, S. Paoletti^a, L. Russo^{a,b}, E. Scarlini^{a,b}, G. Sguazzoni^a, L. Viliani^{a,b}

INFN Sezione di Genova^a, Università di Genova^b, Genova, Italy

S. Cerchi^a, F. Ferro^a, R. Mulargia^{a,b}, E. Robutti^a

INFN Sezione di Milano-Bicocca^a, Università di Milano-Bicocca^b, Milano, Italy

F. Brivio^{a,b}, M.E. Dinardo^{a,b}, P. Dini^a, S. Gennai^a, L. Guzzi, S. Malvezzi^a, D. Menasce^a, L. Moroni^a, D. Pedrini^a, D. Zuolo^{a,b}

INFN Sezione di Padova^a, Università di Padova^b, Padova, Italy

P. Azzi^a, N. Bacchetta^a, D. Bisello^a, T. Dorigo^a, N. Pozzobon^{a,b}, M. Tosi^{a,b}

INFN Sezione di Pavia^a, Università di Bergamo^b, Bergamo, Italy

F. De Canio^{a,b}, L. Gaioni^{a,b}, M. Manghisoni^{a,b}, L. Ratti^a, V. Re^{a,b}, E. Riceputi^{a,b}, G. Traversi^{a,b}

INFN Sezione di Perugia^a, Università di Perugia^b, CNR-IOM Perugia^c, Perugia, Italy

G. Baldinelli^{a,b}, F. Bianchi^{a,b}, M. Biasini^{a,b}, G.M. Bilei^a, S. Bizzaglia^a, M. Caprai^a, C. Cecchi^{a,b}, B. Checcucci^a, D. Ciangottini^a, L. Fanò^{a,b}, L. Farnesini^a, M. Ionica^a, R. Leonardi^{a,b}, E. Manoni^a, G. Mantovani^{a,b}, V. Mariani^{a,b}, M. Menichelli^a, A. Morozzi^a, F. Moscatelli^{a,c}, D. Passeri^{a,b}, P. Placidi^{a,b}, A. Rossi^{a,b}, A. Santocchia^{a,b}, D. Spiga^a, L. Storchi^a, C. Turrioni^{a,b}

INFN Sezione di Pisa^a, Università di Pisa^b, Scuola Normale Superiore di Pisa^c, Pisa, Italy

K. Androsov^a, P. Azzurri^a, G. Bagliesi^a, A. Basti^a, R. Beccherle^a, V. Bertacchi^{a,c}, L. Bianchini^a, T. Boccali^a, L. Borrello^a, F. Bosi^a, R. Castaldi^a, M.A. Ciocci^{a,b}, R. Dell'Orso^a, G. Fedi^a, F. Fiori^{a,c}, L. Giannini^{a,c}, A. Giassi^a, M.T. Grippo^{a,b}, F. Ligabue^{a,c}, G. Magazzu^a, E. Manca^{a,c}, G. Mandorli^{a,c}, E. Mazzoni^a, A. Messineo^{a,b}, A. Moggi^a, F. Morsani^a, F. Palla^a, F. Palmonari^a, F. Raffaelli^a, A. Rizzi^{a,b}, P. Spagnolo^a, R. Tenchini^a, G. Tonelli^{a,b}, A. Venturi^a, P.G. Verdini^a

INFN Sezione di Torino^a, Università di Torino^b, Politecnico di Torino^c, Torino, Italy

R. Bellan^{a,b}, M. Costa^{a,b}, R. Covarelli^{a,b}, G. Dellacasa^a, N. Demaria^a, A. Di Salvo^{a,c}, G. Mazza^a, E. Migliore^{a,b}, E. Monteil^{a,b}, L. Pacher^a, A. Paterno^{a,c}, A. Rivetti^a, A. Solano^{a,b}

Instituto de Física de Cantabria (IFCA), CSIC-Universidad de Cantabria, Santander, Spain

E. Curras Rivera, J. Duarte Campderros, M. Fernandez, G. Gomez, F.J. Gonzalez Sanchez, R. Jaramillo Echeverria, D. Moya, E. Silva Jimenez, I. Vila, A.L. Virto

CERN, European Organization for Nuclear Research, Geneva, Switzerland

D. Abbaneo, I. Ahmed, B. Akgun, E. Albert, J. Bendotti, G. Berruti, G. Blanchot, F. Boyer, A. Caratelli, D. Ceresa, J. Christiansen, K. Cichy, J. Daguin, N. Deelen⁶, S. Detraz, D. Deyrail, N. Emriskova⁷, F. Faccio, A. Filenius, N. Frank, T. French, T. Gadek, R. Gajanec, A. Honma, G. Hugo, W. Hulek, L.M. Jara Casas, J. Kaplon, K. Kloukinas, A. Kornmayer, N. Koss, L. Kottelat, D. Koukola, M. Kovacs, A. La Rosa, P. Lenoir, R. Loos, A. Marchioro, S. Marconi, S. Mersi, S. Michelis, C. Nieto Martin, A. Onnela, S. Orfanelli, T. Pakulski, A. Perez, F. Perez Gomez, J.-F. Perrot, P. Petagna, Q. Piazza, H. Postema, T. Prousalidi, R. Puente Rico⁸, S. Scarf⁹, S. Spathopoulos, S. Sroka, P. Tropea, J. Troska, A. Tsiros, F. Vasey, P. Vichoudis

Paul Scherrer Institut, Villigen, Switzerland

W. Bertl[†], L. Caminada¹⁰, K. Deiters, W. Erdmann, R. Horisberger, H.-C. Kaestli, D. Kotlinski, U. Langenegger, B. Meier, T. Rohe, S. Streuli

Institute for Particle Physics, ETH Zurich, Zurich, Switzerland

F. Bachmair, M. Backhaus, R. Becker, P. Berger, D. di Calafiori, L. Djambazov, M. Donega, C. Grab, D. Hits, J. Hoss, W. Luster mann, M. Masciovecchio, M. Meinhard, V. Perovic, L. Perozzi, B. Ristic, U. Roeser, D. Ruini, V. Tavoraro, R. Wallny, D. Zhu

Universität Zürich, Zurich, Switzerland

T. Aarrestad, C. Amsler¹¹, K. Bösiger, F. Canelli, V. Chiochia, A. De Cosa, R. Del Burgo, C. Galloni, B. Kilminster, S. Leontsinis, R. Maier, G. Rauco, P. Robmann, Y. Takahashi, A. Zucchetta

National Taiwan University (NTU), Taipei, Taiwan

P.-H. Chen, W.-S. Hou, R.-S. Lu, M. Moya, J.F. Tsai

University of Bristol, Bristol, United Kingdom

D. Burns, E. Clement, D. Cussans, J. Goldstein, S. Seif El Nasr-Storey

Rutherford Appleton Laboratory, Didcot, United Kingdom

D. Braga¹², J.A. Coughlan, K. Harder, K. Manolopoulos, I.R. Tomalin

Imperial College, London, United Kingdom

G. Auzinger, R. Bainbridge, J. Borg, G. Hall, T. James, M. Pesaresi, S. Summers, K. Uchida

Brunel University, Uxbridge, United Kingdom

J. Cole, C. Hoad, P. Hobson, I.D. Reid

The Catholic University of America, Washington DC, U.S.A.

R. Bartek, A. Dominguez, R. Uniyal

Brown University, Providence, U.S.A.

G. Altopp, B. Burkle, C. Chen, X. Coubez, Y.-T. Duh, M. Hadley, U. Heintz, N. Hinton, J. Hogan¹³, A. Korotkov, J. Lee, M. Narain, S. Sagir¹⁴, E. Spencer, R. Syarif, V. Truong, E. Usai, J. Voelker

University of California, Davis, Davis, U.S.A.

M. Chertok, J. Conway, G. Funk, F. Jensen, R. Lander, S. Macaуда, D. Pellett, J. Thomson, R. Yohay¹⁵, F. Zhang

University of California, Riverside, Riverside, U.S.A.

G. Hanson, W. Si

University of California, San Diego, La Jolla, U.S.A.

R. Gerosa, S. Krutelyov, V. Sharma, A. Yagil, G. Zevi Della Porta

University of California, Santa Barbara - Department of Physics, Santa Barbara, U.S.A.

O. Colegrove, V. Dutta, L. Gouskos, J. Incandela, S. Kyre, H. Qu, M. Quinnan, D. White

University of Colorado Boulder, Boulder, U.S.A.

J.P. Cumalat, W.T. Ford, E. MacDonald, A. Perloff, K. Stenson, K.A. Ulmer, S.R. Wagner

Cornell University, Ithaca, U.S.A.

J. Alexander, Y. Cheng, J. Chu, J. Conway, D. Cranshaw, A. Datta, K. McDermott, J. Monroy, Y. Bordlemay Padilla, D. Quach, A. Rinkevicius, A. Ryd, L. Skinnari, L. Soffi, C. Strohmaan, Z. Tao, J. Thom, J. Tucker, P. Wittich, M. Zientek

Fermi National Accelerator Laboratory, Batavia, U.S.A.

A. Apresyan, A. Bakshi, G. Bolla[†], K. Burkett, J.N. Butler, A. Canepa, H.W.K. Cheung, J. Chramowicz, G. Derylo, A. Ghosh, C. Gingu, H. Gonzalez, S. Grünendahl, S. Hasegawa, J. Hoff, S.Y. Hoh, Z. Hu, S. Jindariani, M. Johnson, C.M. Lei, R. Lipton, M. Liu, T. Liu, S. Los, M. Matulik, P. Merkel, S. Nahn, J. Olsen, A. Prosser, F. Ravera, L. Ristori, R. Rivera, B. Schneider, W.J. Spalding, L. Spiegel, S. Timpone, N. Tran, L. Uplegger, C. Vernieri, E. Voirin, H.A. Weber

University of Illinois at Chicago (UIC), Chicago, U.S.A.

D.R. Berry, X. Chen, S. Dittmer, A. Evdokimov, O. Evdokimov, C.E. Gerber, D.J. Hofman, C. Mills

The University of Iowa, Iowa City, U.S.A.

M. Alhusseini, S. Durgut, J. Nachtman, Y. Onel, C. Rude, C. Snyder, K. Yi¹⁶

Johns Hopkins University, Baltimore, U.S.A.

N. Eminizer, A. Gritsan, P. Maksimovic, J. Roskes, M. Swartz, M. Xiao

The University of Kansas, Lawrence, U.S.A.

P. Baringer, A. Bean, S. Khalil, A. Kropivnitskaya, D. Majumder, E. Schmitz, G. Wilson

Kansas State University, Manhattan, U.S.A.

A. Ivanov, R. Mendis, T. Mitchell, A. Modak, R. Taylor

University of Mississippi, Oxford, U.S.A.

J.G. Acosta, L.M. Cremaldi, S. Oliveros, L. Perera, D. Summers

University of Nebraska-Lincoln, Lincoln, U.S.A.

K. Bloom, D.R. Claes, C. Fangmeier, F. Golf, I. Kravchenko, J. Siado

State University of New York at Buffalo, Buffalo, U.S.A.

C. Harrington, I. Iashvili, A. Kharchilava, D. Nguyen, A. Parker, S. Rappoccio, B. Roozbahani

Northwestern University, Evanston, U.S.A.

K. Hahn, Y. Liu, K. Sung

The Ohio State University, Columbus, U.S.A.

J. Alimena, B. Cardwell, B. Francis, C.S. Hill

University of Puerto Rico, Mayaguez, U.S.A.

S. Malik, S. Norberg, J.E. Ramirez Vargas

Purdue University, West Lafayette, U.S.A.

S. Das, M. Jones, A. Jung, A. Khatiwada, G. Negro, J. Thieman

Purdue University Northwest, Hammond, U.S.A.

T. Cheng, J. Dolen, N. Parashar

Rice University, Houston, U.S.A.

K.M. Ecklund, S. Freed, M. Kilpatrick, T. Nussbaum

University of Rochester, Rochester, U.S.A.

R. Demina, J. Dulemba, O. Hindrichs

Rutgers, The State University of New Jersey, Piscataway, U.S.A.

E. Bartz, A. Gandrakotra, Y. Gershtein, E. Halkiadakis, A. Hart, S. Kyriacou, A. Lath, K. Nash, M. Osherson, S. Schnetzer, R. Stone

Texas A&M University, College Station, U.S.A.

R. Eusebi

Vanderbilt University, Nashville, U.S.A.

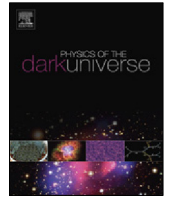
P. D'Angelo, W. Johns, K.O. Padeken

Wayne State University, Detroit, U.S.A.

R. Harr, N. Poudyal

†: Deceased

- 1: Now at CERN, European Organization for Nuclear Research, Geneva, Switzerland
- 2: Also at Vienna University of Technology, Vienna, Austria
- 3: Also at Institute for Theoretical and Experimental Physics, Moscow, Russia
- 4: Also at Université de Haute-Alsace, Mulhouse, France
- 5: Also at Horia Hulubei National Institute of Physics and Nuclear Engineering (IFIN-HH), Bucharest, Romania
- 6: Also at Institut für Experimentelle Kernphysik, Karlsruhe, Germany
- 7: Also at Université de Strasbourg, CNRS, IPHC UMR 7178, Strasbourg, France
- 8: Also at Instituto de Física de Cantabria (IFCA), CSIC-Universidad de Cantabria, Santander, Spain
- 9: Also at École Polytechnique Fédérale de Lausanne, Lausanne, Switzerland
- 10: Also at Universität Zürich, Zurich, Switzerland
- 11: Also at Albert Einstein Center for Fundamental Physics, Bern, Switzerland
- 12: Also at Imperial College, London, United Kingdom
- 13: Now at Bethel University, St. Paul, Minnesota, U.S.A.
- 14: Now at Karamanoglu Mehmetbey University, Karaman, Turkey
- 15: Now at Florida State University, Tallahassee, U.S.A.
- 16: Also at Nanjing Normal University, Nanjing, China



Dark Matter benchmark models for early LHC Run-2 Searches: Report of the ATLAS/CMS Dark Matter Forum

Daniel Abercrombie¹, Nural Akchurin², Ece Akilli³, Juan Alcaraz Maestre⁴, Brandon Allen¹, Barbara Alvarez Gonzalez^{5,a}, Jeremy Andrea¹⁷, Alexandre Arbey^{6,7}, Georges Azuelos⁸, Patrizia Azzi⁹, Mihailo Backović⁵², Yang Bai¹⁰, Swagato Banerjee^{10,b}, James Beacham^{11,c}, Alexander Belyaev¹², Antonio Boveia^{11,*;d,e}, Amelia Jean Brennan¹³, Oliver Buchmueller¹⁴, Matthew R. Buckley¹⁵, Giorgio Busoni^{16,f}, Michael Buttignol¹⁷, Giacomo Cacciapaglia²⁵, Regina Caputo¹⁸, Linda Carpenter¹¹, Nuno Filipe Castro¹⁹, Guillermo Gomez Ceballos¹, Yangyang Cheng^{20,g}, John Paul Chou²¹, Arely Cortes Gonzalez^{22,h}, Chris Cowden², Francesco D'Eramo^{23,i}, Annapaola De Cosa²⁴, Michele De Gruttola⁵, Albert De Roeck⁵, Andrea De Simone¹⁶, Aldo Deandrea²⁵, Zeynep Demiragli^{1,j}, Anthony DiFranzo^{26,k}, Caterina Doglioni^{27,d}, Tristan du Pree^{5,l}, Robin Erbacher²⁸, Johannes Erdmann²⁹, Cora Fischer²², Henning Flaecher³⁰, Patrick J. Fox³¹, Benjamin Fuks^{32,m}, Marie-Helene Genest³³, Bhawna Gomber^{10,n}, Andreas Goudelis^{34,m}, Johanna Gramling^{35,o}, John Gunion²⁸, Kristian Hahn³⁶, Ulrich Haisch^{37,p}, Roni Harnik³⁸, Philip C. Harris^{5,q}, Kerstin Hoepfner⁴⁶, Siew Yan Hoh³⁹, Dylan George Hsu¹, Shih-Chieh Hsu⁸⁹, Yutaro Iiyama¹, Valerio Ippolito^{40,r}, Thomas Jacques^{41,s}, Xiangyang Ju^{10,t}, Felix Kahlhoefer^{42,u}, Alexis Kalogeropoulos^{42,v}, Laser Seymour Kaplan¹⁰, Lashkar Kashif¹⁰, Valentin V. Khoze⁴³, Raman Khurana^{44,w}, Khristian Kotov^{11,x}, Dmytro Kovalskiy¹, Suchita Kulkarni^{45,y}, Shuichi Kunori^{2,z}

* Corresponding author.

E-mail address: boveia.1@osu.edu (A. Boveia).

^a Now at Oviedo U.

^b Now at Louisville U.

^c Now at Duke U.

^d Forum organizer and editor.

^e Previously at CERN

^f Now at Heidelberg U., Max Planck Inst.

^g Now at Cornell U.

^h Now at CERN.

ⁱ Now at INFN Padua.

^j Now at Boston U.

^k Now at Rutgers U.

^l Now at NIKHEF.

^m Now at Paris LPTHE.

ⁿ Now at Hyderabad U.

^o Now at UC Irvine.

^p Now at Munich MPI.

^q Now at MIT.

^r Now at INFN Rome.

^s Now at SISSA Trieste.

^t Now at LBL.

^u Now at RWTH Aachen.

^v Now at Princeton U.

^w Now at Delhi U.

^x Now at Florida U.

^y Editor.

^z Now at Maryland U.

<https://doi.org/10.1016/j.dark.2019.100371>

2212-6864/© 2019 The Authors. Published by Elsevier B.V. This is an open access article under the CC BY license (<http://creativecommons.org/licenses/by/4.0/>).

Viktor Kutzner⁴⁶, Hyun Min Lee⁴⁷, Sung-Won Lee², Seng Pei Liew⁴⁸, Tongyan Lin^{49,aa}, Steven Lowette^{50,d}, Romain Madar⁵¹, Sarah Malik^{14,d}, Fabio Maltoni⁵², Mario Martinez Perez²², Olivier Mattelaer^{53,ab}, Kentarou Mawatari^{54,ac}, Christopher McCabe^{55,ad}, Théo Megy^{56,ae}, Enrico Morgante^{41,af}, Stephen Mrenna^{57,d}, Chang-Seong Moon^{58,ag}, Siddharth M. Narayanan¹, Andy Nelson⁵⁹, Sérgio F. Novaes⁶⁰, Klaas Ole Padeken^{61,ah}, Priscilla Pani^{62,y,af}, Michele Papucci⁶³, Manfred Paulini⁶⁴, Christoph Paus¹, Jacopo Pazzini⁹⁶, Björn Penning^{14,ai}, Michael E. Peskin⁶⁵, Deborah Pinna^{24,j}, Massimiliano Procura⁶⁶, Shamona F. Qazi⁶⁷, Davide Racco^{41,aj}, Emanuele Re^{68,ak}, Antonio Riotto⁴¹, Thomas G. Rizzo⁶⁹, Rainer Roehrig⁷⁰, David Salek^{71,y}, Arturo Sanchez Pineda^{72,h}, Subir Sarkar^{73,74}, Alexander Schmidt^{75,al}, Steven Randolph Schramm³, William Shepherd^{76,77,am}, Gurpreet Singh⁷⁸, Livia Soffi⁷⁹, Norraphat Srimanobhas⁸⁰, Kevin Sung^{81,q}, Tim M.P. Tait⁸², Timothee Theveneaux-Pelzer^{83,af}, Marc Thomas⁸⁴, Mia Tosi⁸⁵, Daniele Trocino^{86,an}, Sonaina Undleeb², Alessandro Vichi^{7,ao}, Fuquan Wang¹⁰, Lian-Tao Wang⁸⁷, Ren-Jie Wang^{88,ap}, Nikola Whallon⁸⁹, Steven Worm^{90,aq}, Mengqing Wu^{91,ar}, Sau Lan Wu¹⁰, Hongtao Yang¹⁰, Yong Yang^{92,as}, Shin-Shan Yu⁹³, Bryan Zaldivar^{94,at}, Marco Zanetti⁹⁶, Zhiqing Zhang⁹⁵, Alberto Zucchetta^{96,au}

¹ MIT, USA

² Texas Tech University, USA

³ Université de Genève, DPNC, Switzerland

⁴ Centro de Investigaciones Energéticas Medioambientales y Tecnológicas (CIEMAT), Spain

⁵ CERN, Switzerland

⁶ Université de Lyon and Centre de Recherche Astrophysique de Lyon, CNRS and Ecole Normale Supérieure de Lyon, France

⁷ CERN Theory Division, Switzerland

⁸ University of Montreal and TRIUMF, Canada

⁹ INFN Padova, Italy

¹⁰ University of Wisconsin-Madison, USA

¹¹ Ohio State University, USA

¹² Rutherford Appleton Laboratory and University of Southampton, United Kingdom

¹³ The University of Melbourne, Australia

¹⁴ Imperial College London, United Kingdom

¹⁵ Department of Physics and Astronomy, Rutgers University, USA

¹⁶ SISSA and INFN, Sezione di Trieste, Italy

¹⁷ Institut Pluridisciplinaire Hubert Curien/Département Recherches Subatomiques, Université de Strasbourg/CNRS-IN2P3, France

¹⁸ Santa Cruz Institute for Particle Physics, Department of Physics and Department of Astronomy and Astrophysics, University of California at Santa Cruz, USA

¹⁹ LIP-Minho, Braga, and Departamento de Física e Astronomia, Faculdade de Ciências da Universidade do Porto, Portugal

²⁰ University of Chicago, USA

²¹ Rutgers University, USA

²² IFAE Barcelona, Spain

²³ University of California and LBNL, Berkeley, USA

²⁴ University of Zurich, Switzerland

²⁵ Université de Lyon and Université Lyon 1, CNRS/IN2P3, UMR5822, IPNL, France

²⁶ Department of Physics and Astronomy, University of California, Irvine and Theoretical Physics Department, Fermilab, USA

²⁷ Lund University, Sweden

aa Now at San Diego U.

ab Now at Louvain CP3.

ac Now at Osaka U.

ad Now at King's College London.

ae Now at Freiburg U.

af Now at DESY.

ag Now at Kyungpook Natl. U.

ah Now at Vanderbilt U.

ai Now at Brandeis U.

aj Now at Perimeter.

ak Now Annecy LAPTH.

al Now at RWTH Aachen U.

am Now at Mainz U.

an Now at U. Gent.

ao Now at LPHE Lausanne.

ap Now at Mainz.

aq Now at Birmingham U.

ar Now at Beijing IHEP.

as Now at Shanghai Jiao Tong U.

at Now at LAPTh.

au Now at Zurich. U.

- ²⁸ University of California, Davis, USA
²⁹ Institut für Experimentelle Physik IV, Technische Universität Dortmund, Germany
³⁰ H.H. Wills Physics Laboratory, University of Bristol, United Kingdom
³¹ Fermilab, USA
³² Institut Pluridisciplinaire Hubert Curien/Département Recherches Subatomiques, Université de Strasbourg/CNRS-IN2P3, France
³³ LPSC, Université Grenoble-Alpes, CNRS/IN2P3, France
³⁴ Institut für Hochenergiephysik, Österreichische Akademie der Wissenschaften, Austria
³⁵ Université de Genève, DPNC, Switzerland
³⁶ Northwestern University, USA
³⁷ Rudolf Peierls Centre for Theoretical Physics, University of Oxford, United Kingdom
³⁸ Theoretical Physics Department, Fermilab, USA
³⁹ National Centre for Particle Physics, Universiti Malaya, Malaysia
⁴⁰ Laboratory for Particle Physics and Cosmology, Harvard University, USA
⁴¹ Department of Theoretical Physics, University of Geneva, Switzerland
⁴² Deutsches Elektronen-Synchrotron (DESY), Germany
⁴³ Institute of Particle Physics Phenomenology, Durham University, United Kingdom
⁴⁴ National Central University, Taiwan
⁴⁵ Institut für Hochenergiephysik, Österreichische Akademie der Wissenschaften, Austria
⁴⁶ RWTH Aachen University, III. Physikalisches Institut A, Germany
⁴⁷ Department of Physics, Chung-Ang University, Korea
⁴⁸ Department of Physics, University of Tokyo, Japan
⁴⁹ Kavli Institute for Cosmological Physics, University of Chicago, USA
⁵⁰ Vrije Universiteit Brussel - IIHE, Belgium
⁵¹ Laboratoire de Physique Corpusculaire, Clermont-Ferrand, France
⁵² Centre for Cosmology, Particle Physics and Phenomenology (CP3), Université catholique de Louvain, Belgium
⁵³ IPPP Durham, United Kingdom
⁵⁴ Theoretische Natuurkunde and IIHE/ELEM, Vrije Universiteit Brussel, and International Solvay Institutes, Belgium
⁵⁵ GRAPPA, University of Amsterdam, Netherlands
⁵⁶ Laboratoire de Physique Corpusculaire, Clermont-Ferrand, France
⁵⁷ FNAL, USA
⁵⁸ Universidade Estadual Paulista, Brazil
⁵⁹ University of California, Irvine, USA
⁶⁰ Universidade Estadual Paulista, Brazil
⁶¹ RWTH Aachen University, III. Physikalisches Institut A, Aachen, Germany
⁶² Stockholm University, Sweden
⁶³ Theoretical Physics Group, Lawrence Berkeley National Laboratory, and Berkeley Center for Theoretical Physics, University of California, Berkeley, USA
⁶⁴ Carnegie Mellon University, USA
⁶⁵ SLAC, Stanford University, USA
⁶⁶ Universität Wien, Austria
⁶⁷ National Centre for Physics, Quaid-i-Azam University, Pakistan
⁶⁸ Rudolf Peierls Centre for Theoretical Physics, University of Oxford, United Kingdom
⁶⁹ SLAC, USA
⁷⁰ Max-Planck-Institut fuer Physik, Germany
⁷¹ Nikhef and GRAPPA, Netherlands
⁷² INFN Sezione di Napoli, and Dipartimento di Fisica, Università di Napoli, Italy
⁷³ Rudolf Peierls Centre for Theoretical Physics, University of Oxford, United Kingdom
⁷⁴ Niels Bohr Institute, Copenhagen, Denmark
⁷⁵ University of Hamburg, Germany
⁷⁶ University of California Santa Cruz Department of Physics and Santa Cruz Institute for Particle Physics, USA
⁷⁷ Niels Bohr International Academy, University of Copenhagen, Denmark
⁷⁸ Chulalongkorn University, Thailand
⁷⁹ Cornell University, USA
⁸⁰ Chulalongkorn University, Faculty of Science, Department of Physics, Thailand
⁸¹ Northwestern University, USA
⁸² Department of Physics and Astronomy, University of California, Irvine, USA
⁸³ Laboratoire de Physique Corpusculaire, Clermont Université and Université Blaise Pascal and CNRS/IN2P3, Clermont-Ferrand, France
⁸⁴ Southampton University, United Kingdom
⁸⁵ University of Padova and INFN, Italy
⁸⁶ Northeastern University, Boston, USA
⁸⁷ Enrico Fermi Institute and Department of Physics and Kavli Institute for Cosmological Physics, University of Chicago, USA
⁸⁸ Department of Physics, Northeastern University, USA
⁸⁹ Physics, University of Washington, Seattle, USA
⁹⁰ Particle Physics Department, Rutherford Appleton Laboratory, United Kingdom
⁹¹ Laboratoire de Physique Subatomique et de Cosmologie, Université Grenoble-Alpes, CNRS/IN2P3, France
⁹² Universität Zurich, Switzerland
⁹³ National Central University, Taiwan
⁹⁴ Université Libre de Bruxelles, Belgium
⁹⁵ Laboratoire de l'Accélérateur Linéaire, University Paris-Sud 11 et IN2P3/CNRS, France
⁹⁶ Università di Padova, Italy

ARTICLE INFO

ABSTRACT

This document is the final report of the ATLAS-CMS Dark Matter Forum, a forum organized by the ATLAS and CMS collaborations with the participation of experts on theories of Dark Matter, to select a minimal basis set of dark matter simplified models that should support the design of the early LHC Run-2 searches. A prioritized, compact set of benchmark models is proposed, accompanied by studies

Article history:
Received 10 July 2019
Accepted 19 August 2019

Keywords:
Dark Matter
Simplified models
EFT
LHC

of the parameter space of these models and a repository of generator implementations. This report also addresses how to apply the Effective Field Theory formalism for collider searches and present the results of such interpretations.

© 2019 The Authors. Published by Elsevier B.V. This is an open access article under the CC BY license (<http://creativecommons.org/licenses/by/4.0/>).

1. Introduction

Dark matter (DM)¹ has not yet been observed in particle physics experiments, and there is not yet any evidence for non-gravitational interactions between DM and the Standard Model (SM) particles. If such interactions exist, particles of DM could be produced at the LHC. Since DM particles themselves do not produce signals in the LHC detectors, one way to observe them is when they are produced in association with a visible SM particle $X(=g, q, \gamma, Z, W, \text{ or } h)$. Such reactions, which are observed at colliders as particles or jets recoiling against an invisible state, are called “mono- X ” or \cancel{E}_T+X reactions (see e.g Refs. [1–5]), where \cancel{E}_T is the missing transverse momentum observable in the detector.

Early Tevatron and LHC Run-1 searches for \cancel{E}_T+X signatures at CDF [6], ATLAS [7–14] and CMS [15–21], employed a basis of contact interaction operators in effective field theories (EFTs) [22,23] to calculate the possible signals. These EFTs assume that production of DM takes place through a contact interaction involving a quark–antiquark pair, or two gluons, and two DM particles. In this case, the missing energy distribution of the signal is determined by the nature and the mass of the DM particles and the Lorentz structure of the interaction. Only the overall production rate is a free parameter to be constrained or measured. Provided that the contact interaction approximation holds, these EFTs provide a straightforward way to compare the results from different collider searches with non-collider searches for DM.

The EFT describes the case when the mediator of the interaction between SM and DM particles are very heavy; if this is not the case, models that explicitly include these mediators are needed [5,22,24,24–28]. Some “simplified models” [29–31] of DM production were constructed, including particles and interactions beyond the SM. These models can be used consistently at LHC energies, and provide an extension to the EFT approach. Many proposals for such models have emerged (see, for example Refs. [32–48]). At the LHC, the kinematics of mono- X reactions occurring via a TeV-scale mediator can differ substantially from the prediction of the contact interaction. The mediator may also produce qualitatively different signals, such as decays back into the SM particles. Thus, appropriate simplified models are an important component of the design, optimization, and interpretation of DM searches at ATLAS and CMS. This has already been recognized in the CDF, ATLAS and CMS searches quoted above, where both EFT and selected simplified model results are presented.

1.1. The ATLAS/CMS dark matter forum

To understand what signal models should be considered for the upcoming LHC Run-2, groups of experimenters from both ATLAS and CMS collaborations have held separate meetings with small groups of theorists, and discussed further at the DM@LHC

workshop [39,40,49]. These discussions identified overlapping sets of simplified models as possible benchmarks for early LHC Run-2 searches. Following the DM@LHC workshop, ATLAS and CMS organized a forum, called the *ATLAS-CMS Dark Matter Forum*, to form a consensus on the use of these simplified models and EFTs for early Run-2 searches with the participation of experts on theories of DM. This is the final report of the ATLAS-CMS Dark Matter Forum.

One of the guiding principles of this report is to channel the efforts of the ATLAS and CMS collaborations towards a minimal basis of dark matter models that should influence the design of the early Run-2 searches. At the same time, a thorough survey of realistic collider signals of DM is a crucial input to the overall design of the search program.

The goal of this report is such a survey, though confined within some broad assumptions and focused on benchmarks for kinematically-distinct signals which are most urgently needed. As far as time and resources have allowed, the assumptions have been carefully motivated by theoretical consensus and comparisons of simulations. But, to achieve such a consensus in only a few months before the start of Run-2, it was important to restrict the scope and timescale to the following:

1. The forum should propose a prioritized, compact set of benchmark simplified models that should be agreed upon by both collaborations for Run-2 searches. The values for the scan on the parameters of the models for which experimental results are provided should be specified, to facilitate theory reinterpretation beyond the necessary model-independent limits that should be provided by all LHC DM searches.
2. The forum should recommend the use of the state of the art calculations for these benchmark models. Such a recommendation will aid the standardization the event generator implementation of the simplified models and the harmonization of other common technical details as far as practical for early Run-2 LHC analyses. It would be desirable to have a common choice of leading order (LO) and next-to-leading order (NLO) matrix elements corresponding to the state of the art calculations, parton shower (PS) matching and merging, factorization and renormalization scales for each of the simplified models. This will also lead to a common set of theory uncertainties, which will facilitate the comparison of results between the two collaborations.
3. The forum should discuss how to apply the EFT formalism and present the results of EFT interpretations.
4. The forum should prepare a report summarizing these items, suitable both as a reference for the internal ATLAS and CMS audiences and as an explanation of early Run-2 LHC benchmark models for theory and non-collider readers. This report represents the views of its endorers, as participants of the forum.

This document constitutes the basis for further recommendations from the LHC Dark Matter Working Group [50–52].

¹ Many theories of physics beyond the Standard Model predict the existence of stable, neutral, weakly-interacting and massive particles that are putative DM candidates. In the following, we refer to such matter as DM, even though the observation of such matter at a collider could only establish that it is neutral, weakly-interactive, massive and stable on the distance-scales of tens of meters.

1.2. Grounding assumptions

We assume that interactions exist between the SM hadrons and the particles that constitute cosmological DM. If this is not the case, then proton collisions will not directly produce DM particles, and DM will not scatter off nuclei in direct detection experiments.

The DM itself is assumed to be a single particle, a Dirac fermion WIMP, stable on collider timescales and non-interacting with the detector. The former assumption is reductionistic. The rich particle content of the SM is circumstantial evidence that the DM sector, which constitutes five times as much of the mass of the universe, may be more complex than a single particle or a single interaction. But, as was often the case in the discoveries of the SM, here only one mediator and one search channel might play a dominant role in the opening stages of an LHC discovery. The latter assumption focuses our work on early LHC searches, where small kinematic differences between models will not matter in a discovery scenario, and with the imminent re-start of the LHC our report relies heavily on a large body of existing theoretical work which assumed Dirac fermionic DM.

Different spins of DM particles will typically give similar results. Exceptions exist: For example, the choice of Majorana fermions forbids some processes that are allowed for Dirac fermions [22]. Aside from these, adjusting the choice of Dirac or Majorana fermions or scalars will produce only minor changes in the kinematic distributions of the visible particle and is expected to have little effect on cut-and-count² analysis. Thus the choice of Dirac fermion DM should be sufficient as benchmarks for the upcoming Run-2 searches.

One advantage of collider experiments lies in their ability to study and possibly characterize the mediator. A discovery of an anomalous \cancel{E}_T signature at the LHC would not uniquely imply discovery of dark matter, while at the same time e.g. discovery of an anomalous and annually-modulated signal in a direct-detection experiment would leave unanswered many questions about the nature of the interaction that could be resolved by the simultaneous discovery of a new mediator particle. Collider, direct, and indirect detection searches provide complementary ways to approach this problem [53], and it is in this spirit that much of our focus is on the mediator.

We systematically explore the basic possibilities for mediators of various possible spins and couplings. All models considered are assumed to produce a signature with pairs of DM particles. Though more varied and interesting possibilities are added to the literature almost daily, these basic building blocks account for much of the physics studied at hadron colliders in the past three decades.

We also assume that Minimal Flavor Violation (MFV) [54–57] applies to the models included in this report. This means that the flavor structure of the couplings between DM and ordinary particles follows the same structure as the SM. This choice is simple, since no additional theory of flavor is required, beyond what is already present in the SM, and it provides a mechanism to ensure that the models do not violate flavor constraints. As a consequence, spin-0 resonances must have couplings to fermions proportional to the SM Higgs couplings. Flavor-safe models can still be constructed beyond the MFV assumption, for example [58], and deserve further study. For a discussion of MFV in the context of the simplified models included in this report, see Ref. [49].

In the parameter scan for the models considered in this report, we make the assumption of a minimal decay width for the particles mediating the interaction between SM and DM. This means that only decays strictly necessary for the self-consistency of the model (e.g. to DM and to quarks) are accounted for in the definition of the mediator width. We forbid any further decays to other invisible particles of the Dark Sector that may increase the width or produce striking, visible signatures. Studies within this report show that, for cut-and-count analyses, the kinematic distributions of many models, and therefore the sensitivity of these searches, do not depend significantly on the mediator width, as long as the width remains smaller than the mass of the particle and that narrow mediators are sufficiently light.

The particle content of the models chosen as benchmarks is limited to one single kind of DM whose self-interactions are not relevant for LHC phenomenology, and to one type of SM/DM interaction at a time. These assumptions only add a limited number of new particles and new interactions to the SM. These simplified models, independently explored by different experimental analyses, can be used as starting points to build more complete theories. Even though this factorized picture does not always lead to full theories and leaves out details that are necessary for the self-consistency of single models (e.g. the mass generation for mediator particles), it is a starting point to prepare a set of distinct but complementary collider searches for DM, as it leads to benchmarks that are easily comparable across channels.

1.3. Choices of benchmarks considered in this report and parameter scans

Contact interaction operators have been outlined as basis set of theoretical building blocks representing possible types of interactions between SM and DM particles in [23]. The approach followed by LHC searches (see e.g. Refs. [7,15] for recent jet+ \cancel{E}_T Run-1 searches with the 8 TeV dataset) so far has been to simulate only a prioritized set of the possible operators with distinct kinematics for the interpretation of the constraints obtained, and provide results that may be reinterpreted in terms of the other operators. This report intends to follow this strategy, firstly focusing on simplified models that allow the exploration of scenarios where the mediating scale is not as large. In the limit of large mediator mass, the simplified models map onto the EFT operators. Secondly, this report considers specific EFT benchmarks whenever neither a simplified model completion nor other simplified models yielding similar kinematic distributions are available and implemented in one of the event generators used by both collaborations. This is the case for dimension-5 or dimension-7 operators with direct DM-electroweak boson couplings.³ Considering these models as separate experimental benchmarks will allow to target new signal regions and help validate the contact interaction limit of new simplified models developed to complete these specific operators. Results from these EFT benchmarks should include the condition that the momentum transfer does not probe the scale of the interaction; whenever there is no model that allows a direct mapping between these two quantities, various options should be tested to ensure a given fraction of events within the range of applicability of the EFT approach. Experimental searches should in any case deliver results that are independent from the specific benchmark tested, such as fiducial cross-sections that are excluded in a given signal region.

When choosing the points to be scanned in the parameter space of the models, this report does not quantitatively consider

² Cut-and-count refers to an analysis that applies a certain event selection and checks the inclusive number of events which pass. This is to be contrasted with a shape analysis, which compares the distribution of events.

³ An example of a dimension-5 operator for scalar DM is described in Appendix A. Dimension-7 operators of DM coupling to gauge bosons exist in the literature, but they require a larger particle spectrum with respect to the models studied in this report.

constraints that are external to the MET+X analyses. This is the case also for results from LHC experiments searching for mediator decays. The main reason for not doing so in this report is the difficulty of incorporating these constraints in a rigorous quantitative way within the timescale of the Forum. However, even if the parameter scans and the searches are not optimized with those constraints in mind, we intend to make all information available to the community to exploit the unique sensitivity of colliders to all possible DM signatures.

1.4. Structure of this report and dissemination of results

The report provides a brief theoretical summary of the models considered, starting from the set of simplified models and contact interactions put forward in previous discussions and in the literature cited above. Its main body documents the studies done within this Forum to identify a kinematically distinct set of model parameters to be simulated and used as benchmarks for early Run-2 searches. The implementation of these studies according to the state of the art calculations is detailed, including instructions on how to estimate theoretical uncertainties in the generators used for these studies. The presentation of results for EFT benchmarks is also covered.

Section 2 of this report is dedicated to simplified models with radiation of a hard object either from the initial state or from the mediator. These models produce primarily monojet signatures, but should be considered for all \cancel{E}_T+X searches. Section 3 contains studies on the benchmark models for final states specifically containing an electroweak boson ($W/Z/\gamma/H$). In this case, both simplified models leading to mono-boson signatures and contact interaction operators are considered. Details of the state of the art calculations and on the implementation of the simplified models in Monte Carlo generators are provided in Section 4. Section 5 is devoted to the treatment of the presentation of results for the benchmark models from contact interaction operators. Section 6 prescribes how to estimate theoretical uncertainties on the simulation of these models. Section 7 concludes the report.

Further models that could be studied beyond early searches and their implementation are described in Appendix A. For these models, either the implementation could not be fully developed by the time of this report, or some of the grounding assumptions were not fully met. Some of these models have been used in previous ATLAS and CMS analyses and discussed thoroughly within the Forum. They are therefore worth considering for further studies and for Run-2 searches, since they lead to unique \cancel{E}_T+X signatures that are not shared by any other of the models included in this report. Appendix B contains the necessary elements that should be included in the results of experimental searches to allow for further reinterpretation.

It is crucial for the success of the work of this Forum that these studies can be employed as cross-check and reference to the theoretical and experimental community interested in early Run-2 searches. For this reason, model files, parameter cards, and cross-sections for the models considered in these studies are publicly available. The Git repository of the Forum [59] contains the models and parameter files necessary to reproduce the studies within this report.

2. Simplified models for all \cancel{E}_T+X analyses

In this Chapter we review models that yield $X+\cancel{E}_T$ signatures, where X is a QCD parton or γ , W , Z or h .

The primary simplified models for Dirac fermion DM studied and recommended by this Forum for early LHC Run-2 searches are detailed in this Chapter, comprising spin-0 and spin-1 mediators.

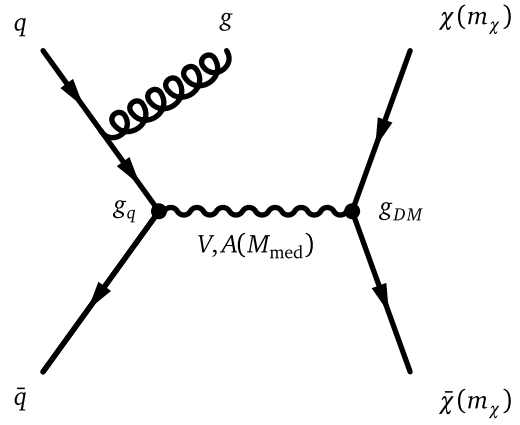


Fig. 1. Representative Feynman diagram showing the pair production of DM particles in association with a parton from the initial state via a vector or axial-vector mediator. The cross section and kinematics depend upon the mediator and DM masses, and the mediator couplings to DM and quarks respectively: $(M_{\text{med}}, m_\chi, g_\chi, g_q)$.

Section 2.1 covers the s -channel exchange of a vector mediator,⁴ while we consider both s -channel and t -channel exchange for scalar mediators in Sections 2.2 and 2.3 respectively. Spin-2 mediators are briefly mentioned in Section 2.4. While these models are general and cover a broad set of signatures, the discussion and studies are focused on the monojet final state. Details on final states with electroweak (EW) boson radiation and with heavy flavor quarks from diagrams arising within these models are also discussed in this Chapter.

A summary of the state of the art calculations and implementations for these models is provided in Table 9. Section 4 details the implementation of these models that have been used for the studies in this Chapter and that will be employed for the simulation of early Run-2 benchmark models for LHC DM searches.

2.1. Vector and axial vector mediator, s -channel exchange

A simple extension of the SM is an additional $U(1)$ gauge symmetry, where a DM candidate particle has charges only under this new group. Assuming that some SM particles are also charged under this group, a new gauge boson can mediate interactions between the SM and DM.

We consider the case of a DM particle χ of mass m_χ that is a Dirac fermion and where the production proceeds via the exchange of a spin-1 mediator of mass M_{med} in the s -channel, illustrated in Fig. 1.

We consider two models with vector and axial-vector couplings between the spin-1 mediator Z' and SM and DM fields, with the corresponding interaction Lagrangians:

$$\mathcal{L}_{\text{vector}} = g_q \sum_{q=u,d,s,c,b,t} Z'_\mu \bar{q} \gamma^\mu q + g_\chi Z'_\mu \bar{\chi} \gamma^\mu \chi \quad (1)$$

$$\mathcal{L}_{\text{axial-vector}} = g_q \sum_{q=u,d,s,c,b,t} Z'_\mu \bar{q} \gamma^\mu \gamma^5 q + g_\chi Z'_\mu \bar{\chi} \gamma^\mu \gamma^5 \chi. \quad (2)$$

The coupling g_q is assumed to be universal to all quarks. It is also possible to consider other models in which mixed vector and axial-vector couplings are considered, for instance the couplings to the quarks are axial-vector whereas those to DM are vector.

⁴ Colored vector mediators can be exchanged in the t -channel, but there are no examples in literature as of this report.

As mentioned in the Introduction, when no additional visible or invisible decays contribute to the width of the mediator, the minimal width is fixed by the choices of couplings g_q and g_χ . The effect of larger widths is discussed in Section 2.5.2. For the vector and axial-vector models, the minimal width is:

$$\Gamma_{\min}^V = \frac{g_\chi^2 M_{\text{med}}}{12\pi} \left(1 + \frac{2m_\chi^2}{M_{\text{med}}^2}\right) \beta_{DM} \theta(M_{\text{med}} - 2m_\chi) \quad (3)$$

$$+ \sum_q \frac{3g_q^2 M_{\text{med}}}{12\pi} \left(1 + \frac{2m_q^2}{M_{\text{med}}^2}\right) \beta_q \theta(M_{\text{med}} - 2m_q),$$

$$\Gamma_{\min}^A = \frac{g_\chi^2 M_{\text{med}}}{12\pi} \beta_{DM}^3 \theta(M_{\text{med}} - 2m_\chi) \quad (4)$$

$$+ \sum_q \frac{3g_q^2 M_{\text{med}}}{12\pi} \beta_q^3 \theta(M_{\text{med}} - 2m_q).$$

$\theta(x)$ denotes the Heaviside step function, and $\beta_f = \sqrt{1 - \frac{4m_f^2}{M_{\text{med}}^2}}$ is the velocity of the fermion f with mass m_f in the mediator rest frame. Note the color factor 3 in the quark terms. Fig. 2 shows the minimal width as a function of mediator mass for both vector and axial-vector mediators assuming the coupling choice $g_q = g_\chi = 1$. With this choice of the couplings, the dominant contribution to the minimal width comes from the quarks, due to the combined quark number and color factor enhancement. We specifically assume that the vector mediator does not couple to leptons. If such a coupling were present, it would have a minor effect in increasing the mediator width, but it would also bring in constraints from measurements of the Drell–Yan process that would unnecessarily restrict the model space.

Therefore, the minimal set of parameters under consideration for these two models is

$$\{g_q, g_\chi, m_\chi, M_{\text{med}}\} \quad (5)$$

together with the spin structure of their couplings.

A thorough discussion of these models and their parameters can also be found in [60].

These simplified models are known and available in event generators at NLO + PS accuracy, as detailed in Section 4.1.1. Results in this Section have been obtained using the model implementation within the POWHEG generator (v3359) [61], interfaced to PYTHIA 8 [62] for the parton shower.

In addition, for the vector models considered, initial and final state radiation of a Z' can occur which can appear as a narrow jet if it decays hadronically and may not be distinguishable from a QCD jet, thus accounting for some fraction of the monojet signal. The ISR and FSR of Z' becomes more important at large values of the couplings [63].

2.1.1. Parameter scan

In order to determine an optimal choice of the parameter grid for the simulation of early Run-2 benchmark models, dependencies of the kinematic quantities and cross sections on the model parameters have been studied. Only points that are kinematically distinct will be fully simulated, while instructions on how to rescale the results according to models with different cross sections are presented in Section 2.5. The following paragraphs list the main observations from the scans over the parameters that support the final proposal for the benchmark signal grid.

Scan over the couplings. To study the dependence of kinematic distributions on the coupling strength, samples were generated where a pair of $m_\chi = 10$ GeV DM particles is produced on-shell from the mediator of $M_{\text{med}} = 1$ TeV. Fig. 3 compares the shapes of the \not{E}_T distribution for the different choices of the coupling

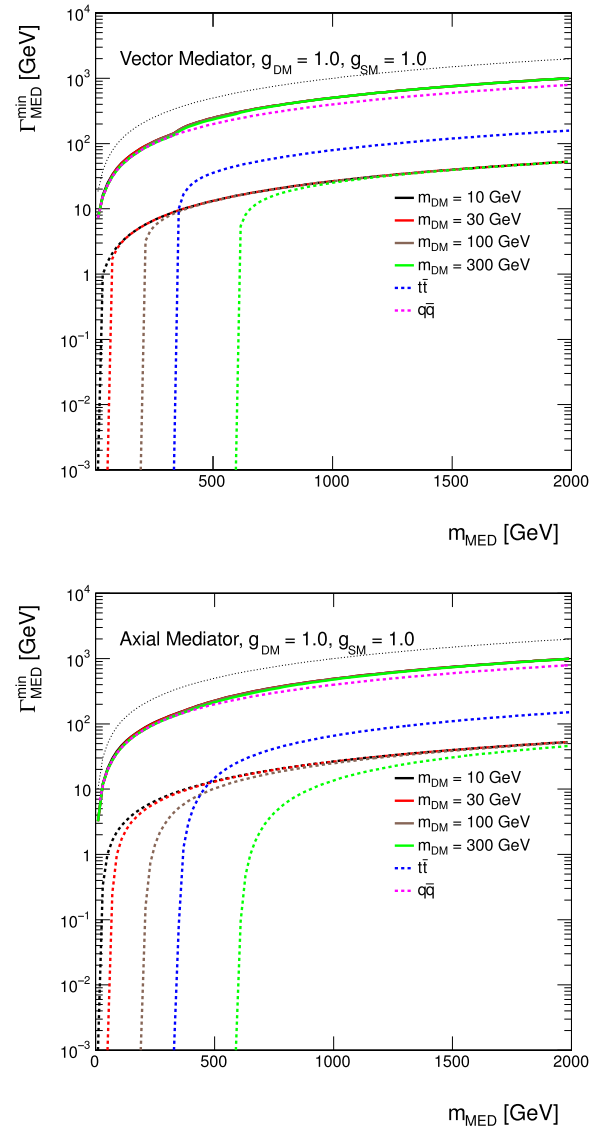


Fig. 2. Minimal width as a function of mediator mass for vector and axial-vector mediator assuming couplings of 1. The total width is shown as solid lines for DM masses of 10 GeV, 30 GeV, 100 GeV and 300 GeV in black, red, brown and green, respectively. The individual contributions from DM are indicated by dotted lines with the same colors. The contribution from all quarks but top is shown as magenta dotted line and the contribution from top quarks only is illustrated by the dotted blue line. The dotted black line shows the extreme case $\Gamma_{\min} = M_{\text{med}}$. (For interpretation of the references to color in this figure legend, the reader is referred to the web version of this article.)

strength. This is a generator-level prediction with no kinematic selections or detector simulation. Coupling values in the scan range 0.1–1.45, fixing $g_q = g_\chi$, correspond to a rough estimate of the lower sensitivity of mono-jet analyses and a maximum coupling value such that $\Gamma_{\min} < M_{\text{med}}$. We observe that the shapes of the \not{E}_T or jet p_T distributions do not depend on the couplings (and consequently the width) in the ranges considered. A large width of the mediator implies a broad integral over the contributing parton distributions, which might not be well approximated by the midpoint of this integral. This study shows that the effect, in the p_T distribution of the observed gluon, is not important.

Based on similar findings for different choices of M_{med} and m_χ , we conclude that the shapes of kinematic distributions are not altered by coupling variations, neither for the on-shell mediator

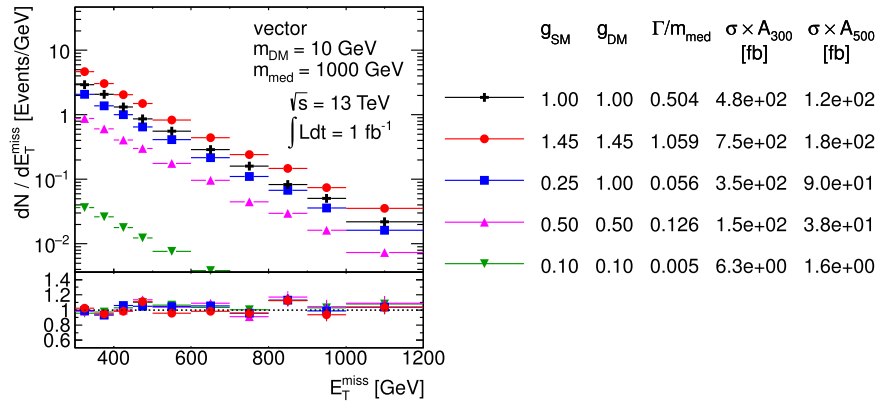


Fig. 3. Scan over couplings. The \tilde{E}_T distribution is compared for the vector mediator models using the parameters as indicated. Ratios of the normalized distributions with respect to the first one are shown. A_{300} and A_{500} in the table denote the acceptance of the $\tilde{E}_T > 300$ GeV and $\tilde{E}_T > 500$ GeV cut, respectively. All figures in this Section have been obtained using the model implementation within the POWHEG generator (v3359) [61], interfaced to PYTHIA 8 [62] for the parton shower.

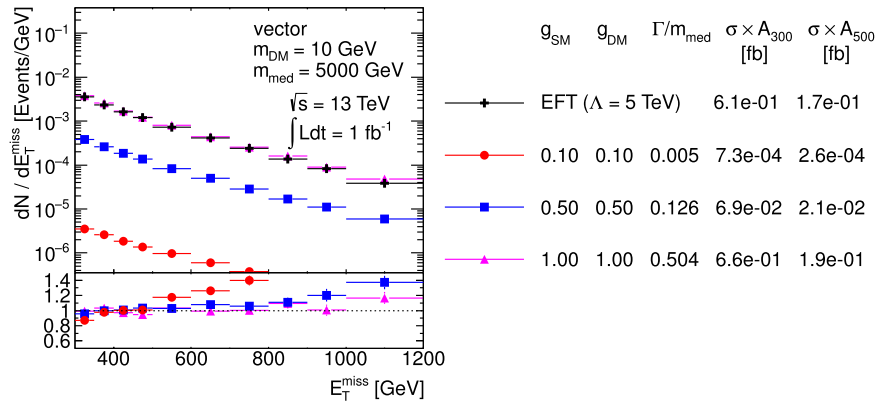


Fig. 4. Comparison of the \tilde{E}_T distributions from the D5 EFT sample and the vector models with 5 TeV heavy mediator of various widths. Ratios of the normalized distributions with respect to the first one are shown. A_{300} and A_{500} in the table denote the acceptance of the $\tilde{E}_T > 300$ GeV and $\tilde{E}_T > 500$ GeV cut, respectively.

case where $M_{\text{med}} > 2m_\chi$, nor for the off-shell case where $M_{\text{med}} < 2m_\chi$. Only the production cross sections change. Differences in kinematic distributions are expected only close to the transition region between on-shell and off-shell mediators.

Special care needs to be taken when coupling strengths are combined with extremely heavy mediators. Fig. 4 suggests a change in the shape of the \tilde{E}_T distribution for a $M_{\text{med}} = 5$ TeV mediator once $\Gamma_{\text{min}}/M_{\text{med}}$ is of the order of a percent or lower.

Such heavy mediators, although inaccessible with early LHC data, are interesting since they provide a good approximation for benchmark EFT models. The observed difference among the simplified models in the plot arises from the fact that the region of low invariant masses of the DM pair, $m_{\tilde{\chi}\chi}$, is suppressed due to narrow Breit–Wigner peak that only probes a narrow window of parton distribution functions. For wider mediators, the low mass region is significantly enhanced by parton distribution functions at low Bjorken x , as illustrated in Fig. 5(a). This explains why the sample with the narrowest mediator in Fig. 4 is heavily suppressed in terms of production cross section and also gives different \tilde{E}_T shape. Furthermore, Fig. 4 compares the vector model with 5 TeV mediator to the D5 EFT sample and reveals that the simplified models with larger mediator widths (e.g. for couplings of 1 where $\Gamma_{\text{min}}/M_{\text{med}} \sim 0.5$) are the ones resembling the kinematics of contact interactions. This reflects the fact that in an EFT there is no enhancement due to on-shell mediators, leading to a closer resemblance to an off-shell regime where no peak in the $m_{\tilde{\chi}\chi}$ distribution is present. In case of narrow width mediators, e.g. $\Gamma_{\text{min}}/M_{\text{med}} \sim 0.05$, even larger mediator masses need to be chosen in order to significantly suppress the peak in the $m_{\tilde{\chi}\chi}$

distribution and reproduce the kinematic shapes of an EFT model. Fig. 5(b) verifies that the choice of 10 TeV mediator mass is sufficient to achieve that.

Since kinematic distributions are robust to changes in the specific values of coupling,⁵ the choice of $g_q = 0.25$ and $g_\chi = 1$ is reasonable to reduce the parameter space to be scanned. There are no complications associated with small couplings, but, also, the early part of Run 2 will not be sensitive to them. The range of couplings we recommend to generate limit the calculated width of the mediator to be near or below M_{med} .

For direct mediator searches, such as $q\bar{q} \rightarrow Z' \rightarrow q\bar{q}$, different couplings ($g_q \neq g_\chi$) might also be considered. A scan in g_χ vs. g_q can then be performed for a fixed mediator mass. Such searches may restrict g_q to a greater degree than g_χ .

Scan over m_χ . For a fixed mediator mass M_{med} and couplings, the DM mass falls into three regimes:

On-shell: When $M_{\text{med}} \gg 2m_\chi$, most mediators are on-shell.

The hardness of the ISR is set by M_{med} , and the kinematic distributions do not strongly depend on m_χ . This is illustrated in Fig. 6 for an example of $M_{\text{med}} = 1$ TeV, $10 \text{ GeV} < m_\chi < 300 \text{ GeV}$. The cross section decreases as the m_χ approaches $M_{\text{med}}/2$. A coarse binning along m_χ is sufficient.

⁵ This applies as long as heavy narrow mediators are generated without any truncation of low-mass tails at the generator-level.

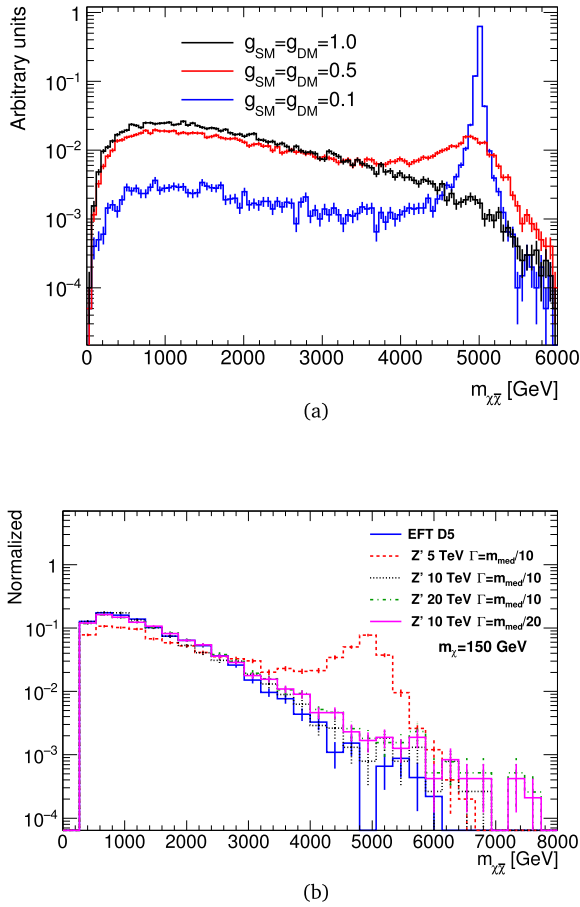


Fig. 5. Invariant mass of the DM pair in the vector mediator samples with $m_\chi = 10$ GeV, $M_{\text{med}} = 5$ TeV and different coupling strengths (a). A similar comparison is shown for the samples with different mediator masses considering $\Gamma_{\text{min}}/M_{\text{med}} = 0.05$ and 0.1 (b). An EFT sample is also displayed in the latter case. The distributions are normalized to unit area.

Threshold: When $M_{\text{med}} \approx 2m_\chi$, the production is resonantly enhanced, and both the cross section and kinematic distributions change more rapidly as a function of the two masses, and finer binning is needed in order to capture the changes.

Off-shell: When $M_{\text{med}} \ll 2m_\chi$, the DM pair is produced by an off-shell mediator. The mediator propagator gives an explicit suppression of $(M_{\text{med}}/Q)^2$ that suppresses hard ISR. The $m_\chi = 1$ TeV case, shown in Figs. 6 and 7 demonstrates that the \cancel{E}_T spectrum hardens with increasing m_χ , accompanied by the gradual decrease of the cross section. Due to the significant cross section suppression, it is not necessary to fully populate the parameter space. Imminent LHC searches are not expected to be sensitive to these signals.

Scan over the mediator mass. Changing the mediator mass for fixed DM mass and couplings leads to significant differences in cross section and shapes of the kinematic variables for the on-shell regime, as shown in Fig. 8. As expected, higher mediator masses lead to harder \cancel{E}_T spectra. On the other hand, the \cancel{E}_T shapes are similar for off-shell mediators. This is illustrated in Fig. 9. Therefore, a coarse binning in M_{med} is sufficient in the off-shell regime.

Spin structure of the couplings. This section compares the kinematic properties of vector, axial-vector and mixed vector/axial-vector models. The samples with pure vector and pure axial-vector couplings are compared for $M_{\text{med}} = 100$ GeV and different DM masses in Fig. 10. No differences in the shape of the \cancel{E}_T distributions are observed between the samples with coincident masses. In the case of the on-shell mediators, where $2m_\chi \ll M_{\text{med}}$, the cross sections of the pure vector and pure axial-vector models are similar. With increasing DM mass towards the $2m_\chi = M_{\text{med}}$ transition and further into the off-shell regime, the relative difference between the cross sections of the two samples is increasing, with the vector ones having larger cross sections.

Fig. 11 shows the samples generated with pure and mixed couplings for $m_\chi = 100$ GeV and $M_{\text{med}} = 1$ TeV, i.e. where the mediator is on-shell. The mediator width between the pure vector and pure axial-vector couplings differ only by 2% in this case, and $<10\%$ agreement between the cross sections is found. The mediator widths for the samples with the same type coupling to quarks agree at better than 1% since the width is dominated by the quark contribution, as expected from Eq. (3). No significant differences between the samples with same type DM coupling are seen, given the statistical precision of the generated samples. This is expected since the mediator is on-shell, and the details of the invisible decay are unimportant in cut-and-count searches.

For the off-shell case, shown in Fig. 12 for $m_\chi = 100$ GeV and $M_{\text{med}} = 100$ GeV, there is approximately a factor 2 difference between the cross-sections of the samples with pure couplings is observed. As in the previous case, the samples with the same type coupling to DM are similar both in terms of cross sections and \cancel{E}_T shape. Since the contribution to the mediator width from DM is closed in this case, only the quark couplings define the width. Only couplings to light quarks are opened in the case of $M_{\text{med}} = 100$ GeV for which the differences between the partial widths of vector and axial-vector couplings are marginal. This explains the similar minimal widths for all four samples stated in Fig. 12.

In general, the coupling to quarks is not expected to play an important role in the kinematics as it is only needed to produce the mediator which is confirmed by the observations above. Based on this argument and on the observations above, we recommend to consider only the models with pure vector couplings or pure axial-vector couplings for simulation.

Proposed parameter grid. The final step in proposing a parameter grid is to evaluate the sensitivity of Run-2 LHC data with respect to rate and/or kinematics. The parameter scan focuses on two important regions, the light mediator region and the heavy mediator limit to reproduce the EFT limit, and takes into account the projected sensitivities for the mono-jet analysis.

Considering simplified models also allows to discuss constraints from different search channels. In the case of the s-channel exchange, the results from the mono-jet final states, where the mediator decays to a DM pair, one can also take into account dijet constraints on the processes where the mediator decays back to the SM particles. The importance of the dijet results depend on the magnitude of the coupling g_q . We recommend to keep the two channels rather independently by choosing $g_q = 0.25$ and $g_\chi = 1$, based on the findings given in Ref. [64]. Furthermore, it is also important to mention this choice leads to $\Gamma_{\text{min}}/M_{\text{med}} \lesssim 0.06$. Note that the usual choice of $g_q = g_\chi = 1$ used in literature leads to $\Gamma_{\text{min}}/M_{\text{med}} \sim 0.5$, questioning the applicability of the narrow width approximation.

The expected upper limit at 95% confidence level on the product of cross section, acceptance and efficiency, $\sigma \times A \times \epsilon$, in the final Run-1 ATLAS mono-jet analysis [7] is 51 fb and 7.2 fb for $\cancel{E}_T > 300$ GeV and $\cancel{E}_T > 500$ GeV, respectively. Projected sensitivities for a 14 TeV mono-jet analysis are available from

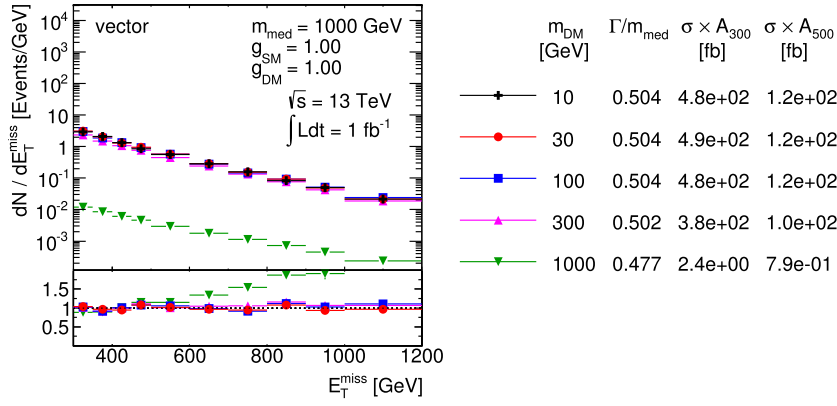


Fig. 6. Scan over DM mass. The E_T distribution is compared for the vector mediator models using the parameters as indicated. Ratios of the normalized distributions with respect to the first one are shown. A_{300} and A_{500} in the table denote the acceptance of the $E_T > 300$ GeV and $E_T > 500$ GeV cut, respectively.

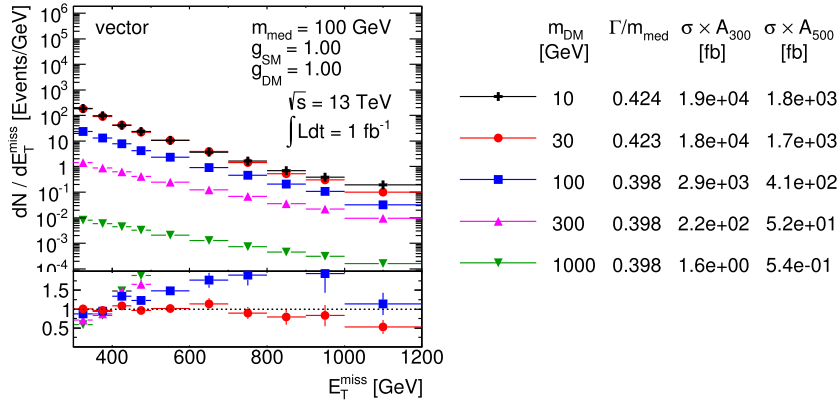


Fig. 7. Scan over DM mass. The E_T distribution is compared for the vector mediator models using the parameters as indicated. Ratios of the normalized distributions with respect to the first one are shown. A_{300} and A_{500} in the table denote the acceptance of the $E_T > 300$ GeV and $E_T > 500$ GeV cut, respectively.

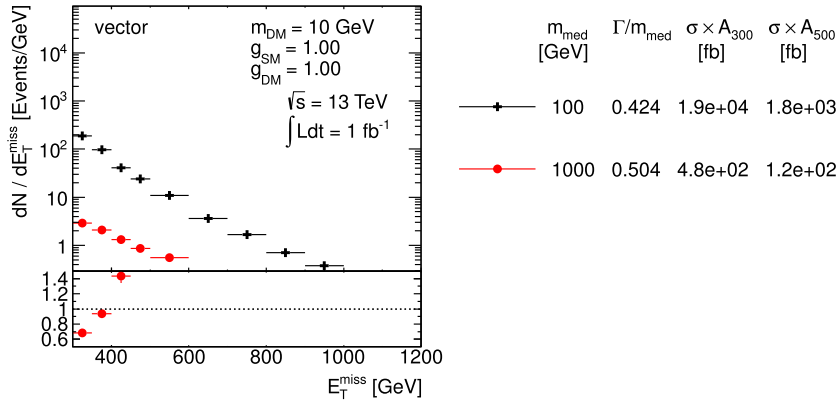


Fig. 8. Scan over mediator mass. The E_T distribution is compared for the vector mediator models using the parameters as indicated. Ratios of the normalized distributions with respect to the first one are shown. A_{300} and A_{500} in the table denote the acceptance of the $E_T > 300$ GeV and $E_T > 500$ GeV cut, respectively.

ATLAS [14]. These ATLAS studies estimate a factor of two increase in sensitivity with the 2015 data. The generator level cross section times efficiency times acceptance at $E_T > 500$ GeV for the model with couplings $g_q = 0.25$ and $g_\chi = 1$, a light DM particle of $m_\chi = 10$ GeV and a $M_{\text{med}} = 1$ TeV vector mediator is at the order of 100fb, i.e. the early Run-2 mono-jet analysis is going to be sensitive to heavier mediators than this. The value of $\sigma \times \epsilon \times A$ at $E_T > 500$ GeV for a 5 TeV vector mediator is at the order of 0.1fb, therefore this model lies beyond the reach of the LHC in the early Run-2. However, models with high enough mediators are still useful to reproduce the EFT result.

Following these arguments, M_{med} grid points are chosen, roughly equidistant in a logarithmic scale: 10 GeV, 20 GeV, 50 GeV, 100 GeV, 200 GeV, 300 GeV, 500 GeV, 1000 GeV and 2000 GeV. In the threshold regime $M_{\text{med}} = 2m_\chi$, the m_χ grid points are taken at approximately $M_{\text{med}}/2$, namely: 10 GeV, 50 GeV, 150 GeV, 500 GeV and 1000 GeV. Points on the on-shell diagonal are always chosen to be 5 GeV away from the threshold, to avoid numerical instabilities in the event generation. The detailed studies of the impact of the parameter changes on the cross section and kinematic distributions presented earlier in this section support removing some of the grid points and relying on interpolation. The optimized grids proposed for the vector and

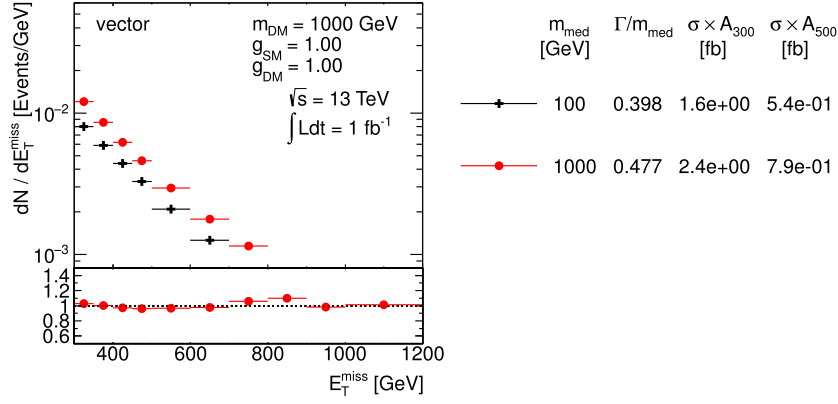


Fig. 9. Scan over mediator mass. The \vec{E}_T distribution is compared for the vector mediator models using the parameters as indicated. Ratios of the normalized distributions with respect to the first one are shown. A_{300} and A_{500} in the table denote the acceptance of the $\vec{E}_T > 300$ GeV and $\vec{E}_T > 500$ GeV cut, respectively.

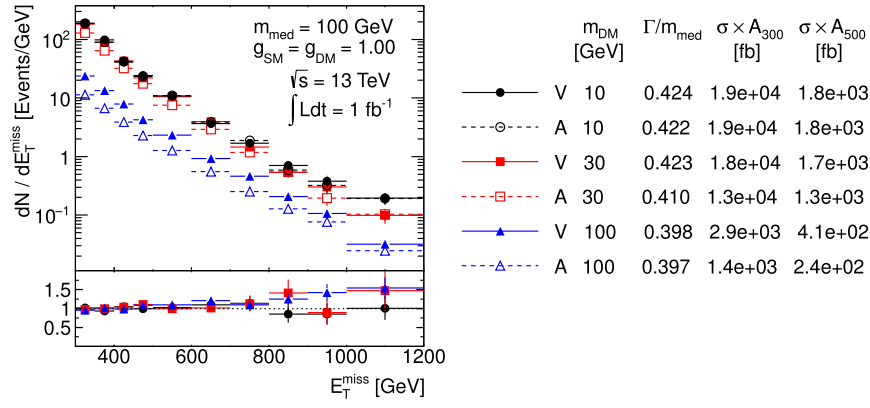


Fig. 10. Comparison of the pure vector and pure axial-vector couplings. The \vec{E}_T distribution is shown for the samples generated with $M_{\text{med}} = 100$ GeV and different DM masses. Ratios of the normalized distributions are shown for between the samples with coincident masses. A_{300} and A_{500} in the table denote the acceptance of the $\vec{E}_T > 300$ GeV and $\vec{E}_T > 500$ GeV cut, respectively.

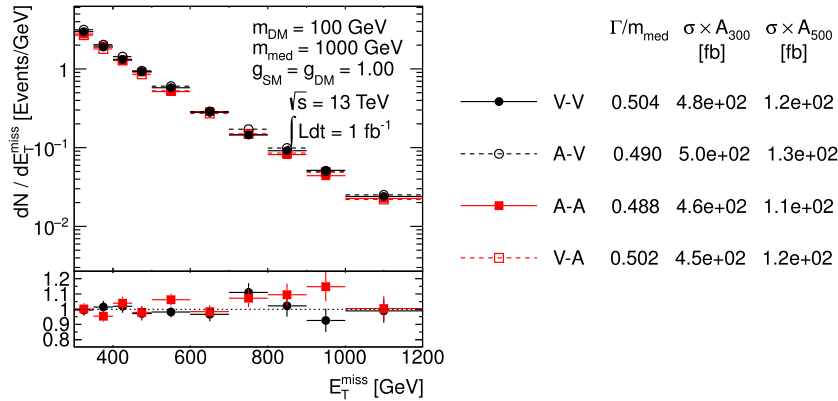


Fig. 11. Comparison of the pure vector, V-V, and pure axial-vector, A-A, couplings with mixed couplings, A-V and V-A where the first (second) letter indicates the SM (dark sector) vertex. The \vec{E}_T distribution is shown for the samples generated with $m_\chi = 100$ GeV and $M_{\text{med}} = 1$ TeV. Ratios of the normalized distributions are shown for A-V over V-V and for V-A over A-A. A_{300} and A_{500} in the table denote the acceptance of the $\vec{E}_T > 300$ GeV and $\vec{E}_T > 500$ GeV cut, respectively.

axial-vector mediators are given in Table 1. One point at very high mediator mass (10 TeV) is added for each of the DM masses scanned, to aid the reinterpretation of results in terms of contact interaction operators (EFTs), as discussed in Section 5.2.

Tables 2 and 3 give the $\Gamma_{\text{min}}/M_{\text{med}}$ ratio for the parameter grid proposed for vector and axial-vector s -channel models, respectively. The numbers range from ~ 0.02 in the off-shell regime at $2m_\chi > M_{\text{med}}$ to ~ 0.06 in the on-shell regime for heavy mediators where all coupling channels contribute.

2.1.2. Additional considerations for $V + \vec{E}_T$ signatures

All models detailed in this Section are applicable to signatures where a photon, a W boson, a Z boson or a Higgs boson is radiated from the initial state partons instead of a gluon. The experimental signature is identified as $V + \vec{E}_T$ and it has been sought by ATLAS and CMS in Refs. [8–11, 16, 17]. This signature is also produced by the models described in Section 3.

Monojet searches are generally more sensitive with respect to final states including EW bosons, due to the much larger rates of signal events featuring quark or gluon radiation with respect to

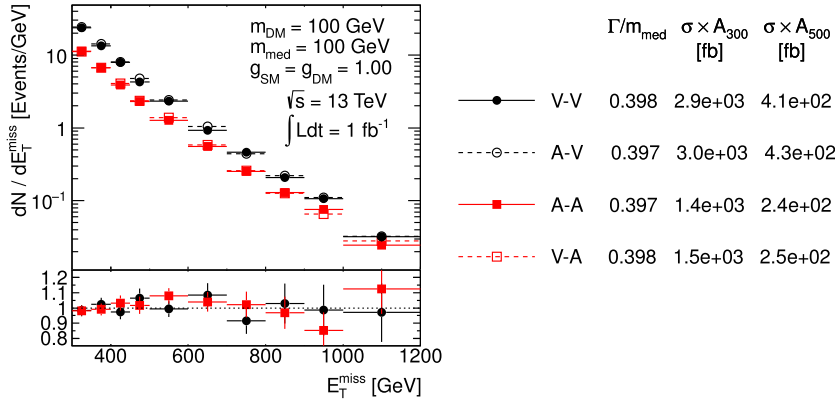


Fig. 12. Comparison of the pure vector, V-V, and pure axial-vector, A-A, couplings with mixed couplings, A-V and V-A where the first (second) letter indicates the SM (dark sector) vertex. The E_T distribution is shown for the samples generated with $m_\chi = 100$ GeV and $M_{\text{med}} = 100$ GeV. Ratios of the normalized distributions are shown for A-V over V-V and for V-A over A-A. A_{300} and A_{500} in the table denote the acceptance of the $E_T > 300$ GeV and $E_T > 500$ GeV cut, respectively. The suppression by β^3 for $m_\chi \sim M_{\text{med}}$ can be seen for the curves representing axial DM coupling.

Table 1

Simplified model benchmarks for s -channel simplified models (spin-1 mediators decaying to Dirac DM fermions in the V and A case, taking the minimum width for $g_q = 0.25$ and $g_x = 1$).

m_χ / GeV	M_{med} / GeV									
	10	20	50	100	200	300	500	1000	2000	10 000
1	10	20	50	100	200	300	500	1000	2000	10 000
10	10	15	50	100						10 000
50	10		50	95	200	300				10 000
150	10				200	295	500	1000		10 000
500	10						500	995	2000	10 000
1000	10							1000	1995	10 000

radiation of bosons [65], in combination with the low branching ratios if leptons from boson decays are required in the final state. The rates for the Higgs boson radiation is too low for these models to be considered a viable benchmark [48]. However, the presence of photons, leptons from W and Z decays, and W or Z bosons decaying hadronically allow backgrounds to be rejected more effectively, making $Z/\gamma/W+\cancel{E}_T$ searches still worth comparing with searches in the jet+ \cancel{E}_T final state (see e.g. Ref. [66]).

In the case of a spin-1 mediator, an example Feynman diagram for these processes can be constructed by taking Fig. 1 and replacing the gluon with γ , W or Z.

When the initial state radiation is a W boson, Run-1 searches have considered three benchmark cases, varying the relative coupling of the W to u and d quarks. The simplified model with a vector mediator exchanged in the s -channel includes only the simplest of these cases, in which the W coupling to u and d quarks is identical, as required naively by SU(2) gauge invariance. With some more complex model building, other cases are possible. The case in which the u and d couplings have opposite sign is particularly interesting, since this enhances the $W+\cancel{E}_T$ signal over the jet+ \cancel{E}_T signal [44,67,68]. An example of a model of this type is discussed in Appendix A.4.

Simulations for the models in this Section have been done at the LO+PS level using MADGRAPH5_AMC@NLO 2.2.3 interfaced to PYTHIA 8, and therefore no special runtime configuration is needed for pythia 8. Even though merging samples with different parton multiplicities is possible, this has not been deemed necessary as the visible signal comes from the production of a heavy SM boson whose transverse momentum distribution is sufficiently well described at LO+PS level.

In these $V+\cancel{E}_T$ models, as in the case of the jet+ \cancel{E}_T models, p_T of the boson or the \cancel{E}_T does not depend strongly on the width of the mediator. An example of the particle-level analysis acceptance using the generator-level cuts from Ref. [8] for the

Table 2

Minimal width of the vector mediator exchanged in s -channel divided by its mass, assuming $g_q = 0.25$ and $g_x = 1$. The numbers tabulated under $2m_\chi = M_{\text{med}}$ correspond to the width calculated for $M_{\text{med}} - 5$ GeV.

m_χ / GeV	M_{med} / GeV									
	10	20	50	100	200	300	500	1000	2000	10 000
1	0.049	0.051	0.051	0.051	0.051	0.051	0.056	0.056	0.056	0.056
10	0.022	0.024	0.054	0.052						0.056
50	0.022		0.025	0.025	0.055	0.053				0.056
150	0.022				0.025	0.025	0.061	0.058		0.056
500	0.022						0.029	0.030	0.060	0.057
1000	0.022							0.030	0.030	0.057

Table 3

Minimal width of the axial-vector mediator exchanged in s -channel divided by its mass, assuming $g_q = 0.25$ and $g_x = 1$. The numbers tabulated under $2m_\chi = M_{\text{med}}$ correspond to the width calculated for $M_{\text{med}} - 5$ GeV.

m_χ / GeV	M_{med} / GeV									
	10	20	50	100	200	300	500	1000	2000	10 000
1	0.045	0.049	0.051	0.051	0.051	0.051	0.053	0.055	0.056	0.056
10	0.020	0.022	0.047	0.050						0.056
50	0.020		0.025	0.025	0.045	0.048				0.056
150	0.020				0.025	0.025	0.044	0.053		0.056
500	0.020						0.027	0.029	0.050	0.056
1000	0.020							0.029	0.030	0.055

Table 4

Analysis acceptance ratios for the photon+ \cancel{E}_T analysis when varying the mediator width, in the case of a vector mediator exchanged in the s -channel. The figures shown in this Section have been obtained using a LO UFO model in MADGRAPH5_AMC@NLO 2.2.3 interfaced to PYTHIA 8 for the parton shower.

Acceptance ratio: $\Gamma = \Gamma_{\min}$ vs. $\Gamma = M_{\text{med}}/3$				
$M_{\text{med}}/\text{GeV}$	m_χ/GeV			
	10	50	200	400
50	0.96	0.99		0.95
100	0.97			
300	1.00	1.02		
600			0.96	
1000	1.01	1.02	1.03	
3000	1.02	1.03		1.01

photon+ \cancel{E}_T analysis, but raising the photon p_T cut to 150 GeV, is shown in Table 4, comparing a width that is set to $\Gamma = M_{\text{med}}/3$ to the minimal width (the ratio between the two widths ranges from 1.05 to 1.5 with increasing mediator masses).

Examples of relevant kinematic distributions for selected benchmark points are shown in Fig. 13.

2.2. Scalar and pseudoscalar mediator, s -channel exchange

In this section, we consider a parallel situation to the vector and axial-vector mediators in the previous sections: a real scalar or a pseudoscalar where the associated scalar is decoupled at higher energies.⁶ This section is largely based on Refs. [41–43] which contain a thorough discussion of these models.

Assuming MFV, spin-0 resonances behave in a similar fashion as the SM Higgs boson. If the mediators are pure singlets of the SM, their interactions with quarks are not $SU(2)_L$ invariant. To restore this invariance, one could include the mixing of such mediators with the Higgs sector. This leads to extra interactions and a more complex phenomenology with respect to what considered in this Section (for a more complete discussion, see Refs. [42,43]). In the interest of simplicity, we do not study models including those interactions in this report as early Run-2 benchmark models, but we give an example of a model of this kind in Appendix A.6.

Relative to the vector and axial-vector models discussed above, the scalar models are distinguished by the special consequences of the MFV assumption: the very narrow width of the mediator and its extreme sensitivity to which decays are kinematically available, and the loop-induced coupling to gluons. The interaction Lagrangians are

$$\mathcal{L}_\phi = g_\chi \phi \bar{\chi} \chi + \frac{\phi}{\sqrt{2}} \sum_i (g_u y_i^u \bar{u}_i u_i + g_d y_i^d \bar{d}_i d_i + g_\ell y_i^\ell \bar{\ell}_i \ell_i), \quad (6)$$

$$\mathcal{L}_a = i g_\chi a \bar{\chi} \gamma_5 \chi + \frac{ia}{\sqrt{2}} \sum_i (g_u y_i^u \bar{u}_i \gamma_5 u_i + g_d y_i^d \bar{d}_i \gamma_5 d_i + g_\ell y_i^\ell \bar{\ell}_i \gamma_5 \ell_i) \quad (7)$$

where ϕ and a are respectively the scalar and pseudoscalar mediators, and the Yukawa couplings y_i^f are normalized to the Higgs vev as $y_i^f = \sqrt{2} m_i^f / v$.

The couplings to fermions are proportional to the SM Higgs couplings, yet one is still allowed to adjust an overall strength of the coupling to charged leptons and the relative couplings of u - and d -type quarks. As in the preceding sections, for the

⁶ This assumption does not hold in a UV-complete model where the two components of the complex scalar mediator would be approximately degenerate. The complex scalar case could be studied separately in the case of heavy flavor final states given the sufficiently different kinematics.

sake of simplicity and straightforward comparison, we reduce the couplings to the SM fermions to a single universal parameter $g_q \equiv g_u = g_d = g_\ell$. Unlike the vector and axial-vector models, the scalar mediators are allowed to couple to leptons.⁷

The relative discovery and exclusion power of each search can be compared in this framework. However, we again emphasize the importance of searching the full set of allowed channels in case violations of these simplifying assumptions lead to significant modifications of the decay rates that unexpectedly favor different channels than the mix obtained under our assumptions. The coupling g_χ parametrizes the entire dependence on the structure between the mediator and the dark sector.

Given these simplifications, the minimal set of parameters under consideration is

$$\{m_\chi, m_{\phi/a} = M_{\text{med}}, g_\chi, g_q\}. \quad (8)$$

Fig. 14 shows the one-loop diagrams producing a jet+X signature. The full calculation of the top loop is available at LO for DM pair production in association with one parton.

The minimal mediator width (neglecting the small contributions from quarks other than top in the loop) is given by

$$\Gamma_{\phi,a} = \sum_f N_c \frac{y_f^2 g_q^2 m_{\phi,a}}{16\pi} \left(1 - \frac{4m_f^2}{m_{\phi,a}^2}\right)^{x/2} + \frac{g_\chi^2 m_{\phi,a}}{8\pi} \left(1 - \frac{4m_\chi^2}{m_{\phi,a}^2}\right)^{x/2} + \frac{\alpha_s^2 g_q^2 m_{\phi,a}^3}{32\pi^3 v^2} \left| f_{\phi,a} \left(\frac{4m_t^2}{m_{\phi,a}^2}\right) \right|^2 \quad (9)$$

where $x = 3$ for scalars and $x = 1$ for pseudoscalars. The loop integrals, with f as complex functions, are

$$f_\phi(\tau) = \tau \left[1 + (1 - \tau) \arctan^2 \left(\frac{1}{\sqrt{\tau - 1}} \right) \right], \quad (10)$$

$$f_a(\tau) = \tau \arctan^2 \left(\frac{1}{\sqrt{\tau - 1}} \right) \quad (11)$$

where $\tau = 4m_t^2 / m_{\phi,a}^2$.

The minimal widths for scalar and pseudo-scalar mediators with $g_q = g_\chi = 1$ are shown in Fig. 20, illustrating the effect of choosing the SM Higgs-like Yukawa couplings for the SM fermions. For the mediator mass above twice the top quark mass m_t , the minimal width receives the dominant contribution from the top quark. For lighter mediator masses, DM dominates as the couplings to lighter quarks are Yukawa suppressed.

As shown in the diagram of Fig. 14, the lowest order process of these models already involves a one-loop amplitude in QCD, and only LO predictions are currently available. The generator used for the studies for the jet+ \cancel{E}_T signature is POWHEG [43,61,69–71], with PYTHIA 8 [62] for the parton shower; within this implementation, the scalar and pseudoscalar mediator benchmark models are known at LO+PS accuracy.

2.2.1. Parameter scan

Similarly as in the case of the vector and axial-vector couplings of spin-1 mediators, scans in the parameter space are performed also for the scalar and pseudo-scalar couplings of the spin-0 mediators in order to decide on the optimized parameter grid for the presentation of Run-2 results. Figs. 15–19 show the scans

⁷ This contribution plays no role for most of the parameter space considered. The choice to allow lepton couplings follows Refs. [41,42].

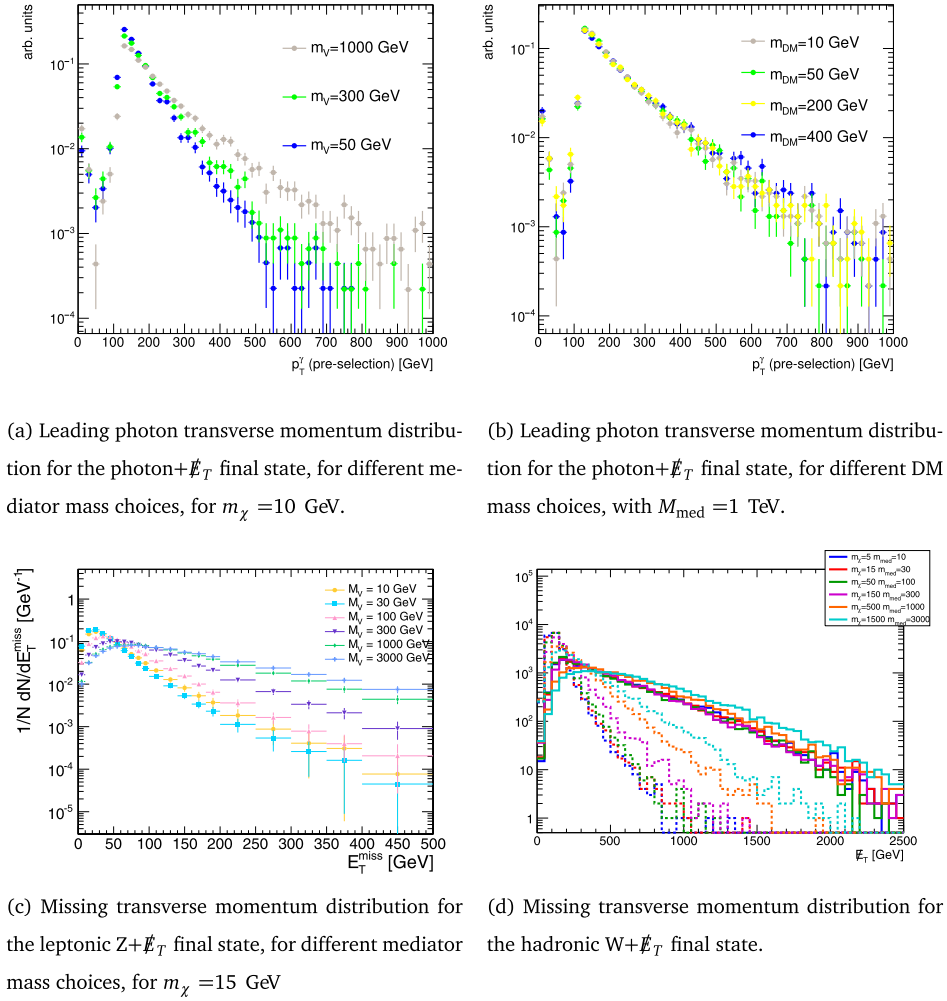


Fig. 13. Kinematic distributions relevant for searches with W, Z and photons in the final state, for the simplified model with a vector mediator exchanged in the s-channel.

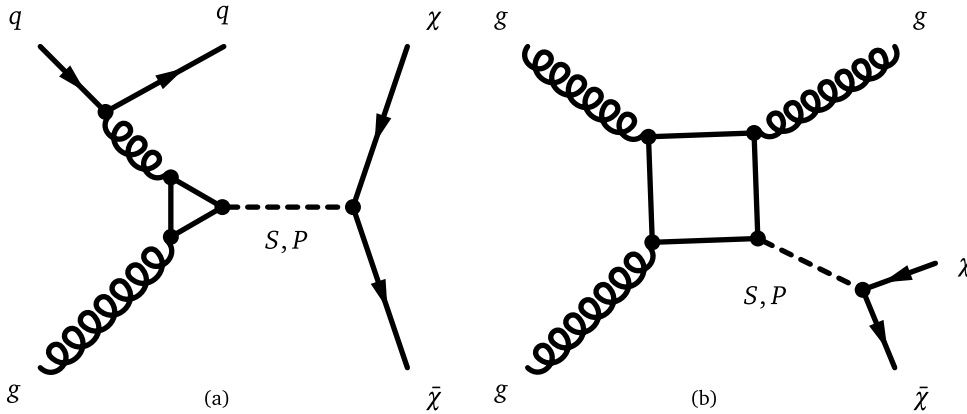


Fig. 14. One-loop diagrams of processes exchanging a scalar (S) or pseudoscalar (P) mediator, leading to a mono-jet signature.

over the couplings, DM mass and mediator mass and the same conclusions apply as in Section 2.1.

A scan over the mediator mass is shown in Fig. 19 where $M_{\text{med}} = 300$ GeV and 500 GeV are chosen to be below and above $2m_t$. The off-shell case is assumed by taking an extreme limit ($m_\chi = 1$ TeV) in order to study solely the effects of the couplings to quarks. No differences in the kinematic distributions are observed and also the cross sections remain similar in this

case. No significant changes appear for mediator masses around the $2m_t$ threshold.

It can be seen in Fig. 21 that the kinematics for the scalar and pseudoscalar models coincides when considering the diagrams in Fig. 14. For this reason, we recommend to fully simulate only one of the two models. No preference is given between the two models as they have the same kinematics, although it is worth noting that the pseudo-scalar model has been used for a DM interpretation of the DAMA signal and of the galactic center

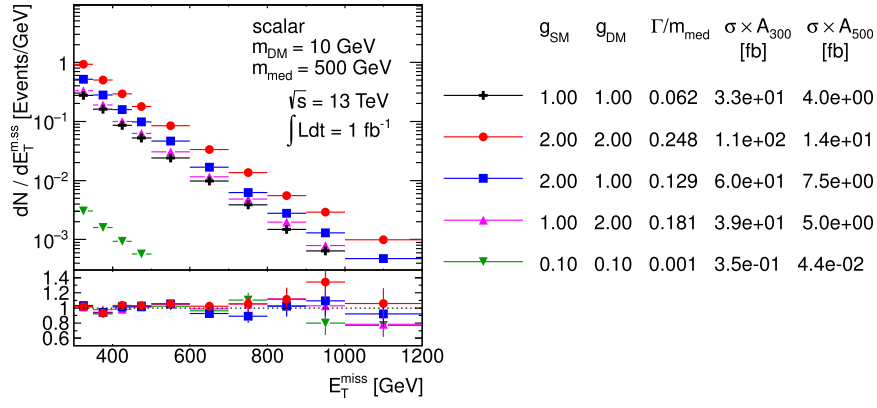


Fig. 15. Scan over couplings. The E_T distribution is compared for the scalar mediator models using the parameters as indicated. Ratios of the normalized distributions with respect to the first one are shown. A_{300} and A_{500} in the table denote the acceptance of the $E_T > 300$ GeV and $E_T > 500$ GeV cut, respectively. Studies in all figures for the jet+ E_T signature is POWHEG, with PYTHIA 8 for the parton shower.

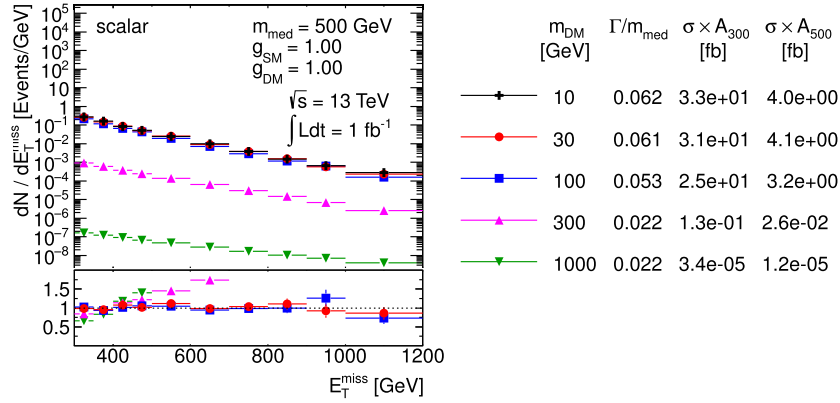


Fig. 16. Scan over DM mass. The E_T distribution is compared for the scalar mediator models using the parameters as indicated. Ratios of the normalized distributions with respect to the first one are shown. A_{300} and A_{500} in the table denote the acceptance of the $E_T > 300$ GeV and $E_T > 500$ GeV cut, respectively.

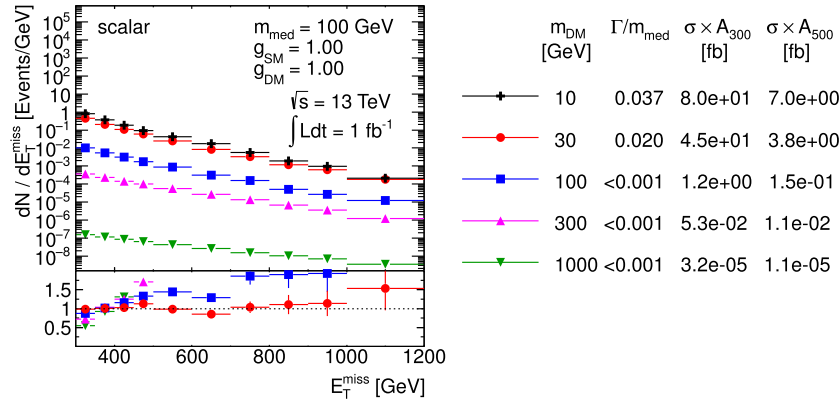


Fig. 17. Scan over DM mass. The E_T distribution is compared for the scalar mediator models using the parameters as indicated. Ratios of the normalized distributions with respect to the first one are shown. A_{300} and A_{500} in the table denote the acceptance of the $E_T > 300$ GeV and $E_T > 500$ GeV cut, respectively.

excess [72]. Like in the case of the vector and axial-vector models described in , the differences between the cross sections for the scalar and pseudo-scalar samples with the same m_χ and M_{med} are increasing with the DM mass for fixed mediator mass, with the pseudo-scalar model yielding larger cross sections. There is an increasing difference between the minimal widths close to the $2m_\chi = M_{med}$ threshold.

Proposed parameter grid. The optimized parameter grid in the $M_{med}-m_\chi$ plane for scalar and pseudo-scalar mediators is motivated by similar arguments as in the previous section. Therefore,

a similar pattern is followed here, with the exception of taking $g_q = g_\chi = 1$. The choice of $g_q = 0.25$ for the vector and axial-vector models is motivated by suppressing constraints from di-jets, which is not a concern in the scalar and pseudo-scalar mediator case. Here a di-jet signal emerges only at the 2-loop level through diagrams where the mediator is produced via gluon-gluon fusion and decays back into two gluons through a top loop. The strong loop suppression renders such signals unobservable at the LHC. Further constraints on the scalar and pseudo-scalar mediators may emerge from searches in $t\bar{t}$ final states. Studies

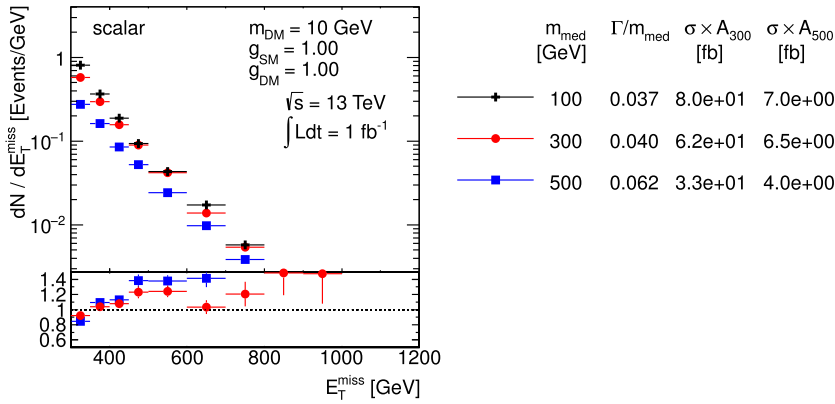


Fig. 18. Scan over mediator mass. The \cancel{E}_T distribution is compared for the scalar mediator models using the parameters as indicated. Ratios of the normalized distributions with respect to the first one are shown. A_{300} and A_{500} in the table denote the acceptance of the $\cancel{E}_T > 300$ GeV and $\cancel{E}_T > 500$ GeV cut, respectively.

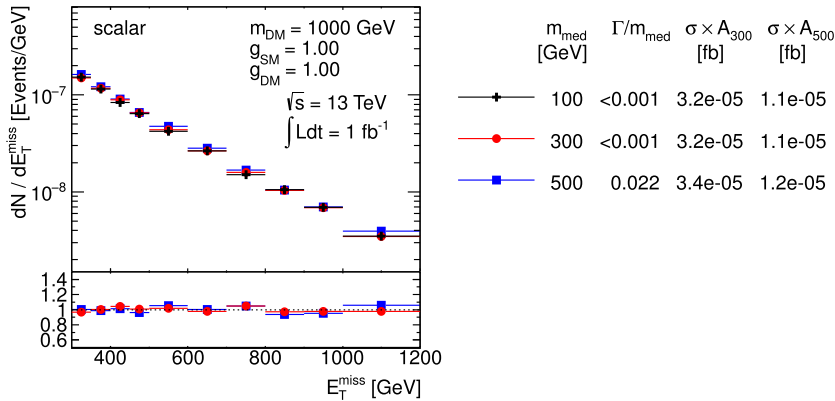


Fig. 19. Scan over mediator mass. The \cancel{E}_T distribution is compared for the scalar mediator models using the parameters as indicated. Ratios of the normalized distributions with respect to the first one are shown. A_{300} and A_{500} in the table denote the acceptance of the $\cancel{E}_T > 300$ GeV and $\cancel{E}_T > 500$ GeV cut, respectively.

of the electroweak effects to $t\bar{t}$ production suggest that one can only expect percent level contributions for $g_q \sim O(1)$ [73]. Therefore, keeping $g_q = g_\chi = 1$ is a reasonable choice in the case of the scalar and pseudo-scalar mediators. Contrary to the vector and axial-vector models, note that couplings of 1 lead to $\Gamma_{\text{min}}/M_{\text{med}} \lesssim 0.1$, ensuring the narrow width approximation is applicable. Furthermore, the sensitivity to the highest mediator masses has to be re-evaluated. The generator level cross section times the acceptance at $\cancel{E}_T > 500$ GeV for the model with couplings $g_q = g_\chi = 1$, light DM of $m_\chi = 10$ GeV and a $M_{\text{med}} = 500$ GeV scalar mediator is at the order of 10 fb, i.e. just at the edge of the early Run-2 sensitivity. Increasing the mediator mass to 1 TeV pushes the product $\sigma \times A$ down to approximately 0.1 fb, below the LHC sensitivity. Therefore, we choose to remove the 2 TeV mediator mass from the grid and present the final grid with 33 mass points only, as shown in Table 5. One point at very high mediator mass (10 TeV) is added for each of the DM masses scanned, to aid the reinterpretation of results in terms of contact interaction operators (EFTs).

For the parameter grid for scalar and pseudo-scalar mediator s-channel exchange, the $\Gamma_{\text{min}}/M_{\text{med}}$ ratio is given in Tables 6 and 7, respectively. In the on-shell regime, the ratio is between 0.04 and 0.1. Very narrow resonances with $\Gamma_{\text{min}}/M_{\text{med}} < 0.001$ correspond to the mass points where the mediator is off-shell. Note that the loop-induced contribution from gluons is ignored in the width calculation.

2.2.2. Additional considerations for $V + \cancel{E}_T$ signatures

The discussion of parameters for the model with a color-singlet, spin-0 mediator parallels that in Section 2.

Table 5

Simplified model benchmarks for s-channel simplified models (spin-0 mediators decaying to Dirac DM fermions in the scalar and pseudoscalar case, taking the minimum width for $g_q = 1$ and $g_\chi = 1$).

m_χ (GeV)	M_{med} (GeV)								
1	10	20	50	100	200	300	500	1000	10000
10	10	15	50	100					10000
50	10		50	95	200	300			10000
150	10				200	295	500	1000	10000
500	10						500	995	10000
1000	10							1000	10000

Even though the sensitivity of mono-boson searches to this model is low and it may not be in reach of early LHC searches, this model can be generated for W, Z and photon searches in order to reproduce the kinematics of contact interaction operators that are further described in Section 3.2.1, to aid later reinterpretation.

Other models of DM that couple dominantly to electroweak gauge bosons through either pseudo-scalar or vector mediators can be found in Ref. [74].

2.2.3. Additional considerations for $t\bar{t}$ and $b\bar{b} + \cancel{E}_T$ signatures

With the MFV assumption, the top and bottom quark can play an important role in the phenomenology. The scalar and pseudo-scalar mediator models predict not only the monojet process described in Section 2.2, but also production of Dark Matter in association with top (or bottom) pairs, as illustrated in Fig. 22. Dedicated searches including jets from heavy flavor quarks in the final state can be designed for this signature. Another class of

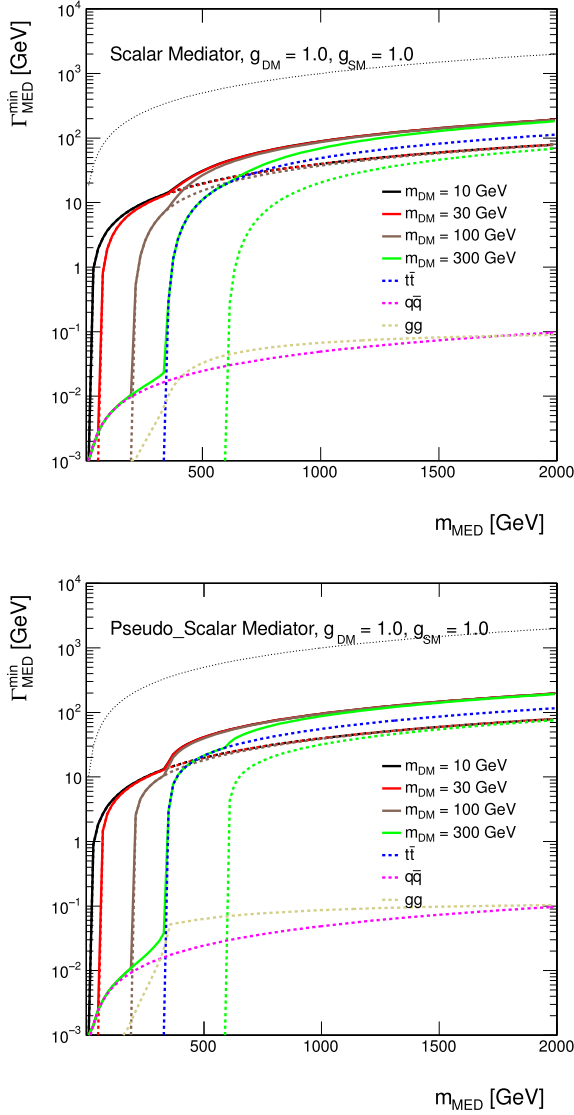


Fig. 20. Minimal width as a function of mediator mass for scalar and pseudo-scalar mediator assuming couplings of 1. The total width is shown as solid lines for DM masses of $m_\chi = 10$ GeV, 30 GeV, 100 GeV and 300 GeV in black, red, brown and green, respectively. The individual contributions from DM are indicated by dotted lines with the same colors. The contribution from all quarks but top is shown as magenta dotted line and the contribution from top quarks only is illustrated by the dotted blue line. The dotted beige line shows the contribution from the coupling to gluons. The dotted black line shows the extreme case $\Gamma_{\min} = M_{\text{med}}$. (For interpretation of the references to color in this figure legend, the reader is referred to the web version of this article.)

simplified models, which includes a Dark Matter interpretation among many others, and yields a single top quark in the final state, is detailed in [Appendix A.1](#).

In addition to the $t\bar{t}$ +DM models illustrated in [Fig. 22](#), some theoretically motivated scenario (e.g. for high $\tan\beta$ in 2HDM in the pMSSM) privilege the coupling of spin-0 mediators to down generation quarks. This assumption motivates the study of final states involving b -quarks as a complementary search to the $t\bar{t}$ +DM models, to directly probe the b -quark coupling. An example of such a model can be found in Ref. [\[42\]](#) and can be obtained by replacing top quarks with b quarks in [Fig. 22](#). Note that, because of the kinematics features of b quark production relative to heavy t quark production, a $b\bar{b}$ +DM final state may only yield one experimentally visible b quark, leading to a mono- b signature in a model that conserves b flavor.

Dedicated implementations of these models for the work of this Forum are available at LO+PS accuracy, even though the state of the art is set to improve on a timescale beyond that for early Run-2 DM searches as detailed in [Section 4.1.5](#). The studies in this Section have been produced using a leading order UFO model within MADGRAPH5_AMC@NLO 2.2.2 [\[75–77\]](#) using PYTHIA 8 for the parton shower.

Parameter scan. The parameter scan for the dedicated $t\bar{t}+\cancel{E}_T$ searches has been studied in detail to target the production mechanism of DM associated with heavy flavor quarks, and shares many details of the scan for the scalar model with a gluon radiation. The benchmark points scanning the model parameters have been selected to ensure that the kinematic features of the parameter space are sufficiently represented. Detailed studies were performed to identify points in the m_χ , $m_{\phi,a}$, g_χ , g_q (and $\Gamma_{\phi,a}$) parameter space that differ significantly from each other in terms of expected detector acceptance. Because missing transverse momentum is the key observable for searches, the mediator p_T spectra is taken to represent the main kinematics of a model. Another consideration in determining the set of benchmarks is to focus on the parameter space where we expect the searches to be sensitive during the 2015 LHC run. Based on a projected integrated luminosity of 30 fb^{-1} expected for 2015, we disregard model points with a cross section times branching ratio smaller than 0.1 fb , corresponding to a minimum of one expected event assuming a 0.1% efficiency times acceptance.

The kinematics is most dependent on the masses m_χ and $m_{\phi,a}$. [Figs. 23](#) and [24](#) show typical dependencies for scalar and pseudoscalar couplings respectively. Typically, the mediator p_T spectrum broadens with larger $m_{\phi,a}$. The kinematics are also different between on-shell ($M_{\text{med}} > 2m_\chi$) and off-shell ($M_{\text{med}} < 2m_\chi$) mediators as discussed in [Section 2.2](#). Furthermore, the kinematic differences in the \cancel{E}_T spectrum between scalar and pseudoscalar are larger for light mediator masses with respect to heavier mediators. It is therefore important to choose benchmark points covering on-shell and off-shell mediators with sufficient granularity, including the transition region between on-shell and off-shell mediators.

Typically only weak dependencies on couplings are observed (see [Fig. 25](#)) where the variation with width of the integral over parton distributions is unimportant. As shown in [Section 2.1.1](#), for couplings $\sim O(1)$ the width is large enough that the p_T of the mediator is determined mainly by the PDF.

At large mediator masses ($\sim 1.5 \text{ TeV}$) or very small couplings ($\sim 10^{-2}$), width effects are significant, but these regimes have production cross sections that are too small to be relevant for 30 fb^{-1} and are not studied here. However, with the full Run 2 dataset, such models may be within reach.

Another case where the width can impact the kinematics is when $m_{\phi,a}$ is slightly larger than $2m_\chi$. Here, the width determines the relative contribution between on-shell and off-shell mediators. An example is given in [Fig. 26](#). As the minimal width choice pursued in this document is the most conservative one, this effect can be neglected in order to reduce the number of benchmark points to be generated.

The points for the parameter scan chosen for this model are listed in [Table 5](#), chosen to be harmonized with those for other analyses employing the same scalar model as benchmark. Based on the sensitivity considerations above, DM masses are only simulated up to 500 GeV (but the 5 TeV mediator point is retained) leading to a total of 24 benchmark points. However for these searches we recommend to generate and simulate scalar and pseudoscalar models separately, as the kinematics differs due to the different coupling of the mediator to the final state top quarks in the two cases, as shown in [Figs. 23](#) and [24](#).

Table 6

Minimal width of the scalar mediator exchanged in s -channel divided by its mass, assuming $g_q = g_\chi = 1$. The loop-induced gluon contribution is ignored. The numbers tabulated under $2m_\chi = M_{\text{med}}$ correspond to the width calculated for $M_{\text{med}} = 5$ GeV.

m_χ/GeV	$M_{\text{med}}/\text{GeV}$								
	10	20	50	100	200	300	500	1000	10000
1	0.040	0.040	0.040	0.040	0.040	0.040	0.062	0.089	0.099
10	<0.001	<0.001	0.040	0.040					0.099
50	<0.001		<0.001	<0.001	0.040	0.040			0.099
150	<0.001				<0.001	<0.001	0.062	0.089	0.099
500	<0.001						0.022	0.049	0.099
1000	<0.001							0.049	0.099

Table 7

Minimal width of the pseudo-scalar mediator exchanged in s -channel divided by its mass, assuming $g_q = g_\chi = 1$. The loop-induced gluon contribution is ignored. The numbers tabulated under $2m_\chi = M_{\text{med}}$ correspond to the width calculated for $M_{\text{med}} = 5$ GeV.

m_χ/GeV	$M_{\text{med}}/\text{GeV}$								
	10	20	50	100	200	300	500	1000	10000
1	0.040	0.040	0.040	0.040	0.040	0.040	0.083	0.095	0.099
10	<0.001	<0.001	0.040	0.040					0.099
50	<0.001		<0.001	<0.001	0.040	0.040			0.099
150	<0.001				<0.001	<0.001	0.083	0.095	0.099
500	<0.001						0.043	0.056	0.099
1000	<0.001							0.056	0.099

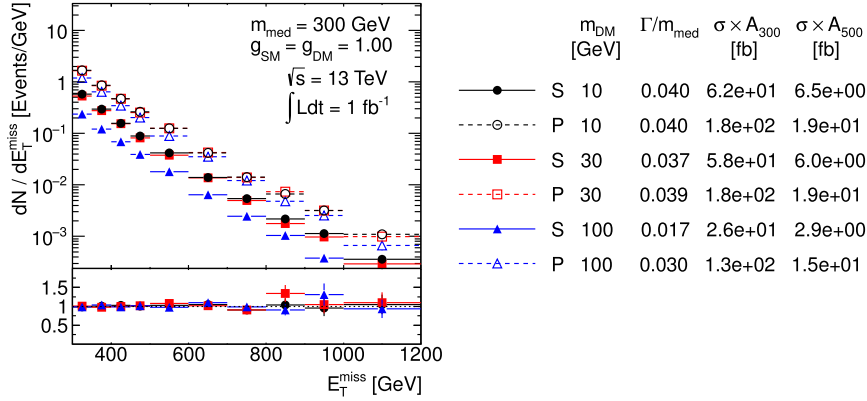


Fig. 21. Comparison of the \vec{E}_T distributions for the scalar and pseudoscalar models for different $M_{\text{med}} = 300$ GeV and different DM masses. Ratios of the normalized distributions with respect to the first one are shown. A_{300} and A_{500} in the table denote the acceptance of the $\vec{E}_T > 300$ GeV and $\vec{E}_T > 500$ GeV cut, respectively.

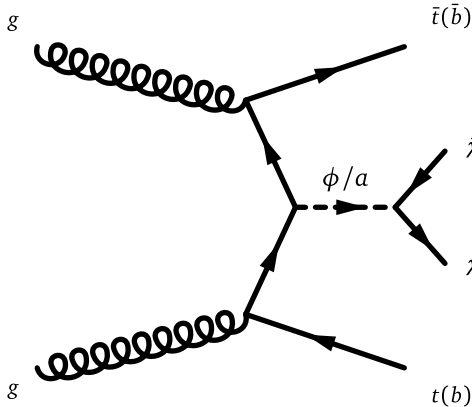


Fig. 22. Representative Feynman diagram showing the pair production of Dark Matter particles in association with $t\bar{t}$ (or $b\bar{b}$).

Similar studies were performed in the $b\bar{b}$ case. It was found that they show the same weak dependence of the kinematics of the event on the mediator width. The same benchmark parameters of the $t\bar{t}$ case could then be chosen.

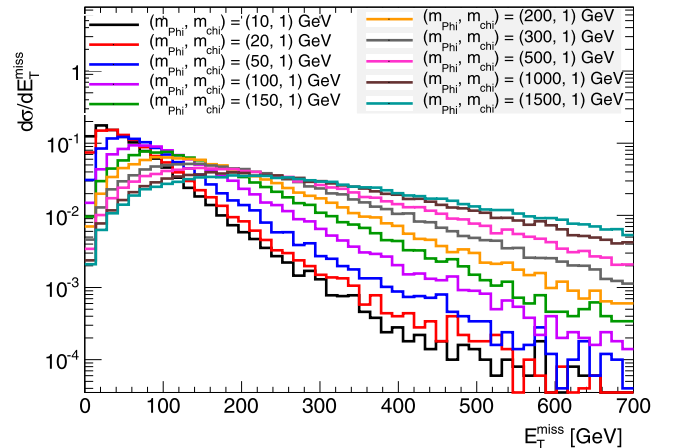


Fig. 23. Example of the dependence of the kinematics on the scalar mediator mass in the $t\bar{t} + \vec{E}_T$ signature. The Dark Matter mass is fixed to be $m_\chi = 1$ GeV.

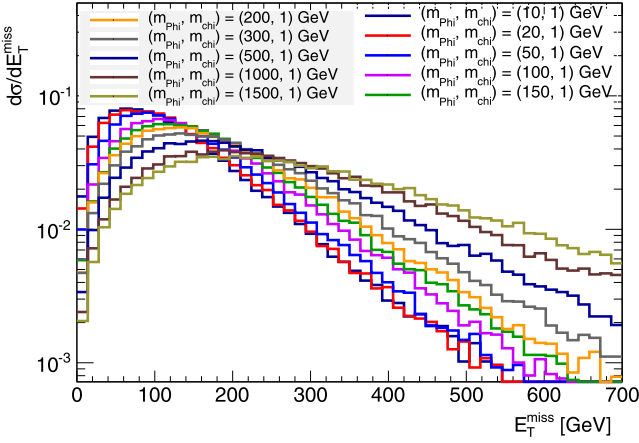


Fig. 24. Example of the dependence of the kinematics on the pseudoscalar mediator mass in the $t\bar{t} + \cancel{E}_T$. The Dark Matter mass is fixed to be $m_\chi = 1\text{ GeV}$. All figures concerning the $t\bar{t} + \cancel{E}_T$ signature have been produced using a leading order model within MADGRAPH5_AMC@NLO 2.2.2, using PYTHIA 8 for the parton shower.

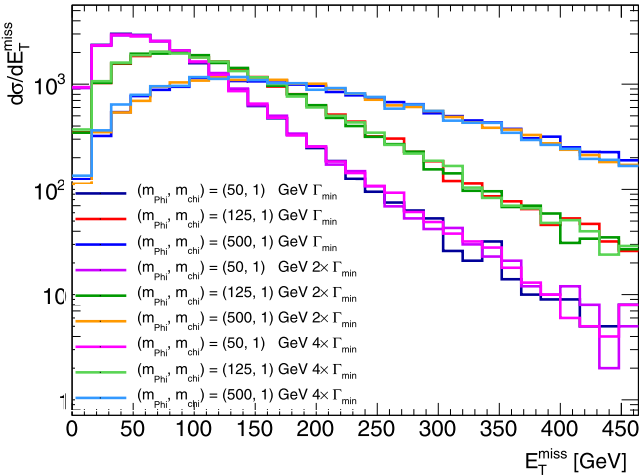


Fig. 25. Study of the dependence of kinematics on the width of a scalar mediator $t\bar{t} + \cancel{E}_T$. The width is increased up to four times the minimal width for each mediator and Dark Matter mass combination.

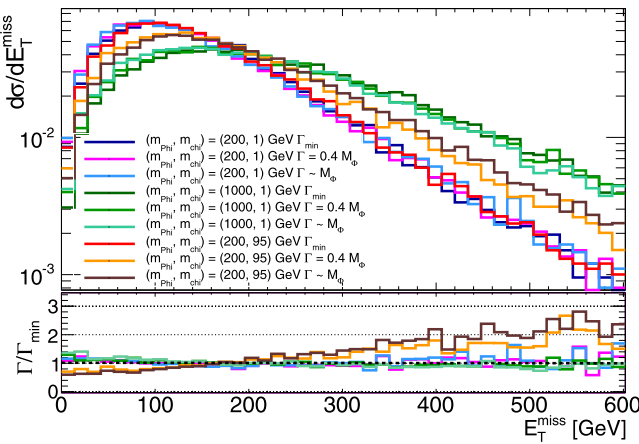


Fig. 26. Dependence of the kinematics on the width of a scalar mediator $t\bar{t} + \cancel{E}_T$. The width is increased up to the mediator mass. Choices of mediator and Dark Matter masses such that $m_{\phi,a}$ is slightly larger than $2m_\chi$ is the only case that shows a sizeable variation of the kinematics as a function of the width.

2.3. Colored scalar mediator, t -channel exchange

The preceding sections address models with a Dirac fermion coupled to the SM through exchange of a neutral spin-0 or spin-1 particle in an s -channel process. A t -channel process may couple the SM and DM directly, leading to a different phenomenology. For completeness, we examine a model where χ is a Standard Model (SM) singlet, a Dirac fermion; the mediating particle, labeled ϕ , is a charged scalar color triplet and the SM particle is a quark. Such models have been studied in Refs. [34,36,38,46,78,79]. However, these models have not been studied as extensively as others in this Forum.

Following the example of Ref. [78], the interaction Lagrangian is written as

$$\mathcal{L}_{\text{int}} = g \sum_{i=1,2} (\phi_{(i),L} \bar{Q}_{(i),L} + \phi_{(i),u,R} \bar{u}_{(i),R} + \phi_{(i),d,R} \bar{d}_{(i),R}) \chi \quad (12)$$

where $Q_{(i),L}$, $u_{(i),R}$ and $d_{(i),R}$ are the SM quarks of the i th generation and $\phi_{(i),L}$, $\phi_{(i),u,R}$ and $\phi_{(i),d,R}$ are the corresponding mediators, which (unlike the s -channel mediators) must be heavier than χ . These mediators have SM gauge representations under $(SU(3), SU(2))_Y$ of $(3, 2)_{-1/6}$, $(3, 1)_{2/3}$ and $(3, 1)_{-1/3}$ respectively. Variations of the model previously studied in the literature include coupling to the left-handed quarks only [79,80], to the $\phi_{(i),u,R}$ [34] or $\phi_{(i),d,R}$ [39,78], or some combination [36,38].

The minimal width of each mediator is expressed, using the example of decay to an up quark, as

$$\Gamma(\phi_{(i)} \rightarrow \bar{u}_{(i)} \chi) = \frac{g_{(i)}^2}{16\pi M_{\phi_{(i)}}^3} (M_{\phi_{(i)}}^2 - m_{u_{(i)}}^2 - m_\chi^2) \times \sqrt{(M_{\phi_{(i)}}^2 - (m_{u_{(i)}} + m_\chi)^2)(M_{\phi_{(i)}}^2 - (m_{u_{(i)}} - m_\chi)^2)}, \quad (13)$$

which reduces to

$$\frac{g_{(i)}^2 M_{\phi_{(i)}}}{16\pi} \left(1 - \frac{m_\chi^2}{M_{\phi_{(i)}}^2}\right)^2 \quad (14)$$

in the limit $M_{\phi_{(i)}}, m_\chi \gg m_{u_{(i)}}$.

The generation index i for $\phi_{(i)}$ is linked to the incoming fermion(s), and it runs on all three quark generations due to the MFV assumption. Ref. [78] considers two extreme cases for this model in terms of cross-sections: the case in which all mediator flavors are present, leading to the maximal cross-section, and the case in which only right-handed down-type mediators are present. Neither of the models in this reference include couplings to the third quark generation, leading to a violation of the MFV assumption. In the case of purely down-type right-handed squarks this is still safe from flavor constraints. Furthermore, reintroducing the third generation squarks would lead to models that produce qualitatively similar signals in the mono-jet and SUSY squark searches, the main difference being the production cross-section. At the same time the presence of third generation squarks will lead to further constraints from other searches such as those for mono-bjets, for stops and for sbottoms, as discussed in Section 2.3.2. The studies in this Section are performed using a model with a mediator coupling to all three generation, following Ref. [46]. Further differences between the two models (hypercharge, chirality) only lead to a change in the cross-section. The LO UFO model is interfaced to MADGRAPH5_AMC@NLO v2.2.3, but it was not possible to go beyond parton-level studies and interface those models to a parton shower in time for the conclusion of this Forum. The state of the art for calculating these models is LO+PS, and the implementation of multi-parton merging has been studied in detail [78,81–83], and further studies should be

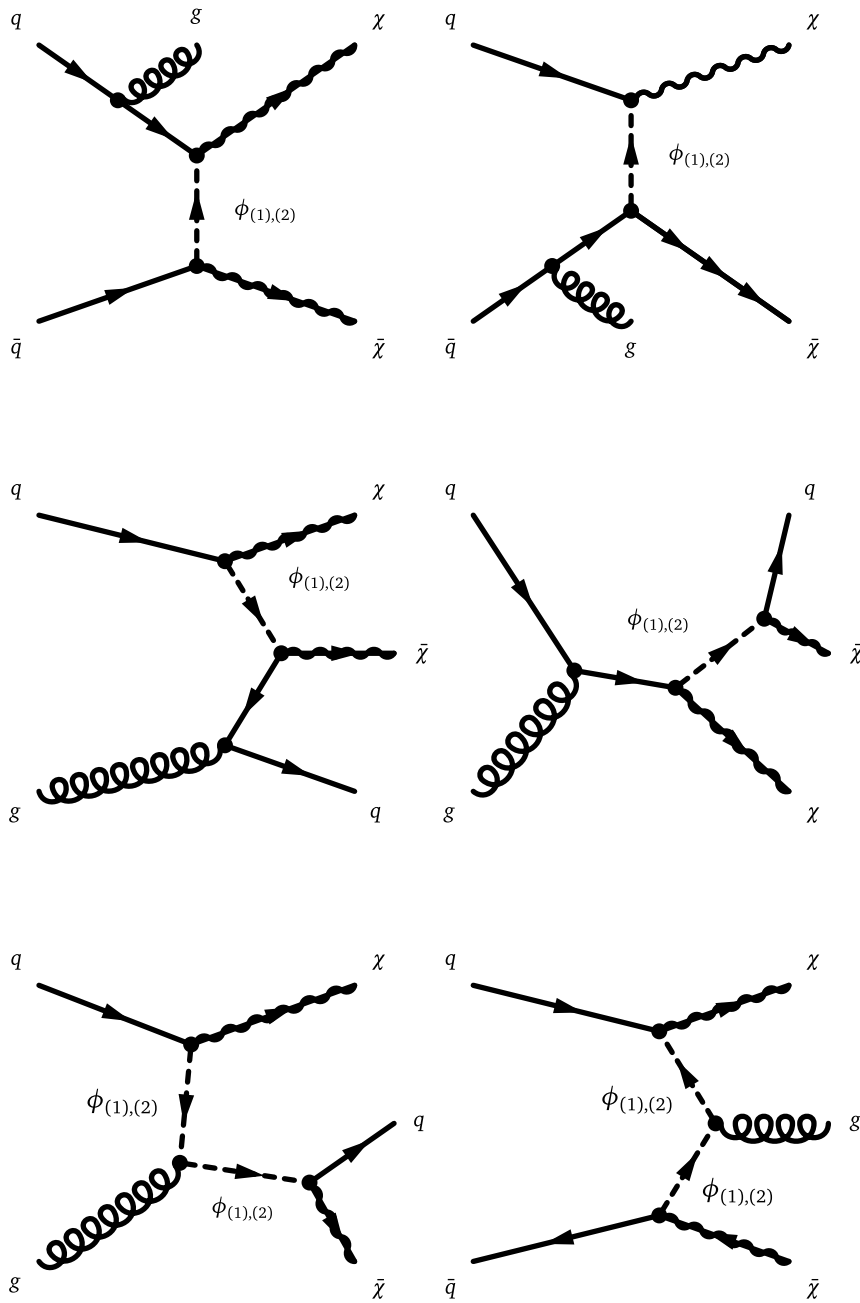


Fig. 27. Leading order mono-jet t -channel processes.

Source: Adapted from [78].

undertaken prior to generating signal samples for early Run-2 LHC searches.

The leading-order processes involved in \cancel{E}_T +jet production are shown in Fig. 27. This model can also give a signal in the \cancel{E}_T + di-jet channel when, for example, the χ is exchanged in the t -channel and the resulting ϕ pair each decay to a jet + χ . Fig. 28 shows the leading order diagrams. Except for the gg induced process, di-jet production through the third-generation mediator $\phi_{(3),u}$ is not possible, and production through $\phi_{(3),d}$ is suppressed. However, if the coupling g includes a Yukawa coupling proportional to the quark mass, and g is sufficiently large, LHC searches will still be sensitive to this model, as explained in Section 2.3.2.

The diagram involving the t -channel exchange of χ is strongly dependent upon the Dirac fermion assumption. For a Majorana

fermion, $q\bar{q}$, $\bar{q}q$, and qq production would be possible with the latter having a pronounced enhancement at the LHC.

This model is similar to the simplified model considered in SUSY searches, implemented as the MSSM with only light squarks and a neutralino, except for two distinct points: the χ is a Dirac fermion and the coupling g is not limited to be weak scale ($g \ll 1$). In the MSSM, most of these processes are sub-dominant, even if resonantly enhanced, because the production is proportional to weak couplings. In the more general theories considered here, g is free to take on large values of order 1 or more, and thus diagrams neglected in MSSM simulation can occur at a much higher rate here. While constraints from SUSY jets+ \cancel{E}_T analyses on MSSM models can be recast to apply to the specific model in this report, DM searches should also directly test their sensitivity to the MSSM benchmark models.

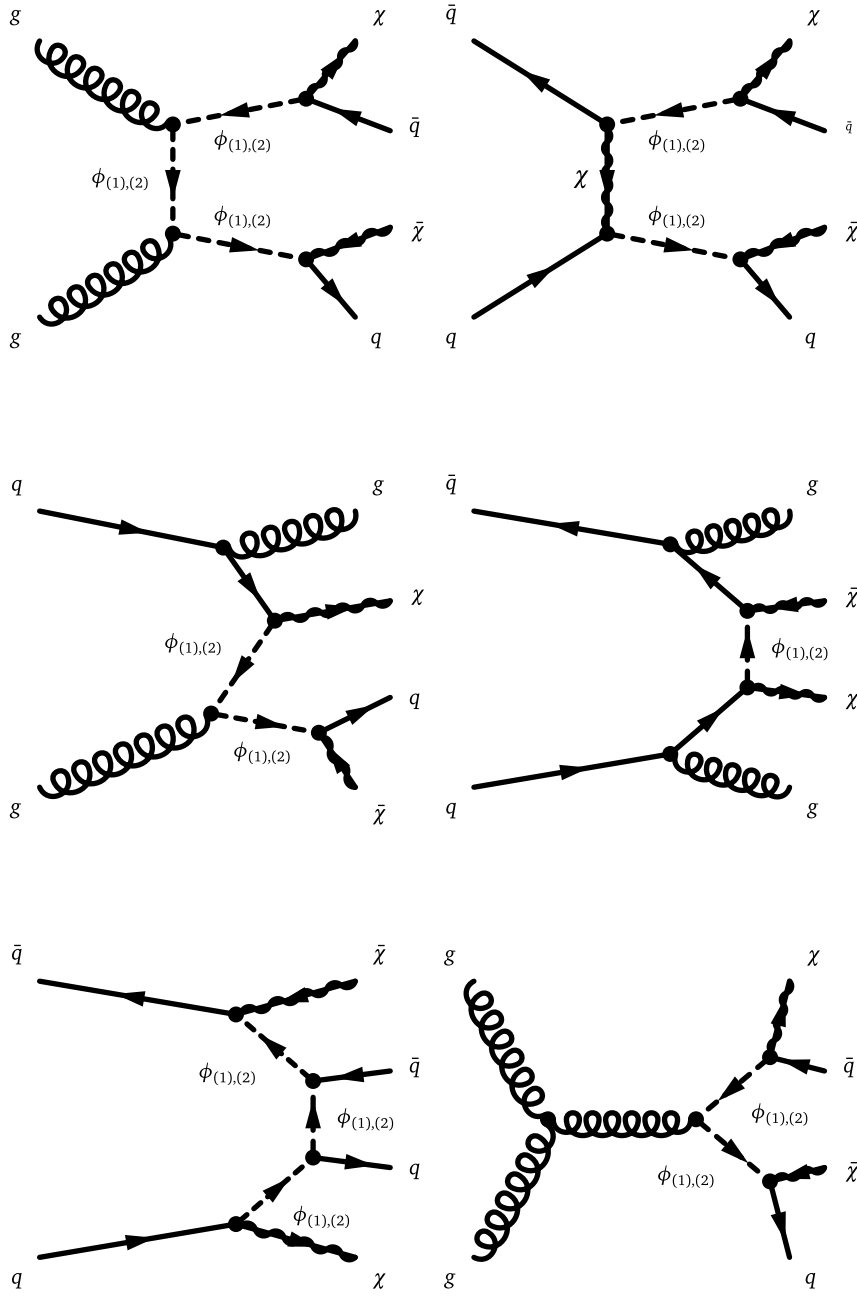


Fig. 28. Leading order two-jet t -channel processes.
Source: Adapted from [78].

The state of the art calculation for these models is LO and they can be interfaced with a parton shower program. The studies in this Section use a LO model implementation within MADGRAPH5_AMC@NLO v2.2.3, but no parton shower could be employed in the time-frame of the conclusions of this Forum. Further implementation details can be found in Section 4.1.3.

2.3.1. Parameter scan

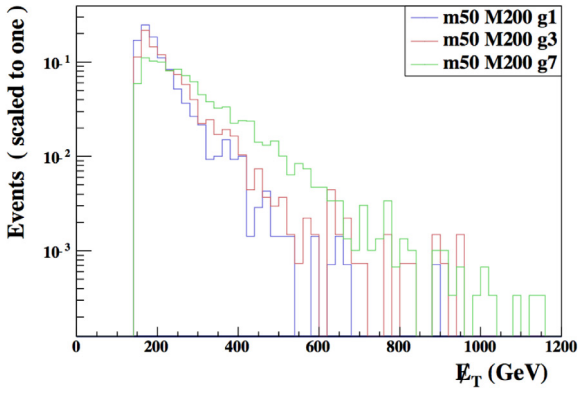
As for the s -channel models, we adopt the simplifying assumption that the mediator masses and couplings are equal for each flavor and handedness. The free parameters are then

$$\{m_\chi, M_\phi, g\}. \tag{15}$$

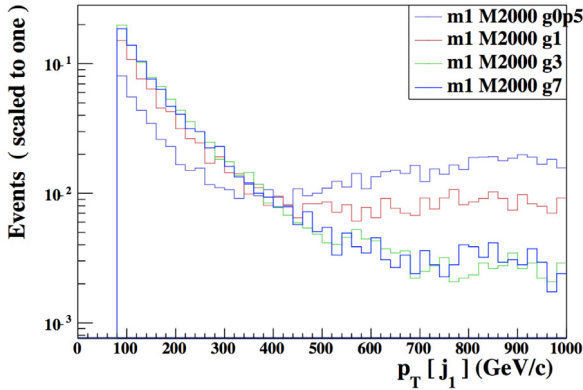
Ref. [78] studies the parameter space and obtains bounds on this model from LHC Run-1 mono-jet and dijets+ \cancel{E}_T data. The Forum did not exhaustively compare the kinematic distributions

of the t -channel models as done in the s -channel case. In particular, the absence of a parton shower simulation can affect some of the conclusions on the points and sensitivity chosen. While this means the conclusions on the parameter scan below should be taken with more caution, the model is plausible and distinctive, and it should be included in the design of early Run-2 LHC searches.

As in the s -channel models, scans should be performed over m_χ and M_ϕ . The viable ranges of both parameters nearly coincide with the scan proposed for the s -channel. For the early Run-2 searches, we recommend to generate and fully simulate a subset of the s -channel mono-jet grid that accounts for the on-shell and off-shell regions. In contrast to the s -channel case, the bounds one obtains from \cancel{E}_T+X searches depend strongly on the width of the mediator, as is visible in Figs. 5 and 6 of Ref. [78] and in



(a) \cancel{E}_T distribution for a 200 GeV t -channel mediator, when varying the couplings.



(b) Leading jet p_T distribution for a 2 TeV t -channel mediator with small ($g=0.5$) to large ($g=7$) couplings with a DM mass of 1 GeV

Fig. 29. Kinematic distributions normalized to unit area from the t -channel model from Ref. [46], using MadAnalysis [84,86] and simplified analysis cuts on the leading jet $p_T > 150$ GeV and $\eta < 2.8$, $\cancel{E}_T > 150$ GeV. For these models, a LO UFO model is interfaced to MADGRAPH5_AMC@NLO v2.2.3, and studies are at parton-level only.

Fig. 29(a), except in the heavy mediator limit ($M_\phi \approx 2$ TeV). This figure has been obtained applying a simplified analysis selection (cuts on the leading jet $p_T > 150$ GeV and $\eta < 2.8$, $\cancel{E}_T > 150$ GeV.) using MadAnalysis [84,85]. Fig. 29(b) also shows that, if the DM mass is low and the mediator is produced on-shell and its width is narrow, the cross-section is dominated by $qg \rightarrow q\chi\chi$ diagram. The mediator energy is then split evenly between the light DM particles and the quark, leading to a broad enhancement at $M_{\text{med}}/2$.

Points with distinct kinematic distributions for a preliminary scan in $\{m_\chi, M_\phi, g\}$ are selected taking into account the expected sensitivity of Run-2 searches, and requiring at least 100 events to pass the kinematic cuts outlined for Fig. 29 in 25 fb^{-1} of collected data, and respect $\Gamma/M_{\text{med}} < 1$. They are outlined in Table 8. The conclusions in this table may change when a parton shower is employed together with multiparton matching.

2.3.2. Additional considerations for $V + \cancel{E}_T$ signatures

The models and parameters with emission of an EW boson generally follow those in Section 2.3. even though different diagrams are involved. A representative Feynman diagram can be constructed by replacing a final-state gluon in Fig. 27 with a γ , W , Z boson, but radiation of electroweak bosons directly from the mediator also leads to a mono-boson signature.

Table 8

Simplified model benchmark points for t -channel simplified model (spin-0 mediators coupling to Dirac DM fermions, taking the minimum width).

m_χ /GeV	$M_{\text{med}}/\text{GeV}$		Couplings		
1	10	50	100	300	0.1, 1, 3, 7
1				500	0.25, 1, 3, 7
1				1000	1, 3, 7
				2000	
50		55			0.1, 1, 3, 4π
50			200	300	0.1, 1, 3, 7
500				550	1, 3
500					0.25, 1, 3
500				1000	3
				2000	
1000					3, 4π
1000				1100	3
				2000	

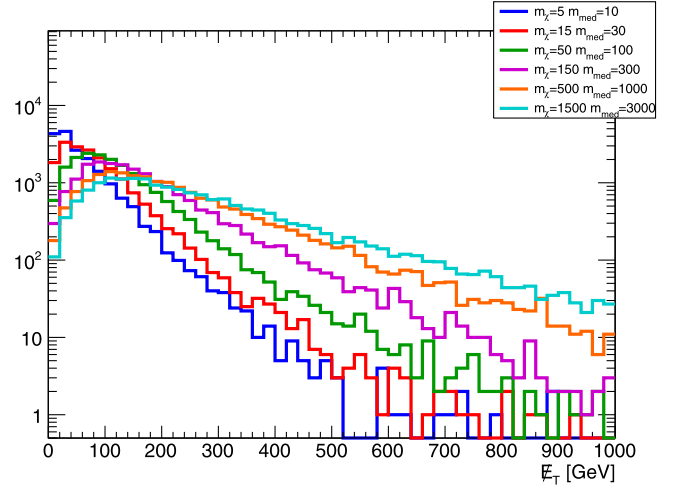


Fig. 30. Missing transverse momentum distribution for the hadronic $Z + \cancel{E}_T$ final state, for the simplified model with a colored scalar mediator exchanged in the t -channel.

The models considered in Section 2.3 present a relevant difference concerning final states with an electroweak boson. In the model in [46], both right- and left-handed mediators can radiate a Z boson, while only the left-handed mediator in [46] allows for W and Z radiation.

The studies in this Section use the LO+PS UFO model from [46] in MADGRAPH5_AMC@NLO v2.2.3, using PYTHIA 8 for the parton shower. Fig. 30 shows the \cancel{E}_T distribution for the hadronic $Z + \cancel{E}_T$ final state, with varying DM and mediator mass, before any selection. The acceptance for a series of basic analysis selections ($\cancel{E}_T > 350$ GeV, leading jet $p_T > 40$ GeV, minimum azimuthal angle between jet and $\cancel{E}_T > 0.4$) applied at the generator level is shown in Fig. 31.

The discussion of the parameter scan for the t -channel model in the case of signatures including EW bosons parallels that of the monojet case for mediator and DM masses, but no kinematic dependence on the width is observed, so a coupling scan is not needed.

Additional considerations for signatures with b -quarks + \cancel{E}_T . Models of bottom-flavored Dark Matter that are closely related to the t -channel mediated model from this Section have been proposed in Refs. [87,88]. We describe the b -FDM model of Ref. [88], created to explain the Galactic Center (GC) gamma-ray excess observed in data collected by the Fermi-LAT collaboration [89,90]. This model favors couplings to third-generation quarks via Yukawa couplings, therefore respecting the MFV assumption.

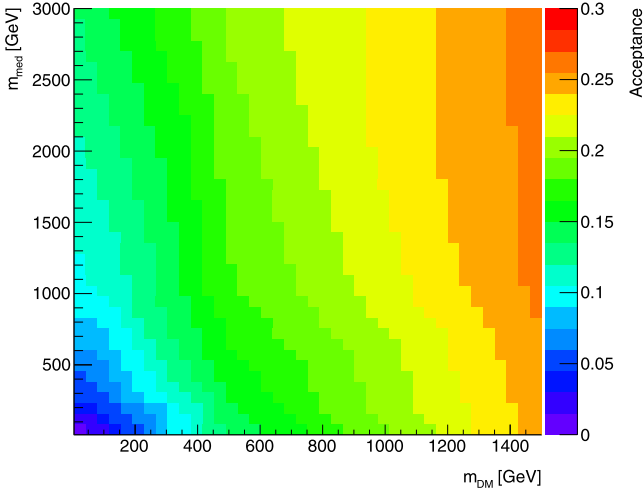


Fig. 31. Acceptance for the hadronic $Z+\ell_T$ final state, for the simplified model with a colored scalar mediator exchanged in the t -channel.

The model contains a Dirac fermion transforming as a flavor triplet, exclusively coupling to right-handed down-type quarks. The third component of the triplet χ_b comprises the cosmological DM. Within the MFV framework, the other fermions in the flavor triplet can be made sufficiently heavy and weakly-coupled that they can be neglected in the analysis. A flavor singlet, color triplet scalar field Φ mediates the interactions between the DM and the Standard Model quarks. The model is similar to the MSSM with a light bottom squark and neutralino, and is thus a flavor-specific example of a t -channel model. Similar top-flavored models can exist, as e.g. in Refs. [91,92]. In the case where the top coupling is the main DM coupling, the signal is very similar to a signal from a stop quark, since unlike the other t -channel cases there is no top in the initial state parton distribution functions (PDFs). This is the reason why it was not considered as an additional model. More recent literature shows that other flavor states could also contribute to LHC signals, as shown in Ref. [93], but such models will have to be investigated on a longer timescale with respect to that of this Forum.

The Lagrangian considered is given by

$$-\mathcal{L} \supset g\Phi^* \bar{\chi}_b b_R + \text{h.c.} \quad (16)$$

This model is known at LO+PS accuracy, and the studies in this Section use a LO model implementation within MADGRAPH5_AMC@NLO v2.2.3 interfaced to PYTHIA 8 for the parton shower. Further implementation details can be found in Section 4.1.5.

Parameter scan. In this model, the interference of diagrams with QCD production of the mediator (which scale as g_s^2) with diagrams that are proportional to the coupling g in the $b+\ell_T$ and $b\bar{b}+\ell_T$ final states. In the case of large couplings, this is not conducive to a simple scaling behavior that would allow us to reduce the number of points to be simulated. This can be seen in Fig. 33.

A full study of the parameter scan for this model was not available for this report; thus for early Run-2 searches we recommend scanning a range of possible widths as discussed in a more limited way than for the t -channel mono-jet, spanning from the minimal width to a value approaching the particle limit, e.g. $g = 0.5, 1, 2, 3$. A coupling benchmark such as $g = 1$ should be considered for each mass point since this would be a distinctive feature of this benchmark from SUSY models with sbottom squarks (see Section 2.3 for further discussion).

A scan of Dark Matter and mediator masses should be done in the on-shell region $M_\Phi > m_\chi + m_b$, since the cross-sections in the off-shell region are too small to be probed with early LHC data, spanning from 10 to 500 GeV in m_χ and from 10 to 1300 GeV in M_Φ . Examples of the kinematic distributions produced by this model are shown in Fig. 32.⁸

2.4. Spin-2 mediator

In models with extra dimensions, the Kaluza–Klein excitations of the graviton could also serve as a mediator between the SM and dark sector physics. This kind of model was not studied in the forum and is not included in the recommendations, but models such as Ref. [94,95] may warrant further study on a longer timescale.

2.5. Presentation of results for reinterpretation of s -channel mediator models

The aim of the parameter grid optimization done for the s -channel models in the previous sections is to reduce the parameter space that must be simulated. We then need a procedure for populating the full parameter space by using the simulated grid points. We recommend doing this as follows:

- When the dependences on parameters are known, the cross sections and efficiencies at general points can be calculated from the grid data.
- In other cases, this information can be obtained by interpolation between the grid points. We have chosen the grid points so that the dependence is sufficiently smooth that this will be possible.

The results of the scan over the couplings presented in the previous sections indicate that there are no changes in kinematic distributions for different choices of the coupling strengths. This means that the acceptance remains the same in the whole g_q – g_χ plane and it is sufficient to perform the detector simulation only for one single choice of g_q, g_χ . The resulting truth-level selection acceptance and the detector reconstruction efficiency can then be applied to all remaining grid points in the g_q – g_χ plane where only the generator-level cross section needs to be known. This significantly reduces the computing time as the detector response is by far the most CPU-intensive part of the Monte Carlo sample production. However, the number of generated samples can be reduced even further if a parameterization of the cross section dependence from one grid point to another exists. In this section, we describe the details of a cross section scaling procedure that can be used to reinterpret results for a fixed coupling for s -channel mediator models. The studies in this section employ the POWHEG [43] generator.

The propagator for the s -channel exchange is written in a Breit–Wigner form as $\frac{1}{q^2 - M_{\text{med}}^2 + iM_{\text{med}}\Gamma}$, where q is the momentum

transfer calculated from the two partons entering the hard process after the initial state radiation, which is equivalent to the momentum of the DM pair.⁹ The size of the momentum transfer with respect to the mediator mass allows us to identify three cases:

⁸ Following the grounding assumptions in this report, the normalization to the relic density is considered only in these example plots rather than as a necessary ingredient for the parameter scan of this model.

⁹ Using a running width and replacing the denominator of the propagator with $q^2 - M_{\text{med}}^2 + iQ^2 \frac{\Gamma}{M_{\text{med}}}$ should be considered in the case of wide mediators [96].

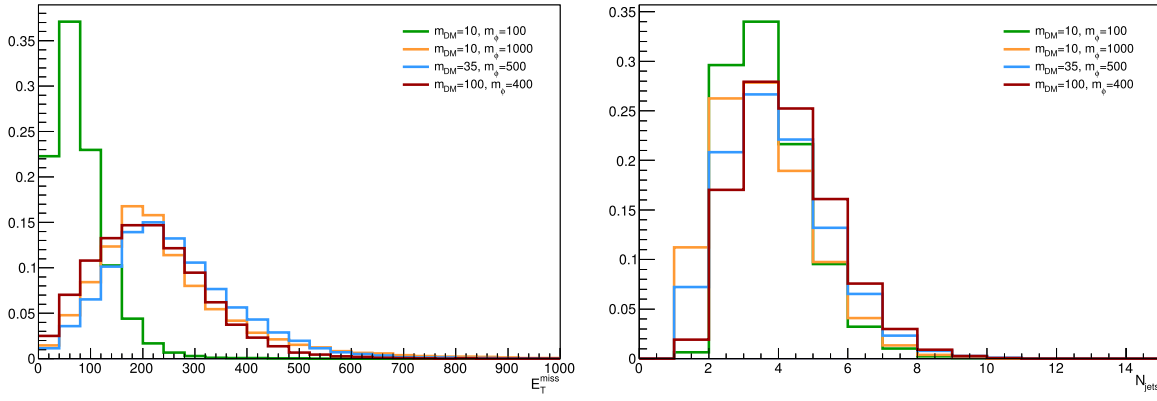


Fig. 32. E_T (left) and jet multiplicity (right) for various DM and mediator masses and couplings normalized to the relic density observed in the early universe. Studies in this section use a LO UFO model implementation within MADGRAPH5_AMC@NLO v2.2.3 interfaced to PYTHIA 8 for the parton shower.

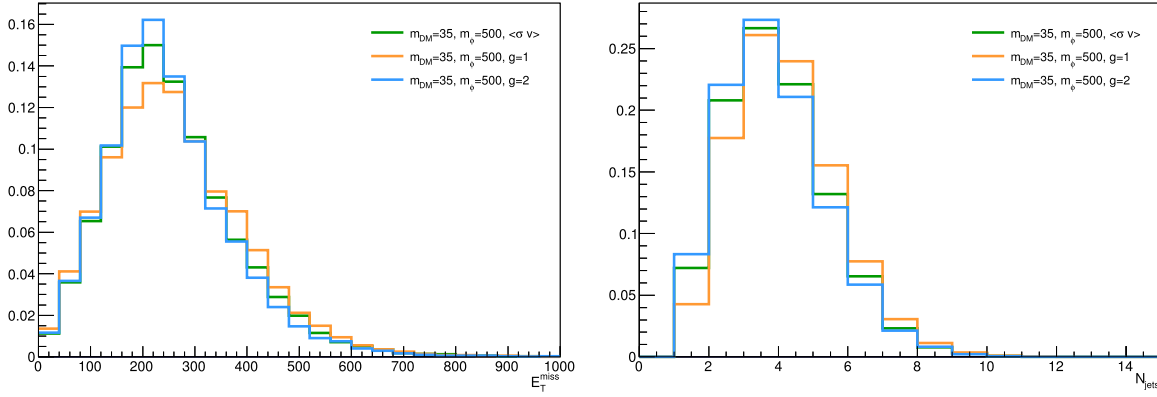


Fig. 33. E_T (left) and jet multiplicity (right) for $m_\chi = 35$ GeV and $M_\phi = 500$ GeV for varying couplings of $g = 1, 2$.

- off-shell mediator, when $q^2 \gg M_{\text{med}}^2$ leading to suppressed cross sections,
- on-shell mediator, when $q^2 \sim M_{\text{med}}^2$ leading to enhanced cross sections,
- effective field theory (EFT) limit when $q^2 \ll M_{\text{med}}^2$.

In the case of the off-shell mediator and the EFT limit, the first and second term in the propagator dominate, respectively, which reduces the dependence on the mediator width. Therefore, in these cases one can approximate the cross section as

$$\sigma \propto g_q^2 g_\chi^2. \quad (17)$$

The on-shell regime is the most interesting one as it gives the best chances for a discovery at the LHC given the cross section enhancement. The propagator term with the width cannot be neglected in this case and, in the narrow width approximation which requires $\Gamma \ll M_{\text{med}}$ (this is not necessarily the case in the benchmarks considered in the scans), one can integrate

$$\int \frac{ds}{(s - M_{\text{med}}^2)^2 + M_{\text{med}}^2 \Gamma^2} = \frac{\pi}{M_{\text{med}} \Gamma} \quad (18)$$

which further implies the cross section scaling

$$\sigma \propto \frac{g_q^2 g_\chi^2}{\Gamma}. \quad (19)$$

The narrow width approximation is important here as it ensures an integration over parton distribution functions (PDFs) can be neglected. In other words, it is assumed the integrand in Eq. (18) is non-zero only for a small region of s , such that the PDFs can be taken to be constant in this range. By simplifying the dependence of the minimal width on the couplings as $\Gamma \sim g_q^2 + g_\chi^2$, one can

approximate this scaling rule in the extreme cases as follows

$$\sigma \propto \frac{g_q^2 g_\chi^2}{g_q^2 + g_\chi^2} \xrightarrow{g_q \ll g_\chi} g_q^2 \quad (20)$$

$$\sigma \propto \frac{g_q^2 g_\chi^2}{g_q^2 + g_\chi^2} \xrightarrow{g_q \gg g_\chi} g_\chi^2. \quad (21)$$

However, it is important to keep in mind that this formula omits color and multiplicity factors as well as possible Yukawa suppression, and there is no simple scaling rule for how the cross section changes with the DM mass and the mediator mass, or for mediators with a large width, because PDFs matter in such cases as well. Therefore, the scaling procedure outlined above is expected to work only for fixed masses and fixed mediator width, assuming the narrow width approximation applies.

Fig. 34 shows the minimal width over the mediator mass in the g_q - g_χ plane for vector and scalar mediators for $M_{\text{med}} = 100$ GeV and 1000 GeV, taking $m_\chi = 10$ GeV. The individual colors indicate the lines of constant width, along which the cross section scaling may work for narrow mediators. The limiting case $\Gamma_{\text{min}} = M_{\text{med}}$ defines the upper values of the couplings below which the narrow width approximation can be considered and provides more stringent constraint than the perturbative limit $g_q = g_\chi = 4\pi$. For vector and axial-vector mediators, the minimal width is predominantly defined by g_q due to the number of quark flavors and the color factor. On the contrary, both the SM and DM partial width have comparable contributions in case of scalar and pseudo-scalar mediators if the top quark channel is open ($M_{\text{med}} > 2m_t$). However, mostly g_χ defines the minimal width for $M_{\text{med}} < 2m_t$ due to the Yukawa-suppressed light quark couplings.

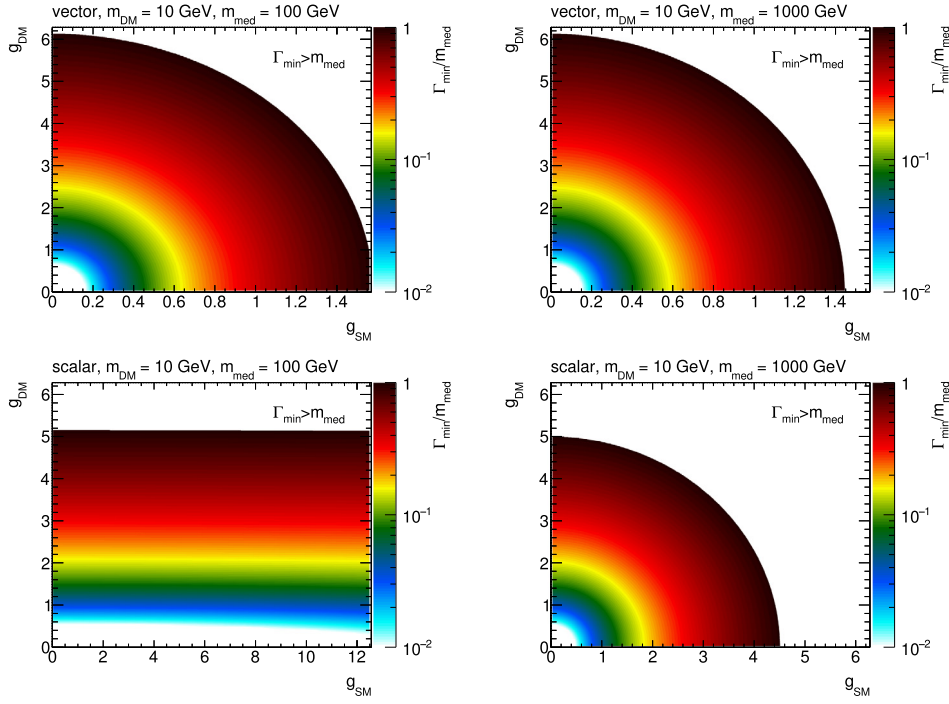


Fig. 34. Minimal width over the mediator mass for vector (top) and scalar (bottom) mediators as a function of the individual couplings g_q and g_χ , assuming $M_{\text{med}} = 100$ GeV (left) and $M_{\text{med}} = 1$ TeV (right). $m_\chi = 10$ GeV is considered in all cases. Only the cases with $\Gamma_{\text{min}} < M_{\text{med}}$ are shown.

The performance of the cross section scaling is demonstrated in Fig. 35 where two mass points $M_{\text{med}} = 100$ GeV and 1 TeV with $m_\chi = 10$ GeV are chosen and rescaled from the starting point $g_q = g_\chi = 1$ according to Eq. (19) to populate the whole g_q - g_χ plane. This means the width is not kept constant in this test and this is done in purpose in order to point out deviations from the scaling when the width is altered. For each mass point, the rescaled cross section is compared to the generator cross section and the ratio of the two is plotted. For the given choice of the mass points, the scaling seems to work approximately within the precision of $\sim 20\%$ in the region where $\Gamma_{\text{min}} < M_{\text{med}}$. Constant colors indicate the lines along which the cross section scaling works precisely and there is a remarkable resemblance of the patterns shown in the plots of the mediator width. To prove the scaling along the lines of constant width works, one such line is chosen in Fig. 36 for a scalar mediator, defined by $M_{\text{med}} = 300$ GeV, $m_\chi = 100$ GeV, $g_q = g_\chi = 1$, and the rescaled and generated cross sections are found to agree within 3%.

2.5.1. Proposed parameter grid for cross-section scaling

We propose to deliver collider results in the g_q - g_χ plane using the following prescription, to ease reinterpretation through cross-section scaling:

- Since the shapes of kinematic quantities do not change for different couplings, use the acceptance and efficiency for the available $m_\chi = 50$ GeV, $M_{\text{med}} = 300$ GeV grid point from the $M_{\text{med}}-m_\chi$ plane for the scalar and pseudo-scalar mediator. In case of the vector and axial-vector mediator, use the grid point $m_\chi = 150$ GeV, $M_{\text{med}} = 1$ TeV.
- Generate additional samples in order to get generator cross sections only. For scalar and pseudo-scalar mediator, choose $m_\chi = 50$ GeV, $M_{\text{med}} = 300$ GeV with the following values for $g_q = g_\chi$: 0.1, 1, 2, 3. For vector and axial vector mediator, choose $m_\chi = 150$ GeV, $M_{\text{med}} = 1$ TeV with the following values for $g_q = g_\chi$: 0.1, 0.25, 0.5, 0.75, 1, 1.25, 1.5. The

upper values are defined by the minimal width reaching the mediator mass.

- Rescale the generator cross sections for on-shell resonance production along the lines of constant width in order to populate the whole g_q - g_χ plane in the region $\Gamma_{\text{min}} < M_{\text{med}}$. The scaling follows from Eq. (19) which for the constant width implies:

$$\sigma' = \sigma \times \frac{g_q^2 g_\chi^2}{g_q^2 g_\chi^2}. \quad (22)$$

2.5.2. Rescaling to different mediator width

In general it is also important to consider a larger mediator width than Γ_{min} in order to accommodate additional interactions of the mediator with the visible and hidden sector particles [41, 42]. If the narrow width approximation applies, the cross section scaling method described above can be used to reinterpret the results presented for the minimal width, since multiplying the width by factor n is equivalent to changing the coupling strength by factor \sqrt{n} , i.e.

$$\sigma(g_q, g_\chi, n\Gamma_{\text{min}}(g_q, g_\chi)) \propto \frac{g_q^2 g_\chi^2}{\Gamma_{\text{min}}(\sqrt{n}g_q, \sqrt{n}g_\chi)}. \quad (23)$$

The cross section for the sample with couplings g_q and g_χ and modified mediator width $\Gamma = n\Gamma_{\text{min}}$ can therefore be rescaled from a sample generated with the minimal width corresponding to the couplings scaled by \sqrt{n} as described in the following formula.

$$\sigma(g_q, g_\chi, n\Gamma_{\text{min}}(g_q, g_\chi)) = \frac{1}{n^2} \sigma(\sqrt{n}g_q, \sqrt{n}g_\chi, \Gamma_{\text{min}}(\sqrt{n}g_q, \sqrt{n}g_\chi)) \quad (24)$$

The advantage of doing this is in the fact that no event selection and detector response needs to be simulated since the changes in couplings do not have an effect on the shapes of kinematic distributions.

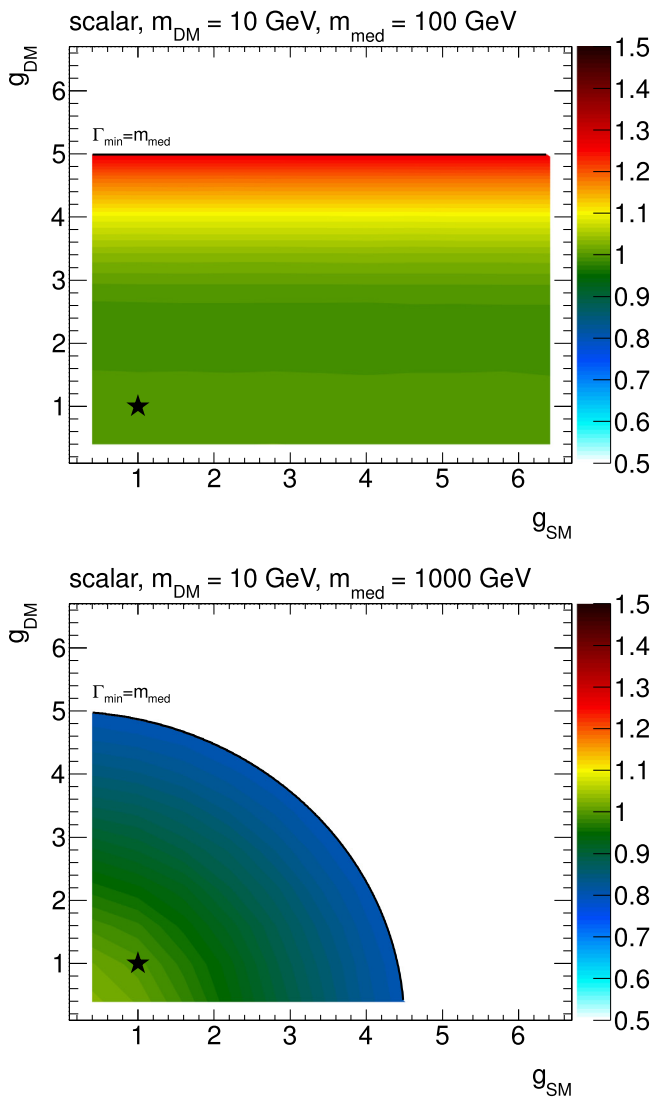


Fig. 35. Ratio of the rescaled and generated cross sections in the g_q - g_χ plane. The point at $g_q = g_\chi = 1$, taken as a reference for the rescaling, is denoted by a star symbol. Scalar model with $M_{\text{med}} = 100$ GeV (left) and 1 TeV (right) is plotted for $m_\chi = 10$ GeV. The limiting case $\Gamma_{\text{min}} = M_{\text{med}}$ is indicated by a black line and no results are shown beyond.

It should be noted again that this procedure is only useful when the narrow width approximation applies. Care must be taken to ensure that is the case. For example, in the vector and axial-vector cases, one quickly breaks this approximation even for small n .

Additional considerations for $t\bar{t}$ and $b\bar{b} + \cancel{E}_T$ signatures. The cross-section scaling considerations shown in Section 2.5 still apply for the reactions in the scalar and pseudoscalar models with explicit b and t quarks. Here we detail the specific studies done for the $t\bar{t}$ model.

Given that the kinematics are similar for all couplings $g \simeq 1$, we recommend to generate only samples with $g_\chi = g_q = 1$. It follows from this that these benchmark points should be a good approximation for non-unity couplings and for $g_\chi \neq g_q$, provided that the sample is rescaled to the appropriate cross section times branching ratio.

While the simple scaling function

$$\sigma' \times BR' = [\sigma \times BR] \times \left(\frac{g'_q}{g_q}\right)^2 \times \left(\frac{g'_\chi}{g_\chi}\right)^2 \times \frac{\Gamma}{\Gamma'} \quad (25)$$

is sufficient for a limited range of coupling values (see Fig. 37 for example), this scaling is only approximate (up to 20%) and relies on the narrow width approximation, ignoring PDFs effects.

3. Specific models for signatures with EW bosons

In this Section, we consider specific models with a photon, a W boson, a Z boson or a Higgs boson in the final state ($V + \cancel{E}_T$ signature), accompanied by DM particles that either couple directly to the boson or are mediated by a new particle. The common feature of those models is that they provide different kinematic distributions with respect to the models described in Section 2.

The models considered in this Section can be divided into two categories:

V-specific simplified models These models postulate direct couplings of new mediators to bosons, e.g. they couple the Higgs boson to a new vector or to a new scalar [48,97].

Models involving a SM singlet operator including a boson pair that couples to DM through a contact interaction Shown on the right-hand side of Fig. 38, these models allow for a contact interaction vertex that directly couples the boson to DM [45,97–99]. The models of this type included in this report are devoted to simplified models since UV completions for most of these operators proceed through loops and are not available to date. These models provide a benchmark to motivate signal regions that are unique to searches with EW final states and would otherwise not be studied. However, we recommend to use these models as placeholders and emphasize model-independent results especially in signal regions tailored to these models. Whenever results are interpreted in terms of these operators, a truncation procedure to ensure the validity of the EFT should be employed, as detailed in Section 5.

The following Sections describe the models within these categories, the chosen parameters for each of the benchmark models and the studies towards the choices of the parameters to be scanned.

3.1. Specific simplified models including EW bosons, tailored to Higgs+MET searches

Three benchmark simplified models [48,97] are recommended for Higgs+ \cancel{E}_T searches:

- A model where a vector mediator (Z'_B) is exchanged in the s -channel, radiates a Higgs boson, and decays into two DM particles (Fig. 39(a)). As in Section 2.1, we conservatively omit couplings of the Z'_B to leptons.
- A model where a scalar mediator S is emitted from the Higgs boson and decays to a pair of DM particles (Fig. 40).
- A model where a vector Z' is produced resonantly and decays into a Higgs boson plus an intermediate heavy pseudoscalar particle A^0 , in turn decaying into two DM particles (Fig. 39(b)).

These models are kinematically distinct from one another, as shown in the comparison of the \cancel{E}_T spectra in Fig. 41 for high and low masses of the pseudoscalar mediator. Fig. 41(a) shows the \cancel{E}_T distribution for models with high mediator masses ($m_S = 1$ TeV, $m_{Z'} = 1$ TeV, $m_{A^0} = 1$ TeV) and DM mass of either 50 (Z'_B and

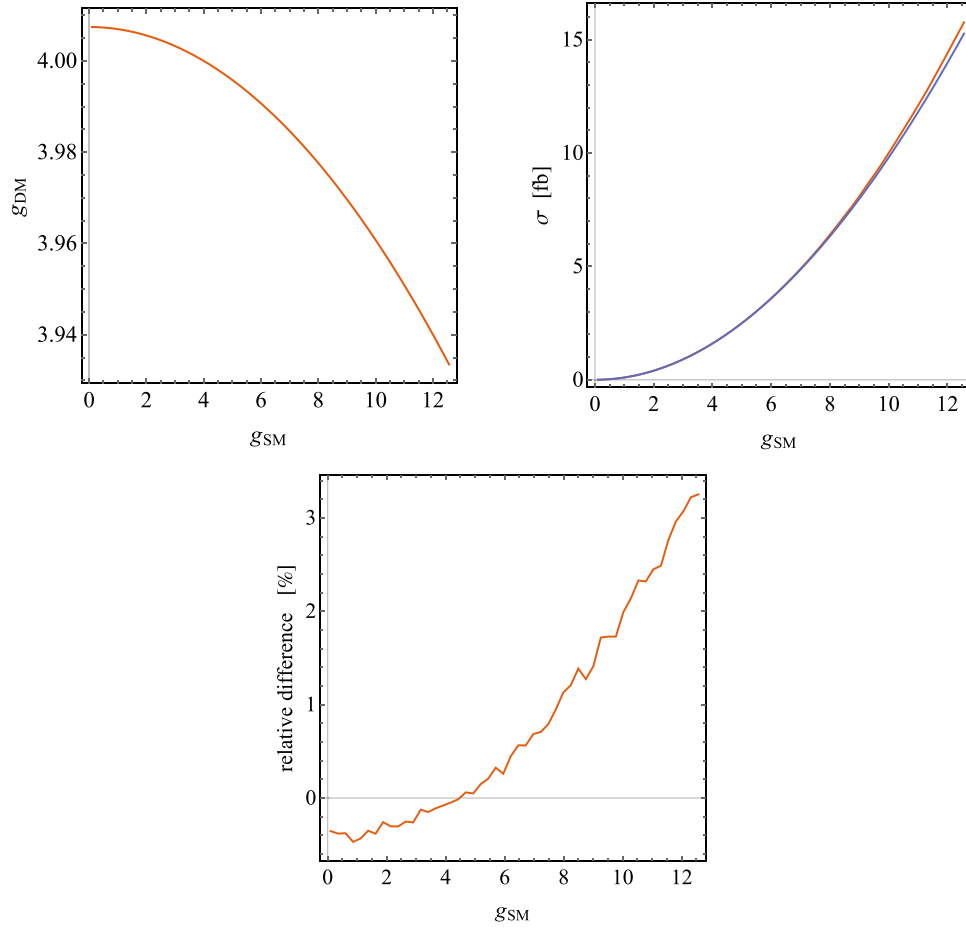


Fig. 36. Scaling along the lines of constant width. The line of constant width for $M_{\text{med}} = 300$ GeV and $m_\chi = 100$ GeV, intercepting $g_q = g_\chi = 4$ is shown on left. The generated and rescaled cross sections are compared in the middle, the corresponding ratio is shown on right.

A^0 models) or 65 GeV (scalar mediator model). Fig. 41(b) shows the \cancel{E}_T distribution for models with low pseudoscalar mediator masses ($m_{Z'_B} = 100$ GeV, $m_{Z'} = 1$ TeV, $m_{A^0} = 100$ GeV) and DM mass of 1 TeV for all models.

Predictions for this class of models have been so far considered at LO+ Parton Shower (PS), even though they could be extended to NLO+PS in the near future. The studies in this Section have been performed using a model within MADGRAPH5_AMC@NLO v5.1.5.12, interfaced to PYTHIA 6 for the parton shower. The implementation details for these models are discussed in Section 4.2.1.

3.1.1. \cancel{E}_T +Higgs from a baryonic Z'

The model shown in Fig. 39(a) postulates a new gauge boson Z' corresponding to a new $U(1)_B$ baryon number symmetry. The stable baryonic states included in this model are the DM candidate particles. The mass of the Z' boson is acquired through a baryonic Higgs h_B , which mixes with the SM Higgs boson.

The interactions between the Z' , the quarks and the DM are described by the following Lagrangian:

$$\mathcal{L} = g_q \bar{q} \gamma^\mu q Z'_\mu + g_\chi \bar{\chi} \gamma^\mu \chi Z'_\mu. \quad (26)$$

The quark couplings g_q are fixed to be equal to one third of the gauge coupling g_B , while the DM coupling to the Z' are proportional to the baryon number and to the gauge coupling ($g_\chi = B g_B$). No leptonic couplings of the Z' are allowed, thus evading dilepton constraints. After incorporating the mixing of the baryonic and SM Higgs bosons, this model is described by the

following Lagrangian term at energies below $m_{Z'}$ ¹⁰:

$$\mathcal{L}_{\text{eff}} = -\frac{g_q g_\chi}{m_{Z'}^2} \bar{q} \gamma^\mu q \bar{\chi} \gamma_\mu \chi \left(1 + \frac{g_{hZ'Z'}}{m_{Z'}^2} h \right), \quad (27)$$

The first term of this equation is the standard DMV model in the large $M_{Z'}$ limit. This term can lead to a monojet signature, which can be also used to constrain this model. The second term describes the interaction between the Z' and the SM Higgs boson, via the coupling $g_{hZ'Z'} = \frac{m_{Z'}^2 \sin \theta}{v_B}$, where $\sin \theta$ is the mixing angle between the SM Higgs and the baryonic Higgs h_B , and v_B is the Baryonic Higgs vacuum expectation value.

In its most general form, this model can contribute to mono-Z signals due to the Z' mixing with the Z or photon. Note that EWSB and $U(1)_B$ breaking do not lead to this mixing at tree-level. Instead, kinetic mixing occurs between the $U(1)_Y$ and $U(1)_B$ gauge bosons due to the gauge invariant term $F_Y^{\mu\nu} F_{B\mu\nu}$. This mixing is a free parameter which we assume to be small in order to focus on the mono-Higgs signature. Mixing may also occur due to radiative corrections, however we choose to ignore this here as it is model dependent.

The predictions of the model depend upon the two additional parameters beyond an s-channel simplified model, namely the mixing angle between baryonic Higgs h_B and the SM-like Higgs boson $\sin \theta$ and the coupling of the mediator to SM-like Higgs

¹⁰ The operator in Eq. (27) is an effective one, to highlight the two main terms. The full dimension-4 simplified model is used in the model for event generation.

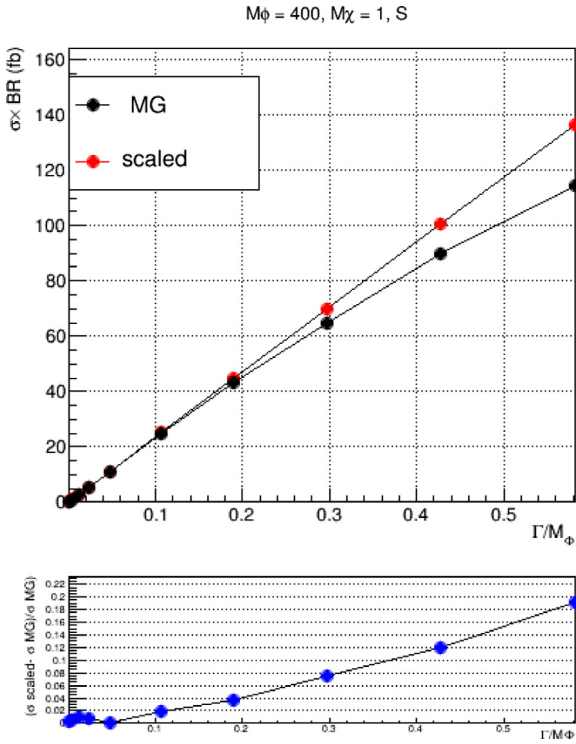


Fig. 37. An example comparing a simple cross section scaling versus the computation from the MADGRAPH5_AMC@NLO generator, for a scalar $t\bar{t} + \cancel{E}_T$ model with $m_\phi = 400$ GeV, $m_\chi = 1$ GeV and all couplings set to unity. In this example, the scaling relationship holds for Γ_ϕ/m_ϕ below 0.2, beyond which finite width effects become important and the simple scaling breaks down.

boson, $g_{hZ'Z'}$. Thus, a full model is specified by:

$$\{M_{\text{med}}, m_\chi, g_\chi, g_q, \sin \theta, g_{hZ'Z'}\}. \quad (28)$$

Parameter scan. The width of the Z' mediator is calculated using all possible decays to SM particles (quarks) and to pairs of DM particles if kinematically allowed as in the DMV model.

The dependence of the missing transverse momentum (\cancel{E}_T) on the model parameters is studied by varying the parameters one at a time. The variation of parameters other than M_{med} and m_χ does not result in significant variations of the \cancel{E}_T spectrum, as shown in Fig. 42. Fig. 43 shows that for an on-shell mediator, varying m_χ with the other parameters fixed does not affect the \cancel{E}_T distribution, while the distribution broadens significantly in the case of an off-shell mediator. For this reason, the same grid in M_{med}, m_χ as for the vector mediator of the jet + \cancel{E}_T search (Table 1)

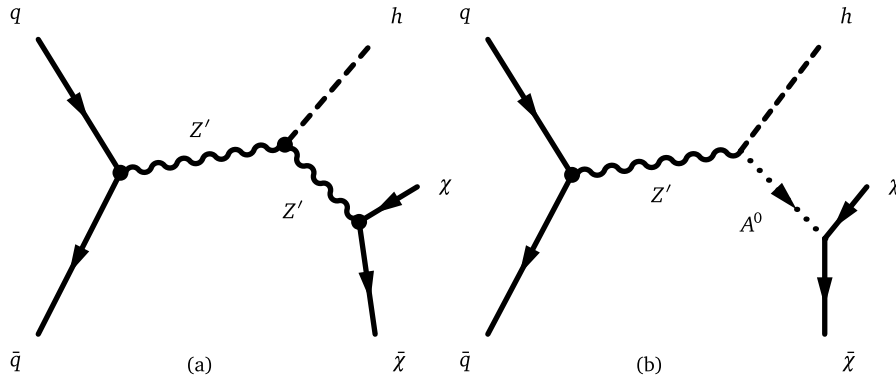


Fig. 39. Examples of Feynman diagrams leading to Higgs + \cancel{E}_T events: (a) a model with a vector mediator (Z') coupling with DM and with the Higgs boson h , and (b) a 2HDM model with a new invisibly decaying pseudoscalar A^0 from the decay of an on-shell resonance Z' giving rise to a Higgs + \cancel{E}_T signature.

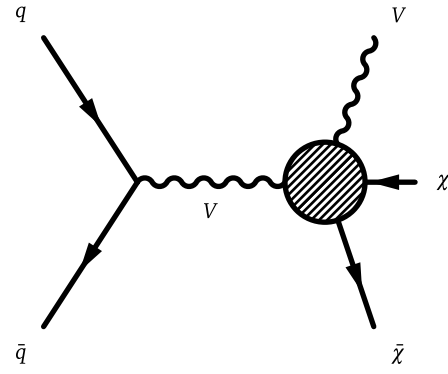


Fig. 38. Sketch of benchmark models including a contact interaction for V+MET searches.

Source: Adapted from [100].

is chosen as a starting point. The coupling $g_{hZ'Z'}$, along with g_q and g_χ , are subject to perturbativity bounds:

$$g_q, g_\chi < 4\pi,$$

and

$$g_{hZ'Z'} < \sqrt{4\pi} m_{Z'} \sin \theta.$$

The value $g_{hZ'Z'}/m_{Z'} = 1$ is chosen as a benchmark value for the generation of Monte Carlo samples since it maximizes the cross section (as shown in the following paragraph) without violating the bounds. The mediator-DM coupling g_χ is fixed to 1, and the mediator-quark g_q coupling is fixed to $1/3$. The kinematic distributions do not change as a function of these parameters, so results for other values of $g_{hZ'Z'}/m_{Z'}$, g_χ and g_q can be obtained through rescaling by the appropriate cross sections.

Figs. 44 and 45 show the kinematic distributions for the two leading jets in the $H \rightarrow \bar{b}b$ decay channel, for two values of the mediator mass and varying the DM mass.

Experimentalists should perform further studies, beyond those studies performed for the forum, to estimate the reach of the analysis with respect to all points in the grid and therefore decide on a smaller set of grid points to be generated.

3.1.2. \cancel{E}_T + Higgs from a scalar mediator

A real scalar singlet S coupling to DM can be introduced as a portal between SM and the dark sector through the Higgs field. The most general scalar potential is detailed in Ref. [101], including terms that break \mathbb{Z}_2 . The \mathbb{Z}_2 symmetry, which causes the new scalar to also be a DM candidate, is not covered in this report, but follows Ref. [48] introducing an additional coupling to

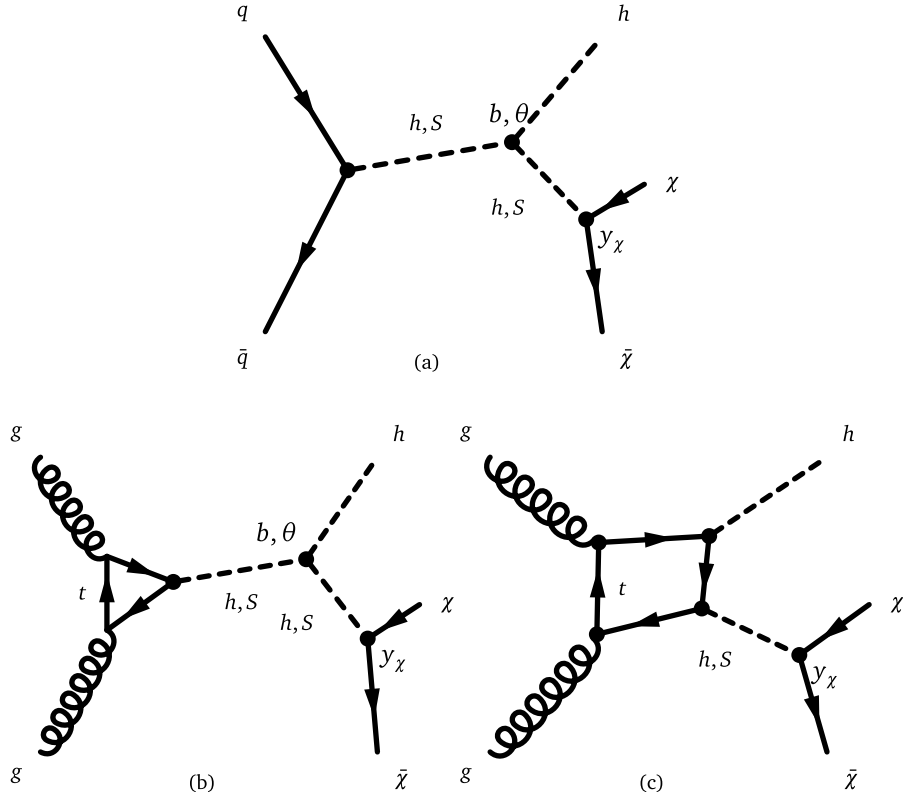


Fig. 40. Examples of Feynman diagrams leading to Higgs+ \bar{E}_T events for a model with a scalar mediator (S) coupling with DM and with the Higgs boson h .

DM that breaks \mathbb{Z}_2 and leads to a new invisible decay of S . For this reason, no symmetry is broken and no new interactions arise, so there is no dependence on the vacuum expectation value of S : a shift in the field leads to a redefinition of the model couplings. The new scalar S mixes with the SM Higgs boson, and couples to DM through a Yukawa term y_χ . The relevant terms in the scalar potential are:

$$V \supset a|H|^2S + b|H|^2S^2 + \lambda_h|H|^4 \\ \longrightarrow \frac{1}{2}a(h+v)^2S + \frac{1}{2}b(h+v)^2S^2 + \frac{\lambda_h}{4}(h+v)^4, \quad (29)$$

where a, b are new physics couplings and λ_h is the Higgs quartic coupling.

The additional Lagrangian terms for this model are:

$$\mathcal{L} \supset -y_\chi \bar{\chi} \chi (\cos \theta S - \sin \theta h) - \frac{m_q}{v} \bar{q} q (\cos \theta h + \sin \theta S) \quad (30)$$

where θ is the mixing angle between the Higgs boson and the new scalar.

Mono-Higgs signals in this second model arise through processes shown in Fig. 40 (a,b), or through the radiation of a Higgs boson from the t quark in the production loop, in Fig. 40(c). The first two processes depend on the h^2S and hS^2 cubic terms in Eq. (29). At leading order in $\sin \theta$, these terms are:

$$V_{\text{cubic}} \approx \frac{\sin \theta}{v} (2m_h^2 + m_S^2) h^2 S + b v h S^2 + \dots, \quad (31)$$

with a and λ_h expressed in terms of $\sin \theta$ and m_h^2 , respectively. At leading order of $\sin \theta$, the h^2S term is fixed once the mass eigenvalues m_h, m_S and mixing angle are specified. The hS^2 term is not fixed and remains a free parameter of the model, depending on the new physics coupling b .

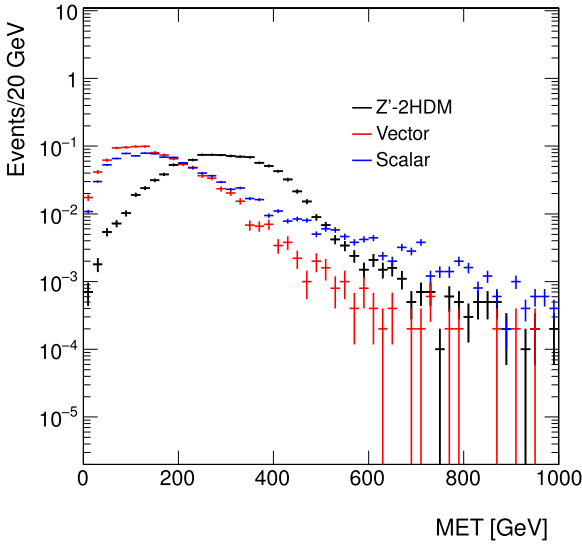
This model also has mono-X signatures through h/S mixing. This model is related to the scalar model discussed in Section 2.2 in the case of $m_S \gg m_h$ or $m_h \gg m_S$ and M_{med} equal to the lighter of the two masses, albeit with different mono-Higgs signatures due to the hS^2 vertex.

Parameter scan. The model is described by five parameters:

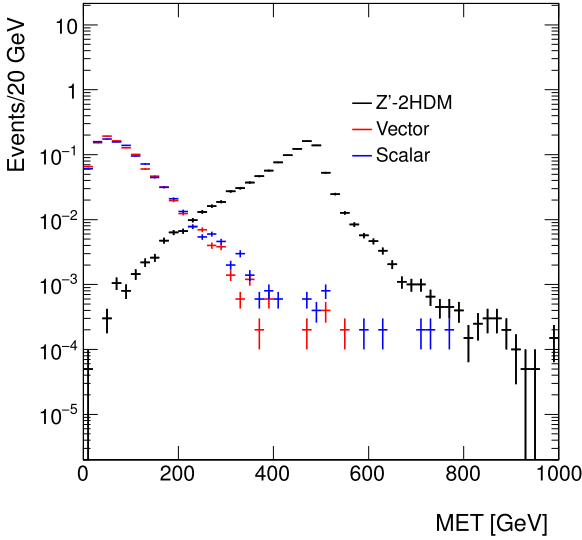
1. the Yukawa coupling of heavy scalar to dark matter, g_χ (also referred to as y_χ)
2. the mixing angle between heavy scalar and SM-like Higgs boson, $\sin \theta$;
3. the new physics coupling, b ;
4. mass of heavy scalar, m_S , also termed M_{med} ;
5. mass of DM, m_χ ;

The mixing angle is constrained from current Higgs data to satisfy $\cos \theta = 1$ within 10% and therefore $\sin \theta \lesssim 0.4$. This provides a starting point for the parameter scan in this model: we recommend to set $\sin \theta = 0.3$.

Fig. 47 shows that the kinematics does not depend on the value of this angle, and results for different values can be obtained via rescaling the results for this mixing angle according to the relevant cross-section. It can also be observed from Figs. 46 and 48 that the kinematics of this model follows that of the equivalent jet+ \bar{E}_T model: only small changes are observed in the on-shell region, while the relevant distributions diverge when the mediator is off-shell. For this reason, the same grid in M_{med}, m_χ as for the scalar mediator of the jet+ \bar{E}_T search (Table 5) is chosen as a starting point. The Yukawa coupling to DM y_{DM} is set to 1, the new physics coupling between scalar and SM Higgs $b = 3$. Results for other values can be obtained via a rescaling of the results for these parameters.



(a) High mediator mass



(b) Low mediator mass

Fig. 41. Comparison of the missing transverse momentum distributions at generator level in different simplified models leading to a Higgs+ \cancel{E}_T signature. The model parameter settings are detailed in the text. The figures in this Section have been obtained using LO UFO models within MADGRAPH5_AMC@NLO v2.2.3, interfaced to PYTHIA 8 for the parton shower.

Figs. 49 and 50 show the kinematic distributions for the two leading jets in the $H \rightarrow b\bar{b}$ decay channel, for two values of the mediator mass and varying the DM mass.

3.1.3. Higgs+ \cancel{E}_T signal from 2HDM model with a Z' and a new pseudoscalar

In this simplified model [97], a new Z' resonance decays to a Higgs boson h plus a heavy pseudoscalar state A^0 in the 2HDM framework, which in turn decays to a DM pair. This model is represented in the diagram in Fig. 39(b).

The motivation for coupling the DM to the pseudoscalar is that DM coupling to a Higgs or Z' boson is generically constrained by other signal channels and direct detection. A reason to consider

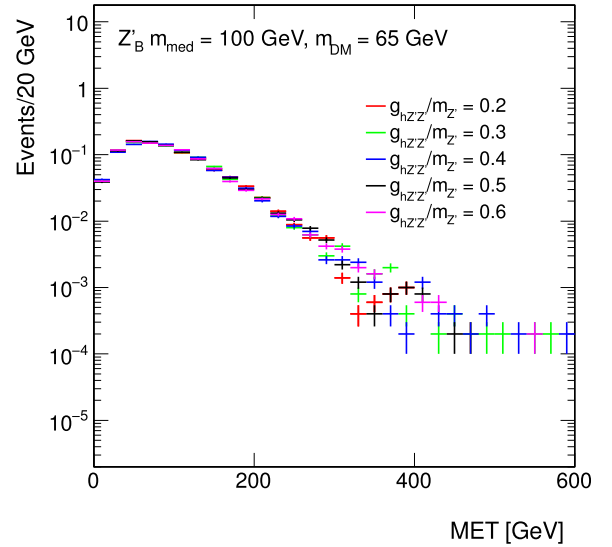
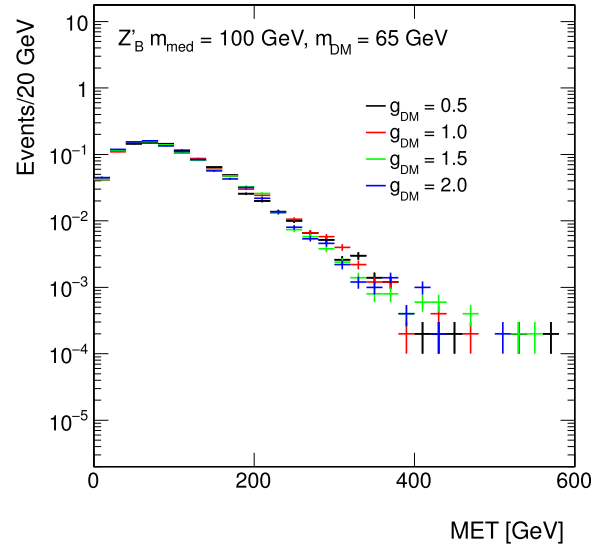


Fig. 42. Missing transverse momentum distributions at generator level in the vector mediator scenario for different values of: the mediator-DM coupling g_x (left), and the coupling between the mediator and the SM-like Higgs boson, scaled by the mediator mass, $g_{hZ'Z'}/m_{Z'}$ (right).

this model is that it has different kinematics due to the on-shell Z' production, where for heavy Z' masses the \cancel{E}_T and p_T spectra are much harder. This model can satisfy electroweak precision tests and constraints from dijet resonance searches, and still give a potentially observable Higgs+ \cancel{E}_T signal.

The model comprises of two doublets, where Φ_u couples to up-type quarks and Φ_d couples to down-type quarks and leptons:

$$-\mathcal{L} \supset y_u Q \tilde{\Phi}_u \bar{u} + y_d Q \Phi_d \bar{d} + y_e L \Phi_d \bar{e} + \text{h.c.} \quad (32)$$

After electroweak symmetry breaking, the Higgs doublets attain vacuum expectation values v_u and v_d , and in unitary gauge the doublets are parameterized as

$$\Phi_d = \frac{1}{\sqrt{2}} \begin{pmatrix} -\sin \beta H^+ \\ v_d - \sin \alpha h + \cos \alpha H - i \sin \beta A^0 \end{pmatrix}, \quad \Phi_u = \frac{1}{\sqrt{2}} \begin{pmatrix} \cos \beta H^+ \\ v_u + \cos \alpha h + \sin \alpha H + i \cos \beta A^0 \end{pmatrix} \quad (33)$$

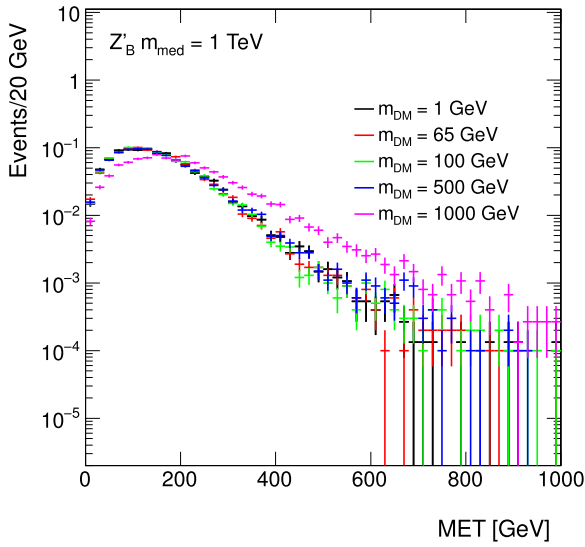
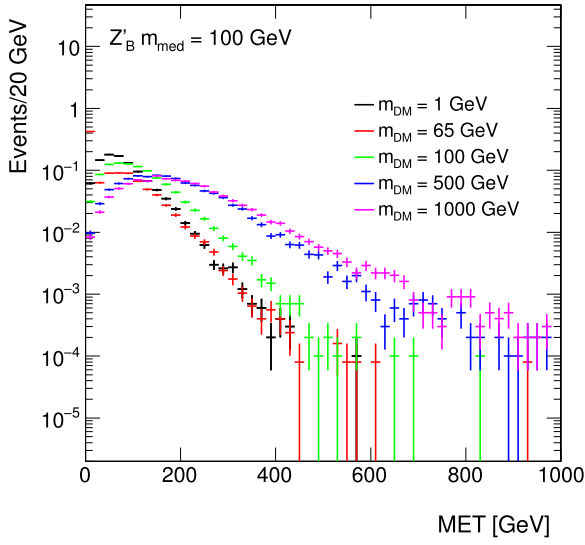
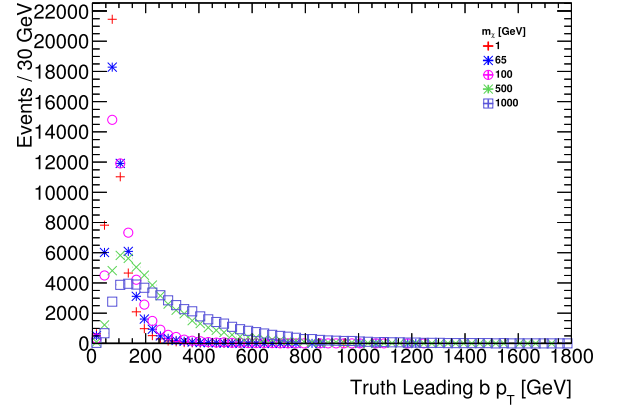


Fig. 43. Missing transverse momentum distributions at generator level in the vector mediator scenario: for different values of the DM mass m_χ and a mediator mass of $M_{\text{med}} = 100$ GeV (left) and $M_{\text{med}} = 1$ TeV (right).

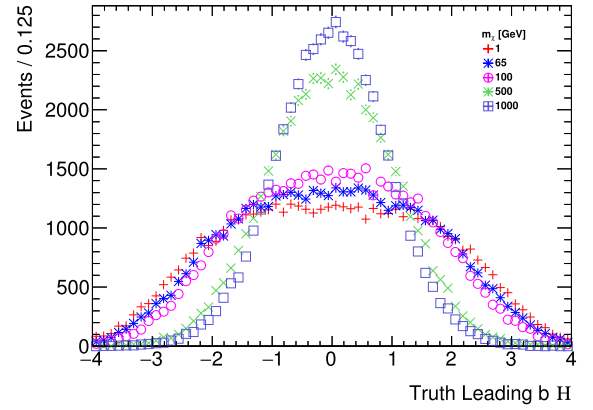
where h, H are neutral CP-even scalars, H^\pm is a charged scalar, and A^0 is a neutral CP-odd scalar. In this framework, $\tan \beta \equiv v_u/v_d$, and α is the mixing angle that diagonalizes the $h-H$ mass squared matrix. This model also contains an additional scalar singlet ϕ that leads to spontaneous symmetry breaking. We take $\alpha = \beta - \pi/2$, in the alignment limit where h has SM-like couplings to fermions and gauge bosons as per Ref. [102], and $\tan \beta \geq 0.3$ as implied from the perturbativity of the top Yukawa coupling. The Higgs vacuum expectation values lead to $Z-Z'$ mass mixing, with a small mixing parameter given by

$$\begin{aligned} \epsilon &\equiv \frac{1}{M_{Z'}^2 - M_Z^2} \frac{g g_z}{2 \cos \theta_w} (z_d v_d^2 + z_u v_u^2) \\ &= \frac{(M_Z^0)^2}{M_{Z'}^2 - M_Z^2} \frac{2 g_z \cos \theta_w}{g} z_u \sin^2 \beta, \end{aligned} \quad (34)$$

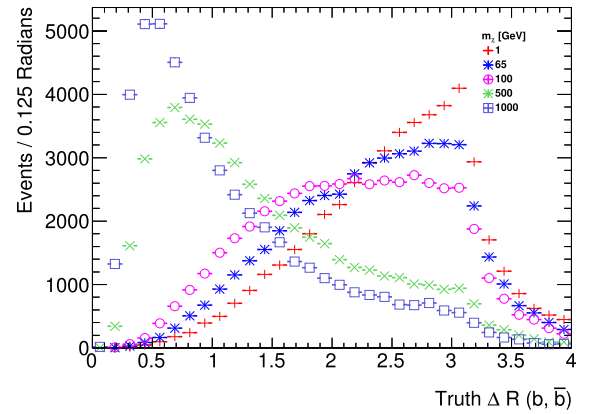
where z_i are the Z' charges of the two Higgs doublets, and g and g_z related to the mass-squared values in absence of mixing $(M_Z^0)^2 = g^2(v_d^2 + v_u^2)/(4 \cos^2 \theta_w)$ and $(M_{Z'}^0)^2 = g_z^2(z_d^2 v_d^2 + z_u^2 v_u^2 + z_\phi^2 v_\phi^2)$.



(a) Leading b -jet transverse momentum



(b) Leading b -jet pseudorapidity



(c) Angular distance between the two leading b -jets

Fig. 44. Comparison of the kinematic distributions for the two leading b -jets (from the Higgs decay) in the vector Z' simplified model, when fixing the Z' mass to 100 GeV and varying the DM mass.

The production cross section for this model scales as $(g_z)^2$, as the decay width for this process to leading order in ϵ (Eq. (34)) is

$$\Gamma_{Z' \rightarrow h A^0} = (g_z \sin \beta \cos \beta)^2 \frac{|p|}{24\pi} \frac{|p|^2}{M_{Z'}^2}. \quad (35)$$

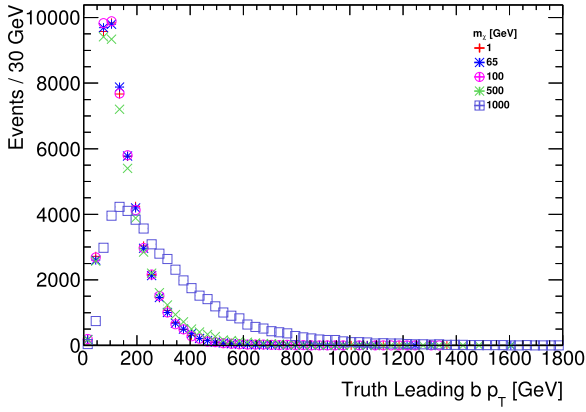
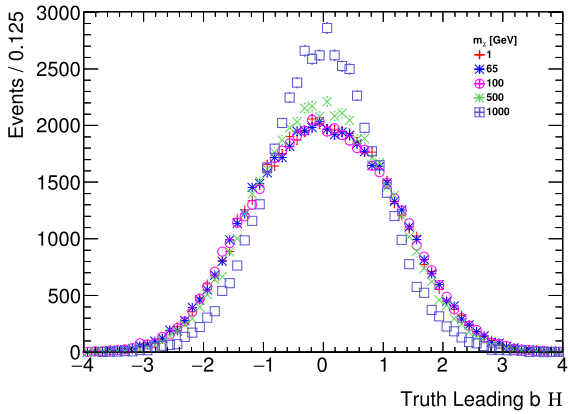
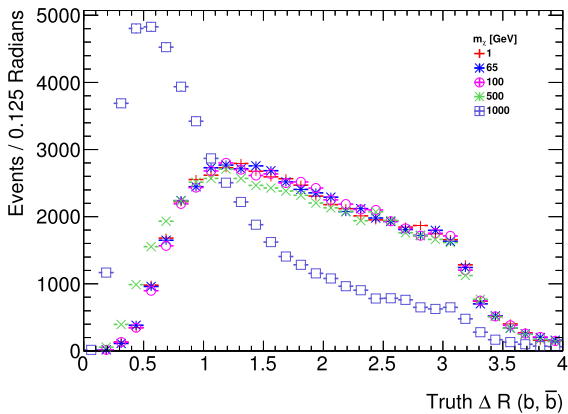
(a) Leading b -jet transverse momentum(b) Leading b -jet pseudorapidity(c) Angular separation of the two leading b -jets

Fig. 45. Comparison of the kinematic distributions for the two leading jets from the Higgs decay in the vector Z' simplified model, when fixing the Z' mass to 1000 GeV and varying the DM mass.

where the center of mass momentum for the decay products is

$$|p| = \frac{1}{2M_{Z'}} \sqrt{(M_{Z'}^2 - (m_h + m_{A^0})^2)(M_{Z'}^2 - (m_h - m_{A^0})^2)}. \quad (36)$$

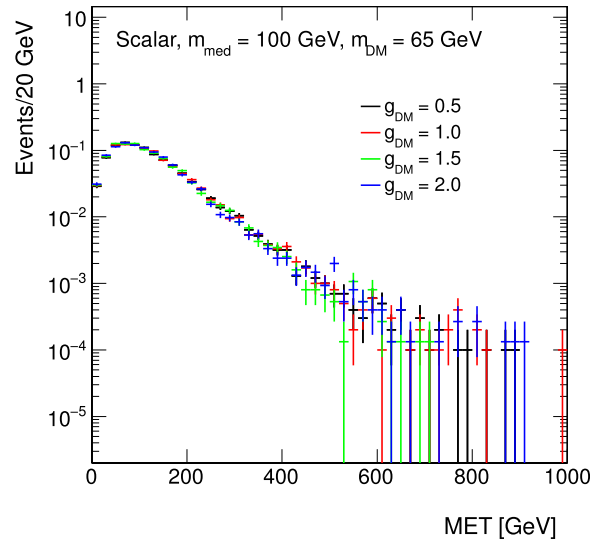
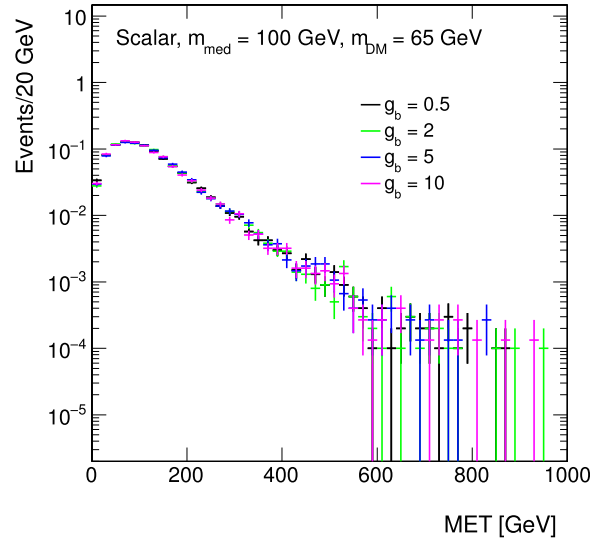


Fig. 46. Missing transverse momentum distributions at generator level in the scalar mediator scenario, for different values of: the new physics coupling g_b (left), and the mediator-DM coupling g_χ (right).

The Z' can also decay to Zh , leading to the same signature if the Z decays invisibly. The partial width for this decay is:

$$\Gamma_{Z' \rightarrow hZ} = (g_z \sin \beta^2)^2 \frac{|p|}{24\pi} \left(\frac{|p|^2}{M_{Z'}^2} + 3 \frac{M_Z^2}{M_{Z'}^2} \right). \quad (37)$$

We recommend to generate these two decays separately and combine them at a later stage.

Parameter scan. The model is described by five parameters:

- the pseudoscalar mass M_{A^0} ,
- the DM mass m_χ ,
- the Z' mass, $M_{Z'}$,
- $\tan \beta (\equiv v_u/v_d)$,
- the Z' coupling strength g_z .

To study the signal production and kinematic dependencies on these parameters, we produced signal samples varying each of the five parameters through MADGRAPH5_AMC@NLO for the matrix element, PYTHIA 8 for the parton shower, and DELPHES [103] for a parameterized detector-level simulation.

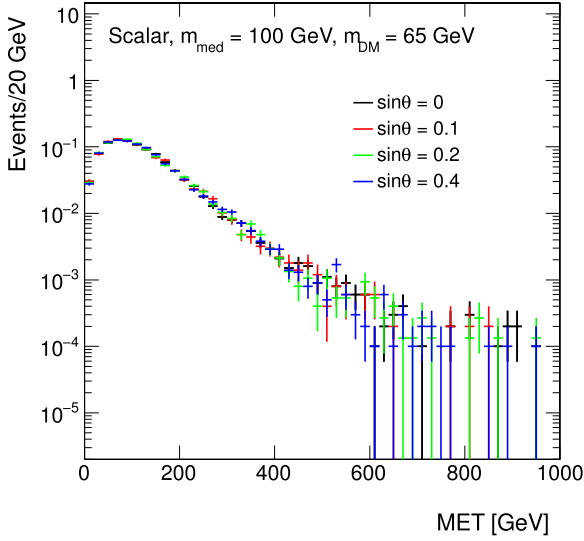


Fig. 47. Missing transverse momentum distributions at generator level in the scalar mediator scenario: for different values of the mixing angle $\sin\theta$.

As seen in Fig. 51, variations of $\tan\beta$ does not lead to any kinematic difference and the production cross section simply scales as a function of $\tan\beta$. Hence we recommend to fix $\tan\beta$ to unity in the signal generation.

Similarly, variations of g_z do not lead to any kinematic changes. The value of g_z for a given $M_{Z'}$ and $\tan\beta$ can be set according to the maximum value allowed by electroweak global fits and dijet constraints, as described in [97]. Since this parameter does not influence the kinematics, we leave it up to individual analyses to decide whether they generate benchmark points only according to these external constraints.

Since the DM pair are produced as a result of the decay of A^0 , there are minimal kinematic changes when varying m_χ as long as $m_\chi < M_{A^0}/2$ so that A^0 production is on-shell, as shown in Figs. 52 and 53 (before detector simulation).

We recommend to produce signal events for a fixed $g_z = 0.8$, $\tan\beta = 1$ and $m_\chi = 100$ GeV. For these values, we scan the 2-D parameter space of $M_{Z'}$, M_{A^0} with $M_{Z'} = 600, 800, 1000, 1200, 1400$ GeV, and $M_{A^0} = 300, 400, 500, 600, 700, 800$ GeV with $M_{A^0} < M_{Z'} - m_h$, for a total of 24 points. The choice of scan is justified by the sensitivity study in [97]: the expected LHC sensitivity for Run-2 is up to $M_{Z'} \sim 1.5$ TeV. For the parameter scan, the DM mass is fixed to 100 GeV. For two $M_{Z'}$, M_{A^0} value sets, we vary the DM mass to obtain sample cross section for rescaling results. All LO cross sections for the various parameter scan points are reported on HEPData. The parameter scan excludes the off-shell region, as the cross-sections are suppressed and the LHC would not have any sensitivity to these benchmark points in early data.

The kinematic distributions with varying $M_{Z'}$ for fixed M_{A^0} are shown in Fig. 54, while the dependency on M_{A^0} is shown in Fig. 55.

This model also allows for an additional source of Higgs plus \cancel{E}_T signal with a similar kinematics (Fig. 56, shown with detector simulation samples) to the signal process from the decay of $Z' \rightarrow hZ$, where the Z decays invisibly. The partial decay width for the Z' is:

$$\Gamma_{Z' \rightarrow hZ} = (g_z \cos\alpha \sin\beta)^2 \frac{|p|}{24\pi} \left(\frac{|p|^2}{M_{Z'}^2} + 3 \frac{M_Z^2}{M_{Z'}^2} \right). \quad (38)$$

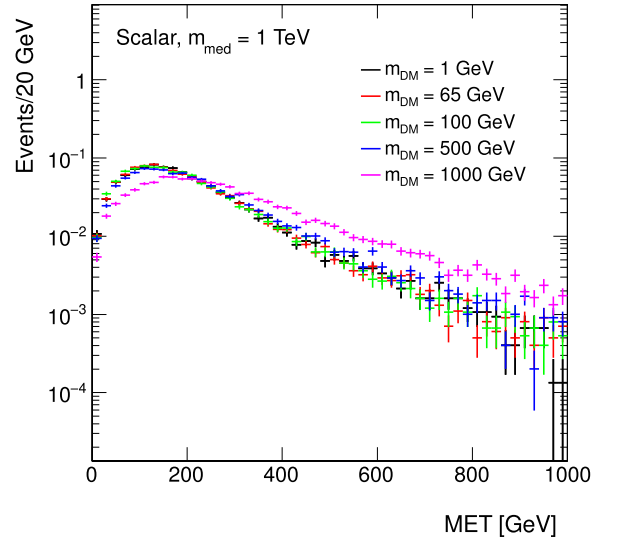
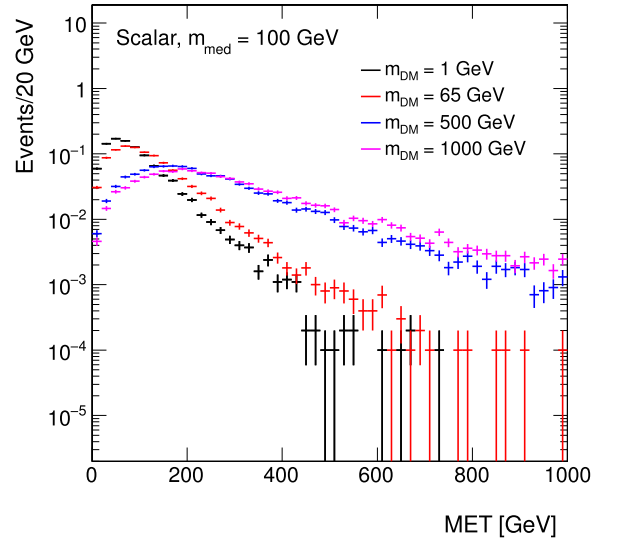


Fig. 48. Missing transverse momentum distributions at generator level in the scalar mediator scenario: for different values of the DM mass m_χ and a mediator mass of $M_{\text{med}} = 100$ GeV (left) and $M_{\text{med}} = 1$ TeV (right).

The values for the Z' masses scanned for those samples should follow those of the previous samples, namely values of $M_{Z'} = 600, 800, 1000, 1200, 1400$ GeV. This signal process has no M_A dependence.

3.2. EFT models with direct DM-boson couplings

The EFT operators considered in this section do not have an implementation of a simplified model completion for Dirac fermion Dark Matter available to date. They provide kinematic distributions that are unique to mono-boson signatures, and that in most cases are not reproduced by an equivalent simplified model.¹¹

A complete list of effective operators with direct DM/boson couplings for Dirac DM, up to dimension 7, can be found in [45, 98, 99]. Higher dimensional operators, up to dimension 8, leading

¹¹ Wherever this is the case, for practical reasons one can only generation a simplified model result in the limiting EFT case, as the results can be rescaled and reinterpreted.

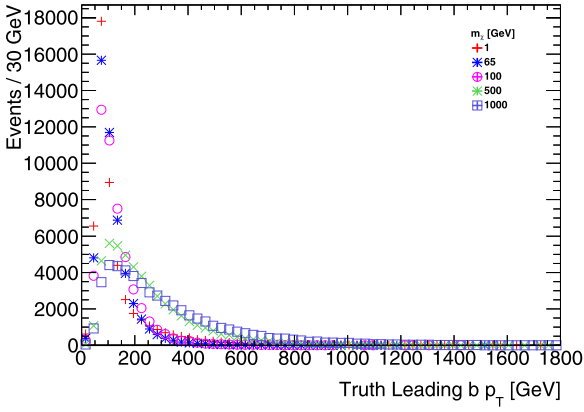
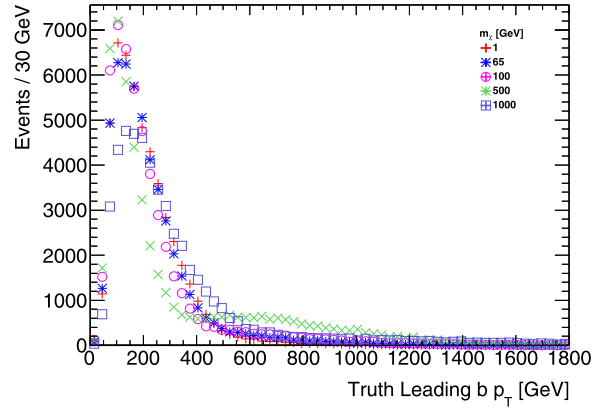
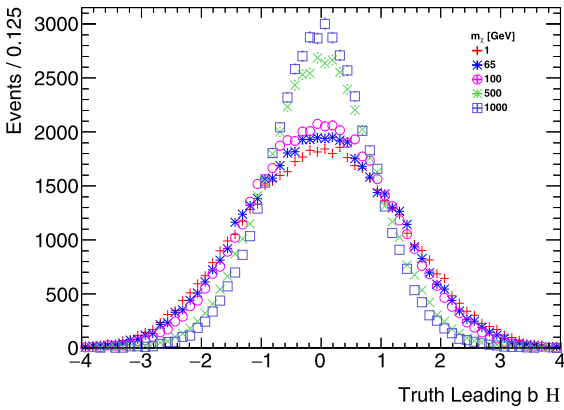
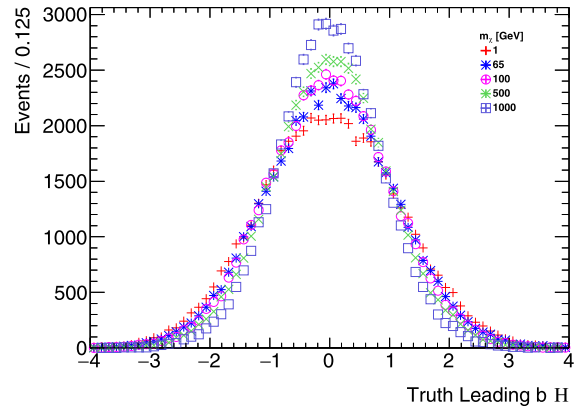
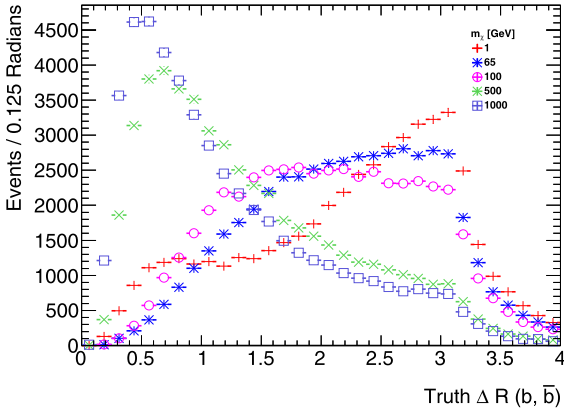
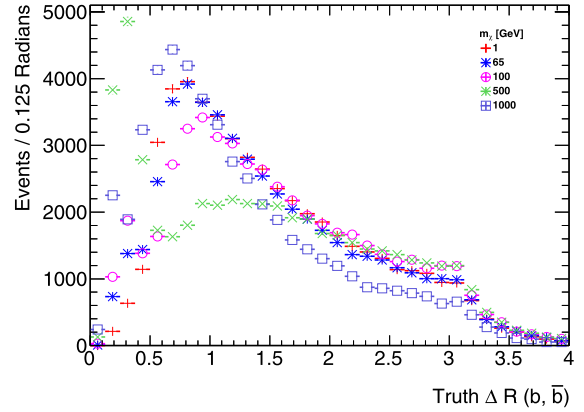
(a) Leading b -jet transverse momentum(a) Leading b -jet transverse momentum(b) Leading b -jet pseudorapidity(b) Leading b -jet pseudorapidity(c) Angular distance between the two leading b -jets(c) Angular distance between the two leading b -jets

Fig. 49. Comparison of the kinematic distributions for the two leading jets from the Higgs decay in the scalar simplified model, when fixing the new scalar mass to 100 GeV and varying the DM mass.

Fig. 50. Comparison of the kinematic distributions for the two leading jets from the Higgs decay in the scalar simplified model, when fixing the new scalar mass to 1000 GeV and varying the DM mass.

to Higgs+ \cancel{E}_T signatures, are mentioned in [45,97]. The first part of this Section outlines the main characteristics for a limited number of these models that could be considered in early Run-2 searches. However, the EFT approximation made for these operators can be

problematic, see Ref. [97] for discussion. For this reason, model-independent results as in Appendix B should be privileged over considering these operators as realistic benchmarks.

However, the Forum discussion highlighted that the EFT approach allows more model-independence when reinterpreting results, and that it is worth still considering interpretation of the

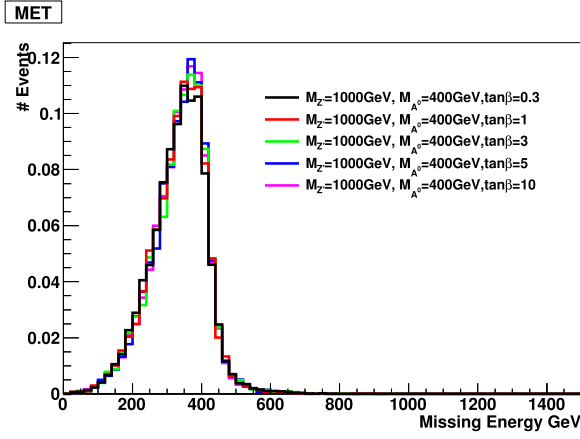
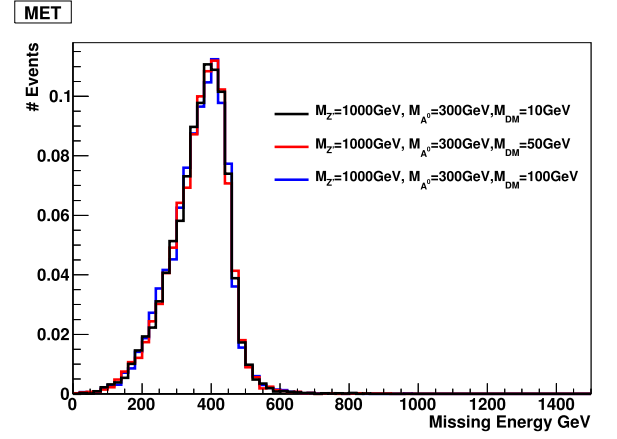
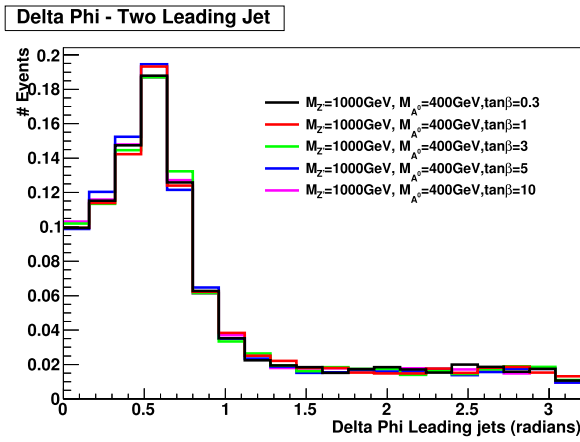
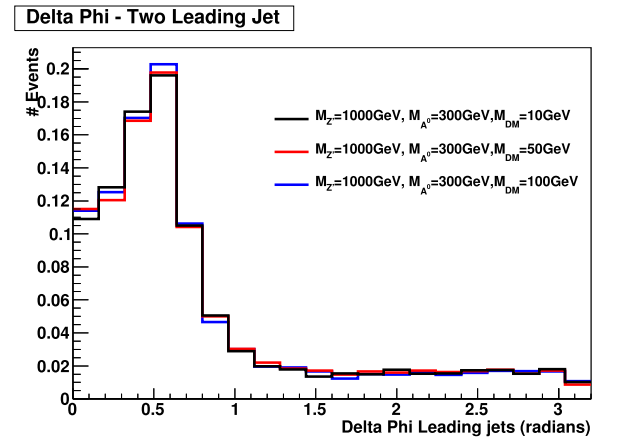
(a) \cancel{E}_T distribution(a) \cancel{E}_T distribution(b) $\Delta\phi$ distance between the two b -jets(b) $\Delta\phi$ distance between the two b -jets

Fig. 51. Kinematic distributions of the signal process varying $\tan\beta$, in the case of a Higgs boson decaying into two b quarks, after parameterized detector simulation: no kinematic dependence is observed on the mixing angle.

Fig. 52. Kinematic distributions of the signal process varying m_χ : minimal kinematic dependency on m_χ as expected when A^0 is produced on-shell. Plots shown for $M_{Z'} = 1000$ GeV, $M_{A^0} = 300$ GeV.

results available in terms of these operators. Furthermore, once simplified models are available for those operators, EFT results can be used as a limiting case for consistency checks. We devote the end of this Section to a discussion on the presentation of results from this model, including an assessment of their reliability using a conservative procedure that is only dependent on EFT parameters.

The studies in this Section have been performed using a UFO model within MADGRAPH5_AMC@NLO v2.2.3, interfaced to PYTHIA 8 for the parton shower. The implementation of these models is discussed further in Section 4.2.2.

3.2.1. Dimension 5 operators

The lowest dimension benchmark operators we consider are effective dimension 5, such as the one depicted in Fig. 57.

Following the notation of [45], models from this category have a Lagrangian that, after electroweak symmetry breaking, includes terms such as:

$$\frac{m_W^2}{\Lambda_5^3} \bar{\chi} \chi W^{+\mu} W_\mu^- + \frac{m_Z^2}{2\Lambda_5^3} \bar{\chi} \chi Z^\mu Z_\mu, \quad (39)$$

where m_Z and m_W are the masses of the Z and W boson, W^μ and Z^μ are the fields of the gauge bosons, χ denotes the Dark Matter

fields and Λ_5 is the effective field theory scale. Note that these operators are of true dimension 7, but reduce to effective dimension 5 once the Higgs vacuum expectation values, contained in the W and Z mass terms, are inserted. As such, one expects that these operators would naturally arise in UV complete models where Dark Matter interacts via a Higgs portal where heavy mediators couple to the Higgs or other fields in an extended Higgs sector. In such models the full theory may be expected to contain additional operators with Higgs-Dark Matter couplings [104]. The above operator also induces signatures with \cancel{E}_T in conjunction with Z and W bosons at tree level, as shown in Fig. 38, while at loop level it induces couplings to photon pairs and $Z\gamma$ through W loops. In these models, a clear relation exists between final states with photons, EW bosons and Higgs boson.

As shown in Fig. 58, the kinematics of this model can be approximated by that of a simplified model including a high-mass scalar mediator exchanged in the s -channel described in Section 2.2.2. For this reason, the list of benchmark models with direct boson-DM couplings for photon, Z and W only includes dimension 7 operators: if the scalar model with initial state radiation of an EW boson is already generated, then its results can be rescaled.

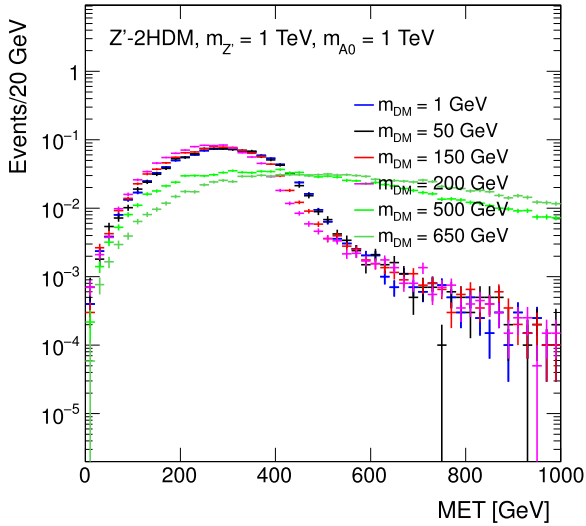
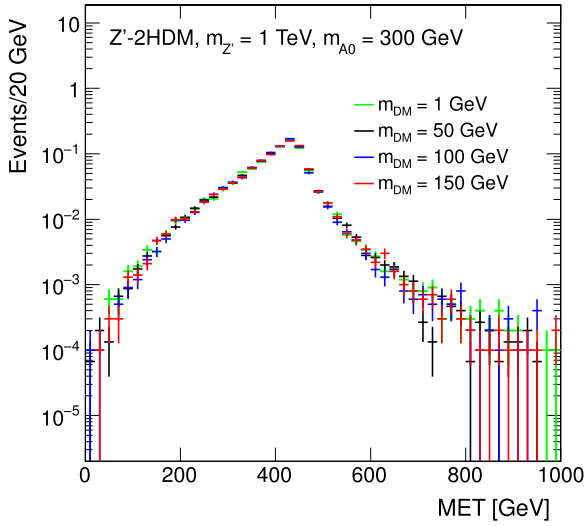


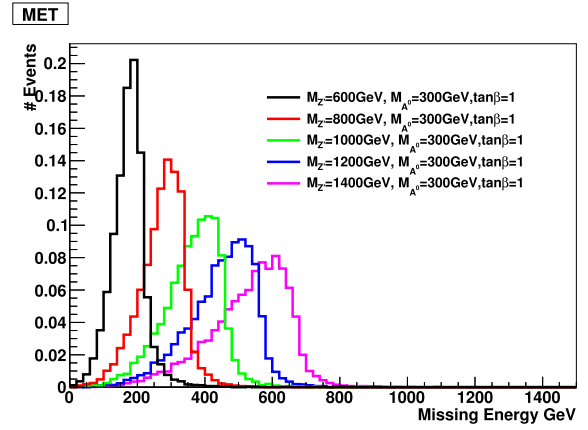
Fig. 53. Missing transverse momentum distributions at generator level in the $Z' + 2\text{HDM}$ scenario for different values of the DM mass m_χ , with $m_{Z'} = 1$ TeV and $m_{A^0} = 300$ GeV (left) and $m_{A^0} = 1$ TeV (right).

The Higgs+ \cancel{E}_T analysis, however, will not consider the scalar simplified model as benchmark, due to the very low sensitivity in early LHC analyses, and will instead use this dimension 5 operator.

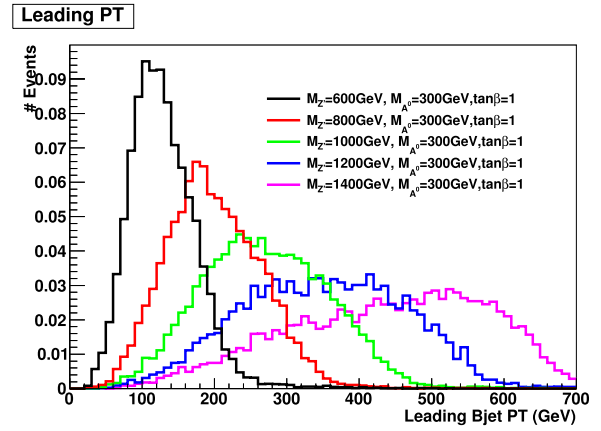
Parameter scan. The two parameters of this model are the scale of new physics λ and the DM particle mass. SM-DM coupling and new physics scale are related by $g_\chi = (246 \text{ GeV})/\lambda$.

The initial value of the new physics scale λ chosen for the sample generation is 3 TeV. This is a convention and does not affect the signal kinematics: the cross-section of the samples can be rescaled when deriving the constraints on this scale. However, more care should be given when rescaling Higgs+ \cancel{E}_T operators of higher dimensions, as different diagrams have a different λ dependence.

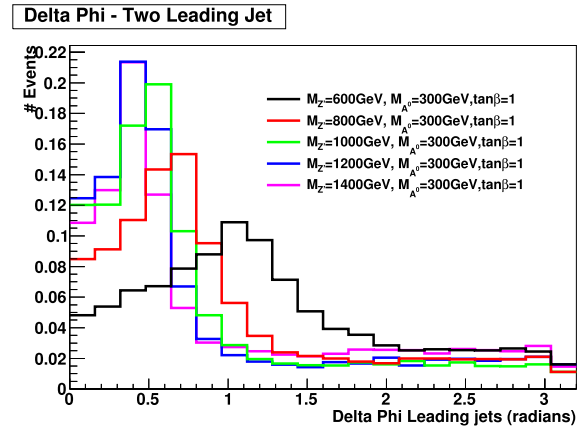
The DM mass values for the benchmark points to be simulated are chosen to span a sufficient range leading to different kinematics, that is within the LHC sensitivity for early searches and that is consistent across the various signatures and EFT operators.



(a) \cancel{E}_T distribution



(b) Leading b -jet p_T distribution



(c) $\Delta\phi$ distance between the two b -jets

Fig. 54. Kinematic distributions of the signal process varying $M_{Z'}$, for $m_\chi = 100$ GeV, $M_{A^0} = 300$ GeV.

We therefore start the mass scan at $m_\chi = 1$ GeV, where collider experiments are complementary to direct and indirect detection and choose the last point corresponding to a DM mass of 1.3 TeV. We recommend a scan in the following mass points:

$m_\chi = 1, 10, 50, 100, 200, 400, 800, 1300$ GeV.

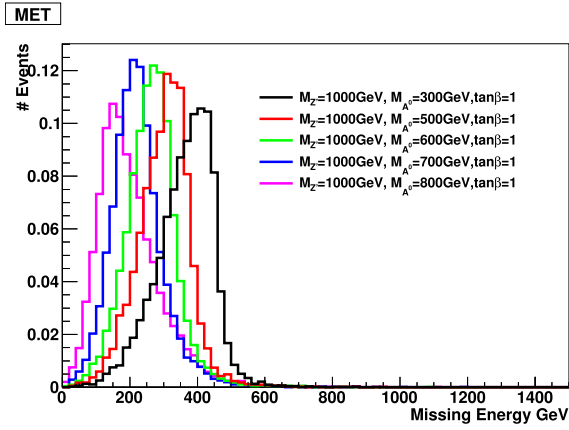
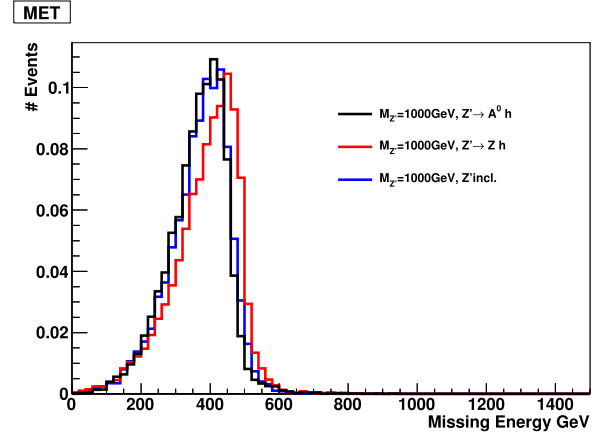
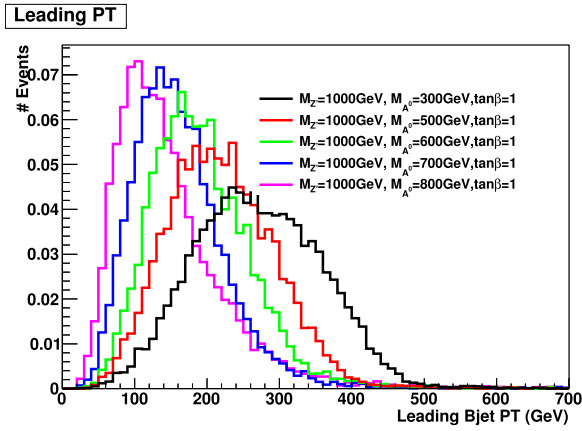
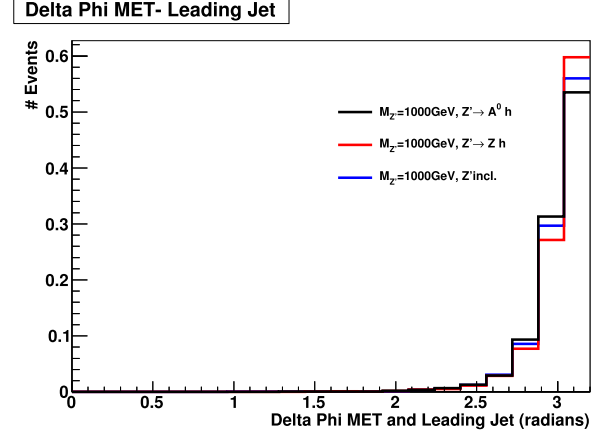
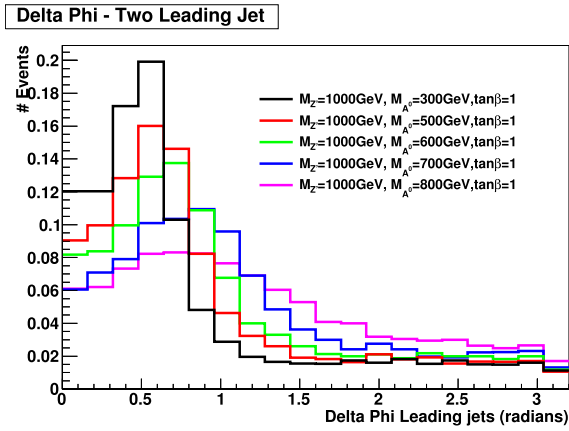
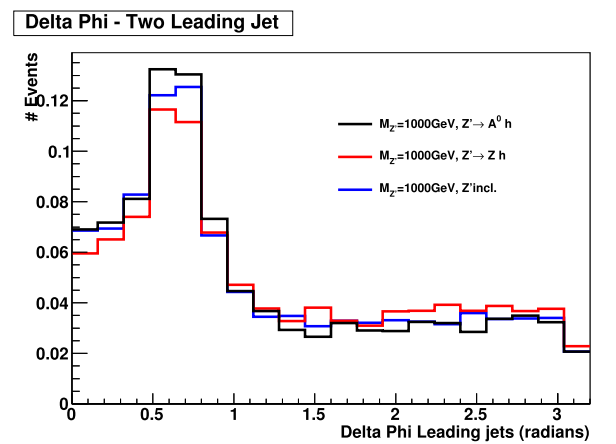

 (a) \cancel{E}_T distribution

 (a) \cancel{E}_T distribution

 (b) Leading b -jet p_T distribution

 (b) Leading b -jet p_T distribution

 (c) $\Delta\phi$ distance between the two b -jets

 (c) $\Delta\phi$ distance between the two b -jets

Fig. 55. Kinematic distributions of the signal process varying M_{A^0} , for $m_\chi = 100$ GeV, $M_{Z'} = 1000$ GeV.

Fig. 56. Kinematic distributions of $Z' \rightarrow A^0 h$ exclusive production, $Z' \rightarrow Zh$ exclusive production and Z' inclusive production for $M_{Z'} = 1000$ GeV and $M_{A^0} = 300$ GeV.

A set of kinematic distributions from the Higgs+ \cancel{E}_T signature where the Higgs decays into two b -quarks is shown in Fig. 59, for points similar to those of the grid scan proposed.

3.2.2. Dimension 7 operators

The dimension-7 benchmark models contain the $SU(2)_L \times U(1)_Y$ gauge-invariant couplings between DM fields and the kinetic terms of the EW bosons. The CP-conserving scalar couplings

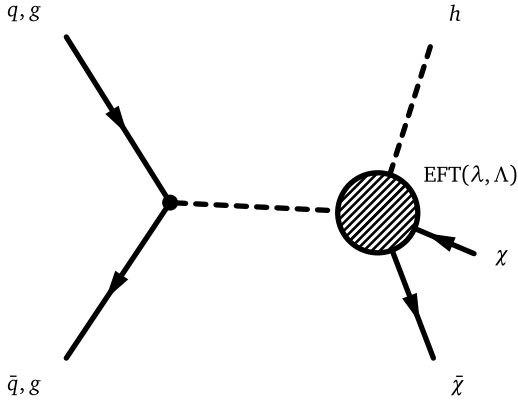


Fig. 57. Diagram for EFT operators giving rise to a Higgs+ \cancel{E}_T signature.

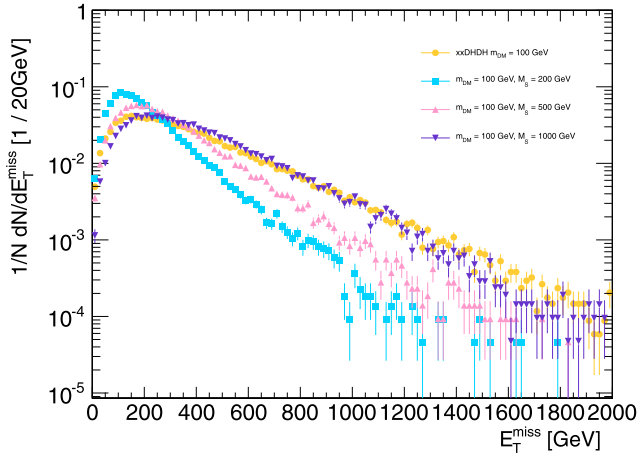


Fig. 58. Comparison of the missing transverse momentum for the simplified model where a scalar mediator is exchanged in the s -channel and the model including a dimension-5 scalar contact operator, in the leptonic $Z + \cancel{E}_T$ final state. All figures in this Section have been performed using a UFO model within MADGRAPH5_AMC@NLO v2.2.3, interfaced to PYTHIA 8 for the parton shower.

of this type can be written as

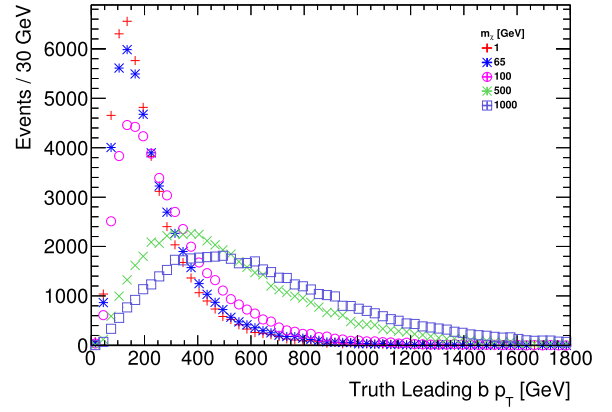
$$\frac{c_1}{\Lambda_S^3} \bar{\chi} \chi B_{\mu\nu} B^{\mu\nu} + \frac{c_2}{\Lambda_S^3} \bar{\chi} \chi W_{\mu\nu}^i W^{i,\mu\nu}. \quad (40)$$

Here $B_{\mu\nu} = \partial_\mu B_\nu - \partial_\nu B_\mu$ and $W_{\mu\nu}^i = \partial_\mu W_\nu^i - \partial_\nu W_\mu^i + g_2 \epsilon^{ijk} W_\mu^j W_\nu^k$ are the $U(1)_Y$ and $SU(2)_L$ field strength tensor, respectively, and g_2 denotes the weak coupling constant. In the case of the pseudoscalar couplings, one has instead

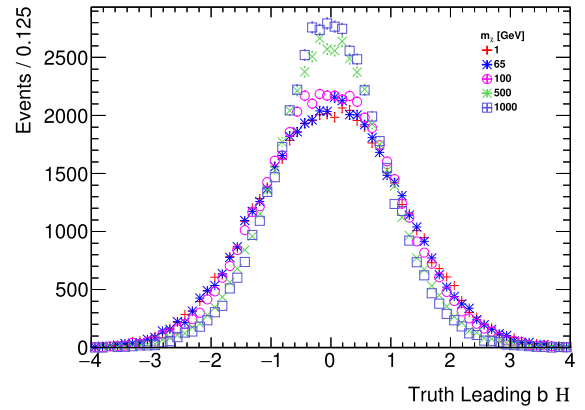
$$\frac{c_1}{\Lambda_P^3} \bar{\chi} \gamma_5 \chi B_{\mu\nu} \tilde{B}^{\mu\nu} + \frac{c_2}{\Lambda_P^3} \bar{\chi} \gamma_5 \chi W_{\mu\nu}^i \tilde{W}^{i,\mu\nu}, \quad (41)$$

where $\tilde{B}_{\mu\nu} = 1/2 \epsilon_{\mu\nu\lambda\rho} B^{\lambda\rho}$ and $\tilde{W}_{\mu\nu}^i = 1/2 \epsilon_{\mu\nu\lambda\rho} W^{i,\lambda\rho}$ are the dual field strength tensors. In addition to the CP-conserving interactions (40) and (41), there are also four CP-violating couplings that are obtained from the above operators by the replacement $\bar{\chi} \chi \leftrightarrow \bar{\chi} \gamma_5 \chi$.

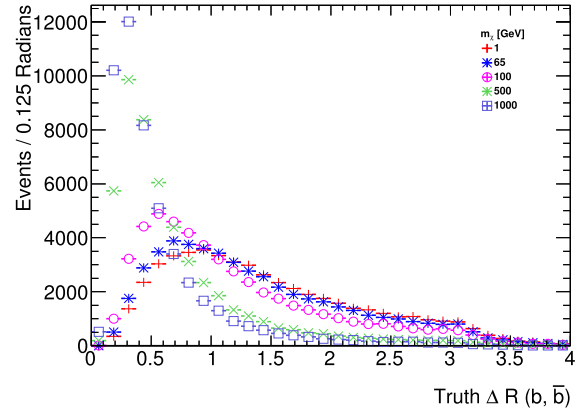
The effective interactions introduced in (40) and (41) appear in models of Rayleigh DM [105]. Ultraviolet completions where the operators are generated through loops of states charged under $U(1)_Y$ and/or $SU(2)_L$ have been proposed in [106] and their LHC signatures have been studied in [107]. If these new charged particles are light, the high- p_T gauge bosons that participate in the \cancel{E}_T processes considered here are able to resolve the substructure of the loops. This generically suppresses the cross sections compared to the EFT predictions [108], and thus will weaken the



(a) Leading b -jet transverse momentum



(b) Leading b -jet pseudorapidity



(c) Angular distance between the two leading b -jets

Fig. 59. Comparison of the kinematic distributions for the two leading b -jets (from the Higgs decay) in the model with direct interactions between the Higgs boson and the DM particle, when varying the DM mass.

bounds on the interaction strengths of DM and the EW gauge bosons to some extent. Furthermore, the light charged mediators may be produced on-shell in pp collisions, rendering direct LHC searches potentially more restrictive than \cancel{E}_T searches. Making the above statements precise would require further studies beyond the timescale of this forum.

Since for $\Lambda_S = \Lambda_P$ the effective interactions (40) and (41) predict essentially the same value of the mono-photon, mono-Z and mono-W cross section [45,99], we consider below only the former couplings. We emphasize however that measurements of the jet-jet azimuthal angle difference in $\cancel{E}_T + 2j$ events may be used to disentangle whether DM couples more strongly to the combination $B_{\mu\nu} B^{\mu\nu}$ ($W_{\mu\nu}^i W^{i,\mu\nu}$) or the product $B_{\mu\nu} \tilde{B}^{\mu\nu}$ ($W_{\mu\nu}^i \tilde{W}^{i,\mu\nu}$) of field strength tensors [98,99].

After EW symmetry breaking the interactions (40) induce direct couplings between pairs of DM particles and gauge bosons. The corresponding Feynman rule reads:

$$\frac{4i}{\Lambda_S^3} g_{V_1 V_2} (p_1^{\mu_2} p_2^{\mu_1} - g^{\mu_1 \mu_2} p_1 \cdot p_2), \quad (42)$$

where p_i (μ_i) denotes the momentum (Lorentz index) of the vector field V_i and for simplicity the spinors associated with the DM fields have been dropped. The couplings $g_{V_1 V_2}$ take the form:

$$\begin{aligned} g_{\gamma\gamma} &= c_w^2 c_1 + s_w^2 c_2, \\ g_{\gamma Z} &= -s_w c_w (c_1 - c_2), \\ g_{ZZ} &= s_w^2 c_1 + c_w^2 c_2, \\ g_{WW} &= c_2, \end{aligned} \quad (43)$$

with s_w (c_w) the sine (cosine) of the weak mixing angle. Note that our coefficients c_1 and c_2 are identical to the coefficients C_B and C_W used in [99], while they are related via $k_1 = c_w^2 c_1$ and $k_2 = s_w^2 c_2$ to the coefficients k_1 and k_2 introduced in [45].

The coefficients c_1 and c_2 appearing in (43) determine the relative importance of each of the \cancel{E}_T channels and their correlations. For example, one observes that:

- Only c_2 enters the coupling between DM and W bosons, meaning that only models with $c_2 \neq 0$ predict a mono- W signal;
- If $c_1 = c_2$ the mono-photon (mono- Z) signal does not receive contributions from diagrams involving Z (photon) exchange;
- Since numerically $c_w^2/s_w^2 \simeq 3.3$ the mono-photon channel is particularly sensitive to c_1 .

Parameter scan. As stated above and shown in Ref. [100], the kinematic distributions for dimension-7 scalar and pseudoscalar operators only shows small differences. This has been verified from a generator-level study: the signal acceptance after a simplified analysis selection ($\cancel{E}_T > 350$ GeV, leading jet $p_T > 40$ GeV, minimum azimuthal angle difference between either of the two jets and the \cancel{E}_T direction > 0.4) is roughly 70% for both models, independent from the coefficients c_1 and c_2 . We therefore only suggest to generate one of the two models.

The differences in kinematics for the various signatures are negligible when changing the coefficients c_1 and c_2 , since these coefficient factorize in the matrix element. Only the case $c_1 = c_2 = 1$ is generated as benchmark; other cases are left for reinterpretation as they will only need a rescaling of the cross-sections (see Fig. 60).

3.2.3. Higher dimensional operators

Many higher dimensional operators can induce signals of photons or $W/Z/H$ bosons in the final state. A complete list can be found in Refs. [47,48,97] and references therein.

Although with lower priority with respect to the operators above, a representative dimension-8 operators can be chosen as benchmark, with the form:

$$\frac{1}{\Lambda^4} \bar{\chi} \gamma^\mu \chi B_{\mu\nu} H^\dagger D^\nu H.$$

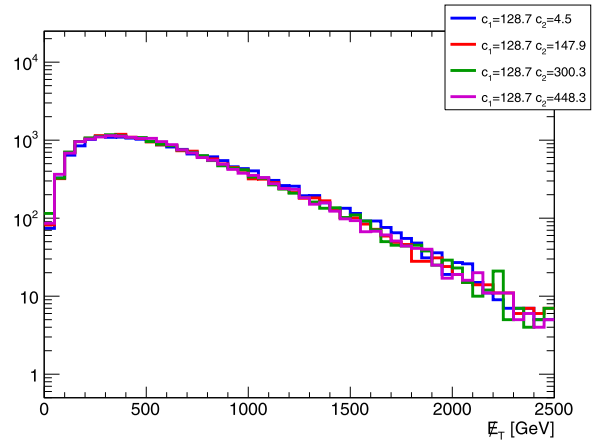


Fig. 60. \cancel{E}_T distribution for the dimension-7 model with a hadronically decaying Z in the final state, for the scalar and pseudoscalar operators representing direct interactions between DM and bosons. The values of the coefficients in the legend are multiplied by 100.

In this case, the new physics scale is Λ is related to the coupling of the DM as $y_\chi = \frac{1}{\Lambda^4}$. An advantage of this operator is that it includes all signatures with EW bosons, allowing to assess the relative sensitivity of the various channels with the same model. The kinematics for this operator is different with respect to other operators, leading to a harder \cancel{E}_T spectrum, as illustrated by comparing the leading b -jet distribution for the dimension 5 operator to the dimension 8 operator (see Fig. 61).

3.2.4. Validity of EW contact operators and possible completions

It is important to remember that the operators described in this section may present problems in terms of the validity of the contact interaction approach for the energy scales reached at the LHC.

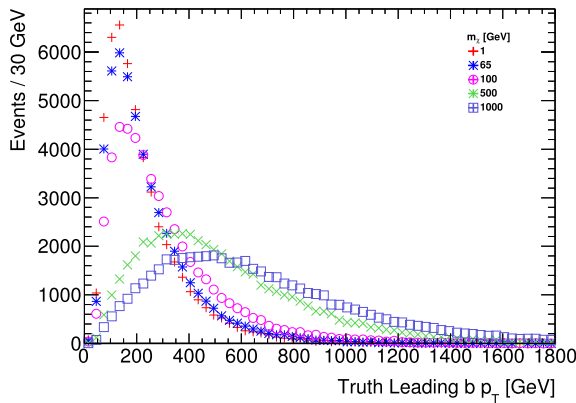
As outlined in [97], designing very high \cancel{E}_T search signal regions that are exclusively motivated by the hard \cancel{E}_T spectra of the dimension 7 and 8 operators will mean that the momentum transfer in the selected events is larger. This in turn means that processes at that energy scale (mediators, particles exchanged in loops) are accessible, and a simple contact interaction will not be able to correctly describe the kinematics of these signals.

Contact interaction operators like the ones in this section remain useful tools for comparison of the sensitivity of different search channels, and for reinterpretation of other models under the correct assumptions. To date, while UV-complete models are known, their phenomenology has not been studied in full detail as their completion involves loops.¹²

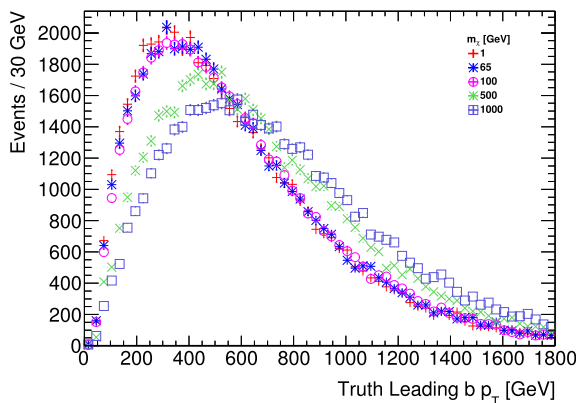
However, this may be the focus of future theoretical exploration, as discussed in Ref. [99]. An example of a complete model for scalar DM corresponding to the dimension-5 operator is provided in the Appendix A. Providing results for the pure EFT limit of these models will prove useful to cross-check the implementation of future.

Given these considerations, we recommend to present results for these models as follows:

¹² An example case for the need of loop completions is a simplified model with an additional scalar exchanged at tree level. The scalar couples to WW and ZZ in a gauge-invariant way, Integrating out the mediator does not lead to the Lorentz structure of a dimension-7 operator, so it is not possible to generate dimension-7 operators that satisfy gauge and Lorentz invariance at the same time. A model with a spin-1 mediator cannot be considered as an candidate for completion either, since dimension-7 operators only have scalar or pseudoscalar couplings.



(a) Dimension 5 operator



(b) Dimension 7 operator

Fig. 61. Comparison of the transverse momentum for the leading b -jet from the Higgs decay for a dimension 5 and dimension 7 operator with direct boson-DM couplings.

- Deliver fiducial limits on the cross section of any new physics events, without any model assumption, according to the guidelines in [Appendix B](#).
- Assess the percentage of events that pass a condition of validity for the EFT approximation that does not depend on a specific completion, and present results removing of the invalid events using the procedure in [Section 5](#) alongside the raw EFT results.

4. Implementation of models

4.1. Implementation of s -channel and t -channel models for $\cancel{E}_T + X$ analyses

In the studies to date, a number of different Monte Carlo tools have been used to simulate DM signals. In this Chapter, we make recommendations on the accuracy at which simulations should be performed for different final states. We also provide explicit examples of codes and implementations (including specific settings) that have been used to obtain the results in this report. We stress that these recommendations are based on the current status of publicly available codes and users should always check whether new results at a better accuracy have appeared in the meantime. We recommend to update the corresponding analyses directly using the new releases and/or codes respectively, and in case this would not be possible, to at least take into account

the new information in the analysis (e.g., via a MC comparison with the latest predictions, or by effectively using global/local K -factors). For all models included in this report, PYTHIA 8 has been used to provide the parton shower simulation. Nevertheless, we note that showering matrix element events with Herwig [[109–112](#)] should be considered as an equally valid alternative.

4.1.1. Implementation of s -channel models for mono-jet signature

These models include those discussed in [Sections 2.1 and 2.2](#). In monojet analyses, i.e. when final states are selected with a few jets and \cancel{E}_T , observables and in particular the \cancel{E}_T spectrum depend upon the accuracy of the simulation of QCD radiation. For the vector and axial vector models, the current state of the art is NLO+PS. It is particularly simple to obtain simulations for these processes at NLO+PS and even for merged samples at NLO accuracy, starting from SM implementations. We therefore recommend simulations to be performed at NLO+PS, and in case multi-jet observables are employed, by merging samples with different multiplicities. Results at such accuracy can be obtained either in dedicated implementations, such as that of POWHEG [[61](#)], or via general purpose NLO tools like MADGRAPH5_AMC@NLO employing available UFO models at NLO. A testing version of the full set of these UFO models has been made available only in June 2015 [[113](#)]. For this reason, it was not used as part of the studies of this Forum on initial Run-2 benchmark models. Nevertheless, we encourage further study of these UFO models by the ATLAS and CMS collaborations.

A study using POWHEG [[61,114](#)] has shown that the NLO corrections result in a substantial reduction in the dependence on the choice of the renormalization and factorization scales and hence a reduced theoretical uncertainty on the signal prediction. For the central choice of renormalization and factorization scales, the NLO corrections also provide a minor enhancement in the cross section due to the jet veto that has been so far employed in Run-1 analyses.

For the scalar and pseudoscalar models, the lowest order process already involves a one-loop amplitude in QCD. Because of the complexity of performing NLO calculations for this class of processes and in particular the absence of general methods for computing two-loop virtual contributions, only LO predictions are currently available. These can be interfaced to shower programs exactly as usual tree-level Born computations, i.e. by considering one parton multiplicity at a time or by merging different parton multiplicities via CKKW or MLM schemes to generate inclusive samples with jet rates at LO accuracy. For spin-0 mediators in the mono-jet final state, the top-quark loop is the most important consideration. The matrix element implementation with exact top-loop dependence of the s -channel spin-0 mediated DM production is available in MCFM [[41,114](#)]¹³ at fixed order and in POWHEG [[43](#)] and MADGRAPH5_AMC@NLO [[113](#)] for event generation at LO+PS level. The POWHEG and MCFM implementations include the finite top quark mass dependence for DM pair production and one extra parton at LO. The same processes are available in MADGRAPH5_AMC@NLO v2.3 and could be made available in the future in codes like SHERPA+OPENLOOPS/GoSAM, including up to two extra partons in the final state. Samples can be merged employing CKKW, K_T -MLM procedures.

Most of the results that have been presented in this document for these processes have been obtained with POWHEG interfaced to PYTHIA 8, matching the state of the art calculation as of Spring 2015. For future reference, we document the specific settings needed to run the POWHEG generation for the dark matter models so they can serve as nominal benchmarks for the early Run-2

¹³ Only the scalar mediator is available in the public release.

ATLAS and CMS DM analyses. POWHEG parameter cards for all models can be found on the Forum Git repository [115–118].

POWHEG configuration for s-channel DM models. The latest POWHEG release is available for download using the instructions at <http://powhegbox.mib.infn.it/>. The Forum recommends using at least version 3059.

- POWHEG can generate either unweighted (uniformly-weighted) or weighted events. The relevant keywords in the input card are `bornsuppfact` and `bornktmin`.

1. unweighted events:

`bornsuppfact`: negative or absent
`bornktmin` PT

This runs the program in the most straightforward way, but it is likely not the more convenient choice, as will be explained below. POWHEG will generate unweighted events using a sharp lower cut (with value PT) on the leading-jet p_T . Since this is a generation cut, the user must check that the choice of `bornktmin` does not change the cross section for signal events passing analysis selections. It is a good practice to use 10–20% smaller \cancel{E}_T value in the input card than the final analysis selection, and check that the final result is independent, by exploring an even smaller value of `bornktmin`. The drawback of using this mode is that it is difficult to populate well, and in a single run, both the low- p_T region as well as the high- p_T tail.

2. weighted events:

`bornsuppfact` PTS
`bornktmin` PT

POWHEG will now produce weighted events, thereby allowing to generate a single sample that provides sufficient statistics in all signal regions. Events are still generated with a sharp lower cut set by `bornktmin`, but the `bornsuppfact` parameter is used to set the event suppression factor according to

$$F(k_T) = \frac{k_T^2}{k_T^2 + \text{bornsuppfact}^2}. \quad (44)$$

In this way, the events at, for instance, low \cancel{E}_T , are suppressed but receive higher weight, which ensures at the same time higher statistics at high \cancel{E}_T . We recommend to set `bornsuppfact` to 1000.

The `bornktmin` parameter can be used in conjunction with `bornsuppfact` to suppress the low \cancel{E}_T region even further. It is recommended to set `bornktmin` to one-half the value of the lowest \cancel{E}_T selection. For instance, for the event selection used in the CMS/ATLAS monojet analyses, assuming the lowest \cancel{E}_T region being defined above 300 GeV, the proposed value for `bornktmin` is 150. However, this parameter should be set keeping in mind the event selection of all the analyses that will use these signal samples, and hence a threshold lower than 150 may be required.

- The POWHEG monojet implementations can generate events using two expressions for the mediator propagators. The default setup (i.e if the keyword `runningwidth` is absent, commented out or set to 0) is such that a normal Breit-Wigner function is used for the propagator: in this case, the expression

$$Q^2 - M^2 + iM\Gamma$$

is used for the propagator's denominator, where Q is the virtuality of the mediator, and M and Γ are its mass and width, respectively. This is the more straightforward, simple and transparent option, and it was used for the Forum studies. It should be the method of choice, unless one approaches regions of parameter space where Γ/M starts to approach order 1 values. In those cases, a more accurate modeling (or at least a check of the validity of the fixed width approach) can be achieved by using a running width: by setting the `runningwidth` token to 1, POWHEG uses as the denominator of the mediator propagator the expression

$$Q^2 - M^2 + iQ^2 \frac{\Gamma}{M},$$

which is known to give a more realistic description. See Ref. [96] for a discussion.

- Set the parameters defining the bounds on the invariant mass of the dark matter pair, `mass_low` and `mass_high`, to -1 . In this way, POWHEG will assign values internally.
- The minimal values for `ncall1`, `itmx1`, `ncall2`, `itmx2` are 250 000, 5, 1 000 000, 5 for the vector model, respectively.
- The minimal values for `ncall1`, `itmx1`, `ncall2`, `itmx2` are 100 000, 5, 100 000, 5 for the scalar top-loop model, respectively.
- When NLO corrections are included (as for instance in the vector model), negative-weighted events could occur and should be kept in the event sample, hence `withnegweights` should be set to 1. If needed, their fraction can be decreased by setting `foldsci` and `foldy` to larger values (2 for instance). `foldphi` can be kept to 1.
- One should use the automatic calculation of systematic uncertainties associated with the choice of hard scale and PDFs as described in Section 6.
- `idDM` is the integer that identifies the DM particle in the Monte Carlo event record. This should be chosen so that other tools can process the POWHEG output properly.

POWHEG in itself is not an event generator and must be interfaced with a tool that provides parton showering, hadronization, etc. For some time, a PYTHIA 8 [119] interface has existed for POWHEG. The PYTHIA 8 runtime configuration is the following:

```
POWHEG: veto = 1
POWHEG: pTdef = 1
POWHEG: emitted = 0
POWHEG: pTemt = 0
POWHEG: pThard = 0
POWHEG: vetoCount = 100
SpaceShower: pTmaxMatch = 2
TimeShower: pTmaxMatch = 2
```

As always, it is recommended to use the latest PYTHIA 8 release, available at <http://home.thep.lu.se/torbjorn/Pythia.html>. At the time of this report, the latest version is 8. 209.

4.1.2. Merging samples with different parton multiplicities

For the models discussed in the previous section, it is important to calculate the hard process as accurately as possible in QCD. For many other signal models, the \cancel{E}_T signature depends more upon the production and decay of the mediator. In some cases, observables built in terms of the jets present in the final state are considered, relying on the assumption that inclusive samples accurate in higher jet multiplicities are available. In these cases, one can employ LO+PS simulations where different parton multiplicities are merged and then matched to parton shower, using schemes such as CKKW or MLM merging.

Here, we consider the example of an EFT model produced in association with up to 2 additional QCD partons. A Monte Carlo sample based on this method could be used in alternative to a NLO+PS sample for describing shapes and jet distributions (but not for the overall normalization which would still be at LO). The methodology described here could also be used for the t -channel model discussed in Section 2.3.

For the calculation of tree-level merged samples for DM signals, tools that can read UFO files and implement multi-parton merging should be employed, such that MADGRAPH5_AMC@NLO (+PYTHIA 8 or HERWIG++) and SHERPA [120]. In this report we have mostly employed MADGRAPH5_AMC@NLO.

MADGRAPH5_AMC@NLO provides a flexible and easy-to-use framework for implementing new models via the FEYNRULES package. MADGRAPH5_AMC@NLO can perform both LO and NLO calculations in QCD, matched/merged to parton showers [83]. For NLO ones, dedicated UFO model implementations at NLO should be used. Several UFO models at NLO are publicly available that although not developed specifically for DM, are suitable to make mode independent simulations at NLO accuracy, including multiparton merging via the FxFx technique [121]. A dedicated DM UFO implementation has been developed and it has been released as a testing version [113].

Merging events generated via matrix elements with different number of partons in the final state can be achieved by a judicious procedure that avoids double counting of the partons from matrix elements and parton showering. Several merging techniques are available. Based on some comparative studies [122], there is some advantage to using the CKKW-L merging scheme [123] implemented in PYTHIA 8. Alternatively, one can use the k_T -MLM scheme also available in PYTHIA 8.

Generation of the LHE file. The example presented here is a D5 EFT model, and includes tree-level diagrams with $\chi\bar{\chi}+0,1,2$ partons. We stress that MADGRAPH5_AMC@NLO, like POWHEG, is not in itself an event generator, but must be interfaced with an event generator through an LHE file. The production of the LHE file proceeds through setting the process parameters and the run parameters.

The process parameters are:

```
import model MODELNAME
generate pp > chi chi ~ [QCD] @0
add process pp > chi chi ~ j [QCD] @1
add process pp > chi chi ~ j j [QCD] @2
```

The runtime parameters are more numerous, and define the collider properties, PDF sets, etc. The specific parameters needed for matching are, for the example of CKKW-L matching:

```
icckw = 0
ktdurham = matching scale
dparameter = 0.4
dokt = T
ptj = 20
drjj = 0
mmjj = 0
ptj1min = 0
```

For different kinds of matching, a different choice of icckw and related parameters would be made.

Implementation of the CKKW-L merging. To illustrate the settings related to merging different multiplicities, the EFT D5 samples were generated with MADGRAPH5_AMC@NLO version 2.2.2 and showered in PYTHIA 8.201, using the Madgraph parameters in the previous section (Section 4.1.2).

The PYTHIA 8 parameters for the CKKW-L k_T -merging scheme are:

```
Merging: ktType = 1
Merging: TMS = matching scale
1000022: all = chi chi ~ 2 0 0 30.0 0.0 0.0 0.0 0.0 0.0
1000022: isvisible = false
Merging: doKTMerging = on
Merging: Process = pp > {chi, 1000022} {chi ~, -1000022}
Merging: nJetMax = 2
```

The matching scales should be the same for the generation and parton showering. In the model implementation, the particle data group ID 1000022 is used for weakly interacting dark matter candidates. Since this is a Majorana particle by default (with no corresponding anti-particle), and the model produces a DM Dirac fermion, the particle properties are changed accordingly. Also, the DM mass is set to 30 GeV. The Merging: Process command specifies the lowest parton emission process generated in MADGRAPH5_AMC@NLO and Merging: nJetMax = 2 gives the maximum number of additional parton emissions with respect to the lowest parton emission process.

In general, it is desired to take the hard parton emissions from the matrix element generation in MADGRAPH5_AMC@NLO and allow PYTHIA 8 to take care of soft emissions only. The transition between these two regimes is defined by the matching scale and its optimal value can be determined by studying the cross-section as a function of the number of jets (differential jet rates). The differential rates $\frac{dN_{i \rightarrow j}}{d \log_{10}(k_{\text{cut}})}$ give the number of events which pass from i jets to j jets as the k_T value increases beyond k_{cut} . An optimal matching scale should lead to smooth differential jet rates.

Two examples of differential jet rates, using matching scale 30 GeV and 80 GeV, from the EFT D5 sample generated as described in the previous section are given in Figs. 62 and 63, respectively. Although a kink is visible around the matching scale value in both cases, the 80 GeV scale leads to smoother distributions. In order to find the optimal matching scale, additional samples with matching scale 50, 70, and 90 GeV are generated as well and a detailed comparison of the differential jet rates close to the transition region is shown in Fig. 64. The largest differences among the samples are visible for the $1 \rightarrow 2$ jets transition where the 30 GeV and 50 GeV scale lead to a drop of the rates around the matching scale values. On the contrary, there is a hint of an increased rate around the matching scale value in the sample generated with the 90 GeV scale. Therefore, we recommend to use 80 GeV as the baseline matching scale.

The prescription for the event generation given in Section 4.1.2 starts with the emission of 0 partons and ends with maximum 2 partons in addition. Producing the samples separately allows to investigate the relative composition of the individual samples in various parts of the phase space. Fig. 65 shows the \cancel{E}_T distribution of the EFT D5 sample with the matching scale at 80 GeV. The plot reveals that the 0-parton sample gives the dominant contribution in the region below the matching scale value that rapidly decreases at higher \cancel{E}_T . Assuming the lowest analysis \cancel{E}_T cut in early Run-2 mono-jet analyses at 300 GeV, the generation of the 0-parton emission sample can be safely omitted as it only gives < 1% contribution at $\cancel{E}_T > 300$ GeV. For the 1- and 2-parton emission samples, one can use a generator cut on the leading parton p_T , ptj1min, in order to avoid generating low \cancel{E}_T events that are irrelevant for the analysis.

In order to describe the signal kinematics correctly and save time during MC production, the parton emissions will only be

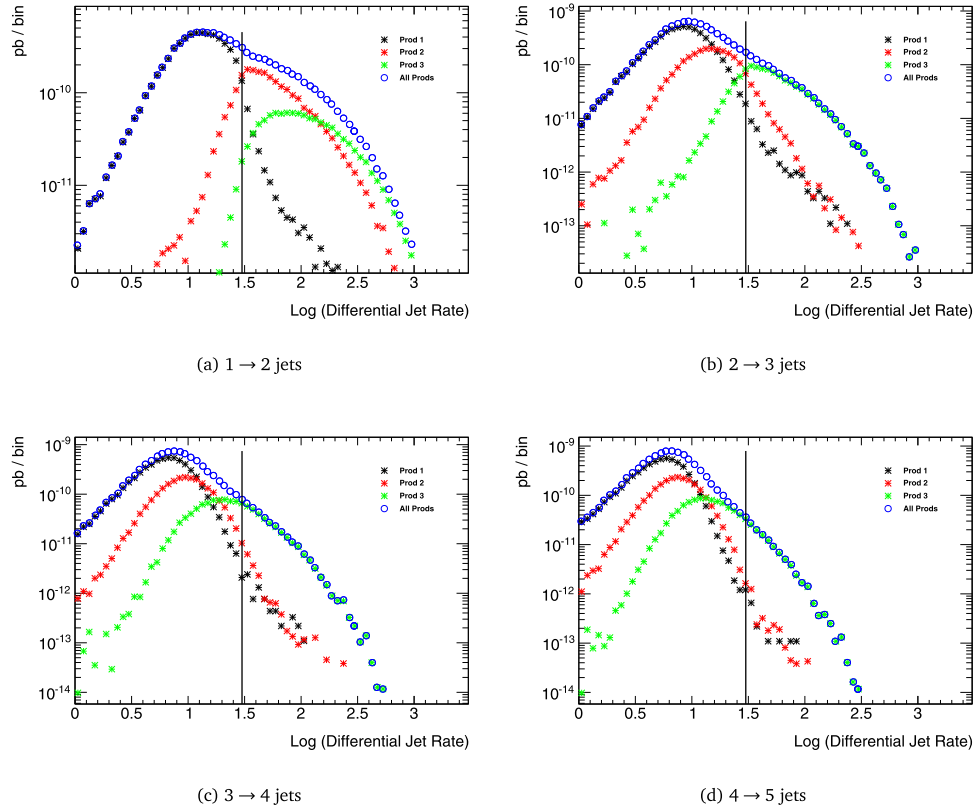


Fig. 62. Distributions of differential jet rates $\frac{dN_{i \rightarrow j}}{d \log_{10}(k_{\text{cut}})}$ for EFT D5 sample with CKKW-L matching scale at 30 GeV. The 0-, 1- and 2-parton emission samples are generated separately and indicated in the plots as Prod 1, Prod 2 and Prod 3, respectively. A vertical line is drawn at the matching scale.

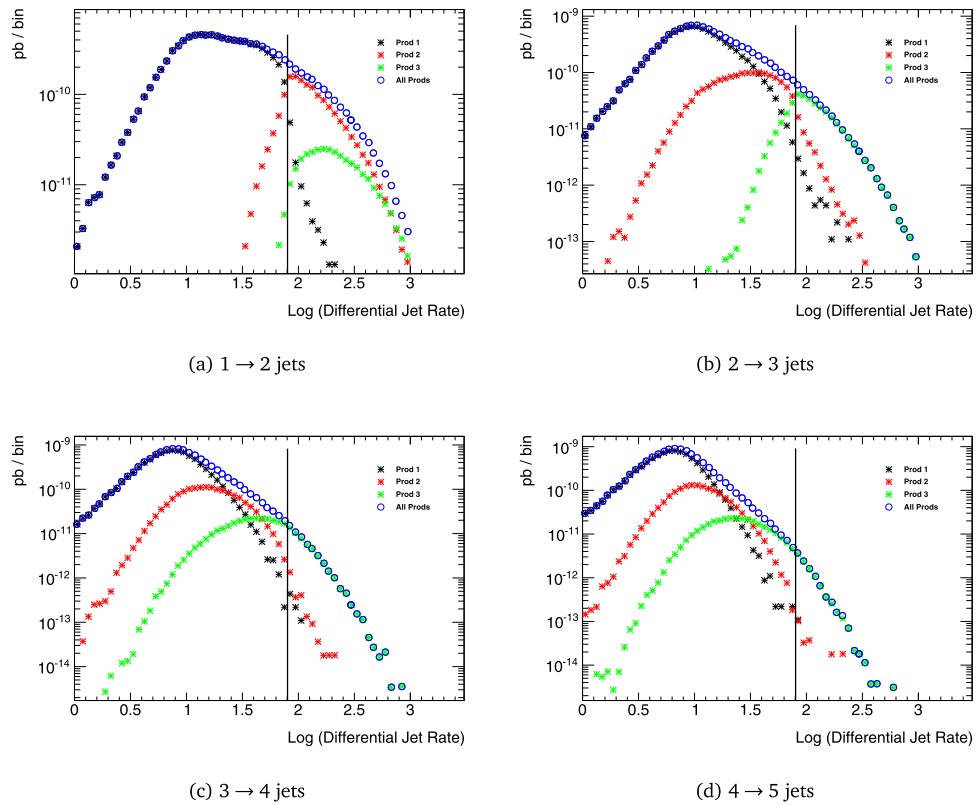
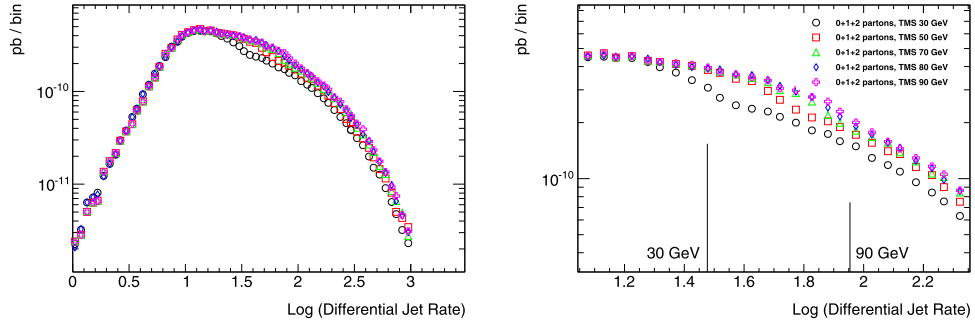
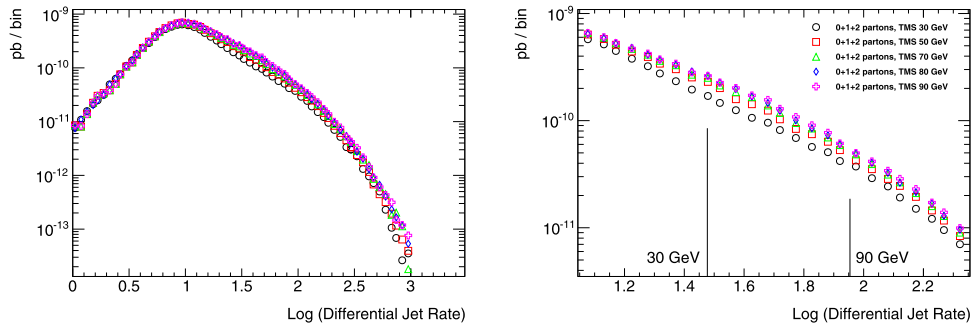


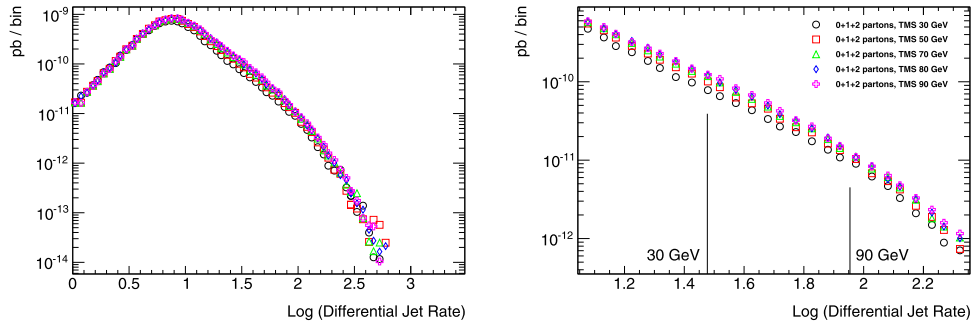
Fig. 63. Distributions of differential jet rates $\frac{dN_{i \rightarrow j}}{d \log_{10}(k_{\text{cut}})}$ for EFT D5 sample with CKKW-L matching scale at 80 GeV. The 0-, 1- and 2-parton emission samples are generated separately and indicated in the plots as Prod 1, Prod 2 and Prod 3, respectively. A vertical line is drawn at the matching scale.



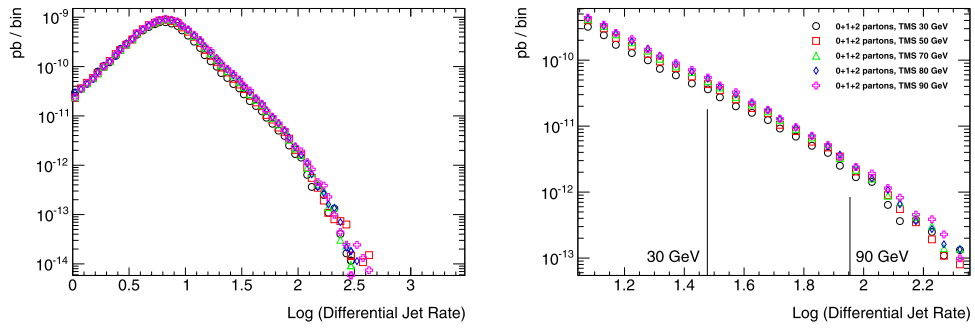
(a) 1 → 2 jets



(b) 2 → 3 jets



(c) 3 → 4 jets



(d) 4 → 5 jets

Fig. 64. Distributions of differential jet rates $\frac{dN_{i \rightarrow j}}{d \log_{10}(k_{cut})}$ for EFT D5 sample with CKKW-L matching scale at 30, 50, 70, 80 and 90 GeV. A zoom of the region around the matching scale values is shown on right.

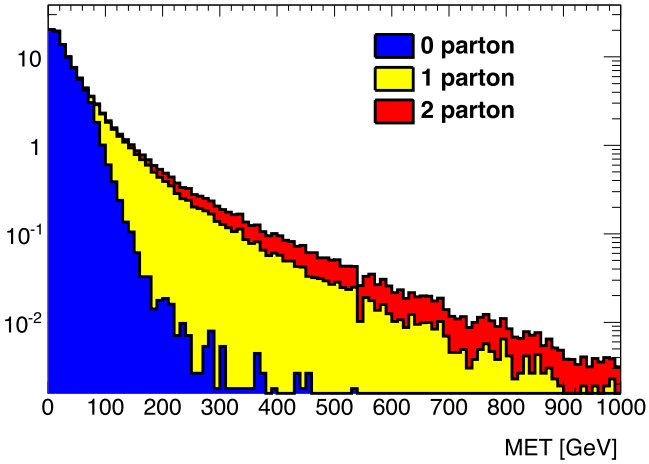


Fig. 65. Missing transverse momentum distributions for EFT D5 sample with CKKW-L matching scale at 80 GeV. Individual contributions from the 0-, 1- and 2-parton emission samples are shown.

generated up to a certain multiplicity. The higher multiplicity samples usually have small enough cross sections and the corresponding parts of the phase space can be sufficiently approximated by parton showering in PYTHIA 8. A dedicated study comparing samples generated with up to 1-, 2-, or 3-parton multiplicities was performed, using again the settings for the CKKW-L k_T -merging with the 80 GeV matching scale and the Merging:nJetMax parameter adjusted accordingly. Fig. 66 shows the \cancel{E}_T distribution of the samples at $\cancel{E}_T > 250$ GeV.

With an event selection requiring \cancel{E}_T and the leading jet p_T being larger than 250 GeV, the sample generated with up to 1 parton has 10.3% larger yield compared to the sample with up to 3 partons, while the yield of the sample with up to 2 partons is only 2.3% larger. If an additional cut is applied allowing for up to 3 jets with $p_T > 30$ GeV, the agreement improves to 3.2% larger for up to 1 parton and 0.7% larger for up to 2 partons, compared with up to 3 partons.

A similar comparison is shown in Fig. 67 for the jet multiplicity in the events with the leading jet $p_T > 250$ GeV, where an agreement at the level of $\sim 3\%$ between the samples with up to 2 and 3 parton emissions is observed for number of jets up to 7. This justifies it is sufficient to produce samples with up to 2 parton emissions only at the generator level and ignore generating higher parton emissions.

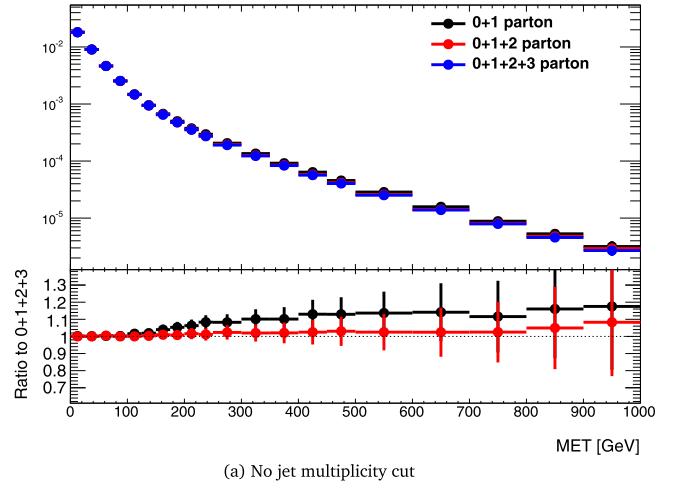
4.1.3. Implementation of t -channel models for the jet+ \cancel{E}_T final state

The simulations for t -channel models are available via LO UFO implementations, where events are generated at LO+PS accuracy. The UFO file and parameter cards for the t -channel models with couplings to light quarks only [78] can be found on the Forum Git repository [124]. The model files from Ref. [46] can also be found on the repository [125]. The latter is the implementation that has been used for the studies in this report: in the monojet case there are only cross section differences between this model and the model in [124].

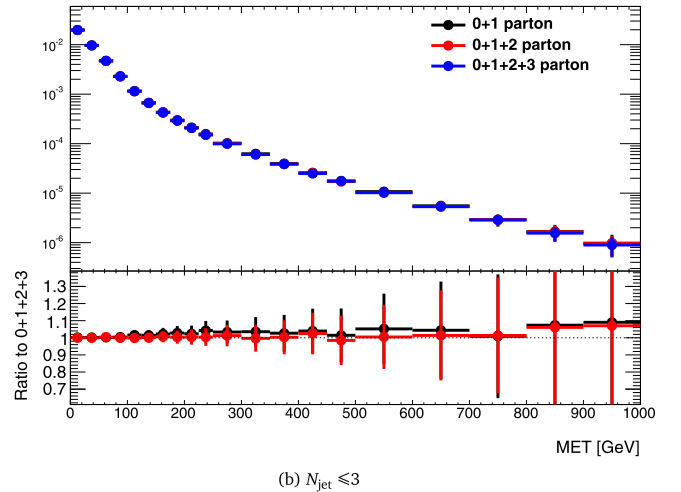
Multi-parton simulation and merging are necessary and require particular care for this model: this has not been a topic of detailed studies within the Forum, and we suggest to follow the procedure outlined in Ref. [78].

4.1.4. Implementation of s -channel and t -channel models with EW bosons in the final state

Currently, simulations for most of these models are available via LO UFO implementations, allowing event generation at the



(a) No jet multiplicity cut



(b) $N_{\text{jet}} \leq 3$

Fig. 66. Missing transverse momentum distributions for EFT D5 sample with CKKW-L matching scale at 80 GeV produced with maximum 1 (black), 2 (red) and 3 (blue) partons emitted at the generator level. The ratios are shown with respect to the latter sample. (For interpretation of the references to color in this figure legend, the reader is referred to the web version of this article.)

LO+PS accuracy. We note, however, that inclusion of NLO corrections would be possible. In MADGRAPH5_AMC@NLO, for example, this amounts to simply upgrading the currently employed UFO models to NLO, where the calculations exist for this class of processes. However, this was not available within the timescale of the Forum towards simulation of early Run-2 benchmarks. As a consequence, in this work we have used LO UFO implementations within MADGRAPH5_AMC@NLO 2.2.3 interfaced to PYTHIA 8 for the parton shower. The corresponding parameter cards used for the Run-2 benchmark models can be found on the Forum Git repository [126]. This is the implementation that will be used for early Run-2 LHC Dark Matter searches.

None of these models requires merging samples with different parton multiplicities since the visible signal comes from the production of a heavy SM boson whose transverse momentum distribution is sufficiently well described at LO+PS level. As a result, no special runtime configuration is needed for PYTHIA 8.

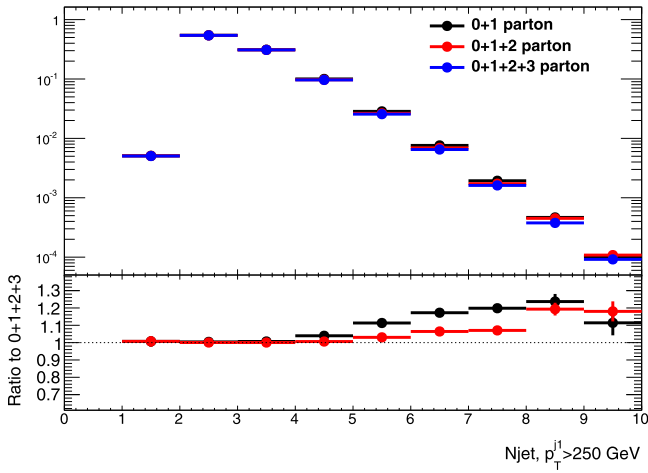


Fig. 67. Multiplicity of jets with $p_T > 30$ GeV and $|\eta| < 2.8$ for EFT D5 sample with CKKW-L matching scale at 80 GeV produced with maximum 1 (black), 2 (red) and 3 (blue) partons emitted at the generator level. The ratios are shown with respect to the latter sample. The leading jet p_T is required to be larger than 250 GeV. (For interpretation of the references to color in this figure legend, the reader is referred to the web version of this article.)

4.1.5. Implementation of s -channel and t -channel models with heavy flavor quark signatures

Dedicated implementations for DM signals in this final state are available at LO+PS accuracy. However, the state of the art of the simulations for $t\bar{t}$ and $b\bar{b}$ with a generic scalar and vector mediator is NLO+PS accuracy. For example, simulations for $t\bar{t} + \text{scalar}$ can be obtained via POWHEG and SHERPA starting from the SM implementations. In MADGRAPH5_AMC@NLO, all final relevant final states, spin-0 (scalar and pseudo scalar) and spin-1, (vector and axial) are available at NLO+PS via the dedicated NLO UFO for DM has been released in June 2015 [113]).

Within the scope of the Forum, simulations for the $t\bar{t}$ and $b\bar{b}$ signatures of the scalar mediator model have been generated starting from a leading order UFO with MADGRAPH5_AMC@NLO 2.2.2, using PYTHIA 8 for the parton shower. The UFO file and parameter cards that will be used as benchmarks for early Run-2 searches in these final states can be found on the Forum Git repository [127]. Multi-parton merging has been used for the $b\bar{b}$ case but it has not been studied in detail within this Forum. The b -flavored DM model of Section 2.3.2 is simulated at LO+PS using MADGRAPH5_AMC@NLO v2.2.3 and PYTHIA 8 for the parton shower. The corresponding UFO and parameter files can be found on the Forum Git repository [128].

Quark flavor scheme and masses. In the case of $b\bar{b}$ final state an additional care should be taken when choosing the flavor scheme generation and whether quarks should be treated as massive or massless.

The production of $DM+b\bar{b}$, dark matter in association with b jets via a decay of a (pseudo) scalar boson, is dominated in simplified mediator models by the gluon–gluon initiated production, similar to the production of $Z+b\bar{b}$ at the LHC. The $Z+b\bar{b}$ process has been studied in detail in the $Z(\text{ll})+b$ -jets final state, which can be used to validate both the modeling of $DM+b\bar{b}$ and, its main background, $Z(\nu\nu)+b\bar{b}$. In this context, the p_T of the Z boson is related to the observed MET, whereas the b -jet kinematics determines the ratio of mono- b /di- b signatures in the detector.

For basic kinematic criteria applied to $Z+b\bar{b}$ production, this process leads in $\sim 90\%$ of the events to a signature with only 1 b -jet in the acceptance ($Z+1b$ -jet production’) and only in $\sim 10\%$ of the events to a signature with 2 b -jets in the detector ($Z+2b$ -jets

production’). The production cross section of the $Z+b\bar{b}$ process can be calculated in the ‘five-flavor scheme’, where b quarks are assumed massless, and the ‘four-flavor scheme’, where massive b quarks are used [129–131]. Data slightly favor the cross-section predictions in the five-flavor scheme [132] for the 1 b -jet signature. In this document we have preferred the 5-flavor scheme due to its simplicity and cross section agreement within the SM. The PDF used to calculate these cross section is NNPDF3.0 (lhaid 263000).

On the other hand, both data [132–134] and theoretical studies [135,136] suggest that the best modeling of an inclusive $Z+b\bar{b}$ sample especially for what concerns b -quark observables, is achieved at NLO+PS using a 4-flavor scheme and a massive treatment of the b -quarks. In Fig. 68 we show that, at LO, as expected, no appreciable difference is visible in the kinematics between either flavor scheme used for $DM+b\bar{b}$. In our generation we have used NNPDF3.0 set (lhaid 263400).

4.2. Implementation of specific models for $V + \cancel{E}_T$ analyses

4.2.1. Model implementation for mono-Higgs models

Currently, simulations for most of these models are available via LO UFO implementations, allowing event generation at the LO+PS accuracy. We note, however, that the inclusion of NLO corrections would be possible but not available in time for the conclusion of these studies. In MADGRAPH5_AMC@NLO, for example, this amounts to simply upgrading the currently employed UFO models to NLO. Simulation of loop-induced associated production of DM and Higgs is also possible with the exact top-quark mass dependence. In MADGRAPH5_AMC@NLO, for example, this can be obtained from the NLO UFO SM and 2HDM implementations.

In this work all three Higgs+ \cancel{E}_T models have been generated at leading order with MADGRAPH5_AMC@NLO 2.2.2, using PYTHIA 8 for the parton shower. No merging procedure has been employed. The LO UFO implementations of the scalar and vector models that will be used as early Run-2 benchmarks can be found on the Forum Git repository [137], while the 2HDM model can be found at this link [138].

As a final technical remark, we suggest always to let the shower program handle the h decay (and therefore to generate a stable h at the matrix element level). In so doing a much faster generation is achieved and the h branching ratios are more accurately accounted for by the shower program.

MADGRAPH5_AMC@NLO details for scalar mediator Higgs+MET model. The case of the associated production of a Higgs and scalar mediator via a top-quark loop can be either considered exactly or via an effective Lagrangian where the top-quark is integrated out. While this latter model has been shown not to be reliable [108,139,140], for simplicity we have chosen to perform the study in this tree-level effective formulation. A full study of the process including finite top-quark mass and parton shower effects is possible yet left for future work.

MADGRAPH5_AMC@NLO details for 2HDM Higgs+MET model. While a 2HDM UFO implementation at NLO accuracy to be used with MADGRAPH5_AMC@NLO has been made available at the end of the work of the Forum [113], in this work we have only considered LO simulations.

The two couplings that can be changed in the implemented model follow the nomenclature below:

- T_b - $\tan \beta$
- g_Z - g_z , gauge coupling of Z' to quarks

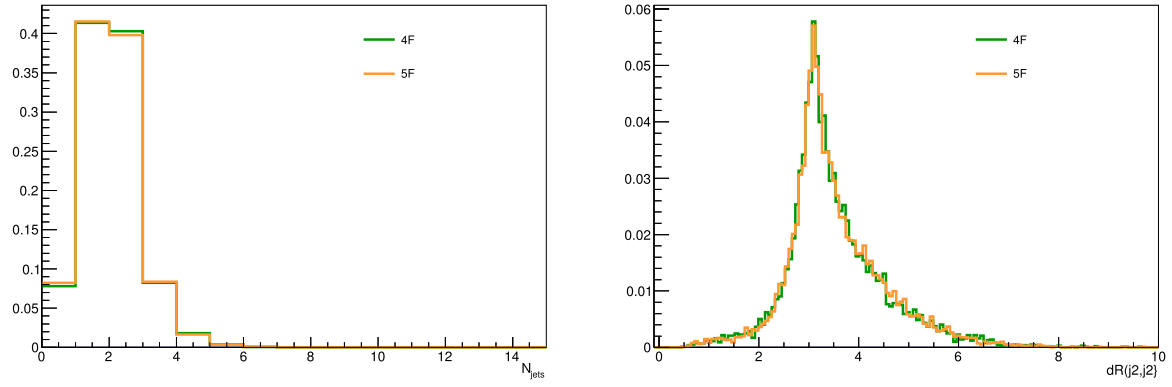


Fig. 68. Comparison of the jet multiplicity (left) and angular correction $\Delta R(j_1, j_2)$ (right) for the DM+ $b\bar{b}$ scalar model generated in the 4-flavor and 5-flavor schemes. The samples are generated for $m_\chi = 1$ GeV and $m_\phi = 10$ GeV.

The other couplings are not changed, including g_X (the $A\bar{\chi}\chi$ coupling) which has little impact on the signal. $\sin\alpha$ is fixed internally such that $\cos(\beta - \alpha) = 0$. The width of the Z' and A can be computed automatically within MADGRAPH5_AMC@NLO. The couplings here do not affect the signal kinematics, so they can be fixed to default values and then the signal rates can be scaled appropriately.

The nomenclature for the masses in the implemented model is:

- MZp - PDG ID 32 - Z'
- MA0 - PDG ID 28 - A
- MX - PDG ID 100022 - dark matter particle

The other masses are unchanged and do not affect the result. Both $Z' \rightarrow hZ(\bar{\nu}\nu)$ and $Z' \rightarrow hA(\bar{\chi}\chi)$ contribute to the final state, scaling different with model parameters. We recommend to generate them separately, and then add the two signal processes together weighted by cross sections.

4.2.2. Implementation of EFT models for EW boson signatures

The state of the art for these models is LO+PS. NLO+PS can be achieved as well, but the corresponding implementation is not yet available. In our simulations we have implemented the models in the corresponding UFO files and generated events at LO via MADGRAPH5_AMC@NLO 2.2.2, using PYTHIA 8 for the parton shower. UFO files and parameter cards that will be used as early Run-2 benchmarks can be found on the Forum Git repository: [137] for operators with Higgs+MET final states and [141] for $W/Z/\gamma$ final states. These models do not require merging.

5. Presentation of EFT results

Most of this report has focused on simplified models of dark matter. In this Chapter, we wish to emphasize the applicability of Effective Field Theories (EFTs) in the interpretation of DM searches at the LHC. Given our current lack of knowledge about the nature of a DM particle and its interactions, it appears mandatory to provide the necessary information for a model independent interpretation of the collider bounds. This approach should be complemented with an interpretation within a choice of simplified models. We note that, even though EFT benchmarks are only valid in given conditions, the results provided by the current list of simplified models cannot always characterize the breadth of SM-DM interactions. In at least one case, composite WIMPs [142–144], the contact interaction framework is the correct one to constrain new confinement scales.

Ideally, experimental constraints should be shown as bounds of allowed signal events in the kinematic regions considered for

the search, as detailed in Appendix B. A problematic situation is the attempt to derive a limit on nucleon–dark matter scattering cross sections from EFT results based on collider data.¹⁴ Experiments that directly probe the nucleon–dark matter scattering cross section are testing the regime of small momentum transfers, where the EFT approximation typically holds. Collider experiments, though, are sensitive to large momentum transfers: We first illustrate the complications that can arise with EFTs at colliders by considering an effective interaction

$$\mathcal{L}_{\text{int}} = \frac{(\bar{q}\gamma_\mu q)(\bar{\chi}\gamma^\mu \chi)}{M_*^2} = (\bar{q}\gamma_\mu q)(\bar{\chi}\gamma^\mu \chi) \frac{g}{\Lambda^2}$$

that couples quarks and DM χ fields.¹⁵ The strength of this interaction is parameterized by $\frac{1}{M_*^2} = \frac{g}{\Lambda^2}$. A monojet signature can be generated from this operator by applying perturbation theory in the QCD coupling. An experimental search will place a limit on M_* . For a fixed M_* , a small value of g will correspond to a small value of Λ . The EFT approximation breaks down if $Q > \Lambda$, where Q is a typical hard scale of the process. The limit on small g can only be reliable if the kinematic region $Q > \Lambda$ is removed from the event generation. However, if a fraction of events is removed from the prediction, the corresponding value of g must increase to match the experimental limit on M_* . On the other hand, if, for the same value of M_* , a large Λ is assumed so that the full set of events fulfill the EFT validity condition, a larger value of g is required. For large enough g , computations based on perturbation theory become unreliable.

In the first part of this Chapter, we summarize two methods that have been advocated to truncate events that do not fulfill the condition necessary for the use of an EFT. These methods are described in detail in Refs. [7,28,80,97,145,146]. We then propose a recommendation for the presentation of EFT results for early Run-2 LHC searches.

5.1. Procedures for the truncation of EFT benchmark models

5.1.1. EFT truncation using the momentum transfer and information on UV completion

In the approach described in Ref. [145], the EFT prediction is modified to incorporate the effect of a propagator for a relatively

¹⁴ Comparisons between constraints from different experiments meant to highlight their complementarity should be expressed as a function of the model parameters rather than on derived observables; however this is a point that should be developed further after the conclusion of the work of this Forum.

¹⁵ The exact operator chosen is not important: as detailed in the following, statements concerning the applicability of an EFT can also be made without a specific relation to simplified models.

light mediator. For a tree-level interaction between DM and the SM via some mediator with mass M_{med} , the EFT approximation corresponds to expanding the propagator for the mediator in powers of $Q_{\text{tr}}^2/M_{\text{med}}^2$, truncating at lowest order, and combining the remaining parameters into a single parameter M_* (connected to the scale of the interaction Λ in the literature). For an example scenario with a Z' -type mediator (leading to some combination of operators D5 to D8 in the notation of [23] for the EFT limit), this corresponds to setting

$$\frac{g_\chi g_q}{Q_{\text{tr}}^2 - M_{\text{med}}^2} = -\frac{g_\chi g_q}{M_{\text{med}}^2} \left(1 + \frac{Q_{\text{tr}}^2}{M_{\text{med}}^2} + \mathcal{O}\left(\frac{Q_{\text{tr}}^4}{M_{\text{med}}^4}\right) \right) \simeq -\frac{1}{M_*^2}, \quad (45)$$

where Q_{tr} is the momentum carried by the mediator, and g_χ , g_q are the DM-mediator and quark-mediator couplings respectively.¹⁶ A minimal condition that must be satisfied for this approximation to be valid is that $Q_{\text{tr}}^2 < M_{\text{med}}^2 = g_\chi g_q M_*^2$. This requirement avoids the regions: $Q_{\text{tr}}^2 \sim M_{\text{med}}^2$, in which case the EFT misses a resonant enhancement; and $Q_{\text{tr}}^2 \gg M_{\text{med}}^2$, in which case the signal cross section should fall according to a power of Q_{tr}^{-1} instead of M_{med}^{-1} . The latter is the problematic kinematic region.

The condition $Q_{\text{tr}}^2 < M_{\text{med}}^2 = g_\chi g_q M_*^2$ was applied to restrict the kinematics of the signal and remove events for which the high-mediator-mass approximation made in the EFT would not be reliable. This leads to a smaller effective cross-section, after imposing the event selection of the analysis. This truncated signal was then used to derive a new, more conservative limit on M_* as a function of $(m_\chi, g_\chi g_q)$.

For the example D5-like operator, where the cross section σ scales as M_*^{-4} , there is a simple rule for converting a rescaled cross section into a rescaled constraint on M_* if the original limit is based on a simple cut-and-count procedure. Defining $\sigma_{\text{EFT}}^{\text{cut}}$ as the cross section truncated such that all events pass the condition $\sqrt{g_\chi g_q} M_*^{\text{rescaled}} > Q_{\text{tr}}$, we have

$$M_*^{\text{rescaled}} = \left(\frac{\sigma_{\text{EFT}}}{\sigma_{\text{EFT}}^{\text{cut}}(M_*^{\text{rescaled}})} \right)^{1/4} M_*^{\text{original}}, \quad (46)$$

which can be solved for M_*^{rescaled} via either iteration or a scan. Similar relations exist for a given UV completion of each operator.

This procedure has been proposed in Ref. [145] and its application to ATLAS results can be found in Ref. [7] for a range of operators. We reiterate: knowledge of the UV completion for a given EFT operator was necessary for this procedure; this introduces a model-dependence that was not present in the non-truncated EFT results.

Currently, simplified models (including the full effect of the mediator propagator) are available for comparison with the data, and since knowledge of the simplified models is needed for the truncation procedure, there is no reason to apply this prescription. Instead, the simplified model limit for large M_* can be presented for interpretation in terms of EFT operators.

5.1.2. EFT truncation using the center of mass energy

The procedure presented in the previous section was predicated on some knowledge of the simplified model. This led to the identification of the mass of the DM pair as the relevant kinematic quantity to use in a truncation procedure. In general, if no assumption is made about the underlying dynamics, it is more conservative to place a limit on the total center of mass energy E_{cm} of the DM production process. Furthermore, the direct

connection between the mass scale of the EFT validity, M_{cut} , and the mass scale that normalizes the EFT operator, M_* , is unknown. For such cases, Refs.[97,146] proposed a procedure to extract model independent and consistent bounds within the EFT that can be applied to any effective Lagrangian describing the interactions between the DM and the SM. This procedure provides conservative limits that can be directly reinterpreted in any completion of the EFT. The condition ensuring that the EFT approximation is appropriate is:

$$E_{\text{cm}} < M_{\text{cut}}. \quad (47)$$

The relationship between M_{cut} and M_* can be parameterized by an *effective coupling strength* g_* , such that $M_{\text{cut}} = g_* M_*$. A scan over values of g_* provides an indication of the sensitivity of the prediction to the truncation procedure. In the Z' -type model considered above, g_* is equal to $\sqrt{g_\chi g_q}$. The resulting plots are shown in [146] for a particular effective operator.

The advantage of this procedure is that the obtained bounds can be directly and easily recast in any completion of the EFT, by computing the parameters M_* , M_{cut} in the full model as functions of the parameters of the complete theory. On the other hand, the resulting limits will be weaker than those obtained using Q_{tr} and a specific UV completion.

5.1.3. Truncation at the generator level

The conditions on the momentum transfer can also be applied directly at the generator level, by discarding events that are invalid and calculating the limits from this truncated shape. This provides the necessary rescaling of the cross section while keeping the information on the change in the kinematic distributions due to the removal of the invalid events. This procedure is more general with respect to rescaling the limit in the two sections above, and it should be followed if a search is not simply a counting experiment and exploits the shapes of kinematic distributions.

5.1.4. Sample results of EFT truncation procedures

An example of the application of the two procedures to the limit on M_* from Ref. [14] as a function of the product of the couplings is shown in Fig. 69. Only the region between the dashed and the solid line is excluded. It can be seen that the procedure from [146] outlined in Section 5.1.2, shown in blue, is more conservative than the procedure from Refs. [7,145], described in Section 5.1.1.

5.1.5. Comments on unitarity considerations

A further consideration applicable to EFT operators at hadron colliders is the potential violation of unitarity. An analysis of the operator $\frac{\bar{q}\gamma_\mu q \bar{\chi}\gamma^\mu \chi}{M_*^2}$ provides the limit:

$$M_* > \beta(s) \sqrt{s} \sqrt{\frac{\sqrt{3}}{4\pi}}, \quad (48)$$

where \sqrt{s} is (maximally) the collider energy and $\beta(s)$ is the DM velocity [24]. Constraints for other operators have also been derived [147]. This constraint on M_* still is open to interpretation, since the relation to M_{cut} is not resolved, except for a specific simplified model. Derived limits on M_* should be compared to this unitarity bound to check for consistency.

5.2. Recommendation for presentation of EFT results

In this report, we make two recommendations for the presentation of collider results in terms of Effective Field Theories for the upcoming Run-2 searches. A full discussion of the presentation of

¹⁶ Here, we ignore potential complications from the mediator width when the couplings are large.

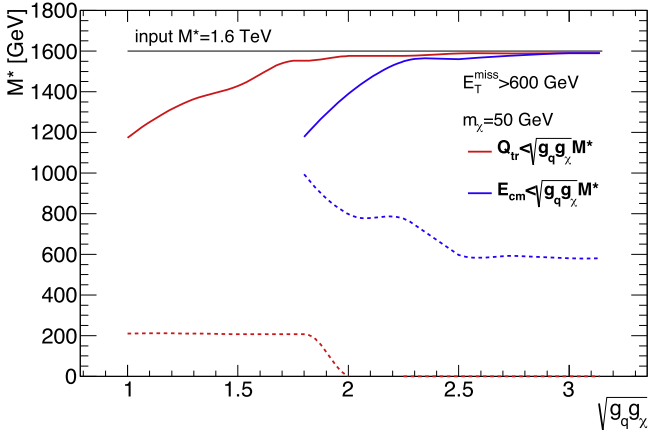


Fig. 69. 95% CL lower limits on the scale of the interaction of the D5 operator at 14 TeV, after the two truncation procedures. The procedure from [146] outlined in Section 5.1.2 is shown in blue, while the procedure from Refs. [7,145], described in Section 5.1.1 is shown in red. Only the region between the dashed and the solid lines is excluded. Even though the intersection between the two lines is not shown in this plot, it should be noted that no limit can be set anymore for sufficiently low couplings, whatever truncation method is used.

collider results in relation to other experiments is left to work beyond this Forum, where ATLAS, CMS, the theory community and the Direct and Indirect Detection communities are to be involved.

We divide the EFT operators in two categories: those that can be mapped to one or more UV-complete simplified models, such as those commonly used in LHC searches so far and detailed in [23], and those for which no UV completion is available to LHC experiments, such as those outlined in Section 3.2.

5.2.1. EFT benchmarks with corresponding simplified models

If a simplified model can be mapped to a given EFT, then the model's high-mediator-mass limit will converge to the EFT. A study of 14 TeV benchmarks for narrow resonances with $g_q = 0.25$ and $g_\chi = 1$ (see Section 2.1.1) shows that a mediator with a mass of at least 10 TeV fully reproduces the kinematics of a contact interaction and has no remaining dependence on the presence of a resonance. A comparison of the main kinematic variables for the s -channel vector mediator model with a width of $0.1 M_{\text{med}}$ is shown in Fig. 70.¹⁷

As already observed in Section 2.1.1, varying the DM mass changes the kinematics, both in the simplified model and in the EFT case. This can be seen in Fig. 71.

Based on these studies, the Forum recommends experimental collaborations to add one grid scan point at very high mediator mass (10 TeV) to the scan, for each of the DM masses for the s -channel simplified models described in Section 2. This will allow to reproduce the results of an equivalent contact interaction as a simple extension of the existing parameter scan.

It should be checked that the high-mass mediator case for the simplified model is correctly implemented

5.2.2. EFT benchmarks with no corresponding simplified models

Whenever a UV completion is not available, an EFT still captures a range of possible theories beyond the simplified models that we already consider. However, in the case of the dimension-7

operators detailed in Section 3.2 we can only roughly control how well the EFT approximation holds, as described in Section 3.2.4. Despite the fact that a propagator was introduced to motivate the truncation procedure for s -channel models, the prescription from Section 5.2.1 depends upon the simplified model to derive the energy scaling that is used for the comparison with the momentum transfer. The simple fact remains that the effective coupling of the operator $-g/\Lambda^n$ should not allow momentum flow $Q > \Lambda$ or $g > 4\pi$. Given our ignorance of the actual kinematics, the truncation procedure recommended for this purpose is the one described in Section 5.1.2, as it is independent from any UV completion details.

Because there is no UV completion, the parameter M_{cut} can be treated more freely than an explicit function of g and Λ . It makes sense to choose M_{cut} such that we identify the transition region where the EFT stops being a good description of UV complete theories. This can be done using the ratio R , which is defined as the fraction of events for which $\hat{s} > M_{\text{cut}}^2$. For large values of M_{cut} , no events are thrown away in the truncation procedure, and $R = 1$. As M_{cut} becomes smaller, eventually all events are thrown away in the truncation procedure, i.e. $R = 0$, and the EFT gives no exclusion limits for the chosen acceptance.

We propose a rough scan over M_{cut} , such that we find the values of M_{cut} for which R ranges from 0.1 to 1. The analysis can then perform a scan over several values of M_{cut} , and show the truncated limit for each one of them.

6. Evaluation of signal theoretical uncertainties

A comprehensive and careful assessment of signal theoretical uncertainties plays in general a more important role for the background estimations (especially when their evaluation is non-entirely data-driven) than it does for signal simulations. Nevertheless, also for signal samples theoretical uncertainties are relevant, and may become even dominant in certain regions of phase space.

The uncertainties on the factorization and renormalization scales are assessed by the experimental collaborations by varying the original scales of the process by factors of 0.5 and 2. The evaluation of the uncertainty on the choice of PDF follows the PDF4LHC recommendation [148] of considering the envelope of different PDF error sets, in order to account for the uncertainty on the various PDFs as well as the uncertainty on the choice of the central value PDF. The Forum has not discussed the uncertainties related to the merging of different samples, nor the uncertainty due to the choice of the modeling of the parton shower. This Chapter provides technical details on how scale and PDF uncertainties can be assessed for events generated with POWHEG and MADGRAPH5_AMC@NLO.

6.1. POWHEG

When using POWHEG [69–71], it is possible to study scale and PDF errors for the dark matter signals. A fast reweighting machinery is available in POWHEG-BOX that allows one to add, after each event, new weights according to different scale or PDF choices, without the need to regenerate all the events from scratch.

To enable this possibility, the variable `storeinfo_rwgt` should be set to 1 in the POWHEG input file when the events are generated for the first time.¹⁸ After each event, a line starting with

```
#rwgt
```

¹⁷ The use of a fixed width rather than the minimal width is exclusive of these plots.

¹⁸ Notice that even if the variable is not present, by default it is set to 1.

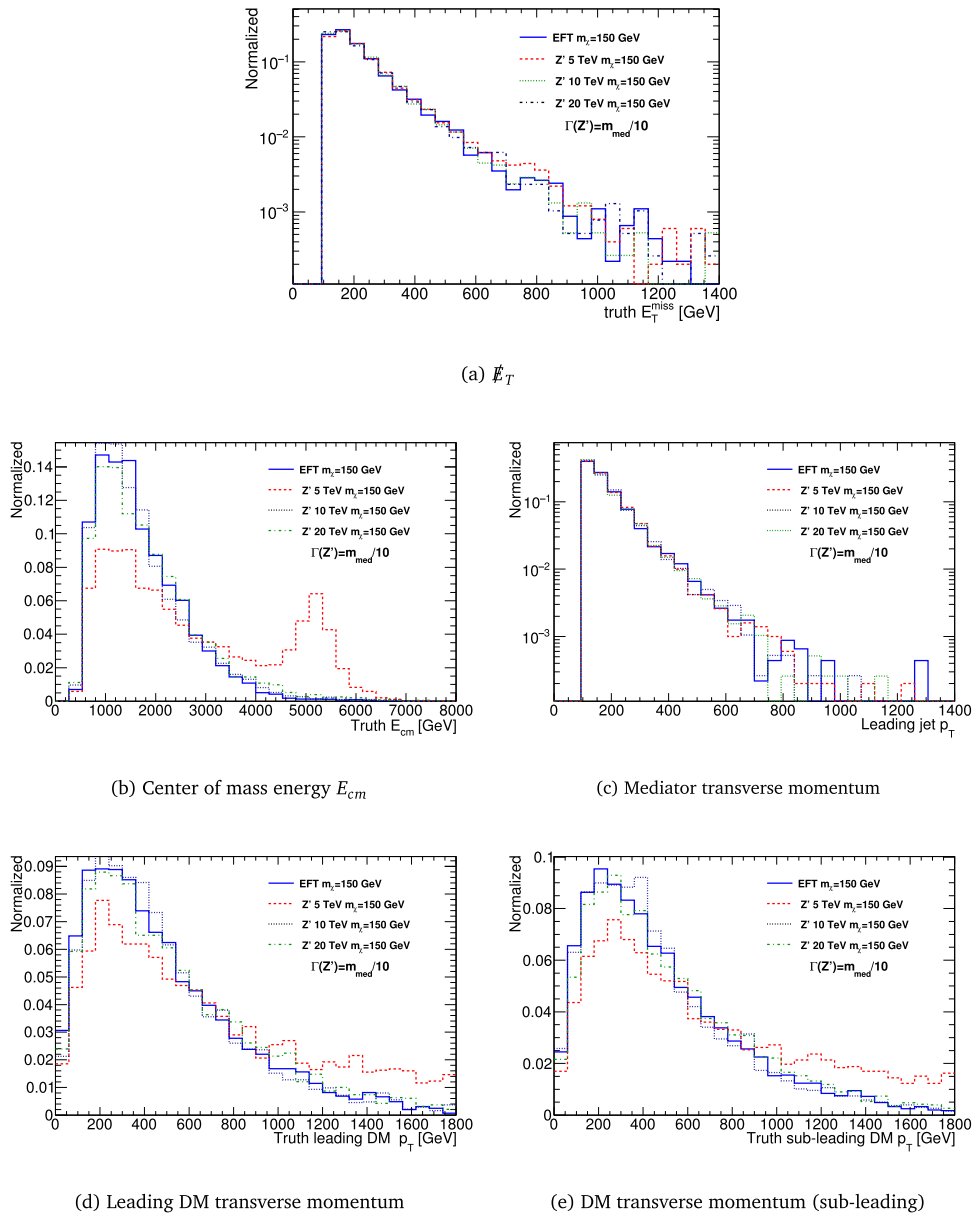


Fig. 70. Comparison of the kinematic distributions at 14 TeV between a narrow s -channel mediator and the corresponding D5 contact operator, at generator level for a $\text{jet}+\cancel{E}_T$ signature.

is appended, containing the necessary information to generate extra weights. In order to obtain new weights, corresponding to different PDFs or scale choice, after an event file has been generated, a line

```
compute_rwgt 1
```

should be added in the input file along with the desired change in parameters. For instance, `renscfact` and `facscfact` allow one to study scale variations on the renormalization and factorization scales around a central value. By running the program again, a new event file will be generated, named `<Original Name>-rwgt.lhe`, with one more line at the end of each event of the form

```
#new weight, renfact, facfact, pdf1, pdf2
```

followed by five numbers and a character string. The first of these numbers is the weight of that event with the new parameters

chosen. By running in sequence the program in the reweighting mode, several weights can be added on the same file. Two remarks are in order.

- The file with new weights is always named `<Original Name>-rwgt.lhe` hence care has to be taken to save it as `<Original Name>.lhe` before each iteration of the reweighting procedure.
- Due to the complexity of the environment where the program is likely to be run, it is strongly suggested as a self-consistency check that the first reweighting is done keeping the initial parameters. If the new weights are not exactly the same as the original ones, then some inconsistency must have happened, or some file was probably corrupted.

It is possible to also have weights written in the version 3 Les Houches format. To do so, in the original run, at least the token `lhweight_id 'ID'`

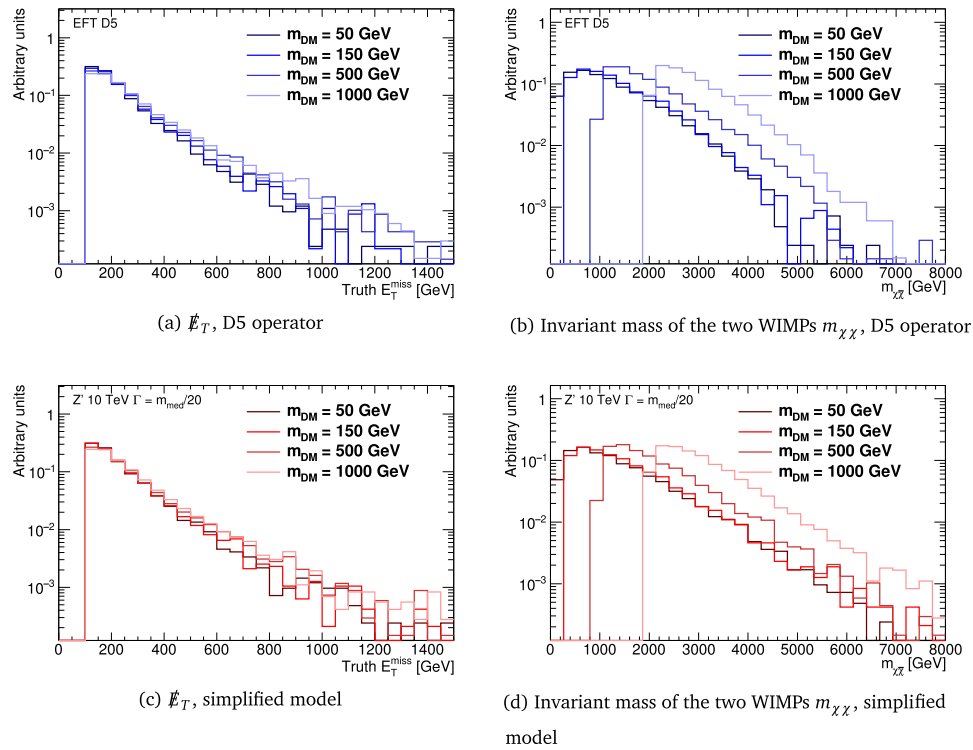


Fig. 71. Comparison of the kinematic distributions for a narrow s -channel mediator, at generator level for a jet+ \cancel{E}_T signature, for varying DM masses.

must be present. The reweighting procedure is the same as described above, but now each new run can be tagged by using a different value for the `lhrwgt_id` keyword. After each event, the following lines will appear:

```
<rwgt>
<wgt id='ID' >
<wgt id='ID1' >
</rwgt>
```

A more detailed explanation of what went into the computation of every single weight can be included in the `<header>` section of the event file by adding/changing the line

```
lhrwgt_descr 'some info'
```

in the input card, before each “reweighting” run is performed. Other useful keywords to group together different weights are `lhrwgt_group_name` and `lhrwgt_group_combine`.

More detailed information can be obtained by inspecting the document in `/Docs/V2-paper.pdf` under the common POWHEG-BOX-V2 directory.

6.2. The SysCalc package in MADGRAPH5_AMC@NLO

SysCALC is a post-processing package for parton-level events as obtained from leading-order calculations in MADGRAPH5_AMC@NLO. It can associate to each event a series of weights corresponding to the evaluation of a certain class of theoretical uncertainties. The event files in input and output are compliant with the Les Houches v3 format. For NLO calculations, PDF and scale uncertainties are instead evaluated automatically by setting corresponding instructions in the `run_card.dat` and no post-processing is needed (or possible).

The requirements of the package as inputs are :

- A systematics file (which can be generated by MadGraph 5 v. 1.6.0 or later) [75,149].
- The Pythia-PGS package (v. 2.2.0 or later) [150]. This is needed only in the case of matching scales variations.

- The availability of LHAPDF5 [151].
- A configuration file (i.e. a text file) specifying the parameters to be varied.

SysCALC supports all leading order computations generated in MADGRAPH5_AMC@NLO including fixed-order computation and matched-merged computation performed in the MLM scheme [152]. MADGRAPH5_AMC@NLO stores additional information inside the event in order to have access to all the information required to compute the convolution of the PDFs with the matrix element for the various supported systematics.

An example configuration file is as follows:

```
# Central scale factors
scalefact:
0.5 1 2
# Scale correlation
# Special value -1: all combination (N**2)
# Special value -2: only correlated variation
# Otherwise list of index N*fac_index + ren_index
# index starts at 0
scalecorrelation:
-1
# alpha_s emission scale factors
alpsfact:
0.5 1 2
# matching scales
matchscale:
30 60 120
# PDF sets and number of members (optional)
PDF:
CT10.LHgrid53
MSTW2008nlo68cl.LHgrid
```

Without matching/merging, SysCALC is able to compute the variation of renormalization and factorization scale (parameter `scalefact`) and the change of PDFs. The variation of the scales

can be done in a correlated and/or uncorrelated way, basically following the value of the scale correlation parameter which can take the following values:

- -1 : to account for all N^2 combinations.
- -2 : to account only for the correlated variations.
- A set of positive values corresponding to the following entries (assuming 0.5, 1, 2 for the scale effect entry):

$$\begin{aligned} 0: & \mu_F = \mu_F^{\text{orig}}/2, \mu_R = \mu_R^{\text{orig}}/2 \\ 1: & \mu_F = \mu_F^{\text{orig}}/2, \mu_R = \mu_R^{\text{orig}} \\ 2: & \mu_F = \mu_F^{\text{orig}}/2, \mu_R = \mu_R^{\text{orig}} * 2 \\ 3: & \mu_F = \mu_F^{\text{orig}}, \mu_R = \mu_R^{\text{orig}}/2 \\ 4: & \mu_F = \mu_F^{\text{orig}}, \mu_R = \mu_R^{\text{orig}} \\ 5: & \mu_F = \mu_F^{\text{orig}}, \mu_R = \mu_R^{\text{orig}} * 2 \\ 6: & \mu_F = \mu_F^{\text{orig}} * 2, \mu_R = \mu_R^{\text{orig}}/2 \\ 7: & \mu_F = \mu_F^{\text{orig}} * 2, \mu_R = \mu_R^{\text{orig}} \\ 8: & \mu_F = \mu_F^{\text{orig}} * 2, \mu_R = \mu_R^{\text{orig}} * 2 \end{aligned}$$

Without correlation, the weight associated to the renormalization scale is the following:

$$\mathcal{W}_{\text{new}}^{\mu_R} = \frac{\alpha_s^N(\Delta * \mu_R)}{\alpha_s^N(\mu_R)} * \mathcal{W}_{\text{orig}}, \quad (49)$$

where Δ is the scale variation considered, $\mathcal{W}_{\text{orig}}$ and \mathcal{W}_{new} are respectively the original/new weights associated to the event. N is the power in the strong coupling for the associated event (interference is not taken account on an event by event basis). The weight associated to the scaling of the factorization scale is:

$$\mathcal{W}_{\text{new}}^{\mu_F} = \frac{f_{1,\text{orig}}(x_1, \Delta * \mu_F) * f_{2,\text{orig}}(x_2, \Delta * \mu_F)}{f_{1,\text{orig}}(x_1, \mu_F) * f_{2,\text{orig}}(x_2, \mu_F)} * \mathcal{W}_{\text{orig}}, \quad (50)$$

where $f_{i,\text{orig}}$ are the probabilities from the original PDF set associated to the incoming partons, which hold a proton momentum fraction x_1 and x_2 for the first and second beam respectively.

The variations for the PDF are given by the corresponding weights associated to the new PDF sets:

$$\mathcal{W}_{\text{new}}^{\text{PDF}} = \frac{f_{1,\text{new}}(x_1, \mu_F) * f_{2,\text{new}}(x_2, \mu_F)}{f_{1,\text{orig}}(x_1, \mu_F) * f_{2,\text{orig}}(x_2, \mu_F)} * \mathcal{W}_{\text{orig}}, \quad (51)$$

where $f_{i,\text{new}}$ is the new PDF probability associated to parton i .

In presence of matching, MADGRAPH5_AMC@NLO associates one history of radiation (initial and/or final state radiation) obtained by a k_T clustering algorithm, and calculates α_s at each vertex of the history to a scale given by the aforementioned clustering algorithm. Furthermore, MADGRAPH5_AMC@NLO reweights the PDF in a fashion similar to what a parton shower would do. SysCALC can perform the associated re-weighting (parameter `alpsfact`) by dividing and multiplying by the associated factor.

For each step in the history of the radiation (associated to a scale $\mu_i = k_{T,i}$), this corresponds to the following expression for a Final State Radiation (FSR):

$$\mathcal{W}_{\text{new}}^{\text{FSR}} = \frac{\alpha_s(\Delta * \mu_i)}{\alpha_s(\mu_i)} * \mathcal{W}_{\text{orig}}, \quad (52)$$

and to the following expression for Initial State Radiation (ISR), associated to a scale μ_i and fraction of energy x_i :

$$\mathcal{W}_{\text{new}}^{\text{ISR}} = \frac{\alpha_s(\Delta * \mu_i) \frac{f_a(x_i, \Delta * \mu_i)}{f_b(x_i, \Delta * \mu_{i+1})}}{\alpha_s(\mu_i) \frac{f_a(x_i, \mu_i)}{f_b(x_i, \mu_{i+1})}} * \mathcal{W}_{\text{orig}}, \quad (53)$$

where μ_{i+1} is the scale of the next step in the (initial state) history of radiation.

SysCALC can include the weight associated to different merging scales in the MLM matching/merging mechanism (for output of the `pythia6` package or `pythia-pgs` package).

In that case, the parton shower does not veto any event according to the MLM algorithm, although in the output file the scale of the first emission is retained. Having this information, SysCALC can test each value of the specified matching scales under the `matchscale` parameter block. SysCALC will then test for each of the values specified in the parameter `matchscale` if the event passes the MLM criteria or not. If it does not, then a zero weight is associated to the event, while if it does, then a weight 1 is kept. As a reminder, those weights are the equivalent of having a (approximate) Sudakov form-factor and removing at the same time the double counting between the events belonging to different multiplicities.

Finally, we give an example of the SysCALC output which follows the LHEF v3 format. The following block appears in the header of the output file:

```
<header>
<ini trwgt>
<weightgroup type="Central scale variation" combine="envelope">
  <weight id="1"> mur=0.5 muf=0.5 </weight>
  <weight id="2"> mur=1 muf=0.5 </weight>
  <weight id="3"> mur=2 muf=0.5 </weight>
  <weight id="4"> mur=0.5 muf=1 </weight>
  <weight id="5"> mur=1 muf=1 </weight>
  <weight id="6"> mur=2 muf=1 </weight>
  <weight id="7"> mur=0.5 muf=2 </weight>
  <weight id="8"> mur=1 muf=2 </weight>
  <weight id="9"> mur=2 muf=2 </weight>
</weightgroup>
<weightgroup type="Emission scale variation" combine="envelope">
  <weight id="10"> alpsfact=0.5</weight>
  <weight id="11"> alpsfact=1</weight>
  <weight id="12"> alpsfact=2</weight>
</weightgroup>
<weightgroup type="CT10nlo.LHgrid" combine="hessian">
  <weight id="13">Member 0</weight>
  <weight id="14">Member 1</weight>
  <weight id="15">Member 2</weight>
  <weight id="16">Member 3</weight>
  ...
  <weight id="65">Member 52</weight>
</weightgroup>
</ini trwgt>
</header>
```

For each event, the weights are then written as follows:

```
<rwt>
<wgt id="1">83214.7</wgt>
<wgt id="2">61460</wgt>
<wgt id="3">47241.9</wgt>
<wgt id="4">101374</wgt>
...
<wgt id="64">34893.5</wgt>
<wgt id="65">41277</wgt>
</rwt>
```

7. Conclusions

The ATLAS/CMS Dark Matter Forum concluded its work in June 2015. Its mandate was focused on identifying a prioritized, compact set of simplified model benchmarks to be used for the design of the early Run-2 LHC searches for $\tilde{E}_T + X$ final states. Its participants included many of the experimenters from both collaborations that are involved in these searches, as well as many of the theorists working actively on these models. This report has documented this basis set of models, as well as studies of the kinematically-distinct regions of the parameter space of the models, to aid the design of the searches. Table 9 summarizes the state of the art of the calculations, event generators, and tools that are available to the two LHC collaborations to simulate

Table 9

Summary table for available benchmark models considered within the works of this Forum. The results in this document have been obtained with the implementations in bold.

Benchmark models for ATLAS and CMS Run-2 DM searches			
Vector/axial vector mediator, s -channel (Section 2.1)			
Signature	State of the art calculation and tools	Implementation	References
jet + \cancel{E}_T	NLO + PS (POWHEG, SVN r3059)	[115,116]	[43,61,69–71]
	NLO+PS (<i>DMsimp</i> UFO + MADGRAPH5_AMC@NLO v2.3.0) NLO (MCFM v7.0)	[113] Upon request	[75–77] [41,114]
$W/Z/\gamma$ + \cancel{E}_T	LO + PS (UFO + MADGRAPH5_AMC@NLO v2.2.3) NLO+PS (<i>DMsimp</i> UFO + MADGRAPH5_AMC@NLO v2.3.0)	[126] [113]	[75–77] [75–77]
Scalar/pseudoscalar mediator, s -channel (Section 2.2)			
Signature	State of the art calculation and tools	Implementation	References
jet + \cancel{E}_T	LO + PS, top loop (POWHEG, r3059)	[117,118]	[43,61,69–71]
	LO+PS, top loop (<i>DMsimp</i> UFO + MADGRAPH5_AMC@NLO v2.3.0) LO, top loop (MCFM v7.0)	[113] Upon request	[75–77,153] [41,114]
$W/Z/\gamma$ + \cancel{E}_T	LO + PS (UFO + MADGRAPH5_AMC@NLO v2.2.3)		[75–77]
$t\bar{t}$, $b\bar{b}$ + \cancel{E}_T	LO + PS (UFO + MADGRAPH5_AMC@NLO v2.2.3) NLO+PS (<i>DMsimp</i> UFO + MADGRAPH5_AMC@NLO v2.3.0)	[127] [113]	[75–77] [75–77]
Scalar mediator, t -channel (Section 2.3)			
Signature	State of the art calculation and tools	Implementation	References
jet(s) + \cancel{E}_T (2-quark gens.)	LO+PS (UFO + MADGRAPH5_AMC@NLO v2.2.3)	[124]	[75–78]
jet(s) + \cancel{E}_T (3-quark gens.)	LO + PS (UFO + MADGRAPH5_AMC@NLO v2.2.3)	[125]	[46,75–77]
$W/Z/\gamma$ + \cancel{E}_T	LO + PS (UFO + MADGRAPH5_AMC@NLO v2.2.3)	TBC	[46,75–77]
b + \cancel{E}_T	LO + PS (UFO + MADGRAPH5_AMC@NLO v2.2.3)	[128]	[75–77,87,88]
Specific simplified models with EW bosons (Section 3.1)			
Signature and model	State of the art calculation and tools	Implementation	References
Higgs + \cancel{E}_T , vector med.	LO + PS (UFO + MADGRAPH5_AMC@NLO v2.2.3)	[137]	[48,75–77,97]
Higgs + \cancel{E}_T , scalar med.	LO + PS (UFO + MADGRAPH5_AMC@NLO v2.2.3)	[137]	[48,75–77,97]
Higgs + \cancel{E}_T , 2HDM	LO + PS (UFO + MADGRAPH5_AMC@NLO v2.2.3)	[138]	[75–77,97]
Contact interaction operators with EW bosons (Section 3.1)			
Signature and model	State of the art calculation and tools	Implementation	References
$W/Z/\gamma$ + \cancel{E}_T , dim-7	LO + PS (UFO + MADGRAPH5_AMC@NLO v2.2.3)	[141]	[45,75–77,97–99]
Higgs + \cancel{E}_T , dim-4/dim-5	LO + PS (UFO + MADGRAPH5_AMC@NLO v2.2.3)	[154]	[47,48,75–77,97]
Higgs + \cancel{E}_T , dim-8	LO + PS (UFO + MADGRAPH5_AMC@NLO v2.2.3)	[137]	[47,48,75–77,97]

these models at the start of Run-2. It also describes some that are known to be under development as the report was finalized.

This document primarily presents studies related to simplified models. The presentation of results for EFT benchmark models is also discussed. The studies contained in this report are meant to highlight the use of EFTs as a benchmark that is complementary to simplified models, and to demonstrate how that collider results could be presented a function of the fraction of events that are valid within the contact interaction approximation.

A number of points remain to be developed beyond the scope of this Forum, in order to fully benefit from LHC searches in the global quest for Dark Matter. First and foremost, to accommodate the urgent need of a basis set of simplified models, this work has made many grounding assumptions, as stated in the introduction. Departures from these assumptions have not been fully explored. As a consequence, the list of models and implementations employed by the ATLAS and CMS collaborations for early LHC Run-2 searches is not meant to exhaust the range of possibilities for mediating processes, let alone cover all plausible models of collider dark matter production. Rather, it is hoped that others will continue the systematic exploration of the most generic possibilities for collider dark matter production, building upon the framework used in this report just as this report has relied heavily on the work of many others. This also applies to models that exist in literature but do not have an implementation yet: we hope that this work will further encourage the theory and generator community to improve the implementation of new models as well as the precision of the calculations of existing ones. The role of constraints on the mediator particles from

direct past and present collider searches should also be developed further.

Furthermore, we see the need for broader discussion on the comparison of experimental results amongst collider and non-collider searches for particle dark matter. This point will have to be addressed before the presentation of Run-2 results: The uncertainties in the comparisons between experiments should be discussed and conveyed, so that the different results can be placed in their correct context, and so we can collectively build a fair and comprehensive picture of our understanding of particle dark matter.

Acknowledgments

The authors would like to thank Daniel Whiteson for helping in the review of this document. This research was supported by the Munich Institute for Astro- and Particle Physics (MIAPP) of the DFG cluster of excellence “Origin and Structure of the Universe”. The authors would like to express a special thanks to the Mainz Institute for Theoretical Physics (MITP) for its hospitality and support. P. Pani wishes to thank the support of the Computing Infrastructure of Nikhef. In addition we thank CERN and acknowledge the support of: DOE and NSF (USA), including grant DE-SC0011726 for the preparation of this manuscript; SER, SNSF and Cantons of Bern and Geneva, Switzerland; MINECO, Spain; European Union, where the preparation of this manuscript is part of a project that has received funding from the European Research Council under the European Union’s Horizon 2020 research and innovation program (grant agreement 679305); IN2P3-CNRS, CEA-DSM/IRFU, France; NSERC,

NRC, and CFI, Canada; INFN, Italy; FNRS and FWO, Belgium; STFC, United Kingdom; ARC, Australia; GRICES and FCT, Portugal; SRC, Sweden; BMBF, DFG, HGF, MPG and AvH Foundation, Germany; Austrian Academy of Sciences, Austria; MOE and UM, Malaysia; National Research Foundation and Ministry of Education, Science and Technology, Korea; MEXT and JSPS, Japan; FOM and NWO, Netherlands; CNPq and FAPESP, Brazil; Atomic Energy Commission, Pakistan; DNRF, DNSRC and Lundbeck Foundation, Denmark; Thailand Center of Excellence in Physics, Institute for the Promotion of Teaching Science and Technology, Special Task Force for Activating Research and National Science and Technology Development Agency, Thailand; MOST, Taiwan.

Appendix A. Additional models for dark matter searches

A.1. Models with a single top–quark + \tilde{E}_T

Many different theories predict final states with a single top and associated missing transverse momentum (monotop), some of them including dark matter candidates. A simplified model encompassing the processes leading to this phenomenology is described in Refs. [155–157], and is adopted as one of the benchmarks for Run 2 LHC searches.

The simplified model is constructed by imposing that the model Lagrangian respects the electroweak $SU(2)_L \times U(1)_Y$ gauge symmetry and by requiring minimality in terms of new states to supplement to the Standard Model fields. As a result, two monotop production mechanisms are possible. In the first case, the monotop system is constituted by an invisible (or long-lived with respect to detector distances) fermion χ and a top quark. It is produced as shown in the diagram of A.72(a) where a colored resonance φ lying in the triplet representation of $SU(3)_C$ decays into a top quark and a χ particle. In the second production mode, the monotop state is made of a top quark and a vector state V connected to a hidden sector so that it could decay invisibly into, e.g., a pair of dark matter particles as studied in [157]. The production proceeds via flavor-changing neutral interactions of the top quark with a quark of the first or second generation and the invisible V boson (see the diagrams of A.72(b) and (c)).

Resonant production. In this case, a colored 2/3-charged scalar (φ) is produced and decays into a top quark and a spin-1/2 invisible particle, χ . The dynamics of the new sector is described by the following Lagrangian:

$$\mathcal{L} = \left[\varphi \bar{d}^c \left[a_{SR}^q + b_{SR}^q \gamma_5 \right] d + \varphi \bar{u} \left[a_{SR}^{1/2} + b_{SR}^{1/2} \gamma_5 \right] \chi + \text{h.c.} \right], \quad (\text{A.1})$$

where u (d) stands for any up-type (down-type) quark, the notation SR refers to the monotop production mechanism via a scalar resonance and all flavor and color indices are understood for clarity.

In the notation of [156], the couplings of the new colored fields to down-type quarks are embedded into the 3×3 antisymmetric matrices a_{SR}^q (scalar couplings) and b_{SR}^q (pseudoscalar couplings) while those to the new fermion χ and one single up-type quark are given by the three-component vectors $a_{SR}^{1/2}$ and $b_{SR}^{1/2}$ in flavor space.

Under the form of Eq. (A.1), the Lagrangian is the one introduced in the original monotop search proposal [155]. It has been used by the CMS collaboration for Run I analyses after neglecting all pseudoscalar components of the couplings and adding the vector resonance case for which minimality requirements are difficult to accommodate [18]. In contrast, the study of Ref. [157] has imposed electroweak gauge invariance and required minimality.

This enforces all new couplings to be right-handed so that

$$a_{SR}^{1/2} = b_{SR}^{1/2} = \frac{1}{2} y_s^* \quad \text{and} \quad a_{SR}^q = b_{SR}^q = \frac{1}{2} \lambda_s, \quad (\text{A.2})$$

where the objects y_s and λ_s are a tridimensional vector and a 3×3 matrix in flavor space respectively. This class of scenarios is the one that has been adopted by the ATLAS collaboration for its Run I monotop searches [12] and will be considered by both collaborations for Run II analyses.

The resulting model can be likened to the MSSM with an R -parity violating of a top squark to the Standard Model down-type quarks and an R -parity conserving interaction of a top quark and a top-squark to a neutralino.

Non-resonant production. For non-resonant monotop production, the monotop state is produced via flavor-changing neutral interactions of the top quark, a lighter up-type quark and a new invisible vector particle V . This is the only case considered, as having a new scalar would involve in particular a mixing with the SM Higgs boson and therefore a larger number of free parameters. The Lagrangian describing the dynamics of this non-resonant monotop production case is:

$$\mathcal{L} = \left[V_\mu \bar{u} \gamma^\mu \left[a_{FC}^1 + b_{FC}^1 \gamma_5 \right] u + \text{h.c.} \right], \quad (\text{A.3})$$

where the flavor and color indices are again understood for clarity. The strength of the interactions among these two states and a pair of up-type quarks is modeled via two 3×3 matrices in flavor space a_{FC}^1 for the vector couplings and b_{FC}^1 for the axial vector couplings, the FC subscript referring to the flavor-changing neutral monotop production mode and the (1) superscript to the vectorial nature of the invisible particle.

As for the resonant case, the Lagrangian of Eq. (A.3) is the one that has been used by CMS after reintroducing the scalar option for the invisible state and neglecting all pseudoscalar interactions [18]. As already mentioned, a simplified setup motivated by gauge invariance and minimality has been preferred so that, as shown in Ref. [157], we impose all interactions to involve right-handed quarks only,¹⁹

$$a_{FC}^1 = b_{FC}^1 = \frac{1}{2} a_R \quad (\text{A.4})$$

where a_R denotes a 3×3 matrix in flavor space. This implies the vector field to be an $SU(2)_L$ singlet.

Model parameters and assumptions. The models considered as benchmarks for the first LHC searches contain further assumptions in terms of the flavor structure of the model with respect to the Lagrangians of the previous subsection. In order to have an observable monotop signature at the LHC, the Lagrangians introduced above must include not too small couplings of the new particles to first and second generation quarks. For simplicity, we assumed that only channels enhanced by parton density effects will be considered, so that we fix

$$\begin{aligned} (a_R)_{13} &= (a_R)_{31} = a, \\ (\lambda_s)_{12} &= -(\lambda_s)_{21} = \lambda \quad \text{and} \quad (y_s)_3 = y, \end{aligned} \quad (\text{A.5})$$

all other elements of the matrices and vectors above being set to zero.

Implementation. In order to allow one for the Monte Carlo simulation of events relevant for the monotop production cases

¹⁹ Ref. [158], which became public only after the conclusion of this Forum, introduces both left- and right-handed couplings.

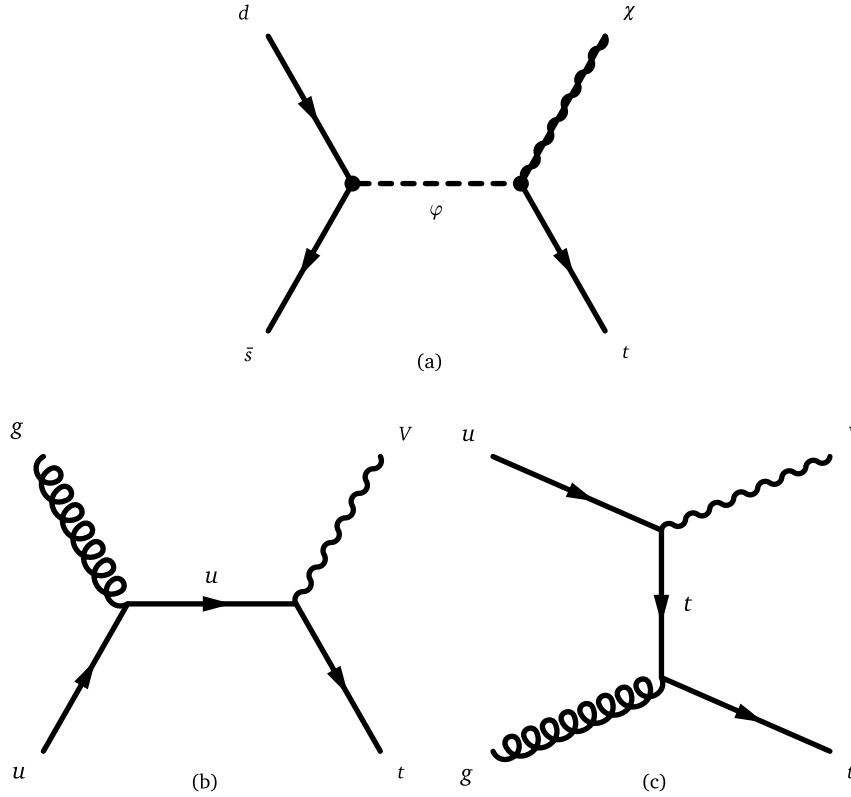


Fig. A.72. Feynman diagrams of leading order processes leading to monotop events: production of a colored scalar resonance φ decaying into a top quark and a spin-1/2 fermion χ (a), s - (b) and t -channel (c) non resonant production of a top quark in association with a spin-1 boson V decaying invisibly.

described above, we consider the Lagrangian

$$\mathcal{L} = \left[aV_\mu \bar{u} \gamma^\mu P_R t + \lambda \varphi \bar{d}^c P_R s + y \varphi \bar{\chi} P_R t + \text{h.c.} \right], \quad (\text{A.6})$$

where P_R stands for the right-handed chirality projector and the new physics couplings are defined by the three parameters a , λ and y . We additionally include a coupling of the invisible vector boson V to a dark sector (represented by a fermion ψ) whose strength can be controlled through a parameter g_{DM} ,

$$\mathcal{L} = g_{DM} V_\mu \bar{\psi} \gamma^\mu \psi. \quad (\text{A.7})$$

This ensures the option to make the V -boson effectively invisible by tuning g_{DM} respectively to a . We implement the entire model in the FEYNRULES package [76] so that the model can be exported to a UFO library [77] to be linked to MADGRAPH5_AMC@NLO [75] for event generation, following the approach outlined in [159].

A.2. Parameter scan

Under all the assumptions of the previous sections, the parameter space of the resonant model is defined by four quantities, namely the mass of the new scalar field φ , the mass of the invisible fermion χ and the strengths of the interactions of the scalar resonance with the monotop system y and with down-type quarks λ . One of both coupling parameters could however be traded with the width of the resonance.

The parameter space of the non-resonant model is defined by two parameters, namely the mass of the invisible state V and its flavor-changing neutral coupling to the up-type quarks a_R .

In the case of the non-resonant model, the invisible vector is connected to a hidden sector that could be, in its simplest form, parameterized by a new fermion [157]. This has effects on the width of the invisible V state.

A consensus between the ATLAS and CMS collaborations has been reached in the case of non-resonant monotop production. The results have been described above. In contrast, discussions in the context of resonant monotop production are still on-going. The related parameter space contains four parameters and must thus be further simplified for practical purposes. Several options are possible and a choice necessitates additional studies that will be achieved in a near future.

It has been verified that the kinematics do not depend on the width of the invisible state in the case where this width is at most 10% of the V -mass. This is illustrated in Fig. A.73, where we show the transverse-momentum spectra of the V -boson when it decays into a top-up final state and for different V -boson masses. The results are independent of the visible or invisible decay modes as we are only concerned with the kinematic properties of the invisible state.

A.3. Single top model implementation

Card files for MADGRAPH5_AMC@NLO are provided on the Forum Git repository [160] and correspond to the Lagrangian that has been implemented in FEYNRULES. Each coupling constant of the model can be set via the block COUPX of the parameter card. Its entries 1, 2 and 3 respectively correspond to the monotop-relevant parameters a , λ and y , while the width (and in particular the invisible partial width) of the V -boson can be tuned via the g_{DM} parameter to given in the entry 10 of the COUPX block.

The masses of the particles are set in the MASS block of the parameter card, the PDG codes of the new states being 32 (the vector state V), 1000006 (the φ colored resonance), 1000022 (the invisible fermion χ) and 1000023 (the fermion ψ connecting the V state to the dark sector). The width of the new vector has to be computed from all open tree-level decays (after fixing g_{DM} to a large value and setting the relevant entry to Auto in the DECAY

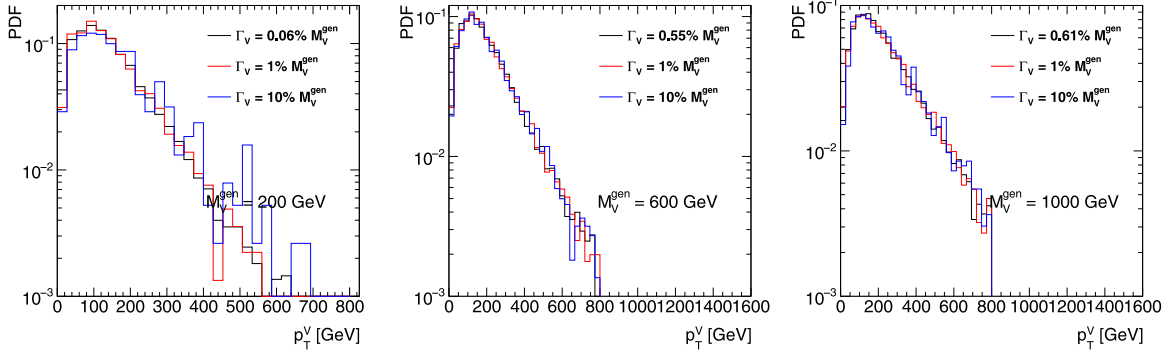


Fig. A.73. Distributions of the transverse momentum of the V boson in the case of the process $pp \rightarrow tV \rightarrow t(\bar{t}u + \text{c.c.})$. We have imposed that the V -boson is produced on-shell and have chosen its mass to be $m_V = 200, 600$ and 1000 GeV (left, central and right panels). We have considered three possible cases for the total width of the V -boson, which has been fixed to 0.61% , 0.1% and 10% of the mass.

block of the parameter card), while the way to calculate the width of the resonance ϕ is under discussion by both the ATLAS and CMS collaborations. The χ and ψ fermions are taken stable so that their width vanishes.

A.4. Further $W + \cancel{E}_T$ models with possible cross-section enhancements

As pointed out in Ref. [67], the mono- W signature can probe the iso-spin violating interactions of dark matter with quarks. The relevant operator after the electroweak symmetry breaking is

$$\frac{1}{\Lambda^2} \bar{\chi} \gamma_\mu \chi (\bar{u}_L \gamma^\mu u_L + \xi \bar{d}_L \gamma^\mu d_L). \quad (\text{A.8})$$

Here, we only keep the left-handed quarks because the right-handed quarks do not radiate a W -gauge boson from the weak interaction. As the LHC constrains the cutoff to higher values, it is also important to know the corresponding operators before the electroweak symmetry. At the dimension-six level, the following operator

$$\frac{c_6}{\Lambda^2} \bar{\chi} \gamma_\mu \chi \bar{Q}_L \gamma^\mu Q_L \quad (\text{A.9})$$

conserves iso-spin and provides us $\xi = 1$ [67]. At the dimension-eight level, new operators appear to induce iso-spin violation and can be

$$\frac{c_8^d}{\Lambda^4} \bar{\chi} \gamma_\mu \chi (H \bar{Q}_L) \gamma^\mu (Q_L H^\dagger) + \frac{c_8^u}{\Lambda^4} \bar{\chi} \gamma_\mu \chi (\tilde{H} \bar{Q}_L) \gamma^\mu (Q_L \tilde{H}^\dagger). \quad (\text{A.10})$$

After inputting the vacuum expectation value of the Higgs field, we have

$$\xi = \frac{c_6 + c_8^d v_{EW}^2 / 2\Lambda^2}{c_6 + c_8^u v_{EW}^2 / 2\Lambda^2}. \quad (\text{A.11})$$

For a nonzero c_6 and $v_{EW} \ll \Lambda$, the iso-spin violation effects are suppressed. On the other hand, the values of c_6 , c_8^d and c_8^u depend on the UV-models.

There is one possible UV-model to obtain a zero value for c_6 and non-zero values for c_8^d and c_8^u . One can have the dark matter and the SM Higgs field charged under a new $U(1)$ symmetry. There is a small mass mixing between SM Z -boson and the new Z' with a mixing angle of $\mathcal{O}(v_{EW}^2 / M_{Z'}^2)$. After integrating out Z' , one has different effective dark matter couplings to u_L and d_L fields, which are proportional to their couplings to the Z boson. For this model, we have $c_6 = 0$ and

$$\xi = \frac{-\frac{1}{2} + \frac{1}{3} \sin^2 \theta_W}{\frac{1}{2} - \frac{2}{3} \sin^2 \theta_W} \approx -2.7 \quad (\text{A.12})$$

and order of unity.

A.5. Simplified model corresponding to dimension-5 EFT operator

As an example of a simplified model corresponding to the dimension-5 EFT operator described in Section 3.2, we consider a Higgs portal with a scalar mediator. Models of this kind are among the most concise versions of simplified models that produce couplings of Dark Matter to pairs of gauge-bosons. Scalar fields may couple directly to pairs of electroweak gauge bosons, but must carry part of the electroweak vacuum expectation value. One may thus consider a simple model where Dark Matter couples to a scalar singlet mediator, which mixes with the fields in the Higgs sector.

$$L \subset \frac{1}{2} m_s S^2 + \lambda S^2 |H|^2 + \lambda' S |H|^2 + y S \chi \bar{\chi} \quad (\text{A.13})$$

where H is a field in the Higgs sector that contains part of the electroweak vacuum expectation value, S is a heavy scalar singlet and χ is a Dark Matter field. There is then an s -channel diagram where DM pairs couple to the singlet field S , which then mixes with a Higgs-sector field, and couples to W and Z bosons. This diagram contains 2 insertions of EW symmetry breaking fields, corresponding in form to the effective dimension-5 operator in Section 3.2.1.

A.6. Inert two-Higgs Doublet Model (IDM)

For most of the simplified models included in this report, the mass of the mediator and couplings/width are non-trivial parameters of the model. In these scenarios, we remain agnostic about the theory behind the dark matter sector and try to parameterize it in simple terms.

We have not addressed how to extend the simplified models to realistic and viable models which are consistent with the symmetries of the Standard Model. Simplified models often violate gauge invariance which is a crucial principle for building a consistent BSM model which incorporates SM together with new physics. For example, with a new heavy gauge vector boson mediating DM interactions, one needs not just the dark matter and its mediator, but also a mechanism which provides mass to this mediator in a gauge invariant way.

Considering both the simplified model and other elements necessary for a consistent theory is a next logical step. The authors of [161] term these Minimal Consistent Dark Matter (MCDM) models. MCDM models are at the same time still toy models that can be easily incorporated into a bigger BSM model and explored via complementary constraints from collider and direct/indirect DM search experiments as well as relic density constraints.

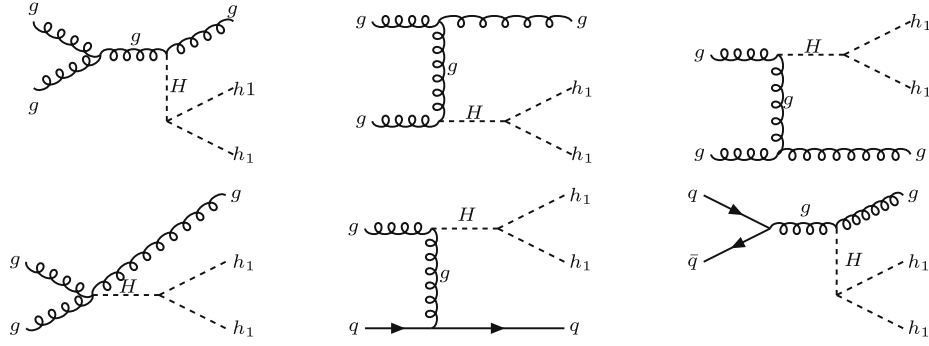


Fig. A.74. Feynman diagrams for $gg \rightarrow h_1 h_1 + g$ process contributing to mono-jet signature.
Source: Adapted from [161].

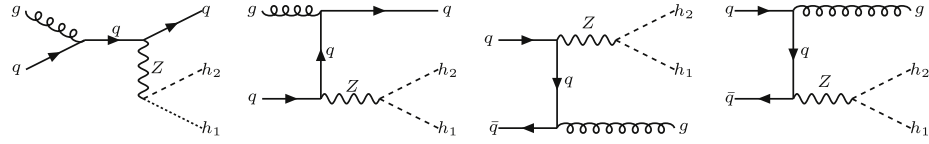


Fig. A.75. Feynman diagrams for $q\bar{q} \rightarrow h_1 h_2 + g$ ($gq \rightarrow h_1 h_2 + q$) process contributing to mono-jet signature.
Source: Adapted from [161].

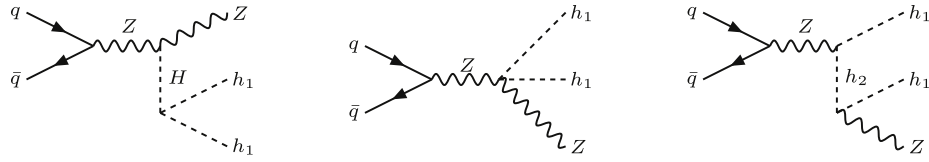


Fig. A.76. Feynman diagrams for $q\bar{q} \rightarrow h_1 h_1 + Z$ process contributing to mono-Z signature.
Source: Adapted from [161].

The idea of an inert Two-Higgs Doublet Model (IDM) was introduced more than 30 years ago in Ref [162]. The IDM was first proposed as a Dark Matter model in Ref. [163] and its phenomenology further studied in Refs. [14,161,164–173]. It is an extension of the SM with a second scalar doublet ϕ_2 with no direct coupling to fermions. This doublet has a discrete Z_2 symmetry, under which ϕ_2 is odd and all the other fields are even. The Lagrangian of the odd sector is,

$$\mathcal{L} = \frac{1}{2}(D_\mu \phi_2)^2 - V(\phi_1, \phi_2) \quad (\text{A.14})$$

with the potential V containing mass terms and $\phi_1 - \phi_2$ interactions:

$$\begin{aligned} V = & -m_1^2(\phi_1^\dagger \phi_1) - m_2^2(\phi_2^\dagger \phi_2) + \lambda_1(\phi_1^\dagger \phi_1)^2 + \lambda_2(\phi_2^\dagger \phi_2)^2 \\ & + \lambda_3(\phi_2^\dagger \phi_2)(\phi_1^\dagger \phi_1) + \lambda_4(\phi_2^\dagger \phi_1)(\phi_1^\dagger \phi_2) \\ & + \frac{\lambda_5}{2} [(\phi_1^\dagger \phi_2)^2 + (\phi_2^\dagger \phi_1)^2], \end{aligned} \quad (\text{A.15})$$

where ϕ_1 and ϕ_2 are SM and inert Higgs doublets respectively carrying the same hypercharge. These doublets can be parameterized as

$$\phi_1 = \frac{1}{\sqrt{2}} \begin{pmatrix} 0 \\ v + H \end{pmatrix} \quad \phi_2 = \frac{1}{\sqrt{2}} \begin{pmatrix} \sqrt{2}h^+ \\ h_1 + ih_2 \end{pmatrix} \quad (\text{A.16})$$

In addition to the SM, the IDM introduces four more degrees of freedom coming from the inert doublet in the form of a Z_2 -odd charged scalar h^\pm and two neutral Z_2 -odd scalars h_1 and h_2 . The lightest neutral scalar, h_1 is identified as the dark matter candidate. Aspects of the IDM collider phenomenology have been studied in [161,163,173–184]. Its LHC signatures include dileptons [179,184], trileptons [180] and multileptons [181] along with

missing transverse energy, modifications of the Higgs branching ratios [173,182,183], as well as $\cancel{E}_T + \text{jet}$, Z , and Higgs and $\cancel{E}_T + \text{VBF}$ signals (see Figs. A.74–A.79).

Based on the various LHC search channels, DM phenomenology issues and theoretical considerations, numerous works have proposed benchmark scenarios for the IDM, see e.g. [173,181] while a FeynRules implementation (including MadGraph, CalcHEP and micrOMEGAs model files) was provided in [181]. An updated analysis of the parameter space has recently been performed in Ref. [161].

The authors suggested to study mono-X signatures that are relevant to model-independent collider DM searches, and evaluated their rates presented below. They have implemented and cross-checked the IDM model into CalcHEP and micrOMEGAs, with an implementation publicly available on the HEPMDB database, including loop-induced HHG and $\gamma\gamma H$ models. They propose an additional set of benchmark points, mostly inspired by mono-X and VBF searches (Table A.10). Though the overall parameter space of IDM is 5-dimensional, once all relevant constraints are applied the parameter space relevant to a specific LHC signature typically reduces to 1–2 dimensional. In the mono-jet case, one can use two separate simplified models, a $gg \rightarrow h_1 h_1 + g$ process (via Higgs mediator) and a $q\bar{q} \rightarrow h_1 h_2 + g$ ($gq \rightarrow h_1 h_2 + q$) process (through a Z -boson mediator) to capture the physics relevant to the search. The cross sections for the various mono-X and VBF signatures produced by this model are displayed in Fig. A.80.

Appendix B. Presentation of experimental results for reinterpretation

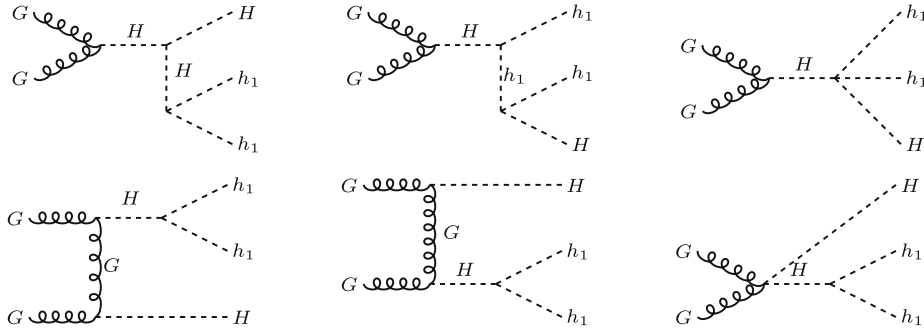


Fig. A.77. Feynman diagrams for $gg \rightarrow h_1 h_1 + H$ process contributing to mono-Higgs signature.
Source: Adapted from [161].

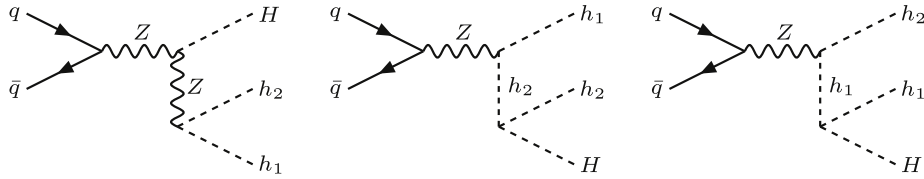


Fig. A.78. Feynman diagrams for $q\bar{q} \rightarrow h_1 h_2 + H$ process contributing to mono-Higgs signature.
Source: Adapted from [161].

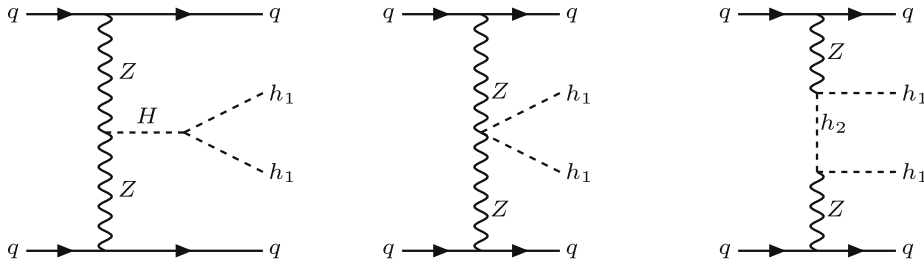


Fig. A.79. Diagrams for $qq \rightarrow qqh_1 h_1$ DM production in vector boson fusion process.
Source: Adapted from [161].

Table A.10

Five benchmarks for IDM in $(M_{h_1}, M_{h_2}, M_{h_{\pm}}, \lambda_2, \lambda_{345})$ parameter space. We also present the corresponding relic density (Ωh^2), the spin-independent cross section for DM scattering on the proton (σ_{SI}), and the LHC cross section at 13 TeV for mono-jet process $pp \rightarrow h_1, h_1 + jet$ for $p_T^{jet} > 100$ GeV cut (σ_{LHC}).

BM	1	2	3	4	5
M_{h_1} (GeV)	48	53	70	82	120
M_{h_2} (GeV)	55	189	77	89	140
$M_{h_{\pm}}$ (GeV)	130	182	200	150	200
λ_2	0.8	1.0	1.1	0.9	1.0
λ_{345}	-0.010	-0.024	+0.022	-0.090	-0.100
Ωh^2	3.4×10^{-2}	8.1×10^{-2}	9.63×10^{-2}	1.5×10^{-2}	2.1×10^{-3}
σ_{SI} (pb)	2.3×10^{-10}	7.9×10^{-10}	5.1×10^{-10}	4.5×10^{-10}	2.6×10^{-9}
σ_{LHC} (fb)	1.7×10^2	7.7×10^2	4.3×10^{-2}	1.2×10^{-1}	2.3×10^{-2}

When collider searches present results with the recommended benchmarks, we suggest the following:

- Provide limits in collider language, on fundamental parameters of the interaction: the couplings and masses of particles in simplified model.
- Translate limits to non-collider language, for a range of assumptions, in order to convey a rough idea of the range of possibilities. The details of this point are left for work beyond the scope of this Forum.

- Provide all necessary material for theorists to reinterpret simplified model results as building blocks for more complete models (e.g. signal cutflows, acceptances, etc.). This point is detailed further in this appendix.
- Provide model-independent results in terms of limits on cross-section times efficiency times acceptance of new phenomena for all cases, but especially when EFTs are employed as benchmarks. This recommendation has been issued before: see Ref. [185] for detailed suggestions.

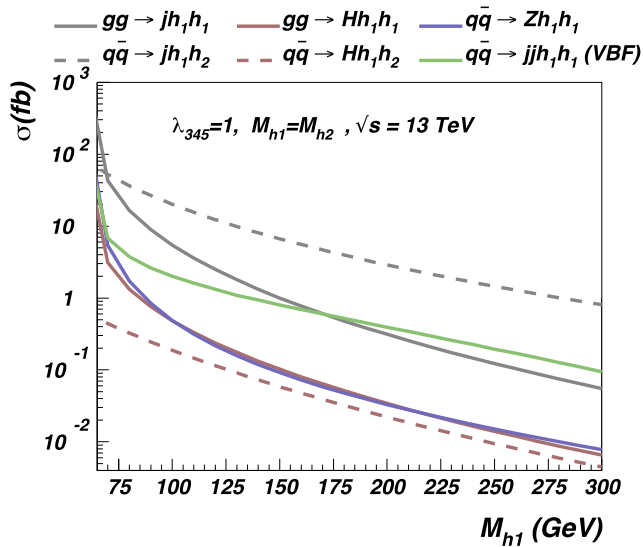


Fig. A.80. LHC cross section at 13 TeV for various signatures, from [161].

- Provide easily usable and clearly labeled results in a digitized format, e.g. [186] entries, ROOT histograms and macros or tables available on analysis public pages.

This appendix describes further considerations for reinterpretation and reimplementing of the analyses, as well as for the use of simplified model results directly given by the collaborations.

B.1. Reinterpretation of analyses

In the case of reinterpretation for models different than those provided by the experimental collaborations, the information needed primarily includes expected and observed exclusion lines along with their $\pm 1\sigma$ uncertainty, expected and observed upper limits in case of simplified models, efficiency maps and kinematic distributions as reported in the analysis. If the kinematics of the new model to be tested in the reinterpretation is similar to that of the original model provided by the collaboration, it will be straight-forward to rescale the results provided to match the new model cross-section using this information.

B.2. Reimplementation of analyses

One of the important developments in recent years is an active development of software codes [84,85,187–190] necessary for recasting analyses. The aim of these codes is to provide a public library of LHC analyses that have been reimplemented and validated, often by the collaborations themselves. Such libraries can then be used to analyze validity of a BSM scenario in a systematic and effective manner. The availability of public libraries further facilitates a unified framework and can lead to an organized and central structure to preserve LHC information long term. The reimplementation of an analysis consists of several stages. Typically, the analysis note is used as a basis for the implementation of the preselection and event selection cuts in the user analysis code within the recasting frameworks. Signal events are generated, and passed through a parameterized detector simulation using software such as Delphes or PGS [103,191]. The reconstructed objects are then analyzed using the code written in the previous step, and the results in terms of number of events are passed through a statistical analysis framework to compare with the backgrounds provided by the collaborations.

In order to be able to effectively use such codes, it is important to get a complete set of information from the collaborations.

For what concerns the generation of the models, it is desirable to have the following items as used by the collaborations:

- Monte Carlo generators: Monte Carlo generators along with the exact versions used to produce the event files should be listed.
- Production cross sections: The order of production cross sections (e.g. LO,NLO,NLL) as well as the codes which were used to compute them should be provided. Tables of reference cross sections for several values of particle masses are useful as well.
- Process Generation: Details of the generated process, detailing number of additional partons generated.
- LHE files: selected LHE files (detailing at least a few events if not the entire file) corresponding to the benchmarks listed in the analysis could also be made available in order to cross check process generation. Experimental collaborations may generate events on-the-fly without saving the intermediate LHE file; we advocate that the cross-check of process generation is straight-forward if this information is present, so we encourage the generation of a few selected benchmark points allowing for a LHE file to be saved. Special attention should be paid to list the parameters which change the production cross section or kinematics of the process e.g. mixing angles.
- Process cards: Process cards including PDF choices, details of matching algorithms and scales and details of process generation. If process cards are not available, the above items should be clearly identified.
- Model files: For models which are not already implemented in MADGRAPH5_AMC@NLO, the availability of the corresponding model files in the UFO format [77] is highly desired. This format details the exact notation used in the model and hence sets up a complete framework. In case MADGRAPH5_AMC@NLO is not used, enough information should be provided in order to clearly identify the underlying model used for interpretations and reproduce the generation.

The ATLAS/CMS Dark Matter Forum provides most of the information needed within its Git repository [59].

Efficiency maps and relevant kinematic distributions as reported in the analysis should be provided, in a digitized format with clearly specified units. If selection criteria cannot be easily simulated through parameterized detector simulation, the collaborations should provide the efficiency of such cuts. Overall reconstruction and identification efficiencies of physics objects are given as an input to the detector simulation software. It is thus very useful to get parameterized efficiencies for reconstructed objects (as a function of the rapidity η and/or transverse momentum p_T), along with the working points at which they were evaluated (e.g. loose, tight selection). Object definitions should be clearly identifiable. Digitized kinematic distributions are often necessary for the validation of the analysis so that the results from the collaboration are obtained, and so are tables containing the events passing each of the cuts.

The availability of digitized data and backgrounds is one of the primary requirements for fast and efficient recasting. Platforms such as HepData [186] can be used as a centralized repository; alternatively, analysis public pages and tables can be used for dissemination of results. Both data and Standard Model backgrounds should be provided in the form of binned histogram that can be interpolated if needed.

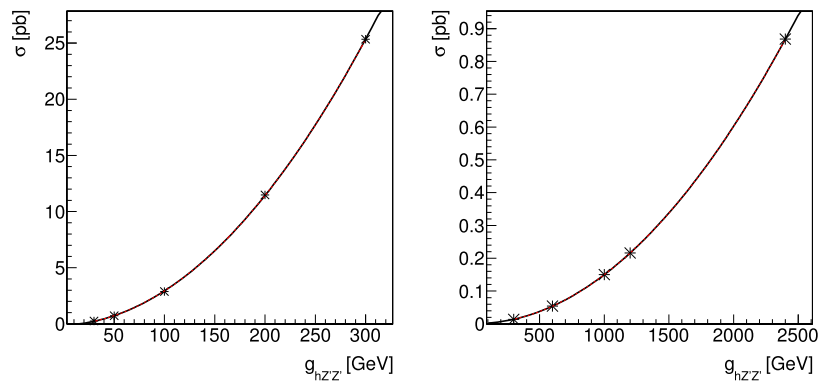


Fig. C.81. Cross section of the $pp \rightarrow H\chi\bar{\chi}$ process as a function of $g_{hZ'Z'}$ for $m_{Z'} = 100$ GeV (left) and $m_{Z'} = 1$ TeV (right). The fit functions are shown in the text.

A detailed description of the likelihood used in order to derive the limits from the comparison of data to signal plus background should be given. This can be inferred from the analysis documentation itself, however direct availability of the limit setting code as a workspace in RooStats or HistFitter [192] is highly desirable.

Finally, the collaborations can also provide an analysis code directly implemented in one of the public recasting codes detailed above. Such codes can be published via INSPIRE [193] in order to track versioning and citations.

B.3. Simplified model interpretations

Dark Matter searches at the LHC will include simplified model interpretations in their search results. These interpretations are simple and can be used for a survey of viability of parameter space. Codes such as [194–196] can make use of the simplified model results given in the form of 95% Confidence Level (CLs) upper limit or efficiency maps in order to test Beyond the Standard Model parameter space. As mentioned above, it will thus be extremely useful if the results are given in a digitized form that is easily usable by the theory community.

The parameter space of these models should be clearly specified. For example, for a simplified model containing dark matter mass m_χ , mediator mass M_{med} and couplings g_χ , g_q it will be very useful to have upper limits on the product of couplings $\sqrt{g_\chi g_q}$ or cross section times branching ratio as a function of m_χ , M_{med} . Limits on visible cross sections of the simplified models considered for interpretations should be made available.

The usage of simplified model results relies on interpolating between upper limit values. In order to facilitate the interpolation, regions where large variation of upper limits is observed should contain denser grid, if a uniform grid over the entire plane is not possible. For simplified model involving more than three parameters (two masses and product of couplings), slices of upper limits in the additional dimensions will be necessary for reinterpretation.

As already mentioned in the introduction to this Chapter, acceptance and efficiency maps for all the signal regions involved in the analysis should be made available. These results are not only useful for model testing using simplified models but also to validate implementation of the analysis. Information about the most sensitive signal regions as a function of new particle masses is also useful in order to determine the validity of approximate limit setting procedures commonly used by theorists.

Appendix C. Additional details and studies within the forum

Further information for baryonic Z' model

Cross-section scaling

The dependence of the cross section of the $pp \rightarrow H\chi\bar{\chi} + X$ process on $g_{hZ'Z'}$ is shown in Fig. C.81. The curves have been fit to second-order polynomials, where y is the cross-section and x is the coupling $g_{hZ'Z'}$.

For $m_{\text{med}} = 100$ GeV, the fit function is

$$y = -0.12 - 3.4 \times 10^{-3}x + 2.7 \times 10^{-4}x^2. \quad (\text{C.1})$$

For $M_{\text{med}} = 1$ TeV, the fit function is:

$$y = 0.0012 - 2.4 \times 10^{-7}x + 1.5 \times 10^{-7}x^2. \quad (\text{C.2})$$

References

- [1] A. Birkedal, K. Matchev, M. Perelstein, Dark matter at colliders: A Model independent approach, *Phys. Rev. D* 70 (2004) 077701, <http://dx.doi.org/10.1103/PhysRevD.70.077701>, [arXiv:hep-ph/0403004](https://arxiv.org/abs/hep-ph/0403004).
- [2] J.L. Feng, S. Su, F. Takayama, Lower limit on dark matter production at the large hadron collider, *Phys. Rev. Lett.* 96 (2006) 151802, <http://dx.doi.org/10.1103/PhysRevLett.96.151802>, [arXiv:hep-ph/0503117](https://arxiv.org/abs/hep-ph/0503117).
- [3] F.J. Petriello, S. Quackenbush, K.M. Zurek, The Invisible Z' at the CERN LHC, *Phys. Rev. D* 77 (2008) 115020, <http://dx.doi.org/10.1103/PhysRevD.77.115020>, [arXiv:0803.4005](https://arxiv.org/abs/0803.4005).
- [4] M. Beltran, D. Hooper, E.W. Kolb, Z.A. Krusberg, T.M. Tait, Maverick dark matter at colliders, *J. High Energy Phys.* 1009 (2010) 037, [http://dx.doi.org/10.1007/JHEP09\(2010\)037](http://dx.doi.org/10.1007/JHEP09(2010)037), [arXiv:1002.4137](https://arxiv.org/abs/1002.4137).
- [5] Y. Bai, P.J. Fox, R. Harnik, The Tevatron at the frontier of dark matter direct detection, *J. High Energy Phys.* 1012 (2010) 048, [http://dx.doi.org/10.1007/JHEP12\(2010\)048](http://dx.doi.org/10.1007/JHEP12(2010)048), [arXiv:1005.3797](https://arxiv.org/abs/1005.3797).
- [6] T. Aaltonen, et al., A search for dark matter in events with one jet and missing transverse energy in $p\bar{p}$ collisions at $\sqrt{s} = 1.96$ TeV, *Phys. Rev. Lett.* 108 (2012) 211804, <http://dx.doi.org/10.1103/PhysRevLett.108.211804>, [arXiv:1203.0742](https://arxiv.org/abs/1203.0742).
- [7] G. Aad, et al., Search for new phenomena in final states with an energetic jet and large missing transverse momentum in pp collisions at $\sqrt{s} = 8$ TeV with the ATLAS detector, *Eur. Phys. J. C* 75 (7) (2015) 299, <http://dx.doi.org/10.1140/epjc/s10052-015-3639-7>, [arXiv:1502.01518](https://arxiv.org/abs/1502.01518), Erratum; *Eur. Phys. J. C* 75 (9) (2015) 408.
- [8] ATLAS Collaboration, Search for new phenomena in events with a photon and missing transverse momentum in pp collisions at $\sqrt{s} = 8$ TeV with the ATLAS detector, *Phys. Rev. D* 91 (2015) 012008.
- [9] ATLAS Collaboration, Search for new particles in events with one lepton and missing transverse momentum in pp collisions at $\sqrt{s} = 8$ TeV with the ATLAS detector, *J. High Energy Phys.* 1409 (2014) 037, [http://dx.doi.org/10.1007/JHEP09\(2014\)037](http://dx.doi.org/10.1007/JHEP09(2014)037), [arXiv:1407.7494](https://arxiv.org/abs/1407.7494).
- [10] ATLAS Collaboration, Search for dark matter in events with a Z boson and missing transverse momentum in pp collisions at $\sqrt{s} = 8$ TeV with the ATLAS detector, *Phys. Rev. D* 90 (2014) 012004, <http://dx.doi.org/10.1103/PhysRevD.90.012004>, [arXiv:1404.0051](https://arxiv.org/abs/1404.0051).
- [11] ATLAS Collaboration, Search for dark matter in events with a hadronically decaying W or Z boson and missing transverse momentum in pp collisions at $\sqrt{s} = 8$ TeV with the ATLAS detector, *Phys. Rev. Lett.* 112 (2014) 041802, <http://dx.doi.org/10.1103/PhysRevLett.112.041802>, [arXiv:1309.4017](https://arxiv.org/abs/1309.4017).

- [12] ATLAS Collaboration, Search for invisible particles produced in association with single-top-quarks in proton–proton collisions at $\sqrt{s} = 8$ TeV with the ATLAS detector, *Eur. Phys. J. C* 75 (2015) 79, <http://dx.doi.org/10.1140/epjc/s10052-014-3233-4>, arXiv:1410.5404.
- [13] ATLAS Collaboration, Search for dark matter in events with heavy quarks and missing transverse momentum in pp collisions with the ATLAS detector, *Eur. Phys. J. C* 75 (2015) 92, <http://dx.doi.org/10.1140/epjc/s10052-015-3306-z>, arXiv:1410.4031.
- [14] ATLAS Collaboration, Sensitivity to WIMP dark matter in the final states containing jets and missing transverse momentum with the ATLAS detector at 14 TeV LHC, Tech. Rep. ATL-PHYS-PUB-2014-007, CERN, Geneva (2014). URL <http://cds.cern.ch/record/1708859>.
- [15] CMS Collaboration, Search for dark matter extra dimensions and unparticles in monojet events in proton–proton collisions at $\sqrt{s} = 8$ TeV, *Eur. Phys. J. C* 75 (2015) 235, <http://dx.doi.org/10.1140/epjc/s10052-015-3451-4>, arXiv:1408.3583.
- [16] CMS Collaboration, Search for new phenomena in monophoton final states in proton–proton collisions at $\sqrt{s} = 8$ TeV, *Phys. Lett. B* 755 (2016) 102–124.
- [17] CMS Collaboration, Search for physics beyond the standard model in final states with a lepton and missing transverse energy in proton–proton collisions at \sqrt{s} TeV, *Phys. Rev. D* 91 (2015) 092005, <http://dx.doi.org/10.1103/PhysRevD.91.092005>, arXiv:1408.2745.
- [18] CMS Collaboration, Search for monotop signatures in proton–proton collisions at $\sqrt{s} = 8$ TeV, *Phys. Rev. Lett.* 114 (2015) 101801, <http://dx.doi.org/10.1103/PhysRevLett.114.101801>, arXiv:1410.1149.
- [19] CMS Collaboration, Search for the production of dark matter in association with top-quark pairs in the single-lepton final state in proton–proton collisions at $\sqrt{s} = 8$ TeV, *J. High Energy Phys.* 06 (2015) 121, [http://dx.doi.org/10.1007/JHEP06\(2015\)121](http://dx.doi.org/10.1007/JHEP06(2015)121), arXiv:1504.03198.
- [20] CMS Collaboration, Search for the production of dark matter in association with top quark pairs in the di-lepton final state in pp collisions at $\sqrt{s} = 8$ TeV, CMS-PAS-B2G-13-004. URL <http://cds.cern.ch/record/1697173>.
- [21] CMS Collaboration, Search for dark matter direct production using razor variables in events with two or more jets in pp collisions at 8 TeV, CMS-PAS-EXO-14-004. URL <http://cds.cern.ch/record/2002861>.
- [22] J. Goodman, M. Ibe, A. Rajaraman, W. Shepherd, T.M. Tait, et al., Constraints on light Majorana dark matter from colliders, *Phys. Lett. B* 695 (2011) 185–188, <http://dx.doi.org/10.1016/j.physletb.2010.11.009>, arXiv:1005.1286.
- [23] J. Goodman, M. Ibe, A. Rajaraman, W. Shepherd, T.M. Tait, et al., Constraints on dark matter from colliders, *Phys. Rev. D* 82 (2010) 116010, <http://dx.doi.org/10.1103/PhysRevD.82.116010>, arXiv:1008.1783.
- [24] I.M. Shoemaker, L. Vecchi, Unitariness and monojet bounds on models for DAMA, CoGeNT, and CRESST-II, *Phys. Rev. D* 86 (2012) 015023, <http://dx.doi.org/10.1103/PhysRevD.86.015023>, arXiv:1112.5457.
- [25] J. Kopp, Collider limits on dark matter arXiv:1105.3248.
- [26] P.J. Fox, R. Harnik, J. Kopp, Y. Tsai, LEP Shines light on dark matter, *Phys. Rev. D* 84 (2011) 014028, <http://dx.doi.org/10.1103/PhysRevD.84.014028>, arXiv:1103.0240.
- [27] P.J. Fox, R. Harnik, J. Kopp, Y. Tsai, Missing energy signatures of dark matter at the LHC, *Phys. Rev. D* 85 (2012) 056011, <http://dx.doi.org/10.1103/PhysRevD.85.056011>, arXiv:1109.4398.
- [28] G. Busoni, A. De Simone, E. Morgante, A. Riotto, On the validity of the effective field theory for dark matter searches at the LHC, *Phys. Lett. B* 728 (2014) 412–421, <http://dx.doi.org/10.1016/j.physletb.2013.11.069>, arXiv:1307.2253.
- [29] J. Alwall, P. Schuster, N. Toro, Simplified models for a first characterization of new physics at the LHC, *Phys. Rev. D* 79 (2009) 075020, <http://dx.doi.org/10.1103/PhysRevD.79.075020>, arXiv:0810.3921.
- [30] J. Goodman, W. Shepherd, LHC bounds on UV-complete models of dark matter arXiv:1111.2359.
- [31] D. Alves, et al., Simplified models for LHC new physics searches, *J. Phys. G* 39 (2012) 105005, <http://dx.doi.org/10.1088/0954-3899/39/10/105005>, arXiv:1105.2838.
- [32] H. An, X. Ji, L.-T. Wang, Light dark matter and Z' dark force at colliders, *J. High Energy Phys.* 1207 (2012) 182, [http://dx.doi.org/10.1007/JHEP07\(2012\)182](http://dx.doi.org/10.1007/JHEP07(2012)182), arXiv:1202.2894.
- [33] H. An, R. Huo, L.-T. Wang, Searching for low mass dark portal at the LHC, *Phys. Dark Univ.* 2 (2013) 50–57, <http://dx.doi.org/10.1016/j.dark.2013.03.002>, arXiv:1212.2221.
- [34] A. DiFranzo, K.I. Nagao, A. Rajaraman, T.M.P. Tait, Simplified models for dark matter interacting with quarks, *J. High Energy Phys.* 1311 (2013) 014, [http://dx.doi.org/10.1007/JHEP11\(2013\)014](http://dx.doi.org/10.1007/JHEP11(2013)014), [http://dx.doi.org/10.1007/JHEP01\(2014\)162](http://dx.doi.org/10.1007/JHEP01(2014)162), arXiv:1308.2679.
- [35] O. Buchmueller, M.J. Dolan, C. McCabe, Beyond effective field theory for dark matter searches at the LHC, *J. High Energy Phys.* 1401 (2014) 025, [http://dx.doi.org/10.1007/JHEP01\(2014\)025](http://dx.doi.org/10.1007/JHEP01(2014)025), arXiv:1308.6799.
- [36] Y. Bai, J. Berger, Fermion Portal Dark matter, *J. High Energy Phys.* 1311 (2013) 171, [http://dx.doi.org/10.1007/JHEP11\(2013\)171](http://dx.doi.org/10.1007/JHEP11(2013)171), arXiv:1308.0612.
- [37] Y. Bai, J. Berger, Lepton Portal Dark matter, *J. High Energy Phys.* 1408 (2014) 153, [http://dx.doi.org/10.1007/JHEP08\(2014\)153](http://dx.doi.org/10.1007/JHEP08(2014)153), arXiv:1402.6696.
- [38] H. An, L.-T. Wang, H. Zhang, Dark matter with t -channel mediator: a simple step beyond contact interaction, *Phys. Rev. D* 89 (2014) 115014, <http://dx.doi.org/10.1103/PhysRevD.89.115014>, arXiv:1308.0592.
- [39] J. Abdallah, et al., Simplified models for dark matter and missing energy searches at the LHC arXiv:1409.2893.
- [40] S.A. Malik, et al., Interplay and characterization of dark matter searches at colliders and in direct detection experiments, *Phys. Dark Univ.* 9–10 (2015) 51–58, <http://dx.doi.org/10.1016/j.dark.2015.03.003>, arXiv:1409.4075.
- [41] P. Harris, V.V. Khoze, M. Spannowsky, C. Williams, Constraining dark sectors at colliders: Beyond the effective theory approach, *Phys. Rev. D* 91 (2015) 055009, <http://dx.doi.org/10.1103/PhysRevD.91.055009>, arXiv:1411.0535.
- [42] M.R. Buckley, D. Feld, D. Goncalves, Scalar simplified models for dark matter, *Phys. Rev. D* 91 (2015) 015017, <http://dx.doi.org/10.1103/PhysRevD.91.015017>, arXiv:1410.6497.
- [43] U. Haisch, E. Re, Simplified dark matter top-quark interactions at the LHC, *J. High Energy Phys.* 1506 (2015) 078, [http://dx.doi.org/10.1007/JHEP06\(2015\)078](http://dx.doi.org/10.1007/JHEP06(2015)078), arXiv:1503.00691.
- [44] Y. Bai, T.M. Tait, Searches with mono-leptons, *Phys. Lett. B* 723 (2013) 384–387, <http://dx.doi.org/10.1016/j.physletb.2013.05.057>, arXiv:1208.4361.
- [45] L.M. Carpenter, A. Nelson, C. Shimmin, T.M. Tait, D. Whiteson, Collider searches for dark matter in events with a Z boson and missing energy, *Phys. Rev. D* 87 (2013) 074005, <http://dx.doi.org/10.1103/PhysRevD.87.074005>, arXiv:1212.3352.
- [46] N.F. Bell, J.B. Dent, A.J. Galea, T.D. Jacques, L.M. Krauss, et al., Searching for dark matter at the LHC with a mono- Z , *Phys. Rev. D* 86 (2012) 096011, <http://dx.doi.org/10.1103/PhysRevD.86.096011>, arXiv:1209.0231.
- [47] A.A. Petrov, W. Shepherd, Searching for dark matter at LHC with mono-Higgs production, *Phys. Lett. B* 730 (2014) 178–183, <http://dx.doi.org/10.1016/j.physletb.2014.01.051>, arXiv:1311.1511.
- [48] L. Carpenter, A. DiFranzo, M. Mulhearn, C. Shimmin, S. Tulin, et al., Mono-Higgs-boson: A new collider probe of dark matter, *Phys. Rev. D* 89 (2014) 075017, <http://dx.doi.org/10.1103/PhysRevD.89.075017>, arXiv:1312.2592.
- [49] J. Abdallah, et al., Simplified models for dark matter searches at the LHC, *Phys. Dark Univ.* 9–10 (2015) 8–23, <http://dx.doi.org/10.1016/j.dark.2015.08.001>, arXiv:1506.03116.
- [50] G. Busoni, et al., Recommendations on presenting LHC searches for missing transverse energy signals using simplified s -channel models of dark matter arXiv:1603.04156.
- [51] A. Albert, et al., Recommendations of the LHC Dark Matter Working Group: Comparing LHC searches for heavy mediators of dark matter production in visible and invisible decay channels arXiv:1703.05703.
- [52] T. Abe, et al., LHC Dark Matter Working Group: Next-generation spin-0 dark matter models arXiv:1810.09420.
- [53] D. Bauer, J. Buckley, M. Cahill-Rowley, R. Cotta, A. Drlica-Wagner, et al., Dark matter in the coming decade: Complementary paths to discovery and beyond, *Phys. Dark Univ.* 7–8 (2013) 16–23, <http://dx.doi.org/10.1016/j.dark.2015.04.001>, arXiv:1305.1605.
- [54] R.S. Chivukula, H. Georgi, Composite technicolor standard model, *Phys. Lett. B* 188 (1987) 99, [http://dx.doi.org/10.1016/0370-2693\(87\)90713-1](http://dx.doi.org/10.1016/0370-2693(87)90713-1).
- [55] L. Hall, L. Randall, Weak scale effective supersymmetry, *Phys. Rev. Lett.* 65 (1990) 2939–2942, <http://dx.doi.org/10.1103/PhysRevLett.65.2939>.
- [56] A. Buras, P. Gambino, M. Gorbahn, S. Jäger, L. Silvestrini, Universal unitarity triangle and physics beyond the Standard Model, *Phys. Lett. B* 500 (2001) 161–167, [http://dx.doi.org/10.1016/S0370-2693\(01\)00061-2](http://dx.doi.org/10.1016/S0370-2693(01)00061-2), arXiv:hep-ph/0007085.
- [57] G. D’Ambrosio, G. Giudice, G. Isidori, A. Strumia, Minimal Flavor Violation: An effective field theory approach, *Nuclear Phys. B* 645 (2002) 155–187, [http://dx.doi.org/10.1016/S0550-3213\(02\)00836-2](http://dx.doi.org/10.1016/S0550-3213(02)00836-2), arXiv:hep-ph/0207036.
- [58] P. Agrawal, M. Blanke, K. Gemmler, Flavored dark matter beyond Minimal Flavor Violation, *J. High Energy Phys.* 1410 (2014) 72, [http://dx.doi.org/10.1007/JHEP10\(2014\)072](http://dx.doi.org/10.1007/JHEP10(2014)072), arXiv:1405.6709.
- [59] Git repository for model, input and parameter cards for models considered in the ATLAS/CMS Dark Matter Forum studies, <https://doi.org/10.5281/zenodo.3260943>, [Online; accessed 28-June-2019] (2015).
- [60] O. Buchmueller, M.J. Dolan, S.A. Malik, C. McCabe, Characterising dark matter searches at colliders and direct detection experiments: Vector mediators, *J. High Energy Phys.* 1501 (2015) 037, [http://dx.doi.org/10.1007/JHEP01\(2015\)037](http://dx.doi.org/10.1007/JHEP01(2015)037), arXiv:1407.8257.
- [61] U. Haisch, F. Kahlhoefer, E. Re, QCD Effects in mono-jet searches for dark matter, *J. High Energy Phys.* 1312 (2013) 007, [http://dx.doi.org/10.1007/JHEP12\(2013\)007](http://dx.doi.org/10.1007/JHEP12(2013)007), arXiv:1310.4491.
- [62] T. Sjöstrand, S. Mrenna, P.Z. Skands, A brief introduction to PYTHIA 8.1, *Comput. Phys. Comm.* 178 (2008) 852–867, <http://dx.doi.org/10.1016/j.cpc.2008.01.036>, arXiv:0710.3820.

- [63] Y. Bai, J. Bourbeau, T. Lin, Dark matter searches with a mono- Z' jet, *J. High Energy Phys.* 06 (2015) 205, [http://dx.doi.org/10.1007/JHEP06\(2015\)205](http://dx.doi.org/10.1007/JHEP06(2015)205), arXiv:1504.01395.
- [64] M. Chala, F. Kahlhoefer, M. McCullough, G. Nardini, K. Schmidt-Hoberg, Constraining dark sectors with Monojets and Dijets, *J. High Energy Phys.* 07 (2015) 089, [http://dx.doi.org/10.1007/JHEP07\(2015\)089](http://dx.doi.org/10.1007/JHEP07(2015)089), arXiv:1503.05916.
- [65] N. Zhou, D. Berge, D. Whiteson, Mono-everything: combined limits on dark matter production at colliders from multiple final states, *Phys. Rev. D* 87 (2013) 095013, <http://dx.doi.org/10.1103/PhysRevD.87.095013>, arXiv:1202.3619.
- [66] Y. Gershtein, F. Petriello, S. Quackenbush, K.M. Zurek, Discovering hidden sectors with mono-photon Z' searches, *Phys. Rev. D* 78 (2008) 095002, <http://dx.doi.org/10.1103/PhysRevD.78.095002>, arXiv:0809.2849.
- [67] N.F. Bell, Y. Cai, J.B. Dent, R.K. Leane, T.J. Weiler, Dark matter at the LHC: Effective field theories and gauge invariance, *Phys. Rev. D* 92 (5) (2015) 053008, <http://dx.doi.org/10.1103/PhysRevD.92.053008>, arXiv:1503.07874.
- [68] K. Hamaguchi, S.P. Liew, T. Moroi, Y. Yamamoto, Isospin-violating dark matter with colored mediators, *J. High Energy Phys.* 1405 (2014) 086, [http://dx.doi.org/10.1007/JHEP05\(2014\)086](http://dx.doi.org/10.1007/JHEP05(2014)086), arXiv:1403.0324.
- [69] S. Alioli, P. Nason, C. Oleari, E. Re, A general framework for implementing NLO calculations in shower Monte Carlo programs: the POWHEG BOX, *J. High Energy Phys.* 1006 (2010) 043, [http://dx.doi.org/10.1007/JHEP06\(2010\)043](http://dx.doi.org/10.1007/JHEP06(2010)043), arXiv:1002.2581.
- [70] P. Nason, A new method for combining NLO QCD with shower Monte Carlo algorithms, *J. High Energy Phys.* 0411 (2004) 040, <http://dx.doi.org/10.1088/1126-6708/2004/11/040>, arXiv:hep-ph/0409146.
- [71] S. Frixione, P. Nason, C. Oleari, Matching NLO QCD computations with parton shower simulations: the POWHEG method, *J. High Energy Phys.* 0711 (2007) 070, <http://dx.doi.org/10.1088/1126-6708/2007/11/070>, arXiv:0709.2092, * Temporary entry *.
- [72] C. Arina, E. Del Nobile, P. Panci, Dark matter with pseudoscalar-mediated interactions explains the DAMA signal and the Galactic Center excess, *Phys. Rev. Lett.* 114 (2015) 011301, <http://dx.doi.org/10.1103/PhysRevLett.114.011301>, arXiv:1406.5542.
- [73] U. Haisch, A. Hibbs, E. Re, Determining the structure of dark-matter couplings at the LHC, *Phys. Rev. D* 89 (2014) 034009, <http://dx.doi.org/10.1103/PhysRevD.89.034009>, arXiv:1311.7131.
- [74] H.M. Lee, M. Park, V. Sanz, Interplay between Fermi gamma-ray lines and collider searches, *J. High Energy Phys.* 1303 (2013) 052, [http://dx.doi.org/10.1007/JHEP03\(2013\)052](http://dx.doi.org/10.1007/JHEP03(2013)052), arXiv:1212.5647.
- [75] J. Alwall, R. Frederix, S. Frixione, V. Hirschi, F. Maltoni, et al., The automated computation of tree-level and next-to-leading order differential cross sections, and their matching to parton shower simulations, *J. High Energy Phys.* 1407 (2014) 079, [http://dx.doi.org/10.1007/JHEP07\(2014\)079](http://dx.doi.org/10.1007/JHEP07(2014)079), arXiv:1405.0301.
- [76] A. Alloul, N.D. Christensen, C. Degrande, C. Duhr, B. Fuks, FeynRules 2.0 - a complete toolbox for tree-level phenomenology, *Comput. Phys. Comm.* 185 (2014) 2250–2300, arXiv:1310.1921.
- [77] C. Degrande, C. Duhr, B. Fuks, D. Grellscheid, O. Mattelaer, et al., UFO - The Universal FeynRules Output, *Comput. Phys. Comm.* 183 (2012) 1201–1214, <http://dx.doi.org/10.1016/j.cpc.2012.01.022>, arXiv:1108.2040.
- [78] M. Papucci, A. Vichi, K.M. Zurek, Monojet versus the rest of the world I: t -channel models, *J. High Energy Phys.* 1411 (2014) 024, [http://dx.doi.org/10.1007/JHEP11\(2014\)024](http://dx.doi.org/10.1007/JHEP11(2014)024), arXiv:1402.2285.
- [79] S. Chang, R. Edezhath, J. Hutchinson, M. Luty, Effective WIMPs, *Phys. Rev. D* 89 (2014) 015011, <http://dx.doi.org/10.1103/PhysRevD.89.015011>, arXiv:1307.8120.
- [80] G. Busoni, A. De Simone, T. Jacques, E. Morgante, A. Riotto, On the validity of the effective field theory for dark matter searches at the LHC part III: analysis for the t -channel, *J. Cosmol. Astropart. Phys.* 1409 (2014) 022, <http://dx.doi.org/10.1088/1475-7516/2014/09/022>, arXiv:1405.3101.
- [81] F. Maltoni, A. Martini, K. Mawatari, B. Oehl, Signals of a superlight gravitino at the LHC, *J. High Energy Phys.* 1504 (2015) 021, [http://dx.doi.org/10.1007/JHEP04\(2015\)021](http://dx.doi.org/10.1007/JHEP04(2015)021), arXiv:1502.01637.
- [82] P. de Aquino, F. Maltoni, K. Mawatari, B. Oehl, Light gravitino production in association with gluinos at the LHC, *J. High Energy Phys.* 1210 (2012) 008, [http://dx.doi.org/10.1007/JHEP10\(2012\)008](http://dx.doi.org/10.1007/JHEP10(2012)008), arXiv:1206.7098.
- [83] J. Alwall, S. de Visscher, F. Maltoni, QCD Radiation in the production of heavy colored particles at the LHC, *J. High Energy Phys.* 0902 (2009) 017, <http://dx.doi.org/10.1088/1126-6708/2009/02/017>, arXiv:0810.5350.
- [84] E. Conte, B. Dumont, B. Fuks, C. Wymant, Designing and recasting LHC analyses with MadAnalysis 5, *Eur. Phys. J. C* 74 (2014) 3103, <http://dx.doi.org/10.1140/epjc/s10052-014-3103-0>, arXiv:1405.3982.
- [85] B. Dumont, B. Fuks, S. Kraml, S. Bein, G. Chalons, et al., Toward a public analysis database for LHC new physics searches using MADANALYSIS 5, *Eur. Phys. J. C* 75 (2015) 56, <http://dx.doi.org/10.1140/epjc/s10052-014-3242-3>, arXiv:1407.3278.
- [86] E. Conte, B. Fuks, G. Serret, MadAnalysis 5, a user-friendly framework for collider phenomenology, *Comput. Phys. Comm.* 184 (2013) 222–256, <http://dx.doi.org/10.1016/j.cpc.2012.09.009>, arXiv:1206.1599.
- [87] T. Lin, E.W. Kolb, L.-T. Wang, Probing dark matter couplings to top and bottom quarks at the LHC, *Phys. Rev. D* 88 (2013) 063510, <http://dx.doi.org/10.1103/PhysRevD.88.063510>, arXiv:1303.6638.
- [88] P. Agrawal, B. Batell, D. Hooper, T. Lin, Flavored dark matter and the Galactic Center gamma-ray excess, *Phys. Rev. D* 90 (2014) 063512, <http://dx.doi.org/10.1103/PhysRevD.90.063512>, arXiv:1404.1373.
- [89] T. Daylan, D.P. Finkbeiner, D. Hooper, T. Linden, S.K.N. Portillo, N.L. Rodd, T.R. Slatyer, The characterization of the gamma-ray signal from the central Milky Way: A case for annihilating dark matter, *Phys. Dark Univ.* 12 (2016) 1–23, <http://dx.doi.org/10.1016/j.dark.2015.12.005>, arXiv:1402.6703.
- [90] F. Calore, I. Cholis, C. Weniger, Background model systematics for the Fermi GeV excess, *J. Cosmol. Astropart. Phys.* 1503 (2015) 038, <http://dx.doi.org/10.1088/1475-7516/2015/03/038>, arXiv:1409.0042.
- [91] A. Kumar, S. Tulin, Top-flavored dark matter and the forward-backward asymmetry, *Phys. Rev. D* 87 (9) (2013) 095006, <http://dx.doi.org/10.1103/PhysRevD.87.095006>, arXiv:1303.0332.
- [92] B. Batell, T. Lin, L.-T. Wang, Flavored Dark Matter And R-parity violation, *J. High Energy Phys.* 1401 (2014) 075, [http://dx.doi.org/10.1007/JHEP01\(2014\)075](http://dx.doi.org/10.1007/JHEP01(2014)075), arXiv:1309.4462.
- [93] C. Kilic, M.D. Klimek, J.-H. Yu, Signatures of top flavored dark matter, *Phys. Rev. D* 91 (5) (2015) 054036, <http://dx.doi.org/10.1103/PhysRevD.91.054036>, arXiv:1501.02202.
- [94] H.M. Lee, M. Park, V. Sanz, Gravity-mediated (or composite) Dark Matter, *Eur. Phys. J. C* 74 (2014) 2715, <http://dx.doi.org/10.1140/epjc/s10052-014-2715-8>, arXiv:1306.4107.
- [95] H.M. Lee, M. Park, V. Sanz, Gravity-mediated (or composite) dark matter confronts astrophysical data, *J. High Energy Phys.* 1405 (2014) 063, [http://dx.doi.org/10.1007/JHEP05\(2014\)063](http://dx.doi.org/10.1007/JHEP05(2014)063), arXiv:1401.5301.
- [96] D.Y. Bardin, S.M. Bilenyk, W. Beenakker, F.A. Berends, W.L. van Neerven, S.C. Van der Marck, G. Burgers, W.F.L. Hollik, T. Riemann, M. Sachwitz, Z Line shape, in: Workshop on Z Physics at LEP1 : General Meetings, Vol. 1 : StandArd Physics, 1989, p. 43, URL <http://cds.cern.ch/record/199969>.
- [97] A. Berlin, T. Lin, L.-T. Wang, Mono-Higgs detection of dark matter at the LHC, *J. High Energy Phys.* 1406 (2014) 078, [http://dx.doi.org/10.1007/JHEP06\(2014\)078](http://dx.doi.org/10.1007/JHEP06(2014)078), arXiv:1402.7074.
- [98] R. Cotta, J. Hewett, M. Le, T. Rizzo, Bounds on dark matter interactions with electroweak gauge bosons, *Phys. Rev. D* 88 (2013) 116009, <http://dx.doi.org/10.1103/PhysRevD.88.116009>, arXiv:1210.0525.
- [99] A. Crivellin, U. Haisch, A. Hibbs, LHC constraints on gauge boson couplings to dark matter, *Phys. Rev. D* 91 (2015) 074028, <http://dx.doi.org/10.1103/PhysRevD.91.074028>, arXiv:1501.00907.
- [100] A. Nelson, L.M. Carpenter, R. Cotta, A. Johnstone, D. Whiteson, Confronting the Fermi Line with LHC data: an effective theory of dark matter interaction with photons, *Phys. Rev. D* 89 (2014) 056011, <http://dx.doi.org/10.1103/PhysRevD.89.056011>, arXiv:1307.5064.
- [101] D. O'Connell, M.J. Ramsey-Musolf, M.B. Wise, Minimal extension of the Standard Model scalar sector, *Phys. Rev. D* 75 (2007) 037701, <http://dx.doi.org/10.1103/PhysRevD.75.037701>, arXiv:hep-ph/0611014.
- [102] N. Craig, J. Galloway, S. Thomas, Searching for signs of the Second Higgs Doublet arXiv:1305.2424.
- [103] J. de Favereau, et al., DELPHES 3, a modular framework for fast simulation of a generic collider experiment, *J. High Energy Phys.* 1402 (2014) 057, [http://dx.doi.org/10.1007/JHEP02\(2014\)057](http://dx.doi.org/10.1007/JHEP02(2014)057), arXiv:1307.6346.
- [104] A. Djouadi, A. Falkowski, Y. Mambrini, J. Quevillon, Direct detection of Higgs-Portal dark matter at the LHC, *Eur. Phys. J. C* 73 (2013) 2455, <http://dx.doi.org/10.1140/epjc/s10052-013-2455-1>, arXiv:1205.3169.
- [105] N. Weiner, I. Yavin, How dark are Majorana WIMPs? signals from MiDM and Rayleigh dark matter, *Phys. Rev. D* 86 (2012) 075021, <http://dx.doi.org/10.1103/PhysRevD.86.075021>, arXiv:1206.2910.
- [106] N. Weiner, I. Yavin, UV completions of magnetic inelastic and Rayleigh dark matter for the Fermi Line(s), *Phys. Rev. D* 87 (2013) 023523, <http://dx.doi.org/10.1103/PhysRevD.87.023523>, arXiv:1209.1093.
- [107] J. Liu, B. Shuve, N. Weiner, I. Yavin, Looking for new charged states at the LHC: Signatures of magnetic and Rayleigh dark matter, *J. High Energy Phys.* 1307 (2013) 144, [http://dx.doi.org/10.1007/JHEP07\(2013\)144](http://dx.doi.org/10.1007/JHEP07(2013)144), arXiv:1303.4404.
- [108] U. Haisch, F. Kahlhoefer, J. Unwin, The impact of heavy-quark loops on LHC dark matter searches, *J. High Energy Phys.* 1307 (2013) 125, [http://dx.doi.org/10.1007/JHEP07\(2013\)125](http://dx.doi.org/10.1007/JHEP07(2013)125), arXiv:1208.4605.
- [109] M. Bahr, S. Gieseke, M. Gigg, D. Grellscheid, K. Hamilton, et al., Herwig++ physics and manual, *Eur. Phys. J. C* 58 (2008) 639–707, <http://dx.doi.org/10.1140/epjc/s10052-008-0798-9>, arXiv:0803.0883.
- [110] G. Corcella, I. Knowles, G. Marchesini, S. Moretti, K. Odagiri, et al., HERWIG 6.5 release note arXiv:hep-ph/0210213.

- [111] G. Corcella, et al., HERWIG 6: An event generator for hadron emission reactions with interfering gluons (including supersymmetric processes), *J. High Energy Phys.* 0101 (2001) 010, <http://dx.doi.org/10.1088/1126-6708/2001/01/010>, arXiv:hep-ph/0011363.
- [112] G. Marchesini, B. Webber, G. Abbiendi, I. Knowles, M. Seymour, L. Stanco, HERWIG 5.1 - a monte carlo event generator for simulating hadron emission reactions with interfering gluons, *Comput. Phys. Comm.* 67 (3) (1992) 465–508, [http://dx.doi.org/10.1016/0010-4655\(92\)90055-4](http://dx.doi.org/10.1016/0010-4655(92)90055-4), <http://www.sciencedirect.com/science/article/pii/0010465592900554>.
- [113] M. Backovic, M. Krämer, F. Maltoni, A. Martini, K. Mawatari, M. Pellen, Higher-order QCD predictions for dark matter production at the LHC in simplified models with s-channel mediators, *Eur. Phys. J. C* 75 (10) (2015) 482, <http://dx.doi.org/10.1140/epjc/s10052-015-3700-6>, arXiv:1508.05327.
- [114] P.J. Fox, C. Williams, Next-to-leading order predictions for dark matter production at hadron colliders, *Phys. Rev. D* 87 (2013) 054030, <http://dx.doi.org/10.1103/PhysRevD.87.054030>, arXiv:1211.6390.
- [115] Git repository for POWHEG input card for model with s-channel exchange of axial vector mediator, https://github.com/LHC-DMWG/model-repository/tree/master/models/Monojet_DMA, [Online; accessed 08-May-2019] (2015). <http://dx.doi.org/10.5281/zenodo.3260943>.
- [116] Git repository for POWHEG input card for model with s-channel exchange of vector mediator, https://github.com/LHC-DMWG/model-repository/tree/master/models/Monojet_DMV, [Online; accessed 08-May-2019] (2015). <http://dx.doi.org/10.5281/zenodo.3260943>.
- [117] Git repository for POWHEG input card for model with s-channel exchange of scalar mediator, https://github.com/LHC-DMWG/model-repository/tree/master/models/Monojet_DMS_tLoop, [Online; accessed 08-May-2019] (2015). <http://dx.doi.org/10.5281/zenodo.3260943>.
- [118] Git repository for POWHEG input card for model with s-channel exchange of pseudo-scalar mediator, coupling to the quarks through a top loop, https://github.com/LHC-DMWG/model-repository/tree/master/models/Monojet_DMP_tloop, [Online; accessed 08-May-2019] (2015). <http://dx.doi.org/10.5281/zenodo.3260943>.
- [119] T. Sjöstrand, S. Ask, J.R. Christiansen, R. Corke, N. Desai, et al., An introduction to PYTHIA 8.2, *Comput. Phys. Comm.* 191 (2015) 159–177, <http://dx.doi.org/10.1016/j.cpc.2015.01.024>, arXiv:1410.3012.
- [120] S. Hoeche, S. Kuttimalai, S. Schumann, F. Siegert, Beyond Standard Model calculations with Sherpa, *Eur. Phys. J. C* 75 (3) (2015) 135, <http://dx.doi.org/10.1140/epjc/s10052-015-3338-4>, arXiv:1412.6478.
- [121] R. Frederix, S. Frixione, Merging meets matching in MC@NLO, *J. High Energy Phys.* 1212 (2012) 061, [http://dx.doi.org/10.1007/JHEP12\(2012\)061](http://dx.doi.org/10.1007/JHEP12(2012)061), arXiv:1209.6215.
- [122] J. Alwall, et al., Comparative study of various algorithms for the merging of parton showers and matrix elements in hadronic collisions, *Eur. Phys. J. C* 53 (2008) 473–500, <http://dx.doi.org/10.1140/epjc/s10052-007-0490-5>, arXiv:0706.2569.
- [123] L. Lonnblad, S. Prestel, Matching tree-level matrix elements with interleaved showers, *J. High Energy Phys.* 1203 (2012) 019, [http://dx.doi.org/10.1007/JHEP03\(2012\)019](http://dx.doi.org/10.1007/JHEP03(2012)019), arXiv:1109.4829.
- [124] Git repository for Madgraph inputs with t-channel exchange of colored scalar mediator, couplings to light quarks only, https://github.com/LHC-DMWG/model-repository/tree/master/models/Monojet_tChannel/contributed_by_PapucciVichiZurek, [Online; accessed 08-May-2019] (2015). <http://dx.doi.org/10.5281/zenodo.3260943>.
- [125] Git repository for Madgraph inputs with t-channel exchange of colored scalar mediator, couplings to all quark generations, https://github.com/LHC-DMWG/model-repository/tree/master/models/Monojet_tChannel/contributed_by_AmeliaBrennan, [Online; accessed 08-May-2019] (2015). <http://dx.doi.org/10.5281/zenodo.3260943>.
- [126] Git repository for Madgraph input cards for model with s-channel exchange of vector mediator, for electroweak boson final states, https://github.com/LHC-DMWG/model-repository/tree/master/models/EW_DMV, [Online; accessed 08-May-2019] (2015). <http://dx.doi.org/10.5281/zenodo.3260943>.
- [127] Git repository for Madgraph inputs for model with s-channel exchange of pseudo-scalar mediator, produced in association with top quarks, https://github.com/LHC-DMWG/model-repository/tree/master/models/HF_S+PS, [Online; accessed 08-May-2019] (2015). <http://dx.doi.org/10.5281/zenodo.3260943>.
- [128] Git repository for Madgraph inputs for simplified model with a colored scalar mediator coupling to DM and b-quarks, https://github.com/LHC-DMWG/model-repository/tree/master/models/HF_S+PS, [Online; accessed 08-May-2019] (2015). <http://dx.doi.org/10.5281/zenodo.3260943>.
- [129] J.M. Campbell, R.K. Ellis, F. Maltoni, S. Willenbrock, Associated production of a Z boson and a single heavy quark jet, *Phys. Rev. D* 69 (2004) 074021, <http://dx.doi.org/10.1103/PhysRevD.69.074021>, arXiv:hep-ph/0312024.
- [130] F. Maltoni, T. McElmurry, S. Willenbrock, Inclusive production of a Higgs or Z boson in association with heavy quarks, *Phys. Rev. D* 72 (2005) 074024, <http://dx.doi.org/10.1103/PhysRevD.72.074024>, arXiv:hep-ph/0505014.
- [131] J.M. Campbell, R.K. Ellis, F. Maltoni, S. Willenbrock, Production of a Z boson and two jets with one heavy-quark tag, *Phys. Rev. D* 73 (2006) 054007, <http://dx.doi.org/10.1103/PhysRevD.73.054007>, arXiv:hep-ph/0510362.
- [132] CMS Collaboration, Measurement of the production cross sections for a Z boson and one or more b jets in pp collisions at $\sqrt{s} = 7$ TeV, *J. High Energy Phys.* 1406 (2014) 120, [http://dx.doi.org/10.1007/JHEP06\(2014\)120](http://dx.doi.org/10.1007/JHEP06(2014)120), arXiv:1402.1521.
- [133] CMS Collaboration, Measurement of the cross section and angular correlations for associated production of a Z boson with b hadrons in pp collisions at $\sqrt{s} = 7$ TeV, *J. High Energy Phys.* 1312 (2013) 039, [http://dx.doi.org/10.1007/JHEP12\(2013\)039](http://dx.doi.org/10.1007/JHEP12(2013)039), arXiv:1310.1349.
- [134] CMS Collaboration, Search for H/A decaying into Z+A/H, with Z to ll and A/H to fermion pair 2015.
- [135] R. Frederix, S. Frixione, V. Hirschi, F. Maltoni, R. Pittau, et al., W and Z/ γ^* boson production in association with a bottom-antibottom pair, *J. High Energy Phys.* 1109 (2011) 061, [http://dx.doi.org/10.1007/JHEP09\(2011\)061](http://dx.doi.org/10.1007/JHEP09(2011)061), arXiv:1106.6019.
- [136] M. Wiesemann, R. Frederix, S. Frixione, V. Hirschi, F. Maltoni, et al., Higgs production in association with bottom quarks, *J. High Energy Phys.* 1502 (2015) 132, [http://dx.doi.org/10.1007/JHEP02\(2015\)132](http://dx.doi.org/10.1007/JHEP02(2015)132), arXiv:1409.5301.
- [137] Git repository for Madgraph inputs for vector and scalar mediator models leading to a mono-Higgs signature, https://github.com/LHC-DMWG/model-repository/tree/master/models/EW_Higgs_all, [Online; accessed 08-May-2019] (2015). <http://dx.doi.org/10.5281/zenodo.3260943>.
- [138] Git repository for Madgraph inputs for 2HDM model leading to a mono-Higgs signature, https://github.com/LHC-DMWG/model-repository/tree/master/models/EW_Higgs_2HDM, [Online; accessed 08-May-2019] (2015). <http://dx.doi.org/10.5281/zenodo.3260943>.
- [139] B. Hespel, D. Lopez-Val, E. Vryonidou, Higgs pair production via gluon fusion in the Two-Higgs-Doublet Model, *J. High Energy Phys.* 1409 (2014) 124, [http://dx.doi.org/10.1007/JHEP09\(2014\)124](http://dx.doi.org/10.1007/JHEP09(2014)124), arXiv:1407.0281.
- [140] U. Baur, E.N. Glover, Higgs boson production at large transverse momentum in hadronic collisions, *Nuclear Phys. B* 339 (1990) 38–66, [http://dx.doi.org/10.1016/0550-3213\(90\)90532-1](http://dx.doi.org/10.1016/0550-3213(90)90532-1).
- [141] Git repository for Madgraph inputs for dimension-7 EFT models with direct DM-EW boson couplings, https://github.com/LHC-DMWG/model-repository/tree/master/models/EW_Fermion_D7/contributed_by_Renjie_Wang, [Online; accessed 08-May-2019] (2015). <http://dx.doi.org/10.5281/zenodo.3260943>.
- [142] S. Nussinov, Technoc cosmology: could a technibaryon excess provide a 'natural' missing mass candidate?, *Phys. Lett. B* 165 (1985) 55, [http://dx.doi.org/10.1016/0370-2693\(85\)90689-6](http://dx.doi.org/10.1016/0370-2693(85)90689-6).
- [143] D.B. Kaplan, A single explanation for both the baryon and dark matter densities, *Phys. Rev. Lett.* 68 (1992) 741–743, <http://dx.doi.org/10.1103/PhysRevLett.68.741>.
- [144] T. Banks, J.-F. Fortin, S. Thomas, Direct detection of dark matter electromagnetic dipole moments arXiv:1007.5515.
- [145] G. Busoni, A. De Simone, J. Gramling, E. Morgante, A. Riotto, On the validity of the effective field theory for dark matter searches at the LHC, part II: Complete analysis for the s-channel, *J. Cosmol. Astropart. Phys.* 1406 (2014) 060, <http://dx.doi.org/10.1088/1475-7516/2014/06/060>, arXiv:1402.1275.
- [146] D. Racco, A. Wulzer, F. Zwirner, Robust collider limits on heavy-mediator dark matter, *J. High Energy Phys.* 1505 (2015) 009, [http://dx.doi.org/10.1007/JHEP05\(2015\)009](http://dx.doi.org/10.1007/JHEP05(2015)009), arXiv:1502.04701.
- [147] M. Endo, Y. Yamamoto, Unitarity bounds on dark matter effective interactions at LHC, *J. High Energy Phys.* 1406 (2014) 126, [http://dx.doi.org/10.1007/JHEP06\(2014\)126](http://dx.doi.org/10.1007/JHEP06(2014)126), arXiv:1403.6610.
- [148] PDF4LHC: Recommendation for LHC cross section calculations, <http://www.hep.ucl.ac.uk/pdf4lhc/>, [Online; accessed 08-May-2019] 2015.
- [149] J. Alwall, M. Herquet, F. Maltoni, O. Mattelaer, T. Stelzer, MadGraph 5 : Going beyond, *J. High Energy Phys.* 1106 (2011) 128, [http://dx.doi.org/10.1007/JHEP06\(2011\)128](http://dx.doi.org/10.1007/JHEP06(2011)128), arXiv:1106.0522.
- [150] T. Sjöstrand, S. Mrenna, P.Z. Skands, PYTHIA 6.4 physics and manual, *J. High Energy Phys.* 0605 (2006) 026, <http://dx.doi.org/10.1088/1126-6708/2006/05/026>, arXiv:hep-ph/0603175.
- [151] M. Whalley, D. Bourilkov, R. Group, The Les Houches accord PDFs (LHAPDF) and LHAGLUE arXiv:hep-ph/0508110.
- [152] M.L. Mangano, M. Moretti, F. Piccinini, M. Treccani, Matching matrix elements and shower evolution for top-quark production in hadronic collisions, *J. High Energy Phys.* 0701 (2007) 013, <http://dx.doi.org/10.1088/1126-6708/2007/01/013>, arXiv:hep-ph/0611129.
- [153] V. Hirschi, R. Frederix, S. Frixione, M.V. Garzelli, F. Maltoni, et al., Automation of one-loop QCD corrections, *J. High Energy Phys.* 1105 (2011) 044, [http://dx.doi.org/10.1007/JHEP05\(2011\)044](http://dx.doi.org/10.1007/JHEP05(2011)044), arXiv:1103.0621.
- [154] Git repository for Madgraph inputs for mono-Higgs EFT models, dimension 4 and 5, https://github.com/LHC-DMWG/model-repository/tree/master/models/EW_Higgs_D4D5, [Online; accessed 08-May-2019] (2015). <http://dx.doi.org/10.5281/zenodo.3260943>.

- [155] J. Andrea, B. Fuks, F. Maltoni, Monotops at the LHC, *Phys. Rev. D* 84 (2011) 074025, <http://dx.doi.org/10.1103/PhysRevD.84.074025>, arXiv:1106.6199.
- [156] J.-L. Agram, J. Andrea, M. Buttignol, E. Conte, B. Fuks, Monotop phenomenology at the Large Hadron Collider, *Phys. Rev. D* 89 (2014) 014028, <http://dx.doi.org/10.1103/PhysRevD.89.014028>, arXiv:1311.6478.
- [157] I. Boucheneb, G. Cacciapaglia, A. Deandrea, B. Fuks, Revisiting monotop production at the LHC, *J. High Energy Phys.* 1501 (2015) 017, [http://dx.doi.org/10.1007/JHEP01\(2015\)017](http://dx.doi.org/10.1007/JHEP01(2015)017), arXiv:1407.7529.
- [158] R. Allahverdi, M. Dalchenko, B. Dutta, A. Flórez, Y. Gao, T. Kamon, N. Kolev, R. Mueller, M. Segura, Distinguishing standard model extensions using monotop chirality at the LHC, *J. High Energy Phys.* 12 (2016) 046, [http://dx.doi.org/10.1007/JHEP12\(2016\)046](http://dx.doi.org/10.1007/JHEP12(2016)046), arXiv:1507.02271.
- [159] N.D. Christensen, P. de Aquino, C. Degrande, C. Duhr, B. Fuks, et al., A comprehensive approach to new physics simulations, *Eur. Phys. J. C* 71 (2011) 1541, <http://dx.doi.org/10.1140/epjc/s10052-011-1541-5>, arXiv:0906.2474.
- [160] Git repository for Madgraph inputs for mono-top models, https://github.com/LHC-DMWG/model-repository/tree/master/models/HF_SingleTop, [Online; accessed 08-May-2019] (2015). <http://dx.doi.org/10.5281/zenodo.3260943>.
- [161] A. Belyaev, G. Cacciapaglia, I.P. Ivanov, F. Rojas-Abatte, M. Thomas, Anatomy of the Inert Two Higgs Doublet Model in the light of the LHC and non-LHC Dark Matter Searches, *Phys. Rev. D* 97 (3) (2018) 035011, <http://dx.doi.org/10.1103/PhysRevD.97.035011>, arXiv:1612.00511.
- [162] N.G. Deshpande, E. Ma, Pattern of symmetry breaking with two Higgs doublets, *Phys. Rev. D* 18 (1978) 2574, <http://dx.doi.org/10.1103/PhysRevD.18.2574>.
- [163] R. Barbieri, L.J. Hall, V.S. Rychkov, Improved naturalness with a heavy Higgs: An alternative road to LHC physics, *Phys. Rev. D* 74 (2006) 015007, <http://dx.doi.org/10.1103/PhysRevD.74.015007>, arXiv:hep-ph/0603188.
- [164] L. Lopez Honorez, E. Nezri, J.F. Oliver, M.H. Tytgat, The Inert Doublet Model: An archetype for dark matter, *J. Cosmol. Astropart. Phys.* 0702 (2007) 028, <http://dx.doi.org/10.1088/1475-7516/2007/02/028>, arXiv:hep-ph/0612275.
- [165] T. Hambye, F.-S. Ling, L. Lopez Honorez, J. Rocher, Scalar Multiplet dark matter, *J. High Energy Phys.* 0907 (2009) 090, [http://dx.doi.org/10.1007/JHEP05\(2010\)066](http://dx.doi.org/10.1007/JHEP05(2010)066), arXiv:0903.4010.
- [166] L. Lopez Honorez, C.E. Yaguna, A new viable region of the Inert Doublet Model, *J. Cosmol. Astropart. Phys.* 1101 (2011) 002, <http://dx.doi.org/10.1088/1475-7516/2011/01/002>, arXiv:1011.1411.
- [167] M. Gustafsson, E. Lundström, L. Bergström, J. Edsjö, Significant gamma lines from Inert Higgs Dark Matter, *Phys. Rev. Lett.* 99 (2007) 041301, <http://dx.doi.org/10.1103/PhysRevLett.99.041301>, arXiv:astro-ph/0703512.
- [168] E.M. Dolle, S. Su, The Inert Dark Matter, *Phys. Rev. D* 80 (2009) 055012, <http://dx.doi.org/10.1103/PhysRevD.80.055012>, arXiv:0906.1609.
- [169] P. Agrawal, E.M. Dolle, C.A. Krenke, Signals of Inert Doublet Dark Matter in neutrino telescopes, *Phys. Rev. D* 79 (2009) 015015, <http://dx.doi.org/10.1103/PhysRevD.79.015015>, arXiv:0811.1798.
- [170] S. Andreas, M.H. Tytgat, Q. Swillens, Neutrinos from Inert Doublet Dark Matter, *J. Cosmol. Astropart. Phys.* 0904 (2009) 004, <http://dx.doi.org/10.1088/1475-7516/2009/04/004>, arXiv:0901.1750.
- [171] E. Nezri, M.H. Tytgat, G. Vertongen, e^+ and anti- p from Inert Doublet model dark matter, *J. Cosmol. Astropart. Phys.* 0904 (2009) 014, <http://dx.doi.org/10.1088/1475-7516/2009/04/014>, arXiv:0901.2556.
- [172] C. Garcia-Cely, A. Ibarra, Novel gamma-ray spectral features in the Inert Doublet Model, *J. Cosmol. Astropart. Phys.* 1309 (2013) 025, <http://dx.doi.org/10.1088/1475-7516/2013/09/025>, arXiv:1306.4681.
- [173] A. Goudelis, B. Herrmann, O. Stål, Dark matter in the Inert Doublet Model after the discovery of a higgs-like boson at the LHC, *J. High Energy Phys.* 1309 (2013) 106, [http://dx.doi.org/10.1007/JHEP09\(2013\)106](http://dx.doi.org/10.1007/JHEP09(2013)106), arXiv:1303.3010.
- [174] C. Burgess, M. Pospelov, T. ter Veldhuis, The Minimal model of non-baryonic dark matter: A singlet scalar, *Nuclear Phys. B* 619 (2001) 709–728, [http://dx.doi.org/10.1016/S0550-3213\(01\)00513-2](http://dx.doi.org/10.1016/S0550-3213(01)00513-2), arXiv:hep-ph/0011335.
- [175] S. Andreas, T. Hambye, M.H. Tytgat, WIMP dark matter, Higgs exchange and DAMA, *J. Cosmol. Astropart. Phys.* 0810 (2008) 034, <http://dx.doi.org/10.1088/1475-7516/2008/10/034>, arXiv:0808.0255.
- [176] A. Arhrib, Y.-L.S. Tsai, Q. Yuan, T.-C. Yuan, An updated analysis of Inert Higgs Doublet Model in light of the recent results from LUX, PLANCK, AMS-02 and LHC, *J. Cosmol. Astropart. Phys.* 1406 (2014) 030, <http://dx.doi.org/10.1088/1475-7516/2014/06/030>, arXiv:1310.0358.
- [177] E. Lundström, M. Gustafsson, J. Edsjö, The Inert Doublet Model and LEP II limits, *Phys. Rev. D* 79 (2009) 035013, <http://dx.doi.org/10.1103/PhysRevD.79.035013>, arXiv:0810.3924.
- [178] Q.-H. Cao, E. Ma, G. Rajasekaran, Observing the Dark Scalar Doublet and its impact on the Standard-Model Higgs boson at colliders, *Phys. Rev. D* 76 (2007) 095011, <http://dx.doi.org/10.1103/PhysRevD.76.095011>, arXiv:0708.2939.
- [179] E. Dolle, X. Miao, S. Su, B. Thomas, Dilepton signals in the Inert Doublet Model, *Phys. Rev. D* 81 (2010) 035003, <http://dx.doi.org/10.1103/PhysRevD.81.035003>, arXiv:0909.3094.
- [180] X. Miao, S. Su, B. Thomas, Trilepton signals in the Inert Doublet Model, *Phys. Rev. D* 82 (2010) 035009, <http://dx.doi.org/10.1103/PhysRevD.82.035009>, arXiv:1005.0090.
- [181] M. Gustafsson, S. Rydbeck, L. Lopez-Honorez, E. Lundstrom, Status of the Inert Doublet Model and the role of multileptons at the LHC, *Phys. Rev. D* 86 (2012) 075019, <http://dx.doi.org/10.1103/PhysRevD.86.075019>, arXiv:1206.6316.
- [182] A. Arhrib, R. Benbrik, N. Gaur, $H \rightarrow \gamma\gamma$ in Inert Higgs Doublet Model, *Phys. Rev. D* 85 (2012) 095021, <http://dx.doi.org/10.1103/PhysRevD.85.095021>, arXiv:1201.2644.
- [183] B. Swiezewska, M. Krawczyk, Diphoton rate in the inert doublet model with a 125 GeV Higgs boson, *Phys. Rev. D* 88 (3) (2013) 035019, <http://dx.doi.org/10.1103/PhysRevD.88.035019>, arXiv:1212.4100.
- [184] G. Belanger, B. Dumont, A. Goudelis, B. Herrmann, S. Kraml, D. Sengupta, Dilepton constraints in the Inert Doublet Model from Run 1 of the LHC, *Phys. Rev. D* 91 (11) (2015) 115011, <http://dx.doi.org/10.1103/PhysRevD.91.115011>, arXiv:1503.07367.
- [185] S. Kraml, B. Allanach, M. Mangano, H. Prosper, S. Sekmen, et al., Searches for new physics: Les Houches recommendations for the presentation of LHC results, *Eur. Phys. J. C* 72 (2012) 1976, <http://dx.doi.org/10.1140/epjc/s10052-012-1976-3>, arXiv:1203.2489.
- [186] The Durham HepData project, <http://hepdata.cedar.ac.uk/abouthepdata>, [Online; accessed 08-May-2019] 2015.
- [187] J.S. Kim, D. Schmeier, J. Tattersall, K. Rolbiecki, A framework to create customised LHC analyses within CheckMATE, *Comput. Phys. Comm.* 196 (2015) 535–562, <http://dx.doi.org/10.1016/j.cpc.2015.06.002>, arXiv:1503.01123.
- [188] K. Cranmer, I. Yavin, RECAST: Extending the impact of existing analyses, *J. High Energy Phys.* 1104 (2011) 038, [http://dx.doi.org/10.1007/JHEP04\(2011\)038](http://dx.doi.org/10.1007/JHEP04(2011)038), arXiv:1010.2506.
- [189] Michele Papucci, Joshua T. Ruderman, Andreas Weiler, Natural susy endures, *JHEP* 09 (2012) 035, [http://dx.doi.org/10.1007/JHEP09\(2012\)035](http://dx.doi.org/10.1007/JHEP09(2012)035), arXiv:1110.6926.
- [190] D. Barducci, A. Belyaev, M. Buchkremer, G. Cacciapaglia, A. Deandrea, et al., Framework for model independent analyses of multiple extra quark scenarios, *J. High Energy Phys.* 1412 (2014) 080, [http://dx.doi.org/10.1007/JHEP12\(2014\)080](http://dx.doi.org/10.1007/JHEP12(2014)080), arXiv:1405.0737.
- [191] PGS: simulation of a generic high-energy physics collider detector, <http://conway.physics.ucdavis.edu/research/software/pgs/pgs4-general.htm>, [Online; accessed 09-May-2019] 2015.
- [192] M. Baak, G. Besjes, D. Căzte, A. Koutsman, J. Lorenz, et al., HistFitter software framework for statistical data analysis, *Eur. Phys. J. C* 75 (2015) 153, <http://dx.doi.org/10.1140/epjc/s10052-015-3327-7>, arXiv:1410.1280.
- [193] INSPIRE: High-energy physics literature database, <http://inspirehep.net>, [Online; accessed 08-May-2019] 2015.
- [194] S. Kraml, S. Kulkarni, U. Laa, A. Lessa, W. Magerl, D. Proschofsky, W. Waltenberger, SModelS: a tool for interpreting simplified-model results from the LHC and its application to supersymmetry, *Eur. Phys. J. C* 74 (2014) 2868, <http://dx.doi.org/10.1140/epjc/s10052-014-2868-5>, arXiv:1312.4175.
- [195] S. Kraml, S. Kulkarni, U. Laa, A. Lessa, V. Magerl, et al., SModelS v1.0: a short user guide arXiv:1412.1745.
- [196] M. Papucci, K. Sakurai, A. Weiler, L. Zeune, Fastlim: a fast LHC limit calculator, *Eur. Phys. J. C* 74 (2014) 3163, <http://dx.doi.org/10.1140/epjc/s10052-014-3163-1>, arXiv:1402.0492.

Publications Krijn de Vries

Coherent transition radiation from the geomagnetically-induced current in cosmic-ray air showers: Implications for the anomalous events observed by ANITA

Krijn D. de Vries^{1,*} and Steven Prohira^{2,†}

¹*Vrije Universiteit Brussel, Dienst ELEM, IIHE, Pleinlaan 2, 1050, Brussel, Belgium*

²*Center for Cosmology and AstroParticle Physics (CCAPP), The Ohio State University, Columbus OH, 43210*

We show that coherent transition radiation from the electrically-neutral transverse geomagnetic current (CTR-GM) in a cosmic-ray air shower provides a natural, standard model, explanation to the recent “anomalous” events observed by the ANITA detector. We demonstrate that for zenith angles less than ~ 70 degrees, combined with high surface elevation, the inclusion of CTR-GM can significantly alter the emitted electric field from a cosmic-ray air shower. CTR-GM therefore has to be included in radio emission models to provide a full description of the radio emission from a high-energy cosmic-ray air shower traversing a dielectric boundary.

Introduction— During propagation through the atmosphere, the electrons and positrons of a cosmic ray air shower will be deflected in Earth’s magnetic field, inducing a net transverse current in the shower front. This results in geomagnetically induced radio emission up to GHz frequencies [1–4], which allows the shower to be detected with radio instruments. A second radio emission source is the net negative excess charge in the shower, first predicted by Askaryan in 1962 [5] and experimentally confirmed in 2001 [6].

Detection of high energy cosmic rays using radio is currently a well established method [7, 8], with development stretching back to the initial efforts of the 1960’s [9]. In addition to cosmic-ray air shower radio detectors, several radio detectors are currently under development to probe particle cascades induced by high-energy (> 10 PeV) cosmic neutrinos interacting in more dense media such as ice or rock [10–13].

In recent works [14–16] another important emission mechanism is discussed, coherent transition radiation (CTR) from a high-energy particle cascade traversing different media. The considered source of the transition radiation is the net excess charge predicted by Askaryan (CTR-A). Other works considering particle cascades moving through dielectrics concern the EXTASIS experiment [17], for which the emission at ground based cosmic-ray detection set-ups due to the absorption of the cosmic-ray air shower by Earth was treated in Ref. [18]. Recently, CTR-A was confirmed experimentally at the Telescope Array Electron Light Source facility, where the emission from a high-energy electron beam leaving the accelerator was quantified in detail [19], earlier works on CTR-A using electron beams are found in Refs. [20, 21].

In this work, we present a second CTR contribution that is expected for cosmic-ray air showers hitting a boundary surface. We show that strong coherent transition radiation from the geomagnetically-induced current (CTR-GM) can be expected once a significantly large particle number crosses a boundary surface. We also show that this condition in general is satisfied for high-energy cosmic-ray air showers with shallow zenith angles ($\lesssim 70^\circ$) incident upon high surface elevations ($\gtrsim 2.5$ km). If these criteria are not satisfied, the particle

content at the boundary is too small for the coherent transition radiation to be significant [14, 18].

We discuss the obtained results in the context of the two so-called ‘anomalous events’ detected by the stratospheric balloon-borne ANITA instrument [22][23]. Though primarily a neutrino detector, ANITA also observes the emission from downward-going cosmic-ray air showers after reflection from the ice. The anomalous cosmic-ray like events detected by ANITA have the same polarization as a typical cosmic-ray, but an inverted polarity. *Polarization* is a measure of the plane of oscillation of the electric field, while *polarity* is a measure of the sign of the dominant peak(s) of this field. Consequently, the inverted polarity of the anomalous events has been interpreted as emission from an upward-going shower of some kind.

Such an upward moving cascade, however, is only possible for primary particles having traversed a long path through the earth. Plausible standard-model explanations for such events are largely ruled out by ANITA exposure limits [24], and other explanations require physics beyond the standard model [25–34].

In this work, we show that CTR-GM from a down-going cosmic ray shower provides a natural explanation for the observed inverted polarity signals. We show that CTR-GM significantly affects the expected electric field pulse shapes and that the two anomalous events have cascade geometries for which strong coherent transition radiation is expected, which is not the case for the majority of the cosmic-ray events observed by the ANITA detector.

Coherent transition radiation— To calculate the coherent transition radiation from the geomagnetically-induced air shower current, we follow the approach presented in Ref. [14]. In what follows, we denote z as the axis normal to the ice surface, the subscript b refers to the air/ice boundary, and primed quantities are ‘retarded’ or ‘emission’ times.

Since the particle cascade is moving relativistically, the emission will be boosted along its direction of motion. In the following we will therefore only consider emission in the forward direction. In the left half of Fig. 1, the forward emission from a cosmic-ray air shower while propagating in air is illustrated by the full black cone. The signal gets ‘split’ at the boundary z_b , where part of the emission gets transmitted into

* krijn.de.vries@vub.ac.be

† prohira.1@osu.edu

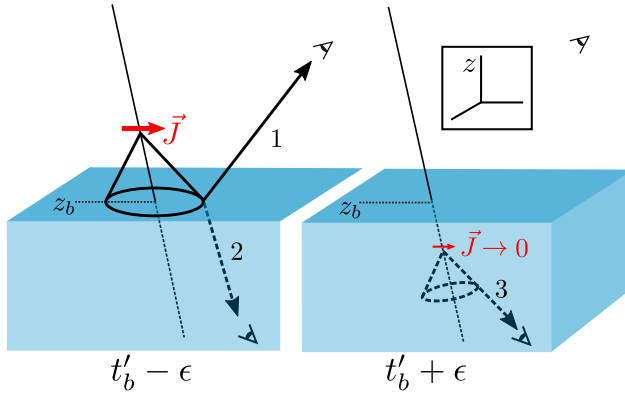


FIG. 1. The geometry for coherent transition radiation just before (left) and just after (right) the relativistic shower front crosses the air/ice boundary z_b at retarded time t'_b . The geomagnetic current is indicated by \vec{J} . The direct emission from this current is given by the solid black cone on the left figure, which reflects up (label 1) for an in-air observer and refracts down for an in-ice observer (label 2). At time $t'_b + \epsilon$, the path to the in-air observer has vanished.

the ice given by the dashed line (label 2) and part of the signal gets reflected off the surface, shown by the full line (label 1). After the cascade penetrates the ice at time t_b (Fig. 1, right), the reflected path completely vanishes and only the direct path remains (label 3).

From Fig. 1, it immediately follows that the observed emission depends strongly on the observer location. For an in-ice observer, one has to consider paths 2 and 3, where for an in-air observer only path 1 has to be considered. In the following, we derive the expected fields due to coherent transition radiation for both situations separately.

CTR for an in-ice observer.— The in-air potential obtained at an infinitesimal distance ϵ above the boundary is observed through a completely different refracted path (Fig. 1, left, label 2), compared to the emission emitted an infinitesimal distance ϵ below the boundary (Fig. 1, right, label 3). A direct consequence of this discontinuity in the path length is a discontinuity in the observed potentials, leading to strong emission from the boundary, coherent transition radiation. It also follows that this is a geometrical effect, and as such is not limited to the net excess charge predicted by Askaryan, but applies equally well to the geomagnetically-induced air shower current.

To calculate the transition radiation from the geomagnetically-induced current for a typical cosmic-ray air shower, we consider the three dimensional current distribution given by $J^x(t', \vec{r}, h) = N_e(t') ev_d w(\vec{r}, h)$. Here, $N_e(t')$ denotes the number of leptons at the emission time t' , to be observed at the observer time t . The drift velocity $v_d = 0.04 c$ is the average velocity induced by Earth's magnetic field for electrons and positrons in a typical cosmic-ray air shower [35]. The function $w(\vec{r}, h)$ gives the particle distribution within the charge cloud, where \vec{r} denotes the lateral distance and h the longitudinal distance within the cloud which moves by definition with the speed of light along

the cascade axis. The total particle number, as well as the particle distributions within the charge cloud are parameterized following Ref. [35] and the detailed parameterizations are presented in the supplementary materials.

Closely following the formalism for a net excess charge presented in Ref. [14], the potential for the geomagnetically-induced air shower current crossing a boundary surface is given by,

$$A^x(\vec{x}, t) = \frac{\mu_0}{4\pi} \int d^2\vec{r} dh \mathcal{T}_{air-ice} \frac{J^x(t', r, h)}{|\mathcal{D}_2|} \theta(z - z_b) \Big|_{t'} + \frac{\mu_0}{4\pi} \int d^2\vec{r} dh \frac{J^x(t', r, h)}{|\mathcal{D}_3|} \theta(z_b - z) \Big|_{t'}. \quad (1)$$

Here, $\mathcal{T}_{air-ice}$ denotes the Fresnel transmission coefficient, and the different path lengths are included in the retarded distance $\mathcal{D} = L \frac{dt}{dt'}$, where L denotes the optical path length from the emission point at emission time t' to the observer, where the signal arrives at the observer time t . The electric fields are now obtained through the standard relation $\vec{E} = -dA^0/d\vec{x} - d\vec{A}/d(ct)$. These derivatives work on all terms under the integral. The specific contribution where the derivatives operate on the Heaviside step function $\theta(z)$ is called CTR and gives rise to the fields

$$E^x(\vec{x}, t) = \frac{\mu_0}{4\pi} \lim_{\epsilon \rightarrow 0} \int d^2\vec{r} \mathcal{T}_{air-ice} \frac{J^x(t', r, h)}{|\mathcal{D}_2|} \Big|_{z=z_b+\epsilon} - \frac{\mu_0}{4\pi} \lim_{\epsilon \rightarrow 0} \int d^2\vec{r} \frac{J^x(t', r, h)}{|\mathcal{D}_3|} \Big|_{z=z_b-\epsilon}. \quad (2)$$

CTR for an in-air observer.— The derivation for coherent transition radiation for an in-air observer is similar to the derivation for an in-ice observer outlined above. For an in-air observer, however, the reflected path through which the potential is observed (Fig. 1, left, label 1) instantly vanishes below the boundary. Though the (backward) emission from the cascade propagation below the ice reaches the detector, due to relativistic beaming this component is negligible compared to the reflected component from the in-air emission. As such, it is safe to ignore this in-ice contribution to the potential. We continue to use the term “transition radiation,” however, because the transition from air to ice is explicitly responsible for the induced shock in the potential. The potential from the geomagnetically-induced air shower current for an in-air observer is thus given by,

$$A^x(\vec{x}, t) = \frac{\mu_0}{4\pi} \int d^2\vec{r} dh \mathcal{R}_{air-ice} \frac{J^x(t', r, h)}{|\mathcal{D}_1|} \theta(z - z_b) \Big|_{t'}, \quad (3)$$

using the Fresnel reflection coefficient $\mathcal{R}_{air-ice}$. We subsequently obtain the field due to the vanishing of the potential at the boundary,

$$\vec{E}^x(\vec{x}, t) = \frac{\mu_0}{4\pi} \lim_{\epsilon \rightarrow 0} \int d^2\vec{r} \mathcal{R}_{air-ice} \frac{J^x(t', r, h)}{|\mathcal{D}_1|} \Big|_{z=z_b+\epsilon}. \quad (4)$$

The ANITA anomalous events.— In this section we investigate if coherent transition radiation from the

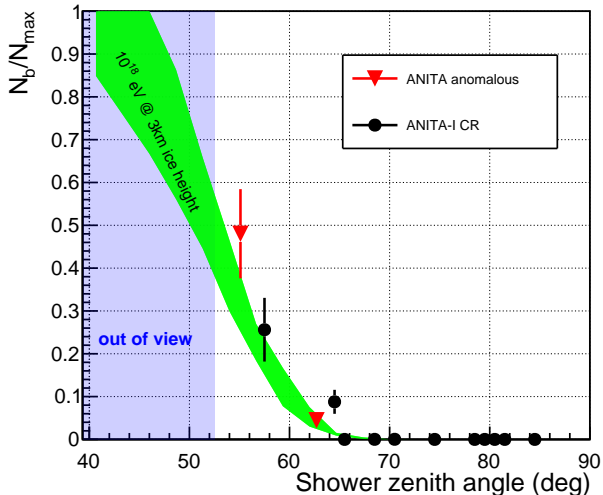


FIG. 2. The ratio of the number of charged particles hitting the ice boundary (N_b) to the maximum number of charged particles in the shower (N_{max}), versus zenith angle of the shower. Both the ANITA-I cosmic rays as well as the ANITA-I and ANITA-III anomalous events are shown. The error on the ANITA-1 CR sample is due to the reported error in the energy estimate. The shaded region is excluded by ANITA’s field of view.

geomagnetically-induced air shower current can provide an explanation for the ANITA anomalous events. For strong coherent transition radiation to occur, a significant part of the cosmic-ray air shower has to hit Earth’s surface. From Fig. 7 in Ref. [14], it follows that this restricts us to cosmic-ray air showers with zenith angles below ~ 70 degrees for the typical environments in which the ANITA detector operates.

To quantify this, a set of Monte-Carlo (MC) showers has been made using the CX-MC-GEO package presented in Ref [35]. This package allows to obtain the three dimensional charge and current distributions located inside the high-energy cascade front and is based on the full MC cascade mode of CONEX [36, 37]. The showers have been produced in the zenith angle range from 40-80 degrees, containing 10 simulations for each degree interval. The considered showers are induced by a 10^{18} eV proton primary, and the air-ice boundary is chosen at 3 km above sea level similar to conditions at Antarctica.

The results are shown by the green plane in Fig. 2. Here we plot the number of particles hitting the air-ice boundary, N_b , with respect to the maximum number of shower particles, N_{max} . From this we indeed confirm that for zenith angles larger than 70 degrees the particle content at the boundary becomes small.

Additionally, the shaded area in Fig. 2 shows the range of zenith angles excluded by the ANITA antenna array field of view [10]. To investigate in more detail if the ANITA anomalous events lie within the region of interest for coherent transition radiation to be significant, we ran 10 Monte-Carlo showers for each anomalous event within their given reconstruction errors. These errors are obtained by using the event param-

eters published by the ANITA collaboration [23], including energy (the reported energies for the anomalous events, provided for a direct shower, have been scaled by the empirically determined surface reflectivity coefficients attained on recent ANITA flights [38]), zenith angle, and surface elevation. A similar procedure has been made for the normal cosmic-ray air shower events detected during the ANITA-1 flight [39, 40].

From Fig. 2, it indeed follows that the ANITA anomalous events lie within the region of interest, separated from the majority of the ANITA cosmic-ray sample. For the CTR-GM signal to be significant, a combination of three variables of each event has to be considered: the event must be high energy, arrive at a zenith angle $\lesssim 70$ degrees, and impact the surface at a high elevation. It happens that in these variables, the ANITA anomalous events are within the region of interest and live in the tails of the typical CR distribution.

To quantify if coherent transition radiation can be an explanation for the ANITA anomalous events, as well as the normal cosmic-ray air showers observed in this region, in Fig. 3, we show the expected field for one of the ANITA anomalous events with a reconstructed zenith angle of 55 degrees and a surface elevation of 2.7 km, that is seen by an observer located 30 km above the air-ice boundary. The field is simulated at different viewing angles of $\alpha = 0, 1.7, 3.9$ degrees with respect to the specular angle of the cascade axis. It follows that, depending on the observer geometry, the expected transition radiation can be large compared to the geomagnetic emission in air, inverting the field polarity (Fig. 3 (b)). Furthermore, the time-ordering of the peaks can be reversed, (Fig. 3 (a)). These effects are absent for observer geometries further out from the specular angle (Fig. 3 (c)). For comparison, in Fig. 3 (d), we show the expected emission observed at a viewing angle of $\alpha = 1.7$ degree for a primary of the same energy and surface elevation, only adapting the zenith angle to 70 degrees, typical of an ANITA-1 CR. As expected in this situation, the transition radiation becomes negligible.

We further note that, being derived from the geomagnetic current, the CTR-GM signal is aligned with the local geomagnetic angle, and thus it has the same polarization—but inverted polarity—to the in-air signal from the induced geomagnetic current, a fact which has so far not been explained without significant tension with the standard model. Additionally, an interesting signature to distinguish the expected CTR-GM signal from the in-air emission is found in the received spectrum, increasing the high-frequency content due to the sharp shock in the potential. As such, a detailed comparison of the spectra of events that satisfy the CTR-GM criteria—anomalous or not—to the spectra of those events which are not expected to be influenced by CTR-GM can be used to confirm the presented hypothesis. Finally, since the CTR-GM signal is expected to dominate at small zenith angles we suggest an increased exposure for the ANITA detector towards these angles in future flights which will increase their cosmic-ray statistics within the region of interest for the CTR-GM signal.

Conclusions— We have shown that coherent transition radiation is not limited to a net excess charge, but applies equally well to a (net charge-neutral) transverse current traversing different media. We investigated if the anoma-

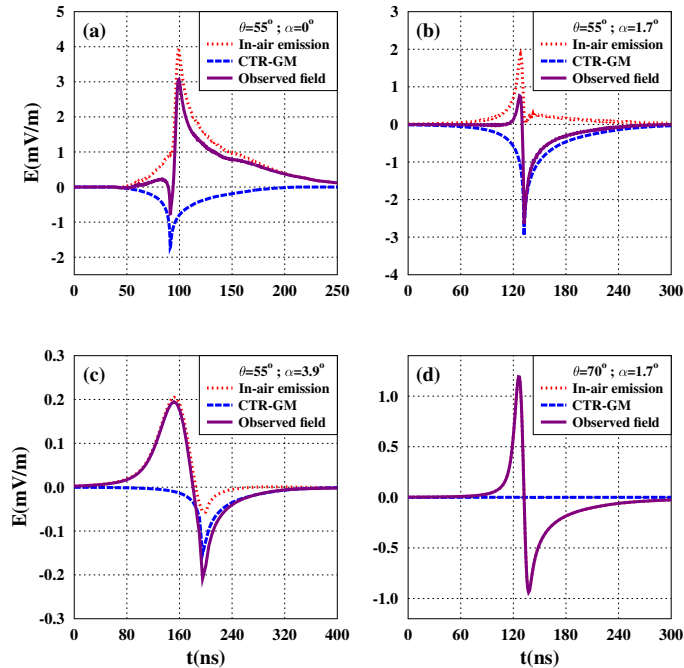


FIG. 3. The expected radio emission (full purple lines) from a downgoing cosmic ray air shower hitting an air-ice boundary at 3 km above sea level for a shower with a zenith angle of 55 degrees observed at: a) the specular angle of the shower axis, the CTR-GM (striped blue line) is seen before the in-air emission (dotted red line), b) 1.7 degrees from the specular angle, the CTR-GM emission is strong and arrives approximately at the same time as the in-air emission, c) 3.9 degrees from the shower axis, the CTR-GM emission is seen after the in-air emission. The situation for a 70 degrees inclined shower at 1.7 degree from the specular angle, is given in d), where it is observed that the CTR-GM emission is negligible.

ous events observed by the ANITA detector can be explained by coherent transition radiation from the geomagnetically-induced air shower current hitting the Antarctic surface. It is shown that the anomalous events have a particularly high particle content at the air-ice boundary compared to the typical cosmic-ray events detected by ANITA. Furthermore, we show that for showers with relatively small zenith angles $\lesssim 70$ degrees, similar to the two anomalous events detected by ANITA, the expected electric field at the detector can be dominated by coherent transition radiation, and even more interestingly, the apparent polarity can be inverted. For larger zenith angles, the particle content at the boundary is too

small to have a significant influence on the expected electric fields. It follows that coherent transition radiation from the geomagnetically-induced air shower current provides a natural, standard model explanation for the ANITA anomalous events. We recommend a more detailed event-by-event investigation to confirm this hypothesis.

Acknowledgements— We express our gratitude to the ANITA collaboration for their informative comments and assistance regarding this work. We also thank A. Connolly, D. Besson, A. Romero-Wolf, O. Scholten, S. Buitink, and J. Beacom for edits and insights. This work was supported by the Flemish Foundation for Scientific Research FWO (FWO-12L3715N - K.D. de Vries) and the European Research Council under the EU-uropean Unions Horizon 2020 research and innovation programme (grant agreement No 805486).

Appendix A: Particle distribution parameterization—

The electric field calculations presented in Fig. 3 are based on the obtained field equations presented in Eq. 6. The three dimensional distribution $J^x(t')$ describing the geomagnetically induced air shower current is parameterized as,

$$J^x(t', \vec{r}, h) = N_e(t') ev_d w(\vec{r}, h). \quad (5)$$

The total particle number as function of the emission time t' is obtained directly from the NKG formalism [41, 42], and outlined in detail in [14]. Following [35], the drift velocity $v_d = 0.04 c$ is taken constant throughout the 3D particle distribution in the cascade front. This distribution is assumed to be radially symmetric and subdivided as $w(\vec{r}, h) = 2\pi w_1(r) w_2(r, h)$. The radial particle distribution $w_1(r)$ is obtained through,

$$w_1(r) = \frac{\Gamma(4.5 - p)}{\Gamma(p)\Gamma(4.5 - 2p)} \left(\frac{r}{r_0}\right)^{p-1} \left(\frac{r}{r_0} + 1\right)^{p-4.5} \quad (6)$$

Here $p = 1.1$, and $r_0 = 80$ m are fit parameters fixed to their values obtained close to shower maximum from the CX-MC-GEO package [35]. The longitudinal particle distribution is a function of distance from the shower axis and given by,

$$w_2(r, h) = \frac{4h}{(h_1)^2} \exp(-2h/h_1). \quad (7)$$

The radial dependence is hidden in the width parameter $h_1(r) = 5(0.02 + 0.1r)$ m fitted by comparison of this parameter with results obtained by the CX-MC-GEO package, corresponding to an effective width of 10 cm at the shower axis up to 10 meters at a radial distance of 100 m away from the shower axis (see Fig [10] of [35]).

[1] F.D. Kahn and I. Lerche, Proc. Royal Soc. London **A289**, 206 (1966).
 [2] O. Scholten, K. Werner, F. Rusydi, Astropart. Phys. **29**, 94-103 (2008)
 [3] N.N. Kalmykov, A.A. Konstantinov, and R. Engel, Nucl. Phys.

B 151, 347 (2006); Phys. of At. Nuclei, **73**, 1191 (2010)
 [4] K.D. de Vries, A.M. van den Berg, O. Scholten, K. Werner, Phys.Rev.Lett. **107**, 061101 (2011)
 [5] G.A. Askaryan, Sov. Phys. JETP **14**, 441 (1962); **21**, 658 (1965)
 [6] D. Saltzberg, P. Gorham, D. Walz, C. Field, R. Iverson, A.

- Odian, G. Resch, P. Schoessow, D. Williams, *Phys. Rev. Lett.* **86**, 2802-2805 (2001)
- [7] F.G. Schröder, *Progress in Particle and Nuclear Physics*, **93**, 1-68, (2017)
- [8] T. Huege, D. Besson, *Progress of Theoretical and Experimental Physics*, **12**, 12A106, (2017)
- [9] H.R. Allan, *Progress in Elementary Particle and Cosmic Ray Physics* **10**, 171 (1971)
- [10] P.W. Gorham *et al.*, ANITA Collaboration, *Astropart. Phys.* **32**, 10 (2009)
- [11] P. Allison *et al.*, ARA Collaboration, *Astropart. Phys.* **35**, 457-477 (2012)
- [12] S.W. Barwick *et al.*, ARIANNA Collaboration, *Astropart. Phys.* **70**, 12-26 (2015)
- [13] GRAND Collaboration, arXiv:1810.09994
- [14] K.D. de Vries *et al.*, *Astropart. Phys.* **74**, 96 (2016).
- [15] P. Motloch, J. Alvarez-Muniz, P. Privitera, *E. Zas*, *Phys. Rev. D* **93**, 043010 (2016).
- [16] P. Motloch, J. Alvarez-Muniz, P. Privitera, *E. Zas*, *Phys. Rev. D* **95**, 043004 (2017).
- [17] H. Carduner, D. Charrier, R. Dallier, L. Denis, A. Escudie, D. García-Fernández, F. Gaté, A. Lecacheux, V. Marin, L. Martin, B. Revenu, M. Tueros, PoS(2017)416, PoS(2017)417, PoS(2017)418, PoS(2017)419, arXiv:1710.02487.
- [18] D. García-Fernández, B. Revenu, D. Charrier, R. Dallier, A. Escudie, L. Martín, *Phys. Rev. D* **97**, 103010 (2018).
- [19] K.D. de Vries, M. DuVernois, M. Fukushima, R. Gaior, K. Hanson, D. Ikeda, Y Inome, A. Ishihara, T. Kuwabara, K. Mase, J.N. Matthews, T. Meures, P. Motloch, I.S. Ohta, A. O'Murchadha, F. Partous, M. Relich, H. Sagawa, T. Shibata, B.K. Shin, G. Thomson, S. Ueyama, N. van Eijndhoven, T. Yamamoto, S. Yoshida, *Phys. Rev. D* **98**, 123020 (2018).
- [20] P.W. Gorham, D. Saltzberg, P. Schoessow, W. Gai, J.G. Power, R. Konecny, M.E. Conde, *Phys. Rev. E* **62**, 8590 (2000).
- [21] P.W. Gorham, D. Saltzberg, R.C. Field, E. Guillian, R. Milincic, P. Miocinovic, D. Walz, D. Williams, *Phys. Rev. D* **72**, 023002 (2005).
- [22] P.W. Gorham *et al.*, ANITA Collaboration, *Phys. Rev. Lett.* **117**, no. 7, 071101 (2016)
- [23] P. W. Gorham *et al.*, ANITA Collaboration, *Phys. Rev. Lett.* **121**, no. 16, 161102 (2018)
- [24] A. Romero-Wolf *et al.*, arXiv:1811.07261
- [25] L.A. Anchordoqui, V. Barger, J.G. Learned, D. Marfatia, T.J. Weiler, *LHEP* **1**, 13, 2018
- [26] G.-Y. Huang, *Phys. Rev. D* **98**, 043019 (2018)
- [27] J.H. Collins, P.S. Bhupal Dev, Y. Sui, *Phys. Rev. D.* **99**, 043009 (2019)
- [28] L.A. Anchordoqui, I. Antoniadis, *Phys. Lett. B* **790**, 578-582 (2019)
- [29] D.B. Fox, S. Sigurdsson, S. Shandera, P. Mészáros, K. Murase, M. Mostafá, S. Coutu, arXiv:1809.09615
- [30] J.F. Cherry, I.M. Shoemaker, arXiv:1802.01611
- [31] L. Heurtier, Y. Mambrini, M. Pierre, arXiv:1902.04584
- [32] A. Connolly, P. Allison, O. Banerjee, arXiv:1807.08892
- [33] T. M. Nieuwenhuizen, arXiv:1810.04613
- [34] B. Chauhan and S. Mohanty, *Phys. Rev. D* **99**, 095018 (2019)
- [35] K. Werner, K.D. de Vries, O. Scholten, *Astropart. Phys.* **37**, 5-16 (2012)
- [36] G. Bossard, H.J. Drescher, N.N. Kalmykov, S.Ostapchenko, A.I. Pavlov, T. Pierog, E.A. Vishnevskaya, and K. Werner, *Phys. Rev.* **D63**, 054030, (2001)
- [37] T. Bergmann R. Engel, D. Heck, N.N. Kalmykov, Sergey Ostapchenko, T. Pierog, T. Thouw, and K. Werner , *Astropart. Phys.* **26**, 420 (2007)
- [38] S. Prohira *et al.*, *Phys. Rev. D* **98**, no. 4, 042004 (2018)
- [39] H. Schoorlemmer *et al.*, *Astropart. Phys.* **77**, 32 (2016)
- [40] private communication, ANITA collaboration
- [41] K. Kamata, J. Nishimura, *Suppl. Progr. Theoret. Phys.* **6**, 93 (1958)
- [42] K. Greisen, in: J.G. Wilson (Ed.), *Prog. Cosmic Ray Phys.*, **3**, 1 (1965)

Observation of Radar Echoes From High-Energy Particle Cascades

S. Prohira,^{1,*} K.D. de Vries,² P. Allison,¹ J. Beatty,¹ D. Besson,^{3,4} A. Connolly,¹ N. van Eijndhoven,² C. Hast,⁵ C.-Y. Kuo,⁶ U.A. Latif,³ T. Meures,⁷ J. Nam,⁶ A. Nozdrina,³ J.P. Ralston,³ Z. Riesen,⁸ C. Sbrocco,¹ J. Torres,¹ and S. Wissel⁸

¹*Center for Cosmology and AstroParticle Physics (CCAPP), The Ohio State University, Columbus OH, USA*

²*Vrije Universiteit Brussel, Brussel, Belgium*

³*University of Kansas, Lawrence, KS, USA*

⁴*National Research Nuclear University, Moscow Engineering Physics Institute, Moscow, Russia*

⁵*SLAC National Accelerator Laboratory, Menlo Park, CA, USA*

⁶*National Taiwan University, Taipei, Taiwan*

⁷*University of Wisconsin-Madison, Madison, WI, USA*

⁸*California Polytechnic State University, San Luis Obispo, CA, USA*

We report the observation of radar echoes from the ionization trails of high-energy particle cascades. These data were taken at the SLAC National Accelerator Laboratory, where the full electron beam ($\sim 10^9$ e⁻ at ~ 10 GeV/e⁻) was directed into a plastic target to simulate an ultra high-energy neutrino interaction. This target was interrogated with radio waves, and coherent radio reflections from the cascades were detected, with properties consistent with theoretical expectations. This is the first definitive observation of radar echoes from high-energy particle cascades, which may lead to a viable neutrino detection technology for energies $\gtrsim 10^{16}$ eV.

Introduction.— Ultra high energy (UHE; $\gtrsim 10^{16}$ eV) astrophysical neutrinos offer great discovery potential. They would probe the accelerators of UHE cosmic rays, which are detected up to $\sim 10^{20}$ eV. Unlike cosmic rays, which are down-scattered on the cosmic microwave background and also deflected in magnetic fields, detected neutrinos will point back to their sources. UHE neutrino-nucleon interactions probe center-of-mass energies above the energy scale of colliders, allowing sensitive tests of new physics. To fully exploit the scientific potential of UHE neutrinos, we ultimately need an observatory with sufficient exposure to collect high statistics even in pessimistic flux scenarios.

When UHE neutrinos interact in matter, they produce a relativistic cascade of particles, as well as a trail of non-relativistic electrons and nuclei produced through the energy loss of the relativistic particles. The time-integrated cascade profile is a ellipsoid of length ~ 10 m and radius ~ 0.1 m, and nearly all of the primary interaction energy goes into ionization of the medium.

The incoherent optical Cherenkov emission from individual cascade electrons and positrons can be detected in TeV–PeV detectors like IceCube [1] and similar experiments [2–4]. However, the optical portion of the proposed successor IceCube-Gen2 [5] is too small to be an adequate UHE observatory, due to the steeply falling neutrino spectrum. Therefore, there are several proposed and implemented methods to detect these cascades from UHE neutrinos. First, the coherent radio-frequency Cherenkov emission from a net charge asymmetry in the cascade (the Askaryan effect [6]) has been observed in the lab [7], and is the focus of a variety of past [8], present [9–11], and proposed [12, 13] experiments. Radio methods can instrument large volumes more sparsely than optical detectors due to the transparency of radio in ice [14–16] making the construction of a large detector more cost-effective. Second, a τ neutrino, interacting in the earth, can produce a τ lepton—carrying much of the primary ν_τ energy—that exits the earth and decays in air, producing a

cascade. A current is induced in this cascade as it moves relativistically through the earth’s geomagnetic field, leading to coherent radio emission [17–21] that might be detected by proposed experiments [22–24]. Third, the optical Cherenkov light from such in-air decays can be detected by balloon-or satellite-borne experiments [25, 26]. All of these methods have potential for discovery at very high energies. However, they all have limited sensitivity at the lower end of the UHE range, between 10-100 PeV, just above the reach of optical Cherenkov detectors like IceCube.

Finally, it has been proposed that cascades can be detected by radar reflections off the ionization trail left in their wake. This technique shows promising projected sensitivity [27, 28], and is the only technique forecasted to have peak sensitivity in the 10-100 PeV range, with the potential to close the gap between optical Cherenkov detectors and the high energy technologies listed above. To that end, several recent experimental efforts [29–31] have made incremental progress toward the detection of a radar echo from a cascade in a dense medium.

In this letter, we present the first definitive observation of a radar echo from a particle cascade. This observation was made by experiment T576 at the SLAC National Accelerator Laboratory, where their electron beam was used to produce a particle cascade with a density equivalent to that of a $\sim 10^{19}$ eV neutrino interaction in ice, and with a similar shower profile. A transmitting antenna (TX) broadcast continuous-wave (CW) radio into the target, and several receiving antennas (RX) monitored the target for a radar reflection. We report on the observation of a signal consistent with theoretical predictions. Below, we detail the experiment, analysis technique, and results.

Experimental setup and data collection.— The experiment, depicted in Fig. 1, took place at End Station A at SLAC, a large, open hall with a rich history of discovery. Designated T576, the experiment had two runs during 2018, one in May after which a suggestion of a reflection was reported [32], and a second run in October, which is the focus of the present

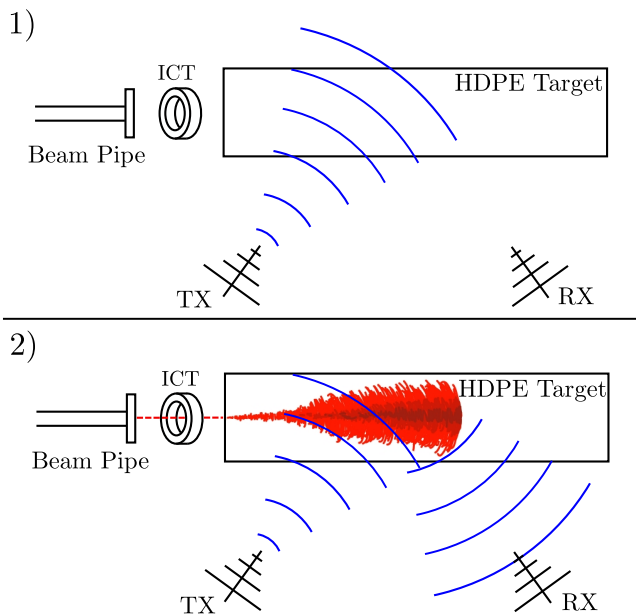


FIG. 1. Cartoon of the radar method and T576. 1) A transmitter (TX) illuminates a target. 2) The beam passes through the integrating current toroid (ICT, to monitor beam charge and align the data during analysis) and creates a cascade inside the target, leaving behind an ionization cloud. The transmitted signal is reflected to a monitoring receiver (RX). Not to scale.

article. We broadcast CW radio at a range of frequencies between 1 and 2.1 GHz and a range of amplitudes, using a signal generator, 50 W power amplifier, and transmitting antenna (TX) toward a target of high-density polyethylene (HDPE), into which the electron beam was directed. Receiving antennas (RX) were also directed at this target to measure the radar reflection. The data presented in this article were captured by a Tektronix 4 channel, 20 GS/s oscilloscope.

Two different types of antennas were used in this analysis. One was a Vivaldi-style, ultra-wide-band antenna (0.6–6 GHz) with a measured forward gain of +12 dBi at 2 GHz, and the other was a custom-built 0.9–4 GHz log-periodic dipole antenna (LPDA). The LPDA was used in conjunction with a parabolic dish reflector, with a measured forward gain of +18 dBi at 2 GHz. Surrounding the beam pipe exit was an integrating current toroid (ICT), which gave a precise measurement of the charge in each bunch, and provided a very stable reference point for post-run alignment of the dataset.

The data taking was separated into sub-runs consisting of 100–500 events. Between sub-runs, certain parameters (TX frequency, TX amplitude, TX position and RX position) were varied. Runs in which data was taken for analysis are called signal-runs. Other sub-runs were reserved for taking background data, which will be discussed in the data analysis section, and are called background-runs. The run lasted 8 days, with over 4 full days of beam time acquired in 12-hour increments.

Expectations.—The radar method had been suggested for

cosmic-ray initiated extensive-air-shower (EAS) detection in the atmosphere as early as 1940 [33, 34], with further development in the 1960s [35], followed by stagnation, and then renewed interest in the early 2000s [36–38]. Recent experimental searches from terrestrial radar systems [39] and a dedicated experiment, Telescope Array Radar (TARA), [40, 41] reported no signal due to collisional losses—which limit the efficiency of the scattering—and insufficient ionization density in air. Short free-electron lifetimes ($\tau \sim \text{ns}$) in air at EAS altitudes cause the ionization to vanish before a sufficient density to reflect incident RF can be achieved. Cascades in ice or other dense media do not suffer from this problem.

The theory for radar is well-established, and models of radar detection of cascades in dense media have evolved to maturity in recent years. Whether built up from a macroscopic [27] or first-principles [28] viewpoint, the properties of a reflection are well-defined, and subject to several properties of the material in which the cascade happens. The maximum density of the ionization is directly proportional to the density of the medium. Another critical parameter is the mean ionization lifetime of the material. This lifetime τ dictates the longitudinal extent of the ionization deposit, and thus the overall length scale of the reflector. For ice, τ ranges from $\mathcal{O}(1 - 10 \text{ ns})$ and is strongly dependent upon the temperature of the ice [42]. For HDPE, the lifetimes are comparable to those of cold polar ice [43].

For a given transmitter and receiver, the spectral content of the reflected signal is a function of τ and the cascade geometry. For a compact cascade, as was the case for T576, any lifetime exceeding 1 ns would produce a significant radar reflection at the transmitted frequency. (In nature, an UHE cascade of similar density would be longer by a factor of $\sim \text{few}$ in ice, which is expected to cause an effective Doppler shift depending upon the radar geometry.) We transmitted at a peak power of 50 W, with no amplification on our receivers. The expected signal for T576 was a radar return of a few ns in duration, at the transmitter frequency, at a level of a few mV.

Data analysis.— The data analysis for T576 was challenging because of the high-amplitude backgrounds. When a charge bunch such as the SLAC beam traverses media with differing indices of refraction, or effective indices of refraction, transition radiation of various forms [44–46] is produced. These signals—which would not be present in nature¹—exceeded our expected radar signal by a factor of 10–100 in amplitude. We call the total RF background caused by the beam ‘beam splash’ owing to its overall messy character. Fortunately, the beam splash was quite stable, and therefore able to be characterized and filtered using a sensitive matrix-decomposition technique, detailed in [47] and based on [48],

¹ Except for the case of a cascade crossing the air/ice boundary, either an in-ice neutrino cascade breaking out into the air, or an in-air cosmic ray cascade breaking into the ice. Sensitivity to such events is subject to the orientation of transmit and receive antennas, and will be explored.

that we call singular-value-decomposition filtration, or SVD-filtration.

There are four nominal components to the signal-run data: CW, beam splash, noise, and signal (a radar reflection). The background-run data contains only beam-splash and thermal noise. Assuming that the response of our system is linear for the range of signals received (which we confirmed subsequently in the lab with independent measurements, discussed below) then the total background to our signal can be formed by a linear combination of CW, beam splash, and thermal noise. We call this linear combination ‘null data.’ To build the null data, we added pre-signal-region CW from signal-run data to signal-region beam splash in background-run data.

SVD-filtration identifies and removes patterns. Patterns are features in the data that are found in multiple individual measurements, such as the beam splash and CW. The SVD-filtration characterizes these patterns within a set of carefully aligned null data, producing a filter basis. Then a filter is produced for each individual event by expanding it in the filter basis. After applying this filter, the only thing remaining in the event should be random, featureless background noise, and any putative signal present in the real data.

The filtration process was a blind procedure, having been tuned on a number of sub-runs comprising $<10\%$ of the data. In addition to the null data produced to build the SVD-filter basis, a null event was constructed for every real event in the full dataset, to serve as the null hypothesis. An SVD-filter was constructed for each signal-run according to its associated background-run, and both datasets (real and null) were filtered using the same SVD-filter basis. The resultant filtered data was then analyzed for excess.

Results.—After filtration, the dataset was further processed using a method devised during the run-1 analysis. To investigate both the time and spectral content of the signal, a time-versus-frequency spectrogram was generated for each filtered event in a signal-run, and these spectrograms were averaged. The result of such a process is shown in Figure 2, where a clear excess is visible in the real data—and not in the null data—at the transmitter frequency of 2.1 GHz with a duration of a few ns. A similar excess was observed at many different transmit frequencies, antenna positions, and in different antennas, but no excess is observed at the same time and frequency point in the null data. Signal and sideband regions are indicated by the solid and dashed lines respectively, used in significance calculations defined below.

The highest amplitude signal was expected and received during runs with a horizontally-polarized, high-gain antenna at the specular angle, where the resultant (SVD-filtered) signal was large enough to extract a time-domain waveform through careful alignment and averaging. The alignment was performed so that the events could shift by no more than a fraction of a transmit period, and they were averaged. A resultant time-domain average is shown in Figure 3, where only events that had high enough SNR for reliable cross-correlation are used in order to facilitate qualitative comparison to simulation. Also in Figure 3 is a comparison to an FDTD sim-

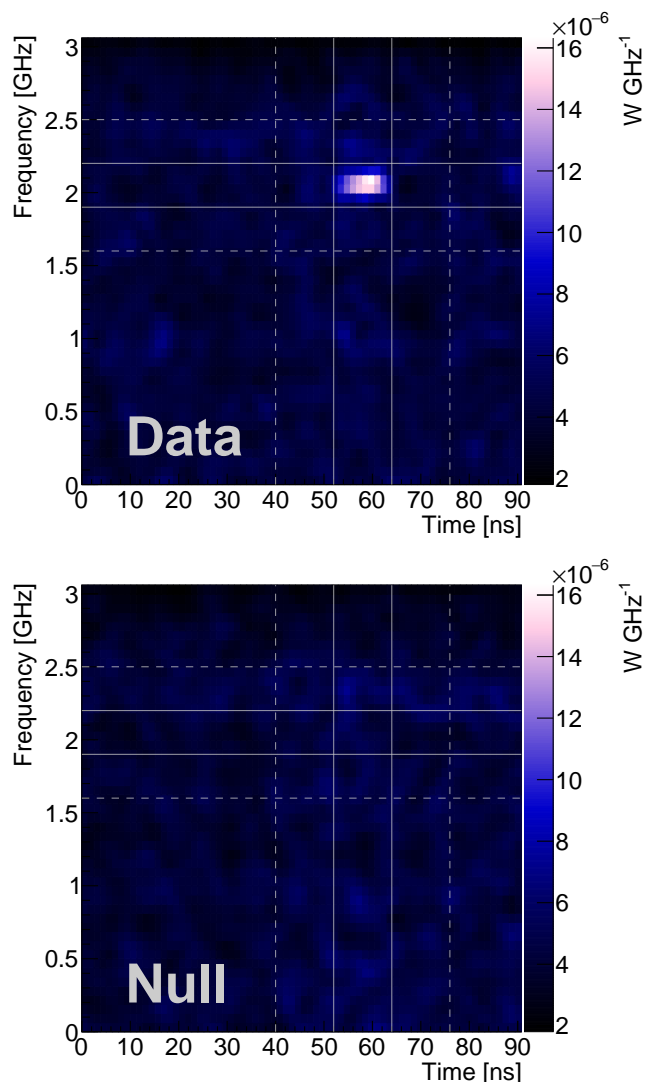


FIG. 2. (Top) Time-versus-frequency (spectrogram) representation of the observed signal in data. This is the average of 200 events in a single signal-run. (Bottom) The same representation for the associated null data set for this sub-run. In both plots, the cross-hairs indicate the signal and sideband regions, used to calculate the significance as described in the main text.

ulation of the same signal-run (including models of the actual antennas used, the same ionization profile, and the same target material), and a comparison to the RadioScatter simulation code [49], which is particle-level and runs within GEANT4 [50]. The simulations have been scaled by a few percent to allow comparison of the waveform shapes and aligned in time with the data. The plasma lifetime is set to $\tau = 3$ ns in the simulation.

Several checks were performed to establish that the observed signal has properties consistent with a radar scatter. The first and most obvious is the observation that the signal scales with the transmitter output power. This is shown in Figure 4, where we plot the effective scattering cross section, σ_{eff} ,

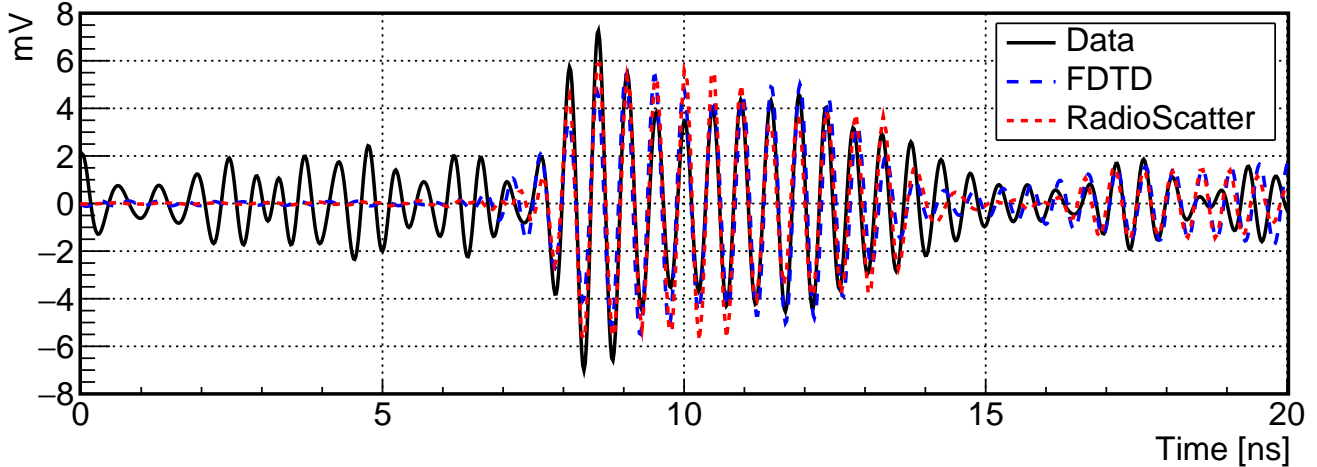


FIG. 3. An example time-domain average of the highest-SNR reflections from a signal-run (solid black), compared to the output of an FDTD simulation for the same signal-run (dashed red), and a RadioScatter simulation for the same signal-run (dashed cyan). The plasma lifetime for the simulation is 3 ns.

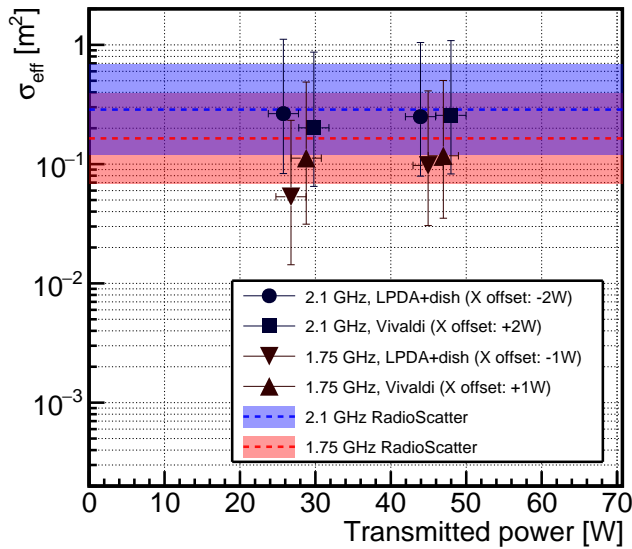


FIG. 4. The effective scattering cross section, σ_{eff} , as a function of transmitter output power, for various receiving antennas (LPDA+dish and Vivaldi) and 2 different frequencies. Errors are statistical and systematic, and dominated by the latter. Each set of 4 points has been clustered around the true X axis value, for clarity, with the offset indicated in the figure legend. The solid bands are σ_{eff} from RadioScatter including statistical and systematic errors.

as a function of transmitter power. This expression, discussed in [28], is a measure of the effective ‘size’ of the reflecting region, should have a weak dependence on frequency at these energies, and should be constant with transmit power. All of these attributes are observed for the signal, which is shown in comparison to RadioScatter simulation (solid bands, including systematic error of HDPE collisional frequency, which is

Systematic	Est. error (dB)	dependence
Room effects	3	A,F,G
Antenna gain/orientation	1	A,F
Cable loss measurement	1	P
TX output power	2	P,G

TABLE I. Sources of systematic error (in dB of received power), and their associated estimated errors, used in Figure 4. Indicated in the right column is the dependence of the individual systematic on the data, either antenna-to-antenna dependent (A), frequency dependent (F), power dependent (P) or globally dependent (G).

ionization energy dependent [51]). The errors in the measurement of σ_{eff} include statistical and systematic uncertainties, and the systematic errors are tabulated in Table I along with the dependence of each error. Some errors affect the overall level of all received signal amplitudes (globally dependent) while others would, for example, introduce systematic offsets between antennas (antenna-to-antenna dependent). Trending of the signal with TX or RX baselines was not observed, owing to the fact that our antennas were not in the diffractive far field. This non-observation of such trends was verified by FDTD simulations.

Because the signal is so small relative to the beam splash, and the null hypothesis relies on a linear combination of background components, an obvious concern is a non-linearity in the overall system. After the run, a series of tests were performed in which CW at the same frequency and amplitude as T576 was amplified and broadcast via a Vivaldi antenna, and another Vivaldi, connected to an oscilloscope, was set up as a receiver. A high-voltage pulse with similar spectral content to the beam splash was broadcast simultaneously. The same analysis technique explained here, involving construction of null data and SVD-filtration, was performed on these data, and no excess was observed.

To establish a significance against a random fluctuation of the background, we generated $N = 10^7$ sets of 100 null events via bootstrapping, made an average spectrogram (like in Figure 2) for each set, and evaluated a test statistic of the sideband-subtracted power excess in the signal region. The signal region, tuned on a discarded subset of the data, is outlined in Figure 2. The value of the test statistic (μW ns) in the null data is $TS_{\text{null}} = 2.20_{-6.20}^{+6.56}$. The value of the test statistic in the measured data is $TS_{\text{data}} = 61.2_{-6.58}^{+7.40}$, well in excess of the 5σ quantile.

Conclusions.— In this letter, we have presented the observation of a radar reflection from a particle-shower induced cascade in a dense material. We have shown that the signal is in good agreement with theoretical expectations, and has a negligible probability of being a background fluctuation. This detection has promising implications for UHE neutrino detection, particularly in the 10-100 PeV range.

Acknowledgments.— We thank the personnel at SLAC for providing us with excellent, stable beam and a safe, productive work environment. We also thank David Saltzberg for invaluable assistance during both runs of T576, and John Beacom for comments and revisions of early drafts of this letter. This work was performed in part under SLAC DOE Contract DE-AC02-76SF00515. SP was partially supported by a US Department of Energy Office of Science Graduate Student Research (SCGSR) award, administered by the Oak Ridge Institute for Science and Education for the DOE under contract DE-SC-0014664. Computing resources were provided by the Ohio Supercomputer Center. KDdV was supported in part by the Flemish Foundation for Scientific Research FWO-12L3715N, and the European Research Council under the European Unions Horizon 2020 research and innovation programme (grant agreement No 805486). JN and CYK were supported by the Vanguard program from the Taiwan Ministry of Science and Technology.

* prohira.1@osu.edu

- [1] M. G. Aartsen *et al.* (IceCube), *Science* **342**, 1242856 (2013), arXiv:1311.5238 [astro-ph.HE].
- [2] M. Ageron *et al.* (ANTARES), *Nucl. Instrum. Meth.* **A656**, 11 (2011), arXiv:1104.1607 [astro-ph.IM].
- [3] A. D. Avrorin *et al.* (BAIKAL), *Nucl. Instrum. Meth.* **A742**, 82 (2014), arXiv:1308.1833 [astro-ph.IM].
- [4] A. Margiotta (KM3NeT), *Nucl. Instrum. Meth.* **A766**, 83 (2014), arXiv:1408.1392 [astro-ph.IM].
- [5] J. van Santen (IceCube Gen2), *PoS ICRC2017*, 991 (2018).
- [6] G. A. Askar'yan, *Sov. Phys. JETP* **14**, 441 (1962), [*Zh. Eksp. Teor. Fiz.*41,616(1961)].
- [7] D. Saltzberg, P. Gorham, D. Walz, C. Field, R. Iverson, A. Odian, G. Resch, P. Schoessow, and D. Williams, *Phys. Rev. Lett.* **86**, 2802 (2001), arXiv:hep-ex/0011001 [hep-ex].
- [8] I. Kravchenko *et al.*, *Phys. Rev.* **D73**, 082002 (2006), arXiv:astro-ph/0601148 [astro-ph].
- [9] P. Allison *et al.*, *Astropart. Phys.* **35**, 457 (2012), arXiv:1105.2854 [astro-ph.IM].
- [10] P. W. Gorham *et al.* (ANITA), *Astropart. Phys.* **32**, 10 (2009), arXiv:0812.1920 [astro-ph].
- [11] S. Klein *et al.*, *IEEE Transactions on Nuclear Science* **60**, 637 (2013).
- [12] C. Deaconu (ANITA), *PoS ICRC2019*, 867 (2019), arXiv:1908.00923 [astro-ph.HE].
- [13] J. A. Aguilar *et al.*, (2019), arXiv:1907.12526 [astro-ph.HE].
- [14] E. Zas, F. Halzen, and T. Stanev, *Phys. Rev.* **D45**, 362 (1992).
- [15] G. M. Frichter, J. P. Ralston, and D. W. McKay, *Phys. Rev.* **D53**, 1684 (1996), arXiv:astro-ph/9507078 [astro-ph].
- [16] S. Barwick, D. Besson, P. Gorham, and D. Saltzberg, *J. Glaciol.* **51**, 231 (2005).
- [17] O. Scholten, K. Werner, and F. Ruyydi, *Astropart. Phys.* **29**, 94 (2008), arXiv:0709.2872 [astro-ph].
- [18] D. Ardouin, A. Belletoile, C. Berat, D. Breton, D. Charrier, J. Chauvin, M. Chendeb, A. Cordier, S. Dagoret-Campagne, R. Dallier, *et al.*, *Astroparticle Physics* **31**, 192 (2009).
- [19] T. Huege *et al.* (LOPES), *Nucl. Instrum. Meth.* **A662**, S72 (2012), arXiv:1009.0345 [astro-ph.HE].
- [20] A. Aab, P. Abreu, M. Aglietta, M. Ahlers, E. Ahn, I. Albuquerque, I. Allekotte, J. Allen, P. Allison, A. Almela, *et al.*, *Physical Review D* **89**, 052002 (2014).
- [21] K. Belov *et al.* (T-510), *Phys. Rev. Lett.* **116**, 141103 (2016), arXiv:1507.07296 [astro-ph.IM].
- [22] J. Alvarez-Muiz *et al.* (GRAND), (2018), arXiv:1810.09994 [astro-ph.HE].
- [23] S. Wissel, J. Alvarez-Muniz, C. Burch, A. Cummings, W. Carvalho, C. Deaconu, G. Hallinan, K. Hughes, A. Ludwig, E. Oberla, C. Paciaroni, A. Rodriguez, A. Romero-Wolf, H. Schoorlemmer, D. Southall, B. Strutt, M. Vasquez, A. Vieregge, and E. Zas, *PoS ICRC2019* (2019).
- [24] J. Nam, P. Chen, Y. Chen, S. Hsu, J. Huang, M. Huang, C. Kuo, C. Leung, T. Liu, B. Shin, Y. Shiao, M. Wang, S. Wang, C. Hornhuber, and A. Novikov, *PoS ICRC2019* (2019).
- [25] J. H. Adams *et al.*, (2017), arXiv:1703.04513 [astro-ph.HE].
- [26] A. V. Olinto *et al.*, *PoS ICRC2017*, 542 (2018), [35.542(2017)], arXiv:1708.07599 [astro-ph.IM].
- [27] K. D. de Vries, K. Hanson, and T. Meures, *Astropart. Phys.* **60**, 25 (2015), arXiv:1312.4331 [astro-ph.HE].
- [28] S. Prohira and D. Besson, *Nucl. Instrum. Meth.* **A922**, 161 (2019), arXiv:1710.02883 [physics.ins-det].
- [29] M. Chiba *et al.*, *SUSY07* (2007), arXiv:0710.4186v1.
- [30] M. Chiba *et al.*, *AIP Conference Proceedings* **1535**, 45 (2013).
- [31] K. DeVries *et al.*, *Proceedings of Science (ICRC2017)*, 1049 (2017).
- [32] S. Prohira *et al.*, *Phys. Rev.* **D100**, 072003 (2019), arXiv:1810.09914 [hep-ex].
- [33] P. Blackett and C. Lovell, *Proc. Roy. Soc A* **177**, 183 (1941).
- [34] A. C. B. Lovell, *Notes and Records of the Royal Society of London* **47**, 119 (1993).
- [35] T. Matano, M. Nagano, K. Suga, and G. Tanahashi, *Canadian Journal of Physics* **46**, S255 (1968).
- [36] P. Gorham, *Astropart. Phys.* **15**, 177 (2001), arXiv:hep-ex/0001041 [hep-ex].
- [37] J. Stasielak *et al.*, *Astroparticle Physics* **73**, 14 (2016).
- [38] M. I. Bakunov, A. V. Maslov, A. L. Novokovskaya, and A. Kryemadhi, *Astropart. Phys.* **33**, 335 (2010).
- [39] T. Terasawa, T. Nakamura, H. Sagawa, H. Miyamoto, H. Yoshida, and M. Fukushima, *Proceedings of the 31st International Cosmic ray Conference* (2009).
- [40] R. Abbasi *et al.*, *Nucl. Instrum. Meth.* **A767**, 322 (2014), arXiv:1405.0057 [astro-ph.IM].
- [41] R. U. Abbasi *et al.*, *Astropart. Phys.* **87**, 1 (2017), arXiv:1603.05217 [astro-ph.IM].

- [42] M. P. De Haas, M. Kunst, J. M. Warman, and J. B. Verberne, *The Journal of Physical Chemistry* **87**, 4089 (1983).
- [43] R. Weingart, R. Barlett, R. Lee, and W. Hofer, *IEEE Transactions on Nuclear Science* **19**, 15 (1972).
- [44] V. L. Ginzburg and I. M. Frank, *J. Phys.(USSR)* **9**, 353 (1945), [*Zh. Eksp. Teor. Fiz.*16,15(1946)].
- [45] K. D. de Vries *et al.*, *Phys. Rev.* **D98**, 123020 (2018), arXiv:1902.02737 [astro-ph.HE].
- [46] P. W. Gorham, D. P. Saltzberg, P. Schoessow, W. Gai, J. G. Power, R. Konecny, and M. E. Conde, *Phys. Rev. E* **62**, 8590 (2000).
- [47] S. Prohira (T576), (2019), arXiv:1910.11314 [astro-ph.IM].
- [48] A. Bean, J. P. Ralston, and J. Snow, *Nucl. Instrum. Meth.* **A596**, 172 (2008), arXiv:1008.0029 [physics.ins-det].
- [49] S. Prohira, <https://github.com/prchyr/RadioScatter> (2017).
- [50] S. Agostineli *et al.*, *Nuclear Instruments and Methods in Physics Research A* **506**, 250 (2003).
- [51] Y.-K. Kim, K. Irikura, M. Rudd, M. Ali, P. Stone, J. Chang, J. Coursey, R. Dragoset, A. Kishore, K. Olsen, A. Sansonetti, G. Wiersma, D. Zucker, and M. Zucker, “Electron-impact ionization cross section for ionization and excitation database (version 3.0),” (2004).

Multi-messenger observations of a flaring blazar coincident with high-energy neutrino IceCube-170922A

The IceCube, *Fermi*-LAT, MAGIC, *AGILE*, ASAS-SN, HAWC, H.E.S.S., *INTEGRAL*, Kanata, Kiso, Kapteyn, Liverpool telescope, Subaru, *Swift*/*NuSTAR*, VERITAS, and VLA/17B-403 teams ^{*†}

Individual astrophysical sources previously detected in neutrinos are limited to the Sun and the supernova 1987A, whereas the origins of the diffuse flux of high-energy cosmic neutrinos remain unidentified. On 22 September 2017 we detected a high-energy neutrino, IceCube-170922A, with an energy of ~ 290 terra-electronvolts. Its arrival direction was consistent with the location of a known γ -ray blazar TXS 0506+056, observed to be in a flaring state. An extensive multi-wavelength campaign followed, ranging from radio frequencies to γ -rays. These observations characterize the variability and energetics of the blazar and include the first detection of TXS 0506+056 in very-high-energy γ -rays. This observation of a neutrino in spatial coincidence with a γ -ray emitting blazar during an active phase suggests that blazars may be a source of high-energy neutrinos.

Since the discovery of a diffuse flux of high-energy astrophysical neutrinos (1, 2), IceCube has searched for its sources. The only non-terrestrial neutrino sources identified previously are the Sun and the supernova 1987A, producing neutrinos with energies millions of times lower than the high-energy diffuse flux, such that the mechanisms and the environments responsible for the high-energy cosmic neutrinos are still to be ascertained (3, 4). Many candidate source types exist, with Active Galactic Nuclei (AGN) among the most prominent (5), in particular the small fraction of them designated as radio-loud (6). In these AGNs, the central super-massive black hole converts gravitational energy of accreting matter and/or the rotational energy of the black hole into powerful relativistic jets, within which particles can be accelerated to

*The full lists of participating members for each team and their affiliations are provided in the supplementary material.

†Email: analysis@icecube.wisc.edu

high energies. If a number of these particles are protons or nuclei, their interactions with the radiation fields and matter close to the source would give rise to a flux of high-energy pions that eventually decay into photons and neutrinos (7). In blazars (8) – AGNs that have one of the jets pointing close to our line of sight – the observable flux of neutrinos and radiation is expected to be greatly enhanced owing to relativistic Doppler boosting. Blazar electromagnetic (EM) emission is known to be highly variable on time scales from minutes to years (9).

Neutrinos travel largely unhindered by matter and radiation. Even if high-energy photons (TeV and above) are unable to escape the source owing to intrinsic absorption, or are absorbed by interactions with the extragalactic background light (EBL) (10, 11), high-energy neutrinos may escape and travel unimpeded to Earth. An association of observed astrophysical neutrinos with blazars would therefore imply that high-energy protons or nuclei up to energies of at least tens of PeV are produced in blazar jets, suggesting that they may be the birthplaces of the most energetic particles observed in the Universe, the ultra-high energy cosmic rays (12). If neutrinos are produced in correlation with photons, the coincident observation of neutrinos with electromagnetic flares would greatly increase the chances of identifying the source(s). Neutrino detections must therefore be combined with the information from broad-band observations across the electromagnetic spectrum (multi-messenger observations).

To take advantage of multi-messenger opportunities, the IceCube neutrino observatory (13) has established a system of real-time alerts that rapidly notify the astronomical community of the direction of astrophysical neutrino candidates (14). From the start of the program in April 2016 through October 2017, 10 public alerts have been issued for high-energy neutrino candidate events with well-reconstructed directions (15).

We report the detection of a high-energy neutrino by IceCube and the multi-wavelength/multi-instrument observations of a flaring γ -ray blazar, TXS 0506+056, which was found to be positionally coincident with the neutrino direction (16). Chance coincidence of the IceCube-170922A event with the flare of TXS 0506+056 is statistically disfavored at the level of 3σ in models evaluated here associating neutrino and γ -ray production.

The neutrino alert

IceCube is a neutrino observatory with more than 5000 optical sensors embedded in 1 km³ of the Antarctic ice-sheet close to the Amundsen-Scott South Pole Station. The detector consists of 86 vertical strings frozen into the ice 125 m apart, each equipped with 60 digital optical modules (DOMs) at depths between 1450 and 2450 m. When a high-energy muon-neutrino interacts with an atomic nucleus in or close to the detector array, a muon is produced moving through the ice at superluminal speed and creating Cherenkov radiation detected by the DOMs. On 22 September 2017 at 20:54:30.43 Coordinated Universal Time (UTC), a high-energy neutrino-induced muon track event was detected in an automated analysis that is part of IceCube’s real-time alert system. An automated alert was distributed (17) to observers 43 seconds later, providing an initial estimate of the direction and energy of the event. A sequence

of refined reconstruction algorithms was automatically started at the same time, using the full event information. A representation of this neutrino event with the best-fitting reconstructed direction is shown in Figure 1. Monitoring data from IceCube indicate that the observatory was functioning normally at the time of the event.

A Gamma-ray Coordinates Network (GCN) Circular (18) was issued ~ 4 h after the initial notice including the refined directional information (offset 0.14° from the initial direction, see Figure 2). Subsequently, further studies were performed to determine the uncertainty of the directional reconstruction arising from statistical and systematic effects, leading to a best-fitting right ascension (RA) $77.43_{-0.65}^{+0.95}$ and declination (Dec) $+5.72_{-0.30}^{+0.50}$ (degrees, J2000 equinox, 90% containment region). The alert was later reported to be in positional coincidence with the known γ -ray blazar TXS 0506+056 (16), which is located at RA 77.36° and Dec $+5.69^\circ$ (J2000) (19), 0.1° from the arrival direction of the high-energy neutrino.

The IceCube alert prompted a follow-up search by the Mediterranean neutrino telescope ANTARES (acronym for Astronomy with a Neutrino Telescope and Abyss environmental RE-Search) (20). The sensitivity of ANTARES at the declination of IceCube-170922A is about one-tenth that of IceCube's (21) and no neutrino candidates were found in a ± 1 day period around the event time (22).

An energy of 23.7 ± 2.8 TeV was deposited in IceCube by the traversing muon. To estimate the parent neutrino energy, we performed simulations of the response of the detector array, considering that the muon-neutrino might have interacted outside the detector at an unknown distance. We assumed the best-fitting power-law energy spectrum for astrophysical high-energy muon neutrinos, $dN/dE \propto E^{-2.13}$ (2) where N is the number of neutrinos as a function of energy E . The simulations yielded a most probable neutrino energy of 290 TeV, with a 90% confidence level (C.L.) lower limit of 183 TeV, depending only weakly on the assumed astrophysical energy spectrum (25).

The vast majority of neutrinos detected by IceCube arise from cosmic-ray interactions within Earth's atmosphere. Although atmospheric neutrinos are dominant at energies below 100 TeV, their spectrum falls steeply with energy, allowing astrophysical neutrinos to be more easily identified at higher energies. The muon-neutrino astrophysical spectrum, together with simulated data, was used to calculate the probability that a neutrino at the observed track energy and zenith angle in IceCube is of astrophysical origin. This probability, the so-called signalness of the event (14), was reported to be 56.5% (17). Although IceCube can robustly identify astrophysical neutrinos at PeV energies, for individual neutrinos at several hundred TeV, an atmospheric origin cannot be excluded. Electromagnetic observations are valuable to assess the possible association of a single neutrino to an astrophysical source.

Following the alert, IceCube performed a complete analysis of relevant data prior to 31 October 2017. Although no additional excess of neutrinos was found from the direction of TXS 0506+056 near the time of the alert, there are indications at the 3σ level of high-energy neutrino emission from that direction in data prior to 2017, as discussed in a companion paper (26).

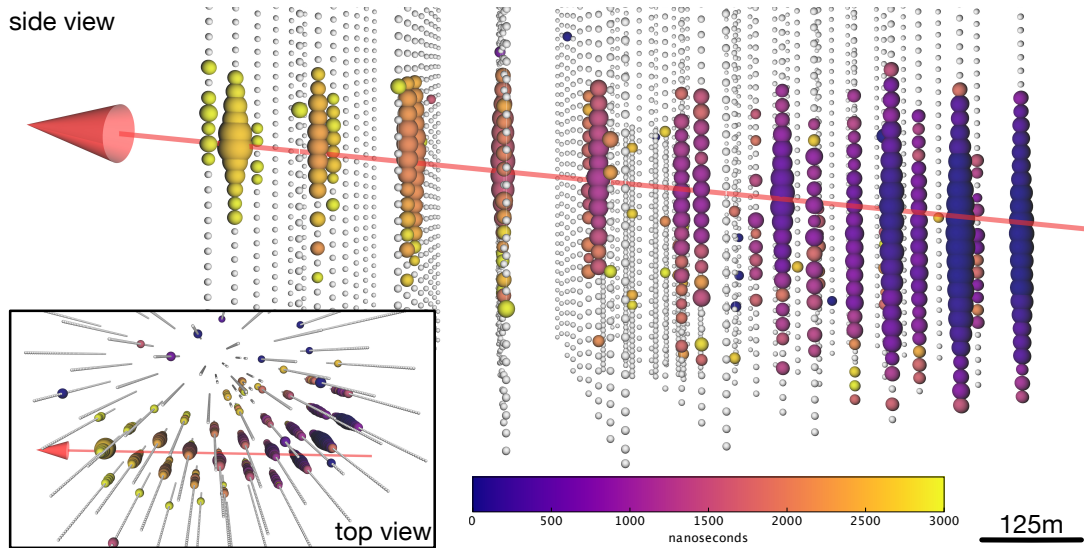


Figure 1: **Event display for neutrino event IceCube-170922A.** The time at which a DOM observed a signal is reflected in the color of the hit, with dark blues for earliest hits and yellow for latest. Time shown are relative to the first DOM hit according to the track reconstruction, and earlier and later times are shown with the same colors as the first and last times, respectively. The total time the event took to cross the detector is ~ 3000 ns. The size of a colored sphere is proportional to the logarithm of the amount of light observed at the DOM, with larger spheres corresponding to larger signals. The total charge recorded is ~ 5800 photoelectrons. Inset is an overhead perspective view of the event. The best-fitting track direction is shown as an arrow, consistent with a zenith angle $5.7^{+0.50}_{-0.30}$ degrees below the horizon.

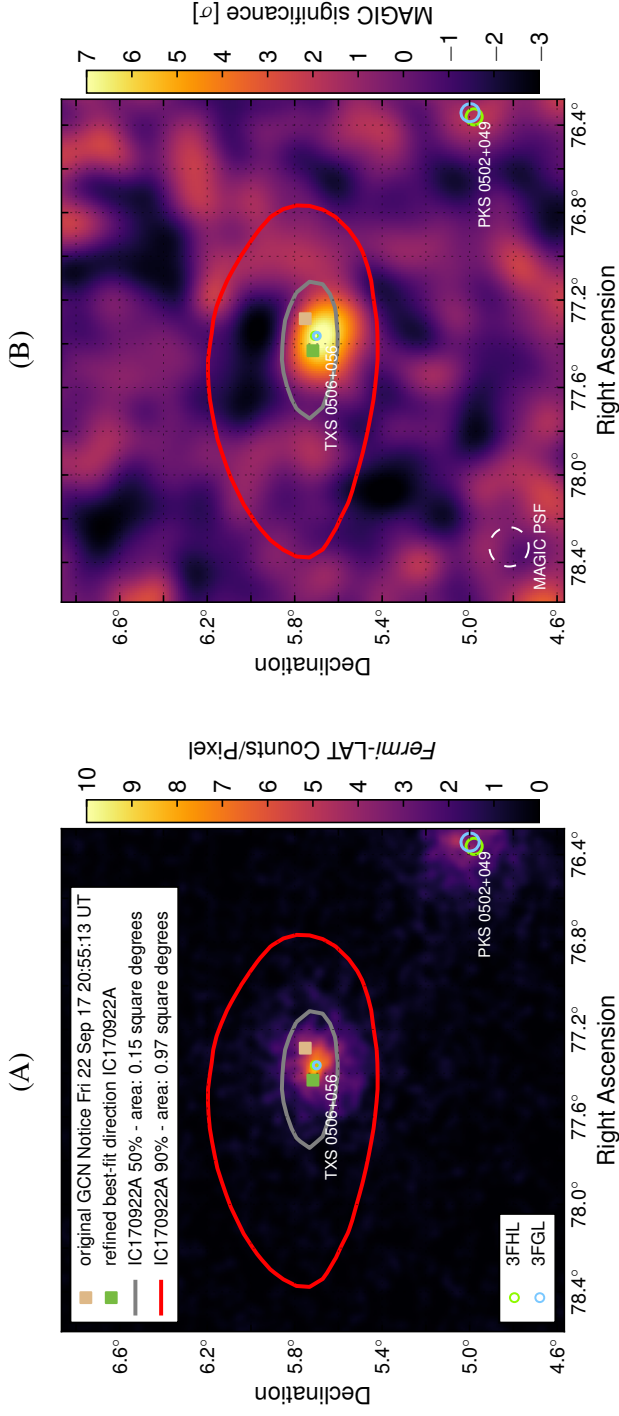


Figure 2: **Fermi-LAT and MAGIC observations of IceCube-170922A's location.** Sky position of IceCube-170922A in J2000 equatorial coordinates overlaying the γ -ray counts from *Fermi*-LAT above 1 GeV (A) and the signal significance as observed by MAGIC (B) in this region. The tan square indicates the position reported in the initial alert and the green square indicates the final best-fitting position from follow-up reconstructions (18). Gray and red curves show the 50% and 90% neutrino containment regions, respectively, including statistical and systematic errors. *Fermi*-LAT data are shown as a photon counts map in 9.5 years of data in units of counts per pixel, using detected photons with energy of 1 to 300 GeV in a 2° by 2° region around TXS0506+056. The map has a pixel size of 0.02° and was smoothed with a 0.02 degree-wide Gaussian kernel. MAGIC data are shown as signal significance for γ -rays above 90 GeV. Also shown are the locations of a γ -ray source observed by *Fermi*-LAT as given in the *Fermi*-LAT Third Source Catalog (3FGL) (23) and the Third Catalog of Hard *Fermi*-LAT Sources (3FHL) (24) source catalogs, including the identified positionally coincident 3FGL object TXS 0506+056. For *Fermi*-LAT catalog objects, marker sizes indicate the 95% C.L. positional uncertainty of the source.

High-energy γ -ray observations of TXS 0506+056

On 28 September 2017, the *Fermi* Large Area Telescope (LAT) Collaboration reported that the direction of origin of IceCube-170922A was consistent with a known γ -ray source in a state of enhanced emission (16). *Fermi*-LAT is a pair-conversion telescope aboard the *Fermi* Gamma-ray Space Telescope sensitive to γ -rays with energies from 20 MeV to greater than 300 GeV (27). Since August 2008, it has operated continuously, primarily in an all-sky survey mode. Its wide field of view of ~ 2.4 steradian provides coverage of the entire γ -ray sky every 3 hours. The search for possible counterparts to IceCube-170922A was part of the *Fermi*-LAT collaboration's routine multi-wavelength/multi-messenger program.

Inside the error region of the neutrino event, a positional coincidence was found with a previously cataloged γ -ray source, 0.1° from the best-fitting neutrino direction. TXS 0506+056 is a blazar of BL Lacertae (BL Lac) type. Its redshift of $z = 0.3365 \pm 0.0010$ was measured only recently based on the optical emission spectrum in a study triggered by the observation of IceCube-170922A (28).

TXS 0506+056 is a known *Fermi*-LAT γ -ray source, appearing in three catalogs of *Fermi* sources (23, 24, 29) at energies above 0.1, 50, and 10 GeV, respectively. An examination of the *Fermi* All-Sky Variability Analysis (FAVA) (30) photometric light curve for this object showed that TXS 0506+056 had brightened considerably in the GeV band starting in April 2017 (16). Independently, a γ -ray flare was also found by *Fermi*'s Automated Science Processing (ASP, (25)). Such flaring is not unusual for a BL Lac object, and would not have been followed up as extensively if the neutrino were not detected.

Figure 3 shows the *Fermi*-LAT light curve and the detection time of the neutrino alert. The light curve of TXS 0506+056 from August 2008 to October 2017 was calculated in bins of 28 days for the energy range above 0.1 GeV. An additional light curve with 7-day bins was calculated for the period around the time of the neutrino alert. The γ -ray flux of TXS 0506+056 in each time bin was determined through a simultaneous fit of this source and the other *Fermi*-LAT sources in a 10° by 10° region of interest along with the Galactic and isotropic diffuse backgrounds, using a maximum likelihood technique (25). The integrated γ -ray flux of TXS 0506+056 for $E > 0.1$ GeV, averaged over all *Fermi*-LAT observations spanning 9.5 years, is $(7.6 \pm 0.2) \times 10^{-8} \text{ cm}^{-2} \text{ s}^{-1}$. The highest flux observed in a single 7-day light curve bin was $(5.3 \pm 0.6) \times 10^{-7} \text{ cm}^{-2} \text{ s}^{-1}$, measured in the week 4 to 11 July 2017. Strong flux variations were observed during the γ -ray flare, the most prominent being a flux increase from $(7.9 \pm 2.9) \times 10^{-8} \text{ cm}^{-2} \text{ s}^{-1}$ in the week 8 to 15 August 2017 to $(4.0 \pm 0.5) \times 10^{-7} \text{ cm}^{-2} \text{ s}^{-1}$ in the week 15 to 22 August 2017.

The Astro-Rivelatore Gamma a Immagini Leggero (*AGILE*) γ -ray telescope (31) confirmed the elevated level of γ -ray emission at energies above 0.1 GeV from TXS 0506+056 in a 13-day window (10 to 23 September 2017). The *AGILE* measured flux of $(5.3 \pm 2.1) \times 10^{-7} \text{ cm}^{-2} \text{ s}^{-1}$ is consistent with the *Fermi*-LAT observations in this time period.

High-energy γ -ray observations are shown in Figures 3 and 4. Details on the *Fermi*-LAT and *AGILE* analyses can be found in (25).

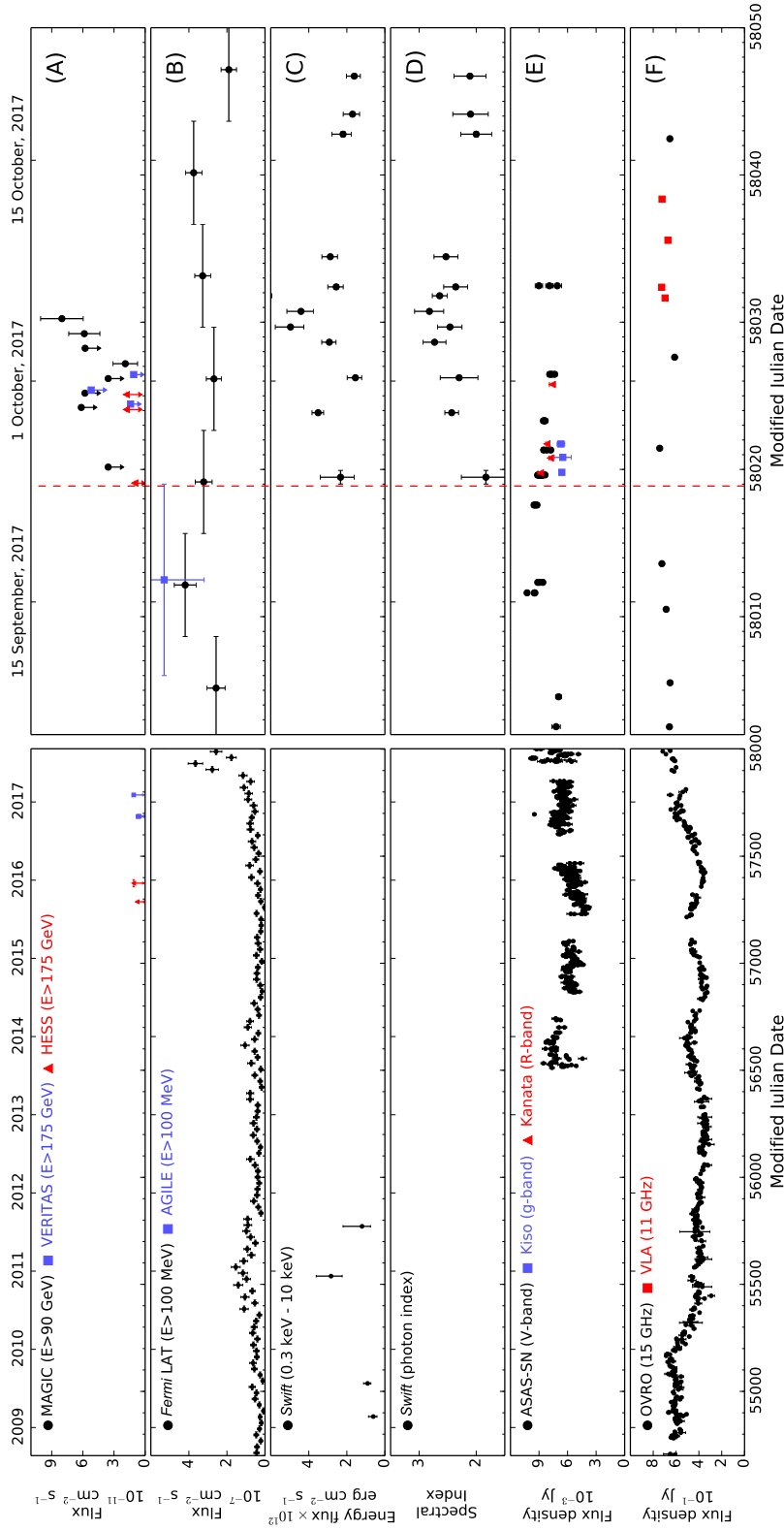


Figure 3: Time-dependent multi-wavelength observations of TXS 0506+056 before and after IceCube-170922A. Significant variability of the electromagnetic emission can be observed in all displayed energy bands, with the source being in a high emission state around the time of the neutrino alert. From top to bottom: (A) VHE γ -ray observations by MAGIC, H.E.S.S. and VERITAS; (B) high-energy γ -ray observations by *Fermi*-LAT and *AGILE*; (C and D) x-ray observations by *Swift* XRT; (E) optical light curves from ASAS-SN, Kiso/KWFC, and Kanata/HONIR; and (F) radio observations by OVRO and VLA. The red dashed line marks the detection time of the neutrino IceCube-170922A. The left set of panels shows measurements between MJD 54700 (22 August, 2008) and MJD 58002 (6 September, 2017). The set of panels on the right shows an expanded scale for time range MJD 58002 – MJD 58050 (24 October, 2017). The *Fermi*-LAT light curve is binned in 28 day bins on the left panel, while finer 7 day bins are used on the expanded panel. A VERITAS limit from MJD 58019.40 (23 September, 2017) of $2.1 \times 10^{-10} \text{ cm}^{-2} \text{ s}^{-1}$ is off the scale of the plot and not shown.

Very-high-energy γ -ray observations of TXS 0506+056

Following the announcement of IceCube-170922A, TXS 0506+056 was observed by several ground based Imaging Atmospheric Cherenkov Telescopes (IACTs). A total of 1.3 hours of observations in the direction of the blazar TXS 0506+056 were taken using the High-Energy Stereoscopic System (H.E.S.S.) (32), located in Namibia, on 23 September, 2017 (Modified Julian Date (MJD) 58019), ~ 4 hours after the circulation of the neutrino alert. A 1-hour follow-up observation of the neutrino alert under partial cloud coverage was performed using the Very Energetic Radiation Imaging Telescope Array System (VERITAS) γ -ray telescope array (33), located in Arizona, USA, later on the same day, ~ 12 hours after the IceCube detection. Both telescopes made additional observations on subsequent nights but neither detected γ -ray emission from the source [see Figure 3 and (25)]. Upper limits at 95% C.L. on the γ -ray flux were derived accordingly (assuming the measured spectrum, see below): $7.5 \times 10^{-12} \text{ cm}^{-2} \text{ s}^{-1}$ during the H.E.S.S. observation period, and $1.2 \times 10^{-11} \text{ cm}^{-2} \text{ s}^{-1}$ during the VERITAS observations, both for energies $E > 175 \text{ GeV}$.

The Major Atmospheric Gamma Imaging Cherenkov (MAGIC) Telescopes (34) observed TXS 0506+056 for 2 hours on 24 September 2017 (MJD 58020) under non-optimal weather conditions and then for a period of 13 hours from 28 September to 4 October 2017 (MJD 58024–58030) under good conditions. MAGIC consists of two 17 m telescopes, located at the Roque de los Muchachos Observatory on the Canary Island of La Palma (Spain).

No γ -ray emission from TXS 0506+056 was detected in the initial MAGIC observations on 24 September 2017, and an upper limit was derived on the flux above 90 GeV of $3.6 \times 10^{-11} \text{ cm}^{-2} \text{ s}^{-1}$ at 95% C.L. (assuming a spectrum $dN/dE \propto E^{-3.9}$). However, prompted by the *Fermi*-LAT detection of enhanced γ -ray emission, MAGIC performed another 13 hours of observations of the region starting 28 September 2017. Integrating the data, MAGIC detected a significant very-high-energy (VHE) γ -ray signal (35) corresponding to 374 ± 62 excess photons, with observed energies up to about 400 GeV. This represents a 6.2σ excess over expected background levels (25). The day-by-day light curve of TXS 0506+056 for energies above 90 GeV is shown in Figure 3. The probability that a constant flux is consistent with the data is less than 1.35%. The measured differential photon spectrum (Figure 4) can be described over the energy range of 80 to 400 GeV by a simple power law $dN/dE \propto E^\gamma$ with a spectral index $\gamma = -3.9 \pm 0.4$ and a flux normalization of $(2.0 \pm 0.4) \times 10^{-10} \text{ TeV}^{-1} \text{ cm}^{-2} \text{ s}^{-1}$ at $E = 130 \text{ GeV}$. Uncertainties are statistical only. The estimated systematic uncertainties are $< 15\%$ in the energy scale, 11 to 18% in the flux normalization and ± 0.15 for the power-law slope of the energy spectrum (34). Further observations after 4 October 2017 were prevented by the full Moon.

An upper limit to the redshift of TXS 0506+056 can be inferred from VHE γ -ray observations using limits on the attenuation of the VHE flux due to interaction with the EBL. Details on the method are available in (25). The obtained upper limit ranges from 0.61 to 0.98 at a 95% C.L., depending on the EBL model used. These upper limits are consistent with the measured redshift of $z = 0.3365$ (28).

No γ -ray source above 1 TeV at the location of TXS 0506+056 was found in survey data of the High Altitude Water Cherenkov (HAWC) γ -ray observatory (36), either close to the time of the neutrino alert, or in archival data taken since November 2014 (25).

VHE γ -ray observations are shown in Figures 3 and 4. All measurements are consistent with the observed flux from MAGIC, considering the differences in exposure, energy range and observation periods.

Radio, optical and x-ray observations

The Karl G. Jansky Very Large Array (VLA) (37) observed TXS 0506+056 starting 2 weeks after the alert in several radio bands from 2 to 12 GHz (38), detecting significant radio flux variability and some spectral variability of this source. The source is also in the long-term blazar monitoring program of the Owens Valley Radio Observatory (OVRO) 40-m telescope at 15 GHz (39). The light curve shows a gradual increase in radio emission during the 18 months preceding the neutrino alert.

Optical observations were performed by the All-Sky Automated Survey for Supernovae (ASAS-SN) (40), the Liverpool telescope (41), the Kanata Telescope (42), the Kiso Schmidt Telescope (43), the high resolution spectrograph (HRS) on the Southern African Large Telescope (SALT) (44), the Subaru telescope Faint Object Camera and Spectrograph (FOCAS) (45) and the X-SHOOTER instrument on the Very Large Telescope (VLT) (46). The V band flux of the source is the highest observed in recent years, and the spectral energy distribution has shifted towards blue wavelengths. Polarization was detected by Kanata in the R band at the level of 7%. Redshift determination for BL Lac objects is difficult owing to the non-thermal continuum from the nucleus outshining the spectral lines from the host galaxies. Attempts were made using optical spectra from the Liverpool, Subaru and VLT telescopes to measure the redshift of TXS 0506+056, but only limits could be derived, [see, e.g., (47)]. The redshift of TXS0506+056 was later determined to be $z = 0.3365 \pm 0.0010$ using the Gran Telescopio Canarias (28).

X-ray observations were made by the x-Ray Telescope (XRT) on the *Neil Gehrels Swift Observatory* (0.3 to 10 keV) (48), *MAXI* Gas Slit Camera (GSC) (2 to 10 keV) (49), Nuclear Spectroscopic Telescope Array (*NuSTAR*) (3 to 79 keV) (50) and the INTERNATIONAL Gamma-Ray Astrophysics Laboratory (*INTEGRAL*) (20 to 250 keV) (51), with detections by *Swift* and *NuSTAR*. In a 2.1 square degree region around the neutrino alert, *Swift* identified nine x-ray sources, including TXS 0506+056.

Swift monitored the x-ray flux from TXS 0506+056 for 4 weeks after the alert, starting 23 September 2017 00:09:16 UT, finding clear evidence for spectral variability (see Figure 3D). The strong increase in flux observed at VHE energies over several days up until MJD 58030 (4 October 2017) correlates well with an increase in the x-ray emission in this period of time. The spectrum of TXS 0506+056 observed in the week after the flare is compatible with the sum of two power-law spectra, a soft spectrum with index -2.8 ± 0.3 in the soft x-ray band covered

by *Swift* XRT and a hard spectrum with index -1.4 ± 0.3 in the hard x-ray band covered by *NuSTAR* (25). Extrapolated to 20 MeV, the *NuSTAR* hard-spectrum component connects smoothly to the plateau (index -2) component observed by the *Fermi*-LAT between 0.1 and 100 GeV and the soft VHE γ -ray component observed by MAGIC (compare Fig. 4). Taken together, these observations provide a mostly complete, contemporaneous picture of the source emissions from 0.3 keV to 400 GeV, more than nine orders of magnitude in photon energy.

Figures 3 and 4 summarize the multi-wavelength light curves and the changes in the broad-band spectral energy distribution (SED), compared to archival observations. Additional details about the radio, optical, and x-ray observations can be found in (25).

Chance coincidence probability

Data obtained from multi-wavelength observations of TXS 0506+056 can be used to constrain the blazar-neutrino chance coincidence probability. This coincidence probability is a measure of the likelihood that a neutrino alert like IceCube-170922A is correlated by chance with a flaring blazar, considering the large number of known γ -ray sources and the modest number of neutrino alerts.

Given the large number of potential neutrino source classes available, no a priori blazar-neutrino coincidence model was selected ahead of the alert. After the observation, however, several correlation scenarios were considered and tested to quantify the a posteriori significance of the observed coincidence. Testing multiple models is important as the specific assumptions about the correlation between neutrinos and γ rays have an impact on the chance coincidence probability. In each case, the probability to obtain, by chance, a degree of correlation at least as high as that observed for IceCube-170922A was calculated using simulated neutrino alerts and the light curves of *Fermi*-LAT γ -ray sources. Given the continuous all-sky monitoring of the *Fermi*-LAT since 2008, all tests utilized 28-day binned γ -ray light curves above 1 GeV from 2257 extragalactic *Fermi*-LAT sources, derived in the same manner as used for the analysis of TXS 0506+056 γ -ray data.

To calculate the chance probabilities, a likelihood ratio test is used that allows different models of blazar-neutrino flux correlation to be evaluated in a consistent manner. All models assume that at least some of the observed γ -ray flux is produced in the same hadronic interactions that would produce high-energy neutrinos within the source. Our first model assumes that the neutrino flux is linearly correlated with the high-energy γ -ray energy flux (4). In this scenario, neutrinos are more likely to be produced during periods of bright, hard γ -ray emission. In the second model, the neutrino flux is modeled as strongly tied to variations in the observed γ -ray flux, regardless of the average flux of γ -rays. Here, a weak or a strong γ -ray source is equally likely to be a neutrino source if the neutrino is temporally correlated with variability in the γ -ray light curve. Third, we consider a correlation of the neutrino flux with the VHE γ -ray flux. Because hadronic acceleration up to a few PeV is required to explain the detected neutrino energy, VHE γ -ray sources are potential progenitors. Full details and results from these

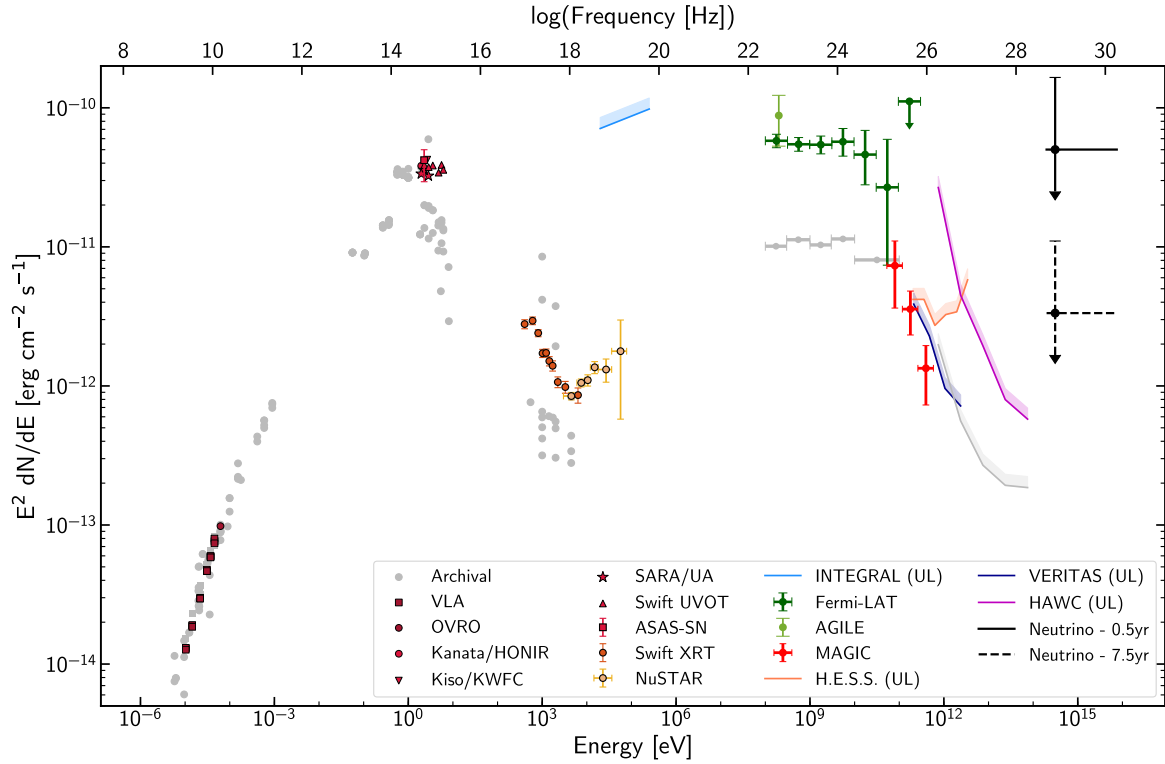


Figure 4: **Broadband spectral energy distribution for the blazar TXS 0506+056.** The SED is based on observations obtained within 14 days of the detection of the IceCube-170922A event. The $E^2 dN/dE$ vertical axis is equivalent to a νF_ν scale. Contributions are provided by the following instruments: VLA (38), OVRO (39), Kanata Hiroshima Optical and Near-Infrared camera (HONIR) (52), Kiso and the Kiso Wide Field Camera (KWFC) (43), South-eastern Association for Research in Astronomy Observatory (SARA/UA) (53), ASAS-SN (54), *Swift* Ultraviolet and Optical Telescope (UVOT) and XRT (55), *NuSTAR* (56), *INTEGRAL* (57), *AGILE* (58), *Fermi-LAT* (16), MAGIC (35), VERITAS (59), H.E.S.S. (60) and HAWC (61). Specific observation dates and times are provided in (25). Differential flux upper limits (shown as colored bands and indicated as “UL” in the legend) are quoted at the 95% C.L. while markers indicate significant detections. Archival observations are shown in gray to illustrate the historical flux level of the blazar in the radio-to-keV range as retrieved from the ASDC SED Builder (62), and in the γ -ray band as listed in the *Fermi-LAT* 3FGL catalog (23) and from an analysis of 2.5 years of HAWC data. The γ -ray observations have not been corrected for absorption owing to the EBL. SARA/UA, ASAS-SN, and Kiso/KWFC observations have not been corrected for Galactic attenuation. The electromagnetic SED displays a double-bump structure, one peaking in the optical-ultraviolet range and the second one in the GeV range, which is characteristic of the non-thermal emission from blazars. Even within this 14-day period, there is variability observed in several of the energy bands shown (see Figure 3) and the data are not all obtained simultaneously. Representative $\nu_\mu + \bar{\nu}_\mu$ neutrino flux upper limits that produce on average one detection like IceCube-170922A over a period of 0.5 (solid black line) and 7.5 years (dashed black line) are shown assuming a spectrum of $dN/dE \propto E^{-2}$ at the most probable neutrino energy (311 TeV).

analyses are presented in (25).

The neutrino IceCube-170922A was found to arrive in a period of flaring activity in high-energy γ -rays. Prior to IceCube-170922A, nine public alerts had been issued by the IceCube real-time system. Additionally, 41 archival events have been identified among the IceCube data recorded since 2010, before the start of the real-time program in April 2016, which would have caused alerts if the real-time alert system had been in place. These events were also tested for coincidence with the γ -ray data.

Chance coincidence of the neutrino with the flare of TXS 0506+056 is disfavored at the 3σ level in any scenario where neutrino production is linearly correlated with γ -ray production or with γ -ray flux variations. This includes look-elsewhere corrections for all 10 alerts issued previously by IceCube and the 41 archival events. One of the neutrino events that would have been sent as an alert and had a good angular resolution ($<5^\circ$) is in a spatial correlation with the γ -ray blazar 3FGL J1040.4+0615. However, this source was not in a particularly bright emission state at the detection time of the corresponding neutrino. Therefore, a substantially lower test statistic would be obtained in the chance correlation tests defined in this paper (25).

We have investigated how typical the blazar TXS 0506+056 is among those blazars that might have given rise to a coincident observation similar to the one reported here. A simulation that assumes that the neutrino flux is linearly correlated with the blazar γ -ray energy flux shows that in 14% of the signal realizations we would find a neutrino coincident with a similarly bright γ -ray state as that observed for TXS 0506+056 (25). The detection of a single neutrino does not allow us to probe the details of neutrino production models or measure the neutrino-to- γ -ray production ratio. Further observations will be needed to unambiguously establish a correlation between high-energy neutrinos and blazars, as well as to understand the emission and acceleration mechanism in the event of a correlation.

Discussion

Blazars have often been suggested as potential sources of high-energy neutrinos. The calorimetric high-energy output of certain candidate blazars is high enough to explain individual observed IceCube events at 100 TeV to 1 PeV energies (63). Spatial coincidences between catalogs of blazars and neutrinos have been examined in (64), while (65) investigated one shower-like event with several thousand square degrees angular uncertainty observed in time coincidence with a blazar outburst. A track-like event, IceCube-160731, has been previously connected to a flaring γ -ray source (66). However, the limited evidence for a flaring source in the multi-wavelength coverage did not permit an identification of the source type of the potential counterpart (66).

Owing to the precise direction of IceCube-170922A, combined with extensive multi-wavelength observations, a chance correlation between a high-energy neutrino and the potential counterpart can be rejected at the 3σ level. Considering the association between IceCube-170922A and TXS 0506+056, γ -ray blazars are strong candidate sources for at least a fraction of the observed astrophysical neutrinos. Earlier studies of the cross-correlation between IceCube events

and the γ -ray blazar population observed by *Fermi*-LAT demonstrated that these blazars can only produce a fraction of the observed astrophysical neutrino flux above 10 TeV (4). Although these limits constrain the contribution from blazars to the diffuse neutrino background, the potential association of one or two high-energy neutrinos to blazars over the total observing time of IceCube is fully compatible with the constraint.

Adopting cosmological parameters (67) $H_0 = 67.8$, $\Omega_m = 0.308$, $\Omega_\lambda = 0.692$, where H_0 is the Hubble constant, Ω_m is the matter density and Ω_λ is the dark energy density, the observed redshift of $z = 0.3365$ implies an isotropic γ -ray luminosity between 0.1 GeV and 100 GeV of 1.3×10^{47} erg s⁻¹ in the ± 2 weeks around the arrival time of the IceCube neutrino, and a luminosity of 2.8×10^{46} erg s⁻¹, averaged over all *Fermi*-LAT observations. Observations in the optical, x-ray, and VHE γ -ray bands show typical characteristics of blazar flares: strong variability on time scales of a few days, and an indication of a shift of the synchrotron emission peak towards higher frequencies. VHE γ -ray emission is found to change by a factor of ~ 4 within just 3 days. Similarly, the high-energy γ -ray energy band shows flux variations up to a factor of ~ 5 from 1 week to the next.

No other neutrino event that would have passed the selection criteria for a high-energy alert was observed from this source since the start of IceCube observations in May 2010. The muon neutrino fluence for which we would expect to detect one high-energy alert event with IceCube in this period of time is 2.8×10^{-3} erg cm⁻². A power-law neutrino spectrum is assumed in this calculation with an index of -2 between 200 TeV and 7.5 PeV, the range between the 90% C.L. lower and upper limits for the energy of the observed neutrino (see (25) for details).

The fluence can be expressed as an integrated energy flux if we assume a time period during which the source was emitting neutrinos. For a source that emits neutrinos only during the ~ 6 month period corresponding to the duration of the high-energy γ -ray flare, the corresponding average integrated muon neutrino energy flux would be 1.8×10^{-10} erg cm⁻² s⁻¹. Alternatively, the average integrated energy flux of a source that emits neutrinos over the whole observation period of IceCube, *i.e.* 7.5 years, would be 1.2×10^{-11} erg cm⁻² s⁻¹. These two benchmark cases are displayed in Figure 4. In an ensemble of faint sources with a summed expectation of order 1, we would anticipate observing a neutrino even if the individual expectation value is $\ll 1$. This is expressed by the downward arrows on the neutrino flux points in Figure 4.

The two cases discussed above correspond to average isotropic muon neutrino luminosities of 7.2×10^{46} erg s⁻¹ for a source that was emitting neutrinos in the ~ 6 month period of the high-energy γ -ray flare, and 4.8×10^{45} erg s⁻¹ for a source that emitted neutrinos throughout the whole observation period. This is similar to the luminosity observed in γ -rays, and thus broadly consistent with hadronic source scenarios (68).

A neutrino flux that produces a high-energy alert event can, over time, produce many lower-energy neutrino-induced muons in IceCube. A study of neutrino emission from TXS 0506+056 prior to the high-energy γ -ray flare, based on the investigation of these lower-energy events, is reported in a companion paper (26).

Supplementary Materials

Supplementary Text

Table S1 — S10
Fig S1 — S7
References (69 — 116)

References

1. M. G. Aartsen, *et al.*, *Science* **342**, 1242856 (2013).
2. M. G. Aartsen, *et al.*, *Astrophys. J.* **833**, 3 (2016).
3. M. G. Aartsen, *et al.*, *Astrophys. J.* **835**, 151 (2017).
4. M. G. Aartsen, *et al.*, *Astrophys. J.* **835**, 45 (2017).
5. F. W. Stecker, C. Done, M. H. Salamon, P. Sommers, *Phys. Rev. Lett.* **66**, 2697 (1991).
6. K. Mannheim, *Astropart. Phys.* **3**, 295 (1995).
7. M. Petropoulou, S. Dimitrakoudis, P. Padovani, A. Mastichiadis, E. Resconi, *Mon. Not. Roy. Astron. Soc.* **448**, 2412 (2015).
8. C. M. Urry, P. Padovani, *Publ. Astron. Soc. Pac.* **107**, 803 (1995).
9. M.-H. Ulrich, L. Maraschi, C. M. Urry, *Ann. Rev. Astron. Astrophys.* **35**, 445 (1997).
10. M. G. Hauser, E. Dwek, *Ann. Rev. Astron. Astrophys.* **39**, 249 (2001).
11. F. W. Stecker, O. C. de Jager, M. H. Salamon, *Astrophys. J. Lett.* **390**, L49 (1992).
12. K. A. Olive, *et al.*, *Chin. Phys.* **C38**, 090001 (2014).
13. M. G. Aartsen, *et al.*, *J. Instrum.* **12**, P03012 (2017).
14. M. G. Aartsen, *et al.*, *Astropart. Phys.* **92**, 30 (2017).
15. GCN/AMON Notices, <https://gcn.gsfc.nasa.gov/amon.html>. Accessed: 26 April 2018.
16. Y. T. Tanaka, S. Buson, D. Kocevski, *The Astronomer's Telegram* **10791** (2017).
17. IceCube Collaboration, *GRB Coordinates Network/AMON Notices* **50579430_130033** (2017).
18. IceCube Collaboration, *GRB Coordinates Network, Circular Service* **21916** (2017).
19. G. E. Lanyi, *et al.*, *Astron. J.* **139**, 1695 (2010).

20. M. Ageron, *et al.*, *Nucl. Instr. Meth. Phys. Res.* **A656**, 11 (2011).
21. A. Albert, *et al.*, *Phys. Rev.* **D96**, 082001 (2017).
22. D. Dornic, A. Coleiro, *The Astronomer's Telegram* **10773** (2017).
23. F. Acero, *et al.*, *Astrophys. J. Suppl.* **218**, 23 (2015).
24. M. Ajello, *et al.*, *Astrophys. J. Suppl.* **232**, 18 (2017).
25. Materials and methods are available as supplementary materials on *Science Online*.
26. IceCube Collaboration, *Science* **this issue** (2018).
27. W. B. Atwood, *et al.*, *Astrophys. J.* **697**, 1071 (2009).
28. S. Paiano, R. Falomo, A. Treves, R. Scarpa, *Astrophys. J.* **854**, L32 (2018).
29. M. Ackermann, *et al.*, *Astrophys. J. Suppl.* **222**, 5 (2016).
30. S. Abdollahi, *et al.*, *Astrophys. J.* **846**, 34 (2017).
31. M. Tavani, *et al.*, *Astron. Astrophys.* **502**, 995 (2009).
32. F. Aharonian, *et al.*, *Astron. Astrophys.* **457**, 899 (2006).
33. J. Holder, *et al.*, *Astropart. Phys.* **25**, 391 (2006).
34. J. Aleksić, *et al.*, *Astropart. Phys.* **72**, 76 (2016).
35. R. Mirzoyan, *The Astronomer's Telegram* **10817** (2017).
36. A. U. Abeysekara, *et al.*, *Astrophys. J.* **843**, 39 (2017).
37. R. A. Perley, C. J. Chandler, B. J. Butler, J. M. Wrobel, *Astrophys. J. Lett.* **739**, L1 (2011).
38. A. J. Tetarenko, G. R. Sivakoff, A. E. Kimball, J. C. A. Miller-Jones, *The Astronomer's Telegram* **10861** (2017).
39. J. L. Richards, *et al.*, *Astrophys. J. Suppl.* **194**, 29 (2011).
40. C. S. Kochanek, *et al.*, *Publ. Astron. Soc. Pac.* **129**, 104502 (2017).
41. I. A. Steele, *et al.*, *Ground-based Telescopes*, J. M. Oschmann, Jr., ed. (2004), vol. 5489 of *Proc. SPIE*, pp. 679–692.
42. H. Akitaya, *et al.*, *Ground-based and Airborne Instrumentation for Astronomy V* (2014), vol. 9147 of *Proc. SPIE*, p. 91474O.

43. S. Sako, *et al.*, *Ground-based and Airborne Instrumentation for Astronomy IV* (2012), vol. 8446 of *Proc. SPIE*, p. 84466L.
44. L. A. Crause, *et al.*, *Ground-based and Airborne Instrumentation for Astronomy V* (2014), vol. 9147 of *Proc. SPIE*, p. 91476T.
45. N. Kashikawa, *et al.*, *Publ. Astron. Soc. Jpn.* **54**, 819 (2002).
46. J. Vernet, *et al.*, *Astron. Astrophys.* **536**, A105 (2011).
47. A. Coleiro, S. Chaty, *The Astronomer's Telegram* **10840** (2017).
48. D. N. Burrows, *et al.*, *Space Sci. Rev.* **120**, 165 (2005).
49. M. Matsuoka, *et al.*, *Publ. Astron. Soc. Jpn.* **61**, 999 (2009).
50. F. A. Harrison, *et al.*, *Astrophys. J.* **770**, 103 (2013).
51. C. Winkler, *et al.*, *Astron. Astrophys.* **411**, L1 (2003).
52. M. Yamanaka, *et al.*, *The Astronomer's Telegram* **10844** (2017).
53. W. Keel, M. Santander, *The Astronomer's Telegram* **10831** (2017).
54. A. Franckowiak, *et al.*, *The Astronomer's Telegram* **10794** (2017).
55. A. Keivani, *et al.*, *The Astronomer's Telegram* **10792** (2017).
56. D. B. Fox, *et al.*, *The Astronomer's Telegram* **10845** (2017).
57. V. Savchenko, *et al.*, *GRB Coordinates Network, Circular Service* **21917** (2017).
58. F. Lucarelli, *et al.*, *The Astronomer's Telegram* **10801** (2017).
59. R. Mukherjee, *The Astronomer's Telegram* **10833** (2017).
60. M. de Naurois, H.E.S.S. Collaboration, *The Astronomer's Telegram* **10787** (2017).
61. I. Martinez, I. Taboada, M. Hui, R. Lauer, *The Astronomer's Telegram* **10802** (2017).
62. G. Stratta, *et al.*, *arXiv e-print astro-ph/1103.0749* (2011).
63. F. Krauß, *et al.*, *Astron. Astrophys.* **566**, L7 (2014).
64. P. Padovani, E. Resconi, P. Giommi, B. Arsioli, Y. L. Chang, *Mon. Notices Royal Astron. Soc.* **457**, 3582 (2016).
65. M. Kadler, *et al.*, *Nature Phys.* **12**, 807 (2016).

66. F. Lucarelli, *et al.*, *Astrophys. J.* **846**, 121 (2017).
67. P. A. R. Ade, *et al.*, *Astron. Astrophys.* **594**, A13 (2016).
68. T. K. Gaisser, F. Halzen, T. Stanev, *Phys. Rept.* **258**, 173 (1995).
69. M. G. Aartsen, *et al.*, *Phys. Rev. Lett.* **117**, 241101 (2016).
70. M. G. Aartsen, *et al.*, *J. of Glaciology* **59**, 1117 (2013).
71. M. G. Aartsen, *et al.*, *Nucl. Instr. Meth. Phys. Res.* **A711**, 73 (2013).
72. R. Abbasi, *et al.*, *Nucl. Instr. Meth. Phys. Res.* **A703**, 190 (2013).
73. M. G. Aartsen, *et al.*, *J. Instrum.* **9**, P03009 (2014).
74. Fermi Science Support Center, <https://fermi.gsfc.nasa.gov/ssc>. Accessed: 26 April 2018.
75. M. Ajello, *et al.*, *arXiv e-print astro-ph/1705.00009* (2017).
76. J. Chiang, J. Carson, W. Focke, *The First GLAST Symposium*, S. Ritz, P. Michelson, C. A. Meegan, eds. (2007), vol. 921 of *American Institute of Physics Conference Series*, pp. 544–545.
77. S. Ciprini, *et al.*, *Proceedings, 2011 Fermi Symposium: Rome, Italy, May 9-12, 2011, SLAC eConf C110509* (2011). ArXiv e-print, **astro-ph/1111.6803**.
78. Fermi LAT Monitor and Transient Information, https://gcn.gsfc.nasa.gov/fermi_lat_mon_trans.html. Accessed: 26 April 2018.
79. F. Damiani, A. Maggio, G. Micela, S. Sciortino, *Astrophys. J.* **483**, 350 (1997).
80. Fermi All-Sky Variability Analysis, <https://fermi.gsfc.nasa.gov/ssc/data/access/lat/FAVA/>. Accessed: 26 April 2018.
81. A. Bulgarelli, *et al.*, *Astron. Astrophys.* **540**, A79 (2012).
82. T.-P. Li, Y.-Q. Ma, *Astrophys. J.* **272**, 317 (1983).
83. W. A. Rolke, A. M. López, J. Conrad, *Nucl. Instr. Meth. Phys. Res.* **A551**, 493 (2005).
84. W. A. Rolke, A. M. López, *Nucl. Instr. Meth. Phys. Res.* **A458**, 745 (2001).
85. A. Domínguez, *et al.*, *Mon. Notices Royal Astron. Soc.* **410**, 2556 (2011).
86. A. Franceschini, G. Rodighiero, M. Vaccari, *Astron. Astrophys.* **487**, 837 (2008).

87. J. D. Finke, S. Razzaque, C. D. Dermer, *Astrophys. J.* **712**, 238 (2010).
88. F. W. Stecker, S. T. Scully, M. A. Malkan, *Astrophys. J.* **827**, 6 (2016).
89. Y. Inoue, Y. T. Tanaka, G. M. Madejski, A. Dominguez, *Astrophys. J. Lett.* **781**, L35 (2014).
90. K. Helgason, M. Ricotti, A. Kashlinsky, *Astrophys. J.* **752**, 113 (2012).
91. C. Hoischen, H.E.S.S. Collaboration, *Lake Baikal Three Messengers Conference* (2016).
92. F. Schüssler, H.E.S.S. Collaboration, *Proceedings, 35th International Cosmic Ray Conference (ICRC 2017): Bexco, Busan, Korea, July 12-20, 2017* (2017).
93. M. de Naurois, L. Rolland, *Astropart. Physics* **32**, 231 (2009).
94. J. Lundberg, J. Conrad, W. Rolke, A. Lopez, *Comput. Phys. Commun.* **181**, 683 (2010).
95. R. D. Parsons, J. A. Hinton, *Astropart. Phys.* **56**, 26 (2014).
96. N. Park, VERITAS Collaboration, *Proceedings, 34th International Cosmic Ray Conference (ICRC2015)* (2015), p. 771.
97. M. Santander, VERITAS Collaboration, *Proceedings of the 38th International Conference on High Energy Physics (ICHEP2016). 3-10 August 2016. Chicago, USA.* (2016), p. 85.
98. R. Mukherjee, VERITAS Collaboration, *GRB Coordinates Network, Circular Service* **19377** (2016).
99. M. G. Aartsen, *et al.*, *Astron. Astrophys.* **607**, A115 (2017).
100. J. McMullin, B. Waters, D. Schiebel, W. Young, K. Golap, *Astronomical Data Analysis Software and Systems XVI*, R. Shaw, F. Hill, D. Bell, eds. (2007), vol. 376 of *Astronomical Society of the Pacific Conference Series*, p. 127.
101. B. J. Shappee, *et al.*, *Astrophys. J.* **788**, 48 (2014).
102. A. A. Henden, D. L. Welch, D. Terrell, S. E. Levine, *American Astronomical Society Meeting Abstracts #214* (2009), p. 669.
103. G. D. Schmidt, R. Elston, O. L. Lupie, *Astron. J.* **104**, 1563 (1992).
104. E. F. Schlafly, D. P. Finkbeiner, *Astrophys. J.* **737**, 103 (2011).
105. K. Serkowski, D. S. Mathewson, V. L. Ford, *Astrophys. J.* **196**, 261 (1975).
106. H. T. Intema, P. Jagannathan, K. P. Mooley, D. A. Frail, *Astron. Astrophys.* **598**, A78 (2017).

107. J. J. Condon, *et al.*, *Astron. J.* **115**, 1693 (1998).
108. T. Morokuma, *et al.*, *Publ. Astron. Soc. Jpn.* **66**, 114 (2014).
109. K. C. Chambers, *et al.*, *arXiv e-print astro-ph/1612.05560* (2016).
110. J. P. Halpern, M. Eracleous, J. R. Mattox, *Astron. J.* **125**, 572 (2003).
111. Image Reduction and Analysis Facility, <http://iraf.noao.edu/>. Accessed: 26 April 2018.
112. P. A. Evans, *et al.*, *Mon. Not. Roy. Astron. Soc.* **397**, 1177 (2009).
113. P. A. Evans, *et al.*, *Astrophys. J. Suppl.* **210**, 8 (2013).
114. A. Keivani, P. A. Evans, J. A. Kennea, Swift Collaboration, *GRB Coordinates Network, Circular Service* **21930** (2017).
115. J. K. Blackburn, *Astronomical Data Analysis Software and Systems IV*, R. A. Shaw, H. E. Payne, J. J. E. Hayes, eds. (1995), vol. 77 of *Astronomical Society of the Pacific Conference Series*, p. 367.
116. M. Ackermann, *et al.*, *Phys. Rev. Lett.* **115**, 231301 (2015).

Acknowledgements

MAGIC: We would like to thank the Instituto de Astrofísica de Canarias for the excellent working conditions at the Observatorio del Roque de los Muchachos in La Palma.

AGILE: We thank ASI personnel involved in the operations and data center of the AGILE mission.

ASAS-SN: We thank Las Cumbres Observatory and its staff for their continued support of ASAS-SN.

VERITAS: We acknowledge the excellent work of the technical support staff at the Fred Lawrence Whipple Observatory and at the collaborating institutions in the construction and operation of the instrument.

Funding

IceCube Collaboration: The IceCube collaboration gratefully acknowledge the support from the following agencies and institutions: USA – U.S. National Science Foundation-Office of Polar Programs, U.S. National Science Foundation-Physics Division, Wisconsin Alumni Research Foundation, Center for High Throughput Computing (CHTC) at the University of Wisconsin–Madison, Open Science Grid (OSG), Extreme Science and Engineering Discovery Environment (XSEDE), U.S. Department of Energy–National Energy Research Scientific Computing Center, Particle astrophysics research computing center at the University of Maryland, Institute for Cyber-Enabled Research at Michigan State University, and Astroparticle physics computational facility at Marquette University; Belgium – Funds for Scientific Research (FRS-FNRS and FWO), FWO Odysseus and Big Science programmes, and Belgian Federal Science Policy Office (Belspo); Germany – Bundesministerium für Bildung und Forschung (BMBF), Deutsche Forschungsgemeinschaft (DFG), Helmholtz Alliance for Astroparticle Physics (HAP), Initiative and Networking Fund of the Helmholtz Association, Deutsches Elektronen Synchrotron (DESY), and High Performance Computing cluster of the RWTH Aachen; Sweden – Swedish Research Council, Swedish Polar Research Secretariat, Swedish National Infrastructure for Computing (SNIC), and Knut and Alice Wallenberg Foundation; Australia – Australian Research Council; Canada – Natural Sciences and Engineering Research Council of Canada, Calcul Québec, Compute Ontario, Canada Foundation for Innovation, WestGrid, and Compute Canada; Denmark – Villum Fonden, Danish National Research Foundation (DNRF); New Zealand – Marsden Fund; Japan - Japan Society for Promotion of Science (JSPS) and Institute for Global Prominent Research (IGPR) of Chiba University; Korea – National Research Foundation of Korea (NRF); Switzerland – Swiss National Science Foundation (SNSF).

Fermi-LAT collaboration: The *Fermi*-LAT Collaboration acknowledges generous ongoing support from a number of agencies and institutes that have supported both the development and the operation of the LAT as well as scientific data analysis. These include the National Aeronautics and Space Administration and the Department of Energy in the United States, the Commissariat à l’Energie Atomique and the Centre National de la Recherche Scientifique / Institut National de Physique Nucléaire et de Physique des Particules in France, the Agen-

zia Spaziale Italiana and the Istituto Nazionale di Fisica Nucleare in Italy, the Ministry of Education, Culture, Sports, Science and Technology (MEXT), High Energy Accelerator Research Organization (KEK) and Japan Aerospace Exploration Agency (JAXA) in Japan, and the K. A. Wallenberg Foundation, the Swedish Research Council and the Swedish National Space Board in Sweden.

Additional support for science analysis during the operations phase is gratefully acknowledged from the Istituto Nazionale di Astrofisica in Italy and the Centre National d'Études Spatiales in France. This work performed in part under DOE Contract DE-AC02-76SF00515.

MAGIC collaboration: The financial support of the German BMBF and MPG, the Italian INFN and INAF, the Swiss National Fund SNF, the ERDF under the Spanish MINECO (FPA2015-69818-P, FPA2012-36668, FPA2015-68378-P, FPA2015-69210-C6-2-R, FPA2015-69210-C6-4-R, FPA2015-69210-C6-6-R, AYA2015-71042-P, AYA2016-76012-C3-1-P, ESP2015-71662-C2-2-P, CSD2009-00064), and the Japanese JSPS and MEXT is gratefully acknowledged. This work was also supported by the Spanish Centro de Excelencia “Severo Ochoa” SEV-2012-0234 and SEV-2015-0548, and Unidad de Excelencia “María de Maeztu” MDM-2014-0369, by the Croatian Science Foundation (HrZZ) Project IP-2016-06-9782 and the University of Rijeka Project 13.12.1.3.02, by the DFG Collaborative Research Centers SFB823/C4 and SFB876/C3, the Polish National Research Centre grant UMO-2016/22/M/ST9/00382 and by the Brazilian MCTIC, CNPq and FAPERJ.

AGILE: AGILE is an ASI space mission developed with scientific and programmatic support from INAF and INFN. Research partially supported through the ASI grant no. I/028/12/2. Part of this work is based on archival data, software or online services provided by the ASI Space Science Data Center (SSDC, previously known as ASDC).

ASAS-SN: ASAS-SN is funded in part by the Gordon and Betty Moore Foundation through grant GBMF5490 to the Ohio State University, NSF grant AST-1515927, the Mt. Cuba Astronomical Foundation, the Center for Cosmology and AstroParticle Physics (CCAPP) at OSU, and the Chinese Academy of Sciences South America Center for Astronomy (CASSACA). A. F. was supported by the Initiative and Networking Fund of the Helmholtz Association. J. F. B. is supported by NSF Grant PHY-1714479. S.D. acknowledges Project 11573003 supported by NSFC. J. L. P. is supported by FONDECYT grant 1151445 and by the Ministry of Economy, Development, and Tourism's Millennium Science Initiative through grant IC120009, awarded to The Millennium Institute of Astrophysics, MAS. This research was made possible through the use of the AAVSO Photometric All-Sky Survey (APASS), funded by the Robert Martin Ayers Sciences Fund.

HAWC: HAWC acknowledges the support from: the US National Science Foundation (NSF) the US Department of Energy Office of High-Energy Physics; the Laboratory Directed Research and Development (LDRD) program of Los Alamos National Laboratory; Consejo Nacional de Ciencia y Tecnología (CONACyT), México (grants 271051, 232656, 260378, 179588, 239762, 254964, 271737, 258865, 243290, 132197, 281653)(Cátedras 873, 1563), Laboratorio Nacional HAWC de rayos gamma; L'OREAL Fellowship for Women in Science 2014; Red HAWC, México; DGAPA-UNAM (grants IG100317, IN111315, IN111716-3, IA102715,

109916, IA102917, IN112218); VIEP-BUAP; PIFI 2012, 2013, PROFOCIE 2014, 2015; the University of Wisconsin Alumni Research Foundation; the Institute of Geophysics, Planetary Physics, and Signatures at Los Alamos National Laboratory; Polish Science Centre grant DEC-2014/13/B/ST9/945; Coordinación de la Investigación Científica de la Universidad Michoacana. Thanks to Scott Delay, Luciano Díaz and Eduardo Murrieta for technical support.

H.E.S.S.: The support of the Namibian authorities and of the University of Namibia in facilitating the construction and operation of H.E.S.S. is gratefully acknowledged, as is the support by the German Ministry for Education and Research (BMBF), the Max Planck Society, the German Research Foundation (DFG), the Helmholtz Association, the Alexander von Humboldt Foundation, the French Ministry of Higher Education, Research and Innovation, the Centre National de la Recherche Scientifique (CNRS/IN2P3 and CNRS/INSU), the Commissariat à l'énergie atomique et aux énergies alternatives (CEA), the U.K. Science and Technology Facilities Council (STFC), the Knut and Alice Wallenberg Foundation, the National Science Centre, Poland grant no. 2016/22/M/ST9/00382, the South African Department of Science and Technology and National Research Foundation, the University of Namibia, the National Commission on Research, Science & Technology of Namibia (NCRST), the Austrian Federal Ministry of Education, Science and Research and the Austrian Science Fund (FWF), the Australian Research Council (ARC), the Japan Society for the Promotion of Science and by the University of Amsterdam. We appreciate the excellent work of the technical support staff in Berlin, Zeuthen, Heidelberg, Palaiseau, Paris, Saclay, Tübingen and in Namibia in the construction and operation of the equipment. This work benefited from services provided by the H.E.S.S. Virtual Organisation, supported by the national resource providers of the EGI Federation.

INTEGRAL: INTEGRAL is an ESA space mission, with its instruments and science data center funded by the ESA member states (specifically the PI countries: Denmark, France, Germany, Italy, Switzerland, Spain), and with additional participation of Russia and the USA. The INTEGRAL SPI instrument was provided through Co-PI institutes IRAP (Toulouse/France) and MPE (Garching/Germany), the SPI project was coordinated and managed by CNES (Toulouse/France). The INTEGRAL IBIS instrument was provided through Co-PI institutes IAPS (Rome/Italy) and CEA (Saclay/France). The SPI-ACS detector system has been provided by MPE Garching/Germany. The SPI team is grateful to ASI, CEA, CNES, DLR, ESA, INTA, NASA and OSTC for their support. The Italian INTEGRAL team acknowledges the support of ASI/INAF agreement n. 2013-025-R.1. JR acknowledges support from the European Union's Horizon 2020 Programme under the AHEAD project (grant n. 654215). RD acknowledges the German INTEGRAL support through DLR grants 50 OG 1101 and 1601.

Kanata, Kiso and Subaru observing teams: Observations with the Kanata and Kiso Schmidt telescopes were supported by the Optical and Near-infrared Astronomy Inter-University Cooperation Program and the Grants-in-Aid of the Ministry of Education, Science, Culture, and Sport JP23740143, JP25800103, JP16H02158, JP17K14253, JP17H04830, JP26800103, JP24103003. This work was also based in part on data collected at Subaru Telescope, which is operated by the National Astronomical Observatory of Japan.

Kapteyn: The Jacobus Kapteyn telescope is operated at the Observatorio del Roque de los

Muchachos on the Spanish island of La Palma by the SARA consortium, whose member institutions (listed at <http://saraobservatory.org>) fund its operation. Refitting for remote operations and instrumentation were funded by the National Science Foundation under grant 1337566 to Texas A&M University—Commerce.

Liverpool telescope: The Liverpool Telescope is operated on the island of La Palma by Liverpool John Moores University in the Spanish Observatorio del Roque de los Muchachos of the Instituto de Astrofísica de Canarias with financial support from the UK Science and Technology Facilities Council.

Swift/NuSTAR: AK and DFC acknowledge support from the National Aeronautics and Space Administration Swift Guest Investigator Program under grant NNX17AI95G. The Swift team at the Mission Operations Center (MOC) at Penn State acknowledges support from NASA contract NAS5-00136. Swift is supported at the University of Leicester by the UK Space Agency.

VERITAS: This research is supported by grants from the U.S. Department of Energy Office of Science, the U.S. National Science Foundation and the Smithsonian Institution, and by NSERC in Canada.

VLA/17B-403 The National Radio Astronomy Observatory (NRAO) is a facility of the National Science Foundation operated under cooperative agreement by Associated Universities, Inc. AJT is supported by a Natural Sciences and Engineering Research Council of Canada (NSERC) Post-Graduate Doctoral Scholarship (PGSD2-490318-2016). AJT and GRS are supported by NSERC Discovery Grants (RGPIN-402752-2011 and RGPIN-06569-2016). JCAMI is the recipient of an Australian Research Council Future Fellowship (FT140101082).

Author contributions

IceCube: The IceCube Collaboration designed, constructed and now operates the the IceCube Neutrino Observatory. Data processing and calibration, Monte Carlo simulations of the detector and of theoretical models, and data analyses were performed by a large number of collaboration members, who also discussed and approved the scientific results presented here. It was reviewed by the entire collaboration before publication, and all authors approved the final version of the manuscript.

Fermi-LAT: The Fermi-LAT contact authors and internal reviewers are SB, AF, YT, KB, EC, and MW.

MAGIC: EB is the MAGIC multi-messenger contact and PI of the neutrino follow-up program. KS is co-convenor of the MAGIC transient working group. LF and MP are the main analyzers of the MAGIC data presented here. AM and EP derived an upper limit to the redshift inferred from MAGIC data.

AGILE: All co-authors contributed to the scientific results presented in the paper. FL and MT wrote the part of the manuscript related to the *AGILE* results.

ASAS-SN: AF, BJS and SH installed an automatic follow up to IceCube triggers which provided additional early data on this event. KZS, CSK, JFB, TAT, TWSH, SD, JLP and BJS built

the telescopes and developed the data processing pipelines.

HAWC: TW is convener of the HAWC extragalactic working group. MH is the HAWC multi-messenger contact. IT, RL and IMC are the main analysers of the HAWC data presented here.

H.E.S.S.: AT is convener of the H.E.S.S. extragalactic working group. FS is the H.E.S.S. multi-messenger contact and PI of the neutrino follow-up program. CH is the main analyser of the H.E.S.S. data presented here. SO provided a cross-check of the presented analysis.

INTEGRAL: VS has performed the INTEGRAL analysis presented here. CF is the PI of INTEGRAL Science Data Center. RD is the co-PI of the SPI instrument. EK is INTEGRAL Project Scientist. PL and PU are co-PIs of INTEGRAL/IBIS instrument. SM is responsible for the INTEGRAL/IBAS. All of the collaborators provided contribution to the text.

Kanata, Kiso and Subaru observing teams: YTT and YU developed the follow-up strategy to search for IceCube counterparts. TN and MK conducted the near-infrared imaging and polarimetric observations of the TXS 0506+056 using the HONIR instrument on the Kanata telescope, which were processed by the data reduction system developed by RI. The reduced images were mainly examined by HM and HN. MY reduced the polarimetric data. KSK supervised all of the above. TM conducted the optical imaging observations of TXS 0506+056 with the KWFC instrument on the Kiso Schmidt telescope. He also reduced the data. These two observations contribute to Figures 3 and 4. YM conducted optical spectroscopic observations of the TXS 0506+056 with the FOCAS spectrograph on the 8.2 m Subaru telescope. The data are reduced and examined by MY, TM, and KO. The spectra are shown in Figure S5.

Kapteyn: WCK obtained and reduced the optical observations at the Kapteyn telescope.

Liverpool telescope: IS and CC obtained, reduced and analysed the Liverpool Telescope spectra presented in this paper.

Swift/NuSTAR: AK led reduction of Swift XRT data, and JJD led reduction of NuSTAR data. DBF carried out the joint Swift XRT + NuSTAR analysis, and AK managed author contributions to this section.

VERITAS: The construction, operation, and maintenance of the VERITAS telescopes, as well as the tools to analyze the VERITAS data, are the work of the the VERITAS Collaboration as a whole. The VERITAS Collaboration contacts for this paper are MS and DAW.

VLA/17B-403: GRS wrote the Director's Discretionary Time proposal whose VLA data are used in this paper (VLA/17B-403). AJT performed the VLA data reduction and analyses in consultation with the rest of the team. AJT and GRS wrote the VLA-related text in consultation with the rest of the team. GRS contributed to significant copy editing of the entire paper.

Competing interests

IceCube: There are no competing interests to declare.

Fermi-LAT: There are no competing interests to declare.

MAGIC: There are no competing interests to declare.

AGILE: There are no competing interests to declare.

ASAS-SN: There are no competing interests to declare.

HAWC: There are no competing interests to declare.

H.E.S.S.: There are no competing interests to declare.

INTEGRAL: There are no competing interests to declare.

Liverpool Telescope: There are no competing interests to declare.

Kanata, Kiso and Subaru observing teams: There are no competing interests to declare.

Kapteyn: There are no competing interests to declare.

Swift/NuSTAR: There are no competing interests to declare.

VERITAS: There are no competing interests to declare.

VLA/17B-403: There are no competing interests to declare.

Data and materials availability

IceCube: All IceCube data related to the the results presented in this paper are provided in (25).

Fermi-LAT: Fermi-LAT data are available from the Fermi Science Support Center (<http://fermi.gsfc.nasa.gov/ssc>) and https://www-glast.stanford.edu/pub_data/1483/.

MAGIC: The MAGIC collaboration routinely releases published graphics, tables and analysis results on a database linked from the official web pages. For this paper we will additionally release underlying data in the form of a list of the MAGIC observed events, after reconstruction and analysis cuts, and simplified instrument response functions.

Both resources (published analysis results as well as data releases for specific publications, like in this case) are accessible at the MAGIC public data website:

<https://magic.mpp.mpg.de/public/public-data/>

We note that the format we choose for our data release, aims to make MAGIC data accessible to the wider community, without requiring the use of internal proprietary software.

To exactly reproduce the published results, advanced software programs are necessary together with training on how to use them. Access to all data, analysis software and necessary training will be made available on request.

AGILE: Data and materials availability: All the *AGILE* data used in this paper are public and available from the *AGILE* Data Center webpage at the following URL: <http://www.ssdsc.asi.it/mmia/index.php?mission=agilemmia>. The *AGILE* data analysis software and calibrations are also public and available at the URL: <http://agile.ssdsc.asi.it/publicsoftware.html>.

ASAS-SN: ASAS-SN light curves are available through the ASAS-SN sky patrol <https://asas-sn.osu.edu>

HAWC: Data used for the presented results are available at:

<https://data.hawc-observatory.org/datasets/ic170922/index.php>.

H.E.S.S.: Data used for the presented results are available at https://www.mpi-hd.mpg.de/hfm/HESS/pages/publications/auxiliary/auxinfo_TXS0506.html

INTEGRAL: Data and software used for the presented results are available at <https://www.isdc.unige.ch/>.

Kanata, Kiso and Subaru observing teams: All the raw data taken with the Kiso, Kanata, and Subaru telescopes are available in the SMOKA, which is operated by the Astronomy Data

Center, National Astronomical Observatory of Japan. The Subaru data were taken in the open-use program S16B-0711.

Kapteyn: The numerical magnitude/flux data to produced the published results here are available in at <http://www.astronomerstelegam.org/?read=10831>

Liverpool Telescope: Data used for the presented results are available in the telescope archive at <http://telescope.livjm.ac.uk>.

Swift/NuSTAR: Link to the archived Swift data:

<http://www.swift.ac.uk/archive/obs.php>

The initial tiling observations (shortly after the IceCube trigger) targetIDs: 10308-10326. Monitoring ObsIDs used for this analysis (from Sept 23 to Oct 23): 00010308001, 00083368001-006, 00010308008-013.

Link to the archived NuSTAR data:

<https://heasarc.gsfc.nasa.gov/FTP/nustar/data/obs/03/9//90301618002/>

ObsID used for this analysis: 90301618002.

VERITAS: Data used for the presented results is available at <https://veritas.sao.arizona.edu/veritas-science/veritas-results-mainmenu-72/490-ic-result>

VLA/17B-403 team: The VLA/17B-403 team would like to thank the NRAO for granting us DDT VLA time to observe this source and the NRAO staff for rapidly executing our observations. The original data from the VLA observations presented in this paper are publicly available through the NRAO Science Data Archive (<https://archive.nrao.edu/archive/advquery.jsp>, using the Project Code 17B-403).

Supplementary Materials for:
Multi-messenger observations of a flaring blazar
coincident with high-energy neutrino IceCube-170922A

IceCube Collaboration[‡]:

M. G. Aartsen¹⁶, M. Ackermann⁵², J. Adams¹⁶, J. A. Aguilar¹², M. Ahlers²⁰, M. Ahrens⁴⁴, I. Al Samarai²⁵, D. Altmann²⁴, K. Andeen³⁴, T. Anderson⁴⁹, I. Anseau¹², G. Anton²⁴, C. Argüelles¹⁴, J. Auffenberg¹, S. Axani¹⁴, H. Bagherpour¹⁶, X. Bai⁴¹, J. P. Barron²³, S. W. Barwick²⁷, V. Baum³³, R. Bay⁸, J. J. Beatty^{18, 19}, J. Becker Tjus¹¹, K.-H. Becker⁵¹, S. BenZvi⁴³, D. Berley¹⁷, E. Bernardini⁵², D. Z. Besson²⁸, G. Binder^{9, 8}, D. Bindig⁵¹, E. Blaufuss¹⁷, S. Blot⁵², C. Boehm⁴⁴, M. Börner²¹, F. Bos¹¹, S. Böser³³, O. Botner⁵⁰, E. Bourbeau²⁰, J. Bourbeau³², F. Bradascio⁵², J. Braun³², M. Brenzke¹, H.-P. Bretz⁵², S. Bron²⁵, J. Brostean-Kaiser⁵², A. Burgman⁵⁰, R. S. Busse³², T. Carver²⁵, E. Cheung¹⁷, D. Chirkin³², A. Christov²⁵, K. Clark²⁹, L. Classen³⁶, S. Coenders³⁵, G. H. Collin¹⁴, J. M. Conrad¹⁴, P. Coppin¹³, P. Correa¹³, D. F. Cowen^{48, 49}, R. Cross⁴³, P. Dave⁶, M. Day³², J. P. A. M. de André²², C. De Clercq¹³, J. J. DeLaunay⁴⁹, H. Dembinski³⁷, S. De Ridder²⁶, P. Desiati³², K. D. de Vries¹³, G. de Wasseige¹³, M. de With¹⁰, T. DeYoung²², J. C. Díaz-Vélez³², V. di Lorenzo³³, H. Dujmovic⁴⁶, J. P. Dumm⁴⁴, M. Dunkman⁴⁹, E. Dvorak⁴¹, B. Eberhardt³³, T. Ehrhardt³³, B. Eichmann¹¹, P. Eller⁴⁹, P. A. Evenson³⁷, S. Fahey³², A. R. Fazely⁷, J. Felde¹⁷, K. Filimonov⁸, C. Finley⁴⁴, S. Flis⁴⁴, A. Franckowiak⁵², E. Friedman¹⁷, A. Fritz³³, T. K. Gaisser³⁷, J. Gallagher³¹, L. Gerhardt⁹, K. Ghorbani³², T. Glauch³⁵, T. Glüsenskamp²⁴, A. Goldschmidt⁹, J. G. Gonzalez³⁷, D. Grant²³, Z. Griffith³², C. Haack¹, A. Hallgren⁵⁰, F. Halzen³², K. Hanson³², D. Hebecker¹⁰, D. Heereman¹², K. Helbing⁵¹, R. Hellauer¹⁷, S. Hickford⁵¹, J. Hignight²², G. C. Hill², K. D. Hoffman¹⁷, R. Hoffmann⁵¹, T. Hoinka²¹, B. Hokanson-Fasig³², K. Hoshina^{31, 53}, F. Huang⁴⁹, M. Huber³⁵, K. Hultqvist⁴⁴, M. Hünnefeld²¹, R. Hussain³², S. In⁴⁶, N. Iovine¹², A. Ishihara¹⁵, E. Jacobi⁵², G. S. Japaridze⁵, M. Jeong⁴⁶, K. Jero³², B. J. P. Jones⁴, P. Kalaczynski¹, W. Kang⁴⁶, A. Kappes³⁶, D. Kappesser³³, T. Karg⁵², A. Karle³², U. Katz²⁴, M. Kauer³², A. Keivani⁴⁹, J. L. Kelley³², A. Kheirandish³², J. Kim⁴⁶, M. Kim¹⁵, T. Kintscher⁵², J. Kiryluk⁴⁵, T. Kittler²⁴, S. R. Klein^{9, 8}, R. Koirala³⁷, H. Kolanoski¹⁰, L. Köpke³³, C. Kopper²³, S. Kopper⁴⁷, J. P. Koschinsky¹, D. J. Koskinen²⁰, M. Kowalski^{10, 52}, K. Krings³⁵, M. Kroll¹¹, G. Krückl³³, S. Kunwar⁵², N. Kurahashi⁴⁰, T. Kuwabara¹⁵, A. Kyriacou², M. Labare²⁶, J. L. Lanfranchi⁴⁹, M. J. Larson²⁰, F. Lauber⁵¹, K. Leonard³², M. Lesiak-Bzdak⁴⁵, M. Leuermann¹, Q. R. Liu³², C. J. Lozano Mariscal³⁶, L. Lu¹⁵, J. Lünemann¹³, W. Luszczak³², J. Madsen⁴², G. Maggi¹³, K. B. M. Mahn²², S. Mancina³², R. Maruyama³⁸, K. Mase¹⁵, R. Maunu¹⁷, K. Meagher¹², M. Medici²⁰, M. Meier²¹, T. Menne²¹, G. Merino³¹, T. Meures¹², S. Miarecki^{9, 8}, J. Micallef²², G. Momenté³³, T. Montaruli²⁵, R. W. Moore²³, R. Morse³², M. Moulai¹⁴, R. Nahnauer⁵², P. Nakarmi⁴⁷, U. Naumann⁵¹, G. Neer²², H. Niederhausen⁴⁵, S. C. Nowicki²³, D. R. Nygren⁹, A. Obertacke Pollmann⁵¹, A. Olivas¹⁷, A. O’Murchadha¹², E. O’Sullivan⁴⁴, T. Palczewski^{9, 8}, H. Pandya³⁷, D. V. Pankova⁴⁹, P. Peiffer³³, J. A. Pepper⁴⁷, C. Pérez de los Heros⁵⁰, D. Pieloth²¹, E. Pinat¹², M. Plum³⁴, P. B. Price⁸, G. T. Przybylski⁹, C. Raab¹², L. Rädcl¹, M. Rameez²⁰, L. Rauch⁵², K. Rawlins³, I. C. Rea³⁵, R. Reimann¹,

B. Relethford⁴⁰, M. Relich¹⁵, E. Resconi³⁵, W. Rhode²¹, M. Richman⁴⁰, S. Robertson², M. Rongen¹, C. Rott⁴⁶, T. Ruhe²¹, D. Ryckbosch²⁶, D. Rysewyk²², I. Safa³², T. Sälzer¹, S. E. Sanchez Herrera²³, A. Sandroock²¹, J. Sandroos³³, M. Santander⁴⁷, S. Sarkar^{20, 39}, S. Sarkar²³, K. Satalecka⁵², P. Schlunder²¹, T. Schmidt¹⁷, A. Schneider³², S. Schoenen¹, S. Schöneberg¹¹, L. Schumacher¹, S. Sclafani⁴⁰, D. Seckel³⁷, S. Seunarine⁴², J. Soedingrekso²¹, D. Soldin³⁷, M. Song¹⁷, G. M. Spiczak⁴², C. Spiering⁵², J. Stachurska⁵², M. Stamatikos¹⁸, T. Stanev³⁷, A. Stasik⁵², R. Stein⁵², J. Stettner¹, A. Steuer³³, T. Stezelberger⁹, R. G. Stokstad⁹, A. Stöbl¹⁵, N. L. Strotjohann⁵², T. Stuttard²⁰, G. W. Sullivan¹⁷, M. Sutherland¹⁸, I. Taboada⁶, J. Tatar^{9, 8}, F. Tenholt¹¹, S. Ter-Antonyan⁷, A. Terliuk⁵², S. Tilav³⁷, P. A. Toale⁴⁷, M. N. Tobin³², C. Toennis⁴⁶, S. Toscano¹³, D. Tosi³², M. Tselengidou²⁴, C. F. Tung⁶, A. Turcati³⁵, C. F. Turley⁴⁹, B. Ty³², E. Unger⁵⁰, M. Usner⁵², J. Vandenbroucke³², W. Van Driessche²⁶, D. van Eijk³², N. van Eijndhoven¹³, S. Vanheule²⁶, J. van Santen⁵², E. Vogel¹, M. Vraeghe²⁶, C. Walck⁴⁴, A. Wallace², M. Wallraff¹, F. D. Wandler²³, N. Wandkowsky³², A. Waza¹, C. Weaver²³, M. J. Weiss⁴⁹, C. Wendt³², J. Werthebach³², S. Westerhoff³², B. J. Whelan², N. Whitehorn³⁰, K. Wiebe³³, C. H. Wiebusch¹, L. Wille³², D. R. Williams⁴⁷, L. Wills⁴⁰, M. Wolf³², J. Wood³², T. R. Wood²³, K. Woschnagg⁸, D. L. Xu³², X. W. Xu⁷, Y. Xu⁴⁵, J. P. Yanez²³, G. Yodh²⁷, S. Yoshida¹⁵, T. Yuan³²

¹ III. Physikalisches Institut, RWTH Aachen University, D-52056 Aachen, Germany

² Department of Physics, University of Adelaide, Adelaide, 5005, Australia

³ Dept. of Physics and Astronomy, University of Alaska Anchorage, 3211 Providence Dr., Anchorage, AK 99508, USA

⁴ Dept. of Physics, University of Texas at Arlington, 502 Yates St., Science Hall Rm 108, Box 19059, Arlington, TX 76019, USA

⁵ CTSPS, Clark-Atlanta University, Atlanta, GA 30314, USA

⁶ School of Physics and Center for Relativistic Astrophysics, Georgia Institute of Technology, Atlanta, GA 30332, USA

⁷ Dept. of Physics, Southern University, Baton Rouge, LA 70813, USA

⁸ Dept. of Physics, University of California, Berkeley, CA 94720, USA

⁹ Lawrence Berkeley National Laboratory, Berkeley, CA 94720, USA

¹⁰ Institut für Physik, Humboldt-Universität zu Berlin, D-12489 Berlin, Germany

¹¹ Fakultät für Physik & Astronomie, Ruhr-Universität Bochum, D-44780 Bochum, Germany

¹² Université Libre de Bruxelles, Science Faculty CP230, B-1050 Brussels, Belgium

¹³ Vrije Universiteit Brussel (VUB), Dienst ELEM, B-1050 Brussels, Belgium

¹⁴ Dept. of Physics, Massachusetts Institute of Technology, Cambridge, MA 02139, USA

¹⁵ Dept. of Physics and Institute for Global Prominent Research, Chiba University, Chiba 263-8522, Japan

¹⁶ Dept. of Physics and Astronomy, University of Canterbury, Private Bag 4800, Christchurch, New Zealand

¹⁷ Dept. of Physics, University of Maryland, College Park, MD 20742, USA

¹⁸ Dept. of Physics and Center for Cosmology and Astro-Particle Physics, Ohio State University, Columbus, OH 43210, USA

¹⁹ Dept. of Astronomy, Ohio State University, Columbus, OH 43210, USA

- ²⁰ Niels Bohr Institute, University of Copenhagen, DK-2100 Copenhagen, Denmark
- ²¹ Dept. of Physics, TU Dortmund University, D-44221 Dortmund, Germany
- ²² Dept. of Physics and Astronomy, Michigan State University, East Lansing, MI 48824, USA
- ²³ Dept. of Physics, University of Alberta, Edmonton, Alberta, Canada T6G 2E1
- ²⁴ Erlangen Centre for Astroparticle Physics, Friedrich-Alexander-Universität Erlangen-Nürnberg, D-91058 Erlangen, Germany
- ²⁵ Département de physique nucléaire et corpusculaire, Université de Genève, CH-1211 Genève, Switzerland
- ²⁶ Dept. of Physics and Astronomy, University of Gent, B-9000 Gent, Belgium
- ²⁷ Dept. of Physics and Astronomy, University of California, Irvine, CA 92697, USA
- ²⁸ Dept. of Physics and Astronomy, University of Kansas, Lawrence, KS 66045, USA
- ²⁹ SNOLAB, 1039 Regional Road 24, Creighton Mine 9, Lively, ON, Canada P3Y 1N2
- ³⁰ Dept. of Physics and Astronomy, University of California, Los Angeles, CA 90095, USA
- ³¹ Dept. of Astronomy, University of Wisconsin, Madison, WI 53706, USA
- ³² Dept. of Physics and Wisconsin IceCube Particle Astrophysics Center, University of Wisconsin, Madison, WI 53706, USA
- ³³ Institute of Physics, University of Mainz, Staudinger Weg 7, D-55099 Mainz, Germany
- ³⁴ Department of Physics, Marquette University, Milwaukee, WI, 53201, USA
- ³⁵ Physik-department, Technische Universität München, D-85748 Garching, Germany
- ³⁶ Institut für Kernphysik, Westfälische Wilhelms-Universität Münster, D-48149 Münster, Germany
- ³⁷ Bartol Research Institute and Dept. of Physics and Astronomy, University of Delaware, Newark, DE 19716, USA
- ³⁸ Dept. of Physics, Yale University, New Haven, CT 06520, USA
- ³⁹ Dept. of Physics, University of Oxford, 1 Keble Road, Oxford OX1 3NP, UK
- ⁴⁰ Dept. of Physics, Drexel University, 3141 Chestnut Street, Philadelphia, PA 19104, USA
- ⁴¹ Physics Department, South Dakota School of Mines and Technology, Rapid City, SD 57701, USA
- ⁴² Dept. of Physics, University of Wisconsin, River Falls, WI 54022, USA
- ⁴³ Dept. of Physics and Astronomy, University of Rochester, Rochester, NY 14627, USA
- ⁴⁴ Oskar Klein Centre and Dept. of Physics, Stockholm University, SE-10691 Stockholm, Sweden
- ⁴⁵ Dept. of Physics and Astronomy, Stony Brook University, Stony Brook, NY 11794-3800, USA
- ⁴⁶ Dept. of Physics, Sungkyunkwan University, Suwon 440-746, Korea
- ⁴⁷ Dept. of Physics and Astronomy, University of Alabama, Tuscaloosa, AL 35487, USA
- ⁴⁸ Dept. of Astronomy and Astrophysics, Pennsylvania State University, University Park, PA 16802, USA
- ⁴⁹ Dept. of Physics, Pennsylvania State University, University Park, PA 16802, USA
- ⁵⁰ Dept. of Physics and Astronomy, Uppsala University, Box 516, S-75120 Uppsala, Sweden
- ⁵¹ Dept. of Physics, University of Wuppertal, D-42119 Wuppertal, Germany

⁵² DESY, D-15738 Zeuthen, Germany

⁵³ Earthquake Research Institute, University of Tokyo, Bunkyo, Tokyo 113-0032, Japan

‡E-mail: analysis@icecube.wisc.edu

Fermi-LAT collaboration:

S. Abdollahi¹, M. Ajello², R. Angioni³, L. Baldini⁴, J. Ballet⁵, G. Barbiellini^{6,7}, D. Bastieri^{8,9}, K. Bechtol¹⁰, R. Bellazzini¹¹, B. Berenji¹², E. Bissaldi^{13,14}, R. D. Blandford¹⁵, R. Bonino^{16,17}, E. Bottacini^{15,18}, J. Bregeon¹⁹, P. Bruel²⁰, R. Buehler²¹, T. H. Burnett²², E. Burns^{23,24}, S. Buson^{23,24}, R. A. Cameron¹⁵, R. Caputo²⁵, P. A. Caraveo²⁶, E. Cavazzuti²⁷, E. Charles¹⁵, S. Chen^{8,18}, C. C. Cheung²⁸, J. Chiang¹⁵, G. Chiaro²⁶, S. Ciprini^{29,30}, J. Cohen-Tanugi¹⁹, J. Conrad^{31,32,33}, D. Costantin⁹, S. Cutini^{29,30}, F. D'Ammando^{34,35}, F. de Palma^{14,36}, S. W. Digel¹⁵, N. Di Lalla⁴, M. Di Mauro¹⁵, L. Di Venere^{13,14}, A. Domínguez³⁷, C. Favuzzi^{13,14}, A. Franckowiak²¹, Y. Fukazawa¹, S. Funk³⁸, P. Fusco^{13,14}, F. Gargano¹⁴, D. Gasparrini^{29,30}, N. Giglietto^{13,14}, M. Giomi²¹, P. Giommi²⁹, F. Giordano^{13,14}, M. Giroletti³⁴, T. Glanzman¹⁵, D. Green^{39,23}, I. A. Grenier⁵, M.-H. Grondin⁴⁰, S. Guiriec^{41,23}, A. K. Harding²³, M. Hayashida^{42,72}, E. Hays²³, J.W. Hewitt⁴³, D. Horan²⁰, G. Jóhannesson^{44,45}, M. Kadler⁴⁶, S. Kensei¹, D. Kocevski²³, F. Krauss^{47,48}, M. Kreter⁴⁶, M. Kuss¹¹, G. La Mura⁹, S. Larsson^{49,32}, L. Latronico¹⁶, M. Lemoine-Goumard⁴⁰, J. Li²¹, F. Longo^{6,7}, F. Loparco^{13,14}, M. N. Lovellette²⁸, P. Lubrano³⁰, J. D. Magill³⁹, S. Maldera¹⁶, D. Malyshev³⁸, A. Manfreda⁴, M. N. Mazziotta¹⁴, J. E. McEnery^{23,39}, M. Meyer^{15,15,15}, P. F. Michelson¹⁵, T. Mizuno⁵⁰, M. E. Monzani¹⁵, A. Morselli⁵¹, I. V. Moskalenko¹⁵, M. Negro^{16,17}, E. Nuss¹⁹, R. Ojha²³, N. Omodei¹⁵, M. Orienti³⁴, E. Orlando¹⁵, M. Palatiello^{6,7}, V. S. Paliya², J. S. Perkins²³, M. Persic^{6,52}, M. Pesce-Rollins¹¹, F. Piron¹⁹, T. A. Porter¹⁵, G. Principe³⁸, S. Rainò^{13,14}, R. Rando^{8,9}, B. Rani²³, M. Razzano^{11,53}, S. Razzaque⁵⁴, A. Reimer^{55,15}, O. Reimer^{55,15}, N. Renault-Tinacci^{5,56}, S. Ritz⁵⁷, L. S. Rochester¹⁵, P. M. Saz Parkinson^{57,58,59}, C. Sgrò¹¹, E. J. Siskind⁶⁰, G. Spandre¹¹, P. Spinelli^{13,14}, D. J. Suson⁶¹, H. Tajima^{62,15}, M. Takahashi⁶³, Y. Tanaka⁵⁰, J. B. Thayer¹⁵, D. J. Thompson²³, L. Tibaldo⁶⁴, D. F. Torres^{65,66}, E. Torresi⁶⁷, G. Tosti^{30,68}, E. Troja^{23,39}, J. Valverde²⁰, G. Vianello¹⁵, M. Vogel¹², K. Wood⁶⁹, M. Wood¹⁵, G. Zaharijas^{70,71}

¹ Department of Physical Sciences, Hiroshima University, Higashi-Hiroshima, Hiroshima 739-8526, Japan

² Department of Physics and Astronomy, Clemson University, Kinard Lab of Physics, Clemson, SC 29634-0978, USA

³ Max-Planck-Institut für Radioastronomie, Auf dem Hügel 69, D-53121 Bonn, Germany

⁴ Università di Pisa and Istituto Nazionale di Fisica Nucleare, Sezione di Pisa I-56127 Pisa, Italy

⁵ Laboratoire AIM, CEA-IRFU/CNRS/Université Paris Diderot, Service d'Astrophysique, CEA Saclay, F-91191 Gif sur Yvette, France

⁶ Istituto Nazionale di Fisica Nucleare, Sezione di Trieste, I-34127 Trieste, Italy

⁷ Dipartimento di Fisica, Università di Trieste, I-34127 Trieste, Italy

⁸ Istituto Nazionale di Fisica Nucleare, Sezione di Padova, I-35131 Padova, Italy

⁹ Dipartimento di Fisica e Astronomia "G. Galilei", Università di Padova, I-35131 Padova, Italy

- ¹⁰ Large Synoptic Survey Telescope, 933 North Cherry Avenue, Tucson, AZ 85721, USA
- ¹¹ Istituto Nazionale di Fisica Nucleare, Sezione di Pisa, I-56127 Pisa, Italy
- ¹² California State University, Los Angeles, Department of Physics and Astronomy, Los Angeles, CA 90032, USA
- ¹³ Dipartimento di Fisica “M. Merlin” dell’Università e del Politecnico di Bari, I-70126 Bari, Italy
- ¹⁴ Istituto Nazionale di Fisica Nucleare, Sezione di Bari, I-70126 Bari, Italy
- ¹⁵ W. W. Hansen Experimental Physics Laboratory, Kavli Institute for Particle Astrophysics and Cosmology, Department of Physics and SLAC National Accelerator Laboratory, Stanford University, Stanford, CA 94 305, USA
- ¹⁶ Istituto Nazionale di Fisica Nucleare, Sezione di Torino, I-10125 Torino, Italy
- ¹⁷ Dipartimento di Fisica, Università degli Studi di Torino, I-10125 Torino, Italy
- ¹⁸ Department of Physics and Astronomy, University of Padova, Vicolo Osservatorio 3, I-35122 Padova, Italy
- ¹⁹ Laboratoire Univers et Particules de Montpellier, Université Montpellier, CNRS/IN2P3, F-34095 Montpellier, France
- ²⁰ Laboratoire Leprince-Ringuet, École polytechnique, CNRS/IN2P3, F-91128 Palaiseau, France
- ²¹ Deutsches Elektronen Synchrotron DESY, D-15738 Zeuthen, Germany
- ²² Department of Physics, University of Washington, Seattle, WA 98195-1560, USA
- ²³ NASA Goddard Space Flight Center, Greenbelt, MD 20771, USA
- ²⁴ NASA Postdoctoral Program Fellow, USA
- ²⁵ Center for Research and Exploration in Space Science and Technology (CRESST) and NASA Goddard Space Flight Center, Greenbelt, MD 20771, USA
- ²⁶ INAF-Istituto di Astrofisica Spaziale e Fisica Cosmica Milano, via E. Bassini 15, I-20133 Milano, Italy
- ²⁷ Italian Space Agency, Via del Politecnico snc, 00133 Roma, Italy
- ²⁸ Space Science Division, Naval Research Laboratory, Washington, DC 20375-5352, USA
- ²⁹ Space Science Data Center - Agenzia Spaziale Italiana, Via del Politecnico, snc, I-00133, Roma, Italy
- ³⁰ Istituto Nazionale di Fisica Nucleare, Sezione di Perugia, I-06123 Perugia, Italy
- ³¹ Department of Physics, Stockholm University, AlbaNova, SE-106 91 Stockholm, Sweden
- ³² The Oskar Klein Centre for Cosmoparticle Physics, AlbaNova, SE-106 91 Stockholm, Sweden
- ³³ Wallenberg Academy Fellow
- ³⁴ INAF Istituto di Radioastronomia, I-40129 Bologna, Italy
- ³⁵ Dipartimento di Astronomia, Università di Bologna, I-40127 Bologna, Italy
- ³⁶ Università Telematica Pegaso, Piazza Trieste e Trento, 48, I-80132 Napoli, Italy
- ³⁷ Grupo de Altas Energías, Universidad Complutense de Madrid, E-28040 Madrid, Spain
- ³⁸ Friedrich-Alexander-Universität Erlangen-Nürnberg, Erlangen Centre for Astroparticle Physics, Erwin-Rommel-Str. 1, 91058 Erlangen, Germany
- ³⁹ Department of Astronomy, University of Maryland, College Park, MD 20742, USA

- ⁴⁰ Centre d'Études Nucléaires de Bordeaux Gradignan, IN2P3/CNRS, Université Bordeaux 1, BP120, F-33175 Gradignan Cedex, France
- ⁴¹ The George Washington University, Department of Physics, 725 21st St, NW, Washington, DC 20052, USA
- ⁴² Dept. of Physics and Institute for Global Prominent Research, Chiba University, Chiba 263-8522, Japan
- ⁴³ University of North Florida, Department of Physics, 1 UNF Drive, Jacksonville, FL 32224, USA
- ⁴⁴ Science Institute, University of Iceland, IS-107 Reykjavik, Iceland
- ⁴⁵ KTH Royal Institute of Technology and Stockholm University, Roslagstullsbacken 23, SE-106 91 Stockholm, Sweden
- ⁴⁶ Institut für Theoretische Physik and Astrophysik, Universität Würzburg, D-97074 Würzburg, Germany
- ⁴⁷ Anton Pannekoek Institute for Astronomy, University of Amsterdam, Postbus 94249, NL-1090 GE Amsterdam, The Netherlands
- ⁴⁸ GRAPPA, University of Amsterdam, Science Park 904, 1098XH Amsterdam, Netherlands
- ⁴⁹ Department of Physics, KTH Royal Institute of Technology, AlbaNova, SE-106 91 Stockholm, Sweden
- ⁵⁰ Hiroshima Astrophysical Science Center, Hiroshima University, Higashi-Hiroshima, Hiroshima 739-8526, Japan
- ⁵¹ Istituto Nazionale di Fisica Nucleare, Sezione di Roma "Tor Vergata", I-00133 Roma, Italy
- ⁵² Osservatorio Astronomico di Trieste, Istituto Nazionale di Astrofisica, I-34143 Trieste, Italy
- ⁵³ Funded by contract FIRB-2012-RBFR12PM1F from the Italian Ministry of Education, University and Research (MIUR)
- ⁵⁴ Department of Physics, University of Johannesburg, PO Box 524, Auckland Park 2006, South Africa
- ⁵⁵ Institut für Astro- und Teilchenphysik and Institut für Theoretische Physik, Leopold-Franzens-Universität Innsbruck, A-6020 Innsbruck, Austria
- ⁵⁶ UPMC-CNRS, UMR7095, Institut d'Astrophysique de Paris, F-75014 Paris, France
- ⁵⁷ Santa Cruz Institute for Particle Physics, Department of Physics and Department of Astronomy and Astrophysics, University of California at Santa Cruz, Santa Cruz, CA 95064, USA
- ⁵⁸ Department of Physics, The University of Hong Kong, Pokfulam Road, Hong Kong, China
- ⁵⁹ Laboratory for Space Research, The University of Hong Kong, Hong Kong, China
- ⁶⁰ NYCB Real-Time Computing Inc., Lattingtown, NY 11560-1025, USA
- ⁶¹ Purdue University Northwest, Hammond, IN 46323, USA
- ⁶² Solar-Terrestrial Environment Laboratory, Nagoya University, Nagoya 464-8601, Japan
- ⁶³ Max-Planck-Institut für Physik, D-80805 München, Germany
- ⁶⁴ IRAP, Université de Toulouse, CNRS, UPS, CNES, F-31028 Toulouse, France
- ⁶⁵ Institute of Space Sciences (CSICIEEC), Campus UAB, Carrer de Magrans s/n, E-08193 Barcelona, Spain
- ⁶⁶ Institució Catalana de Recerca i Estudis Avançats (ICREA), E-08010 Barcelona, Spain

⁶⁷ INAF-Istituto di Astrofisica Spaziale e Fisica Cosmica Bologna, via P. Gobetti 101, I-40129 Bologna, Italy

⁶⁸ Dipartimento di Fisica, Università degli Studi di Perugia, I-06123 Perugia, Italy

⁶⁹ Praxis Inc., Alexandria, VA 22303, resident at Naval Research Laboratory, Washington, DC 20375, USA

⁷⁰ Istituto Nazionale di Fisica Nucleare, Sezione di Trieste, and Università di Trieste, I-34127 Trieste, Italy

⁷¹ Center for Astrophysics and Cosmology, University of Nova Gorica, Nova Gorica, Slovenia

⁷² current address Konan University, 8 Chome-9-1 Okamoto, Higashinada Ward, Kobe, Hyōgo Prefecture 658-0072, Japan

MAGIC collaboration^{||}:

M. L. Ahnen¹, S. Ansoldi^{2,20}, L. A. Antonelli³, C. Arcaro⁴, D. Baack⁵, A. Babić⁶, B. Banerjee⁷, P. Bangale⁸, U. Barres de Almeida^{8,9}, J. A. Barrio¹⁰, J. Becerra González¹¹, W. Bednarek¹², E. Bernardini^{4,13,23}, A. Berti^{2,24}, W. Bhattacharyya¹³, A. Biland¹, O. Blanch¹⁴, G. Bonnoli¹⁵, A. Carosi³, R. Carosi¹⁵, G. Ceribella⁸, A. Chatterjee⁷, S. M. Colak¹⁴, P. Colin⁸, E. Colombo¹¹, J. L. Contreras¹⁰, J. Cortina¹⁴, S. Covino³, P. Cumani¹⁴, P. Da Vela¹⁵, F. Dazzi³, A. De Angelis⁴, B. De Lotto², M. Delfino^{14,25}, J. Delgado¹⁴, F. Di Pierro⁴, A. Domínguez¹⁰, D. Dominis Prester⁶, D. Dorner¹⁶, M. Doro⁴, S. Einecke⁵, D. Elsaesser⁵, V. Fallah Ramazani¹⁷, A. Fernández-Barral^{4,14}, D. Fidalgo¹⁰, L. Foffano⁴, K. Pfrang⁵, M. V. Fonseca¹⁰, L. Font¹⁸, A. Franceschini²⁸, C. Fruck⁸, D. Galindo¹⁹, S. Gallozzi³, R. J. García López¹¹, M. Garczarczyk¹³, M. Gaug¹⁸, P. Giammaria³, N. Godinović⁶, D. Gora^{13,27}, D. Guberman¹⁴, D. Hadasch²⁰, A. Hahn⁸, T. Hassan¹⁴, M. Hayashida²⁰, J. Herrera¹¹, J. Hose⁸, D. Hrupec⁶, S. Inoue²⁹, K. Ishio⁸, Y. Konno²⁰, H. Kubo²⁰, J. Kushida²⁰, D. Lelas⁶, E. Lindfors¹⁷, S. Lombardi³, F. Longo^{2,24}, M. López¹⁰, C. Maggio¹⁸, P. Majumdar⁷, M. Makariev²¹, G. Maneva²¹, M. Manganaro¹¹, K. Mannheim¹⁶, L. Maraschi³, M. Mariotti⁴, M. Martínez¹⁴, S. Masuda²⁰, D. Mazin^{8,20}, M. Minev²¹, J. M. M¹⁵, R. Mirzoyan⁸, A. Moralejo¹⁴, V. Moreno¹⁸, E. Moretti⁸, T. Nagayoshi²⁰, V. Neustroev¹⁷, A. Niedzwiecki¹², M. Nieves Rosillo¹⁰, C. Nigro¹³, K. Nilsson¹⁷, D. Ninci¹⁴, K. Nishijima²⁰, K. Noda^{14,20}, L. Nogués¹⁴, S. Paiano⁴, J. Palacio¹⁴, D. Paneque⁸, R. Paoletti¹⁵, J. M. Paredes¹⁹, G. Pedalletti¹³, M. Peresano², M. Persic^{2,26}, P. G. Prada Moroni²², E. Prandini⁴, I. Puljak⁶, J. Rodriguez Garcia⁸, I. Reichardt⁴, W. Rhode⁵, M. Ribó¹⁹, J. Rico¹⁴, C. Righi³, A. Rugliancich¹⁵, T. Saito²⁰, K. Satalecka¹³, T. Schweizer⁸, J. Sitarek^{12,20}, I. Šnidarić⁶, D. Sobczynska¹², A. Stamerra³, M. Strzys⁸, T. Suric⁶, M. Takahashi²⁰, F. Tavecchio³, P. Temnikov²¹, T. Terzić⁶, M. Teshima^{8,20}, N. Torres-Albà¹⁹, A. Treves², S. Tsujimoto²⁰, G. Vanzo¹¹, M. Vazquez Acosta¹¹, I. Vovk⁸, J. E. Ward¹⁴, M. Will⁸, D. Zarić⁶

¹ ETH Zurich, CH-8093 Zurich, Switzerland

² Università di Udine, and INFN Trieste, I-33100 Udine, Italy

³ National Institute for Astrophysics (INAF), I-00136 Rome, Italy

⁴ Università di Padova and INFN, I-35131 Padova, Italy

- ⁵ Technische Universität Dortmund, D-44221 Dortmund, Germany
- ⁶ Croatian MAGIC Consortium: University of Rijeka, 51000 Rijeka, University of Split - FESB, 21000 Split, University of Zagreb - FER, 10000 Zagreb, University of Osijek, 31000 Osijek and Rudjer Boskovic Institute, 10000 Zagreb, Croatia
- ⁷ Saha Institute of Nuclear Physics, HBNI, 1/AF Bidhannagar, Salt Lake, Sector-1, Kolkata 700064, India
- ⁸ Max-Planck-Institut für Physik, D-80805 München, Germany
- ⁹ now at Centro Brasileiro de Pesquisas Físicas (CBPF), 22290-180 URCA, Rio de Janeiro (RJ), Brasil
- ¹⁰ Unidad de Partículas y Cosmología (UPARCOS), Universidad Complutense, E-28040 Madrid, Spain
- ¹¹ Inst. de Astrofísica de Canarias, E-38200 La Laguna, and Universidad de La Laguna, Dpto. Astrofísica, E-38206 La Laguna, Tenerife, Spain
- ¹² University of Łódź, Department of Astrophysics, PL-90236 Łódź, Poland
- ¹³ Deutsches Elektronen-Synchrotron (DESY), D-15738 Zeuthen, Germany
- ¹⁴ Institut de Física d'Altes Energies (IFAE), The Barcelona Institute of Science and Technology (BIST), E-08193 Bellaterra (Barcelona), Spain
- ¹⁵ Università di Siena and INFN Pisa, I-53100 Siena, Italy
- ¹⁶ Universität Würzburg, D-97074 Würzburg, Germany
- ¹⁷ Finnish MAGIC Consortium: Tuorla Observatory and Finnish Centre of Astronomy with ESO (FINCA), University of Turku, Vaisalantie 20, FI-21500 Piikkiö, Astronomy Division, University of Oulu, FIN-90014 University of Oulu, Finland
- ¹⁸ Departament de Física, and CERES-IEEC, Universitat Autònoma de Barcelona, E-08193 Bellaterra, Spain
- ¹⁹ Universitat de Barcelona, ICC, IEEC-UB, E-08028 Barcelona, Spain
- ²⁰ Japanese MAGIC Consortium: ICRR, The University of Tokyo, 277-8582 Chiba, Japan; Department of Physics, Kyoto University, 606-8502 Kyoto, Japan; Tokai University, 259-1292 Kanagawa, Japan; The University of Tokushima, 770-8502 Tokushima, Japan
- ²¹ Inst. for Nucl. Research and Nucl. Energy, Bulgarian Academy of Sciences, BG-1784 Sofia, Bulgaria
- ²² Università di Pisa, and INFN Pisa, I-56126 Pisa, Italy
- ²³ Humboldt University of Berlin, Institut für Physik D-12489 Berlin Germany
- ²⁴ also at Dipartimento di Fisica, Università di Trieste, I-34127 Trieste, Italy
- ²⁵ also at Port d'Informació Científica (PIC) E-08193 Bellaterra (Barcelona) Spain
- ²⁶ also at INAF-Trieste and Dept. of Physics & Astronomy, University of Bologna
- ²⁷ also at Institute of Nuclear Physics Polish Academy of Sciences, PL-31342 Krakow, Poland
- ²⁸ Department of Physics and Astronomy, University of Padova, E-35131 Padova, Italy
- ²⁹ RIKEN, 2-1 Hirosawa, Wako, Saitama 351-0198, Japan
- ||E-mail: elisa.bernardini@desy.de, konstancja.satalecka@desy.de, luca.foffano@pd.infn.it, pere-sano.michele@gmail.com, moralejo@ifae.es, prandini@pd.infn.it

AGILE:

F. Lucarelli^{1,2}, M. Tavani^{3,4,5}, G. Piano³, I. Donnarumma⁶, C. Pittori^{1,2}, F. Verrecchia^{1,2}, G. Barbiellini⁷, A. Bulgarelli⁸, P. Caraveo⁹, P. W. Cattaneo¹⁰, S. Colafrancesco^{11,2}, E. Costa^{3,6}, G. Di Cocco⁸, A. Ferrari¹², F. Gianotti⁸, A. Giuliani⁹, P. Lipari¹³, S. Mereghetti⁹, A. Morselli¹⁴, L. Pacciani³, F. Paoletti^{15,3}, N. Parmiggiani⁸, A. Pellizzoni¹⁶, P. Picozza¹⁷, M. Pilia¹⁶, A. Rappoldi¹⁰, A. Trois¹⁶, S. Vercellone¹⁸, V. Vittorini³,

¹ ASI Space Science Data Center (SSDC), Via del Politecnico snc, I-00133 Roma, Italy

² INAF–OAR, via Frascati 33, I-00078 Monte Porzio Catone (Roma), Italy

³ INAF/IAPS–Roma, Via del Fosso del Cavaliere 100, I-00133 Roma, Italy

⁴ Univ. “Tor Vergata”, Via della Ricerca Scientifica 1, I-00133 Roma, Italy

⁵ Gran Sasso Science Institute, viale Francesco Crispi 7, I-67100 L’Aquila, Italy

⁶ Agenzia Spaziale Italiana (ASI), Via del Politecnico snc, I-00133 Roma, Italy

⁷ Dipartimento di Fisica, Università di Trieste and INFN, via Valerio 2, I-34127 Trieste, Italy

⁸ INAF/IASF–Bologna, Via Gobetti 101, I-40129 Bologna, Italy

⁹ INAF/IASF–Milano, via E. Bassini 15, I-20133 Milano, Italy

¹⁰ INFN–Pavia, Via Bassi 6, I-27100 Pavia, Italy

¹¹ University of Witwatersrand, Johannesburg, South Africa

¹² CIFS, c/o Physics Department, University of Turin, via P. Giuria 1, I-10125 Torino, Italy

¹³ INFN–Roma Sapienza, Piazzale Aldo Moro 2, 00185 Roma, Italy

¹⁴ INFN–Roma Tor Vergata, via della Ricerca Scientifica 1, 00133 Roma, Italy

¹⁵ East Windsor RSD, 25a Leshin Lane, Hightstown, NJ 08520, USA

¹⁶ INAF – Osservatorio Astronomico di Cagliari, via della Scienza 5, I-09047 Selargius (CA), Italy

¹⁷ INFN–Roma Tor Vergata, via della Ricerca Scientifica 1, I-00133 Roma, Italy

¹⁸ INAF – Oss. Astron. di Brera, Via E. Bianchi 46, I-23807 Merate (LC), Italy

ASAS-SN:

A. Franckowiak¹, K. Z. Stanek², C. S. Kochanek^{2,3}, J. F. Beacom^{3,4,2}, T. A. Thompson², T. W.-S. Holoien⁵, S. Dong⁶, J. L. Prieto^{7,8}, B. J. Shappee⁹, S. Holmbo¹⁰,

¹ DESY, D-15738 Zeuthen, Germany

² Department of Astronomy, The Ohio State University, 140 West 18th Avenue Columbus, OH 43210 USA

³ Center for Cosmology and Astroparticle Physics, The Ohio State University, 191 W. Woodruff Avenue, Columbus, OH 43210, USA

⁴ Department of Physics, The Ohio State University, 191 W. Woodruff Avenue, Columbus, OH 43210 USA

⁵ The Observatories of the Carnegie Institution for Science, 813 Santa Barbara St., Pasadena, CA 91101, USA

⁶ Kavli Institute for Astronomy and Astrophysics, Peking University, 5 Yiheyuanlu, Haidian District Beijing, China 100871

⁷ Núcleo de Astronomía de la Facultad de Ingeniería y Ciencias, Universidad Diego Portales, Av. Ejército 441, Santiago, Chile

⁸ Millennium Institute of Astrophysics, Santiago, Chile

⁹ Institute for Astronomy, University of Hawai'i, 2680 Woodlawn Drive, Honolulu, HI 96822, USA

¹⁰ Department of Physics and Astronomy, Aarhus University, Ny Munkegade 120, 8000 Aarhus C, Denmark

HAWC:

A. U. Abeysekara¹, A. Albert², R. Alfaro³, C. Alvarez⁴, R. Arceo⁴, J. C. Arteaga-Velázquez⁵, D. Avila Rojas³, H. A. Ayala Solares⁶, A. Becerril³, E. Belmont-Moreno³, A. Bernal⁷, K. S. Caballero-Mora⁴, T. Capistrán⁸, A. Carramiñana⁸, S. Casanova⁹, M. Castillo⁵, U. Cotti⁵, J. Cotzomi¹⁰, S. Coutiño de León⁸, C. De León¹⁰, E. De la Fuente¹¹, R. Diaz Hernandez⁸, S. Dichiaro⁷, B. L. Dingus², M. A. DuVernois¹², J. C. Díaz-Vélez¹¹, R. W. Ellsworth¹³, K. Engel¹⁴, D. W. Fiorino¹⁴, H. Fleischhack¹⁵, N. Fraija⁷, J. A. García-González³, F. Garfias⁷, A. González Muñoz³, M. M. González⁷, J. A. Goodman¹⁴, Z. Hampel-Arias¹², J. P. Harding², S. Hernandez³, B. Hona¹⁵, F. Hueyotl-Zahuantitla⁴, C. M. Hui¹⁶, P. Hütemeyer¹⁵, A. Iriarte⁷, A. Jardin-Blicq¹⁷, V. Joshi¹⁷, S. Kaufmann⁴, G. J. Kunde², A. Lara¹⁸, R. J. Lauer¹⁹, W. H. Lee⁷, D. Lennarz²⁰, H. León Vargas³, J. T. Linnemann²¹, A.L. Longinotti⁸, G. Luis-Raya²², R. Luna-García²³, K. Malone⁶, S. S. Marinelli²¹, O. Martinez¹⁰, I. Martinez-Castellanos¹⁴, J. Martínez-Castro²³, H. Martínez-Huerta²⁴, J. A. Matthews¹⁹, P. Miranda-Romagnoli²⁵, E. Moreno¹⁰, M. Mostafá⁶, A. Nayerhoda⁹, L. Nellen²⁶, M. Newbold¹, M. U. Nisa²⁷, R. Noriega-Papaqui²⁵, R. Pelayo²³, J. Pretz⁶, E. G. Pérez-Pérez²², Z. Ren¹⁹, C. D. Rho²⁷, C. Rivière¹⁴, D. Rosa-González⁸, M. Rosenberg⁶, E. Ruiz-Velasco³, E. Ruiz-Velasco¹⁷, F. Salesa Greus⁹, A. Sandoval³, M. Schneider²⁸, H. Schoorlemmer¹⁷, G. Sinnis², A. J. Smith¹⁴, R. W. Springer¹, P. Surajbali¹⁷, O. Tibolla⁴, K. Tollefson²¹, I. Torres⁸, L. Villaseñor¹⁰, T. Weisgarber¹², F. Werner¹⁷, T. Yapici²⁷, Y. Gaurang²⁹, A. Zepeda²⁴, H. Zhou², J. D. Álvarez⁵,

¹ Department of Physics and Astronomy, University of Utah, Salt Lake City, UT, USA

² Physics Division, Los Alamos National Laboratory, Los Alamos, NM, USA

³ Instituto de Física, Universidad Nacional Autónoma de México, Ciudad de Mexico, Mexico

⁴ Universidad Autónoma de Chiapas, Tuxtla Gutiérrez, Chiapas, Mexico

⁵ Universidad Michoacana de San Nicolás de Hidalgo, Morelia, Mexico

⁶ Department of Physics, Pennsylvania State University, University Park, PA, USA

⁷ Instituto de Astronomía, Universidad Nacional Autónoma de México, Ciudad de Mexico, Mexico

⁸ Instituto Nacional de Astrofísica, Óptica y Electrónica, Puebla, Mexico

⁹ Institute of Nuclear Physics Polish Academy of Sciences, PL-31342 IFJ-PAN, Krakow, Poland

¹⁰ Facultad de Ciencias Físico Matemáticas, Benemérita Universidad Autónoma de Puebla,

Puebla, Mexico

¹¹ Departamento de Física, Centro Universitario de Ciencias Exactas e Ingenierías y Centro Universitario de los Valles (CUValles), Universidad de Guadalajara, Guadalajara, Mexico

¹² Department of Physics, University of Wisconsin-Madison, Madison, WI, USA

¹³ School of Physics, Astronomy, and Computational Sciences, George Mason University, Fairfax, VA, USA

¹⁴ Department of Physics, University of Maryland, College Park, MD, USA

¹⁵ Department of Physics, Michigan Technological University, Houghton, MI, USA

¹⁶ NASA Marshall Space Flight Center, Astrophysics Office, Huntsville, AL 35812, USA

¹⁷ Max-Planck Institute for Nuclear Physics, 69117 Heidelberg, Germany

¹⁸ Instituto de Geofísica, Universidad Nacional Autónoma de México, Ciudad de México, Mexico

¹⁹ Dept of Physics and Astronomy, University of New Mexico, Albuquerque, NM, USA

²⁰ School of Physics and Center for Relativistic Astrophysics - Georgia Institute of Technology, Atlanta, GA, USA 30332

²¹ Department of Physics and Astronomy, Michigan State University, East Lansing, MI, USA

²² Universidad Politécnica de Pachuca, Pachuca, Hgo, Mexico

²³ Centro de Investigación en Computación, Instituto Politécnico Nacional, México City, Mexico

²⁴ Physics Department, Centro de Investigación y de Estudios Avanzados del IPN, Mexico City, DF, Mexico

²⁵ Universidad Autónoma del Estado de Hidalgo, Pachuca, Mexico

²⁶ Instituto de Ciencias Nucleares, Universidad Nacional Autónoma de México, Ciudad de México, Mexico

²⁷ Department of Physics & Astronomy, University of Rochester, Rochester, NY, USA

²⁸ Santa Cruz Institute for Particle Physics, University of California, Santa Cruz, Santa Cruz, CA, USA

²⁹ Department of Physics and Astronomy, University of California, Irvine, CA 92697, USA

H.E.S.S.††:

H. Abdalla¹, E.O. Angüner², C. Armand³, M. Backes¹⁵, Y. Becherini⁴, D. Berge⁵, M. Böttcher¹, C. Boisson⁶, J. Bolmont⁷, S. Bonnefoy⁵, P. Bordas⁸, F. Brun⁹, M. Büchele¹⁰, T. Bulik¹¹, S. Caroff¹², A. Carosi³, S. Casanova^{8,13}, M. Cerruti⁷, N. Chakraborty⁸, S. Chandra¹, A. Chen¹⁴, S. Colafrancesco¹⁴, I.D. Davids¹⁵, C. Deil⁸, J. Devin¹⁶, A. Djannati-Ataï¹⁸, K. Egberts¹⁹, G. Emery⁷, S. Eschbach¹⁰, A. Fiasson³, G. Fontaine¹², S. Funk¹⁰, M. Füßling⁵, Y.A. Gallant¹⁶, F. Gaté³, G. Giavitto⁵, D. Glawion¹⁷, J.F. Glicenstein²⁰, D. Gottschall²¹, M.-H. Grondin⁹, M. Haupt⁵, G. Henri²², J.A. Hinton⁸, C. Hoischen¹⁹, T. L. Holch²³, D. Huber²⁴, M. Jamrozy²⁵, D. Jankowsky¹⁰, F. Jankowsky¹⁷, L. Jouvin¹⁸, I. Jung-Richardt¹⁰, D. Kerszberg⁷, B. Khélifi¹⁸, J. King⁸, S. Klepser⁵, W. Kluźniak²⁶, Nu. Komin¹⁴, M. Kraus¹⁰, J. Lefaucheur²⁰, A. Lemièrre¹⁸, M. Lemoine-Goumard⁹, J.-P. Lenain⁷,

E. Leser¹⁹, T. Lohse²³, R. López-Coto⁸, M. Lorentz²⁰, I. Lypova⁵, V. Marandon⁸, G. Guillem Martí-Devesa²⁴, G. Maurin³, A.M.W. Mitchell⁸, R. Moderski²⁶, M. Mohamed¹⁷, L. Mohrmann¹⁰, E. Moulin²⁰, T. Murach⁵, M. de Naurois¹², F. Niederwanger²⁴, J. Niemiec¹³, L. Oakes²³, P. O'Brien²⁷, S. Ohm⁵, M. Ostrowski²⁵, I. Oya⁵, M. Panter⁸, R.D. Parsons⁸, C. Perennes⁷, Q. Piel³, S. Pita¹⁸, V. Poireau³, A. Priyana Noel²⁵, H. Prokoph⁵, G. Pühlhofer²¹, A. Quirrenbach¹⁷, S. Raab¹⁰, R. Rauth²⁴, M. Renaud¹⁶, F. Rieger^{8,28}, L. Rinchiuso²⁰, C. Romoli⁸, G. Rowell²⁹, B. Rudak²⁶, D.A. Sanchez³, M. Sasaki¹⁰, R. Schlickeiser³⁰, F. Schüssler²⁰, A. Schulz⁵, U. Schwanke²³, M. Seglar-Arroyo²⁰, N. Shafi¹⁴, R. Simoni³¹, H. Sol⁶, C. Stegmann^{5,19}, C. Steppa¹⁹, T. Tavernier²⁰, A.M. Taylor⁵, D. Tiziani¹⁰, C. Trichard², M. Tsirou¹⁶, C. van Eldik¹⁰, C. van Rensburg¹, B. van Soelen³², J. Veh¹⁰, P. Vincent⁷, F. Voisin²⁹, S.J. Wagner¹⁷, R.M. Wagner³³, A. Wierzycholska¹², R. Zanin⁸, A.A. Zdziarski²⁶, A. Zech⁶, A. Ziegler¹⁰, J. Zorn⁸, N. Żywucka²⁵,

¹ Centre for Space Research, North-West University, Potchefstroom 2520, South Africa

² Aix Marseille Université, CNRS/IN2P3, CPPM, Marseille, France

³ Laboratoire d'Annecy de Physique des Particules, Univ. Grenoble Alpes, Univ. Savoie Mont Blanc, CNRS, LAPP, 74000 Annecy, France

⁴ Department of Physics and Electrical Engineering, Linnaeus University, 351 95 Växjö, Sweden

⁵ DESY, D-15738 Zeuthen, Germany

⁶ LUTH, Observatoire de Paris, PSL Research University, CNRS, Université Paris Diderot, 5 Place Jules Janssen, 92190 Meudon, France

⁷ Sorbonne Université, Université Paris Diderot, Sorbonne Paris Cité, CNRS/IN2P3, Laboratoire de Physique Nucléaire et de Hautes Energies, LPNHE, 4 Place Jussieu, F-75252 Paris, France

⁸ Max-Planck-Institut für Kernphysik, P.O. Box 103980, D 69029 Heidelberg, Germany

⁹ Université Bordeaux, CNRS/IN2P3, Centre d'Études Nucléaires de Bordeaux Gradignan, 33175 Gradignan, France

¹⁰ Friedrich-Alexander-Universität Erlangen-Nürnberg, Erlangen Centre for Astroparticle Physics, Erwin-Rommel-Str. 1, D 91058 Erlangen, Germany

¹¹ Astronomical Observatory, The University of Warsaw, Al. Ujazdowskie 4, 00-478 Warsaw, Poland

¹² Laboratoire Leprince-Ringuet, Ecole Polytechnique, CNRS/IN2P3, F-91128 Palaiseau, France

¹³ Instytut Fizyki Jądrowej PAN, ul. Radzikowskiego 152, 31-342 Kraków, Poland

¹⁴ School of Physics, University of the Witwatersrand, 1 Jan Smuts Avenue, Braamfontein, Johannesburg, 2050 South Africa

¹⁵ University of Namibia, Department of Physics, Private Bag 13301, Windhoek, Namibia

¹⁶ Laboratoire Univers et Particules de Montpellier, Université Montpellier, CNRS/IN2P3, CC 72, Place Eugène Bataillon, F-34095 Montpellier Cedex 5, France

¹⁷ Landessternwarte, Universität Heidelberg, Königstuhl, D 69117 Heidelberg, Germany

¹⁸ APC, AstroParticule et Cosmologie, Université Paris Diderot, CNRS/IN2P3, CEA/Irfu, Observatoire de Paris, Sorbonne Paris Cité, 10, rue Alice Domon et Léonie Duquet, 75205 Paris Cedex 13, France

¹⁹ Institut für Physik und Astronomie, Universität Potsdam, Karl-Liebknecht-Strasse 24/25, D 14476 Potsdam, Germany

²⁰ IRFU, CEA, Université Paris-Saclay, F-91191 Gif-sur-Yvette, France

²¹ Institut für Astronomie und Astrophysik, Universität Tübingen, Sand 1, D 72076 Tübingen, Germany

²² Univ. Grenoble Alpes, CNRS, IPAG, F-38000 Grenoble, France

²³ Institut für Physik, Humboldt-Universität zu Berlin, Newtonstr. 15, D 12489 Berlin, Germany

²⁴ Institut für Astro- und Teilchenphysik, Leopold-Franzens-Universität Innsbruck, A-6020 Innsbruck, Austria

²⁵ Obserwatorium Astronomiczne, Uniwersytet Jagielloński, ul. Orła 171, 30-244 Kraków, Poland

²⁶ Nicolaus Copernicus Astronomical Center, Polish Academy of Sciences, ul. Bartycka 18, 00-716 Warsaw, Poland

²⁷ Department of Physics and Astronomy, The University of Leicester, University Road, Leicester, LE1 7RH, United Kingdom

²⁸ Heisenberg Fellow (DFG), ITA Universität Heidelberg, Germany

²⁹ School of Physical Sciences, University of Adelaide, Adelaide 5005, Australia

³⁰ Institut für Theoretische Physik, Lehrstuhl IV: Weltraum und Astrophysik, Ruhr-Universität Bochum, D 44780 Bochum, Germany

³¹ GRAPPA, Anton Pannekoek Institute for Astronomy, University of Amsterdam, Science Park 904, 1098 XH Amsterdam, The Netherlands

³² Department of Physics, University of the Free State, PO Box 339, Bloemfontein 9300, South Africa

³³ Oskar Klein Centre, Department of Physics, Stockholm University, Albanova University Center, SE-10691 Stockholm, Sweden

††E-mail: contact.hess@hess-experiment.eu

INTEGRAL^{††}:

V. Savchenko¹, C. Ferrigno¹, A. Bazzano², R. Diehl³, E. Kuulkers⁴, P. Laurent^{5,6}, S. Mereghetti⁷, L. Natalucci², F. Panessa², J. Rodi², P. Ubertini²

¹ISDC, Department of astronomy, University of Geneva, chemin d'Écogia, 16 CH-1290 Versoix, Switzerland

²INAF-Institute for Space Astrophysics and Planetology, Via Fosso del Cavaliere 100, 00133-Rome, Italy

³Max-Planck-Institut für Extraterrestrische Physik, Garching, Germany

⁴European Space Research and Technology Centre (ESA/ESTEC), Keplerlaan 1, 2201 AZ Noordwijk, The Netherlands

⁵APC, AstroParticule et Cosmologie, Université Paris Diderot, CNRS/IN2P3, CEA/Irfu, Ob-

servatoire de Paris Sorbonne Paris Cité, 10 rue Alice Domont et Léonie Duquet, 75205 Paris Cedex 13, France.

⁶DSM/Irfu/Service d'Astrophysique, Bat. 709 Orme des Merisiers CEA Saclay, 91191 Gif-sur-Yvette Cedex, France

⁷INAF, IASF-Milano, via E.Bassini 15, I-20133 Milano, Italy

^{##}E-mail: Volodymyr.Savchenko@unige.ch

Kanata, Kiso and Subaru observing teams^{|||}:

T. Morokuma¹, K. Ohta², Y. T. Tanaka³, H. Mori⁴, M. Yamanaka³, K. S. Kawabata³, Y. Utsumi⁵, T. Nakaoka⁴, M. Kawabata⁴, H. Nagashima⁴, M. Yoshida⁶, Y. Matsuoka⁷, R. Itoh⁸

¹ Institute of Astronomy, Graduate School of Science, The University of Tokyo, 2-21-1 Osawa, Mitaka, Tokyo 181-0015, Japan

² Department of Astronomy, Graduate School of Science, Kyoto University, Sakyo-ku, Kyoto, Kyoto 606-8502, Japan

³ Hiroshima Astrophysical Science Center, Hiroshima University, 1-3-1 Kagamiyama, Higashi-Hiroshima, Hiroshima 739-8526, Japan

⁴ Department of Physical Science, Hiroshima University, 1-3-1 Kagamiyama, Higashi-Hiroshima, Hiroshima 739-8526, Japan

⁵ Kavli Institute for Particle Astrophysics and Cosmology, SLAC National Accelerator Laboratory, Stanford University, 2575 Sand Hill Road, Menlo Park, CA 94025, USA

⁶ Subaru Telescope, National Astronomical Observatory of Japan, National Institutes of Natural Sciences, 650 North A'ohoku Place, Hilo, HI 96720, USA

⁷ Research Center for Space and Cosmic Evolution, Ehime University, Matsuyama, Ehime 790-8577, Japan

⁸ Department of Physics, Tokyo Institute of Technology, 2-12-1 Ohokayama, Meguro, Tokyo 152-8551, Japan

^{|||}E-mail: tmorokuma@ioa.s.u-tokyo.ac.jp

Kapteyn^{¶¶}:

W. Keel¹,

¹ Department of Physics and Astronomy, University of Alabama, Box 870324, Tuscaloosa, AL 35487, USA

^{¶¶}E-mail: keel@ua.edu

Liverpool telescope:

C. Copperwheat¹, I. Steele¹,

¹ Astrophysics Research Institute, Liverpool John Moores University, IC2, Liverpool Science Park, Liverpool L3 5RF, UK

Swift/NuSTAR:

S. B. Cenko^{1, 2}, D. F. Cowen^{3, 4, 5}, J. J. DeLaunay^{3, 4}, P. A. Evans⁶, D. B. Fox^{4, 5, 7}, A. Keivani^{3, 4}, J. A. Kennea⁵, F. E. Marshall⁸, J. P. Osborne⁶, M. Santander⁹, A. Tohuvavohu⁵, C. F. Turley^{3, 4},

¹ Astrophysics Science Division, NASA Goddard Space Flight Center, Mail Code 661, Greenbelt, MD 20771, USA

² Joint Space-Science Institute, University of Maryland, College Park, MD 20742, USA

³ Department of Physics, Pennsylvania State University, University Park, PA 16802, USA

⁴ Center for Particle & Gravitational Astrophysics, Institute for Gravitation and the Cosmos, Pennsylvania State University, University Park, PA 16802, USA

⁵ Department of Astronomy & Astrophysics, Pennsylvania State University, University Park, PA 16802, USA

⁶ University of Leicester, X-ray and Observational Astronomy Research Group, Leicester Institute for Space and Earth Observation, Department of Physics & Astronomy, University Road, Leicester, LE1 7RH, UK

⁷ Center for Theoretical & Observational Cosmology, Institute for Gravitation and the Cosmos, Pennsylvania State University, University Park, PA 16802, USA

⁸ NASA Goddard Space Flight Center, Mail Code 660.1, Greenbelt, MD 20771, USA

⁹ Department of Physics and Astronomy, University of Alabama, Tuscaloosa, AL 35487, USA

VERITAS:

A. U. Abeysekara¹, A. Archer², W. Benbow³, R. Bird⁴, A. Brill⁵, R. Brose^{6, 7}, M. Buchovecky⁴, J. H. Buckley², V. Bugaev², J. L. Christiansen⁸, M. P. Connolly⁹, W. Cui^{10, 11}, M. K. Daniel³, M. Errando², A. Falcone¹², Q. Feng¹³, J. P. Finley¹⁰, L. Fortson¹⁴, A. Furniss¹⁵, O. Gueta⁷, M. Hütten⁷, O. Hervet¹⁶, G. Hughes³, T. B. Humensky⁵, C. A. Johnson¹⁶, P. Kaaret¹⁷, P. Kar¹, N. Kelley-Hoskins⁷, M. Kertzman¹⁸, D. Kieda¹, M. Krause⁷, F. Krennrich¹⁹, S. Kumar²⁰, M. J. Lang⁹, T. T.Y. Lin¹³, G. Maier⁷, S. McArthur¹⁰, P. Moriarty⁹, R. Mukherjee²¹, D. Nieto⁵, S. O'Brien²², R. A. Ong⁴, A. N. Otte²³, N. Park²⁴, A. Petrashyk⁵, M. Pohl^{6, 7}, A. Popkow⁴, E. Pueschel⁷, J. Quinn²², K. Ragan¹³, P. T. Reynolds²⁵, G. T. Richards²³, E. Roache³, C. Rulten¹⁴, I. Sadeh⁷, M. Santander²⁶, S. S. Scott¹⁶, G. H. Sembroski¹⁰, K. Shahinyan¹⁴, I. Sushch⁷, S. Trépanier¹³, J. Tyler¹³, V. V. Vassiliev⁴, S. P. Wakely²⁴, A. Weinstein¹⁹, R. M. Wells¹⁹,

P. Wilcox¹⁷, A. Wilhelm^{6,7}, D. A. Williams¹⁶, B. Zitzer¹³

¹ Department of Physics and Astronomy, University of Utah, Salt Lake City, UT 84112, USA

² Department of Physics, Washington University, St. Louis, MO 63130, USA

³ Fred Lawrence Whipple Observatory, Harvard-Smithsonian Center for Astrophysics, Amado, AZ 85645, USA

⁴ Department of Physics and Astronomy, University of California, Los Angeles, CA 90095, USA

⁵ Physics Department, Columbia University, New York, NY 10027, USA

⁶ Institute of Physics and Astronomy, University of Potsdam, 14476 Potsdam-Golm, Germany

⁷ DESY, Platanenallee 6, 15738 Zeuthen, Germany

⁸ Physics Department, California Polytechnic State University, San Luis Obispo, CA 94307, USA

⁹ School of Physics, National University of Ireland Galway, University Road, Galway, Ireland

¹⁰ Department of Physics and Astronomy, Purdue University, West Lafayette, IN 47907, USA

¹¹ Department of Physics and Center for Astrophysics, Tsinghua University, Beijing 100084, China.

¹² Department of Astronomy and Astrophysics, 525 Davey Lab, Pennsylvania State University, University Park, PA 16802, USA

¹³ Physics Department, McGill University, Montreal, QC H3A 2T8, Canada

¹⁴ School of Physics and Astronomy, University of Minnesota, Minneapolis, MN 55455, USA

¹⁵ Department of Physics, California State University - East Bay, Hayward, CA 94542, USA

¹⁶ Santa Cruz Institute for Particle Physics and Department of Physics, University of California, Santa Cruz, CA 95064, USA

¹⁷ Department of Physics and Astronomy, University of Iowa, Van Allen Hall, Iowa City, IA 52242, USA

¹⁸ Department of Physics and Astronomy, DePauw University, Greencastle, IN 46135-0037, USA

¹⁹ Department of Physics and Astronomy, Iowa State University, Ames, IA 50011, USA

²⁰ Department of Physics and Astronomy and the Bartol Research Institute, University of Delaware, Newark, DE 19716, USA

²¹ Department of Physics and Astronomy, Barnard College, Columbia University, NY 10027, USA

²² School of Physics, University College Dublin, Belfield, Dublin 4, Ireland

²³ School of Physics and Center for Relativistic Astrophysics, Georgia Institute of Technology, 837 State Street NW, Atlanta, GA 30332-0430

²⁴ Enrico Fermi Institute, University of Chicago, Chicago, IL 60637, USA

²⁵ Department of Physical Sciences, Cork Institute of Technology, Bishopstown, Cork, Ireland

²⁶ Department of Physics and Astronomy, University of Alabama, Tuscaloosa, AL 35487, USA

VLA/17B-403 team:

A. J. Tetarenko¹, A. E. Kimball², J. C. A. Miller-Jones³, G. R. Sivakoff¹

¹ Department of Physics, CCIS 4-181, University of Alberta, Edmonton, Alberta, Canada T6G 2E1

² National Radio Astronomy Observatory, 1003 Lopezville Rd, Socorro, NM, 87801, USA

³ International Centre for Radio Astronomy Research – Curtin University, GPO Box U1987, Perth, WA 6845, Australia

Contents

IceCube	S18
Calculations of systematic uncertainties for IceCube-170922A	S18
Calculation of the neutrino energy	S20
High-energy γ-ray observations	S20
Generation of the <i>Fermi</i> -LAT light curves of TXS 0506+056	S20
<i>Fermi</i> -LAT real-time follow up pipelines	S22
<i>AGILE</i>	S23
Very-high-energy γ-ray observations	S23
MAGIC	S23
H.E.S.S.	S26
VERITAS	S27
HAWC	S29
Radio, optical and X-ray observations	S30
VLA	S30
ASAS-SN	S31
Kanata/HONIR	S32
Kiso/KWFC	S32
Liverpool Telescope	S33
Subaru/FOCAS	S33
<i>Swift</i> and <i>NuSTAR</i>	S34
<i>INTEGRAL</i>	S36
Neutrino-blazar coincidence analysis	S36
Correlation analysis sensitivity	S40
Previous high-energy IceCube events	S40

IceCube

IceCube is a cubic-kilometer-sized neutrino detector (13) installed in the ice at the geographic South Pole, Antarctica between depths of 1450 m and 2450 m. The detector consists of 5160 digital optical modules (DOMs) attached to 86 cables (called strings), each instrumented with 60 DOMs. The strings are arranged in a hexagonal pattern with 125 m average horizontal spacing. Each DOM consists of a glass pressure-resistant sphere containing a photomultiplier and electronics, and operates independently producing digital signals, which are transmitted to the surface along the string. Detector construction was completed in 2010, and IceCube has operated with an $\sim 99\%$ duty cycle since then.

IceCube does not directly observe neutrinos, but rather the secondary particles produced in the neutrino interaction with matter. IceCube detects these particles by observing the Cherenkov light emitted as they travel through the ice. The ability to accurately determine the direction of a neutrino event recorded in IceCube is highly dependent on the ability to reconstruct the trajectories of these secondary particles. The secondary particles produce two distinct classes of signals within the instrumented volume: tracks and cascades. Track events, the primary focus of the IceCube alert system, are produced by muons, arising primarily from the charged-current interaction of muon-type neutrinos, which produce tracks with lengths of the order of a few kilometers. These tracks can be reconstructed with a directional uncertainty less than 1 deg, but with a large uncertainty on the neutrino energy since an unmeasured fraction of their energy is deposited outside the instrumented volume.

The IceCube neutrino alerts are generated in real time by applying direction and energy estimates to all events as the data are collected (14), and notifying the astronomical community immediately of a candidate astrophysical neutrino event. IceCube-170922A was generated by the “EHE” through-going track selection in the real-time alert system. The event selection was inspired by the event requirements used to search for cosmogenic/GZK neutrinos (69) and was modified for online use to give a larger number of astrophysical neutrinos. The sensitivity of this event selection is highlighted by the effective area for several zenith angle ranges, shown in Figure S1. The zenith angle of IceCube-170922A ($\cos(\text{zenith}) = -0.1$) was in the most sensitive zenith acceptance range, a direction where atmospheric muons are easily blocked, but neutrino absorption in the Earth has not depleted the high-energy neutrino flux.

Calculations of systematic uncertainties for IceCube-170922A The directional resolution of muon tracks passing through the IceCube detector is limited by the stochastic nature of the detected light, the finite density of DOMs where Cherenkov light is detected and the uncertainty in the optical properties of the glacial ice (70). We modeled the expected uncertainty due to these statistical and systematic effects by re-simulating a large sample of candidate events similar to the observed event, and studying the distance of their best-fitting directions from their true simulated direction.

A dedicated simulation set was generated containing muon tracks passing through the same part of the detector as the originally observed event (closer than 30 m from the original best-

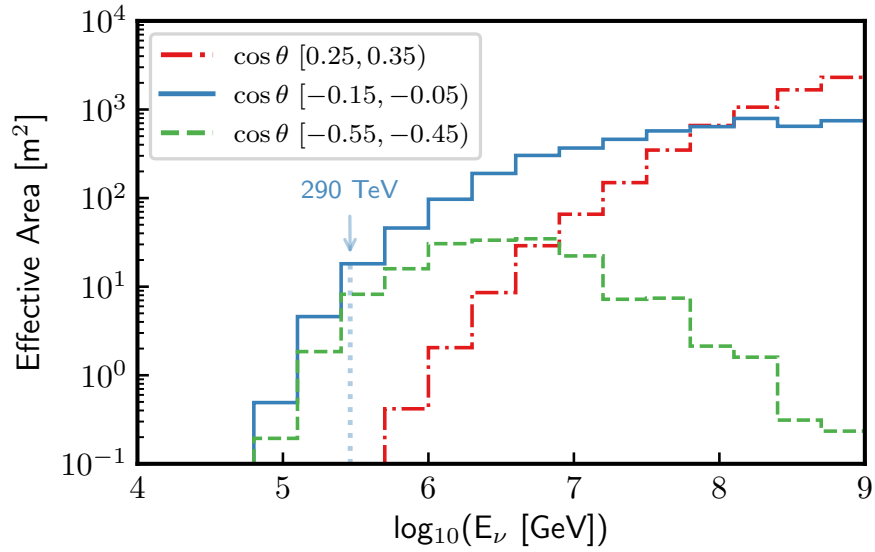


Figure S1: **Neutrino effective area for the through-going track alert channel.** Effective area for the online through-going track (“EHE”) selection in three zenith angle ranges. The zenith angle of IceCube-170922A was $\cos(\text{zenith}) = -0.1$, a preferred direction for this event selection. In the range -0.55 to -0.45 (~ 30 deg below the horizon) a strong absorption by the Earth at the highest neutrino energies is seen, while in the interval 0.25 to 0.35 (~ 20 deg above the horizon) strong cuts on track energy are needed to suppress the background from cosmic-ray muons, limiting sensitivity below 1 PeV. The most probable neutrino energy of 290 TeV is also shown.

fitting track at any point within the instrumented volume and within 2 deg of the best-fitting direction) and with a similar energy loss pattern (total deposited charge within $\pm 20\%$ of the original charge). Each event was simulated using an ice model sampled from the space of ice models compatible with the current baseline best-fitting ice model (71).

Each event in this simulation set is reconstructed using the same method as is applied to the observed event and a test statistic (TS), defined as the difference in log-likelihood (L) between the best-fitting direction and the true direction is recorded as $TS = 2(\log L_{\text{true}} - \log L_{\text{best}})$. The 50% and 90% percentiles of the distribution of TS over this simulation set are recorded and used to draw the 50% and 90% contour lines in the reconstructed likelihood fit at the corresponding likelihood ratios.

This algorithm allows us to include the uncertainty in the modeling of optical properties of the glacial ice into the fit uncertainty providing a combined statistical and systematic error (taking into account ice model systematics only). By construction, this method is not able to shift the best-fitting direction of the reconstruction and will include systematic bias on average only.

Calculation of the neutrino energy As IceCube detects the secondary muon produced in the neutrino's interaction in or near the instrumented volume, a precise determination of the neutrino energy is generally not possible for track events. However, for high-energy muons, a robust estimation of the energy of the muon as it traverses the instrumented volume is available (72, 73). Muons above ~ 1 TeV experience large stochastic energy losses due to pair production, bremsstrahlung, and photo-nuclear interactions. These energy losses grow with muon energy and can be used to estimate the energy as the muon passes through the detector.

Figure S2 presents the measured muon energy (72) observed in simulation of neutrino track events for a wide range of neutrino energies. The exact distribution of muon energies will depend on the assumed neutrino spectral index. For the observed muon energy of the IceCube-170922A track, the most-probable neutrino energy and the 90% C.L. lower limit can be calculated, and is shown in Figure S2 for three spectral indices. Using the measured spectral index of -2.13 (-2.0) for the estimated diffuse astrophysical muon neutrino spectrum (2), the most-probable neutrino energy of 290 TeV (311 TeV), a 90% C.L. lower limit on the neutrino energy of 183 TeV (200 TeV), and a 90% C.L. upper limit on the neutrino energy of 4.3 PeV (7.5 PeV) are determined.

High-energy γ -ray observations

Generation of the *Fermi*-LAT light curves of TXS 0506+056 The light curve is based on Pass 8 SOURCE class photons detected in the time interval from the start of the science phase of the mission in 4 August, 2008 to 24 October, 2017. This is the recommended class for most analyses and provides good sensitivity for analysis of point sources. Standard good-time intervals were selected excluding time intervals when the field of view of the LAT intersected the Earth, and during which bright γ -ray bursts and solar flares were observed.

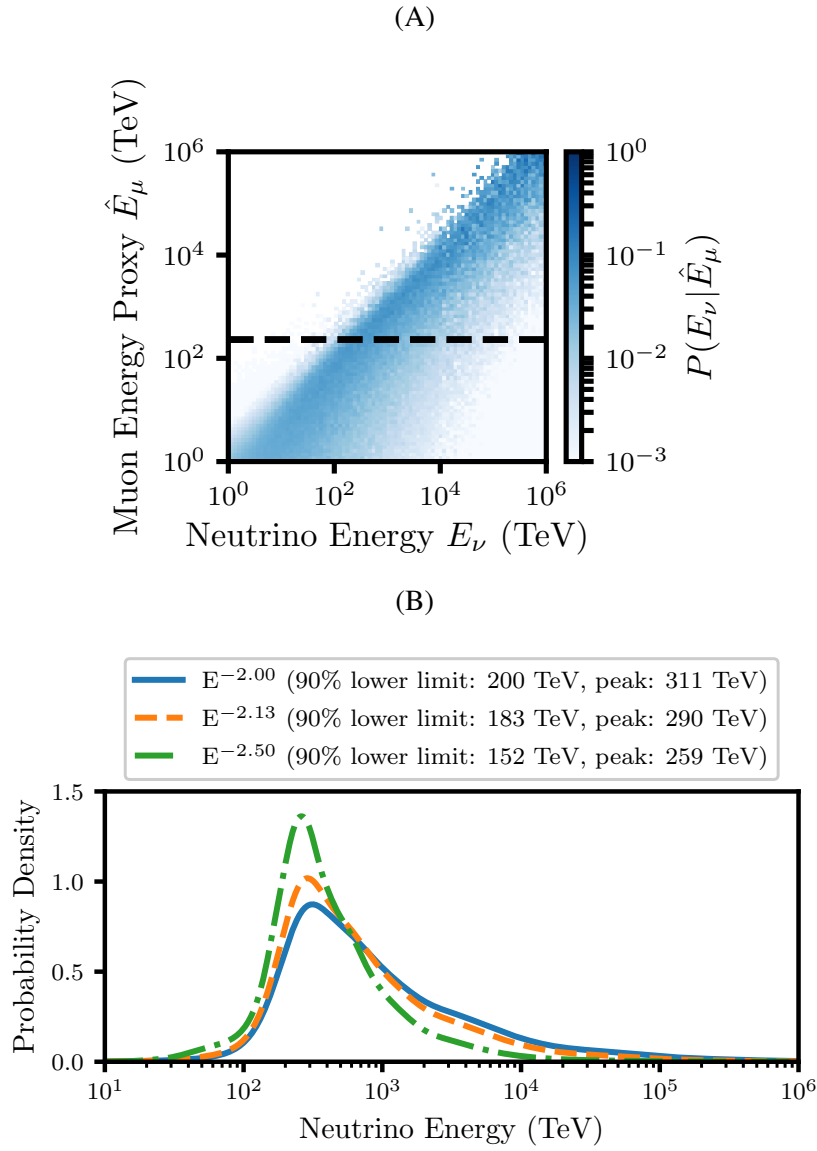


Figure S2: **Estimate of neutrino energy for IceCube-170922A.** Estimate of the neutrino energy of IceCube-170922A derived from an estimator of the muon energy in the detector (72). Note that the muon energy estimator is not equivalent to the deposited energy as the muon passed through the detector. The deposited muon energy sets a lower limit on the neutrino and muon energies. Panel A presents the 2-D distribution of neutrino energy vs. muon energy estimator (“Muon Energy Proxy”) from simulation. The observed energy estimator is indicated by a horizontal dashed black line. Assuming a prior distribution of true neutrino energies (modeled as power-law spectra with various indices), a probability distribution of true neutrino energies for the event can be derived (Panel B). For each neutrino spectral index, the 90% C.L. lower limit and most probable (“peak”) neutrino energies are listed. The result is only weakly dependent on the chosen spectral index.

A binned maximum likelihood technique (binned in space and energy) was applied using the standard *Fermi*-LAT Science-Tools package version v11r05p02 available from the *Fermi* Science Support Center (FSSC) (74) and the P8R2_SOURCE_V6 instrument response functions. Data in the energy range of 100 MeV to 1 TeV were binned into eight equally spaced logarithmic energy intervals per decade. To minimize the contamination from the γ -rays produced in Earth's upper atmosphere, a zenith angle cut of < 90 deg was applied.

A $10 \text{ deg} \times 10 \text{ deg}$ region of interest (ROI) was selected centered on the assumed source position and binned in 0.1 deg pixels. The input model for the ROI included all known γ -ray sources from the *Fermi*-LAT Third Source Catalog (3FGL) (23). We refined the best-fitting position of TXS 0506+056, including the additional data taken since the release of the 3FGL catalog. Similarly, we searched for additional sources in the ROI that may be significantly detected in the current data set, but were too faint to be included in this catalog, a standard procedure (75). The model of the ROI included the isotropic and Galactic diffuse components (gll_iem_ext_v06.fits and iso_P8R2_SOURCE_V6_v06.txt). To build the light curve, the spectral functional forms given in the 3FGL/3FHL (24) catalog for each source in the ROI were adopted. For each time interval analyzed for the light curve, the flux normalization of TXS 0506+056 and of other sources within 3 deg of it were free parameters, while the spectral shapes were fixed to their forms in the overall best-fitting model for the entire 9.5-year dataset starting in August 2008. Light curves for TXS 0506+056 were created with a time binning of 28 days over the full *Fermi*-LAT observation period, and a binning of 7 days around the time of the IceCube neutrino alert.

Similar light curves, but with an energy threshold of 1 GeV and using 28 day bins only, were compiled for all extragalactic *Fermi*-LAT sources (time binning and energy threshold were chosen to reduce the required computing resources). All sources from the four-year source catalog (3FGL) and the six-year hard source catalog (3FHL) (24) which are classified as extragalactic objects were included. Unclassified sources were added if they were more than 5 deg from the Galactic equator. Sources that were marked with an analysis flag (23), were removed. In total, 2257 sources were selected. These light curves were used in the calculation of the chance coincidence probability of the apparent neutrino-flaring blazar correlation. Very bright sources were modeled with log-parabolic spectra. For the light curve generation, the spectra of the sources were kept fixed to the values obtained from a fit over the total observation period. The limited statistics in the 28 day time bins do not allow fitting bin-by-bin spectral parameters for most sources.

***Fermi*-LAT real-time follow up pipelines** Following the neutrino alert, the quick recognition of the coincident blazar flare was made possible by automated high-level software pipelines developed by the LAT collaboration that provide continuous monitoring of the γ -ray sky. The Automated Science Processing (ASP) (76) and the *Fermi* All-sky Variability Analysis (FAVA) (30) are model independent techniques that search for variations in γ -ray flux, on timescales from hours to one week. The statistical significances of the candidate sources identified by ASP and FAVA are subsequently evaluated with the more robust maximum-likelihood technique, and

further inspected by the so-called Flare Advocates in the LAT collaboration, who communicate significant results to the external scientific community through the *Fermi* multi-wavelength mailing list, Astronomer’s Telegrams, and direct e-mail (77). Significant flares seen with ASP are reported automatically as Gamma-ray Coordinates Network notices (78).

ASP is based on the source detection algorithm PGWave (79), used also in the *Fermi*-LAT catalog pipeline to identify candidate sources. PGWave applies a two-dimensional Mexican Hat wavelet filtering to find significant clusters of photons in the LAT data from different intervals (6-hour, 1-day and 1-week) and in three energy ranges (0.1 GeV – 300 GeV, 0.1 GeV – 1 GeV and 1 GeV – 300 GeV).

FAVA searches for γ -ray variability on a weekly time scale in a low and high energy bands, *i.e.*, from 0.1 GeV to 0.8 GeV and from 0.8 GeV to 300 GeV. A photometric technique is used to compare the weekly flux to the long-term average flux over the first four years of the mission in a grid of regions covering the entire sky. If the photometric technique finds a deviation from the average in at least one of the two energy bands with a significance greater than 4σ , a maximum likelihood analysis is applied. This models the ROI, including background sources and the diffuse emission, taking into account the LAT PSF that is applied to accurately assess the statistical significance.

The FAVA results are updated in real time and are displayed in a public web interface (80). FAVA has been used as a tool to quickly find potentially variable sources in the neutrino error circle. In the time bin during which IceCube-170922A arrived, FAVA reported a significance at the position of TXS 0506+056 obtained in the likelihood analysis of 6.5σ in the low-energy band and 6.9σ in the high-energy band.

AGILE The γ -ray satellite *AGILE* (31) monitors the sky in spinning mode in the energy range 30 MeV–30 GeV. *AGILE* detected enhanced γ -ray emission above 100 MeV from the IceCube-170922A/TXS 0506+056 region and reported this in an Astronomer’s Telegram, issued 7 days after the neutrino detection (58).

A refined analysis of the data acquired with the *AGILE* imaging γ -ray detector leads to significant detections from this region on short and long timescales before and near the time of the IceCube neutrino alert, compatible with the flaring activity observed by *Fermi*-LAT from TXS 0506+056.

The *AGILE* γ -ray flux above 100 MeV from TXS 0506+056, estimated with the *AGILE* Maximum Likelihood (ML) algorithm (81) in a time window of 13 days centered at MJD 58012.5 (16 September, 2017) is found to be $(5.3 \pm 2.1) \times 10^{-7} \text{ cm}^{-2} \text{ s}^{-1}$. The corresponding energy flux density of this *AGILE* observation, scaled at 200 MeV assuming a power-law index of -2, is $(8.8 \pm 3.5) \times 10^{-11} \text{ erg cm}^{-2} \text{ s}^{-1}$.

Very-high-energy γ -ray observations

MAGIC MAGIC followed-up 4 of the 10 IceCube alerts that had been issued by 1 October, 2017. The properties of the events that were followed-up are listed in Table S1. For the alerts

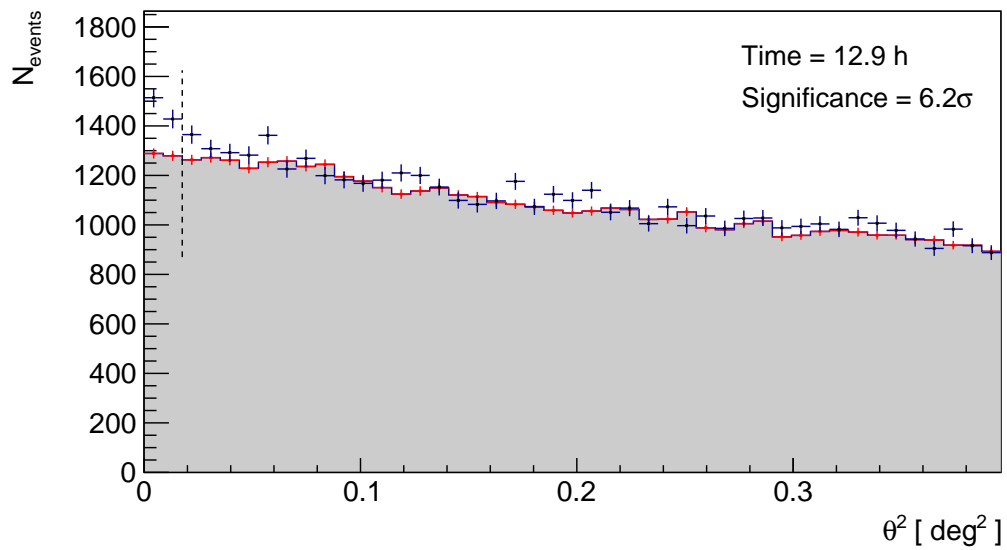


Figure S3: **Significance of the VHE γ -ray signal from TXS 0506+056 as measured by MAGIC.** Distribution of the squared angular distance, θ^2 , between the re-constructed source position and the nominal source position (blue points) or the background estimation position (shaded area) for the direction of the blazar TXS 0506+056. Statistical uncertainties on the number of signal (blue markers) or background (red markers) events are shown as vertical error bars. The number of excess events ($N_{\text{ex}} = 374 \pm 62$) and significance (82) are calculated in the region from 0 to the vertical dashed line. The estimated energy threshold is 90 GeV.

issued before September 2017 no signal was detected by MAGIC within the 50% containment radius reported by IceCube (15).

Table S1: **Neutrino alerts selected as MAGIC targets.** For each set of targeted observations, the position, directional uncertainty and reported deposited energy from the neutrino alert are listed. Additionally, MAGIC zenith angle ranges and times over which observations were made are listed.

IceCube-	160427A	160731A	170321A	170922A
<i>From IceCube:</i>				
Right Ascension [deg]	240.57	214.54	98.33	77.43
Declination [deg]	9.34	-0.33	-14.48	5.72
Median angular resolution [deg]	0.60	0.33	0.33	0.25
Deposited energy [TeV]	~140	<100	>120	>23
<i>MAGIC data taking:</i>				
Zenith angle range [deg]	18 - 26	45-65	45-60	22-52
Effective observation time [h]	1.85	1.3	1.0	12.9

MAGIC performed the first observations of the reported IceCube-170922A event direction for 2 hours on 24 September, 2017 (32 hours after the IceCube alert was issued), under non-optimal weather conditions. The standard MAGIC analysis framework MARS was used for the data analysis (34). After data quality selection, 1.07 hours of observations were used to derive an upper limit on the TXS 0506+056 flux above 90 GeV of $3.56 \times 10^{-11} \text{ cm}^{-2} \text{ s}^{-1}$ at 95% C.L. The upper limit was calculated (83) assuming a 30% systematic uncertainty in the estimated γ -ray detection efficiency of MAGIC. Observations were resumed on 28 September, 2017. With good observational conditions, data from 28 September, 2017 and 29 September, 2017 revealed hints of a signal, with an excess observed at the $\sim 3.5 \sigma$ significance level. The significance of this signal grew steadily over the following nights, motivating the long exposure. Analysis cuts optimized for Crab Nebula detection above 90 GeV were applied to the data. Integrating 12.9 hours of good quality data, MAGIC detected a clear signal with 374 ± 62 excess events at the location of the blazar TXS 0506+056 (RA: 77.36 deg, Dec: +5.69 deg (J2000) (19)). The combined signal is shown in Figure S3. The day-to-day results from the MAGIC observations are provided in Table S2. Observations with a detection significance of less than 2σ are reported as flux upper limits at 95% C.L., again including a 30% systematic uncertainty on the detection efficiency.

The MAGIC VHE γ -ray observations can be used to determine an upper limit for the redshift of TXS 0506+056 constraining the attenuation of the VHE flux due to interaction with the EBL (10, 11). These redshift limits are derived from assumed properties of the intrinsic spectrum, the measured VHE spectrum from MAGIC and models for the EBL. Here, the intrinsic spectrum is assumed to be a simple power-law $dN/dE \propto E^\gamma$, with the index constrained to be $\gamma < -1.5$. For each assumed redshift value, the VHE gamma-ray spectrum is evaluated including attenuation with the EBL and the expected rate of γ -ray events is calculated using the

MAGIC instrument response. A likelihood test is constructed by comparing the expected event rates to those observed in the source region and in the background control regions. The likelihood (L) is maximized by allowing the intrinsic spectral model parameters to vary and treating uncertainties in the cosmic-ray induced background as nuisance parameters. Performing a scan in redshift, at each step the profile likelihood following (84) is used to derive an upper limit to the source redshift at 95% C.L. When the maximum likelihood value is obtained for $z=0$, the so-called "bounded likelihood" approach is followed, *i.e.* the increase in $-2 \ln \mathcal{L}$ is computed relative to its value at $z=0$. The dominant experimental systematics are evaluated by varying the simulated total light throughput of the instrument (including effects in the atmosphere) by $\pm 15\%$. The most conservative value derived from all realizations is taken as a result for the upper limit.

For TXS 0506+056, the redshift upper limit ranges from 0.61 to 0.67 at 95% C.L, adopting the EBL models from (85–87). More conservative are the results obtained using the models from (88–90) for which the redshift upper limit ranges from 0.83 to 0.98 at 95% C.L. Considering a lower confidence level of 90% C.L. the results are in better agreement, the full range of upper limits values for all EBL models considered here being 0.41 to 0.57. Conservatively, the resulting 95% confidence level upper limit on the source redshift is $z < 0.98$ taking into account a 15% systematic uncertainty on the total light throughput of the instrument (11). These results are consistent with the measured redshift of $z=0.3365$ (28).

Table S2: **MAGIC nightly observations of TXS 0506+056.** Summary of MAGIC observations for each night’s observation of TXS 0506+056, including: date corresponding to the middle of the observation window; effective observation time after quality cuts; integral photon flux above 90 GeV, with flux upper limits (indicated by $<$) given at 95% C.L.; and per-night significance.

Date MJD	Effective time [hours]	Flux $>$ 90 GeV [ph cm $^{-2}$ s $^{-1}$]	Significance σ
58020.16	1.07	$< 3.6 \times 10^{-11}$	0
58024.21	1.25	$< 6.2 \times 10^{-11}$	1.8
58025.18	2.9	$< 5.8 \times 10^{-11}$	1.0
58026.17	3.0	$< 3.6 \times 10^{-11}$	0.95
58027.18	2.9	$1.9 \pm 1.2 \times 10^{-11}$	2.5
58028.23	0.8	$< 5.8 \times 10^{-11}$	1.7
58029.22	1.3	$5.9 \pm 1.5 \times 10^{-11}$	4.3
58030.24	0.65	$8.0 \pm 2.0 \times 10^{-11}$	5.4

H.E.S.S. The High Energy Stereoscopic System (H.E.S.S.) of imaging atmospheric Cherenkov telescopes has been routinely performing follow-up observations of high-energy neutrinos detected by IceCube and ANTARES since 2015. The H.E.S.S. system has been designed to automatically react to neutrino alerts, allowing for a search for VHE γ -ray sources in coincidence with a neutrino detection on timescales that range from a few tens of seconds to several

days (91). In the past, several neutrino alerts were followed up by H.E.S.S. (92). All follow-up observations of IceCube alerts performed by H.E.S.S. are summarized in Table S3.

Table S3: Neutrino follow-up observations performed by H.E.S.S. IceCube-170922A represents the IceCube alert which was followed up with the longest exposure and the shortest delay. The long exposure was taken following the *Fermi*-LAT announcement of TXS 0506+056 being in a high emission state (16).

Date	Alert identifier	Delay of observations	Duration of observations
Apr 27, 2016	IceCube-160427A	2d 15h	2h
Jul 31, 2016	IceCube-160731A	16h	2h
Nov 3, 2016	IceCube-161103A	12h	2h
Sep 22, 2017	IceCube-170922A	4h	3h 14m

H.E.S.S. performed follow-up observations towards the direction of the blazar TXS 0506+056 during the nights of 22 September, 2017 and 23 September, 2017 after the detection of a high-energy neutrino by IceCube. Initial observations started ~ 4 hours after the circulation of the neutrino alert (18). A preliminary on-site analysis did not reveal any significant γ -ray emission (60) for this data set. A second set of observations was acquired during the nights of 27 September, 2017 and 28 September, 2017 following the announcement of *Fermi*-LAT that TXS 0506+056 was in an active state and positionally coincident with the direction of the neutrino event (16). In total 3.25 hours of high-quality observations including the central large telescope (CT5) were obtained at zenith angles ranging from 31 deg to 46 deg.

The 3.25 hours of CT5 data were analyzed in mono mode using the Model Analysis (93) with *loose* cuts to achieve a low energy threshold. No γ -ray emission at a significant level was detected and upper limits on the VHE γ -ray flux have been calculated. The best fit spectral index of -3.9 as measured from the MAGIC data was used as the spectral assumption. Limits at 95% C.L. were derived using the Rolke method (94) and assuming a systematic uncertainty of 30%. Negative excess fluctuations of the measured counts in the signal region were taken into account by replacing them with the measured background counts, scaled with the signal region exposure time.

The limits and fluxes were calculated for each night of the data set individually. They are shown in Figure 3 and summarized in Table S4 above an energy threshold of 175 GeV. The table and figure also include flux upper limits from two archival observation campaigns from September 2015 and December 2015 to January 2016. Additionally, differential flux upper limits were calculated for the whole 3.25 hour dataset. They are depicted in Figure 4 and summarized in Table S5. All results have been cross-checked with an independent calibration and analysis chain (95), which showed consistent results.

Table S4: **Flux upper limits from H.E.S.S. for TXS 0506+056.** Archival and nightly γ -ray flux upper limits at 95% confidence level for TXS 0506+056 derived from the H.E.S.S. observations assuming an $E^{-3.9}$ energy spectrum.

MJD [days]	Observation time [h]	Flux > 175 GeV [ph cm ⁻² s ⁻¹]
57286 – 57288	5.4	$< 7.2 \times 10^{-12}$
57358 – 57390	4.4	$< 1.1 \times 10^{-11}$
58019.07	1.35	$< 1.0 \times 10^{-11}$
58024.08	0.48	$< 1.8 \times 10^{-11}$
58025.08	1.65	$< 1.8 \times 10^{-11}$

Table S5: **H.E.S.S. differential γ -ray flux upper limits for TXS 0506+056.** Flux upper limits (f_γ) at 95% C.L. obtained for the full TXS 0506+056 H.E.S.S. data set and assuming an $E^{-3.9}$ energy spectrum. E_{\min} and E_{\max} define the energy range over which the differential flux upper limit is derived.

E_{\min} [TeV]	E_{\max} [TeV]	f_γ [cm ⁻² s ⁻¹ TeV ⁻¹]
0.16	0.28	$< 6.6 \times 10^{-11}$
0.28	0.48	$< 2.1 \times 10^{-11}$
0.48	0.85	$< 4.5 \times 10^{-12}$
0.85	1.50	$< 1.8 \times 10^{-12}$
1.50	2.63	$< 5.9 \times 10^{-13}$
2.63	4.62	$< 3.3 \times 10^{-13}$

VERITAS The Very Energetic Radiation Imaging Telescope Array System (VERITAS) (33), was used to perform follow-up observations of IceCube-170922A. Observations started on 23 September 2017 at 09:06 UTC, 12.2 hours after the IceCube detection, accumulating an exposure of one hour under partial cloud coverage in normal observation mode. Additional VERITAS observations were collected following the *Fermi*-LAT report of the detection of a hard GeV γ -ray flare from the blazar TXS 0506+056 located within the neutrino error region. Five additional hours were collected during the period between 28 September 2017 at 08:57 UTC and 30 September 2017 at 11:04 UTC (5.5 to 7.6 days after the neutrino detection), resulting in a total exposure of 5.5 hours for the entire data set after quality cuts.

An analysis of the data optimized for soft-spectrum sources shows no evidence of γ -ray emission at the blazar location or anywhere else in the 3.5 deg VERITAS field of view. The integral γ -ray flux upper limit derived from the VERITAS observations at the TXS 0506+056 position is $1.2 \times 10^{-11} \text{ cm}^{-2} \text{ s}^{-1}$ at 95% C.L. above an energy threshold of 175 GeV assuming the power-law photon spectral index of -3.9 from the MAGIC data.

All limits were calculated using the method described in (84) with the requirement of a minimum of 10 events present in the off-source region to reduce the uncertainty in the estimation of the background rate. The systematic uncertainty in the energy scale of VERITAS is 15% to 20% (96). Differential γ -ray flux upper limits are listed in Table S7 at 95% C.L. for observations obtained within two weeks of the neutrino alert. These observations, with the addition of historical observations of the blazar TXS 0506+056 performed by VERITAS prior to the detection of IceCube-170922A, were used to calculate light-curve integral flux upper limits above a threshold of 175 GeV which are listed in Table S6. For observation periods where the VERITAS energy threshold was higher than 175 GeV, the upper limits were scaled to this value by conservatively assuming a photon spectral index of -4.3 based on a 1σ deviation of the index from the MAGIC data (-3.9 ± 0.4).

VERITAS observations of IceCube-170922A were performed as part of the VERITAS neutrino follow-up program (97). Prompt follow-up observations performed by VERITAS under this program in response to alerts prior to the IceCube-170922A are included in Table S8.

HAWC The High-Altitude Water Cherenkov (HAWC) γ -ray observatory (36) has a very wide field of view (~ 2 sr) and operates with $>95\%$ uptime, enabling it to survey $2/3$ of the sky above ~ 1 TeV. The IceCube-170922A location was not in the field of view of HAWC at the time of the event. Three time periods were searched for VHE γ -rays with no evidence for a source in any of the studies. For all these searches, the 95% C.L. upper limits on the flux above 1 TeV assume a spectral index of -3.9 . The 1 TeV threshold for flux limits was chosen so that the limit depends very weakly on the spectral index.

First, a time integrated search at the location of TXS 0506+056 was made using archival data from 26 November 2014 to 27 August 2017. The upper limit on the flux is $1.6 \times 10^{-13} \text{ cm}^{-2} \text{ s}^{-1}$. Second, the transits of TXS 0506+056, in HAWC, right before and right after the time stamp of IceCube-170922A (22 September 2017, from 08:37:15 to 14:29:45 UTC and 23 Septem-

Table S6: **Flux upper limits from VERITAS for TXS 0506+056.** Nightly γ -ray flux upper limits at 95% confidence level from VERITAS above an energy threshold of 175 GeV, assuming an $E^{-3.9}$ energy spectrum.

MJD [days]	Time window (half width) [days]	Flux > 175 GeV [ph cm ⁻² s ⁻¹]
57685.4392	± 0.0104	$< 6.8 \times 10^{-12}$
57686.4500	± 0.0200	$< 5.7 \times 10^{-12}$
57786.1544	± 0.0142	$< 1.1 \times 10^{-11}$
58019.3971	± 0.0124	$< 2.1 \times 10^{-10}$
58024.4380	± 0.0653	$< 1.4 \times 10^{-11}$
58025.3932	± 0.0219	$< 5.2 \times 10^{-11}$
58026.4399	± 0.0211	$< 1.1 \times 10^{-11}$

Table S7: **VERITAS differential γ -ray flux upper limits for TXS 0506+056.** Differential γ -ray flux upper limits (f_γ) derived from VERITAS observations of the TXS 0506+056 blazar position. E_{\min} and E_{\max} define the energy range over which the differential flux upper limit is derived and are based on observations obtained within 2 weeks of the neutrino alert.

E_{\min} [TeV]	E_{\max} [TeV]	f_γ [cm ⁻² s ⁻¹ TeV ⁻¹]
0.141	0.316	$< 5.4 \times 10^{-11}$
0.316	0.708	$< 6.4 \times 10^{-12}$
0.708	1.585	$< 5.3 \times 10^{-13}$
1.585	3.548	$< 8.0 \times 10^{-14}$

ber 2017, from 08:33:19 to 14:25:49 UTC) were used. The upper limit on the flux is 3.6×10^{-12} cm⁻² s⁻¹. Finally, data from 9 September 2017 09:28:22 to 19 September 2017 14:41:33 UTC and from 21 September 2017 08:41:11 to 6 October 2017 13:34:43 UTC was used (the time gap was due to a power outage after Mexico’s earthquake on 19 September 2017), roughly coinciding with the *Fermi*-LAT reported flare (16), results in an upper limit of the flux of 2.1×10^{-12} cm⁻² s⁻¹. Quasi-differential upper limits on $E^2 dN/dE$ using HAWC data are presented in Figure 4 using the method described in (99).

Radio, optical and X-ray observations

VLA The Karl G. Jansky Very Large Array (VLA) (37) was used to obtain radio frequency observations of the blazar TXS 0506+056, following its identification as the potential astrophysical origin of IceCube-170922A (18). The VLA observations were taken over six epochs between 5 October 2017 and 21 November 2017, in *S* (2 – 4 GHz), *C* (4 – 8 GHz) and *X* (8 – 12 GHz) bands. The array was split into 3 sub-arrays, with 8 antennas observing at *C* band, 9 antennas at *X* band, and 10 antennas observing at *S* band, to simultaneously sample the source

Table S8: **Neutrino follow-up observations performed by VERITAS.**

IceCube Alert ID	UTC Date	Obs delay [hr]	Exposure [hr]	VERITAS publication
IceCube-160427A	27 April 2016	0.05	3.15	(98)
IceCube-161103A	3 November 2016	0.06	1.5	-
IceCube-170321A	21 March 2017	19.3	0.5	-
IceCube-170922A	22 September 2017	12.2	5.5	(59)

flux density across the three receiver sets. The antennas for each sub-array were selected so that all sub-arrays had similar beam patterns. A total of 10.8 minutes on target were acquired in each band, per epoch, cycling continuously between the calibrator (1 min) and target (5.4 min). All observations were made with the 8-bit samplers, using 2 base-bands with 8 spectral windows of 64 2 MHz channels each, giving a total bandwidth of 1.024 GHz per base-band. The flagging, calibration, and imaging were carried out within the Common Astronomy Software Application package (CASA, v5.1.1; (100)) using standard procedures.

For all sub-arrays, 3C 138 (QSO J0521+166) was applied as the flux calibrator, and QSO J0502+0609 as the phase calibrator. When imaging, a natural weighting scheme was used to maximize sensitivity. A phase-only self-calibration was performed on the data (with 10 second solution intervals) to correct for phase de-correlation of the unresolved emission. No self-calibration was performed when the preliminary flux densities of the first 4 epochs were reported in (38). As expected, phase de-correlation was strongest at higher frequencies, and on 6 October 2017, that was measured to have significantly stronger tropospheric contribution to the interferometric phase.

TXS 0506+056 was detected significantly in all bands/epochs. Observation times and flux densities for TXS 0506+056 are shown in Table S9, where a point source was fitted in the image plane (with the CASA imfit task) to obtain each of these measurements. The reported uncertainties on the flux density do not include the $\sim 5\%$ systematic uncertainty on the absolute flux scale calibration. This uncertainty should be included when comparing these flux density measurements to those with other facilities. Flux densities and the measured $\nu^{\sim 0.2}$ spectra were relatively constant from 5 - 12 October 2017 (epochs 1–4). The source brightened slightly above 4 GHz on 24 October 2017. The final data (on 21 November 2017) indicate a ($\sim 20\%$) brighter source at frequencies below 6 GHz, and spectral steepening at higher frequencies ($\nu^{\sim 0.2}$ at lower frequencies and $\nu^{\sim -0.1}$ at higher frequencies). This peak may be due to synchrotron self-absorption. An injection of energy (*e.g.*, jet ejecta) that moves downstream and reaches the radio photosphere for $\nu \sim 10$ GHz by 21 November 2017, could provide a spectral turnover.

ASAS-SN The All-Sky Automated Survey for Supernovae (ASAS-SN) consists of two units — one at Haleakala, Hawaii and one at Cerro Tololo in Chile — each comprising four robotic 14 cm telescopes. ASAS-SN has been monitoring the visible sky to ~ 17 mag in the *V* band on a 2–3 day cadence (101).

An initially extracted light curve spanning from August 2013 to October 2017 from the ASAS-SN Sky Patrol (40) interface indicated that TXS 0506+056 had brightened by $\Delta V \sim 0.5$ mag over the 50 days prior to the neutrino event (54). While the source shows significant variability, the recent data indicate this is the brightest this object has been in several years. This source was observed at higher cadence compared to the regular survey for a few days after the neutrino detection thanks to automated ASAS-SN target-of-opportunity observations triggered by the public IceCube alerts.

The ASAS-SN V band light curve is shown in Figure 3 and is extracted using aperture photometry on the difference images and combining the multiple images obtained at each epoch. Proximity to the Sun prevented observations from April to July 2017. The source had a relatively steady flux of $V \sim 14.5$ mag in the previous observing season (August 2016 to April 2017) and brightened from a minimum of $V \simeq 15.0$ mag in the season before that (July 2015 to March 2016). ASAS-SN images have $\sim 15''$ FWHM PSF. There is a modest dilution of the variability amplitude through the contributions of a nearby source to the photometry aperture.

Kanata/HONIR TXS 0506+056 was monitored in the imaging mode with the Hiroshima Optical and Near-InfraRed camera (HONIR) (42) installed at the Cassegrain focus of the 1.5-m Kanata telescope at the Higashi-Hiroshima Observatory, starting ~ 20 hours after the IceCube-170922A alert. Polarimetric observation with HONIR was also performed since 30 September 2017, revealing that TXS 0506+056 was highly polarized ($\sim 7\%$ in R band). The magnitude was measured by relative photometry with respect to the nearby reference stars listed in the AAVSO Photometric All-Sky Survey (102). For polarimetry of TXS 0506+056, strongly-polarized standard stars (BD +64 106 and BD +59 389; (103)), and several unpolarized standard stars, were observed for calibration. The instrumental polarization for HONIR was confirmed to be negligibly small ($\lesssim 0.1\%$), and no correction was applied. The foreground Galactic extinction ($E_{B-V} = 0.096$, (104)) indicates that the interstellar polarization is $p_R \leq 0.9\%$ (105), suggesting the observed large polarization is predominantly intrinsic to the blazar. Possible blazar candidates were selected from flat spectrum radio sources of $\alpha > -0.5$ (where α is a spectral index defined as $F_\nu \propto \nu^\alpha$) from 0.15 GHz TGSS (106) and 1.4 GHz NVSS (107) catalogs. Four flat-radio-spectrum objects (including TXS 0506+056) found within the IceCube-170922A error region were examined. Visual inspection of differenced images taken on 23 September 2017 and 24 September 2017 showed a clear fading of blazar TXS 0506+056 (52).

Kiso/KWFC Monitoring observations of TXS 0506+056 in optical g , r , and i bands commenced after the neutrino alert with the Kiso Wide Field Camera (43) attached to the 1.05 m Kiso Schmidt telescope. The point spread function sizes are 4-6 arcsec FWHM, well separated from a nearby bright star in the KWFC images. The data were reduced in the same manner as that for a previous supernova survey (108). Compared with previous observations (109), the flux of the object increased by approximately 1.0 mag and remained in a bright phase until at least November 2017.

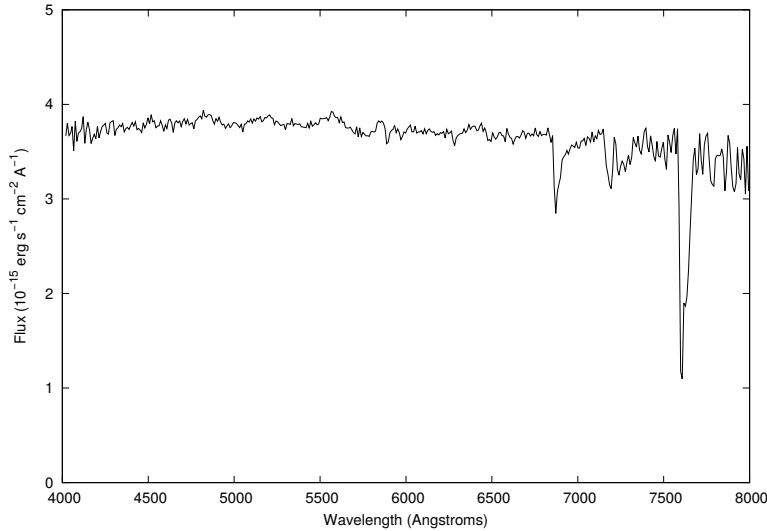


Figure S4: **Liverpool Telescope measured spectrum of TXS 0506+056.** Spectrum of TXS 0506+056 obtained with the low resolution ($R \approx 350$) spectrograph SPRAT on the Liverpool Telescope on 29 September 2017. The spectrum shows a smooth continuum typical of a BL Lac object, with absorption features that are telluric or attributable to Galactic interstellar Na I absorption.

Liverpool Telescope Low resolution (resolving power ~ 350 , $4000 - 8000 \text{ \AA}$) optical spectra of TXS 0506+056 were obtained with the SPRAT spectrograph of the 2.0 m Liverpool Telescope (41) on 29 September 2017 02:31 UTC and 30 September 2017 02:15 UTC. The spectra, shown in Figure S4, showed no sign of variation and are typical of a BL Lac object, showing a smooth continuum. The only feature seen is attributable to Galactic interstellar Na I absorption. No redshift measurement is possible from the optical spectra. Both spectra have a flat spectral energy distribution with $F_\lambda \sim 4 \times 10^{-15} \text{ ergs s}^{-1} \text{ cm}^{-2} \text{ \AA}^{-1}$, which is bluer than the (similarly featureless) spectrum presented in (110), indicating a likely “bluer-when-brighter” behavior.

Subaru/FOCAS Low resolution (resolving power ~ 400 in $4700-8200 \text{ \AA}$ and ~ 1200 in $7500-10500 \text{ \AA}$) optical spectra were obtained with the Faint Object Camera and Spectrograph (45) on the 8.2-m Subaru telescope on 30 September 2017 and 1 October 2017, respectively, and are shown in Figure S5. The data was reduced with IRAF software in the standard manner (111). The signal-to-noise ratios are roughly 350 per pixel. The spectra are almost featureless smooth continua over the entire wavelength range except for a weak emission line is marginally detected around $8,800 \text{ \AA}$, corresponding [NII] detected in (28).

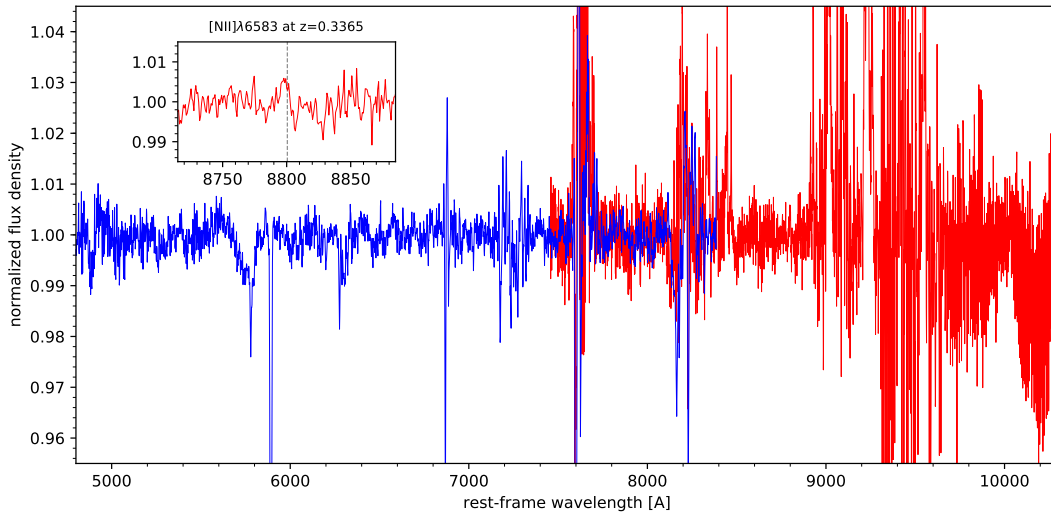


Figure S5: **Subaru/FOCAS spectra of TXS 0506+056.** Normalized spectra taken with FOCAS on the 8.2-m Subaru telescope on 30 September 2017 (blue) and 1 October 2017 (red), in two different settings of the grism and order-sort filters. Note that some atmospheric absorption effects remain. The [NII] line detected by Paiano et al. (28) is marginally detected as shown in the inset figure.

Swift and NuSTAR *Swift* carried out rapid-response follow-up observations of IceCube-170922A as a mosaic of 19 pointings beginning 3.25 hours after the neutrino detection, lasting 22.5 hours, and accumulating approximately 800 s exposure per pointing. The tiled *Swift* XRT observations together cover a roughly circular region centered on RA, Dec (J2000) = (77.2866 deg, +5.7537 deg), with radius of approximately 0.8 deg and sky area 2.1 deg². XRT data was analyzed automatically as data was received at the University of Leicester, via the reduction routines described in (112, 113). Nine sources were detected in the covered region down to a typical achieved depth of 3.8×10^{-13} erg cm⁻² s⁻¹ (0.3 keV – 10.0 keV). All of the detected sources were identified as counterparts to known and cataloged stars, X-ray sources, or radio sources (114). Source 2 from these observations, located 0.077 deg from the center of the neutrino localization, was identified as the likely X-ray counterpart to TXS 0506+056.

Following the *Fermi*-LAT report that TXS 0506+056 was in an enhanced GeV-flaring state, a *Swift* monitoring campaign was initiated (55) and a single *NuSTAR* observation (56) was requested. *Swift* monitoring observations began on 27 September 2017 with 12 epochs (and 24.7 ks total exposure time) completed by 23 October 2017 (Table S10). *NuSTAR* observations over 02:23 to 17:48 UTC on 29 September 2017 yielded 23.9 ks (24.5 ks) exposure in the A (B) units, respectively, after processing with *NuSTAR* standard software tools (115) (SAAMODE=strict). With count rates of 21.3 ct ks⁻¹ (20.8 ct ks⁻¹) in the A (B) units, TXS 0506+056 is well detected in these data.

For joint analysis purposes, the *Swift* XRT data from the 27 September 2017 and 30 Septem-

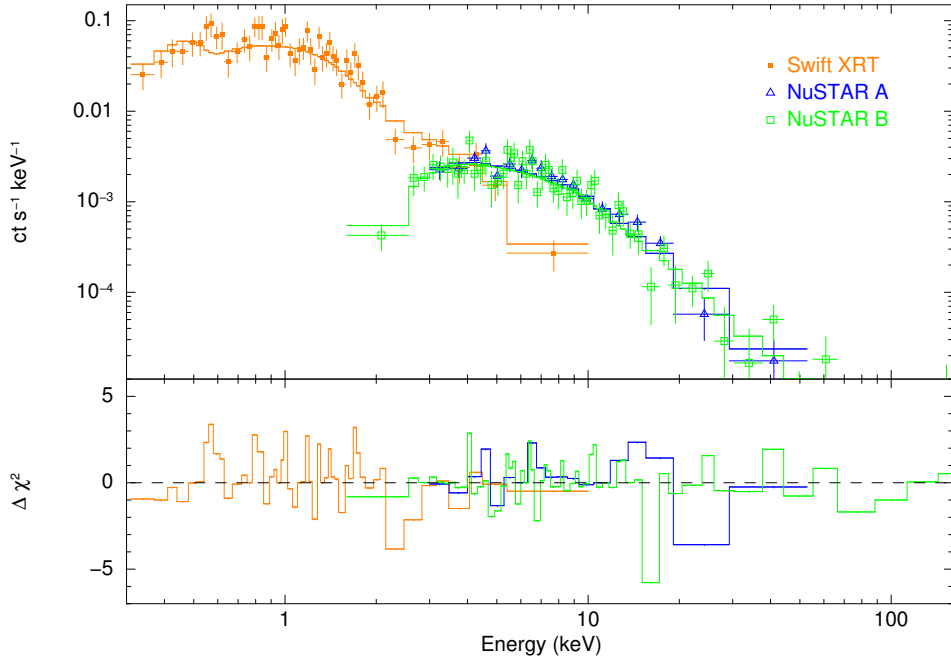


Figure S6: **Swift-XRT and NuSTAR observations of TXS 0506+056.** The spectrum of TXS 0506+056 from a joint fit to Swift-XRT data with the NuSTAR spectrum of TXS 0506+056. Swift-XRT data are shown with orange markers and the two NuSTAR units are shown with blue and green markers.

ber 2017 monitoring observations were selected; processing of these data occurred with the online tools of the UK *Swift* Science Data Centre (112), yielding a 6.9 ks exposure, with the source exhibiting a count rate of 88 ct ks^{-1} .

The resulting TXS 0506+056 spectrum over 0.3 keV – 100 keV is adequately fit with a double power-law spectral model with the galactic hydrogen column density (N_{H}) fixed at the expected Galactic value, $N_{\text{H}} = 1.11 \times 10^{21} \text{ cm}^{-2}$ (Fig. S6).

The soft power-law component has the photon index $\Gamma_s = -2.78 \pm 0.30$ and yields a flux of $(1.78 \pm 0.41) \times 10^{-12} \text{ erg cm}^{-2} \text{ s}^{-1}$ over 0.3 keV – 10 keV, while the hard power-law component has the photon index $\Gamma_h = -1.43 \pm 0.25$ and yields a flux of $(4.7 \pm 2.4) \times 10^{-12} \text{ erg cm}^{-2} \text{ s}^{-1}$ over 3 keV – 100 keV. The hard power-law component that dominates over the NuSTAR bandpass extrapolates to $\nu F_\nu = 5.8 \times 10^{-11} \text{ erg cm}^{-2} \text{ s}^{-1}$ at $E_\gamma = 20 \text{ MeV}$, consistent with the flux observed over the *Fermi*-LAT bandpass (0.1 GeV – 100 GeV) at that epoch.

To characterize the X-ray flux and spectral variability of TXS 0506+056, we performed a power-law fit to each individual *Swift* XRT observation (Table S10), as well as to the summed spectrum from all listed epochs. The 14 October 2017 observation is excluded from the spectral analysis due to low exposure time. The summed spectrum (24.7 ks total exposure) is adequately fitted with a single power-law spectral model having $N_{\text{H}} = 1.11 \times 10^{21} \text{ cm}^{-2}$, resulting in a pho-

ton index $\Gamma = -2.46 \pm 0.06$ and mean flux of $3.06 \times 10^{-12} \text{ erg cm}^{-2} \text{ s}^{-1}$ (0.3 keV – 10.0 keV). This source has been observed on multiple previous occasions with the *Swift* XRT (113). In past observations, TXS 0506+056 exhibits a typical count rate of 40 ct ks⁻¹, with one observation at approximately 90 ct ks⁻¹. The source was therefore in an active X-ray flaring state by comparison to historical X-ray measurements (cf. Figure 3).

Individual monitoring observations show evidence of spectral variability; photon indices and X-ray flux measurements for each epoch are provided in Table S10, and the variations in photon index are shown in Figure 3. The χ^2 statistic for photon index variations (compared to a fixed $\Gamma = -2.46$ from the summed spectrum) is 33.91 for 11 degrees of freedom ($p = 3.7 \times 10^{-4}$).

INTEGRAL The *INTEGRAL* observatory (51) has surveyed the sky in hard X-rays and soft γ -rays at energies above 20 keV since October 2002. At the time of the IceCube-170922A detection, *INTEGRAL* was performing a slew between two pointings, and the sensitivity to emission from the IceCube neutrino direction depends on time. Combining data from the Spectrometer on *INTEGRAL* - Anti-Coincidence Shield (SPI-ACS) and Imager on Board the *INTEGRAL* Satellite - Veto (IBIS/Veto) instruments, we set a limit on the 8-second peak flux at any time within ± 30 minutes from the time of the alert at a level of $10^{-7} \text{ erg cm}^{-2} \text{ s}^{-1}$, assuming a power-law spectrum with a slope of -2 (57).

The location of IceCube-170922A was serendipitously in the field of view of *INTEGRAL* from 30 September 2017, 05:36:04 UTC (MJD 58026.23) to 24 October 2017, 16:20:25 UTC (MJD 58050.68). Due to the large off-axis angle, the resulting effective exposure was only 32 ks. In the combined mosaicked images of *INTEGRAL* Soft Gamma-Ray Imager data we did not detect the source, and set an upper limit (3σ C.L.) on the average flux from the position of TXS 0506+056 of $7.1 \times 10^{-11} \text{ erg cm}^{-2} \text{ s}^{-1}$ in the 20 keV – 80 keV energy range and $9.8 \times 10^{-11} \text{ erg cm}^{-2} \text{ s}^{-1}$ in the 80 keV – 250 keV energy range.

Neutrino-blazar coincidence analysis

In order to calculate the chance probability of a coincidence between a neutrino alert, such as IceCube-170922A, and a flaring blazar, several hypothesis tests have been performed covering a range of assumptions on the spatial and temporal signal distribution and neutrino emission scenarios. For each hypothesis we create a test statistic (TS) that we use in a likelihood ratio test to compare the signal hypothesis to the null hypothesis. In each case our null hypothesis assumes no correlation between a cataloged γ -ray source and high-energy neutrino events (including atmospheric neutrinos and misidentified muons, and the astrophysical neutrinos). The signal hypothesis assumes that neutrino events originate from cataloged *Fermi*-LAT blazars, given a particular model for the correlation between the neutrino and γ -ray emission.

As a common framework for all the analyses, we start with an unbinned likelihood function defined in a similar way to previous IceCube point source analyses (3, 4):

$$\mathcal{L} = \prod_i^N \left(\frac{n_s}{N} \mathcal{S} + \left(1 - \frac{n_s}{N}\right) \mathcal{B} \right), \quad (\text{S1})$$

with signal and background probability density functions (PDFs) denoted as \mathcal{S} and \mathcal{B} , respectively. N is the total number of events and n_s the number of signal events. Additionally, there is one constrained nuisance parameter included in the likelihood for the γ -ray energy flux (or flux ratio) normalization of each source using the method from (116), treating the flux error as a normal distribution. Including the nuisance factor does not have a significant influence on the results. In the simple case considered here, only a single event enters the analysis, i.e. $N = 1$.

We define a test statistic of the form

$$TS = 2 \log \frac{\mathcal{L}(n_s = 1)}{\mathcal{L}(n_s = 0)} = 2 \log \frac{\mathcal{S}}{\mathcal{B}}. \quad (\text{S2})$$

In this definition the likelihood ratio test reduces to a test between two fixed alternate hypotheses and TS can take negative values for background-like events. The signal PDF consists of three independent parts, a spatial factor, a flux weight factor, and a factor for the detector acceptance:

$$\mathcal{S}(\vec{x}, t) = \sum_s \frac{1}{2\pi\sigma^2} e^{-|\vec{x}_s - \vec{x}|^2 / (2\sigma^2)} w_s(t) w_{\text{acc}}(\theta_s), \quad (\text{S3})$$

where the sum runs over all 2257 extragalactic *Fermi*-LAT sources, s . Their light curves were constructed as described above for the analysis of the *Fermi*-LAT light curves for TXS 0506+056, where 28-day wide bins are used to characterize the γ -ray activity at time t . The term w_{acc} is the IceCube acceptance as a function of zenith angle (normalized over all zenith angles, θ_s), assuming a neutrino signal spectral index $\gamma = -2.13$. This factor accounts for the zenith-dependent sensitivity of the IceCube detector. The function $w_s(t)$ derived from the *Fermi*-LAT light curve, describes the model-dependent relation between the γ -ray emission and the expected neutrino flux from source s as a function of time.

The leading factor inside the summation is the spatial weight accounting for the distance of a source at position, \vec{x}_s , to the reconstructed neutrino direction, \vec{x} , in terms of the reconstruction uncertainty σ of the neutrino direction, which is found on a per-event basis (3). The uncertainty of the γ -ray source position is negligible compared to the neutrino angular uncertainty. Sources at large angular distances from the neutrino are assigned a negligible weight by the spatial factor, which models the IceCube point-spread function (PSF). The ‘‘signalness’’ of a neutrino event, as mentioned in the main text, is a quantity constructed by the realtime system from the energy and zenith angle estimates, to rapidly allow an assessment of whether an event is a worthy target of opportunity. It does not enter into the likelihood.

The background PDF is described by the zenith acceptance, $\mathcal{P}_{BG}(\sin \theta)$, which is a probability density function describing the zenith distribution of the alert events that are due to background.

$$\mathcal{B}(\vec{x}) = \frac{\mathcal{P}_{BG}(\sin \theta)}{2\pi}, \quad (\text{S4})$$

where θ is the zenith angle of the reconstructed neutrino direction \vec{x} . To construct a background TS distribution we randomly draw neutrino events from an IceCube all-sky Monte Carlo sample containing muon-neutrinos and misidentified muons from air-showers and astrophysical neutrinos with energies according to the spectral shape presented in (2).

The final p-value is then determined by calculating the fraction of background TS values larger than the measured one for IceCube-170922A. Note that the overall normalization of \mathcal{S} and \mathcal{B} does not influence the final p-value, but only shifts the TS distribution.

As the production mechanisms of neutrinos and γ -rays in astrophysical environments are poorly understood, three models connecting the γ -ray and the neutrino flux are considered for $w_s(t)$. All models are based on the assumption that at least part of the γ -ray emission is of hadronic origin. In all cases the extragalactic sources from the *Fermi*-LAT catalog are used.

Model 1: The neutrino energy flux is proportional to the γ -ray energy flux of the source in the time bin where the neutrino arrives (4). This is motivated by the fact that a similar amount of energy is expected to be channeled into the neutrino and γ -ray emission, if pion decays from pp or p γ interactions dominate at high energies. Alternatively, it can be relevant even if emission from electrons dominate, as long as protons and electrons are accelerated at a fixed power ratio.

In this case the weight is equal to the γ -ray energy flux defined as:

$$w_s(t) = \phi_E(t) = \int_{1 \text{ GeV}}^{100 \text{ GeV}} E_\gamma \frac{d\phi_\gamma(t)}{dE_\gamma} dE_\gamma, \quad (\text{S5})$$

where $\phi_\gamma(t)$ is the photon flux from the γ -ray light curves, at time t . The resulting pre-trial p-value is $2.1 \cdot 10^{-5}$, corresponding to a Gaussian equivalent one-sided probability of 4.1σ .

Model 2: The neutrino production and detection probability depend only on the relative flux change of the γ -ray source emission around the neutrino event time, t . This prevents missing a correlation with γ -dim sources that may be much brighter in neutrinos than γ -rays, at the cost of some sensitivity to bright sources.

Here,

$$w_s(t) = \phi_\gamma(t) / \langle \phi_\gamma \rangle, \quad (\text{S6})$$

where $\langle \phi_\gamma \rangle$ is the time averaged γ -ray flux from the source. The resulting pre-trial p-value is $2.5 \cdot 10^{-5}$ (4.1σ).

Model 3: The neutrino energy flux is proportional to the γ -ray energy flux predicted in the very-high-energy (VHE) γ -ray regime (100 GeV – 1 TeV). This approach is triggered by the detection of VHE γ -ray emission by MAGIC.

If a similar amount of energy is channeled into neutrinos and γ -rays in the sources (as in Model 1) the energy flux is expected to be correlated with the neutrino energy flux. The VHE γ -ray emission is closer in energy to the observed neutrino and might therefore be a better indicator for high-energy particle acceleration.

As no unbiased survey of the sky exists at energies above 100 GeV, the 2257 extragalactic *Fermi*-LAT sources were considered. The VHE spectral functional form was obtained through extrapolations of the spectrum measured by *Fermi*-LAT in the energy range from 1 GeV – 100 GeV over the entire 9.5-year *Fermi*-LAT exposure. The VHE spectral normalization was scaled to match each monthly bin of the *Fermi*-LAT light-curve. Since any additional softening of the spectrum in the VHE energy band due to limitations in the acceleration capabilities of the source, limitations in the radiative efficiency, absorption within the source or in the extragalactic background light (EBL) would yield a lower flux, these extrapolations represent a conservative assumption.

The pre-trial p-value in this case is $4.9 \cdot 10^{-5}$ (3.9σ). Including absorption by the extragalactic background light for the extrapolations does not change the p-value significantly. Extrapolations to VHE energies are potentially uncertain for weaker, hard-spectrum sources with a spectral shape not well constrained in the high-energy band. For the sources within the Fermi 3FHL catalog, the results obtained with the best fit from 9.5 years of *Fermi*-LAT data (*e.g.* power-law or log-parabola or power-law with exponential cutoff) were compared to extrapolations based on the power-law fit. Minimal impact was found on the weights in the energy band considered.

A test was applied to assess the impact of the flux weight on the chance coincidence probability, and to quantify the probability of a simple spatial coincidence between a neutrino alert and a cataloged source. To achieve that, the flux weight was set to one for all cataloged sources ($w_s(t) = 1$). This choice implies that the intensities of the neutrino and γ -ray emission are not correlated for LAT catalog sources. In this case, the pre-trial p-value is reduced to 0.0017 (2.9σ). Another set of tests was applied to check the impact of the spatial factor in the likelihood description above, given that IceCube-170922A was found very close to the source (at a distance of 0.1 deg, much smaller than the 90% angular error typical for IceCube through-going track events). The Gaussian PSF factor is replaced by 1 in this test for neutrino events within 0.5 deg of the source and by 0 otherwise. If the full PSF information is not used, the significance values drop by $0.4\sigma - 0.5\sigma$ for the three models described above.

Prior to 22 September 2017, IceCube had publicly issued 9 alerts. In addition 41 archival events (before April 2016) were inspected, which would have triggered alerts if the realtime system had been operational. Since no *Fermi*-LAT source comparable in energy flux to TXS 0506+056 was found within the 90% error region of any of the potential previous alerts, the global p-value, corrected for all trials, can be obtained from the pre-trial local p-value $p_{\text{global}} = 1 - (1 - p_{\text{local}})^N$, where $N = 51$ is the number of trials. For $p_{\text{local}} \ll 1$ this simplifies to $p_{\text{global}} \approx p_{\text{local}}N$. For Model 1 and 2, the trial factor correction yields a global p-value of 3.0σ . Five of the 10 IceCube alerts were followed-up by VHE observations. With the exception of IceCube-170922A,

no alert has been observed by an IACT more than 3.2 hours. Considering 5 alerts only, the global p-value for Model 3 based on the formula above becomes 3.5σ . For 10 (51) alerts the corresponding p-values are 3.3σ (2.8σ). Since IACTs do not follow up all IceCube alerts, it is not clear if these values are relevant in this case.

Correlation analysis sensitivity To demonstrate that the test described above is sensitive to our signal hypothesis, an ensemble of simulated IceCube observations was generated assuming a proportionality between the instantaneous γ -ray and neutrino emission, corresponding to Model 1 above.

In these simulations, the signal normalization is set such that the expected number of IceCube real-time alerts originating from cataloged extragalactic *Fermi*-LAT sources is equal to 1. Here we have assumed that the purity of the IceCube real-time stream is $\sim 40\%$ and that blazars produce $\sim 5\%$ of the diffuse neutrino flux, which is consistent with the current upper limits in (4). With a total of 51 alerts, we expect roughly one coincidence. In each realization of these signal simulations, one IceCube event is injected on a cataloged extragalactic *Fermi*-LAT source. The probability to select each individual source is set proportional to its energy flux.

For each injected IceCube event, we calculate the TS as described above using the observed γ -ray light curves.

The resulting signal and background TS distributions are compared in Figure S7. Defining sensitivity as the fraction of the signal realizations correctly identified as such, the figure shows that for a reasonable cut at e.g. $TS = 9$, a sensitivity $> 50\%$ is obtained for a p-value less than 1%. The pre-trial p-value shown for IceCube-170922A is $2.1 \cdot 10^{-5}$, corresponding to Model 1. This test has been applied for the assumption of one signal event and can therefore be directly compared with the pre-trial p-values of the energy flux weighting scenario described above.

Furthermore the energy flux distribution of γ -ray sources with simulated neutrino coincidences was inspected assuming that all sources produce neutrinos proportional to their γ -ray energy flux. It is found that 14% of all sources have an equal to or larger γ -ray energy flux than TXS 0506+056 during the time of IceCube-170922A (see Fig. S7). This shows that if the neutrino flux is in fact highly correlated with the γ -ray flux it is not surprising that we detect a neutrino in coincidence with this particular source and flaring incident. This test neglects dim γ -ray sources below the detection threshold of the *Fermi*-LAT, which would also contribute to the neutrino flux.

Previous high-energy IceCube events Prior to IceCube-170922A, the IceCube real-time system sent 9 public high-energy neutrino alerts. IceCube data recorded prior to the start of the real-time system in April 2016, starting from 2010, has been inspected for events that would have passed the selection criteria of the real-time stream. An additional 41 events were identified. The 90% error contours of all 51 events were searched for γ -ray sources in spatial coincidence. The angular resolution for those events varies strongly with the topology and energy of the event. Only events with an angular uncertainty of less than 5 deg^2 are considered, excluding 4 events from the pre-alert time period. Events with larger uncertainty would get

a small spatial weight assigned in the likelihood analysis and would not yield a significant p-value. One neutrino (9 December 2014) is found with a 90% location uncertainty region of 1.76 deg^2 in spatial coincidence with the γ -ray source 3FGL J1040.4+0615. The best-fitting neutrino position is 0.27 deg from the position of the γ -ray source. In the monthly time bin around the neutrino arrival time, the source was detected with an energy flux of $1.3 \times 10^{-11} \text{ erg cm}^{-2} \text{ s}^{-1}$ between 1 GeV and 100 GeV, more than an order of magnitude lower than the energy flux at TXS 0506+056 during the time of IceCube-170922A of $1.9 \times 10^{-10} \text{ erg cm}^{-2} \text{ s}^{-1}$, and about a factor of 2 below the brightest emission period ($2.7 \times 10^{-11} \text{ erg cm}^{-2} \text{ s}^{-1}$) observed for this particular source. Therefore, this event would have produced substantially lower test statistic values in the statistical tests for chance coincidence described above, where a correlation between the gamma-ray and neutrino emission is assumed.

Table S9: **VLA Radio Frequency Flux Densities of TXS 0506+056.** A $\sim 5\%$ systematic uncertainty in the absolute flux scale should be included when comparing these to flux densities measured with other facilities.

Epoch	MJD	Sub-array Receiver Band	Frequency (GHz)	Flux Density mJy
1	58031.6429 ± 0.0104	S	2.50	519.7 ± 1.3
		S	3.50	540.4 ± 0.9
		C	5.25	565.3 ± 1.0
		C	7.45	624.9 ± 1.1
		X	9.00	663.2 ± 1.5
		X	11.00	695.9 ± 1.4
2	58032.3724 ± 0.0104	S	2.50	522.8 ± 0.8
		S	3.50	543.6 ± 0.5
		C	5.25	569.8 ± 1.0
		C	7.45	640.2 ± 1.3
		X	9.00	662.8 ± 3.5
		X	11.00	725.7 ± 6.1
3	58035.5662 ± 0.0104	S	2.50	507.5 ± 0.9
		S	3.50	529.4 ± 0.6
		C	5.25	563.3 ± 1.1
		C	7.45	625.9 ± 1.5
		X	9.00	650.1 ± 1.2
		X	11.00	670.9 ± 1.1
4	58038.3585 ± 0.0104	S	2.50	520.4 ± 0.8
		S	3.50	535.0 ± 0.6
		C	5.25	571.3 ± 1.0
		C	7.45	631.9 ± 1.0
		X	9.00	661.9 ± 1.1
		X	11.00	722.8 ± 1.1
5	58050.3048 ± 0.0104	S	2.50	511.4 ± 1.6
		S	3.50	549.7 ± 0.8
		C	5.25	607.2 ± 1.4
		C	7.45	699.4 ± 1.6
		X	9.00	723.8 ± 1.7
		X	11.00	753.0 ± 1.6
6	58078.5534 ± 0.0104	S	2.50	606.0 ± 1.6
		S	3.50	658.4 ± 1.3
		C	5.25	696.2 ± 1.2
		C	7.45	669.3 ± 1.5
		X	9.00	667.0 ± 1.4
		X	11.00	646.2 ± 1.0

Table S10: **Swift XRT Monitoring Campaigns of TXS 0506+056.** R_X and $F_{X,-12}$ indicate count rate and energy flux (0.3-10 keV), in units of ct ks^{-1} and $10^{-12} \text{ erg cm}^{-2} \text{ s}^{-1}$, respectively. Uncertainties are 90%-confidence regions. The * indicates that UT end was during the following day. The energy flux reported here is not corrected for Galactic absorption.

Epoch	UT start	UT end	Exposure [ks]	R_X [ct ks^{-1}]	Photon Index	$F_{X,-12}$ [$10^{-12} \text{ erg cm}^{-2} \text{ s}^{-1}$]
2017-09-23	00:09:16	22:24:03	0.8	65.8 ± 10.1	$1.83^{+0.43}_{-0.42}$	$2.33^{+1.07}_{-0.72}$
2017-09-27	18:51:08	22:04:26	4.9	121.2 ± 5.3	2.43 ± 0.12	$3.51^{+0.32}_{-0.29}$
2017-09-30	04:27:57	06:24:00	2.0	66.2 ± 7.8	2.30 ± 0.33	$1.55^{+0.43}_{-0.33}$
2017-10-02	15:04:30	15:41:32	2.0	117.3 ± 8.2	2.73 ± 0.20	$2.92^{+0.40}_{-0.35}$
2017-10-03	13:38:57	18:41:00	1.1	182.4 ± 14.1	$2.46^{+0.22}_{-0.21}$	$4.96^{+0.80}_{-0.70}$
2017-10-04	16:42:57	18:37:00	1.2	186 ± 16.1	$2.82^{+0.26}_{-0.25}$	$4.41^{+0.74}_{-0.65}$
2017-10-05	16:32:57	21:32:00	2.3	255.1 ± 11.7	2.64 ± 0.13	$6.47^{+0.57}_{-0.53}$
2017-10-06	13:16:57	05:48:00*	2.1	90.1 ± 7.1	2.36 ± 0.21	$2.56^{+0.44}_{-0.37}$
2017-10-08	09:51:57	11:34:00	1.9	108.1 ± 8.1	2.53 ± 0.21	$2.87^{+0.44}_{-0.38}$
2017-10-16	14:21:57	22:30:00	2.2	61.9 ± 5.8	2.0 ± 0.27	$2.20^{+0.59}_{-0.44}$
2017-10-18	01:23:57	04:48:00	1.8	52.6 ± 6.0	2.10 ± 0.31	$1.70^{+0.49}_{-0.37}$
2017-10-20	13:47:57	20:23:00*	2.3	49.6 ± 5.1	2.11 ± 0.28	$1.61^{+0.41}_{-0.32}$

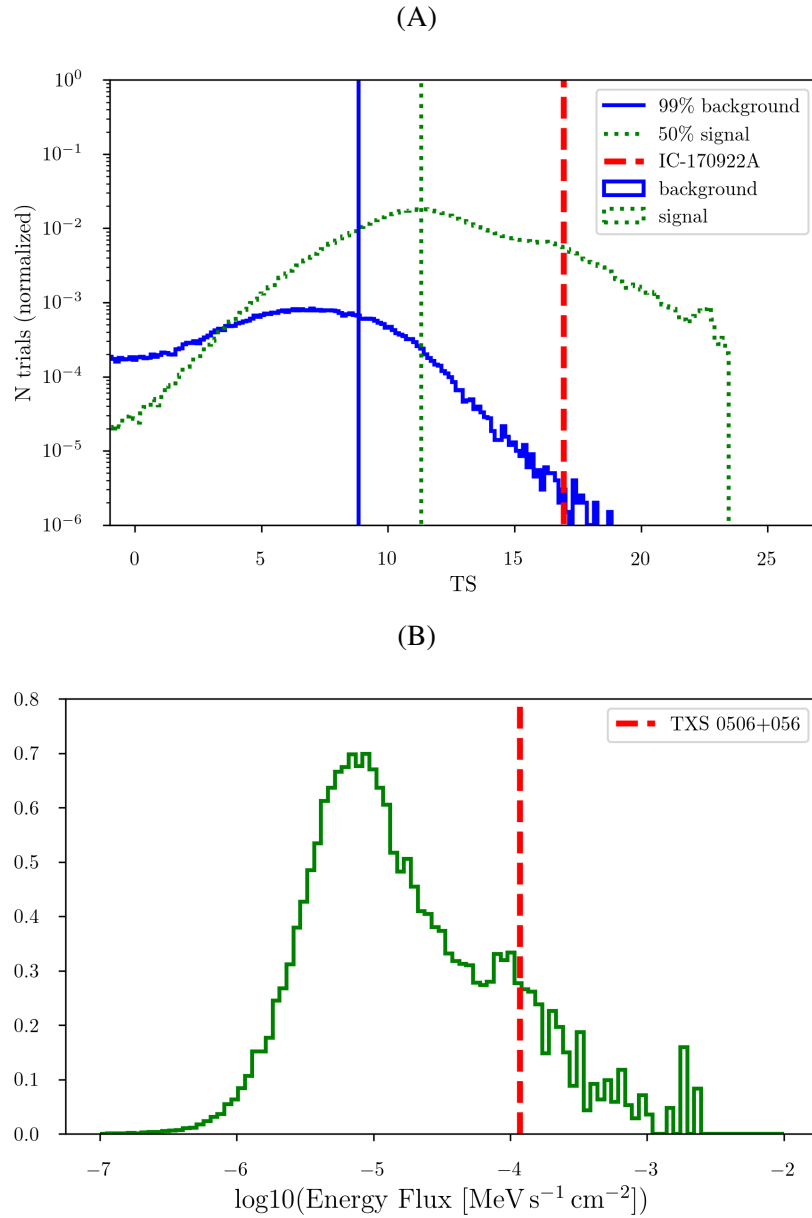


Figure S7: γ -ray energy flux and neutrino correlation study sensitivity. Panel A: TS distribution for background trials (blue) and signal trials (green dashed) assuming a linear correlation of γ -ray energy flux and neutrino flux. The solid blue line indicates the TS value below which 99% of the background trials lie. The green dotted line shows the median TS of the signal trial distribution. The red dashed line shows the measured TS value for IceCube-170922A. The x-axis is suppressed in order to show only the relevant tail of the background distribution. Panel B: distribution of γ -ray energy flux (for γ -ray energies >1 GeV) for found neutrino γ -ray correlations assuming that all sources produce neutrinos proportionately to their energy fluxes in the range 1 GeV – 100 GeV.

The Radar Echo Telescope for Cosmic Rays: Pathfinder Experiment for a Next-Generation Neutrino Observatory

S. Prohira,^{1,*} K.D. de Vries,^{2,†} P. Allison,¹ J. Beatty,¹ D. Besson,^{3,4} A. Connolly,¹ P. Dasgupta,⁵ C. Deaconu,⁶ S. De Kockere,² D. Frikken,¹ C. Hast,⁷ E. Huesca Santiago,² C.-Y. Kuo,⁸ U.A. Latif,^{3,2} V. Lukic,² T. Meures,⁹ K. Mulrey,² J. Nam,⁸ A. Nozdrina,³ E. Oberla,⁶ J.P. Ralston,³ C. Sbrocco,¹ R.S. Stanley,² J. Torres,¹ S. Toscano,⁵ D. Van den Broeck,² N. van Eijndhoven,² and S. Wissel^{10,11}

(Radar Echo Telescope)

¹Department of Physics, Center for Cosmology and AstroParticle Physics (CCAPP), The Ohio State University, Columbus OH, USA

²Vrije Universiteit Brussel, Brussel, Belgium

³University of Kansas, Lawrence, KS, USA

⁴National Research Nuclear University, Moscow Engineering Physics Institute, Moscow, Russia

⁵Université Libre de Bruxelles, Brussels, Belgium

⁶Enrico Fermi Institute, Kavli Institute for Cosmological Physics, Department of Physics, University of Chicago, Chicago, IL, USA

⁷SLAC National Accelerator Laboratory, Menlo Park, CA, USA

⁸National Taiwan University, Taipei, Taiwan

⁹University of Wisconsin-Madison, Madison, WI, USA

¹⁰Departments of Physics and Astronomy & Astrophysics,

Institute for Gravitation and the Cosmos, Pennsylvania State University, University Park, PA, USA

¹¹California Polytechnic State University, San Luis Obispo CA, USA

The Radar Echo Telescope for Cosmic Rays (RET-CR) is a recently initiated experiment designed to detect the englacial cascade of a cosmic-ray initiated air shower via in-ice radar, toward the goal of a full-scale, next-generation experiment to detect ultra high energy neutrinos in polar ice. For cosmic rays with a primary energy greater than 10 PeV, roughly 10% of an air-shower's energy reaches the surface of a high elevation ice-sheet ($\gtrsim 2$ km) concentrated into a radius of roughly 10 cm. This penetrating shower core creates an in-ice cascade many orders of magnitude more dense than the preceding in-air cascade. This dense cascade can be detected via the radar echo technique, where transmitted radio is reflected from the ionization deposit left in the wake of the cascade. RET-CR will test the radar echo method in nature, with the in-ice cascade of a cosmic-ray initiated air-shower serving as a test beam. We present the projected event rate and sensitivity based upon a three part simulation using CORSIKA, GEANT4, and RadioScatter. RET-CR expects ~ 1 radar echo event per day.

I. INTRODUCTION

Ultra high energy cosmic rays (UHECR) and neutrinos (UHEN) are important messengers from the most energetic astrophysical sources. Identifying and understanding these sources is a key goal of current multi-messenger astronomy, a burgeoning field with exciting recent breakthroughs and many discoveries to be made [1–3].

The primary challenge to detecting UHECR and particularly UHEN is the low flux at the highest energies. This low flux requires an observatory that can efficiently probe a large target volume, in order to acquire a statistically significant sample of events. There are several current and proposed experimental strategies to achieve this large volume [4–10]. In this paper we discuss the *radar echo* method. This method has promising projected sensitivity to neutrinos in the 10-100 PeV range, providing complementarity with existing and future techniques for measuring UHEN. [11–16]

A high energy particle (e.g. neutrino) interacting in a dense medium (e.g. ice) creates a cascade of relativistic particles that ionize atoms in the target medium. A short-lived cloud of

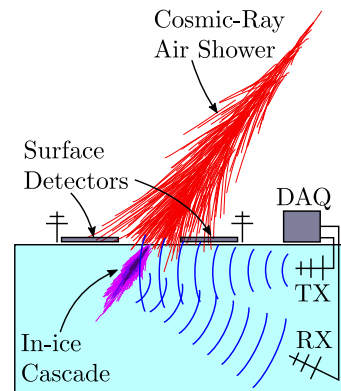


FIG. 1. The RET-CR concept. A surface detector triggers on the charged in-air cascade particles as they reach the surface. The energy of this in-air cascade is deposited into the ice, where a denser in-ice cascade is produced. Radio is broadcast from the transmitter (TX) and reflected from the in-ice cascade to the embedded receiver (RX).

charge is left behind, which can, if sufficiently dense, reflect incident radio waves. RET proposes to illuminate a volume of ice with a transmitter radio-frequency antenna and monitor that same volume for reflections with a receiving antenna. To improve reconstruction of the geometry of a cascade, and therefore the progenitor source direction, a target volume can

* prohira.1@osu.edu

† Krijn.de.Vries@vub.be

be illuminated with multiple transmitters, and monitored with multiple receivers. Overall, the radar echo method allows for the coverage of a large volume with minimal apparatus and station layout optimized for a given neutrino energy, making it an attractive option for UHEN detection.

The radar echo method has been verified in the lab [11, 12], with first observations of radar echoes from particle cascades recently reported [15, 16]. These lab tests are critical steps in developing an ultimate radar echo neutrino observatory. The final step in validating the technique is to translate the laboratory tests into nature, and test the method *in situ* with a known test beam: the in-ice cascade produced when the extensive air shower (EAS) of an UHECR impacts the ice.

In this paper we describe the Radar Echo Telescope for Cosmic Rays (RET-CR) (Figure 1) which will serve as a testbed for the radar echo method, and a final stepping stone toward the eventual construction of a full-scale radar echo telescope for UHEN.

II. HISTORY, THEORY, AND BACKGROUND.

First efforts on the radar echo method were chronicled by Lovell [17]. With collaborator Blackett, the Jodrell bank observatory was constructed in the UK, anticipating that radar echoes from UHECR might explain “sporadic radio reflexions” from the upper atmosphere. Ultimately, those signals were determined to be from meteors, which ionize similar, far denser trails in the upper atmosphere. After several experimental efforts (including the Telescope Array RADar (TARA)) failed to detect UHECR via radar [18–21], and theoretical work explaining the lack of observed reflections [22, 23], the in-air method was finally deemed not viable due to short ionization lifetimes in the atmosphere at EAS altitudes, and damping from collisions between ionized electrons and neutral air molecules (an issue first raised by Eckersley in 1941 [17], though largely subsequently ignored.)

Neutrino interactions in the ice produce ionization densities many orders of magnitude more dense than those in-air, owing to the $\sim 10^3$ greater density of ice relative to air. Therefore, while the ionization lifetime remains short in ice (roughly 10 ns [24]) and the collision rate is extremely high, so too is the underlying ionization density, allowing for a possible scatter. Several models now exist for the in-ice radar echo [13, 14] and show promising experimental sensitivity. Laboratory tests have shown good agreement with theory, but in order to test the radar echo method in nature, a source of *in-ice* ionization is required; EAS offer such a source.

The EAS of a UHECR expands radially outward from the shower axis, such that an EeV cascade has a $\mathcal{O}(100\text{ m})$ footprint on the ground. However, nearly all of the cascade energy is contained within $\sim 10\text{ cm}$ of the shower axis, as illustrated below [25]. The sought-after signal depends on the total number of particles in the shower core, as well as the geometry of the shower. In Figure 2, we plot the ratio of the number of particles at the air/ground boundary (N_b) to the maximum number in the cascade (N_{max}) for different primary UHECR energies for different ice elevations as a function of zenith an-

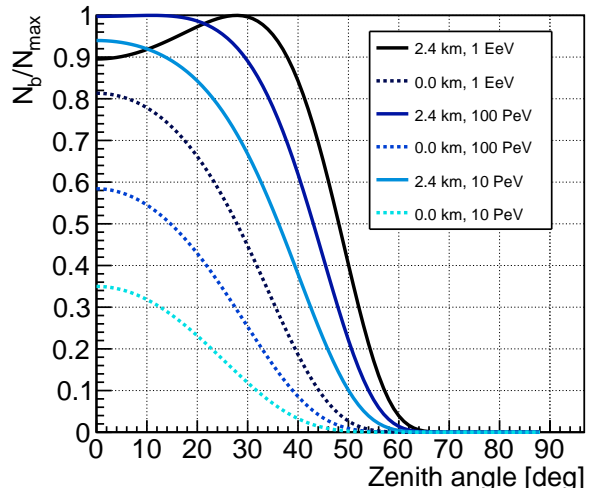


FIG. 2. The ratio of the number of cascade particles, N_b , arriving at the air/ground boundary relative to the maximum number in the cascade, N_{max} , for various energies and ground elevations. At 2.4 km elevation and 1 EeV primary energy, shower maximum at normal incidence is in-ice.

gle using the NKG approximation [26]. For a high elevation (such as the interior Antarctic plateau), this ratio is ≥ 0.9 for energies $\geq 10\text{ PeV}$ for a wide zenith angle range, indicating that a significant fraction of the energy of the primary particle will arrive at the air/ice boundary.

The core of a UHECR when it impacts the ice can be used as an in-nature test beam. Though TARA demonstrated that UHECR detection *in air* via radar echo was not feasible, the *in-ice* cascade produced by the remaining EAS particles, as demonstrated by our beam tests, should be detectable via radar echo. For energies above 10 PeV, we expect an ionized column with a density that decreases rapidly with radius, and an in-ice length of about 10 m. The effective radius along this column at which radar will scatter depends on the transmitter frequency (discussed below); for frequencies in the 100s of MHz range, this radius is approximately 10 cm. The profile of this ionization deposit is similar to that which would be produced by a neutrino-induced cascade, the primary difference being that neutrino events are more likely to occur in deep ice rather than near the surface.

The properties of the *in-ice* cascade from EAS have been studied using CORSIKA [27] to simulate the extensive air shower evolution, GEANT-4 [28] to simulate the propagation of these cascades once they enter the ice, and RadioScatter [29] to calculate the reflected signals from the ionization deposits left in the wake of the cascades. We next discuss our planned detector layout and design, and then describe our simulation and projected sensitivity.

III. EXPERIMENTAL CONCEPT

The experimental concept is shown in Figure 1. A transmitter illuminates the region of ice just below the surface, with receivers monitoring this same region. The EAS of a UHECR with a primary energy greater than 10^{16} eV deposits a fraction ($\gtrsim 10\%$) of the primary energy at the surface of a high-elevation ice sheet. This energy is largely centered around the cascade axis, resulting in a dense secondary in-ice cascade roughly 10-20 m long. The charged particles from the EAS are detected by a surface scintillator array, triggering a radio receiver waveform to be recorded in the radar data acquisition system (DAQ). This simple setup closely parallels that already employed for the laboratory test-beam experiment, with the focus of the experiment on post-run, offline analysis of the data. This relative simplicity also allows for testing various radar based trigger routines, which can be optimized for efficacy against the charged particle trigger. Such testing is critical, as an eventual neutrino detector will be triggered by the radar signal itself.

When the cascade leaves the air and enters the ice, the density of the resultant ionization increases dramatically. This results in an ionization deposit in the ice with a plasma frequency $\omega_p = \sqrt{4\pi n_e q^2/m}$ far higher than any point in air. The plasma frequency, with n_e the number density of the ionization, q the electric charge, and m the electron mass, is a measure of the density of an ionization deposit. To first order, incident fields with interrogating frequencies lower than ω_p are reflected efficiently.¹ The profile of ω_p from a primary cosmic ray as it moves through air into the ice is shown in Figure 3, where the in-air and in-ice components of an EAS are indicated, as well as a vertical line indicating 100 MHz. The plasma frequency for the in-ice portion of EAS with primary energies greater than 10^{16} eV exceeds 100 MHz, indicating efficient scattering for interrogating frequencies in this range.

In the following sections, we describe the various subsystems of RET-CR. We provide a detail of the experimental layout in the Appendix.

A. Surface detector

The RET-CR surface detector is designed to detect the air shower incident on the surface of the radar detector, providing both an external trigger to the radar DAQ, and an independent reconstruction of the air shower. Using the surface detector as a trigger for the radar system will ensure that an UHECR has entered the radar detector volume with sufficient energy to be detected through the radar echo technique. The independent reconstruction of shower parameters by the surface detector will provide values for the core position, energy, and arrival

direction of the incident UHECR. These values will then be used to validate the reconstruction parameters obtained by the radar echo system.

The primary component of the surface detector is a scintillator plate array. The plates will be grouped in pairs following the design of the Cosmic-Ray Energy Cross-Calibration Array [30]. The plates in each pair of scintillators will be separated by 20 m and will be accompanied by a radio antenna operating in the frequency band 30-300 MHz, to form a station. Each station will have its own DAQ and power system. The combination of a radio and scintillator signal at each station will be beneficial in providing event reconstruction and energy estimates. The current deployment layout is shown in Appendix A, where the stations are grouped into two sets of three stations, separated by the central radar system. Additionally, a system diagram is provided in Appendix B. The station layout has been optimized for trigger efficiency, discussed below.

For the current prototyping and development of the RET-CR surface detector, and the current simulation work, the scintillators used are those from the KASCADE experiment [31]. The radio antennas have been donated by the CODALEMA/EXTASIS experiment [32, 33]. As such, for modelling the polyvinyl-toluene scintillator in GEANT4 we use a carbon:hydrogen ratio of 9:10 [34]. The panels deployed to the field will be similar in size and composition, and we do not expect any difference in performance from the panels simulated here.

The scintillator trigger threshold is tuned to maximize the radar echo detections. Simulations indicate that air showers with energy less than $10^{15.5}$ eV are inadequate to produce an in-ice cascade detectable via radar echo (and the rate of such showers would overwhelm the DAQ storage and may cause interesting events at higher energies to be lost). Additionally,

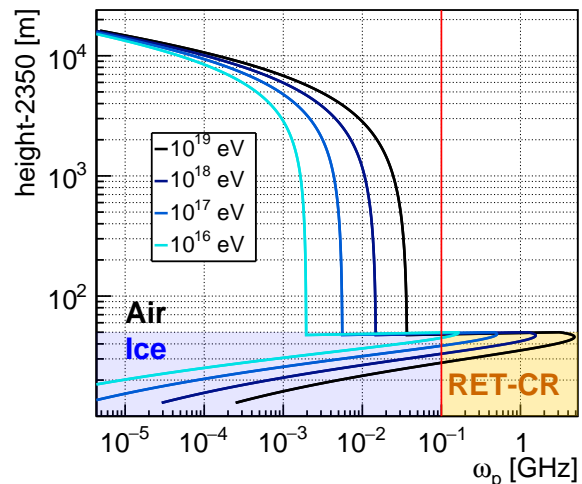


FIG. 3. The peak plasma frequency (ω_p) of the cascade as it develops in-air and then in-ice, at normal incidence. The in-ice cascade is far more dense than the in-air cascade, making it detectable via radar for primary energies greater than 10^{16} eV. The red line indicates the point at which $\omega_p > 100$ MHz.

¹ In a collisionless plasma, ω_p is a hard cutoff between the 'overdense' and 'underdense' regimes, which indicate fully coherent and incoherent scattering respectively. When taking collisions into account, this boundary is smeared, but ω_p is still a useful discriminator for the underlying ionization density.

simulations of the air shower radio footprint show that radio reconstruction of the air shower is not possible for showers with an energy less than approximately $10^{16.0}$ eV. Therefore we target 100% efficiency at $10^{16.5}$ eV, with efficiency defined as the percentage of cosmic ray air showers traversing the instrumented area that trigger the surface detector. We aim for a trigger rate of order 10^5 events per month, leading to approximately 300 surface triggered events a day. This is a manageable rate for both the surface and radar DAQ systems.

Simulation studies have been conducted to determine an appropriate triggering scheme for the surface detector. Events have been simulated with energies in the range $10^{15.0}$ eV to $10^{19.0}$ eV and zenith angles in the range 0-30 degrees. We limit ourselves to this zenith range because in-ice energy deposition decreases dramatically beyond 30 degrees zenith. The simulations were made using the CORSIKA and CoREAS [35] software for air shower simulation with a ground elevation set to 2400 m, that of an optimal deployment site, Taylor Dome, Antarctica. A change in this altitude will affect the point within the shower development at which the air shower passes through the detector. Showers at sea level are generally developed beyond shower maximum before reaching the ground. At the altitude of Taylor Dome, whether the shower has developed to a point before or after the shower maximum is strongly dependent on the energy and zenith angle of the air shower (Figure 2).

The stations of the surface detector will trigger independently. Each scintillator will be required to contain a deposit of 6 MeV (1 minimally ionizing particle) or greater per event and both scintillators in a station must trigger coincidentally within an event (an L0 trigger). The final trigger requirement is that all stations within one cluster must have coincident (restricting our zenith angle to $< 30^\circ$ zenith), above threshold energy deposits in all scintillators (an L1 trigger). A timing diagram is provided in Appendix C. The resulting trigger efficiency is shown in Figure 4. In this figure, we show that we achieve 100% efficiency at $10^{16.5}$ eV, as desired. Decreasing a half-decade in energy, at $10^{16.0}$ eV the efficiency decreases to $\sim 90\%$. In the lowest energy bin simulated, the efficiency is approximately 5%. This rapid turn-on in our trigger threshold allows us to target our desired event rate.

B. Radar echo detector

1. Data Acquisition System

The primary element of the radar echo detector DAQ is a Xilinx RFSoc [36]. This device serves as both our transmitter and our receiver. The transmit portion comprises 8 channels, each with a 6 GS/s digital-to-analog converter (DAC) capable of producing a phased, modulated output to an array of transmitters. The receive portion has 8 channels, each channel with a 4 GS/s analog-to-digital converter (ADC). A Virtex-7 FPGA provides transmit and receive functions and trigger logic, and an on-board ARM processor facilitates information transfer between the FPGA and the communication subsystems, also described below. This array is centrally located, and will be

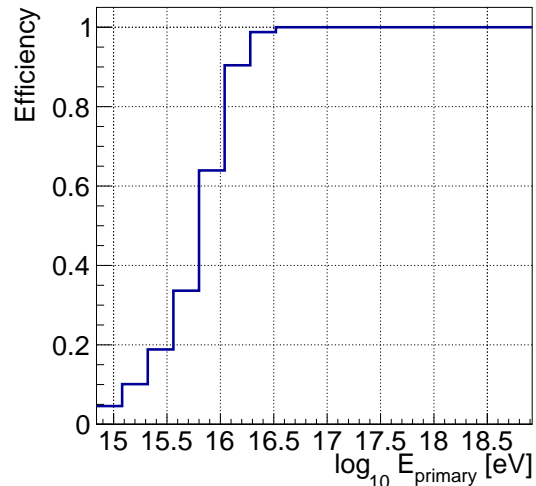


FIG. 4. Trigger efficiency curve for the surface system as a function of primary UHECR energy.

described below.

The DAQ will have local storage for buffering data and a prioritizer system for telemetry, with a design expectation that our data transfer rate will be the primary bottleneck in getting data from the station. The most promising events are sent via communication link as well as being stored locally on disk. The criteria for this can include i) measured primary energy from the surface detectors or ii) the proximity of the in-ice vertex to a receive antenna, or a combination of the two. The disks will be retrieved at the end of the season.

The FPGA will host a number of radar “triggers” with potentially varying topologies, even though these triggers do not actually signal an event snapshot. These triggers will be trained against the surface detector trigger to determine their efficacy for eventual use in the successor neutrino detector, where the radar signal itself must trigger the DAQ. One such trigger under investigation is a heterodyne trigger (also called a “chirp trigger”) based upon a method developed for the TARA remote stations [37, 38] that exploits the frequency shift of the return signal. The geometry of RET-CR is such that all of the received radar echoes will exhibit this frequency shifting behavior. Other triggers based on the unique radar signature are also being explored. The sensitivity studies in this article employ a simple threshold trigger for the radar component.

2. Transmit array and transmitter modulation

The transmitter for RET-CR will be a vertical phased array of 8 vertically polarized antennas buried 2-20 m below the ice surface. This phased array serves 2 critical functions. The first is directionality—a phased array governed by an FPGA can form high gain beams in a defined direction, achieved via adjusting the relative phases of the transmit signal being delivered to each of the antennas in the array. A vertical phased

array has azimuthal symmetry with a high gain beam at a defined zenith angle, defined by the relative phase delays of each antenna. Since our reflectors are confined to the top ~ 10 m of the ice just below the surface, we can steer the beam slightly upward and waste virtually no power to the region below, where we do not expect to receive UHECR core reflections. Recent studies in Antarctica have shown that in-ice phased arrays are highly efficient receivers [39], and phased transmitter arrays are common in use throughout the world, including the TARA experiment. The second critical function of a phased array is to lower the single-amplifier gain for the transmit power amplifier. In lieu of a single 160 W power amplifier, each antenna will have its own 20 W power amplifier. This distributes the ohmic heating losses over 8 antennas instead of 1 and provides some redundancy: in the event that a power amplifier malfunctions, the experiment loses some efficiency, but does not shut down entirely.

The antennas will be based upon the simple bicones or biconical dipoles used by the RICE, ARA, and ARIANNA experiments in Antarctica. These antennas are small enough to fit down a borehole but are sufficiently broadband as to allow for a range of transmit frequencies and modulations. Studies are underway to determine if antennas with an asymmetric zenith angle gain can increase transmitter efficiency in the direction the beam is ‘steered’.

The modulation scheme is currently being defined. We plan to frequency hop or frequency shift around a central carrier of 100-300 MHz, with a transmitter bandwidth of 50-100 MHz. The central frequency is determined by maximizing the signal to noise ratio of a radar signal to the background noise. The signal has an optimal frequency dependent on the cascade dimensions and density, and the noise decreases with increasing frequency as thermal noise begins to dominate over galactic noise above ~ 150 MHz.

This frequency and the ultimate modulation strategy will be determined via simulations that are already underway. Modulation, as opposed to pulsing, increases detector livetime, as long as the carrier signal can be removed from the receivers. We discuss this below in section III B 4.

3. Receive array

The receiver array will be laid out in the configuration shown in Appendix A. Two different TX-RX baselines allow for a wide range of primary particle energies to be detected. Similar to the transmitter array, the receiver antennas will be buried 2-20 m below the surface of the ice. Each receive antenna will be a vertical phased array, similar to the transmit array, in order to maximize near-surface gain with full azimuthal coverage.

The receivers will not trigger the DAQ, but will form triggers as a testbed for eventual use in a neutrino array.

4. Amplification and active filtration

We will have a limiter and high-gain, low-noise amplifier on each receive channel, providing protection during transmitter turn-on and approximately 70 dB of gain, respectively. This amount of gain is sufficient to attain the galactic noise floor at our frequency, location, and receiver bandwidth of ~ 100 MHz.

Because radar receivers will be illuminated by the transmitter, it is essential to filter the transmitter or gate the receivers such that amplifier saturation does not occur. We plan to adopt an adaptive filtration scheme, whereby we will record an amplifier-bypassed snapshot of the transmitted signal over a horizon-distance window in time at each receiver, and then inject it time-delayed and phase-inverted into the receiver stream before the amplifier chain. The delay and output amplitude are tuneable, allowing for an iterative reduction of the input amplitude until the carrier is fully eliminated. This procedure will be updated at intervals throughout the day to account for environmental changes such as snow accumulation, which have been shown to introduce measurable changes in reflection times on \sim day timescales [40].

5. Power, system health, calibration, and communications

The detector will be fully autonomous and powered by three 1.2 kW solar arrays arranged in a triangle, such that at any time of (a sunny) day the station is provided with approximately 1 kW of power, with the majority of this power being used by the transmit power amplifiers. A bank of batteries will buffer power to assist in running the stations during adverse weather conditions. Each surface station will be powered by an individual photovoltaic. RET-CR will run only during the austral summer.

The system health, including power consumption, DAQ enclosure temperature, power amplification health, and local weather will all be monitored remotely, in real-time.

We will deploy a small, autonomous calibration unit that sends out a broadband pulse at regular intervals. This unit will serve as a regular baseline for thresholds and ensure global time synchronization, as well as for active monitoring of the above mentioned environmental changes, such as snow accumulation.

The communication system will be a 2-way satellite-based internet link. Through this link we will telemeter the prioritized data and system health information back to the lab, and, from the Northern Hemisphere, new trigger schemes and other station software and commanding to RET-CR. Alternative communications links via point-to-point Ethernet may be possible if there are line-of-sight repeater stations between a major base and the remote RET-CR.

IV. PROJECTED SENSITIVITY

The approximate sensitive surface area instrumented by RET-CR is 50×10^3 m². Through this area we can expect

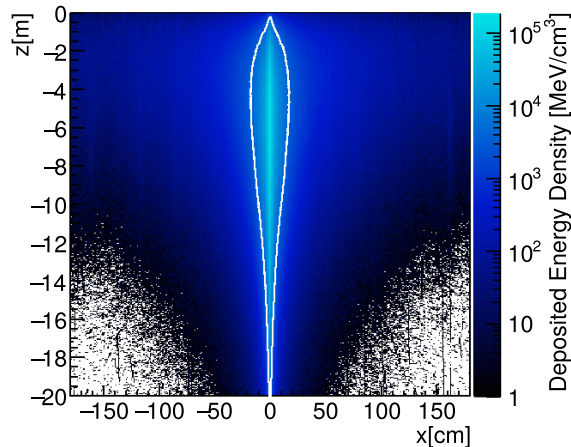


FIG. 5. A one centimeter wide, two-dimensional slice of the in-ice energy density distribution along the cascade axis for a primary proton with $E = 10^{17}$ eV. The solid white line outlines the region for which the plasma frequency exceeds 100 MHz.

a flux of roughly 1 event at 100 PeV per day. The surface system will trigger on every cosmic ray with a primary energy above this, with decreasing efficiency at lower energies, as described in section III A. To simulate our radar echo detection efficiency, we performed a detailed multi-step Monte Carlo which we describe here using (in order) CORSIKA, GEANT4, and RadioScatter.

A. CORSIKA cascades and the surface stations

A CORSIKA-based Monte Carlo simulation for optimizing the surface array location was described in section III A. This same distribution of events (core positions, zenith angles, and energies) was used to simulate the radar sensitivity of RET-CR. A separate set of CORSIKA simulations was prepared specifically for producing the GEANT4 output used in subsequent simulation steps. These CORSIKA showers were produced at 0, 15, and 30 degrees zenith for each half-decade energy, with a ground elevation of 2400 m, as before. For 10^{16} eV and $10^{16.5}$ eV, no thinning was employed. For higher energies, thinning is set to 10^{-7} of the primary particle energy. For 10^{17} eV and $10^{17.5}$ eV the CORSIKA ‘weight’ of a single particle will never be larger than 10, for 10^{18} eV it will never be larger than 100. Thinning retains the overall energy of a cascade, such that the total in-ice ionization number will be the same for any thinning, but it changes the distribution of low-energy particles in the final footprint (which is then used as the input to GEANT4). We therefore minimized thinning as much as possible, subject to computing constraints.

B. GEANT4 simulations from CORSIKA output

The CORSIKA particle output at the surface of the ice was subsequently used as input for the GEANT4 simulation code configured to propagate particles into the ice. For this a realistic density profile similar to that found at South Pole was used, $\rho(z) = 0.460 + 0.468 \cdot (1 - e^{-0.02z})$ with ρ the density in g/cm^3 and z the depth in m. In each step of the simulation, the ionization energy loss is recorded; taking a typical ionization energy of 50 eV allowed us to obtain the free charge density profile in the ice [41]. An example of this profile is shown in Figure 5 for an air shower induced by a 10^{17} eV proton primary incident on an ice sheet at 2400 m elevation. The plasma frequency is a good indicator of the reflective properties of the induced plasma, as discussed previously. The solid white line in Figure 5 outlines the region for which the plasma frequency has a value larger than 100 MHz, where fully coherent scattering is expected.

C. RadioScatter simulations of GEANT4 output

To simulate the overall sensitivity, we use the RadioScatter [29] code. RadioScatter is a particle-level c++ code to simulate radio scattering from ionization deposits. It calculates the received radio signal reflected from an ionization deposit (from e.g. a particle cascade) for an arbitrary geometry of transmitter(s) and receiver(s).

The energy deposition calculated by GEANT4 was used as the input to RadioScatter. An example of a triggered event from a $10^{16.5}$ eV primary at normal incidence is shown in Figure 6. Clearly visible is the characteristic frequency shift expected for the RET-CR geometry, which can be exploited in trigger routines. At each cascade position in the surface scintillator simulation set, we simulated two different GEANT4 cascades: 1) the cascade with the closest half-decade energy *below* the primary energy of the surface simulation and 2) the cascade with the closest half-decade energy *above* the primary energy of the surface simulation. This is done because generating the GEANT4 cascades from the CORSIKA output is computationally expensive, so each discrete energy and zenith angle cannot be simulated individually. This method bounds the amount of energy that could arrive at the surface and accounts for shower-to-shower fluctuations. Both energies were simulated at each cascade position at one of three zenith angles, 0, 15, and 30 degrees selected according to their proximity to the ‘true’ zenith angle of the cascade from the surface simulation. These cascades were generated with a uniform distribution in $\cos \theta$ because cosmic rays arrive isotropically at earth, and a uniform distribution in $\cos \theta$ ensures that any zenith angle dependencies of the trigger are reflected in the sensitivity. The horizon distance for an in-ice transmitter is finite owing to the changing index of refraction in the firm (the top ~ 100 m of an ice sheet where snow is being compacted into ice) [42–45]. We therefore put a hard cut on a horizon distance of 150 m, which is commensurate with the point at which the in-ice shower maximum is out of view for a transmitter depth of ~ 20 m. The simulations in this paper eschew

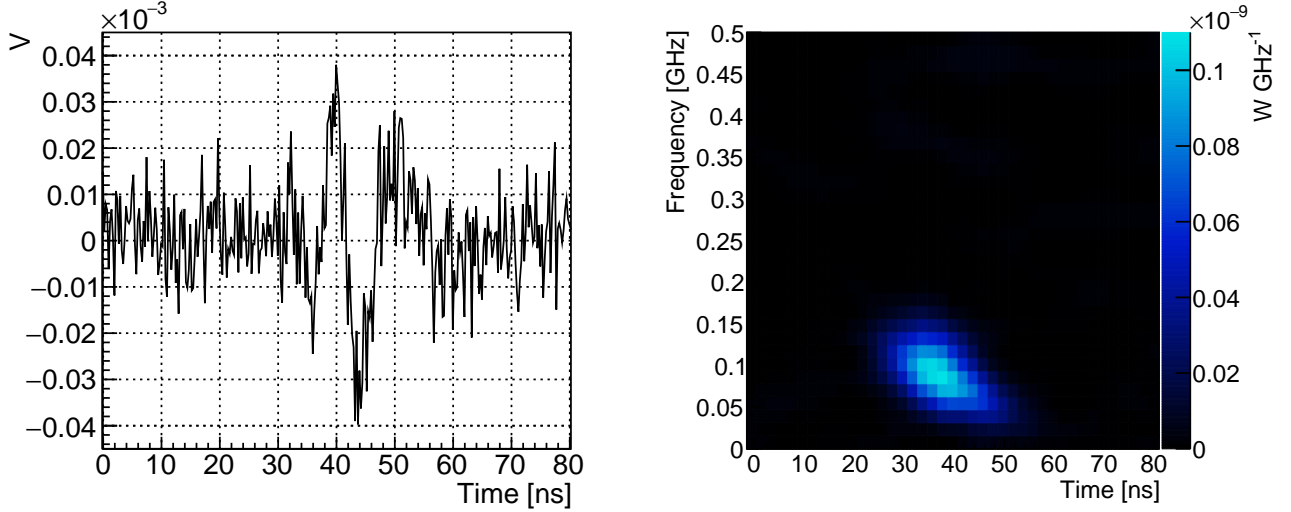


FIG. 6. An example event simulated using CORSIKA+GEANT4+RadioScatter, as described in the text. This is a $10^{16.5}$ eV primary at normal incidence with a 10 ns plasma lifetime, simulated with a 160 W transmitter at 100 MHz.

the typical ray-tracing approach for studying propagation in the firm since this has recently been shown to be incomplete without in-situ studies of the ice density profile [46, 47]. The hard horizon cutoff for the results presented here are a proxy for the loss in efficiency due to propagation effects. These effects will be explored in detail in a future work.

D. Calculation of the event rate for RET-CR

The two components of the event rate are the effective area of the detector and the cosmic ray flux. We define both of these over an energy bin E_i with index i and width dE . The effective area $\mathcal{A}_i^{eff}(E_i)[m^2]$ for energy bin i is a function of the cross sectional area \mathcal{A}_\perp over which the sensitivity is calculated and a dimensionless trigger efficiency for the same bin, $\mathcal{T}_i(E_i)$.

To detail the effective area we first introduce the boxcar function, \mathbf{B} , which bounds a number $x_1 < x < x_2$:

$$\mathbf{B}(x, x_1, x_2) = \Theta(x - x_1)\Theta(x_2 - x), \quad (1)$$

where Θ is the Heavyside step function. Then we define our trigger conditions δ^S (for surface) and δ^R (for radar) which are 1 if the trigger condition is satisfied, and 0 if not. For example,

$$\delta^R = \Theta(v^{peak} - v^{thresh}) \quad (2)$$

for a peak waveform voltage v^{peak} and threshold voltage v^{thresh} , and δ^S is 1 when the surface system trigger logic is satisfied (a coincidence between surface stations with a certain per-station energy threshold, as described in Section III A). We then define the number of detected events, for event index k , energy bin with index i and θ bin with index j , as a matrix n_{ij} . These events are weighted by $\cos\theta_k$ to account for the

correction to the perpendicular cross-sectional area \mathcal{A}_\perp seen by a cosmic ray at zenith angles greater than zero.

$$n_{ij}(E_i, \theta_j) = \sum_k \delta_k^S \delta_k^R \cos(\theta_k) \mathbf{B}(E_k, E_i, E_{i+1}) \mathbf{B}(\theta_k, \theta_j, \theta_{j+1}) \quad (3)$$

n_{ij} will be zero for bins in zenith outside of the aperture of the instrument. For RET-CR, this aperture is 0-30 degrees as discussed in section III A. The total number of simulated events N_{ij} , also as a matrix in E and θ is

$$N_{ij}(E_i, \theta_j) = \sum_k \mathbf{B}(E_k, E_i, E_{i+1}) \mathbf{B}(\theta_k, \theta_j, \theta_{j+1}). \quad (4)$$

The trigger efficiency \mathcal{T}_{ij} in energy and zenith bins is represented as the ratio of these two,

$$\mathcal{T}_{ij}(E_i, \theta_j) = \frac{n_{ij}}{N_{ij}} \quad (5)$$

and we can then sum over all θ to get this expression as a function of energy only,

$$\mathcal{T}_i(E_i) = \sum_j \frac{n_{ij}}{N_{ij}}, \quad (6)$$

meaning that the effective area for energy bin E_i is

$$\mathcal{A}_i^{eff}(E_i) = \mathcal{T}_i \mathcal{A}_\perp \quad (7)$$

The flux as a function of energy $\mathcal{F}(E)[m^{-2}s^{-1}sr^{-1}eV^{-1}]$ is a broken power-law fit to the measured CR flux by many experiments [41, 48, 49]. To get a number of events per square meter, per second, per steradian, in energy bin E_i , we integrate $\mathcal{F}(E)$ over the energy range of bin i ,

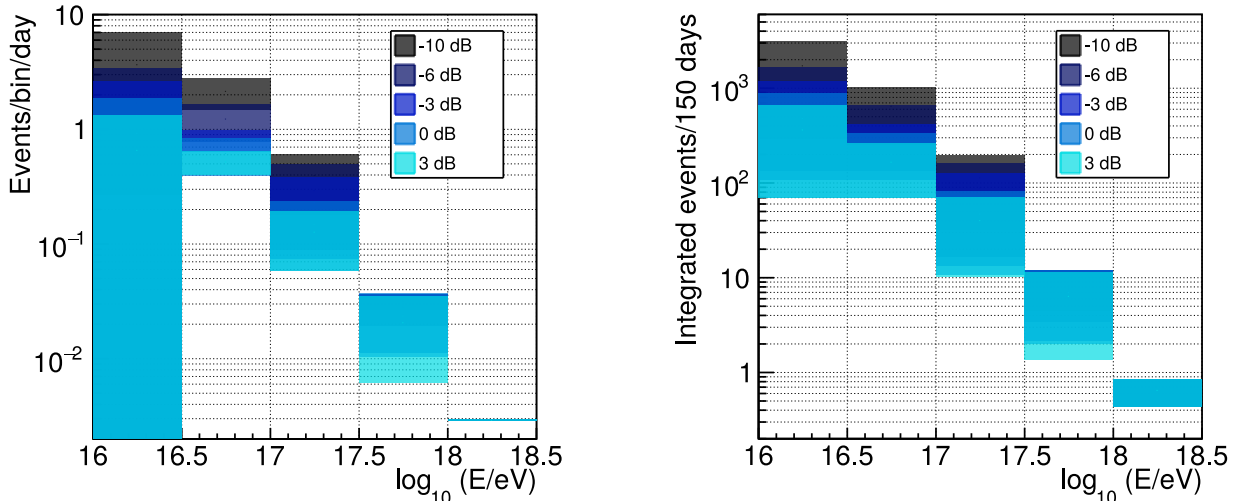


FIG. 7. (Left) Event rates per day as a function of energy for the RET-CR detector. Colors correspond to different signal-to-noise relative to thermal noise of $8\mu\text{V}$ for a 100 MHz bandwidth. Width of the bands are explained in the text. (Right) Integrated event rates per 150 days as a function of energy for the RET-CR detector. Each bin represents the total integrated number of events per 150 days at and above that energy. Colors correspond to different signal-to-noise relative to thermal noise.

$$\mathcal{F}_i(E_i) = \int_{E_i}^{E_{i+1}} \mathcal{F}(E) dE. \quad (8)$$

Finally, the expression we use to calculate the event rate as a function of energy, for energy bin index i , $\mathcal{R}_i(E_i)$ is given in Eq. 9,

$$\mathcal{R}_i(E_i) = \mathcal{A}_i^{eff} \mathcal{F}_i \int dt \int d\Omega, \quad (9)$$

where the integral over time is the detector live time, and $\int d\Omega = \int d\phi d(\cos\theta) = \int d\phi \sin\theta d\theta$ is the integral over the aperture of the instrument. For an experiment sensitive to cosmic rays from the full sky, $\int d\Omega = 2\pi$ sr; the aperture for RET-CR is from 0-30 degrees zenith, $\int d\Omega \approx 0.26\pi$ sr.

We note that the measured flux of cosmic rays differs per experiment. A global study seeking to quantify this fluctuation between experiments [50] shows roughly 20% spread in measured energies between various experiments in our range of interest, leading to an uncertainty in the true flux. Therefore, to account for this uncertainty, we use the cosmic ray flux normalization in line with the mean of the global fit. A goal of the forthcoming Cross-Calibration Array [30] is to mitigate this uncertainty between experiments.

Figure 7, left, presents our expected event rate per day as a function of energy for various signal-to-noise levels relative to a thermal noise RMS of $8\mu\text{V}$. This is for a 160 W transmitter at 100 MHz with a 10 ns plasma lifetime, a likely plasma lifetime for polar ice near the surface [24]. The upper and lower bounds of the bands correspond to the over and underestimated energy simulation respectively. The mean of the 0 dB SNR curve integrates to roughly 1 event per day.

Figure 7, right, shows the integrated event rate for one austral running season, approximately 150 days. To produce this

figure, we have integrated the daily event rate histograms in Figure 7 at all energies. An entry here represents the integrated number of events detected per 150 days at and above that energy, at that SNR. We expect e.g. ~ 50 events at and above 10^{17} eV per season at the 0 dB threshold level.

For comparison to RET-N, the in-ice cascade energy for a 10^{17} eV primary detected by RET-CR is roughly 10^{16} eV. This cascade energy would correspond to that of a charged-current neutrino-nucleon interaction of 10^{16} eV, or a neutral current neutrino-nucleon interaction at $\sim 5 \times 10^{16}$ eV for inelasticity $y \sim 0.2$. Thus, the primary cosmic ray energies probed with RET-CR are similar to those of neutrinos to be targeted with RET-N.

V. CONCLUSION

We have presented the Radar Echo Telescope for Cosmic Rays, a pathfinder *in-situ* detector to test the radar echo method. Using the dense in-ice shower core of a cosmic ray air shower as a test beam, RET-CR will train trigger routines, energy and direction reconstruction methods, and analysis techniques to be employed by an eventual full-scale next-generation neutrino detector.

SOFTWARE

CORSIKA version 7.7400 (with QGSJETII-04 and URQMD 1.3cr), CORSIKA 7.7100 (with QGSJETII-04 and GHEISHA 2002d), CoREAS version 1.4 with a typical Taylor Dome, Antarctica atmosphere, GEANT4 versions 10.5 and 9.6, and RadioScatter version 1.1.0 were used to produce results for this paper.

ACKNOWLEDGEMENTS

RET-CR is supported by the National Science Foundation under award numbers NSF/PHY-2012980 and NSF/PHY-2012989. This work is also supported by the Flemish Foundation for Scientific Research FWO-12ZD920N, the European Research Council under the EU-ropean Unions Horizon 2020 research and innovation programme (grant agreement No 805486), and the Belgian Funds for Scientific Research

(FRS-FNRS). A. Connolly acknowledges support from NSF Award #1806923. S. Wissel was supported by NSF CAREER Awards #1752922 and #2033500. DZB is grateful for support from the U.S. National Science Foundation-EPSCoR (RII Track-2 FEC, award ID 2019597). We express our gratitude to R. Dallier, L. Martin, J-L. Beney and the CODALEMA experiment for providing electronics and hardware to be used in the surface radio stations of RET-CR. Computing resources were provided by the Ohio Supercomputer Center.

-
- [1] M. Aartsen, M. Ackermann, J. Adams, J. A. Aguilar, M. Ahlers, M. Ahrens, I. Al Samarai, D. Altmann, K. Andeen, and et al., *Science* **361**, eaat1378 (2018).
- [2] B. P. Abbott, R. Abbott, T. D. Abbott, F. Acernese, K. Ackley, C. Adams, T. Adams, P. Addesso, R. X. Adhikari, V. B. Adya, and et al., *The Astrophysical Journal* **848**, L12 (2017).
- [3] *Science* **361**, 147 (2018).
- [4] I. Kravchenko *et al.*, *Phys. Rev.* **D73**, 082002 (2006), arXiv:astro-ph/0601148 [astro-ph].
- [5] P. Allison *et al.*, *Astropart. Phys.* **35**, 457 (2012), arXiv:1105.2854 [astro-ph.IM].
- [6] P. W. Gorham *et al.* (ANITA), *Astropart. Phys.* **32**, 10 (2009), arXiv:0812.1920 [astro-ph].
- [7] S. R. Klein *et al.*, *IEEE Transactions on Nuclear Science* **60**, 637 (2013).
- [8] S. Wissel *et al.*, *JCAP* **11**, 065 (2020), arXiv:2004.12718 [astro-ph.IM].
- [9] A. V. Olinto *et al.*, *PoS ICRC2017*, 542 (2018), [35,542(2017)], arXiv:1708.07599 [astro-ph.IM].
- [10] J. Alvarez-Muñiz *et al.* (GRAND), (2018), arXiv:1810.09994 [astro-ph.HE].
- [11] M. Chiba *et al.*, *SUSY07* (2007), arXiv:0710.4186v1.
- [12] M. Chiba *et al.*, *AIP Conference Proceedings* **1535**, 45 (2013).
- [13] K. D. de Vries, K. Hanson, and T. Meures, *Astropart. Phys.* **60**, 25 (2015), arXiv:1312.4331 [astro-ph.HE].
- [14] S. Prohira and D. Besson, *Nucl. Instrum. Meth.* **A922**, 161 (2019), arXiv:1710.02883 [physics.ins-det].
- [15] S. Prohira *et al.*, *Phys. Rev.* **D100**, 072003 (2019), arXiv:1810.09914 [hep-ex].
- [16] S. Prohira *et al.*, *Phys. Rev. Lett.* **124**, 091101 (2020), arXiv:1910.12830 [astro-ph.HE].
- [17] A. C. B. Lovell, *Notes and Records of the Royal Society of London* **47**, 119 (1993).
- [18] T. Matano, M. Nagano, K. Suga, and G. Tanahashi, *Canadian Journal of Physics* **46**, S255 (1968).
- [19] T. Terasawa, T. Nakamura, H. Sagawa, H. Miyamoto, H. Yoshida, and M. Fukushima, *Proceedings of the 31st International Cosmic ray Conference* (2009).
- [20] R. Abbasi *et al.*, *Nucl. Instrum. Meth.* **A767**, 322 (2014), arXiv:1405.0057 [astro-ph.IM].
- [21] R. U. Abbasi *et al.*, *Astropart. Phys.* **87**, 1 (2017), arXiv:1603.05217 [astro-ph.IM].
- [22] J. Stasielak *et al.*, *Astroparticle Physics* **73**, 14 (2016).
- [23] M. I. Bakunov, A. V. Maslov, A. L. Novokovskaya, and A. Kryemadhi, *Astropart. Phys.* **33**, 335 (2010).
- [24] M. P. De Haas, M. Kunst, J. M. Warman, and J. B. Verberne, *The Journal of Physical Chemistry* **87**, 4089 (1983), <https://doi.org/10.1021/j100244a019>.
- [25] S. de Kockere *et al.*, To be submitted, Private communication (2021).
- [26] K. Kamata and J. Nishimura, *Progress of Theoretical Physics Supplement* **6**, 93–155 (1958).
- [27] D. Heck, J. Knapp, J. Capdevielle, G. Schatz, T. Thouw, *et al.*, *Report fzka* **6019** (1998).
- [28] S. Agostinelli *et al.*, *Nuclear Instruments and Methods in Physics Research A* **506**, 250 (2003).
- [29] S. Prohira, <https://github.com/prchyr/RadioScatter> (2017).
- [30] K. Mulrey *et al.*, *JCAP* **11**, 017 (2020), arXiv:2005.13441 [astro-ph.HE].
- [31] H. Bozdog *et al.*, *Nucl. Instrum. Meth. A* **465**, 455 (2001).
- [32] B. Revenu, D. Charrier, R. Dallier, A. Escudie, D. García-Fernández, A. Lecacheux, and L. Martin, *PoS ICRC2017*, 416 (2018).
- [33] D. Ardouin, A. Belletoile, D. Charrier, R. Dallier, L. Denis, P. Eschstruth, T. Gousset, F. Haddad, J. Lamblin, P. Lautridou, *et al.*, *Astroparticle Physics* **26**, 341 (2006).
- [34] S. Thoudam *et al.*, *Nucl. Instrum. Meth. A* **767**, 339 (2014), arXiv:1408.4469 [physics.ins-det].
- [35] T. Huege, M. Ludwig, and C. W. James, *AIP Conf. Proc.* **1535**, 128 (2013), arXiv:1301.2132 [astro-ph.HE].
- [36] Xilinx, <https://www.xilinx.com/products/silicon-devices/soc/rfsoc.html> (2021).
- [37] S. Kunwar *et al.*, *Nucl. Instrum. Meth.* **A797**, 110 (2015), arXiv:1504.00779 [astro-ph.IM].
- [38] S. Prohira, S. Kunwar, K. Ratzlaff, R. Young, and D. Besson, *Nucl. Instrum. Meth.* **A890**, 126 (2018), arXiv:1709.08587 [astro-ph.IM].
- [39] P. Allison *et al.*, *Nucl. Instrum. Meth.* **A930**, 112 (2019), arXiv:1809.04573 [astro-ph.IM].
- [40] A. Anker *et al.*, *JCAP* **11**, 030 (2019), arXiv:1909.02677 [astro-ph.IM].
- [41] P. Zyla *et al.* (Particle Data Group), *PTEP* **2020**, 083C01 (2020).
- [42] K. C. Kuivinen, *Antarct. J. US* **18**, 113 (1983).
- [43] R. L. Hawley, E. M. Morris, and J. R. McCONNELL, *Journal of Glaciology* **54**, 839 (2008).
- [44] R. J. Arthern, H. F. J. Corr, F. Gillet-Chaulet, R. L. Hawley, and E. M. Morris, *Journal of Geophysical Research: Earth Surface* **118**, 1257 (2013), <https://agupubs.onlinelibrary.wiley.com/doi/pdf/10.1002/jgrf.20089>.
- [45] G. d. Q. Robin, *Journal of Glaciology* **15**, 151 (1975).
- [46] C. Deaconu, A. G. Viereg, S. A. Wissel, J. Bowen, S. Chipman, A. Gupta, C. Miki, R. J. Nichol, and D. Saltzberg, *Phys. Rev.* **D98**, 043010 (2018), arXiv:1805.12576 [astro-ph.IM].
- [47] S. Prohira *et al.* (Radar Echo Telescope), (2020), arXiv:2011.05997 [astro-ph.IM].

- [48] M. G. Aartsen *et al.* (IceCube), *Phys. Rev. D* **88**, 042004 (2013), arXiv:1307.3795 [astro-ph.HE].
- [49] A. Aab *et al.* (Pierre Auger), *Phys. Rev. Lett.* **125**, 121106 (2020), arXiv:2008.06488 [astro-ph.HE].
- [50] H. P. Dembinski, R. Engel, A. Fedynitch, T. Gaisser, F. Riehn, and T. Stanev, *PoS ICRC2017*, 533 (2018), arXiv:1711.11432 [astro-ph.HE].

Appendix A: Station Layout

The station layout for RET-CR is shown in Figure 8. A phased transmitter is centrally located along with a data acquisition system and an amplifier enclosure for the transmitter. Three 1 kW solar power arrays are oriented in a triangle to maximize power over the full austral summer day. Satellite communications are shown near the solar power array. Each receive antenna is a vertical phased dipole array to maximize gain in an azimuthally symmetric region near the surface. The

cosmic ray detector system is shown in blue, where each of the six, two-panel stations is shown in blue. The receive antennas are arranged in two sets, near at 20 m from the TX and far at 100 m from the TX. The drawing is not to scale.

Appendix B: System diagram

A schematic of the RET-CR system, including the surface system, is shown in Figure 9.

Appendix C: Timing diagram

A schematic of the RET-CR trigger timing is shown in Figure 10. Each of three surface stations outputs an L0 trigger. If all three of these happen within the coincident window, here set to 170 ns, then an L1 trigger is satisfied, and the data is read out.

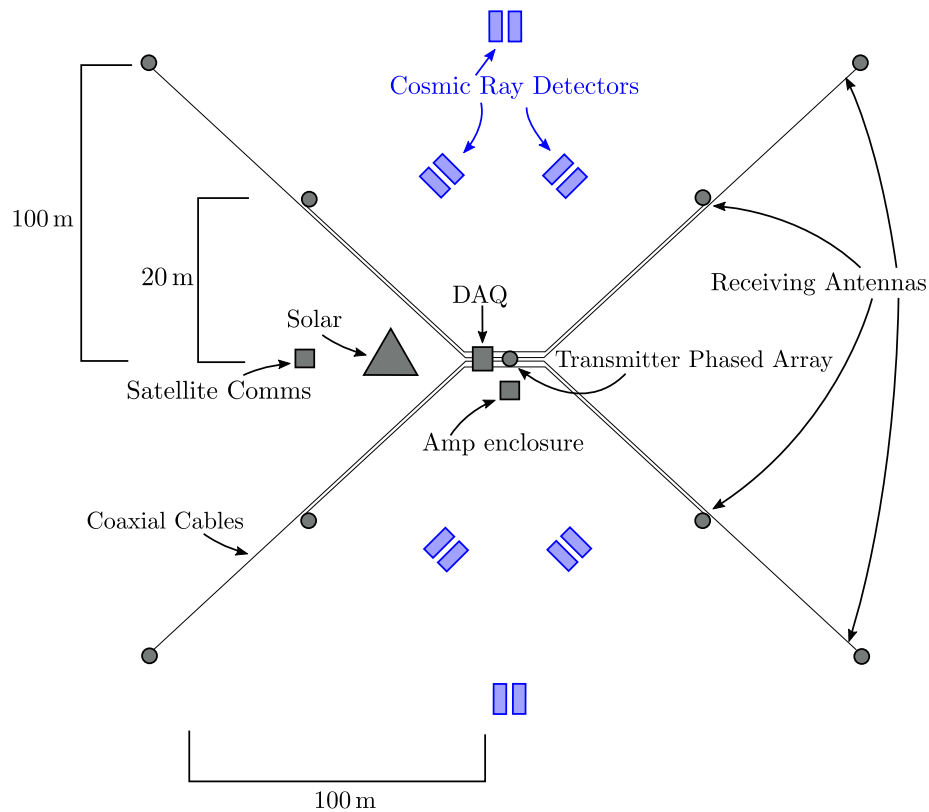


FIG. 8. The station layout for RET-CR. A phased transmitter array is centrally located along with a data acquisition system (DAQ) and an amplifier enclosure for the transmitter power amplifier(s). Three 1 kW solar power arrays oriented in a triangle are indicated along with satellite communications. The cosmic ray detector system is shown in blue. These serve to trigger the DAQ. The dimensions of the station are also indicated.

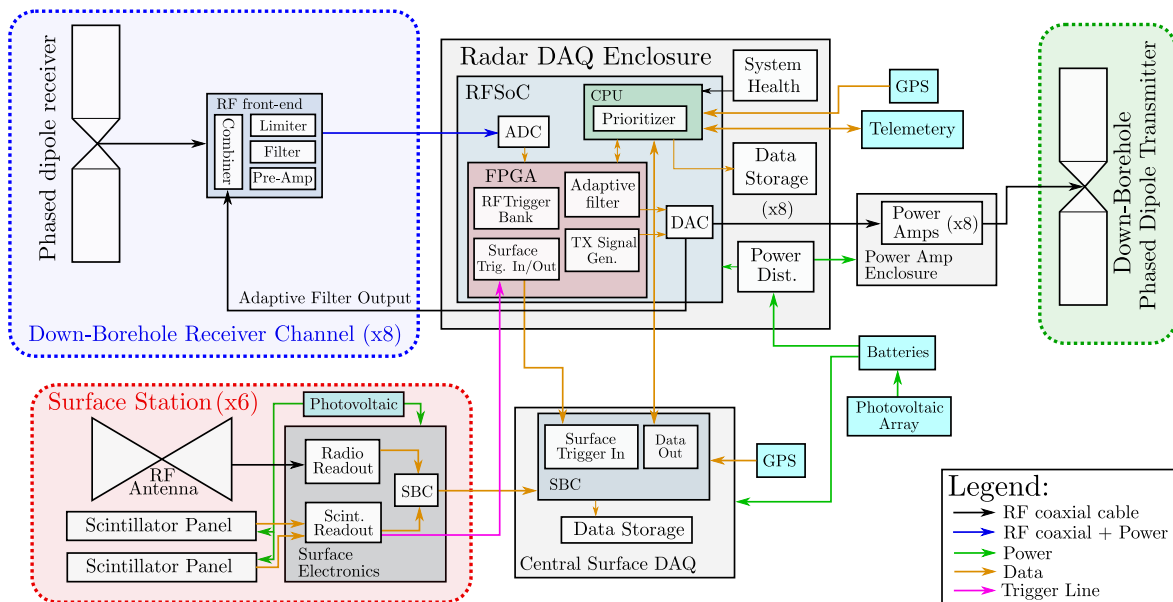


FIG. 9. The system diagram for RET-CR. The down-borehole receiver system is indicated on the left. There are 8 identical receivers placed according to the layout shown in Figure 8. The line indicating RF cable + power going to the receiver channel is powered via the bias-tee. The down-borehole transmitter is an 8-channel phased array, each antenna having its own DAC channel and power amplifier. The surface system, shown on the bottom, has 6 identical individual stations (bottom left).

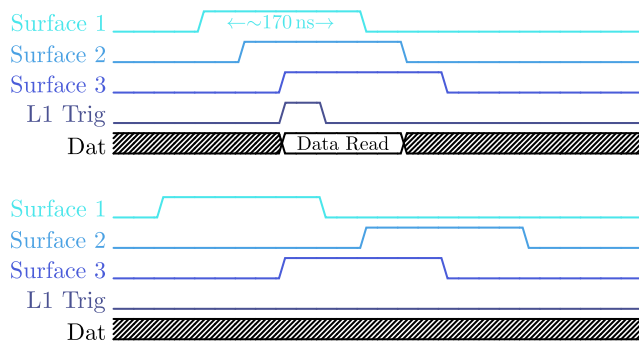


FIG. 10. The timing diagram for the RET-CR trigger. Top: all 3 surface stations in one quadrant provide an L0 trigger within the coincident window, forming a global L1 trigger, which triggers an event record. Bottom: all 3 surface stations provide an L0 trigger, but not within the coincident window, meaning this event is unlikely to have a radar echo and therefore not recorded.

The cosmic-ray air-shower signal in Askaryan radio detectors

Krijn D. de Vries^a, Stijn Buitink^a, Nick van Eijndhoven^a, Thomas Meures^b, Aongus Ó Murchadha^b, Olaf Scholten^{a,c}

^a*Vrije Universiteit Brussel, Dienst ELEM, B-1050 Brussels, Belgium*

^b*Université Libre de Bruxelles, Department of Physics, B-1050 Brussels, Belgium*

^c*University Groningen, KVI Center for Advanced Radiation Technology, Groningen, The Netherlands*

Abstract

We discuss the radio emission from high-energy cosmic-ray induced air showers hitting Earth's surface before the cascade has died out in the atmosphere. The induced emission gives rise to a radio signal which should be detectable in the currently operating Askaryan radio detectors built to search for the GZK neutrino flux in ice. The in-air emission, the in-ice emission, as well as a new component, the coherent transition radiation when the particle bunch crosses the air-ice boundary, are included in the calculations.

Key words: Cosmic rays, Neutrinos, Radio detection, Coherent Transition Radiation, Askaryan radiation

1. Introduction

We calculate the radio emission from cosmic-ray-induced air showers as a possible (background) signal for the Askaryan radio-detection experiments currently operating at Antarctica [1, 2, 3]. A high-energy neutrino interacting in a medium like (moon)-rock, ice, or air will induce a high-energy particle cascade. In 1962 Askaryan predicted that during the development of such a cascade a net negative charge excess arises mainly due to Compton scattering [4]. This net excess charge by itself will induce a radio signal that can be used to measure the original neutrino. This Askaryan radio emission [4, 5, 6] has been confirmed experimentally at SLAC [7], and more recently the Askaryan effect was also confirmed in nature by the radio emission from cosmic-ray induced air showers [8, 9, 10].

For high-energy cosmic-ray air showers, along with the Askaryan emission, there is another emission mechanism due to a net transverse current that is induced in the shower front by Earth's magnetic field [11-14]. Recently the radio emission from cosmic-ray air showers has been measured in great detail by the LOFAR collaboration [10, 15, 16], confirming the predictions from several independent radio emission models [17-20].

Most Askaryan radio detectors [1-3, 21-23] search for so-called GZK neutrinos that are expected from the interaction of ultra-high-energy cosmic-ray protons with the cosmic microwave background [24, 25]. The expected GZK neutrinos are extremely energetic with energies in the EeV range, while the flux at these energies is expected to fall below one neutrino interaction per cubic kilometer of ice per year. Therefore, to detect these neutrinos an extremely large detection volume, even larger than the cubic kilometer currently covered by the IceCube experiment, is

needed. Due to its long attenuation length, the induced radio signal is an excellent means to detect these GZK neutrinos. This has led to the development of several radio-detection experiments [1-6, 26-30]. Nevertheless, the highest-energy neutrinos detected so-far are those observed recently by the IceCube collaboration [31] and have energies up to several PeV, just below the energies expected from the GZK neutrino flux.

In this article we calculate the radio emission from cosmic-ray-induced air showers as a possible (background) signal for the Askaryan radio-detection experiments currently operating at Antarctica [1, 2, 3]. Besides the emission during the cascade development also transition radiation should be expected when the cosmic ray air shower hits Earth's surface [32, 33]. It follows that the induced emission is very hard to distinguish from the direct Askaryan emission from a high-energy neutrino induced cascade in a dense medium such as ice.

2. Radio emission from a particle cascade

We start from the Liénard-Wiechert potentials for a point-like four current from classical electrodynamics and closely follow the macroscopic MGMR [34] and EVA [20] models. Both models were developed to describe the radio emission from cosmic-ray-induced air showers. The Liénard-Wiechert potentials for a point charge, $A_{PL}^\mu(t, \vec{x})$, as seen by an observer positioned at \vec{x} at an observer time t are obtained directly from Maxwell's equations after fixing the Lorenz gauge [35],

$$A_{PL}^\mu(t, \vec{x}) = \frac{1}{4\pi\epsilon_0} \left. \frac{J^\mu}{|\mathcal{D}|} \right|_{ret}. \quad (1)$$

The point-like current is defined by $J^\mu = eV^\mu$, where e is the charge, and V^μ is the four-velocity for a particle at

Email address: krijndeVries@gmail.com (Krijn D. de Vries)

$\vec{\xi}(t_r)$ where the retarded emission time is denoted by t_r . The denominator of the vector potential, \mathcal{D} , is the retarded four-distance. For an extended current with longitudinal dimension h and lateral dimensions \vec{r} , the vector potential has to be convolved with the charge distribution given by the weight function $w(\vec{r}, h)$,

$$A^\mu(t, \vec{x}) = \frac{1}{4\pi\epsilon_0} \int dh d^2r \frac{J^\mu w(\vec{r}, h)}{|\mathcal{D}|} \Big|_{ret}, \quad (2)$$

where the vector potential has to be evaluated at the retarded emission time t_r . The corresponding geometry is

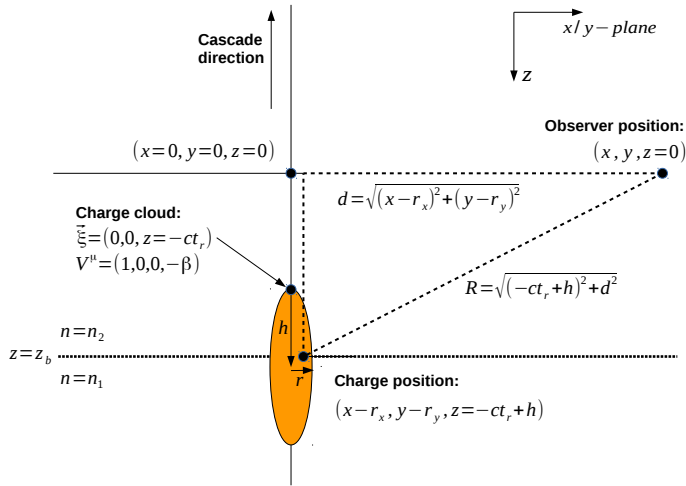


Figure 1: The geometry used to calculate the radiation emitted from a charge cloud crossing a boundary at $z = z_b$. The observer is positioned at an impact parameter $d = \sqrt{(x - r_x)^2 + (y - r_y)^2}$.

denoted in Fig. 1. We consider an observer positioned at an impact parameter $d = \sqrt{(x - r_x)^2 + (y - r_y)^2}$ perpendicular to the charge track, where r_x , and r_y denote the lateral position of the considered charge within the charge cloud. Defining the element in the plane of the observer perpendicular to the charge-track as $z = 0$, we can define the time at which the front of the charge cloud crosses this plane to be $t = 0$. Using these definitions the position of the charge along the track is now given by $z = -ct_r + h$.

Fixing the geometry, the vector potential can now be evaluated. The retarded emission time is obtained from the light-cone condition with respect to the optical path length L ,

$$c(t - t_r) = L, \quad (3)$$

from which the relation between the observer time and the emission time, $t_r(t)$, can be obtained. It should be noted that t_r is a negative quantity. For a medium consisting out of m layers with different index of refraction n_i , the optical path length can be defined by

$$L = \sum_{i=1}^m n_i d_i, \quad (4)$$

where the distance d_i , the distance covered by the emission in layer i , is obtained by using a ray-tracing procedure based on Snell's law. Following [36], the retarded distance for a signal traveling through different media is given by,

$$\mathcal{D} = L \frac{dt}{dt_r}. \quad (5)$$

In this work the index of refraction is assumed to be independent of frequency within the radio frequency range starting from a few MHz, up to several GHz. In the simplified situation where the signal travels through a medium with constant index of refraction n , the retarded distance can be written in the more common form,

$$\mathcal{D} = nR(1 - n\beta \cos(\theta)), \quad (6)$$

where θ denotes the opening angle between the line of sight from the emission point to the observer and the direction of movement of the emitting charge.

2.1. Cherenkov effects for a single electron

For a single electron moving at a highly relativistic velocity $\vec{\beta} = \vec{v}/c \approx 1$ along the z -axis (by definition), the current is given by $J^\mu = e(1, 0, 0, -\beta)$. The electric field is now obtained directly from the Liénard-Wiechert potentials through,

$$E^i(t, \vec{x}) = -\frac{dA^0}{dx^i} - \frac{dA^i}{dct}, \quad (7)$$

where $i = x, y$ gives the polarization of the field in the transverse direction, and x^i denotes the observer position in the transverse plane ($x^1 = x, x^2 = y$). For the moment we will ignore the electric field in the longitudinal direction and, since $A^i \propto J^i = 0$ for $i = 1, 2$ (there is no transverse current), we only have to consider the spatial derivative of the scalar potential. The electric field in the longitudinal direction will in general be small and can easily be calculated following the gauge condition $\vec{k} \cdot \vec{\epsilon} = 0$, where \vec{k} is the momentum vector of the photon and $\vec{\epsilon}$ the polarization. Hence the photon cannot be polarized along its direction of motion. Starting at the zeroth component of the vector potential, the spatial derivative can be evaluated by,

$$\frac{dA^0}{dx^i} = \frac{\partial}{\partial x^i} A^0, \quad (8)$$

which corresponds to the radiation from a net charge moving through the medium. For a relativistic electron ($\beta \approx 1$) moving in a medium with a refractive index $n > 1$ this term becomes,

$$\begin{aligned} E_{st}^i(t, \vec{x}) &= -\frac{\partial}{\partial x^i} A^0 \\ &= \frac{-e}{4\pi\epsilon_0} \frac{(1 - n^2)x^i}{|\mathcal{D}|^3}. \end{aligned} \quad (9)$$

Where the label 'st', denotes that the field is due to a highly relativistic non time-varying steady charge. The emission shows a radial polarization direction and vanishes

linearly with the distance of the observer to the shower core. This component of the electric field is suppressed by the factor $1 - n^2$, which vanishes in vacuum. In a medium with an index of refraction larger than unity however, this factor does not vanish and Cherenkov radiation is observed at the point where the retarded distance vanishes, $\mathcal{D} = \sqrt{t^2 + (1 - n^2\beta^2)(x^2 + y^2)} = 0$.

The retarded distance vanishes at the finite Cherenkov angle $\cos(\theta_{CH}) = \frac{1}{n\beta}$ (see Eq. (6)) where the electric field diverges. One intuitive way to understand the Cherenkov effect follows from the more general definition of \mathcal{D} given in Eq. (5). For a vanishing retarded distance, the derivative dt/dt_r has to vanish. It follows that the function $t(t_r)$ is flat at this point. Hence at an observer time t , signals emitted at different emission times t_r will be observed at once, leading to a boosted electric field. The vanishing of the retarded distance leads to a divergence in the electric field expressions. These divergences are integrable and therefore disappear for coherent emission by performing an integration over the finite charge and current distributions in the shower front [20].

2.2. Transition radiation for a single electron

So far we calculated the component of the electric field due to a relativistically moving net charge in a medium with a refractive index equal to n . How does this compare to the transition radiation for a relativistic charge crossing from a medium with refractive index n_1 to a medium with refractive index n_2 ? The vector potential for a single electron now becomes,

$$A^0(t, \vec{x}) = \frac{e}{4\pi\epsilon_0} \left(\frac{x^i}{|\mathcal{D}|} \theta(z - z_b) + \frac{x^i}{|\mathcal{D}|} \theta(z_b - z) \right), \quad (10)$$

where the discontinuity at a distance $z_b = -ct_b$, corresponding to the retarded emission time t_b when the electron crosses the boundary, is reflected by the step function $\theta(x)$ which is defined by,

$$\theta(x) = \begin{cases} 0 & \text{if } x < 0 \\ 1 & \text{if } x > 0 \end{cases}. \quad (11)$$

Since the step function is a function of the retarded emission time,

$$\theta(z - z_b) = \theta(-c(t_r - t_b)), \quad (12)$$

an additional term has to be added to Eq. (8). The full electric field is now given by,

$$\frac{dA^0}{dx^i} = \frac{\partial}{\partial x^i} A^0 + \frac{\partial t_r}{\partial x^i} \frac{\partial}{\partial t_r} A^0, \quad (13)$$

where in case of a single electron the second term on the right hand side of Eq. (13) will correspond to the transition radiation. The transition radiation can therefore be

evaluated as,

$$E_{tr}^i(t, \vec{x}) = \frac{\partial t_r}{\partial x^i} \frac{\partial}{\partial t_r} A^0 = \frac{e\delta(c(t_r - t_b))}{4\pi\epsilon_0 c} \lim_{\epsilon \rightarrow 0} \left(\frac{x^i}{|\mathcal{D}|_{t_r+\epsilon}^2} - \frac{x^i}{|\mathcal{D}|_{t_r-\epsilon}^2} \right). \quad (14)$$

It follows that when there is no boundary, hence $n_1 = n_2$, the transition radiation vanishes as it should. Looking more closely at the obtained expression in Eq. (14), it can be described as the superposition of the emission just before the particle crosses the boundary and the field just after the particle crossed the boundary. The two terms interfere destructively. This corresponds well to the mirror-charge approach for determining the transition radiation as applied by Ginzburg et al. [37] and the expressions obtained in [23, 38] and references therein.

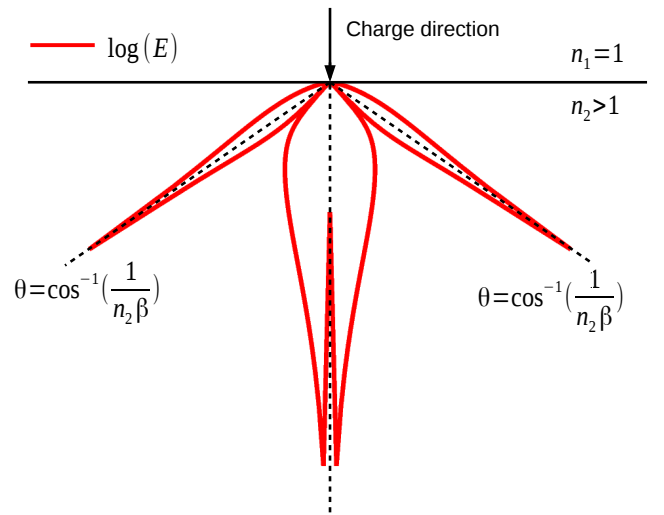


Figure 2: The angular intensity of the transition radiation seen from a charge moving from vacuum, $n_1 = 1$, to a dense medium $n_2 > 1$.

In Fig. 2 the intensity of the transition radiation is shown as function of angle. Since in vacuum the retarded distance vanishes at forward angles the first term dominates in the forward direction. At very small angles the intensity is suppressed due to the factor x in Eq. (14). With increasing angle $1/|\mathcal{D}|_{t_r+\epsilon}^2$ drops in magnitude while the contribution from below the surface, proportional to $1/|\mathcal{D}|_{t_r-\epsilon}^2$ increases in magnitude. Since the two interfere destructively there is a cancellation at a certain angle after which the second term dominates. At the Cherenkov angle in the medium, θ_2 , the second term diverges.

2.2.1. The sudden appearance signal

Another effect which is similar to transition radiation is the sudden appearance signal. One example of such a signal is found in accelerator experiments [39, 40]. Here the charged particle beam is accelerated, but during the acceleration process the charge is (partly) blocked from an

observer. The consequence is that when the beam leaves the accelerator, the observer suddenly observes a charge. This effect can be described in a similar way as transition radiation. The vector potential simply becomes,

$$A^0(t, \vec{x}) = \frac{e}{4\pi\epsilon_0} \frac{1}{|\mathcal{D}|} \theta(z_b - z), \quad (15)$$

for a beam traveling in a medium with refractive index n . Following the transition radiation calculation, the electric field is now directly obtained by,

$$\begin{aligned} E_{sa}^i(t, \vec{x}) &= \frac{\partial t_r}{\partial x^i} \frac{\partial}{\partial t_r} A^0 \\ &= \lim_{\epsilon \rightarrow 0} \frac{e\delta(c(t_r - t_b))}{4\pi\epsilon_0 c} \frac{x^i}{|\mathcal{D}|_{t_r+\epsilon}^2}. \end{aligned} \quad (16)$$

It should be noted that the delta-function is a function of the retarded emission time, t_r . The functional dependence can be shifted to the observer time, t , after which the field is given by the more common expression,

$$E_{sa}^i(t, \vec{x}) = \frac{e\delta(ct + z_b - L_b)}{4\pi\epsilon_0 c} \frac{x^i}{LD}, \quad (17)$$

where L_b denotes the optical path length for the signal emitted at the boundary point toward the observer.

2.3. Time varying current emission

So far we considered radiation from a single electron. In case of an electron bunch, there will be another radiation component due to the time variation of the total number of charges. In general this time variation can be linked to the net contribution of coherent bremsstrahlung emission of charges dropping out of the high-energy charge cloud and the emission of Compton electrons which are suddenly accelerated to relativistic speed. More generally, we can define the total number of particles at the retarded emission time t_r by the distribution $N_e(t_r)$. Defining the four-current as,

$$J^\mu(t_r) = eN_e(t_r)V^\mu, \quad (18)$$

the vector potential becomes,

$$A^\mu(t, \vec{x}) = \frac{1}{4\pi\epsilon_0} \frac{J^\mu(t_r)}{|\mathcal{D}|} \Big|_{ret}, \quad (19)$$

which gives the point-like vector potential for a non extended current. For a cosmic-ray air shower, the two main emission mechanisms are due to a time-varying transverse current which is induced by Earth's magnetic field, and the Askaryan emission due to the time-variation of the net negative charge-excess in the cascade. Nevertheless, for the geometry considered in this article, describing the emission for a perpendicular incoming shower hitting the ice surface at the South-Pole, the cascade will be aligned with Earth's magnetic field and the transverse current vanishes. Therefore, in this section we focus on the emission from a time varying charge. For more information about

the radio emission arising from the transverse current the reader is referred to [20, 34].

In case of a point-like time varying charge $Q(t_r) = eN_e(t_r)$, the partial derivative with respect to the retarded time of the second term on the right hand side of Eq. (13) will now also get a contribution where the derivative acts on this current. This leads to the varying charge emission,

$$E_{vc}^i(t, \vec{x}) = \frac{-1}{4\pi\epsilon_0 c} \frac{nx^i}{|\mathcal{D}|^2} \frac{dQ}{dt_r}, \quad (20)$$

which is the far-field radiation component. It should be noted that also here the signal scales like $1/|\mathcal{D}|^2$ and hence Cherenkov or equivalently relativistic time-compression effects apply equally well for this component of the radiation. Furthermore, a similar polarization behavior as for the emission from a highly relativistic steady charge as well as the transition radiation is obtained.

3. Coherent emission

To obtain the coherent emission we need to consider the spatial extent of the particle cascade. This is done by inclusion of the weight function $w(\vec{r}, h)$. The weight function is normalized such that $\int dh d^2r w(\vec{r}, h) = 1$. In a realistic situation, there will also be emission from the charged trail which is left behind after the cascade has passed. A detailed calculation including this can be found in [34]. The expressions given below for the coherent emission are obtained including this positive trail.

The electric field is now obtained by convolving the point-like current with the particle distributions in the shower front which can be evaluated numerically,

$$\begin{aligned} \vec{E}_{st}(t, \vec{x}) &= \frac{-e d}{4\pi\epsilon_0} \int dh d^2r \frac{(1-n^2)}{|\mathcal{D}|^3} \\ &\times N_e(t_r) w(\vec{r}, h) \hat{p} \end{aligned} \quad (21)$$

$$\begin{aligned} \vec{E}_{vc}(t, \vec{x}) &= \frac{-e d}{4\pi\epsilon_0 c} \int dh d^2r \frac{n}{|\mathcal{D}|^2} \\ &\times w(\vec{r}, h) \frac{dN_e(t_r)}{dt_r} \hat{p}. \end{aligned} \quad (22)$$

Here $\hat{p} = \vec{e}_r \times (\vec{e}_r \times \vec{e}_\beta)$ is the polarization of the signal, \vec{e}_r is the unit vector pointing from the emission point to the observer, and \vec{e}_β is the unit vector denoting the direction of the cascade. For the transition radiation the delta-function in Eq. (14) can be rewritten as,

$$\delta(z - z_b) = \delta(h - c(t_r - t_b)). \quad (23)$$

The electric field can now be solved analytically by integrating the delta-function and is given by,

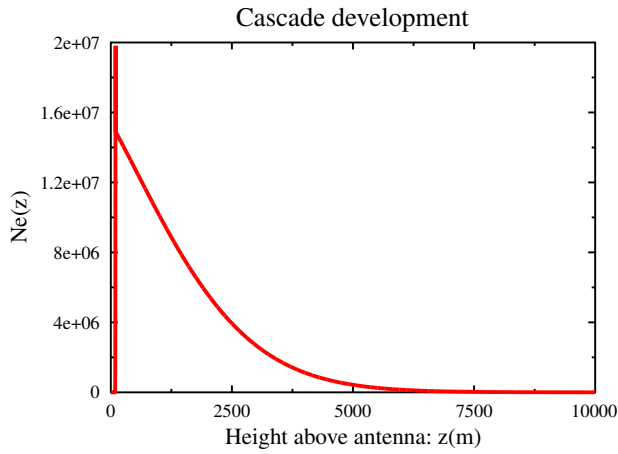
$$\begin{aligned} \vec{E}_{tr}(t, \vec{x}) &= \lim_{\epsilon \rightarrow 0} \int dh d^2r \left[\frac{e d N_e(t_r) w(\vec{r}, h)}{4\pi\epsilon_0 c} \right. \\ &\times \left. \left(\frac{1}{|\mathcal{D}|_{t_r-\epsilon}^2} - \frac{1}{|\mathcal{D}|_{t_r+\epsilon}^2} \right) \right] \\ &\times \delta(h - c(t_r - t_b)) \hat{p} \end{aligned}$$

$$\begin{aligned}
&= \lim_{\epsilon \rightarrow 0} \int d^2r \frac{e dN_e(t_r) w(\vec{r}, h)}{4\pi\epsilon_0 c} \\
&\times \left(\frac{1}{|\mathcal{D}|_{t_r-\epsilon}^2} - \frac{1}{|\mathcal{D}|_{t_r+\epsilon}^2} \right) \hat{p} \Big|_{h=c(t_r-t_b)} \quad (24)
\end{aligned}$$

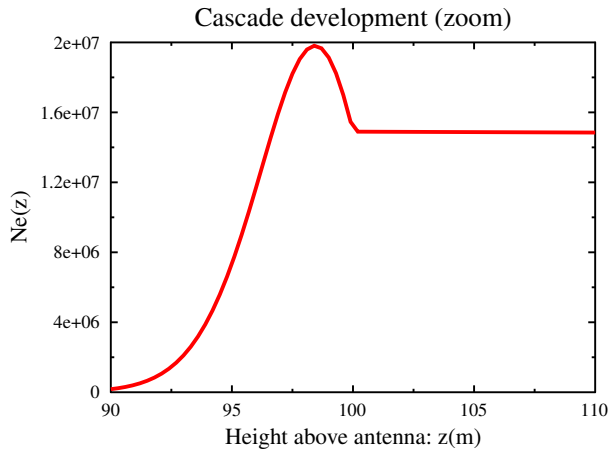
Following the same procedure the sudden appearance signal is given by,

$$\vec{E}_{sa}(t, \vec{x}) = \lim_{\epsilon \rightarrow 0} \int d^2r \frac{e dN_e(t_r) w(\vec{r}, h)}{4\pi\epsilon_0 c |\mathcal{D}|_{t_r+\epsilon}^2} \hat{p} \Big|_{h=c(t_r-t_b)} \quad (25)$$

4. The cosmic-ray air shower signal in Askaryan radio detectors



(a)



(b)

Figure 3: The number of charges N_e as a function of height z above the antenna as simulated for a cosmic-ray air shower with primary particle energy of 10^{17} eV. The antenna is positioned at an observer level 2900 m above sea level in ice. The ice-air boundary is at 3000 m above sea level.

In the previous section, we obtained the electric field expressions for the transition radiation from a particle cascade traversing the boundary between two different media. We also considered the steady charge emission as well as the varying current emission. We now have all ingredients to solve for the the emission from a high-energy cosmic-ray air shower which penetrates a surface.

4.1. The particle cascade

As an example we consider a shower which is induced by a 10^{17} eV primary cosmic ray, where the shower will hit an ice surface. The shower profile can be expressed as a function of the penetration depth $X(\text{g/cm}^2) = \int \rho(z) dz$, given by the line integral over the density which the shower has passed through. This allows us to naturally take into account for the air-ice boundary by simply writing the density as,

$$\rho(z) = \rho_{air} \theta(z - z_b) + \rho_{ice} \theta(z_b - z), \quad (26)$$

again using the step function $\theta(x)$. We will assume a density profile $\rho_{air}(z) = \rho_0 \exp[-C(z + z_0)]$ for an observer positioned at a height $z = z_0$ above sea level. Here $C = 1.160 \times 10^{-4} \text{ m}^{-1}$, and $\rho_0 = 1.168 \times 10^{-3} \text{ g cm}^{-3}$ [34]. The ice density is assumed to be constant over the few meters in which the cascade will die out and taken as $\rho_{ice} = 0.92 \text{ g cm}^{-3}$.

Since the radiation length $X_0 = 36 \text{ g/cm}^2$, as well as the critical energy $E_{crit} = 80 \text{ MeV}$ for electrons is approximately equal in air and ice, we can now take a NKG approximation [41, 42] given by,

$$N(X) = \frac{0.31 \exp[(X/X_0)(1 - 1.5 \ln s)]}{\sqrt{\ln(E/E_{crit})}} \quad (27)$$

for the total number of particles as a function of depth. The shower age s is given by [43],

$$s(X) = \frac{3X/X_0}{(X/X_0) + 2 \ln(E/E_{crit})}. \quad (28)$$

The excess charge as function of shower depth can be approximated by $N_{ch}(X) \approx 0.23 N(X)$ [34]. The total number of excess electrons as function of depth is shown in Fig. 3. Taking a geometry with the observer positioned at 2900 m above sea level with the air-ice boundary at 3000 m, the boundary at $z_b = 100$ m is clearly visible.

The particle distribution in the shower front is given by the weight function $w(r, h) = \delta(r) f(h)$, where $\int dh f(h) = 1$. The radial extension of the particles in the shower front is taken to be a delta function at the shower axis. To compensate for the loss of the lateral coherence scale, we use an effective width h_1 for the longitudinal particle distribution in the shower front. This width therefore reflects the coherence scale due to the full extension of the shower front. The longitudinal distribution of particles in the shower front is parametrized by [43, 44],

$$f(h) = (4/h_1^2) h e^{-2h/h_1}. \quad (29)$$

The effective width h_1 is chosen to be $h_1^{air} = 0.5$ m following [45] for the in-air development, while for the in-ice part of the cascade a width $h_1^{ice} = 0.1$ m is chosen.

4.2. The refractive index

In [45] it was shown that in determining the radio signal from cosmic-ray air showers it is crucial to take into account a realistic index of refraction. Therefore, in the following we model the index of refraction in air by the Gladstone-Dale law,

$$n_{air}(z) = 1 + 0.226 \frac{\text{g}}{\text{cm}^3} \rho_{air}(z). \quad (30)$$

Furthermore, in [36] it was shown that the bending of the emission in air can safely be neglected. The index of refraction in ice is taken as a constant equal to

$$n_{ice} = 1.78. \quad (31)$$

4.3. Results

Since we now have our electric field expressions, as well as the particle distributions, we can calculate the electric field at different observer positions in ice. We consider two different boundary levels at 500 m and 3000 m above sea level. The shower profile is given in Fig. 3 for a geometry where the air-ice boundary is 3000 m above sea level. In Fig. 3a the full shower profile is given. It follows that the shower hits the ice surface before it reaches its maximum. This is more clear from Fig. 3b where we zoom in on the boundary. In the ice the shower quickly reaches its maximum and dies out within 10 meters.

We consider the emission as seen by an observer positioned at several distances, $d = 40$ m, $d = 80$ m, and $d = 240$ m, from the shower axis, 100 m below the air-ice boundary. The obtained electric fields are shown in Fig. 4 a, c, and e. The full red line gives the electric field generated by the in-air development of the cascade, the striped purple line gives the transition radiation, and the dotted blue line gives the emission from the in-ice development of the cascade. Next to the obtained electric fields, in Fig. 4 b, d, and f we also show the total number of particles as function of height. Furthermore, in these figures we show the observer time for a signal emitted from a certain height. The full green line gives the total number of particles as function of height. It should be noted that the vertical axis is shifted by 90 m for plotting purposes. The full red line gives the emission height as function of the observer time for the in-air emission, where the striped purple line gives the same quantity for the in-ice emission.

The emission observed at $d = 40$ m is shown in Fig. 4a. As follows from Fig. 4b, the in-air emission from large heights is observed before the emission from lower heights. For the in-ice emission, this picture is completely reversed. In-ice signals emitted from large heights are delayed by the medium, while the cascade continues to propagate with the speed of light. Hence signals emitted at later times (lower heights) arrive before signals emitted early and the

observer is positioned inside the Cherenkov cone for the full in-ice emission.

For the transition radiation, it is important to notice that the electric field as given in Eq. (14) can be seen as a superposition of the emission just above, and just below the boundary which interferes destructively. The emission scales with $1/|\mathcal{D}| \sim |dt_r/dt| \sim |dz/dt|$, which is reflected in Fig. 4b by the slopes of the full red and striped purple lines at the boundary. At the boundary, there will be a sudden change of the particle distributions in the shower front. To take this into account in our modeling, the emission just above the boundary is evaluated using the particle distributions for the in-air shower, where the component just below the boundary is modeled using the particle distribution for the in-ice cascade. From this point of view one might also consider the transition radiation from just above the boundary as the sudden-death signal from the emission in air, where the transition radiation from just below the boundary can be seen as the sudden appearance signal for the in-ice emission.

For an observer positioned at $d = 80$ m, see Fig. 4c and d, a similar picture is obtained. The in-air emission is observed over a longer time-scale since we move further away from the Cherenkov cone for the emission emitted in air. For the in-ice emission, however, we shift closer to the Cherenkov angle. It follows that the in-ice emission is observed within a much shorter time-span and becomes much stronger. The transition radiation is now dominated by the emission from just below the boundary.

Finally we consider an observer positioned at $d = 240$ m. From Fig. 4e and f it follows that both the in-air emission as well as the in-ice emission are observed outside the Cherenkov cone. The emission is observed over a rather long time-scale, although the in-air component starts to be rather weak. One interesting feature is that the emission just above the boundary does not arrive at the same time as the emission just below the boundary. The transition radiation component just above the boundary is highly suppressed, and arrives just before $t = 1000$ ns, where the component emitted just below the boundary is much stronger and arrives at a much later time around $t = 1200$ ns. The time difference arises due to the fact that the signal emitted just above the air-ice boundary will first travel a significant part of its path almost horizontally before breaking into the ice under the critical angle, which in this case is equal to the in-ice Cherenkov angle. The signal emitted just below the air-ice boundary will travel its full path through the ice and hence obtain a large delay with respect to the signal emitted just above the boundary. It should be noted that this effect occurs in the situation of a perfectly flat and smooth surface. In a realistic experiment, the emission from just above the boundary however will not be able to travel almost perfectly horizontally along the surface and hence will lose coherence and become suppressed (already in the present case it is almost negligible in magnitude). The signal emitted just below the surface will not be affected and keep its

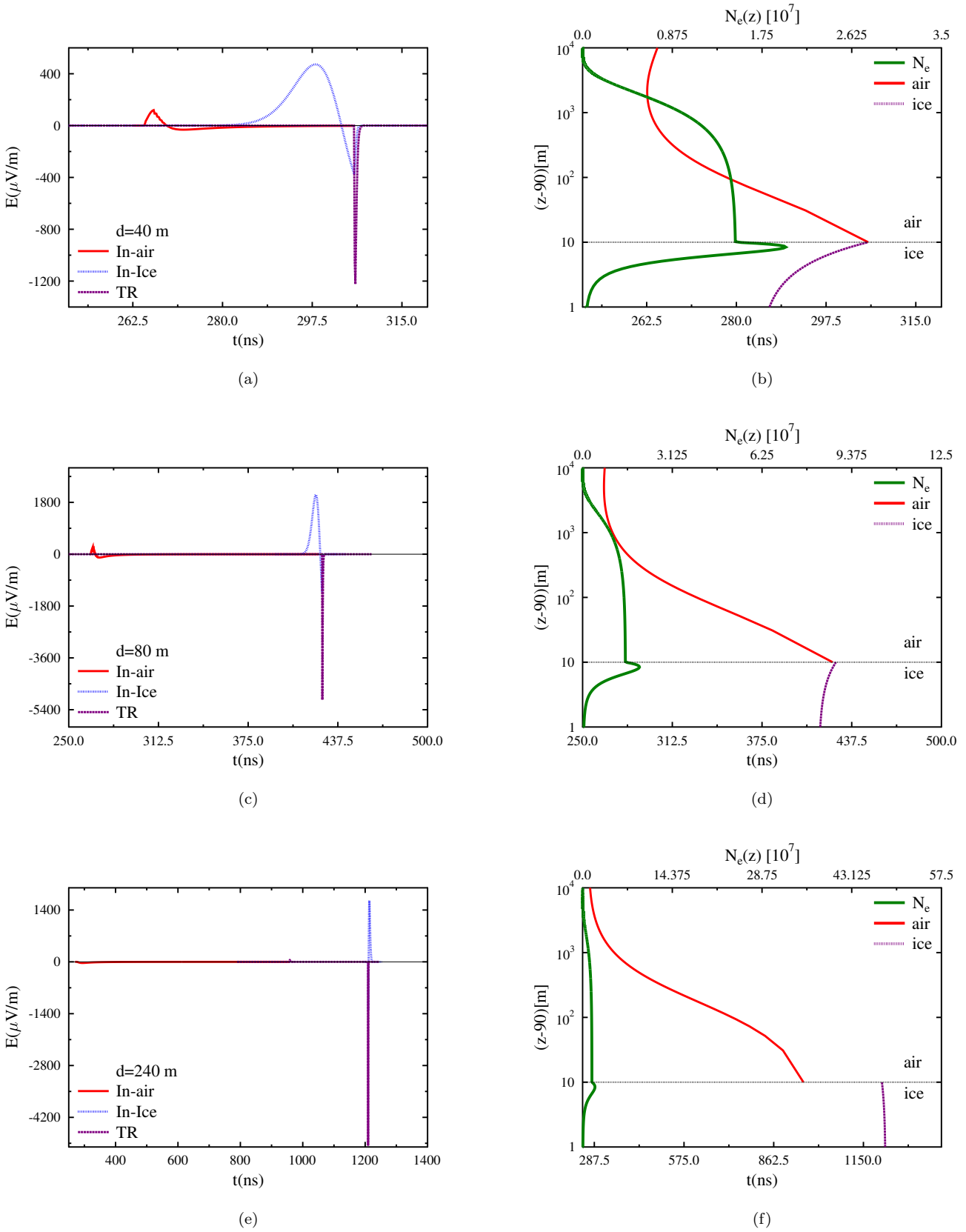


Figure 4: The electric field at different observer distances equal to, a) $d = 40$ m, b) $d = 80$ m, c) $d = 240$ m. The figures on the right show the emission height, plotted as function of the observer time. The full red line gives the emission in air, the dotted purple line gives the transition radiation, and the dashed blue line gives the in-ice emission. For the figures on the right, the total number of particles is given by the full green line.

coherence.

The emission will be coherent up to relatively high frequencies. This is also seen in Fig. 5a where we plot the frequency spectrum of the different components of the emission when the observer is positioned at a distance of $d = 240$ m. In Fig. 5b, we plot the frequency spectrum for the same geometry shifting the ice-air boundary to 500 m above sea level. Coherence of the in-ice emission as well

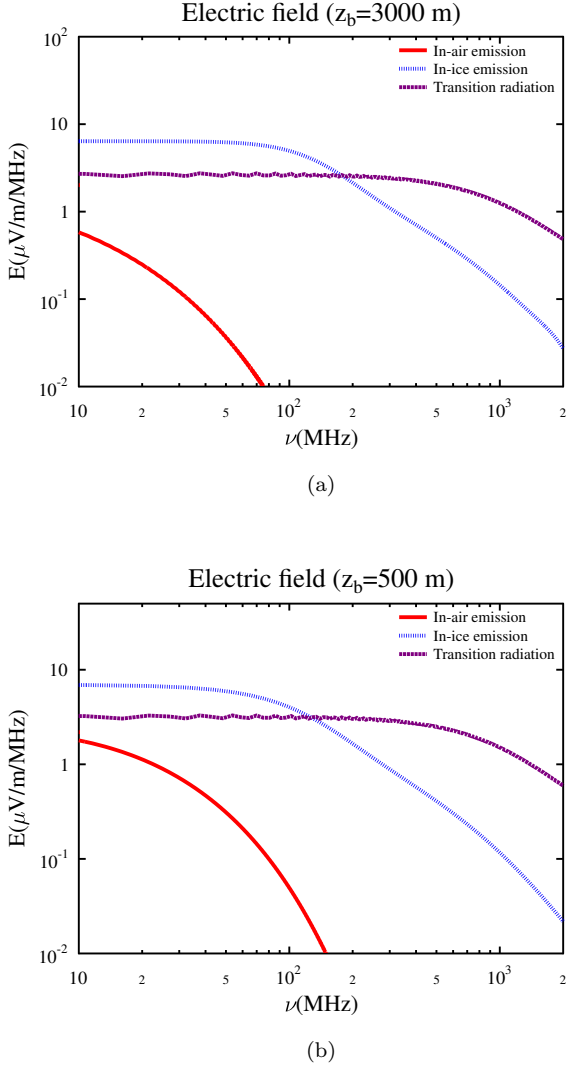


Figure 5: The frequency spectrum of the different components to the electric field as seen by an observer positioned 100 m below the ice-air boundary and $d = 250$ m from the shower axis. The simulation is performed for a 10^{17} eV primary energy cosmic-ray air shower.

as the in-air emission away from the Cherenkov angle is typically determined by the length of the shower trajectory leading to a suppression at the highest frequencies. The transition radiation, however, is emitted from a single point at the boundary, and hence its coherence is fully determined by the particle distributions in the shower front

which gives a cut-off at relatively high-frequencies in the GHz range. Each of the several different components has a finite response at zero frequency. One should note however that the combined response of all different components vanishes at zero frequency.

In Fig. 4, and Fig. 5, the detailed properties of the emission in time and frequency space were shown. This allows us to understand the angular distribution of the different components of the emission shown in Fig. 6. Here we plot the integrated absolute value of electric field $I = \int |E| dt$. It follows that the in-air emission given by the full red

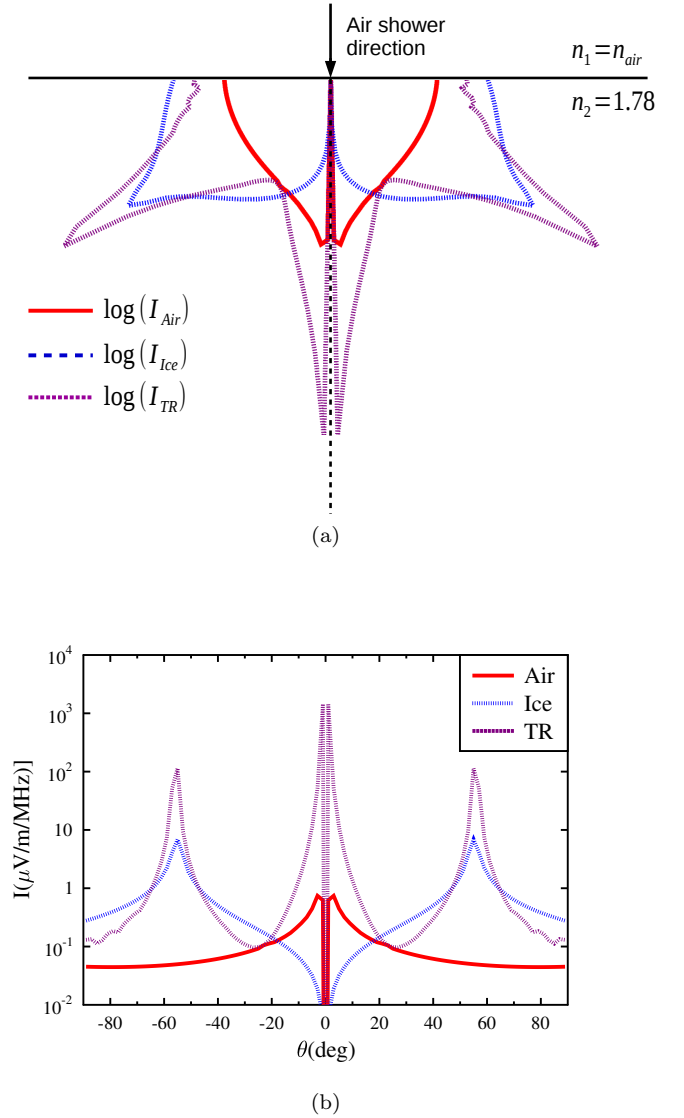


Figure 6: The angular distribution of the integrated field for a radial observer distance of $R = \sqrt{z^2 + d^2} = 300$ m. The full red line gives the angular distribution for the in-air emission, the dotted purple line gives the transition radiation, and the dashed blue line shows the in-ice emission.

line in Fig. 6, as expected, peaks toward a highly forward angle ($\theta = 0^\circ$), after which the emission drops rapidly to

ward larger angles. The transition radiation, shown by the dotted purple line in Fig. 6, shows a similar behavior as observed in Fig. 2. There is a strong forward peak, after which the transition radiation gets suppressed due to the destructive interference between the emission just above the air-ice boundary and the emission just below the air-ice boundary. When the destructive interference is maximal, contrary to Fig. 2, the field does not vanish completely. This is due to the different particle distributions for the in-air emission and the in-ice emission which is taken into account for in the evaluation of the transition radiation. The in-ice emission, as expected, peaks at the in-ice Cherenkov angle. Nevertheless, the emission pattern is rather broad toward smaller angles due to the longitudinal extent of the cascade.

4.4. Zenith angle dependence

Up to now we only considered a perpendicular incoming cosmic-ray induced air shower. Since a shower coming in under a finite zenith angle can be treated by a direct rotation of the geometry, we do not expect the emission to change significantly. One effect that is to be expected for an inclined shower, or in case of a non-perpendicular boundary, is that the transition radiation from different radial parts of the shower is emitted at different times. In case of an observer positioned underneath the shower axis this will lead to a small additional spread in the arrival time of signals emitted from different positions in the shower front, and hence a slight decrease of pulse-strength can be expected. For an observer positioned away from the shower axis however, this effect is reversed, leading to a slightly enhanced pulse-strength in the detector. Furthermore, it should also be noted that for more inclined geometries, a larger part of the signal created in air will be reflected off of the surface suppressing the in-air emission over the in-ice emission even more.

The most important effect, however, will be due to the change of the total number of charges hitting the air-ice boundary. Since for larger zenith angles the shower traverses a longer distance through air, the total number of particles actually hitting the air-ice boundary changes. Other effects influencing the total number of particles hitting the air-ice surface are the chemical composition and the energy of the primary cosmic ray. An iron induced shower typically develops earlier in the atmosphere than a proton induced shower, where cosmic rays of higher energy typically peak deeper in the atmosphere. In Fig. 7 we show the total number of particles hitting the air-ice surface for boundary layers at $z_b = 3000$ m (full lines) and $z_b = 500$ m (dotted lines) for a typical proton shower with a primary energy of $E_p = 10^{17}$ eV (red lines) and $E_p = 10^{18}$ eV (blue lines).

For an air-ice boundary at $z_b = 3000$ m, the air shower is still below shower maximum for both considered energies. It follows that the total number of particles peaks at a zenith angle of approximately $\theta \approx 40 - 50$ degrees, where the air shower is fully developed at the boundary. For

larger zenith angles, the total number of particles hitting the air-ice boundary becomes smaller, and for zenith angles larger than $\theta \gtrsim 60$ degrees the shower dies out before hitting the air-ice boundary. Hence no transition radiation and in-ice emission will be observed for showers at zenith angles larger than approximately $\theta \approx 60$ degrees.

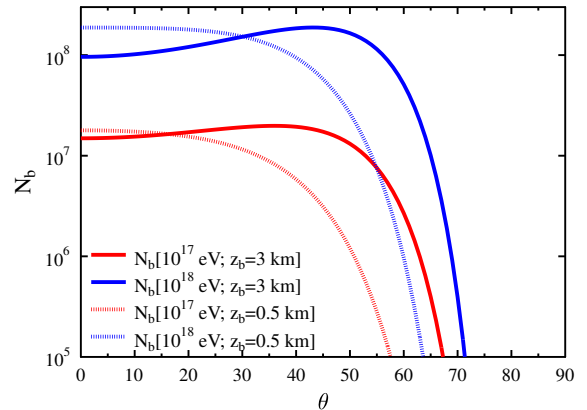


Figure 7: The total number of particles hitting the air-ice surface for boundary layers at $z_b = 3000$ m (full lines) and $z_b = 500$ m (dotted lines) for a typical proton shower with a primary energy of $E_p = 10^{17}$ eV (red lines) and $E_p = 10^{18}$ eV (blue lines).

4.5. Cosmic-ray air shower or neutrino induced cascade?

One important question to consider is how the cosmic-ray air shower signal compares to the emission from a neutrino induced cascade in ice. This is shown in Fig. 8. For the cosmic-ray air shower signal, we consider both the in-ice emission as well as the transition radiation component just below the boundary. As follows from Fig. 4, the in-air emission is very small and will therefore be ignored for this comparison.

The neutrino induced cascade is modeled by taking a 10^{17} eV primary neutrino interacting at the surface of the air-ice boundary, after which the cascade develops in ice. The observer is positioned 100 m below the ice surface at a distance $d = 240$ m perpendicular to the shower axis. The effective width of the particle distribution is taken as $h_1 = 0.1$ m, approximately corresponding to the dimensions of the cascade front in ice.

It follows that the emission from a typical proton induced high-energy cosmic ray air shower hitting the ice surface is of similar magnitude compared to the Askaryan signal from a neutrino induced particle cascade in ice of the same energy. Since the total number of particles hitting the air-ice interface is slightly larger at $z_b = 500$ m for the considered geometry of a vertical cosmic-ray air shower (see Fig. 7), the transition radiation gets slightly enhanced with respect to the emission seen at $z_b = 3000$ m.

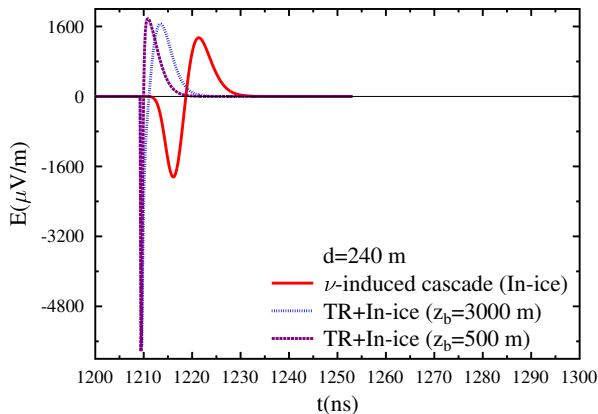


Figure 8: The electric field from a neutrino induced particle cascade in ice (full red line), compared to the transition radiation just below the boundary layer and the in-ice emission from a vertical, proton induced, cosmic-ray air shower of the same energy. The electric field is shown for ice-air boundaries equal to $z_b = 3000$ m (dashed blue line) and $z_b = 500$ m (dotted purple line). The observer is positioned at a lateral distance $d = 250$ m perpendicular to the shower axis.

The direct consequence is that the radio emission from a high-energy cosmic ray air shower will be very hard to distinguish from the emission of a high-energy neutrino induced particle cascade without directional information about the signal. Another possible method to separate the cosmic-ray air shower from the neutrino induced cascade might be obtained by adding a surface veto to the array.

5. Summary and conclusions

We derived an analytical expression for coherent transition radiation from a particle bunch with a net charge which is traversing from one medium to another. In addition to the transition radiation also the emission due to a highly-relativistic steady charge and a time-varying current are given.

As a first application we calculate the radio emission from a cosmic-ray-induced air shower hitting an ice layer before the shower has died out. It is shown that a relatively strong transition radiation component can be expected from an air shower when taking an air-ice boundary in the range between 500-3000 m above sea level. The emission from such a cosmic-ray air shower is calculated to be of similar strength as the Askaryan signal obtained from an in-ice cascade induced by a GZK-neutrino of similar energy. Furthermore, the polarization of the transition radiation will be similar to the polarization of the Askaryan signal. It follows that without directional information or a surface veto, it will be very hard to distinguish between both signals. Therefore, the emission from

cosmic-ray air showers might induce a significant (background) signal in the currently operating Askaryan neutrino detectors at Antarctica.

Next to the discussed application for cosmic-ray air showers hitting a dense medium, the transition radiation from neutrino induced particle cascades traveling from a dense medium to air or vacuum is also expected to give a strong signal. This signal might be a promising probe to detect high-energy neutrino-induced particle cascades escaping dense media. A more detailed calculation for this component will be given in future work.

6. Acknowledgments

The authors wish to thank The Flemish Foundation for Scientific Research (FWO-12L3715N - Krijn D. de Vries), and the FWO Odysseus program (G.0917.09. - N. van Eijndhoven), and the FRS-FNRS (Aongus Ó Murchadha) for making this research possible.

References

- [1] P.W. Gorham et al., *Phys. Rev. Lett.* **103**, 051103 (2009)
- [2] P. Allison et al., ARA Collaboration, *Astropart. Phys.* **35**, 457-477 (2012)
- [3] ARIANNA Collaboration, Proc. 32nd ICRC Rio De Janeiro, Brasil, to be published
- [4] G.A. Askaryan, *Sov. Phys. JETP* **14**, 441 (1962); **21**, 658 (1965)
- [5] E. Zas, F. Halzen, and T. Stanev, *Phys. Rev. D* **45**, 362 (1992)
- [6] J. Alvarez-Muñiz and E. Zas, *Phys. Lett. B* **411**, 218 (1997)
- [7] D. Saltzberg et al., *Phys. Rev. Lett.* **86**, 2802 (2001)
- [8] V. Marin, CODALEMA Collaboration, Proc. 32nd ICRC, Beijing, China
- [9] A. Aab et al., Pierre Auger Collaboration, *Phys. Rev. D* **89**, 052002 (2014)
- [10] P. Schellart et al., arXiv:1406.1355
- [11] F.D. Kahn and I. Lerche, *Proc. Royal Soc. London* **A289**, 206 (1966)
- [12] O. Scholten, K. Werner, F. Rusydi, *Astropart. Phys.* **29**, 94-103 (2008)
- [13] H. Falcke et al., *Nature* **435**, 313 (2005)
- [14] D. Ardouin et al., *Astropart. Phys.* **26**, 341 (2006)
- [15] A. Nelles et al., *Astropart. Phys.* **65**, 11-21 (2015)
- [16] S. Buitink et al., *Phys. Rev. D* **90**, 082003 (2014)
- [17] J. Alvarez-Muniz, W. R. Carvalho, Jr., E. Zas, *Astropart. Phys.* **35**, 325-341 (2012)
- [18] V. Marin, B. Revenu, *Astropart. Phys.* **35**, 733-741 (2012)
- [19] T. Huege, M. Ludwig, C. James, *AIP Conf. Proc.* **1535**, 128-132 (2013)
- [20] K. Werner, K.D. de Vries, O. Scholten, *Astropart. Phys.* **37**, 5-16 (2012)
- [21] O. Scholten et al., *Phys. Rev. Lett.* **103**, 191301 (2009)
- [22] C.W. James et al., *MNRAS* **410**(2), 885-889 (2011)
- [23] S. ter Veen et al., *Phys. Rev. D* **82**, 103014 (2010)
- [24] K. Greisen, *Phys. Rev. Lett.* **16**, 748 (1966)
- [25] G.T. Zatsepin, V.A. Kuzmin, *Pisma Zh. Eksp. Teor. Fiz.* **4**, 114 (1966)
- [26] R. Dagesamanski and I. Zheleznyk, *Sov. Phys. J.E.T.P.* **50**, 233 (1989)
- [27] T. Hankins, R. Ekers, and J. OSullivan, *MNRAS* **283**, 1027 (1996)
- [28] H. Lethinen et al., *Phys. Rev. D* **69**, 013008 (2004)
- [29] P. Gorham et al., *Phys. Rev. Lett.* **93**, 41101 (2004)
- [30] A. Beresnyak et al., *Astronomy Reports* **49**, 127 (2005)
- [31] IceCube Collaboration, *Science* **342**, 1242856 (2013)

- [32] M.A. Markov, I.M. Zheleznykh, Nucl. Instrum. Meth. Res. A **248**, 242 (1986)
- [33] B. Revenu, V. Marin, arXiv:1211.3305
- [34] K.D. de Vries, A.M. van den Berg, Olaf Scholten, Klaus Werner, Astropart. Phys. **34**, 267 (2010)
- [35] J.D. Jackson, Classical Electrodynamics, Wiley, New York, 1999
- [36] K. Werner, O. Scholten, Astropart.Phys. **29**, 393 (2008)
- [37] V.L. Ginzburg, V.N. Tsytovich, Transition Radiation and Transition Scattering, Adam Hilger Press, New York, 1990
- [38] C.W. James, H. Falcke, T. Huege, M. Ludwig, Phys. Rev. E **84**, 056602 (2011)
- [39] Y. Shibata et. al, Phys. Rev. E **50**, 1479 (1994)
- [40] P.W. Gorham et. al, Phys. Rev. E **62**, 8590 (2000)
- [41] K. Kamata, J. Nishimura, Suppl. Progr. Theoret. Phys. **6**, 93 (1958)
- [42] K. Greisen, in: J.G. Wilson (Ed.), Prog. Cosmic Ray Phys., vol. III, North Holland, Amsterdam, 1965, p. 1
- [43] T. Huege, H. Falcke, Astronomy & Atrophys. **19**, 412 (2003)
- [44] G. Agnetta et al., Astropart. Phys.**6**, 301 (2003)
- [45] K.D. de Vries, A.M. van den Berg, O. Scholten, K. Werner, Phys. Rev. Lett. **107**, 061101 (2011)

Publications Ben Craps

Entwinement in discretely gauged theories

V. Balasubramanian,^{a,b} A. Bernamonti,^{c,d} B. Craps,^b T. De Jonckheere^b and F. Galli^{c,d}

^aDavid Rittenhouse Laboratory, University of Pennsylvania,
Philadelphia, PA 19104, U.S.A.

^bTheoretische Natuurkunde, Vrije Universiteit Brussel, and International Solvay Institutes,
Pleinlaan 2, B-1050 Brussels, Belgium

^cPerimeter Institute for Theoretical Physics,
31 Caroline Street North, ON N2L 2Y5, Canada

^dInstitute for Theoretical Physics, Katholieke Universiteit Leuven,
Celestijnenlaan 200D, B-3001 Leuven, Belgium

E-mail: vijay@physics.upenn.edu, abernamonti@perimeterinstitute.ca,
Ben.Craps@vub.ac.be, Tim.De.Jonckheere@vub.ac.be,
fgalli@perimeterinstitute.ca

ABSTRACT: We develop the notion of “entwinement” to characterize the amount of quantum entanglement between internal, discretely gauged degrees of freedom in a quantum field theory. This concept originated in the program of reconstructing spacetime from entanglement in holographic duality. We define entwinement formally in terms of a novel replica method which uses twist operators charged in a representation of the discrete gauge group. In terms of these twist operators we define a non-local, gauge-invariant object whose expectation value computes entwinement in a standard replica limit. We apply our method to the computation of entwinement in symmetric orbifold conformal field theories in 1+1 dimensions, which have an S_N gauging. Such a theory appears in the weak coupling limit of the D1-D5 string theory which is dual to AdS_3 at strong coupling. In this context, we show how certain kinds of entwinement measure the lengths, in units of the AdS scale, of non-minimal geodesics present in certain excited states of the system which are gravitationally described as conical defects and the $M = 0$ BTZ black hole. The possible types of entwinement that can be computed define a very large new class of quantities characterizing the fine structure of quantum wavefunctions.

KEYWORDS: AdS-CFT Correspondence, Gauge Symmetry, Gauge-gravity correspondence, Long strings

ARXIV EPRINT: [1609.03991](https://arxiv.org/abs/1609.03991)

Contents

1	Introduction	1
2	Defining entwinement	4
2.1	Replica trick — generalities	5
3	Entwinement in symmetric orbifold CFTs	9
3.1	Single interval entwinement	10
3.2	Entanglement entropy of a spatial region	12
4	D1-D5 CFT	12
4.1	Conical defects	13
4.2	Zero mass BTZ black hole	14
5	Discussion and outlook	15
A	Twist correlator	18
B	Dominant contributions to the entwinement of $M = 0$ BTZ	21

1 Introduction

When a quantum system finds itself in a pure state $|\psi\rangle$, the entanglement between a part A of the system and its complement \bar{A} is quantified by the entanglement entropy. In most applications, A and \bar{A} describe the degrees of freedom in complementary spatial regions. In systems with localized degrees of freedom such as spin chain models or local quantum field theory, this corresponds to a natural separation of the total Hilbert space. However, it is also fruitful to consider other ways of separating the Hilbert space.

In [1, 2], the degrees of freedom of a local quantum field theory were separated into high and low spatial momentum modes. It was demonstrated that in a generic interacting field theory, even in the vacuum state, the long wavelength (low energy) degrees of freedom necessarily find themselves in a nontrivial reduced density matrix because of entanglement with the short wavelength (high energy) degrees of freedom. This gives rise to finite entanglement entropy, which was computed explicitly in perturbative scalar field theories. The more traditional way of describing the low energy degrees of freedom is Wilsonian renormalization. In this language, the vacuum state of a Wilsonian low energy theory is necessarily a density matrix with finite entropy [1, 2]. This phenomenon of UV-IR entanglement in quantum field theories could be particularly important in theories of gravity (in which ultraviolet and infrared degrees of freedom are known to couple in nontrivial ways), as well as in the ground states of strongly correlated electronic systems (see, e.g. [3]).

This also raises the question whether it is fruitful to consider other non-spatial ways of dividing the degrees of freedom of quantum field theories. One interesting way to separate energy scales is by imagining a collection of local observers who have a finite duration T over which they can make measurements. This is a natural situation to consider, as it describes the practical constraints of most measurements. Intuitively, given Heisenberg’s energy-time uncertainty relation, such observers will be insensitive to energies smaller than the inverse duration of the experiment, so that those low energy degrees of freedom are effectively traced out, turning the accessible part of the state into a nontrivial density matrix. Thinking in this way, [4–7] proposed a new information theoretic quantity, the *differential entropy*, as a measure of UV-IR entanglement, at least for two-dimensional theories.

These effects should become stronger for theories with an energy gap that is smaller than the inverse spatial size of the system. For example, consider relativistic theories where the local degrees of freedom are matrices, e.g. $SU(N)$ gauge theories. In such systems the energy gap can be much smaller than the inverse spatial size of the system so that even a set of observers with enough time to observe the entire spatial domain will not have access to the lowest energy excitations. Another example which is easier to visualize is a “long string” theory, where strings or spin chains are multiply wound around a spatial circle, allowing for excitation wavelengths that exceed the system size. In both these examples, the key to the physics lies in entanglement between “internal” degrees of freedom (matrix components, or strands of string) that are not spatially organized.

One way to study the entanglement of gauge degrees of freedom in an $SU(N)$ theory is to break the gauge group into $SU(m) \times SU(N - m)$ while allowing for interactions between the two sectors. This could be realized holographically by separating a stack of N branes into a stack of m and one of $N - m$ branes and studying entangling surfaces in the $AdS_d \times S^{10-d}$ geometry which arises in the low energy limit. Such a set-up was first considered in [8] and later refined in [9–11]. The authors of [9, 10] also considered global symmetries and in case of an $SO(11 - d)$ global symmetry they proposed a quantity in the field theory which would holographically be represented by the area of caps on the internal S^{10-d} .

One important complication that we have glossed over so far is that in systems exhibiting gauge symmetry, even the association of degrees of freedom to spatial regions is subtle. For example, some of the fundamental degrees of freedom, such as Wilson loops, are not local in space, making it more complicated to split up the Hilbert space according to spatial regions. Interesting work on how to define entanglement entropy in gauge theories has recently appeared (see e.g. [12–21]), but a complete understanding is still lacking.

These questions about entanglement in quantum field theory are also linked to equally deep questions about the nature of black hole horizons and the holographic emergence of spacetime. It was proposed in [22–24] that the entanglement entropy of a spatial region A in the field theory is proportional to the area of the minimal surface in AdS space that ends on the boundary of A . Furthermore, [4–7] showed that the area of closed surfaces in the bulk of AdS can be related to a measure of UV-IR entanglement, the differential entropy discussed above, at least for two-dimensional boundary theories and higher dimensional cases with translational symmetries — some of the limitations were discussed in [25]. Fi-

nally, in [26–31] it was suggested that spacetime connectedness is related to entanglement of the underlying quantum degrees of freedom, and that the linearized equations of motion of gravity can be derived from the dynamics of entanglement perturbations.

In general, can all of spacetime geometry be reconstructed from spatial entanglement entropy in the AdS/CFT correspondence? At least when we do not consider bulk quantum corrections to the entanglement entropy [32], the answer is no — in some asymptotically AdS spacetimes, the minimal surfaces anchored on the boundary that geometrically reproduce the entanglement entropy will not penetrate a region [33, 34] which has been called the *entanglement shadow* [35, 36]. It is argued in [35] that in such systems entanglement can be dominated by “internal” degrees of freedom (e.g. the matrix components, or strands of string discussed above) that are not spatially organized, and that these entanglements can measure the areas of non-minimal, extremal surfaces that can penetrate part of the entanglement shadows of the gravitational dual. In the examples arising in the AdS/CFT correspondence, such internal degrees of freedom are usually gauged. Thus, reconstructing the emergent space in gauge/gravity duality will involve entanglement between “internal”, gauged degrees of freedom — a notion that was named *entwinement* in [35]. While we will not address the question of which part of a general spacetime can be probed by extremal surfaces (see, for instance, [33, 34, 36]), it is clear that entwinement will often allow the reconstruction of a larger part of spacetime than spatial entanglement entropy. Entwinement also plays a key role in the description of holographic spacetimes using methods of integral geometry based in kinematic space [37–39].

In summary, both in quantum field theory and in quantum gravity, we are driven to consider a new notion of “entwinement” — non-spatial quantum entanglement between gauged degrees of freedom. In this paper we will define entwinement formally in discretely gauged theories, and discuss how it can be explicitly computed. Section 2 develops the general formalism. For two-dimensional theories, we define entwinement in terms of a replica method using twist operators that are charged under the discrete gauge group. We use these operators to construct a new non-local, gauge invariant object whose expectation value is defined to be the entwinement in a standard replica limit. Section 3 applies this formalism to symmetric orbifold conformal field theories in two dimensions. By explicitly applying uniformization maps, obtained by generalizing a construction of [40], to the Riemann surfaces arising from the replica method we directly compute entwinement in generic microstates of these theories. We also comment on how to recover the usual spatial entanglement entropy as a special limit of entwinement.

In section 4, we apply our formalism to the weak coupling limit of the D1-D5 CFT, a theory with a holographic dual. Ordinary spatial entanglement entropy in generic classes of the D1-D5 CFT was considered before in [40–42]. For generic microstates, entanglement entropy was computed approximately using both a short interval expansion [41] and large c methods [42]. In [40], a specific state corresponding to a local quench was considered, and the evolution of the entanglement entropy was computed using a uniformization map — we generalize the construction for use with other microstates. Although this uniformization map will work for computing single interval entwinement in general microstates, in section 4 to compare with holography we focus on two examples of microstates, which are

gravitationally related to conical defects and the $M = 0$ BTZ black hole, respectively. We demonstrate that the lengths of non-minimal geodesics that penetrate entanglement shadows of the spacetime are computed by certain entwinements. In the same way as spatial entanglement entropy corresponds to minimal extremal area surfaces in the bulk, here entwinement provides a direct field theory interpretation for non-minimal extremal surfaces.

The paper concludes with a discussion of possible directions forward to develop the notion of entwinement in more general situations, and comments on the relation with the appearance of non-minimal geodesics in the semiclassical Virasoro conformal blocks discussed in [43]. A number of technical results are collected in appendices.

2 Defining entwinement

In a gauge theory, states are required to be symmetric under identifications by the gauge group. The main complication in discussing entanglement entropy in gauge theories is that the Hilbert space does not factorize. For example, for a $U(1)$ gauge theory there is a Gauss law constraint which requires that the electric flux entering a region should determine the flux leaving it. We will be interested in situations where the gauge symmetry is discrete.

Recently various authors have developed a formalism for dealing with this lack of factorization in gauge theories. One method is to consider an extended Hilbert space in which the gauge constraints are temporarily relaxed [12, 13, 16–18, 20, 21]. A way of achieving this is by introducing “edge modes” on the entangling surface [13]. In this approach, the Hilbert space splits into superselection sectors defined by the fluxes at the entangling surface, making the reduced density matrix block-diagonal. The entanglement entropy then becomes a sum of two contributions, a Shannon entropy associated to the distribution over superselection sections and a distillable piece arising from entanglement within each superselection sector. In the same spirit, the approach to entwinement suggested in [35] was to ungauged the theory, compute, and then symmetrize.

An alternative approach is to define a subalgebra of gauge invariant observables \mathcal{O}_A associated to the region A . Then, given a density matrix ρ for the full theory, the reduced density matrix ρ_A is defined as the element of the subalgebra of region A such that $\text{Tr}(\rho_A \mathcal{O}_A) = \text{Tr}(\rho \mathcal{O}_A)$ for all \mathcal{O}_A [14, 15, 19]. In this formalism, the reduced density matrix splits into blocks according to superselection sectors determined by the center of the subalgebra. An algebraic approach to entwinement was recently proposed in [44], where it was shown that for a spin system the entwinement could be recovered from a state-dependent subalgebra.

A third approach, which works for states that can be constructed by a Euclidean path integral, is the replica trick. In this case, the entanglement entropy is computed by analytically continuing the Rényi entropies. In two dimensions this approach is particularly convenient and the Rényi entropies can be defined in terms of the correlation functions of twist operators that splice together replicated copies of the CFT. At least for the case of 2d Yang-Mills theory in de Sitter space, it was verified in [16] that the replica method gives the same result as the extended Hilbert space method described above. Below we will define entwinement along these lines.

As a working example, consider a CFT with target space M^N/S_N . The CFT contains N sets of fields, where each set can be viewed as coordinates on one copy of the manifold M , together with companion fermions in case of a supersymmetric theory. The S_N indicates that we identify configurations that differ by permutations of these N sets of fields. This is similar to the way one treats indistinguishable particles in quantum mechanics: wavefunctions need to be appropriately symmetrized under permutations. The S_N identification is really a discrete gauge symmetry. We can gauge fix the local symmetry and think of the fields as changing continuously from point to point (i.e., each of the N copies of M has a continuous string embedded in it). The theory has so-called “twisted sectors” in which strings are only periodic up to permutations. A twisted sector is labeled by a conjugacy class, which is characterized by the lengths of its permutation cycles: there will be N_m cycles of length m such that $\sum_m N_m m = N$. Each cycle is referred to as a “long string” because it can be visualized as a string winding m times. We will refer to each winding of the long string as a “strand”.

The conventional spatial entanglement entropy of an angular interval of size α can be thought of as the entanglement entropy of the union of intervals of size α in each of the N strands of the system. Following the proposal of [35], we want to define entwinement as the entanglement of intervals that extend over some strands and not others. For example, one can talk about the entwinement of an interval on a single strand. If one considers the entwinement of a union of identical intervals in each strand, then it reduces to the conventional spatial entanglement. Because there is a gauge symmetry, we cannot invariantly specify which strand we are talking about. But, as we will argue below, we can meaningfully talk about things like “the entanglement of one and a half connected strands”. Likewise, while one cannot invariantly ask for the entanglement of a particular strand, one can ask for the entanglement of a single strand if we do not specify which one it is. This invariance can be made manifest by simply averaging the computation of entanglement of a single strand over all the strands. It is worth emphasizing that this average is *not* the same thing as the entanglement of the union of such intervals. Below, we will give a mathematical definition of such quantities.

2.1 Replica trick — generalities

A useful method for computing entanglement entropy in two-dimensional conformal field theories is the replica trick. In this method, the entanglement entropy of an interval $[0, \alpha]$ is computed from the reduced density matrix for this region ρ_α by taking a limit of the Rényi entropies:

$$S(\alpha) = \lim_{n \rightarrow 1} \frac{1}{1-n} \log \text{Tr}(\rho_\alpha^n). \quad (2.1)$$

Consider a two-dimensional CFT in the plane in Euclidean signature. In radial quantization, circles of fixed radius become equal time slices. An operator σ acting at the origin creates a pure state, and we can find the wavefunction at $t = 0$ by performing the path integral with the operator inserted and fixed boundary conditions at the unit circle. The density matrix $\rho(\phi, \phi')$ corresponding to such a pure state is then computed by inserting operators at the origin and at infinity in the path integral, and imposing boundary condi-

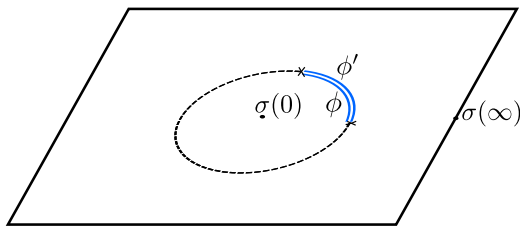


Figure 1. Path integral in radial quantization. The path integral is left open on the cut (indicated in full blue lines) with boundary conditions ϕ on the lower cut and ϕ' on the upper cut. The dashed lines define the complementary interval along which boundary conditions are matched $\phi = \phi'$. The operator σ prepares the state.

tions ϕ and ϕ' on the interior and the exterior of the unit circle, respectively. The reduced density matrix for the interval $[0, \alpha]$ is computed by tracing over the complementary part of the unit circle (i.e., setting $\phi = \phi'$ in the complementary region and then integrating over ϕ there). This leaves us with a path integral over the entire plane, except over the arc corresponding to the interval $[0, \alpha]$, as depicted in figure 1. To compute $\text{Tr}(\rho_\alpha^n)$ we consider n copies of the plane cyclically glued together over the cut $[0, \alpha]$ producing an n -sheeted Riemann surface as in figure 2 (left). This can alternatively be obtained as a correlator of Rényi twist operators $\Sigma^{(n)}$ computed on a single sheet of the n -fold cover of the theory, $\text{CFT}^n/\mathbb{Z}_n$, as represented in figure 2 (right). The n fictitious copies of the CFTs are called “replicas”. Each of the n copies of the CFT is placed in the same state. The Rényi twist cyclically splices together the n CFT copies, such that dragging a field from one CFT around the cut produces a field in the next copy of the CFT.

Below we will illustrate this procedure in symmetric product CFTs with target space M^N/S_N and show how entwinement in these theories can be defined in a similar manner. We will then generalize the definition to apply to more general discretely gauged theories in two dimensions.

Now take the CFT to be a symmetric orbifold with target space M^N/S_N for some M . As discussed above, this CFT can be regarded as having N elementary strands spliced together into series of cycles (“long strings”) determined by the twisted sector. The twist operator can therefore be regarded as a product of elementary twists

$$\Sigma^{(n)} = \Sigma_1^{(n)} \Sigma_2^{(n)} \dots \Sigma_N^{(n)}, \tag{2.2}$$

where each $\Sigma_i^{(n)}$ splices together the n replica copies of the i th strand. Each elementary twist is in the fundamental representation of S_N . Thus we can write for any $g \in S_N$

$$g[\Sigma_i^{(n)}] \equiv g \Sigma_i^{(n)} g^{-1} = \Sigma_{g(i)}^{(n)}, \tag{2.3}$$

where $g(i)$ is the strand produced by permuting i by the action of g . The twist operator appearing in the computation of entanglement entropy (2.2) is a product of all the elementary twists and hence is invariant under the action of S_N . The twists configuration that computes the entanglement entropy is depicted in figure 3 (left).

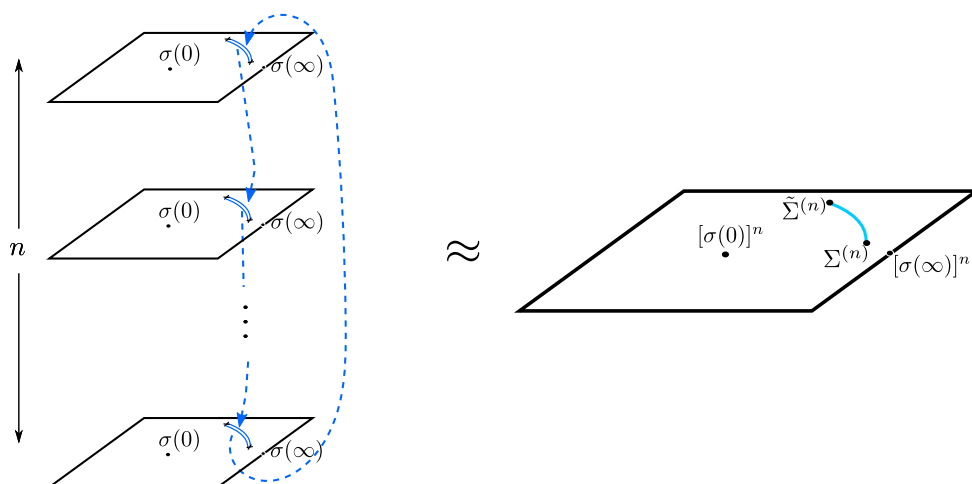


Figure 2. (Left) The n -sheeted Riemann surface from cyclically gluing n copies of the plane. The dashed arrows denote how to sew fields across the cuts. (Right) Correlator in the plane. The Σ insertions represent Rényi twist operators, while the σ insertions define the replicated state.

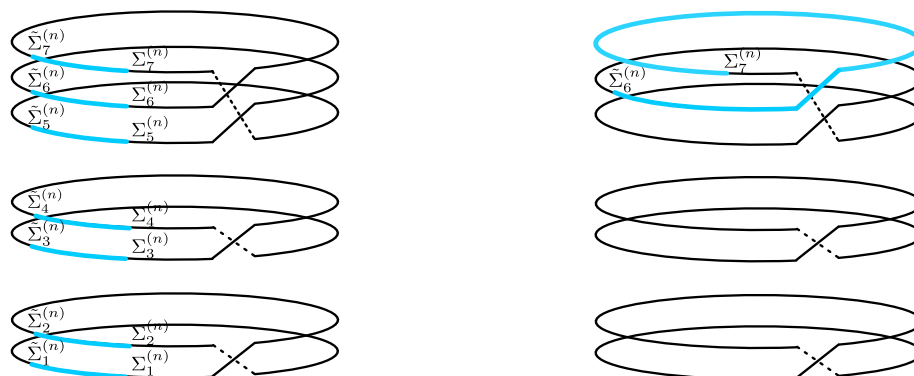


Figure 3. Multiwound strings, each consisting of m strands. There are N_m m -wound strings such that the total number of strands is N . Here we depict $N = 7$, $N_2 = 2$, $N_3 = 1$. (Left) The entanglement entropy is computed by inserting Rényi twist operators at the endpoints of the interval on every strand. The entangling region can be visualized in the long string picture as a union of disjoint intervals on all strands. (Right) Configuration of twists corresponding to the bilocal operator of single interval entwinement. The entangling region extends across different strands of the 3-cycle.

We can define entwinement formally in terms of the elementary twists. Take Σ_i to be an elementary twist operator for strand i and consider the bilocal combination

$$\tilde{\Sigma}_i^{(n)}(1) \Sigma_i^{(n)}(e^{i(\alpha+2\pi\ell)}) \tag{2.4}$$

where for compactness we have only written the holomorphic coordinate and $\tilde{\Sigma}_i$ is the conjugate twist. In this bilocal operator the Σ_i is taken around the complex plane relative to $\tilde{\Sigma}_i$ by an amount $\alpha + 2\pi\ell$. In a specific state of the symmetric orbifold the i th strand is

generally spliced with k other strands into a long string. In such a state the twist Σ will be inserted on a different strand, as represented on the right of figure 3. We then consider the bilocal, gauge-invariant quantity

$$\frac{1}{|S_N|} \sum_{g \in S_N} \tilde{\Sigma}_{g(i)}^{(n)}(1) \Sigma_{g(i)}^{(n)}(e^{i(\alpha+2\pi\ell)}), \quad (2.5)$$

where $|S_N|$ is the cardinality of S_N , i is any reference strand of the CFT, and $g(i)$ is the strand to which i is transported when all the strands are permuted by $g \in S_N$. Because we are summing over all permutations in S_N , the final quantity is independent of i . Its expectation value computes the Rényi analog of entwinement of single intervals.

When $\ell > k$ (k being the number of strands of the specific cycle, i.e. long string, in which the strand $g(i)$ lives) we mean the operator in the sum in (2.5) to represent the twisted boundary conditions of the replicated set of fields on the full long string. Intuitively, we can imagine starting from a short interval on a single strand and putting twisted boundary conditions on the fields inside the interval. Enlarging the interval until it eventually covers the full string, i.e. $\alpha + 2\pi\ell = 2\pi k$, represents putting twisted boundary conditions on the fields on the full string. Further increasing the interval to $\alpha + 2\pi\ell > 2\pi k$ does not change this picture and just keeps all fields on the long string twisted, nothing more. Keeping this in mind, we can define the entwinement as

$$E_\ell(\alpha) = \lim_{n \rightarrow 1} \frac{1}{1-n} \log \left[\langle \Psi | \frac{1}{|S_N|} \sum_{g \in S_N} \tilde{\Sigma}_{g(i)}^{(n)}(1) \Sigma_{g(i)}^{(n)}(e^{i(\alpha+2\pi\ell)}) | \Psi \rangle \right]. \quad (2.6)$$

For symmetric product orbifolds this is just a formal way of saying that we are calculating the entanglement entropy of a connected set of partial strands in a long string. This definition of single interval entwinement can be generalized to multi-interval entwinements by taking a product of operators like (2.5) defined at different locations and strands. A particular example of multi-interval entwinement is entanglement, where we take a product of the same interval with $\alpha < 2\pi$ in each of the N strands.

The formalism described above is general. We can consider theories with any discrete gauge symmetry H , and elementary twist operators in any representation R of H that is useful. These can be used to define bilocal, gauge invariant twist operators of the form (2.5) and products of such operators. Entwinements defined as expectation values of these quantities are a very general new class of gauge-invariant objects than can be used to characterize quantum wavefunctions in two-dimensional theories. Conceptually we can also talk about the entanglement of subsets of degrees of freedom in a spatial region even in higher dimensional theories on any manifold, but we need a formalism for calculating such quantities efficiently.

In the next section we will use the replica method to explicitly compute entwinements in symmetric orbifold conformal field theories in two dimensions.

3 Entwinement in symmetric orbifold CFTs

In the following we analyze symmetric orbifold CFTs on a circle of length L . These are obtained starting with a seed CFT with target space M and central charge c . The orbifold theory $\mathcal{C} = \text{CFT}^N/S_N$ has target space M^N/S_N and central charge $c_N = cN$. Because of the S_N identification, states need only be periodic up to the action of a group element. In a sector twisted by $h \in S_N$, the boundary conditions are

$$\phi_i(L) = \phi_{h(i)}(0) \quad i = 1, \dots, N, \quad (3.1)$$

where here ϕ_i collectively indicates the fields in the i -th copy of the CFT. All physical states should be invariant under the action of S_N . Since acting with a group element g maps the sector twisted by h to that twisted by ghg^{-1} , twisted sectors should really be labeled by conjugacy classes $[h]$, as mentioned in the previous section.

Twisted states can be conveniently obtained through the action of *orbifold twist operators* on untwisted states. An orbifold twist operator $\sigma_m(0)$ at the origin of the complex plane causes m copies of the target space M to be linked together by the periodicity condition

$$\sigma_m(0) : \quad \phi_j(ze^{2\pi i}) = \phi_{j'}(z) ; \quad j' = (j + 1) \pmod{m}. \quad (3.2)$$

Here $j = 1, \dots, m$, and the twist operator can be thought of as linking m strands of string, each with period 2π , into a single long string with period $2m\pi$. We will be interested in twisted states of the form

$$|\psi\rangle = \prod_{m=1}^N [\sigma_m(0)]^{N_m} |0\rangle, \quad (3.3)$$

where each σ_m acts on a different subset of the N copies of the target space M . Thus, there will be N_m long strings of period $2m\pi$ and $\sum_m mN_m = N$. In radial quantization this prepares a state on the spatial circle, and the corresponding out state is

$$\langle\psi| = \langle 0| \prod_{m=1}^N [\tilde{\sigma}_m(\infty)]^{N_m} \equiv \langle 0| \prod_{m=1}^N \lim_{z, \bar{z} \rightarrow \infty} \left[z^{2h_m} \bar{z}^{2\bar{h}_m} \tilde{\sigma}_m(z, \bar{z}) \right]^{N_m}, \quad (3.4)$$

where $\tilde{\sigma}_m$ has opposite action to σ_m . The twists transform as primaries with conformal weights

$$h_m = \bar{h}_m = \frac{c}{24} \left(m - \frac{1}{m} \right). \quad (3.5)$$

We wish to define entwinement in such twisted states of the symmetric product CFT.

In radial quantization we can specify a connected entangling region at a fixed time $t = 0$ by an arc on the unit circle. As explained in the previous section, entwinement in twisted states of the form (3.3) can be computed using the replica trick, by inserting *elementary replica twist operators*, Σ_i . Such twists act each on a single strand out of the N strands in the CFT and can be thought of as connecting the n -fold Rényi replicates of that strand. The elementary replica twists, Σ_i , have conformal weights

$$H_n = \bar{H}_n = \frac{c}{24} \left(n - \frac{1}{n} \right). \quad (3.6)$$

We insert the elementary twists at the endpoints of the chosen interval of length $\alpha + 2\pi\ell$ and average over the symmetric group, which moves the left boundary of the interval over all strands while keeping the length of the interval fixed. The state of the replicated theory, $|\Psi\rangle$, is obtained inserting orbifold twist operators for each of the n replica copies of the theory,

$$|\Psi\rangle = \left[\prod_{m=1}^N [\sigma_m(0)]^{N_m} \right]^n |0\rangle, \quad (3.7)$$

i.e., by taking products of (3.3) for each of the n replicated theories. In terms of $|\Psi\rangle$, we can write

$$E_\ell(\alpha) = \lim_{n \rightarrow 1} \frac{1}{1-n} \log \left[\frac{1}{|S_N|} \sum_{g \in S_N} \langle \Psi | \tilde{\Sigma}_{g(i)}^{(n)}(1) \Sigma_{g(i)}^{(n)}(e^{2\pi i \ell} x, e^{-2\pi i \ell} \bar{x}) | \Psi \rangle \right], \quad (3.8)$$

where we have taken the entwinement interval to extend between 1 and x in the complex plane; in the notation of the previous section, $x = e^{i\alpha}$. As before, since we are averaging over S_N , the result is independent of the arbitrary choice of the initial strand i , which can run from 1 to N . This correlator is a four-point function in the cyclic orbifold theory $\mathcal{C}^n/\mathbb{Z}_n$ obtained taking n replicas of the original symmetric orbifold $\mathcal{C} = \text{CFT}^N/S_N$.

At the practical level then, the computation above simplifies drastically. Consider a term in (3.8) where the strand $g(i) = k$ is embedded in a particular long string with m strands, which we relabel here as $1, 2, \dots, m$ for convenience. Let us define a notation

$$\Sigma_k^{(n)}(e^{2\pi i \ell} x, e^{-2\pi i \ell} \bar{x}) \equiv \Sigma_{k+\ell}(x, \bar{x}), \quad (3.9)$$

where the subscripts k and $k + \ell$ are understood modulo m because of the cyclic symmetry of the m -stranded long string. Then we have to compute terms like

$$\langle \Psi | \tilde{\Sigma}_k^{(n)}(1) \Sigma_{k+\ell}^{(n)}(x, \bar{x}) | \Psi \rangle = \langle [\tilde{\sigma}_m(\infty)]^n \tilde{\Sigma}_k^{(n)}(1) \Sigma_{k+\ell}^{(n)}(x, \bar{x}) [\sigma_m(0)]^n \rangle. \quad (3.10)$$

As discussed in the previous section, if the long string is shorter than the interval in question, i.e., $2\pi m < \alpha + 2\pi\ell$, (3.10) is understood as computing how the entire long string is entangled with the rest of the system.

3.1 Single interval entwinement

To evaluate the entwinement of a single interval we must therefore compute the correlator

$$\langle [\tilde{\sigma}_m(\infty)]^n \tilde{\Sigma}_k^{(n)}(1) \Sigma_{k+\ell}^{(n)}(x, \bar{x}) [\sigma_m(0)]^n \rangle. \quad (3.11)$$

The branching structure of the correlator is effectively mn -dimensional as illustrated in figure 4, and we can label the twist fields in terms of these mn sheets involved in the correlator:

$$[\sigma_m]^n = \sigma_{(1\dots m)\sigma_{(m+1\dots 2m)} \cdots \sigma_{(m(n-1)+1\dots mn)}, \quad (3.12)$$

$$\Sigma_k^{(n)} = \sigma_{(k, k+m, \dots, k+(n-1)m)} \quad (3.13)$$

in the cycles notation $\sigma_{(\dots)}$ of S_{mn} .

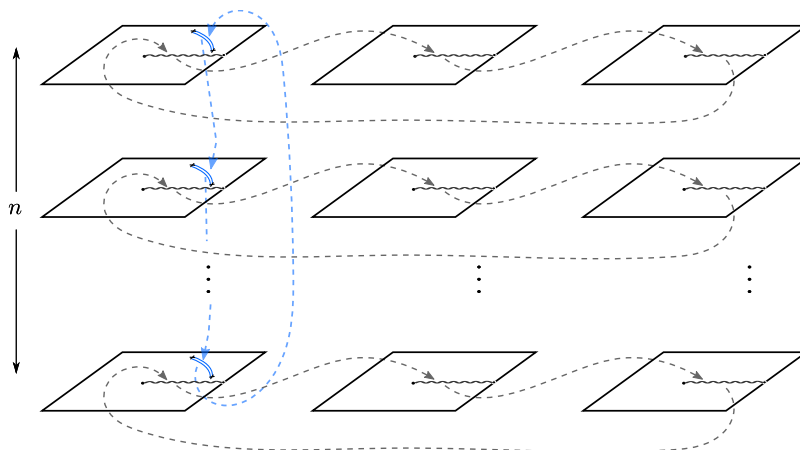


Figure 4. Representation of the branching structure of a correlator of the form (3.11) in the simple case of a single strand entwinement, $\ell = 0$, on a 3-cycle factor, $m = 3$.

The correlator (3.11) can be evaluated through a uniformization map to a covering space. To compute the map we extend a calculation of [40], which dealt with the case $m = 2$. We first observe that the branched covering has spherical genus, as determined by the Riemann-Hurwitz formula

$$g = \frac{1}{2} \sum_i (r_i - 1) - s + 1 = \frac{1}{2} [2n(m - 1) + 2(n - 1)] - mn + 1 = 0. \quad (3.14)$$

The sum is over the twist insertions in (3.11) of length r_i , and $s = mn$ is the total number of sheets involved in the correlator. An explicit formula for such twist correlation function in terms of the properties of the uniformization map to a genus zero surface is worked out in appendix D of [45] (see also [46, 47]). In appendix A, we review these results and apply them to the computation of single interval entwinement. Our final result is (see eq. (A.26) in the appendix)

$$\langle [\tilde{\sigma}_m(\infty)]^n \tilde{\Sigma}_k^{(n)}(1) \Sigma_{k+\ell}^{(n)}(x, \bar{x}) [\sigma_m(0)]^n \rangle = \left[m^2 |A|^{m-1} |A - 1|^2 \right]^{-\frac{c}{12} \left(n - \frac{1}{n} \right)}, \quad (3.15)$$

with $A = x^{1/m} e^{2\pi i \ell / m}$ and c the central charge of a single copy.

To obtain the entwinement of an interval of opening angle α on the spatial circle $w \sim w + L$, we only need to relate the result (3.15) obtained on the plane to the computation on the cylinder, with elementary replica twists inserted at $w = 0$ and $w = \alpha L / (2\pi)$. Using the map $z = e^{\frac{2\pi i w}{L}}$:

$$\langle \Psi | \tilde{\Sigma}_k^{(n)}(0) \Sigma_{k+\ell}^{(n)} \left(\frac{\alpha L}{2\pi} \right) | \Psi \rangle_{\text{cylinder}} = \left(\frac{2\pi}{L} \right)^{4H_n} \langle \Psi | \tilde{\Sigma}_k^{(n)}(1) \Sigma_{k+\ell}^{(n)}(x, \bar{x}) | \Psi \rangle \quad (3.16)$$

with $x = e^{i\alpha}$, $\bar{x} = e^{-i\alpha}$. If we explicitly insert a UV cutoff ϵ_{UV} to regulate the twist operators and work out the sum over all elements in S_N , we obtain

$$E_\ell(\alpha) = \lim_{n \rightarrow 1} \frac{1}{1 - n} \log \left[\frac{1}{N} \sum_{m=\ell+1}^N m N_m \left| \frac{mL}{\pi \epsilon_{\text{UV}}} \sin \left(\frac{\alpha + 2\pi \ell}{2m} \right) \right|^{-\frac{c}{6} \left(n - \frac{1}{n} \right)} \right] + O(\epsilon_{\text{UV}}^0). \quad (3.17)$$

The sum in the first term extends over long strings with $\ell + 1$ and more strands, because shorter strings are completely covered by intervals of length $\alpha + 2\pi\ell$. The contribution from each of these shorter strings computes the entanglement of the string with the rest of the theory. Since the short string is by construction disconnected from all other strands in this particular twisted sector, its entanglement entropy will not have the dominant UV-divergent contributions that are present for the longer strings with $\ell + 1$ and more strands. In formulas, if one sets $\alpha + 2\pi\ell \approx 2\pi m$ up to a contribution of order ϵ_{UV} , the occurrences of the cutoff will cancel in (3.17) between $1/\epsilon_{UV}$ and the sine, yielding a cutoff-independent result, which is small compared to the cutoff-dependent terms arising from long strings longer than the interval.

3.2 Entanglement entropy of a spatial region

The entanglement entropy of an interval is a specific case of computing entwinement. The gauge invariant twist operators are decomposed into products of twist operators on each strand as in (2.2), and the entanglement entropy of a spatial interval can be expressed as

$$S(\alpha) = \lim_{n \rightarrow 1} \frac{1}{1-n} \log \left[\langle \Psi | \tilde{\Sigma}_1^{(n)}(1) \Sigma_1^{(n)}(x, \bar{x}) \tilde{\Sigma}_2^{(n)}(1) \Sigma_2^{(n)}(x, \bar{x}) \dots \tilde{\Sigma}_N^{(n)}(1) \Sigma_N^{(n)}(x, \bar{x}) | \Psi \rangle \right]. \tag{3.18}$$

In the perspective of entwinement, entanglement entropy coincides with the entwinement of the union over all strands of an interval that fits within a single strand. Clearly, as this quantity is already gauge invariant, the sum over S_N appearing in the entwinement definition exactly cancels the normalization $|S_N|^{-1}$.

In fact the entanglement entropy for a state of the form (3.3) is not known in general. For instance the branching structure of the correlator leads generically to a covering space of non-trivial genus, and thus one cannot straightforwardly apply the same techniques we used for computing entwinement. However, in the limit of a short interval ($x, \bar{x} \rightarrow 1$), using the OPE of the elementary twists $\tilde{\Sigma}_i^{(n)}(1) \Sigma_i^{(n)}(x, \bar{x}) \sim \mathbb{1}/|1-x|^{2H_n}$ the correlator factorizes. Via the conformal map to the cylinder, the result reproduces the short interval expansion of the entanglement entropy for a CFT on a circle of length L with central charge $c_N = cN$,

$$S(\alpha) \approx \frac{c_N}{3} \log \frac{\alpha L}{\pi \epsilon_{UV}}. \tag{3.19}$$

This is N times the single strand ($\ell = 0$) short interval expansion ($\alpha \rightarrow 0$) of the entwinement result given in (3.17). This reflects the fact that $\ell = 0$ entwinement computes the entanglement for a single factor in the symmetric product orbifold theory, while entanglement entropy simultaneously involves fields in all N factors.

4 D1-D5 CFT

A well-known example of a symmetric orbifold CFT is the D1-D5 CFT. This is realized in type IIB string theory compactified on $S^1 \times T^4$ (or $S^1 \times K3$), with N_1 D1-branes wrapping the circle and N_5 D5-branes wrapping the entire compact product space. The near horizon geometry of the D1-D5 brane system is $AdS_3 \times S^3 \times T^4$, and one can formulate

a two-dimensional CFT at the conformal boundary of the AdS₃. This is an $\mathcal{N} = (4, 4)$ supersymmetric sigma model with $SU(2) \times SU(2)$ R-symmetry, corresponding to the isometry group of the S^3 , another $SU(2) \times SU(2)$ global symmetry and central charge equal to $6N_1N_5$ (see for instance [45] for a review). The moduli space of the CFT contains an orbifold point where the theory consists of $N \equiv N_1N_5$ copies of a $c = 6$ free CFT of 4 real bosons and their fermionic superpartners with target space $(T^4)^N/S_N$.

We will work at the orbifold point of the D1-D5 CFT and focus on the Ramond ground states. These can be constructed by multiplying together bosonic and fermionic twist operators to achieve a total twist of N . The theory contains eight bosonic and eight fermionic twists labeled in terms of the global symmetries. Since we are only interested in computing correlators of bosonic quantities that do not carry R-charge, we can simplify the discussion and generically consider the normalized symmetric orbifold microstates (3.3). In this section we will consider two examples of such states, which in the large N limit are dual to conical defects and zero mass BTZ black holes in the bulk (see [48] for discussion of the map between Ramond ground states of the D1-D5 system and AdS₃ gravity).¹ Points in the moduli space with a geometric supergravity description are actually far from the orbifold point where we perform our computations, and agreement with semiclassical gravity is not to be expected a priori. However protected BPS quantities can be computed exactly at the orbifold point and it has been proposed that agreement should extend also to observables computed in terms of covering space constructions [49].

4.1 Conical defects

Simple Ramond ground states of the D1-D5 CFT are of the form [46, 47, 50]

$$|\psi\rangle = [\sigma_{\tilde{m}}(0)]^{N/\tilde{m}} |0\rangle, \tag{4.1}$$

where N/\tilde{m} is an integer. The holographically dual bulk geometries are conical defects

$$ds^2 = -\left(\frac{1}{\tilde{m}^2} + \frac{r^2}{R_{\text{AdS}}^2}\right) dt^2 + \left(\frac{1}{\tilde{m}^2} + \frac{r^2}{R_{\text{AdS}}^2}\right)^{-1} dr^2 + r^2 d\theta^2, \tag{4.2}$$

where θ is a periodic coordinate and the AdS radius is related to the length of the spatial circle introduced in the previous section via $R_{\text{AdS}} = L/(2\pi)$. These geometries can be obtained from empty AdS₃ in global coordinates via $\mathbb{Z}_{\tilde{m}}$ identifications. For a single interval of opening angle α on the boundary, there exist multiple geodesics connecting the endpoints of the interval. These have regulated lengths [35]

$$\mathcal{L}_\ell(\alpha) = 2R_{\text{AdS}} \log \left[\frac{2\tilde{m}r_\infty}{R_{\text{AdS}}} \sin \left(\frac{\alpha + 2\pi\ell}{2\tilde{m}} \right) \right]. \tag{4.3}$$

The index $\ell = 0, \dots, \tilde{m} - 1$ counts the number of times the geodesics winds around the conical defect at $r = 0$. Here r_∞ is an IR gravitational cutoff. Identifying it with the field

¹The BTZ black hole is actually dual to an ensemble of states; we will comment on this point and on the notion of typical states in section 4.2.

theory cutoff ϵ_{UV} via $r_\infty = \frac{L}{2\pi} \frac{R_{AdS}}{\epsilon_{UV}}$ and substituting $c = 6$ in (3.17), we find the relation between entwinement in the state (4.1) and geodesic lengths

$$E_\ell(\alpha) = \frac{\mathcal{L}_\ell(\alpha)}{R_{AdS}}. \tag{4.4}$$

Therefore in this case, the field theory notion of entwinement computes the length of geodesics in AdS, in agreement with the idea advanced in [35] that non-minimal geodesics in the bulk capture the entanglement of internal degrees of freedom. Ordinary entanglement entropy on the other hand is related to the length of minimal geodesics, in agreement with the Ryu-Takayanagi formula [22]

$$S(\alpha) = \frac{\mathcal{L}_0(\alpha)}{4G_N}. \tag{4.5}$$

Since the D1-D5 central charge is $cN = 3R_{AdS}/(2G_N)$, the entanglement entropy of an interval coincides with N times the $\ell = 0$ single interval entwinement E_0 .

4.2 Zero mass BTZ black hole

One could wonder whether the length of long geodesics also captures entwinement in a black hole background. We will show this is indeed the case in the zero mass BTZ black hole

$$ds^2 = -\frac{r^2}{R_{AdS}^2} dt^2 + \frac{R_{AdS}^2}{r^2} dr^2 + r^2 d\theta^2, \tag{4.6}$$

which arises in the $\tilde{m} \rightarrow \infty$ limit of the conical defect geometry (4.2). The $M = 0$ black hole has a horizon of zero size which coincides with the singularity.

The $M = 0$ black hole geometry is not dual to a particular CFT microstate, but rather to an ensemble of states of the D1-D5 CFT with fixed N . Following [50], instead of working with the microcanonical ensemble, it is more convenient to work in the canonical description where N_m as well as the total number of strands fluctuate, but the ensemble average is fixed to N . The average number of m -cycles is [50]

$$\langle N_m \rangle = \frac{8}{\sinh \beta m}, \tag{4.7}$$

where the inverse fictitious temperature β is determined in terms of the average N of the total number of strands, as

$$N = \left\langle \sum_{m=1}^{\infty} m N_m \right\rangle \simeq \frac{2\pi^2}{\beta^2}. \tag{4.8}$$

In the large N limit, typical states in the ensemble have individual twist distributions that lie very close to (4.7) and expectation values of observables in a typical state deviate by only a small amount from those computed in the ensemble. In the following, we therefore compute entwinement in a typical state with representative distribution (4.7), rather than in the ensemble.

The single interval entwinement in a typical microstate is again given by (3.17). As we prove in appendix B, for fixed α and ℓ , the sum over m is dominated by the terms with $m \sim O(\sqrt{N})$. For $\ell \ll \sqrt{N}$, we obtain

$$E_\ell(\alpha) \approx \frac{c}{3} \log \left[\frac{L}{2\pi\epsilon_{\text{UV}}} (\alpha + 2\pi\ell) \right]. \tag{4.9}$$

Black holes admit a region outside the horizon which is not penetrated by minimal geodesics, which we can call the entanglement shadow of the black hole. Just as in the case of the conical defect, non-minimal geodesics penetrate the entanglement shadow. The non-minimal geodesics wind around the horizon and the bigger their winding number, the closer they wrap the horizon. The $M = 0$ BTZ black hole has a horizon that shrinks to zero size, but nevertheless it has a finite entanglement shadow. The lengths of non-minimal geodesics in the $M = 0$ BTZ black hole background are given by

$$\mathcal{L}_\ell(\alpha) = 2R_{\text{AdS}} \log \left[\frac{r_\infty}{R_{\text{AdS}}} (\alpha + 2\pi\ell) \right]. \tag{4.10}$$

Using again that $c = 6$ and $r_\infty = \frac{L}{2\pi} \frac{R_{\text{AdS}}}{\epsilon_{\text{UV}}}$, we recover that entwinement and geodesic length are related by

$$E_\ell(\alpha) = \frac{\mathcal{L}_\ell(\alpha)}{R_{\text{AdS}}}. \tag{4.11}$$

As $\ell \rightarrow \sqrt{N}$, the relation between entwinement and geodesic length breaks down. But the corresponding long geodesics, which wind very many times around the black hole, approach the horizon to within a Planck length. It is not clear that they are well defined in the quantum theory where we expect classical geometry to be ill-defined at the Planck scale. Hence it is not surprising that the lengths of these geodesics do not match the corresponding entwinements.

5 Discussion and outlook

We have verified the correspondence between single-interval entwinement and lengths of non-minimal geodesics in conical defects and $M = 0$ BTZ black holes, which correspond to specific states of the D1-D5 system. We studied these configurations because there are explicit constructions of the corresponding states in the literature [50]. Furthermore, these states are BPS-protected ground states in the Ramond sector of the theory [48, 49], so that we can expect non-renormalization of some quantities as we deform the theory away from its orbifold point. Of course this does not mean that all correlation functions extrapolate from weak to strong coupling, but we were essentially computing partition sums after a conformal map, which might help explain the agreements we found between field theory and gravity. It has also been seen that certain graviton correlators computed at the orbifold point do match the gravitational results which are related to the strongly coupled theory [50]. Possible general reasons for such matching are discussed in [49]. It should be possible to extend our computations in at least two interesting directions. First, we can consider the general R-charged Ramond ground states of the D1-D5 CFT. The $M = 0$

BTZ black hole and the conical defects considered here were two specific examples of such states, but a more general class is discussed in [50], including candidate states describing “black ring” geometries. Another interesting extension is to consider rotating, but extremal, AdS_3 black holes. These are represented in the D1-D5 CFT by adding energy to the left moving sector alone. One approach would be to add a small left-moving temperature; another would be to perturb the theory with a holomorphic stress tensor. Both of these are settings where it would be very interesting to compute both spatial entanglement and entwinement.

While in this paper we have mostly focused on 2d symmetric orbifold CFTs, our definition (2.6) of entwinement can be extended to more general discretely gauged theories. Consider, for instance, the discrete rotation orbifold $\mathbb{R}^2/\mathbb{Z}_N$ with $N > 2$. In the sector twisted by the generator of \mathbb{Z}_N , the target space coordinates satisfy

$$X(\tau, 2\pi) = \cos\left(\frac{2\pi}{N}\right) X(\tau, 0) - \sin\left(\frac{2\pi}{N}\right) Y(\tau, 0), \quad (5.1)$$

$$Y(\tau, 2\pi) = \sin\left(\frac{2\pi}{N}\right) X(\tau, 0) + \cos\left(\frac{2\pi}{N}\right) Y(\tau, 0). \quad (5.2)$$

We can extend the range of the σ coordinate in $X(\tau, \sigma)$ to $0 \leq \sigma < 4\pi$ by defining

$$X(\tau, \sigma) \equiv \cos\left(\frac{2\pi}{N}\right) X(\tau, \sigma - 2\pi) - \sin\left(\frac{2\pi}{N}\right) Y(\tau, \sigma - 2\pi), \quad 2\pi \leq \sigma < 4\pi. \quad (5.3)$$

A twisted sector string is then determined by the “long string” profile $X(\tau, \sigma)$ with $0 \leq \sigma < 4\pi$, which satisfies the boundary condition

$$X(\tau, 4\pi) = -X(\tau, 0) + 2 \cos\left(\frac{2\pi}{N}\right) X(\tau, 2\pi). \quad (5.4)$$

Entwinement defined in analogy with (2.6) then quantifies how one part of this long string is entangled with its complement. There does seem to be an important difference, however, with symmetric orbifold theories. For the above rotation orbifold, we could equally well have defined entwinement by considering target space coordinates X', Y' related to X, Y by rotation in field space over an arbitrary angle. Entwinement defined using long string profiles $X'(\sigma)$ would generically be different from that defined using $X(\sigma)$, reflecting the basis dependence of measures of quantum entanglement in general. In contrast, for symmetric orbifolds the requirements that the target space coordinates should be mapped into each other by permutations and should have diagonal kinetic terms does select a preferred notion of entwinement. It is interesting to ask for which gauge theories our definition of entwinement leads to “natural” quantities, including quantities with a clear geometrical meaning in a holographic dual. Other generalizations worth studying are continuous gauge theories, higher dimensional theories and matrix models.

Note that entwinement, as we defined it, measured the lengths of geodesics in units of the AdS scale, rather than in units of the Planck length (which is related to the three dimensional Newton constant G_N). In the original formulation of holographic entanglement entropy [22, 23], it seemed natural that G_N should appear in the formulas, in analogy

with black hole entropy which is measured by horizon area in units of G_N . Of course field theories with a holographic dual having a classical description generally have a large number of local degrees of freedom arising from e.g. dynamical variables that are large matrices. The entwinement that we are defining seeks to piece apart the entanglement of some of these local degrees of freedom (e.g. parts of the local matrices) with other elements of the Hilbert space. As such, we are extracting the elementary parts out of which spatial entanglement arises in such quantum field theories. These elementary entanglements are correspondingly smaller, and are thus related to geodesic lengths measured relative to a length scale that is much larger than the Planck length. One might ask if single interval entwinement can ever be of the same order of magnitude as the spatial entanglement as we make the interval size larger. At least in the 2d CFT states we considered, this cannot happen because entanglement between different long strings is negligible and within a single long string entanglement only depends logarithmically on the interval size. This could be different in excited or thermal states where there could be extensive contributions to entanglement, or in theories with less local interactions such as matrix models. It is also interesting that the fundamental object (2.6) from which we construct entwinement is non-local. This recalls the discussion in [51] of the relevance of non-local observables in field theory for reconstructing local physics in AdS space in a gauge-invariant manner.

One of our goals in this paper has been to define the field theoretic dual of extremal, non-minimal geodesics in AdS_3 . These geodesics also appear in the semiclassical CFT computation of Rényi entropies in terms of the conformal block expansion of heavy-heavy-light-light correlators [43]. There it was shown that the single interval entanglement entropy in a state created by heavy operator insertions, and dual to an AdS_3 conical defect or BTZ, is well approximated by the semiclassical identity block and reproduces the Ryu-Takayanagi minimal geodesic result. This leading answer for the four-point function however has monodromies as the Rényi twists are moved around the heavy operators in the CFT. These monodromies transform the minimal geodesic result into quantities related to the length of non-minimal geodesics. Therefore in this context non-minimal geodesics are also related in the dual CFT to analytic properties of semiclassical Virasoro blocks.

Acknowledgments

We thank Alexandre Belin, Netta Engelhardt, Jutho Haegeman, Volkher Scholz, Norbert Schuch, Karel Van Acoleyen, Henri Verschelde, and Frank Verstraete for very helpful discussions. We are also particularly grateful to Bartek Czech, Lampros Lamprou, Sam McCandlish, and Jamie Sully for discussing details of their ongoing work on related questions with us. This work was supported in part by a grant from the Simons Foundation (#385592, Vijay Balasubramanian) through the It From Qubit Simons Collaboration, by the Belgian Federal Science Policy Office through the Interuniversity Attraction Pole P7/37, by FWO-Vlaanderen through projects G020714N, G044016N and Odysseus grant G.001.12, by the European Research Council grant no. ERC-2013-CoG 616732 HoloQosmos, by COST Action MP1210 The String Theory Universe, and by Vrije Universiteit Brussel through the Strategic Research Program “High-Energy Physics”. It was performed

in part at the Aspen Center for Physics, which is supported by National Science Foundation grant PHY-1066293. Research at Perimeter Institute is supported by the Government of Canada through Industry Canada and by the Province of Ontario through the Ministry of Research & Innovation. T.D.J. is Aspirant FWO-Vlaanderen. F.G. is a Postdoctoral Researcher of FWO-Vlaanderen and acknowledges support from a JuMo grant of KU Leuven. V.B., A.B., and F.G. thank YITP for support during the program “Quantum Information in String Theory and Many-body Systems” and conference “Quantum Matter, Spacetime and Information”. V.B. and T.D.J. also thank the Perimeter Institute for hospitality during the It From Qubit workshop and school. B.C. thanks the organizers of the Nordita program “Black Holes and Emergent Spacetime” for hospitality while this work was in progress.

A Twist correlator

In this appendix we briefly review the result described in [45] for general bare twists correlators with covering space of spherical genus, and apply them explicitly to the computation of the correlator in eq. (3.11),

$$\langle [\tilde{\sigma}_m(\infty)]^n \tilde{\Sigma}_1^{(n)}(1) \Sigma_{1+\ell}^{(n)}(x, \bar{x}) [\sigma_m(0)]^n \rangle, \tag{A.1}$$

where, since the strands are indistinguishable, we have set without loss of generality $k = 1$.

Consider a general correlator of $P + Q$ normalized twists,

$$\langle \sigma_{p_1}(z_1) \sigma_{p_2}(z_2) \dots \sigma_{p_P}(z_P) \sigma_{q_1}(\infty) \sigma_{q_2}(\infty) \dots \sigma_{q_Q}(\infty) \rangle, \tag{A.2}$$

where p_i, q_j denote the lengths of the symmetric group cycles of the corresponding operators, inserted in the finite z -plane and at infinity, respectively. We restrict attention to correlators of genus zero,

$$g = \frac{1}{2} \sum_{i=1}^P (p_i - 1) + \frac{1}{2} \sum_{j=1}^Q (q_j - 1) - s + 1 = 0, \tag{A.3}$$

where, as in the main text, s denotes the total number of copies.

The map to the covering space $z = z(t)$ should be meromorphic and reproduce the correct monodromies corresponding to the twist insertions

$$\begin{aligned} z - z_i &\approx a_i (t - t_i)^{p_i} && \text{for } z \approx z_i, \quad t \approx t_i && \forall i = 1, \dots, P \\ z &\approx b_1 t^q && \text{for } z \rightarrow \infty, \quad t \rightarrow \infty \\ z &\approx b_j (t - t_j^\infty)^{-q_j} && \text{for } z \rightarrow \infty, \quad t \approx t_j^\infty && \forall j = 2, \dots, Q \end{aligned} \tag{A.4}$$

to leading order near each branch point. The correlator (A.2) can then be shown to depend only on the coefficients a_i, b_j and parameters p_i, q_j and to be given by [45]

$$\begin{aligned} &\langle \sigma_{p_1}(z_1) \sigma_{p_2}(z_2) \dots \sigma_{p_P}(z_P) \sigma_{q_1}(\infty) \sigma_{q_2}(\infty) \dots \sigma_{q_Q}(\infty) \rangle = && \tag{A.5} \\ &= \left(\prod_{i=1}^P p_i^{-\frac{c}{12}(p_i+1)} \right) \left(\prod_{j=1}^Q q_j^{\frac{c}{12}(q_j-1)} \right) \left(\prod_{i=1}^P |a_i|^{-\frac{c}{12} \frac{p_i-1}{p_i}} \right) \left(\prod_{j=1}^Q |b_j|^{-\frac{c}{12} \frac{q_j+1}{q_j}} \right) |b_1|^{\frac{c}{6}} q_1^{\frac{c}{6}}, \end{aligned}$$

where

$$F = s + Q - \sum_{j=1}^Q q_j \quad (\text{A.6})$$

is the number of distinct images of infinity and c denotes the central charge of the seed CFT.

Specializing to the correlator (A.1), we have

$$\begin{aligned} z &\approx a_i(t - t_i)^m && \text{for } z \approx 0, && t \approx t_i && \forall i = 1, \dots, n \\ z - 1 &\approx a_{n+1}t^n && \text{for } z \approx 1, && t \approx 0 \\ z - x &\approx a_{n+2}(t - 1)^n && \text{for } z \approx x, && t \approx 1 \\ z &\approx b_1t^m && \text{for } z \rightarrow \infty, && t \rightarrow t_1^\infty = \infty \\ z &\approx b_j(t - t_j^\infty)^{-m} && \text{for } z \rightarrow \infty, && t \approx t_j^\infty && \forall j = 2, \dots, n \end{aligned} \quad (\text{A.7})$$

and a map that satisfies these properties is

$$z = \left[\frac{At^n - (t - 1)^n}{t^n - (t - 1)^n} \right]^m \quad (\text{A.8})$$

with

$$x = A^m. \quad (\text{A.9})$$

In order to completely fix the map that computes the correlator (3.11), we choose the branch requiring that for two elementary replica twists in (A.1) acting on the same strand, i.e. for $\ell = 0$, $A \rightarrow 1$ as the interval size goes to zero. We then impose continuity as we increase the interval size and take x ℓ times around the unit circle in the complex plane, that is

$$A = e^{\frac{2\pi i \ell}{m}} x^{\frac{1}{m}}. \quad (\text{A.10})$$

In the t -plane, the insertions map to

$$t_k = \frac{1}{1 - A^{\frac{1}{n}} e^{\frac{2\pi i k}{n}}}, \quad t_j^\infty = \frac{1}{1 - e^{\frac{2\pi i (j-1)}{n}}}, \quad (\text{A.11})$$

and

$$At^n - (t - 1)^n = (A - 1) \prod_{i=1}^n (t - t_i), \quad t^n - (t - 1)^n = n \prod_{j=2}^n (t - t_j^\infty), \quad (\text{A.12})$$

so that the conformal map can also be written as

$$z = \frac{(A - 1)^m \prod_{i=1}^n (t - t_i)^m}{n^m \prod_{j=2}^n (t - t_j^\infty)^m}. \quad (\text{A.13})$$

From this expression we can directly determine the coefficients

$$b_1 = \left(\frac{A - 1}{n} \right)^m, \quad b_j = \left[\frac{A - 1}{n} \frac{\prod_{k=1}^n (t_j^\infty - t_k)}{\prod_{k=2, k \neq j}^n (t_j^\infty - t_k^\infty)} \right]^m. \quad (\text{A.14})$$

To work out the remaining coefficients a_i , we consider the first derivative

$$\frac{dz}{dt} = \frac{mn(A-1)^m}{[t^n - (t-1)^n]^{m+1}} t^{n-1} (t-1)^{n-1} \prod_{i=1}^n (t-t_i)^{m-1}. \quad (\text{A.15})$$

Near $t \approx 0, 1, t_i$ the first derivative vanishes. In fact, the first $m-1$ derivatives vanish near $t = t_i$, and the first $n-1$ near $t = 0, 1$. This implies that in a Taylor expansion near these points we have

$$\begin{aligned} z &= \frac{1}{m!} \left. \frac{d^m z}{dt^m} \right|_{t=t_i} (t-t_i)^m + \dots, \\ z &= 1 + \frac{1}{n!} \left. \frac{d^n z}{dt^n} \right|_{t=0} t^n + \dots, \\ z &= x + \frac{1}{n!} \left. \frac{d^n z}{dt^n} \right|_{t=1} (t-1)^n + \dots, \end{aligned} \quad (\text{A.16})$$

from which we read

$$\begin{aligned} a_i &= \frac{n(A-1)^m}{[t_i^n - (t_i-1)^n]^{m+1}} t_i^{n-1} (t_i-1)^{n-1} \prod_{k=1, k \neq i}^n (t_i - t_k)^{m-1}, \\ a_{n+1} &= m(-1)^{-(n+1)}(A-1), \\ a_{n+2} &= mA^{m-1}(A-1). \end{aligned} \quad (\text{A.17})$$

Substituting in (A.5), we obtain

$$\begin{aligned} &\langle [\tilde{\sigma}_m(\infty)]^n \tilde{\Sigma}_1^{(n)}(1) \Sigma_{1+\ell}^{(n)}(x, \bar{x}) [\sigma_m(0)]^n \rangle \\ &= m^{\frac{c}{6}(1-n)} n^{-\frac{c}{6}(n+1)} \left(\prod_{i=1}^n |a_i|^{-\frac{c}{12} \frac{m-1}{m}} \right) |a_{n+1}|^{-\frac{c}{12} \frac{n-1}{n}} |a_{n+2}|^{-\frac{c}{12} \frac{n-1}{n}} \left(\prod_{j=1}^n |b_j|^{-\frac{c}{12} \frac{m+1}{m}} \right) |b_1|^{\frac{c}{6}}. \end{aligned} \quad (\text{A.18})$$

To evaluate explicitly the products, observe that from (A.11), (A.12), (A.15) we can derive the following identities

$$\prod_{k=1}^n |t_k^n - (t_k-1)^n| = \prod_{k=1}^n \frac{|1-A|}{\left| 1 - A^{\frac{1}{n}} e^{\frac{2\pi i k}{n}} \right|^n} = |1-A|^n \prod_{k=1}^n |t_k|^n = 1, \quad (\text{A.19})$$

$$\prod_{k=1}^n |t_k - 1| = |A| \prod_{k=1}^n |t_k| = \frac{|A|}{|A-1|}, \quad (\text{A.20})$$

$$\begin{aligned} \prod_{k=1}^n \prod_{j=1, j \neq k}^n |t_k - t_j| &= \prod_{k=1}^n \frac{1}{|A-1|} \left| \frac{d}{dt} (At^n - (t-1)^n) \right|_{t=t_k} \\ &= \prod_{k=1}^n \frac{n}{|A-1|} |At_k^{n-1} - (t_k-1)^{n-1}| \\ &= \prod_{k=1}^n \frac{n}{|A-1|} \left| \frac{A^{1-\frac{1}{n}}}{\left(1 - A^{\frac{1}{n}} e^{\frac{2\pi i k}{n}} \right)^{n-2}} \right| \\ &= \frac{n^n |A|^{n-1}}{|A-1|^n} \prod_{k=1}^n |t_k|^{n-2} = n^n |A|^{n-1} |A-1|^{2(1-n)}, \end{aligned} \quad (\text{A.21})$$

$$\begin{aligned} \prod_{j=2}^n \prod_{k=1}^n |t_j^\infty - t_k| &= \prod_{k=1}^n \frac{1}{n} |t_k^n - (t_k - 1)^n| = n^{-n} \prod_{k=1}^n \frac{|1 - A|}{\left|1 - A^{\frac{1}{n}} e^{\frac{2\pi i k}{n}}\right|^n} \\ &= n^{-n} |1 - A|^n \prod_{k=1}^n |t_k|^n = n^{-n}, \end{aligned} \tag{A.22}$$

$$\begin{aligned} \prod_{j=2}^n \prod_{k=2, k \neq j}^n |t_j^\infty - t_k^\infty| &= \prod_{j=2}^n \frac{1}{n} \left| \frac{d}{dt} (t^n - (t-1)^n) \right|_{t=t_j^\infty} \\ &= \prod_{j=2}^n \left| (t_j^\infty)^{n-1} - (t_j^\infty - 1)^{n-1} \right| \\ &= \prod_{j=2}^n \left| 1 - e^{\frac{2\pi i(j-1)}{n}} \right|^{2-n} = \prod_{j=2}^n |t_j^\infty|^{n-2} = n^{2-n}. \end{aligned} \tag{A.23}$$

Using these identities we can write the expressions (A.14) and (A.17) as

$$\prod_{i=1}^n |a_i| = n^{mn} |A|^{m(n-1)} |A - 1|^{m(2-n)}, \tag{A.24}$$

$$\prod_{j=1}^n |b_j| = n^{-m(n+2)} |A - 1|^{nm}, \tag{A.25}$$

and substituting in the correlator gives

$$\langle [\tilde{\sigma}_m(\infty)]^n \tilde{\Sigma}_1^{(n)}(1) \Sigma_{1+\ell}^{(n)}(x, \bar{x}) [\sigma_m(0)]^n \rangle = \left[m^2 |A|^{m-1} |A - 1|^2 \right]^{-\frac{c}{12} \left(n - \frac{1}{n} \right)}. \tag{A.26}$$

B Dominant contributions to the entanglement of $M = 0$ BTZ

In this appendix, we show that in a typical state of the zero mass BTZ black hole the sum

$$\sum_m m N_m \left| 2m \sin \left(\frac{\alpha + 2\pi\ell}{2m} \right) \right|^{-\frac{c}{6} \left(n - \frac{1}{n} \right)} \tag{B.1}$$

appearing in the correlator (3.17) is dominated by strings with $m \sim O(\sqrt{N})$.

We assume we are working at large enough N , such that deviations from typicality are small. The total number of strings of length m in a typical state is

$$N_m = \frac{8}{\sinh \beta m} \tag{B.2}$$

with $\beta \simeq \sqrt{2}\pi/\sqrt{N}$ [50]. Since m is an integer, we can write the total number of strands as

$$N = \sum_m m N_m \Delta m, \tag{B.3}$$

with $\Delta m = 1$, and by redefining $m \equiv xN$, $\Delta m \equiv \Delta xN$:

$$1 = N \sum_x x N_x \Delta x. \tag{B.4}$$

In the limit $N \rightarrow \infty$ this becomes the integral

$$1 = N \int_0^\infty dx \frac{8x}{\sinh(\sqrt{2\pi x\sqrt{N}})}, \quad (\text{B.5})$$

which can be split as

$$1 = N \int_0^{N^{\gamma-1}} dx \frac{8x}{\sinh(\sqrt{2\pi x\sqrt{N}})} + N \int_{N^{\gamma-1}}^{N^{\gamma'-1}} dx \frac{8x}{\sinh(\sqrt{2\pi x\sqrt{N}})} + N \int_{N^{\gamma'-1}}^\infty dx \frac{8x}{\sinh(\sqrt{2\pi x\sqrt{N}})} \quad (\text{B.6})$$

with $\gamma < 1/2$ and $\gamma' > 1/2$. We now observe that the first and last integral vanish in the large N limit.

- For $x \in [0, N^{\gamma-1})$, or $m \in [0, N^\gamma)$, and $\gamma < 1/2$:

$$N \int_0^{N^{\gamma-1}} dx \frac{8x}{\sinh(\sqrt{2\pi x\sqrt{N}})} \sim \int_0^{N^{\gamma-1}} dx \frac{8\sqrt{N}}{\sqrt{2\pi}} = \frac{8N^{\gamma-1/2}}{\sqrt{2\pi}} \rightarrow 0, \text{ as } N \rightarrow \infty. \quad (\text{B.7})$$

- For $x \in [N^{\gamma'-1}, \infty)$, or $m \in [N^{\gamma'}, \infty)$, and $\gamma' > 1/2$:

$$N \int_{N^{\gamma'-1}}^\infty dx \frac{8x}{\sinh(\sqrt{2\pi x\sqrt{N}})} \sim N \int_{N^{\gamma'-1}}^\infty dx \frac{16x}{e^{\sqrt{2\pi x\sqrt{N}}}} \quad (\text{B.8})$$

$$\sim \frac{8\sqrt{2}}{\pi} N^{\gamma'-1/2} e^{-\sqrt{2\pi} N^{\gamma'-1/2}} \rightarrow 0, \text{ as } N \rightarrow \infty. \quad (\text{B.9})$$

It follows that

$$1 \approx N \int_{N^{\gamma-1}}^{N^{\gamma'-1}} dx \frac{8x}{\sinh(\sqrt{2\pi x\sqrt{N}})} = \frac{1}{N} \sum_{m \sim N^\gamma}^{N^{\gamma'}} \frac{8m}{\sinh \beta m} \quad (\text{B.10})$$

and

$$N \approx \sum_{m \sim N^\gamma}^{N^{\gamma'}} m N_m \quad (\text{B.11})$$

for any $\gamma < 1/2$ and $\gamma' > 1/2$, and especially for γ, γ' arbitrarily close to $1/2$ proving that indeed strings with $m \sim O(\sqrt{N})$ dominate the sum (B.3).

To complete the proof, we observe that for fixed α and l

$$2m \sin\left(\frac{\alpha + 2\pi\ell}{2m}\right) \sim O(1) \quad (\text{B.12})$$

is of the same order regardless of m . Therefore

$$\sum_m m N_m \left| 2m \sin\left(\frac{\alpha + 2\pi\ell}{2m}\right) \right|^{-\frac{\epsilon}{6}(n-\frac{1}{n})} \sim N \left| 2\sqrt{N} \sin\left(\frac{\alpha + 2\pi\ell}{2\sqrt{N}}\right) \right|^{-\frac{\epsilon}{6}(n-\frac{1}{n})} \quad (\text{B.13})$$

for all finite ℓ not scaling with N .

Open Access. This article is distributed under the terms of the Creative Commons Attribution License ([CC-BY 4.0](https://creativecommons.org/licenses/by/4.0/)), which permits any use, distribution and reproduction in any medium, provided the original author(s) and source are credited.

References

- [1] V. Balasubramanian, M.B. McDermott and M. Van Raamsdonk, *Momentum-space entanglement and renormalization in quantum field theory*, *Phys. Rev. D* **86** (2012) 045014 [[arXiv:1108.3568](https://arxiv.org/abs/1108.3568)] [[INSPIRE](#)].
- [2] C. Agon, V. Balasubramanian, S. Kasko and A. Lawrence, *Coarse Grained Quantum Dynamics*, [arXiv:1412.3148](https://arxiv.org/abs/1412.3148) [[INSPIRE](#)].
- [3] R. Lundgren, J. Blair, M. Greiter, A. Läuchli, G.A. Fiete and R. Thomale, *Momentum-Space Entanglement Spectrum of Bosons and Fermions with Interactions*, *Phys. Rev. Lett.* **113** (2014) 256404 [[arXiv:1404.7545](https://arxiv.org/abs/1404.7545)] [[INSPIRE](#)].
- [4] V. Balasubramanian, B. Czech, B.D. Chowdhury and J. de Boer, *The entropy of a hole in spacetime*, *JHEP* **10** (2013) 220 [[arXiv:1305.0856](https://arxiv.org/abs/1305.0856)] [[INSPIRE](#)].
- [5] V. Balasubramanian, B.D. Chowdhury, B. Czech, J. de Boer and M.P. Heller, *Bulk curves from boundary data in holography*, *Phys. Rev. D* **89** (2014) 086004 [[arXiv:1310.4204](https://arxiv.org/abs/1310.4204)] [[INSPIRE](#)].
- [6] R.C. Myers, J. Rao and S. Sugishita, *Holographic Holes in Higher Dimensions*, *JHEP* **06** (2014) 044 [[arXiv:1403.3416](https://arxiv.org/abs/1403.3416)] [[INSPIRE](#)].
- [7] M. Headrick, R.C. Myers and J. Wien, *Holographic Holes and Differential Entropy*, *JHEP* **10** (2014) 149 [[arXiv:1408.4770](https://arxiv.org/abs/1408.4770)] [[INSPIRE](#)].
- [8] A. Mollabashi, N. Shiba and T. Takayanagi, *Entanglement between Two Interacting CFTs and Generalized Holographic Entanglement Entropy*, *JHEP* **04** (2014) 185 [[arXiv:1403.1393](https://arxiv.org/abs/1403.1393)] [[INSPIRE](#)].
- [9] A. Karch and C.F. Uhlemann, *Holographic entanglement entropy and the internal space*, *Phys. Rev. D* **91** (2015) 086005 [[arXiv:1501.00003](https://arxiv.org/abs/1501.00003)] [[INSPIRE](#)].
- [10] M. Taylor, *Generalized entanglement entropy*, *JHEP* **07** (2016) 040 [[arXiv:1507.06410](https://arxiv.org/abs/1507.06410)] [[INSPIRE](#)].
- [11] M.R. Mohammadi Mozaffar and A. Mollabashi, *On the Entanglement Between Interacting Scalar Field Theories*, *JHEP* **03** (2016) 015 [[arXiv:1509.03829](https://arxiv.org/abs/1509.03829)] [[INSPIRE](#)].
- [12] P.V. Buividovich and M.I. Polikarpov, *Entanglement entropy in gauge theories and the holographic principle for electric strings*, *Phys. Lett. B* **670** (2008) 141 [[arXiv:0806.3376](https://arxiv.org/abs/0806.3376)] [[INSPIRE](#)].
- [13] W. Donnelly, *Decomposition of entanglement entropy in lattice gauge theory*, *Phys. Rev. D* **85** (2012) 085004 [[arXiv:1109.0036](https://arxiv.org/abs/1109.0036)] [[INSPIRE](#)].
- [14] H. Casini, M. Huerta and J.A. Rosabal, *Remarks on entanglement entropy for gauge fields*, *Phys. Rev. D* **89** (2014) 085012 [[arXiv:1312.1183](https://arxiv.org/abs/1312.1183)] [[INSPIRE](#)].
- [15] D. Radicevic, *Notes on Entanglement in Abelian Gauge Theories*, [arXiv:1404.1391](https://arxiv.org/abs/1404.1391) [[INSPIRE](#)].
- [16] W. Donnelly, *Entanglement entropy and nonabelian gauge symmetry*, *Class. Quant. Grav.* **31** (2014) 214003 [[arXiv:1406.7304](https://arxiv.org/abs/1406.7304)] [[INSPIRE](#)].

- [17] W. Donnelly and A.C. Wall, *Entanglement entropy of electromagnetic edge modes*, *Phys. Rev. Lett.* **114** (2015) 111603 [[arXiv:1412.1895](#)] [[INSPIRE](#)].
- [18] S. Ghosh, R.M. Soni and S.P. Trivedi, *On The Entanglement Entropy For Gauge Theories*, *JHEP* **09** (2015) 069 [[arXiv:1501.02593](#)] [[INSPIRE](#)].
- [19] D. Radićević, *Entanglement in Weakly Coupled Lattice Gauge Theories*, *JHEP* **04** (2016) 163 [[arXiv:1509.08478](#)] [[INSPIRE](#)].
- [20] R.M. Soni and S.P. Trivedi, *Aspects of Entanglement Entropy for Gauge Theories*, *JHEP* **01** (2016) 136 [[arXiv:1510.07455](#)] [[INSPIRE](#)].
- [21] K. Van Acoleyen, N. Bultinck, J. Haegeman, M. Marien, V.B. Scholz and F. Verstraete, *The entanglement of distillation for gauge theories*, *Phys. Rev. Lett.* **117** (2016) 131602 [[arXiv:1511.04369](#)] [[INSPIRE](#)].
- [22] S. Ryu and T. Takayanagi, *Holographic derivation of entanglement entropy from AdS/CFT*, *Phys. Rev. Lett.* **96** (2006) 181602 [[hep-th/0603001](#)] [[INSPIRE](#)].
- [23] S. Ryu and T. Takayanagi, *Aspects of Holographic Entanglement Entropy*, *JHEP* **08** (2006) 045 [[hep-th/0605073](#)] [[INSPIRE](#)].
- [24] V.E. Hubeny, M. Rangamani and T. Takayanagi, *A Covariant holographic entanglement entropy proposal*, *JHEP* **07** (2007) 062 [[arXiv:0705.0016](#)] [[INSPIRE](#)].
- [25] N. Engelhardt and S. Fischetti, *Covariant Constraints on Holography*, *Class. Quant. Grav.* **32** (2015) 195021 [[arXiv:1507.00354](#)] [[INSPIRE](#)].
- [26] M. Van Raamsdonk, *Building up spacetime with quantum entanglement*, *Gen. Rel. Grav.* **42** (2010) 2323 [[arXiv:1005.3035](#)] [[INSPIRE](#)].
- [27] E. Bianchi and R.C. Myers, *On the Architecture of Spacetime Geometry*, *Class. Quant. Grav.* **31** (2014) 214002 [[arXiv:1212.5183](#)] [[INSPIRE](#)].
- [28] N. Lashkari, M.B. McDermott and M. Van Raamsdonk, *Gravitational dynamics from entanglement 'thermodynamics'*, *JHEP* **04** (2014) 195 [[arXiv:1308.3716](#)] [[INSPIRE](#)].
- [29] T. Faulkner, M. Guica, T. Hartman, R.C. Myers and M. Van Raamsdonk, *Gravitation from Entanglement in Holographic CFTs*, *JHEP* **03** (2014) 051 [[arXiv:1312.7856](#)] [[INSPIRE](#)].
- [30] J. Maldacena and L. Susskind, *Cool horizons for entangled black holes*, *Fortsch. Phys.* **61** (2013) 781 [[arXiv:1306.0533](#)] [[INSPIRE](#)].
- [31] B. Swingle and M. Van Raamsdonk, *Universality of Gravity from Entanglement*, [[arXiv:1405.2933](#)] [[INSPIRE](#)].
- [32] T. Faulkner, A. Lewkowycz and J. Maldacena, *Quantum corrections to holographic entanglement entropy*, *JHEP* **11** (2013) 074 [[arXiv:1307.2892](#)] [[INSPIRE](#)].
- [33] V.E. Hubeny, *Extremal surfaces as bulk probes in AdS/CFT*, *JHEP* **07** (2012) 093 [[arXiv:1203.1044](#)] [[INSPIRE](#)].
- [34] N. Engelhardt and A.C. Wall, *Extremal Surface Barriers*, *JHEP* **03** (2014) 068 [[arXiv:1312.3699](#)] [[INSPIRE](#)].
- [35] V. Balasubramanian, B.D. Chowdhury, B. Czech and J. de Boer, *Entwinement and the emergence of spacetime*, *JHEP* **01** (2015) 048 [[arXiv:1406.5859](#)] [[INSPIRE](#)].
- [36] B. Freivogel, R.A. Jefferson, L. Kabir, B. Mosk and I.-S. Yang, *Casting Shadows on Holographic Reconstruction*, *Phys. Rev. D* **91** (2015) 086013 [[arXiv:1412.5175](#)] [[INSPIRE](#)].

- [37] B. Czech and L. Lamprou, *Holographic definition of points and distances*, *Phys. Rev. D* **90** (2014) 106005 [[arXiv:1409.4473](#)] [[INSPIRE](#)].
- [38] B. Czech, L. Lamprou, S. McCandlish and J. Sully, *Integral Geometry and Holography*, *JHEP* **10** (2015) 175 [[arXiv:1505.05515](#)] [[INSPIRE](#)].
- [39] B. Czech, L. Lamprou, S. McCandlish and J. Sully, *Tensor Networks from Kinematic Space*, *JHEP* **07** (2016) 100 [[arXiv:1512.01548](#)] [[INSPIRE](#)].
- [40] C.T. Asplund and S.G. Avery, *Evolution of Entanglement Entropy in the D1 – D5 Brane System*, *Phys. Rev. D* **84** (2011) 124053 [[arXiv:1108.2510](#)] [[INSPIRE](#)].
- [41] S. Giusto and R. Russo, *Entanglement Entropy and D1 – D5 geometries*, *Phys. Rev. D* **90** (2014) 066004 [[arXiv:1405.6185](#)] [[INSPIRE](#)].
- [42] A. Galliani, S. Giusto, E. Moscato and R. Russo, *Correlators at large c without information loss*, *JHEP* **09** (2016) 065 [[arXiv:1606.01119](#)] [[INSPIRE](#)].
- [43] C.T. Asplund, A. Bernamonti, F. Galli and T. Hartman, *Holographic Entanglement Entropy from 2d CFT: Heavy States and Local Quenches*, *JHEP* **02** (2015) 171 [[arXiv:1410.1392](#)] [[INSPIRE](#)].
- [44] J. Lin, *A Toy Model of Entwinement*, [arXiv:1608.02040](#) [[INSPIRE](#)].
- [45] S.G. Avery, *Using the D1D5 CFT to Understand Black Holes*, [arXiv:1012.0072](#) [[INSPIRE](#)].
- [46] O. Lunin and S.D. Mathur, *Correlation functions for M^N/S_N orbifolds*, *Commun. Math. Phys.* **219** (2001) 399 [[hep-th/0006196](#)] [[INSPIRE](#)].
- [47] O. Lunin and S.D. Mathur, *Three point functions for M^N/S_N orbifolds with $N = 4$ supersymmetry*, *Commun. Math. Phys.* **227** (2002) 385 [[hep-th/0103169](#)] [[INSPIRE](#)].
- [48] V. Balasubramanian, J. de Boer, E. Keski-Vakkuri and S.F. Ross, *Supersymmetric conical defects: Towards a string theoretic description of black hole formation*, *Phys. Rev. D* **64** (2001) 064011 [[hep-th/0011217](#)] [[INSPIRE](#)].
- [49] E.J. Martinec and W. McElgin, *Exciting AdS orbifolds*, *JHEP* **10** (2002) 050 [[hep-th/0206175](#)] [[INSPIRE](#)].
- [50] V. Balasubramanian, P. Kraus and M. Shigemori, *Massless black holes and black rings as effective geometries of the D1 – D5 system*, *Class. Quant. Grav.* **22** (2005) 4803 [[hep-th/0508110](#)] [[INSPIRE](#)].
- [51] E. Mintun, J. Polchinski and V. Rosenhaus, *Bulk-Boundary Duality, Gauge Invariance and Quantum Error Corrections*, *Phys. Rev. Lett.* **115** (2015) 151601 [[arXiv:1501.06577](#)] [[INSPIRE](#)].

Echoes of chaos from string theory black holes

Vijay Balasubramanian,^{a,b} Ben Craps,^b Bartłomiej Czech^c and Gábor Sárosi^{a,b}

^a*David Rittenhouse Laboratory, University of Pennsylvania,
Philadelphia, PA 19104, U.S.A.*

^b*Theoretische Natuurkunde, Vrije Universiteit Brussel (VUB),
and International Solvay Institutes,
Pleinlaan 2, B-1050 Brussels, Belgium*

^c*Institute for Advanced Study,
Princeton, NJ 08540, U.S.A.*

E-mail: vijay@physics.upenn.edu, Ben.Craps@vub.ac.be, czech@ias.edu,
gsarosi@vub.ac.be

ABSTRACT: The strongly coupled D1-D5 conformal field theory is a microscopic model of black holes which is expected to have chaotic dynamics. Here, we study the weak coupling limit of the theory where it is integrable rather than chaotic. In this limit, the operators creating microstates of the lowest mass black hole are known exactly. We consider the time-ordered two-point function of light probes in these microstates, normalized by the same two-point function in vacuum. These correlators display a universal early-time decay followed by late-time sporadic behavior. To find a prescription for temporal coarse-graining of these late fluctuations we appeal to random matrix theory, where we show that a progressive time-average smooths the spectral form factor (a proxy for the 2-point function) in a typical draw of a random matrix. This coarse-grained quantity reproduces the matrix ensemble average to a good approximation. Employing this coarse-graining in the D1-D5 system, we find that the early-time decay is followed by a dip, a ramp and a plateau, in remarkable qualitative agreement with recent studies of the Sachdev-Ye-Kitaev (SYK) model. We study the timescales involved, comment on similarities and differences between our integrable model and the chaotic SYK model, and suggest ways to extend our results away from the integrable limit.

KEYWORDS: Black Holes in String Theory, AdS-CFT Correspondence, Random Systems, Sigma Models

ARXIV EPRINT: [1612.04334](https://arxiv.org/abs/1612.04334)

Contents

1	Introduction	1
2	Correlators in the D1-D5 CFT at the orbifold point	3
3	Random matrices and progressive time-averaging	6
3.1	Ergodicity in random matrix theory	7
3.2	Progressive time-averaging	8
4	Echoes of chaos in D1-D5 two-point functions	10
4.1	Plateau	12
4.2	Ramp	13
4.3	Dip	15
4.4	Variances	16
5	Discussion	17
A	D1-D5 two-point functions echo the spectral form factor	19
B	More detailed ramp estimate	20

1 Introduction

Black holes are the most entropic objects in the universe. Their entropy $S_{\text{BH}} = \frac{A_{\text{BH}}}{4G_N\hbar}$ is proportional to the horizon area and implies that the energy spectrum of microstates has a miniscule gap ($\delta E \sim e^{-A_{\text{BH}}/4G_N\hbar}$), which becomes infinitesimal in the classical $\hbar \rightarrow 0$ limit. Various lines of evidence also suggest that the dynamics of the Hamiltonian acting on these microstates is chaotic [1–3], implying that the spectrum of excitations must be irregular [4]. Around a typical state of such a bounded system, general arguments from quantum mechanics suggest that the gapped, irregular spectrum will lead to temporal correlations showing a universal initial decay which gives way at very late times to rapid, small fluctuations whose precise structure is determined by the actual microstate.

Random matrix theory (RMT), where the Hamiltonian is drawn from a fixed ensemble, has been proposed as a universal description of this sort of behavior. In this theory it has been shown that the ensemble average of the spectral form factor, a proxy for the two-point function related to the ‘easy’ version of the information paradox [5–7], exhibits a characteristic initial decay, followed by an increasing ramp, and then a plateau. Recently, it was shown that the Sachdev-Ye-Kitaev (SYK) model [8–10], which is a strongly coupled

model of quenched disorder inspired by black hole physics,¹ also displays the decay, ramp and plateau phenomena [16].² Like random matrix theory, the SYK model contains an average over Hamiltonians — the coupling of the theory is drawn from a distribution and the smooth ramp and plateau arise after averaging over this ensemble. We would like to understand whether this behavior occurs generally in black hole physics.

String theory contains many examples of black holes whose microscopic descriptions are well understood. The simplest setting is Type IIB string theory compactified on a torus with five asymptotically flat dimensions. This theory contains charged black holes whose extremal limit still has a large entropy. The low-energy excitations of such a black hole are described by a two-dimensional conformal field theory [18], the “D1-D5 CFT”, which is a marginal deformation of a sigma model on the symmetric product target space $(T^4)^N/S_N$. Here S_N is the permutation group acting on N copies of T^4 . The marginal deformation parameter acts as the coupling in the theory. When it is large the theory is expected to be chaotic as it describes a macroscopic black hole. When it goes to zero, the theory approaches the symmetric product limit where it is integrable.

These five dimensional black holes can be reduced through a sequence of near-horizon, low-energy limits to extremal black holes in three and two dimensional Anti-de Sitter space. Indeed, through these limits, the D1-D5 CFT is known to be exactly dual to type IIB string theory on $\text{AdS}_3 \times S^3 \times T^4$ [19, 20]. The SYK model was inspired by AdS_2 black holes, and hence it may be that the D1-D5 CFT at finite coupling has a reduction to an SYK-like model [13, 15]. Here, we instead study the weak coupling limit of the theory. In this limit, the theory is integrable rather than chaotic but, remarkably, we show that many of the qualitative features of the chaotic RMT and SYK dynamics are already present.

Specifically, we consider dynamics around Ramond ground states of the D1-D5 theory which are typical microstates of the lightest black hole. These black holes have a large microscopic entropy, although it is not large enough to produce a classical black hole horizon. The temporal correlation function of graviton operators in these states shows an initial universal decay followed by sporadic fluctuations [21]. A similar structure occurs in observables computed with a *single* draw of a Hamiltonian in a random matrix theory. We argue, and numerically demonstrate, that the ensemble average in RMT can be mimicked by a progressive time-average in a single draw from the theory, over windows that scale proportionally to time. Applying this progressive time average to correlators in a typical ground state of the D1-D5 theory reveals an initial decay, followed by a long ramp and a plateau, qualitatively resembling both the RMT and SYK theories. The initial decay exactly reproduces the expected results in a black hole background [21]. We present analytic calculations of the plateau height and the shape of the ramp, and comment on the reasons for the quantitative differences between our results and those in fully chaotic theories like RMT and SYK. An interesting challenge for the future is to perturbatively turn on the marginal deformation that takes the integrable limit of the D1-D5 theory into a chaotic regime.

The paper is organized as follows. In section 2 we give a short review of the D1-D5 system at the orbifold point and the two point functions in the Ramond ground states

¹This model exhibits a tractably broken Virasoro symmetry [11] and its effective action takes a form which also arises in two-dimensional dilaton gravity [12–15].

²In fact, the level statistics in SYK is well approximated by RMT around the mean level spacing [16, 17].

based on [21]. In section 3 we introduce progressive time averaging in the context of random matrix theory and present evidence that it is capable of capturing both qualitative and quantitative features of the ensemble average. In section 4 we apply this time average to the D1-D5 graviton two point function and present the main results of the paper, including analytic estimates for the ramp and the plateau. In section 5 we conclude the paper. We include two appendices with some additional details of the discussion in section 4.

2 Correlators in the D1-D5 CFT at the orbifold point

We will consider Type IIB string theory compactified to five dimension on $S^1 \times T^4$ with N_1 D1-branes wrapped on the S^1 and N_5 D5-branes wrapped on the entire compact space. At low energies, the effective theory describing the dynamics of excitations is a certain marginal deformation of an $\mathcal{N} = (4, 4)$ supersymmetric sigma model on the symmetric product target space $\mathcal{M}_0 = (T^4)^N/S_N$, where $N = N_1N_5$ and S_N is the permutation group acting on the N copies of T^4 [18]. The sigma model on \mathcal{M}_0 describes N “strands” of string propagating on T^4 . While this is a free orbifold theory, it has an interesting spectrum and correlation functions, as we will see. The marginal deformation corresponds to turning on an interaction that allows splitting and joining of strings.

Taking an appropriate limit isolates the part of the spacetime that is exactly described by the CFT. In this low-energy limit we say that the D1-D5 CFT is holographically dual to Type IIB string theory on $\text{AdS}_3 \times S^3 \times T^4$. To have a large, weakly coupled AdS_3 space, N must be large and, in addition, the CFT must be strongly coupled, i.e. deformed far from the orbifold point. We are going to study the theory in the opposite, weakly coupled limit, but still at large N .

The extremal, supersymmetric black holes in the five dimensional asymptotically flat theory descend in this construction to the BTZ black holes of AdS_3 with periodic boundary conditions for fermions around the asymptotic circle in the AdS_3 geometry, i.e., they are in the Ramond sector of the theory. The lightest black hole, which is massless, has the quantum numbers of a ground state in this sector.

The construction of Ramond ground states of the D1-D5 CFT at the orbifold point is reviewed in detail in appendix A of [21]; here we provide a brief summary. We think of the CFT as describing N distinct “strands” of string, each of which propagates on T^4 . The ground states of the theory are formed by joining strands into various closed strings, which may be “short” (consisting of one strand) or “long” (consisting of multiple strands). The strands are attached together by applying elementary bosonic (σ) and fermionic (τ) twist operators which create n -wound string sectors. Each twist operator has 8 polarizations associated with the global symmetries of the theory. A general Ramond sector ground state is created by multiplying together bosonic and fermionic twist operators to achieve a total twist of $N = N_1N_5$:

$$\sigma = \prod_{n,\mu} (\sigma_n^\mu)^{N_{n\mu}} (\tau_n^\mu)^{N'_{n\mu}}, \tag{2.1}$$

$$\sum_{n\mu} n(N_{n\mu} + N'_{n\mu}) = N, \quad N_{n\mu} = 0, 1, 2, \dots, \quad N'_{n\mu} = 0, 1, \tag{2.2}$$

where $\mu = 1, \dots, 8$ labels the polarizations, and $n = 1, 2, \dots, N$ labels the possible lengths of strings (i.e. the number of strands a string is made of). For our purposes, the integers $N_{n\mu}$ and $N'_{n\mu}$, which count the various twist operators, uniquely specify a Ramond ground state of the theory.

Note that while Ramond ground states all have the same energy, the spectrum of excitations around each of them is different. For example, consider a case with $N = 4$ strands. Three possible states are four strings of length 1 ($N_1 = 4$), two long strings of length 2 ($N_2 = 2$), and one string of length 3 with another of length 1 ($N_3 = 1, N_1 = 1$). If we take the CFT to be on a circle of circumference L , the momentum spectrum of excitations is very different in these sectors — the first has modes gapped by $1/L$ with four-fold degeneracy, the second has modes gapped by $1/2L$ with 2-fold degeneracy and the third spectrum is a union of modes gapped by $1/L$ and $1/3L$ each with unit degeneracy. Thus correlation functions computed in each of the microstates will be different and will depend on the twist distributions $\{N_{n\mu}, N'_{n\mu}\}$.

Now observe that the number of Ramond ground states is given by counting (colored) partitions of the integer N . When $N \gg 1$, there are $O(e^{2\sqrt{2\pi N}})$ such partitions, leading to an enormous ground state degeneracy in the theory, corresponding to an entropy $S = 2\sqrt{2\pi N}$. Nearly all partitions of a large integer lie very close to a certain “typical partition” [21]. This means that most Ramond states will in fact have twist distributions $\{N_{n\mu}, N'_{n\mu}\}$ that lie close to a certain typical distribution. Thus, although correlation functions measured in individual microstates will depend on the precise form of the state, for almost all microstates the generic correlation functions will take a typical form, which we seek to investigate. Microcanonically, we should study all partitions of integers that lead to a total twist of N . The easiest way, however, to derive the form of the typical state is to use the grand canonical ensemble with a “chemical potential” η to fix the total “charge” N for eight types ($\mu = 1 \dots 8$) of bosons (σ_n^μ) and fermions (τ_n^μ) with integral charges n . When N is large, the grand canonical average populations for $\{N_{n\mu}, N'_{n\mu}\}$ will also be typical, in the sense that most configurations will be very close to the average (the standard deviation over the mean will tend to zero). Thus we can derive that most of the Ramond ground states have twist distributions close to the Bose-Einstein and Fermi-Dirac forms:

$$N_{n\mu} = \frac{1}{e^{\eta n} - 1}, \quad N'_{n\mu} = \frac{1}{e^{\eta n} + 1}, \quad N_n = \sum_{\mu} (N_{n\mu} + N'_{n\mu}) = \frac{8}{\sinh \eta n}, \quad (2.3)$$

with η set by

$$N = \sum_n n N_n \approx \frac{2\pi^2}{\eta^2}. \quad (2.4)$$

For further reference, we note that the entropy scales as $S \sim 1/\eta$.

Now that we know the form of the typical Ramond ground state in the D1-D5 system it remains to calculate the correlation function. Again following [21], we will consider bosonic non-twist operators, which do not cut and join the N strands of the CFT. (An operator describing a fluctuation of the metric in the T^4 directions is an example.) We focus on S_N

invariant operators obtained as sums of copies acting on each strand,

$$\mathcal{O} = \frac{1}{\sqrt{N}} \sum_{a=1}^N \mathcal{O}_a. \tag{2.5}$$

We are interested in two-point functions of the form

$$\langle \sigma^\dagger \mathcal{O}^\dagger \mathcal{O} \sigma \rangle. \tag{2.6}$$

Since the state as a whole splits into a product of strings of lengths n , the correlator splits into a sum of terms, each of which reduces to a two point function in a CFT on a spatial circle that is n times as long. After some algebra (see [21] for details), the correlation function becomes

$$\langle \sigma^\dagger \mathcal{O}^\dagger \mathcal{O} \sigma \rangle = G(w, \bar{w}) = \frac{1}{N} \sum_{n=1}^N n N_n \sum_{k=0}^{n-1} \frac{C}{[2n \sin(\frac{w-2\pi k}{2n})]^{2h} [2n \sin(\frac{\bar{w}-2\pi k}{2n})]^{2\bar{h}}}. \tag{2.7}$$

Here h and \bar{h} are the left and right conformal dimensions, C is a constant, the sum on n accounts for the contribution from strings of length n , and the sum on k accounts for the placement of operators on different strands of a long string. Also, $w = w_1 - w_2$ and $\bar{w} = \bar{w}_1 - \bar{w}_2$ are differences in the lightcone positions of the probe operators. In Lorentzian signature we will set

$$w = \phi - t, \quad \bar{w} = \phi + t, \tag{2.8}$$

where ϕ and t are dimensionless angular and time coordinates in the CFT, normalized by setting the length of the spatial circle to be equal to 2π .

The correlator $G(w, \bar{w})$ exhibits physical lightcone divergences on the cylinder. We can regularize these divergences by dividing by the vacuum correlation function, which is fixed by conformal invariance. Focusing, for definiteness, on operators with conformal dimensions $h = \bar{h} = 1$ this results in [21]

$$\hat{G}(w, \bar{w}) = \frac{1}{N} \sum_{n=1}^N n N_n \sum_{k=0}^{n-1} \left(\frac{4 \sin \frac{w}{2} \sin \frac{\bar{w}}{2}}{2n \sin(\frac{w-2\pi k}{2n}) 2n \sin(\frac{\bar{w}-2\pi k}{2n})} \right)^2. \tag{2.9}$$

Setting $\phi = 0$, we can evaluate the temporal correlation function numerically — the result is plotted in figure 1. We see a smooth initial decay followed by sporadic behavior, which is qualitatively similar to the behavior of observables in a single draw from a random matrix theory or in the SYK model before the average over disorder.

What is the origin of this sporadic behavior? As shown in appendix A, the two-point function (2.9) for $\phi = 0$ receives contributions from frequencies of the form m/n , with n an integer labeling the length of a component string (so $1 \leq n \leq N$). This is a dense spectrum consisting of all rational numbers with denominators smaller than $N + 1$. The mixing of this large number of incommensurate frequencies produces the rapid late time oscillations. A feature of the theory is that excitations on different long strings do not interact at the orbifold point. This means that the smallest frequencies that occur in the

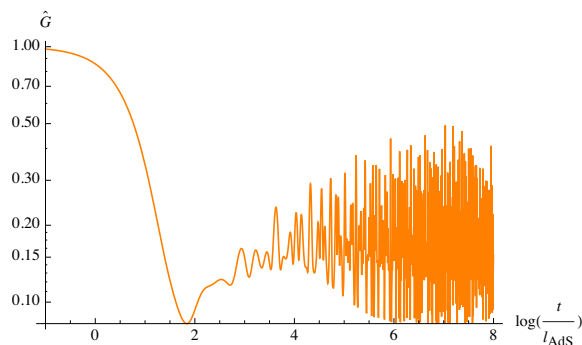


Figure 1. The regularized two-point function (2.9).

two-point function are much larger than implied by the dense spectrum because no terms depend on the energy *differences* between excitations of strings of different lengths. (Hence, while the spectrum contains excitations with energies $1/(N - 1)$ and $1/N$ the two point function does not contain the difference $1/(N - 1) - 1/N$.) If we were dealing with a fully chaotic system, we would expect all the degeneracies in the spectrum to be broken, leading to exponentially small energy spacings. When we later analyze smooth, time-averaged versions of our two-point function, we will see that the relatively large frequency gap will cause the late-time plateau value to be reached earlier than would have been the case for smaller gaps.

One might wonder why the averaging over states we have performed by going to the grand canonical ensemble has not led to a smoothing of the sporadic behavior, in the way that ensemble averaging does for random matrix theory and SYK. The reason is that every state in the ensemble has exactly the same spectrum, albeit with different degeneracies. Our ensemble average therefore does not have the same effect as the averaging over different spectra that produces smoothing in random matrix theory and SYK. Thus, to obtain smooth late-time behavior, we will need another way of coarse graining, to which we turn next.

3 Random matrices and progressive time-averaging

The sporadic late-time fluctuations of the two-point correlation function (2.9) are reminiscent of similar behavior found in [16] for the SYK model. There, smooth curves were obtained by averaging over random couplings. The main object of study in [16] was the spectral form factor

$$F_\beta(t) = \sum_{m,n} e^{-\beta(E_m + E_n)} e^{-i(E_m - E_n)t}, \tag{3.1}$$

where the sum runs over all the eigenvalues E_n of a Hamiltonian drawn from an ensemble. The spectral form factor displays sporadic late-time behavior, which can be smoothed by averaging over the ensemble of Hamiltonians. The main result of [16] is that the result agrees very well with the spectral form factor in random matrix theory, again after averaging over the random Hamiltonians. One motivation for studying the spectral form factor is

found in the spectral decomposition of the thermal two point function,

$$\langle O(t)O(0) \rangle \sim \sum_{m,n} |\langle m|O(0)|n \rangle|^2 e^{-\beta E_m + i(E_m - E_n)t}. \quad (3.2)$$

It is believed that the late-time behavior is controlled by the phases $e^{i(E_m - E_n)t}$, so that some features of the two point function in this regime are captured by the spectral form factor (3.1). Another motivation is that the spectral form factor is a more primitive quantity than two-point functions, in that it can be obtained directly from the partition function and does not require the introduction of operators. As a result, it can be straightforwardly studied in random matrix theory.

Our D1-D5 CFT has a definite Hamiltonian, so we cannot resort to disorder averaging for smoothing the sporadic late-time behavior of two-point functions. Is there any other meaningful way in which the late-time oscillations can be smoothed? A natural idea is to coarse-grain the correlator over time. One quickly notices, however, that averaging with any fixed time window either fails to remove the late-time oscillations or significantly distorts the early-time decay. This leads to the idea of using a time-window that grows with time, which we refer to as progressive time-averaging. In order to motivate a specific prescription we turn to random matrix theory. We will ask whether the well-known result of ensemble averaging could be alternatively obtained by progressive time-averaging applied to a single Hamiltonian drawn from the ensemble. We will find that this is the case for a time window that grows linearly with time, which will motivate our use of this procedure in the context of the D1-D5 CFT.

3.1 Ergodicity in random matrix theory

We consider Hamiltonians that are $L \times L$ matrices drawn from a random matrix ensemble. An important phenomenon in random matrix theory is self-averaging of certain quantities, i.e. the agreement of a quantity evaluated on a typical instance of the ensemble with the ensemble average of the same quantity. An interesting generalization of self-averaging quantities are ergodic quantities. For ergodic quantities the result of averaging over random Hamiltonians can be approximately reproduced by using a single Hamiltonian drawn from the ensemble and coarse-graining in time.

It is known in random matrix theory that the spectral form factor is self-averaging for sufficiently short times but not for longer times [22]. On the other hand, we can study the ergodicity of the form factor by considering suitable time averages

$$\bar{F}_\beta(t, \Delta t) = \int_{-\infty}^{\infty} dt' g(t - t', \Delta t) F_\beta(t'), \quad (3.3)$$

where $g(t, \Delta t)$ is some smearing function with peak at $t = 0$, width Δt and $\int dt g(t, \Delta t) = 1$. We could imagine it to be a Gaussian

$$g(t, \Delta t) = \frac{1}{\sqrt{2\pi}\Delta t} e^{-\frac{t^2}{2(\Delta t)^2}}, \quad (3.4)$$

or a step function, but its details should not matter too much. The spectral form factor for a Gaussian random matrix ensemble, which is related to the late time behavior of the SYK model, is not ergodic for any fixed time window Δt [22].³

3.2 Progressive time-averaging

We will now provide evidence suggesting that a progressive time average with $\Delta t \sim t$ gives a good approximation to the ensemble average for Gaussian random matrices. This is equivalent to averaging over fixed windows in $\log t$. We first present a heuristic motivation, followed by numerical evidence.

In Gaussian random matrix ensembles, the probability distribution for the difference of two neighboring energy levels $s = E_{n+1} - E_n$ with $s > 0$ is given by [24]

$$p(s) = \frac{A}{s_0} \left(\frac{s}{s_0}\right)^\beta e^{-\alpha\left(\frac{s}{s_0}\right)^2}, \tag{3.5}$$

where s_0 is the average value of s , A is the normalization, and the constants α and β depend on the specific ensemble. In the spectral form factor (3.1), the phases $\exp(\pm ist)$ appear with the same weight and so add to give a term proportional to $\cos(st)$. Let us ask what happens to this cosine upon ensemble averaging:

$$\int_0^\infty ds p(s) \cos(st) \sim \partial_t^\beta e^{-\frac{s_0^2 t^2}{4\alpha}}. \tag{3.6}$$

We see a cancellation of the random phases in the average, resulting in Gaussian decay. Can we reproduce this with a time average? Consider for example a Gaussian smearing function applied to a typical phase $e^{is_0 t}$ and its conjugate:

$$\int_{-\infty}^\infty dt' \frac{1}{\sigma} e^{-\frac{(t-t')^2}{2\sigma^2}} \cos(s_0 t') \sim \cos(s_0 t) e^{-\frac{s_0^2 \sigma^2}{2}}. \tag{3.7}$$

We see that we need to set $\sigma = \frac{t}{\sqrt{2\alpha}}$ in order to reproduce the decay of the ensemble average. At the qualitative level the argument depends relatively little on the smearing function. For instance, for a step function we find

$$\frac{1}{\sigma} \int_{t-\sigma/2}^{t+\sigma/2} dt \cos(s_0 t) = 2 \cos(s_0 t) \frac{\sin\left(\frac{s_0 \sigma}{2}\right)}{s_0 \sigma}, \tag{3.8}$$

which for $\sigma \sim t$ is again a decaying function with width of order $\frac{1}{s_0}$.

The argument above focuses on time dependences associated to differences of *neighboring* energy levels rather than generic energy differences, so that we may really trust it only at very late times. While it would be interesting to find a more precise analytic argument, in the present paper we will simply use the heuristic argument as motivation, verify numerically that the resulting prescription produces good results in random matrix theory, and then apply it to our system of interest.

³Note that for sufficiently large, fixed values of Δt and L the spectral form factor is ergodic for circular ensembles [23].

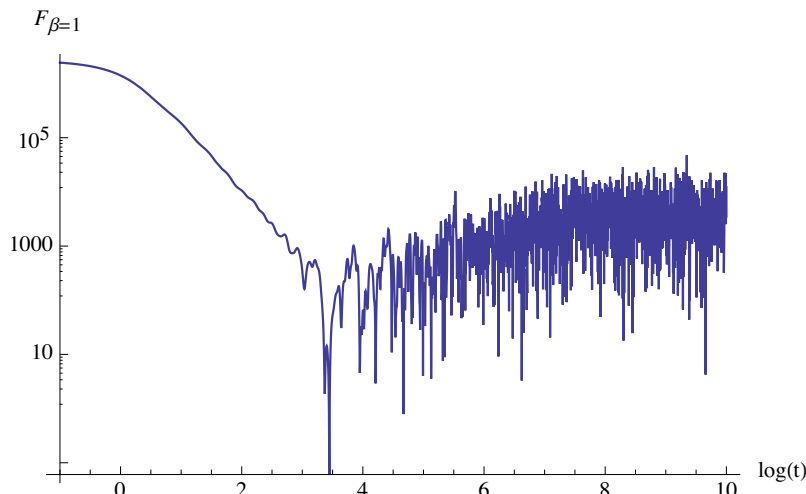


Figure 2. Log-log plot of the spectral form factor (3.1) with $\beta = 1$ for a single 1024×1024 matrix drawn from the Gaussian Unitary Ensemble (GUE). The early part is self-averaging but the late part is superseded by noise.

Now we present numerical evidence suggesting that the progressive time-average with window $\Delta t \sim t$ of the spectral form factor (3.1) is ergodic. We work with 1024×1024 matrices and — for numerical speed up — discretized time averages

$$\bar{F}_\beta(t, \Delta t) = \frac{1}{100} \sum_{k=-50}^{49} F_\beta \left(t + \frac{k}{100} \Delta t \right). \quad (3.9)$$

We draw a single pseudorandom Hermitian matrix H from the Gaussian Unitary Ensemble (GUE), $p(H) = \frac{1}{2^{L/2} \pi^{L^2/2}} e^{-\frac{L}{2} \text{Tr} H^2}$ with $L = 2^{10}$. The spectral form factor for such a single matrix is plotted in figure 2. We see self-averaging for early times which is quickly overtaken by noise for late times.

The ensemble average of the spectral form factor for Gaussian ensembles is a well studied quantity. In particular, it behaves universally for large L , exhibiting an early slope from an initial value $\sim L^2$, followed by a dip, a linear rise over time scale $\sim L$, and finally a plateau which is the infinite-time average and is of order L [25]. We plot this ensemble average for 500 random matrices in figure 3 and figure 4, with the results of time-averaging for a single matrix drawn from GUE superposed, with various fixed windows and a progressive window $\Delta t = 0.8t$, respectively.⁴ It is clear that the progressive time window provides a much better approximation to the ensemble average than the fixed time windows.

⁴The order one coefficient in front of t should be smaller than 2 because otherwise, in (3.9), we are calculating the total integral of the function. Other than this constraint, the late part of the ramp and the plateau are rather insensitive to this coefficient, as follows from the argument presented around (3.6). On the other hand, the location of the dip depends slightly on the choice of the coefficient. The coefficient could be tuned to minimize deviations from the early self-averaging part of the curve in order extract the dip time.

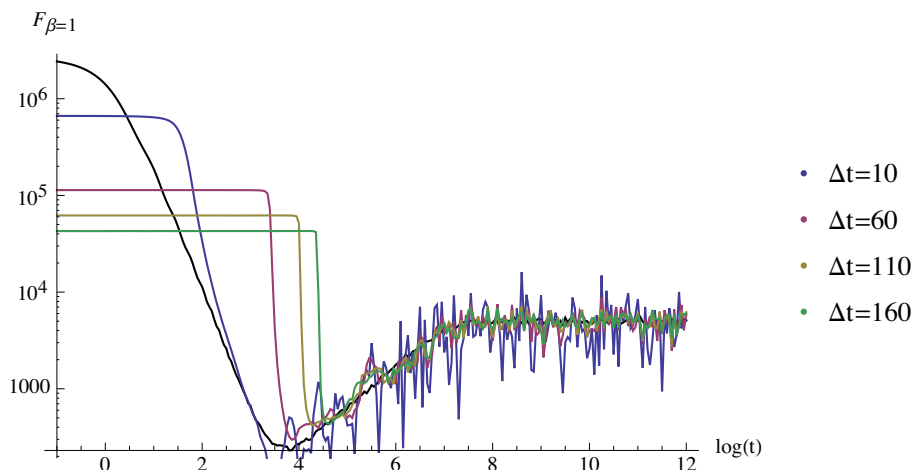


Figure 3. Log-log plot of the average spectral form factor with $\beta = 1$ for five hundred 1024×1024 matrices drawn from the Gaussian unitary ensemble (GUE) (black), and the sliding window average (3.9) with fixed time windows $\Delta t = 10, 60, 110, 160$ (color) for a single instance of a random matrix. Notice that for averaging with a fixed time window there is tension between preserving the dip and having a sufficiently smooth ramp and plateau.

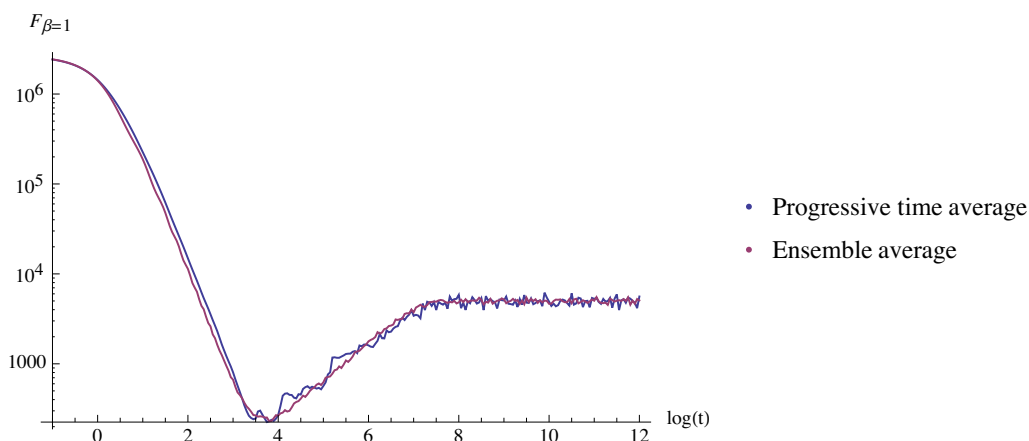


Figure 4. Log-log plot of the average spectral form factor with $\beta = 1$ for five hundred 1024×1024 matrices drawn from the Gaussian unitary ensemble (GUE) (purple), and the sliding window average (3.9) for a progressive time window $\Delta t = 0.8t$ (blue) for a single instance of a random matrix. The progressive window captures the behavior of the ensemble average, in particular the dip, the ramp and the plateau.

4 Echoes of chaos in D1-D5 two-point functions

Our examination of the D1-D5 theory at the orbifold point will focus on the regularized Lorentzian two-point function (2.9) evaluated at temporal distance t and equal location in space:

$$\hat{G}(t) = \frac{1}{N} \sum_{n=1}^N n N_n \sum_{k=0}^{n-1} \frac{\sin^4 \frac{t}{2}}{n^4 \sin^2 \left(\frac{t+2\pi k}{2n} \right) \sin^2 \left(\frac{t-2\pi k}{2n} \right)} \equiv \frac{1}{N} \sum_{n=1}^N N_n C_n(t). \quad (4.1)$$

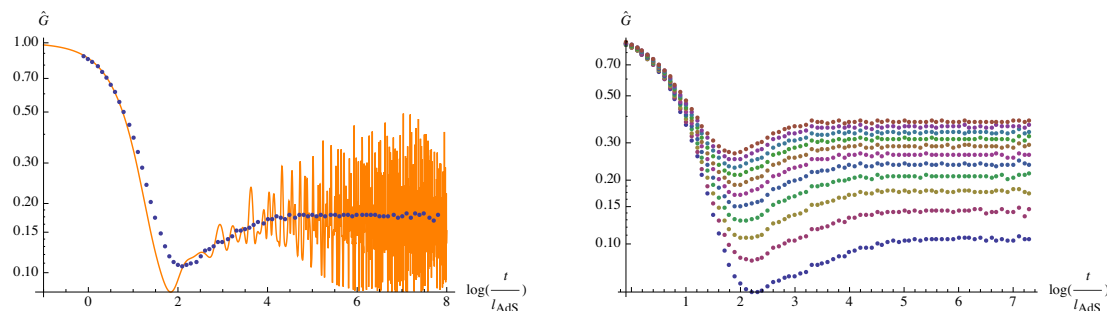


Figure 5. Left: the continuous orange line represents the regularized two-point function (4.1). The blue dotted line is its progressive time-average. Right: the progressive time-average of (4.1) for $\eta = 0.05 + 0.025j$, $j = 0, \dots, 10$. Smaller values of η correspond to larger N and smaller plateau height.

We start by applying the progressive time average of the previous section to this two point function. For numerical simplicity, we will use the pointwise averaging⁵ of (3.9) with $\Delta t = t$. The results are presented in figure 5. The smoothed curve has a dip that is lower than the late time average (plateau), which it reaches after climbing a ramp whose length increases with N . This is in qualitative agreement with random matrix theory and the SYK model. The remainder of this section is devoted to an analytic study of the late time ramp and plateau, highlighting the quantitative differences from random matrix theory.

In the following, we will find two ways of rewriting $C_n(t)$ useful. The first was obtained in [21] by explicitly evaluating the sum over k :

$$C_n(t) = 2n \left(\frac{\sin \frac{t}{2}}{n \sin \frac{t}{n}} \right)^2 \left(1 + \frac{\sin t}{n \tan \frac{t}{n}} \right). \quad (4.2)$$

The second rewriting (worked out in appendix A) will be handy for deriving analytically the late-time behavior of the correlator (4.1). In addition, it emphasizes the similarity between the D1-D5 two-point function and the spectral form factor:

$$C_n(t) = \frac{1}{n^3} \sum_{m_1=0}^{2n-2} \sum_{m_2=0}^{2n-2} \rho_n(m_1) \rho_n(m_2) e^{it \frac{(m_1 - m_2)}{n}} \mathcal{G}_n(m_1 + m_2 + 2). \quad (4.3)$$

Here the ‘spectral weights’ follow a ‘triangle law’ (see figure 6)

$$\rho_n(m) = \begin{cases} m + 1 & m < n \\ 2n - 1 - m & m \geq n \end{cases} \quad (4.4)$$

and

$$\mathcal{G}_n(x) = \begin{cases} n & n \text{ divides } x \\ 0 & \text{otherwise.} \end{cases} \quad (4.5)$$

Below, we analyze the behavior of (4.1) after progressive time-averaging.

⁵One might expect a Gaussian kernel to produce smoother curves but it is numerically more challenging.

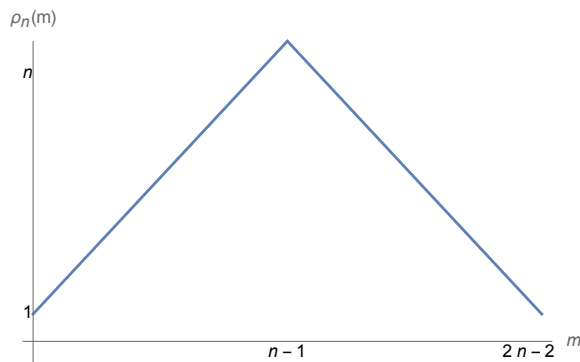


Figure 6. The spectral weights (4.4) follow a ‘triangle law’.

4.1 Plateau

At very late times, the progressive time averages of the quantities $C_n(t)$ tend to limiting values:

$$\bar{C}_n = \lim_{T \rightarrow \infty} \frac{1}{T} \int_0^T dt C_n(t) = \frac{1}{n^3} \sum_{m=0}^{2n-2} \rho_n(m)^2 \mathcal{G}_n(2m+2). \quad (4.6)$$

The function $\mathcal{G}_n(2m+2)$ vanishes unless $2m+2$ is a multiple of n . This requires that

$$m = \frac{n}{2} - 1, n-1, \frac{3n}{2} - 1 \quad (4.7)$$

for even n and $m = n-1$ for odd n . This leads to

$$\bar{C}_{n(\text{even})} = \frac{3}{2} \quad \text{and} \quad \bar{C}_{n(\text{odd})} = 1, \quad (4.8)$$

from which we obtain:

$$\bar{G} \equiv \lim_{T \rightarrow \infty} \frac{1}{T} \int_0^T dt \hat{G}(t) = \frac{1}{N} \left(\frac{3}{2} \sum_{n \text{ even}}^N N_n + \sum_{n \text{ odd}}^N N_n \right) = \frac{1}{N} \left(\sum_{\text{all } n}^N N_n + \frac{1}{2} \sum_{n \text{ even}}^N N_n \right). \quad (4.9)$$

We may approximate \bar{G} for the typical state using the grand canonical ensemble in which the total twist N is fixed with a chemical potential η according to equations (2.3) and (2.4). In this approximation, we may let the sums in (4.9) run to infinity,

$$\bar{G} \approx \frac{1}{N} \left(\sum_{s=1}^{\infty} \frac{8}{\sinh(\eta s)} + \frac{1}{2} \sum_{s=1}^{\infty} \frac{8}{\sinh(2\eta s)} \right), \quad (4.10)$$

and then, when N is large, approximate them with integrals:

$$\bar{G} \approx \frac{1}{N} \cdot \frac{8}{\eta} \int_{\delta\eta}^{\infty} \frac{du}{\sinh u} + \frac{1}{N} \cdot \frac{1}{2} \cdot \frac{8}{2\eta} \int_{2\delta\eta}^{\infty} \frac{du}{\sinh u}. \quad (4.11)$$

Here δ is an $O(1)$ number that parameterizes the discretization error at the lower limit. Evaluating the integrals gives:

$$\bar{G} \approx \frac{8\eta}{2\pi^2} \left[\log \coth \left(\frac{\eta\delta}{2} \right) + \frac{1}{4} \log \coth(\eta\delta) \right]. \quad (4.12)$$

Remembering that $\delta = O(1)$ and $\eta = O(1/\sqrt{N})$, we further approximate and get:

$$\bar{G} \approx \frac{5\eta}{\pi^2} \log\left(\frac{1}{\eta}\right) + O(1). \tag{4.13}$$

Thus, at late times, the coarse-grained temporal 2-point function approaches a constant plateau that scales as $\log(\sqrt{N})/\sqrt{N} \sim \log(S)/S$, where S is the entropy of the black hole.

4.2 Ramp

To exhibit the ramp behavior of the correlator (4.1), we again employ progressive time averaging. For numerical convenience, we use a simple step-function averaging reminiscent of eq. (3.9):

$$\tilde{G}(t) = \frac{1}{t} \int_{t/2}^{3t/2} dt' \hat{G}(t'). \tag{4.14}$$

The progressively time-averaged $\tilde{G}(t)$ decomposes into progressively time-averaged contributions from individual modes,

$$\tilde{G}(t) = \frac{1}{N} \sum_n N_n \tilde{C}_n(t), \tag{4.15}$$

each of which takes the form:

$$\tilde{C}_n(t) = \frac{1}{t} \cdot \frac{2}{n} \int_{t/2}^{3t/2} \left(\frac{\sin t'/2}{\sin t'/n}\right)^2 \left(1 + \frac{\sin t'}{n \tan t'/n}\right) dt'. \tag{4.16}$$

This rewriting follows from eq. (4.2).

An intuitive approach to estimate the ramp is to recognize that for each individual n , the contribution of $\tilde{C}_n(t)$ to the correlator jumps fairly quickly from the low point in the dip to the plateau. This is because there is only one timescale, as the gap (which sets the plateau time as $\gamma \times 1/\text{gap}$ for some constant γ) and the level spacing are the same.⁶ We also know from the above that for odd n the contribution to the plateau is 1 and for even n it is 3/2. This suggests that we can write the ramp part of the correlator as:

$$\tilde{G}(t) \approx \frac{1}{N} \left(\frac{3}{2} \sum_{n \text{ even}}^{t/\gamma} N_n + \sum_{n \text{ odd}}^{t/\gamma} N_n \right) = \frac{1}{N} \left(\sum_{\text{all } n}^{t/\gamma} N_n + \frac{1}{2} \sum_{n \text{ even}}^{t/\gamma} N_n \right). \tag{4.17}$$

In this equation we have taken into account that by a time t the contribution of any n with $n < t/\gamma$ will have hit its plateau, and we approximate the other modes as being 0. Here γ is some $O(1)$ number that relates the scale of the gap to the precise timescale of the plateau. This may depend on the spectrum and on the operator. The sum includes a unit contribution from the plateau for any n and the second sum includes the additional 1/2 that is present for even n . Putting in the occupation numbers, we get

$$\tilde{G}(t) = \frac{1}{N} \sum_{n=1}^{t/\gamma} \frac{8}{\sinh(\eta n)} + \frac{1}{N} \sum_{n=1}^{t/(2\gamma)} \frac{1}{2} \frac{8}{\sinh(2\eta n)}. \tag{4.18}$$

We plot this function on top of the time averaged two point function on figure 7 with⁷

⁶For further justification of this intuition and a slight improvement of the simple estimate below, see appendix B.

⁷To see better why this value works so well, see appendix B.

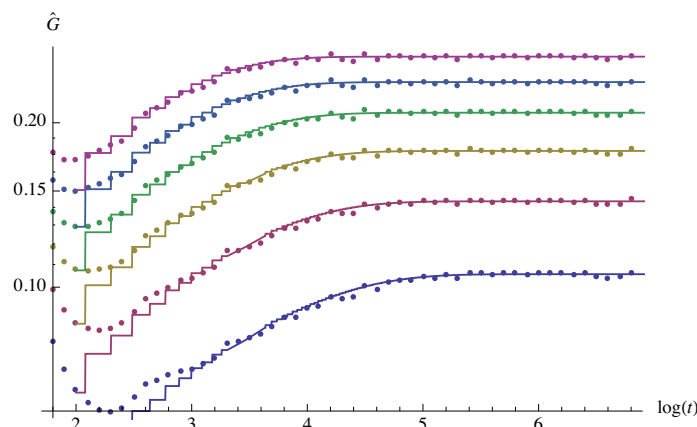


Figure 7. The estimate (4.18) for the ramp and the plateau with $\gamma = 2$ (solid lines) versus the numerically evaluated progressive time averaged regularized two point function (dots) for $\eta = 0.05, 0.075, 0.1, 0.125, 0.15, 0.175$ (from bottom to top).

$\gamma = 2$. For large N we again approximate the sum as an integral,

$$\sum_{n=1}^{\tau} \frac{8}{\sinh(\eta n)} \approx \frac{8}{\eta} \log \left[\frac{\tanh\left(\frac{\tau\eta}{2}\right)}{\tanh\left(\frac{\delta\eta}{2}\right)} \right]. \quad (4.19)$$

For the first sum $\tau = t/\gamma$ and for the second sum $\tau = t/(2\gamma)$. Also, note that η in second sum is multiplied by a factor of 2. Putting this all together and doing some elementary algebra gives

$$\tilde{G}(t) = \frac{5\eta}{\pi^2} \log \left[\frac{1}{\eta\delta} \tanh\left(\frac{t\eta}{2\gamma}\right) \right] + \frac{8\eta}{2\pi^2} \log 2, \quad (4.20)$$

where we can ignore the last term for our purposes. The characteristic time scale is the plateau time $t_p \sim 1/\eta \sim \sqrt{N}$.

Let us understand the time dependence. First, note that t cannot be taken to zero since the integral approximation is invalid in that case. Thus, t is at least $\mathcal{O}(1)$ and $\tilde{G}(t) \geq 0$. We can consider two useful limits. First

$$1 < t \ll \sqrt{N} : \quad \tilde{G}(t) = \frac{5\eta}{\pi^2} \log \frac{t}{\gamma\delta}, \quad (4.21)$$

so the ramp rises logarithmically, in contrast to the linear rise for random matrices. In this range,

$$1 < t \ll \sqrt{N} : \quad \frac{d\tilde{G}}{dt} \sim \frac{\eta}{t} \sim \frac{1}{t\sqrt{N}}. \quad (4.22)$$

As a check also note that at late times

$$t \gg \sqrt{N} : \quad \tilde{G}(t) = \frac{5\eta}{\pi^2} \log \frac{2}{\eta\delta}, \quad (4.23)$$

which reproduces the plateau value from eq. (4.13).

From (4.22), we see that when $t \sim O(1)$, then $d\tilde{G}/dt \sim O(1/\sqrt{N})$, while when $t \sim O(\sqrt{N})$ at central times in the ramp, $d\tilde{G}/dt \sim 1/N$. So the plateau height will be parametrically controlled by $d\tilde{G}/dt$ at central times in the ramp, multiplied by the duration of the ramp (which is determined by the inverse of the typical gap size, which is $1/\sqrt{N}$). This gives the estimate $1/N \times \sqrt{N} \sim 1/\sqrt{N}$ for the plateau height. The more rapid growth with slope of $O(1/\sqrt{N})$ in the early part of the ramp gives a logarithmic correction, resulting in a plateau height of $\log N/\sqrt{N} \sim \eta \log(1/\eta)$.

4.3 Dip

In this subsection, we consider the temporal coarse graining of (4.1) with generic progressive time window of width $\Delta t = at$ (generalizing (4.14)), which we will denote by

$$\tilde{G}_a(t) = \frac{1}{at} \int_{t-at/2}^{t+at/2} dt' \hat{G}(t'). \quad (4.24)$$

Such a generalization does not modify the conclusions about the late part of the ramp and the plateau time. However, we do expect the precise location of the dip to be sensitive to the parameter a and therefore the specific coarse graining that we pick. As we will see, the scaling with the entropy is independent of a .

The strategy we use is to approximate (4.24) as the sum of the contribution coming from the regularized $M = 0$ BTZ two point function [21]⁸

$$\hat{G}_{\text{BTZ}}(t) = 2 \sin^2\left(\frac{t}{2}\right) \frac{t + \sin t}{t^3}, \quad (4.25)$$

and our ramp estimate (4.20), i.e.

$$\tilde{G}_a(t) \approx \frac{1}{at} \int_{t-at/2}^{t+at/2} dt' \hat{G}_{\text{BTZ}}(t') + \frac{5\eta}{\pi^2} \log\left[\frac{1}{\eta\delta} \tanh\left(\frac{t\eta}{2\gamma}\right)\right] + \frac{8\eta}{2\pi^2} \log 2. \quad (4.26)$$

We illustrate on the left of figure 8 how remarkably well this naive estimate works. The very precise match indicates that there is no extra physics going on at intermediate time scales.

In order to extract the dip time, we want to find the minimum of this curve. Let us assume that the dip happens at $1 \ll t_d \ll \sqrt{N}$. In this case, we can approximate the ramp part with the logarithmic rise of (4.21). On the other hand, the BTZ part asymptotes to⁹

$$\frac{1}{at} \int_{t-at/2}^{t+at/2} dt' \hat{G}_{\text{BTZ}}(t') \approx \frac{4}{4-a^2} \frac{1}{t^2}, \quad t \gg 1, \quad a < 2, \quad (4.27)$$

so that for times $1 \ll t \ll \sqrt{N}$ we have

$$\tilde{G}_a(t) \approx \frac{4}{4-a^2} \frac{1}{t^2} + \frac{5\eta}{\pi^2} \log \frac{t}{\gamma\delta}, \quad (4.28)$$

⁸To arrive at this expression, take (2.14) of [21], set $w = -\bar{w} = -t$ and divide by the two point function in the NS vacuum.

⁹For $a \geq 2$ the asymptote crosses over to $1/t$. In this case, the lower end of the integral moves to the left, so we no longer have a good temporal coarse graining.

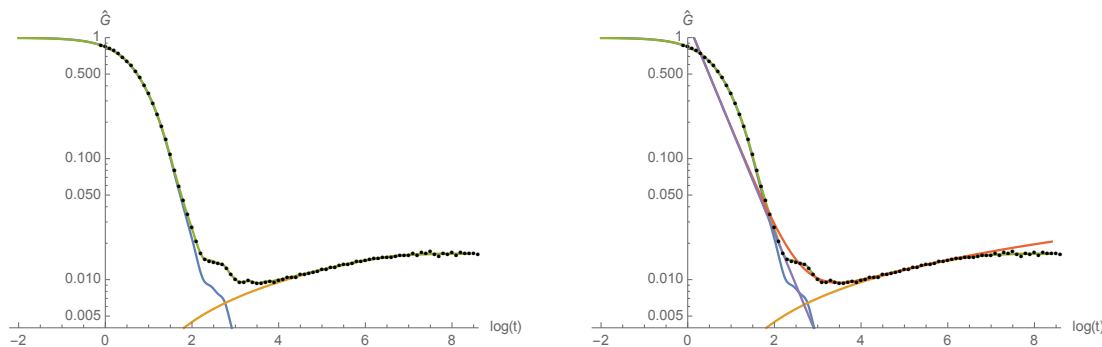


Figure 8. Left: the black dots represent the progressive time-average of the regularized two point function (4.1), the blue line is the progressive time-average of the BTZ two point function (4.25), the yellow line is the ramp estimate (4.18), while the green line is the sum of the latter two, i.e. the function (4.26). Right: same as the left, with the addition of: purple line is the BTZ asymptote (4.27); the dark orange line is the curve (4.28). Both figures are for $\eta = 0.005$ and use $\gamma = 2$, $\delta = 0.55$ and $a = 1$.

see the right panel of figure 8 for an illustration. The minimum of this curve is at

$$t_d = \sqrt{\frac{8\pi^2}{5(4-a^2)\eta}}, \tag{4.29}$$

which scales as $t_d \sim \sqrt{S}$ with the entropy. Note that we indeed have $1 \ll t_d \ll \sqrt{N}$. This establishes a parametrically long ramp. Notice that we have $t_d \sim \sqrt{t_p}$ which is also valid for random matrices.

4.4 Variances

Eqs. (4.13) and (4.18) apply to the typical Ramond ground state of the D1-D5 system. We may ask by how much other Ramond ground states differ from these typical values.

We start by considering eigenstates of the occupation numbers N_n . The middle expression in eq. (4.17) casts $\tilde{G}(t)$ as a linear combination of distinct occupation numbers N_n , which in the grand canonical ensemble are independent random variables. Thus, the variance in the ramp part of progressively time-averaged correlator, $\tilde{G}(t)$, can be approximated in terms of variances in N_n :

$$\text{var } \tilde{G}(t) \approx \frac{1}{N^2} \left(\frac{9}{4} \sum_{n \text{ even}}^{t/\gamma} \text{var } N_n + \sum_{n \text{ odd}}^{t/\gamma} \text{var } N_n \right). \tag{4.30}$$

Using

$$\text{var } N_{n\mu} = \frac{e^{\eta n}}{(e^{\eta n} - 1)^2} \quad \text{and} \quad \text{var } N'_{n\mu} = \frac{e^{\eta n}}{(e^{\eta n} + 1)^2}, \tag{4.31}$$

we get:

$$\text{var } N_n = \frac{8 \cosh \eta n}{\sinh^2 \eta n}. \tag{4.32}$$

Substituting, we obtain:

$$\begin{aligned} \text{var } \tilde{G}(t) &\approx \frac{8}{N^2} \left(\frac{1}{\eta} \int_{\eta\delta}^{\eta t/\gamma} \frac{du \cosh u}{\sinh^2 u} + \frac{5}{4} \cdot \frac{1}{2\eta} \int_{2\eta\delta}^{\eta t/\gamma} \frac{du \cosh u}{\sinh^2 u} \right) \\ &= \frac{8}{N^2\eta} \left(\frac{1}{\sinh \eta\delta} + \frac{5}{8 \sinh 2\eta\delta} - \frac{13}{8 \sinh \eta t/\gamma} \right). \end{aligned} \quad (4.33)$$

The variance in the plateau height is obtained by taking the late time limit of the above expression:

$$\text{var } \tilde{G}(\infty) \approx \left(\frac{\eta^2}{2\pi^2} \right)^2 \cdot \frac{8}{\eta} \left(\frac{1}{\sinh \eta\delta} + \frac{5}{8 \sinh 2\eta\delta} \right) \propto \eta^2, \quad (4.34)$$

where we have expanded in small η (large N) in the last expression. So the standard deviation in the plateau height divided by the mean (4.13) scales as $1/\log(1/\eta) \sim 1/\log N$. Note that the primary sources of the deviation are the ‘relatively short long strings’ with $n \gtrsim 1$.

We can also estimate the variance of the slope of the ramp. From (4.17), we recognize that after sufficient coarse-graining, $d\tilde{G}(t)/dt \propto N_{t/\gamma}/N$. Therefore,

$$\text{var} \left(\frac{d\tilde{G}(t)}{dt} \right) \propto \frac{\text{var } N_{t/\gamma}}{N^2} \propto \frac{\eta^4 \cosh(\eta t/\gamma)}{\sinh^2(\eta t/\gamma)}. \quad (4.35)$$

At central times in the ramp $t \sim \sqrt{N}$. Since $\eta \sim 1/\sqrt{N}$ this means that the hyperbolic functions on the right hand side are $O(1)$. So the standard deviation in the slope is $O(1/N)$. At central times in the ramp, we showed above that the slope is also $O(1/N)$. Thus the slope varies significantly between occupation number eigenstates.

However, a typical Ramond ground state is a *superposition* of these eigenstates. Since $\tilde{G}(t)$ is not an eigenvalue, but an expectation value of a quantum mechanical operator, it makes sense to discuss the variances among all ensemble members, including superpositions. Such a variance, with superposition states weighted with a uniform measure over $\mathbb{C}\mathbb{P}^{\exp S}$, was computed in [26]. This paper showed that the variance in the expectation value of a quantum mechanical operator is suppressed relative to the variance among its eigenstates by an extra factor of the dimension of the Hilbert space. Thus, all the variances computed in the preceding paragraphs receive an additional factor:

$$\text{var}_{\text{superpositions}} = e^{-S} \text{var}_{N_n \text{ eigenstates}} = e^{-2\pi\sqrt{2N}} \text{var}_{N_n \text{ eigenstates}}. \quad (4.36)$$

Thus we can conclude that over the entire Hilbert space, almost all states will show a coarse-grained two point function that lies very close to the results that we have computed in the typical state.

5 Discussion

We have studied the time-ordered two-point correlation function of certain operators in typical states of the Ramond sector of the D1-D5 CFT. At strong coupling these are black hole microstates and the theory is expected to be chaotic. Here, we studied the weak coupling

limit of this theory, where it is integrable. After temporal coarse-graining, the late time two-point function displays a characteristic dip, ramp and plateau. These features are remarkably similar to those seen in random matrix theory (RMT) and the SYK model, showing that the qualitative form does not specifically arise from the chaos present in those models.

A key quantitative difference is that the slopes of the ramps in RMT and SYK are constant, while in our model the slope decreases with time. Also, while the RMT and SYK plateaus are exponentially suppressed in the entropy S , our plateau scales as $\log S/S$. Finally, the plateau in RMT and SYK is reached at a time that is exponential in the entropy, while in our case it is reached at times proportional to the entropy.

These quantitative differences arise from the different structures of the excitation spectra. In a chaotic theory the energy eigenvalues are typically non-degenerate and have spacings that are exponentially small in the entropy. Random matrix theories also demonstrate a phenomenon of spectral rigidity, in which repulsion between eigenvalues of the Hamiltonian produces long-range correlations in the spectrum. The exponentially small gap leads to the exponentially large plateau time, and the linear ramp is partially a consequence of the spectral rigidity [16]. By contrast, although the D1-D5 theory at the orbifold point has a dense spectrum, there is a very large degeneracy of each energy level and the gaps are not exponentially small. This leads to a much shorter timescale for the plateau. The plateau is also much higher because the theory explores its phase space less completely than a chaotic model.

The authors of [27] argue that in general 2d CFTs, the dip occurs at times proportional to the entropy. Likewise the authors of [28] predict a breakdown of the semiclassical description of the two point function at entropy times. (See also [29] for related work in the context of the D1-D5 system.) In contrast, the location of our dip scales with the entropy as \sqrt{S} . The reason for the difference is that all of these works address finite temperature states, and require generalization to apply to the zero temperature, large entropy system that we examine.¹⁰ It would also be useful to see what the results in [27, 28] imply for the late time, finite temperature two-point function in the orbifold D1-D5 theory.

It would be very interesting to see how these phenomena change as the D1-D5 theory is deformed from the integrable point that we studied to the strongly coupled region where it is expected to be chaotic and dual to weakly coupled AdS₃ gravity. One strategy for making progress is to turn on this marginal deformation perturbatively [30], although it may be challenging to sum the perturbation series with sufficient accuracy to capture the late time physics. Another interesting avenue is to consider correlation functions of twist operators that induce interaction between the long string components of the state. The resulting mixing should break degeneracies between energy levels and lead to much smaller gaps. This will in turn lead to much longer timescales for the ramp and the plateau in the two point function.

¹⁰In SYK, the range of parameters where there is both chaotic behavior and IR conformal symmetry is $1 \ll \beta J \ll N$, where β is the inverse temperature and J is the coupling [11]. We see that in the zero temperature limit we need to switch off the coupling to stay in this regime. Our situation is somewhat similar to this.

Acknowledgments

We thank Paweł Caputa, Federico Galli, Aitor Lewkowycz, Alex Maloney, Márk Mezei, Onkar Parrikar, Charles Rabideau and Douglas Stanford for helpful discussions. This work was supported in part by a grant from the Simons Foundation (#385592, Vijay Balasubramanian) through the It From Qubit Simons Collaboration, by the U.S. Department of Energy under contract DOE DE-FG02-05ER-41367, by the Belgian Federal Science Policy Office through the Interuniversity Attraction Pole P7/37, by FWO-Vlaanderen through projects G020714N and G044016N, and by Vrije Universiteit Brussel through the Strategic Research Program “High-Energy Physics”. The work of B. Czech is supported by the Peter Svennilsson Membership in the Institute for Advanced Study.

A D1-D5 two-point functions echo the spectral form factor

To highlight the similarity between

$$\hat{G}(t) = \frac{1}{N} \sum_{n=1}^N n N_n \sum_{k=0}^{n-1} \frac{\sin^4 \frac{t}{2}}{n^4 \sin^2 \left(\frac{t+2\pi k}{2n} \right) \sin^2 \left(\frac{t-2\pi k}{2n} \right)} \equiv \frac{1}{N} \sum_{n=1}^N N_n C_n(t) \quad (\text{A.1})$$

and the spectral form factor, we start by noting that

$$\frac{\sin \frac{t}{2}}{\sin \left(\frac{t-2\pi k}{2n} \right)} = (-1)^k \frac{q^n - q^{-n}}{q - q^{-1}} = (-1)^k \sum_{\ell=0}^{n-1} q^{2\ell+1-n} = (-1)^k \sum_{\ell=0}^{n-1} e^{i \frac{t-2\pi k}{2n} (2\ell+1) - i \frac{t-2\pi k}{2}}, \quad (\text{A.2})$$

where $q = \exp \left(i \frac{t-2\pi k}{2n} \right)$. Substituting into (A.1) yields

$$C_n(t) = \frac{1}{n^3} \sum_{\ell_1, \ell_2, \ell'_1, \ell'_2=0}^{n-1} e^{i \frac{\ell_1 + \ell'_1 - \ell_2 - \ell'_2}{n} t} \mathcal{G}_n(\ell_1 + \ell'_1 + \ell_2 + \ell'_2 + 2) \quad (\text{A.3})$$

with

$$\mathcal{G}_n(x) = \sum_{k=0}^{n-1} e^{2\pi i \left(2 - \frac{x}{n} \right) k} = \frac{e^{-2\pi i x} - 1}{e^{-2\pi i \frac{x}{n}} - 1}. \quad (\text{A.4})$$

Because x only takes integer values in (A.3), we effectively have $\mathcal{G}_n(x) = \sum_{q \in \mathbb{Z}} n \delta_{qn, x}$, which is eq. (4.5) in the main text.

Since the summand in (A.3) depends only on the combinations $m_1 = \ell_1 + \ell'_1$ and $m_2 = \ell_2 + \ell'_2$, we change two of the summation variables to these new variables. We exchange the sums according to

$$\sum_{\ell_1=0}^{n-1} \sum_{m_1=\ell_1}^{\ell_1+n-1} = \sum_{m_1=0}^{n-1} \sum_{\ell_1=0}^{m_1} + \sum_{m_1=n}^{2n-2} \sum_{\ell_1=m_1-n+1}^{n-1} = \sum_{m_1=0}^{n-1} (m_1+1) + \sum_{m_1=n}^{2n-2} (2n-1-m_1), \quad (\text{A.5})$$

where in the last step we perform the ℓ_1 sums as the (suppressed) summand does not depend on it. After a similar manipulation for ℓ_2 and m_2 , we find

$$C_n(t) = \frac{1}{n^3} \sum_{m_1=0}^{2n-2} \sum_{m_2=0}^{2n-2} \rho_n(m_1) \rho_n(m_2) e^{i t \frac{(m_1 - m_2)}{n}} \mathcal{G}_n(m_1 + m_2 + 2), \quad (\text{A.6})$$

where the spectral weights are given by

$$\rho_n(m) = \begin{cases} m + 1 & m < n \\ 2n - 1 - m & m \geq n. \end{cases} \quad (\text{A.7})$$

We plot this function in figure 6.

B More detailed ramp estimate

For all except very small values of n , the quantities $\tilde{C}_n(t)$ defined in (4.16) show a universal behavior.¹¹ Following a rapid decay from their initial values, the $\tilde{C}_n(t)$ hover near zero for a time $\sim 0.67n\pi$. At that time, the even n quantities undergo one sharp jump to near their asymptotic value of $3/2$ and, thereafter, many smaller jumps and gentle decays that keep the $\tilde{C}_n(t)$ near $3/2$. For odd n , the $\tilde{C}_n(t)$ rise to near their asymptotic value of 1 in two distinct sharp jumps that happen at approximately $0.67n\pi$ and $1.34n\pi$, also followed by many smaller jumps and gentle decays which keep the $\tilde{C}_n(t)$ near 1 . We have not derived these statements analytically, but they are manifest from the plots in figure 9.

As a coarse approximation to the time dependence of $\tilde{G}(t)$, we may model the $\tilde{C}_n(t)$ as simple step functions:

$$C_{n \text{ even}} = \frac{3}{2}\Theta(t - 0.67n\pi) \quad \text{and} \quad C_{n \text{ odd}} = 0.54\Theta(t - 0.67n\pi) + 0.46\Theta(t - 1.34n\pi). \quad (\text{B.1})$$

In this treatment, the ramp is built up as successive modes shoot up from zero to their final values. This leads to

$$\tilde{G}(t) \approx \frac{1}{N} \left(\frac{3}{2} \sum_{n \text{ even}}^{t/0.67\pi} N_n + 0.54 \sum_{n \text{ odd}}^{t/0.67\pi} N_n + 0.46 \sum_{n \text{ odd}}^{t/1.34\pi} N_n \right). \quad (\text{B.2})$$

As a next step, we substitute the occupation numbers for the typical state and replace the sums with integrals. After these approximations, it will not be meaningful to keep track of the various $\mathcal{O}(1)$ coefficients appearing in (B.2). Thus, we introduce a single $\mathcal{O}(1)$ coefficient γ that parameterizes the average rate at which the successive modes join the ramp:

$$\tilde{G}(t) \approx \frac{1}{N} \cdot \frac{5}{4} \sum_{n=1}^{t/\gamma} \frac{8}{\sinh \eta n} \approx \frac{10}{N\eta} \int_{\delta\eta}^{t\eta/\gamma} \frac{du}{\sinh u} = \frac{10}{N\eta} \log \frac{\tanh t\eta/2\gamma}{\tanh \delta\eta/2}. \quad (\text{B.3})$$

The factor of $5/4$ is the average height of the jumps undergone by the even ($3/2$) and odd ($1 = 0.54 + 0.46$) modes. Since $N = 2\pi^2/\eta^2 \gg 1$, this reduces to:

$$\tilde{G}(t) \approx \frac{5\eta}{\pi^2} \log \left(\frac{2}{\delta\eta} \tanh \frac{t\eta}{2\gamma} \right). \quad (\text{B.4})$$

¹¹Most features we discuss are clearly discernible already at $n \gtrsim 10$. We will not need to set the range of n more precisely, because our use of the grand canonical ensemble and approximating sums by integrals are greater sources of error.

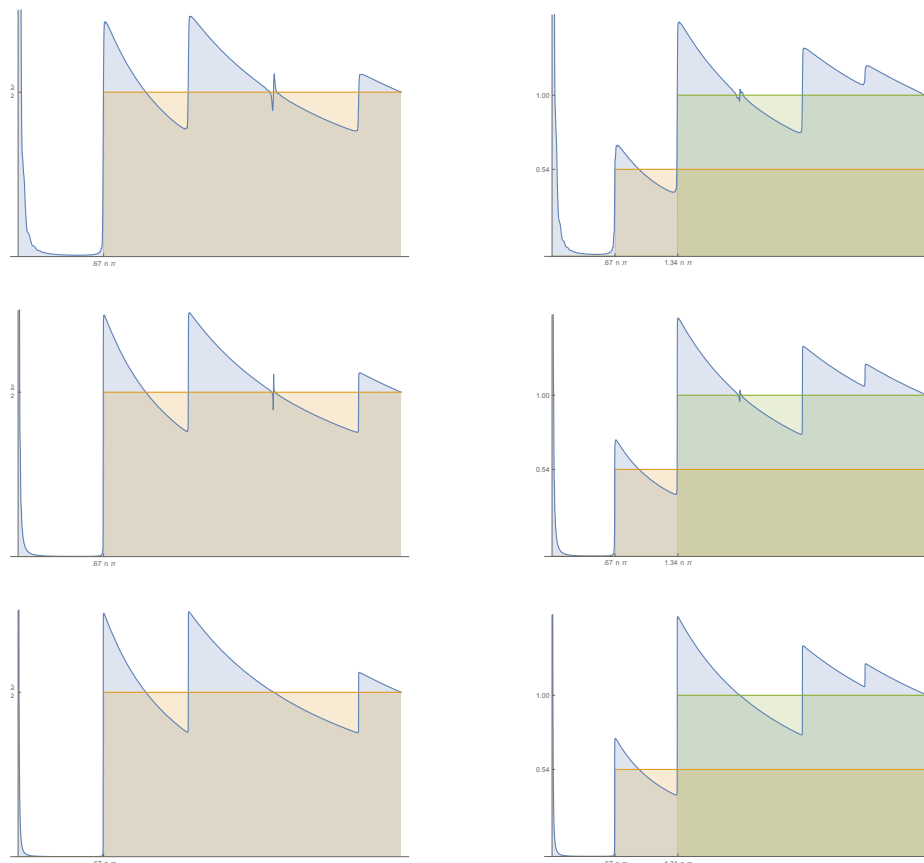


Figure 9. The progressively time-averaged correlator contributions of individual modes $\tilde{C}_n(t)$ for even n (left; $n = 100, 500, 1500$) and odd n (right; $n = 101, 501, 1501$). We have also marked the Θ -functions from eq. (B.1).

Open Access. This article is distributed under the terms of the Creative Commons Attribution License ([CC-BY 4.0](https://creativecommons.org/licenses/by/4.0/)), which permits any use, distribution and reproduction in any medium, provided the original author(s) and source are credited.

References

- [1] Y. Sekino and L. Susskind, *Fast Scramblers*, *JHEP* **10** (2008) 065 [[arXiv:0808.2096](https://arxiv.org/abs/0808.2096)] [[INSPIRE](#)].
- [2] S.H. Shenker and D. Stanford, *Black holes and the butterfly effect*, *JHEP* **03** (2014) 067 [[arXiv:1306.0622](https://arxiv.org/abs/1306.0622)] [[INSPIRE](#)].
- [3] J. Polchinski, *Chaos in the black hole S-matrix*, [arXiv:1505.08108](https://arxiv.org/abs/1505.08108) [[INSPIRE](#)].
- [4] O. Bohigas, M.J. Giannoni and C. Schmit, *Characterization of chaotic quantum spectra and universality of level fluctuation laws*, *Phys. Rev. Lett.* **52** (1984) 1 [[INSPIRE](#)].
- [5] J.M. Maldacena, *Eternal black holes in anti-de Sitter*, *JHEP* **04** (2003) 021 [[hep-th/0106112](https://arxiv.org/abs/hep-th/0106112)] [[INSPIRE](#)].

- [6] K. Papadodimas and S. Raju, *Local Operators in the Eternal Black Hole*, *Phys. Rev. Lett.* **115** (2015) 211601 [[arXiv:1502.06692](#)] [[INSPIRE](#)].
- [7] K. Papadodimas and S. Raju, *Remarks on the necessity and implications of state-dependence in the black hole interior*, *Phys. Rev. D* **93** (2016) 084049 [[arXiv:1503.08825](#)] [[INSPIRE](#)].
- [8] S. Sachdev and J. Ye, *Gapless spin fluid ground state in a random, quantum Heisenberg magnet*, *Phys. Rev. Lett.* **70** (1993) 3339 [[cond-mat/9212030](#)] [[INSPIRE](#)].
- [9] A. Kitaev, *A simple model of quantum holography*, seminar at KITP, (2015) [<http://online.kitp.ucsb.edu/online/entangled15/kitaev/>] [<http://online.kitp.ucsb.edu/online/entangled15/kitaev2/>].
- [10] J. Polchinski and V. Rosenhaus, *The Spectrum in the Sachdev-Ye-Kitaev Model*, *JHEP* **04** (2016) 001 [[arXiv:1601.06768](#)] [[INSPIRE](#)].
- [11] J. Maldacena and D. Stanford, *Remarks on the Sachdev-Ye-Kitaev model*, *Phys. Rev. D* **94** (2016) 106002 [[arXiv:1604.07818](#)] [[INSPIRE](#)].
- [12] K. Jensen, *Chaos in AdS₂ Holography*, *Phys. Rev. Lett.* **117** (2016) 111601 [[arXiv:1605.06098](#)] [[INSPIRE](#)].
- [13] J. Maldacena, D. Stanford and Z. Yang, *Conformal symmetry and its breaking in two dimensional Nearly Anti-de-Sitter space*, *PTEP* **2016** (2016) 12C104 [[arXiv:1606.01857](#)] [[INSPIRE](#)].
- [14] J. Engelsöy, T.G. Mertens and H. Verlinde, *An investigation of AdS₂ backreaction and holography*, *JHEP* **07** (2016) 139 [[arXiv:1606.03438](#)] [[INSPIRE](#)].
- [15] M. Cvetič and I. Papadimitriou, *AdS₂ holographic dictionary*, *JHEP* **12** (2016) 008 [Erratum *ibid.* **01** (2017) 120] [[arXiv:1608.07018](#)] [[INSPIRE](#)].
- [16] J.S. Cotler et al., *Black Holes and Random Matrices*, [arXiv:1611.04650](#) [[INSPIRE](#)].
- [17] A.M. García-García and J.J.M. Verbaarschot, *Spectral and thermodynamic properties of the Sachdev-Ye-Kitaev model*, *Phys. Rev. D* **94** (2016) 126010 [[arXiv:1610.03816](#)] [[INSPIRE](#)].
- [18] A. Strominger and C. Vafa, *Microscopic origin of the Bekenstein-Hawking entropy*, *Phys. Lett. B* **379** (1996) 99 [[hep-th/9601029](#)] [[INSPIRE](#)].
- [19] J.M. Maldacena, *The large-N limit of superconformal field theories and supergravity*, *Int. J. Theor. Phys.* **38** (1999) 1113 [[hep-th/9711200](#)] [[INSPIRE](#)].
- [20] J.M. Maldacena and A. Strominger, *AdS₃ black holes and a stringy exclusion principle*, *JHEP* **12** (1998) 005 [[hep-th/9804085](#)] [[INSPIRE](#)].
- [21] V. Balasubramanian, P. Kraus and M. Shigemori, *Massless black holes and black rings as effective geometries of the D1 – D5 system*, *Class. Quant. Grav.* **22** (2005) 4803 [[hep-th/0508110](#)] [[INSPIRE](#)].
- [22] R. Prange, *The spectral form factor is not self-averaging*, *Phys. Rev. Lett.* **78** (1997) 2280 [[chao-dyn/9606010](#)].
- [23] F. Haake, H.-J. Sommers and J. Weber, *Fluctuations and ergodicity of the form factor of quantum propagators and random unitary matrices*, *J. Phys. A* **32** (1999) 6903 [[chao-dyn/9906024](#)].
- [24] F.J. Dyson, *Statistical theory of the energy levels of complex systems. II*, *J. Math. Phys.* **3** (1962) 157.

- [25] E. Brézin and S. Hikami, *Spectral form factor in a random matrix theory*, *Phys. Rev.* **E 55** (1997) 4067 [[cond-mat/9608116](#)].
- [26] V. Balasubramanian, B. Czech, V.E. Hubeny, K. Larjo, M. Rangamani and J. Simon, *Typicality versus thermality: An analytic distinction*, *Gen. Rel. Grav.* **40** (2008) 1863 [[hep-th/0701122](#)] [[INSPIRE](#)].
- [27] E. Dyer and G. Gur-Ari, *2D CFT Partition Functions at Late Times*, [arXiv:1611.04592](#) [[INSPIRE](#)].
- [28] A.L. Fitzpatrick, J. Kaplan, D. Li and J. Wang, *On information loss in AdS_3/CFT_2* , *JHEP* **05** (2016) 109 [[arXiv:1603.08925](#)] [[INSPIRE](#)].
- [29] A. Galliani, S. Giusto, E. Moscato and R. Russo, *Correlators at large c without information loss*, *JHEP* **09** (2016) 065 [[arXiv:1606.01119](#)] [[INSPIRE](#)].
- [30] Z. Carson, S. Hampton and S.D. Mathur, *Full action of two deformation operators in the $D1D5$ CFT*, [arXiv:1612.03886](#) [[INSPIRE](#)].



Conformal Flow on S^3 and Weak Field Integrability in AdS_4

Piotr Bizon^{1,4}, Ben Craps², Oleg Evnin^{2,3}, Dominika Hunik¹, Vincent Luyten², Maciej Maliborski⁴

¹ Institute of Physics, Jagiellonian University, Kraków, Poland.

E-mail: bizon@th.if.uj.edu.pl; dominika.hunik@uj.edu.pl

² Theoretische Natuurkunde, Vrije Universiteit Brussel and The International Solvay Institutes, Brussels, Belgium. E-mail: Ben.Craps@vub.ac.be; Vincent.Luyten@vub.ac.be

³ Department of Physics, Faculty of Science, Chulalongkorn University, Bangkok, Thailand.

E-mail: oleg.evnin@gmail.com

⁴ Max-Planck-Institut für Gravitationsphysik, Albert-Einstein-Institut, Golm, Germany.

E-mail: maciej.maliborski@aei.mpg.de

Received: 30 August 2016 / Accepted: 20 March 2017

Published online: 13 May 2017 – © The Author(s) 2017. This article is an open access publication

Abstract: We consider the conformally invariant cubic wave equation on the Einstein cylinder $\mathbb{R} \times S^3$ for small rotationally symmetric initial data. This simple equation captures many key challenges of nonlinear wave dynamics in confining geometries, while a conformal transformation relates it to a self-interacting conformally coupled scalar in four-dimensional anti-de Sitter spacetime (AdS_4) and connects it to various questions of AdS stability. We construct an effective infinite-dimensional time-averaged dynamical system accurately approximating the original equation in the weak field regime. It turns out that this effective system, which we call the *conformal flow*, exhibits some remarkable features, such as low-dimensional invariant subspaces, a wealth of stationary states (for which energy does not flow between the modes), as well as solutions with nontrivial exactly periodic energy flows. Based on these observations and close parallels to the cubic Szegő equation, which was shown by Gérard and Grellier to be Lax-integrable, it is tempting to conjecture that the conformal flow and the corresponding weak field dynamics in AdS_4 are integrable as well.

1. Introduction

Propagation of nonlinear waves in confining geometries presents significant challenges because the key mechanism stabilizing the evolution of waves on unbounded domains, which is the dispersion of energy by radiation, is missing in confined settings. Consequently, an arbitrarily small perturbation of a ground state can lead to complicated long-time behavior. The central physical problem in this context is that of energy transfer, namely, understanding how the energy injected into the system gets distributed over the degrees of freedom in the course of its evolution. This problem has been studied in the physics literature from a statistical viewpoint under the name of wave (weak) turbulence [1, 2], but it has only recently emerged as an active research topic in dispersive PDE theory. In this deterministic mathematical approach, the energy cascades from low to high modes are quantified by the growth of higher Sobolev norms of solutions, and

the main question is whether these norms can become unbounded in finite or infinite time. The past few years have witnessed significant progress in the understanding of this issue in the context of nonlinear Schrödinger equations (and their variations) on tori [3–5]. However, almost nothing is known, as far as we can tell, about manifestations of these phenomena in other interesting evolution equations of mathematical physics.

Our attention in this article will be focused on the weak field dynamics for the conformally invariant cubic wave equation on the three-sphere. This very natural geometrical model describes relativistic scalar waves propagating on a compact manifold and interacting with the background geometry and among themselves. The spherical geometry prevents the waves from dispersing to infinity and thus ensures that the nonlinear self-interactions remain important for all times, inducing complicated energy transfer patterns. Another important circumstance is that all normal mode frequencies of the corresponding linearized theory are integer in appropriate units. Such a fully resonant spectrum ensures that nonlinearities can produce significant effects over long times for arbitrarily small perturbation amplitudes, generating highly nontrivial weak field dynamics.

The weak field dynamics of the system we are considering is closely related to investigations of nonlinear stability of anti-de Sitter (AdS) spacetime initiated in [6] (see [7, 8] for brief reviews and further references). A conformal transformation relates our considerations to the dynamics of the cubic Klein–Gordon equation with mass $m^2 = -2$ (conformally coupled self-interacting probe scalar) on the four-dimensional AdS space. In contrast to the bulk of AdS stability research, we do not consider the backreaction of perturbations on the AdS geometry. However, a number of features of the weak field dynamics remain unaffected by our simplification. (The weak field dynamics of a massless self-interacting probe scalar in AdS was introduced as a toy model for the AdS stability problem in [9].)

Our main tool for analyzing the weak field dynamics, given a fully resonant spectrum of the linearized system, is the time averaging method that goes back to Bogoliubov and Krylov and is described in many books on perturbation theory (e.g., [10]). For a contemporary treatment adapted to studies of nonlinear PDEs, see [11]. Applied to the PDE we are considering, the time averaging method produces a simplified infinite-dimensional dynamical system, which we shall refer to as the *conformal flow*. By standard theorems underlying time averaging, this effective system (in PDE theory sometimes called the *resonant* system) accurately approximates the dynamics of the original PDE for small amplitude fields of order $O(\varepsilon)$ on long time-scales of order $O(1/\varepsilon^2)$, and in particular it accurately captures the energy transfer patterns on such time scales. (Time averaging and related techniques were introduced to the AdS stability problem closely related to our current studies in [12–14].) The conformal flow displays a number of highly special features not apparently present in the original PDE and suggestive of integrability. This includes additional conserved quantities, low-dimensional invariant subspaces, a variety of stationary states without any energy transfer, as well as solutions with exactly periodic energy transfer patterns.

Our original PDE can be viewed as an infinite system of oscillators with integer frequencies and a quartic potential. We do not see any indications that it might be integrable; only the time-averaged system describing its weak field dynamics displays signs of integrability. While extensive searches for quartic integrable systems (i.e., integrable mechanical analogs of our original PDE) have been conducted in the past (see [15] for a review and references to earlier work and [16, 17] for some later contributions), we are

not aware of any broad scans for systems displaying *weak field integrability* of the type suggested by our results.

The conformal flow introduced in this paper bears a strong resemblance to the cubic Szegő equation that has been designed and studied in a series of papers by Gérard and Grellier, of which [18–21] are particularly relevant for our purposes. This equation also emerges as the resonant approximation of a nonlocal transport equation, called the cubic half-wave equation [19], which is a special case of one-dimensional models of wave turbulence introduced in [22]. In [18–21] and related publications, a number of remarkable properties were established for the cubic Szegő equation, in particular, a Lax pair structure, existence of finite-dimensional invariant subspaces, as well as some weak turbulence phenomena. The bulk of our effort will be directed at recovering analogs of a subset of these results for the conformal flow, a system with a natural geometric origin. We furthermore believe that the analogy goes deeper than what we are able to explicitly demonstrate in this article.

There are also close similarities between the conformal flow and resonant approximations for the cubic Schrödinger equation, either with harmonic trapping [23] or in the infinite volume limit on the 2-dimensional torus [24,25]. Another system that shares some properties with the conformal flow and the cubic Szegő equation is the Lowest Landau Level evolution equation, which appears in the studies of rapidly rotating Bose-Einstein condensates (see [26] and references therein). We furthermore mention the curious case of the Charney–Hasegawa–Mima (CHM) equation explored in [11]. Also in that case, effective integrable dynamics emerges in the time-averaged approximation (which the authors call the ‘effective equation’). However, a substantial difference is that the linearized spectrum of the CHM equation is not fully resonant and splits into disconnected resonant clusters. In such a situation, the resulting effective time-averaged system literally separates into independent finite-dimensional integrable subsystems. This simplification does not happen in our case because our linearized spectrum is fully resonant.

We comment on how our work is related to extensive investigations of the last decade in the area of ‘AdS/CFT Integrability’ (see [27] for a review). One of the central ingredients of that line of research is integrability of sigma models (describing string world-sheets) on target spaces involving AdS factors. While we are also presently talking about integrability emerging due to special features of the AdS geometry, there are also essential differences. We are considering a field system evolving in AdS, rather than a sigma model (whose fields are maps from a two-dimensional surface into AdS). We are furthermore not talking about exact integrability of our AdS field system, but rather about the integrability of the effective weak field theory (conformal flow) emerging from it within the standard time-averaged approximation.

Our exposition is organized as follows. In Sect. 2, we formulate our scalar field dynamics on a three-sphere, describe its connection to AdS stability problems and apply time averaging to derive the corresponding effective system, which we name the conformal flow. In Sect. 3, we give a very elementary pragmatic summary of some properties of the cubic Szegő equation relevant in our context, aimed mostly at the physics audience. In Sect. 4, we construct a three-dimensional invariant subspace of the conformal flow and discuss some complex plane properties of the generating functions that encode the conformal flow amplitudes. In Sect. 5, we analyze stationary states of the conformal flow, in which the initial conditions are adjusted to ensure that no energy transfer occurs. In Sect. 6, we exhibit explicit solutions with periodic energy flows on the three-dimensional invariant subspace of the conformal flow and discuss their properties. Finally, in Sect. 7,

we give a summary of what we have practically demonstrated and an outlook on more ambitious directions, keeping the likelihood of Lax-integrability in mind.

2. Conformally Coupled Scalar Field on the Einstein Cylinder and in AdS₄ and Its Weak Field Dynamics

As a simple model of confining geometry we consider the Einstein cylinder, which is the globally hyperbolic spacetime (\mathcal{M}, g) with topology $\mathbb{R} \times \mathbb{S}^3$ and metric

$$g = -dt^2 + r^2 \left(dx^2 + \sin^2 x d\omega^2 \right), \tag{1}$$

where $x \in [0, \pi]$, $d\omega^2$ is the round metric on the unit 2-sphere and r is the radius of \mathbb{S}^3 . This spacetime has a constant scalar curvature $R(g) = 6/r^2$.

As a model of nonlinear dynamics on \mathcal{M} , we consider the semilinear wave equation for the real scalar field $\phi : \mathcal{M} \mapsto \mathbb{R}$

$$\left(\square_g - \frac{1}{6} R(g) \right) \phi - \lambda \phi^3 = 0, \tag{2}$$

where $\square_g := g^{\mu\nu} \nabla_\mu \nabla_\nu$ is the wave operator associated with g and λ is a constant. For concreteness, we assume that $\lambda > 0$ (which corresponds to a defocusing nonlinearity); however, in the small data regime that we focus upon here, all the results below hold true in the focusing case $\lambda < 0$ as well. Due to the identity

$$\left(\square_{\Omega^2 g} - \frac{1}{6} R(\Omega^2 g) \right) (\Omega^{-1} \phi) = \Omega^{-3} \left(\square_g - \frac{1}{6} R(g) \right) \phi, \tag{3}$$

Eq. (2) is conformally invariant. After rescaling $t \rightarrow t/r$ and $\phi \rightarrow r\sqrt{\lambda} \phi$, it takes the dimensionless form

$$\phi_{tt} - \Delta_{\mathbb{S}^3} \phi + \phi + \phi^3 = 0, \tag{4}$$

which can be interpreted as the cubic Klein–Gordon equation on the unit \mathbb{S}^3 with a unit mass. For simplicity, we shall restrict our analysis to rotationally symmetric fields, which depend only on (t, x) . Substituting $\phi(t, x) = v(t, x) / \sin(x)$ into (4) we obtain a nonlinear string equation

$$v_{tt} - v_{xx} + \frac{v^3}{\sin^2 x} = 0, \tag{5}$$

with Dirichlet boundary conditions $v(t, 0) = v(t, \pi) = 0$, which are enforced by regularity of $\phi(t, x)$ on \mathcal{M} .

Remark 1. We could have arrived at the same equation considering the conformally coupled self-interacting scalar (2) in the 4-dimensional anti-de Sitter (AdS₄) spacetime with the metric

$$\tilde{g} = \frac{1}{\cos^2 x} \left(-dt^2 + dx^2 + \sin^2 x d\omega^2 \right), \tag{6}$$

where x varies between 0 and $\pi/2$. Indeed, $g = \cos^2 x \tilde{g}$, hence it follows from (3) that the field redefinition $\tilde{\phi}(t, x) = \phi(t, x) \cos x$ converts Eq. (2) from the Einstein cylinder to AdS. In order to define the evolution, one has to impose a boundary condition at $x = \pi/2$. Here, we shall impose the Dirichlet condition $\phi(\pi/2) = 0$ on the equator,

corresponding to the reflecting boundary conditions most commonly used in the AdS research context. This model is just a subsector of the model on the full Einstein cylinder, which can be implemented by imposing the reflection symmetry $\phi(t, x) = -\phi(t, \pi - x)$. We emphasize this connection because problems involving nonlinear dynamics of small AdS perturbations have received a significant amount of attention in recent years, and our objectives here have much in common with that body of work.

Our goal is to understand the evolution of small smooth initial data $v(0, x), \partial_t v(0, x)$. Decomposing the solution into a Fourier series,

$$v(t, x) = \sum_{n=0}^{\infty} c_n(t) \sin(n + 1)x, \tag{7}$$

we get from (5) an infinite system of coupled oscillators

$$\frac{d^2 c_n}{dt^2} + (n + 1)^2 c_n = - \sum_{jkl} S_{jkl n} c_j c_k c_l, \tag{8}$$

with the interaction coefficients

$$S_{jkl n} = \frac{2}{\pi} \int_0^\pi \frac{dx}{\sin^2 x} \sin(j + 1)x \sin(k + 1)x \sin(l + 1)x \sin(n + 1)x. \tag{9}$$

To factor out fast linear oscillations in (8), we change the variables using variation of constants

$$c_n = \beta_n e^{i(n+1)t} + \bar{\beta}_n e^{-i(n+1)t}, \tag{10}$$

$$\frac{dc_n}{dt} = i(n + 1) \left(\beta_n e^{i(n+1)t} - \bar{\beta}_n e^{-i(n+1)t} \right). \tag{11}$$

This transforms the system (8) into

$$2i(n + 1) \frac{d\beta_n}{dt} = - \sum_{jkl} S_{jkl n} c_j c_k c_l e^{-i(n+1)t}, \tag{12}$$

where each c_j in the sum is given by (10). Thus, each term in the sum has a factor $e^{-i\Omega t}$, where $\Omega = (n + 1) \pm (j + 1) \pm (k + 1) \pm (l + 1)$, with all the three plus-minus signs independent. The terms with $\Omega = 0$ correspond to resonant interactions, while those with $\Omega \neq 0$ are non-resonant.

Passing to slow time $\tau = \varepsilon^2 t$ and rescaling $\beta_n(t) = \varepsilon \alpha_n(\tau)$, we see that for ε going to zero the non-resonant terms $\propto e^{-i\Omega\tau/\varepsilon^2}$ are highly oscillatory, and therefore expected to be negligible (in a sense we are about to specify). Keeping only the resonant terms in (12) (which is equivalent to time-averaging), we obtain an infinite autonomous dynamical system

$$2i(n + 1) \frac{d\alpha_n}{d\tau} = -3 \sum_{jkl} S_{jkl n} \alpha_j \alpha_k \bar{\alpha}_l, \tag{13}$$

where the summation runs over the set of indices $\{j, k, l\}$ for which $\Omega = 0$. Evaluating the integrals for the S -coefficients, one finds that this set reduces to $\{jkl \mid j + k - l = n\}$ and for such resonant combinations of indices,

$$S_{jkl n} = \min(j, k, l, n) + 1. \tag{14}$$

Note that terms with $n = j + k + l + 2$ could have been present in principle, but the corresponding S -coefficients vanish, which can be verified by direct calculation. This is directly parallel to the selection rules that have been extensively discussed in the AdS stability literature [13, 14, 28, 29].

It is part of the standard lore in nonlinear perturbation theory that solutions to (12) starting from small initial data of size $\mathcal{O}(\varepsilon)$ are well approximated by solutions of (13) on timescales of order $\mathcal{O}(\varepsilon^{-2})$. More precisely, if $\beta_n(t)$ and $\alpha_n(\tau)$ are solutions of (12) and (13), respectively, and $\beta_n(0) = \varepsilon\alpha_n(0)$ for each n , then $|\beta_n(t) - \varepsilon\alpha_n(\tau(t))| \lesssim \mathcal{O}(\varepsilon^2)$ for $t \lesssim \mathcal{O}(\varepsilon^{-2})$. In other words, on this timescale the dynamics of solutions of Eq. (5) is dominated by resonant interactions. Straightforward proofs (normally phrased for systems with a finite number of degrees of freedom) can be found in textbooks on nonlinear perturbation theory, e.g., [10].

For convenience, we shall henceforth rescale τ to remove the numerical factors 2 and -3 from (13). Renaming so rescaled τ back to t and using $\dot{} = d/dt$, we finally arrive at the following system, which we call the *conformal flow*

$$i(n+1)\dot{\alpha}_n = \sum_{j=0}^{\infty} \sum_{k=0}^{n+j} [\min(n, j, k, n+j-k) + 1] \bar{\alpha}_j \alpha_k \alpha_{n+j-k}. \tag{15}$$

Remark 2. Note that the AdS formulation described in *Remark 1* simply corresponds to setting all even-numbered modes to 0, while only keeping odd-numbered modes α_{2m+1} with m running from 0 to infinity. It is easy to see that if one implements this constraint in (15) and expresses everything through the new mode counting index m , one gets back Eq. (15). Thus, the conformal flow is equally applicable to the dynamics in $\mathbb{R} \times \mathbb{S}^3$ and in AdS_4 .

The conformal flow (15) is Hamiltonian with

$$H = \sum_{n=0}^{\infty} \sum_{j=0}^{\infty} \sum_{k=0}^{n+j} [\min(n, j, k, n+j-k) + 1] \bar{\alpha}_n \bar{\alpha}_j \alpha_k \alpha_{n+j-k} \tag{16}$$

and symplectic form $\sum_n 2i(n+1) d\bar{\alpha}_n \wedge d\alpha_n$:

$$i(n+1)\dot{\alpha}_n = \frac{1}{2} \frac{\partial H}{\partial \bar{\alpha}_n}. \tag{17}$$

It enjoys the following one-parameter groups of symmetries (where λ, θ are real parameters):

$$\text{Scaling: } \alpha_n(t) \rightarrow \lambda \alpha_n(\lambda^2 t), \tag{18}$$

$$\text{Global phase shift: } \alpha_n(t) \rightarrow e^{i\theta} \alpha_n(t), \tag{19}$$

$$\text{Mode-dependent phase shift: } \alpha_n(t) \rightarrow e^{in\theta} \alpha_n(t). \tag{20}$$

The latter two symmetries respect the Hamiltonian structure and give rise to two conserved quantities (in addition to the Hamiltonian itself):

$$\text{‘Charge:’ } Q = \sum_{n=0}^{\infty} (n+1) |\alpha_n|^2, \tag{21}$$

$$\text{‘Linear energy:’ } E = \sum_{n=0}^{\infty} (n+1)^2 |\alpha_n|^2. \tag{22}$$

We emphasize that these two conservation laws have no obvious counterparts in the original wave equation (4). Their prototypes were presented in the AdS stability context in [9, 14].

3. An Elementary Introduction to the Cubic Szegő Equation

The main content of our current treatment will be in presenting a range of remarkably simple dynamical behaviors of the conformal flow system (15). In anticipation of these results, it is useful to contemplate for a moment the apparent special features of Eq. (15) itself.

One can trivially rewrite (15) as

$$i\dot{\alpha}_n = \sum_{j=0}^{\infty} \sum_{k=0}^{n+j} \frac{\min(n, j, k, n+j-k) + 1}{n+1} \bar{\alpha}_j \alpha_k \alpha_{n+j-k}. \tag{23}$$

One notable property of this representation is that many coefficients of the trilinear form on the right hand side are simply 1. Indeed, this happens for the contribution of any triplet of modes with all frequencies higher than the recipient mode n . It turns out useful to consider the following simpler equation, in which *all* numerical coefficients are set to 1,

$$i\dot{\alpha}_n = \sum_{j=0}^{\infty} \sum_{k=0}^{n+j} \bar{\alpha}_j \alpha_k \alpha_{n+j-k}. \tag{24}$$

We shall see that, while the systems (23) and (24) are distinct, their dynamics is qualitatively similar, with a number of parallels between the emerging algebraic structures.

Actually, the simplified system (24) is the Fourier representation of a simple paradifferential equation that has been studied before. To show this, let $u(t, e^{i\theta})$ be a complex function on the circle whose nonnegative Fourier coefficients are given by $\alpha_n(t)$ and negative Fourier coefficients vanish, i.e.

$$u(t, e^{i\theta}) = \sum_{n=0}^{\infty} \alpha_n(t) e^{in\theta}, \tag{25}$$

and assume that $\sum_{n=0}^{\infty} |\alpha_n|^2 < \infty$. Mathematically, this means that u belongs to the Hardy space on the circle $L^2_+(S^1) \subset L^2(S^1)$ [30]. Furthermore, we define an orthogonal projector $\Pi : L^2(S^1) \mapsto L^2_+(S^1)$ (called the Szegő projector) that filters out negative frequencies

$$\Pi \left(\sum_{n=-\infty}^{\infty} \alpha_n e^{in\theta} \right) := \sum_{n=0}^{\infty} \alpha_n e^{in\theta}. \tag{26}$$

Then, it is easy to see that the system (24) is equivalent to

$$i\partial_t u = \Pi(|u|^2 u). \tag{27}$$

This equation was introduced by Gérard and Grellier in [18] under the name of the cubic Szegő equation. They showed that this equation has a remarkably deep structure, including a Lax pair, finite-dimensional invariant subspaces and weakly turbulent solutions. We shall demonstrate below that the conformal flow exhibits at least some of this structure (in a modified form), and conjecture that the similarity goes even further. In view of these parallels, we shall present below a very elementary summary of the features of the cubic Szegő equation that are important to us. Readers interested in more details are referred to the original publications [18–21].

The cubic Szegő equation is Hamiltonian with

$$H = \sum_{n=0}^{\infty} \sum_{j=0}^{\infty} \sum_{k=0}^{n+j} \bar{\alpha}_n \bar{\alpha}_j \alpha_k \alpha_{n+j-k} = \frac{1}{2\pi} \int_0^{2\pi} |u|^4 d\theta \tag{28}$$

and symplectic form $\sum_n 2i d\bar{\alpha}_n \wedge d\alpha_n$, and has the same symmetries (18–20) as (15). Hence, it possesses two conserved quantities analogous to (21) and (22), in addition to the Hamiltonian itself:

$$M = \sum_{n=0}^{\infty} |\alpha_n|^2 = \frac{1}{2\pi} \int_0^{2\pi} |u|^2 d\theta, \tag{29}$$

$$P = \sum_{n=0}^{\infty} n |\alpha_n|^2 = \frac{1}{2\pi} \int_0^{2\pi} (-i \partial_\theta u) \bar{u} d\theta. \tag{30}$$

Borrowing terminology from studies of the nonlinear Schrödinger equation, we shall refer to these charges as ‘mass’ and ‘momentum,’ respectively.

Note that $M + P = \|u\|_{H_{1/2}}^2$, where $H_s \subset L^2_+$ is the Sobolev space on the circle equipped with the norm

$$\|u\|_{H_s}^2 = \sum_{n=0}^{\infty} (n + 1)^{2s} |\alpha_n(t)|^2. \tag{31}$$

This fact can be used to control the growth in time of higher Sobolev norms and thereby prove that the Cauchy problem for the Szegő equation is globally well posed for smooth initial data in H_s with $s > 1/2$ [18].

Any function $u(e^{i\theta})$ of the form (25) in $L^2_+(S^1)$ can be identified with a holomorphic function $u(z)$ inside the unit disk $|z| < 1$ in the complex plane [30], hence we can write

$$u(t, z) = \sum_{n=0}^{\infty} \alpha_n(t) z^n. \tag{32}$$

In terms of $u(t, z)$, the cubic Szegő equation (27) takes the form

$$i \partial_t u(t, z) = \frac{1}{2\pi i} \oint_{|w|=1} \frac{dw}{w - z} \tilde{u}(t, w) u(t, w)^2, \tag{33}$$

where

$$\tilde{u}(t, z) = \sum_{n=0}^{\infty} \bar{\alpha}_n z^{-n}. \tag{34}$$

General properties of the Cauchy-type integral appearing in (33) suggest the existence of meromorphic solutions for u with a finite number of isolated poles moving in the complex plane outside the unit disk. Indeed, it was shown in [18] that the cubic Szegő equation admits finite-dimensional invariant subspaces given by rational functions of arbitrarily high degree. Moreover, due to the Lax-integrability (and, consequently, infinitely many conserved quantities), the Szegő flow restricted to such subspaces is completely integrable in the sense of Liouville. The simplest invariant manifold with nontrivial dynamics is parametrized by the following single pole ansatz

$$u(t, z) = \frac{b(t) + a(t)z}{1 - p(t)z}, \quad |p| < 1. \tag{35}$$

We shall now demonstrate explicitly by elementary means that the subspace given by such functions is indeed dynamically invariant under the flow, and analyze its evolution. The Fourier coefficients corresponding to (35) are

$$\alpha_0 = b \quad \text{and} \quad \alpha_n = (a + bp)p^{n-1} \quad \text{for } n \geq 1. \tag{36}$$

Expressed through the parameters of our ansatz, the mass and momentum take the form

$$M = |b|^2 + \frac{|a + bp|^2}{1 - |p|^2}, \quad P = \frac{|a + bp|^2}{(1 - |p|^2)^2}. \tag{37}$$

Substitution of (35) into (33) produces exactly three distinct dependences on z on both sides, namely, $(1 - pz)^{-2}$, $(1 - pz)^{-1}$ and a z -independent term, resulting in the following three equations for $a(t)$, $b(t)$, and $p(t)$

$$i\dot{a} = Ma, \tag{38}$$

$$i\dot{b} = (M + P)b + Pa\bar{p}, \tag{39}$$

$$i\dot{p} = Mp + a\bar{b}, \tag{40}$$

where we used the conservations laws (37) to simplify some terms. These equations describe a three-dimensional Liouville-integrable system which can be easily solved (in [20] an explicit formula for the general solution was derived using harmonic analysis tools). One first integrates (38) to find a , whereupon the remaining equations become linear. The solution corresponding to initial conditions $a(0) = a_0$, $b(0) = b_0$, $p(0) = p_0$ (for simplicity assumed to be real) is

$$a(t) = a_0 e^{-iMt}, \tag{41}$$

$$b(t) = \left(b_0 \cos \omega t - i \frac{b_0(M + P) + 2a_0 p_0 P}{2\omega} \sin \omega t \right) e^{-\frac{i}{2}(M+P)t}, \tag{42}$$

$$p(t) = \left(p_0 \cos \omega t - i \frac{p_0(M + P) + 2a_0 b_0}{2\omega} \sin \omega t \right) e^{-\frac{i}{2}(M-P)t}, \tag{43}$$

where $\omega = \frac{1}{2}\sqrt{(M + P)^2 - 4Pa_0^2}$ and the expressions for M and P in terms of (a_0, b_0, p_0) are given in (37). Thus, the solution is quasiperiodic for all initial conditions, while the corresponding ‘mass’ spectrum,

$$|\alpha_0|^2 = M - P(1 - |p|^2) \quad \text{and} \quad |\alpha_n|^2 = P(1 - |p|^2)^2 |p|^{2(n-1)} \quad \text{for } n \geq 1, \tag{44}$$

is expressible through $|p|^2$ and the conserved quantities, and hence exactly periodic. In the special case $M = P = a_0^2$, we have $\omega = 0$ and then

$$a(t) = a_0 e^{-iMt}, \quad b(t) = -a_0 p_0 e^{-iMt}, \quad p(t) = p_0. \tag{45}$$

The evolution of two-mode initial data $a_0 = 1, b_0 = 2\varepsilon, p_0 = 0$ was used in [18] to illustrate a very interesting instability phenomenon. For these data, (43) gives

$$p(t) = -\frac{i}{\sqrt{1 + \varepsilon^2}} \sin(\omega t) e^{-2i\varepsilon^2 t}, \quad \omega = 2\varepsilon\sqrt{1 + \varepsilon^2}, \tag{46}$$

hence, in the regime of $\varepsilon \rightarrow 0, |p(t_n)| \sim 1 - \varepsilon^2/2$ for a sequence of times $t_n = \frac{n\pi}{2\omega}$, meaning that the energy goes periodically to arbitrarily high modes. Put differently, although all solutions are quasiperiodic, their radius of analyticity is not uniformly bounded from below. Note that (46) implies instability of the one-mode stationary state $u(t, z) = a_0 e^{-iMt} z$.

As mentioned above, one can consider more general meromorphic solutions with an arbitrary number of time-dependent simple poles outside the unit disk

$$u(t, z) = \sum_{k=1}^N \frac{b_k(t)}{1 - p_k(t)z}, \quad |p_k| < 1, \quad N \geq 2. \tag{47}$$

One can convince oneself that the ansatz is consistent in the sense that substituting it in (33) results only in z -dependences of the form $(1 - p_k z)^{-1}$ and $(1 - p_k z)^{-2}$ on both sides, producing $2N$ ordinary differential equations for the $2N$ functions b_k and p_k . It is possible to consistently impose $p_N = 0$, producing an ansatz with one parameter less. The single pole ansatz (35) is precisely of such a form. The equations of motion within the subspace defined by (47) were written down explicitly in [18]. As in the simplest case of the three-dimensional invariant subspace discussed above, the dynamics on all finite-dimensional invariant subspaces is Liouville-integrable and bounded, and hence quasiperiodic.

Among the quasiperiodic solutions there exist special solutions with time-independent amplitudes $|\alpha_n|$. Such solutions, which we call stationary states, were classified in [18] in the case of finite dimensional invariant manifolds. They are given by either finite Blaschke products

$$u(t, z) = c e^{-i|c|^2 t} \prod_{k=1}^N \frac{\bar{p}_k - z}{1 - p_k z}, \quad |p_k| < 1, \quad c \in \mathbb{C}, \tag{48}$$

or

$$u(t, z) = \frac{cz^\ell}{1 - p^N z^N} e^{-i\lambda t}, \quad p(t) = p(0) e^{-i\omega t}, \quad \lambda = \frac{|c|^2}{(1 - |p|^{2N})^2},$$

$$N\omega = \frac{|c|^2}{1 - |p|^{2N}}, \tag{49}$$

where $N \geq 1$ and $\ell \leq N - 1$ are nonnegative integers.

It was recently shown in [21] that outside the finite-dimensional invariant subspaces there exists a dense set of smooth solutions whose radius of analyticity tends to zero for a sequence of times $t_n \rightarrow \infty$. Consequently, the Sobolev norms with $s > 1/2$ are

unbounded. Such a weakly turbulent behavior is somewhat surprising in a completely integrable model. The coexistence of integrability and turbulence is possible because the infinitely many conserved quantities are too weak to control higher regularity properties of solutions.

4. Three-Dimensional Invariant Subspaces of the Conformal Flow

We now return to the conformal flow (15) and attempt to treat it along the lines applied above to the cubic Szegő equation. While the treatment is closely parallel, we shall be able to immediately recover only a part of the results available for the cubic Szegő equation. Using the generating function $u(t, z)$ and its conjugate $\tilde{u}(t, z)$ defined as in (32) and (34), we find that the system (15) is equivalent to the integro-differential equation

$$i \partial_t \partial_z(zu) = \frac{1}{2\pi i} \oint_{|w|=1} \frac{dw}{w} \tilde{u}(w) \left(\frac{wu(w) - zu(z)}{w - z} \right)^2. \tag{50}$$

The following summation formula has been used while obtaining this complex plane representation:

$$\begin{aligned} \sum_{j=0}^{\infty} \sum_{k=0}^{n+j} [\min(n, j, k, n + j - k) + 1] \rho^j \theta^k &= \frac{1 - \theta^{n+1}}{(1 - \theta)(1 - \rho)(1 - \theta\rho)} \\ &= \frac{1 + \theta + \dots + \theta^n}{(1 - \rho)(1 - \theta\rho)}. \end{aligned} \tag{51}$$

Derivations of (50) and (51) and further comments are given in Appendix A.

Although Eq. (50) looks like a somewhat more elaborate version of (33), we do not see an immediate way to characterize its meromorphic solutions and defer it to future work. Nonetheless, the lowest-dimensional nontrivial invariant subspace is easy to construct, as we shall explicitly demonstrate now.

The ansatz relevant for the three-dimensional invariant subspace, analogous to (36), is

$$\alpha_n = (b + an)p^n, \tag{52}$$

where b, a, p are complex-valued functions of time. The corresponding generating function has the following combination of poles outside the unit disk

$$u(t, z) = \frac{b(t) - a(t)}{1 - p(t)z} + \frac{a(t)}{(1 - p(t)z)^2} = \frac{b(t) + (a(t) - b(t))p(t)z}{(1 - p(t)z)^2}. \tag{53}$$

We note that the two-mode initial data ($\alpha_n = 0$ for $n \geq 2$) are accommodated within this ansatz as a special limiting case $p \rightarrow 0$ with b and $(a - b)p$ finite. All of our general statements about the dynamics on the three-dimensional invariant subspace apply to solutions starting with such initial configurations.

While we could have used the complex plane representation (50) to establish the validity of our ansatz, it is instructive to apply brute force summations in this case. Substitution of (52) into (15) yields

$$\begin{aligned}
 & i(1+n) \left(\dot{b} + \dot{a}n + n(b+an) \frac{\dot{p}}{p} \right) \\
 &= \sum_{j=0}^{\infty} \sum_{k=0}^{n+j} [\min(n, j, k, n+j-k) + 1] (\bar{b} + \bar{a}j)(b+ak)(b+a(n+j-k)) |p|^{2j}.
 \end{aligned} \tag{54}$$

Note that the p^n factor has consistently cancelled on the two sides. It remains to show that different n -dependences on both sides can be matched and produce a sufficiently small number of equations. All summations in (54) can be performed by applying the relation

$$\begin{aligned}
 & \sum_{j=0}^{\infty} \sum_{k=0}^{n+j} [\min(n, j, k, n+j-k) + 1] j^K k^L |p|^{2j} \\
 &= (\rho \partial_{\rho})^K (\theta \partial_{\theta})^L \frac{1 + \theta + \dots + \theta^n}{(1 - \rho)(1 - \theta\rho)} \Big|_{\substack{\theta=1 \\ \rho=|p|^2}},
 \end{aligned} \tag{55}$$

which follows from (51). While we give explicit expressions for the sums involved in (54) in Appendix B, the only thing one needs to know about these sums to establish the validity of our ansatz is that they are all polynomials of degree L in n , times $(n+1)$, the latter factor coming from Faulhaber’s sums $1 + 2^l + \dots + n^l$, with $l \leq L$, originating from $1 + \theta + \dots + \theta^n$ in (55). Therefore, explicit counting tells us that, upon substituting the summation formulas of Appendix B in (54), the factor $(n+1)$ will cancel on the two sides, leaving behind a statement that two quadratic polynomials in n equal each other. Matching the coefficients of these polynomials produces three ordinary differential equations for three functions b, a, p , confirming the validity of our ansatz.

The explicit equations for b, a and p are given by

$$\frac{i \dot{p}}{(1+y)^2} = \frac{p}{6} \left(2y|a|^2 + \bar{b}a \right), \tag{56}$$

$$\frac{i \dot{a}}{(1+y)^2} = \frac{a}{6} \left(5|b|^2 + (18y^2 + 4y)|a|^2 + (6y - 1)\bar{b}a + 10y\bar{a}b \right), \tag{57}$$

$$\frac{i \dot{b}}{(1+y)^2} = b \left(|b|^2 + (6y^2 + 2y)|a|^2 + 2yb\bar{a} \right) + a \left(2y|b|^2 + (4y + 2)y^2|a|^2 + y^2\bar{b}a \right), \tag{58}$$

where we have introduced the following notation, which will turn out to be useful later:

$$y = \frac{|p|^2}{1 - |p|^2}. \tag{59}$$

The conservation laws (21) and (22) take the form

$$Q = (1+y)^2 \left(|b|^2 + 4y \operatorname{Re}(\bar{b}a) + 2y(3y+1)|a|^2 \right), \tag{60}$$

$$E = (1+y)^2 \left((1+2y)|b|^2 + 4y(3y+2) \operatorname{Re}(\bar{b}a) + 4y(6y^2+6y+1)|a|^2 \right). \tag{61}$$

We remark that if $u(t, z)$ is a solution of the conformal flow, so is $z^N u(t, z^{N+1})$ for any non-negative integer N . This automatically generates an infinite number of other three-dimensional invariant subspaces of the conformal flow, in which only subsets of modes are activated.

We shall return to equations (56–58) in sect. 6, and analyze the dynamics within the three-dimensional dynamically invariant subspace (52) explicitly. Before proceeding in that direction, we shall discuss special solutions for which $|\alpha_n|$ are time-independent.

5. Stationary States

The conformal flow (15) admits solutions of the form

$$\alpha_n(t) = A_n e^{-i\lambda_n t}, \tag{62}$$

where the frequencies λ_n and complex amplitudes A_n are time-independent, and λ_n are linear in n , that is $\lambda_n = \lambda - n\omega$ for some real λ and ω . For such solutions there is no energy transfer between the modes, hence we call them *stationary states*. The cubic Szegő equation admits a variety of stationary states [18]; such solutions have also been considered in the context of AdS stability [12,31,32], where they were referred to as ‘quasiperiodic’ solutions.

Substituting (62) into (15) we get a nonlinear ‘eigenvalue’ problem

$$(n + 1)(\lambda - n\omega)A_n = \sum_{j=0}^{\infty} \sum_{k=0}^{n+j} [\min(n, j, k, n + j - k) + 1] \bar{A}_j A_k A_{n+j-k}. \tag{63}$$

The simplest solutions of this algebraic system, easily seen by inspection, $A_n = c \delta_{Nn}$, $\lambda = |c|^2$, $\omega = 0$ for $c \in \mathbb{C}$, give the one-mode stationary states for any non-negative integer N

$$\alpha_n = c \delta_{Nn} e^{-i|c|^2 t}. \tag{64}$$

We will see shortly that these trivial solutions are the endpoints of two-parameter families of stationary solutions. We note in passing that they are seeds for time-periodic solutions of the original equation (5) whose construction will be described elsewhere along the lines of [33].

Within the ansatz (52), stationary states take the form

$$b(t) = b(0)e^{-i\lambda t}, \quad a(t) = a(0)e^{-i\lambda t}, \quad p(t) = p(0)e^{i\omega t}. \tag{65}$$

Plugging this into the system (56–58), we obtain a system of algebraic equations that can be solved explicitly. The case $a(0) = 0$ yields

$$b(t) = c \exp\left(-\frac{i|c|^2 t}{(1 - |p|^2)^2}\right). \tag{66}$$

For this solution $Q = \frac{|c|^2}{(1 - |p|^2)^2}$, hence $\lambda = Q$. The corresponding generating function reads

$$u(t, z) = \frac{c}{1 - pz} e^{-i\lambda t}. \tag{67}$$

For nonzero a we get the following two-parameter family of stationary states with $\omega = 0$

$$b(0) = -2c|p|^2, \quad a(0) = c(1 - |p|^2), \quad \lambda = \frac{|c|^2|p|^2}{(1 - |p|^2)^2} \tag{68}$$

For this solution

$$Q = \frac{2|c|^2|p|^2}{(1 - |p|^2)^2}, \quad E = \frac{4|c|^2|p|^2(1 + |p|^2)}{(1 - |p|^2)^3}, \tag{69}$$

hence $\lambda = \frac{1}{2}Q$. The corresponding generating function reads

$$u(t, z) = c \frac{-2|p|^2 + (1 + |p|^2) pz}{(1 - pz)^2} e^{-i\lambda t}. \tag{70}$$

In addition, for $|p| \leq p_* := 2 - \sqrt{3} \approx 0.268$, there is a pair of two-parameter families of stationary states with nonzero ω . The range of $|p|$ is restricted by the condition that $\kappa := \sqrt{|p|^4 - 14|p|^2 + 1}$ should be real, so we have a tangential bifurcation at p_* . These two solutions (labelled by \pm) are given by

$$b_{\pm}(0) = -c(1 + 5|p|^2 \pm \kappa), \quad a_{\pm}(0) = 2c(1 - |p|^2), \tag{71}$$

$$\omega_{\pm} = \frac{|c|^2}{3} \frac{1 + |p|^2 \pm \kappa}{1 - |p|^2}, \tag{72}$$

$$\lambda_{\pm} = \frac{2|c|^2}{3} \left(\frac{3 - 4|p|^2}{1 - |p|^2} \pm \frac{(3 + 4|p|^2)\kappa}{(1 - |p|^2)^2} \right), \tag{73}$$

and their conserved quantities are

$$Q_{\pm} = \frac{6}{7}(\lambda_{\pm} + \omega_{\pm}), \quad E_{\pm} = 6\omega_{\pm}. \tag{74}$$

The corresponding generating function reads

$$u(t, z) = c \frac{-(1 + 5|p|^2 \pm \kappa) + (3 + 3|p|^2 \pm \kappa) pz}{(1 - pz)^2} e^{-i\lambda_{\pm} t}, \tag{75}$$

where $p(t) = p(0)e^{i\omega_{\pm} t}$.

Outside the three-dimensional invariant subspace given by (52) there exist many other stationary states. For instance, we verified that, in close parallel to the cubic Szegő equation, any finite Blaschke product

$$u(t, z) = c e^{-i|c|^2 t} \prod_{k=1}^N \frac{\bar{p}_k - z}{1 - p_k z} \tag{76}$$

yields a stationary state. There are also stationary states where only every N th mode is activated, for instance

$$u(t, z) = \frac{cz^{N-1}}{1 - p^N z^N} e^{-i\lambda t}, \quad \lambda = \frac{|c|^2}{(1 - |p|^2)^2}. \tag{77}$$

Remark 3. For all the above stationary states with $\omega = 0$ we have $\lambda = \frac{Q}{N+1}$, where N is the number of zeroes of the generating function (counted with multiplicity). It would be interesting to find a reason that underlies this ‘quantization’ structure.

It is well known that stationary states of Hamiltonian systems admit a variational characterization. In our case, it follows from the Hamilton equation (17) that stationary states (62) are the critical points of the functional

$$K := \frac{1}{2}H - \lambda Q + \omega(E - Q), \tag{78}$$

hence stationary states with $\omega = 0$ are extrema of H for fixed Q , while stationary states with nonzero ω are extrema of H for fixed Q and E . This fact is very helpful in determining stability properties of stationary states, as will be described elsewhere.

6. Dynamics on the Three-Dimensional Invariant Subspace

We now return to equations (56–58) describing the dynamics on the three-dimensional invariant subspace of the conformal flow and demonstrate how to solve them explicitly. Once again, the situation is closely parallel to the three-dimensional invariant subspace of the cubic Szegő equation with its underlying one-dimensional periodic motion.

From (56), we obtain for y defined by (59)

$$\dot{y} = \frac{1}{3}y(1+y)^3 \operatorname{Im}(\bar{b}a). \tag{79}$$

This equation and (57) imply that

$$S = |a|^2 y(1+y)^3 \tag{80}$$

is conserved. This quantity is related to the conformal flow Hamiltonian (16) by

$$H = Q^2 - 2S^2. \tag{81}$$

Equations (60), (61) and (80) can be resolved to express $|b|^2$, $|a|^2$ and $\operatorname{Re}(\bar{b}a)$ through Q , E , S and y as follows

$$\begin{aligned} |b|^2 &= \frac{2Q - E + 3y(Q + 2S)}{(1+y)^3}, & |a|^2 &= \frac{S}{y(1+y)^3}, \\ \operatorname{Re}(\bar{b}a) &= \frac{E - Q - 2S - 2y(Q + 6S)}{4y(1+y)^3}. \end{aligned} \tag{82}$$

From these relations, together with (79), one obtains

$$\dot{y}^2 = -\frac{Q^2 + 12S^2}{36} \left(y^2 + \left(1 - \frac{E(Q + 2S)}{Q^2 + 12S^2} \right) y + \frac{(E - Q - 2S)^2}{4(Q^2 + 12S^2)} \right). \tag{83}$$

Note that this equation has the algebraic form of energy conservation for an ordinary one-dimensional harmonic oscillator. The solution of (83) reads

$$y(t) = B + A \sin(\Omega t + \psi), \quad \Omega = \frac{1}{6} \left(Q^2 + 12S^2 \right)^{1/2}, \tag{84}$$

where B and A are constants depending on E , Q , and S ; ψ is a phase that must be determined from the entire set of initial conditions. By Eq. (82), this exactly periodic motion is transferred to $|b|^2$, $|a|^2$ and $\text{Re}(\bar{b}a)$, and hence to the mode energy spectrum

$$|\alpha_n|^2 = |b + na|^2 |p|^{2n} = \left(|b|^2 + 2n \text{Re}(\bar{b}a) + n^2 |a|^2 \right) |p|^{2n}. \tag{85}$$

One will thus observe exact returns of the energy spectrum to the initial configurations for *all* solutions within the three-dimensional invariant subspace of the conformal flow.

The turning points of the periodic motion of y described by (84), $y_{\pm} = B \pm A$, are given by the roots of the quadratic polynomial appearing on the right-hand side of (83) (the special case $A = 0$ corresponds to stationary states). In terms of the energy spectrum (85), these turning points provide lower and upper bounds for the inverse and direct cascades of energy, respectively. One of the key questions in this context is how large can y grow starting from some small y . To answer this question, we consider the ratio

$$\frac{1 + y_+}{1 + y_-} = \frac{(1 + y_+)^2}{(1 + y_-)(1 + y_+)} \leq \frac{(1 + y_+ + y_-)^2}{1 + y_- + y_+ + y_- y_+}. \tag{86}$$

An advantage of the last representation is that it only contains combinations of y_+ and y_- directly expressible through the coefficients of the quadratic polynomial on the right-hand side of (83). One thus gets

$$\frac{(1 + y_+ + y_-)^2}{1 + y_- + y_+ + y_- y_+} = \frac{4E^2(Q + 2S)^2}{(Q^2 + 12S^2)(E + Q + 2S)^2} \leq \frac{4(Q + 2S)^2}{Q^2 + 12S^2}. \tag{87}$$

We furthermore notice that

$$Q = (1 + y)^2 |b + 2ya|^2 + 2S \geq 2S. \tag{88}$$

Therefore, dividing the numerator and denominator of (87) by Q^2 and replacing the numerator by its maximum and denominator by its minimum, we obtain a simple uniform upper bound (which very likely can be tightened with extra work)

$$\frac{1 + y_+}{1 + y_-} \leq 16. \tag{89}$$

This proves that the transfer of energy to high frequencies (or, equivalently, the growth of the higher Sobolev norms (31)) is uniformly bounded. We recall from Sect. 3 that there is no such bound for the Szegő flow on the three-dimensional invariant subspace (35). In this sense, the conformal flow is much less ‘turbulent’ than the Szegő flow. Heuristically, this is not very surprising in view of the fact that the interaction coefficients in (23)

$$\frac{\min(n, j, k, n + j - k) + 1}{n + 1} \tag{90}$$

decay when the recipient mode number n is large and at least one of the source mode numbers is small, undermining the efficiency of energy transfer from low to high frequencies. This is in contrast to the Szegő flow where all coupling coefficients are equal to 1.

7. Summary and Open Questions

Starting with a naturally defined geometric PDE (4) on a three-sphere describing a self-interacting conformally coupled scalar field, we have considered its effective time-averaged weak field dynamics, arriving at the conformal flow (15). The conformal flow is both structurally similar and displays a number of dynamical parallels to the previously known cubic Szegő equation (24). Building on these analogies, we have revealed the dynamics on the three-dimensional invariant subspace of the conformal flow described by the ansatz (52). Within this subspace, the dynamics is Liouville-integrable and bounded, and hence quasiperiodic, with exactly periodic energy flows (85) displaying an alternating sequence of direct and inverse cascades. Unlike the cubic Szegő case, the conformal flow dynamics within the three-dimensional invariant subspace does not display turbulent behaviors (not even the ‘weak weak turbulence’ of [3]). Other similar three-dimensional subspaces can be immediately constructed, as follows from simple properties of the conformal flow equation. There are furthermore direct parallels between the structure of stationary states of the Szegő and conformal flows (these states are special solutions for which no energy transfer between the modes occurs). Of these, the Blaschke product states (76) are particularly intriguing, as they clearly demonstrate that the parallels between the Szegő and conformal flows extend beyond the three-dimensional invariant subspaces that have been our main focus here.

We conclude with a list of open questions that we leave for future investigations:

- Is the conformal flow (15) Lax-integrable?
- Is there a way to re-express the conformal flow through a projector similar to the Szegő projector? Apart from the conceptual importance, such a projector should make calculations easier. The complex plane representation of the conformal flow (50) can be seen as a first step in this direction.
- Are there higher dimensional invariant subspaces? The three-dimensional subspace we have considered, with its double-pole generating function (53), and parallels to the cubic Szegő case strongly suggest that more elaborate meromorphic ansätze should work; however, we have not been able to find them.
- Are there weakly turbulent solutions? We have explicitly demonstrated that no turbulent behavior occurs within the three-dimensional invariant subspace (52). This does not in principle exclude turbulence for other initial conditions; however, we find it unlikely because the conformal flow generally appears to display less energy spread than the Szegő flow.
- Complete classification of stationary states and analysis of their stability properties would contribute to the overall picture of the conformal flow dynamics.
- To what extent can the properties of the conformal flow, both explicitly demonstrated and putative, be structurally stable with respect to variations of the flow equation? Do these dynamical patterns have applications to the weak field limit of other related systems? Can the Szegő and conformal flows be just two representative members of a large hierarchy of equations?
- To what extent can the highly structured dynamics of the conformal flow be transferred to the original conformally invariant cubic wave equation (5) on the three-sphere? Standard results on time averaging guarantee that in the weak field regime the conformal flow accurately approximates our original wave equation for a long but limited time. Can our findings have further implications on longer time scales?

Acknowledgements. P.B. gratefully acknowledges the stimulating atmosphere at the trimestre “Ondes Non Linéaires” in IHES, where part of this work was done; he is particularly indebted to Patrick Gérard for

helpful discussions. The work of P.B., D.H., and M.M. was supported by the Polish National Science Centre grant no. DEC-2012/06/A/ST2/00397. P.B. and M.M. gratefully acknowledge the support of the Alexander von Humboldt Foundation. D.H. acknowledges a scholarship of Marian Smoluchowski Research Consortium Matter Energy Future from KNOW funding. The work of B.C. and V.L. is supported in part by the Belgian Federal Science Policy Office through the Interuniversity Attraction Pole P7/37, by FWO-Vlaanderen through projects G020714N and G044016N, and by Vrije Universiteit Brussel (VUB) through the Strategic Research Program “High-Energy Physics”. V.L. is supported by a PhD fellowship from the VUB Research Council. B.C. thanks the organizers of the NumHol2016 meeting at Santiago de Compostela and of the Nordita program “Black Holes and Emergent Spacetime” for hospitality while this work was in progress. The work of O.E. is funded under the CUniverse research promotion project by Chulalongkorn University (grant reference CUAASC). O.E. would like to thank Latham Boyle, Stephen Green and especially Luis Lehner for stimulating discussions and warm hospitality during his visit to the Perimeter Institute (Waterloo, Canada). The part of this research conducted during that visit was supported by the Perimeter Institute for Theoretical Physics. (Research at Perimeter Institute is supported by the Government of Canada through the Department of Innovation, Science and Economic Development and by the Province of Ontario through the Ministry of Research and Innovation.)

Open Access This article is distributed under the terms of the Creative Commons Attribution 4.0 International License (<http://creativecommons.org/licenses/by/4.0/>), which permits unrestricted use, distribution, and reproduction in any medium, provided you give appropriate credit to the original author(s) and the source, provide a link to the Creative Commons license, and indicate if changes were made.

A. Complex Plane Representation for the Conformal Flow

We first introduce the generating functions u and \tilde{u} according to (32) and (34). It is true for any contour enclosing the origin but not enclosing the singularities of u , and any contour enclosing all singularities of \tilde{u} that

$$\alpha_m = \frac{1}{2\pi i} \oint \frac{dz}{z} u(z) z^{-m}, \quad \bar{\alpha}_m = \frac{1}{2\pi i} \oint \frac{dz}{z} \tilde{u}(z) z^m. \tag{91}$$

Substituting these expressions to the right-hand side of conformal flow (15), one gets

$$\begin{aligned} i(n+1)\dot{\alpha}_n &= \frac{1}{(2\pi i)^3} \oint \frac{ds}{s} \frac{dv}{v} \frac{dw}{w^{n+1}} \tilde{u}(s)u(v)u(w) \\ &\times \sum_{j=0}^{\infty} \sum_{k=0}^{n+j} [\min(n, j, k, n+j-k) + 1] \left(\frac{s}{w}\right)^j \left(\frac{w}{v}\right)^k. \end{aligned} \tag{92}$$

The summation can be performed using the following master formula

$$\begin{aligned} &\sum_{j=0}^{\infty} \sum_{k=0}^{n+j} [\min(n, j, k, n+j-k) + 1] \rho^j \theta^k \\ &= \frac{1 - \theta^{n+1}}{(1-\theta)(1-\rho)(1-\theta\rho)} = \frac{1 + \theta + \dots + \theta^n}{(1-\rho)(1-\theta\rho)}. \end{aligned} \tag{93}$$

This summation formula can be derived by many methods, for example, by noticing that

$$2 \min(n, j, k, n+j-k) = n + j - |k-n| - |k-j|, \tag{94}$$

and performing brute force resummations of geometric series. The best way to understand it, however, is essentially combinatorial in nature. The right-hand side of (93) can be rewritten as

$$(1 + \theta + \dots + \theta^n) \sum_{m=0}^{\infty} \rho^m (1 + \theta + \dots + \theta^m). \tag{95}$$

The coefficient of $\rho^j \theta^k$ in this expression is just the coefficient of θ^k in the product

$$(1 + \theta + \dots + \theta^n) (1 + \theta + \dots + \theta^j). \tag{96}$$

Counting the number of relevant pairings of powers of θ in the two polynomials of the product reproduces the coefficient on the left-hand side of (93), thus verifying the summation formula.

Using (93), one can rewrite (92) as

$$i(n+1)\dot{\alpha}_n = \frac{1}{(2\pi i)^3} \oint \frac{ds}{s} \frac{dv}{v} dw \tilde{u}(s)u(v)u(w) \frac{w^{-(n+1)} - v^{-(n+1)}}{(1-s/v)(1-s/w)(1-w/v)}. \tag{97}$$

(One must have $|s| < |v|$ and $|s| < |w|$ in order for the sum to converge.) Multiplying by z^n (with $|z| < |v|$ and $|z| < |w|$) and summing over n , one obtains after elementary simplification

$$i\partial_t\partial_z(zu) = \frac{1}{2\pi i} \oint \frac{ds}{s} \tilde{u}(s) \left[\frac{1}{2\pi i} \oint dv \frac{u(v)}{(1-s/v)(v-z)} \right]^2. \tag{98}$$

Since by construction, the v -integration contour must not enclose any singularities of u , the integral inside the square brackets is simply given by a sum of two residues, resulting in the complex plane representation we have quoted in the main text:

$$i\partial_t\partial_z(zu) = \frac{1}{2\pi i} \oint \frac{ds}{s} \tilde{u}(s) \left(\frac{su(s) - zu(z)}{s-z} \right)^2. \tag{99}$$

B. A Few Summation Formulas

We assemble below the explicit summation formulas necessary for deriving (56–58) from (54). A crucial feature of these expressions in our context is that all of them are proportional to $(n+1)$.

$$\sum_{j=0}^{\infty} \sum_{k=0}^{n+j} [\min(n, j, k, n+j-k) + 1] |p|^{2j} = \frac{n+1}{(1-|p|^2)^2}, \tag{100}$$

$$\sum_{j=0}^{\infty} \sum_{k=0}^{n+j} [\min(n, j, k, n+j-k) + 1] j |p|^{2j} = \frac{2(n+1)|p|^2}{(1-|p|^2)^3}, \tag{101}$$

$$\sum_{j=0}^{\infty} \sum_{k=0}^{n+j} [\min(n, j, k, n+j-k) + 1] k |p|^{2j} = \frac{n(n+1)}{2(1-|p|^2)^2} + \frac{(n+1)|p|^2}{(1-|p|^2)^3}, \tag{102}$$

$$\sum_{j=0}^{\infty} \sum_{k=0}^{n+j} [\min(n, j, k, n+j-k) + 1] j^2 |p|^{2j} = \frac{2(n+1)|p|^2}{(1-|p|^2)^3} + \frac{6(n+1)|p|^4}{(1-|p|^2)^4}, \tag{103}$$

$$\begin{aligned} \sum_{j=0}^{\infty} \sum_{k=0}^{n+j} [\min(n, j, k, n+j-k) + 1] k^2 |p|^{2j} \\ = \frac{n(n+1)(2n+1)}{6(1-|p|^2)^2} + \frac{(n+1)^2|p|^2}{(1-|p|^2)^3} + \frac{2(n+1)|p|^4}{(1-|p|^2)^4}, \end{aligned} \tag{104}$$

$$\sum_{j=0}^{\infty} \sum_{k=0}^{n+j} [\min(n, j, k, n+j-k) + 1] jk |p|^{2j} = \frac{(n+1)^2|p|^2}{(1-|p|^2)^3} + \frac{3(n+1)|p|^4}{(1-|p|^2)^4}, \tag{105}$$

$$\begin{aligned} \sum_{j=0}^{\infty} \sum_{k=0}^{n+j} [\min(n, j, k, n+j-k) + 1] j^2 k |p|^{2j} \\ = \frac{(n+1)^2|p|^2}{(1-|p|^2)^3} + \frac{3(n+1)(n+3)|p|^4}{(1-|p|^2)^4} + \frac{12(n+1)|p|^6}{(1-|p|^2)^5}, \end{aligned} \tag{106}$$

$$\sum_{j=0}^{\infty} \sum_{k=0}^{n+j} [\min(n, j, k, n+j-k) + 1] jk^2 |p|^{2j}$$

$$= \frac{(n+1)(2n^2+4n+3)|p|^2}{3(1-|p|^2)^3} + \frac{(n+1)(3n+7)|p|^4}{(1-|p|^2)^4} + \frac{8(n+1)|p|^6}{(1-|p|^2)^5}. \quad (107)$$

References

1. Zakharov, V.E., L'vov, V.S., Falkovich, G.: Kolmogorov Spectra of Turbulence I: Wave Turbulence. Springer, Berlin (1992)
2. Nazarenko, S.: Wave Turbulence. Springer, Berlin (2011)
3. Colliander, J., Keel, M., Staffilani, G., Takaoka, H., Tao, T.: Transfer of energy to high frequencies in the cubic defocusing nonlinear Schrödinger equation. *Invent. Math.* **181**, 39 (2010). [arXiv:0808.1742](#) [math.AP]
4. Hani, Z.: Long-time instability and unbounded Sobolev orbits for some periodic nonlinear Schrödinger equations. *Arch. Ration. Mech. Anal.* **211**, 929 (2014). [arXiv:1210.7509](#) [math.AP]
5. Guardia, M., Kaloshin, V.: Growth of Sobolev norms in the cubic defocusing nonlinear Schrödinger equation. *J. Eur. Math. Soc.* **17**, 71 (2015). [arXiv:1205.5188](#) [math.AP]
6. Bizoń, P., Rostworowski, A.: On weakly turbulent instability of anti-de Sitter space. *Phys. Rev. Lett.* **107**, 031102 (2011). [arXiv:1104.3702](#) [gr-qc]
7. Bizoń, P.: Is AdS stable? *Gen. Rel. Grav.* **46**, 1724 (2014). [arXiv:1312.5544](#) [gr-qc]
8. Craps, B., Evnin, O.: AdS (in)stability: an analytic approach. *Fortsch. Phys.* **64**, 336 (2016). [arXiv:1510.07836](#) [gr-qc]
9. Basu, P., Krishnan, C., Saurabh, A.: A stochasticity threshold in holography and the instability of AdS. *Int. J. Mod. Phys. A* **30**, 1550128 (2015). [arXiv:1408.0624](#) [hep-th]
10. Murdock, J.A.: *Perturbations: Theory and Methods*. SIAM, Philadelphia (1987)
11. Kuksin, S., Maiocchi, A.: The effective equation method. In: *New Approaches to Nonlinear Waves*. Springer, Berlin (2016). [arXiv:1501.04175](#) [math-ph]
12. Balasubramanian, V., Buchel, A., Green, S. R., Lehner, L., Liebling, S. L.: Holographic thermalization, stability of anti-de Sitter space, and the Fermi-Pasta-Ulam paradox. *Phys. Rev. Lett.* **113**, 071601 (2014). [arXiv:1403.6471](#) [hep-th]
13. Craps, B., Evnin, O., Vanhooft, J.: Renormalization group, secular term resummation and AdS (in)stability. *JHEP* **1410** (2014) 48. [arXiv:1407.6273](#) [gr-qc]
14. Craps, B., Evnin, O., Vanhooft, J.: Renormalization, averaging, conservation laws and AdS (in)stability. *JHEP* **1501** (2015) 108. [arXiv:1412.3249](#) [gr-qc]
15. Lakshmanan, M., Sahadevan, R.: Painlevé analysis, Lie symmetries and integrability of coupled nonlinear oscillators of polynomial type. *Phys. Rep.* **224**, 1 (1993)
16. Bruschi, M., Calogero, F.: Integrable systems of quartic oscillators. *Phys. Lett. A* **273**, 173 (2000)
17. Bruschi, M., Calogero, F.: Integrable systems of quartic oscillators II. *Phys. Lett. A* **327**, 320 (2004). [arXiv:nlin/0403011](#) [nlin.SI]
18. Gérard, P., Grellier, S.: The cubic Szegő equation. *Ann. Scient. Éc. Norm. Sup.* **43**, 761 (2010). [arXiv:0906.4540](#) [math.CV]
19. Gérard, P., Grellier, S.: Effective integrable dynamics for a certain nonlinear wave equation. *Anal. PDE* **5**, 1139 (2012). [arXiv:1110.5719](#) [math.AP]
20. Gérard, P., Grellier, S.: An explicit formula for the cubic Szegő equation. *Trans. Am. Math. Soc.* **367**, 2979 (2015). [arXiv:1304.2619](#) [math.AP]
21. Gérard, P., Grellier, S.: The cubic Szegő equation and Hankel operators. [arXiv:1508.06814](#) [math.AP]
22. Majda, A.J., McLaughlin, D.W., Tabak, E.G.: A one-dimensional model for dispersive wave turbulence. *J. Nonlinear Sci.* **7**, 9 (1997)
23. Hani, Z., Thomann, L.: Asymptotic behavior of the nonlinear Schrödinger equation with harmonic trapping. *Commun. Pur. App. Math.* **69**, 1727 (2016). [arXiv:1408.6213](#) [math.AP]
24. Faou, E., Germain, P., Hani, Z.: The weakly nonlinear large box limit of the 2D cubic nonlinear Schrödinger equation. *J. Am. Math. Soc.* **29**, 915 (2016). [arXiv:1308.6267](#) [math.AP]
25. Germain, P., Hani, Z., Thomann, L.: On the continuous resonant equation for NLS: I. Deterministic analysis. *J. Math. Pure Appl.* **105**, 131 (2016). [arXiv:1501.03760](#) [math.AP]
26. Germain, P., Thomann, L.: On the high frequency limit of the LLL equation. *Quart. Appl. Math.* **74**, 633 (2016). [arXiv:1509.09080](#) [math.AP]
27. Beisert, N. et al.: Review of AdS/CFT integrability: an overview. *Lett. Math. Phys.* **99**, 3 (2012). [arXiv:1012.3982](#) [hep-th]
28. Yang, I-S.: Missing top of the AdS resonance structure. *Phys. Rev. D* **91**, 065011 (2015). [arXiv:1501.00998](#) [hep-th]
29. Evnin, O., Nivesvivat, R.: AdS perturbations, isometries, selection rules and the Higgs oscillator. *JHEP* **1601**, 151 (2016). [arXiv:1512.00349](#) [hep-th]
30. Garnett, J.B.: *Bounded Analytic Functions*. Springer, Berlin (2007)

31. Green, S. R., Maillard, A., Lehner, L., Liebling, S. L.: Islands of stability and recurrence times in AdS. *Phys. Rev. D* **92**, 084001 (2015). [arXiv:1507.08261](#) [gr-qc]
32. Craps, B., Evnin, O., Jai-akson, P., Vanhoof, J.: Ultraviolet asymptotics for quasiperiodic AdS_4 perturbations. *JHEP* **1510**, 080 (2015). [arXiv:1508.05474](#) [gr-qc]
33. Maliborski, M., Rostworowski, A.: Time-periodic solutions in an Einstein AdS-Massless-Scalar-Field system. *Phys. Rev. Lett.* **111**, 051102 (2013). [arXiv:1303.3186](#) [gr-qc]

Communicated by P. T. Chrusciel

Slow scrambling in extremal BTZ and microstate geometries

Ben Craps,^a Marine De Clerck,^a Philip Hacker,^a Kévin Nguyen^b
and Charles Rabideau^a

^a*Theoretische Natuurkunde, Vrije Universiteit Brussel (VUB)
and The International Solvay Institutes,
Pleinlaan 2, B-1050 Brussels, Belgium*

^b*Black Hole Initiative, Harvard University,
Cambridge, MA 02138, U.S.A.*

E-mail: Ben.Craps@vub.be, Marine.Alexandra.De.Clerck@vub.be,
Philip.Hacker@vub.be, kevin_nguyen@g.harvard.edu,
Charles.Rabideau@vub.be

ABSTRACT: Out-of-time-order correlators (OTOCs) that capture maximally chaotic properties of a black hole are determined by scattering processes near the horizon. This prompts the question to what extent OTOCs display chaotic behaviour in horizonless microstate geometries. This question is complicated by the fact that Lyapunov growth of OTOCs requires nonzero temperature, whereas constructions of microstate geometries have been mostly restricted to extremal black holes.

In this paper, we compute OTOCs for a class of extremal black holes, namely maximally rotating BTZ black holes, and show that on average they display “slow scrambling”, characterized by cubic (rather than exponential) growth. Superposed on this average power-law growth is a sawtooth pattern, whose steep parts correspond to brief periods of Lyapunov growth associated to the nonzero temperature of the right-moving degrees of freedom in a dual conformal field theory.

Next we study the extent to which these OTOCs are modified in certain “superstrata”, horizonless microstate geometries corresponding to these black holes. Rather than an infinite throat ending on a horizon, these geometries have a very deep but finite throat ending in a cap. We find that the superstrata display the same slow scrambling as maximally rotating BTZ black holes, except that for large enough time intervals the growth of the OTOC is cut off by effects related to the cap region, some of which we evaluate explicitly.

KEYWORDS: AdS-CFT Correspondence, Black Holes in String Theory, Gauge-gravity correspondence

ARXIV EPRINT: [2009.08518](https://arxiv.org/abs/2009.08518)

Contents

1	Introduction	1
2	Geodesic approximation to the OTOC	9
3	OTOC in extremal BTZ	15
3.1	Highly energetic particles	16
3.2	Eikonal phase	18
4	Microstate geometries	24
4.1	(1,0,n) superstrata	24
4.2	Black hole limit of the superstrata	26
4.3	Geodesics of the superstrata	27
4.4	OTOC in the superstrata	30
5	Discussion	37
A	Oscillations and decay in the OTOC	38
B	Center-of-mass energy in generic BTZ	42
C	Shock wave in extremal BTZ	43

1 Introduction

The nature of the microstates of black holes in quantum gravity is a matter of ongoing debate. Some take recent progress on recovering the Page curve of evaporating black holes from semiclassical gravity [1–4] (see [5] for a review) as evidence that black hole microstates have a smooth horizon and an interior region. Others are convinced that many or all black hole microstates correspond to horizonless geometries (see [6] for a review), and point to explicit constructions of increasingly large families of such geometries in string theory (see e.g. [7]).

If black hole microstates correspond to horizonless geometries, one expects that observables computed in such geometries should approximately reproduce those computed in the “naïve” black hole geometry. Nevertheless, sufficiently accurate computations or measurements should be able to distinguish them. Examples include studies of the approximate thermality of probes in ensembles of gravitational microstates [8, 9], an analogue of Hawking radiation in special microstate geometries of a non-extremal black hole [10], and the behaviour of retarded two-point functions in certain microstates of extremal black holes [11].

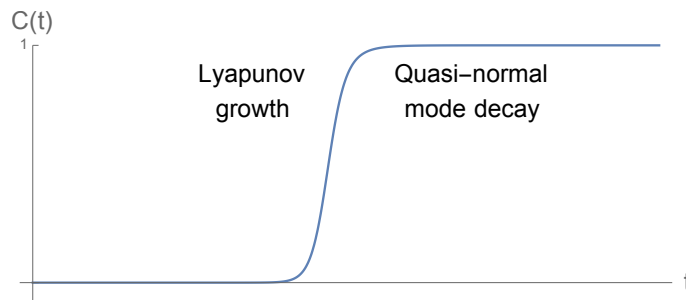


Figure 1. Schematic plot (based on [14]) of the expected behaviour of the normalized commutator squared $C(t)$ over time.

Black hole horizons have played a central role in recent connections between gravity and quantum chaos. Out-of-time-order correlators (OTOCs) in holographic field theories in a thermal ensemble display transient Lyapunov growth, with Lyapunov exponent equal to 2π times the temperature [12]. Such systems have been argued to be maximally chaotic [13]. In the dual gravitational description, the OTOC corresponds to a scattering process very close to a black hole horizon. In contrast to quasinormal mode (QNM) decay, which depends on what happens within a few Schwarzschild radii of the horizon, chaos probes what happens *at* the horizon [14]. This makes it very interesting to investigate how OTOCs distinguish between black hole geometries and horizonless microstate geometries.

An important complication is that so far constructions of microstate geometries that closely resemble black holes have been mostly restricted to extremal black holes, which are under better control due to supersymmetry. Such black holes have zero temperature, which requires modification of the above discussion. While it would be interesting from various points of view to have microstate geometries corresponding to non-extremal black holes, constructing them is not an easy task. In the present paper, we will therefore extend computations of chaos as measured by OTOCs to the case of certain extremal black holes and associated microstate geometries.

To set the stage, we briefly review some aspects of quantum chaos and OTOCs, mainly following [14]. In classically chaotic systems, neighboring phase space trajectories diverge exponentially, $\partial q(t)/\partial q(0) \sim \exp(\lambda t)$. Since $\partial q(t)/\partial q(0) = \{q(t), p(0)\}$, this motivates the study in quantum mechanics of commutators of operators at different times. More specifically, one is interested in $-\langle [V(0), W(t)]^2 \rangle_\beta$, which we will refer to as the commutator squared, and where β is the inverse temperature. As displayed in figure 1, in theories with a chaotic semi-classical limit and for operators that commute at $t = 0$ this quantity typically displays two exponential behaviours, namely transient Lyapunov growth followed by saturation, where the latter is described by Ruelle resonances. Holographically, Ruelle resonances correspond to quasinormal mode decay, also visible in two-point functions, while the Lyapunov growth is due to near-horizon blueshifts, which manifest themselves in 2-to-2 scattering amplitudes that can be associated to OTOCs [15]. For times large compared to the inverse temperature, the normalized commutator squared $C(t)$ is simply given by 1

minus the real part of the out-of-time-order correlator,

$$C(t) \equiv \frac{-\langle [V(0), W(t)]^2 \rangle_\beta}{2\langle VV \rangle_\beta \langle WW \rangle_\beta} \approx 1 - \text{Re OTOC}(t) \quad (t \gg \beta), \quad (1.1)$$

where the normalized OTOC is defined as

$$\text{OTOC}(t) \equiv \frac{\langle V(0)W(t)V(0)W(t) \rangle_\beta}{\langle VV \rangle_\beta \langle WW \rangle_\beta}. \quad (1.2)$$

This is due to the fact that contributions like $\langle V(0)W(t)W(t)V(0) \rangle_\beta$ can be interpreted as the 2-point function of $W(t)$ in a state created by acting with $V(0)$ on the thermal state; this state behaves thermally after one waits a few thermal times, so this contribution factorizes.

In fact, the commutator squared contains more structure than shown in figure 1. In a 2d holographic Conformal Field Theory (CFT), if the conformal dimensions satisfy $h_W \gg h_V \gg 1$ and the time is large compared to both the spatial separation and the inverse temperature, the OTOC was computed in [16],

$$\frac{\langle V(i\epsilon_1, x)W(t + i\epsilon_3, 0)V(i\epsilon_2, x)W(t + i\epsilon_4, 0) \rangle_\beta}{\langle V(i\epsilon_1, 0)V(i\epsilon_2, 0) \rangle_\beta \langle W(i\epsilon_3, 0)W(i\epsilon_4, 0) \rangle_\beta} \approx \left(\frac{1}{1 - \frac{24\pi i h_W}{\epsilon_{12}^* \epsilon_{34} c} e^{\frac{2\pi}{\beta}(t-|x|)}} \right)^{2h_V}. \quad (1.3)$$

Here c is the central charge, which is large, and

$$\epsilon_{ij} = i \left(e^{\frac{2\pi}{\beta} i\epsilon_i} - e^{\frac{2\pi}{\beta} i\epsilon_j} \right). \quad (1.4)$$

At sufficiently early times, one gets Lyapunov behaviour from the $1/c$ expansion,

$$\frac{\langle V(i\epsilon_1, x)W(t + i\epsilon_3, 0)V(i\epsilon_2, x)W(t + i\epsilon_4, 0) \rangle_\beta}{\langle V(i\epsilon_1, 0)V(i\epsilon_2, 0) \rangle_\beta \langle W(i\epsilon_3, 0)W(i\epsilon_4, 0) \rangle_\beta} \approx 1 + \frac{48\pi i h_W h_V}{\epsilon_{12}^* \epsilon_{34} c} e^{\frac{2\pi}{\beta}(t-|x|)}. \quad (1.5)$$

Note that this exponential growth is suppressed by a prefactor that is small in the large- c semi-classical limit. This growth will persist until it competes with the small prefactor at the scrambling time

$$t_s = |x| + \frac{\beta}{2\pi} \log \frac{|\epsilon_{12}^* \epsilon_{34}| c}{48\pi h_W h_V}, \quad (1.6)$$

which is the time at which the commutator squared, $C(t)$, first becomes $O(1)$.

After the scrambling time there is a region of oscillatory behaviour, which subsequently decays away. This decay is also controlled by the Lyapunov exponent and occurs well before the quasi-normal regime. Nonetheless, at sufficiently late times one sees the faster exponential quasi-normal mode decay in the tail of this decay. The details of this intermediate regime are described in more detail in appendix A and the behaviour of the OTOC described by (1.3) is depicted in figure 2.

At very late times, the quasi-normal mode decay is expected to stop as the OTOC cannot continue to decay forever in a unitary theory [17]. The result (1.3) was derived

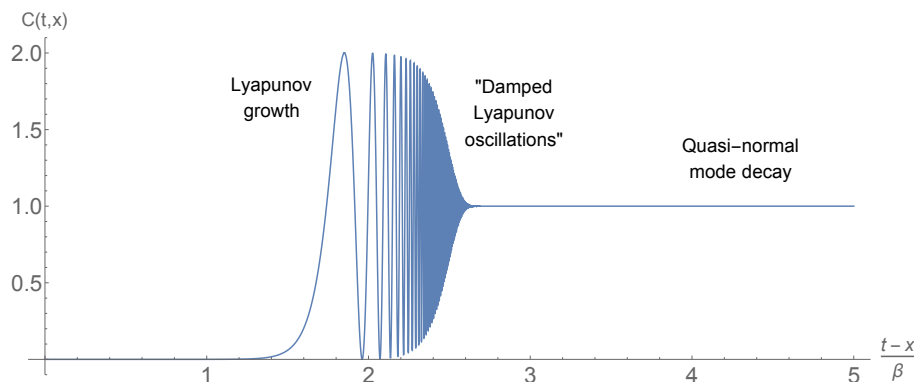


Figure 2. Behaviour of the normalized commutator squared in a 2d holographic CFT. In this plot, $\frac{h_W}{c\epsilon_{12}\epsilon_{34}} = \exp(-24.5)$ and $h_V = \exp(9)$.

assuming that only the contribution from the Virasoro conformal block of the identity is important and this approximation is expected to breakdown at very late times [18–21].

To get a feeling for what to expect for extremal black holes, which involve zero temperature, we first review what happens in vacuum. In [16] it was found that for infinite β and $t \gg |x|$

$$\frac{\langle V(i\epsilon_1, x)W(t+i\epsilon_3, 0)V(i\epsilon_2, x)W(t+i\epsilon_4, 0) \rangle}{\langle V(i\epsilon_1, 0)V(i\epsilon_2, 0) \rangle \langle W(i\epsilon_3, 0)W(i\epsilon_4, 0) \rangle} \approx \left(\frac{1}{1 - \frac{24\pi i h_W}{c(\epsilon_1 - \epsilon_2)(\epsilon_3 - \epsilon_4)}(t - |x|)^2} \right)^{2h_V}. \quad (1.7)$$

At early times, we again see a period of growth suppressed by a small prefactor,

$$\left(\frac{1}{1 - \frac{24\pi i h_W}{c(\epsilon_1 - \epsilon_2)(\epsilon_3 - \epsilon_4)}(t - |x|)^2} \right)^{2h_V} \approx 1 + \frac{48\pi i h_V h_W}{c(\epsilon_1 - \epsilon_2)(\epsilon_3 - \epsilon_4)}(t - |x|)^2. \quad (1.8)$$

This result for the OTOC is qualitatively similar to the finite temperature case, except that the exponential Lyapunov growth is replaced by quadratic growth in time. The link between the OTOC and the commutator squared is now less straightforward, because contributions like $\langle V(0)W(t)W(t)V(0) \rangle$ need not factorize at zero temperature.

In this paper, we will focus on maximally rotating BTZ black holes and some of their microstate geometries. In the dual CFT, the left-movers are at zero temperature while the right-movers are at finite temperature T_R . To guide our expectations for computing OTOCs in BTZ geometries, we refer to earlier studies of non-maximally rotating BTZ black holes, including [22, 23], where Lyapunov growth alternates between the left and right-moving temperatures [23] at small time scales, yet the overall growth is controlled by the Bekenstein-Hawking temperature. These results cannot be applied directly to the extremal case, since they assume the regime where $t \gg \beta$ whereas β diverges in the extremal limit. Yet our results are compatible with extrapolating their conclusion to our setting, since for sufficiently high right-moving temperature one finds a small sawtooth-like modulation on top of power law growth, where the steep parts of the sawtooth correspond to brief periods of Lyapunov growth at the nonzero right-moving temperature. Nonetheless, on average

the scrambling is slow. It is worth emphasizing that the sawtooth-like modulation is tied to the compactness of the spatial direction of the dual CFT. In contrast, the results (1.3) and (1.7) obtained in [16] were derived in the decompactified limit such that they do not display such a sawtooth-like modulation.

In [24], the gravitational modes responsible for scrambling corresponding to the zero left moving temperature and the non-zero right moving temperature were identified using an effective action. However, as emphasised in [23], identifying the overall rate of growth relevant for scrambling requires the detailed computation of the OTOC we present in this work. The instantaneous Lyapunov exponent in rotating ensembles has been bounded in [25]. Scrambling in BTZ has also been studied from the perspective of mutual information in [26]. In the context of microstate geometries resembling maximally rotating BTZ black holes, note that an interesting recent paper [27] has described a different kind of Lyapunov behaviour associated to geodesic instability near photon spheres. This latter Lyapunov exponent is related to quasi-normal decay [28], while the focus of our work is on the Lyapunov growth displayed by OTOCs, which is of a different nature.

A method to compute OTOCs within AdS/CFT, which is based on the geodesic approximation to the propagation of bulk fields in asymptotically AdS spacetimes, has been developed in [29]. We give a brief summary thereof in section 2. In practice, this method requires one to consider a particle falling in from the earlier boundary insertion point of the OTOC, together with the linearised gravitational shock wave that it sources. Similarly, an outgoing particle reaching the later boundary insertion point needs to be considered. Within the geodesic approximation, the OTOC is then determined by

$$\text{OTOC} \sim e^{i\delta}, \quad (1.9)$$

where the *eikonal phase* δ encodes the interaction of each particle with the gravitational shock wave emitted by the other one. Compared to the original method put forward by Shenker and Stanford [15] or follow up works such as [22, 23], this approach allows us to work at zero temperature. The difference is that the original method makes the approximation, well motivated at finite temperature, that the shock wave propagates exactly on the horizon. However, this approximation clearly does not apply in the vacuum where there is no horizon. The applicability of the new approach summarized in section 2 to the zero temperature case was demonstrated in [29] where the quadratic growth associated to *slow scrambling* in vacuum was obtained, finding agreement with earlier CFT results [16]. Similarly, the results of [23] show that the shock wave diverges in the extremal limit when the approximation of placing it on the horizon is made. Therefore, working with a method valid at zero temperature which accurately computes the shock wave without making the approximation of placing it on the horizon, is again crucial to the study of extremal BTZ and microstate geometries which we initiate in this paper.

The gravitational scattering amplitude of highly energetic particles turns out to be generically proportional to the corresponding center-of-mass energy. Hence, at finite temperature a rough estimate of the time-dependence of an OTOC may be obtained by computing this simple quantity; see also [30]. We will find that the story is more subtle in the zero temperature case, nevertheless the center-of-mass energy gives useful intuition in

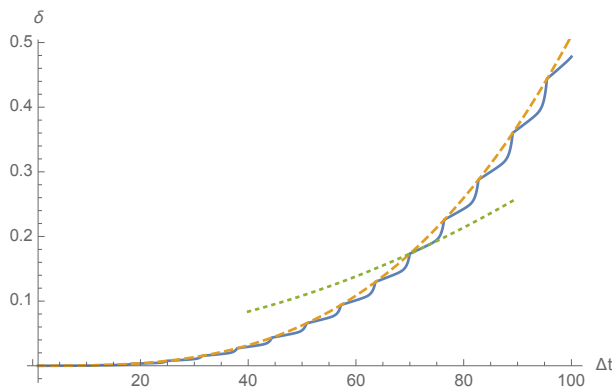


Figure 3. The growth of the eikonal phase δ , related to the OTOC through (1.9), of two scalar operators at a fixed spatial separation in extremal BTZ, computed within the geodesic approximation (solid blue line). The growth is cubic on average and can be very well approximated by the functional dependence depicted in orange (dashed), which scales as $\sim \frac{4r_+^2 t^3}{3\pi} - \frac{2r_+}{\pi} t^2 \log(4r_+ t) + 2r_+^2 t^2$. On top of this average growth, we find a sawtooth-like modulation that starts with a quadratically growing piece, followed by an exponential growth that catches up with the overall t^3 growth. One of the phases of t^2 growth is depicted by superimposing the dashed green (dotted) line, obtained by summing the quadratic contributions of a fixed 20 images. This figure is discussed in detail in section 3.2.

instances where gravitational shock waves are difficult to compute, as is the case when the source particles propagate in microstate geometries. In appendix B, we compute the center of mass energy in rotating BTZ and find an early time period of power-law growth. This early time period persists for longer and longer as we approach the extremal BTZ limit, leading to slow scrambling.

In section 3 we provide a detailed holographic computation of the OTOC of scalar operators within the geodesic approximation, in CFT states dual to maximally rotating BTZ black holes. First, we review the properties of geodesics in this spacetime. Then we consider the shock waves emitted by the scattered particles along their trajectories, computed in appendix C. We deal with the angular periodicity in BTZ by first computing the shock wave in the black brane geometry and then using the method images to find the periodic solution. We find that a large but finite number of these images contribute to the shock wave at any given time and that the number of images grows linearly with time. This explains the divergence found when taking the zero-temperature limit of the result found using the earlier approach — the late time approximation necessary to place the shock wave on the horizon leads to a diverging sum over images. This sum over images yields an enhancement factor in the strength of the gravitational interaction which, controlled by the center-of-mass energy of the interaction, would otherwise have grown quadratically with time. All in all, we find that the OTOC displays approximately cubic growth in time, with a sawtooth-like modulation that alternates between quadratic and exponential growth. In addition, the latter exponential Lyapunov growth is associated to the nonzero right-moving temperature T_R . This is displayed in figure 3. The scrambling associated to scalar operators is therefore slow on average. In particular, for the scrambling time defined

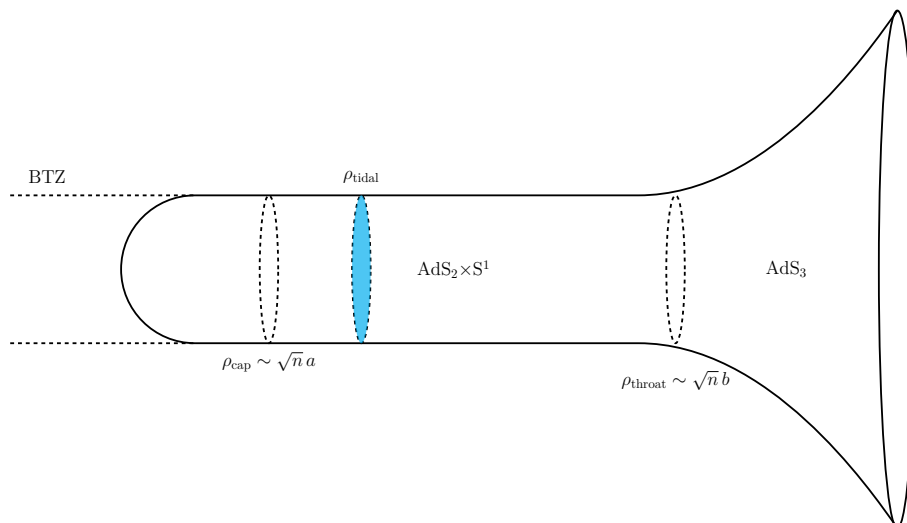


Figure 4. Schematic representation of a spatial slice of the superstrata geometry described by the metric (4.1). Each point in the picture corresponds to an S^3 in the six-dimensional geometry. Coming in from infinity, there is an asymptotic $\text{AdS}_3 \times S^3$ region, followed by an $\text{AdS}_2 \times S^1 \times S^3$ throat region which then ends in a smooth cap region. For geodesics falling in from a large radius in the asymptotic region, the tidal forces are in danger of invalidating the geodesic approximation at a radius ρ_{tidal} in the throat region.

as the time at which the eikonal phase δ becomes $O(1)$, we obtain

$$t_s \simeq \left(\frac{c \varepsilon^2}{16 h_V h_W} \right)^{\frac{1}{3}}. \tag{1.10}$$

Here, the time is expressed in units such that the spatial circle on which the boundary CFT lives has unit radius and ε is a holographic regulator to be introduced in (3.3).

Next, in section 4, we turn to the microstate geometries studied in [7, 11]. We focus on the $(1, 0, n)$ -superstrata whose salient geometric features are described in section 4.1. They are constructed from a BPS configuration of N_1 D1-branes and N_5 D5-branes. These geometries have an asymptotic $\text{AdS}_3 \times S^3 \times T^4$ region. They closely approximate an $S^3 \times T^4$ trivially fibred over an extremal BTZ outside of a cap region. In the cap region, the fibration becomes non-trivial and the S^3 pinches off in a smooth way. This allows the geometry to smoothly end outside of the would-be horizon of extremal BTZ. This geometry can be pictured by considering a spatial slice like that of figure 4. In extremal BTZ, this spatial slice is comprised of a near-horizon $\text{AdS}_2 \times S^1$ throat of infinite proper length attached to the asymptotic AdS_3 region. These microstates also exhibit a long throat attached to an asymptotic region, but this throat is capped off at a finite proper distance, before the would-be horizon is reached. These geometries are dual to a class of states in a two-dimensional CFT with central charge $c = 6N_1 N_5$ [7].

In section 4.4 we describe the first steps towards computing the OTOC within the geodesic approximation in these microstate geometries. First, we study null geodesics with zero angular momentum in order to understand what regions of the geometry are probed

by the OTOC as a function of the time separation between the operator insertions on the boundary. We find that for early times the interaction happens in the region of the geometry well described by extremal BTZ and so we expect the OTOC to be well described by the computations of section 3. At a time scale

$$t_{\text{cap}} \simeq \frac{N_1 N_5}{T_R}, \tag{1.11}$$

the OTOC starts to probe the cap region of the geometry and so we expect it to strongly deviate from the extremal BTZ answer. There are two main effects that will cause it to deviate: the blueshift in the center-of-mass energy will stop increasing since the geodesics cannot fall any further into the throat and the shock wave controlling the gravitational interaction between the scattered geodesics will be modified by the presence of the cap. These effects are discussed further in section 4.4.

Another effect can invalidate the geodesic approximation before either of these effects of the cap manifest themselves. In [31], it was found that the tidal forces in the throat region become Planckian well before the cap region. These tidal forces have been subsequently studied in a number of works including [32–34]. The geodesic approximation requires that the volume expansion of a particular congruence of geodesics be much smaller than the mass of the particle, which will generically be violated in a region of large tidal forces. These tidal forces become important, and are therefore in danger of invalidating the geodesic approximation, at a time scale

$$t_{\text{tidal}} \simeq \sqrt{\frac{\pi T_R}{\pi^2 T_R^2 + 1} \min(h_V, h_W) \varepsilon N_1 N_5}. \tag{1.12}$$

We have not tried to compute the shock wave produced by these geodesics in the cap region, since in any case the geodesic approximation does not hold in that region. Instead, the exact bulk-to-boundary propagators would need to be combined with the bulk-to-bulk graviton propagators to access the cap region, a computation we leave for future work.

The most relevant question for our purposes is whether the effects of the cap appear before or after the scrambling time. Indeed, given (1.10) with the appropriate central charge, we find that $t_s \ll t_{\text{tidal}}$ for large black holes in the semi-classical limit as long as the right-moving temperature is not too high

$$T_R \ll \min(h_V, h_W) \left(\frac{h_V^2 h_W^2 N_1 N_5}{\varepsilon} \right)^{\frac{1}{3}}. \tag{1.13}$$

As long as this condition holds, we expect the commutator squared to stop growing well before the interaction region reaches the part of the superstrata geometry where it deviates from extremal BTZ. In this case, we do not expect the details of the cap to affect the scrambling behaviour. They only come in far into the tail of the decay of the OTOC in the details of how the commutator squared saturates. However, for sufficiently high right-moving temperature, there does seem to be a regime where the effects of the cap will be felt before the scrambling time. We are not aware of any limit on the parameter n appearing in the superstrata solutions, which means that such large temperatures are allowed. This

region of large temperature would be an interesting regime to probe more precisely with a computation that goes beyond the geodesic approximation so that it can take into account the effects of the cap.

In section 5, we collect a number of open problems and directions for future work.

Conventions. We work in units such that the AdS length $\ell_{\text{AdS}} = 1$. The time coordinate in terms of which we express the various time scales agrees with the time coordinate of the dual CFT on a spatial circle with unit radius.

2 Geodesic approximation to the OTOC

We consider an asymptotically AdS background spacetime on which two massive Klein-Gordon real scalar fields ϕ_V and ϕ_W propagate. We are interested in computing the out-of-time-order correlator

$$\text{OTOC} \equiv \langle \psi | \phi_V(X_1) \phi_W(X_2) \phi_V(X_3) \phi_W(X_4) | \psi \rangle, \tag{2.1}$$

where the insertion points X_2, X_4 lie in the future of X_1, X_3 or are spacelike-separated from them. The state $|\psi\rangle$ corresponds to the background geometry on which the scalar fields propagate. All insertion points are also taken to lie asymptotically close to the spacetime conformal boundary in order to reproduce the OTOC of a dual conformal field theory. A method based on the geodesic approximation has been developed in a previous paper [29], which may be viewed as a position-space version of the one originally presented by Shenker and Stanford [15]. It was similarly constructed as the overlap

$$\text{OTOC} = \langle \text{out} | \text{in} \rangle, \tag{2.2}$$

between the in- and out-states

$$|\text{in}\rangle \equiv \phi_V(X_3) \phi_W(X_4) | \psi \rangle, \quad |\text{out}\rangle \equiv \phi_W(X_2) \phi_V(X_1) | \psi \rangle. \tag{2.3}$$

The operator $\phi_W(X_4)$ used to create the in-state is represented on an early time slice Σ_- by free propagation backward in time using the advanced propagator. In the same way, the operator $\phi_V(X_1)$ used to create the out-state is represented on a late time slice Σ_+ by free propagation forward in time using the retarded propagator. Note that the choice of these time slices is completely arbitrary and does not affect the end result. The overlap (2.2) then equals the *time-ordered* transition amplitude

$$\langle \psi | \phi_V(X_+) \phi_W(X_2) \phi_V(X_3) \phi_W(X_-) | \psi \rangle \sim e^{i\delta}, \tag{2.4}$$

convoluted with boundary-bulk propagators encoding the backward and forward propagation in time described above. Within the geodesic approximation $m_V, m_W \gg 1$ and the high-energy (eikonal) regime $G_N s \lesssim 1$, where s is the center-of-mass energy of the corresponding 2-to-2 scattering, the time-ordered amplitude (2.4) reduces to a simple phase $e^{i\delta}$ which we describe below in more detail. This whole construction, originally presented in [29], is illustrated for the case of an extremal BTZ background geometry in figure 5. For

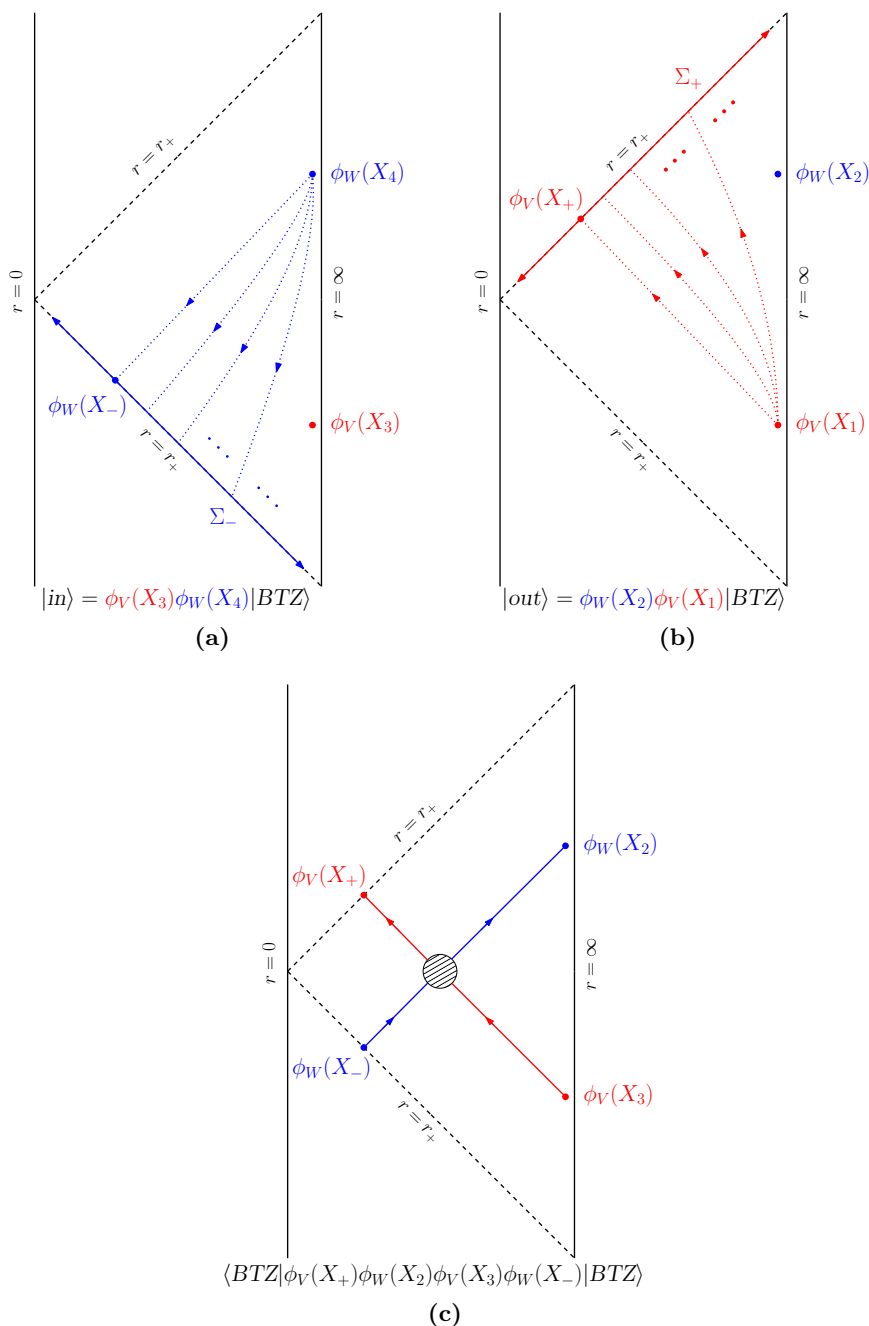


Figure 5. Steps involved in the derivation of formula (2.5) for the OTOC written as the state overlap $\langle out|in\rangle$, illustrated in the case where the background geometry is an extremal BTZ black hole, i.e. $|\psi\rangle = |BTZ\rangle$. (a)-(b) The operator $\phi_W(X_4)$ ($\phi_V(X_1)$) used to create the in-state (out-state) may be represented on the early (late) time slice Σ_- (Σ_+) by free propagation backward (forward) in time. The slices Σ_- and Σ_+ are chosen to coincide with the past and future horizons, respectively. (c) The state overlap $\langle out|in\rangle$ reduces to *time-ordered* transition amplitudes involving all points $X_- \in \Sigma_- \cap J^-(X_4)$ and $X_+ \in \Sigma_+ \cap J^+(X_1)$.

a more detailed description of the extremal BTZ geometry, we refer the reader to section 3, where we apply the general method presented here to this particular background spacetime. All in all, this construction yields the formula

$$\begin{aligned} \text{OTOC} &= -4m_W m_V \int_{\Sigma_- \cap J^-(X_4)} d\Sigma \cdot k_W \Psi_W(X_2, X_-) \Psi_W(X_4, X_-)^* \\ &\quad \times \int_{\Sigma_+ \cap J^+(X_1)} d\Sigma \cdot k_V \Psi_V(X_+, X_3) \Psi_V(X_+, X_1)^* e^{i\delta}, \end{aligned} \quad (2.5)$$

where $J^+(X_1)$ ($J^-(X_4)$) denotes the causal future (past) of the insertion point X_1 (X_4).

In the geodesic approximation which we consider, boundary-bulk propagators appearing in the above formula are given by

$$\Psi(X, Y) \equiv \langle \psi | \phi(X) \phi(Y) | \psi \rangle = A(X, Y) e^{imS(X, Y)}, \quad (2.6)$$

where the point X is assumed to lie in the causal future of the point Y , and with the phase given by the action of a timelike geodesic going from Y to X with velocity k ,

$$S(X, Y) = \int_Y^X dx \cdot k. \quad (2.7)$$

According to (2.5), each point X_- (X_+) within the time slice Σ_- (Σ_+) that can be connected by a timelike geodesic to the future (past) insertion points X_2, X_4 (X_1, X_3) must be considered. Finally, the *eikonal phase shift* δ encodes the gravitational interaction between the outgoing geodesic going from X_- to X_2 and the ingoing geodesic going from X_3 to X_+ . The stress-energy tensor $T_{\mu\nu}^V$ of an ingoing V particle is the source of a gravitational field $h_{\mu\nu}^V$ that propagates and interacts with the outgoing geodesic, and conversely. For the eikonal phase shift, this yields the formula [29]

$$\delta = \frac{1}{4} \int \left(h_{\mu\nu}^V T_W^{\mu\nu} + h_{\mu\nu}^W T_V^{\mu\nu} \right) + O(G_N^2). \quad (2.8)$$

If it were not for the eikonal phase factor, the OTOC (2.5) would simply factorize into the product of two boundary propagators,

$$\langle \psi | \phi_V(X_1) \phi_V(X_3) | \psi \rangle = 2m_V \int_{\Sigma_+ \cap J^+(X_1)} d\Sigma \cdot k_V \Psi_V(X_+, X_3) \Psi_V(X_+, X_1)^*, \quad (2.9a)$$

$$\langle \psi | \phi_W(X_2) \phi_W(X_4) | \psi \rangle = -2m_W \int_{\Sigma_- \cap J^-(X_4)} d\Sigma \cdot k_W \Psi_W(X_2, X_-) \Psi_W(X_4, X_-)^*. \quad (2.9b)$$

Stress tensor and shock wave of a particle. The stress-energy tensor of a massive particle with trajectory $x^\mu(\tau)$ and velocity $k^\mu(\tau)$ may be conveniently written [29]

$$T_{\mu\nu} = \frac{m}{\sqrt{-g}} \left(\frac{dx^0}{d\tau} \right)^{-1} k_\mu k_\nu \delta(x^1 - x^1(\tau)) \dots \delta(x^d - x^d(\tau)) \Big|_{x^0=x^0(\tau)}. \quad (2.10)$$

It sources a gravitational field which one may compute by solving the linearized Einstein's equations

$$D_{\text{lin}} h_{\mu\nu} = 8\pi G_N T_{\mu\nu}, \quad (2.11)$$

where D_{lin} is a differential operator whose definition involves the background geometry. For a single particle source with arbitrarily high energy, $h_{\mu\nu}$ is known as a gravitational *shock wave*. Although it is found by solving the above linearized Einstein's equations, it is usually also a nonlinear solution [35].

Ultraviolet regulators. We further restrict our attention to a configuration of infinitesimally separated boundary insertion points of the form

$$X_3^\mu = X_1^\mu - \epsilon_V \xi^\mu, \quad X_4^\mu = X_2^\mu - \epsilon_W \xi^\mu, \quad (2.12)$$

where ξ is a future-directed timelike vector of our choice that is tangent to the conformal boundary.¹ The role of ϵ_V, ϵ_W is to avoid UV divergences due to the insertion of operators at the same boundary points. When working in the limit of small UV regulators $\epsilon_W, \epsilon_V \ll 1$, the WKB phases in the overlap formula (2.5) simply differ by

$$S_V(X_+, X_3) = S_V(X_+, X_1) + \epsilon_V \xi \cdot k_V(X_1) + \mathcal{O}(\epsilon_V^2), \quad (2.13a)$$

$$S_W(X_4, X_-) = S_W(X_2, X_-) - \epsilon_W \xi \cdot k_W(X_4) + \mathcal{O}(\epsilon_W^2), \quad (2.13b)$$

such that

$$\Psi_V(X_+, X_3)\Psi_V(X_+, X_1)^* = |A_V(X_+, X_1)|^2 e^{im_V \epsilon_V \xi \cdot k_V(X_1)}, \quad (2.14a)$$

$$\Psi_W(X_2, X_-)\Psi_W(X_4, X_-)^* = |A_W(X_4, X_-)|^2 e^{im_W \epsilon_W \xi \cdot k_W(X_4)}. \quad (2.14b)$$

Hence, the OTOC (2.5) simplifies to

$$\begin{aligned} \text{OTOC} &= -4m_W m_V \int_{\Sigma_- \cap J^-(X_4)} d\Sigma \cdot k_W |A_W(X_4, X_-)|^2 e^{im_W \epsilon_W \xi \cdot k_W(X_4)} \\ &\quad \times \int_{\Sigma_+ \cap J^+(X_1)} d\Sigma \cdot k_V |A_V(X_+, X_1)|^2 e^{im_V \epsilon_V \xi \cdot k_V(X_1)} e^{i\delta}. \end{aligned} \quad (2.15)$$

It is customary to perform this integral by stationary phase approximation in the regime of large field masses m_V, m_W [15, 29].²

Early-time saddle point. If one is only interested in the early-time Lyapunov growth, the eikonal phase can be neglected in determining the saddle point of the integral (2.15), and one simply has to extremize the initial component velocities $\xi \cdot k_V(X_1)$ and $\xi \cdot k_W(X_4)$ over the whole set of timelike geodesics connecting the boundary insertion points X_1 and X_4 to the time slices Σ_- and Σ_+ . We present a significant simplification in the determination of the dominant pair of geodesics compared to the method used in a previous publication [29]. This new method highlights that the arbitrary choice of time slices Σ_- and Σ_+ does not affect the location of the saddle, since they do not enter the determination process at any

¹More precisely, $X_3 = \exp(-\epsilon_V \xi)$, where \exp is the exponential map at the point X_1 .

²As we explain in section 3.1, the velocities $k_{V,W}$ of particles inserted at a radial Schwarzschild coordinate $r = \epsilon^{-1}$ scale like $O(\epsilon^{-1})$ in the regime $\epsilon \ll 1$. Thus, the stationary phase approximation to the integral (2.15) holds within the regime $m_{V,W} \epsilon_{V,W} \gg \epsilon$. Since $\epsilon_{V,W}$ and ϵ both act as UV regulators, it is natural to consider them on the same footing, in which case the stationary phase approximation can be performed within the regime of large field masses $m_{V,W} \gg 1$.

point. Instead of extremizing directly over the geodesic endpoints $X_- \in \Sigma_-$ and $X_+ \in \Sigma_+$, we equivalently extremize over their initial velocities k_V and k_W , respectively. Thus, we need to determine the geodesic whose initial velocity k^μ is an extremum of the ‘energy’ functional

$$E_\xi \equiv \xi \cdot k. \quad (2.16)$$

Its variation with respect to the initial velocity is given by

$$\delta E_\xi = \xi \cdot \delta k, \quad (2.17)$$

which is required to vanish for all allowed velocity variations δk^μ . In fact, the only restriction on δk^μ comes from the timelike condition $k^2 = -1$, whose variation yields

$$k \cdot \delta k = 0. \quad (2.18)$$

From (2.17) and (2.18), we conclude that the initial velocity k^μ is a saddle point of E_ξ if

$$k^\mu \propto \xi^\mu, \quad (2.19)$$

where we recall that ξ is the future-directed timelike vector introduced in (2.12), and the normalization is easily found by imposing $k^2 = -1$. The interpretation of this result is clear: the initial velocity of the geodesic inserted at X_3 (X_4) must point towards X_1 (X_2). Note that the same condition determines the saddle point of the two-point functions (2.9). As a result, the *normalized* OTOC takes a particularly simple form,

$$\frac{\langle \phi_V(t_{\text{in}}, x_-) \phi_W(t_{\text{out}}, x_+) \phi_V(t_{\text{in}}, x_-) \phi_W(t_{\text{out}}, x_+) \rangle}{\langle \phi_V \phi_V \rangle \langle \phi_W \phi_W \rangle} \approx e^{i\delta} \Big|_{\text{saddle}}, \quad (2.20)$$

where we have made implicit that all insertions happen arbitrarily close to the conformal boundary. The pair of geodesics corresponding to the dominant saddle in (2.20) is determined from the condition (2.19) on their initial velocity at the boundary insertion points. In the limit where their insertion points are taken to the conformal boundary, these geodesics become approximately null. This is also precisely the regime in which the geodesic approximation to field propagation is most reliable and the gravitational field they create takes the form of shock waves [29]. However, note that the parameter ε measuring how close to the conformal boundary the operators are inserted, to be introduced in section 3, acts as another UV regulator and cannot be taken to zero without introducing an appropriate renormalization scheme. We will not attempt to do this in the present paper.

The above approximation scheme breaks down in the regime where the eikonal phase shift itself significantly contributes to the determination of the dominant saddle of the integral (2.5), i.e., when $\delta \gg 1$. Since δ is a growing function of time, which we describe in the next paragraph, this usually happens for late enough times. In particular, the quasi-normal decay of an OTOC (if it happens at all) lies within this late-time regime [15]. We refer the reader to appendix A for further comments and details on the treatment needed in order to describe the quasi-normal decay of OTOCs.

Early-time Lyapunov growth. Computation of OTOCs in the early-time regime through formula (2.20) instructs one to consider the stress tensor and gravitational field associated to one pair of highly energetic geodesics reaching the associated boundary insertion points, and to evaluate the eikonal phase shift (2.8) encoding their gravitational interaction. In the context of non-rotating BTZ black holes, it has been previously found that the latter scales with the center-of-mass energy s of the 2-to-2 particle scattering [15, 30]

$$\delta \sim G_N s, \tag{2.21}$$

where

$$s = -(m_V k_V + m_W k_W)^2 \approx -2m_V m_W k_V \cdot k_W, \quad k_W^2 = k_V^2 = -1. \tag{2.22}$$

The exponential Lyapunov growth originates from the exponential blueshift experienced by these particles in the neighborhood of a black hole. Indeed, one has

$$k_V(t_*) \sim e^{\kappa(t_* - t_{in})} k_V(t_{in}), \quad k_W(t_*) \sim e^{\kappa(t_{out} - t_*)} k_W(t_{out}), \tag{2.23}$$

where t_* is the time of interaction and κ is the surface gravity of the black hole background. Hence, one generically finds

$$\delta \sim G_N s \sim G_N m_W m_V e^{\kappa(t_{out} - t_{in})}, \tag{2.24}$$

which yields an exponential growth in the commutator squared, with Lyapunov exponent

$$\lambda_L = \kappa = \frac{2\pi}{\beta}. \tag{2.25}$$

This simple reasoning is useful to estimate the exponential Lyapunov growth, but is in no way rigorous nor accurate. As an example, it has been shown that (2.25) only holds on average in the context of non-maximally rotating BTZ black holes [23].

The above description does not apply to states at zero temperature $\beta \rightarrow \infty$, however. In the case of empty AdS dual to the CFT ground state, it has been shown that the eikonal phase δ grows quadratically with time [29], finding agreement with earlier results obtained by CFT techniques [16]. This sort of polynomial growth has been associated to a form of *slow scrambling*, in contrast to fast scrambling in case of exponential growth. In this paper we focus on extremal black holes to which a zero temperature is also associated. We study the case of a maximally rotating BTZ black hole in section 3, and show that the growth in time of the eikonal phase alternates between quadratic and exponential — with Lyapunov exponent associated to the nonzero ‘right-moving’ temperature. On average, the growth is cubic so that the scrambling may be qualified as slow. We will phrase this latter result in terms of the center-of-mass energy of the corresponding 2-to-2 particle scattering together with the topology of the black hole. We turn to superstratum microstate geometries in section 4, and point to the various effects that potentially distinguish the behaviour of the eikonal phase and OTOC, compared to the case of an extremal BTZ geometry.

3 OTOC in extremal BTZ

We now focus on the OTOC computation in the particular case of maximally rotating BTZ black holes. The latter being extremal and therefore having zero temperature, we expect additional subtleties compared to the computation of OTOCs in non-extremal BTZ black holes [15, 22, 23, 29].

The exterior region of extremal BTZ is commonly described using Schwarzschild coordinates (t, r, φ) with metric³

$$ds^2 = \ell_{\text{AdS}}^2 \left[- (r^2 - 2r_+^2) dt^2 + \frac{r^2 dr^2}{(r^2 - r_+^2)^2} - 2r_+^2 dt d\varphi + r^2 d\varphi^2 \right], \quad (3.1)$$

where the angular coordinate is periodically identified, $\varphi \sim \varphi + 2\pi$. The black hole horizon lies at $r = r_+$ while a timelike singularity lies at $r = 0$. The AdS conformal boundary lies at $r \rightarrow \infty$, has cylinder topology and is covered by the coordinate system (t, φ) . The Penrose diagram of extremal BTZ is displayed in figure 5. See [37, 38] for thorough reviews of three-dimensional BTZ black holes. In what follows, we will display time scales in terms of the time coordinate t , which is also the time coordinate of the dual CFT with a spatial circle of unit radius.

Being extremal, this black hole has zero Bekenstein-Hawking temperature. However, because it corresponds to a rotating ensemble, one can associate distinct temperatures to right- and left-moving modes,

$$T_L = 0, \quad T_R = \frac{r_+}{\pi}. \quad (3.2)$$

In particular, right-movers are at nonzero temperature. Extrapolating earlier results found in the case of non-maximally rotating BTZ black holes [22, 23], we can expect that the OTOC of scalar operators alternates between a polynomial growth associated to a zero left-moving temperature T_L and an exponential growth associated to a nonzero right-moving temperature T_R . We will show in section 3.2 that this is indeed the case.

We specify the coordinates of the boundary insertion points X_1 and X_2 of the OTOC as follows:

$$t_1 \equiv t_{\text{in}}, \quad \varphi_1 \equiv \varphi_{\text{in}}, \quad r_1 = \varepsilon^{-1}, \quad (3.3)$$

$$t_2 \equiv t_{\text{out}}, \quad \varphi_2 \equiv \varphi_{\text{out}}, \quad r_2 = \varepsilon^{-1}. \quad (3.4)$$

Here, we consider $\varepsilon \ll 1$ as a holographic regulator measuring how close to the conformal boundary operators are inserted. The specification of the other two boundary insertion points X_3 and X_4 is made through a choice of point-splitting regulator ξ of the type (2.12), which we make in such a way that both ingoing and outgoing geodesics connecting the above insertion points have zero angular momentum. This is always possible to achieve, and we leave the expression of ξ implicit. Following the geodesic approximation described in section 2, the computation of the OTOC at early times $\delta \lesssim 1$ (see section 2) amounts

³Useful formulae may be found in [36].

to the evaluation of the eikonal phase factor (2.8) encoding the gravitational interaction of the two geodesics. As we will show, the energy E of the associated particles scales like $E \sim \varepsilon^{-1}$ such that, in the limit $\varepsilon \rightarrow 0$, they follow null trajectories.

3.1 Highly energetic particles

Evaluation of the OTOC through the geodesic approximation scheme presented in section 2 requires one to consider the ingoing timelike geodesic connecting the insertion point $(\varepsilon^{-1}, t_{\text{in}}, \varphi_{\text{in}})$, with initial velocity k^μ proportional to the point-splitting regulator ξ^μ as shown in (2.19). The outgoing timelike geodesic connecting the insertion point $(\varepsilon^{-1}, t_{\text{out}}, \varphi_{\text{out}})$ has to be considered similarly. We start by showing that at leading order in $\varepsilon \ll 1$, we can switch to a description in terms of null geodesics. We then give the expressions of the stress tensor and gravitational shock wave associated to each one of these null geodesics, which will be needed in section 3.2 in order to compute the eikonal phase and OTOC.

Timelike geodesics. A timelike geodesic with velocity $k^\mu = \dot{x}^\mu = dx^\mu/d\tau$ has conserved energy⁴ E and angular momentum L associated to the Killing vectors ∂_t and ∂_φ of the extremal BTZ metric (3.1),

$$E = -(\partial_t)^\mu k_\mu, \quad L = (\partial_\varphi)^\mu k_\mu, \quad k^2 = -1. \quad (3.5)$$

In terms of these conserved quantities, the radial velocity of a timelike geodesic satisfies [39]

$$r^2 \dot{r}^2 = -(r^2 - r_+^2)^2 + (E^2 - L^2) r^2 + 2(L^2 - EL) r_+^2. \quad (3.6)$$

The choice of point-splitting regulator ξ^μ determines the velocity k^μ of the geodesics at the insertion points. Since ξ^μ is tangent to the (cutoff) boundary, the latter necessarily has vanishing radial component, $\dot{r} = 0$. In addition, we choose the orientation of ξ^μ in such a way that these geodesics also have zero angular momentum $L = 0$. Plugging these requirements into (3.6), we find the value of the energy,

$$E = \varepsilon^{-1} \left(1 - \varepsilon^2 r_+^2\right). \quad (3.7)$$

In the limit $\varepsilon \rightarrow 0$ where the insertion points are taken to the conformal boundary, the energy of these geodesics simply diverges and their trajectories coincide with those of the corresponding null geodesics; see also [29]. In the following, we work at leading order in $\varepsilon \ll 1$, at which we can simply approximate the trajectories of the highly energetic particles of interest by null geodesics with energy $E = \varepsilon^{-1}$ and angular momentum $L = 0$. We switch to this leading order approximation in what follows.

Null geodesics and shock waves. We thus restrict our attention to null geodesics. In terms of the null velocity k^μ , the conserved energy and angular momentum are

$$E = -(\partial_t)^\mu k_\mu, \quad L = (\partial_\varphi)^\mu k_\mu, \quad k^2 = 0. \quad (3.8)$$

⁴Following the choice of normalization $k^2 = -1$, E and L are the conserved energy and angular momentum *per unit mass*.

The null geodesic equations are then given by [39]

$$\dot{t} = \frac{Er^2 - Lr_+^2}{(r^2 - r_+^2)^2}, \quad (3.9a)$$

$$\dot{\phi} = \frac{Er_+^2 + L(r^2 - 2r_+^2)}{(r^2 - r_+^2)^2}, \quad (3.9b)$$

$$r^2\dot{r}^2 = (E^2 - L^2)r^2 + 2(L^2 - EL)r_+^2. \quad (3.9c)$$

To describe the ingoing geodesic, it is convenient to define retarded coordinates (r, v, ϕ) through

$$t = v + \frac{r}{2(r^2 - r_+^2)} - \frac{1}{4r_+} \ln \frac{r - r_+}{r + r_+}, \quad (3.10a)$$

$$\varphi = \phi + v + \frac{r}{2(r^2 - r_+^2)} + \frac{1}{4r_+} \ln \frac{r - r_+}{r + r_+}, \quad (3.10b)$$

such that the extremal BTZ metric becomes

$$ds^2 = 2drdv + 2(r^2 - r_+^2)d\phi dv + r^2d\phi^2. \quad (3.11)$$

In these coordinates, the coefficient of $d\phi dv$ vanishes at the horizon so that these coordinates give the co-rotating frame for infalling particles at the horizon. In retarded coordinates, the ingoing geodesic of interest with $E = \varepsilon^{-1}$ and $L = 0$ takes a particularly simple form. By differentiating equations (3.10a) and (3.10b) and using the negative root of (3.9c) for \dot{r} , one finds that its velocity is purely radial,

$$k_V = -\varepsilon^{-1}\partial_r, \quad (3.12)$$

such that its trajectory is

$$v(r) = v_{\text{in}} = t_{\text{in}}, \quad \phi(r) = \phi_{\text{in}} = \varphi_{\text{in}} - t_{\text{in}}. \quad (3.13)$$

From (2.10), its stress tensor has only one non-trivial component,

$$T_V^{rr} = -\frac{m_V \varepsilon^{-1}}{\sqrt{-g}} \delta(v - v_{\text{in}}) \delta(\phi - \phi_{\text{in}}). \quad (3.14)$$

On the other hand, the velocity of the outgoing geodesic with $E = \varepsilon^{-1}$ and $L = 0$ is

$$k_W = \varepsilon^{-1} \left(\frac{2r^2\partial_v}{(r^2 - r_+^2)^2} + \partial_r - \frac{2\partial_\phi}{r^2 - r_+^2} \right), \quad (3.15)$$

while its trajectory can be found by integrating the velocity and can be parametrized by

$$v(r) = t_{\text{out}} - \frac{r}{r^2 - r_+^2} + \frac{1}{2r_+} \ln \frac{r - r_+}{r + r_+}, \quad (3.16a)$$

$$\phi(r) = \varphi_{\text{out}} - t_{\text{out}} - \frac{1}{r_+} \ln \frac{r - r_+}{r + r_+}. \quad (3.16b)$$

Retarded coordinates are well suited to compute the term $h_{\mu\nu}^W T_V^{\mu\nu}$ in the eikonal phase (2.8), due to the simple form of the stress tensor (3.14). On the other hand, to compute the other term $h_{\mu\nu}^V T_W^{\mu\nu}$ in (2.8), it is more convenient to turn to the advanced coordinate system (r, u, ϕ') defined through

$$t = u - \frac{r}{2(r^2 - r_+^2)} + \frac{1}{4r_+} \ln \frac{r - r_+}{r + r_+}, \quad (3.17a)$$

$$\varphi = \phi' + u - \frac{r}{2(r^2 - r_+^2)} - \frac{1}{4r_+} \ln \frac{r - r_+}{r + r_+}. \quad (3.17b)$$

In the following we focus on the $h_{\mu\nu}^W T_V^{\mu\nu} = h_{rr}^W T_V^{rr}$ contribution. We have checked that, as in previous work [15], this is also equal to the $h_{\mu\nu}^V T_W^{\mu\nu}$ contribution.

The relevant component of the shock wave sourced by the outgoing particle is computed in appendix C and is obtained from (C.17),

$$h_{rr}^W = -\frac{4\pi G_N m_W}{r_+^2 \varepsilon} \sum_{n \in \mathbb{Z}} f(r_+ \Delta v, r_+ (\Delta v + \Delta \phi_n)) \delta(r - r_0(v, \phi)) \Theta(-\Delta \phi_n) \Theta(2\Delta v + \Delta \phi_n), \quad (3.18)$$

with

$$r_0(v, \phi) = \frac{1}{2\Delta v + \Delta \phi_n} - r_+ \coth(r_+ \Delta \phi_n), \quad (3.19)$$

and

$$f(t, x) \equiv \begin{cases} (t+x)^2, & t+x < \sinh(t-x), \\ \sinh^2(t-x), & t+x \geq \sinh(t-x), \end{cases} \quad (3.20)$$

where $\Delta v = v_{\text{out}} - v$, $\Delta \phi_n = \phi_{\text{out}} - \phi + 2\pi n$ and Θ denotes the Heaviside function. Note that, due to the ϕ -direction being periodic, the shock wave includes the contribution of many ‘images’ of the outgoing geodesic, appearing in (3.18) through the summation over $n \in \mathbb{Z}$. The shock wave of a single image geodesic has support on a surface determined by the Dirac delta function and the Heaviside functions in (3.18), in such a way that a given bulk point (v, r, φ) lies at most on a finite number of shock wave images. Indeed, for fixed values of the coordinates, only a finite number of images satisfy $-2\Delta v \leq \Delta \phi_n \leq 0$.

3.2 Eikonal phase

With the analysis of the previous section, we are in a position to compute the eikonal phase (2.8). Using (3.14) and (3.18), we find

$$\delta = \frac{1}{4} \int \sqrt{-g} (h_{\mu\nu}^V T_W^{\mu\nu} + h_{\mu\nu}^W T_V^{\mu\nu}) = \frac{2\pi G_N m_V m_W}{r_+^2 \varepsilon^2} \sum_{\substack{n \in \mathbb{Z} \\ |\Delta \varphi_n| \leq \Delta t}} f(r_+ \Delta t, r_+ \Delta \varphi_n), \quad (3.21)$$

with $\Delta t = t_{\text{out}} - t_{\text{in}}$ and $\Delta \varphi_n = \varphi_{\text{out}} - \varphi_{\text{in}} + 2\pi n$. Note that in terms of the boundary coordinates (t, φ) , the condition $-2\Delta v \leq \Delta \phi_n \leq 0$ on the sum translates to $|\Delta \varphi_n| \leq \Delta t$. Thus boundary causality determines which images should be included in the sum. Figure 6 displays the level sets of the eikonal phase. In figure 6 (a), we see the contribution of the first image. The orange line tracks the cusp in the eikonal phase, and corresponds to boundary insertions such that the dual particles collide in the bulk. The distinct accumulation of contour lines on each side of this orange line is due to the piecewise behaviour of the

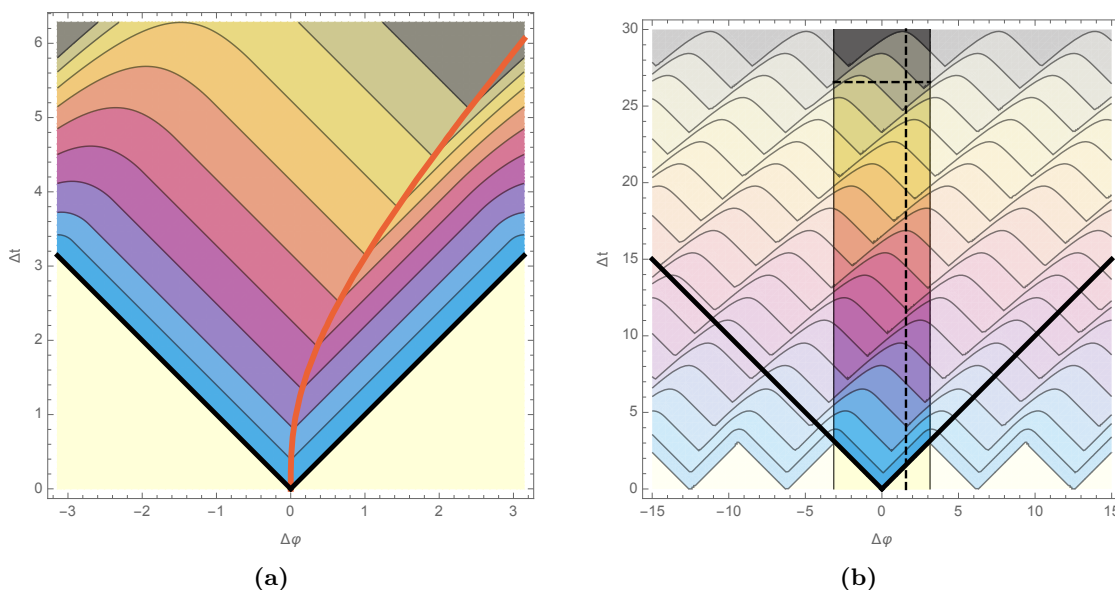


Figure 6. Contour plots of the eikonal phase $\delta(\Delta\varphi, \Delta t)$ in extremal BTZ, for $r_+ = 1$, and where the n^{th} contour level is given by a cubic function $(cn + d)^3$ with $c = 10^{-7}$ and $d = 10^{-7}$ in (a) and $(cn + d)^3$ with $c = 10^{-7}$ and $d = 15 \cdot 10^{-7}$ in (b). A cubic function would therefore have equidistant contour lines. (a) At small times, a single image contributes to the eikonal phase. The orange line characterizes the spatial separation for which δ is maximal at a fixed time separation, which corresponds to the boundary insertions for which the two geodesics cross with zero impact parameter in the bulk. On the right of this line, the growth as a function of time is exponential, while on the left there is power law growth. (b) The contour plot is extended for larger time separations, involving multiple images, while highlighting the physical domain $\Delta\varphi \in]-\pi, \pi]$. The behaviour of the eikonal phase along the vertical and horizontal dashed lines are shown in figures 3 and 7, respectively.

function $f(t, x)$ defined in (3.20), which is quadratic on the left and exponential on the right. Figure 6 (b) shows the full result which involves a sum over images. The fictitious region from which ‘image particles’ are emitted is represented in lighter colors, while the physical periodic region corresponding to $\Delta\varphi \in]-\pi, \pi]$ is brighter, with $\Delta\varphi = \varphi_{\text{out}} - \varphi_{\text{in}}$.

The time-dependence of the eikonal phase is easier to visualize from figure 3, which corresponds to the dashed vertical cut of figure 6. To properly understand the various features that appear, it is useful to further analyze the result (3.21). Consider the sum appearing in (3.21). It can be split into two elementary sums according to the two cases of the piecewise function,

$$\sum_{\substack{n \in \mathbb{Z} \\ |\Delta\varphi_n| \leq \Delta t}} f(r_+ \Delta t, r_+ \Delta\varphi_n) = \text{II} + \text{III}, \tag{3.22}$$

$$\text{II} = \sum_{n = -\lfloor \frac{\Delta t + \Delta\varphi}{2\pi} \rfloor}^{\lfloor n_* \rfloor} r_+^2 (\Delta t + \Delta\varphi + 2\pi n)^2, \quad \text{III} = \sum_{n = \lfloor n_* \rfloor}^{\lfloor \frac{\Delta t - \Delta\varphi}{2\pi} \rfloor} \sinh^2 [r_+ (\Delta t - \Delta\varphi - 2\pi n)], \tag{3.23}$$

where n_* is the real number at which the transition between the two cases occurs, and satisfies

$$r_+(\Delta t + \Delta\varphi + 2\pi n_*) = \sinh[r_+(\Delta t - \Delta\varphi - 2\pi n_*)]. \quad (3.24)$$

These sums are simple to evaluate, but the full expression is a bit involved so we will not write it out in full here. We will focus instead on the behaviour in the late time regime. The transition point n_* can be approximated in the large $\Delta t \gg 1$ regime by,

$$2\pi n_* = \Delta t - \Delta\varphi - \frac{\log(4r_+\Delta t)}{r_+} + O\left(\frac{\log(r_+\Delta t)}{r_+^2\Delta t}\right). \quad (3.25)$$

Using this approximation along with the fact that $[x] = x - (x \bmod 1)$, we obtain

$$\delta = \frac{4\pi G_N m_V m_W}{\varepsilon^2} \left\{ \frac{2\Delta t^3}{3\pi} - \frac{\Delta t^2 \log(4r_+\Delta t)}{\pi r_+} + \left(1 - \frac{\left[\left(\Delta t - \Delta\varphi - \frac{\log(4r_+\Delta t)}{r_+} \right) \bmod 2\pi \right]}{\pi} + 2 \frac{e^{2r_+ \left[\left(\Delta t - \Delta\varphi - \frac{\log(4r_+\Delta t)}{r_+} \right) \bmod 2\pi \right]}}{e^{4\pi r_+} - 1} \right) \Delta t^2 + O(\Delta t) \right\}. \quad (3.26)$$

Average slow scrambling. The average growth of the eikonal phase for times $\Delta t \gg 1$ is well described by equation (3.26). In particular, it is cubic up to subleading contributions. One of these subleading contributions is of the form (periodic function) $\times \Delta t^2$, which suggests a sawtooth-like behaviour around this average cubic growth. Indeed, we can observe in figure 3 that the average value of the eikonal phase follows the cubic orange dashed line, with sawtooth-modulation around this cubic growth. The scrambling time Δt_s defined as the time at which $\delta \sim 1$, is inferred from this average cubic growth,

$$\Delta t_s \simeq \left(\frac{3\varepsilon^2}{8G_N m_V m_W} \right)^{\frac{1}{3}} = \left(\frac{c\varepsilon^2}{16h_V h_W} \right)^{\frac{1}{3}}. \quad (3.27)$$

The second equality gives the expression of the scrambling time in terms of CFT quantities, namely the central charge $c = \frac{3}{2G_N}$ and the conformal weights $2h_{V,W} \approx m_{V,W} \gg 1$ and reproduces (1.10) from the introduction.

The average cubic growth could have been obtained in a much simpler fashion by considering the dependence of the center-of-mass energy of the scattered particles on the time separation of their boundary insertion points, together with the angular periodicity of the background spacetime leading to contributions from multiple image particles. Indeed, the center-of-mass energy s associated to the scattering of the two null geodesics with momentum (3.12) and (3.15) and colliding at $r = r_*$ is proportional to

$$k_V \cdot k_W = -\frac{2r_*^2}{\varepsilon^2(r_*^2 - r_+^2)^2}. \quad (3.28)$$

From the trajectories of the geodesics given by (3.13) and (3.16), one can relate r_* to the time separation of the boundary points,

$$\Delta t = t_{\text{out}} - t_{\text{in}} = \frac{r_*}{r_*^2 - r_+^2} - \frac{1}{2r_+} \ln \frac{r_* - r_+}{r_* + r_+}. \quad (3.29)$$

At late times, the geodesics scatter close to the horizon so that the separation is given at leading order by

$$\Delta t = \frac{1}{2(r_* - r_+)} + O\left(\ln\left(\frac{r_*}{r_+} - 1\right)\right), \quad (3.30)$$

such that the center-of-mass energy scales like

$$k_V \cdot k_W = \frac{\varepsilon^{-2}}{2(r_* - r_+)^2} + O\left(\left(\frac{r_*}{r_+} - 1\right)^{-1}\right) \approx 2\varepsilon^{-2}\Delta t^2. \quad (3.31)$$

Hence, the center-of-mass energy of the particle scattering grows quadratically with Δt . The discrepancy between this estimate and the cubic growth found from (3.26) is explained by the angular periodicity of the solution. Indeed, the number n of image particles contributing to the sum (3.22) actually grows linearly with time. Equivalently, the two physical scattered particles are seen to circle around the black hole and the number of times they meet grows linearly with Δt . In summary, the average cubic growth of the eikonal phase δ may be inferred from the quadratic growth of the center-of-mass energy s together with the linear growth in the number of particle images.

Sawtooth pattern. We would now like to understand the sawtooth pattern appearing on top of the average growth in figure 3. For this it is useful to analyze (3.22) in more detail. The two sums, II and III, have very different behaviours. First, we note that for $\Delta t \gg 1$ the range of n in II scales as $\Delta t/\pi$ whereas in III it scales as $r_+^{-1} \log(4r_+\Delta t)$. Since the summand in II is a $O(\Delta t^2)$ polynomial, a sum over Δt terms leads to a Δt^3 scaling. On the other hand, the summand in III is exponential and so its scaling is controlled by the largest term at $n = \lceil n_* \rceil$. The logarithmic term in n_* leads to an overall Δt^2 growth for this sum,

$$\sinh^2[r_+(\Delta t - \Delta\varphi - 2\pi\lceil n_* \rceil)] \sim 4r_+^2\Delta t^2 e^{-4\pi r_+} e^{2r_+ \left[\left(\Delta t - \Delta\varphi - \frac{\log 4r_+\Delta t}{r_+} \right) \bmod 2\pi \right]}. \quad (3.32)$$

This explains why II dominates the overall value of the eikonal phase.

Let us now consider the sum II in more detail. On small time intervals, this sum has a fixed number of terms, each contributing an $O(\Delta t^2)$ growth, so it exhibits quadratic growth. An example of such quadratic growth is represented by the dotted green line in figure 3. On larger time scales, the number of terms jumps discretely as additional images are included, and grows on average as $O(\Delta t)$. Thus the locally quadratic but overall cubic growth comes from a behaviour that can be schematically written as

$$\text{II} \sim \lfloor \Delta t \rfloor \Delta t^2. \quad (3.33)$$

A sawtooth pattern appears because both sums compete in the time derivative of the eikonal phase. First, note that the bounds of the sums involve floors such that they are mostly constant except for discontinuities when a new image must be included. Therefore, except at these cusps in δ , a time derivative only acts on the summands. This means that the time derivative of the sum \mathbb{I} is reduced to $O(\Delta t^2)$, at which order it will have to compete with the time derivative of \mathbb{III} . Indeed,

$$\frac{d\delta}{d\Delta t} \sim \frac{4G_N m_V m_W}{\varepsilon^2} \left(1 + 4\pi r_+ \frac{e^{2r_+ \left[\left(\Delta t - \Delta\varphi - \frac{\log 4r_+ \Delta t}{r_+} \right) \bmod 2\pi \right]}}{e^{4\pi r_+} - 1} \right) \Delta t^2 + O(\Delta t), \quad (3.34)$$

where the two terms in parentheses come from the two sums, respectively. The relative size of the two terms changes depending on whether we look right before or after the cusp. These correspond to whether $\left[\left(\Delta t - \Delta\varphi - \frac{\log 4r_+ \Delta t}{r_+} \right) \bmod 2\pi \right]$ is just below 2π or just above 0, respectively,

$$\frac{d\delta}{d\Delta t} = \frac{4G_N m_V m_W}{\varepsilon^2} \begin{cases} \left(1 + \frac{4\pi r_+}{1 - e^{-4\pi r_+}} \right) \Delta t^2 + O(\Delta t), & \left[\left(\Delta t - \Delta\varphi - \frac{\log 4r_+ \Delta t}{r_+} \right) \bmod 2\pi \right] \lesssim 2\pi, \\ \left(1 + \frac{4\pi r_+}{e^{4\pi r_+} - 1} \right) \Delta t^2 + O(\Delta t), & \left[\left(\Delta t - \Delta\varphi - \frac{\log 4r_+ \Delta t}{r_+} \right) \bmod 2\pi \right] \gtrsim 0. \end{cases}$$

Right before the cusp, the contribution to the derivative from \mathbb{III} is biggest since $\frac{4\pi r_+}{1 - e^{-4\pi r_+}} > 1$ for $r_+ > 0$. Conversely, right after the cusp, the contribution to the derivative from \mathbb{I} is biggest since $\frac{4\pi r_+}{e^{4\pi r_+} - 1} < 1$ for $r_+ > 0$. At $r_+ = 0$ the two terms become equal, as we return to the vacuum answer. The sawtooth is sharpest when r_+ is large and there is a sharp hierarchy between the two contributions.

The cross-over between the two behaviours, seen in figure 7, occurs when the two terms in (3.34) are equal, i.e.

$$\left[\left(\Delta t - \Delta\varphi - \frac{\log 4r_+ \Delta t}{r_+} \right) \bmod 2\pi \right] = \pi + \frac{1}{2r_+} \log \left(\frac{\sinh(2\pi r_+)}{2\pi r_+} \right), \quad (3.35)$$

such that the part of the sawtooth with exponential growth decreases as r_+ increases. This is compatible with the fact that the rate of exponential growth is $2r_+$ and so when r_+ is increased the same amount of catch-up growth to interpolate between the local quadratic and overall cubic growth can be achieved in a shorter time.

The OTOC in non-maximally rotating BTZ. We would also like to comment on a connection with previous work which has studied the OTOC in rotating ensembles [22, 23]. In those works the OTOC was computed by multiplying the center-of-mass energy with a shock wave profile computed by assuming that the scattering occurs on the horizon. In the finite temperature case, this is a good approximation in the regime $\Delta t \gg \beta$. However, in the extremal limit, this shock wave profile (denoted $f(\phi)$ in [22] and $h(\phi)$ in [23]) diverges. This can be seen by looking at equation (5.17) in [23] for example. This is why in our approach, it was important that we did not approximate the shock wave by putting it on the horizon in the description of the gravitational scattering. Nonetheless, the shock wave profile from [23] can be regulated by subtracting a term that diverges in the near extremal

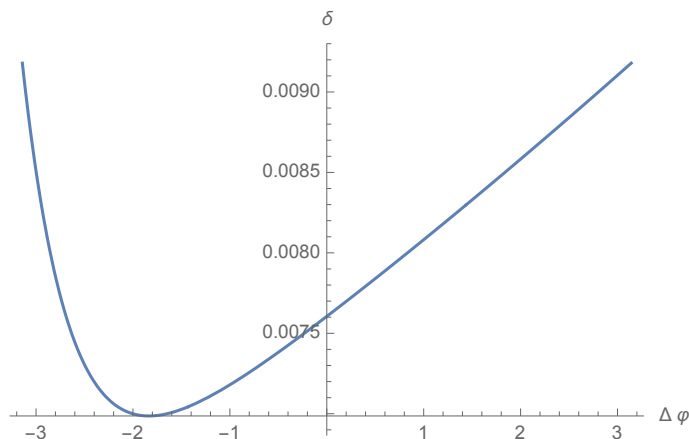


Figure 7. The spatial dependence of the eikonal phase in extremal BTZ at $r_+ = 1$, for a fixed time separation, $\Delta t \gg 1$, corresponding to the horizontal dashed line in figure 6. The time separation has been chosen such that the cusp would be on the edges $\Delta\varphi = \pm\pi$. The cross-over between the exponential and power-law behavior is also visible in this figure, with the location of the trough given by (3.35). The φ -dependence of the eikonal phase is encoded in the subleading $O(t^2)$ terms of (3.26). Up to a redefinition $\phi \rightarrow \Delta t - \Delta\varphi - \frac{\log 4r_+ \Delta t}{r_+}$, this precisely matches the shape of the shockwave in the extremal limit in [23], after subtracting the divergent piece (although the latter shockwave is a priori only valid for $t \gg \beta \rightarrow \infty$).

limit, yet is constant in Δt and $\Delta\varphi$.⁵ The regulated shock wave then corresponds to the terms of $O(\Delta t^2)$ in parentheses in (3.26). This regulated shock wave does not help with computing the leading growth of Δt^3 in (3.26), which arose from the sum of an interaction of strength $O(\Delta t^2)$ over Δt images. The number of images is controlled by how deep the interaction happens in the bulk and taking the approximation that the scattering happens on the horizon would correspond to including an infinite number of these images. Since in the extremal case the shock wave has a power-law tail, this cutoff regulating the sum over images is important to track. On the other hand, the sawtooth pattern on top of this overall growth, contained in the $O(\Delta t^2)$ term, does correspond to considering the regulated

⁵Using the conventions of (5.17) in [23], in the near extremal limit,

$$h(\phi) \simeq \frac{1}{2\pi(r_+ - r_-)} + \frac{1}{2} \left(1 - \frac{(\phi \bmod 2\pi)}{\pi} + \frac{2e^{2r_+(\phi \bmod 2\pi)}}{e^{4\pi r_+} - 1} \right) + O(r_+ - r_-).$$

Notice that this matches the $O(\Delta t^2)$ term in parentheses in (3.26) up to the replacement $\phi \rightarrow \Delta t - \Delta\varphi - \frac{\log(4r_+ \Delta t)}{r_+}$. The constant factors multiplying the parentheses can be understood by comparing the relevant conventions and using the expression (3.31) for the center-of-mass energy in extremal BTZ. The variable ϕ in that work corresponded to a co-rotating coordinate. In the extremal limit, that co-rotating coordinate becomes null. Similarly, the expression $\Delta t - \Delta\varphi - \frac{\log(4r_+ \Delta t)}{r_+}$ appearing in our result can be thought of as a type of co-rotating coordinate slightly regulated so that it does not become null in the extremal limit. This is also related to the retarded coordinates defined in (3.10), where an additional logarithmic term was required compared to the similar coordinates in the non-extremal case. This term was required to ensure that a radially infalling null geodesic stays at constant ϕ . Alternatively, it can be understood as the term required for the infalling coordinates to be co-rotating at the horizon rather than at the boundary. Notice that the $d\varphi dt$ term is subleading at the conformal boundary in (t, r, φ) coordinates, (3.1), whereas the $d\phi dv$ vanishes at the horizon in (v, r, ϕ) coordinates, (3.11).

extremal limit of the shock wave computed on the horizon in the non-extremal geometry times the center-of-mass energy of two colliding geodesics in extremal BTZ. The spatial dependence of the eikonal phase, which coincides with the dependence of the shockwave, is displayed in figure 7.

4 Microstate geometries

We have seen above that the OTOC can be computed within a WKB approximation by studying the exchange of a gravitational shock wave between two boundary anchored geodesics. The strength of the interaction was controlled by the energy of the interacting geodesics in the center-of-mass frame. The form of the gravitational shock wave also played an important role in controlling the sum over images that appears due to the periodic spatial direction on the boundary.

In this section, we will consider a family of three-charge microstate geometries constructed in [7, 40]. These are 10-dimensional IIB supergravity solutions reduced to 6 dimensions on a T^4 dual to BPS states of $\mathcal{N} = 4$ SYM. These geometries have the form of a 3-sphere fibred over an extremal BTZ black hole. At large radial coordinate of the BTZ base, they approach an asymptotic $\text{AdS}_3 \times S^3$. At intermediate radii they have a throat region which approximates the $\text{AdS}_2 \times S^1 \times S^3$ characteristic of the near horizon region of extremal BTZ. However at small radius, the throat region ends in a smooth cap at a finite proper distance.

In section 4.1, we introduce the metric of these geometries. In section 4.2, we discuss the black hole limit of the superstrata and how the quantities derived in this section can be compared to the computations in extremal BTZ black holes. In section 4.3, we study null geodesics in the superstrata, which will be required to compute the OTOC within the WKB approximation. In section 4.4, we use these results to discuss how the presence of the cap potentially modifies the behaviour of the OTOC in different regimes and identify a time scale where our geodesic approximation breaks down due to tidal forces. We find that these effects only become relevant after the time scale associated with scrambling when the commutator squared becomes $\mathcal{O}(1)$.

4.1 (1,0,n) superstrata

The superstrata are solutions of six-dimensional supergravity, with metric given by [11]

$$\begin{aligned}
 ds_6^2 = \sqrt{Q_1 Q_5} \Lambda \left[\frac{d\rho^2}{\rho^2 + a^2} - \frac{F_1(\rho)}{a^2(2a^2 + b^2)^2 F_2(\rho)} \left(dt - d\varphi + \frac{a^2(a^4 + (2a^2 + b^2)\rho^2)}{F_1(\rho)} (dt + d\varphi) \right)^2 \right. \\
 + \frac{a^2 \rho^2 (\rho^2 + a^2)}{F_1(\rho)} (dt + d\varphi)^2 + d\theta^2 + \frac{1}{\Lambda^2} \sin^2 \theta \left(d\phi_1 - \frac{2a^2}{(2a^2 + b^2)} dt \right)^2 \\
 \left. + \frac{F_2(\rho)}{\Lambda^2} \cos^2 \theta \left(d\phi_2 - \frac{1}{(2a^2 + b^2) F_2(\rho)} \left[-2a^2 dt + b^2 F_0(\rho) (dt - d\varphi) \right] \right)^2 \right], \tag{4.1}
 \end{aligned}$$

where φ goes around an S^1 with periodicity $\varphi \sim \varphi + 2\pi$. We have made the coordinate redefinition $t \rightarrow R_y t$ and $y \rightarrow R_y \varphi$ compared to the notation in [11]. This eliminates the parameter R_y from their solution in order to be consistent with the conventions used in the previous section. The following functions enter the above metric:

$$F_0(\rho) = 1 - \frac{\rho^{2n}}{(\rho^2 + a^2)^n}, \tag{4.2a}$$

$$F_1(\rho) = a^6 - b^2(2a^2 + b^2)\rho^2 F_0(\rho), \tag{4.2b}$$

$$F_2(\rho) = 1 - \frac{a^2 b^2}{2a^2 + b^2} \frac{\rho^{2n}}{(\rho^2 + a^2)^{n+1}}, \tag{4.2c}$$

$$\Lambda = \sqrt{1 - \frac{a^2 b^2}{2a^2 + b^2} \frac{\rho^{2n}}{(\rho^2 + a^2)^{n+1}} \sin^2 \theta}. \tag{4.2d}$$

In addition to the metric, there are various other supergravity fields turned on which we will not need here.

The superstrata solution is specified by the 3 parameters (a, b, n) . There are a number of conserved charges in supergravity which have non-zero values in this solution. The D-brane charges Q_1 and Q_5 only appear in the metric in the combination $Q_1 Q_5$, which is fixed in terms of the parameters of the superstrata solution by the regularity condition

$$Q_1 Q_5 = \left(a^2 + \frac{1}{2} b^2 \right). \tag{4.3}$$

This solution also has momentum charge along the S^1 parametrized by φ and angular momentum $J_L = J_R = J$ in planes that straddle both the BTZ and S^3 parts of the fibration. These charges are given by

$$Q_P = \frac{1}{2} b^2, \quad J = \frac{1}{2} \mathcal{N} a^2, \quad \mathcal{N} = \frac{\text{Vol}(T^4)}{\ell_{10}^8}, \tag{4.4}$$

where $\text{Vol}(T^4)$ is the normalised volume of the T^4 as defined in [11] and ℓ_{10} is the 10-dimensional Planck length. An effective 6-dimensional Planck length can be introduced

$$\ell_6^4 \equiv \frac{\ell_{10}^8}{\text{Vol}(T^4)}, \tag{4.5}$$

in terms of which

$$J = \frac{a^2}{2\ell_6^4}. \tag{4.6}$$

These supergravity solutions have well understood CFT duals which are described in [7, 11]. Their central charge is controlled by two quantised numbers N_1 and N_5 corresponding to the number of units of D-brane charge in the supergravity solution. We will not discuss these CFTs in detail here except to note that the supergravity charges $Q_{1,5}$ are related to the central charge of the CFT by

$$c = 6N_1 N_5 = 6 \frac{Q_1 Q_5}{\ell_6^4}. \tag{4.7}$$

Note that we can also relate the central charge to the three-dimensional Newton constant through the Brown-Henneaux formula [41],

$$c = \frac{3}{2G_N}. \tag{4.8}$$

4.2 Black hole limit of the superstrata

We now study the $a \rightarrow 0$ limit of the superstrata, where it approaches the extremal BTZ black hole. This allows the parametrization of the superstrata used so far to be related to r_+ parametrizing the extremal BTZ black hole.

In the limit $a \rightarrow 0$, the metric (4.1) becomes

$$ds^2 = \sqrt{Q_1 Q_5} \left[\frac{d\rho^2}{\rho^2} - \frac{2\rho^2}{b^2} (dt^2 - d\varphi^2) + n(dt - d\varphi)^2 + d\theta^2 + \sin^2 \theta d\phi_1^2 + \cos^2 \theta d\phi_2^2 \right]. \tag{4.9}$$

To make contact with the extremal BTZ black hole in the form (3.1), one can use the regularity condition (4.3) and the fact that $a \ll b$, to identify

$$\rho^2 = \frac{b^2}{2}(r^2 - n), \quad n = r_+^2, \quad Q_1 Q_5 = \ell_{\text{AdS}}^4 \simeq \frac{1}{2} b^2. \tag{4.10}$$

In other words, b controls the overall scale of the geometry through ℓ_{AdS} and n controls the right-moving temperature (3.2) of the approximate extremal BTZ geometry,

$$T_R = \frac{\sqrt{n}}{\pi}. \tag{4.11}$$

At the conformal boundary, $r \rightarrow \infty$, t is equal to the dimensionless time on the boundary measured in units of the radius of the boundary circle (taken to be unity), while φ is an angular coordinate on that same circle. To be consistent with the previous section, we should set $\ell_{\text{AdS}} = 1$ which means that $b = \sqrt{2}$, however since the existing literature on these geometries keeps b in expressions we will do so as well.

The remaining parameter, a , controls the deviations from this extremal BTZ. More concretely, let us investigate the region where the superstrata closely approximates the throat of extremal BTZ. This throat sets in for

$$\rho \ll \frac{\sqrt{nb}}{\sqrt{2}} \equiv \rho_{\text{throat}}, \tag{4.12}$$

which is where the radius of the S^1 is approximately constant. In BTZ, this translates to $r^2 - r_+^2 \ll r_+^2$. It provides a good approximation for the geometry as long as $\rho \gg \sqrt{na}$, after which the radius of the throat starts to shrink again until it pinches off at the tip of this cap region as described in detail in [11]. Therefore the relevant length scale associated with the start of the cap region is

$$\rho_{\text{cap}} \equiv \sqrt{na}. \tag{4.13}$$

The proper length along the radial direction of the throat region, depicted in figure 4, is

$$(Q_1 Q_5)^{\frac{1}{4}} \log \left(\frac{\rho_{\text{throat}}}{\rho_{\text{cap}}} \right). \tag{4.14}$$

The ratio controlling the depth of the throat can also be expressed as

$$\frac{\rho_{\text{throat}}^2}{\rho_{\text{cap}}^2} = \frac{b^2}{2a^2} = \frac{Q_1 Q_5}{2\ell_6^4 J} = \frac{N_1 N_5}{2J}. \quad (4.15)$$

For a fixed value of the central charge, or equivalently $N_1 N_5$, the longest throats are obtained by setting J to be as small as possible. Since it is quantised, this is $J = \frac{1}{2}$ [11]. This corresponds to the regime of superstrata parameter space which is closest to the extremal BTZ ensemble, since it has the minimal extra angular momentum in the extra dimensions. In the following, we set $J = \frac{1}{2}$.

With this top-down understanding of how an extremal BTZ appears as a limit of these microstate geometries, the scrambling time computed in (3.27) can be expressed in terms of the parameters of the dual CFT state,

$$\Delta t_s = \left(\frac{3\varepsilon^2 N_1 N_5}{8h_V h_W} \right)^{\frac{1}{3}}. \quad (4.16)$$

Note that in this section we have worked in the regime $a \ll b$, where the physical identification of a long extremal BTZ throat makes sense. In extending the definition of these parameters away from this regime, it may be natural to include additional terms that are subleading in the $a \ll b$ limit.

4.3 Geodesics of the superstrata

The geodesic method for computing the OTOC, outlined in section 2 and applied in section 3 to extremal BTZ, involves an ingoing and an outgoing null geodesic that are both anchored on the boundary and interact in the bulk of the geometry. In this section, we will analyze such geodesics in the microstate geometries described by (4.1). Geodesics in the superstrata geometries were studied in [27, 32]. The present analysis is based on the results of [32], which analyzed timelike geodesics dropped into the throat region of these geometries. As was done there, we will also restrict ourselves to geodesics with $\theta = \frac{\pi}{2}$, which is a fixed point of the $\theta \rightarrow \pi - \theta$ symmetry.

Working in $(t, \varphi, \rho, \theta, \phi_1, \phi_2)$ coordinates, the Killing vectors associated to the isometries of the metric (4.1) are given by ∂_t , ∂_φ , ∂_{ϕ_1} and ∂_{ϕ_2} , with associated conserved momenta

$$E = -(\partial_t)^\mu k_\mu, \quad P_\varphi = (\partial_\varphi)^\mu k_\mu, \quad L_1 = (\partial_{\phi_1})^\mu k_\mu, \quad L_2 = (\partial_{\phi_2})^\mu k_\mu, \quad (4.17)$$

where $x^\mu(\tau)$ is a parametrization of the geodesic in question and $k^\mu = dx^\mu/d\tau$. We set $P_\varphi = 0$ as was done in the previous section when studying the extremal BTZ black hole. We also set $L_1 = 0$ and $L_2 = 0$ so that the geodesic does not have extra angular momentum in the S^3 .

The equations (4.17) can be solved to express components of the velocity in terms of the energy E ,

$$\frac{dt}{d\tau} = \frac{(2a^2 + b^2)((2a^2 + b^2)(\rho^2 + a^2)^n - b^2\rho^{2n})}{2\sqrt{2}a^2(\rho^2 + a^2)^{n+1}\sqrt{(2a^2 + b^2) - a^2b^2\rho^{2n}(\rho^2 + a^2)^{-(n+1)}}} E, \quad (4.18a)$$

$$\frac{d\varphi}{d\tau} = \frac{(2a^2 + b^2)b^2(\rho^2 + a^2)^{-\frac{1}{2}(n+1)}((\rho^2 + a^2)^n - \rho^{2n})}{2\sqrt{2}\sqrt{(2a^2 + b^2)(\rho^2 + a^2)^{n+1} - a^2b^2\rho^{2n}}} E, \quad (4.18b)$$

$$\frac{d\phi_1}{d\tau} = \frac{(2a^2 + b^2)(\rho^2 + a^2)^n - b^2\rho^{2n}}{\sqrt{2}(\rho^2 + a^2)^{n+1}\sqrt{(2a^2 + b^2)(\rho^2 + a^2)^{n+1} - a^2b^2\rho^{2n}}} E, \quad (4.18c)$$

and $d\theta/d\tau = d\phi_2/d\tau = 0$. The condition that the geodesic be null, $k^2 = 0$, can be solved for the remaining component of the velocity

$$\left(\frac{d\rho}{d\tau}\right)^2 = \frac{2a^2 + b^2}{2a^2} \frac{(\rho^2 + a^2)((2a^2 + b^2)(\rho^2 + a^2)^n - b^2\rho^{2n})}{(2a^2 + b^2)(\rho^2 + a^2)^{n+1} - a^2b^2\rho^{2n}} E^2. \quad (4.19)$$

In order to find the trajectory of the geodesics we simply need to integrate the ratio of the velocities (4.18a) and (4.19)

$$t(\rho) - t(\infty) = \pm \int_{\rho}^{\infty} d\rho \frac{\sqrt{2a^2 + b^2}\sqrt{(2a^2 + b^2)(\rho^2 + a^2)^n - b^2\rho^{2n}}}{2a(\rho^2 + a^2)^{\frac{n}{2}+1}}. \quad (4.20)$$

This expression gives the coordinate time at which a null geodesic emitted from the boundary will probe a given radius of the geometry. Now consider two geodesics, one which leaves the boundary at t_{in} and one that is absorbed at the boundary at t_{out} . These two geodesics will rotate around the compact φ and ϕ_1 directions, but they will most strongly interact in the bulk when the ingoing and outgoing geodesics meet at the same radius, ρ_* .

A full computation of their interaction would require computing the dependence on the compact directions of the gravitational shock wave produced by geodesics in the superstrata geometry. However, here we will simply take the first steps towards understanding the difference between the superstrata and the extremal BTZ black hole. We will therefore focus on the motion in the ρ - t directions in order to better understand the effect of the cap in the superstrata geometry without the additional complication of the effects of these compact directions.

The radius where the two geodesics meet, ρ_* , is related to the difference of their insertion times at the boundary by

$$\Delta t(\rho_*) \equiv t_{\text{out}} - t_{\text{in}} = 2 \int_{\rho_*}^{\infty} d\rho \frac{\sqrt{2a^2 + b^2}\sqrt{(2a^2 + b^2)(\rho^2 + a^2)^n - b^2\rho^{2n}}}{2a(\rho^2 + a^2)^{\frac{n}{2}+1}}. \quad (4.21)$$

We will now proceed to study this expression in various regimes.

BTZ region. First, let us consider the region well outside the cap, where the geometry is well approximated by extremal BTZ $\times S^3$, for $\rho_*, b \gg a$,

$$\Delta t \simeq 2 \int_{\rho_*}^{\infty} \frac{\sqrt{2\rho^2 + nb^2}b}{2\rho^3} d\rho = \frac{b}{2\rho_*^2} \sqrt{2\rho_*^2 + nb^2} + \frac{1}{\sqrt{n}} \operatorname{arcsinh} \frac{\sqrt{nb}}{\sqrt{2}\rho_*}. \quad (4.22)$$

The OTOC will start probing the throat when $\rho_* = \rho_{\text{throat}}$, corresponding to a time separation on the boundary of

$$\Delta t_{\text{throat}} \simeq \left(\sqrt{2} + \text{arcsinh } 1\right) \frac{1}{\sqrt{n}} \implies \Delta t_{\text{throat}} \propto T_R^{-1}. \quad (4.23)$$

This timescale is controlled by the right-moving temperature of the extremal BTZ black hole approximated by this geometry. As expected, this time scale only depends on BTZ parameters and does not involve details of the cap region.

In this regime the motion of the geodesic along the BTZ factor of the geometry closely follows the trajectory of a geodesic in extremal BTZ, that is $(t(\rho), \varphi(\rho))_{\text{superstrata}} \simeq (t(\rho), \varphi(\rho))_{\text{BTZ}}$. In this asymptotic region, the geometry is approximately a product of BTZ and a homogeneous S^3 . The geodesics we consider do not have any angular momentum along the S^3 , such that they sit at a constant value of the sphere coordinates (θ, ϕ_1, ϕ_2) .

To understand where the corrections to the geometry first start to significantly affect the trajectory, the ratio of the first subleading term to this leading term must be examined. In the regime where $a \ll \rho_* \ll b$, by expanding $t(\rho)$ in (4.21) to subleading order, we find that this ratio is

$$-\frac{(n+5)a^2}{8\rho^2}. \quad (4.24)$$

By using a similar approach to compute $\varphi(\rho)$, we find the same ratio. The perturbative expansion used in (4.22) breaks down when this ratio is $O(1)$ at $\rho \sim \sqrt{n+5}a \sim \rho_{\text{cap}}$.

Cap region. In order to access the cap region, we can instead expand (4.21) in the regime where $\rho_*, a \ll b$. To do so, we must split the integral into two parts somewhere in the overlap of the applicability of the two approximations, at a radius ρ_{split} obeying both $\rho_{\text{split}}, b \gg a$ and $\rho_{\text{split}}, a \ll b$, i.e. $a \ll \rho_{\text{split}} \ll b$,

$$\Delta t \simeq 2 \int_{\rho_{\text{split}}}^{\infty} \frac{\sqrt{2\rho^2 + nb^2}b}{2\rho^3} d\rho + 2 \int_{\rho_*}^{\rho_{\text{split}}} \frac{\sqrt{(\rho^2 + a^2)^n - \rho^{2n}b^2}}{2a(\rho^2 + a^2)^{\frac{n}{2}+1}} d\rho \simeq \frac{b^2}{a^2} \chi_n \left(\frac{\rho_*}{a}\right) \quad (4.25)$$

where only the leading term in $\frac{b}{a} \gg 1$ has been kept and the following dimensionless integral was introduced,

$$\chi_n(x) \equiv \int_x^{\infty} \frac{\sqrt{(\xi^2 + 1)^n - \xi^{2n}}}{(\xi^2 + 1)^{\frac{n}{2}+1}} d\xi. \quad (4.26)$$

The minimal separation between the insertions on the boundary so that the OTOC can directly probe the cap occurs when $\rho_* = \rho_{\text{cap}}$, so that

$$\Delta t_{\text{cap}} \simeq \frac{b^2}{a^2} \chi_n(\sqrt{n}). \quad (4.27)$$

At large x , $\chi_n(x) \simeq \frac{\sqrt{n}}{2x^2}$, so that at large n , $\chi_n(\sqrt{n}) \simeq \frac{1}{2\sqrt{n}}$. In fact, numerical investigation shows that for any $n \geq 1$,

$$\frac{1}{4} < \sqrt{n} \chi_n(\sqrt{n}) < \frac{1}{2}. \quad (4.28)$$

Therefore the time scale to reach the cap region is given by

$$\Delta t_{\text{cap}} \propto \frac{1}{\sqrt{n}} \frac{b^2}{a^2} \propto \frac{N_1 N_5}{T_R}, \tag{4.29}$$

reproducing the result quoted in the introduction in (1.11).

4.4 OTOC in the superstrata

Now that we have understood the trajectory of the relevant geodesics, we can see how this affects the computation of the OTOC in the superstrata geometry. First of all, we should be clear about the OTOC we wish to compute. In the asymptotic region, reducing on the compact $S^3 \times T^4$ of the 10-dimensional geometry leads to a Kaluza-Klein tower of fields from the 3-dimensional BTZ perspective. Each of the 3-dimensional fields in this tower corresponds to an operator in the dual 2-dimensional CFT. We will restrict ourselves to considering OTOCs of operators dual to the lowest field in this tower of Kaluza-Klein modes, which are completely delocalised along these extra compact dimensions. More precisely, this means that in the bulk-to-boundary propagators used to compute the OTOC, such as in equation (2.6), the boundary insertion point is integrated over $S^3 \times T^4$. In the part of the geometry well approximated by extremal BTZ $\times S^3 \times T^4$, this leads to fields which are completely homogeneous in the compact dimensions and which source a homogeneous shock wave. This is compatible with the fact that the geodesics in this region with no angular momentum along the S^3 follow BTZ geodesics as discussed in the previous section, so that the WKB approximation applied to the 3-dimensional reduction is consistent with the 6-dimensional picture. With this set up in mind, there are three major effects which will cause the computation of the OTOC in the superstrata to differ from the computation in extremal BTZ and we will discuss each one in turn.

First, the center-of-mass energy of the interacting geodesics will be modified once the bottom of the throat is reached. In BTZ, the center-of-mass energy continues to grow in an unbounded fashion as the interaction gets closer and closer to the horizon. In the superstrata, this growth is cut off by the depth of the throat once the interaction moves into the cap region. Below, we will compute the center-of-mass energy of two colliding geodesics as they fall down the throat of the superstrata and see how the growth in this quantity saturates. This will occur at the time scale set by Δt_{cap} . This time scale can be compared to the scrambling time, to determine whether the effect of the cap will be felt before scrambling,

$$\frac{\Delta t_{\text{cap}}}{\Delta t_s} = \left(\frac{8h_V h_W (N_1 N_5)^2}{3\epsilon T_R^3} \right)^{\frac{1}{3}}. \tag{4.30}$$

We conclude that the OTOC will have exited the slow scrambling regime before the interaction reaches the cap, unless the right-moving temperature is very large,

$$T_R \gtrsim \left(\frac{h_V h_W (N_1 N_5)^2}{\epsilon} \right)^{\frac{1}{3}}. \tag{4.31}$$

Second, the shock wave will be modified by the presence of the cap. The geometry away from the cap is well approximated by a geometry with an extremal BTZ factor. Within this part of the geometry, all the fields remain homogeneous in the extra compact dimensions. Therefore the gravitational shock wave does not depend on these extra dimensions and the BTZ result can be used. In particular, the average time growth is cubic since the number of images contributing to the gravitational interaction grows linearly while each individual contribution is proportional to the center-of-mass energy $s \sim \Delta t^2$. Once the cap region is reached, the fibration of the S^3 over BTZ becomes non-trivial and the shock wave must be computed using the full 6-dimensional geometry.⁶

In the following, we will argue more carefully that the deformation of the geometry in the cap region does not affect the gravitational shock wave relevant to the OTOC at times before the interaction reaches the cap region. Consider the time slice where the first operator is inserted at t_{in} . On this slice we can find a solution to Einstein's equations that is compatible with this source and that is only supported near the boundary. As we evolve time forward, the shock wave will not probe deeper into the geometry than the null geodesic that sources it (the support of the shock wave is depicted in figure 9 in appendix C for non-compact φ). We can stop evolving time once we reach the interaction region. If this interaction occurs well outside the cap, $\rho_* \gg a$, the shock wave we needed to consider is only supported in the region where $\rho \gg a$. Since we know that this shock wave is a solution to Einstein's equations with a source at the geodesic for an extremal BTZ background and that the metric of the superstrata for $\rho \gg a$ is well approximated by extremal BTZ, then the shock wave will still be a solution in the superstrata up to subleading terms in a/ρ and a/b . The same argument can be run in reverse for the shock wave sourced by the outgoing geodesic, by starting at the time where it reaches the boundary, t_{out} and evolving the shock wave backwards in time to the interaction region.

Once the interaction reaches the cap region, this approximation will no longer be valid. Since the number of images included in the sum was essentially controlled by boundary causality, one may not expect this to change the overall scaling with Δt . However, the detailed form of the OTOC once the interaction reaches the cap region will be affected by the precise form of the shock wave in the 6 dimensional geometry. We will not compute this precise form in this work, but we are optimistic that it may be tractable to do so due to the successes in computing two-point functions in the superstrata in [11] thanks to the approximately separable form of the wave equation.

Finally, [31–34] found that probes falling into the throat of the superstrata feel strong tidal forces well before reaching the cap region. In fact, these strong tidal forces potentially invalidate the WKB approximation we have made in computing the OTOC. In particular, we expect the expansion of the geodesic congruence to quickly grow in the presence of strong tidal forces, violating the assumption that it is much smaller than the mass of the probe required for the WKB approximation to hold, as described in more detail below. Below,

⁶Note that the OTOC of an operator localised in the S^3 would correspond to a computation using a single geodesic in the 6-dimensional geometry with no smearing and the resulting gravitational shock wave would propagate in the S^3 . From the perspective of the boundary CFT, localising the insertion in the S^3 requires a sum over a tower of primary operators so this is not the most natural OTOC to consider.

we adapt their computation to the present setup and find that the tidal stresses are in danger of invalidating the WKB approximation at a time scale Δt_{tidal} , given in (4.54), well before the center-of-mass energy of the interaction starts to saturate at Δt_{cap} . Since we lose control of the computation beyond Δt_{tidal} , we cannot say for certain what the behaviour of the OTOC will be past this time. We expect, however, that whatever happens beyond this point, the OTOC cannot continue to grow beyond the bound identified below in (4.44), since the center-of-mass energy, which controls the strength of gravitational interactions, is bounded by the presence of the cap in any case.

In the above discussion, we have focused on boundary time scales. In the bulk, it is more natural to think instead of the radial coordinate at which the interaction occurs. Although the cap deforms the near-horizon region, in the careful treatment of the OTOC needed for zero temperature states, we find that the OTOC is controlled by an interaction centered at a small but finite distance from the horizon. The scrambling time is reached when this interaction is at a radial coordinate

$$r_{\text{sat}} - r_+ \sim \left(\frac{G_N m_W m_V}{\varepsilon^2} \right)^{\frac{1}{3}}, \quad (4.32)$$

whereas the tidal forces become important at a radial coordinate

$$r_{\text{tidal}} - r_+ \sim \sqrt{\frac{G_N(\pi^2 T_R^2 + 1)}{\pi T_R \varepsilon \min(h_V, h_W)}}, \quad (4.33)$$

these are both intermediate distance scales between the Planck and AdS scales away from the horizon.

Center-of-mass energy. Given the relationship between the velocities and the conserved quantities in (4.18) and (4.19), the center-of-mass energy can be expressed in terms of the conserved quantities and the radius, ρ_* , where the collision occurs,

$$s = -(m_V k_V + m_W k_W)^2 \Big|_{\rho=\rho_*}, \quad (4.34)$$

$$= \frac{b(2a^2 + b^2) ((2a^2 + b^2)(\rho_*^2 + a^2)^n - b^2 \rho_*^{2n})}{a^2(\rho_*^2 + a^2)^{n+1} \sqrt{2a^2 + b^2 - a^2 b^2 \rho_*^{2n} (\rho_*^2 + a^2)^{-(n+1)}}} \frac{m_V m_W}{\varepsilon^2} + O(\varepsilon^0), \quad (4.35)$$

where m_V and m_W are the masses of the in- and outgoing geodesics respectively and we set $E_V = E_W = \sqrt{\frac{b}{\sqrt{2}}}\varepsilon^{-1}$ where we have restored the factors of b in the energy computed in (3.7). In order to make the connection with the OTOC, the location of the collision must be re-expressed in terms of the times at which the perturbations are inserted at the boundary. This is straightforward in principle by inverting (4.21), however it is not tractable to perform this inversion analytically. The relation between s and Δt is plotted in figure 8.

We can find approximate answers by dividing the microstate geometry into three regions: an asymptotic region $\rho \gg \sqrt{n}b$, a throat region $\sqrt{n}a \ll \rho \ll \sqrt{n}b$ and a cap region $\rho \ll \sqrt{n}a$. We emphasize again that the overall time growth of the OTOC also depends on the number of images contributing to the gravitational interaction. As argued above,

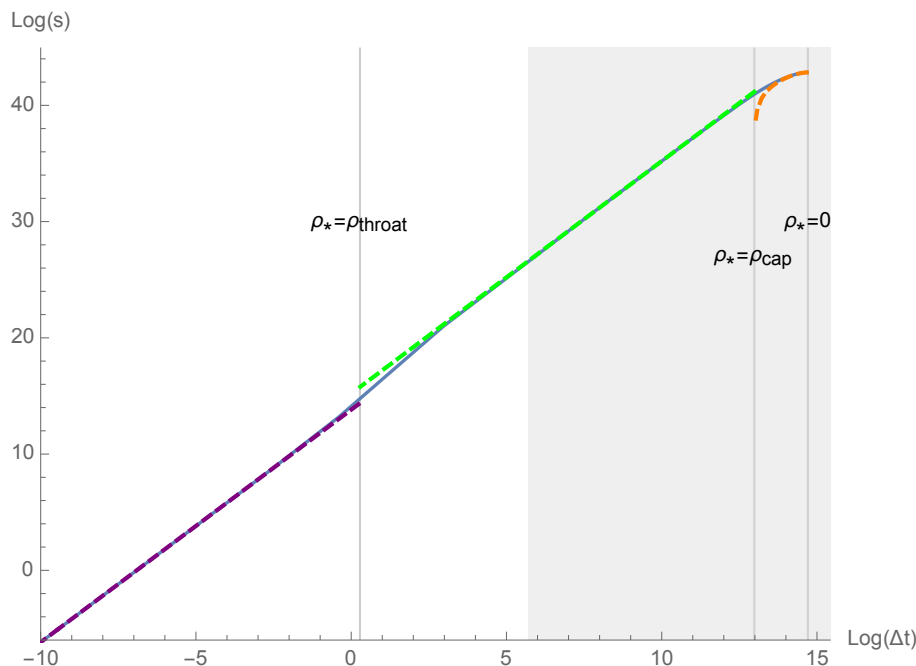


Figure 8. The solid blue line is the full numeric answer for the center-of-mass energy, while the dashed lines are the analytic approximations in the respective regimes. In the grey area, the tidal forces become large. The parameters used are $n = 3$, $a = 10^{-3}$, $b = \sqrt{2}$, $m_V = m_W = 10$ and $\varepsilon = 10^{-2}$.

the BTZ result should apply in the asymptotic and throat regions, yielding an additional factor of Δt . With this in mind, below we only study the behavior of the center-of-mass energy.

- In the asymptotic region, $\rho_* \gg \sqrt{n}b \gg \sqrt{n}a$, we can approximate the integral (4.21) by

$$\Delta t \simeq 2 \int_{\rho_*}^{\infty} d\rho \frac{b}{\sqrt{2}\rho^2} = \frac{\sqrt{2}b}{\rho_*}. \quad (4.36)$$

For the center-of-mass energy this yields quadratic growth in this region:

$$s \simeq 2 \frac{b^2}{\rho_*^2} \frac{m_V m_W}{\varepsilon^2} \simeq \frac{m_V m_W}{\varepsilon^2} \Delta t^2 = \frac{4\sqrt{2}}{b} \frac{h_V h_W}{\varepsilon^2} \Delta t^2. \quad (4.37)$$

In the last equality we have used $2h_{V,W} = \sqrt{b/\sqrt{2}}m_{V,W}$ where we have again restored factors of b compared to section 3.

- In the throat region, $\sqrt{n}a \ll \rho_* \ll \sqrt{n}b$, we get

$$\Delta t \simeq \Delta t_{\text{throat}} + 2 \int_{\rho_*}^{\sqrt{\frac{n}{2}}b} d\rho \frac{\sqrt{n}b^2}{2\rho^3} \simeq \frac{\sqrt{n}b^2}{2\rho_*^2}, \quad (4.38)$$

which, for the center-of-mass energy, yields

$$s \simeq \frac{nb^4}{\rho_*^4} \frac{m_V m_W}{\varepsilon^2} = \frac{16\sqrt{2}}{b} \frac{h_V h_W}{\varepsilon^2} \Delta t^2. \quad (4.39)$$

This leads again to a growth in the center-of-mass energy that is quadratic in time.

- In the deep cap region, $\rho_* \ll \sqrt{n} a \ll \sqrt{n} b$, we get

$$\Delta t \simeq \Delta t_{\text{bottom}} - 2 \int_0^{\rho_*} d\rho \frac{b^2}{2a^3} \simeq \frac{b^2}{a^2} \left(\chi_n(0) - \frac{\rho_*}{a} \right), \quad (4.40)$$

where Δt_{bottom} was approximated using (4.25)

$$\Delta t_{\text{bottom}} \equiv 2 \int_0^\infty \frac{dt}{d\rho} \simeq \chi_n(0) \frac{b^2}{a^2} \sim \frac{b^2}{a^2}, \quad (4.41)$$

and where $\chi_n(0)$ was estimated by using

$$\frac{1}{2\sqrt{n}} < \frac{\pi}{2} - \chi_n(0) < \frac{2}{3\sqrt{n}}, \quad (4.42)$$

which can be verified numerically. The behaviour of the center-of-mass energy in this regime is then approximated by

$$s \simeq \begin{cases} \frac{(2a^2 - 3\rho_*^2)b^4}{2a^6} \frac{m_V m_W}{\varepsilon^2} & \text{for } n = 1 \\ \frac{(a^2 - \rho_*^2)b^4}{a^6} \frac{m_V m_W}{\varepsilon^2} & \text{for } n > 1 \end{cases} \quad (4.43a)$$

$$\simeq \begin{cases} \left(\frac{b^4}{a^4} - \frac{3}{2} (\Delta t_{\text{bottom}} - \Delta t)^2 \right) \frac{m_V m_W}{\varepsilon^2} & \text{for } n = 1 \\ \left(\frac{b^4}{a^4} - (\Delta t_{\text{bottom}} - \Delta t)^2 \right) \frac{m_V m_W}{\varepsilon^2} & \text{for } n > 1 \end{cases} \quad (4.43b)$$

At the bottom of the cap, the center-of-mass energy is given by

$$s_{\text{bound}} \simeq \frac{m_V m_W b^4}{\varepsilon^2 a^4} = \frac{16\sqrt{2}}{b} \frac{h_V h_W (N_1 N_5)^2}{\varepsilon^2}. \quad (4.44)$$

After the geodesics reach the bottom of the cap, they bounce off and start to move back up the throat. This therefore gives an upper bound on the center-of-mass energy of the interaction in the superstrata geometry.

These various approximate regimes are compared to the numeric answer in figure 8.

Tidal stress. The geodesic approximation to field propagation, used in this work to compute OTOCs, has a limit of validity. Indeed, as any WKB-type approximation, it rests on the assumption that the amplitude variation of the wavefunction (2.6) does not compete with that of its phase factor (2.7),

$$|\partial_\mu A| \ll m |k_\mu A|, \quad (4.45)$$

where this condition must hold for each of the components individually, and so in particular it must hold for the component along the velocity k^μ of the geodesic,

$$\frac{d}{d\tau} A \equiv k^\mu \partial_\mu A. \tag{4.46}$$

By expanding the Klein-Gordon equation to first subleading order in $1/m$, it may be shown that the variation of the amplitude A along k^μ is related to the *volume expansion* θ of a congruence of geodesics [29]

$$\frac{d}{d\tau} A = -\frac{\theta}{2} A, \quad \theta \equiv \nabla_\mu k^\mu. \tag{4.47}$$

Therefore, the validity of the geodesic approximation through (4.45) requires in particular

$$|\theta| \ll m. \tag{4.48}$$

The evolution of the expansion θ is controlled by the Raychaudhuri equation

$$\dot{\theta} = -\frac{1}{2}\theta^2 - \sigma_{\mu\nu}\sigma^{\mu\nu} + \omega_{\mu\nu}\omega^{\mu\nu} - R_{\mu\nu}k^\mu k^\nu, \tag{4.49}$$

where $\sigma_{\mu\nu}$ and $\omega_{\mu\nu}$ are the *shear* and *rotation* tensors, respectively; for more details, see textbooks such as [42]. The quantity $R_{\mu\nu}k^\mu k^\nu$ is known as the trace of the tidal tensor and quantifies the tidal forces felt by a congruence of geodesics. In the context of superstratum microstates, it has been shown that tidal forces on infalling particles are Planckian long before they reach the cap region [31–34]. In the presence of such Planckian tidal forces, one may quickly expect a violation of the condition (4.48) and a breakdown of the validity of the geodesic approximation.

The leading term in the trace of the tidal tensor can be computed in the throat region of the geometry, where $\sqrt{na} \ll \rho \ll \sqrt{nb}$,

$$-R_{\mu\nu}k^\mu k^\nu \sim -\frac{2\sqrt{2}}{b} - \frac{n(n+1)a^2b^2E^2}{\rho^6} = -\frac{2\sqrt{2}}{b} - \frac{n(n+1)a^2b^3}{\sqrt{2}\epsilon^2\rho^6}, \tag{4.50}$$

where all higher order terms in the small parameters $\frac{\rho}{b}$, $\frac{a}{\rho}$ and $\frac{a}{b}$ have been dropped. These two terms can compete depending on how deep into the throat we look. The first term does not depend on a and so it is what we would get for an extremal BTZ black hole. For $\rho \sim \sqrt{nb}$ the second term is suppressed by $\frac{a^2}{b^2} \sim (N_1N_5)^{-1}$ and so it is very small and cannot cause a large expansion. However, as the geodesic falls into the throat this second term grows and eventually gets bigger than the first.

Assuming that our congruence of geodesics obeys the condition (4.48) for BTZ,⁷ the danger comes from the additional term in the tidal tensor that grows as the geodesic falls

⁷We do not generically expect the condition (4.48) to be violated in the near horizon region of BTZ. Since the geometry is locally AdS, the tidal tensor is never large in BTZ (this fact was pointed out by [31]). Also, neglecting the shear and rotation in the Raychaudhuri equation allows it to be integrated in BTZ and the solutions are approximately constant in the throat region.

down the throat. As this additional term grows, it causes $\dot{\theta}$ to grow, which will cause a potential violation of the condition (4.48) when

$$\left| \int \frac{n(n+1)a^2b^3}{\sqrt{2}\varepsilon^2\rho^6} d\tau \right| \sim m. \tag{4.51}$$

We change variables from τ to ρ in this integral by using our known expressions for the velocity of the geodesic. Expanding (4.19) in the throat regime, $\sqrt{na} \ll \rho \ll \sqrt{nb}$,

$$\frac{d\rho}{d\tau} = -\frac{\sqrt{n}b^{\frac{3}{2}}}{2^{\frac{3}{4}}\varepsilon\rho}. \tag{4.52}$$

This will cause (4.48) to be violated at a radial coordinate,

$$\rho_{\text{tidal}}^4 \sim \frac{a^2b^{\frac{3}{2}}\sqrt{n}(n+1)}{2^{\frac{7}{4}}\varepsilon m}. \tag{4.53}$$

Using (4.38), this translates into a boundary time separation of

$$\Delta t_{\text{tidal}} \sim \sqrt{\frac{\pi T_R}{\pi^2 T_R^2 + 1} \min(h_V, h_W) \varepsilon N_1 N_5}, \tag{4.54}$$

where $\min(h_V, h_W)$ denotes the minimum of the conformal weights of the operators in the OTOC and appears because the condition (4.48) must be imposed on both the in- and outgoing geodesics. This reproduces the result (1.12) quoted in the introduction.

This time scale can be compared to the scrambling time,

$$\frac{\Delta t_{\text{tidal}}}{\Delta t_s} \sim \frac{2}{3^{\frac{1}{3}}} \sqrt{\frac{\pi T_R}{(\pi^2 T_R^2 + 1)}} \sqrt{\min(h_V, h_W)} \left(\frac{h_V^2 h_W^2 N_1 N_5}{\varepsilon} \right)^{\frac{1}{6}}. \tag{4.55}$$

In this expression, $N_1 N_5 \gg 1$ in order to have a hierarchy between the Planck and AdS scales (semi-classical regime), $\varepsilon \ll 1$ since it is the holographic regulator and $h_{V,W} \gg 1$ for the validity of the WKB approximation. All these scalings contribute to ensuring that $\Delta t_s \ll \Delta t_{\text{tidal}}$ so that we can reliably approximate the superstrata by BTZ during the slow scrambling phase of the OTOC. The only way this condition can be violated is for very small or very large right-moving temperature. Since the superstrata solutions only exist for integer n , the temperature is bounded from below by $\pi T_R \geq 1$ and we only need to worry about large temperatures. In that case, $\Delta t_{\text{tidal}} \lesssim \Delta t_s$ when

$$T_R \gtrsim \min(h_V, h_W) \left(\frac{h_V^2 h_W^2 N_1 N_5}{\varepsilon} \right)^{\frac{1}{3}}. \tag{4.56}$$

As far as we are aware, there is no obstruction to considering superstrata with arbitrarily large right-moving temperature. In this large right-moving temperature regime, we expect the WKB approximation to break down, leading to deviations from the BTZ result, before the scrambling time is reached.

5 Discussion

In the following, we point to some open problems and possible future directions.

Late-time regime and quasi-normal decay. We have described OTOCs in extremal geometries within the geodesic approximation scheme presented in section 2. This approach requires improvement if it is to accurately describe the late-time regime where quasi-normal decay may occur. It is very likely that the latter coincides with a regime where the assumption (4.45) does not hold anymore. This would be in line with earlier study of black hole quasi-normal modes within related WKB-type approximations [43]. We also refer the reader to [11, 44] for a description of quasi-normal decay of two-point functions in states dual to extremal BTZ and superstratum microstates.

Shock waves in microstate geometries. As described in section 4.4, we expect OTOCs in superstratum geometries to coincide with those in extremal BTZ as long as the dual particle scattering does not probe some of its distinctive features, including strong tidal forces and the existence of a cap region. This assumes that shock waves emitted by particles falling from infinity in these microstate geometries do not significantly differ from their analogue in extremal BTZ, at least far away from the throat region where strong tidal forces occur. Once the interaction probes sufficiently deep into the throat, we would need to understand the shock wave in the full 6-dimensional geometry of the cap. Two-point functions have been computed in the superstrata geometry by exploiting the almost separable form of the wave equation in [11], which suggests that the computation of this shock wave may be tractable.

Breakdown of the geodesic approximation due to tidal forces. The analysis performed in section 4.4 strongly suggests that tidal forces invalidate the geodesic approximation to field propagation at the timescale Δt_{tidal} given in (4.54). A fully rigorous proof of this fact would require a more detailed study of the Raychaudhuri equation describing the congruence of geodesics used to propagate bulk fields from their boundary insertion points, including the effect of shear and rotation associated to this congruence.

Right-moving operators. We have discovered that the OTOC of scalar operators, when evaluated in a state dual to extremal BTZ, displays a time-dependence which alternates between a quadratic growth associated to the zero left-moving temperature T_L and an exponential Lyapunov growth associated to the non-zero right-moving temperature T_R . It is interesting to contemplate the possibility that the OTOC of purely right-moving CFT operators could display a purely exponential growth. In the gravitational description, these right-moving CFT operators correspond to high spin fields with equal spin s and right conformal weight h_R . Since the geodesic approximation holds for large masses $m \gg 1$, high spin fields would have to be considered in order to see this purely exponential Lyapunov growth at the temperature T_R within this approximation.

Probes of higher complexity. Two-point functions in the superstrata were studied in [11], and were found to closely approximate the decay found in extremal BTZ until a

time scale $\sqrt{N_1 N_5}$, where they start to deviate. At a time scale equal to $\Delta t_{\text{cap}} \sim \frac{N_1 N_5}{T_R}$, they start to grow again and exhibit a sharp echo at a time scale $t_{\text{echo}} = N_1 N_5$. Thus, these probes exhibit the effects of the difference between the superstrata and extremal BTZ geometries at similar time scales as the OTOC. One might have expected more complex probes to be more sensitive to the difference between a microstate or a statistical ensemble, but that does not seem to be the case here. This may be related to the fact that the relevant time scales are powers rather than exponentials of $N_1 N_5$ so that the difference between $N_1 N_5$ and $2N_1 N_5$ is lost.

The new feature of the OTOC is the appearance of a new time scale, the scrambling time. We expect more complex probes to take longer to scramble and so it would be interesting to compare their scrambling time to the time where they start to feel the effects of the microstate.

Extremal black holes in higher spacetime dimensions. It would also be interesting to study the OTOC in higher dimensional black holes. The gravitational modes responsible for scrambling in these black holes have been identified in [45]. It would be interesting to determine whether there is a similar saw-tooth behaviour in the OTOC and whether the overall growth of the OTOC is consistent with slow scrambling or whether the mode with the largest rate of growth comes to dominate in that case.

Acknowledgments

Some of the ideas on which this paper is based were discussed at the “Microstates and Chaos” panel of the Black-Hole Microstructure Conference (Saclay, 2020). BC thanks I. Bena, E. Martinec, D. Stanford and N. Warner for the organization and for discussions. BC also thanks S. Khetrpal for collaboration on a related project.

This work is supported in part by FWO-Vlaanderen through project G006918N and by Vrije Universiteit Brussel through the Strategic Research Program “High-Energy Physics.” MDC is supported by a PhD fellowship from the Research Foundation Flanders (FWO). PH is supported by a PhD fellowship from the VUB Research Council. KN is supported by a Fellowship of the Belgian American Educational Foundation and by a grant from the John Templeton Foundation. CR is supported by a postdoctoral fellowship from the Research Foundation Flanders (FWO).

A Oscillations and decay in the OTOC

In this appendix, we describe in more detail the existence of an intermediate region of damped rapid oscillatory behaviour for the OTOC in non-rotating BTZ, which lies between the Lyapunov growth and the quasi-normal mode decay. These damped oscillations appear before the quasi-normal mode decay whenever there is a hierarchy, controlled by the weight h_V , between the scrambling time t_s and the time scale t_{QN} at which the quasi-normal mode decay kicks in.

For a non-rotating BTZ black hole, the OTOC is given by ($h_W \gg h_V \gg 1$) [15]

$$\frac{\langle V(-i\epsilon_V, 0)W(t-i\epsilon_W, x)V(i\epsilon_V, 0)W(t+i\epsilon_W, x) \rangle_\beta}{\langle V(-i\epsilon_V, 0)V(i\epsilon_V, 0) \rangle_\beta \langle W(t-i\epsilon_W, x)W(t+i\epsilon_W, x) \rangle_\beta} = \left(1 - \frac{6\pi i h_W e^{\frac{2\pi}{\beta}(t-|x|)}}{c \sin\left(\frac{2\pi}{\beta}\epsilon_V\right) \sin\left(\frac{2\pi}{\beta}\epsilon_W\right)} \right)^{-2h_V}, \quad (\text{A.1})$$

where h_V and h_W are the conformal weights of the operators. It is well known that (A.1) describes both the early-time Lyapunov growth and the quasi-normal mode decay of the OTOC. In the following, we will discuss the presence of an intermediate regime where the OTOC shows rapid damped oscillations, with a decay that is doubly-exponential.

We start by noting that for $x \ll 1$

$$\log(1+x) \simeq x - \frac{1}{2}x^2 + O(x^3). \quad (\text{A.2})$$

Therefore, in the regime where $\frac{6\pi h_W e^{\frac{2\pi}{\beta}(t-|x|)}}{c \sin\left(\frac{2\pi}{\beta}\epsilon_V\right) \sin\left(\frac{2\pi}{\beta}\epsilon_W\right)} \ll 1$, we can write (A.1) as

$$\begin{aligned} & \left(1 - \frac{6\pi i h_W e^{\frac{2\pi}{\beta}(t-|x|)}}{c \sin\left(\frac{2\pi}{\beta}\epsilon_V\right) \sin\left(\frac{2\pi}{\beta}\epsilon_W\right)} \right)^{-2h_V} \simeq \exp\left(i \frac{12\pi h_W h_V}{c \sin\left(\frac{2\pi}{\beta}\epsilon_V\right) \sin\left(\frac{2\pi}{\beta}\epsilon_W\right)} e^{\frac{2\pi}{\beta}(t-|x|)} \right) \\ & \times \exp\left(-\frac{36\pi^2 h_W^2 h_V}{c^2 \sin^2\left(\frac{2\pi}{\beta}\epsilon_V\right) \sin^2\left(\frac{2\pi}{\beta}\epsilon_W\right)} e^{\frac{4\pi}{\beta}(t-|x|)} + O\left(\frac{h_W^3 h_V e^{3t}}{c^3}\right) \right). \quad (\text{A.3}) \end{aligned}$$

Normally the second term in the exponent would be subleading, but since the first term is purely imaginary it does not contribute to the magnitude of the OTOC. Taking the real part of this expression, we obtain

$$\text{Re}(\text{OTOC}) \simeq \cos\left(\frac{12\pi h_W h_V e^{\frac{2\pi}{\beta}(t-|x|)}}{c \sin\left(\frac{2\pi}{\beta}\epsilon_V\right) \sin\left(\frac{2\pi}{\beta}\epsilon_W\right)} \right) \exp\left(-\frac{36\pi^2 h_W^2 h_V}{c^2 \sin^2\left(\frac{2\pi}{\beta}\epsilon_V\right) \sin^2\left(\frac{2\pi}{\beta}\epsilon_W\right)} e^{\frac{4\pi}{\beta}(t-|x|)} \right). \quad (\text{A.4})$$

This starts very near 1 and decreases exponentially, as is well known. The first zero of the cosine, which corresponds to the time scale at which the commutator squared first becomes order 1 and is known as the scrambling time, t_s , occurs at

$$t_s \simeq |x| - \frac{\beta}{2\pi} \log\left(\frac{24 h_W h_V}{c \sin\left(\frac{2\pi}{\beta}\epsilon_V\right) \sin\left(\frac{2\pi}{\beta}\epsilon_W\right)} \right). \quad (\text{A.5})$$

After this time scale, the OTOC oscillates with a rapidly increasing frequency. At a time scale t_d the OTOC starts to decay double-exponentially,

$$t_d \simeq |x| - \frac{\beta}{2\pi} \log\left(\frac{6\pi h_W \sqrt{h_V}}{c \sin\left(\frac{2\pi}{\beta}\epsilon_V\right) \sin\left(\frac{2\pi}{\beta}\epsilon_W\right)} \right). \quad (\text{A.6})$$

The separation between these timescales is controlled by the conformal weight of the lighter V operator:

$$t_d - t_s \sim \frac{\beta}{\pi} \log h_V. \tag{A.7}$$

Finally at late times, $t \sim t_{QN}$, quasi-normal decay takes over

$$t_{QN} = |x| - \frac{\beta}{2\pi} \log \left(\frac{6\pi h_W}{c \sin\left(\frac{2\pi}{\beta} \epsilon_V\right) \sin\left(\frac{2\pi}{\beta} \epsilon_W\right)} \right). \tag{A.8}$$

In this regime, the OTOC decays exponentially at a rate controlled by h_V/β

$$\text{OTOC} \simeq \left(\frac{6\pi i h_W}{c \sin\left(\frac{2\pi}{\beta} \epsilon_V\right) \sin\left(\frac{2\pi}{\beta} \epsilon_W\right)} \right)^{-2h_V} e^{-\frac{4\pi h_V}{\beta}(t-|x|)}. \tag{A.9}$$

Note however that by this time, the OTOC has already been decaying doubly exponentially since t_d . This time scale is separated from the earlier decay by the same amount as the scrambling time was separated from the doubly-exponential decay,

$$t_{QN} - t_d \sim \frac{\beta}{\pi} \log h_V. \tag{A.10}$$

Although the geodesic approximation to the computation of the OTOC is not sensitive to the quasi-normal decay regime, we will show that in addition to the leading early-time behaviour given by

$$\text{OTOC} \simeq e^{i\delta} \Big|_{\text{saddle}}, \tag{A.11}$$

it correctly reproduces the first correction, i.e., the second factor in (A.3). The leading term is obtained by ignoring the back reaction of the geodesics on their trajectories and computing the dominating saddle point in (A.11) by a choice of point-splitting regulators together with condition (2.19), which is a local condition that does not include the effect of the eikonal phase factor. In [15], the late-time quasi-normal type decay arises by taking the eikonal phase into account when computing the saddle point, which can be interpreted in terms of the propagation of the light particle (V) in the background of the heavier particle (W). In the WKB approach used in this paper, a first correction to the OTOC in non-rotating BTZ can similarly be found by including the eikonal phase factor in the computing of the saddle of the V particle, such that one finds⁸

$$\frac{\langle V(0,0)W(t,x)V(-\epsilon_V,0)W(t-\epsilon_W,x) \rangle_\beta}{\langle V(0,0)V(-\epsilon_V,0) \rangle_\beta \langle W(t,x)W(t-\epsilon_W,x) \rangle_\beta} \simeq e^{i\frac{\beta^2 G_N m_W m_V}{2\pi \epsilon^2} e^{\frac{2\pi}{\beta}(t-|x|)} + i\frac{\beta^4 G_N^2 m_W^2 m_V}{2(2\pi)^3 \epsilon^3 \epsilon_V} e^{\frac{4\pi}{\beta}(t-|x|)}}, \tag{A.12}$$

with $m_i = 2h_i$ and where G_N is related to the central charge c of the CFT by the Brown-Henneaux relation $c = \frac{3}{2G_N}$, in units where the AdS length is set to 1. A few differences

⁸In [29], a detailed derivation of the saddles was given (without including the eikonal phase factor). (A.12) can be derived following those steps while including the effect of the eikonal phase.

are to be noted with respect to (A.3). First, a feature of our approach that is already present in the leading term, is that the (holographic) cutoff surface regulator ε appears in the denominator of the eikonal phase instead of the time regulators. Second, the regulators ϵ_i are taken to be real shifts to the times (see (2.12)). This type of time regulator leads to a correction to the phase of the OTOC and does not change its amplitude. In order to connect more directly with the result from [15], we need to consider Euclidean time regulators⁹ and send $\epsilon_i \rightarrow -i\epsilon_i$. Putting both types of regulators on the same footing, equations (A.3) and (A.12) are in agreement, provided we consider small shifts ϵ_i . As a consequence, the exact behaviour of the intermediate regime of the OTOC seems to be strongly dependent on the choice of regulator.

Note that the corrections to the leading early-time behaviour of the OTOC break the symmetry between V and W , because a hierarchy was chosen between the two particles ($h_W \gg h_V$). As a result, the two series (A.3) and (A.12) contain an increasing number of factors of h_W together with a single factor of h_V .

Slow scrambling in the vacuum The OTOC has been computed for the vacuum state of a CFT₂ on an infinite line, in the vacuum block approximation [16]:

$$\frac{\langle V(-i\epsilon_V, 0)W(t - i\epsilon_W, x)V(i\epsilon_V, 0)W(t + i\epsilon_W, x) \rangle_\infty}{\langle V(-i\epsilon_V, 0)V(i\epsilon_V, 0) \rangle_\beta \langle W(t - i\epsilon_W, x)W(t + i\epsilon_W, x) \rangle_\infty} = \left(1 - \frac{6\pi i h_W}{\epsilon_W \epsilon_V c} (t - |x|)^2\right)^{-2h_V}. \tag{A.13}$$

Again the same approximation scheme can be used in the regime where $\frac{6\pi h_W}{\epsilon_W \epsilon_V c} (t - |x|)^2 \ll 1$ to write this as

$$\left(1 - \frac{6\pi i h_W}{\epsilon_W \epsilon_V c} (t - |x|)^2\right)^{-2h_V} \simeq e^{i \frac{12\pi h_W h_V}{\epsilon_W \epsilon_V c} (t - |x|)^2 - \frac{36\pi^2 h_W^2 h_V}{\epsilon_W^2 \epsilon_V^2 c^2} (t - |x|)^4 + O\left(\frac{h_W^3 h_V t^6}{c^3}\right)}. \tag{A.14}$$

Taking the real part of the OTOC, we see the same sort of damped oscillations, but with a power law instead of exponential dependence on t in the argument,

$$\text{Re}(\text{OTOC}) \simeq \cos\left(\frac{12\pi h_W h_V}{\epsilon_W \epsilon_V c} (t - |x|)^2\right) e^{-\frac{36\pi^2 h_W^2 h_V}{\epsilon_W^2 \epsilon_V^2 c^2} (t - |x|)^4}. \tag{A.15}$$

The same time scales can be identified,

$$t_s \simeq |x| + \sqrt{\frac{\epsilon_W \epsilon_V c}{24 h_W h_V}}, \tag{A.16}$$

$$t_d \simeq |x| + \sqrt{\frac{\epsilon_W \epsilon_V c}{6\pi h_W \sqrt{h_V}}}, \tag{A.17}$$

$$t_{QN} \simeq |x| + \sqrt{\frac{\epsilon_W \epsilon_V c}{6\pi h_W}}, \tag{A.18}$$

where, once again, the weight h_V controls the time separation between the different regimes.

⁹This is a natural choice from the CFT point of view, because the ordering of the operators inside the four-point function is fixed by the euclidean time ordering of the operators.

B Center-of-mass energy in generic BTZ

In this appendix, we show that the center-of-mass energy of two colliding geodesics in a non-extremal BTZ black hole already contains an initial period of power law growth, followed by an exponential growth set by the temperature. As the angular momentum of the black hole is tuned towards extremality, this region of power law growth extends to larger separation times until the exponential behaviour disappears completely at extremality.

The metric of a rotating BTZ black hole is given by

$$ds^2 = -f(r)dt^2 + \frac{dr^2}{f(r)} + r^2 \left(d\varphi - \frac{r_+ r_-}{r^2} dt \right)^2, \quad f(r) = \frac{(r^2 - r_+^2)(r^2 - r_-^2)}{r^2}, \quad (\text{B.1})$$

where the angular coordinate φ is periodically identified, $\varphi \sim \varphi + 2\pi$. The angular velocity of the black hole is given by $\Omega = r_-/r_+$ and extremal BTZ corresponds to setting $r_+ = r_-$.

As explained in the main text, we consider a collision between radially infalling null geodesics. One geodesic falls in at time t_1 and $\varphi = 0$ and the other moves outwards and reaches the boundary at t_2 and the same $\varphi = 0$. The two cross at a radius r_* and we will compute their center-of-mass energy at this point

$$s = -2m_V m_W k_V \cdot k_W|_{r=r_*}, \quad (\text{B.2})$$

where k_V^μ and k_W^μ are the velocities associated to the two geodesics.

This geometry has two Killing vectors, ∂_t and ∂_φ , with associated conserved quantities

$$E = -(\partial_t)^\mu k_\mu = \left(f(r) - \frac{r_+^2 r_-^2}{r^2} \right) \dot{t} + r_+ r_- \dot{\varphi}, \quad (\text{B.3})$$

$$L = (\partial_\varphi)^\mu k_\mu = r^2 \dot{\varphi} - r_+ r_- \dot{t}. \quad (\text{B.4})$$

Setting $L = 0$ and using the null condition $k^2 = 0$, the final coordinate can be fixed to be

$$\dot{r}^2 = E^2, \quad (\text{B.5})$$

so that the center-of-mass energy of two geodesics with $L_i = 0$ and $E_V = E_W = E$, at the collision, can be written in terms of only the energy and the position of the collision,

$$s = \frac{4m_V m_W E^2}{f(r_*)}. \quad (\text{B.6})$$

The horizon is located at the outermost zero of $f(r)$. For non-extremal BTZ, this is a simple zero, whereas for extremal BTZ it becomes a double zero. For $r_* \sim r_+$, the center-of-mass energy can be approximated by

$$s \sim \frac{2m_V m_W r_+ E^2}{(r_+^2 - r_-^2)(r_* - r_+)}, \quad r_*^2 - r_+^2 \ll r_+^2 - r_-^2, \quad (\text{B.7})$$

$$\sim \frac{m_V m_W E^2}{(r_* - r_+)^2}, \quad r_+^2 - r_-^2 \ll r_*^2 - r_+^2 \ll r_+^2. \quad (\text{B.8})$$

The remaining task is to relate the position of the collision to the location at which the geodesics meet the boundary,

$$t_\infty - t_* = \int_{r_*}^{\infty} \frac{dt}{dr} dr = \int_{r_*}^{\infty} \frac{\dot{t}}{\dot{r}} dr = \pm \int_{r_*}^{\infty} \frac{dr}{f(r)}. \quad (\text{B.9})$$

Once again, we distinguish two regimes, depending on the value of the ratio of the distance between the two horizons and the distance between the collision and the outer horizon,

$$\int_{r_*}^{\infty} \frac{dr}{f(r)} \sim \frac{r_+}{2(r_+^2 - r_-^2)} \int_{r_*}^{\infty} \frac{dr}{r - r_+} = -\frac{r_+ \log(r_* - r_+)}{2(r_+^2 - r_-^2)}, \quad r_*^2 - r_+^2 \ll r_+^2 - r_-^2, \quad (\text{B.10})$$

$$\sim \frac{1}{4} \int_{r_*}^{\infty} \frac{dr}{(r - r_+)^2} = \frac{1}{4(r_* - r_+)}, \quad r_+^2 - r_-^2 \ll r_*^2 - r_+^2 \ll r_+^2. \quad (\text{B.11})$$

In other words, for non-extremal black holes we find that the depth inside the geometry explored by probes separated by a distance Δt on the boundary scales like

$$r_* - r_+ \sim e^{-\frac{r_+^2 - r_-^2}{r_+} \Delta t}, \quad r_*^2 - r_+^2 \ll r_+^2 - r_-^2, \quad (\text{B.12})$$

$$\sim \frac{1}{2\Delta t}, \quad r_+^2 - r_-^2 \ll r_*^2 - r_+^2 \ll r_+^2. \quad (\text{B.13})$$

This leads to

$$s \sim \frac{2m_V m_W r_+ E^2}{(r_+^2 - r_-^2)} e^{\frac{r_+^2 - r_-^2}{r_+} \Delta t}, \quad r_*^2 - r_+^2 \ll r_+^2 - r_-^2, \quad (\text{B.14})$$

$$\sim 4m_V m_W E^2 \Delta t^2, \quad r_+^2 - r_-^2 \ll r_*^2 - r_+^2 \ll r_+^2. \quad (\text{B.15})$$

Note that for a non-rotating black hole, $r_- = 0$, and the second regime never applies. In that case, r_* approaches the horizon exponentially. As the spin of the black hole increases, a region of power law approach to the horizon appears before the exponential approach begins. As the extremal limit is approached this power law regime persists for longer until at extremality, $r_- = r_+$, the exponential regime disappears completely and only the power law regime remains.

C Shock wave in extremal BTZ

Following the method presented in [29], we construct the shock wave solutions used in the main text, which are associated to geodesics with zero angular momentum in extremal BTZ. We make use of the fact that extremal BTZ is just a patch of pure AdS₃, where the latter may be viewed as a hyperboloid in four-dimensional flat space through the constraint

$$\eta_{MN} X^M X^N = -1, \quad \eta_{MN} = \text{diag}(-1, 1, 1, -1). \quad (\text{C.1})$$

We refer to X^M as ‘embedding coordinates’. We then choose the following set of independent lightcone coordinates,

$$\mathcal{V} = X^0 + X^1, \quad \mathcal{U} = X^0 - X^1, \quad \mathcal{Z} = X^2, \quad (\text{C.2})$$

while the remaining embedding coordinate X^3 is determined from either one of the two branches

$$X^3 = \pm\sqrt{1 - \mathcal{UV} + \mathcal{Z}^2}. \tag{C.3}$$

A choice of branch corresponds to a choice of either one of the two ‘hemispheres’ of the AdS hyperboloid.

A highly energetic particle following a null trajectory along $\mathcal{V} = \mathcal{Z} = 0$ in the lower hemisphere ($X^3 = -1$) has a stress tensor given by

$$T_{\mathcal{V}\mathcal{V}} = -mk_{\mathcal{V}} \delta(\mathcal{V})\delta(\mathcal{Z})\Theta(-X^3), \tag{C.4}$$

where its velocity $k_{\mathcal{V}}$ is a constant of motion. The Heaviside step function $\Theta(-X^3)$ explicitly restricts the source to lie in the lower hemisphere of the AdS hyperboloid. It has the effect of discarding a second null geodesic at $\mathcal{V} = \mathcal{Z} = 0$, but lying in the upper hemisphere ($X^3 = 1$) instead. When going to the extremal BTZ patch, this second geodesic simply coincides with the ‘reflected’ continuation at the AdS conformal boundary of the geodesic of interest. This will be made explicit later on. Here, we are interested in null geodesics either created or absorbed at the AdS conformal boundary such that we don’t consider such boundary ‘reflections’. The associated shock wave geometry is found by solving Einstein’s equations sourced by the above stress tensor. It takes the form

$$ds^2 = ds_{\text{AdS}}^2 + ds_{\text{SW}}^2, \quad ds_{\text{SW}}^2 = -16\pi G_{\text{NM}} k_{\mathcal{V}} \Pi(\mathcal{Z})\delta(\mathcal{V})\Theta(-X^3)d\mathcal{V}^2, \tag{C.5}$$

where $\Pi(\mathcal{Z})$ solves

$$\left[(1 + \mathcal{Z}^2) \partial_{\mathcal{Z}}^2 + \mathcal{Z} \partial_{\mathcal{Z}} - 1 \right] \Pi(\mathcal{Z}) = -\delta(\mathcal{Z}). \tag{C.6}$$

Before solving this equation, we first need to determine the appropriate boundary conditions.

The shock wave sourced by a highly energetic particle in any locally AdS₃ spacetime can be mapped to the solution (C.5) written in embedding coordinates X^M . In particular, shock waves in maximally rotating BTZ black hole backgrounds may be found by appropriate coordinate transformation. To achieve this, we first give the map¹⁰ between some other *intermediate* embedding coordinate system \bar{X}^M and retarded BTZ coordinates (v, r, ϕ) ,

$$\bar{X}^0 = \frac{1}{2}e^{-r+\phi}(1 + (r + r_+)(2v + \phi)) - \frac{(r - r_+)e^{r+\phi}}{4r_+}, \tag{C.7a}$$

$$\bar{X}^1 = \frac{1}{2}e^{-r+\phi}(1 + (r + r_+)(2v + \phi)) + \frac{(r - r_+)e^{r+\phi}}{4r_+}, \tag{C.7b}$$

$$\bar{X}^2 = \frac{e^{r+\phi}(1 + (r - r_+)(2v + \phi))}{4r_+} - \frac{1}{2}(r + r_+)e^{-r+\phi}, \tag{C.7c}$$

$$\bar{X}^3 = \frac{e^{r+\phi}(1 + (r - r_+)(2v + \phi))}{4r_+} + \frac{1}{2}(r + r_+)e^{-r+\phi}. \tag{C.7d}$$

¹⁰It may be found by performing the following chain of coordinate transformations: $\bar{X}^M \rightarrow$ Poincaré patch of AdS $\rightarrow (t, r, \varphi) \rightarrow (v, r, \phi)$; see [36].

Any null geodesic in extremal BTZ then maps to a null ray in the intermediate coordinate system \bar{X}^M . Depending on the null geodesic of interest, as a final step we need to find the isometry relating these intermediate coordinates \bar{X}^M to the coordinates X^M described above, in such a way that the null geodesic lies at $\mathcal{V} = \mathcal{Z} = 0$ in the lower hemisphere of the AdS hyperboloid ($X^3 = -1$).

Outgoing shock wave. The trajectory of an outgoing geodesic with zero angular momentum has been described in section 3.1. It can be mapped to the null ray

$$\mathcal{V} = \mathcal{Z} = 0, \quad (X^3 = -1), \quad (\text{C.8})$$

through the following AdS isometry,

$$\begin{pmatrix} X^0 \\ X^1 \\ X^2 \\ X^3 \end{pmatrix} = \begin{pmatrix} 1 & 0 & 0 & 0 \\ 0 & 1 & 0 & 0 \\ 0 & 0 & \cosh c_2 & \sinh c_2 \\ 0 & 0 & \sinh c_2 & \cosh c_2 \end{pmatrix} \begin{pmatrix} a & 0 & 0 & -b \\ 0 & 1 & 0 & 0 \\ 0 & 0 & 1 & 0 \\ b & 0 & 0 & a \end{pmatrix} \begin{pmatrix} 1 & 0 & 0 & 0 \\ 0 & 1 & 0 & 0 \\ 0 & 0 & \cosh c_1 & \sinh c_1 \\ 0 & 0 & \sinh c_1 & \cosh c_1 \end{pmatrix} \begin{pmatrix} \bar{X}^0 \\ \bar{X}^1 \\ \bar{X}^2 \\ \bar{X}^3 \end{pmatrix}, \quad (\text{C.9})$$

with parameters

$$a = \frac{e^{2r_+ \phi_{\text{out}}} - 2r_+(2v_{\text{out}} + \phi_{\text{out}})}{e^{2r_+ \phi_{\text{out}}} + 2r_+(2v_{\text{out}} + \phi_{\text{out}})}, \quad b = \frac{e^{r_+ \phi_{\text{out}}} \sqrt{8r_+(2v_{\text{out}} + \phi_{\text{out}})}}{e^{2r_+ \phi_{\text{out}}} + 2r_+(2v_{\text{out}} + \phi_{\text{out}})}, \quad (\text{C.10a})$$

$$c_1 = -r_+ \phi_{\text{out}} - \frac{1}{2} \log \frac{2v_{\text{out}} + \phi_{\text{out}}}{2r_+}, \quad c_2 = \frac{1}{2} \log 2r_+(2v_{\text{out}} + \phi_{\text{out}}). \quad (\text{C.10b})$$

One may check that $a^2 + b^2 = 1$ such that the associated isometry is a rotation in the X^0 - X^3 plane. Using (C.7) and (C.9), we get a final expression for the null coordinate \mathcal{V} ,

$$\mathcal{V} = \frac{e^{-r_+ \Delta \phi} [1 + (r - r_+)(2\Delta v + \Delta \phi)] - e^{r_+ \Delta \phi} [1 + (r + r_+)(2\Delta v + \Delta \phi)]}{e^{r_+ \phi_{\text{out}}} + 2r_+(2v_{\text{out}} + \phi_{\text{out}})e^{-r_+ \phi_{\text{out}}}}, \quad (\text{C.11})$$

with $\Delta \phi \equiv \phi_{\text{out}} - \phi$ and $\Delta v \equiv v_{\text{out}} - v$. We can now explicitly check that the null ray lying at $\mathcal{V} = \mathcal{Z} = 0$ in the upper hemisphere ($X^3 = 1$) maps to a ‘reflected’ ingoing null geodesic with zero angular momentum and trajectory $v(r) = v_{\text{out}}$, $\phi(r) = \phi_{\text{out}}$.

In the main text, we only need the rr -component of the shock wave created by the outgoing geodesic. It is found from (C.5) by use of the coordinate transformation (C.11), and by plugging the relation between one component of the velocity (3.15) and the conserved energy E defined in (3.8),

$$k_r = \frac{2r^2}{(r^2 - r_+^2)^2} E, \quad (\text{C.12})$$

yielding

$$h_{rr} = \frac{8\pi G_N m E}{r_+} (2\Delta v + \Delta \phi) \sinh(r_+ \Delta \phi) \Pi(\mathcal{Z}) \delta(r - r_0(v, \phi)) \Theta(-X^3), \quad (\text{C.13})$$

with

$$r_0(v, \phi) = \frac{1}{2\Delta v + \Delta \phi} - r_+ \coth r_+ \Delta \phi, \quad (\text{C.14})$$

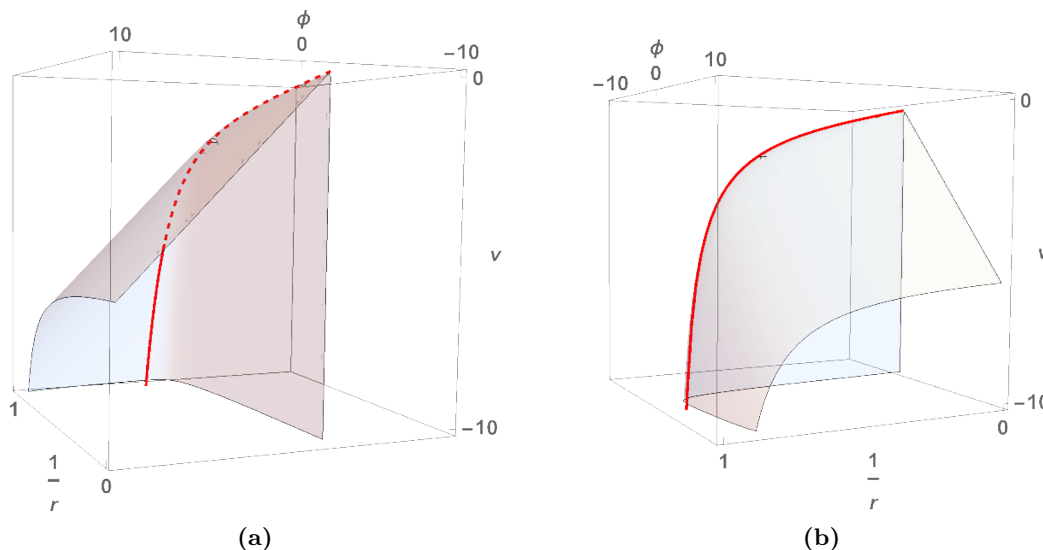


Figure 9. Support of the shock wave (C.13) emitted by a null outgoing geodesic with boundary insertion point $v_{\text{out}} = 0$, $\phi_{\text{out}} = -2$, viewed in retarded coordinates (v, r, ϕ) from two different perspectives. The horizon radius has been set to $r_+ = 1$ and the outgoing geodesic is indicated by the red line. The shock wave is emitted from the geodesic towards the conformal boundary. The shock wave (C.17) associated with a conformal boundary with cylinder topology used in the main text, is found by adding images in order to implement the periodic identification $\phi \sim \phi + 2\pi$.

and

$$\mathcal{Z}(v, r_0(v, \phi), \phi) = -\frac{\sinh^2(r_+ \Delta\phi) - r_+^2 (2\Delta v + \Delta\phi)^2}{2r_+ \sinh(r_+ \Delta\phi) (2\Delta v + \Delta\phi)}, \quad (\text{C.15a})$$

$$X^3(v, r_0(v, \phi), \phi) = \frac{\sinh^2(r_+ \Delta\phi) + r_+^2 (2\Delta v + \Delta\phi)^2}{2r_+ \sinh(r_+ \Delta\phi) (2\Delta v + \Delta\phi)}. \quad (\text{C.15b})$$

The restriction $X^3 < 0$ in (C.13) is equivalent to $\Delta\phi(2\Delta v + \Delta\phi) < 0$. From (C.14), we find that only $-2\Delta v < \Delta\phi < 0$ yields a positive value for r_0 . Since the BTZ radial coordinate r ranges over positive values, only a positive r_0 can contribute to the support of the shock wave (C.13). The support of this outgoing shock wave is depicted in figure 9.

Let us now come back to the boundary conditions that one needs to impose on (C.6). The support of the shock wave stretches out from the outgoing geodesic towards the boundary and reaches the boundary when $\Delta\phi = 0$ or $\Delta\phi = -2\Delta v$, as may be seen from (C.14). Those values correspond to $\mathcal{Z} \rightarrow \pm\infty$ in embedding space. We therefore impose that $\Pi(\mathcal{Z})$ should decay at infinity. Together with a continuity constraint on $\Pi(\mathcal{Z})$ at $\mathcal{Z} = 0$, one finds the following solution

$$\Pi(\mathcal{Z}(v, r_0(v, \phi), \phi)) = \begin{cases} \frac{1}{2} \left(\sqrt{1 + \mathcal{Z}^2} + \mathcal{Z} \right) = -\frac{\sinh r_+ \Delta\phi}{2r_+ (2\Delta v + \Delta\phi)} & \text{for } \mathcal{Z} \leq 0 \\ \frac{1}{2} \left(\sqrt{1 + \mathcal{Z}^2} - \mathcal{Z} \right) = -\frac{r_+ (2\Delta v + \Delta\phi)}{2 \sinh r_+ \Delta\phi} & \text{for } \mathcal{Z} > 0, \end{cases} \quad (\text{C.16})$$

where we assumed $-2\Delta v < \Delta\phi < 0$ in the last equality.

Equation (C.13) represents the rr -component of the shock wave of an outgoing null geodesic in the decompactified limit. When the coordinate ϕ is periodic with period 2π , one should sum over images,

$$h_{rr}^{(2\pi)} = \sum_{n \in \mathbb{Z}} h_{rr}(r, \Delta v, \Delta \phi_n), \quad \Delta \phi_n \equiv \phi_{\text{out}} - \phi + 2\pi n. \quad (\text{C.17})$$

The shock wave of a single image of the geodesic only has support at bulk points $(v, r_0(v, \phi), \phi)$ satisfying $-2\Delta v < \Delta \phi < 0$, such that only finitely many images will contribute to the shock wave considered at any given bulk point.

Ingoing shock wave. The derivation of the shock wave sourced by an ingoing particle with zero angular momentum is identical, provided that one uses advanced coordinates (3.17). The relevant rr -component is thus obtained from (C.17) by making the replacements

$$\Delta v \rightarrow \Delta u \equiv u - u_{\text{in}}, \quad \Delta \phi_n \rightarrow \Delta \phi'_n \equiv \phi' - \phi'_{\text{in}} + 2\pi n. \quad (\text{C.18})$$

Comparison with earlier literature. It is worth contrasting the shock wave expression (C.17) to the one obtained in the case of non-extremal BTZ in [23]; see also [22]. These authors considered the shock waves sourced by geodesics lying on the past and future horizons of a non-maximally rotating BTZ black hole, respectively. As already mentioned, this allows one to compute the leading contribution to the OTOC in the regime $\Delta t \gg \beta$ but precludes the study of zero temperature states which include vacuum AdS and extremal BTZ. For these, it is crucial that one considers shock waves sourced by geodesics away from horizons instead. In particular, (C.17) cannot be straightforwardly obtained as the zero-temperature limit of the shock wave presented in [22, 23], which simply diverges. A similar qualitative feature, however, is the appearance of a sum over images due to the angular periodicity. Each image may be thought of as being associated to an additional winding of the shock wave around the black hole. More images are being generated as the time separation Δv with the source particle increases. In particular, an infinite number of images contribute to (C.17) in the limit $\Delta v \rightarrow \infty$. The shock wave described in [23] may be similarly expressed as an infinite sum over images, although it has been explicitly resummed in that case. We refer the reader to section 3.2 for further comments on the relation between shock waves in maximally and non-maximally rotating BTZ black holes.

Open Access. This article is distributed under the terms of the Creative Commons Attribution License ([CC-BY 4.0](https://creativecommons.org/licenses/by/4.0/)), which permits any use, distribution and reproduction in any medium, provided the original author(s) and source are credited.

References

- [1] G. Penington, *Entanglement Wedge Reconstruction and the Information Paradox*, *JHEP* **09** (2020) 002 [[arXiv:1905.08255](https://arxiv.org/abs/1905.08255)] [[INSPIRE](#)].
- [2] A. Almheiri, N. Engelhardt, D. Marolf and H. Maxfield, *The entropy of bulk quantum fields and the entanglement wedge of an evaporating black hole*, *JHEP* **12** (2019) 063 [[arXiv:1905.08762](https://arxiv.org/abs/1905.08762)] [[INSPIRE](#)].
- [3] G. Penington, S.H. Shenker, D. Stanford and Z. Yang, *Replica wormholes and the black hole interior*, [arXiv:1911.11977](https://arxiv.org/abs/1911.11977) [[INSPIRE](#)].
- [4] A. Almheiri, T. Hartman, J. Maldacena, E. Shaghoulian and A. Tajdini, *Replica Wormholes and the Entropy of Hawking Radiation*, *JHEP* **05** (2020) 013 [[arXiv:1911.12333](https://arxiv.org/abs/1911.12333)] [[INSPIRE](#)].
- [5] A. Almheiri, T. Hartman, J. Maldacena, E. Shaghoulian and A. Tajdini, *The entropy of Hawking radiation*, [arXiv:2006.06872](https://arxiv.org/abs/2006.06872) [[INSPIRE](#)].
- [6] S.D. Mathur, *The Information paradox: A Pedagogical introduction*, *Class. Quant. Grav.* **26** (2009) 224001 [[arXiv:0909.1038](https://arxiv.org/abs/0909.1038)] [[INSPIRE](#)].
- [7] I. Bena et al., *Smooth horizonless geometries deep inside the black-hole regime*, *Phys. Rev. Lett.* **117** (2016) 201601 [[arXiv:1607.03908](https://arxiv.org/abs/1607.03908)] [[INSPIRE](#)].
- [8] V. Balasubramanian, J. de Boer, V. Jejjala and J. Simon, *The Library of Babel: On the origin of gravitational thermodynamics*, *JHEP* **12** (2005) 006 [[hep-th/0508023](https://arxiv.org/abs/hep-th/0508023)] [[INSPIRE](#)].
- [9] V. Balasubramanian, B. Czech, V.E. Hubeny, K. Larjo, M. Rangamani and J. Simon, *Typicality versus thermality: An Analytic distinction*, *Gen. Rel. Grav.* **40** (2008) 1863 [[hep-th/0701122](https://arxiv.org/abs/hep-th/0701122)] [[INSPIRE](#)].
- [10] B.D. Chowdhury and S.D. Mathur, *Radiation from the non-extremal fuzzball*, *Class. Quant. Grav.* **25** (2008) 135005 [[arXiv:0711.4817](https://arxiv.org/abs/0711.4817)] [[INSPIRE](#)].
- [11] I. Bena, P. Heidmann, R. Monten and N.P. Warner, *Thermal Decay without Information Loss in Horizonless Microstate Geometries*, *SciPost Phys.* **7** (2019) 063 [[arXiv:1905.05194](https://arxiv.org/abs/1905.05194)] [[INSPIRE](#)].
- [12] S.H. Shenker and D. Stanford, *Black holes and the butterfly effect*, *JHEP* **03** (2014) 067 [[arXiv:1306.0622](https://arxiv.org/abs/1306.0622)] [[INSPIRE](#)].
- [13] J. Maldacena, S.H. Shenker and D. Stanford, *A bound on chaos*, *JHEP* **08** (2016) 106 [[arXiv:1503.01409](https://arxiv.org/abs/1503.01409)] [[INSPIRE](#)].
- [14] J. Polchinski, *Chaos in the black hole S-matrix*, [arXiv:1505.08108](https://arxiv.org/abs/1505.08108) [[INSPIRE](#)].
- [15] S.H. Shenker and D. Stanford, *Stringy effects in scrambling*, *JHEP* **05** (2015) 132 [[arXiv:1412.6087](https://arxiv.org/abs/1412.6087)] [[INSPIRE](#)].
- [16] D.A. Roberts and D. Stanford, *Two-dimensional conformal field theory and the butterfly effect*, *Phys. Rev. Lett.* **115** (2015) 131603 [[arXiv:1412.5123](https://arxiv.org/abs/1412.5123)] [[INSPIRE](#)].
- [17] J.M. Maldacena, *Eternal black holes in anti-de Sitter*, *JHEP* **04** (2003) 021 [[hep-th/0106112](https://arxiv.org/abs/hep-th/0106112)] [[INSPIRE](#)].

- [18] A.L. Fitzpatrick and J. Kaplan, *Conformal Blocks Beyond the Semi-Classical Limit*, *JHEP* **05** (2016) 075 [[arXiv:1512.03052](#)] [[INSPIRE](#)].
- [19] A.L. Fitzpatrick, J. Kaplan, D. Li and J. Wang, *On information loss in AdS_3/CFT_2* , *JHEP* **05** (2016) 109 [[arXiv:1603.08925](#)] [[INSPIRE](#)].
- [20] A.L. Fitzpatrick and J. Kaplan, *On the Late-Time Behavior of Virasoro Blocks and a Classification of Semiclassical Saddles*, *JHEP* **04** (2017) 072 [[arXiv:1609.07153](#)] [[INSPIRE](#)].
- [21] A. Bombini, A. Galliani, S. Giusto, E. Moscato and R. Russo, *Unitary 4-point correlators from classical geometries*, *Eur. Phys. J. C* **78** (2018) 8 [[arXiv:1710.06820](#)] [[INSPIRE](#)].
- [22] V. Jahnke, K.-Y. Kim and J. Yoon, *On the Chaos Bound in Rotating Black Holes*, *JHEP* **05** (2019) 037 [[arXiv:1903.09086](#)] [[INSPIRE](#)].
- [23] M. Mezei and G. Sárosi, *Chaos in the butterfly cone*, *JHEP* **01** (2020) 186 [[arXiv:1908.03574](#)] [[INSPIRE](#)].
- [24] R.R. Poojary, *BTZ dynamics and chaos*, *JHEP* **03** (2020) 048 [[arXiv:1812.10073](#)] [[INSPIRE](#)].
- [25] I. Halder, *Global Symmetry and Maximal Chaos*, [arXiv:1908.05281](#) [[INSPIRE](#)].
- [26] A. Štikonas, *Scrambling time from local perturbations of the rotating BTZ black hole*, *JHEP* **02** (2019) 054 [[arXiv:1810.06110](#)] [[INSPIRE](#)].
- [27] M. Bianchi, A. Grillo and J.F. Morales, *Chaos at the rim of black hole and fuzzball shadows*, *JHEP* **05** (2020) 078 [[arXiv:2002.05574](#)] [[INSPIRE](#)].
- [28] V. Cardoso, A.S. Miranda, E. Berti, H. Witek and V.T. Zanchin, *Geodesic stability, Lyapunov exponents and quasinormal modes*, *Phys. Rev. D* **79** (2009) 064016 [[arXiv:0812.1806](#)] [[INSPIRE](#)].
- [29] V. Balasubramanian, B. Craps, M. De Clerck and K. Nguyen, *Superluminal chaos after a quantum quench*, *JHEP* **12** (2019) 132 [[arXiv:1908.08955](#)] [[INSPIRE](#)].
- [30] J. Maldacena, *Chaos and black holes*, Harvard Physics Morris Loeb Lectures in Physics, 25 March 2016 [<https://www.youtube.com/watch?v=7Dd51agJCcU>].
- [31] A. Tyukov, R. Walker and N.P. Warner, *Tidal Stresses and Energy Gaps in Microstate Geometries*, *JHEP* **02** (2018) 122 [[arXiv:1710.09006](#)] [[INSPIRE](#)].
- [32] I. Bena, E.J. Martinec, R. Walker and N.P. Warner, *Early Scrambling and Capped BTZ Geometries*, *JHEP* **04** (2019) 126 [[arXiv:1812.05110](#)] [[INSPIRE](#)].
- [33] I. Bena, A. Houppe and N.P. Warner, *Delaying the Inevitable: Tidal Disruption in Microstate Geometries*, *JHEP* **02** (2021) 103 [[arXiv:2006.13939](#)] [[INSPIRE](#)].
- [34] E.J. Martinec and N.P. Warner, *The Harder They Fall, the Bigger They Become: Tidal Trapping of Strings by Microstate Geometries*, [arXiv:2009.07847](#) [[INSPIRE](#)].
- [35] K. Sfetsos, *On gravitational shock waves in curved space-times*, *Nucl. Phys. B* **436** (1995) 721 [[hep-th/9408169](#)] [[INSPIRE](#)].
- [36] S.E. Gralla, A. Ravishankar and P. Zimmerman, *Horizon Instability of the Extremal BTZ Black Hole*, *JHEP* **05** (2020) 094 [[arXiv:1911.11164](#)] [[INSPIRE](#)].
- [37] S. Carlip, *The (2 + 1)-Dimensional black hole*, *Class. Quant. Grav.* **12** (1995) 2853 [[gr-qc/9506079](#)] [[INSPIRE](#)].

- [38] G. Compère and A. Fiorucci, *Advanced Lectures on General Relativity*, [arXiv:1801.07064](#) [[INSPIRE](#)].
- [39] N. Cruz, C. Martinez and L. Pena, *Geodesic structure of the (2 + 1) black hole*, *Class. Quant. Grav.* **11** (1994) 2731 [[gr-qc/9401025](#)] [[INSPIRE](#)].
- [40] I. Bena et al., *Asymptotically-flat supergravity solutions deep inside the black-hole regime*, *JHEP* **02** (2018) 014 [[arXiv:1711.10474](#)] [[INSPIRE](#)].
- [41] J.D. Brown and M. Henneaux, *Central Charges in the Canonical Realization of Asymptotic Symmetries: An Example from Three-Dimensional Gravity*, *Commun. Math. Phys.* **104** (1986) 207 [[INSPIRE](#)].
- [42] E. Poisson, *A Relativist's Toolkit: The Mathematics of Black-Hole Mechanics*, Cambridge University Press (2009) [[DOI](#)] [[INSPIRE](#)].
- [43] G. Festuccia and H. Liu, *A Bohr-Sommerfeld quantization formula for quasinormal frequencies of AdS black holes*, *Adv. Sci. Lett.* **2** (2009) 221 [[arXiv:0811.1033](#)] [[INSPIRE](#)].
- [44] D. Birmingham, I. Sachs and S.N. Solodukhin, *Conformal field theory interpretation of black hole quasinormal modes*, *Phys. Rev. Lett.* **88** (2002) 151301 [[hep-th/0112055](#)] [[INSPIRE](#)].
- [45] A. Banerjee, A. Kundu and R.R. Poojary, *Rotating black holes in AdS spacetime, extremality, and chaos*, *Phys. Rev. D* **102** (2020) 106013 [[arXiv:1912.12996](#)] [[INSPIRE](#)].

Submerging islands through thermalization

Vijay Balasubramanian,^{a,b} Ben Craps,^b Mikhail Khramtsov^c and Edgar Shaghoulian^a

^a*David Rittenhouse Laboratory, University of Pennsylvania,
Philadelphia, PA 19104, U.S.A.*

^b*Theoretische Natuurkunde, Vrije Universiteit Brussel (VUB)
and The International Solvay Institutes,
Brussels, Belgium*

^c*Department of Mathematical Methods for Quantum Technologies,
Steklov Mathematical Institute of Russian Academy of Sciences,
Gubkin str. 8, 119991 Moscow, Russia*

E-mail: vijay@physics.upenn.edu, Ben.Craps@vub.be,
khramtsov@mi-ras.ru, eshag@sas.upenn.edu

ABSTRACT: We illustrate scenarios in which Hawking radiation collected in finite regions of a reservoir provides temporary access to the interior of black holes through transient entanglement “islands.” Whether these islands appear and the amount of time for which they dominate — sometimes giving way to a thermalization transition — is controlled by the amount of radiation we probe. In the first scenario, two reservoirs are coupled to an eternal black hole. The second scenario involves two holographic quantum gravitating systems at different temperatures interacting through a Rindler-like reservoir, which acts as a heat engine maintaining thermal equilibrium. The latter situation, which has an intricate phase structure, describes two eternal black holes radiating into each other through a shared reservoir.

KEYWORDS: 2D Gravity, Black Holes, AdS-CFT Correspondence

ARXIV EPRINT: [2107.14746](https://arxiv.org/abs/2107.14746)

Contents

1	Introduction	1
2	An eternal black hole coupled to a reservoir	3
2.1	Radiation entropy	3
2.2	The entanglement entropy of finite segments	5
3	Two holographic quantum dots connected by a reservoir	7
3.1	Black hole phase	9
3.2	Asymmetric wormhole phase	12
4	Page curves of two connected black holes	15
4.1	The two black hole setup	15
4.2	Entanglement entropy of segments including the second black hole	17
4.2.1	Page curves	19
4.3	Entanglement entropy of segments in reservoir	20
4.3.1	Page curves	22
5	Discussion	24

1 Introduction

The fine-grained entropy of any quantum system A entangled with its complement \bar{A} satisfies the unitarity bound $S(A) \leq \min\{\log \dim \mathcal{H}_A, \log \dim \mathcal{H}_{\bar{A}}\}$ in terms of the dimensions of the corresponding Hilbert spaces. In a holographic theory, the entropy may be geometrized in terms of the areas of extremal surfaces in spacetime [1–6]. As the system evolves, entanglement structure can change dynamically, and be reflected in exchange of dominance between different extremal surfaces. Beautiful work has shown that this exchange can be necessary for the satisfaction of the bound on $S(A)$ as time evolves [4–17].

One example [13] involves holographic CFTs entangled in a thermofield double state dual to eternal black holes connected behind their horizons by a wormhole. The entropy of a pair of subregions in these theories is initially associated to an extremal surface passing through the wormhole. The area of this surface grows in time, threatening violation of the entropy bound, a fate avoided by a thermalization transition after which the two regions no longer share mutual information. After this time, their entropy is geometrized by a pair of disconnected extremal surfaces of constant area outside the horizons. A second example occurs in the same setup of eternal black holes, this time coupled to reservoirs collecting the Hawking radiation escaping the black holes [4–6, 8, 11]. In this case, at early times the entropy of the radiation increases in time exactly as computed by Hawking. At the Page time,

a nontrivial quantum extremal surface (QES) [1–3, 18] appears in the spacetime. This leads to a saturation of the entropy by requiring us to include the interior Hawking modes in the computation of the entropy. The nontrivial QES occurs due to the replica wormhole saddle points in the quantum gravity path integral [8, 11]. It bounds an “island” and is responsible for information recovery from Hawking radiation via access to the black hole interior.

In this paper, we study what occurs when one considers finite-sized portions of the radiation. For sufficiently small portions, the radiation may thermalize before or after it has a chance to encode the black hole interior. We will probe this competition between thermalization and the island mechanism — realizing both examples discussed above in the same physical system — by examining the time-dependence of entanglement entropy. The various transitions can be predicted by a careful application of the unitarity bound described above. In short, island regions will appear when the entropy of quantum fields on the black hole background threatens the unitarity bound set by its Bekenstein-Hawking entropy, whereas thermalization will occur when the entropy of the radiation approaches the maximal amount dictated by the size of the radiation region’s Hilbert space. We will exhibit a nontrivial phase structure transitioning between these possibilities in two scenarios, which we now summarize.

Summary of results. Our first scenario, studied in section 2, involves finite regions in two reservoirs coupled to a thermofield double black hole in AdS_2 , see figure 1 (the entropy of infinite radiation regions in this model was studied in [7, 8]). The entropy initially grows linearly as time evolves, then (depending on the region size and boundary conditions) there may be a transition to half the initial rate, and finally the growth stabilizes; see figure 3. If we treat the radiation as holographic in its own right, the transition between the initial and the final phase involves an exchange between an extremal surface passing between the reservoirs through the induced dimension, and a pair of disconnected extremal surfaces of constant area, as in [13]; see figure 2. However the “island formula” (reviewed below) dictates a new intermediate phase, which includes an island, although the entropy does not stabilize but instead grows with only half the initial slope. The eventual stabilization of entanglement entropy of finite intervals then happens not because of entanglement islands, but because of the thermalization of the segments. When the entanglement entropy saturates, the island is no longer accessible.

Our second scenario involves two holographic quantum dots at different temperatures, each dual to an eternal AdS_2 black hole, in local equilibrium with a finite radiation reservoir. The reservoir is modeled by Rindler space, which acts as a heat engine maintaining local equilibrium by redshifting warmer modes approaching the cooler black hole and vice versa; see the beginning of section 3 and figure 4. The radiation theory will itself be holographic. The phase structure includes transitions between an asymmetric wormhole (the “confined” phase; see section 3.2 and figure 7) and two black holes of different temperature (the “deconfined” phase; see section 3.1 and figure 5). In the deconfined phase, many extremal surfaces vie to dominate the entropy of reservoir regions in this model. This is studied in section 4; see figure 9, 10, 11 for the case where we include one pair of thermofield double quantum dots in the region whose entropy we are computing and figure 12, 13, 14 for the case where

we do not. As time evolves, these surfaces exchange dominance to maintain the unitary upper bound on entropy. In particular, unlike the single black hole case, in this model it is possible to have both temporary island configurations and permanent island configurations.

2 An eternal black hole coupled to a reservoir

Consider an AdS₂ eternal black hole with flat, non-gravitating radiation reservoirs glued to the two boundaries (figure 1) [7, 8]. In the AdS₂ region we have Jackiw-Teitelboim (JT) gravity, along with transparent boundary conditions for conformal matter in the black hole and reservoirs. The action is:

$$I = -\frac{\phi_0}{4\pi} \left[\int_{\Sigma_2} R + 2 \int_{\partial\Sigma_2} K \right] - \frac{1}{4\pi} \left[\int_{\Sigma_2} \phi(R+2) + 2\phi_b \int_{\partial\Sigma_2} (K-1) \right] + I_{\text{CFT}}, \quad (2.1)$$

where the first term is topological, the last term is a Conformal Field Theory (CFT) with central charge c , ϕ_0 gives the Bekenstein-Hawking entropy of the extremal black hole (we have set $4G_N = 1$), and ϕ_b is the asymptotic value of the dilaton on Σ_2 , the region of spacetime where gravity is dynamical. Varying (2.1) with respect to the dilaton fixes the metric to be locally AdS₂. Globally we consider the eternal black hole (figure 1), with each of the two exterior regions described by

$$ds_{\text{grav}}^2 = \frac{4\pi^2}{\beta^2} \frac{-dt^2 + d\sigma^2}{\sinh^2 \frac{2\pi\sigma}{\beta}}, \quad t \in \mathbb{R}, \quad \sigma \in (-\infty, -\epsilon]. \quad (2.2)$$

We glue the surface $\sigma = -\epsilon$ continuously to the reservoir [7], so the latter's metric is:

$$ds_{\text{bath}}^2 = \frac{-dt^2 + d\sigma^2}{\epsilon^2}, \quad t \in \mathbb{R}, \quad \sigma \in [-\epsilon, +\infty). \quad (2.3)$$

Varying with respect to the metric yields the dilaton equation of motion:

$$D_\mu D_\nu \phi - g_{\mu\nu} \square \phi + g_{\mu\nu} \phi + 2\pi T_{\mu\nu} = 0. \quad (2.4)$$

With the stress tensor given by $T_{\mu\nu} = \frac{c}{24\pi} g_{\mu\nu}$, the dilaton in the gravitational region (2.2) is

$$\phi(\sigma) = \frac{2\pi\phi_r}{\beta} \coth \frac{2\pi\sigma}{\beta}, \quad (2.5)$$

where ϕ_r is an integration constant.

2.1 Radiation entropy

The island formula [4–6, 8, 11] says that the entanglement entropy of reservoir region A is

$$\mathcal{S}(A) = \min_{\mathcal{I}} \text{ext} [S_{\text{CFT}}(A \cup \mathcal{I}) + \text{Area}(\partial\mathcal{I})], \quad (2.6)$$

where \mathcal{I} is an “island” in the gravitating region. In JT gravity the area term equals the dilaton value on the corresponding surface plus the constant ϕ_0 , while, for a general 2d CFT, the entropy on $A \cup \mathcal{I}$ is related to the (generically non-universal) correlator of twist

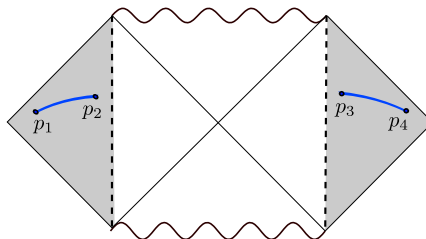


Figure 1. Penrose diagram of an eternal AdS₂ black hole with flat reservoirs glued to the boundaries, and identical equal-time segments $[p_1, p_2]$ and $[p_3, p_4]$. We compute the entanglement entropy of the union of these segments.

operators. We take the CFT to be holographic following [6],¹ and compute $S_{\text{CFT}}(A \cup \mathcal{I})$ through the Ryu-Takayanagi formula [1, 2] in a 3d gravity theory dual to this CFT on a fixed curved background.

In Euclidean signature, the CFT on the 2d boundary of the 3d gravity theory is defined on a Euclidean black hole attached to reservoirs with fixed metrics. The dynamical part of the 2d boundary is referred to as a “Planck brane”, which corresponds to a cut-off boundary of the 3d geometry. Given a specific dynamical 2d metric ds_2^2 and stress tensor, it is convenient to introduce a complex coordinate w on the 2d boundary so that $T_{ww} = 0$ in the flat Weyl-transformed metric $dwd\bar{w}$ [6]. Since the stress tensor vanishes, the dual 3d spacetime can be described by Poincaré coordinates in Euclidean AdS₃:

$$ds^2 = \frac{dwd\bar{w} + dz^2}{z^2}. \tag{2.7}$$

Writing the original boundary metric (before Weyl transformation) as

$$ds_2^2 = \Omega^{-2}(w, \bar{w})dwd\bar{w}, \tag{2.8}$$

the holographic relation

$$g_{\mu\nu}^{(3)}|_{\text{bdy}} = \frac{1}{\varepsilon^2}g_{\mu\nu}^{(2)} \tag{2.9}$$

leads to

$$\frac{dwd\bar{w}}{z(w)^2} = \frac{1}{\varepsilon^2}\Omega^{-2}(w, \bar{w})dwd\bar{w} \Rightarrow z(w) = \varepsilon\Omega(w, \bar{w}), \tag{2.10}$$

which determines the embedding of the Planck brane in the 3d geometry [6]. Note that the regulator ε is distinct from the 2d cutoff ϵ where the reservoir is glued to the AdS₂ black hole.

Following [1, 2] the CFT entropies $S_{\text{CFT}}(A \cup \mathcal{I})$ are computed by lengths of geodesics in (2.7) ending on boundary points of $A \cup \mathcal{I}$, with $z(w)$ treated as a cutoff. Physical quantities will depend nontrivially on Ω , e.g., the entropy of a single interval between w_1 and w_2 is [27, 28]:

$$S(w_1, w_2) = \frac{c}{6} \log \left(\frac{|w_1 - w_2|^2}{\varepsilon_1 \varepsilon_2 \Omega(w_1, \bar{w}_1) \Omega(w_2, \bar{w}_2)} \right), \tag{2.11}$$

¹For further developments of the doubly holographic approach to the entanglement entropy of radiation, see e.g. [14, 19–26], especially [20] for a pedagogical treatment.

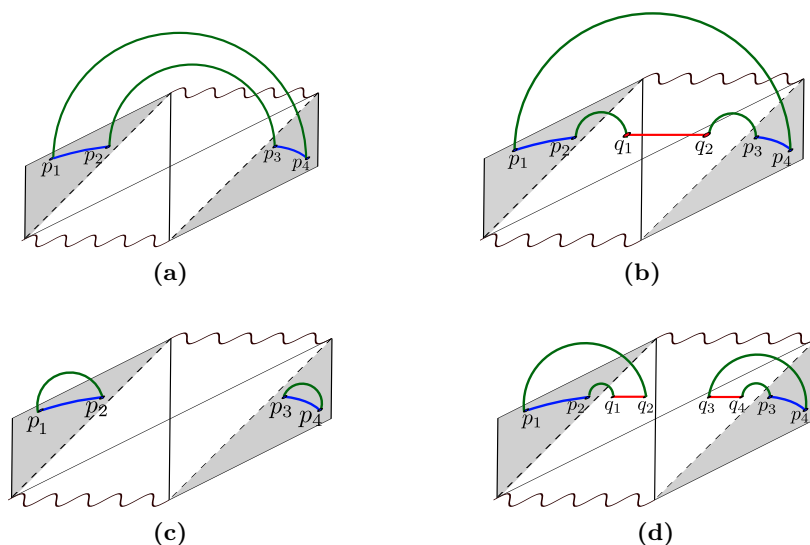


Figure 2. Extremal surfaces that extend into the 3d bulk from the Penrose diagram in figure 1 playing the role of the 2D boundary. (a) \rightarrow (c) is a thermalization transition, which can be interrupted by the island configuration (b). Surface (d) is always subleading.

To return to Lorentzian coordinates (2.2), we write $w = e^{\frac{2\pi}{\beta}(\sigma+i\tau)}$ and Wick rotate $\tau = it$. The single interval entropy is universal for 2d CFTs [27] but we consider a union of intervals. Typically, several combinations of geodesics end on such unions, with each geodesic length given by (2.11). For fixed $A \cup \mathcal{I}$ the minimal total geodesic length gives the entropy. Thus, we identify possible 3d geodesic configurations computing $S_{\text{CFT}}(A \cup \mathcal{I})$, extremize the functional in (2.6) for each choice, and select the minimizing choice.

2.2 The entanglement entropy of finite segments

To compute the entropy of the region $A = [p_1, p_2] \cup [p_3, p_4]$ in figure 1, we will use a time that continuously glues global AdS₂ to the reservoirs, reversing Schwarzschild time t (2.2) in one of the exterior regions of the black hole. Thus we choose endpoint coordinates

$$p_1 = (b, -t + i\pi); \quad p_2 = (a, -t + i\pi); \quad p_3 = (a, t); \quad p_4 = (b, t). \quad (2.12)$$

Figure 2 shows 3d geodesics between interval endpoints $p_{1,2,3,4}$ and a possible island in the black hole region.² The green curves are Ryu-Takayanagi surfaces, while red regions inside the black hole are islands whose endpoints are the quantum extremal surfaces found by extremizing (2.6).

Configuration (a): linear growth. Two 3d geodesics connect $p_1 \leftrightarrow p_4$ and $p_2 \leftrightarrow p_3$, respectively. There are no islands and the entropy is given by

$$\mathcal{S}_a = S_{\text{connected}}^{\text{no island}}(p_1, p_2; p_3, p_4) = 2 \frac{c}{3} \log \left[\frac{\pi}{\beta} \cosh \frac{2\pi t}{\beta} \right]. \quad (2.13)$$

This expression grows approximately linearly in time.

²UV divergences are associated with endpoints of $p_{1,2,3,4}$ and possible islands. The first kind are the same for any choice of geodesic, so we omit them. The second kind renormalize ϕ_0 .

Configuration (b): island. This fully connected configuration includes an island in the black hole region between $[q_1, q_2]$. The location is obtained by extremizing (2.6) with respect to $q_{1,2} = (x, t_x)$ in their respective black hole exterior patches. The entropy is

$$S_{\text{connected}}^{\text{island}} = 2 \left(\phi_0 + \frac{2\pi\phi_r}{\beta} \coth \left(-\frac{2\pi}{\beta} x \right) \right) + \frac{c}{3} \log \left(\frac{\beta \left(\cosh \left[\frac{\pi}{\beta} (x-a) \right] - \cosh \left[\frac{2\pi}{\beta} (t-t_x) \right] \right)}{\pi \sinh \left(-\frac{2\pi x}{\beta} \right)} \right) + \frac{c}{3} \log \left[\frac{\pi}{\beta} \cosh \frac{2\pi t}{\beta} \right]. \quad (2.14)$$

The extrema for the time and space decouple, and the time equation yields $t_x = t$. The solution for x is cumbersome, but in the regime $\frac{\phi_r}{c\beta} \gg 1$ there is a simplified expression

$$x \approx a + \frac{\beta}{2\pi} \log \left[24\pi \frac{\phi_r}{c\beta} \right], \quad \frac{\phi_r}{c\beta} \gg 1. \quad (2.15)$$

The first line in (2.14) determines the time-independent island contribution. The second line, which grows linearly with half the slope compared to the configuration (a), comes from the long geodesic that goes across the Einstein-Rosen bridge.

Configuration (c): thermalization. This configuration gives the sum of thermalized CFT entanglement entropies for the thermofield double copies of the reservoir segment:

$$S_{\text{thermalized}} = 2 \frac{c}{3} \log \left(\frac{\beta}{\pi} \sinh \frac{\pi|a-b|}{\beta} \right). \quad (2.16)$$

Configurations (d): disconnected islands. Here two islands lie in exterior regions of the black hole, connected with the RT geodesics to their respective copies of the radiation segment. One can show that this configuration is always subleading compared to (c) while also being time independent.

Summary. Varying the size of the reservoir regions with other parameters fixed, we see in figure 3 that for large regions we have transitions (a) \rightarrow (b) \rightarrow (c), accessing an island region for a finite period of time before losing it. For smaller regions we directly make the thermalization transition (a) \rightarrow (c) as in [13]. Thus, finite radiation segments give temporary access to the black hole interior, unlike infinite segments which give permanent access at late times [7–9, 11]. This happens because during the entanglement evolution any finite segment will eventually thermalize, scrambling information from the island. From the path integral point of view the transition (a) \rightarrow (b) arises by including replica wormholes [7, 11], and will be smoothed by also summing over replica non-symmetric manifolds [11, 29, 30].

By utilizing the unitarity bound discussed in section 1, the qualitative nature of these transitions can be predicted without much computation. In particular, (a) and (b) will eventually threaten the unitarity bound set by the size of the Hilbert space of our radiation region, so must eventually transition. What about the transition (a) \rightarrow (b)? Clearly this need not come close to saturating the unitarity bound of our radiation region, since the entropy continues to increase in phase (b) due to interior Hawking modes being captured by the island while their exterior partners escape away into the infinite region of the bath.

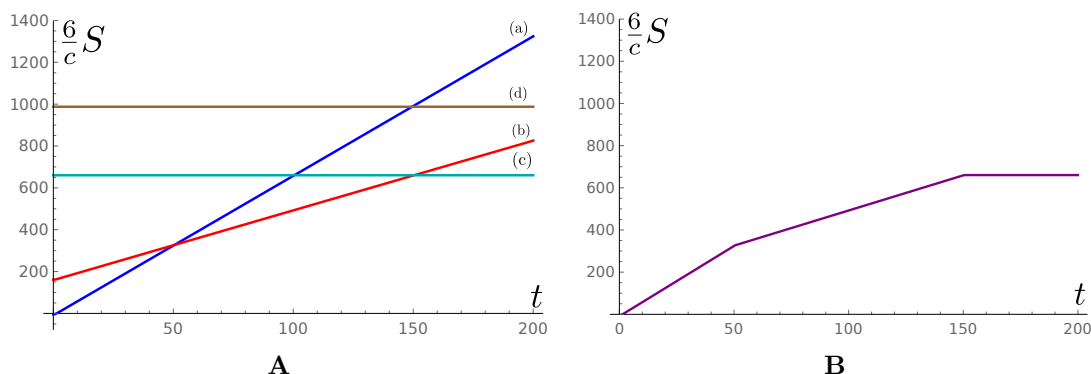


Figure 3. **A.** The entanglement entropy curves for the configurations (a), (b), (c) and (d) for region size much larger than the distance from the interface and comparable to ϕ_r/c . **B.** The Page curve of a finite segment, obtained by minimizing between the saddles shown in plot A.

However, the structure of the geodesics in figure 2(a) indicates that the mutual information vanishes between (i) the gravitational region and the adjoining baths up to the radiation region, and (ii) the rest of the complement of the radiation region A . In particular, this means that each region of the complement is subject to its own unitarity bound. The relevant bound here is the one set by the gravitational region (plus some of the adjoining baths, which we take to be a small correction): once the entropy of this region comes close to $2S_{\text{BH}}$, a transition must occur.

3 Two holographic quantum dots connected by a reservoir

The quantum-mechanical setup we consider next involves two thermofield double pairs of a holographic quantum mechanical system (which we refer to as the quantum dot) interacting through a common reservoir. The quantum dots are dual to JT gravity described by the action (2.1). They are coupled to a CFT₂ of central charge c , which lives in the reservoir. We will not specify the exact Hamiltonian of the quantum dots; however a common example of a quantum mechanical system holographically dual to JT gravity (in an appropriate limit) is the SYK model [31–33].

The temperatures of the quantum dots are treated as independent parameters, and so for this setup to be in the equilibrium, we have the reservoir working as a heat engine which cools the matter CFT quanta being emitted from the hotter quantum dot and going into the cooler one. The action of the heat engine is caused by the nontrivial metric in the reservoir. Such a reservoir in Euclidean signature has a boundary consisting of two thermal circles of different lengths (figure 4). One can write down a metric for such a reservoir as follows:³

$$ds^2 = \frac{dr^2 + f(r)^2 d\tau^2}{\epsilon^2}, \quad \tau \sim \tau + 2\pi\alpha, \quad r \in (r_1, r_2). \quad (3.1)$$

Notice that the thermal periodicity changes from $2\pi f(r_1)\alpha/\epsilon$ to $2\pi f(r_2)\alpha/\epsilon$. So, as advertised, such a spacetime acts as a heat engine which equilibrates the radiation between the

³We include the regulator ϵ so that the metric in the gravity dual is manifestly continuous throughout the spacetime, similarly to the discussion in section 2.

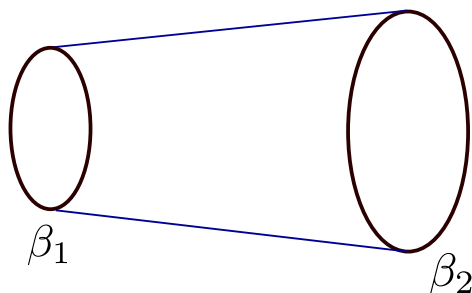


Figure 4. Euclidean picture of the two quantum dots living on the thermal circles of different lengths coupled by the conical reservoir.

two systems with different temperature. This is similar to considering different radial positions in a black hole in thermal equilibrium: the physical temperature for static observers at each location is different, yet the entire system is in thermal equilibrium.

In the present paper we consider the simplest case and assume that $f(r) = r$ and the reservoir has the metric of a cone:

$$ds_R^2 = \frac{dr^2 + r^2 d\tau^2}{\epsilon^2}, \quad \tau \sim \tau + 2\pi\alpha. \quad (3.2)$$

The results in this model can be extended to a general $f(r)$ in a straightforward manner. The position-dependent temperature is precisely that of Rindler space, obtained by continuing to Lorentzian signature $\tau \rightarrow it$.

By choosing an interval of size L_R and inverse temperatures β_1 and β_2 , we fix the radial coordinates of boundaries in figure 4 and the solid angle of the cone. Choosing $\beta_2 > \beta_1$, this yields the relations

$$r_1 = \frac{L_R \beta_1}{\beta_2 - \beta_1}, \quad r_2 = \frac{L_R \beta_2}{\beta_2 - \beta_1}, \quad \alpha = \frac{\beta_2 - \beta_1}{2\pi L_R}. \quad (3.3)$$

For $\alpha \neq 1$ there is a conical singularity, although it is excised from the region we are considering. The parameter α has a physical interpretation as the strength of the heat engine which equilibrates the two sides, and it must be tuned as we vary the temperatures or the distance over which we want to equilibrate the temperatures. Some formulas will be simpler to write in terms of α , but fixing α and $\beta_{1,2}$ fixes L_R . The equal-temperature limit can be realized by taking $\alpha \rightarrow 0$ while keeping L_R fixed, in which case $r_{1,2} \rightarrow \infty$. Physically we are taking the strength of the equilibrator to zero (equal temperatures are already equilibrated), but to keep finite-sized circles we need to scale the coordinates to infinity.

We can rewrite the cone metric as conformally flat:

$$ds_R^2 = \Omega_R(\xi)^{-2} \frac{d\xi^2 + d\theta^2}{\epsilon^2}, \quad \xi \in [0, L], \quad \theta \sim \theta + 2\pi. \quad (3.4)$$

Note that the dimensionless coordinate ξ plays the role of the spatial coordinate, and θ plays the role of Euclidean time. The Weyl factor is given by the formula

$$\Omega_R(\xi) = \frac{1}{\alpha r} = \frac{2\pi}{\beta_1} e^{-\alpha\xi}, \quad r = r_1 e^{\alpha\xi}, \quad L = \alpha^{-1} \log \frac{\beta_2}{\beta_1}. \quad (3.5)$$

There are two possible two-dimensional gravitational duals for our Rindler reservoir coupled to holographic quantum dots living on thermal circles at each end. We can either complete the circular boundaries of the reservoir into a torus, or we can have independent disks at the two boundaries. The first possibility represents a confined phase, described by a wormhole, shown schematically in figure 7. The second possibility represents a deconfined phase, described by independent thermofield double black holes, shown schematically in figure 4.

The partition sum of the theory will undergo transitions between these confined and deconfined phases as the parameters change. We expect that the phase structure will be similar to the one in [34]. The wormhole solution should be global AdS₂ as in [34], except that the dilaton profile will be a one-parameter generalization of the usual one: the solution has a free constant that is usually fixed by the \mathbb{Z}_2 symmetry, but in our case this constant will be fixed by the choice of temperatures. This allows us to cut the solution off at slightly different coordinate values on either side of the wormhole, which leads to equal values of ϕ_r , but with different temperatures. In other words, the boundary conditions from the bulk perspective are given by

$$ds_{1,2}^2 = \frac{du^2}{\epsilon^2}, \quad u \sim u + \beta_{1,2}, \quad \phi_{1,2} = \frac{\phi_r}{\epsilon} \tag{3.6}$$

at leading order in ϵ . The other novelty is the Rindler region. As we reviewed above, a Weyl transformation maps this to the usual case of a finite cylinder with constant thermal periodicity. The Weyl anomaly then makes a contribution to the partition sum, but since the transformation is the same in both solutions, the anomaly does not affect the phase structure.

3.1 Black hole phase

The action is given in (2.1) and the solution that describes the geometry (figure 4) involves two Euclidean copies of the gravitational solution in (2.2)–(2.5), with different temperatures:

$$ds_1^2 = \frac{4\pi^2}{\beta_1^2} \frac{d\tau_1^2 + d\sigma^2}{\sinh^2 \frac{2\pi\sigma}{\beta_1}}; \quad \sigma \in (-\infty, -\epsilon], \quad \tau_1 \sim \tau_1 + \beta_1, \tag{3.7}$$

$$ds_2^2 = \frac{4\pi^2}{\beta_2^2} \frac{d\tau_2^2 + d\sigma^2}{\sinh^2 \left[\frac{2\pi\sigma}{\beta_2} - L \right]}; \quad \sigma \in \left[\frac{\beta_2}{2\pi} L + \epsilon, +\infty \right), \quad \tau_2 \sim \tau_2 + \beta_2. \tag{3.8}$$

The reservoir metric is given by (3.4), with $L = \alpha^{-1} \log \frac{\beta_2}{\beta_1}$ being the size of the reservoir in the cylinder coordinates. The reservoir coordinate ξ is dimensionless, hence the extra conversion factor of $\frac{\beta_2}{2\pi}$. The dilaton profile in the disk regions is given by the equations

$$\phi(\sigma)_1 = -\frac{2\pi}{\beta_1} \phi_r \coth \frac{2\pi\sigma}{\beta_1}; \tag{3.9}$$

$$\phi(\sigma)_2 = \frac{2\pi}{\beta_2} \phi_r \coth \left(\frac{2\pi\sigma}{\beta_2} - L \right). \tag{3.10}$$

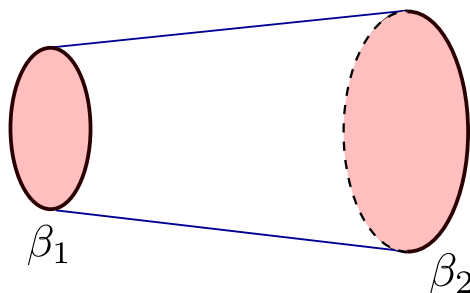


Figure 5. The schematic picture of the black hole phase in the Euclidean signature. The spacetime is two hyperbolic disks connected by the conical reservoir.

We can break up the on-shell partition function for this solution into two main pieces. The first is the gravitational contribution on the disks; it is obtained by directly evaluating the pure JT gravity part of the action on the solution, and reads

$$Z_{\text{disks,grav}} = e^{2\phi_0 + \pi\phi_r \left(\frac{1}{\beta_1} + \frac{1}{\beta_2} \right)}. \quad (3.11)$$

The second piece of the on-shell partition function comes from the matter CFT living on the curved background. The spacetime metric can be written as $ds^2 = e^{2\omega} d\hat{s}_{\text{flat}}^2$ everywhere in the spacetime, and so the nontrivial Weyl factor ω gives a Weyl anomaly contribution [35]:

$$Z_{\text{anomaly}} = \exp \left[\frac{c}{24\pi} \int \sqrt{\hat{g}} (\partial\omega)^2 \right]. \quad (3.12)$$

The computation of this partition function involves a step which will also be used in the computations of entanglement entropy in this model, so we discuss it in detail.

Our spacetime is a closed manifold, so there are no physical boundaries to generate boundary terms. We perform the conformal transformation from the disks and the conical reservoir shown in figure 4 to the plane with metric of the form $ds^2 = e^{2\omega} d\hat{s}_{\text{flat}}^2$. We write the flat reference metric in polar coordinates:

$$d\hat{s}_{\text{flat}}^2 = dw d\bar{w} = d\rho^2 + \rho^2 d\varphi^2, \quad (3.13)$$

where $w = \rho e^{i\varphi}$ is the complex coordinate, $\rho \in [0, +\infty)$ and $\varphi \sim \varphi + 2\pi$. The explicit form of the conformal transformation is given by

$$\text{Disk 1 : } w = e^{\frac{2\pi}{\beta_1}(\sigma + i\tau_1)}; \quad (3.14)$$

$$\text{Reservoir : } w = e^{\xi + i\theta}; \quad (3.15)$$

$$\text{Disk 2 : } w = e^{\frac{2\pi}{\beta_2}(\sigma + i\tau_2)}. \quad (3.16)$$

As shown in figure 6, the plane is divided into three regions where the Weyl factor ω is

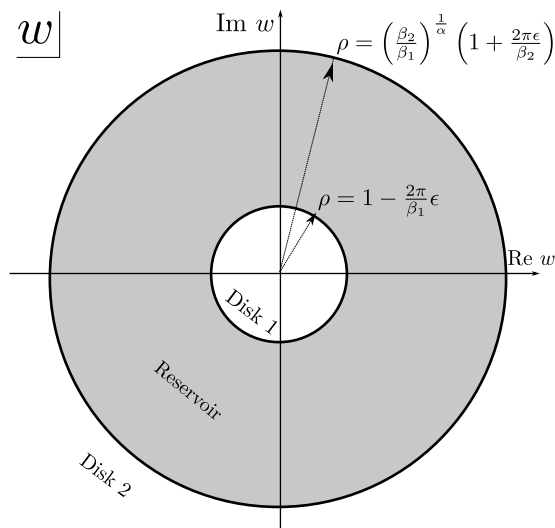


Figure 6. Euclidean geometry of two black holes coupled via a reservoir conformally mapped to a plane. The shaded region is the reservoir.

given by different functions:

$$\text{Disk 1: } e^{\omega_1} = \Omega_1^{-1} = \frac{2}{1-\rho^2}, \quad \rho \in \left[0, 1 - \frac{2\pi\epsilon}{\beta_1}\right]; \quad (3.17)$$

$$\text{Reservoir: } e^{\omega_{\text{bath}}} = \Omega_{\text{bath}}^{-1} = \frac{\beta_1}{2\pi\epsilon} \rho^{\alpha-1}, \quad \rho \in \left(1 - \frac{2\pi\epsilon}{\beta_1}\epsilon, \left(\frac{\beta_2}{\beta_1}\right)^{\frac{1}{\alpha}} \left(1 + \frac{2\pi\epsilon}{\beta_2}\right)\right); \quad (3.18)$$

$$\text{Disk 2: } e^{\omega_2} = \Omega_2^{-1} = \frac{2\left(\frac{\beta_2}{\beta_1}\right)^{\frac{1}{\alpha}}}{\rho^2 - \left(\frac{\beta_2}{\beta_1}\right)^{\frac{2}{\alpha}}}, \quad \rho \in \left[\left(\frac{\beta_2}{\beta_1}\right)^{\frac{1}{\alpha}} \left(1 + \frac{2\pi\epsilon}{\beta_2}\right), \left(\frac{\beta_2}{\beta_1}\right)^{\frac{1}{\alpha}} \Lambda\right], \quad (3.19)$$

where the bottom line includes the Weyl factor from the Rindler geometry in the reservoir defined in (3.5) written in terms of $w = e^{\xi+i\theta}$, and $\Lambda \gg 1$ is the cutoff. The cutoff is defined with the $(\beta_2/\beta_1)^{1/\alpha}$ prefactor to ensure the ratio of radii defining disk 2 is independent of β_1 , which means the contribution of disk 2 to the partition function will be independent of β_1 (see (3.21) below). We now compute the contributions from the three regions to (3.12) separately.

Disk 1. We integrate from $\rho = 0$ to $\rho = 1 - \frac{2\pi\epsilon}{\beta_1}$ and get

$$Z_1 = \exp \left[\frac{c\beta_1}{24\pi\epsilon} + \frac{c}{6} \log \frac{4\pi\epsilon}{\beta_1} - \frac{c}{8} \right] \tilde{Z}_1, \quad (3.20)$$

where \tilde{Z}_1 is the partition function of the theory on the portion $\rho \in [0, 1 - 2\pi\epsilon/\beta_1]$ of flat space.

Disk 2. We integrate from $\rho = \left(\frac{\beta_2}{\beta_1}\right)^{\frac{1}{\alpha}} \left(1 + \frac{2\pi\epsilon}{\beta_2}\right)$ to $\rho = \Lambda \gg 1$ and get

$$Z_2 = \exp \left[\frac{c\beta_2}{24\pi\epsilon} - \frac{c}{6} \log \frac{4\pi\epsilon}{\beta_2} - \frac{c}{24} + \frac{c}{3} \log \Lambda \right] \tilde{Z}_2, \quad (3.21)$$

where \tilde{Z}_2 is the partition function of the theory on the portion $\rho \in \left[\left(\frac{\beta_2}{\beta_1} \right)^{\frac{1}{\alpha}} \left(1 + \frac{2\pi\epsilon}{\beta_2} \right), \left(\frac{\beta_2}{\beta_1} \right)^{\frac{1}{\alpha}} \Lambda \right]$ of flat space.

Reservoir region. Here we integrate from $\rho = 1 - \frac{2\pi\epsilon}{\beta_1}$ to $\rho = \left(\frac{\beta_2}{\beta_1} \right)^{\frac{1}{\alpha}} \left(1 + \frac{2\pi\epsilon}{\beta_2} \right)$ and get

$$Z_{\text{reservoir}} = \exp \left[\frac{c(\alpha - 1)^2}{12\alpha} \log \frac{\beta_2}{\beta_1} \right] \tilde{Z}_{\text{reservoir}}, \quad (3.22)$$

where $\tilde{Z}_{\text{reservoir}}$ is the partition function of the theory on the portion $\rho \in \left[1 - 2\pi\epsilon/\beta_1, \left(\frac{\beta_2}{\beta_1} \right)^{\frac{1}{\alpha}} \left(1 + 2\pi\epsilon/\beta_2 \right) \right]$ of flat space. Combining (3.20)–(3.22) and using the normalization $\tilde{Z}_1 \tilde{Z}_2 \tilde{Z}_{\text{reservoir}} = 1$, we get the total result for the CFT anomaly contribution:

$$Z_{\text{anomaly}} = \exp \left[-\frac{c}{6} + \frac{c}{12} \left(\alpha + \frac{1}{\alpha} \right) \log \frac{\beta_2}{\beta_1} + \frac{c(\beta_1 + \beta_2)}{24\epsilon} + \frac{c}{3} \log \Lambda \right]. \quad (3.23)$$

Next we combine this result with the gravitational partition function (3.11):

$$Z = \exp \left(2\phi_0 - \frac{c}{6} + \pi\phi_r \left(\frac{1}{\beta_1} + \frac{1}{\beta_2} \right) + \frac{c}{12} \left(\alpha + \frac{1}{\alpha} \right) \log \frac{\beta_2}{\beta_1} \right). \quad (3.24)$$

This is the final result for the partition function of the disconnected black hole phase. We removed two terms from (3.23): a $1/\epsilon$ divergence proportional to the sum of lengths of the boundary of the hyperbolic disk which was removed by a local counterterm, and a divergence in Λ that is expected to renormalize ϕ_0 .⁴

3.2 Asymmetric wormhole phase

The asymmetric wormhole solution is a quotient of Euclidean AdS₂ spacetime with the metric [34, 36]

$$ds^2 = \frac{d\chi^2 + d\sigma^2}{\sin^2 \sigma}, \quad \phi = -2\pi T_{\sigma\sigma}^{\text{traceless; bulk}} \left(\frac{\gamma - \sigma}{\tan \sigma} + 1 \right), \quad (3.25)$$

where $\chi \sim \chi + b$ is a periodic coordinate which plays the role of Euclidean time direction and $\sigma \in [\epsilon_1, \pi - \epsilon_2]$ is the spatial coordinate with $\epsilon_{1,2}$ being small cutoffs to be determined below. The two boundaries of AdS₂ are glued to the Rindler reservoir with the metric (3.4). The spacetime is thus a conformally flat manifold with the topology of a torus, as shown in figure 7.

It remains to compute $T_{\sigma\sigma}^{\text{traceless; bulk}}$ and fix γ . Ignoring the curved metric for a moment, the torus has circumferences b and $d = \pi + (2\pi\alpha)^{-1} b \log \frac{\beta_2}{\beta_1}$ along the χ and σ directions of the AdS₂ bulk, and along the θ and ξ directions of the reservoir, respectively. For the wormhole solution to exist, we take $b > d$. If we consider a holographic CFT on this

⁴Note that if we chose the cutoff in the plane as Λ instead of $(\beta_2/\beta_1)^{1/\alpha} \Lambda$, it would modify the coefficient of the term $\alpha^{-1} \log \frac{\beta_2}{\beta_1}$ and give the wrong answer in the equal-temperature limit where $\alpha \rightarrow 0$ and $\alpha^{-1} \log \frac{\beta_2}{\beta_1} \rightarrow 2\pi L_R/\beta$, where we denote the limiting value of β_1 and β_2 as β .

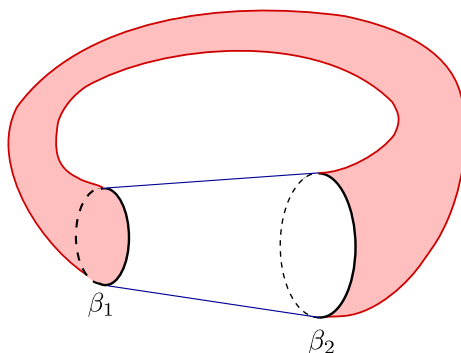


Figure 7. Schematic of the wormhole phase. The asymmetry of the wormhole is caused by the different sizes of the thermal circles which are glued to the regulated AdS₂ boundaries. Correspondingly, the two boundary regulators are different.

background, and quantize along the χ direction of the AdS₂ (θ direction of the reservoir), we are in the vacuum. The vacuum stress tensor on such a cylinder of circumference d , evaluated for a torus with the flat metric $\hat{g}_{\mu\nu}$ is therefore:

$$T_{\sigma\sigma}^{\hat{g}} = -T_{\chi\chi}^{\hat{g}} = -\frac{\pi c}{6d^2} = -\frac{c}{6\pi} \frac{1}{\left(1 + \frac{b \log \frac{\beta_2}{\beta_1}}{2\pi^2\alpha}\right)^2}. \quad (3.26)$$

Now recall that the gravitational part of the manifold has a curved metric (3.25) of the form $g_{\mu\nu} = e^{2\omega} \hat{g}_{\mu\nu}$, where $\hat{g}_{\mu\nu}$ is the flat metric. This gives an anomalous contribution to the stress tensor which has a traceless piece and a piece proportional to the metric. The traceless piece coming from the combination of the flat torus and the anomaly is what enters in the dilaton solution above and is given as

$$T_{\sigma\sigma}^{\text{traceless; bulk}} = -T_{\chi\chi}^{\text{traceless; bulk}} = -\frac{c}{6\pi} \frac{1}{\left(1 + \frac{b \log \frac{\beta_2}{\beta_1}}{2\pi^2\alpha}\right)^2} + \frac{c}{24\pi}. \quad (3.27)$$

Unlike previous works we have a free parameter γ in the solution for the dilaton; without this free parameter the solution would only exist for equal temperatures on the two sides. We want to match the lengths of the different thermal circles at the interfaces between the wormhole and the Rindler bath while maintaining equal ϕ_r values (see eq. (3.6)). This requires asymmetric cutoffs $\sigma_1 = \epsilon_1 \ll 1$, $\pi - \sigma_2 = \epsilon_2 \ll 1$:

$$\frac{b}{\epsilon_{1,2}} = \frac{\beta_{1,2}}{\epsilon} \implies \epsilon_{1,2} = \frac{b}{\beta_{1,2}} \epsilon, \quad \phi|_{\sigma_1} = \phi|_{\sigma_2} \implies \gamma = \frac{\pi\beta_2}{\beta_1 + \beta_2}. \quad (3.28)$$

So the choice of temperatures β_1, β_2 dictates the cutoffs σ_1, σ_2 and the dilaton solution. In the symmetric case $\beta_1 = \beta_2$ we would find $\gamma = \pi/2$. The dilaton boundary condition fixes b through

$$\phi|_{\sigma_1} = \frac{\phi_r}{\epsilon} \implies \left(\frac{c}{3 \left(1 + \frac{b \log \frac{\beta_2}{\beta_1}}{2\pi^2\alpha}\right)^2} - \frac{c}{12} \right) = \frac{\phi_r b (\beta_1 + \beta_2)}{\pi \beta_1 \beta_2}. \quad (3.29)$$

Having established the dilaton solution, we are now ready to discuss the full partition function of the wormhole phase. We can break up the partition function in this phase into three pieces:

- (i) The gravitational contribution from the AdS₂ wormhole, computed using the action (2.1) evaluated on the solution (3.25).
- (ii) The CFT anomaly from the Weyl transform from cylinder $\chi \in [0, b)$, $\sigma \in [\epsilon_1, \pi - \epsilon_2]$ to the AdS₂ metric in the gravitational region. It is computed using equation (3.12) with $e^\omega = \frac{1}{\sin \sigma}$.
- (iiia) The contribution of the CFT on a torus of lengths d and b . Recall that we assume $b > d$ to project onto the vacuum for a holographic CFT. Under this assumption the partition function is the thermal partition function of a CFT on the circle of size $d = \pi + (2\pi\alpha)^{-1}b \log \frac{\beta_2}{\beta_1}$.
- (iiib) The CFT anomaly from Weyl transforming from the cylinder to the cone in the reservoir region with the Weyl factor given by (3.5).

Altogether we get

$$Z = Z_{(i)}Z_{(ii)}Z_{(iii)} = \exp \left(\underbrace{-\frac{\phi_r b^2}{4\pi} \left(\frac{1}{\beta_1} + \frac{1}{\beta_2} \right)}_{(i)} - \underbrace{\frac{cb}{24}}_{(ii)} + \underbrace{\frac{c}{6} \frac{b}{1 + \frac{b \log \frac{\beta_2}{\beta_1}}{2\pi^2 \alpha}}}_{(iiia)} + \underbrace{\frac{c\alpha}{12} \log \frac{\beta_2}{\beta_1}}_{(iiib)} \right). \quad (3.30)$$

Note that the contribution (i) is accompanied by a $1/\epsilon$ -divergence proportional to the length of AdS boundaries, which is identical to the $1/\epsilon$ -divergence that appeared in (3.23) in the disconnected phase and is removed in the same way. Note that the equation (3.29) can be reproduced by extremizing (3.30) over b .

The contribution (iiib) is the same between the two phases, and can hence be ignored in determining which phase is dominant. The phases are easy to compare in two limits for which the equation (3.29) has a simple solution. In the first limit we have (trading α for L_R)

$$L_R \ll \phi_r/c: \quad b \approx \frac{\beta_1 \beta_2 c \pi}{4\phi_r(\beta_1 + \beta_2)} \quad (3.31)$$

$$\implies Z_{WH} \approx \exp \left(\frac{\beta_1 \beta_2 c^2 \pi}{64\phi_r(\beta_1 + \beta_2)} + I_R \right), \quad Z_{BH} \approx \exp \left(2\phi_0 + \left(\frac{1}{\beta_1} + \frac{1}{\beta_2} \right) \pi \phi_r + I_R \right), \quad (3.32)$$

where $I_R = \frac{c}{24\pi} \frac{\beta_2 - \beta_1}{L_R} \log \frac{\beta_2}{\beta_1}$ is the contribution from the reservoir which is common for the two phases. Equating the two expressions, we find that the wormhole dominates for

$$\frac{\beta_1 \beta_2}{\beta_1 + \beta_2} \gtrsim \frac{128\phi_r \phi_0}{c^2 \pi}. \quad (3.33)$$

In the second limit we have

$$L_R \gg \phi_r/c: \quad b \approx \frac{\pi(\beta_2 - \beta_1)}{L_R \log \frac{\beta_2}{\beta_1}} \quad (3.34)$$

$$\implies Z_{WH} \approx \exp\left(\frac{c\pi(\beta_2 - \beta_1)}{24L_R \log \frac{\beta_2}{\beta_1}} + I_R\right), \quad Z_{BH} \approx \exp\left(2\phi_0 - \frac{\pi c L_R \log \frac{\beta_2}{\beta_1}}{6(\beta_2 - \beta_1)} + I_R\right). \quad (3.35)$$

Equating the two expressions, we find that the wormhole dominates for

$$\frac{\beta_2 - \beta_1}{\log \frac{\beta_2}{\beta_1}} \gtrsim \frac{48L_R \phi_0}{c\pi}. \quad (3.36)$$

Notice that in this limit it is sufficient to take β_2 large at any value of β_1 for the wormhole to dominate.

4 Page curves of two connected black holes

We can now analyze the structure of entanglement entropy in our model to ask when island configurations appear, and whether and how they compete with other quantum extremal surfaces to saturate the entropy.

A priori, we can study this question in either of the two phases discussed in the previous section. However, we will argue that the wormhole phase does not have any island saddles. First we show that, for a holographic theory, we have to be in the vacuum channel, i.e. in the doubly holographic picture the three-dimensional bulk filling in the torus is thermal AdS₃. To see this, if we were instead in the vacuum in the dual channel, i.e. the three-dimensional bulk filling in the torus being the BTZ black hole, this would imply a positive stress-energy tensor. Such a stress tensor would not consistently solve the equation of motion (2.4) with the boundary conditions needed for the dilaton. This is the familiar statement that we need a negative stress-energy to support the wormhole [36, 37].⁵ To complete the argument, note that in the vacuum channel the 2d entanglement entropy is $O(c)$ and constant for intervals in the bath and their thermofield double partners. Any nontrivial QES will come with a cost of ϕ_0 , which we assume to be much larger than the CFT central charge c . Hence the nontrivial QES will never dominate. In the rest of this section we therefore focus on the phase with two black holes.

4.1 The two black hole setup

We are interested in the temporal behavior of the entanglement entropy of the two thermofield double copies of a segment that includes some portion of radiation in the reservoir and may or may not include one of the quantum dots dual to black holes. The metric of the exterior regions of the black hole is given by the Lorentzian version of the solution (3.7)–(3.8). We rescale the coordinates in such a way that they are dimensionless and continuous

⁵The spacetime wormhole can be converted into an (eternally) traversable spatial wormhole by analytic continuation, e.g. in equation (3.25) continue $\chi \rightarrow it$.

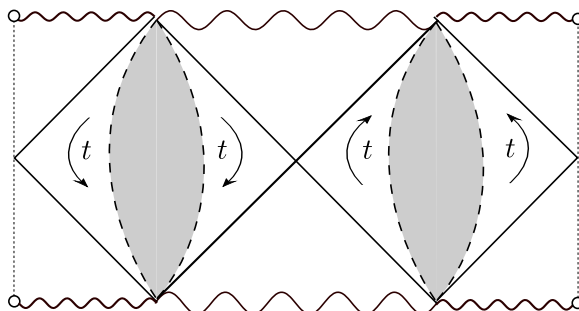


Figure 8. The Penrose diagram for two eternal black holes with different inverse temperatures β_1, β_2 connected by two copies of the reservoir (shown by the shaded regions) with the conical metric (3.4). The arrows show the direction of the coordinate time in the external regions of the black holes. The diagram is identified across the dashed line which goes through the bifurcation surface of the second black hole.

across the pairs of exterior regions connected to their corresponding reservoirs. The metric in the external black hole region then reads:

$$ds_1^2 = \frac{-dt^2 + d\xi^2}{\sinh^2 \xi}; \quad \xi \in \left(-\infty, -\frac{2\pi}{\beta_1}\epsilon\right] \quad (4.1)$$

$$ds_2^2 = \frac{-dt^2 + d\xi^2}{\sinh^2(\xi - L)}; \quad \xi \in \left[L + \frac{2\pi}{\beta_2}\epsilon, +\infty\right), \quad (4.2)$$

and the reservoir metric is the Lorentzian continuation of the metric (3.4):

$$ds_R^2 = \frac{\beta_1^2}{4\pi^2} e^{\alpha\xi} \frac{-dt^2 + d\xi^2}{\epsilon^2}, \quad \xi \in \left[-\frac{2\pi}{\beta_1}\epsilon, L + \frac{2\pi}{\beta_2}\epsilon\right]. \quad (4.3)$$

Note that temperature dependence is now contained in the cutoffs for ξ . Thus the lengths of thermal circles on the boundaries in the Euclidean continuation of the metric are the same and are equal to $\beta_{1,2}/\epsilon$. The dilaton solution in these rescaled coordinates reads

$$\phi(\sigma)_1 = -\frac{2\pi}{\beta_1} \phi_r \coth(-\xi); \quad (4.4)$$

$$\phi(\sigma)_2 = \frac{2\pi}{\beta_2} \phi_r \coth(\xi - L). \quad (4.5)$$

In terms of the Schwarzschild-like coordinate t , the right side of the TFD evolves forward and the left side evolves backward, as indicated by arrows in figure 8. This setup generalizes the eternal black hole version of the information paradox discussed in [7, 8, 11] and in section 2 of the present paper to the case of two eternal black holes instead of one. Correspondingly, at late times we can expect islands to appear in both black hole regions. Similar models were considered in [11, 25, 26]. See [38, 39] for a discussion of entanglement between disjoint gravitating universes.

To compute the generalized entropy functional, we again assume that the matter CFT is holographic and dual to some asymptotically AdS₃ geometry, and we follow the approach explained in section 2.1. The CFT entanglement entropy can be computed by (2.11) using

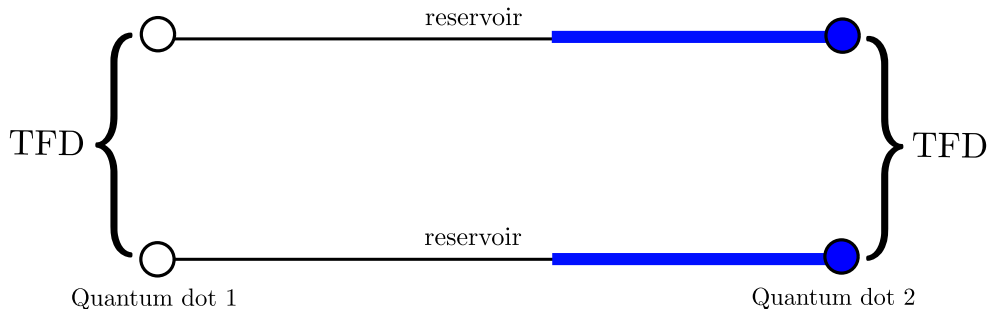


Figure 9. We collect the radiation in the bold blue segments of radiation that include the boundary duals (quantum dots) of the second eternal black hole.

the conformal transformation to the plane from section 3.1. This transformation maps a pair of black hole exterior regions connected by a reservoir on the same side of the thermofield double (in Euclidean signature) to the complex w -plane with the conformally flat metric $\Omega^{-2}(w, \bar{w})dw d\bar{w}$, with the Weyl factor Ω in the three regions given by (3.17)–(3.18):

$$\text{Black hole 1 : } \quad \Omega_1 = \frac{1 - |w|^2}{2}; \quad (4.6)$$

$$\text{Black hole 2 : } \quad \Omega_2 = \frac{|w|^2 - \left(\frac{\beta_2}{\beta_1}\right)^{\frac{2}{\alpha}}}{2 \left(\frac{\beta_2}{\beta_1}\right)^{\frac{1}{\alpha}}}; \quad (4.7)$$

$$\text{Reservoir : } \quad \Omega_{\text{bath}} = \frac{2\pi}{\beta_1} |w|^{1-\alpha}. \quad (4.8)$$

Finally, to compute the area terms in the island formula (2.6) we need also the dilaton profile, which is given by equations (3.9)–(3.10).

4.2 Entanglement entropy of segments including the second black hole

We begin by treating the second black hole as a detector which collects the radiation from the first black hole. This detector also radiates back into the reservoir, at a rate which creates an equilibrium with the reservoir heat engine. The Hilbert space available to the black hole detector is finite, but nevertheless it is large enough to be comparable to the Hilbert space of the first black hole. This means that it should be able to gain access to the island.

In the microscopic description, we want to compute the entanglement entropy of a quantum dot and its thermofield double partner, plus some of their adjoining baths (figure 9). The coordinates of the reservoir endpoints in terms of the ξ, t variable are chosen as

$$p_2 = (a, -t + i\pi); \quad p_3 = (a, t). \quad (4.9)$$

In the two-dimensional effective gravitational description we need to search for QESs which extend the regions into the bulk, plus possible QESs in the other gravitational region which

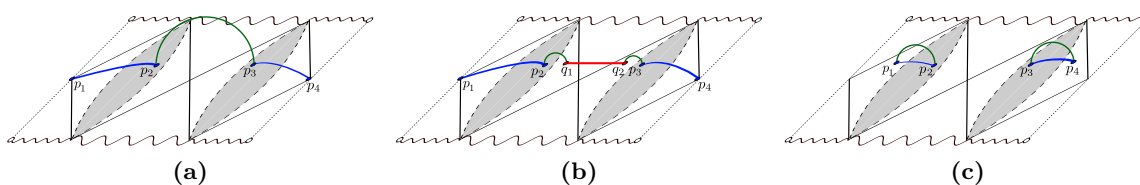


Figure 10. Configurations of the RT geodesics extending into the 3d bulk which determine the competing generalized entropy channels with the second black hole included in the region being probed. The drawings are identified across the dashed line which goes through the bifurcation surface of the second black hole. Multiple-island configurations, which turn out to be always subleading, are not shown. For the connected configurations (a) and (b) the blue segments join across the bifurcation surface and the QES is empty surface.

bound islands. Three configurations⁶ can dominate the Page curve; they are shown in figure 10 (other configurations are subleading). As we assume the CFT is holographic, it is straightforward to identify the channels in the CFT entanglement entropy which define the competing generalized entropy functionals and quantum extremal island configurations.

Configuration (a): linear growth. This is a fully connected no-island configuration, with a trivial (empty) QES in the second black hole region. The endpoints $p_2 = (a, -t + i\pi)$ and $p_3 = (a, t)$ are connected by a geodesic in the 3D bulk. With this in mind, the entanglement entropy of the configuration (a) is given just by one geodesic shown in figure 10(a), and reads

$$\mathcal{S}_a = S_{\text{conn.}}^{\text{no island}}(p_2, p_3) = \frac{c}{3} \log \left(\frac{\beta_1 e^{\alpha a}}{\pi} \cosh t \right). \quad (4.10)$$

Configuration (b): the island. This is a fully connected configuration that includes an island in the first black hole region and an empty QES in the second black hole region. The location of the island $[q_1, q_2]$ is again defined by the QESs. Since the points p_2 and p_3 are located symmetrically with respect to the bifurcation surface of the first black hole, that means that the QES points will have the same coordinates $q_{1,2} = (x, t_x)$. The generalized entropy is

$$\mathcal{S}_b = \text{Ext}_{q_1} S_{\text{gen}}^{\text{island}}(q_1, p_2) + \text{Ext}_{q_2} S_{\text{gen}}^{\text{island}}(q_2, p_3), \quad (4.11)$$

where the generalized entropy functional reads

$$\begin{aligned} S_{\text{gen}}^{\text{island}}(q_2, p_3) &= \phi_0 + \frac{2\pi\phi_r}{\beta_1} \coth(-x) \\ &+ \frac{c}{6} \log \left(\frac{\beta_1 e^{\alpha a} (\cosh(x-a) - \cosh(t-t_x))}{\pi \sinh(-x)} \right). \end{aligned} \quad (4.12)$$

Extremizing t_x gives $t_x = t$, and so the island contribution is time-independent.

⁶We omit the usual UV divergences in the generalized entropy functionals and other formulae for the entanglement entropy as we did in section 2.

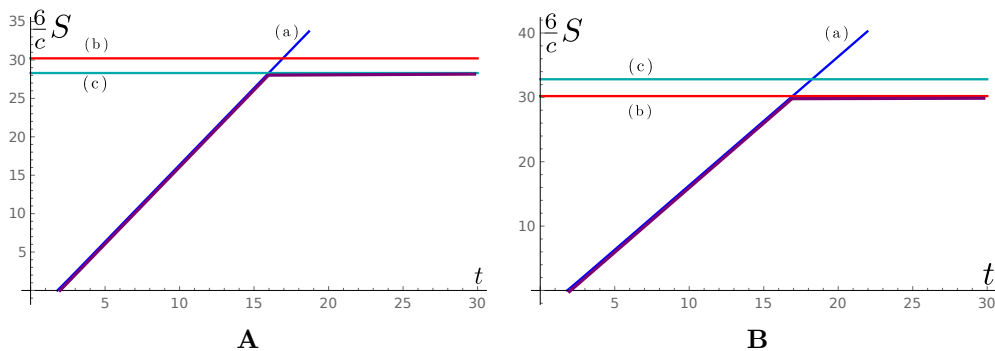


Figure 11. Page curves for the radiation segments plus the second black hole. We fix the physical reservoir size $L_R = 0.5$, physical location of $p_{2,3}$ endpoints $r = r_1 + 0.01L_R$, $\beta_1 = 1$, $\phi_0 = 10\frac{c}{6}$ and $\phi_r = \frac{c}{6}$. (A) $\beta_2 = 2$. The no-island phase dominates at late times. (B) $\beta_2 = 1.3$. The island phase dominates at late times.

Configuration (c): disconnected QES configuration. This configuration corresponds to two times the entropy of the segment. The corresponding generalized entropy functional reads

$$S_{\text{gen}}(p_3, p_4) = \phi_0 + \frac{2\pi\phi_r}{\beta_2} \coth\left(y - \alpha^{-1} \log \frac{\beta_2}{\beta_1}\right) + \frac{c}{6} \log\left(\frac{2\beta_1 e^{\alpha a + y} \frac{\beta_2^{1/\alpha}}{\beta_1} [\cosh(y - a) - \cosh(t - t_y)]}{\pi \left(e^{2y} - \left(\frac{\beta_2}{\beta_1}\right)^{2/\alpha}\right)}\right), \quad (4.13)$$

where (y, t_y) are the coordinates of the QES p_4 . The total entropy in this configuration reads

$$\mathcal{S}_c = 2 \times \underset{p_4}{\text{Ext}} S_{\text{gen}}(p_3, p_4). \quad (4.14)$$

It is worth noting that for this configuration the QES points $p_{1,4}$ end up at finite distance between the AdS_2 boundary and the horizon in the corresponding external regions of the second black hole. This quantity is also time-independent.

4.2.1 Page curves

The possible behaviors in the case of the black hole detector involve a competition between the two phases of constant entanglement entropy at late times — namely, between configurations (b) and (c). Let us fix the physical size of the reservoir L_R . Then we can have a transition between (b) and (c) at late times if we vary the temperature ratio β_2/β_1 or the physical position of the points $p_{2,3}$ at the Rindler coordinate $r = \frac{\beta_1}{2\pi\alpha} e^{\alpha a}$. We show this transition in figure 11 for the case when we vary the temperature of the “detector” β_2 while keeping r fixed. We see that adjusting this temperature can reveal the island of the first black hole. A similar results were obtained in [23, 26].

This transition has a simple interpretation, if we think of the island configuration (b) as the entanglement entropy of the first black hole plus the segments $[0, a]$. It competes against configuration (c), which is the entropy of the second black hole plus segments $[a, L]$.

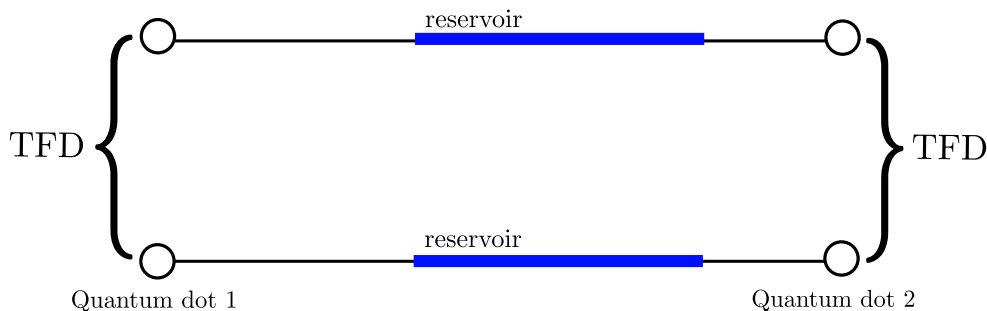


Figure 12. We consider the radiation in the bold blue segments of the reservoir.

Then the island of the first black hole reveals itself if the entropy of the first black hole becomes smaller than the entanglement entropy of the probed system (which includes the second black hole and the radiation segment $[a, L]$). This means that this system, which we can think of as a detector, has enough room to effectively accommodate all states of the radiation. If the detector’s entropy is not large enough, however, it effectively thermalizes before gaining access to the island, which is expressed by the phase (c). In other words, the no-island phase 9(c) and the island phase 9(b) can be interpreted, respectively, as the island phase and the no-island phase of the computation of entanglement entropy of the complementary subsystem. Note that the key property in the evolution of the entanglement entropy of radiation regions which include one of the black holes is that the Hilbert space of the radiation is large. Because of this, there are no finite size effects that would introduce an intermediate phase into the Page curve for any choice of parameters, as we saw in the case of a single black hole in section 2. Below, we exclude both black holes from the radiation region, so that the radiation segment belongs to the interior of the reservoir only. We will then see that the Page curve structure becomes richer.

4.3 Entanglement entropy of segments in reservoir

We compute the entanglement entropy of the union of two identical segments $A = [p_1, p_2] \cup [p_3, p_4]$ positioned inside corresponding copies of the reservoir, as shown in figure 12. The coordinates of these endpoints are chosen as:

$$p_1 = (b, -t + i\pi); \quad p_2 = (a, -t + i\pi); \quad p_3 = (a, t); \quad p_4 = (b, t). \quad (4.15)$$

We now have 5 possible generalized entropy configurations which can dominate, shown in figure 13.

Configuration (a): linear growth. This is a fully connected no-island configuration, where two RT geodesics connect the endpoints $p_1 \leftrightarrow p_4$ and $p_2 \leftrightarrow p_3$, respectively. The entanglement entropy of this configuration is given by the formula

$$\mathcal{S}_a = S_{\text{conn.}}^{\text{no island}}(p_1, p_2; p_3, p_4) = 2\frac{c}{3} \log \left(\frac{\beta_1 e^{\frac{\alpha(a+b)}{2}}}{\pi} \cosh t \right). \quad (4.16)$$

This expression grows in time approximately linearly, and in the general case the entropy depends on the segment location when $\alpha \neq 0$.

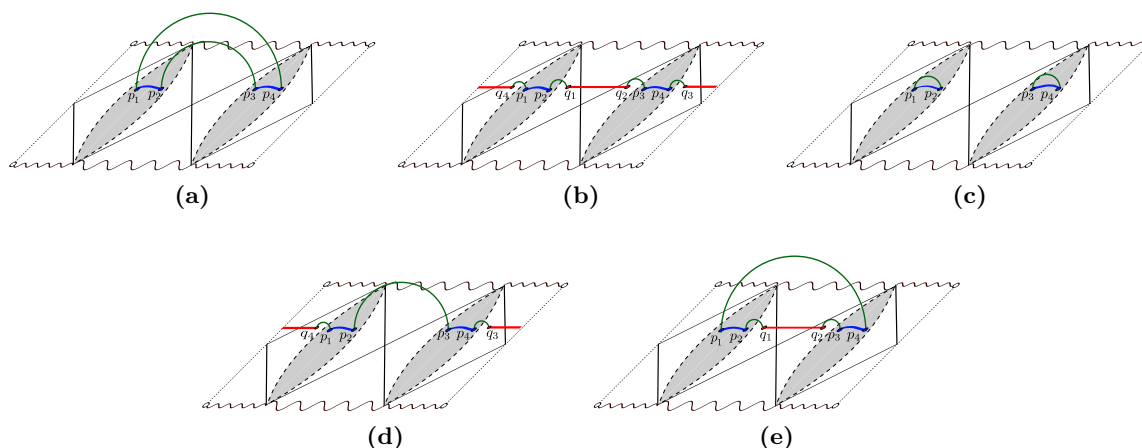


Figure 13. Configurations of the RT geodesics extending into the 3d bulk which determine the competing generalized entropy channels. The drawings are identified across the dashed line which goes through the bifurcation surface of the second black hole. Multiple-island configurations that are always subleading are not shown.

Configuration (b): two islands. This is a fully connected configuration that includes an island in every black hole region. The location of the islands $[q_{1,3}, q_{2,4}]$ is defined by the QESs, obtained by extremizing the generalized entropy functionals. These generalized entropy functionals are exactly the same ones as (4.12) for the island in the first black hole and (4.13) for the island in the second black hole. We write down the corresponding formulae for the QESs on the right side of the thermofield double, the points $q_2 = (x, t_x)$ and $q_3 = (y, t_y)$. The QESs q_1 and q_4 on the left are determined analogously.

$$S_{\text{gen}}^{\text{island}}(q_2, p_3) = \phi_0 + \frac{2\pi\phi_r}{\beta_1} \coth(-x) + \frac{c}{6} \log \left(\frac{\beta_1 e^{\alpha a} (\cosh(x-a) - \cosh(t-t_x))}{\pi \sinh(-x)} \right); \quad (4.17)$$

$$S_{\text{gen}}^{\text{island}}(q_3, p_4) = \phi_0 + \frac{2\pi\phi_r}{\beta_2} \coth \left(y - \alpha^{-1} \log \frac{\beta_2}{\beta_1} \right) + \frac{c}{6} \log \left(\frac{2\beta_1 e^{\alpha b + y} \frac{\beta_2}{\beta_1}^{1/\alpha} [\cosh(y-b) - \cosh(t-t_y)]}{\pi \left(e^y - \left(\frac{\beta_2}{\beta_1} \right)^{2/\alpha} \right)} \right). \quad (4.18)$$

The total entropy in this configuration is given by the sum of the two island contributions, or four quantum extremal surfaces:

$$\mathcal{S}_b = \text{Ext}_{q_2} S_{\text{gen}}^{\text{island}}(q_2, p_3) + \text{Ext}_{q_3} S_{\text{gen}}^{\text{island}}(q_3, p_4) + \text{Ext}_{q_4} S_{\text{gen}}^{\text{island}}(q_4, p_1) + \text{Ext}_{q_1} S_{\text{gen}}^{\text{island}}(q_1, p_2). \quad (4.19)$$

The two-island contribution is time-independent, and $t_x = t_y = t$.

Configuration (c): generalized thermalization. This is a disconnected configuration, which is the sum of the CFT entanglement entropy for the two thermofield double

copies of the reservoir segment. The entanglement entropy of a copy is given by the formula

$$S_{\text{disc.}}(p_1, p_2) = \frac{c}{3} \log \left(\frac{\beta_1 e^{\alpha(a+b)}}{\pi} \sinh \frac{|a-b|}{2} \right). \quad (4.20)$$

This configuration can be interpreted as describing the extension of the notion of thermalization to the case of the varying temperature. The entropy of the segment on the left of TFD $[p_3, p_4]$ is given by an analogous formula, and the total entropy in this configuration is given by

$$\mathcal{S}_c = S_{\text{disc.}}(p_1, p_2) + S_{\text{disc.}}(p_3, p_4). \quad (4.21)$$

Configurations (d) and (e): single island. In these configurations we have an island in one of the black holes while the other black hole still produces linear growth:

$$\mathcal{S}_d = \text{E}_{q_4}^{\text{Ext}} S_{\text{gen}}^{\text{island}}(q_4, p_1) + \text{E}_{q_3}^{\text{Ext}} S_{\text{gen}}^{\text{island}}(q_3, p_4) + \frac{c}{3} \log \left(\frac{\beta_1 e^{a\alpha}}{\pi} \cosh t \right); \quad (4.22)$$

$$\mathcal{S}_e = \text{E}_{q_1}^{\text{Ext}} S_{\text{gen}}^{\text{island}}(q_1, p_2) + \text{E}_{q_2}^{\text{Ext}} S_{\text{gen}}^{\text{island}}(q_2, p_3) + \frac{c}{3} \log \left(\frac{\beta_1 e^{ab}}{\pi} \cosh t \right). \quad (4.23)$$

These expressions grow linearly with half the slope of configuration (a).

Let us note that there are also configurations that have two islands in black hole regions, similarly to the case (d) in section 2 (see figure 2). Just as in that case of a single eternal black hole, such configurations are always subleading, so we do not consider them.

4.3.1 Page curves

We have four qualitatively different possibilities for the Page curve, which are determined by the competition between the two-island phase (b) and the disconnected phase (c) at very late times, and by the possibility of one of the two single-island phases (d) or (e) dominating for a finite time between the early and very late times.

First, let us consider the equal-temperature case, which is achieved in the limit $\alpha \rightarrow 0$, $\frac{\beta_2}{\beta_1} \rightarrow 1$ with $L = 2\pi L_R/\beta$ fixed. The four qualitatively different Page curves are shown in figure 14. More specifically, we plot the contributions of the five phases (a)–(e) described above.

- In figure 14A the linear growth generated by the connected no-island phase (a) transitions into the two-island phase (b), which keeps the entanglement entropy constant. The segment is large enough so that the island phase saturates the entanglement entropy before the disconnected phase (c) has a chance to become relevant.
- In figure 14B the connected phase (a) also dominates at early time, but because of the de-centered position of the segment in the reservoir, at some time the transition to the mixed phase (e) happens. This phase has an island in the first black hole but continues to grow linearly with halved slope due to the active remaining ER bridge across the second black hole. At later times, another transition happens, where the entanglement entropy is completely saturated by the two-island phase. Thus, the single-island phase persists only for finite time.

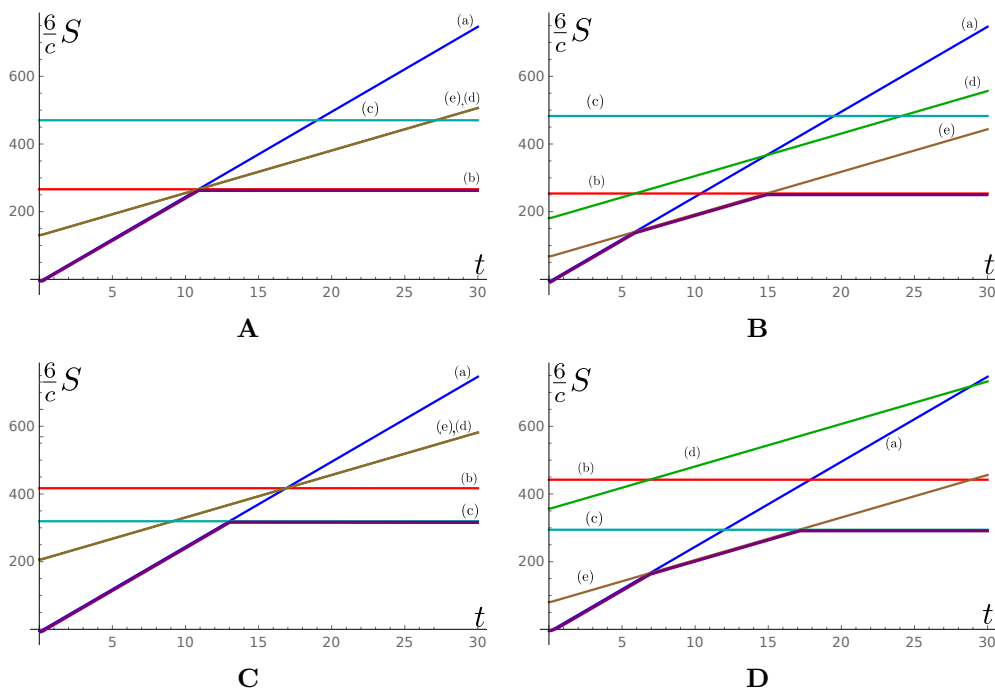


Figure 14. Page curves for the radiation segments in the reservoir in the equal temperature case with $\beta_1 = \beta_2 = 1$. (A) $a = 0.12L$, $b = 0.88L$. (B) $a = 0.02L$, $b = 0.78L$. (C) $a = 0.24L$, $b = 0.76L$. (D) $a = 0.04L$, $b = 0.52L$. We have set $\frac{c}{6}\phi_0 = 20$ and $\frac{\pi\phi_r}{3} = 10$.

- In figure 14C, the segment is small enough so that the entanglement entropy is saturated by the disconnected phase (c) before any islands get involved.
- In figure 14D, the early-time growth (a) transitions into the mixed phase (e) with slower growth and an island in one of the black holes. However, later the entanglement entropy is saturated by the disconnected phase (c) again, so the island is no longer accessible. Thus, this behavior only allows for temporary access to an island.

When the temperatures are different, $\beta_1 \neq \beta_2$, the qualitative behavior is the same. The main difference is that now temporary single-island phases are possible even for segments centered in the reservoir, because there is an additional non-uniform contribution in the entanglement entropy arising from the heat engine, which is represented, e.g., by the second term in (4.20). Because of this, a Page curve for any fixed pair of segments can include a temporary single island phase if we adjust the temperature difference and/or the reservoir size and positions of endpoints of A .

By utilizing the unitarity bound $S(A) \leq \min\{\log \dim \mathcal{H}_A, \log \dim \mathcal{H}_{\bar{A}}\}$ discussed in section 1 and applied at the end of section 2, the qualitative nature of these transitions can be predicted. In our setting, both $\dim \mathcal{H}_A$ and $\dim \mathcal{H}_{\bar{A}}$ are finite, and so these Hilbert spaces enforce distinct unitarity bounds. When the former is threatened, there is a thermalization transition (c), whereas when the latter is threatened, we are led to the two-island phase (b). There is also the possibility of transition to one-island phases (d) or (e), which have growing entropy and therefore are not explained by the simple unitarity bound. As in section 2,

this case can be explained by a unitarity bound applied to the two gravitational regions (plus the adjoining baths up to the radiation region A) separately. When the entropy of this region approaches the entropy of the two black holes in the given gravitational region $2S_{BH}$, a transition must occur.

5 Discussion

We have investigated the effects of competition between the thermalization mechanism and the island information recovery mechanism in the time evolution of entanglement entropy of Hawking radiation. We considered finite radiation regions in the classic example of a thermofield double black hole coupled to two semi-infinite baths. We also introduced a new model, where we have two pairs of thermofield double black holes at different temperatures radiating into a finite shared bath (and its thermofield double). To maintain equilibrium this required a Rindler-like bath which operated as a heat engine equilibrating the two sides. A summary of our results can be found in section 1.

The two-temperature system provides a tunable parameter which models thermal loss from engineered quantum dots in the lab, such as the SYK system. In relation to this, it should also be possible to write down an explicit coupling between two SYK systems at different temperatures leading to asymmetric wormholes, generalizing the Maldacena-Qi solution [36].⁷

It would be interesting to study the generalization of our two-temperature model to higher dimensions. In two dimensions we saw that we can have transitions from the asymmetric wormhole (the “confined” phase) to two thermofield double black holes (the “deconfined” phase). In higher dimensions, by picking the bath and boundary CFTs appropriately, one can more cleanly probe the confining structure of the model as the temperatures are varied through an order parameter like center symmetry [43], which does not have much meaning in $(0+1)$ dimensions. In the two-temperature model considered in this paper, the fate of one of the thermofield double quantum dots was tied to the other one, since the confining phase was a gravitational solution which linked the two systems. In higher dimensions, however, the confining phase of a single thermofield double boundary pair is two copies of thermal AdS, and it need not link to the other thermofield double. Thus we can have one of the thermofield double boundary pairs in the confined phase while the other pair is in the deconfined phase. It would be interesting to work out whether this actually occurs, and, if so, what the doubly holographic solution looks like; it would need to have nontrivial topology to accommodate the change from confined to deconfined phases.

The computations of entanglement entropy in the black hole phase would also take on a different structure in higher dimensions. The closest analogy to our results would be obtained by taking the bath CFT $_d$ to be placed on \mathbb{R}^d and considering infinite strips,

⁷There are avatars of the asymmetric wormhole in contexts where it is not the leading saddle of a path integral; for example in the matrix model description of JT gravity [40, 41] it is an off-shell configuration captured by $\langle Z(\beta_1)Z(\beta_2) \rangle$, while in systems with multiple uncoupled SYK dots there may exist subleading saddles which link the various systems (such subleading saddles have been exhibited for the case of equal temperatures in [42]).

which would allow the “halfway” surfaces seen in two dimensions, as in figure 2(b). Such surfaces would not appear for compact regions. One way to see this is to note that in figure 2(b) the two endpoints of an interval are treated differently, which would not work for the boundary of a higher-dimensional ball, which is connected.

Acknowledgments

The authors would like to thank Raghu Mahajan for valuable discussions. This work has been supported in part by FWO-Vlaanderen through project G006918N and by Vrije Universiteit Brussel through the Strategic Research Program “High-Energy Physics.” Research at the University of Pennsylvania was supported by the Simons Foundation It From Qubit collaboration (385592) and the DOE QuantISED grant DESC0020360. VB thanks the Santa Fe Institute for hospitality as this work was completed. The work of M.K. was funded by Russian Federation represented by the Ministry of Science and Higher Education (grant number 075-15-2020-788).

Open Access. This article is distributed under the terms of the Creative Commons Attribution License ([CC-BY 4.0](https://creativecommons.org/licenses/by/4.0/)), which permits any use, distribution and reproduction in any medium, provided the original author(s) and source are credited.

References

- [1] S. Ryu and T. Takayanagi, *Holographic derivation of entanglement entropy from AdS/CFT*, *Phys. Rev. Lett.* **96** (2006) 181602 [[hep-th/0603001](https://arxiv.org/abs/hep-th/0603001)] [[INSPIRE](#)].
- [2] V.E. Hubeny, M. Rangamani and T. Takayanagi, *A Covariant holographic entanglement entropy proposal*, *JHEP* **07** (2007) 062 [[arXiv:0705.0016](https://arxiv.org/abs/hep-th/0705.0016)] [[INSPIRE](#)].
- [3] N. Engelhardt and A.C. Wall, *Quantum Extremal Surfaces: Holographic Entanglement Entropy beyond the Classical Regime*, *JHEP* **01** (2015) 073 [[arXiv:1408.3203](https://arxiv.org/abs/1408.3203)] [[INSPIRE](#)].
- [4] G. Penington, *Entanglement Wedge Reconstruction and the Information Paradox*, *JHEP* **09** (2020) 002 [[arXiv:1905.08255](https://arxiv.org/abs/1905.08255)] [[INSPIRE](#)].
- [5] A. Almheiri, N. Engelhardt, D. Marolf and H. Maxfield, *The entropy of bulk quantum fields and the entanglement wedge of an evaporating black hole*, *JHEP* **12** (2019) 063 [[arXiv:1905.08762](https://arxiv.org/abs/1905.08762)] [[INSPIRE](#)].
- [6] A. Almheiri, R. Mahajan, J. Maldacena and Y. Zhao, *The Page curve of Hawking radiation from semiclassical geometry*, *JHEP* **03** (2020) 149 [[arXiv:1908.10996](https://arxiv.org/abs/1908.10996)] [[INSPIRE](#)].
- [7] A. Almheiri, R. Mahajan and J. Maldacena, *Islands outside the horizon*, [arXiv:1910.11077](https://arxiv.org/abs/1910.11077) [[INSPIRE](#)].
- [8] A. Almheiri, T. Hartman, J. Maldacena, E. Shaghoulian and A. Tajdini, *Replica Wormholes and the Entropy of Hawking Radiation*, *JHEP* **05** (2020) 013 [[arXiv:1911.12333](https://arxiv.org/abs/1911.12333)] [[INSPIRE](#)].
- [9] A. Almheiri, R. Mahajan and J.E. Santos, *Entanglement islands in higher dimensions*, *SciPost Phys.* **9** (2020) 001 [[arXiv:1911.09666](https://arxiv.org/abs/1911.09666)] [[INSPIRE](#)].
- [10] H.Z. Chen, Z. Fisher, J. Hernandez, R.C. Myers and S.-M. Ruan, *Information Flow in Black Hole Evaporation*, *JHEP* **03** (2020) 152 [[arXiv:1911.03402](https://arxiv.org/abs/1911.03402)] [[INSPIRE](#)].

- [11] G. Penington, S.H. Shenker, D. Stanford and Z. Yang, *Replica wormholes and the black hole interior*, [arXiv:1911.11977](#) [[INSPIRE](#)].
- [12] D. Marolf and H. Maxfield, *Transcending the ensemble: baby universes, spacetime wormholes, and the order and disorder of black hole information*, *JHEP* **08** (2020) 044 [[arXiv:2002.08950](#)] [[INSPIRE](#)].
- [13] T. Hartman and J. Maldacena, *Time Evolution of Entanglement Entropy from Black Hole Interiors*, *JHEP* **05** (2013) 014 [[arXiv:1303.1080](#)] [[INSPIRE](#)].
- [14] M. Rozali, J. Sully, M. Van Raamsdonk, C. Waddell and D. Wakeham, *Information radiation in BCFT models of black holes*, *JHEP* **05** (2020) 004 [[arXiv:1910.12836](#)] [[INSPIRE](#)].
- [15] R. Bousso and M. Tomašević, *Unitarity From a Smooth Horizon?*, *Phys. Rev. D* **102** (2020) 106019 [[arXiv:1911.06305](#)] [[INSPIRE](#)].
- [16] V. Balasubramanian, A. Kar, O. Parrikar, G. Sárosi and T. Ugajin, *Geometric secret sharing in a model of Hawking radiation*, *JHEP* **01** (2021) 177 [[arXiv:2003.05448](#)] [[INSPIRE](#)].
- [17] T. Hartman, E. Shaghoulian and A. Strominger, *Islands in Asymptotically Flat 2D Gravity*, *JHEP* **07** (2020) 022 [[arXiv:2004.13857](#)] [[INSPIRE](#)].
- [18] T. Faulkner, A. Lewkowycz and J. Maldacena, *Quantum corrections to holographic entanglement entropy*, *JHEP* **11** (2013) 074 [[arXiv:1307.2892](#)] [[INSPIRE](#)].
- [19] J. Sully, M.V. Raamsdonk and D. Wakeham, *BCFT entanglement entropy at large central charge and the black hole interior*, *JHEP* **03** (2021) 167 [[arXiv:2004.13088](#)] [[INSPIRE](#)].
- [20] H.Z. Chen, R.C. Myers, D. Neuenfeld, I.A. Reyes and J. Sandor, *Quantum Extremal Islands Made Easy, Part I: Entanglement on the Brane*, *JHEP* **10** (2020) 166 [[arXiv:2006.04851](#)] [[INSPIRE](#)].
- [21] H.Z. Chen, R.C. Myers, D. Neuenfeld, I.A. Reyes and J. Sandor, *Quantum Extremal Islands Made Easy, Part II: Black Holes on the Brane*, *JHEP* **12** (2020) 025 [[arXiv:2010.00018](#)] [[INSPIRE](#)].
- [22] J. Hernandez, R.C. Myers and S.-M. Ruan, *Quantum extremal islands made easy. Part III. Complexity on the brane*, *JHEP* **02** (2021) 173 [[arXiv:2010.16398](#)] [[INSPIRE](#)].
- [23] H.Z. Chen, Z. Fisher, J. Hernandez, R.C. Myers and S.-M. Ruan, *Evaporating Black Holes Coupled to a Thermal Bath*, *JHEP* **01** (2021) 065 [[arXiv:2007.11658](#)] [[INSPIRE](#)].
- [24] H. Geng and A. Karch, *Massive islands*, *JHEP* **09** (2020) 121 [[arXiv:2006.02438](#)] [[INSPIRE](#)].
- [25] H. Geng et al., *Information Transfer with a Gravitating Bath*, *SciPost Phys.* **10** (2021) 103 [[arXiv:2012.04671](#)] [[INSPIRE](#)].
- [26] H. Geng, S. Lüster, R.K. Mishra and D. Wakeham, *Holographic BCFTs and Communicating Black Holes*, *jhep* **08** (2021) 003 [[arXiv:2104.07039](#)] [[INSPIRE](#)].
- [27] P. Calabrese and J.L. Cardy, *Entanglement entropy and quantum field theory*, *J. Stat. Mech.* **0406** (2004) P06002 [[hep-th/0405152](#)] [[INSPIRE](#)].
- [28] T.M. Fiola, J. Preskill, A. Strominger and S.P. Trivedi, *Black hole thermodynamics and information loss in two-dimensions*, *Phys. Rev. D* **50** (1994) 3987 [[hep-th/9403137](#)] [[INSPIRE](#)].
- [29] S. Colin-Ellerin, X. Dong, D. Marolf, M. Rangamani and Z. Wang, *Real-time gravitational replicas: Low dimensional examples*, [arXiv:2105.07002](#) [[INSPIRE](#)].

- [30] S. Colin-Ellerin, X. Dong, D. Marolf, M. Rangamani and Z. Wang, *Real-time gravitational replicas: Formalism and a variational principle*, *JHEP* **05** (2021) 117 [[arXiv:2012.00828](#)] [[INSPIRE](#)].
- [31] S. Sachdev and J. Ye, *Gapless spin fluid ground state in a random, quantum Heisenberg magnet*, *Phys. Rev. Lett.* **70** (1993) 3339 [[cond-mat/9212030](#)] [[INSPIRE](#)].
- [32] A. Kitaev, *A simple model of quantum holography (part 1)*, talk at KITP, April 7, 2015, <http://online.kitp.ucsb.edu/online/entangled15/kitaev/>.
- [33] A. Kitaev, *A simple model of quantum holography (part 2)*, talk at KITP, May 27, 2015, <http://online.kitp.ucsb.edu/online/entangled15/kitaev2/>.
- [34] Y. Chen, V. Gorbenko and J. Maldacena, *Bra-ket wormholes in gravitationally prepared states*, *JHEP* **02** (2021) 009 [[arXiv:2007.16091](#)] [[INSPIRE](#)].
- [35] A.M. Polyakov, *Gauge Fields and Strings*, *Contemp. Concepts Phys.* **3** (1987) 1 [[INSPIRE](#)].
- [36] J. Maldacena and X.-L. Qi, *Eternal traversable wormhole*, [arXiv:1804.00491](#) [[INSPIRE](#)].
- [37] P. Gao, D.L. Jafferis and A.C. Wall, *Traversable Wormholes via a Double Trace Deformation*, *JHEP* **12** (2017) 151 [[arXiv:1608.05687](#)] [[INSPIRE](#)].
- [38] L. Anderson, O. Parrikar and R.M. Soni, *Islands with Gravitating Baths: Towards $ER = EPR$* , [arXiv:2103.14746](#) [[INSPIRE](#)].
- [39] V. Balasubramanian, A. Kar and T. Ugajin, *Entanglement between two gravitating universes*, [arXiv:2104.13383](#) [[INSPIRE](#)].
- [40] P. Saad, S.H. Shenker and D. Stanford, *JT gravity as a matrix integral*, [arXiv:1903.11115](#) [[INSPIRE](#)].
- [41] D. Stanford and E. Witten, *JT gravity and the ensembles of random matrix theory*, *Adv. Theor. Math. Phys.* **24** (2020) 1475 [[arXiv:1907.03363](#)] [[INSPIRE](#)].
- [42] I. Aref'eva, M. Khramtsov, M. Tikhonovskaya and I. Volovich, *Replica-nondiagonal solutions in the SYK model*, *JHEP* **07** (2019) 113 [[arXiv:1811.04831](#)] [[INSPIRE](#)].
- [43] E. Witten, *Anti-de Sitter space, thermal phase transition, and confinement in gauge theories*, *Adv. Theor. Math. Phys.* **2** (1998) 505 [[hep-th/9803131](#)] [[INSPIRE](#)].

5 Publications Alexandre SEVRIN

Integrable asymmetric λ -deformations

Sibylle Driezen,^{a,b} Alexander Sevrin^b and Daniel C. Thompson^{a,b}

^a*Department of Physics, Swansea University,
Singleton Park, Swansea SA2 8PP, U.K.*

^b*Theoretische Natuurkunde, Vrije Universiteit Brussel & The International Solvay Institutes,
Pleinlaan 2, B-1050 Brussels, Belgium*

E-mail: Sibylle.Driezen@vub.be, Alexandre.Sevrin@vub.be,
D.C.Thompson@swansea.ac.uk

ABSTRACT: We construct integrable deformations of the λ -type for asymmetrically gauged WZW models. This is achieved by a modification of the Sfetsos gauging procedure to account for a possible automorphism that is allowed in G/G models. We verify classical integrability, derive the one-loop beta function for the deformation parameter and give the construction of integrable D-brane configurations in these models. As an application, we detail the case of the λ -deformation of the cigar geometry corresponding to the axial gauged $SL(2, R)/U(1)$ theory at large k . Here we also exhibit a range of both A-type and B-type integrability preserving D-brane configurations.

KEYWORDS: D-branes, Integrable Field Theories, Sigma Models

ARXIV EPRINT: [1902.04142](https://arxiv.org/abs/1902.04142)

Contents

1	Introduction	1
2	Left-right asymmetrical λ-deformations	3
2.1	Classical integrability	7
2.2	One-loop beta functions	8
2.3	Integrable boundary conditions	10
3	Deforming the Euclidean black hole and Sine-Liouville	11
3.1	The parafermionic $SL(2,R)/U(1)$ WZW theory	12
3.2	Asymmetrical λ -deformed $SL(2,R)/U(1)$	13
3.3	Integrable branes in the λ -cigar	16
3.4	Connection to Sine-Liouville theory	19
4	Conclusion	20
A	Conventions and sigma models (WZW, PCM and SSSM)	22

1 Introduction

Since the observation of worldsheet integrability in the $AdS_5 \times S^5$ superstring [1], integrable two-dimensional non-linear sigma-models have played a prominent role in the gauge-gravity correspondence. In the planar limit in particular, the simplicity offered by integrability allows one to go beyond perturbation theory and interpolate at finite 't Hooft coupling between known results at both sides of the correspondence (for a review see [2, 3]).

For the purpose of the present paper, we are interested in the application of bosonic integrable sigma models as building blocks of worldsheet theories¹ describing strings propagating in curved backgrounds. Well known examples in this context are the Wess-Zumino-Witten (WZW) model [4], which has an exact worldsheet CFT formulation, and the Principal Chiral Model (PCM) [5], which has worldsheet integrability, on a non-Abelian group manifold. Closely related are the gauged WZW model and the Symmetric Space Sigma Model (SSSM) which can be obtained by gauging an appropriate subgroup of the global symmetry group. These gauged theories retain some desirable properties; the gauged WZW model gives a Lagrangian description of coset CFT's [6, 7] and the SSSM retains integrability [8]. Both provide highly symmetrical target spaces which have been key in the construction of amenable string duals.

¹When supplemented with a fermionic field content, as in a Green-Schwarz formulation for instance, they should describe consistent string configurations.

An interesting question in recent years has been to deform known holographic theories while maintaining worldsheet integrability.² Prominent examples include the η - [10–12], β - [9, 13, 14]³ and λ -deformations [16–18]. Our focus will be on the λ -deformation which is an integrable two-dimensional QFT for all values $\lambda \in [0, 1]$. For $\lambda \rightarrow 0$ the model traces back to the WZW model (or gauged WZW model) while for $\lambda \rightarrow 1$ one finds the non-Abelian T-dual of the PCM (or SSSM). There has been significant evidence from both a worldsheet [18, 19] and target space [20–22] perspective that, when applied to supercoset geometries, the λ -model is a marginal deformation introducing no Weyl anomaly. In [23, 24] it was also shown one can promote bosonic coset λ -models to type IIB supergravity backgrounds when a suitable ansatz is made for the RR fields.

We will focus our attention here on bosonic coset λ -deformations of G/H gauged WZW models. A limitation to the standard construction so far is that it is deforming WZW models where only the vector subgroup is gauged [16, 17]. When the subgroup H is Abelian, however, gauging an axial action in the WZW leads to a topologically distinct target space [25, 26]. For H non-Abelian, particular asymmetrical gaugings can be of interest in the case of higher rank groups [25, 27]. The present note will fill this gap by deforming spacetimes obtained from asymmetrically gauged WZW models on a general footing.⁴

A physical motivation of this line of study is the two-dimensional Euclidean black hole in string theory [31–33] corresponding to the $SL(2, R)/U(1)_k$ WZW model [31, 34]. When the gauged $U(1)$ is compact and vector one obtains the so-called trumpet geometry, while for an axial gauging one finds the so-called cigar.⁵ Analytical continuation of the Euclidean time gives the Minkowskian black hole where the trumpet corresponds to the region within the singularity and the cigar to the region outside the horizon [31, 37]. In particular the cigar approaches asymptotically a flat space cylinder while the tip describes the horizon itself. These regions are known to be T-dual [37–40] to the \mathbb{Z}_k orbifold of one another and are indeed described by an equivalent coset CFT [37].

The stringy origin of a black hole horizon has been an attractive asset for the study of the axial $SL(2, R)/U(1)_k$ WZW. In two target space dimensions the only low energy closed string modes are tachyons winding around the periodic direction of the cigar. However, when these states enter the region of the horizon at the tip, winding number conservation breaks, leading to the existence of a tachyonic condensate in that region. This has been understood in [41] using the (bosonic) FZZ duality [41–43] between the cigar geometry and Sine-Liouville theory where the latter is an interacting theory in a flat space cylinder geometry. Here it is an exponentially growing potential that breaks winding conservation explicitly and only allows high momentum tachyon modes to penetrate through the dual

²One ambition here is to have gravity duals that reduce the amount of (super)symmetries on the gauge theory side as in e.g. [9].

³See also the recent [15] and references therein.

⁴Similar ideas of an asymmetric deformation have been developed in [28, 29] where a tensor product of coset manifolds is considered with either different levels or an asymmetrical gauging between the tensor product terms (see also the recently appeared [30]). The novelty of our approach includes deforming an asymmetric gauging of one factor in the tensor product.

⁵These backgrounds are only valid for large k , receiving (quantum) corrections for finite k [35, 36].

of the region behind the horizon [44]. The machinery developed in this note allows one to study the effects of the λ -deformation to the cigar geometry and the Sine-Liouville potential explicitly. At this point the interested reader might be enticed by the success of integrability in going beyond perturbation theory to study quantum gravity effects associated to the horizon. Moreover, using the large N matrix model description of the cigar through Sine-Liouville theory [41], this particular application opens the route to a tractable interpretation of the integrable λ -deformations in holography.

In section 2 we develop the λ -deformation of the asymmetrically gauged WZW model. We show that the model is classically integrable and that, when the asymmetrical gauging respects the symmetric space decomposition,⁶ the one-loop beta function of the λ -parameter match those obtained in the case of symmetric gaugings. We conclude this section by describing integrable boundary conditions of the worldsheet theory where we develop the method of [45] to accommodate for coset spaces and asymmetric gaugings.

We then briefly introduce the $SL(2, R)/U(1)_k$ WZW and apply the λ -deformation to the cigar geometry⁷ in section 3. To first order we will see the deformation to explicitly break the axial-vector duality of the undeformed case. The analysis of our method for the integrable boundary conditions, however, shows the D-brane configurations of [46–50] to persist the deformation albeit with isometries being lost. We find D1-branes extending to asymptotic infinity, but allowed only at particular angles in the deformed cigar, D0-branes at the tip and D2-branes covering the whole or part of the space. In the undeformed case these branes are distinguished, in the nomenclature of [51], as the former being of A-type, while the latter two being of B-type. Finally, after a small review on FZZ duality, we give the starting point to the study of a deformed Sine-Liouville theory by extracting the first order perturbation.

We conclude in section 4 with a short summary and outlook of our results.

2 Left-right asymmetrical λ -deformations

In this section we generalise the construction of λ -deformations of symmetric coset manifolds G/H developed in [16–18] to incorporate the possibility of deforming the left-right asymmetrical gauged WZW model [25, 27].

This *asymmetric* coset λ -deformation is constructed in a number of steps based on the Sfetsos gauging procedure [16]. First one combines⁸ the Wess-Zumino-Witten (WZW) model [4] on a group manifold G ,

$$S_{\text{WZW},k}(g) = -\frac{k}{2\pi} \int_{\Sigma} d\sigma d\tau \langle g^{-1} \partial_+ g, g^{-1} \partial_- g \rangle - \frac{k}{24\pi} \int_{M_3} \langle \bar{g}^{-1} d\bar{g}, [\bar{g}^{-1} d\bar{g}, \bar{g}^{-1} d\bar{g}] \rangle, \quad (2.1)$$

⁶It seems only a technical issue to relax this requirement.

⁷Although the region of the deformed cigar geometry was captured globally in [23] and can be obtained from analytical continuations of the $SU(2)/U(1)$ case of [16], the methodology developed here is more fundamental and, moreover, applicable to a wide range of models.

⁸For a summary of our conventions and more details on the WZW and SSSM we refer the reader to the appendix A.

with the Symmetric Space Sigma Model (SSSM) on G/H ,

$$S_{\text{SSSM}, \kappa^2}(\hat{g}, B_{\pm}) = -\frac{\kappa^2}{\pi} \int d\sigma d\tau \langle (\hat{g}^{-1} \partial_+ \hat{g} - B_+), (\hat{g}^{-1} \partial_- \hat{g} - B_-) \rangle, \quad (2.2)$$

where the latter is invariant under an $H_R \subset G$ action $\hat{g} \rightarrow \hat{g}h$ with $h \in H$ when the gauge fields $B_{\pm} \in \mathfrak{h}$ transform as $B_{\pm} \rightarrow h^{-1}(B_{\pm} + \partial_{\pm})h$. Note that these models are realised through distinct group elements $g \in G$ and $\hat{g} \in G$ respectively which we assume to be connected to the identity. Next, we reduce back to $\dim G - \dim H$ degrees of freedom by gauging simultaneously the left-right asymmetric G -action in the WZW model (generalising the usual λ -model construction [16–18] where the vector action is gauged) and the G_L -action in the SSSM given by,

$$\begin{aligned} g &\rightarrow g_0^{-1} g \tilde{g}_0, \\ \hat{g} &\rightarrow g_0^{-1} \hat{g}. \end{aligned} \quad (2.3)$$

Here $g_0 = \exp(G^A T_A) \in G$ and $\tilde{g}_0 = \exp(G^A \tilde{T}_A) \in G$ have the same parameters G^A but are generated by different embeddings T_A and \tilde{T}_A of a representation of the Lie algebra \mathfrak{g} of G . Their relation can be packaged into an object W as $\tilde{T}_A = W(T_A) = W^B{}_A T_B$. To find a gauge-invariant action we introduce the gauge fields $A_{\pm} = A_{\pm}^A T_A$ transforming as,

$$A_{\pm} \rightarrow g_0^{-1} (A_{\pm} - \partial_{\pm}) g_0, \quad W(A_{\pm}) \rightarrow \tilde{g}_0^{-1} (W(A_{\pm}) - \partial_{\pm}) \tilde{g}_0, \quad (2.4)$$

and we perform the usual minimal substitution (i.e. replacing derivatives by $\partial_{\pm} \cdot - A_{\pm} \cdot$) in the SSSM term and replace the WZW term by the left-right asymmetrical gauged WZW model⁹ [25, 27] on the coset G/G_{AS} given by,

$$\begin{aligned} S_{\text{WZW}, k}(g, A_{\pm}^A, W) &= S_{\text{WZW}, k}(g) + \frac{k}{\pi} \int_{\Sigma} d\sigma d\tau \langle A_-, \partial_+ g g^{-1} \rangle - \langle W(A_+), g^{-1} \partial_- g \rangle \\ &+ \langle A_-, g W(A_+) g^{-1} \rangle - \frac{1}{2} \langle A_-, A_+ \rangle - \frac{1}{2} \langle W(A_-), W(A_+) \rangle. \end{aligned} \quad (2.5)$$

The latter is gauge-invariant¹⁰ provided that $W : \mathfrak{g} \rightarrow \mathfrak{g}$ is a metric-preserving automorphism of the Lie algebra \mathfrak{g} [25, 27] i.e.,

$$W([T_A, T_B]) = [W(T_A), W(T_B)] \quad \text{and} \quad \langle W(T_A), W(T_B) \rangle = \langle T_A, T_B \rangle. \quad (2.6)$$

Finally, one can fix the gauge symmetry by setting $\hat{g} = \mathbf{1}$, which allows one to integrate out the gauge fields B_{\pm} easily. The result is a generalised version¹¹ of the λ -deformed gauged

⁹In the following, we will abbreviate the left-right asymmetrical gauged WZW model with G/H_{AS} WZW when the subgroup $H \subset G$ is gauged.

¹⁰The invariance under the gauge transformations (2.3) can be easily checked when rewriting the action (2.5) using the Polyakov-Wiegmann identity [52], which in our conventions takes the form,

$$S_{\text{WZW}, k}(g_1 g_2) = S_{\text{WZW}, k}(g_1) + S_{\text{WZW}, k}(g_2) - \frac{k}{\pi} \int d\sigma d\tau \langle g_1^{-1} \partial_- g_1, \partial_+ g_2 g_2^{-1} \rangle,$$

for $g_1, g_2 \in G$. One obtains $S_{\text{WZW}, k}(g, A_{\pm}^A, W) = S_{\text{WZW}, k}(g_L^{-1} g \tilde{g}_R) - S_{\text{WZW}, k}(g_L^{-1} g_R)$, where $g_{L,R} \in G$ and one identifies $A_+ = \partial_+ g_R g_R^{-1}$ and $A_- = \partial_- g_L g_L^{-1}$. The gauge transformations are given by $g \rightarrow g_0^{-1} g \tilde{g}_0$ and $g_{L,R} \rightarrow g_0^{-1} g_{L,R}$.

¹¹When the automorphism $W = \mathbf{1}$ one finds the usual λ -model on the G/H coset [16, 17] which is deforming the *vectorially* gauged G/H_V WZW model.

WZW given by,

$$S_\lambda(g, A_\pm^A, W) = S_{\text{wzw},k}(g) + \frac{k}{\pi} \int d\sigma d\tau \langle A_-, \partial_+ g g^{-1} \rangle - \langle W(A_+), g^{-1} \partial_- g \rangle + \langle A_-, g W(A_+) g^{-1} \rangle - \langle A_+, \Omega(A_-) \rangle, \quad (2.7)$$

where we introduced the operator $\Omega(\mathfrak{g}) = \mathfrak{g}^{(0)} \oplus \frac{1}{\lambda} \mathfrak{g}^{(1)}$ with $\mathfrak{g}^{(0)} \equiv \mathfrak{h}$. The deformation parameter λ is defined as $\lambda = \frac{k}{\kappa^2 + k}$.

The action (2.7) still has a residual $\dim H$ left-right asymmetrical gauge symmetry inherited from the G/G_{AS} WZW model (2.5) which acts as,

$$g \rightarrow h^{-1} g \tilde{h}, \quad A_\pm^{(0)} \rightarrow h^{-1} \left(A_\pm^{(0)} - \partial_\pm \right) h, \quad A_\pm^{(1)} \rightarrow h^{-1} A_\pm^{(1)} h, \quad (2.8)$$

with $h = \exp(X)$, $\tilde{h} = \exp(W(X))$ connected to the identity and where $X \in \mathfrak{g}^{(0)}$. Consequently under the gauge transformation we have $W(A_\pm^{(0)}) \rightarrow \tilde{h}^{-1} (W(A_\pm^{(0)}) - \partial_\pm) \tilde{h}$ and $W(A_\pm^{(1)}) \rightarrow \tilde{h}^{-1} W(A_\pm^{(1)}) \tilde{h}$. This shows that the fields $A_\pm^{(0)}$ are still genuine (but non-propagating) gauge fields while the fields $A_\pm^{(1)}$ are auxiliary. Both can be integrated out, yielding the constraints,

$$A_+ = - (D_g W - \Omega)^{-1} \partial_+ g g^{-1}, \quad A_- = (D_{g^{-1}} - W \Omega)^{-1} g^{-1} \partial_- g. \quad (2.9)$$

Once the gauge fields are eliminated in favour of these equations, the resulting action is given by,

$$S_\lambda(g, W) = S_{\text{wzw},k}(g) + \frac{k}{\pi} \int d\sigma d\tau \langle \partial_+ g g^{-1}, (\mathbf{1} - D_g W \Omega)^{-1} \partial_- g g^{-1} \rangle, \quad (2.10)$$

accompanied with a non-constant dilaton profile, coming from the Gaussian integral over gauge fields, given by,

$$e^{-2\Phi} = e^{-2\Phi_0} \det(D_g W - \Omega), \quad (2.11)$$

with Φ_0 constant.

In the $\lambda \rightarrow 0$ limit one reproduces the G/H_{AS} WZW (i.e. the action (2.5) but with $A_\pm^{(1)} = 0$) which can be seen directly from the constraint equations. For small λ one finds, by integrating out the auxiliary fields $A_\pm^{(1)}$ in (2.7), the first order correction to the G/H_{AS} WZW to be,

$$S_\lambda(g, A_\pm^{(0)}, W) = S_{\text{wzw},k}(g, A_\pm^{(0)}, W) + \frac{\lambda}{\pi k} \int d\sigma d\tau \langle \mathcal{J}_+^{(1)}, W^{-1} \mathcal{J}_- \rangle + \mathcal{O}(\lambda^2), \quad (2.12)$$

where we introduced the Kac-Moody currents \mathcal{J}_\pm of the G/H_{AS} WZW¹² defined as

$$\mathcal{J}_+ = -k(\partial_+ g g^{-1} + g W(A_+^{(0)}) g^{-1} - A_-^{(0)}), \quad \mathcal{J}_- = k(g^{-1} \partial_- g - g^{-1} A_-^{(0)} g + W(A_+^{(0)})), \quad (2.13)$$

¹²Although we are not aware of an occurrence in the literature of these currents in the case of the G/H_{AS} WZW, they can be derived analogously to [53] showing that their Poisson brackets satisfy two commuting classical versions of a Kac-Moody algebra.

Hence, the perturbation term away from the CFT point is a particular coupling between these currents. Under the residual gauge transformation (2.8) the currents transform as,¹³

$$\mathcal{J}_+ \rightarrow h^{-1}\mathcal{J}_+h + kh^{-1}\partial_\sigma h, \quad \mathcal{J}_- \rightarrow \tilde{h}^{-1}\mathcal{J}_-\tilde{h} - kW(h^{-1}\partial_\sigma h), \quad (2.14)$$

so that the perturbation term is gauge invariant as is indeed required for consistency.

Another interesting limit to consider is the $\lambda \rightarrow 1$ scaling limit (sending $k \rightarrow \infty$) for which in the usual vectorial gauged case of [16] one reproduces the non-Abelian T-dual of the SSSM. This fact can be traced back to the property that the G/G_V WZW under the scaling limit reduces to a Langrange multiplier term. For the G/G_{AS} WZW (2.5) this is not true for general W which strongly suggests there is no interpretation of this limit as a non-Abelian T-dual.

The novelty of the constructed coset λ -model (2.7) is that it deforms the left-right asymmetrically gauged G/H_{AS} WZW model (2.5) instead of solely the vectorial gauged G/H_V WZW. As advertised, this will allow us to deform also target spaces obtained by an axial gauging when the subgroup H is abelian. However, even in the undeformed case, as noted in [27], not all W that satisfy the conditions (2.6) will produce interesting and novel spacetimes. Indeed, if W is an inner automorphism of the Lie algebra, where one can always find a constant $w \in G$ so that $W(T_A) = wT_Aw^{-1}$, the action (2.7) can be rewritten as,

$$S_\lambda(g, A_\pm^A, W) = S_\lambda(gw, A_\pm^A, \mathbf{1}), \quad (2.15)$$

where we used the $G_L \times G_R$ invariance of the WZW term. Hence, in this case only a trivial redefinition of the fields $g \in G$ to $gw \in G$ has been performed. Nevertheless, if $w \in G^{\mathbb{C}}$ or a different outer automorphism of the Lie algebra the generalisation is non-trivial as we will see later in section 3.

To conclude this section, we note that the construction as described above is also applicable to the group manifold and super-coset case. For the former one can perform the gauging procedure starting with a combination of a WZW and an ordinary PCM model on a Lie group G . The formulae in this section then continue to persist upon the redefinition $\Omega = \lambda^{-1}$. We believe this asymmetrical λ -model can have an interest for higher rank group manifolds allowing Dynkin outer automorphisms such as for instance when $G = \text{SU}(N)$, $N > 2$. Moreover, one can view this λ -model as one with a single but anisotropic coupling matrix $\lambda^{AB} = \lambda W^{AB}$ as discussed for instance in [29, 54]. In the super-coset case, where G is a Lie supergroup, the Sfetsos gauging procedure is not applicable anymore, but one can follow straightforwardly the construction of [18] and replace the G/G_V WZW with the G/G_{AS} WZW. The conditions on the automorphism W are analogous to (2.6) but here the inner product on the Lie supergroup will be taken to be the supertrace STr instead of an ordinary trace. When, moreover, the Lie superalgebra has a semi-symmetric space decomposition defined by a \mathbb{Z}_4 grading $\mathfrak{g} = \oplus_{i=0}^3 \mathfrak{g}^{(i)}$ where $\mathfrak{g}^{(0)} \equiv \mathfrak{h}$ and $[\mathfrak{g}^{(i)}, \mathfrak{g}^{(j)}] \subset \mathfrak{g}^{(i+j \bmod 4)}$, the formulae in this section are again similar upon the redefinition $\Omega(\mathfrak{g}) = \mathfrak{g}^{(0)} \oplus \lambda^{-1}\mathfrak{g}^{(1)} \oplus \lambda^{-2}\mathfrak{g}^{(2)} \oplus \lambda\mathfrak{g}^{(3)}$ and upon the usage of the supertrace. Note

¹³Note that the Kac-Moody currents \mathcal{J}_\pm are not Lorentz invariant by definition.

that, with respect to the supertrace, Ω is not symmetric anymore, so that the constraint equations (2.9) are however altered as,

$$\begin{aligned} A_+ &= -(D_g W - \Omega^T)^{-1} \partial_+ g g^{-1}, \\ A_- &= (D_{g^{-1}} - W \Omega)^{-1} g^{-1} \partial_- g, \end{aligned} \quad (2.16)$$

with $\Omega^T(\mathfrak{g}) = \mathfrak{g}^{(0)} \oplus \lambda \mathfrak{g}^{(1)} \oplus \lambda^{-2} \mathfrak{g}^{(2)} \oplus \lambda^{-1} \mathfrak{g}^{(3)}$.

2.1 Classical integrability

To check the integrability of the asymmetrical λ -model we follow the method of [17]¹⁴ starting from the action (2.7). As in the SSSM it is necessary here to assume the Lie algebra to have a symmetric space decomposition defined by $\mathfrak{g} = \mathfrak{g}^{(0)} \oplus \mathfrak{g}^{(1)}$, with $\mathfrak{g}^{(0)} \equiv \mathfrak{h}$, and a \mathbb{Z}_2 grading $[\mathfrak{g}^{(i)}, \mathfrak{g}^{(j)}] \subset \mathfrak{g}^{(i+j \bmod 2)}$.

The equations of motion of the group fields g can be written as,

$$[\partial_+ - W(A_+), \partial_- + g^{-1} \partial_- g - g^{-1} A_-] = 0, \quad (2.17)$$

or equivalently,

$$[\partial_+ - \partial_+ g g^{-1} - g W(A_+) g^{-1}, \partial_- - A_-] = 0. \quad (2.18)$$

Using the constraints (2.9) and W being a constant Lie algebra automorphism these can be rewritten as,

$$\begin{aligned} [\partial_+ - A_+, \partial_- - \Omega(A_-)] &= 0, \\ [\partial_+ - \Omega(A_+), \partial_- - A_-] &= 0. \end{aligned} \quad (2.19)$$

The above equations of motion can be represented through a $\mathfrak{g}^{\mathbb{C}}$ -valued Lax connection depending on a spectral parameter $z \in \mathbb{C}$ that satisfies a zero-curvature condition,

$$[\partial_+ + \mathcal{L}_+(z), \partial_- + \mathcal{L}_-(z)] = 0, \quad \forall z \in \mathbb{C}, \quad (2.20)$$

when it is given by,

$$\mathcal{L}_{\pm}(z) = -A_{\pm}^{(0)} - z^{\pm 1} \lambda^{-1/2} A_{\pm}^{(1)}. \quad (2.21)$$

This fact shows the left-right asymmetrical λ -theories on G/H manifolds to be classically integrable models [55] for general automorphisms W . These λ -models therefore supplement the list of [29] of integrable λ -models with a general single coupling matrix for $\lambda^{\alpha\beta} = \lambda W^{\alpha\beta}$ with W satisfying (2.6). Additionally, along similar lines, one can show integrability for the asymmetrical λ -model on group and super-coset manifolds for which the Lax connection will take the form,

$$\mathcal{L}_{\pm}(z) = -\frac{2}{1+\lambda} \frac{1}{1 \mp z} A_{\pm}, \quad (2.22)$$

and,

$$\mathcal{L}_{\pm}(z) = -A_{\pm}^{(0)} - z^{-1} \lambda^{\pm 1/2} A_{\pm}^{(1)} - z^{\pm 2} \lambda^{-1} A_{\pm}^{(2)} - z \lambda^{\mp 1/2} A_{\pm}^{(3)}, \quad (2.23)$$

respectively.

¹⁴Note that to translate to [17] one should identify the group fields as $g = \mathcal{F}^{-1}$. The method of [17] consists of relating the equations of motions of the fields in the λ -model to the equations of motions of the SSSM for which the Lax pair is known.

2.2 One-loop beta functions

To compute the one-loop beta functions of the λ -parameter of the above asymmetrically deformed theories, we follow the method of [19], but see also [56, 57] for possibly different approaches. The authors of [19] consider fluctuations around a background field for the currents rather than the fundamental field g and applied the background field approach to the PCM and the SSSM. They efficiently generalise their results to the usual λ -deformed theories on group or (super)-coset manifolds by identifying the appropriate fields such that the classical equations of motion take an identical form to those of the PCM or SSSM models respectively. With minor adjustments we can follow the same path here.

To begin we choose for the group valued field g the same background as [19], namely,

$$g = \exp(\sigma^+ \Lambda_+ + \sigma^- \Lambda_-), \quad (2.24)$$

with Λ_{\pm} constant commuting elements of $\mathfrak{g}^{(1)}$. Hence, on the background we have $\partial_{\pm} g g^{-1} = g^{-1} \partial_{\pm} g = \Lambda_{\pm}$. Through the constraints (2.9) the background of the gauge fields A_{\pm} then becomes,

$$A_+^{bg} = (\Omega - W)^{-1} \Lambda_+, \quad A_-^{bg} = (\mathbf{1} - W\Omega)^{-1} \Lambda_-, \quad (2.25)$$

and, after passing to Euclidean signature, the tree-level contribution of the asymmetrical λ -model Lagrangian (2.7) on the background (2.24), (2.25) evaluates simply to,

$$L^0(\lambda) = \frac{k}{2\pi} \langle \Lambda_+, (W\Omega + \mathbf{1})(W\Omega - \mathbf{1})^{-1} \Lambda_- \rangle. \quad (2.26)$$

To compute the one-loop contribution one introduces a fluctuation around the background and integrates it out in the path integral by a saddle point approximation. Doing so, one needs to calculate the functional determinant of the operator that describes the equations of motion of the fluctuation. Rather than carrying this out directly on the λ -model it is useful to observe that their equations of motion can be identified with those of the SSSM (2.2) where the computation is easier and described in detail in [19].

To see this, let us consider the SSSM (2.2) and define for now $\widehat{L}_{\pm} = \widehat{g}^{-1} \partial_{\pm} \widehat{g} - B_{\pm}$. The equations of motion of the gauge field B_{\pm} take the form of a constraint equation,

$$\widehat{L}_{\pm}^{(0)} = 0. \quad (2.27)$$

Subjected to this constraint, the equations of motion and the Maurer-Cartan identity of the group-valued field $\widehat{g} \in G$ become, projected onto $\mathfrak{g}^{(0)}$ and $\mathfrak{g}^{(1)}$,

$$\begin{aligned} \partial_{\pm} \widehat{L}_{\mp}^{(1)} + [B_{\pm}, \widehat{L}_{\mp}^{(1)}] &= 0, \\ \partial_+ B_- - \partial_- B_+ + [B_+, B_-] + [\widehat{L}_+^{(1)}, \widehat{L}_-^{(1)}] &= 0. \end{aligned} \quad (2.28)$$

One can, moreover, fix the gauge by a covariant gauge choice,

$$\partial_+ B_- + \partial_- B_+ = 0. \quad (2.29)$$

The equations of motion (2.28) can be recast in terms of a flat Lax connection $\mathcal{L}(z)$,

$$\mathcal{L}_{\pm}(z) = B_{\pm} + z^{\pm 1} \widehat{L}_{\pm}^{(1)}, \quad (2.30)$$

satisfying $[\partial_+ + \mathcal{L}_+(z), \partial_- + \mathcal{L}_-(z)] = 0$ for all $z \in \mathbb{C}$ and ensuring the classical integrability of the SSSM. The SSSM Lax connection then indeed takes an identical form to the Lax (2.21) of the λ -deformed theory if we identify,

$$B_{\pm} = -A_{\pm}^{(0)}, \quad \widehat{L}_{\pm}^{(1)} = -\lambda^{-1/2} A_{\pm}^{(1)}, \quad (2.31)$$

where the fields A_{\pm} satisfy the constraints (2.9).

For the one-loop contribution we can now proceed with the SSSM as in section 2.2 of [19] and subject the result to the identification (2.31). Let us denote the background fields for the gauge field B_{\pm} and the current $\widehat{L}_{\pm}^{(1)}$ by B_{\pm}^{bg} and Θ_{\pm} respectively, so that,

$$\begin{aligned} B_{\pm}^{bg} &= 0, \\ \Theta_+ &= -\lambda^{-1/2}(\Omega - W)^{-1}\Lambda_+, \quad \Theta_- = -\lambda^{-1/2}(\mathbf{1} - W\Omega)^{-1}\Lambda_-, \end{aligned} \quad (2.32)$$

where we assumed that W respects the \mathbb{Z}_2 -grading of $\mathfrak{g} = \mathfrak{g}^{(0)} \oplus \mathfrak{g}^{(1)}$ (as will be the case for the vector or axial deformed cases of section 3).¹⁵ Varying the equations of motion (2.28) and the covariant gauge fixing (2.29) the operator that governs the fluctuations can be found, after Fourier transforming to momentum space, to be,

$$\mathcal{D} = \begin{pmatrix} p_- & 0 & 0 & -\Theta_+^{\text{adj}} \\ 0 & p_+ & -\Theta_-^{\text{adj}} & 0 \\ -\Theta_-^{\text{adj}} & \Theta_+^{\text{adj}} & -p_- & p_+ \\ 0 & 0 & p_- & p_+ \end{pmatrix}, \quad (2.33)$$

acting on the fluctuations in the order $(\delta\widehat{L}_+^{(1)}, \delta\widehat{L}_-^{(1)}, \delta B_+, \delta B_-)$. Here we have $(\Theta_{\pm}^{\text{adj}})_B{}^C = \Theta_{\pm}^A (T_A^{\text{adj}})_B{}^C = i\Theta_{\pm}^A F_{AB}{}^C$. The one-loop contribution to the Lagrangian,

$$L^1(\lambda) = \frac{1}{2} \int^{\mu} \frac{d^2 p}{(2\pi)^2} \text{Tr} \log \mathcal{D}, \quad (2.34)$$

will have a logarithmic divergence given by [19],

$$L^1(\lambda) = -\frac{c_2(G)}{2\pi} \langle \Theta_+, \Theta_- \rangle \log \mu + \dots \quad (2.35)$$

where $c_2(G) \equiv x_{\text{adj}}$ is the index of the adjoint representation. Substituting (2.32) and using the property (2.6) that W preserves the Lie algebra metric we find,

$$L^1(\lambda) = \frac{c_2(G)}{2\pi} \frac{1}{\lambda} \langle \Lambda_+, (W\Omega - \mathbf{1})^{-1} W (W\Omega - \mathbf{1})^{-1} \Lambda_- \rangle \log \mu + \dots \quad (2.36)$$

The one-loop beta function of the λ -parameter then follows from demanding that the one-loop effective Lagrangian $L(\lambda) = L^0(\lambda) + L^1(\lambda)$ is independent of the scale μ ,

$$\mu \partial_{\mu} \left[k \langle \Lambda_+, \left(\frac{W\Omega + 1}{W\Omega - 1} \right) \Lambda_- \rangle + \frac{c_2(G)}{\lambda} \langle \Lambda_+, (W\Omega - 1)^{-1} W (W\Omega - 1)^{-1} \Lambda_- \rangle \log \mu \right] = 0, \quad (2.37)$$

¹⁵When W does not respect the \mathbb{Z}_2 -grading one will generate non-zero background fields for the gauge fields B_{\pm} and the calculation of [19] is not directly applicable anymore. In this case it seems that one needs to choose a different but appropriate background field for the group elements $g \in G$ than the one chosen in (2.24). We will not consider this technical issue here further.

This yields (recall that $\Omega(\mathfrak{g}^{(1)}) = \lambda^{-1}$) to first order in $1/k$,

$$\mu \partial_\mu \lambda = -\frac{c_2(G)}{2k} \lambda + \mathcal{O}\left(\frac{1}{k^2}\right). \quad (2.38)$$

We find agreement with [19] and with [56] for the case $G = \text{SU}(2)$, $H = \text{U}(1)$. We conclude that including an automorphism W of the Lie algebra $\mathfrak{g} = \mathfrak{g}^{(0)} \oplus \mathfrak{g}^{(1)}$ which respects the \mathbb{Z}_2 -grading does not affect the one-loop beta function of the asymmetrical λ -model. As with the conventional symmetric λ -model, the deformation for compact groups is marginally relevant driving the model away from the CFT point and marginally irrelevant for non-compact groups (as then one should send $k \rightarrow -k$, see appendix A).

2.3 Integrable boundary conditions

In this section we derive the (open string) boundary conditions that preserve integrability for the asymmetrical coset λ -model from the boundary monodromy method of [45, 58–60] to interpret them later as integrable D-brane configurations in the deformed background.

We define the generalised transport matrix,

$$T^{\mathcal{W}}(b, a; z) = \overleftarrow{P} \exp \left(- \int_a^b d\sigma \mathcal{W}[\mathcal{L}_\sigma(\tau, \sigma; z)] \right), \quad (2.39)$$

with an explicit dependence on the worldsheet coordinates (τ, σ) included and where \mathcal{W} is a constant metric-preserving Lie algebra automorphism (\mathcal{W} is not to be confused with the automorphism W used in the asymmetric gauging). Generally speaking, under periodic boundary conditions (when $\partial\Sigma = 0$) and with a flat Lax connection, one finds classical integrability by generating a tower of conserved charges from the *monodromy matrix* $T^{\mathcal{W}}(2\pi, 0; z)$ as $\partial_\tau \text{Tr} T^{\mathcal{W}}(2\pi, 0; z)^n = 0$ with $n \in \mathbb{Z}$, see e.g. [61]. This is not the case under open boundary conditions. Instead, we build the *boundary monodromy matrix* $T_b(z)$ by gluing the usual ($\mathcal{W} = \mathbf{1}$) transport matrix $T(\pi, 0; z)$ (from the $\sigma = 0$ to the $\sigma = \pi$ end) to the generalised transport matrix $T_R^{\mathcal{W}}(2\pi, \pi; z)$ in the reflected region:

$$T_b(z) = T_R^{\mathcal{W}}(2\pi, \pi; z) T(\pi, 0; z), \quad (2.40)$$

where $T_R^{\mathcal{W}}(2\pi, \pi; z)$ is constructed from the Lax (2.21) under the reflection $\sigma \rightarrow 2\pi - \sigma$ so that,

$$T_R^{\mathcal{W}}(2\pi, \pi; z) = T^{\mathcal{W}}(0, \pi; z^{-1}). \quad (2.41)$$

One finds an infinite set of conserved charges given by $\text{Tr} T_b(z)^n = 0$ with $n \in \mathbb{Z}$ when $\partial_\tau T_b(z) = [T_b(z), N(z)]$ for some $N(z)$. This is satisfied sufficiently when $N(z) = \mathcal{L}_\tau(0; z)$ and when we impose the boundary conditions [45, 60]:

$$\mathcal{L}_\tau(z)|_{\partial\Sigma} = \mathcal{W}[\mathcal{L}_\tau(z^{-1})]|_{\partial\Sigma}, \quad (2.42)$$

on both the open string ends. Explicitly, for the Lax connection (2.21) of the λ -coset model, we find by expanding order by order in the arbitrary parameter z the conditions,

$$\mathcal{O}(z) : \quad A_+^{(1)} \Big|_{\partial\Sigma} = \mathcal{W}[A_-^{(1)}] \Big|_{\partial\Sigma}, \quad (2.43a)$$

$$\mathcal{O}(z^0) : \quad A_\tau^{(0)} \Big|_{\partial\Sigma} = \mathcal{W}[A_\tau^{(0)}] \Big|_{\partial\Sigma}, \quad (2.43b)$$

$$\mathcal{O}(z^{-1}) : \quad A_-^{(1)} \Big|_{\partial\Sigma} = \mathcal{W}[A_+^{(1)}] \Big|_{\partial\Sigma}. \quad (2.43c)$$

Note from the above that the automorphism \mathcal{W} should respect the \mathbb{Z}_2 grading. Moreover, from (2.43b) one deduces that $\mathcal{W}(\mathfrak{g}^{(0)}) = \mathbf{1}$ unless $A_\tau^{(0)}|_{\partial\Sigma} = 0$ and using (2.43c) in (2.43a) that $\mathcal{W}^2(\mathfrak{g}^{(1)}) = \mathbf{1}$. Taking these restrictions on \mathcal{W} into account we continue with (2.43a) as describing the *integrable* boundary conditions. In components, and using the constraint equations (2.9), it translates to conditions on the local coordinates X^μ as,

$$[(D_g W - \Omega)^{-1}]^\alpha \, {}_B R^B{}_\mu \partial_+ X^\mu|_{\partial\Sigma} = -\mathcal{W}^\alpha{}_\beta [(D_{g^{-1}} - W\Omega)^{-1}]^\beta \, {}_C L^C{}_\mu \partial_- X^\mu|_{\partial\Sigma}. \quad (2.44)$$

Given a G/H model one can now continue by studying the eigensystem and derive the corresponding D-brane configurations in the target space background. This will be illustrated in section 3.3 for $G = \text{SL}(2, R)$ and $H = \text{U}(1)$.

In [45] we described also the possibility to glue $T(\pi, 0; z)$ to a gauge transformed reflected transport matrix $T_R^{\mathcal{W}g}(2\pi, \pi; z)$. Here we have the residual gauge symmetry (2.8) under which the Lax (2.21) transforms as $\mathcal{L}(z) \rightarrow h^{-1}\mathcal{L}h + h^{-1}dh$ with $h \in H$. The integrable boundary conditions then read,

$$\mathcal{L}_\tau(z)|_{\partial\Sigma} = \mathcal{W} [h^{-1}\mathcal{L}_\tau(z^{-1})h + h^{-1}\partial_\tau h]|_{\partial\Sigma}, \quad (2.45)$$

which allows a gluing of the gauge fields that is field-dependent. We will see in the explicit example of section 3 that this possibility will prove to be of significant importance to exhibit distinct D-brane configurations.

3 Deforming the Euclidean black hole and Sine-Liouville

We now illustrate the general story above with a simple example. The simplest example one could consider is the $\text{SU}(2)/\text{U}(1)$ case, however, there are no non-trivial outer automorphisms here and all that is achieved is simply a coordinate redefinition as seen from (2.15). One could go on to look at compact theories based on e.g. $\text{SU}(3)$ which does have such a symmetry however we choose here instead to pursue directly the $\text{SL}(2, R)/\text{U}(1)$ theories given their interest towards black hole physics.

For $G = \text{SL}(2, R)$ we take our generators T_A , $A = \{1, 2, 3\}$ to be,

$$T_1 = \frac{1}{\sqrt{2}} \begin{pmatrix} 1 & 0 \\ 0 & -1 \end{pmatrix}, \quad T_2 = \frac{1}{\sqrt{2}} \begin{pmatrix} 0 & 1 \\ 1 & 0 \end{pmatrix}, \quad T_3 = \frac{1}{\sqrt{2}} \begin{pmatrix} 0 & 1 \\ -1 & 0 \end{pmatrix}, \quad (3.1)$$

such that $\text{Tr}(T_A T_B) = \text{diag}(+1, +1, -1)$ and adopt the following parameterisation of a group element $g \in \text{SL}(2, R)$ connected to the identity,

$$g = e^{\frac{\tau-\theta}{\sqrt{2}} T_3} e^{\sqrt{2}\rho T_1} e^{\frac{\tau+\theta}{\sqrt{2}} T_3} = \cosh \rho \begin{pmatrix} \cos \tau & \sin \tau \\ -\sin \tau & \cos \tau \end{pmatrix} + \sinh \rho \begin{pmatrix} \cos \theta & \sin \theta \\ \sin \theta & -\cos \theta \end{pmatrix}, \quad (3.2)$$

with $\rho \in [0, +\infty)$, $\theta, \tau \in [0, 2\pi]$. We take the subgroup $H = \text{U}(1)$ to be generated by T_3 .

3.1 The parafermionic $SL(2, R)/U(1)$ WZW theory

Let us first consider gauging the $U(1)_k$ subgroup in the WZW model on (a single cover of) $SL(2, R)_k$. As a coset CFT this model can be understood as being generated by a set of non-compact *parafermionic* currents introduced in [62] which are semi-local chiral fields with fractional spin (see also [63] and for the compact analogues [64]). In terms of these [63] showed the symmetry algebra to be the non-linear infinite W-algebra $\hat{W}_\infty(k)$. Although obscured as a non-rational CFT it is expected that, as in the compact $SU(2)/U(1)$ theory [51, 64], the level k parafermion theory and its \mathbb{Z}_k orbifold are equivalent for k integral [37, 65].

For large k we can view these theories as sigma models for strings propagating in a two-dimensional target space equipped with a non-constant dilaton originating from the action (2.5). If we perform an axial gauging $g \rightarrow hgh$ with $h \in H$ the τ -coordinate is gauge and we obtain, up to finite $1/k$ corrections, the *cigar* geometry,

$$ds_A^2 = k (d\rho^2 + \tanh^2 \rho d\theta^2), \quad e^{-2\Phi_A} = e^{-2\Phi_0} \cosh^2 \rho, \quad (3.3)$$

and zero B-field. The geometry is semi-infinite and terminates at $\rho = 0$ where the dilaton field is of maximum but finite value. The Ricci scalar computed from this metric is $R = \frac{4}{k \cosh^2 \rho}$ so that $\rho = 0$ is only a coordinate singularity.

If instead we perform the vector gauging $g \rightarrow h^{-1}gh$ the coordinate θ is gauge and we find at large k the *trumpet* geometry,

$$ds_V^2 = k (d\rho^2 + \coth^2 \rho d\tau^2), \quad e^{-2\Phi_A} = e^{-2\Phi_0} \sinh^2 \rho, \quad (3.4)$$

and zero B-field. The Ricci scalar is now $R = -\frac{4}{k \sinh^2 \rho}$ and, therefore, $\rho = 0$ is a true curvature singularity where the dilaton field reaches $+\infty$. Notice that both solutions (3.3) and (3.4) are related by the transformation,

$$\rho \rightarrow \rho + \frac{i\pi}{2}, \quad \theta \rightarrow \tau. \quad (3.5)$$

which, because it involves a complexification, is obviously not a standard field redefinition. Below we will understand it as originating from an outer automorphism. When performing an analytical continuation to Lorentzian signature the above solutions can be interpreted as a two-dimensional black hole for which the global Kruskal coordinates were written down in [31]. The cigar and trumpet solutions correspond to the region outside the horizon and inside the singularity respectively and are described by an equivalent coset CFT [37] with a central charge,

$$c = \frac{3k}{k-2} - 1. \quad (3.6)$$

As we will see shortly, the cigar is known to be T-dual to the \mathbb{Z}_k orbifold of the trumpet solution, and vice versa, where in the Euclidean picture the orbifolding can be understood as changing the temperature of the black hole [37–40].

The axial gauged $SL(2, R)/U(1)$ WZW (3.3) has a $U(1)_\theta$ isometry shrinking to zero size at $\rho = 0$ breaking the conservation of winding number. Nevertheless one can associate

a classically conserved current J_{\pm}^{θ} to $U(1)_{\theta}$ given by,

$$J_{\pm}^{\theta} = k \tanh^2 \rho \partial_{\pm} \theta, \quad \partial_+ J_-^{\theta} + \partial_- J_+^{\theta} = 0. \quad (3.7)$$

Using the conservation equation together with the equations of motion for ρ, θ , one can give semi-classical analogues of the non-compact parafermions which furnish chiral algebra's,

$$\partial_- \Psi_{(\pm)}^A = \partial_+ \bar{\Psi}_{(\pm)}^A = 0, \quad (3.8)$$

in terms of phase space variables [66, 67],

$$\Psi_{(\pm)}^A = (\partial_+ \rho \mp i \tanh \rho \partial_+ \theta) e^{\mp i \left(\theta + \frac{\tilde{\theta}}{k} \right)}, \quad \bar{\Psi}_{(\pm)}^A = (\partial_- \rho \pm i \tanh \rho \partial_- \theta) e^{\pm i \left(\theta - \frac{\tilde{\theta}}{k} \right)}, \quad (3.9)$$

where $\tilde{\theta}$ is a non-local expression in terms of ρ and θ defined by,

$$\partial_{\pm} \tilde{\theta} = \pm J_{\pm}^{\theta}. \quad (3.10)$$

This relation corresponds precisely to the canonical T-duality rule found when performing a standard Buscher procedure [68–70] on the $U(1)_{\theta}$ isometry. In the dual picture $\tilde{\theta}$ becomes a local coordinate with a periodicity of 2π [40]. The T-dual background is,

$$ds_{\mathcal{O}}^2 = k \left(d\rho^2 + \frac{1}{k^2} \coth^2 \rho d\tilde{\theta} \right), \quad e^{-2\Phi_{\mathcal{O}}} = e^{-2\Phi_0} \sinh^2 \rho, \quad (3.11)$$

and thus corresponds to the \mathbb{Z}_k orbifold of the vectorial gauged theory (3.4). Acting with the T-duality action (3.10) the non-compact parafermions of the dual background become,

$$\begin{aligned} \Psi_{(\pm)}^A &\rightarrow \Psi_{(\pm)}^{\mathcal{O}} = \left(\partial_+ \rho \mp i \coth \rho \frac{\partial_+ \tilde{\theta}}{k} \right) e^{\mp i \left(\frac{\tilde{\theta}}{k} + \theta \right)}, \\ \bar{\Psi}_{(\pm)}^A &\rightarrow \bar{\Psi}_{(\pm)}^{\mathcal{O}} = \left(\partial_- \rho \pm i \coth \rho \frac{\partial_- \tilde{\theta}}{k} \right) e^{\pm i \left(\frac{\tilde{\theta}}{k} - \theta \right)}, \end{aligned} \quad (3.12)$$

in which now θ is a non-local expression in the fields ρ and $\tilde{\theta}$ satisfying,

$$\partial_{\pm} \theta = \pm J_{\pm}^{\tilde{\theta}}, \quad J_{\pm}^{\tilde{\theta}} = \coth^2 \rho \frac{\partial_{\pm} \tilde{\theta}}{k}, \quad (3.13)$$

with $J_{\pm}^{\tilde{\theta}}$ the $U(1)_{\tilde{\theta}}$ classically conserved current of the background (3.11). Together with the classical equations of motions, this ensures again the dual parafermions to be holomorphically conserved, $\partial_- \Psi_{(\pm)}^{\mathcal{O}} = \partial_+ \bar{\Psi}_{(\pm)}^{\mathcal{O}} = 0$.

3.2 Asymmetrical λ -deformed $SL(2, \mathbf{R})/U(1)$

Let us now consider the asymmetrically deformed λ -theories. The metric preserving automorphisms W satisfying (2.6) are elements of $SO(2, 1)$ (including elements disconnected from the identity). They can for instance act as,

$$W : \{T_1, T_2, T_3\} \mapsto \{T_1, \cosh \alpha T_2 + \sinh \alpha T_3, \sinh \alpha T_2 + \cosh \alpha T_3\}, \quad (3.14)$$

induced from the action on $g \in \text{SL}(2, R)$ by $g \mapsto wgw^{-1}$ with,

$$w = \exp\left(\frac{\alpha}{\sqrt{2}}T_1\right). \quad (3.15)$$

When the parameter $\alpha \in \mathbb{R}$ the asymmetric gauging involves an inner automorphism which from (2.15) can clearly be absorbed by a trivial field redefinition. When instead we take for instance $\alpha = i\pi$ we have $w \in \text{SL}(2, \mathbb{C})$ and hence the automorphism W is outer. It is an element of $\text{SO}(2, 1)$ corresponding to a reflection of the T_2 and T_3 directions (i.e. $W = \text{diag}(+1, -1, -1)$) and is thus disconnected from the identity. The corresponding asymmetrical λ -theory then defines a background that deforms the axial gauged $\text{SL}(2, R)/\text{U}(1)$ WZW (since $W(T_3) = -T_3$) or *cigar* geometry of (3.3). Under the residual gauge symmetry (2.8) the τ -coordinate is then indeed gauge so that we can adopt the gauge fixing choice $\tau = 0$. Introducing the complex coordinates $\zeta = \sinh \rho e^{i\theta}$ and $\bar{\zeta} = \sinh \rho e^{-i\theta}$ the group element can then be written as,

$$\begin{aligned} g &= \begin{pmatrix} \cosh \rho + \cos \theta \sinh \rho & \sin \theta \sinh \rho \\ \sin \theta \sinh \rho & \cosh \rho - \cos \theta \sinh \rho \end{pmatrix}, \\ &= \frac{1}{2} \begin{pmatrix} \zeta + \bar{\zeta} - 2\sqrt{\zeta\bar{\zeta} + 1} & -i(\zeta - \bar{\zeta}) \\ -i(\zeta - \bar{\zeta}) & -\zeta - \bar{\zeta} - 2\sqrt{\zeta\bar{\zeta} + 1} \end{pmatrix}. \end{aligned} \quad (3.16)$$

The gauge field equations of motion (2.9) are,

$$\begin{aligned} (1 - \lambda)A_+^1 + i(1 + \lambda)A_+^2 &= -\frac{\sqrt{2}\lambda}{\sqrt{1 + \zeta\bar{\zeta}}}\partial_+\zeta, \\ (1 - \lambda)A_-^1 + i(1 + \lambda)A_-^2 &= \frac{\sqrt{2}\lambda}{\sqrt{1 + \zeta\bar{\zeta}}}\partial_-\bar{\zeta}, \end{aligned} \quad (3.17)$$

with A_\pm^3 determined in terms of A_\pm^1 and A_\pm^2 . The deformed background can be computed from (2.10) and (2.11) to be,

$$\begin{aligned} ds_{A,\lambda}^2 &= k \left(\frac{1 - \lambda}{1 + \lambda} (d\rho^2 + \tanh^2 \rho d\theta^2) + \frac{4\lambda}{1 - \lambda^2} (\cos \theta d\rho - \sin \theta \tanh \rho d\theta)^2 \right), \\ &= \frac{k}{1 - \lambda^2} \frac{(\lambda (d\zeta^2 + d\bar{\zeta}^2) + (1 + \lambda^2)d\zeta d\bar{\zeta})}{1 + |\zeta|^2}, \\ e^{-2\Phi} &= e^{-2\Phi_0} \cosh^2 \rho = e^{-2\Phi_0} (1 + |\zeta|^2), \end{aligned} \quad (3.18)$$

and zero B-field. Notice that the deformation has broken the $\text{U}(1)_\theta$ isometry to a \mathbb{Z}_2 . As before, $\rho = 0$ is only a coordinate singularity where the dilaton is constant.

Note that for $\lambda = 0$ we have that the metric is of the form $ds_A^2 = k\partial\bar{\partial}V(\zeta\bar{\zeta})d\zeta d\bar{\zeta}$ with $V(x) = -\text{Li}_2(-x) = \int_0^x ds s^{-1} \log(1 + s)$ and the geometry is indeed Kähler [34] allowing $\mathcal{N} = (2, 2)$ worldsheet supersymmetry. Let us see if we can find a similar form in the deformation, i.e. as $ds_{A,\lambda}^2 = k\partial\bar{\partial}V^\lambda(\zeta, \bar{\zeta})d\zeta d\bar{\zeta}$, with an eye on future applications to extended worldsheet supersymmetry. First, let us bring the metric into canonical form by defining $\zeta = Z - \lambda\bar{Z}$ such that,

$$ds_{A,\lambda}^2 = k \frac{(1 - \lambda^2)dZ d\bar{Z}}{1 - \lambda(Z^2 + \bar{Z}^2) + (1 + \lambda^2)Z\bar{Z}}, \quad (3.19)$$

Although performing directly a double integral of the function $(1 + \lambda^2)(1 - \lambda(Z^2 + \bar{Z}^2) + (1 + \lambda^2)Z\bar{Z})^{-1}$ appears to be inaccessible one can however do an expansion in λ and integrate each term in this evolution. To first order we find,

$$V^\lambda(Z, \bar{Z}) = -\text{Li}_2(-Z\bar{Z}) + \lambda \left(\frac{1}{Z^2} + \frac{1}{\bar{Z}^2} \right) \log(1 + Z\bar{Z}) - \lambda \left(\frac{Z}{\bar{Z}} + \frac{\bar{Z}}{Z} \right) + \mathcal{O}(\lambda^2). \quad (3.20)$$

Whilst a series expansion can doubtless be found, the resummation of such a result is not evident. However, this first-order perturbed potential can be the starting point for the development of the notion of integrability in an $\mathcal{N} = (2, 2)$ superspace setting, a totally uncharted topic. We hope to come back to this in a future publication.

For the remains of the paper we will see it to be more useful to reformulate the deformation in terms of the axial parafermions (3.9). The Lagrangian L_A of the sigma model corresponding to the deformed geometry (3.18) is a perturbation of the CFT point $L_{A,\text{wzw}}$ by a bilinear in the axial parafermions (as in [16]) given to all orders by,

$$L_A = k \left(\frac{1 + \lambda^2}{1 - \lambda^2} L_{A,\text{wzw}} + \frac{\lambda}{1 - \lambda^2} (\Psi_{(+)}^A \bar{\Psi}_{(-)}^A + \Psi_{(-)}^A \bar{\Psi}_{(+)}^A) \right). \quad (3.21)$$

Notice that the non-local phases $\tilde{\theta}$ of the parafermions drop out of this bilinear combination. Furthermore, this perturbation is clearly a non-compact analogue of the one considered in [71].

When instead we take $\alpha = 0$ in (3.15) and thus W the identity (that is trivially inner) one obtains the background known from [23], or from an analytical continuation of the $\text{SU}(2)/\text{U}(1)$ case of [16],

$$ds_{V,\lambda}^2 = k \left(\frac{1 - \lambda}{1 + \lambda} (d\rho^2 + \coth^2 \rho d\tau^2) + \frac{4\lambda}{1 - \lambda^2} (\cos \tau d\rho - \sin \tau \coth \rho d\tau)^2 \right), \quad (3.22)$$

$$e^{-2\Phi} = e^{-2\Phi_0} \sinh^2 \rho,$$

and zero B-field, deforming the vectorial gauged *trumpet* geometry of (3.4). Here $\rho = 0$ is again representing the curvature singularity.¹⁶ After taking the \mathbb{Z}_k orbifold, where the coordinate τ is replaced by the $2\pi/k$ periodic coordinate $\tilde{\theta}/k$, the first order correction to the corresponding Lagrangian L_O becomes a bilinear in terms of the orbifold parafermions Ψ_{\pm}^O of (3.12) as [16],

$$L_O = k \left(\frac{1 + \lambda^2}{1 - \lambda^2} L_{O,\text{wzw}} + \frac{\lambda}{1 - \lambda^2} (\Psi_{(+)}^O \bar{\Psi}_{(+)}^O + \Psi_{(-)}^O \bar{\Psi}_{(-)}^O) \right), \quad (3.23)$$

in which again the non-local phases drop out. One might at first sight think this indicates the axial-vector duality of the CFT point ($\lambda = 0$) [37–40] to persist in the deformation. However, one needs to be more careful here: when performing the T-duality transformation (3.12) on (3.21) the $\Psi_{(\pm)}^O$ enter in a combination where the non-local θ does not drop out and so the deformation term (3.23) is not recovered. Indeed this can be expected as the deformation destroys the isometries of the background.

¹⁶After analytical continuation, reference [23] derived the global Kruskal coordinates of the vectorially deformed theory to interpret the background as a deformed two-dimensional black hole capturing therefore also the region outside the horizon. However, a systematic analysis to obtain this region from an axial gauged deformation was lacking there.

3.3 Integrable branes in the λ -cigar

Let us now consider integrable boundary conditions defined in the λ -cigar geometry. Even in the undeformed case, this is a challenging question because of the well known difficulties with non-rational CFT. However, the expectation is (and based on a semi-classical analysis of the DBI action) that the cigar geometry allows D0-, D1- and D2-brane configurations [46–50]. Except for the D0, these branes can be understood as descending from the ungauged $SL(2, R)$ WZW model [72]. Geometrically, the D0 is located at the tip of the cigar, the D1 covers a so-called *hairpin* and the D2 is either space-filling or extends from the circle at some value $\rho_\star > 0$ to infinity. The D1-branes are understood to be non-compact analogues of the A-branes of [51] in the $SU(2)/U(1)$ WZW while the D0 and D2 are analogues of the B-branes. The latter are an interesting type as they provide a way to derive symmetry breaking branes in the parent theory which are non-obvious to obtain from first principles, see for instance [73] and references therein. Here we will find the above D-brane configurations by employing the classical integrability technique outlined in section 2.3.

We start with analysing the simplest case given in equations (2.42), (2.44) for the cigar, i.e. taking $W = \text{diag}(1, -1, -1)$, and for $\mathcal{W} = \mathbf{1}_3$ (which is trivially satisfying the restrictions given below (2.43)). After a straightforward computation this leads to the integrable boundary conditions,

$$\begin{aligned} \cos \theta \partial_\tau \rho - \sin \theta \tanh \rho \partial_\tau \theta &= 0, \\ \sin \theta \partial_\sigma \rho + \cos \theta \tanh \rho \partial_\sigma \theta &= 0, \end{aligned} \tag{3.24}$$

which describe static D1-branes. These boundary conditions notably do not depend on the deformation parameter and indeed match precisely those of the CFT point [46–48]. In terms of the complex coordinates $\zeta = \sinh \rho e^{i\theta}$, $\bar{\zeta} = \sinh \rho e^{-i\theta}$ they simplify to,

$$\partial_\tau (\zeta + \bar{\zeta}) = 0, \quad \partial_\sigma (\zeta - \bar{\zeta}) = 0. \tag{3.25}$$

The Dirichlet condition gives the embedding equation in the two-dimensional (ρ, θ) space such that the D1-branes cover so-called *hairpins* on the cigar as visualised in figure 1 in the undeformed case. In the limit $\rho \rightarrow \infty$ the branes reach the asymptotic circle at two opposite positions, $\theta = \pi/2, 3\pi/2$. Another possibility in the λ -cigar is taking the gluing automorphism $\mathcal{W} = \text{diag}(-1, -1, 1)$. In this case the integrable boundary conditions (2.44) are an exchange of the Dirichlet and Neumann direction,

$$\partial_\tau (\zeta - \bar{\zeta}) = 0, \quad \partial_\sigma (\zeta + \bar{\zeta}) = 0, \tag{3.26}$$

corresponding to a rotation along the circle of the static D1-branes over an angle $\pi/2$. In contrast to the undeformed case, the extra restrictions on the automorphism \mathcal{W} prevents the branes to be rotated smoothly into each other while preserving the integrability properties, essentially since the deformation destroys such isometry of the background.

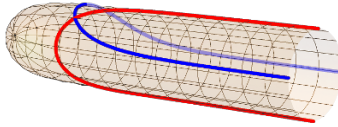


Figure 1. The D1-brane configurations in the undeformed cigar manifold embedded in \mathbb{R}^3 . Heuristically, one can think of the deformation as to convert the $U(1)_\theta$ circle into an ellipse. However, visualising this exactly is surprisingly challenging.¹⁷

Let us consider the D1-branes found above also from the semi-classical perspective. If we let y be the spatial coordinate of the D1-brane¹⁸ and introduce $u = |\zeta| = \sinh(\rho)$ then the DBI action reads,

$$S_{\text{DBI}} = T_1 \int dy e^{-\Phi} \sqrt{\det \hat{G}}, \quad (3.27)$$

where,

$$e^{-2\Phi} \det \hat{G} \propto u'(y)^2 (1 + \lambda^2 + 2\lambda \cos(2\theta(y))) - 4\lambda u(y)u'(y)\theta'(y) \sin(2\theta(y)) + u(y)^2 \theta'(y)^2 (1 + \lambda^2 - 2\lambda \cos(2\theta(y))). \quad (3.28)$$

Although the action evidently depends on the deformation parameter, this drops out in the classical Euler-Lagrange equations, which have a solution,

$$u(y) = v \csc(\theta_0 + \theta(y)), \quad (3.29)$$

with v, θ_0 integration constants. Hence, the D1-branes are semi-infinite with $u \in (v, \infty)$. Plugging this solution back into the DBI action yields,

$$S_{\text{DBI}} \propto \lim_{u \rightarrow \infty} \sqrt{u^2 - v^2} \sqrt{1 + \lambda^2 + 2\lambda \cos(2\theta_0)}. \quad (3.30)$$

Whilst this is clearly diverging, for any UV cut-off the action is minimised by $\theta_0 = \frac{\pi}{2}, \frac{3\pi}{2}$. Asymptotically as $\rho \rightarrow \infty$ these special configurations match precisely to the integrable D-branes described in (3.25).

As is the case in the undeformed cigar we anticipate¹⁹ here also $D0$ -branes localised at the tip. The corresponding worldsheet boundary conditions read,

$$\partial_\tau \theta = \partial_\tau \rho = 0, \quad \rho = 0. \quad (3.31)$$

To ascertain if these constitute integrable boundary conditions we shall reverse the logic compared to the $D1$ case described above; we shall start with these boundary conditions on the field and from this infer a boundary condition on the Lax connection. A first step is

¹⁷Whilst it is easy to find an explicit isometric embedding in \mathbb{R}^3 for the undeformed cigar geometry, finding the same for the deformed cigar proved to be an engrossing, deceptively challenging, and ultimately frustrating activity, at least for the present authors. Solutions to this problem would be welcomed.

¹⁸As is commonplace in the topic we assume that there is an auxiliary time direction and assume some static gauge.

¹⁹Inspired by [45] where a generic geometrical approach was taken for group manifolds, we anticipate the brane configurations of the CFT to persist in the deformed theory.

to use the gauge field equations eq. (3.17) of motion evaluated with the gauge fixing choice eq. (3.16). Then the D0 boundary condition reads simply,

$$A_+^1 = A_-^1, \quad A_+^2 = -A_-^2, \quad A_+^3 = A_-^3 = 0, \quad (3.32)$$

where the latter equality follows on $\rho = 0$. In terms of the Lax connection (2.21),

$$\mathcal{L}_\tau(z) = \frac{1}{\sqrt{2\lambda}z} \begin{pmatrix} -(1+z^2)A_+^1 & (1-z^2)A_+^2 \\ (1-z^2)A_+^2 & (1+z^2)A_+^1 \end{pmatrix} \quad (3.33)$$

we find that this satisfies the condition $\mathcal{L}_\tau(z)| = \mathcal{W}[\mathcal{L}_\tau(z^{-1})]$ of (2.42) when $\mathcal{W} = \text{diag}(1, -1, -1)$. In this case \mathcal{W} satisfies all necessary requirements when $\rho = 0$ (since then $A_+^3 = 0$): it is a constant metric-preserving automorphism of $\mathfrak{sl}(2, R)$ and $\mathcal{W}^2(\mathfrak{g}^{(1)}) = \mathbf{1}$.

In [46, 47] it was shown that there is also a D2-brane configuration supported by a worldvolume gauge field \mathcal{A} with field strength $F_{\rho\theta} \equiv f = \partial_\rho \mathcal{A}_\theta$ (in which the gauge $\mathcal{A}_\rho = 0$ is adopted). In the deformed scenario we might again anticipate finding such a configuration. Indeed from the DBI action,

$$S_{\text{DBI}} \propto \int d\rho d\sigma e^{-\Phi} \sqrt{\det(G + F)}, \quad (3.34)$$

we find that the λ -dependence drops from the equation of motion for the gauge field which is solved with,

$$f^2 = \frac{\beta^2 \tanh^2 \rho}{-\beta^2 + \cosh^2 \rho}. \quad (3.35)$$

Here we see that when the constant $\beta > 1$, the field strength f is critical outside the region $\cosh \rho \geq \beta$ so that the D2-brane extends from the asymptotic circle to a minimum value in ρ given by $\cosh \rho_* = \beta$. When $\beta < 1$, however, the D2 is space-filling.

The question now comes if this corresponds to an integrable boundary condition. Recall that a volume-filling brane should consist of generalised Neumann type boundary conditions that incorporate the gauge field F :

$$G_{ab} \partial_\sigma X^a = F_{ab} \partial_\tau X^b. \quad (3.36)$$

In terms of the coordinates $X = (\rho, \theta)$ these are quite inelegant and have explicit dependence on λ . However, we may recast this result in terms of the gauge fields $A_\pm^{(1)}$ using the on-shell equations of motion (3.17). We find that upon doing so the λ -dependence is again removed and yields,

$$(1 + f^2 \coth^2 \rho) \{A_-^1, A_-^2\} = (1 - f^2 \coth^2 \rho) \{-A_+^1, A_+^2\} - 2f \coth \rho \{A_+^2, A_+^1\}. \quad (3.37)$$

This tells us the gluing between the gauge fields should be field-dependent and therefore hints towards a boundary condition of the form (2.45) where one includes a gauge transformation in the boundary monodromy matrix. Indeed, after a tedious but straightforward computation we find that gauge transforming the Lax (2.21),

$$\mathcal{L}(z) \rightarrow h^{-1} \mathcal{L}(z) h + h^{-1} dh, \quad (3.38)$$

by,

$$h = \exp(v(\rho, \beta)T_3) \in H, \quad v(\rho, \beta) = \sqrt{2} \arcsin(\coth^2 \rho f^2 + 1)^{-1/2}, \quad (3.39)$$

the integrable boundary condition (2.45) agrees with the D2 boundary conditions (3.37) when $\mathcal{W} = \text{diag}(1, -1, -1)$.

Concluding, we see here integrable D-branes corresponding to D0-, D1- and D2-configurations which are all obtained differently from a boundary condition on the Lax connection. We see also that not all of the D1-branes of the undeformed theory preserve integrability: instead of having the continuous $U(1)_\theta$ isometry, only two configurations at specific angles survive the integrable deformation.

3.4 Connection to Sine-Liouville theory

We are now in a position to discuss the deformation to the dual Sine-Liouville (SL) background, which in the undeformed case has the action (see for instance [41, 74]),

$$S_{\text{SL},k}(x, \phi) = \frac{1}{\pi} \int_{\Sigma} d\tau d\sigma \partial_+ \phi \partial_- \phi + \partial_+ x \partial_- x + QR^{(2)}\phi + \mu e^{b\phi} \cos(R\tilde{x}), \quad (3.40)$$

with $R^{(2)}$ the worldsheet Ricci scalar. The target space has the topology of cylinder with $\phi \in (-\infty, +\infty)$ the radial coordinate and x a 2π periodic coordinate with radius R and a dual \tilde{x} . The parameters Q , b and R are related as $Q = -1/b$ and $R^2 - b^2 = 2$ ensuring Sine-Liouville is an exact CFT with central charge,

$$c = 2 + 6Q^2, \quad (3.41)$$

and a potential $V(\phi, \tilde{x}) = \mu e^{b\phi} \cos(R\tilde{x})$ with scaling dimension 1. The central charge of the Euclidean cigar (3.6) matches with that of SL when $Q^2 = \frac{1}{k-2}$, hence (taking the positive root of Q) we have $b = -\sqrt{k-2}$ and $R = \sqrt{k}$.

A dictionary between the (undeformed) Euclidean cigar black hole and Sine-Liouville theory can be made in the asymptotic flat space limit $\rho \rightarrow \infty$ where the cigar approaches the topology of a cylinder and its dilaton falls off linearly, $\Phi_A - \Phi_0 \rightarrow -\rho$. On the SL side, this limit corresponds to the region $\phi \rightarrow \infty$ in which the potential $V(\phi, \tilde{x})$ as well as the string coupling constant go to zero given the dilaton $\Phi_{\text{SL}} = Q\phi$. The identification is therefore at large k given by,

$$\rho \sim -Q\phi, \quad \theta \sim \frac{x}{\sqrt{k}}, \quad \tilde{\chi} \sim \sqrt{k}\tilde{x}. \quad (3.42)$$

At finite ρ and ϕ , the duality between both theories can be demonstrated as an exact match between the symmetry algebra's, vertex operators and n -point functions [41–43] (see also [74]) where they look both topologically and dynamically very different. Indeed, it can be understood that the dynamics is governed by the geometry in the cigar picture and by the potential $V(\phi, \tilde{x})$ in the SL picture. Additionally, the tip of the cigar is the end of space corresponding to the horizon of the Euclidean black hole and hence cutting off the strong string coupling region, while on the SL side this region is protected by the potential $V(\phi, \tilde{x})$. On the worldsheet the duality can be viewed as a strong-weak coupling

duality. However, the sigma model point of view taken here forces us in the small coupling (large k) regime on the cigar side.

For us the power of the duality lies in the observation that the semi-classical cigar parafermions (3.9) in the flat space limit under the identification (3.42),

$$\Psi_{(\pm)}^{\text{SL}} = \left(-\frac{\partial_+\phi}{\sqrt{k-2}} \mp i\frac{\partial_+x}{\sqrt{k}} \right) e^{\mp \frac{2ix_L}{\sqrt{k}}}, \quad \bar{\Psi}_{(\pm)}^{\text{SL}} = \left(-\frac{\partial_-\phi}{\sqrt{k-2}} \pm i\frac{\partial_-x}{\sqrt{k}} \right) e^{\pm \frac{2ix_R}{\sqrt{k}}}, \quad (3.43)$$

commute²⁰ with the SL potential $V(\phi, \tilde{x})$ [74]. Here $x(\sigma^+, \sigma^-) = x_L(\sigma^+) + x_R(\sigma^-)$ and $\tilde{x}(\sigma^+, \sigma^-) = x_L(\sigma^+) - x_R(\sigma^-)$. Therefore, one can rely on the expression (3.43) for all values of ϕ . Since the parafermion fields induce the deformation (3.21) we can now easily extract the perturbation on the SL theory side. To first order in λ the deforming term in the large k regime becomes,

$$\begin{aligned} \delta L_{\text{SL}} = \lambda & \left(2 \cos\left(\frac{2x}{R}\right) \partial_+\phi \partial_-\phi - 2 \cos\left(\frac{2x}{R}\right) \partial_+x \partial_-x \right. \\ & \left. + 2 \sin\left(\frac{2x}{R}\right) (\partial_+x \partial_-\phi + \partial_-x \partial_+\phi) \right) + \mathcal{O}(\lambda^2). \end{aligned} \quad (3.44)$$

A similar structure is expected for finite λ , as (3.21) is exact in λ , so that one deforms the flat space SL theory to a curved background. We anticipate this is the starting point of an integrable deformation of the SL theory. Moreover, it appears to be in a different class to the integrable deformations studied in [74]. We will leave this as an open problem to be fully understood.

4 Conclusion

The Sfetsos procedure [16] to construct the λ -deformation of a G/H coset realised as a gauged WZW model actually requires the G/G model as a starting point. To date, even when H is abelian, attention has been restricted to the case in which in the G/G model the G symmetry, and consequently that of H , acts vectorially. Here we explore the asymmetric gauging of G in which the left and right actions differ by the application of an algebra automorphism. When this is an outer automorphism what results can not be trivially removed via field redefinitions. In this way, we are able to produce new λ -type deformations leading to topologically distinct target spaces in a robust and fundamental manner. Using the similarities between this asymmetric λ -model and its vectorial cousin we demonstrate classical integrability and show the one-loop beta functions to stay marginally relevant for compact groups and irrelevant for non-compact groups. To end our general discussion of this model, we present a simple technique to construct integrable boundary conditions in which we, moreover, exploit the residual asymmetric gauge symmetry.

As an example we consider the $\text{SL}(2, R)/\text{U}(1)$ model where unlike the compact $\text{SU}(2)$ there is such a non-trivial outer automorphism. We show that employing our procedure

²⁰After analytical continuation to Euclidean worldsheet signature one should check that $\oint_w dz \Psi_{(\pm)}^{\text{SL}}(z) V(\phi(w), \tilde{x}(w)) = \oint_{\bar{w}} d\bar{z} \bar{\Psi}_{(\pm)}^{\text{SL}}(\bar{z}) V(\phi(\bar{w}), \tilde{x}(\bar{w}))$. Note that a translation to [74] should be done in the large k limit and by the substitution $\phi \rightarrow \varphi/2$, $x \rightarrow \phi/2$, $b \rightarrow 2b$, $R \rightarrow 2a$. Doing so one indeed finds $\Psi_{(\pm)}^{\text{SL}} \propto \Psi_{(\mp)}^{\text{Fateev}}$ up to an irrelevant overall factor.

we are able to find an integrable deformation of the theory in which the gauged symmetry acts axially. Geometrically, and at large k , we have an integrable deformation of the cigar geometry corresponding to the Euclideanised Witten black hole. The cigar geometry itself receives $\frac{1}{k}$ corrections and it would be doubtless valuable to find a description of the λ -deformation that takes these corrections into account. Continuing at large k , we analyse also the boundary conditions preserving integrability in the deformed cigar. We see this can be done straightforwardly and observe the D-branes proposed at the (non-rational) CFT point to be integrable in the deformation.

As well as demonstrating the concept for this broader class of deformations we believe this example could hold some further interest in its own right. Let us entertain some speculation about how the deformation translates to both the Sine-Liouville (SL) dual and in turn to the matrix model description of this picture. An initial step is made here by identifying for small deformation parameters in the cigar a bilinear of the non-compact parafermions as the operators that drive the deformation. Demanding agreement between the SL at large values of the radial coordinate suggests strongly the same parafermionic bilinear deformation should be considered in the SL model. However the λ -model goes much further since it provides a resummation to all orders in λ of this deformation; what this looks like in the SL theory is far from clear. One possible root to shed light on this could be to combine the Sfetsos procedure with the path integral derivation of FZZ. When successful, one can continue and probe, using the deformed SL theory and integrability, the region behind the horizon.

It is also interesting to ask what the deformation does at the level of the S-matrix. For the case of similar deformations of *compact* parafermionic theories it has long been known that the S-matrix has a kink structure and in the $k \rightarrow \infty$ limit matches that of the O(3) sigma-model [71]. A similar expectation holds for general λ -deformations, the underlying S-matrix has a q root-of-unity quantum group symmetry associated to a face model [75, 76]. Here it is less clear due to the non-compactness of the theory but one might well anticipate a similar q -deformation to hold. Further one might ask what this structure might relate to in the postulated dual matrix model description of the cigar [41].

A final enticing direction is to employ similar techniques in the context of geometries relevant to black hole microstates. For instance a static configuration of NS5-branes on a circle admits a description as a gauged WZW model [77, 78], and more general solutions (supertubes and spectral flows of supertubes) can also be realised as gauged WZW models [79, 80]. It seems quite possible that the techniques developed here may be applicable to such situations. We leave that for future work.

Acknowledgments

We thank Ben Hoare, Tim Hollowood, Carlos Nunez and Kostas Sfetsos for useful discussions that aided this project and to Panagiotis Betzios, Gaston Giribet, Olga Papadoulaki and David Turton for useful communications on the manuscript. DCT is supported by a Royal Society University Research Fellowship *Generalised Dualities in String Theory and Holography* URF 150185 and in part by STFC grant ST/P00055X/1. SD is supported

by the “FWO-Vlaanderen” through an aspirant fellowship. This work is additionally supported in part by the “FWO-Vlaanderen” through the project G006119N and by the Vrije Universiteit Brussel through the Strategic Research Program “High-Energy Physics”.

A Conventions and sigma models (WZW, PCM and SSSM)

In this appendix, we briefly introduce some basic ingredients and conventions for the gauging procedure of section 2.

For the general formulae of this paper we adopt conventions for compact and semi-simple groups G , although they should be changed conveniently when working out the non-compact $SL(2, R)/U(1)$ example in section 3. We denote the generators of the Lie algebra \mathfrak{g} of G by T_A and pick a basis in which they are Hermitean, i.e. $[T_A, T_B] = iF_{AB}^C T_C$ with real structure constants F_{AB}^C and $A = \{1, \dots, \dim G\}$. They are normalised in such a way that the ad-invariant Cartan-Killing metric $\langle \cdot, \cdot \rangle : \mathfrak{g} \times \mathfrak{g} \rightarrow \mathbb{R}$, taken to be $\langle T_A, T_B \rangle = \frac{1}{x_R} \text{Tr}(T_A T_B)$ with x_R the index of the representation R , has unit entries. The left-(right-)invariant Maurer-Cartan one-forms are expanded in the Lie algebra as $g^{-1}dg = -iL^A T_A$ ($dg g^{-1} = -iR^A T_A$) and in explicit local coordinates X^μ , $\mu \in \{1, \dots, \dim G\}$ as $g^{-1}dg = -iL^A_\mu(X) T_A dX^\mu$ ($dg g^{-1} = -iR^A_\mu(X) T_A dX^\mu$). The adjoint action is denoted by $D_g T_A = g T_A g^{-1} = (D_g)^B{}_A T_B$, hence $(D_g)_{AB} = \langle T_A, g T_B g^{-1} \rangle$ and $R^A = (D_g)^A{}_B L^B$.

Finally, considering the G/H coset, we denote the generators of the subgroup $H \subset G$ with Lie algebra \mathfrak{h} by T_a , $a = \{1, \dots, \dim H\}$ and the remaining generators by T_α , $\alpha = \{\dim H + 1, \dots, \dim G\}$. We assume the Lie algebra \mathfrak{g} to have a symmetric space decomposition $\mathfrak{g} = \mathfrak{g}^{(0)} \oplus \mathfrak{g}^{(1)}$, with $\mathfrak{g}^{(0)} \equiv \mathfrak{h}$, defined by a \mathbb{Z}_2 grading $[\mathfrak{g}^{(i)}, \mathfrak{g}^{(j)}] \subset \mathfrak{g}^{(i+j \bmod 2)}$.

We consider the WZW model on a Lie group manifold G at level k [4] with the action,

$$S_{\text{WZW},k}(g) = -\frac{k}{2\pi} \int_{\Sigma} d\sigma d\tau \langle g^{-1} \partial_+ g, g^{-1} \partial_- g \rangle - \frac{k}{24\pi} \int_{M_3} \langle \bar{g}^{-1} d\bar{g}, [\bar{g}^{-1} d\bar{g}, \bar{g}^{-1} d\bar{g}] \rangle, \quad (\text{A.1})$$

with $g : \Sigma \rightarrow G$ a Lie group element and \bar{g} an extension of g into $M_3 \subset G$ such that $\partial M_3 = g(\Sigma)$. To cancel ambiguities from the choice of M_3 in the path integral the level k should be integer quantised for compact groups while for non-compact cases it can be free [4, 81]. The two-dimensional manifold Σ can be thought of as a worldsheet on which we have fixed the metric as $\text{diag}(+1, -1)$, the Levi-Civita as $\epsilon_{\tau\sigma} = 1$ and we have units in which $\alpha' = 1$. We analytically continue to Euclidean coordinates by taking $\sigma_+ = \tau + \sigma \rightarrow -iz$ and $\sigma_- = \tau - \sigma \rightarrow -i\bar{z}$ and will use the term *holomorphic* abusively to mean either $f(\sigma^+)$ or $f(z)$. The WZW model on group manifolds is known to have an exact CFT formulation originating from the $G_L(\sigma^+) \times G_R(\sigma^-)$ symmetry generated by the holomorphically conserved currents $J_+(\sigma^+) = -k \partial_+ g g^{-1}$ and $J_-(\sigma^-) = k g^{-1} \partial_- g$ whose components satisfy two commuting Kac-Moody algebra's.

We consider moreover the PCM model on a Lie group manifold G with a coupling constant κ^2 ,

$$S_{\text{PCM},\kappa^2}(\hat{g}) = -\frac{\kappa^2}{\pi} \int d\sigma d\tau \langle \hat{g}^{-1} \partial_+ \hat{g}, \hat{g}^{-1} \partial_- \hat{g} \rangle, \quad \hat{g} \in G, \quad (\text{A.2})$$

which has a global $G_L \times G_R$ symmetry. From the PCM model the SSSM model on the G/H coset manifold can be obtained by gauging an $H_R \subset G$ subgroup acting as,

$$\widehat{g} \rightarrow \widehat{g}h. \tag{A.3}$$

The gauge-invariant action is then,

$$S_{\text{SSSM},\kappa^2}(\widehat{g}, B_{\pm}) = -\frac{\kappa^2}{\pi} \int d\sigma d\tau \langle (\widehat{g}^{-1} \partial_+ \widehat{g} - B_+), (\widehat{g}^{-1} \partial_- \widehat{g} - B_-) \rangle, \tag{A.4}$$

with B_{\pm} the gauge fields taking values in the Lie algebra $\mathfrak{g}^{(0)} \equiv \mathfrak{h}$ of H and transforming under the gauge transformation as $B_{\pm} \rightarrow h^{-1} (B_{\pm} + \partial_{\pm}) h$. This model is easily shown to be classically integrable when $\mathfrak{g} = \mathfrak{g}^{(0)} \oplus \mathfrak{g}^{(1)}$ has a symmetric space decomposition [8, 17].

Note that when working with non-compact groups, where one usually picks a generator basis $[T_A, T_B] = F_{AB}^C T_C$ with F_{AB}^C real, one should analytically continue in the above models $k \rightarrow -k$ and $\kappa^2 \rightarrow -\kappa^2$.

Open Access. This article is distributed under the terms of the Creative Commons Attribution License ([CC-BY 4.0](https://creativecommons.org/licenses/by/4.0/)), which permits any use, distribution and reproduction in any medium, provided the original author(s) and source are credited.

References

- [1] I. Bena, J. Polchinski and R. Roiban, *Hidden symmetries of the $AdS_5 \times S^5$ superstring*, *Phys. Rev. D* **69** (2004) 046002 [[hep-th/0305116](#)] [[INSPIRE](#)].
- [2] N. Beisert et al., *Review of AdS/CFT Integrability: An Overview*, *Lett. Math. Phys.* **99** (2012) 3 [[arXiv:1012.3982](#)] [[INSPIRE](#)].
- [3] G. Arutyunov and S. Frolov, *Foundations of the $AdS_5 \times S^5$ Superstring. Part I*, *J. Phys. A* **42** (2009) 254003 [[arXiv:0901.4937](#)] [[INSPIRE](#)].
- [4] E. Witten, *Nonabelian Bosonization in Two-Dimensions*, *Commun. Math. Phys.* **92** (1984) 455 [[INSPIRE](#)].
- [5] A.M. Polyakov, *Interaction of Goldstone Particles in Two-Dimensions. Applications to Ferromagnets and Massive Yang-Mills Fields*, *Phys. Lett. B* **59** (1975) 79 [[INSPIRE](#)].
- [6] K. Gawedzki and A. Kupiainen, *G/h Conformal Field Theory from Gauged WZW Model*, *Phys. Lett. B* **215** (1988) 119 [[INSPIRE](#)].
- [7] D. Karabali, Q.-H. Park, H.J. Schnitzer and Z. Yang, *A GKO Construction Based on a Path Integral Formulation of Gauged Wess-Zumino-Witten Actions*, *Phys. Lett. B* **216** (1989) 307 [[INSPIRE](#)].
- [8] H. Eichenherr and M. Forger, *On the Dual Symmetry of the Nonlinear σ -models*, *Nucl. Phys. B* **155** (1979) 381 [[INSPIRE](#)].
- [9] O. Lunin and J.M. Maldacena, *Deforming field theories with $U(1) \times U(1)$ global symmetry and their gravity duals*, *JHEP* **05** (2005) 033 [[hep-th/0502086](#)] [[INSPIRE](#)].
- [10] C. Klimčík, *On integrability of the Yang-Baxter σ -model*, *J. Math. Phys.* **50** (2009) 043508 [[arXiv:0802.3518](#)] [[INSPIRE](#)].

- [11] F. Delduc, M. Magro and B. Vicedo, *On classical q -deformations of integrable σ -models*, *JHEP* **11** (2013) 192 [[arXiv:1308.3581](#)] [[INSPIRE](#)].
- [12] F. Delduc, M. Magro and B. Vicedo, *An integrable deformation of the $AdS_5 \times S^5$ superstring action*, *Phys. Rev. Lett.* **112** (2014) 051601 [[arXiv:1309.5850](#)] [[INSPIRE](#)].
- [13] I. Kawaguchi, T. Matsumoto and K. Yoshida, *Jordanian deformations of the $AdS_5 \times S^5$ superstring*, *JHEP* **04** (2014) 153 [[arXiv:1401.4855](#)] [[INSPIRE](#)].
- [14] D. Osten and S.J. van Tongeren, *Abelian Yang-Baxter deformations and TsT transformations*, *Nucl. Phys.* **B 915** (2017) 184 [[arXiv:1608.08504](#)] [[INSPIRE](#)].
- [15] R. Borsato and L. Wulff, *Marginal deformations of WZW models and the classical Yang-Baxter equation*, [arXiv:1812.07287](#) [[INSPIRE](#)].
- [16] K. Sfetsos, *Integrable interpolations: From exact CFTs to non-Abelian T -duals*, *Nucl. Phys.* **B 880** (2014) 225 [[arXiv:1312.4560](#)] [[INSPIRE](#)].
- [17] T.J. Hollowood, J.L. Miramontes and D.M. Schmidt, *Integrable Deformations of Strings on Symmetric Spaces*, *JHEP* **11** (2014) 009 [[arXiv:1407.2840](#)] [[INSPIRE](#)].
- [18] T.J. Hollowood, J.L. Miramontes and D.M. Schmidt, *An Integrable Deformation of the $AdS_5 \times S^5$ Superstring*, *J. Phys.* **A 47** (2014) 495402 [[arXiv:1409.1538](#)] [[INSPIRE](#)].
- [19] C. Appadu and T.J. Hollowood, *β -function of k deformed $AdS_5 \times S^5$ string theory*, *JHEP* **11** (2015) 095 [[arXiv:1507.05420](#)] [[INSPIRE](#)].
- [20] R. Borsato, A.A. Tseytlin and L. Wulff, *Supergravity background of λ -deformed model for $AdS_2 \times S^2$ supercoset*, *Nucl. Phys.* **B 905** (2016) 264 [[arXiv:1601.08192](#)] [[INSPIRE](#)].
- [21] Y. Chervonyi and O. Lunin, *Supergravity background of the λ -deformed $AdS_3 \times S^3$ supercoset*, *Nucl. Phys.* **B 910** (2016) 685 [[arXiv:1606.00394](#)] [[INSPIRE](#)].
- [22] R. Borsato and L. Wulff, *Target space supergeometry of η and λ -deformed strings*, *JHEP* **10** (2016) 045 [[arXiv:1608.03570](#)] [[INSPIRE](#)].
- [23] K. Sfetsos and D.C. Thompson, *Spacetimes for λ -deformations*, *JHEP* **12** (2014) 164 [[arXiv:1410.1886](#)] [[INSPIRE](#)].
- [24] S. Demulder, K. Sfetsos and D.C. Thompson, *Integrable λ -deformations: Squashing Coset CFTs and $AdS_5 \times S^5$* , *JHEP* **07** (2015) 019 [[arXiv:1504.02781](#)] [[INSPIRE](#)].
- [25] E. Witten, *On Holomorphic factorization of WZW and coset models*, *Commun. Math. Phys.* **144** (1992) 189 [[INSPIRE](#)].
- [26] P.H. Ginsparg and F. Quevedo, *Strings on curved space-times: Black holes, torsion and duality*, *Nucl. Phys.* **B 385** (1992) 527 [[hep-th/9202092](#)] [[INSPIRE](#)].
- [27] I. Bars and K. Sfetsos, *Generalized duality and singular strings in higher dimensions*, *Mod. Phys. Lett.* **A 7** (1992) 1091 [[hep-th/9110054](#)] [[INSPIRE](#)].
- [28] G. Georgiou, K. Sfetsos and K. Siampos, *λ -Deformations of left-right asymmetric CFTs*, *Nucl. Phys.* **B 914** (2017) 623 [[arXiv:1610.05314](#)] [[INSPIRE](#)].
- [29] G. Georgiou and K. Sfetsos, *A new class of integrable deformations of CFTs*, *JHEP* **03** (2017) 083 [[arXiv:1612.05012](#)] [[INSPIRE](#)].
- [30] G. Georgiou and K. Sfetsos, *The most general λ -deformation of CFTs and integrability*, *JHEP* **03** (2019) 094 [[arXiv:1812.04033](#)] [[INSPIRE](#)].
- [31] E. Witten, *On string theory and black holes*, *Phys. Rev.* **D 44** (1991) 314 [[INSPIRE](#)].

- [32] S. Elitzur, A. Forge and E. Rabinovici, *Some global aspects of string compactifications*, *Nucl. Phys. B* **359** (1991) 581 [[INSPIRE](#)].
- [33] G. Mandal, A.M. Sengupta and S.R. Wadia, *Classical solutions of two-dimensional string theory*, *Mod. Phys. Lett. A* **6** (1991) 1685 [[INSPIRE](#)].
- [34] M. Roček, K. Schoutens and A. Sevrin, *Off-shell WZW models in extended superspace*, *Phys. Lett. B* **265** (1991) 303 [[INSPIRE](#)].
- [35] A.A. Tseytlin, *Effective action of gauged WZW model and exact string solutions*, *Nucl. Phys. B* **399** (1993) 601 [[hep-th/9301015](#)] [[INSPIRE](#)].
- [36] I. Bars and K. Sfetsos, *Exact effective action and space-time geometry in gauged WZW models*, *Phys. Rev. D* **48** (1993) 844 [[hep-th/9301047](#)] [[INSPIRE](#)].
- [37] R. Dijkgraaf, H.L. Verlinde and E.P. Verlinde, *String propagation in a black hole geometry*, *Nucl. Phys. B* **371** (1992) 269 [[INSPIRE](#)].
- [38] A. Giveon, *Target space duality and stringy black holes*, *Mod. Phys. Lett. A* **6** (1991) 2843 [[INSPIRE](#)].
- [39] E.B. Kiritsis, *Duality in gauged WZW models*, *Mod. Phys. Lett. A* **6** (1991) 2871 [[INSPIRE](#)].
- [40] M. Roček and E.P. Verlinde, *Duality, quotients and currents*, *Nucl. Phys. B* **373** (1992) 630 [[hep-th/9110053](#)] [[INSPIRE](#)].
- [41] V. Kazakov, I.K. Kostov and D. Kutasov, *A Matrix model for the two-dimensional black hole*, *Nucl. Phys. B* **622** (2002) 141 [[hep-th/0101011](#)] [[INSPIRE](#)].
- [42] V.A. Fateev, A.B. Zamolodchikov and A.B. Zamolodchikov, unpublished.
- [43] Y. Hikida and V. Schomerus, *The FZZ-Duality Conjecture: A Proof*, *JHEP* **03** (2009) 095 [[arXiv:0805.3931](#)] [[INSPIRE](#)].
- [44] A. Giveon, N. Itzhaki and D. Kutasov, *Stringy Horizons*, *JHEP* **06** (2015) 064 [[arXiv:1502.03633](#)] [[INSPIRE](#)].
- [45] S. Driezen, A. Sevrin and D.C. Thompson, *D-branes in λ -deformations*, *JHEP* **09** (2018) 015 [[arXiv:1806.10712](#)] [[INSPIRE](#)].
- [46] A. Fotopoulos, *Semiclassical description of D-branes in $SL(2)/U(1)$ gauged WZW model*, *Class. Quant. Grav.* **20** (2003) S465 [[hep-th/0304015](#)] [[INSPIRE](#)].
- [47] S. Ribault and V. Schomerus, *Branes in the 2 – D black hole*, *JHEP* **02** (2004) 019 [[hep-th/0310024](#)] [[INSPIRE](#)].
- [48] A. Fotopoulos, V. Niarchos and N. Prezas, *D-branes and extended characters in $SL(2, \mathbb{R})/U(1)$* , *Nucl. Phys. B* **710** (2005) 309 [[hep-th/0406017](#)] [[INSPIRE](#)].
- [49] D. Israel, A. Pakman and J. Troost, *D-branes in $N = 2$ Liouville theory and its mirror*, *Nucl. Phys. B* **710** (2005) 529 [[hep-th/0405259](#)] [[INSPIRE](#)].
- [50] S. Ribault, *Discrete D-branes in AdS_3 and in the 2 – D black hole*, *JHEP* **08** (2006) 015 [[hep-th/0512238](#)] [[INSPIRE](#)].
- [51] J.M. Maldacena, G.W. Moore and N. Seiberg, *Geometrical interpretation of D-branes in gauged WZW models*, *JHEP* **07** (2001) 046 [[hep-th/0105038](#)] [[INSPIRE](#)].
- [52] A.M. Polyakov and P.B. Wiegmann, *Goldstone Fields in Two-Dimensions with Multivalued Actions*, *Phys. Lett. B* **141** (1984) 223 [[INSPIRE](#)].

- [53] P. Bowcock, *Canonical Quantization of the Gauged Wess-Zumino Model*, *Nucl. Phys. B* **316** (1989) 80 [INSPIRE].
- [54] K. Sfetsos, K. Siampos and D.C. Thompson, *Generalised integrable λ - and η -deformations and their relation*, *Nucl. Phys. B* **899** (2015) 489 [arXiv:1506.05784] [INSPIRE].
- [55] V.E. Zakharov and A.V. Mikhailov, *Relativistically Invariant Two-Dimensional Models in Field Theory Integrable by the Inverse Problem Technique* (In Russian), *Sov. Phys. JETP* **47** (1978) 1017 [INSPIRE].
- [56] G. Itsios, K. Sfetsos and K. Siampos, *The all-loop non-Abelian Thirring model and its RG flow*, *Phys. Lett. B* **733** (2014) 265 [arXiv:1404.3748] [INSPIRE].
- [57] K. Sfetsos and K. Siampos, *Gauged WZW-type theories and the all-loop anisotropic non-Abelian Thirring model*, *Nucl. Phys. B* **885** (2014) 583 [arXiv:1405.7803] [INSPIRE].
- [58] I.V. Cherednik, *Factorizing Particles on a Half Line and Root Systems*, *Theor. Math. Phys.* **61** (1984) 977 [INSPIRE].
- [59] E.K. Sklyanin, *Boundary Conditions for Integrable Quantum Systems*, *J. Phys. A* **21** (1988) 2375 [INSPIRE].
- [60] A. Dekel and Y. Oz, *Integrability of Green-Schwarz σ -models with Boundaries*, *JHEP* **08** (2011) 004 [arXiv:1106.3446] [INSPIRE].
- [61] O. Babelon, D. Bernard and M. Talon, *Introduction to Classical Integrable Systems*, *Cambridge Monographs on Mathematical Physics*, Cambridge University Press, Cambridge U.K. (2003).
- [62] J.D. Lykken, *Finitely Reducible Realizations of the $N = 2$ Superconformal Algebra*, *Nucl. Phys. B* **313** (1989) 473 [INSPIRE].
- [63] I. Bakas and E. Kiritsis, *Beyond the large N limit: Nonlinear $W(\infty)$ as symmetry of the $SL(2, \mathbb{R})/U(1)$ coset model*, *Int. J. Mod. Phys. A* **7S1A** (1992) 55 [hep-th/9109029] [INSPIRE].
- [64] V.A. Fateev and A.B. Zamolodchikov, *Parafermionic Currents in the Two-Dimensional Conformal Quantum Field Theory and Selfdual Critical Points in $Z(n)$ Invariant Statistical Systems*, *Sov. Phys. JETP* **62** (1985) 215 [INSPIRE].
- [65] D. Israel, C. Kounnas and M.P. Petropoulos, *Superstrings on $NS5$ backgrounds, deformed AdS_3 and holography*, *JHEP* **10** (2003) 028 [hep-th/0306053] [INSPIRE].
- [66] K. Bardakci, M.J. Crescimanno and E. Rabinovici, *Parafermions From Coset Models*, *Nucl. Phys. B* **344** (1990) 344 [INSPIRE].
- [67] P. Marios Petropoulos and K. Sfetsos, *$NS5$ -branes on an ellipsis and novel marginal deformations with parafermions*, *JHEP* **01** (2006) 167 [hep-th/0512251] [INSPIRE].
- [68] T.H. Buscher, *A Symmetry of the String Background Field Equations*, *Phys. Lett. B* **194** (1987) 59 [INSPIRE].
- [69] T.H. Buscher, *Path Integral Derivation of Quantum Duality in Nonlinear σ -models*, *Phys. Lett. B* **201** (1988) 466 [INSPIRE].
- [70] E. Alvarez, L. Álvarez-Gaumé and Y. Lozano, *A Canonical approach to duality transformations*, *Phys. Lett. B* **336** (1994) 183 [hep-th/9406206] [INSPIRE].
- [71] V.A. Fateev and A.B. Zamolodchikov, *Integrable perturbations of $Z(N)$ parafermion models and $O(3)$ σ -model*, *Phys. Lett. B* **271** (1991) 91 [INSPIRE].

- [72] C. Bachas and M. Petropoulos, *Anti-de Sitter D-branes*, *JHEP* **02** (2001) 025 [[hep-th/0012234](#)] [[INSPIRE](#)].
- [73] T. Quella and V. Schomerus, *Symmetry breaking boundary states and defect lines*, *JHEP* **06** (2002) 028 [[hep-th/0203161](#)] [[INSPIRE](#)].
- [74] V.A. Fateev, *Integrable Deformations of Sine-Liouville Conformal Field Theory and Duality*, *SIGMA* **13** (2017) 080 [[arXiv:1705.06424](#)] [[INSPIRE](#)].
- [75] T.J. Hollowood, J.L. Miramontes and D.M. Schmidtt, *S-Matrices and Quantum Group Symmetry of k -Deformed σ -models*, *J. Phys. A* **49** (2016) 465201 [[arXiv:1506.06601](#)] [[INSPIRE](#)].
- [76] C. Appadu, T.J. Hollowood and D. Price, *Quantum Inverse Scattering and the Lambda Deformed Principal Chiral Model*, *J. Phys. A* **50** (2017) 305401 [[arXiv:1703.06699](#)] [[INSPIRE](#)].
- [77] K. Sfetsos, *Branes for Higgs phases and exact conformal field theories*, *JHEP* **01** (1999) 015 [[hep-th/9811167](#)] [[INSPIRE](#)].
- [78] D. Israel, C. Kounnas, A. Pakman and J. Troost, *The Partition function of the supersymmetric two-dimensional black hole and little string theory*, *JHEP* **06** (2004) 033 [[hep-th/0403237](#)] [[INSPIRE](#)].
- [79] E.J. Martinec and S. Massai, *String Theory of Supertubes*, *JHEP* **07** (2018) 163 [[arXiv:1705.10844](#)] [[INSPIRE](#)].
- [80] E.J. Martinec, S. Massai and D. Turton, *String dynamics in NS5-F1-P geometries*, *JHEP* **09** (2018) 031 [[arXiv:1803.08505](#)] [[INSPIRE](#)].
- [81] J.M. Figueroa-O'Farrill and S. Stanciu, *D-brane charge, flux quantization and relative (co)homology*, *JHEP* **01** (2001) 006 [[hep-th/0008038](#)] [[INSPIRE](#)].

D-branes in λ -deformations

Sibylle Driezen,^{a,b} Alexander Sevrin^{a,c} and Daniel C. Thompson^{a,b}

^a*Theoretische Natuurkunde, Vrije Universiteit Brussel & The International Solvay Institutes,
Pleinlaan 2, B-1050 Brussels, Belgium*

^b*Department of Physics, Swansea University,
Singleton Park, Swansea SA2 8PP, U.K.*

^c*Physics Department, Universiteit Antwerpen,
Campus Groenenborger, 2020 Antwerpen, Belgium*

E-mail: Sibylle.Driezen@vub.be, Alexandre.Sevrin@vub.be,
D.C.Thompson@Swansea.ac.uk

ABSTRACT: We show that the geometric interpretation of D-branes in WZW models as twisted conjugacy classes persists in the λ -deformed theory. We obtain such configurations by demanding that a monodromy matrix constructed from the Lax connection of the λ -deformed theory continues to produce conserved charges in the presence of boundaries. In this way the D-brane configurations obtained correspond to “integrable” boundary configurations. We illustrate this with examples based on $SU(2)$ and $SL(2, \mathbb{R})$, and comment on the relation of these D-branes to both non-Abelian T-duality and Poisson-Lie T-duality. We show that the D2 supported by D0 charge in the λ -deformed theory map, under analytic continuation together with Poisson-Lie T-duality, to D3 branes in the η -deformation of the principal chiral model.

KEYWORDS: D-branes, Integrable Field Theories, String Duality

ARXIV EPRINT: [1806.10712](https://arxiv.org/abs/1806.10712)

Contents

1	Introduction	1
2	λ-deformations	4
3	Integrable boundary conditions	6
3.1	General methodology	6
3.2	Applied to λ -deformations	9
3.3	Interpretation as twisted conjugacy classes	10
4	Examples	12
4.1	The S^3 deformation	12
4.2	The AdS_3 deformation	15
5	Relation to generalised T-dualities	19
5.1	The non-Abelian T-dual limit	19
5.2	The pseudo-dual limit	20
5.3	Poisson-Lie dual interpretation	21
6	Conclusions	24
A	General sigma models with boundaries	26
B	WZW models and conventions	27

1 Introduction

The study of two-dimensional quantum field theories with boundaries has rich physical and mathematical significance. In the context of open string theory, the boundary conditions describe D-branes, an essential non-perturbative ingredient of string theory. More generally 2d conformal field theories with boundaries have applications in condensed matter systems including boundary critical behaviour, percolation models and quantum impurity problems (see e.g. [1–3]). When the correct CFT description is available the application of boundary conformal field theory (BCFT) can render the physics tractable [4, 5]. Another interesting class of theories comes from integrable systems;¹ here one is lead to ask (both classically and quantum mechanically) what boundary conditions can be implemented such that the integrability of the system is preserved. The present paper will in some way consider both contexts; we aim to study boundary effects in field theories that are integrable and at some point in the parameter space are connected to conformal field theories.

¹See [6] or for a recent set of useful lecture notes [7].

Our primary motivation will be that of string theory; i.e. we are interested in understanding the D-branes admitted by a given curved closed string background. In general this is a very demanding problem since one would like to have a precise CFT formulation, see e.g. [8, 9]. A simple example is provided by the Wess-Zumino-Witten (WZW) model [10] describing closed strings propagating in a group manifold supported by Neveu-Schwarz flux. Whilst BCFT can be employed here to give an algebraic description of the D-brane [11] our interest will lie in the elegant geometric picture developed through a number of works [12–15]. By identifying possible gluing conditions at the boundary it is determined that D-branes are described by (twisted) conjugacy classes. For example in the $SU(2)_k$ WZW model one finds two D0-branes and a further $k - 1$ D2-branes that are blown up to wrap the conjugacy classes described by $S^2 \subset S^3$.

When an explicit CFT description is unknown and one has just a non-linear sigma-model describing strings in a curved background, giving a precise description of D-branes is challenging. However in a special circumstance, namely when the sigma-model is integrable, progress can be made. One can seek boundary conditions that preserve integrability and hope that they are amenable to a simple interpretation as D-branes. What is meant by *preserve integrability*? At a classical level it is natural to demand that the boundary condition preserves a large number of conserved charges. There are typically two sorts of conserved charges at play, higher spin local charges and non-local charges (e.g. for the principal chiral model (PCM) see [16] for local charges and the construction of a non-local Yangian \times Yangian structure starts with [17–19]). In this work we will focus our attention on the boundary conditions that preserve some portion of the tower of non-local charges obtained from a monodromy matrix. We anticipate that the same boundary conditions will also preserve higher spin local charges. We shall see that this quite naturally generalises the gluing conditions used in the case of the WZW model. This approach has its origins in [20, 21] and has been used in a variety of contexts including the identification of integrable boundary conditions for strings in bosonic sigma models [22], in Green-Schwarz sigma models [23],² for the $O(N)$ sigma model [25, 26], the principal chiral model [27, 28], open spin chains (e.g. [29, 30] although the literature is vast) and affine Toda field theories [31]. For methods based on the conservation of local spin charges see e.g. [32–35].

The present manuscript will seek to make a bridge between the two above ways of determining boundary conditions. The λ -deformed WZW model introduced by Sfetsos in [36] provides an ideal arena to do this. At a classical level the λ -deformation is an integrable 1+1 dimensional field theory that depends on a parameter $\lambda \in [0, 1]$. At $\lambda = 0$ the WZW model is recovered while in a scaling limit as $\lambda \rightarrow 1$ one find the non-Abelian T-dual to the principal chiral model. For generic values of λ the dynamics can be encoded by means of a Lax connection and so a natural question to ask is what boundary conditions can be placed on a λ -model that preserve integrability. Should one wish, once such boundary conditions are established, the limit $\lambda \rightarrow 0$ can be taken providing an alternative route to the D-brane configurations of the WZW model. It is tricky to apply integrability techniques directly to the WZW model due to the chiral nature of the current, so one can think of λ as providing

²In the context of the AdS/CFT correspondence see also [24] and references therein.

a convenient alleviation of this. What we shall see in this paper is that, through a number of pleasing algebraic cancelations, the twisted conjugacy classes define integrable boundary conditions even in the deformed model.³ Moreover, when a quantisation condition is required on the worldvolume flux of D-branes the cancellations are such that the result is independent of the (continuous) deformation parameter λ as it must indeed be for consistency.

A further motivation for the present study comes from duality. To fully establish a duality one would like to have access to its action on both perturbative and non-perturbative degrees of freedom. Consider conventional Abelian target space duality in the absence of any NS two-form potential: here the interpretation is quite simple, a T-duality transverse to a Dp brane produces a $D(p+1)$ brane whilst when performed along a direction of the worldvolume a $D(p-1)$ is produced. This can be seen rather simply by considering the open string boundary conditions; since T-duality acts as a reflection on right-movers, Neumann N and Dirichlet D boundary conditions are interchanged. For more exotic notions of target space duality, e.g. non-Abelian [45, 46] or Poisson-Lie [47, 48], such an understanding is less refined (although see [49–55] and recent work in [56–58]) one reason being that the geometries concerned are not flat making it harder to identify the appropriate boundary conditions. Here however we will have access to an elegant description of D-brane boundary conditions in the λ -model whose interplay with duality can be readily studied. For instance by taking the $\lambda \rightarrow 1$ limit on our D-brane configurations we will gain information about the brane spectrum of the non-Abelian T-dual theory. It is also known that after appropriate analytic continuations the λ -model produces a geometry that is Poisson-Lie T-dual to the integrable η -deformed principal chiral model [59–62]. By examining this analytic continuation on our D-brane configurations we will too gain information about the brane spectrum of the Poisson-Lie T-dual theory. We study this interplay of duality with D-brane configurations in the case of the $SU(2)$ theory. Here we find that under either the “ $\lambda \rightarrow 1 +$ non-Abelian T-duality” or “analytic continuation + PL T-duality” procedures, the D2 branes discovered in the λ -model are transformed to space-filling D3 branes.

The structure of the paper is as follows. We will briefly review in section 2 the salient features of integrable λ -deformations of WZW models, in section 3 we will explain the strategy used to derive integrable boundary conditions and then apply it directly to the λ -deformed WZW. We illustrate this in section 4 in the context of examples based on both $SU(2)$ and $SL(2, \mathbb{R})$ theories, where in the latter case we see the possibility of twisting conjugacy classes by an algebra outer automorphism. In section 5 we explore the relation of these D-brane configurations to both non-Abelian and Poisson-Lie T-duality. In the appendices we establish our conventions and the necessary ingredients of the general sigma model and the WZW model.

³When taken in isolation the λ -deformation is actually a marginally relevant deformation of the WZW and is not a CFT [37]. However we continue to use the terminology of D-branes to describe boundary conditions. It is expected that when applied to super-cosets the λ -deformation becomes a true marginal integrable deformation [37–39] which hopefully makes this usage somewhat acceptable to a string theorist. Moreover, they provide genuine supergravity solutions when a suitable ansatz is made for the RR fluxes and the dilaton [40–44].

2 λ -deformations

First, we will briefly review the construction of [36] in order to set up the sigma model action from which the background fields can be read off and a Lax connection representing the equations of motion can be found. The isotropic λ deformation from group manifolds is obtained by starting with a sum of a PCM on G for a group element $\tilde{g} \in G$,⁴

$$S_{\text{PCM}}(\tilde{g}) = -\frac{\kappa^2}{\pi} \int d\sigma d\tau \langle \tilde{g}^{-1} \partial_+ \tilde{g} \tilde{g}^{-1} \partial_- \tilde{g} \rangle, \quad (2.1)$$

and a WZW model on G for a different group element $g \in G$ as in eq. (B.1). Altogether, this action has a global $G_L \times G_R$ symmetry for the PCM and a $G_L(z) \times G_R(\bar{z})$ symmetry group for the WZW. One continues by gauging simultaneously the left symmetry action of the PCM and the diagonal action of the WZW acting as,

$$G_L: \quad \tilde{g} \rightarrow h^{-1} \tilde{g}, \quad G_{\text{diag}}: g \rightarrow h^{-1} g h, \quad (2.2)$$

with $h \in G$, using a common gauge field $A = A^A T_A$ transforming as,

$$A \rightarrow h^{-1} A h - h^{-1} dh. \quad (2.3)$$

The total model is made gauge invariant by replacing the derivatives in the PCM by a covariant derivative $\tilde{D}_\pm \tilde{g} = \partial_\pm \tilde{g} - A_\pm \tilde{g}$ (i.e. by minimal substitution), and by replacing the WZW model (B.1) with the G/G gauged WZW model,

$$S_{\text{gWZW},k}(g, A) = S_{\text{WZW},k}(g) + \frac{k}{\pi} \int d\sigma d\tau \langle A_- \partial_+ g g^{-1} - A_+ g^{-1} \partial_- g + A_- g A_+ g^{-1} - A_- A_+ \rangle. \quad (2.4)$$

Finally, we can fix the gauge to $\tilde{g} = 1$ to find,

$$S_{k,\lambda}(g, A) = S_{\text{WZW},k}(g) - \frac{k}{\lambda\pi} \int d\sigma d\tau \langle A_+ O_{g^{-1}} A_- \rangle + \frac{k}{\pi} \int d\sigma d\tau \langle A_- \partial_+ g g^{-1} - A_+ g^{-1} \partial_- g \rangle, \quad (2.5)$$

where we introduced the useful operator,

$$O_g = (\mathbf{1} - \lambda D)^{-1}, \quad (2.6)$$

given in terms of the adjoint action $D(T_A) = \text{ad}_g T_A = g T_A g^{-1} = T_B D^B_A(g)$. For the isotropic λ -model, which is the model we consider throughout this paper, we have,

$$\lambda_{AB} = \lambda \langle T_A, T_B \rangle \equiv \lambda \eta_{AB}, \quad \lambda = \frac{k}{k + \kappa^2}. \quad (2.7)$$

The gauge fields are now auxiliary and can be integrated out. Varying the action $S_{k,\lambda}(g)$ with respect to A_\pm we find the constraints,

$$A_+ = \lambda O_g \partial_+ g g^{-1}, \quad A_- = -\lambda O_{g^{-1}} g^{-1} \partial_- g, \quad (2.8)$$

⁴See appendix B for conventions.

Substituting these constraints into eq. (2.5) gives,

$$\begin{aligned}
S_{k,\lambda}(g) &= S_{\text{WZW},k}(g) + \frac{k\lambda}{\pi} \int d\sigma d\tau R_+^A (O_{g^{-1}})_{AB} L_-^B \\
&= \frac{k}{2\pi} \int_{\Sigma} d\sigma d\tau L_+^A \eta_{AB} L_-^B + \frac{k\lambda}{\pi} \int d\sigma d\tau R_+^A (O_{g^{-1}})_{AB} L_-^B \\
&\quad + \frac{k}{24\pi} \int_{M_3} F_{ABC} L^A \wedge L^B \wedge L^C,
\end{aligned} \tag{2.9}$$

in which Lie algebra indices out of position are raised and lowered with the metric $\eta = \langle \cdot, \cdot \rangle$ and we work in term of the Maurer-Cartan forms $L = g^{-1}dg = -iL^A T_A$ and $R = dgg^{-1} = -iR^A T_A$. From the above λ action it is straightforward to read off the target space data which can be expressed in terms of the left-invariant forms L^A as:

$$\begin{aligned}
ds_{\lambda}^2 &= k (O_{g^{-1}} + O_g - \eta)_{AB} L^A \otimes L^B, \\
B_{\lambda} &= B_{\text{WZW}} + \frac{k}{2} (O_{g^{-1}} - O_g)_{AB} L^A \wedge L^B,
\end{aligned} \tag{2.10}$$

where we have used that $R^A = D^A_B(g)L^B$ and in which $dB_{\text{WZW}} = \frac{k}{6} F_{ABC} L^A \wedge L^B \wedge L^C$. Equivalently we can use the identity (and this will proof useful later),

$$O_{g^{-1}} + O_g - \eta = (1 - \lambda^2) O_g \eta O_{g^{-1}} = (1 - \lambda^2) O_{g^{-1}} \eta O_g, \tag{2.11}$$

to express the target space metric as,

$$ds_{\lambda}^2 = k \eta_{AB} E^A \otimes E^B, \quad E = \sqrt{1 - \lambda^2} O_{g^{-1}} L, \tag{2.12}$$

with E the vielbein bringing us to the flat frame. In addition the Gaussian elimination of the gauge fields, when performed in a path integral, results in a non-constant dilaton profile,

$$\Phi = \Phi_0 + \frac{1}{2} \log \det O_{g^{-1}}, \tag{2.13}$$

in which constants are absorbed into Φ_0 . Finally, one can derive the classical energy momentum tensor of the λ -model to find,

$$T_{\pm\pm} = k (1 - \lambda^2) \langle A_{\pm}, A_{\pm} \rangle. \tag{2.14}$$

There are two interesting limits at play here [36]; for $\lambda \rightarrow 0$ we see from eq. (2.8) that the fields A_{\pm} will freeze out and, hence, one will reproduce the well-understood WZW model (see appendix B), allowing consistency checks of analyses of the deformation. For small λ the WZW is deformed by a current-current bilinear. In the $\lambda \rightarrow 1$ limit one reproduces the non-Abelian T-dual of the principal chiral model. This limit is more subtle and should be taken by $k \rightarrow \infty$ in eq. (2.7) and expanding group elements around the identity (but see section 5 for more details).

To establish the classical integrability of the λ model it is convenient to work with eq. (2.5) but where we take the gauge fields on-shell eq. (2.8) (although see [36] for the proof of integrability starting from eq. (2.9)). In this way any variation of the action with

respect to A_{\pm} vanishes and calculations simplify. From eq. (2.5) we then find the equation of motion for the group element g to be,

$$D_+(g^{-1}D_-g) = F_{+-}, \tag{2.15}$$

where we introduced the derivative $D_{\pm}\cdot = \partial_{\pm}\cdot - [A_{\pm}, \cdot]$ and the field strength $F_{+-} = \partial_+A_- - \partial_-A_+ - [A_+, A_-]$. Using the on-shell expression for A_{\pm} , eq. (2.8), this can be rewritten as,

$$\partial_{\pm}A_{\mp} = \pm \frac{1}{1+\lambda} [A_+, A_-]. \tag{2.16}$$

Hence, effectively we have recast one second order equation for the field g , by the constraints, as two first order equations for A_{\pm} . It is now straightforward to show that the following Lax connection,

$$\mathcal{L}_{\pm}(z) = -\frac{2}{1+\lambda} \frac{A_{\pm}}{1 \mp z}, \quad z \in \mathbb{C}, \tag{2.17}$$

satisfying the flatness condition $d\mathcal{L} + \mathcal{L} \wedge \mathcal{L} = 0$ is equivalent to the equations of motion (2.16) thereby ensuring its classical integrability [63] (see also the next section).

3 Integrable boundary conditions

3.1 General methodology

This section closely follows [22, 23] for obtaining open string boundary conditions that preserve integrability based on a method first introduced by Cherdnik and Sklyanin [20, 21] in the context of two-dimensional integrable systems. We add here a slightly more general procedure applicable to integrable sigma models which has not been clearly spelled out yet in the literature (however, see [28] for a recent usage hereof in the case of the PCM) but which can lead to distinct integrable D-brane configurations.

Consider first a general (1+1)-dimensional field theory in a spacetime (or worldsheet) Σ parametrised by (τ, σ) on a periodic or infinite line with a global symmetry group G . The model is said to be classically integrable when its equations of motion can be recast in a zero curvature condition of a $\mathfrak{g}^{\mathbb{C}}$ -valued Lax connection one-form $\mathcal{L}(z)$ depending on a spectral parameter $z \in \mathbb{C}$ [63],

$$d\mathcal{L}(z) + \mathcal{L}(z) \wedge \mathcal{L}(z) = 0. \tag{3.1}$$

The Lax $\mathcal{L}(z)$ is defined up to a local gauge transformation by a Lie group element $g(\tau, \sigma) \in G$ given by,

$$\mathcal{L}(z) \rightarrow \mathcal{L}^g(z) = g\mathcal{L}(z)g^{-1} - dg g^{-1}, \tag{3.2}$$

leaving the zero curvature condition (3.1) invariant. In this case, an infinite set of conserved charges can be obtained from the usual transport matrix $T(b, a; z)$ defined by,

$$T(b, a; z) = \overleftarrow{P} \exp \left(- \int_a^b d\sigma \mathcal{L}_{\sigma}(\tau, \sigma; z) \right), \tag{3.3}$$

where we included the explicit dependence on the (worldsheet) coordinates and the arrow specifies the ordering of the integral as per [6]. The transport matrix satisfies the following useful properties,

$$\delta T(b, a; z) = - \int_a^b d\sigma T(b, \sigma; z) \delta \mathcal{L}_\sigma(\tau, \sigma; z) T(\sigma, a; z), \quad (3.4)$$

$$\partial_\sigma T(\sigma, a; z) = - \mathcal{L}_\sigma(\tau, \sigma; z) T(\sigma, a; z), \quad (3.5)$$

$$\partial_\sigma T(b, \sigma; z) = T(b, \sigma; z) \mathcal{L}_\sigma(\tau, \sigma; z), \quad (3.6)$$

$$T(a, a; z) = 1, \quad (3.7)$$

and under the gauge transformation (3.2) it transforms as,

$$T(b, a; z) \rightarrow T^g(b, a; z) = g(\tau, b) T(b, a; z) g^{-1}(\tau, a). \quad (3.8)$$

Using the flatness of the Lax $\mathcal{L}(z)$ together with the above properties, one can now show that,

$$\partial_\tau T(b, a; z) = T(b, a; z) \mathcal{L}_\tau(\tau, a; z) - \mathcal{L}_\tau(\tau, b; z) T(b, a; z). \quad (3.9)$$

Therefore, under periodic boundary conditions $\sigma \simeq \sigma + 2\pi$ (for e.g. the closed string) we find that the trace of the *monodromy matrix* $T(2\pi, 0; z)$ is conserved,⁵

$$\partial_\tau \text{Tr} T(2\pi, 0; z)^n = 0 \quad \forall n \in \mathbb{N}. \quad (3.10)$$

Different sets of conserved charges (local or non-local) can then be obtained from expanding the monodromy matrix or its gauge transformed form around suitable values of the spectral parameter leading typically to Yangian algebra's or quantum groups for the non-local sets of charges, see e.g. [64].

For later convenience, we define here also a generalised transport matrix,

$$T^\Omega(b, a; z) = \overleftarrow{P} \exp \left(- \int_a^b d\sigma \Omega [\mathcal{L}_\sigma(\tau, \sigma; z)] \right), \quad (3.11)$$

where Ω is a constant Lie algebra automorphism. This generalised transport matrix behaves under time derivation as,

$$\partial_\tau T^\Omega(b, a; z) = T^\Omega(b, a; z) \Omega [\mathcal{L}_\tau(\tau, a; z)] - \Omega [\mathcal{L}_\tau(\tau, b; z)] T^\Omega(b, a; z), \quad (3.12)$$

such that $\partial_\tau \text{Tr} T^\Omega(2\pi, 0; z)^n = 0$ for all $n \in \mathbb{Z}$, and under gauge transformations as,

$$T^\Omega(b, a; z) \rightarrow \omega(g(b)) T^\Omega(b, a; z) \omega(g^{-1}(a)), \quad (3.13)$$

where the map $\omega : G \rightarrow G$ is defined as $\omega(e^{tX}) = e^{t\Omega[X]}$ for t small and $X \in \mathfrak{g}$. Here we assumed the corresponding Lie group G to be connected to the identity (in this case ω is a constant Lie *group* automorphism also).

⁵Alternatively, on the infinite line with suitable asymptotic fall-off conditions we find immediately that $\partial_\tau T(+\infty, -\infty; z) = 0$.

When the model is considered on a finite line, e.g. $\sigma \in [0, \pi]$ in the context of sigma models describing open strings, the charges obtained from the above procedure are generically not conserved. Similarly to the loss of conservation of momentum along the spatial direction, integrability might be spoiled. However, with the appropriate boundary conditions one can still obtain an infinite set of conserved charges from the so called *boundary monodromy* object $T_b(z)$ that involves the transport matrix T from the $\sigma = 0$ end of the open string to the $\sigma = \pi$ end *glued* to the generalised transport matrix T^Ω in the reflected region, i.e. going in the other direction. At the boundaries we include the possibility of non-trivial effects incorporated by the so-called reflection matrices U_0 and U_π that are in the Lie group G . Hence we define,⁶

$$T_b(z) = U_0 T_R^\Omega(2\pi, \pi; z) U_\pi^{-1} T(\pi, 0; z), \tag{3.14}$$

where the allowed boundary conditions are encoded in conditions on the reflection matrices and the automorphism Ω . As discussed in [22, 23] the reflection matrices are taken to be constant in time and independent of the spectral parameter.⁷ The transport matrix $T_R(2\pi, \pi; z)$ in the reflected region is constructed from the transformation $\sigma \rightarrow \sigma_R = 2\pi - \sigma$ when $\sigma \in [\pi, 2\pi]$. We will assume in the following the reflected generalised transport matrix to have the form,

$$T_R^\Omega(2\pi, \pi; z) = T^\Omega(0, \pi; -z), \tag{3.15}$$

which will indeed be the case for the λ model.

In general this strongly depends on the specific form of the Lax connection $\mathcal{L}(z)$ but the following procedure can be easily adapted to other cases. Similar to the bulk model, we impose integrability by requiring that the time derivative of the boundary monodromy matrix is given by a commutator,

$$\partial_\tau T_b(z) = [T_b(z), N(z)], \tag{3.16}$$

for some matrix $N(z)$, such that $\text{Tr} T_b(z)^n$ is conserved for any $n \in \mathbb{N}$. Explicitly we find using the formulae (3.9) and (3.12) that,

$$\begin{aligned} \partial_\tau T_b(z) = & U_0 [T^\Omega(0, \pi; -z) \mathcal{L}_\tau^\Omega(\pi; -z) - \mathcal{L}_\tau^\Omega(0; -z) T^\Omega(0, \pi; -z)] U_\pi^{-1} T(\pi, 0; z) \\ & + U_0 T^\Omega(0, \pi; -z) U_\pi^{-1} [T(\pi, 0; z) \mathcal{L}_\tau(0; z) - \mathcal{L}_\tau(\pi; z) T(\pi, 0; z)], \end{aligned} \tag{3.17}$$

discarding here the τ -dependence and using the notation $\mathcal{L}^\Omega(z) = \Omega[\mathcal{L}(z)]$. One can show that the integrability condition (3.16) sufficiently holds for $N(z) = \mathcal{L}_\tau(0; z)$ when we require the following boundary conditions on both the open string ends:

$$\mathcal{L}_\tau(\tau, 0; z) = U_0 \Omega[\mathcal{L}_\tau(\tau, 0; -z)] U_0^{-1}, \tag{3.18}$$

⁶When the Lie algebra automorphism Ω is taken to be inner we recover the discussion of [22] up to a suitable redefinition of the reflection matrices. The possibility of Ω to be outer, however, leads to interesting non-trivial boundary conditions.

⁷These conditions are preferred for the interpretation of the boundary conditions as physical D-brane configurations. However the spectral parameter independence e.g. might be relaxed as in [28] where the objective is to map the boundary conditions to known boundary scattering matrices of the quantum theory containing a free parameter.

and similarly on $\sigma = \pi$ (but where in principal the reflection matrix U_π can be different allowing the open string to connect different D-branes). Substituting the Lax connection of the considered model in eq. (3.18) imposes integrable boundary conditions on the field variables, together with consistency conditions on the automorphism Ω and the reflection matrix U as will be clear in the coming subsection.

However this is not the end of the story: the above procedure leads to sufficient conditions for integrability of the boundary model but they are not necessary. We can cook up any exotic boundary monodromy matrix $T_b(z)$; as long as it satisfies $\partial_\tau T_b(z) = [T_b(z), N(z)]$ for some $N(z)$ an infinite set of conserved charges can be constructed. It is e.g. an interesting possibility to consider also a gauge transformation in the reflected region,

$$\begin{aligned} T_b(z, \delta) &= U_0 T_R^{g\Omega} \left(2\pi, \pi; \tilde{\delta}_R; w \right) U_\pi^{-1} T(\pi, 0; \delta; z) \\ &= U_0 \omega(g(0)) T^\Omega \left(0, \pi; \tilde{\delta}; -w \right) \omega(g(\pi))^{-1} U_\pi^{-1} T(\pi, 0; \delta; z), \end{aligned} \quad (3.19)$$

where we used eq. (3.13) and eq. (3.15) and we included in the transport matrix⁸ the possible dependence on δ representing (multiple) deformation parameters. Moreover, in the reflected region there is the possibility that the spectral parameter and the deformation parameters change, meaning $w = F(z)$ and $\tilde{\delta} = G(\delta)$ for some suitable functions F and G . Although we will not consider this for the λ -deformed model, we are convinced that a detailed investigation of this possibility in other integrable models will lead to interesting results and we hope to return to this point in the future.

3.2 Applied to λ -deformations

Having the Lax connection of the isotropic λ -deformation on group manifolds at hand one can now derive the integrable boundary conditions corresponding to the boundary monodromy matrix $T_b(z)$ given in eq. (3.14). One can check that eq. (3.15) indeed holds for the Lax (2.17). Using now the constraints (2.8) we can write the Lax in a convenient form in terms of the Maurer-Cartan forms $L_- = g^{-1} \partial_- g$ and $R_+ = \partial_+ g g^{-1}$,

$$\mathcal{L}_\tau(z) = \frac{2\lambda}{1+\lambda} \frac{1}{1-z^2} \left(O_{g^{-1}}[L_-] - O_g[R_+] - z \left(O_{g^{-1}}[L_-] + O_g[R_+] \right) \right), \quad (3.20)$$

where recall $O_g = (\mathbf{1} - \lambda D)^{-1}$. Plugging the above into the result (3.18) and requiring the reflection matrices to be z -independent leads to the following boundary conditions,⁹

$$O_{g^{-1}}[L_-]|_{\partial\Sigma} = -\Omega \cdot O_g[R_+]|_{\partial\Sigma}, \quad (3.21)$$

where, for consistency, Ω should be a constant *involutive* Lie algebra automorphism. A further restriction comes from demanding the (classical) conformal boundary condition (see eq. (A.7)) which requires the energy-momentum tensor to satisfy $T_{++}| = T_{--}|$. Using the

⁸The cumbersome notation $T_R^{g\Omega}$ represents the gauge transformed transport, acted on by the automorphism Ω and reflected.

⁹Here we absorbed the reflection matrices $U_{0/\pi}$ (which are essentially an additional inner automorphism action) into the definition of the automorphism Ω and discarded the indication of the open string end. However one should keep in mind that in principle Ω can be different on each end.

form of the stress tensor of the λ model (2.14) we require that Ω preserves the inner product $\langle \cdot, \cdot \rangle$. This is important for the boundary conditions to preserve conformal invariance in the WZW limit $\lambda \rightarrow 0$ [4, 5, 11–15]. Summarising, Ω is a constant Lie algebra metric-preserving involutive automorphism:

$$\Omega \in \text{Aut}(\mathfrak{g}), \quad \Omega^2 = 1, \quad \Omega^T \eta \Omega = \eta. \tag{3.22}$$

The integrable boundary conditions thus obtained reduce in the $\lambda \rightarrow 0$ limit exactly to chiral-algebra preserving symmetric D-branes of the WZW model [4, 5, 11–14] (in the terminology of [14] the type D conditions (B.8)).

3.3 Interpretation as twisted conjugacy classes

Like in the WZW case, we desire a geometrical interpretation of the (integrable) boundary conditions (3.21) as Dirichlet and Neumann conditions on $g : \partial\Sigma \rightarrow N$ defining a D-brane N . In this regard it is important to realise that eq. (3.21) takes values in the tangent space of G at the identity $T_e G \simeq \mathfrak{g}$. To interpret the geometry of the D-brane configurations one needs local conditions on an arbitrary point $g \in G$ obtained by translating eq. (3.21) to $T_g G$ (which is non-trivial for non-Abelian group manifolds). However, as λ deformations of WZW theories deform only the target space data while the tangent space $T_g G$ is independent of the choice of metric, it is clear that only the size of the classical D-branes can change while their topology must be unaffected compared to the well-known WZW branes. We will show here that this is indeed the case leading to (integrable) boundary conditions corresponding to D-brane configurations that are (twisted) conjugacy classes [12–14].

First, we should split the tangent space $T_g G$ at $g \in G$ orthogonally to the D-brane N with respect to the λ -deformed metric (2.12) (assuming the metric restricts non-degenerately to N),

$$T_g G = T_g N \oplus T_g N^\perp. \tag{3.23}$$

Important here is that the object $\tilde{\Omega}_g \equiv O_{g^{-1}}^{-1} \cdot \Omega \cdot O_g$ gluing left to right currents in eq. (3.21) is easily shown to preserve the deformed metric (2.12) at g provided that Ω preserves the inner product $\eta = \langle \cdot, \cdot \rangle$. Indeed, writing the metric as

$$G_\lambda = k E^T \eta E = k (1 - \lambda^2) L^T O_{g^{-1}} \eta O_g L = k (1 - \lambda^2) L^T O_g \eta O_{g^{-1}} L, \tag{3.24}$$

we have $\tilde{\Omega}_g^T G_\lambda \tilde{\Omega}_g = G_\lambda$. Moreover, it is straightforward to show that the deformed metric at g is invariant under an adjoint action by g , i.e. $D^T G_\lambda D = G_\lambda$.

With these properties of the deformed metric at hand we can now exactly follow the procedure used in the WZW case of [14, 15] for finding the tangent space $T_g N$ to the D-brane when treating $\tilde{\Omega}_g$ as the gluing matrix. This leads to,

$$T_g N = \left\{ u - O_{g^{-1}}^{-1} \cdot \Omega \cdot O_g [g^{-1} u] g \mid \forall u \in T_g G \right\}. \tag{3.25}$$

Using the transitivity property of left and right translations on group manifolds, together with Ω being an automorphism (and thus bijective), there exists for every $u \in T_g G$ a Lie algebra element X such that,

$$u = -g O_{g^{-1}}^{-1} \Omega [X]. \tag{3.26}$$

Hence, $T_g N$ is equivalently given by,

$$\begin{aligned} T_g N &= \left\{ O_g^{-1} [X] g - g O_{g^{-1}}^{-1} \Omega [X] \mid \forall X \in \mathfrak{g} \right\} \\ &= \left\{ (\mathbf{1} + \lambda \Omega) [X] g - g (\lambda \mathbf{1} + \Omega) [X] \mid \forall X \in \mathfrak{g} \right\}. \end{aligned} \quad (3.27)$$

Contrary to the WZW case, we have here the extra property on the Lie algebra automorphism Ω that it is involutive, $\Omega^2 = 1$, and thus defines a symmetric space decomposition of the Lie algebra \mathfrak{g} :

$$\mathfrak{g} = \mathfrak{h} \oplus \mathfrak{k}, \quad (3.28)$$

where $\Omega[\mathfrak{h}] = \mathfrak{h}$, $\Omega[\mathfrak{k}] = -\mathfrak{k}$ and,

$$[\mathfrak{h}, \mathfrak{h}] \subset \mathfrak{h}, \quad [\mathfrak{h}, \mathfrak{k}] \subset \mathfrak{k}, \quad [\mathfrak{k}, \mathfrak{k}] \subset \mathfrak{h}. \quad (3.29)$$

Hence, also $T_g N$ splits accordingly,

$$T_g N = \left\{ (1 + \lambda) (Hg - gH) \mid \forall H \in \mathfrak{h} \right\} \oplus \left\{ (1 - \lambda) (Kg + gK) \mid \forall K \in \mathfrak{k} \right\}, \quad (3.30)$$

It is now possible to rescale $(1 + \lambda)H \rightarrow H$ and $(1 - \lambda)K \rightarrow K$ such that,

$$\begin{aligned} T_g N &= \left\{ Hg - gH \mid \forall H \in \mathfrak{h} \right\} \oplus \left\{ Kg + gK \mid \forall K \in \mathfrak{k} \right\} \\ &= \left\{ Xg - g\Omega[X] \mid \forall X \in \mathfrak{g} \right\}. \end{aligned} \quad (3.31)$$

As expected, this is exactly the tangent space to the twisted conjugacy class $C_\omega(g)$ defined by,¹⁰

$$C_\omega(g) = \left\{ h g \omega(h^{-1}) \mid \forall h \in G \right\}, \quad (3.32)$$

shown explicitly in [14, 15]. Hence, the worldvolumes N of the integrable D-brane configurations lie on twisted conjugacy classes $C_\omega(g)$ of the group G on which the deformation is based. In the λ -deformed background only the size of the branes (determined by the induced deformed metric) change, as also illustrated in the following section. The twisted conjugacy classes are classified by the quotient $\text{Out}_0(G) = \text{Aut}_0(G)/\text{Inn}_0(G)$ of metric-preserving outer automorphisms of G since two automorphisms that are related by an inner automorphism in $\text{Inn}_0(G)$ lead to twisted conjugacy classes that differ simply by a group translation [15]. However, the involution condition $\omega^2 = 1$ from integrability does not allow these group translation to be arbitrary and in practice there will only be a small number of them, depending on the dimensionality of G . When the group automorphism ω is taken to be the identity element of $\text{Out}_0(G)$, the twisted conjugacy classes reduce to regular conjugacy classes [12].

Note finally that, using Frobenius' integrability theorem and Ω being an automorphism, the D-brane N is a submanifold of G eliminating the possibility of intersecting integrable D-brane configurations [14, 15] using the methodology outlined in section 3.1.

¹⁰Recall the definition of the map $\omega : G \rightarrow G$ under eq. eq. (3.13).

4 Examples

In this section we will apply the above observations explicitly in two simple examples: the λ deformation based on the $SU(2)$ and $SL(2, \mathbb{R})$ Lie groups. In the compact $SU(2)$ case only regular conjugacy classes exist and we will derive the boundary equations explicitly for them (necessary for section 5). Moreover we will show that the flux quantisation condition remains independent of λ . We will perform a semi-classical analysis of the spectrum of quadratic fluctuations and demonstrate that turning on λ will lift the zero modes of the WZW branes. In the non-compact $SL(2, R)$ the study of both regular and twisted conjugacy classes is possible. Here we will focus on the classical aspects showing only the twisted conjugacy classes to be (classically) physical in contrary to the regular conjugacy classes. Moreover we find again the flux quantisation to remain independent of λ .

4.1 The S^3 deformation

For $\mathfrak{su}(2)$ the metric-preserving algebra automorphisms form the group of rotations $SO(3)$ while $Out_0(SU(2))$ is known to be trivial. The D-branes in the S^3 manifold therefore lie on regular conjugacy classes. In light of this we choose the following convenient parametrisation for the $SU(2)$ group element,

$$\begin{pmatrix} \cos \alpha + i \cos \beta \sin \alpha & e^{-i\gamma} \sin \alpha \sin \beta \\ -e^{i\gamma} \sin \alpha \sin \beta & \cos \alpha - i \cos \beta \sin \alpha \end{pmatrix}, \quad (4.1)$$

such that the S^3 is given by an S^2 parametrised by $\beta \in [0, \pi]$ and $\gamma \in [0, 2\pi]$ fibred over an interval $\alpha \in [0, \pi]$. Regular conjugacy classes are distinguished by $\text{Tr}(g) = 2 \cos \alpha$ constant and so correspond to this S^2 . Note that integrability only allows group translations from involutive inner automorphisms that correspond here to rotations over an angle π . For the WZW analysis of these D2-branes see we refer to [65, 67–69].

We first recall the target space geometry of the λ -deformed theory [36],

$$\begin{aligned} ds_\lambda^2 &= 2k \left(\frac{1+\lambda}{1-\lambda} d\alpha^2 + \frac{1-\lambda^2}{\Delta} \sin^2 \alpha (d\beta^2 + \sin^2 \beta d\gamma^2) \right), \\ H_\lambda &= 4k \frac{2\lambda\Delta + (1-\lambda^2)^2}{\Delta^2} \sin^2 \alpha \sin \beta d\alpha \wedge d\beta \wedge d\gamma, \\ e^{-2\Phi} &= e^{-2\Phi_0} \Delta, \end{aligned} \quad (4.2)$$

where $\Delta = 1 + \lambda^2 - 2\lambda \cos 2\alpha$. Here we note that in performing the Gaussian integration to arrive at the λ model a dilaton (2.13) is produced. In the metric observe that, and this will be important, that the deformation leaves the S^2 intact changing only the radius of this sphere as it is fibred over α .

The integrable boundary condition obtained from (3.21) with $\Omega = 1$ reads,

$$\begin{aligned} \partial_- \alpha| &= -\partial_+ \alpha|, \\ (1 + \lambda^2 - 2\lambda \cos 2\alpha) \partial_- \beta| &= (2\lambda - (1 + \lambda^2) \cos 2\alpha) \partial_+ \beta - (1 - \lambda^2) \sin \beta \sin 2\alpha \partial_+ \gamma|, \\ (1 + \lambda^2 - 2\lambda \cos 2\alpha) \partial_- \gamma| &= (2\lambda - (1 + \lambda^2) \cos 2\alpha) \partial_+ \gamma + (1 - \lambda^2) \csc \beta \sin 2\alpha \partial_+ \beta|. \end{aligned} \quad (4.3)$$

It is immediately clear that α obeys a Dirichlet boundary condition and $X^a = \{\beta, \gamma\}$ obey (generalised) Neumann boundary conditions (A.4) which should take the standard form,

$$\widehat{G}_{ab}(X)\partial_\sigma X^b = \mathcal{F}_{ab}\partial_\tau X^b, \tag{4.4}$$

in which $\mathcal{F}_{ab} = \widehat{B}_{ab} + 4\pi F_{ab}$ ¹¹ (see also appendix A). We first re-express the Neumann boundary condition as,

$$\partial_\sigma \beta| = -\frac{\lambda-1}{\lambda+1} \cot \alpha \sin \beta \partial_\tau \gamma|, \quad \partial_\sigma \gamma| = \frac{\lambda-1}{\lambda+1} \cot \alpha \csc \beta \partial_\tau \beta|, \tag{4.5}$$

and making use of the metric restricted to $\alpha = \text{const}$ we extract the two-form,

$$\mathcal{F} = \frac{k}{2\Delta}(1-\lambda)^2 \sin 2\alpha \sin \beta d\beta \wedge d\gamma. \tag{4.6}$$

We can now evaluate the DBI action (A.10),

$$S_{\text{DBI}} = T_2 \int e^{-\Phi} \sqrt{\widehat{G} + \mathcal{F}} = 4\pi k T_2 e^{-\Phi_0} \sin \alpha. \tag{4.7}$$

where we absorbed a factor of $1-\lambda$ into the constant dilaton $e^{-\Phi_0}$. Naively this would suggest that the only stable D-branes are the ones for which this quantity is minimised i.e. the D0 branes located at $\alpha = 0$ and $\alpha = \pi$. However the flux quantisation stabilises the branes in other locations in a slightly subtle way. There are two well defined forms at play; the NS three form H and a two-form on the D-brane submanifold ω which is, by virtue of the construction, equal to the two-form \mathcal{F} locally. The quantisation is now a statement that the relative cohomology class $[(H, \omega)]/2\pi$ be integral [51, 70–72] demanded by consistency for the definition of the WZ term in the action (2.5) (see also appendix B). Put plainly, the difference in periods of ω over the D2-brane worldvolume N and H on an extension B whose boundary is the D2-brane $\partial B = N$ should be integral i.e.

$$\frac{1}{4\pi} \int_N \omega - \frac{1}{4\pi} \int_B H \in 2\pi \mathbb{Z}. \tag{4.8}$$

For the case at hand, let us locate the D2 brane at $\alpha = \alpha_*$ and integrate H over an extension $\alpha \in [0, \alpha_*]$. This yields

$$\frac{1}{4\pi} \int_B H = -2k\alpha_* + \frac{k(1-\lambda)^2 \sin 2\alpha_*}{\Delta_*}. \tag{4.9}$$

At the same time we have

$$\frac{1}{4\pi} \int_N \omega = \frac{k(1-\lambda)^2 \sin 2\alpha_*}{\Delta_*}, \tag{4.10}$$

so that in the combination entering the quantisation condition eq. (4.8) all dependence on the deformation parameter λ drops out and one recovers the conventional result for the WZW model; there are, in addition to the D0-branes, stabilised D2's located at¹²

$$\alpha_* = \frac{n\pi}{k}, \quad n = 1 \dots k-1. \tag{4.11}$$

¹¹For the level k to obey the conventional quantisation we have used units in which $\alpha' = 2$.

¹²We are assuming throughout that we are in the semi-classical regime and so ignore any consequences of the shift $k \rightarrow k+2$ [1].

Let us now evaluate the dynamics of fluctuations of this D-brane. For that we need to consider dependence on the target space time coordinate; i.e. we need to introduce an extra time-like dimension to the target space. We will choose a synchronous gauge and let the coordinates of the worldvolume of the D2 be $X^a = (t, \beta, \gamma)$. Following [65] we examine fluctuations of the transverse scalar and worldvolume gauge field in the DBI action,

$$S = T_2 \int e^{-\Phi} \sqrt{-\det(\widehat{G}_{ab} + \mathcal{F}_{ab})}, \tag{4.12}$$

where,

$$\mathcal{F}_{ab} = B_{ab} + 2\pi\alpha'(\partial_a A_b - \partial_b A_a). \tag{4.13}$$

For direct comparison to [65] we reinstate explicit factors of α' . It should be emphasised that the metric \widehat{G} needs to be pulled back to the worldvolume according to,

$$\widehat{G}_{ab} = G_{\mu\nu} \partial_a X^\mu \partial_b X^\nu, \tag{4.14}$$

which induces derivatives for fluctuations in the transverse scalar. To perform this analysis it is helpful to pick a gauge for the antisymmetric field [36],

$$B = -k\alpha' \left(\alpha - \frac{(1-\lambda)^2}{\Delta} \cos \alpha \sin \alpha \right) \sin \beta d\beta \wedge d\gamma. \tag{4.15}$$

Then we make the ansatz for fluctuations,

$$\alpha = \alpha_* + \delta(X), \quad A_t = 0, \quad A_\beta = \frac{k}{2\pi} a_\beta(X), \quad A_\gamma = \frac{k}{2\pi} \alpha_* (\cos \beta - 1) + \frac{k}{2\pi} a_\gamma(X). \tag{4.16}$$

Now the procedure is to expand the DBI action to quadratic order in the fluctuation and to extract classical equations of motion.¹³ The intermediate steps of this calculation are extremely unedifying and made algebraically complicated by the appearance of the function $\Delta(\alpha)$ in various places. However, somewhat remarkably to a large extent all of the complications cancel out to leave a very simple result. In terms of the covariant fluctuation $g(t, \beta, \gamma) = -\frac{1}{\sin \beta} (\partial_\beta \alpha_\gamma - \partial_\gamma \alpha_\beta)$ we find equations of motion,

$$\frac{d^2}{dt^2} \begin{pmatrix} \delta \\ g \end{pmatrix} = -\frac{1}{k\alpha'} \frac{1+\lambda^2}{1-\lambda^2} \begin{pmatrix} 2 + \frac{(1+\lambda)^2}{1+\lambda^2} \square & 2 \\ 2\square & \frac{(1+\lambda)^2}{1+\lambda^2} \square \end{pmatrix} \begin{pmatrix} \delta \\ g \end{pmatrix}, \tag{4.17}$$

in which \square is the Laplacian on the S^2 . This operator can be diagonalised in terms of an expansion in spherical harmonics. In the l^{th} sector (i.e. where $\square = l(l+1)$) we find that the eigenvalues are,

$$\frac{1}{k(1-\lambda^2)} (1+l) ((1+\lambda)^2 l + 2(1+\lambda^2)), \quad \frac{1}{k(1-\lambda^2)} l (l(1+\lambda)^2 - (1-\lambda)^2). \tag{4.18}$$

These are all positive, hence stable fluctuations of positive mass. Since g carries no s -wave as a consequence of flux-quantisation and that the s -wave of δ has a frequency squared of

¹³As in [65] in the expansion there is a linear term proportional to the fluctuation of the quantised D0 charge which must necessarily vanish and so we neglect it in what follows.

$\frac{2}{k\alpha} \frac{1+\lambda^2}{1-\lambda^2}$ — it is not a moduli. It is interesting to notice that the p -wave triplet (i.e. $l = 1$) acquires a positive mass for $\lambda \neq 0$; this lifting of zero modes is a reflection of the fact that one of the $SU(2)$ symmetries is broken in the target space metric and so we are not longer free to move the S^2 of the D-brane about the S^3 . Put another way, in the undeformed theory these zero modes on the worldvolume are associated Goldstone modes from breaking the $SU(2)$ global symmetry of the target space by the D-brane; in the deformed theory there is no longer such an $SU(2)$ symmetry to be broken and hence no corresponding Goldstone. A further feature of the spectrum is that it inherits a \mathbb{Z}_2 invariance $\lambda \rightarrow \lambda^{-1}$, $k \rightarrow -k$ displayed by the λ -deformed worldsheet theory [66].

4.2 The AdS_3 deformation

For the $\mathfrak{sl}(2, \mathbb{R})$ algebra it can be shown that the metric-preserving automorphisms form the group $SO(1, 2) = SO(1, 2)^+ \cup SO(1, 2)^-$ where $SO(1, 2)^+$ correspond to the usual rotations and boosts, while $SO(1, 2)^-$ transformations are obtained from an additional reflection and time-reversal. The metric-preserving outer automorphism group $Out_0(SL(2, \mathbb{R}))$ descends from the latter and can be shown to have, besides the identity, one non-trivial element given in convenient representation by the conjugation $\omega(g) = \omega_1 g \omega_1^{-1}$ with

$$\omega_1 = \begin{pmatrix} 1 & 0 \\ 0 & -1 \end{pmatrix} \notin SL(2, \mathbb{R}). \tag{4.19}$$

The corresponding Lie algebra automorphism Ω defined by $\Omega[T_A] = \Omega^B{}_A T_B = \omega_1 T_A \omega_1^{-1}$ is readily shown to be an involution and therefore defining with (3.21) consistent integrable boundary conditions. Note that we might as well represent the non-trivial $Out_0(SL(2, \mathbb{R}))$ element by a conjugation with,

$$\omega_2 = \begin{pmatrix} 0 & 1 \\ 1 & 0 \end{pmatrix} \notin SL(2, \mathbb{R}), \tag{4.20}$$

which is connected to ω_1 with an involutive inner automorphism that corresponds in $SO(1, 2)$ with a rotation over π . Moreover, it is important to emphasise that this inner automorphism is the only allowed group translation leading to integrable D-brane configurations in AdS_3 . We are thus allowed to make two distinguished cases in the analysis of D-branes in the λ -deformed AdS_3 corresponding to regular and twisted conjugacy classes.

First, let us parametrise the $SL(2, \mathbb{R})$ in a general way as,

$$g = \begin{pmatrix} X_0 + X_1 & X_2 + X_3 \\ X_2 - X_3 & X_0 - X_1 \end{pmatrix} \tag{4.21}$$

with X_i , $i = \{0, 1, 2, 3\}$, real and with the defining relation $-X_0^2 + X_1^2 + X_2^2 - X_3^2 = -1$, making apparent the AdS_3 embedding.

The regular conjugacy classes (obtained by taking ω the identity) are distinguished by $Tr(g) = 2X_0$ constant and substituting this into the defining relation one finds the geometry of the corresponding D-branes (see also [68, 69, 73]). The geometry will depend

on the values of X_0 ; for $X_0 > 1$ the conjugacy classes correspond to de Sitter D1-strings, for $X_0 < 1$ they correspond to H_2 instantons and for $X_0 = 1$ to the future- and past light-cone. In the next, we will consider only the former de Sitter D1-strings since the study of instantons is beyond the goal of this paper and for the latter case the metric will be degenerate. However, as shown by [73], the de Sitter WZW-branes are tachyonic and, as we will shortly touch upon, they will stay so when turning on the deformation.

The twisted conjugacy classes (3.32) are obtained by conjugation with ω_1 ,

$$C_\omega(g) = \{h g \omega_1 h^{-1} \mid \forall h \in G\} \omega_1^{-1}, \tag{4.22}$$

and are thus distinguished by $\text{Tr}(g \omega_1) = 2X_1$ constant. The corresponding D-brane configurations are, for any $X_1 \in \mathbb{R}$, two-dimensional Anti de Sitter D1-strings (see also [73]). Equivalently, when conjugating with ω_2 , twisted conjugacy classes will be distinguished by $\text{Tr}(g \omega_2) = 2X_2$ constant corresponding again to AdS D1-strings. The choice of representation depends on how one wants to analyse these D-brane configurations together with the choice of parametrisation of the $\text{SL}(2, \mathbb{R})$ group element. In both cases, however, one sees from the defining AdS₃ relation that the *integrable* AdS₂ branes are static configurations. In the WZW case, these D-branes configurations are shown to be physical in [73].

dS D1-strings. A convenient parametrisation to describe the dS D1-strings is one where we replace in (4.21) the elements by,

$$X_0 = \cosh \psi, \quad X_3 = \sinh \psi \sinh \tau, \quad X_1 + iX_2 = \sinh \psi \cosh \tau e^{i\phi} \tag{4.23}$$

with $\psi \in [0, \infty[$, $\tau \in]-\infty, \infty[$ and $\phi \in [0, 2\pi]$ (although, they are not good global coordinates). Here the AdS₃ is build up out of fixed ψ -slices of dS₂ spacetimes parametrised by τ and ϕ corresponding to the dS D1-strings. Note that in this coordinate system we describe D1-strings that are static configurations in AdS₃.

The target space geometry of the λ -deformed AdS₃ is,

$$\begin{aligned} ds_\lambda^2 &= 2k \left(\frac{1+\lambda}{1-\lambda} d\psi^2 + \frac{1-\lambda^2}{\widehat{\Delta}} \sinh^2 \psi (-dt^2 + \cosh^2 t d\phi^2) \right) \\ H_\lambda &= 4k \frac{2\lambda \widehat{\Delta} + (1-\lambda^2)^2}{\widehat{\Delta}^2} \sinh^2 \psi \cosh \tau d\psi \wedge d\tau \wedge d\phi \\ e^{-2\Phi} &= e^{-2\Phi_0} \widehat{\Delta} \end{aligned} \tag{4.24}$$

with $\widehat{\Delta} = 1 + \lambda^2 - 2\lambda \cosh 2\psi$. In these coordinates it is obvious that the deformation leaves the dS₂ D1-strings intact but changing the radius with a squashing factor $\frac{1-\lambda^2}{\widehat{\Delta}}$.

Comparing the integrable boundary conditions obtained from (3.21) with $\Omega = 1$ with the boundary conditions from the sigma model approach, i.e. Dirichlet (A.3) and (generalised) Neumann (A.4), one can extract the two-form \mathcal{F} on the dS D1-brane to find,

$$\mathcal{F} = k \frac{(1-\lambda)^2}{\widehat{\Delta}} \sinh 2\psi \cosh \tau d\tau \wedge d\phi. \tag{4.25}$$

See also [12, 70, 71] for a general formula in terms of the gluing matrix. The induced metric \widehat{G} on the D1-brane is obtained simply by enforcing $\psi = \text{constant}$ in eq. (4.24). The DBI action now evaluates to (absorbing a factor $1 - \lambda$ into the constant dilaton),

$$S_{\text{DBI}} = T_1 \int e^{-\Phi} \sqrt{-\det(\widehat{G}_{ab} + \mathcal{F}_{ab})} = 4\pi k T_1 e^{-\Phi_0} \int d\tau \sqrt{-\sinh^2 \psi \cosh^2 \tau} \quad (4.26)$$

and, hence, is supercritical.

One could equally perform this analysis in the global cylindrical coordinates along the lines of [73] to describe dynamical configurations of a circular D1-string and argue that these are unphysical trajectories. We expect however no new information to be gained.

Anti de Sitter D1-strings. At first sight a logical coordinate system to describe the AdS D1-strings seems to be the global AdS coordinates where the elements of (4.21) are replaced by,

$$X_0 + iX_3 = \cosh \psi \cosh \omega e^{i\tau}, \quad X_1 = \sinh \psi, \quad X_2 = \cosh \psi \sinh \omega \quad (4.27)$$

with $\{\psi, \tau, \omega\} \in \mathbb{R}^3$. The twisted conjugacy class (4.22) (obtained by conjugation with ω_1 of eq. (4.19)) lie along fixed ψ -slices which correspond to AdS₂ spacetimes parametrised by τ and ω .

In this coordinate system the target space geometry of the λ -deformed theory is,

$$\begin{aligned} ds_\lambda^2 = & 2k \frac{1 + \lambda}{1 - \lambda} \left(\frac{\widetilde{\Delta} + 4\lambda(\cos^2 \tau \cosh^2 \omega - 1)}{\widetilde{\Delta}} d\psi^2 + 2\lambda \frac{\sin 2\tau \cosh^2 \omega \sinh 2\psi}{\widetilde{\Delta}} d\psi d\tau \right. \\ & - 2\lambda \frac{\cos^2 \tau \sinh 2\omega \sinh 2\psi}{\widetilde{\Delta}} d\psi d\omega + \cosh^2 \psi \left(-\frac{(1 + \lambda)^2 - 4\lambda \cos^2 \tau}{\widetilde{\Delta}} \cosh^2 \omega d\tau^2 \right. \\ & \left. \left. + 2\lambda \frac{\sin 2\tau \sinh 2\omega}{\widetilde{\Delta}} d\tau d\omega + \frac{(1 - \lambda)^2 - 4\lambda \cos^2 \tau \sinh^2 \omega}{\widetilde{\Delta}} d\omega^2 \right) \right) \\ H_\lambda = & 4k \frac{2\lambda \widetilde{\Delta} + (1 - \lambda^2)^2}{\widetilde{\Delta}} \cosh^2 \psi \cosh \omega d\psi \wedge d\tau \wedge d\omega \\ e^{-2\Phi} = & e^{-2\Phi_0} \widetilde{\Delta} \end{aligned} \quad (4.28)$$

with $\widetilde{\Delta} = (1 + \lambda^2) - 4\lambda \cos^2 \tau \cosh^2 \omega \cosh^2 \psi$. One can readily verify that in the WZW $\lambda \rightarrow 0$ limit the metric reduces to the obvious slicing of AdS₃ by AdS₂ spacetimes along ψ . However, when turning on the deformation this slicing becomes obscure and one can not read of a “squashing” factor of the AdS D1-strings in contrary to the dS case of above. An explicit analysis of the integrable boundary conditions (3.21) with the conjugation by ω_1 teaches us however that it is indeed the ψ direction that is Dirichlet. The induced metric \widehat{G} on the brane is thus obtained by enforcing ψ constant in (4.28). Comparing again the integrable boundary conditions to the ones obtained from the general sigma model, we can extract the gauge invariant two-form \mathcal{F} on the AdS D1-string,

$$\mathcal{F} = k \frac{(1 + \lambda)^2}{\widetilde{\Delta}} \sinh 2\psi \cosh \omega d\tau \wedge d\omega. \quad (4.29)$$

The DBI action simply gives,

$$S_{\text{DBI}} = T_1 \int e^{-\Phi} \sqrt{-\det(\widehat{G}_{ab} + \mathcal{F}_{ab})} = 2k T_1 e^{-\Phi_0} \int d\tau d\omega \cosh \psi \cosh \omega, \quad (4.30)$$

where we absorbed a factor of $1 + \lambda$ into the constant $e^{-\Phi_0}$. The action is readily minimised when $\psi_0 = 0$ where the D1-string is still of finite size. However, when making appropriate gauge choices for the induced antisymmetric field \widehat{B} and the U(1) field strength F , in particular one where $A_\tau = 0$, one can identify the usual quantisation condition from the Gauss constraint of QED₂ (following [73]) given by,

$$4\pi T_1 e^{-\Phi_0} \frac{\widetilde{\Delta} \mathcal{F}_{\tau\omega}}{\sqrt{-\widetilde{\Delta} \det(\widehat{G}_{ab} + \mathcal{F}_{ab})}} = 4\pi T_1 e^{-\Phi_0} \sinh \psi = q \in \mathbb{Z} \quad (4.31)$$

with the integer q known to be the number of fundamental strings bound to the D1-string [74]. Similar to the SU(2) example we thus have again, due to a flux quantisation condition, additional locations where the D1-strings are stabilised, independent of the value of λ . However, contrary to the SU(2) case, this does not descend from topological conditions of the boundary WZW (see also appendix B) as AdS₃ is topologically trivial.

One could instead also consider the twisted conjugacy class obtained from conjugation by ω_2 of eq. (4.20). The corresponding worldvolume is then characterised by $X_2 = \cosh \psi \sinh \omega$ constant and is obtained from the previous fixed ψ -slices by a rotation over π in the spatial directions. The analysis of these worldvolumes are easily done in the Poincaré coordinates $(t, x, u) \in \mathbb{R}^3$ that are obtained by,

$$X_0 + X_1 = u, \quad X_0 - X_1 = \left(\frac{1}{u} + u(x+t)(x-t) \right), \quad X_2 \pm X_3 = u(x \pm t). \quad (4.32)$$

Eliminating then the coordinate u by $ux = C$ with C a constant one can identify the gauge-invariant two-form \mathcal{F} to be,

$$\mathcal{F} = 2k \frac{(1 + \lambda)^2}{\Delta_P} \frac{C^2}{x^2} dt \wedge dx, \quad (4.33)$$

with the dilaton factor Δ_P in Poincaré coordinates. The Gauss constraint similarly quantises the constant C as,

$$4\pi T_1 e^{-\Phi_0} C = q \in \mathbb{Z}, \quad (4.34)$$

where again a factor of $1 + \lambda$ was absorbed in the constant $e^{-\Phi_0}$.

We conclude that from a classical point of view the AdS D1-strings in the λ background are still physical. Moreover they are stabilised in the same manner as in the WZW case, i.e. due to flux quantisation. Semi-classically it would be interesting to perform a stability analysis of the quadratic fluctuations as was done for SU(2) in section 4.1. In the λ case we expect the same stability conclusion as the WZW case (see e.g. [75, 76]) accompanied with a lifting of zero modes. However, we will not pursue this interesting point here.

5 Relation to generalised T-dualities

5.1 The non-Abelian T-dual limit

In a scaling limit $\lambda \rightarrow 1$ the λ -deformation recovers the non-Abelian T-dual of the principal chiral model [36]. To achieve this limit one expands the group element around the identity,

$$g = \mathbf{1} + \frac{i}{k} v^A T_A + \mathcal{O}\left(\frac{1}{k^2}\right), \quad (5.1)$$

and takes $k \rightarrow \infty$ to find,

$$L_-^A = -\frac{\partial_- v^A}{k} + \mathcal{O}\left(\frac{1}{k^2}\right), \quad R_+^A = -\frac{\partial_+ v^A}{k} + \mathcal{O}\left(\frac{1}{k^2}\right), \quad D_{AB} = \eta_{AB} + \frac{F_{AB}{}^C v_C}{k}. \quad (5.2)$$

In this limit the λ -deformed action (2.9) becomes the non-Abelian T-dual with respect to the G_L action of the PCM (2.1),

$$S = \frac{1}{\pi} \int \partial_+ v_A (\mathcal{M}^{-1})^{AB} \partial_- v_B + \mathcal{O}\left(\frac{1}{k}\right), \quad \text{with } \mathcal{M} = \kappa^2 \eta_{AB} + F_{AB}{}^C v_C. \quad (5.3)$$

For the case of SU(2) in the parametrisation used in eq. (4.1) this limit is achieved by taking $\alpha = \frac{r}{2k}$ with

$$v_1 = -\frac{r}{\sqrt{2}} \sin \beta \sin \gamma, \quad v_2 = \frac{r}{\sqrt{2}} \sin \beta \cos \gamma, \quad v_3 = \frac{r}{\sqrt{2}} \cos \beta. \quad (5.4)$$

The metric becomes

$$ds_{NAIT}^2 = \frac{1}{\kappa^2} \left(dr^2 + \frac{r^2 \kappa^4}{r^2 + \kappa^4} ds^2(S^2) \right). \quad (5.5)$$

where $ds^2(S^2) = d\beta^2 + \sin^2 \beta d\gamma^2$. The first point to note is that in the limit the two-sphere remains intact so one anticipates that the D-branes described previously are preserved. Performing the $\lambda \rightarrow 1$ limit procedure on the boundary conditions of eq. (4.3) yields,

$$\begin{aligned} \partial_- r| &= -\partial_+ r|, \\ (r^2 + \kappa^4) \partial_- \beta| &= (r^2 - \kappa^4) \partial_+ \beta - 2r\kappa^2 \sin \beta \partial_+ \gamma| \\ (r^2 + \kappa^4) \partial_- \gamma| &= 2r\kappa^2 \csc \beta \partial_+ \beta + (r^2 - \kappa^4) \partial_+ \gamma|. \end{aligned} \quad (5.6)$$

To understand these conditions it is useful to work instead with the following combination of worldsheet derivatives

$$\mathring{L}_+ = -\mathcal{M}^{-T} \partial_+ v, \quad \mathring{L}_- = +\mathcal{M}^{-1} \partial_- v, \quad (5.7)$$

which can be used to construct a Lax connection for the dynamics of the non-Abelian T-dual theory eq. (5.3):

$$\mathring{L}_\pm[z] = \frac{1}{1 \mp z} \mathring{L}_\pm, \quad [\partial_+ + \mathring{L}_+, \partial_- + \mathring{L}_-] = 0. \quad (5.8)$$

In terms of these the boundary conditions of eq. (5.6) take a remarkably simple form

$$\mathring{L}_+| = \mathring{L}_-|. \quad (5.9)$$

This property of the boundary conditions holds in general, at least in the case where we set the extra automorphism $\Omega = 1$, and follows due to the limit

$$\frac{1}{k + \kappa^2} O_g \rightarrow \mathcal{M}^{-T}, \tag{5.10}$$

from eq. (3.21).

Now for the punchline. The non-Abelian T-dual theory described by eq. (5.3) is classically equivalent to the principal chiral theory

$$S_{\text{PCM}} = -\frac{\kappa^2}{\pi} \int d\sigma d\tau \langle \tilde{g}^{-1} \partial_+ \tilde{g} \tilde{g}^{-1} \partial_- \tilde{g} \rangle. \tag{5.11}$$

The T-duality transformation rules are non-local in terms of the coordinates of the sigma-models but in terms of world sheet derivatives are a canonical transformation of the form

$$\tilde{L}_\pm^a = \dot{L}_\pm, \quad \tilde{g}^{-1} \partial_\pm \tilde{g} = -i \tilde{L}_\pm^a T_a. \tag{5.12}$$

Thus we can immediately conclude that under non-Abelian T-duality the D2-brane described by the boundary condition (5.6) results in

$$\tilde{g}^{-1} \partial_\sigma \tilde{g} | = 0, \tag{5.13}$$

i.e. a space-filling D3-brane.

This analysis agrees exactly with the integrable boundary conditions that we would obtain for the principal chiral model by substituting the Lax (5.8) into the result (3.18) (note that this holds as the Lax (5.8) satisfies eq. (3.15)) which leads to the boundary conditions,

$$\dot{L}_\pm | = \Omega(\dot{L}_\mp) | = \Omega \cdot D^T(\dot{R}_\mp) |. \tag{5.14}$$

Interestingly, these have the form of type N gluing conditions. In the context of the WZW, these type N gluings eq. (B.9) preserve conformal invariance but break the chiral-algebra (and for which a good understanding is still lacking to our knowledge). It would be interesting to relate these observations to the recently appeared [56].

5.2 The pseudo-dual limit

A second interesting limit described in [77] is a scaling limit as $\lambda \rightarrow -1$ which results in the pseudo-dual [78] of the principal chiral model. The pseudo-dual theory is obtained by replacing the currents of the PCM with scalars according to

$$\tilde{g}^{-1} \partial^\mu \tilde{g} = \epsilon^{\mu\nu} \partial_\nu \phi, \tag{5.15}$$

such that the conservation of the currents becomes a trivial consequence of the commutation of partial derivatives. The Bianchi identities and equations of motion written in terms of ϕ can be obtained from a “dual” action. However this is not a true dualisation [78] — even at the classical level the two theories are not related by a canonical transformation and at the quantum level they have striking differences. The PCM is asymptotically free where as the pseudo-dual is not. The PCM is quantum integrable whereas the pseudo-dual displays

particle production. Nonetheless it is intriguing that the pseudo-dual action follows from the λ -theory upon the scaling

$$\lambda = -1 + \frac{\kappa^2}{k^{\frac{1}{3}}}, \quad g = \mathbf{1} + \frac{i}{k^{\frac{1}{3}}} \phi^A T_A + \dots, \quad k \rightarrow \infty. \quad (5.16)$$

Evidently in taking this limit one needs to relax the requirement that $\lambda \in [0, 1]$ required of the original construction of the λ -model.

Let us see the effect of this on the boundary conditions in the context of the SU(2) theory. The scaling is quite similar; we define $\alpha = \frac{r}{2k^{\frac{1}{3}}}$ and

$$\phi^1 = -\frac{r}{\sqrt{2}} \sin \beta \sin \gamma, \quad \phi^2 = \frac{r}{\sqrt{2}} \sin \beta \cos \gamma, \quad \phi^3 = \frac{r}{\sqrt{2}} \cos \beta. \quad (5.17)$$

The limit $k \rightarrow \infty$ can then be taken in the boundary conditions of eq. (4.3) resulting simply in

$$\partial_\tau \phi^i| = 0. \quad (5.18)$$

In terms of the PCM variables we recover, as with the non-Abelian T limit, a D3-brane described by

$$\tilde{g}^{-1} \partial_\sigma \tilde{g}| = 0. \quad (5.19)$$

5.3 Poisson-Lie dual interpretation

The λ -deformed theory is closely connected to a class of integrable deformations of the principal chiral model known as η -deformation (also known as Yang-Baxter deformations) [79, 80]. To establish the relation between the λ and η theories one first performs an analytic continuation of the coordinates parameterising the λ -theory and also of the deformation parameter itself. Performing this analytic continuation in the λ -deformed action of (2.9) results in a new (real) sigma-model that is the Poisson-Lie T-dual to the η -deformation [59–62]. Our goal here is to track this connection through with the boundary conditions considered here. To make this rather technical procedure accessible we first introduce the rudiments of Poisson-Lie technology.

Poisson-Lie T-duality [47, 48] is a generalised notion of T-duality between a pair of σ -models on group manifolds \widehat{G} and \check{G} (with corresponding algebras $\widehat{\mathfrak{g}}$ and $\check{\mathfrak{g}}$) that do not enjoy isometries but instead possess a set of currents that are non-commutatively conserved with respect to the dual algebra $\check{\mathfrak{g}}$ ($\widehat{\mathfrak{g}}$). For this construction to be consistent $\mathfrak{d} = \widehat{\mathfrak{g}} \oplus \check{\mathfrak{g}}$ must define a Drinfeld double [81]. The two Poisson-Lie dual sigma-models defined in this way are of the form,

$$\begin{aligned} \widehat{S}[\widehat{g}] &= \frac{1}{t\eta} \int d^2\sigma \widehat{L}_+^T (E_0^{-1} - \widehat{\Pi})^{-1} \widehat{L}_-, \\ \check{S}[\check{g}] &= \frac{1}{t\eta} \int d^2\sigma \check{L}_+^T (E_0 - \check{\Pi})^{-1} \check{L}_-, \end{aligned} \quad (5.20)$$

in which $\widehat{L}_\pm(\check{L}_\pm)$ are pullbacks of left-invariant one-forms for $\widehat{G}(\check{G})$, E_0 is a constant matrix of freely chosen moduli, and $\widehat{\Pi}(\check{\Pi})$ is a matrix formed by the combination of the adjoint action of $\widehat{G}(\check{G})$ on itself and $\check{G}(\widehat{G})$ according to,

$$\widehat{g}^{-1} \widehat{T}_a \widehat{g} = a_a{}^b \widehat{T}_b, \quad \widehat{g}^{-1} \check{T}^b \widehat{g} = b^{ab} T_b + (a^{-1})_b{}^a \check{T}^b, \quad \widehat{\Pi}^{ab} = b^{ca} a_c{}^b, \quad (5.21)$$

where \widehat{T}_a and \check{T}^a resp. are the generators of $\widehat{\mathfrak{g}}$ and $\check{\mathfrak{g}}$ resp. The overall tension of the sigma-models has been introduced for later convenience. What will be useful in our consideration is that the two PL models are canonically equivalent [82, 83] with the canonical transformation defined by,

$$\widehat{P} = -\check{\Pi}\check{P} + \frac{t\eta}{2}\check{L}_\sigma, \quad \check{P} = -\widehat{\Pi}\widehat{P} + \frac{t\eta}{2}\widehat{L}_\sigma, \quad (5.22)$$

in which, if we let X^μ be local coordinates on \widehat{G} , we define the momentum $\widehat{P}_a = \widehat{L}_a^\mu \frac{\delta S}{\delta \dot{X}^\mu}$.¹⁴

In the context of the λ - η connection the relevant Drinfeld double is $\mathfrak{d} = \mathfrak{g}^{\mathbb{C}}$ and $\check{\mathfrak{g}}$ is identified with a Borel sub-algebra coming from the Iwasawa decomposition $\mathfrak{g}^{\mathbb{C}} = \mathfrak{g} + \mathfrak{a} + \mathfrak{n}$. The action \check{S} is defined on the group manifold $\check{G} \cong AN$ and is the one obtained by analytic continuation of the λ -deformation. The dual action, i.e. the first of eq. (5.20), is defined on the group manifold \widehat{G} and can be recast as,

$$\widehat{S} = \frac{1}{t} \int d^2\sigma \widehat{R}_+^T (\mathbf{1} - \eta \mathcal{R})^{-1} \widehat{R}_-, \quad (5.23)$$

in which \widehat{R}_\pm are right-invariant one forms (pulled back) and \mathcal{R} solves the modified classical Yang-Baxter equation. For the isotropic single parameter deformations considered here $E_0^{-1} = \frac{1}{\eta} \mathbf{1} + \mathcal{R}$. This is the integrable η -deformation [79, 80].

For didactic purpose we consider the case of the $SU(2)$ λ -deformation. In the parametrisation used in eq. (4.1) this analytic continuation amounts to a mapping between coordinates $(\alpha, \beta, \gamma) \rightarrow (y_1, y_2, \chi)$ and parameters $(k, \lambda) \rightarrow (t, \eta)$ given by,

$$y_1 + iy_2 = i \sin \alpha \sin \beta e^{i\gamma}, \quad e^\chi = \cos \alpha + i \sin \alpha \cos \beta, \quad k = \frac{i}{4t\eta}, \quad \lambda = \frac{i - \eta}{i + \eta}. \quad (5.24)$$

In this case the $\widehat{\mathfrak{g}} = \mathfrak{su}(2)$ and $\check{\mathfrak{g}} = \mathfrak{e}_3$ (Bianchi II) and we will work with group elements parametrised by,

$$\check{g} = \begin{pmatrix} e^{\frac{\chi}{2}} & e^{-\frac{\chi}{2}}(y_1 - iy_2) \\ 0 & e^{-\frac{\chi}{2}} \end{pmatrix}, \quad \widehat{g} = \begin{pmatrix} e^{\frac{1}{2}i(\phi+\psi)} \cos\left(\frac{\theta}{2}\right) & e^{\frac{1}{2}i(\phi-\psi)} \sin\left(\frac{\theta}{2}\right) \\ -e^{-\frac{1}{2}i(\phi-\psi)} \sin\left(\frac{\theta}{2}\right) & e^{-\frac{1}{2}i(\phi+\psi)} \cos\left(\frac{\theta}{2}\right) \end{pmatrix}. \quad (5.25)$$

Applying the analytic continuation eq. (5.24) to the boundary conditions eq. (4.3) yields a result that is real (as required to be a consistent boundary condition) and rather elegant when written in terms of the momentum \check{P} :

$$\begin{aligned} \check{P}_1| &= \frac{4}{t\eta} \frac{e^{2\chi}}{1 + e^{2\chi} + r^2} \check{L}_{2\sigma}|, \\ \check{P}_2| &= -\frac{4}{t\eta} \frac{e^{2\chi}}{1 + e^{2\chi} + r^2} \check{L}_{1\sigma}|, \\ \check{P}_3| &= 0. \end{aligned} \quad (5.26)$$

Notice that in these conditions all the complicated dependence on the deformation parameter η (notwithstanding the factors of $t\eta$) is subsumed into the momenta \check{P} . In this form

¹⁴We adapt the results of the [36] to our conventions and restore the overall normalisation of the sigma models.

we can now immediately apply the canonical transformation of eq. (5.22) to deduce the corresponding boundary condition for the η -deformed theory. Actually something rather special happens; the canonical transformation eq. (5.22) depends explicitly not only on the momenta \check{P}, \hat{P} and the left-invariant forms $\check{L}_\sigma, \hat{L}_\sigma$ but also on all the coordinates through the matrices $\check{\Pi}$ and $\hat{\Pi}$ in a rather complicated fashion. It is then by no means guaranteed that when the canonical transformation is applied to the boundary conditions of eq. (5.26) that what results will depend only on the coordinates (θ, ϕ, ψ) that parametrise \hat{G} . Reassuringly, however, this does indeed transpire to be the case!

We are now in a position to present the boundary conditions of the η -deformed principal chiral model obtained in this fashion. In terms of the coordinates themselves the boundary condition takes a rather simple form,

$$\begin{aligned} \partial_\sigma \psi + \sec \theta \partial_\sigma \phi &= 0, \\ \eta \partial_\tau \theta + \tan \theta \partial_\sigma \phi &= 0, \\ \eta \partial_\tau \psi - \sec \theta \partial_\sigma \theta &= 0. \end{aligned} \tag{5.27}$$

For reference the geometry corresponding to the η -deformed theory reads

$$\begin{aligned} ds^2 &= \frac{1}{t} \left((d\phi + \cos \theta d\psi)^2 + \frac{1}{1 + \eta^2} (d\theta^2 + \sin^2 \theta d\psi^2) \right), \\ B &= \frac{\eta}{t(1 + \eta^2)} \sin \theta d\theta \wedge d\psi, \quad H = dB = 0. \end{aligned} \tag{5.28}$$

Since all the coordinates enjoy (generalised) Neumann boundary condition we are describing here a space-filling brane supported by a worldvolume two-form $\mathcal{F} = B + 2\pi\alpha' F$. Making use of the above metric we can readily extract this two-form,

$$\mathcal{F} = \frac{\eta}{t(1 + \eta^2)} \sin \theta d\theta \wedge d\psi, \tag{5.29}$$

showing that $F = dA = 0$.

It is also illuminating to express the results in terms of right invariant forms,

$$\hat{R}^1 = -\cos \phi \sin \theta d\psi + \sin \phi d\theta, \quad \hat{R}^2 = \sin \phi \sin \theta d\psi + \cos \phi d\theta, \quad \hat{R}^3 = d\phi + \cos \theta d\psi. \tag{5.30}$$

such that the boundary conditions take the conventional form of a gluing,

$$\hat{R}_+^i = \mathbb{R}^i_j \hat{R}_-^j, \tag{5.31}$$

with

$$\mathbb{R} = \mathbb{O}_+^{-1} \mathbb{O}_-, \quad \mathbb{O}_\pm = \frac{1}{\mathbf{1} \pm \eta \mathcal{R}}. \tag{5.32}$$

It is easily verified that \mathbb{R} so defined is an algebra automorphism. It is worth emphasising that here the gluing between currents after the generalised duality is again with an overall plus sign (it is of the form of a WZW N-type boundary condition eq. (B.9)) whereas in the original λ -deformed WZW the gluing between currents was with an overall minus sign (i.e. of WZW D-type eq. (B.8)).

To close the circle we can again relate these boundary conditions to the general integrable boundary condition construction. First we recall that the Lax for the η -deformed PCM eq. (5.23) is given by [79, 80],

$$\mathcal{L}_{\pm}(\eta, z) = \frac{1 + \eta^2}{1 \pm z} \text{ad}_{\hat{g}^{-1}} \cdot \mathbb{O}_{\pm} \cdot \hat{R}_{\pm}. \tag{5.33}$$

Using this we can readily see that boundary condition above is obtained from,

$$\mathcal{L}_{\tau}(\eta, z)| = \mathcal{L}_{\tau}(\eta, -z)|, \tag{5.34}$$

and hence is of the form of the integrable boundary condition that one would obtain from eq. (3.14) in which the extra automorphism $\Omega = 1$ and when would choose the freedom to change the deformation parameter conveniently (see also the discussion at the end of section 3.1). Actually there is a second possibility,

$$\mathcal{L}_{\tau}(\eta, z)| = \mathcal{L}_{\tau}(-\eta, -z)|, \tag{5.35}$$

which also gives an integrable condition; this is just $\hat{R}_{+}| = \hat{R}_{-}|$.¹⁵

6 Conclusions

We have seen that integrable boundary conditions of the λ -deformed theory can be obtained by demanding that the monodromy matrix of the Lax connection generates conserved charges even in the presence of a boundary. Rather elegantly these boundary conditions can be described by (twisted) conjugacy classes, independent of the deformation parameter and indeed as the deformation is turned off the known D-brane configurations in WZW models are recovered. For the $SU(2)$ theory the picture is nice; viewing S^3 as a two-sphere fibred over an interval the conjugacy classes correspond to D2-branes wrapping the two-sphere (that shrink at the end points of the interval to D0-branes), and the effect of the λ -deformation is in essence to determine the size of the two-spheres. The quantisation of the world-volume flux remains consistent in the deformed theory — all occurrences of the deformation parameter cancel — and enforce that the D-branes sit at localised positions along the interval.

Armed with the integrable D-branes of the λ -model we were then able to show their connection to D-branes in the PCM and its η -deformation. First we could track the D-brane boundary condition through to the non-Abelian T-dual point ($\lambda = 1$) and dualise them to an N-type boundary condition of the PCM, which is also integrable. Alternatively we could perform analytical continuation to ascertain boundary conditions for a Poisson-Lie sigma model on the group manifold AN appearing in the Iwasawa decomposition $G^{\mathbb{C}} = GAN$. The boundary conditions produced in this fashion were then Poisson-Lie T-dualisable and produced N-type boundary conditions of the η -deformed PCM. Again we saw explicitly

¹⁵This later choice however appears incompatible with PL T-duality, this is easily seen since the boundary condition is equivalent to $\hat{L}_{\sigma} = 0$ and making use of the canonical transformation eq. (5.22) this leads to a PL dual condition $0 = \frac{t\eta}{2}(1 - \hat{\Pi}\check{\Pi})\check{P} + \hat{\Pi}\check{L}_{\sigma}$ which still depends on the coordinates of \hat{g} and is thus non-local.

that these D-branes of the η -deformed PCM are integrable. The exchange of N -type and D -type boundary conditions in this approach is a phenomenon that seems generic in the context of non-Abelian and Poisson-Lie theories.

Let us comment on a few interesting open problems triggered by this study.

The concerns and analysis of this paper have been predominantly classical. An important next direction is to make more precise the quantum description corresponding to the boundary conditions considered here. Assuming no Goldschmidt-Witten anomaly is encountered one might anticipate that the integrability transfers to the quantum theory. Here the situation is rather intriguing. A bulk S-matrix is conjectured — and to a certain extent derived via quantum inverse scattering — for the λ -deformation and has a factorised product form $S(\theta) = X(\theta)S^{\text{SU}(2)}(\theta) \otimes S^{\text{RSOS}_k}(\theta)$ (for the SU(2) theory), in which the first factor is the SU(2) rational solution of the Yang-Baxter equation and the second is an interaction round a face type block that is thought of as describing kink degrees of freedom [84]. A quantum integrable boundary should supplement this bulk S-matrix with a boundary ‘K-matrix’ that obeys a boundary version of the Yang-Baxter equation [20, 21]. It will be interesting, and the subject of further investigation, to establish the boundary K-matrix corresponding to integrable boundary conditions found within. Developing this line further, the quantum inverse scattering construction shows how the λ -theory can be quantised on a lattice as a spin k XXX Heisenberg chain with impurities [84]. It is appealing to establish a match between integrable boundary conditions of such spin chains (studied e.g. in [30]) and the boundary conditions of the continuum theory we constructed here.

Here we have considered just bosonic λ -theory on a group manifold. These λ -deformations have an analogue in the context of symmetric spaces [38] (i.e. deformations of gauged WZW models) which will be of interest to study, with the anticipation that the geometric description of D-branes of [85–88] persists in the deformed theory. Going further one can consider λ -deformations of theories based on supercosets with applications to the $AdS_5 \times S^5$ superstring [37, 39]. Here the deformation is expected to be truly marginal and conjectured to correspond to a root-of-unity deformation of the holographic dual gauge theory. The study of the integrable D-branes in this arena also seems profitable.

One way to introduce fermionic degrees of freedom is by considering supergroups or supercosets as target manifolds as outlined in the previous paragraph. Another way is through the supersymmetrization of the deformed σ -model thereby introducing worldsheet fermions. We expect that the results obtained in this paper carry over unchanged to the $N = (1, 1)$ supersymmetric version of the isotropically λ -deformed theory. However as is well known, going to $N = (2, 1)$ or $N = (2, 2)$ supersymmetry, which is needed when one has string theoretical applications in mind, requires additional geometrical structure(s) thereby strongly restricting the allowed target manifolds and the choices of metric and torsion on it. For example, on the integrable Yang-Baxter deformation of the PCM with a Wess-Zumino term (which is a generalization of the η -deformed PCM) it is highly unlikely that one can go beyond $N = (1, 1)$ supersymmetry [89]. As far as we know, the question whether λ -deformed theories allow for extended supersymmetry, even in the absence of boundaries, has not been addressed yet and forms an interesting open question.

Acknowledgments

DCT is supported by a Royal Society University Research Fellowship *Generalised Dualities in String Theory and Holography* URF 150185 and in part by STFC grant ST/P00055X/1. This work is supported in part by the “FWO-Vlaanderen” through the project G020714N and one “aspirant” fellowship (SD), and by the Vrije Universiteit Brussel through the Strategic Research Program “High-Energy Physics”. We thank Saskia Demulder, Tamás Gombor, Tim Hollowood, Marios Petropoulos and Kostas Sfetsos for useful conversations/communications that aided this project.

A General sigma models with boundaries

To establish our sigma model conventions we briefly review the necessary basics of bosonic open strings in general curved backgrounds (see for instance [8, 9]). We discard the dilaton in this brief discussion and adapt throughout this paper the open string picture.

The string sigma model is a theory of maps $X^\mu(\tau, \sigma)$ from the worldsheet Σ parametrised by (τ, σ) to a target space manifold \mathcal{M} parametrised by X^μ with $\mu \in \{0, \dots, D-1\}$. Considering open strings, the worldsheet Σ has a boundary $\partial\Sigma$ that is mapped in the target space to a $p+1$ -dimensional submanifold¹⁶ $N \subset \mathcal{M}$ known as a Dp-brane. For a target space with metric $G_{\mu\nu}(X)$ and anti-symmetric 2-form $B_{\mu\nu}(X)$ the sigma model action is

$$S_\sigma = \frac{1}{4\pi\alpha'} \int d^2\sigma \sqrt{-g} \partial_\alpha X^\mu \left(g^{\alpha\beta} G_{\mu\nu}(X) + \epsilon^{\alpha\beta} B_{\mu\nu}(X) \right) \partial_\beta X^\nu + \int_{\partial\Sigma} d\tau A_a(X) \frac{dX^a}{d\tau}, \quad (\text{A.1})$$

with $A_a(X)$ the U(1) gauge field coupling to the end-points of the open string and $a \in \{0, \dots, p\}$ denoting the tangent directions to the worldvolume of the Dp-brane. In conformal gauge, $g_{\alpha\beta} = \text{diag}(+1, -1)$, and lightcone coordinates, $\sigma^\pm = \tau \pm \sigma$, we have

$$S_\sigma = \frac{1}{\pi\alpha'} \int d\sigma d\tau \partial_+ X^\mu (G_{\mu\nu}(X) + B_{\mu\nu}(X)) \partial_- X^\nu + \int_{\partial\Sigma} d\tau A_a(X) \frac{dX^a}{d\tau}. \quad (\text{A.2})$$

Varying the action with respect to the fields X^μ (to obtain the equations of motion) one encounters a boundary term leading to Dirichlet and (generalised) Neumann directions provided the metric splits orthogonally:

$$\text{Dirichlet: } \delta X^{\hat{a}}|_{\partial\Sigma} = 0 \quad \Rightarrow \quad \partial_\tau X^{\hat{a}}|_{\partial\Sigma} = 0, \quad (\text{A.3})$$

$$\text{Neumann: } G_{ab}(X) \partial_\sigma X^b|_{\partial\Sigma} = (B_{ab}(X) + 2\pi\alpha' F_{ab}(X)) \partial_\tau X^b|_{\partial\Sigma}, \quad (\text{A.4})$$

with $\hat{a} = p+1, \dots, D-1$ the directions normal to the Dp-brane and where we introduced the Abelian field strength $F_{ab}(X) = \partial_a A_b(X) - \partial_b A_a(X)$. The classical energy momentum tensor of the sigma model is given by

$$T_{\alpha\beta} = \partial_\alpha X^\mu G_{\mu\nu}(X) \partial_\beta X^\nu - \frac{1}{2} g_{\alpha\beta} g^{\gamma\delta} \partial_\gamma X^\mu G_{\mu\nu}(X) \partial_\delta X^\nu. \quad (\text{A.5})$$

¹⁶We do not consider the possibility of intersecting D-branes nor a stack of D-branes here.

and in light cone coordinates we have,

$$T_{\pm\pm} = \partial_{\pm} X^{\mu} G_{\mu\nu}(X) \partial_{\pm} X^{\nu}, \quad T_{+-} = 0. \quad (\text{A.6})$$

It is straightforward to see that on the boundary, imposing either Dirichlet conditions (A.3) or generalised Neumann conditions (A.4), the energy-momentum tensor satisfies

$$T_{++}|_{\partial\Sigma} = T_{--}|_{\partial\Sigma} \rightarrow T_{10}|_{\partial\Sigma} = 0. \quad (\text{A.7})$$

which we will call the (classical) conformal boundary condition. Hence, there is no momentum flow through the boundary (although A and B charge can be interchanged). If we now summarise the Dirichlet and Neumann conditions (A.3), (A.4) using a map W that combines them as,

$$\partial_{+} X^{\mu}|_{\partial\sigma} = W^{\mu}_{\nu} \partial_{-} X^{\nu}|_{\partial\sigma}, \quad (\text{A.8})$$

then the Dirichlet conditions correspond to -1 eigenvalues of W while the generalised Neumann conditions are described by all other eigenvalues. The classical conformal boundary condition eq. (A.7) then requires that W preserves the target space metric G ,

$$W^T G W = G. \quad (\text{A.9})$$

The dynamics of the Dp -brane with tension T_p is governed by the DBI action (throughout this paper we ignore the scalar fields parameterizing the fluctuations transversal to the brane),

$$S_{\text{DBI}} = T_p \int e^{-\Phi} \sqrt{\det(\widehat{G}_{ab}(X) + \mathcal{F}_{ab}(X))}, \quad (\text{A.10})$$

where $\widehat{G}_{ab}(X)$ is the induced metric on the worldvolume and $\mathcal{F}_{ab}(X)$ is the gauge-invariant worldvolume flux given by

$$\mathcal{F}_{ab}(X) = \widehat{B}_{ab}(X) + 2\pi\alpha' F_{ab}(X), \quad (\text{A.11})$$

with $\widehat{B}_{ab}(X)$ the induced anti-symmetric 2-form.

B WZW models and conventions

In this appendix we collect a number of conventions together with a short review concerning (boundary) WZW models. The WZW model is a non-linear sigma model of maps $g(\tau, \sigma)$ from a 1+1 dimensional Riemann surface Σ (with or without boundary) to a Lie group G . The model is exact conformal invariant and hence simple enough to describe strings propagating in curved backgrounds.

Before writing down the action let us make our conventions clear. We pick for the Lie algebra a basis of hermitian generators $\{T_A\}$, with $A = 1, \dots, \text{Dim}(G)$, that satisfy $[T_A, T_B] = iF_{AB}^C T_C$. The ad-invariant metric on the Lie algebra is given by $\langle T_A, T_B \rangle = \frac{1}{x_r} \text{Tr}(T_A T_B) = \eta_{AB}$ with x_r the index of the representation r . The left and right-invariant Maurer-Cartan one-forms are expanded in the Lie algebra as $L = g^{-1} dg = -iL^A T_A$ and $R = dg g^{-1} = -iR^A T_A$ respectively. They are related by an adjoint action $D(g)[T_A] =$

$D^B{}_A(g)T_B = gT_Ag^{-1}$ so that $D_{AB}(g) = \text{Tr}(g^{-1}T_AgT_B)$ and $D^T_{AB}(g) = D_{AB}(g^{-1})$. Hence, $R^A = D^A{}_B(g)L^B$.

The WZW action [10] is

$$S_{\text{WZW},k}(g) = -\frac{k}{2\pi} \int_{\Sigma} d\sigma d\tau \langle g^{-1}\partial_+g, g^{-1}\partial_-g \rangle - \frac{k}{4\pi} \int_{M_3} H, \tag{B.1}$$

where H is the closed torsion 3-form (locally satisfying $H = dB$) given by

$$H = \frac{1}{6} \langle \bar{g}^{-1}d\bar{g}, [\bar{g}^{-1}d\bar{g}, \bar{g}^{-1}d\bar{g}] \rangle, \tag{B.2}$$

with \bar{g} the extension of g into $M_3 \subset G$ such that $\partial M_3 = g(\Sigma)$. There are two topological obstructions for the consistency of the definition of the WZW action and its quantum theory.¹⁷ First, the existence of M_3 is guaranteed only when the second homology group $H_2(G)$ is empty. Second, the path integral based on this action is insensitive to the choice of extension provided that the third cohomology class $[H]/2\pi \in H^3(G)$ is integral. For $SU(2)$ we have $H^3(SU(2)) \cong \mathbb{Z}$ requiring the level k to be integer quantised while on the other hand for $SL(2, \mathbb{R})$ we have $H^3(SL(2, \mathbb{R}))$ empty which allows the level k to be free. We want to emphasise here that comparing the WZW action, which in terms of vielbeins is,

$$S_{\text{WZW},k}(g) = \frac{k}{2\pi} \int_{\Sigma} d\sigma d\tau L^A_+ \eta_{AB} L^B_- + \frac{k}{24\pi} \int_{M_3} F_{ABC} L^A \wedge L^B \wedge L^C, \tag{B.3}$$

to a worldsheet model (A.2) we have units in which $\alpha' = 2$, crucial for $k \in \mathbb{Z}$ when $G = SU(2)$.

The WZW model is invariant under a global $G(z) \times G(\bar{z})$ action leading to an infinite-dimensional symmetry group described by the chirally conserved holomorphic Kac-Moody currents¹⁸

$$J(z) = -k \partial g g^{-1}, \quad \bar{J}(\bar{z}) = k g^{-1} \bar{\partial} g, \tag{B.4}$$

in the conventions $z = x^0 + ix^1 = i\sigma^+$ and $\bar{z} = x^0 - ix^1 = i\sigma^-$ with the Euclidean worldsheet coordinates $(x^0, x^1) = (i\tau, \sigma)$ and lightcone coordinates $\sigma^{\pm} = \tau \pm \sigma$. At the quantum level the current algebra takes the form,

$$J^A(z)J^B(w) = \frac{iF^{AB}{}_C J^C(w)}{z-w} + \frac{k\eta^{AB}}{(z-w)^2} + \text{reg.}, \tag{B.5}$$

and analogous for the $\bar{J}\bar{J}$ OPE (hence the sign difference in the definition (B.4)). The exact conformal invariance is established through the energy-momentum tensor obtained via the Sugawara construction based on the current algebra [1],

$$T(z) = T_{zz}(z) = \frac{1}{2(k + h\nu)} \eta_{AB} (J^A J^B)(z), \tag{B.6}$$

¹⁷By construction it is obvious that these obstructions still apply for the λ model (2.5).

¹⁸Note that whether the left current is holomorphic or anti-holomorphic depends on the sign of the WZ term.

where h^\vee is the dual Coxeter number of G (here we assumed for simplicity G to be semi-simple). The central charge of the theory can then be found to be,

$$c = \frac{k \dim(G)}{k + h^\vee}, \tag{B.7}$$

and all analogous for $\bar{T}(\bar{z})$.

When considering a boundary in the WZW model one will seek boundary conditions that preserve its exact conformal invariance. Since the CFT is easily described in terms of the chiral currents (B.4) it is convenient to express these boundary conditions as a class of gluing conditions¹⁹ for the currents at $z = \bar{z}$,

$$J(z)| = \Omega \bar{J}(\bar{z})|, \tag{B.8}$$

with $\Omega : \mathfrak{g} \rightarrow \mathfrak{g}$. To preserve the exact conformal invariance the gluing condition should satisfy the conformal boundary condition $T(z)| = \bar{T}(\bar{z})|$. This translates into the condition that the gluing map Ω should be an isometry of the ad-invariant Lie algebra metric. One could further require Ω to be an algebra automorphism and, hence, the gluing condition to preserve also the infinite-dimensional current algebra (B.5). The corresponding D-brane configurations are well-understood and geometrically wrap the twisted conjugacy classes of the group [12–14]. They are known as symmetric D-branes or of ‘type D’ [14], a terminology that we will adapt. Another possibility analysed in [14, 68], where it was dubbed ‘type N’, is to consider,

$$J(z)| = -\Omega \bar{J}(\bar{z})|. \tag{B.9}$$

with Ω a metric-preserving automorphism. They preserve the conformal invariance but do not preserve the current algebra which makes them somewhat more difficult to analyse. However, as suggested in section 5 they seem to be related to the type D by generalised T-dualities in the context of the λ deformation of the WZW model.

From the sigma model point of view the WZW action (B.1) is necessarily modified when the Riemann surface Σ has a boundary $\partial\Sigma$ [51, 70–72]. The image of $g(\partial\Sigma)$ is a (D-brane) submanifold N of G on which a two-form ω lives such that the restriction of H on N coincides with $d\omega$. Locally the two-form coincides with the gauge-invariant worldvolume flux \mathcal{F} , i.e. $\omega = \hat{B} + 4\pi dA$ [72]. The action of the boundary WZW model is,

$$S_{\text{WZW},k}(g) = -\frac{k}{2\pi} \int_{\Sigma} d\sigma d\tau \langle g^{-1} \partial_+ g, g^{-1} \partial_- g \rangle - \frac{k}{4\pi} \int_{M_3} H + \frac{k}{4\pi} \int_{D_2} \omega, \tag{B.10}$$

where $M_3 \subset G$ with boundary $\partial M_3 = g(\Sigma) + D_2$ and $D_2 \subset N$. Note that only the boundary equations of motion will depend on the two-form ω . Demanding that the boundary conditions obtained from the gluing conditions that preserve conformal invariance (B.8) coincides with the boundary conditions from the sigma model approach (A.3) and (A.4) will completely determine the two-form ω on the D-brane in terms of the gluing map Ω as in [12, 70, 71].

¹⁹To compare these gluing conditions (which take value in $T_e G$) to sigma model boundary conditions of the form (A.9) one should still translate them to $T_g G$.

Again, there are two topological obstructions for the consistency of the definition of the boundary WZW action and its quantum theory (for a detailed exposition see [51, 70, 72]). The existence of M_3 and D_2 is guaranteed only when the second relative homology $H_2(G, N)$ vanishes. The path integral is insensitive to the choice of M_3 and ω provided that the third relative cohomology class $[(H, \omega)] / 2\pi \in H^3(G, N)$ is integral. As seen in section 4 this condition enforces for $G = \text{SU}(2)$ the position of D2-branes to sit on only a discrete number of values. Locally this quantisation condition coincides with the quantisation of the worldvolume flux of the U(1) gauge-field A on the brane [65, 72]. For $G = \text{SL}(2, \mathbb{R})$ the position of the D1-strings will not be constrained by this particular topological obstruction; however, the D1-strings carry a natural quantisation descending from the Gauss constraint of two-dimensional gauge theory on the brane [73, 74].

Open Access. This article is distributed under the terms of the Creative Commons Attribution License ([CC-BY 4.0](https://creativecommons.org/licenses/by/4.0/)), which permits any use, distribution and reproduction in any medium, provided the original author(s) and source are credited.

References

- [1] P. Di Francesco, P. Mathieu and D. Senechal, *Conformal field theory*, Springer-Verlag, New York, U.S.A., (1997) [[INSPIRE](#)].
- [2] J.L. Cardy, *Boundary conformal field theory*, [hep-th/0411189](#) [[INSPIRE](#)].
- [3] J.L. Cardy, *Lectures on conformal invariance and percolation*, in *New trends of mathematical physics and probability theory*, Tokyo, Japan, 5–6 March 2001 [[math-ph/0103018](#)] [[INSPIRE](#)].
- [4] N. Ishibashi, *The boundary and crosscap states in conformal field theories*, *Mod. Phys. Lett. A* **4** (1989) 251 [[INSPIRE](#)].
- [5] J.L. Cardy, *Boundary conditions, fusion rules and the Verlinde formula*, *Nucl. Phys. B* **324** (1989) 581 [[INSPIRE](#)].
- [6] O. Babelon, D. Bernard and M. Talon, *Introduction to classical integrable systems*, volume 1, Cambridge University Press, Cambridge, U.K., (2003) [[INSPIRE](#)].
- [7] K. Zarembo, *Integrability in σ -models*, in *Les Houches Summer School. Integrability: from statistical systems to gauge theory*, Les Houches, France, 6 June–1 July 2016 [[arXiv:1712.07725](#)] [[INSPIRE](#)].
- [8] V. Schomerus, *Lectures on branes in curved backgrounds*, *Class. Quant. Grav.* **19** (2002) 5781 [[hep-th/0209241](#)] [[INSPIRE](#)].
- [9] A. Recknagel and V. Schomerus, *Boundary conformal field theory and the worldsheet approach to D-branes*, Cambridge University Press, Cambridge, U.K., (2013) [[INSPIRE](#)].
- [10] E. Witten, *Non-Abelian bosonization in two-dimensions*, *Commun. Math. Phys.* **92** (1984) 455 [[INSPIRE](#)].
- [11] M. Kato and T. Okada, *D-branes on group manifolds*, *Nucl. Phys. B* **499** (1997) 583 [[hep-th/9612148](#)] [[INSPIRE](#)].
- [12] A. Yu. Alekseev and V. Schomerus, *D-branes in the WZW model*, *Phys. Rev. D* **60** (1999) 061901 [[hep-th/9812193](#)] [[INSPIRE](#)].

- [13] G. Felder, J. Fröhlich, J. Fuchs and C. Schweigert, *The geometry of WZW branes*, *J. Geom. Phys.* **34** (2000) 162 [[hep-th/9909030](#)] [[INSPIRE](#)].
- [14] S. Stanciu, *D-branes in group manifolds*, *JHEP* **01** (2000) 025 [[hep-th/9909163](#)] [[INSPIRE](#)].
- [15] J.M. Figueroa-O'Farrill and S. Stanciu, *More D-branes in the Nappi-Witten background*, *JHEP* **01** (2000) 024 [[hep-th/9909164](#)] [[INSPIRE](#)].
- [16] J.M. Evans, M. Hassan, N.J. MacKay and A.J. Mountain, *Local conserved charges in principal chiral models*, *Nucl. Phys.* **B 561** (1999) 385 [[hep-th/9902008](#)] [[INSPIRE](#)].
- [17] M. Lüscher, *Quantum nonlocal charges and absence of particle production in the two-dimensional nonlinear σ -model*, *Nucl. Phys.* **B 135** (1978) 1 [[INSPIRE](#)].
- [18] D. Bernard, *Hidden Yangians in 2D massive current algebras*, *Commun. Math. Phys.* **137** (1991) 191 [[INSPIRE](#)].
- [19] N.J. MacKay, *On the classical origins of Yangian symmetry in integrable field theory*, *Phys. Lett.* **B 281** (1992) 90 [*Erratum ibid.* **B 308** (1993) 444] [[INSPIRE](#)].
- [20] I.V. Cherednik, *Factorizing particles on a half line and root systems*, *Theor. Math. Phys.* **61** (1984) 977 [*Teor. Mat. Fiz.* **61** (1984) 35] [[INSPIRE](#)].
- [21] E.K. Sklyanin, *Boundary conditions for integrable quantum systems*, *J. Phys.* **A 21** (1988) 2375 [[INSPIRE](#)].
- [22] N. Mann and S.E. Vazquez, *Classical open string integrability*, *JHEP* **04** (2007) 065 [[hep-th/0612038](#)] [[INSPIRE](#)].
- [23] A. Dekel and Y. Oz, *Integrability of Green-Schwarz σ -models with boundaries*, *JHEP* **08** (2011) 004 [[arXiv:1106.3446](#)] [[INSPIRE](#)].
- [24] K. Zoubos, *Review of AdS/CFT integrability, chapter IV.2: deformations, orbifolds and open boundaries*, *Lett. Math. Phys.* **99** (2012) 375 [[arXiv:1012.3998](#)] [[INSPIRE](#)].
- [25] E. Corrigan and Z.-M. Sheng, *Classical integrability of the $O(N)$ nonlinear σ -model on a half line*, *Int. J. Mod. Phys.* **A 12** (1997) 2825 [[hep-th/9612150](#)] [[INSPIRE](#)].
- [26] I. Aniceto, Z. Bajnok, T. Gombor, M. Kim and L. Palla, *On integrable boundaries in the 2 dimensional $O(N)$ σ -models*, *J. Phys.* **A 50** (2017) 364002 [[arXiv:1706.05221](#)] [[INSPIRE](#)].
- [27] G.W. Delius, N.J. MacKay and B.J. Short, *Boundary remnant of Yangian symmetry and the structure of rational reflection matrices*, *Phys. Lett.* **B 522** (2001) 335 [*Erratum ibid.* **B 524** (2002) 401] [[hep-th/0109115](#)] [[INSPIRE](#)].
- [28] T. Gombor, *New boundary monodromy matrices for classical σ -models*, [arXiv:1805.03034](#) [[INSPIRE](#)].
- [29] D. Arnaudon, J. Avan, N. Crampé, A. Doikou, L. Frappat and É. Ragoucy, *General boundary conditions for the $sl(N)$ and $sl(M|N)$ open spin chains*, *J. Stat. Mech.* **0408** (2004) P08005 [[math-ph/0406021](#)] [[INSPIRE](#)].
- [30] H.J. de Vega and A. González-Ruiz, *Boundary K matrices for the XYZ, XXZ and XXX spin chains*, *J. Phys.* **A 27** (1994) 6129 [[hep-th/9306089](#)] [[INSPIRE](#)].
- [31] P. Bowcock, E. Corrigan, P.E. Dorey and R.H. Rietdijk, *Classically integrable boundary conditions for affine Toda field theories*, *Nucl. Phys.* **B 445** (1995) 469 [[hep-th/9501098](#)] [[INSPIRE](#)].

- [32] S. Ghoshal and A.B. Zamolodchikov, *Boundary S matrix and boundary state in two-dimensional integrable quantum field theory*, *Int. J. Mod. Phys. A* **9** (1994) 3841 [Erratum *ibid.* **A 9** (1994) 4353] [[hep-th/9306002](#)] [[INSPIRE](#)].
- [33] N.J. MacKay and B.J. Short, *Boundary scattering, symmetric spaces and the principal chiral model on the half line*, *Commun. Math. Phys.* **233** (2003) 313 [Erratum *ibid.* **245** (2004) 425] [[hep-th/0104212](#)] [[INSPIRE](#)].
- [34] N.J. MacKay and C.A.S. Young, *Classically integrable boundary conditions for symmetric space σ -models*, *Phys. Lett. B* **588** (2004) 221 [[hep-th/0402182](#)] [[INSPIRE](#)].
- [35] M. Moriconi, *Integrable boundary conditions and reflection matrices for the $O(N)$ nonlinear σ -model*, *Nucl. Phys. B* **619** (2001) 396 [[hep-th/0108039](#)] [[INSPIRE](#)].
- [36] K. Sfetsos, *Integrable interpolations: from exact CFTs to non-Abelian T-duals*, *Nucl. Phys. B* **880** (2014) 225 [[arXiv:1312.4560](#)] [[INSPIRE](#)].
- [37] C. Appadu and T.J. Hollowood, *β -function of k deformed $AdS_5 \times S^5$ string theory*, *JHEP* **11** (2015) 095 [[arXiv:1507.05420](#)] [[INSPIRE](#)].
- [38] T.J. Hollowood, J.L. Miramontes and D.M. Schmidt, *Integrable deformations of strings on symmetric spaces*, *JHEP* **11** (2014) 009 [[arXiv:1407.2840](#)] [[INSPIRE](#)].
- [39] T.J. Hollowood, J.L. Miramontes and D.M. Schmidt, *An integrable deformation of the $AdS_5 \times S^5$ superstring*, *J. Phys. A* **47** (2014) 495402 [[arXiv:1409.1538](#)] [[INSPIRE](#)].
- [40] K. Sfetsos and D.C. Thompson, *Spacetimes for λ -deformations*, *JHEP* **12** (2014) 164 [[arXiv:1410.1886](#)] [[INSPIRE](#)].
- [41] R. Borsato and L. Wulff, *Target space supergeometry of η and λ -deformed strings*, *JHEP* **10** (2016) 045 [[arXiv:1608.03570](#)] [[INSPIRE](#)].
- [42] S. Demulder, K. Sfetsos and D.C. Thompson, *Integrable λ -deformations: squashing coset CFTs and $AdS_5 \times S^5$* , *JHEP* **07** (2015) 019 [[arXiv:1504.02781](#)] [[INSPIRE](#)].
- [43] R. Borsato, A.A. Tseytlin and L. Wulff, *Supergravity background of λ -deformed model for $AdS_2 \times S^2$ supercoset*, *Nucl. Phys. B* **905** (2016) 264 [[arXiv:1601.08192](#)] [[INSPIRE](#)].
- [44] Y. Chervonyi and O. Lunin, *Supergravity background of the λ -deformed $AdS_3 \times S^3$ supercoset*, *Nucl. Phys. B* **910** (2016) 685 [[arXiv:1606.00394](#)] [[INSPIRE](#)].
- [45] X.C. de la Ossa and F. Quevedo, *Duality symmetries from non-Abelian isometries in string theory*, *Nucl. Phys. B* **403** (1993) 377 [[hep-th/9210021](#)] [[INSPIRE](#)].
- [46] A. Giveon and M. Roček, *On non-Abelian duality*, *Nucl. Phys. B* **421** (1994) 173 [[hep-th/9308154](#)] [[INSPIRE](#)].
- [47] C. Klimčík and P. Ševera, *Dual non-Abelian duality and the Drinfeld double*, *Phys. Lett. B* **351** (1995) 455 [[hep-th/9502122](#)] [[INSPIRE](#)].
- [48] C. Klimčík and P. Ševera, *Poisson-Lie T duality and loop groups of Drinfeld doubles*, *Phys. Lett. B* **372** (1996) 65 [[hep-th/9512040](#)] [[INSPIRE](#)].
- [49] S. Förste, A.A. Kehagias and S. Schwager, *Non-Abelian duality for open strings*, *Nucl. Phys. B* **478** (1996) 141 [[hep-th/9604013](#)] [[INSPIRE](#)].
- [50] J. Borlaf and Y. Lozano, *Aspects of T duality in open strings*, *Nucl. Phys. B* **480** (1996) 239 [[hep-th/9607051](#)] [[INSPIRE](#)].

- [51] C. Klimčík and P. Ševera, *Open strings and D-branes in WZNW model*, *Nucl. Phys. B* **488** (1997) 653 [[hep-th/9609112](#)] [[INSPIRE](#)].
- [52] C. Klimčík and P. Ševera, *Poisson Lie T duality: open strings and D-branes*, *Phys. Lett. B* **376** (1996) 82 [[hep-th/9512124](#)] [[INSPIRE](#)].
- [53] C. Albertsson and R.A. Reid-Edwards, *Worldsheet boundary conditions in Poisson-Lie T-duality*, *JHEP* **03** (2007) 004 [[hep-th/0606024](#)] [[INSPIRE](#)].
- [54] C. Albertsson, L. Hlavaty and L. Snobl, *On the Poisson-Lie T-plurality of boundary conditions*, *J. Math. Phys.* **49** (2008) 032301 [[arXiv:0706.0820](#)] [[INSPIRE](#)].
- [55] L. Hlavaty and L. Snobl, *Description of D-branes invariant under the Poisson-Lie T-plurality*, *JHEP* **07** (2008) 122 [[arXiv:0806.0963](#)] [[INSPIRE](#)].
- [56] B. Fraser, *D-branes (or not) in the non-Abelian T-dual of the SU(2) WZW model*, *Phys. Lett. B* **784** (2018) 307 [[arXiv:1806.00713](#)] [[INSPIRE](#)].
- [57] F. Cordonier-Tello, D. Lüst and E. Plauschinn, *Open-string T-duality and applications to non-geometric backgrounds*, [arXiv:1806.01308](#) [[INSPIRE](#)].
- [58] R. Borsato and L. Wulff, *Non-Abelian T-duality and Yang-Baxter deformations of Green-Schwarz strings*, *JHEP* **08** (2018) 027 [[arXiv:1806.04083](#)] [[INSPIRE](#)].
- [59] B. Hoare and A.A. Tseytlin, *On integrable deformations of superstring σ -models related to $AdS_n \times S^n$ supercosets*, *Nucl. Phys. B* **897** (2015) 448 [[arXiv:1504.07213](#)] [[INSPIRE](#)].
- [60] K. Sfetsos, K. Siampos and D.C. Thompson, *Generalised integrable λ - and η -deformations and their relation*, *Nucl. Phys. B* **899** (2015) 489 [[arXiv:1506.05784](#)] [[INSPIRE](#)].
- [61] C. Klimčík, *η and λ deformations as E-models*, *Nucl. Phys. B* **900** (2015) 259 [[arXiv:1508.05832](#)] [[INSPIRE](#)].
- [62] B. Hoare and F.K. Seibold, *Poisson-Lie duals of the η deformed symmetric space σ -model*, *JHEP* **11** (2017) 014 [[arXiv:1709.01448](#)] [[INSPIRE](#)].
- [63] V.E. Zakharov and A.V. Mikhailov, *Relativistically invariant two-dimensional models in field theory integrable by the inverse problem technique* (in Russian), *Sov. Phys. JETP* **47** (1978) 1017 [*Zh. Eksp. Teor. Fiz.* **74** (1978) 1953] [[INSPIRE](#)].
- [64] F. Loebbert, *Lectures on Yangian symmetry*, *J. Phys. A* **49** (2016) 323002 [[arXiv:1606.02947](#)] [[INSPIRE](#)].
- [65] C. Bachas, M.R. Douglas and C. Schweigert, *Flux stabilization of D-branes*, *JHEP* **05** (2000) 048 [[hep-th/0003037](#)] [[INSPIRE](#)].
- [66] G. Itsios, K. Sfetsos and K. Siampos, *The all-loop non-Abelian Thirring model and its RG flow*, *Phys. Lett. B* **733** (2014) 265 [[arXiv:1404.3748](#)] [[INSPIRE](#)].
- [67] J. Pawelczyk, *SU(2) WZW D-branes and their noncommutative geometry from DBI action*, *JHEP* **08** (2000) 006 [[hep-th/0003057](#)] [[INSPIRE](#)].
- [68] S. Stanciu, *D-branes in an AdS_3 background*, *JHEP* **09** (1999) 028 [[hep-th/9901122](#)] [[INSPIRE](#)].
- [69] J.M. Figueroa-O'Farrill and S. Stanciu, *D-branes in $AdS_3 \times S^3 \times S^3 \times S^1$* , *JHEP* **04** (2000) 005 [[hep-th/0001199](#)] [[INSPIRE](#)].
- [70] K. Gawedzki, *Conformal field theory: a case study*, [hep-th/9904145](#) [[INSPIRE](#)].

- [71] S. Stanciu, *A note on D-branes in group manifolds: flux quantization and D0-charge*, *JHEP* **10** (2000) 015 [[hep-th/0006145](#)] [[INSPIRE](#)].
- [72] J.M. Figueroa-O'Farrill and S. Stanciu, *D-brane charge, flux quantization and relative (co)homology*, *JHEP* **01** (2001) 006 [[hep-th/0008038](#)] [[INSPIRE](#)].
- [73] C. Bachas and M. Petropoulos, *Anti-de Sitter D-branes*, *JHEP* **02** (2001) 025 [[hep-th/0012234](#)] [[INSPIRE](#)].
- [74] E. Witten, *Bound states of strings and p-branes*, *Nucl. Phys. B* **460** (1996) 335 [[hep-th/9510135](#)] [[INSPIRE](#)].
- [75] P.M. Petropoulos and S. Ribault, *Some remarks on anti-de Sitter D-branes*, *JHEP* **07** (2001) 036 [[hep-th/0105252](#)] [[INSPIRE](#)].
- [76] P. Lee, H. Ooguri, J.-W. Park and J. Tannenhauser, *Open strings on AdS₂ branes*, *Nucl. Phys. B* **610** (2001) 3 [[hep-th/0106129](#)] [[INSPIRE](#)].
- [77] G. Georgiou, K. Sfetsos and K. Siampos, *All-loop correlators of integrable λ -deformed σ -models*, *Nucl. Phys. B* **909** (2016) 360 [[arXiv:1604.08212](#)] [[INSPIRE](#)].
- [78] C.R. Nappi, *Some properties of an analog of the nonlinear σ model*, *Phys. Rev. D* **21** (1980) 418 [[INSPIRE](#)].
- [79] C. Klimčík, *On integrability of the Yang-Baxter σ -model*, *J. Math. Phys.* **50** (2009) 043508 [[arXiv:0802.3518](#)] [[INSPIRE](#)].
- [80] F. Delduc, M. Magro and B. Vicedo, *On classical q -deformations of integrable σ -models*, *JHEP* **11** (2013) 192 [[arXiv:1308.3581](#)] [[INSPIRE](#)].
- [81] V.G. Drinfeld, *Quantum groups*, *J. Sov. Math.* **41** (1988) 898 [*Zap. Nauchn. Semin.* **155** (1986) 18] [[INSPIRE](#)].
- [82] K. Sfetsos, *Poisson-Lie T duality and supersymmetry*, *Nucl. Phys. Proc. Suppl.* **B 56** (1997) 302 [[hep-th/9611199](#)] [[INSPIRE](#)].
- [83] K. Sfetsos, *Canonical equivalence of nonisometric σ -models and Poisson-Lie T duality*, *Nucl. Phys. B* **517** (1998) 549 [[hep-th/9710163](#)] [[INSPIRE](#)].
- [84] C. Appadu, T.J. Hollowood and D. Price, *Quantum inverse scattering and the lambda deformed principal chiral model*, *J. Phys. A* **50** (2017) 305401 [[arXiv:1703.06699](#)] [[INSPIRE](#)].
- [85] J.M. Maldacena, G.W. Moore and N. Seiberg, *Geometrical interpretation of D-branes in gauged WZW models*, *JHEP* **07** (2001) 046 [[hep-th/0105038](#)] [[INSPIRE](#)].
- [86] K. Gawedzki, *Boundary WZW, G/H, G/G and CS theories*, *Annales Henri Poincaré* **3** (2002) 847 [[hep-th/0108044](#)] [[INSPIRE](#)].
- [87] S. Fredenhagen and V. Schomerus, *D-branes in coset models*, *JHEP* **02** (2002) 005 [[hep-th/0111189](#)] [[INSPIRE](#)].
- [88] S. Stanciu, *D-branes in Kazama-Suzuki models*, *Nucl. Phys. B* **526** (1998) 295 [[hep-th/9708166](#)] [[INSPIRE](#)].
- [89] S. Demulder, S. Driezen, A. Sevrin and D.C. Thompson, *Classical and quantum aspects of Yang-Baxter Wess-Zumino models*, *JHEP* **03** (2018) 041 [[arXiv:1711.00084](#)] [[INSPIRE](#)].

Generalized Kähler structures on group manifolds and T-duality

J.P. Ang,^a Sibylle Driezen,^{b,c} Martin Roček^a and Alexander Sevrin^{b,d}

^a*C.N. Yang Institute for Theoretical Physics, Stony Brook University,
Stony Brook, NY 11794, U.S.A.*

^b*Theoretische Natuurkunde, Vrije Universiteit Brussel and The International Solvay Institutes,
Pleinlaan 2, B-1050 Brussels, Belgium*

^c*Department of Physics, Swansea University,
Singleton Park, Swansea SA2 8PP, U.K.*

^d*Physics Department, Universiteit Antwerpen,
Campus Groenenborger, B-2020 Antwerpen, Belgium*

E-mail: JianPeng.Ang@gmail.com, Sibylle.Driezen@vub.be,
Martin.Rocek@stonybrook.edu, Alexandre.Sevrin@vub.be

ABSTRACT: We study generalized Kähler structures on $N = (2, 2)$ supersymmetric Wess-Zumino-Witten models; we use the well known case of $SU(2) \times U(1)$ as a toy model and develop tools that allow us to construct the superspace action and uncover the highly nontrivial structure of the hitherto unexplored case of $SU(3)$; these tools should be useful for studying many other examples. We find that *different* generalized Kähler structures on $N = (2, 2)$ supersymmetric Wess-Zumino-Witten models can be found by T-duality transformations along affine isometries.

KEYWORDS: Sigma Models, Superspaces, Supersymmetry and Duality

ARXIV EPRINT: [1804.03259](https://arxiv.org/abs/1804.03259)

Contents

1	Introduction	1
2	Generalized Kähler geometry on group manifolds	3
2.1	(2,2) sigma model description of bihermitian geometry	3
2.2	(1,1) WZW models	5
2.3	(2,2) WZW models	6
2.4	Isometries	7
2.5	T-duality along Kac-Moody isometries	7
2.6	General strategy for finding the generalized Kähler potential	8
3	$SU(2) \times U(1)$	9
3.1	Coordinates and generalized Kähler potential	9
3.1.1	Type (0,0)	9
3.1.2	Type (1,1)	11
3.2	Isometries	12
3.3	T-duality: relating the two types	12
3.3.1	Type (0,0) to type (1,1)	13
3.3.2	Using the group coordinates to find the T-dual	14
4	$SU(3)$	15
4.1	Complex coordinates and generalized Kähler potential	15
4.1.1	Type (0,0)	16
4.1.2	Type (1,1)	18
4.2	T-duality: relating the two generalized Kähler structures	21
4.2.1	Isometries	21
4.2.2	T-duality from type (0,0) to type (1,1)	21
4.2.3	Type (1,1) to type (0,0)	23
5	Discussion and conclusion	23
5.1	Results	23
5.2	Possible future developments	23
5.2.1	Type change	23
5.2.2	(4,4) supersymmetry	23
5.2.3	Other groups	24
A	Sigma models and supersymmetry	24
B	Local description of bihermitian geometry	25

C	Isometries and T-duality	28
C.1	Large vector multiplet (LVM)	28
C.2	Semichiral vector multiplet (SVM)	30
D	Finding complex coordinates	32
E	Other type (0,0) potentials for $SU(2) \times U(1)$	34
F	T-duality from type (1,1) to type (0,0) on $SU(2) \times U(1)$	35
G	$SU(2) \times SU(2)$	37
G.1	Type (1,0)	37
G.2	Type (0,1)	38
G.3	T-duality	39

1 Introduction

Almost since its inception it was recognized that supersymmetry and geometry go hand in hand [1]. Supersymmetric non-linear σ -models in two dimensions (NLSM) are a class of field theories where the geometric aspects are under control and can be studied both at the classical and the quantum mechanical level. They are interesting in their own right, and have many applications, including as the building blocks for type II string theories, as the description of certain moduli spaces, condensed matter physics, etc.

A non-supersymmetric NLSM is fully characterized by its target manifold, which is endowed with a metric and a closed 3-form. These models can always be supersymmetrized as long as the number of supersymmetries is bounded by $(N_+, N_-) \leq (1, 1)$ where N_+ (N_-) is the number of right-handed (left-handed) supersymmetries. No further geometric structure arises at the classical level. However, any additional supersymmetry past the first introduces a covariantly constant complex structure,¹ with respect to which the metric is hermitian. In addition, if $(N_+, N_-) \geq (2, 2)$, there are complex structures of each handedness.

In the current paper we will mostly focus on the $(N_+, N_-) = (2, 2)$ case, which requires besides the metric and the closed 3-form, two covariantly constant complex structures that both preserve metric, hence the name “bihermitian geometry”. A simple dimensional argument shows that the Lagrange density in $(2, 2)$ superspace can only be a function of a number of (constrained) scalar superfields. The Lagrange density encodes the full local geometry. In the simplest case where only chiral superfields appear, the two complex structures coincide, the 3-form vanishes and the geometry is Kähler. The Lagrange density is then precisely the Kähler potential. This suggests that the generic case describes a far reaching generalization of Kähler manifolds where the Lagrange density gets the interpretation of a

¹In general, covariantly constant with respect to a connection with torsion related to the closed 3-form.

generalized Kähler potential. This was understood to be the case in the bihermitian language of [2] in a series of papers from the NLSM perspective [3–6]. This was reinterpreted by Hitchin when he introduced the concept of generalized Kähler geometry [7], a natural generalization of Kähler geometry acting non-trivially on the sum of the tangent and cotangent bundle, and which was shown by Gualtieri [8] to coincide with bihermitian geometry. A subclass of generalized Kähler manifolds, generalized Calabi-Yau manifolds, are conformally invariant at the quantum level and provide an important class of supergravity solutions [9, 10].

The off-shell completion of a $(2, 2)$ NLSM depends on the precise choice of the right and left complex structures J_+ and J_- ; when different choices are possible, they correspond to different bihermitian structures and thus to different generalized Kähler structures. This is reflected in the supersymmetry algebra: one finds it closes off-shell modulo terms proportional to the commutator of the two complex structures $[J_+, J_-]$. As a consequence one expects that $\ker[J_+, J_-] = \ker(J_+ - J_-) \oplus \ker(J_+ + J_-)$ can be described in a manifestly supersymmetric way without introducing any further off-shell degrees of freedom. This is indeed achieved by means of chiral and twisted chiral superfields [2]. To close the supersymmetry algebra off-shell when the image $[J_+, J_-]$ is nonvanishing, one must introduce additional $(1, 1)$ auxiliary fields; in $(2, 2)$, they arise from semi-chiral superfields [3]. Any $(2, 2)$ NLSM can be described in terms of these three classes of superfields: chiral, twisted chiral and semi-chiral [6]. However, as the off-shell completion of a $(2, 2)$ NLSM fully depends on the choice made for J_+ and J_- and as this choice is not always unique, one finds that a given target manifold often admits different generalized Kähler structures.

If the generalized Kähler manifold possesses an isometry, one can T-dualize the model along that isometry [11]. Generically one ends up with a different manifold. T-duality not only affects the metric and closed 3-form, but also acts non-trivially on the complex structures [12]. Hence, T-duality alters the superfield content of a $(2, 2)$ NLSM. Two cases appear: a chiral superfield can be interchanged for a twisted chiral superfield (and vice-versa) [2] or a pair of chiral and twisted chiral superfields gets exchanged for a semi-chiral multiplet (and vice-versa) [5]. A particularly interesting case arises when the isometry is actually a Kac-Moody symmetry — then the metric and closed 3-form remain unchanged, but the complex structures still transform [13]. This is precisely the case we investigate in this paper.

A simple but non-trivial class of generalized Kähler manifolds where many of the issues discussed above can be studied quite explicitly are even-dimensional reductive Lie group manifolds [14]. The resulting σ -models are $(2, 2)$ supersymmetric Wess-Zumino-Witten (WZW) models. A complex structure on a reductive group manifold is fully determined by its action on the Lie algebra where it is almost equivalent to a Cartan decomposition of the Lie algebra: it has eigenvalue $+i$ ($-i$) on positive (negative) roots. The only freedom remains in its action on the Cartan subalgebra where the only restriction is the requirement that the Cartan-Killing metric should be hermitian. Given a choice for J_+ there is still a considerable freedom in choosing J_- , giving rise to various generalized Kähler structures on reductive even-dimensional Lie groups. For groups of low rank this can be studied systematically.

In the current paper we explore and elucidate the relation between various generalized Kähler structures on the same Lie group. We start with the well-known example of $SU(2) \times U(1)$, which allows for two generalized Kähler structures: one in terms of a chiral and a twisted chiral field [15] and one in terms of semi-chiral multiplet [4]. We show that the two generalized Kähler structures are related through T-duality transformation along an affine isometry. This can be understood as follows. Only the maximal abelian subgroup of the left and right-handed affine group acts trivially on the complex structures and thus are manifest in $(2, 2)$ superspace. T-dualizing along an affine isometry does not alter the metric or the closed 3-form [13] but it does alter the complex structures, mapping one generalized Kähler structure on $SU(2) \times U(1)$ into the other one! As a far more difficult example, we study the hitherto unexplored case of $SU(3)$; this also has (at least) two inequivalent generalized Kähler structures: one in terms of two semi-chiral multiplets and one in terms of a single semi-chiral multiplet, one chiral and one twisted chiral superfield.²

The outline of the rest of the paper is as follows. Section 2 reviews supersymmetric WZW models, which form an important class of generalized Kähler manifolds. Section 3 comprises a review of the generalized Kähler structures carried by $SU(2) \times U(1)$, in particular concentrating on relating generalized Kähler structures of different types via T-duality. Section 4 studies the generalized Kähler structures on $SU(3)$. Generalized Kähler potentials for both types of generalized Kähler structures on $SU(3)$ are derived. Section 5 has a brief summary of our results and discusses possibilities for further research. Appendix A reviews sigma models and their supersymmetric extensions to $(1, 1)$ superspace. Appendix B gives details of the $(2, 2)$ superspace description of bihermitian geometry, including explicit formulae for the complex structures J_{\pm} in terms of the generalized Kähler potential K . Appendix C discusses isometries, T-duality, and generalized $(2, 2)$ supersymmetric vector multiplets. Appendix D attempts to give insight into the art of finding holomorphic coordinates on WZW-models. Appendix E presents some particular choices of holomorphic coordinates for $SU(2) \times U(1)$ that we found but are not discussed in section 3. Appendix F describes the T-duality transformation from type $(1, 1)$ to $(0, 0)$ using the Large Vector Multiplet discussed in appendix C. Appendix G discusses another rank 2 group, $SU(2) \times SU(2)$, which admits only type $(1, 0)$ and type $(0, 1)$ generalized Kähler structures.

2 Generalized Kähler geometry on group manifolds

2.1 $(2, 2)$ sigma model description of bihermitian geometry

We briefly recap the $(2, 2)$ superspace formulation of a two-dimensional sigma model with bihermitian target space and establish the notation used in the rest of this paper.³

As always, $(2, 2)$ superspace has two commuting coordinates $\sigma^{\text{++}} = \tau + \sigma$, $\sigma^{\text{--}} = \tau - \sigma$ and four anticommuting coordinates θ^+ , $\bar{\theta}^+$, θ^- , $\bar{\theta}^-$. There are two complex spinorial

²Actually, both $SU(2) \times U(1)$ and $SU(3)$ have $(4, 4)$ supersymmetry, so in principle there are $S^2 \times S^2$ generalized Kähler structures. We expect these to fall into two deformation classes, so that our examples should be generic, but further investigation might be worthwhile.

³For background and more details about sigma models in general, see appendix A.

covariant derivatives \mathbb{D}_\pm which satisfy the algebra

$$\{\mathbb{D}_\pm, \bar{\mathbb{D}}_\pm\} = 2i\partial_\pm, \quad \mathbb{D}_\pm^2 = \bar{\mathbb{D}}_\pm^2 = 0. \quad (2.1)$$

The three types of (2, 2) superfields required to describe a generic generalized Kähler manifold are the following:

- chiral superfields $\phi, \bar{\phi}$ satisfying

$$\begin{aligned} \bar{\mathbb{D}}_+\phi &= 0, & \bar{\mathbb{D}}_-\phi &= 0, \\ \mathbb{D}_+\bar{\phi} &= 0, & \mathbb{D}_-\bar{\phi} &= 0, \end{aligned} \quad (2.2)$$

- twisted chiral superfields $\chi, \bar{\chi}$ satisfying

$$\begin{aligned} \bar{\mathbb{D}}_+\chi &= 0, & \mathbb{D}_-\chi &= 0, \\ \mathbb{D}_+\bar{\chi} &= 0, & \bar{\mathbb{D}}_-\bar{\chi} &= 0, \end{aligned} \quad (2.3)$$

- left and right semi-chiral superfields $\ell, \bar{\ell}, r, \bar{r}$ satisfying

$$\begin{aligned} \bar{\mathbb{D}}_+\ell &= 0, & \bar{\mathbb{D}}_-\bar{r} &= 0, \\ \mathbb{D}_+\bar{\ell} &= 0, & \mathbb{D}_-r &= 0. \end{aligned} \quad (2.4)$$

The action in (2, 2) superspace has the form

$$I = \int d^2\sigma d^4\theta K = \int d^2x \mathbb{D}^2 \bar{\mathbb{D}}^2 K, \quad (2.5)$$

where K is a real local function, the generalized Kähler potential, of the superfields $\ell, \bar{\ell}, r, \bar{r}, \phi, \bar{\phi}, \chi, \bar{\chi}$. The potential is defined modulo generalized Kähler transformations

$$K \mapsto K + f(\ell, \phi, \chi) + \bar{f}(\bar{\ell}, \bar{\phi}, \bar{\chi}) + g(r, \phi, \bar{\chi}) + \bar{g}(\bar{r}, \bar{\phi}, \chi), \quad (2.6)$$

which give rise to total derivatives in the component sigma model Lagrangian density.

This single function K fully encodes the local geometry of the target manifold \mathcal{M} which must be even-dimensional and has geometric structures (g, H, J_+, J_-) where⁴

- J_+ and J_- are two integrable complex structures on \mathcal{M} compatible with the metric g

$$\begin{aligned} J_+^2 &= J_-^2 = -\mathbf{1}, \\ [X, Y] + J_\pm[J_\pm X, Y] + J_\pm[X, J_\pm Y] - [J_\pm X, J_\pm Y] &= 0, \\ g(J_\pm X, J_\pm Y) &= g(X, Y), \end{aligned} \quad (2.7)$$

where X, Y are arbitrary vector fields, and

- $H = d_+^c \omega_+ = -d_-^c \omega_-$ is a closed 3-form, where d_\pm^c are the d^c operators with respect to J_\pm , and $\omega_\pm = gJ_\pm$ are the hermitian forms of the respective complex structures.

⁴See appendix B for the formulas expressing these structures in terms of the generalized potential.

A manifold carrying such a structure is known as bihermitian [2], and has been shown to be equivalent to generalized Kähler geometry [8]. Note that the second condition is equivalent to the covariant constancy

$$\nabla^{(\pm)} J_{\pm} = 0 \tag{2.8}$$

of the complex structures J_{\pm} with respect to the Bismut connections $\nabla^{(\pm)}$, which are metric connections with torsions $\pm g^{-1}H$ (first introduced by Yano — see [16], pp. 150-151). Explicitly,

$$\Gamma^{(\pm)\mu}_{\nu\rho} = \Gamma^{(0)\mu}_{\nu\rho} \pm \frac{1}{2}g^{\mu\sigma}H_{\sigma\nu\rho}, \tag{2.9}$$

where $\Gamma^{(0)}$ is the Levi-Civita connection. The torsion 3-form H enters the sigma model description via a local 2-form potential b known as the Kalb-Ramond field, with $H = db$.

A bihermitian manifold is equipped with three Poisson structures

$$\pi_{\pm} = (J_{+} \pm J_{-})g^{-1}, \tag{2.10}$$

$$\sigma = [J_{+}, J_{-}]g^{-1}. \tag{2.11}$$

The superfields (2.2)–(2.4) arising from the (2, 2) superspace description may be interpreted as coordinates adapted to these Poisson structures. More specifically, near a regular point,⁵ chiral superfields are complex coordinates along $\ker \pi_{-}$, twisted chiral superfields are complex coordinates along $\ker \pi_{+}$, and semi-chiral coordinates are holomorphic Darboux coordinates along the symplectic leaves of the foliation defined by σ [6]. The type of the generalized Kähler geometry at a point is $(\dim_{\mathbb{C}} \ker \pi_{-}, \dim_{\mathbb{C}} \ker \pi_{+})$; equivalently, a geometry of type (N_c, N_t) at a point admits a (2, 2) sigma model description with N_c chiral superfields and N_t twisted chiral superfields near that point. In general, the type is not constant on the manifold: there may be subvarieties, known as type-change loci, on which the type increases; these must have strictly positive codimension.

2.2 (1, 1) WZW models

A Wess-Zumino-Witten (WZW) model is a theory of maps from a Riemann surface Σ to a Lie group G equipped with an invariant metric and a normalized torsion form. The (1, 1) WZW model is a theory of maps from a (1, 1) super-Riemann surface to G , and has action⁶

$$kI[g] = -\frac{k}{\pi} \int_{\Sigma} d^2\sigma d^2\theta \operatorname{tr}(g^{-1}\nabla_{+}g g^{-1}\nabla_{-}g) - \frac{k}{\pi} \int_B d^3\tilde{\sigma} d^2\theta \operatorname{tr}(\tilde{g}^{-1}\partial_t\tilde{g}\{\tilde{g}^{-1}\nabla_{+}\tilde{g}, \tilde{g}^{-1}\nabla_{-}\tilde{g}\}), \tag{2.12}$$

where k is an integer (the level),⁷ “tr” is a normalized invariant bilinear form on the Lie algebra $\mathfrak{g} := \operatorname{Lie}(G)$, B is a 3-dimensional manifold with boundary $\partial B = \Sigma$ with local coordinates $\tilde{\sigma} = (t, \sigma)$, and \tilde{g} is an extension of g to B . Modulo multiples of $2\pi i$, $I[g]$ is independent of the choice of B and extension \tilde{g} .

⁵At a regular point on a manifold with a Poisson structure, the rank of the structure is constant in a sufficiently small neighborhood of the point. Here we consider a point that is regular with respect to all three Poisson structures.

⁶See appendix A for a review of (1, 1) superspace.

⁷Nonconformal models with separate normalizations of the two terms can also be studied; their extensions to (2, 2) superspace are not understood.

The Maurer-Cartan forms e_L^a, e_R^a , defined by

$$g^{-1} dg = e_L^a T_a, \quad dg g^{-1} = e_R^a T_a, \quad (2.13)$$

where T_a is a basis for the Lie algebra \mathfrak{g} , allow one to push forward tensors on the Lie algebra to the group.

The (1, 1) WZW model has symmetry group $G_L \times G_R$, acting as $g \mapsto h_L g h_R^{-1}$ (only the subgroup $(G_L \times G_R)/Z(G)$ acts nontrivially, where $Z(G)$ is the center of the group). The model also has superconformal symmetry, so the parameters h_L and h_R are allowed to be semilocal, satisfying

$$\nabla_+ h_L = 0, \quad \nabla_- h_R = 0. \quad (2.14)$$

2.3 (2, 2) WZW models

All even dimensional reductive Lie groups admit (2, 2) extensions [14]. The complex structures corresponding to the extended supersymmetries (2.7) may be pulled back to the Lie algebra

$$(\mathbb{J}_+)^a_b = (e_L)^a_\mu (J_+)^{\mu\nu} (e_L^{-1})^\nu_b, \quad (\mathbb{J}_-)^a_b = (e_R)^a_\mu (J_-)^{\mu\nu} (e_R^{-1})^\nu_b, \quad (2.15)$$

and in terms of the Lie algebra complex structures \mathbb{J}_\pm , the conditions for (2, 2) supersymmetry may be reformulated as [14]

- \mathbb{J}_\pm are constant and satisfy $\mathbb{J}_\pm^2 = -\mathbb{1}$ as well as $\eta(\mathbb{J}_\pm X, \mathbb{J}_\pm Y) = \eta(X, Y)$ where η is the Killing form and X, Y are arbitrary Lie algebra elements.
- Further, they obey $f(X, \mathbb{J}_\pm Y, \mathbb{J}_\pm Z) + f(\mathbb{J}_\pm X, Y, \mathbb{J}_\pm Z) + f(\mathbb{J}_\pm X, \mathbb{J}_\pm Y, Z) = f(X, Y, Z)$, where $f(X, Y, Z) = \eta([X, Y], Z)$ is the alternating form constructed from the structure constants and η .

These conditions were solved in [14] where it was shown that \mathbb{J}_\pm may be characterized by a choice of Cartan subalgebra and positive direction. The complex structures are diagonal on the positive and negative roots with eigenvalue $+i$ and $-i$ respectively, and map the Cartan subalgebra to itself in a way that makes the Killing form hermitian. Since any two Cartan decompositions of a Lie algebra are related by group conjugation, the only freedom lies in the choice of the action on the Cartan subalgebra.

Let us now turn to the superfield content, or type, allowed for a particular WZW model. A choice of \mathbb{J}_+ and \mathbb{J}_- on the Lie algebra fixes the superfield content. The numbers of chiral (2.2) and twisted chiral superfields (2.3)

$$N_c = \dim_{\mathbb{C}} \ker(J_+ - J_-), \quad N_t = \dim_{\mathbb{C}} \ker(J_+ + J_-) \quad (2.16)$$

can be computed by noting that $\ker(J_+ \pm J_-) = \ker(\mathbb{J}_+ \pm e_L e_R^{-1} (\mathbb{J}_-) e_R e_L^{-1})$ and that $e_L e_R^{-1}$ is a transformation in the adjoint representation. The number of sets of semi-chiral superfields (2.4) is then $(N - N_c - N_t)/2$, where $2N$ is the (real) dimension of the Lie group.

This can be easily analyzed for rank two groups. Here, one has essentially two choices for the Lie algebra complex structures: either they are equal $\mathbb{J}_+ = \mathbb{J}_-$, or they are opposite on the Cartan subalgebra $\mathbb{J}_+|_{\text{CSA}} = -\mathbb{J}_-|_{\text{CSA}}$. For the former case, $N_t = \dim_{\mathbb{C}} \ker(\mathbb{J}_+ +$

Group	N	$\mathbb{J}_+ = \mathbb{J}_-$			$\mathbb{J}_+ \neq \mathbb{J}_-$		
		N_s	N_c	N_t	N_s	N_c	N_t
$SU(2) \times U(1)$	2	1	0	0	0	1	1
$SU(2) \times SU(2)$	3	1	1	0	1	0	1
$SU(3)$	4	2	0	0	1	1	1
$SO(5)$	5	2	1	0	1	2	1
G_2	7	3	1	0	2	2	1

Table 1. The coordinate content for the rank 2 non-abelian reductive Lie groups either taking the complex structures to be equal on the Lie algebra ($\mathbb{J}_+ = \mathbb{J}_-$) or having the opposite sign on the CSA ($\mathbb{J}_+ \neq \mathbb{J}_-$). The number of semi-chiral, chiral and twisted chiral coordinates are denoted N_s , N_c and N_t respectively.

$e_L e_R^{-1}(\mathbb{J}_-) e_R e_L^{-1} = 0$ always, while $N_c = \ker(\mathbb{J}_+ - e_L e_R^{-1}(\mathbb{J}_-) e_R e_L^{-1})$ can be analyzed by writing $e_L e_R^{-1} = \exp(\alpha)$ and expanding through first nontrivial order in α . A similar analysis can be done for the latter choice. The results are given in table 1. Notice that each of the rank two groups admit generalized Kähler structures of two different types.

2.4 Isometries

Of the $G_L \times G_R$ symmetry of the (2, 2) WZW model, only the subgroup $G_L \times H_R$ preserves the left complex structure J_+ , where $H_R \subset G_R$ is the maximal torus corresponding to the action of \mathbb{J}_+ on the Lie algebra as described in section 2.3. A similar statement holds for J_- , so the group of isometries preserving both complex structures of the (2, 2) extended WZW is $H_L \times H_R$.⁸ Due to the superconformal invariance of the WZW model, these are in fact Kac-Moody symmetries.

2.5 T-duality along Kac-Moody isometries

Consider the T-dual sigma model of a (2, 2) supersymmetric WZW model along some isometry $U(1) \subset H_L \times H_R$. Since the isometry preserves the bihermitian structure, the T-duality can be performed in (2, 2) superspace, and the dual model also exhibits (2, 2) supersymmetry.⁹

If, furthermore, the T-duality is along a left (right) Kac-Moody isometry $U(1) \subset H_L$, then in fact the metric, torsion and left (right) complex structure of the sigma model is unchanged [12, 13]. Indeed, for a left Kac-Moody isometry with Killing field k^μ , normalized so that it has unit norm, the chiral component of the Noether current (see (3.1) of [13])

$$J = (k^\mu (g_{\mu\nu} - b_{\mu\nu}) + \omega_\nu) \partial^\nu \Phi \tag{2.17}$$

vanishes, where ω is a one-form defined by $\mathcal{L}_k b = d\omega$. We assume that the b field is chosen to be invariant under k , so that $\omega = d\alpha$ is locally exact, so

$$k^\mu (g_{\mu\nu} - b_{\mu\nu}) + \partial_\nu \alpha = 0. \tag{2.18}$$

⁸As before, the group which acts faithfully is actually $(H_L \times H_R)/Z(G)$.

⁹See appendix C below for a review of T-duality in (2, 2) superspace.

Choose a coordinate system Φ^I such that $\Phi^0 = -\alpha$ and the other Φ^i are k -invariant. Contracting (2.18) with k^ν shows that in this coordinate system, the Killing field is $k = \partial/\partial\Phi^0$. Taking $\nu = I$ in (2.18) then shows that the metric and b field satisfy $e_{00} = g_{00} = 1$ and $e_{i0} = (g-b)_{0i} = 0$. Substituting $e_{00} = 1$ and $e_{i0} = 0$ into the formulas (12), (15), (16) of [12] then shows that the metric, torsion and left complex structure are unchanged by T-duality.

For a right Kac-Moody isometry, the antichiral component of the Noether current

$$\bar{J} = (k^\mu(g_{\mu\nu} + b_{\mu\nu}) - \omega_\nu) \bar{\partial}\Phi^\nu \tag{2.19}$$

vanishes. The discussion proceeds analogously: assuming that b is invariant, $\omega = d\alpha$ is exact, and in a coordinate system $\Phi^0 = \alpha$ and Φ^i such that $\mathcal{L}_k\Phi^i = 0$, we have $e_{00} = 1$ and $e_{0i} = 0$. The formulas (13), (15) and (16) of [12] then show that the metric, torsion and right complex structure are unchanged by T-duality (after a change of coordinates $\tilde{\Phi}^0 \mapsto -\tilde{\Phi}^0$ of the dual model).

However, T-duality along a left (right) isometry does change the right (left) complex structure. In particular, the structures $J_+ \pm J_-$ and $[J_+, J_-]$ are changed. Therefore, T-duality along a Kac-Moody isometry changes the type of the generalized geometry and relates the different generalized Kähler structures on the same Lie group.

In the following sections, we will perform these T-dualities in $(2, 2)$ superspace. Since in $(2, 2)$ superspace, gauging an isometry complexifies the gauge group (with respect to both complex structures), T-dualizing along isometries related by the complex structures gives rise to the same T-dual model in superspace. This also implies that isometries related by complex structures cannot be simultaneously gauged [17]. For the rank 2 Lie groups which we consider in this paper, this means that T-duality along *any* Kac-Moody isometry always leads to the same T-dual model.

2.6 General strategy for finding the generalized Kähler potential

Given the bihermitian data (g, H, J_+, J_-) , the generalized Kähler potential K can in principle be found by solving the equations (B.12)–(B.13), which relate nonlinearly the Hessian of K to g and H in adapted coordinates. This is a nonlinear second order differential equation — a difficult equation to solve. However, on the symplectic leaves of σ (2.11), there is a simplification. On each symplectic leaf, K generates the symplectomorphism between left holomorphic Darboux coordinates (left semi-chiral superfields) and right holomorphic coordinates (right semi-chiral superfields), which means that it satisfies the *first order linear* differential equations (B.9)–(B.11).

This simplification, coupled with the observation about T-duality noted above, allows one to find the generalized Kähler potentials for all the generalized Kähler structures supported by a Lie group admitting a type $(0, 0)$ structure. The strategy is as follows. First, we find left and right holomorphic coordinates on the Lie group. This can be done by expanding the left and right invariant frames about the origin, taking the leading term to be given by the holomorphic Lie algebra generators, and solving for the higher order terms order by order using the Maurer-Cartan equations. (See appendix D for more details.) Next, for the type $(0, 0)$ structure, identify combinations $\ell, \tilde{\ell}$ and r, \tilde{r} of left and right

holomorphic coordinates that are Darboux for σ . This yields one-form symplectic potentials $\theta_L = \tilde{\ell} d\ell + \bar{\tilde{\ell}} d\bar{\ell}$ and $\theta_R = r d\tilde{r} + \bar{r} d\bar{\tilde{r}}$ for the (local) symplectic form σ^{-1} . The difference $\theta_L - \theta_R$ is closed, and can be integrated to give the generalized Kähler potential $K = \int \theta_L - \theta_R$. Next, the potentials for the generalized geometries of other types on the Lie group can be obtained by T-duality, as discussed above.

We illustrate this strategy for $SU(2) \times U(1)$ by first computing the type (0, 0) structure, and then T-dualizing along a Kac-Moody isometry to obtain the type (1, 1) generalized Kähler potential, reproducing a previously known result. We then apply this to $SU(3)$, constructing the type (1, 1) generalized Kähler potential from the type (0, 0) potential.

3 $SU(2) \times U(1)$

The generalized Kähler geometry of $SU(2) \times U(1)$ has been studied in detail [15, 18]. In this section, we revisit these results as a warm up for the $SU(3)$ model.

The outline of the section is as follows. First, we choose complex structures J_{\pm} on the Lie group and find complex coordinates. As discussed in section 2.3, generalized Kähler structures of two types are admissible depending on the choice of complex structures. Next, we find generalized Kähler potentials for each of the two types. These potentials can be written down in various different forms, differing from one another by generalized Kähler transformations and coordinate transformations. Different choices of potentials suit different purposes and the relations between them are illuminating. Finally, we relate the generalized geometries of the two different types by T-duality.

3.1 Coordinates and generalized Kähler potential

On the Lie algebra, take the basis $\{h, \bar{h}, e, \bar{e}\}$ where

$$h = \begin{pmatrix} \zeta & 0 \\ 0 & -\bar{\zeta} \end{pmatrix}, \quad \bar{h} = \begin{pmatrix} \bar{\zeta} & 0 \\ 0 & -\zeta \end{pmatrix}, \quad e = \begin{pmatrix} 0 & 1 \\ 0 & 0 \end{pmatrix}, \quad \bar{e} = \begin{pmatrix} 0 & 0 \\ 1 & 0 \end{pmatrix}, \quad (3.1)$$

$\zeta = \frac{1}{2}(1+i)$, $\bar{\zeta} = \frac{1}{2}(1-i)$. The two complex structures on the Lie algebra compatible with the choice of Cartan subalgebra h, \bar{h} are

$$\mathbb{J}_1 = \text{diag}(i, -i, i, -i), \quad \mathbb{J}_2 = \text{diag}(-i, i, i, -i). \quad (3.2)$$

Depending on whether one takes J_{\pm} induced from the same or from different Lie algebra complex structures $\mathbb{J}_1, \mathbb{J}_2$, one gets generalized Kähler structures of different types on $SU(2) \times U(1)$.

3.1.1 Type (0, 0)

If one takes J_+ and J_- both induced from the same Lie algebra complex structure, say \mathbb{J}_1 , then generically the resulting generalized Kähler structure has type (0, 0); in other words, $[J_+, J_-]$ has full rank at generic points of the group.¹⁰ In this case, J_+ and J_- induce the

¹⁰There are loci of positive codimension on which $\ker[J_+, J_-]$ is nontrivial.

same orientation on $SU(2) \times U(1)$. The sigma model description is in terms of one set of semi-chiral superfields.

In terms of the group element in the defining representation

$$g = \begin{pmatrix} g_{11} & g_{12} \\ g_{21} & g_{22} \end{pmatrix}, \tag{3.3}$$

the J_{\pm} holomorphic coordinates can be chosen to be¹¹

$$\begin{aligned} z_+^1 &= \log g_{12}^{\zeta} \bar{g}_{21}^{\bar{\zeta}}, \\ z_+^2 &= \log g_{22}^{\zeta} \bar{g}_{11}^{\bar{\zeta}}, \\ z_-^1 &= \log g_{12}^{\bar{\zeta}} \bar{g}_{21}^{\zeta}, \\ z_-^2 &= \log g_{11}^{\bar{\zeta}} \bar{g}_{22}^{\zeta}. \end{aligned} \tag{3.4}$$

Note that neither the set $(z_+^1, \bar{z}_+^1, z_-^1, \bar{z}_-^1)$ nor the set $(z_+^2, \bar{z}_+^2, z_-^2, \bar{z}_-^2)$ is nondegenerate (in each case, unitarity of g implies one real relation between these functions). These holomorphic coordinates are chosen to be Darboux with respect to the Poisson structure σ :

$$\sigma(dz_{\pm}^1, dz_{\pm}^2) = \pm 1, \quad \sigma(d\bar{z}_{\pm}^1, d\bar{z}_{\pm}^2) = \pm 1. \tag{3.5}$$

One choice of semi-chiral coordinates is

$$\ell = z_+^2, \quad \bar{\ell} = z_+^1, \quad r = z_-^2 - z_-^1, \quad \bar{r} = z_-^2, \tag{3.6}$$

satisfying $d(\tilde{\ell} d\ell + \bar{\tilde{\ell}} d\bar{\ell} + \tilde{r} dr + \bar{\tilde{r}} d\bar{r}) = 0$. Choosing polarizations such that the adapted coordinates are $\tilde{\ell}, \bar{\tilde{\ell}}$ and r, \bar{r} results in the parametrization [18]

$$g = e^{-\zeta\theta} \begin{pmatrix} e^{\tilde{\ell}+r} & e^{\bar{\tilde{\ell}}} \\ -e^{\tilde{\ell}} & e^{\tilde{\ell}+\bar{r}} \end{pmatrix}, \quad \theta = \tilde{\ell} + \bar{\tilde{\ell}} + \log(1 + e^{r+\bar{r}}) \tag{3.7}$$

and potential

$$\begin{aligned} K_0^{(0,0)} &= \int -\ell d\tilde{\ell} - \bar{\ell} d\bar{\tilde{\ell}} + \tilde{r} dr + \bar{\tilde{r}} d\bar{r} \\ &= -(\tilde{\ell} + r)(\bar{\tilde{\ell}} + \bar{r}) + \int^{-r-\bar{r}} \log(1 + e^q) dq \end{aligned} \tag{3.8}$$

satisfying $\frac{\partial K}{\partial \tilde{\ell}} = -\ell, \frac{\partial K}{\partial \bar{\tilde{\ell}}} = \bar{\tilde{\ell}}$. This potential is valid on the coordinate patch away from the off-diagonal matrices. On the other coordinate patch, away from the diagonal matrices, we choose the polarizations spanned by $\ell, \bar{\ell}$ and r, \bar{r} , which results in the parametrization

$$g = e^{-\zeta\theta} \begin{pmatrix} e^{\bar{\ell}} & e^{\bar{\ell}-r} \\ -e^{\ell-\bar{r}} & e^{\ell} \end{pmatrix}, \quad \theta = \ell + \bar{\ell} + \log(1 + e^{-(r+\bar{r})}) \tag{3.9}$$

¹¹See appendix D for a discussion of how to find such coordinates.

and potential

$$\begin{aligned}
 K_1^{(0,0)} &= \int \tilde{\ell} d\ell + \bar{\ell} d\bar{\ell} + \tilde{r} dr + \bar{r} d\bar{r} \\
 &= (\ell - \bar{r})(\bar{\ell} - r) - \int^{r+\bar{r}} \log(1 + e^q) dq + \frac{1}{2}(r^2 + \bar{r}^2)
 \end{aligned}
 \tag{3.10}$$

satisfying $\frac{\partial K}{\partial \ell} = \tilde{\ell}$, $\frac{\partial K}{\partial r} = \tilde{r}$. On the overlap of the two patches (comprising the group elements with nonvanishing entries), (3.8) and (3.10) differ by a Legendre transform

$$K_0^{(0,0)}(\tilde{\ell}, \bar{\ell}, r, \bar{r}) = K_1^{(0,0)}(\ell, \bar{\ell}, r, \bar{r}) - \ell\tilde{\ell} - \bar{\ell}\bar{r}.
 \tag{3.11}$$

This appears to be the choice of parametrization and polarization giving the simplest expression for the potential. Some other choices are given in appendix E.

3.1.2 Type (1, 1)

If one instead takes J_+ and J_- induced from different Lie algebra complex structures, say J_+ from \mathbb{J}_1 and J_- from \mathbb{J}_2 , one finds $[J_+, J_-] = 0$ everywhere. In other words, the resulting generalized Kähler structure has type (1, 1), and can be parametrized by a chiral coordinate ϕ and a twisted chiral coordinate χ . Furthermore, J_+ and J_- induce opposite orientations. In this case, the conditions that ϕ is holomorphic with respect to both J_{\pm} determine it uniquely up to a simple redefinition $\phi \rightarrow \phi'(\phi)$. Similarly, χ is also essentially unique.

One choice of parametrization of the group element is given by

$$g = e^{-\zeta\theta} \begin{pmatrix} e^{\bar{\chi}} & e^{\phi} \\ -e^{\bar{\phi}} & e^{\chi} \end{pmatrix}, \quad \theta = \log(e^{\phi+\bar{\phi}} + e^{\chi+\bar{\chi}}).
 \tag{3.12}$$

where we recall that $\zeta = \frac{1}{2}(1 + i)$. Equivalently, the chiral and twisted chiral coordinates are given by

$$\begin{aligned}
 \phi &= \log g_{12}^{\zeta} \bar{g}_{21}^{\bar{\zeta}}, \\
 \chi &= \log g_{22}^{\zeta} \bar{g}_{11}^{\bar{\zeta}}.
 \end{aligned}
 \tag{3.13}$$

This coordinate patch covers the region where all the entries of the group are nonzero. A redefinition $\hat{\phi} = e^{\phi}$, $\hat{\chi} = e^{\chi}$ allows one to reach the diagonal elements ($\hat{\phi} = 0$) and the off-diagonal elements ($\hat{\chi} = 0$).

The generalized potential for the type (1, 1) structure is known [15]

$$K_0^{(1,1)} = \frac{1}{2}(\chi - \bar{\chi})^2 + \int^{\phi+\bar{\phi}-\chi-\bar{\chi}} dq \log(1 + e^q).
 \tag{3.14}$$

By redefining $\hat{\phi} = e^{\phi}$ and checking that the limit $\hat{\phi} \rightarrow 0$ is well-defined, one can verify that this potential is valid on the coordinate patch away from the off-diagonal matrices.¹² The following potential

$$K_1^{(1,1)} = -\frac{1}{2}(\phi - \bar{\phi})^2 - \int^{-\phi-\bar{\phi}+\chi+\bar{\chi}} dq \log(1 + e^q).
 \tag{3.15}$$

¹²In [15], the variables used correspond to $\hat{\phi}, \hat{\chi}$.

is valid on the coordinate patch away from diagonal matrices, as can be seen by redefining $\hat{\chi} = e^\chi$ and checking that the limit $\hat{\chi} \rightarrow 0$ is well-defined. These two patches cover $SU(2) \times U(1)$. On the overlap of the two patches, comprising the group elements with nonvanishing entries, (3.14) and (3.15) differ by a generalized Kähler transformation $K_0^{(1,1)} - K_1^{(1,1)} = -(\chi + \bar{\chi})(\phi + \bar{\phi})$.

The generalized potentials (3.14), (3.15) were obtained by solving the second order differential equations (B.12)–(B.13)¹³ In the next subsection, we shall make use of the discussion in the previous section to derive the type (1, 1) potentials (3.14), (3.15) from the type (0, 0) potentials (3.8), (3.10) via T-duality.

3.2 Isometries

The $SU(2) \times U(1)$ WZW model has isometry group $SU(2)_L \times SU(2)_R \times U(1)$, and the subgroup preserving both complex structures J_\pm is $U(1)_L \times U(1)_R \times U(1)$. It acts on the group element g as

$$g \mapsto h_L g h_R^{-1}, \tag{3.16}$$

with

$$h_L = e^{-i(\epsilon h + \bar{\epsilon} \bar{h})}, \quad h_R = e^{i(\eta \bar{h} + \bar{\eta} h)}, \tag{3.17}$$

where h is defined in (3.1), and ϵ and η are complex parameters.

In the type (0, 0) parametrization (3.6), this corresponds to

$$\begin{aligned} \ell &\mapsto \ell + \bar{\epsilon} + \eta, & \tilde{\ell} &\mapsto \tilde{\ell} + \epsilon + \eta \\ r &\mapsto r - \eta + \bar{\eta}, & \tilde{r} &\mapsto \tilde{r} - \bar{\epsilon} - \eta. \end{aligned} \tag{3.18}$$

The parameters ϵ and η can be promoted to Kac-Moody parameters satisfying

$$\begin{aligned} \bar{\mathbb{D}}_+ \epsilon &= 0, & \mathbb{D}_\pm \epsilon &= 0, \\ \bar{\mathbb{D}}_\pm \eta &= 0, & \mathbb{D}_- \eta &= 0. \end{aligned} \tag{3.19}$$

In the type (1, 1) parametrization (3.12), this corresponds to

$$\phi \mapsto \phi + \epsilon + \eta, \quad \chi \mapsto \chi + \bar{\epsilon} + \eta. \tag{3.20}$$

The parameters ϵ and η can be promoted to Kac-Moody parameters satisfying (note the chirality constraints on ϵ differ from above)

$$\begin{aligned} \bar{\mathbb{D}}_\pm \epsilon &= 0, & \mathbb{D}_+ \epsilon &= 0, \\ \bar{\mathbb{D}}_\pm \eta &= 0, & \mathbb{D}_- \eta &= 0. \end{aligned} \tag{3.21}$$

3.3 T-duality: relating the two types

As discussed in section 2.5, T-duality along a Kac-Moody isometry relates the two generalized structures on $SU(2) \times U(1)$. This T-duality may be realized in (2, 2) superspace using the gauging prescription of [13].

¹³For special case of $SU(2) \times U(1)$, which has no semi-chiral coordinates, these equations turn out to be linear. For generic Lie groups, these equations are nonlinear and difficult to solve.

3.3.1 Type (0, 0) to type (1, 1)

We begin with the type (0, 0) generalized Kähler structure (3.8), and T-dualize along any factor of the $U(1)_L \times U(1)_R \times U(1)$ Kac-Moody isometry group. The complex structures J_{\pm} map these isometries into one another, so in superspace, where the gauge group is complexified, the gauging of any of these isometries is equivalent (up to reparametrizations).

Along $U(1)_R$. Consider first T-duality along $U(1)_R$, which acts on the semi-chiral coordinates as in (3.18) with $\epsilon = 0, \eta = i\lambda$, where λ is a real parameter. This isometry is gauged with an Semichiral Vector Multiplet (SVM) [23] (see appendix C). The combinations invariant under the $U(1)_R$ isometry are $\tilde{\ell} + \bar{\tilde{\ell}}, -\frac{1}{2}(r + \bar{r})$ and $i(\tilde{\ell} - \bar{\tilde{\ell}} + \frac{1}{2}(\bar{r} - r))$, and are respectively gauged with the potentials V^L, V^R and V' of the SVM. Starting from $K_0^{(0,0)}$ in (3.8), we add the generalized Kähler transformation term

$$K^{(0,0)} = K_0^{(0,0)} + \frac{1}{2}(\tilde{\ell}^2 + \bar{\tilde{\ell}}^2) - \frac{1}{4}(r^2 + \bar{r}^2) \tag{3.22}$$

to make the potential exactly invariant.¹⁴ The generalized Kähler transformation terms amount to redefining ℓ and \tilde{r} to the invariant combinations $\ell \mapsto \ell - \tilde{\ell}, \tilde{r} \mapsto \tilde{r} - r/2$. The resulting invariant potential is

$$K^{(0,0)} = \frac{1}{2} \left(\bar{\tilde{\ell}} - \tilde{\ell} + \frac{1}{2}(\bar{r} - r) \right)^2 - \frac{3}{8}(r + \bar{r})^2 - \frac{1}{2}(\tilde{\ell} + \bar{\tilde{\ell}})(r + \bar{r}) + \int^{-r-\bar{r}} dq \log(1 + e^q). \tag{3.23}$$

Gauging with an SVM, enforced to be flat by Lagrange multipliers Φ_I , and gauge fixing $\tilde{\ell} = \bar{\tilde{\ell}} = r = \bar{r} = 0$ yields

$$\tilde{K}^{(0,0)} = -\frac{1}{2}(V')^2 - \frac{3}{2}(V^R)^2 + V^L V^R + \int^{2V^R} dq \log(1 + e^q) - V^I \Phi_I, \tag{3.24}$$

where the Lagrange multipliers are

$$\begin{aligned} \Phi_L &= \frac{1}{2}(\phi + \bar{\phi} - \chi - \bar{\chi}), \\ \Phi_R &= \frac{1}{2}(-\phi - \bar{\phi} - \chi - \bar{\chi}), \\ \Phi' &= \frac{i}{2}(\phi - \bar{\phi} + \bar{\chi} - \chi). \end{aligned} \tag{3.25}$$

Eliminating the SVM gauge fields yields the T-dual potential

$$\begin{aligned} \tilde{K}^{(0,0)} &= -\frac{1}{2}(\chi + \bar{\chi})^2 + \int^{\phi + \bar{\phi} - \chi - \bar{\chi}} dq \log(1 + e^q) - \frac{1}{2}((\phi - \chi)^2 + (\bar{\phi} - \bar{\chi})^2) \\ &\quad + \frac{1}{4}((\phi + \bar{\chi})^2 + (\bar{\phi} + \chi)^2), \end{aligned} \tag{3.26}$$

which is precisely $K_0^{(1,1)}$ (3.14) up to a generalized Kähler transformation.

¹⁴This is not necessary but simplifies the discussion somewhat.

Along $U(1)_L$. Consider now T-duality along the $U(1)_L$ factor of $U(1)_L \times U(1)_R \times U(1)$, which acts on the coordinates as in (3.18) with $\epsilon = i\lambda, \eta = 0$, where λ is a real parameter. In this case, there is a complication because r, \bar{r} are invariant - how does the potential (3.8) couple to the SVM in this case? One way to do so is to perform a Legendre transform from r, \bar{r} to $\tilde{r}, \tilde{\bar{r}}$ (corresponding to a change in polarization), yielding the potential (we also add the generalized Kähler transformation $-\frac{1}{2}(\tilde{\ell}^2 + \tilde{\bar{\ell}}^2)$ to render the potential invariant - this amounts to redefining $\ell \rightarrow \ell + \tilde{\ell}$)

$$\begin{aligned} K^{(0,0)}(\tilde{\ell}, \tilde{\bar{\ell}}, \tilde{r}, \tilde{\bar{r}}) &= K_0^{(0,0)}(\tilde{\ell}, \tilde{\bar{\ell}}, r, \bar{r}) - \frac{1}{2}(\tilde{\ell}^2 + \tilde{\bar{\ell}}^2) - r\tilde{r} - \bar{r}\tilde{\bar{r}} \\ &= -\frac{1}{2}(\tilde{\ell} + \tilde{\bar{\ell}})^2 - r(\tilde{\ell} + \tilde{r}) - \bar{r}(\tilde{\bar{\ell}} + \tilde{\bar{r}}) - r\bar{r} + \int^{-r-\bar{r}} dq \log(1 + e^q). \end{aligned} \quad (3.27)$$

Note that \tilde{r} does indeed transform as $\tilde{r} \mapsto \tilde{r} + i\lambda$, so now the invariant combinations $\tilde{\ell} + \tilde{\bar{\ell}}$, $\tilde{\ell} + \tilde{\bar{r}}$ and $\tilde{\bar{\ell}} + \tilde{r}$ can be respectively gauged with the components $V^L, \tilde{\mathbb{V}}$ and $\tilde{\bar{\mathbb{V}}}$ of the SVM. The T-dual potential is

$$\tilde{K}^{(0,0)} = -\frac{1}{2}(V^L)^2 - r\bar{r} - r\tilde{\bar{\mathbb{V}}} - \bar{r}\tilde{\mathbb{V}} + \int^{-r-\bar{r}} dq \log(1 + e^q) - V^I \Phi_I, \quad (3.28)$$

where

$$V^I \Phi_I = V^L i(\bar{\phi} - \phi) + \tilde{\mathbb{V}}(\bar{\phi} - \chi) + \tilde{\bar{\mathbb{V}}}(\phi - \bar{\chi}). \quad (3.29)$$

Note that the variational equations of V^I are

$$0 = \left(\frac{\partial K_0^{(0,0)}}{\partial r} + \tilde{r} \right) \frac{\partial r}{\partial V^I} + \left(\frac{\partial K_0^{(0,0)}}{\partial \bar{r}} + \tilde{\bar{r}} \right) \frac{\partial \bar{r}}{\partial V^I} + \frac{\partial K^{(0,0)}}{\partial V^I}, \quad (3.30)$$

where the derivative in the last term is taken with r, \bar{r} held fixed. The two terms in parentheses vanish. In particular, the variational equation of $\tilde{\mathbb{V}}$ sets $\bar{r} = \chi - \bar{\phi}$. The T-dual potential then simplifies to

$$\tilde{K}^{(0,0)} = \frac{1}{2}(\chi - \bar{\chi})^2 + \int^{\phi + \bar{\phi} - \chi - \bar{\chi}} dq \log(1 + e^q) - \frac{1}{2}((\phi - \chi)^2 + (\bar{\phi} - \bar{\chi})^2), \quad (3.31)$$

which we recognize as (3.14) up to a generalized Kähler transformation. We have obtained the type (1, 1) potential without the need to solve second order differential equations.

3.3.2 Using the group coordinates to find the T-dual

We make an observation of the T-dualities which we performed, which we will apply to simplify the discussion in the $SU(3)$ case.

In the type (0, 0) structure, both complex structures J_{\pm} were induced from the Lie algebra structure \mathbb{J}_1 . As discussed in section 2.5, T-duality along the left Kac-Moody isometry $U(1)_L$ does not change the metric, torsion and left complex structure. Therefore, on the dual type (1, 1) structure, we know exactly what the complex structures are: J_+ is unchanged and is still induced from \mathbb{J}_1 , while J_- is changed and is now induced from \mathbb{J}_2 . The adapted coordinates for this particular generalized Kähler structure are already

known and given in (3.12). The solution to the SVM equations of motion must therefore be given by the original type (0, 0) coordinates (3.6),¹⁵ expressed in terms of the type (1, 1) coordinates of the dual (3.12), to wit

$$\begin{aligned} \ell &= \chi + \phi, & \tilde{\ell} &= \phi, \\ r &= \bar{\chi} - \phi, & \tilde{r} &= \phi - \theta, \end{aligned} \quad \text{where } \theta = \log(e^{\phi+\bar{\phi}} + e^{\chi+\bar{\chi}}). \quad (3.32)$$

Notice also that, when the isometries act as translations (all the examples we encounter in this paper are translational isometries), the Lagrange multiplier term may be written as

$$V^I \Phi_I = -\ell(\Phi) \tilde{\ell} - \bar{\ell}(\Phi) \tilde{\bar{\ell}} - r(\Phi) \tilde{r} - \bar{r}(\Phi) \tilde{\bar{r}}, \quad (3.33)$$

where $\ell(\Phi), \bar{\ell}(\Phi), r(\Phi), \bar{r}(\Phi)$ are functions of $\Phi = (\phi, \bar{\phi}, \chi, \bar{\chi})$ given in (3.32). This yields a simple integral expression for the type (1, 1) potential

$$\begin{aligned} K^{(1,1)}(\phi, \bar{\phi}, \chi, \bar{\chi}) &= \left(-\int \ell d\tilde{\ell} + \bar{\ell} d\tilde{\bar{\ell}} + r d\tilde{r} + \bar{r} d\tilde{\bar{r}} \right) - V^I \Phi_I \\ &= \int \tilde{\ell} d\ell + \tilde{\bar{\ell}} d\bar{\ell} + \tilde{r} dr + \tilde{\bar{r}} d\bar{r}, \end{aligned} \quad (3.34)$$

where the semi-chiral fields $\tilde{\ell}, \tilde{\bar{\ell}}, \tilde{r}, \tilde{\bar{r}}$ are to be understood as functions of ϕ, χ through (3.32). It is straightforward to verify, via direct substitution, that this exactly reproduces (3.31).

For another illustration of using the group coordinates to solve the vector multiplet moment map equations, see appendix F where the T-duality in the other direction, which is done with an Large Vector Multiplet (LVM) [23], is discussed.

4 SU(3)

4.1 Complex coordinates and generalized Kähler potential

On the Lie algebra, take the basis $\{h, \bar{h}, e_3, \bar{e}_3, e_1, \bar{e}_1, e_2, \bar{e}_2\}$, where

$$h = \begin{pmatrix} \frac{1}{2} + \frac{i}{2\sqrt{3}} & & & \\ & -\frac{i}{\sqrt{3}} & & \\ & & -\frac{1}{2} + \frac{i}{2\sqrt{3}} & \\ & & & \end{pmatrix}, \quad e_3 = \begin{pmatrix} 1 \\ & & & \\ & & & \\ & & & \end{pmatrix}, \quad e_1 = \begin{pmatrix} 1 \\ & & & \\ & & & \\ & & & \end{pmatrix}, \quad e_2 = \begin{pmatrix} & & & \\ & & & \\ & & & \\ & & & 1 \end{pmatrix}, \quad (4.1)$$

and the bar denotes hermitian conjugation. The two complex structures on the Lie algebra compatible with the choice of Cartan subalgebra h, \bar{h} are

$$\mathbb{J}_1 = \text{diag}(i, -i, i, -i, i, -i, i, -i), \quad \text{and} \quad \mathbb{J}_2 = \text{diag}(-i, i, i, -i, i, -i, i, -i). \quad (4.2)$$

As discussed in section 2.3, SU(3) admits generalized Kähler structures of two different types depending on whether one takes J_{\pm} induced from the same or from different Lie algebra complex structures $\mathbb{J}_1, \mathbb{J}_2$.

¹⁵With ℓ replaced with $\ell + \tilde{\ell}$ corresponding to the addition of the generalized Kähler transformation term $-\frac{1}{2}(\tilde{\ell}^2 + \bar{\tilde{\ell}}^2)$.

4.1.1 Type (0, 0)

If one takes J_+ and J_- both to be induced from the same Lie algebra complex structure, say \mathbb{J}_1 , then generically the resulting generalized Kähler structure has type (0, 0).¹⁶ The J_{\pm} complex coordinates take the simplest form when presented in an overcomplete basis,

$$\begin{aligned} z_+^{\phi} &= \log \bar{g}_{31}^{\omega} g_{13}^{\omega}, & z_+^{\chi} &= \log \bar{g}_{11}^{\omega} g_{33}^{\omega}, \\ z_+^1 &= \log \frac{g_{13}}{g_{23}}, & z_+^2 &= \log \frac{g_{23}}{g_{33}}, & z_+^3 &= \log \frac{\bar{g}_{11}}{\bar{g}_{21}}, & z_+^4 &= \log \frac{\bar{g}_{21}}{\bar{g}_{31}}, \end{aligned} \quad (4.3)$$

$$\begin{aligned} z_-^{\phi} &= \log \bar{g}_{31}^{\omega} g_{13}^{\omega}, & z_-^{\bar{\chi}} &= \log \bar{g}_{11}^{\omega} \bar{g}_{33}^{\omega}, \\ z_-^1 &= \log \frac{g_{11}}{g_{12}}, & z_-^2 &= \log \frac{g_{12}}{g_{13}}, & z_-^3 &= \log \frac{\bar{g}_{31}}{\bar{g}_{32}}, & z_-^4 &= \log \frac{\bar{g}_{32}}{\bar{g}_{33}}, \end{aligned} \quad (4.4)$$

where g_{ij} is the (i, j) th entry of the group element g in the defining representation of $SU(3)$, and $\omega = e^{i\pi/3} = \frac{1}{2}(1 + i\sqrt{3})$. For each of $+$ and $-$, the six complex coordinates satisfy two relations

$$\begin{aligned} e^{z_{\pm}^1 + z_{\pm}^3} + e^{-z_{\pm}^2 - z_{\pm}^4} + 1 &= 0, \\ z_+^{\phi} - z_+^{\chi} &= \omega(z_+^1 + z_+^2) - \bar{\omega}(z_+^3 + z_+^4), \\ z_-^{\phi} - z_-^{\bar{\chi}} &= -\bar{\omega}(z_-^1 + z_-^2) + \omega(z_-^3 + z_-^4). \end{aligned} \quad (4.5)$$

Semichiral coordinates are holomorphic coordinates that are Darboux with respect to the Poisson structure σ : $\sigma(d\ell^j, d\bar{\ell}^k) = \delta^{jk}$, $\sigma(d\ell^j, d\ell^k) = \sigma(d\bar{\ell}^j, d\bar{\ell}^k) = 0$, $\sigma(dr^j, d\bar{r}^k) = -\delta^{jk}$ and $\sigma(dr^j, dr^k) = \sigma(d\bar{r}^j, d\bar{r}^k) = 0$. One choice of semi-chiral coordinates is given by

$$\begin{aligned} \hat{\ell}^1 &= \frac{1}{3}(z_+^{\chi} + 2z_+^{\phi} - \omega z_+^1 + \bar{\omega} z_+^4) = \frac{1}{3} \log(\bar{g}_{11} \bar{g}_{21} \bar{g}_{31})^{\bar{\omega}} (g_{13} g_{23} g_{33})^{\omega}, \\ \hat{\bar{\ell}}^1 &= (\bar{\omega} - \omega)(z_+^1 + z_+^2 + z_+^3 + z_+^4) = (\bar{\omega} - \omega) \log \frac{\bar{g}_{11} g_{13}}{\bar{g}_{31} g_{33}}, \\ \hat{\ell}^2 &= z_+^{\chi} = \log \bar{g}_{11}^{\omega} g_{33}^{\omega}, \\ \hat{\bar{\ell}}^2 &= z_+^{\phi} = \log \bar{g}_{31}^{\omega} g_{13}^{\omega}, \\ \hat{r}^1 &= (\bar{\omega} - \omega)(z_-^1 + z_-^2 + z_-^3 + z_-^4) = (\bar{\omega} - \omega) \log \frac{g_{13} \bar{g}_{33}}{g_{11} \bar{g}_{31}}, \\ \hat{r}^1 &= \frac{1}{3}(z_-^{\bar{\chi}} + 2z_-^{\phi} + \bar{\omega} z_-^2 - \omega z_-^3) = \frac{1}{3} \log(g_{11} g_{12} g_{13})^{\bar{\omega}} (\bar{g}_{31} \bar{g}_{32} \bar{g}_{33})^{\omega}, \\ \hat{r}^2 &= z_-^{\bar{\chi}} = \log \bar{g}_{11}^{\omega} \bar{g}_{33}^{\omega}, \\ \hat{\bar{r}}^2 &= z_-^{\phi} = \log \bar{g}_{13}^{\omega} \bar{g}_{31}^{\omega}. \end{aligned} \quad (4.6)$$

(Recall $\omega = e^{i\pi/3} = \frac{1}{2}(1 + i\sqrt{3})$.) Choosing the polarizations defined by $\hat{\ell}^j, \hat{\bar{\ell}}^j$ and $\hat{r}^j, \hat{\bar{r}}^j$, the group element is parametrized as

$$g = \begin{pmatrix} \exp(\hat{\bar{\ell}}^2 + u\hat{h}_1) & \exp(3\hat{r}^1 - \hat{\bar{\ell}}^2 - \hat{r}^2 - \hat{h}_1 + \bar{u}\hat{h}_4) & \exp(\hat{r}^2 - \bar{u}\hat{h}_2) \\ -\exp(3\hat{\bar{\ell}}^1 - \hat{\bar{\ell}}^2 - \hat{r}^2 - \hat{h}_2 + u\hat{h}_3) & g_{22} & \exp(3\hat{\ell}^1 - \hat{\bar{\ell}}^2 - \hat{r}^2 - \hat{h}_2 + u\hat{h}_3) \\ \exp(\hat{r}^2 - \bar{u}\hat{h}_2) & -\exp(3\hat{\bar{r}}^1 - \hat{\bar{r}}^2 - \hat{\bar{\ell}}^2 - \hat{h}_1 + \bar{u}\hat{h}_4) & \exp(\hat{\bar{\ell}}^2 + u\hat{h}_1) \end{pmatrix} \quad (4.7)$$

¹⁶There are loci of positive codimension on which $\ker[J_+, J_-]$ is nontrivial.

where $u = \frac{1}{\sqrt{3}}e^{i\pi/6} = \frac{1}{2}(1 + \frac{i}{\sqrt{3}})$ and $\hat{h}_1, \hat{h}_2, \hat{h}_3, \hat{h}_4$ are functions of $\hat{\ell}^j, \bar{\ell}^j, \hat{r}^j, \bar{r}^j$, determined by the orthonormality of the first and third rows and columns;¹⁷ and finally g_{22} may be determined by unimodularity.

To find the potential, we need to express $\hat{\ell}^j, \hat{r}^j$ in terms of $\bar{\ell}^j, \bar{r}^j$. It is straightforward to verify that

$$\begin{aligned}\hat{\ell}^1 &= -\bar{h}_1 + \hat{h}_2, \\ \hat{\ell}^2 &= \hat{r}^2 - \hat{h}_2, \\ \hat{r}^1 &= -\hat{h}_1 + \hat{h}_2, \\ \hat{r}^2 &= \bar{\ell}^2 + \hat{h}_1.\end{aligned}\tag{4.8}$$

The difference between the one-form symplectic potentials adapted to the left and right semi-chiral coordinates is the closed one-form $\hat{\theta}_1 + \hat{\theta}_2$, where

$$\hat{\theta}_j = \hat{\ell}^j d\hat{\ell}^j + \bar{\ell}^j d\bar{\ell}^j - \hat{r}^j d\hat{r}^j - \bar{r}^j d\bar{r}^j \quad (\text{no sum over } j).\tag{4.9}$$

The potential is given by

$$K = \int_{\mathcal{O}}^{(\hat{\ell}^j, \bar{\ell}^j, \hat{r}^j, \bar{r}^j)} \hat{\theta}_1 + \hat{\theta}_2,\tag{4.10}$$

where \mathcal{O} is some base point. The closure condition $d(\hat{\theta}_1 + \hat{\theta}_2) = 0$ ensures that the integral is independent of path. K generates the symplectomorphism between left and right semi-chiral coordinates

$$\begin{aligned}\frac{\partial K}{\partial \hat{\ell}^j} &= \hat{\ell}^j, & \frac{\partial K}{\partial \bar{\ell}^j} &= \bar{\ell}^j, \\ \frac{\partial K}{\partial \hat{r}^j} &= -\hat{r}^j, & \frac{\partial K}{\partial \bar{r}^j} &= -\bar{r}^j.\end{aligned}\tag{4.11}$$

A different choice. In section 4.2, it will prove convenient to choose instead the following Darboux coordinates (these are adapted to the isometry considered later in section 4.2)

$$\begin{aligned}\ell^1 &= \frac{1}{3}(z_+^\chi + 2z_+^\phi - \omega z_+^1 + \bar{\omega} z_+^4) = \frac{1}{3} \log(\bar{g}_{11}\bar{g}_{21}\bar{g}_{31})^{\bar{\omega}}(g_{13}g_{23}g_{33})^\omega, \\ \bar{\ell}^1 &= (\bar{\omega} - \omega)(z_+^1 + z_+^2 + z_+^3 + z_+^4) = (\bar{\omega} - \omega) \log \frac{\bar{g}_{11}g_{13}}{\bar{g}_{31}g_{33}}, \\ \ell^2 &= z_+^\chi = \log \bar{g}_{11}g_{33}^\omega, \\ \bar{\ell}^2 &= z_+^\phi + z_+^\chi = \log(\bar{g}_{11}\bar{g}_{31})^{\bar{\omega}}(g_{13}g_{33})^\omega, \\ r^1 &= (\omega - 2\bar{\omega})(z_-^1 + z_-^2) + (2\omega - \bar{\omega})(z_-^3 + z_-^4) = (2\bar{\omega} - \omega) \log \frac{g_{13}}{g_{11}} + (\bar{\omega} - 2\omega) \log \frac{\bar{g}_{33}}{\bar{g}_{31}}, \\ \bar{r}^1 &= \frac{1}{6}(z_-^\chi - z_-^\phi + \bar{\omega} z_-^2 - \omega z_-^3) = \frac{1}{6} \log \left(\frac{g_{11}g_{12}}{g_{13}^2} \right)^{\bar{\omega}} \left(\frac{\bar{g}_{32}\bar{g}_{33}}{\bar{g}_{31}^2} \right)^\omega, \\ r^2 &= \omega(z_-^1 + z_-^2) - \bar{\omega}(z_-^3 + z_-^4) = \log \frac{g_{11}^\omega \bar{g}_{33}^{\bar{\omega}}}{g_{13}^\omega \bar{g}_{31}^{\bar{\omega}}}, \\ \bar{r}^2 &= \frac{1}{6}(z_-^\chi + 5z_-^\phi + \bar{\omega} z_-^2 - \omega z_-^3) = \frac{1}{6} \log(g_{11}g_{12}g_{13}^4)^{\bar{\omega}}(\bar{g}_{31}^4\bar{g}_{32}\bar{g}_{33})^\omega.\end{aligned}\tag{4.12}$$

¹⁷Unfortunately, it seems that $\hat{h}_1, \hat{h}_2, \hat{h}_3, \hat{h}_4$ cannot be written down in terms of elementary functions, so we have to work implicitly.

In the polarizations defined by $\ell^j, \bar{\ell}^j$ and $\tilde{r}^j, \bar{\tilde{r}}^j$, the group element is parametrized as

$$g = \begin{pmatrix} \exp(\bar{\ell}^2 + u h_1) & \exp(4\tilde{r}^1 - \bar{\ell}^2 + 2\tilde{r}^2 - h_1 + \bar{u} h_4) & \exp(-\tilde{r}^1 + \tilde{r}^2 - \bar{u} h_2) \\ -\exp(3\bar{\ell}^1 - \bar{\ell}^2 + \tilde{r}^1 - \tilde{r}^2 - \bar{h}_2 + u h_3) & g_{22} & \exp(3\ell^1 - \ell^2 + \tilde{r}^1 - \tilde{r}^2 - h_2 + u \bar{h}_3) \\ \exp(-\tilde{r}^1 + \tilde{r}^2 - \bar{u} \bar{h}_2) & -\exp(4\bar{\tilde{r}}^1 + 2\bar{\tilde{r}}^2 - \ell^2 - \bar{h}_1 + \bar{u} \bar{h}_4) & \exp(\ell^2 + u \bar{h}_1) \end{pmatrix}, \quad (4.13)$$

where h_1, h_2, h_3, h_4 are once again functions of $\ell^j, \bar{\ell}^j, \tilde{r}^j, \bar{\tilde{r}}^j$ determined by the orthonormality of the first and last rows and columns. The Darboux partners are expressed in this mixed coordinate system as

$$\begin{aligned} \tilde{\ell}^1 &= -\bar{h}_1 + h_2, \\ \tilde{\ell}^2 &= -\tilde{r}^1 + \tilde{r}^2 + \ell^2 - h_2, \\ r^1 &= -\bar{\ell}^2 - \tilde{r}^1 + \tilde{r}^2 - 2h_1 + h_2, \\ r^2 &= \bar{\ell}^2 + \tilde{r}^1 - \tilde{r}^2 + h_2. \end{aligned} \quad (4.14)$$

The generalized potential is given by

$$K^{(0,0)} = \int_{\mathcal{O}}^{(\ell^j, \bar{\ell}^j, \tilde{r}^j, \bar{\tilde{r}}^j)} \theta_1 + \theta_2, \quad \text{where } \theta = \theta_1 + \theta_2, \quad (4.15)$$

$$\theta_j = \tilde{\ell}^j d\ell^j + \bar{\tilde{\ell}}^j d\bar{\ell}^j - r^j d\tilde{r}^j - \bar{r}^j d\bar{\tilde{r}}^j \quad (\text{no sum over } j) \quad (4.16)$$

4.1.2 Type (1, 1)

If one instead takes J_+ and J_- induced from different Lie algebra complex structures, say J_+ from \mathbb{J}_1 and J_- from \mathbb{J}_2 , then generically the resulting generalized Kähler structure has type (1, 1). The biholomorphic coordinate is

$$\phi = \log \bar{g}_{31}^{\bar{\omega}} g_{13}^{\omega}, \quad (4.17)$$

and represents a chiral superfield in the (2, 2) sigma model, while the J_+ -holomorphic and J_- -antiholomorphic coordinate is

$$\chi = \log \bar{g}_{11}^{\bar{\omega}} g_{33}^{\omega}, \quad (4.18)$$

and represents a twisted chiral superfield. The other holomorphic coordinates once again take the simplest form in an overcomplete basis

$$w_+^1 = \log \frac{g_{13}}{g_{23}}, \quad w_+^2 = \log \frac{g_{23}}{g_{33}}, \quad w_+^3 = \log \frac{\bar{g}_{11}}{g_{21}}, \quad w_+^4 = \log \frac{\bar{g}_{21}}{\bar{g}_{31}}, \quad (4.19)$$

$$w_-^1 = \log \frac{g_{11}}{g_{12}}, \quad w_-^2 = \log \frac{g_{12}}{g_{13}}, \quad w_-^3 = \log \frac{\bar{g}_{31}}{\bar{g}_{32}}, \quad w_-^4 = \log \frac{\bar{g}_{32}}{\bar{g}_{33}}, \quad (4.20)$$

satisfying

$$e^{w_{\pm}^1 + w_{\pm}^3} + e^{-w_{\pm}^2 - w_{\pm}^4} + 1 = 0, \quad (4.21)$$

$$\phi - \chi = \omega(w_+^1 + w_+^2) - \bar{\omega}(w_+^3 + w_+^4), \quad (4.22)$$

$$\phi - \bar{\chi} = -\omega(w_-^1 + w_-^2) + \bar{\omega}(w_-^3 + w_-^4). \quad (4.23)$$

One choice of semi-chiral coordinates is

$$\begin{aligned}
 \hat{\ell} &= \phi - \omega w_+^1 + \bar{\omega} w_+^4 = \log g_{23}^\omega \bar{g}_{21}^{\bar{\omega}}, \\
 \hat{\bar{\ell}} &= -w_+^1 - w_+^2 + w_+^3 + w_+^4 = \log \frac{\bar{g}_{11} g_{33}}{\bar{g}_{31} g_{13}}, \\
 \hat{r} &= -w_-^1 - w_-^2 + w_-^3 + w_-^4 = \log \frac{\bar{g}_{31} g_{13}}{g_{11} \bar{g}_{33}}, \\
 \hat{\bar{r}} &= \phi + \omega w_-^2 - \bar{\omega} w_-^3 = \log g_{12}^\omega \bar{g}_{32}^{\bar{\omega}}.
 \end{aligned}
 \tag{4.24}$$

In the polarizations defined by $\hat{\ell}, \hat{\bar{\ell}}$ and $\hat{r}, \hat{\bar{r}}$, the parametrization looks relatively uncluttered

$$g = \begin{pmatrix} e^{\bar{\chi}+u\hat{f}_1} & e^{\hat{r}+u\hat{f}_4} & e^{\phi+u\hat{f}_2} \\ -e^{\bar{\ell}+u\hat{f}_3} & g_{22} & e^{\hat{\ell}+u\hat{f}_3} \\ e^{\bar{\phi}+u\hat{f}_2} & -e^{\hat{\bar{r}}+u\hat{f}_4} & e^{\chi+u\hat{f}_1} \end{pmatrix}.
 \tag{4.25}$$

(Recall $u = \frac{1}{\sqrt{3}}e^{i\pi/6} = \frac{1}{2}(1 + \frac{i}{\sqrt{3}})$.) The conditions of orthonormality on the first and third rows and columns are

$$\begin{aligned}
 e^{\phi+\chi}(e^{\bar{u}\hat{f}_1+u\hat{f}_2} + e^{u\hat{f}_1+\bar{u}\hat{f}_2}) - e^{2\hat{\ell}+\sqrt{3}\hat{f}_3} &= 0, \\
 e^{\phi+\bar{\chi}}(e^{\bar{u}\hat{\bar{f}}_1+u\hat{f}_2} + e^{u\hat{\bar{f}}_1+\bar{u}\hat{f}_2}) - e^{2\hat{\bar{r}}+\sqrt{3}\hat{f}_4} &= 0, \\
 e^{2\text{Re}(\chi+u\hat{f}_1)} + e^{2\text{Re}(\phi+u\hat{f}_2)} + e^{2\text{Re}(\hat{\ell}+u\hat{f}_3)} &= 1, \\
 e^{2\text{Re}(\chi+\bar{u}\hat{f}_1)} + e^{2\text{Re}(\phi+\bar{u}\hat{f}_2)} + e^{2\text{Re}(\hat{\bar{\ell}}+\bar{u}\hat{f}_3)} &= 1, \\
 e^{2\text{Re}(\chi+\bar{u}\hat{f}_1)} + e^{2\text{Re}(\phi+u\hat{f}_2)} + e^{2\text{Re}(\hat{r}+u\hat{f}_4)} &= 1, \\
 e^{2\text{Re}(\chi+u\hat{f}_1)} + e^{2\text{Re}(\phi+\bar{u}\hat{f}_2)} + e^{2\text{Re}(\hat{\bar{r}}+\bar{u}\hat{f}_4)} &= 1.
 \end{aligned}
 \tag{4.26}$$

The first equation of (4.26) is complex, and may be solved for \hat{f}_3 in terms of $\phi, \chi, \hat{\ell}, \hat{f}_1, \hat{f}_2$. This may then be substituted into the third and fourth equations, which are real. Similarly, the second complex equation may be solved for \hat{f}_4 in terms of $\phi, \bar{\chi}, \hat{\bar{r}}, \hat{\bar{f}}_1, \hat{f}_2$, and substituted into the fifth and sixth equations. This yields four real equations, from which we may solve for $\hat{f}_1, \hat{f}_2, \hat{\bar{f}}_1$ and $\hat{\bar{f}}_2$.¹⁸ It is not obvious, at first glance, that these 8 real equations (4.26) are independent — for instance, the equations $gg^\dagger = \mathbb{1}$ and $g^\dagger g = \mathbb{1}$ are equivalent — but we have checked that they indeed are, and hence uniquely determine the $\hat{f}_i, \hat{\bar{f}}_i$ s.

Note that these equations (4.26) exhibit two involutive symmetries. There is first a left-right symmetry given by exchanging $\chi \leftrightarrow \bar{\chi}, \hat{\ell} \leftrightarrow \hat{\bar{r}}, \hat{f}_1 \leftrightarrow \hat{\bar{f}}_1, \hat{f}_3 \leftrightarrow \hat{f}_4$, which exchanges the first, third, fourth equations with the second, fifth and sixth equations. Under this symmetry, the Darboux partners

$$\hat{\bar{\ell}} = \log \frac{\bar{g}_{11} g_{33}}{\bar{g}_{31} g_{13}} = 2\chi - 2\phi + \hat{f}_1 - \hat{f}_2,
 \tag{4.27}$$

$$\hat{r} = \log \frac{\bar{g}_{31} g_{13}}{g_{11} \bar{g}_{33}} = 2\phi - 2\bar{\chi} - \hat{\bar{f}}_1 + \hat{f}_2
 \tag{4.28}$$

¹⁸As before, it is not possible to write down $\hat{f}_1, \hat{f}_2, \hat{\bar{f}}_1, \hat{\bar{f}}_2$ using elementary functions, so we work implicitly.

are interchanged with a twist, $\hat{\ell} \leftrightarrow -\hat{r}$. Second, there is a local mirror symmetry which exchanges $\phi \leftrightarrow \chi, \hat{r} \leftrightarrow \bar{\hat{r}}, \hat{f}_1 \leftrightarrow \hat{f}_2, \hat{f}_4 \leftrightarrow \bar{\hat{f}}_4, \hat{\ell} \leftrightarrow -\hat{\ell}, \hat{r} \leftrightarrow -\bar{\hat{r}}$. This exchanges the second equation with its conjugate, and the fifth with the sixth equation, and preserves the other equations.

On top of symplectomorphisms on each symplectic leaf, the semi-chiral coordinates may also be redefined by arbitrary functions of chiral and twisted chiral coordinates (with the appropriate holomorphy)

$$\begin{aligned}\hat{\ell} &\mapsto \hat{\ell}'(\hat{\ell}, \bar{\hat{\ell}}, \phi, \chi), \\ \hat{r} &\mapsto \hat{r}'(\hat{r}, \bar{\hat{r}}, \phi, \bar{\chi}).\end{aligned}\tag{4.29}$$

There is therefore a large amount of freedom in the choice of holomorphic Darboux coordinates $\hat{\ell}, \bar{\hat{\ell}}, \hat{r}, \bar{\hat{r}}$.

A different choice. In section 4.2 we will find it convenient to use a different choice of semi-chiral coordinates (adapted to an isometry introduced later in section 4.2), given by

$$\begin{aligned}\ell &= \frac{1}{3}(w_+^\chi + 2w_+^\phi - \omega w_+^1 + \bar{\omega} w_+^4) = \frac{1}{3} \log(\bar{g}_{11} \bar{g}_{21} \bar{g}_{31})^{\bar{\omega}} (g_{13} g_{23} g_{33})^\omega, \\ \tilde{\ell} &= (\bar{\omega} - \omega)(w_+^1 + w_+^2 + w_+^3 + w_+^4) = (\bar{\omega} - \omega) \log \frac{\bar{g}_{11} g_{13}}{\bar{g}_{31} g_{33}}, \\ r &= (\omega - 2\bar{\omega})(w_-^1 + w_-^2) + (2\omega - \bar{\omega})(w_-^3 + w_-^4) = (\omega - 2\bar{\omega}) \log \frac{g_{11}}{g_{13}} + (\bar{\omega} - 2\omega) \log \frac{\bar{g}_{33}}{\bar{g}_{31}}, \\ \tilde{r} &= \frac{1}{6}(\bar{\omega} w_-^1 + 2\bar{\omega} w_-^2 - 2\omega w_-^3 - \omega w_-^4) = \frac{1}{6} \log \left(\frac{g_{11} g_{12}}{g_{13}^2} \right)^{\bar{\omega}} \left(\frac{\bar{g}_{32} \bar{g}_{33}}{\bar{g}_{31}^2} \right)^\omega.\end{aligned}\tag{4.30}$$

Note that they coincide with $\ell^1, \bar{\ell}^1, r^1, \bar{r}^1$ in (4.12). The parametrization of the group element is

$$g = \begin{pmatrix} \exp(\bar{\chi} + u f_1) & \exp(6\tilde{r} + 2\phi - \bar{\chi} - f_1 + 2f_2 + \bar{u} f_4) & \exp(\phi + u f_2) \\ -\exp(3\ell - \bar{\phi} - \bar{\chi} + u f_3) & g_{22} & \exp(3\ell - \phi - \chi + u \bar{f}_3) \\ \exp(\bar{\phi} + u \bar{f}_2) & -\exp(6\bar{\tilde{r}} + 2\bar{\phi} - \chi - \bar{f}_1 + 2\bar{f}_2 + \bar{u} \bar{f}_4) & \exp(\chi + u \bar{f}_1) \end{pmatrix},\tag{4.31}$$

with the Darboux partners given by

$$\begin{aligned}\tilde{\ell} &= -\bar{f}_1 + f_2, \\ r &= \phi - \bar{\chi} - 2f_1 + 2f_2.\end{aligned}\tag{4.32}$$

On each symplectic leaf, the generating function of the symplectomorphism (4.11) $(\ell, \bar{\ell}, \tilde{\ell}, \bar{\tilde{\ell}}) \rightarrow (r, \bar{r}, \tilde{r}, \bar{\tilde{r}})$ is formally

$$K^{(1,1)} = \int_{\mathcal{O}}^{(\ell, \bar{\ell}, \tilde{\ell}, \bar{\tilde{\ell}})} \theta_1, \quad \text{where } \theta_1 = \tilde{\ell} d\ell + \bar{\tilde{\ell}} d\bar{\ell} - r d\tilde{r} - \bar{r} d\bar{\tilde{r}},\tag{4.33}$$

where $\mathcal{O} = \mathcal{O}(\phi, \bar{\phi}, \chi, \bar{\chi})$ is collection of base points, one on each symplectic leaf. To find the explicit dependence of K on $\phi, \bar{\phi}, \chi, \bar{\chi}$, one has to, as discussed above, solve the second order nonlinear differential equations (B.12)–(B.13). However, this can be circumvented, as discussed in section 2.6, by relating the type (1, 1) generalized Kähler structure to the type (0, 0) structure (4.15).

4.2 T-duality: relating the two generalized Kähler structures

4.2.1 Isometries

The group of isometries preserving both complex structures of $SU(3)$ is $U(1)_L^2 \times U(1)_R^2$, acting on the group element as

$$g \mapsto h_L g h_R^{-1} \equiv e^{\epsilon \bar{h} - \bar{\epsilon} h} g e^{\bar{\eta} \bar{h} - \eta h}, \quad (4.34)$$

where h and \bar{h} are defined in (4.1), and ϵ and η are complex Kac-Moody parameters. In the type (0,0) structure, they obey the constraints

$$\bar{\mathbb{D}}_+ \epsilon = 0, \quad \mathbb{D}_\pm \epsilon = 0, \quad \bar{\mathbb{D}}_\pm \eta = 0, \quad \mathbb{D}_- \eta = 0, \quad (4.35)$$

and the coordinates (4.12) transform as

$$\begin{aligned} \ell^1 &\mapsto \ell^1 + \eta, & \tilde{\ell}^1 &\mapsto \tilde{\ell}^1, \\ \ell^2 &\mapsto \ell^2 + \bar{\epsilon} + \eta, & \tilde{\ell}^2 &\mapsto \tilde{\ell}^2 + \epsilon + \bar{\epsilon} + 2\eta, \\ r^1 &\mapsto r^1 + \eta - \bar{\eta}, & \tilde{r}^1 &\mapsto \tilde{r}^1 + \frac{1}{2}\bar{\eta}, \\ r^2 &\mapsto r^2 - \eta + \bar{\eta}, & \tilde{r}^2 &\mapsto \tilde{r}^2 - \bar{\epsilon} - \frac{1}{2}\bar{\eta}. \end{aligned} \quad (4.36)$$

Meanwhile, in the type (1,1) structure, ϵ and η obey (note that, as in the $SU(2) \times U(1)$ case, the chirality constraint on ϵ differs from that in the type (0,0) structure)

$$\bar{\mathbb{D}}_\pm \epsilon = 0, \quad \mathbb{D}_+ \epsilon = 0, \quad \bar{\mathbb{D}}_\pm \eta = 0, \quad \mathbb{D}_- \eta = 0, \quad (4.37)$$

and the coordinates (4.30) transform as

$$\begin{aligned} \phi &\mapsto \phi + \epsilon + \eta, & \chi &\mapsto \chi + \bar{\epsilon} + \eta, \\ \ell &\mapsto \ell + \eta, & \tilde{\ell} &\mapsto \tilde{\ell}, \\ r &\mapsto r + \eta - \bar{\eta}, & \tilde{r} &\mapsto \tilde{r} + \frac{1}{2}\bar{\eta}. \end{aligned} \quad (4.38)$$

4.2.2 T-duality from type (0,0) to type (1,1)

In this subsection, we T-dualize from the type (0,0) structure (4.15) to the type (1,1) structure along the left Kac-Moody $U(1)_L$ isometry defined by setting $\epsilon = i\lambda$ and $\eta = 0$ in (4.34), where λ is a real parameter. Under this isometry, $\ell^1, \bar{\ell}^1, \tilde{r}^1, \bar{\tilde{r}}^1$ are invariant spectator fields, while $\ell^2 \mapsto \ell^2 - i\lambda$, $\tilde{r}^2 \mapsto \tilde{r}^2 + i\lambda$. The invariance of the Darboux partners $\tilde{\ell}^j, \bar{\tilde{\ell}}^j, r^j, \tilde{r}^j$ guarantees that the potential (4.15) is invariant this isometry.

The Killing field of the isometry is

$$k = i(-\partial_{\ell^2} + \partial_{\bar{\ell}^2} + \partial_{\tilde{r}^2} - \partial_{\bar{\tilde{r}}^2}); \quad (4.39)$$

and the invariant combinations $-\ell^2 - \bar{\ell}^2$, $\tilde{r}^2 + \bar{\tilde{r}}^2$ and $i(\ell^2 - \bar{\ell}^2 + \tilde{r}^2 - \bar{\tilde{r}}^2)$ can be gauged respectively by the components V^L, V^R and V^I of the SVM. The T-dual potential is obtained by constraining the SVM to be flat using Lagrange multipliers Φ_I

$$\tilde{K}(\ell^1, \bar{\ell}^1, \tilde{r}^1, \bar{\tilde{r}}^1, \Phi_I) = K^g(\ell^1, \bar{\ell}^1, \tilde{r}^1, \bar{\tilde{r}}^1, V^I) - V^I \Phi_I, \quad (4.40)$$

where V^I are to be eliminated using their equations of motion. We make use of the observation in section 3.3.2: since the T-duality is along a left Kac-Moody isometry, the left complex structure is preserved and continues to be induced by \mathbb{J}_1 , and therefore the relation between the type (0,0) coordinates (4.12) and type (1,1) coordinates (4.17), (4.18), (4.30) is a solution to the SVM equations of motion. This relation is

$$\begin{aligned}\ell^2 &= \chi, \\ \tilde{\ell}^2 &= \phi + \chi, \\ r^2 &= \bar{\chi} - \phi, \\ \tilde{r}^2 &= \tilde{r}^1 + \phi + f_2.\end{aligned}\tag{4.41}$$

It is easily verified that this relation is consistent with (4.14). The moment maps are linear combinations of the Darboux partners since the isometry acts translationally, so the SVM equations of motion are

$$\begin{aligned}\Phi_L &= -\frac{1}{2}(\tilde{\ell}^2 + \bar{\tilde{\ell}}^2), \\ \Phi_R &= -\frac{1}{2}(r^2 + \bar{r}^2), \\ \Phi' &= \frac{i}{4}(-\tilde{\ell}^2 + \bar{\tilde{\ell}}^2 + r^2 - \bar{r}^2),\end{aligned}\tag{4.42}$$

which is once again consistent with (4.41).

As in the $SU(2) \times U(1)$ case, we can write the dual potential as an integral. Note that the invariance of the type (0,0) potential implies

$$\mathcal{L}_k K = i(-\tilde{\ell}^2 + \bar{\tilde{\ell}}^2 - r^2 + \bar{r}^2) = 0,\tag{4.43}$$

which means that the Lagrange multiplier term is

$$V^I \Phi_I = \tilde{\ell}^2(\Phi)\ell^2 + \bar{\tilde{\ell}}^2(\Phi)\bar{\ell}^2 - r^2(\Phi)\tilde{r}^2 - \bar{r}^2(\Phi)\bar{\tilde{r}}^2,\tag{4.44}$$

where $\tilde{\ell}^2, \bar{\tilde{\ell}}^2, r^2, \bar{r}^2$ are understood as functions of $\Phi = (\phi, \bar{\phi}, \chi, \bar{\chi})$ given by (4.41). Therefore, the dual potential can be written as

$$\tilde{K} = \int \theta_1 - \ell^2 d\tilde{\ell}^2 - \bar{\ell}^2 d\bar{\tilde{\ell}}^2 + \tilde{r}^2 dr^2 + \bar{\tilde{r}}^2 d\bar{r}^2.\tag{4.45}$$

In terms of the functions f_1, f_2 defined in (4.13),

$$\begin{aligned}\tilde{K} &= \left(\int (-\bar{f}_1 + f_2) d\ell + 2(f_1 - f_2) d\tilde{r} - (\chi + f_2) d\phi + (\bar{\phi} + \bar{f}_2) d\chi \right) \\ &\quad - \frac{1}{2}(\phi^2 + \chi^2) + \tilde{r}(\bar{\chi} - \phi) + \text{cc}.\end{aligned}\tag{4.46}$$

Note that the two terms on the last line are generalized Kähler transformations. In contrast to (4.33), this is an unambiguous potential for the type (1,1) structure, obtained without having to solve the nonlinear differential equations (B.12)–(B.13).

4.2.3 Type (1, 1) to type (0, 0)

One can also perform the T-duality in the other direction, gauging the same left Kac-Moody isometry of the type (1, 1) geometry with an LVM and enforcing it to be flat with semi-chiral Lagrange multipliers, and then integrating out the LVM. This would return (4.46) to the type (0, 0) potential (4.15).

5 Discussion and conclusion

5.1 Results

In this paper, we studied the generalized Kähler structures of two rank 2 groups, $SU(2) \times U(1)$ and $SU(3)$, in detail. We found coordinates that were holomorphic with respect to left-invariant and right-invariant complex structures, and formulae (in one case explicit, in the other implicit) for their generalized Kähler potentials (which have an interpretation as the Lagrange density of the sigma model in (2, 2) superspace).

We explained how rank two groups carry generalized Kähler structures of two different types, related to one another by T-duality along a Kac-Moody isometry, and how a clever trick trivializes the Legendre transform that is usually needed to relate their generalized Kähler potentials. We also gave a wealth of computational details that may be useful for future investigations.

5.2 Possible future developments

5.2.1 Type change

Apart from $SU(2) \times U(1)$, $U(1)^2$ and their products, left and right complex structures on Lie groups do not commute, and therefore semi-chiral superfields are generically present. Semichiral coordinates are accompanied by type change loci, which are loci of positive codimension on which the type of the generalized geometry changes. For $SU(2) \times U(1)$, an analysis of the type change locus for the type (0, 0) generalized geometry was performed in [18]. For $SU(3)$, this has not yet been done and is a direction for future work.

5.2.2 (4, 4) supersymmetry

The WZW models on both $SU(2) \times U(1)$ and $SU(3)$ admit a further enhancement of supersymmetry to (4, 4). Such bi-hypercomplex Lie groups were classified [14], and the whole list of them are $SU(n+1)$, $SU(2n) \times U(1)$, $SO(4n) \times U(1)^{2n}$, $SO(4n+2) \times U(1)^{2n-1}$, $SO(2n+1) \times U(1)^n$, $Sp(2n) \times U(1)^n$, $E_6 \times U(1)^2$, $E_7 \times U(1)^7$, $E_8 \times U(1)^8$, $F_4 \times U(1)^4$, $G_2 \times U(1)^2$ (and products). There always exists a choice of left and right complex structures that gives rise to a type (0, 0) generalized geometry - fully parametrized by semi-chiral coordinates. For such generalized Kähler structures, the potential is an integral of a tautological one-form and can be easily computed without having to solve nonlinear second order PDEs. Generalized geometries of other types on these Lie groups can be obtained from the type (0, 0) geometry via T-duality and (possibly repeated) applications of the technique detailed above.

Another direction for the study of (4, 4) supersymmetric models is the problem of manifestly realizing all the supersymmetries. For $SU(2) \times U(1)$, a (4, 4) formulation of

the type (1, 1) generalized geometry in biprojective superspace is known [15] (although it is not known how to define the contour for the generalized potential), while for the type (0, 0) geometry, the extra supersymmetries are not compatible with (2, 2) superspace [19]. Preliminary investigations of the SU(3) model seem to indicate that it is not compatible with the multiplet structure of biprojective superspace. It is worthwhile to conduct a more thorough investigation of off-shell (4, 4) supersymmetry for WZW models.

5.2.3 Other groups

Another obvious direction is to investigate other groups. The holomorphic structures on SU(3) are surprisingly subtle and we can expect more surprises as we investigate higher rank groups.

Acknowledgments

The work of JPA and MR is supported in part by NSF grant PHY1620628. The work of SD and AS is supported in by the “FWO-Vlaanderen” through the project G020714N and an “aspirant” fellowship, and by the Vrije Universiteit Brussel through the Strategic Research Program “High-Energy Physics”. We are grateful to the Simons Center for Geometry and Physics for providing a stimulating environment during the conference “Generalized Geometry and T-dualities” where part of this work was performed.

A Sigma models and supersymmetry

The $d = 2$ non-linear sigma model is a Lagrangian field theory of maps φ from a two-dimensional worldsheet (Σ, h) to a target Riemannian manifold (M, g) , equipped with a closed 3-form H , known as the torsion. Let b be a local 2-form potential (the Kalb-Ramond 2-form) for H , $db = H$. The action is the sum of the integrals of the pullback (via φ) of g , with respect to the volume form of h , and the pullback (via φ) of b

$$I[\varphi] = \int_{\Sigma} \sqrt{h} d^2\sigma h^{\alpha\beta} \partial_{\alpha}\varphi^{\mu} g_{\mu\nu} \partial_{\beta}\varphi^{\nu} + \int_{\Sigma} d^2\sigma \epsilon^{\alpha\beta} \partial_{\alpha}\varphi^{\mu} b_{\mu\nu} \partial_{\beta}\varphi^{\nu}. \tag{A.1}$$

The action depends only on the conformal class of h .

Any sigma model admits an (1, 1) supersymmetric extension, which moreover can be written in (1, 1) superspace as

$$I[\Phi] = \int_{\Sigma} d^2\sigma d^2\theta \nabla_{+}\Phi^{\mu} (g_{\mu\nu} + b_{\mu\nu}) \nabla_{-}\Phi^{\nu} \tag{A.2}$$

where ∇_{\pm} are the (1, 1) supercovariant derivatives satisfying the algebra

$$\{\nabla_{\pm}, \nabla_{\pm}\} = 2i\partial_{\pm}, \quad \{\nabla_{\pm}, \nabla_{\mp}\} = 0, \tag{A.3}$$

and $\Phi^{\mu}(\sigma, \theta)$ is the (1, 1) superfield which has φ^{μ} as its bottom component.

To look for extended supersymmetries, one considers the most general transformations

$$\delta\Phi^{\mu} = \epsilon_{(A)}^{+} (J_{+}^{(A)})^{\mu}_{\nu} \nabla_{+}\Phi^{\nu} + \epsilon_{(\tilde{A})}^{-} (J_{-}^{(\tilde{A})})^{\mu}_{\nu} \nabla_{-}\Phi^{\nu}, \tag{A.4}$$

where $A = 2, \dots, \mathcal{N}_+$ and $\tilde{A} = 2, \dots, \mathcal{N}_-$ indexes the extended supersymmetries. Demanding that these transformations satisfy the supersymmetry algebra implies that the $J_+^{(A)}$ and $J_-^{(\tilde{A})}$ are integrable complex structures on M , and moreover satisfy the Clifford-like relations

$$\{J_+^{(A)}, J_+^{(B)}\} = -2\delta^{AB}\mathbb{1}, \quad \{J_-^{(\tilde{A})}, J_-^{(\tilde{B})}\} = -2\delta^{\tilde{A}\tilde{B}}\mathbb{1}. \quad (\text{A.5})$$

Demanded that the action (A.2) is invariant under these transformations further implies that the metric g is hermitian with respect to all the complex structures $J_\pm^{(A)}$, and that the complex structures are covariantly constant

$$\nabla^{(+)}J_+^{(A)} = 0, \quad \nabla^{(-)}J_-^{(\tilde{A})} = 0 \quad (\text{A.6})$$

with respect to the Bismut connections $\nabla^{(\pm)}$, which are metric connections with torsions $\pm g^{-1}H$. Explicitly, the connection coefficients of the Bismut connections are

$$\Gamma^{(\pm)\mu}_{\nu\rho} = \Gamma^{(0)\mu}_{\nu\rho} \pm \frac{1}{2}g^{\mu\sigma}H_{\sigma\nu\rho}, \quad (\text{A.7})$$

where $\Gamma^{(0)}$ is the Levi-Civita connection.

For (2, 2) supersymmetry, which is the subject of discussion in this paper, this implies that the target geometry is bihermitian [2], which is equivalent to generalized Kähler geometry [8]. In the more specific case $J_+ = \pm J_-$, the manifold is Kähler [1].

For (4, 4) supersymmetry, the target geometry is bi-hypercomplex (or bi-hyperKähler with torsion). The $SU(2) \times U(1)$ and $SU(3)$ WZW models are in fact bi-hypercomplex [14], and therefore has (4, 4) supersymmetry, but the off-shell formulation of the supersymmetry is more challenging and will not be addressed in this paper.

B Local description of bihermitian geometry

The bihermitian data (g, H, J_+, J_-) of the generalized Kähler manifold may be expressed in terms of generalized Kähler potential K . Consider a (2, 2) sigma model with N_c chiral, N_t twisted chiral and N_s sets of semi-chiral superfields, which locally describes a type (N_c, N_t) generalized Kähler manifold of real dimension $2N_c + 2N_t + 4N_s$. The generalized Kähler potential, which also serves as the (2, 2) superspace Lagrange density, is a real function of the superfields

$$K = K(\ell, \bar{\ell}, \tilde{r}, \bar{\tilde{r}}, \phi, \bar{\phi}, \chi, \bar{\chi}). \quad (\text{B.1})$$

We use a convention where $c, \bar{c} = 1, \dots, N_c$ label the chiral and antichiral superfields, $t, \bar{t} = 1, \dots, N_t$ label the twisted chiral and twisted antichiral superfields, and $l, \bar{l}, r, \bar{r} = 1, \dots, N_s$ label the left, anti-left, right and anti-right semi-chiral superfields respectively. Furthermore, capital indices label the collective set of chiral, twisted chiral and semi-chiral superfields

$$L = (l, \bar{l}), \quad R = (r, \bar{r}), \quad C = (c, \bar{c}), \quad T = (t, \bar{t}). \quad (\text{B.2})$$

To express the bihermitian data in terms of the potential, we introduce the notation

$$K_{AB} = \begin{pmatrix} K_{ab} & K_{a\bar{b}} \\ K_{\bar{a}b} & K_{\bar{a}\bar{b}} \end{pmatrix}, \quad (\text{B.3})$$

where $A, B = L, R, C, T$, and K_{ab} is shorthand for the second derivative $\partial_a \partial_b K$. For example, K_{CL} is the $2N_c \times 2N_s$ matrix of second derivatives

$$K_{CL} = \begin{pmatrix} \partial_c \partial_l K & \partial_c \partial_{\bar{l}} K \\ \partial_{\bar{c}} \partial_l K & \partial_{\bar{c}} \partial_{\bar{l}} K \end{pmatrix}. \quad (\text{B.4})$$

We write $K_{AB}^{-1} = (K_{BA})^{-1}$. We also define

$$C_{AB} = JK_{AB} - K_{AB}J, \quad A_{AB} = JK_{AB} + K_{AB}J, \quad (\text{B.5})$$

where J is the square matrix

$$J = \begin{pmatrix} i\mathbf{1} & 0 \\ 0 & -i\mathbf{1} \end{pmatrix}, \quad (\text{B.6})$$

whose size varies depending on the context.

By reducing the $(2, 2)$ superspace formulation of the sigma model to $(1, 1)$ superspace and eliminating auxiliary fields arising from the semi-chiral sector, one can obtain explicit expressions for the bihermitian data in terms of the potential K (for more details, see [6]). The complex structures are (in the order L, R, C, T)

$$J_+ = \begin{pmatrix} J & & & \\ K_{RL}^{-1} C_{LL} & K_{RL}^{-1} J K_{LR} & K_{RL}^{-1} C_{LC} & K_{RL}^{-1} C_{LT} \\ & J & & \\ & & J & \end{pmatrix},$$

$$J_- = \begin{pmatrix} K_{LR}^{-1} J K_{RL} & K_{LR}^{-1} C_{RR} & K_{LR}^{-1} C_{RC} & K_{LR}^{-1} A_{RT} \\ & J & & \\ & & J & \\ & & & -J \end{pmatrix}, \quad (\text{B.7})$$

and the Poisson structure σ is

$$\sigma = \begin{pmatrix} 0 & K_{LR}^{-1} & 0 & 0 \\ -K_{RL}^{-1} & 0 & 0 & 0 \\ 0 & 0 & 0 & 0 \\ 0 & 0 & 0 & 0 \end{pmatrix}. \quad (\text{B.8})$$

Note that a change of coordinates from $(\ell, \bar{\ell}, \tilde{r}, \bar{\tilde{r}}, \phi, \bar{\phi}, \chi, \bar{\chi})$ to $(\ell, \bar{\ell}, \tilde{\ell}, \bar{\tilde{\ell}}, \phi, \bar{\phi}, \chi, \bar{\chi})$, where

$$\tilde{\ell} := \frac{\partial K}{\partial \ell}, \quad \bar{\tilde{\ell}} := \frac{\partial K}{\partial \bar{\ell}} \quad (\text{B.9})$$

diagonalizes J_+ and puts the Poisson structure in the canonical form

$$\sigma = \begin{pmatrix} 0 & \mathbf{1} & 0 & 0 \\ -\mathbf{1} & 0 & 0 & 0 \\ 0 & 0 & 0 & 0 \\ 0 & 0 & 0 & 0 \end{pmatrix}; \quad (\text{B.10})$$

while a coordinate change to $(r, \bar{r}, \tilde{r}, \bar{\tilde{r}}, \phi, \bar{\phi}, \chi, \bar{\chi})$, where

$$r := -\frac{\partial K}{\partial \tilde{r}}, \quad \bar{r} := -\frac{\partial K}{\partial \bar{\tilde{r}}} \tag{B.11}$$

diagonalizes J_- and again puts σ in the canonical form. In other words, the generalized potential K serves as the generating function of the symplectomorphism between the J_+ -holomorphic Darboux coordinates $(\ell, \bar{\ell}, \tilde{\ell}, \bar{\tilde{\ell}})$ and J_- -holomorphic Darboux coordinates $(r, \bar{r}, \tilde{r}, \bar{\tilde{r}})$ on the symplectic leaves of σ . This is an important characterization of the generalized Kähler potential which will be repeatedly used in this paper.

The metric g and 2-form potential b can be obtained from the local symplectic forms

$$\mathcal{F}_+ = \frac{1}{2}(b_+ - g)J_+ = \frac{1}{2} \begin{pmatrix} d\ell^L \\ dr^R \\ d\phi^C \\ d\chi^T \end{pmatrix}^T \begin{pmatrix} -C_{LL} & -A_{LR} & -A_{LC} & -C_{LT} \\ A_{RL} & C_{RR} & C_{RC} & A_{RT} \\ A_{CL} & C_{CR} & C_{CC} & A_{CT} \\ -C_{TL} & -A_{TR} & -A_{TC} & -C_{TT} \end{pmatrix} \begin{pmatrix} d\ell^L \\ dr^R \\ d\phi^C \\ d\chi^T \end{pmatrix} \tag{B.12}$$

$$\mathcal{F}_- = \frac{1}{2}(b_- + g)J_- = -\frac{1}{2} \begin{pmatrix} d\ell^L \\ dr^R \\ d\phi^C \\ d\chi^T \end{pmatrix}^T \begin{pmatrix} C_{LL} & C_{LR} & C_{LC} & C_{LT} \\ C_{RL} & C_{RR} & C_{RC} & C_{RT} \\ C_{CL} & C_{CR} & C_{CC} & C_{CT} \\ C_{TL} & C_{TR} & C_{TC} & C_{TT} \end{pmatrix} \begin{pmatrix} d\ell^L \\ dr^R \\ d\phi^C \\ d\chi^T \end{pmatrix}. \tag{B.13}$$

Here, b_+ and b_- are different two-form potentials for H , $db_{\pm} = H$, chosen such that b_{\pm} are $(2, 0) + (0, 2)$ forms with respect to J_{\pm} . b_+ and b_- differ by an exact form

$$\mathcal{G} = \frac{1}{2}(b_+ - b_-) = d\lambda. \tag{B.14}$$

The local symplectic two-forms \mathcal{F}_{\pm} may be interpreted as connections for flat gerbes [20].

Finally, we turn to the quantum properties of the underlying $(2, 2)$ sigma model. Denoting

$$N_+ = \begin{pmatrix} K_{\ell\bar{\ell}} & K_{l\bar{r}} & K_{l\bar{\ell}} \\ K_{\bar{r}\bar{\ell}} & K_{\bar{r}\bar{r}} & K_{\bar{r}\bar{\ell}} \\ K_{t\bar{\ell}} & K_{t\bar{r}} & K_{t\bar{\ell}} \end{pmatrix}, \quad N_- = \begin{pmatrix} K_{\ell\bar{\ell}} & K_{l\bar{r}} & K_{l\bar{c}} \\ K_{\bar{r}\bar{\ell}} & K_{\bar{r}\bar{r}} & K_{\bar{r}\bar{c}} \\ K_{c\bar{\ell}} & K_{c\bar{r}} & K_{c\bar{c}} \end{pmatrix}, \tag{B.15}$$

the one loop beta function vanishes if [21]

$$\log \frac{\det N_+}{\det N_-} = f(\ell, \phi, \chi) + \bar{f}(\bar{\ell}, \bar{\phi}, \bar{\chi}) + g(r, \phi, \bar{\chi}) + \bar{g}(\bar{r}, \bar{\phi}, \chi), \tag{B.16}$$

while the target manifold is generalized Calabi-Yau if it satisfies the stronger condition [22]

$$\log \frac{\det N_+}{\det N_-} = \text{const.} \tag{B.17}$$

We end this section with a final remark. Mapping the bihermitian data,

$$(g, H, J_+, J_-) \rightarrow (g, H, J_+, -J_-), \tag{B.18}$$

merely amounts to mapping the corresponding generalized Kähler potential

$$K(\ell, \bar{\ell}, \tilde{r}, \bar{\tilde{r}}, \phi, \bar{\phi}, \chi, \bar{\chi}) \rightarrow -K(\ell, \bar{\ell}, \bar{\tilde{r}}, \tilde{r}, \chi, \bar{\chi}, \bar{\phi}, \phi), \tag{B.19}$$

leaving any of the expressions above unchanged. This is a general symmetry of (2,2) supersymmetric sigma models.

C Isometries and T-duality

T-duality is an equivalence of the underlying physics of sigma models describing different geometries. The duality can be realized by gauging an isometry of the sigma model, and then adding a Lagrange multiplier enforcing flatness of the gauge connection, so that it is equivalent to the original model. Integrating out instead the non-dynamical gauge connection yields the T-dual model, which in general describes a different geometry [13].

In (2, 2) superspace, T-duality also changes the complex structures [12], and therefore also the type of the generalized Kähler geometry. Isometries of (2, 2) supersymmetric sigma models fall into three categories: in appropriate local coordinates, they act either on (i) a chiral or a twisted chiral coordinate, (ii) a pair of chiral and twisted chiral coordinates, or (iii) a set of semi-chiral coordinates.¹⁹ The isometries can then be gauged using an appropriate gauge connection: for (i), a usual vector multiplet; for (ii), a large vector multiplet (LVM); and for (iii) a semi-chiral vector multiplet (SVM) [23–25].

T-duality along isometries of type (i) exchanges a chiral superfield for a twisted chiral (or vice versa), so if the original generalized geometry is of type (p, q) , then the dual geometry has type $(p - 1, q + 1)$ (or $(p + 1, q - 1)$). T-dualizing along a type (ii) isometry exchanges a pair of chiral and twisted chiral coordinates for a set of semi-chirals, so the dual model has type $(p - 1, q - 1)$. Finally, for type (iii), a set of semi-chirals is exchanged for a chiral and twisted chiral, so the dual model has type $(p + 1, q + 1)$.

The LVM and SVM are novel vector multiplets which do not arise in the Kähler (torsionless) case. We briefly review these vector multiplets.

C.1 Large vector multiplet (LVM)

A type (i) isometry $k = k^\phi \partial_\phi + k^{\bar{\phi}} \partial_{\bar{\phi}} + k^\chi \partial_\chi + k^{\bar{\chi}} \partial_{\bar{\chi}}$ acts on both chiral ϕ and twisted chiral χ coordinates and is gauged with a large vector multiplet (LVM), consisting of three real vector multiplets $V^I = (V^\phi, V^\chi, V')$. Since the isometry preserves the generalized Kähler structure $\mathcal{L}_k g = \mathcal{L}_k H = \mathcal{L}_k J_\pm = 0$, the potential transforms into a generalized Kähler transformation

$$\mathcal{L}_k K = f(\phi, \chi) + \bar{f}(\bar{\phi}, \bar{\chi}) + g(\phi, \bar{\chi}) + \bar{g}(\bar{\phi}, \chi). \tag{C.1}$$

The preservation of both complex structures J_\pm implies that the components of k depend only on coordinates of the appropriate chirality

$$k^\phi = k^\phi(\phi), \quad k^{\bar{\phi}} = k^{\bar{\phi}}(\bar{\phi}), \quad k^\chi = k^\chi(\chi), \quad k^{\bar{\chi}} = k^{\bar{\chi}}(\bar{\chi}). \tag{C.2}$$

¹⁹More generally, isometries of type (i) and (ii) can also act on semi-chiral coordinates.

In this paper we deal only with invariant potentials, so we shall assume $f = \bar{f} = g = \bar{g} = 0$. Therefore,

$$\begin{aligned}
 k^\phi \partial_\phi K &= i\mu_\phi + \mu', \\
 k^{\bar{\phi}} \partial_{\bar{\phi}} K &= -i\mu_\phi + \mu', \\
 k^\chi \partial_\chi K &= i\mu_\chi - \mu', \\
 k^{\bar{\chi}} \partial_{\bar{\chi}} K &= -i\mu_\chi - \mu',
 \end{aligned} \tag{C.3}$$

for some real functions $\mu_I = (\mu_\phi, \mu_\chi, \mu')$. These functions have the interpretation as (local) moment maps with respect to the 2-form gerbe potentials \mathcal{F}_\pm of the generalized geometry, and another symplectic form \mathcal{G} we define below. Recall that generalized Kähler geometry may be reformulated as a flat biholomorphic gerbe [20] with local two-form potentials

$$\mathcal{F}_\pm = \frac{1}{2}(b_\pm J_\pm \mp \omega_\pm) = \frac{i}{2}d(\mp K_\phi d\phi \pm K_{\bar{\phi}} d\bar{\phi} + K_\chi d\chi - K_{\bar{\chi}} d\bar{\chi}) = \mp \frac{1}{2}dd_\mp^c K, \tag{C.4}$$

where subscripts of K denote derivatives, and b_\pm are local torsion potentials $db_\pm = H$ which are chosen to be $(2, 0) + (0, 2)$ with respect to the complex structures J_\pm . We also introduce the local symplectic form

$$\mathcal{G} = \frac{1}{2}(b_+ - b_-) = \frac{1}{2}d(-K_\phi d\phi - K_{\bar{\phi}} d\bar{\phi} + K_\chi d\chi + K_{\bar{\chi}} d\bar{\chi}) = \frac{1}{2}d(K_\mu J_+ J_- dX^\mu). \tag{C.5}$$

For an invariant potential K ,

$$\begin{aligned}
 \iota_k \mathcal{F}_\pm &= \mp \frac{1}{2} \mathcal{L}_k(K_\mu J_\mp dX^\mu) \pm \frac{1}{2} d\iota_k(K_\mu J_\mp dX^\mu) \\
 &= -\frac{1}{2}d(\pm\mu_\phi - \mu_\chi),
 \end{aligned} \tag{C.6}$$

$$\iota_k \mathcal{G} = \frac{1}{2} \mathcal{L}_k(K_\mu J_+ J_- dX^\mu) - \frac{1}{2} d\iota_k(K_\mu J_+ J_- dX^\mu) = d\mu', \tag{C.7}$$

which shows that the μ_I are indeed moment maps with respect to \mathcal{F}_\pm and \mathcal{G} .

Gauging the isometry in $(2, 2)$ superspace promotes the parameter to chiral and twisted chiral parameters

$$\begin{aligned}
 \delta_\Lambda &= \Lambda^\phi k^\phi \partial_\phi + \Lambda^{\bar{\phi}} k^{\bar{\phi}} \partial_{\bar{\phi}} + \Lambda^\chi k^\chi \partial_\chi + \Lambda^{\bar{\chi}} k^{\bar{\chi}} \partial_{\bar{\chi}} \\
 &= \frac{1}{4}(\Lambda^\phi + \Lambda^{\bar{\phi}} + \Lambda^\chi + \Lambda^{\bar{\chi}}) \mathcal{L}_k + i(\Lambda^\phi - \Lambda^{\bar{\phi}}) \mathcal{L}_{k_{(\phi)}} \\
 &\quad + i(\Lambda^\chi - \Lambda^{\bar{\chi}}) \mathcal{L}_{k_{(\chi)}} + (\Lambda^\phi + \Lambda^{\bar{\phi}} - \Lambda^\chi - \Lambda^{\bar{\chi}}) \mathcal{L}_{k_{(\prime)}}.
 \end{aligned} \tag{C.8}$$

where the complex conjugate vector fields k_I are defined by

$$\begin{aligned}
 k_{(\phi)} &= -\frac{1}{4}(J_+ + J_-)k = \frac{i}{2}(k^{\bar{\phi}} \partial_{\bar{\phi}} - k^\phi \partial_\phi), \\
 k_{(\chi)} &= -\frac{1}{4}(J_+ - J_-)k = \frac{i}{2}(k^{\bar{\chi}} \partial_{\bar{\chi}} - k^\chi \partial_\chi), \\
 k_{(\prime)} &= -\frac{1}{4}J_+ J_- k = \frac{1}{4}(k^\phi \partial_\phi + k^{\bar{\phi}} \partial_{\bar{\phi}} - k^\chi \partial_\chi - k^{\bar{\chi}} \partial_{\bar{\chi}}).
 \end{aligned} \tag{C.9}$$

The gauged potential is

$$\begin{aligned}
 K^g(\phi, \bar{\phi}, \chi, \bar{\chi}, V^\phi, V^\chi, V') &= K(\phi, \bar{\phi}, \chi, \bar{\chi}) + \int_0^1 dt \exp(tV^I \mathcal{L}_{k_I}) V^K \mu_K \\
 &= \exp(V^I \mathcal{L}_{k_I}) K(\phi, \bar{\phi}, \chi, \bar{\chi}),
 \end{aligned}
 \tag{C.10}$$

with implicit sums over repeated indices I, J, K (over $\phi, \chi, \bar{\phi}, \bar{\chi}$). Note that $\mathcal{L}_{k_I} K = \mu_I$.

The equations of motion of V^I from (C.10) are

$$\frac{\partial K^g}{\partial V^I} = \exp(V^J \mathcal{L}_{k_J}) \mathcal{L}_{k_I} K = \exp(V^J \mathcal{L}_{k_J}) \mu_I.
 \tag{C.11}$$

Since

$$\delta_\Lambda K^g = \exp(V^J \mathcal{L}_{k_J}) (\delta_\Lambda K + \mathcal{L}_{k_I} K \delta_\Lambda V^I),
 \tag{C.12}$$

gauge invariance of (C.10) follows provided

$$\begin{aligned}
 \delta_\Lambda V^\phi &= i(\Lambda^{\bar{\phi}} - \Lambda^\phi), \\
 \delta_\Lambda V^\chi &= i(\Lambda^{\bar{\chi}} - \Lambda^\chi), \\
 \delta_\Lambda V' &= -\Lambda^\phi - \Lambda^{\bar{\phi}} + \Lambda^\chi + \Lambda^{\bar{\chi}}.
 \end{aligned}
 \tag{C.13}$$

It is convenient to combine the gauge fields into complex combinations

$$\mathbb{V} = \frac{1}{2}(-V' + i(V^\phi - V^\chi)), \quad \tilde{\mathbb{V}} = \frac{1}{2}(-V' + i(V^\phi + V^\chi)),
 \tag{C.14}$$

which transform with semi-chiral parameters $\delta_\Lambda \mathbb{V} = \Lambda^\phi - \Lambda^\chi, \delta_\Lambda \tilde{\mathbb{V}} = \Lambda^\phi + \Lambda^\chi$. Therefore, the following are four gauge invariant semi-chiral field strengths

$$\begin{aligned}
 \mathbb{G}_+ &= \bar{\mathbb{D}}_+ \mathbb{V}, & \bar{\mathbb{G}}_+ &= \mathbb{D}_+ \mathbb{V}, \\
 \mathbb{G}_- &= \bar{\mathbb{D}}_- \tilde{\mathbb{V}}, & \bar{\mathbb{G}}_- &= \mathbb{D}_- \tilde{\mathbb{V}}.
 \end{aligned}
 \tag{C.15}$$

To enforce the flatness of the LVM, one constrains its field strengths with Lagrange multipliers of the appropriate semi-chirality,

$$\begin{aligned}
 K_{LM} &= -\frac{1}{2} V^I X_I = -(\ell \mathbb{V} + r \tilde{\mathbb{V}} + \bar{\ell} \bar{\mathbb{V}} + \bar{r} \bar{\tilde{\mathbb{V}}}) \\
 &= -\frac{1}{2} (V' X' + V^\phi X_\phi + V^\chi X_\chi),
 \end{aligned}
 \tag{C.16}$$

where $X' = -(\ell + \bar{\ell} + r + \bar{r}), X_\phi = i(\ell - \bar{\ell} + r - \bar{r}), X_\chi = i(-\ell + \bar{\ell} + r - \bar{r})$. Here I runs over the components $\phi, \chi, \bar{\phi}, \bar{\chi}$ of the vector multiplet.

To obtain the T-dual sigma model, one eliminates the flat vector fields V^I by their equations of motion, which set the moment maps μ_I equal to the Fayet-Iliopolous terms X_I .

C.2 Semichiral vector multiplet (SVM)

A type (ii) isometry $k = k^\ell \partial_\ell + k^{\bar{\ell}} \partial_{\bar{\ell}} + k^r \partial_r + k^{\bar{r}} \partial_{\bar{r}}$ acting on semi-chiral coordinates $\ell, \bar{\ell}, r, \bar{r}$ is gauged with a semi-chiral vector multiplet (SVM) consisting of three real vector multiplets $V^I = (V^L, V^R, V')$. As discussed in section 2.1, the choice of coordinates $\ell, \bar{\ell}, r, \bar{r}$ encodes

a choice of polarization on the symplectic leaves of the generalized Kähler manifold; we demand that the isometry k preserves this polarization (on top of the usual conditions of a generalized Kähler isometry). This implies

$$\mathcal{L}_k K = f(\ell) + \bar{f}(\bar{\ell}) + g(r) + \bar{g}(\bar{r}), \tag{C.17}$$

$$k^\ell = k^\ell(\ell), \quad k^r = k^r(r), \quad k^{\bar{\ell}} = k^{\bar{\ell}}(\bar{\ell}), \quad k^{\bar{r}} = k^{\bar{r}}(\bar{r}). \tag{C.18}$$

For the cases encountered in this paper, the potential K is invariant, so we shall set $f = \bar{f} = g = \bar{g} = 0$. Note that the mixed coordinate system $(\ell, \bar{\ell}, r, \bar{r})$ is not holomorphic with respect to either complex structure, so that e.g. k^ℓ may not be J_+ holomorphic despite it depending only on ℓ .

From (C.17) it follows that

$$\begin{aligned} k^\ell \partial_\ell K &= i\mu_L + \mu', \\ k^{\bar{\ell}} \partial_{\bar{\ell}} K &= -i\mu_L + \mu', \\ k^r \partial_r K &= i\mu_R - \mu', \\ k^{\bar{r}} \partial_{\bar{r}} K &= -i\mu_R - \mu', \end{aligned} \tag{C.19}$$

where $\mu_I = (\mu_L, \mu_R, \mu')$ are three real functions. In fact, the μ_I may be interpreted as moment maps. Recall that on a symplectic leaf of a generalized Kähler manifold, the inverse of the Poisson structure π is a symplectic form $\Omega = g[J_+, J_-]^{-1}$ which may be thought of as the real part of a holomorphic symplectic form with respect to *either* complex structure, $\Omega = \Omega_L + \bar{\Omega}_L = \Omega_R + \bar{\Omega}_R$, where $\Omega_L = -d(\partial_\ell K d\ell)$, $\Omega_R = -d(\partial_r K dr)$. Then, using subscripts to denote derivatives of K , we may compute

$$\begin{aligned} \iota_k \Omega_L &= k^\ell dK_\ell - (k^{\bar{\ell}} K_{\ell\bar{\ell}} + k^r K_{\ell r} + k^{\bar{r}} K_{\ell\bar{r}}) d\ell \\ &= d(k^\ell K_\ell) - \partial_\ell(k^\ell K_\ell + k^{\bar{\ell}} K_{\bar{\ell}} + k^r K_r + k^{\bar{r}} K_{\bar{r}}) d\ell \\ &= d(k^\ell K_\ell) = d(i\mu_L + \mu'), \end{aligned} \tag{C.20}$$

and similarly for Ω_R . This shows that (μ^L, μ^R, μ') are moment maps for the symplectic forms $\text{Im}(\Omega_L), \text{Im}(\Omega_R)$ and $\text{Re}(\Omega_L) = \text{Re}(\Omega_R)$ respectively.

Upon gauging, each J_\pm -(anti)holomorphic and polarized sector acquires its own gauge parameter, $\Lambda^L, \bar{\Lambda}^L, \Lambda^R, \bar{\Lambda}^R$, so that the gauge variation is

$$\begin{aligned} \delta\Lambda &= \Lambda^L k^\ell \partial_\ell + \bar{\Lambda}^L k^{\bar{\ell}} \partial_{\bar{\ell}} + \Lambda^R k^r \partial_r + \bar{\Lambda}^R k^{\bar{r}} \partial_{\bar{r}} \\ &= \frac{1}{4}(\Lambda^L + \bar{\Lambda}^L + \Lambda^R + \bar{\Lambda}^R) \mathcal{L}_k + i(\Lambda^L - \bar{\Lambda}^L) \mathcal{L}_{k_L} \\ &\quad + i(\Lambda^R - \bar{\Lambda}^R) \mathcal{L}_{k_R} + (\Lambda^L + \bar{\Lambda}^L - \Lambda^R - \bar{\Lambda}^R) \mathcal{L}_{k'}, \end{aligned} \tag{C.21}$$

where

$$\begin{aligned} k_L &= \frac{i}{2}(k^{\bar{\ell}} \partial_{\bar{\ell}} - k^\ell \partial_\ell) \\ k_R &= \frac{i}{2}(k^{\bar{r}} \partial_{\bar{r}} - k^r \partial_r) \\ k' &= \frac{1}{4}(k^\ell \partial_\ell + k^{\bar{\ell}} \partial_{\bar{\ell}} - k^r \partial_r - k^{\bar{r}} \partial_{\bar{r}}). \end{aligned} \tag{C.22}$$

Note that $\mathcal{L}_{k_I}K = \mu_I$. The gauged action is

$$\begin{aligned} K^g(\ell, \bar{\ell}, r, \bar{r}, V^L, V^R, V') &= K(\ell, \bar{\ell}, r, \bar{r}) + \int_0^1 \exp(tV^I \mathcal{L}_{k_I})(V^K \mu_K) \\ &= \exp(V^I \mathcal{L}_{k_I})K. \end{aligned} \tag{C.23}$$

The equations of motion of V^I from (C.23) are

$$\frac{\partial K^g}{\partial V^I} = \exp(V^J \mathcal{L}_{k_J}) \mathcal{L}_{k_I} K = \exp(V^J \mathcal{L}_{k_J}) \mu_I. \tag{C.24}$$

The gauge variation of K^g is

$$\delta_\Lambda K^g = \exp(V^J \mathcal{L}_{k_J}) (\delta_\Lambda K + \mathcal{L}_{k_I} K \delta_\Lambda V^I). \tag{C.25}$$

Using (C.21) and $\mathcal{L}_k K = 0$, we see that $\delta_\Lambda K^g$ vanishes provided the SVM transforms as

$$\begin{aligned} \delta_\Lambda V^L &= i(\bar{\Lambda}^L - \Lambda^L), \\ \delta_\Lambda V^R &= i(\bar{\Lambda}^R - \Lambda^R), \\ \delta_\Lambda V' &= -\Lambda^L - \bar{\Lambda}^L + \Lambda^R + \bar{\Lambda}^R. \end{aligned} \tag{C.26}$$

The gauge invariant field strengths are built out of the complex combinations

$$\mathbb{V} = \frac{1}{2}(-V' + i(V^L - V^R)), \quad \tilde{\mathbb{V}} = \frac{1}{2}(-V' + i(V^L + V^R)) \tag{C.27}$$

which transform as $\delta_\Lambda \mathbb{V} = \Lambda^L - \Lambda^R$, $\delta_\Lambda \tilde{\mathbb{V}} = \Lambda^L - \bar{\Lambda}^R$. The complex field strengths are

$$\begin{aligned} \mathbb{F} &= \bar{\mathbb{D}}_+ \bar{\mathbb{D}}_- \mathbb{V}, & \bar{\mathbb{F}} &= \mathbb{D}_+ \mathbb{D}_- \bar{\mathbb{V}}, \\ \tilde{\mathbb{F}} &= \bar{\mathbb{D}}_+ \mathbb{D}_- \tilde{\mathbb{V}}, & \bar{\tilde{\mathbb{F}}} &= \mathbb{D}_+ \bar{\mathbb{D}}_- \bar{\tilde{\mathbb{V}}}, \end{aligned} \tag{C.28}$$

which are respectively chiral and twisted chiral.

To enforce the flatness of the SVM, one constrains its field strengths with Lagrange multipliers of the appropriate chirality,

$$\begin{aligned} K_{LM} &= -\frac{1}{2} V^I \Phi_I = -(\phi \mathbb{V} + \bar{\phi} \bar{\mathbb{V}} + \chi \tilde{\mathbb{V}} + \bar{\chi} \bar{\tilde{\mathbb{V}}}) \\ &= -\frac{1}{2} (V' \Phi' + V^L \Phi_L + V^R \Phi_R), \end{aligned} \tag{C.29}$$

where $\Phi' = -(\phi + \bar{\phi} + \chi + \bar{\chi})$, $\Phi_L = i(\phi - \bar{\phi} + \chi - \bar{\chi})$, $\Phi_R = i(-\phi + \bar{\phi} + \chi - \bar{\chi})$.

To obtain the T-dual sigma model, one eliminates the flat vector fields V^I by their equations of motion, which set the moment maps μ_I equal to the Fayet-Iliopolous terms Φ_I .

D Finding complex coordinates

Suppose we have a Lie algebra complex structure (with $T_\alpha = (T_a, T_{\bar{a}})$ denoting respectively the holomorphic and antiholomorphic generators) which induces a complex structure on the Lie group, with holomorphic coordinates $x^\mu = (z^i, \bar{z}^{\bar{i}})$. For definiteness, suppose we

are working with the left complex structure, so the complex structures on the Lie algebra and group are related by conjugation by the left Maurer-Cartan frame $g^{-1}dg = e^\alpha T_\alpha$. In this appendix, we discuss how to obtain the holomorphic coordinates $z^i, \bar{z}^{\bar{i}}$ in some neighborhood around the origin from the Lie algebra complex structure.

Compatibility of the complex structures of the group and algebra implies that the Maurer-Cartan frames corresponding to the holomorphic Lie algebra generators lie in the holomorphic cotangent bundle:

$$e_i^a d\bar{z}^{\bar{i}} = 0, \quad e_{\bar{i}}^{\bar{a}} dz^i = 0. \tag{D.1}$$

Suppose we parametrize the group element as $g = \exp(\xi^\alpha(z, \bar{z})T_\alpha - \bar{\xi}^{\bar{a}}(z, \bar{z})T_{\bar{a}})$. In the cases encountered in this paper, the group is unitary, and if T_a are chosen to be hermitian, then $\bar{\xi}^{\bar{a}} = (\xi^a)^*$. The Maurer-Cartan frames are

$$\begin{aligned} e^\alpha T_\alpha &= \exp(-\mathcal{L}_{\xi-\bar{\xi}})d = \sum_{n=0}^{\infty} \frac{1}{(n+1)!} (-\mathcal{L}_{\xi-\bar{\xi}})^n d(\xi-\bar{\xi}) \\ &= d(\xi-\bar{\xi}) + \frac{1}{2}[d(\xi-\bar{\xi}), \xi-\bar{\xi}] + \frac{1}{3!}[[d(\xi-\bar{\xi}), \xi-\bar{\xi}], \xi-\bar{\xi}] + \dots, \end{aligned} \tag{D.2}$$

where $\mathcal{L}_X(Y) = [X, Y]$. In a neighborhood around the origin, we can solve for $\xi(z, \bar{z})$ order by order, by imposing (D.1). Suppose that $z = \bar{z} = 0$ at the origin, and expand ξ around it

$$\xi^\alpha(z, \bar{z}) = A_i^\alpha z^i + A_{\bar{i}}^{\bar{\alpha}} \bar{z}^{\bar{i}} + A_{ij}^\alpha z^i z^j + A_{\bar{i}\bar{j}}^{\bar{\alpha}} \bar{z}^{\bar{i}} \bar{z}^{\bar{j}} + A_{ij}^{\bar{\alpha}} \bar{z}^{\bar{i}} z^j + A_{\bar{i}\bar{j}}^\alpha z^i \bar{z}^{\bar{j}} + \dots \tag{D.3}$$

Using a holomorphic diffeomorphism, we can set $A_i^a = \delta_i^a$ and $A_{ij\dots k}^a = 0$. This allows us to identify the holomorphic coordinates z^i with the holomorphic directions at the origin $e^a|_{g=1}$ determined by the Lie algebra complex structure. We substitute this expansion into (D.2) and apply the constraint (D.1), order by order in z and \bar{z} . At leading order, we obtain

$$A_i^a = 0, \quad A_{\bar{i}}^{\bar{a}} = 0, \tag{D.4}$$

and the next order yields

$$A_{\bar{i}j}^a = 0, \quad A_{ij}^a = \frac{1}{2}f_{ij}^a, \quad A_{\bar{i}\bar{j}}^{\bar{a}} = 0, \quad A_{\bar{i}j}^{\bar{a}} = \frac{1}{2}f_{\bar{i}j}^{\bar{a}}, \tag{D.5}$$

where the integrability condition (see section 2.3) $f_{bc}^{\bar{a}} = 0, f_{b\bar{c}}^a = 0$ has been used. This process can be iterated, and in principle yields all the coefficients $A_{ij\dots kl}^{\alpha}$ in terms of the structure constants. The integrability condition ensures that solutions for the coefficients always exists. This yields a series for $\xi(z, \bar{z})$ and therefore a complex parametrization of the group in a neighborhood of the origin within the radius of convergence.

An important check on our expressions for the holomorphic coordinates comes from the integrability condition that the form

$$\Omega = \bigwedge_a \text{tr}(T_a g^{-1} dg), \tag{D.6}$$

is proportional to the holomorphic top form, and hence annihilates all holomorphic differentials dz^a .

E Other type (0, 0) potentials for $SU(2) \times U(1)$

In section 3.1.1, we found a type (0, 0) generalized Kähler potential for $SU(2) \times U(1)$ corresponding to a particular choice of parametrization and polarization. Here we explore other choices.

One choice of parametrization is

$$\ell = z_+^2, \quad \tilde{\ell} = z_+^1, \quad r = -z_-^1, \quad \tilde{r} = z_-^2, \quad (\text{E.1})$$

satisfying $\text{Re } d(\tilde{\ell} d\ell + \tilde{r} dr) = 0$. In the polarization spanned by $\tilde{\ell}, \bar{\tilde{\ell}}$ and $\tilde{r}, \bar{\tilde{r}}$, the group element is parametrized as

$$g = \begin{pmatrix} e^{\zeta\theta + \tilde{r}} & e^{-\zeta\theta + \tilde{\ell}} \\ -e^{-\zeta\theta + \bar{\tilde{\ell}}} & e^{\zeta\theta + \bar{\tilde{r}}} \end{pmatrix}. \quad (\text{E.2})$$

Unimodularity of the $SU(2)$ factor implies that θ satisfies

$$e^{\theta + \tilde{r} + \bar{\tilde{r}}} + e^{-\theta + \bar{\tilde{\ell}} + \tilde{\ell}} = 1, \quad (\text{E.3})$$

which is solved by

$$\theta = \tilde{\ell} + \bar{\tilde{\ell}} + \log f(e^{\tilde{\ell} + \bar{\tilde{\ell}} + \tilde{r} + \bar{\tilde{r}}}), \quad (\text{E.4})$$

where $f(x)$ solves the quadratic equation

$$x f^2(x) - f(x) + 1 = 0. \quad (\text{E.5})$$

The potential, satisfying $\frac{\partial K}{\partial \tilde{\ell}} = -\ell$, $\frac{\partial K}{\partial \tilde{r}} = -r$ is

$$K_2^{(0,0)} = \tilde{\ell}\tilde{r} + \bar{\tilde{\ell}}\bar{\tilde{r}} + \frac{1}{2}(\tilde{r} + \bar{\tilde{r}})^2 + \int^{\tilde{\ell} + \bar{\tilde{\ell}} + \tilde{r} + \bar{\tilde{r}}} dx \log f(e^x). \quad (\text{E.6})$$

Note that this parametrization (E.2) is related to the parametrization (3.7) in section 3.1.1 by the symplectomorphism $(r, \tilde{r}) \mapsto (r', \tilde{r}')$ with $r' = r + \tilde{r}$, $\tilde{r}' = \tilde{r}$, so we expect the potentials (E.6) and (3.8) to be related by a generalized Kähler transformation followed by a change in polarization. Indeed, it can be checked that

$$K_0^{(0,0)}(\tilde{\ell}, \bar{\tilde{\ell}}, r, \tilde{r}) = K_2^{(0,0)}(\tilde{\ell}, \bar{\tilde{\ell}}, \tilde{r}, \bar{\tilde{r}}) - \frac{1}{2}(\tilde{r}^2 + \bar{\tilde{r}}^2) + r\tilde{r} + \bar{\tilde{r}}\bar{\tilde{r}}. \quad (\text{E.7})$$

This potential (E.6) can be obtained via T-duality along $U(1)$ from the type (1, 1) potential (3.14), provided the following generalized Kähler transformation is added

$$\begin{aligned} & K_0^{(1,1)} - \frac{1}{2}(\phi - \chi)^2 - \frac{1}{2}(\bar{\phi} - \bar{\chi})^2 \\ &= -\frac{1}{2}(\phi - \bar{\phi})^2 + \frac{1}{4}(\chi - \bar{\chi} - \phi + \bar{\phi})^2 - \frac{1}{4}(\phi + \bar{\phi} - \chi - \bar{\chi})^2 + \int^{\phi + \bar{\phi} - \chi - \bar{\chi}} dq \log(1 + e^q). \end{aligned} \quad (\text{E.8})$$

Another family of parametrizations, indexed by a nonzero real parameter γ , is given by

$$\begin{aligned} \ell &= \frac{1}{2}(\gamma z_+^1 - (\gamma + 1)z_+^2), & \tilde{\ell} &= 2(-z_+^1 + z_+^2), \\ r &= \frac{1}{2}(-\gamma z_-^1 + (\gamma - 1)z_-^2), & \tilde{r} &= 2(-z_-^1 + z_-^2). \end{aligned} \quad (\text{E.9})$$

In the polarization $\ell, \bar{\ell}$ and r, \bar{r} , the potential is

$$K_3^{(0,0)} = \frac{1}{2\gamma^2}(\ell - \bar{\ell} + r - \bar{r})^2 + \frac{1}{\gamma}((r - \bar{r})^2 - (\ell - \bar{\ell})^2) - \int^{\ell + \bar{\ell} + r + \bar{r}} dx \log(e^x - 1). \quad (\text{E.10})$$

This potential can be obtained via T-duality along U(1) from the type (1,1) potential (3.14), with the addition of the generalized Kähler transformation

$$\begin{aligned} K_0^{(1,1)} + \frac{\gamma}{2}((\phi - \chi)^2 - (\phi - \bar{\chi})^2 + (\bar{\phi} - \bar{\chi})^2 - (\bar{\phi} - \chi)^2) = \\ = \frac{1}{2}(\chi - \bar{\chi})^2 - \gamma(\chi - \bar{\chi})(\phi - \bar{\phi}) + \int^{\phi + \bar{\phi} - \chi - \bar{\chi}} dq \log(1 + e^q). \end{aligned} \quad (\text{E.11})$$

F T-duality from type (1,1) to type (0,0) on SU(2) × U(1)

We begin with the type (1,1) generalized Kähler structure, with group element parametrized as in (3.12). We may perform the T-duality along any factor of the U(1)_L × U(1)_R × U(1) Kac-Moody isometry group. The complex structures J_{\pm} map these isometries into one another, so in superspace, where the gauge group is complexified, the gauging of any the isometries is equivalent up to reparametrizations.

For definiteness, let us dualize along U(1)_R, which corresponds to $\epsilon = 0, \eta = i\lambda$ in (3.20), with λ a real parameter. This isometry can be gauged with a LVM (see appendix C). The invariant combinations of fields are $\phi + \bar{\phi}, \chi + \bar{\chi}$ and $i(\bar{\phi} - \phi + \chi - \bar{\chi})$, which are respectively gauged with the components V^{ϕ}, V^{χ} and V' of the LVM. There is a subtlety involved in dualizing from $K_0^{(1,1)}$ (3.14): performing the gauging prescription of [13] on $K_0^{(1,1)}$ (and gauge fixing $\phi \rightarrow 0, \chi \rightarrow 0$) yields

$$\tilde{K}_0^{(1,1)} = -\frac{1}{2}(V^{\chi})^2 + \int^{V^{\phi} - V^{\chi}} dq \log(1 + e^q) - V^I X_I, \quad (\text{F.1})$$

in which V' appears only linearly and hence cannot be solved for. To get around this issue, we restrict the potential to be defined only on the overlap of the two patches (where all the entries of the group element are nonzero), and add generalized Kähler transformations to the potential.²⁰ For simplicity, we shall consider only invariant potentials, and in that case, the generalized Kähler transformations which can be added must be functions of $i(\phi - \chi), i(\phi + \bar{\chi})$ (and complex conjugates),

$$K^{(1,1)} \mapsto K^{(1,1)} + f(i(\phi - \chi)) + \bar{f}(-i(\bar{\phi} - \bar{\chi})) + g(i(\phi + \bar{\chi})) + \bar{g}(-i(\bar{\phi} + \chi)). \quad (\text{F.2})$$

These combinations are gauged by the complex gauge fields \mathbb{V} and $\bar{\mathbb{V}}$ respectively, so the T-dual potential is now

$$\tilde{K}^{(1,1)} = -\frac{1}{2}(V^{\chi})^2 + f(\mathbb{V}) + \bar{f}(\bar{\mathbb{V}}) + g(\tilde{\mathbb{V}}) + \bar{g}(\bar{\tilde{\mathbb{V}}}) + \int^{V^{\phi} - V^{\chi}} dq \log(1 + e^q). \quad (\text{F.3})$$

²⁰Adding these terms, which in general shifts the b -field of the original geometry, correspond to holomorphic symplectomorphisms of the T-dual geometry.

If we restrict to the case where $f(x) = \alpha x^2$ and $g(x) = \beta x^2$ are quadratic monomials, then solutions for all the gauge fields V^ϕ, V^χ, V' exist if

$$8\beta\bar{\beta} + 2(\alpha + \bar{\alpha})(\beta + \bar{\beta}) + (\alpha + \bar{\alpha} + \beta + \bar{\beta}) \neq 0. \quad (\text{F.4})$$

In order to arrive at the type $(0,0)$ potential $K_0^{(0,0)}$ obtained in (3.8), we choose $\alpha = \frac{1}{2}$ and $\beta = -\frac{1}{4}$. The dual potential becomes

$$\tilde{K}^{(1,1)} = \frac{1}{8}(V')^2 - \frac{3}{8}(V^\phi - V^\chi)^2 + \frac{1}{4}(V^\phi - V^\chi)(V^\phi + V^\chi) + \int^{V^\phi - V^\chi} dq \log(1 + e^q) - V^I X_I. \quad (\text{F.5})$$

Defining the Lagrange multipliers by

$$\begin{aligned} \frac{1}{2}(X_\phi + X_\chi) &= -\frac{1}{4}(r + \bar{r}), \\ \frac{1}{2}(X_\phi - X_\chi) &= -\frac{1}{2}(\tilde{\ell} + \bar{\tilde{\ell}}), \\ X' &= \frac{i}{4}(-r + \bar{r} - 2\tilde{\ell} + 2\bar{\tilde{\ell}}), \end{aligned} \quad (\text{F.6})$$

after some simplification the dual potential may be written as

$$\tilde{K}^{(1,1)} = -(\tilde{\ell} + r)(\bar{\tilde{\ell}} + \bar{r}) + \int^{-r - \bar{r}} dq \log(1 + e^q) + \frac{1}{2}(\tilde{\ell}^2 + \bar{\tilde{\ell}}^2) - \frac{1}{4}(r^2 + \bar{r}^2), \quad (\text{F.7})$$

which agrees with (3.8) up to a generalized Kähler transformation.

Performing the duality along the $U(1)$ factor requires a subtle maneuver (due to the fact that r is invariant - see (3.18)) which we shall illustrate here. The $U(1)$ isometry corresponds to $\text{Im } \epsilon = 0$, $\text{Im } \eta = 0$ and $\epsilon + \eta = \lambda$ with λ a real parameter. The invariant combinations $i(\phi - \bar{\phi})$, $i(\chi - \bar{\chi})$ and $\phi + \bar{\phi} - \chi - \bar{\chi}$ are gauged with V^ϕ , V^χ and V' respectively. Starting with (3.14), we add the generalized Kähler transformation $\frac{1}{2}(\phi - \bar{\chi})^2 + \frac{1}{2}(\bar{\phi} - \chi)^2$, resulting in the T-dual potential

$$\tilde{K}^{(1,1)} = -\frac{1}{2}(V^\chi)^2 + \frac{1}{2}\tilde{\mathbb{V}}^2 + \frac{1}{2}\bar{\tilde{\mathbb{V}}}^2 + \int^{-\tilde{\mathbb{V}} - \bar{\tilde{\mathbb{V}}}} dq \log(1 + e^q) - V^I X_I \quad (\text{F.8})$$

with Lagrange multipliers defined such that

$$V^I X_I = V^\chi i(\ell - \bar{\ell}) + \tilde{\mathbb{V}}(\ell + \bar{r}) + \bar{\tilde{\mathbb{V}}}(\bar{\ell} + \bar{r}). \quad (\text{F.9})$$

At this point, we can eliminate V^χ using its variational equation $V^\chi = i(\bar{\ell} - \ell)$, while $\tilde{\mathbb{V}}$ and $\bar{\tilde{\mathbb{V}}}$ are somewhat more complicated functions of $(\tilde{r} + \ell)$ and $(\bar{\tilde{r}} + \bar{\ell})$. Rather than solve them explicitly, we instead change the polarization²¹ from $\tilde{r}, \bar{\tilde{r}}$ to r, \bar{r} :

$$\begin{aligned} \tilde{K}'(\ell, \bar{\ell}, r, \bar{r}) &= \tilde{K}^{(1,1)}(\ell, \bar{\ell}, \tilde{r}, \bar{\tilde{r}}) + \tilde{r}r + \bar{\tilde{r}}\bar{r} \\ &= -\frac{1}{2}(\ell - \bar{\ell})^2 + \frac{1}{2}\tilde{\mathbb{V}}^2 + \frac{1}{2}\bar{\tilde{\mathbb{V}}}^2 + \int^{-\tilde{\mathbb{V}} - \bar{\tilde{\mathbb{V}}}} dq \log(1 + e^q) \\ &\quad - \tilde{\mathbb{V}}(\ell + \bar{r}) - \bar{\tilde{\mathbb{V}}}(\bar{\ell} + \bar{r}) + \tilde{r}r + \bar{\tilde{r}}\bar{r} \end{aligned} \quad (\text{F.10})$$

²¹In superspace language, changing the polarization is a semi-chiral duality.

Since

$$\frac{\partial \tilde{K}^{(1,1)}}{\partial \tilde{r}} = \left(\frac{\partial K^{(1,1)}}{\partial V^I} - X_I \right) \frac{\partial V^I}{\partial \tilde{r}} - \tilde{\nabla}, \quad (\text{F.11})$$

and the expression in the parentheses vanishes, the variational equation of \tilde{r} sets $r = \tilde{\nabla}$. This yields

$$\tilde{K}' = \ell \bar{\ell} - \ell r - \bar{\ell} \bar{r} + \int^{-r-\bar{r}} dq \log(1 + e^q) + \frac{1}{2}(-\ell^2 - \bar{\ell}^2 + r^2 + \bar{r}^2). \quad (\text{F.12})$$

A generalized Kähler transformation cancelling the last term on the line above, and a further change of polarization, this time on the left semi-chiral fields, brings this to (3.8):

$$K_0^{(0,0)}(\tilde{\ell}, \bar{\tilde{\ell}}, r, \bar{r}) = \tilde{K}'(\ell, \bar{\ell}, r, \bar{r}) + \frac{1}{2}(\ell^2 + \bar{\ell}^2 - r^2 - \bar{r}^2) - \ell \tilde{\ell} - \bar{\ell} \bar{\tilde{\ell}}. \quad (\text{F.13})$$

G SU(2) × SU(2)

In this appendix, we examine the two types of generalized Kähler structures on SU(2) × SU(2) and relate them by T-duality along an affine isometry. The complex structures on SU(2) × SU(2) were first written down in [12] and the generalized geometry is discussed in great detail in [18].

As discussed in section 2.3, SU(2) × SU(2) admits generalized Kähler structures of two types: choosing the complex structures to be equal on the Lie algebra leads to a type $(N_c, N_t) = (1, 0)$ generalized Kähler structure while choosing them to be opposite on the Cartan subalgebra leads to a type $(0, 1)$ structure.

We choose the basis $\{h, \bar{h}, e_1, \bar{e}_1, e_2, \bar{e}_2\}$ for the Lie algebra of SU(2) × SU(2), where

$$h = \frac{1}{2}(\sigma_{1,3} + i\sigma_{2,3}), \quad e_1 = \frac{1}{2}(\sigma_{1,1} + i\sigma_{1,2}), \quad e_2 = \frac{1}{2}(\sigma_{2,1} + i\sigma_{2,2}) \quad (\text{G.1})$$

and $\sigma_{1,i}$ (respectively $\sigma_{2,i}$), $i = 1, 2, 3$, are the sigma matrices of the first (second) SU(2) factor, and the bar denotes hermitian conjugation. The two complex structures on the Lie algebra compatible with the choice of Cartan subalgebra h, \bar{h} are

$$\mathbb{J}_1 = \text{diag}(i, -i, i, -i, i, -i) \quad \text{and} \quad \mathbb{J}_2 = \text{diag}(-i, i, i, -i, -i, i). \quad (\text{G.2})$$

G.1 Type (1, 0)

If one takes J_+ and J_- both induced from the same Lie algebra complex structure, say \mathbb{J}_1 , then generically the resulting generalized Kähler structure has type $(1, 0)$ (there are once again positive codimension type change loci). Denoting the group element in the defining representation by (g_{ij}^1, g_{ij}^2) , $i, j = 1, 2$, the chiral coordinate is

$$\phi = -\log g_{12}^1 + i \log g_{12}^2, \quad (\text{G.3})$$

while J_{\pm} coordinates on each symplectic leaf can be chosen to be

$$\begin{aligned} z_+^1 &= \log \frac{g_{12}^1}{g_{22}^1}, & z_+^2 &= \log \frac{g_{12}^2}{g_{22}^2}, \\ z_-^1 &= \log \frac{g_{12}^1}{g_{11}^1}, & z_-^2 &= \log \frac{g_{12}^2}{g_{11}^2}. \end{aligned} \quad (\text{G.4})$$

The Poisson structure in these coordinates is

$$\sigma(dz_{\pm}^1, dz_{\pm}^2) = \pm i. \tag{G.5}$$

We choose the semi-chiral coordinates

$$\begin{aligned} \ell &= z_+^1, & \tilde{\ell} &= -iz_+^2, \\ r &= z_-^2, & \tilde{r} &= iz_-^1, \end{aligned} \tag{G.6}$$

which satisfy $d(\tilde{\ell}d\ell + \bar{\tilde{\ell}}d\bar{\ell} + \tilde{r}dr + \bar{\tilde{r}}d\bar{r}) = 0$. In the polarization determined by ℓ and r , the generalized potential is²²

$$\begin{aligned} K &= F(\phi, \bar{\phi}) + \int^{(\ell, \bar{\ell}, r, \bar{r})} \tilde{\ell} d\ell + \bar{\tilde{\ell}} d\bar{\ell} + \tilde{r} dr + \bar{\tilde{r}} d\bar{r} \\ &= \frac{1}{2}(\bar{\phi} - \phi)^2 - (r + i\ell)(\bar{r} - i\bar{\ell}) - (\phi + \bar{\phi})(\ell + \bar{\ell}) + i(\bar{\phi} - \phi)(r + \bar{r}) \\ &\quad + \int^{\ell + \bar{\ell}} dq \log(1 + e^q) + \int^{r + \bar{r}} dq \log(1 + e^q) - \frac{1}{2}(\ell^2 + \bar{\ell}^2 + r^2 + \bar{r}^2). \end{aligned} \tag{G.7}$$

Here, $F(\phi, \bar{\phi}) = \frac{1}{2}(\bar{\phi} - \phi)^2$ is determined by solving the second order differential equations (B.12)–(B.13). For our later discussion of T-duality, it is convenient to add generalized Kähler transformation terms so that

$$\begin{aligned} K^{(1,0)}(\ell, \bar{\ell}, r, \bar{r}, \phi, \bar{\phi}) &= \frac{1}{2}(\bar{\phi} - \phi)^2 - (r + i\ell)(\bar{r} - i\bar{\ell}) + i(\bar{\phi} - \phi)(r + \bar{r} + i\ell - i\bar{\ell}) \\ &\quad + \int^{\ell + \bar{\ell}} dq \log(1 + e^q) + \int^{r + \bar{r}} dq \log(1 + e^q) - \frac{1}{2}(r^2 + \bar{r}^2), \end{aligned} \tag{G.8}$$

which corresponds to shifting $\tilde{\ell} \rightarrow \tilde{\ell}' = \tilde{\ell} + 2\phi + \ell = -iz_+^2 + z_+^1 + 2\phi$.

G.2 Type (0, 1)

If one takes J_+ induced from the Lie algebra complex structure \mathbb{J}_1 and J_- induced from \mathbb{J}_2 , then generically the resulting generalized Kähler structure has type (0, 1). The twisted chiral coordinate is

$$\chi = -\log g_{22}^1 + i \log g_{22}^2 \tag{G.9}$$

while J_{\pm} coordinates on the symplectic leaves can be chosen to be the same as those for the type (1, 0) structure (G.4). The Poisson structure in these coordinates, however, is now different

$$\sigma(dz_{\pm}^1, dz_{\pm}^2) = i. \tag{G.10}$$

We choose now

$$\ell = z_+^1, \quad r = z_-^2, \quad \tilde{r} = iz_-^1, \tag{G.11}$$

as before, but now

$$\tilde{\ell} = iz_+^2 \tag{G.12}$$

²²Note that, due to the relations $z_+^j + \bar{z}_+^j = z_-^j + \bar{z}_-^j$ for each $j = 1, 2$, the combinations $(\ell, \bar{\ell}, \tilde{r}, \bar{\tilde{r}})$ and $(\tilde{\ell}, \bar{\tilde{\ell}}, r, \bar{r})$ are not functionally independent.

has an extra minus sign compared to the above. This is necessary to preserve $d(\tilde{\ell}d\ell + \bar{\tilde{\ell}}d\bar{\ell} + \tilde{r}dr + \bar{\tilde{r}}d\bar{r}) = 0$. In the polarization determined by ℓ and r , the generalized potential is

$$\begin{aligned}
 K &= G(\chi, \bar{\chi}) + \int^{(\ell, \bar{\ell}, r, \bar{r})} \tilde{\ell} d\ell + \bar{\tilde{\ell}} d\bar{\ell} + \tilde{r} dr + \bar{\tilde{r}} d\bar{r} \\
 &= -\frac{1}{2}(\bar{\chi} - \chi)^2 + i(\ell r - \bar{\ell} \bar{r}) - (\chi + \bar{\chi})(\ell + \bar{\ell}) + i(\bar{\chi} - \chi)(r + \bar{r}) \\
 &\quad + \int^{\ell + \bar{\ell}} dq \log(1 + e^q) + \int^{r + \bar{r}} dq \log(1 + e^q), \tag{G.13}
 \end{aligned}$$

where $G(\chi, \bar{\chi}) = -\frac{1}{2}(\bar{\chi} - \chi)^2$ is determined by (B.12), (B.13).

For later discussion of T-duality, it is convenient to add generalized Kähler transformation terms so that

$$\begin{aligned}
 K^{(0,1)}(\ell, \bar{\ell}, r, \bar{r}, \chi, \bar{\chi}) &= -\frac{1}{2}(\bar{\chi} - \chi)^2 + i(\bar{\chi} - \chi)(r + \bar{r} + i\ell - i\bar{\ell}) \\
 &\quad + \int^{\ell + \bar{\ell}} dq \log(1 + e^q) + \int^{r + \bar{r}} dq \log(1 + e^q) - \frac{1}{2}(\ell^2 + \bar{\ell}^2) \tag{G.14}
 \end{aligned}$$

which corresponds to shifting $\tilde{\ell} \rightarrow \tilde{\ell}' = \tilde{\ell} + 2\chi - \ell = iz_+^2 - z_+^1 + 2\chi$. This matches with $\tilde{\ell}$ in (G.8) since $iz_+^2 - z_+^1 + 2\chi = -iz_+^2 + z_+^1 + 2\phi$.

G.3 T-duality

The subgroup of the isometry group preserving both complex structures is $(U(1) \times U(1))_L \times (U(1) \times U(1))_R$, acting as $g \mapsto e^{\epsilon h - \bar{\epsilon} \bar{h}} g e^{\bar{\eta} \bar{h} - \eta h}$. Under this action, the coordinates transform as

$$\begin{aligned}
 \phi &\mapsto \phi - i\bar{\epsilon} + i\eta, & \chi &\mapsto \chi + i\bar{\epsilon} + i\eta, \\
 z_+^1 &\mapsto z_+^1 + i\epsilon + i\bar{\epsilon} & z_-^1 &\mapsto z_-^1 - i\eta - i\bar{\eta}, \\
 z_+^2 &\mapsto z_+^2 + \epsilon - \bar{\epsilon} & z_-^2 &\mapsto z_-^2 + \bar{\eta} - \eta.
 \end{aligned} \tag{G.15}$$

For the type (1, 0) structure, the parameters satisfy

$$\bar{\mathbb{D}}_+ \epsilon = 0, \quad \mathbb{D}_\pm \epsilon = 0, \quad \bar{\mathbb{D}}_\pm \eta = 0, \quad \mathbb{D}_- \eta = 0, \tag{G.16}$$

while for the type (0, 1) structure, they satisfy

$$\bar{\mathbb{D}}_\pm \epsilon = 0, \quad \mathbb{D}_+ \epsilon = 0, \quad \bar{\mathbb{D}}_\pm \eta = 0, \quad \mathbb{D}_- \eta = 0. \tag{G.17}$$

In both cases, it is clear that these isometries are affine, $\partial_+ \epsilon = 0 = \partial_- \eta$.

Let us perform T-duality along the isometry with parameter $\epsilon = -i\lambda, \eta = 0$, with λ real. This isometry transforms $\phi \mapsto \phi + \lambda$ and $\chi \mapsto \chi - \lambda$ and leaves $\ell, \bar{\ell}, r, \bar{r}$ invariant. The potential (G.8) is invariant under this isometry, and can be gauged by a standard vector multiplet. Constraining the gauge field to be flat using a twisted chiral Lagrange multiplier χ returns one to the original model

$$\begin{aligned}
 \tilde{K}^{(1,0)} &= -\frac{1}{2}V^2 - (r + i\ell)(\bar{r} - i\bar{\ell}) + V(r + \bar{r} + i\ell - i\bar{\ell}) \\
 &\quad + \int^{\ell + \bar{\ell}} dq \log(1 + e^q) + \int^{r + \bar{r}} dq \log(1 + e^q) - \frac{1}{2}(r^2 + \bar{r}^2) - i(\bar{\chi} - \chi)V, \tag{G.18}
 \end{aligned}$$

where we have gauge fixed $\phi = 0$. It is now straightforward to check that integrating out the gauge field V yields the type $(0, 1)$ potential $K^{(0,1)}$ (G.14).

Open Access. This article is distributed under the terms of the Creative Commons Attribution License ([CC-BY 4.0](https://creativecommons.org/licenses/by/4.0/)), which permits any use, distribution and reproduction in any medium, provided the original author(s) and source are credited.

References

- [1] B. Zumino, *Supersymmetry and Kähler manifolds*, *Phys. Lett.* **B 87** (1979) 203 [[INSPIRE](#)].
- [2] S.J. Gates, Jr., C.M. Hull and M. Roček, *Twisted multiplets and new supersymmetric nonlinear σ -models*, *Nucl. Phys.* **B 248** (1984) 157 [[INSPIRE](#)].
- [3] T. Buscher, U. Lindström and M. Roček, *New supersymmetric σ models with Wess-Zumino terms*, *Phys. Lett.* **B 202** (1988) 94 [[INSPIRE](#)].
- [4] A. Sevrin and J. Troost, *Off-shell formulation of $N = 2$ nonlinear σ -models*, *Nucl. Phys.* **B 492** (1997) 623 [[hep-th/9610102](#)] [[INSPIRE](#)].
- [5] M.T. Grisaru, M. Massar, A. Sevrin and J. Troost, *Some aspects of $N = (2, 2)$, $D = 2$ supersymmetry*, *Fortsch. Phys.* **47** (1999) 301 [[hep-th/9801080](#)] [[INSPIRE](#)].
- [6] U. Lindström, M. Roček, R. von Unge and M. Zabzine, *Generalized Kähler manifolds and off-shell supersymmetry*, *Commun. Math. Phys.* **269** (2007) 833 [[hep-th/0512164](#)] [[INSPIRE](#)].
- [7] N. Hitchin, *Generalized Calabi-Yau manifolds*, *Quart. J. Math.* **54** (2003) 281 [[math.DG/0209099](#)] [[INSPIRE](#)].
- [8] M. Gualtieri, *Generalized complex geometry*, Ph.D. thesis, Oxford U., Oxford U.K., (2003) [[math.DG/0401221](#)] [[INSPIRE](#)].
- [9] M. Graña, R. Minasian, M. Petrini and A. Tomasiello, *Supersymmetric backgrounds from generalized Calabi-Yau manifolds*, *JHEP* **08** (2004) 046 [[hep-th/0406137](#)] [[INSPIRE](#)].
- [10] C. Jeschek and F. Witt, *Generalised G_2 -structures and type IIB superstrings*, *JHEP* **03** (2005) 053 [[hep-th/0412280](#)] [[INSPIRE](#)].
- [11] T.H. Buscher, *Path integral derivation of quantum duality in nonlinear σ -models*, *Phys. Lett.* **B 201** (1988) 466 [[INSPIRE](#)].
- [12] I.T. Ivanov, B.-B. Kim and M. Roček, *Complex structures, duality and WZW models in extended superspace*, *Phys. Lett.* **B 343** (1995) 133 [[hep-th/9406063](#)] [[INSPIRE](#)].
- [13] M. Roček and E.P. Verlinde, *Duality, quotients and currents*, *Nucl. Phys.* **B 373** (1992) 630 [[hep-th/9110053](#)] [[INSPIRE](#)].
- [14] P. Spindel, A. Sevrin, W. Troost and A. Van Proeyen, *Extended supersymmetric σ -models on group manifolds. 1. The complex structures*, *Nucl. Phys.* **B 308** (1988) 662 [[INSPIRE](#)].
- [15] M. Roček, K. Schoutens and A. Sevrin, *Off-shell WZW models in extended superspace*, *Phys. Lett.* **B 265** (1991) 303 [[INSPIRE](#)].
- [16] K. Yano, *Differential geometry on complex and almost complex spaces*, Pergamon Press, Oxford U.K., (1965).
- [17] C.M. Hull, A. Karlhede, U. Lindström and M. Roček, *Nonlinear σ models and their gauging in and out of superspace*, *Nucl. Phys.* **B 266** (1986) 1 [[INSPIRE](#)].

- [18] A. Sevrin, W. Staessens and D. Terry, *The generalized Kähler geometry of $N = (2, 2)$ WZW-models*, *JHEP* **12** (2011) 079 [[arXiv:1111.0551](#)] [[INSPIRE](#)].
- [19] U. Lindström, *Extended supersymmetry of semichiral σ -models in 4D*, *JHEP* **02** (2015) 170 [[arXiv:1411.3906](#)] [[INSPIRE](#)].
- [20] C.M. Hull, U. Lindström, M. Roček, R. von Unge and M. Zabzine, *Generalized Kähler geometry and gerbes*, *JHEP* **10** (2009) 062 [[arXiv:0811.3615](#)] [[INSPIRE](#)].
- [21] M.T. Grisaru, M. Massar, A. Sevrin and J. Troost, *The quantum geometry of $N = (2, 2)$ nonlinear σ -models*, *Phys. Lett. B* **412** (1997) 53 [[hep-th/9706218](#)] [[INSPIRE](#)].
- [22] C.M. Hull, U. Lindström, M. Roček, R. von Unge and M. Zabzine, *Generalized Calabi-Yau metric and generalized Monge-Ampere equation*, *JHEP* **08** (2010) 060 [[arXiv:1005.5658](#)] [[INSPIRE](#)].
- [23] U. Lindström, M. Roček, I. Ryb, R. von Unge and M. Zabzine, *New $N = (2, 2)$ vector multiplets*, *JHEP* **08** (2007) 008 [[arXiv:0705.3201](#)] [[INSPIRE](#)].
- [24] U. Lindström, M. Roček, I. Ryb, R. von Unge and M. Zabzine, *T-duality and generalized Kähler geometry*, *JHEP* **02** (2008) 056 [[arXiv:0707.1696](#)] [[INSPIRE](#)].
- [25] U. Lindström, M. Roček, I. Ryb, R. von Unge and M. Zabzine, *Non-Abelian generalized gauge multiplets*, *JHEP* **02** (2009) 020 [[arXiv:0808.1535](#)] [[INSPIRE](#)].

RECEIVED: November 6, 2017

REVISED: February 7, 2018

ACCEPTED: February 28, 2018

PUBLISHED: March 7, 2018

Classical and quantum aspects of Yang-Baxter Wess-Zumino models

Saskia Demulder,^a Sibylle Driezen,^a Alexander Sevrin^{a,b} and Daniel C. Thompson^{a,c}

^a*Theoretische Natuurkunde, Vrije Universiteit Brussel & The International Solway Institutes,
Pleinlaan 2, B-1050 Brussels, Belgium*

^b*Physics Department, Universiteit Antwerpen,
Campus Groenenborger, 2020 Antwerpen, Belgium*

^c*Department of Physics, Swansea University,
Singleton Park, Swansea SA2 8PP, U.K.*

E-mail: Saskia.Demulder@vub.be, Sibylle.Driezen@vub.be,
Alexandre.Sevrin@vub.be, D.C.Thompson@Swansea.ac.uk

ABSTRACT: We investigate the integrable Yang-Baxter deformation of the 2d Principal Chiral Model with a Wess-Zumino term. For arbitrary groups, the one-loop β -functions are calculated and display a surprising connection between classical and quantum physics: the classical integrability condition is necessary to prevent new couplings being generated by renormalisation. We show these theories admit an elegant realisation of Poisson-Lie T-duality acting as a simple inversion of coupling constants. The self-dual point corresponds to the Wess-Zumino-Witten model and is the IR fixed point under RG. We address the possibility of having supersymmetric extensions of these models showing that extended supersymmetry is not possible in general.

KEYWORDS: Integrable Field Theories, Sigma Models, String Duality

ARXIV EPRINT: [1711.00084](https://arxiv.org/abs/1711.00084)

Contents

1	Introduction	1
2	Yang-Baxter and Yang-Baxter Wess-Zumino models	3
3	Renormalisation of the YB-WZ model	6
3.1	Case I: general group G and restriction to the integrable locus	9
3.2	Case II: simply laced groups and general parameters	13
4	Poisson-Lie T-duality of the YB-WZ model	17
5	The supersymmetric YB-WZ model	19
6	Summary, conclusions and outlook	25
A	Conventions	27
B	Charges in $SU(2)$	28
C	Properties of \mathcal{R}	30
D	Geometry in the non-orthonormal frame	31

1 Introduction

Two-dimensional non-linear sigma models hold great interest for two key reasons. First, they can provide prototypes with which to study strong coupling dynamics in a simpler setting than four-dimensional non-abelian gauge theories. Second, they are the building blocks of the worldsheet description of string theory. Under certain circumstances these theories can have a dramatic additional simplicity — that of integrability — allowing one to transcend the usual perturbative tool kit. A rather long standing question has been to establish the complete landscape of integrable sigma models.

A substantial breakthrough was made by Klimcik with the explicit demonstration that the Yang-Baxter sigma models [1] are integrable [2]; thereby providing a one-parameter integrable deformation of the principal chiral theory associated to any semi-simple Lie algebra. These theories, now often called η -deformations, have taken great prominence since they provide a Lagrangian description of a theory whose symmetry is deformed to a quantum group [3]. When extended to theories on symmetric spaces and to super-cosets, this has yielded a remarkable quantum group deformation of the $AdS_5 \times S^5$ superstring [4] opening the door to an intriguing interpretation within holography.

A surprising feature of the η -deformed theory in the context of the $AdS_5 \times S^5$ superstring is that it appears to describe a scale invariant but not Weyl invariant theory. This is seen directly by the target spacetime's failure to satisfy the equations of Type IIB supergravity but instead to obey a set of “generalised” supergravity equations [5]. Recent work has started to place these η -theories, and the generalised supergravity that govern their target spacetimes, in the context of double/exceptional field theory [6, 7] and make explicit the link to T-folds and non-geometric configurations [8]. A link between the r-matrix, satisfying a (modified) classical Yang-Baxter equation, that defines Yang-Baxter sigma models and the spacetime non-commutativity parameter has been developed in [9, 10] using the open-closed map.

Notably, the η -theory displays a so-called Poisson-Lie (PL) symmetry. This means that it possesses a generalised T-dual in the Poisson-Lie sense proposed by Klimcik and Severa [11]. The Poisson-Lie dual model, modulo an analytic continuation, has been established to be a well-known integrable deformation called the λ -deformation. Introduced by Sfetsos [12] these theories interpolate between a Wess-Zumino-Witten (WZW) [13] or a gauged WZW model and the non-abelian T-dual of the principal chiral model on a group manifold or symmetric coset space respectively. The connection between the η - and the λ -theories was first shown for explicit $SU(2)$ based examples [14, 15] and established in generality by [16, 17].

Like the η -theories, λ -models can also be applied to cosets [18] and semi-symmetric spaces [19] and are thought to encapsulate quantum group deformations with q a root of unity. In contrast to the η -theory, the target spacetimes associated to the λ -model provide genuine solutions of supergravity (with no modification) [20–24].

Given these successes a natural recent focus has been to understand potential generalisations of these approaches to include multi-parameter families of integrable models. On the side of the η -deformation (or Yang-Baxter model) notable are the two-parameter bi-Yang-Baxter deformations [25], the inclusion of a Wess-Zumino term [26] and indeed the recent synthesis of these [27]. On the λ side, multi-parameter deformations have been constructed and studied in [15, 28–30]. There is also some evidence that a Poisson-Lie connection should be present between multi-parameter η - and λ -models; for example the bi-Yang Baxter model has been shown to be related to a generalised λ -model [31]. The Yang-Baxter theory with a WZ term (YB-WZ) appears amenable to similar treatment since it can be written as an \mathcal{E} -model [32] (though the corresponding λ theory is not clearly spelt out as yet). The construction of Lax pairs directly from the \mathcal{E} -model has recently been studied in [33].

In this work we will provide further study of the multi-parameter YB-WZ model. For the case of $SU(2)$ this system was studied in [34, 35]. Specifically we shall,

- Study the one-loop renormalisation of the general YB+WZ model extending results in the literature from $SU(2)$ [34] to arbitrary groups. We will find that the conditions placed on a sigma model by integrability have an interesting interplay with renormalisation. The condition required of classical integrability is preserved by RG flow. Second, when dealing with non-simply laced algebras one finds the classical integrability condition is necessary for the renormalisation of the model not to introduce new

couplings in addition to those of the bare theory. That a classical property seems to be so tied to a very quantum calculation is notable.

- We will clarify some details of the quantum group symmetries in these models and in particular show that the parameters defining the symmetry algebra are invariants of the RG flow.
- We comment on the role of Poisson-Lie dualisation for the YB-WZ model. Considered within the framework of the \mathcal{E} -model [32], the YB-WZ can be seen as being part of a pair of Poisson-Lie dual models. In particular, it admits a formulation as an \mathcal{E} -model associated to the Drinfeld double $\mathfrak{d} = \mathfrak{g}^{\mathbb{C}}$. When the integrability condition is satisfied, the Poisson-Lie T-duality transformation preserves the structure of the action (2.2) while the coupling parameters follow very simple “radial inversion” transformation rules.
- We will examine the possible worldsheet supersymmetrisation of the YB-WZ model associated to $SU(2) \times U(1)$ which is the simplest but non-trivial example that allows $N = (2, 2)$ in the undeformed (WZW) case. While $N = (1, 1)$ supersymmetry is always possible, going beyond that requires the introduction of additional geometric structures. We show that $N = (2, 2)$ is forbidden for generic values of the deformation parameters while $N = (2, 0)$ or $N = (2, 1)$ is possible only for specific values. This leads us to conjecture that an $N = (2, 2)$ YB-WZ model is not possible in general.

The paper is organised as follows. Section 2 introduces the Yang-Baxter Wess-Zumino model together with its integrability properties relevant to the subsequent discussions. In section 3 we give an explicit derivation of the one-loop β -functions of the YB-WZ model in the case of arbitrary groups. Given the result, we find that one needs to carefully distinguish between two cases: when the group is simply-laced or not. In the former case, a consistent renormalisation does not require the model to be integrable. For the latter case, the classical integrability condition turns out to be necessary to prevent the creation of new couplings in the theory by renormalisation. A detailed discussion of the RG behaviour is given in both cases. Section 4 formulates the YB-WZ action (2.2) within the framework of the \mathcal{E} -model and derives the Poisson-Lie T-dual model. In section 5 we study the possibility of extended supersymmetry of the YB-WZ model. We end with a summary and conclusions in section 6. The conventions used throughout this paper are given in appendix A. Appendix B reviews the construction [35] of the charges of the $SU(2)$ YB-WZ model paying particular care to the overall normalisations required to expose the correct RG properties. In appendix C and D we collate a set of useful expressions which were used in the calculations of the β -functions.

2 Yang-Baxter and Yang-Baxter Wess-Zumino models

In this first section, we present the Yang-Baxter Wess-Zumino model (YB-WZ) as constructed in [26], which will be the main topic of the remainder of this paper. Given a Lie algebra \mathfrak{g} , we introduce an endomorphism $\mathcal{R} : \mathfrak{g} \rightarrow \mathfrak{g}$ skew symmetric with respect to

the Cartan-Killing product $\langle \cdot, \cdot \rangle$ ($\langle \mathcal{R}x, y \rangle = -\langle x, \mathcal{R}y \rangle$) and obeying the modified classical Yang-Baxter (mCYBE) equation,

$$[\mathcal{R}x, \mathcal{R}y] - \mathcal{R}([x, \mathcal{R}y] + [\mathcal{R}x, y]) = [x, y] \quad \forall x, y \in \mathfrak{g}, \quad (2.1)$$

which further satisfies $\mathcal{R}^3 = -\mathcal{R}$. The canonical realization of \mathcal{R} is most easily seen in a Cartan-Weyl basis for the Lie algebra where it maps generators belonging to the CSA to zero and where it acts diagonally on generators corresponding to positive (negative) roots with eigenvalue $+i$ ($-i$). Equipped with this structure, we define the YB-WZ action in worldsheet light-cone coordinates as,

$$\begin{aligned} \mathcal{S} = & -\frac{1}{2\pi} \int d\sigma d\tau \langle g^{-1} \partial_+ g, (\alpha \mathbb{1} + \beta \mathcal{R} + \gamma \mathcal{R}^2) g^{-1} \partial_- g \rangle \\ & + \frac{k}{24\pi} \int_{M_3} \langle \bar{g}^{-1} d\bar{g}, [\bar{g}^{-1} d\bar{g}, \bar{g}^{-1} d\bar{g}] \rangle. \end{aligned} \quad (2.2)$$

Here as usual the coefficient of the Wess-Zumino term, k , is an integer, quantised such that the path integral based on this action is insensitive to the choice of the extension $\bar{g} : M_3 \rightarrow G$.

A short calculation yields, after integration by parts and discarding the total derivative, the equations of motion,

$$\delta S = \frac{\alpha - \gamma}{2\pi} \int d\sigma d\tau \langle \delta g g^{-1}, \partial_+ \mathcal{K}_- + \partial_- \mathcal{K}_+ \rangle, \quad (2.3)$$

with,

$$\mathcal{K}_\pm = \frac{1}{\alpha - \gamma} ((\alpha \mp k) \mp \beta \mathcal{R}_g + \gamma \mathcal{R}_g^2) v_\pm, \quad (2.4)$$

in which we recall $v = dg g^{-1}$ are the right invariant one-forms and,

$$\mathcal{R}_g = \text{ad}_g \circ \mathcal{R} \circ \text{ad}_{g^{-1}}, \quad (2.5)$$

which, like \mathcal{R} , obeys the mCYBE and is skew symmetric with respect to the ad-invariant Cartan-Killing form $\langle \cdot, \cdot \rangle$. Using the inverse of eq. (2.4),

$$\begin{aligned} v_\pm = & (\alpha - \gamma) \left(\frac{1}{\alpha \mp k} \pm \frac{\beta}{\beta^2 + (\alpha \mp k - \gamma)^2} \mathcal{R}_g \right. \\ & \left. + \frac{\beta^2 - \gamma(\alpha \mp k - \gamma)}{(\alpha \mp k)(\beta^2 + (\alpha \mp k - \gamma)^2)} \mathcal{R}_g^2 \right) \mathcal{K}_\pm, \end{aligned} \quad (2.6)$$

in $dv - v \wedge v = 0$, one easily gets,

$$\begin{aligned} \partial_+ \mathcal{K}_- - \partial_- \mathcal{K}_+ - [\mathcal{K}_+, \mathcal{K}_-] = & \left(\frac{k}{\alpha} + \frac{\sqrt{\gamma(\alpha^2 - \alpha\gamma - k^2)}}{\sqrt{\alpha}(\alpha - \gamma)} \mathcal{R}_g \right. \\ & \left. - \frac{k\gamma}{\alpha(\alpha - \gamma)} \mathcal{R}_g^2 \right) (\partial_+ \mathcal{K}_- + \partial_- \mathcal{K}_+), \end{aligned} \quad (2.7)$$

if and only if the coefficients are related via [26],

$$\beta^2 = \frac{\gamma}{\alpha} (\alpha^2 - \alpha\gamma - k^2). \quad (2.8)$$

So we conclude that the currents \mathcal{K}_\pm are on-shell flat provided eq. (2.8) holds. This is sufficient to guarantee classical integrability as the equations of motion follow then from the flatness of the standard $\mathfrak{g}^{\mathbb{C}}$ -valued Zakharov-Mikhailov Lax connection [42],

$$\mathcal{L}_\pm(z) = \frac{1}{1 \mp z} \mathcal{K}_\pm. \tag{2.9}$$

We call the solutions to eq. (2.8) the *integrable locus*.¹ From eqs. (2.7) and (2.4) one deduces the further conditions $\alpha \neq 0$ and $\gamma \neq \alpha$, ensuring that the kinetic term is properly defined. In addition, as all parameters α, β, γ, k are real and the kinetic term should have the right sign ($\alpha > 0$), we conclude from eq. (2.8) that the allowed values of α and γ are $\alpha \in [|k|, \infty[$ and $\gamma \in [0, \frac{\alpha^2 - k^2}{\alpha}]$ or $\alpha \in]0, |k|]$ and $\gamma \in [-\frac{k^2 - \alpha^2}{\alpha}, 0]$, where on $\alpha = |k|$ we find the WZW point [13]: $\gamma = \beta = 0$.

For the particular subset of the integrable locus given by [1],

$$k = 0, \quad \alpha = \frac{1}{\tau}, \quad \beta = \frac{\eta}{\tau(1 + \eta^2)}, \quad \gamma = \frac{\eta^2}{\tau(1 + \eta^2)}, \tag{2.11}$$

the action eq. (2.2) reduces to what has become known as the η -deformed principal chiral model which is integrable [2] with the dynamics encoded in the flatness of a $\mathfrak{g}^{\mathbb{C}}$ -valued Lax connection $\mathcal{L}(z)$ depending on a spectral parameter $z \in \mathbb{C}$. This theory displays a fascinating structure of infinite symmetries [3]. At the Lagrangian level the left acting G symmetry is preserved and is complemented, as in the undeformed principal chiral model, with non-local charges furnishing a Yangian $\mathcal{Y}(\mathfrak{g})$. The right acting G symmetry is broken to its Cartan in the action eq. (2.2), but is enhanced by non-local charges to form a classical version of a quantum group $\mathcal{U}_q(\mathfrak{g})$ [3] (actually further extended to an affine $\mathcal{U}_q(\hat{\mathfrak{g}})$ [36]). Schematically, for a given simple root there exists a local charge \mathfrak{Q}^H and non-local charges \mathfrak{Q}^\pm that obey,

$$\{\mathfrak{Q}^+, \mathfrak{Q}^-\} = i \frac{q^{\mathfrak{Q}^H} - q^{-\mathfrak{Q}^H}}{q - q^{-1}}, \quad \{\mathfrak{Q}^\pm, \mathfrak{Q}^H\} = \pm i \mathfrak{Q}^\pm. \tag{2.12}$$

The quantum group parameter is given simply by $q = \exp(8\pi\tau\eta)$ which is an invariant under the renormalisation group flow of couplings [15].

The charges that generate these symmetries can be obtained by expansions around suitable values of the spectral parameter of the monodromy matrix,

$$U(z) = P \exp \left[\int d\sigma \mathcal{L}_\sigma(z) \right], \tag{2.13}$$

which is conserved by virtue of the flatness of \mathcal{L} . The Yangian left acting symmetries are found through expansions around $z = \infty$ whereas the right acting quantum group

¹To translate to [26] we have the dictionary of parameters $(\alpha, \beta, \gamma, k) \rightarrow (\eta^2, R, k', K)$

$$A = \frac{\beta}{\alpha - \gamma}, \quad \eta^2 = \frac{\gamma}{\alpha - \gamma}, \quad k' = \frac{k}{\alpha - \gamma}, \quad K = \frac{\alpha - \gamma}{4\pi}, \tag{2.10}$$

however we shall continue with the $(\alpha, \beta, \gamma, k)$ such that k gives the level of the WZW model that will appear at IR fixed points.

symmetries are found [3] via the expansion of the gauge transformed Lax around special points corresponding to poles in the twist function of the Maillet algebra [37].

Much of the story for the general η -deformed model was first established for the case of $\mathfrak{g} = \mathfrak{su}(2)$ which corresponds to the sigma model on a squashed S^3 (the Kalb-Ramond potential encoded by eq. (2.2) is pure gauge in this case and though it doesn't effect the equation of motions it corresponds to an improvement term to ensuring flatness of currents). The integrability was established many years ago by Cherednik [38]. Somewhat later the classical Yangian symmetry was shown in [39] and the (affine) quantum group symmetry in [40, 41].²

Now we turn to the case where $k \neq 0$ which is the main focus of this paper. Again historically this was first well explored for the case of $\mathfrak{g} = \mathfrak{su}(2)$. The left acting symmetry is still a Yangian [34] but the right acting symmetry is more mysterious [35] (we review the construction of the charges generating these generalised symmetries in appendix B). One finds a structure similar to an affine quantum group $\mathcal{U}_q(\widehat{\mathfrak{su}(2)})$ with,³

$$q = \exp \left[\frac{8\pi\Theta}{\Theta^2 + k^2} \right], \tag{2.14}$$

but with a modification in how the affine tower of charges is build up. Namely, instead of taking successively the Poisson bracket to access the next charges in the tower, the Poisson bracket is multiplied at each step by an additional factor,

$$\frac{\gamma^-}{\gamma^+} = -\frac{k + i\Theta}{k - i\Theta}. \tag{2.15}$$

To move down, the Poisson bracket needs to be multiplied by its inverse (see figure 2 of [35] for further details). Here the combination,

$$\Theta^2 = \frac{\alpha(\alpha - \gamma) - k^2}{\gamma}, \tag{2.16}$$

will play a distinguished role in what follows; it will be seen to be an RG invariant.

As mentioned above, several partial results were already obtained for the YB-WZ model in the particular case where $\mathfrak{g} = \mathfrak{su}(2)$. In this paper we mostly focus on the case where \mathfrak{g} is arbitrary. As we will see the general case shows several features which are absent when $\mathfrak{g} = \mathfrak{su}(2)$.⁴

3 Renormalisation of the YB-WZ model

Our aim is to calculate the β -functions for the couplings $\{\alpha, \beta, \gamma\}$ in the theory defined by eq. (2.2) without first assuming that the couplings lie on the integrable locus eq. (2.8).

²There is a small but potentially important subtlety here. In [41] the affine charges are constructed from the expansion of a trigonometric Lax at infinity and appear in the principal gradation. When the charges are extracted from the gauge transformation of the rational Lax evaluated around the poles in the twist function as in [36] they appear in the homogeneous gradation; to go between the two gradations requires a spectral parameter dependent redefinition of generators.

³Here we restore the overall normalisations to the results in [35] and map to our conventions.

⁴Mathematically all differences between the general case and the simpler case where $\mathfrak{g} = \mathfrak{su}(2)$ arise from the fact that $\mathfrak{su}(2)$ is the only simple Lie algebra where all roots are simple roots.

The coupling k being integer quantised evidently does not run. To do so we will proceed geometrically; for a general two-dimensional non-linear sigma model the β -function for the metric $G_{\mu\nu}$ and Kalb-Ramond two-form potential $B_{\mu\nu}$ in local coordinates x^μ are given by, at one-loop,

$$\begin{aligned} \mu \frac{d}{d\mu} G_{\mu\nu} &= \hat{\beta}_{\mu\nu}^G = \alpha' \left(R_{\mu\nu} - \frac{1}{4} H_{\mu\nu}^2 \right) + O(\alpha')^2, \\ \mu \frac{d}{d\mu} B_{\mu\nu} &= \hat{\beta}_{\mu\nu}^B = \alpha' \left(-\frac{1}{2} \nabla^\lambda H_{\lambda\mu\nu} \right) + O(\alpha')^2, \end{aligned} \tag{3.1}$$

where $H = dB$ is the torsion 3-form and the connections and curvatures are to be calculated using G . However, the diffeomorphism and gauge covariance of G and B means that these β -functions are ambiguous (even at one-loop order) [43, 44] allowing us to modify them by,⁵

$$\begin{aligned} \bar{\beta}_{\mu\nu}^G &= \hat{\beta}_{\mu\nu}^G + \nabla_{(\mu} W_{\nu)}, \\ \bar{\beta}_{\mu\nu}^B &= \hat{\beta}_{\mu\nu}^B + (\iota_W H)_{\mu\nu} + (d\Lambda)_{\mu\nu}, \end{aligned} \tag{3.2}$$

with W and Λ arbitrary target space one-forms. For the sigma model defined in eq. (2.2), of which the left acting G symmetry is unaltered by the deformation, the target space data is most naturally expressed in a non-orthonormal frame formalism with frames defined by the left-invariant one-forms $u = g^{-1}dg = -iu^A T_A$ as,

$$G_{AB} = \alpha \kappa_{AB} + \gamma \mathcal{R}_{AB}^2, \tag{3.3}$$

and torsion,

$$H_{ABC} = 3\beta F_{[AB}{}^D \mathcal{R}_{C]D} - k F_{ABC}. \tag{3.4}$$

Here $\kappa_{AB} = \langle T_A, T_B \rangle$, $\mathcal{R}(T_A) = \mathcal{R}^B{}_{AT_B}$ and algebra indices out of position are lowered with κ_{AB} . To completely fix things one should set $\alpha' = 2$ so that the standard normalisation of the WZW models is recovered in the case $\alpha = |k|, \beta = \gamma = 0$.

After a long battle making use of the properties listed in appendix C and the expressions of the geometry in the non-orthonormal frame listed in appendix D one finds that the β -functions are given by,

$$\begin{aligned} \hat{\beta}_{AB}^G &= -c_G \left(\frac{k^2(\alpha - 2\gamma)}{2\alpha(\gamma - \alpha)^2} - \frac{\beta^2}{(\gamma - \alpha)^2} - \frac{\gamma^2}{2(\gamma - \alpha)^2} - \frac{1}{2} \right) \kappa_{AB} - \frac{c_G}{2} \left(1 - \frac{\alpha^2 + \beta^2}{(\gamma - \alpha)^2} \right) \mathcal{R}_{AB}^2 \\ &\quad - \left(\frac{\gamma}{\alpha} \frac{k^2}{(\gamma - \alpha)^2} + \frac{\beta^2}{(\gamma - \alpha)^2} + \frac{\gamma}{(\gamma - \alpha)} \right) F_{AD}{}^C F_{BC}{}^E (\mathcal{R}^2)^D{}_E, \end{aligned} \tag{3.5}$$

$$\hat{\beta}_{AB}^B = \frac{2\beta}{\alpha - \gamma} F_{AD}{}^C F_{BC}{}^E \mathcal{R}^D{}_E + c_G \frac{\beta}{\alpha - \gamma} \mathcal{R}_{AB}. \tag{3.6}$$

The terms in blue involve tensor structures that are not present in the metric ansatz. If these terms are not removed it would mean that under the RG flow the metric would flow out of the ansatz specified by eq. (3.3). Let us exploit the diffeomorphism symmetry to

⁵Note that the Lie derivative acts on $L_W B = \iota_W H + d\iota_W B$ and the latter term being a total derivative can be discarded within the action.

try and ameliorate the situation. With this in mind, note that for a one-form W whose components W_A are constant in frame indices we have:

$$\begin{aligned} \nabla_{(A} W_{B)} &= \frac{1}{2} \frac{\gamma}{\alpha - \gamma} (F_{AD}{}^C (\mathcal{R}^2)^D{}_B + F_{BD}{}^C (\mathcal{R}^2)^D{}_A) W_C, \\ (i_W H)_{AB} &= 3\beta F_{[AB}{}^D \mathcal{R}_{C]D} G^{CE} W_E - k F_{ABC} G^{CD} W_D. \end{aligned} \tag{3.7}$$

First, we try to use an appropriate choice of W to remove the offending blue term in $\hat{\beta}^G$. However, using the properties listed in appendix C, one can show that the only sensible choice of $G^{-1}W$ involving the structure constants and the \mathcal{R} -matrix will always be Killing. Nevertheless, by taking the components W_A proportional to $F_{AB}{}^C \mathcal{R}^B{}_C$, one can show that it is again Killing but can now in fact absorb the offending first term in $\hat{\beta}^B$. Finally, we remark that for the case of $\mathfrak{g} = \mathfrak{su}(2)$ ($c_G = 4$ in our conventions) the contribution of the parameter β cancels exactly in $\hat{\beta}^G$ and can be gauged away by an appropriate gauge choice Λ in $\bar{\beta}^B$ eq. (3.2) since $\mathcal{R}_{AB} u^A \wedge u^B$ is a pure gauge improvement term for $\mathfrak{su}(2)$.

We now consider the remaining offending term in $\hat{\beta}^G$ eq. (3.5). Using a Cartan-Weyl basis for the Lie algebra and calling Lie algebra indices corresponding to positive (negative) roots as $a, b, \dots (\bar{a}, \bar{b}, \dots)$ and those corresponding to directions in the CSA by m, n, \dots one gets,

$$F_{AD}{}^C F_{BC}{}^E (\mathcal{R}^2)^D{}_E = c_G \kappa_{AB} + F_{Am}{}^C F_{BC}{}^m. \tag{3.8}$$

The second term is non-vanishing only if the index A corresponds to a positive root and the index B to the corresponding negative root (or vice-versa) so one would expect it to be proportional to \mathcal{R}_{AB}^2 . Explicit computation gives,

$$F_{am}{}^C F_{\bar{a}C}{}^m = -\kappa_{a\bar{a}} \vec{a} \cdot \vec{a} = \vec{a} \cdot \vec{a} \mathcal{R}_{a\bar{a}}^2, \tag{3.9}$$

where $\vec{a} \cdot \vec{a}$ is the length squared of the root a . In our normalization it is always equal to 2 for simply laced groups ($\mathfrak{g} = A_n, D_n, E_6, E_7$ and E_8). For the non-simply laced groups its either 2 or 1 (for $\mathfrak{g} = B_n, C_n$ and F_4) or 2 or 1/3 (for $\mathfrak{g} = G_2$). So the term in blue in eq. (3.5) can be rewritten as,

$$F_{AD}{}^C F_{BC}{}^E (\mathcal{R}^2)^D{}_E = c_G \kappa_{AB} + 2x(A, B) \mathcal{R}_{AB}^2, \tag{3.10}$$

where for simply laced groups $x(A, B) = 1$ holds. For non-simply laced groups $x(A, B)$ assumes two different values pending the values of the indices A and B . This implies that only for simply laced groups the RG stays within the ansatz specified by eq. (3.3).

However, there is a second way to remain within the ansatz eq. (3.3). Till now we did not impose any restriction on the parameters α, β, γ and k . Looking at the bothersome term in the last line of eq. (3.5) we see that it precisely vanishes at the integrable locus eq. (2.8) and we remain within the ansatz eq. (3.3) for any group (simply laced and non-simply laced)! So we should distinguish two cases: case I, a restriction to the integrable locus for general groups, and case II, a restriction to simply laced groups where we can keep the parameters general.

Before analysing both cases, we will consider a useful quantity to understand the RG flow: the Weyl anomaly coefficient $\tilde{\beta}^\Phi$. It is defined through the expectation value of the trace of the stress tensor,

$$\langle T \rangle = \frac{1}{4\pi} \tilde{\beta}^\Phi R^{(2)} + \dots, \quad \tilde{\beta}^\Phi = \frac{D}{6} - \alpha' \frac{1}{4} \left(R + 4\nabla^2 \Phi - 4(\partial\Phi)^2 - \frac{1}{12} H^2 \right) + O(\alpha')^2. \quad (3.11)$$

with D the dimension of \mathfrak{g} . The quantity $\tilde{\beta}^\Phi$, which one recognises in the spacetime effective Lagrangian for bosonic strings, can serve as a c-function for the models we are considering [45].⁶ Here we find for arbitrary groups in general,

$$\tilde{\beta}^\Phi = \frac{D}{6} + \frac{c_G D}{8} \left(\frac{1}{(\gamma - \alpha)} - \frac{k^2 + \beta^2}{3(\gamma - \alpha)^3} \right) + \frac{c_G l}{8} \left(\frac{\gamma}{(\gamma - \alpha)^2} + \frac{k^2 \gamma + \alpha \beta^2}{\alpha(\gamma - \alpha)^3} \right) \quad (3.12)$$

where l is the rank of \mathfrak{g} . Focusing on the particular case of the integrable locus (i.e. case I) this equation reduces to,

$$\tilde{\beta}^\Phi = \frac{D}{6} + \frac{c_G D}{24} \left(\frac{(\Theta^2 + \alpha^2)(\alpha^4 + k^2(\Theta^2 - 3\alpha^2) - 3\Theta^2\alpha^2)}{\alpha^3(\Theta^2 + k^2)^2} \right). \quad (3.13)$$

Whilst perhaps not so elegant, after applying the RG equations for this case we have,

$$\frac{d}{dt} \tilde{\beta}^\Phi = \frac{c_G^2 D (k^2 - \alpha^2)^2 (\alpha^2 + \Theta^2)^2 (3\alpha^4 - 2\alpha^2\Theta^2 + 3\Theta^4)}{48\alpha^6 (\Theta^2 + k^2)^4}. \quad (3.14)$$

Notice that because $(3\alpha^4 + 3\Theta^4 - 2\alpha^2\Theta^2)$ has no real roots for $\alpha^2 \in \mathbb{R}$ and $\Theta^2 \in \mathbb{R}$ we explicitly see the monotonicity of the flow $d_t \tilde{\beta}^\Phi > 0$ with $t \rightarrow \infty$ in the UV giving as required $\tilde{\beta}^\Phi|_{UV} > \tilde{\beta}^\Phi|_{IR}$. The IR is no more than the WZW CFT at $\alpha = |k|, \gamma = \beta = 0$ (for which of course $\tilde{\beta}^\Phi = \frac{D}{6} - \frac{Dh^v}{6k} + O(\frac{1}{k})^2$ in accordance with the large level expansion of $\frac{1}{6}$ times the central charge $c = \frac{k \dim G}{k+h^v}$).

3.1 Case I: general group G and restriction to the integrable locus

We will now restrict ourselves to the integrable locus, i.e. the coupling constant β satisfies eq. (2.8),

$$\beta = \pm \sqrt{\frac{\gamma}{\alpha}} \sqrt{\alpha^2 - \alpha\gamma - k^2}, \quad (3.15)$$

whilst keeping the group G arbitrary. Eqs. (3.5) and (3.6) now become,

$$\begin{aligned} \hat{\beta}_{AB}^G &= -c_G \left(\frac{k^2(\alpha - 2\gamma)}{2\alpha(\gamma - \alpha)^2} - \frac{\beta^2}{(\gamma - \alpha)^2} - \frac{\gamma^2}{2(\gamma - \alpha)^2} - \frac{1}{2} \right) \kappa_{AB} - \frac{c_G}{2} \left(1 - \frac{\alpha^2 + \beta^2}{(\gamma - \alpha)^2} \right) \mathcal{R}_{AB}^2 \\ &= -\frac{c_G}{2} \frac{k^2 - \alpha^2}{(\alpha - \gamma)^2} \kappa_{AB} - \frac{c_G}{2} \frac{\gamma}{\alpha(\alpha - \gamma)^2} (2\alpha\gamma - 3\alpha^2 + k^2) \mathcal{R}_{AB}^2, \end{aligned} \quad (3.16)$$

$$\begin{aligned} \hat{\beta}_{AB}^B &= c_G \frac{\beta}{\alpha - \gamma} \mathcal{R}_{AB} \\ &= \pm c_G \frac{1}{\alpha - \gamma} \sqrt{\frac{\gamma}{\alpha}} \sqrt{\alpha^2 - \alpha\gamma - k^2} \mathcal{R}_{AB}. \end{aligned} \quad (3.17)$$

⁶In general one would need to average, i.e. integrate this over spacetime coordinates but the special form of the metric on a group manifold means that is not needed here.

Eq. (3.16) yields the RG equations for the independent coupling constants α and γ ,

$$\begin{aligned}\frac{d\alpha}{dt} &= -\frac{c_G}{2} \frac{k^2 - \alpha^2}{(\alpha - \gamma)^2}, \\ \frac{d\gamma}{dt} &= -\frac{c_G}{2} \frac{\gamma}{\alpha(\alpha - \gamma)^2} (2\alpha\gamma - 3\alpha^2 + k^2).\end{aligned}\tag{3.18}$$

Note that eq. (3.18) is simply a rescaling of that obtained for $\mathfrak{su}(2)$ in [34]. Therefore, the group dependence in the flow equations is limited to the rate of the flow. Indeed, absorbing the factor c_G in the RG time, $t \rightarrow c_G t$, the flow can be made independent of the Lie group G . Eq. (3.17) also consistently yields the flow of the dependent parameter β ,

$$\frac{d\beta}{dt} = c_G \frac{\beta}{\alpha - \gamma}.\tag{3.19}$$

Using these equations one immediately gets,

$$\frac{d}{dt} \left(\beta^2 - \frac{\gamma}{\alpha} (\alpha^2 - \alpha\gamma - k^2) \right) = \frac{2c_G}{\alpha - \gamma} \left(\beta^2 - \frac{\gamma}{\alpha} (\alpha^2 - \alpha\gamma - k^2) \right),\tag{3.20}$$

showing that the integrable locus is preserved by the RG!

Moreover, this system has an RG invariant aside from the coefficient of the WZ term,

$$\Theta^2 = \frac{\alpha (\alpha^2 - \alpha\gamma - k^2)}{\gamma},\tag{3.21}$$

in terms of which we have a single independent RG equation,

$$\frac{d}{dt} \alpha = \frac{c_G}{2} \frac{(\alpha^2 - k^2) (\alpha^2 + \Theta^2)^2}{\alpha^2 (k^2 + \Theta^2)^2}.\tag{3.22}$$

Returning to the discussion in section 2 we see that the parameters entering the charge algebra are RG invariants since they are functions of Θ and k alone.

Discussion of the RG behaviour at the integrable locus. The case of $SU(2)$ was already considered in [34], where at first sight it appears to be different because the β coupling is a total derivative in the Lagrangian and serves merely as an improvement term in the currents. The renormalisation of this coupling in the case of $SU(2)$ can be absorbed by a gauge transformation generated by Λ of eq. (3.2). So in fact the analysis of the RG phase portraits performed in [34] is equally valid here, corroborating the group dependence of the flow. However, for completeness and later discussion we present in figure 1 the RG behaviour of the $G = SU(3)$ YB-WZ model at level $k = 4$ restricted to the integrable locus.

In this case, we have an RG invariant Θ given by eq. (3.21) which labels the RG trajectories. The only fixed point is now the WZW at $\alpha = |k| = 4$, $\beta = \gamma = 0$ in the IR. Again, on the $\alpha = \gamma$ line the one-loop result blows up and the metric is degenerate. Since we are restricted to the integrable locus, where β satisfies eq. (2.8), the physically allowed theories are located in the regions where β , or equivalently the RG invariant Θ , is real. There are two such regions indicated in green.

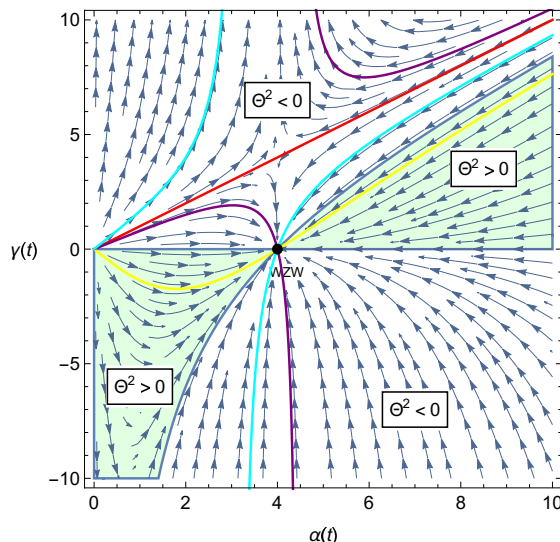


Figure 1. The RG evolution for the $G = \text{SU}(3)$ and $k = 4$ YB-WZ model restricted on the integrable locus of the couplings α vs. γ . The arrows point towards the IR. The red line $\alpha = \gamma$ depicts the points where the one-loop result blows up and it is labeled by $\Theta^2 = -k^2 = -16$. The black dot represents the WZW point ($\alpha = 4, \beta = \gamma = 0$) which is an IR fixed point with only irrelevant directions. The green regions are those where the coupling $\beta(\alpha, \gamma)$ and the RG invariant Θ are real. The yellow line portrays $\Theta^2 = 10$, the cyan line $\Theta^2 = -10$ and the purple line $\Theta^2 = -20$.

A physically allowed trajectory is portrayed by the yellow line in figure 1, along which the RG invariant has the constant real value. By varying the value of the RG invariant $\Theta \in \mathbb{R}$, we can cover the full region of physically allowed trajectories. In the green region where $\gamma < 0$, we start from the trivial fixed point at $\alpha = \gamma = 0$ in the UV and end up at the WZW in the IR in a finite RG time. In the green region where $\gamma > 0$, the WZW is again an IR fixed point but the asymptotic behaviour is not yet apparent. However, as we will see in the coming section, these two green regions are to be physically identified by a duality.

In the other regions, we have either $0 > \Theta^2 > -k^2$, represented by the cyan line, or $\Theta^2 < -k^2$, represented by the purple line. The crossover is given by $\Theta^2 = -k^2$ which corresponds to the red $\alpha = \gamma$ line. In any case, we flow either to the WZW or to a strongly γ -coupled theory in the IR. Conversely, flowing towards the UV leads either to the trivial fixed point or to an unsafe theory.

Let us analyse the behaviour around the IR WZW fixed point. If we linearise the flow around the fixed point, i.e. let $\alpha = k + \bar{\alpha}$ and $\beta = 0 + \bar{\beta}$, $\gamma = 0 + \bar{\gamma}$, we see from eqs. (3.18),

$$\frac{d\bar{\alpha}}{dt} = \frac{c_G}{k} \bar{\alpha}, \quad \frac{d\bar{\beta}}{dt} = \frac{c_G}{k} \bar{\beta}, \quad \frac{d\bar{\gamma}}{dt} = \frac{c_G}{k} \bar{\gamma}. \quad (3.23)$$

Since they all have positive sign's on the right-hand side we conclude that these are indeed irrelevant. Making use of the RG invariant eq. (3.21) and the integrable locus eq. (2.8) we can express the action as,

$$\mathcal{S} = -\frac{1}{2\pi} \int d\sigma d\tau \text{Tr} \left(g^{-1} \partial_+ g, \left(\alpha \mathbb{1} + \frac{\Theta(\alpha^2 - k^2)}{\alpha^2 + \Theta^2} \mathcal{R} + \frac{\alpha(\alpha^2 - k^2)}{\alpha^2 + \Theta^2} \mathcal{R}^2 \right) g^{-1} \partial_- g \right) + I_{WZ}, \quad (3.24)$$

where we choose the positive sign for the β -coupling. Now expanding around the IR fixed point to leading order in $\bar{\alpha}$ we have,

$$\mathcal{S} = S_{WZW_k}[g] - \frac{\bar{\alpha}}{2\pi} \int d\sigma d\tau \text{Tr} \left(g^{-1} \partial_+ g, \left(\mathbb{1} + \frac{2k\Theta}{k^2 + \Theta^2} \mathcal{R} + \frac{2k^2}{k^2 + \Theta^2} \mathcal{R}^2 \right) g^{-1} \partial_- g \right). \quad (3.25)$$

To interpret this let us now go to the Euclidean setting and define the usual WZW CFT currents,

$$J(z) = J^a(z)t^a = -\frac{k}{2} \partial g g^{-1}, \quad \bar{J}(\bar{z}) = \frac{k}{2} g^{-1} \bar{\partial} g, \quad (3.26)$$

which obey a current algebra, and are Virasoro primary with weights $(1, 0)$ and $(0, 1)$ with respect to the Sugawara stress tensor. Consider a composite field $\phi_{\ell\bar{\ell}}(z, \bar{z})$ transforming in representations labelled by ℓ and $\bar{\ell}$ under the affine $G_L \times G_R$ symmetry. This field will also be Virasoro primary and will have an anomalous dimensions $(\Delta_\ell, \bar{\Delta}_{\bar{\ell}})$. As explained in [46] the associated representation of the full Virasoro \times KM algebra is degenerate with a null vector. Because of this the anomalous dimension can be extracted as,

$$\Delta_\ell = \frac{c_\ell}{c_G + k}, \quad (3.27)$$

where $c_\ell \mathbb{I} = t_\ell^a t_\ell^a$. Examples of such primaries are $g(z, \bar{z})$, the group element itself, but also composites including the adjoint action,

$$\mathcal{D}^{ab}(z, \bar{z}) = \text{tr}(g^{-1} t^a g t^b), \quad (3.28)$$

that transforms in the adjoint of G_L on the first index and the adjoint of G_R on the second. This operator has anomalous dimension $\Delta_{\mathcal{D}} = \bar{\Delta}_{\mathcal{D}} = \frac{c_G}{c_G + k}$ and can be used to define the “wrong” currents i.e.,

$$K = K^a t^a = -\frac{k}{2} g^{-1} \partial g = g^{-1} J g \Rightarrow K^a = J^b \mathcal{D}^{ba}, \quad (3.29)$$

with dimensions $(1 + \Delta_\ell, \bar{\Delta}_{\bar{\ell}})$.

Now we can see that the deforming operator is of the form,

$$\mathcal{O}(z, \bar{z}) \sim K^a(z, \bar{z}) \mathcal{M}_{ab} \bar{J}^b(\bar{z}), \quad \mathcal{M} = \left(\mathbb{1} + \frac{2k\Theta}{k^2 + \Theta^2} \mathcal{R} + \frac{2k^2}{k^2 + \Theta^2} \mathcal{R}^2 \right), \quad (3.30)$$

and has total dimension $2 + 2\Delta_{\mathcal{D}} > 2$ and is irrelevant even without any further corrections. Suppose that we send $\Theta \rightarrow \infty$ then we are in exactly the situation considered in [13, 46] of the flow of the PCM plus a Wess-Zumino term with the WZW as the IR fixed point.

Now recall that the Callan-Symanzik equation can be used to relate the beta function to the anomalous dimension and indeed we see that in the large k limit (in which loop corrections are suppressed) the anomalous dimension of \mathcal{O} , $\gamma_{\mathcal{O}} \rightarrow \frac{c_G}{k}$ precisely in agreement with the leading order of the beta functions eq. (3.23).

It would be interesting to develop this line further and to try and ascertain all loop summation of the anomalous dimension following similar techniques to those adopted in the context of λ -models in [47]. There is however an added complexity that the deforming operator is not diagonal in the algebra indices but mixed with the inclusion of the \mathcal{M} matrix.

3.2 Case II: simply laced groups and general parameters

Although it is outside the primary purpose of this paper — which is to study integrable deformations — it is intriguing to look at the case of simply laced groups for which a consistent renormalisation did not require the model to lie on the integrable locus. It is then possible to rewrite eqs. (3.5) and (3.6) as,

$$\begin{aligned}\hat{\beta}_{AB}^G &= -\frac{c_G}{2} \frac{k^2 - \alpha^2}{(\alpha - \gamma)^2} \kappa_{AB} - \left[\frac{c_G}{2} \left(1 - \frac{\alpha^2 + \beta^2}{(\gamma - \alpha)^2} \right) + 2 \left(\frac{\gamma k^2 + \alpha \beta^2}{\alpha(\gamma - \alpha)^2} + \frac{\gamma}{(\gamma - \alpha)} \right) \right] \mathcal{R}_{AB}^2, \\ \hat{\beta}_{AB}^B &= c_G \frac{\beta}{\alpha - \gamma} \mathcal{R}_{AB}.\end{aligned}\tag{3.31}$$

This gives the following RG equations for the coupling constants α , β and γ (with RG time $t = \log \mu$):

$$\begin{aligned}\frac{d\alpha}{dt} &= -\frac{c_G}{2} \frac{k^2 - \alpha^2}{(\alpha - \gamma)^2}, \\ \frac{d\beta}{dt} &= c_G \frac{\beta}{\alpha - \gamma}, \\ \frac{d\gamma}{dt} &= -\frac{c_G}{2} \left(1 - \frac{\alpha^2 + \beta^2}{(\gamma - \alpha)^2} \right) - 2 \left(\frac{\gamma k^2 + \alpha \beta^2}{\alpha(\gamma - \alpha)^2} + \frac{\gamma}{(\gamma - \alpha)} \right).\end{aligned}\tag{3.32}$$

We will analyse the RG behaviour in some detail below. However one already notices a remarkable fact. Besides the standard WZW fixed point ($\alpha = |k|$, $\beta = \gamma = 0$), a second fixed point seems to emerge at $\alpha = |k|$, $\beta = 0$ and $\gamma = 2c_G|k|/(c_G + 4)$ iff. $c_G \neq 4$ or thus $G \neq \text{SU}(2)$. We call this point FP2. When $G = \text{SU}(2)$ the RG equations blow up on the FP2 values (since then $\alpha = \gamma$) and the second fixed point is removed. Furthermore, for $\text{SU}(2)$ one sees that the terms involving β cancel in the flow equation for $\dot{\gamma}$ and the general RG equations of the remaining α and γ will coincide with the corresponding RG equations when restricted to the integrable locus (see above).

The RG behaviour when not restricted to the integrable locus. To illustrate the existence of the second fixed point FP2, we consider the RG flow for the case of the group $G = \text{SU}(3)$, setting $k = 4$. We plot the flow in two slices of the three-dimensional coupling space (α, β, γ) in order to visualise various directions around the fixed points. Figure 2a shows the flow of α vs. γ in the $\beta = 0$ slice and figure 2b the flow of γ vs. β in the $\alpha = 4$ slice.

From the above figures 2a and 2b, we see qualitatively that the WZW fixed point exhibits three independent irrelevant directions and the FP2 fixed point one irrelevant and two relevant independent directions. This can be made precise by again analysing the linearised flows in the neighbourhood of the fixed points. In a more compact notation, denoting $\xi_i = \{\alpha, \beta, \gamma\}$ with $i \in \{1, 2, 3\}$, the linearised flow can be written as,

$$\frac{\partial \xi_i}{\partial \log \mu} = A_{ij} \delta \xi_j + \mathcal{O}(\delta \xi_i^2).\tag{3.33}$$

In the neighbourhood of the WZW point we find,

$$A_{ij}^{\text{WZW}} = \frac{c_G}{|k|} \delta_{ij},\tag{3.34}$$

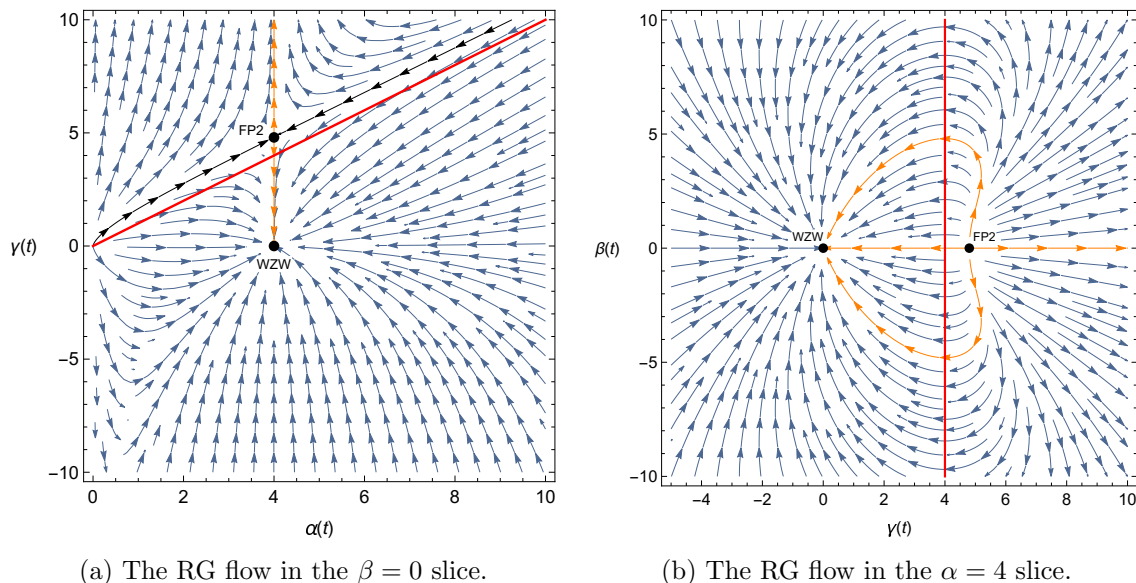


Figure 2. The RG evolution of (α, β, γ) for $G = \text{SU}(3)$ and $k = 4$. The arrows point towards the IR. The red line $\alpha = \gamma$ depicts the points where the one-loop result blows up. The black dots represent the RG fixed points WZW and FP2. We see that FP2 exhibits two relevant (orange lines) and one irrelevant (black line) direction. The WZW is a true IR fixed point with only irrelevant directions.

which gives indeed three independent irrelevant directions (they have positive eigenvalues). On the other hand, in the neighbourhood of the second fixed point we find,

$$A_{ij}^{FP2} = \frac{c_G(c_G + 4)}{|k|(c_G - 4)} \begin{pmatrix} \frac{c_G+4}{c_G-4} & 0 & 0 \\ 0 & -1 & 0 \\ \frac{2(c_G+4)}{c_G-4} & 0 & -\frac{c_G+4}{c_G-4} \end{pmatrix}, \quad (3.35)$$

for which the eigenvalues read:

$$\left\{ \frac{c_G(c_G + 4)^2}{|k|(c_G - 4)^2}, -\frac{c_G(c_G + 4)}{|k|(c_G - 4)}, -\frac{c_G(c_G + 4)^2}{|k|(c_G - 4)^2} \right\}. \quad (3.36)$$

Thus, from the second fixed point indeed two relevant and one irrelevant independent directions emerge.

At the two fixed points the Ricci curvature R (D.12) evaluates to,

$$R_{\text{WZW}} = \frac{c_G D}{4|k|},$$

$$R_{\text{FP2}} = -\frac{c_G}{4(c_G - 4)^2} \left((c_G^2 - 16) D + 2c_G(c_G + 4) l \right) \frac{1}{|k|},$$

with D the dimension and l the rank of G such that the target spaces are weakly curved for large enough k and for which the one-loop result is trustworthy. Whilst there is no reason to believe that the location of FP2 (i.e. the value of γ at the fixed point) is one-loop exact, it seems likely that its existence is robust to loop corrections. It is then conceivable that

FP2 may define a CFT. This being the case, from the general dilaton β -function eq. (3.12) we can read off the effective central charge c_{eff} of FP2 at one-loop to find,

$$c_{\text{eff}} = D + \frac{c_G(c_G + 4) \left((16 + (c_G - 16)c_G)D + 6c_G^2 l \right)}{2|k|(c_G - 4)^3}. \quad (3.37)$$

Before further discussing this possibility let us explore other aspects of the RG flow.

At first sight, and consistent with $c_{UV} > c_{IR}$, is that FP2 defines a UV fixed point from which in the deep IR one arrives at the WZW theory. However, care has to be taken when traveling over the line $\alpha = \gamma$, displayed in red in the figures. In the vicinity of this line the one-loop approximation is evidently not trustworthy; the target space curvatures blow up for small values of $|\gamma - \alpha|$ as is clear from the curvature R eq. (D.12) and indeed the metric G_{AB} (3.3) becomes degenerate. In light of the apparent singularity of the one-loop flow equations where $\gamma - \alpha$ appears in denominators, it is then quite surprising that numerically a global picture emerges with flows that transgress the red line. We are then led to ask if such an RG trajectory can cross the $\alpha = \gamma$ line in a finite RG time. To show that this is possible we concentrate on the slice of $\alpha = |k|$ illustrated in figure 2b and for further simplicity consider going backwards along the orange direction $\beta = 0$ starting near to the WZW point. Along this trajectory we can calculate the RG time Δt , with $t = \log \mu$, by evaluating,

$$\Delta t = \int_{\gamma=\gamma_i}^{\gamma=\gamma_f} \frac{dt}{d\gamma} d\gamma. \quad (3.38)$$

One can show that there is no pathology associated with $\gamma = \alpha = |k|$ in this quantity. Given this, one is encouraged to take seriously the quantity $\tilde{\beta}^\Phi$ defined in eq. (3.12) as a would-be c-function for the flow connecting FP2 and WZW. For simplicity we again consider this quantity along the orange direction $\beta = 0, \alpha = |k|$ in figure 2b and plot the result in figure 3. What we see is that $\tilde{\beta}^\Phi$ is sensitive, unsurprisingly, to the singularity at $\gamma = k$. Whilst $\tilde{\beta}^\Phi|_{UV} > \tilde{\beta}^\Phi|_{IR}$ and its derivative is strictly positive, it is not a positive definite quantity and diverges at $\gamma = k$. Of course one should not read too much into this; the singularity is just symptomatic of the breakdown of the perturbative approximation. One could still expect that a correct strictly positive monotonic function exists and it agrees with this one-loop approximate result where the one-loop result is valid.

Combining the observation that the one-loop approximation is robust around the fixed points (for large k) and the unexpected global continuity of the numerical solutions in figures 2a and 2b leads us to tentatively suggest that there is indeed an RG flow between a new fixed point FP2 and an IR WZW model but that the sigma model description may not be the correct variables to reveal this.

There are several points that merit investigation:

- At FP2, $\det(G_{AB}) < 0$. This means that some currents occur in the action with a negative coefficient of their kinetic term. A conservative viewpoint would be to regard this as non-physical but this then begs the question what is the UV completion of the model? Let us instead take FP2 seriously. Should FP2 define a CFT, it is presumably non-unitary. In this case we would have an RG flow between a non-unitary UV theory and an unitary IR theory. Perhaps this suggestion is not

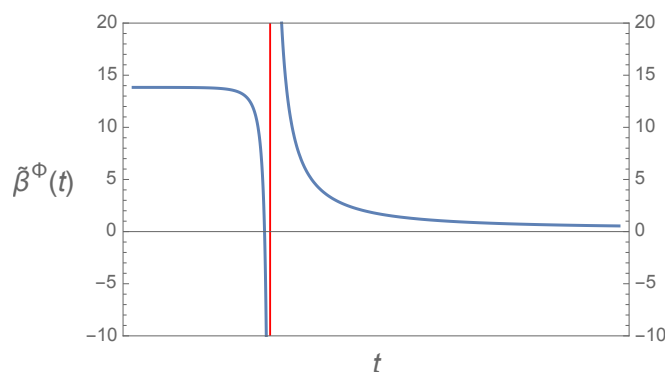


Figure 3. The Weyl anomaly coefficient $\tilde{\beta}^\Phi$ evaluated for $G = \text{SU}(3)$ and $k = 4$ along the orange RG trajectory $\beta = 0, \alpha = |k|$ shown in figures 2a and 2b that connects the UV FP2 to the WZW in the IR.

as outlandish as might first seem. By way of example we could consider RG flows in minimal models. It is well known [48, 49] that the $\phi_{(1,3)}$ deformation of the p^{th} minimal model $\mathcal{M}_{(p,p+1)}$ triggers an RG flow resulting in the $(p-1)^{\text{th}}$ minimal model IR.⁷ Less familiar perhaps are the RG flows involving non-unitary minimal models, i.e. $\mathcal{M}_{(p,q)}$ with p, q co-prime and $q \neq p+1$, whose study was initiated in [50–52]. More generally [53], chains of non-unitary minimal models can be connected by RG flows triggered by alternating deformations of $\phi_{(1,5)}$ and $\phi_{(2,1)}$ which then terminate in an unitary minimal model. One example from [53] is,⁸

$$\dots \mathcal{M}_{(5,12)} \xrightarrow{\phi_{(1,5)}} \mathcal{M}_{(5,8)} \xrightarrow{\phi_{(2,1)}} \mathcal{M}_{(3,8)} \xrightarrow{\phi_{(1,5)}} \mathcal{M}_{(3,4)}. \quad (3.39)$$

An other example in [53] terminates in a flow from the Yang-Lee edge singularity to the trivial $c = 0$ theory. Recently in [54] it was shown that it is possible to relax the requirement of unitary and still show the existence of a monotonic decreasing c -function along such flows. So the learning here is that it is not a manifest impossibility to conceive an RG flow between a non-unitary UV CFT and a unitary IR CFT.

- The fate of FP2 with regard to higher loop corrections needs to be established; does it persist?
- Is the postulated FP2 both scale *and* Weyl invariant?⁹
- What are the corresponding affine symmetries and the exact value of the central charge at FP2?
- What is the spectrum of primaries for this postulated CFT at FP2?

⁷More precisely this occurs when the deformation parameter is negative, when the deformation parameter is positive the flow results in a massive theory.

⁸Notice that this terminates in the unitary critical Ising model with $c = \frac{1}{2}$ and, just as with the flow between tri-critical Ising and critical Ising, the single massless Majorana fermion of the final IR theory can be interpreted as the goldstino for the spontaneous breaking of the supersymmetry present in $\mathcal{M}_{(3,8)}$.

⁹For instance in η -deformed $\text{PSU}(2, 2|4)$ current understanding is that only scale invariance holds [5].

These are evidently interesting challenges that we hope to return to in a future paper. For the present we continue with our principle concern; the YB-WZ model on the integrable locus.

4 Poisson-Lie T-duality of the YB-WZ model

Motivated by the Poisson-Lie symmetric structure of the η -deformation, one could wonder how the YB-WZ action (2.2) behaves under Poisson-Lie symmetry. Remarkably the YB-WZ model at the integrable locus features an example of the most simple realisation of PL. The Poisson-Lie duality transformation preserves the structure of the action, reshuffling the coupling constant in a surprisingly Buser-rule like manner. At the RG fixed point (the WZW) the action is self-dual. This section, being somewhat technical, can safely be omitted at a first reading and the reader can jump directly to the resulting “effective” transformation rules of the Poisson-Lie transformation of the YB-WZ model in equations (4.10).

When restricted to the integrable locus, the YB-WZ model admits a 1st order formulation as an \mathcal{E} -model [32]. We refer the reader to the original paper for full details of this construction but note here the essential ingredients of an \mathcal{E} -model, and its connection to sigma models, are:

- (i) An even dimensional real Lie-algebra \mathfrak{d}
- (ii) An ad-invariant inner product $(\cdot, \cdot)_{\mathfrak{d}} : \mathfrak{d} \otimes \mathfrak{d} \rightarrow \mathbb{R}$
- (iii) An idempotent involution \mathcal{E} that is self-adjoint with respect to the inner product
- (iv) A maximally isotropic subalgebra \mathfrak{h} (i.e. $(z_1, z_2)_{\mathfrak{d}} = 0 \forall z_{1,2} \in \mathfrak{h}$ and $\dim \mathfrak{h} = \frac{1}{2} \dim \mathfrak{d}$).

Given the data of (i)-(iii) one can construct a 1st order action known as the \mathcal{E} -model. Given further (iv) one can integrate out auxiliary fields from the \mathcal{E} -model to arrive at a non-linear sigma model. The field variables of this sigma model are sections (defined patchwise if needed) of the coset D/H (with D, H the groups corresponding to \mathfrak{d} and \mathfrak{h}). If a second maximally isotropic subalgebra $\tilde{\mathfrak{h}}$ can be found then the procedure can be repeated to yield a second non-linear sigma model on D/\tilde{H} — this is the Poisson-Lie dual.

For both the YB (η -theory) and the present case of interest, the YB-WZ theory, the relevant algebra is $\mathfrak{d} = \mathfrak{g}^{\mathbb{C}}$, viewed as a real Lie algebra with elements $z = x + iy$ with $x, y \in \mathfrak{g}$. The addition of the WZ term requires that the inner product be modified to [32],

$$(z_1, z_2)_{\mathfrak{d}} = C \text{Im} \langle e^{i\rho} z_1, z_2 \rangle, \tag{4.1}$$

where the parameters used in [32] translate to,

$$C = \frac{k^2 + \Theta^2}{8\pi\Theta}, \quad e^{i\rho} = -\frac{k + i\Theta}{k - i\Theta} = \frac{\gamma^-}{\gamma^+}, \tag{4.2}$$

which are both RG invariant and match the parameters determining the (affine tower) charge algebra in the case of $SU(2)$ established in [35], see also appendix B. The involution \mathcal{E} , whose precise definition will not be illuminating for us and can be found in eq. (3.8)

of [32], dresses up the swapping of real and imaginary parts of $z \in \mathfrak{g}^{\mathbb{C}}$ with parametric dependence on ρ and also on $e^p = -\frac{\alpha}{\mathfrak{O}}$. So unlike the innerproduct, \mathcal{E} is RG variant.

We have two maximal isotropics given by the embeddings of \mathfrak{g} :

$$\begin{aligned} \tilde{\mathfrak{h}}_{\rho} &= \left(\mathcal{R} - \tan \frac{\rho}{2} (\mathcal{R}^2 + 1) - i \right) \mathfrak{g}, \\ \tilde{\tilde{\mathfrak{h}}}_{\rho} &= \left(\mathcal{R} - \cot \frac{\rho}{2} (\mathcal{R}^2 + 1) + i \right) \mathfrak{g}. \end{aligned} \tag{4.3}$$

That these are subalgebras follows immediately since \mathcal{R} satisfies the mCYBE and $\mathcal{R}^2 + 1$ projects into the Cartan. That they are isotropic with respect to (4.1) fixes the trigonometric functions. Since $\mathfrak{h}_{\rho} = e^{i\rho} \mathfrak{a} + \mathfrak{n}$ where \mathfrak{a} and \mathfrak{n} are the corresponding algebras in the Iwasawa decomposition $D = KAN$, we can think of \mathfrak{h}_{ρ} as a twisted upper triangular subalgebra and the other, $\tilde{\tilde{\mathfrak{h}}}_{\rho}$, as lower triangular. Locally at least we can decompose,

$$D = H_{\rho} \cdot \tilde{H}_{\rho} = \tilde{H}_{\rho} \cdot H_{\rho}, \tag{4.4}$$

and because the standard Iwasawa decomposition can be modified to incorporate the twisting by ρ as in [32] we can identify $D \equiv G^{\mathbb{C}} = G \cdot \tilde{H}_{\rho} = G \cdot H_{\rho}$. Thus the cosets D/H_{ρ} and D/\tilde{H}_{ρ} can be identified with G and so $g \in G$ can serve as field variables on either of the two dual models. To extract the sigma models one needs to specify projectors \mathcal{P} and $\tilde{\mathcal{P}}$ such that,¹⁰

$$\text{Im}\mathcal{P} = \mathfrak{h}_{\rho}, \quad \text{Ker}\mathcal{P} = (1 + \mathcal{E})\mathfrak{d}, \quad \text{Im}\tilde{\mathcal{P}} = \tilde{\tilde{\mathfrak{h}}}_{\rho}, \quad \text{Ker}\tilde{\mathcal{P}} = (1 + \mathcal{E})\mathfrak{d}. \tag{4.5}$$

Explicitly if we let (making use of the definition of \mathcal{E} in eqs. (3.7,3.8) of [32]),

$$w = e^{-i\rho} + i \cosh(p) + i e^{-i\rho} \sinh(p) = w_1 + i w_2, \quad x = \frac{w_1}{w_2}, \tag{4.6}$$

and define,

$$\mathcal{O} = \mathcal{R} - \tan \frac{\rho}{2} (\mathcal{R}^2 + 1), \quad \tilde{\mathcal{O}} = \mathcal{R} - \cot \frac{\rho}{2} (\mathcal{R}^2 + 1), \tag{4.7}$$

then,

$$\mathcal{P}(g^{-1}dg) = (\mathcal{O} - i)(\mathcal{O} + x)^{-1} g^{-1}dg, \quad \tilde{\mathcal{P}}(g^{-1}dg) = (\tilde{\mathcal{O}} + i)(\tilde{\mathcal{O}} - x)^{-1} g^{-1}dg. \tag{4.8}$$

Equipped with all of this we can now simply specify the non-linear sigma models obtained after integrating out the auxiliary fields from the \mathcal{E} models. They read,

$$\begin{aligned} S &= S_{WZW,k}^{\mathfrak{d}}[g] + \frac{k}{\pi} \int d\sigma d\tau \left(\mathcal{P}(g^{-1}\partial_+g), g^{-1}\partial_-g \right)_{\mathfrak{d}}, \\ \tilde{S} &= S_{WZW,k}^{\mathfrak{d}}[g] + \frac{k}{\pi} \int d\sigma d\tau \left(\tilde{\mathcal{P}}(g^{-1}\partial_+g), g^{-1}\partial_-g \right)_{\mathfrak{d}}, \end{aligned} \tag{4.9}$$

where we emphasise that the deformed inner product on $\mathfrak{g}^{\mathbb{C}}$ of eq. (4.1) is used to define the WZW models and that the term depending on the projectors has coefficient -2 times

¹⁰There is a slight simplification here of the general formulas of [32] since $g \in G$ the adjoint action ad_g commutes in this case with the idempotent \mathcal{E} .

that of the kinetic term of the WZW model. Using $\mathcal{R}^3 = -\mathcal{R}$ it was established in [32] that the first of these actions matches the general model in eq. (2.2) with parameters α , β and γ obeying the integrable locus relation. What of the Poisson-Lie dual theory? After some tedious trigonometry and using the relations eq. (4.2) together with the definition of the inner product eq. (4.1) one finds the action \tilde{S} is also of the form of eq. (2.2) but the T-duality acts on the parameters as,

$$\begin{aligned} \alpha &\rightarrow \tilde{\alpha} = \frac{k^2}{\alpha}, \\ \beta &\rightarrow \tilde{\beta} = -\beta, \\ \gamma &\rightarrow \tilde{\gamma} = \frac{k^2 + \alpha\gamma - \alpha^2}{\alpha} = -\frac{\beta^2}{\gamma}. \end{aligned} \tag{4.10}$$

This is a truly elegant result; recall that $\frac{1}{k}$ plays the role of α' so that these Poisson-Lie T-duality rules really do resemble the radial inversion of abelian T-duality. Being canonically equivalent it must be the case that the T-dual model is also integrable, and indeed one sees that $\tilde{\alpha}, \tilde{\beta}, \tilde{\gamma}$ also sit on the integrable locus; this serves as a check of the T-duality rules.

We can see that the WZW point is rather special; it is the self-dual point of the duality transformation.¹¹ As remarked earlier in the RG portrait figure 1 there are two regions that corresponding to a real action, shaded in green and for which $\Theta^2 > 0$. The Poisson-Lie duality action simply maps the region for $\alpha < k$ one-to-one with that of $\alpha > k$; these two regions of course touch at the self-dual WZW fixed point.

The action of this T-duality on the charge algebra is also of note. It follows immediately that the RG invariant combination is transformed as,

$$\Theta \rightarrow \tilde{\Theta} = \frac{k^2}{\Theta}. \tag{4.11}$$

Then we see that the quantum group parameter $q = \exp\left[\frac{8\pi\Theta}{k^2+\Theta^2}\right]$ is invariant under T-duality. However recall that the affine tower of charges (at least in the $\mathfrak{su}(2)$ where it has been established explicitly) differs from the standard affine quantum group by a multiplicative factor between gradations of $-\frac{k+i\Theta}{k-i\Theta}$. This factor undergoes an S-transformation, i.e it is mapped to negative its inverse. This illustrates that whilst the T-duality rules look quite trivial, at the level of charges the canonical transformation that maps the two T-dual theories can have quite an involved action.

5 The supersymmetric YB-WZ model

This section falls a bit outside the main line of the paper but is motivated by the following observation. It is clear from the previous discussion that starting from a generic $d = 2$ non-linear σ -model and requiring (classical) integrability, imposes severe restrictions on the target manifold and its metric and torsion 3-form. However another way to restrict the allowed background geometries is by requiring the existence of extended worldsheet supersymmetries. Indeed asking that the non-linear σ -model exhibits $N > (1, 1)$ supersymmetry

¹¹Self-duality under PL of WZW models (with no deformations) was exhibited already in [55].

introduces additional geometric structure which only exists for particular background geometries. A hitherto unexplored terrain is the eventual relationship between integrable models on the one hand and extended supersymmetry on the other (however see [56] for some early work in this direction).

In this section we explore the possibility of having $N > (1, 1)$ supersymmetry in the YB-WZ models studied in this paper. This is an interesting point in itself because if one thinks about the potential use of these integrable models as backgrounds for type II superstrings in the NS worldsheet formulation then the existence of an $N = (2, 2)$ supersymmetric extension is necessary as well. As we will see, the integrable deformations of the WZW-model studied in this paper do generically not allow for an extended supersymmetry.

Given is a non-linear sigma model with target manifold \mathcal{M} endowed with a metric G and a closed 3-form H (the torsion). Locally we write $H = dB$. Passing to an $N = (1, 1)$ supersymmetric extension of the model does not require any further geometric structure. Indeed the action for the $N = (1, 1)$ supersymmetric non-linear sigma model written in $N = (1, 1)$ superspace is remarkably similar to the non-supersymmetric one,¹²

$$\mathcal{S} = \int d^2\sigma d^2\theta D_+ X^\mu (G_{\mu\nu} + B_{\mu\nu}) D_- X^\nu, \tag{5.1}$$

where X^μ are some local coordinates on the target manifold.

However asking for more supersymmetry does introduce additional geometrical structure. E.g. $N = (2, 2)$ supersymmetry requires the existence of two complex structures \mathcal{J}_+ and \mathcal{J}_- which are endomorphisms of the tangent space $T\mathcal{M}$ and which are such that $(\mathcal{M}, G, H, \mathcal{J}_\pm)$ is a bihermitian structure [57, 58], i.e. \mathcal{M} is even-dimensional and the complex structures \mathcal{J}_\pm satisfy,

1. $\mathcal{J}_\pm^2 = -\mathbf{1}$,
2. $[X, Y] + \mathcal{J}_\pm [\mathcal{J}_\pm X, Y] + \mathcal{J}_\pm [X, \mathcal{J}_\pm Y] - [\mathcal{J}_\pm X, \mathcal{J}_\pm Y] = 0$ for all $X, Y \in T\mathcal{M}$, which is the integrability condition for the complex structures,
3. $G(\mathcal{J}_\pm X, Y) = -G(X, \mathcal{J}_\pm Y)$ for all $X, Y \in T\mathcal{M}$, so G is a hermitian metric with respect to both complex structures,
4. $\nabla^{(+)} \mathcal{J}_+ = \nabla^{(-)} \mathcal{J}_- = 0$ with $\nabla^{(\pm)}$ covariant derivatives which use the Bismut connections:

$$\Gamma^{(\pm)} = \{ \} \pm \frac{1}{2} G^{-1} H, \tag{5.2}$$

such that in a local coordinate bases,

$$\nabla_\rho \mathcal{J}_{\pm\nu}^\mu = \pm \frac{1}{2} \left(G^{\kappa\lambda} H_{\lambda\rho\nu} \mathcal{J}_{\pm\kappa}^\mu - G^{\mu\lambda} H_{\lambda\rho\kappa} \mathcal{J}_{\pm\nu}^\kappa \right), \tag{5.3}$$

where the covariant derivative ∇ in the above is taken with the Christoffel symbol as connection. This condition is equivalent to the requirement that the exterior derivative of the two-forms $\omega_\pm(X, Y) = -G(X, \mathcal{J}_\pm Y)$ are given by:

$$d\omega_\pm(X, Y, Z) = \mp H(\mathcal{J}_\pm X, \mathcal{J}_\pm Y, \mathcal{J}_\pm Z). \tag{5.4}$$

¹²A brief summary of our superspace conventions can be found in appendix A.

Using the covariant constancy of the complex structure one can rewrite the integrability condition (condition 2) as,

$$H(X, \mathcal{J}_\pm Y, \mathcal{J}_\pm Z) + H(Y, \mathcal{J}_\pm Z, \mathcal{J}_\pm X) + H(Z, \mathcal{J}_\pm X, \mathcal{J}_\pm Y) = H(X, Y, Z). \quad (5.5)$$

Note that demanding $N = (2, 0)$ or $N = (2, 1)$ instead of $N = (2, 2)$ supersymmetry only requires the existence of \mathcal{J}_+ satisfying the above conditions.

We now rewrite these conditions for the deformed models studied in this paper. Since at the level of the action the deformation preserves the left acting G symmetry while it breaks the right acting G symmetry (to its Cartan subgroup), the geometry and the $\mathcal{N} = (2, 2)$ conditions are most naturally presented in the basis of left-invariant one-forms u^A . Given the deformed metric G_{AB} eq. (3.3) and the torsion H_{ABC} eq. (3.4), we find that the above conditions for $\mathcal{N} = (2, 2)$ supersymmetry translate in this basis to the following:

1. The first condition is simply,

$$\mathcal{J}_\pm^A{}_C \mathcal{J}_\pm^C{}_B = -\delta_B^A. \quad (5.6)$$

2. The second condition (using the form in eq. (5.5)) results in:

$$3\mathcal{J}_\pm^D{}_{[A} \mathcal{J}_\pm^E{}_B H_{C]DE} = H_{ABC}, \quad (5.7)$$

where H_{ABC} is given in eq. (3.4).

3. The third condition yields, $G_{AB} = \mathcal{J}_\pm^C{}_A \mathcal{J}_\pm^D{}_B G_{CD}$ or using eq. (3.3):

$$\mathcal{J}_\pm^C{}_A \kappa_{CB} = -\mathcal{J}_\pm^C{}_B \kappa_{CA} - \frac{\gamma}{\alpha} (\mathcal{J}_\pm^C{}_B \mathcal{R}_{CA}^2 + \mathcal{J}_\pm^C{}_A \mathcal{R}_{CB}^2). \quad (5.8)$$

4. After a little bit of work, the covariant constancy of the complex structures (the fourth condition), translates to,

$$u_C{}^\mu \partial_\mu \mathcal{J}_\pm^A{}_B = \mathcal{J}_\pm^A{}_D M_\pm^D{}_{CB} - M_\pm^A{}_{CD} \mathcal{J}_\pm^D{}_B, \quad (5.9)$$

where,

$$M_\pm^A{}_{BC} = \Gamma_{BC}^A \pm \frac{1}{2} G^{AD} H_{DBC}, \quad (5.10)$$

and where the spin connection Γ_{BC}^A is given by eq. (D.7). Eq. (5.9) implies an integrability condition,

$$\mathcal{J}_\pm^A{}_E R_\pm^E{}_{BCD} = R_\pm^A{}_{ECD} \mathcal{J}_\pm^E{}_B, \quad (5.11)$$

where the curvature tensors R_\pm are given by,

$$R_\pm^A{}_{BCD} = M_\pm^E{}_{DB} M_\pm^A{}_{CE} - M_\pm^E{}_{CB} M_\pm^A{}_{DE} - F_{CD}{}^E M_\pm^A{}_{EB}. \quad (5.12)$$

The integrability condition eq. (5.11) is the requirement that the complex structures commute with the generators of the holonomy group defined by the connections in eq. (5.10).

While the first three conditions are given by algebraic equations eqs. (5.6)–(5.7), which can be analyzed in a way similar to what was done in [59, 60], the last one, eq. (5.9), is involved. However, the integrability conditions for the latter are algebraic again and can be explicitly analyzed.

In [59, 60] these conditions were analyzed for the undeformed case, $\alpha = |k|$, $\beta = \gamma = 0$, *i.e.* the standard WZW model and it was found that on any even-dimensional group manifolds there exist solutions to the above equations. Let us briefly review those results. In the undeformed case the connections in eq. (5.10) are simply,

$$M_{+BC}^A = 0, \quad M_{-BC}^A = F_{BC}^A. \quad (5.13)$$

With this one verifies that the curvature tensors in eq. (5.12) vanish (reflecting the fact group manifolds are parallelizable), either trivially or by virtue of the Jacobi identities, and as a consequence the integrability conditions, eq. (5.11), are automatically satisfied. Turning then to eq. (5.9) one finds that \mathcal{J}_{+B}^A is constant while \mathcal{J}_{-B}^A satisfies,

$$u_C^\mu \partial_\mu \mathcal{J}_{-B}^A = \mathcal{J}_{-D}^A F_{CB}^D - F_{CD}^A \mathcal{J}_{-B}^D. \quad (5.14)$$

In order to analyze the latter one introduces a group element in the adjoint representation,

$$S^A{}_B = v_\mu^A u_B^\mu, \quad (5.15)$$

which can easily be shown to satisfy,

$$u_C^\mu \partial_\mu S^A{}_B = F_{CB}^D S^A{}_D. \quad (5.16)$$

Using this and eq. (5.14) one shows that $S^A{}_C \mathcal{J}_{-D}^C (S^{-1})^D{}_B$ (which is \mathcal{J}_- in the right invariant frame) is constant as well. In this way the remaining conditions for $N = (2, 2)$ supersymmetry, eq. (5.6)–(5.8), all reduce to algebraic equations on the Lie algebra which were solved in [59, 60]. The result is remarkably simple: any complex structure pulled back to the Lie algebra is almost completely equivalent to a choice for a Cartan decomposition. Indeed the complex structure acts diagonally on generators corresponding to positive (negative roots) with eigenvalue $+i$ ($-i$). It maps the CSA to itself so that it squares to minus one and so that the Cartan-Killing metric restricted to the CSA is hermitian.

In the deformed case the integrability conditions eq. (5.11) become non-trivial and need to be investigated first. While in principle this can be done for general groups (resulting in not particularly illuminating complex expressions) we limit ourselves in this paper to a detailed analysis of the simplest case: $SU(2) \times U(1)$. A more systematic analysis of the relation extended supersymmetry and integrability in general is currently underway and will be reported on elsewhere.

For $SU(2) \times U(1)$ the β deformation is a total derivative and can be ignored in the present analysis. We choose a basis for the Lie algebra where $t_0 = (\sigma_3 + i\sigma_0)/2$, $t_{\bar{0}} = (\sigma_3 - i\sigma_0)/2$, $t_1 = (\sigma_1 + i\sigma_2)/2$ and $t_{\bar{1}} = (\sigma_1 - i\sigma_2)/2$. In this basis the non-vanishing components of the Cartan-Killing metric are given by $\kappa_{0\bar{0}} = \kappa_{1\bar{1}} = 1$ and those of \mathcal{R} by $\mathcal{R}^1{}_1 = -\mathcal{R}^{\bar{1}}{}_{\bar{1}} = i$. The non-vanishing components of the deformed metric in the left invariant frame, eq. (3.3),

are $G_{0\bar{0}} = \alpha$ and $G_{1\bar{1}} = \alpha - \gamma$. For the torsion, eq. (3.4), we get $H_{01\bar{1}} = H_{\bar{0}1\bar{1}} = ik$. The hermiticity condition eq. (5.8) and the integrability condition eq. (5.11) are both linear in the complex structures and as a consequence are easily analyzed. The hermiticity condition eliminates 10 of the 16 components of each complex structure. A straightforward but somewhat tedious calculation shows the following result for the integrability condition:

1. It is identically satisfied without any further conditions if $\alpha = |k|$ and $\gamma = 0$. This is just the undeformed $SU(2) \times U(1)$ WZW model known to be $N = (2, 2)$ supersymmetric (in fact it is even $N = (4, 4)$ supersymmetric).
2. It is satisfied if $\alpha = |k|$ and only $\mathcal{J}_{\pm 0}^0 = -\mathcal{J}_{\pm 0}^{\bar{0}}$ and $\mathcal{J}_{\pm 1}^1 = -\mathcal{J}_{\pm 1}^{\bar{1}}$ are non-vanishing.
3. Otherwise, for generic values of α, γ and k it has *no* solutions.

So we can conclude that in general the deformed $SU(2) \times U(1)$ YB-WZ model does not allow for an $N = (2, 2)$ supersymmetric extension. Remains of course case 2 in the above.

From now on we take $\alpha = |k|$. Checking eq. (5.14) one finds that only a vanishing \mathcal{J}_- is consistent with eqs. (5.6) and (5.7) while \mathcal{J}_+ is constant and its non-vanishing components are given by e.g. $\mathcal{J}_{+0}^0 = -\mathcal{J}_{+0}^{\bar{0}} = \mathcal{J}_{+1}^1 = -\mathcal{J}_{+1}^{\bar{1}} = i$. This choice for \mathcal{J}_+ also satisfies eqs. (5.6) and (5.7). So we conclude that the model is indeed $N = (2, 1)$ or $N = (2, 0)$ supersymmetric but does not allow for $N = (2, 2)$ supersymmetry.

To end this section we formulate this model in $N = (2, 1)$ superspace thereby making the $N = (2, 1)$ supersymmetry explicit. In general one starts with a set of $N = (2, 1)$ superfields z^α and $z^{\bar{\alpha}}$ satisfying the constraints $\hat{D}_+ z^\alpha = +i D_+ z^\alpha$ and $\hat{D}_+ z^{\bar{\alpha}} = -i D_+ z^{\bar{\alpha}}$ which are a consequence of the fact that the non-vanishing components of the complex structure \mathcal{J}_+ are $\mathcal{J}_{+\beta}^\alpha = +i \delta_\beta^\alpha$ and $\mathcal{J}_{+\bar{\beta}}^{\bar{\alpha}} = -i \delta_{\bar{\beta}}^{\bar{\alpha}}$. The action is expressed in terms of a vector on the target manifold ($iV_\alpha, -iV_{\bar{\alpha}}$),

$$\mathcal{S} = \frac{1}{2} \int d^2\sigma d^2\theta d\hat{\theta}^+ \left(iV_\alpha D_- z^\alpha - iV_{\bar{\alpha}} D_- z^{\bar{\alpha}} \right). \quad (5.17)$$

Passing to $N = (1, 1)$ superspace,

$$\begin{aligned} \mathcal{S} = \int d^2\sigma d^2\theta & \left(G_{\alpha\bar{\beta}} (D_+ z^\alpha D_- z^{\bar{\beta}} + D_+ z^{\bar{\beta}} D_- z^\alpha) + \right. \\ & \left. + B_{\alpha\bar{\beta}} (D_+ z^\alpha D_- z^{\bar{\beta}} - D_+ z^{\bar{\beta}} D_- z^\alpha) \right), \end{aligned} \quad (5.18)$$

one identifies the metric,

$$G_{\alpha\bar{\beta}} = G_{\bar{\beta}\alpha} = \frac{1}{2} \left(\partial_\alpha V_{\bar{\beta}} + \partial_{\bar{\beta}} V_\alpha \right), \quad (5.19)$$

and the Kalb-Ramond 2-form,

$$B_{\alpha\bar{\beta}} = -B_{\bar{\beta}\alpha} = \frac{1}{2} \left(\partial_\alpha V_{\bar{\beta}} - \partial_{\bar{\beta}} V_\alpha \right). \quad (5.20)$$

Now let us apply this to the deformed $SU(2) \times U(1)$ model where $\alpha = |k|$. The group element $g \in SU(2) \times U(1)$ is parameterized in a standard way by,

$$g = e^{\frac{i}{2}\rho} \begin{pmatrix} e^{\frac{i}{2}(\varphi_1 + \varphi_2)} \cos \frac{\psi}{2} & e^{\frac{i}{2}(\varphi_1 - \varphi_2)} \sin \frac{\psi}{2} \\ -e^{-\frac{i}{2}(\varphi_1 - \varphi_2)} \sin \frac{\psi}{2} & e^{-\frac{i}{2}(\varphi_1 + \varphi_2)} \cos \frac{\psi}{2} \end{pmatrix}, \quad (5.21)$$

where,

$$0 \leq \psi \leq \pi, \quad \varphi_1 \in \mathbb{R} \bmod 2\pi, \quad \varphi_2, \rho \in \mathbb{R} \bmod 4\pi. \quad (5.22)$$

We introduce complex coordinates $z^\alpha = (z, w)$ and $\bar{z}^{\bar{\alpha}} = (\bar{z}, \bar{w})$ with $\alpha, \bar{\alpha} = \{1, 2\}$ such that \mathcal{J}_+ acts as $+i$ on dz and dw . The complex structure in this case is exactly the same as the one studied originally in [61, 62] (for a more detailed treatment see [63, 64]), so we can use the results obtained there to write the group element in terms of the complex coordinates as,

$$g = (z\bar{z} + w\bar{w})^{-\frac{1}{2}(1+i)} \begin{pmatrix} \bar{w} & z \\ -\bar{z} & w \end{pmatrix}, \quad (5.23)$$

where the complex coordinates are related to the original coordinates as,

$$z = e^{-\frac{1}{2}\rho} e^{\frac{i}{2}(\varphi_1 - \varphi_2)} \sin \frac{\psi}{2}, \quad w = e^{-\frac{1}{2}\rho} e^{-\frac{i}{2}(\varphi_1 + \varphi_2)} \cos \frac{\psi}{2}. \quad (5.24)$$

Note that in the undeformed case, which allows for $N = (2, 2)$ supersymmetry, z and w are the chiral and the twisted chiral $N = (2, 2)$ superfield resp. [61, 62]. In the undeformed case we can readily derive the $N = (2, 1)$ vector V_z and V_w appearing in the action eq. (5.17) as it directly descends from the generalized $N = (2, 2)$ Kähler potential K obtained in [61, 62],

$$K(z, \bar{z}, w, \bar{w}) = -k \left(\frac{1}{2} (\ln w\bar{w})^2 + Li_2 \left(-\frac{z\bar{z}}{w\bar{w}} \right) \right), \quad (5.25)$$

from which we get,

$$\begin{aligned} V_z^0 &= +\partial_z K = \frac{k}{z} \ln \left(1 + \frac{z\bar{z}}{w\bar{w}} \right), \\ V_w^0 &= -\partial_w K = \frac{k}{w} \ln(z\bar{z} + w\bar{w}), \end{aligned} \quad (5.26)$$

where the upper index 0 on V points to the fact that we are dealing with the undeformed case $\alpha = |k|$ and $\gamma = 0$.

In order to extend this to the deformed case, i.e. $\gamma \neq 0$, we first rewrite the deformed geometry in terms of complex coordinates,

$$\begin{aligned} ds^2 &= \frac{k}{z\bar{z} + w\bar{w}} (dz d\bar{z} + dw d\bar{w}) - \frac{\gamma}{(z\bar{z} + w\bar{w})^2} (w dz - z dw) (\bar{w} d\bar{z} - \bar{z} d\bar{w}), \\ H &= \frac{k}{(z\bar{z} + w\bar{w})^2} (dz \wedge d\bar{z} \wedge (\bar{w} dw - w d\bar{w}) + dw \wedge d\bar{w} \wedge (\bar{z} dz - z d\bar{z})), \end{aligned} \quad (5.27)$$

where we put $\alpha = k$. From the expression for the torsion one gets the Kalb-Ramond 2-form as well,

$$B = \frac{k}{z\bar{z} + w\bar{w}} \left(\frac{\bar{z}}{\bar{w}} dz \wedge d\bar{w} - \frac{z}{w} dw \wedge d\bar{z} \right). \quad (5.28)$$

From this we obtain V_z and V_w ,

$$V_z = V_z^0 + \frac{\gamma}{z} \frac{w\bar{w}}{z\bar{z} + w\bar{w}}, \quad V_w = V_w^0 + \frac{\gamma}{w} \frac{z\bar{z}}{z\bar{z} + w\bar{w}}, \quad (5.29)$$

where V_z^0 and V_w^0 were given in eq. (5.26). Using eqs. (5.19) and (5.20) one verifies that eq. (5.29) indeed reproduces eq. (5.27) and (5.28). Combining eq. (5.29) with eq. (5.17) gives the action of the deformed theory explicitly in $N = (2, 1)$ superspace.

Concluding: as the generic $SU(2) \times U(1)$ YB-WZ model does not allow for $N = (2, 2)$ supersymmetry, it looks highly improbable that deformed models for other groups would allow for $N = (2, 2)$ supersymmetry. Even when only requiring $N = (2, 0)$ or $N = (2, 1)$ supersymmetry, one finds that this is only possible for specific values of the deformation parameters. However, it is important to note that the above derivation is based on the canonical form of the \mathcal{R} -matrix. There is still an $GL(2, \mathbb{C})$ freedom on the CSA directions of \mathcal{R} which, together with the possibility of going beyond a single Yang-Baxter to a bi-Yang-Baxter deformation, could still reveal extended supersymmetry (but since these geometries are more complicated it would seem unlikely that they are more amenable to supersymmetries).

6 Summary, conclusions and outlook

In this paper we investigated various properties of the Yang-Baxter deformation of the Principal Chiral model with a Wess-Zumino term introduced in [26].

As the undeformed model, the WZW model, exhibits rather unique features at the quantum level, we made a one-loop renormalisation group analysis of this class of models. For general groups and for generic values of the deformation parameters, the RG flow drives the theory outside the classical sigma model ansatz given in eq. (3.3) and (3.4). However, when the classical integrability condition is invoked, the renormalisation does remain within the sigma model ansatz and moreover the integrability condition is preserved along the RG flow. The fact that a very quantum property — the RG equations — are sensitive to the consideration of classical integrability is rather suggestive. It is therefore natural to conjecture that these models are quantum mechanically integrable. However, the non-ultralocal property of such theories precludes a direct application of the Quantum Inverse Scattering method. It would be very interesting to examine how the alleviation approach, used in the context of the related λ -models [65], might be applied here in order to unravel the quantum S-matrix.

Another interesting aspect is that the WZW model is the IR fixed point; in comparison the integrable λ -deformed WZW has the CFT situated as an UV fixed point. This model then seems closer in spirit to the irrelevant double trace integrable deformations of 2d CFTs constructed recently in [66]. Recently λ type deformations have been studied in the context of $G_k \times G_l / G_{k+l}$ coset theories [67]; curiously there the CFT is recovered as an IR fixed point in the same way as we have here.

An unanticipated feature of this class of models is that when restricting to simply laced groups but staying outside of the integrable locus, we found a second fixed point of the one-loop β -functions which is UV with respect to the IR WZW model. Around this fixed point, the curvatures of the target space geometry are small leading us to anticipate that the existence of this fixed point is robust to higher loops. However, at this fixed point a number of the currents have wrong sign kinetic terms. A conservative view would be to discard this as non-physical but this then begs the question of the UV completion

of the deformation we are considering. Tentatively we might suppose that the fixed point corresponds to a non-unitary CFT and that we have an exotic RG flow from this in the UV to the WZW in the IR. Comparable flows have been discovered in the context of minimal models. Needless to say it would be interesting to examine this more robustly. A technique that might help here could be to rephrase the entire discussion of these theories in terms of the free field representations of WZW models.

An obvious exercise which remains to be done is an RG analysis of the integrable models introduced in [27] that incorporate both bi-Yang-Baxter deformations and TST transformations. We expect this to be significantly more involved than the analysis performed in the current paper as the deformations in [27] destroy both the left and right acting group symmetry rendering the choice of a good basis to calculate the β -functions non-trivial.

An appealing feature of the landscape of η , Yang-Baxter and λ deformations is that they provide tractable examples of sigma models that are Poisson-Lie T-dualisable. The theories considered here also share this feature; in fact the Poisson-Lie duality (which normally results in quite convoluted geometries) has a remarkably simple form. It results in a set of “Buscher rules” that resemble Abelian T-duality in that coupling constants are simply inverted. We see quite explicitly the compability of Poisson-Lie duality and RG flow and in particular we find that the self-dual point of the duality and the fixed point of RG are coincident. At this self-dual point the symmetries are enhanced and the theory becomes the WZW CFT. With the understanding that the Heisenberg anti-ferromagnetic $XXX_{\frac{k}{2}}$ chain has a gapless regime in the same universality class as the $SU(2)_k$ WZW model [68] an intriguing question is whether this PL duality can also be given an interpretation in spin-chains.

Finally we studied the possibility of supersymmetrising these models. As for any non-linear sigma model in two dimensions an $N = (1, 1)$ supersymmetric extension is always possible. Going beyond $N = (1, 1)$ requires extra geometric structure, in particular every additional supersymmetry requires the existence of a complex structure satisfying various properties outlined in section 5 of this paper. Compared to the undeformed WZW model these conditions turn out to be rather involved. We solved them explicitly in the simplest non-trivial example: $SU(2) \times U(1)$. For generic values of the deformation parameters no supersymmetry beyond $N = (1, 1)$ is allowed. For the particular case where the deformation parameter α , defined in eq. (2.2), satisfies $\alpha = |k|$ with k the level of the WZ term an $N = (2, 1)$ extension is still possible while $N = (2, 2)$ is forbidden. We provided the manifest supersymmetric formulation of this model in $N = (2, 1)$ superspace.

The above analysis showed no obvious connection between integrability and the existence of extended supersymmetries (perhaps this is not so surprising, see e.g. [56]). A useful exercise in this context would be the following. All bi-hermitian complex surfaces have been classified [69, 70]. Those with the topology of $SU(2) \times U(1)$ are the primary Hopf surfaces. A detailed analysis of the $N = (2, 2)$ superspace formulations of those models combined with their integrability properties would be most interesting, in particular a characterization of the notion of integrability directly in $N = (2, 2)$ superspace would be quite exciting. In view of the results obtained in the current paper we expect that if a

connection between extended supersymmetry and integrability can be obtained it would probably not fall in the class of the models introduced in [26], however other possibilities remain, e.g. the models developed in [27] and through the inclusion of an action on the Cartan in the \mathcal{R} -matrix. We will come back to this issue in a future publication.

Acknowledgments

DCT is supported by a Royal Society University Research Fellowship *Generalised Dualities in String Theory and Holography* URF 150185 and in part by STFC grant ST/P00055X/1. This work is supported in part by the Belgian Federal Science Policy Office through the Interuniversity Attraction Pole P7/37, and in part by the “FWO-Vlaanderen” through the project G020714N and two “aspirant” fellowships (SD and SD), and by the Vrije Universiteit Brussel through the Strategic Research Program “High-Energy Physics”. SD and SD would like to thank Swansea University for hospitality during a visit in which part of this research was conducted. We thank Vestislav Apostolov, Benjamin Doyon, Tim Hollowood, Chris Hull, Ctirad Klimcik, Prem Kumar, Martin Roček and Kostas Sfetsos for useful conversations/communications that aided this project.

A Conventions

Let us establish our conventions. In this article we consider only semi-simple Lie groups G . For the corresponding Lie algebra \mathfrak{g} we pick a basis of Hermitian generators,

$$[T_A, T_B] = i F_{AB}{}^C T_C, \tag{A.1}$$

where $F_{AB}{}^C$ are the structure constants which satisfy the Jacobi identity:

$$F_{AB}{}^D F_{DC}{}^E + F_{CA}{}^D F_{DB}{}^E + F_{BC}{}^D F_{DA}{}^E = 0. \tag{A.2}$$

We denote by $\langle \cdot, \cdot \rangle : \mathfrak{g} \times \mathfrak{g} \rightarrow \mathbb{R}$ the ad-invariant Cartan-Killing form on \mathfrak{g} whose components are $\langle T_A, T_B \rangle = \frac{1}{x_R} \text{Tr}(T_A T_B) = \kappa_{AB}$ (with x_R the index of the representation R). In particular one gets for the adjoint representation,

$$F_{AC}{}^D F_{BD}{}^C = -c_G \kappa_{AB}, \tag{A.3}$$

with $c_G = 2h^\vee$ where h^\vee is the dual Coxeter number of the group.

Going now to a Cartan-Weyl basis where we call the generators in the Cartan subalgebra (CSA) H_m , the generators corresponding to positive (negative) roots T_a ($T_{\bar{a}}$), where we have $[H_m, T_a] = a_m T_a$ and $[H_m, T_{\bar{a}}] = -a_m T_{\bar{a}}$. Using this one immediately gets from eq. (A.3),

$$\kappa_{mn} = \frac{1}{h^\vee} \sum_a a_m a_n, \tag{A.4}$$

where the sum runs over the positive roots. With this we define the length squared of a root \vec{a} by¹³ $\vec{a} \cdot \vec{a} = a_m \kappa^{mn} a_n$. With our choice for the normalization of the Cartan-Killing

¹³ κ^{mn} is the inverse of κ_{mn} .

form the length squared of the long roots is always 2 and for the non-simply laced groups the length squared of the short roots is either 1 or 1/3.

We define left-invariant forms $u = -iu^A T_A = g^{-1} dg$ which thus obey $du^A = -\frac{1}{2} F_{BC}^A u^B \wedge u^C$ whilst right-invariant forms $v = -iv^A T_A = dg g^{-1}$ obey $dv^A = +\frac{1}{2} F_{BC}^A v^B \wedge v^C$. The Wess-Zumino-Witten action [13] is,

$$S = -\frac{k}{2\pi} \int_{\Sigma} d\sigma d\tau \langle g^{-1} \partial_+ g, g^{-1} \partial_- g \rangle + \frac{k}{24\pi} \int_{M_3} \langle \bar{g}^{-1} d\bar{g}, [\bar{g}^{-1} d\bar{g}, \bar{g}^{-1} d\bar{g}] \rangle, \quad (\text{A.5})$$

in which $g : \Sigma \rightarrow G$ and with \bar{g} the extension of g into M_3 such that $\partial M_3 = \Sigma$. We adopt light-cone coordinates $\sigma^{\pm} = \tau \pm \sigma$. For compact G , and demanding that the action is insensitive to the choice of action, requires $k \in \mathbb{Z}$.

In section 5 we deal with non-linear sigma models in $N = (1, 1)$ and $N = (2, 1)$ superspace. Let us briefly review some of the notations appearing there and refer to e.g. [63, 64] for more details. Denoting for this section the bosonic worldsheet light-cone coordinates by,

$$\sigma^{\ddagger} = \tau + \sigma, \quad \sigma^{\bar{}} = \tau - \sigma, \quad (\text{A.6})$$

and the $N = (1, 1)$ (real) fermionic coordinates by θ^+ and θ^- , we introduce the fermionic derivatives which satisfy,

$$D_{\ddagger}^2 = -\frac{i}{2} \partial_{\ddagger}, \quad D_{\bar{}}^2 = -\frac{i}{2} \partial_{\bar{}}, \quad \{D_+, D_-\} = 0. \quad (\text{A.7})$$

The $N = (1, 1)$ integration measure is given by,

$$\int d^2\sigma d^2\theta = \int d\tau d\sigma D_+ D_-. \quad (\text{A.8})$$

Passing from $N = (1, 1)$ to $N = (2, 1)$ superspace requires the introduction of one more real fermionic coordinates $\hat{\theta}^+$ where the corresponding fermionic derivative satisfies,

$$\hat{D}_{\ddagger}^2 = -\frac{i}{2} \partial_{\ddagger}, \quad (\text{A.9})$$

and all other — except for (A.7) — (anti-)commutators do vanish. The $N = (2, 1)$ integration measure is,

$$\int d^2\sigma d^2\theta d\hat{\theta}^+ = \int d\tau d\sigma D_+ D_- \hat{D}_+. \quad (\text{A.10})$$

B Charges in SU(2)

In this appendix we review the construction [35] of charges satisfying a quantum group algebra for the case of $\mathfrak{g} = \mathfrak{su}(2)$ paying rather careful attention to the normalisation of canonical momenta so as to obtain the quantum group parameters expressed in terms of RG invariant quantities.

In this appendix we use $\mathfrak{su}(2)$ generators $[T^{\pm}, T^3] = iT^{\pm}$, $[T^+, T^-] = -iT^3$ and define components of the left invariant one-forms via $g^{-1} dg \equiv u_+ T^+ + u_- T^- + u_3 T^3$.

To orientate ourselves we begin with the Lagrangian eq. (2.2) specialised to the case of the η -deformation, i.e. $\alpha = \frac{1}{\tau}$, $\beta = \frac{\eta}{1+\eta^2} \frac{1}{\tau}$, $\gamma = \frac{\eta^2}{1+\eta^2} \frac{1}{\tau}$ with $k = 0$ incorporating some of the key points of [3, 41]. Let us define some at first sight non-obvious currents,

$$j_{\pm} = -\frac{1}{2} \frac{\eta}{1+\eta^2} \frac{1}{\Sigma} (\eta u_{\sigma\pm} \pm i u_{\tau\pm}), \quad j_3 = \frac{\eta}{2\Sigma} u_{\tau 3}, \quad (\text{B.1})$$

in which $\Sigma = 4\pi\tau\eta$. These have simple Poisson brackets,

$$\begin{aligned} \{j_3(\sigma_1), j_3(\sigma_2)\} &= 0, \\ \{j_{\pm}(\sigma_1), j_3(\sigma_2)\} &= \pm i j_{\pm}(\sigma_2) \delta(\sigma_1 - \sigma_2), \\ \{j_{\pm}(\sigma_1), j_{\mp}(\sigma_2)\} &= \mp i j_3(\sigma_2) \delta(\sigma_1 - \sigma_2). \end{aligned} \quad (\text{B.2})$$

That these are indeed the correct objects to work with becomes evident if we look at the Lax connection of eq. (2.9). Recall that the path-ordered exponential integral of the spatial component of the Lax defines conserved charges. Expanding around particular values of the spectral parameter gives expressions for the charges. In particular if we expand the gauge transformed Lax $\mathcal{L}^g(z) = g^{-1} \mathcal{L}_{\sigma}(z) g - g^{-1} \partial_{\sigma} g$ around certain points $z = \pm i\eta$ — these correspond to poles in the twist function of the Maillet r/s kernels — we find that these currents occur naturally as,

$$\mathcal{L}^g(z = \mp i\eta) = 4\Sigma j_{\pm} T^{\pm} \pm 2i\Sigma j_3 T^3. \quad (\text{B.3})$$

Using the fact that the Cartan element can be factored in the path ordered exponential occurring in the monodromy matrix [71] one is led to construct (non-local) currents,

$$\begin{aligned} \tilde{\mathfrak{J}}_+(\sigma, \tau) &= j_+(\sigma, \tau) \exp \left[-2\Sigma \int_{\sigma}^{\infty} j_3(\hat{\sigma}, \tau) d\hat{\sigma} \right], \\ \tilde{\mathfrak{J}}_-(\sigma, \tau) &= j_-(\sigma, \tau) \exp \left[2\Sigma \int_{-\infty}^{\sigma} j_3(\hat{\sigma}, \tau) d\hat{\sigma} \right], \\ \tilde{\mathfrak{J}}_3(\sigma, \tau) &= j_3(\sigma, \tau). \end{aligned} \quad (\text{B.4})$$

The equations of motion imply $\partial_{\tau} \tilde{\mathfrak{J}} = \partial_{\sigma} \tilde{\mathfrak{J}}$ for some $\tilde{\mathfrak{J}}$ whose explicit form is not important to us and thus that the charges $\mathfrak{Q} = \int_{-\infty}^{\infty} \tilde{\mathfrak{J}} d\sigma$ are conserved subject to standard boundary fall off. The Poisson brackets give,

$$\{\tilde{\mathfrak{J}}_+(\sigma_1), \tilde{\mathfrak{J}}_-(\sigma_2)\} = \frac{i}{4\Sigma} \delta(\sigma_1 - \sigma_2) \partial_{\sigma_2} \exp \left[-2\Sigma \left(\int_{\sigma_2}^{\infty} - \int_{-\infty}^{\sigma_2} \right) j_3(\hat{\sigma}) d\hat{\sigma} \right], \quad (\text{B.5})$$

where we note that “cross terms” involving the non-local exponentials cancel. Thus one finds that, with suitable normalisation,

$$\{\mathfrak{Q}_+, \mathfrak{Q}_-\} = i \frac{q^{\mathfrak{Q}_3} - q^{-\mathfrak{Q}_3}}{q - q^{-1}}, \quad \{\mathfrak{Q}_{\pm}, \mathfrak{Q}_3\} = \pm i \mathfrak{Q}_{\pm}, \quad q = e^{2\Sigma}. \quad (\text{B.6})$$

Now we turn to the full theory including the WZ term. For this case we have the definitions,

$$j_{\pm} = -\frac{k \mp i\Theta}{8\pi(\alpha^2 + \Theta^2)} ((\pm i\alpha^2 + k\Theta)u_{\sigma\pm} + \alpha(\pm ik + \Theta)u_{\tau\pm}), \quad j_3 = \frac{1}{8\pi} (k u_{\sigma 3} + \alpha u_{\tau 3}), \quad (\text{B.7})$$

which obey a non-ultralocal algebra,

$$\begin{aligned} \{j_3(\sigma_1), j_3(\sigma_2)\} &= -\frac{k}{4\pi} \partial_{\sigma_1} \delta(\sigma_1 - \sigma_2), \\ \{j_{\pm}(\sigma_1), j_3(\sigma_2)\} &= \pm i j_{\pm}(\sigma_2) \delta(\sigma_1 - \sigma_2), \\ \{j_{\pm}(\sigma_1), j_{\mp}(\sigma_2)\} &= \mp i j_3(\sigma_2) \delta(\sigma_1 - \sigma_2) - \frac{k}{4\pi} \partial_{\sigma_1} \delta(\sigma_1 - \sigma_2), \end{aligned} \tag{B.8}$$

and from which we can build in the same way as above *mutatis mutandis* (non-local) conserved currents as,

$$\begin{aligned} \mathfrak{J}_+(\sigma, \tau) &= j_+(\sigma, \tau) \exp \left[\frac{8\pi}{\Theta - ik} \int_{\sigma}^{\infty} j_3(\hat{\sigma}, \tau) d\hat{\sigma} \right], \\ \mathfrak{J}_-(\sigma, \tau) &= j_-(\sigma, \tau) \exp \left[-\frac{8\pi}{\Theta + ik} \int_{-\infty}^{\sigma} j_3(\hat{\sigma}, \tau) d\hat{\sigma} \right], \\ \mathfrak{J}_3(\sigma, \tau) &= j_3(\sigma, \tau). \end{aligned} \tag{B.9}$$

At the WZW fixed point ($\alpha = |k|, \Theta = 0$) these currents just reduce to the currents generating the right acting affine $\mathfrak{su}(2)$. As with the case above these currents appear in the gauge transformed Lax expanded around the poles of its twist function, i.e.,

$$\mathcal{L}^g \left(z = \frac{\mp ik\Theta + \alpha^2}{k\alpha + \mp i\Theta\alpha} \right) = \frac{16\pi\Theta}{k^2 + \Theta^2} j_{\pm} T^{\pm} + \frac{8\pi}{k \mp i\Theta} j_3 T^3. \tag{B.10}$$

For completeness we make the identification with the parameters γ_+ and γ_- used in the analysis of [35]:

$$\gamma_+ = \frac{8i\pi}{k - i\Theta}, \quad \gamma_- = -\frac{8\pi i}{k + i\Theta}, \tag{B.11}$$

such that,

$$\frac{\gamma_-}{\gamma_+} = -\frac{k - i\Theta}{k + i\Theta}, \quad \Delta = \frac{\gamma^+ + \gamma^-}{2} = \frac{-8\pi\Theta}{\Theta^2 + k^2}. \tag{B.12}$$

Even though the currents have a non-ultra-local algebra, the charge algebra is not ambiguous [35] (there is no order of limits problem in regulating the spatial integrals) and the commutator of charges (up to overall normalisations of \mathcal{Q}^{\pm}) still obeys eq. (B.6) with $q = e^{-\Delta}$.

C Properties of \mathcal{R}

We collate here a number of identities used in the massaging of the calculation of the β -functions. The strategy of deriving these identities is practically always the same: we expand the mCYBE eq. (2.1) or related versions in the generators T_A of the Lie algebra and contract two free indices with two from the structure constants F_{AB}^C or from $F_{AB}^D \mathcal{R}^C_D$.

For completeness, we repeat here the mCYBE:

$$[\mathcal{R}x, \mathcal{R}y] - \mathcal{R}([x, \mathcal{R}y] + [\mathcal{R}x, y]) = [x, y] \quad \forall x, y \in \mathfrak{g}. \tag{C.1}$$

From this we can derive a related identity,

$$[\mathcal{R}^2x, \mathcal{R}y] - [\mathcal{R}x, \mathcal{R}^2y] = \mathcal{R}([\mathcal{R}^2x, y] - [x, \mathcal{R}^2y]) + [\mathcal{R}x, y] - [x, \mathcal{R}y], \tag{C.2}$$

and using $\mathcal{R}^3 = -\mathcal{R}$ we can also derive:

$$[\mathcal{R}^2 x, \mathcal{R}^2 y] = \mathcal{R}^2 ([\mathcal{R}^2 x, y] + [x, \mathcal{R}^2 y]) + (1 + 2\mathcal{R}^2)[x, y], \quad (\text{C.3})$$

$$[\mathcal{R}^2 x, \mathcal{R} y] + [\mathcal{R} x, \mathcal{R}^2 y] = \mathcal{R} ([\mathcal{R}^2 x, y] + [x, \mathcal{R}^2 y] + 2[x, y]) + \mathcal{R}^2 ([\mathcal{R} x, y] + [x, \mathcal{R} y]), \quad (\text{C.4})$$

for all $x, y \in \mathfrak{g}$. This gives the following (non-exhaustive) list of properties of the \mathcal{R} -matrix all of which were used in the derivation of the β -functions:

$$\mathcal{R}^D{}_A \mathcal{R}^E{}_B F_{DEC} + \mathcal{R}^D{}_B \mathcal{R}^E{}_C F_{DEA} + \mathcal{R}^D{}_C \mathcal{R}^E{}_A F_{DEB} - F_{ABC} = 0, \quad (\text{C.5})$$

$$(\mathcal{R}^2)^D{}_A \mathcal{R}^E{}_B F_{DE}{}^C + (\mathcal{R}^2)^D{}_A \mathcal{R}^C{}_E F_{BD}{}^E + \mathcal{R}^D{}_A F_{BD}{}^C + (A \leftrightarrow B) = 0, \quad (\text{C.6})$$

$$(\mathcal{R}^2)^D{}_A (\mathcal{R}^2)^E{}_B F_{DEC} - (\mathcal{R}^2)^D{}_C (\mathcal{R}^2)^E{}_A F_{DEB} - (\mathcal{R}^2)^D{}_B (\mathcal{R}^2)^E{}_C F_{DEA} - 2(\mathcal{R}^2)^E{}_C F_{ABE} - F_{ABC} = 0, \quad (\text{C.7})$$

$$\mathcal{R}^C{}_E \mathcal{R}^F{}_D F_{CA}{}^D F_{FB}{}^E + 2\mathcal{R}^C{}_E \mathcal{R}^F{}_B F_{CA}{}^D F_{DF}{}^E - c_G \kappa_{AB} = 0, \quad (\text{C.8})$$

$$(\mathcal{R}^2)^D{}_A \mathcal{R}^E{}_F F_{DE}{}^C F_{CB}{}^F = \mathcal{R}^C{}_D F_{AE}{}^D F_{CB}{}^E, \quad (\text{C.9})$$

$$(\mathcal{R}^2)^E{}_C \mathcal{R}^F{}_A F_{EF}{}^D F_{DB}{}^C + (\mathcal{R}^2)^E{}_C \mathcal{R}^F{}_D F_{AE}{}^D F_{FB}{}^C + \mathcal{R}^C{}_D F_{AE}{}^D F_{CB}{}^E + c_G \mathcal{R}_{AB} = 0, \quad (\text{C.10})$$

$$(\mathcal{R}^2)^D{}_F \mathcal{R}^C{}_E F_{CB}{}^F F_{AD}{}^E - (\mathcal{R}^2)^D{}_F \mathcal{R}^C{}_A F_{EB}{}^F F_{CD}{}^E + \mathcal{R}^C{}_D F_{AE}{}^D F_{CB}{}^E + c_G \mathcal{R}_{AB} = 0, \quad (\text{C.11})$$

$$(\mathcal{R}^2)^D{}_F (\mathcal{R}^2)^E{}_C F_{DA}{}^C F_{BE}{}^F + 2(\mathcal{R}^2)^E{}_C F_{DA}{}^C F_{BE}{}^D + c_G \kappa_{AB} = 0, \quad (\text{C.12})$$

$$(\mathcal{R}^2)^D{}_F (\mathcal{R}^2)^E{}_C F_{EA}{}^F F_{BD}{}^C + 2(\mathcal{R}^2)^E{}_C (\mathcal{R}^2)^D{}_A F_{DE}{}^F F_{BF}{}^C - 2c_G (\mathcal{R}^2)_{AB} - c_G \kappa_{AB} = 0, \quad (\text{C.13})$$

$$(\mathcal{R}^2)^G{}_C \mathcal{R}^D{}_A \mathcal{R}^E{}_F F_{DG}{}^E F_{BF}{}^C - \mathcal{R}^F{}_C (\mathcal{R}^E{}_D F_{AF}{}^D + \mathcal{R}^D{}_A F_{FD}{}^E) F_{BE}{}^C - (\mathcal{R}^2)^E{}_C F_{EA}{}^D F_{BD}{}^C = 0, \quad (\text{C.14})$$

$$(\mathcal{R}^2)^C{}_F (\mathcal{R}^2)^D{}_G \mathcal{R}^E{}_A F_{DE}{}^F F_{BC}{}^G + 2(\mathcal{R}^2)^C{}_D \mathcal{R}^E{}_A F_{FE}{}^D F_{BC}{}^F - c_G \mathcal{R}_{AB} = 0, \quad (\text{C.15})$$

$$(\mathcal{R}^2)^E{}_A \mathcal{R}^F{}_B \mathcal{R}^D{}_G F_{DE}{}^C F_{CF}{}^G = \mathcal{R}^E{}_B \mathcal{R}^C{}_D F_{FA}{}^D F_{CE}{}^F, \quad (\text{C.16})$$

$$(\mathcal{R}^2)^D{}_G \mathcal{R}^H{}_A \mathcal{R}^E{}_B F_{HD}{}^C F_{CE}{}^G + (\mathcal{R}^2)^E{}_D F_{BC}{}^D F_{AE}{}^C - c_G (\mathcal{R}^2)_{AB} - c_G \kappa_{AB} = 0, \quad (\text{C.17})$$

$$(\mathcal{R}^2)^C{}_G (\mathcal{R}^2)^D{}_F \mathcal{R}^H{}_A \mathcal{R}^E{}_B F_{DE}{}^G F_{CH}{}^F + 2(\mathcal{R}^2)^D{}_E F_{BC}{}^E F_{AD}{}^C - c_G (\mathcal{R}^2)_{AB} - 2c_G \kappa_{AB} = 0, \quad (\text{C.18})$$

$$(\mathcal{R}^2)^G{}_A (\mathcal{R}^2)^D{}_E \mathcal{R}^F{}_B F_{DG}{}^C F_{FC}{}^E - (\mathcal{R}^2)^D{}_F \mathcal{R}^E{}_C F_{AD}{}^C F_{EB}{}^F + \mathcal{R}^C{}_D F_{CA}{}^E F_{BE}{}^D = c_G \mathcal{R}_{AB}, \quad (\text{C.19})$$

$$(\mathcal{R}^2)^G{}_A (\mathcal{R}^2)^D{}_E \mathcal{R}^F{}_C F_{DG}{}^C F_{FB}{}^E = (\mathcal{R}^2)^D{}_F \mathcal{R}^E{}_C F_{AE}{}^F F_{BD}{}^C, \quad (\text{C.20})$$

$$\mathcal{R}^C{}_A \mathcal{R}^D{}_B F_{CD}{}^B = 0. \quad (\text{C.21})$$

D Geometry in the non-orthonormal frame

Consider a general Riemannian target manifold \mathcal{M} with local coordinates x^μ and endowed with a curved metric G . We work in a frame formalism $\hat{e}_A = e_A^\mu \partial_\mu$ where the metric is constant but non-orthonormal:

$$G_{\mu\nu}(x) = e^A{}_\mu(x) G_{AB} e^B{}_\nu(x). \quad (\text{D.1})$$

Requiring the spin-connection to be metric-compatible and torsion-free gives the following connection coefficients:

$$\Gamma_{BC}^A = \frac{1}{2}G^{AE} (\Omega_{EB}{}^D G_{DC} + \Omega_{EC}{}^D G_{DB}) + \frac{1}{2}\Omega_{BC}{}^A, \quad (\text{D.2})$$

where $\Omega_{AB}{}^C$ are the anholonomy coefficients determined by,

$$[\hat{e}_A, \hat{e}_B] = \Omega_{AB}{}^C \hat{e}_C, \quad \Omega_{AB}{}^C = e_A{}^\mu e_B{}^\nu (\partial_\nu e^C{}_\mu - \partial_\mu e^C{}_\nu). \quad (\text{D.3})$$

In our case, the target manifold is a Lie manifold G endowed with a deformed geometry. Introducing left-invariant one-forms $u = g^{-1}dg = -iu_\nu^A T_A dx^\nu$ which satisfy,

$$du^A = -\frac{1}{2}F_{BC}{}^A u^B \wedge u^C, \quad (\text{D.4})$$

we go to the frames $\hat{e}_A = u_A^\mu \partial_\mu$. The deformed geometry in this frame is given by the constant non-orthonormal metric eq. (3.3) and by the torsion eq. (3.4),

$$G_{AB} = \alpha \kappa_{AB} + \gamma \mathcal{R}_{AB}^2, \quad H_{ABC} = 3\beta F_{[AB}{}^D \mathcal{R}_{C]D} - k F_{ABC}. \quad (\text{D.5})$$

The inverse metric is then (using $\mathcal{R}^3 = -\mathcal{R}$):

$$G^{AB} = \frac{1}{\alpha} \kappa^{AB} + \frac{\gamma}{\alpha(\gamma - \alpha)} (\mathcal{R}^2)^{AB}. \quad (\text{D.6})$$

For the spin-connection coefficients we find from eq. (D.4) that $\Omega_{AB}{}^B = F_{AB}{}^C$ and thus,

$$\Gamma_{BC}^A = \frac{1}{2}G^{AE} (F_{EB}{}^D G_{DC} + F_{EC}{}^D G_{DB}) + \frac{1}{2}F_{BC}{}^A. \quad (\text{D.7})$$

Noting that the spin-connections are constant, the Riemann tensor can be calculated from,

$$R^A{}_{BCD} = \Gamma_{DB}^E \Gamma_{CE}^A - \Gamma_{CB}^E \Gamma_{DE}^A - \Omega_{CD}{}^E \Gamma_{EB}^A, \quad (\text{D.8})$$

and the Ricci tensor from,

$$R_{AB} = R^C{}_{ACB} = -\Gamma_{CA}^E \Gamma_{BE}^C - F_{CB}{}^E \Gamma_{EA}^C. \quad (\text{D.9})$$

With the β -functions in mind we end this appendix with a set of useful expressions which are found by plugging in the expressions of the metric eq. (3.3) and the torsion eq. (3.4) and by making use of the properties of the \mathcal{R} -matrix listed in appendix C:

- The spin-connection:

$$\Gamma_{BC}^A = \frac{1}{2} \frac{\gamma}{\alpha - \gamma} (F_{BD}{}^A (\mathcal{R}^2)^D{}_C + F_{CD}{}^A (\mathcal{R}^2)^D{}_B) + \frac{1}{2} F_{BC}{}^A. \quad (\text{D.10})$$

- The Ricci tensor:

$$\begin{aligned} R_{AB} &= \frac{c_G}{4} \left(1 + \left(\frac{\gamma}{\gamma - \alpha} \right)^2 \right) \kappa_{AB} - \frac{c_G}{4} \left(1 - \left(\frac{\alpha}{\gamma - \alpha} \right)^2 \right) \mathcal{R}_{AB}^2 \\ &\quad + \frac{1}{2} \left(\frac{\gamma}{\alpha - \gamma} \right) F_{AD}{}^C F_{BC}{}^E (\mathcal{R}^2)^D{}_E. \end{aligned} \quad (\text{D.11})$$

- The Ricci curvature:

$$R = R_{AB}G^{AB} = -\frac{c_G}{4} \left(\frac{1}{(\gamma - \alpha)} D + \frac{\gamma}{(\gamma - \alpha)^2} l \right), \quad (\text{D.12})$$

where D is the dimension and l is the rank of the Lie algebra \mathfrak{g} . Hence, we have $\text{Tr}(\mathcal{R}^2) = -(D - l)$.

- Expressions from the torsion tensor:

$$\begin{aligned} H_{AB}^2 &= H_{ACD}H_{BEF}G^{CE}G^{DF} \\ &= c_G \left(\frac{\alpha k^2 - 2(\gamma k^2 + \alpha\beta^2)}{\alpha(\gamma - \alpha)^2} \right) \kappa_{AB} - c_G \frac{\beta^2}{(\gamma - \alpha)^2} \mathcal{R}_{AB}^2 \\ &\quad + \left(\frac{2(\gamma k^2 + \alpha\beta^2)}{\alpha(\gamma - \alpha)^2} \right) (\mathcal{R}^2)^D{}_E F_{BC}{}^E F_{AD}{}^C, \end{aligned} \quad (\text{D.13})$$

$$H^2 = -c_G \left(\frac{k^2 + \beta^2}{(\gamma - \alpha)^3} D - \frac{3(\gamma k^2 + \alpha\beta^2)}{\alpha(\gamma - \alpha)^3} l \right), \quad (\text{D.14})$$

$$\begin{aligned} \nabla_C H^C{}_{AB} &= G^{DE} (\Gamma_{DA}^C H_{EBC} - \Gamma_{DB}^C H_{EAC}) \\ &= c_G \frac{\beta}{\gamma - \alpha} \mathcal{R}_{AB} + \frac{2\beta}{\gamma - \alpha} \mathcal{R}^D{}_E F_{AD}{}^C F_{BC}{}^E. \end{aligned} \quad (\text{D.15})$$

Open Access. This article is distributed under the terms of the Creative Commons Attribution License ([CC-BY 4.0](https://creativecommons.org/licenses/by/4.0/)), which permits any use, distribution and reproduction in any medium, provided the original author(s) and source are credited.

References

- [1] C. Klimčík, *Yang-Baxter σ -models and dS/AdS T duality*, *JHEP* **12** (2002) 051 [[hep-th/0210095](https://arxiv.org/abs/hep-th/0210095)] [[INSPIRE](#)].
- [2] C. Klimčík, *On integrability of the Yang-Baxter σ -model*, *J. Math. Phys.* **50** (2009) 043508 [[arXiv:0802.3518](https://arxiv.org/abs/0802.3518)] [[INSPIRE](#)].
- [3] F. Delduc, M. Magro and B. Vicedo, *On classical q -deformations of integrable σ -models*, *JHEP* **11** (2013) 192 [[arXiv:1308.3581](https://arxiv.org/abs/1308.3581)] [[INSPIRE](#)].
- [4] F. Delduc, M. Magro and B. Vicedo, *An integrable deformation of the $AdS_5 \times S^5$ superstring action*, *Phys. Rev. Lett.* **112** (2014) 051601 [[arXiv:1309.5850](https://arxiv.org/abs/1309.5850)] [[INSPIRE](#)].
- [5] G. Arutyunov, S. Frolov, B. Hoare, R. Roiban and A.A. Tseytlin, *Scale invariance of the η -deformed $AdS_5 \times S^5$ superstring, T-duality and modified type-II equations*, *Nucl. Phys. B* **903** (2016) 262 [[arXiv:1511.05795](https://arxiv.org/abs/1511.05795)] [[INSPIRE](#)].
- [6] Y. Sakatani, S. Uehara and K. Yoshida, *Generalized gravity from modified DFT*, *JHEP* **04** (2017) 123 [[arXiv:1611.05856](https://arxiv.org/abs/1611.05856)] [[INSPIRE](#)].
- [7] A. Baguet, M. Magro and H. Samtleben, *Generalized IIB supergravity from exceptional field theory*, *JHEP* **03** (2017) 100 [[arXiv:1612.07210](https://arxiv.org/abs/1612.07210)] [[INSPIRE](#)].
- [8] J.J. Fernandez-Melgarejo, J.-I. Sakamoto, Y. Sakatani and K. Yoshida, *T-folds from Yang-Baxter deformations*, *JHEP* **12** (2017) 108 [[arXiv:1710.06849](https://arxiv.org/abs/1710.06849)] [[INSPIRE](#)].

- [9] T. Araujo, E.Ó. Colgáin, J. Sakamoto, M.M. Sheikh-Jabbari and K. Yoshida, *I in generalized supergravity*, *Eur. Phys. J. C* **77** (2017) 739 [[arXiv:1708.03163](#)] [[INSPIRE](#)].
- [10] I. Bakhmatov, Ö. Kelekci, E.Ó. Colgáin and M.M. Sheikh-Jabbari, *Classical Yang-Baxter equation from supergravity*, [arXiv:1710.06784](#) [[INSPIRE](#)].
- [11] C. Klimčík and P. Ševera, *Dual non-Abelian duality and the Drinfeld double*, *Phys. Lett. B* **351** (1995) 455 [[hep-th/9502122](#)] [[INSPIRE](#)].
- [12] K. Sfetsos, *Integrable interpolations: from exact CFTs to non-Abelian T-duals*, *Nucl. Phys. B* **880** (2014) 225 [[arXiv:1312.4560](#)] [[INSPIRE](#)].
- [13] E. Witten, *Non-Abelian bosonization in two-dimensions*, *Commun. Math. Phys.* **92** (1984) 455 [[INSPIRE](#)].
- [14] B. Hoare and A.A. Tseytlin, *On integrable deformations of superstring σ -models related to $AdS_n \times S^n$ supercosets*, *Nucl. Phys. B* **897** (2015) 448 [[arXiv:1504.07213](#)] [[INSPIRE](#)].
- [15] K. Sfetsos, K. Siampos and D.C. Thompson, *Generalised integrable λ - and η -deformations and their relation*, *Nucl. Phys. B* **899** (2015) 489 [[arXiv:1506.05784](#)] [[INSPIRE](#)].
- [16] C. Klimčík, *η and λ deformations as E-models*, *Nucl. Phys. B* **900** (2015) 259 [[arXiv:1508.05832](#)] [[INSPIRE](#)].
- [17] B. Hoare and F.K. Seibold, *Poisson-Lie duals of the η deformed symmetric space σ -model*, *JHEP* **11** (2017) 014 [[arXiv:1709.01448](#)] [[INSPIRE](#)].
- [18] T.J. Hollowood, J.L. Miramontes and D.M. Schmidt, *Integrable deformations of strings on symmetric spaces*, *JHEP* **11** (2014) 009 [[arXiv:1407.2840](#)] [[INSPIRE](#)].
- [19] T.J. Hollowood, J.L. Miramontes and D.M. Schmidt, *An integrable deformation of the $AdS_5 \times S^5$ superstring*, *J. Phys. A* **47** (2014) 495402 [[arXiv:1409.1538](#)] [[INSPIRE](#)].
- [20] K. Sfetsos and D.C. Thompson, *Spacetimes for λ -deformations*, *JHEP* **12** (2014) 164 [[arXiv:1410.1886](#)] [[INSPIRE](#)].
- [21] R. Borsato and L. Wulff, *Target space supergeometry of η and λ -deformed strings*, *JHEP* **10** (2016) 045 [[arXiv:1608.03570](#)] [[INSPIRE](#)].
- [22] S. Demulder, K. Sfetsos and D.C. Thompson, *Integrable λ -deformations: squashing coset CFTs and $AdS_5 \times S^5$* , *JHEP* **07** (2015) 019 [[arXiv:1504.02781](#)] [[INSPIRE](#)].
- [23] R. Borsato, A.A. Tseytlin and L. Wulff, *Supergravity background of λ -deformed model for $AdS_2 \times S^2$ supercoset*, *Nucl. Phys. B* **905** (2016) 264 [[arXiv:1601.08192](#)] [[INSPIRE](#)].
- [24] Y. Chervonyi and O. Lunin, *Supergravity background of the λ -deformed $AdS_3 \times S^3$ supercoset*, *Nucl. Phys. B* **910** (2016) 685 [[arXiv:1606.00394](#)] [[INSPIRE](#)].
- [25] C. Klimčík, *Integrability of the bi-Yang-Baxter σ -model*, *Lett. Math. Phys.* **104** (2014) 1095 [[arXiv:1402.2105](#)] [[INSPIRE](#)].
- [26] F. Delduc, M. Magro and B. Vicedo, *Integrable double deformation of the principal chiral model*, *Nucl. Phys. B* **891** (2015) 312 [[arXiv:1410.8066](#)] [[INSPIRE](#)].
- [27] F. Delduc, B. Hoare, T. Kameyama and M. Magro, *Combining the bi-Yang-Baxter deformation, the Wess-Zumino term and TsT transformations in one integrable σ -model*, *JHEP* **10** (2017) 212 [[arXiv:1707.08371](#)] [[INSPIRE](#)].
- [28] K. Sfetsos and K. Siampos, *The anisotropic λ -deformed $SU(2)$ model is integrable*, *Phys. Lett. B* **743** (2015) 160 [[arXiv:1412.5181](#)] [[INSPIRE](#)].

- [29] Y. Chervonyi and O. Lunin, *Generalized λ -deformations of $AdS_p \times S^p$* , *Nucl. Phys. B* **913** (2016) 912 [[arXiv:1608.06641](#)] [[INSPIRE](#)].
- [30] C. Appadu, T.J. Hollowood, D. Price and D.C. Thompson, *Yang Baxter and anisotropic sigma and lambda models, cyclic RG and exact S-matrices*, *JHEP* **09** (2017) 035 [[arXiv:1706.05322](#)] [[INSPIRE](#)].
- [31] C. Klimčík, *Poisson-Lie T-duals of the bi-Yang-Baxter models*, *Phys. Lett. B* **760** (2016) 345 [[arXiv:1606.03016](#)] [[INSPIRE](#)].
- [32] C. Klimčík, *Yang-Baxter σ -model with WZNW term as E-model*, *Phys. Lett. B* **772** (2017) 725 [[arXiv:1706.08912](#)] [[INSPIRE](#)].
- [33] P. Ševera, *On integrability of 2-dimensional σ -models of Poisson-Lie type*, *JHEP* **11** (2017) 015 [[arXiv:1709.02213](#)] [[INSPIRE](#)].
- [34] I. Kawaguchi, D. Orlando and K. Yoshida, *Yangian symmetry in deformed WZNW models on squashed spheres*, *Phys. Lett. B* **701** (2011) 475 [[arXiv:1104.0738](#)] [[INSPIRE](#)].
- [35] I. Kawaguchi and K. Yoshida, *A deformation of quantum affine algebra in squashed Wess-Zumino-Novikov-Witten models*, *J. Math. Phys.* **55** (2014) 062302 [[arXiv:1311.4696](#)] [[INSPIRE](#)].
- [36] F. Delduc, T. Kameyama, M. Magro and B. Vicedo, *Affine q -deformed symmetry and the classical Yang-Baxter σ -model*, *JHEP* **03** (2017) 126 [[arXiv:1701.03691](#)] [[INSPIRE](#)].
- [37] J.M. Maillet, *New integrable canonical structures in two-dimensional models*, *Nucl. Phys. B* **269** (1986) 54 [[INSPIRE](#)].
- [38] I.V. Cherednik, *Relativistically invariant quasiclassical limits of integrable two-dimensional quantum models*, *Theor. Math. Phys.* **47** (1981) 422 [*Teor. Mat. Fiz.* **47** (1981) 225] [[INSPIRE](#)].
- [39] I. Kawaguchi and K. Yoshida, *Hidden Yangian symmetry in σ -model on squashed sphere*, *JHEP* **11** (2010) 032 [[arXiv:1008.0776](#)] [[INSPIRE](#)].
- [40] I. Kawaguchi and K. Yoshida, *Hybrid classical integrability in squashed σ -models*, *Phys. Lett. B* **705** (2011) 251 [[arXiv:1107.3662](#)] [[INSPIRE](#)].
- [41] I. Kawaguchi, T. Matsumoto and K. Yoshida, *The classical origin of quantum affine algebra in squashed σ -models*, *JHEP* **04** (2012) 115 [[arXiv:1201.3058](#)] [[INSPIRE](#)].
- [42] V.E. Zakharov and A.V. Mikhailov, *Relativistically invariant two-dimensional models in field theory integrable by the inverse problem technique* (in Russian), *Sov. Phys. JETP* **47** (1978) 1017 [*Zh. Eksp. Teor. Fiz.* **74** (1978) 1953] [[INSPIRE](#)].
- [43] G.M. Shore, *A local renormalization group equation, diffeomorphisms and conformal invariance in σ models*, *Nucl. Phys. B* **286** (1987) 349 [[INSPIRE](#)].
- [44] A.A. Tseytlin, *σ model Weyl invariance conditions and string equations of motion*, *Nucl. Phys. B* **294** (1987) 383 [[INSPIRE](#)].
- [45] A.A. Tseytlin, *Conditions of Weyl invariance of two-dimensional σ model from equations of stationarity of ‘central charge’ action*, *Phys. Lett. B* **194** (1987) 63 [[INSPIRE](#)].
- [46] V.G. Knizhnik and A.B. Zamolodchikov, *Current algebra and Wess-Zumino model in two-dimensions*, *Nucl. Phys. B* **247** (1984) 83 [[INSPIRE](#)].
- [47] G. Georgiou, K. Sfetsos and K. Siampos, *All-loop anomalous dimensions in integrable λ -deformed σ -models*, *Nucl. Phys. B* **901** (2015) 40 [[arXiv:1509.02946](#)] [[INSPIRE](#)].

- [48] A.W.W. Ludwig and J.L. Cardy, *Perturbative evaluation of the conformal anomaly at new critical points with applications to random systems*, *Nucl. Phys. B* **285** (1987) 687 [INSPIRE].
- [49] A.B. Zamolodchikov, *Renormalization group and perturbation theory near fixed points in two-dimensional field theory*, *Sov. J. Nucl. Phys.* **46** (1987) 1090 [*Yad. Fiz.* **46** (1987) 1819] [INSPIRE].
- [50] M. Lassig, *New hierarchies of multicriticality in two-dimensional field theory*, *Phys. Lett. B* **278** (1992) 439 [INSPIRE].
- [51] C.-R. Ahn, *RG flows of nonunitary minimal CFTs*, *Phys. Lett. B* **294** (1992) 204 [hep-th/9202028] [INSPIRE].
- [52] M.J. Martins, *Renormalization group trajectories from resonance factorized S matrices*, *Phys. Rev. Lett.* **69** (1992) 2461 [hep-th/9205024] [INSPIRE].
- [53] P. Dorey, C. Dunning and R. Tateo, *New families of flows between two-dimensional conformal field theories*, *Nucl. Phys. B* **578** (2000) 699 [hep-th/0001185] [INSPIRE].
- [54] O.A. Castro-Alvaredo, B. Doyon and F. Ravanini, *Irreversibility of the renormalization group flow in non-unitary quantum field theory*, *J. Phys. A* **50** (2017) 424002 [arXiv:1706.01871] [INSPIRE].
- [55] C. Klimčík and P. Ševera, *Open strings and D-branes in WZNW model*, *Nucl. Phys. B* **488** (1997) 653 [hep-th/9609112] [INSPIRE].
- [56] F.E. Figueirido, *Particle creation in a conformally invariant supersymmetric model*, *Phys. Lett. B* **227** (1989) 392 [INSPIRE].
- [57] S.J. Gates, Jr., C.M. Hull and M. Roček, *Twisted multiplets and new supersymmetric nonlinear σ -models*, *Nucl. Phys. B* **248** (1984) 157 [INSPIRE].
- [58] P.S. Howe and G. Sierra, *Two-dimensional supersymmetric nonlinear σ -models with torsion*, *Phys. Lett. B* **148** (1984) 451 [INSPIRE].
- [59] P. Spindel, A. Sevrin, W. Troost and A. Van Proeyen, *Complex structures on parallelized group manifolds and supersymmetric σ models*, *Phys. Lett. B* **206** (1988) 71 [INSPIRE].
- [60] P. Spindel, A. Sevrin, W. Troost and A. Van Proeyen, *Extended supersymmetric σ -models on group manifolds. 1. The complex structures*, *Nucl. Phys. B* **308** (1988) 662 [INSPIRE].
- [61] M. Roček, K. Schoutens and A. Sevrin, *Off-shell WZW models in extended superspace*, *Phys. Lett. B* **265** (1991) 303 [INSPIRE].
- [62] M. Roček, C.-H. Ahn, K. Schoutens and A. Sevrin, *Superspace WZW models and black holes*, in *Workshop on Superstrings and Related Topics*, Trieste Italy, 8–9 August 1991, pg. 995 [hep-th/9110035] [INSPIRE].
- [63] A. Sevrin, W. Staessens and D. Terry, *The generalized Kähler geometry of $N = (2, 2)$ WZW-models*, *JHEP* **12** (2011) 079 [arXiv:1111.0551] [INSPIRE].
- [64] J.P. Ang, S. Driezen, M. Roček and A. Sevrin, *The SU(3) WZW model in (2, 2) superspace*, in preparation.
- [65] C. Appadu, T.J. Hollowood and D. Price, *Quantum inverse scattering and the lambda deformed principal chiral model*, *J. Phys. A* **50** (2017) 305401 [arXiv:1703.06699] [INSPIRE].
- [66] F.A. Smirnov and A.B. Zamolodchikov, *On space of integrable quantum field theories*, *Nucl. Phys. B* **915** (2017) 363 [arXiv:1608.05499] [INSPIRE].

- [67] K. Sfetsos and K. Siampos, *Integrable deformations of the $G_{k_1} \times G_{k_2}/G_{k_1+k_2}$ coset CFTs*, *Nucl. Phys. B* **927** (2018) 124 [[arXiv:1710.02515](#)] [[INSPIRE](#)].
- [68] I. Affleck and F.D.M. Haldane, *Critical theory of quantum spin chains*, *Phys. Rev. B* **36** (1987) 5291 [[INSPIRE](#)].
- [69] V. Apostolov and M. Gualtieri, *Generalized Kähler manifolds, commuting complex structures, and split tangent bundles*, *Commun. Math. Phys.* **271** (2007) 561 [[math.DG/0605342](#)].
- [70] V. Apostolov and G. Dloussky, *Bihermitian metrics on Hopf surfaces*, *Math. Res. Lett.* **15** (2008) 827 [[arXiv:0710.2266](#)].
- [71] I. Kawaguchi, T. Matsumoto and K. Yoshida, *On the classical equivalence of monodromy matrices in squashed σ -model*, *JHEP* **06** (2012) 082 [[arXiv:1203.3400](#)] [[INSPIRE](#)].

Aspects of the doubled worldsheet

Sibylle Driezen, Alexander Sevrin¹ and Daniel C. Thompson

*Theoretische Natuurkunde, Vrije Universiteit Brussel and The International Solvay Institutes,
Pleinlaan 2, B-1050 Brussels, Belgium*

E-mail: Sibylle.Driezen@vub.ac.be, Alexandre.Sevrin@vub.ac.be,
Daniel.Thompson@vub.ac.be

ABSTRACT: We clarify the relation between various approaches to the manifestly T-duality symmetric string. We explain in detail how the PST covariant doubled string arises from an unusual gauge fixing. We pay careful attention to the role of “spectator” fields in this process and also show how the T-duality invariant doubled dilaton emerges naturally. We extend these ideas to non-Abelian T-duality and show they give rise to the duality invariant formalism based on the semi-Abelian Drinfeld Double. We then develop the $\mathcal{N} = (0, 1)$ supersymmetric duality invariant formalism.

KEYWORDS: String Duality, Superspaces, Superstrings and Heterotic Strings, Supersymmetry and Duality

ARXIV EPRINT: [1609.03315](https://arxiv.org/abs/1609.03315)

¹Also at: the Physics Department, Universiteit Antwerpen, Campus Groenenborger, 2020 Antwerpen, Belgium.

Contents

1	Introduction	1
2	Bosonic abelian doubled string	5
2.1	Deriving the covariant doubled string	5
2.2	Gauge symmetries and the origin of PST symmetry	8
2.3	Equations of motion in the PST doubled formalism	10
2.4	Gauge fixing and the dilaton	11
2.5	A comment on chiral gauging	13
3	Application to non-abelian T-duality	14
3.1	Relation to Poisson Lie doubled formalism	16
4	Towards the supersymmetric doubled string	18
4.1	The covariant formulation	18
4.2	The Tseytlin formulation	20
4.3	Component form	22
5	Discussion and open problems	22
A	Conventions	24
B	PST symmetry in the $\mathcal{N} = (0, 1)$ case	25

1 Introduction

A central theme in recent years has been to understand the ways in which dualities of string and M-theory may be promoted to manifest symmetries and indeed the extent to which they may be used to determine the structure of the underlying theory.

The idea of a T-duality invariant worldsheet description, *the doubled worldsheet (DWS)*, of strings goes back to pioneering work of Duff [1] and Tseytlin [2, 3]. The study of this approach was reignited following the proposal of Hull [4, 5] to use such a formalism to define strings in a class of non-geometric backgrounds known as T-folds. Parallel to this has been the development of a spacetime T-duality invariant theory, often now dubbed *double field theory (DFT)*, whose origins date to the seminal works of Tseytlin [2, 3] and Siegel [6, 7]. This approach was derived from the perspective of closed string field theory on a torus by Hull and Zwiebach [8]. These ideas have also been explored in the context of M-theory [9, 10] where *exceptional field theory (EFT)* seeks to promote the U-duality

group to a manifest symmetry of a spacetime action and in the E_{11} program of West [11] and collaborators.¹

A common theme of the *doubled worldsheet*, *double field theory* and *exceptional field theory* is that in order to make the duality act as a linearly realised symmetry, the dimensionality of spacetime is augmented by the introduction of additional coordinates. For instance, in the case of T-duality of strings on a d -dimensional torus, we have a $2d$ -dimensional extended spacetime consisting of d -regular coordinates x^i and d -dual coordinates \tilde{x}_i . Just as position is conjugate to momenta one can think of these extra coordinates as conjugate to winding of the string. For strings in a curved background, the components of the background metric g_{ij} and NS two-form fields b_{ij} in the internal toroidal directions are united into a *generalised metric*,

$$\mathcal{H}_{IJ} = \begin{pmatrix} g - b g^{-1} b & -b g^{-1} \\ g^{-1} b & g^{-1} \end{pmatrix}, \tag{1.1}$$

on the doubled space parametrised by coordinates $\mathbb{X}^I = \{x^i, \tilde{x}_i\}$. The T-duality group, which is $O(d, d; \mathbb{Z})$ in this case, acts on this *generalised metric* as,

$$\mathcal{H} \rightarrow \mathcal{H}' = \mathcal{O}^T \mathcal{H} \mathcal{O}, \tag{1.2}$$

where the group element preserves the inner product, $\mathcal{O}^T \eta \mathcal{O} = \eta$, given in this basis by,

$$\eta_{IJ} = \begin{pmatrix} 0 & \mathbf{1} \\ \mathbf{1} & 0 \end{pmatrix}. \tag{1.3}$$

From the generalised metric we see that the doubled space is equipped with an almost product structure $\mathcal{S} = \eta \mathcal{H}$ such that $\mathcal{S}^2 = \mathbf{1}$ which one can think of as giving rise to a “chiral structure” specified by the projection operators,

$$P_{\pm} = \frac{1}{2} (\mathbf{1} \pm \mathcal{S}). \tag{1.4}$$

This doubled space is also equipped with a natural symplectic product Ω given in this basis as,

$$\Omega_{IJ} = \begin{pmatrix} 0 & \mathbf{1} \\ -\mathbf{1} & 0 \end{pmatrix}. \tag{1.5}$$

The existence of the objects \mathcal{S} , η and Ω are central to the recent proposal of Born geometries [15, 16].

In all of these duality symmetric approaches, there is a price to pay; action principles based on the doubled or extended spacetimes require supplementary constraints. In *DFT* and *EFT* gauge invariance of the theory requires a constraint, also known as the section condition, that essentially declares the field content of the theory to depend on only a

¹Our focus in this note will be on the worldsheet rather than spacetime so for further introduction to the *DFT* and *EFT* we refer the reader to the review articles [12–14].

physical spacetime’s worth of coordinates.² In the case of *DWS*, the worldsheet bosons are required to obey a chirality constraint meaning that of the $2d$ bosons \mathbb{X}^I exactly half are left-movers and half are right-movers and thereby give the correct contribution to the physical central charge. In this note we will be focussed on the variety of ways in which the chirality constraint of *DWS* has been handled.

To explain this let us momentarily restrict ourselves to a simple case; a doubled torus T^{2d} with coordinates \mathbb{X}^I and a generalised metric \mathcal{H} possibly depending on some other “spectator” coordinates y parametrising a base manifold over which the doubled torus is trivially fibered with vanishing connection. In this situation the constraints are given in terms of the chiral projections by,

$$(P_+)^I{}_J \partial_- \mathbb{X}^J = 0, \quad (P_-)^I{}_J \partial_+ \mathbb{X}^J = 0. \quad (1.6)$$

Chiral scalars are notoriously tricky objects to describe, the main reason is that these constraints are first order differential equations and in the terminology of Dirac second class constraints and can not be imposed easily with Lagrange multipliers. One approach is to simply consider a non-linear σ -model in the doubled spacetime,

$$S_{\text{Hull}} = \frac{1}{2} \int d^2 \sigma \partial_+ \mathbb{X}^I \mathcal{H}_{IJ} \partial_- \mathbb{X}^J + \dots, \quad (1.7)$$

in which, and in the following, the ellipsis indicate terms depending on the spectators and also a topological term involving Ω_{IJ} both of which we shall detail later. One can then implement the constraints supplementary to the action for instance by using Dirac brackets and then performing canonical quantisation [27] or by holomorphic factorisation of the resulting partition function [28, 29]. Whilst this is certainly a viable route, one should very much like to have an action principle from which eq. (1.6) follows. Without introducing extra field content this is possible only at the expense of sacrificing manifest Lorentz invariance leading to the action pioneered by Tseytlin [2, 3],

$$S_{\text{Tseytlin}} = \frac{1}{4} \int d^2 \sigma - \partial_\sigma \mathbb{X}^I \mathcal{H}_{IJ} \partial_\sigma \mathbb{X}^J + \partial_\sigma \mathbb{X}^I \eta_{IJ} \partial_\tau \mathbb{X}^J + \dots, \quad (1.8)$$

which essentially employs a Floreanini-Jackiw [30] construction for chiral bosons. The equations of motion that follow from eq. (1.8) may be integrated and using a gauge invariance of the form $\delta X^I = f^I(\tau)$ give rise to the desired chirality constraints of eq. (1.6). Despite its apparent non-covariance one can still employ some conventional field theory techniques, for instance one-loop beta functions of this action have been calculated [31, 32] and shown to give rise to background field equations for \mathcal{H} which are indeed compatible with the equations that follow from *DFT* in the present context (other attempts to make more precise the linkage between *DFT* and the worldsheet theory by allowing \mathcal{H} to depend on the internal coordinates are found in [33, 34] and [35]). However multi-loop calculations are at best very difficult without Lorentz covariance.

²Upon solving this section condition for type II DFT [17] globally, one recovers the generalised geometry [18, 19] reformulation of supergravity of [20, 21]. Ways in which the section condition can be consistently relaxed are of great interest and connect to gauged supergravities see [22–26].

A further approach is to include extra fields so as to furnish the action with a gauge redundancy which promotes the second class constraint to a first class one. This is the spirit of the Pasti-Sorokin-Tonin (PST) approach to chiral fields³ [36]. In the present context this leads to a doubled action,

$$S_{\text{PST}} = \frac{1}{2} \int d^2\sigma \partial_{\pm}\mathbb{X}^I \mathcal{H}_{IJ} \partial_{\pm}\mathbb{X}^J - \frac{\partial_{\pm}f}{\partial_{\pm}f} (P_{+}\partial_{\pm}\mathbb{X})^I \eta_{IJ} (P_{+}\partial_{\pm}\mathbb{X})^J + \frac{\partial_{\pm}f}{\partial_{\pm}f} (P_{-}\partial_{\pm}\mathbb{X})^I \eta_{IJ} (P_{-}\partial_{\pm}\mathbb{X})^J + \dots \quad (1.9)$$

The symmetries of this action are,

$$1) \quad \delta\mathbb{X}^I = \Lambda^I(f), \quad \delta f = 0, \quad (1.10)$$

$$2) \quad \delta\mathbb{X}^I = \frac{\epsilon}{\partial_{\pm}f} (P_{-}\partial_{\pm}\mathbb{X})^I + \frac{\epsilon}{\partial_{\pm}f} (P_{+}\partial_{\pm}\mathbb{X})^I, \quad \delta f = \epsilon. \quad (1.11)$$

Upon using the second symmetry to fix $f = f(\tau)$ one recovers the Tseytlin action eq. (1.8).

Whilst this overall picture is correct, the literature has been rather sketchy in places about many of the details concerning the derivations of the covariant forms of the doubled worldsheet and in particular has omitted a careful treatment of spectator fields (i.e. exactly the terms in ellipsis in the above discussion). In the following we will resolve many of these outstanding issues and by giving the complete derivation of the covariant bosonic doubled formalism achieved by adopting an unusual gauge fixing in a Buscher procedure. A version of this idea was suggested in [37] wherein an axial gauge fixing gives rise to the non-covariant action eq. (1.8) and more recently explored in [38, 39] wherein covariant gauge fixing choices were adopted (though those are not directly relevant to the present discussion). We further this approach by making direct the linkage to the PST form of the action and will then be able to clarify some surprising features concerning the origin of the PST symmetries. These ideas will then be generalised to the case of non-Abelian T-dualities [40] and we will recover a covariant version of the Poisson-Lie duality symmetric action of Klimčík and Ševera [41, 42].

This work arose out of an ongoing attempt to better understand the supersymmetric doubled formalism. It is quite clear in this case how to generalise the chirality constraints to $\mathcal{N} = 1$ supersymmetry; one promotes partial derivatives to super covariant derivatives acting on superfields,

$$(P_{+})^I{}_J D_{-}\mathbb{X}^J = 0, \quad (P_{-})^I{}_J D_{+}\mathbb{X}^J = 0. \quad (1.12)$$

Previous work in the literature has followed the route of imposing the constraints by hand either via Dirac brackets as in [27] or via holomorphic factorisation of a partition function [43]. However the implementation of these constraints at the level of the action has rarely been considered; there is no known covariant formalism in the style of eq. (1.9)

³A different approach based upon gauging the the symmetries generated by the constraints was followed in [5] however at the cost of losing manifest $O(d, d; \mathbb{Z})$ invariance. This approach can be extended to superspace (at least to $\mathcal{N} = (1, 1)$) and higher genus worldsheets.

and even a non-covariant Tseytlin style action has only been considered for the case of a constant generalised metric i.e. assuming no dependence on spectator coordinates. Naive attempts to generalise this appear to fail badly and addressing this short coming seems essential for the doubled worldsheet to have a life in superstring theory.

Here we take a step in this direction by carefully analysing the simplest supersymmetric model, i.e. the one which exhibits an $\mathcal{N} = (0, 1)$ supersymmetry on the worldsheet. It turns out that even a first order formulation comes accompanied by external constraints. These extra constraints are similar in nature to nilpotency constraints on superfields, so at the level of the components of the superfields they are algebraic and, as a consequence, they can simply be imposed using Lagrange multipliers. We do give both the PST and the Tseytlin like description of the $\mathcal{N} = (0, 1)$ system. Note that a Hamiltonian perspective was given in [44] in which only bosonic degrees of freedom are doubled making supersymmetry less evident; here we will instead work in superspace.

2 Bosonic abelian doubled string

2.1 Deriving the covariant doubled string

Our starting point is some compact D -dimensional manifold \mathcal{M} endowed with a metric g and a closed 3-form H . Locally we introduce the Kalb-Ramond 2-form b : $H = db$. Choosing local coordinates X^A , $A \in \{1, \dots, D\}$, the non-linear σ -model Lagrange density is given by,

$$\mathcal{L} = \partial_{\neq} X^A (g_{AB} + b_{AB}) \partial_{=} X^B. \tag{2.1}$$

We now assume the existence of d isometries ($d \leq D$) and introduce adapted coordinates x^i , $i \in \{1, \dots, d\}$, such that the background fields g and b *do not depend on* x . The spectator coordinates are called y^α , $\alpha \in \{1, \dots, D-d\}$. In an obvious matrix notation the Lagrange density becomes,

$$\mathcal{L} = \partial_{\neq} x^T E \partial_{=} x + \partial_{\neq} x^T M \partial_{=} y + \partial_{\neq} y^T N \partial_{=} x + \partial_{\neq} y^T K \partial_{=} y. \tag{2.2}$$

A special role is accorded to $E_{ij} = g_{ij} + b_{ij}$. We denote the inverse of g_{ij} (g) by g^{ij} (g^{-1}): $g_{ik} g^{kj} = \delta_i^j$ ($g g^{-1} = g^{-1} g = \mathbf{1}$). We introduce ‘‘connections’’ \mathcal{B} and $\tilde{\mathcal{B}}$,

$$\begin{aligned} \mathcal{B}^i &= g^{ij} g_{j\beta} \partial y^\beta, \\ \tilde{\mathcal{B}}_i &= b_{i\beta} \partial y^\beta - b_{ij} g^{jk} g_{k\beta} \partial y^\beta, \end{aligned} \tag{2.3}$$

which are adapted coordinate representations of (pull backs of) one-forms detailed in [5] that are horizontal and invariant with respect to the Killing vectors generating the isometry. With these we may rewrite eq. (2.2) as,

$$\mathcal{L} = \nabla_{\neq} x^T E \nabla_{=} x + \partial_{\neq} x^T \tilde{\mathcal{B}}_{=} - \partial_{=} x^T \tilde{\mathcal{B}}_{\neq} - \mathcal{B}_{\neq}^T E \mathcal{B}_{=} + \partial_{\neq} y^T K \partial_{=} y, \tag{2.4}$$

where,

$$\nabla x = \partial x + \mathcal{B}. \tag{2.5}$$

In order to obtain the T-dual model we gauge the isometries,

$$x \rightarrow x' = x + \zeta, \quad y \rightarrow y' = y. \quad (2.6)$$

For this we introduce $2d$ gauge fields A_{\pm} and A_{\pm}' transforming as,

$$A_{\pm} \rightarrow A_{\pm}' = A_{\pm} - \partial_{\pm} \zeta, \quad A_{\pm}' \rightarrow A_{\pm} = A_{\pm}' + \partial_{\pm} \zeta, \quad (2.7)$$

together with d Lagrange multipliers \tilde{x} which are inert under the gauge transformations. The gauge invariant Lagrange density is then,⁴

$$\begin{aligned} \mathcal{L}_{\text{gauged}} = & (\nabla_{\pm} x + A_{\pm})^T E (\nabla_{\pm} x + A_{\pm}) + (\partial_{\pm} x + A_{\pm})^T \tilde{\mathcal{B}}_{\pm} - (\partial_{\pm} x + A_{\pm})^T \tilde{\mathcal{B}}_{\pm} \\ & - \mathcal{B}_{\pm}^T E \mathcal{B}_{\pm} + \partial_{\pm} y^T K \partial_{\pm} y + \tilde{x}^T (\partial_{\pm} A_{\pm} - \partial_{\pm} A_{\pm}'). \end{aligned} \quad (2.8)$$

Integrating over the Lagrange multipliers sets the field strengths to zero, so we can gauge away the gauge fields and we recover the original model. However making the gauge choice $x = 0$, integrating by parts on the Lagrange multiplier term and integrating out the gauge fields yields the dual model,

$$\tilde{\mathcal{L}}_{\text{dual}} = \nabla_{\pm} \tilde{x}^T \tilde{E} \nabla_{\pm} \tilde{x} + \partial_{\pm} \tilde{x}^T \tilde{\mathcal{B}}_{\pm} - \partial_{\pm} \tilde{x}^T \tilde{\mathcal{B}}_{\pm} - \tilde{\mathcal{B}}_{\pm}^T \tilde{E} \tilde{\mathcal{B}}_{\pm} + \partial_{\pm} y^T \tilde{K} \partial_{\pm} y, \quad (2.9)$$

with,

$$\nabla \tilde{x} = \partial \tilde{x} + \tilde{\mathcal{B}}. \quad (2.10)$$

The dual background fields are given by the Buscher rules [46, 47],

$$\tilde{E} = E^{-1}, \quad \tilde{M} = E^{-1} M, \quad \tilde{N} = -N E^{-1}, \quad \tilde{K} = K - N E^{-1} M, \quad (2.11)$$

together with a shift in the dilaton that is seen when the dualisation procedure is carried out in a path integral.

Let us now turn to the manifest T-dual invariant or doubled formulation of the model. In fact our starting point, the gauged Lagrange density eq. (2.8) is already “doubled” as both the original coordinates x and the dual coordinates \tilde{x} appear. This was suggested in [37] (see also [48] for a detailed development) where it was shown that by making the non-Lorentz covariant gauge choice $A_{\pm} = A_{\pm}' \equiv A$ and subsequently integrating out A one recovers Tseytlin’s non-Lorentz covariant doubled formulation [2, 3]. This is very reminiscent of the Floreanini-Jackiw formulation of a chiral boson [30]. Just as the Floreanini-Jackiw formalism can be covariantized [36, 49] we expect the same for Tseytlin’s action. In the next we show how by making a judicious gauge choice in eq. (2.8) one indeed obtains a Lorentz invariant doubled worldsheet formulation.

Starting from the gauge invariant Lagrange density in eq. (2.8) we impose the gauge fixing condition,

$$\partial_{\pm} f A_{\pm} = \partial_{\pm} f A_{\pm}', \quad (2.12)$$

⁴Note that in order to avoid nontrivial holonomies around non-contractible loops, \tilde{x} should satisfy appropriate periodicity conditions. In addition, a surface term $\partial_{\pm}(\tilde{x}^T A_{\pm}) - \partial_{\pm}(\tilde{x}^T A_{\pm}')$ should be added to eq. (2.8) [45] which is important to keep in mind as we treat boundary contributions in what follows.

where f is some scalar field. In writing the gauge fixing choice as in eq. (2.12) we are emphasising that the function f should be suitably chosen so as to have nowhere vanishing derivatives — we will discuss this requirement further in the discussion section. Making a coordinate transformation,

$$\sigma^\ddagger \rightarrow \hat{\sigma}^\ddagger = \sigma^\ddagger, \quad \sigma^\bar{=} \rightarrow \hat{\sigma}^\bar{=} = f, \quad (2.13)$$

the above gauge choice simplifies to $\hat{A}_\ddagger = 0$. From this we immediately identify the residual gauge symmetry. It is given by eqs. (2.6) and (2.7) where the gauge parameter ξ is of the form $\xi = \xi(f(\sigma^\ddagger, \sigma^\bar{=}))$. A full and detailed discussion of the residual symmetries will be given in section 2.2. In addition to this, one verifies that the Lagrange density eq. (2.8) is invariant under,

$$\tilde{x} \rightarrow \tilde{x}' = \tilde{x} + \tilde{\xi}(f), \quad (2.14)$$

as well.

Now the strategy is clear. We adopt this gauge choice and parameterize the gauge fields as,

$$A_\ddagger = A \partial_\ddagger f \quad A_\bar{=} = A \partial_\bar{=} f, \quad (2.15)$$

where A is a $d \times 1$ column matrix of scalar fields. Implementing this gauge fixing in eq. (2.8) and eliminating A through its equations of motion,

$$A = -\frac{1}{2\partial_\bar{=} f} g^{-1} \mathcal{J}_\bar{=} - \frac{1}{2\partial_\ddagger f} g^{-1} \mathcal{J}_\ddagger, \quad (2.16)$$

where,

$$\mathcal{J}_\bar{=} = E \nabla_\bar{=} x + \nabla_\bar{=} \tilde{x}, \quad \mathcal{J}_\ddagger = E^T \nabla_\ddagger x - \nabla_\ddagger \tilde{x}, \quad (2.17)$$

yields, after a little manipulation, the desired covariant doubled Lagrange density,⁵

$$\begin{aligned} \mathcal{L}_{\text{doubled}} = & \frac{1}{2} \nabla_\ddagger \mathbb{X}^T \mathcal{H} \nabla_\bar{=} \mathbb{X} - \frac{1}{2} \partial_\ddagger \mathbb{X}^T \Omega \partial_\bar{=} \mathbb{X} - \frac{1}{2} \frac{\partial_\bar{=} f}{\partial_\ddagger f} \nabla_\ddagger \mathbb{X}^T \mathcal{H} P_- \nabla_\ddagger \mathbb{X} \\ & - \frac{1}{2} \frac{\partial_\ddagger f}{\partial_\bar{=} f} \nabla_\bar{=} \mathbb{X}^T \mathcal{H} P_+ \nabla_\bar{=} \mathbb{X} + \frac{1}{2} \partial_\ddagger \mathbb{X}^T \eta \mathbb{B}_\bar{=} - \frac{1}{2} \partial_\bar{=} \mathbb{X}^T \eta \mathbb{B}_\ddagger + \partial_\ddagger y^T \hat{K} \partial_\bar{=} y, \end{aligned} \quad (2.18)$$

where,

$$\mathbb{B} = \begin{pmatrix} \mathcal{B} \\ \tilde{\mathcal{B}} \end{pmatrix}, \quad \nabla \mathbb{X} = \partial \mathbb{X} + \mathbb{B}. \quad (2.19)$$

This action is now (almost) manifestly invariant under global $O(d, d; \mathbb{R})$ transformations acting as,

$$\mathcal{H} \rightarrow \mathcal{H}' = \mathcal{O}^T \mathcal{H} \mathcal{O}, \quad \mathbb{X} \rightarrow \mathcal{O}^{-1} \mathbb{X}, \quad \mathbb{B} \rightarrow \mathcal{O}^{-1} \mathbb{B}. \quad (2.20)$$

⁵Note that a Lagrange density somewhat similar to this one has been obtained in the context of heterotic strings compactified on a Narain torus [53].

This invariance is further reduced to $O(d, d; \mathbb{Z})$ by demanding that the periodicities of the coordinates \mathbb{X} are preserved [4, 8].

Note that other than the initial integration by parts on the Lagrange multiplier term (and, see footnote 4, in a careful gauging any boundary terms from this are canceled by a boundary contribution), we have not discarded any total derivatives in this manipulation and the topological term, $\partial_{\pm} \mathbb{X}^T \Omega \partial_{\pm} \mathbb{X}$, appears automatically. One might be tempted to ignore such a piece however this term is vital for instance in getting a correct factorisation of the partition function and in [5] this topological term ensures invariance under certain large gauge transformations that are used to define the quantum theory (as originally emphasized in [54]). We will see later that when generalised to non-Abelian T-duality it will no longer remain topological and rather play the role of a potential for a WZ term. Strictly speaking this topological term spoils the invariance of the action under $O(d, d; \mathbb{Z})$ unless $\mathcal{O}^T \Omega \mathcal{O} = \Omega$. Evidently the $GL(d, \mathbb{Z})$ subgroup of the duality group preserves Ω , but for the remaining components of $O(d, d; \mathbb{Z})$, namely B-field shifts and Buscher dualities, one needs to exercise more care. Properly normalised this topological term [5] evaluates to the sum of products of winding numbers around canonically dual cycles and in a fixed winding sector evaluates to $\pi \mathbb{Z}$ contributing a sign in the path integral. B-field shifts have the effect of adding $2\pi \mathbb{Z}$ to this contribution and thus leave the path integral invariant. For T-dualities that simply swap n coordinates the coefficient of the topological term is multiplied by $(-1)^n$ and again the path integral is invariant.

The Lagrange density governing the spectator coordinates is altered as well — a fact often ignored in the literature. Indeed the $O(d, d; \mathbb{Z})$ non-invariant background field K is replaced by \hat{K} which is invariant and explicitly given by,

$$\hat{K} = K - \frac{1}{2} N g^{-1} M - \frac{1}{4} M^T g^{-1} M - \frac{1}{4} N g^{-1} N^T. \tag{2.21}$$

The action of parity is slightly non-standard. Since parity acts as $\mathcal{P} : \{\sigma^{\pm}, \sigma^{\mp}\} \rightarrow \{\sigma^{\mp}, \sigma^{\pm}\}$ leaving the one-form gauge connection $A_{\mu} dx^{\mu}$ invariant, we require that $\mathcal{P} : \{x, \tilde{x}\} \rightarrow \{x, -\tilde{x}\}$ for the gauged Lagrangian to have definite parity. In terms of the doubled space we have $\mathcal{P} : \mathbb{X}^I \rightarrow \mathcal{P}^I{}_J \mathbb{X}^J$ with $\mathcal{P}^I{}_J = -(\Omega \eta)^I{}_J$. In addition, for the term $E_{ij} \partial_{\pm} x^i \partial_{\pm} x^j$ to have definite parity we should also insist that $\mathcal{P} : b_{ij} \rightarrow -b_{ij}$ which implies that the generalised metric must transform as $\mathcal{P} : \mathcal{H} \rightarrow \mathcal{P} \cdot \mathcal{H} \cdot \mathcal{P}$. Making use of the identity $\mathcal{P} \cdot \eta \cdot \mathcal{P} = -\eta$ we see $\mathcal{P} : (P_{+} \partial_{-} \mathbb{X})^I \rightarrow (\mathcal{P} \cdot P_{-} \partial_{+} X)^I$ and thus both the Tseytlin and PST actions have definite parity.

2.2 Gauge symmetries and the origin of PST symmetry

In this section we investigate the symmetries of the manifest $O(d, d; \mathbb{Z})$ invariant Lagrange density. Upon gauge fixing the original gauge symmetry eqs. (2.6) and (2.7) and passing to the second order formalism, the residual gauge symmetry extended by the symmetry eq. (2.14) is given by,

$$\mathbb{X} \rightarrow \mathbb{X}' = \mathbb{X} + \Lambda(f), \quad f \rightarrow f' = f, \tag{2.22}$$

where $\Lambda(f)$ is a $2d \times 1$ column matrix of arbitrary functions of f . This explains the origin of the first of the symmetries of eq. (1.10). However the appearance of the PST symmetry which acts as,

$$\begin{aligned} \delta f &= \varepsilon, \\ \delta \mathbb{X} &= \frac{\varepsilon}{\partial_{\mp} f} P_{-} \nabla_{\mp} \mathbb{X} + \frac{\varepsilon}{\partial_{=} f} P_{+} \nabla_{=} \mathbb{X}, \end{aligned} \quad (2.23)$$

in the second order formulation eq. (2.18) is quite mysterious. It looks as if it is unrelated to the original gauge symmetry eqs. (2.6) and (2.7). In the remainder we explain how the PST symmetry originates from the gauged σ -model in eq. (2.8).

Given an infinitesimal vector, ξ^{μ} , $\mu \in \{\mp, =\}$, we introduce the variations,

$$\begin{aligned} \delta A_{\mu} &= \mathcal{L}_{\xi} A_{\mu} = \partial_{\mu}(\xi^{\nu} A_{\nu}) + \xi^{\nu} F_{\nu\mu}, \\ \delta x &= -\xi^{\mu} A_{\mu}, \\ \delta \tilde{x} &= -\xi^{\mp}(\mathcal{J}_{\mp} + E^T A_{\mp}) + \xi^{=}(\mathcal{J}_{=} + EA_{=}), \end{aligned} \quad (2.24)$$

where $F_{\mu\nu} = \partial_{\mu} A_{\nu} - \partial_{\nu} A_{\mu}$, \mathcal{L}_{ξ} is the Lie derivative along ξ and \mathcal{J} was given in eq. (2.17). One easily verifies that the gauged σ -model in eq. (2.8) is invariant under these transformations. This is not so surprising as these transformations can be rewritten as,

$$\begin{aligned} \delta x &= -\xi^{\mu} A_{\mu}, \\ \delta A_{\mp} &= \partial_{\mp}(\xi^{\mu} A_{\mu}) - \xi^{=} \frac{\delta \mathcal{S}}{\delta \tilde{x}}, \\ \delta A_{=} &= \partial_{=}(\xi^{\mu} A_{\mu}) + \xi^{\mp} \frac{\delta \mathcal{S}}{\delta \tilde{x}}, \\ \delta \tilde{x} &= -\xi^{\mp} \frac{\delta \mathcal{S}}{\delta A_{=}} + \xi^{=} \frac{\delta \mathcal{S}}{\delta A_{\mp}}, \end{aligned} \quad (2.25)$$

where we introduced the action $\mathcal{S} = \int d^2\sigma \mathcal{L}_{\text{gauged}}$. So one sees that this is not a new symmetry: it is a combination of a (field dependent) gauge transformation eqs. (2.6), (2.7) with parameter $\zeta = -\xi^{\mu} A_{\mu}$ and a (trivial) equations of motion symmetry.

However the situation changes when making the gauge choice $A_{\mp} = \partial_{\mp} f A$, $A_{=} = \partial_{=} f A$. The residual gauge symmetry is now,

$$x \rightarrow x' = x + \varepsilon(f), \quad f \rightarrow f' = f, \quad A \rightarrow A' = A - \frac{d\varepsilon(f)}{df}, \quad (2.26)$$

and the symmetries in eq. (2.25) survive provided we assign the following transformation rules to A and f ,

$$\begin{aligned} \delta f &= \xi^{\mu} \partial_{\mu} f, \\ \delta A &= \xi^{\mu} \partial_{\mu} A. \end{aligned} \quad (2.27)$$

Introducing the parameters ε and \varkappa ,

$$\varepsilon \equiv \xi^{\mp} \partial_{\mp} f + \xi^{=} \partial_{=} f, \quad \varkappa \equiv \xi^{\mp} \partial_{\mp} f - \xi^{=} \partial_{=} f, \quad (2.28)$$

one rewrites the transformation rules as,

$$\begin{aligned}
 \delta f &= \varepsilon, \\
 \delta x &= -\varepsilon A, \\
 \delta \tilde{x} &= \frac{\varepsilon}{2} \left(-\frac{\mathcal{J}_\oplus}{\partial_\oplus f} + \frac{\mathcal{J}_\ominus}{\partial_\ominus f} + 2b A \right) - \frac{\varkappa}{2\partial_\oplus f \partial_\ominus f} \frac{\delta \mathcal{S}}{\delta A}, \\
 \delta A &= \frac{\varepsilon}{2} \left(\frac{\partial_\oplus A}{\partial_\oplus f} + \frac{\partial_\ominus A}{\partial_\ominus f} \right) + \frac{\varkappa}{2\partial_\oplus f \partial_\ominus f} \frac{\delta \mathcal{S}}{\delta \tilde{x}}.
 \end{aligned} \tag{2.29}$$

So one sees that the symmetry parameterized by ε corresponds to a genuine gauge symmetry while the one parameterized by \varkappa is a trivial equations of motion symmetry. Eliminating A through its equations of motion, eq. (2.16) the \varkappa dependent term in $\delta \tilde{x}$ drops out and the transformations rules for x , \tilde{x} and f exactly reduce to the PST transformations in eq. (2.23).

Concluding: we initially had $2d$ gauge fields and d abelian gauge symmetries. Imposing the gauge choice $\partial_\oplus f A_\ominus = \partial_\ominus f A_\oplus$ eliminates half of the gauge fields but introduces one new degree of freedom f leaving one unfixed gauge symmetry which appears as the PST gauge symmetry in the way outlined above. The PST symmetry acts as a shift on f allowing it to be used to put $f = \tau$ which leads to the Tseytlin doubled formulation.

2.3 Equations of motion in the PST doubled formalism

We can now see how the desired chirality constraints, eq. (1.6), follow as equations of motion in this approach. For a single chiral boson a clear explanation of this was provided in [55] and we adapt this to the doubled string taking into account the twisted nature of the constraints.

The equations of motion that follows from a variation in \mathbb{X} of the doubled action (2.18) can be expressed as,

$$0 = \partial_\oplus \left(\mathcal{H} P_+ \nabla_\ominus \mathbb{X} - \frac{\partial_\ominus f}{\partial_\oplus f} P_- \nabla_\oplus \mathbb{X} \right) + \partial_\ominus \left(\mathcal{H} P_- \nabla_\oplus \mathbb{X} - \frac{\partial_\oplus f}{\partial_\ominus f} P_+ \nabla_\ominus \mathbb{X} \right). \tag{2.30}$$

Introducing a one-form with components,

$$v_\oplus = \frac{\partial_\oplus f}{\sqrt{\partial_\oplus f \partial_\ominus f}}, \quad v_\ominus = \frac{\partial_\ominus f}{\sqrt{\partial_\oplus f \partial_\ominus f}}, \tag{2.31}$$

allows the equations of motion to be recast as,

$$0 = d(v\Lambda), \quad \Lambda = v_\oplus \mathcal{H} P_+ \nabla_\ominus \mathbb{X} - v_\ominus \mathcal{H} P_- \nabla_\oplus \mathbb{X}. \tag{2.32}$$

The homogenous solution $\Lambda = 0$ corresponds exactly, after making use of the chiral projectors P_\pm , to the chirality constraint,

$$P_+ \nabla_\ominus \mathbb{X} = 0, \quad P_- \nabla_\oplus \mathbb{X} = 0, \tag{2.33}$$

i.e. the covariant version of eq. (1.6) that incorporates the connection. There is also an inhomogeneous solution of the form $\Lambda_I = \Gamma_I(f) \sqrt{\partial_\oplus f \partial_\ominus f}$ since then $v\Lambda = df\Gamma(f)$ is

trivially closed. However this is a pure gauge piece; under the residual gauge symmetry $\delta\mathbb{X} = \mathbb{T}(f)$ we have,

$$\begin{aligned}\delta\Lambda &= \frac{1}{\sqrt{\partial_{\pm}f\partial_{\mp}f}} (\partial_{\pm}f\mathcal{H}P_{+}\partial_{\mp}\mathbb{T} - \partial_{\mp}f\mathcal{H}P_{-}\partial_{\pm}\mathbb{T}) \\ &= \sqrt{\partial_{\pm}f\partial_{\mp}f} (\mathcal{H}P_{+} - \mathcal{H}P_{-})\mathbb{T}' = \sqrt{\partial_{\pm}f\partial_{\mp}f}\eta\mathbb{T}',\end{aligned}\tag{2.34}$$

which is of the correct form to be gauged away with $\Gamma_I(f) = \eta\mathbb{T}'$.

Performing the variation with respect to f yields an equation of motion,

$$\begin{aligned}0 &= \partial_{\pm} \left[\frac{1}{\partial_{\mp}f} (P_{+}\nabla_{\mp}\mathbb{X})^T \mathcal{H}(P_{+}\nabla_{\mp}\mathbb{X}) - \frac{\partial_{\mp}f}{(\partial_{\pm}f)^2} (P_{-}\nabla_{\pm}\mathbb{X})^T \mathcal{H}(P_{-}\nabla_{\pm}\mathbb{X}) \right] \\ &\quad - \partial_{\mp} \left[\frac{\partial_{\pm}f}{(\partial_{\mp}f)^2} (P_{+}\nabla_{\mp}\mathbb{X})^T \mathcal{H}(P_{+}\nabla_{\mp}\mathbb{X}) - \frac{1}{\partial_{\pm}f} (P_{-}\nabla_{\pm}\mathbb{X})^T \mathcal{H}(P_{-}\nabla_{\pm}\mathbb{X}) \right].\end{aligned}\tag{2.35}$$

Here the projectors P_{\pm} come in handy to show that this equation can be recast as

$$0 = d \left(v \frac{\Lambda^T \eta \Lambda}{\sqrt{\partial_{\pm}f\partial_{\mp}f}} \right),\tag{2.36}$$

and hence follows as a consequence of the field equation for \mathbb{X} . That this does not give rise to extra dynamical equations is a manifestation of the PST gauge symmetry.

2.4 Gauge fixing and the dilaton

In our above derivations we introduced a gauge fixing condition,

$$0 = \partial_{\pm}f A_{=} - \partial_{\mp}f A_{\pm}.\tag{2.37}$$

Let us consider how this should be done in a path integral. We begin with the ill-defined,

$$Z = \int [d\mathbb{X}][dA_{\pm}][dA_{=}] e^{-i \int \mathcal{L}[A_{\pm}, A_{=}, \mathbb{X}]},\tag{2.38}$$

and insert the gauge fixing condition and Jacobian,

$$Z = \int [d\mathbb{X}][dA_{\pm}][dA_{=}] \delta(\partial_{\pm}f A_{=} - \partial_{\mp}f A_{\pm}) \det(\partial_{\pm}f\partial_{\mp} - \partial_{\mp}f\partial_{\pm}) e^{-i \int \mathcal{L}[A_{\pm}, A_{=}, \mathbb{X}]}. \tag{2.39}$$

At this stage the function f should not be considered dynamical but rather it is a fixed background object that defines a gauge fixing. The delta function restricts the path integral and since this is just an algebraic equation one can solve it by replacing $A_{=}$ with $A_{\pm} \frac{\partial_{\mp}f}{\partial_{\pm}f}$. Hence,

$$\begin{aligned}Z[f] &= \int [d\mathbb{X}][dA_{\pm}][dA_{=}] \frac{1}{\partial_{\pm}f} \delta \left(A_{=} - \frac{\partial_{\mp}f}{\partial_{\pm}f} A_{\pm} \right) \det(\partial_{\pm}f\partial_{\mp} - \partial_{\mp}f\partial_{\pm}) e^{-i \int \mathcal{L}[A_{\pm}, A_{=}, \mathbb{X}]} \\ &= \int [d\mathbb{X}][dA_{\pm}] \frac{1}{\partial_{\pm}f} \det(\partial_{\pm}f\partial_{\mp} - \partial_{\mp}f\partial_{\pm}) e^{-i \int \mathcal{L}[A_{\pm}, A_{\pm} \frac{\partial_{\mp}f}{\partial_{\pm}f}, \mathbb{X}]} \\ &= \int [d\mathbb{X}][dA][db][dc] e^{-i \int \mathcal{L}[A, \mathbb{X}; f] + \mathcal{L}_{gh}[b, c; f]},\end{aligned}\tag{2.40}$$

in which we made the final change of variables $A_{\pm} = A\partial_{\pm}f$ and the ghost Lagrangian is given by

$$\mathcal{L}_{gh} = \partial_{\pm}f b \partial_{=}c - \partial_{=}f b \partial_{\pm}c . \tag{2.41}$$

The PST symmetry, which extends to the ghost sector as,

$$\begin{aligned} \delta f &= \varepsilon , \\ \delta \mathbb{X} &= \frac{\varepsilon}{\partial_{\pm}f} P_{-} \nabla_{\pm} \mathbb{X} + \frac{\varepsilon}{\partial_{=}f} P_{+} \nabla_{=} \mathbb{X} , \\ \delta b &= \frac{1}{2} \varepsilon \left(\frac{\partial_{\pm}b}{\partial_{\pm}f} - \frac{\partial_{=}b}{\partial_{=}f} \right) , \\ \delta c &= \frac{1}{2} \varepsilon \left(\frac{\partial_{\pm}c}{\partial_{\pm}f} - \frac{\partial_{=}c}{\partial_{=}f} \right) , \end{aligned} \tag{2.42}$$

can now be re-interpreted as saying nothing more than $Z[f]$ does not depend on the gauge fixing choice. We can then simply choose to integrate over choices of the gauge fixing function f in much the same way as one averages over gauge choices to obtain R_{ξ} gauge in QED. That is we can consider,

$$Z = \frac{1}{\text{vol}_{\text{PST}}} \int [df] Z[f] , \tag{2.43}$$

in which we divide by the volume of the PST group. Since the PST symmetry acts a simple shift on f , it can be fixed without the need for further ghost terms.

To progress to the doubled formalism we now need to integrate out the gauge fields A in this path integral. As is well known, under T-duality, the dilaton receives a shift which in the Buscher procedure can be attributed to the determinant that comes from the Gaussian integral over the gauge fields. A useful mnemonic to obtain the correct shift is that the string frame supergravity measure $\sqrt{|g|}e^{-2\phi}$ should be invariant. For $g \rightarrow g^{-1}$ this means that T-dual dilaton is given by

$$\phi' = \phi - \frac{1}{2} \ln \det g . \tag{2.44}$$

On the other hand a T-duality invariant ‘‘doubled dilaton’’ is given by

$$\Phi = \phi - \frac{1}{4} \ln \det g . \tag{2.45}$$

We can see that in the above derivation it is this doubled dilaton that emerges automatically in the covariant doubled formalism for elementary reasons; whereas in a tradition Buscher procedure one integrates out *two* components of a gauge field in the Gaussian term $A_{\pm}gA_{\pm}$ giving essentially a factor of $\det(g)^{-1}$, in the covariant fixing we have a Gaussian term $AgA\partial_{\pm}f\partial_{=}f$ and we integrate over a *single* mode, A , giving rise to a determinant factor $\det(g)^{-\frac{1}{2}} \times (\partial_{\pm}f\partial_{=}f)^{-\frac{d}{2}}$. The determinant of the metric enters with half the power and thus will give rise to a Fradkin Tseytlin coupling of to the doubled dilaton eq. (2.45). Note that even if we begin with a non-flat geometry in which the normal dilaton is constant the doubled dilaton will not be.

2.5 A comment on chiral gauging

In the derivation above we started with the usual string σ -model and performed an unusual gauge fixing in a Buscher procedure to obtain the manifestly Lorentz covariant doubled sigma model whose equations of motion imply chirality conditions. One might wish to adopt a different tactic namely to begin with a *doubled* sigma-model from the outset and invoke the constraints via a gauging procedure. In a previous paper, [49], two of the present authors emphasized that PST style actions for (supersymmetric) chiral bosons can be obtained by gauging a chiral (super)-conformal symmetry and by then specifying a Beltrami parametrisation for the corresponding gauge field. This approach also works in the current case although in a rather surprising way which we will now illustrate (suppressing spectators for simplicity).

We start with a Hull style σ -model on the doubled space,

$$S_{Hull} = \frac{1}{2} \int d^2\sigma \mathcal{H}_{IJ}(y) \partial_{\mp} \mathbb{X}^I \partial_{\pm} \mathbb{X}^J + \dots, \quad (2.46)$$

in which the ellipses indicate spectator terms that will play no role in what follows. We want to furnish the action with a gauge invariance,

$$\delta \mathbb{X} = \varepsilon^{\mp} P_{-} \partial_{\mp} \mathbb{X} + \varepsilon^{\pm} P_{+} \partial_{\pm} \mathbb{X}, \quad (2.47)$$

such that only the field configurations obeying the constraint eq. (1.6) are physical. *A priori* the gauge parameters ε^{\pm} correspond to independent symmetries however as we shall soon see gauge invariance will force them to be related. It is curious that in the ungauged action that this putative symmetry does not correspond to a rigid invariance (unless $\partial_y \mathcal{H} = 0$); this is one of the features that makes the following gauging procedure rather atypical. We proceed by introducing gauge fields $h_{\mp\mp}$ and $h_{\pm\pm}$ (not to be confused with the usual worldsheet metric components) with the usual conformal transformation rules,

$$\begin{aligned} \delta h_{\mp\mp} &= \partial_{\mp} \varepsilon^{\pm} + \varepsilon^{\pm} \partial_{\pm} h_{\mp\mp} - \partial_{\pm} \varepsilon^{\mp} h_{\mp\mp}, \\ \delta h_{\pm\pm} &= \partial_{\pm} \varepsilon^{\mp} + \varepsilon^{\mp} \partial_{\mp} h_{\pm\pm} - \partial_{\mp} \varepsilon^{\pm} h_{\pm\pm}, \end{aligned} \quad (2.48)$$

and “covariant” derivatives,

$$\nabla_{\mp}^h \mathbb{X}^I = \partial_{\mp} \mathbb{X}^I - h_{\mp\mp} (P_{+} \partial_{\pm} \mathbb{X})^I, \quad \nabla_{\pm}^h \mathbb{X}^I = \partial_{\pm} \mathbb{X}^I - h_{\pm\pm} (P_{-} \partial_{\mp} \mathbb{X})^I. \quad (2.49)$$

In fact, though their structure is informed by the usual conformal covariant derivative, these derivatives are not at all covariant as e.g. $\delta \nabla_{\pm}^h \mathbb{X} |_{\nabla_{\pm}^h \mathbb{X} = 0} \neq 0$. That these derivatives are not actually covariant makes the fact that the following construction works even more surprising. We continue regardless of this and consider the “gauged” action,

$$S_{\text{gauged}} = \frac{1}{2} \int d^2\sigma \mathcal{H}_{IJ} \nabla_{\mp}^h \mathbb{X}^I \nabla_{\pm}^h \mathbb{X}^J + \dots. \quad (2.50)$$

Performing a gauge variation, integrating by parts all terms containing $\partial_{\mp\mp} \mathbb{X}$ and $\partial_{\pm\pm} \mathbb{X}$ and making use of the identities obeyed by the projectors eq. (A.13) results in a variation

of the Lagrange density,

$$\begin{aligned} \frac{1}{2} \delta \mathcal{L}_{\text{gauged}} = & -\varepsilon^\dagger \partial_\mp \mathcal{H}_{IJ} (P_- \partial_\mp \mathbb{X})^I \partial_- \mathbb{X}^J + 2\varepsilon^\dagger h_{==} \eta_{IJ} (P_- \partial_\mp P_+ \partial_- \mathbb{X})^I \partial_\mp \mathbb{X}^J \\ & - \varepsilon^\dagger \partial_- \mathcal{H}_{IJ} \partial_\mp \mathbb{X}^I (P_+ \partial_- \mathbb{X})^J - 2\varepsilon^\dagger h_{\mp\mp} \eta_{IJ} \partial_- \mathbb{X}^I (P_+ \partial_- P_- \partial_\mp) \mathbb{X}^J \end{aligned} \quad (2.51)$$

To cancel this we see that the gauge variation parameters are not independent and one must enforce,

$$h_{\mp\mp} h_{==} = 1, \quad \varepsilon^\dagger h_{\mp\mp} = \varepsilon^\dagger, \quad \varepsilon^\dagger h_{==} = \varepsilon^\dagger. \quad (2.52)$$

It is easy to see that these are consistent with the gauge transformations rules. With these identifications and the definitions of the projectors we find that indeed action eq. (2.50) is gauge invariant. Solving the first of these relations with a Beltrami parametrisation

$$h_{\mp\mp} = \frac{\partial_\mp f}{\partial_- f}, \quad h_{==} = \frac{\partial_- f}{\partial_\mp f}. \quad (2.53)$$

and noting that the quadratic term in gauge fields vanishes by virtue of $(P_+)^T \mathcal{H} P_- = 0$, one immediately recovers from eq. (2.50) the Lorentz covariant action PST action of eq. (1.9).

3 Application to non-abelian T-duality

Let us now consider the generalisation of these ideas to a non-Abelian group⁶ of isometries, and for clarity we ignore spectator fields first and then give the result with their inclusion after. Let us consider a σ -model on a d -dimensional group space G specified by the Lagrange density,

$$\mathcal{L} = L_\mp^a E_{ab} L_+^b, \quad (3.1)$$

in which E_{ab} is a constant (or possibly spectator dependant) matrix and the L^a are the pull back to the worldsheet of the left invariant Maurer-Cartan forms for a group element $g \in G$ with conventions,

$$L^a = -i \delta^{ab} \text{Tr} T_b g^{-1} dg, \quad dL^a = \frac{1}{2} f^a{}_{bc} L^b \wedge L^c, \quad [T_a, T_b] = i f_{ab}{}^c T_c, \quad \text{Tr} T_a T_b = \delta_{ab}. \quad (3.2)$$

This σ -model has a global G_L invariance that we can gauge by introducing a connection one-form $A = i A^a T_a$ in the algebra of G which minimally couples through the introduction of covariant derivatives,

$$\partial g \rightarrow Dg = \partial g - Ag. \quad (3.3)$$

The connection has a field strength,

$$F_{\mp=} = \partial_\mp A_- - \partial_- A_\mp - [A_\mp, A_-]. \quad (3.4)$$

⁶In this work we restrict our attention to the cases in which the structure constants of the group dualised are traceless; this is to avoid the occurrence of a mixed gravitational-gauge anomaly when coupled to a curved background which upon dualisation can give rise to a Weyl anomaly i.e. a dual background that does not obey the (super)gravity equations. For discussion of this and related issues see [50–52].

We see then that the gauging replaces the Maurer-Cartan forms with,

$$L^a \rightarrow L^a - A^a D_{ab}, \quad D_{ab} = \text{Tr}(T_a g T_b g^{-1}), \quad (3.5)$$

in which we have defined the adjoint action D_{ab} which obeys $D.D^T = \mathbf{1}$. Then the action is invariant under the G_L local transformations,

$$g \rightarrow h^{-1}g, \quad A \rightarrow h^{-1}Ah - h^{-1}\partial h. \quad (3.6)$$

In addition we introduce a Lagrange multiplier term $\text{Tr} v F_{\pm} =$ to enforce a flat connection which is gauge invariant provided the Lagrange multipliers transforms in the adjoint,

$$v \rightarrow h^{-1}vh. \quad (3.7)$$

After integration by parts of the Lagrange multiplier term one finds a gauged Lagrange density,

$$\begin{aligned} \mathcal{L}_{\text{gauged}} = & L_{\pm}^T E L_{\pm} - A_{\pm}^T D E L_{\pm} - L_{\pm}^T E D^T A_{\pm} + A_{\pm} D E D^T A_{\pm} \\ & + A_{\pm}^T \partial_{\pm} v - A_{\pm}^T \partial_{\pm} v + A_{\pm} F A_{\pm}, \end{aligned} \quad (3.8)$$

in which $F_{ab} = -i f_{ab}^c v_c$. Obtaining the non-Abelian T-dual is then achieved by gauge fixing g to the identity and integrating out the gauge fields to yield,

$$\mathcal{L}_{\text{dual}} = \partial_{\pm} v^T (E + F)^{-1} \partial_{\pm} v. \quad (3.9)$$

Now we invoke the covariant gauge fixing choice,

$$A_{\pm}^a = A^a \partial_{\pm} f, \quad A_{\pm}^a = A^a \partial_{\pm} f, \quad (3.10)$$

and integrate out the field A . Since the non-Abelian term in the field strength $[A_{\pm}, A_{\pm}]$ vanishes in this gauge the manipulations are actually quite similar to the Abelian case described earlier.

If we define,

$$\mathbb{L}^A = \begin{pmatrix} L^a \\ \tilde{L}_a \end{pmatrix}, \quad \tilde{L}_a = D_{ba}(g) \partial v^b, \quad (3.11)$$

then one finds a doubled action,

$$\mathcal{L} = \frac{1}{2} \mathbb{L}_{\pm}^T \mathcal{H} \mathbb{L}_{\pm} - \frac{1}{2} \mathbb{L}_{\pm}^T \Omega \mathbb{L}_{\pm} - \frac{1}{2} \frac{\partial_{\pm} f}{\partial_{\pm} f} \mathbb{L}_{\pm}^T (\mathcal{H} P_{-}) \mathbb{L}_{\pm} - \frac{1}{2} \frac{\partial_{\pm} f}{\partial_{\pm} f} \mathbb{L}_{\pm}^T (\mathcal{H} P_{+}) \mathbb{L}_{\pm}. \quad (3.12)$$

Notice that the pull back of $\Omega_{AB} \mathbb{L}^A \wedge \mathbb{L}^B = 2L^a \wedge \tilde{L}_a$ which entered the action as a purely topological term in the Abelian case is no-longer topological, instead it serves as a Kalb-Ramond potential. Since,

$$d\tilde{L}_a = d(D_{ba} \partial v^b) = f_{ab}^c L^b \wedge \tilde{L}_c, \quad (3.13)$$

this implies a three-form flux

$$H = d(L^a \wedge \tilde{L}_a) = -\frac{1}{2} f_{bc}^a L^b \wedge L^c \wedge \tilde{L}_a. \quad (3.14)$$

It is quite straightforward to extend these considerations to include a fibration and spectator coordinates. Starting with the Lagrangian,

$$\mathcal{L} = L_{\mp}^T E L_{=} + L_{\mp}^T M \partial_{=} y + \partial_{\mp} y^T N L_{=} + \partial_{\mp} y^T K \partial_{=} y, \quad (3.15)$$

in which E, M, N, K may have arbitrary dependence on the coordinates y , and repeating the above procedure yields the doubled action,

$$\begin{aligned} \mathcal{L} = & \frac{1}{2} \mathbb{L}_{\mp}^{\nabla T} \mathcal{H} \mathbb{L}_{=}^{\nabla} - \frac{1}{2} \mathbb{L}_{\mp}^T \Omega \mathbb{L}_{=} - \frac{1}{2} \frac{\partial_{=} f}{\partial_{\mp} f} \mathbb{L}_{\mp}^{\nabla T} (\mathcal{H} P_{-}) \mathbb{L}_{\mp}^{\nabla} - \frac{1}{2} \frac{\partial_{\mp} f}{\partial_{=} f} \mathbb{L}_{=}^{\nabla T} (\mathcal{H} P_{+}) \mathbb{L}_{=}^{\nabla} \\ & + \frac{1}{2} \mathbb{L}_{\mp}^T \eta \mathbb{B}_{=} - \frac{1}{2} \mathbb{B}_{\mp}^T \eta \mathbb{L}_{=} + \hat{K}_{\mu\nu} \partial_{\mp} y^{\mu} \partial_{=} y^{\nu}, \end{aligned} \quad (3.16)$$

in which we defined,

$$\mathbb{L}^{\nabla} = \mathbb{L} + \mathbb{B}, \quad P_{+} \mathbb{B} = \begin{pmatrix} g^{-1} M \\ E^T g^{-1} M \end{pmatrix}, \quad P_{-} \mathbb{B} = \begin{pmatrix} g^{-1} N^T \\ -E g^{-1} N^T \end{pmatrix}, \quad (3.17)$$

and the modified Lagrangian on the base involves \hat{K} defined as in the Abelian case in eq. (2.21).

3.1 Relation to Poisson Lie doubled formalism

There is an existing formulation for a non-Abelian T-duality double formalism, which in fact also accommodates a further generalisation known as Poisson Lie T-duality [41, 42]. The result we obtained in eq. (3.12) can be understood in this context. To do so we remind the reader of a little technology — the Drinfeld double [62].

The Drinfeld double \mathcal{D} is a Lie algebra that can be decomposed as the sum of two sub algebras $\mathcal{D} = \mathcal{G} \oplus \tilde{\mathcal{G}}$ that are maximally isotropic with respect to an inner product $\langle \cdot | \cdot \rangle$. If T_a are the generators of \mathcal{G} and \tilde{T}^a those of $\tilde{\mathcal{G}}$, then the generators of the double $\mathbb{T}_A = \{T_a, \tilde{T}^a\}$ obey $\eta_{AB} = \langle \mathbb{T}_A | \mathbb{T}_B \rangle$ i.e.,

$$\langle T_a | T_b \rangle = \langle \tilde{T}^a | \tilde{T}^b \rangle = 0, \quad \langle T_a | \tilde{T}^b \rangle = \delta_a^b. \quad (3.18)$$

The structure constants of the double $[\mathbb{T}_A, \mathbb{T}_B] = i F_{AB}^C \mathbb{T}_C$ decompose as,

$$[T_a, T_b] = i f_{ab}^c T_c, \quad [\tilde{T}^a, \tilde{T}^b] = i \tilde{f}^{ab}_c \tilde{T}^c, \quad [T_a, \tilde{T}^b] = i \tilde{f}^{bc}_a T_c - i f_{ac}^b \tilde{T}^c, \quad (3.19)$$

and the Jacobi identity places further constraints on the admissible choices of \mathcal{G} and $\tilde{\mathcal{G}}$. We also need to define some matrices for $g \in G$ the group of \mathcal{G} ,

$$g^{-1} T_a g = a_a^b T_b, \quad g^{-1} \tilde{T}^a g = b^{ab} T_b + (a^{-1})_b^a \tilde{T}^b, \quad \Pi^{ab} = b^{ca} a_c^b, \quad (3.20)$$

and tilde analogues, $\tilde{a}, \tilde{b}, \tilde{\Pi}$, for $\tilde{g} \in \tilde{G}$. The statement of Poisson-Lie T-duality then is the equivalence between the two σ -models,

$$S = \int d^2 \sigma (E^{-1} + \Pi)_{ab}^{-1} L_{\mp}^a L_{=}^b, \quad \tilde{S} = \int d^2 \sigma [(E + \tilde{\Pi})^{-1}]^{ab} \tilde{L}_{\mp a} \tilde{L}_{=}^b, \quad (3.21)$$

where L and \check{L} refer to the left-invariant one-forms of G and \check{G} respectively (a háček is used to distinguish \check{L} from \tilde{L} introduced above).

If $G = \check{G} = U(1)^d$ we have an Abelian double and the dual pairs of σ -models correspond to Abelian T-duals. If \mathcal{G} is the algebra of some d -dimensional non-Abelian Lie group and $\check{\mathcal{G}} = u(1)^d$, the double is said to be semi-Abelian and the two dual models in eq. (3.21) reduce exactly to non-Abelian T-dual related actions of eq. (3.1) and eq. (3.9). The case where neither \check{G} nor G are Abelian corresponds to a dualisation of non-isometric σ -models and has recently found new applications in the context of the relation between certain classes of integrable models in two dimensions known as η and λ deformations.⁷

That the actions in eq. (3.21) are dual was established in [41, 42] by constructing an action on the Drinfeld double given by,

$$S_{\text{PLT}} = \frac{1}{2} \int_{\Sigma} \langle l^{-1} \partial_{\sigma} l | l^{-1} \partial_{\tau} l \rangle + \frac{1}{12} \int_{M_3} \langle l^{-1} dl | [l^{-1} dl, l^{-1} dl] \rangle - \frac{1}{2} \int_{\Sigma} \langle l^{-1} \partial_{\sigma} l | \mathcal{H} | l^{-1} \partial_{\sigma} l \rangle, \quad (3.22)$$

in which l is group element of the Drinfeld double, $\mathcal{H}_{AB} = \langle \mathbb{T}_A | \mathcal{H} | \mathbb{T}_B \rangle$ is just the $O(d, d)$ coset generalised metric and M_3 is a suitable three-manifold whose boundary is the worldsheet Σ . This action can be thought of as deforming the chiral WZW model of Sonnenschein [56] and is essentially a doubled action in a Tseytlin style non-covariant gauge. Parametrising $l = \tilde{g}g$ with $\tilde{g} \in \check{G}$ and $g \in G$ and integrating out \tilde{g} will give the action S of eq. (3.21) and doing the converse with $l = g\tilde{g}$ gives the dual action \tilde{S} .

There also exists a PST version of the doubled action eq. (3.22) given by [57],⁸

$$\begin{aligned} S_{\text{PLT-PST}} = & \frac{1}{2} \int_{\Sigma} \langle l^{-1} \partial_{\pm} l | \mathcal{H} | l^{-1} \partial_{\pm} l \rangle + \frac{1}{12} \int_{M_3} \langle l^{-1} dl | [l^{-1} dl, l^{-1} dl] \rangle \\ & - \frac{1}{2} \int_{\Sigma} \frac{\partial_{\pm} f}{\partial_{\pm} f} \langle l^{-1} \partial_{\pm} l | \mathcal{H} P_{\pm} | l^{-1} \partial_{\pm} l \rangle + \frac{1}{2} \int_{\Sigma} \frac{\partial_{\pm} f}{\partial_{\pm} f} \langle l^{-1} \partial_{\pm} l | \mathcal{H} P_{\mp} | l^{-1} \partial_{\pm} l \rangle. \end{aligned} \quad (3.23)$$

Let us now restrict our attention to the semi-Abelian double appropriate for non-Abelian T-duality. The first thing to note is that if we express the group element on the double as $l = \tilde{g}g$ then,

$$l^{-1} dl = g^{-1} \tilde{g}^{-1} d\tilde{g}g + g^{-1} dg = idv_a g^{-1} \tilde{T}^a g + g^{-1} dg = ia^{-1}(g)_b^a dv_a \tilde{T}^b + iL^a T_a, \quad (3.24)$$

in which we parametrised $\tilde{g} = \exp(iv_a \tilde{T}^a)$. However since $a^{-1}(g)$ is no more than the adjoint action, $D^T(g)$, we see that,

$$l^{-1} dl = i\check{L}_a \tilde{T}^a + iL^a T_a = i\mathbb{L}^A \mathbb{T}_A \quad (3.25)$$

coinciding with the definition in eq. (3.11). One can now see that all the terms involving \mathcal{H} in (3.12) directly match those in eq. (3.23). All that remains is to understand the WZ term for which we observe,

$$\langle l^{-1} dl | [l^{-1} dl, l^{-1} dl] \rangle = F_{AB}{}^C \eta_{CD} \mathbb{L}^A \wedge \mathbb{L}^B \wedge \mathbb{L}^C = 3f_{ab}{}^c L^a \wedge L^b \wedge \check{L}_c \quad (3.26)$$

⁷For a brief summary of this direction the reader may consult [63] and references within.

⁸To the best of our knowledge this has not appeared in the literature and we are grateful to K. Sfetsos for sharing his notes in which it was derived.

which is in agreement with eq. (3.14), thus confirming what started off as a topological term in the Abelian doubled theory is precisely what is needed as a potential for the WZ in the non-Abelian doubled theory.

To close this section let us finally note that actions of this style have been used in [64–67] to describe strings whose doubled target space is a twisted torus and have been conjectured to give a world sheet description of $\mathcal{N} = 4$ electrically gauged supergravities. The works [64, 65] have the chirality constraint as supplementary to the action and those of [66, 67] use the Tseytlin style formulation. It will be of interest to make more precise the linkage between the spacetime violation of section condition leading to gauged supergravities as in [23–26] and the generalised notions of Poisson-Lie duality whose worldsheet generalised metric has dependence on both coordinates and their duals.

4 Towards the supersymmetric doubled string

A supersymmetric first order manifest T-dual invariant worldsheet formulation is still lacking. Even a non-covariant Tseytlin type description has not been given yet. We provide here a first step by constructing the simplest model which has an $\mathcal{N} = (0, 1)$ worldsheet supersymmetry. While extremely simple it already exhibits all subtleties which also occur in models with more supersymmetry. We will keep supersymmetry manifest by working in $\mathcal{N} = (0, 1)$ superspace (conventions can be found at the beginning of appendix A).

4.1 The covariant formulation

For simplicity we restrict ourselves to a trivial bundle structure. All results can rather straightforwardly be generalized to a non-trivial bundle structure. The starting point is the Lagrange density,

$$\mathcal{L} = 2i \partial_{\mp} x E D_{-} x + \mathcal{L}_S(y), \tag{4.1}$$

where x is a set of adapted coordinates such that the background field $E = E(y)$ depends only on the spectator coordinates y whose dynamics is governed by \mathcal{L}_S . In order to gauge the isometries $x \rightarrow x + \varepsilon$ we introduce gauge fields A_{\mp} and A_{-} and using Lagrange multipliers \tilde{x} we impose flatness. The gauged σ -model is given by,⁹

$$\mathcal{L} = 2i \partial_{\mp} x E D_{-} x + 2i A_{\mp} E A_{-} + 2i A_{\mp} \mathcal{J}_{-} + 2i \mathcal{J}_{\mp} A_{-} + \mathcal{L}_S(y), \tag{4.2}$$

where,

$$\mathcal{J}_{\mp} = E^T \partial_{\mp} x - \partial_{\mp} \tilde{x}, \quad \mathcal{J}_{-} = E D_{-} x + D_{-} \tilde{x}. \tag{4.3}$$

Integrating over \tilde{x} gives the original model back. Motivated by the non-supersymmetric case we impose the gauge choice,

$$A_{\mp} = \partial_{\mp} f A, \quad A_{-} = D_{-} f A, \tag{4.4}$$

⁹Note that we could as well have introduced the full $\mathcal{N} = (0, 1)$ gauge multiplet which consists of A_{\mp} , A_{-} and A_{+} . Introducing Lagrange multipliers which constrain all fieldstrengths $F_{\mp+}$, $F_{\mp-}$, F_{+-} and F_{--} to zero, one finds that upon making a field redefinition on \tilde{x} this reduces to the current case.

where f is an arbitrary function and A is a set of $d\mathcal{N} = (0,1)$ scalar superfields. The Lagrange density becomes so,

$$\mathcal{L} = 2i \partial_{\pm} x E D_- x + 2i \partial_{\pm} f D_- f A g A + 2i A (\partial_{\pm} f \mathcal{J}_- + D_- f \mathcal{J}_{\pm}) + \mathcal{L}_S(y). \quad (4.5)$$

The residual gauge invariance is given by,

$$x \rightarrow x + \varepsilon(f), \quad A \rightarrow A - \partial_f \varepsilon(f), \quad f \rightarrow f. \quad (4.6)$$

In addition the action is invariant under,

$$\tilde{x} \rightarrow \tilde{x} + \tilde{\varepsilon}(f), \quad (4.7)$$

as well. The equations of motion for A are given by,

$$D_- f A = -\frac{1}{2} g^{-1} \mathcal{J}_- - \frac{1}{2} \frac{D_- f}{\partial_{\pm} f} g^{-1} \mathcal{J}_{\pm}, \quad (4.8)$$

which, because of the fermionic nature of $D_- f$, *cannot* directly be solved for A . However one notes that by multiplying the equations of motion by $D_- f$ one obtains the constraint,

$$D_- f \mathcal{J}_- = 0. \quad (4.9)$$

Acting with D_- on this one gets,

$$\mathcal{J}_- = 2i \frac{D_- f}{\partial_{\pm} f} D_- \mathcal{J}_-. \quad (4.10)$$

Despite appearances, eq. (4.9) is an algebraic constraint on the components of the superfields. Indeed writing the superspace components of x and \tilde{x} , $x = x + i\theta^- \psi_-$ and $\tilde{x} = \tilde{x} + i\theta^- \tilde{\psi}_-$, one readily verifies using eq. (4.10) that the constraint can be solved for half of the component fields ψ and $\tilde{\psi}$. As such this constraint can simply be imposed using Lagrange multipliers. This is very reminiscent of the nilpotent superfield constraints ([58, 59]; a systematic treatment and review of nilpotent superfields can be found in [60]). Using this in the equations of motion eq. (4.8) one solves for A ,

$$A = -\frac{1}{2} \frac{1}{\partial_{\pm} f} g^{-1} \mathcal{J}_{\pm} - \frac{i}{\partial_{\pm} f} g^{-1} D_- \mathcal{J}_- + D_- f (\dots), \quad (4.11)$$

where the terms following $D_- f$ remain undetermined but they will not play any role in what follows. Using this to eliminate A in the first order Lagrange density eq. (4.5) one gets,

$$\begin{aligned} \mathcal{L} = & 2i \partial_{\pm} x E D_- x - i \mathcal{J}_{\pm} g^{-1} \mathcal{J}_- - \frac{i}{2} \frac{D_- f}{\partial_{\pm} f} \mathcal{J}_{\pm} g^{-1} \mathcal{J}_{\pm} \\ & + \frac{\partial_{\pm} f}{\partial_{\pm} f} \mathcal{J}_- g^{-1} D_- \mathcal{J}_- + \mathcal{L}_S(y), \end{aligned} \quad (4.12)$$

together with the constraint given in eq. (4.9). Repeatedly using eqs. (4.9) and (4.10), one rewrites this as,

$$\begin{aligned} \mathcal{L} = & 2 \frac{\partial_{\pm} f}{\partial_{\pm} f} \left(D_- - \frac{D_- f}{\partial_{\pm} f} \partial_{\pm} \right) \mathbb{X} \eta P_+ D_- (P_+ D_- \mathbb{X}) - i \left(D_- - \frac{D_- f}{\partial_{\pm} f} \partial_{\pm} \right) \mathbb{X} \eta P_- \partial_{\pm} \mathbb{X} \\ & + 2i \frac{D_- f}{\partial_{\pm} f} \Psi_+ \eta P_+ D_- \mathbb{X} + \mathcal{L}_S(y), \end{aligned} \quad (4.13)$$

where the topological term has been dropped. The Lagrange multiplier Ψ_+ , which transforms under $O(d, d; \mathbb{Z})$ in the same way as \mathbb{X} , enforces the constraint,

$$\mu_- \equiv D_- f P_+ D_- \mathbb{X} = 0, \quad (4.14)$$

which is equivalent to the constraint in eq. (4.9). Note that because of the presence of the projection operator P_+ only d components of the Lagrange multiplier Ψ_+ effectively appear in the lagrangian.

The covariant action has two classes of symmetries,

The residual gauge symmetry Even after we gauge fixed the gauged non-linear σ -model there is a residual gauge invariance left:

$$\begin{aligned} f &\rightarrow f \\ \mathbb{X} &\rightarrow \mathbb{X} + \Lambda(f) \\ \Psi_+ &\rightarrow \Psi_+ - \frac{i}{2} D_- S \partial_{\mp} \Lambda, \end{aligned} \quad (4.15)$$

where $\Lambda(f)$ is a $2d \times 1$ column matrix of arbitrary functions of f .

The PST symmetry As the gauge fixing function f was randomly chosen, we expect that it can be shifted in an arbitrary way which is the origin of the PST symmetry. To see this first consider the action defined by eq. (4.13) in the absence of the Lagrange multiplier term. After some significant effort one determines that under the variation,

$$\begin{aligned} \delta f &= \varepsilon \\ \delta \mathbb{X} &= \frac{\varepsilon}{\partial_{\mp} f} P_- \partial_{\mp} \mathbb{X} + \frac{2i\varepsilon}{\partial_- f} P_+ D_- (P_+ D_- \mathbb{X}) - \frac{2i\varepsilon}{\partial_- f} D_- f P_+ D_- \left(\frac{1}{\partial_{\mp} f} P_- \partial_{\mp} \mathbb{X} \right), \end{aligned} \quad (4.16)$$

one produces only terms that are proportional to the constraint μ defined in eq. (4.14) or derivatives thereof. Moreover, this property is shared by the variation of the constraint itself. As a result, one is then guaranteed a transformation of the Lagrange multiplier that renders the whole Lagrangian (4.13) invariant. For pedagogical purpose we illustrate this in the simplest case of constant background fields in the appendix.

4.2 The Tseytlin formulation

We now pass to a Lorentz non-covariant gauge for the PST symmetry in order to recover a Tseytlin like formulation. Choosing $f = f(\tau)$ [49] we get that the Lagrange density eq. (4.13) becomes,

$$\begin{aligned} \mathcal{L} &= -\frac{i}{2} \hat{D} \mathbb{X} \eta \partial_{\tau} \mathbb{X} + \frac{i}{2} \hat{D} \mathbb{X} \mathcal{H} \partial_{\sigma} \mathbb{X} + \hat{D} \mathbb{X} \eta P_+ D_- S D_- \mathbb{X} \\ &\quad + \theta^- \Psi_+ \eta P_+ D_- \mathbb{X} + \mathcal{L}_S(y), \end{aligned} \quad (4.17)$$

where,

$$\hat{D} \equiv D_- + \frac{i}{2} \theta^- \partial_{\mp} = \partial_- + \frac{i}{2} \theta^- \partial_{\sigma}, \quad \hat{D}^2 = \frac{i}{2} \partial_{\sigma}, \quad \theta^- D_- = \theta^- \hat{D}. \quad (4.18)$$

The equations of motion for Ψ_+ and \mathbb{X} read,

$$\begin{aligned} \theta^- P_+ D_- \mathbb{X} = \theta^- P_+ \hat{D} \mathbb{X} = 0, \\ \hat{D} \left(\partial_\tau \mathbb{X} - S \partial_\sigma \mathbb{X} + i \hat{D} S \hat{D} \mathbb{X} + i P_+ D_- S D_- \mathbb{X} \right. \\ \left. - i D_- S P_+ \hat{D} \mathbb{X} + \theta^- P_+ \Psi_+ \right) = 0. \end{aligned} \quad (4.19)$$

The second of these equations immediately implies,

$$\partial_\tau \mathbb{X} - S \partial_\sigma \mathbb{X} + i \hat{D} S \hat{D} \mathbb{X} + i P_+ D_- S D_- \mathbb{X} - i D_- S P_+ \hat{D} \mathbb{X} + \theta^- P_+ \Psi_+ = F(\tau), \quad (4.20)$$

with $F(\tau)$ an arbitrary function of τ . Using the residual gauge invariance, eq. (4.15), which assumes now the form,

$$\begin{aligned} \mathbb{X} &\rightarrow \mathbb{X} + \Lambda(\tau) \\ \Psi_+ &\rightarrow \Psi_+ - \frac{i}{4} D_- S \partial_\tau \Lambda(\tau), \end{aligned} \quad (4.21)$$

this function can be put to zero leaving us with,

$$\partial_\tau \mathbb{X} - S \partial_\sigma \mathbb{X} + i \hat{D} S \hat{D} \mathbb{X} + i P_+ D_- S D_- \mathbb{X} - i D_- S P_+ \hat{D} \mathbb{X} + \theta^- P_+ \Psi_+ = 0. \quad (4.22)$$

The first equation in eq. (4.19) implies,

$$P_+ \hat{D} \mathbb{X} = \theta^- P_+ \hat{D} (P_+ \hat{D} \mathbb{X}). \quad (4.23)$$

Acting with P_- on eq. (4.22) and using eq. (4.23) one obtains,

$$P_- \partial_+ \mathbb{X} = 0. \quad (4.24)$$

Acting with P_+ on eq. (4.22) allows one to solve for $\theta^- P_+ \Psi_+$. However multiplying this equation with θ^- gives,

$$\theta^- P_+ D_- (P_+ D_- \mathbb{X}) = 0. \quad (4.25)$$

From the first equation in eq. (4.19) one also gets,

$$P_+ D_- \mathbb{X} = \theta^- P_+ D_- (P_+ D_- \mathbb{X}) \quad (4.26)$$

which combined with eq. (4.25) gives,

$$P_+ D_- \mathbb{X} = 0. \quad (4.27)$$

So the equations of motion of the model in the Tseytlin gauge indeed reproduce the constraints eqs. (4.24) and (4.27) as expected.

4.3 Component form

For convenience we now give the results expanded into components as defined by the superfield expansion $\mathbb{X} = \mathbb{X} + i\theta^-\Xi_-$. We use that $D_-\hat{D}|_{\theta=0} = \frac{i}{2}\partial_\sigma$ to find that the lagrangian can be expressed as,

$$D_-\mathcal{L}|_{\theta=0} = \frac{1}{4}\partial_\sigma\mathbb{X}\eta\partial_\tau\mathbb{X} - \frac{1}{4}\partial_\sigma\mathbb{X}\mathcal{H}\partial_\sigma\mathbb{X} - i\Xi_-\eta(\partial_\pm\Xi_- + iD_-S\partial_\sigma\mathbb{X}) + \frac{1}{2}\Xi_-\eta D_-SD_-S\Xi_- + i\Psi_+\eta P_+\Xi_- . \quad (4.28)$$

Here, and in the following component expressions, we adopt the implicit notation that $D_-S \equiv D_-S|_{\theta=0}$ and $\mathbb{X} \equiv \mathbb{X}|_{\theta=0}$. Note the presence of a four-fermi interaction term that would have been hard to guess from the bosonic case; this term will prove essential in what follows. As above, the variation with respect to the Lagrange multiplier enforces,

$$P_+\Xi_- = 0 . \quad (4.29)$$

The variation with respect to \mathbb{X} gives an equation of motion that is a total ∂_σ derivative which, using the residual gauge redundancy, can be integrated to yield,

$$P_+(\partial_-\mathbb{X} - D_-S\Xi_-) = 0 , \quad P_-\partial_\pm\mathbb{X} = 0 . \quad (4.30)$$

The variation with respect to the fermion is more intricate and yields,

$$2\partial_\pm\Xi_- + iD_-S\partial_\sigma\mathbb{X} + iD_-SD_-S\Xi_- + P_+\Psi_+ = 0 . \quad (4.31)$$

The P_+ projection of this equation fixes the Lagrange multiplier however the P_- projection provides a fermion equation of motion,

$$\begin{aligned} 0 &= P_-\left(\partial_\pm\Xi_- + \frac{i}{2}D_-S\partial_\sigma\mathbb{X} + \frac{i}{2}D_-SP_+D_-S\Xi_-\right) \\ &= P_-\left(\partial_\pm\Xi_- + \frac{i}{2}D_-S\partial_\sigma\mathbb{X} + \frac{i}{2}D_-S\partial_-\mathbb{X}\right) \\ &= P_-\left(\partial_\pm\Xi_- + \frac{i}{2}D_-S\partial_\pm\mathbb{X}\right) , \end{aligned} \quad (4.32)$$

in which we used that $P_-D_-S = D_-SP_+$ and the equation of motion eq. (4.30) to pass to the final line. Together the equations (4.29), (4.30), and (4.32) are exactly the component content of the superspace equations,

$$P_+D_-\mathbb{X} = P_-\partial_\pm\mathbb{X} = 0 . \quad (4.33)$$

5 Discussion and open problems

In this paper we have clarified many missing details in the construct of the manifestly T-duality symmetric worldsheet theory and shown how such a formulation can be obtained through a novel gauge fixing choice. This procedure allowed us to make the generalisation to

the supersymmetric case in the most minimal, but still non-trivial, extension to $\mathcal{N} = (0, 1)$ supersymmetry. The essential reason for the complexity comes from having in the theory chiral bosons whose chirality is mis-aligned with that of the supersymmetry.

The natural next direction here is to extend this work to both $\mathcal{N} = (1, 1)$ and $\mathcal{N} = (2, 2)$ supersymmetry. The $\mathcal{N} = (1, 1)$ case is already under study and will directly follow from the techniques outlined within. The $\mathcal{N} = (2, 2)$ remains less obvious but should be an exciting arena to make a direct link to Hitchin’s generalised geometry. Initial results in this direction have recently been reported by one of us [61]. It will also be of interest to consider spacetime supersymmetry generalising the result of [68] to curved backgrounds.

Our discussion has been local in nature and there are sensitive issues, even in the bosonic theory, that will have to be addressed if the derivation used is to be implemented in full Polyakov sum over genus at the quantum level. At first sight our gauge fixing choice $\partial_{\pm} f A_{\pm} = \partial_{\mp} f A_{\mp}$ looks to require the introduction of a globally defined exact form $u = df$. In fact this is too strong, as is known from previous studies of the PST formalism [69] it is sufficient to work with a closed form $du = 0$. Put another way [70], the residual gauge invariance is sufficient to eliminate cohomological contributions that come from integrating the equation of motion to produce the constraint. However one still requires in the manipulations that f has nowhere vanishing first derivatives so as to allow such terms to appear in the denominator of fractions in a PST approach. Since this necessitates the existence of a nowhere vanishing vector field, it is not obvious how to extend from \mathbb{R}^2 to a compact Riemann surfaces of non-vanishing Euler character. The appearance of the function f was via a gauge fixing, the interpretation here is that the gauge fixing choice adopted can not be globally extended and is only locally well defined. A possible resolution is to find a suitable global fixing or to work patchwise. Understanding this will be an interesting topic for further investigation

This formulation may have great utility; by calculating the β -functions in a perhaps naive manner one could hope to find background field equations for the generalised metric which relate to the target space formulation of *DFT*. Whilst the non-covariant Tseytlin style action allows for such progress to be made at 1-loop order [31–33], it is very hard to extend this to higher loops — the non-Lorentz invariant structure makes the regularisation of Feynman diagrams taxing at best. Using the covariant formulation may alleviate some of this trouble. Optimistically we hope that the techniques in this paper could prove to be a valuable starting point for the calculation of duality covariant corrections to *DFT*.

Acknowledgments

This work is supported in part by the Belgian Federal Science Policy Office through the Interuniversity Attraction Pole P7/37, and in part by the “FWO-Vlaanderen” through the project G020714N and a postdoctoral fellowship, and by the Vrije Universiteit Brussel through the Strategic Research Program “High-Energy Physics”. We are grateful to J.P. Ang, David Berman, Chris Blair and Martin Roček and for numerous illuminating discussions, and to K. Sfetsos for discussions and sharing with us his work on the PST formulation of Poisson-Lie duality. We would like to thank the Simons Center for Geometry

and Physics for providing a stimulating environment during the conference “Generalized Geometry and T-dualities” while part of this work was finalized.

A Conventions

Throughout the paper we use worldsheet lightcone coordinates,

$$\sigma^{\pm} = \tau + \sigma, \quad \sigma^{\mp} = \tau - \sigma. \tag{A.1}$$

In $N = (0, 1)$ superspace this is extended by adding one one-component real fermionic coordinate θ^- . The fermionic derivative D_- satisfies,

$$D_-^2 = -\frac{i}{2} \partial_- . \tag{A.2}$$

The T-duality group $O(d, d; \mathbb{Z})$ plays a central role. In the present context $\mathcal{O} \in O(d, d; \mathbb{Z})$ is a $2d \times 2d$ matrix with integer entries satisfying,

$$\mathcal{O}^T \eta \mathcal{O} = \eta, \tag{A.3}$$

where,

$$\eta = \begin{pmatrix} 0 & \mathbf{1} \\ \mathbf{1} & 0 \end{pmatrix}. \tag{A.4}$$

In the current paper we use adapted coordinates x^i and their T-duals \tilde{x}_i , $i \in \{1, \dots, d\}$ together with spectator coordinates y^μ , $\mu \in \{1, \dots, D - d\}$. We write the adapted coordinates together with the dual ones into a single $O(d, d; \mathbb{Z})$ multiplet,

$$\mathbb{X} = \begin{pmatrix} x \\ \tilde{x} \end{pmatrix}, \tag{A.5}$$

which transforms under the action of $\mathcal{O} \in O(d, d; \mathbb{Z})$ as,

$$\mathbb{X} \rightarrow \mathbb{X}' = \mathcal{O}^{-1} \mathbb{X}. \tag{A.6}$$

Writing $\mathcal{O} \in O(d, d; \mathbb{Z})$ as,

$$\mathcal{O} = \begin{pmatrix} A & B \\ C & D \end{pmatrix}, \tag{A.7}$$

the background fields $E_{ij}(y) = g_{ij}(y) + b_{ij}(y)$ transform non-linearly,

$$E \rightarrow E' = (EB + D)^{-1}(EA + C), \tag{A.8}$$

however, the *generalised metric* \mathcal{H} ,

$$\mathcal{H} = \begin{pmatrix} 1 & -b \\ 0 & 1 \end{pmatrix} \begin{pmatrix} g & 0 \\ 0 & g^{-1} \end{pmatrix} \begin{pmatrix} 1 & 0 \\ b & 1 \end{pmatrix} = \begin{pmatrix} g - b g^{-1} b & -b g^{-1} \\ g^{-1} b & g^{-1} \end{pmatrix}, \tag{A.9}$$

transforms linearly,

$$\mathcal{H} \rightarrow \mathcal{H}' = \mathcal{O}^T \mathcal{H} \mathcal{O}. \quad (\text{A.10})$$

From \mathcal{H} we construct an almost product structure S ,

$$S = \eta \mathcal{H}, \quad (\text{A.11})$$

such that $S^2 = +\mathbf{1}$. Using this we introduce the orthogonal projection operators P_+ and P_- ,

$$P_{\pm} = \frac{1}{2} (\mathbf{1} \pm S). \quad (\text{A.12})$$

Some often used identities include,

$$\mathcal{H} P_{\pm} = P_{\pm}^T \mathcal{H} = \pm \eta \mathcal{H}, \quad P_{\pm} \partial_y S = \partial_y S P_{\mp}. \quad (\text{A.13})$$

B PST symmetry in the $\mathcal{N} = (0, 1)$ case

We assume constant background fields and for notation convenience define,

$$\sigma = \frac{1}{\partial_- f} P_+ \partial_- \mathbb{X}, \quad \rho = \frac{1}{\partial_+ f} P_- \partial_+ \mathbb{X}. \quad (\text{B.1})$$

In terms of these quantities we can recast the Lagrangian as,

$$\mathcal{L} = -i \partial_+ f D_- X \eta (\sigma + \rho) + i D_- f \partial_+ \mathbb{X} \eta (\sigma + \rho) + i \Psi_{\mp\mp} \eta \mu_-, \quad (\text{B.2})$$

where we have defined $\Psi_{\mp\mp} \partial_- f = 2\Psi_{\mp}$ and in which the constraint, and its derivative are given by,

$$\mu_- = D_- f P_+ D_- \mathbb{X}, \quad \nu_- = \frac{2i}{\partial_- f} D_- \mu_- = P_+ D_- X - \sigma D_- f. \quad (\text{B.3})$$

The PST transformations in the case of constant backgrounds reduce to,

$$\delta f = \varepsilon, \quad \delta \mathbb{X} = \varepsilon (\sigma + \rho), \quad (\text{B.4})$$

which exactly replicate those already seen in the bosonic $\mathcal{N} = (0, 0)$ case. Under these transformation one finds,

$$\delta \mu_- = D_- (\varepsilon \nu_-), \quad (\text{B.5})$$

and the variation of the Lagrangian reads,

$$\delta \mathcal{L} = i \delta \Psi_{\mp\mp} \eta \mu_- + \Lambda_{\mp} \eta \nu_- - \Lambda_{\mp\mp} \eta \partial_- \nu_-, \quad (\text{B.6})$$

in which we defined

$$\begin{aligned} \Lambda_{\mp} &= i \varepsilon \left(D_- \Psi_{\mp\mp} - \frac{\partial_+ f}{\partial_- f} \partial_- \sigma + \partial_+ \sigma \right), \\ \Lambda_{\mp\mp} &= -i \varepsilon \left(\frac{\partial_+ f}{\partial_- f} \sigma - \frac{\partial_+ \mathbb{X}}{\partial_- f} \right). \end{aligned} \quad (\text{B.7})$$

Then invariance of the action is recovered with,

$$\delta\Psi_{\pm\pm} = D_- \left(\frac{2\Lambda_{\pm}}{\partial_- f} \right) + D_- \left(\frac{2}{\partial_- f} \partial_- \Lambda_{\pm\pm} \right). \quad (\text{B.8})$$

One could choose other rewritings of the action by adding on terms proportional to the constraint, but due to eq. (B.5) the transformation rule of the Lagrange multiplier can be modified to ensure the resulting action still possesses the PST symmetry.

Open Access. This article is distributed under the terms of the Creative Commons Attribution License ([CC-BY 4.0](https://creativecommons.org/licenses/by/4.0/)), which permits any use, distribution and reproduction in any medium, provided the original author(s) and source are credited.

References

- [1] M.J. Duff, *Duality rotations in string theory*, *Nucl. Phys. B* **335** (1990) 610 [[INSPIRE](#)].
- [2] A.A. Tseytlin, *Duality symmetric formulation of string world sheet dynamics*, *Phys. Lett. B* **242** (1990) 163 [[INSPIRE](#)].
- [3] A.A. Tseytlin, *Duality symmetric closed string theory and interacting chiral scalars*, *Nucl. Phys. B* **350** (1991) 395 [[INSPIRE](#)].
- [4] C.M. Hull, *A geometry for non-geometric string backgrounds*, *JHEP* **10** (2005) 065 [[hep-th/0406102](#)] [[INSPIRE](#)].
- [5] C.M. Hull, *Doubled geometry and T-folds*, *JHEP* **07** (2007) 080 [[hep-th/0605149](#)] [[INSPIRE](#)].
- [6] W. Siegel, *Superspace duality in low-energy superstrings*, *Phys. Rev. D* **48** (1993) 2826 [[hep-th/9305073](#)] [[INSPIRE](#)].
- [7] W. Siegel, *Two vierbein formalism for string inspired axionic gravity*, *Phys. Rev. D* **47** (1993) 5453 [[hep-th/9302036](#)] [[INSPIRE](#)].
- [8] C. Hull and B. Zwiebach, *Double field theory*, *JHEP* **09** (2009) 099 [[arXiv:0904.4664](#)] [[INSPIRE](#)].
- [9] D.S. Berman and M.J. Perry, *Generalized geometry and M-theory*, *JHEP* **06** (2011) 074 [[arXiv:1008.1763](#)] [[INSPIRE](#)].
- [10] O. Hohm and H. Samtleben, *Exceptional form of D = 11 supergravity*, *Phys. Rev. Lett.* **111** (2013) 231601 [[arXiv:1308.1673](#)] [[INSPIRE](#)].
- [11] P.C. West, *E₁₁ and M-theory*, *Class. Quant. Grav.* **18** (2001) 4443 [[hep-th/0104081](#)] [[INSPIRE](#)].
- [12] G. Aldazabal, D. Marques and C. Núñez, *Double field theory: a pedagogical review*, *Class. Quant. Grav.* **30** (2013) 163001 [[arXiv:1305.1907](#)] [[INSPIRE](#)].
- [13] O. Hohm, D. Lüst and B. Zwiebach, *The spacetime of double field theory: review, remarks and outlook*, *Fortsch. Phys.* **61** (2013) 926 [[arXiv:1309.2977](#)] [[INSPIRE](#)].
- [14] D.S. Berman and D.C. Thompson, *Duality symmetric string and M-theory*, *Phys. Rept.* **566** (2014) 1 [[arXiv:1306.2643](#)] [[INSPIRE](#)].
- [15] L. Freidel, R.G. Leigh and D. Minic, *Born reciprocity in string theory and the nature of spacetime*, *Phys. Lett. B* **730** (2014) 302 [[arXiv:1307.7080](#)] [[INSPIRE](#)].

- [16] L. Freidel, R.G. Leigh and D. Minic, *Metastring theory and modular space-time*, *JHEP* **06** (2015) 006 [[arXiv:1502.08005](#)] [[INSPIRE](#)].
- [17] O. Hohm, S.K. Kwak and B. Zwiebach, *Double field theory of type II strings*, *JHEP* **09** (2011) 013 [[arXiv:1107.0008](#)] [[INSPIRE](#)].
- [18] N. Hitchin, *Generalized Calabi-Yau manifolds*, *Quart. J. Math.* **54** (2003) 281 [[math/0209099](#)] [[INSPIRE](#)].
- [19] M. Gualtieri, *Generalized complex geometry*, [math/0401221](#) [[INSPIRE](#)].
- [20] A. Coimbra, C. Strickland-Constable and D. Waldram, *Supergravity as generalised geometry I: type II theories*, *JHEP* **11** (2011) 091 [[arXiv:1107.1733](#)] [[INSPIRE](#)].
- [21] A. Coimbra, C. Strickland-Constable and D. Waldram, *Supergravity as generalised geometry II: $E_{d(d)} \times \mathbb{R}^+$ and M-theory*, *JHEP* **03** (2014) 019 [[arXiv:1212.1586](#)] [[INSPIRE](#)].
- [22] O. Hohm and S.K. Kwak, *Massive type II in double field theory*, *JHEP* **11** (2011) 086 [[arXiv:1108.4937](#)] [[INSPIRE](#)].
- [23] D. Geissbuhler, *Double field theory and $N = 4$ gauged supergravity*, *JHEP* **11** (2011) 116 [[arXiv:1109.4280](#)] [[INSPIRE](#)].
- [24] G. Aldazabal, W. Baron, D. Marques and C. Núñez, *The effective action of Double Field Theory*, *JHEP* **11** (2011) 052 [*Erratum ibid.* **11** (2011) 109] [[arXiv:1109.0290](#)] [[INSPIRE](#)].
- [25] M. Graña and D. Marques, *Gauged double field theory*, *JHEP* **04** (2012) 020 [[arXiv:1201.2924](#)] [[INSPIRE](#)].
- [26] D.S. Berman, E.T. Musaev, D.C. Thompson and D.C. Thompson, *Duality invariant M-theory: gauged supergravities and Scherk-Schwarz reductions*, *JHEP* **10** (2012) 174 [[arXiv:1208.0020](#)] [[INSPIRE](#)].
- [27] E. Hackett-Jones and G. Moutsopoulos, *Quantum mechanics of the doubled torus*, *JHEP* **10** (2006) 062 [[hep-th/0605114](#)] [[INSPIRE](#)].
- [28] D.S. Berman and N.B. Copland, *The String partition function in Hull's doubled formalism*, *Phys. Lett. B* **649** (2007) 325 [[hep-th/0701080](#)] [[INSPIRE](#)].
- [29] H.S. Tan, *Closed string partition functions in toroidal compactifications of doubled geometries*, *JHEP* **05** (2014) 133 [[arXiv:1403.4683](#)] [[INSPIRE](#)].
- [30] R. Floreanini and R. Jackiw, *Selfdual fields as charge density solitons*, *Phys. Rev. Lett.* **59** (1987) 1873 [[INSPIRE](#)].
- [31] D.S. Berman, N.B. Copland and D.C. Thompson, *Background field equations for the duality symmetric string*, *Nucl. Phys. B* **791** (2008) 175 [[arXiv:0708.2267](#)] [[INSPIRE](#)].
- [32] D.S. Berman and D.C. Thompson, *Duality symmetric strings, dilatons and $O(d, d)$ effective actions*, *Phys. Lett. B* **662** (2008) 279 [[arXiv:0712.1121](#)] [[INSPIRE](#)].
- [33] N.B. Copland, *A double σ -model for double field theory*, *JHEP* **04** (2012) 044 [[arXiv:1111.1828](#)] [[INSPIRE](#)].
- [34] K. Lee and J.-H. Park, *Covariant action for a string in "doubled yet gauged" spacetime*, *Nucl. Phys. B* **880** (2014) 134 [[arXiv:1307.8377](#)] [[INSPIRE](#)].
- [35] A. Betz, R. Blumenhagen, D. Lüst and F. Rennecke, *A note on the CFT origin of the strong constraint of DFT*, *JHEP* **05** (2014) 044 [[arXiv:1402.1686](#)] [[INSPIRE](#)].

- [36] P. Pasti, D.P. Sorokin and M. Tonin, *On Lorentz invariant actions for chiral p forms*, *Phys. Rev. D* **55** (1997) 6292 [[hep-th/9611100](#)] [[INSPIRE](#)].
- [37] M. Roček and A.A. Tseytlin, *Partial breaking of global $D = 4$ supersymmetry, constrained superfields and three-brane actions*, *Phys. Rev. D* **59** (1999) 106001 [[hep-th/9811232](#)] [[INSPIRE](#)].
- [38] S. Groot Nibbelink and P. Patalong, *A Lorentz invariant doubled world-sheet theory*, *Phys. Rev. D* **87** (2013) 041902 [[arXiv:1207.6110](#)] [[INSPIRE](#)].
- [39] S. Groot Nibbelink, F. Kurz and P. Patalong, *Renormalization of a Lorentz invariant doubled worldsheet theory*, *JHEP* **10** (2014) 114 [[arXiv:1308.4418](#)] [[INSPIRE](#)].
- [40] X.C. de la Ossa and F. Quevedo, *Duality symmetries from nonAbelian isometries in string theory*, *Nucl. Phys. B* **403** (1993) 377 [[hep-th/9210021](#)] [[INSPIRE](#)].
- [41] C. Klimčík and P. Ševera, *Dual non-Abelian duality and the Drinfeld double*, *Phys. Lett. B* **351** (1995) 455 [[hep-th/9502122](#)] [[INSPIRE](#)].
- [42] C. Klimčík and P. Ševera, *Poisson-Lie T duality and loop groups of Drinfeld doubles*, *Phys. Lett. B* **372** (1996) 65 [[hep-th/9512040](#)] [[INSPIRE](#)].
- [43] S.P. Chowdhury, *Superstring partition functions in the doubled formalism*, *JHEP* **09** (2007) 127 [[arXiv:0707.3549](#)] [[INSPIRE](#)].
- [44] C.D.A. Blair, E. Malek and A.J. Routh, *An $O(d, d)$ invariant Hamiltonian action for the superstring*, *Class. Quant. Grav.* **31** (2014) 205011 [[arXiv:1308.4829](#)] [[INSPIRE](#)].
- [45] M. Roček and E.P. Verlinde, *Duality, quotients and currents*, *Nucl. Phys. B* **373** (1992) 630 [[hep-th/9110053](#)] [[INSPIRE](#)].
- [46] T.H. Buscher, *A symmetry of the string background field equations*, *Phys. Lett. B* **194** (1987) 59 [[INSPIRE](#)].
- [47] T.H. Buscher, *Path integral derivation of quantum duality in nonlinear σ -models*, *Phys. Lett. B* **201** (1988) 466 [[INSPIRE](#)].
- [48] P. Patalong, *Aspects of non-geometry in string theory*, Ph.D. thesis, University of Munich, Munich, Germany (2013).
- [49] A. Sevrin and D.C. Thompson, *A note on supersymmetric chiral bosons*, *JHEP* **07** (2013) 086 [[arXiv:1305.4848](#)] [[INSPIRE](#)].
- [50] A. Giveon and M. Roček, *On non-Abelian duality*, *Nucl. Phys. B* **421** (1994) 173 [[hep-th/9308154](#)] [[INSPIRE](#)].
- [51] E. Alvarez, L. Álvarez-Gaumé and Y. Lozano, *On non-Abelian duality*, *Nucl. Phys. B* **424** (1994) 155 [[hep-th/9403155](#)] [[INSPIRE](#)].
- [52] S. Elitzur, A. Giveon, E. Rabinovici, A. Schwimmer and G. Veneziano, *Remarks on non-Abelian duality*, *Nucl. Phys. B* **435** (1995) 147 [[hep-th/9409011](#)] [[INSPIRE](#)].
- [53] S.A. Cherkis and J.H. Schwarz, *Wrapping the M -theory five-brane on $K3$* , *Phys. Lett. B* **403** (1997) 225 [[hep-th/9703062](#)] [[INSPIRE](#)].
- [54] A. Giveon and M. Roček, *Generalized duality in curved string backgrounds*, *Nucl. Phys. B* **380** (1992) 128 [[hep-th/9112070](#)] [[INSPIRE](#)].
- [55] K. Lechner, *Selfdual tensors and gravitational anomalies in $4n + 2$ -dimensions*, *Nucl. Phys. B* **537** (1999) 361 [[hep-th/9808025](#)] [[INSPIRE](#)].

- [56] J. Sonnenschein, *Chiral bosons*, *Nucl. Phys. B* **309** (1988) 752 [INSPIRE].
- [57] K. Sfetsos, *Notes on Poisson-Lie T-duality*, private communication (1997).
- [58] M. Roček, *Linearizing the Volkov-Akulov model*, *Phys. Rev. Lett.* **41** (1978) 451 [INSPIRE].
- [59] U. Lindström and M. Roček, *Constrained local superfields*, *Phys. Rev. D* **19** (1979) 2300 [INSPIRE].
- [60] G. Dall'Agata, E. Dudas and F. Farakos, *On the origin of constrained superfields*, *JHEP* **05** (2016) 041 [arXiv:1603.03416] [INSPIRE].
- [61] A. Sevrin, *Some comments on supersymmetry and the doubled formalism from a worldsheet perspective*, talk given at *Generalized Geometry and T-dualities*, May 13, Simons Center For Geometry and Physics, U.S.A. (2010).
- [62] V.G. Drinfeld, *Quantum groups*, *J. Sov. Math.* **41** (1988) 898 [*Zap. Nauchn. Semin.* **155** (1986) 18] [INSPIRE].
- [63] D.C. Thompson, *Generalised T-duality and integrable deformations*, *Fortsch. Phys.* **64** (2016) 349 [arXiv:1512.04732] [INSPIRE].
- [64] C.M. Hull and R.A. Reid-Edwards, *Gauge symmetry, T-duality and doubled geometry*, *JHEP* **08** (2008) 043 [arXiv:0711.4818] [INSPIRE].
- [65] C.M. Hull and R.A. Reid-Edwards, *Non-geometric backgrounds, doubled geometry and generalised T-duality*, *JHEP* **09** (2009) 014 [arXiv:0902.4032] [INSPIRE].
- [66] G. Dall'Agata and N. Prezas, *Worldsheet theories for non-geometric string backgrounds*, *JHEP* **08** (2008) 088 [arXiv:0806.2003] [INSPIRE].
- [67] S.D. Avramis, J.-P. Derendinger and N. Prezas, *Conformal chiral boson models on twisted doubled tori and non-geometric string vacua*, *Nucl. Phys. B* **827** (2010) 281 [arXiv:0910.0431] [INSPIRE].
- [68] I. Bandos, *Superstring in doubled superspace*, *Phys. Lett. B* **751** (2015) 408 [arXiv:1507.07779] [INSPIRE].
- [69] D. Berman, *M5 on a torus and the three-brane*, *Nucl. Phys. B* **533** (1998) 317 [hep-th/9804115] [INSPIRE].
- [70] I. Bandos, *On Lagrangian approach to self-dual gauge fields in spacetime of nontrivial topology*, *JHEP* **08** (2014) 048 [arXiv:1406.5185] [INSPIRE].